JOURNAL
OF THE
PHYSICAL SOCIETY
OF JAPAN

Volume 9
1954

Published by the
PHYSICAL SOCIETY OF JAPAN

Digitized by the Internet Archive
in 2024

https://archive.org/details/physical-society-of-japan-journal_1954_9

JOURNAL OF THE PHYSICAL SOCIETY OF JAPAN Vol. 9, No. 1, JAN.—FEB., 1954

Internal Conversion Coefficient of Ba^{137}

By Toshio AZUMA

Physics Department, Naniwa University, Sakai, Osaka

(Received June 8, 1953)

Internal conversion coefficient of Ba^{137} has been investigated with a double coil, magnetic lens beta-ray spectrometer. The relative intensities of the internal conversion electrons of the 663 KeV gamma-ray for K and L, L and M energy levels have been estimated as 4.62 ± 0.18 and 15.0 ± 0.8, respectively. The value of K/L is in accored with the previous experimental values and that of L/M is presented as a new value.

§ 1. Introduction

The radioactive decay of Cs^{137} was determined by Waggoner[1] as shown in Fig. 1. The spin of the metastable state of Ba^{137} was determined by the analysis of the 518 KeV beta-ray spectrum and of the internal conversion of the 663 KeV gamma-ray. The shape of the 518 KeV beta-ray spectrum was found to be first forbidden of either tensor or axial vector form[2][3][4]. The experimental α_K was in accord with the theoretical value of the magnetic 2^4-pole radiation. But the value of K/L obtained experimentally was lower than the theoretical value[5][6], the latter, however, is supposed to be erroneous owing to the approximation method used in the calculation.

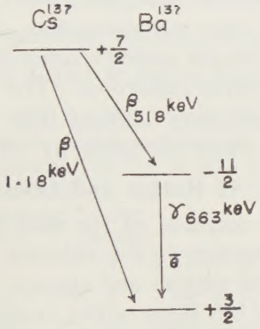

Fig. 1. Decay scheme of Cs^{137} with spins and parities to the nuclear levels in its decay.

Recently semi-empirical curve of K/L of magnetic 2^4-pole radiation was presented by Goldhaber and Sunyar[7]. There exist many isomers which deviate from it. The experimental value of K/L of Ba^{137} is one of those which deviate from it, which is 10 percent lower than their semi-empirical value. The amount of deviation seems to be beyond the experimental erros. There are none of accurate theoretical and semi-empirical values of K/L of Ba^{137}, and also none who tried to check these values after Goldhaber and Sunyar. We have intended to so with the beta-ray spectrometer of 1.4 percent resolution, and also estimate the value of L/M.

§ 2. Experimental Arrangement

A double coil, magnetic lens beta-ray spectrometer was used in these measurements. The aluminium baffle system in the chamber was arranged as almost the same as those of Van Atta *et al*[8], so the effect of scattering in the chamber could be eliminated almost entirely. The axis of the spectrometer was improved by the final alignment of the chamber with the K peak of the internal conversion electrons from Ba^{137}, and was ascertained by the photograph of the x-ray film which was set at the position of the counter window and exposed during five hours.

The radioactive isotope used was obtained from the Oak Ridge National Laboratory. The sources were prepared by first defining the source area with insulin on a thin Aquadack Zapon film of about 30 $\mu g/cm^2$ thick to avoid the source charging up[9]. The active material in solution was then applied to this area and dried quickly under an infra red lamp. The resolution of the spectrometer used was 1.4 per cent with the source size of 2 mm in diameter and the counter window of 3 mm in diameter. The G-M counter used for the detection of beta-particles was one of end window type whose mica thickness was 2.9 mg/cm^2.

The coil current was stabilized at better than 1/50,000 by the stabilizer circuit of

Lawson and Tylor type[10], and was measured by the potensiometer and galvanometer system, using the standard resistance of 0.1 ohm, 15 ampere. The sensitivity of the galvanometer system was such that the 10 mm division on the lamp scale correspond to the 1 miliampere deviation of the coil current. The steady state of the coil temperature was attained by the method of water cooling which was flowed in the space between the aluminium frame and the chamber. The measurement was performed after it was ascertained that its steady state was reached.

§ 3. Shape of the 518 KeV Beta-ray Spectrum and the Value of α_K

We have reinvestigated the shape of the 518 KeV beta-ray spectrum and obtained the value of the internal conversion coefficient α_K. The uncorrected Fermi plot, and the Fermi plot corrected with two kinds of correction factors (a) and (c) are shown in Fig. 2 A, B and C respectively. The correction factors (a) and (c) are

$$(a)\sim (W^2-1)+(W_0-W)^2\,,$$
$$(c)\sim 3(W^2-1)^2+3(W_0-W)^4+10(W^2-1)(W_0-W)^2\,,$$

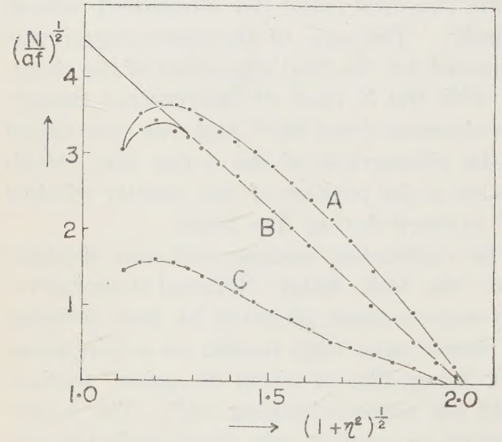

Fig. 2. The Fermi plot of the 518 KeV beta-ray spectrum from Cs^{137}. A; The uncorrected Fermi plot, B; The Fermi plot corrected with the correction factor (a), C; The Fermi plot corrected with the correction factor (c).

where W is the electron energy in unit of m_0c^2, and W_0 is the total energy available for the beta-ray transition in unit of m_0c^2. A rather good fit of the correction factor (a) was in agreement with the previous results[2][3][4], and indicate that the interaction is of either tensor or axial form, obeyed the selection rule of $\Delta I=\pm 2$, and change of parity.

There are two methods to evaluate the experimental value of α_K[1]. Waggoner tried both of them and estimated the value of α_K of Ba^{137} within the errors of 4 percents, which agreeded the theoretical value for magnetic 2^4-pole radiation, $M(2^4)$.[11] The spin of the Ba^{137} isomer was assumed to be $-11/2$ from the selection rule of the 518 KeV beta-ray spectrum and that of the radiation type of the 663 Kev gamma-ray.

We have evaluated the value of α_K in these measurements following the method of the comparison of area. The momentum plot of the beta-ray spectrum was reconstructed from the corrected Fermi plot with the correction factor (a). The effect of the thickness of the counter window in the energy region below 120 KeV was eliminated by this procedure. The value of α_K was then obtained as the ratio of the reconstructed area of the beta-ray spectrum and the area of the internal K conversion electrons. The mean value of α_K obtained was 0.096 ± 0.005. This value agrees with those obtained by others[1][2].

§ 4. K/L, L/M Ratios and Discussions

A typical example of the data obtained for the determination of the relative intensities, K/L and L/M ratios, are shown in Fig. 3 a and b. Fig. 3 b depicts the counts of the L and M region enlarged. Observation records are taken at an interval of 5.6 gauss-cm which corresponds to 5 miliampere of the coil current and 2.3 gauss-cm around the M conversion peak. The M conversion peak could be detected clearly when we used the stronger sources of about 30 and 60 micro-curie equivalent intensities, with the resolution of 1.4 percents. The relative intensities of these conversion peaks are estimated from the area under each peaks. We met sometimes some ambiguities in estimating the area, but the values of the ratios K/L and L/M obtained in 5 runs agreed with each other within the error of about 5 percents. The results obtained are shown in Table I together with the diameter of the source in mm and the intensities in micro-curie. The mean values obtained are 4.62 ± 0.18 for K/L and 15.0 ± 0.8 for L/M. The value of K/L obtained is in general accord with those of previous authors, which are 4.7[1], 4.8[4], and 5.0[2]. The value of L/M is presented as a new value.

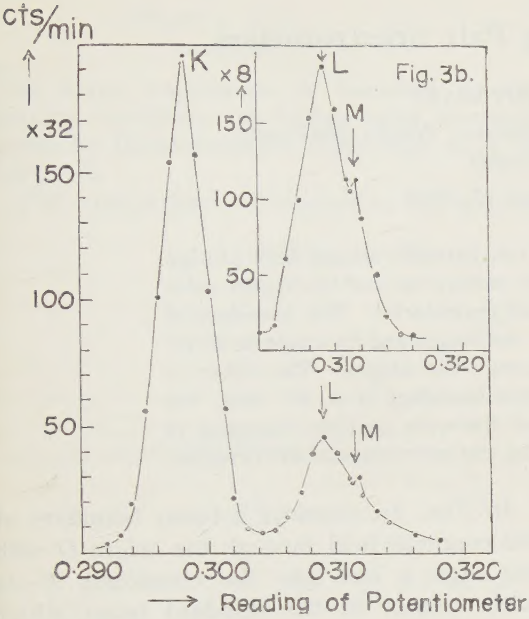

Fig. 3. The internal conversion lines for the gamma-ray from Ba^{137}. Fig. 3b depicts the counts of L and M region enlarged.

Table 1. The relative intensities of the internal conversion electrons of the 663 KeV gamma-ray for K and L, L and M energy levels.

Source No.	Intensity μ.c.	Size mmϕ	K/L.	L/M.
1	5	3	4.68±0.18	—
2	8	3	4.70±0.19	--
3	14	2	4.54±0.17	—
4	30	2	4.61±0.18	14.5±0.7
5	60	2	4.63±0.18	15.4±0.8
mean			4.62±0.18	15.0±0.8

The experimental values of K/L hitherto obtained are, therfore, agrees among themselves, but if they are compared with the theoretical calculations, rather distinct discrepancy appears. The existing theoretical calculations are expected to involve considerable errors owing to the approximations used, and the values obtained by them may not be accurate. If we estimate the value of K/L for Ba^{137} from the theoretical curves of Tralli and Lowen5), and Hebb and Nelson6) for the magnetic 2^4-pole radiation, we get 8.2 and 6.2 respectively. This is in contrast with the fact that the value of α_K obtained experimentally agrees well with, in this case, the accurate theoretical value within the experimental errors.

The value of K/L of magnetic 2^4-pole radiation for a number of elements are summarized recently by Goldhaber and Sunyar7). In their paper semi-empirical curve of K/L versus Z^2/E is shown, which gives the values of K/L for quite a number of elements very well. But there are also many elements where experimental K/L values deviate from the curve and Ba^{137} is one of them.

It may be possible that the experimental value of K/L for Ba^{137} came out too small for some reasons, but it may also be possible that the values for Sr^{87}, In^{113}, and In^{115} which are used to construct the curve in the neighbourhood of Ba^{137} had been estimated too large. It may be necessary to check the values of K/L of these isomers to see if they were really accurate, especially because of their very short half lifes. It seems that latter case is rather probable as a cause for their deviation considering the experimental values which are hitherto obtained, and their semi-empirical curve of K/L versus Z^2/E of magnetic 2^4-pole radiation is 10 percents too high at the position of Ba^{137}.

The value of L/M which was obtained in the present experiment by the same method as used for K/L is 15.0±0.8. No theoretical and experimental values of L/M to be compared with this, however, exist.

In conclusion the author express his sincere gratitude to Professor K. Kimura of the University of Kyoto for his encouragements and valuable discussions, and also to Dr. K. Shinohara for his kind instructions during the publication. Acknowledgement should also be made to Mr. K. Tsumori and Mr. S. Sato for their assistances with the operation of the instrument.

This work was financially supported by the special fund of the Ministry of Education.

References

1) M. A. Waggoner: Phys. Rev. **82** (1951) 906.

2) J. S. Osoba: Phys. Rev. **76** (1949) 345.

3) L. Langer and H. Price: Phys. Rev. **76** (1949) 641.

4) C. Peacock and A. Mitchel: Phys. Rev. **75** (1949) 197, 1272.

5) N. Trally and I. S. Lowen: Phys. Rev. **76** (1949) 1541.

6) M. H. Hebb and E. Nelson: Phys. Rev. **58** (1940) 486.

7) M. Goldhaber and A. W. Sunyar: Phys. Rev. **83** (1951) 906.

8) C. M. Van Atta, S. D. Warshaw, J. J. L. Chen and S. I. Taimuty: Rev. Sci. Inst. **21** (1950) 985.

9) C. H. Braden, G. E. Owen, J. Townsend, C. S. Cook and F. B. Shull: Phys. Rev. **74** (1948) 1539.

10) J. L. Lawson and A. W. Tylor: Rev. Sci. Inst. **10** (1939) 304.

11) Rose, Goertzel, Harr, Spinrad, and Strong: Phys. Rev. **83** (1951) 79.

JOURNAL OF THE PHYSICAL SOCIETY OF JAPAN Vol. 9, No. 1, JAN.—FEB., 1954

Higher Order Focusing Pair Spectrometers

By Toshio KITAGAKI

Physical Institute, Faculty of Science, Tohoku University,
Sendai, Japan

(Received August 17, 1953)

For the field of pair spectrometer two batterfly shaped fields of high character are shown. One is for low energy use and the higher order focusing is achieved for all radii of trajectories. The boundary of the magnetic field is a line through the origin and its angle is 35°16′ and the focal plane is also a line through the origin. The other is for the use of high energy. When the boundary is a 45° line, the boundary is the focal plane itself, and the wide position focusing is given at a point, which is determined by the curverture of the coverter.

For the electron pair spectrometer the direction focusing should be provided when the energy of gamma ray is low. 180° focusing uniform magnetic field is conventionally used. We studied the pair spectrometer which has a sharp focusing for all radii of the beam and has a linear focal plane, with a comparatively small magnet.

§ 1. Low Energy Pair Spectrometer

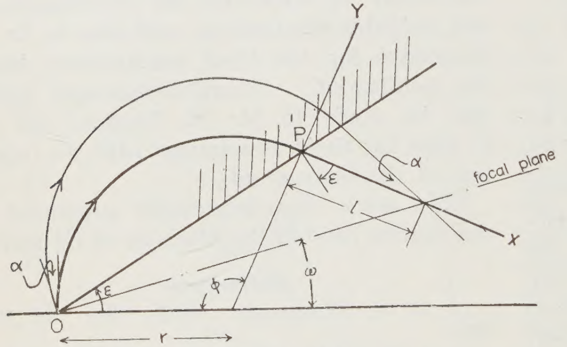

Fig. 1. (a)

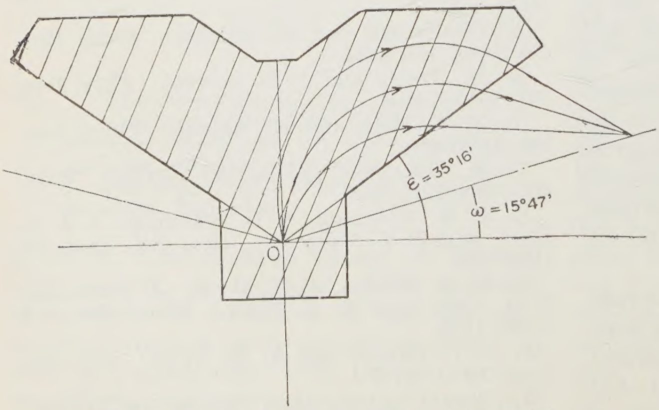

Fig. 1. (b) Low energy pair spectrometer.

In Fig. 1a, consider a linear boundary of the magnetic field through the origin O with the angle ε, and take the coordinate $P-xy$ with respect to the standard beam which starts the origin O with incident angle $\alpha=0$. In the coordinate, the trajectory of a general beam (incident angle α) is expressed as:

$$\begin{aligned} y=\alpha&[-x+r\sin 2\varepsilon] \\ &+\alpha^2 r[1/2-(3/2)\cos 2\varepsilon] \\ &-\alpha^3[(x/3)+(2r/3)\sin 2\varepsilon] \\ &+\alpha^4(r/24)[5-3\cos 2\varepsilon]+O(\alpha^5)\,, \end{aligned}$$

the first order focusing point, $x=l$, is given by

$$l=r\sin 2\varepsilon\,. \qquad (1)$$

The second order focusing is fulfilled when

$$\left.\begin{aligned} \cos 2\varepsilon&=1/3\,, \\ \varepsilon&=35°16'\,, \end{aligned}\right\} \qquad (2)$$

$$\phi=\pi-2\varepsilon=109°28'\,, \qquad (3)$$

where ϕ is the angle of deflection and the deflection is comparatively large for the size of the magnet. In the case, 3rd order y-aberration is,

$$\Delta=-l\,\alpha^3\,. \qquad (4)$$

The focusing is applied for all radii of trajectories and the focal plane is a line through the origin O with the angle ω.

In general,

$$\tan\omega=\frac{\sin 2\varepsilon\cdot(1-\cos 2\varepsilon)}{(2-\cos 2\varepsilon)(1+\cos 2\varepsilon)}\,.$$

In the special case of (2), (3),

$$\left.\begin{aligned}\tan\omega&=\sqrt{2}/5\,,\\ \omega&=15°47'\,.\end{aligned}\right\}\qquad(5)$$

The above calculation is included in the general condition for higher order focusing given by Hintenberger⁽¹⁾ (The sign of ε is inverted).

The comparison of aberration for several types of focusing graphically obtained is shown in Fig. 2. The pole piece is practically made as shown in Fig. 1b and the correction for stray field effect may be done by shifting the position of the slit O along the incident direction of gamma ray experimentally.

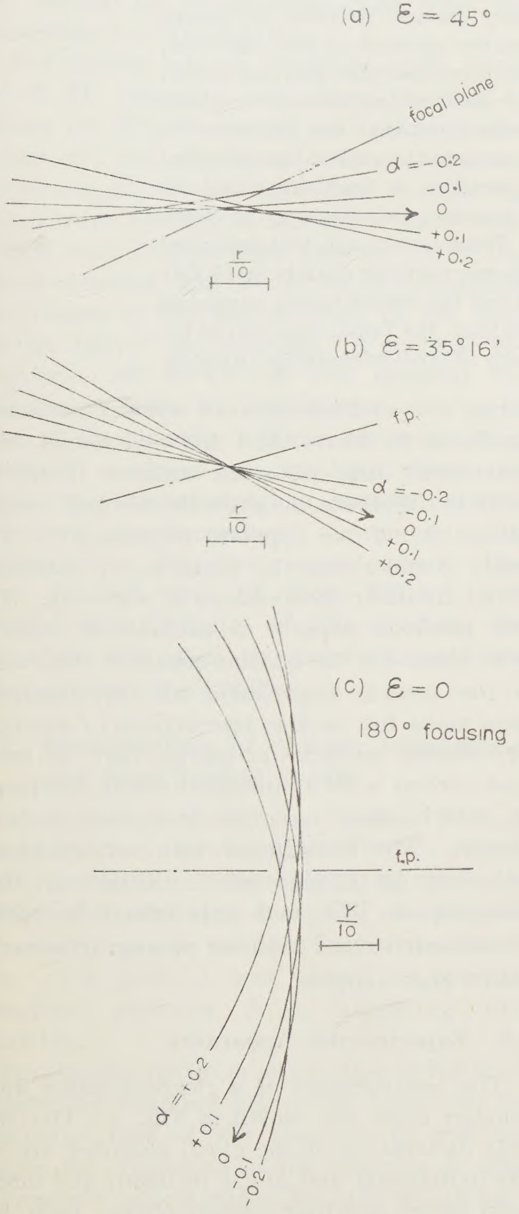

Fig. 2. Graphical comparison of several focusings.

This pair spectrometer is now being constructed and the results will be published later. These results of focusing may be applied for the beam analyzer or massspectrograph and -meter.

§ 2. High Energy Pair Spectrometer

When the energy of gamma ray is extremely high, the ejected angle of the electron is very small ($\alpha\approx mc^2/h\nu\ll1$). In this case the direction focusing may be abandoned and the wide position focusing may be possible with large area converter. In a similar way as in Fig. 1, the first order position focusing is achived for all radius on a line. Especially when the angle ε is taken to be 45°, the focal plane concurs with the field boundary. (Fig. 3) In this case at the point, $r=R$, (r; the radius of the trajectory. R; the radius of curverture of the converter), the perfect focusing is obtained. A very intense pair spectrometer for high energy may be possible by this method.

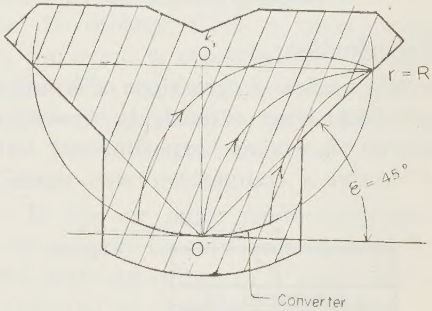

Fig. 3. High energy pair spectrometer.

This type of pair spectrometer has been used by De Wire, Ashkin and Beach in a somewhat different way⁽²⁾. This type of focusing is the limited case where the radius of the inner circule of Smythe analyser⁽³⁾ is reduced to zero, and has been used by Bothe⁽⁴⁾ to get a parallel beam of beta-ray. The author wishes to thanks Prof. M. Kimura of Tohoku University and also to Prof. Nishiwaki of Osaka City Medical University.

References

1) H. Hintenberger: Rev. Sci. Inst. **20** (1949) 748.

2) J. W. DeWire, A. Ashkin and L. A. Beach: Phys. Rev. **83** (1951) 505.

3) W. R. Smythe L. H. Rumbaugh S. S. West: Phys. Rev. **45** (1934) 724.

4) W. Bothe: Z. f. Naturforsch, **4a** (1948) 88.

JOURNAL OF THE PHYSICAL SOCIETY OF JAPAN Vol. 9, No. 1, JAN.—FEB., 1954

Nuclear Interactions of Secondary Shower Particles of Cosmic Rays in Lead and Carbon

By Isao KITA and Osamu MINAKAWA

Department of Physics, Kobe University

(Received August 12, 1953)

Nuclear events produced by secondary shower particles of cosmic rays have been observed in a cloud chamber operated at Mt. Norikura, 2,840 meters altitude. In the chamber were mounted lead and carbon plates, and a comparison was made for penetrating showers originating in these two materials. The results show that the nuclear cross sections for lead and carbon are given to be in the ratio of geometrical values. The multiplicities of shower particles in lead are difenitely larger than those in carbon, and the angular distributions, however, show no differences in both cases. These results can be interpreted quite naturally if we consider that the shower particles contain inevitably high energy protons besides mesons and that the created meson or recoiled proton which is emitted at large angle from the initial direction of the colliding particle has no sufficient energy to produce energetic particles.

§ 1. Introduction

Recently nuclear interactions of cosmic ray particles have been extensively investigated by means of various experimental techniques1)-6), and a comparison was made for penetrating showers produced in a heavy element as lead and in a light element as carbon. The results are at qualitative variance with each other, however, especially when the multiplicities of shower particles produced in heavy and light elements are compared; that is, some authors found a definite difference between them3) and some others found no apparent difference7)8). In order to make clear this problem, we intended cloud chamber observations of showers. In the previous paper10) a preliminary result was given for the nuclear events in lead, and in the present experiment an investigation was made for nuclear interactions of secondary shower particles of cosmic rays in lead and carbon with a multiplate cloud chamber, in which were mounted lead and carbon plates. The experiment was performed at Mt. Norioka (2,840 meters altitude) in the summer of 1952 and approximately 5,000 stereo-scopic cloud chamber photographs were taken and analyzed.

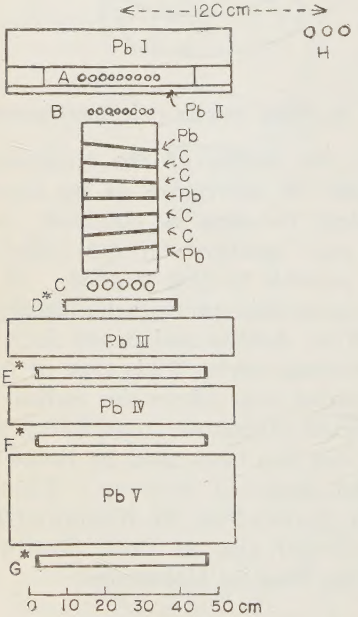

Fig. 1. Diagram of counter and cloud chamber arrangement.

§ 2. Experimental Apparatus

The arrangement of a cloud chamber and counter trays are shown in Fig. 1. The inside dimensions of the cloud chamber are 38 cm in diameter and 20 cm in depth and three lead plates and four carbon plates, each 10 mm thick, are mounted in the chamber, as shown in the figure. In order to compare the nuclear interactions in lead and carbon, it is desirable that the charged particles have the same range in the plates of two different materials and so the lead plates should be much thinner. But such a thin plate can hardly distinguish heavy charged particles such as protons from electrons and consequently the lead plates as well as the carbon plates were made to be 10 mm thick.

The chamber was filled with 88 cm argon saturated with the mixture of alcohol-water. This was situated in a constant temperature box so that the temperature inside could be controlled to about 0.2°C.

The counter system contained eight trays of G. M. counters, as shown in Fig. 1. Trays D*, E*, F* and G* were used in hodoscope and the coincidence between a master pulse and any of the individual counter in those trays resulted in flashing a neon lamp which was photographed together with the cloud chamber, and this allows us to estimate the ranges of charged particles in the lead blocks below the chamber. A sextuple coincidence $A^{\geqq 3}B^{\geqq 2}C^{\geqq 1}-H$ was required for the master pulse which triggered an expansion of the chamber. Hence the penetrating showers produced in the lead above the chamber were detected and nuclear interactions of the secondary shower particles entering the chamber were observed. The tray H with area of about 400 cm^2, was located at a distance of 120 cm from the chamber and used as an anti-coincidence tray against air shower.

§ 3. Identifications of Nuclear Interactions and Some Typical Events

As described above, the chamber is triggered by the coincidence $A^{\geqq 3}B^{\geqq 2}C^{\geqq 1}-H$ and then are detected the penetrating showers produced by the high energy N components of cosmic rays in the lead I above the chamber. The lead II was placed to prevent knock-on electrons from triggering the chamber.

Penetrating particles originating in the lead I enter the chamber below and have only to discharge one of the counters in tray C. Hence the triggering of the chamber is not necessarily accompained by nuclear interactions in the slabs mounted in the chamber, and most of penetrating particles pass through the chamber without any nuclear interactions, giving the poor efficiency for detecting secondary events produced in the chamber. But such a loose triggering has an advantage to avoid a bias to energetic events and enables us to detect low energy events as well as high energy penetrating showers.

Secondary particles of evaporation stars, however, are of about 10 Mev. in the average energy and very few of them exceed 20 Mev.[11], while the range of a proton of about 10 Mev. is 0.1 mm in lead and 0.7 mm in carbon. Hence most of these small stars with only evaporation particles escape from observations.

In order for any event to be classified as a nuclear event produced in the chamber and to eliminate electrons, one of the following criteria is required to be fulfilled.[12][13][14] If these criteria are too severe, we may fail to take all of genuine nuclear events and if too loose we cannot separate electron showers from nuclear events.

(1) If two or more heavy tracks are observed to emerge from a point within a plate, the event is classified as a nuclear disruption. The requirement that two or more heavily ionizing particles are ejected rules out the possibility that this event be electromagnetic.

(2) If one or more penetrating particles and one or more heavily ionizing particles are ejected from an origin in a plate this event is considered as a nuclear collision.

(3) If two or more penetrating particles emerge this event is classified as a nuclear collision.

(4) If a penetrating particle exhibits a sharply defined single scattering, larger than 15° in a lead or carbon plate, it is assumed that the scattering is due to a single nuclear encounter.

A penetrating particle is a lightly ionizing particle that passes through a lead plate without producing any secondary particles. A lead plate has about two cascade units and when an electron hits the plate, the average number of emerging electrons is 1.5 and 3 for the incident energies of 100 Mev and 500 Mev respectively[15]. Particles which ionize less than about two times the minimum ionization were classed lightly ionizing particles. These particles, if they are protons, have energies above 260 Mev and if π-mesons, above 40 Mev. We designate these particles as shower particles and the number of these shower particles in a nuclear event as the multiplicity of the event. But the energy range of the shower particles in the present experiment is somewhat different from that of nuclear plate experiments.[16)]

Even when an event is identified as a nuclear interaction, some lightly ionizing particles of shower may get away from illumination without penetrating a lead plate. These particles may be electrons. Electrons were not found to be ejected directly in nuclear interactions[17)], but the neutral π-meson produced in the event may give rise to electrons in the same plate. Such a probability is quite negligible in case of the shower produced in carbon, but the apparent shower particles produced in lead may include some electrons which must be strictly corrected when a comparison is made between the showers originating in lead and carbon. This will be described subsequently. Since a considerable variety of cosmic ray events was photographed in the course of this experiment, it seems desirable to show some typical photographs demonstrating the nature of these events.

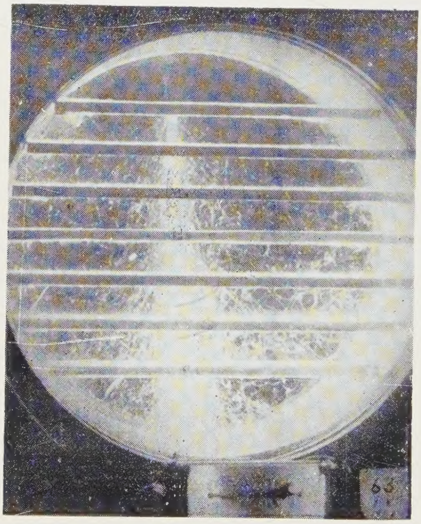

Fig. 2.

Fig. 2 shows the core of a penetrating shower originating in the lead above the chamber. Many electron showers appear. The nuclear events which probably have taken place in the plates are invisible, being covered by electron showers. Almost all of the counters in the trays below the chamber are tripped.

In Fig.3 several penetrating particles traverse the plates in the chamber. The event at the fourth lead plate is produced by a non-ionizing particle, and two regressive particles appear. At the second carbon plate a small nuclear disruption is seen. The event at the fifth plate is not classed as a nuclear disruption according to our criteria.

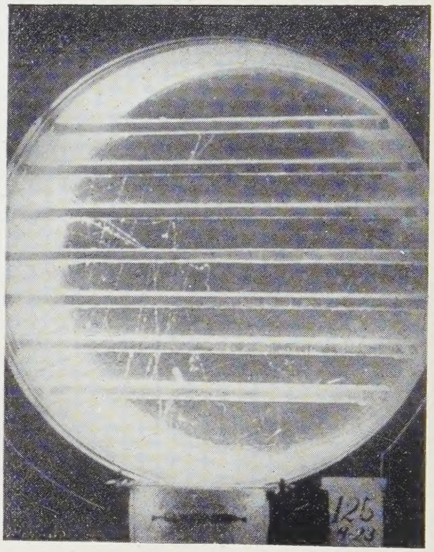

Fig. 3.

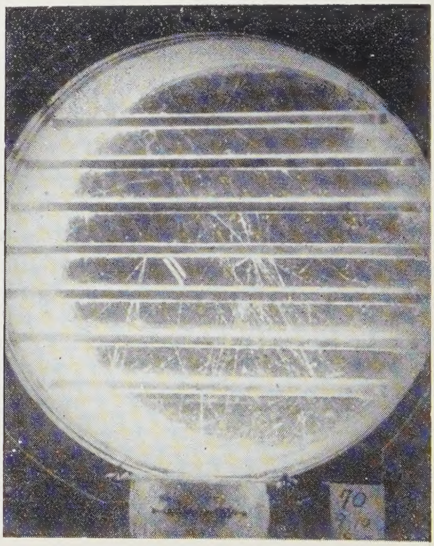

Fig. 4.

Fig. 4 shows complicated nuclear events including many ionizing and non-ionizing particles. At the fourth plate an event with many lightly and heavily iozing particles appears. The shower at the fourth plate is presumably an electron shower produced by a decayed photon of a neutral π-meson in the event at the second plate, that is not clear by poor illuminations.

§ 4. The Ratio of Protons and Pi-Mesons in Penetrating Showers Produced by Primary Nucleons

The values of mean free path, multiplicities and angular distributions obtained in the present experiment can be considered to be average values for the mixture of protons and mesons which are present in the secondaries of penetrating showers. Fowler[17] has shown that more than 90% of the minimum ionization particles emitted from high energy nuclear events observed in photographic emulsions are π-mesons and that majority of the remaining 10% are protons. However in this experiment the fraction of π-mesons among the secondary shower particles emitted from nuclear events originating in the lead I differs from 0.9, as described just below.

An estimate of the fractions of protons and π-mesons among the secondary shower particles can be made by observing the number of secondary neutrons that give rise to further nuclear interactions in the chamber since the numbers of protons and neutrons produced are expected to be roughly equal or proportional to those contained in target nuclei*.

For this purpose the numbers of secondary nuclear interactions produced by ionizing or nonionizing particles are given in Table I.

Table I. Character of the initiating particles

no. of secondary nuclear interactions produced by	no. of tertiary shower particles			Total
	$n=0$	$n\geq1$	$n\geq2$	
non-ionizing particles	27	42	27	69
ionizing particles	51	97	57	148
quetionable	15	22	18	37
Total	93	161	102	254

We assume that the numbers of protons and neutrons are equal and the nuclear interaction cross sections of neutrons, protons and π-mesons are the same also for the secondary showers with two or more shower particles.[1][14] Then from the table we obtain the ratio of the numbers of secondary protons and π-mesons among the secondary shower particles as follows.

$$27:30=47\pm9\%:53\pm10\% .$$

In the same way for the secondary events with one or more shower particles, the ratio is found to be

$$42:52=44\pm7\%:56\pm7\% .$$

These figures show the smaller fraction of π-mesons among the secondary shower particles than that of Fowler[17]. This is due presumably to the differences between the energies of initiating particles and between the probabilities of plural collisions of secondary particles within the nuclei of lead and emulsion materials. Sitte[1] found that 65% of secondary shower particles consisted of π-mesons.

The stars with no penetrating particles ($n=0$ in Table I) are produced by rather low energy particles among which some of protons will stop in the absorbers due to ionization loss. Hence we cannot expect the same number of protons and neutrons and moreover it is known that in such a low energy events the nuclear interaction cross sections of protons and π-mesons may be different[18]. And the probabilities of detecting the stars in lead and carbon will not be same due to the absorption in the plates. In consequence, large errors are inevitable for estimating the meson fraction among shower particles producing such low energy stars.

§ 5. Interaction Mean Free Paths of Charged Shower Particles in Lead and Carbon

In order to determine the mean free paths for nuclear collisions in lead or carbon, the numbers of nuclear events and traversals of penetrating charged particles through the plates in the chamber are necessary and presented in Table II.

The corrections for the nuclear events produced by undiscerned particles were made, as shown in the table. Moreover, the corrections for the stars absorbed in the plate and the unidentified genuine nuclear events by the criteria given in § 3 should be made. Since it is difficult to find the absolute values of these corrections[19], the absolute value of

---

* Among these secondary particles some V-particles are included and 4-shaped tracks were photographed in the experiment. But these are very few as compared with other particles and are not taken into account here.

Table II. Numbers of secondary interactions produced in lead and carbon

	Pb		C	
Traversals of charged particles	4,567		6,894	
Nuclear events produced				
by charged particles	96 $\begin{cases}38 & n\geqq 2\\ 58 & n=0,1\end{cases}$	124	52 $\begin{cases}19\\ 33\end{cases}$	56
by neutral particles	38	46	31	33
by undiscern-ed particles	31	0	6	0
	Observed number	Corrected	Observed number	Corrected

the mean free path subjects always to rather large errors, as is the case with other cloud chamber experiments. Hence in the present paper corrections are made for the difference between the efficiencies for detecting the showers in lead and carbon, so that a comparison between the nuclear events produced in the both materials can be made, and only the relative value of the two mean free paths will be discussed.

Generally the detecting efficiency is a function of the number and energies of the shower particles in nuclear interactions and of the location of points of origins. We may, however, assume that the efficiencies for detecting the high energy penetrating showers with two or more shower particles are equal for the showers produced in lead and carbon, since the penetrating particles takes a main part in identifying the nuclear event. On the contrary, the nuclear disruptions or stars without or with only one shower particle will have a larger probability to be detected in carbon than in lead, because of the absorption of heavily ionizing particles in plates. Hence let us assume that the small nuclear events without or with only one shower particle in lead should be detected in the same efficiency in compared with small nuclear events in carbon. Then we obtain the corrected number of relatively low energy nuclear interactions in lead to be $38\times(33/19)=66$ from Table II, and a total of 124 nuclear interactions in lead are obtained. Then, the apparent mean free paths in lead and carbon are given as follows.

$$\begin{aligned}\text{Pb}: &\quad 4567\times 11.34\times 1.06/124=442\pm 40\ \text{gcm}^{-2}\,,\\ \text{C}: &\quad 6894\times\ 1.66\times 1.06/56\ =217\pm 30\ \text{gcm}^{-2}\,.\end{aligned}$$

A small correction totalling 6% was applied to the values of traversals because of the inclination of the tracks in the chamber.

These values are obviously too large, because of the undetectable nuclear interactions, though it is difficult to find the absolute corrections. Hence, by taking the mean free path in lead to be 142 gcm^{-2} and considering the ratio of those in lead and carbon to be given by the above values, the mean free path in carbon is determined to be 70 ± 16 gcm^{-2}. Consequently it is concluded that the nuclear interaction cross sections of shower particles in lead and carbon are given to be in the ratio of geometrical values for the both materials within the experimental errors.

§ 6. Multiplicity Spectra of Secondary Showers Produced in Lead and Carbon

The numbers of nuclear interactions without or with one, two three, etc. penetrating shower particles were compared for different producing materials. For each material a histogram of the number of showers with *n* shower particles *versus n* has been plotted in Fig. 5.

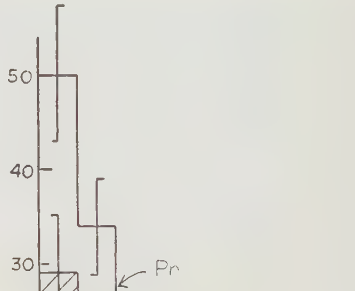

Fig. 5. Uncorrected differential multiplicity spectra of nuclear events in lead and carbon.

From the figure, the multiplicity of shower particles produced in lead seems to be larger than that in carbon, but in order to ascertain this conclusion, we have to make the following corrections. The frequency of small nuclear interactions without or with one shower particle was corrected in §5. The most serious error to be considered in addition arises from the fact that some electrons may be present among the apparent shower particles. As described above, from all of the lightly ionizing particles of the identified nuclear interactions, the electrons which may exist among them have to be removed statistically.

Let us consider n_s, the number of protons and π-mesons among n lightly ionizing particles in an identified nuclear event and α, the fraction of π-mesons in n_s. Then the decayed photons amount to $n_s\alpha\times\frac{1}{2}\times 2=n_s\alpha$, where we assume the neutral π-meson to be half as frequent as the charged mesons1)2). When such a photon of about 300 Mev is emitted in the lead plate20), it will be materialized into two electrons when going through the plate5). Hence electrons in a penetrating shower are increased in number to $2n_s\alpha$, and so the electron fraction in a nuclear event is estimated to be $2n_s\alpha/n=2\alpha/(1+2\alpha)$. In Table III are presented the electron fractions and corrected multiplicities for various observed multiplicities, using the results of the nuclear plates6)7), and the corrected integral multiplicity spectra are plotted in Fig. 6.

Table III. Estimates of corrected multiplicities

Observed multiplicity	1	2	3	4	5	6	7
Electron fraction	0.04	0.10	0.16	—	—	0.20	—
Corrected multiplicity	1	1.8	2.5	3.3	4.1	4.8	5.6
No. of observed showers	33	16	12	8	6	4	10
Corrected no. of showers	35	21	12	8	4	3	5

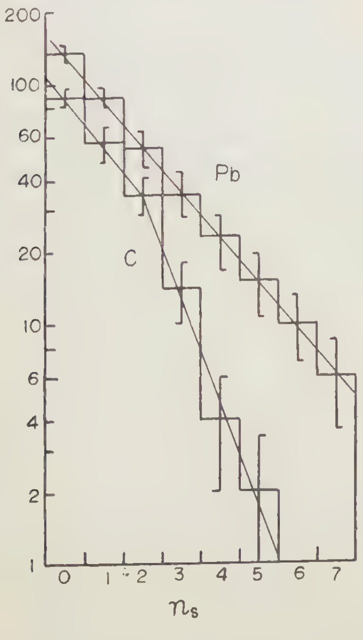

Fig. 6. Corrected integral multiplicity spectra of nuclear events in lead and carbon.

The figures show a large difference between the multiplicity spectra of the showers produced in lead and in carbon. Comparing this result with that of the nuclear plates, the average energy of the initiating particle is estimated to be about 3 Bev6). It is well known that the number of created mesons in a penetrating shower is not alway a good measure of the shower energy, but on the average 1.5~2 mesons have to be produced in the showers described above6). Hence it must be noted that among the shower particles obserbed in this experiment a considerable fraction of protons is included, while each of them cannot be identified as a proton or a π-meson. For the showers with one or more shower particles, average multiplicities are given

$$\text{Pb}: \quad \langle n_s\rangle=2.9\pm0.2\,,$$
$$\text{C}: \quad \langle n_s\rangle=2.4\pm0.2\,.$$

§7. Angular Distributions of Shower Particles Produced in Lead and Carbon

In the experiment of the nuclear plates the angular distributions of the shower particles with respect to the line of motion of an initiating particle have been determined, separating into two classes according to the number of heavy tracks6), where the showers with seven or more heavy tracks are considered to be produced from such heavy elements as Ag and Br, and the showers with six or less heavy tracks, from light elements as C, N and O. In the present experiment a comparison was made for the angular distributions of shower particles for nuclear events in lead and in carbon. The integrated angular distributions of shower particles with respect to the shower axes were ploted in Fig. 7. From the figures it is seen that there is no definite difference between the angular distributions of the shower particles produced in lead and in carbon. This would seem to be in agreement with the results of the nuclear plate investigations⁽⁶⁾.

The average projected angles are determined as follows,

$$\text{Pb}: \quad \langle\Theta\rangle = 18.4^\circ \pm 2^\circ ,$$
$$\text{C}: \quad \langle\Theta\rangle = 18.4^\circ \pm 2^\circ ,$$

giving the same value.

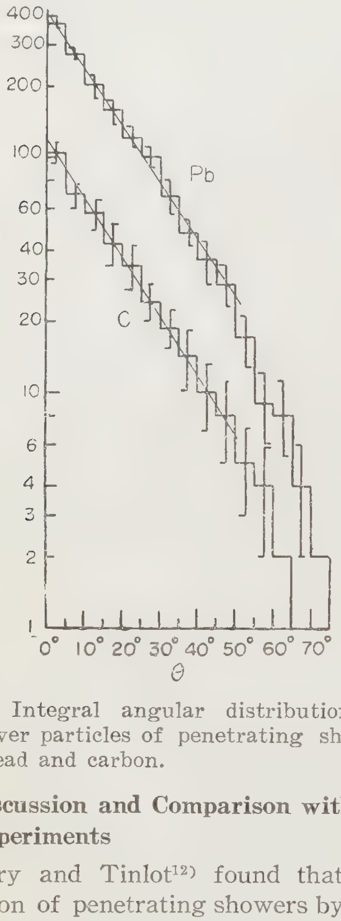

Fig. 7. Integral angular distributions of shower particles of penetrating showers in lead and carbon.

§ 8. Discussion and Comparison with Other Experiments

Gregory and Tinlot⁽¹²⁾ found that for the production of penetrating showers by secondary penetrating particles, the cross section in lead was more than a factor of $(208/27)^{2/3}$ greater than that in aluminium, and the explained the result by the theory of transparency. This agreed qualitatively with the experimental result of Lavati *et al*⁽⁹⁾. In the present experiment, however, it was found that the ratio of the mean free paths in lead and carbon is given by that of geometrical values within large experimental errors. This result agrees with that of Walker *et al*⁽³⁾ whereas the initiating particles in their experiment were primary nucleons. C. Chedester *et al*⁽²¹⁾ showed that the nuclear interaction mean free paths of 85 Mev negative π-mesons in various matters (Li, Be, C, O, Al, Cu, Cd and Pb) were found to be geometrical values approximately, with the exception of hydrogen.

In the following table are presented the mean free paths of secondary penetrating particles in several materials, obtained by many workers. The apperent mean free path in carbon in the present experiment is given by 217 ± 30 gcm^{-2} and is in agreement with that of Green⁽⁸⁾.

As described above, the energies of the penetrating showers investigated in the present experiment are about 3 Bev, and 1.5 ~2 mesons are created in the events. Consequently the multiplicity spectra in Fig. 6 must be accounted for by one or two created mesons and several recoiled protons, and it is not appropriate to discuss the problem that mesons are emerged by the process of multiple or plural productions in the high energy nuclear interactions.

Fretter⁽⁷⁾, Green⁽⁸⁾, Chang *et al*⁽²³⁾ and others have concluded that lead and carbon are about equivalent as generators for penetrating showers. This seems to indicate that mesons are produced from nucleon-nucleon collisions according to the process of multiple productions and plural collisions do not occur in the nuclei. If, on the other hand, successive collisions occure fairly frequently within the same nucleus, appreciably higher multiplicity of shower particles would be expected from lead than from carbon. From comparison of showers starting in lead and carbon in Fig. 6, it seems apparent that in the showers observed secondary collision occurs inside the target nucleus. Walker *et al*⁽³⁾ found large differences in comparison of showers produced in lead and carbon, in agreement with our result.

As seen in the figures the multiplicity spectrum of lead decreases exponentially with increasing n_s but, on the contrary that of carbon has a knee at $n_s=2$ or 3. This will be explained qualitatively as follows. If a penetrating shower in carbon has four or more shower particles, the scattered nucleon

Table IV. Some determination of the interaction mean free path of shower particles

Authors	MFP in gcm^{-2}	Observed MFP / Geometrical MFP	Experimental method
Lovati *et al*4)	200±50 Pb	1.25±0.3	cloud chamber
Hartzler14)	230±60 Au	1.5 ±0.4	〃
Lock & Yekutieli18)	120±20 emul.	1.4 ±0.2	emulsion
Brown & Mckay19)	316±70 Pb	2.0 ±0.4	cloud chamber
Green8)	237±29 C	3.7 ±0.5	〃
Gregory & Tinlot12)	172±30 Pb	1.1 ±0.2	〃
〃	164±50 Al	2.0 ±0.6	〃
Cool & Piccioni22)	208±38 Pb	1.3 ±0.2	counter
〃	74± 7 C	1.2 ±0.1	〃
Kita & Minakawa	442±40 Pb	2.8 ±0.3	cloud chamber
〃	217±30 C	3.4 ±0.5	〃
〃	78±16 C*	1.2 ±0.2	〃
Walker *et al*3)	76± 8 C*†	1.2 ±0.1	〃

* The nuclear interaction mean free path in lead is assumed to be geometrical value.

† The result of Waeker *et al* is that for primary nuclear.

or the created meson must have had successive collisions in the nucleus, but such a particle is supposed to have rather lower energy and has a long mean free path for recoiling another nucleon, and hence the multiplicity spectrum decreases steeply from $n_s=2$ or 3. For a penetrating shower in lead, on the contrary, the energetic particle with a little change in its direction can have succesive collisions several times, and so the spectrum does not show a knee as in carbon.

As for the angular distribution, there is no definite difference between the two multiplicity spectra. This fact seems to indicate that recoiled nucleons or created mesons which are emitted at large angles with respect to the colliding particle have a quite long mean free path in nuclear matter for successive collisions and they do not repeat nucleonic collisions in the target nuclei, so that such particles do presumably not contribute to change the angular distribution. Thus, since the particles which are scattered at large angle from the initiating particles have no successive collisions in the struck nuclei, it is expected that the angular distributions of shower particles produced in lead and carbon do not exhibit a definite difference, as verified in the present experiment.

The present work was supported in part by the research expenditure from the Ministry of Education.

References

1) F. E. Froehlich, E. M. Harth and K. Sitte: Phys. Rev. **87** (1952) 504.

2) G. Salvini and Y. B. Kim: Phys. Rev. **88** (1952) 40.

3) W. O. Walker, N. M. Duller and J. O. Sorrels: Phys. Rev. **86** (1952) 865.

4) A. Lovati, A. Mura, C. Succi and G. Tagliaferri: Nuovo Cimento **8** (1951) 271, ibid **9** (1952) 205.

5) W. Y. Chang, G. D. Castillo and G. Grodzins: Phys. Rev. **89** (1953) 408.

6) U. Camerini *et al*: Phil. Mag. **42** (1951) 1241, 1261.

7) W. B. Fretter: Phys. Rev. **76** (1949) 511.

8) J. R. Green: Phys. Rev. **80** (1950) 832.

9) A. Lovati, A. Mura, G. Salvini and G. Tagliaferri: Phys. Rev. **77** (1950) 284.

10) I. Kita and O. Minakawa: Journ. Phys. Soc. Japan **8** (1953) 139.

11) K. Le Couteur: Proc. Phys. Soc. **A63** (1950) 259.

12) B. P. Gregory and J. H. Tinlot: Phys. Rev. **81** (1951) 667, 675.

13) M. B. Gottlieb: Phys. Rev. **82** (1951) 349.

14) A. J. Hartzler: Phys. Rev. **82** (1951) 359.

15) R. R. Wilson: Phys. Rev. **86** (1952) 261.

16) R. H. Brown *et al*: Phil. Mag. **40** (1949) 862.

17) P. H. Fowler: Phil. Mag. **41** (1950) 169.

18) W. O. Lock and C. Yekutieli: Phil. Mag. **43** (1952) 231.

19) R. R. Brown: Phys. Rev. **87** (1952) 999.

20) A. G. Carlson, J. E. Hooper and D. T. King: Phil. Mag. **41** (1950) 701.

21) C. Chedester, P. Isaacs, A. Sachs and J. Steinberger: Phys. Rev. **82** (1951) 958.

22) R. L. Cool and O. Piccioni: Phys. Rev. **87** (1952) 531.

23) W. Y. Chang and G. D. Castillo: Phys. Rev. **84** (1951) 582, 584.

JOURNAL OF THE PHYSICAL SOCIETY OF JAPAN Vol. 9, No. 1, JAN.—FEB., 1954

Notes on Fermi and Bose Statistics

By Morikazu TODA and Fumihiko TAKANO

Institute of Physics, Tokyo University of Education

(Received March 19, 1953)

By expanding the grand partition function, we obtain the expression for partition function of two dimensional free particles which is seen to be of the same form as that of one dimensional harmonic oscillators. For such systems it is shown that the difference in statistics does not appear in thermal behavior. When the energy levels of the particles are modified as $\varepsilon_{n_1,n_2}=\Delta+b(n_1^2+n_2^2)$, $\Delta>0$, the Bose condensation occurs and, if we set $\Delta=2b$, the condensation temperature qualitatively agrees with that of Osborne. The speciffic heat of free Bosons in a narrow box is calculated as the function of temperature, its width d being taken 7.1 Å and 14.2 Å. The results show that the maximum of the specific heat occurs at higher temperatures than that of the case $d=\infty$, and its height becomes lower.

The weak excitation of a Fermi system can be treated as excitons which obey Bose statistics. And we can show, by the method analogous to that of Ward and Wilks and Dingle, that the sound wave in a Fermi gas should be considered as the second sound, or the propagation of fluctuation in exciton distribution. Its propagation velocity is shown to become $p_0/\sqrt{3}m$, where p_0 is the momentum at the Fermi surface.

§ 1. Introduction

Recent development of the theories of superconductivity and of liquid helium is pressing new attentions on the quantum statistics of Fermi- as well as Bose-systems. Especially the problem of the Bose-condensation was attacked with some doubts in customary methods, e. g., the method of steepest descent or so. By several authors, however, it is justified that the Bose-condensation actually takes place and that despite of the apparent uncertainty conventional method leads to correct results.

On the other hand, statistical treatment of system of particles with strong mutual interaction seems to be of much difficulty. Even the question whether the difference in statistics (Fermi and Bose) has nothing to do with the apparent parallelism between the phase transitions of superconductor and of liquid helium, or the super-flow of electrons and of helium II, is not solved yet. The only one fact which will be reliable in this connection is that the isotope He^3, obeying Fermi statistics, has no helium II region.

It seems difficult to approach these problems by the usual methods in statistics and perturbation theory. The method of sound quanta developed by Tomonaga[1)] threw light upon the relation between the two statistics. It is likely that Fermi and Bose statistics are, contrary to what is believed, intimately connected to each other. In these notes we begin with the special cases where the both statistics are equivalent, and then apply the results to some problems.

§ 2. Systems for which Both Statistics are Equivalent

We shall seek now for compact expressions of the partition functions for systems of Bosons as well as of Fermions. Formally speaking we can do so by expanding grand partition functions and taking up the term for the given numbers of particles. But it is convenient to make use of the fact that a strict expression can be obtained in the case of particles in a common parabollic field.

1) System of oscillators.[2)] Let Z_N denote the partition function for N particles. The grand partition function is given, for non-interacting particles whose energy levels are ε_j, by

$$\Xi=\sum_{N=0}^{\infty}\lambda^N Z_N=\prod_j(1\pm\lambda e^{-\beta\varepsilon_j})^{\pm}\,, \qquad (1)$$

where $\beta=1/kT$ and the upper sign is for

Fermions and lower for Bosons. By the Euler's theorem

$$\prod_{n=1}^{\infty}(1\pm\lambda z^n)^{\pm}=\sum_{N=0}^{\infty}\lambda^N\begin{Bmatrix}z^{N(N-1)/2}\\1\end{Bmatrix}\Big/\prod_{s=1}^{N}(1-z^s)\,, \tag{2}$$

we obtain for the system of oscillators in a common field, $\mathcal{E}_n=n\hbar\omega$,

$$\left.\begin{aligned}&Z_N=e^{-\beta E_0(N)}\Big/\prod_{s=1}^{N}(1-e^{-s\beta\hbar\omega})\,,\\&E_0(N)=\begin{cases}\dfrac{N(N-1)}{2}\hbar\omega & F.\\0 & B.\end{cases},\end{aligned}\right\} \tag{3}$$

where $E_0(N)$ is the zero point energy. This result is rigorous and is generalized as follows: If the level is quasi-continuous and its density g is constant, the excitation of the system can be described by the partition function of the form

$$Z^*=\prod_{s=1}^{N}(1-e^{-s\beta/g})^{-1}\,, \tag{4}$$

for both Fermi and Bose statistics.

2) Two dimensional free particles. When the quasicontinuous energy levels can be written as

$$\mathcal{E}_n=(n_1^2+n_2^2)b\,,\qquad n_1\,,\ n_2=1,\ 2,\ 3,\ \cdots$$

the level density is a constant, given by $g=\pi/4b$. Then we can use the above formula (4), and the partition function is written as

$$\left.\begin{aligned}&Z_N=e^{-\beta E_0(N)}\Big/\prod_{s=1}^{N}(1-e^{-s\beta 4b/\pi})\,,\\&E_0=\begin{cases}2N(N-1)b/\pi & F.\\0 & B.\end{cases}\end{aligned}\right\} \tag{5}$$

This result can be considered rigorous if $b\beta\gg1$ and $N\gg1$.

For a system of free particles in a two dimensional box of length L, we have $b=h^2/8mL^2$.

It is trivial to justify the classical limit where $N^2b\beta\ll1$, Z_N approaches the well known formula :

$$\lim_{\beta\to0}Z_N=1\Big/\prod_{s=1}^{N}s\frac{4b}{\pi}\beta=\left(\frac{2\pi m}{h^2\beta}\right)^N\frac{L^{2N}}{N!}\,.$$

§ 3. Application

1) Two dimensional Bose condensation. We have seen above that thermal behaviors f the two-dimensional free particles obeying Fermi and Bose statistics exhibit no difference. And it is shown that two-dimensional free Bosons do not show Bose condensation (see lso Eq. (12), below).

If we assume that the energy levels are modified as

$$\mathcal{E}_0=0\,,\qquad \mathcal{E}_{n_1,n_2}=\Delta+b(n_1^2+n_2^2)\,,$$
$$(n_1\,,\ n_2=1,\ 2,\ 3,\ \cdots\ )\,,$$

we have

$$\left.\begin{aligned}&Z_N=1+\sum_{n=1}^{N}e^{-\beta n\Delta}\Big/\prod_{s=1}^{n}(1-e^{s\beta\kappa})\\&\kappa=4b/\pi\,,\end{aligned}\right\} \tag{6}$$

we shall replace the summation by the largest term, which is given by

$$\bar{n}=\frac{1}{\kappa\beta}\log(1-e^{-\beta\Delta})^{-1}\,. \tag{7}$$

Thus as the temperature is raised from the absolute zero, the number $\bar{n}$ of excited particles increases. As it is bounded, however, Bose condensation will take place at the temperature given by $\bar{n}=N$, provided that the number of particles is sufficiently large. The conventional method gives for the condensation point

$$N=\int_0^{\infty}\frac{g(\mathcal{E})\,d\mathcal{E}}{e^{\beta\mathcal{E}}-1}=\frac{\pi}{4b}\int_{\Delta}^{\infty}\frac{d\mathcal{E}}{e^{\beta\mathcal{E}}-1}$$
$$=\frac{\pi}{4b\beta}\log(1-e^{-\beta\Delta})^{-1}\,,$$

which is same as Eq. (7).

Osborne[3] pointed out that the conventional method failed when the temperature was sufficiently low as the summation could be no longer replaced by the integration and that the lowest level must be separated from the integral. In such a way he obtained an apparent Bose condensation, or a beginning of the abrupt accumulation in the ground state. In our treatment setting $\Delta=2b$, we obtain for the condensation temperature,

$$e^{-4b\beta/\pi}=1-e^{-2b\beta}\,.$$

In the notation of Osborne, $4b\beta N/\pi=T_{01}'/T$, so the left hand side becomes $\alpha'\equiv\exp(-T_{01}'/T)$. Thus the Osborne's conditions for an abrupt accumulation $\alpha'=5b\beta/2$ is compared with the above equation $\alpha'=1-e^{-2b\beta}\approx2b\beta$ if $b\beta\ll1$. The difference of the factore 5/2 and 2 comes from the fact that in replacing a summation by an integral he used the formula

$$\sum_{m=a}^{b}f(m)\cong\int_{a-1/2}^{b+1/2}f(m)\,dm\,,$$

whereas we have used

$$\sum_{m=a}^{b}f(m)\cong\int_a^b f(m)\,dm\,.$$

2) Bose condensation in a narrow box. Let us consider a system of free particles in a parallelpiped box of dimensions L, L, and d energy levels are given by

$$\varepsilon_n = b(n_1^2+n_2^2)+cn^2, \quad (n,\ n_1,\ n_2=1,\ 2,\ 3,\cdots), \tag{8}$$

$$b=h^2/8mL^2\,, \qquad c=h^2/8md^2\,.$$

We must pay a special attention to the lowest state, and so it is convenient to take the lowest state as the zero of energy, which involves

$$\varepsilon_n = b(n_1^2+n_2^2)+cn^2-(2b+c)\,. \tag{9}$$

Extracting the zero state, we have

$$\begin{aligned}\Xi &= (1-\lambda)^{-1}\prod_{n}\prod_{n_1,n_2}(1-\lambda e^{-\beta\varepsilon_n})^{-1}\\ &= \left(\sum_{\nu=0}^{\infty}\lambda^{\nu}\right)\left\{1+\sum_{\mu=1}^{\infty}\lambda^{\mu}\sum_{\Sigma N_n=\mu}\prod_{n=1}^{\infty}\right.\\ &\quad\left.\cdot\exp\Big(-\beta N_n c(n^2-1)\Big)\Big/\prod_{s=1}^{N_n}(1-e^{-4b\beta s/\pi})\right\}.\end{aligned}$$

Thus we obtain

$$\begin{aligned}Z_N = 1+\sum_{N'=1}^{N}e^{N'c\beta}\sum_{\Sigma N_n=N'}\prod_{n=1}^{\infty}\prod_{s=1}^{N_n}\\ \cdot\,[e^{-c\beta n^2}/(1-e^{-4b\beta s/\pi})]\end{aligned} \tag{10}$$

It is trivial to show that these expressions coincide with the classical ones in the limit of high temperature.

We shall replace the summation in (10) by the maximum term, which is given by

$$N'=N \quad\text{and}\quad \overline{N}_n=\frac{\pi}{4b\beta}\log\,(1-e^{-\alpha-c\beta n^2})^{-1}, \tag{11}$$

where α is the factor determined by the total number of particles, $\overline{N}_n$ means the number of particles on the level n, $(n_1,\ n_2=1,\ 2,\ 3,\cdots)$. Customary method leads to the same result, i. e.,

$$\begin{aligned}\overline{N}_n = \sum_{n_1,n_2}N_{n,n_1,n_2} &= \iint\frac{dn_1\,dn_2}{e^{\alpha+c\beta n^2+b\beta(n_1^2+n_2^2)}-1}\\ &= \frac{\pi}{4b\beta}\log\,(1-e^{-\alpha-c\beta n^2})^{-1}.\end{aligned}$$

From Eq. (11), the total number of particles is given by

$$N=\sum_n\overline{N}_n=\frac{\pi}{4b\beta}\sum_{n=1}^{\infty}\log\,(1-e^{-\alpha-c\beta n^2})^{-1}\,. \tag{12}$$

This equation, determining α, has always a solution $\alpha > -b\beta$, which means that the so-called Bose condensation cannot take place when the width d of the box is finite. An abrupt transition of phases occurs only in the limit $d\to\infty$.

We calculate the value of α and then the specific heat as a function of the temperature. To do so we use the following equations.

$$Z=\prod_n e^{-\overline{N}_n c\beta n^2}\Big/\prod_{s=1}^{\overline{N}_n}(1-e^{-4b\beta s/\pi})\,,$$

$$E=\sum_n\left\{\overline{N}_n cn^2+\sum_{s=1}^{\overline{N}_n}\frac{4bs}{\pi}\Big/(e^{4b\beta s/\pi}-1)\right\}\cong\sum_n\left\{\overline{N}_n cn^2+\frac{\pi}{4b\beta^2}\int_0^{x_n}\frac{xdx}{e^x-1}\right\},$$

$$\frac{\beta^2}{N}\frac{\partial E}{\partial\beta}=-\frac{C_v}{Nk}=\sum_n\left\{\left(c\beta n^2+\frac{x_n}{e^{x_n}-1}\right)\frac{\beta}{N}\frac{\partial\overline{N}_n}{\partial\beta}+\frac{\overline{N}_n}{N}\frac{x_n}{e^{x_n}-1}-2\frac{\pi}{4b\beta N}\int_0^{x_n}\frac{xdx}{e^x-1}\right\},$$

Table 1.

$d=7.11$Å	T/T_0	0.35	0.87	1.15	1.73	3.46	8.65	17.3
	α	3.15	2.04	0.58	−0.52	−1.25	−1.85	−5.00
	$-\frac{\beta^2}{N}\frac{\partial E}{\partial\beta}$	0.61	0.95	1.08	1.31	1.54	1.68	1.50
$d=14.2$Å	T/T_0	0.87	1.15	1.73	3.46			
	α	0.025	−0.28	−0.48	−1.25			
	$-\frac{\beta^2}{N}\frac{\partial E}{\partial\beta}$	1.11	1.36	1.91	1.33			

where

$$x_n=4b\beta\overline{N}_n/\pi\,.$$

The ratio A of $4b\beta N/\pi$ to $c\beta$ determines the width d of the box, and the value of $c\beta$ determines the temperature. We take $A=1$ and 8, which correspond to $d=7.11$Å and 14.2Å, respectively. The results are shown in Table I and Fig. 1.

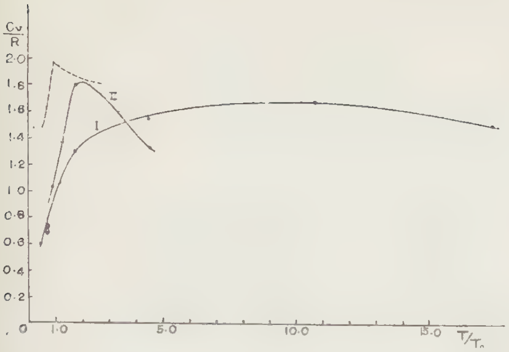

Fig. 1. The specific heat of free Bosons in a narrow box. Its width d is taken 7.11 Å (curve I) and 14.2 Å (curve II). The dotted curve corresponds to $d=\infty$. T_0 is the condensation temperature in the case of $d=\infty$.

From the Fig 1, we see that the maximum of the specific heat occurs at a higher temperature and its height becomes lower when the width of the box becomes thinner.

3) Fermi system. The energy expression of Fermi particles, i. e.,

$$E=\int_0^\infty \frac{\mathcal{E}\, g(\mathcal{E})\, d\mathcal{E}}{e^{(\mathcal{E}-\mu)/kT}+1},$$

can be written as

$$E=E_0-\int_\mu^{\mu_0}(\mathcal{E}-\mu)g(\mathcal{E})d\mathcal{E}+\left\{\int_0^{\mu_0}g(\mu-x)+\int_0^\infty g(\mu+x)\right\}\frac{x}{e^{x/kT}+1}\,dx\,, \qquad (13)$$

the first term is the zero point energy. Analogous computation for the total number immediately shows that $\mu-\mu_0$ is proportional T^3. The second term in the right hand side of Eq. (13) is therefore proportional to T^4. Expanding the third term, we have, up to the term T^2.

$$E-E_0=2g(\mu_0)(kT)^2\int_0^\infty \xi d\xi/(e^\xi+1)\,. \qquad (14)$$

This gives the well-known Sommerfeld's term $(\pi^2/6)(kT)^2 g(\mu_0)$.

Now, Eq. (14) is written as

$$E^*=E-E_0=g(\mu_0)\int_0^\infty \frac{\mathcal{E}\, d\mathcal{E}}{e^{\mathcal{E}/kT}-1}\,, \qquad (15)$$

by using the identity

$$(e^\xi+1)^{-1}=(e^\xi-1)^{-1}-2(e^{2\xi}-1)^{-1}\,,$$

or

$$\int_0^\infty \frac{\xi d\xi}{e^\xi+1}=\frac{1}{2}\int_0^\infty \frac{\xi d\xi}{e^\xi-1}\,.$$

Eq. (15) shows that the weak excitation of a Fermi system can be regarded as the excitation of Bosons at the Fermi surface.

§ 4. Sound

1) In the first instance, let us consider free Fermions in a one-dimensional box of length L. The energy levels are given by

$$\mathcal{E}_n=h^2n^2/8mL^2, \quad n=1,\ 2,\ 3,\ \cdots\ .$$

If there are N particles, the levels, are occupied up to the Fermi surface $n_m=N$; the zero point energy of the system is

$$E_0=\frac{h^2}{8mL^2}\sum_1^N n^2 \cong \frac{h^2 N^3}{24mL^2}\,.$$

Since the level density at the Fermi surface is given by

$$g(n_m)=1\bigg/\left[\frac{d\mathcal{E}}{dn}\right]_{n_m}=\frac{4mL^2}{h^2 n_m}\,,$$

the Sommerfeld's term of excitation energy is

$$E_1{}^*=\frac{2\pi^2}{3}\frac{mL^2}{h^2N}(kT)^2\,. \qquad (16)$$

It is shown that this is the excitation energy of the "Hohlraum" for sound waves whose propagation velocity is given by

$$c=\frac{Nh}{2mL}=\frac{p_0}{m}\,, \qquad p_0=\frac{h}{2L}N\,, \qquad (17)$$

and whose energy is

$$\mathcal{E}=cp,\ p=h/\lambda,\ \lambda=L/|n|,\ n=\pm1,\pm2,\cdots,\ \pm N/2,$$

periodic condition being used. Indeed such an sound system has an energy at sufficiently low temperature

$$\int_{-\infty}^\infty \frac{|cp|\, d(cp)}{e^{|cp|/kT}-1}\frac{L}{hc}\cong\frac{\pi^2}{3}\frac{L}{hc}(kT)^2\,, \qquad (18)$$

which coincides Eq. (16) when Eq. (17) is used.

It is important to note that the above coincidence shows that the excitations near the Fermi surface may be regarded as excitons, which obey Bose statistics and have the energy $\mathcal{E}=(p^2/2m)-(p_0{}^2/2m)\sim(p_0/m)(p-p_0)$. The excitons belong to each electron and move with the velocity of electrons near the Fermi surfrce, which is equated to sound velocity.

2) Sound velocity. It has been pointed out in a preceding paragraph that the exciton in one dimensional Fermi gas propagates with the velocity of sound p_0/m. In three dimensional Fermi gas, the velocity of

exciton is again p_0/m, whereas the velocity of sound is $p_0/\sqrt{3}\,m$. The factor $1/\sqrt{3}$ is due to the fact that the "sound" is the propagation of fluctuations in excitons. The direct proof is quite analogous to a treatment of second sound in liquid helium, where the disturbance or the fluctuation in phonon distribution at very low temperature propagates with the velocity $1/\sqrt{3}$ times the velocity of sound. The sound in a Fermi gas is rather the second sound, the propagation of the fluctuation in distribution of excitons.

In Landau's treatment of liquid helium it was predicted that as the temperature approaches to absolute zero, the velocity of second sound would become the value $1/\sqrt{3}$ times the velocity of ordinary sound. But as Ward and Wilks[4] and Dingle[5] have pointed out, one gets the above results starting from the Maxwell's general equation for transfer. In fact, the equations for energy and momentum transfer along the x direction are, respectively,

$$\frac{\partial}{\partial t}\int E f_0 p^2 dp = -\frac{\partial}{\partial x}\int E v f' p^2 dp\ , \qquad \text{(19a)}$$

$$\frac{\partial}{\partial t}\int f' p^3 dp = -\frac{1}{3}\frac{\partial}{\partial x}\int v f_0 p^3 dp\ , \qquad \text{(19b)}$$

where E, p and v denote respectively the energy, momentum and velocity of a particle or an exciton, f_0 the equilibrium distribution function and f' a measure of its distorsion. For a phonon gas ($v=c=\text{const.}$, $E=pc$) we can readily eliminate f' from the above equations (19), and the wave equation thus obtained leads to a velocity $c_2=c/\sqrt{3}$.

For a gas of particles, we have an equation for the number density of particles in addition to Eq. (19); that is

$$\left.\begin{aligned} n &= \int f p^2 dp\ , \\ \frac{\partial}{\partial t}\int f_0 p^2 dp &= -\frac{\partial}{\partial x}\int v f' p^2 dp\ . \end{aligned}\right\} \qquad \text{(20)}$$

The energy and velocity of a particle are given by

$$E=p^2/2m, \quad v=\partial E/\partial p = p/m\ .$$

We can eliminate f' from Eqs. (20) and (19b), the result being

$$\frac{\partial^2}{\partial t^2}\int f_0 p^2 dp = \frac{1}{3m^2}\frac{\partial^2}{\partial x^2}\int f_0 p^4 dp\ . \qquad \text{(21)}$$

For a degenerate Fermi gas,

$$\frac{\partial^2}{\partial t^2}\int f_0 p^2\, dp \sim p_0{}^2\frac{\partial^2 p_0}{\partial t^2}\ , \quad \frac{\partial^2}{\partial x^2}\int f_0 p^4 dp \sim p_0{}^4\frac{\partial^2 p_0}{\partial x^4}$$

where p_0 denotes the maximum momentum. Thus the wave equation $\partial^2 p_0/\partial t^2 = c^2\partial^2 p_0/\partial x^2$ is obtained, leading to a velocity $c=p_0/\sqrt{3}\,m$.

For a classical gas $f_0 \sim Ce^{-p^2/2mkT}$, and Eq. (21) gives

$$m\frac{\partial^2 n}{\partial t^2} = \frac{\partial^2(nkT)}{\partial x^2}\ .$$

If the change is adiabatic as is widely known, $T\sim n^{2/3}$ and thus we see that for a classical gas the velocity of sound is given by the well-known formula $(5kT/3m)^{1/2}$.

Acknowledgement

In conclusion we should like to express our thanks to the theoretical group for low temperature physics in Tokyo and especially to Mr. T. Tsuzuki for valuable discussions. This works is indebted to the Scientific Research Expenditure of the Ministry of Education.

References

1) S. Tomonaga: Prog. Theor. Phys. **5** (1950) 544.

2) M. Toda: J. Phys. Soc. Japan **7** (1952) 230.

3) M. F. M. Osborne: Phys. Rev. **76** (1949) 396.

4) J. C. Ward and J. Wilks: Phil. Mag. **42** (1951) 314; **43** (1952) 48.

5) R. B. Dingle: Proc. Phys. Soc **A65** (1952) 374.

JOURNAL OF THE PHYSICAL SOCIETY OF JAPAN Vol. 9, No. 1, JAN.—FEB., 1954

Some Physical Properties of Nickel Oxides*

By Yasumitsu SHIMOMURA and Ichiro TSUBOKAWA

Department of Physics, Naniwa University

(Received July 20, 1953)

Variation of the magnetic susceptibility, electric resistivity and specific heat with temperature have been observed for various nickel oxides containing different amounts of copper. The anomaly temperatures of these properties and also of their lattice generally differ from one another. Among these temperatures the last one is the lowest and the magnetic one is the highest, and the higher is the copper content the larger is the difference. It may be concluded from these results that the deformation of nickel oxide must be originated from the antiferro-magnetic exchange interaction as proposed by Greenwald and Smart,[4] but at the same time it seems to be affected by the other factors *e.g.* the ionic radius ratio and the vacancies.

§ 1. Introduction

Nickel oxide has, at room temperature, a face centered rhombohedral structure deformed slightly from the rocksalt type,[1] and at higher temperatures, it becomes cubic.[2] Similar phenomena have been found in some other antiferromagnetic compounds[3], and considered to be originated from the exchange interaction between magnetic atoms of these substances[4]. But the lattice deformation of cobaltous oxide cannot be explained in such a way[5]. Moreover it must be noticed that, at the ordinary temperature, the surface oxide film of nickel is cubic, the composition of which is nearly the same as that of the ordinary rhombohedral oxide. If the lattice deformation arises only from the exchange force, the Néel point of the oxide film should be lower than the room temperature which is much deeper than that of the rhombohedral oxide.

It is, therefore, very important to know how high the Néel point of the oxide film is, but it is very difficult because of the presence of the ferromagnetic substratum.

The rhombohedrality of nickel oxide, however, can be controlled by dissolving copper in it, and it is able to obtain even a cubic oxide similar to that in the oxide film (as shown by the dotted line in Fig. 3)[6]. If the oxides thus obtained are used, it will be possible to determine the Néel point of the cubic oxides as well as those oxides having various rhombohedralities. This paper reports the results of such determinations and also of the observations for the specific heat and the electric resistance.

§ 2. Method of Experiments

The specimen was made from nitrates in the following way. A definite amount of nickel nitrate and that of copper nitrate were dissolved together into water in the same vessel, stirred thoroughly and boiled down nearly to dryness. Then the nitrates were calcinated to become oxides, each of which was verified to be in the state of a complete solid solution, by the method mentioned in the previous reports[6].

The magnetic susceptibility was measured by an apparatus of Hirone's type[7], and the specific heat by Sykes' method modified by Nagasaki and Takagi[8]. For the observation of electric resistivity change with temperature, sintered specimens of about 3.5 mm. in diameter and 6 mm. in length were employed.

§ 3. Results of Experiments

The magnetic susceptibility change with temperature for all the specimens investigated is similar to that of pure nickel oxide observed by Foëx and Blanchtais[9]**. For example, the results of two specimens containing 0 and 24 at. % Cu*, which have a rhombohedral and a cubic structure respectively, are illustrated in Fig. 1, where the anomaly points are indicated by arrows. The heating curves do not coincide with the cooling ones, perhaps owing partly to the rather rapid change of temperature. The mean anomaly temperatures in both curves are plotted against the copper content in Fig. 3.

---

* This paper was read before the 7th annual meeting of the Physical Society of Japan held in Kyoto, in October, 1952.

** As for a specimen calcinated at a rather low temperature, the susceptibility decreases monotonically with temperature as in the case of ferromagnetics.

The electric resistivity depends greatly on the degree of sintering but its anomaly point does not**. The two typical examples are shown also in Fig. 1. It can easily be verfied that the decrease of the resistivity with temperature is exponential in the region far from the critical point.

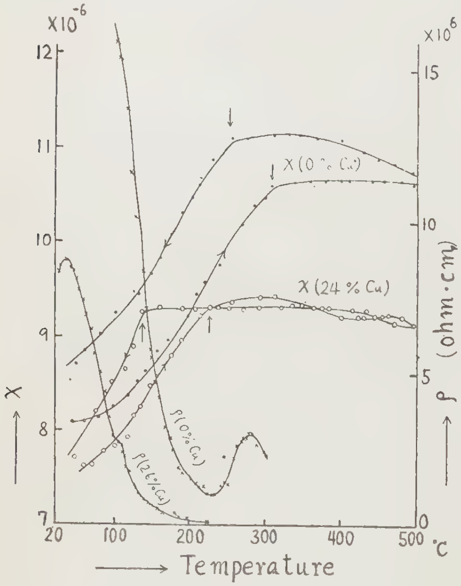

Fig. 1. Variation of the magnetic susceptibility (χ) and the electric resistivity (ρ) with temperature.

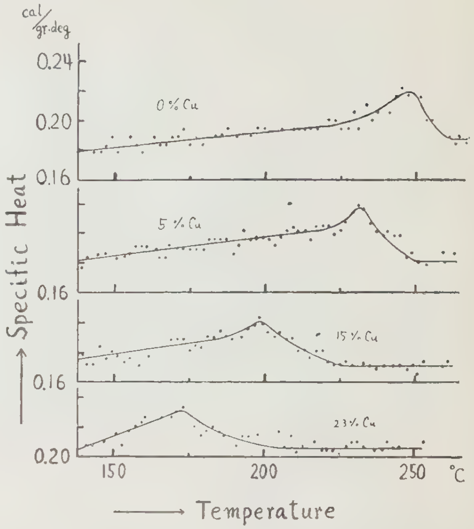

Fig. 2. Variation of the specific heat with temperature.

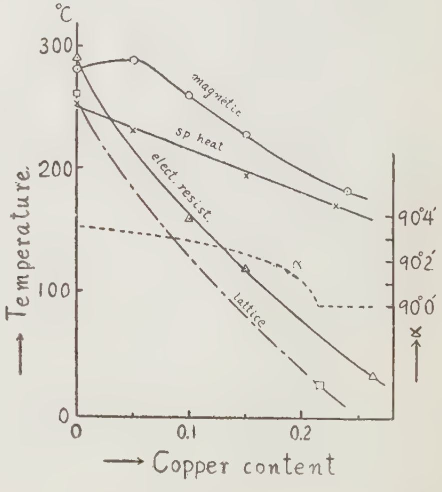

Fig. 3. Anomaly temperatures for physical properties of nickel oxides containing copper. (The dotted line indicates the variation of lattice constant α with the copper content).

The specific heat varies with temperature as shown in Fig. 2, the change is not so large but the anomaly showing a distinct peak is always found. This anomaly temperature as well as that of the resistance are also plotted in Fig. 3.

§ 4. Discussion

The lattice transformation point of pure nickel oxide may be considered to be 250°C., because a sharp anomaly was observed at this temperature in the dilatometric measurement by Foëx[10]***. On the other hand, the copper concentration of the oxide having a lattice transformation point at the ordinary temperature (25°C.) should be 21.5 at. %⁽⁶⁾. These two points are marked with ⊡ in Fig. 3*. Then it becomes clear that there generally exist marked differences among the anomally temperatures for the different kinds of physical properties**. Such a phenomenon has not been hitherto observed on the ordinary phase transitions. This is perhaps due to the reason that the transformation of this oxide owes to the antiferromagnetic origin as reported by Greenwald and Smart⁽⁴⁾.

---

* The copper content is referred to the cation only. The same expression will be used hereafter in this paper.

** In this case, the results of both measurements, heating and cooling coincide with each other.

*** It is difficult to determine precisely this temperature by means of X-ray crystal analysis.

However it must be also noticed that the magnetic transformation point of the specimen containing 24 at. % Cu is observed to be as high as 182°C., the structure of which is cubic at room temperature***. This fact shows that, in some cases, the nickel oxide lattice does not deform under the action of antiferromagnetic exchange force. Moreover when the oxide contains aluminium, it becomes to have a tendency to increase its lattice deformation inspite of lowering of the number of magnetic ions⁽⁶⁾. These phenomena may be explained only from the exchange interaction. Another consideration may be also possible that the lattice deformation owes not only the exchange force but also the other factors *e. g.* the ionic radius ratio and vacancies. That is, if there is no deformation force, the lattice does not deform even though the oxide has vacancies or the ionic radius ratio unfavourable to its crystal structure as in the case of the ordinary crystal, but when the force acts, the lattice deformation must depend on the ratio or the vacancies. Thus, if the ratio is too large as in the case of the oxide of rather high copper content, or if there are very few vacancies as in the case of the oxide film, the lattice can not deform inspite of the presence of the exchange force.****

References

1) Y. Shimomura and Z. Nishiyama: Memoirs of the Institute of Scientific and Industrial Research, Osaka University **6** (1948) 30; J. Japan Inst. Met. **13** (1949) No. 4, p. 2.

2) H. P. Rooksby: Acta Cryst. **1** (1948) 226.

3) N. C. Tombs and H. P. Rooksby: Nature **165** (1950) 442.

4) S. Greenwald and J. S. Smart: Nature **166** (1950) 523.

5) J. S. Smart and S. Greenwald: Phys. Rev. **82** (1951) 113.

6) Y. Shimomura: J. Japan Inst. Met. **17** (1953) 421.

7) T. Hirone, S. Maeda, I. Tsubokawa and N. Tsuya delivered at the meeting of the Phys. Soc. of Japan held in Sendai, in May, 1952.

8) S. Nagasaki and U. Takagi: J. Appl. Phys. Jap. **17** (1948) No. 5, p. 104.

9) M. Foëx et C. H. la Blanchtais: Compt rend. **228** (1948) 1344.

10) M. Foëx: Compt rend. **227** (1948) 193.

---

* The two points seem to have an intimate relation with the resistivity curve, so it may be possible to consider that the lattice transformation point changes as shown by a broken line.

** But the higher one of the two temperatures at which the anomaly of specific heat vanishes can be considered to coincide with the magnetic anomaly point.

*** It may be considered that the lattice transformation point is generally much lower than the magnetic one. The difference can be estimated by comparing the broken line with the magnetic curve in Fig. 3.

**** When there is a special (*e.g.* ordered) distribution of vacancies, the lattice may deform in the direction different from that of the exchange force as in the case of cobaltous oxide.

JOURNAL OF THE PHYSICAL SOCIETY OF JAPAN Vol. 9, No. 1, JAN.—FEB., 1954

External Photo-Emission of Thin Films Deposited by Evaporation from Barium Oxide

By Sin-ichiro NARITA

Kobe Kogyo Corporation, Hyogo-ku, Kobe

(Received March 26, 1953)

The properties of thin films, deposited onto clean metal surfaces by evaporation from barium oxide cathode, were studied simultaneously by means of photo-electric and thermionic procedures. Both photo-electric and thermionic emission had close dependence upon the concentration of atomic barium in the barium oxide source cathode. So far as the deposited layer was very thin, the spectral distribution of photo-emission fitted well to Fowler's plot, but as the layer became thicker, semiconductor type photo-emission appeared gradually. The maximum sensitivity of photo-emission from several molecular layers of BaO displaced 2.72 to 2.30 ev., together with the decrease in thermionic work function from 1.7 to 1.0 ev by increasing barium density of the layer.

§ 1. Introduction

The evaporation from an oxide coated cathode and the properties of thin film, deposited by evaporation onto clean metal surfaces from the cathode, were recently studied by many investigators.

Several ten years ago Davisson and Pidgeon[1] studied the properties of the thin film, concluding that the thermionic emission occurs through the agency of aggregates of BaO molecules. Kawamura[2] evaluated the heat of evaporation of BaO through measuring thermionic emission from the thin film assuming that the initial increase of emission with evaporated time is due to the formation of BaO dipoles. Arizumi and the author[3] investigated the properties of thin film concluding that its thermionic emission is influenced by barium atoms contained in deposited layer. On the contrary, Moore and Allison[4] asserted that only alkali-earth oxide can be evaporated from the evaporator and their dipoles moment reduce the work function. Noga[5] mentioned that the first rapid increase of thermionic emission with the increasing of contamination may be ascribed to BaO dipoles, however, as the layer become thicker semiconductor type emission may appear.

In the present paper both photo-electric and thermionic properties of thin films, deposited on molybdenum and tantalum by evaporation from BaO were studied to obtain more accurate knowledge on the properties of the films.

§ 2. Experimental Procedure

(*1*) *Construction of experimental tubes*

One of representative structure of experimental tubes is shown in Fig. 1. The surface of the receiver filament F, was polished, if necessary, and mounted on a plane at angle of 45° to the incident light beam for studing the effect of electrical vector of the incident beam upon the photo-electric emission current.

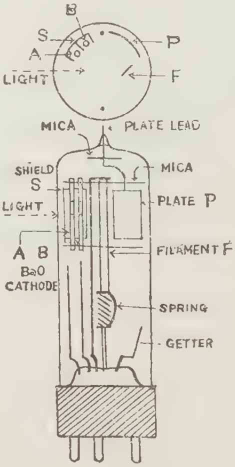

Fig. 1. Experimental tube.

The activator in base nickel of the evaporator cathodes was silicon to avoid the evaporation of other kinds of material than barium and barium oxide, and sleeve nickel of the cathode B was richer in silicon than that of the cathode A.

Thus the cathode B usually had a better activity than the cathode A and the thermionic emission was taken as a measure of their activities. At the same temperature the same amount of barium oxide evaporated from both cathodes, but the amount of barium evaporated differed largely from one to the other. This construction was convenient for obtaining the deposited films, differing in relative composition of barium and barium oxide.

(*2*) *Measurement*

After againg BaO coated source cathodes, the receiver F was flashed up to about 2,000°C to make free from involved gases. The source cathode A or B was then heated at 1,250°K to evaporate some amount of active materials for a certain interval, with the receiver F being kept at 800°K. Then the thermionic emission from F was measured near at 800°K. The spectral distribution of photo-emission was studied at room temperature. Such a procedure was repeated for each evaporation until the thickness of the contaminated layer grew to nearly ten molecular layers of BaO.

The light source for the photo-electric measurement was an incandescent lamp whose white light was resolved through an infra-red monochrometer with a quartz prism to focus on the filament F. A DuBridge-Brown amplifier and a galvanometer were used for the reading of photo-electric current. The relative intensity of the light source was calibrated by a vacuum thermo-couple, connected to a galvanometer of high sensitivity and low resistance.

Temperature of the source and the receiver was determined pyrometrically and necessary corrections were made for emissivity of the radiator and transmissivity of glass bulb.

The amount of deposited barium oxide on the receiver was computed from the vapour pressure-temperature curve of barium oxide and tube geometry. When the temperature of evaporator fixed to 1,250°K, the surface of the receiver was covered by a mono-molecular layer of barium oxide after evaporation of about 7 mins.

§ 3. Experimental results

(*1*) *Tantalum*

The tube used for this experiment had an evaporator cathode, and tantalum receiver surface was not polished. No essential difference in both photo-electric and thermionic emission from deposited thin films could be found between tantalum and molybdenum receiver.

(a) Effect of amount of contamination.

The thermionic emission from the receiver filament usually increased with the contamination of active substances (Fig. 2) and the emission current could be always expressed in term of Richardson equation

$$I = AT^2 \exp(-\varphi e/kT) .$$

I, A and φ are tabulated in Table 1. The spectral distribution curves of photo-electric emission are shown in Fig. 3 with linear scale and in Fig. 4 with logarithmic scale.

As far as the contamination was small, the curves obtained fitted fairly well to Fowler plots (I and II in Fig. 3) as plotted in Fig. 5, but it became to deviate more and more (III–VIII) with the appearance of tails.

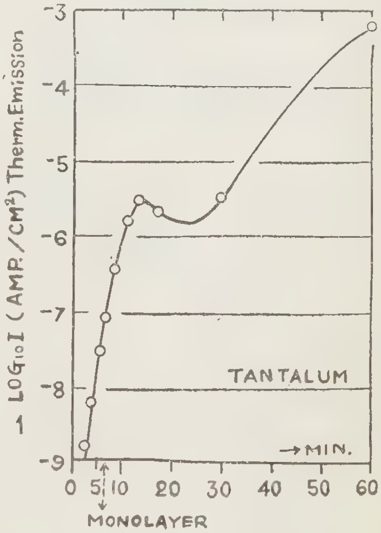

Fig. 2. Thermionic emission current from oxide thin film at 800°K vs. evaporated time curve 1.

In the present work the photoelectric work functions were determined, for convenience, under the assumption that the photoelectric emission could be expressed by Fowler equation, so long as the considered region

Table I.

No.	Evap. time t min.	Therm. Curr. i (800°K) Amp./cm^2	Richard. Const. A Amp./cm^2 degree^2	Work Function φ (therm.) ev	φ (photo.) ev
I	6	2.8×10^{-8}	15	2.35	2.35
II	7	9.8×10^{-8}	8	2.23	2.25
III	9	4.0×10^{-7}	1.2	2.03	2.10
IV	10	7.0×10^{-7}	0.8	1.94	1.99
V	12	1.5×10^{-6}	2.2×10^{-2}	1.61	1.87
VI	19	1.4×10^{-6}	1.5×10^{-1}	1.75	1.85
VII	30	4.0×10^{-6}	6.0×10^{-2}	1.61	1.87
VIII	60	9.9×10^{-4}	5.7×10^{-3}	1.20	1.69

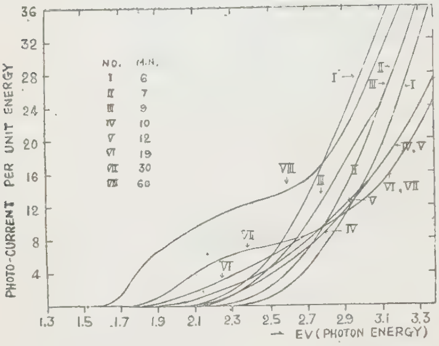

Fig. 3. Spectral distribution of photoemission from oxide thin film on tantalum.

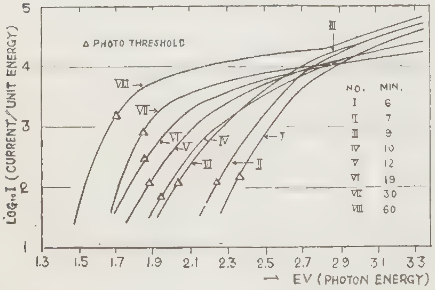

Fig. 4. Logarithmic photocurrent vs. photon energy curves.

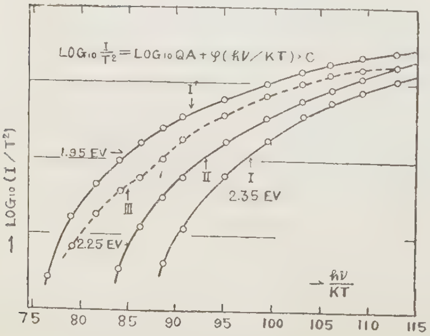

Fig. 5. Fowler plot.

Table II.

Heater Volt. Ef	Thermionic Emission A (Inactive)	B (Active)
3.5 V	0.055 mA	0.37 mA
3.25	0.025	0.20
3.0	0.012	0.095

was sufficient narrow near at the threshold. The results are appended to Table I, but they agreed well with those obtained by applying Nishibori et al's methode[6].

The photoelectric work function at which the photo-current began to deviate from a Fowler plot depended upon the activity of the evaporator cathode. Generally in the case of more active source, the photo-emission curve fitted to Fowler plot until the work function became smaller. The curves I' in Figs. 3 and 5 are the example in which the work function was estimated 1.95 ev.

(2) *Molybdenum*

In the case of molybdenum receiver, two source cathodes A and B with different activities were mounted in the same tube. The thermionic activities of both sources are shown in Table 2. The surface of the molybdenum receiver was polished carefully and it was settled at angle of 45° to the incident light.

(a) Activity of source cathodes.

Fig. 6 shows the time change of the thermionic emission from a molybdenum filament onto which evaporated substances deposited from the cathodes A and B respectively. Figs. 7 (a) and (b) are their spectral distribution curves of photoemission, and corresponding thermionic data are summarized in Table 3.

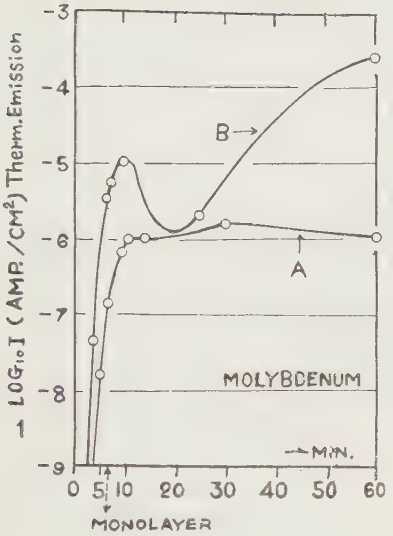

Fig. 6. Thermionic emission current from oxide thin films at 845°K vs. evaporated time curves 2.
A: evap. from inactive cathode
B: evap. from active cathode

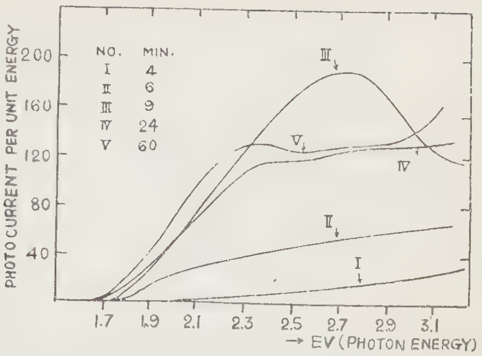

Fig. 7 (a). Spectral distribution of photoemission from oxide thin film on molybdenum evaporated from active cathode B.

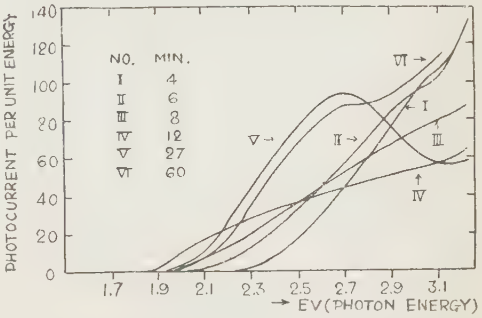

Fig. 7 (b). Spectral distribution of photoemission from oxide thin film on molybdenum evaporated from inactive cathode A.

Table III.

Evap. Cathode	No.	Evap. Time t min.	Therm. Curr. i (845°K) Amp./cm²	Richard. Const. A Amp./cm² degree²	Work Function φ (therm) ev	φ (photo) ev
From Inactive (A)	I	4	3.2×10^{-8}	—	—	2.15
	II	6	2.1×10^{-7}	4.0	2.20	2.15
	III	8	8.9×10^{-7}	2.7	2.09	2.10
	IV	12	1.3×10^{-6}	5.2×10^{-1}	1.94	1.90
	V	27	1.8×10^{-6}	1.05×10^{-1}	1.83	2.00
	VI	60	1.1×10^{-6}	1.6×10^{-1}	1.85	2.00
From Active (B)	I	4	3.4×10^{-7}	3.9×10^{-1}	2.00	2.00
	II	6	4.0×10^{-6}	2.2	1.97	1.95
	III	9	8.0×10^{-5}	1.1×10^{-3}	1.35	1.80
	IV	24	2.3×10^{-6}	2.4×10^{-3}	1.57	1.80
	V	60	2.0×10^{-4}	5.7×10^{-4}	1.0	1.70

When the filament was exposed to the evaporation from the active source, the photocurrent was represented by a Fowler equation at first (I in Fig. 7 (a)), but then began to deviate from this equation. On the other hand, when the filament was exposed to the evaporation from the inactive source, the photocurrent did not follow Fowler plot from the beginning. (where the thermionic emission showed initial rapid increase) and the current maximum in the long wave length did not displace to 2.3 ev even after deposition of several molecular layers, but it remained 2.72 ev. (Fig. 7 (b)). Parallelly the thermionic emission remained much lower (Table 3) however, such an inactive state could be activated by evaporation of active substances from the active source as will be mentioned in the next paragraph.

(b) Displacement of maximum sensitivity.

Preceeding to this experiment the active source cathode B was flashed at 1,470°K in order to increase the content of barium atoms and the molybdenum receiver was cleaned by flashing. At first the active substances evaporated from the inactive source A at 1,250°K was deposited on the receiver at 800°K. The spectral distribution curve obtained is shown by the curve I in Fig. 8 together with the thermionic data, then lighting the cathode B at 1,250°K and the receiver at 800°K, the active substances were evaporated further on to the receiver for 1 min. The spectral distribution curve changed to the curve II in the same figure. The current maximum displaced from 2.72 to 2.3 ev and at the same time the thermionic work function lowered down from 1.73 to 1.06 ev. corresponding to a large increase of thermionic emission at 800°K by the factor of 5,000 times.

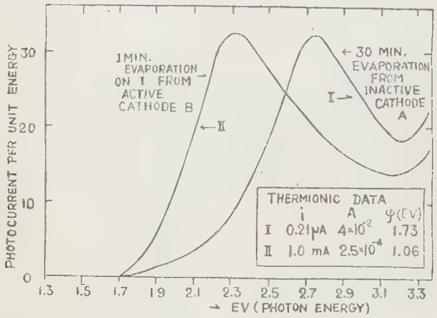

Fig. 8. Displacement of sensitive maximum of photoemission from oxide thin film on molybdenum. Thermionic datas are obtained from Richardson's formula,

$I=AT^2\exp(-\varphi e/kT)$ $(T_i: 800°\mathrm{K})$.

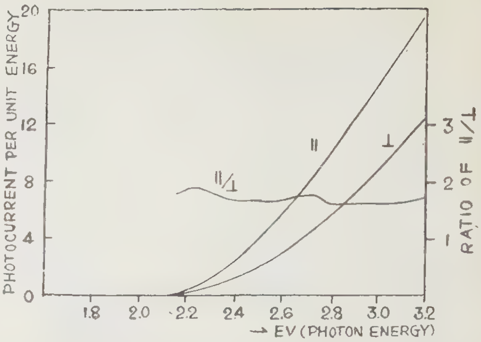

Fig. 9 (a). Effect of the direction of electric vector of the incident light on the metallic photoemission.

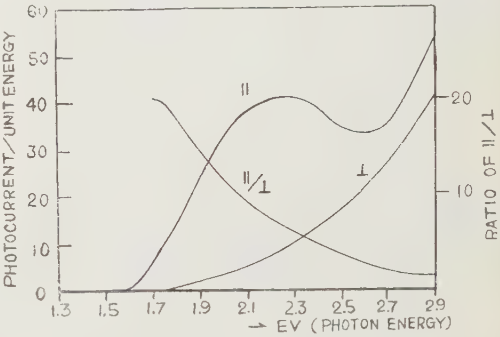

Fig. 9 (b). Effect of the direction of electric vector of the incident light on the selective photoemission.

(c) Vector effect of the incident light

For simplicity the light polarized with the electric vector parallel and perpendicular to the plane of metal are symbolized by ⊥ and // respectively. In Fig. 9 (a) are shown photo-emission curves for ⊥ and // for a thin film deposited by 4 mins evaporation. Both curves fit to Fowler plots, but the current for // is usually about twice larger than that for ⊥. Fig. 9 (b) are photo-emission curves by 30 mins evaporation, in which the selective photoemission whose maximum situates at 2.3 ev is clearly observed only for // and the ratio of ∥/⊥ often exceed by the factor of ten in the low energy region.

§ 4. Discussion

(1) *On the curves fitting to Fowler Plots*

The photoemission current from a clean metal has been known to be expressed by Fowler equation,

$$I=AQT^2\varphi\{h(\nu-\nu_0)/kT\}\,.$$

When a metal surface is covered by a mono-atomic layer of other kind of metal and the surface dipoles reduce the work function of the base metal, its photo-current should have the similar expression, because electrons participated to the emission may be free electrons in the base metal, as supported by many investigators[7].

The present study revealed that the photoemission from thin films deposited by evaporation from BaO initially expressed by Fowler equation. This suggests that the dipoles of BaO or Ba are formed on the surface of receiver at the beginning of evaporation. If BaO dipoles are assumed to be formed, the photoelectric and thermionic emission at the beginning of the evaporation must be independent of the source cathodes, standing against the experimental results shown in Fig. 6 and 7. Also the present photo-electric work showed that the active evaporators give the Fowler plots having smaller work-function. These results seems to lead to the conclusion that barium atoms evaporate from a source cathode and form their dipoles on the receiver surface locating independently upon barium oxide molecules at the first stage of contamination.

(2) *Selective photo-emission*

As the amount of contamination became larger, the photo-emission curve became to have an abnormal tail in low energy side and began to deviate from the Fowler plot. Finally the curve had the maximum of photo-sensitivity at the lower energy region. It may give an evidence for denying the formation of BaO dipoles at the stage. Perhaps evaporated barium oxide molecules combine with barium atoms on the surface of the receiver to have a crystal structure of semi-conductor type. The displacement of maximum of sensitivity also indicate the powerful role of barium atoms in the emission.

In the case of (K)—KH—K cathode, reported by Fleisher8), the photo-sensitive maximum at 427 $m\mu$ has an abnormally vector effect and correspond to the absorption maximum of light. DeBoer8) explained this results by the anisotropy of the layer. In the present work, the maximum of sensitivity at 2.3 ev showing abnormally vector effect may have some relation with the absorption by F center of BaO single crystal observed by Kane10), and the anisotropy of the present layer may be attributed to surface barium on BaO layer.11) It seems, however, difficult to give a complete interpretation for the present experimental results in term of energy level diagram.

The vector effect of the photoemission seems to suggest additionally that the aggregation of the evaporated materials may not occur on the receiver.

(3) *Thick Oxide Coating*

It is quite interesting that the photo-electric threshold of active thin film of several molecular layers quite resembles to that of the thick oxide coating of good activation reported by Nishibori et al's6) as is the case for the thermionic work function3)4).

These resemblance may be explained by the conception that these work functions of both emitters are determined by the structure near the surfaces.

The writer wishes to express his thanks to Dr. T. Arizumi for his helpful suggestions and discussions.

References

1) C. Davisson and H. A. Pigeon: Phys. Rev. **15** (1920) 553.

2) H. Kawamura: J. Phys. Soc. Japan **1** (1946) 8.

3) T. Arizumi and S. Narita: J. Phys. Soc. Japan **4** (1949) 300.

4) G. E. Moore and H. W. Allison: Phys. Rev. **77** (1950) 246.

5) K. Noga: J. Phys. Soc. Japan **4** (1949) 360.

6) E. Nishibori, H. Kawamura and K. Hirano: Proc. Phys-Math. Soc. Japan **23** (1941) 37.

7) A. King: Phys. Rev. **53** (1938) 570.
J. J. Brady: Phys. Rev. **46** (1934) 768.
C. L. Henshaw: Phys. Rev. **52** (1937) 854.

8) R. Fleisher: Ann. Phys. LPZ **82** (1927) 75.

9) J. H. DeBoer: Electron Emission and Adsorption Phenomena, Cambridge, (1935) P. 212.

10) O. Kane: J. Appl. Phys. **22** (1951) 1214.

11) S. Narita: J. Appl. Phys. **23** (1952) 599; J. Phys. Soc. Japan **8** (1953) 331.

JOURNAL OF THE PHYSICAL SOCIETY OF JAPAN Vol. 9, No. 1, JAN.—FEB., 1954

On the Electron Bombardment Effect for Deposited Barium Oxide Films

By Tetsuji IMAI

Electrical Communication Laboratory, Nippon Telegraph and Telephone Public Corporation, Tokyo, Japan

(Received August 27, 1953)

Several phenomena caused by electron bombardment for barium oxide films deposited from oxide coated cathode are described. Oxide cathode used as electron source is largely deactivated by electron bombardment applied for deposited film. Origin of emission decay is found to be ascribed to evolved gas from deposited film under bombardment.

Furthermore, details of change of deposited film's activity under bombardment are described. Emission of film increases or decreases by electron bombardment due to whether deposition is carried out at low or at high cathode temperature. Change of work function is also measured. In connection with the electron bombardment, temperature effect for films are studied and an activation or a deactivation phenomenon was found. These results obtained for nickel and molybdenum sleeves are applicable for the case of grid emission in commercial tubes.

§ 1. Introduction

Effect of the "contamination of positive electrodes" on cathode emission is investigated from several points of view. Some descriptions[1] are already given of the emission decay phenomenon due to the anode contamination. For the contamination of anode material itself, gas evolution from the anode under electron bombardment and the effect of pretreatment of the anode material on emission decay were also investigated[2]. To prevent the emission decay, clean-up of positive electrode is quite important and appropriate methods in pumping, activation and aging process are desirable.

Another interesting problem originated from the contamination due to deposition from oxide cathode is the variation of emission in deposited film under electron bombardment. In this article, activation and deactivation phenomena in the deposited films under bombardment and temperature effect for films after bombardment are mentioned in detail. These provide a very interesting clue which clarify the mechanism of emission of the thin film composed of evaporated substance from the oxide cathode.

In order to outline the full behaviour of electron bombardment effect, main points of phenomena observed at bombarding cathode and of gas evolution data will be added before the description of phenomena in the deposited film.

§ 2. Survey on Previous Results

It was found that if an anode is contaminated by deposited film from oxide cathode, d.c. emission of the latter is smaller than that which is faced to noncontaminated anode. Further investigations indicated that, in former case, large emission decay took place by the dissociation of deposited barium oxide.[1] In some extreme cases, it is difficult to draw sufficient anode current necessary for normal operation, unless adequate aging process is applied after thermal activation.[3] This result implies that one purpose of drawing emission during thermal activation and of aging process after activation lines in cleaningup of contamination on the positive electrodes.[4],[5] Mechanism of emission decay due to the presence of contaminated anode was also confirmed by founding the threshold potential for dissociation of deposited barium oxide. Anode voltage at which abrupt change in saturated anode current occur is 6.0 V and in considering the contact potential difference between cathode and contaminated anode it was concluded that dissociation of deposited barium oxide will occur at about 5.0 eV. In practice, life test data indicated a very interesting result, that is, one batch carried out with Ep=3.0 V has stable emission while the other one carried out with Ep=8.0 V has a seriously slamped emission in spite of same anode current (10 mA) for both cases.3)

Furthermore, when an anode contaminated with deposited film is employed, a particular phenomenon appeared in decay process, i.e., emission decay curve has a hump. Degree of humping is different from case to case according to circumstances, e.g., the proportion of barium to barium oxide in deposited film, activity, temperature of bombarding cathode, etc.

§ 3. Gas Evolution under Electron Bombardment

Experiments were performed to ascertain whether gas evolution takes place at contaminated anode. Test tube used is shown in Fig 1. in which A and B are diodes, C is Pirani gauge and D getter chamber. At first, saturation current is drawn in diode A and after steady state is established, emission current is drawn in diode B having an anode with deposited film, thus emission current of a diode is measured in function of gas pressure and the emission current of another diode. Fig. 2 is an example of the results obtained and shows increase of gas pressure and decrease of the emission current in A due to current drawing in B. In diode B, anode material is cleaned up by electron bombardment for long hours, and deposition from oxide cathode is made after the gas evolution has ceased. Increase of gas pressure in Fig. 2 is, therefore, ascribed reasonably to deposited film, and origin of emission decay for both cathodes will be ascribed to the evolved gas. Furthermore, it was found that the higher the bombarding voltage and the larger the time of deposition, the greater the gas evolution. An example is illustrated in Fig. 3 and this curve implies enhancement of dissociation as bombarding energy increases.

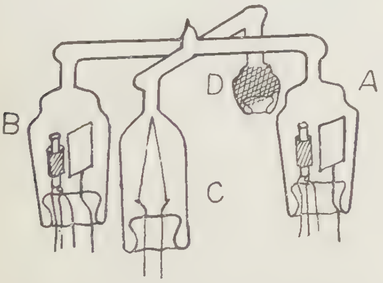

Fig. 1. Experimental tube for measuring the variations of emission and gas pressure shown in Fig. 2. A and B are diodes, C is Pirani gauge and D is getter chamber.

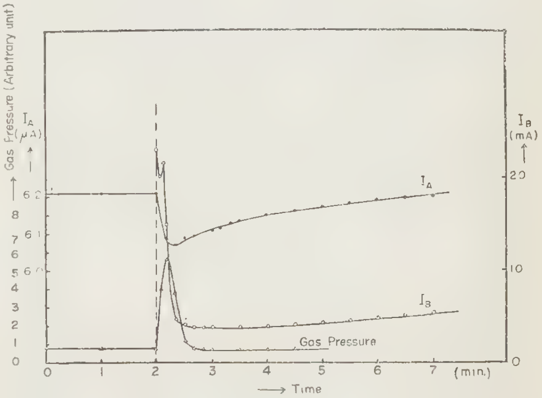

Fig. 2. Variations of emission and gas pressure caused by electron bombardment applied for contaminated anode with deposited film.

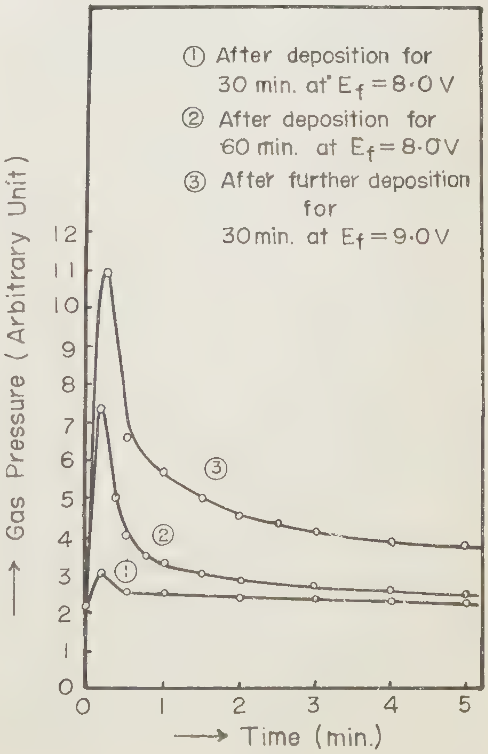

Fig. 3. Evolution of gas from the deposited anode under electron bombardment for various quantities of deposition.

Comparison of gas evolution for the deposited nickel and tantalum anodes are also examined. In the same test tube nickel and tantalum anode were deposited with cathode materials by flashing the oxide cathode in equal conditions e.g. at about 1200°K for 10 minutes, then bombarded at an equal anode voltage (=200 V). Gas evolution result is given in Fig. 4, which represents marked difference for two anodes. This marked difference in gas evolution for two anodes will be due to the difference of dissociation probability for deposited barium oxide.

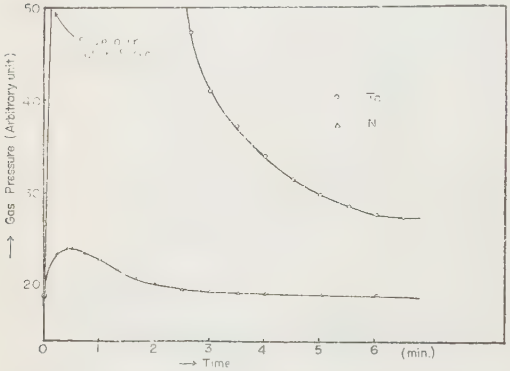

Fig. 4. Comparision of gas-evolutions from Ta and Ni anodes on which deposition from oxide cathode were made.

It is obvious from these results that deposited film from oxide cathode liberates some gas, probably oxygen, under electron bombardment and the liberated gas affects the cathode to cause emission decay.

§ 4. Change of Emission at the Deposited Film

We can suppose, from what we saw in previous sections, that a marked change of activity would be brought about in the deposited film by electron bombardment. Measurements of emission and work function of deposited film during bombardment were carried out associated with the observation of the temperature effect of the film. Preliminary experiment gave such inconsistent results as indicating increase and decrease of emission from case to case by bombardment. Detailed systematic experiments were, therefore, undertaken and a consistent explanation for various experimental results were obtained. Test tube, shown in Fig. 5, have two sleeves, the one coated and the another uncoated, of which normal rating of heater is 6.3 V. The uncoated sleeve is attached by P_t—P_t-R_h thermo-junction and is shielded by sliding plate from the coated sleeve whenever undesirable deposition takes place.

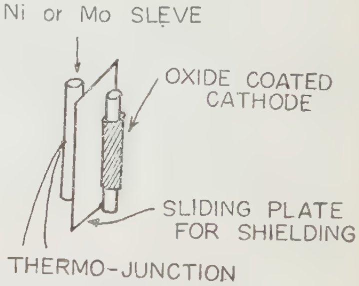

Fig. 5. Experimental tube for measuring the behaviour of activity in deposited film caused by electron bombardment.

Experiments were carried out for nickel and molybdenum sleeves and for commercial tube's grid. Emission from the deposited film was measured by a galvanometer, whose sensitivity is 2.3×10^{-10} A.

(4-1) *Variation of Contact Potential and of Asscciated Emission during Deposition*

In order to get a measure of deposited quantity, measurements are performed for the variation of contact potential between deposited film and cathode as well as for the emission of deposited film during deposition. One of these results obtained for nickel sleeve is illustrated in Fig. 6. Contact potential is measured by so called method of "initial velocity characteristic". If we assume that emission current is saturated when monolayer is formed, then, in the case shown in Fig. 6, formation of monolayer would be completed in several minutes. The behabiour shown in Fig. 6 are qualitatively similar to those obtained with molybdenum sleeve.

(4-2) *Activation and Deactivation by Electron Bombardment*

The fact that electron bombardment effect is different for individual cases even under the same bombarding condition, means that there will be some difference in the nature of deposited film before bombardment. This "difference in nature" will be ascribed to the difference of composition in deposited films, and this difference of composition would be originated from the fact that each cathode is flashed at different activity and maintained at different temperature on depositon. In this experiment, test tube has good activity of the order of 100 mA/cm^2 at about 800°K. To ascertain the above consideration experiments were performed at various temperatures of cathode during deposition. Results are classified into two general groups. (1) When deposition was made at high cathode temperature, deactivation is caused by electron bombardment. (2) On the other hand, when deposition was made at low temperature, electron bombardment causes activation. In the case of activation, however, further successive bombardment brings about deactivation. An example of the first case is shown in Fig. 7. After deposition for 20 min. at Ef=7.5 V (about 1150°K), marked decrease in emission accompanied by the increase in work function appeared by bombardment as shown by Richardson plot ①, ②, ③ in Fig. 7 (a). These variation of emission and work function are re-illustrated in Fig. 7 (b) as a function of time of bombardment at a certain temperature. An example of the second case is represented similarly in Fig. 8 (a), (b). The latter result is obtained for deposited film after deposition of 2 hours at Ef=7.1 V, and shows marked activation due to bombardment, though farther bombardment brings about deactivation. If the deposition time is longer, activation process is transformed into deactivation process in much shorter time of bombardment though bombarding and depositing conditions remained the same. This means that it becomes easier to deactivate as the deposited quantity becomes larger. In the above examples, conditiones of bombardment are 100 V. for bombarding voltage and 7 mA for bombarding current in all cases, but if bombarding condition is less severe, e. g. 50 V, 1 mA, activation process becomes much more gradual. In this series of experiments, medium temperature range was also examined. It was found that, if deposition is made at Ef=7.3 V (even for 1 hour) activation appeared by bombardment and if temperature exceeds that corresponds to Ef=7.4 V, deactivation takes place except for very short time of deposition (shorter that about 5 min.)

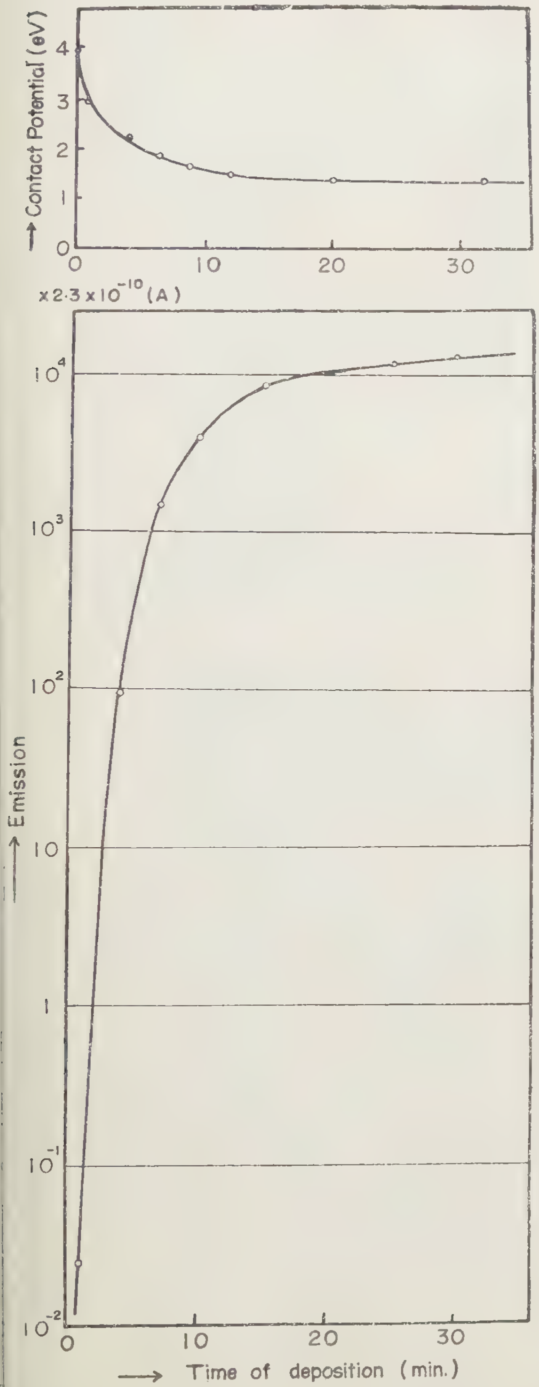

Fig. 6. Variations of emission in the deposited film and of contact potential difference between film and oxide cathode during deposition. Emission is measured at 600°C. (Ni sleeve used).

For molybdenum sleeve, activation-deacti-

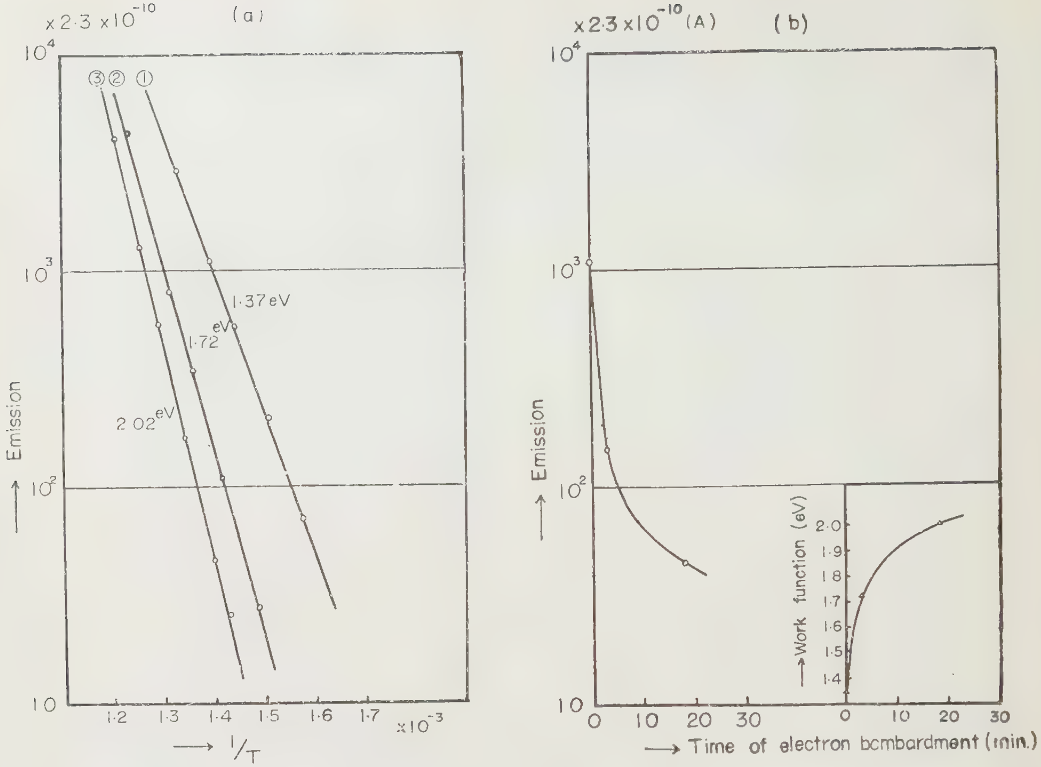

Fig. 7. Electron bombardment effect for Ni sleeve on which deposition was made at Ef=7.5 V for 20 min.

(a) Logarithmic emission vs. $1/T$ plots. ①: Immediately after deposition. ②: After electron bombardment at 100 V, 7 mA for 3 min. ③: After further bombardment at 100 V, 7 mA for 15 min.

(b) Variations of emission at 440°C and of work function as a function of bombarding time.

vatirn critical temperature is much higher than that for nickel sleeve. Even when deposition temperature is about 1200°K (Ef=8.0 V) activation due to bombardment appeared. If deposition is made at Ef=9.0 V, deactivation due to bombardment is appeared excepted for a very little deposition.

Effect of temperature of sleeve on which deposition is made is also examined for molybdenum sleeve. Curves ① and ② in Fig. 9 indicate the electron bombardment effect for molybdenum sleeve which maintained at room temperature and 600°C respectively during deposition. In the latter case, initial emission is smaller than that for the former and activation process appeares at first, though flashing temperature and bombarding conditions are kept same for both cases. The mechanism for this difference will be considered later.

(4-3) *Temperature Effect*

Marked temperature effect was observed which represents a serious decrease in emission together with a appreciable increase in work function by raising the film temperature momentarily after activation due to bombardment. Detailed study of emission decay phenomenon was made and the decay is found to become more rapid as temperature increases. Fig. 10 (a) indicates this behaviour and if we plot the quantity of decrease in emission per unit time against $1/T$, on a assumption that emission decay is in proportion to time, a straight line shown in Fig. 10 (b) is obtained. Slope of this line corresponds to energy of about 2.0~2.2 eV.

On the other hand, after deactivation due to bombardment, activation appears by raising film temperature slightly. Even in this case, however, raising film temperature further, strong decrease in emission is caused in the same manner as mentioned above.

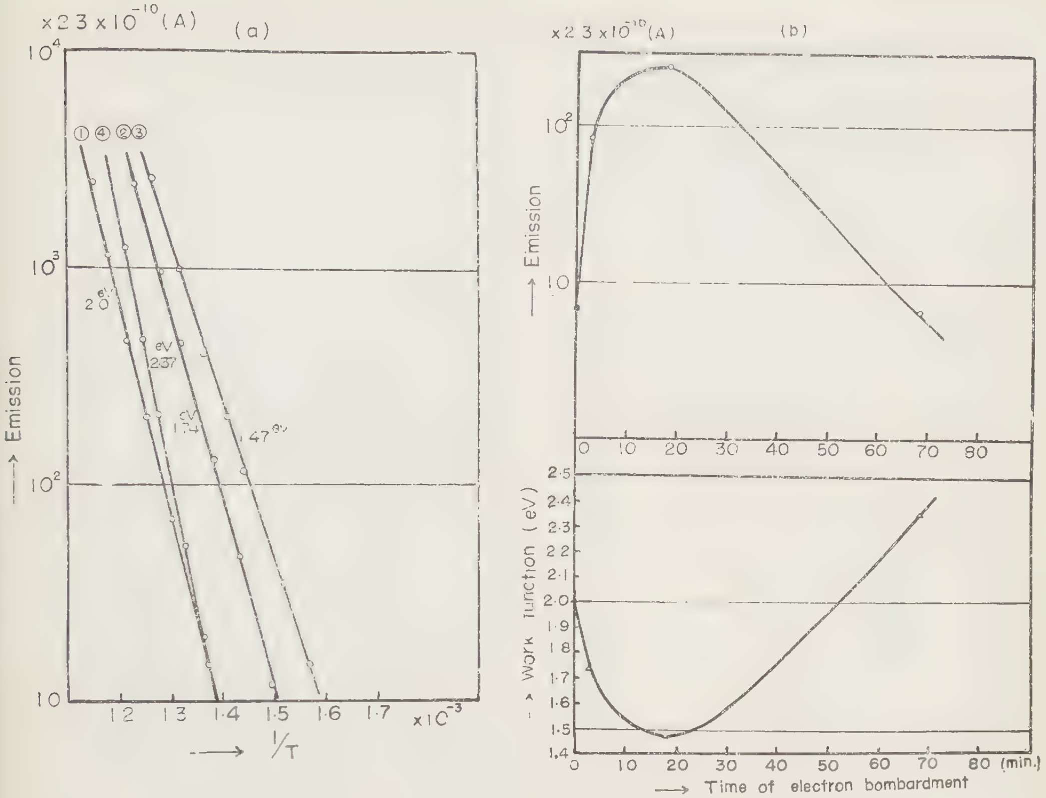

Fig. 8. Electron bombardment effect for Ni sleeve on which deposition was made at Ef = 7.1 V for 120 min.

(a) Logarithmic emission vs. 1/*T* plots. ①: Immediately after deposition. ②: After electron bombardment at 100 V, 7 mA for 3 min. ③: After further electron bombardment at 100 V, 7 mA for 15 min. ④: After further electron bombardment at 100 V, 7 mA for 50 min.

(b) Variations of emission at 440°C and of work function as a function of bombarding time.

Degree of this activation is comparatively small for nickel, while for molybdenum marked. An example of result obtained for molybdenum sleeve is shown in Fig. 11. In Fig. 11 (a), emission was measured at a certain temperature after film was heated at more higher temperature for several minutes. Aspect of the emission increase against time is shown in Fig. 11 (b), which represents a strong increase in emission after equilibrium is established in temperature. Difference of degrees of this emission increase for nickel and molybdenum will be ascribed to the difference of reduction ability for these two sleeve materials.

(4–4) *Adoptation for Grid Emission*

Phenomena similar to that mentioned in previous sections must be found also in grids of commercial tubes. Results obtained for CZ–504–D, a repeater power amplifier pentode, after an over-heated life test at nearly 1300°K of cathode temperature for several hours is quite similar to that of Fig. 7 obtained for sleeves on which deposition were made at high cathode temperature. On the other hand, result obtained for CZ–501–D, a repeater voltage amplifier pentode, operated at normal rating for several thousands hours indicates strong increase in grid emission by bombardment. In this case, the behaviour is analogous to these obtained for sleeves on which deposition were made at low cathode temperature. In (4–3), we found that large decrease in emission would be brought about by raising the temperature of film even when marked activation is caused by bombardment. In the case of grid emission, however, direct heating of grid wire is impossible. Heating is carried out, therefore, by flashing the cathode momentarily, for example at about 1350°K for 1 minute, thus raising the temperature of grid wire by radiated heat from the cathode. This heat treatment is very sensitive to decrease the grid emission as shown in Fig. 12. It is very interesting and important fact that grid emission decreases to a value lower than initial value.

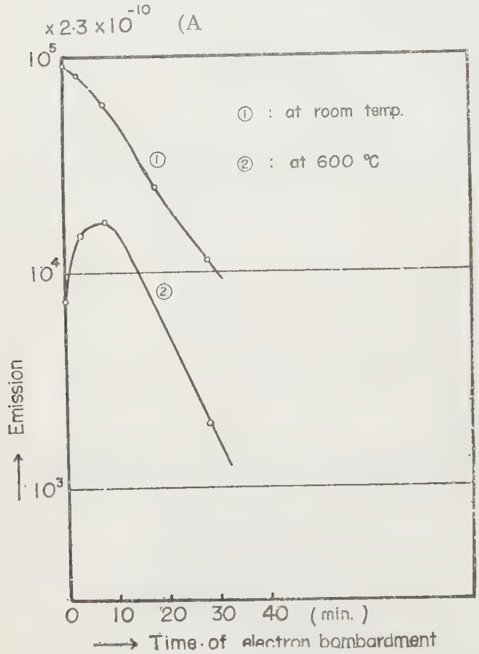

Fig. 9. Effect of temperature of sleeve on which deposition is made. Deposition is made on Mo sleeve at Ef=9.0 V for 30 min. Bombarding condition is 100 V, 7 mA and emission is compared at 380°C.

(4–5) *Consideration*

It will be expected from the results mentioned above that there is optimum condition for thermionic emission from deposited film. Our present interest lies in finding the main factor which affects this optimum condition. Deposited materials from oxide coated cathode are considered to be a mixture consisted of a large number of barium oxide molecules and a few barium atoms.⁶⁾,⁷⁾ If this is the case, gas evolved at electron bombardment should be oxygen and it is quite natural to expect the production of free barium atom in the deposited film by electron bombardment. For the electron bombardment effect to oxide cathode, Becker⁸⁾ as well as Yoshida, Takeda and Arata⁹⁾ have performed already very interesting works and pointed out that activation or deactivation phenomenon appeared owing to the production of free barium atoms in the cathode under bombardment.* In present experiment also, if we assume that emission of deposited film has a maximum value at the appropriate quantity of surface free barium atom, the results obtained will be explained.

If the flashing temperature is high, deposited film will be at optimum state from the beginning and so free barium produced by bombardment will bring about deactivation. On the other hand, if the flashing temperature is low, deposited film will not reach to an optimum state even if deposition quantity is much larger. Free barium produced by bombardment will then activate the deposited film. It is clear from these considerations that even in the case of activation, successive bombardment will deactivate the film owing to the over production of free barium. Result shown in Fig. 10 representing a difference of electron bombardment effect for molybdenum sleeve maintained at room temperature and 600°C will be explained in terms of re-evaporation of free barium. In the later case, quantity of barium atom in the deposited film is smaller than that in the former case, and so the emission in the latter is smaller and increases by bombardment. The dependency of activation due to bombardment on whether the evaporating material composing thin film comes from the cathode with inactive core metal, e.g. platinum, or comes from that with active core metal, e.g. tantalum, furnishes a powerful proof for the free barium theory mentioned above.**

Temperature effect also seems to be explained by diffusion or evaporation of free barium, and variation of density of surface free barium will cause activation or deactivation. For the temperature dependency of emission decay mentioned in (4–3), the following consideration is possible.

If decreasing velocity of suaface density of

---

* More recently, Wood and Right¹⁰⁾ performed similar experiment for deposited BaO film. Ishikawa, Sato, Okumura and Sasaki also carried out the electron bombardment effect for oxide cathode in a different point of view (Presented orally at the meeting of the Society of Electronic Emission, Tokyo, Japan, 29th. Sept. 1950.)

** These results will be reported later.

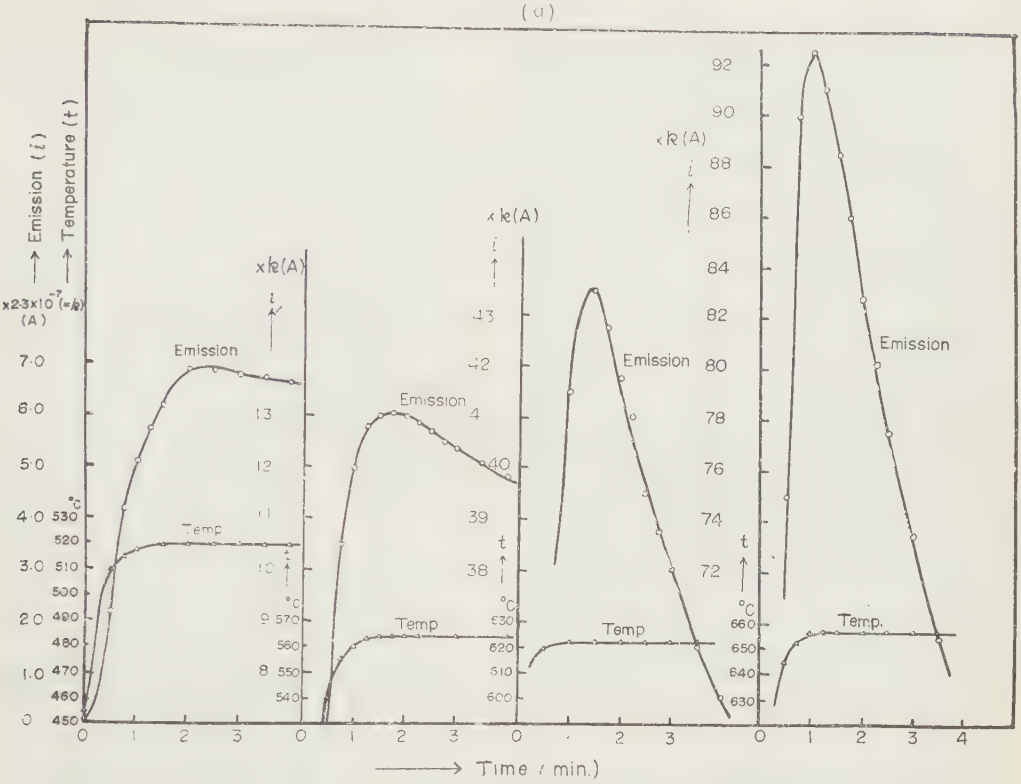

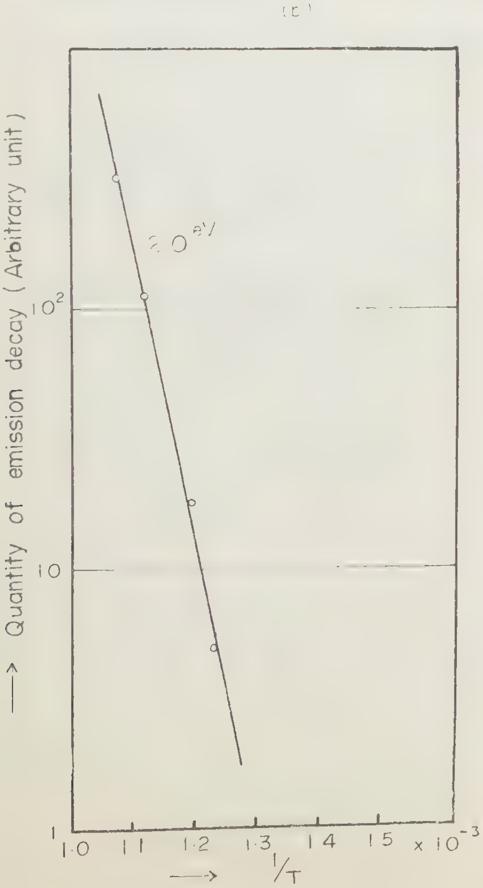

Fig. 10. Degree of emission decay affected by film temperature (Ni sleeve).

(a) Decrease of emission as a function of time after raising film temperature.

(b) Logarithmic plot of degree of emission decay per unit time vs. $1/T$ obtained from (a).

free barium (n_0) in the deposited film is considered to be proportional to n_0 and also emission (I) from the film is considered to be proportional to n_0, as a first approximation, we obtain

$$dI/dt=-KI\,, \qquad (1)$$

where

$$K=K_0\exp(-E/kT)\,. \qquad (2)$$

If we denote the maximum emission before decay starts as I_0, then, I/I_0 plotted against time in a semi-log. paper gives a straight line, of which slope coincides with K. Thus if we take the slope K for various temperature and plot this value against the reciprocal of temperature in a semi-log. paper, we obtain E. Value of E thus obtained for the result shown in Fig. 10, is 0.7 eV. and this value is considered to correspond much more naturally to diffusion energy of free barium. From this consideration, variation of emission

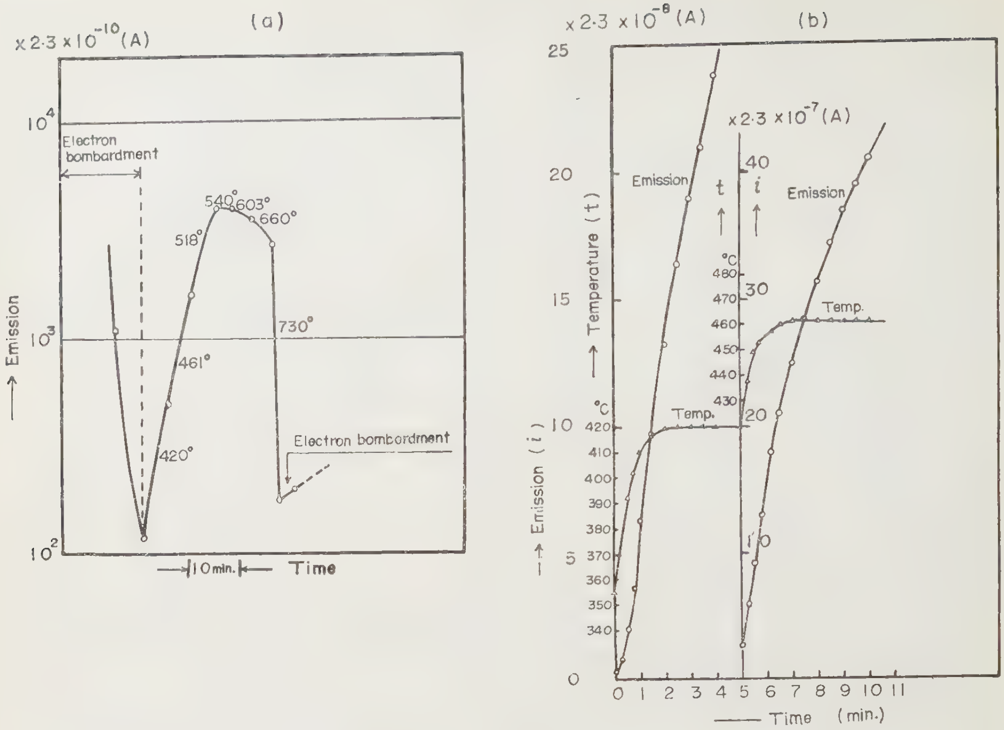

Fig. 11. Activation due to raising of film temperature after deactivation caused by electron bombardment. (Mo sleeve)
(a) Variation of emission is measured at 380°C.
(b) Increase of emission continues after establishment of equilibrium in film temperature.

will be ascribed to the variation of n_0 due to diffusion into deposited film. The value of 2.0~2.2 eV. obtained for the same data on an assumption that emission decreases linearly against time, indicates that the value of work function of the film corresponds to about 1.3~1.5 eV. This value is seemed to certify the validity of the assumption $I \propto n_0$ as a first approximation.

Increase of emission caused by raising temperature would be explained similarly in terms of the diffusion of free barium atoms. Raising of film temperature after over production of free barium by electron bombardment would cause the decrease of surface free barium due to it's diffusion towards sleeve. Increase of emission, thus, continues until the density of surface barium decreases below the optimum value.

The fact that variation of emission is always associated with variation of work function is analogous to that for oxide cathode, in which activity is affected by density of excess barium. Increase of work function due to over-bombardment will be ascribed, however, to metallic barium at the film surface owing to the excess production of free barium.

Above considerations appear to provide consistently a good explanation for results obtained, but following points will remain unexplained in the present experiment. The deposited film has, unless quantity of deposition is not sufficient,* an amorphous structure. From the result shown in Fig. 6, if the formation of monolayer takes place at saturation point in emission, it will be natural to consider that the deposited layer remains at the amorphous state. If the emission mechanism of these thin films and role of the free barium in it are unknown, therefore, above considerations do not hold.

On the other hand, Arizumi and Narita** recently performed photo-electric investigations for deposited film. They found that

---

* More than about 100 Å.

** Report of the Society of Electronic Emission of Japan, March, 1953.

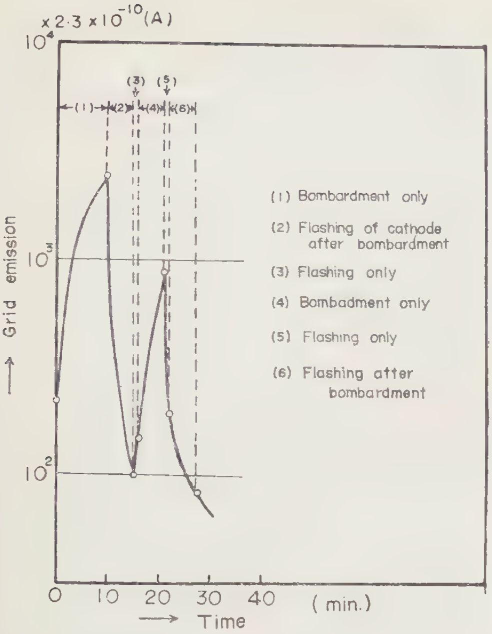

Fig. 12. Logarithmic grid emission vs. bombarding time plots for repeater pentode CZ-501-D. Bombarding condition is 50 V, 100 mA. Temperature effect also clearly appeared in this case.

maximum point of photo-emission from films made of evaporated materials from active cathode lies at 2.3 eV. This result obtained for very thin film, even at about several molecular layer thickness, is quite similar to that obtained for oxide cathode. In considering this result and our electron bombardment result, emission mechanism for both deposited thin film and oxide cathode seems to coincide. It may not be unreasonable, therefore, to doubt the validity of semiconductor model of electron emission in oxide cathodes. If this is not the case, it may be reasonable to assume the formation of crystalized non-uniform thick layer in Patch form during a short deposition time.

§ 5. Conclusion

In a vacuum tube with oxide coated cathode, evaporated film of cathode materials contaminates other electrodes during the pumping, activation and normal operating processes. When the deposited films of positive electrodes such as anode and screen grid are subjected to electron impact, they liberate gas which causes the decrease in electron emission from cathode.

The fact that the emission from evaporated thin layer exhibits various behaviours due to electron bombardment will become an effective clue for the clarification of emission mechanism of thin deposited film. In practice, these result will suggest a measure to lower grid emission and also to renovate tubes having failure with respect to excessive grid emission.

In conclusion the author wishes to express his sincere thanks to Mr. Z. Oda for his friendly cooperation on the gas evolution experiment. He wishes to Dr. Y. Takeda and Mr. K. Amakasu for their kindly guidance and encouragement. Thanks are due to Mr. Y. Nakamura of the Laboratory for his cordial assistance in preparing English text.

References

1) K. Amakasu, T. Imai: J. App. Phys. **24** (1953) 107.

2) K. Amakasu, T. Imai: Month. J. Elect. Comm. Lab., Japan **6** (1953) 327.

3) Presented by Amakasu, Imai and Asano at the Joint Meeting of the Tokyo annexes of three Institutes of Electrical Engineers of Japan, Nov., 1953.

4) G. Herrman, S. Wagener: The Oxide Coated Cathode, Chapman and Hall, London, 1951.

5) G. H. Metson, S. Wagener, M. F. Holmes and M. R. Cild: Proc. I.E.E. **99** Pt. III (1952) 69.

6) G. E. Moore and H. W. Allison: Phys. Rev. **77** (1950) 246.

7) L. T. Aldrich: J. App. Phys. **22** (1950) 1168.

8) J. A. Becker: Phys Rev. **34** (1929) 1323.

9) S. Yoshida, I. Takeda and H. Arata: J. Phys. Soc. Japan, **7** (1952) 430.

10) J. Wood and D. A. Wright: British J. App. Phys. **4** (1953) 56.

JOURNAL OF THE PHYSICAL SOCIETY OF JAPAN Vol. 9, No. 1, JAN.—FEB., 1954

Transient Phenomenon in the Oxide Cathode Layer

By Takuzo SHINDO

The Electrical Communication Laboratory, Tokyo, Japan

(Received August 25, 1953)

In the previous paper, it was shown by the writer that the space charge may be formed up in the oxide cathode layer near the surface. In this paper the theory was extended to clarify the transient phenomenon in oxide layer forming up this space charge. The theory shows some short time transient phenomena having $10^{-8}\sim10^{-9}$ second transit time.

§ 1. Introduction

In the previous papers[1]* the writer has shown that the space charge may be formed up in the oxide cathode layer near the surface and the static character of a planar diode can be well understood as an effect of this space charge. Recently Wright and Woods[2] have proposed similar theory independent of the writer's work. Unfortunately, however, their theory was somewhat restricted and mathematical treatment was unfavorable in some detail.

In recent years porous characters of the oxide layer have been studied by many investigators and it would be certain that the oxide layer may have some porous characters in well activated state[3]. In the present status of affairs, however, it would be worth while to publish a theory based upon the bulk conduction of the oxide layer. The essential parts of the theory that follows have been accomplished about three years ago to clarify the short time emission decay observed by Sproull[4] and others without any knowledge of the pore conduction.

§ 2. Fundamental Equations

Considering one dimensional model of the oxide layer and, for simplicity, an interface which usually exists between the base metal and oxide layer shall be neglected (see Fig. 1).

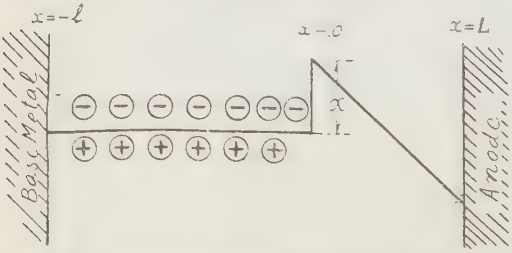

Fig. 1. A Simple Model of the Oxide Cathode.

When the diode acts stationary a space charge may be formed up in the oxide layer near the surface, as was shown in (I) and (II). As an initial condition we shall suppose that the density of conduction electron in the oxide layer is uniformly distributed across the layer if the anode potential is properly chosen. When fairly large anode potential is suddenly applied at any instant, the cathode will show some transient phenomenon forming up the space charge in the cathode layer. It is the purpose of this article to develope a theory concerning these transient phenomenon.

The density, $n^-(x,t)$, of the conduction electron at any point, x, in the cathode layer at any time, t, will satisfy the continuity equation :

$$\frac{\partial n^-}{\partial t}=-\frac{\partial}{\partial x}(\mu n^- E_r^{(i)})+\frac{\partial}{\partial x}\left(D\frac{\partial n^-}{\partial x}\right)+\frac{n_0-n^-}{\tau}, \tag{2.1'}$$

where

$E_r^{(i)}$: resultant electric field at that point in the cathode layer,
e,μ,D : charge, mobility and diffusion coefficient of the conduction electron,
τ : recombination time of excess conduction electron,
n : the density of the conduction electron at thermal equilibrium.

The third term in the right hand side of Eq. (2.1′) denotes the increase (decrease) of conduction electrons due to thermal equilibrium. When the transient phenomena due to the drift of conduction electrons occurs rapidly compared to the time, τ, as in our case**, we may safely omitt this term without serious error. A transient phenomena tending to the thermal equilibrium may be regarded to occur when the drift of the conduction electron has attained to its stationary state. Accordingly, Eq. (2.1′) may be written as

---

* These papers will be referred hereafter as (I) and (II).

** In § 6 some numerical evidences will be shown.

$$\frac{\partial n^-}{\partial t}=-\frac{\partial}{\partial x}(\mu n^- E_r^{(i)})+\frac{\partial}{\partial x}\left(D\frac{\partial n^-}{\partial x}\right). \tag{2.1}$$

The electric field, $E_r^{(i)}$, is composed of two parts, the one is that due to the conduction electron E^-, and the other is due to the vacant, active center, E^+; that is

$$E_r^{(i)}=E^- - E^+ .$$

These fields are in turn related to the charge densities by Poisson equations:

$$\left.\begin{aligned}\frac{dE^-}{dx}&=\frac{4\pi e}{K}n^-=N_0[1+f(x)]\\ \frac{dE^+}{dx}&=-N_0\,,\end{aligned}\right\}\quad(2.2)^*$$

$$\left(N_0=\frac{4\pi e}{K}n_0=\text{constant}\right)$$

where K is the dielectric constant of the oxide layer, n_0 is the density of the conduction eleciron at the time $t\leq-0$ and a function $f(x,t)$ denotes the excess electron in the conduction band. The resultant field, $E_r^{(i)}$, can be obtained from Eqs. (2.2) as

$$E_r^{(i)}=E^-+E^+=N_0\left[\int f(x,t)dx+E_0(t)\right], \tag{2.3}$$

in which $E_0(t)$ is a constant of integration. The constant, $E_0(t)$, is related to the anode voltage, V, and the distance, L, between the electrodes by an equation:

$$V=\int_{-l}^{0}E_r^{(i)}dx+KL[E_r^{(i)}]_{x=0}\,,$$

where l is the thickness of cathode layer (see Fig. 1). Inserting (2.3) in above equation, we obtain

$$V=N_0\left[\int_{-l}^{0}\int_{-l}^{x}f(\xi)d\xi\cdot dx+E_0 l\right]$$
$$+N_0KL\left[\int_{-l}^{0}f(x)dx+E_0\right]. \tag{2.4′}$$

Usually the thickness, l, is much smaller than the distance, L, and we have

$$LK+l\simeq LK.$$

Solving the Eq. (2.4′), we obtain

$$\left.\begin{aligned}E_0&=E_{00}+E_{0t}\,,\\ E_{00}&=V/(N_0LK)\,,\\ E_{0t}&=-\frac{1}{KL}\int_{-l}^{0}\int_{-l}^{x}f(\xi)d\xi\cdot dx-\int_{-l}^{0}f(x)\,dx\,.\end{aligned}\right\} \tag{2.4}$$

Inserting the Eqs. (2.3) and (2.4) in (2.1) and neglecting all but the first order terms in f, we obtain

$$\frac{\partial^2 f}{\partial x^2}-\frac{1}{D}\frac{\partial f}{\partial t}-\frac{\mu N_0 E_{00}}{D}\frac{\partial f}{\partial t}-\frac{\mu N_0}{D}=0. \tag{2.5}$$

This is a partial differential equation to determine the function $f(x,t)$.

The boundary conditions to be imposed on (2.5) are

$$f(0,t)=f_0(t)\qquad f(-l,t)=0\,, \tag{2.6}$$

where $f_0(t)$ is an unknown function, for the moment, which can be determined by the other condition (see § 3). As an initial condition we have

$$f(x,0)=0\qquad t\leq-0\,. \tag{2.7}$$

A solution of the Eq. (2.5) satisfying the conditions (2.6) and (2.7) can be easily obtained and we have**

$$f(X,t)=e^{-BX}\int_0^t e^{-C(t-\tau)-\frac{X^2}{4(t-\tau)}}\frac{X}{2\sqrt{\pi}(t-\tau)^{3/2}}f_0(\tau)d\tau$$
$$=\frac{2}{\sqrt{\pi}}e^{-BX}\int_{X/2\sqrt{t}}^{\infty}e^{-\left(v^2+\beta^2\frac{X^2}{v^2}\right)}f_0\left(t-\frac{X^2}{4v^2}\right)dv\,, \tag{2.8***}$$

where

$$X=-x/\sqrt{D}\,,\qquad B=(\mu N_0E_{00})/2\sqrt{D}\,,$$
$$C=B^2+\mu N_0\,,\qquad \beta=\sqrt{C}\,/2\,.$$

§ 3. Continuity Equation at the Emitting Surface

The function $f_0(t)$ in Eq. (2.8) is an unknown function which can be determined by the continuity of the conduction electron at the emitting surface. The electron emission from hot cathode obeys the well known Fowler-Dushman equation and, therefore, we must set up another continuity equation than (2.1) at the emitting surface.

---

* It should be kept in mind that the conduction electron is not in thermal equilibrium in the course of the drift.

** cf., for instance, Bayerly, "Fourier Series and Spherical Harmonics" Ginn and Company (1893), p. 90.

*** The solution (2.8) satisfies a boundary condition at $x=-l$ approximately.

Considering a thin layer below the emitting surface whose width, λ, is equal to the mean free path of the conduction electron, the continuity of the electron in this layer can be written as follows.

Inflow of the electron :

$$\left(n^{-}\mu E_r^{(i)}-D\frac{\partial n^{-}}{\partial x}\right)_{x=-\lambda}, \tag{3.1}$$

Out flow of the electron :

$$\left.\begin{aligned}&(n^{-}\Phi)_{x=0}\\&\Phi=\Phi_0\exp\left(\frac{b}{T}\sqrt{E_r^{(e)}}\right),\end{aligned}\right\} \tag{3.2}$$

where

$$\Phi_0=D_0\sqrt{\frac{kT}{2\pi m}}e^{-\chi/kT} \text{ and } E_r^{(e)}=KE_r^{(i)}(0),$$

in which k is the Boltzmann constant, T is the cathode temperature in °K, m is the mass of the electron, χ is the hight of the surface potential barrier and D_0 the mean transmission coefficient for electron at the emitting surface. An exponential term in Eq. (3.2) is due to the Schottky effect and a coefficient b should be chosen as 4.39 if the field strength, $E_r^{(e)}$, is measured in volts per centimeter. The continuity equation can be written, therefore, as

$$\left[n^{-}\mu E_r^{(i)}-D\frac{\partial n^{-}}{\partial x}\right]_{x=-\lambda}-[n^{-}\Phi]_{x=0}=\lambda\frac{\partial n^{-}}{\partial t}. \tag{3.3}$$

The quantity (3.1) can be written in terms of $f(x,t)$ as

$$\left(n^{-}\mu E_r^{(i)}-D\frac{\partial n^{-}}{\partial x}\right)=\mu n_0 N_0\left[E_{00}(1+f)+E_{0t}+\int f dx\right]-Dn_0\frac{\partial f}{\partial x}. \tag{3.4}$$

Similarly, $\sqrt{E_r^{(e)}}$ can be written as

$$\sqrt{E_r^{(e)}}=\sqrt{KN_0E_{00}}(1+F)^{1/2}\simeq\sqrt{KN_0E_{00}}(1+\tfrac{1}{2}F),$$

where

$$F=\frac{1}{E_{00}}\left(\int_{-l}^{0}f(x)dx+E_{0t}\right).$$

Whereby

$$\begin{aligned}\Phi&\simeq\Phi_0e^{\gamma}\left(1+\frac{1}{2}\gamma F\right), \quad \left(\gamma=\frac{b}{T}\sqrt{\frac{V}{L}}\right)\\&=\Phi_0e^{\gamma}\left[1+\frac{\gamma}{2E_{00}}\left\{\int_{-l}^{0}fdx-\frac{1}{LK}\right.\right.\\&\qquad\left.\left.\times\int_{-l}^{0}\int_{-l}^{x}fd\xi\cdot dx-\int_{-l}^{0}fdx\right\}\right].\end{aligned} \tag{3.5}$$

Inserting Eqs. (3.4) and (3.5) into (3.3), we obtain

$$\begin{aligned}&\nu E_{00}(1+f)+\frac{1}{KL}\left(\Phi_1\frac{\gamma}{2E_{00}}-\nu\right)\int_{-l}^{0}\int_{-l}^{x}f(\xi)d\xi\cdot dx\\&\qquad-D\frac{\partial f}{\partial x}-\Phi_1(1+f)=\lambda\frac{\partial f}{\partial t}\\&\qquad\qquad(\Phi_1=\Phi_0e^{\gamma},\ \nu=\mu N_0).\end{aligned} \tag{3.6}$$

The function $f(x,t)$ in Eq. (3.6) is a slowly varing function of x and we can take approximately

$$[f(x,t)]_{x=-\lambda}\simeq f(0,t)=f_0(t).$$

Thus we obtain an equation to determine the function $f_0(t)$:

$$\begin{aligned}&\nu E_{00}(1+f_0)+\frac{1}{KL}\left(\Phi_1\frac{\gamma}{2E_{00}}-\nu\right)\int_{-l}^{0}\int_{-l}^{x}f(\xi)d\xi\cdot dx\\&\qquad-D\left[\frac{\partial f}{\partial x}\right]_{x=0}-\Phi_1(1+f_0)=\lambda\frac{df_0}{dt}.\end{aligned} \tag{3.7}$$

§ 4. Determination of the Function $f_0(t)$

We are now in position to solve the Eq. (3.7). It is very convenient to use the Laplace transformation and we define the l-Functions of $f(x,t)$ and $f_0(t)$ as follows :

$$\left.\begin{aligned}h(s,x)&=\int_0^{\infty}e^{-st}f(x,t)dt\\h_0(s)&=\int_0^{\infty}e^{-st}f_0(t)dt.\end{aligned}\right\} \tag{4.1}$$

From the Eq. (2.8), we have

$$h(s,x)=e^{x(B+\sqrt{s+C})/\sqrt{D}}\cdot h_0(s). \tag{4.2}$$

By the use of Eqs. (4.1) and (4.2), the Eq. (3.7) can be transformed as

$$h_0\left[\nu E_{00}-\frac{D}{KL}\left(\nu-\Phi_1\frac{\gamma}{2E_{00}}\right)\frac{1}{(B+\sqrt{s+c})^2}-\sqrt{D}(B+\sqrt{s+c})\Phi_1-\lambda s\right]=\frac{1}{s}(\Phi_1-\nu E_{00}). \tag{4.3}$$

The l-Function $h_0(s)$ can be obtained at once :

$$\left.\begin{aligned} h_0(s)&=\frac{(1/s)\,(\Phi_1-\nu E_{00})\,(B+\sqrt{s+c})^2}{(\nu E_{00}-\Phi_1-\lambda s)\,(B+\sqrt{s+c})^2-\sqrt{D}\,(B+\sqrt{s+c})^3-\dfrac{\nu_1 D}{KL}} \\ \nu_1&=\nu-\Phi_1\gamma/2E_{00}\;. \end{aligned}\right\} \quad (4.4)$$

We have, now, to transform the l-Function, $h_0(s)$, to L-Function, $f_0(t)$. For this purpose it is convenient to rearrange the Eq. (4.4) as follows. Putting

$$h_0(s)=\frac{(\nu E_{00}-\Phi_1)}{\lambda}\cdot\frac{p(s)}{sq(s)}\;, \qquad (4.5a)$$

we have

$$\begin{aligned} p(s)&=\begin{vmatrix} s^2+ds+e & 2B\sqrt{s+c} \\ (as+b)\sqrt{s+c} & B^2+s+c \end{vmatrix} + \begin{vmatrix} s^2+ds+e & B^2+s+c\,\sqrt{s+c} \\ (as+b) & 2B \end{vmatrix} \\ &=p_1(s)+p_2(s)\;, \end{aligned} \qquad (4.5b)$$

and

$$q(s)=(s^2+ds+e)^2-(s+c)(as+b)^2, \quad (4.5c)$$

where the coefficients a,b,d and e are

$$\left.\begin{aligned} a&=\frac{\sqrt{D}}{\lambda}\left(1+\lambda\frac{\nu E_{00}}{D}\right)\,, \\ b&=\frac{\sqrt{D}}{\lambda}\left(\nu+\Phi_1\frac{\nu E_{00}}{D}\right)\,, \\ d&=\Phi_1/\lambda+\nu^2E_{00}{}^2/2D+\nu+\nu E_{00}/2\lambda\;, \\ e&=\nu^2E_{00}/2\lambda+(\Phi_1/\lambda)\left(\nu+\frac{\nu^2E_{00}{}^2}{2D}\right)+\nu_1D/\lambda KL\;. \end{aligned}\right\} \qquad (4.5d)$$

The function $q(s)$ is a quadratic function in s and we can put

$$q(s)=(s+a_1)(s+a_2)(s+a_3)(s+a_4)\;.$$

Consequently we have

$$\frac{p(s)}{sq(s)}=\sum_{k=0}^{4}\frac{A_k}{s+a_k}+\frac{1}{\sqrt{s+c}}\sum_{k=0}^{4}\frac{B_k}{s+a_k} \qquad (a_0=0) \qquad (4.6a)$$

where
$$\left.\begin{aligned} A_k&=p_1(-a_k)/q'(-a_k) \\ B_k&=p_2(-a_k)/q'(-a_k)\;. \end{aligned}\right\} \qquad (4.6b)$$

From the Eqs. (4.6) we can obtain the L-Function, $f_0(t)$, of $h_0(s)$ as follows. By the well known transformations:

$$\mathfrak{L}^{-1}\left[\frac{1}{s+a_k}\right]=e^{-a_kt}\;,$$

$$\mathfrak{L}^{-1}\left[\frac{1}{\sqrt{s+c}}\right]=\frac{1}{\sqrt{\pi t}}e^{-ct}\;,$$

$$\mathfrak{L}^{-1}\left[\frac{1}{\sqrt{s+c}(s+a_k)}\right]=\varphi(\sqrt{(c-a_k)t})e^{-a_kt}/\sqrt{\pi t},$$

where $\mathfrak{L}^{-1}$ denotes inverse Laplace transformation and $\varphi(x)$ is an Error integral defined by

$$\varphi(x)=\frac{2}{\sqrt{\pi}}\int_0^x e^{-x^2}dx\;,$$

we have finally

$$\begin{aligned} f_0(t)&=A_0+\sum_k A_ke^{-a_kt}+B_0\frac{1}{\sqrt{c}}\varphi(\sqrt{ct}) \\ &\quad+\sum_k B_ke^{-a_kt}/\sqrt{c-a_k}\cdot\varphi(\sqrt{(c-a_k)t})\;. \end{aligned} \qquad (4.7)$$

The coefficients in Eq. (4.7) can be rewritten as follows. We can subdivide the roots of the equation, $q(s)=0$, into two groups; that is, those satisfying an equation

$$s^2+ds+e=(as+b)\sqrt{s+c}=\alpha_i \quad (\alpha_i>0)\;,$$

and others satisfying

$$s^2+ds+e=-(as+b)\sqrt{s+c}=-\alpha_k \quad (\alpha_k>0)\;.$$

Denoting the first group of the root as $-a_i$ and the second as a_k, the coefficients A's and B's in Eq. (4.7) can be written as

$$\begin{cases} A_i=\dfrac{\alpha_i(\beta_i-\gamma_i)}{q'(-a_i)} \\ B_i=\alpha_i\sqrt{c-a_i}\,\dfrac{(\gamma_i-\beta_i)}{q'(-a_i)} \end{cases} \qquad \begin{cases} \gamma_i=2B\sqrt{c-a_i} \\ \beta_i=B^2+c-a_i \end{cases}$$

and

$$\begin{cases} A_k=-\dfrac{\alpha_k(\beta_k+\gamma_k)}{q'(-a_k)} \\ B_k=-\alpha_k\sqrt{c-a_k}\,\dfrac{(\beta_k+\gamma_k)}{q'(-a_k)} \end{cases} \qquad \begin{cases} \gamma_k=2B\sqrt{c+a_k} \\ B_k=B^2+c+a_k. \end{cases}$$

With these expressions the Eq. (4.7) can be written in the form

$$\begin{aligned} f_0(t)=A_0+B_0\varphi(\sqrt{ct})&+\sum_i\frac{\alpha_i(\beta_i-\gamma_i)}{q'(-a_i)} \\ &\times e^{-a_it}[1-\varphi(\sqrt{(c-a_i)t})] \\ -\sum_k\frac{\alpha_k(\beta_k+\gamma_k)}{q'(-a_k)}&e^{a_kt}[1+\varphi(\sqrt{(c+a_k)t})]\;. \end{aligned} \qquad (4.8)$$

In our case, the equation, $q(s)=0$, have only such the roots as $-a_i$ and we can omit the last term in Eq. (4.8). On the other hand, from the asymptotic expansion of the Error integral*, we see that the third term in Eq. (4.8) can be written as

$$e^{-a_i t}[1-\varphi(\sqrt{(c-a_i)t})]\simeq e^{-ct}/[(c-a_i)\pi t]^{1/2},$$

and we have for the function $f_0(t)$

$$f_0(t)=A_0+B_0\varphi(\sqrt{ct})+\sum_i \frac{\alpha_i(\beta_i-\gamma_i)}{q'(-a_i)}\frac{e^{-ct}}{\sqrt{(c-a_i)\pi t}}. \tag{4.9}$$

The emission current ratio, $j(t)/j(0)$, where $j(0)$ denotes emission current at $t=0$, can, therefore, be written as

$$j(t)/j(0)=1+f_0(t)\,. \tag{4.10}$$

§ 5. Relaxation tending to Thermal Equilibrium

In the previous sections we have concerned only with the transient phenomena due to the drift of conduction electrons in the oxide layer. The electron distribution given by the Eq. (4.9) is not in thermal equilibrium with donors at any time. As was remarked in § 2, these treatments will be correct so long as the transit time of the drift motion is far shorter than the relaxation time, τ. In this section we shall concern ourselves with the relaxation tending to thermal equilibrium.

According to our assumption we shall consider such a process that the excess of electrons, over thermal equilibrium, be caught by vacant donor centers. First of all, we shall estimate a difference of the emission current given by the expression

$$j=e\Phi n^-=[e\Phi n_0(1+f_0(t))]_{t=\infty}\,, \tag{5.1}$$

and the steady state current j_s, which is given by the Eqs. (3.1) and (3.2) of (II), taking into account of the thermal equilibrium. The emission current (5.1) has been given by the Eqs. (3.1) and (3.2) of (I) and in the present notation we have

$$\left.\begin{aligned} j&=en^-\Phi_0\exp\left(\frac{4.39}{T}\sqrt{E_r^{(e)}}\right)\\ n^-&=n_0e^{-g_l}\end{aligned}\right\} \tag{5.1a}$$

$$\left.\begin{aligned} E_r^{(e)}&=K(e^{-g_l}\Phi/\mu-\beta_1 g_l/\alpha_1^*)\\ \beta_1&=\sqrt{\frac{4\pi n_0kT}{K}}\,.\end{aligned}\right\} \tag{5.1b}$$

On the other hand the Eqs. (3.1) and (3.2) of (II) can be written as

$$j_s=en_0e^{-g_l}\Phi\,, \tag{5.2a}$$

$$\left.\begin{aligned} E_r^{(e)}&=K(e^{-g_l}\Phi/\mu-\beta g_l/\alpha^*)\\ \beta&=\sqrt{\frac{8\pi n_0kT}{K}}\,.\end{aligned}\right\} \tag{5.2b}$$

Comparing the Eqs. (5.1) and (5.2), we see that the values of g_l given by the two equations, for a given value of $E_r^{(e)}$, are almost same for small value of g_l. In other words, we can expect such a small relaxation phenomena in the transition to the thermal equilibrium that we can neglect this phenomena, for small values of g_l as considered here. Of course, for larger values of g_l, these relaxations should be accounted for, but, unfortunately, for such a large value the linearized theory, as developed here, cease to be valid and more elaborate treatments should be required.

The physical understanding of these facts would be clear enough if one considers the mechanism of the space charge emission given in (I) and (II).

§6. Numerical Calculations

In line with the general theory developed above, the transient phenomeon in the cathode layer shall be calculated numerically. In this paper we shall employ a value, 10 cm²/volt. sec., as a reasonable value of the electron mobility in the cathode layer⁵⁾. This value may be considered as a constant independent of the temperature. The other constants are same as those given by (I) and (II); that is,

$K=10$,
$\Delta E/2=0.7$ ev.,
$\chi=0.3$ ev.,
$D_0=1.0$
$n_0=5\times10^{14}\,\mathrm{cm}^{-3}$ at 1000°K .

The values of g_l, in the quasi-equilibrium ate, given by the Eq. (5.1), employing the onstants quoted above, are given in Table

---

* cf., for instance, Jahnke-Emde, "Funktionentafeln" S. 98.

From these values of g_l we see that the alue of g_l in the quasi-equilibrium may have onsiderable dependency on the plate voltages nd may have negative values as well as ositive values, for the case may be. For e negative value of g_l the emission increase ould be expected. The values given above e restricted to small values of g_l in order fit with our linearised theory. In the actical case, however, much larger values ould be expected.

Table I.

T (°K)	Vp (KV)	ge
800	10	−0.016
850	10	0.230
900	10	0.454
800	10	−0.016
800	8	0.147
800	6	0.363

$\mu = 10\ \mathrm{cm^2/volt.\ sec.}$　　$L = 1$ cm.
Vp: Plate voltages

Table II.

(°K)	Vp (KV)	a_1	τ (sec.)
900	10	-3.43×10^8	2.92×10^{-9}
850	10	-1.85×10^8	5.41×10^{-9}
800	10	no decay	—
800	8	-0.948×10^8	1.05×10^{-8}
800	6	Imaginary	Oscillatory

For the values of g_l given in Table I, the decay constants (reciprocals of $|a_i|$'s) were calculated taking the constant λ to be 100Å for all temperatures. In Table II these values are shown. As is seen from these data the transit time of the conduction electron is extremly short and it may be far shorter than the life time, τ, of the excess conduction electron. Concerning the values of τ we have as yet no reliable value. In the non-polar crystals, such as Si and Ge, we have $\tau \sim 10^{-6}$ second as a reasonable value and this is much larger than the transit time given above. Considering these data, it would not be much in error to neglect the last term in the Eq. (2.1′).

In conclusion we can advocate the view that the microsecond emission decay observed by Sproull and others is quite different phenomena from that considered here.

References

1) T. Shindo: Jour. Phys. Soc. Japan **6** (1951) 352; ibid. **8** (1953) 494.

2) D. A. Wright and J. Woods: Proc. Phys. Soc. B LXV (1952) 134.

3) J. R. Young: Jour. App. Phys. **23** (1952) 1129.

4) R. L. Sproull: Phys. Rev. **67** (1945) 166.

5) E. M. Pell: Phys. Rev. **87** (1952) 457.

JOURNAL OF THE PHYSICAL SOCIETY OF JAPAN Vol. 9, No. 1, JAN.—FEB., 1954

Observation of the Grain Boundary in Soap Bubble Raft

Part II. Dynamical Behaviour of the Grain Boundary

By Einosuke FUKUSHIMA*
Department of Physics, Tokyo Metropolitan University, Tokyo
and Akiya OOKAWA*
Department of Physics and Chemistry, Gakushuin University, Mejiro, Tokyo

(Read May 18, and Received July 21, 1953)

The dynamical behaviour of the grain boundary is observed in the process of relative displacement between the two grains. Each type of the grain boundaries, classified into three types in respect to their statical transition structure, behaves in discriminatively different manner from each other.

The relative displacement between two grains separated by the grain boundary of type A has the issue of shifting the array of constituent parallel dislocations normal to the boundary. The relative displacement between two grains separated by a straight boundary of type B is accommodated wholly by the independent rearrangement of the bubbles in the boundary layer of a few bubble diameters thickness. As to the grain boundary of type C, the dynamical benaviours of the constituent dislocations can be analysed into two modes. In the mode (i), rather similar to that of type A, the constituent dislocations displace themselves as a whole. In the mode (ii), rather similar to that of type B, the constituent dislocations remain stationary but change frequently their characteristic Burgers' vectors, which is accompanied by local yielding in portions along the grain boundary.

The statical feature as well as the dynamical behaviour in the mode (ii) of the grain boundary of type C has much analogies with the Mott's theory on the viscous flow along the grain boundary. To interpret the mode (ii), it is proposed to introduce transient dislocations, traversing along the grain boundary and reacting with the constituent dislocations. In terms of the transient dislocations the activated state in the process of viscous flow corresponds, to an intermediate stage involving transient dislocations, whence the rate of flow is determined by the energy required to decompose a constituent dislocation to activate a transient dislocation, under favourable influence of the local strain.

§ 1. Introduction

The grain boundaries observed in the soap bubble raft can be classified into three types[1)2)], in respect to the statical feature of the transition structure. The grain boundary between two grains with the angle of disorientation smaller than about 10° is constituted of dislocations all on parallel slip planes (type A)**, the boundary between the grains with the disorientation angle ranging from 20° to 40° is composed of disordered groups of atoms or the diffused holes (type B)**, and the grain boundary between the grains with the disorientation angle greater than about 50° is constituted of two sorts of dislocations each on non-parallel slip planes (type C).

Under shearing stress along the grain boundary, each type of the grain boundary according the above statical classification responds in discriminatively different manner[3]. The observed dynamical behaviour of the grain boundary of type A has been predicted theoretically, qualitatively by Bragg[4] and quantitatively by Read and Shockley[5], and detected experimentally, by Lomer and Nye[6] in the soap bubble raft and by Washburn and Parker[7] with the bicrystal of zinc. The observed dynamical behaviour of the grain boundary of type B has features corresponding to the viscous flow mechanism along the grain boundary, proposed by Kê[8] concerning the anelasticity in the polycrystalline metals, and is detected in the soap bubble raft by Lomer-Nye[6]. The grain boundary of type C is predicted by Read-Shockley[5] but the fuller account of the dynamical behaviour of this type boundary is yet available neither theoretically nor experimentally.

---

* Member of the Kobayashi Institute of Physical Research, Kokubunji, Tokyo.

** The nomenclature of type A and B is the same with that in reference (2). Henceforward the nomenclature in referenc (3) below is abandoned.

The present paper reports in the main on the observed dynamical behaviours of the boundary of type C, including some short accounts on those of type A and B on the benefit of explaining and comparing the dynamical features of the three types of the grain boundary.

The apparatus used is the same as that reported in Part I.

§ 2. Observations

I. *Grain Boundary of Type A.*

Fig. 1 shows a grain boundary of type A between two grains with an angle of disorientation $\theta=12^\circ$. The left grain is fixed and the right grain can be shifted upwards or downwards by driving the right frame by micro-manipulator. In Fig. 1 the upper half (a) corresponds to the state before displacement and the lower half (b) to the state after displacement of the right grain upwards in distance amounting to 1.5 times the bubble diameter. It can easily be observed that the array of parallel dislocations constituting the boundary displaces itself rightwards in perfect cooperation in the process of upwards displacement of the right grain.

The amount of displacement of the grain boundary is measured conveniently referring to some fixed point, such as the light spot on top of the left frame in the lowest part of the figure. In Fig. 1, the amount of displacement d of the grain boundary amounts to 7 times the bubble diameter.

As to the dynamical behaviour of the grain boundary of type A, it is predicted[5] that the geometrical relation

$$D_1=2d\sin(\theta/2)\,, \qquad (1)$$

where D_1 is the corresponding amount of relative displacement between the two grains.

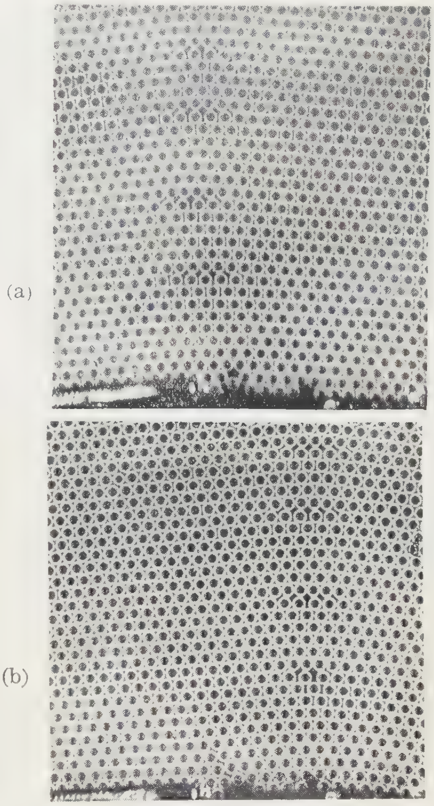

Fig. 1. Grain boundary of type A with disorientation angle $\theta=12^\circ$, (a) before and (b) after upwards displacement of the right grain.

With $\theta=12^\circ$ and D_1 amounting to 1.5 times the bubble diameter, we expect d, according to Eq. (1), amounting to 7.2 times the bubble diameter. This is in fair agreement with the observed value.

II. *Grain Boundary of Type B.*

Fig. 2 shows a nearly straight grain boundary of type B between two grains with disorientation angle $\theta=28^\circ30'$, (a) and (b) corresponding, respectively, to the states before and after downwards displacement of the right grain. It can be seen that the grain boundary remains stationary, which signifies that the two grains behave as rigid bodies in the process and that the relative displacement between the two grains is wholly accommodated by rearrangement of the bubbles in a thin boundary layer of a few bubble diameters thickness. The observed dynamical behaviour of the boundary is believed to correspond to the viscous flow along the grain boudary in polycrystalline metals[8]).

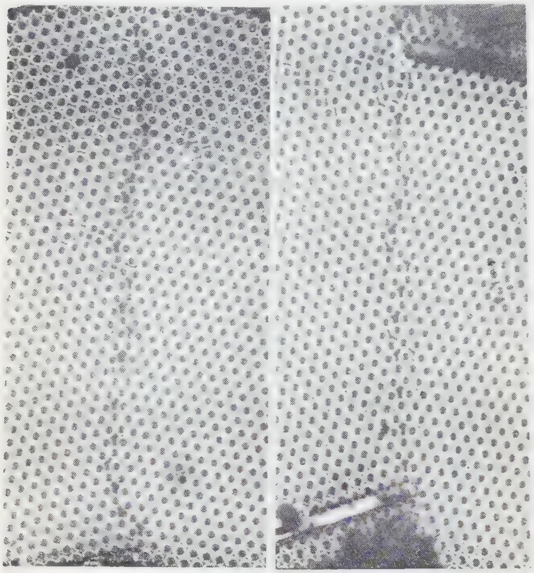
(a) (b)

Fig. 2. Nearly straight grain boundary of type B with disorientation angle $\theta=28°30'$, (a) before and (b) after downward displacement of the right grain.

In the process of relative displacement between the two grains along the straight grain boundary, the bubbles in a thin boundary layer are observed to change frequently their allignance from one grain to another grain. It is worth noting with the grain boundary of type B that the changing allignance of each of the bubbles is nearly independent to each other, in marked contrast to the rather cooperative dynamical behaviour of bubbles along the stationary grain boundary of type C (see later).

The viscous flow mechanism along the grain boundary of type B is obscured in case of non-straight boundary. When the boundary is not straight, it can be observed the generation of new dislocations at turning points of the boundary (see upper left in Fig. 2b). In an extreme case, a portion of the sharp grain boundary degenerates into a diffuse bended raft portion, as is shown in the central part of Fig. 3b which corresponds to an upwards displacement of the right grain in Fig. 3a. In some cases, it can also be observed the rearrangement of bubbles in a hump portion of one grain to allign with the other grain such as to effect a straight boundary, which may correspond to some stress induced grain boundary migration.

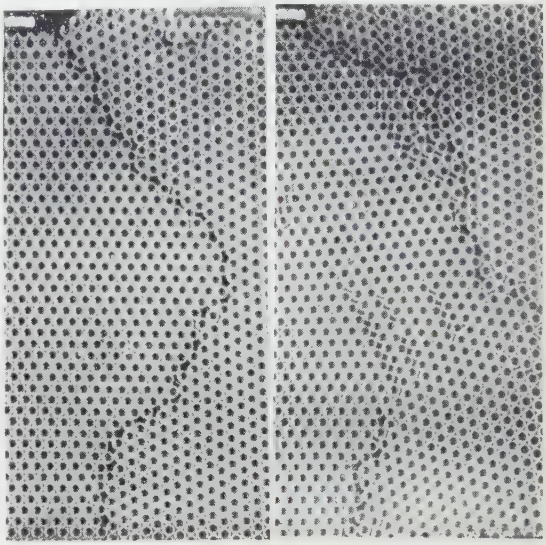
(a) (b)

Fig. 3. Non-straight grain boundary of type B, (a) before and (b) after upward displacement of the right grain.

III. *Grain Boundary of Type C*

The grain boundaries of type C are conveniently subdivided into two cases in regard of their dynamical feature.

Type C_1 : the case of large spacing between the constituent dislocations and of zig-zag arrangement of them.

An example of this case, with the angle of disorientation $\theta=53°$, is shown in Fig. 4, where the grain boundary is constituted of six dislocations, each characterized by alternating Burgers' vectors and with centers nearly on a straight line. Specifying the dislocations from upper to lower by contracted notations $1D, 2D, \cdots, 6D$, respectively, the spacings between each neighbouring dislocations are

$1D-2D=11$ bubbles
$2D-3D=6$,, ,
$3D-4D=8$,, ,
$4D-5D=7$,, ,
$5D-6D=6$,, .

Displacing the right grain in Fig. 4a upwards 0.75 mm (about 3/4 times the bubble diameter), we have the state shown by (b). In the process of the relative displacement of the two grains from the state of (a) to that of (b), the dislocations $1D, 2D, 3D$, and $6D$ displace themselves leftwards in amounts of 6, 6, 3, and 5 bubbles respectively, without change of each characteristic Burgers' vector, while the dislocation $4D$ moves rightwards amounting 1 bubble and the dislocation $5D$ moves leftwards amounting 3 bubbles, both with change of each characteristic Burgers' vector.

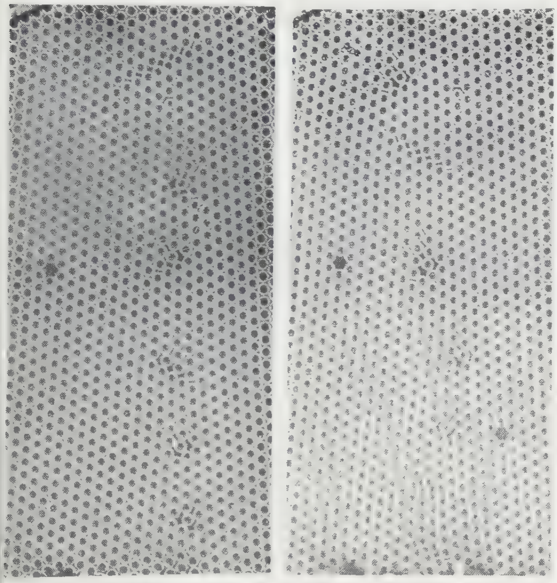
(a) 1st stage (b) 2nd stage

Fig. 4. Grain boundary of type C_1 with disorientation angle $\theta=53°$, (a) before and (b) after upwards displacement of the right grain by amount of about 3/4 times the bubble diameter.

The displacement as well as the changing ature of the constituent dislocations are chematically depicted in Fig. 5, where the ite of the dislocation is shown by the site of he representative short line, in reference to n arbitrarily chosen ground line in the fixed left) grain, and the characteristic slip plane f the dislocation is shown by the direction f the representative short line. The numberng suffixes 1, 2, and 3, attached to under ight of the dislocation notation D, signify he each stage of displacement; the suffix 1 or the stage before displacement (Fig, 4a), e suffix 2 for the stage of 0.75 mm upwards isplacement of the right grain (Fig. 4b), and e suffix 3 for the stage of further 0.25 mm upwards displacement.

Fig. 5. Map representing constituent dislocations of grain boundary of type C_1, for each stage of upwards displacement of the right grain.

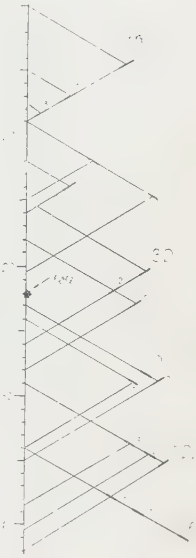

The rather complicated dynamical behaviour of the dislocations constituting the grain boundary of type C_1 can be analysed into two modes :

(i) The displacement as a whole of the constituent dislocations along each characteristic slip plane, the leftwards displacement of the dislocations coupled with the upwards displacement of the right grain.

(ii) The alternation of the characteristic Burgers' vector or the slip plane of the constituent dislocations from type $(01\bar{1})\perp(1\bar{1}0)$ to type $(10\bar{1})'\perp(01\bar{1})$ and vice versa (refer to the notation given in Part I).

Speaking in general, the mode (i) is predominant so long as the spacing between the constituent dislocations is large, and the total displacement of the dislocations is the larger the wider the initial spacing between them. This mode can be understood with the mechanism analogous to that underlying the parallel displacement of the grain boundary of type A.

However, in contrast to the boundary of type A, the displacement of the dislocations constituting the grain boundary of type C has in the mode (i) the consequence of decreasing the spacing between some pairs of dislocations, as they approach the crossing point of their characteristic slip planes. This pair of dislocations repulsive to each other can not approach nearer than a minimum spacing, of about 5 bubbles in the present case of raft of bubble diameter of about 1 mm. The further relative displacement between the two grains is always accompanied with the mode (ii). For the study of this mode, the second case, type C_2, is more convenient.

Type C_2: the case of small spacing between the constituent dislocations and of nearly straight arrangement of them.

Fig. 6a shows the initial stage of the grain boundary of type C_2 with an angle of disorientation $\theta=49°$, constituted of eight dislocations $1D$, $2D$, $\cdots$, and $8D$, each characterized by alternative Burgers' vector and with the centers nearly on a straight line. The spacings between the successively neighbouring dislocations are 3, 5, 6, 5, 4, 5, and 4 bubbles respectively, and the displacement of the dislocations as a whole (mode (i)) is expected almost prohibited already in the initial stage.

The right grain in Fig. 6a is shifted upwards successively, in each stage by amount of 0.5 mm (about 1/2 times the bubble diameter), the second stage and the fifth stage being shown in (b) and (c), respectively. The general view of affairs involved in the process can be obtained with the aid of Eig. 7, which is analogous to Fig. 5. We see that the grain boundary is nearly stationary throughout the stages while the alternation in nature of the constituent dislocation is rather frequent. This process in the mode (ii) can be continuated until the two grains depart from each other.

In the respect that the relative displacement between the two grains is wholly accommodated by the rearrangement of the bubbles in a relatively thinner boundary layer, the dynamical behaviour of the grain boundary of type C_2 is thus much analogous to that of the grain boundary of type B. It deserves noting, however, that between stages a local yielding in portions of the grain boundary can be detected with caution. This cooperative rearrangement of a group of bubbles along the grain boundary ot type C_2 is in marked contrast to the nearly independent rearrangement of bubbles along the grain boundary of type B (see above). This point of contrast is discussed below, in connection with the theoretical interpretation of the process of viscous flow along the grain boundary.

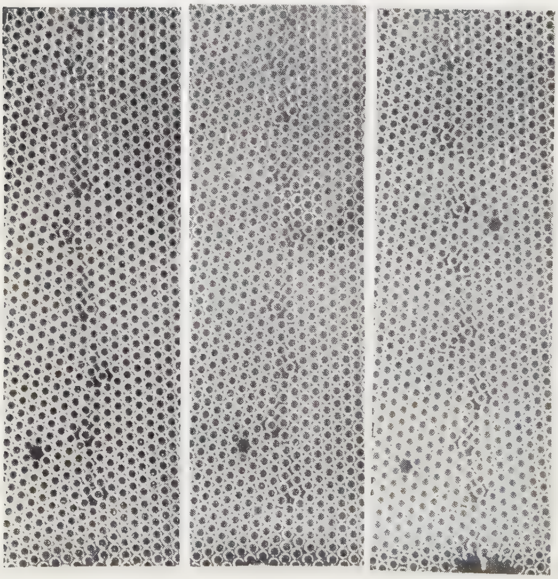
(a) 1st stage (b) 2nd stage (c) 5th stage

Fig. 6. Grain boundary of type C_2 with disorientation angle $\theta=49°$, (a) before and (b) and (c) after upwards displacement of the right grain by amount of about 1/2 and about 2 bubbles respectively.

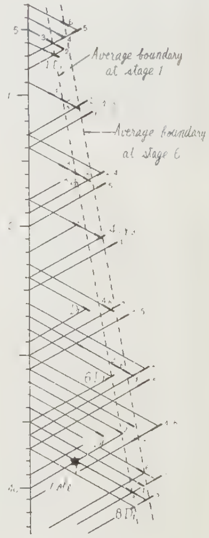

Fig. 7. Map representing constituent dislocations of grain boundary of type C_2, for each stages of upwards displacement of the right grain.

§ 3. Discussions

The dynamical behaviour of the grain boundary of type A, constitued of parallel dislocations, has been discussed, as was related in the introduction, by many authors. The dynamical behaviour of the grain boundary of type C_1 in the mode (i) may be understood in the similar line. In contrast with these, it n be detected discriminatively different haracteristics with the viscous flow along the rain boundary of type B and with the relave displacement of the two grains along the ationary grain boundary of type C_2 in the ode (ii).

In his theory on the viscous flow along the rain boundary, Mott[9] has proposed a grain oundary model composed of regions in good t and of regions in bad fit, where the ementary process of viscous flow under ress is ascribed to local yielding of regions good fit. It is easy to see that the grain oundary of type C has the static features orresponding to those postulated in Mott's heory, the region near the center of dislocaon corresponding to the region in bad fit and he region between the dislocations correspondg to region in good fit. Moreover, the ynamical characteristics postulated in Mott's heory have correspondences in the dynamical ehaviours detected with the grain boundary f type C in the mode (ii). Under the rcumstances, it is believed interesting to iscuss on the details of the mode.

The most characteristic feature associated ith the relative displacement of the grains long the grain boundary of type C in the ode (ii) is the alternation in successive strain ages of the Burgers' vector or the slip plane haracterizing the constituent dislocations. he general view of the alternating nature of haracteristic slip planes can be obtained by the aid of the schematical Table I.

Table I.

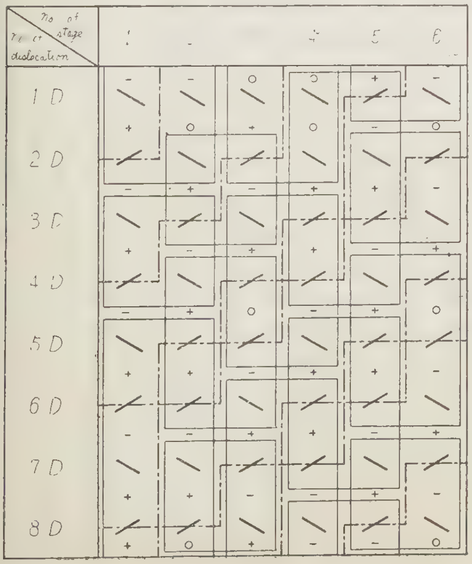
No of stage
No of dislocation
1 D
2 D
3 D
4 D
5 D
6 D
7 D
8 D

In connection with the characteristics, the previous remark in the last paragraph relating the observation deserves to be taken into account. It was noted that with much caution a local yielding in portions of the grain boundary can be detected between stages. We propose accordingly to introduce *transient* dislocations traversing along the grain boundary with characteristic Burgers' vector or slip plane parallel to $(\bar{1}01)$ of the right grain or to $(\bar{1}01)'$ of the left grain, both directions coinciding with the average direction of the grain boundary in its vicinity. The introduced transient dislocations are to traverse between stages through only local portions of the grain boundary, such as to effect the detected local yielding.

The alternation in nature of the *constituent* dislocations between successive stages is then understood straight forwards as the issue of reaction between the constituent dislocation and the transient dislocation. The dislocation reaction involved are, with the notation defined in Part I, the followings :

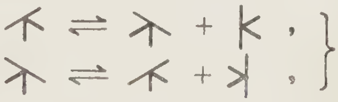
(2)

where, in each case, an energy is required to decompose a dislocation.

The spatial process of a transient dislocation traversing a region between two neighbouring constituent dislocations is shown in Fig. 8, where the two alternatives (b′) and (b″) are shown as the intermediate stages. From the view point of the theory of rate process, any one of the intermediate stages corresponds to the activated state, the relevant activation energy being primarily determined by the energy required to decompose the constituent dislocation according to Eq. (2). In Table I, in each rectangle are shown the constituent dislocations taking part in the relevant dislocation reactions with a transient dislocation in each successive stages. At any rate, the constituent dislocation changing its characteristic Burgers' vector between two stages marks, so to speak, the initial or the terminal point of a transient dislocation activated between the stages.

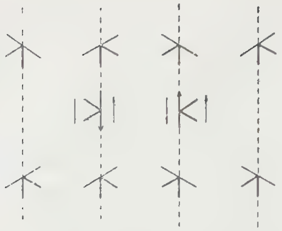
(a) (b) (b′) (c)

initial stage, intermediate stage, final stage

Fig. 8. The spatial process of a transient dislocation traversing a region between two constituent dislocations, thereby changing the characteristic Burgers' vectors of the two dislocations.

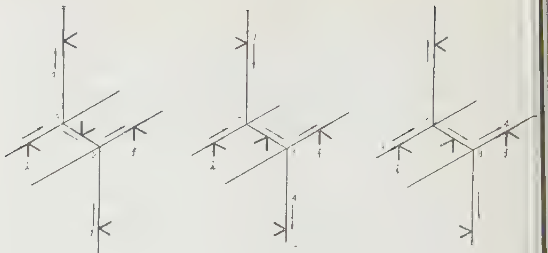
(a) upward traversing of a transient dislocation

(b) downward traversing of a transient dislocation

(c) pair creation of transient dislocations

Fig. 9. Three alternatives of dislocation reactions involved in the process of shifting a constituent dislocation normal to the slip plane, taking account of transient dislocations.

We note in some rectangle the dislocations which do not change its Burgers' vector. It is of course natural that the characteristic Burgers' vector of a constituent dislocation shall be preserved, notwithstanding a transient dislocation passing through the constituent dislocation. The conservation of the Burgers' vector of a constituent dislocation does not, however, necessarily mean that the constituent dislocation is indifferent to the transient dislocation. In the respect we remark the feature displayed by the dislocations, such as $1D$, $6D$, and $7D$ between the stage 1 and the stage 2 (see Fig. 7). They preserve in the process their characteristic Burgers' vectors, but are shifted on other slip planes parallel to the initial ones. As the current view of forming or of annihilating vacant sites at the dislocation center associated with the climbing motion of an edge dislocation is untenable with the soap bubble model, this character can only be understood by the process of dislocation reactions with the transient dislocation. The three alternatives of the dislocation reactions concerned are shown in Fig. 9.

As the characteristic Burgers' vector of a constituent dislocation is unaltered in the process of a transient dislocation passing through the dislocation, there remains undermined whether an excess transient dislocation traverses through the whole length of the grain boundary. The relevant ambiguity can be decided in reference to the total amount of the relative displacement between the two grains. With the experiment abstracted in Fig. 7 and in Table I, the right grain is shifted, from the stage 1 to the stage 6, upwards in amount of 0.5 mm × 5 = 2.5 mm o of about 2.5 times the bubble diameter. This amount is to be accommodated in main by the relative displacement D_2 in the mode (ii) induced by the traversing transient dislocations, with minor correction of the relative displacement D_1 in the mode (i), induced by the displacement as a whole of the constituent dislocation array. The relative displacement D_2 due to the transient dislocation is estimated according to the formula

$$D_2 = (l/L) \times (\text{bubble diameter})\,, \quad (3)$$

where L is the whole length of the grain boundary and l is the total length traversed by transient dislocations. In accordance with Table I, without any excess transient dislocations traversing through the whole length of the grain boundary, we have D_2 of about 3.2 times the bubble diameter. The relative displacement D_1 due to the constituent dislocation array is estimated by formula analogous to Eq. (1). Referring to Fig. 7, we have D_1 of about 0.4 times the bubble diameter, in opposite sign to D_2, corresponding to the rightwards displacement in average of the dislocation array. The estimated relative displacement, $D_2 - D_1$, amounting in total to about 2.8 times the bubble diameter, is in fair agreement with the output displacement of 2.5 times the bubble diameter, which excludes the possibility of any transient dislocation traversing through the whole length of the boundary. With the foregoings, it can be traced with some confidence the trajectories of the transient dislocations, which are shown by vertical chain line segments in Table I.

Table I has another feature, that a local region between neighbouring dislocations which has not yielded just before a stage does yield just after the stage, and that a local region which does not yield just after a stage has yielded just before the stage. Such a temporal correlation between the local yielding processes in successive stages is in sympathy with the inhomogeneous distribution of the local strain along the grain boundary, alternating with elementary unit traverse of the transient dislocations. The distribution of the local strain is necessarily determined by the configuration of the constituent dislocations in each stage. In a rather crude yet direct estimation, we have the convenience in detecting the sense of the local strain along the grain boundary by direct observation of the relative arrangement of the bubbles there. The plus and minus signs in Table I signify, in respective regions, the local strain in the same sense and that in the opposite sense to the applied strain.

In an ideal case where yielding proceeds over a single region, it can be expected[10] that the region under local gtrain in the same sense with the applied strain before yielding is put over into local strain in the opposite sense after yielding, and that the local strain in regions not yielding is shifted towards the same sense with the applied strain. In the present observation, from a stage to the next yielding proceeds in several regions, and the mode of changing local strain is not so simple as in the ideal case. Speaking qualitatively, however, it is evident that the local strain in regions traversed (not traversed) by transient dislocation is shifted towards the opposite (same) sense to the applied strain.

The above mentioned correlation between the local yielding processes is understood, in terms of the alternating inhomogeneous distribution of the local strain, in the line that for the site of yielding a region under local strain in the same sense with the applied strain is preferred to a region under local strain in the opposite sense. In this concern, it is note-worthy that the local strain favours the dislocation reaction decomposing a constituent dislocation according to Eq. (2) and that we have an expectancy of decreasing the necessary activation energy substantially under the influence of the local strain field.

In terms of the transient dislocations, the temporal correlation between yielding processes signifies the temporal continuation of the trajectories of them. A tentative manner of continuating the trajectories is shown by horizontal chain line segments in Table 1, which are legitimate only provided the upwards traverse of all the transient dislocations. But this is admittedly not the unique possibility. We have then the problem of deciding between numerous possibilities in the manner of continuating the trajectories. For the problem to be clarified, we must decide with the respective constituent dislocations between the alternatives as to the intermediate stages of the dislocation reactions, such as shown in Figs. 8 and 9. In the present stage of experiment, it can not be decided between the alternatives, and a cinematographic photograph of the processes is under preparation.

In concluding the discussions, at any rate, it may be said that the activated state in the process of 'viscous flow' along the grain boundary of type C in the mode (ii) corresponds to an intermediate stage involving transient dislocation, whence the rate of flow is determined by the energy required to decompose, under favourable influence of the local strain, a constituent dislocation to activate a transient dislocation.

References

1) E. Fukushima, A. Ookawa: J. Phys. Soc. Japan **8** (1953) 129.

2) E. Fukushima, A. Ookawa: J. Phys. Soc. Japan **8** (1953) 609.

3) E. Fukushima, A. Ookawa: J. Phys. Soc. Japan **8** (1953) 280.

4) W. L. Bragg: Proc. Phys. Soc. London **52** (1940) 54.

5) W. T. Read, W. Shockley: Phys. Rev. **78** (1950) 275.

6) W. M. Lomer, J. F. Nye: Proc. Roy. Soc. **A212** (1952) 576.

7) J. Washburn, E. R. Parker: J. Metals **4** (1952) 1076.

8) T. S. Kê: Phys. Rev. **73** (1948) 267.

9) N. F. Mott: Proc. Phys. Soc. London **60** (1948) 391.

10) W. L. Bragg: Proc. Camb. Phil. Soc. **45** (1948) 125.

JOURNAL OF THE PHYSICAL SOCIETY OF JAPAN Vol. 9, No. 1, JAN.—FEB., 1954

The Scattering of Slow Electrons by the Diatomic Molecules

II : Elastic Scattering by the Hydrogen Molecules

By Sigeru NAGAHARA

Department of Physics, Faculty of Literature and Science,
Toyama University

(Received October 18, 1952)

The author has applied the general theory developed in the preceding paper[1] to the elastic scattering of slow electrons by the hydrogen molecule, using the more exact molecular potential than those used in J. B. Fisk's paper.[2] The calculation has been made for the following energies of the incident electron : 27.2 ev, 17.1 ev, 6.8 ev and 1.7 ev : the corresponding total cross sections being 9.163, 19.43, 43.84 and 33.23 atomic unit. The remaining discrepancy with the observed values may be attributable to the effect of exchange and of inelastic collisions.

§ 1. Introduction

The problem of the elastic scattering of slow electrons by the hydrogen molecules has been studied by J. B. Fisk. Although he has obtained fairly good results, especially in low-energy domain, his method is still open to question, because he modified the molecular field for the purpose of obtaining separability of the wave equation. Since a fairly accurate molecular potential is available in the case of the hydrogen molecule, it seems to us worthwhile to calculate the scattering cross-section more accurately, applying the general method developed in the preceding paper.

§ 2. Interaction Field between the Incident Electron and the Hydrogen Molecule

As the wave function of the hydrogen molecule, we use the one obtained by T. Inui[3] i.e.,

$$\Psi=\frac{2}{N}e^{-\alpha(\xi_1+\xi_2)}\cosh\beta(\eta_1-\eta_2)\,, \qquad (1)$$

where ξ_i and η_i denote the elliptic coordinates of the ith electron ($i=1,2$), α, β, numerical parameters, and N, the normalization factor. In the present paper we assume the following values for these parameters

$$\alpha=1.75\,, \qquad \beta=1.375$$

and $\quad R=1.42\text{Å}$

for the internuclear distance.

With the use of the wave function (1), the electronic charge density in the hydrogen molecule is calculated as

$$\rho(\boldsymbol{r})=-2\int|\Psi(\boldsymbol{r},\boldsymbol{r}')|^2d\tau'\,, \qquad (2)$$

and the potential energy of the incident electron due to the molecular electrons is given by

$$V_e(\boldsymbol{r})=-\int\frac{\rho(\boldsymbol{r}')}{|\boldsymbol{r}-\boldsymbol{r}'|}d\tau'=2\iint\frac{|\Psi(\boldsymbol{r}',\boldsymbol{r}'')|^2}{|\boldsymbol{r}-\boldsymbol{r}''|}d\tau'd\tau''. \qquad (3)$$

Substituting the Neumann expansion for $1/(|\boldsymbol{r}-\boldsymbol{r}'|)$ and carrying out the integrations with the use of elliptic coordinates, $V_e(\boldsymbol{r})$ can be expressed in the following form :

$$V_e(\boldsymbol{r})=\sum_{\tau=0}^{\infty}\{a_\tau R_\tau(2,\xi)-b_\tau R_\tau(0,\xi)\}P_\tau(\eta)\,, \qquad (4)$$

where $P_\tau(\eta)$ are Legendre polynomials and a_τ, b_τ are numerical constants.* The auxiliary functions

$$R_\tau(m,\xi)=\int_1^\infty Q_\tau(\xi_+)P_\tau(\xi_-)e^{-\alpha\xi'}\xi'^m d\xi'\,, \qquad (5)$$

have been calculated numerically with the use of tables published by M. Kotani and his collaborators.*[4]

§ 3. Integration of the Wave Function

In this case, for simplification of the calculation, the wave function is expanded in terms of the function $\mathrm{P}_l^m(\eta)$ (Legendre function), instead of the function $pe_l^m(\eta)$:

$$\Phi_l^m(\xi,\eta)=\sum g_{lj}^m(\xi)P_j^m(\eta)\,. \qquad (6)$$

The relation between the function $g_{lj}^m(\xi)$

---

* Numerical tables of these constants and functions $[jj':0]$, $b_{jj'}{}^m(\xi)$, etc., will be sent on request.

nd the function $f_{lj}{}^{m}(\xi)$ defined in I is obtained ith the use of transformation matrix be-veen $pe_l{}^m(\eta)$ and $P_l{}^m(\eta)$ as follows

Table I.

=0	$\kappa=0.25$	$\kappa=0.50$	$\kappa=0.75$	$\kappa=1.0$
'00	1	1	1	1
'02	−0.0069307	−0.027556	−0.061366	−0.10748
'04	0.000074	0.0001179	0.0005890	0.001828
'20	0.0013861	0.00551	0.01227	0.02150
'22	1	1	1	1
'24	−0.0015307	−0.0061237	−0.013778	−0.024479
40	0	0	0	0
'42	0	0	0	0
44	1	1	1	1
11	1	1	1	1
13	−0.002501	−0.010022	−0.02261	−0.04035
15	−0.00000177	−0.000028	−0.000143	−0.000453
31	0.001072	0.004295	0.010137	0.10729
33	1	1	1	1
35	−0.0021226	−0.008504	−0.020071	−0.034247
51	0	0	0	0
53	0	0	0	0
55	1	1	1	1

$$pe_l{}^m(\eta)=\sum d_{lj}{}^m P_j{}^m(\eta)\ , \qquad (7)$$

$$g_{lj}{}^m(\xi)=\sum f_{l,j'}{}^m(\xi) d_{j',j}{}^m\ . \qquad (8)$$

ıbstituting (6) in (2) given in I, we obtain :

$$\sum P_j{}^m(\eta)\{L_\xi-j(j+1)+\kappa^2(\xi^2-\eta^2)$$
$$-W(\xi,\eta)(\xi^2-\eta^2)\}g_{lj}{}^m(\xi)=0\ , \quad (9)$$

ıere

$$W(\xi,\eta)=-\frac{2R\xi}{\xi^2-\eta^2}+\frac{R^2}{2}V_e(\xi,\eta)\ .$$

Integrating (9) with respect to η on multiply-g by $P_{j'}{}^m(\eta)$, the following equations are ıtained :

$$\{L_\xi-j(j+1)\}g_{lj}{}^m(\xi)+\sum_{j'}\{\kappa^2 b_{jj'}{}^m(\xi)$$
$$-w_{jj'}{}^m(\xi)\}g_{lj}{}^m(\xi)=0\ , \quad (10)$$

ere

$$b_{jj'}{}^m(\xi)=\int P_j{}^m(\eta)(\xi^2-\eta^2)P_{j'}{}^m(\eta)d\eta\ . \quad (11)$$

$$w_{jj'}{}^m=\int P_j{}^m(\eta)W(\xi,\eta)P_{j'}{}^m(\eta)d\eta\ , \quad (12)$$

se are numerically calculated.

ntroducing the function $\sqrt{\xi^2-1}\,g_{lj}{}^m(\xi)=$ $^m(\xi)$, (10) can be written as follows :

$$\frac{d^2G_{lj}{}^m(\xi)}{d\xi^2}+\sum[jj':\kappa]G_{lj'}{}^m(\xi)=0\ , \quad (13)$$

ere

$$[jj':\kappa]=[jj':0]+\kappa^2\frac{b_{jj'}{}^m(\xi)}{\xi^2-1}\ , \qquad (14)$$

$$[jj':0]=\delta_{jj'}\left\{\frac{1-m^2}{(\xi^2-1)^2}-\frac{j(j+1)}{\xi^2-1}\right\}+\frac{w_{jj'}{}^m}{\xi^2-1}\ . \qquad (15)$$

To obtain the wave function, we integrate (13) in the following three different ways according as the domain of the variable ξ.

Firstly when ξ is in the neighbourhood of 1, we substitute $(1+y)$ for ξ and expand $[jj':k]$ and $G_{lj}{}^m(\xi)$ in power of y, i.e.,

$$[jj':\kappa]=\sum_{h=-2}^{\infty}c_{jj':h}{}^m y^h\ , \qquad (16)$$

$$G_{ll}{}^m(\xi)=y^{(1+m)/2}(1+a_{ll,1}{}^m y+a_{ll,2}{}^m y^2+\cdots)$$
$$G_{lj}{}^m(\xi)=\qquad a_{lj,1}{}^m y^{(3+m)/2}+\cdots \qquad (17)$$

where

$$c_{jj':-2}{}^m=\tfrac{1}{4}(1-m^2)\delta_{jj'}\ , \qquad c_{jj':h}{}^m=c_{j'j:h}{}^m$$
$$a_{ll,0}{}^m=1 \qquad a_{lj,0}{}^m=0 \qquad (l\neq j)$$

Substituting (16) and (17) in (13), we can obtain $a_{lj,h}{}^m$.

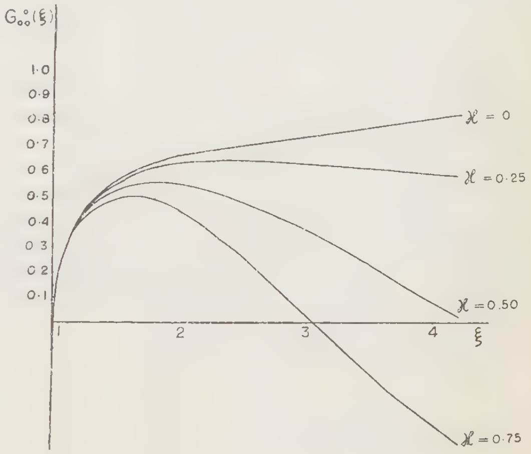

Fig. 1. $G_{00}{}^0(\xi)$ curve.

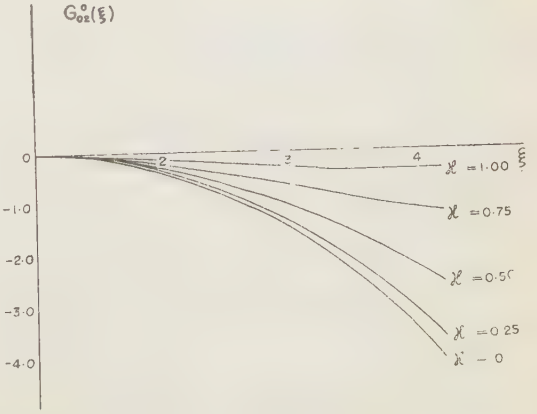

Fig. 2. $G_{02}{}^0(\xi)$.

Secondly, using the numerical values of $[jj':\kappa]$ and applying Störmer-Levy's method

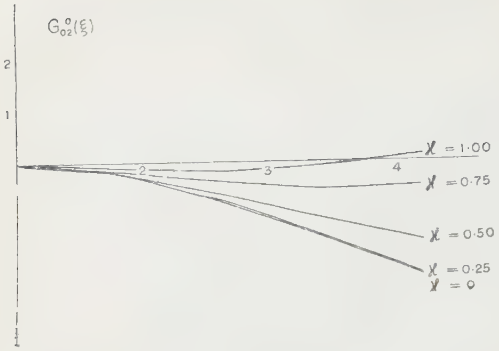

Fig. 3. $G_{20}{}^0(\xi)$.

to (13), the functions $G_{lj}{}^m$ are numerically integrated onwards, starting with the values obtained by the first method. We have integrated eleven functions $G_{00}{}^0(\xi)$, $G_{02}{}^0(\xi)$, $G_{04}{}^0(\xi)$, $G_{06}{}^0(\xi)$, $G_{20}{}^0(\xi)$, $G_{22}{}^0(\xi)$, $G_{24}{}^0(\xi)$, $G_{26}{}^0(\xi)$, $G_{11}{}^0(\xi)$, $G_{13}{}^0(\xi)$ and $G_{15}{}^0(\xi)$ numerically for $\kappa=0$, 0.25, 0.5, 0.75 and 1.00. $G_{00}{}^0(\xi)$, $G_{02}{}^0(\xi)$ and $G_{20}{}^0(\xi)$ are given in Figures 1—3 as examples.

Thirdly, when ξ is very large, (which is realized practically for $\xi=4$) the poteintial $W(\xi,\eta)$ becomes negligible and the equation (13) reduces to the differential equation of the spheroidal wave function so that its general solution is expressed as a linear combination of $S_l{}^m(\xi)$ and $C_l{}^m(\xi)$ defined in Stier's paper.[5]

$$f_{lj}{}^m(\xi)=\alpha_{lj}{}^m S_l{}^m(\xi)+\beta_{lj}{}^m C_l{}^m(\xi)$$

$$\sim B_{lj}{}^m\,\frac{2}{a_{jm}N_{jm}}\,\frac{\sin\left(\kappa\xi-\dfrac{\pi}{2}j+\delta_{lj}{}^m\right)}{\kappa\xi}\,. \tag{18}$$

§ 4. Calculation of Phase Shifts and the Total Cross Section

If we find the transformation formulae $P_l{}^m(\eta)$ into $pe_l{}^m(\eta)$ and apply them to the following equation,

$$\begin{aligned}\Phi(\xi,\eta)&=\sum g_{lj}{}^m(\xi)P_l{}^m(\eta)=\sum f_{lj}{}^m(\xi)pe_l{}^m(\eta)\\&=\sum\frac{G_{lj}{}^m(\xi)}{\sqrt{\xi^2-1}}P_l{}^m(\eta)=\sum\frac{F_{lj}{}^m(\xi)}{\sqrt{\xi^2-1}}pe_l{}^m(\eta)\end{aligned} \tag{19}$$

we obtain $F_{lj}{}^m$ respectively from $G_{lj}{}^m$ obtained by the first and second methods, thus, let us equal $f_{lj}{}^m(\xi)$, $f_{lj}{}'{}^m(\xi)$ above obtained by the two methods at the adequately large value of ξ (which the author takes to be 4.0), then the phase shifts are obtained as follows:

Table II.

$\dfrac{a_{jm}{}^2N_{jm}}{a_{j'm}{}^2N_{j'm}}|\sigma_{jj'}|^2$:

(jj')	$\kappa=\frac{1}{4}$	$\kappa=\frac{1}{2}$	$\kappa=\frac{3}{4}$	$\kappa=1$
(00)	0.16497	0.84337	0.84830	0.38278
(02)	0.00005	0.00000	0.00000	0.00000
(20)	0.00004	0.00573	0.01660	0.01141
(22)	0.00017	0.02292	0.00468	0.01415
(11)	0.00004	0.00003	0.00000	0.32080
Σ	0.16527	0.87205	0.86958	0.72914

$$Q=\frac{4\pi}{\kappa^2}\sum\varepsilon_m\frac{a_{jm}{}^2N_{jm}}{a_{j'm}{}^2N_{j'm}}|\sigma_{jj'}|^2$$

Q:	33.23	43.84	19.43	9.163

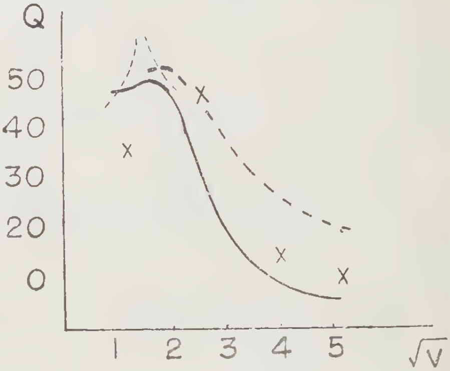

Fig. 4. Total cross section.

——— Calc. (J. B. Fisk)
- - - - } Expt.
× Calc. (The author)

$$\tan\delta_{lj}{}^m=\beta_{lj}{}^m/\alpha_{lj}{}^m,\quad B_{lj}{}^m=\sqrt{(\alpha_{lj}{}^m)^2+(\beta_{lj}{}^m)^2}. \tag{20}$$

In calculating the inverse matrix $\sigma_{jj'}{}^m$, although the order of the matrix is infinite, the author takes only the first several terms and neglects the others, i.e.,

$$\begin{aligned}m&=0, & j&=0,2, & j'&=0,2\\ & & j&=1, & j'&=1\end{aligned}$$

The results are given in Table 2. The total cross section is obtained by substituting above obtained values for $\sigma_{jj'}{}^m$ in (15) given in I. The results are given in Fig. 4.

§ 5. Discussion and Conclusion

The comparision of the results obtained here with those by J. B. Fisk and with the experimental values is given in Fig. 4. Closer approachment is obtained to the experimental values than Fisk's values. Also in the molecule Ramsauer's effect is acturally proved as in the case of atom. In the case of the hydrogen molecule, this effect is caused lower in the low-energy domain than in the case of, for instance, nitrogen and oxygen molecules. Herein lie experimental difficulties and is to be found the reason why few experiments have been made in this field up to now. Therefore, it is, henceforth, desirable that more experiments should be made in the low-energy domain.

§ 6. Acknowledgment

I wish to express my sincere thanks to Prof. M. Kotani for his much helpful advice and continuous encouragement throughout this work. I should also like to thank Hattori-Hōkōkai for financial support.

References

1) S. Nagahara: "Scattering of slow electrons by the diatomic molecules. I: General theory" J. Phys. Soc. Japan **8** (1953) 165. This paper is herin referred to as I.

2) J. B. Fisk: Phys. Reg. **49** (1936) 790.

3) T. Inui: Proc. Phys. -Math. Soc. Japan **20** (1938) 790.

4) M. Kotani etc.: Proc. Phys. -Math. Soc. Japan **20** (1938), **22** (1940) Extra No.

* Those who are interested in the numerical values of the functions and also of other functions and parameters in the present paper may obtain a mimeographed copy on application.

5) Stier: Zeits. f. Phys. **76** (1932) 439.

6) Brode: Rev. Mod. Phys. **5** (1933) 257.
Brücke: Ann. d. Physik **82** (1927) 912.
Ergeb. d. exp. Naturwiss. **8** (1929) 185.
Ramsauer, Kollath: Handbuch der physik 22/11.

Journal of the Physical Society of Japan Vol. 9, No. 1, Jan.—Feb., 1954

The Viscoelasticity of Linear Polymeric Substance

By Shizuo Hayashi

University of Gumma

(Received October 25, 1952)

The viscoelasticity of highpolymeric substance is discussed from the stand point of a molecular theory. The strain of a substance consists of the elongation of polymer and the intermolecular slipping. These two kinds of strain of substance and the elongation of polymer are named the macroscopic elongation and the microscopic elongation respectively. Supposing the rate of the intermoleclar slipping obeys the Eyring's formula the relation between the macroscopic elongation-factor λ and the microscopic elongation-factor α is obtained as follow

$$\frac{d\lambda}{dt}=\frac{d\alpha}{dt}+Ab\varepsilon(\alpha-1)\ .$$

Where A, b and ε are physical constants. Solving the equation above we obtain the following results. First; at the constant strain the retractive force decays exponentially against the time as expected. Second; when the velocity of elongation is constant the retractive force shows a maximum against the elongation and decays gradually as elongation goes on.

§ 1. Introduction

It is considered that the viscoelatic behavior of the polymeric substance results from the elongation of polymers which construct the subtance and the intermelecular slipping of polymer. The elongation of the substance and the elongation of polymers are named macroscopic elongation (or strain) and the microscopic elongation respectively. The macroscopic elongation is expressed by the superposition of microscopic elongation and the intermolecular slipping. Therefore we would be able to investigate the viscoelastic behavior by examing the relation between the macroscopic elongation and the microscopic elongation.

In this article it is supposed that the linear polymers are arranged as sticks make a faggot and when the substance is elonged each polymer in the substance is not only elonged but also slips each other, these microscopic elongation and the intermolecular slipping results the macroscopic elongation of the substance. According to the consideration above, the relation of retractive force to the elongation-velocity and to the time are investigated.

When the elongation-velocity is constant the retractive force shows a maximum and decays gradually against the elongation, in the other hand, the experimental results show that the retractive force has a maximum against the elongation and then increase as the elongation goes on. This second increase of stress will result from the effect of crystallization of polymer at the large elongation. When the macroscopic elongation of substance is constant the retractive force decays exponentially against the time as expected. From the results above this theory seems to explain qulitatively the viscoelastic behavior of the high polymeric substance.

§ 2. Theory

When a sample is streched along a direction by a factor λ, each linear polymer is assumed to be streched by a factor α and to slip by a factor β, and the relation

$$d\lambda=d\alpha+d\beta\ , \tag{1}$$

is obtained. Where, α relates to the elasticity and β relates viscocity. The time derivertive of Eq. (1) becomes

$$\frac{d\lambda}{dt}=\frac{d\alpha}{dt}+\frac{d\beta}{dt}\ . \tag{2}$$

The second term of the right hand side $d\beta/dt$ means the rate of slipping per unit time, so it is proportional to

$$\frac{2kT}{h}e^{-F^+}\sinh\left(\frac{fx}{2kT}\right), \qquad (3)$$

after Eyring's textbook1), provided that the slipping occurs when a polymer is acted by the force f. Therefore

$$\frac{d\beta}{dt}=A\sinh(b.f), \qquad (3')$$

is obtained where A and b are constants.

As the force contained in Eq. (3′) can be regarded to be the retractive force of a linear polymer it might be regarded to be a microscopic force which acts on a linear polymer, so f might be set by

$$f=\mathcal{E}(\alpha-1), \qquad (4)$$

where, α means the degree of microscopic elongation of linear polymer.

From Eq. (2) and Eq. (4) it becomes

$$\frac{d\lambda}{dt}=\frac{1}{\mathcal{E}}\frac{df}{dt}+A\sinh(b\cdot f), \qquad (5)$$

which has the identical form with Tobolsky-Eyring's formula2), accordingly Eq. (5) is idential with Maxwell's formula when bf is small enough. But the force contained in Eq. (5) expresses the microscopic force and in this point Eq. (5), though it is identical in form, has the different concept from Tobolsky-Eyring's formula.

As the macroscopic force is not contained in Eq. (5), in order to obtain the results which relate to the macroscopic force we must return to Eq. (2). Letting bf be small enough $d\beta/dt$ is nearly equal to Abf and Eq. (2) becomes

$$\frac{d\lambda}{dt}=\frac{d\alpha}{dt}+Ab\mathcal{E}(\alpha-1). \qquad (6)$$

Solving the Eq. (6), we obtain some results.

Letting the elongation-velocity be constant it becomes

$$\alpha=\delta(1-e^{-\kappa t})+1, \qquad (7)$$

$$\kappa=Ab\mathcal{E}, \qquad \delta=\dot{\lambda}/\kappa, \qquad (8)$$

under the condition that $\alpha=1$ for $t=0$, where $\dot{\lambda}$ denotes the elongation-velocity.

When λ is constant and equal to λ_0 it becomes

$$\alpha=C(\lambda_0)e^{-\kappa t}+1 \qquad (9)$$

where $C(\lambda_0)$ is constant of integral and means that it contains the initial elongation-factor λ_0 as a parameter.

From the consideration above we obtain the microscopic elongation α at the special case, then we must investigate how the retractive force becomes through the parameter α.

§ 3. Retractive Force

Letting unit volume of the substance contain N linear molecules the free energy of the substance per unit volume will becomes

$$\Psi=\tfrac{1}{2}N\mathcal{E}(\alpha-1)^2, \qquad (10)$$

using Eq. (4). Differentiating Eq. (10) by λ, the retractive force σ per unit initial cross-sectional area is obtained.

$$\sigma=\left(\frac{\partial\Psi}{\partial\lambda}\right)_T=\left(\frac{\partial\Psi}{\partial\alpha}\right)_T\left(\frac{\partial\alpha}{\partial\lambda}\right). \qquad (11)$$

When the elongation-velocity is constant, from Eq. (11) and Eq. (7) the retractive force becomes

$$\sigma=\frac{N\mathcal{E}\dot{\lambda}}{\kappa}\left(1-e^{-\kappa t}\right)e^{-\kappa t}. \qquad (12)$$

And when the length is constant, from Eq. (11) and Eq. (9)

$$\sigma=N\mathcal{E}C\left(\frac{dC}{d\lambda_0}\right)e^{-2\kappa t}, \qquad (13)$$

is obtained.

The results computed from Eq. (12) and Eq. (13) are shown in Fig. 1 and Fig. 2. In Fig. 1 the strain-stress curve for constant elongation-velocity are shown. The curves from below correspond to the rate of elongation-velocity *1, 1.3, 1.5, 2. 3* and *4* respectively. The times which correspond to the maximum stress in Eq. (12) are equal for all curves, but if the elongation-velocity becomes greater the elongation correspond to the maximum stress becomes greater. The greater the elongation-velocity is the greater the retractive force becomes against the same elongation.

In Fig. 2 the stress-time curves for constant elongation are shown. From below the curves correspond to the rate of elongation 1, 2 and 3 respectively. The retractive force decays exponentially as expected. It is the evident fact that the greater the elongation is the greater the retractive force becomes against the same elongation.

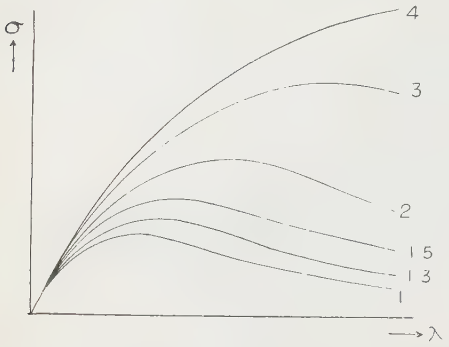

Fig. 1. Strain-stress curve in arbitary scale.

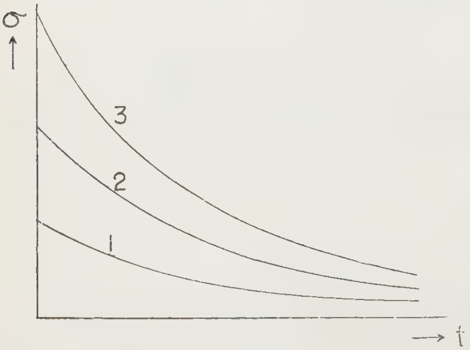

Fig. 2. Stress-time curve in arbitary scale.

§ 4. Conclusion

From the consideration above this theory can explain qualitatively the viscoelastic behavior of high polymeric substance. This idea had already been presented by Dr. Sakai in his work[3], but the method treated in this theory is different from his work. Accordingly, we have a little different results, but the qualitative property is seemed to be identical. For instance when the elongation is constant Dr. Sakai's formula is expressed by

$$\sigma = \frac{N\varepsilon}{\lambda_0} C e^{-\kappa t}(e^{-\kappa t}+1),$$

in which the notations in this theory is used. The formula is a little different from Eq. (13), but it is identical qualitatively except the additional term, because, if $C \propto \lambda_0$ is assumed $C^2/\lambda_0 \sim C(dC/d\lambda_0)$.

If the substance is subjected to a constant stress, the macroscopic elongation λ is expressed, through the parameter α, by the time t. In this case the elongation becomes greater and greater as the time goes on, and it is easily shown that the elongation increases more rapidly than expected from Maxwell's equation.

In conclusion the author wants to express his cordial thanks to Professor K. Fuchino for his kind discussion about this problem.

References

1) H. Eyring: Theory of Rate process.

2) A. V. Tobolsky and H. Eyring: J. Chem. Phys. **11** (1943)

3) T. Sakai: High polymetric Substance (Compiled by S. Mizushima).

JOURNAL OF THE PHYSICAL SOCIETY OF JAPAN Vol. 9, No. 1, JAN.—FEB., 1954

On Molecular Sound Velocity of Liquids. I

Consideration on the Rao's Relation between the Temperature Coefficient of Sound Velocity in and the Coefficient of Thermal Expansion of Liquids

By Tadashi KISHIMOTO and Otohiko NOMOTO

Kobayasi Institute of Physical Research, Kokubunzi, Tokyo

(Read April 29, 1953; Received August 15, 1953)

(a) The temperature coefficient of the isothermal compressibility $(1/\beta_T)(d\beta_T/dT)$ and the coefficient of thermal expansion α have been computed for liquids employing Lennard-Jones and Devonshire's equation of state as improved by Wentorf, Buehler, Hirschfelder and Curtiss and employing the numerical tables by these authors. The computed value of the ratio of these two coefficients is about 6.5 at temperatures corresponding to $0.9\ T_b$, where T_b means the boiling points. This gives a rough explanation of the Rao's relation between the temperature coefficient of the adiabatic compressibility β_S and the coefficient of thermal expansion α; i.e., $(1/\beta_s)(d\beta_s/dT)=7\alpha$. (b) Re-examination of Rao's relation has been performed on many organic liquids, some liquified gases, and some molten metals employing existing ultrasonic velocity data. The ratios $(1/\beta_s)(d\beta_s/dT):\alpha$ are about 7 in organic liquids, about 5 in liquified gases and rather scattered in molten metals.

1. Introduction

It has been pointed out by Rao[1] that the mperature coefficient of sound velocity in ch organic liquid is proportional to the ermal expansion coefficient of this liquids, e ratio being nearly independent of tem- rature and nearly common (=3) fomany ganic liquids, i.e.,

$$\frac{1}{V}\left(\frac{\partial V}{\partial T}\right)_p=-3\left(\frac{1}{v}\frac{\partial v}{\partial T}\right)_p=-3\alpha\,, \qquad (1.1)$$

here T means the asbolute temperature, V e sound velocity, v the molar volume, and the coefficient of thermal expansion.

As the sound velocity is related to the nsity ρ, and the adiabatic compressibility by

$$V=1/\sqrt{\rho\beta_s}\,, \qquad (1.2)$$

have from (1.1) the relation:

$$\frac{1}{\beta_s}\left(\frac{\partial \beta_s}{\partial T}\right)_p=-7\frac{1}{\rho}\left(\frac{\partial \rho}{\partial T}\right)_p=7\alpha\,. \qquad (1.3)$$

Although the Rao's relation (1.1) or (1.3) known to be valid for many organic liquids proximately well, the theoretical back- ound of this rule is not clear as yet. This per intends to interprete this rule from nnard-Jones and Devonshire's liquid model. Also a re-examination of this rule has been performed in § 4, employing existing ultrasonic velocity data on many organic liquids, some liquified gases and some molten metals.

§ 2. Relation between the Temperature Coefficient of the Isothermal Compressibility and the Coefficient of thermal Expansion of Liquids

Although the adiabatic compressibility

$$\beta_s=-\frac{1}{v}\left(\frac{\partial v}{\partial p}\right)_s\,, \qquad (2.1)$$

of the liquid is also to be computed from the equation of state of the liquid directly, it is more convenient to compute the isothermal compressibility

$$\beta_T=-\frac{1}{v}\left(\frac{\partial v}{\partial p}\right)_T\,. \qquad (2.2)$$

at first and obtain the adiabatic compressibility therefrom by adding a small correction term, i.e., by employing the well-known relation:

$$\beta_s=\beta_T-\frac{T\alpha^2}{\rho c_p}\,. \qquad (2.3)$$

Here c_p means the specific heat at constant pressure.

We will employ the Lennard-Jones and Devonshire's liquid model[2], postulating the intermolecular potential of force

$$\mathcal{E}(r)=4\mathcal{E}_m\left[\left(\frac{r_0}{r}\right)^{12}-\left(\frac{r_0}{r}\right)^{6}\right], \tag{2.4}$$

where r means the intermolecular distance and $-\mathcal{E}_m$ the minimum value of $\mathcal{E}(r)$. r_0 is the value of r for which $\mathcal{E}(r)=0$, and means the collision radius at low temperature.

The equation of state of liquid (and compressed gas) has been obtained by Lennard-Jones and Devonshire using their liquid model. This equation has been improved by Wentorf, Buehler, Hirschfelder and Curtiss³⁾ (in the following, cited as WBHC) by taking the effect of the second layer and the third layer molecules also into consideration. The molecules are assumed to be spheres and the arrangements as closest packings, so that the number of nearest neighbours are 12.

The WBHC's equation of state is as follows:

$$p=\frac{NkT}{v}\left[1-\frac{12\mathcal{E}_m}{kT}\left\{2.4090\left(\frac{v_0}{v}\right)^2-2.0219\left(\frac{v_0}{v}\right)^4\right\}+4\frac{12\mathcal{E}_m}{kT}\left\{\left(\frac{v_0}{v}\right)^4\frac{g_L}{G}-\left(\frac{v_0}{v}\right)^2\frac{g_M}{G}\right\}\right], \tag{2.5}$$

where p means the pressure, N the Loschmidt number, k the Boltzmann constant, and G, g_L, and g_M are the functions of T and (v_0/v) given by

$$G=\int_0^{0.30544} y^{1/2}\exp\left\{-\frac{12\mathcal{E}_m}{kT}\left(\frac{v_0}{v}\right)^4 L(y)+\frac{24\mathcal{E}_m}{kT}\left(\frac{v_0}{v}\right)^2 M(y)\right\}dy\,,$$

$$g_L=\int_0^{0.30544} y^{1/2}L(y)\exp\left\{-\frac{12\mathcal{E}_m}{kT}\left(\frac{v_0}{v}\right)^4 L(y)+\frac{24\mathcal{E}_m}{kT}\left(\frac{v_0}{v}\right)^2 M(y)\right\}dy\,,$$

$$g_M=\int_0^{0.30544} y^{1/2}M(y)\exp\left\{-\frac{12\mathcal{E}_m}{kT}\left(\frac{v_0}{v}\right)^4 L(y)+\frac{24\mathcal{E}_m}{kT}\left(\frac{v_0}{v}\right)^2 M(y)\right\}dy\,, \tag{2.6}$$

where

$$L(y)=l(y)+\frac{1}{128}\,l(y/2)+\frac{2}{729}\,l(y/3)\,,$$

$$M(y)=m(y)+\frac{1}{16}m(y/2)+\frac{2}{27}m(y/3)\,, \tag{2.7}$$

with

$$l(y)=(1+12y+25.2y^2+12y^3+y^4)(1-y)^{-10}-1,$$

$$m(y)=(1+y)(1-y)^{-4}-1\,.$$

In these equations, y denotes

$$y=r^2/a^2\,, \tag{2.8}$$

where a means the molecular distance (W have $Na^3=\sqrt{2}\,v$).

In the following, we employ the simplifie notations:

$$\varphi_L=4g_L/G\,,\quad \varphi_M=4g_M/G\,, \tag{2.9}$$

which transforms the equation of state (2.5 into

$$p=(NkT/v)[1-(12\mathcal{E}_m/kT)\{(2.4090+\varphi_M)(v_0/v)^2-(2.0219+\varphi_L)(v_0/v)^4\}]\,. \tag{2.5a}$$

By differentiating this equation with respec to p under constant T, we have, considering (2.2), the relation

$$1=N\left[\frac{kT}{v}\beta_T+\frac{12\mathcal{E}_m}{kT}\left\{-(7.2270+3\varphi_M)\left(\frac{v_0}{v}\right)^2\beta_T+(10.1095+5\varphi_L)\left(\frac{v_0}{v}\right)^4\beta_T+\left(\frac{v_0}{v}\right)^4\left(\frac{\partial\varphi_L}{\partial p}\right)_T-\left(\frac{v_0}{v}\right)^2\left(\frac{\partial\varphi_M}{\partial p}\right)_T\right\}\right]. \tag{2.10}$$

As we have further the relation:

$$\left(\frac{\partial\varphi_i}{\partial p}\right)_T=\left(\frac{\partial\varphi_i}{\partial v}\right)_T\left(\frac{\partial v}{\partial p}\right)_T=-v\left(\frac{\partial\varphi_i}{\partial v}\right)_T\cdot\beta_T\,,\quad (i=L,\ M)\,, \tag{2.11}$$

we have from (2.10) the equation giving the value of the isothermal compressibility:

$$\frac{1}{\beta^T}=N\left[\frac{kT}{v}+\frac{12\mathcal{E}_m}{v}\left\{-(7.2270+3\varphi_M)\left(\frac{v_0}{v}\right)^2+(10.1095+5\varphi_L)\left(\frac{v_0}{v}\right)^4+\left(\frac{v_0}{v}\right)^2 v\left(\frac{\partial\varphi_M}{\partial v}\right)_T-\left(\frac{v_0}{v}\right)^4 v\left(\frac{\partial\varphi_L}{\partial v}\right)_T\right\}\right]. \tag{2.12}$$

Differentiating the both sides of this equation with respect to T under constant p, and taking into consideration the relations

$$\left(\frac{\partial\varphi_i}{\partial T}\right)_p=\left(\frac{\partial\varphi_i}{\partial T}\right)_v+\left(\frac{\partial\varphi_i}{\partial T}\right)_T\left(\frac{\partial v}{\partial T}\right)_p=\left(\frac{\partial\varphi_i}{\partial T}\right)_v+v\left(\frac{\partial\varphi_i}{\partial v}\right)_T\cdot\alpha\,,$$

$$\left\{\frac{\partial}{\partial T}\left(\frac{\partial\varphi_i}{\partial v}\right)_T\right\}_p=\frac{\partial^2\varphi_i}{\partial T\partial v}+v\left(\frac{\partial^2\varphi_i}{\partial v^2}\right)_T\cdot\alpha\,, \tag{2.13}$$

we have as the temperature coefficient of the isothermal compressibility:

$$\frac{1}{\beta_T}\left(\frac{\partial\beta_T}{\partial T}\right)_p = -N\beta_T\Bigg[\frac{k}{v}+\frac{12\,\mathcal{E}_m}{v}\Bigg\{-3\left(\frac{v_0}{v}\right)^2 \times\left(\frac{\partial\varphi_M}{\partial T}\right)_v + 5\left(\frac{v_0}{v}\right)^4\left(\frac{\partial\varphi_L}{\partial T}\right)_v + \left(\frac{v_0}{v}\right)^2 v\left(\frac{\partial^2\varphi_M}{\partial v\partial T}\right) - \left(\frac{v_0}{v}\right)^4 v\left(\frac{\partial^2\varphi_L}{\partial v\partial T}\right)\Bigg\}\Bigg] -N\beta_T\alpha\Bigg[-\frac{kT}{v}+\frac{12\,\mathcal{E}_m}{v}\Bigg\{(21.6810+9\varphi_M) \times\left(\frac{v_0}{v}\right)^2 - (50.5975+25\varphi_L)\left(\frac{v_0}{v}\right)^4 - 5\left(\frac{v_0}{v}\right)^2 v\left(\frac{\partial\varphi_M}{\partial v}\right) - 9\left(\frac{v_0}{v}\right)^4 v\left(\frac{\partial\varphi_L}{\partial v}\right)_T + \left(\frac{v_0}{v}\right)^2 v^2\left(\frac{\partial^2\varphi_M}{\partial v^2}\right)_T - \left(\frac{v_0}{v}\right)^4 v^2\left(\frac{\partial^2\varphi_L}{\partial v^2}\right)_T\Bigg]. \tag{2.14}$$

The right-hand side of this equation consists of terms containing $\alpha\beta_T$ and those containing β_T only. We make use of the thermodynamic relation

$$\beta_T = \frac{\alpha}{\left(\frac{\partial p}{\partial T}\right)_v}, \tag{2.15}$$

to transform the later terms so as to contain α. We obtain from the equation of state (2.5) by differentiation with respect to T under v=constant, the relation

$$\left(\frac{\partial p}{\partial T}\right)_v = N\left[\frac{k}{v}+\frac{12\mathcal{E}_m}{v}\left\{\left(\frac{v_0}{v}\right)^4\left(\frac{\partial\varphi_L}{\partial T}\right)_v - \left(\frac{v_0}{v}\right)^2\left(\frac{\partial\varphi_M}{\partial T}\right)_v\right\}\right]. \tag{2.16}$$

By substituting (2.15) and (2.16) into the β_T-terms of equation (2.14) (but not into $\alpha\beta_T$-terms), and dividing by α, we obtain the ratio of the temperature coefficient of the isothermal compressibility to the coefficient of thermal expansion:

$$\frac{1}{\beta_T}\left(\frac{\partial\beta_T}{\partial T}\right)_p : \alpha = -\frac{A}{B} - \frac{C}{D}, \tag{2.17}$$

where

$$A = \frac{k}{v}+\frac{12\,\mathcal{E}_m}{v}\left\{-3\left(\frac{v_0}{v}\right)^2\left(\frac{\partial\varphi_M}{\partial T}\right)_v + 5\left(\frac{v_0}{v}\right)^4\left(\frac{\partial\varphi_L}{\partial T}\right)_v + \left(\frac{v_0}{v}\right)^2 v\,\frac{\partial^2\varphi_M}{\partial v\partial T} - \left(\frac{v_0}{v}\right)^4 v\,\frac{\partial^2\varphi_L}{\partial v\partial T}\right\}, \tag{2.18}$$

$$B = \frac{1}{N}\left(\frac{\partial p}{\partial T}\right)_v = \frac{k}{v}+\frac{12\,\mathcal{E}_m}{v}\left\{\left(\frac{v_0}{v}\right)^4\left(\frac{\partial\varphi_L}{\partial T}\right) - \left(\frac{v_0}{v}\right)^2\left(\frac{\partial\varphi_M}{\partial T}\right)_v\right\}, \tag{2.19}$$

$$C = -\frac{kT}{v}+\frac{12\,\mathcal{E}_m}{v}\left\{(21.6810+9\,\varphi_M)\left(\frac{v_0}{v}\right)^2 - (50.5975+25\varphi_L)\left(\frac{v_0}{v}\right)^4 - 5\left(\frac{v_0}{v}\right)^2 v\left(\frac{\partial\varphi_M}{\partial v}\right)_T + 9\left(\frac{v_0}{v}\right)^4 v\left(\frac{\partial\varphi_L}{\partial v}\right)_T + \left(\frac{v_0}{v}\right)^2 v^2\frac{\partial^2\varphi_M}{\partial v^2} - \left(\frac{v_0}{v}\right)^4 v^2\left(\frac{\partial^2\varphi_L}{\partial v^2}\right)\right\}, \tag{2.20}$$

$$D = \frac{1}{N\beta_T} = \frac{kT}{v}+\frac{12\,\mathcal{E}_m}{v}\left\{-(7.2270+3\,\varphi_M)\left(\frac{v_0}{v}\right)^2 + (10.1095+5\varphi_L)\left(\frac{v_0}{v}\right)^4 + \left(\frac{v_0}{v}\right)^2 v\left(\frac{\partial\varphi_M}{\partial v}\right)_T - \left(\frac{v_0}{v}\right)^4 v\left(\frac{\partial\varphi_L}{\partial v}\right)_T\right\}. \tag{2.21}$$

WBHC have computed the values of G, g_L, g_M and pv/NkT as functions of

$$\left.\begin{aligned} &x = kT/\mathcal{E}_m, \\ \text{and}\quad &z = v/v_0. \end{aligned}\right\} \tag{2.22}$$

We have computed the values of φ_L and φ_M from WBHC's tables and obtained the values reproduced in Table I.

Table I. The values of φ_L and φ_M as functions of x and z.

	φ_L				φ_M			
z	x=0.70	x=0.75	x=0.80	x=0.85	x=0.70	x=0.75	x=0.80	x=0.85
0.8485	0.2592	0.2826	0.2988	0.3149	0.0601	0.0656	0.9691	0.0726
0.9899	0.5328	0.5652	0.5972	0.6289	0.1203	0.1272	0.1340	0.1408
1.0607	0.7380	0.7703	0.8115	0.8520	0.1635	0.1702	0.1786	0.1869
1.1314	0.9876	1.0421	1.0985	1.1495	0.2140	0.2249	0.2354	0.2459
1.2728	1.728	1.8136	1.8950	1.9747	0.3544	0.3696	0.3839	0.3978
1.4142	2.805	2.920	3.0340	3.1412	0.5381	0.5563	0.5739	0.5905

The substitution (2.22) transforms (2.17) into

$$\frac{1}{\beta_T}\left(\frac{\partial\beta_T}{\partial T}\right)_p : \alpha = -\frac{a}{b} - \frac{c}{d}\,, \tag{2.23}$$

where

$$\left.\begin{aligned} a &= A\frac{v}{k} = 1+12\left\{-3\frac{1}{z^2}\frac{\partial\varphi_M}{\partial x} + 5\frac{1}{z^4}\frac{\partial\varphi_L}{\partial x} + \frac{1}{z}\frac{\partial^2\varphi_M}{\partial z\partial x} - \frac{1}{z^3}\frac{\partial^2\varphi_L}{\partial z\partial x}\right\},\\ b &= \frac{v}{k}B = 1+12\left\{\frac{1}{z^4}\frac{\partial\varphi_L}{\partial x} - \frac{1}{z^2}\frac{\partial\varphi_M}{\partial x}\right\},\\ c &= \frac{v}{\mathcal{E}_m}C = -x+12\left\{\frac{1}{z^2}(21.6810+9\varphi_M) - \frac{1}{z^4}(50.5975+25\varphi_L)\right.\\ &\qquad \left. -5\frac{1}{z}\frac{\partial\varphi_M}{\partial z} + 9\frac{1}{z^3}\frac{\partial\varphi_L}{\partial z} + \frac{\partial^2\varphi_M}{\partial z^2} - \frac{1}{z^2}\frac{\partial^2\varphi_L}{\partial z^2}\right\},\\ d &= \frac{v}{\mathcal{E}_m}D = x+12\left\{-\frac{1}{z^2}(7.2270+3\varphi_M) + \frac{1}{z^4}(10.1095+5\varphi_L)\right.\\ &\qquad\qquad \left. + \frac{1}{z}\frac{\partial\varphi_M}{\partial z} - \frac{1}{z^3}\frac{\partial\varphi_L}{\partial z}\right\}. \end{aligned}\right\} \tag{2.24}$$

We have to know the values of $x=kT/\mathcal{E}_m$ and $z=v/v_0$ to perform the numerical computation. As the ordinary experiments are performed under atmospheric pressure, the value of z is determined when the value of x is given. In case of liquid under atmospheric pressure, the equation of state (2.5a) takes simple form

$$\frac{12\,\mathcal{E}_m}{kT}\left\{(2.4090+\varphi_M)\left(\frac{v_0}{v}\right)^2 - (2.0219+\varphi_L)\left(\frac{v_0}{v}\right)^4\right\} = 1\,, \tag{2.25}$$

by omitting pv/NkT as compared to unity. This means

$$(pv/NkT)^* = 0\,, \tag{2.25a}$$

where $(pv/NkT)^*$ means the value of (pv/NkT) computed from (2.5a) employing the known values of G, g_L and g_M, and given in WBHC's tables.

The value of the parameter $x=kT/\mathcal{E}_m$ depends on the value of the potential $\mathcal{E}_m$ and the temperature T, so that an appropriate value must be appointed to x according to the nature of the liquid examined and the temperature of observation. We have, however, selected the value

$$x=kT/\mathcal{E}_m=0.70\,, \tag{2.26}$$

from the following two reasons.

In the first place, our computation was limited by the computed range of the WBHC's tables, the lower limit of x for these tables being $x=0.70$. The second reason is that this value of x corresponds to the state of liquid at temperature roughly equal to

$$T=0.90T_b\,, \tag{2.27}$$

where T_b means the boiling point; and this was so to speak the upper limit of our desired range of x, the liquid at room temperatures corresponding to lower values of x than given in (2.26).

The relation (2.27) follows from the following considerations. We have the values of $\mathcal{E}_m/k$ for various gases determined from viscosity data and second virial coefficients, among others. Table II indicates the values of this ratio taken from the paper of Hirschfelder, Bird and Spotz[5]. The values of the boiling point T_b and the ratio $T_b:\mathcal{E}_m/k$ are also indicated in this table. We see that this ratio is constant in rough approximation and is given by

$$T_b=0.78\mathcal{E}_m/k. \tag{2.28}$$

On the other hand we have from WBHC's theory that the critical temperature T_c is proportional to $\mathcal{E}_m/k$ and given by

$$T_c=1.30\mathcal{E}_m/k\,, \tag{2.29}$$

while the original Lennard-Jones and Devonshire's thory gives a similar relation $T_c=4/3\cdot\mathcal{E}_m/k=1.33\mathcal{E}_m/k$. There is also a relation between the critical temperature and the boiling point, i.e.,

$$T_b=0.60T_c\,, \tag{2.30}$$

(cf. Fowler and Guggenheim[4]), so that we have from (2.29) and (2.30) the relation (2.28) again.

The relation (2.28) may be considered to hold true also for ordinary organic liquids, because of the fact that the Trouton's rule

$$S=10.3k\ , \tag{2.31}$$

is known to hold true in these liquids, indicating the constancy of the entropy of evaporation

$$S=0.628\times 12\varepsilon_m/T_b\ , \tag{2.32}$$

for all the liquids. Here we will assume that the relation (2.28) holds true for ordinary liquids and liquified metals.

The relation (2.27) follows from (2.28) and (2.26) immediately.

We have computed the values of the functions φ_L, φ_M and their differential coefficients from the values of φ_L and φ_M indicated in Table I, for the value of $x=0.70$ and for the corresponding value of $z=1.040$ as determined from the equation of state (2.25) or (2.25a), by approximate numerical calculation including graphical interpolation and extrapolation. These are as follows:

$$\left.\begin{aligned} \varphi_L&=0.672\ , & \varphi_M&=0.150\ , \\ \left(\frac{\partial\varphi_L}{\partial x}\right)_z&=0.56\ , & \left(\frac{\partial\varphi_M}{\partial x}\right)_z&=0.137\ , \\ \left(\frac{\partial\varphi_L}{\partial z}\right)_x&=2.99\ , & \left(\frac{\partial\varphi_M}{\partial z}\right)_x&=0.624\ , \\ \frac{\partial^2\varphi_L}{\partial z\partial x}&=1.4\ , & \frac{\partial^2\varphi_M}{\partial z\partial x}&=0.20\ , \\ \left(\frac{\partial^2\varphi_L}{\partial z^2}\right)_x&=6.55\ , & \left(\frac{\partial^2\varphi_M}{\partial z^2}\right)_x&=0.83\ , \end{aligned}\right\} \tag{2.33}$$

Table II. The values of T_b, ε_m/k and their ratios in various gases (see Hirschfelder, Bird and Spotz[5]) for literatures)

gases	ε_m/k from viscosity	ε_m/k from second virial coefficients	ε_m/k mean values	T_b (°K)	$T_b:\varepsilon_m/k$
H_2	33.3	37.02	35.2	20.4	0.58
N_2	91.46	95.9	93.68	77.5	0.83
N_2O	220	189	204.5	184.5	0.90
NO	119	131	120	121.4	1.01
CH_4	136.5	142.7	139.6	109.2	0.78
O_2	113.2	117.5	115.4	90.2	0.78
CO	110.3	95.33	102.8	81.7	0.79
A	124.0	119.5	121.8	87.2	0.72
Ne	35.7	35.7	35.7	27.3	0.77
He	6.03	6.03	6.03	4.4	0.73
					mean 0.789

The values of the functions defined in (2.24) are obtained from (2.33) as

$$\left.\begin{aligned} a&=12.5\ , \\ b&=5.22\ , \\ c&=-248\ , \\ d&=29.0\ . \end{aligned}\right\} \tag{2.34}$$

Finally, the ratio between the temperature coefficient of isothermal compressibility and the coefficient of thermal expansion is obtained from (2.23) as

$$\frac{1}{\beta_T}\left(\frac{\partial\beta_T}{\partial T}\right)_p : \alpha=6.16\pm1\ , \tag{2.35}$$

This result is only approximate, because of the inevitable interpolations and extrapolations employed in the calculation. Especially, the values of the coefficients $(\partial^2\varphi_L/\partial z\partial x)$ and $(\partial^2\varphi_M/\partial z\partial x)$ determined in this manner are not precise, and a slight variation in these values affects the result in a serious manner. The deviation of ±1 is perhaps rather an underestimation for the ratio (2.35). The ratio of (2.35) is also affected by a slight variation of the value of x. For example, $x=0.75$ gives 8.6 and $x=0.80$ gives 10.2 as the values of this ratio. We may write

$$\frac{1}{\beta_T}\left(\frac{\partial\beta_T}{\partial_T}\right)_p : \alpha=6.5\ , \tag{2.36}$$

considering the approximate nature of our computation. This means, perhaps, that the ratio is between 6 and 7, approximately.

§ 3. Relation between the Temperature Coefficient of the Adiabatic Compressibility and the Coefficient of Thermal Expansion

We have from the relation (2.3) between

the adiabatic and the isothermal compressibilities, the relation

$$\frac{1}{\beta_s}\left(\frac{\partial\beta_s}{\partial T}\right)_p=\frac{\beta_T}{\beta_s}\frac{1}{\beta_T}\left(\frac{\partial\beta_T}{\partial T}\right)_p-\frac{1}{\beta_s}\left\{\frac{\alpha^2}{\rho c_p}-\frac{T\alpha^2}{\rho c_p{}^2}\left(\frac{\partial c_p}{\partial T}\right)_p+2\frac{T\alpha}{\rho c_p}\left(\frac{\partial\alpha}{\partial T}\right)_p+\frac{T\alpha^3}{\rho c_p}\right\}. \tag{3.1}$$

The value of $(1/\beta_s)(\partial\beta_s/\partial T)_p:\alpha$ have been computed by assuming (2.36) and employing the experimental values of Freyer, Hubbard and Andrews[6] and others for β_s, β_T, c_p and ρ on the right hand side of the above equation. These values are indicated in Table III together with the experimental values. The result indicates a rough correspondence between the calculated and the experimental values and shows the approximate validity of the Rao's relation (1.3). The Rao's relation is, also experimentally, an approximate relation, and the ratio is scattered between 5.8 and 7.2.

Table III. The ratio between the temperature coefficient of the adiabatic compressibility and the coefficient of thermal expansion of various liquids.

Liquids	temperature	ratio $(1/\beta_s)(\partial\beta_s/\partial T)_p:\alpha$ (calc.)	(exp.)	difference
carbon disulfide	20°C	6.00	5.8	0.2
acetone	30	6.33	6.2	0.13
benzene	20	7.25	7.1	0.15
carbon tetrachloride	30	7.20	6.6	0.6
chloroform	30	6.68	6.6	0.08
toluene	30	8.00	7.2	0.8
ether	20	6.40	7.2	−0.8
chlorobenzene	30	7.48	6.9	0.58

§ 4. Experimental Relation between the Temperature Coefficient of Adiabatic Compressibility and the Coefficient of Thermal Expansion: Discussion of the Results

In the following, we will examine the validity of the Rao's relation (1.3), which is known to hold true approximately in organic liquids, as is also indicated in Table III, on more organic liquids, some liquified gases, and some molten metals. Fig. 1 indicates the relation between $(1/\beta_s)(\partial\beta_s/\partial T)_p$ and α in these liquid substances. The numerical tables and the literature of data are reproduced in Part II of the paper together with other results (cf. Table III in Part II). The straight line in the figure corresponds to the ratio $(1/\beta_s)(\partial\beta_s/\partial T)_p:\alpha=6.85$. The experimental results for organic liquids correspond roughly to this value, the mean value for 28 organic liquids (except glycerine) being 6.85. (Glycerine is an exceptional example with extremely low value of this ratio, 2.56. This may be due to the OH-bonds of this molecule.)

The results for liquified gases indicate definitely smaller values of this ratio, the mean value being approximately 5.5. The values of this ratio are various in molten metals, ranging between 2.68 of Cd and 7.2 of Sn. (cf. Table III, Part II).

Our calculation is based on the Lennard-Jones and Devonshire's type liquid model, assuming spherical molecules, and the closest packing arrangement of molecules with 12 nearest neighbours. Experimentally, the relation (1.3) holds true also in organic liquids with somewhat longer molecules or with dipole moments.

Smaller values of the ratio in liquified gases and in some of the molten metals may presumably be ascribed to structures with many holes, especially at temperatures near the boiling point.

So far, we can conclude that the Rao's relation (1.3) is also to be expected theoretically on Lennard-Jones and Devonshire's liquid model, at temperatures corresponding to $0.9T_b$, where T_b means the boiling point. It is, however, not clear whether this relation holds true or not independently of temperature. In order to check this point, it is necessary to make calculations at smaller

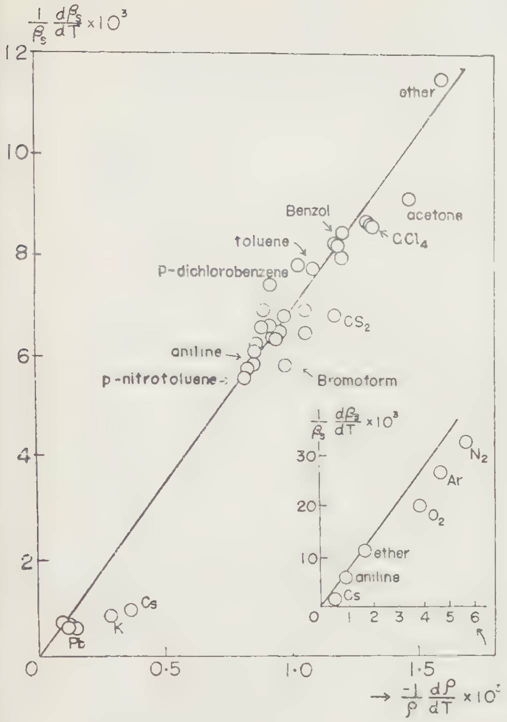

Fig. 1. Relation between the coefficient of thermal expansion and the temperature coefficient of adiabatic compressibility in various organic liquids, some liquified gases and some molten metals.

values of $x=kT/\varepsilon_m$ than 0.70. We could not perform this computation because the calculated range of WBHC's table does not cover this range. At higher temperatures than 0.90 T_b, however, the Rao's relation does not seem to be valid from Lennard-Jones and Devonshire's liquid model, because the ratio between the temperature coefficient of adiabatic compressibility and the thermal expansion coefficient increases with increase in temperature in this range.

References

1) M. Rama Rao: Indian J. Phys. **14** (1940) 109.

2) J. E. Lennard-Jones and A. F. Devonshire: Proc. Roy. Soc. **163A** (1937) 53; **165A** (1938) 1; **169A** (1939) 317; **170A** (1939) 469.

3) R. H. Wentorf, jr., R. J. Buehler, J. O. Hirschfelder and C. F. Curtiss: J. Chem. Phys. **18** (1950) 1484.

4) R. H. Fowler and E. A. Guggenheim, "Statistical Thermodynamics". (1939) p. 336.

5) J. O. Hirschfelder, R. B. Bird and E. L. Spotz, J. Chem. Phys. **16** (1948) 968.

6) E. B. Freyer, J. C. Hubbard and D. H. Andrews: J. Amer. Chem. Soc. **51** (1929) 759.

JOURNAL OF THE PHYSICAL SOCIETY OF JAPAN Vol. 9, No. 1, JAN.—FEB., 1954

On Molecular Sound Velocity of Liquids. II

Dependence of the Thermal Expansion Coefficient and the Temperature Coefficient of Compressibility of Liquids on the Boiling Point

By Tadashi KISHIMOTO and Otohiko NOMOTO

Kobayasi Institute of Physical Research, Kokubunzi, Tokyo

(Received August 15, 1953)

The coefficient of thermal expansion α and the temperature coefficient of isothermal compressibility $(1/\beta_T)(\partial\beta_T/\partial T)_p$ of liquids calculated on the basis of the Lennard-Jones and Devonshire's equation of state as improved by Wentorf, Buehler, Hirschfelder and Curtiss have been shown to be inversely proportional to the boiling point of the liquids, if we consider the liquids at absolute temperatures $T=\text{constant}\times T_b$, where T_b means the boiling points. At temperatures $T=0.9\ T_b$, we have theoretically $\alpha=0.140/T_b$ and $(1/\beta_T)(\partial\beta_T/\partial T)_p=0.865/T_b$. If we assume the same temperature dependence for the adiabatic compressibility β_S as for β_T, we have for the temperature dependence of the sound velocity in liquids $(1/V)(\partial V/\partial T)_p=-0.36/T_b$. These linear dependency of the coefficient of thermal expansion, the temperature coefficient of the adiabatic compressibility, and the temperature coefficient of the sound velocity on the reciprocal of the boiling point have been investigated in many organic liquids, some liquified gases and some molten metals employing existing ultrasonic velocity data and proved to be true in rough approximation, though the measurements do not correspond to temperatures satisfying $T=\text{const.}\times T_b$. The experimental values of the proportionality factors, however, proved to be about three times larger than the calculated ones, i.e., $\alpha=0.41/T_b$, $(1/\beta_S)(\partial\beta_S/\partial T)_p=2.8/T_b$ and $(1/V)(\partial V/\partial T)_p=-1.2/T_b$.

§ 1. Dependence of the Coefficient of Thermal Expansion, the Temperature Coefficient of the Compressibility, and the Temperature Coefficient of Sound Velocity on the Boiling Point

As described in the previous paper¹⁾ (in the following cited with (I)), we have from the equation of state of Wentorf, Buehler, Hirschfelder and Curtiss²⁾ (WBHC) based on the Lennard-Jones and Devonshire's liquid model³⁾

$$p=\frac{NkT}{v}\left[1+\frac{12\varepsilon_m}{kT}\left\{-2.4090\left(\frac{v_0}{v}\right)^2+2.0219\left(\frac{v_0}{v}\right)^4+\left(\frac{v_0}{v}\right)^4\varphi_L-\left(\frac{v_0}{v}\right)^2\varphi_M\right\}\right] \tag{1.1}$$

the reciprocal of the isothermal compressibility β_T, ((I), (2.12)),

$$\frac{1}{\beta_T}=N\left[\frac{kT}{v}+\frac{12\varepsilon_m}{v}\left\{\left(-7.2270+3\varphi_M-v\left(\frac{\partial\varphi_M}{\partial v}\right)_T\right)\left(\frac{v_0}{v}\right)^2+\left(10.1095+5\varphi_L-v\left(\frac{\partial\varphi_L}{\partial v}\right)_T\right)\left(\frac{v_0}{v}\right)^4\right\}\right] \tag{1.2}$$

and the coefficient of thermal expansion (cf. (I), (2.15))

$$\alpha=(\partial p/\partial T)_v\cdot\beta_T\ , \tag{1.3}$$

where (cf. (I), (2.16))

$$\left(\frac{\partial p}{\partial T}\right)_v=N\left[\frac{k}{v}+\frac{12\varepsilon_m}{v}\left\{\left(\frac{v_0}{v}\right)^4\left(\frac{\partial\varphi_L}{\partial T}\right)_v-\left(\frac{v_0}{v}\right)^2\left(\frac{\partial\varphi_M}{\partial T}\right)_v\right\}\right]\ . \tag{1.4}$$

There is further a relation between α and the temperature coefficient of β_T (cf. (I), (2.17)):

$$\frac{1}{\beta_T}\left(\frac{\partial\beta_T}{\partial T}\right)_p=-\left(\frac{A}{B}+\frac{C}{D}\right)\alpha\ , \tag{1.5}$$

where (cf. (I), (2.18)–(2.21))

$$A=\frac{k}{v}+\frac{12\mathcal{E}_m}{v}\left[\left\{-3\left(\frac{\partial\varphi_M}{\partial T}\right)_v+v\frac{\partial^2\varphi_M}{\partial v\partial T}\right\}\left(\frac{v_0}{v}\right)^2\right.$$
$$\left.+\left\{5\left(\frac{\partial\varphi_L}{\partial T}\right)_v-v\frac{\partial^2\varphi_L}{\partial v\partial T}\right\}\left(\frac{v_0}{v}\right)^4\right], \qquad (1.6)$$

$$B=\frac{1}{N}\left(\frac{\partial p}{\partial T}\right)_v, \qquad (1.7)$$

$$C=-\frac{kT}{v}+\frac{12\mathcal{E}_m}{v}\left[\left\{21.6810+9\varphi_M-5v\left(\frac{\partial\varphi_M}{\partial v}\right)_T\right.\right.$$
$$\left.+v^2\frac{\partial^2\varphi_M}{\partial v^2}\right\}\left(\frac{v_0}{v}\right)^2-\left\{50.5975+25\varphi_L\right.$$
$$\left.\left.-9v\left(\frac{\partial\varphi_L}{\partial v}\right)_T+v^2\frac{\partial^2\varphi_L}{\partial v^2}\right\}\left(\frac{v_0}{v}\right)^4\right]. \qquad (1.8)$$

$$D=\frac{1}{N\beta_T}. \qquad (1.9)$$

The relation (1.5) can also be written as

$$\frac{1}{\beta_T}\left(\frac{\partial\beta_T}{\partial T}\right)_p=-(A+C\alpha)\cdot\beta_T. \qquad (1.10)$$

In these equations φ_L and φ_M are defined by

$$\varphi_L=4g_L/G, \quad \varphi_M=4g_M/G, \qquad (1.11)$$

where G, g_L and g_M are the functions of $\mathcal{E}_m/kT$ and v_0/v as defined in (I), Eq. (2.10). As these functions are rather complex in form, it is not easy to evaluate the variations of φ_L and φ_M by variation of $\mathcal{E}_m/kT$ and v_0/v from analytical expressions of these functions.

It is, however, possible to evaluate these variations from the numerical tables calculated by WBHC. The numerical values of the functions φ_L and φ_M have been reproduced in (I), Table I. These are nearly proportional to $x(=kT/\mathcal{E}_m)$ at least in the narrow range of parametars here employed. If we put

$$\varphi_L=\frac{kT}{\mathcal{E}_m}f_L, \quad \varphi_M=\frac{kT}{\mathcal{E}_m}f_M, \qquad (1.12)$$

we have for the values of f_L and f_M the Table I, indicating that these functions are nearly independent of x and mainly determined by the value of $z(=v_0/v)$.

Table I. Values of the functions f_L and f_M as functions of x and z.

	f_L				f_M			
$z=v_0/v$	$x=0.70$	$x=0.75$	$x=0.80$	$x=0.85$	$x=0.70$	$x=0.75$	$x=0.80$	$x=0.85$
0.8485	0.3703	0.3768	0.3735	0.3705	0.0859	0.0875	0.0864	0.0854
0.9899	0.7609	0.7535	0.7463	0.7399	0.1717	0.1696	0.1675	0.1656
1.0607	1.0543	1.0269	1.0143	1.0024	0.2336	0.2268	0.2233	0.2199
1.1314	1.4107	1.3893	1.3698	1.3524	0.3056	0.2999	0.2943	0.2893
1.2728	2.469	2.418	2.369	2.3232	0.5063	0.4928	0.4799	0.4680
1.4142	4.007	3.893	3.7925	3.696	0.7687	0.7417	0.7174	0.6947

It follows, therefore, that the derivatives $(\partial\varphi_L/\partial v)$, $(\partial\varphi_M/\partial v)$, $(\partial^2\varphi_L/\partial v^2)$ and $(\partial^2\varphi_M/\partial v^2)$ are also approximately proportional to $x(=kT/\mathcal{E}_m)$.

It follows also that in the neighbourhood of $x=0.70$ the variation of the functions φ_L and φ_M are approximately linear with respect to x as is indicated in Table II, or

$$(\partial\varphi_L/\partial x)_z=\text{const.}, \quad (\partial\varphi_M/\partial x)_z=\text{const.}, \qquad (1.13)$$

i.e., we have from (1.12)

$$\frac{\partial\varphi_L}{\partial T}\cong\frac{k}{\mathcal{E}_m}f_L\infty\frac{k}{\mathcal{E}_m}, \quad \frac{\partial\varphi_M}{\partial T}\cong\frac{k}{\mathcal{E}_m}f_M\infty\frac{k}{\mathcal{E}_m}. \qquad (1.14)$$

First we will consider about β_T. Eq. (1.2) becomes by substitution of (1.12) as

$$\frac{1}{\beta_T}=\frac{12N\mathcal{E}_m}{v}\left\{-7.2270\left(\frac{v_0}{v}\right)^4+10.1095\left(\frac{v_0}{v}\right)^4\right\}$$
$$+\frac{12NkT}{v}\left[\frac{1}{12}-\left\{3f_M-v\left(\frac{\partial f_m}{\partial v}\right)_T\left(\frac{v_0}{v}\right)^2\right\}\right.$$
$$\left.+\left\{5f_L-v\left(\frac{\partial f_L}{\partial v}\right)_T\right\}\left(\frac{v_0}{v}\right)^4\right]. \qquad (1.15)$$

As was also the case in (I), we will consider the temperature corresponding to

$$kT=0.70\,\mathcal{E}_m=0.90\,kT_b \qquad (1.16)$$

(cf. (I), (2.26), (2.27)), then we can transform (1.15) into

$$\frac{1}{\beta_T}=\frac{12NkT_b}{v}\left[1.28\left\{-7.2270\left(\frac{v_0}{v}\right)^2\right.\right.$$
$$\left.+10.1095\left(\frac{v_0}{v}\right)^4\right\}$$
$$+0.90\left\{\frac{1}{12}-\left(3f_M-v\left(\frac{\partial f_M}{\partial v}\right)_T\right)\left(\frac{v_0}{v}\right)^2\right.$$
$$\left.\left.+\left(5f_L-v\left(\frac{\partial f_L}{\partial v}\right)_T\right)\left(\frac{v_0}{v}\right)^4\right\}\right]. \qquad (1.17)$$

This equation shows that β_T is approximately inversely proportional to T_b/v, i.e.,

$$\beta_T \propto v/T_b \,. \qquad (1.18)$$

Table II. The variation of φ_L and φ_M with x in the neighbourhood of $x=0.70$ ($v/v_0=1.040$)

$\Delta x=0.05$	$\Delta\varphi_L$	$\Delta\varphi_M$
$x=0.70\sim0.75$	0.032	0.07
$x=0.75\sim0.80$	0.038	0.07
$x=0.80\sim0.85$	0.038	0.08

For the practical calculation of the proportionality factor it is more convenient to substitute the relation (1.16) and the relation

$$kT_b/\mathcal{E}_m=0.78, \quad \text{or} \quad \mathcal{E}_m=1.28\,kT_b \qquad (1.19)$$

(cf. (I), (2.28)) into (1.2) and write

$$\frac{1}{\beta_T}=T_b\frac{N}{v}k\Big[0.90+12\times1.28\Big\{-(7.2270+3\varphi_M)\left(\frac{v_0}{v}\right)^2+(10.1095+5\varphi_L)\left(\frac{v_0}{v}\right)^4+\left(\frac{v_0}{v}\right)^2 v\left(\frac{\partial\varphi_M}{\partial v}\right)_T-\left(\frac{v_0}{v}\right)^4 v\left(\frac{\partial\varphi_L}{\partial v}\right)_T\Big\}\Big]. \qquad (1.20)$$

Next we will consider about α, the coefficient of thermal expansion. This is given by (1.3) as product of β_T and $(\partial p/\partial T)_p$, the latter being given by (1.4). We have on the right-hand side of this equation the term proportional to $\mathcal{E}_m/v$. The coefficient of this term, however, is proportional to $k/\mathcal{E}_m$ by (1.14), so that the right-hand side of (1.4) is approximately independent of $\mathcal{E}_m$ or T_b. The quantity $(\partial p/\partial T)_v$ is, therefore, approximately independent of $\mathcal{E}_m$ or T_b, and inversely proportional to v. Now that β_T is approximately proportional to v/T_b by (1.20), we have the relation

$$\alpha\cong K/T_b\propto 1/T_b \,. \qquad (1.21)$$

The constant of proportionality K is given by (1.4) and (1.20) as

$$K=(B/D)T_b \,, \qquad (1.22)$$

taking (1.7) and (1.9) also into consideration. If we define the functions b and d as in (I), Eq. (2.24), i.e., by

$$B=(k/v)b \,, \quad \text{and} \quad D=(\mathcal{E}_m/v)d \,, \qquad (1.23)$$

we have by (1.19)

$$K=0.78\,b/d \qquad (1.23)$$

where b and d are the known functions and computed in (I), (2.34) for the case when $kT/\mathcal{E}_m=0.70$ or $T=0.90\,T_b$.

We have in this case

$$K=0.140 \qquad (1.24)$$

or

$$\alpha\sim0.140/T_b \qquad (1.25)$$

by (1.21).

Finally, we will consider about

$$(1/\beta_T)(\partial\beta_T/\partial T)_p \,,$$

given in (1.10). In this equation, the coefficient of β_T on the right-hand side, $A+C\alpha$, is independent of T_b and inversely proportional to v from following reasons. The quantity A, given by (1.6), is inversely proportional to v and independent of $\mathcal{E}_m$, because the coefficient of $\mathcal{E}_m$ in (1.6), $(\partial\varphi_L/\partial T)$, $(\partial^2\varphi_L/\partial v\partial T)$, etc., are inversely proportional to $\mathcal{E}_m$ by (1.14). The quantity C, given in (1.8), is inversely proportional to v and proportional to $\mathcal{E}_m$ or T_b at any given temperature, where $kT/\mathcal{E}_m$ is constant (cf. (1.12)). So the quantity $C\alpha$ is also independent of T_b and inversely proportional to v.

Thus the quantity $(1/\beta_T)(\partial\beta_T/\partial T)_p$ is proportional to β_T/v and accordingly inversely proportional to T_b by (1.18), i.e.,

$$(1/\beta_T)(\partial\beta_T/\partial T)_p\cong K'/T_b\propto 1/T_b \,. \qquad (1.26)$$

The proportionality factor K' is given by

$$K'=-(A/B+C/D)K$$

by (1.5); or

$$K'=-0.78(a/b+c/d)(b/d) \qquad (1.27)$$

if we use the quantities b, d, given in (1.23), and a, c given in (I), (2.24), i.e., by

$$A=a(k/v), \quad C=c(\mathcal{E}_m/v), \qquad (1.28)$$

and use (1.24) for K.

As we have

$$(1/\beta_T)(\partial\beta_T/\partial T)_p : \alpha=6.16 \qquad (1.29)$$

by (I), (2.35), we have at temperatures corresponding to $T=0.90\,T_b$,

$$K'=0.865 \,, \qquad (1.30)$$

or

$$(1/\beta_T)(\partial\beta_T/\partial T)_p=0.865/T_b \,. \qquad (1.31)$$

The temperature coefficient of the adiabatic compressibility is to be computed from (I), (3.1) from the temperature coefficient of the isothermal compressibility. Though it is not simple to compute $(1/\beta_s)(\partial\beta_s/\partial T)_p$, the correction term being different for each liquid, the correction is usually not so great, as is seen

Table III. Values of the boiling point (t_b), $1/T_b$, the thermal expansion coefficient α, the temperature coefficient of the adiabatic compressibility $(1/\beta_s)(d\beta_s/dT)_p$, the temperature coefficient of the sound velocity $(1/V)(dV/dT)$, and the ratio between $(1/\beta_s)(d\beta_s/dT)$ and α for some liquified gases, many organic liquids, and some molten metals; arranged after increasing order of the boiling point.

liquids	boiling point t_b(°C)	$1/T_b$ in 10^{-3} deg^{-1}K	α in 10^{-3}	$\frac{1}{\beta_s}\frac{d\beta_s}{dT}$ in 10^{-3}	$\frac{1}{V}\frac{dV}{dT}$ in 10^{-3}	ratio $\frac{1}{\beta_s}\frac{d\beta_s}{\alpha T}:\alpha$	range of temperature (°C)	authors of sound velocity or other data
I. liquified gases								
N_2	−195.8	12.8	5.60	32.6	13.5	5.7	−197 ∼ −203	Liepmann9)
A	−185.8	11.3	4.71	27.2	11.25	6.00	−186 ∼ −189	Liepmann9)
				24.4			−186 ∼ −189	Itterbeek-Verhaegen11)
O_2	−183.0	11.0	3.8	20.5	8.55	5.4	−193 ∼ −183	Liepmann8)
			4.20	20.2	8.00	4.8	−193 ∼ −183	Itterbeek, de Bock, and Verhaegen10)
propane	− 45	4.35	1.85				− 78 ∼ − 24	I.C.T.12)
NH_3	− 33.4	4.00	2.1				− 78 ∼ − 33	I.C.T.12)
II. organic liquids								
ethyl ether	35	3.24	1.60	11.6	5.00	7.2	10 ∼ 30	Freyer, Hubbard and Andrews4)
carbon disulfide	46	3.13	1.189	6.8	2.81	5.75	10 ∼ 30	F.H.A.4)
acetone	56	3.05	1.48	9.2	3.86	6.2	20 ∼ 40	F.H.A.4)
chloroform	61	2.99	1.30	8.53	3.62	6.6	20 ∼ 40	F.H.A.4)
carbon tetrachloride	76	2.86	1.21	8.0	3.395	6.6	20 ∼ 40	F.H.A.4)
n-butyl chloride	78	2.85	1.31	8.72	3.71	7.00	20 ∼ 40	Lagemann, McMillan, Woolf5)
methyl-ethyl ketone	80	2.83	1.32	8.60	3.64	6.50	20 ∼ 40	L.McM.W.5)
benzene	80	2.83	1.206	8.50	3.65	7.05	10 ∼ 40	F.H.A.4)
fluorobenzene	85	2.79	1.19	8.25	3.53	6.92	20 ∼ 40	L.McM.W.5)
methylene bromide	99	2.69	1.06	6.50	2.72	6.15	20 ∼ 40	L.McM.W.5)
n-butyl bromide	100	2.68	1.04	7.85	3.36	6.90	20 ∼ 40	L.McM.W.5)
toluene	111	2.60	1.09	7.8	3.35	7.2	20 ∼ 40	F.H.A.4)
n-oktane	125	2.50	1.16	8.27	3.55	7.4	10 ∼ 30	F.H.A.4)
n-butyl iodide	130	2.48	1.06	6.95	2.95	6.55	20 ∼ 30	L.McM.W.5)
chlorobenzene	132	2.47	0.90	6.90	3.53	6.92	10 ∼ 30	L.McM.W.5)
			0.985	6.8	2.917	6.90	20 ∼ 40	F.H.A.4)
propyl bromide	142	2.41	0.955	6.50	2.77	6.83	20 ∼ 40	L.McM.W.5)
bromoform	149.6	2.36	0.99	5.80	2.41	5.8	10 ∼ 30	F.H.A.4)
bromobenzene	156	2.33	0.92	6.41	2.75	6.99	20 ∼ 40	L.McM.W.5)
o-chloro-toluene	159.5	2.31	0.89	6.60	2.85	7.40	20 ∼ 40	L.McM.W.5)
p-chloro-toluene	162	2.30	0.915	6.62	2.85	7.25	20 ∼ 40	L.McM.W.5)
m-chloro-toluehe	161.6	2.30	0.925	6.45	2.85	6.97	20 ∼ 40	L.McM.W.5)
p-dichloro-benzene	173	2.24	0.92	7.45	3.27	8.0	72 ∼ 94	Schaags7)
o-bromo toluene	181	2.20	0.86	6.10	2.62	7.10	20 ∼ 40	L.McM.W.5)
p-bromotoluene	183.6	2.19	0.87	6.25	2.69	7.20	30 ∼ 50	L.McM.W.5)
aniline	184	2.18	0.85	5.82	2.486	6.7	10 ∼ 30	F.H.A.4)
iodobenzene	189	2.16	0.83	5.80	2.49	7.00	20 ∼ 40	L.McM.W.5)
p-nitrotoluene	225	2.00	0.83	5.60	2.385	6.8	74 ∼ 123	Schaaffs6a)
glycerine	290	1.77	0.96	2.46	0.75	2.56	20 ∼ 40	F.H.A.4)
sulphric acid	330	1.66	0.53					I.C.T.1)
III. molten metals, etc.								
S	444.55	1.39			1.08			Kleppa14)
Cs	670	1.06	0.37	0.99	0.31	2.69	29 ∼ 130	Kleppa12)
K	759	0.97	0.29	0.84	0.28	2.90	64 ∼ 160	Kleppa12)
Cd	766	0.96	0.15	0.60	0.23	4.00	321 ∼ 360	Kleppa12)
Bi	1560	0.580	0.12	0.73	0.31	6.1	271 ∼ 365	Kleppa12)
Pb	1755	0.528	0.12	0.67	0.28	5.6	327 ∼ 380	Kleppa12)
Sn	2362	0.395	0.10	0.72	0.31	7.2	232 ∼ 380	Kleppa12)

in (I), Table III. The average value of $(1/\beta_s)\times(\partial\beta_s/\partial T)_p$ is not so different from that of $(1/\beta_T)(\partial\beta_T/\partial_T)_p$; the average computed value for 8 liquids tabulated in (I), Table III is $(1/\beta_s)(\partial\beta_s/\partial T)_p=6.92\,\alpha$ when the value of $(1/\beta_T)(\partial\beta_T/\partial T)_p=6.5\,\alpha$ is assumed. It may, therefore, presumably be permitted to assume the same temperature dependence for β_s as for β_T and write

$$(1/\beta_s)(\partial\beta_s/\partial T)_p=0.865/T_b \qquad (1.32)$$

in first approximation.

Now that the sound velocity is given by

$$V=1/(\rho\beta_s)^{1/2}=(v/M\beta_s)^{1/2} \qquad (1.33)$$

the temperature coefficient of the sound velocity is given by

$$(1/V)(\partial V/\partial T)_p=\tfrac{1}{2}\{\alpha-(1/\beta_s)(\partial\beta_s/\partial T)_p\}, \quad (1.34)$$

and we have from (1.25) and (1.32)

$$(1/V)(\partial V/\partial T)_p=-0.36/T_b\,, \qquad (1.35)$$

a relation, which is to be expected at temperatures corresponding to $kT/\mathcal{E}_m=0.70$, or $T=0.90\,T_b$ for each liquid.

The equations (1.25), (1.32) and (1.35) are expected to hold true only at temperatures corresponding to constant values of $kT/\mathcal{E}_m$ $(=0.70)$, or $T/T_b=0.90$. If the temperature is different from this, α and $(1/\beta_T)(\partial\beta_T/\partial T)_p$ become approximately proportional to

$$P_i(v/v_0)T_b+Q_i(v/v_0)T\,,\ (i=1,2)\,, \quad (1.36)$$

where P_i and Q_i are the known functions of (v/v_0) and $i=1,2$ corresponds to α and $(1/\beta_T)(\partial\beta_T/\partial T)_p$ respectively.

As, however, these functions become dependent on T through the equation of state, if the experiment is performed at constant pressure, the temperature dependence are not simple for both α and $(1/\beta_T)(\partial\beta_T/\partial T)_p$. The circumstance is similar also for $(1/\beta_s)(\partial\beta_s/\partial T)_s$ and $(1/V)(\partial V/\partial T)_p$.

§ 2. Comparison with Experiments

We have made use of the existing ultrasonic velocity data by Freyer, Hubbard and Andrews[4], Lagemann, McMillan and Woolf[5], Schaaffs[6][7] and others[8]-[11],[13]-[16] in order to test the validity of our results, eq. (1.35), (1.25) and (1.32).

Table III shows the values of $1/T_b$, α, $(1/\beta_s)(\partial\beta_s/\partial T)_p$, and $(1/V)(\partial V/\partial T)_p$ in many organic liquids, some liquified gases and some molten metals. Table IV shows some more results on the temperature coefficient

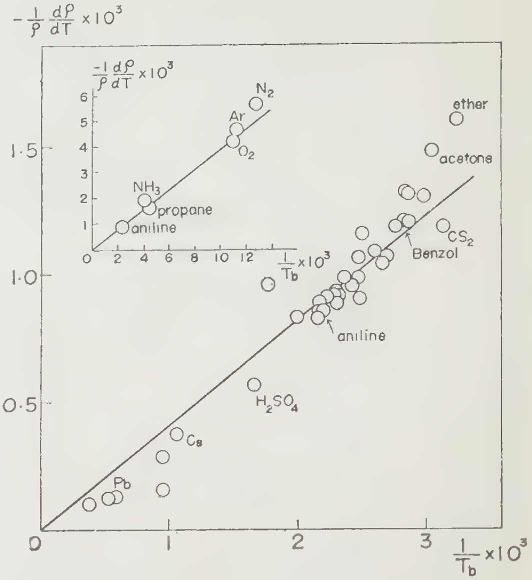

Fig. 1. The relation between the coefficient of thermal expansion α and the boiling point T_b in organic liquids, liquified gases and molten metals.

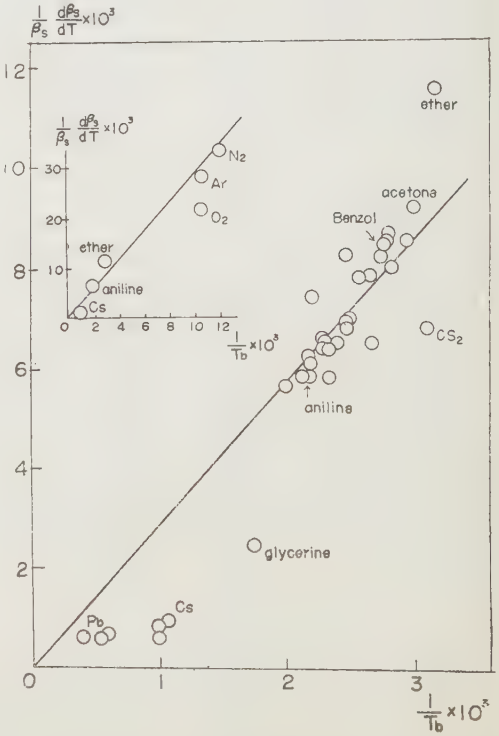

Fig. 2. The relation between the temperature coefficient of the adiabatic compressibility $(1/\beta_s)(\partial\beta_s/\partial T)_p$ and the boiling point T_b in organic liquids, liquified gases and molten metals.

Table IV. Relation between the boiling point and the temperature coefficient of ultrasonic velocity in organic liquids (after measurements of Willard (W)15) and Schaaffs (S)6))

liquids	boiling point t_b(°C)	$\frac{1}{T_b}$	$\frac{1}{V}\frac{dV}{dT}$	author
ethyl ether	35	3.25	5.4	S
pentane	36	3.24	4.2	S
iso-pentane			4.8	W
n-propylchloride	46	3.14	4.03	S
tert-butyl chloride	52	3.08	4.3	W
acetylendichloride	55	3.05	3.7	W
acetone	56	3.03	4.6	S
methanol	65	2.96	2.9	W
n-butyl chloride	78	2.85	4.1	S
ethanol	78	2.85	3.3	W
benzene	80	2.84	3.9	S
methyl ethyl ketone	80	2.84	4.1	S
cyclohexane	81	2.82	4.4	S
acetonitrile	82	2.82	3.8	S
cyclohexene	84	2.80	4.1	S
trichloro ethylene	87	2.78	4.2	S
diacetyl	88	2.77	3.70	W
n-butyl bromide	100	2.69	4.0	S
dioxane	101	2.68	4.5	S
methyl cyclohexane	101	2.68	4.5	S
crotonaldehyde	102	2.67	3.0	S
nitromethane	102	2.67	3.6	S
formamide	114	2.58	1.4	W
propyl iodide	116	2.57	3.0	S
n-butyl alchol	117	2.56	2.7	W
paraldehyde	124	2.52	4.2	S
tetranitro methane	126	2.51	3.8	S
n-octane	126	2.51	3.7	S
morpholine	129	2.49	2.6	W
n-butyl iodide	130	2.49	3.7	S
n-amyl bromide	130	2.49	3.7	S
chlorobenzene	132	2.47	3.4	S
p-xylol	136	2.45	3.6	S
ethyl benzene	136	2.45	3.3	S
acetylacetone	137	2.44	3.8	S
cyclohexyl chloride	142	2.41	3.6	S
cyclohexanone	155	2.33	2.8 3.7	W S
cyclohexanol	161	2.30	2.45 3.3	W S
mesitylene	163	2.29	3.5	S
furfuryl alcohol	170	2.25	2.35	W
benzaldehyde	179	2.21	2.7	S
benzylchloride	179	2.21	3.2	S
n-octyl chloride	180	2.21	3.3	S
aniline	184	2.20	2.8	S
o-cresol	191	2.16	2.3	W
dimethyl aniline	194	2.14	2.4	S
acetonyl acetohe	194	2.14	3.4	S
acetophenone	202	2.11	2.5	S
n-octyl bromide	202	2.11	4.1	S
tetraline	206	2.09	3.0	S
nitrobenzene	211	2.06	2.6	S
diethyl aniline	216	2.04	2.7	S
citral	223	2.01	2.6	S
carvacrol	238	1.95	3.4	S
quinoline	238	1.95	3.0	S
nicotine	247	1.92	3.4	S
diethylene glycol	250	1.91	1.5	W
cinnamaldehyde	252	1.90	2.05	W
triethylene glycol	285	1.79	2.4	W
glycerine	290	1.77	1.1	Hunter16)
Acids				
valeric acid	187	2.17	3.6	S
caproic acid	205	2.09	3.9	S
oenanthylic acid	223	2.01	3.8	S
caprylic acid	237	1.96	3.7	S

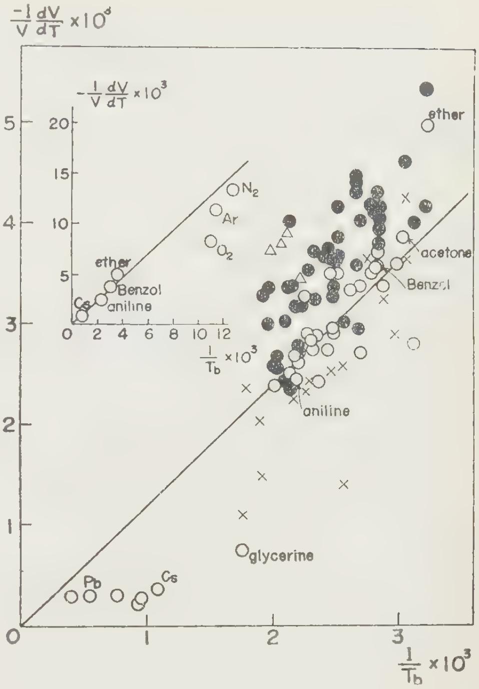

Fig. 3. The relation between the temperature coefficient of sound velocity $(1/V)(\partial V/\partial T)_p$ and the boiling point T_b in organic liquids, liquified gases and molten metals.
○: data taken from Table III; ●: Schaaffs' data; △: Schaaffs' data on acids; ×: Willard's data.

of ultrasonic velocity in organic liquids, the data being taken from Schaaffs6) and Willard's paper15).

Fig. 1 shows the relation between $1/T_b$ and $\alpha(=-(1/\rho)(\partial\rho/\partial T)_p)$ and Fig. 2 shows the relation between $1/T_b$ and $(1/\beta_s)(\partial\beta_s/\partial T)_p$. These figures correspond to the data represented in Table III. Fig. 3 shows the relation between $1/T_b$ and $(1/V)(\partial V/\partial T)_p$ for all the substances tabulated in Table III and Table IV. The straight lines in the figures represent rough averages of experimental slopes. In drawing the straight line in Fig. 3, the data of Schaaffs (marked with black circles for ordinary liquids and with triangles for acids) and those of Willard (marked with ×) are not taken into consideration, It seems that Schaaffs' value of the tamperature coefficient of ultrasonic velocity are about 10% higher than other results as far as comparison is possible on the same substances. Also Schaaffs himself admits, that his temperature coefficients are not so exact as compared to other data, because the temperature range of his measurements was rather narrow (5 degrees interval). On the other hand, Willard's values of the temperature coefficients are too low, as far as comparison is possible.

The approximately straight line relationships are perceptible in all the three figures though the molten metals do not lie on the same straight line. The experimental data, however, are rather scattered. This may be due, at least partly, to the fact that the straight line relationship is to be expected only at temperatures corresponding to $kT/\mathcal{E}_m=$ constant ($=0.70$ for example), or $T/T_b=$ constant ($=0.90$ for example), while the experiments do not correspond to this condition. As regards the temperature coefficient of β_s, scattering is also to be expected from omittion of the correction terms, because the linear relationship is expected, strictly speaking, only for β_T and not for β_s. The same source of error is included also in the temperature variation of the ultrasonic velocity.

Thus we may conclude that the expectations of our theory, the linear relationships between $1/T_b$ and the coefficient of thermal expansion, temperature coefficient of the adiabatic compressibility, and the temperature coefficient of the sound velocity, respectively, are also observed experimentally.

The slopes of these straight lines, however, are not in accord with predictions of the theory, the experimental relations being

$$\alpha=0.41/T_b\,, \tag{2.1}$$

$$(1/\beta_s)(\partial\beta_s/\partial T)_p=2.8/T_b\,, \tag{2.2}$$

and

$$(1/V)(\partial V/\partial T)_p=-1.2/T_b \tag{2.3}$$

respectively as compared with theoretical relations (1.25), (1.32) and (1.35) respectively. The experimental proportionality constants are larger than the theoretical ones by factors of 2.93, 3.24 and 3.33 respectively, or roughly about 3.

The reason of this discrepancy is not clear. It is perhaps partly attributable to the inadequacy of the Lennard-Jones and Devonshire's liquid model and the equation of state (including that of WBHC).

References

1) T. Kishimoto and O. Nomoto: J. Phys. Soc. Japan **9** (1954) 59.

2) R. B. H. Wentorf, jr., R. J. Buehler, J. O. Hirschfelder and C. F. Curtiss: J. Chem. Phys. **18** (1950) 1484.

3) J. E. Lennard-Jones and A. F. Devonshire: Proc. Roy. Soc. **163A** (1937) 53; **165A** (1948) 1; **169A** (1939) 317; **170A** (1939) 469.

4) E. B. Freyer, J. C. Hubbard and D. H. Andrews: J. Amer. Chem. Soc. **51** (1929) 759.

5) R. T. Lagemann, D. R. McMillan, jr., and W. E. Woolf, J. Chem. Phys. **17** (1949) 369.

6) W. Schaaffs: Zeits. Phys. Chem. **194** (1944) 28.

7) W. Schaaffs: Zeits. Phys. **105** (1937) 658.

8) H. W. Liepmann: Helv. Phys. Acta **9** (1936) 507; **11** (1938) 381.

9) H. W. Liepmann: Helv. Phys. Acta **12** (1939) 421.

10) A. Van Itterbeek, A. de Bock, and L. Verhaegen: Physica **15** (1949) 624.

11) A. Van Itterbeek and L. Verhaegen: Proc. Phys. Soc. **B62** (1949) 800.

12) International Critical Tables of Numerical Data.

13) O. J. Kleppa: J. Chem. Phys. **18** (1950) 1303.

14) O. J. Kleppa: J. Chem. Phys. **18** (1950) 1331.

15) G. W. Willard: J. Acous. Soc. Amer. **19** (1949) 235.

16) J. L. Hunter: J. Acous. Soc. Amer. **13** (1941) 36.

JOURNAL OF THE PHYSICAL SOCIETY OF JAPAN Vol. 9, No. 1, JAN.—FEB., 1954

On Molecular Sound Velocity of Liquids. III

Consideration on the Rao's Relation on the Dependence of Molecular Sound Velocity on Critical Constants

By Otohiko NOMOTO and Tadashi KISHIMOTO

Kobayasi Institute of Physical Research, Kokubunzi, Tokyo

(Received August 15, 1953)

(a) Theoretical derivation of the Rao's relation $R_V=a(T_c/M)^{1/6}v_c$ has been performed on the basis of the Lennard-Jones and Devonshire's liquid model and using Wentorf, Buehler, Hirschfelder and Curtiss' equation of state. Here R_V means the molecular sound velocity defined by $R_V=(M/\rho)V^{1/3}$, with M the molecular weight, ρ the density and V the sound velocity; T_c and v_c mean the critical temperature and the critical volume respectively, and a is an empirical constant with average value 2.68, according to Rao. The theoretical value of a obtained in this paper is 4.64.

(b) Re-examination of Rao's relation has been performed on organic liquids and on some liquified gases employing existing ultrasonic velocity data and the following average values have been obtained: $a_{\text{exp}}=2.86$ (on five liquified gases), $a_{\text{exp}}=2.69$ (on 21 organic liquids except alcohols, acids and acetonitrile). The a_{exp} for alcohols and acids are somewhat lower, the lowest example being $a_{\text{exp}}=1.825$ for acetic acid. These substances are known to be associated liquids and show extremely low values of R_V, deviating from the additivity rule of R_V for atomic increments or bond increments. This is also the cause for the low values of a_{exp} in alcohols and acids. The average value for 27 organic liquids including alcohols, acids and acetonitrile are $a_{\text{exp}}=2.60$.

(c) A modification of Rao's relation has been proposed in the form $R_V=b(\gamma T_c/M)^{1/6}v_c$, where γ means the ratio of the specific heats. The constant b is theoretically 4.44 and the average experimental value for 3 liquified gases proved to be 2.53, and for 13 organic liquids 2.53. The average value for 11 organic liquids excluding alcohols and acids proved to be 2.56.

§1. Introduction

There are proposed two experimental formulas relating the molecular sound velocity R_V of organic liquid with critical temperature and/or critical volume. The relation obtained by Rao¹⁾* (cited in Rao²⁾) is

$$R_V=a(T_c/M)^{1/6}v_c \tag{1.1}$$

where T_c means the critical temperature, v_c the critical volume and M the molecular weight, and a an empirical constant with average value 2.68 for organic liquids. As is well known, the molecular sound velocity R_V is defined by

$$R_V=(M/\rho)V^{1/3}\,, \tag{1.2}$$

where M means the molecular weight, ρ the density of the liquid and V the sound velocity in it. It is known to be a quantity satisfying additivity rules with respect to constitutive elements of the molecule, i.e., with respect to atomic inrements a_i (Rao³⁾) or bond increments b_i (Lagemann and Corey)⁴⁾.

$$R_V=\sum_i a_i\,, \tag{1.3}$$

$$R_V=\sum_i b_i\,. \tag{1.4}$$

The relations proposed by Lagemann and Dunbar⁵⁾

$$T_b=A+B\log R\,, \tag{1.5}$$

and

$$T_c=C+D\log R \tag{1.6}$$

are applicable only to those substances which constitute homologous series and we will not

---

* The present authors have no occasion of seeing Rao's paper as yet.

Table I. Values of the constants a, b and other related quantities for organic liquids and liquified gases

liquids	critical constants t_c (°C)	critical constants p_c (atm.)	critical constants ρ_c (g/cm³)	molecular weight M	$\frac{M}{\rho_c}\left(\frac{T_c}{M}\right)^{1/6}$	sound velocity V (m/sec)	density ρ (g/cm³)	temp. t	molecular sound velocity $R_{exp.}$	molecular sound velocity $R_{cal.}$	ratio of the specific heats γ	coefficients a	coefficients b	author of ultrasonic velocity data
liquified gases														
He	−267.9	2.26	0.0693	4.002	60.52	188^a	0.129^a	4°K	177.7	(185.0)		2.936		Findlay, Pitt, Smith, Wilhelm[8]
H_2	−239.9	12.8	0.0310	2.0156	103.8	1127	0.0709	−252°.7C	296.0			2.852		Pitt and Jackson[9]
N_2	−147.1	33.5	0.3110	28.016	115.7	880.3	0.811	77°K	331.1		1.96	2.862	2.56	Itterbeek, Bock and Verhaegen[10]
A	−122	48	0.531	75.22	93.90	863	1.424	−186°C	267.1		2.21	2.845	2.49	Liepmann[11]
O_2	−118.8	49.7	0.430	32.000	96.74	909	1.142	90°K	271.4	(148)	1.79	2.805	2.55	Itterbeek and Bock[12]
CH_4	− 82.5	45.8	0.162	16.0312	149.5	1418		111°.4K		(380)		(2.54)		Itterbeek and Verhaegen[22]
												$\bar{a}=2.86$	$\bar{b}=2.53$	
organic liquids														
ethyl ether	193.8	35.5	0.2625	74.08	383.5	1006	0.7135	20°C	1040	1039	1.33	2.712	2.56	Freyer, Hubbard and Andrews[13]
n-pentane	197.2	33.0	0.232	72.09	424.7	1182	0.891	26°C	1169	1160	1.2	2.752	2.67	Schaaffs[14]
ethyl bromide	231		0.513	108.96	274.2	900	1.4606	20°C	720.3	727.5		2.627		Lagemann, McMillan, Woolf[15]
methyl acetate	233.7	46.3	0.325	74.05	313.9	1154.4	0.928	25°C	837.1	843		2.667		Schreuer[16]
acetone	235.0	47	0.268	58.05	311.0	1190	0.7905	20°C	778.4	769	1.46	2.503	2.35	Freyer, Hubbard, and Andrews[13]
ethyl formate	235.3	46.65	0.323	74.05	316.2	1263	0.9048	23°.5C	884.7	843		2.798		Parthasarathy[17]
methanol	240.0	78.7	0.272	32.03	186.9	1121	0.7913	20°C	420.6	454	1.21	2.250*	2.18*	Ereyer, Hubbard and Andrews[13]
ethyl acetate	250.1	37.8	0.308	88.06	384.8	1176	0.900	20°C	1033	1038		2.744		Schaaffs[18]
methyl propionate	257.4	39.3	0.312	88.06	380.7	1215	0.9112	24°.5C	1031	1038		2.708		Parthasarathy[17]
chloroform	263		0.516	119.38	297.1	1002.5	1.488	20°C	803.1	783.5	1.48	2.703	2.53	Freyer, Hubbard and Andrews[13]
n-propyl alcohol	263.7	49.95	0.273	60.06	317.0	1193.2	0.7966	30°C	800.0	844	1.16	2.524*	2.46*	Weissler[19]
n-heptane	266.8	26.8	0.234	100.12	566.5	1154	0.684	20°C	1536	1550	1.19	2.711	2.63	Freyer, Hubbard and Andrews[13]
ethyl propionate	272.9	33.0	0.2965	102.08	455.5	1185	0.8837	23°.5C	1222	1233		2.683		Parthasarathy[17]
propyl acetate	276.2	32.9	0.296	102.08	454.6	1182	0.891	26°C	1211	1233	1.21	2.664	2.53	Parthasarathy[18]
iso-butyl formate	278	38	0.288	102.08	469.6	1199^b	0.9066^b	24°C	1196	1233		(2.547)		Parthasarathy[17]
acetonitrile	274.7	47.7	0.240	41.03	263.4	1305	0.785	20°C	571.3	572.5^c		2.169*		Lagemann, McMillan and Woolf[15]
cyclohexane	281.0	40.4	0.270	84.09	426·3	1284	0.779	20°C	1173	1170		2.752		Schaaffs[19]
carbon tetrachloride	283.1	45.0	0.558	153.83	341.6	920.6	1.584	25°C	944.7	909	1.46	2.766	2.60	Seifen[20]
fluorobenzene	286	44.6	0.354	96.04	363.8	1189	1.0249	20°C	992.4			2.728		Lagemann, McMillan and Woolf[15]
iso-butyl acetate	294	32	0.279	116.09	542.2	1179^d	0.871^d	26°C	1408	1374		(2.597)		Parthasarathy[18]
ethyl butyrate	293	30	0.276	116.09	547.6	1171	0.8768	23°.5C	1395	1374	1.25	2.547	2.45	Parthasarathy[17]

n-octane	296	24.6	0.234	114.22	637.9	1192	0.702	20° C	1725	1745	1.15	2.704	2.64	Freyer, Hubbard and Andrews[13]
isoamyl formate	303	34	0.282	116.09	537.7	1201^e	0.869^e	26° C	1420	1428		(2.641)		Parthasarathy[18]
toluene	320.6	41.6	0.292	92.06	430.1	1304.9	0.861	25° C	1168	1140	1.34	2.716	2.59	Schreuer[16]
acetic acid	321.6	57.2	0.351	60.03	250.6	1141	1.3718	20° C	457.3	648		1.825*		Lamb and Pinkerton[21]
propionic acid	339.5	53.0	0.315	74.05	334.4	1176	0.992	20° C	788.3	843		2.357*		Schaaffs[19]
n-butyric acid	355		0.302	88.06	404.6	1203	0.959	20° C	977.0	1038		2.415*		Schaaffs[19]
chlorobenzene	359	44.6	0.365	112.50	411.0	1289	1.104	20° C	1109	1079.5	1.35	2.698	2.57	Lagemann, McMillan and Woolf[15]
bromobenzene	397	44.6	0.486	156.96	411.5	1170	1.4953	20° C	1107	1097.5		2.690		Lagemann, McMillan and Woolf[15]
iodobenzene	448	44.6	0.581	203.96	433.3	1114	1.8280	20° C	1157	1156.5		2.670		Lagemann, McMillan and Woolf[15]
												$\bar{a}=2.692$	$\bar{b}=2.56$	(excluding alcohols, acids and acetonitrile)
												$\bar{a}=2.595$	$\bar{b}=2.53$	(including alcohols, acids and acetonitrile)

remarks	a	V and ρ under vapour pressure, ρ obtained from Keesom's "Helium" (1942)
	b	Data of V and ρ are not for the iso-compound
	c	R computed by bond increments (cf. (3))
	d	Data for V and ρ are for the n-compound
	e	Data for V and ρ are not for the iso-compound

take these into account in this paper. Here T_b means the boiling point, and T_c the critical temperature, and A, B, C, D are the constants for each homologous series.

It is the purpose of this paper to make a theoretical examination whether the Rao's relation (1.1) can be explained from the basis of the Wentorf, Buehler, Hirschfelder and Curtiss' (WBHC) equation of state[6] based on the Lennard-Jones and Devonshire's liquid model.

§ 2. Theoretical Derivation of the Rao's Relation

As the sound velocity is related to the density ρ and the adiabatic compressibility β_s with

$$V=(\rho\beta_s)^{-1/2}=(v/M\beta_s)^{1/2}\,, \qquad (2.1)$$

where v denotes the molar volume, we have as the expression of the molecular sound velocity in terms of these quantities the relation

$$R_v=v(v/M\beta_s)^{1/6}\,. \qquad (2.2)$$

Although the relation between the adiabatic and the isothermal compressibilities is not common for all the liquids, the ratio

$$\gamma=\beta_T/\beta_s \qquad (2.3)$$

for average organic substances is between 1.15 and 1.50. (The γ for liquified gases are generally larger than this; for example, $\gamma=2$ for N_2 and 2.2 for A). We will assume here

$$\gamma=1.30 \qquad (2.4)$$

as representing the average value of the ratio of the specific heats.

The value of $1/\beta_T$ has been calculated in part (I) of our paper[7] employing WBHC's equation of state as

$$\frac{1}{\beta_T}=N\Bigg[\frac{kT}{v}+\frac{12\varepsilon_m}{v}\Bigg\{-(7.2270+3\varphi_M)\left(\frac{v_0}{v}\right)^2 +(10.1095+5\varphi_L)\left(\frac{v_0}{v}\right)^4+\left(\frac{v_0}{v}\right)^2 v\left(\frac{\partial\varphi_M}{\partial v}\right)_T -\left(\frac{v_0}{v}\right)^4 v\left(\frac{\partial\varphi_L}{\partial v}\right)_T\Bigg\}\Bigg] \qquad (2.5)$$

(cf. (I), (2.12)).

In terms of the quantity D, defined in (I), (2.21), or in terms of the quentity d, defined in (I), (2.24), this becomes simply

$$\frac{1}{\beta_T}=ND=N\frac{\varepsilon_m}{v}d\,, \qquad (2.6)$$

where N means the Loschmidt number, and ε_m the Lennard-Jones and Devonshire's potential constant of the liquid (cf. (I), (2.4)).

If we consider further that the temperature is such that $T=0.9\,T_b$, where T_b denotes the absolute temperature of the boiling point, we have by (I), (2.34)

$$d=29.0\,, \qquad (2.7)$$

while we have

$$\varepsilon_m=kT_c/1.30 \qquad (2.8)$$

after WBHC, where k means the Boltzmann's constant and T_c the critical temperature. We have accordingly as the quantity inside the bracket of eq. (2.2)

$$v/M\beta_s=\gamma v/M\beta_T=Nk\gamma dT_c/1.30M$$
$$=Rd\gamma T_c/1.30M\,, \quad (2.9)$$

where R ($=8.3136\times10^7$ erg/deg.) means the universal gas constant. Substituting (2.4) and (2.7) we have

$$v/M\beta_s=2.411\times10^9 Tc/M\,. \qquad (2.10)$$

On the other hand, we have in this case of $kT/\varepsilon_m=0.70$, or $T=0.90T_b$, the molar volume

$$v=1.040\,v_0 \qquad (2.11)$$

from the equation of state for liquids (cf. (I), (2.25)), while we have

$$v_c=1.768\,v_0 \qquad (2.12)$$

for the critical volume (cf. WBHC,[6] Eq. (14)).

With substitution of (2.10), (2.11) and (2.12) in (2.2) we have as the value of R_V expressed in CGS-units

$$(R_V)_{\text{cgs}}=21.541v_c(T_c/M)^{1/6}\,. \quad (2.13)$$

As it is customary to express R_V in such a unit that in eq. (1.2) the density ρ is expressed in CGS unit but the sound velocity V is expressed in m/sec, we have the relation

$$R_V=(1/100)^{1/3}(R_V)_{\text{cgs}}=(1/4.64159)(R_V)_{\text{cgs}}\,, \qquad (2.14)$$

and we have finally as the theoretical formulation of Rao's relation (1.1)

$$R_V=4.64v_c(T_c/M)^{1/6}\,. \qquad (2.15)$$

This relation is derived on the assumption that $\gamma=1.30$ (cf. (2.4)), but the result is only slightly dependent on the value of γ, and we have as the value of the coefficient $a_{\text{cal}}=4.44$ in case $\gamma=1$, and $a_{\text{cal}}=4.99$ in case $\gamma=2$.

Thus the Rao's empirical relation (1.1) is to be expected also theoretically from the basis of the WBHC's equation of state based on Lennard-Jones and Devonshire's liquid model. But the value of the proportionality constant a is greater by a factor of about 7/4 than the experimental one.

As the theoretical expression of Rao's constant

$$a=(100)^{1/3}\frac{v/v_0}{v_c/v_0}\left(\frac{Rd\gamma}{kT_c/\varepsilon_m}\right)^{1/6}$$
$$=\frac{1.040}{4.642\times1.768}\left(\frac{Rd\gamma}{1.30}\right)^{1/6} \quad (2.16)$$

is dependent on γ, it may be better to use a formula

$$R_V=b(\gamma T_c/M)^{1/6}v_c \qquad (2.17)$$

in place of the Rao's relation (1.1), if the value of γ is known. The theoretical value of the coefficient b is given by

$$b=\frac{1.040}{4.642\times1.768}\left(\frac{Rd}{1.30}\right)^{1/6}=4.44 \qquad (2.18)$$

though also this may be greater than the experimental coefficient in the same ratio as in the case of a.

§ 3. Comparison with Experiments

As the Rao's original paper[1] is not available to us as yet, and as our theoretical result (2.15) was not in full agreement with Rao's empirical formula (1.1), we have performed a re-examination of the Rao's formula employing existing ultrasonic velocity data. At the same time we have intended to extend the formula on liquified gases.

The result is reproduced in Table I, which contains the values of the critical constants t_c, p_c, ρ_c taken from the "International Critical Tables" and the molecular weight M, the values of the quantity $(T_c/M)^{1/6}v_c$ calculated therefrom, and the ultrasonic velocity V, density ρ, and the experimental value of the molecular sound velocity obtained $(R_V)_{\text{exp}}$ therefrom, and the calculated value of the molecular sound velocity $(R_V)_{\text{cal}}$ obiained from the additivity rule (1.3) employing Rao's values of the atomic inrements or from the additivity rule (1.4) using the Lagemann and Corey's (cf. also Lagemann and Dunbar) values of the bond increments, values of γ (taken from Hiedemann's book[23]), and finally the empirical value of a and b. The authors for ultrasonic data are also indicated in the table.

As is to be seen in the table, the values of the proportionality factor a is fairly constant in many of the organic liquids and liquified gases. The value of a is slightly greater in liquified gases, the average for 5 liquified gases being

$$a_{\text{liq.gas}}=2.86 \tag{3.1}$$

while the average for 21 organic liquids excluding alcohols, acids and acetonitrile are

$$a_{\text{org. liq.}}(n)=2.69 \text{ . (except alcohols, acids)} \tag{3.2}$$

The values of a are lower in such compounds as alcohols and acetic acids and marked with asterisks in the table, the lowest value investigated being $a=1.825$ of acetic acid. These liquids are known to be associated liquids possessing unusually low molecular sound velocity $(R_V)_{\text{exp}}$ as compared to $(R_V)_{\text{cal}}$, the value computed from the additivity rule (cf. Table I). If we include also these liquids into consideration, we have as the average for 27 organic liquids

$$a_{\text{org. liq.}}=2.60 \text{ .} \tag{3.3}$$

The value for ordinary organic liquids is in good agreement with Rao's orginal result ($a=2.68$).

The slightly higher value of the constant a for liquified gases is to be attributed to the higher values of γ for these substances, because the values of the constant b are nearly the same for liquified gases as for organic liquids, the average values being

$$\left.\begin{aligned}&b_{\text{liq. gas}}=2.53 \text{ (3 liquified gases) ,}\\ &\text{and}\\ &b_{\text{org. liq.}}=2.56 \text{ (11 organic liquids except alcohols, acids) ,}\\ &b_{\text{org. liq.}}=2.53 \text{ (13 organic liquids including alcohols) .}\end{aligned}\right\} \tag{3.4}$$

The absolute values of the constants a and b, however, are not explicable by our theory.

Conclusion

Although the Rao's relation (1.1) is also to be derived theoretically on the basis of the Lennard-Jones and Devonshire's liquid model, the theoretical value of the proportionality factor a is larger by a factor of about 7/4 as compared with the experimental value. On the other hand, the re-examination of experimental data affords a value in good agreement with Rao's orginal result. Rao's relation is also applicable to liquified gases with a slightly higher constant. The associated liquids as alcohols and acetic acids show lower values of a, which is presumably due to the lower values of R_V in these substances.

References

1) M. Rama Rao: J. Mysore Univ. **12** (1942) 896.

2) M. Rama Rao: J. Chem. Phys. **14** (1946) 699.

3) M. Rama Rao: J. Chem. Phys. **9** (1941) 682.

4) R. T. Lagemann and J. E. Corey: J. Chem. Phys. **10** (1942) 759.

5) R. T. Lagemann and W. S. Dunbar: J. Phys. Chem. **49** (1945) 428.

6) R. H. Wentorf, jr., R. J. Buehler, J. O. Hirschfelder and C. F. Curtiss: J. Chem. Phys. **18** (1950) 1484.

7) T. Kishimoto and O. Nomoto: J. Phys. Soc. Japan **9** (1954) 59.

8) J. C. Findlay, A. C. Pitt, H. G. Smith and J. O. Wilhelm: Phys. Rev. **56** (1939) 122.

9) A. Pitt and W. J. Jackson: Canad. J. Res. **12A** (1935) 686.

10) A. Van Itterbeek, A. de Bock and L. Verhaegen, Physica **15** (1949) 624.

11) H. W. Liepmann: Helv. Phys. Acta **12** (1939) 421.

12) A. Van Itterbeek and A. de Bock: Physica, **14** (1948) 542.

13) E. B. Freyer, J. C. Hubbard and D. H. Andrews: J. Amer. Chem. Soc. **51** (1929) 759.

14) W. Schaaffs: Zeits. Phys. **114** (1939) 110.

15) R. T. Lagemann, D. R. McMillan, jr., and W. E. Woolf: J. Chem. Phys. **17** (1949) 369.

16) E. Schreuer: Akus. Zeits. **4** (1939) 215.

17) S. Parthasarathy: Proc. Indian Acad. Sci. **2A** (1935) 497.

18) S. Parthasarathy: Proc. Indian Acad. Sci. **3A** (1936) 482.

19) W. Schaaffs: Zeits. Phys. Chem. **194** (1944) 28.

20) N. Seifen: Zeits. Phys. **108** (1938) 681.

21) J. Lamb and J. M. M. Pinkerton: Proc. Roy. Soc. **199A** (1949) 114.

22) A. Van Itterbeek and L. Verhaegen: Proc. Phys. Soc. **62B** (1949) 800.

23) E. Hiedemann: "Ultraschallforschung" (Berlin, 1939).

JOURNAL OF THE PHYSICAL SOCIETY OF JAPAN Vol. 9, No. 1, JAN.—FEB., 1954

The Density and the Ultrasonic Velocity in Benzene Solutions of Methyl Methacrylate at Different Polymerization Stages

By Yasaku WADA and Sotoshi SHIMBO

Department of Applied Physics, Faculty of Engineering,
University of Tokyo

(Received July 31, 1953)

Measurements of density and ultrasonic velocity have been performed in dilute benzene solutions of methyl methacrylate of different polymerization stages, including the monomer and the final product of polymerization. The apparent molal volume and the apparent molal compressibility have been computed from the experimental results. The amount of polymerization (the ratio of reacted monomers to initial ones) of each intermediate product has been estimated from the molal properties respectively, taking account of the fact that these molal properties of polymer with high polymerization degree are independent of polymerization degree. The values of the amount of polymerization, estimated from each of the molal properties, are in satisfactory agreement with each other and also with the value computed from the ultrasonic absorption in the previous paper.

§ 1. Introduction

In an intermediate stage of polymerization process, a mixture of polymer molecules and unreacted monomer is formed. A physical property of a dilute solution of such a mixture may be derived from the property of solutions including polymer alone and monomer alone, if the interaction between polymer and monomer can be neglected at a high dilution. Furthermore, in the case that the property of the solution of polymer alone be independent of polymerization degree, the property of the mixture of polymer and monomer would depend only upon the fraction of polymer and monomer in the solute and would be independent of the molecular weight distribution in the polymer.

As well established in the earlier paper,[1] the ultrasonic absorption in benzene solutions of methyl methacrylate corresponds to the above case. In that paper, the ultrasonic absorption in dilute benzene solutions of methyl methacrylate monomer, perfect polymer and several intermediate products was measured and the amount of polymerization was estimated for each specimen.

In the present paper, the density and the ultrasonic velocity of the same solutions are measured and the amount of polymerization is estimated from them. The values thus obtained are compared with those from the ultrasonic absorption.

§ 2. Experimental

The specimens were prepared in the same way as the previous experiment[1] and were denoted as follows: A the monomer, B (rather viscous), C (highly viscous), D (soft) and E (hard) the intermediate products and F the perfect polymer. The specimen F is the precipitate from acetone solution of the final product of polymerization. Benzene solutions of three or four different concentrations are prepared for each specimen.

All the measurements were performed relatively to the solvent at room temperature, ca. 10°C. The measurement of density and viscosity was carried by a pyknometer and a viscometer of the Ostwald design respectively.

An ultrasonic interferometer of a new type was used for the measurement of ultrasonic velocity. The schematic circuit diagram and the details of the vessel are illustrated in Fig. 1. The interferometer, whose essential feature consists in making use of the free liquid surface as a reflector, is of a simplified form of that developed by Hunter[2] and has following advantages to usual ones:

(1) The interferometer is quite simple in construction, because it lacks a reflecting plate and a precise screw which drives it.

(2) The setting of parallelism between the

quartz and the liquid surface can be assured in a simple manner by the optical method which has been described in the earlier paper[1].

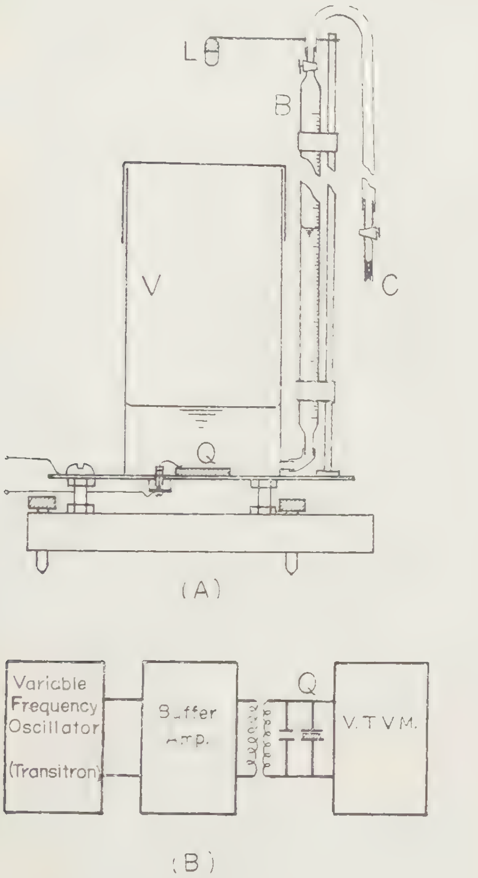

Fig. 1. Ultrasonic interferometer.
(A) The essential details of the vessel. V: vessel. Q: quartz. L: lamp for parallelism setting. B: burette. C: capillary.
(B) The schematic circuit diagram.

(3) If the vacuum tube voltmeter is sensitive enough, the radiofrequency potential applied to the quartz transducer can be lowered to a few tenths of volt and the local warming of the liquid can be avoided.

The height of the liquid column in the vessel is changed by adding the liquid from the 50 cc burette through the inlet which is below the reflecting surface. The rate of raising the liquid column height is regulated to any desired rate by a capillary tube which is connected with the top of the burette by a rubber tube. The readings of the liquid volume in the burette are taken when the rf voltage across the quartz falls to minimum, answering to the formation of the standing wave in the column.

The vessel is a cylinder of 76 mm diameter and the change of liquid volume by unit cubic centimeter results in the change of column height by 0.220 mm. The tranducer used in the present work is an X-cut quartz plate, 3×3 cm^2 and 3 mm thick, whose resonant frequency is about 927 kc/s. As half wave length of ultrasonic waves in benzene is about 0.755 mm at this frequency, forteen resonant points can be observed in the course of adding liquid of 50 cc.

The error of the relative value of wave length caused by this equipment is usually 0.02% or less. The frequency of ultrasonic waves, the sectional area of the vessel and the calibration of the burette are not required, because only the relative value of sound velocity of solutions to that of the solvent is necessary to the present work.

§ 3. Results

All the experimental data are listed in Table I. The unit of concentration is gram per 100 cc solution throughout this parper.

As illustrated in Fig. 2, the density of the solution increases linearly with concentration within the range studied and the apparent molal volume of solute $\overline{V}_2$, computed from the equation,

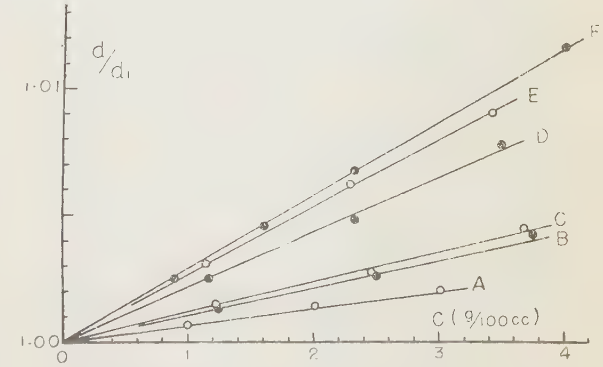

Fig. 2. Concentration dependence of density of methly methacrylate solutions relative to benzene.

$$\overline{V}_2=\frac{M}{d_1}\left[1-\frac{100}{c}(d-d_1)\right], \qquad (1)$$

becomes independent of concentration. In Eq. (1), M is the molecular weight of monomer, c concentration and d and d_1 are density of solution and solvent respectively. The com-

Table I.
(All the data are relative to benzene. ca. 10°C)

Specimen	Concentration	Density	Sound velocity	Adiabatic compressibility	Viscosity
A	1.00	1.00068	0.9970	1.0053	1.00
	2.01	1.00137	0.9948	1.0090	1.00
	3.01	1.00203	0.9935	1.0110	1.00
B	1.25	1.00130	0.9972	1.0043	1.16
	2.50	1.00258	0·9950	1.0074	1.22
	3.75	1.00424	0.9936	1.0086	1.43
C	1.23	1.00150	—	—	1.26
	2.46	1.00275	0.9952	1.0069	1.60
	3.68	1.00448	0.9938	1.0079	1.74
D	1.17	1.00250	0.9996	0.9983	2.17
	2.33	1.00481	0.9992	0.9968	3.80
	3.50	1.00779	1.0001	0.9920	6.3
E	1.15	1.00306	0.9998	0.9971	2.70
	2.29	1.00620	1.0002	0.9936	5.3
	3.43	1.00903	1.0024	0.9888	9.6
F	0.90	1.00248	1.0002	0.9971	3.26
	1.61	1.00456	1.0019	0.9916	6.3
	2.33	1.00676	1.0034	0.9866	11.2
	4.02	1.01169	1.0087	0.9715	27.5

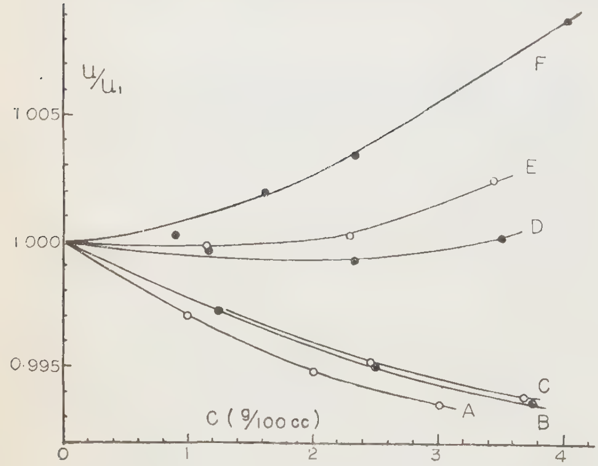

Fig. 3. Concentration dependence of sound velocity of methyl methacrylate solutions relative to benzene.

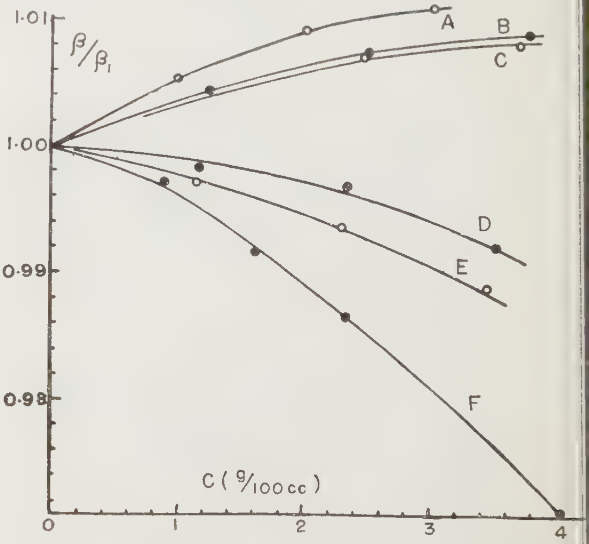

Fig. 4. Concentration dependence of adiabatic compressibility of methyl methacrylate solutions relative to benzene.

puted values of $\overline{V}_2$ for each specimen are listed in Table II.

Fig. 3 shows how the sound velocity varies as a function of concentration. The adiabatic compressibility β, calculated from the sound velocity u and density d by the equation $\beta=1/u^2d$, is plotted in Fig. 4. The apparent molal adiabatic compressibility of solute, $\overline{K}_2$, varies almost linearly with concentration. $\overline{K}_2$ can be computed from the following equation,

$$\overline{K}_2=M\beta_1\left[\frac{100}{c}\left(\frac{\beta}{\beta_1}-\frac{d}{d_1}\right)+\frac{1}{d_1}\right], \qquad (2)$$

where β and β_1 are compressibility of solution and solvent respectively. The extrapolated value of $\overline{K}_2$ to infinite dilution is shown in the second column of Table II. In the calculation of $\overline{V}_2$ and $\overline{K}_2$, d_1 and β_1 are assumed as 0.8896 g/cc and 59.5×10^{-12} cm²/dyne respectively, taken from a current table.

It is interesting to note that the plot of compressibility against concentration is convex upwards contrary to the case of aqueous solution of electrolyte, and the value of $\overline{K}_2$ differs so markedly for monomer and polymer.

Table II. Apparent molal volume and compressibility and amount of polymerization estimated from them

Specimen	$\overline{V}_2$ (cc)	$\overline{K}_2$ (10^{-10} cgs)	Amount of polymerization estimated from			Viscosity average molecular weight (relative to F)
			$\overline{V}_2$	$\overline{K}_2$	ultrasonic absorption	
A	105.7	99	0	0	0	0
B	101.7	85	0.17	0.19	0.19	0.05
C	100.8	83	0.23	0.21	0.25	0.10
D	91.6	49	0.62	0.67	0.66	0.44
E	85.7	38	0.88	0.83	0.80	0.69
F	83.0	26	1	1	1	1

No attempt will be made in this paper, however, to give explanations about this fact.

§4. Discussions

If the interaction between polymer and monomer can be neglected in highly dilute solutions of mixture of them, the apparent molal volume and compressibility of an intermediate product of polymerization can be expressed as linear combinations of those of monomer and polymer. It follows thus

$$\overline{V}_2=(\overline{V}_2)_M(1-x)+(\overline{V}_2)_P\cdot x\,, \qquad (3)$$

and

$$\overline{K}_2=(\overline{K}_2)_M(1-x)+(\overline{K}_2)_P\cdot x\,, \qquad (4)$$

where x is the amount of polymerization, here defined as the ratio of reacted monomers to initial monomers, and the subscript M is for monomer and P for polymer.

As ascertained from our preliminary experiment and others[3], the apparent molal volume and compressibility of polymer at a high dilution, $(\overline{V}_2)_P$ and $(\overline{K}_2)_P$ in Eq. (3) and (4), are independent of the polymerization degree except the polymers of very low degree such as dimer, trimer etc.. The values of $\overline{V}_2$ and $\overline{K}_2$ of the specimen F can be substituted in $(\overline{V}_2)_P$ and $(\overline{K}_2)_P$ in Eqs. (3) and (4) respectively and so it follows

$$\overline{V}_2=105.7(1-x)+83.0\cdot x \qquad (5)$$

and

$$\overline{K}_2=99(1-x)+26x\,. \qquad (6)$$

The effect on density and compressibility of polymers of such a low degree of polymerization as dimer, trimer etc. may be intermediate between monomer and high polymer. If the intermediate product of polymerization contains such low polymers, the value of $(1-x)$ in Eqs. (5) and (6) means not only the fraction of monomer, but also a part of the fraction of the low polymer.

The values of x computed from Eqs. (5) and (6) are tabulated in Table II, together with those estimated from ultrasonic absorption in the previous paper. In the previous paper, the fraction of unreacted monomer has been estimated, corresponding to $(1-x)$ in this case. The specimen A in the present experiment corresponds to A in the previous experiment, B to intermediate of B and C, C to D, D to E, E to intermediate of F and G, and F to H and I. Three values of the estimated amount of polymerization are in satisfactory agreement with each other for each specimen.

The last column of the Table II shows the relative values of average molecular weight, calculated on the assumption that the intrinsic viscosity is proportional to the 0.76th power of the average molecular weight[4]. The values are much smaller than the amount of polymerization for each intermediate product. This may be ascribed to the fact that the polymerized part of an intermediate product has a smaller average molecular weight than the final product.

In conclusion, the authors wish to thank Professor Yoshio Suge for his continuous encouragement.

References

1) Y. Wada and S. Shimbo: J Acous. Soc. Am. **25** (1953) 549.

2) J. L. Hunter: J. Acous. Soc. Am. **22** (1950) 243.

3) T. Ooi: Busseiron Kenkyu No. 44 (1951) 52.

4) Baxendale, Bywater and Evans: J. Polymer Sci. **1** (1946) 237.

JOURNAL OF THE PHYSICAL SOCIETY OF JAPAN Vol. 9, No. 1, JAN.—FEB., 1954

Concentration Shift of Nuclear Magnetic Resonances in Some Concentrated Acids

By Yoshika MASUDA and Teinosuke KANDA

Department of Physics, Kobe University

(Received July 23, 1953)

Chemical shifts of nuclear magnetic resonances are caused when two nuclei of the same kind have different magnetic shieldings caused by their environments. When there are two species of molecules having a chemical shift between them and if they are exchanging their states very rapidly by chemical reaction, we cannot observe their nuclear magnetic resonances separately but we observe a single resonance at the position of the field averaged over the two states with a weight of their populations. We observed such resonances for N^{14}, Cl^{35}, Br^{81} and I^{127} in concentrated aqueous solutions of HNO_3, $HClO_4$, HCl, HBr and HI, respectively. In these cases, the chemically exchanging states are ions and undissociated molecules and from the measurements of the shifts we can get some knowledge of the concentrated acid solutions, such as the degrees of dissociation, the type of the undissociated molecule and so on. All the nuclei examined here have the quadrupole moments, and from the measured line width in HCl, HBr and HI, we concluded that the undissociated molecules are not the HCl, HBr and HI molecules which possess large quadrupole couplings but some other molecules which have much smaller quadrupole couplings.

§ 1. Introduction

It was noted in a preliminary note¹⁾ that the N^{14} nuclear magnetic resonance frequency in nitric acid was concentration dependent.

Independently, Gutowsky and Saika²⁾ observed that the position of the proton magnetic resonance is concentration dependent in aqueous solutions of electrolytes yielding hydrogen containing ions.*

A resonance frequency shift exists between the dissociated ion and the undissociated molecule, because the nuclei should experience a different magnetic shielding in the dissociated and the molecular states. In aqueous solution, a dissociation equilibrium between the undissociated molecule and the dissociated ion is set up. Gutowsky and Saika²⁾ showed that when the correlation time for life times, τ_{ion} and τ_{mol}, of the dissociated and the moleecular states is extremly shorter than the inverse frequency separation of the chemically shifted components, the nuclear resonance will be observed at the frequency corresponding to the average shielding for the states. The frequency shift S measured from the resonance frequency of the dissociated ion is given by

$$S=S_{\text{mol}}\frac{\tau_{\text{mol}}}{\tau_{\text{mol}}+\tau_{\text{ion}}}\,, \qquad (1)$$

where S_{mol} is the shift of the undissociated molecule. The apparent degree of the dissociation α is given by

$$\alpha=\frac{\tau_{\text{ion}}}{\tau_{\text{mol}}+\tau_{\text{ion}}}\,. \qquad (2)$$

Then

$$S=S_{\text{mol}}(1-\alpha)\,. \qquad (3)$$

Since the changes in concentration will alter the degrees of the dissociation, the resonance frequency should be concentration dependent.

We have found the magnetic resonance to be concentration dependent in aqueous solutions of some strong acids and obtained results which may be correlated with the dissociation of the electrolyte.

§ 2. The Experimental Procedure

Apparatus and Procedure

Fig. 1 is a block diagram of the experi-

---

* We are indebted to Dr. Gutowsky for sending us a copy of his article prior to publication.

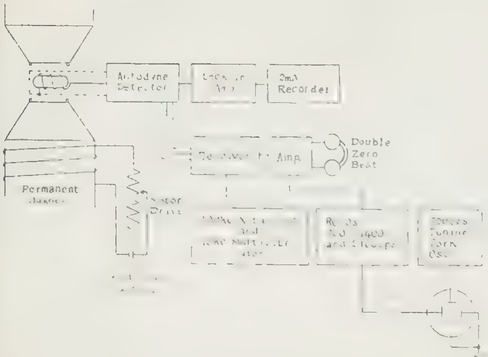

Fig. 1. Block diagram of experimental device.

mental arrangement. All the experiments were performed with a large permanent magnet made of 110 kgs. NKS–1 steel with a total weight of approximately 1,300 kg delivering 6,220 gauss. Each of the permanent magnets (① in Fig. 2), weighing 55 kgs., is a cylinder of 23 cm in diameter and 20 cm in length, and consists of ten bar magnets of NKS–1 arranged parallel to the directron of the magnetic field. The pole pieces (② in Fig. 2) were machined from low carbon iron with a 37° taper leading from the 25 cm-diameter to the pole face, which is finished below 0.01 mm and kept parallel to the another by three distant pieces (③ in Fig. 2) of non-magnetic steel, 3 cm in length. Ring shims of Rose type (④ in Fig. 2), 2.5 mm in height and 1.5 mm in width, are attached to the pole faces fixed by magnetic force. The frame of the magnet is 970 cm by 860 cm in its outside dimensions, and 25 cm thick of low carbon iron.

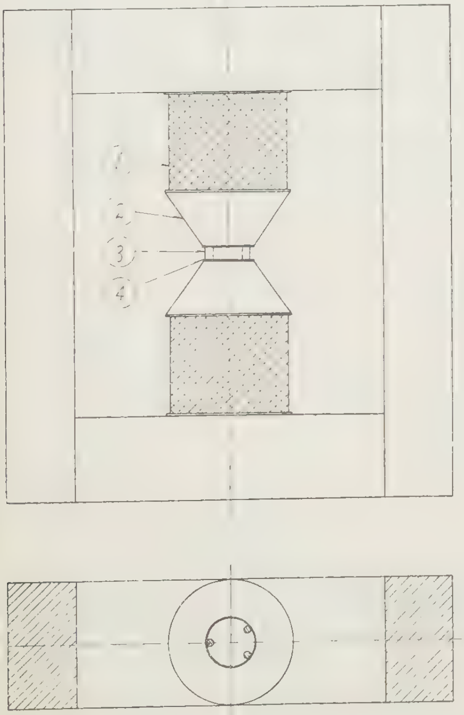

Fig. 2. Permanent magnet.

The assembly was magnetized by passing approximately 160 amperes through a total of 4,000 turns of 3.2 mm copper wire about the NKS–1 poles. It was magnetized to saturation.

The magnetic field distribution is almost circular in the meridian plane. The measured variation of the magnetic field along a horizontal line passing through the center of the gap amounts to 0.012, 0.06, and 0.18 gauss at diameters of about 1, 2, and 3 cm, respectively. The field appears to be homogeneous within 0.05 gauss over the sample, (10 mm in diameter and 12 mm in length) at the center of the gap. Further attempts of improving the field homogeneity have not been done.

The magnetic field is biased linearly by a pair of coils with one milliampere producing a change in field of 0.269±0.010 gauss.

The spectroscope used was an authodyne detector[3]. To investigate the concentration shifts in N^{14}, Cl^{35}, Br^{81}, and I^{127}, the autodyne detector at fixed radiofrequencies of 1,920, 2,598, 7,140, and 5,290 kcs., respectively, corresponding to a field of 6,221 gauss, was employed, and a sweeping magnetic field was superposed upon the permanent field. However, hysteresis of one twentieth of a gauss results when large currents are applied first in one direction and then reversed. All the measurements were made at an identical position in the magnetic field, at room temperature.

The chemical shifts were measured as

$$S=(H_{\text{sample}}-H_{\text{ref}})/H_{\text{ref}}\times 10^5 ,$$

where H_{ref} and H_{sample} are the applied magnetic fields required for resonance, at fixed frequency, of nuclei in the reference sample which showed no concentration dependence and in the solutions, respectively. In these experiments the maximum experimental error in S was about ±0.3.

Materials

The nitric acid samples were obtained by diluting anhydrous nitric acid which had been prepared by vacuum distillation from a sulphuric acid solution. Titration with sodium hydroxide solution gave values of 100 percent.

For the preparation of anhydrous perchloric acid the distillation was performed under the following conditions.[4] A mixture of 40 ml. chilled sulphuric acid and 10 ml. of chilled perchloric acid (60%) was sealed in a distilling flask and distilled at about 58° in the vacuum of an oil pump. In a period of 3 hours, approximately 5 ml. of colorless anhydrous acid was collected in a receiver cooled by means of dry ice. The samples were obtained by diluting the anhydrous perchloric acid.

The hydrochloric acid samples were obtained by diluting the saturated solution at 15°C which was prepared by passing gaseous HCl through commercial hydrochloric acid.

The hydrobromic acid samples were obtained by diluting the chemically pure acid of the highest concentration commercially obtainable.

Hydroiodic acid is quite rapidly decomposed to I_3^- ion becoming reddish colored, and a slightly colored sample does not show magnetic resonance. To obtain colorless samples we adopted the following procedure. Hydrogen sulphide gas prepared from pyrites and hydrochloric acid was passed through commercial, colored hydroiodic acid (S.G. = 1.48). After an hour the sample became transparent by the reaction $I_2+H_2S=2HI+S$. Removing the free sulphur by filtration, H_2S was passed again through the sample for half an hour and finally we got the sample slightly colored yellow, perhaps owing to colloidal sulphur not removed by filtration. The concentration was determined to be 5.0 Normal according to the Mohr titration. The sample contained a small quantity of H_2S gas and this is of use to prevent the oxidation of HI. The measurements of the chemical shift were performed soon after the preparation of the samples.

§ 3. Results and Discussions

Nitric Acid

The results observed for nitric acid are plotted against the concentration in moles per liter in Fig. 3, where the 0-origin was taken at the resonance position of $NaNO_3$ aq., which indicated no concentration dependence within experimental error. We obtained the chemical shift of the "molecular" nitric acid, $S_{mol}=5.2\pm0.3$. Using this value, Eq. (3) can be used to evaluate the apparent degrees of dissociation α from the S observed at intermediate concentrations.

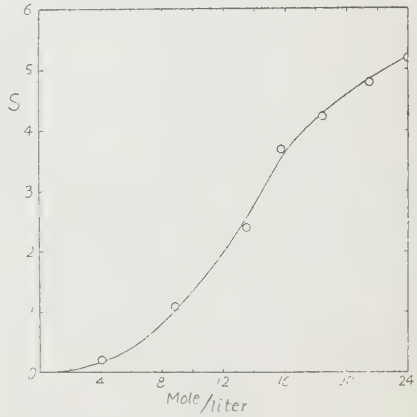

Fig. 3. Chemical shift of N^{14} magnetic resonance signals of HNO_3 dissolved in water from those of $NaNO_3$ aq.

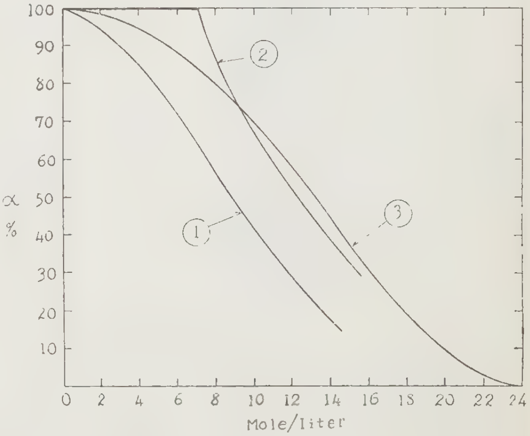

Fig. 4. Apparent degrees of dissociation of HNO_3 aq.

1 Redlich and Bigeleisen, Reference 6
2 Gutowsky and Saika, Reference 2
3 Masuda and Kanda, Reference 1.

Gutowsky and Saika[2] also obtained the degrees of dissociation of nitric acid from the measurement of the proton chemical shift of nitric acid.

Another criterion which can be used to distinguish sharply between molecules and interacting ions is a shift of vibration spectra.[5][6] Raman experiment distinguishes molecules and the dissociation products when their life times are much longer than the molecular vibration period, between 10^{-12} and 10^{-14} seconds, and separate Raman lines are obtained. In concentrated nitric acid, Raman lines corresponding to a nitrate ion and a nitric acid molecule appear. The presence of a shifted single line in N^{14} magnetic resonance and of the separate two lines in Raman experiment shows that the life times of the interacting ion and molecule are between 10^{-2} sec. (inverse frequency shift) and 10^{-12} sec. (molecular vibration period).

The degrees of dissociation of nitric acid versus its concentration obtained by three different experiments are plotted in Fig. 4 showing a qualitative agreement between them.

Perchloric Acid

The shifts are given in Fig. 5. The 0-origin was taken at the Cl^{35} resonance position of $NaClO_4$ dil. aq. which showed no concentration dependence within experimental error. The most concentrated acid commercially obtained (60% or 9.2 moles per liter) is almost completely ionized and the degrees of dissociation is much greater than that of nitric acid.

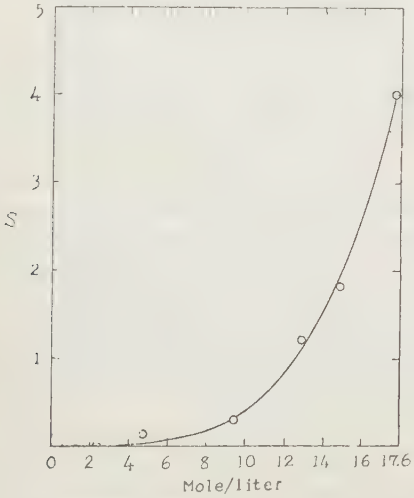

Fig. 5. Chemical shift of Cl^{35} nuclear magnetic resonance signals of $HClO_4$ dissolved in water from those of $NaClO_4$ aq.

We obtained the chemical shift of anhydrous perchloric acid, $S_{mol}=4.0\pm0.3$. Inserting this value into Eq. (3), we can determine the apparent degrees of dissociation α from the S observed at intermediate concentrations. The values computed in this manner are listed in Table I. Gutowsky's experiment[2] showed also the existence of the undissociated molecules.

Table I. Apparent degrees of dissociation of $HClO_4$

Concentration %	Normality	S	α
21	2.3	0	1.00
37	4.7	0.05	0.99
60	9.2	0.30	0.92
78	12.8	1.22	0.72
84	14.8	1.87	0.49

The Raman spectrum of perchloric acid furnishes a fairly general and unambiguous criterion of the existence of molecules, also.[4] Apparent degrees of dissociation obtained from the Raman experiment and from the present study are compared in Fig. 7.

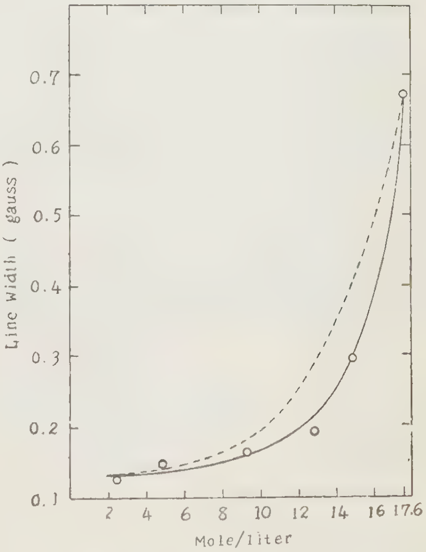

Fig. 6. Resonance line width of $HClO_4$ aq. Circles are experimental points, dotted line is theoretical curve.

The observed line width varies from 0.12 gauss in extreme dilute solution to 0.67 gauss in 100% $HClO_4$ as shown in Fig. 6. In the mixed state of ClO_4^- and $HClO_4$, if their spin-spin relaxation times are assumed to be the same as in extreme dilute solution, $(T_2)_{ion}$, and in 100% $HClO_4$, $(T_2)_{mol}$, respectively, the line width is given by the weighted mean,

$$\frac{1}{T_2}=\alpha\left(\frac{1}{T_2}\right)_{ion}+(1-\alpha)\left(\frac{1}{T_2}\right)_{mol}. \quad (4)$$

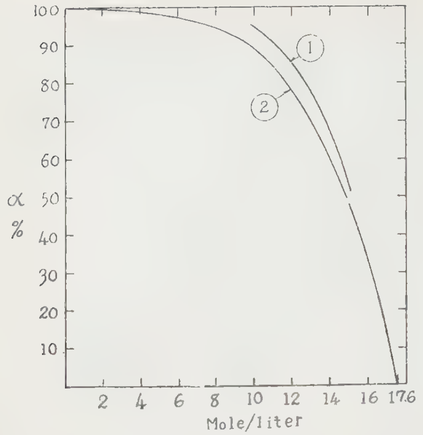

Fig. 7. Apparent degrees of dissociation of $HClO_4$ aq.
1 Redlich, Holt, and Bigeleisen, Reference 4
2 This research.

Eq. (20) of Gutowsky and Saika[2] leads to the same formula. The line width calculated from this formula using the α values obtained from the shift is plotted in Fig. 6 by a dotted line. The discrepancies between theory and experiment are much greater than the experimental errors and this fact shows us that $(T_2)_{\mathrm{ion}}$ and $(T_2)_{\mathrm{mol}}$ depend upon the concentration appreciably.

Hydrochloric Acid

The S values observed are plotted against the concentration up to the saturated solution at 15°C, in Fig. 8, where the 0-origin was taken at the Cl^{35} resonance position of NaCl aq. which showed no concentration dependence. There are chemical shifts proportional to the concentration of the hydrochloric acid. Therefore, we may point out the appearance of the undissociated molecule.

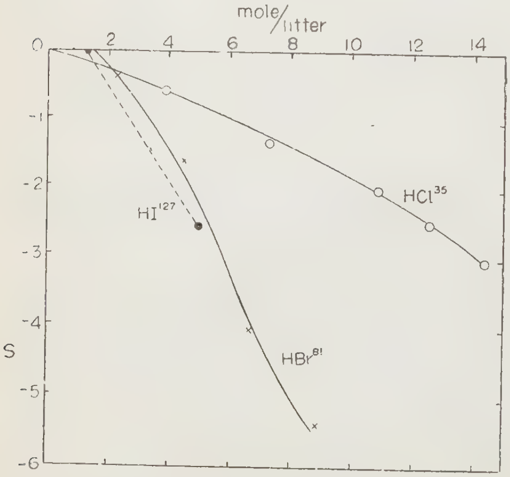

Fig. 8. Chemical shifts of Cl^{35}, Br^{81}, and I^{127} magnetic resonance signals of HCl, HBr and HI solutions from those of NaCl, NaBr and and KI solutions, respectively.

In the Raman data on HCl at concentrations greater than 9 normal, a diffuse Raman line appears at 2,630 cm^{-1} characteristic of molecular HCl showing the existence of an appreciable amount of undissociated molecules HCl.[7] But from our experiment, for the reason stated below, these undissociated molecules can not be regarded as HCl molecules. A recent experiment of pure nuclear quadrupole resonance showed that the Cl^{35} quadrupole resonance frequency in solid HCl is about 26.5 Mc.[8] Spin lattice relaxation time T_1 due to quadrupole coupling was given by N. Bloembergen,[9]

$$\frac{1}{T_1}=\frac{1}{4}\,\frac{e^2Q^2}{\hbar}\,\frac{\tau_c}{1+16\pi^2\nu^2\tau_c^2}\left\{\overline{\left(\frac{\partial E_x}{\partial x}\right)^2}+\overline{\left(\frac{\partial E_y}{\partial y}\right)^2}+\frac{1}{4}\overline{\left(\frac{\partial E_x}{\partial y}+\frac{\partial E_y}{\partial x}\right)^2}\right\}$$
$$+\frac{1}{16}\,\frac{e^2Q^2}{\hbar}\,\frac{\tau_c}{1+4\pi^2\nu^2\tau_c^2}\times\left\{\frac{1}{4}\overline{\left(\frac{\partial E_x}{\partial z}+\frac{\partial E_z}{\partial x}\right)^2}+\frac{1}{4}\overline{\left(\frac{\partial E_y}{\partial z}+\frac{\partial E_z}{\partial y}\right)^2}\right\}. \qquad (5)$$

A rough estimate using this formulas and Meal and Allen's data gives a resonance line width of 15 kc. for pure liquid hydrogen chloride. In the most concentrated HCl solution (14.3N), if the degree of dissociation is assumed to be 80% the resonance width would be 3 kc. which entirely disagrees with our experiment (0.15 kc.). Undissociated molecules in concentrated solution may not be HCl molecules but certain molecules having quadrupole coupling much smaller than HCl. On the other hand, Gutowsky and Saika[2] showed that HCl solution is completely dissociated up to 12N. To interpret, without contradiction, the results of the three experiments, first the complete dissociation by Gutowsky and Saika, secondly the existence of the undissociated molecules by the Raman experiment and thirdly our result indicating the existence of undissociated molecules having small quadrupole coupling, we assume the undissociated molecules to be ion pairs $(H_3O)^+Cl^-$. Cl^- in this ion pair is assumed to be in such a state different from the free ion Cl^- that it suffers a chemical shift and small quadrupole coupling. The protons in this ion pair keep a nearly equivalent state to the free hydronium ion H_3O^+ and so will not show a chemical shift. Concerning this problem, further evidences are expected.

Hydrobromic Acid and Hydroiodic Acid

The shifts are plotted in Fig. 8, where the 0-origin was taken at the resonance positions of Br^{81} in NaBr aq. and of I^{127} in KI aq., respectively, each indicating no concentration dependence. HBr and HI show the chemical shifts similar to HCl in character (H is decreasing for increasing concentrations) indicating that the undissociated molecules in these solutions are alike. For HI, the results are not so precise as for HCl and HBr owing to the large line width (Fig. 9) and to the chemical instability of the sample.

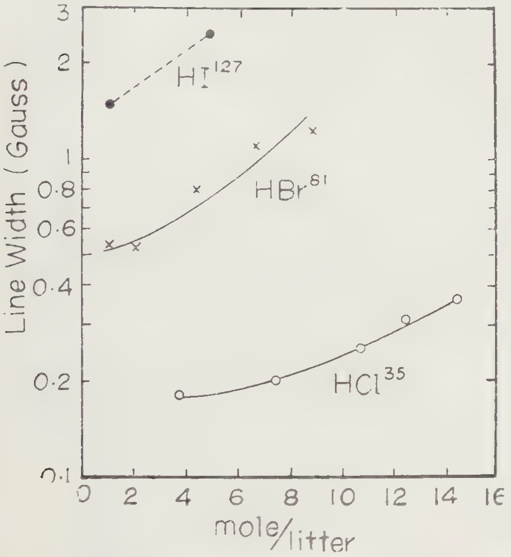

Fig. 9. Line width of Cl^{35}, Br^{81}, and I^{127} magnetic resonances in HCl, HBr and HI solutions, respectively.

In conclusion, we wish to express our appreciation to Dr. Y. Inoue and Y. Kitano of the Department of Chemistry, Kobe University, for the preparation and the chemical analysis of all the samples in the present study. This work has been supported in part by the Scientific Research Expenditure of the Ministry of Education.

References

1) Y. Masuda and T. Kanda: J. Phys. Soc. Japan **8** (1953) 432.

2) H. S. Gutowsky and A. Saika: J. Chem. Phys. **21** (1953) 1688.

3) N. J. Hopkins: Rev. Sci. Instr. **20** (1949) 401.

4) O. Redlich, E. K. Holt and J. Bigeleisen: J. Am. Chem. Soc. **66** (1944) 13.

5) J. H. Hibben: "The Raman Effect and its Chemical Applications", Reinhold Pub. Co., N. Y., (1939), p. 365. H. S. Harned and B. B. Owen: "The Physical Chemistry of Electrolytic Solutions", Reinhold Pub. Co., N. Y., (1950), p. 609.

6) O. Redlich and J. Bigeleisen: J. Am. Chem. Soc. **65** (1943) 1883.

7) L. Ochs, J. Guéron and M. Magat: J. Phys. Rad. **1** (1940) 85.

8) H. C. Meal and H. C. Allen: Phys. Rev. **90** (1953) 348.

9) N. Bloembergen: Nuclear Magnetic Relaxation, Thesis, Leiden (1948).

JOURNAL OF THE PHYSICAL SOCIETY OF JAPAN Vol. 9, No. 1, JAN.—FEB., 1954

On the Excitation of Oscillations in a Thermal Plasma

By Masao SUMI

Electrical Communication Laboratory, Tokyo

(Received October 9, 1953)

In an ionized gas neutrized on the average plasma oscillations are considered for an arbitrary distribution of electron beams. Under the assumption of small signal and of the absence of any static fields, the fundamental equations are derived in one-dimensional treatment. The dispersion relation obtained from the fundamental equations is found to describe the behavior of propagation of localized initial disturbances with electron beams. It is applied to the case of excitation of thermal plasma by an injected electron beam and the rate of wave growth is obtained. The numerical results are compared with the circumstances corresponding to the investigation by Merrill and Webb. Abrupt scattering of electron beam observed may be ascribed to the excitation of plasma oscillations.

§ 1. Introduction

Relating to the problems of gaseous discharge tubes and solar enhanced noise, the excitation of plasma with Maxwellian distribution of electron velocity have been treated by several authors1)−4). In particular the excitation of thermal plasma by an injected uniform homogeneous beam has been discussed by Feinstein and Sen3). They employed, as model of thermal plasma, first sharp cutoff distribution of electron velocity and second a Maxwellian velocity distribution. In the latter case, however, questionable is the approximation which they employed for the integration including the Maxwellian distribution function. Furthermore in both cases the ranges over which wave growth can exist was shown in figures. but the magnitude of the rate of wave growth itself was not provided. In this paper the dispersion relation is separated into real and imaginary parts for the complex frequency and the integration including the Maxwellian distribution function can be carried out with use of appropriate approximations. Then the magnitude of the rate of wave growth is given as a function of several parameters. In the later section this will be applied to the problem of electron scattering by the plasma oscillations.

§ 2. Fundamental Equations

In an ionized gas containg a suitably high density of electrons and positive ions, it is assumed that the medium is uniformly smeared-out by the positive charge of ions and is neutrized by the time-averaged negative charge of electrons. Therefore, the total stationary space charge is always absent ; that is, $\rho_0^+ + \rho_0 = 0$, where ρ_0^+ and ρ_0 represents the stationary density of positive ions and that of electrons respectively. Thus the density of total charge becomes equal to the oscillating density of electrons ρ, and hence no electrostatic field is considered to be present.

Let a distribution function of electron velocity be $f(\boldsymbol{v}, \boldsymbol{x}, t)$ which can written as

$$f(\boldsymbol{v},\boldsymbol{x},t) = f_0(\boldsymbol{v},\boldsymbol{x},t) + f_1(\boldsymbol{v},\boldsymbol{x},t) ,$$

where f_0 and f_1 correspond to the stationary and oscillating part respectively. In terms of these functions the densities and current of electrons can be represented as follows

$$\rho_0(\boldsymbol{x}) = -e\int f_0(\boldsymbol{v},\boldsymbol{x})d\boldsymbol{v} ,$$

$$\rho(\boldsymbol{x},t) = -e\int f_1(\boldsymbol{v},\boldsymbol{x},t)d\boldsymbol{v} ,$$

$$\boldsymbol{J} = \boldsymbol{J}_0 + \boldsymbol{J}_1 = -e\int \boldsymbol{v} f_0(\boldsymbol{v},\boldsymbol{x})d\boldsymbol{v} - e\int \boldsymbol{v} f_1(\boldsymbol{v},\boldsymbol{x},t)d\boldsymbol{v} ,$$

where $-e$ is charge of an electron and $d\boldsymbol{v} = dv_x dv_y dv_z$.

The distribution function $f(\boldsymbol{v},\boldsymbol{x},t)$ changes with time in accordance with the Boltzmann equation

$$\frac{\partial f}{\partial t} + \boldsymbol{v}\nabla f - \frac{e}{m}[\boldsymbol{E} + \mu_0(\boldsymbol{v}\times\boldsymbol{H})]\frac{\partial f}{\partial \boldsymbol{v}} = \left(\frac{\delta f}{\delta t}\right)_{\text{coll}} , \tag{1}$$

where μ_0 is the permeability of vacuum* and $(\delta f/\delta t)_{\text{coll}}$ the rate of change of f by interparticle collisions. In general the electromagnetic fields E and H satisfy Maxwell's equations, but, since we are only concerned with the longitudinal wave in one-dimension throughout this paper, the field can be represented by the electric field only satisfying the Poisson Equation

---

* Throughout this article we use the rationalized m.k.s. system of units.

$$\nabla\cdot E=\frac{1}{\varepsilon_0}\rho\ , \tag{2}$$

where ε_0 is the permittivity of vacuum. It will be assumed in Eq. (1) that the function f_0 is uniform in space and the collisional term on the right hand side $(\partial f/\partial t)_{\mathrm{coll}}$ will be neglected. If the static magnetic field is taken in the same direction as those of electron-flows and wave propagations, it does not affect on the oscillatory behaviour of the system. In this case, therefore, the static magnetic field is not needed to be taken into consideration. Furthermore the oscillating parts of equations are linearized under the assumption that one is concerned with only small amplitude oscillations, so that terms quadratic in f, E, and H are neglected. (Hereater all the oscillatory parts of the quantities concerned are denoted by the letters without suffices, e.g., f, E and H.)

The linearized Boltzmann equation becomes, in absence of collisions,

$$\frac{\partial f}{\partial t}+\nu\nabla f-\frac{e}{m}E\frac{\partial f_0}{\partial \nu}=0\ . \tag{3}$$

If all the quantities are considered to be one-dimensional, then Eqs. (2) and (3) reduce to

$$\frac{\partial E}{\partial x}=-\frac{e}{\varepsilon_0}\int_{-\infty}^{\infty}f(u,x,t)\,du\ , \tag{4}$$

$$\left(\frac{\partial}{\partial t}+u\frac{\partial}{\partial x}\right)f-\frac{e}{m}E\frac{df_0}{du}=0 \tag{5}$$

where u is the x-component of electron velocity and E the longitudinal component of the electric field. Eqs. (4) and (5) can be used as the fundamental equations in this case.

§ 3. Dispersion Relation

In an infinite medium a dispersion relation can be obtained by taking that f and E have the space-time factor $\exp i(\omega t-kx)$. The dispersion relation $D(k,\omega)=0$ thus obtained from the fundmental equations is solved for ω as a function of k or inversely for k as a function of ω. The former solution corresponds to that for the spatial initial condition extending to infinity and the disturbance considered is always of the standing-wave form. The latter corresponds to a steady state solution for the temporal boundary condition and the space charge wave is amplified as it is conveyed in space. In an actual case, on the other hand, the spatial initial disturbance is confined within a finite region. How the disturbance localized in a small region can be propagated through the medium may be seen by solving Eqs. (4) and (5) by means of Laplace transform method. Twiss⁵⁾ has discuscussed the case of propagation through double beams. It has been analysed that the disturbance localized in a bounded region at an initial instant is propagated with the flow of space charge and is seen to be amplified exponentially with time due to the mutual interaction of beams. The propagation in this case can be described by a solution of the dispersion equation for ω as a function of real k.

In order to obtain the dispersion relation connecting ω and k, let E and f be proportional to $\exp i(\omega t-kx)$. Then the fundamental equations (4) and (5) can be written as

$$i(\omega-uk)f-\frac{e}{m}E\frac{df_0}{du}=0\ , \tag{6}$$

$$ikE=\frac{e}{\varepsilon_0}\int_{-\infty}^{\infty}f\,du\ . \tag{7}$$

From (6) we get $f=(e/m)E(df_0/du)/i(\omega-uk)$ which is substituted into (7). Then (7) becomes

$$\left\{k+\frac{e^2}{m\varepsilon_0}\int_{-\infty}^{\infty}\frac{1}{(\omega-uk)}\frac{df_0}{du}du\right\}E=0\ . \tag{8}$$

Consequently, for non-vanishing field the sum in the parenthesis in (8) must be equal to zero and it gives the dispersion relation required:

$$D(k,\omega)=k+\frac{e^2}{m\varepsilon_0}\int_{-\infty}^{\infty}\frac{1}{(\omega-uk)}\frac{df_0}{du}du=0\ . \tag{9}$$

Hence if the steady distribution function f_0 is given, the relation between ω and k is determined from (9).

§ 4. Excitation of Plasma by an Injected Beam

We consider the case where a homogeneous beam of electron density n_1 is injected with uniform velocity u_1 into a plasma of density n_p with Maxwellian velocity distribution of electrons. The steady distribution function f_0 in this case is given by

$$f_0(u)=\{n_1\delta(u-u_1)+n_p(m/2\pi\kappa T)^{1/2} \times\exp\,(-mu^2/2\kappa T)\}\,, \qquad (10)$$

where δ is the usual delta function and κ is the Boltzmann constant. When (10) is inserted into (9), the following characteristics of δ-function is used :

$$\int_{-\infty}^{\infty} g(u)\frac{d}{du}\delta(u-a)du=-\left[\frac{d}{du}g(u)\right]_{u=a}.$$

Then we get from (9) after simple calculations,

$$\frac{\omega_1{}^2}{(\omega-u_1k)^2}-\frac{m}{\kappa T}\left(\frac{\omega_p}{k}\right)^2+\frac{1}{\sqrt{2\pi}}\left(\frac{m}{\kappa T}\right)^{3/2} \times\left(\frac{\omega_p}{k}\right)^2\int_{-\infty}^{\infty}\frac{\omega}{\omega-uk}e^{-\frac{mu^2}{2\kappa T}}du=1\,, \qquad (11)$$

where $\omega_1{}^2=n_1e^2/m\varepsilon_0$ and $\omega_p{}^2=n_pe^2/m\varepsilon_0$. In (11) suppose k as real and ω as complex. If we put $\omega=\omega_0+i\sigma$, then we can divide (11) into real and imaginary parts. The real part yields

$$1+\frac{m}{\kappa T}\left(\frac{\omega_p}{k}\right)^2=\frac{\{(\omega_0-u_1k)^2-\sigma^2\}\omega_1{}^2}{\{(\omega_0-u_1k)^2+\sigma^2\}^2} +\frac{1}{\sqrt{2\pi}}\left(\frac{m}{\kappa T}\right)^{3/2}\left(\frac{\omega_p}{k}\right)^2\int_{-\infty}^{\infty}\frac{\omega_0(\omega_0-uk)+\sigma^2}{(\omega_0-uk)^2+\sigma^2} \times e^{-\frac{mu^2}{2\kappa T}}du\,, \qquad (12)$$

while imaginary part yields

$$0=\frac{2(\omega_0-u_1k)\omega_1{}^2}{\{(\omega_0-u_1k)^2+\sigma^2\}^2}+\frac{1}{\sqrt{2\pi}}\left(\frac{m}{\kappa T}\right)^{3/2}\left(\frac{\omega_p}{k}\right)^2 \times\int_{-\infty}^{\infty}\frac{uk}{(\omega_0-uk)^2+\sigma^2}e^{-\frac{mu^2}{2kT}}du\,. \qquad (13)$$

Integrations appeared in the right hand sides of (12) and (13) can be carried out approximately if the following condition is satisfied

$$4\frac{|\sigma|}{\omega_0}\frac{m}{2\kappa T}\left(\frac{\omega^0}{k}\right)^2\lesssim 1\,. \qquad (14)$$

(14) is obtained when the gaussian function in the intergrands does not change appreciably in the domain where other factors in the integrands have main contributions. Then integrations appeared in (12) and (13) can be approximated as follows respectively :

$$\int_{-\infty}^{\infty}\frac{\omega_0(\omega_0-uk)+\sigma^2}{(\omega_0-uk)^2+\sigma^2}e^{-\frac{mu^2}{2\kappa T}}du\doteqdot\frac{\pi\sigma}{k}e^{-\frac{m\omega_0{}^2}{2\kappa Tk^2}}\,, \qquad (15)$$

and

$$\int_{-\infty}^{\infty}\frac{uk}{(\omega_0-uk)^2+\sigma^2}e^{-\frac{mu^2}{2kT}}du\doteqdot\frac{\pi\omega_0}{\sigma k}e^{-\frac{m\omega_0{}^2}{2\kappa T^2k^2}}\,, \qquad (16)$$

Furthermore assuming $|\sigma|/\omega_0\ll 1$, the quantities higher than the second order of $|\sigma|/\omega_0$ can be neglected. As a result, we get from (13)

$$\frac{\sigma}{\omega_0}=\sqrt{\pi}\left(\frac{m}{2\kappa T}\right)^{3/2}\left(\frac{\omega_p}{\omega_1}\right)^2\left(u_1-\frac{\omega_0}{k}\right)^3e^{-\frac{m\omega_0{}^2}{2\kappa Tk^2}}\,, \qquad (17)$$

and from (12) we obtain

$$1+\frac{m}{2\kappa T}\left(\frac{\omega_p}{\omega_1}\right)^2\doteqdot\frac{\omega_1{}^2}{(\omega_0-u_1k)^2}\,, \qquad (18)$$

since with use of (17) the second term in the right hand side of (12) is found to be of higher order for σ/ω_0. For an growing wave σ must take a negative value, and it is seen from (17) $u_1-\omega_0/k$ must also be negative since ω_0 is taken as positive. Furthermore the value of k is needed to be positive so that the growing wave is found to be propagated in the beam direction. If u_0 is defined as the absolute value of $(u_1-\omega_0/k)$;

$$u_0\equiv|u_1-\omega_0/k|\,, \qquad (19)$$

we get from (18) ,

$$u_0=\left[\frac{(\omega_1/\omega_0)^2(\omega_0/k)^2}{1+(m/\kappa T)(\omega_0/k)^2(\omega_p/\omega_0)^2}\right]^{\frac{1}{2}}. \qquad (20)$$

When the mean square speed for a one-dimensional distribution, $2\kappa T/m$, is denoted by $v_0{}^2$ and when the relation (20) is taken into account, (17) can be written as

$$\frac{\sigma}{\omega_0}=-\sqrt{\pi}\left(\frac{\omega_p}{\omega_1}\right)^2\left(\frac{u_1}{v_0}\right)^3\left(\frac{u_0}{u_1}\right)^3e^{-\left(\frac{u_1}{v_0}\right)^2\left(1+\frac{u_0}{u_1}\right)^2}. \qquad (21)$$

The relation (20) which gives u_0 is then rewritten in the form

$$\left(\frac{\omega_1}{\omega_0}\right)^2\left[\left(\frac{u_1}{u_0}\right)^2-2\left(\frac{\omega_p}{\omega_1}\right)^2\left(\frac{u_1}{v_0}\right)^2\right]=\left(1+\frac{u_0}{u_1}\right)^{-2}. \qquad (22)$$

The condition (14) under which the approximation is valid becomes

$$4\frac{|\sigma|}{\omega_0}\left(\frac{u_1}{v_0}\right)^2\left(1+\frac{u_0}{u_1}\right)^2\lesssim 1\,. \qquad (23)$$

If (21) and (22) are compatible under the condition of (23) it is concluded that the growing wave can exist in the beam direction and the wave phase velocity $\omega_0/k=u_0+u_1$ is greater than the velocity of injected uniform beam u_1.

To get the value of σ/ω_0, it is necessary first to solve Eq. (22) for u_0/u_1. Denoting ω_0/ω_1 and $[2(\omega_p/\omega_1)^2(u_1/v_0)^2]^{-1/2}$ as a and b respectively, u_0/u_1 can be obtained from the intersecting points of two groups of curves with parameters a and b; $y=a^2/(1+x)^2$ and $y=(1/x)^2-(1/b)^2$ where $x=u_0/u_1$. They are drawn in Fig. 1 and abscissas of intersecting points indicate the needed values of u_0/u_1 corresponding to two parameters a and b. For the values of a smaller than 1, u_0/u_1 are a little smaller than the corresponding values of b. The larger the values as a become, the more the required values of u_0/u_1 are reduced. For the values of b much smaller than 1 the needed values of u_0/u_1 are little changed with the variation of a. As mentioned in the previous section, $(1+u_0/u_1)$ is the ratio of the wave phase velocity (u_0+u_1) to the injected beam velocity u_1 and is greater than 1 in these cases.

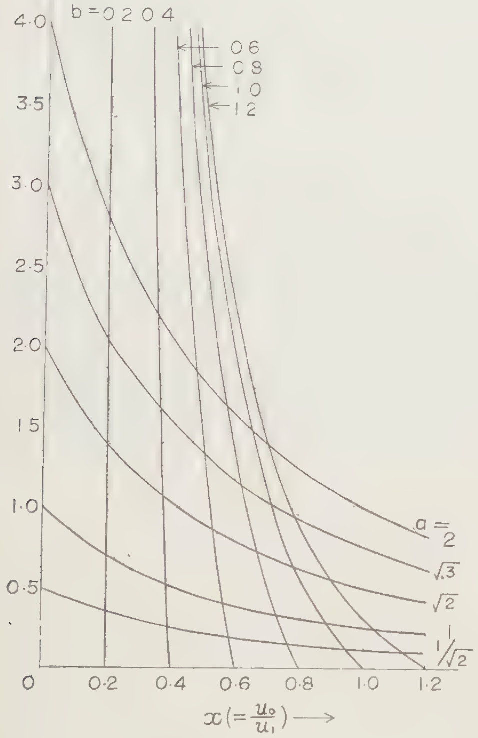

Fig. 1. Two groups of curves; $y=a^2/(1+x)^2$ and $y=(1/x^2)-(1/b)^2$. The needed values of x correspond to the intersecting points of two curves. $(1+x)$ means the ratio of the wave phase velocity to the injected beam velocity.

The formula (21), the ratio of wave growth rate σ to oscillating frequency ω_0, is expressed in terms of three parameters: e.g., ω_1/ω_p, u_1/v_0 and u_0/u_1. In Fig. 2, $|\sigma|/\omega_0$ is plotted against ω_1/ω_p for the value of ω_0/ω_1 and for the values of parameter b from 0.2 to 1.2. The value of $|\sigma|/\omega_0$ grows up from zero at $\omega_1/\omega_p=0$, reaches its maximum at $\omega_1/\omega_p=b/(1+u_0/u_1)$ and beyond the maximum it decreases rather rapidly with the increasing values of ω_1/ω_p. The maximum value of $|\sigma|/\omega_0$ increases gradually with the increasing value of b. It is readily seen that even for the values of b below 0.2 or beyond 1.2, $|\sigma|/\omega_0$ is found to have as similar tendency as in Fig. 2.

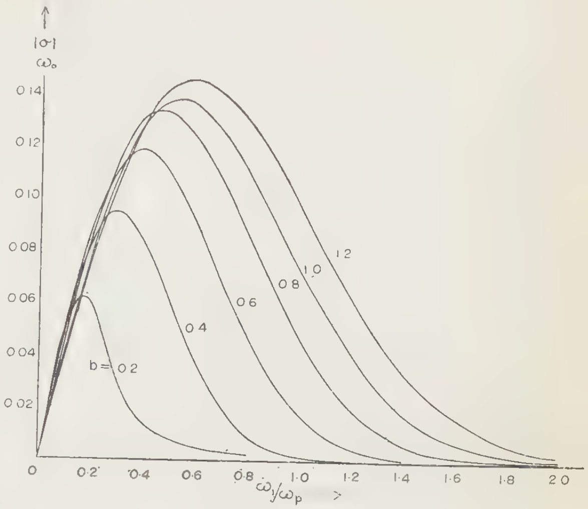

Fig. 2. The ratio of wave growth rate to oscillating frequency, $|\sigma|/\omega_0$, as a function of ω_1/ω_p for different values of b.

§ 5. Discussions

In the preceding section we have discussed the rate of wave growth in a plasma injected by an electron beam under various conditions.

In this section we shall compare the results obtained thus far with the investigation by Merrill and Webb[6]. Electron beams injected into a plasma has long been known to be scattered much more rapidly than can be accounted for collisions with other particles. It has already been suggested that plasma oscillations causes such a rapid scattering. We shall give an explanation of abrupt scattering, such that in a plasma injected by an electron beam a localized disturbance builds up to large amplitude as it proceeds in a medium and the oscillations thus growing up causes the scattering of beams in a sharply narrow region.

In an investigation made by Merrill and Webb, it has been found that an electron beam of about 20 ev. energy near the cathode and of about 10^{10} electron concentration is scattered to have a uniform distribution of energy from zero to 30 ev. at a distance of about 4.3 mm to 6.1 mm from the cathode. Oscillations picked up was about 10^{10} r.p.s. and the electron temperature in the plasma about 30,000°K.

Corresponding to the experimental data, we get the following values: $\omega_p=1\times10^{10}$, $\omega_1=\omega_0=7.5\times10^9$, $(u_1/v_0)^2=0.8$. These leads to $a=1$, $b=0.6$ and $\omega_1/\omega_p=0.75$. This gives $|\sigma|=4.8\times10^8$ per second. The wave phase velocity $u=u_1(1+u_0/u_1)$ is found to be 4.0×10^6 meters per second. The time of wave growth is of the order of $1/|\sigma|$ and in the meanwhile the wave travels the distance $x=u/|\sigma|$ which becomes about 8 mm in this case. This implies that the disturbance localized initially in the vicinity of the cathode plane is propagated with the electron beam and it grows up to a large amplitude at a distance of about 8 mm from the cathode plane where electrons in the beam can be abruptly scattered. The distance thus calculated corresponds to that obtained from the experiment of Merrill and Weeb. Fairly good agreement of the distance seems to be satisfactory for the interpretation presented here.

§ 6. Conclusions and Summary

In an ionized gas neutrized on the average, the electromagnetic oscillations are considered in an arbitrary distribution of electron beams. The fundmental equations are derived in one-dimensional treatment under the assumption of small signal and in the absence of any static fields. The initial disturbance in a localized region can be found to be propagated with electron beam and to be amplified exponentially with time. The behaviours of propagation are described by the dispersion relation which connects wave frequency ω and propagation constant k.

This is applied to the case of the excitation of thermal plasma by an injected uniform beam. From the dispersion relation we can get the rate of wave growth as a function of several parameters specified by the characteristics of the plasma and the beam. The results thus obtained are compared with the investigation by Merrill and Webb. Fairly good agreement is attained as to the distance from the cathode where electron beam scattering takes place.

Finally the author is indebted to Mr. Y. Honda for computing and drawing the curves in figures.

References

1) D. Bohm and E. P. Gross: Phys. Rev. **75** (1949) 1864.
2) E. P. Gross: Phys. Rev. **82** (1951) 232.
3) J. Feinstein and H. K. Sen: Phys. Rev. **83** (1951) 405.
4) H. K. Sen: Phys. Rev. **88** (1952) 816.
5) R. Q. Twiss: Proc. Phys. Soc. **64** (1951) 654.
6) H. J. Merrill and H. W. Webb: Phys. Rev. **55** (1939) 1911.

JOURNAL OF THE PHYSICAL SOCIETY OF JAPAN Vol. 9, No. 1, JAN.—FEB., 1954

Hyperfine Structure of the Spectrum of Pr II

By Kiyoshi MURAKAWA and Shigeki SUWA

Institute of Science and Technology, Komaba-machi, Meguro-ku, Tokyo

(Received August 15, 1953)

Analysis of the hyperfine structure of the term $4f^3(^4I)6s$ of Pr II resulted $a(6s)=0.426\,\mathrm{cm}^{-1}$, $a_{4f}=0.0227\,\mathrm{cm}^{-1}$. From the value of $a(6s)$ the nuclear magnetic moment of Pr was deduced to be $\mu=+4.0$ n.m., in agreement with the value given in the literature. From the value of a_{4f} the screening constant σ of the $4f$ electron was deduced to be 32.9. The quadrupole moment of Pr was found to be $Q=(0.0\pm0.2)\times10^{-24}\,\mathrm{cm}^2$. This is in agreement with the value $Q=-0.05\times10^{-24}\,\mathrm{cm}^2$ calculated from the data published by Lew regarding the hyperfine structure of the ground term of Pr I.

§ 1. Introduction

The hyperfine structure (hfs) of the spectrum of Pr II was published by White[1] who took the photograph with a large grating and concluded the nuclear spin to be 5/2. Using atomic beam magnetic resonance method, Lew[2] analysed the hfs of the $4f^3\,{}^4I_{9/2}$ level of Pr I and deduced the nuclear magnetic moment to be $\mu=+3.8$ n.m. Using the data of White[1] and the value of a_{4f} published by Lew[2], Brix[3] deduced the value $\mu=+3.9\pm0.3$ n.m.

Since the hfs of the Pr II spectrum is a prototype of the hfs of rare-earth spectrum, it seemed worth while to photograph the Pr II spectrum with an instrument having a larger resolution than the grating of White and analyse the hfs more fully than Brix did. This is the purpose of the present work.

§ 2. Experimental Arrangement

The spectrum of Pr II was excited by a hollow cathode discharge tube, and the hfs was examined with a Fabry-Perot etalon.

Fig. 1 is a reproduction of some of the interference patterns of the spectrum of Pr II.

§ 3. Nuclear Magnetic Moment

The gross multiplet structure of Pr II was analysed by Rosen, Harrison and McNally[4]. Fig. 2 shows schematically the deepest terms of Pr II that arise from the configuration $4f^36s$. The Zeeman effect data published by the above-mentioned authors show that the terms $4f^3(^4I)6s\ {}^5I$ and ${}^3I$ are of Jj-coupling rather than LS-coupling.

Each of the strong lines of Pr II was found to consist of six components* having a flag pattern. This is to be expected when the J-values involved are sufficiently high. However, in order to know the hfs splitting of each level, some off-diagonal components must be detected, and this was met with success at least in the cases of λ4225 and λ4101. The hfs of these two lines are shown schematically in Fig. 3 and 4 respectively. When the J-values are larger than 13/2, the existing tables of hfs component intensities are useless, so the authors prepared a table[5] useful for larger J-values.

For other lines it was sometimes possible to detect off-diagonal components but difficult to measure them accurately. Table 1 gives the result of measurement of the lines other than λ4225 and λ4101. White's measurement is also listed as W for the sake of comparison.

Specially from the hfs of λ4225, we get for the level $4f^3(^4I_{9/2})6s\,{}^5I_4$:

$$A=-0.0100\,\mathrm{cm}^{-1}, \quad B=0.0\times10^{-6}\,\mathrm{cm}^{-1}.$$

All the hfs constants that can be deduced from Fig. 3 and Fig. 4 and Table I are summarized in Table II.

The level $4f^3(^4I_{15/2})6s\,{}^5I_8^0$ has a hfs constant independent of coupling and it is given by**

---

* Of course this refers to the number of diagonal components; there are more components when the off-diagonal components are taken into account.

** The same notations as those of Breit and Wills[6] are used here.

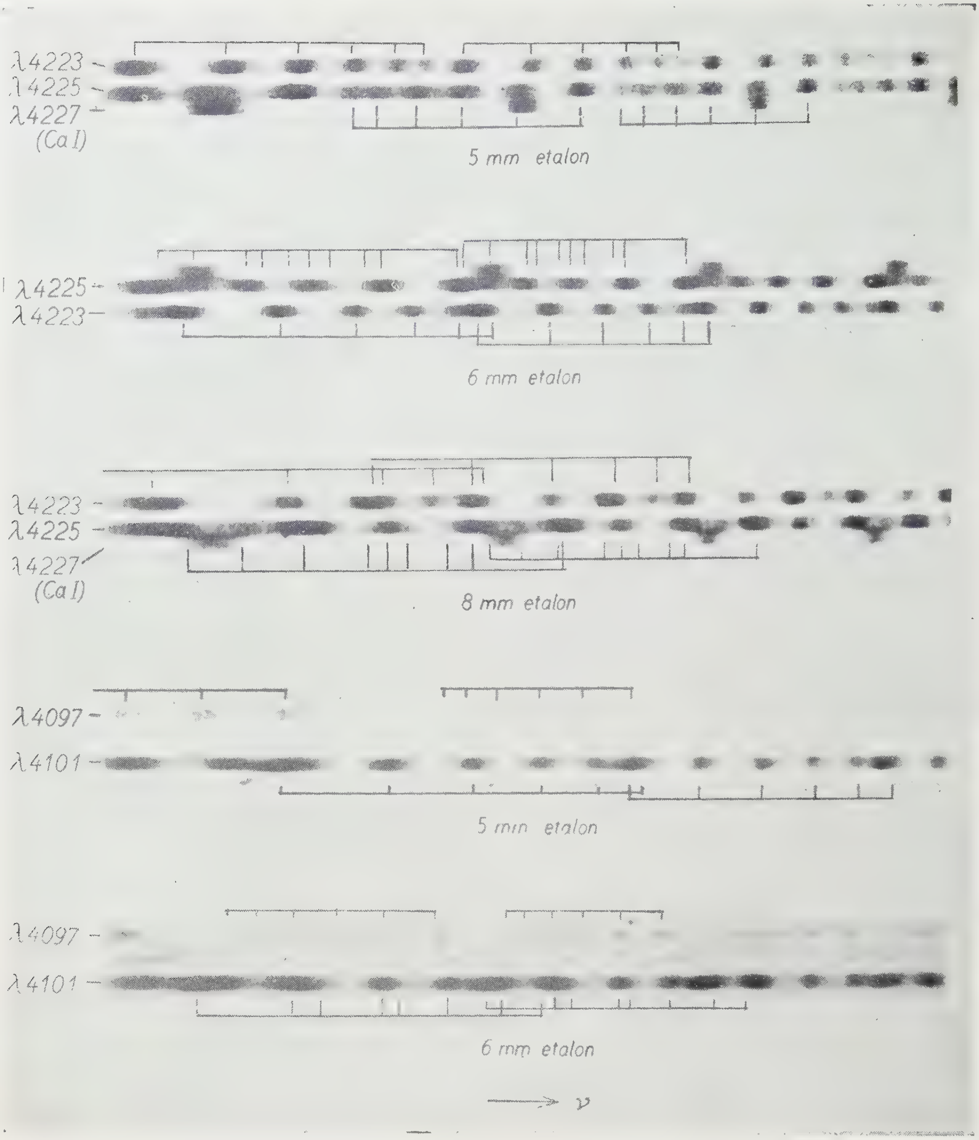

Fig. 1. Enlargement of some of the interference patterns of the spectrum of Pr II.

$$A({}^5I_8)=\frac{15}{16}A({}^4I_{15/2})+\frac{1}{16}a(s)\,,$$

$$A({}^4I_{15/2})=\frac{2}{15}\left(\frac{47}{7}a'+\frac{11}{14}a''+\frac{32}{7}a'''\right).\;*$$

As shown in Table III, the relativity corrections for the $4f$ electron can be neglected, so we can put

$$a'=\frac{16}{21}a_f\,,\quad a''=\frac{48}{35}a_f\,,\quad a'''=-\frac{1}{14}a_f\,.$$

We get, therefore,

$$A({}^4I_{15/2})=\frac{176}{15^2}a_f$$

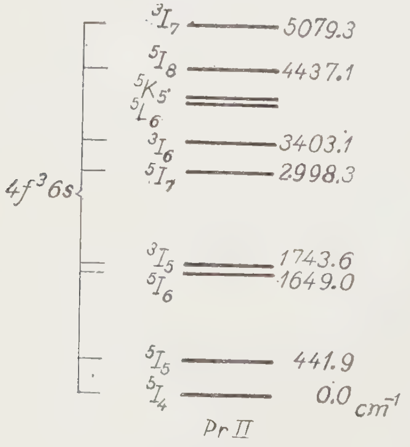

Fig. 2. Deepest levels of Pr II.

---

* The term $4f^3\,{}^4I$ is assumed to be of an LS-coupling.

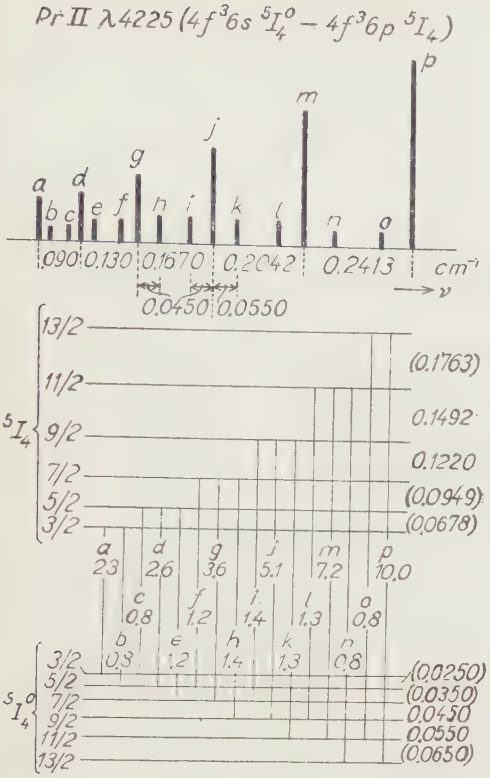
Pr II λ4225 (4f³6s ⁵I₄⁰ – 4f³6p ⁵I₄)
a b c d e f g h i j k l m n o p
.090 0.130 0.1670 0.2042 0.2413 cm⁻¹
→ ν
0.0450 0.0550
⁵I₄
13/2 11/2 9/2 7/2 5/2 3/2
(0.1763) 0.1492 0.1220 (0.0949) (0.0678)
a 2.3 d 2.6 g 3.6 j 5.1 m 7.2 p 10.0
c 0.8 f 1.2 i 1.4 l 1.3 o 0.8
b 0.3 e 1.2 h 1.4 k 1.3 n 0.8
⁵I₄⁰
3/2 5/2 7/2 9/2 11/2 13/2
(0.0250) (0.0350) 0.0450 0.0550 (0.0650)

Fig. 3. Hfs of the line Pr II λ4225.

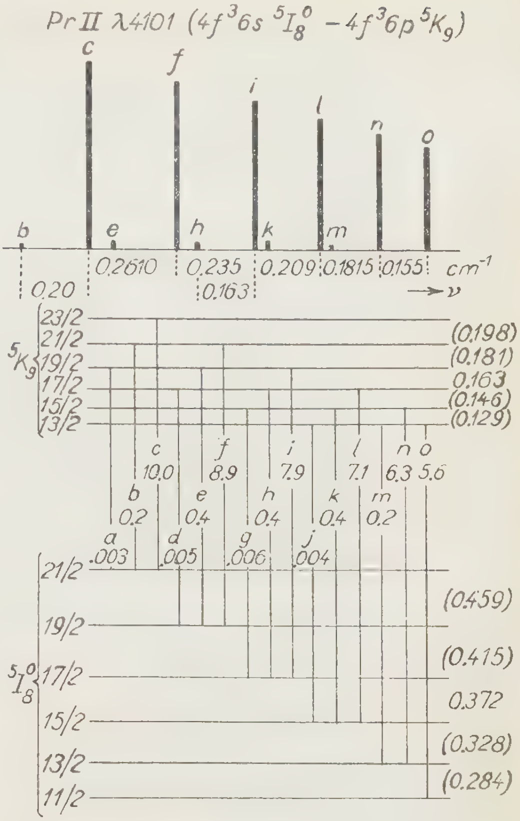
Pr II λ4101 (4f³6s ⁵I₈⁰ – 4f³6p ⁵K₉)
b c e f h i k l m n o
0.20 0.2610 0.235 0.163 0.209 0.1815 0.155 cm⁻¹
→ ν
⁵K₉
23/2 21/2 19/2 17/2 15/2 13/2
(0.198) (0.181) 0.163 (0.146) (0.129)
c 10.0 f 8.9 i 7.9 l 7.1 n 6.3 o 5.6
b 0.2 e 0.4 h 0.4 k 0.4 m 0.2
a .003 d .005 g .006 j .004
⁵I₈⁰
21/2 19/2 17/2 15/2 13/2 11/2
(0.459) (0.415) 0.372 (0.328) (0.284)

Fig. 4. Hfs of the line Pr II λ4101.

and consequently

$$A(^5I_8)=\frac{11}{15}\,a_f+\frac{1}{16}\,a(s)\ .$$

In a similar way we get

$$A(^5I_7)+A(^3I_7)=\frac{1306}{1575}a_f+\frac{1}{14}a(s)$$

$$+\frac{187}{225}a_f-\frac{1}{16}\,a(s)=1.66032\,a_f+\frac{1}{112}a(s)\ .$$

$$A(^5I_6)+A(^3I_6)=\frac{3730}{3861}a_f+\frac{1}{12}a(s)$$

$$+\frac{1306}{1365}a_f-\frac{1}{14}\,a(s)=1.92286\,a_f+\frac{1}{84}\,a(s)\ .$$

$$A(^5I_5)+A(^3I_5)=\frac{1428}{1210}a_f+\frac{1}{10}\,a(s)$$

$$+\frac{3730}{3267}a_f-\frac{1}{12}a(s)=2.3219\,a_f+\frac{1}{60}a(s)\ .$$

$$A(^5I_4)=\frac{476}{330}a_f-\frac{1}{10}a(s)\ .$$

From the values of A listed in Table II, fairly consistent values of $a(s)$ and a_f can be obtained:

$$a(6s)=0.426\ \text{cm}^{-1},\quad a_{4f}=0.0227\ \text{cm}^{-1}.$$

Table I. Measured hfs of the Pr II spectrum

(A) Flag-pattern structure degrading towards the violet

λ	Combination	$\Delta\nu_1$	$\Delta\nu_2$	$\Delta\nu_3$	$\Delta\nu_4$	$\Delta\nu_5$
4334	$^5I_6{}^0-{}^5I_5$	0.283 W: 0.29	0.252 0.25	0.222 0.21	0.191 0.19	0.159 0.17
4306	$^5I_5{}^0-{}^5I_4$	0.290	0.255	0.221	0.185	0.068
4223	$^5I_5{}^0-{}^5K_6$	0.2436 W: 0.25	0.2076 0.21	0.172 0.18	0.136 0.15	0.096 0.13
4207	$^5I_8{}^0-{}^5I_8$	0.266 W: 0.27	0.241 0.25	0.215 0.23	0.190 0.21	0.165 0.17
4164	$^5I_6{}^0-{}^5I_6$	0.275 W: 0.30	0.243 0.26	0.210 0.22	0.177 0.18	0.149 0.14
4118	$^5I_5{}^0-{}^5I_5$	0.294 W: 0.28	0.255 0.25	0.216 0.21	0.175 0.18	0.135 0.15
3877*	$^5I_5{}^0-X_4$	0.334	0.292	0.250	0.208	0.166

(B) Flag-pattern structure degrading towards the red

λ	Combination	$\Delta\nu_1$	$\Delta\nu_2$	$\Delta\nu_3$	$\Delta\nu_4$	$\Delta\nu_5$
4352	$^3I_5{}^0-{}^5I_5$	0.196 W: 0.19	0.170 0.17	0.144 0.14	0.118 0.11	(0.092) 0.08

* Newly classified by the authors. $X_4=26226.5$.

This value of $a(6s)$ is to be compared with that of Brix $a(6s)=0.416\pm0.015\ \text{cm}^{-1}$.

Table II. Observed hfs constants of the terms $4f^3(^4I)6s$ of Pr II.

Term	A (cm^{-1})	Term	A (cm^{-1})
$^5I_4{}^0$	-0.0100	$^3I_5$	-0.0032
$^5I_5{}^0$	0.0622		
$^5I_6{}^0$	0.0536		
$^5I_8$	0.0437		

Table III. Relativity correction for the f-electron.*

Z_i	F'	F''	G
20	1.002	1.004	1.001
30	1.005	1.008	1.003
35	1.006	1.011	1.004
40	1.008	1.015	1.006
50	1.013	1.023	1.009
60	1.018	1.033	1.012
70	1.025	1.046	1.017

* Relativity correction for $a'(f_{7/2})$:

$$F'=252/\rho'(4\rho'^2-1).$$

Relativity correction for $a''(f_{5/2})$:

$$F''=105/\rho''(4\rho''^2-1).$$

Relativity correction for a''':

$$G=[24\sin\pi(\rho'-\rho''-1)]/\pi Z^2\alpha^2.$$

$\rho=\sqrt{k^2-Z^2\alpha^2}$, $\alpha=0.007284$.

$k=l+1$ for $j=l+\frac{1}{2}$; $k=-l$ for $j=l-\frac{1}{2}$.

The authors' $a(6s)$ gives the nuclear magnetic moment

$$\mu=+4.0\pm0.1\text{ n.m.}$$

This is in agreement with Lew's $\mu=+3.8\pm10\%$ n.m. and with Brix's $\mu=+3.9\pm0.3$ n.m.

$a_{4f}=0.0227\text{ cm}^{-1}$ is in fairly good agreement with $a_{4f}(\text{Pr I})=0.02356\text{ cm}^{-1}$ deduced by Lew. However, we should expect a_{4f} (Pr II) to be slightly larger than a_{4f} (Pr I). At present the authors are unable to find reason for the slightly smaller value of a_{4f} (Pr II) than a_{4f} (Pr I).

From the value of a_{4f} we can deduce the value of the screening constant σ defined by $Z_i=Z-\sigma$. Putting $\mu=4.0$ n.m., $I=5/2$, $\delta=2392.3\text{ cm}^{-1}$ (Pr II) in the formula

$$a_f=\frac{\mu}{I}\frac{\delta}{(7/2)HZ_i}\frac{1}{1838}$$

δ =doublet splitting of the f electron,

we get

$$Z_i=26.1,\quad \sigma=32.9\,.$$

This is to be compared with Lew's $\sigma=35.5$.

It will be interesting to compare the hfs constants with calculation, and this is done in Table IV. It is clear that in this case Jj-coupling is a better approximation than LS-coupling.* In the authors' calculation it was assumed that the ion $4f^3$ forms the term ^4I by an LS-coupling.

Table IV. Comparison of observed hfs constants (in unit of cm^{-1}) with calculations.

	obs.	calc.		calc.* Brix
		Jj-coupling	LS-coupling	
$A(^5I_5{}^0)$	0.0622	0.0694	0.0149	0.0647
$A(^3I_5{}^0)$	-0.0032	-0.0096	0.0449	-0.0006
$A(^5I_6{}^0)$	0.0536	0.0574	0.02895	0.0552
$A(^3I_6{}^0)$	(-0.0049)	-0.0087	0.01975	-0.0057

* Deduced by Brix from the measurement of White.

§4. Nuclear Quadrupole Moment

As mentioned above, $B=0.0\times10^{-6}\text{ cm}^{-1}$ was obtained for the level $4f^3(^4I_{9/2})6s\,^5I_4$. This level is independent of coupling and we get

$$Q=B\frac{Z_iHI(2I-1)J(2J-1)1988}{\zeta_f(28/121)(14/15)}\,.$$

Putting the above-mentioned value of B in the formula, we get

$$Q(\text{Pr})=(0.0\pm0.2)\times10^{-24}\text{ cm}^2.$$

On the other hand, Lew found $B=-0.00045\times10^{-3}\text{cm}^{-1}$, $a_{4f}=0.02356\text{ cm}^{-1}$ for the level $4f^3\,^4I_{9/2}$(Pr I). When these values are put in the formula

$$Q=\frac{BI(2I-1)J(2J-1)1988}{(28/121)\,1838\,a_f}\cdot\frac{\mu}{I}\,,$$

the following value of Q is obtained:

$$Q(\text{Pr})=-0.05\times10^{-24}\text{ cm}^2.$$

The value of Q obtained from the Pr II spectrum is in agreement with this, and we will consider $-0.05\times10^{-24}\text{ cm}^2$ as the final value of Q(Pr) at present.

References

1) H. E. White: Phys. Rev. **34** (1929) 1397.
2) H. Lew: Phys. Rev. **89** (1953) 530.
3) P. Brix: Phys. Rev. **89** (1953) 1245.
4) N. Rosen, G. R. Harrison and J. R. McNally: Phys. Rev. **60** (1941) 722.
5) K. Murakawa and S. Suwa: Report of the Institute of Science and Technology **7** (1953) 139 (in Japanese).
6) G. Breit and L. A. Wills: Phys. Rev. **44** (1933) 470.

---

* This is in agreement with the Zeeman effect data of ref. 4.

Journal of the Physical Society of Japan Vol. 9, No. 1, Jan.—Feb., 1954

The Optical and Electrical Properties of Cadmium Sulphide Films

By Goro Kuwabara

Department of Physics, Faculty of Science, University of Tokyo

(Received September 2, 1953)

The optical and electrical properties of evaporated CdS film were measured. The optical properties are similar to those of the single crystal, that is, the absorption edge lies at 2.4 eV; the photosensitivity peaks near the edge; with temperature decrease, the absorption edge and photosensitivity maximum shift towards shorter wave length; while the electrical properties show wide variation from sample to sample and by heat treatment. The photoresponse shows large dependence on the temperature and is closely related with the dark conductivity. By baking in the air, the conductivity at room temperature decreases by a great deal and the activation energy increases. By baking in the reduced atmosphere, the conductivity, the activation energy and photoresponse almost restore their initial values. In this process, the adsorption or desorption of oxygen on the surfaces of microcrystals plays an important role. The bimolecular recombination argument for the interpretation of spectral sensitivity curves seems inadequate.

§ 1. Introduction

In the last ten years, much attension has been paid to the photoconducting semi-conductors concerning infrared sensitive detectors and television pick up tubes, and many experimental results have been reported. Mott and Gurney[1] gave a fundamental explanation on the relation between optical and electrical properties of insulators and semiconductors. There remain, however, many inportant problems yet unsolved, such as the interpretation of spectral sensitivity curves and the mechanism of the so called sensitization with oxygen, and more over it seems to us that, for photoconductors of practical importance, which are used in the most cases as thin films, these relations are far more complicated. It is generally supposed that the optical or electrical properties of thin films differ appreciably from those of single crystals, and it is necessary to distinguish whether the observed phenomena may be attributed to the properties of single crystals or to the peculiarities of thin films. This paper is intended to clarify these problems, and the evaporated film of cadmium sulphide, whose properties in the single crystal have been extensively studied[2], is chosen as a typical photoconductive film.

§ 2. Optical Constants

Cadmium sulphide powder used in the present experiment was prepared by passing H_2S gas through the cadmium sulphate solution at p.H 2 to 6, and the precipitate was purified. The colours of the precipitates vary from yellow to orange according with p.H of the solution, but the properties of the evaporated films show no difference. The film was obtained by evaporating the powder from a tungsten coil onto a glass substrate in the vacuum of ca. 5×10^{-5} mm Hg. For optical measurements, the film was evaporated on the half of a polished glass (BK-7, 20×20 mm), and then in order to measure the thickness of the film by the method of mul-

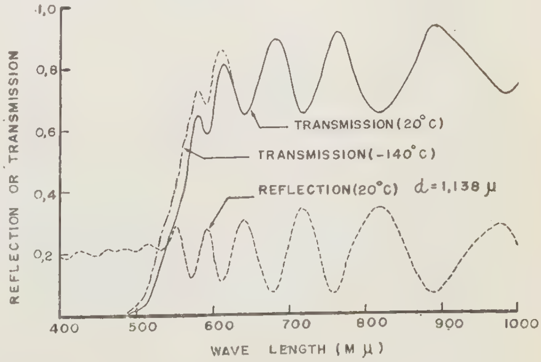

Fig. 1. Reflection and transmission of CbS film.

tiple beam interference, silver was evaporated on the halves of the film and the transparent part of the substrate. Five specimens of 90 mμ to 1.2 μ in thickness were prepared. The transmittance and reflectance between 400 mμ and 1000 mμ were measured with the photoelectric photometer reffering to the transparent part, and the effect of reflections within the glass was corrected as in the previous paper³⁾. One of the results wa shown in Fig. 1. In the long wave lengt region, a few maxima and minima due t interference can be perceived. Let the refractive index of the film be $n-ik$, then th reflection and transmission coefficients of th film on a substrate in the air are expresse by the following formulas⁴⁾.

$$T=\frac{16n_0(n^2+k^2)}{l_2\exp\left(\frac{4\pi k}{\lambda}d\right)+m_2\exp\left(-\frac{4\pi k}{\lambda}d\right)+p_2\cos\frac{4\pi n}{\lambda}d+q_2\sin\frac{4\pi n}{\lambda}d} \tag{1}$$

$$R=\frac{l_1\exp\left(\frac{4\pi k}{\lambda}d\right)+m_1\exp\left(-\frac{4\pi k}{\lambda}d\right)+p_1\cos\frac{4\pi n}{\lambda}d+q_1\sin\frac{4\pi n}{\lambda}d}{l_2\exp\left(\frac{4\pi k}{\lambda}d\right)+m_2\exp\left(-\frac{4\pi k}{\lambda}d\right)+p_2\cos\frac{4\pi n}{\lambda}d+q_2\sin\frac{4\pi n}{\lambda}d} \tag{2}$$

$$l_1=[(n-1)^2+k^2][(n+n_0)^2+k^2] \qquad l_2=[(n+1)^2+k^2][(n+n_0)^2+k^2]$$
$$m_1=[(n+1)^2+k^2][(n-n_0)^2+k^2] \qquad m_2=[(n-1)^2+k^2][(n-n_0)^2+k^2]$$
$$p_1=2[(n_0^2+1)(n^2+k^2)-(n^2+k^2)^2-n_0^2-4n_0k^2]$$
$$p_2=2[(n_0^2+1)(n^2+k^2)-(n^2+k^2)^2-n_0^2-4n_0k^2]$$
$$q_1=4k(n-1)(n^2+k^2+n_0) \qquad q_2=4k(n+1)(n^2+k^2-n_0)$$

where d is the thickness of the film, and n_0 is the refractive index of the substrate. In the non-absorbing region, n at the wave length, where the reflection or transmission shows the extremum can be easily obtained. In the region, where the film shows strong absorption k and n were determined by the successive approximation with the formulas

$$k=\frac{\lambda}{4\pi d}\log\frac{(1-R)}{T}, \tag{3}$$

$$R=\frac{[(n-1)^2+k^2]}{[(n+1)^2+k^2]}, \tag{4}$$

$$k=\frac{\lambda}{4\pi d}\left\{\log\frac{1}{T}\right.$$
$$\left.+\log\frac{16n_0(n^2+k^2)}{[(n+1)^2+k^2][(n+n_0)^2+k^2]}\right., \tag{5}$$

and (1), (2). In the region near the absorption edge, a pair of n and k which gives the measured values of T and R was determined by try and error using the rigorous formulas. With these procedures, the refractive index and absorption coefficient between 400 mμ and 1000 mμ were determined within the error of 3% and were shown in Fig. 2.

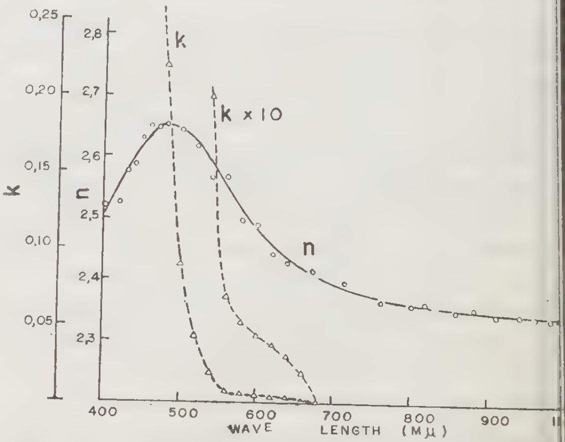

Fig. 2. Refractive index and absorption coefficient.

The absorption coefficient, rising steeply at 520 mμ, attains to 1.5×10^4 mm^{-1} at 400 mμ and the absorption edge lies at 2.4 eV., which is supposed to be the energy gap between the filled and the conduction band.

The main features of the absorption curve is similar to that reported by Frerichs and others for a single crystal. However, the weak absorption, which may be due to excess Cd atoms, extends to rather longer wave length and the colour of thick films appears orange rather than green.

The absorption at the lower temperature were measured with the Dewar vessel as shown in Fig. 3. By decreasing the temperature, the absorption edge shift towards shorter wave length with the rate of ca. 1 Å/1°C

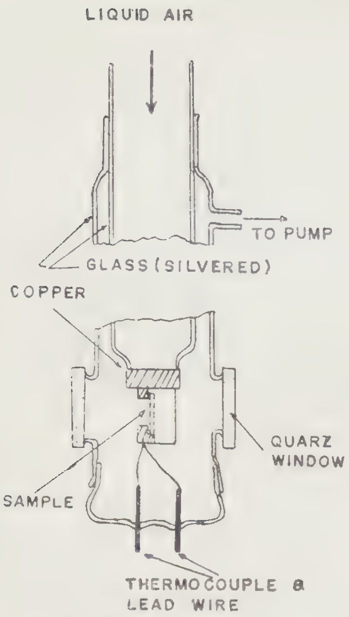

Fig. 3. Dewar vessel for mersurements at low temperature.

between the room temperature and −140°C, conforming to the result for the single crystal. The refractive index, increasing from 2.35 at 1000 mμ towards shorter wave length, attains the maximum value of 2.65 near the absorption edge, and then decreasing steeply shows an anomalous dispersion in the region of lattice absorption. The general rule that the high refractive index is associated with good photoconductivity is valid for CdS.

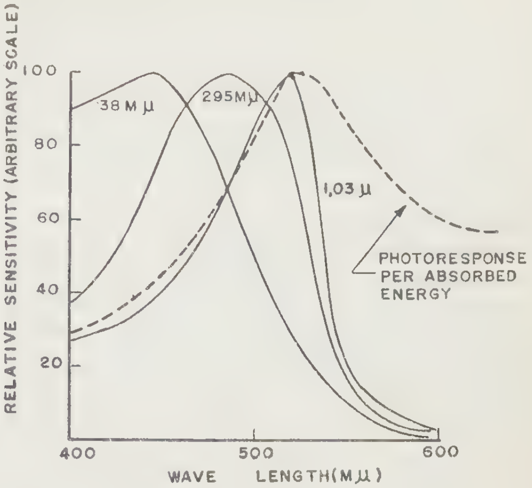

Fig. 4. Spectral sensitivity of photoconductivity.

§ 3. Electrical Properties

(a) *Spectral Sensitivity*

In order to measure the conductivity and the photoconductivity, the two aquadag electrodes with the separation of 2 mm were drawn on a glass substrate and the film was evaporated on it. In the measurement of photoconductivity, the film between the electrodes was illuminated uniformly and the D.C. voltage was applied. The relative spectral sensitivities for the specimens of different thickness were shown in Fig. 4. In the case of thick films, the photoconductivity peaks at the absorption edge i.e. 520 mμ as in the case of the single crystal. The spectral sensitivity including the peak, however, is independent on the applied voltage between 50 and 500 volt/cm and shows no anomalous behavior. As the thickness of the film is decreased, the peak of the photoconductivity shifts towards shorter wave length according with the shift of absorption, and the relative height of the maximum also decreases until it almost disappears for the film of 90 mμ in thickness. The photoresponse varied considerably even among the specimens of nearly the same thickness. The relative quantum yield, that is, the photocurrent per absorbed energy was also shown in Fig. 4 which is almost independent on the thickness of the film. The quantum yield peaks near the absorption edge. The decrease of spectral sensitivity on the red side of the peak is mainly due to the decrease of absorption, while the reason for the drop of sensitivity on the blue side is not clear. As will be stated in the next section, however, the usual bimolecular recombination argument often reffered seems inadequate.

The threshold of the photoconductivity extends to as long as 0.8 μ, where the absorption can be hardly measured with the evaporated films. The photocurrent rises or decays with the time constant as long as a few seconds or more, and while decaying, neither stimulation nor quenching of the current with infrared radiation can be perceived. The spectral sensitivity is independent on the temperature except the shift of sensitivity maximum according with that of the absorption edge at low temperature.

(b) *Correlation between the Dark Conductivity and Photosensitivity*

In Fig. 5, the dark- and photo-currents

were plotted versus the applied voltage. Both of them show non-ohmic character and can be expressed as $I=kV^n$, where the power n is nearly equal to 1 for the specimens with high conductivity and approaches to 2 for specimens with low conductivity. If we define the sensitivity as $S=(\sigma_L-\sigma_D)/\sigma_D$ instead of photoresponse $(\sigma_L-\sigma_D)$, where σ_D and σ_L are the dark- and the illuminated-conductivity, the sensitivity is independent on the applied voltage. The non-linearity of the conductivity suggests the granuality of the film and existence of the potential barrier between crystallites.

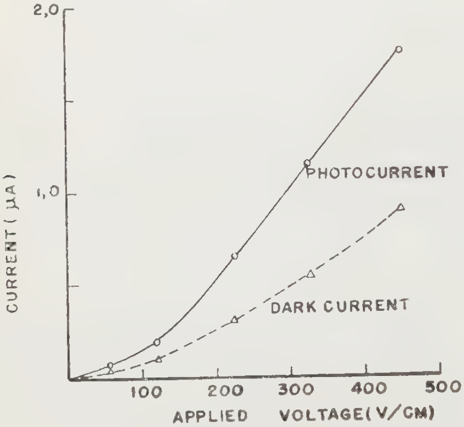

Fig. 5. Dark- and photo-current versus applied voltage.

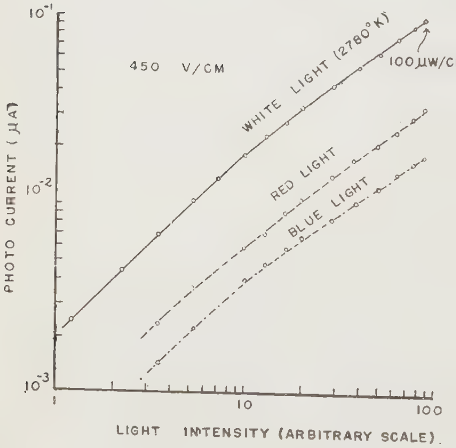

Fig. 6. Photocurrent versus light intensity.

The specimen was illuminated with white light from the tungsten lamp of the colour temperature of 2780°K and the photocurrent was measured as a function of light intensity. The results were shown in Fig. 6. At low light level, the photocurrent varies linearly with the light intensity, while at high light level, the deviation from the linearity occurs and can be expressed as $(\sigma_L-\sigma_D)=kI^n$ where I is the light intensity and n is 0.8 for high intensity. This relation was also measured for 3 monochromatic lights, that is, the light shorter than 460 mμ, longer than 570 mμ and that with the intensity maximum at 540 mμ, which were obtained by the combination of the tungsten lamp and Wratten filters. The relation between the light intensity and photocurrent is the same for these four kinds of lights.

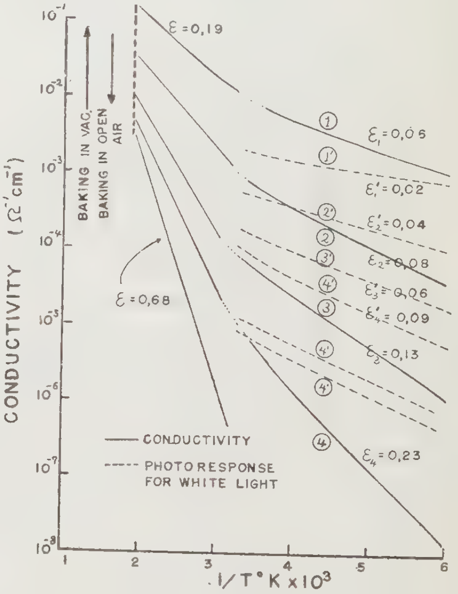

Fig. 7. Temperature dependence of conductivity and photoresponse.

In Fig. 7 the logarithm of the dark conductivity was plotted versus $1/T$ between the room temperatnre and -140°C. With temperature decrease, the conductivity varies according to the formula $\sigma_D=ae^{-\varepsilon/kT}$ as is usual with the semiconductors. However, the activation energy ε shows rather large variation between 0.06 eV and 0.28 eV among the samples of different thickness, and the activation energy decreases as the conductivity at room temperature increases. The temperature dependence of photoresponse is also expressed as $(\sigma_L-\sigma_D)=Ae^{-\varepsilon'/kT}$. The activation energy for photocurrent is generally smaller than that for the dark conductivity. Accordingly, $(\sigma_L-\sigma_D)/\sigma_D$ increases as the temperature de pendence of the photocurrent is quite the same for all wave length on either the blue or the red side of the absorption edge, that is, the spectral sensitivity is independent on the temperature except the shift of the sensitivity peak accompanied with the shift of the absorption edge. Therefore, taking the photocurrent-light intensity relation into consideration, it can be supposed that the low sensitivity on the blue side is due to the inherent low efficiency in creation of free carriers. The thermal activation energy determined by the measurement at low temperature is far smaller than the half of that corresponding to the absorption edge or threshold wave length of photoconductivity. In the high temperature range, the thermal activation energy attains to 0.8 eV or more and approaches to the half of that determined optically. As will be shown in the next section, however, it is quite doubtful that the energy determined from the conductivity in the present experiment corresponds directly to the energy between the filled band or impurity levels and the conduction band.

(*c*) *The Effect of Baking*

The thick films freshly prepared show high conductivity, low activation energy and large photoresponse. The temperature dependence of the photocurrent is also quite small. Up to 150°C, the film shows quite reproducible behavior either in the open air or in the vacuum. However, when these specimens are heated above ca. 200°C in the open air, the conductivity at room temperature decreases by as much as $10^{-1} \sim 10^{-5}$ times and the activation energy greatly increases. By this treatment the photoresponse also decreases, but its decrement is less than that of the conductivity and $(\sigma_L - \sigma_D)/\sigma_D$ increascs. As the conductivity decreases, the temperature dependence of the dark conductivity and that of the photoresponse increase, always keeping the relation $\mathcal{E} > \mathcal{E}'$, and the close correlation exists between the dark- and photo-conductivity. This process is reversible, that is, the specimen, which has been baked in the open air, can almost restores its initial conductivity, thermal activation energy and photosensitivity by baking above 200°C in the reduced atomosphere of 10^{-4} mm Hg. As above stated, according to the conditions of baking, the conductivity at room temperature shows wide variation, which is, for the most part, due to the change in the activation energy. It is supposed that the oxygen plays an important role in this process. Meyer and others⁵⁾ have also reported the large changes in conductivity and activation energy of ZnO, TiO_2 and other oxides caused by baking and found an experimental relation between $\mathcal{E}$ and a. In the present experiment on CdS, however, a shows only a little variation, while $\mathcal{E}$ varies as much as 4 times or more. By baking, the thickness and spectral sensitivity show no appreciable change, but the absorption edge becomes slightly steeper. The electron diffraction study shows that the fresh specimens consist of hexagonal microcrystals, and by baking either in the open air or in the vacuum, the diffraction pattern turns to more diffuse halo corresponding to far finer polycrystalline structure without orientation. This remarkable change in the submicroscopic structure, however, seems to have little effect on the electrical properties of the film.

§ 4. Discussions

The main features of the electrical properties are the wide variation of activation energy by baking and the close correlation between the conductivity and photoelectric sensitivity. In order to explain the former, there are four hypotheses:

(1) Before baking, the activation energy $\mathcal{E}$ is equal to $E/2$, where E is the energy gap between the conduction and the impurity levels, and by baking in the air $\mathcal{E}$ tends to E.

(2) According with the impurity concentration, the impurity level is shifted upwards relative to the conduction band due to the interaction between impurity centers⁶⁾. By baking in the air, the impurity centers (Cd atoms) decrease as a consequence of oxidation and the impurity level is lowered.

(3) The change of the submicroscopic structure or the crystallization of the film by baking.

(4) The change in the height of the potential barrier between microcrystals due to the adsorption or desorption of oxygen on the polycrystalline surfaces.

The first and the second hypothesis can not explain the large change of activation energy observed in our cxperiment. Because, by the first hypothesis, $\mathcal{E}$ can not change by more than 2 times. If we assume that the mobility of charge carriers is nearly constant throughout baking, and analyse the curves using the conventional model of n-type semiconductor, the ratio of the impurity concentrations can be obtained by the square of the ratio of a, i.e. the conductivity extraporated to $T=\infty$. The change of the impurity concentration by baking is less than a few tens, which may not cause the large change of interaction between them. The third hypothesis fails to explain the experimental results, because, according to the electron diffraction study, the change in the submicroscopic structure is caused by baking in the open air as well as in the vacuum, and is irreversible. The fourth hypothesis seems to be the most plausible. The evaporated film is consisted of microcrystals, and there will be a potential barrier between them, which is formed by the adsorbed oxygen on the surface.7) The carrier concentration within the microcrystals varies exponentially with the inverse of the temperature and in D.C. measurements, the carrier must pass through or over these potential barriers, which increase the resistance by a great deal. The probability of passing through the potential barrier depends upon the temperature and the height of the barrier, which will be greatly modified by the amount of oxygen adsorbed on the surface. The non-ohmic character of the film of low conductivity suggests the existence of such barrier. If we assume that the probability of creation of free carrier by photon is independent on the temperature, the activation energy of the photosensitivity, $\mathcal{E}'$, is the energy associated with the probability of passing through the potential barrier, while the thermal activation energy $\mathcal{E}$ determined by the conductivity is the sum of the energy to raise the electrons from the bound levels to the conduction band and that is needed to pass through the barrier. It is uncertain whether the photocurrent is caused by the modification of potential barrier due to the absorption of light near the surface8) or by the increase of carrier inside the microcrystals. In order to clarify these points, the measurements of Hall effect, A.C. conductivity and rise or decay process of the photoresponse are desirable. It may be certain, however, that the photon does not directly eject the electron from the surface level and modify the barrier as assumed in the explanation of long wave tail of PbS9), because by baking in the open air or in the vacuum, no appreciable change is observed in the spectral sensitivity.

§ 5. Conclusions

The optical and electrical properties of the evaporated CdS are measured. The optical properties, such as the absorption edge, spectral sensitivity or their temperature dependence are reproducible and can be regarded the same as those of the single crystal; while the electrical properties, such as the conductivity, the photosensitivity and their temperature dependence are sensitive to the conditions of evaporation, and vary according with the after-treatment; they are much more complicated than those of the ideal crystal. The drop of the photosensitivity on the blue side of the absorption edge may be due to the inherent low efficiency in creation of free carriers. There exists close correlation between the conductivity and photosensitivity, in which the potential barrier between the microcrystals probably due to the adsorbed oxygen seems to play an important role, and there is little correlation between the energies determined by conductivity, optical absorption in the visible or the threshold wave length of photoconductivity.

In conclnsion, the author wishes to express his thanks to Dr. G. Honzyo for the electron diffraction analysis, to Prof. Z. Koana, Prof. K. Isiguro and Dr. H. Miyazawa for their encouragements and discussions.

References

1) N. F. Mott and R. W. Gurney: Electronic Processes in Ionic Crystals. Clarendon Press. London, 1940.

2) R. Frerichs: Phys. Rev. **72** (1947) 594.

3) G. Kuwabara and K. Isiguro: J. Phys. Soc. Jap. **7** (1952) 72.

4) H. Mayer: Physik dünner Schichten, p. 154. Wissenschaftliche Ver. Stuttgart, 1950.

5) W. Meyer and H. Neldel: Phys. Zs. **38** (1938) 1014.
O. Fritsch: Ann. d. Phys. **22** (1935) 375.

6) G. L. Pearson and J. Bardeen: Phys. Rev. **75** (1949) 865.
N. F. Mott and R. W. Gurney: l.c.

7) J. Bardeen: Phys. Rev. **71** (1947) 717.
R. A. Smith: Henisch; The Semiconducting Materials. p. 198. Butterworths, London, 1951.
R. P. Chasman and E. H. Putley: ibid. p. 208.

8) A. F. Gibson: Proc. Phys. Soc. B. **64** (1951) 603.

9) R. A. Smith: l.c.

JOURNAL OF THE PHYSICAL SOCIETY OF JAPAN Vol. 9, No. 1, JAN.—FEB., 1954

Extension of von Kármán's Transonic Similarity Rule*

By Isao IMAI

Department of Physics, Faculty of Science, University of Tokyo

(Received August 28, 1953)

An attempt is made to extend von Kármán's transonic similarity theory so as to cover the whole range of Mach number from subsonic to supersonic. First, the equations for the two-dimensional compressible flow past a slender body are reduced to

$$\frac{\partial G}{\partial \bar{\zeta}}=B\left(\frac{\partial \phi_1}{\partial \xi}\right)^2 \quad (1) \qquad \text{or} \qquad \frac{\partial^2 \phi_2}{\partial \eta^2}=4B\frac{\partial \phi_2}{\partial \xi}\frac{\partial^2 \phi_2}{\partial \xi^2} \quad (2)$$

by assuming that the perturbation velocity is small of order ε and neglecting small quantities of $O(\varepsilon^3)$. Here we have written $\Phi=U(x+\phi)$, $\Psi=U(y+\psi)$, $\zeta=\xi+i\eta=x+i\mu y$, $\psi=\mu\chi$, $\phi+i\chi=A(\phi_1+i\chi_1)=AG$, $\phi_1=\phi_2+\xi/4B$, $B=\nu A/4$, $\mu=\sqrt{1-M^2}$, $\nu=4M^2[1+(\gamma+1)M^2/4\mu^2]$, where Φ is the stream function, U and M are respectively the free stream velocity and Mach number, γ is the ratio of specific heats, A is a constant of order $O(\varepsilon)$, and $G(\zeta,\bar{\zeta})$, $\phi_1(\xi,\eta)$, $\chi_1(\xi,\eta)$ are $O(1)$.

Then, it is shown that $B=O(t)$ for $M\not\doteqdot 1$, and that $(\nu/\mu)t$ is an appropriate parameter for $M\doteqdot 1$, where t is the thickness ratio of the body. For the case $M\not\doteqdot 1$, either subsonic or supersonic, the procedure of successive approximation can be applied to Eq. (1). It is to be noted that Eq. (2) is exact to the order $O(\varepsilon^2)$ in contrast to the fact that the similar equation in the usual transonic approximation theory is correct only to the order $O(\varepsilon)$. Hence it is suggested that the parameter $(\nu/\mu)t$ may be used with advantage in place of the usual transonic parameter $(\gamma+1)t/\mu^3$ or $(\gamma+1)t/(1-M^2)^{3/2}$.

Finally, Liepmann and Bryson's experimental data on the transonic flow past wedge sections are analyzed using the parameter $(\nu/\mu)t$.

§ 1. Introduction and Summary

It is well known that von Kármán's transonic similarity rule [5] is based on the two assumptions, namely, that the perturbation velocity due to the presence of an obstacle is small and that the free stream velocity is very near to the sound velocity. In this paper, an attempt is made to extend von Kármán's approximation theory so as to cover the whole range of Mach number from subsonic to supersonic. For this purpose, only the assumption of small perturbation velocity is made, without making any special assumption concerning the free stream Mach number. Moreover, in contrast to the usual transonic approximation, second order perturbations are also taken into account. Thus, the theory reduces to the usual transonic approximation for $M\doteqdot 1$ and goes over smoothly to the second approximation of Prandtl-Glauert's theory for $M<1$ and to Busemann's second order approximation for $M>1$. In particular, it is found that the usual linearized theory yields result correct to the second order for the special Mach number $M=[4/(3-\gamma)]^{1/2}$, γ being the ratio of specific heats.

As examples of application of the theory, we can deal with subsonic flow along a sinusoidal wall and past an elliptic cylinder at zero angle of attack; and the result will be reported in a separate paper. Also, Liepmann and Bryson's experimental data on the transonic flow past wedge sections [4] are analyzed by using the transonic parameter introduced in the present approximation theory.

§ 2. Basic Equation for the Small Perturbation Theory

The two-dimensional irrotational flow of a compressible fluid is governed by the equations:

$$u=\frac{\partial \Phi}{\partial x}=\frac{\rho_\infty}{\rho}\frac{\partial \Psi}{\partial y}, \qquad (2.1)$$

---

* Presented at the Eighth International Congress on Theoretical and Applied Mechanics held in Istanbul in August, 1952.

$$v=\frac{\partial\Phi}{\partial y}=-\frac{\rho_\infty}{\rho}\frac{\partial\Psi}{\partial x}\,, \tag{2.2}$$

$$\frac{\rho}{\rho_\infty}=\left\{1-\frac{\gamma-1}{2}M^2\left(\frac{q^2}{U^2}-1\right)\right\}^{1/(\gamma-1)}\,, \tag{2.3}$$

$$q^2=u^2+v^2\,, \tag{2.4}$$

where (u,v) are the component velocities in the x- and y-directions, q is the magnitude of velocity, ρ is the density, Φ is the velocity potential, Ψ is the stream function, U, M, and ρ_∞ are respectively the velocity, Mach number, and density of the free stream, and γ is the ratio of specific heats.

If the disturbance due to the presence of an obstacle is small, we can write

$$\Phi=U(x+\phi)\,,\quad \Psi=U(y+\psi)\,, \tag{2.5}$$

where ϕ and ψ can be assumed to be small, say of order $O(\varepsilon)$. Then we have, from (2.4) and (2.3),

$$\frac{q^2}{U^2}=1+2\phi_x+\phi_x^2+\phi_y^2\,, \tag{2.6}$$

$$\frac{\rho}{\rho_\infty}=1-M^2\phi_x-\frac{M^2}{2}\{1-(2-\gamma)M^2\}\phi_x^2 -\frac{M^2}{2}\phi_y^2+O(\varepsilon^3)\,, \tag{2.7}$$

where $\phi_x=\partial\phi/\partial x$, $\phi_y=\partial\phi/\partial y$. From (2.1) and (2.2), we obtain

$$\frac{\rho}{\rho_\infty}(1+\phi_x)-(1+\psi_y)=0,$$

$$\frac{\rho}{\rho_\infty}\phi_y+\psi_x=0\,.$$

Employing (2.7) and putting

$$\xi=x,\quad \eta=\mu y,\quad \psi=\mu\chi\,, \tag{2.8}$$

$$\mu=\sqrt{1-M^2}\,, \tag{2.9}$$

$$\phi=A\phi_1\,,\quad \chi=A\chi_1\,, \tag{2.10}$$

we have

$$\phi_{1\xi}-\chi_{1\eta}=\frac{M^2}{2}\{3-(2-\gamma)M^2\}\frac{A}{\mu^2}\phi_{1\xi}^2 -\frac{M^2}{2}A\phi_{1\eta}^2+O\left(\frac{\varepsilon^3}{A\mu^2}\right),$$

$$\phi_{1\eta}+\chi_{1\xi}=M^2A\phi_{1\xi}\phi_{1\eta}+O\left(\frac{\varepsilon^3}{A\mu}\right).$$

Here A is a certain constant to be determined later on.

In the first place, we shall consider the subsonic case: $M<1$. The supersonic case: $M>1$ will be considered in § 6.

Putting

$$\zeta=\xi+i\eta\,,\quad \bar\zeta=\xi-i\eta\,, \tag{2.11}$$

$$G=\phi_1+i\chi_1\,, \tag{2.12}$$

the above two equations can be combined into a single equation:

$$\frac{\partial G}{\partial\bar\zeta}=\frac{\nu}{4}A\phi_{1\xi}^2-M^2A\left(\frac{\partial\phi_1}{\partial\zeta}\right)^2 +O\left[\frac{\varepsilon^3}{A}\left(\frac{1}{\mu}+\frac{1}{\mu^2}\right)\right], \tag{2.13}$$

where

$$\nu=4M^2\left(1+\frac{\gamma+1}{4}\frac{M^2}{1-M^2}\right). \tag{2.14}$$

We now assume that ϕ_1, χ_1, and G (hence $\phi_{1\xi}$ and $\phi_{1\zeta}$, but not ψ_1) can be taken to be $O(1)$ by suitable choice of the constant A. Then, remembering that $\phi=O(\varepsilon)$ and $\phi\fallingdotseq A\phi_1$, we must have

$$A=O(\varepsilon)\,. \tag{2.15}$$

Now (2.13) gives

$$\frac{\partial G}{\partial\bar\zeta}=O\left(\frac{\varepsilon}{\mu^2}+\varepsilon+\frac{\varepsilon^2}{\mu}+\frac{\varepsilon^2}{\mu^2}\right)=O\left(\frac{\varepsilon}{\mu^2}\right),$$

where only the most significant terms for $M\fallingdotseq 1$ are retained on the right-hand side. Hence

$$G=f(\zeta)+O(\varepsilon/\mu^2)\,,$$

where $f(\zeta)$ is an arbitrary analytic function of ζ. Hence we have

$$\frac{\partial\phi_1}{\partial\zeta}=\frac{1}{2}\frac{\partial}{\partial\zeta}(G+\bar G)=\frac{1}{2}f'(\zeta)+O\left(\frac{\varepsilon}{\mu^2}\right).$$

Substituting this into (2.13), we have

$$\frac{\partial G}{\partial\bar\zeta}=\frac{\nu}{4}A\phi_{1\xi}^2-\frac{M^2}{4}A\left(\frac{df}{d\zeta}\right)^2+O\left(\frac{\varepsilon^2}{\mu^2}\right),$$

which, on integration, gives

$$G=\frac{M^2}{4}A\left(\frac{df}{d\zeta}\right)^2(\zeta-\bar\zeta) +\frac{\nu}{4}A\int\phi_{1\xi}^2d\bar\zeta+O\left(\frac{\varepsilon^2}{\mu^2}\right).$$

Usually we are only interested in the state of affairs on or near the surface of the obstacle, where $\zeta-\bar\zeta=2i\eta=O(\mu t)$, t being the thickness parameter of the obstacle. Therefore

$$G=\frac{\nu}{4}A\int\phi_{1\xi}^2d\bar\zeta+O\left(\varepsilon\mu t+\frac{\varepsilon^2}{\mu^2}\right).$$

It will be seen later that $\varepsilon=O(t/\mu)$. Thus, neglecting $O(t^2/\mu^4)$, we have finally

$$\frac{\partial G}{\partial\bar\zeta}=B\left(\frac{\partial\phi_1}{\partial\xi}\right)^2, \tag{2.16}$$

with

$$B=\frac{\nu}{4}A\,. \tag{2.17}$$

The equation (2.16) will be useful as a basic equation for compressible flow past thin obstacles. Indeed, remembering that $\phi+i\chi=AG$, $A=O(\mathcal{E})$, it will be seen that the error caused by the adoption of (2.16) instead of the exact equations of motion (2.1) and (2.2) is only of the order $O(\mathcal{E}^3/\mu^2)=O(t^3/\mu^5)$.

§ 3. Comparison with the Usual Transonic Approximation Theory

Separating real and imaginary parts of (2.16) we have

$$\phi_{1\xi}-\chi_{1\eta}=2B\phi_{1\xi}{}^2\,, \tag{3.1}$$

$$\phi_{1\eta}+\chi_{1\xi}=0\,, \tag{3.2}$$

whence, eliminating χ_1, we obtain

$$\phi_{1\xi\xi}+\phi_{1\eta\eta}=4B\phi_{1\xi}\phi_{1\xi\xi}\,. \tag{3.3}$$

If we put

$$\phi_1=\phi_2+\frac{\xi}{4B}\,, \tag{3.4}$$

the equation (3.3) becomes

$$\frac{\partial^2\phi_2}{\partial\eta^2}=4B\frac{\partial\phi_2}{\partial\xi}\frac{\partial^2\phi_2}{\partial\xi^2}\,. \tag{3.5}$$

This is exactly the same as the basic equation of the usual transonic approximation theory. But, whereas in the usual theory the equation is derived by assuming $M\doteqdot 1$ and neglecting $O(\mathcal{E}^2)$, the present analysis shows that it is also valid for any Mach number, and, moreover, it is correct to the order $O(\mathcal{E}^2)$.

§ 4. Boundary Condition

The boundary condition at the surface of the obstacle is

$$\Psi=0 \quad \text{for} \quad y=tg(x)\,, \tag{4.1}$$

t being the thickness parameter. (4.1) can be written as

$$\chi_1(\xi,\eta)=-\frac{t}{A\mu}g(\xi) \quad \text{for} \quad \eta=\mu tg(\xi)\,. \tag{4.2}$$

Expanding $\chi_1(\xi,\eta)$ in Taylor series in η, we have

$$\chi_1(\xi,0)=-\frac{t}{A\mu}g(\xi)-\mu tg(\xi)\chi_{1\eta}(\xi,0)+O(\mu^2t^2)\,. \tag{4.3}$$

Putting

$$k=\frac{t}{A\mu}=\frac{1}{4B}\frac{\nu}{\mu}t\,, \tag{4.4}$$

and neglecting $O(\mu t)$, we have from (4.3)

$$\chi_1(\xi,0)=-kg(\xi)\,. \tag{4.5}$$

The equation (2.16) together with the boundary condition (4.5) gives similar flow patterns for the same value of k. This is well known as von Kármán's transonic similarity rule [5].

By assumption $\chi_1(\xi,0)=O(1)$, $g(\xi)=O(1)$, so that

$$k=O(1)\,. \tag{4.6}$$

Combining $A=O(\mathcal{E})$ with (4.4) and (4.6) we have

$$\mathcal{E}=O(t/\mu)\,, \tag{4.7}$$

which has been used in deriving the equation (2.16). Now, it follows from (2.17) that

$$B=O(\nu A)=O(\mathcal{E}/\mu^2)=O(t/\mu^3)\,. \tag{4.8}$$

Therefore, two cases can be distinguished as follows.

(i) The case: $M\not\doteqdot 1$. Here we have

$$B=O(t)\,.$$

(ii) The case: $M\doteqdot 1$. Now the case $B=O(1)$ can take place, if $t=O(\mu^3)$ so that

$$\mathcal{E}=O(\mu^2)=O(t^{2/3})\,.$$

Here we have

$$\nu\sim\frac{\gamma+1}{\mu^2}\,, \qquad k\sim\frac{1}{4B}\frac{(\gamma+1)t}{\mu^3}\,;$$

the latter combination $(\gamma+1)t/\mu^3$ is well known in von Kármán's transonic similarity theory. (As seen from (3.5), von Kármán's treatment corresponds to the adoption of the special value $B=1/2$. If this value of B is adopted not only for $M\doteqdot 1$, but also for $M\not\doteqdot 1$, we have $k=O(t)$ for $M\not\doteqdot 1$, so that k is equivalent to the thickness parameter in the usual thin-wing-expansion method.)

§ 5. Specialization for the Case $M<1$

Equation (2.16) can be expressed as

$$\frac{\partial G}{\partial\bar\zeta}=\beta\left(\frac{\partial G}{\partial\zeta}+\frac{\partial G}{\partial\bar\zeta}+\frac{\partial\bar G}{\partial\zeta}+\frac{\partial\bar G}{\partial\bar\zeta}\right)^2\,, \tag{5.1}$$

with

$$\beta=\frac{B}{4}=\frac{\nu}{16}A\,. \tag{5.2}$$

Since $\beta=O(t)$ for $M \not\approx 1$, (5.1) can be integrated by successive iterations. Thus, for the zero approximation, we have

$$\frac{\partial G}{\partial \bar{\zeta}}=0\ ,$$

so that

$$G=f(\zeta)\ , \tag{5.3}$$

where $f(\zeta)$ is an arbitrary analytic function of ζ.

Inserting (5.3) in (5.1), we have

$$\frac{\partial G}{\partial \bar{\zeta}}=\beta(f'+\bar{f}')^2\ ,$$

where $f'=f'(\zeta)=df/d\zeta$ and $\bar{f}'=\bar{f}'(\bar{\zeta})=d\bar{f}/d\bar{\zeta}$.

Integrating we get

$$G=\beta[2f'\bar{f}+\textstyle\int\bar{f}'^2 d\bar{\zeta}+(\bar{\zeta}-\zeta)f'^2]+F(\zeta)\ ,$$

where $F(\zeta)$ is another arbitrary function of ζ. It may be remarked here that although in the above expression the term $-\zeta f'^2$ could be absorbed in the arbitrary function $F(\zeta)$, the combination $(\bar{\zeta}-\zeta)f'^2$ has been preferred to the simpler expression $\bar{\zeta}f'^2$; the reason will be made clear below. Further, remembering that $f(\zeta)$ itself is arbitrary, we may conveniently take $F(\zeta)\equiv f(\zeta)$.

Repeating similar calculations we obtain

$$\begin{aligned}
G=f&+\beta\left(2f'\bar{f}+\int\bar{f}'^2 d\bar{\zeta}\right)\\
&+\beta^2\left(10f'^2\bar{f}+4ff'\bar{f}'+2f''\bar{f}^2+2f\bar{f}'^2+12f'\int\bar{f}'^2d\bar{\zeta}+\frac{10}{3}\int\bar{f}'^3d\bar{\zeta}\right)\\
&+\beta^3\left\{\frac{200}{3}f'^3\bar{f}+20ff'^2\bar{f}'+40f'f''\bar{f}^2+44ff'\bar{f}'^2+8(ff')'\bar{f}\bar{f}'+8f^2\bar{f}'\bar{f}''+20f\bar{f}'^3\right.\\
&\qquad+4f'\bar{f}\bar{f}'^2+\frac{4}{3}f'''\bar{f}^3+130f'^2\int\bar{f}'^2d\bar{\zeta}+12\bar{f}'^2\int f'^2d\zeta+24f''\bar{f}\int\bar{f}'^2d\bar{\zeta}+24\bar{f}'f'\int f'^2d\zeta\\
&\qquad\left.+\frac{260}{3}f'\int\bar{f}'^3d\bar{\zeta}+\frac{47}{3}\int\bar{f}'^4d\bar{\zeta}\right\}+\cdots\\
&+\beta(\bar{\zeta}-\zeta)\Bigl[f'^2+\beta\left\{2f'^3+4f'f''\bar{f}-2f'\bar{f}'^2-\frac{4}{3}\bar{f}'^3\right\}\\
&\qquad+\beta^2\left\{\frac{23}{3}f'^4+4f'^3\bar{f}'+8ff'f''\bar{f}'+52f'^2f''\bar{f}-8ff'\bar{f}'\bar{f}''-8f'^2\bar{f}'^2+4(f'f'')'\bar{f}^2\right.\\
&\qquad\quad\left.-8f\bar{f}'^2\bar{f}''-20f'\bar{f}'^3-4f''\bar{f}\bar{f}'^2-2\bar{f}'^4+24f'f''\int\bar{f}'^2d\bar{\zeta}\right\}+\cdots\Bigr]\\
&+\beta^2(\bar{\zeta}-\zeta)^2[2f'^2f''+\beta\{12f'^3f''+4(f'^2f'')'\bar{f}-4f'f''\bar{f}'^2+4f'\bar{f}'^2\bar{f}''+4\bar{f}'^3\bar{f}''\}+\cdots]\\
&+\beta^3(\bar{\zeta}-\zeta)^3\left[\frac{4}{3}(f'^3f'')'+\beta\{\cdots\}+\cdots\right]\\
&+\cdots
\end{aligned} \tag{5.4}$$

It is to be noted that near the surface of the obstacle $\bar{\zeta}-\zeta=O(\mu t)$ and so the terms involving $\beta(\bar{\zeta}-\zeta)$ as a factor can be neglected in our approximation; indeed (5.2), (4.7), and (4.8) give $O(\beta(\bar{\zeta}-\zeta))=O(B\mu t)=O(t^2/\mu^2)=O(\varepsilon^2)$, which has already been omitted in deriving the basic equation (2.16). Further, it may be mentioned that f would in general involve terms of order $O(\mu t)$, on account of the boundary condition at the surface of the obstacle.

In a previous paper [1] the author has developed a convenient procedure of the thin-wing-expansion method in order to deal with the subsonic flow past arbitrary thin aerofoils. Thus, the expressions correct to $O(t^2)$ were obtained in explicit forms for the velocity distribution round the aerofoil as well as for the lift and moment. Later, in collaboration with Ōyama, the author [2] obtained the expression for the complex velocity potential which is correct to $O(t^3)$, and, as an application, investigated the flow along a sinusoidal wall [3].

It can be seen that (5.4) is in perfect agreement with the previous result up to the term of $O(\beta)$. Moreover, it should be mentioned that the terms of $O(\beta^2)$ represent the most significant terms, for high subsonic speeds, among those of order $O(t^3)$ in the (complete) thin-wing-expansion method; and hence (5.4) is particularly suited for treating transonic flow past very thin aerofoils.

The procedure to be taken for this "transonic thin-wing-expansion method" is the same in principle as for the usual (complete) thin-wing-expansion method, but the labour involved in the practical calculation is considerably less with the former than with the latter. Application of the method to flow along a sinusoidal wall and past an elliptic cylinder at zero angle of attack will be presented in a separate paper.

§ 6. Specialization for the Case $M>1$

For supersonic free stream velocity, the analysis proceeds in a similar manner. We have only to make the following substitutions in the various formulae.

$$\mu = i\bar{\mu}\,, \quad \eta = i\bar{\eta}\,, \quad \bar{\eta} = \bar{\mu} y\,, \tag{6.1}$$

$$\bar{\mu} = \sqrt{M^2-1}\,, \tag{6.2}$$

$$\left.\begin{aligned} \zeta &= x - \bar{\mu} y = \xi - \bar{\eta}\,, \\ \bar{\zeta} &= x + \bar{\mu} y = \xi + \bar{\eta}\,, \end{aligned}\right\} \tag{6.3}$$

$$G = \phi_1 + \bar{\chi}_1\,, \quad \bar{G} = \phi_1 - \bar{\chi}_1\,, \quad \bar{\chi}_1 = \phi_1/\bar{\mu}\,. \tag{6.4}$$

And thus we have

$$\frac{\partial G}{\partial \bar{\zeta}} = B\phi_{1\xi}{}^2\,, \quad \frac{\partial \bar{G}}{\partial \zeta} = B\phi_{1\xi}{}^2\,. \tag{6.5}$$

(It should be noted that the bars do not mean the complex conjugate in this case.) Corresponding to (5.4), we have two equations: (5.4) and its complex conjugate (of course in formal sense).

For flow past a thin obstacle whose equation is

$$y = tg(x)\,, \tag{6.6}$$

the flow field in the upper half plane can be shown to be given by

$$G = f + O(\beta^2)\,, \tag{6.7}$$

$$\bar{G} = \beta \int f'^2 d\zeta + O(\beta^2)\,, \tag{6.8}$$

in view of the fact that the incoming wave $\bar{f}(\bar{\zeta}) = \bar{f}(x+\bar{\mu}y)$ should not appear in this case. Thus we find

$$\phi = \frac{A}{2}\left(f + \beta \int f'^2 d\zeta\right) + O(t^3)\,. \tag{6.9}$$

From the boundary condition similar to (4.3) we get

$$f = -\frac{2}{\bar{\mu}A}g - \frac{2}{A}gg' + \beta\left(\frac{2}{\bar{\mu}A}\right)^2 \int g'^2 d\zeta\,. \tag{6.10}$$

Introducing (2.7) in the adiabatic relation $p/p_\infty = (\rho/\rho_\infty)^\gamma$, we can find the pressure coefficient in the form:

$$\begin{aligned} C_p &= \frac{p-p_\infty}{\frac{1}{2}\rho_\infty U^2} \\ &= -2\phi_x + \bar{\mu}^2\phi_x{}^2 - \phi_y{}^2 + O(\varepsilon^3)\,. \end{aligned} \tag{6.11}$$

Substituting (6.9) and (6.10) into (6.11), we finally arrive at

$$C_p = \frac{2t}{\bar{\mu}}\frac{dg}{dx} + \left(2 - \frac{\nu}{2\bar{\mu}^2}\right)t^2\left(\frac{dg}{dx}\right)^2. \tag{6.12}$$

This is in complete agreement with Busemann's pressure formula derived by the use of an entirely different method.

§ 7. Simplification Obtained for the Special Mach Number $M=[4/(3-\gamma)]^{1/2}$

It is readily seen from (2.14) and (5.2) that

$$\nu = B = 0 \quad \text{for} \quad M^2 = 4/(3-\gamma)\,.$$

In this case (6.5) gives

$$G = f(\zeta) + O(\varepsilon^2)\,, \quad \bar{G} = \bar{f}(\bar{\zeta}) + O(\varepsilon^2)\,.$$

Hence

$$\begin{aligned} \phi &= \frac{A}{2}(G+\bar{G}) \\ &= \frac{A}{2}[f(x-\bar{\mu}y) + \bar{f}(x+\bar{\mu}y)] + O(\varepsilon^3)\,. \end{aligned}$$

For this special Mach number, therefore, the usual linearized theory gives result correct to the order $O(\varepsilon^2)$. For air $\gamma=1.4$, and so such a Mach number is given by $M=\sqrt{5/2}=1.5811$.

§ 8. Analysis of Experimental Data on Transonic Flow past Wedge Sections

Recently Liepmann and Bryson [4] made an experimental study of transonic flow past wedge sections, and compared the results with recent theoretical work of Guderley and Yoshihara and especially of Vincenti and

Wagoner and of Cole. The semi-apex angles θ of the wedge sections investigated were 4.5°, 7.5°, and 10° respectively. They plotted the measured drag coefficients by using von Kármán's transonic parameters. Thus they employed the reduced drag coefficient $\tilde{C}_D$ defined as

$$\tilde{C}_D=\frac{(\gamma+1)^{1/3}}{\theta^{5/3}}C_D\,, \tag{8.1}$$

together with the parameter

$$\xi=\frac{-\mu^2}{[(\gamma+1)\theta]^{2/3}}\,. \tag{8.2}$$

According to the present theory, it is suggested to change the definitions a little, thus

$$\tilde{C}_{D1}=\frac{(\mu^2\nu)^{1/3}}{\theta^{5/3}}C_D\,, \tag{8.3}$$

$$\xi_1=\left(\frac{\mu}{\nu\theta}\right)^{2/3}, \tag{8.4}$$

which reduce to (8.1) and (8.2) respectively for $M\fallingdotseq 1$.

If Liepmann and Bryson's experimental data are plotted using the new parameters $\tilde{C}_{D1}$ and ξ_1, the values for the three wedges lie nearly on a single curve, though some systematic deviations still exist, just as when using original parameters $\tilde{C}_D$ and ξ (Fig. 1). However, with our new parameters, the deviations are solely ascribable to the large values of θ, whereas in the $\tilde{C}_D-\xi$ plot the deviations may have arisen partly from the large departure of the Mach number from 1.

Therefore, it is expected that the effect of finite values of θ may be taken into account by considering the more accurate boundary condition (4.3). This problem will be considered in a future paper.

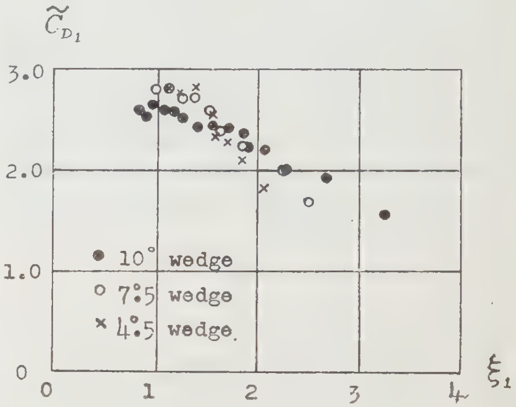

Fig. 1. Drag coefficients of wedge sections (Liepmann and Bryson's experiment).

References

1) I. Imai: Report Aeron. Res. Inst. Tokyo Imp. Univ. No. **294** (1944).

2) I. Imai and S. Ōyama: Report Inst. Sci. Technol. Tokyo Univ. **2** (1948) 37.

3) I. Imai and S. Ōyama: Report Inst. Sci. Technol. Tokyo Univ. **2** (1948) 39.

4) H. W. Liepmann and A. E. Bryson: J. Aero. Sci. **17** (1950) 745.

5) Th. von Kármán: J. Math. Phys. **26** (1947) 182.

JOURNAL OF THE PHYSICAL SOCIETY OF JAPAN Vol. 9, No. 1, JAN.—FEB., 1954

Electromicroscopie de la Surface d'une Cassure de Verre (II)*

Par Nobuzo TERAO
Institut de Physique, Faculté des Sciences, Université de Tokyo
et Shigeo SAKATA
Institut du Microscope Electronique, Université de Tokyo

(Reçu le 27 juin 1953)

The mirror surface appearing at the starting point of a crack produced in a glass rod is observed through the electron microscope by the method of the methyl methacrylate-aluminium-chrome shadow casting replica. First, photographs were taken of the entire view of the replica sample with the low magnification and then each part of mirror surface with the magnification of 400∼500 and next with the much higher magnification. Comparing these photographs with each other, we are led to notice the morphological variation of the glass fracture surface from place to place. We observed especially the small circular bodies which appeared on the flat part of the fracture surface. It is presumed that these small bodies do not exist actually on the fracture surface but arise from some secondary reaction between the fresh smooth fracture surface of glass and the replica material. Special forms of cracks such as fiber, comb, foil, feather, arch etc. were observed.

Nous avons rendu compte par la note précédente[1] de l'observation au microscope électronique d'une cassure de verre appelée le foyer d'éclatement. Nous y avons signalé surtout les petits corps ronds qui se trouvent dans le domiane spécialement plan. La conclusion était la suivante : Si ces petits corps existent réellement dans une cassure de verre, on peut considérer qu'ils sont des cassures en forme de lentilles qui se produisent localement avant que la surface principale de rupture se développe. Mais, d'un autre côté, il y a encore une possibilité que ce soit un phénomène produit par l'effet secondaire dû à la réaction particulière entre la matière de réplique et la surface de la cassure. Pour éclairer ce sujet nous avons fait encore les essais suivants.

Après avoir fait une réplique en aluminium de la surface du foyer d'éclatement d'une baguette de verre suivant la méthode du méthacrylate de méthyl-aluminium, nous l'avons ombrée avec le chrome comme précédemment. Nous avons mis cet échantillon de réplique sur un réseau mince de cuivre qui a beaucoup de trous ronds rangés régulièrements, d'environ 0.1 mm de diamètre (Fig. 0) et nous l'avons observé avec le microscope électronique. Le microscope électronique employé ici est de type électromagnétique de Hitati HU 4 amélioré, dont le voltage accélerateur est de 50kV. Ce microscope n'est pas convenable pour l'observation des grossissements très faibles parce qu'il n'a que l'objectif et le projectif en outre du condenseur. Cependant nous avons d'abord photographié l'ensemble de la réplique avec un grossissement d'environ 100 en mettant l'échantillon dans une position plus proche du condenseur que d'habitude et sans action du projectif. La Fig. 0 est un de ces exemples. Puis, nous avons photographié chacun des trous du réseau métallique avec un grossissement de 400 à 500 à peu près en approchant l'éhantillon de la position habituelle et en utilisant un peu l'action du projectif. Les figures 28 et 33 montrent ces exemples. Dans ces deux sortes de clichés on trouve inévitablement une distorsion assez remarquable. Nons avons enfin observé les places qui se trouvent dans une répliqne, chacune à son tour, avec un grossissement d'environ 3,000. La Fig. 29, par exemple, correspond à l'endroit entouré par un cercle dans la Fig. 28. (La Fig. 28 est une partie de la circonférence du foyer d'éclatement et une flèche montre la direction de croissance de la cassure.) Nous avons ainsi pu identifier l'endroit observé plus nettement que précédemment par comparaison l'une avec l'autre des photographies de grossissement plus fort et plus faible. Les figures 1 à 27 sont des microphotographies électroniques qui représentent respectivement les points marqués par les chiffres correspondants dans la Fig. 0. Nous avons aussi arrangé ces 27 figures de sorte qu'elles indiquent la même direction que la Fig. 0. On sait de cette façon la variation morphologique de la surface d'un foyer d'éclatement.

---

* Séance de la Société de Physique, le 2 avril 1953.

Le point A dans la Fig. 0 montre le point de départ d'un foyer d'éclatement. Les nombreux petits corps ronds signalés par la note précédente et qui sont convexes par rapport au plan de réplique, existent dans la partie spécialement lisse près du point A, comme on les voit dans les figures 1, 2, 3, 4, 5 et 13. A mesure que la surface de sectionnement s'approche de la circonférence, elle devient de plus en plus inégale et orientée comme les figures 6, 9, 12, 14, 15, 19, 20, 23 etc.. La cassure se ramifie près de la circonférence du foyer d'éclatement et il se produit localement à nouveau une surface assez plane.²⁾ On y trouve encore une fois les petits corps comme l'indiquent les figures 7, 8, 10, 11, 16, 17, 18, 21, 22, 24, 25, 26, 27 etc.. Le fait que la forme de ces corps est moins régulière que précédement doit être causé par ce que la polymériésation du méthacrylate de méthyl est insuffisante. Les corps ronds spécialement géants que l'on voit dans les figures 3 et 27 nous donnent l'idée qu'ils proviennent d'une sorte de bulle. La cassure ne se développe pas toujours en forme simple du rayon du point A et, de plus, la vitesse de croissance d'une cassure semble différente d'une place à l'autre. Par exemple les figures 21, 22 et 25 montrent que la direction de croissance change localement. Et on remarquera une relation géométrique entre la direction de croissance et les figures d'arc ogival que montrent les figures 9, 12, 15, 19, 20, 23 et 37. (La flèche dans la Fig. 37 montre la direction de croissance de la cassure.) La cassure comme celle-ci est celle que l'on observe souvent macroscopiquement et microscopiquement dans la cassure d'une dalle de verre, de bitume ou de résine. La cassure en forme de peigne, observée dans les figures 21, 22, 24, 25, 26, 29, 35 etc., se trouve près de la circonférence du foyer d'éclatement et les dents du peigne sont à peu près perpendiculaires à la direction de croissance de la cassure. Les corps noirs en forme de cheveux des figures 25, 26, 29, 35 sont du verre fibreux lui-même détaché de la partie de dent du peigne et qui s'attache à la surface de la réplique d'aluminium. On voit de même dans la Fig. 24 un fragment mince de verre qui n'est pas divisé en cheveux. La cassure en forme de plume comme la Fig. 7 est une forme que nous avons quelquefois observée.

Les petits corps qui apparaissent dans l'endroit plan de la surface d'une cassure de verre se rattachent étroitement à la polymériésation du méthacrylate de méthyl. La Fig. 30 a été obtenue quand la polymériésation semblait plus ou moins insuffisante et elle ressemble à un liquide gluant adhérant à la surface du corps solide. La Fig. 38 représente le cas où l'on a fait la réplique de métal par l'évaporation dans le vide après avoir laissé à l'abandon la réplique de méthacrylate de méthyl polymérisée sur la surface d'une cassure pendant environ 20 jours; on y voit des corps ronds dont les surface sont déformées comme des fleurs de chrysanthème sauvage. Si le temps de polymériésation est long, le contour du petit corps devient un cercle plus complet, comme dans la note précédente, et des corps concaves par rapport au plan de réplique, apparaissent de temps en temps. Les figures 31, 32, 33, 34 etc. sont de ces exemples. On trouve dans les figures 31, 32 et 33 de grandes surfaces concaves sphériques qui contiennent des corps convexes plus petits. La Fig. 32 correspond à la partie marquée --→ dans la Fig. 33 à un grossissement plus faible. La flèche dans la Fig. 33 montre la direction de la croissance de la cassure. Nous avons essayé de faire des répliques à plusieurs reprises sur une surface du foyer d'éclatement, mais nous n'avons pas réussi à obtenir des figures coïncidant complètement. En effet, les figures 31, 32, 33 et 34 sont toutes celles que nous avons obtenues dans une réplique de la même surface de rupture que la Fig. 0. Les corps spécialement géants sont si grands que nous pouvons les observer aisément avec le microscope optique, mais il va sans dire qu'ils n'existent pas réellement sur la surface elle-même d'une cassure de verre. Lorsqu'on observe une réplique que l'on a faite de la même façon que précedemment, après avoir recouvert la surface de rupture du verre avec une couche mince d'aluminium par l'évaporation dans le vide, on ne peut presque jamais trouver ces petits corps ronds. La Fig. 39 est un de ces exemples. Cependant les corps ronds paraissent même dans ce cas très rarement comme on les voit dans la Fig. 40 (marquée →). Quand après avoir recouvert la surface de rupture du verre par une couche d'aluminium on fait la membrane polymérisée de méthacrylate de méthyl et qu'on arrache cette membrane, il arrive quelquefois que la couche d'aluminium est arrachée de la surface du verre et s'attache à la membrane polymérisée. On peut faire ainsi une réplique métallique en ombrant cette membrane avec le chrome. La Fig. 41 est un de ces exemples. La partie P est constituée par une couche double d'aluminium et de chrome et la partie Q est seulement formée de chrome. Même dans ce cas, les corps ronds n'apparaissent que très rarement. La Fig. 36 est celle que nous avons obtenue par hasard sur l'observation de la surface du monocristal d'aluminium par la même méthode de replique que ci-dessus ; il s'y trouve un corps rond. Ce serait le même que ceux que l'on voit dans la réplique de la surface d'une cassure de verre. Donc, bien qu'il ne soit pas vrai que l'on ne puisse jamais trouver un petit corps rond sur la réplique du méthacrylate de méthyl sur d'autres objets, c'est en général très rare. En conclusion, nous supposons que les corps concaves et convexes qui apparaissent abondamment sur la partie plane de la réplique d'une cassure de verre, n'existent pas en réalité sur la surface de rupture du verre, mais sont causés secondairement par quelque réaction spéciale entre la surface de rupture fraîche du verre et la matière de réplique. Et la distribution des points de réaction comme ceux-ci serait liée intimement avec l'inégalité de la surface de rupture du verre.

Nous tenons à remercier le Professeur M. Hirata pour les conseils bienveillants qu'il nous a donnés au cours de ce travail : enfin c'est grâce aux allocations du Ministère du l'Instruction Publique que nous avons pu le mener à bien.

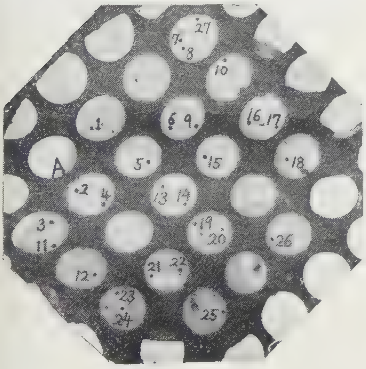

Fig. 0.

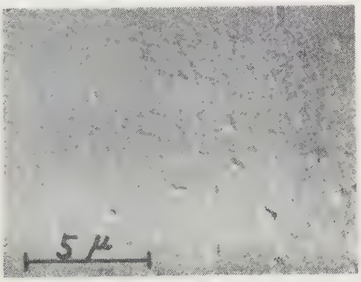

Fig. 1.

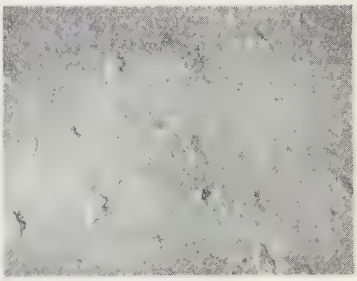

Fig. 2.

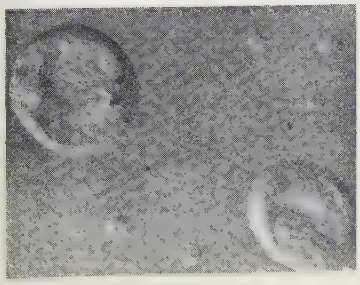

Fig. 3.

Fig. 4.

Fig. 5.

Fig. 6.

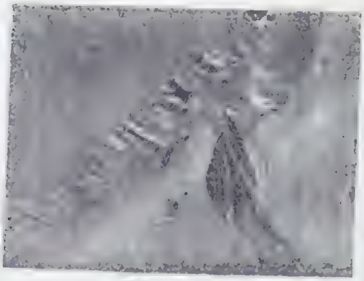
Fig. 7.

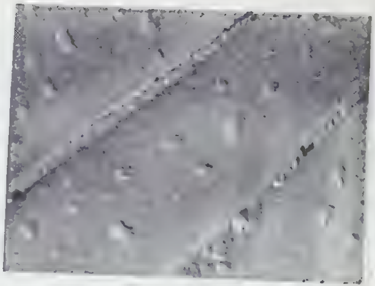
Fig. 8.

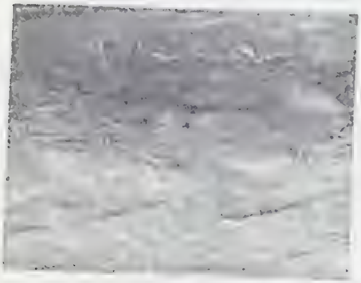
Fig. 9.

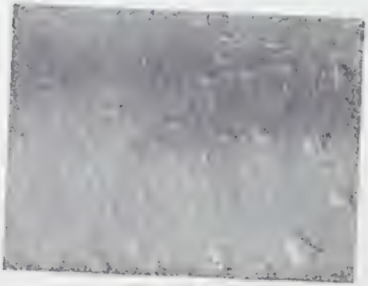
Fig. 10.

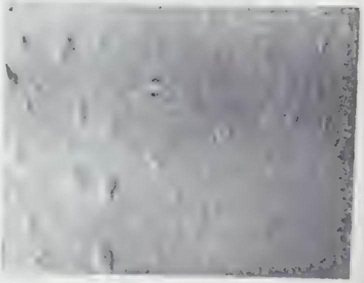
Fig. 11.

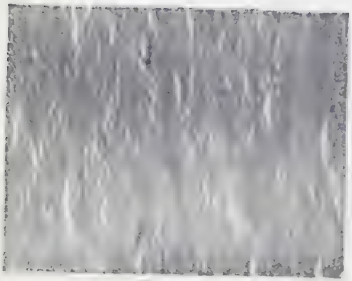
Fig. 12.

Fig. 13.

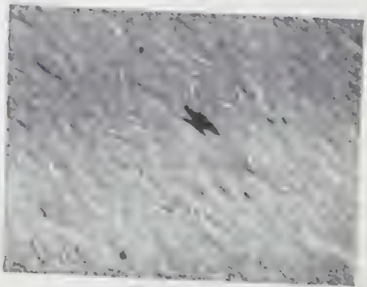
Fig. 14.

Fig. 15.

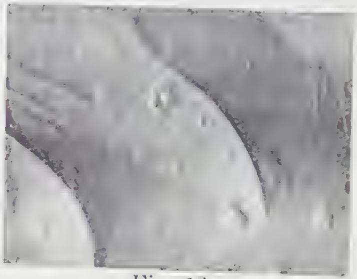
Fig. 16.

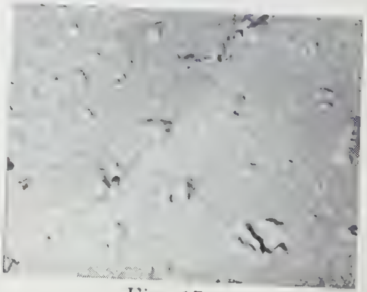
Fig. 17.

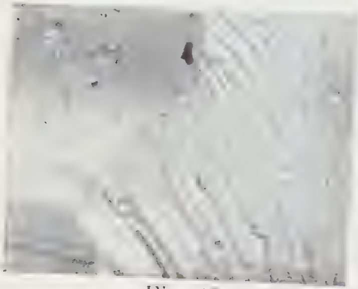
Fig. 18.

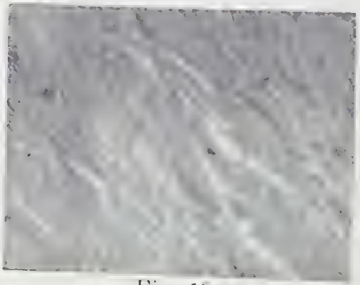
Fig. 19.

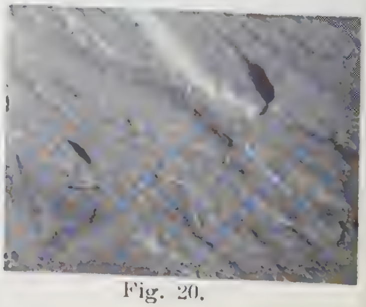
Fig. 20.

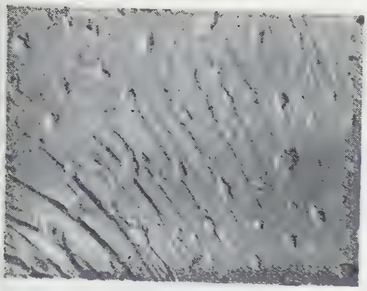
Fig. 21.

Fig. 22.

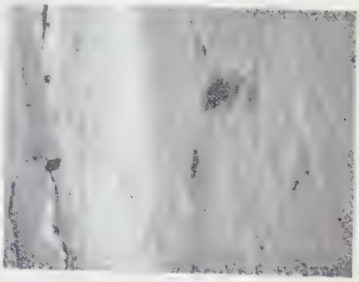
Fig. 23.

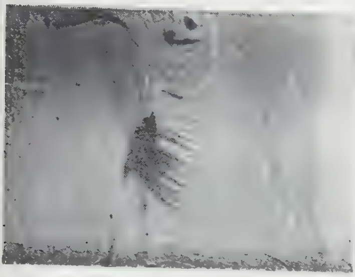
Fig. 24.

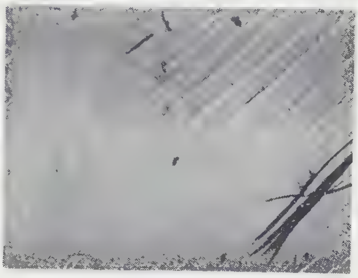
Fig. 25.

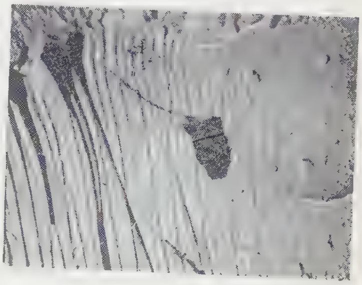
Fig. 26.

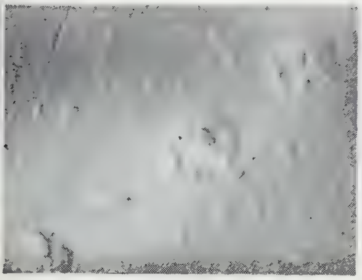
Fig. 27.

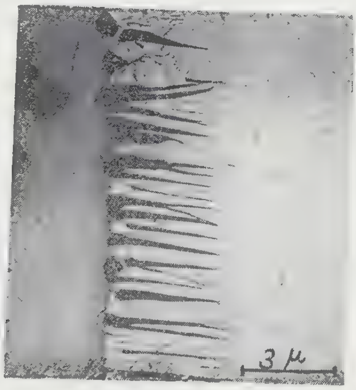

Fig. 28.

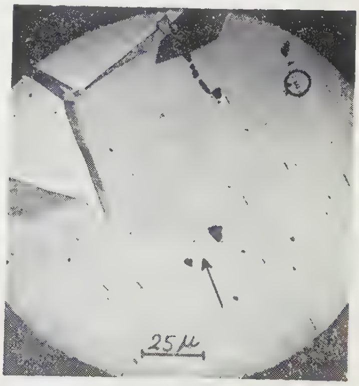

Fig. 29.

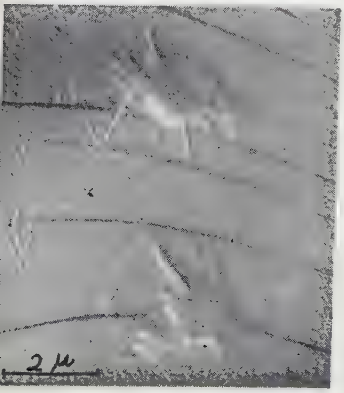

Fig. 30.

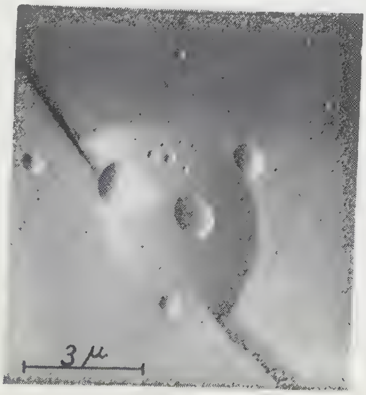

Fig. 31.

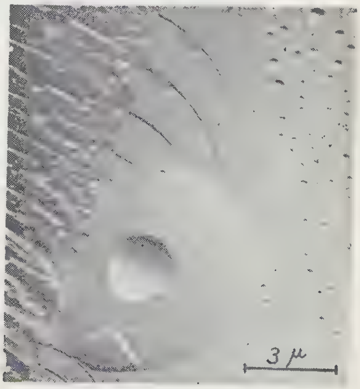

Fig. 32.

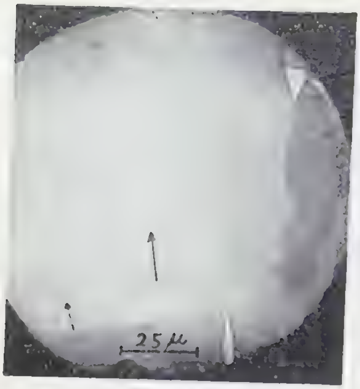

Fig. 33.

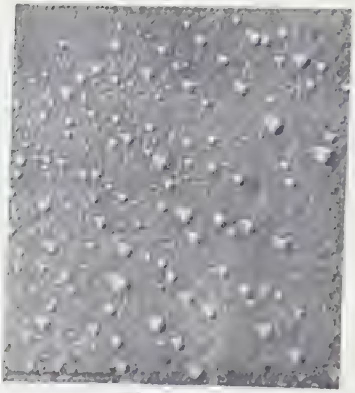

Fig. 34.

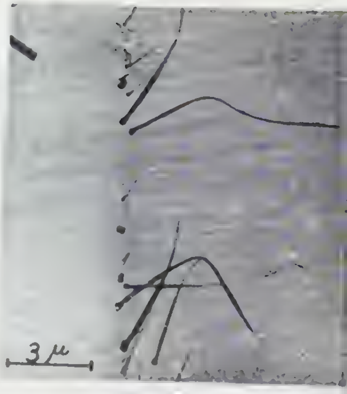

Fig. 35.

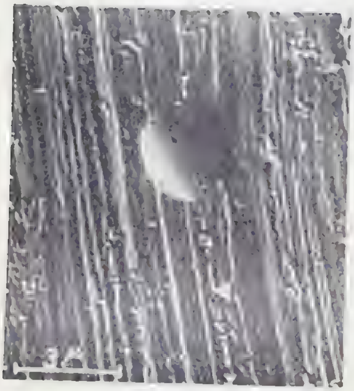

Fig. 36.

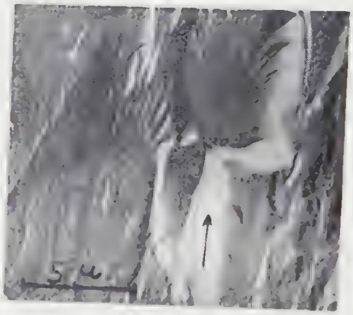

Fig. 37.

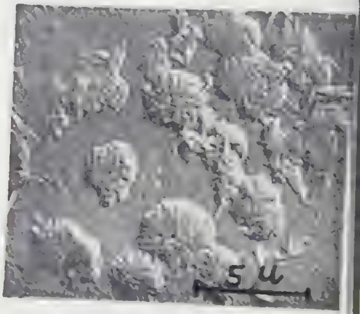

Fig. 38.

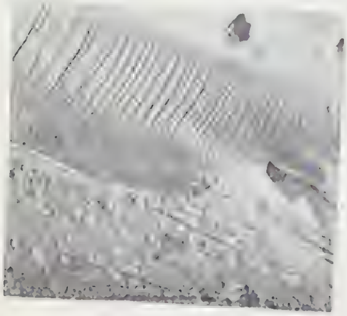

Fig. 39.

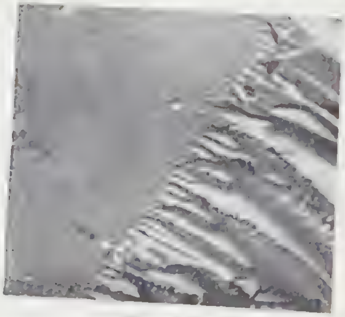

Fig. 40.

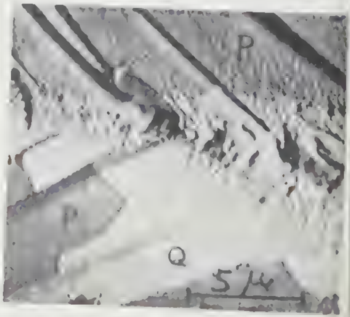

Fig. 41.

Bibliographie

1) N. Terao et S. Okada: J. Phys. Soc. Japan **7** (1952) 427.

2) N. Terao: J. Phys. Soc. Japan **8**(1953) 545.

JOURNAL OF THE PHYSICAL SOCIETY OF JAPAN Vol. 9, No. 1, JAN.—FEB., 1954

Feed-Back Resonance Amplifier for the Infrared Spectrometry
Part I

By Kuniya FUKUDA
Department of Physics, Faculty of Science, Kyoto University

(Received May 23, 1953)

The amplifying system employing two galvanometers was successfully used for the infrared spectrometry in Firestone's periodic radiometer. Our amplifier, having also two galvanometers, is characterized by the negative feed-back circuit, which connects the photovoltaic cell-secondary galvanometer circuit with the primary galvanometer so that the latter may oscillate under the resonance condition analogous to the resonance radiometer of Hardy. In this case the primary galvanometer has much higher sensitivity for a signal frequency than in its ordinary use, and then the whole amplifying system can be exerted free from both zero-drift and noises. In this paper will be given the theoretical analysis of the feed-back circuit, especially of the motion of the primary galvanometer.

§ 1. Introduction

The amplification with galvanometers for the infrared spectroscopic purpose was successfully accomplished by Firestone¹⁾ and numerous data of infrared molecular spectra were obtained by Randall and others²⁾. Firestone's "periodic radiometer" consists of two electric circuits; the thermocouple—primary galvanometer circuit and the photocell—secondary galvanometer one. These two parts are connected by the wellknown simple optical system³⁾, which converts the oscillation of the primary galvanometer to the photo-current in the photocell. This photocurrent, amplified by the amplifying circuit employing FP–54, makes the secondary galvanometer oscillate, whose deflections can be recorded on the photographic paper. In this system the primary galvanometer is used under approximate critical damping, and not in resonance, to get a short time of response. When used in resonance as in Hardy's resonance radiometer⁴⁾, the galvanometer has high sensitivity and low noises, but a long time of response, which is unsuitable for the spectroscopic purpose. The brief descriptions of a galvanometer will be given below, for it may be useful in understanding of our method of amplification.

In general the motion of a galvanometer is expressed by the following equation;

$$I\ddot{\varPhi}+P\dot{\varPhi}+D\varPhi=BJ\,,\quad P=\frac{B^2}{r}+f\,. \qquad (1)$$

The symbols used in this equation are as follows:

$\varPhi$: angular deflection of a galvanometer coil in radian.
I : moment of inertia of a galvanometer coil in gram cm².
P : moment of damping, which is the sum of electro-magnetic damping B^2/r and damping by mechanical causes f.
B : moment of displacement in dyne cm.
f : resisting torque per unit angular velocity due to mechanical resistances in dyne cm per radian per sec.
D : torsion constant of coil suspension in dyne cm per radian.
r : total resistance of galvanometer and external circuit in emu.
J : signal current in emu of current.

When the signal current J is expressed as $i_0\cos\omega t$, the solution of Eq. (1) is given by⁵⁾

$$\left.\begin{aligned}\varPhi&=\frac{Bi_0\sin(\omega t+\sigma)}{\sqrt{I^2(\omega_0{}^2-\omega^2)^2+P^2\omega^2}}-Ce^{-P/2I\cdot t}\sin\left\{\sqrt{\omega_0{}^2-\frac{P^2}{4I^2}}\cdot t+C'\right\}.\\ \sigma&=\tan^{-1}\frac{I(\omega_0{}^2-\omega^2)}{P\omega}\,.\end{aligned}\right\}\qquad(2)$$

Here ω_0 is 2π times the natural frequency of galvanometer in radian per sec and equal to $\sqrt{D/I}$.

In the ordinary usage of a galvanometer under critical damping (i.e. $P=2\sqrt{ID}$) the expression (2) becomes

$$\Phi=\frac{Bi_0\sin(\omega t+\sigma)}{I(\omega_0{}^2+\omega^2)}-Ce^{-\omega_0 t}\,. \qquad (3)$$

In this case the sensitivity, which is defined by $\delta\Phi/\delta i_0$,* decreases with increase of signal frequency.

In another case, when a galvanometer is brought to extreme under damping (i.e. $P\ll 2\sqrt{ID}$) by means of weakening its magnetic field, the expression (2) has a maximum value approximately at the natural frequency of galvanometer and yet this maximum sensitivity becomes highest by making the electromagnetic damping equal to the resisting torque due to mechanical causes (i.e. $B^2/r=f$); that is, under the condition $B^2/r=f$ the sensitivity of galvanometer has the highest value at $\omega=\omega_0$ and falls off for lower and higher frequencies, which makes the galvanometer free from zero-drift and noises. The maximum sensitivity for ω_0 is given by

$$S_r=\frac{\delta\Phi_r}{\delta i_0}=\frac{1}{2\omega_0}\sqrt{\frac{r}{f}}$$

(for current sensitivity), (4)

where the suffix r means that the magnetic field of the galvanometer satisfies the condition $B^2/r=f$, for which B will be designated below as B_r. This is Hardy's use of a galvanometer.

For an ordinary galvanometer, however, the high sensitivity enough for practical use cannot be necessarily obtained, as described later, even if the magnetic field is diminished to the point $B_r=\sqrt{rf}$. In Hardy's radiometer a galvanometer was newly constructed and its constants were suitably adjusted so that the actual high sensitivity could be secured. In spite of its high sensitivity and small noises (zero-drift and Brownian error) this resonant galvanometer is so sharply tuned that the steady state of oscillation cannot be reached till about thirty seconds or more. In Firestone's periodic radiometer Hardy's method is improved for spectroscopic purpose; the primary galvanometer is adjusted to approximate critical damping in order to shorten the response time, say to 6 or 8 sec. On the other hand, this method makes the sensitivity of the primary galvanometer lower and its noises (zero-drift and Brownian limit) higher to some extent, but these disadvantages are compensated by the FP-54 amplifying system.

The amplifier described in this paper has also two low resistance galvanometers, the primary and secondary ones, and a spescially deviced photovoltaic cell. These are connected by the simple electrical circuit, which feeds the optically induced current on the photovoltaic cell back to the primary galvanometer and makes it act under the state analogous to Hardy's resonant galvanometer. Then the primary galvanometer has the maximum sensitivity at a certain resonance frequency, which can be arbitrarily selected, and its value is much higher than that under critical damping or in Hardy's use. The zero-drift and the Brownian error also become much smaller in the primary galvanometer and are completely eliminated in the secondary galvanometer by the same way as in Firestone's method; the out-put current is fed through the condenser to the secondary galvanometer under critical damying**. Thus it may be expected that the stable amplification with high sensitivity can be realized by the feed-back resonance amplifier.

§ 2. Arrangement of Amplifier

The whole system of our amplifier is schematically depicted in Fig. 1. The wire-type thermocouple (Th) in the spectrometer impresses onto the primary galvanometer (G_1) the simple harmonic signal emf produced by the radiation chopped immediately before the entrance slit. The oscillation of the

---

* The current sensitivity is defined by $\delta\Phi/\delta i_0$ and the voltage sensitivity by $\delta\Phi/\delta E_0$. Here Φ is, of course, the amplitude of galvanometer deflection (half the full swing) and E_0 (or i_0) that of the simple impressed emf. In another definition of the sensitivity E is taken in the effective value, but, when this sensitivity is compared with that of the steady deflection, Φ and E must be rewritten in the double amplitude and the voltage change respectively; that is, the sensitivity must be written by our definition.

** The resonance of the two galvanometers at the same frequency, which is the case of the resonance radiometer, makes the Brownian error of the whole system increase.

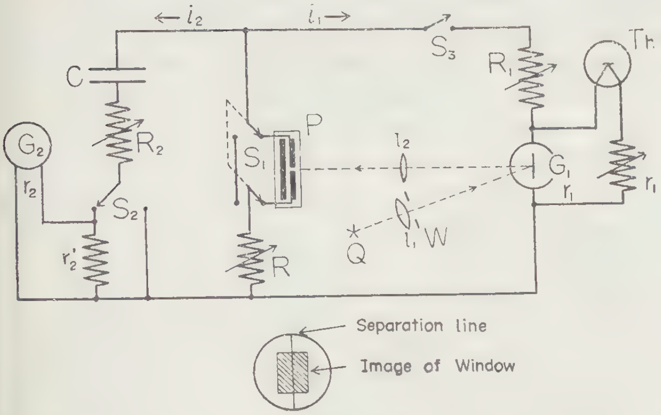

Fig. 1. The whole system of the feed-back resonance amplifier.

primary galvanometer is transferred to that of the image of the window (W) on the photovoltaic cell (P) by the simple optical system; that is, the image of the light source (Q) is focused on the mirror of the primary galvanometer through the lens l_1 and that of the window on the photovoltaic cell through the lens l_2 after reflection on the galvanometer mirror. The photo-conducting surface of the photovoltaic cell is cut off into two parts along its diameter by blade and the rectangular image of the window is placed symmetrically with respect to the separation line as shown below in Fig. 1. Thus, when the window image translates transversally, the voltage on the photovoltaic cell may be considered as the difference of those induced by the image in each part and accordingly, on the oscillation of the galvanometer, the momentary voltage may be proportional to the angular deflection of galvanometer.* This voltage supplys the feed-back current i_1 to the primary galvanometer through the resistance R_1 and the out-put current i_2 to the secondary galvanometer (G_2) through the condenser C and the resistance R_2. R is the series resistance to the photovoltaic cell, r_1, r_2, are the coil reistances, and r_1', r_2' the critical damping resistances of the primary and the secondary galvanometer respectively, the thermocouple resistance being, of course, contained in r_1'.

§ 3. Theoretical Analysis

On discussing the behavior of the primary galvanometer in the feed-back circuit the equation of motion is given by Eq. (1), where as the signal current J the current $i_1(t)$ fed from the photovoltaic cell must be taken into account in addition to the intrinsic signal current $i(t)$ from the thermocouple.

The momentary voltage $E(t)$ of the photovoltaic cell is proportional to the angular deflection Φ_1 of the primary galvanometer as mentioned in the preceding section and so defined by

$$E(t)=\chi\cdot\Phi_1(t)\,, \qquad (5)$$

where χ is the proportional constant, characteristic of the photovoltaic cell employed. For this photo-voltage the following equations hold, as easily understood from Fig. 1:

$$E(t)=(i_1+i_2)R+\frac{1}{c}\int i_2\cdot dt+i_2R_2\,,$$

$$E(t)=(i_1+i_2)R+i_1R_1\,.$$

By using the operator d/dt the feed-back current i_1 and the out-put current i_2 are expressed as follows:

$$\left.\begin{aligned} i_1&=\frac{1}{1+C\left(\dfrac{RR_1}{R+R_1}+R_2\right)\dfrac{d}{dt}}\cdot\frac{E(t)+CR_2\dfrac{d}{dt}E(t)}{R+R_1}\,,\\ i_2&=\frac{E(t)}{R}-\frac{1}{1+C\left(\dfrac{RR_1}{R+R_1}+R_2\right)\dfrac{d}{dt}}\cdot\frac{E(t)+CR_2\dfrac{d}{dt}E(t)}{R}\,. \end{aligned}\right\} \qquad (6)$$

Here, strictly speaking, the resistance symbols R_1 and R_2 have to be written as

$$R_1+\frac{1}{\dfrac{1}{r_1}+\dfrac{1}{r_1'}} \quad\text{and}\quad R_2+\frac{1}{\dfrac{1}{r_2}+\dfrac{1}{r_2'}}$$

respectively, but they may be used for simplicity.

The current fed to the primary galvanometer must be considered as the sum or the difference of $i(t)$ and $ni_1(t)$ according to positive or negative feed-back: $J=i(t)\pm ni_1(t)$, where n is the ratio $r_1'/(r_1+r_1')$ and so $ni_1(t)$

---

* The validity of these considerations will be experimentally proved in Part II.

is the net current fed back to the primary galvanometer from the photovoltaic cell. The current $i(t)$ is, of course, the sine wave having the chopping frequency ω of the sector; that is,

$$i(t)=i_0\sin\omega t=i_0(e^{i\omega t}-e^{-i\omega t})/2i\,.$$

Expressing the signal current J in terms of Φ_1 by using the expressions (5) and (6) and substituting it into Eq. (1), we obtain the equation of motion about Φ_1, the solution of which is given as follows*;

$$\left.\begin{aligned}\Phi_{1,f}(t)&=\frac{B_1i_0\sin(\omega t-\tan^{-1}\theta_\omega)}{\sqrt{\left\{-\omega^2I_1+D_1\mp\dfrac{B_1n\chi\cdot\dfrac{1+CR_2\omega^2A}{R+R_1}}{1+\omega^2A^2}\right\}^2+\omega^2\left\{P_1\pm\dfrac{B_1n\chi\dfrac{CRR_1}{(R+R_1)^2}}{1+\omega^2A^2}\right\}^2}}\,,\\ \theta_\omega&=\frac{\omega\left\{P_1\pm\dfrac{B_1n\chi\dfrac{CRR_1}{(R+R_1)^2}}{1+\omega^2A^2}\right\}}{-\omega^2I_1+D_1\mp\dfrac{B_1n\chi\cdot\dfrac{1+CR_2\omega^2A}{R+R_1}}{1+\omega^2A^2}}\,,\end{aligned}\right\}\qquad(7)$$

with the abbreviation $A=\{RR_1/(R+R_1)+R_2\}C$, where the suffix 1 is attached to distinguish the constants of the primary galvanometer from those of the secondary one and the suffix f means that the galvanometer is put in the feed-back circuit.

From the form of the expression (7) it may be expected that the sensitivity of the primary galvanometer has the maximum value near a certain frequency ω_f for which the first parenthesis term in the root of the denominator is equal to zero. This is the condition analogous to the resonance of Hardy's galvanometer. We call this condition the "feed-back resonance" and ω_f the "feed-back resonance frequency". Under this condition, in order to obtain high sensitivity, the second parenthesis term in the root of the denominator must be made considerably small for the frequeucy ω_f. This requirement for high sensitivity cannot be satisfied in the case of positive feed-back, but can be satisfied in the case of negative feed-back.

In order to realize the feed-back resonance in experiments, the circuit constants of the amplifier must be determined for a certain frequency ω_f so that the above-mentioned two conditions may be fulfiled, but it is difficult to carry out this process directly on the complicated expression (7) containing many parameters. For the sake of simplicity, R_2 in the expression (7) is made of the negligible order compared with the other circuit constants; that is, R_2 in Fig. 1 being taken away, then R_2 in the expression (7) becomes equal to $1/(1/r_2+1/r_2')$, of the order ten ohms. Then the expression (7) takes the following form for negative feed-back;

$$\Phi_{1,f}=\frac{B_1i_0\sin(\omega t-\tan^{-1}\theta_\omega)}{\sqrt{\left\{-\omega^2I_1+D_1+\dfrac{\dfrac{B_1n\chi}{R+R_1}}{1+\omega^2A^2}\right\}^2+\omega^2\left\{P_1-\dfrac{\dfrac{B_1n\chi}{R+R_1}\cdot A}{1+\omega^2A^2}\right\}^2}}\qquad(8)$$

with the abbreviation $A=RR_1C/(R+R_1)$. For a given resonance frequency ω_f the condition of the feed-back resonance is

$$-\omega_f{}^2I_1+D_1+\frac{\dfrac{B_1n\chi}{R+R_1}}{1+\omega_f{}^2A^2}=0\,,\qquad(8.1)$$

and the condition for high sensitivity is that

$$l=P_1-\frac{\dfrac{B_1n\chi}{R+R_1}\cdot A}{1+\omega_f{}^2A^2}\qquad(8.2)$$

is small. Accordingly the circuit constants, which give to the primary galvanometer a high maximum sensitivity at the resonance frequency ω_f, can be calculated from the expressions (8.1) and (8.2) by selecting a suitable small value for l. (In practice, the resistances R and R_1 were calculated by fixing the capacity of the condenser C to a proper value under a small l-value**.) Thus, in the feed-back resonance use of the primary galvanometer the sensitivity distribution in square frequency takes such a shape as shown in curves *I* of Fig. 2. The maximum sensitivity at the resonance frequency ω_f is given by $(S_{1,f})_{\omega_f}=\delta(\Phi_{1,f})_{\omega_f}/\delta i_0$, where $(\Phi_{1,f})_{\omega_f}$ is the maximum deflection at ω_f;

---

* See Appendix I.

** See the experimental procedures in Part II.

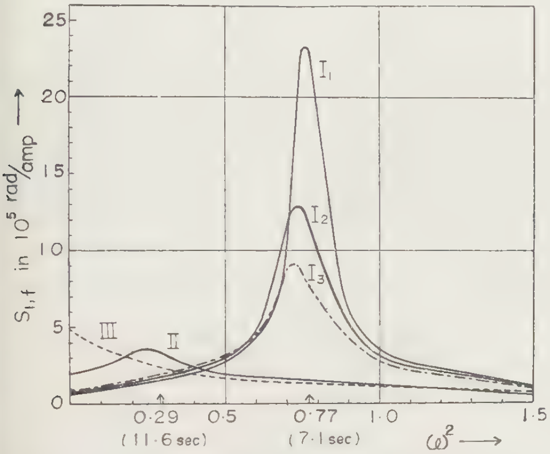

Fig. 2.* The sensitivity distribution curves in various uses of a galvanometer.

$$(\Phi_{1,f})_{\omega_f}=\frac{B_1 i_0 \sin\left(\omega_f t-\dfrac{\pi}{2}\right)}{\omega_f\cdot l}\,. \qquad (9)$$

In this case the sensitivity for the direct current ($\omega=0$) is

$$(S_{1,f})_{\omega=0}\equiv(S_{1,f})_{\text{drift}}$$
$$=\frac{\delta(\Phi_{1,f})_0}{\delta i_0}=\frac{B_1}{D_1+\dfrac{B_1 n\chi}{R+R_1}}\,. \qquad (10)^{**}$$

This indicates the zero-drift of the primary galvanometer in the negative feed-back circuit. Fig. 2 shows also two sensitivity curves II and III for Hardy's method and the critical damping use, as applied to the primary galvanometer employed in our experiments. In Hardy's method the sensitivity distribution follows the expression (2) and its maximum value at the natural frequency ω_0 is given by the expression (4). The expression (4) can be rewritten in the form $\delta\Phi_{1,r}/\delta i_0=B_{1r}/2f_1\omega_0$, where B_{1r} is the value of B_1 satisfying the condition $B_1^2/r=f_1$. When the sensitivity $(S_{1,f})_{\omega_f}=B_1/\omega_f\cdot l$ is compared with this in consideration of the fact $B_1\gg B_{1r}$, it is expected that the sensitivity in the negative feed-back resonance can be brought up to a much higher value than that in Hardy's resonance by making l comparable to f_1. The sensitivity for zero frequency, i.e. the zero-drift, is given by B_{1r}/D_1 for Hardy's use and by B_1/D_1 for critical damping, each of which can be derived from the expressions (2) and (3) for $\omega=0$. It is easily seen that the expression (10), representing the zero-drift in the negative feed-back, is smallerthan B_1/D_1, but it cannot be easily estimated without numerical calculations, which is larger, the expression (10) or B_{1r}/D_1 in Hardy's use. From the considerations just described it has been clear that the primary galvanometer in the negative feed-back circuit has very high sensitivity and suffers extremely small zero-drift.

The out-put current i_2 can be derived by substituting the expressions (7) or (8) into Eq. (6) according as R_2 is negligible or not. Writing the complicated terms in the root of the denominator of (7) as Q, the current i_2 has the subsequent form***;

$$i_2=\frac{B_1\chi i_0}{R\sqrt{Q}}\cdot\Big[\sin(\omega t-\tan^{-1}\theta_\omega)$$
$$-\frac{1+\omega CR_2}{\sqrt{1+\omega^2A^2}}\sin\{\omega t-\tan^{-1}\theta_\omega-\tan^{-1}(A\omega)\}\Big].$$

In our case, when R_2 is negligible, the expression of i_2 for the negative feed-back resonance becomes

$$i_2=\frac{\chi}{R}\cdot(S_{1,f})_{\omega_f}\cdot\frac{A\omega_f}{\sqrt{1+\omega_f^2A^2}}$$
$$\cdot i_0\sin\left\{\omega_f t-\frac{\pi}{2}+\tan^{-1}\left(\frac{1}{A\omega_f}\right)\right\} \quad (11)^{****}$$

at the resonance frequency ω_f, where $(S_{1,f})_{\omega_f}$ is, of course, $B_1/\omega_f\cdot l$. From this formula the current gain i_2'/i_0 can be easily estimated, i_2' being the net current fed to the secondary galvanometer, i.e. the product of i_2 and the ratio $n'=r_2'/(r_2+r_2')$.

The sensitivity of the amplifier can be defined by the deflection of the secondary galvanometer per the intrinsic signal current from the thermocouple, that is, $\delta(\Phi_{2,f})_{\omega_f}/\delta i_0$ and this is the product of the current gain and the sensitivity of the secondary galvanometer at the frequency ω_f. The value of the amplifier sensitivity will be computed in Part II by the experimental examinations.

---

* Fig. 2 will be explained again according to the experimental results in Part II.

** See Appendix I.

*** See Appendix II.

**** See Appendix II.

§ 4. Brownian Limit

The deflection error produced by the Brownian motion of the galvanometer coil is one of the most serious noise in the amplifying system using galvanometers. The Brownian motion of the coil can be estimated from the fact that in the degree of freedom under consideration each of the mean kinetic and the mean potential eneries of the coil is equal to the mean kinetic energy of a air molecule per degree of freedom; that is⁶⁾,

$$\tfrac{1}{2}I\overline{\dot{\Phi}^2}=\tfrac{1}{2}D\overline{\Phi^2}=\tfrac{1}{2}kT\,, \quad \text{or} \quad \sqrt{\overline{\Phi^2}}=\sqrt{kT/D}\,, \tag{12}$$

where k is the Boltzman constant and $\overline{\Phi^2}$ is the mean square deflection of the galvanometer due to the Brownian motion. $\sqrt{\overline{\Phi^2}}$ is also called the "mean Brownian deflection".

In the same way as Hardy's definition the Brownian error is defined by the root-mean-square of the periodic emf of the working frequeney, which will produce a periodic deflection of the galvanometer whose root-mean-square is equal to the mean Brownian deflection. Thus in Hardy's use the Brownian limit of the galvanometer can be obtained from the expressions (4) and (12) for the resonance frequency ω_0; it is

$$E_B=2B_r\omega_0\sqrt{kT/D}\,, \tag{13}$$

under the condition $B_r^2/r=f$. From the expressions (3) and (12) the Brownian limit in the critical damping use is given by

$$E_B=\alpha\cdot B\omega_0\sqrt{kT/D} \tag{14}$$

for a working frequency ω under the conditions $P=2\sqrt{ID}$ and $B^2/r\gg f$, where $\alpha=(\omega_0^2+\omega^2)/2\omega_0^2$. For the natural frequency of the galvanometer this becomes

$$E_B=B\omega_0\sqrt{kT/D}\,. \tag{15}$$

As for the primary galvanometer in the negative feed-back circuit the expression (12) must be somewhat modified. In this case the torsion constant of the primary galvanometer may be considered as

$$D_1+[\{B_1n\chi/(R+R_1)\}/(1+\omega^2A^2)]$$

for an arbitrary frequency ω from the expression (8), which is also proved by the fact that it becomes $D_1+[B_1n\chi/(R+R_1)]$ for zero frequency as shown in the expression (10). Accordingly the mean Brownian deflection becomes

$$\sqrt{\overline{\Phi^2}}=\sqrt{\frac{kT}{D_1+\frac{\frac{B_1n\chi}{R+R_1}}{1+\omega^2A^2}}}\,.$$

From this expression and the expression (8) the Brownian limit for the resonance frequency ω_f can be written as

$$E_B=\frac{lr\omega_0}{B_1}\sqrt{\frac{kT}{D_1}} \tag{16}$$

under the conditions (8.1) and (8.2) because of a very large maximum value (9) of the expression (8) at ω_f.⁷⁾ Taking into account that the constants of the primary galvanometer satisfy approximately the relations of critical damping, $P_1=2\sqrt{I_1D_1}$ and $B_1^2/r\gg f_1$, we can write the expression (16) in the following form;

$$E_B=\beta\cdot B_1\omega_0\sqrt{kT/D_1}\,, \tag{17}$$

where

$$\beta=l/P_1\,.$$

It is easily seen from the expressions (13) and (15) that the Brownian error in Hardy's resonance is lower than that of the critical damping use at the natural frequency of galvanometer because of $B_r\ll B$. This Brownian advantage of the resonant galvanometer, however, comes at the expense of an increase in response time, for the time of response is defined by $2I/P$ of the exponential factor of the expression (2). The Brownian limit in the negative feed-back resonance (17) is also much smaller than that of critical damping for the feed-back resonance frequency ω_f; in the frequency ω_f near to the natural one of the galvanometer α in the expression (14) is of the order 1, whereas β in the expression (17) is much smaller than unity. Next, when the expressions (13) and (17) are compared with one another, it cannot be easily determined without experimental examinations which is larger, but it will be possible for the Brownian error in the negative feed-back to become lower if β is bronght to a smaller value than $B_{1r}/B_1=\sqrt{f_1/P_1}$, that is, if l is made smaller than f_1. This is realized by the sharp tuning of the galvanometer in the negative feed-back circuit, but in this case it must be examined whether the time of response is prolonged as in Hardy's resonance or not. At the sharp tuning, which gives low noises (Brownian error and zero-drift) as well as a high sensitivity, the response time tends in general to become long.

§ 5. Conclusions

From the whole discussions described above it may be expected that the primary galvanometer in the negative feed-back circuit has the superior properties as compared to the other uses of galvanometer and that our amplifier is successfully used with high sensitivity and low noises. Furthermore our amplifier has the advantage that the feed-back resonance frequency and the sensitivity at this frequency are adjustable at will to considerable extent, which will give much convenience in practice. In this paper remains undiscussed the problem of the response time of amplifier, which will become important with respect to the scanning rate and the resolving power in the spectroscopic measurements. In the subsequent papers will be given the experimental procedures, by which the feed-back resonance is realized, as well as the discussions of response time.

The author wishes to express his sincere thanks to Prof. Y. Uchida for his continual interest and directions in this research and is indebted to Mr. H. Yoshimura for his helpful discussions in the course of this work.

Appendix I

The equation of motion of the primary galvanometer is given by

$$I_1\ddot{\Phi}_1+P_1\dot{\Phi}_1+D_1\Phi_1=B_1J\,,\qquad J=i(t)\pm ni_1(t)\,,\tag{1}$$

where

$$i_1=\frac{1}{1+C\left(\dfrac{RR_1}{R+R_1}+R_2\right)\dfrac{d}{dt}}\cdot\frac{E(t)+CR_2\dfrac{d}{dt}E(t)}{R+R_1}\,,\tag{6}$$

and $E=\chi\Phi_1(t)$ (5)

By using these expressions Eq. (1) becomes

$$I_1\ddot{\Phi}_1+P_1\dot{\Phi}_1+D_1\Phi_1\mp\frac{B_1}{1+A\cdot\dfrac{d}{dt}}\cdot\frac{n\chi(\Phi_1+CR_2\dot{\Phi}_1)}{R+R_1}=B_1i(t)\,,\tag{1'}$$

with the abbreviation $A=\left(\dfrac{RR_1}{R+R_1}+R_2\right)C$. To solve this equation, first $\Phi_1(t)$ is expanded into Fourier series as $\Phi_1(t)=\dfrac{1}{2\pi}\displaystyle\int_{-\infty}^{+\infty}\Phi_1(\omega)e^{i\omega t}\cdot d\omega$ and then this is substituted into Eq. (1′). Thus we obtain

$$\frac{1}{2\pi}\int_{-\infty}^{+\infty}\Phi_1(\omega)\left[-\omega^2I_1+i\omega P_1+D_1\mp\frac{B_1}{1+iA\omega}\cdot\frac{n\chi(1+iCR_2\omega)}{R+R_1}\right]e^{i\omega t}\cdot d\omega=B_1i(t)\,.$$

Multiplying the both sides of this equation by $e^{-i\omega' t}$ and integrating with respect to t, we obtain

$$\frac{1}{2\pi}\iint_{-\infty}^{+\infty}\Phi_1(\omega)\left[-\omega^2I_1+i\omega P_1+D_1\pm\frac{B_1}{1+iA\omega}\cdot\frac{n\chi(1+iCR_2\omega)}{R+R_1}\right]e^{i(\omega-\omega')t}\cdot d\omega\cdot dt=\int_{-\infty}^{+\infty}B_1i(t)e^{-i\omega' t}\cdot dt\,.$$

Then by using δ-function

$$\Phi_1(\omega)=\frac{B_1\displaystyle\int_{-\infty}^{+\infty}i(t)e^{-i\omega t}\cdot dt}{-\omega^2I_1+D_1\mp\dfrac{B_1n\chi\dfrac{1+CR_2\omega^2A}{R+R_1}}{1+\omega^2A^2}+i\omega\left\{P_1\pm\dfrac{B_1n\chi\dfrac{CRR_1}{(R+R_1)^2}}{1+\omega^2A^2}\right\}}\,.$$

When this is substituted into $\Phi_1(t)$ as expanded into Fourier series, the following expression is obtained;

$$\Phi_1(t)=\frac{1}{2\pi}\int_{-\infty}^{+\infty}\left[\int_{-\infty}^{+\infty} i(t)\,e^{-i\omega t}\cdot dt\right]$$

$$\cdot\frac{B_1 e^{i\omega t}}{-\omega^2 I_1+D_1\mp\dfrac{B_1 n\chi\dfrac{1+CR_2\omega^2 A}{R+R_1}}{1+\omega^2A^2}+i\omega\left\{P_1\pm\dfrac{B_1 n\chi\dfrac{CRR_1}{(R+R_1)^2}}{1+\omega^2A^2}\right\}}\cdot d\omega\,.$$

When the intrinsic signal current from the thermocouple is the sinsoidal one of the chopping frequency ω_0, that is, when $i(t)$ is expressed by $i(t)=\frac{i_0}{2i}(e^{+i\omega_0 t}-e^{-i\omega_0 t})\equiv i_0\sin\omega_0 t$, $\Phi_1(t)$ becomes

$$\Phi_1(t)=\frac{1}{2\pi}\int_{-\infty}^{+\infty}\left[\frac{1}{2i}\int_{-\infty}^{+\infty} i_0\{e^{i(\omega_0-\omega)t}-e^{-i(\omega_0+\omega)t}\}dt\right]$$

$$\times\frac{B_1 e^{i\omega t}}{-\omega^2 I_1+D_1\mp\dfrac{B_1 n\chi\dfrac{1+CR_2\omega^2 A}{R+R_1}}{1+\omega^2A^2}+i\omega\left\{P_1\pm\dfrac{B_1 n\chi\dfrac{CRR_1}{(R+R_1)^2}}{1+\omega^2A^2}\right\}}\cdot d\omega\,.$$

Using the δ-function again and writing the denominator of this expression in the exponential form, we obtain

$$\Phi_1(t)=\frac{1}{2i}\int_{-\infty}^{+\infty}\frac{i_0B_1\{\delta(\omega_0-\omega)-\delta(\omega_0+\omega)\}e^{i\omega t}}{-\omega^2 I_1+D_1\mp\dfrac{B_1 n\chi\dfrac{1+CR_2\omega^2 A}{R+R_1}}{1+\omega^2A^2}+i\omega\left\{P_1\pm\dfrac{B_1 n\chi\dfrac{CRR_1}{(R+R_1)^2}}{1+\omega^2A^2}\right\}}\cdot d\omega$$

$$=\frac{1}{2i}\cdot\frac{i_0B_1\{e^{i(\omega_0 t-\tan^{-1}\theta_{\omega_0})}-e^{-i(\omega_0 t-\tan^{-1}\theta_{\omega_0})}\}}{\sqrt{\left\{-\omega_0^2 I_1+D_1\mp\dfrac{B_1 n\chi\dfrac{1+CR_2\omega_0^2 A}{R+R_1}}{1+\omega_0^2A^2}\right\}^2+\omega_0^2\left\{P_1\pm\dfrac{B_1 n\chi\dfrac{CRR_1}{(R+R_1)^2}}{1+\omega_0^2A^2}\right\}^2}}\,, \tag{7'}$$

where

$$\theta_{\omega_0}=\frac{\omega_0\left\{P_1\pm\dfrac{B_1 n\chi\dfrac{CRR_1}{(R+R_1)^2}}{1+\omega_0^2A^2}\right\}}{-\omega_0^2 I_1+D_1\mp\dfrac{B_1 n\chi\dfrac{1+CR_2\omega_0^2 A}{R+R_1}}{1+\omega_0^2A^2}}\,.$$

The real part of this expression becomes the expression (7), in which the signal frequency is written as ω. The solution (7) is the particular one of Eq. (1′) and corresponds to the steady state of motion.

As for the zero-drift, setting the signal current $i(t)$ as i_0 in Eq. (1′), we obtain the expression (10).

Appendix II

Substituting the expression (7′) for $\Phi_1(t)$ into the expression of i_2 in (6) under $E=\chi\cdot\Phi_1(t)$, we can easily calculate the out-put current i_2.

When R_2 is negligible and the negative feed-back resonance consists at the frequency ω_f, the expression of i_2 becomes

$$i_2=\frac{\chi}{R}\cdot(S_{1,f})_{\omega_f}\cdot i_0\left[\sin(\omega_f t-\pi/2)-\frac{1}{\sqrt{1+\omega_f^2A^2}}\sin\{\omega_f t-\pi/2-\tan^{-1}(\omega_f A)\}\right]$$

$$=\frac{\chi}{R}\cdot(S_{1,f})_{\omega_f}\cdot i_0\left[\left\{1-\frac{\cos\{\tan^{-1}(\omega_f A)\}}{\sqrt{1+\omega_f^2A^2}}\right\}\sin(\omega_f t-\pi/2)+\frac{\sin\{\tan^{-1}(\omega_f A)\}}{\sqrt{1+\omega_f^2A^2}}\cos(\omega_f t-\pi/2)\right].$$

This leads to the expression (11).

References

1) F. A. Firestone: Rev. Sci. Inst. **3** (1932) 163.

2) H. M. Randall, R. G. Fowler, N. Fuson and J. R. Dangel: "Infrared Determination of Organic Structures." (D. Van Nostrand Co., Inc., 1949)

3) For example, R. B. Barnes and F. Mattossi: Zeits. f. Physik **76** (1932) 24.

4) J. D. Hardy: Rev. Sci. Inst. **1** (1930) 429.

5) F. Wenner: Bull. of Bureau of Stand. **6** (1909) 347.

6) F. A. Firestone, loc. cit.; J. D. Hardy, loc. cit.; G. E. Uhlenbeck and S. Goudsmit: Phys. Rev. **34** (1929) 145.

7) G. E. Uhlenbeck and S. Goudsmit: loc. cit.

JOURNAL OF THE PHYSICAL SOCIETY OF JAPAN Vol. 9, No. 1, JAN.—FEB., 1954

Feed-Back Resonance Amplifier for the Infrared Spectrometry
Part II

By Kuniya FUKUDA

Department of Physics, Faculty of Science, Kyoto University

(Received May 23, 1953)

The negative feed-back resonance has been brought about at the resonance frequencies of about 0.9 sec^{-1} and 1.65 sec^{-1} according to the numerical computations carried out on the discussions of Part I with experimental corrections and the circuit constants of the amplifier for various sensitivities at these frequencies have been determined. Our amplifier can be worked under resonance at any frequency in a wide range with sensitivity up to the order of 1×10^{-10} volt by adjusting the circuit constants. The spectroscopic works with the amplifier have been carried out at the resonance frequency 1.65 sec^{-1} with the sensitivity of 1×10^{-9} volt and fine absorption curves have been obtained.

§ 1. Introduction

In part I it was theoretically proved that the primary galvanometer in the negative feed-back circuit resonated under the suitable circuit constants at any signal (or resonance) frequency in a considerably wide range and that the amplifier had adjustable high sensitivity and low noises. In this paper the experimental procedures, by which the negative feed-back resonance is realized, will be described in detail, as well as the properties of the amplifier constructed in our laboratory. In order to find the circuit constants for the feed-back resonance, the constants of the primary galvanometer and the constant χ of the photovoltaic cell must be first determined by the experimental examinations.

§ 2. Determination of Primary Galvanometer Constants

When a galvanometer is set in under damping, its transient behavior can be expressed by the second term of the expression (2) of Part I; after the switch-off of an impressed voltage the galvanometer oscillates with the period $T=2\pi/\sqrt{\omega_0{}^2-(P/2I)^2}$ and the amplitude of this oscillation decreases according to $e^{-P/2I}$, where $P=f+B^2/r$, $\omega_0=\sqrt{D/I}$, and R is the total resistance of the galvanometer coil and the outer circuit. The galvanometer constants can be easily determined by observing the above two constants, the time swing and the decay constant, for various values of R. In our case

$R=\infty$: $f/2I=0.074$ sec^{-1},

$$T=2\pi\Big/\sqrt{\left(\frac{D}{I}\right)^2-\left(\frac{f}{2I}\right)^2}=11.64 \text{ sec},$$

$R=300\ \Omega$: $P/2I=0.115$ sec^{-1},

$$T=2\pi\ \sqrt{\left(\frac{D}{I}\right)^2-\left(\frac{P}{2I}\right)^2}=11.95 \text{ see},$$

$R=100\ \Omega$: $P/2I=0.191$ sec^{-1},

$$T=2\pi\Big/\sqrt{\left(\frac{D}{I}\right)^2-\left(\frac{P}{2I}\right)^2}=12.54 \text{ sec}.$$

From these observed values the values of D/I, B^2/I, and f/I can be calculated. Using these values, we can derive the galvanometer constants for its given sensitivity. For the sensitivity $D/B=2.2\times10^{-6}$ amp/rad of our primary galvanometer the following values of the constants were obtained; $I=15.5\times10^{-3}$ gr.cm², $B=2.04\times10^4$ dyne.cm/emu. of current, $f=2.30\times10^{-3}$ dyne.cm/rad/sec, $D=4.50\times10^{-3}$ dyne.cm/rad. By using the condition $P=2\sqrt{ID}=B^2/r_c+f$ for critical damping $P=16.8\times10^{-3}$ dyne.cm/rad/sec and $r_c=29$ ohm, where r_c is the total resistance under critical dampin. ω_0, 2π times of the natural frequency of the galvanometer, becomes 0.54 sec^{-1} from $\omega_0=\sqrt{D/I}$ and accordingly the characteristic period of the galvanometer is 11.6 sec.

§ 3. Linearity Constant χ of Photovoltaic Cell

The photovoltaic cell used in our amplifier is the selenium one and the relation between its induced voltage and the deflection of the primary galvanometer was measured by the statical method employing a quadrant electrometer. The optical system, which converts the oscillation of galvanometer to that of the window image on the photovoltaic cell, is depicted with its dimensions in Fig. 1. The rectangular window of 2 cm width and 3 cm long is illuminated through the leng l_1 from the light source Q (head light lamp 6 volt-5 amp.) and focused on the photovoltaic cell through the lens l_2 at the rate of two-thirds.

The procedure of the measurements of photo-voltage is as follows. First the mirror of the primary galvanometer is fixed so that the image of the window may take a symmetrical position with respect to the cutting line of the photo-conducting surface and then the photovoltaic cell is moved to right and left. Thus the photo-voltage caused by the translation of the photovoltaic cell was measured by the quadrant electrometer, the sensitivity of which was 350 div/volt. Fig. 2 shows the results of this measurements. It is found here that the range, in which the linear relation between the induced voltage and the translation of the photovoltaic cell holds, becomes wider with lowering of the resistance R inserted parallel to the photovoltaic cell; for $R=\infty$ the linearity is destroyed at the distance of about 2 mm and for R from 50 kΩ to 20 kΩ it holds up to 3 mm or more from the symmetrical position of the window image.

Now it is necessary to find the relation between the galvanometer deflection and the translation of the photovoltaic cell, which may be considered as that of the window image. Provided that the window image translates from one point a to another point b on the photovoltaic cell by the galvanometer deflection Φ_1, it may be considered that this translation ab is caused by the translation $a'b'$ of the window in lieu of the galvanometer deflection (see Fig. 1). Then the relation between the translations ab and $a'b'$ is easily comprehended by forming the mirror image of $a'b'$ with respect to the plane of the galvanometer mirror as shown by dotted line in Fig. 1. (There $\overline{W}$, $\overline{a'}$ and $\overline{b'}$ are the mirror images of W, a', and b' respectively.) It follows that $2\Phi_1$ can be calculated as the ratio $a'b'/a'G_1=3/2(ab/a'G_1)$. Under the dimensions of the optical system indicated in Fig. 1 the deflection of the galvanometer 1/470 rad. causes the translation 1 mm of the

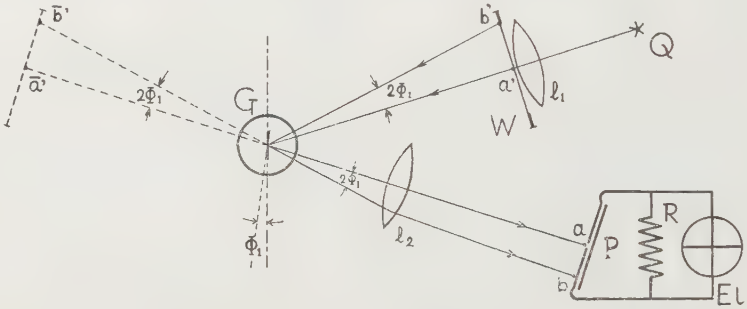

Fig. 1. The optical system converting the galvanometer deflection to the photovoltaic cell voltage

$l_1:f=10$ cm, $l_2:f=24$ cm, $WG_1=35$ cm $(=\overline{W}G_1)$, $G_1l_2=25$ cm, $l_2P=40$ cm, $Ql_1=14$ cm.

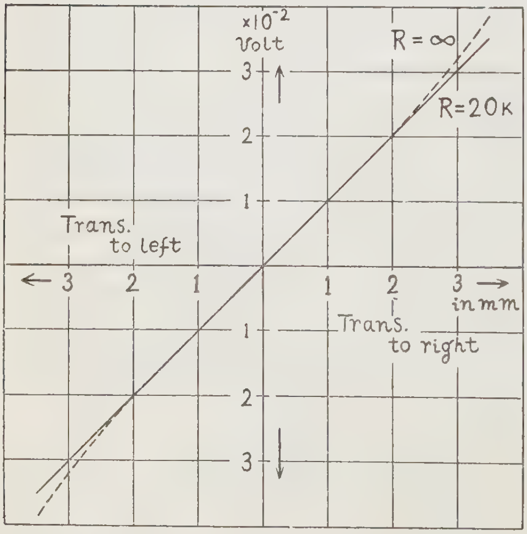

Fig. 2. The relation between the induced photo-voltage and the translation distance of the photo-voltaic cell.

window image, which induces the photovoltage about 0.01 volt as shown in Fig. 2. Accordingly the expression (5) of Part I becomes

$$E(t)=\chi\Phi_1(t)\ , \text{ and } \chi=4.7 \text{ volt/rad.} \qquad (5.1)$$

The value of χ essentially contains the factors concerning the intensity of illumination on the window, the dimensions of the window and the optical system, and the sensitivity of the photovoltaic cell. It is, however, rather important that there is the dependence of the linearity relation on the outer circuit of the photovoltaic cell, which limits the magnitude of the primary galvanometer deflection in practice.

§ 4. Negative Feed-back Resonance and Correction of χ-value

Now the circuit constants of amplifier must be determined by applying the values of the galvanometer constants and the linearity constant to the expression (8). For the constants given above, however, there remain still four variables ω, C, R, and R_1. Hence the values of ω and C were fixed to 0.88 sec^{-1} or 0.86 sec^{-1} (7.1 sec or 7.3 sec in period) and 72 μF respectively and then the resistance R and R_1 for the feed-back resonance were calculated for a given value of l. In selection of these ω- and C-values there was no spescial reason except the presumptions that the sensitivity of the primary galvanometer, accordingly that of the amplifier, would considerably fall down for a higher signal frequency and that the condenser of small capacity would not fit for such a low frequency current as used in our amplification.

As was described in Part I, the conditions for the negative feed-back resonance and the high sensitivity are given by

$$-\omega_f^2 I_1+D_1+\frac{B_1\, n\, \chi/(R+R_1)}{1+\omega_f^2 A^2}=0\ , \qquad (8.1)$$

and

$$P_1-\frac{\{B_1 n\chi/(R+R_1)\}\, A}{1+\omega_f^2 A^2}=l\ , \qquad (8.2)$$

for the resonance frequency ω_f with the abbreviation $A=RR_1C/(R+R_1)$. Here n is the ratio $r_1'/(r_1+r_1')$ and becomes 6/13 in our case, where the coil resistance (r_1) of the primary galvanometer is 16Ω and the resistance of the thermocouple circuit 13.7 Ω. For the frequency ω_f the deflection of the primary galvanometer is given by

$$(\Phi_{1,f})_{\omega_f}=\frac{B_1\, i_0 \sin(\omega_f t-\pi/2)}{\omega_f\, l}\ , \qquad (9)$$

and the sensitivity by $(S_{1,f})_{\omega f}=\delta(\Phi_{1,f})_{\omega f}/\delta i_0=B_1/w_f l$. l may be considered as the sensitivity parameter of the primary galvanometer in the negative feed-back resonance.

In our case the numerical computations gave the following results; for $l=2\times10^{-10}$* $R=36$ kΩ, $R_1=167$ kΩ at $\omega_f=0.88\ \text{sec}^{-1}$ and $R=38$ kΩ, $R_1=120$ kΩ at $\omega_f=0.86\ \text{sec}^{-1}$**, where $C=72\ \mu$F on both cases, while $l=2\times10^{-10}$ gives the sensitivity 1.16×10^6 rad/amp and 1.19×10^6 rad/amp to the primary galvanometer in each case. In experiments, however, the feed-back resonance could not be realized just at these calculated values of the resistances, but in the neighbourhood of them within ten kilo-ohms. This error resulted chiefly from the ambiguity contained in the χ-value (4.7 volt/rad) measured by the statical method and so the χ-value had to be corrected so as to be consistent with the experimental results.

The negative feed-back resonance was found in experiments by observing the following three conditions of the amplifier. i) If the switch S_3 for the feed-back current is off (see Fig. 1 of Part I), the primary galvanometer deflects under critical damping only for the signal current from the thermocouple. Then the sensitivity of the galvanometer $(S_1)_{\omega f}$ becomes 1.23×10^5 rad/amp for $\omega_f=0.88\ \text{sec}^{-1}$ and 1.27×10^5 rad/amp for $\omega_f=0.86\ \text{sec}^{-1}$ by calculating from the expression (3) of Part I***. On the other hand the sensitivity for the feed-back resonance is given by the above calculated value of $(S_{1,f})_{\omega f}$ for $l=2\times10^{-10}$ and, therefore, the ratio of $(S_{1,f})_{\omega f}/(S_1)_{\omega f}$ becomes equal to about 9.5 for both ω_f, which is also the ratio of the linear deflections of the primary galvanometer on feed-back and on no-feed-back. Thus the resonance can be testfied by observing the magnitudes of the window-image translation on the photovoltaic cell for these both cases by a telescope. ii) The primary galvanometer has the maximum deflection approximately at the resonance frequency ω_f. This can be examined by observing the primary (or the secondary) galvanometer deflection for the variation of chopping frequency of the sector. iii) In the feed-back resanance the phase difference between the chopping sector (i.e. the signal current) and the deflection of the primary galvanometer is $\pi/2$ as shown in the expression (9). This fact can be confirmed with some exactness on visual observations.

---

* The unit of l-value is the same as P.

** From the expressions (8.1) and (8.2) the quadratic equation of R can be derived, the larger root of which may be taken as the value of R_1 and the smaller as that of R because of the gain in the out-put current for a smaller value of R (see the expression (11) of Part I).

*** Under critical damping the galvanometer sensitivity at a frequency ω is given by $(S)_\omega=(S)_0\cdot\omega_0^2/(\omega_0^2+\omega^2)$, where $(S)_0$ is the sensitivity for $\omega=0$.

For the chopping frequencies $\omega_f=0.88\ \text{sec}^{-1}$ and $\omega_f=0.86\ \text{sec}^{-1}$ the negative feed-back resonance was found by the above method and then the resistances R and R_1 were measured for each case. As the result the following values were obtained ; $R=33$ kΩ, $R_1=167$ kΩ for $\omega_f=0.88$ sec^{-1} and $R=36$ kΩ, $R_1=163$ kΩ for $\omega_f=0.86$ sec^{-1}. By applying these resistance values to the expressions (8.1) and (8–2) the χ-value was calculated as 6.5 volt/rad for both frequencies. Under this value of χ it was found that the calculated values of the amplifier sensitivities and the circuit constants fairly coincided with the experimental results and accordingly it was concluded that this χ-value was correct.

$$E(t)=\chi\cdot\Phi_1(t) \text{ aud } \chi=6.5 \text{ volt/rad} . \qquad (5.2)$$

§ 5. Properties of Amplifier and Noises

Table I shows the characteristic values of the amplifier for $\omega_f=0.88$ sec^{-1} and $C=72$ μF. The listed values are the calculated ones for various l-values under $\chi=6.5$ volt/rad. The values of R and R_1 can be calculated from the expressions (8.1) and (8.2) for each l-value and $(S_{1,f})_{\omega f}$ and $(S_1)_{\omega f}$ are the sensitivities of the primary galvanometer on feed-back and on no-feed-back, the ratio of which was proved to be in good agreement with the observed one. The cucves I_1, I_2, and I_3 in Fig. 2 of Part I indicate the sensitivity distribution for $l=1$, 2, and 3, respectively. If Hardy's method were applied to our primary galvanometer, the maximum sensitivity S_r for ω_0 would become 3.3×10^5 rad/amp from the expression (4) in Part I. It follows that the sensitivity of an ordinary galvanometer cannot be made so high in Hardy's use.

The current through the secondary galvanometer $n'i_2$ is calculated from the expression (11), where n' is the ratio $r_2'/(r_2+r_2')$ and becomes 30/43.7 for the coil resistance 13.7 Ω of the secondary galvanometer and its external parallel resistence 30 Ω. The ratio $n'i_2/i_0$ is the amplification factor of current. The sensitivity $(S_{2,f})_{\omega f}$ is defined by $\delta(\Phi_{2,f})_{\omega f}/\delta i_0$, that is, the deflection of the seeondary galvanometers for the resonance frequency ω_f per the intrinsic signal current from the thermocouple. The galvanometer, used as the secondary one in the amplifier, has the sensitivity $(S_2)_{\omega f}$. Hence the sensitivity $(S_{2,f})_{\omega f}$ can be calculated from the product of $(S_2)_{\omega f}$ and $n'i_2/i_0$. From the above definition $(S_{2,f})_{\omega f}$ gives the sensitivity of the whole amplifying system. When the deflections of the secondary galvanometer are recorded at the distance of 1 m, the sensitivity of the amplifier is about 1×10^{-9} volt as shown in Table I, which is superior to the sensitivity 3×10^{-9} volt of Firestone's type amplifier used by Randall and others.

$(S_{1,f})_{\text{drift}}$ in Table I is the current sensitivity

Table I. The characteristic constants of the amplifier for 0.8 sec^{-1} (7.1 sec in period) and $C=72\mu$F

l	R	R_1	$(S_{1,f})_{\omega f}$	$n'i_2/i_0$	$(S_{2,f})_{\omega f}$		$(S_{1,f})_{\text{drift}}$	E_B
$\times10^{-10}$	in kΩ	in kΩ	in $\times10^5$ rad/amp	$\times10^2$	in $\times10^5$ rad/amp	in $\times10^{-9}$ volt/mm	in $\times10^5$ rad/amp	in $\times10^{-11}$ volt
1	37	147	23.2	2.4	182	0.8	0.53	2.1
2	33	167	11.6	1.3	99	1.5	0.58	4.1
3	30	195	7.7	1.1	74	2.0	0.64	6.2

$(S_1)_0 =4.5 \times10^5$ rad/amp ($\equiv3.3\times10^{-8}$ volt/mm)
$(S_1)_{\omega f}=1.23\times10^5$ rad/amp, $\omega_0=0.54$ sec^{-1} (11.6 sec in period)
$(S_2)_0 =1.66\times15^5$ rad/amp ($\equiv1.1\times10^{-7}$ volt/mm)
$(S_2)_{\omega f}=0.76\times10^5$ rad/amp, $\omega_0=0.80_5$ sec^{-1} (7.8 sec in period)

of the primary galvanometer for $\omega=0$, which indicates the zero-drift, and its listed values are very small compared with the same quantities for the galvanometer under critidamping and in Hardy's use ; the zero-drift is calculated as 4.5×10^5 rad/amp from $(S_1)_0$ for the former and as 2×10^5 rad/amp from B_{1r}/D_1 for the latter. Table I shows that the value of $(S_{1.f})_{\mathrm{drift}}$ becomes smaller with decrease of l-value, that is, with increase of the sensitivity of the primary galvanometer. Although the secondary galvanometer is free from zero-drift by the condenser in the amplifier circuit, the large magnitude of zero-drift in the primary galvanometer makes the long time measurements impossible, because the window image goes away from the cutting line of the photovoltaic cell*. In our case any disturbance from zero-drift does not occur during the measurements of one day long. The Brownian limit, which is designated as E_B in Table I, is calculated from the expression (16) of Part I for the resonance frequency ω_f and the listed values are one-tenth as small as those under critical damping and in Hardy's use ; the Brownian limit of the primary galvanometer becomes 6.1×10^{-10} volt at the frequency ω_f from the expression (14) for the former and 2.7×10^{-10} volt at the frequency ω_0 from the expression (13) for the lattar. The Brownian error of the primary galvanometer in the amplifier, which also falls down with increase of the galvanometer sensitivity, has the magnitude of the order 5×10^{-11} volt and this does not cause any noise in measurements under the condition of the amplifier with the sensitivity of about 1×10^{-9} volt. In practice the detected noises seem to be produced by the other various causes than the Brownian random motions.

When the chopping sector was driven by the phono-motor, the long-time measurements were impossible because of the unsteadiness of the motor caused by the line-voltage change. This noise, however, was avoided by using the synchronous motor employed in an electric clock. Under the ordinary working condition of the amplifier the fluctuation produced by the cycle change did not cause any remarkable noise in measurements. Besides the noise induced by the rotating sector there is the most serious noise produced by the mechanical causes. This noise is considerably reduced by the negative feed-back circuit, but the whole amplifying system cannot be operated free from the mechanical vibration without the vibrationless support for the primary galvanometer. Although no spescial device was applied to stabilize the globar, the signal to noise ratio could be brought down to about 1/100 by taking cautions against the above two points. Fig. 3 shows the magnitude of the noise detected under the working condition of the amplifier with the sensitivity of about 1×10^{-9} volt for the resonance frequency $\omega_f=0.88$ sec^{-1} (7.1 sec in period), for which the deflection of the secondary galvanometer is 100 mm. The amplification at the resonance frequency $\omega_f=1.65$ sec^{-1} (3·8 sec in period) was carried out by the same way as described above and the good coincidence between the calculated and the experimental values of the amplifier constants was found for various sensitivities (say from the order of 1×10^{-9} volt to 1×10^{-10} volt).

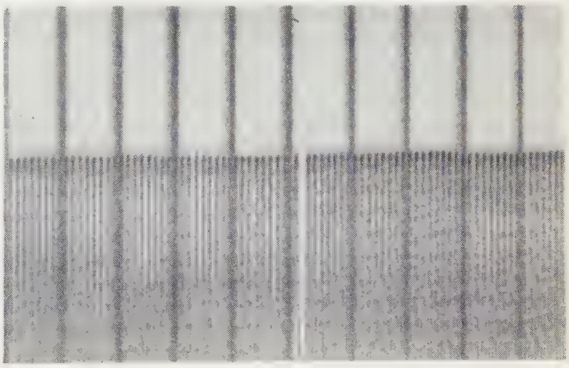

Fig. 3. The magnitude of the noise recorded by the amplifier (of full size).

Lastly the capacity of the condenser C will be examined. In our experiments the capacity was fixed at 72 μF, but this value can be varied in a wide range. However, there is a lower limit in the capacity value, which is determined by the quadratic equation of R derived from the expressions (8–1) and (8–2); it is the lower limit that makes the discriminant of the equation equal to zero, and then the equal roots correspond to the values of R and R_1. For a capacity larger than this lower limit there are two distinct roots in the quadratic equation, the larger of which is taken as R_1 and the smaller as R. As the out-put current i_2 increases for smaller R-value, it is desirable to make the capacity of the condenser as large as possible.

---

* In the Firestone-type amplifier the primary galvanometer suffers from this disturbance.

§ 6. Response Time

It was experimentally found that under the resonance frequency 0.88 $\sec^{-1}$ the time of response varied from more than 40 sec. to about 30 sec. in the range of l-value from 1×10^{-10} to 3×10^{-10} and that it became longer with sharp tuning of the primary galvanometer. Even with these values of response time, the amplifier may be used satisfactorily for the automatic measurements of absorption, combined with slow rotation of the Littrow mirror in a monochromator. However, in order to secure a high resolving power and a high scanning rate, a compromise between the two incompatible factors, high sensitivity and short response time, is necessary, and the best working condition of the amplifier should be so selected as to give as short a response time as possible under a reasonably high sensitivity.

The response time of the amplifier is determined by the time constant of the primary galvanometer according to the general solution of Eq. (1) of Part I for the negative feed-back. The computations of the response time and the sensitivity for various resonance frequencies indicate in accordance with the experimental results that the best working condition of the amplifier exists in the neighbourhood of the resonance frequency of 1.25 $\sec^{-1}$ (5 sec in period); for example, the response time is about 30 sec., 10 sec., and 15 sec. for response periods 7.1 sec., 5 sec., and 3.8 sec. respectively under the same sensitivity of the amplifier of about 1×10^{-9} volt/mm, where the deflection of the secondary galvanometer is recorded at the distance of 2 m.

Table II. The properties of the amplifier at the resonance period of 3.8 sec.

$T=3.8$ sec., $C=72$ μF.

l in $\times10^{-10}$	R_1 in kΩ	R in kΩ	$(S_{1,f})_{\omega f}$ in $\times10^5$ rad/amp	$(S_{2,f})_{\omega f}$ in $\times10^5$ rad/amp	in $\times10^{-9}$ volt/mm	$(S_{1,f})_{\text{drift}}$ in $\times10^5$ rad/amp	E_B in $\times10^{-11}$ volt	Resp. time in sec.
1	103	6	12.4	160	0.9	0.34	2.5	33
2	110	5.5	6.2	86	1.7	0.35	4.8	20
3	111.5	5.5	4.1	54	2.7	0.36	7.3	14~13
4	117	5	3.1	42	3.5	0.37	9.6	10
5	123.5	4.5	2.5	35	4.2	0.39	12.0	8~7

§ 7. Spectroscopic Work with the Amplifier

For the spectroscopic works our amplifier has been used at the resonance frequency of 1.65 $\sec^{-1}$ (3.8 sec. in period). Table II shows the various properties of the amplifier at this resonance frequency. The working condition of the amplifier at this frequency is somewhat out of the best one, but good enough to make the practical fine measurements possible. In our case the secondary galvanometer has been used at a scale distance of 2 m so that a high sensitivity may be secured with a short response time. The sensitivities of the amplifier $(S_{2,f})_{\omega f}$ listed in Table II are, of course, for the scale distance of 1 m and so the sensitivity was twice higher in our real scale.

Our spectrometer is of Beckman-Littrow type; 60° prism is of 6 cm in edge and of 5 cm in height and the main concave mirror has the focal length of 80 cm and $F=10$. For the automatization the wavelength drum and the recording one are connected by a gear system and driven by the synchronous-motor. The entrance and the exit slit, simultaneously operated by a gear system, are coupled to the wavelength drum for a continuous slit drive. As this coupling is linear in our case, the compensation for intensity change with wavelength is not complete, but it has become possible to a considerably extent by separating the whole range of wavelengths ($3\sim15\mu$) into three stages ($3\sim6\mu$, $5\sim10\mu$, and $9\sim15\mu$) and by changing the coupling ratio in each stage.

The automatic absorption measurements were carried out under the amplifier condition with the sensitivity of about 1×10^{-9} volt and the response time of about 15 sec. The exact trace of absorptions was successfully obtained as shown in the recorded curve for pyroxyline film (see Fig. 4); the whole measurements can be worked out completely free from the zero-drift and with extremely low noises and the scanning time from 3μ to 15μ (for the region of NaCl prism) is about one and a half hours. Under the best working condition of the amplifier at the resonance period of 5 sec. a greater scanning speed with the same sensitivity would be obtainable.

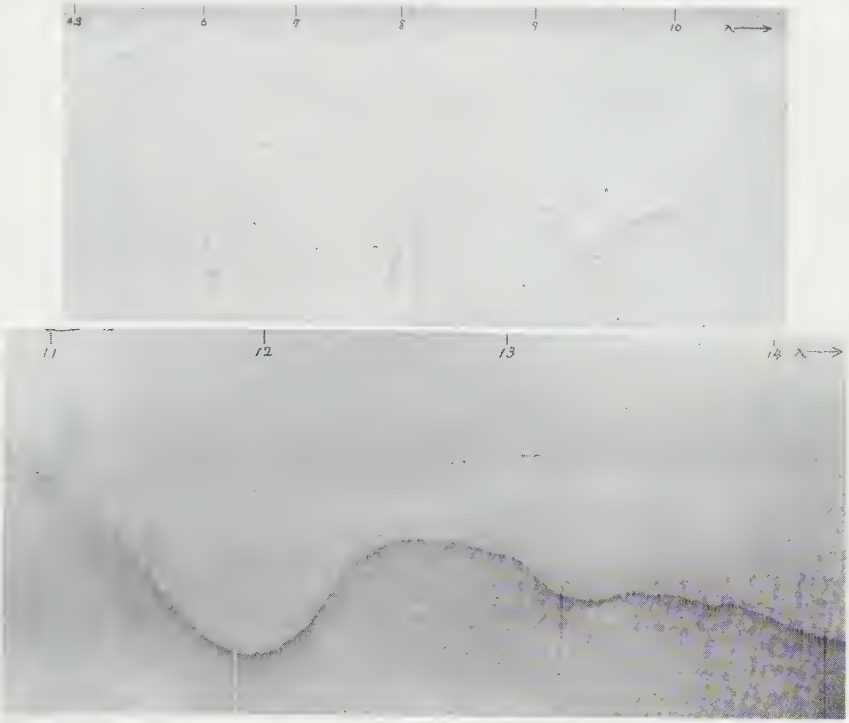

Fig. 4. The recorded absorption curve of pyroxyline film (from 4μ to 15μ).

§ 8. Conclusions

It has been experimentally proved with good agreement to the theoretical results that the stable amplification with high sensitivity is possible by applying the negative feed-back device to the amplifying system of galvanometers. In practice it may be somewhat troublesome to determine the galvanometer constants and the linearity constant of the photovoltaic cell, but, once these constants have been known, the negative feed-back resonance can easily be realized by adjusting the circuit constants (the resistances in our case), in accordance with their calculated values for various sensitivities at any resonance frequency. The adjustable resonance frequency and the adjustable sensitivity will give much convenience to the practical use of our amplifier. In some range of the circuit constants a complicated transient phenomenon appears, but this range can be easily found in experiments.

In ordinary use for the automatic absorption measurements our amplifier has been employed at the resonance period of 3.8 sec. The negative feed-back device, in fact, has extremely reduced the noises (those by mechanical causes, zero-drift, and Brownian error); contrary to the case of the periodic radiometer, no disturbance occurs from the zero-drift of the primary galvanometer in the course of a long-time automatic measurement. The extremely small Brownian limit enables a spectroscopic work with very high sensitivity (of the order of 1×10^{-10} volt).

The author wishes to express his sincere thanks to Prof. Y. Uchida for his continual interest and directions in this research and is indebted to Mr. H. Yoshimura for his helpful collaboration in this work.

J. Phys. Soc. Japan 9 (1954) 130~131

The "Photo-Aftereffect" of Germanium Crystal Rectifiers

By Makoto Kikuchi and Tomio Onishi
Electrotechnical Laboratory, Tokyo, Japan

(Received June 5, 1953)

It has been found that the resistance of the Ge crystal rectifiers can be reduced by the illumination of the contact point. This phenomenon is different from the so-called photoeffects. (See Fig. 1) As shown in Fig. 2, the current at the bias voltage of -0.2 V is increased about 6 times larger than the normal value i_0 by the illumination of 90 seconds, and it decreases to i_0 with time. The currents were measured with the bias voltage which were applied instantaneously to avoid the creeping effect. These curves could not be expressed either by the form of $\exp(-t/\tau)$ or $\exp(-\alpha\sqrt{\tau})$.

The half-value time $T_{1/2}$, which is defined as the time required for the current increment $(i-i_0)$ to decrease to half the initial value, is independent of the applied voltages, time of illumination, but depends on the temperature as shown in the Table I.

The possible physical processes underling this phenomenon are as follows;

(1) The temperature rise of the contact by the illumination.

(2) The polarization of the barrier caused by the impurity migration.

(3) The action of the remainder of the hole-electron pairs produced by the light quantums.

(4) The modulation of the shape of the barrier,
  (a) caused by the action of the surface states,
  (b) caused by the increase of the space charges.

These possibilities were inquired experimentally as follows:

(1) The temperature rise at the vicinity of the contact was measured by the thermocouple inserted into the wax protecting the contact. The measured temperature rise was smaller than 0.5°C. The temperature rise at the contact point itself must be less than this value so we cannot explain the experimental results on this picture.

(2) We could not find any indication of the current by shorting the rectifier through a galvanometer just after the illumination. This implies that the phenomenon is "conductive" but not "voltaic". Therefore, the possibilities of (2) and (3) mentioned above can be eliminated.

We tried to analyze the experimental results on the following physical picture;

(1) There is a "Schottky" barrier at the contact.

(2) The top of the barrier is lowered by the "image force".

(3) Thus, the effective barrier height ϕ_0 is expressed for the first approximation as follows;

$$\phi_0=\phi_\sigma-\sqrt{\frac{e}{\kappa}}\left(\frac{8\pi Ne}{\kappa}\right)^{1/4}(\phi_\sigma+V)^{1/4}, \qquad (1)$$

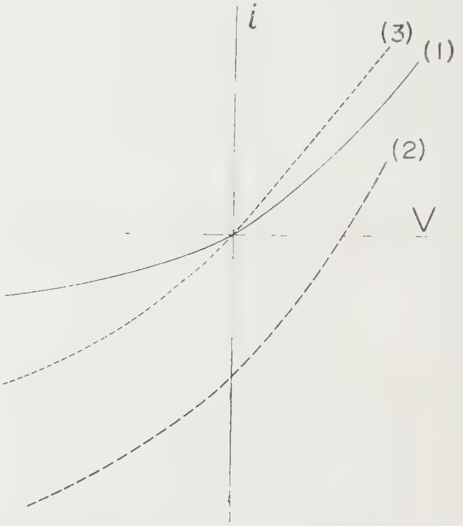

Fig. 1. Graphical description of the photoeffect and photoaftereffect.
(1) before the illumination.
(2) under the illumination. (so-called photoeffect).
(3) after the prolonged illumination. (photoaftereffect).

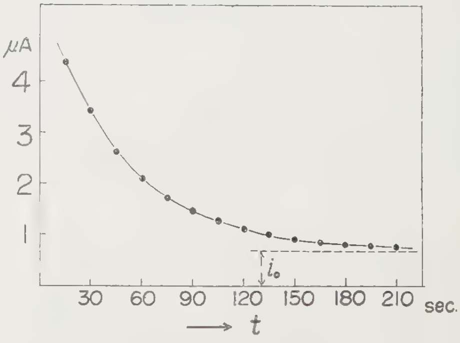

Fig. 2. Recovery of the current at -0.2 V after the illumination. (time of illumination Ti=90 sec.)

where ϕ_σ is the barrier height of the Schottky barrier without the effect of the image force, N the space charge density, κ the dielectric constant, and V is the applied reverse voltage.

(4) Only the portion $\beta(<1)$ of the total contact area A is illuminated. The value of β is expected to be between 0.04 and 0.4 theoretically.

(5) The current depends on the effective barrier height ϕ_0 mainly by the form of $\exp(-e\phi_0/kT)$.

(6) ϕ_0 is lowered to $\phi_0-\phi_s$ by the illumination, and ϕ_s decays to zero exponentially after the

illumination.

From these assumptions the current variation after the illumination could be obtained as a function of time as follows,

$$i(t)=i_0\left\{\beta\exp\left(\frac{e}{kT}\phi_s e^{-t/\tau}\right)+1-\beta\right\}. \qquad (2)$$

The analysis of the results gave the value of β about 0.1, and the experimental points showed fair agreement with the theoretical curve. The decrease of $\phi_0(=\phi_s)$, is shown as a function of the time of illumination T_1 in Fig. 3. It tends to saturate for the prolonged illumination.

Table I.

	Temperature	
	1.84°C	11.5°C
$T_{1/2}$	100±30 sec.	30±15 sec.

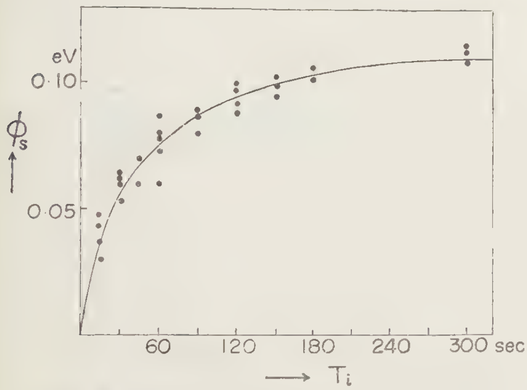

Fig. 3. ϕ_s as a function of the time of illumination Ti.

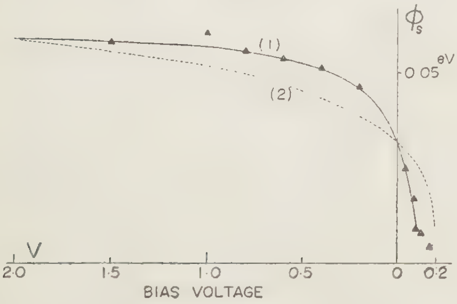

Fig. 4. Dependence of ϕ_s on the bias voltage. Ti=30 sec. ▲ is the experimental points, (1) and (2) are theoretical curves.

As shown in Fig. 4, ϕ_s depends on the bias voltage for fixed T_1. The curve (1) in Fig. 4 is calculated from the physical picture assuming that the illumination lowers ϕ_σ primarily, and ϕ_0 decreases by the relation of Eq. (1). In this case, the impurity concentration N chosen to fit the theoretical curve with the experimental points was $10^{20}\sim10^{21}$ cm^{-3} which is considerably larger than the reasonable value.

This phenomenon was observed also in the p-n junction[1] so the explanation with the action of the surface states mentioned above seems to be inappropriate. It must, however, be noted that if we use the model of the p-n junction given by Stuetzer[2] the explanation need not be rejected.

The curve (2) in Fig. 4 is calculated assuming that the space charge density N is increased by the illumination. The agreement is worse than (1). In this case N and $\varDelta N$ (the increase of N by illumination) were determined to be 10^{18} and $0.1\sim0.5\times10^{18}$ cm^{-3}, respectively.

All of these experiments were performed on 1N34 Ge diodes. We found out four phenomena in these units, i.e.,

(1) The photo-aftereffect (mentioned above).

(2) The positive current creep in the backward direction.

(3) The "photo-creep". (The remarkable creep *under illumination.*

(4) The positive creep of photocurrent.

It must be noted that a unit showed *all or none* of these four phenomena and these phenomena occurred with the time constant of the same order of magnitude. Therefore, the photo-aftereffect seems to be closely related with the creep phenomena.

We are proposing that something like "surface states" or "traps" which have large time constants in ionization and trapping processes[3] must be considered in the barrier to explain those experimental results.

It might be curious that the traps have such a large time constants as observed but it is helpless to explain the results with any existing theories on existing models.

There are evidences that these results are caused neither by moisture nor by impurity migration.

(1) The contact point was protected with wax during experiments. Moreover, if these results are caused by moisture, they must be observed on every unit of 1N34 diodes.

(2) Even if one uses the model of impurity migration which causes the change of the effective barrier height, he will come to the conclusion in the end that it is necessary to consider the large time constant in their ionization processes.

Our results are qualitative rather than quantitative, but we believe that there are some keys in these phenomena to solve the essential problem of "creep" and other related phenomena which might also be relateb with the action of some kind of "traps".

References

1) The p-n junction used here is the Si p-n junction reported in the paper by M. Hatoyama; Researches of the Electrotech. Lab. No. 533.

(2) O. M. Stuetzer: Proc. I.R.E. **40** (1952) 1377.

(3) Shockley; "*Electrons and Holes in Semi. conductors*" 1950. p. 342. The "traps" which are of hypothetical character are introduced there to consider the noise behaviour of Germanium.

J. PHYS. SOC. JAPAN **9** (1954) 132~133

On the Electrical Properties of Silicon Single Crystals (I)

By Yasuo KANAI

The Electrical Communication Laboratory, Nippon Telegraph and Telephone Public Corporation, Tokyo, Japan

(Read Oct. 31, 1952, Received June 26, 1953)

Recently remarkable progress has been made on the researches of the electrical properties of germanium[1] to develope the transistor electronics. Silicon has the same crystal structure (diamond type) as germanium, it is, therefore, very interesting to investigate the electrical properties of silicon to compare with those of germanium. Several years ago, Pearson and Bardeen[2] have studied the electrical properties of pure, n-, and p-type silicon, but unfortunately their studies were made on the polycrystalline materials. Since the grain boundaries between cristalites will affects seriously the electrical properties of the polycrystals, it is desireable to study the single

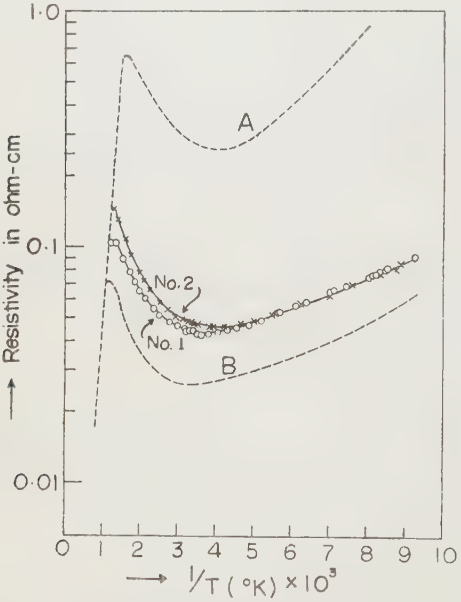

Fig. 1. The curves of resistivity as a function of the inverse absolute temperature.

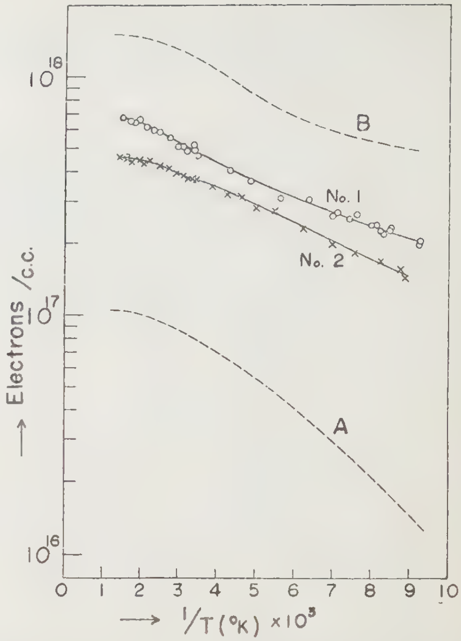

Fig. 2. The curves of electron densities as a function of the inverse absolute temperature.

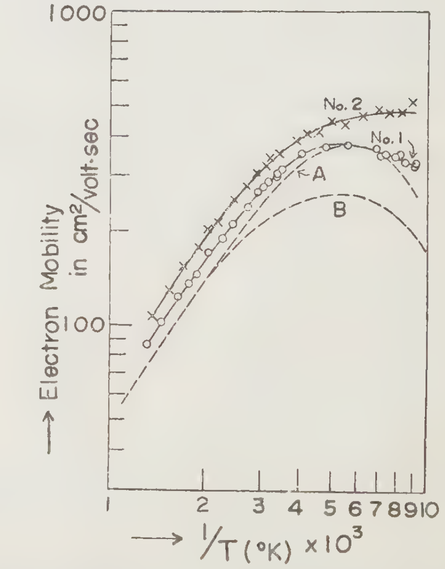

Fig. 3. The curves of electron mobility as a function of the inverse absolute temperature.

Table I.

Sample	type	Carriers/c.c. in saturation range		Experimental arrangement
No. 1	n	6.6×10^{17}	Single crystal	Applied electric field is in the [122]-direction
No. 2	n	4.5×10^{17}	Single crystal	[110]-direction
A	n	1.05×10^{17}	Polycrystal	Pearson and Bardeen's data
B	n	1.25×10^{18}	Polycrystal	Pearson and Bardeen's data

crystals of silicon.

Electrical conductivity and Hall effect of the n-type silicon single crystals, which were made by the author's method[3], were measured between +500°C and −150°C. The experimental results are plotted in Figs. 1, 2 and 3. Pearson and Bardeen's results for polycrystals are also plotted on the same figures for comparison. Some characters of the samples are listed in Table I. In Fig. 2 the electron concentrations (n) are calculated from the Hall coefficient (R) by the equation

$$n=3\pi/8eR\,,$$

where, for simplicity, the coefficient $3\pi/8$ was used in all temperature ranges.

The experimental results show that the electron mobility in silicon single crystals are larger than in polycrystals. Especially at lower temperatures the descrepancy becomes much larger, and this descrepancy may be interpreted by the grain boundary scattering.

References

1) W. Shockley. "Electrons and Holes in Semiconductors" Van Nostrand Company Inc. New York, (1950).

2) G. L. Pearson and J. Bardeen. Phys. Rev. **75** (1949) 865.

3) Y. Kanai: J. Phys. Soc. Japan **7** (1952) 534.

J. Phys. Soc. Japan **9** (1954) 133~134

On the Delocalization Energy in Molecules

By Kenji Nukasawa

Research Institute of Applied Electricity, Hokkaido University, Sapporo

(Received September 4, 1953)

The merit of the MO theory combined with the perturbation method for the purpose of estimating the delocalization energy in molecules, has been appreciated by several authors. Many successful results are being obtained also in the chemical field according to this course.[1] But there are many ambiguous points, setting aside for the moment the question of configuration interaction. One of the most controversial problems is how to decide the orbital energies of localized molecular orbitals. The usual procedure where we assume the energies α and β for each atom and each bond respectively, seems to require much careful consideration, even if the problem be limited to π orbitals of C atoms.[2] The situation is much more serious when we come to the system containing hetero-atoms or σ orbitals. Another treatment using the experimental values of ionization energy and electronic spectra,[3] is more reasonable, but has its own weakness too. For instance, in order to assign the orbitals responsible for the transition, we are obliged to take some kind of averaging process because the electron interaction splits the degeneracies. But the usual method of arithmetical average seems to have no sound base, and after all these data cannot supply the knowledge for the electron affinity of each orbital.

On the other hand, there will be no trouble at least theoretically to calculate the delocalization energy non-empirically within the LCAO approximation. We shall only have to solve Roothaan's SCF equation and to compare this energy with another one which may be obtained for the localized orbitals. Thus Mulliken and Parr have sucesfully calculated the delocalization energy of the π electrons of 1,3-butadiene and benzene in this way.[4] But to solve the SCF equation rigorougly is neither always easy nor able to give far-reaching views in general cases.

Delocalization energies (in e.v.)

	1, 3-butadiene *cis*	*trans*	benzene
M-P	0.34	0.28	3.17
I	0.36	0.31	1.35
II	0.83	0.79	3.10
I′	0.40	0.43	0.87
II′	0.89	0.94	2.63

The numerical values necessary for the energy integrals were taken from Parr-Mulliken[5] and Parr-Craig-Ross.[6]

Making allowance for these circumstances, we examined to apply the perturbation method to Roothaan's equation. The electronic energy of the molecules containing $2n$ electrons which lie on orthogonalized orbitals ψ_1, ψ_2, $\cdots$ ψ_n making a closed shell, can be expressed as

$$E=\sum_{i=1}^{n}(I_i+L_i), \tag{1}$$

where $-I_i$ and $-L_i$ are the energies necessary to take off one electron from ψ_i, the former leaving bare atom-cores while the latter leaving cores plus $n-1$ remaining electrons without changing their orbitals. The delocalization energy can be obtained as the sum of the changes of I's and L's. The approximate non-localized molecular orbital ϕ_i may be expressed, applying the second order perturbation method to Roothaan's equation, as

$$\phi_i=N_i(\psi_i+\sum_{j=1}^{m}\lambda_{ij}\psi_j')\,, \tag{2}$$

$$\lambda_{ij}=(L_{ij}-S_{ij}L_{ii})/(L_{jj}-L_{ii})\,, \tag{3}$$

where ψ_1', ψ_2', $\cdots$ ψ_m' mean the available vacant orbitals of the system and the quantities such as L_{ij} have the same meaning as given by Parr and Mulliken.[5] The orbitals which are contained in the integrand of the L_{ij} are supposed to be unperturbed ones. The change of the orbital energies will become approximately

$$\Delta I_i = \sum_{j=1}^{m} \lambda_{ij}(I_{ij} - S_{ij} I_{ii}) \,, \qquad (4)$$

$$\Delta L_i = \sum_{j=1}^{m} \lambda_{ij}(L_{ij} - S_{ij} L_{ii}) \,. \qquad (5)$$

The values in the row I of the table are the delocalization energies of 1, 3-butadiene and benzene calculated by the use of Eqs. (1), (3), (4) and (5). For butadiene they agree fairly well with those due to Mulliken and Parr (M-P),[4] while for benzene not. This results should have been anticipated because in benzene the delocalization energy would be too large to permit the simple perturbation method. If we use $\frac{1}{2}S_{ij}(I_{ii}+I_{jj})$ and $\frac{1}{2}S_{ij}(L_{ii}+L_{jj})$ instead of $S_{ij}I_{ii}$ and $S_{ij}L_{ii}$ respectively, we can have a better result for benzene as shown in the row II.

The values listed in the rows I′ and II′ are those which were obtained starting with the non-orthogonal orbitals which reflect directly the localized bonds. The difference between I′ and II′ correspond to that between I and II. Eqs. (1), (4) and (5) are not precise for these cases. However, the calculations are much easier and able to be interpreted into empirical quantities. Thus the values of L_{ii} and L_{jj} have close relation with ionization energy ε_i of occupied orbital ψ_i and electron affinity ε_j of vacant orbital ψ_j', respectively, of the localized system. This procedure could be expected to get more reliability if we should treat the cases of intermolecular complexes or the others where the non-orthogonality would become smaller.

It should be noticed that ε_j which Mulliken called "unacceptable"[5] has this clear physical meaning in fact. However, no exact way has been ever found to obtain this value from empirical data, even though there exists a relation such as Eq. (39) of reference 5) connecting ε_j to absorption spectra. The correction terms for the inter-electronic energy would be unfortunately too large to be replaced by some constants.

References

1) M. J. S. Dewar: J. Am. Chem. Soc. **74** (1952) 3341.
2) R. S. Mulliken: Phys. Rev. **74** (1948) 736.
3) K. Nukasawa: J. Phys. Soc. Japan **8** (1953) 132.
4) R. S. Mulliken and R. G. Parr: J. Chem. Phys. **19** (1951) 1271.
5) R. G. Parr and R. S. Mulliken: J. Chem. Phys. **18** (1950) 1338.
6) R. G. Parr, D. P. Craig and I. G. Ross: J. Chem. Phys. **18** (1950) 1561.

J. Phys. Soc. Japan **9** (1954) 134~135

The Magneto-resistance Effect in a Cubic Semiconductor with the Spheroidal Energy Surfaces

By Motoichi Shibuya
Electrotechnical Laboratory, Tokyo

(Received September 30, 1953)

In order to discuss the magneto-resistance effect in oriented single crystals of germanium observed by G. L. Pearson and H. Suhl,[1] we must use the idea of the nonspherical energy surfaces in the Brillouin zone, as suggested by W. Shockley.[1] As an example of such a model we use here the spheroidal surfaces which may be expected in germanium from the study of the electronic energy band structure.[2]

The collision frequency of electrons, whose energy surface is the spheroidal one, with the lattice vibration has been treated approximately along the same line as in Seitz's theory[3] and we have found that the collision frequency of rather high energy electrons is approximately proportional to the square root of their energy.

Using this result, we can easily discuss the magneto-resistance effect in semiconductors in closed form with the same procedure as that used by D. Blochinzev and L. Nordheim[4] who discussed that effect in divalent metals.

We treat here only three special cases, namely, those in which the bottom of the conduction band (or the top of the valence band) appear along (a) six (100) axes, (b) twelve (110) axes and (c) eight (111) axes. The rotation axes of those spheroidal surfaces are also assumed to coincide with the above mentioned axes in each case. Those assumptions satisfy the condition of the cubic symmetry.

Weak magneto-resistance constants introduced by F. Seitz can be obtained with series expansion in H, and are tabulated in Table I, where the constants having a suffix 0 are those that have been obtained with scalar electron mass m_0 under the assumption of the constant mean free path; $M = m_1/m_0$ and $r = m_2/m_1$, here m_1 is the component of mass tensor along the rotation axis and m_2 is that along two other principal axes.

Saturation values of $\Delta\rho/\rho$ or ρ_∞/ρ at infinite magnetic field can be obtained with asymptotic expansion, and some results are shown in Table II.

Saturation Hall coefficient R_∞ becomes in those three cases $\pm(\mathrm{Nec})^{-1}$ which is independent upon the directions of both current vector and magnetic field.

The ratio of the Hall mobility to the conductivity mobility is equal to the ratio of the normal weak field constant R to R_∞,

Table I.

$\sigma,\alpha,\beta,\gamma,\delta,\varepsilon',\lambda',\eta'$	Case (a)	Case (b)	Case (c)
$M^{5/2}r^2\sigma/\sigma_0$	$(2+r)/3$	$(2+r)/3$	$(2+r)/3$
$M^5r^4\alpha/\alpha_0$	$(1+2r)/3$	$(1+2r)/3$	$(1+2r)/3$
*$M^{15/2}r^6\beta/\gamma_0$	$-(1+r+r^2)/3$	$-(1+r)^2/4$	$-(2+r)(1+2r)/9$
$M^{15/2}r^6\gamma/\gamma_0$	r	$(1+4r+r^2)/6$	$(2+r)(1+2r)/9$
$\mathrm{M}^{15/2}r^6\delta/\gamma_0$	$(1-r)^2/3$	$-(1-r)^2/12$	$-2(1-r)^2/9$
$M^{10}r^8\varepsilon'/\lambda_0'$	$(1+2r^2)/3$	$(1+2r+3r^2)/6$	$(1+2r)^2/9$
$M^{10}r^8\lambda'/\lambda_0'$	$r(2+r)/3$	$(3+2r+7r^2)/12$	$(1+2r^2)/3$
$M^{10}r^8\eta'/\lambda_0'$	$r(2+r)/3$	$(3+2r+7r^2)/12$	$(1+2r^2)/3$

* $\gamma_0>0$. About the sign of γ_0, one may find some confusion in the paper referred (1).

Table II.

Longitudinal Effect, $H \parallel I$.	$\Delta\rho/\rho$		
Direction of H.	Case (a)	Case (b)	Case (c)
(100)	0	$(1-r)^2/(1+5r)$	$2(1-r)^2/9r$
(110)	$(1-r)^2/(1+5r)$	$3(1-r)^2/(1+20r+3r^2)$	$(1-r)^2/3(1+2r)$
(111)	$2(1-r)^2/9r$	$(1-r)^2/3(2r+1)$	$2(1-r)^2/3r(7+2r)$

Transverse Effect, $H \perp I$.		$(9\pi/32)(\rho_\infty/\rho)$		
Direction of		Case (a)	Case (b)	Case (c)
H	I			
(100)	$I \perp H$	$(2+r)(1+2r)/9r$	$\dfrac{(2+r)(1+8r+3r^2)}{18(1+r)r}$	$(2+r)^2/3(1+2r)$
(110)	(001)	$(2+r)(1+2r)/9r$	$\dfrac{(2+r)(2+r+r^2)}{3(1+3r)r}$	$(1+7r+r^2)/9r$
(110)	$(0\bar{1}1)$	$\dfrac{(2+r)(5+r)}{9(1+r)}$	$\dfrac{(2+r)(1+r)(11r+1)}{18r(1+3r)}$	$(2+r)(1+2r)/9r$

$$(\mu_H/\mu_\sigma)=(R/R_\infty)=(9\pi/8)(1+2r)/(2+r)^2.$$

In conclusion we may say the large magnetoresistance effects including the longitudinal effect in germanium observed by Pearson and Suhl are qualitatively understood with this spheroidal model. For instance, the effects observed at room temperature in p-type sample are analyzed pretty well by the case (a) putting 2 or 0.5 as the value of r, and those in n-type sample are analyzed by the case (c) with $r=10$ or 0.1. However there are some quantitative discrepancy between this theory and the experiments. We suppose that they may be overwhelmed in future better theory, if one consider the more complicated nonspherical energy surfaces and the complicated collision frequency due to the transitions of electrons between different families of energy surfaces which are neglected in this calculation.

The writer is much indebted to G. M. Hatoyama under whom this research was planned and carried out and to W. Sasaki, for valuable discussions.

References

1) G. L. Pearson and H. Suhl: Phys. Rev. **83** (1951) 768.
2) F. Herman and J. Callaway: Phys. Rev. **89** (1953) 518.
3) F. Seitz: Phys. Rev. **73** (1948) 549.
4) D. Blochinzev and L. Nordheim: Z. Physik, **84** (1933) 168.
5) F. Seitz: Phys. Rev. **79** (1950) 372.

J. PHYS. SOC. JAPAN **9** (1954) 135~136

New Spectra of $H_2C^{12}O$ in 6 mm Wave Range*)

By Akira OKAYA
Department of Physics, Kyoto University

(Received November 24, 1953)

The author has observed two new rotational spectra of formaldehyde in 48,000 Mc/s and 45,000 Mc/s frequency range, and has compared the measured frequencies of these spectra with the values which are calculated by the continued fraction method of King, Hainer, and Cross[1] about the

Table I.

Assignment (J, K_{-1}, K_{+1})	Measurement Freq. (Mc/s)	Calculated Freq. (Mc/s)	Correction (Mc/s)	Residual Error (Mc/s)
$11_{2,10}-11_{2,9}$	48,612.70±0.1	48,615.39	−120.13	+2.69
$19_{3,17}-19_{3,16}$	45,063.10±0.1	45,064.82	−438.56	+1.72

asymmetric rotor, and corrected by taking into account the four correction terms X_j, X_{jk}, X_k, and X_{kk} of centrifugal distortion, semi-empirically introduced by Lawrance and Strandberg[2]. The measured and the calculated values and the corrections of the new lines are given in Table I.

The residual error which is the difference between the measured and the calculated values is about 4~5×10⁻⁵ in ratio against the measured value. The author has succeeded in observing the Stark patterns of $4_{1,4}-4_{1,3}$ and $1_{0,1}-0_{0,0}$ lines in 6 mm and 4 mm wave ranges.

All these spectral lines have been observed by use of the Stark effect spectrograph which includes new devices. The frequency multiplier is constructed such that the crystal is demountably situated in a K-Band wave guide section and driven by a 2K33A klystron oscillator.

The harmonic components are led into the wave guide section with variable gap and taper (squeeze section) and the desired component is matched into the K-Band absorption cell by it.

The Sark cell is composed of one meter long K-Band copper wave guide, on the narrow side of which the groove is cut and the aluminium foil Stark electrode on both sides of which mica plates are pasted using melanin resin, is inserted through the groove into the wave guide.

In conclusion, the author wishes to thank Prof. I. Takahashi for his encouragement and helpful advices and also Mr. T. Nishikawa for his valuable assistance in calculation and Mr. T. Ogawa for his useful collaboration in experiments.

References

1) G. W. King, R. M. Hainer, and P. C. Cross: J. Chem. Phys. **11** (1943) 27.

2) R. B. Lawrance and M. W. P. Strandberg: Phys. Rev. **85** (1951) 363.

---

* Read at an informal meeting on microwave spectroscopy of the International Conference on Theoretical Physics, (Sept. 19, 1953).

J. PHYS. SOC. JAPAN **9** (1954) 136~137

A Filter Transmitting near the Mercury Line, 2537A

By Kikusaburo OSADA

Faculty of Engineering, Nagoya University

(Received November 26, 1953)

In the case of study for the photo-luminescent phenomena of materials, we have frequently used a monochromatic light at 2537A, because a low pressure mercury lamp emits very intensive radiation at this wave-length. Accordingly, many investigations in order to obtain some filters which can isolate this mercury line, have been carried out, and we have obtained several sorts of filter[1][2][3] available for this purpose. One of these filters[2] is made from starch solution containing iodine. This liquid filter, however, makes its treatment inconvenient. So, we wish to make this filter in a solid state, if possible. If we coat a quartz plate with gelatine film containing soluble starch and make iodine adsorb to the starch, then we may obtain a required solid filter, gelatine being transparent to 2300A.

Therefore, a filter was prepared by the following process: Soluble starch (1g) is dissolved in hot water (15 cc). Gelatine (1g) is dissolved in another hot water (15 cc). By mixing these two solutions, we coat a quartz plate with this mixture. Instead of the quartz plate, if we wish, we can take special glass used in the bulb-wall of germicidal lamp. After drying, this plate is dipped for a few

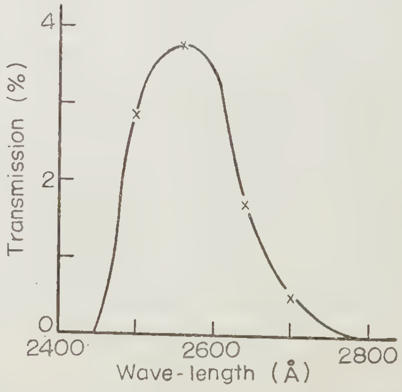

Fig. 1. Transmission in ultraviolet region.

seconds in a solution (20 cc) containing iodine (0.8g) and potassium iodide (1.6g), in order to adsorb the iodine in this solution to the starch. Then we can obtain a required filter.

Optical properties of this filter were measured in the range: $0.18\sim3\ \mu$.

In Ultraviolet Region:—An ultraviolet absorption spectrum was measured to 1800A with a small quartz spectrograph4), and density of photographic plate was measured with a microphotometer. The result obtained is shown in Fig. 1.

This filter is transmissive in the range: 2800 ~2440A, and a maximum of the transmission is 3.7% at about 2560A.

In Visible and Infrared Regions:—Absorption spectra in these regions were measured to $3\ \mu$ with a self-recording infrared quartz spectrophotometer.5) A tungsten lamp was used as a light source, and as a detector we used a photomultiplier tube (931A) under the wave-length $0.8\ \mu$ and a thermopile over $0.8\ \mu$. The result obtained is shown in Fig. 2.

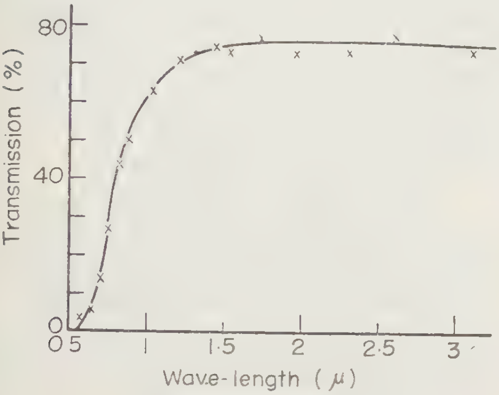

Fig. 2. Transmission in visible and infrared regions.

This filter is transmissive over $0.55\ \mu$ and the transmission is 75% over $1.5\ \mu$.

From these results, we know that this filter is transmissive not only near 2537A, but also in the infrared region.

In conclusion the author wishes to express his sincere thanks to Prof. S. Hattori at the Aichi Liberal Arts College for his approvement of using his infrared spectrophotometer.

References

1) P. Pringsheim u. M. Vogel: *Lumineszenz von Flüssikeiten und festen Körpern* (Verlag Chemie, 1951) p. 48.

2) Y. Hoshino: J. Electrochem. Soc. Japan **18** (1950) 6. (in Japanese)

3) Y. Hoshino & S. Yoshida: *ibid.* **17** (1949) 221.

4) K. Osada: J. Phys. Soc. Japan **8** (1953) 226.

5) S. Hattori: Memoirs Aichi Liber. Arts Coll. **1** (1952) 64. (in Japanese)

J. PHYS. SOC. JAPAN **9** (1954) 137~139

On " An Unusual Star " by Nakagawa et al

O. MINAKAWA and J. NISHIMURA
Department of Physics, Kobe University

(Received December 2, 1953)

In a recent note, Nakagawa et al.1) concluded that they obtained an example of nuclear capture in *flight* of a ***K***-meson from the analysis of the grain density variation of a track in G5 emulsion, exposed to upper air cosmic rays by free balloon. However, because of the importance of such a conclusion, as explained later, we think it is justified to examine their analysis in an especially critical manner.

The production of stars by ***K***-mesons coming to rest, is one of the most important problems in the present cosmic ray physics, and was discussed several times and especially at the Bagnères conference in this summer by Rossi, Powell, and others. At that time, generally accepted examples of ***K***-meson capture were only 6 cases (4 from Peters at Bombay, 2 from Manchester and Ecole Polytechnique). Obviously the most clear case attributable to ***K***-meson capture is that in which one can find out the original nuclear event from which the track in question is emitted, besides the proper length of the track. In the case of unknown origin and of track length less than a mm in G5 emulsion, even when the grain density is so large that the gap counting method is available, it is not generally accepted that the star is definitely caused by ***K***-particles, because one cannot be ready to put full confidence in finding the direction of motion of the particle.2)

The conclusion of Nakagawa et al. rests on the following two points:

(1) The variation of grain density of a track of 2.9 mm in G5 emulsion,

(2) energy consideration.

We wish first to note that in the case of ***K***-meson or proton it is hardly possible to decide with certainty the direction of a particle from the variation of grain density in the region of 3~4 times minimum ionization along a track of only 3 mm in G5 emulsion even when it was carefully processed. We have met with such examples frequently, and an example, the grain density of which is just the same as the track (1) of Nakagawa et al. is shown in Fig. 1. (a) represents the direct observed plots of grain density/100μ, and in (b) grain density/100μ averaged over 500μ is plotted with (×) along the track length.3) Original data of Nakagawa et al. are also shown in the figure with (○). (The similarity of both observations is quite accidental.) From the figure it seems to us that it is not sufficient to decide definitely the direction of particles which produce these tracks from the observed change of grain density in 3 mm track length.

To ascertain the observed rapid variation of grain density of their track (1), Nakagawa et al. compared the variation of grain density of tracks of a μ-meson (1 cm long) and of a proton (1.6 cm long) with the curve obtained from Goldschmidt-Clermont in Fig. 3, and they seem to believe that in the case of protons the grain density changes more rapidly than in the case of μ-mesons in these density regions. But in our opinion it is not appropriate to use the rewritten curve of Goldschmidt-Clermont to discuss such small region, because the original curve of the latter author is calculated for the grain density versus scattering parameter, and ranges are shown only as a calibration, and consequently in converting the original curve into grain density versus range curve, some error might be introduced in detailed portion. This curve, however, is in good accord with the curve obtained by Fowler4) as a whole, except the small unevenness due to the above mentioned reason, which does not correspond to any real physical meaning. To show these circumstances clearly, we compare the results obtained by Nakagawa et al. with grain density versus range curve of proton established by Fowler in Fig. 2. From the figure it may be clear that their observed points are interpreted as due to fluctuations.

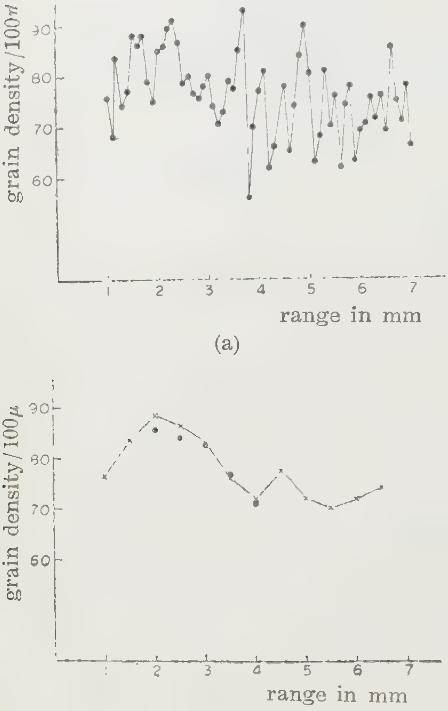

(a)

(b)

Fig. 1.

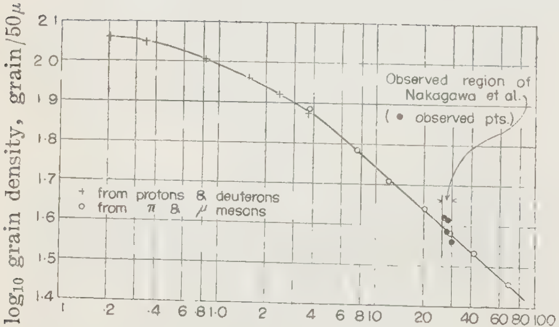

Fig. 2.

Contrary to the above, if we accepted their data shown in Fig. 3 as a real fact not due to fluctuations, with Nakagawa et al., then it would be obvious that the fundamental relation

$$\frac{R_{p(v)}}{M_p}=\frac{R_{\mu(v)}}{M_\mu} \quad (R\text{: range,} \quad M\text{: mass}).$$

would be invalid, in other expression, the relation

$$\text{grain density}=f(e,v) \quad e\text{: charge,} \quad v\text{: velocity}$$

would not hold in this case. Inspite of these circumstances Nakagawa et al. used the above relation implicitly (mass ratio displacement), in the process of estimation of the mass of the particle. So their argument is self-inconsistent, because there are no reason, in their case, to justify to use the method of mass ratio displacement.

Even if we ignore their estimation of mass of the particle, their data in Fig. 3 are quite insufficient to deny the above basic relations which are very well established from experimental and theoretical backgrounds and on which all mass estimations in cosmic-ray work are based.

From the above discussions it seems quite natural to attribute their results concerning the grain density measurements to the fluctuation or the instability of grain density in G5 emulsion.

Apart from the decisive criteria mentioned above, there are further several points which seem to us not so convincing in their interpretation of the star. The first of all is the track (6). Nakagawa et al. interpreted it as a recoil track of 2.7μ but it has a very thin density with a gap. This is quite an unusual interpretation. The second point is the momentum balance. It is very improbable that the charged and neutral projectiles are so separated in space. The third point is the direction of their "K-meson." It comes upwards from the side, independently of the paraffin block situated above.

Considering the above points it seems to us that this star is naturally interpreted as an "usual" star induced by high energy neutron which comes from right above, contrary to their "unusual" interpretation.

References

1) Nakagawa, Hujita and Okudaira: J. Phys. Soc. Japan **8** (1952) 801.

2) This problem was discussed in Bagnères conference and the above circumstances were generally accepted by many specialists for emulsion work, and one of us wrote to Prof. Nakagawa immediately after the conference.

3) We wish to thank here Dr. Tokunaga at Saikyo University for permission to present his data (Fig. 1).

4) P. H. Fowler: Phil. Mag. 41 (1950) 169.

J. PHYS. SOC. JAPAN **9** (1954) 139

On the Photocurrent of High Purity SiC Single Crystal

By Kinzo SATO and Masaharu NAMBA

Fuji Denki Seizo K.K., Material Laboratory, Kawasaki

(Received June 3, 1953)

In studing the various characteristics of SiC single crystals we observe currents flow by illumination of suitable wavelength. The direction of currents is the direction of easy flow by metal-SiC point contact rectifiers. This effect is observed only by very pure SiC crystal (*P*-type, $\rho-10^4$ ohm cm) and not by impure black SiC crystals. According to Brattain1) the surface of the *P*-type semiconducting crystals becomes negatively charged when illuminated by radiasion of the wavelength shorter than the wavelenhgt limit for the photoelectric effect of the crystals. Then we must expect the currents flow in the easy direction of the metal-crystal contact rectifiers and the current-voltage characteristics very similar to the forward characteristics of this rectifiers. This arguments are confirmed by our experiments as shown in Fig. 1. Fig. 1, shows the photopotential vs. photocurrent at various temperatures. Furthermore from the activation energy of the acceptors of the SiC crystal we must expect the absorption to lie in the infrared and actually in this sample the photocurrents are observed in this region and not in ultra-violet. The photocurrents are proportional to the light intensities but the photopotentials are not. The relation between the current and exposure times is shown in Fig. 2.

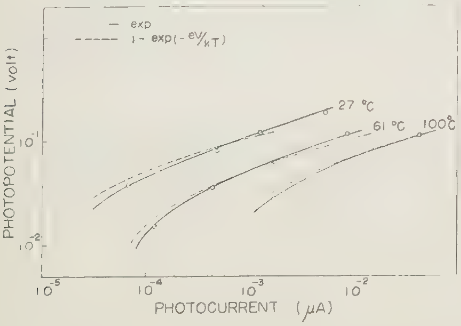

Fig. 1. Change in photopotential with photocurrent at various temperatures.

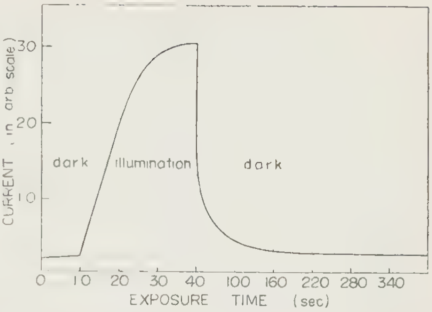

Fig. 2. Photocellaction of SiC rectifier under applied voltage (forward direction).

Reference

1) W. H. Brattain: Semiconducting materials P. 40.

J. PHYS. SOC. JAPAN **9** (1954) 139~140

On the Change of Density of Copper Single Crystals by Cold Working

By Sadabumi ISSIKI and Hiroshi KIMURA

Institute of Industrial Science, University of Tokyo, Chiba City

(Received June 11, 1953)

It is well known that the density of metals is decreased by cold working,1)2)3) and we may find two causes for this effect. The one is the lattice-strain due to dislocations and the other is vacancies produced by cold working.

C. Zener4) calculated the decrease of density by cold working as a result of the elastic strain of iattice. That is,

$$\varDelta V=\frac{1}{n+1}(C_d+nC_s)\cdot W,$$

where ΔV is the increase of volume by cold working (cm^3/g), W is the stored energy in specimens by cold working (erg/g), C_d and C_s are constants for each metals — in the case of copper $C_d=7.3\times10^{-12}$ cm^3/erg and $C_s=2.3\times10^{-12}$ cm^3/erg, and n is a positive number showing the ratio how the strain energy is distributed to the normal component of and to the tangential component of lattice strain.

n can be calculated by the measurements of decrease of density and stored energy by cold working. If n calculated is positive, we may conclude that the decrease of density is caused by the lattice-strain.

The energy required to form a vacancy has been estimated[5] 30 cal/mol for copper by the study of diffusion in metals. On the other hand, we can estimate the number of vacancies produced by cold working from the change of density. Then we can calculate the stored energy. Comparing this calculated value for stored energy with the measured one, we can examine whether the decrease of density is due to vacancies or not.

We have used copper single crystals as specimens for the following two reasons. The first: As most of studies ever performed were with polycrystalline metals, the results obtained are not suitable for the theoretical consideration because of an effect of grain boundaries. The second: Stored energies for the working of various degrees have been measured only in copper single crystal by H. Kanzaki.[6]

Three crystals, about 10 cm in length and 1.8 cm in diameter, were made by Tammann's method. Specimens, 2 cm in height, were cut off from the bottoms of each crystal, polished smoothly and pressed. The density was calculated by the comparison of weights measured in the air and in the water. These values were corrected with every precision according to temperature and the atmospheric pressure. The changes of density were so slight that the measurement were repeated ten times.

The specimens were pressed and decreased about 15% in height' which corresponded to about 30% slip. The results obtained are shown in the Table I.

Table I. Change of Density

Specimen number	1	2	3
Initial values (at 20°C)	8.92969	8.92868	8.92579
99% Confidence Limit	0.00011	0.00018	0.00110
Values after			
Compression (at 20°C)	8.92964	8.92848	8.92549
99% Confidence Limit	0.00008	0.00038	0.00016
Decrease of Density	0.00005	0.00020	0.00030

The difference between the values before and after the compression was found to the significant in more than 90% confidence degree by the satistical treament of data.

From these results it may be concluded that the change of density does not exceed 3×10^{-3}% by cold working as large as 30% slip.

According to H. Kanzaki, energy, 0.018 cal/g, is stored in copper single crystals by the slip 30%, and by heating are 0.016 cal/g and 0.002 cal/g of this energy released respectively in the successive two stages.

If we assume that the decrease of density is due to lattice-strain, we must take the total energy values as W in Eq. (1). Then, it is obtained that $\Delta V/W=4.4\times10^{-12}$ cm^3/erg and $n=1.4$. Now, n is positive, so it can be concluded that lattice strain decreases density.

On the other hand, if we assume that the vacancies are the cause of density decrease, it is better to think that the energy released in the first stage is associated with vacancies because the activation energy of diffusion of vacancy is less than these of dislocation and others.

The energy value is found 0.016 cal/g by H. Kanzaki's measurement, and the energy corresponding to 3×10^{-3}% decrease of density is calculated 0.014 cal/g by the number of vacancies required to decrease density 3×10^{-3}% and by the energy required to form a vacancy. An agreement between these two values is so well that we can conclude that the vacancies are the cause of the decrease of density, too.

From the above experiments alone it cannot be concluded whether the main cause of density decrease is lattice strain or vacancies. It is desirable to perform any other studies.

References

1) D. Hanson and M. A. Wheeler: J. Inst. Metals **45** (1931) 229.
2) W. E. Alkins: J. Inst. Metals **23** (1920) 381.
3) T. Ueda: Sci Rep. Tohoku Univ. **19** (1930) 473.
4) C. Zener: Trans. AIME **147** (1942) 361.
5) N. F. Mott: Phil. Mag. **43** (1952) 1151.
6) H. Kanzaki: J. Phys. Soc. Japan **6** (1951) 456.

J. PHYS. SOC. JAPAN **9** (1954) 141~142

Magneto-Resistance of Cs_3Sb Photo-Cathodes

By Toshimichi SAKATA and Seiji MUNESUE
The Electrical Communication Laboratory

(Received August 25, 1953)

The experimental studies on the physical properties of Cs_3Sb have been reported several times[1)-3)] by the author with the conclusion that the thermo-electromotive force for Cs_3Sb indicates that this is P type and the acceptor concentration must be approximately $10^{20}cm^{-3}$. The purpose of this investigation was to get the mobility b as a function of temperature from the reliable values of the change of resistivity in a magnetic field $\Delta\rho/\rho_0$.

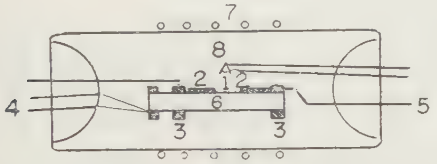

Fig. 1. Typical experimental tube; 1 Cs_3Sb; 2 aquadag; 3 copper bar; 4 thermo-junction; 5 Mo wire; 6 hard glass; 7 heater; 8 Sb.

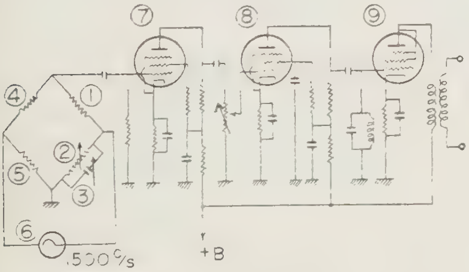

Fig. 2. Circuit diagram of the pre-amplifier (1) sample (150–200 KΩ); (2)–(5) dial resistor (1 KΩ); (3) variable mica condenser (several $\mu\mu F$); (4) resistor (150–200 KΩ); (6) Oscillator: (7) (8) (9) CZ-501-D.

The tube used in this experiment is schematically shown in Fig. 1. Cs_3Sb was evaporated on a narrow space, 2 to 3 mm long and 5 mm wide. Aquadag was used to make electrodes for the film. Both ends of the sample coated with aquadag were connected to small strips of copper through which A.C. current was supplied. The resistivity of specimens was of the order of 150-200 KΩ at room temperature. In order to avoid electrolytic conduction in Cs_3Sb, A.C. method was adopted. The resistance measurements were made by means of null method with impedance bridge circuit at 1500 *c/s*. The outputs of the bridge circuit were fed into a narrow band amplifier, which was followed by a low and high pass filters and a main amplifier. The amplified signals were led into an oscilloscope or a vacuum tube voltmeter. The circuit diagram of the preamplifier used is given in Fig. 2.

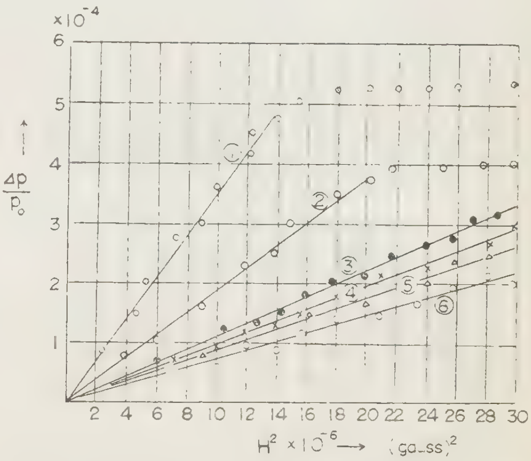

Fig. 3. Magneto-resistance of Cs_3Sb with magnetic fields: (1) 216°K; (2) 273°K; (3) 289°K; (4) 325°K; (5) 344°K; (6) 364°K.

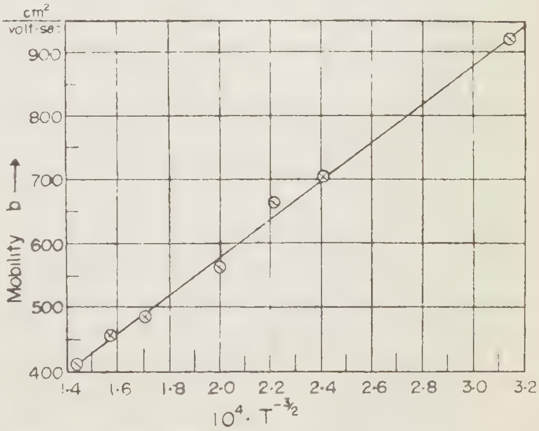

Fig. 4. Mobility of charge carriers in Cs_3Sb, as a function of $T^{-3/2}$.

Applying A.C. voltage of several volts to the sample, the change of resistivity with temperature was examined in the temperature range from 213°K to 364°K. $\Delta E/2$, given by the equation $\rho=\rho_0 \exp(\Delta E/2kT)$, was found to be 0.2-0.3 eV, in accordance with that obtained by the D.C. method previously performed and no appreciable anomaly appeared in the measurement by A.C. method. The change of resistivity in a magnetic field $\Delta\rho/\rho_0$ was measured in the same range of temperature as that for resistivity measurement. Since the resistivity is strongly temperature-dependent, small fluctuations of the temperature in the sample may obscure the effect of the variation dependent on magnetic field. So the measurements were carefully carried out at temperature available as constant as possible. But fluctuation of the signals of the output was not suppressed entirely. This is presumed to be caused by films themselves. The contacts of Cs_3Sb-aquadag-copper were found to play an important role in the stability. Measurements were made in the magnetic field from 200 to 6000 gausses.

The magnitude of the observed effect is considerably different from sample to sample. In the region of low fields, however, the H^2 law is valid as may be seen in Fig. 3. The effects for high fields were not investigated in further details. For weak fields[4], the change of the resistivity in magnetic field is given by

$$\Delta\rho/\rho_0 = B(T)\times H^2 .$$

The coefficient B(T) which depends an temperature, is proportional to the square of the mobility i.e.

$$B(T) = r_H \times b^2 ,$$

Where r_H is a numerical factor. Using the value given by Seitz[5] and Estermann and Foner[6], the mobility is approximately given by

$$b = 1.616\times 10^8\times(\Delta\rho/\rho_0)^{1/2}\times H^{-1}\ \mathrm{cm^2/volt\cdot sec}.$$

The results for several samples calculated in this way are shown in table I.

Table I.

Tube No.	°K	$\Delta\rho/\rho_0$	$b\left(\frac{\mathrm{cm^2}}{\mathrm{volt\cdot sec}}\right)$	H(gauss)
1	301	1.9×10^{-5}	213	3.30×10^3
2	289	2.6×10^{-5}	330	2.50×10^3
3	289	1.1×10^{-4}	564	3.16×10^3

Table II shows the change of the mobility with temperature in a sample.

Table II.

Tube No.	°K	$\Delta\rho/\rho_0$	$b\left(\frac{\mathrm{cm^2}}{\mathrm{volt\cdot sec}}\right)$	$T^{-3/2}$
3	216	3.25×10^{-4}	922	3.15
	258	1.89 〃	703	2.41
	273	1.70 〃	664	2.22
	289	1.10 〃	564	2.04
	325	0.91 〃	484	1.71
	344	0.79 〃	457	1.57
	364	0.65 〃	412	1.44

According to the theory of lattice scattering the temperature dependence of the mobility should go with $T^{-3/2}$. As may be seen in Fig. 4 linear relation holds for Cs_3Sb approximately. It will be noticed that considerably higher values of $\Delta\rho/\rho_0$ were found even at room temperature. The results so far obtained may be roughly checked by calculating the conductivity, for instance, for the room temperature, making use of the results found for the mobility and the concentration of charge carriers. Though we cannot know the exact value of conductivity, it will be shown that the order of conductivity is about $10^{-1}\mathrm{ohm^{-1}cm^{-1}}$. With $b=300\ \mathrm{cm^2/volt\cdot sec}$ and $n\sim10^{16}\mathrm{cm^{-3}}$, we get $\sigma=4.8\times10^{-1}\mathrm{ohm^{-1}cm^{-1}}$ for $T=300$°K. (The present values of n are based on the previous report[1-3]). This value turns out to be too high by a factor of at least 3–4. At low temperatures, further studies are necessary in order to confirm the effect of the impurity scattering. In order to get still more reliable quantitative results, considerable improvement of experimental techniques will be necessary. We communicate these results to indicate some of the difficulties inherent in the measurements of $\Delta\rho/\rho_0$.

References

1)–2) T. Sakata: J. Phys. Soc. Japan **8** (1953) 125 see also J. Phys. Soc. Japan **8** (1953) 272 (No. 2).

3) T. Takata: Studies on the Cs_3Sb Photo-Cathodes; unpublished.

4) "Semi-conducting materials" (1951) 194.

5) F. Seitz: Phys. Rev. **79** (1950) 372.

6) I. Estermann and A. Foner: Phys. Rev. **79** (1950) 365.

J. PHYS. SOC. JAPAN **9** (1954) 142~143

Decay of Shear Turbulence

By Yutaka SHIGEMITSU

Transportation Technical Research Institute, Tokyo

(Received October 27, 1953)

Recently, it has been proved experimentally that in a turbulent wake with a uniform undisturbed velocity the distributions of turbulent intensities, $\overline{u'^2}$, $\overline{v'^2}$, $\overline{u'v'}$, across the flow have their respectively similar forms at any point along the mean flow. When the x-axis is taken parallel to the mean flow, the following expressions hold independently upon the value of x; $\overline{u'^2}/\overline{u_0'^2}=f_1(y/b)$, $\overline{v'^2}/\overline{v_0'^2}=f_2(y/b)$, $\overline{u'v'}/\overline{u'v_0'}=f_3(y/b)$, where $\overline{u_0'^2}$, $\overline{v_0'^2}$, $\overline{u'v_0'}$ and b are their representative (for instance, their maximum) values and the width of wake at a section across the x-axis. As for their changes along x-direction the experimental result of $b^2\propto t$ is widely known, but the changes of $\overline{u_0'^2}$, etc. have not been clarified. We made measurements of distribution of $\overline{u'^2}$ across the flow at many points along the x-axis, and have found that the following relation

$$\overline{u}_0'^2 \infty t^{-1}$$

holds in a fairly wide range behind a body. It is significant that this decay law of shear turbulence has the same form as that of isotropic turbulence in its initial period. The present experiments were made concerning u'-fluctuation but it is expected that there is the same relation also in the cases of $\overline{v}_0'^2$ and $\overline{u'v_0'}$. Measurements were done on the wakes behind a circular cylinder ($d=1.5$ cm, $\overline{U}_0=3.74$ m/s) and an airfoil (NACA-2412, $c=17$ cm, $\alpha=5°$, $\overline{U}_0=7.28$ m/s), and the aspects of change of u' maximum value at many sections are shown in the figure. Detailed descriptions of the above experimental results and of theoretical derivation of decay law of shear turbulence will bep ublished in this journal.

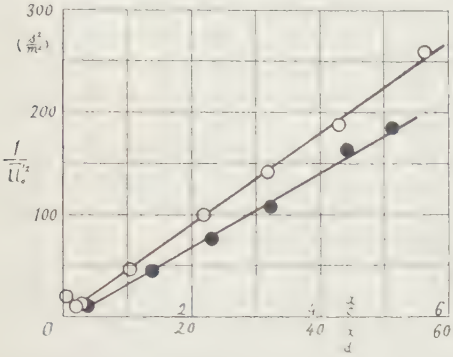

Experimental measurements of decay of shear turbulence. $\overline{u}_0'^2$ is the maximum value of u'-intensity across a turbulent wake. ○ is measured point behind a circular cylinder and ● is behind an airfoil.

J. PHYS. SOC. JAPAN 9 (1954) 143~144

On the A. C. Characteristics of Silicon p-n Junction Alloy Diodes

By Yasuo KANAI

The Electrical Communication Laboratory
Tokyo, Japan

(Received November 9, 1953)

Silicon p-n junction diodes were prepared by the method[1] of alloying aluminium to the n-type silicon. As reported previously by Pearson et al,[1] the d.c. characteristics of our silicon p-n junction diodes were well fitted by the theoretical formula $I=I_0(e^{eV/kT}-1)$ in the low level forward direction, but in the reverse direction there were no saturation parts.

The low voltage a.c. admittances of these junction diodes were measured at room temperature in the frequency range from 0.3 k.c.p.s. to 150 k.c.p.s. The typical chracteristics of these admittances are shown in Fig. 1 and Fig. 2, and these are quite similar to the theoretical curves which were derived by Shockley.[2] From the characteristic shown in Fig. 1, which corresponds to the case of the uniform n-region, the lifetime of excess holes in n-type silicon was calculated as was done in the case of germanium p-n junction,[3] and we have obtained approximately 27 μsec. in this sample. From the characteristic shown in Fig. 2, which corresponds to the case of the retarding field in n-region, we could calculate the lifetime of excess holes by the formula:

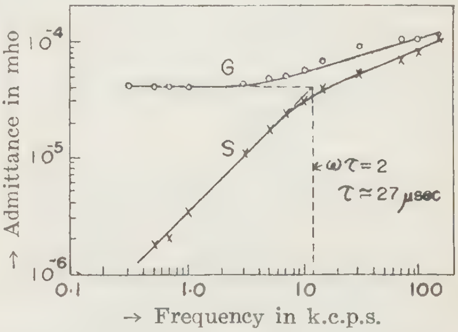

Fig. 1. Real and imaginary parts, G and S, of the admittance versus frequency curves.

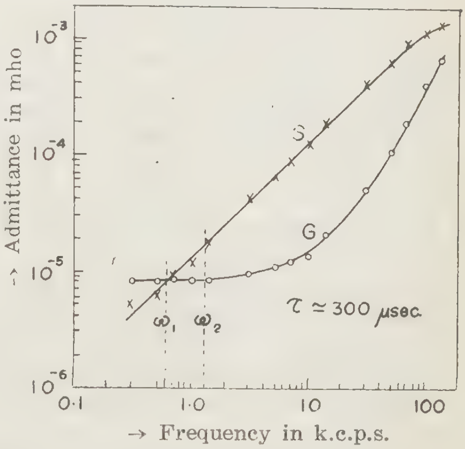

Fig. 2. Real and imaginary parts, G and S, of the admittance versus frequency curves.

$$\frac{\omega_2\tau-2}{\omega_1\tau-1}=\frac{5}{4}\left(\frac{S_2}{S_1}\right)^2$$

where

τ: the liftetime of excess holes in n-region.

ω_1, S_1: the angular frequency and susceptance at the point where the conductance is equal to the susceptance; $G_1=S_1$.

$\omega_2. S_2$: the angular frequency and susceptance at the point where the conductance is one half of the susceptance; $2G_2=S_2$.

This formula gave approximately 300 μsec. in this sample.

Further investigations are now in progress.

References

1) Pearson and Sawyer: Proc. I.R.E. **40** (1952) 1348.

2) Shockley: Bell Sys. Tech. Jour. **28** (1949) 435.

3) Goucher, Pearson, Spark, Teal and Shockley: Phys. Rev. **81** (1951) 637.

J. PHYS. SOC. JAPAN **9** (1954) 144~145

On the Lattice Anomaly of Bismuth Film deposited from its Vapour

By Yoshibumi FUJIKI and Ryōji SUGANUMA

Department of Physics, Faculty of Science, University of Kyoto

(Received November 16, 1953)

In a previous note[1] the writers reported that the structure loosening of bismuth film deposited from its vapour in vacuum occurs at a temperature appreciably below its melting point in the massive state. While the study on the cause of this phenomenon was going on, some anomalies of the axial ratio and the lattice constant of bismuth film were found.

By the transmission method, the electron diffraction study was carried out, both at room and higher temperatures, on bismuth films deposited from their vapour on quartz or on collodion films in the vacuum ($2\times10^{-4}\sim6\times10^{-5}$ mmHg.) of the diffraction apparatus.

To examine the probable deviations of the axial ratio and lattice constant from their normal values, the writers employed the following method. The lattice spacing $d_0(hk\cdot l)$ of normal bismuth, referred to the hexagonal axes of $a_0=9.0735$Å and c_0/a_0 $(=C_0)=1.3047$ (at 25°C)[2], is given by the following equation:

$$\frac{1}{d_0{}^2(hk\cdot l)}=\frac{4}{3a_0{}^2}\left(h^2+k^2+hk+\frac{3}{4}\frac{l^2}{C_0{}^2}\right). \qquad (1)$$

If small deviations of the lattice constant and the axial ratio from their normal values are Δa and ΔC respectively, and that of the lattice spacing d_0 is Δd, the following equation would be obtained by putting $a_0+\Delta a$, $C_0+\Delta C$ and $d_0+\Delta d$ in place of a_0, C_0 and d_0 in equation (1):

$$\frac{\Delta d}{d_0}=\frac{\Delta a}{a_0}+\frac{1}{a_0{}^2C_0{}^2}d_0{}^2l_0{}^2\,. \qquad (2)$$

If the values of $\Delta d/d_0$ for some spacings of a specimen were plotted against their values of $d_0{}^2l_0{}^2$, these points would lie on a straight line. Then $\Delta a/a_0$ would be given by the ordinate where the straight line intercepts the verticel axis, and $\Delta C/C_0$ by the slope of the straight line.

One of the graphs obtained from experiments at room temperature is shown in Fig. 1, from which one may obtain the numerical values of about -0.15% and $+1.48\%$ for $\Delta a/a_0$ and $\Delta C/C_0$ respectively. These deviations showed no change even after the annealing for about an hour at about 225°C.

Then the temperature dependence of these deviations was examined, but little change was observed till the temperature attained to just below that of the structure loosening.

When the specimen was heated up to the temperature of the structure loosening and the amorphous halo pattern began to superpose on the crystalline pattern, $\Delta C/C_0$ of the remaining crystalline pattern became negative, $\Delta a/a_0$ having been unchanged.* The circles in Fig. 2 show $\Delta C/C_0$ in such a state for some specimens. The densities calculated from these data showed intermediate values between that of the crystalline and liquid state (about 9.70 and 10.04 respectively[3]) of bismuth in massive state at the melting point. This seems to show that the crystalline bismuth of these films passes through such intermediate states in the process of structure loosening.

Though it may not be allowed to suppose the direct relation between the anomalies of the axial ratio and the lattice constant at room temperature, and the lowering of the temperature at which the structure loosening takes place, the relation between the observed values of $\Delta C/C_0$ of some specimens at room temperature and the temperatures of their structure loosenings are shown by crosses in Fig. 2.

It is seen from Fig. 1 that the errors introduced in the measurements of diffraction rings are about 0.1% and those of $\Delta a/a_0$ may be somewhat larger than 0.1% because of the difficulty of setting the reference material in just the same position with the specimen. Though this order of accuracy is not sufficient to perform the detailed examination as to how $\Delta C/C_0$ and $\Delta a/a_0$ change their values with temperature and thickness of film, it is highly probable that these values will depend upon the temperature, thickness of film and conditions of the preparation of specimens, and perhaps be one of the causes of variation of temperature at which the structure loosening occurs.

Considering the facts that the axial ratio becomes smaller than that of the normal one, which means that crystal symmetry of the film approaches to the cubic one, and also the density takes

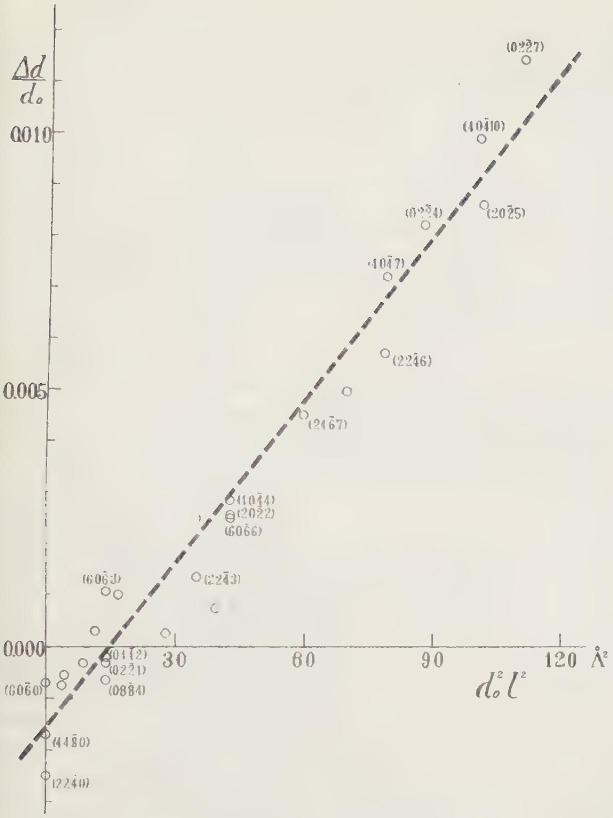

Fig. 1.

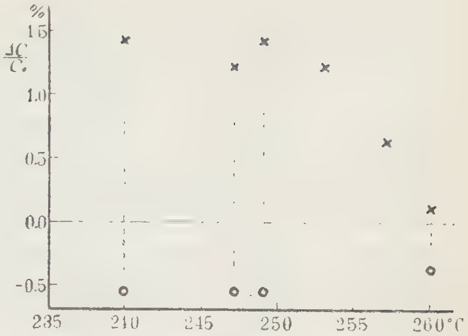

Fig. 2.
Temperature of structure loosening
Crosses: $\frac{\Delta C}{C_0}$ at room temperature
Circles: $\frac{\Delta C}{C_0}$ at the temperature of structure loosening.

intermediate value between solid and liquid state when the structure loosening begins, it is suggested that crystals do not change their states abruptly but through such certain intermediate states as nearly cubic structures in the process of the structure loosening.

For the purpose of detailed investigation, the improvement of the diffraction apparatus and further experiments are now proceeding.

References

1) Y. Fujiki and R. Suganuma: J. Phys. Soc. Japan **8** (1953) 427.

2) A. Jevins, M. Straumanis and K. Karlsons: Z. Phys. Chem. **40B** (1938) 347.

3) A. B. van Arkel: *Reine Metalle* (Berlin, Julius Springer, 1939) 534.

---

* The values of a_0 and C_0 in this case involve the correction for the thermal expansion.

Errata

Application of the Thin-Wing-Expansion Method to the Compressible Flow past an Elliptic Cylinder

By Hidenori HASIMOTO

J. PHYS. SOC. JAPAN **7** (1952) 322–328

Page line				
323 – 10 left	in G_2	α	should be read	d
– 8	in G_3	c	〃	C
– 5 right	in G_2	z^2 $\bar{\sigma}^2$	〃	Z^2 $\bar{Z}$
– 1		$\bar{Z}^2$	〃	Z^2

324	12 left		$\cdots\nu f'^2\cdots$	″	$\cdots\nu^2 f'^2\cdots$
	15		$\cdots\nu\bar{f}'$	″	$\cdots\nu f'$
	2 right		$\cdots(1+\nu)8$	″	$\cdots(1+\nu)/8$
	4		a_2	″	a_3
	5		a_3	″	a_4
	13	in G_3	$\sum$	″	$\varepsilon^3\sum$
	14		$f_3\zeta)$	″	$f_3(\zeta)/\varepsilon^3$
		in b_2	$M^2/4$	″	$M^2D/4$
		in b_3	$\{\cdots\cdots\}$	″	$\{(5\nu+4)\sigma^4+4(3\nu+2)\sigma^2+3\nu\}$
		in b_5	$b_5=\cdots\cdots$	″	$b_5=3B+(M^2D/4)\{4+7\nu-3(\nu+2)\sigma^2\}$
		in b_6, h_6	17, Z	″	7, $\bar{Z}$
		in h_7	Z/V^2	″	$\bar{Z}/\bar{V}^3$
		in h_{11}	V^2	″	V^4
		in b_{12}	$-M^4\nu/2$	″	$M^4\nu/4$
		in b_{14}	$(M^2/4)(D-M^2/2)$	″	$M^4\nu/8$
325		in b_{15}	α^4	″	σ^4
		in b_{16}	$-1/2$	″	$-1/6$
		in h_{17}	$\bar{\zeta}/Z$	″	$\bar{\zeta}/\bar{Z}$
		in b_{18}	$M^4\nu^2/2$	″	$M^4\nu^2/4$
		in b_{21}	$M^2(6+7\nu)/4$	″	$M^2D(6+7\nu)/4-$
		in g_{21}	$g_{21}=\cdots\cdots$	″	$g_{21}=\frac{1}{2\sigma}\frac{Z^2}{1-\sigma^2Z^2}\log\frac{Z-\sigma}{Z+\sigma}$ $+\frac{1}{2\sigma^2}\log\frac{1+\sigma^2}{1-\sigma^2}\left[\frac{Z}{Z^2-\sigma^2}+\frac{Z}{1-\sigma^2Z^2}\right]$
		in h_{22}	$+\bar{Z}/(V\bar{V})$	″	$-\bar{Z}/(V\bar{V})$
		in h_{23}	$h_{23}=\cdots\cdots$	″	$h_{23}=\{\zeta-(1+\sigma^2\bar{Z}^2)/\bar{Z}\}(V\bar{V}^2)$
	−14	in G_3/ε^3	A_1	″	A_1Z
	−11	in A_5	$-A_6/\sigma^2$		should be removed
	−10	in A_1, A_6	M^9D, $D(5+6\nu)$	″	M^2D, $D(6+7\nu)$
326	4	in (3.16)	$I_m(\cdots\cdot)$	″	$I_m(Z\partial G_n/\partial Z-\bar{Z}\partial G_n/\partial\bar{Z})$
	9		$\cdots)\}/\Theta-B_1\sigma^2(\sigma^2+3)/\Theta^2$	″	$\cdots)-A_6\}/\Theta+(2\sigma^2+\sigma^4)(2\sigma^2A_1+3A_2)$
	12		$-\frac{A_5}{\sigma}\cdot\cdot\left[\cdots\cos\theta\log\cdots\tan^{-1}\frac{2\sigma}{1-\sigma^2}\right]$	″	$-\frac{A_6}{\sigma\Theta^2}\left[\frac{1}{2}(1-\sigma^4)\sin 2\theta\log\cdots\right.$ $\left.\cdots\cdot\tan^{-1}\frac{2\sigma\sin\theta}{1-\sigma^2}\right]$
	−11	in F	$3(2-\gamma)M^4$	″	$3(3-\gamma)M^4$
	−1		$\cos\theta$, β^3	″	$\sin^2\theta$, β^2

On the Flow of a Viscous Fluid past an Inclined Elliptic Cylinder at Small Reynolds Numbers

By Hidenori HASIMOTO

J. PHYS. SOC. JAPAN **8** (1953) 653–661

Page	line			
654	2	$[K_1(kr)+K_0(kr)]$	should be read	$[K_1(kr)+K_0(kr)\cos\theta]$
	−8	$=e^{-n\xi}$	″	$\sim e^{-n(\xi-\xi_0)}$
655	18	$2\pi B_0$	″	$2\pi A_0$
657	20	$\{\cos a$	″	$\{\cos\alpha$
658	−7	$4\sigma^6\cos\alpha$	″	$4\sigma^6\cos 4\alpha$
	−5	$-\{(3\sigma^6-12\sigma^4\cdots)\cdots$	″	$+\{3\sigma^6-12\sigma^4\cdots$
	−2	$-(s/24)\{\cdots$	″	$+(s/24)\{\cdots$
	−1	$(12\sigma^4-12\sigma^2)\cos 4\alpha$	″	$(-2\sigma^8+12\sigma^4-12\sigma^2)\cos 4\alpha$
659	12	$-(s/24)\{\cdots$	″	$+(s/24)\{\cdots$
	13	$+(1/48)\{\cdots$	″	$-(1/48)\{\cdots$
661	16	$\cdots+\sigma^4-1]$	″	$\cdots-\sigma^4+1]$
	17	$4s(\sigma^4+1)$	″	$4s(\sigma^2+1)$
	19	$2s(\sigma^2-1)$	″	$2s(\sigma^4-1)$

JOURNAL OF THE PHYSICAL SOCIETY OF JAPAN Vol. 9, No. 2, MAR.—APR., 1954

Frequency of Slow Cosmic-ray μ-Mesons Stopped in the Photographic Emulsions at 23 m.w.e. Underground

By Shin-ichi KANEKO, Tadayoshi KUBOZOE
Institute of Polytechnics, Osaka City University, Osaka
and Masaomi TAKAHATA
Department of Physics, Osaka University, Osaka

(Received October 5, 1953)

The absolute frequency of slow μ-mesons stopped in the photographic emulsions at a depth of 23 m.w.e. underground was measured. The result is 0.22 ± 0.03 particles $\mathrm{cm}^{-3}\,\mathrm{day}^{-1}$, which is greater than the value published by George and Evans by a factor of about 2.5.

§ 1. Introduction

The photographic observations below ground were carried out by George and Evans[1)2)3)] at various depths. They have obtained the results which indicate that the most of slow particles came to rest in emulsions are μ-mesons and also that the fast charged particles produced nuclear disintegrations are energetic μ-mesons. To draw further decisive conclusions, we have undertaken to accumulate more extensive data concerning the underground events with photographic emulsions.

In the course of our observations, we found out that the result obtained on the frequency of slow μ-mesons is considerably different from that published by George and Evans, although the statistical accuracy of our result is poor. In this paper, the result we obtained is described and discussed in detail.

§ 2. Experimental Details

The coating of emulsion was performed in an observing station at about 300 m.w.e. depth of the Underground Cosmic Ray Observatory, Osaka City University in the disused Isohama Railway Tunnel, Shizuoka Prefecture (24° N geomagnetic latitude). The emulsion used for coating was Ilford G5 in gel form, from which two plates of 600 microns thick were prepared.

The plates were exposed vertically at about 23 m.w.e. depth, and after having been exposed for 68 days they were processed according to the usual temperature cycle method at about 300 m.w.e. depth.

The observations were made under the total magnification of ×225. The single particles came to rest in emulsions were carefully examined with oil immersion objectives and those of which projected residual ranges are longer than 100 microns were recorded.

§ 3. The Frequency of Slow μ-Mesons

In the examination of 6.9 cm³ of emulsion (assuming that the shrinkage factor of the emulsion is 2.5), a total of 134 meson tracks have been observed to come to rest. In almost all cases, the tracks of stopped particles allow easily to discriminate whether they are due to mesons or to heavier particles by inspecting of the characteristics of the track, i.e., meson tracks have a large amount of small angle scattering and a greater rate of change of grain density with residual range. Individual meson tracks observed are classified phenomenologically as follows: (i) μ-e decays, (ii) σ-mesons and (iii) ρ-mesons. No π-μ decays have been observed. The observed numbers and the frequencies of various particles are shown in Table I.

(i) μ-e decays.... An electron from μ-e decay would be observed only if it is emitted at a sufficiently small angle to the plane of the emulsion. Thus, the frequency of μ-e decays given in Table I is the value corrected on the basis of the geometrical consideration, and its proportion to that of all the stopped μ-mesons is 60 per cent, which agrees reasonably with the results of Cosyns *et al.*[4)] and of Fry.[5)] We may then conclude that the loss of minimum ionization tracks after 68 days exposure was negligible under our

Table I. The observed numbers and the uncorrected frequencies of various particles stopped in the emulsions.

Type of particle	Observed number	Frequency ($cm^{-3}day^{-1}$)	Percentage of the frequency to that of all the μ-mesons stopped
μ-e decay	81	0.17 ± 0.02	60
σ-meson	5	0.011 ± 0.005	4
ρ-meson	48	0.10 ± 0.02	36
total of μ-mesons	134	0.29 ± 0.03	100

condition.

(ii) σ-mesons.... The proportion of frequency of σ-mesons to that of all the stopped μ-mesons, 4 per cent, is consistent with the result of George and Evans.[2] It seems also that the σ-mesons observed are not π-mesons, as described by George and Evans.[2]

(iii) ρ-mesons.... The mesons excluded both μ-e decays and σ-mesons are grouped together as the ρ-meson. Among this group, 6 mesons emitted Auger electrons at their ends of range are included, and the frequency of these mesons is about 5 per cent of that of all the mesons stopped.

Since no π-μ decays and no π^--meson star were observed, it may be assumed that the ρ-mesons we observed are exclusively μ-mesons. In order to obtain a direct evidence of this view, an attempt was made to measure the multiple Coulomb scatterings along the tracks of ρ-mesons. The experimental distribution of angles of multiple scattering is in well agreement with the one expected for the μ-meson. It is therefore found that the observed frequency of μ-mesons stopped at 23 m.w.e. is $0.29 \pm 0.03\ cm^{-3}\ day^{-1}$ from Table I.

It is now necessary to correct the observed frequency taking into account of the configuration of our tunnel. Although the configuration is complicate, the earth surface is thought to be nearly flat in the region inside the cone with half-angle of 33° about the vertical. In the total number of stopped μ-mesons observed, there are 38 mesons at actual zenith angles (not projected) smaller than 33°. Assuming the zenith angle distribution[6] of $\cos^2\theta$, it is able to obtain the frequency of stopped μ-mesons in vertical direction. The frequency of all μ-mesons stopped in the case of the flat surface of earth is then obtained from this vertical frequency assuming $\cos^2\theta$ distribution; thus the frequency is $0.20 \pm 0.03\ cm^{-3}\ day^{-1}$.

Moreover, the observed number of stopped μ-mesons must be corrected geometrically since the tracks whose projected ranges are smaller than 100 microns have not been recorded in order to avoid misidentifying the particles. Lattes, Occhialini and Powell[7] have determined the geometrical correction factor in the case of high altitude observation assuming the isotropic angular distribution of slow mesons. This correction factor is inapplicable to a case of underground mesons because the angular distribution of these mesons is considerably different from the isotropic. According to a similar calculation, however, we can obtain the corresponding geometrical factor to the case when the angular distribution of slow mesons is assumed to be $\cos^2\theta$ and the plates are exposed vertically:

$$\frac{N_0}{N_t}=\frac{2d\sqrt{d^2+t^2}}{2d^2+t^2-t\sqrt{d^2+t^2}},$$

where, N_0 is the total number of tracks, N_t the observed number of tracks whose projected ranges are longer than t microns, and d the thickness of emulsion in microns. In our case, this correction factor is then $N_0/N_{100}=1.1$. It is therefore found that the corrected frequency of all the μ-mesons stopped at 23 m.w.e. depth is $0.22 \pm 0.03\ cm^{-3}\ day^{-1}$.

§ 4. Discussions

In order to compare our result with the theoretically predicted value, we have roughly calculated the expected number of μ-mesons stopped in emulsions at 23 m.w.e. using the intensity-depth relation of μ-mesons in vertical direction given by George (Fig. 4, p. 403 of the ref. 3). By differentiation of the intensity-depth relation the expected vertical frequency of stopped μ-mesons is obtained, from which the total frequency can be determined assuming the $\cos^2\theta$ distribution. Thus, the frequency of slow μ-mesons expected from the intensity-depth relation is $0.69\ cm^{-3}day^{-1}$.

Comparing this with our value of $0.22 \pm 0.03\ cm^{-3}day^{-1}$, it seems to be discrepancy of a factor of about three. However, since uncertainties in the prediction and in the experiment are considerably great, any decisive conclusion may not be drawn from this discrepancy.

George[3] has given the frequencies of μ-mesons stopped at 0, 20, 34 and 60 m.w.e. depth. By interpolating his values, it is found that the frequency at 23 m.w.e. is about 0.088 ± 0.005 cm^{-3}day^{-1}. Our value is greater than that of George by a factor of about 2.5. This discrepancy may be, however, mainly attributed to the difference of thickness of emulsions used; i.e., it seems that in the George's observation (200 microns emulsion) a greater number of μ-mesons had escaped from the detection as a result of their short lengths. According to the George's new data[8], in fact, he obtained the corrected value of 0.20 ± 0.01 cm^{-3}day^{-1} at 23 m.w.e. using 400 and 600 microns emulsions, which is in well agreement with our value. In Table II are shown the values of ours and of George together with the one expected from the intensity-depth curve.

Table II. Frequencies of μ-mesons stopped in emulsions at a depth of 23 m.w.e. in cm^{-3}day^{-1}.

George's value uncorrected[3]	George's value corrected[8]	Our value corrected	Value expected from intensity-depth curve
0.088 ± 0.005	0.20 ± 0.01	0.22 ± 0.03	0.69

§ 5. Conclusions

The slow particles stopping in emulsions at 23 m.w.e. depth are mainly μ-mesons as pointed out by George and Evans. The corrected frequency of μ-mesons stopping at 23 m.w.e. is 0.22 ± 0.03 cm^{-3}day^{-1}, which is greater than the value published by George and Evans by a factor of about 2.5.

Acknowledgements

We wish to express our sincere thanks to Prof. Y. Watase for his continual encouragements and valuable criticisms, and to Messrs. Y. Koseki and H. Iwamoto of the Research Laboratory, Fuji Photo-Film Co., Ltd. for their instruction during the underground coating. Thanks are due to Dr. E. P. George, University of Sydney for his kind letter, in which he has informed us the new result and given precious criticisms. We are also indebted to Dr. C. Waller, Ilford Ltd. for his advices and suggestions about the coating and the processing of emulsions. In conclusion, we are grateful to the members of the Research Group of Cosmic-Ray Underground, Osaka City University for their helpful discussions, and especially to Mr. K. Watanabe for his calculation in deriving the geometrical correction factor.

References

1) E. P. George and J. Evans: Proc. Phys. Soc. **A63** (1950) 1248.

2) E. P. George and J. Evans: Proc. Phys. Soc. **A64** (1951) 193.

3) E. P. George: "Progress in Cosmic Ray Physics", edited by J. G. Wilson, p. 393, North-Holland Publishing Co., Amsterdam, 1952.

4) M. G. E. Cosyns *et al.*: Proc. Phys. Soc. **A62** (1949) 801.

5) W. F. Fry: Phys. Rev. **83** (1951) 594.

6) R. Creamer: M. Sci. Thesis, London, 1951 cited in the ref. 3.

7) C. M. G. Lattes, G. P. S. Occhialini and C. F. Powell: Nature **160** (1947) 453.

8) E. P. George: Private communication (1953).

JOURNAL OF THE PHYSICAL SOCIETY OF JAPAN Vol. 9, No. 2 MAR.—APR., 1954

Study of Thin Crystalline Films by Universal Electron Diffraction Microscope*

By Hatsujiro HASHIMOTO

Kyoto Technical University, Matsugasaki, Sakyoku, Tokyo

(Received February 5, 1953)

In ordinary electron micrographs of MoO_3 crystals and mica films, which were obtained by using our universal electron diffraction microscope as ordinary electron microscope unit, there observed the well-known patterns which may be called "a group of closed contours", "dark spots" and "feather-like patterns" and further some patterns were also observed which may be called "wave-like patterns". These patterns could be analysed by using the universal electron diffraction microscope as shadow microscope unit and high resolution electron diffraction camera.

In the high resolution electron diffraction patterns and in the diffracted parts of shadow micrographs of bent films of the crystals obtained by the universal electron diffraction microscope, the subsidiary maxima were observed which correspond to the intensity region in the reciprocal lattice extended in the direction normal to the film surface, and from the angular distances of the subsidiary maxima, the thickness of the film, Fourier coefficient of periodic electric field in the crystal and the external form of bent film could be obtained.

Takagi and König observed that MoO_3 crystal transforms into minute MoO_2 cystals when MoO_3 crystal is irradiated by intense electron beam. Besides the transformation of MoO_3 to MoO_2, another type of transformation $MoO_3 \rightarrow MoO_2' \rightarrow MoO_2$ was observed in our experiment. The intermediate substance MoO_2' is observed as homogeneous parts in ordinary electron micrographs. By using the universal electron diffraction microscope as micro-diffraction unit, it has been possible to show that the intermediate substance belongs to monoclinic system and that some hexagonal holes produced in it are bounded by its net planes.

§ 1. Introduction

In ordinary electron microscope images of thin crystalline films such as split mica films, MoO_3 smoke and chemically produced MoO_3 crystals having thin plate-like shape, it is easy to observe the extinction contour lines due to Bragg reflection, so that many observations have been done with these specimens.1),2),3),4),5) In such electron micrographs some patterns were often observed which may be called "a group of closed contours"6),7) and "dark spots"8) and in the case of MoO_3 crystals "feather-like patterns"3) similar to "Fiedelung" named by König4) were observed. In order to clarify the nature of these patterns, some observations have been carried out by using the universal electron diffraction microscope devised by K. Tanaka and the present writer.9)**

In the course of observation, the so-called "wave-like patterns" as well as the subsidiary maxima of electron diffraction patterns by thin crystalline films illuminated by parallel beam were observed.*** The external form of the film in which such "wave-like patterns" were observed was surmised from the shape of extinction parts due to Bragg reflections and the surmise was further confirmed by the shadow micrograph and high resolution electron diffraction pattern of the film. The subsidiary maxima of electron diffraction pattern by thin crystalline film are due to the intensity region in the reciprocal lattice extended in the direction normal to the film surface as have already been observed in divergent beam diffraction patterns of thin crystals[13),14)] as well as in ordinary electron microscope images.[5)] In the case of parallel beam diffraction patterns, Finch and Wilman[15)] observed fractional order rings due to polycrystalline graphite and attributed them to the subsidiary maxima above mentioned. But it was reported later[16)] that these rings might preferably be attributed to the particular structure of graphite. Further, they obtained very beautiful rotational patterns of single crystals of graphite and molybdenite[17),18),19)] and mentioned that some subsidiary maxima were observed, but they did not analyse the series of maxima in detail. As will be mentioned later, the angular distances between the observed subsidiary maxima in this case are very small compared with those in the case of divergent beam. In order to carry out refined observation, therefore, the high resolution electron diffraction pattern is necessary. Thus, we have measured, on such a high resolution electron diffraction pattern, the angular distances between the observed subsidiary maxima and the thickness of the film, Fourier coefficient of the periodic electric field in the crystal and angle of bending of the film have been obtained.

---

* Presented before the Society of Electron Microscope of Japan held at the Nagoya University on Oct. 16, 1952 and at the annual meeting of Physical Society of Japan held at the Kyoto University on Nov. 1, 1952.

** The universal electron diffraction microscope can be operated either as the three stage electron lens microscope10) or the high resolution electron diffraction apparatus11).

*** The similar subsidiary maxima of MoS_2 film were also observed independently by R. Uyeda and his co-workers12).

Takagi[3)] and König[4)] observed in electron micrographs that MoO_3 crystal transforms into minute black crystals when MoO_3 crystal is irradiated by intense electron beam, concluding, by electron diffraction method, that these minute crystals are MoO_2 crystals. We have observed in electron microscope images that, besides the direct transformation of MoO_3 into MoO_2, there exists another type of transformation. Namely, we have observed that some homogeneous parts are formed in the original MoO_3 crystal and in these parts are produced some hexagonal holes. The homogeneous parts have been analysed by microdiffraction method and it has been found that they are composed of an intermediate substance between MoO_3 and MoO_2, which may be called MoO_2' and also that the edges of the hexagonal holes are parallel to some definite net planes of this substance.

§ 2. Experimental Observation

(*a*) *A group of closed contours and dark spots*

In ordinary electron microscope images as well as in shadow microscope images of thin crystalline film, we observe the extinction contour lines due to Bragg reflection of electron beams[1),3),5)] and often "a group of closed contours"[6)] and "dark spots",[8)] and it is supposed that the latters are certain modifications of the extinction contour lines. In order to ensure this supposition, the writer has carried out detailed observation by using the universal electron diffraction microscope as shadow microscope unit. Fig. 1 (a) and Fig. 2 (a) are the examples of shadow micrographs of mica film and MoO_3 respectively. Since these micrographs are shadow ones, the reflected images can also be observed at the same time.[20)] Fig. 1 (b) and Fig. 2 (b) are the enlarged photographs of the shadow images observed at the centers of Fig. 1 (a) and Fig. 2 (a) respectively, where "a group of closed contours" and "dark spots" can be observed respectively. Fig. 1 (c) and Fig. 2 (c) are the enlarged photographs of the reflected patterns as shown in Fig. 1 (a) and Fig. 2 (a) respectively, in which we can see bright closed contours and a bright spots which correspond respectively to "a group of closed contours" in Fig. 1 (b) and one of "dark spots" in Fig. 2 (b) (a dark spot as shown by a large mark ↑ in Fig. 2 (b) corresponding to a bright spot in Fig. 2 (c)). From these correspondences, it can be concluded that these patterns are due to Bragg reflections and the indices of the net planes which reflect the electron beams are determined.

From these reflected parts of shadow micrographs as shown in Fig. 1 (c) we can suppose that the shape of the film in which are observed "a group of closed contours" is such that one region of the film is projected so as to form nearly hemi spherical shell as shown in Fig. 3 (a). In Fig. 1 (c) a bright closed contour due to (220) reflection is divided into two by a line contour of the same reflection, so that a ϕ-shape contour is observed. In such bright ϕ-shape contour, which is due

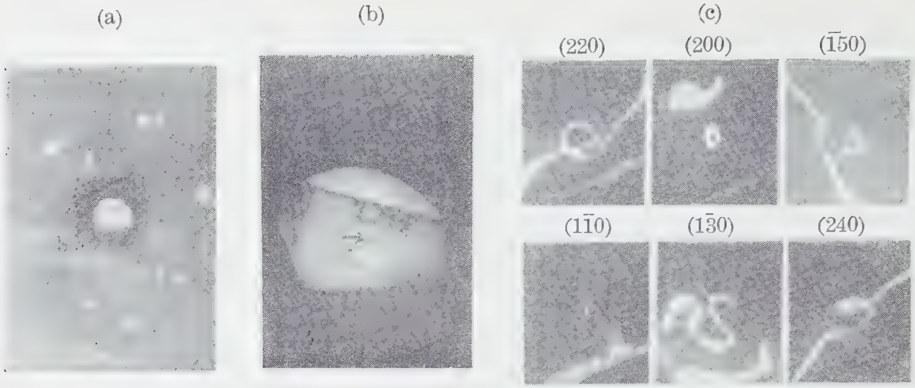

Fig. 1.

(a) Shadow micro-diffraction pattern of split mica film, showing extinction contours and its reflected patterns.
(b) Enlarged shadow image at the centre of (a), showing "a group of closed contours" as shown by mark ↑.
(c) Enlarged reflected patterns corresponding to "a group of closed contours".

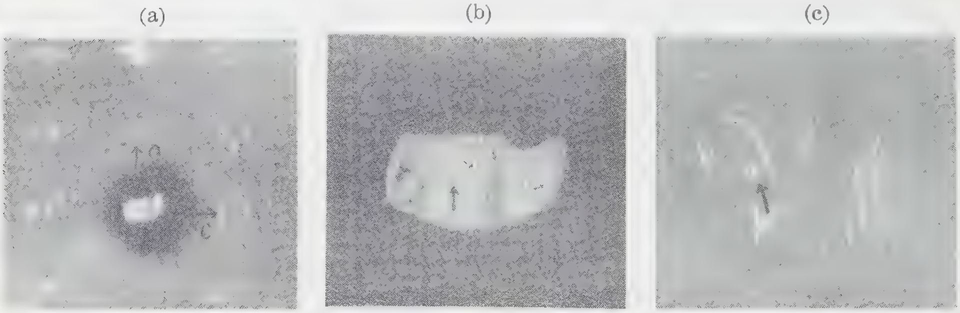

Fig. 2.

(a) Shadow micro-diffraction pattern of MoO_3 film.
(b) Enlarged photograph of the shadow image at the centre of (a) showing "dark spots" as shown by mark ↑.
(c) Enlarged reflected patterns of $(2\ n\ 1)$, $n=0, 1, 2, 3$, showing a reflected bright spot image as shown by mark ↑.

to reflection by a net plane normal to the surface of the film (in this case it is a part of (220) plane), a line contour is caused by the reflection from a part of narrow band which passes through near the top of the projected part of the film and along this contour Bragg condition is always satisfied, though the azimuth of the net plane to the incident beam varies continuously. The trace of such line contour on the film is shown in Fig. 3 (a) as curve 1. A closed contour due to reflection of the same plane, is shown in Fig. 3 (a) as curve 2 and is caused by the Bragg reflection in an annular part of the film, ditch or projection, near the base of the main projection. Along this contour, the azimuth of the net plane to the incident beam is not varied. When the Bragg condition is satisfied by certain other net plane at a portion which aparts a little from the top of the film, the locus of such a portion forms a *D*-shape closed contour between the top and the base of the main projection, because the film takes the same orientation to the incident beams near the base of main projection. In this case, (200) ($\bar{1}$50) (1$\bar{1}$0) plane satisfies this condition. If a very small portion of the projected part further project abruptly, an extinction contour line passing through this portion forms a very small closed contour there and as the result it seems as if the contour line vanishes there so that ϕ-shape contour becomes *S*-shape as is seen in (1$\bar{3}$0) contour. And other contour line passing near this portion varies its form abruptly and a contour with a loop is obtained such as (240) contour. If the indices of the two nearest extinction contours can be known,

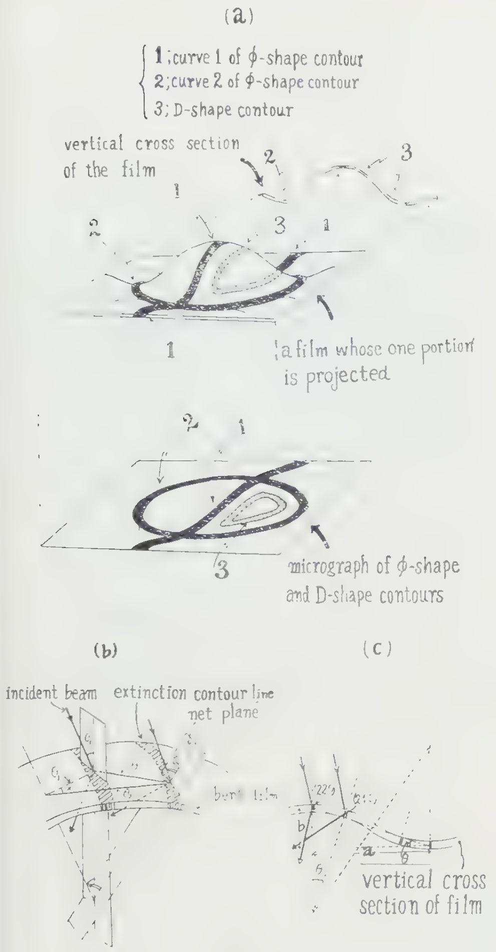
(a)
1;curve 1 of φ-shape contour
2;curve 2 of φ-shape contour
3; D-shape contour
vertical cross section of the film
a film whose one portion is projected
micrograph of φ-shape and D-shape contours
1
2
3
(b)
(c)
incident beam
extinction contour line
net plane
bent film
b
a
vertical cross section of film

Fig. 3.

(a) Geometrical construction of the relation between a film whose one portion is projected and a group of closed contours.
(b) The relation between the angle of bending of the film and two points either of which is on each two extinction contours.
(c) The vertical cross section of the film whose one part is projected and composed of uniformly concave and convex part.

the angle of bending of the film between any two points either of which is on each contours is given, from Fig. 3 (b), as :

$$\cos\theta=\cos\theta_2\cos\theta_1+\sin\theta_2\sin\theta_1\cos\alpha,$$

when the part of the film can be regarded as a portion of a spherical shell. Here, θ_1, θ_2 are the Bragg angles of the net planes corresponding to the two contours and α is the angle between two planes each of which includes the incident beam and one of the reflected beams from the point on the extinction contour. In the case of $\alpha=0$, θ is equal to $(\theta_2-\theta_1)$. From the above relation, the angle of bending of the uniformly bent portion of the projected part of the film can be known. For example, from ϕ-shape contour corresponding to (220) plane and closed contour corresponding to (240) plane which is included in one half of the ϕ, the angle of bending in the neighbourhood of the top and the base of the projection can be given as $\theta=5.50\times10^{-3}$ rad., since in this case $\theta_1=\lambda/2d_{220}$, $\theta_2=\lambda/2d_{240}$ and $\alpha=17°$. If the above calculation is applied to the whole extinction contours, the shape of projected part of the film can be known completely. Since, in the present case, all the net planes corresponding to the closed contours are normal to the film surface, the gradient of the surface of the projected part to the base is in the range of the Bragg angle ($\simeq10^{-2}$rad.). If the shape of film is nearly the one as shown in Fig. 3 (c), the ratio of the height, b, of projected part to the diameter, $2a$, of the base is given as :

$$b/2a=\tan\theta/2\fallingdotseq\theta/2=2.72\times10^{-3}.$$

In the neighbourhoods of "dark stops" it is observed that the shapes of extinction contours are distorted. For example, it can be seen in Fig. 2 (b) that many contour lines meet at "dark spots" or one of "dark spots" is situated at the centre of a group of closed contours. From the forms of the extinction contour lines around "dark spots", whose indices are different from those of contour lines, it can be supposed that a small portion of the film is projected and the curvature of the projected part varies abruptly. So it can be concluded that the dark spot is an extreme case of a closed contours.

(*b*) *Feather-like pattern*

In the ordinary electron microscope images of MoO_3 crystals, many small parallel stripes such as shown in Fig. 4 are observed when the specimens are irradiated a little while by electron beams. Similar stripes have already been observed by H. König$^{4)}$ and R. Takagi$^{3)}$. These patterns may be conveniently called "feather-like patterns". The size of such stripes differs slightly from each other for different specimens, but they make equal angle of about 33.5° with the direction of *c*-axis of MoO_3 crystal. The large stripes as shown in Fig. 4 (b) have the harpoon-like shape and the edges of this harpoon are parallel to the net planes (102) and (304) of MoO_3 (Fig. 5) and in each harpoon small streaks are observed along *c*-axis.

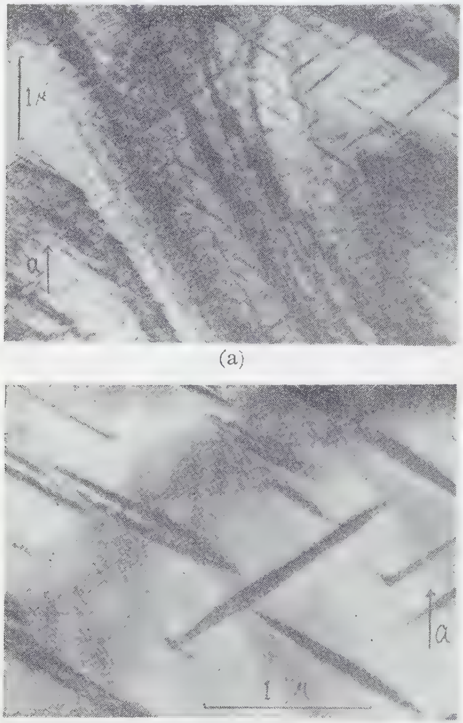

(a)

(b)

Fig. 4. Electron micrographs of the "feather-like patterns" of MoO_3 crystals. Many parallel stripes are observed in (a) and large stripes having harpoon-like shape are observed in (b).

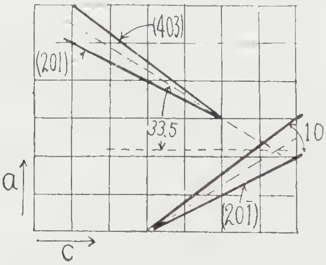

Fig. 5. (010) plane of MoO_3 showing the relation between the edges of harpoon and net planes.

The positions of these stripes do not change even when the orientation of the specimen to the incident beam is varied, but their brightness, which differs from that due to the part of the base crystal, varies. Thus, it can be supposed that the orientation of the stripes differs from that of the base crystal.

The high resolution electron diffraction pattern of this specimen is the *N*-pattern of MoO_3 as shown in Fig. 6 (a) and on each spot the needle-like intensity region is observed which elongates in the direction normal to the stripes. In some cases, this needle-like intensity region is splitted up into small spots as shown in Fig. 6 (b). This can be explained as follows; since all the stripes have almost the same width and are parallel to each other, the electron beam will be diffracted by these parallel narrow windows and will give splitted spots around each *N*-spot which is caused by reflection by Bragg condition. If the stripes are not the same for different ones, the difiraction patterns will not be splitted up into small spots, but will become spikycross pattern. From these splitted spots, the width of stripes can be calculated. From the observed value of the intervals of the splitted small spots, the width of stripes is obtained to be 325Å. On the other hand, from electron micrographs of the same specimen, the width of stripes is obtained to be about 300~350Å, in good agreement with the above value obtained from splitted spots.

(a) (b)

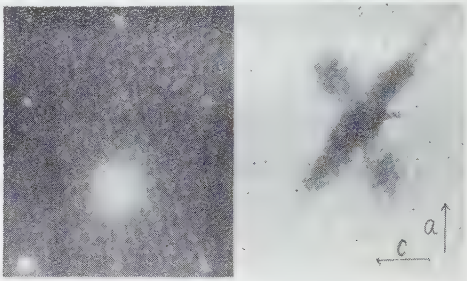

Fig. 6. The high resolution electron diffraction patterns of MoO_3 films whose micrographs show the "feather-like patterns"; (a) shows the *N*-pattern of MoO_3 and needle-like intensity regions are observed on each spot; (b) is the pattern of (100) plane showing, on enlarged scale, that the intensity region is split up into small spots.

(c) *Wave-like patterns*

In ordinary electron microscope images, as shown in Fig. 7 (a), many lines are observed with specimen of MoO_3 crystals chemically produced which are nearly straight and parallel to each other and which seem to be some boundary lines of crystalline film. Many small parallel stripes are the "feather-like patterns" as stated above. Since, in such micrographs, the extinction parts due to

Bragg reflection overlap on them, the patterns become very curious, which may be called the " wave-like parterns "*[7]. By varying the orientation of specimen to the incident beams, the extinction parts due to Bragg reflection vary continuously, but the situation of the boundary lines do not change. In case when the film is bent uniformly, it is expected that the extinction parts due to Bragg reflection become continuous dark bands. However, it is observed, in Fig. 7 (a), that the extinction parts are discontinuous at the boundary lines and their fringes are like the blade of a saw. From the appearance of these extinction parts, it can be supposed that each sections between the boundary lines are bent along its boundaries and at the same time the whole films is bent uniformly as shown in Fig. 7 (b). (By this bending broad extinction band is caused.) As the result, the film is in the state of periodic bending.

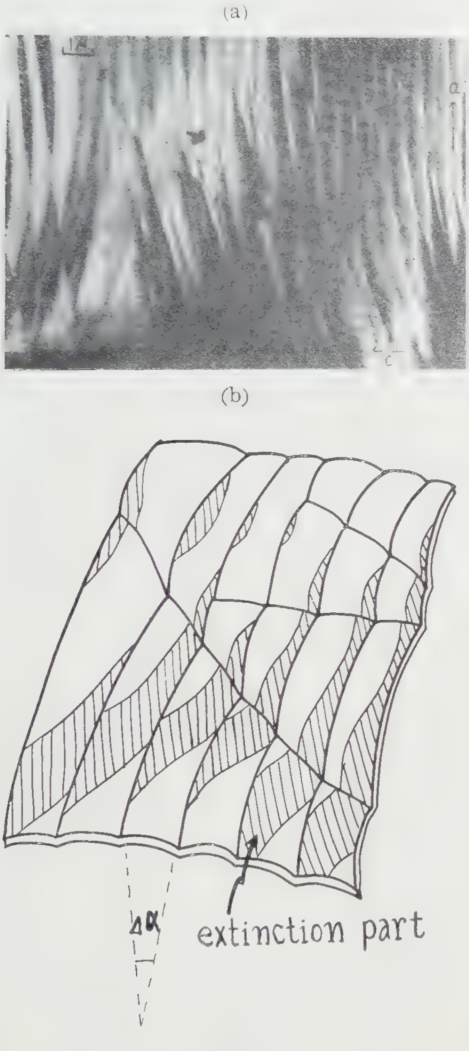

Fig. 7.

(a) Electron micrograph of MoO_3, showing the wave-like pattern composed of many lines which seem to be some boundary lines of crystal sections, and the extinction parts due to Bragg reflection (dark parts).

(b) The relation of the periodic bending of crysal and extinction parts due to Bragg reflection.

This fact also be ascertained in the reflected parts of shadow microgragh (Fig. 8 (a)) as well as in the high resolution electron diffraction pattern (Fig. 8 (b)) as follows. Fig. 8 (a) is an enlarged reflected part of (002) plane of shadow micrograph of MoO_3 film, in which is observed a part corresponding to the wave-like pattern as indicated by mark ↑. As will be seen in this part, since the reflection of (002) plane occurs periodically, it can be concluded that the film is in the state of periodic bending. Also it can be estimated that the angle of bending ($\Delta\alpha$) of the periodic bending as shown in Fig. 7 (b) is at least not greater than $\lambda/2(1/d_{002}-1/d_{012}) = 1.8\times10^{-4}$rad., because in each section only one reflection of (002) plane satisfies the Bragg condition and if the section is further bent, (012) reflection will occur. Fig. 8 (b) shows an enlarged part of high resolution electron diffraction pattern of the same plane with the one as shown in Fig. 8 (a). Since these photographs are taken at the same

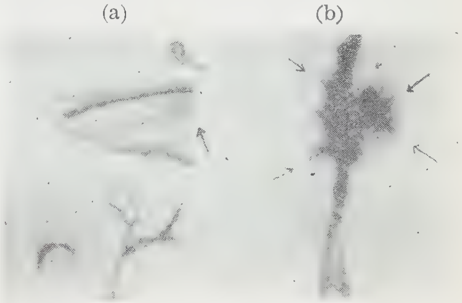

Fig. 8.

(a) Enlarged reflected part of (002) plane of shadow micrograph of MoO_3 film, showing the wave-like pattern.

(b) Enlarged part of high resolution electron diffraction pattern of the same plane (002) of the same specimen, showing a cross spiky part corresponding to the wave-like bending of the film.

---

* The similar pattern was also observed independently by T. Hibi (1952) in the case of split mica films.

situation of the same specimen, a cross spiky part observed in the diffraction patterd corresponds to the wave-like pattern of a reflected part of shadow micrograph. The three direction of the cross as shown by mark ↑ coincide with the directions which are normal to the parallel lines in the reflected part of shadow micrograph of the wave-like pattern in Fig. 8 (a). Since, as will be shown later, the diffraction spots of thin crystalline film elongate in the direction along which the film is bent, it can be concluded that one of the directions of the cross coincides with the direction of the bending of film and the specimen is in the state of periodic bending.

(*d*) *Bent specimen and subsidiary maxima of electron diffraction.*

From the electron micrograph of MoO_3 film as shown in Fig. 9, it is supposed that the film is bent uniformly, because its extinction contours are nearly straight lines, though the angle of bending is not known from this micrograph. The external form of this bent film can easily be seem from the diffraction pattern as follows. In high resolution elec-

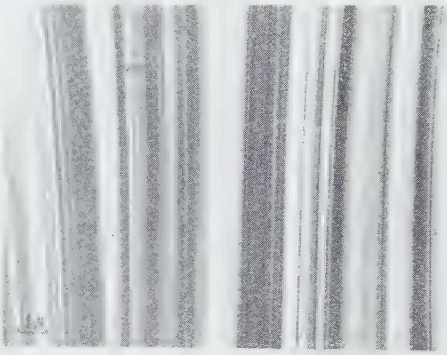

Fig. 9. Electron micrograph of bent MoO_3 films.

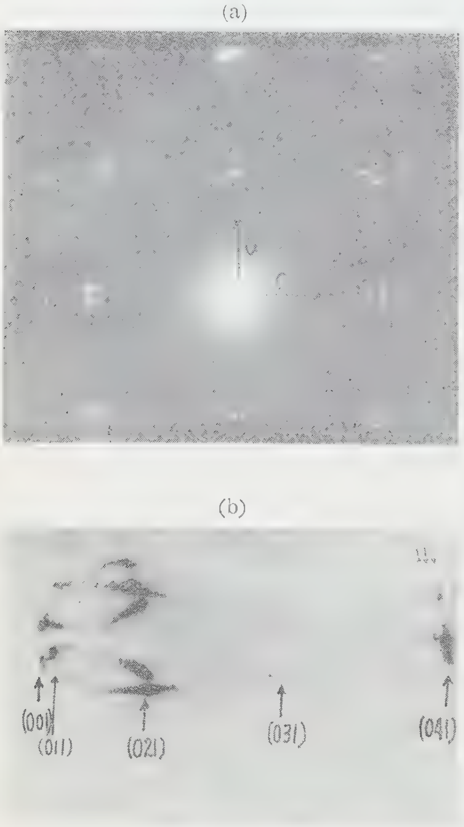

Fig. 10.
(a) The high resolution electron diffraction pattern of bent MoO_3 film.
(b) An enlarged part of (a), showing the subsidiary maxima of a group of indices (0 k 1), k=0, 1, 2, 3, 4.

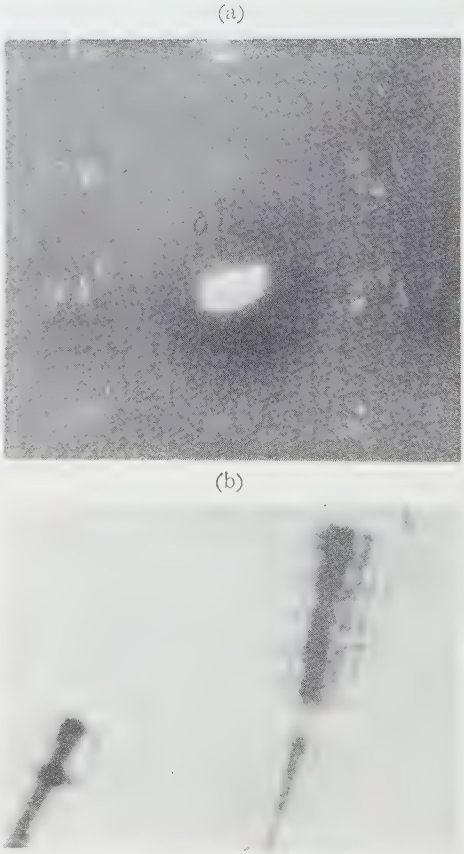

Fig. 11.
(a) The shadow micro-diffraction patterns of bent MoO_3 film.
(b) An enlarged part of (0 k 1) group showing subsidiary maxima.

tron diffraction pattern and shadow micro-diffraction pattern of uniformly bent film of MoO_3, a series of diffraction spots were observed whose indices of reflection plane are not only (h 0 l) but also (h k l) k=1, 2, 3, 4, ... , . From these diffraction patterns the angle of bending of the specimen can be known. In Fig. 10 (a), a high resolution electron diffraction pattern of MoO_3 is shown and in Fig. 10 (b) a group of indices (0 k 1) k=0, 1, 2, 3, 4 are shown. From this Fig. 10 (b), it can be found that the angle of bending is nearly 46°27′ in the range of irradiation (this being the angle between the planes (001) and (041)). In this pattern, the subsidiary maxima were observed around each spots and similar subsidiary maxima were observed in diffracted parts of shadow micrographs of Fig. 11 (a) and one part of which is shown enlarged in Fig. 11 (b). These subsidiary maxima of electron diffraction can be similarly observed in split mica film. According to the theory of electron diffraction, it is expected that a series of subsidiary maxima can be observed around the reflected spots of N-pattern in the case of thin bent film, and from those subsidiary maxima the Fourier coefficient of the periodic electric field in crystal and the thickness of the film can be computed, as will be discussed in the following section.

(e) *Transformation of MoO_3 crystal, MoO_2' and hexagonal holes*

When the intensity of the incident electron beam is increased, the temperature of the specimen becomes higher, and in the case of MoO_3 specimen the transformation of the structure takes place. The fact that the original MoO_3 crystal transforms into the minute MoO_2 crystals by electron irradiation is well known.3),4)

We have observed in detail changes of the structure in the course of such a transferma-tion. When the intensity of electron irradiation was increased, it was observed that many small black grains were created in some parts of the original MoO_3 and simultaneously some homogeneous parts were produced in other parts of the specimen as shown in Fig. 12. In high resolution electron diffraction pattern of such specimens we have been able to see not only an N-pattern due to MoO_3 and Debye-Scherrer rings due to MoO_2 but also another N-pattern due to an unknown substance which belongs to monoclinic system and whose lattice constants are a=3.92Å c=3.44Å β=93°. (The length of b-axis could not be determined.) The first N-pattern is surely due to a part of the original MoO_3 crystal which has remained unchanged. By the electron micro-diffraction method, the second N-pattern has been proved to be due to the homogeneous parts. Therefore, it is seen that the Debye-Scherrer rings corrospond to the black grains.

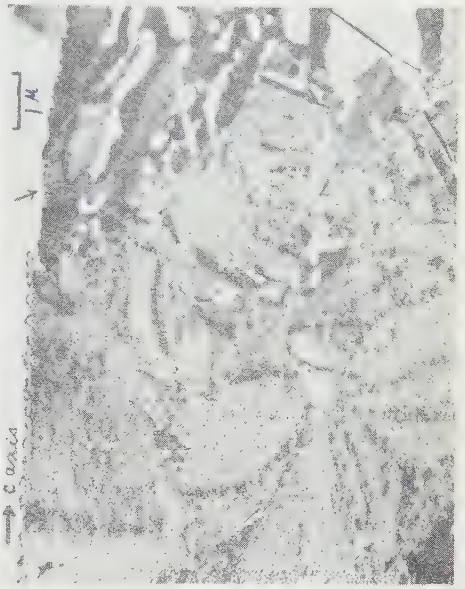

Fig. 12. Electron micrographs of thin MoO_3 crystal, showing the reduction process by electron bombardment. Minute grain crystals are those of MoO_2 and homogeneous parts having hexagonal holes are MoO_2' crystals.

By continuous irradiation of electron beams, many black grains of MoO_2 crystal grew larger to about 0.2μ in diameter and there produced around them irregular holes which grew larger as the black grains in them became larger. From these observations it can be supposed that the MoO_2 crystals grow by sublimation or diffusion of the original MoO_3 crystal and in these processes reduction of MoO_3 to MoO_2 may take place. On the other hand the homogeneous parts become larger and in them some holes of nearly hexagonal shape were produced at the same time. When the former overspread to small grains of MoO_3 crystal, irregular holes around them vanished and MoO_2 crystals were surrounded by the homogeneous parts and stayed there as black spots. As to the monoclinic crystal stated above its value of a (=3.92Å) coincides with the spacing of (100) plane of MoO_3 and the value of c (=3.44Å) coincides with the spacing of (110) plane of MoO_2. Two intermediate substances between MoO_3 and MoO_2 have already been known[21], but the present monoclinic crystal differs from either of these two and it may conveniently be called MoO_2' because of the fact that such crystal is also finally changed, by further illumination of electron beam, to black small grain of MoO_2. The angles between the edges of hexagonal holes as produced in homogeneous parts are 90°, 110°, 130° and 138°, and therefore the holes are supposed to be bounded by the net planes (201), (301) and (103) of MoO_2' crystal.

From the above observations, we can conclude that the changes produced by electron irradiation in vaccum consist of the indirect transformation $MoO_3 \rightarrow MoO_2' \rightarrow MoO_2$ and the direct transformation $MoO_3 \rightarrow MoO_2$. In the case of thick specimens of MoO_3, they become dark and small holes are also formed by intense illumination of electrons. The shadow micro-diffraction image and electron diffraction pattern of the film in this state show the formation of MoO_2' crystal only.

§ 3. Discussion

The dynamical theory of electron diffraction developed by Bethe[22] was extended by other workers[13),23] to the Laue case. According to their results, in case when there is only one reflection, the ratio of the intensity of the reflected beam to that of the incident beam is, for a crystal slab of thickness D, given by

$$\frac{I_h}{I_0}=\frac{V_{12}^2}{\kappa^2\cos\theta_0\cos\theta_h}\,\frac{\sin^2\frac{1}{2}D\sqrt{\left(\frac{V_{11}}{2\kappa\cos\theta_0}-\frac{V_{22}}{2\kappa\cos\theta_h}+\frac{\zeta_h}{\cos\theta_h}\right)^2+\frac{V_{12}^2}{\kappa^2\cos\theta_0\cos\theta_h}}}{\left(\frac{V_{11}}{2\kappa\cos\theta_0}-\frac{V_{22}}{2\kappa\cos\theta_h}+\frac{\zeta_h}{\cos\theta_h}\right)^2+\frac{V_{12}^2}{\kappa^2\cos\theta_0\cos\theta_h}} \qquad (1)$$

where the notations are almost the same as Bethe's one, namely:

θ_0=the angle between the normal of the film and the incident beam,

θ_h=the angle between the normal of the film and the reflected beam,

θ_B=the Bragg angle,

$\boldsymbol{h}$ and $\boldsymbol{g}$=reciprocal lattice vactors,

E= accelerating potential,

V=inner potential of the crystal,

V_0=mean inner potential of the crystal,

$K=\sqrt{\frac{8\pi^2me}{h^2}E}=\frac{2\pi}{\lambda}$= wave vector of electron beam,

$$\frac{8\pi^2me}{h^2}V_0=v_0,\quad \sqrt{K^2+v_0}=\kappa,$$

$$V_{11}=\sum_g\frac{v_gv_{-g}}{\kappa^2-k_g^2},\quad V_{12}=-v_{-h}+\sum_g\frac{v_{-g}v_{g-h}}{\kappa^2-k_g^2},$$

$$V_{21}=-v_h+\sum_g\frac{v_{h-g}v_g}{\kappa^2-k_g^2},\quad V_{22}=\sum_g\frac{v_{h-g}v_{g-h}}{\kappa^2-k_g^2}.$$

The potential $V(r)$ can be expanded in a Fourier series as follow:

$$\frac{8\pi^2me}{h^2}V=\sum_h\sum_k\sum_l v_{gkl}\exp 2\pi i(\boldsymbol{g}_{gkl}\cdot\boldsymbol{r}),$$

$$v_{gkl}=\frac{8\pi^2me}{h^2}\,\frac{d_{hkl}\cdot e}{\pi Q}\sum_j(Z_j-f_j)\exp 2\pi i(\boldsymbol{g}_{hkl}\cdot\boldsymbol{r})$$
$$=\frac{8\pi^2me}{h^2}V_{hkl}.$$

In the last expression Q is the volume of the unit cell and $\sum_j$ the electronic structure factor for the $(h\,k\,l)$ reflection. The quantity ζ_h is the "excitation error"[22] and the geometrical relation to $(\theta_0-\theta_B)$ is given by MacGillavry as $\zeta_h=\kappa(\theta_0-\theta_B)\sin 2\theta_B$ to the net plane normal to the crystal surface.

For our present discussion, however, it is convenient to construct the geometrical relation between θ_h and $\Delta\varphi$ to all the net plane, where $\Delta\varphi$ is the angular deviation of the reflection from the angle $2\theta_B$ when the crystal is illuminated by parallel beams. From the geometrical construction of bent crystal and wave vector of electron beams as shown in Fig. 13, the deviation angle $\Delta\theta_0$ of the incident beam from that corresponding to the exact Bragg condition, which is equal to the angle of bending $\Delta\alpha$ of the crystal, is given as:

$$\Delta\theta_0=\angle L_0OL=\Delta\alpha=\frac{LL_0}{\kappa}=\frac{\zeta_h}{\kappa\sin 2\theta_B}, \qquad (2)$$

and the deviation angle $\Delta\theta_h$ of reflected beam that corresponding to the exact Bragg condition is given as:

$$\Delta\theta_h=\angle L_0HL=\frac{L_0L_h}{\kappa}=\frac{L_0L'}{\kappa}+\frac{L'L_h}{\kappa}$$

$$=\frac{\zeta_h}{\kappa}(\cot 2\theta_B+\tan\theta_h)\,. \qquad (3)$$

Now, from Fig. 13 $\Delta\varphi$ is given by

$$\Delta\varphi=(\theta_h-\theta_0)-2\theta_B=\varphi-2\theta_B=\Delta\theta_h-\Delta\theta_0\,. \qquad (4)$$

The value of $\Delta\varphi$ can be computed by Eqs. (2) and (3).

$$\Delta\varphi=\frac{\zeta_h}{\kappa}\left(\tan\theta_h+\cot 2\theta_B-\frac{1}{\sin 2\theta_B}\right)$$

$$=\frac{\zeta_h}{\kappa}(\tan\theta_h-\tan\theta_B)\,. \qquad (5)$$

From Eq. 5, the intensity of reflected beam can be written as

$$\frac{I_h}{I_0}=\frac{v_h{}^2}{\kappa^4\cos\theta_0\cos\theta_h}\;\frac{\sin^2\frac{1}{2}\kappa D\sqrt{\left(\dfrac{\Delta\varphi}{\cos\theta_h(\tan\theta_h-\tan\theta_B)}\right)^2+\dfrac{v_h{}^2}{\kappa^4\cos\theta_0\cos\theta_h}}}{\left(\dfrac{\Delta\varphi}{\cos\theta_h(\tan\theta_h-\tan\theta_B)}\right)^2+\dfrac{v_h{}^2}{\kappa^4\cos\theta_0\cos\theta_h}}\,. \qquad (6)$$

The relative maxima in the reflected intensity will occur

$$\frac{1}{2}\kappa D\sqrt{\left(\frac{\Delta\varphi}{\cos\theta_h(\tan\theta_h-\tan\theta_B)}\right)^2+\frac{v_h{}^2}{\kappa^4\cos\theta_0\cos\theta_h}}=m\frac{\pi}{2}\,,\quad m=3,\,5,\,7,\,\ldots,. \qquad (7)$$

Therefore

$$(\Delta\varphi)_m=\pm\left[\left(\frac{m\lambda}{2D}\right)^2-\left(\frac{V_{hkl}}{E\sqrt{\cos\theta_0}\sqrt{\cos\theta_h}}\right)^2\right]^{1/2}\cos\theta_h[\tan\theta_h-\tan\theta_B]\,, \qquad (8)$$

and when $\theta_B\ll\theta_h$ this becomes

$$(\Delta\varphi)_m=\pm\left[\left(\frac{m\lambda}{2D}\right)^2-\left(\frac{V_{hkl}}{E\sqrt{\cos\theta_0}\sqrt{\cos\theta_h}}\right)^2\right]^{1/2}\sin\theta_h\,. \qquad (9)$$

As can be seen from Eq. (8), if θ_h is equal to θ_B, $(\Delta\varphi)_m$ becomes zero. Since this condition is satisfied on a plane which is normal to the crystal surface, e.g. in electron diffraction spot of (001) plane of MoO_3 film, the subsidiary maxima can hardly be observed as shown in Fig. 10.

For large m and $\theta_h\gg\theta_B$, the angular spacing of adjacent maxima is given by

$$(\Delta\varphi)_{m+2}-(\Delta\varphi)_m\simeq(\lambda/D)\sin\theta_h\,. \qquad (10)$$

From the angular distance of the subsidiary maxima of electron diffraction of bent MoO_3 film, the thickness of the film and Fourier coefficient of inner potential can be computed by using Eq. (9) as

$$D=\frac{2\lambda\cos\theta_h[\tan\theta_h-\tan\theta_B]}{\sqrt{(\Delta\varphi)_5{}^2-(\Delta\varphi)_3{}^2}}\,,$$

$$V_{hkl}=\frac{\sqrt{9(\Delta\varphi)_5{}^2-25(\Delta\varphi)_3{}^2}\sqrt{\cos\theta_0}\sqrt{\cos\theta_h}}{4\cos\theta_h[\tan\theta_h-\tan\theta_B]}\,. \qquad (11)$$

For example, the values for (041) plane are computed by using the values of $\cos\theta_0=d_{041}/d_{001}=0.689$, $2\theta_B=\lambda/d_{041}=0.0246$, $\cos\theta_h=\cos(\theta_0+2\theta_B)=0.671$, $\tan\theta_h=1.104$, $\tan\theta_B=0.0116$, $E=40\times10^3$ volts and $\lambda=0.062\times10^{-8}$ cm. Making use of the values $(\Delta\varphi)_3=18.46\times10^{-5}$ rad. and $(\Delta\varphi)_5=31.31\times10^{-5}$ rad. as measured on the enlarged photograph whose effective camera length of electron diffraction is 3608 cm, the values of $D=360$Å and $V_{041}=1.6$ volts are obtained, while the calculated value of V_{041} from the values of structure factors is 1.57 volts. It will be seen that the agreement is fairly good. From the shadow micro-diffraction pattern of a specimen, the value of $(\Delta\varphi)$ can be measured and the values $D=230$Å and $V_{021}=3.13$ volts have been obtained, while the calculated value of V_{021} is 3.16 volts. The agreement between theory and experiment is again satisfactory.

If an ideal thin crystalline film of thickness D is bent into a form of cylinder of radius R, the location of relative maxima, S, measured from the point A in Fig. 13 (a) will be given from the figure as $S=\Delta\alpha(R+D/2)$. From Eqs. (2), (5) and (9), $\Delta\alpha$ can be given as

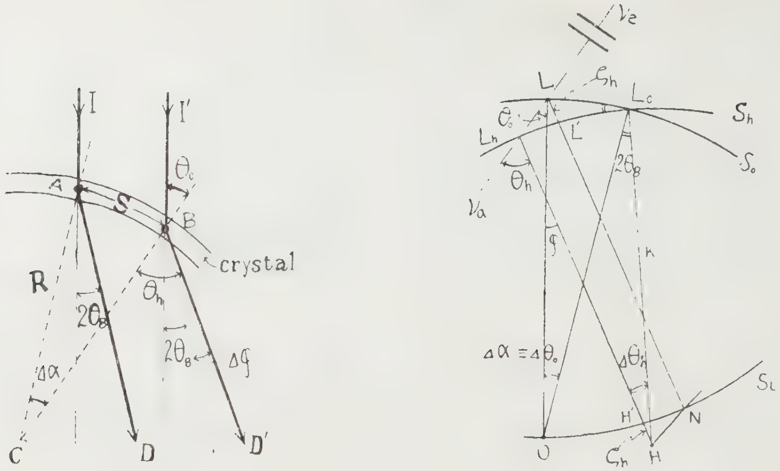

(a) (b)

Fig. 13.

(a) Geometrical construction of bent crystal and electron beams.

IA and AD: Incident beam and reflected beam at a point A respectively where the Bragg condition is satisfied exactly.

I'B and BD': Incident beam and reflected beam respectively at a point A which is apart from *A* at a distance *s*, where the Bragg condition is not satisfied exactly.

The angular deviation of *BD'* from the direction *AD* is $\Delta\varphi$.

(b) Wave vectors of electron beams in reciprocal space of crystal.

O and *H*: The origin and a reciprocal lattice point respectively. $OH=2\pi\boldsymbol{h}$.

Plane of this figure is determined by the vector $\boldsymbol{h}$ and $\kappa=L_0O$.

S_0 and S_h: Spheres of radius κ, drawn *O* and *H* as centres respectively.

L_0: Laue circle, i.e. intersection of S_0 and S_h.

L_0O: The direction along which the incident beam *IA* (Fig. 13 (a)) will proceed in the crystal after the refraction of an amount given by Snell's law.

L_0H: The direction of reflected beam in the crystal when the Bragg condition is satisfied exactly.

LO: The direction along which the incident beam *I'B* (Fig. 13 (a)) will proceed in the crystal.

At the point *B*, as the crystal is bent through an angle $\Delta\alpha$ from the point *A*, the reciprocal point *H* must be rotated around *O* through the same angle. $\Delta\alpha=\angle BCA=\angle L_0OL$.

$\nu_e\nu_a$: Normal of the crystal surface which passes through a point *L* and intersects with S_h at point L_h.

L_hH: The direction of reflected beam in the crystal which corresponds to *BD'*.

S_L: Sphere of radius κ, with *L* as centre.

H': Intersection of S_L and L_hH.

LN: Parallel line to L_hH.

L': Intersection of S_h and *LN*. $\zeta_h=HH'=LL'$.

$$\Delta\alpha=\frac{LL_0}{\kappa}=\frac{\zeta_h}{\kappa\sin 2\theta_B}=\frac{\Delta\varphi}{(\tan\theta_h-\tan\theta_B)\sin 2\theta_B}$$

$$=\pm\left[\left(\frac{md_{hkl}}{2D}\right)^2-\left(\frac{V_{hkl}d_{hkl}}{\lambda E\sqrt{\cos\theta_0}\sqrt{\cos\theta_h}}\right)^2\right]^{1/2}\times\cos\theta_h\,, \tag{12}$$

and *S* is given as

$$S=\Delta\alpha\left(R+\frac{D}{2}\right)=\pm\left(R+\frac{D}{2}\right)\left[\left(\frac{md_{hkl}}{2D}\right)^2-\left(\frac{V_{hkl}d_{hkl}}{\lambda E\sqrt{\cos\theta_0}\sqrt{\cos\theta_h}}\right)^2\right]^{1/2}\cos\theta_h\,. \tag*{(13)*}$$

---

* On the plane normal to the crystal surface, $\cos\theta_0\simeq\cos\theta_h\simeq1$, but on the plane inclined to the crystal surface normal, $\cos\theta_0\simeq\cos\theta_h\neq1$. For example, in some planes of MoO_3 the values of $\cos\theta_0$ are given as 0.967, 0.887, 0.788 and 0.689 respectively for (011), (021), (031) and (041).

If the value of D and the indices of net plane can be known by other methods, the value of R can be computed by measuring the value of S on the electron micrograph. Since, in the case of divergent beam diffraction method, the deviation angle of transmitted dark parts from that corresponding to the exact Bragg condition in the central image is equal to $\Delta\theta_0$ and the deviation of reflected beam from that corresponding to the exact Bragg condition is given as $\Delta\theta_h$, it can be known that $\Delta\varphi$ is given as the difference of them as shown in Eq. (4) and is very small compared with $\Delta\theta_h$ or $\Delta\theta_0$.

§ 4. Acknowledgement

The present paper is the first report on the results obtained by using the universal electron diffraction microscope constructed in the University of Kyoto. The author wishes to express his sincere thanks to Prof. K. Tanaka of the University of Kyoto for his kind guidance and also to Dr. Shimazu and Mr. M. Kurokawa of the Shimazu Seisakusho Co. Ltd. and Mr. H. Kawakatsu of the University of Kyoto for their aids in carrying our experiments. The author's thanks are also due to Mr. R. Takagi of the Mechanical Laboratory, Prof. R. Uyeda of the Nagoya University, Mr. N. Kato of the Kobayashi Institute, and Assist. Prof. K. Kōra of the Tokyo University for their kind discussions.

This work is supported financially by the Ministry of Education.

References

1) R. D. Heidenreich and L. Sturkey: J. Appl. Phys. **16** (1945) 97.

2) R. Takagi: Journal of the Mechanical Laboratory **5** (1951) 107.

3) R. Takagi: Ibid. (in Japanese) **6** (1952) 131.

4) H. Hönig: Zeit. f. Phys. **130** (1951) 483. Optik **7** (1950) 261.

5) R. D. Heidenreich: J. Appl. Phys. **20** (1949) 993.

6) R. Bernard & E. Pernoux: Compt. Rend. **235** (1952) 1488.

7) T. Hibi: Read at the annual meeting of Physical Society of Japan at Kyoto on Oct. 31, 1952.

8) K. Sasagawa: Densikenbikyo (in Japanese), Honda shoten (1951) 370.

9) K. Tanaka & H. Hashimoto: Rev. Sci. Inst. **24** (1953) 669.

10) J. B. le Poole: Philips Tech. Rev. **9** (1947) No. 2.

M. E. Haine, R. S. Page & R. G. Garfitt: J. Appl. Phys. **21** (1950) 173.

11) J. Hillier & R. F. Baker: J. Appl. Phys. **17** (1946) 12.

G. Picard, C. Smith & H. Reisner: Rev. Sci. Inst. **22** (1946) 601.

12) R. Uyeda. T. Ichinokawa & Y. Fukano: Private communication to the writer on Oct. 1952 and read at the annual meeting of the Physical Society of Japan, at Kyoto on Nov. 1, 1952.

13) W. Kossel & G. Möllenstedt: Ann. d. Phys. **36** (1929) 113.

14) C. H. MacGillavry: Physica **7** (1940) 333.

15) G. I. Finch. & H. Wilman: Nature **138** (1936) 1010.

16) H. Lipson & A. R. Stokes: Proc. Roy. Soc. **A181** (1942) 101.

17) G. I. Finch & H. Wilman: Proc. Roy. Soc. **A155** (1936) 345.

18) G. I. Finch & H. Wilman: Trans Faraday. Soc. **32** (1936) 1539.

19) G. I. Finch & H. Wilman: Erg. Exact. Naturw. **16** (1937) 353.

20) N. Davidson & J. Appl. Phys. **18** (1947) 499.

21) R. Uyeda: Proc. Phys. Soc. Japan **21** (1939) 517.

22) H. A. Bethe: Ann. d. Phys. **87** (1928) 55.

23) M. Blackman: Proc. Roy. Soc. **A173** (1939) 68.

JOURNAL OF THE PHYSICAL SOCIETY OF JAPAN Vol. 9, No. 2, MAR.—APR., 1954

Morphology of ZnO Crystals formed on the Surface of Brass or Zinc at High Temperatures

By Riitsu TAKAGI

Government Mechanical Laboratory, Sumiyoshi-cho, Suginamiku, Tokyo

(Read November 2, 1952; Received July 10, 1953)

It was electron-microscopically observed that thin needles are projecting on the surface of brass or zinc heated in the air. Electron diffraction diagrams proved that they are needle-shaped crystals of hexagonal ZnO with axes parallel to [110] direction; which presents an interesting contrast to the ZnO smoke needles having axes parallel to [001]. For brass, needle-shaped crystals begin to form at about 300°C, and the largest crystals grow at 550–650°C. At temperatures higher than 700°C the growth of the needles is suppressed and no oxide is found at all near the melting point. In the case of zinc, the largest crystals are obtained at 450–550°C (melting point 419°C), where dendritic crystals having 60° branching are observed together with flat sword-like crystals. When the substrate brass or zinc is mechanically distorted heavily, plate-shaped ZnO crystals showing rotational slips are obtained.

§ 1. Introduction

Ever since the advent of high resolution electron microscope more than ten years ago, the white smoke produced from burning zinc in the air has attracted general attention because of its fantastic aggregates of submicroscopically thin needle-shaped crystals. In 1944, Fuller$^{1)}$ reported that the needle axis of these crystals is coincident with [001] direction of ZnO. Anomalies in intensity of the electron diffraction Debye-Scherrer rings obtained from these needle-shaped crystals as reported previously$^{2)}$ were explained by Cowley, Rees and Spink from the refraction effect$^{3)}$ and the shape factor of the crystals$^{4)}$. Similar conclusions were reached independently by Honjo *et al.*$^{5)}$; these authors further clarified that the needle-shaped crystals are bounded by six ((100)) planes. Later observations of Cowley *et al.*$^{6)}$ elucidated the structure of webbing stretched between needles.

On the other hand, it has been revealed by electron diffraction studies that the surfaces of polycrystalline zinc$^{7)}$, zinc single crystal$^{8)9)}$, zinc evaporated on to copper surface$^{10)}$, zinc alloy such as brass$^{11)}$, and zinc mineral such as zincblende$^{12)}$, are covered with minute crystals of ZnO when heated in the air. There has been given, however, no direct observation on size and shape of such surface oxide by electron microscope. We found recently the fact that though ZnO crystals formed on the surfaces of brass and zinc at high temperatures in the air possess electron-microscopically either needle- or plate-like shape analogous to the habit of ZnO smoke particles, their electron diffraction patters are such that which correspond to a quite different crystal habit. Thereupon detailed investigations were made about the size, shape and structure of ZnO which forms on surfaces of zinc and brass heated in an electric furnace or by a flame.

§ 2. Experimental Methods

As brass specimen, commercial brass meshes (200 ♯) were employed. The chemical analysis showed: Cu 80% and Zn 20%. Their surface had a characteristic brass lustre. Brass meshes of a little different constituent ratio gave almost the same results. The clean meshes punched into discs, 3 mm in diameter, were put into an electric furnace and heated at 250–1000°C for a period from an hour up to twenty days, the furnace being kept automatically at a desired temperature with a precision of ±15°C. Some of them were heated by an alcohol lamp. They were then examined by a magnetic electron microscope or electron diffraction camera. Accelerating voltage of about 70 kV was used in either case.

As zinc specimen, commercial extra pure granular zinc was generally used. Zinc was iled into fine particles, 0.1–0.3 mm in diameter. A number of the particles were placed on nickel meshes (200 ♯), which were then heated and examined in just the same way as for brass*. High purity zinc (99.99%) gave quite the same results.

In order to observe the oxide on zinc single crystal, the following method was attempted. A thin zinc single crystal, 0.4 mm in diameter and 3 mm in length, was fixed to a specimen holder of an electron microscope, so that its cleavage surface stood parallel to the electron beam. This crystal was heated together with the holder in the furnace, and then mounted n the electron microscope. In this way, ircumference of the cleavage surface could be observed from a direction parallel to the urface.

To make sure the correspondence between lectron microscopical image of a certain rystal and its diffraction pattern, a three-tage electron microscope of Japan Electron Optics Laboratory Co., Ltd., was used.** Its ccelerating voltage was about 50 kV.

3. Needle-shaped ZnO Crystals

When brass was heated at 450°C for an hour, nany needle-shaped crystals grew from the urface (Fig. 1). Dimension of most of these

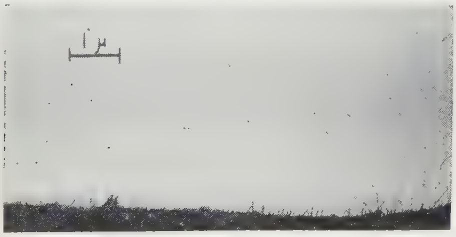

ig. 1. Needle-shaped ZnO crystals projecting from brass surface after 1 hr heating at 450°C.

rystals was 10–20 mμ in thickness and 1–2 μ length. Some of them were as long as μ, and vibrating incessantly during observation in the electron microscope.

It is very likely that the axes of these eedle-shaped crystals have a definite crystallographic direction while their azimuth distributes at random on the substrate. Their ectron diffraction pattern obtained by the ree-stage electron microscope is shown in g. 2, where an arrow indicates normal direction of the brass surface. The spacings are those of hexagonal ZnO. From the arcing direction of the rings from plane (002) which is parallel to the basal plane and from planes (103) and (102) which make small angles with the basal plane, it may be supposed that the direction of the axis of needle crystals, which are lying mostly nearly parallel to the arrow, is parallel to the basal plane. Absence of the orientation which may be expected to exist in the (100) ring is ascribed to the circumstance that the angles between the needle crystals and the substrate normal are distributed in a wide range (considerably over 30°). On the other hand every diffraction spot is more or less elongated into a streak because of the peculiarity in crystal shape. Among the spots on the (110) ring, those which are elongated along the ring circumference show an appreciable arcing, while the others on the same ring are not distinctly arced; the former spots can be interpreted to be due to reflections from planes perpendicular to the axis of the needle crystals which are actually directed to the position of the spots from the direct spot in the pattern.

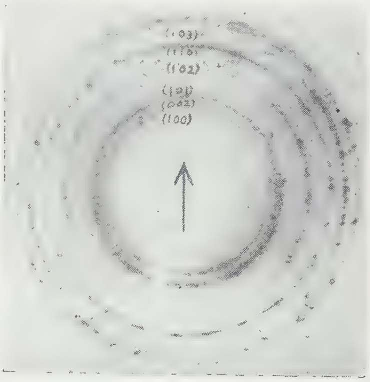

Fig. 2. Electron diffraction pattern of needle-shaped ZnO crystals. Arrow indicates direction perpendicular to Brass surface.

The same habit was ascertained for the needle-shaped crystals grown on zinc surface at elevated temperature.

---

* On the surface of nickel heated above 400°C, plate-like oxide of spotty appearance was sometimes observed with an electron microscope, which was identified as an assembley of minute crystals of NiO. But this NiO was easily discernible from zinc oxide, and offered no trouble in the present investigation.

** The author is very much indebted to Mr. K. Ito and Mr. T. Ito for kindly allowing him to use their three-stage electron microscope.

§ 4. Effect of Temperature

1. *Brass*

Brass was heated for an hour at temperatures 250–1000°C, and observed in an electron microscope. Needle-shaped crystals began to appear at about 300°C. The largest crystals, 3–5 μ in length, grew densely at 550–650°C. Some of them were apparently flat; the flat surfaces are supposed to be parallel to (001) plane as will be mentioned later for the oxidation of zinc. At 750°C, a few thick needles were seen here and there; at temperatures higher than 850°C no oxide crystal was seen up to the melting point (about 995°C).

2. *Zinc*

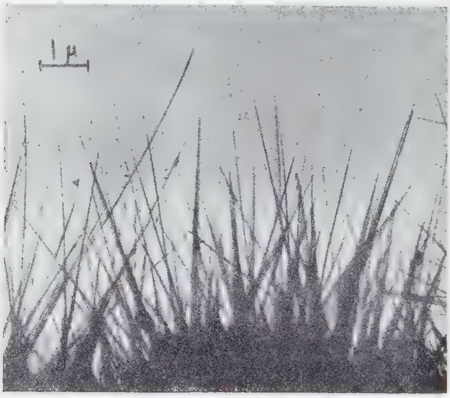

Fig. 3. ZnO crystals grown on zinc surface after 1 hr heating at 550°C.

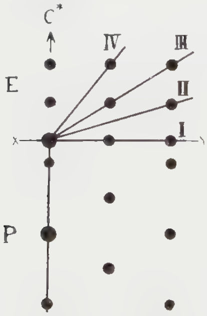

Fig. 4. Elevation (E) and plan (P) representation of ZnO in reciprocal spare. c^*-axis is perpendicular to P and parallel to E. Four planes described by sections I, II, III and IV are perpendicular to E.

When zinc was heated for an hour at various temperatures below melting point (419°C), needle-shaped or flat crystals began to appear in an electron microscope at about 300°C and grew larger at higher temperatures, but neither branching nor any other complicated shape was noticed.

On the other hand, when zinc was heated above melting point (419°C) for an hour, the electron microscope image revealed various shapes of oxide crystals. Between 450°C and 550°C, the growth of ZnO crystals was most remarkable, the zinc surfaces being covered with long, flat sword-like ZnO crystals throughout (Fig. 3). From these specimens single crystal electron diffraction patterns such as those corresponding to the cross sections of the reciprocal lattice by the sphere of reflection as illustrated in Fig. 4 by I, II, III and IV were often observed, but no single crystal pattern corresponding to the cross sections parallel to c^*-axis was obtained. In view of these facts as well as that ZnO seems habitually to grow parallel to (001) plane as will be described in later paragraphs, it will be quite reasonable to suppose that the flat sword-like crystals in Fig. 3 are parallel to (001) plane, having [110] axes. Some of them had a dendritic appearance (Fig. 5). All of the branchings are practically included in a common plane (*i.e.*, basal plane) and they make angles of about 60° with one another, as was found by stereoscopic electron micrographs.

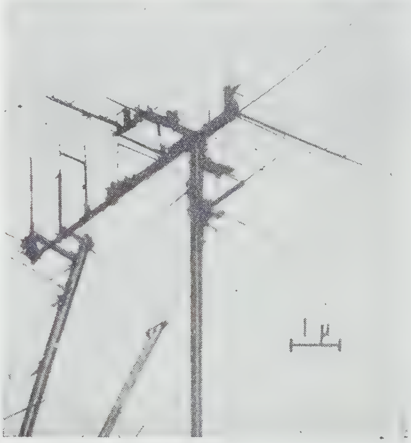

Fig. 5. Dendritic ZnO crystal grown on zinc surface after 1 hr heating at 450°C.

Behaviors of the oxidation at higher temperatures were as follows: The growth of ZnO became less prominent at 650°C; only a few thick crystals, about 5 μ in length, were seen at 750°C, and then still fewer crystals, about 1 μ in length, remained visible at 850°C. Finally at 950°C, no needle crystal but irregularly shaped minute crystals, about 0.1 μ in diameter, aggregating on the surface was observed.

§ 5. Effect of Heating Time

1. Brass

When brass was heated for five hours at 550°C, a number of rape leaf-shaped ZnO crystals were obtained (Fig. 6), besides normally shaped needle crystals. These curiously shaped crystals must be a modification of the needle crystals produced by developing laterally in the basal plane as assumed before. Heating for a day at the same temperature generally resulted in rod-like crystals (Fig. 7). By a further heating for more than six days, though there was found no striking change in their external shape except for considerable increase in length, the corresponding electron diffraction pattern became as shown in Fig. 8 ; in which all the diffraction spots extend in direction perpendicular to the needle crystal, forming almost a pattern of equal-spaced parallel lines. The space changed from crystal to crystal ; their minimum value seems to be half the reciprocal of the spacing of the (110) plane. This anomalous pattern may be ascribed to imperfections along a longitudinal direction of the needle crystal similar to those reported by Cowley *et al.*[6] for the webbing of ZnO smoke particles.

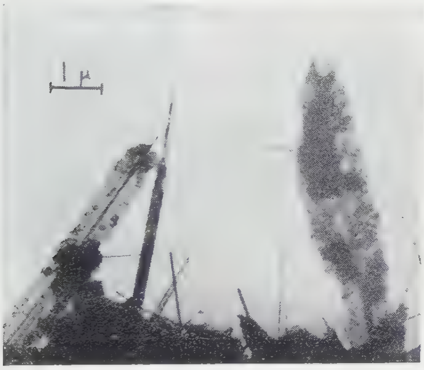

Fig. 6. Rape leaf-shaped ZnO crystals on brass after 5 hr heating at 550°C.

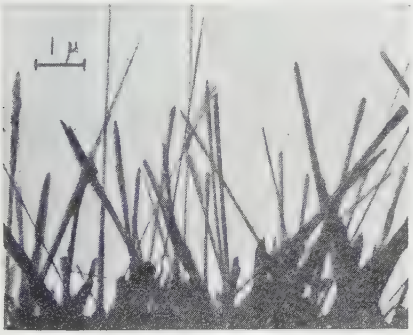

Fig. 7 Rod-like crystals on brass after 1 day heating at 550°C.

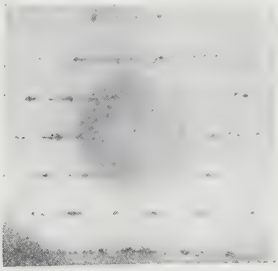

Fig. 8. Electron diffraction pattern of a rod-like ZnO crystal formed on brass after over 6 days heating at 550°C. Taken by the three-stage electron microscope.

2. Zinc

On heating zinc for several hours at 300°C, below melting point, only the needle-shaped or small flat ZnO crystals were observed, but after heating it for more than ten hours, circular flat crystals, about 1 μ in diameter, were also detected.

When zinc was heated for twenty days at 450°C, above melting point, some large crystals, 1 μ in diameter and more than 10 μ in length, were produced.

§ 6. Heating in an Oxidizing Flame

When brass was lightly heated in an oxidizing flame of an alcohol lamp and immediately withdrawn, needle-shaped crystals projecting from the surface with somewhat rounded heads were observed (Fig. 9) ; their electron diffraction pattern exhibited, naturally, a clear fiber diagram of ZnO. But after strong heating in a similar flame, the surface was covered with irregularly shaped ZnO crystals, about 0.1 μ in diameter ; their electron diffraction pattern showed normal ZnO rings.

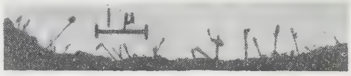

Fig. 9. ZnO crystals on brass after heated lightly with an alcohol lamp.

When zinc was similarly heated with an alcohol lamp, thick and short rod-like ZnO crystals projecting from the surface were observed.

§ 7. Flat ZnO Crystals

When a brass surface was hit heavily with a clean hammer, and then kept for more than ten hours at 500–600°C, seaweed-like flat crystals, 5–10 μ in diameter, as well as needle-shaped crystals were found to form (Fig. 10). In their images many fringes due to Bragg reflections[13] are running irregularly, corresponding to severe distortion of the crystals. When an electron beam was directed approximately normal to the surface of such a flat crystal, either one of the two diffraction patterns as shown in Fig. 11, a, b, and schematically drawn in Fig. 12, a, b, was obtained. In each diagram of Fig. 12, it is easily seen that two sets of hexagonal single crystal patterns expressed by ● and ○ are superposed on each other with a definite angle of rotation, 27°48′ or 38°13′ (or 21°47′), having additional weak spots. Both of the two diagrams can be explained in the following way by the idea of the rotational slip of crystals introduced by Wilman[14].

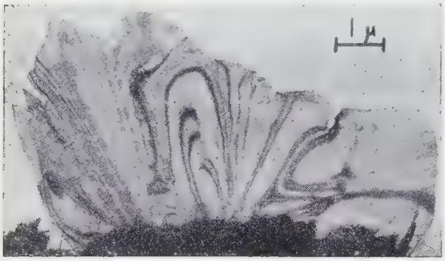

Fig. 10. Flat ZnO crystal formed on the surface of deformed brass after 1 day heating at 550°C.

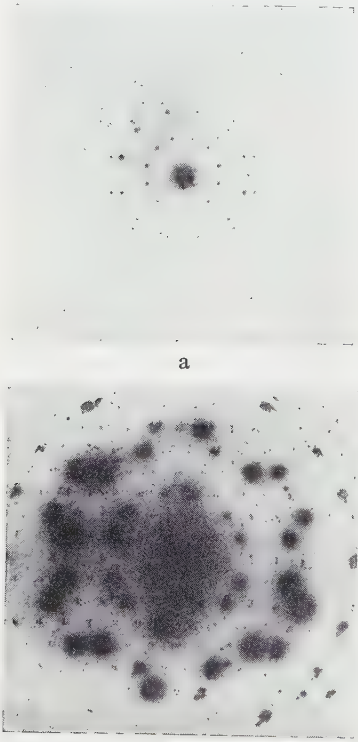
a

b

Fig. 11. Two kinds of electron diffraction patterns taken by a. ordinary diffraction camera, and b. three-stage electron microscope.

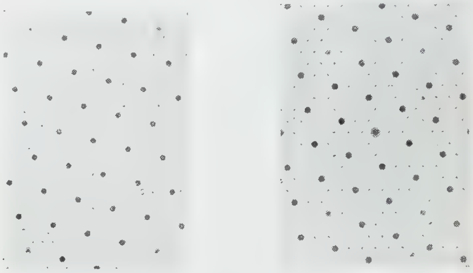
a b

Fig. 12. Schematic diagrams of Fig. 11, a and b.

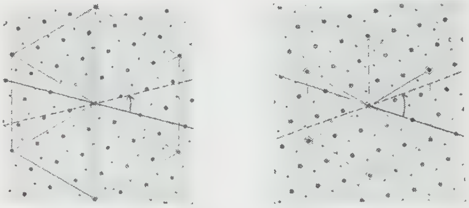
a b

Fig. 13. Atomic arrangement of ZnO crystal projected on basal plane. [100] directions are indicated by a full line (before slip) and a dotted line (after slip).

Let Fig. 13, a, b, represent the basal planes of ZnO crystals. For the sake of simplicity we consider the arrangement of zinc atoms only, and denote their possible positions by ◉, • and ○. It may be easily seen that in the normal structure of ZnO crystal a two-dimensional arrangement of atoms expressed by ◉ and that by • lie alternately in planes with a distance $c/2$ in the c-direction. We represent the crystal of this orientation by ◉. We assume that there are two contacting crystals, each represented by ◉ and ○, related by a rotation about a common lattice direction, *i.e.*, the direction of c-axis. Boundary plane where two crystals meet is here normal to the common lattice direction. Then these two crystals, each of which is represented by ◉ and ○, give single crystal patterns denoted in Fig. 12 by ● and ○, respectively. Weak spots in Fig. 12, which look as if they were originated from large unit cells enclosed in Fig. 13, may be ascribed to the secondary reflection similar to that observed by Wilman in $n\text{-C}_{32}\text{H}_{66}$ crystalized from solution on a collodion film13).

The flat crystals as shown in Fig. 10 always gave diffraction patterns with the rotational slip. In the pattern as Fig. 11, a, short arcs of (hk1) can often be seen just outside of (hk0) spots. This is indicative of the distortion of crystals already mentioned. Appearance of forbidden spots such as (111), (301), (303) and (411) in Fig. 11 may probably owe to the multiple reflection of electrons.

The plate-shaped ZnO crystals formed on highly distorted zinc surface mentioned before gave sometimes the evidence of the same rotational slip, but in other cases no trace of rotational slip was found. Thus it seems to be that the growth of ZnO with rotational slip takes place only when the substrate crystal is in a state of excessive distortion. Hence it may be suggested that here the distortion in the substrate crystal led the surface oxide to rotational slip. Wilman cited many examples of occurrence of rotational slip14)15), but no such case as described here was ever reported.

In connection with the rotational slip occurring in crystals grown from solution, Wilman said that *rotational slip is generally along the atomic or molecular layers which are first formed on the substrate*14). That the basal plane of ZnO, where we observed rotational slip, is one of such layers can be seen also from the following experiment: Thin transparent film of ZnO was obtained from molten zinc by the copper loop method16); this film has a fiber structure with the surface normal parallel to [001] direction17). Observation of this film with an electron microscope revealed that it is generally a flat plate, though it is constituted of domains, about $0.1\,\mu$ in diameter, corresponding to very sharp electron diffraction Debye-Scherrer rings at normal incidence.

§ 8. Discussions

It is worth mentioning to find that oxide formed by atmospheric oxidation of brass or zinc is really a needle projecting from the surface, since the previous investigations performed by means of electron diffraction have overlooked it. For instance, Miyake,11) studied oxidized surface of brass by reflection and merely reported *very clear* pattern of ZnO; Tanaka and Hashimoto10) found *ZnO* pattern on oxidized surface of copper evaporated by zinc in vacuum and explained it with a ring fiber structure in which [001] direction of ZnO distributed at random in the surface. These results may be readily understood from the consideration that ZnO needles of [110] direction were growing on the surfaces.

As mentioned before, Cowley *et al.*6) reported *faults* running in a definite direction in the webbing of ZnO smoke crystals. It will be remarkable that their direction is coincident with that of the needle axis of ZnO in the present experiment.

Vernon *et al.*18) reported, in their study of atmospheric oxidation of zinc below melting point, that below 225°C the surface was covered with smooth amorphous zinc oxide film accompanied by a little weight increment, whereas above 225°C crystalline zinc oxide was formed with far more rapid weight increment wherein the surface showed no interference color on account of roughness. In our electron microscopic experiment, small needle-shaped crystals of ZnO were barely observed by heating zinc up to 250–300°C for an hour. But it may be plausible to suppose that the critical temperature of 225°C found by Vernon *et al.* is the temperature at which the needle-shaped crystals of ZnO begin to grow. Accordingly it can be said that the *crystalline island* of ZnO assumed by Mott in the theory of logarithmic oxidation of zinc19) seems to be a reasonable assumption.

As for the oxidation of the cleavage surface of zinc single crystal, Raether8) investigated, after heating for thirteen hours at 250–400°C, by electron diffraction and deduced that needle crystals with [001] axes were distributed irregularly in the oxidized surface. We also obtained a diffraction pattern of ZnO shown in Fig. 14 from a cleavage surface of zinc single crystal of high purity heated for six hours at 350°C. This pattern is a superposition of an orientated spots with [100] direction perpendicular to the surface on a fiber diagram with [001] direction tending to be parallel to the surface. We suppose that the latter fiber diagram is ascribed to the needle-shaped crystals with [110] axes projecting from the surface, naturally explaining the circumstance remarked by Raether that the intensity of (110) is stronger than that of (103), and the former orientated spots are probably due to small flat crystals growing upright from the surface. Actually in the circumference of the surface flat crystals can be observed among needles.

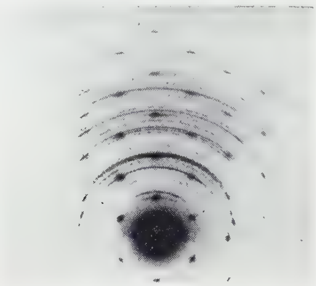

Fig. 14. Electron diffraction pattern of cleavage surface of zinc single crystal after 6 hr heating at 350°C.

In the course of this experiment, no positive evidence of pseudomorphic zinc oxide(17) was obtained. Though some of oxidized brass surfaces gave diffraction pattern showing an extra ring composed of spots just outside of (110) ring, we are interpreting it as (100) ring of Zn(10). No further pursuit of this phenomenon has been attempted.

In conclusion the author wishes to thank Mr. T. Kawada and Mr. S. Yoshida for many helpful advices. He also thanks Prof. S. Miyake and Prof. R. Uyeda for useful discussions.

References

1) M. L. Fuller: J. Appl. Phys. **15** (1944) 164.

2) H. J. Yearian: Phys. Rev. **48** (1935) 631.

3) J. M. Cowley and A. L. G. Rees: Nature **158** (1946) 550; Proc. Phys. Soc. **59** (1947) 287.

4) A. L. G. Rees and J. A. Spink: Acta Cryst. **3** (1950) 316.

5) G. Honjo, S. Miyake and K. Mihama: Report of Congrès International de Microscopie Électronique, Paris, Sept. 1950.

6) J. M. Cowley, A. L. G. Rees and J. A. Spink: Proc. Phys. Soc. B **64** (1951) 638.

7) G. Shearer: Unpublished; quoted in the paper 17).

8) H. Raether: J. Phys. Radium **11** (1950) 11.

9) L. N. D. Lucas: Proc. Roy. Soc. A **215** (1952) 162.

10) K. Tanaka and H. Hashimoto: X-Rays **6** (1950) 1. (In Japanese)

11) S. Miyake: Sc. Pap. I. P. C. R. **29** (1936) 167.

12) R. Uyeda, S. Takagi and H. Hagihara: Proc. Phys. Math. Soc. Jap. **23** (1941) 1049.

13) R. D. Heidenreich: J. Appl. Phys. **20** (1949) 993.

14) H. Wilman: Nature **165** (1950) 321; Proc. Phys. Soc. A **64** (1951) 329.

15) D. M. Evans and H. Wilman: Proc. Phys. Soc. A **63** (1950) 298.

16) W. L. Bragg and J. A. Darbyshire: Trans. Faraday Soc. **28** (1932) 522.

17) G. I. Finch and A. G. Quarrell: Proc. Phys. Soc. **46** (1934) 148.

18) W. H. J. Vernon, E. I. Akeroyd and E. G. Stroud: J. Inst. Metals **65** (1939) 301.

19) N. F. Mott: Trans. Faraday Soc. **36** (1940) 472.

JOURNAL OF THE PHYSICAL SOCIETY OF JAPAN Vol. 9, No. 2, MAR.—APR., 1954

Intensity of X-ray Diffraction by a One-dimensionally Disordered Crystal

(II) General Derivation in the Case of the Correlation Range $s \geq 2$.*

By Jiro KAKINOKI and Yukitomo KOMURA

Institute of Polytechnics, Osaka City University
12 Minami-Ogimachi, Kita-ku, Osaka, Japan

(Received July 31, 1953)

The general intensity equation for X-rays diffracted by a one-dimensionally disordered crystal i.e. $I=N\,\mathrm{Spur}\,\boldsymbol{VF}+\sum_{n=1}^{N-1}(N-n)\,\mathrm{Spur}\,\boldsymbol{VFQ}^n$ +conj. which was derived for the correlation range $s=1$ was found to be valid for any s-value by modifying slightly the elements of the matrices. $\overline{S_jS_{j+n}^*}$ as used by Wilson and Jagodzinski was shown to be equal to Spur $\boldsymbol{VFP}^n$ for any s-value. In our present method, layer form factors are refered to single layers and the preceding $(s-1)$ layers are used only to classify them into rl subgroups where r is the number of the kinds of layers and l that of combinations of $(s-1)$ preceeding layers. This method which we call the "antecedent" one is found to be equivalent to another one as used by Hendricks and Teller in which each layer form factor is taken over the whole s layers hence there are $R=rl$ different layer form factors and which we call the "whole s layers" method. We discussed the relation between the cases of ranges s and $(s-1)$. A simple example is shown in the case of $r=2$ and $s=2$.

§ 1. Introduction

In the first report[1] the general intensity equation for X-rays diffracted by a one-dimensionally disordered crystal was derived as

$$I=N\,\mathrm{Spur}\,\boldsymbol{VF}+\sum_{n=1}^{N-1}(N-n)\,\mathrm{Spur}\,\boldsymbol{VFQ}^n+\text{conjugate}\,, \tag{1}$$

which was derived at first by S. Hendricks and E. Teller[2] and rearranged by us from a rather intuitive standpoint[1]. The symbols in (1) are

$$\boldsymbol{V}=\begin{pmatrix} V_1^*V_1 & V_1^*V_2 & \cdots & V_1^*V_R \\ V_2^*V_1 & V_2^*V_2 & \cdots & V_2^*V_R \\ \vdots & \vdots & & \vdots \\ V_R^*V_1 & V_R^*V_2 & \cdots & V_R^*V_R \end{pmatrix}_R, \qquad \boldsymbol{P}=\begin{pmatrix} P_{11} & P_{12} & \cdots & P_{1R} \\ P_{21} & P_{22} & \cdots & P_{2R} \\ \vdots & \vdots & & \vdots \\ P_{R1} & P_{R2} & \cdots & P_{RR} \end{pmatrix}_R,$$

$$\boldsymbol{F}=\begin{pmatrix} f_1 & & & \\ & f_2 & & \\ & & \ddots & \\ & & & f_R \end{pmatrix}_R, \qquad \boldsymbol{\Phi}=\begin{pmatrix} e^{-i\varphi_1} & & & \\ & e^{-i\varphi_2} & & \\ & & \ddots & \\ & & & e^{-i\varphi_R} \end{pmatrix}_R,$$

$$\boldsymbol{Q}=\boldsymbol{\Phi P}\,.$$

n which V_s is the layer form factor of the ayer of s-kind, φ_s the phase shift due to the isplacement of the layer s along the $\vec{c}$ di- ection, f_s the probability of finding V_s at ny q-th position, P_{st} the probability of finding V_t after V_s, and N the number of layers.

---

* In the first report[1] we used "S" for the "Reichweighte" i.e. the correlation range but in the present and following reports we use "s", as was used by Jagodzinski[4], not to confuse with the layer form factor S.

$\boldsymbol{F}$ and $\boldsymbol{P}^n$ were shown to have the following properties;

$$\text{Spur}\,\boldsymbol{F}=1\,, \tag{2}$$

$$\boldsymbol{P}^n\boldsymbol{M}_0=\boldsymbol{M}_0\,, \tag{3}$$

$$\text{and}\quad \boldsymbol{H}_0\boldsymbol{P}^n=\boldsymbol{H}_0 \quad (\boldsymbol{H}_0=\boldsymbol{M}_0\boldsymbol{F})\,. \tag{4}$$

where $\boldsymbol{M}_0$ is a matrix whose elements are all 1.

$\overline{S_jS_{j+n}^*}$, as used by A. J. C. Wilson[3] and H. Jagodzinski[4], was shown to be equal to

$$\overline{S_jS_{j+n}^*}=\text{Spur}\,\boldsymbol{VFP}^n,\quad \overline{S_jS_{j-n}^*}=\text{Spur}\,(\boldsymbol{VFP}^n)^*$$
$$\text{and}\quad \overline{S_jS_j^*}=\text{Spur}\,\boldsymbol{VF}\,. \tag{5}$$

In the present report it will be shown that (1) and (5) are also valid for $s\geq 2$ provided the elements of the above matrices are slightly modified. We shall discuss the relation between the cases of ranges s and $(s-1)$, the agreement between our antecedent method and the "whole s layers" method used by Hendricks and Teller[2], and a simple example of the case of $r=2$ and $s=2$.

§ 2. The Validity of (1) in the Case of $s\geq 2$

Assume that there are r kinds of layers the layer form factors of which are $S_1, S_2, \ldots, S_r$. When $s\geq 2$, the probability of finding S_p following on S_q depends not only on the kind q but also on the kinds of the $(s-1)$ layers preceding to q. There are $l=r^{s-1}$ combinations of these preceding layers; then we classify, for convenience, the S_q layers into lV's according to their l sets of antecedents as follows:

$$V_{(q-1)l+1}=V_{(q-1)l+2}=\cdot\;\cdot\;\cdot\;\cdot\;\cdot=V_{ql}=S_q\,. \tag{6}$$

Hence there are $R=lr=r^s$ V's with which we can construct such a $\boldsymbol{V}$ matrix of the R-th order as $(\boldsymbol{V})_{st}=V_s^*V_t$ or

$$\boldsymbol{V}=\begin{pmatrix} S_1^*S_1\boldsymbol{M} & S_1^*S_2\boldsymbol{M} & \cdots & S_1^*S_r\boldsymbol{M} \\ S_2^*S_1\boldsymbol{M} & S_2^*S_2\boldsymbol{M} & \cdots & S_2^*S_r\boldsymbol{M} \\ \vdots & \vdots & & \vdots \\ S_r^*S_1\boldsymbol{M} & S_r^*S_2\boldsymbol{M} & \cdots & S_r^*S_r\boldsymbol{M} \end{pmatrix}_R . \tag{7}$$

where $\boldsymbol{M}$ is a matrix of the l-th order with elements all 1. Corresponding to this $\boldsymbol{V}$ matrix, $\boldsymbol{F}$ and $\boldsymbol{\Phi}$ must be taken as

$$\boldsymbol{F}=\begin{pmatrix} \boldsymbol{F}_1 & & & & \\ & \boldsymbol{F}_2 & & & \\ & & \cdot & & \\ & & & \cdot & \\ & & & & \boldsymbol{F}_r \end{pmatrix}_R \quad \text{and} \quad \boldsymbol{F}_p=\begin{pmatrix} f_{(p-1)l+1} & & & & \\ & f_{(p-1)l+2} & & & \\ & & \cdot & & \\ & & & \cdot & \\ & & & & f_{pl} \end{pmatrix}_l , \tag{8}$$

and

$$\boldsymbol{\Phi}=\begin{pmatrix} e^{-i\varphi_1}\mathbf{1}_l & & & & \\ & e^{-i\varphi_2}\mathbf{1}_l & & & \\ & & \cdot & & \\ & & & \cdot & \\ & & & & e^{-i\varphi_r}\mathbf{1}_l \end{pmatrix}_R , \tag{9}$$

in which $\mathbf{1}_l$ is an unit matrix of the l-th order.

The way to classify S_p layers into l subgroups according to their antecedents is shown in Table I in which an example of S_1 is shown in the case of $r=4$ and $s=3$. In Table I each triangle shown by a circle has a counter clockwise order of $1, 2, \ldots, r$ in which, however, the number at the right side vertex of each triangle is doubled.

Let us consider the probabilities of finding S_1 after S_1. If one of V_1, V_2, V_3 and V_4, whose antecedents are (1,1), (2,1), (3,1) and and (4,1), respectively, for example, is followed by S_1, the antecedent of this S_1 becomes (1,1) for each case of V_1, V_2, V_3 and V_4. Therefore these four V's can not be followed by any one of V's from V_2 to V_{16} but only by V_1 because none of V's except V_1 has the antecedent (1,1). Similary V_5, V_6, V_7 and V_8 can be followed only by V_2. In such a way we can construct $\boldsymbol{P}_{11}$ matrix of the l-th order as

Table I.

An example of the way to classify S_1 layers into lV's according to their antecedents is shown in the case of $r=4$ and $s=3$ then $l=16$ and $R=64$.

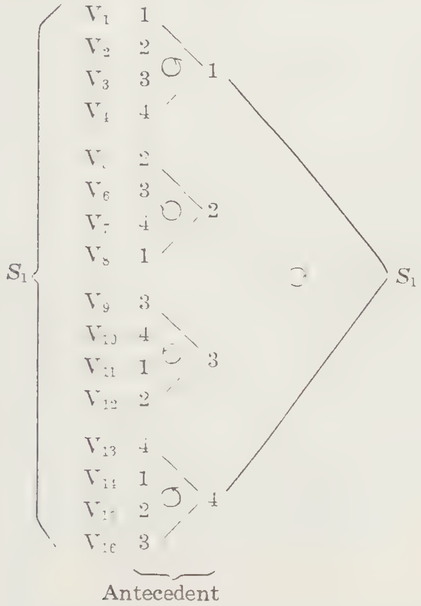

$$P_{11}=\left(\begin{array}{ccccc}\alpha_1 &&&& \\ \alpha_2 &&&& \\ \alpha_3 &&&& \\ \alpha_4 &&&& \text{the other elements} \\ & \alpha_5 &&& \\ & \alpha_6 &&& \text{are all 0.} \\ & \alpha_7 &&& \\ & \alpha_8 &&& \\ && \alpha_9 && \\ && \alpha_{10} && \\ && \alpha_{11} && \\ && \alpha_{12} && \\ &&& \alpha_{13} & \\ &&& \alpha_{14} & \\ &&& \alpha_{15} & \\ &&& \alpha_{16} & \end{array}\right)_l .$$

$$\underbrace{\qquad\qquad\qquad}_{\frac{l}{r}}\qquad\underbrace{\qquad\qquad\qquad\qquad}_{(r-1)\frac{l}{r}}$$

Similary we can obtain $r^2 P_{pq}$'s $(p,q\,;\,1,2,\ldots,r)$ with which we can construct the P matrix of the R-th order as

$$P=\begin{pmatrix} P_{11} & P_{12} & \cdot\;\cdot\;\cdot & P_{1r} \\ P_{21} & P_{22} & \cdot\;\cdot\;\cdot & P_{2r} \\ \cdot & \cdot & & \cdot \\ \cdot & \cdot & & \cdot \\ P_{r1} & P_{r2} & \cdot\;\cdot\;\cdot & P_{rr} \end{pmatrix}_R . \tag{10}$$

As a result of such modifications of defining elements in V, F, Φ and P, we have been able to reduce the case of $s\geq 2$ to that of $s=1$ for RV's. In this meaning, the intensity equation (1) is also valid for the case of $s\geq 2$.

§ 3. Notes on F and P Matrices

Using (8) and (10) we can transform (2), (3) and (4) into

$$\text{Spur } F=1 \longrightarrow \sum_{p=1}^{r} \text{Spur } F_p=1\,, \tag{11}$$

$$P^n M_0=M_0 \longrightarrow \left\{\sum_{q=1}^{r}(P^n)_{pq}\right\} M=M \qquad p=1,2,\ldots,r. \tag{12}$$

and

$$H_0 P^n=H_0 \longrightarrow \sum_{p=1}^{r} H_p (P^n)_{pq}=H_q \qquad q=1,2,\ldots,r. \tag{13}$$

where

$$H_p=MF_p\,, \tag{14}$$

and $(P^n)_{pq}$ does not mean the individual pq-element of P^n but the pq-minor matrix of the l-th order in the expression of P^n similar to (10).

The general structure of P is that each column contains $r\alpha$'s whose suffices are $\alpha_{(j-1)r+1}$, $\alpha_{(j-1)r+2}, \ldots, \alpha_{jr}$ for the j-th column $(j=1,2,\ldots,R)$ and that each α_i from $\alpha_{(q-1)R+1}$ to $\alpha_{qR-(q-1)l}$ belongs to the $\{i-(q-1)(R-l)\}$-th row where $q=1,2,\ldots,r$ and each α_i from $\alpha_{qR-(q-1)l+1}$ to α_{qR} to the $\{i-qR+(q-1)l\}$-th row where $q=2,3,\ldots,r$ all such α_i's giving P_{pq} where $p=1,2,\ldots,r$.

§ 4. The Validity of (5) in the Case of $s\geq 2$

As was seen from the papers of Wilson[3] and Jagodzinski[4] $\overline{S_j S_{j+n}{}^*}$ used by them can be expressed by

$$\overline{S_j S_{j+n}{}^*}=\sum_{p=1}^{r}\sum_{q=1}^{r} F_p S_p S_q{}^* P_{pq}{}^{(n)}\,,$$

in which F_p is the probability of finding S_p at the j-th position and $P_{pq}{}^{(n)}$ that of finding S_q at the $(j+n)$-th position when the j-th position is already occupied by S_p.

On the other hand, our Spur VFP^n can be expressed by

$$\text{Spur } VFP^n=\sum_{q=1}^{r}\sum_{p=1}^{r} S_q{}^* S_p \,\text{Spur } H_p (P^n)_{pq}\,,$$

from (7), (8), (14) and the expression of P^n similar to (10). Then the proof will be given when

$$A_{pq}{}^{(n)} \equiv F_p P_{pq}{}^{(n)}=\text{Spur } H_p (P^n)_{pq}\,, \tag{15}$$

will have been verified where $A_{pq}{}^{(n)}$ is the probability of finding S_p and S_q at the j-th and $(j+n)$-th positions, respectively, at the same time. Since the layer form factors of lV's from $V_{(p-1)l+1}$ to V_{pl} are all S_p from (6) in our case then

$$F_p=\sum_{i=1}^{l} f_{(p-1)l+i}=\text{Spur}\,\boldsymbol{F}_p\,, \tag{16}$$

from (8). The ik-element of $(\boldsymbol{P}^n)_{pq}$ is the $\{(p-1)l+i\}$, $\{(q-1)l+k\}$-element of $\boldsymbol{P}^n$ which is the probability of finding $V_{(q-1)l+k}$ at the $(j+n)$-th position when the j-th position is already occupied by $V_{(p-1)l+i}$. Hence the probability $A^{(n)}{}_{(p-1)l+i,(q-1)l+k}$ of finding $V_{(p-1)l+i}$ and $V_{(q-1)l+k}$ at the j-th and $(j+n)$-th positions, respectively, at the same time is expressed by

$$A^{(n)}{}_{(p-1)l+i,\,(q-1)l+k}=f_{(p-1)l+i}\{(\boldsymbol{P}^n)_{pq}\}_{ik}\,.$$

Therefore we can obtain

$$\begin{aligned}A_{pq}{}^{(n)}&=\sum_{i=1}^{l}\sum_{k=1}^{l}A^{(n)}{}_{(p-1)l+1,(q-1)l+k}\\&=\sum_{i=1}^{l}\sum_{k=1}^{l}(\boldsymbol{H}_p)_{ki}\{(\boldsymbol{P}^n)_{pq}\}_{ik}=\text{Spur}\,\boldsymbol{H}_p(\boldsymbol{P}^n)_{pq}\,,\end{aligned}$$

from (8) and (14) what is the same as (15). From (15) and (16) we can abtain

$$P_{pq}{}^{(n)}=\text{Spur}\,\boldsymbol{H}_p(\boldsymbol{P}^n)_{pq}/\,\text{Spur}\,\boldsymbol{F}_p\,.$$

§ 5. A Simple Example

In this section a simple example is solved in the case of $r=2$ and $s=2$ by the difference equation method.*

In this case, $\boldsymbol{P}$ can be generally expressed as

$$\begin{array}{c|l} & \begin{array}{cc}\overset{1\ \ 2}{\vee} & \overset{2\ \ 1}{\vee}\\ 1 & 2\end{array}\\ \begin{array}{l}S_1\left\{\begin{array}{ll}V_1 & 1\\ V_2 & 2\end{array}\right\rangle S_1\\ S_2\left\{\begin{array}{ll}V_3 & 2\\ V_4 & 1\end{array}\right\rangle S_2\\ \qquad\quad\uparrow\\ \quad\text{Antecedent}\end{array} & \left(\begin{array}{cccc}\alpha_1 & & & 1-\alpha_1\\ \alpha_2 & & & 1-\alpha_2\\ & \alpha_3 & 1-\alpha_3 & \\ & \alpha_4 & 1-\alpha_4 & \end{array}\right)_4=\boldsymbol{P}\,,\end{array}$$

in which the condition (3) is already included. We treat here the special case of $\alpha_1=1-\alpha_3\equiv\alpha$ and $\alpha_2=1-\alpha_4\equiv\beta$. Hence $\boldsymbol{P}$ becomes

$$\boldsymbol{P}=\left(\begin{array}{cccc}\alpha & & & 1-\alpha\\ \beta & & & 1-\beta\\ & 1-\alpha & \alpha & \\ & 1-\beta & \beta & \end{array}\right)_4.$$

From (2), (4) and the above $\boldsymbol{P}$ we can obtain

$$f_1=f_3=\frac{\beta}{2(1-\alpha+\beta)}$$

$$\text{and}\quad f_2=f_4=\frac{1-\alpha}{2(1-\alpha+\beta)}\,.$$

The necessary quantities, therefore, may be expressed as

$$\boldsymbol{V}=\left(\begin{array}{cc}S_1{}^*S_1\boldsymbol{M} & S_1{}^*S_2{}^*\boldsymbol{M}\\ S_2{}^*S_1\boldsymbol{M} & S_2{}^*S_2\boldsymbol{M}\end{array}\right)_4,\qquad \boldsymbol{M}=\left(\begin{array}{cc}1 & 1\\ 1 & 1\end{array}\right)_2,$$

$$\boldsymbol{F}=\frac{1}{2}\left(\begin{array}{cc}\boldsymbol{F}_0 & 0\\ 0 & \boldsymbol{F}_0\end{array}\right)_4,\qquad \boldsymbol{F}_0=\frac{1}{1-\alpha+\beta}\left(\begin{array}{cc}\beta & 0\\ 0 & 1-\alpha\end{array}\right)_2,$$

$$\boldsymbol{H}=\boldsymbol{M}\boldsymbol{F}_0=\frac{1}{1-\alpha+\beta}\left(\begin{array}{cc}\beta & 1-\alpha\\ '' & ''\end{array}\right)_2,\qquad \boldsymbol{H}_0=\frac{1}{2}\left(\begin{array}{cc}\boldsymbol{H} & \boldsymbol{H}\\ '' & ''\end{array}\right)_4,$$

and $\quad\boldsymbol{\Phi}=e^{-i\varphi}\boldsymbol{1}_4\,.$

If we put

$$\boldsymbol{A}=\left(\begin{array}{cc}\alpha & 1-\alpha\\ \beta & 1-\beta\end{array}\right)_2,\quad \boldsymbol{v}_1=\left(\begin{array}{cc}1 & 0\\ 0 & 0\end{array}\right)_2$$

$$\text{and}\quad \boldsymbol{v}_2=\left(\begin{array}{cc}0 & 0\\ 0 & 1\end{array}\right)_2.$$

$\boldsymbol{P}$ may be expressed by

$$\boldsymbol{P}=\left(\begin{array}{cc}\boldsymbol{A}\boldsymbol{v}_1 & \boldsymbol{A}\boldsymbol{v}_2\\ \boldsymbol{A}\boldsymbol{v}_2 & \boldsymbol{A}\boldsymbol{v}_1\end{array}\right)_4.$$

By mathematical induction we can show

$$\boldsymbol{P}^n=\left(\begin{array}{cc}\boldsymbol{X}_n & \boldsymbol{Y}_n\\ \boldsymbol{Y}_n & \boldsymbol{X}_n\end{array}\right)_4.$$

---

* We can solve the problem also by the diagonalizing matrix method[5].

Substituting this and H_0 into (4), we get

$$\boldsymbol{H}(\boldsymbol{X}_n+\boldsymbol{Y}_n)=\boldsymbol{H}, \tag{17}$$

from which $\boldsymbol{HA}=\boldsymbol{H}$ and Spur $\boldsymbol{HX}_n+$Spur$\boldsymbol{HY}_n=1$ can be obtained by the use of the relations of $\boldsymbol{X}_1=\boldsymbol{A}\boldsymbol{\nu}_1$, $\boldsymbol{Y}_1=\boldsymbol{A}\boldsymbol{\nu}_2$, $\boldsymbol{\nu}_1+\boldsymbol{\nu}_2=\boldsymbol{1}$, and Spur $\boldsymbol{H}=1$. Using above relations we can calculate Spur $\boldsymbol{VFQ}^n$ as follows;

$$\text{Spur } \boldsymbol{VFQ}^n=e^{-in\varphi}\tfrac{1}{2}\{S_1{}^*S_2+S_2{}^*S_1+(S_1-S_2)(S_1{}^*-S_2{}^*)\text{ Spur }\boldsymbol{HX}_n\}.$$

Comparing the corresponding minor matrices on both sides of the equation $\boldsymbol{P}^n=\boldsymbol{P}^{n-1}\boldsymbol{P}$ and multiplying the equation just obtained with $\boldsymbol{H}$ from the left side we can get

$$\boldsymbol{HX}_n=\boldsymbol{HX}_{n-1}\boldsymbol{A}\boldsymbol{\nu}_1+\boldsymbol{HY}_{n-1}\boldsymbol{A}\boldsymbol{\nu}_2.$$

Eliminating $\boldsymbol{HY}_{n-1}$ from this equation and (17) and using $\boldsymbol{HA}=\boldsymbol{H}$ we obtain the difference equation of

$$\boldsymbol{HX}_n-\boldsymbol{HX}_{n-1}\boldsymbol{A}(\boldsymbol{\nu}_1-\boldsymbol{\nu}_2)=\boldsymbol{H}\boldsymbol{\nu}_2.$$

Solving this equation we can obtain

$$\text{Spur } \boldsymbol{HX}_n=c_1x_1{}^n+c_2x_2{}^n+\tfrac{1}{2},$$

where

$$\left.\begin{array}{l} x_1=-(1-\alpha-\beta-\sqrt{\gamma})/2 \\ x_2=-(1-\alpha-\beta+\sqrt{\gamma})/2 \end{array}\right\}$$

$$\gamma=(1-\alpha-\beta)^2+4(\alpha-\beta),$$

and

$$\left.\begin{array}{l} c_1=\dfrac{1}{4}\left\{1+\dfrac{\alpha^2-(1-\beta)^2}{(1-\alpha+\beta)\sqrt{\gamma}}\right\} \\ c_2=\dfrac{1}{4}\left\{1-\dfrac{\alpha^2-(1-\beta)^2}{(1-\alpha+\beta)\sqrt{\gamma}}\right\} \end{array}\right\}.$$

Hence Spur $\boldsymbol{VFQ}^n$ becomes

$$\text{Spur } \boldsymbol{VFQ}^n=e^{-in\varphi}\left\{\frac{(S_1+S_2)(S_1{}^*+S_2{}^*)}{4}+\frac{(S_1-S_2)(S_1{}^*-S_2{}^*)}{2}(c_1x_1{}^n+c_2x_2{}^n)\right\}.$$

After all (1) becomes

$$I=\frac{(S_1+S_2)(S_1{}^*+S_2{}^*)}{4}\frac{\sin^2 N(\varphi/2)}{\sin^2\varphi/2}+\frac{(S_1-S_2)(S_1{}^*-S_2{}^*)}{2}(H+ND), \tag{18}$$

where D is the diffuse term and expressed by

$$D_r=c_1\frac{1-x_1{}^2}{1+x_1{}^2-2x_1\cos\varphi}+c_2\frac{1-x_2{}^2}{1+x_2{}^2-2x_2\cos\varphi} \quad \text{for } \gamma\geq 0,$$

and

$$D_c=c_0\left\{\frac{(1-x_0{}^2)\cos\rho-2x_0\sin\rho\sin(\varphi-\theta)}{1+x_0{}^2-2x_0\cos(\varphi-\theta)}+\frac{(1-x_0{}^2)\cos\rho+2x_0\sin\rho\sin(\varphi+\theta)}{1+x_0{}^2-2x_0\cos(\varphi+\theta)}\right\} \quad \text{for } \gamma<0,$$

in which we put $x_1=x_0e^{i\theta}$, $x_2=x_0e^{-i\theta}$, $c_1=c_0e^{i\rho}$ and $c_2=c_0e^{-i\rho}$, and H is the higher term and expressed by

$$H_r=\sum_{i=1}^{2}2c_i\frac{x_i{}^{N+1}\{\cos(N+1)\varphi-2x_i\cos N\varphi+x_i{}^2\cos(N-1)\varphi\}+2x_i{}^2-x_i(1+x_i{}^2)\cos\varphi}{(1+x_i{}^2-2x_i\cos\varphi)^2} \quad \text{for } \gamma\geq 0,$$

and

$$H_c=H_c{}^{(1)}\cos\rho+H_c{}^{(2)}\sin\rho \qquad \text{for } \gamma<0,$$

in which

$H_c{}^{(1)}=$(replace c_i and x_i in H_r by c_0 and x_0 and replace φ by $(\varphi-\theta)$ and $(\varphi+\theta)$ for $i=1$ and 2, respectively.)

$$H_c{}^{(2)}=2c_0\frac{x_0{}^{N+1}\{\sin(N+1)(\varphi-\theta)-2x_0\sin N(\varphi-\theta)+x_0{}^2\sin(N-1)(\varphi-\theta)\}-x_0(1-x_0{}^2)\sin(\varphi-\theta)}{\{1+x_0{}^2-2x_0\cos(\varphi-\theta)\}^2}$$

$-$(replace θ in the former by $-\theta$).

Several special cases are summarized here.

1) $\alpha=1$ and $0<\beta\leq 1$.

$$I_{1\beta}=\frac{S_1S_1{}^*+S_2S_2{}^*}{2}\frac{\sin^2 N(\varphi/2)}{\sin^2\varphi/2},$$

which corresponds to the mixed structure of the regular $S_1S_1S_1\ldots$ and $S_2S_2S_2\ldots$ with the same ratio.

2) $0\leq\alpha<1$ and $\beta=0$.

$$I_{\alpha 0}=\frac{(S_1+S_2)(S_1{}^*+S_2{}^*)}{4}\frac{\sin^2 N(\varphi/2)}{\sin^2\varphi/2}+\frac{(S_1-S_2)(S_1{}^*-S_2{}^*)}{4}\frac{\sin^2 N(\varphi+\pi)/2}{\sin^2(\varphi+\pi)/2},$$

which corresponds to the regular structure of $S_1S_2S_1S_2\ldots$.

3) $\alpha=0$ and $\beta=1$.

$$I_{01}=\frac{(S_1+S_2)(S_1^*+S_2^*)}{4}\frac{\sin^2 N(\varphi/2)}{\sin^2\varphi/2}+\frac{(S_1-S_2)(S_1^*-S_2^*)}{8}\left\{\frac{\sin^2 N\cdot(\varphi-\pi/2)/2}{\sin^2(\varphi-\pi/2)/2}+\frac{\sin^2 N\cdot(\varphi+\pi/2)/2}{\sin^2(\varphi+\pi/2)/2}\right\},$$

which corresponds to the regular structure of $S_1S_1S_2S_2S_1S_1S_2S_2\dots$.

4) $\alpha=1$ and $\beta=0$. This is the only case that makes f_i indefinite but we can easily directly calculate (1) obtaining

$$I_{10}=(f_1S_1^*S_1+f_3S_2^*S_2)\frac{\sin^2 N(\varphi/2)}{\sin^2\varphi/2}+2f_2\left\{\frac{(S_1+S_2)(S_1^*+S_2^*)}{4}\frac{\sin^2 N(\varphi/2)}{\sin^2\varphi/2}+\frac{(S_1-S_2)(S_1^*-S_2^*)}{4}\frac{\sin^2 N\cdot(\varphi+\pi)/2}{\sin^2(\varphi+\pi)/2}\right\}\quad(f_4=f_2),$$

which corresponds to the mixed structure of regular $S_1S_1S_1\dots$, $S_2S_2S_2\dots$ and $S_1S_2S_1S_2\dots$ with a ratio of $(f_1\colon f_3\colon 2f_2)$. On the other hand, when $\alpha=1$ and $\beta=0$, $x_1=1$ and $x_2=-1$, (18) becomes

$$I=c_1(S_1^*S_1+S_2^*S_2)\frac{\sin^2 N(\varphi/2)}{\sin^2\varphi/2}+2c_2\left\{\frac{(S_1+S_2)(S_1^*+S_2^*)}{4}\frac{\sin^2 N(\varphi/2)}{\sin^2\varphi/2}+\frac{(S_1-S_2)(S_1^*-S_2^*)}{4}\frac{\sin^2 N(\varphi+\pi)/2}{\sin^2(\varphi+\pi)/2}\right\},$$

which is a special case of I_{10} in which $f_1=f_3$.

Now as seen from the expression of $\gamma=(1-\alpha-\beta)^2+4(\alpha-\beta)$, the curve of $\gamma=0$ is such a parabola as shown by the broken line in Fig. 1. γ is positive under the parabola and negative above it.

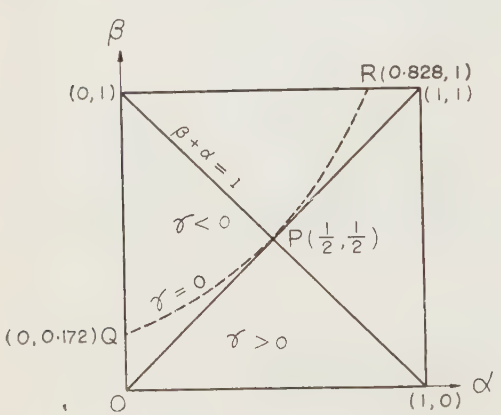

Fig. 1. The locus of $\gamma=(1-\alpha-\beta)^2+4(\alpha-\beta)=0$ is shown by the broken line which is a parabola whose vertex is at $P(\frac{1}{2},\frac{1}{2})$ and whose axis is the line $\alpha+\beta=1$. It passes through $Q(0,3-\sqrt{8})$ and $R(\sqrt{8}-2,1)$.

Keeping this curve and the four special cases mentioned above in mind, (18) can be plotted for any set of α and β giving Fig. 2. In Fig. 2 the four special cases in which there are Laue functions only without giving any diffuse line are shown by vertical lines. The other curves show only the diffuse term D in (18) and we omit the first Laue term for simplicity, the higher term H being neglected.

In Fig. 2, the curves corresponding to $\alpha=\beta$ show the case of $s=1$ as will be expected from § 6. When $\gamma\geq 0$, the maxima of the diffuse line appear at $\varphi=0$ or $\varphi=\pi$ or both but when $\gamma<0$, they appear at the other places which become nearer $\varphi=\pi/2$ and $3\pi/2$ at which the regular structure $S_1S_1S_2S_2S_1S_1S_2S_2\dots$ gives Laue maxima as β goes nearer 1 and α nearer 0. As a result of examing the expressions of D_r and D_c the two curves whose parameters are $\{\alpha,\beta\}$ and $\{1-\beta,1-\alpha\}$ are found to be the same except that φ of the one proceeds that of the other by π.

§ 6. Discussion

The general intensity equation (1) which was derived for the case of $s=1$ and was found to be available also for $s=0$ by putting $\boldsymbol{P}=\boldsymbol{H}_0$ in the first report[1)] was found to be available also for $s\geq 2$ by taking the elements of $\boldsymbol{V}$, $\boldsymbol{F}$, $\boldsymbol{\Phi}$ and $\boldsymbol{P}$ as (7), (8), (9) and (10), respectively. After all (1) is available for any value of s.

The $R=r^s$ elements in $\boldsymbol{F}$ and the $rR=r^{s+1}$ elements in $\boldsymbol{P}$ were not independent on each other but connected by the relations of (2), (3) and (4) or (11), (12) and (13). These relations are well used to solve the problem as shown in § 5, to prove some general relations as will be discussed in following and especially to solve the problem on the close-packed structure which will be discussed in the third report.

We could prove that $\overline{S_jS_{j+n}^*}$ used by Wilson[3)] and Jagodzinski[4)] was equal to Spur $\boldsymbol{VFP}^n$. At the same time it was shown that the probability $A_{pq}^{(n)}$ of finding the two layers of p- and q-kinds at the j-th and $(j+n)$-th positions, respectively, at the same

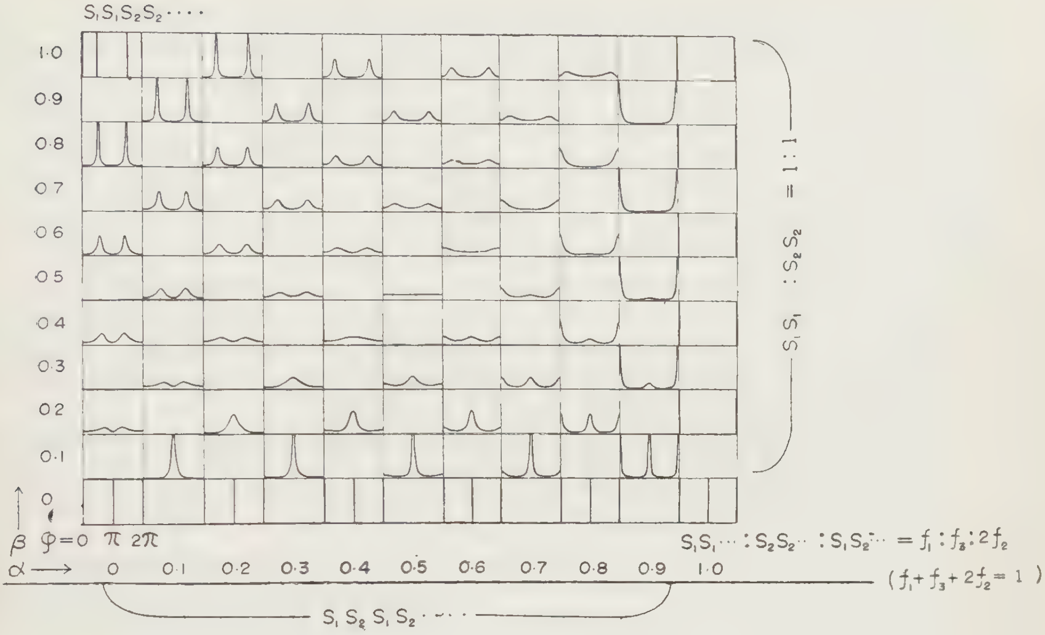

Fig. 2. The diffuse lines are shown for all sets of α and β. When $\gamma=(1-\alpha-\beta)^2+4(\alpha-\beta)\geq 0$, they are expressed by $D_r=\sum_{i=1}^{2} c_i \dfrac{1-x_i^2}{1+x_i^2-2x_i\cos\varphi}$ and when $\gamma<0$, they are expressed by $D_c=c_0\left\{\dfrac{(1-x_0^2)\cos\rho-2x_0\sin\rho\sin(\varphi-\theta)}{1+x_0^2-2x_0\cos(\varphi-\theta)}+\dfrac{(1-x_0^2)\cos\rho+2x_0\sin\rho\sin(\varphi+\theta)}{1+x_0^2-2x_0\cos(\varphi+\theta)}\right\}$. The first Laue term and the higher term H are omitted here. The vertical lines show the Laue maxima corresponding to the four special cases mentioned above.

time, was equal to Spur $\boldsymbol{H}_p(\boldsymbol{P}^n)_{pq}$ and that the probability $P_{pq}{}^{(n)}$ of finding the layer of q-kind at the $(j+n)$-th position when the j-th position was already known to be occupied by the layer of p-kind is equal to Spur $\boldsymbol{H}_p(\boldsymbol{P}^n)_{pq}$/Spur $\boldsymbol{F}_p$.

The case of range $(s-1)$ should correspond to the special case of range s. Namely when

$$\alpha^{(s)}{}_{(j-1)r+1}=\alpha^{(s)}{}_{(j-1)r+2}=\cdots\cdots=\alpha_{jr}{}^{(s)}, \quad j \;\; 1,2\cdots, R, \qquad {}^{*)} \quad (19)$$

the case of range s may be reduced to the case of range $(s-1)$ in which

$$\alpha_j{}^{(s-1)}=\alpha_{jr}{}^{(s)}$$

$$\text{and} \quad f_p{}^{(s-1)}=\sum_{i=1}^{r} f^{(s)}{}_{(p-1)r+i}, \quad p=1,2\cdots, l. \qquad {}^{*)}$$

This conclusion can be verified at least for the case of $r=4$ and $s=3$[5] but we think that it may hold in the case of any values of r and s because (19) means that the kind of the furthest antecedent has no effect upon the probability of P_{st} this fact being equivalent to reduce s to $(s-1)$.

Another method of treating the case of $s\geq 2$ was given in the case of the close-packed structure with $s=2$ for graphite by Hendricks and Teller[2] who took the layer form factor over the whole s layers including $(s-1)$ antecedent layers which method we will call the "whole s layers" method in distinction from our antecedent one. The agreement between both methods was at first suggested by Mr. I. Shōji**) and can be verified by us for the case of $r=4$ and $s=3$[5]. We think that it may hold for any values of r and s[5]. In the "whole s layers" method, the corresponding matrices $\boldsymbol{V}_{(s)}$, $\boldsymbol{\Phi}_{(s)}$ and $\boldsymbol{P}_{(s)}$***) have the much complicated forms comparing with those in our antecedent method[5]. For example, there is not or little zero element in $\boldsymbol{P}_{(s)}(=\boldsymbol{P}^s)$ while there are many zero elements in our $\boldsymbol{P}$. The facts that there are many zero elements in the matrix to be used and that the forms of the matrices are simple are very much desirable in performing the calculation of matrix. These points will become clearer when the close-packed structure will be discussed in the third report.

---

* The number in the bracket of the superscript on α and f shows the correlation range.

** Here we wish to express our hearty thanks to him (in Osaka University).

*** The subscript (s) shows the corresponding quantity in the "whole s layers" method.

In a simple example discussed in § 5 the relation (4) namely (17) were well used to obtain the difference equation and its special solution. In such a simple example many intensity curves corresponding to all sets of two parameters α and β can easily be calculated as plotted in Fig. 2. But when there are many parameters for larger s value it may not always be easy to show all curves corresponding to all sets of many parameters. However, as will be seen from the third report and especially from the following report in which hc-$(s=3)$ and hcc-$(s=4)$ structure of the close-packed structure will be discussed, many parameters may be sometimes much reduced to a few parameters according to the problem or by the use of the experimental data given. In conclusion it depends on what symmetrical properties the matrix $\boldsymbol{P}$ has if it is easy or difficult for the given problem to solve.

References

1) J. Kakinoki and Y. Komura: J. Phys. Soc. Japan **7** (1952) 30; J. Inst. Polytech., Osaka City University, B **2** (1951) 1; and X-rays (in Japanese) **6** (1951) 95.

2) S. Hendricks and E. Teller: J. Chem. Phys. **10** (1942) 147.

3) A. J. C. Wilson: Proc. Roy. Soc. A **180** (1942) 277.

4) H. Jagodzinski: Acta Cryst. **2** (1949) 201.

5) J. Kakinoki and Y. Komura: J. Inst. Polytech. Osaka City University B **3** (1952) 1.; and X-rays (in Japanese) **7** (1952) 25.

JOURNAL OF THE PHYSICAL SOCIETY OF JAPAN Vol. 9, No. 2, MAR.—APR., 1954

Intensity of X-ray Diffraction by a One-dimensionally Disordered Crystal

(III) The Close-packed Structure.*)

By Jiro KAKINOKI and Yukitomo KOMURA

Institute of Polytechnics, Osaka City University
12 Minami-Ogimachi, Kita-ku, Osaka, Japan

(Received July 31, 1953)

The general intensity equation for X-rays diffracted by a one-dimensionally disordered crystal with any value of the correlation range s i.e. $I=N\,\mathrm{Spur}\,\boldsymbol{VF}+\sum_{n=1}^{N-1}(N-n)\,\mathrm{Spur}\,\boldsymbol{VFQ}^n+\mathrm{conj.}$ was applied to the case of the close-packed structure. The obtained result is

$$I=V_0V_0^*\left\{N\sum_{\nu=1}^{l}c_{\nu_0}\frac{(1-x_{\nu_0}{}^2)\cos\rho_\nu+2x_{\nu_0}\sin\rho_\nu\sin(\varphi-\theta_\nu)}{1+x_{\nu_0}{}^2-2x_{\nu_0}\cos(\varphi-\theta_\nu)}\right.$$
$$\left.+\sum_{\nu=1}^{l}c_{\nu_0}(H_\nu{}^{(1)}\cos\rho_\nu+H_\nu{}^{(2)}\sin\rho_\nu)\right\}\qquad\text{for}\quad 2h+k=3m\pm1\,,$$

in which V_0 is the layer from factor, N the number of layers, $l=2^{s-1}$, $x_\nu=x_{\nu_0}e^{i\theta_\nu}$ which are the l roots of the characteristic equation of

$$\det\left[x^2\boldsymbol{1}+x\boldsymbol{\alpha\beta}+\{\boldsymbol{\alpha\beta}+(\boldsymbol{1}-\boldsymbol{\alpha})\boldsymbol{\beta u}\}\{\boldsymbol{\alpha\beta}-(\boldsymbol{1}-\boldsymbol{\alpha})\boldsymbol{\beta u}\}\right]=0\,,$$

$c_\nu=c_{\nu_0}e^{i\rho_\nu}$ which are the roots of the l simultaneous equations of $\sum_{i=1}^{l}x_i{}^\lambda c_i=\frac{3}{2}\,\mathrm{sp.}\,\boldsymbol{x}_\lambda-\frac{1}{2}$ (λ: 0.1,..., $l-1$) and two H's the higher terms which, when $|x_\nu|=1$, give the Laue function whose maximum is at $\varphi=\theta_\nu$. The characteristic equation is derived from the general difference equation

$$\boldsymbol{x}_n+\boldsymbol{x}_{n-1}\boldsymbol{\alpha\beta}+\boldsymbol{x}_{n-2}\{\boldsymbol{\alpha\beta}+(\boldsymbol{1}-\boldsymbol{\alpha})\boldsymbol{\beta u}\}\{\boldsymbol{\alpha\beta}-(\boldsymbol{1}-\boldsymbol{\alpha})\boldsymbol{\beta u}\}=\boldsymbol{h\alpha\beta}\,,$$

from which we can easily obtain the difference equations that Wilson and Jagodzinski derived in the cases of $s=2$ and 3 by the use of rather complicated genealogical tables. We showed the correspondence of our results in the cases of $s=2$ and 3 with those obtained by Wilson, Jagodzinski, Hendricks and Teller. The above matrices are those of $l/2$-th order. The elements in $\boldsymbol{x}_n$ are the probabilities of finding the same kind of layer at the $(j+n)$-th position as that at the j-th position and $\boldsymbol{h}=\boldsymbol{x}_0$. Those in $\boldsymbol{\alpha\beta}$ and $(\boldsymbol{1}-\boldsymbol{\alpha})\boldsymbol{\beta u}$ are the probabilities of finding the layer after the other layers in the cubic and hexagonal manners respectively. When $2h+k=3m$, $I=V_0V_0^*(\sin^2N\varphi/2)/(\sin^2\varphi/2)$ without giving any diffuse line.

§ 1. Introduction

In the second report[1] the general intensity equation for X-rays diffracted by a one-dimensionally disordered crystal was derived as

$$I=N\,\mathrm{Spur}\,\boldsymbol{VF}+\sum_{n=1}^{N-1}(N-n)\,\mathrm{Spur}\,\boldsymbol{VFQ}^n+\text{conjugate}\,,\qquad(1)$$

for any value of the correlation range ("Reichweite") s. The symbols in (1) are

$$\boldsymbol{V}=\begin{pmatrix}S_1{}^*S_1\boldsymbol{M} & S_1{}^*S_2\boldsymbol{M} & \cdots & S_1{}^*S_r\boldsymbol{M}\\ S_2{}^*S_1\boldsymbol{M} & S_2{}^*S_2\boldsymbol{M} & \cdots & S_2{}^*S_r\boldsymbol{M}\\ \vdots & \vdots & & \vdots\\ S_r{}^*S_1\boldsymbol{M} & S_r{}^*S_2\boldsymbol{M} & \cdots & S_r{}^*S_r\boldsymbol{M}\end{pmatrix}_R,$$

---

* This paper was read at the Second International Congress of Crystallography in Stockholm (July (1951) by Dr. S. Miyake (representative)).

$$F=\begin{pmatrix} f_1 & & & \\ & f_2 & & \\ & & \ddots & \\ & & & f_R \end{pmatrix}_R=\begin{pmatrix} F_1 & & & \\ & F_2 & & \\ & & \ddots & \\ & & & F_r \end{pmatrix}_R,$$

$$\Phi=\begin{pmatrix} e^{-i\varphi_1}\mathbf{1}_l & & & \\ & e^{-i\varphi_2}\mathbf{1}_l & & \\ & & \ddots & \\ & & & e^{-i\varphi_r}\mathbf{1}_l \end{pmatrix}_R,$$

$$P=\begin{pmatrix} P_{11} & P_{12} & \cdots & P_{1r} \\ P_{21} & P_{22} & \cdots & P_{2r} \\ \vdots & \vdots & & \vdots \\ P_{r1} & P_{r2} & \cdots & P_{rr} \end{pmatrix}_R \quad \text{and} \quad Q=\Phi P.$$

Expression (1) is based on the assumption that there are r kinds of layers whose layer form factors are $S_1, S_2, \ldots, S_r$ and whose phase shifts along the $\vec{c}$ direction are $\varphi_1, \varphi_2, \ldots, \varphi_r$. N is the number of layers. M is a matrix of the l-th order whose elements are all 1, $\mathbf{1}_l$ an unit matrix of the l-th order, where l is the number of combinations of $(s-1)$ antecedents, namely $l=r^{s-1}$, and $R=r^s$. Each S_p group is conveniently classified into lV's from $V_{(p-1)l+1}$ to V_{pl} according to their antecedents, f_s the probability of finding V_s at any q-th position and P_{st} that of finding V_t after V_s.

F and P^n have the following properties:

$$\mathrm{Spur}\, F=1, \tag{2}$$

$$P^n M_0=M_0, \tag{3}$$

$$H_0 P^n=H_0 \quad (H_0=M_0 F), \tag{4}$$

where M_0 is a matrix of the R-th order whose elements are all 1.

In the preceding report[1)] a simple example of the case of $r=2$ and $s=2$ was shown but the most suitable example will be found in the case of the close-packed structure with any s-value; this will be discussed in detail in the present report.

§ 2. The Close-packed Structure

As seen from Fig. 1, in the close-packed structure, there are three positions

A (0, 0), B ($\frac{2}{3}$, $\frac{1}{3}$) and C ($\frac{1}{3}$, $\frac{2}{3}$),

for the origin of each layer whose layer form factor, therefore, may be expressed by

$$S_A \equiv V_0, \quad S_B=V_0\varepsilon \quad \text{or} \quad S_C=V_0\varepsilon^*,$$

according to taking its origin at A, B or C where $\varepsilon=e^{i(2\pi/3)(2h+k)}$.

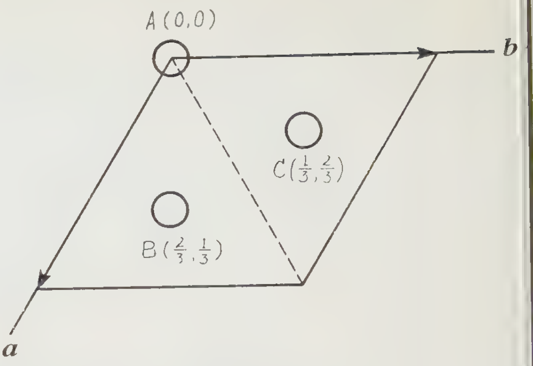
A (0,0)
b
C($\frac{1}{3}$,$\frac{2}{3}$)
B($\frac{2}{3}$,$\frac{1}{3}$)
a

Fig. 1.

Table I.
$s=4$, $l=8$

S_A	V_1	A	C	B	S_A
	V_2	B			
	V_3	B	A		
	V_4	C			
	V_5	B	A	C	
	V_6	C			
	V_7	C	B		
	V_8	A			

Antecedent

Table II.
ch-order

c	c
h	
h	h
c	
c	h
h	
h	c
c	

Since two adjoining layers of the same kind are prohibited in the close-packed structure, then $l=2^{s-1}$ and $R=rl=3\times 2^{s-1}$. The antecedent diagram of S_A corresponding to Table I in the preceding report[1)] is shown in Table I in the case of $s=4$ hence $l=8$. As was done by Jagodzinski[2)3)], each order of A, B, C,-letters belonging to each V may be conveniently rewritten according to the cubic order (c) or the hexagonal one (h) as shown in Table II which we will call *ch*-order. *ch*-orders for S_B and S_C are found to be the same as in Table II.

Following Jagodzinski[2)] we assume that the layers with the same *ch*-order are equivalent to each other. Then V, F, Φ and P may be conveniently expressed as

$$V=V_0^* V_0 \begin{pmatrix} M & \varepsilon M & \varepsilon^* M \\ \varepsilon^* M & M & \varepsilon M \\ \varepsilon M & \varepsilon^* M & M \end{pmatrix}_{R=3\times 2^{s-1}},$$

$$F=1/6\begin{pmatrix} W & & \\ & W & \\ & & W \end{pmatrix}_R ,$$

$$W=\begin{pmatrix} w_1 & & & & & & & & \\ & w_2 & & & & & & & \\ & & \ddots & & & & & & \\ & & & w_{l/2} & & & & & \\ & & & & w_{l/2} & & & & \\ & & & & & \ddots & & & \\ & & & & & & w_2 & \\ & & & & & & & w_1 \end{pmatrix}_{l=2^{s-1}} ,$$

$$\Phi=e^{-i\varphi}\mathbf{1}_R$$

and

$$P=\begin{pmatrix} 0 & UAU & A \\ A & 0 & UAU \\ UAU & A & 0 \end{pmatrix}_R ,$$

in which

$$U=\begin{pmatrix} 0 & & & & 1 \\ & & & 1 & \\ & & \cdot & & \\ & \cdot & & & \\ 1 & & & & 0 \end{pmatrix}_l , \qquad U^2=\mathbf{1}_l ,$$

$$A=\underbrace{\begin{pmatrix} \alpha_1 & & & & & & & & \\ \alpha_2 & & & & & & & & \\ & \alpha_3 & & & & & & & \\ & \alpha_4 & & & & & & & \\ & & \ddots & & & & & & \\ & & & \alpha_{l/2-1} & & & & & \\ & & & \alpha_{l/2} & & & & & 0 \\ & & & & 1-\alpha_{l/2} & & & & \\ & & & & 1-\alpha_{l/2-1} & & & & \\ & & & & & \ddots & & & \\ & & & & & & 1-\alpha_4 & & \\ & & & & & & 1-\alpha_3 & & \\ & & & & & & & 1-\alpha_2 & \\ & & & & & & & 1-\alpha_1 & \end{pmatrix}_l}_{l/2} ,$$

and the condition (3) is already included.

By mathematical induction we can easily show that P^n has such a form as

$$P^n=\begin{pmatrix} X_n & UY_nU & Y_n \\ Y_n & X_n & UY_nU \\ UY_nU & Y_n & X_n \end{pmatrix}_R$$

and $X_n=UX_nU$.

Substituting these F and P^n into (2) and (4), we get

$$\text{Spur } W=\text{Spur } H=2 , \qquad (5)$$

and

$$H(X_n+Y_n+UY_nU)=H , \qquad (6)$$

where $H=MW$, from which $\text{Spur } HY_n=1-1/2 \text{ Spur } HX_n$ can be obtained. With these quantities and relations the intensity equation (1) can be calculated as

$$I=V_0V_0^*\frac{\sin^2 N\varphi/2}{\sin^2\varphi/2} , \qquad \text{for} \quad 2h+k=3m ,$$

which gives only the Laue spot without giving rise to any diffuse line, and

$$I=V_0V_0^*\Big\{N+\sum_{n=1}^{N-1}(N-n)e^{-in\varphi} \times 1/2(3/2 \text{ Spur } HX_n-1)+\text{conj.}\Big\} . \qquad (7)$$

$$\text{for } 2h+k=3m\pm1.$$

Hence we shall calculate (7) only for $2h+k=3m\pm1$.

§ 3. Calculation of (7)

In order to perform the calculation of (7), each matrix of the l-th order used in the preceding section is conveniently devided into four minor matrices of the $l/2$-th order as following :

$$W=\begin{pmatrix} w & 0 \\ 0 & uwu \end{pmatrix}_l , \qquad w=\begin{pmatrix} w_1 & & & \\ & w_2 & & \\ & & \ddots & \\ & & & w_{l/2} \end{pmatrix}_{l/2} ,$$

$$U=\begin{pmatrix}0 & \boldsymbol{u}\\ \boldsymbol{u} & 0\end{pmatrix}_l\ ,\qquad \boldsymbol{u}=\begin{pmatrix}0 & & & 1\\ & & 1 & \\ & \cdot^{\cdot^{\cdot}} & & \\ 1 & & & 0\end{pmatrix}_{l/2}\ ,\qquad \boldsymbol{u}^2=\mathbf{1}_{l/2}\ ,$$

$$\boldsymbol{M}=\begin{pmatrix}\boldsymbol{m} & \boldsymbol{m}\\ \boldsymbol{m} & \boldsymbol{m}\end{pmatrix}_l\ ,\qquad \boldsymbol{m}=\begin{pmatrix}1 & 1 & \cdots & 1\\ 1 & 1 & \cdots & 1\\ \cdot & \cdot & & \cdot\\ \cdot & \cdot & & \cdot\\ 1 & 1 & \cdots & 1\end{pmatrix}_{l/2}\ ,$$

$$\boldsymbol{H}=\begin{pmatrix}\boldsymbol{h} & \boldsymbol{hu}\\ {}'' & {}''\end{pmatrix}_l\ ,\qquad \boldsymbol{h}=\boldsymbol{mw}=\begin{pmatrix}w_1 & w_2 & \cdots & w_{l/2}\\ {}'' & {}'' & & {}''\\ \cdot & \cdot & & \cdot\\ \cdot & \cdot & & \cdot\\ {}'' & {}'' & \cdots & {}''\end{pmatrix}_{l/2}\ ,$$

$$\boldsymbol{X}_n=\begin{pmatrix}\boldsymbol{\xi}_n & \boldsymbol{\xi}_n'\\ \boldsymbol{u}\boldsymbol{\xi}_n'\boldsymbol{u} & \boldsymbol{u}\boldsymbol{\xi}_n\boldsymbol{u}\end{pmatrix}_l\ ,\qquad \boldsymbol{Y}_n=\begin{pmatrix}\boldsymbol{\eta}_n^{(11)} & \boldsymbol{\eta}_n^{(12)}\\ \boldsymbol{\eta}_n^{(21)} & \boldsymbol{\eta}_n^{(22)}\end{pmatrix}_l\ ,$$

$$\boldsymbol{HX}_n=\begin{pmatrix}\boldsymbol{x}_n & \boldsymbol{x}_n\boldsymbol{u}\\ {}'' & {}''\end{pmatrix}_l\ ,\qquad \boldsymbol{x}_n=\boldsymbol{h}(\boldsymbol{\xi}_n+\boldsymbol{\xi}_n'\boldsymbol{u})_{l/2}\ ,$$

$$\boldsymbol{HY}_n=\begin{pmatrix}\boldsymbol{y}_n^{(1)} & \boldsymbol{y}_n^{(2)}\\ {}'' & {}''\end{pmatrix}_l\ ,\qquad \begin{aligned}\boldsymbol{y}_n^{(1)}&=\boldsymbol{h}(\boldsymbol{\eta}_n^{(11)}+\boldsymbol{u}\boldsymbol{\eta}_n^{(21)})_{l/2}\ ,\\ \boldsymbol{y}_n^{(2)}&=\boldsymbol{h}(\boldsymbol{\eta}_n^{(12)}+\boldsymbol{u}\boldsymbol{\eta}_n^{(22)})_{l/2}\ ,\end{aligned}$$

$$\boldsymbol{A}=\begin{pmatrix}\boldsymbol{\alpha\beta} & 0\\ \boldsymbol{u}(\mathbf{1}_{l/2}-\boldsymbol{\alpha})\boldsymbol{\beta u} & 0\end{pmatrix}_l\ ,\qquad \boldsymbol{\alpha}=\begin{pmatrix}\alpha_1 & & & \\ & \alpha_2 & & \\ & & \ddots & \\ & & & \alpha_{l/2}\end{pmatrix}_{l/2}\ ,\qquad \boldsymbol{\beta}=\left(\begin{matrix}\underbrace{\begin{matrix}1 & & & \\ 1 & & & \\ & 1 & & \\ & 1 & & \\ & & \ddots & \\ & & & 1\\ & & & 1\end{matrix}}_{l/4} & 0\end{matrix}\right)_{l/2}\ ,$$

considering their properties. Then (7) can be rewritten immediately as

$$I=V_0V_0^*\Big\{N+\sum_{n=1}^{N-1}(N-n)e^{-in\varphi}\times(3/2\ \mathrm{Spur}\ \boldsymbol{x}_n-1/2)+\text{conj.}\Big\}\ ,\qquad (8)$$

and (5) and (6) can be found to be equivalent to

$$\mathrm{Spur}\ \boldsymbol{h}=1\ ,\qquad (9)$$

and $$\boldsymbol{x}_n+\boldsymbol{y}_n^{(1)}+\boldsymbol{y}_n^{(2)}\boldsymbol{u}=\boldsymbol{h}\ ,\qquad (10)$$

respectively, which becomes

$$\boldsymbol{h}\{\boldsymbol{\alpha\beta}+(\mathbf{1}_{l/2}-\boldsymbol{\alpha})\boldsymbol{\beta u}\}=\boldsymbol{h}\ ,\qquad (11)$$

when $n=1$.

Comparing the corresponding minor matrices of the l-th order on both sides of the relation $\boldsymbol{P}^n=\boldsymbol{P}^{n-1}\boldsymbol{P}$, multiplying the equations just obtained with $\boldsymbol{H}$ from the left side and substituting the above minor matrices of the $l/2$-th order, we can obtain

$$\boldsymbol{x}_n=\boldsymbol{y}_{n-1}^{(1)}(\mathbf{1}_{l/2}-\boldsymbol{\alpha})\boldsymbol{\beta u}+\boldsymbol{y}_{n-1}^{(2)}\boldsymbol{u\alpha\beta}\ ,\qquad (12)$$

$$\boldsymbol{y}_n^{(1)}=\boldsymbol{x}_{n-1}\{\boldsymbol{\alpha\beta}+(\mathbf{1}_{l/2}-\boldsymbol{\alpha})\boldsymbol{\beta u}\}\ ,\qquad (13)$$

and

$$\boldsymbol{y}_n^{(2)}=\boldsymbol{y}_{n-1}^{(1)}\boldsymbol{\alpha\beta u}+\boldsymbol{y}_{n-1}^{(2)}\boldsymbol{u}(\mathbf{1}_{l/2}-\boldsymbol{\alpha})\boldsymbol{\beta}\ .$$

Eliminating $\boldsymbol{y}_n^{(1)}$ and $\boldsymbol{y}_n^{(2)}$ from (10), (12) and (13) we obtain the following general difference equation for $\boldsymbol{x}_n$

$$\begin{aligned}\boldsymbol{x}_n+\boldsymbol{x}_{n-1}\boldsymbol{\alpha\beta}+\boldsymbol{x}_{n-2}&\{\boldsymbol{\alpha\beta}+(\mathbf{1}_{l/2}-\boldsymbol{\alpha})\boldsymbol{\beta u}\}\\ &\times\{\boldsymbol{\alpha\beta}-(\mathbf{1}_{l/2}-\boldsymbol{\alpha})\boldsymbol{\beta u}\}=\boldsymbol{h\alpha\beta}\ .\end{aligned}\qquad (14)$$

Solving this difference equation*)7) we get

---

* Concerning the way to solve the difference equation Prof. and Dr. T. Nagamiya (Osaka University) gave us some hints whom we wish to express our hearty thanks in this place.

$$\mathrm{Spur}\,\boldsymbol{x}_n=\frac{2}{3}\sum_{\nu=1}^{l}c_\nu x_\nu^n+\frac{1}{3}\,, \qquad (15)$$

where lx_ν's are the roots of the characteristic equation

$$\det \boldsymbol{C}=0\,, \qquad (16)$$

in which

$$\boldsymbol{C}=x^2\mathbf{1}_{l/2}+x\boldsymbol{\alpha}\boldsymbol{\beta}+\{\boldsymbol{\alpha}\boldsymbol{\beta}+(\mathbf{1}_{l/2}-\boldsymbol{\alpha})\boldsymbol{\beta}\boldsymbol{u}\}\times\{\boldsymbol{\alpha}\boldsymbol{\beta}-(\mathbf{1}_{l/2}-\boldsymbol{\alpha})\boldsymbol{\beta}\boldsymbol{u}\}\,,$$

and lc_ν's can be determined from the l simultaneous equations

$$\left.\begin{aligned}
c_1+c_2+c_3+\cdots+c_l&=1\,,\\
x_1c_1+x_2c_2+x_3c_3+\cdots+x_lc_l&=-\frac{1}{2}\,,\\
x_1^2c_1+x_2^2c_2+x_3^2c_3+\cdots+x_l^2c_l&=1-\frac{3}{2}\sum_{i=1}^{l/4}w_i\,,\\
x_1^3c_1+x_2^3c_2+x_3^3c_3+\cdots+x_l^3c_l&=\frac{3}{2}\sum_{i=1}^{l/4}\alpha_iw_i-\frac{1}{2}\,,\\
\cdots\cdots\cdots\cdots\cdots\cdots&\cdots\cdots\\
x_1^{l-1}c_1+x_2^{l-1}c_2+x_3^{l-1}c_3+\cdots+x_l^{l-1}c_l&=\frac{3}{2}\,\mathrm{Spur}\,\boldsymbol{x}_{l-1}-\frac{1}{2}\,.
\end{aligned}\right\} \qquad (17)$$

Substituting (15) into (8) we obtain

$$I=V_0V_0^*\left\{N+\sum_{\nu=1}^{l}c_\nu\sum_{n=1}^{N-1}(N-n)e^{-in\varphi}x_\nu^n+\text{conj.}\right\}\,,$$

which can be calculated as

$$\begin{aligned}I=V_0V_0^*\Bigg[N\left\{\sum_{\nu=2\mu+1}^{l}c_\nu\frac{1-x_\nu^2}{1+x_\nu^2-2x_\nu\cos\varphi}+\sum_{\nu=1}^{2\mu}c_{\nu0}\frac{(1-x_{\nu0}^2)\cos\rho_\nu+2x_{\nu0}\sin\rho_\nu\sin(\varphi-\theta_\nu)}{1+x_{\nu_0}^2-2x_{\nu_0}\cos(\varphi-\theta_\nu)}\right\}\\
+\sum_{\nu=2\mu+1}^{l}c_\nu H_\nu+\sum_{\nu=1}^{2\mu}c_{\nu_0}(H_\nu^{(1)}\cos\rho_\nu+H_\nu^{(2)}\sin\rho_\nu)\Bigg]\,,\end{aligned} \qquad (18)$$

where

$$\left.\begin{aligned}
H_\nu&=2\frac{x_\nu^{N+1}\{\cos(N+1)\varphi-2x_\nu\cos N\varphi+x_\nu^2\cos(N-1)\varphi\}+\{2x_\nu^2-x_\nu(1+x_\nu^2)\cos\varphi\}}{(1+x_\nu^2-2x_\nu\cos\varphi)^2}\,,\\
H_\nu^{(1)}&=(\text{replace } x_\nu \text{ and } \varphi \text{ in } H_\nu \text{ by } x_{\nu_0} \text{ and } (\varphi-\theta_\nu)\text{, respectively})\,,\\
H_\nu^{(2)}&=2\\
&\times\frac{x_{\nu_0}^{N+1}\{\sin(N+1)(\varphi-\theta_\nu)-2x_{\nu_0}\sin N(\varphi-\theta_\nu)+x_{\nu_0}^2\sin(N-1)(\varphi-\theta_\nu)\}-x_{\nu0}(1-x_{\nu_0}^2)\sin(\varphi-\theta_\nu)}{\{1+x_{\nu_0}^2-2x_{\nu_0}\cos(\varphi-\theta_\nu)\}^2}\,,
\end{aligned}\right\}$$

in which the real roots of x_ν, hence the real coefficients of c_ν, are labeled with $\nu=2\mu+1, \ldots, l$ and the complex ones with $\nu=1,\ldots, 2\mu$ the latter being put in the form

$$x_\nu=x_{\nu0}e^{i\theta_\nu} \qquad \text{and} \qquad c_\nu=c_{\nu_0}e^{i\rho_\nu}\,.$$

In (18) the terms with N give the diffuse line and the remaining terms are the higher terms which, when $|x_\nu|=1$, give the Laue function whose maximum is at $\varphi=\theta_\nu$[7].

§ 4. $s=2$. Comparisons with Wilson's and Hendricks-Teller's Results

This case is treated by Wilson[4] and Hendricks-Teller[5] their corresponding quantities and equations being put in [ ].

When $s=2$ hence $l=2$, we may put

$$\boldsymbol{\alpha}=\alpha(\equiv[\alpha])$$

$$\boldsymbol{q}=\boldsymbol{u}=\boldsymbol{w}=\boldsymbol{h}=\boldsymbol{m}=1$$

$$\boldsymbol{x}_n=x_n(\equiv[P_{j+n}])$$

and

$$\boldsymbol{P}=\begin{array}{c|cc:cc:cc}
 & \mathrm{BA} & \mathrm{CA} & \mathrm{CB} & \mathrm{AB} & \mathrm{AC} & \mathrm{BC}\\
\hline
\mathrm{BA} & & & & 1-\alpha & \alpha & \\
\mathrm{CA} & & & & \alpha & 1-\alpha & \\
\hdashline
\mathrm{CB} & \alpha & & & & & 1-\alpha\\
\mathrm{AB} & 1-\alpha & & & & & \alpha\\
\hdashline
\mathrm{AC} & & 1-\alpha & \alpha & & & \\
\mathrm{BC} & & \alpha & 1-\alpha & & &
\end{array} \qquad (19)$$

then (16) becomes

$$\left.\begin{aligned}&\det \boldsymbol{C}=x^2+\alpha x-(1-2\alpha)=0\\ &\quad(\text{the characteristic equation of [7]})\,,\end{aligned}\right\} \qquad (20)$$

whose roots are

$$x_1=\frac{-\alpha+\sqrt{4-8\alpha+\alpha^2}}{2}(\equiv[\rho_e]),$$

$$x_2=\frac{-\alpha-\sqrt{4-8\alpha+\alpha^2}}{2}(\equiv[\rho_0]),$$

$\boldsymbol{c}_\nu$ can be calculated from (17) as

$$c_1=\frac{1}{2}\left(1-\frac{1-\alpha}{\sqrt{4-8\alpha+\alpha^2}}\right)\left(\equiv\left[\frac{3}{2}Q_e\right]\right),$$

$$c_2=\frac{1}{2}\left(1+\frac{1-\alpha}{\sqrt{4-8\alpha+\alpha^2}}\right)\left(\equiv\left[\frac{3}{2}Q_0\right]\right).$$

The diffuse term in (18) may be calculated as

$$\boldsymbol{D}=NV_0V_0^*\times\frac{3\alpha(1-\alpha)}{4-8\alpha+5\alpha^2+4\alpha^2\cos\varphi-4(1-2\alpha)\cos^2\varphi},\tag{21}$$

for both real and complex cases of $\sqrt{4-8\alpha+\alpha^2}$. (21) can be derived also from the equation [14] given by Wilson by using the corresponding quantities shown above, $[K]=(\varepsilon+\varepsilon^*)/2$ and $[n]=\frac{1}{2}N$.

Hendricks and Teller's treatment is what we called the "whole s layers" method in § 6 of the preceding report[1]. Then their quantities may be expressed by our quantities as

$$2N^{(H\cdot T)}=N,\quad \varphi^{(H\cdot T)}=2\varphi,\quad \boldsymbol{P}^{(H\cdot T)}=\boldsymbol{P}^2$$

and

$$X=\frac{\alpha}{1-\alpha}.$$

Using these quantities their complicated equation [34] for the diffuse term can be found to be the same as our (21)[7].

§ 5. $s=3$. Comparison with Jagodzinski's Result

This case was treated by Jagodzinski[3] by using a complicated genealogical table.

When $s=3$, $l=4$. He took the probabilities as

$$hh\longrightarrow 1-\alpha,\qquad ch\longrightarrow 1-\beta,$$

$$hc\longrightarrow \alpha,\qquad cc\longrightarrow \beta,$$

which correspond to

$$\alpha_1=\beta\quad\text{and}\quad\alpha_2=\alpha,$$

in our expression. Then we may put

$$\boldsymbol{\alpha}=\begin{pmatrix}\beta & \\ & \alpha\end{pmatrix},\quad \boldsymbol{\beta}=\begin{pmatrix}1 & 0\\ 1 & 0\end{pmatrix},\quad \boldsymbol{w}=\begin{pmatrix}w_c & 0\\ 0 & w_h\end{pmatrix},$$

$$\boldsymbol{u}=\begin{pmatrix}0 & 1\\ 1 & 0\end{pmatrix},\quad \boldsymbol{h}=\begin{pmatrix}w_c & w_h\\ '' & ''\end{pmatrix},$$

from which we can calculate

$$w_c=\frac{\alpha}{1+\alpha-\beta}\quad\text{and}\quad w_h=\frac{1-\beta}{1+\alpha-\beta},$$

referring to (9) and (11). If we put

$$\boldsymbol{x}_n=\begin{pmatrix}q_n & p_n\\ '' & ''\end{pmatrix}_2,$$

we can easily show[7]

$$p_n=[p_n],\qquad p_n+q_n=[P_n],$$

and (14) becomes

$$\begin{cases} q_n+\beta q_{n-1}+\alpha p_{n-1}+q_{n-2}\{\beta^2+\alpha(1-\beta)\} \\ \qquad\qquad +p_{n-2}\alpha(1-\alpha+\beta)=\dfrac{\alpha}{1+\alpha-\beta}, \\ p_n \qquad\qquad -q_{n-2}(1-\beta)(1-\alpha+\beta) \\ \qquad\qquad -p_{n-2}\{\alpha(1-\beta)+(1-\alpha)^2\}=0, \end{cases}$$

from which we can eliminate q_n obtaining

$$p_n+\beta p_{n-1}-(1-\alpha+\beta)(1-\alpha-\beta)p_{n-2}+(1-\alpha)(\alpha-\beta)p_{n-3}-(\alpha-\beta)^2p_{n-4}=\frac{\alpha(1-\beta)(1-\alpha+\beta)}{1+\alpha-\beta}.\tag{22}$$

If we add (22) to (22) multiplied by $(\alpha-\beta)$ in which n is replaced by $(n-1)$, we get

$$p_n+\alpha p_{n-1}+\{2\alpha-1-\alpha(\alpha-\beta)\}p_{n-2}+(\alpha-\beta)(\alpha-\alpha^2+\beta^2)p_{n-3}-\alpha(\alpha-\beta)^2p_{n-4}-(\alpha-\beta)^3p_{n-5}=\alpha(1-\beta)(1-\alpha+\beta),\tag{23}$$

which is the same as his equation [7]. Hence he obtained a difference equation of unnecessarily high order.

(16) becomes

$$x^4+\beta x^3-(1-\alpha+\beta)(1-\alpha-\beta)x^2+(1-\alpha)(\alpha-\beta)x-(\alpha-\beta)^2=0,\tag{24}$$

which is the same as his equation [10]. If we put $\alpha=\beta$ in (24), it becomes

$$x^2+\alpha x-(1-2\alpha)=0,\tag{25}$$

which is the same as (20) in conformity with § 6 of the preceding report.[1]

§ 6. Discussion

In the present report the general treatment of the close-packed structure was discussed but concerning its applications to the individual cases as $s=2$ and 3 we showed only the correspondence of our results to those obtained by other investigators the detailed applications to these cases being omitted here. One of the important results obtained is that the general difference equation (14) could be obtained. In the case of $s=3$ Jagodzinski obtained the difference equation (23) using such a complicated genealogical table as Table II in his 2nd report.[3] But such a table is so complicated that he could not obtain the difference equation in the case of $s=4$ which would serve to calculate such an intensity curve as plotted in Fig. 6 in his 3rd report[6] and also that he obtained a difference equation of unnecessarily high order as seen from the comparison of (22) with (23). On the other hand the general difference equation obtained by us has no such fears although it may become more difficult or practically impossible to solve det $\boldsymbol{C}=0$ (16) as s becomes much larger. But when we use well the experimental data given and an appropriate approximation it will be not always so difficult as thought at first to solve the equation of the l-th order with respect to x and also to determine c_ν. Namely, as seen from § 3, we can know some roots of det $\boldsymbol{C}=0$ for the fundamental regular structure from the positions of the Laue spots since they are found at $\varphi=\pm\theta_\nu$ when $|x_\nu|=1$ including real roots. When these roots substituted into det $\boldsymbol{C}=0$, some of α's can be determined hence the equation to be solved actually is not of the l-th order but of much lower order with respect to x. Namely if the identity period is n times of that of φ then the order of the equation to be solved is $(l-n)$ since other n roots are $x_\mu=e^{i(2\pi/n)\mu}$, μ being $1,2,\dots,n$. And if the Laue spots corresponding to some of these x_μ's do not appear, it may be enough only to put c_μ's accompanying such x_μ's as zero since c_μ is proportional to the intensity. Then we can put

$$\det \boldsymbol{C}=\prod_{\mu=1}^{n}(x-e^{i(2\pi/n)\mu})\prod_{\nu=1}^{l-n}(x-x_\nu)\,, \qquad (26)$$

from which we can determine n α's, the remainning $(l-n)$ α's being undeterminate in which case the corresponding w_l's to these α_l's may be put zero.*)

Next we assume that the true values of α's, x's and c's may deviate so slightly from those just determined for the fundamental regular structure that the higher term of these deviations can be neglected in (11), (17) and the equation corresponding to (26). As a result of such an approximation the determinations of x's, c's and some of α's will be comparatively easily made and moreover the number of the remaining α's may be sometimes further reduced when the intensities at the special points along the observed diffuse line will be zero.

The detailed and numerical discussions will be reported in the following report where the cases of $s=3$ and 4 will be treated for the *hc* (4 layers and $s=3$) and *hcc* (6 layers and $s=4$) structures of SiC. It will be shown there that the curve in the case of $s=3$ will be in agreement with that shown in Fig. 5 in the third report by Jagodzinski⁶⁾ when the values of parameters given by him will be used and that our curve, however, will be a little more excellent than his because his omission of the small quantities will be found to be larger than ours.

In the present treatment, because of the assumption in § 2 that the layers with the same *ch*-order are equivalent to each other both intensity equations for the cases of $2h+k=3m\pm1$ are identical with one another as seen from (7). Therefore the intensity equation in the case of $s=1$ will be derived from such a $\boldsymbol{P}$ as obtained from (19) by putting $\alpha=1-\alpha$ $\therefore$ $\alpha=\frac{1}{2}$, namely

$$\boldsymbol{P}=\frac{1}{2}\begin{pmatrix} 0 & 1 & 1 \\ 1 & 0 & 1 \\ 1 & 1 & 0 \end{pmatrix}.$$

A more and the most general expression of $\boldsymbol{P}$ in the case of $s=1$ may be

$$\boldsymbol{P}=\frac{1}{2}\begin{pmatrix} 0 & 1+\alpha & 1-\alpha \\ 1-\alpha & 0 & 1+\alpha \\ 1+\alpha & 1-\alpha & 0 \end{pmatrix}$$

$$\text{and}\quad \boldsymbol{P}=\frac{1}{2}\begin{pmatrix} 0 & 1+\alpha & 1-\alpha \\ 1-\beta & 0 & 1+\beta \\ 1+\gamma & 1-\gamma & 0 \end{pmatrix},$$

respectively, when the above assumption is not considered. With respect to these points (especially the rhombohedral structure) we may discuss in future.

As was shown in § 4 our antecedent method was found to be simpler than the "whole s layers" method (Hendricks and Teller) also in the close packed structure although both methods were generally equivalent to one another as was shown in § 6 in the preceding report.¹⁾

The agreement of (20) and (25) can be considered to show again the validity of the result in § 6 of the preceding report¹⁾ where the relation between the cases of ranges s and $(s-1)$ was discussed.

In conclusion the general treatment of our antecedent method discussed in the preceding report¹⁾ has found one of the suitable applications in the close packed structure.

References

1) J. Kakinoki and Y. Komura: J. Phys. Soc. Japan **9** (1954) 169; J. Inst. Polytech. Osaka City University *B* **3** (1952) 1; and X-rays (in Japanese) **7** (1952) 25.

2) H. Jagodzinski: Acta Cryst. **2** (1949) 201–207.

3) H. Jagodzinski: Acta Cryst. **2** (1949) 208–214.

4) A. J. C. Wilson: Proc. Roy. Soc. *A* **180** (1942) 277–285.

5) S. Hendricks and E. Teller: J. Chem. Phys. **10** (1942) 147–167.

6) H. Jagodzinski: Acta Cryst. **2** (1949) 298–304.

7) J. Kakinoki and Y. Komura: J. Inst. Polytech. Osaka City University, *B* **3** (1952) 35.

---

* Concerning the fundamental regular structure with any *ch*-order, we shall discuss in more detail in the following paper.

JOURNAL OF THE PHYSICAL SOCIETY OF JAPAN Vol. 9, No. 2, MAR.—APR., 1954

Fine Structure due to Refraction Effect in Electron Diffraction Pattern of Powder Sample

Part II. Multiple Structures due to Double Refraction given by Randomly Oriented Smoke Particles of Magnesium and Cadmium Oxide

By Goro HONJO and Kazuhiro MIHAMA*

Tokyo Institute of Technology, Ohokayama, Tokyo

(Received September 22, 1953)

Fine structures composed of sets of doublets as expected by the double refraction effect, an effect concluded by the dynamical theory of electron diffraction, are studied in details for reflexions given by individual smoke particles of magnesium and cadmium oxides having random orientations. The configurations of doublets vary according not only to the azimuths of the crystallites but also to the angles of deviations from Bragg condition, namely, the errors of resonance of Bragg reflexions. By determining these two parameters from the configuration, the mean and periodic terms of the Fourier expansion of the inner potentials of the crystals are obtained from the inter-doublets and intra-doublets separations in the fine structures. The results show a reasonable agreement with the theoretical values.

The intensity anomaly of the double refraction effect, suggested in Part I, are found to be a general phenomenon. It is observed that between the two spots of a doublet, that of larger deviation is always weaker in intensity than its companion of smaller deviation, and that the intensity difference is more conspicuous for strong reflexions, that is to say, reflexions which show large double refractions. This anomaly seems to be explained when we assume for crystals complex periodic inner potentials.

§ 1. Introduction

In this paper** we will be concerned with the fine structure due to the double refraction effect. This is an effect expected from the dynamical theory of electron diffraction due to Bethe.[1] A reflexion given by a particle of a particular shape will split by the effect into a set of doublets. Sturkey[2] has pointed out, at first, such fine structures for reflexions given by smoke particles of magnesium and cadmium oxides, the particles which are well-known by electronmicroscopy to have clean-cut cubic shape. Kato[3] has extended Bethe's theory, which was confined originally to plane parallel crystal plate, to wedge shaped crystal relevant to the fine structure. Photographs showing the fine structures given by smoke particle of magnesium oxide have been published by Cowley and Rees[4] and by the present authors.[5] In the followings we will call a set of doublets of this kind given by a particle "a double refraction multiplet" or briefly "a multiplet".

Sturkey has applied the observation of the double refraction multiplets to a determination of mean inner potentials, V_0, of crystals, and reported a reasonable result. In his consideration, however, it was assumed that Bragg condition is to be satisfied exactly, while, as well-known by the dynamical theory, a reflexion by a lattice plane may take place with an appreciable intensity not only at the exact Bragg condition but within a finite angular width, that is to say, within a finite range of the error of resonance. As is seen from the more refined theory of Kato and really observed in our previous photographs, the aspect of the double refraction multiplets should depend on the resonance error on account of the corresponding dispersion of electron waves in crystal.

---

* Now at Japan Electron Optics Laboratory Co., Ltd., Kamirenjaku, Mitaka, Tokyo.

** This paper is to be read in conjunction with the previous paper, Part I, of one of the present authors (G.H.) (J. Phys. Soc. J. 8 (1953) 776).

Detailed observations of the double refraction effect for magnesium and cadmium oxide smokes and their comparison with Kato's theory will be presented in this paper*. Hereupon we will mention that an important interest about the double refraction effect consists in the fact that we can determine thereby not only V_0 but also V_h, the Fourier coefficient of the periodic potentials of crystal, for which Sturkey has assumed calculated values and the experimental determination of which can be performed, in usual, only by intensity measurements. Our special interest in the investigation for the smoke having a fibrous orientation, reported in Part I of the present paper, was the determination by taking advantage of the simple condition furnished by the sample that azimuths of crystallites participating in reflexions are easily known and the effect of the resonance error needs not be concerned. But the result was not successful except for (002) reflexion of magnesium oxide on account of a reason as will be mentioned in § 2.

In general a crystal giving rise to reflexion may have an arbitrary azimuth around the normal of the reflecting net plane, and any angle of deviation from the exact Bragg condition, that is, the resonance error. In the following paper we will see, at first, in what way the configuration of the double refraction multiplets varies according to these parameters and then V_0 and V_h will be determined by eliminating the parameters.

In Part I we have mentioned a fact that, though well-separable double refraction effect is expected, it is hard to be observed for cadmium oxide smoke. Concerning this fact we have called attention, as mentioned in Part I, to the intensity anomaly found for (002) reflexion of magnesium oxide, that doubly refracted rays are different in intensity, and suggested a fact that the anomaly might be predominant for cadmium oxide making one of spots of double refraction vanishingly weak. It will be found that the anomaly is a general phenomenon and, in fact, very conspicuous for cadmium oxide. This point will be mentioned and discussed in later sections (§ 6, 7).

§ 2. Experimentals

In the earlier period of the present experiment the same camera as mentioned in Part I, which has a specimen plate distance $L=15$ cm, was utilized. In the later period, a camera** with $L=38$ cm and capable of a much higher resolution, was utilized. To the former camera comparatively low accelerating voltages about 25∼30 kV. and to the latter camera higher voltages about 30∼50 kV. were applied.

The advantage to utilize the smoke sample deposited on a flat substrate to have a fibrous orientation was found to be limited, in practice, by the following condition. When we reduce very much the amount of deposition in order to prepare the sample aligned in the orientation as well as possible, it was found that the fibrous reflexions themselves become spotty, as seen in Photo. I.

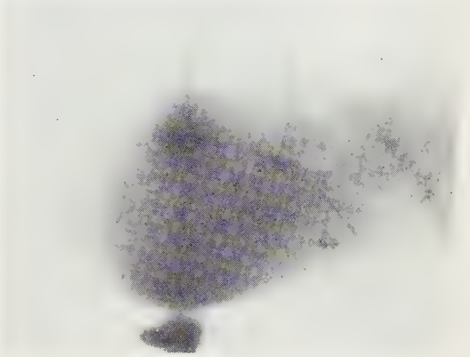

Photo. I.

Such a sampling was favourable, however, to observe the multiplets due to particles of arbitrary orientations, since the effective number of such particles is so small in the sample than usual that individual multi-

---

* The authors overlooked the fact that H. L. Altenhein, K. Molière & H. Niehrs (Naturwiss. **39** (1952) 447) had been published obserbations and discussion of the double refraction effect for magnesium oxide smoke similar to that given in the present paper. The works in the present paper were carried out independently therefrom and the results were reported for several times at meetings of Japan Physical Society in 1949∼1952 and at the second international congress of crystallography (July, 1951, Stockholm).

** An electronmicroscope of three lenses$^{6)}$ furnished with an additional specimen holder between 2nd and 3rd lenses. With a specimen on this holder and the 3rd lens unexcited, a high resolution diffraction pattern can be obtained following the scheme of Hillier & Baker$^{6)}$.

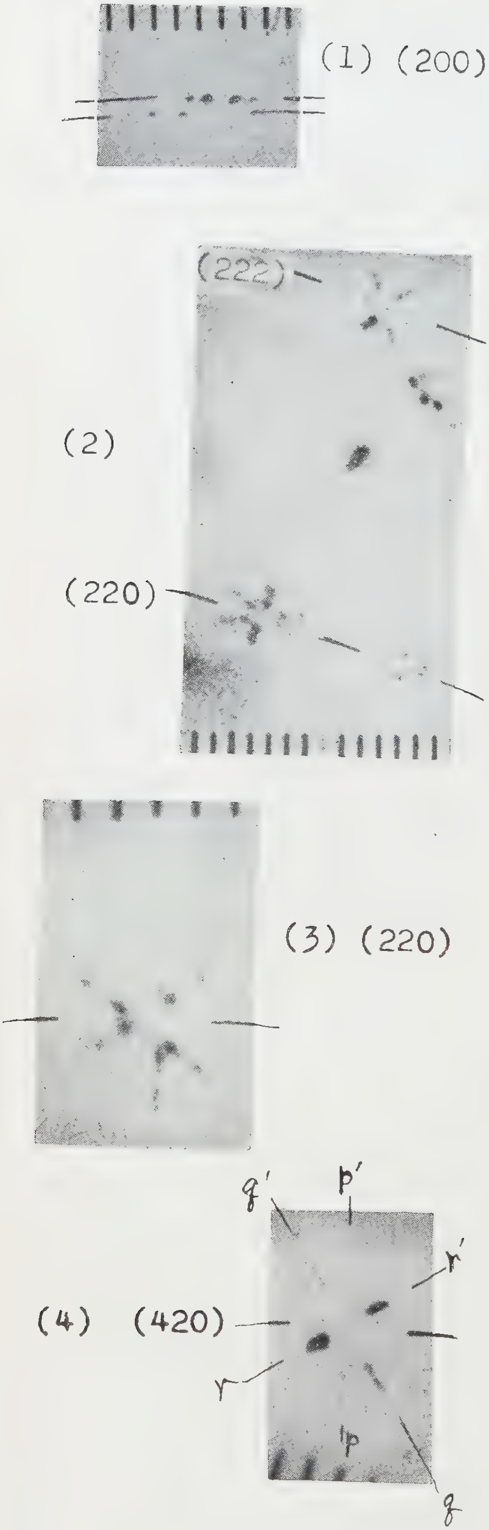

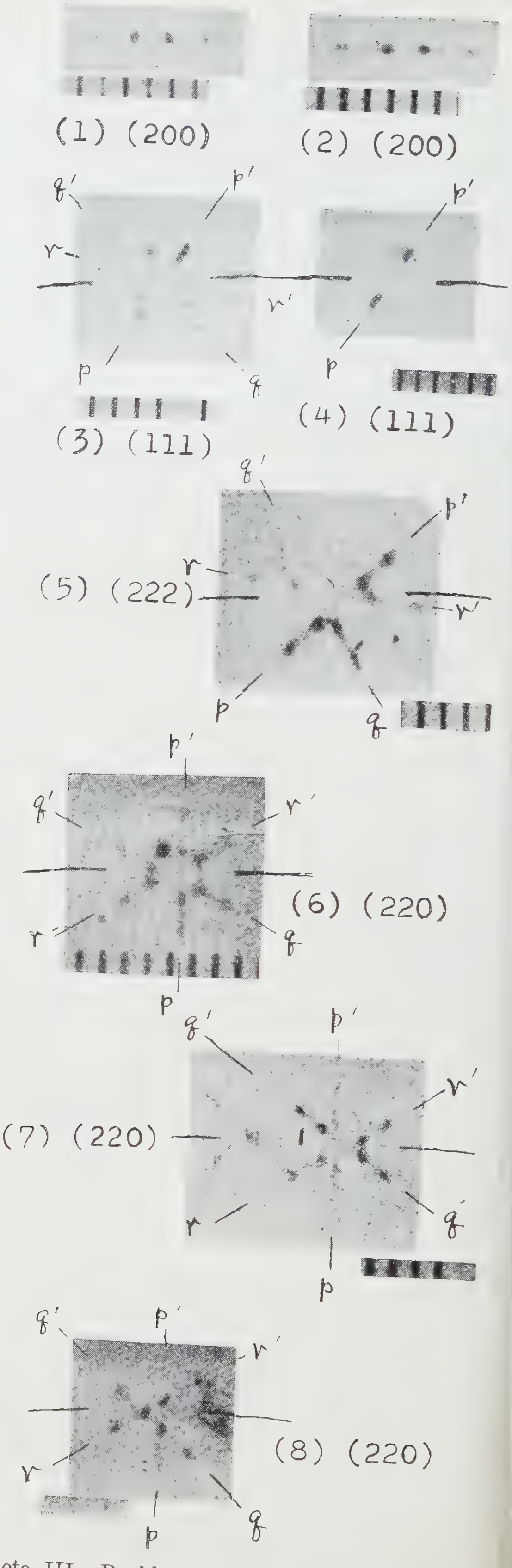

Photo. II. Double Refraction Multiplets of MgO. Photo. III. Double Refraction Multiplets of MgO.

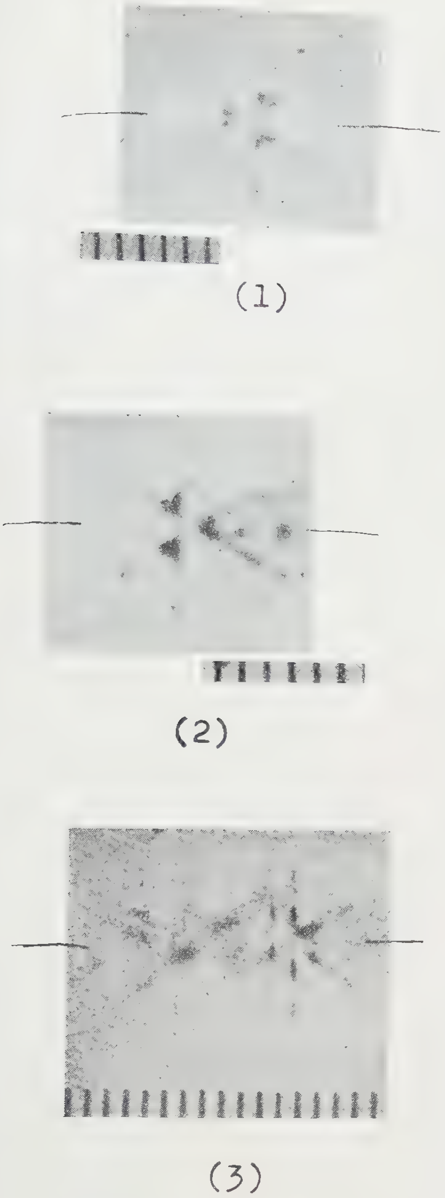

Photo. IV. Double Refraction Multiplets of (220) of CdO.

plets are easily obtainable well-separated from the others without confusions. When we deposite the sample on a mesh to take photographs by the transmission method, it was found to be useful to insert the mesh between wo screening fine meshes in order to reduce he effective number of the particles.

We have thus observed a number of multiplets well-separated from each other as reproduced in Photo. II∼V. Those in Photo. II were obtained by the camera of $L=15$ cm, while the others, by the camera of $L=38$ cm.

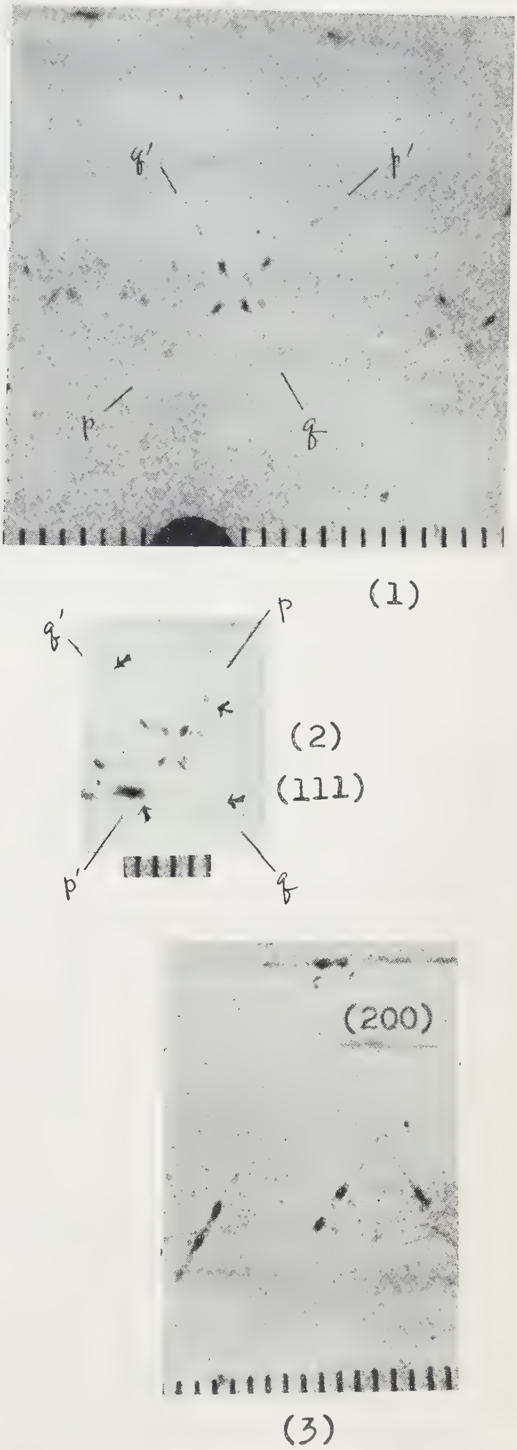

Photo. V. Double Refraction Multiplets of (111)- and (200) of CdO.

One division of the scale in the photographs corresponds to 0.1 mm. on the original plates and the arcs drawn indicate the position of the corresponding Debye rings.

§ 3. Results of the Observation

An electron beam impinging on a cube of the smoke particle will run across it, in general, by (a) six paths as defined in Table I and (b) the paths through two parallel surfaces.

Table I.

Path	Entrance Surface	Exit Surface
p	(100)	(010)
p'	$(0\bar{1}0)$	$(\bar{1}00)$
q	(001)	(010)
q'	$(0\bar{1}0)$	$(00\bar{1})$
r	(100)	$(00\bar{1})$
r'	(001)	$(\bar{1}00)$

We can find that each multiplet reproduced in our photographs composed of a set of doublets which show a configuration characteristic of the index of reflexion and correspond to the paths (a) as seen below, while spots corresponding to the paths (b) are, in general, not found on account of absorption (Cf. 4 (ii) of Part I).

Concerning refraction effect of powder pattern it is convenient, in general, to look for the deviation of a reflexion from the point of the reflexion expected when there were no refraction effect, which we will call, for brevity, "a L_s-point" in the followings. The deviation may be accounted for by the prism action of a wedge of a path on the electron ray which may be considered to run almost along the reflecting lattice plane, because Bragg angles in electron diffraction and the deviation due to refraction itself are very small (Cf. § 4 (i) of Part I). One of the present authors has previously discussed the configuration of refraction multiples by taking account of the ordinary refraction effect in this way⁷⁾. According to it the one to one correspondence of doublets in the observed multiplets to the paths mentioned in Table I can easily be seen as depicted in Fig. 1: the deviation by a path takes place along the direction perpendicular to the projection on the screen of the edge of the wedge and the deviations due to a pair of paths, (p, p'), (q, q') or (r, r'), occur in directions opposite to each other so that the corresponding pair of doublets lie in a line forming a linear quartet. Speaking in details, for (200) reflexion only (q, q') quartet, which is always tangential to the Debye ring, is observed, while the other paths, as easily seen, do not contribute to this reflexion. (Photo. II (1), III (1), (2), V (3)). In (220) multiplets, (p, p') quartet is always radial to the Debye ring, while (q, q'), and (r, r') quartets run across the former making equal angle, the angle varying from one multiplet to another, certainly, on account of varying azimuths of the participating crystallites (Photo. II (2), (3), III (6), (7), (8), IV (1), (2), (3)). In $(11\bar{1})$ and (222) multiplets, (p, p') and (q, q') quartets run across the Debye ring making angles about 35∼45° to the radial direction, while (r, r') making angles about 80° to the direction. (Photo. II (2), III (3), (4), (5), V (1), (2), (3)).

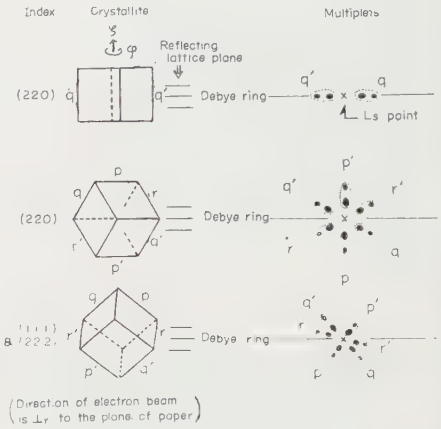

Fig. 1.

Sturkey has assumed, as mentioned above, always exact fulfilment of Bragg condition so that concluded two refractive indices of crystal as given by Equ. (3) of Part I, which are constant for reflexions of a certain index of a substance. Then the angular deviations of doubly refracted reflexion from L_s-point might be proportional to the constant unit increments of the refractive indices

$$\delta_0 \pm \delta_h = \frac{1}{2E}\{V_0 \pm |V_h|\}, \qquad (1)$$

where E is the accelerating voltage of the electron beam, and to a geometrical factor similar to that of the ordinary refraction effect given in the previous paper⁷⁾. The geometrical factor dependent upon the external shape of the crystal varies according to the azimuth of crystal, but is identical in magnitude for a pair of paths mentioned above. Thus Sturkey has considered that, for linear quartets of **h**-reflexion, the ratio of the intra-doublet separation a, which may be then equal for the pair of doublets, to the inter-doublets separation b, is given by

$$\delta_h/\delta_0 = |V_h|/V_0 .$$

We can see that such a pair of doublets have in fact almost equal intra-doublet separations, but our observation deviates from Sturkey's proposition in the following points, which may be, as supposed well, on account of the resonance error. A number of (200) quartets found for magnesium oxide are plotted in Fig. 2, where the ordinate and abscissa correspond respectively to a and b multiplied with $E/2L$. The plots evidently do not show constant a/b. In the left half of Table II, observed values of a and b, multiplied with E/L, together with that of the angle γ between the line of quartet and the radial

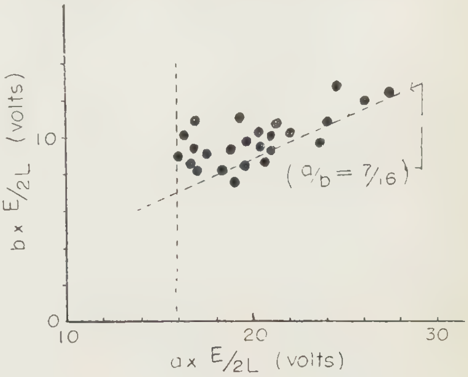

Fig. 2.

Table II.*

Sub-stances	Reflex.	Photo.	E	Quartet.	$a\cdot E/L$	$b\cdot E/L$	γ	φ_{mean}	t	V_0	$\lvert V_h\rvert\sqrt{1+\varepsilon^2}$	ε_{es}
MgO	(111)	III(3)	40.5	pp'	*	33.1	35	17.5	2.10	15.7	*	
				qq'	8.5	67.2	46		4.34	15.1	1.8	
				rr'	9.6	69.4	75		4.60	15.0	2.1	
MgO	(220)	II(2)	24.7	pp'	11.5	34.6	0	21	2.15	16.0	5.8	~0
				qq'	16.5	*	69		3.17	16.5	5.2	
				rr'	17.5	49.2	70			15.5	5.7	
MgO	(220)	III(7)	48.0	pp'	18.9	45.5	0	47	2.93	15.5	6.5	~2/3
				qq'	16.4	39.2	53		2.46	15.9	6.7	
				rr'	15.2	40.4	55			16.4	6.2	
MgO	(220)	III(6)	41.0	pp'	16.2	38.8	0	33	2.39	16.3	6.8	~2/3
				qq'	16.2	38.8	61		2.48	15.7	6.5	
				rr'	17.2	39.9	62			16.1	7.0	
MgO	(220)	III(3)	40.5	pp'	25.6	44.8	0	47	2.99	15.3	8.7	~1 (>)
				qq'	22.4	40.5	55		2.46	16.5	9.2	
				rr'	21.3	38.4	53			15.6	8.8	
MgO	(222)	II(2)	24.7	pp'	9.9	37.9	37	22.5	2.30	16.4	4.3	~0
				qq'	13.1	51.0	42		3.40	15.0	3.8	
				rr'	14.8	57.6	80		3.72	15.4	4.0	
MgO	(222)	III(5)	40.5	pp'	16.0	43.7	38	28	2.60	16.8	6.1	~1
				qq'	18.1	*	39		2.69	*	6.3	
				rr'	21.3	55.4	87		3.45	16.1	6.2	
CdO	(111)	V(1)	44.0	pp'	35.9	75.2	41	37.5	3.45	22.4	10.4	~1/3
				qq'	24.3	51.0	38		2.35	22.2	10.3	
				rr'	*	*	*		3.75	*	*	
CdO	(111)	V(2)	44.0	pp'	25.5	48.6	38	22.5	2.35	20.6	10.8	~1/3
				qq'	35.9	71.8	41		3.45	20·8	10.4	
				rr'	*	*	*		3.75	*	*	
CdO	(220)	IV(3)	34.5	pp'	20.0	45.5	0	41.5	2.60	17.2	7.7	~0
				qq'	19.1	*	57		2.40	*	7.9	
				rr'	20.0	*	56			*	7.6	
CdO	(220)	IV(1)	40.0	pp'	21.1	44.2	0	32.5	2.38	18.8	8.9	~1/3 (<)
				qq'	23.2	48.4	61		2.50	19.4	9.3	
				rr'	22.1	46.3	62			18.5	8.8	
CdO	(220)	IV(2)	39.0	pp'	24.6	45.1	0	35	2.45	18.5	10.1	~1/3 (>)
				qq'	23.6	43.1	58		2.45	17.6	9.6	
				rr'	22.6	42.1	60			17.2	9.2	

(* E in kV, $a\cdot E/L$, $b\cdot E/L$, V_0, $|V_h|\sqrt{1+\varepsilon^2}$ in volts, γ, φ in degrees.)

direction of the Debye ring, are tabulated for the linear quartets found in the multiplets of our photographs. It may be seen that also for these quartets the ratio a/b are not a constant of a reflexion.

A more apparent disagreement of the observation against Sturkey's theory can be found when we observe the symmetry of the configuration of doublets in multiplets. According to the theory, the configuration of doublets given by cubic particles should have in general a centre of symmetry at L_s-point; especially the configuration in (220) multiplets should have symmetries across the radial axis as well as the tangential axis. However, observed multiplets show such symmetries only in exceptional cases and certain distortions from the symmetric form are noted in general. (220) multiplets in our photographs show more or less asymmetry across the radial axis, while the symmetry across the tangential axis is always almost preserved. For example, a slight distortion of this kind can be seen in Photo. II (2), and considerable ones in II (3), III (6), (7), (8), IV (1), (2). (222) multiplet of Photo. II (2) and (111) multiplet of Photo. III (3) have the centrosymmetry, while (222) of Photo. III (5) and (111) of Photo. V (1), (2) show apparent asymmetries.

As the matter of fact, it was rather seldom to find full set of component doublets expected for multiplets, though it was not so difficult to observe only certain component doublets. By taking a hundred of plates we found 6, 10, 7, 4 and 9 multiplets of fuller set of component doublets, respectively for (111), (220), (220) reflexions of magnesium oxide and (111), (220) reflexions of cadmium oxide. These will be utilized in a detailed analysis of the observation given in § 5. For (200) reflexion of cadmium oxide it was very seldom to find tangential quartets as that of Photo. V (3), which has $a\cdot E/2L=16$ and $b\cdot E/2L=22$ volts. We found more frequently pairs of spots along the Debye ring having equal intensity and separations, multiplied with $E/2L$, about 5∼10 volts (Phot. V (1)). As will be seen in later sections, the pair of spots should be considered to be two inner spots of the tangential quartet.

§ 4. Theoretical Consideration

We will now give a theoretical consideration on the configuration of the double refraction multiplet according to Kato's theory of wedge shaped crystal. In the theory the double refraction effect is constructed by the wave vector relation in the reciprocal space (See Appendix). When we utilize the approximation mentioned in the last section, the effect is accounted for by assuming double refractive indices of crystal, the unit increments of which are given by

$$\left.\begin{aligned}&\delta_p^{(1),(2)}=\delta_0+\delta_h(\varepsilon\pm\sqrt{1+\varepsilon^2})\\ &\text{for primary ray and by}\\ &\delta_r^{(1),(2)}=\delta_0+\delta_h(-\varepsilon\pm\sqrt{1+\varepsilon^2})\end{aligned}\right\}\qquad(2)$$

for the reflected ray, where (1) and (2) correspond respectively to + and − signs and ε is a parameter representing the error of resonance, which is defined by the relation:

$$\varepsilon\cdot\delta_h=\Theta\cdot\varDelta\Theta\,,\qquad(2')$$

Θ being the Bragg angle of the reflexion concerned and $\varDelta\Theta$, the angular deviation of the given electron incidence from the direction which satisfies exactly the Bragg condition in the case when there were no refraction effect.

Now let us define (ξ, η, ζ)-axes in such a way that ζ-axis is the normal to the lattice plane which gives rise to the reflexion concerned, ξ-axis the intersection of the lattice plane with the plane containing ζ-axis and the direction of the incident electron, and η-axis perpendicular to the former two. Then $\eta\zeta$-plane is nearly parallel to the photographic plate and the η- and ζ-axis are parallel respectively to the axes which are tangential and radial to the Debye ring through L_s-point. We denote the tangential and radial deviations of the reflexion due to refraction from the L_s-point by angles α_η and α_ζ respectively, then those for a reflexion doubly refracted by a path can be given by

$$\left.\begin{aligned}\alpha_\eta^{(1),(2)}&=\varepsilon\cdot\delta_h\cdot s_\eta-(\delta_0\pm\delta_h\cdot\sqrt{1+\varepsilon^2})\cdot t_\eta\,,\\ \alpha_\zeta^{(1),(2)}&=\varepsilon\cdot\delta_h\cdot s_\zeta-(\delta_0\pm\delta_h\cdot\sqrt{1+\varepsilon^2})\cdot t_\zeta\,.\end{aligned}\right\}\qquad(3)$$

Here $s_{\eta,\zeta}$ and $t_{\eta,\zeta}$ or (s,β) and (t,γ) are given by

$$\left.\begin{aligned}s_\eta&\equiv s\cdot\sin\beta=(m/l+m'/l')\,,\\ s_\zeta&\equiv s\cdot\cos\beta=(n/l+n'/l')\,,\end{aligned}\right\}\qquad(3')$$

$$\left.\begin{aligned}t_\eta&\equiv t\cdot\sin\gamma=(m/l-m'/l')\,,\\ t_\zeta&\equiv t\cdot\cos\gamma=(n/l-n'/l')\,,\end{aligned}\right\}\qquad(3'')$$

(l, m, n) and (l', m', n') being the direction cosines of the outwards normals to the entrance and exit boundaries respectively, and are determined if the azimuth of the crystal relative to the incident electron beam are given. The azimuth can be represented by the angle, φ, of rotation of the crystal around the normal ζ of the reflecting lattice plane from such a zero position that a certain zone axis of the crystal, contained in the lattice plane, coincides with ξ-axis.

Utilizing the above relation we can construct the double refraction multiplet given by a particle of any external shape in terms of two parameters φ and $\mathcal{E}$, provided δ_0 and δ_h. The only task is to find the expressions of $t_{\eta,\zeta}$ and $s_{\eta,\zeta}$ in terms of φ, which are dependent on the external shape and the reflecting lattice plane. The expressions for (110) lattice plane of cubic particles are shown, for example, in Table II, where φ is assumed to be zero when the electron ray is parallel to $[\bar{1}10]$ axis.

Table III.

	s_η	s_ζ	t_η	t_ζ
p	$-2\tan\varphi$	0	0	$-2\sec\varphi$
p'	$-2\tan\varphi$	0	0	$-2\sec\varphi$
q	$-2\cot 2\varphi$	$-\sec\varphi$	$-2\operatorname{cosec} 2\varphi$	$-\sec\varphi$
q'	$-2\cot 2\varphi$	$-\sec\varphi$	$-2\operatorname{cosec} 2\varphi$	$-\sec\varphi$
r	$-2\cot 2\varphi$	$-\sec\varphi$	$-2\operatorname{cosec} 2\varphi$	$-\sec\varphi$
r'	$-2\cot 2\varphi$	$-\sec\varphi$	$-2\operatorname{cosec} 2\varphi$	$-\sec\varphi$

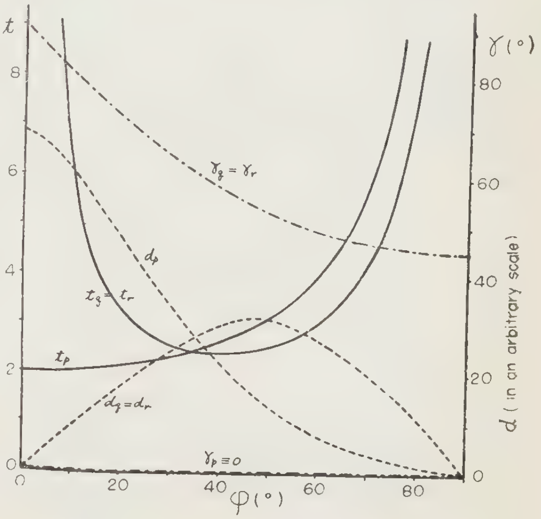

Fig. 3 (a). t, γ, d for (110) lattice plane.

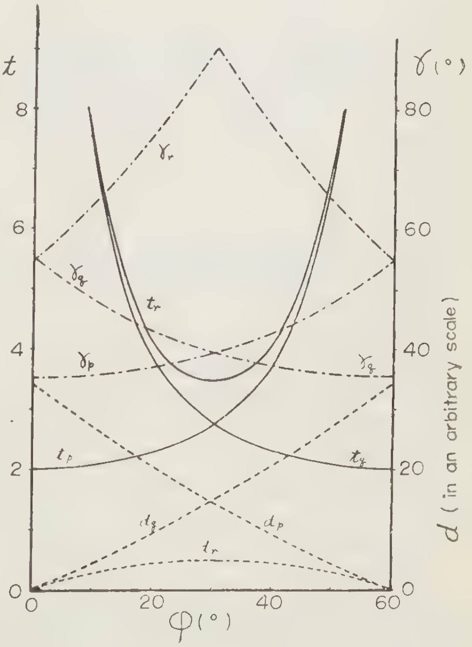

Fig. 3 (b). t, γ, d for (111) lattice plane.

In general for cubic particles, a pair of doublets corresponding to a pair of paths as mentioned in the last section form a linear quartet, because, for the pair, $t_{\eta,\zeta}$ merely reverse their signs and $s_{\eta,\zeta}$ are identical. The intra-doublet separations are given by

$$a=2\cdot\frac{|V_h|\cdot\sqrt{1+\mathcal{E}^2}}{2E}\cdot L\cdot t\,, \qquad (4)$$

while the inter-doublets separations, by

$$b=2\cdot\frac{V_0}{2E}\cdot L\cdot t\,, \qquad (5)$$

the angle γ between the line of quartet and the radial direction, together with t in the above expressions, being given by Equ. (3''). On account of the effect of resonance error the centre of the linear quartet deviates in general from L_s-point: to give the deviation it is convenient to define s and β as Equ. (3'). For the sake of the next section, t and γ are plotted against φ in Fig. 3 (a), (b) for (110) and (111) lattice planes, for the latter lattice plane also $\varphi=0$ when the electron ray is parallel to $[\bar{1}10]$ axis. Similar plots of s and β can be easily obtained. Thus, in Fig. 4 (a), (b), theoretical configurations of double refraction multiplets for (220) reflexion of magnesium oxide and (111) reflexion of cadmium oxide are illustrated for different values of φ and $\mathcal{E}$, anticipating for δ_h/δ_0 the values 5.5/15 and 10/20, respectively, which are in an accordance with our experimental values obtained in the next section. It may be seen that the theoretical configuration can reproduce very well the general features, as mentioned in the last section, of the observed refraction multiplets. As the results of different displacements of centres of different quartets, the configuration is distorted when $\varepsilon \neq 0$ from the symmetric forms of $\varepsilon=0$. For reflexions due to the same lattice plane but with different values of δ_h/δ_0, the intra-doublet separations relative to inter-doublets separations and the degree of the distortion are different, but the main characteristics of the configuration dependent on (t, γ) and (s, β) are similar: the larger δ_h/δ_0 is, the more conspicuous the intra-doublet separations and the degrees of the distortion.

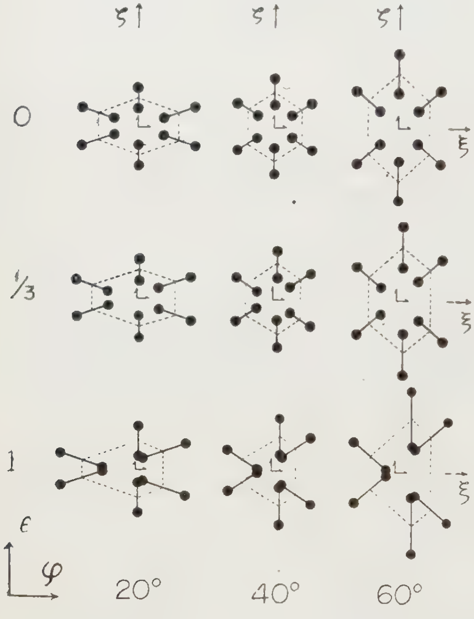

Fig. 4 (a). Double Refraction Multiplet of (220) of MgO (theoretical).

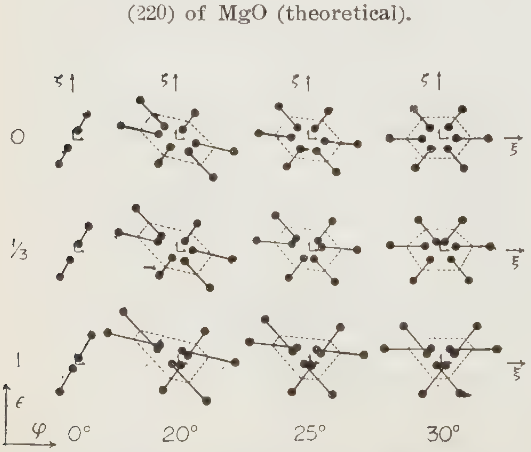

Fig. 4 (b). Double Refraction Multiplet of (111) of CdO (theoretical).

§ 5. Determination of V_0 and V_h

We will now determine V_0 and V_h from the observation and compare them with their theoretical values.

Except for (200) multiplet which consists of only one tangential quartet, the analysis goes as follows. The results for the multiplets reproduced in our photographs are tabulated in the right half of Table II. At first, the value of φ for an observed multiplet can be known from the observed angle γ utilizing the plots as Fig. 2 (9th column of Table II). Then the corresponding values of t can be known by the same plots (10th column), and V_0 and $|V_h|\cdot\sqrt{1+\varepsilon^2}$ are obtained from the observed values of a and b according to Equ. (4) and (5) (11 and 12th columns). The agreement in each multiplet among the values of V_0 and $|V_h|\cdot\sqrt{1+\varepsilon^2}$ from different quartets is fairly satisfactory.

In principle, $\varepsilon\cdot|V_h|$ might be obtained by measuring the displacements of centres of quartets relative to L_s-point utilizing the known values of (s, γ) so that $|V_h|$ can be calculated. However, the position of L_s-point is not given directly and the analysis of the displacements is somewhat involved. We preferred, therefore, an alternative method; namely, ε is estimated roughly (13th column) by comparing the observed configuration of the multiplet with the theoretical ones, as given in Fig. 3, drawn for $\varepsilon=0$, 1/3, 2/3 and 1, assuming approximate values of δ_h/δ_0.

The values of V_0 and $|V_h|\cdot\sqrt{1+\varepsilon^2}$ obtained from multiplets observed with fuller components for (220), (222) reflexions of magnesium oxide and (111), (220) reflexions of cadmium oxide are plotted against the values of ε, estimated as above, in Fig. 5 (a), (b), (c), (d).

The mean values of V_0 and $|V_h|$, the latter being obtained from the above $|V_h|\cdot\sqrt{1+\varepsilon^2}$ utilizing the estimated ε, are tabulated in Table IV. In the same table are tabulated the values of $|V_h|$ and V_0 calculated utilizing the known atom form factors[8], the former by the equation given by Bethe[1] (Equ. (2) of Part I) and the latter by the method given by Tull[9]. The full lines drawn in Fig. (5) represent the theoretical values of $|V_h|\cdot$

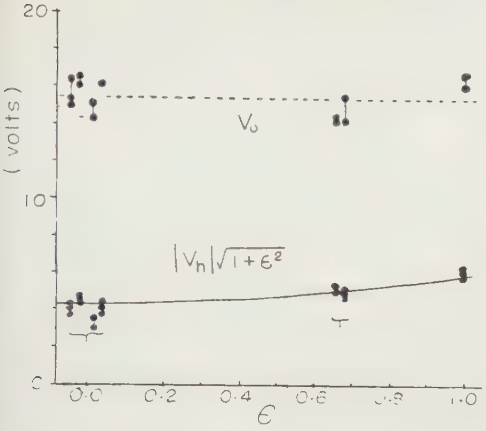

Fig. 5 (a). (220) of MgO.

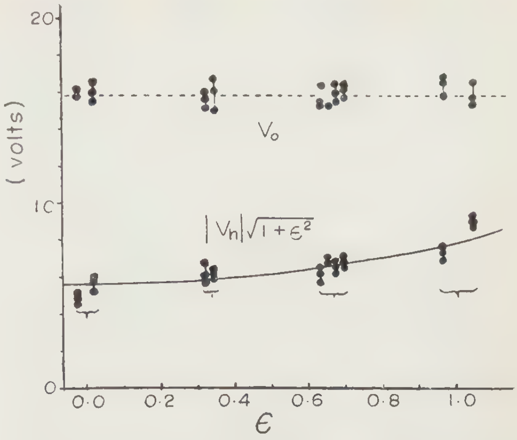

Fig. 5 (b). (222) of MgO.

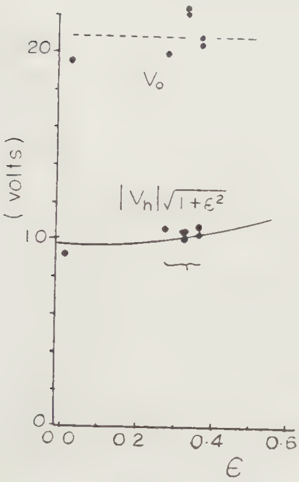

Fig. 5 (c). (111) of CdO.

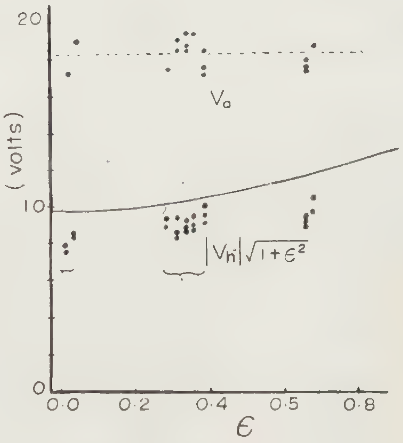

Fig. 5 (d). (220) of CdO.

Table IV.

	Reflexions	Observation		Calculation		V_0 (Sturkey)	Correction	
		$\lvert V_h \rvert$	V_0	$\lvert V_h \rvert$	V_0		V_h'	V_0'
MgO	(111)	~1.7	15.5	1.25			0.22	0.51
	(200)	~7	~16	7.66	12.8	13.0	0.90	1.21
	(220)	5.5	15.8	5.47		12.7	0.17	0.26
	(222)	4.2	15.4	4.23		—	−0.01	−0.10
CdO	(111)	9.9	20.9	9.68		—	2.85	3.06
	(220)	8.2	18.3	9.86		18.1	0.51	0.71
	(200)	—	—	13.75		20.0	3.63	4.61

$\sqrt{1+\varepsilon^2}$ for varying ε.

For (200) quartet a and b are given by Equ. (4) and (5) with $t=2\sec\varphi$ ($\varphi=0$ when electron ray is parallel to [10$\bar{1}$]). For each observed quartet we can not know ε and φ. However, the distribution of plots in Fig. 2 seems to be reasonable when we assme 16 volts for V_0 and 7 volts for $|V_h|$.

Thus we can obtain the values of V_0 and $|V_h|$ which show an agreement with their calculated values. In details, however, there are considerable fluctuations in individual values and those for V_0 of magnesium oxide and for V_h of (220) reflexion of cadmium oxide show systematic deviations from the calculated values.

When the detailed values are concerned, the following circumstances must be taken into account. In the above consideration only one reflexion is considered to exit. As the matter of fact, however, a reflexion may be accompanied by other reflexions, strong or weak, and influenced by the presence of the laters. When some other strong reflexions occur simultaneously the influence may be considerable. The anomalous values for V_0 of magnesium oxide obtained from (111) and (113) reflexions of the sample having [001]-fibrous orientation (§ 4 of Part I) seem to be typical examples of such cases. By this sample, the crystallites giving rise to a certain (h, h, l) reflexion assume such an azimuth that is very favourable for the other (h, h, l) reflexions to occur simultaneously.

The crystallites participating in the reflexions concerned in this paper are in general not in such especial condition, but it is very much probable that the considerable fluctuations of individual values of observed V_0 and V_h are due to the effect of simultaneous occurrence of some other reflexions. It was observed, moreover, that sometimes a component doublet corresponding to a path show higher multiplicity than simple doublet as, for example, p, r, q'-components in Photo. II (3), p-component of Photo. II (4). This is supposed to be due to strong coupling of other reflexions.

Even for arbitrary any azimuth of crystal, a reflexion is always accompanied by reflexions of the other orders at the same lattice plane, though the latters may not become strong. It has been known that the values of mean inner potential obtained from rotation spectrum of single crystals show always anomaly at lower order reflexions which may be attributed to the effect of simultaneous weak reflexions of this kind.[10] Therefore, it seems to be natural to take into account of similar effects also for our values of V_0 and V_h. The corrections, V_h' and V_0', which are to be substracted from our values in 3rd and 4th columns of Table IV, are calculated by means of the summation correction for weak rays in Bethe's theory, assuming exact Bragg condition for the main reflexion concerned, and tabulated in the last two column of the table. When we make these corrections, the agreement with the calculated values of our values of V_h for (220) and (222) of magnesium oxide is damaged somewhat, the discrepancy of $V_{(220)}$ of cadmium oxide is enlarged and our value of $V_{(111)}$ of cadmium oxide becomes also to be discrepant with the calculated value. In the mean while, our values of V_0 of magnesium oxide higher than the calculated values are not improved sufficiently.

In might be impossible, especially for cadmium oxide, to speak of such details up to one or two volts, since there were sometimes uncertainty in locating the spots in multiplets and the observed multiplets were not sufficiently numerous. On the other hand, the weak rays correction itself does not seem to be satisfactory to such extend also for the values of mean inner potential obtained from very low order reflexions of the rotation spectrum. But, in our case the correction is not satisfactory even in its tendency. As to V_0 of magnesium oxide, Sturkey's result, listed in 7th column of Table IV, seems, at a glance, to be in a better agreement with the theoretical values than ours, but it is evident that his method of analysis is obliged to give too lower values than really obtainable ones from the observation. From the photographs given by Cowley and Rees (Fig. 3, 1947), we obtain also about 15 volts. Therefore, the discrepancy of our values does not seem to be only a fortuitous one. We can not find at present any reasonable explanation of the minor discrepancies of our results against the theoretical values.

§ 6. Intensity Relation in the Double Refraction Multiplets

We will now turn our attention to the intensity relation in the double refraction multiplets.

According to Kato's formulation, the intensities of doubly refracted rays relative to that of the incident ray are equal to each other, being given in the present approximation by

$$I_h^{(1)}/I_0=I_h^{(2)}/I_0=\frac{1}{4}\,\frac{1}{1+\varepsilon^2}\,. \qquad (6)$$

(i) *Relative Intensity of Doublets*

At first, we will discuss the relative intensity between each other doublet of a multiplet assuming the above expression. Since this expression depends only upon the common parameter ε for all the doublets of a multiplet, the relative intensity is considered to be proportional to the cross section of the corresponding paths, namely the area common to the entrance and exit surfaces looked along the ray direction. It is expected, then, that the pair of doublets forming a linear quartet should have equal intensities, while the relative intensities among different quartets vary with the azimuth φ. For the latter, the following relations are expected as known from the plots of the cross sections, d, against φ given in Fig. 3. In the multiplet due to (111) lattice plane, (r, r') quartet should be always very weak, while either quartet (p, p') or (q, q') is the more predominating corresponding to φ being either the smaller or the larger than 30°. In the multiplet due to (110) lattice plane, it should be that the smaller the azimuth φ is than 35°, the more dominant is the radial quartet (p, p'), while (q, q') and (r, r') quartet become predominating in the neighbourhood of 45°.

As mentioned in § 3, it was seldom in practice to find the double refraction multiplets of full set of components, some doublets being often absent or distinctly weak even when considerable intensity are expected. For example, p'-doublet and q-doublet are distinctly weaker than p doublet and q'-doublet, respectively, in (222) and (220) multiplets in Photo. II (2) and p', q' and q', r are absent, respectively, in Photo. II (4), III (5), IV (3). However, we can see that the remainders show reasonable intensity relation and it was found that the absence takes place quite at random except when very small intensity is expected according to the very small cross sections of paths. It is very much conceivable that the erratical extinction is due to the fact that the corresponding path is shielded by the other particles in the sample on account of the insufficient dispersion of the particles.

(ii) *Relative Intensity between two Spots of a Doublet*

According to Equ. (6), the intensities of two spots of a doublet should be almost exactly equal.

We have mentioned in Part I a fact that, contradicting the theory, outer two spots are considerably weaker than the inner two spots in (002) quartet of magnesium oxide. A similar fact can be observed, more or less, for all multiplets reproduced in our photographs. As far as we have observed, there was no exception to the tendency of the intensity difference.

Moreover, we can see that the degree of the intensity difference has certain relations to substances and indices of reflexions as seen from our photographs. In general, it is very much conspicuous for cadmium oxide than for magnesium oxide. Among the reflexions of the former, it is so conspicuous for (200) quartets that the outer two spots of the quartets are almost vanishingly weak. It is nearly so also for (111) and (220) reflexions, but the outer spots of quartets of these reflexions can be observed more easily than those of (200). Among the reflexions of magnesium oxide, it is conspicuous for (200) reflexion, becomes less conspicuous for (220), (222), (420) reflexions, in this order, and, finally, is almost indiscernible for (111) reflexion. It is a notable fact that the degree of the intensity difference shows a similar tendency as the magnitude of the double refraction effect according to substances and indices of reflexions.*

---

* Altenhein et al. seems to have overlooked such intensity anomaly. This is presumably due to the fact that the accelerating voltages applied for their electrons were higher than those for our electrons.

§ 7. Discussion on the Intensity Anomaly of Double Refraction

In Bethe-Kato's theories the crystal is assumed to be nonabsorptive. But, as the matter of fact, it is recognized that real crystals are more or less absorptive, so that the inner potential V may be considered as complex quantity, V_r+iV_i, as assumed by Molière[11]. Then, let the mean inner potential and the Fourier coefficient of the potential be given by

$$\left.\begin{aligned} V_0&=V_{0r}+iV_{0i}\,,\\ V_h&=V_{hr}+iV_{hi}\,,\\ V_{\bar{h}}&=V_{\bar{h}r}+iV_{\bar{h}i}\,,\end{aligned}\right\} \qquad (7)$$

V_h and $V_{\bar{h}}$ are not conjugate to each other as in nonabsorptive crystal. For centrosymmetric crystals like magnesium and cadmium oxide, $V_{hr}=V_{\bar{h}r}$ and $V_{hi}=V_{\bar{h}i}$ and these four quantities are all real.

The explanation of the intensity anomaly mentioned in the last section may be naturally sought in the absorption corresponding to such a complex inner potential. The intensity relation in an analogous case in X-ray diffraction was discussed by von Laue[12] and his result may be utilized here[3]. The complex inner potential amounts to assuming double values not only for the refractive index but also for the absorption coefficient of electrons within crystals. When we utilize an approximation similar as that for Equ. (2), the double values of the absorption coefficient are given by

$$\sigma^{(1),(2)}=\frac{4\pi}{2K}\left\{V_{0i}\pm\frac{V_{hr}\cdot V_{hi}}{|V_{hr}|\cdot\sqrt{1+\varepsilon^2}}\right\}, \qquad (8)$$

where the superfix (1) and (2) and ± signs correspond respectively to those as used formerly for the refractive indices and K is the wave number of electrons in vacuum (See Appendix).

Consider a beam of electrons which run across the crystallite through a part where the total path length within the crystal is l, then its contribution to the doubly refracted spots, (1) and (2), will be proportional to $\exp(-\sigma^{(1)}\cdot l)$ and $\exp(-\sigma^{(2)}\cdot l)$ respectively. Since the particles in our sample are supposed to be sufficiently large on account of the reason mentioned at the beginning of § 3, the intensities of the double spots can be obtained by summing up the above contributions from $l=0$ to ∞. Then the intensity ratio R of (2) spot to (1) spot is given by

$$R=\int_0^\infty \exp(-\sigma^{(2)}\cdot l)dl\Big/\int_0^\infty \exp(-\sigma^{(1)}\cdot l)\cdot dl$$
$$=\frac{|V_{hr}|\cdot V_{0i}\cdot\sqrt{1+\varepsilon^2}+V_{hr}\cdot V_{hi}}{|V_{hr}|\cdot V_{0i}\cdot\sqrt{1+\varepsilon^2}-V_{hr}\cdot V_{hi}}\,.$$

Here, V_{0i} representing the ordinary absorption must be naturally considered to be positive and V_{hi}, as well, be smaller than V_{0i}, because otherwise it results in a negative intensity. Our observation that always $R\geqq 1$, requires that V_{hi} should have the same sign as V_{hr}, thereby R being given by

$$R=\frac{\sqrt{1+\varepsilon^2}+|V_{hi}|/V_{0i}}{\sqrt{1+\varepsilon^2}-|V_{hi}|/V_{0i}}\,. \qquad (9)$$

When we assume further that the magnitude V_{hi} varies similarly as V_{hr} according to indices of reflexions, as supposed by Molière, the observed features of the intensity anomaly can be explained by the periodic imaginary potential.

If we assume the potential, the measurement of the intensity ratio amounts to giving the values of $|V_{hi}|/V_{0i}$. For example, the ratio seems to be about 10 or higher for the lowest three reflexions of cadmium oxide, where (1)-spot is almost vanishingly weak compared to (2)-spot, then values of $|V_{hi}|/V_{0i}$, about 9/11 or nearer to 1, might be concluded. The observed ratio R should vary depending upon the reasonance error ε, decreasing with increasing values of ε and the variation being more conspicuous when the value of $|V_{hi}|/V_{0i}$ is larger. At the present stage of our observation, we can hardly speak of the latter variation definitely and work out the analysis through on account of difficulties of the intensity measurement.

As the matter of fact, the periodic imaginary potential of crystal to electrons is only a phenomenological assumption, the theoretical basis being not yet so obvious as the analogous quantity in X-ray diffraction. The intensity anomaly of double refraction seems to require more through experimental as well as theoretical investigations.

§ 8. Conclusion

The duplicated multiple fine structure due to the double refraction effect of electrons at Bragg reflexions are studied in details for reflexions given by cubic smoke particles of magnesium and cadmium oxides. Thereby the following facts were found.

1. The structure of the double refraction multiplets vary according to not only the azimuths of the crystallites but also the angle of deviations from the Bragg condition in a way characteristic of the index of reflecting lattice plane.

2. Thus, for fuller understandings of the structure, Sturkey's first simple consideration is not sufficient and Kato's more refined theory of wedge shaped crystal taking account of the error of resonance is neccessary.

3. According to the latter theory, the deviations of a reflexion due to the effect by a wedge are represented by simple expressions, with a reasonable approximation, in terms of the Fourier coefficients, V_0 and V_h, of the periodic inner potential of crystal and two parameters corresponding to the above mentioned two angles. By the expressions, V_h as well as V_0 can be determined by measuring separations in the multiplet, yielding values in an agreement with calculated values.

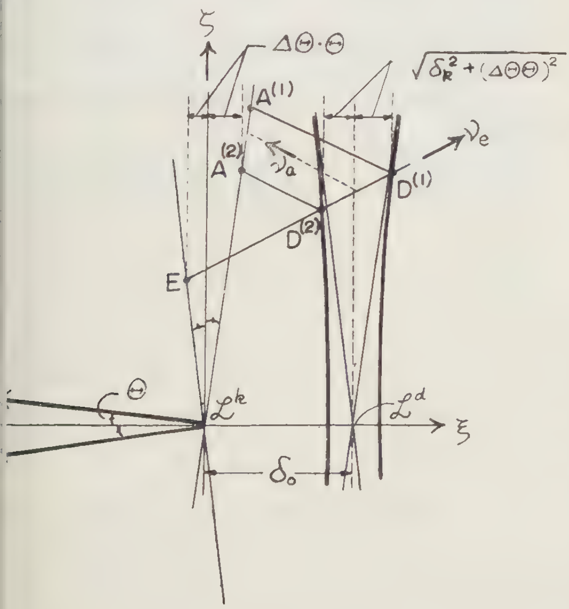

Fig. 6.

4. The double refraction show an intensity anomaly of certain regularities which is not expected by Bethe-Kato's theory and seems to be explainable when periodic absorptive potential, as mentioned by Molière, are assumed for crystal.

The method to determine V_0 and V_h can be applied to other substances of arbitrary external shape containing non-parallel clean cut surfaces ; the refraction effect itself gives an usefull information to know the neccessary crystallographic relation of the external shape, which might be difficult to be known only by electronmicroscopy. In practice, however, the application of the method might be limited on account of the following reasons. The double refraction effect is difficult to separate for higher order reflexions of small V_h. It is considerably influenced by simultaneous existences of other reflexions, especially in lower orders. Finally, for reflexions of large V_h the intensity anomaly may make difficult the separation measurements.

Appendix

Fig. 6 dipicts the wave vector relation of the double refraction effect according to Kato's theory (Cf. Fig. 1 of Kato (1952)) : E ; $D^{(1)}$, $D^{(2)}$; $A^{(1)}$, $A^{(2)}$ represent the wave points, respectively, of the incident vacuum wave, the doubly refracted waves in crystal and the doubly refracted reflexion emergent from crystal, they being connected successively by the lines parallel to the ourwards normals ν_e and ν_a of the entrance and exit surfeces. (In the figure the wave number of incident vacuum wave $K=\overline{EO}(=\overline{L^kO}=\overline{L^kH})$ is taken to be the unit of length). According to the condition that Bragg angle and the refraction effect itself are very small, the relative position along ξ-axis of the wave points is given as indicated in the figure. From this relation

Equ. (2) and (3) can be drawn immediately. Here it is assumed that the electron ray is not grazing to the surfaces of the wedge. If the ray becomes grazing to the surfaces up to a glancing angles $\sim 5°$, the errors of the approximate Equ. (3) amounts to serveral percent, but in such case the intensity of the deviated reflexion is vanishingly weak (Cf. § 4 (i) of Part I).

When imaginary inner potential is assumed for crystal, the displacements of the wave points of crystal waves from those of the vacuum waves contain imaginary parts. From ξ-components of these the linear absorption coefficients along ξ-direction result in as Equ. (8). Here $|V_{hr}| \gg |V_{hi}|$ is assumed following von Laue and according to Molière's estimation that $|V_{hi}|/|V_{hr}| \sim V_{0i}|V_{0r} \sim 0.1$. If this ratio is not sufficiently small, the intra-doublet separation might be dependent also upon $|V_{hi}|$, being proportional to $\sqrt{|V_{hr}|^2 - |V_{hi}|^2}$.

Acknowledgement

The authors wish to express their sincere thanks and appreciation to Prof. S. Miyake for his valuable advices and encouragements in the whole course of our study and to Prof. R. Uyeda and Dr. N. Kato for their interest to our study and valuable discussions. The authors are indebted to these and Dr. Akiyama, Mr. Mitsuishi and Mr. Kondo of Hitachi Central Research Laboratory for much helps and to the Asahi Bunka-Jigyo-Dan in the Asahi Press and Ministry of Education for financial aids in the construction of the camera of a new design.

Literatures

1) H. A. Bethe: Ann. d. Phys. **87** (1928) 55

2) L. Sturkey: Phys. Rev. **73** (1948) 183.

3) N. Kato: Proc. Jap. Acad. **25** (1949) 41.
N. Kato & R. Uyeda: Acta Cryst. **4** (1951) 227.
N. Kato: J. Phys. Soc. Jap. **7** (1952) 397.

4) J. M. Cowley & A. L. G. Rees: Proc. Phys. Soc. **59** (1947) 287.

5) G. Honjo & K. Mihama: Acta Cryst. **4** (1951) 282.

6) J. B. le Poole: Philips Tech. Rev. **9** No. 2 (1947) 33.
M. E. Haine, R. S. Page & R. G. Garfitt: J. App. Phys. **21** (1950) 173.
J. Hillier & R. F. Baker: J. Appl. Phys. **17** (1946) 12.

7) G. Honjo: J. Phys. Soc. Jap. **2** (1947) 133.

8) International Tabellen zur Kristallstrukturbestimmung, Berlin 1935.

9) V. F. D. Tull: Proc. Roy. Soc. A**206** (1951) 232.

10) T. Yamaguchi: Proc. Phys.-Math. Soc. Jap. **16** (1934) 95.
R. Uyeda: Proc. Phys. -Math. Soc. Jap. **20** (1938) 284.

11) K. Molière: Ann. d. Phys. **34** (1939) 461.

12) M. von Laue: Acta Cryst. **2** (1949) 106.

JOURNAL OF THE PHYSICAL SOCIETY OF JAPAN Vol. 9, No. 2, MAR.—APR., 1954

Inelastic Collisions between Two Molecules

By Takechiyo INOUE
Faculty of Engineering, Meiji University, Tokyo
and Takehito TAKAHASHI
Seizyo University, Setagaya, Tokyo

(Received September 25, 1953)

The collision between two diatomic molecules is treated quantum-mechanically. Group theoretical arguments are used, and the differential equations for the internal wave functions are derived. The procedure is due originally to Curtiss and Adler, but is more direct and suitable for collision problems. The equations are solved by Zener's method, and transition probabilities are obtained in terms of integrals of interaction potential and a set of phase shifts. It is also shown that the collision between two polyatomic molecules can be treated in quite similar way.

1. Introduction

The collisions under gas kinetic conditions were discussed by various authors, e.g., Zener[1], Devonshire[2], Jackson and Mott[2] and Schwartz, Slawsky and Herzfeld[3]. In most cases the problmes were treated one-dimensionally. Curtiss, Hirshfelder and Adler[4] developed a useful theory, separating the rotational coordinates from many particle Schroedinger equations, and applied it to the scattering of atoms by diatomic molecules. Though their method is very comprehensive, it seems somewhat indirect and lengthy so far as the impact problems are concerned. In the following sections the more straightforward method is used for collisions between two diatomic molecules and between polyatomic molecules. (The notations similar to those in reference (4) are used as far as possible.)

2. Collisions between two diatomic molecules

i] *Wave equations*

The Schroedinger equation for two diatomic molecules may be written as

$$\left\{\frac{\hbar^2}{2}\sum_{n=1}^{4}\frac{1}{m_n}\Delta_{x_n}+E'-V\right\}\Psi=0\,. \quad (1)$$

If we introduce the vectors ξ_i, ρ, X illustrated in Fig. 1., and the reduced masses M_1, M_2, M, defined by

$$\left.\begin{aligned}
&\boldsymbol{\xi}_1=\boldsymbol{X}_1-\boldsymbol{X}_2\,, \qquad \boldsymbol{\xi}_2=\boldsymbol{X}_3-\boldsymbol{X}_4\,,\\
&\boldsymbol{\rho}=\frac{m_1\boldsymbol{X}_1+m_2\boldsymbol{X}_2}{m_1+m_2}-\frac{m_3\boldsymbol{X}_3+m_4\boldsymbol{X}_4}{m_3+m_4}\,,\\
&\frac{1}{M_1}=\frac{1}{m_1}+\frac{1}{m_2}\,, \qquad \frac{1}{M_2}=\frac{1}{m_3}+\frac{1}{m_4}\,,\\
&\frac{1}{M}=\frac{1}{m_1+m_2}+\frac{1}{m_3+m_4}\,,\\
&(\sum_n m_n)\boldsymbol{X}=\sum m_n\boldsymbol{X}_n\,,
\end{aligned}\right\} \quad (2)$$

we have

$$\sum_n\frac{1}{m_n}\Delta_X=\frac{1}{\sum m_n}\Delta_X+\frac{1}{M}\Delta_{\boldsymbol{\rho}}+\frac{1}{M_1}\Delta_{\boldsymbol{\xi}_1}+\frac{1}{M_2}\Delta_{\boldsymbol{\xi}_2}.$$

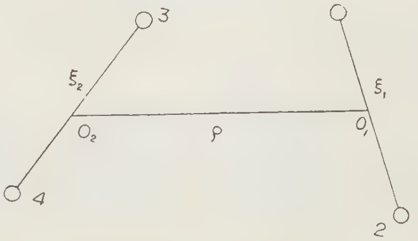

Fig. 1. Vectors specifying the configuration. Atoms 1, 2 belong to molecule 1, and atoms 3, 4 to molecule 2, O_1, O_2 being the centers of mass of the respective molecules.

On separating the motion of the center of mass, equation (1) becomes

$$\left\{\frac{1}{M}\Delta_{\boldsymbol{\rho}}+\frac{1}{M_1}\Delta_{\boldsymbol{\xi}_1}+\frac{1}{M_2}\Delta_{\boldsymbol{\xi}_2}+\frac{2}{\hbar^2}(E-V)\right\}\psi=0. \quad (3)$$

We assume that the potential energy function

V is made up of three parts

$$V=V_1(\xi_1)+V_2(\xi_2)+W(\boldsymbol{\xi}_1,\boldsymbol{\xi}_2,\rho)\,, \qquad (4)$$

where $W(\boldsymbol{\xi}_1,\boldsymbol{\xi}_2,\rho)$ is the collision potential and $V_i(\xi_i)$ is the potential of each isolated molecule. Making use of the wave functions $\psi_{p_iq_im_i}$, $i=1, 2$, and $Y_{j\nu}(\theta_3\varphi_3)$ (surface harmonics of degree j), satisfying the respective equations,

$$\left\{\frac{1}{M_i}\Delta_{\boldsymbol{\xi}_i}+\frac{2}{\hbar^2}(E_{p_iq_i}-V_i(\xi_i))\right\}\psi_{p_iq_im_i}=0\,. \qquad (5)$$

and

$$\left\{\Delta_{(\theta_3\varphi_3)}+\frac{j(j+1)}{\rho^2}\right\}Y_{j\nu}(\theta_3\varphi_3)=0\,, \qquad (6)$$

where $\Delta_{(\theta_3\varphi_3)}$ is related to $\Delta_{\boldsymbol{\rho}}$ by the equations

$$\Delta_{\boldsymbol{\rho}}=\Delta_{(\theta_3\varphi_3)}+\Delta_\rho\,, \quad \Delta_\rho=\frac{d^2}{d\rho^2}+\frac{2}{\rho}\frac{d}{d\rho}\,, \qquad (7)$$

we may expand ψ as

$$\psi=\sum_{p_iq_ijm_i\nu}\psi_{p_1q_1m_1}(\theta_1\varphi_1\xi_1)\psi_{p_2q_2m_2}(\theta_2\varphi_2\xi_2)$$
$$\times Y_{j\nu}(\theta_3\varphi_3)g_{m_i\nu}(p_iq_i\,j)\,, \qquad (8)$$

where $g_{m_i\nu}(p_iq_i\,j)$ stands for $g_{m_1m_2\nu}(p_1p_2q_1q_2\,j)$.

In these equations $\theta_1, \varphi_1; \theta_2, \varphi_2; \theta_3, \varphi_3$ are polar and azimuthal angles of ξ_1, ξ_2 and ρ respectively. Substitution of (8) into Eq. (3) yields

$$\sum_{p_iq_ijm_i\nu}\psi_{p_1q_1m_1}(\theta_1\varphi_1\xi_1)\psi_{p_2q_2m_2}(\theta_2\varphi_2\xi_2)Y_{j\nu}(\theta_3\varphi_3)$$
$$\times\left\{\frac{1}{M}\Delta_\rho-\frac{j(j+1)}{M\rho^2}+\frac{2}{\hbar^2}(E-E_{p_1q_1}\right.$$
$$\left.-E_{p_2q_2}-W)\right\}g_{m_i\nu}(p_iq_i\,j)=0\,. \qquad (9)$$

The eigen-function of each molecule $\psi_{p_iq_im_i}$ may be expressed as

$$\psi_{p_iq_im_i}=Y_{q_im_i}(\theta_i\varphi_i)Z_{p_iq_i}(\xi_i)\,. \qquad (10)$$

If R is the rotation of coordinates system, which brings the system of particles to the standard configuration,

$$Y_{lm}(\theta\varphi)=\sum_{m'}D(R)^*{}_{l,mm'}Y_{lm'}(\theta'\varphi')\,,$$

where $D(R)_l$ is the l-th irreducible representation of the three dimensional rotation group, and the primed coordinates are the coordinates after rotation. Now we specify the standard configuration as follows: $\boldsymbol{\rho}$ is in the positive direction of z-axis. The polar and azimuthal angles of $\boldsymbol{\xi}_1$ and $\boldsymbol{\xi}_2$ are θ, φ and θ', $\pi/2$ respectively. (The azimuthal angles are mesured from yz plane.) Then we have

$$\left.\begin{aligned}
&Y_{j\nu}(\theta_3\varphi_3)=(-1)^j\left(\frac{2j+1}{4\pi}\right)^{1/2}D(R)^*{}_{j,\nu 0}\,,\\
&Y_{q_1m_1}(\theta_1\varphi_1)=\sum_{\alpha_1}D(R)^*{}_{q_1,m_1\alpha_1}Y_{q_1\alpha_1}(\theta\varphi)\,,\\
&Y_{q_2m_2}(\theta_2\varphi_2)=\sum_{\alpha_2}(-i)^{\alpha_2}\\
&\qquad\qquad\times D(R)^*{}_{q_2,m_2\alpha_2}Y_{q_2\alpha_2}(\theta'0)\,.
\end{aligned}\right\} \qquad (11)$$

We may also use the following relations.

$$D(R)^*{}_{q_1,m_1\alpha_1}D(R)^*{}_{q_2,m_2\alpha_2}$$
$$=\sum_{|q_1-q_2|\leqq q\leqq q_1+q_2}S_{q_1q_2,q(m-m_2)m_2}$$
$$\times S_{q_1q_2,(\alpha-\alpha_2)\alpha_2}D(R)^*{}_{q,m\alpha} \qquad (12)$$

$$D(R)^*{}_{j,\nu 0}D(R)^*{}_{q,m\alpha}$$
$$=\sum_{|q-j|\leqq J\leqq q+j}S_{jq,J(\mu-m)m}$$
$$\times S_{jq,J0\alpha}D(R)^*{}_{J,\mu\alpha} \qquad (13)$$

where $m=m_1+m_2$, $\alpha=\alpha_1+\alpha_2$ and $\mu=\nu+m$. On substituting Eqs. (11), (12), (13) in Eq. (9), we multiply both sides by $D(R)_{J',\mu's}$ and integrate them over R. On account of the orthogonality relation of the irreducible representation matrix elements, we have (after dropping the primes)

$$\sum_{p_iq_ijm}\ \sum_{qm_2\alpha_2}(-1)^j(-i)^{\alpha_2}\left(\frac{2j+1}{4\pi}\right)^{1/2}$$
$$\times S_{jq,J(\mu-m)m}S_{q_1q_2,q(m-m_2)m_2}S_{q_1q_2,q(s-\alpha_2)\alpha_2}$$
$$\times Y_{q_1(s-\alpha_2)}(\theta\varphi)Y_{q_2\alpha_2}(\theta'0)Z_{p_1q_1}(\xi_1)Z_{p_2q_2}(\xi_2)$$
$$\times\left\{\frac{1}{M}\Delta_\rho-\frac{j(j+1)}{M\rho^2}+\frac{2}{\hbar^2}(E-E_{p_1q_1}\right.$$
$$\left.-E_{p_2q_2}-W)\right\}g_{(m-m_2)m_2(\mu-m)}(p_iq_i\,j)=0\,. \qquad (14)$$

If we put

$$(-1)^j\left(\frac{2j+1}{4\pi}\right)^{1/2}\sum_{m_1m_2}S_{jq,J(\mu-m)m}S_{q_1q_2,q(m-m_2)m_2}$$
$$\times g_{(m-m_2)m_2(\mu-m)}=G_{Jq\mu}(p_iq_i\,j)\,, \qquad (15)$$

Eq. (14) becomes

$$\sum_{p_iq_ij\alpha q}(-i)^\alpha S_{jq,J0S}S_{q_1q_2,q(S-\alpha)S}Y_{q_1(S-\alpha)}(\theta\varphi)$$
$$\times Y_{q_2\alpha}(\theta'0)Z_{p_1q_1}(\xi_1)Z_{p_2q_2}(\xi_2)$$
$$\times\left\{\frac{1}{M}\Delta_\rho-\frac{j(j+1)}{M\rho^2}+\frac{2}{\hbar^2}(E-E_{p_1q_1}\right.$$
$$\left.-E_{p_2q_2}-W)\right\}G_{Jq\mu}(p_iq_i\,j)=0\,, \qquad (14')$$

where we write α instead of α_2. Eq. (14′) is multiplied by

$$Z_{p_1'q_1'}(\xi_1)^*Z_{p_2'q_2'}(\xi_2)^*Y_{q_1'(S-\alpha')}(\theta\varphi)^*Y_{q_2'\alpha'}(\theta'0)^*$$

$\sin\theta\ \sin\theta'$ and integrated with the result (after dropping the primes)

$$\sum_{jq} S_{jq,JOS} S_{q_1q_2,q(S-\alpha)\alpha}\left\{\frac{1}{M}\Delta_\rho-\frac{j(j+1)}{M\rho^2}\right.$$
$$\left.+\frac{2}{\hbar^2}(E-E_{p_1q_1}-E_{p_2q_2})\right\}G_{Jq\mu}(p_iq_ij)$$
$$=\sum_{p_i'q_i'\alpha'}\sum_{jq} S_{jq,JOS}S_{q_1'q_2',q(S-\alpha')\alpha'}$$
$$\times G_{Jq\mu}(p_i'q_i'j)W_S(p_iq_i\alpha|p_i'q_i'\alpha')\ , \quad (16)$$

where

$$W_S(p_iq_i\alpha|p_i'q_i'\alpha')=\frac{4\pi i^{\alpha-\alpha'}}{\hbar^2}\int WZ_{p_1'q_1'}(\xi_1)$$
$$\times Z_{p_1q_1}(\xi_1)^*Z_{p_2'q_2'}(\xi_2)Z_{p_2q_2}(\xi_2)^*Y_{q_1'(S-\alpha')}(\theta\varphi)$$
$$\times Y_{q_1(S-\alpha)}(\theta\varphi)^*Y_{q_2\alpha'}(\theta'0)Y_{q_2\alpha}(\theta'0)^*\xi_1^2\xi_2^2$$
$$\times\sin\theta\sin\theta' d\xi_1 d\xi_2 d\theta d\theta' d\varphi\ . \quad (17)$$

Operating first $\sum_{\alpha'} S_{q_1q_2,q'(S-\alpha)\alpha}\times$ (multiply by $S_{q_1q_2,q'(S-\alpha)\alpha}$ then sum over α), then $\sum_S S_{j'q',JOS}\times$ on Eq. (16), and making use of the orthogonality relations given by Curtiss and Adler, we obtain (changing q' to q and j' to j after operation)

$$\left\{\frac{1}{M}\Delta_\rho-\frac{j(j+1)}{M\rho^2}+\frac{2}{\hbar^2}(E-E_{p_1q_1}-E_{p_2q_2})\right\}$$
$$\times G_{Jq\mu}(p_iq_ij)$$
$$=\sum_{p_i'q_i'j'}\sum_{q'} W_J(p_iq_ijq|p_i'q_i'j'q')$$
$$\times G_{Jq'\mu}(p_i'q_i'j')\ , \quad (18)$$

where

$$W_J(p_iq_ijq|p_i'q_i'j'q')$$
$$=\frac{2j+1}{2J+1}\sum_S\left(\sum_{\alpha\alpha'}S_{q_1q_2,q(S-\alpha)\alpha}S_{q_1'q_2',q'(S-\alpha')\alpha'}\right)$$
$$\times S_{jq,JOS}S_{j'q',JOS}W_S(p_iq_i\alpha|p_i'q_i'\alpha')\ . \quad (19)$$

[ii] *Approximate solution*

We can get a solution of Eq. (18) by perturbation method assuming that the coupling is weak, by the method similar to that used by Curtiss and Adler, which is originally due to Zener.

Now we consider the equation

$$\left\{\frac{1}{M}\Delta_\rho-\frac{j(j+1)}{M\rho^2}+\frac{k^2}{M}\right.$$
$$\left.-W_J(p_iq_ijq|p_iq_ijq)\right\}f=0\ . \quad (20)$$

with $k^2/M=(\hbar^2/2)(E-E_{p_1q_1}-E_{p_2q_2})$. Let U be the solution of Eq. (20) which is bounded at $\rho=0$ and is normalized so that asymptotically

$$U\to\frac{1}{k\rho}\sin(k\rho+\theta)\ , \quad (21a)$$

θ being a phase angle defined by the asymptotic form. Further let X be the solution which is asymptotically

$$X\to\frac{1}{k\rho}\exp\{i(k\rho+\theta)\}. \quad (21b)$$

To the zero approximation we take

$$G=AU\ , \quad (22)$$

and substituting this into Eq. (18), we have

$$\left\{\frac{1}{M}\Delta_\rho-\frac{j(j+1)}{M\rho^2}+\frac{k^2}{M}\right.$$
$$\left.-W_J(p_iq_ijq|p_iq_ijq)\right\}G$$
$$=\sum_{p_i'q_i'j'q'\neq p_iq_ijq}A'U'W_J(p_iq_ijq|p_i'q_i'j'g')\ .$$
$$(23)$$

U, X, θ, A, G are the abbreivations of U_{Jq,p_iq_ij} etc. and $A_{Jq\mu,p_iq_ij}$, $G_{Jq\mu}(p_iq_ij)$; U', A' etc. of $U_{Jq',p_i'q_i'j'}$, $A_{Jq'\mu,p_i'q_i'j'}$ etc.

We obtain the exact solutions of Eq. (23) as follows

$$G=AU-\sum_{\neq}MkA'\left[X\int_0^\rho U(\rho')W_J(|')(\rho')\right.$$
$$\times U'(\rho')\rho'^2d\rho'+U\int_\rho^\infty X(\rho')W_J(|')(\rho')$$
$$\left.\times U'(\rho')\rho'^2d\rho'\right]. \quad (24)$$

The asymptotic form of this function is

$$G\to A\frac{1}{k\rho}\sin(k\rho+\theta)-\sum_{\neq}A'\frac{1}{k\rho}$$
$$\times\exp\{i(k\rho+\theta)\}\beta_J(|')$$
$$=-\frac{i}{2k\rho}\exp\{i(k\rho+\theta)\}\{A-2i\sum_{\neq}A'\beta_J(|')\}$$
$$+\frac{i}{2k\rho}\exp\{-i(k\rho+\theta)\}A\ , \quad (25)$$

where

$$\beta_J(|')=\beta_J(p_iq_ijq|p_i'q_i'j'q')$$
$$=Mk\int_0^\infty UW_J(|')U'\rho^2d\rho\ . \quad (26)$$

[III] *Asymptotic form of the wave function*

As the procedure to obtain the asymptotic form of the wave function and the scattering amplitude in this and next subsections is quite similar to that used by Curtiss and Adler, only a brief description will be given.

The wave function correct in the region in which the two molecules are not interacting may be expressed as

$$\Psi^{(0)}=\exp(i\boldsymbol{k}_1\boldsymbol{X}_1')\exp(i\boldsymbol{k}_2\boldsymbol{X}_2')Z_{n_1l_1}(\xi_1)$$
$$\times Z_{n_2l_2}(\xi_2)Y_{l_1m_1}(\theta_1\varphi_1)Y_{l_2m_2}(\theta_2\varphi_2)\ , \quad (27)$$

where $\boldsymbol{X}_1'$ and $\boldsymbol{X}_2'$ are the coordinates of the centers of gravity of respective molecules. Using the relations

$$\boldsymbol{X}_1'=\boldsymbol{X}+\frac{m_3+m_4}{\sum m_k}\boldsymbol{\rho},\quad \boldsymbol{X}_2'=\boldsymbol{X}-\frac{m_1+m_2}{\sum m_k}\boldsymbol{\rho},$$
$$(28)$$

we have

$$\exp(i\boldsymbol{k}_1\boldsymbol{X}_1')\exp(i\boldsymbol{k}_2\boldsymbol{X}_2') = \exp\{i(\boldsymbol{k}_1+\boldsymbol{k}_2)\boldsymbol{X}\}\exp(i\boldsymbol{k}\boldsymbol{\rho}) ,$$

where

$$\boldsymbol{k} = \frac{(m_3+m_4)\boldsymbol{k}_1-(m_1+m_2)\boldsymbol{k}_2}{\sum m_k} \tag{29}$$

represents the relative momentum. The wave function which describes the relative motion in the center of gravity coordinate system can be written as

$$\begin{aligned}\psi^{(0)} &= \exp(i\boldsymbol{k}\boldsymbol{\rho})Z_{n_1l_1}(\xi_1)Z_{n_2l_2}(\xi_2) \\ &\qquad \times Y_{l_1m_1}(\theta_1\varphi_1)Y_{l_2m_2}(\theta_2\varphi_2) \\ &= 2\pi(2\pi/k\rho)^{1/2}\sum_{L\nu} i^L Y_{L\nu}(\theta_3\varphi_3\ Y_{l_1m_1}(\theta_1\varphi_1) \\ &\qquad \times Y_{l_2m_2}(\theta_2\varphi_2\ Y_{L\nu}(\Theta\Phi)J_{L+1/2}(k\rho) \\ &\qquad \times Z_{n_1l_1}(\xi_1)Z_{n_2l_2}(\xi_2) ,\end{aligned} \tag{30}$$

where Θ rnd Φ are the direction angles of k. We suppose that the incoming wave is along the z-axis (in the positive direction, $\Theta=0$) with relative momentum k and that the collision may cause the transition in the states of molecules from states specified by $(n_{i_0}, l_{i_0}, m_{i_0})$ to states (n_i, l_i, m_i). Considering the asymptotic behavior we have

$$\begin{aligned}\psi \to -2\pi i &\sum_{n_il_im_iL\nu} Y_{L\nu}(\theta_3\varphi_3)Y_{l_1m_1}(\theta_1\varphi_1) \\ &\times Y_{l_2m_2}(\theta_2\varphi_2)Z_{n_1l_1}(\xi_1)Z_{n_2l_2}(\xi_2) \\ \times\Bigg[&\frac{1}{k\rho}\exp(ik\rho)\Big\{\alpha_{L\nu,n_il_im_i}+(-1)^L\left(\frac{2L+1}{4\pi}\right)^{1/2} \\ &\times\delta_{n_in_{i0}}\delta_{l_il_{i0}}\delta_{m_im_{i0}}\delta_{\nu0}\Big\}-\frac{1}{k\rho}\exp(-ik\rho) \\ &\times\left(\frac{2L+1}{4\pi}\right)\delta_{n_in_{i0}}\delta_{l_il_{i0}}\delta_{m_im_{i0}}\delta_{\nu0}\Bigg] ,\end{aligned} \tag{31}$$

where $\alpha_{L\nu,n_il_im_i}$ is the scattering amplitude. Comparing (8) and (31) we have

$$\begin{aligned}g_{m_i\nu}(n_il_i\,j) \to -\frac{2\pi i}{k\rho}\Bigg[&\exp(ik\rho)\Big\{\alpha_{j\nu,n_il_im_i} \\ &+(-1)^j\left(\frac{2j+1}{4\pi}\right)^{1/2}\delta_{n_in_{i0}}\delta_{l_il_{i0}}\delta_{m_im_{i0}}\delta_{\nu0}\Big\} \\ &-\exp(-ik\rho)\left(\frac{2j+1}{4\pi}\right)^{1/2}\delta_{n_in_{i0}}\delta_{l_il_{i0}}\delta_{m_im_{i0}}\delta_{\nu0}\Bigg].\end{aligned} \tag{32}$$

[IV] *Scattering coefficients*

If we operate first $\sum_J S_{jq,J(\mu-m')m'}\times$ and then $\sum_q S_{q_1q_2,q(m'-m_2')m_2'}\times$ on Eq. (15) and put $\mu-m=\nu$, we have

$$\begin{aligned}g_{m_1m_2\nu}(p_iq_i\,j) &= (-1)^j\left(\frac{4\pi}{2j+1}\right)^{1/2} \\ &\times\sum_{Jq} S_{jq,J\nu m}S_{q_1q_2,qm_1m_2}G_{Jq(m+\nu)}(p_iq_i\,j) .\end{aligned} \tag{33}$$

Substituting Eqs. (25), (32) in Eq. (15), and equating the coefficients of $\exp(-ik\rho)$ on both sides, we obtain

$$\begin{aligned}A = (-1)^j(2j+1)&S_{jq,J0\mu}S_{q_1q_2,q(\mu-m_{20})m_{20}} \\ &\times\delta_{p_in_{i0}}\delta_{q_il_{i0}}\delta_{\mu m_0}\exp(i\theta) .\end{aligned} \tag{34}$$

If we substitute Eqs. (25), (32) in Eq. (33) and compare the coefficients of $\exp(ik\rho)$, we obtain

$$\begin{aligned}\alpha_{j\nu,n_il_im_i} &= -(-1)^j\left(\frac{2j+1}{4\pi}\right)^{1/2} \\ &\qquad\times\delta_{n_in_{i0}}\delta_{l_il_{i0}}\delta_{m_im_{i0}}\delta_{\nu0} \\ &+(-1)^j\{4\pi(2j+1)\}^{-1/2}\sum_{Jl} S_{jl,J\nu m}S_{l_1l_2,lm_1m_2} \\ &\times\exp(i\theta)\{A-2i\sum_{\neq} A'\beta_J(n_il_i\,jl\,|\,n_i'l_i'\,j'l')\}.\end{aligned} \tag{35}$$

Using (34), the scattering amplitude is obtained in the following form, which is similar to that appears in reference (4).

$$\begin{aligned}\alpha_{j\nu,n_il_im_i} &= \{4\pi(2j+1)\}^{-1/2}\delta_{\nu(m_0-m)}\sum_{Jj_0ll_0}(2j_0+1) \\ &\times S_{jl,J\nu m}S_{l_1l_2,lm_1m_2}S_{j_0l_0,J0m_0}S_{l_{10}l_{20},l_0m_{10}m_{20}} \\ &\times\exp(i\theta_0)[\delta_{n_in_{i0}}\delta_{l_il_{i0}}\delta_{jj_0}\delta_{ll_0} \\ &\times\{\exp(i\theta_0)-(-1)^j\exp(-i\theta_0)\} \\ &-2i(1-\delta_{n_in_{i0}}\delta_{l_il_{i0}}\delta_{jj_0}\delta_{ll_0})(-1)^{j+j_0} \\ &\times\exp(i\theta)\beta_J(n_il_i\,jl\,|\,n_{i0}l_{i0}\,j_0l_0)] .\end{aligned} \tag{36}$$

In the Eqs. (35), (36) we put

$$\theta=\theta_{Jl,n_il_ij} , \qquad \theta_0=\theta_{Jl_0,n_{i0}l_{i0}j_0} ,$$
$$A=A_{Jl(m+\nu),n_il_ij} , \quad A'=A_{Jl'(m+\nu),n_i'l_i'j'} .$$

As a special case this involves the scattering amplitude of atoms by diatomic molecules, in which case the result is the same as that obtained by Curtiss and Adler.

§ 3. Collision between polyatomic molecules

Consider two particle systems (polyatomic molecules) 1 and 2. The Schroedinger equation for the whole system is

$$\begin{aligned}\Bigg[\sum_{i=1,2}\Big\{\sum_{k=1}^{Ni}\frac{1}{m_{ik}}\Delta_{X_{ik}}-\frac{2}{\hbar^2}V_i(\cdots X_{ik}\cdots)\Big\} \\ +\frac{2}{\hbar^2}\{E'-W(\cdots X_{ik}\cdots)\}\Bigg]\Psi=0 ,\end{aligned} \tag{37}$$

where W is the interaction potential between two systems ; we consider that W is invariant under the rotation of the whole system.

Changing the variables as follows

$$\left.\begin{aligned}\boldsymbol{X}_i &= \frac{\sum_k m_{ik}\boldsymbol{X}_{ik}}{\sum_k m_{ik}} , \quad \sum_k m_{ik}=m_i,\ m_1+m_2=m, \\ &\qquad \boldsymbol{X}_{ik}=\boldsymbol{X}_i+\boldsymbol{\xi}_{ik}, \\ \boldsymbol{X} &= \frac{m_1\boldsymbol{X}_1+m_2\boldsymbol{X}_2}{m} , \quad \boldsymbol{\rho}=\boldsymbol{X}_1-\boldsymbol{X}_2 , \\ &\qquad \frac{1}{M}=\frac{1}{m_1}+\frac{1}{m_2} ,\end{aligned}\right\} \tag{38}$$

we have

$$\frac{1}{m_1}\Delta x_1+\frac{1}{m_2}\Delta x_2=\frac{1}{m}\Delta x+\frac{1}{m}\Delta_{\boldsymbol{\rho}} . \qquad (39)$$

On separating the motion of the center of gravity, Eq. (37) becomes

$$\left[\frac{1}{M}\Delta_{\boldsymbol{\rho}}+\sum_{i=1,2}\left\{\sum_{k=1}^{Ni-1}\frac{1}{m_{ik}}\frac{\partial^2}{\partial\boldsymbol{\xi}_{ik}{}^2}-\sum_{k,h}\frac{\partial}{\partial\boldsymbol{\xi}_{ik}}\frac{\partial}{\partial\boldsymbol{\xi}_{ih}}\right.\right.$$
$$\left.\left.-\frac{2}{\hbar^2}V_i(\cdots\boldsymbol{\xi}_{ik}\cdots)\right\}+\frac{2}{\hbar^2}\{E-W(\boldsymbol{\rho},\boldsymbol{\xi}_{ik})\}\right]\psi$$
$$=0 , \qquad (40)$$

where $\partial^2/\partial\boldsymbol{\xi}^2$ means $\Delta_{\boldsymbol{\xi}}$.

As before

$$\Delta_{\boldsymbol{\rho}}=\Delta_R+\Delta_\rho , \quad \Delta_\rho=\frac{\partial^2}{\partial\rho^2}+\frac{2}{\rho}\frac{\partial}{\partial\rho} , \qquad (41)$$

$$\left(\Delta_R+\frac{j(j+1)}{\rho^2}\right)Y_{j\nu}(R)=0 , \qquad (42)$$

$$\left\{\sum_{k=1}^{Ni-1}\frac{1}{m_{ik}}\frac{\partial^2}{\partial\boldsymbol{\xi}_{ik}{}^2}-\sum_{kh}\frac{1}{m}\frac{\partial}{\partial\boldsymbol{\xi}_{ik}}\frac{\partial}{\partial\boldsymbol{\xi}_{ih}}\right.$$
$$\left.+\frac{2}{\hbar^2}(E_{p_i}-V_i)\right\}\psi_{p_iq_im_i}(\cdots\boldsymbol{\xi}_{ik}\cdots)=0 .$$
$$(43)$$

$\psi_{p_iq_im_i}$ being the bases of the q-th irreducible representations of the rotation group, we can express them as

$$\psi_{p_iq_im_i}(\cdots\boldsymbol{\xi}_{ik}\cdots)=\sum_{\nu_i}D(R_i)^*{}_{q_i,m_i\nu_i}$$
$$\times Z_{p_iq_i\nu_i}(\cdots\boldsymbol{\eta}_{ih}\cdots) , \quad h=1, 2, \cdots N_i-2.$$
$$(44)$$

where

$$\boldsymbol{\eta}_{ik}=R_i{}^{-1}\boldsymbol{\xi}_{ik} . \qquad (45)$$

The meanings of the rotations R and R_i are as follows:

Operate first the rotation R^{-1} around the center of gravity which brings the whole system to its standard configuration, then the rotation $\omega_i{}^{-1}$ $(i=1, 2)$ around the center of gravity of i-th molecule which brings the one definite particle of i-th molecule on the z axis and another one in the xz plane with positive x.—thus obtaining the standard configuration of i-th molecule. (Notice that among (3+3) parameters of ω_1 and ω_2 5 of them are independent.) The rotation R is expressed by

$$R_i=R\omega_i . \qquad (46)$$

We can specify the internal configuration of the system by the distance between centers of gravity of the molecules ρ, the rotations ω_i, and the position vectors of the consisting particles $\boldsymbol{\eta}_{ik}$ defined by Eq. (45). The accurate differential equation for $Z_{p_iq_i\nu_i}$ is deduced in the first part of reference (4), but in case of practical applications we could neglect the interaction between vibration and rotation of each molecule.

By these functions we can expand ψ as

$$\psi=\sum_{p_iq_ijm_i\nu_i\nu}D(R_1)^*{}_{q_1,m_1\nu_1}\cdot D(R_2)^*{}_{q_2,m_2\nu_2}$$
$$\times Y_{j\nu}(R)Z_{p_1q_1\nu_1}Z_{p_2q_2\nu_2}g_{m_i\nu_i\nu}(p_iq_i\,j) . \ (47)$$

Putting (47) in (40), we have

$$\sum_{p_iq_ijm_i\nu_i\nu}D(R_1)^*{}_{q_1,m_1\nu_1}D(R_2)^*{}_{q_2,m_2\nu_2}Y_{j\nu}(R)$$
$$\times Z_{p_1q_1\nu_1}Z_{p_2q_2\nu_2}\left(\Delta_\rho-\frac{j(j+1)}{\rho^2}+k^2-\frac{2}{\hbar^2}MW\right)$$
$$\times g_{m_i\nu_i\nu}(p_iq_i\,j)=0 , \qquad (48)$$

where

$$k^2=\frac{2M}{\hbar^2}(E-E_{p_1q_1}-E_{p_2q_2}) . \qquad (49)$$

Corresponding formulas to § 1 (11) are

$$Y_{j\nu}(R)=(-1)^j\left(\frac{2j+1}{4\pi}\right)^{1/2}D(R)^*{}_{j,\nu0} , \qquad (50)$$

$$D(R_i)^*{}_{q_i\ m_i\nu_i}=\sum_{\alpha_i}D(R)^*{}_{q_i,m_i\alpha_i}\cdot D(\omega_i)^*{}_{q_i,\alpha_i\nu_i} .$$
$$(51)$$

As the further calculations can be carried out quite analoguously to those of the foregoing section, we should like to omit all the results except a little remark that normalization coefficients for $Z_{p_iq_i\nu_i}$ must be added in the expansion of W_S.

We are now attempting to calculate the probabilities of transition in the states of molecules of several species using appropriate potential functions, and to discuss the problems concerning the relaxation time and supersonic absorption.

References

1) C. Zener: Phys. Rev. **37** (1931) 556; Proc. Cambridge Phil. Soc. **29** (1932) 136.

2) Jackson and Mott: Proc. Roy. Soc. **A137** (1932) 703.

A. F. Devonshire: Proc. Roy. Soc. **A158** (1937) 269.

3) Schwartz, Slawsky and Hertzfeld: J. Chem. Phys. **20** (1952) 1951.

4) Curtiss, Hirschfelder and Adler: J. Chem. Phys. **18** (1950) 1638.

Curtiss and Adler: J. Chem. Phys. **20** (1952) 249.

Relating to the collisions between diatomic molecules, we must add the following papers, in which the energy transfer between the translatioual and vibrational or rotational degrees of freedom is dealt with.

K. Takayanagi: Prog. theor. Phys. **8** (1952) 111, **8** (1952) 497, **9** (1953) 578.

JOURNAL OF THE PHYSICAL SOCIETY OF JAPAN Vol. 9, No. 2, MAR.—APR., 1954

The Production of Single Crystals of Metals and Alloys with any Desired Orientation by Solidification at High Temperature*

By Hideo TAKAKI, Shigeo NAKAMURA, Yoji NAKAMURA,
Jun-ichi HAYASHI, Kazuo FURUKAWA**
and Masato ASO***

Faculty of Science, University of Kyoto, Kyoto, Japan

(Received August 4, 1953)

In order to grow single crystals of metals and alloys with fairly high melting point in large rods with any desired orientation, a method is developed from the Bridgman method, using a vacuum Tammann furnace and porcelain crucibles with no bottom, sometimes with a perforated sectorial plate, and inserting a seed into the lowest part of the crucible. We have succeeded in obtaining single crystals of 3.2% and 4.0% silicon steel, and pure nickel, 3 mm diam and 25 cm in length. The rod axes can be fixed in any desired direction. It is noted that the maximum velocity to lower the crucible and its contents, below which a large crystal can grow at each orientation, shows very large anisotropy.

§ 1. Introduction

For the study of anisotropic properties of ferromagnetic metals and alloys it is desired to prepare their long rods of single crystals, properly oriented with respect to the crystal axes. As a rule, because these materials have melting points as high as 1500°C, special methods are necessary to prepare their long single crystals. For iron, which has transformations in solid phase, Fujiwara and Tatsumoto[1] developed the strain-annealing method for growing single crystals with the above condition; and for silicon steel with less than 2% silicon we used their method successfully[2]. On the other hand, for nickel, its alloys and iron alloys, which have no transformation in solid phase, and, by the above method, tend to produce some twins during annealing, Williams and Bozorth[3] proposed a technique for growing rather large crystals by slow cooling from the melted state and for cutting them in the desired form and accurate orientation. The single crystals thus obtained are not so long as several centimeters. For copper, silver and gold, though these are not ferromagnetic and have rather low melting points, Graf and Glocker[4] developed the Bridgman method[5] for properly orientating single crystals to grow by seeding in the bottom of graphite crucible. Furthermore, he suggested that for nickel, the same method would succeed, using the porcelain crucible instead of the graphite. A method herein described is also a modified form of the Bridgman method for large rods of single crystal to grow in the selected orientations, using a Tammann furnace and long narrow porcelain tubes with no bottom, sometimes with a perforated sectorial plate, and inserting into the lowest part of the tube a seed, a portion of which melts and constructs the bottom. We have successfully obtained long rods, 3 mm diam and 25 cm in length, of single crystal of 3.2% and 4.0% silicon steel and pure nickel with three principal directions and some selected ones. The orientation of their rod axes with respect to the crystal axes is determined by the back-reflection Laue pattern.

---

* Read at the annual meeting of the Physical Society of Japan, November 1950.

** Present address: The Research Institute for Iron, Steel and other Metals, Tohoku Univ., Sendai, Japan.

*** Present address: Saganoseki Factory, Nippon Mining Co., Ltd., Saganoseki, Japan.

§ 2. Apparatus

A Tammann furnace is mounted with its axis vertical in the casing of 16 in. steel tube of 1/4 in. wall thickness, on the outside of which is welded electrically a thin steel jacket to form a water cooling chamber. The upper and lower plates are held in place on each end of the tube, are sealed gas-tight and insulated electrically with rubber gaskets, and are water-cooled, using brass boxes in place. On the central holes of these plates are welded electrically outwards 3 in. steel tubes of respectively 350 and 200 mm in length, among of which the upper cylinder mounts gas-tightly a similar cylinder providing a glass window and an apparatus to lower specimens through the furnace and the lower one is sealed by a brass bottom with a rubber gasket. The power input is led through two fittings, welded on the walls of the 16 in. steel tube and the lower plate, into the heating element of carbon tube. The constructionn is show in Fig. 1. The casing is held in vacuum, about 0.1 mm Hg, by a rotary vacuum pump during operations. The temperature is checked with an optical pyrometer through the top glass window. The velocity lowering the crucible through the furnace can be controled from 0.03 to 10 cm/min, using reduction gears and motor. Porcelain crucsbles prepared* are all 3 mm i.d. and 6 mm o.d. and are classified in three classes ; straight one, 20 cm in length, with a bottom, straight one, 50 cm in length, with no bottom, and straight one, 15 cm in length, with a sectorial plate of 6 mm thickness on the one end (Fig. 2 a). They are sintered at about 1400°C and porous adequately so that they can be removed easily from the specimen by the sliding grind cloth after operation and the sectional plate can be perforated easily by a dental so-called "Hand piece" with an abrasive point, held in place, before operation. During the operation, in order to keep the temperature constant, we must hold the voltage of current constant between the ends of the heating element within ±0.1%,

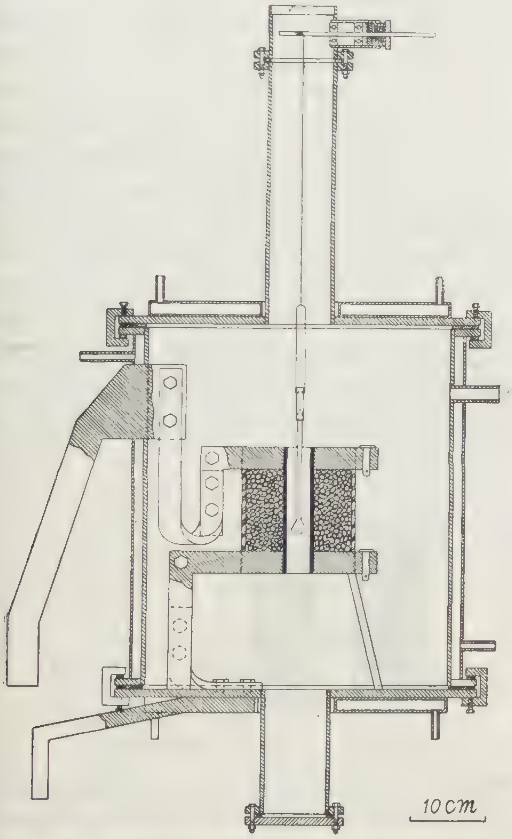

Fig. 1. Apparatus.

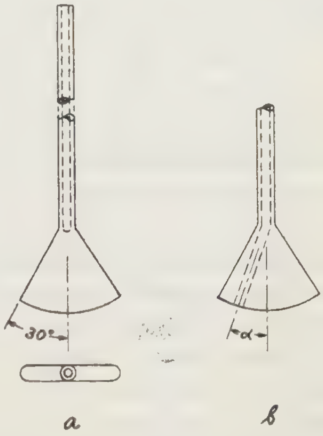

Fig. 2. Porcelain crucible with a sectorial plate; *a*, unperforated. *b*, perforated by an abrasive point with a proper angle to the axis of its upper straight tube.

---

* The crucibles was prepered through the kindness of the late Mr. T. Nakamura, managing director of Nippon Tokushu Togyo Kaisha Ltd., Japan.

which is performed by regulating the resistance by hand. We are planning to remove this hand regulation by obtaining an apparatus keeping at constant voltage at 5 KW.

§ 3. Materials and Procedure

Materials to be melted are commercial 3.2 % and 4.0% silicon steels and nickel of high purity. These chemical analyses are as follows (Table 1):

Table 1. Chemical analyses of materials.

3.2% silicon steel (in %)							
Si	Mn	Cr	Ni	other elements, unanalysed.			
3.2	0.019	Trace	0.045				
4.0% silicon steel (before annealing, in %)							
Si	C	Mn	P	Cr	Cu	S	Ni
4.03	0.08	0.07	0.02	0.026	0.31	0.07	0.031
nickel (in %)							
Ni	C	Si	Mn	Cu	Mg	Fe	
99.36	0.02	Trace	0.22	0.01	0.18	0.21	

The silicon steel was purified by annealing in a wet hydrogen atmosphere at 750°C for 3 hr.

The first procedure is a preparation of seed with any orientation which was performed by usual Bridgman method, using the crucible of 20 cm length with a bottom. The seed thus prepared is ascertained by etching and is cut off to become a rod of 2~3 cm length and its crystal axes are determined by the back-reflection Laue pattern. Then, the second procedure is to obtain the rod of seed with a given orientation with respect to the crystal axes. A crucible with a sectorial part is used and is perforated through the sectrial part by the dental hand piece with an abrasive point, fixed on the table, with a proper angle to the axis of its upper straight tube (Fig. 2 b). The proper angle is determined from the orientations of the above seed and the desired one, and is limited to less than 30° to make an easy process. Then, the crucible is filled with the seed in the sectorial part with a proper position and with a polycrystalline wire in the upper straight tube. The bottom of the crucible is stopped slightly with an angled plate of molybdenum. On the other hand, the distribution of temperature along the furnace is measured at the operating stationary state, and its lower position, indicating the melting point of metal or alloy, is determined exactly (Fig. 3). In our case, the maximum temperature in the furnace was raised to over 100°C above the melting point and the temperature gradient in the crystallizing region was about 80°C/cm. Thus the crucible was hung from the apparatus lowering it by the 0.1 mm diam molybdenum wire in the position where the middle point of the seed would be just situated at the position of melting point. When the temperature is raised and the stationary state is reached, the crucible is lowered through the furnace at an appropriate velocity. It is noted that as soon as the lower portion of molten metal, before the lowering process, is dropped below the position indicating melting point through the narrow gap lying between the seed and the crucible, it is solidified to become the bottom of the crucible, while the seed becomes the nucleus for growing of a single crystal. The molten metal usually becomes a perfect single crystal, exept sometimes near its uppermost end. In the latter case, it would be explained by the repelling of impurities. The crucible being 15 cm in length, the rod of single crystal is about 10 cm, that is short for our purpose. Then, the third procedure is to obtain a long rod of single crystal, using the 50 cm straight crucible with no bottom and the seed with a given orientation. The detail of the procedure is similar to the second one, exept for

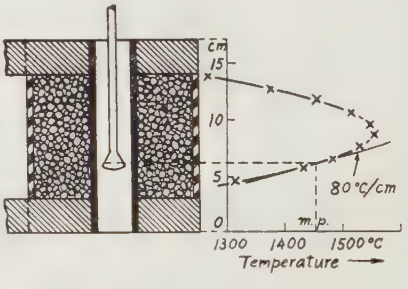

Fig. 3. The distribution of temperature along the furnace and the position of a crucible held in the furnace before lowering it.

using a different crucible. It is necessary that the polycrystalline wire of specimen inserted in the crucible be slid down easily and smoothly through the tube as it is being partly melted, and the crucible is lowered through the furnace at the appropriate velocity for growing of a single crystal. The appropriate velocity depends upon the rod orientation of the single crystal. We can, however, produce single crystals of every orientation by certain very slow velocities, but when the velocity is rather fast we can not obtain single crystal rods with some orientation. That is to say, the single crysral has the maximum velocity for growing largely in each crystallographic orientation. We could succeed for 3.2% silicon steel and nickel in near [001] at 10 mm/min and 8.8 mm/min, in near [101] at 5 mm/min and 1.8 mm/min, and in near [111] at 0.4 mm/min and 1.4 mm/min respectively. These values are not the maximum velocities exactly, the determination of which is in progress. It is noted that the anisotropy of the maximum velocity seems to be very large.

After each procedure, the specimen is carefully removed from the crucible by using a sliding grind cloth, etched in a concentrated nitric acid to ascertain the domain of a single crystal and its crystallographic axes are determined by the back-reflection Laue pattern. Great care must be taken to prevent any straining of the crystal by excessive pressure or heat.

§ 4. Results

In the first procedure, the lowering velocity of the crucible and its contents has been rather fast so that one among differently oriented seeds that were produced in the bottom of the crucible, would assume superiority over the others and seed the remaiving bulk of the melt. In our case of 3.2% silicon steel and nickel, the surviving seeds had their [001] axes near the rod axis (No. 0 in Fig. 4 and No. 2 in Fig. 5).

In the second procedure we have succeeded in obtaining seeds of new orientations indicated in Fig. 4 on 3.2% silicon steel and in Fig. 5 on nickel respectively. The signs of the arrows in the figures indicate the successive changes of orientations of seeds thus obtained. Then, in the third procedure we obtained long rods, 3 mm diam and 25 cm in length, of single crystal with the same orientations as the above seeds. The efficiency of the growing seed was almost perfect, provided that the lowering velocity was within the above maximum values for each orientation. To accurately bring the orientation of the new seed in the desired one depends upon the determination of the orientation of crystals by X-ray, the processing of the perforation in the sectorial part, the setting of the seed into the bottom of the crucible and the

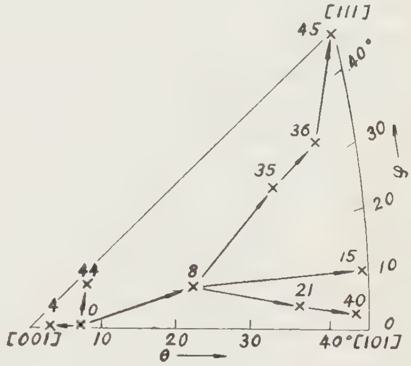

Fig. 4. The orientations of seeds obtained by the second procedure on 3.2% silicon steel. The signs of the arrows indicate the successive changes of orientations of seeds.

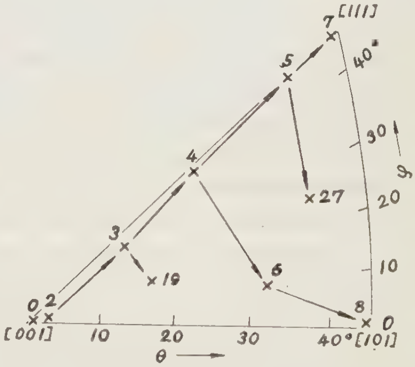

Fig. 5. The orientations of seeds obtained by the second procedure on nickel. The signs of the arrows indicate the successive changes of orientations of seeds.

slight bend of the crucible during the heating in the furnace. Our accuracy for the both materials is about ±2°, when carefully treated.

We have also succeeded in obtaining single crystals of 4.0% silicon steel, using the seed of 3.2% silicon steel and the straight crucible with no bottom. There was no change in the orientation between the seed and the new single crystal but there was a change in concentration through the specimen from the seed to the other end, which was determined by the analysis of the spectrum as indicated by the example in Fig. 6. A new seed of 4.0% silicon steel was cut off from the upper part of the above specimen; and by the third procedure we have obtained long rods of 4.0% silicon steel with the same orientations as the 3.2% silicon steel.

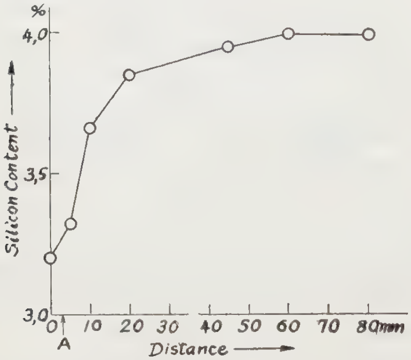

Fig. 6. The change in concentration through the specimen from the seed (3.2% Si) to the other end (4.0% Si). A in the figure indicates the position of melt in the seed.

We are interested in that the anisotropy of the maximum velocity is very large and the maximum velocity in [001] is largest in both the body-centered and the face-centered cubic crystals, where in the former the anisotropy seemed to be larger than in the latter, and these facts correspond to the data that the fibre structure of the columnar crystals in cast has [001] axis along the columnar axes in both cubic types. About this fibre structure in the cast silicon steel we have studied in more detail[6].

In conclusion we wish to thank Professor S. Kaya of the University of Tokyo for his kind interest and encouragement throughout the work and Professor K. Iwase of the University of Kyoto for his kind permission to employ some apparatus in his laboratory and encouragement. We should also like to thank Mr. Y. Deguchi and Mr. K. Nakamura for their helpful assistance. The expense of this research has been partly defrayed by the Scientific Research Expenditure of the Educational Ministry.

References

1) T. Fujiwara and E. Tatsumoto: Sci. Rep. Hiroshima Univ. of Litera. Sci. **12** (1942) 169.

2) H. Takaki and Y. Nakamura: unpublished.

3) J. W. Walker, H. J. Williams and R. M. Bozorth: Rev. Sci. Inst. **20** (1949) 947.

4) R. Grocker and L. Graf: Z. Anorg. Chem. **188** (1930) 232; L. Graf: Z. Physik **67** (1931) 388.

5) P. Bridgman: Proc. Am. Acad. Arts Sci. **60** (1925) 305.

6) H. Takaki, M. Koyama and H. Fujihira: Bulletin Inst. Chem. Research, Kyoto Univ. **31** (1953) 182.

JOURNAL OF THE PHYSICAL SOCIETY OF JAPAN Vol. 9, No. 2, MAR.—APR., 1954

The Electric Quadrupole Splitting of the Nuclear Magnetic Resonance Lines of Sodium in a Single Crystal of $Na_2S_2O_3 \cdot 5H_2O$

By Junkichi ITOH, Riichiro KUSAKA and Yukio YAMAGATA

Department of Physics, Osaka University, Osaka

(Received August 13, 1953)

Splitting of the nuclear magnetic resonance lines of sodium due to the nuclear electric quadrupole interaction was measured in a single crystal of sodium thiosulphate pentahydrate. Since each molecule contains two sodium nuclei which have different electric quadrupole interactions, and there are two groups of molecules with different orientations in a unit cell, twelve lines were observed in general. The experimental results were compared with the theoretical calculation of Bersohn and the values of e^2qQ, η and the directions of the principal axes of the field gradient tensor were determined for each nucleus. The values of e^2qQ and η are 2.26 Mc/sec and 0.334, and 0.830 Mc/sec and 0.41 respectively for two nuclei in the molecule.

§ 1. Introduction

The electric quadrupole splitting of the nuclear magnetic resonance lines was first observed by Pound[1]. He also developed the theoretical calculation and his experimental results fit well with the theory in the case of axially symmetric electric field gradient. Since then, Volkoff et al[2][3], Becker[4] and some others[5] observed similar electric quadruple splitting in some other single crystals. Volkoff et al[2][3] extended the calculation to the case of non-axially symmetric electric field gradient and applied it to the explanation of their experimental results. Lately, Bersohn[6] made the theoretical calculation of the electric quadrupole splitting more extensively upto the third order perturbation terms in quadrupole interaction energy.

We have made an experiment of the electric quadrupole splitting of the nuclear magnetic resonance lines of sodium in a single crystal of sodium thiosulphate pentahydrate. The experimental results shall be compared with the calculation of Bersohn.

§ 2. The Experimental Apparatus and Procedure

The detector of nuclear magnetic resonance is similar to that already described in our previous paper[7]. Briefly speaking, it consists of an autodyne detector, resonance amplifier, phase sensitive detector, and recording milliammeter. With the use of small modulation of the magnetic field, the derivative of the absorption curve is recorded on the recording milliammeter chart, when the static magnetic field is swept very slowly over the resonance field. The magnetic current is read by a potentiometer and recorded simultaneously on the recording milliammeter chart. The frequency used throughout in our experiment is 6.1 Mc/sec calibrated by a standard quartz oscillator.

The electromagnet used is a closed-yoke type magnet, similar to that designed by Bitter and Reed[8]. It has cobalt steel pole pieces of 8 cm in diameter with the magnetic gap of 2.2 cm. The magnetic field is almost linear with the magnet current upto 20,000 gauss and the magnetic field of 24,000 gauss is easily obtained at about 16 ampere of the magnet current. Relation between the magnetic field strength and the current has been calibrated precisely by observing nuclear magnetic resonance lines of sodium or lithium at various frequencies and the hysteresis effect of about 0.3% has been found to exist in our magnet. Therefore, our measurement used to be done after the field strength was increased upto a certain definite higher value in advance of attaining the value where the measurement was performed, in order to reduce the effect of irregularity in the hysteresis. By this procedure the magnetic field has been able to be reproduced within 0.03%. The values of the magnetic field strength where nuclear magnetic resonances occured is expressed by the magnet currents in Figs. 3, 4, 5 and 6. Very slight effect of non-linearity between the field strength and the current is corrected in the final results.

The single crystal has been cut in a desired shape and mounted on a rotative rod which was screwed on a shielding box of the radiofrequency coil which covers the crystal. The box was made rectangular, its upper and lower surfaces being made parallel with each other, and also parallel to the axis of the rotating rod. The box was inserted in the pole gap of the magnet so as to make the upper and the lower surfaces parallel to the pole faces. The cutting and mounting of the crystal and the setting of the box were performed carefully, but on account of being the delicate procedures, the angle may be in error within 1 to 1.5 degrees. The effect of these errors in angles will be discussed in § 5.

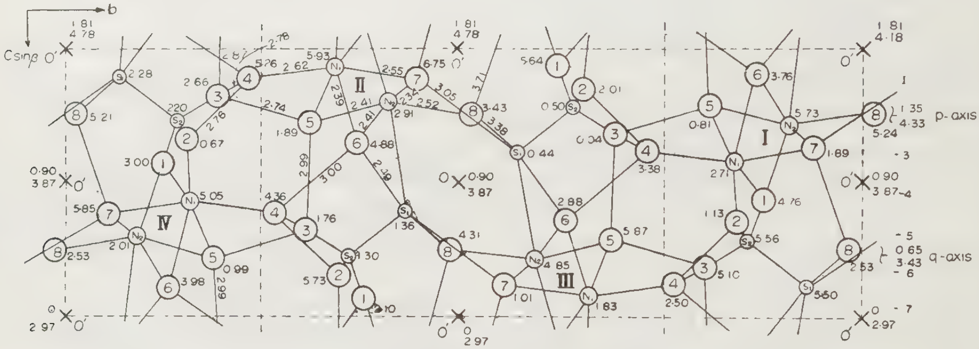

Fig. 1. Projection of a unit cell of $Na_2S_2O_3 \cdot 5H_2O$ on a plane which is perpendicular to the *a*-axis, given by Taylor and Beavers (ref. 9). 1, 2, and 3 are the oxygen atoms in S_2O_3 group, 4, 5, 6, 7, and 8 are the hydrated water molecules, S_1 and S_2 are the sulphur atoms, and N_1 and N_2 are the sodium atoms. *p*- and *q*-axes are the twofold screw axes and *O* and *O′* are the points of symmetry. Two dash-lines are the gliding planes. *I, II, III* and *IV* mean four molecules in a unit cell.

§ 3. The Crystal Structure

The crystal structure of sodium thiosulphate pentahydrate, $Na_2S_2O_3 \cdot 5H_2O$, was determined by the X-ray analysis of Taylor and Beavers[9]. It has monoclinic symmetry with $a=5.94$, $b=21.57$, $c=7.53$Å, and $\beta=103°58'$, and its space group belongs to $C_{2h}^5-P2_1/c$. A unit cell contains four formula units. Fig. 1 shows the projection diagram of the crystal on a plane perpendicular to the *a*-axis. As shown in the figure, there exist four twofold screw axes, *p* and *q*, which are parallel to the *b*-axis, and eight centers of symmetry at *O* and *O′*. Therefore, the four molecules in a unit cell are equivalent: The molecule *II* can be derived from the molecule *I* by the screw operation around the *p*-axis, the molecule *IV* can be derived from *I* by the inversion with respect to the center of symmetry *O* and the molecule *III* can be derived from *IV* by the screw operation around the *q*-axis. By the symmetry character with respect to the point *O*, it is easily shown that, for arbitrary orientation of the crystal, the nuclear magnetic resonance lines, including the quadrupole splitting, of the molecules *I* and *IV* coincide exactly with each other and also the similar situation is valid for the molecules *II* and *III*, since, by the inversion with respect to the point *O*, an orthogonal axis system *X, Y, Z* fixed in the molecule *I*, of which the Y-axis is chosen parallel to the *b*-axis, is transformed to −X, −Y, −Z axes in the molecule *IV* and, further, this change has no effect on the nuclear magnetic resonance fields. On the other hand, by the screw operation around the *p*-axis, X, Y, Z axes in the molecule *I* are transformed to −X, Y, −Z axes in the molecule *II*. This means that, when the crystal is rotated around the *b*-axis (that is, the static field is rotated in the *b*-plane), the magnetic resonance lines, including the quadrupole splitting, of the molecules *I* and *II* coincide exactly with each other. Therefore, in the case of *b*-axis rotation, it is sufficient to consider only one molecule in a unit cell. On the contrary, when the crystal is rotated around the X- or Z-axis, that is, around an arbitrary axis which is perpendicular to the *b*-axis, the magnetic resonance lines of the molecule *I*, which are splitted by the quadrupole interaction, and those of the molecule *II* do not coincide, but the angular dependence of either one of them is just the inversion of the other with respect to the *b*-axis and also to the axis which is perpendicular to both the *b*-axis and the axis of rotation.

We have used two crystals, one of which was cut in a plane perpendicular to the *b*-axis and the other was cut in a plane perpendicular to the *c*-axis. In the former case, the crystal was rotated around the *b*-axis, while in the latter case, it was rotated around the *c*-axis.

Since each molecule contains two independent sodium nuclei, two different sets of the nuclear magnetic resonance lines will be observed for each molecule.

§ 4. The Theoretical Calculation

Theoretical calculations of the electric quadrupole splitting of the nuclear magnetic resonance lines have been carried out by Pound[1], Volkoff et al[2][3], Becker[4] and Bersohn[6]. Among these authors, Bersohn treated the problem most extensively, the energy formulae upto the third order perturbation terms in quadrupole coupling energy being given in his paper. However, since his formulae are too general to be applied to the direct comparison with our experimental result, the reduction to the suitable form has been made in the following.

The Hamiltonian of the nucleus which is rigidly bound in the lattice will be

$$\mathfrak{H}=g\beta \boldsymbol{H}\boldsymbol{I}+\boldsymbol{Q}\cdot\nabla\boldsymbol{E} \qquad (1)$$

apart from the terms which have no contribution in our problem, where $\boldsymbol{H}$ is the applied static magnetic field, g the nuclear g-factor, β the nuclear magneton, $\boldsymbol{I}$ the nuclear spin vector, $\boldsymbol{Q}$ the electric quadrupole moment tensor of the nucleus and $\nabla\boldsymbol{E}$ is the electric field gradient tensor at the nucleus. $\nabla\boldsymbol{E}$, which is irreducible, has five components which are given by

$$\left.\begin{aligned}(\nabla E)_0&=-\frac{1}{2}\left(\frac{\partial E_z}{\partial z}\right)\\(\nabla E)_{\pm1}&=\pm\frac{1}{\sqrt{6}}\left[\frac{\partial E_x}{\partial z}\pm i\frac{\partial E_y}{\partial z}\right]\\(\nabla E)_{\pm2}&=-\frac{1}{2\sqrt{6}}\left[\frac{\partial E_x}{\partial x}-\frac{\partial E_y}{\partial y}\pm 2i\frac{\partial E_x}{\partial y}\right].\end{aligned}\right\} \qquad (2)$$

We assume that the second term in (1) is much smaller than the first term. Then, according to Bersohn, in the representation that diagonalizes the Zeeman energy (the direction of the static magnetic field is chosen as the z-axis), the eigen-energy of the Hamiltonian upto the second order terms in the electric quadrupole moment, Q, is given by

$$\begin{aligned}E_m=&\,mg\beta H+A[3m^2-I(I+1)](\nabla E)_0\\&+3A^2\frac{(\nabla E)_1(\nabla E)_{-1}}{g\beta H}m[4I(I+1)-1-8m^2]\\&+3A^2\frac{(\nabla E)_2(\nabla E)_{-2}}{g\beta H}m[2I(I+1)-1-2m^2]\end{aligned} \qquad (3)$$

where $A=eQ/2I(2I-1)$. In our case, since sodium nucleus has the value of spin 3/2, there are four separated terms, and by the selection rule $\Delta m=\pm1$, three resonance lines are expected to appear in general, which are given by

$$\left.\begin{aligned}E_{3/2}\longleftrightarrow E_{1/2}&=g\beta H+6A(\nabla E)_0-\frac{36A^2}{g\beta H}(\nabla E)_1(\nabla E)_{-1}\\E_{1/2}\longleftrightarrow E_{-1/2}&=g\beta H+\quad 0\quad+\frac{36A^2}{g\beta H}[(\nabla E)_1(\nabla E)_{-1}+\frac{1}{2}(\nabla E)_2(\nabla E)_{-2}]\\E_{-1/2}\longleftrightarrow E_{-3/2}&=g\beta H-6A(\nabla E)_0-\frac{36A^2}{g\beta H}(\nabla E)_1(\nabla E)_{-1}\end{aligned}\right\} \qquad (4)$$

Though Bersohn calculated upto the third order terms in A, it is sufficient to take only the first and the second order terms in our case, since the value of $A(\nabla E)$ is considerably smaller than the Zeeman energy and then the third order terms in A are quite negligible.*

Now, we must calculate the quantities $(\nabla E)_0$ etc. in more explicit form. Let the principal axes of the field gradient tensor be x^*, y^*, and z^*, in which the direction of the largest field gradient be z^*. The irreducible tensor of the field gradient referred to the principal axes has the components

$$\left.\begin{aligned}
&(\nabla E)_0{}^* = -\frac{1}{2}\left(\frac{\partial E_z{}^*}{\partial z^*}\right)\\
&(\nabla E)_{\pm 1}{}^* = 0\\
&(\nabla E)_{\pm 2}{}^* = -\frac{\eta}{2\sqrt{6}}\left(\frac{\partial E_z{}^*}{\partial z^*}\right)
\end{aligned}\right\} \tag{5}$$

where η is the asymmetry factor of the field gradient, e.i.,

$$\eta = [\partial E_x{}^*/\partial x^* - \partial E_y{}^*/\partial y^*]/(\partial E_z{}^*/\partial z^*) \tag{6}$$

Now, in the crystal, we express a fixed coordinate system by X, Y, Z and let the Eulerian angles between (x^*, y^*, z^*) and (X, Y, Z) be α, β, and γ. The Z-axis is chosen as the axis of rotation, and the angle of rotation, which is equal to the angle between the Y-axis and the direction of the static field $\boldsymbol{H}$, is denoted as ϕ. Mutual relations among (x^*, y^*, z^*) system, (X, Y, Z) system and the direction of $\boldsymbol{H}$ are shown in Fig. 2.**

Following the general theory of Bersohn, $(\nabla E)_0$, $(\nabla E)_1(\nabla E)_{-1}$ and $(\nabla E)_2(\nabla E)_{-2}$ in (4) are calculated respectively to be

$$\left.\begin{aligned}
&(\nabla E)_0 = \left[\frac{3}{2}\sin^2\beta\cos^2(\gamma+\phi) - \frac{1}{2}\right](\nabla E)_0{}^* - \frac{\sqrt{6}}{4}\sin^2\beta\cos 2\alpha(\nabla E)_2{}^*\\
&\qquad + \frac{\sqrt{6}}{4}[(1+\cos^2\beta)\cos 2\alpha\cos 2(\phi+\gamma) - 2\cos\beta\sin 2\alpha\sin 2(\phi+\gamma)](\nabla E)_2{}^*\ ,\\
&(\nabla E)_1(\nabla E)_{-1} = -[A^2+B^2]\ ,\\
&(\nabla E)_2(\nabla E)_{-2} = [C^2+D^2]\ ,
\end{aligned}\right\} \tag{7}$$

where

$$\left.\begin{aligned}
&A = \frac{\sqrt{6}}{4}\sin^2\beta\sin 2(\phi+\gamma)(\nabla E)_0{}^* + \left[\frac{1}{2}(1+\cos^2\beta)\sin 2(\phi+\gamma)\cos 2\alpha\right.\\
&\qquad \left. + \cos\beta\sin 2\alpha\cos 2(\phi+\gamma)\right](\nabla E)_2{}^*\ ,\\
&B = \frac{\sqrt{6}}{2}\sin\beta\cos\beta\cos(\phi+\gamma)(\nabla E)_0{}^* + [\sin\beta\cos\beta\cos 2\alpha\cos(\phi+\gamma)\\
&\qquad - \sin\beta\sin 2\alpha\sin(\phi+\gamma)](\nabla E)_2{}^*\ ,\\
&C = \left[\frac{\sqrt{6}}{8}\sin^2\beta\cos 2(\phi+\gamma) + \frac{\sqrt{6}}{4}\left(\frac{3}{2}\cos^2\beta - \frac{1}{2}\right)\right](\nabla E)_0{}^*\\
&\qquad + \left[\frac{3}{4}\sin^2\beta\cos 2\alpha + \frac{1}{4}(1+\cos^2\beta)\cos 2\alpha\cos 2(\phi+\gamma)\right.\\
&\qquad \left. - \frac{1}{2}\cos\beta\sin 2\alpha\sin 2(\phi+\gamma)\right](\nabla E)_2{}^*,\\
&D = \frac{\sqrt{6}}{2}\sin\beta\cos\beta\sin(\phi+\gamma)(\nabla E)_0{}^* + [\sin\beta\cos\beta\cos 2\alpha\sin(\phi+\gamma)\\
&\qquad + \sin\beta\sin 2\alpha\cos(\phi+\gamma)](\nabla E)_2{}^*\ ,
\end{aligned}\right\} \tag{8}$$

In our experiment, the frequency of the r-f field was kept constant, while the magnetic field strength was varied. Therefore, by transforming (4), the expressions for the resonance fields H_1, H_2, and H_3 in case of the fixed frequency should be computed, which correspond to the transitions $3/2 \longleftrightarrow 1/2$, $1/2 \longleftrightarrow -1/2$, and $-1/2 \longleftrightarrow -3/2$ respectively. However, since the electric quadrupole interaction energy is considerably smaller than the Zeeman energy in our case, H in the second order perturbation terms can be replaced with good approximation by the Zeeman field, H_0, for the frequency ν, and then the expressions for H_1, H_2, and H_3 can be easily obtained.*

---

* See appendix.

** Bersohn used the coordinate system given in the book of Winger (Gruppentheorie und ihre Anwendung auf die Quantenmechnik der Atomspektren), where the left-hand system is used in the discussion of the rotational group. Therefore the angle ϕ is defined as the angle between the Y-axis and the direction of H.

Making use of the expression (7), the final results for the resonance fields are given by

$$\left.\begin{aligned}
H_1 \text{ or } H_3 = {} & H_0 \pm \left[\frac{1}{\sqrt{6}}\,p - \frac{\sqrt{6}}{4}\{a\cos 2(\phi+\gamma) - b\sin 2(\phi+\gamma)\}\right]\Delta H \\
& + \frac{(\Delta H)^2}{8H_0}[-(a^2+b^2+c^2+d^2) + \{(a^2-b^2)\cos 4(\phi+\gamma) - 2ab\sin 4(\phi+\gamma)\} \\
& -\{(c^2-d^2)\cos 2(\phi+\gamma) - 2cd\sin 2(\phi+\gamma)\}] \\
H_2 = {} & H_0 + \frac{(\Delta H)^2}{8H_0}\left[\left\{\frac{7}{8}(a^2+b^2) - p^2 + \frac{1}{2}(c^2+d^2)\right\} - \frac{9}{8}\{(a^2-b^2)\cos 4(\phi+\gamma)\right. \\
& \left. -2ab\sin 4(\phi+\gamma)\} - \left\{\left[pa + \frac{3}{2}(d^2-c^2)\right]\cos 2(\phi+\gamma) + (3cd - pb)\sin 2(\phi+\gamma)\right\}\right]
\end{aligned}\right\} \quad (9)$$

where

$$\left.\begin{aligned}
\Delta H &= \frac{1}{g\beta}(e^2qQ) = \frac{1}{g\beta}(-eQ\partial E_z{}^*/\partial z^*) \\
a &= \frac{\sqrt{6}}{4}\sin^2\beta + \frac{\eta}{2\sqrt{6}}(1+\cos^2\beta)\cos 2\alpha \\
b &= \frac{\eta}{\sqrt{6}}\cos\beta\sin 2\alpha \\
c &= \frac{\sqrt{6}}{2}\sin\beta\cos\beta + \frac{\eta}{\sqrt{6}}\sin\beta\cos\beta\cos 2\alpha \\
d &= \frac{\eta}{\sqrt{6}}\sin\beta\sin 2\alpha \\
p &= \frac{\sqrt{6}}{4}\left(1 - \frac{3}{2}\sin^2\beta\right) + \frac{3\eta}{4\sqrt{6}}\sin^2\beta\cos 2\alpha\,.
\end{aligned}\right\} \quad (10)$$

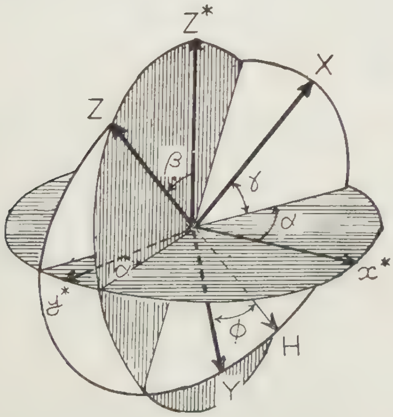

Fig. 2. Definition of the Eulerian angles, rotational angle, and the relative orientation of (X, Y, Z) and (x^*, y^*, z^*) axes. Ellipses are the intersections of a unit sphere and x^*y^*-, XY-, and z^*Z-planes.

Eulerian angles α, β, and γ, the electric quadrupole energy e^2qQ, and the asymmetry factor η will be obtained from the experimental results for H_1, H_2, and H_3, together with (9) and (10).

Equations (9) and (10) are seen to coincide with the formula given by Volkoff et al[2], when applied to the case treated by them.

§ 5. The Experimental Results and Discussions

In Fig. 3 and Fig. 4, the results of the experiments when the crystal was rotated about the b-axis and the c-axis are shown respectively. The experimental plots are indicated with the circular marks, while the solid curves in Fig. 3, a and b, and those in Fig. 4, b are the calculated ones which will be discussed later. On the contrary, the curves in Fig. 4, a are simply those connected smoothly the experimental plots and the comparison with the theory will be shown later. In these figures, the ordinates are the values of the potensiometer readings. The potentiometer reading of 3,000 corresponds to the magnetic field strength of 4730 gauss.

---

* See appendix.

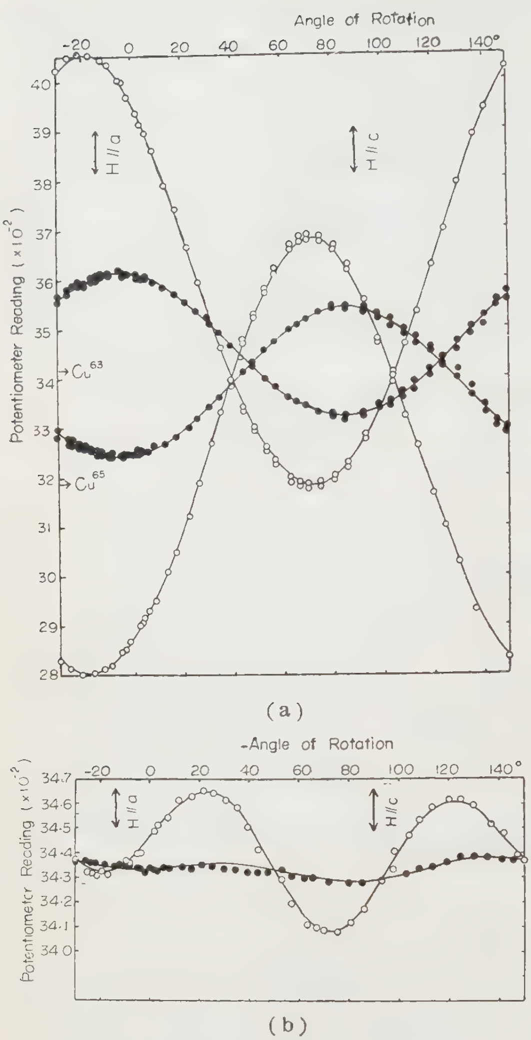

Fig. 3. Resonance fields observed in the case of b-axis rotation. Fig. 3a shows the components which are largely separated while Fig. 3b shows the central components in an enlarged scale. Circular marks are the experimental plots, while the solid curves are those calculated using the constants given in Table I.

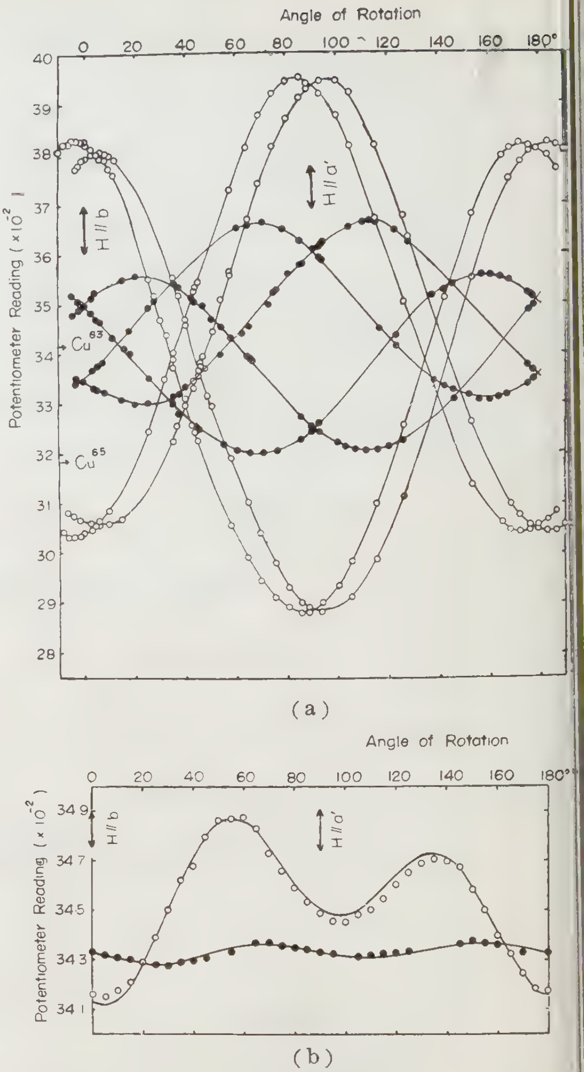

Fig. 4. Resonance fields observed in the case of c-axis rotation. Fig. 4a shows the components which are largely separated, while Fig. 4b shows the central components in an enlarged scale. Circular marks are the experimental plots. The solid curves in Fig. 4a are simply those joining the experimental plots, while curves in Fig. 4b are those calculated theoretically with the constants given in Table I. a' is the projection of the a-axis on the plane perpendicular to the c-axis. In Fig. 4b only two of four components are shown, the other two being just the inversion of those shown in the figure with respect to the line $\phi=0°$ (or $\phi=90°$).

Now, as discussed in § 3, in the case of the b-axis rotation, the resonance lines for all of four molecules in the unit cell are expected to coincide with each other. But, since there exist two independent sodium nuclei in each molecule, six resonance lines are expected to appear in general. Beside these six lines, there appeared two more lines which correspond to the resonance lines due to Cu^{63} and Cu^{65} nuclei contained in the winding wire of the r-f coil. To eliminate small irregular effect due to the hysteresis, the values of H_2 line, which lies very close to the Cu^{63} resonance line, are determined by observing the difference between H_2 and the Cu^{63} resonance field, since the latter is independent of the rotation of the crystal. Intensity of H_2 line is stronger than those of H_1 and H_3, but owing to the non-constancy of the sensitivity of our instrument, the quantitative comparison was not possible. The width of each line is of few gauss for any orientation of the crystal.

As shown in Fig. 3, there appeared, contrary to the discussion given above, closely spaced doublets in H_1 and H_3 lines for some range of the angle of rotation. This splitting into doublet was caused by the small errors in the cutting of the crystal along the desired plane, in the setting of the crystal on the rotating rod, or in the setting of the shield box perpendicular to the direction of the static field. Slight discrepancies due to the same origin can be seen also in Fig. 4, a. The effect of these errors in the instrumental setting and material-cutting upon the values of the resonance fields shall be considered briefly.

As the error in the angle will be quite small, only its effect on the first order perturbation term, which is proportional to $\varDelta H$, is to be considered. Thus it has no effect on H_2 line. If the direction of the axis of rotation has the polar angle (δ', φ_0) with respect to the Z-axis and if the static field makes an angle of $\pi/2+\mathcal{E}'$ with respect to the axis of rotation, where $\mathcal{E}'$ and δ' are very small angles, then δH given by the following equation should be added to H_1 and H_3 of (9) (− for H_1 and + for H_3).

$$\delta H \doteqdot \mp\sqrt{6}\,\varDelta H[c\cos(\phi+\gamma) - d\sin(\phi+\gamma)][\mathcal{E}'+\delta'\cos(\phi-\phi_0)]/2 \tag{11}$$

Now, in the case of the b-axis rotation if the Eulerian angles for the molecule *I* or *IV* be*

$$\left.\begin{array}{l} (\alpha,\ \beta,\ \gamma) \\ \text{where the X-axis is chosen in the direction of the } c\text{-axis, then those for the molecule } II \text{ or } III \text{ are given by} \\ (\alpha,\ \beta,\ \gamma+\pi) \end{array}\right\} \tag{12}$$

Therefore, though H_1 and H_3 in (9) are identical for these two, δH changes its sign for each of them, with the same absolute values. By this consideration, it is concluded that the mean value of resonance fields for doublet corresponds to that for the exact b-axis rotation with $\mathcal{E}'=\delta'=0$.

Similar consideration holds for the case of c-axis rotation. In this case, the Eulerian angles, which are denoted with dash to be discriminated from the case of b-axis rotation, are

$$(\alpha', \beta', \gamma') \text{ and } (\pi+\alpha', \pi-\beta', 2\pi-\gamma') \tag{13}$$

for the molecule *I* or *IV* and for that *II* or *III*, respectively, where the Y-axis is chosen in the direction of the b-axis. For the rotation angle ϕ for the molecule *I* and the angle $-\phi$ for the molecule *II*, H_1 and also H_3 given by (9) have the identical values respectively, but δH has the different value for each of them. The situation is not so simple as in the case of the b-axis rotation, but, by comparing the calculated formula for δH with its experimental value, $\mathcal{E}'$, δ', and ϕ_0 can be determined, and H_1 and H_3 for the case of $\mathcal{E}'=\delta'=0$ can be easily calculated. Since these corrected values of H_1 and H_3 for the molecule *II* at the rotation angle of $-\phi$, coincide exactly with those for the molecule

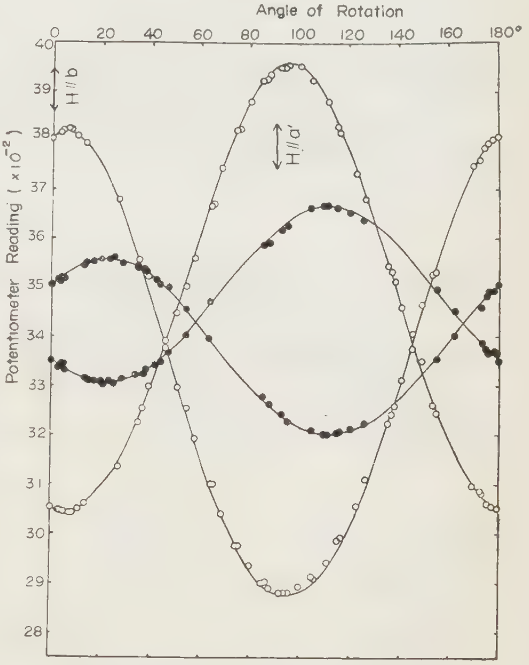

Fig. 5. Resonance fields in the case of c-axis rotation, after corrected in the way given in the text. Circular marks are the experimental plots while the solid curves are those calculated theoretically. Only one of two groups are shown, the other one being the inversion curves with respect to $\phi=0°$ (or $\phi=90°$).

---

* Only the direction of the axes is to be considered, so the Eulerian angles for the molecule *I* and *IV* can be regarded as the same. The similar situation holds for *II* and *III*.

I at the angle of ϕ, it is sufficient to compare the experimental data for one of these two molecules with the theoretical values. In Fig. 5, the corrected values of H_1 and H_3 are plotted with circular marks for one of two groups of the resonance lines. The values of ε' and δ' are within about 1.5° in both cases.

Now, for the analysis of the experimental results, some convenient relations will be obtainable from (9). These are

$$\left.\begin{aligned}
&(H_1-H_3\left(\phi+\frac{\pi}{2}\right)+(H_1-H_3)(\phi)=2<H_1-H_3>_{\mathrm{AV}}=\frac{4}{\sqrt{6}}p\\
&(H_1-H_3)\left(\phi+\frac{\pi}{2}\right)-(H_1-H_3)(\phi)=\sqrt{6}\,\Delta H\sqrt{a^2+b^2}\cos\left[2(\phi+\gamma)+\delta\right]\\
&<\frac{H_1+H_3}{2}>_{\mathrm{AV}}=H_0-\frac{1}{8}\frac{(\Delta H)^2}{H_0}(a^2+b^2+c^2+d^2)\\
&\left(\frac{H_1+H_3}{2}\right)\left(\phi+\frac{\pi}{2}\right)-\left(\frac{H_1+H_3}{2}\right)(\phi)=\frac{(\Delta H)^2}{4H_0}(c^2+d^2)\cos 2(\phi+\gamma+\varepsilon)\\
&\left(\frac{H_1+H_3}{2}\right)\left(\phi+\frac{\pi}{2}\right)+\left(\frac{H_1+H_3}{2}\right)(\phi)-2<\frac{H_1+H_3}{2}>_{\mathrm{AV}}\\
&\qquad\qquad\qquad\qquad=\frac{(\Delta H)^2}{4H_0}(a^2+b^2)\cos\left[4(\phi+\gamma)+2\delta\right]\\
&<H_2>_{\mathrm{AV}}=H_0+\frac{(\Delta H)^2}{4H_0}\left[\frac{7}{16}(a^2+b^2)-\frac{1}{2}p^2+\frac{1}{4}(c^2+d^2)\right]\\
&H_2\left(\phi+\frac{\pi}{2}\right)-H_2(\phi)=\frac{(\Delta H)^2}{4H_0}\sqrt{\left\{pa-\frac{3}{2}(c^2-d^2)\right\}^2+(3cd-pb)^2}\cos\left[2(\phi+\gamma)-\xi\right]\\
&H_2\left(\phi+\frac{\pi}{2}\right)+H_2(\phi)-2<H_2>_{\mathrm{AV}}=-\frac{9}{8}(a^2+b^2)\frac{(\Delta H)^2}{4H_0}\cos\left[4(\phi+\gamma)+2\delta\right]
\end{aligned}\right\}\quad(14)$$

where

$$\left.\begin{aligned}
&\delta=\mathrm{arctg}\frac{b}{a}\\
&\varepsilon=\mathrm{arctg}\frac{d}{c}\\
&\xi=\mathrm{arctg}\frac{3cd-pb}{pa-3/2(c^2-d^2)}
\end{aligned}\right\}\quad(15)$$

and, for example, $(H_1-H_3)(\phi)$ means the value of H_1-H_3 at the angle ϕ. By these relations, the values of a, b, c, d and p can be easily obtained from the experimental results. As an example, the experimental values of the left hand sides of (14) in the case of b-axis rotation are plotted in Fig. 6 for the group of the larger separation in H_1 and H_3*. All of these plots except that for

$$\left(\frac{H_1+H_3}{2}\right)\left(\phi+\frac{\pi}{2}\right)-\left(\frac{H_1+H_3}{2}\right)(\phi)$$

lie exactly on sine curves, as expected from the theoretical consideration. The plots for

$$\left(\frac{H_1+H_3}{2}\right)\left(\phi+\frac{\pi}{2}\right)-\left(\frac{H_1+H_3}{2}\right)(\phi)$$

have very small amplitude, almost within the experimental errors and a definite conclusion is unobtainable. By the amplitudes and the phase angles of the curves joining the plots in Fig. 6, the quantities a to p are calculable easily by using (14). But, since the experimental values of the left hand sides of (14) containing the factor $(\Delta H)^2/H_0$ are not accurate enough, so that a to p thus calculated are not so reliable. Therefore, the similar analysis was made for the case of the c-axis rotation, and using the relations for the Eulerian angles in both cases, the most consistent values for ΔH, η, H_0 and the direction of the principal axes with respect to the crystal ones were determined. The same procedure was made for the group having the smaller separation. The final results obtained are shown in Tab. I. ΔH given in the table are the values corrected allowing for slight non-linearity of the magnetic field.

---

* It is not known *a priori* which one of two curves in Fig. 3, b or Fig. 4, b corresponds to H_2 line of nucleus having the larger separation in H_1 and H_3. This correspondence is made clear only after these analyses have been performed.

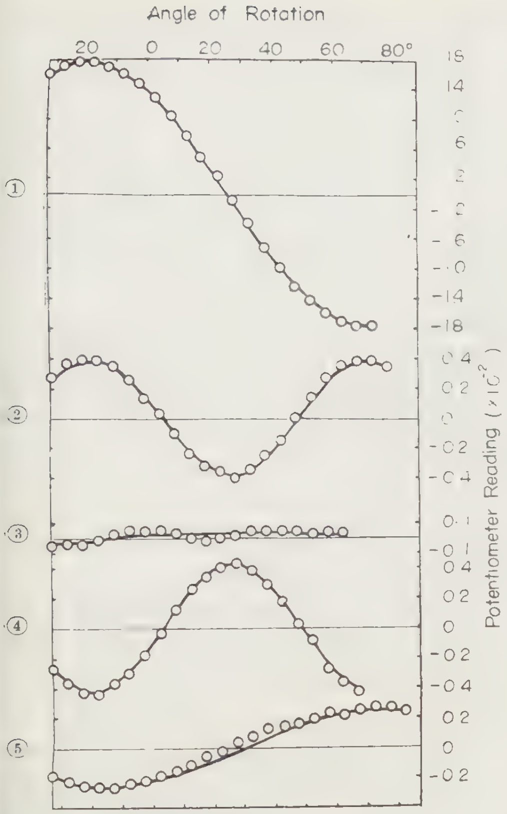

Fig. 6. Comparison of the experimental and the theoretical values of

$$(H_1-H_3)(\phi+\pi/2)-(H_1-H_3)(\phi)$$

and other similar quantities given in (14). Circular marks are the experimental plots while the curves are the calculated ones.

① $(H_1-H_3)(\phi+\pi/2)-(H_1-H_3)(\phi)$
② $((H_1+H_3)/2)(\phi+\pi/2)+((H_1+H_3)/2)(\phi)-2\langle(H_1+H_3)/2\rangle_{Av}$
③ $((H_1+H_3)/2)(\phi+\pi/2)-((H_1+H_3)/2)(\phi)$
④ $H_2(\phi+\pi/2)+H_2(\phi)-2\langle H_2\rangle_{Av}$
⑤ $H_2(\phi+\pi/2)-H_2(\phi)$.

The solid curves shown in Fig. 3, a and b, Fig. 4, b, Fig. 5 and Fig. 6 are those calculated by these values using Eqs. (9), (10) and (14). The agreement with the experimental plots seems satisfactory. The values of α, β and γ for the molecule derived by the screw operation are obtained by the relations (12) and (13).

Now, since the positions of atoms in this crystal were well determined by the X-ray analysis[9)], except those of hydrogen atoms, it will be interesting to compare the atomic configuration around sodium nuclei and the direction of the principal axes of the electric field gradient. Configuration of the nearest neighbors around two sodium nuclei is shown

Table I.

Sodium nucleusha ving the larger quadrupole interaction energy.		
For one molecule	$\alpha=66.8°\pm3°$	$\alpha'=154.6°\pm3°$
	$\beta=96.5°\pm1°$	$\beta'=71.6°\pm1°$
	$\gamma=18.5°\pm1°$	$\gamma'=276.9°\pm1°$
For the other molecule	$\alpha=66.8°\pm3°$	$\alpha'=334.6°\pm3°$
	$\beta=96.5°\pm1°$	$\beta'=108.4°\pm1°$
	$\gamma=198.5°\pm1°$	$\gamma'=83.1°\pm1°$
	$\Delta H=1270\pm10$	$\eta=0.334\pm0.015$
	$e^2qQ=2.258\pm0.018$ Mc/sec.	
Sodium nucleus having the smaller quadrupole interaction energy.		
For one molecule	$\alpha=131.0°\pm3°$	$\alpha'=220.4°\pm3°$
	$\beta=111.5°\pm1°$	$\beta'=88.4°\pm1°$
	$\gamma=1.7°\pm1°$	$\gamma'=291.6°\pm1°$
For the other molecule	$\alpha=131.0°\pm3°$	$\alpha'=40.4,\pm3°$
	$\beta=111.5°\pm1°$	$\beta'=91.6°\pm1°$
	$\gamma=181.7°\pm1°$	$\gamma'=68.4°\pm1°$
	$\Delta H=466\pm5$	$\eta=0.409\pm0.015$
	$e^2qQ=0.830\pm0.010$ Mc/sec.	

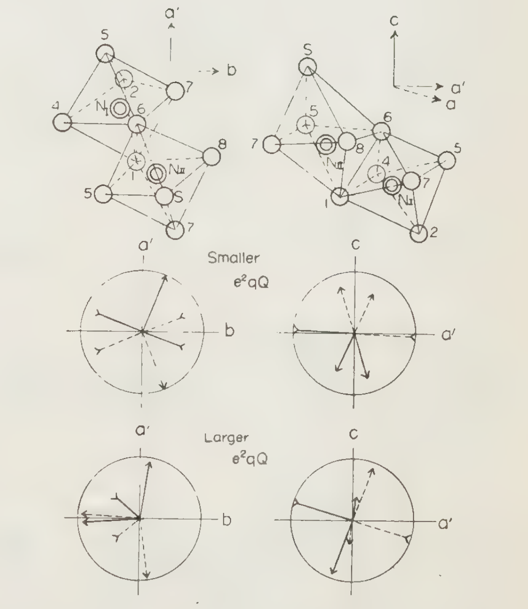

Projection on the plane perdendicular to the c-axis

projection on the plane perpendicular to the b-axis

Fig. 7. Projections of sodium nuclei and their surrounding atoms in one of four molecules in a unit cell, on the planes which are perpendicular to the b- and the c-axis respectively. The lower figures show the projection of unit vectors in the directions of the principal axes of the field gradient on the same planes, for both two groups having the larger and the smaller quadrupole interaction energies. Arrows indicate the signs of the axes, the head of the arrows indicating the upward direction. The dotted lines are the projections of the axes derived from the solid groups by 180° rotation with respect to the b-axis. Solid and dotted axes correspond to those for two types of molecules in a unit cell, respectively. a' is the projection of the a-axis on the plane perpendicular to the c-axis.

in Fig. 7. One of sodium nuclei is surrounded by six oxygen atoms forming a slightly deformed octahedron, while the other one is surrounded by five oxygen atoms and one sulphur atom forming a more deformed octahedron. Direction of the principal axes of the field gradient determined by our experiment is also shown in the figure. (Since it is not known which of two cases given in (12) or (13) corresponds to the molecule shown in Fig. 7, the principal axes for these two cases are shown with full and dotted lines in the figure). No simple correlation between the atomic configuration and the direction of the principal axes is seen to exist in this figure. It may be expected that the group having the larger value of ΔH corresponds to the sodium nucleus No. 2, since the surrounding atomic configuration is more deformed for this nucleus than that of the other and thus may give rise to the larger value of electric field gradient. But it is not clear whether this expectation is the actual case or not. To get some more knowledge about the electric field gradient at the nuclei, proton resonance experiment was performed, and proton-proton distances and proton-proton directions for five water molecules in a unit cell were determined. The results of the proton magnetic resonance experiment together with some discussions will be given in the forthcoming paper.

In conclusion, we would like to thank Dr. R. Kiriyama and Mr. Y. Saito for providing us the single crystal of this salt, and also for some discussions in the last part of this paper.

Appendix

Third order perturbation terms in the expressions of the resonance fields

According to the theory of Bersohn[6], the third order perturbation terms, which must be added to the eqations given by (4), are

$$\left.\begin{array}{l} (6A)^3/(g\beta H)^2\cdot(\nabla E)_0(\nabla E)_1(\nabla E)_{-1}-{}^1/_4\cdot(6A)^3/(g\beta H)^2\cdot(\nabla E)_0(\nabla E)_2(\nabla E)_{-2} \\ \qquad\qquad\qquad\qquad\qquad\qquad\qquad\qquad \text{for } E_{3/2}\longleftrightarrow E_{1/2} \\ 0 \qquad \text{for } E_{1/2}\longleftrightarrow E_{-1/2}, \text{ and} \\ -[(6A)^3/(g\beta H)^2\cdot(\nabla E)_0(\nabla E)_1(\nabla E)_{-1}-{}^1/_4\cdot(6A)^3/(g\beta H)^2\cdot(\nabla E)_0(\nabla E)_2(\nabla E)_{-2}] \\ \qquad\qquad\qquad\qquad\qquad\qquad\qquad\qquad \text{for } E_{-1/2}\longleftrightarrow E_{-2/3} \end{array}\right\} \qquad (16)$$

respectively. When we transform these formulae for the resonance energies to those for resonance fields, the following relations are obtained :

$$\left.\begin{array}{l} H_{1,3}=H_0\pm F+S/H_{1,3}\pm T/H_{1,3}{}^2 \\ H_2\ \ =H_0+0+S'/H_2+0\,. \end{array}\right\} \quad (17)$$

F is the term which is proportional to ΔH, S and S' to $(\Delta H)^2$, and T to $(\Delta H)^3$, the former three of which are given in (9). Now, since $T/H_{1,3}{}^2 \ll (S/H_{1,3}$ and $S'/H_2) \ll F$, $H_{1,3}$ in the denominator of S can be replaced by $H_0\pm F$, and H_2 in the denominator of S' and $H_{1,3}$ in the denominator of T both by H_0. Moreover term T can be expressed as

$$F\cdot(3/2\cdot S+1/2\cdot S'),$$

while

$$S/H_{1,3}\cong S/H_0\cdot(1\mp F/H_0)\,.$$

Therefore (17) can be rewritten with good approximation as

$$\left.\begin{array}{l} H_{1,3}=H_0\pm F+S/H_0\pm{}^1/_2\cdot F/H_0\cdot(S+S')/H_0 \\ H_2\ \ =H_0+S'/H_0 \end{array}\right\} \quad (18)$$

The forth term in the right hand side of $H_{1,3}$, which corresponds to the third order term in (ΔH), was calculated with the numerical values given in Tab. I to be less than 1/3,000 of H_0, which is about the order of experimental inaccuracy for the determination of the resonance fields, and can be neglected in our case.

References

1) R. V. Pound: Phys. Rev. **79** (1950) 685.

2) G. M. Volkoff, H. E. Petch and D. W. L. Smillie: Can. J. Phys. **30** (1952) 270.
H. E. Petch, D. W. L. Smillie and G. M. Volkoff: Phys. Rev. **84** (1951) 602.

3) H. E. Petch, G. M. Volkoff and N. G. Cranna: Phys. Rev. **88** (1952) 1201.

4) G. Becker: Z. Phys. **130** (1951) 415.

5) J. Hatton, B. V. Rollin and E. F. W. Seymour: Phys. Rev. **83** (1951) 672.
N. A. Schuster and G. E. Pake: Phys. Rev. **81** (1951) 157.
N. A. Schuster and G. E. Pake: Phys. Rev. **81** (1951) 886.

6) R. Bersohn: J. Chem. Phys. **20** (1952) 1505.

7) J. Itoh, R. Kusaka, Y. Yamagata, R. Kiriyama, H. Ibamoto, K. Kanda and Y. Masuda: J. Phys. Soc. Japan **8** (1953) 287.

8) F. Bitter and F. E. Reed: Rev. Sci. Instr. **22** (1951) 171.

9) P. G. Taylor and C. A. Beavers: Acta Cryst. **5** (1952) 341.

JOURNAL OF THE PHYSICAL SOCIETY OF JAPAN Vol. 9, No. 2, MAR.—APR., 1954

Simultaneous Excitation and Dissociation of Water Molecule by Hydrogen Canal Ray Impact

By Tadao HORIE and Masamoto OTSUKA

Faculty of Science, Osaka University

(Read November 4, 1950; Received August 29, 1951)

By electron impact, a water molecule dissociates into an OH radical in the excited state and a H atom in the ground state. Immediately after the dissociation, the excited radical makes a transition into the ground state, emitting the intensive (0, 0)-band of OH. According to the studies on intensity measurement of the rotational lines of the band, it has so far been shown that the excited radicals have an exceedingly abnormal distribution of rotational energy. Any sufficient interpretation of this phenomenon, however, has not yet been given from a theoretical standpoint. In order to obtain a key to solve the problem, the present paper is concerned with the measurement of the rotational intensity distribution of the fragment molecule OH dissociated from water molecule by hydrogen canal ray impact.

According to the experiment, it does not show so much abnormality as in the case of electron impact, but up to a certain extent it fades into a normal Maxwellian distribution in the case of hydrogen canal ray impact.

§ 1. Introduction

Experimental studies on the abnormal rotation in the process of the simultaneous excitation and dissociation of water molecule have already been published by many authors[1]. Several attempts at theoretical interpretation of the experimental results have also been reported[2]. In all of the studies mentioned above, however, collision between *electron* and water molecule seems to play the leading part. To obtain any other available key in order to approach to the mechanism of abnormal rotation, the rotational energy distribution of the fragment molecule OH in collision between *proton* and water molecule is desired. The present paper is concerned with the first report on this study which is now in progress.

§ 2. Experimental Procedure

Collisions in which a water molecule is excited and dissociated by hydrogen canal ray are observed in the apparatus as shown schematically in Fig. 1. Hydrogen gas is supplied through the side tube *a*, and glow discharge takes place between the anode *A* and the cathode *C*. Hydrogen canal ray squeezed into the two narrow rectangular slits S_1 and S_2 (0.5 mm in width, 5 cm in length) shoots through the two rooms *U* and *L*. The upper

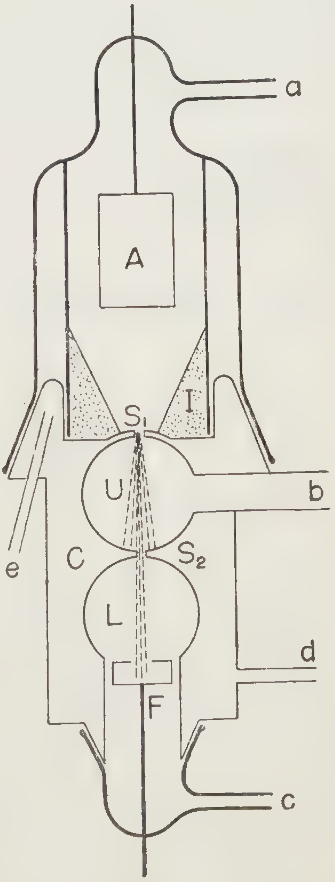

Fig. 1. Experimental apparatus.

room U is connected to a pumping system through the side tube b. Water vapour is sent into the lower room L under the pressure of 2/100 to 3/100 mmHg through the side tube c. The band-spectra emitted from the fragment molecule OH created along the path of canal ray passing through water vapour in the room L is observed through a window with a fused quartz plate.

Canal ray is captured by the Faraday cage F and its intensity can also be known. In order to observe collisions between electron and water molecule, A is used as cathode and C as anode. To increase the intensity of canal ray, the surface of cathode is covered by the insulator I except the neighbourhood of the slit. The surface exposed to glow discharge is made of Al and moreover cooled by water running from d to e, in order to depress sputtering at the cathode.

§ 3. Band Intensity and Anode Potential

The intensity of the band-spectra emitted from the fragment molecule OH depends on the vapour pressure of water in the room L, the intensity and the energy of the positive ion beam. The intensity and the energy of hydrogen canal ray vary with the discharge voltage. Both the canal ray intensity I_c and the band intensity I_b increase along with the anode potential V. The relation obtained between I_b/I_c and V is shown in Fig. 2, in comparison with the excitation function in the case of electron impact[3]. The anode potential V does not represent the energy of the incident canal ray in itself. Therefore, the curve in Fig. 2 tells us approximately only the excitation function, that is, the relation between the excitation probability and the energy of the incident particle.

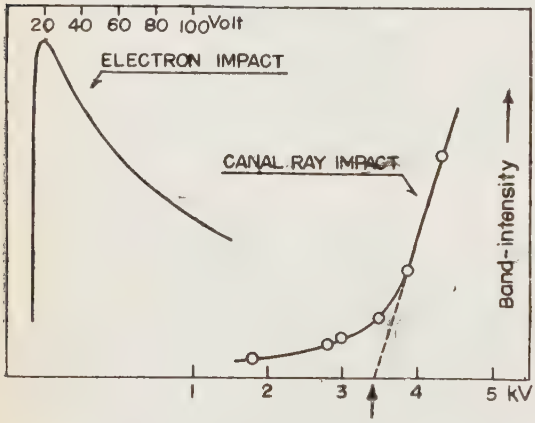

Fig. 2. Excitation function.

Under constant pressure, the band intensity is plotted against the intensity of canal ray in Fig. 3. It shows a linear increase of the band intensity with increase in the positive ion current captured by the Faraday cage up to 100 μA. Therefore, the band-spectra measured may be attributable to the fragment molecule OH created in the process of the simultaneous dissociation and excitation of water molecule by canal ray impact. If the re-excitation of free radicals remained unevacuated in the gas room L by canal ray impact were being essential, the band intensity should increase in proportion to the square of the positive ion current.

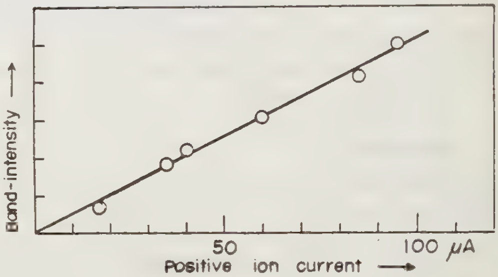

Fig. 3. Band intensity and positive ion current.

§ 4. Rotational Intensity Distribution

It needs a rather long exposure for ten hours or more to make a photographic photometry measurement of the rotational lines of the (0, 0)-band emitted from the fragment molecule OH. The anode voltage is desirable to be taken as high as possible, also other conditions being necessary to be kept unchanged in the course of such a long exposure. Photographs are taken fairly easily under the anode voltage ranging from 4,000 to 4,500 volts.

The rotational intensity distribution curve due to canal ray impact is shown in Fig. 4 in comparison to that of electron impact. It may be admitted that the intensities of the lines with higher rotational quantum numbers are fairly weak in the case of canal ray impact. Such a fact can be acknowledged even by the naked eye, if we compare two plates having equal densities in the neighbourhood of the band-head, the former one due to canal ray and the latter electron impact. Observing from one to the other, it is noticeable at once that the P_1 and P_2 branches extending to the band-tail vanish more rapidly in the plate of the former one than the latter.

In conclusion, it may be said experimentally that the rotational intensity distribution in the case of hydrogen canal ray impact does not show so much abnormality as in the case of electron impact, but to a certain extent it fades into a normal Maxwellian distribution.

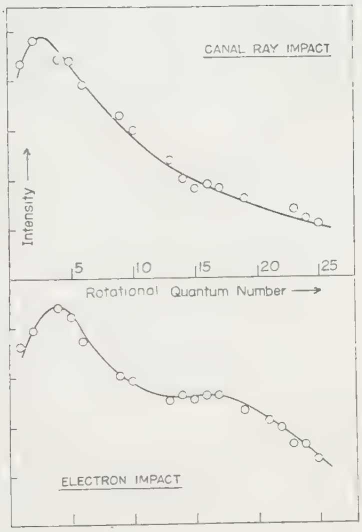

Fig. 4. Rotational intensity distribution of Q_1-branch.

§ 5. Some Considerations

As regards to the excitation function of the atom by electron and canal ray impact, quite similar differences as shown in Fig. 2 have already been known, for example, in the collisions of He with electron and H.[4)] The problems of collisions between such massive particles should be ploughed in the light of quantum mechanics, unfortunately, while the theory in this direction is at present not so well developed as that of electronic collisions. According to London and Massey-Smith[5)], the colliding system makes a quasi-molecule and the excitation probability is negligible until the energy of the incident particle exceeds a certain value, which is considerably greater than the excitation energy. Above this 'activation energy' the excitation probability increases rapidly, therefore we take the anode potential as high as possible.

According to the experimental result, the striking abnormality which is characteristic of electron impact fades remarkably into a normal Maxwellian distribution in the case of canal ray impact. It may, however, be too early to attempt any theoretical interpretation on this point because the canal ray used may be considered to contain not only proton but also H_2^+, H_3^+ and neutral particles created by recombination processes in the course of flight.

§ 6. Origins of Errors

In the emission spectrum of OH molecule, the most prominent (0, 0)-band is accompanied by the (1, 1)-band of the same system with a considerable intensity, which is overlapped in the portion of the band-tail of the preceding one. As a matter of course, each of the (0, 0)-band lines with higher rotational quantum numbers are apt to be misread somewhat higher than its true intensity. Let us call this the (1, 1)-overlapping briefly.

The relative intensity of the (1, 1)-band to (0, 0) may vary considerably from electronic excitation to canal ray impact. The question may, therefore, arise whether the (1, 1)-band appears more strongly in electronic excitation than in canal ray impact. If so, it may be doubted whether the result obtained is only due to the (1, 1)-overlapping or not. In order to make this ambiguity clear, it is necessary to examine the overlapping effect from the view-points of both the dispersion of spectrograph used and the relative intensity of the (1, 1)-band in detail.

The microphotometer figure of the (0, 0)-band taken in the dispersion of 3 Å/mm, by making use of the fourth order of a 1.5 meter concave grating, is shown in Fig. 5. The Q_1-branch lines are marked with circles. The quantum number K'' of each line is indicated in parenthesis[6)]. The lines ranging from Q_1 (14) to Q_1 (26) are of great importance to the abnormal intensity distribution. According to Fig. 5, owing to the (1, 1)-overlapping, among the thirteen lines ranging from Q_1 (14) to Q_1 (26), the number of lines which can surely be reliable in intensity estimation seems to be reduced to only seven as follows, Q_1 (14), Q_1 (15), Q_1 (19), Q_1 (23), Q_1 (24), Q_1 (25) and Q_1 (26). Among the lines ranging from Q_1 (1) to Q_1 (13), it may also be seen readily that the number of the lines with

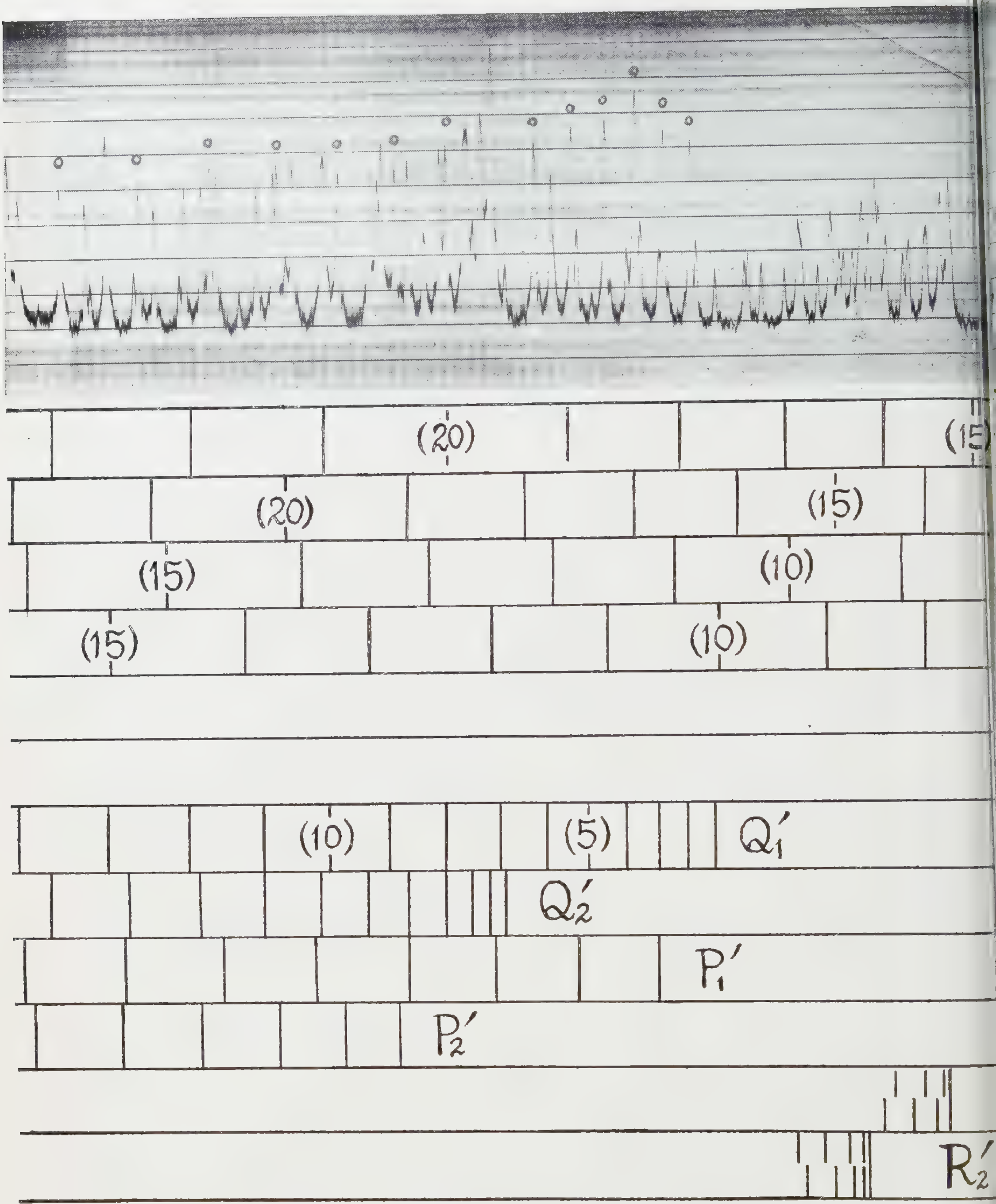

Fig. 5. Microphotometer figure of (0, 0)-band

The (0, 0)-band emitted by a Geissler discharge is taken by the fourth order of a 1.5 meter concave grating with a dispersion of 3 A/mm. The spectrogram obtained is traced by a microphotometer of Riken B type. The Q_1-branch lines of the (0, 0)-band are most free from

higher reliabilities is only three as follows, Q_1 (4), Q_1 (5) and Q_1 (6). Any of the other lines is interfered in some degree with the R_1-, R_2-, P_1-, P_2- and Q_2-branches of the (0, 0)-band. Let us call this the (0, 0)-overlapping briefly.

If the dispersion is much poorer, or if the intensity of the (1, 1)-band is much more intensive, it is to be expected that not only the reliability of the line affected by the

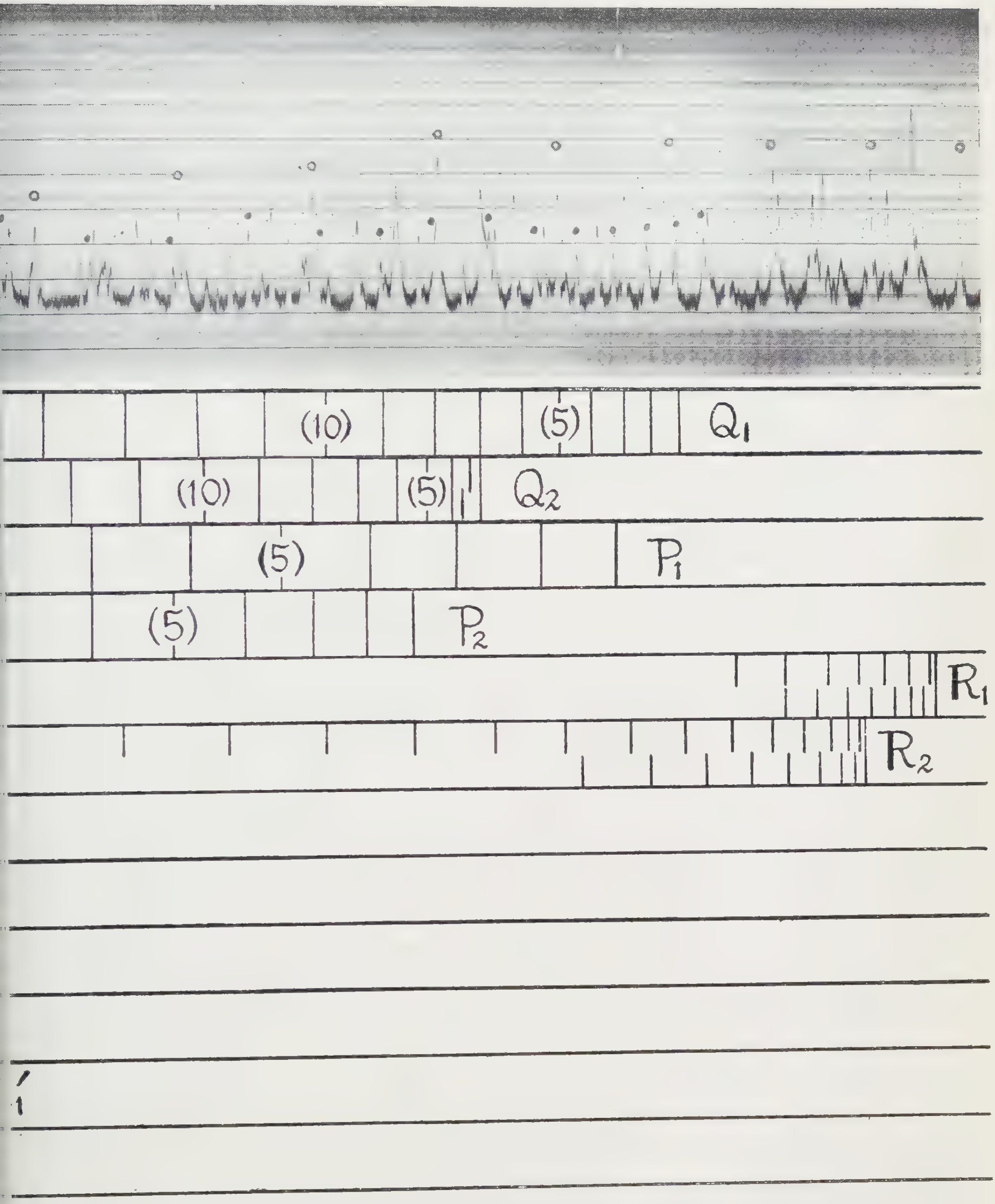

superposition with other lines and marked with circles. The rotational quantum number, K'', is assigned in reference with the paper of M. R. Fortrat; Jour. d. Phys., **5** (1924) 20, and shown in parenthesis. The Q_1' branch lines of the (1, 1)-band are marked with dots. The relative intensity of the line, Q_1' (4), to the line, Q_1 (4), is equal to 28.5/100.

(1, 1)- or (0, 0)-overlapping will decrease further, but also some of the ten lines chosen will happen to lose their reliabilities.

§ 7. Influence of Dispersion

The effective intensities of the Q_1-branch lines of the (0, 0)-band emitted by a Geissler discharge are plotted intentionally without regard to their true values in Fig. 6. The upper is obtained in the dispersion of 3 Å/mm and the lower in a dispersion of 8 Å/mm. In comparison with each other, it may be seen that the influence of dispersion is very great, since the poorer is dispersion the more serious are the overlapping effects. It is, however, quite fortunate that the ten lines mentioned above persist in the same curve irrespective of dispersion. As far as the ten lines are concerned, they may be considered not to lose their reliabilities considerably until the dispersion decreases down to 8 Å/mm.

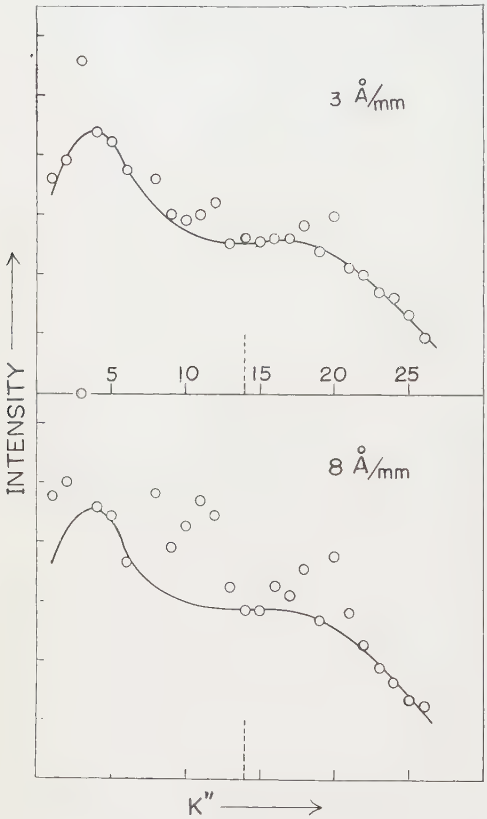

Fig. 6. Overlapping effect.

§ 8. Intensity of (1, 1)-Band

The Q_1-branch lines of the (1, 1)-band are marked with dots in Fig. 5. To avoid confusions, the branches belonging to the (1, 1)-band are denoted by ′ such as Q_1'. Both of the lines, Q_1' (4) and Q_1 (4), are isolated sufficiently from other lines and therefore taken as the representatives for the (1, 1)- and (0, 0)-bands respectively in order to estimate the relative intensity with each other. According to the photometry measurements, the relative intensity of the line, Q_1' (4), to the line, Q_1 (4), equals 28,5/100 for electronic excitation and 36/100 for canal ray impact. This difference seems to indicate that the (1, 1)-band appears more strongly in canal ray excitation.

Smith-Arnott⁷⁾ studied on the excitation of nitrogen molecule by electronic and canal ray impacts. The bands with higher vibrational quantum numbers were shown to appear more intensively in the case of canal ray excitation. The present result in the collision of water molecule with canal ray is quite analogous to the case of nitrogen.

If the rise and fall of the second maximum in the intensity curve were due to the (1, 1)-overlapping, the plateau should be much more high, since the (1, 1)-band is more intense in canal ray excitation. Actually while this does not take place, all doubts as to the (1, 1)-overlapping are removed.

The authors wish to express their thanks to National Research Council, Ministry of Education, for the financial aid.

References

1) O. Oldenberg: Phys Rev. **37** (1931) 1550.
K. F. Bonhoeffer and T. G. Pearson: Z.f.P.C. **14** (1931) 3.
E. R. Lyman: Phys. Rev. **53** (1938) 379.
H. Wakeshima: Proc. Phys. -Math. Soc. Japan **24** (1942) 367.
G. Hayakawa: Proc. Phys. -Math. Soc. Japan **26** (1944) 78.
T. Horie, T. Nagura and Y. Honda: Scientific Paper from the Osaka Univ., No. 21, Feb., 1951.
2) O. Oldenberg: Phys. Rev. **46** (1934) 210.
K. Niira: J. Phys. Soc. Japan **4** (1949) 230.
3) G. Hayakawa: *loc. cit.*
4) W. Maurer: Phys. Zeits. **11** (1939) 161.
5) J. F. London: Z.f.P. **74** (1932) 143.
H. S. Massey and R. A. Smith: Proc. Roy. Soc. (A) **142** (1933) 142.
6) W. Jevons: *Report on Band-spectra of Diatomic Molecules*, The University Press, Cambridge (1932) 164.
7) H. D. Smith and E. G. F. Arnott: Phys. Rev. **36** (1930) 1023.

JOURNAL OF THE PHYSICAL SOCIETY OF JAPAN Vol. 9, No. 2, MAR.—APR., 1954

Studies of Light Absorption under Conditions productive of Joshi Effect in Mercury Vapour under Ozoniser Discharge

By V. VENKATESWARLU and N. A. RAMAIAH

Faculty of Science, Delhi University, Delhi, India

(Received October 12, 1953)

A new phenomenon called Joshi effect (Δi) which involved a marked diminution of gaseous conductivity under irradiation, was described. Data for the production of Δi corresponding to 100 per cent photoreduction of the conductivity in mercury vapour excited by potentials near 'threshold potential' V_m, were presented. Light absorption of mercury vapour was studied against hydrogen discharge when a fine absorption line occurred at 2536Å whose intensity remained sensibly the same for the excited vapour; that excited near V_m and also when irradiated to give appreciable Δi. Results using the tungsten lamp and mercury arc also showed no noticeable difference between normal and excited vapour under conditions causing large Δi. It is considered that Joshi effect is not a consequence of selective light absorption by the gaseous phase.

§ 1. The New Phenomenon—Joshi Effect

While a few theoretical considerations on photo- and thermo-electric effects require that the conductivity of a gas should be enhanced under light, it has been observed by Prof. Joshi[1][2] that the current (i) passing through a gas excited by electrical fields decrease under external light. This current-decrease (Δi) under irradiation, called Joshi effect, is sensibly instantaneous and completely reversible in the sense that when the external radiation is cut off, the initial value of i is restored. The phenomenon is observed in all gases which are electronegative in character like chlorine, bromine, iodine, etc.[2][3] and in those which give under excitation atoms or/and radicals with large electron affinity, *e.g.* OH radicals from H_2O vapour.[4] For other characteristics of the phenomenon, the reader is referred to the reviews thereon published elsewhere.[2][5]

§ 2. A Mechanism of the Phenomenon

For the occurrence of the effect Δi, Joshi[6] postulates that (i) an adsorption-like layer consisting of excited particles, ions and electrons is formed under discharge; (ii) light releases electrons from this boundary layer; and (iii) negative ion formation due to capture of photo-electrons by excited neutral particles reduces the current to give Δi, as a space charge effect.

The adsorption-like layer postulate (i) was found helpful in elucidation of a number of observed facts especially the influence on Δi of 'ageing' (*vide infra*).[7][8] The finding that Δi is pronounced in vessels containing coating materials which possess inherently the photo-sensitive character or increase the photo-electric effect from the electrode surface,[4][9] follows simply from (ii). That the phenomenon is observed markedly in electronegative gases and vapours, is to be anticipated from (iii). The recent observation of appreciable Δi in mercury vapour is attributed[10] on the above mechanism to the excited Hg atoms produced under discharge; it is argued, following the observation of Franck and coworkers especially Compton,[11] that excitation of even atoms of metallic vapours increases appreciably their electron affinity. On Joshi's mechanism, the observed Δi in mercury vapour is due to the conversion of excited mercury atoms into negative ions which on account of their low mobility form a space charge and therefore, inhibit the current.

§ 3. The Present Investigation

A significant feature of the above hypothesis is a deduction therefrom that Δi does not originate principally from light absorption of the homogeneous gas phase. It was, however, observed[12] that the magnitude of

Δi in chlorine was comparatively large in blue—violet region of the spectrum (4750—4000 Å); this appeared to suggest the correlation of Δi in chlorine with the corresponding light absorption. Production of Δi in chlorine of appreciable magnitude under X-rays,[13)] light from sodium vapour lamp and especially at 7700 Å[14)] where the selective absorption by chlorine is practically negligible; and also in gases like oxygen[2)] under visible light, pointed out, on the other hand, that absorption of the gaseous medium is not fundamental to Δi. The object of the present communication is to investigate this factor, in some detail, in mercury vapour; the well established data on the absorption of excited Hg vapour and the remarkably large Joshi effect corresponding to 95 to 100% current suppression observed therein, as also other characteristics of the system mentioned later, were found highly suitable to obtain results of decisive nature.

§ 4. Experimental

The experimental arrangement and the electrical circuit are shown in Fig. 1. Modified Siemen's ozonisers were employed as the discharge tubes. Two glass tubes were sealed internally at one side, as shown in Fig. 1; their disposition was a symetrical in the sense that their axes were parallel but not identical. This caused the annular space between the cylinders narrower at one end than at the other (see the cross section of the ozoniser, Fig. 1). This type of arrangement of the cylinders of the discharge tube resulted in concentrating the discharge in the lower part of the ozoniser from where the absorption of the excited mercury vapour could be studied with relatively short exposure periods. The inner tube was filled with NaCl soln. and constituted as one of the electrodes. A thin copper wire wound tightly in the form of a solenoid on the outer surface of the outer cylinder, served as the other electrode. The ends of the outer tube was flattened or cemented with suitable windows.

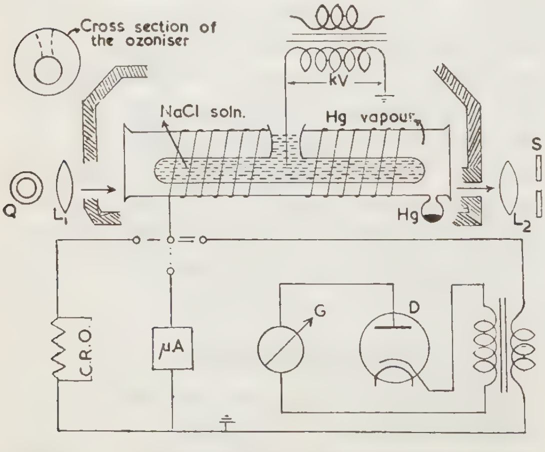

Fig. 1. Experimental set up for the studies of light absorption and Joshi effect in Hg vapour.

Two such modified Siemen's ozonisers (*A* and *B*) were employed. Discharge tube *A* was an all glass vessel (with a light absorbing column of 45 cm) and was used for the studies in the visible. *B* had (an absorbing column of 65 cm and) quartz windows suitable for the investigations in ultra-violet. They contained pure mercury vapour in contact with a pellet of mercury well outside the discharge space (Fig. 1) and were excited by alternating potentials in the range 0.2 to 6 kV of 50 and 500 cycles/sec. The discharge current was studied by a cathode ray oscillograph and its rms value (i) measured by a microammeter or a galvanometer actuated by a diode. Further details of the experimental technique were given in previous communications.[15)][16)]

A 200 watt, 200 volt tungsten bulb, quartz mercury vapour lamp and hydrogen discharge tube were used as the light sources. With these, the discharge tube could be irradiated in two ways: (*a*) longitudinally, *i.e.* in the end-on position; and (*b*) transversely, *i.e.* in the broad side-on position. In both *a* and *b*, the entire gas phase was illuminated but with a difference in the intensity of light falling at different parts of the annular space. While in *b* the intensity of the light falling on the system was sensibly constant throughout, as computed by a thermopile, the same in *a*, *i.e.* in the longitudinal mode of irradiation, decreased with the distance from the source along the axis of the discharge tube.

The studies of light absorption of Hg vapour were made at different applied fields as follows: Light from the source *Q* (Fig. 1) which was herein after referred to as the 'background', was collimated with a lens (L_1), passed along the annular space charged with Hg vapour and then focussed on the slit (S) of the spectrograph by another lens L_2, Fig. 1). For the investigations in the visible (ozoniser *A*), Hilger's constant deviation instrument and Kodak P1200 plates were used, while for those in the ultra-violet ozoniser *B*), Hilger's 'baby' quartz spectrograph and Kodak B20 plates were employed. Microphotometric records were obtained with 25 magnification.

§ 5. Results

Typical series of results on the variation of the discharge current (i) with the potential applied to the ozonisers *A* and *B* are returned in Figs. 2 and 3; these represent also the characteristic variation of Joshi effect with pplied potential and other parameters nentioned below. These data were principally obtained to select the applied potentials t which the absorption of Hg vapour under conditions productive of maximum Joshi effect, could be made.

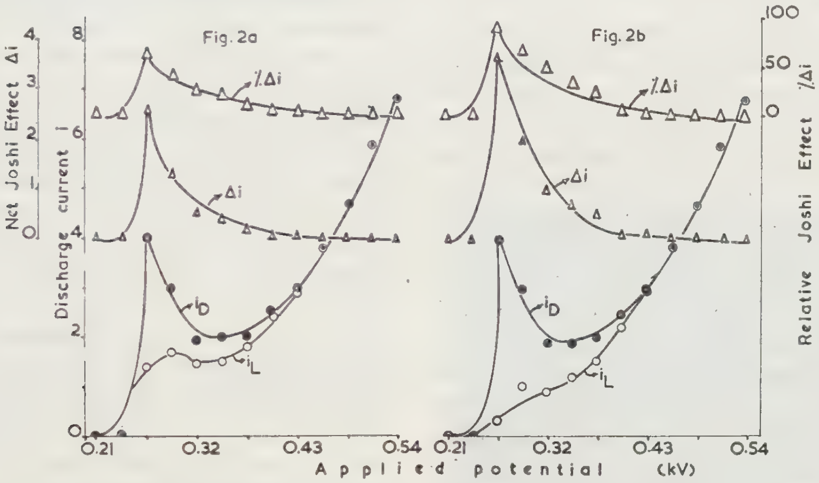

Fig. 2. Potential variation of Joshi effect under (a) longitudinal and (b) transverse irradiations (Ozoniser *A*, 200 watt tungsten bulb).

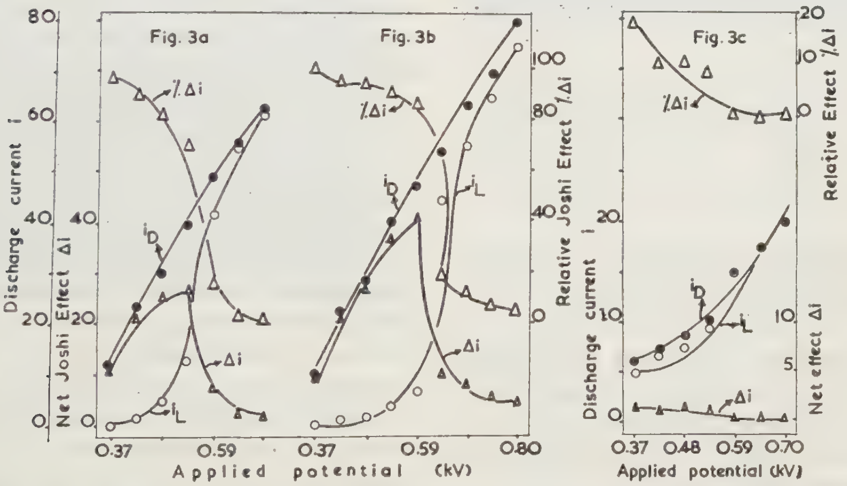

Fig. 3. Comparative studies of Joshi effect in Hg vapour with (a) tungsten bulb, (b) quartz Hg vapour lamp and (c) hydrogen discharge tube as the light sources (ozoniser *B*, transverse illumination).

In Fig. 2a, the curve marked i_D denotes the change of i with applied voltage V; while the curve i_L shows the same when the discharge tube is irradiated with the light source, say 200 watt bulb. In actual experimentation, the current i at a fixed V was noted in dark (i_D) and then under light (i_L). From these, the net decrease of the current due to irradiation ($i_D - i_L = \Delta i$) termed as net Joshi effect and the relative values ($100\Delta i/i_D = \%\Delta i$) referred to as relative Joshi effect were calculated and represented graphically in Figs. 2 and 3.

It was interesting to note that above a critical potential called ' threshold potential ', V_m at which due to the dielectic breakdown of the medium, the rms value (i) of the current increased rapidly, the Joshi effect could but be detected. When observations were made with a cathode ray oscillograph, the above potential corresponded to that voltage from which the discharge attained self-maintained nature, giving rise to self-sustaining current pulses due to well-known secondary mechanisms especially those concerned with the liberation of electrons from the cathode due to bombardment by positive ions and photons ;[17)18)] the effect Δi was represented by marked inhibition of the height of the pulses (cf. Fig. 4). Both the net and relative effects were maximum at potentials just above V_m *e.g.* at 0.28 in *A* and at 0.37 in *B*. They decreased markedly rapidly with increase of the applied potential and could not be detected at $V > 1.5$ kV.

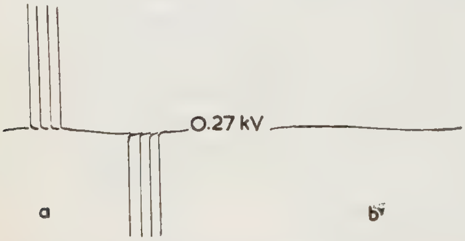

Fig. 4. Oscillograms representing Joshi effect in Hg vapour, (a) in dark and (b) under light from 200 watt bulb.

Further, the effect was appreciably more with transverse illumination than with longitudinal irradiation. Thus *e.g.* at 0.28 kV, $\%\Delta i$ was 100 when the ozoniser *A* was exposed to light in broad side-on position (Fig. 2b) and about 50 when the same was irradiated longitudinally (Fig. 2a) with the light from 200 watt bulb. Similar results were recorded in iodine vapour :[19)] *ceteris paribus*, $\%\ \Delta i$ was 20 under longitudinal and about three times its value *i.e.* 60 under transverse illumination. This markedly low value of Joshi effect in the former case was attributed to the low und progressively decreasing intensity of light falling on every unit volume of the gas or area of the electrode surface of the system. That the intensity of the light used, alters the magnitude of Δi is substantiated by the data obtained with the other sources of irradiation (Fig. 3). At 0.37 kV (ozoniser *B*), $\%\Delta i$ was 70, 100 and 15 with tungsten bulb (Fig. 3a), Hg arc (Fig. 3b) and hydrogen discharge tube (Fig. 3c) respectively ; in all these experiments, the system was irradiated transversely. The intensity, as computed from the measurements by a thermopile, of the light from Hg arc was about 45 times greater than that from hydrogen discharge tube.

The above data were obtained in systems which were tested for the constancy and reproducible nature of the results, by letting them in use for long time. In freshly prepared vessels, the conditions were, however, unstable and the diminution of the current under light *i.e.* Joshi effect, was inappreciable. When the discharge tubes ware ' aged ' *i.e.* exposed continuously to discharge due to a fixed potential,[4)7)] the effect Δi was found to increase progressively to a maximum value. The time needed for obtaining saturation in the magnitude of Δi was of the order of 15 to 20 hrs depending upon the potential employed for ' ageing '. Unlike in other systems such as iodine vapour,[20)] prolonged exposure to discharge did not inhibit Δi in Hg vapour. Furthermore, a rest period[5)] had little influence on Δi especially in the present medium. The details of these results and the significance thereof were given and discussed in previous communications[4)7)8)] and therefore, not reiterated here. The constancy of the data on Δi in mercury vapour was remarkably suitable for the present investigation since one could mention with good certainty, the magnitude of Δi characteristic of the system and applied voltage employed for absorption studies.

Plate 1 gives the absorption spectra of mercury vapour using the tungsten bulb as the background, while Plate 2 shows the corresponding results using Hg vapour lamp ;

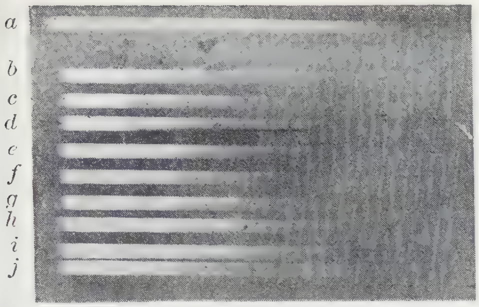

Plate 1: Spectrograms representing the absorption of Hg vapour under conditions productive of Joshi effect.

- *a.* Spectrum of the light source—200 watt tungsten bulb
- *b.* Absorption spectrum of unexcited Hg vapour
- *c.* Absorption spectrum of excited vapour, 0.27 kV; $\%\Delta i=66$
- *d.*—: 0.53 kV; $\%\Delta i=0$
- *e.*—: 1.34 kV; $\%\Delta i=0$ (50 cycles/sec.)
- *f.*—: 0.18 kV; $\%\Delta i=10$
- *g.*—: 0.53 kV; $\%\Delta i=0$
- *h.*—: 1.07 kV; $\%\Delta i=0$ (500 cycles/sec.)
- *i.* Absorption spectrum of unexcited vapour.
- *j.* Spectrum of iron arc.

(Ozoniser *A*)

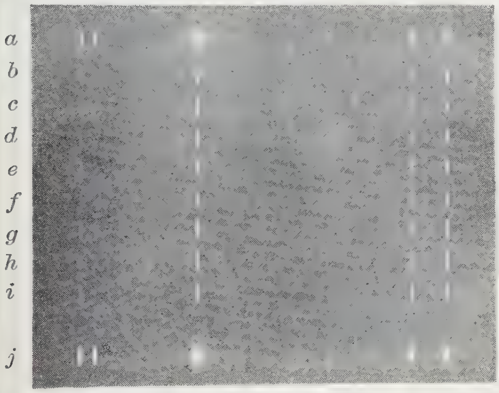

Plate 2. Spectra representing the absorption of Hg vapour under conditions productive of Joshi effect. (Visible region)

- *a.* Spectrum of the light source (background) —Hg arc lamp.
- *b.* Absorption spectrum of unexcited mercury vapour.
- *c.* Absorption Spectrum of vapour excited at 0.27 kV; $\%\Delta i=90$
- *d.*—: 0.53 kV; $\%\Delta i=0$
- *e.*—: 1.34 kV; $\%\Delta i=0$ (50 cycles/sec.)
- *f.*—: 0.18 kV: $\%\Delta i=16$
- *g.*—: 0.53 kV; $\%\Delta i=0$
- *h.*—: 1.07 kV; $\%\Delta i=0$ (500 cycles/sec.)
- *i.* Absorption spectrum of unexcited Hg vapour.
- *j.* Spectrum of Hg arc lamp.

(Ozoniser *A*)

ozoniser *A* was used as the discharge tube. In these, *a* refers to the spectrum of light source. The spectrum *b* gives the absorption of Hg vapour in the unexcited state; that is, in this case the ozoniser was interposed (in its position as indicated in Fig. 1) between the slit *S* and the background *Q* (Fig. 1). *c* indicates the same when the discharge tube was excited and irradiated transversely so as to give appreciable negative Joshi effect as shown against the spectra. The details of *d*–*i* were given in the caption of the plates. Similar data were obtained with the ozoniser *B* and Hg vapour lamp as the background; these are given in Plate 3.

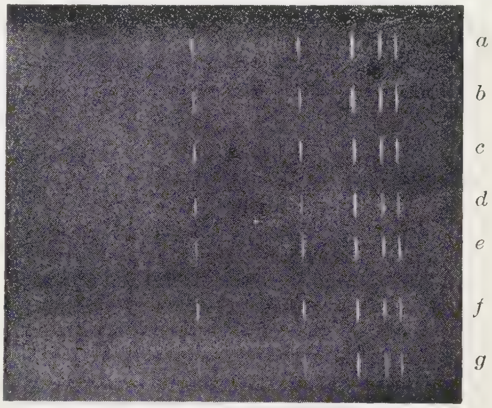

Plate 3. Studies of light absorption in Hg vapour in ultra violet under conditions productive of Joshi effect. (Ozoniser *B*)

The spectra *a*, *c*, *e* and *g* refer to absorption of unexcited Hg vapour.

The spectra *b*, *d* and *f* refer to absorption of Hg vapour excited at 0.37 kV (50 cycles/sec.) —$\%\Delta i=100$.

It was remarkable that in the range of applied potentials 0.3–0.8 kV (in which region the current suppression under irradiation —Joshi effect—was maximum) no difference in the nature and intensity of the absorption between the normal state and excited and irradiated conditions of the vapour (cf. *b* and *c* of Plates 1 and 2, *a* and *b*, *c* and *d*, etc. of Plate 3) was noticeable within the limits of the accuracy of the available instruments. At these potentials the current density was approximately 1μA per cm^2 and the glow in the discharge tube was whitish blue.

The results of the absorption of the mercury vapour in the ultra-violet region using hydrogen discharge tube which provides a continuum in the region 2000–4000 Å, as the background and ozoniser B, are returned in Plate 4. In this, the spectrogram (i) was that of unexcited vapour ; (ii) that of vapour excited near threshold potential V_m ; and (iii) that of excited vapour irradiated transversely to give Joshi effect corresponding to 97% current diminution. The spectra (iv–vi) and (vii–ix) were similar to (i–iii) and afforded to show the reproducibility of the data. The absorption spectra obtained at large voltages (>2.0 kV) are given in (x and xi) of Plate 4. These data also showed that irradiation of the excited system to produce appreciable Joshi effect, caused no difference in the absorption of the excited or/and unexcited mercury atoms.

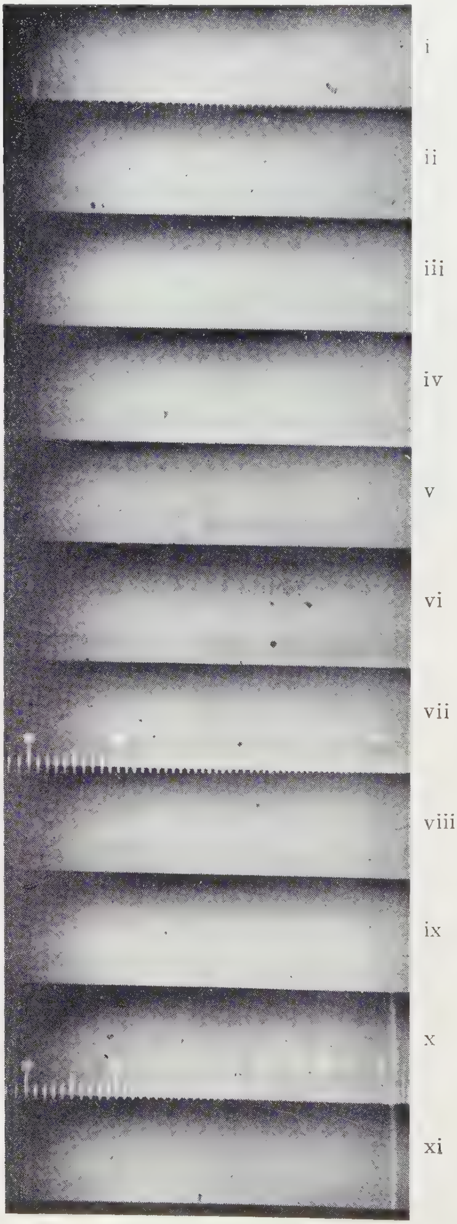

Plate 4. Absorption spectra of Hg vapour against hydrogen discharge tube, under conditions productive of Joshi effect.

It may be pointed out that the comparison of the Plates 3 and 4 shows a marked discrepancy in the absorption at 2536 Å : While the data in Plate 4 revealed absorption at 2536 Å due to mercury atoms in the ground state, $^1S_0$ (*cf.* the micro-photometric curves in Plate 5—the inappreciable depression at 2536Å was due to low pressure of Hg vapour), the spectrograms in Plate 3 indicated that there was no absorption at the reversed line. This discrepancy was but due to the comparatively large intensity of light from mercury vapour lamp used as the background, which masked the appearence of absorption at 2536 Å detected in Plate 4 with hydrogen discharge tube with feeble intensity of light as the background. Nevertheless, the data revealed that there was no difference between the absorption of excited vapour and that under excited and irradiated conditions.

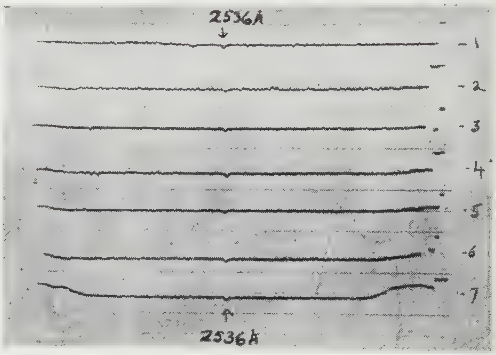

Plate 5. Microphotometric curves for the spectra given in Plate 4.

§ 6. Discussion

Mercury vapour absorbs chiefly at 5790, 5770, 5461 and 4047 Å in the visible and at 3663, 3342, 2536 Å, etc. in the ultra-violet. The absorption, apart from the resonance line—2536 Å, by mercury atoms occurs only when they are excited to higher energy levels;

excitation can be brought about by a number of processes, say collisions of the second kind, electron impact under discharge; this last type is principally controlled by the current density of the system. The unexcited mercury atoms can, however, absorb 2536Å; in fact, the intensity of the absorption at 2536Å gives a measure of the normal or unexcited Hg atoms in a system.

Metcalfe and Venkateshachar[21] observed strong absorption of the lines 5461, 4047, 3342 and 3663Å by excited mercury vapour carrying a current density of about 10 mA/cm². Later, they reported[22] the absorption of the yellow lines 5790 and 5770Å, employing greater length of the light absorbing column, higher current density and with widened lines as the background. They observed that the light absorption, especially the green line, 5461Å, increased with the current density of the discharge, the optimum value being near about 10 mA/cm². If this value was decreased, the absorption diminished appreciably and approached that of the normal vapour at low values of current density. These findings were confirmed by Turner and Compton[23] who claimed that their apparatus was more effective in producing excited atoms and therefore, were able to record greater absorption of light with much shorter absorbing column and greater current density; these were 4 cm and 40 mA/cm² respectively as compared with 100 cm and 10 mA/cm² employed in the earlier investigations.[21][22] These results show that the concentration of the excited atoms which determine the extent of selective absorption of mercury vapour, is controlled chiefly by the density of the discharge current. Since this last in present experiments was of the order of 1μA/cm² compatible with the occurrence of measurable Δi, that the absorption of the vapour under discharge differed negligibly from that in the unexcited state, was not unexpected.

McLennan, Ainsle and Cale[24] and also Metcalfe and Venkateshachar[21][22] found that the vapour showed pronounced absorption when the colour of the discharge was bluish green or pink when viewed end-on; and slight absorption when it was pale blue colour. In the present investigation, the colour of the discharge was invariably pale, whitish blue; it was not therefore, as mentioned above, incompatible with the absence of selective light absorption of excited mercury atoms.* It was interesting to note from the results in Plate 1–4 that during irradiation of the system to produce appreciable Joshi effect, no enhancement in the absorption of the excited Hg vapour, could be detected within the limits of experimental accuracy of the available instruments.

As mentioned earlier, the intensity of the absorption at 2536Å is a measure of the ground state Hg atoms; it decreases with their excitation. At large potentials, $V>2.0$ kV (spectrograms x and xi, Plate 4, the line 2536Å was not reversed, indicating thereby that practically the entirety of the ground state atoms was raised to higher excitation levels. The spectrograms (ii) and (iii) or (v) and (vi) of Plate 4 (*cf.* the corresponding micro-photometric curves, Plate 5) pointed out that the external light did not cause excitation of the normal or ground state atoms in causing appreciable change in the current flowing through the system. It may therefore be concluded that the action of light in causing Δi, is not linked with absorption or excitation of the homogeneous gas phase but presumably with the adsorbed layers on the electrode surface.[2] It may be admitted that the results presented in this communication give no elucidation of the factors that may be taking place on the electrode surface.

Further, the data given in this paper which shows that selective light absorption by excited mercury vapour is not a prerequisite for the production of Δi, point out, however, a marked discrepancy in the argument put forward earlier[10] for the elucidation of the observation of Δi in the system under investigation. It may be recalled that on Joshi's mechanism, Δi in mercury vapour is attributed to excited mercury atoms which according to Franck and coworkers, possess enhanced electron affinity. At large V, the spectrograms (x and xi, Plate 4) show appreciable absorption due to excited atoms. From this, one anticipates that at large applied potentials, the magnitude of Δi should be marked. It was, however, observed that at enhanced fields, no Joshi effect could be noticed. These observations, *viz.* (a) Δi is undetectable at large potentials where excited atoms are found to be appreciable, and (b) Δi is marked at voltages where excited atoms are seemingly inappreciable, lead one to doubt the validity of the mechanism or appear to point out at least a limitation to the hypothesis.

---

* The fundamental object of the present investigation was to find out whether there was any selective absorption or a change therein due to irradiation of the system giving Δi, but not to explore conditions where absorption was maximum. The data were therefore restricted to limited voltage region or current density conditions where Δi was detectable.

§ 7. Acknowledgement

Grateful thanks are due to Professor Joshi for suggesting the problem, kind interest and valuable guidance during the work and to Professor R. K. Asundi for advice.*

References

1) Joshi: Nature **154** (1944) 147.
2) Ramaiah: Jour. Sci. industri. Res. **10A** (1951) 182.
3) Ramaiah: Jour. Sci. Res. (B. H. U.) **1** (1950–51) 91.
4) Ramaiah: Jour. Phys. Chem. **56** (1952) 218.
5) Saxena and Ramaiah: Jour. Sci. industri Res. **12A** (1953) 130.
6) Joshi: Curr. Sci. **16** (1947) 19.
7) Ramaiah: Jour. Chim. Phys. (Paris) **49** (1952) 327.
8) Ramaiah, Ratnam and Devi: Jour. Sci. industri. Res. **12B** (1952) 524.
9) Shukla: Proc. Ind. Sci. Cong. Chem. Sec. (1951).
10) Prasad: Nature **164** (1949) 69.
11) cf. Ref. 6.
12) Joshi and Deo: Nature **151** (1943) 561; Deo: Ind. Jour. Phys. **18** (1944) 83; Proc. Ind. Acad. Sci. **29** (1949) 28.
13) Joshi: Curr. Sci. **13** (1944) 278.
14) Joshi: Pres. Address, Proc. Ind. Sci. Cong. (1943).
15) Ramaiah: Jour. Sci. Res. (B. H. U.) **2** (1951–52) 1.
16) Dogra and Ramaiah: Jour. Sci. industri. Res. **12B** (1953) 29.
17) Saxena, Bhatawdekar and Ramaiah: Jour. Chem. Phys. **21** (1953) 365.
18) Dogra, Bhatawdekar and Ramaiah: Proc. Phys. Soc. (London) **66** (1953) 431.
19) Rao: Proc. Ind. Acad. Sci. **29** (1949) 211.
20) Ramaiah: unpublished results.
21) Metcalfe and Venkateshachar: Proc. Roy. Soc. **A 100** (1922) 149.
22) Metcalfe and Venkateshachar: ibid. **A 105** (1924) 520.
23) Turner and Compton: Phys. Rev. **25** (1924) 606.
24) McLennan, Ainsle and Cale: Proc. Roy. Soc. **A 102** (1923) 33.

---

* The work reported here was carried out in Department of Physical Chemistry, Banaras Hindu University.

JOURNAL OF THE PHYSICAL SOCIETY OF JAPAN Vol. 9, No. 2, MAR.—APR., 1954

The Lift on the Symmetrical Joukowski Aerofoil in a Stream bounded by a Plane Wall

By Hiroomi FUJIKAWA

Junior College of Engineering, Naniwa University

(Received June 1, 1953)

In this paper the lift on the symmetrical Joukowski aerofoil of small thickness in the presence of a plane rigid wall is obtained in the form of a power-series, with the intention of discussing the manner in which the ground-effect on the lift of an aerofoil is modified by its thickness. The calculation of the lift is carried out by extending Green's analysis.

It is found that in case when the symmetrical Joukowski aerofoil of small thickness is placed in the vicinity of the wall at small angles of attack as used in practice, the wall-effect on the lift is quite similar to that in the case of a plane aerofoil. Namely, as the symmetrical Joukowski aerofoil approaches the wall, the lift first decreases and then tends to increase to values which are greater than the corresponding values for the symmetrical Joukowski aerofoil in an infinite stream, especially when the angle of attack is sufficiently small.

Further it is found that for any value of the distance of the aerofoil from the wall, the lift ratio Y/Y_0 decreases as the thickness increases even for small values of the angle of attack.

§1. Introduction and Summary

The investigation of the manner in which the effect of the ground on the lift of an aerofoil is modified by its thickness is of great interest not only from the theoretical point of view but also from the practical standpoint. The problem has already been discussed in some detail by Tomotika, Hasimoto and Urano¹⁾, by evaluating the forces acting on some aerofoils (especially approximately symmetrical aerofoils) of approximate Joukowski type with small camber placed in a stream bounded by an infinite plane rigid wall. It has thus been shown that when an aerofoil is placed in the very vicinity of the ground at small angles of attack as used in practice, the lift on the aerofoil is in general increased by the presence of the ground, but the rate of increase of the lift becomes smaller as the thickness of the aerofoil increases.

In the present paper, we reinvestigate the modifications introduced by the thickness of an aerofoil on the ground-effect upon its lift, by evaluating the lift Y on the symmetrical Joukowski aerofoil of chord length l placed obliquely in a stream bounded by a plane wall by applying Green's new method²⁾, which has been somewhat extended by the present writer. The power-series solution in powers of l/b, correct to the order of $(l/b)^4$, is obtained for the ratio Y/Y_0, where Y_0 is the lift on the symmetrical Joukowski aerofoil of chord length l when placed at the same angle of attack in an unlimited stream, and b is the distance of the centre of the aerofoil from the bounding wall.

The values of the ratio Y/Y_0 have been calculated numerically in three cases in which the thickness parameter of the aerofoil takes the values 0, 0.1 and 0.2 respectively, the corresponding thickness ratios being 0, 0.118 and 0.215 respectively. The values of the angle of attack have been taken to be 5° and 10°.

It is thus shown that the ground-effect on the lift is quite similar to that in the case of a plane aerofoil³⁾. Namely, as the symmetrical Joukowski aerofoil approaches the wall, the lift first decreases and then tends to increase to values which are greater than the corresponding values for the symmetrical Joukowski aerofoil in an unbounded stream, especially when the angle of attack is sufficiently small. Further it is shown that, in accordance with the prediction made by Tomotika *et al.*,¹⁾ the value of the ratio Y/Y_0 becomes smaller as the thickness of the aerofoil increases even for small values of the angle of attack.

OUTLINE OF GREEN'S METHOD

§ 2. The Transformations

We shall begin with the transformations necessary for our present problem. If we take the plane of two-dimensional fluid motion as the z-plane, the symmetrical Joukowski aerofoil is derived from a circle of radius $r(1+\varepsilon)$ with the centre at $M(r\varepsilon, 0)$ in a t-plane by the well-known transformation:

$$z=t+r^2/t\,, \tag{1}$$

where r is the radius of the base circle O and ε is a non-dimensional real small quantity (Fig. 1). As is well known, this quantity ε gives a measure of the thickness of the aerofoil. Thus, the thickness becomes larger as the value of the thickness parameter ε increases.

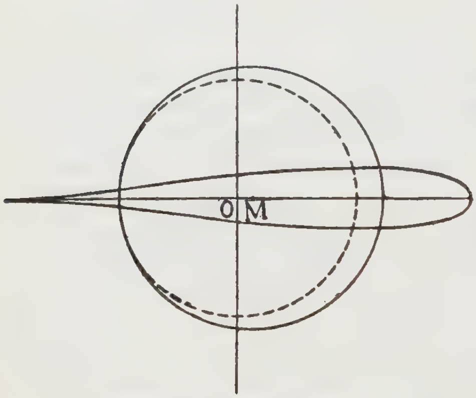

Fig. 1. t and z-plane.

After some reduction, the transformation (1) can be written in the form:

$$z=e^{-i\zeta}\sum_{n=0}^{\infty}a_n e^{in\zeta} \quad (\zeta=\xi+i\eta)\,, \tag{2}$$

where the coefficients a_n are given by

$$\left.\begin{aligned}&a_0=r(1+\varepsilon)\,,\quad a_1=r\varepsilon\,,\\&a_n=(-1)^n r\varepsilon^{n-2}(1+\varepsilon)^{1-n}.\quad (n\geqq 2)\end{aligned}\right\} \tag{3}$$

Then, the circle M in the t-plane corresponds to a straight line:

$$\eta=0\,,\quad \xi=0\longrightarrow -2\pi \tag{4}$$

in the ζ-plane.

Thus, the symmetrical Joukowski aerofoil in the z-plane is obtained from the straight line (4) by means of the transformation (2) with the coefficients a_n given by (3).*

§ 3. The Complex Velocity Potential

We now consider a steady irrotational continuous flow of an incompressible perfect fluid past the symmetrical Joukowski aerofoil placed at an angle of attack θ in the vicinity of a plane rigid wall (Fig. 2). With the origin at the centre of the aerofoil, we take the x-axis parallel to the wall which is defined by $y=-b$. We assume that the fluid at infinity flows with a constant velocity c parallel to the wall in the negative direction of the x-axis, and that there is a circulation round the aerofoil in the counterclockwise sense.

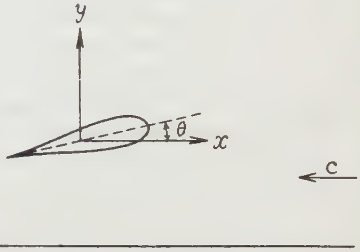

Fig. 2. z-plane.

Then, a suitable complex velocity potential w which makes the bounding wall a streamline is

$$w=cz+iA_0\{\log z-\log(z+2ib)\}+\sum_{n=1}^{\infty}\left\{\frac{A_n}{z^n}+\frac{\bar{A}_n}{(z+2ib)^n}\right\}, \tag{5}$$

where $\bar{A}_n$ denotes the complex conjugate of A_n.

Apart from a constant, equation (5) may be written in the form

$$w=cz+iA_0\log z+\sum_{n=1}^{\infty}\frac{A_n}{z^n}+\sum_{n=1}^{\infty}B_n z^n\,, \tag{6}$$

where

$$B_n=\frac{{}^n\alpha_0 A_0}{b^n}+\sum_{r=1}^{n}\frac{{}^n\alpha_r\bar{A}_r}{b^{n+r}}\,, \tag{7}$$

and

$$ {}^n\alpha_0=\frac{i^{n+1}}{2^n\cdot n}\,,\quad {}^n\alpha_r=\binom{n+r-1}{n}\frac{i^{n-r}}{2^{n+r}} \qquad (n, r\geqq 1)\,. \tag{8}$$

---

* In general, the straight line (4) in the ζ-plane is transformed into an aerofoil in the z-plane by the transformation (2), the shape of the aerofoil being determined by the values of the coefficients a_n. For a plane aerofoil with chord length l, for instance, all, but two, of the coefficients a_n are zero and the two nonvanishing coefficients a_0 and a_2 are both equal to γ or $l/4$.

Substituting (6) in the well-known Blasius's formula for the components (X, Y) of the force acting on the aerofoil under discussion, namely :

$$X-iY=\frac{1}{2}i\rho\oint\left(\frac{dw}{dz}\right)^2 dz\ , \qquad (9)$$

we find that

$$Y+iX=2\pi\rho\left\{cA_0+A_0B_1\right.$$
$$\left.+i\sum_{n=1}^{\infty}n(n+1)A_nB_{n+1}\right\}\ , \qquad (10)$$

ρ being the density of the fluid concerned.

§ 4. Determination of the Quantities A_n and $\bar{A}_n$

Next, we shall determine the quantities A_n and $\bar{A}_n$ so as to satisfy the boundary conditions at the surface of the aerofoil. To do this, it is better to consider the matter in the ζ-plane rather than in the z-plane.

We shall first express, using (2), z^{-r}, z^r and $\log z$ in the forms :

$$\left.\begin{array}{l} z^{-r}=\sum\limits_{n=r}^{\infty}{}^r\beta_n e^{in\zeta}\ , \quad z^r=\sum\limits_{n=-r}^{\infty}{}^r\gamma_n e^{in\zeta}\ , \\ \log z=-i\zeta+\sum\limits_{n=0}^{\infty}{}^0\beta_n e^{in\zeta}\ , \end{array}\right\} \qquad (11)$$

where constant terms, which will not be needed, are ignored. Some of the early coefficients in these expansions, which are necessary for our problem, are given below.

$$\left.\begin{array}{lll} {}^0\beta_1=\dfrac{a_1}{a_0}\ , & {}^0\beta_2=\dfrac{a_2}{a_0}-\dfrac{a_1^2}{2a_0^2}\ , & {}^0\beta_3=\dfrac{a_3}{a_0}-\dfrac{a_1a_2}{a_0^2}+\dfrac{a_1^3}{3a_0^3}\ , \\ {}^1\beta_1=\dfrac{1}{a_0}\ , & {}^1\beta_2=-\dfrac{a_1}{a_0^2}\ , & {}^1\beta_3=\dfrac{a_1^2}{a_0^3}-\dfrac{a_2}{a_0^2}\ , \\ {}^2\beta_2=\dfrac{1}{a_0^2}\ , & {}^2\beta_3=-\dfrac{2a_1}{a_0^3}\ , & {}^3\beta_3=\dfrac{1}{a_0^3}\ , \\ {}^1\gamma_1=a_2\ , & {}^1\gamma_2=a_3\ , & {}^2\gamma_1=2a_0a_3+2a_1a_2\ , \\ {}^1\gamma_{-1}=a_0\ , & {}^2\gamma_{-1}=2a_0a_1\ , & {}^2\gamma_{-2}=a_0^2\ , \\ {}^3\gamma_{-1}=3a_0(a_1^2+a_0a_2)\ , & {}^3\gamma_{-2}=3a_0^2a_1\ , & {}^3\gamma_{-3}=a_0^3\ , \\ \multicolumn{3}{l}{{}^4\gamma_{-1}=4a_0(a_0^2a_3+3a_0a_1a_2+a_1^3)\ ,} \\ {}^4\gamma_{-2}=2a_0^2(2a_0a_2+3a_1^2)\ , & {}^4\gamma_{-3}=4a_0^3a_1\ , & {}^4\gamma_{-4}=a_0^4\ . \end{array}\right\} \qquad (12)$$

Making use of the expansions (11) and ssuming that orders of summations may be nterchanged, the complex velocity potential v can be expressed, after some reductions, s :

$$w=A_0\zeta+\sum_{n=1}^{\infty}C_n e^{in\zeta}+\sum_{n=1}^{\infty}D_n e^{-in\zeta}\ , \qquad (13)$$

here

$$\left.\begin{array}{l} C_n=ca_{n+1}+i\,{}^0\beta_nA_0+\sum\limits_{r=1}^{n}{}^r\beta_nA_r+\sum\limits_{r=1}^{\infty}{}^r\gamma_nB_r \\ \hfill (n\geqq1)\ , \\ D_1=ca_0+\sum\limits_{r=1}^{\infty}{}^r\gamma_{-1}B_r\ , \quad D_n=\sum\limits_{r=n}^{\infty}{}^r\gamma_{-n}B_r \\ \hfill (n\geqq2)\ . \end{array}\right\} \qquad (14)$$

Since the surface of the aerofoil, which is xpressed by the equation $\eta=0$ in the ζ-lane, must coincide with a part of a partiular stream-line which may be defined by =0, we have

$$[\mathfrak{I}(w)]_{\eta=0}=0\ , \qquad (15)$$

which gives immediately

$$C_n=\bar{D}_n\ , \quad (n\geqq1)\ . \qquad (16)$$

Our next problem is to determine the coefficients A_n. Inspection of the equations indicates that it seems possible to express A_n as a power-series in $1/b$. We therefore assume, with Green, that

$$A_n=\sum_{k=0}^{\infty}{}^nA_k/b^k\ , \quad (n\geqq0)\ . \qquad (17)$$

Then we have, from (7),

$$B_n=\sum_{k=0}^{\infty}\left\{{}^n\alpha_0{}^0A_k+\sum_{r=1}^{\infty}\frac{{}^n\alpha_r{}^r\bar{A}_k}{b^r}\right\}\cdot\frac{1}{b^{n+k}}\ . \qquad (18)$$

Substituting these series in the right-hand sides of (14) and assuming that orders of summations in the resulting double and triple series may be changed, we have

$$\begin{aligned}C_n=ca_{n+1}&+\sum_{k=0}^{\infty}\left(i\,{}^0\beta_n{}^0A_k+\sum_{r=1}^{n}{}^r\beta_n{}^rA_k\right)\frac{1}{b^k}\\&+\sum_{k=1}^{\infty}\sum_{m=1}^{k}{}^m\gamma_n{}^m\alpha_0\frac{{}^0A_{k-m}}{b^k}\\&+\sum_{k=2}^{\infty}\sum_{r=1}^{k-1}\sum_{m=1}^{r}{}^m\gamma_n{}^m\alpha_{k-r}\frac{{}^{k-r}\bar{A}_{r-m}}{b^k}\,,\end{aligned}\qquad(n\geqq 1)\quad(19)$$

$$\begin{aligned}D_1=ca_0&+\sum_{k=1}^{\infty}\sum_{m=1}^{k}{}^m\gamma_{-1}{}^m\alpha_0\frac{{}^0A_{k-m}}{b^k}\\&+\sum_{k=2}^{\infty}\sum_{r=1}^{k-1}\sum_{m=1}^{r}{}^m\gamma_{-1}{}^m\alpha_{k-r}\frac{{}^{k-r}\bar{A}_{r-m}}{b^k}\,,\end{aligned}\qquad(20)$$

$$\begin{aligned}D_n=&\sum_{k=n}^{\infty}\sum_{m=n}^{k}{}^m\gamma_{-n}{}^m\alpha_0\frac{{}^0A_{k-m}}{b^k}\\&+\sum_{k=n+1}^{\infty}\sum_{r=n}^{k-1}\sum_{m=n}^{r}{}^m\gamma_{-n}{}^m\alpha_{k-r}\frac{{}^{k-r}\bar{A}_{r-m}}{b^k}\,,\end{aligned}\qquad(n\geqq 2)\,.\quad(21)$$

The boundary conditions (16) must be true for every value of b, so that, using (19)—(21) and equating coefficients of corresponding powers of $1/b$, we obtain the relations:

$$ca_2+i\,{}^0\beta_1{}^0A_0+{}^1\beta_1{}^1A_0=c\bar{a}_0\,,\qquad(22)$$

$$ca_{n+1}+i\,{}^0\beta_n{}^0A_0+\sum_{r=1}^{n}{}^r\beta_n{}^rA_0=0\,,\quad(n\geqq 2)\qquad(23)$$

$$\begin{aligned}&i\,{}^0\beta_n{}^0A_1+\sum_{r=1}^{n}{}^r\beta_n{}^rA_1+{}^1\gamma_n{}^1\alpha_0{}^0A_0\\&\qquad=\begin{cases}{}^1\bar{\gamma}_{-1}{}^1\bar{\alpha}_0{}^0A_0\,, & (n=1)\\ 0\,, & (n>1)\end{cases}\end{aligned}\qquad(24)$$

$$\begin{aligned}&i\,{}^0\beta_n{}^0A_k+\sum_{r=1}^{n}{}^r\beta_n{}^rA_k+\sum_{m=1}^{k}{}^m\gamma_n{}^m\alpha_0{}^0A_{k-m}\\&\qquad+\sum_{r=1}^{k-1}\sum_{m=1}^{r}{}^m\gamma_n{}^m\alpha_{k-r}{}^{k-r}\bar{A}_{r-m}\\&=\begin{cases}\displaystyle\sum_{m=n}^{k}{}^m\bar{\gamma}_{-n}{}^m\bar{\alpha}_0{}^0A_{k-m}\\ \qquad\displaystyle+\sum_{r=n}^{k-1}\sum_{m=n}^{r}{}^m\bar{\gamma}_{-n}{}^m\bar{\alpha}_{k-r}{}^{k-r}A_{r-m}\,, & (n\geqq 2,\ k>2)\\ {}^k\bar{\gamma}_{-k}{}^k\bar{\alpha}_0{}^0A_0\,, & (n=k\geqq 2)\\ 0\,, & (n>k\geqq 2)\,.\end{cases}\end{aligned}\qquad(25)$$

From these equations the coefficients ${}^nA_k$ for $n\geqq 1$ can be expressed successively in terms of the circulation coefficients ${}^0A_k$. Six of these coefficients are given below. Thus

$$\left.\begin{aligned}{}^1A_0&=ca_0(\bar{a}_0-a_2)-ia_1\,{}^0A_0\,,\\ {}^1A_1&=\frac{1}{2}a_0(a_2-\bar{a}_0)\,{}^0A_0-ia_1\,{}^0A_1\,,\\ {}^1A_2&=\frac{1}{4}ca_0\bar{a}_0(a_0\bar{a}_0-2a_0a_2+a_2\bar{a}_2)\\&\quad+\frac{1}{4}ia_0\{a_0a_3+(\bar{a}_0-a_2)(\bar{a}_1-a_1)\}\,{}^0A_0\\&\quad-\frac{1}{2}a_0(\bar{a}_0-a_2)\,{}^0A_1-ia_1\,{}^0A_2\,,\\ {}^2A_0&=ca_0\{a_1(\bar{a}_0-a_2)-a_0a_3\}\\&\qquad-i\left(a_0a_2+\frac{1}{2}a_1^2\right){}^0A_0\,,\\ {}^2A_1&=\frac{1}{2}a_0\{a_0a_3-a_1(\bar{a}_0-a_2)\}\,{}^0A_0\\&\qquad-i\left(a_0a_2+\frac{1}{2}a_1^2\right){}^0A_1\,,\\ {}^3A_0&=ca_0\{(\bar{a}_0-a_2)(a_0a_2+a_1^2)-2a_0a_1a_3-a_0^2a_4\}\\&\qquad-i\left(a_0^2a_3+2a_0a_1a_2+\frac{1}{3}a_1^3\right){}^0A_0\,.\end{aligned}\right\}\qquad(26)$$

With the help of (17) and (7), the expression (10) for the forces on the aerofoil gives $X=0$ and

$$\begin{aligned}\frac{Y}{\pi\rho}=2cA_0-\frac{A_0^2}{b}&-2A_0\sum_{r=1}^{\infty}\frac{r}{(2i)^{r+1}b^{r+1}}\\&\times\{\bar{A}_r+(-1)^{r+1}A_r\}\\&-\sum_{n=1}^{\infty}\sum_{r=1}^{\infty}\frac{(n+r)!\,i^{n-r}}{(n-1)!\,(r-1)!\,2^{n+r}}\cdot\frac{A_n\bar{A}_r}{b^{n+r+1}}\,,\end{aligned}\qquad(27)$$

so that, by writing

$$Y=\sum_{k=0}^{\infty}Y_k/b^k\,,\qquad(28)$$

the coefficients Y_k can be found once and for all for any given shape of an aerofoil. The first five coefficients are given below.

$$\frac{Y_0}{\pi\rho}=2c\,{}^0A_0\,,\qquad(29)$$

$$\frac{Y_1}{\pi\rho}=2c\,{}^0A_1-({}^0A_0)^2\,,\qquad(30)$$

$$\begin{aligned}\frac{Y_2}{\pi\rho}=&2c\,{}^0A_2-2\,{}^0A_0{}^0A_1\\&+\frac{1}{2}c\{a_0(\bar{a}_0-a_2)+\bar{a}_0(a_0-\bar{a}_2)\}\,{}^0A_0\\&-\frac{1}{2}i(a_1-\bar{a}_1)({}^0A_0)^2\,,\end{aligned}\qquad(31)$$

$$\begin{aligned}\frac{Y_3}{\pi\rho}=&-\frac{1}{2}c^2a_0\bar{a}_0(\bar{a}_0-a_2)(a_0-\bar{a}_2)\\&+\frac{1}{2}ic\{(a_1-\bar{a}_1)(2a_0\bar{a}_0-a_0a_2-\bar{a}_0\bar{a}_2)\\&\qquad-a_0^2a_3+\bar{a}_0^2\bar{a}_3\}\,{}^0A_0\\&+\frac{1}{2}c(2a_0\bar{a}_0-a_0a_2-\bar{a}_0\bar{a}_2)\,{}^0A_1\\&+\frac{1}{4}\{(a_1-\bar{a}_1)^2+3(a_0a_2+\bar{a}_0\bar{a}_2)\\&\qquad-2a_0\bar{a}_0\}({}^0A_0)^2\\&-i(a_1-\bar{a}_1)\,{}^0A_0{}^0A_1-2\,{}^0A_0{}^0A_2-({}^0A_1)^2\\&\qquad+2c\,{}^0A_3\,,\end{aligned}\qquad(32)$$

$$
\begin{aligned}
\frac{Y_4}{\pi\rho}=&\frac{3}{4}ic^2a_0\bar{a}_0\{(\bar{a}_1-a_1)(a_0-\bar{a}_2)(\bar{a}_0-a_2)\\
&\quad+(a_0{}^2a_3-\bar{a}_0{}^2\bar{a}_3)+(\bar{a}_0a_2\bar{a}_3-a_0\bar{a}_2a_3)\}\\
&+\frac{3}{8}c[2a_0\bar{a}_0\{a_0\bar{a}_0+2a_2\bar{a}_2-(a_1-\bar{a}_1)^2\}\\
&\quad+(a_0a_2+\bar{a}_0\bar{a}_2)\{(a_1-\bar{a}_1)^2-5a_0\bar{a}_0\}\\
&\quad+(a_0a_2+\bar{a}_0\bar{a}_2)^2+2(a_1-\bar{a}_1)(a_0{}^2a_3\\
&\quad-\bar{a}_0{}^2\bar{a}_3)+(a_0{}^3a_4+\bar{a}_0{}^3\bar{a}_4)]\,{}^0A_0\\
&+\frac{1}{2}ic\{(a_1-\bar{a}_1)(2a_0\bar{a}_0-a_0a_2-\bar{a}_0\bar{a}_2)\\
&\quad-(a_0{}^2a_3-\bar{a}_0{}^2\bar{a}_3)\}\,{}^0A_1\\
&+\frac{1}{2}c\{2a_0\bar{a}_0-(a_0a_2+\bar{a}_0\bar{a}_2)\}\,{}^0A_2\\
&+\frac{1}{8}i[(a_1-\bar{a}_1)\{9(a_0a_2+\bar{a}_0\bar{a}_2)-6a_0\bar{a}_0\\
&\quad+(a_1-\bar{a}_1)^2\}+6(a_0{}^2a_3-\bar{a}_0{}^2\bar{a}_3)]({}^0A_0)^2\\
&+\frac{1}{2}\{3(a_0a_2+\bar{a}_0\bar{a}_2)+(a_1-\bar{a}_1)^2\\
&\quad-2a_0\bar{a}_0\}\,{}^0A_0{}^0A_1\\
&-i(a_1-\bar{a}_1)\,{}^0A_0{}^0A_2-\frac{1}{2}i(a_1-\bar{a}_1)({}^0A_1)^2\\
&-2\,{}^0A_1{}^0A_2-2\,{}^0A_0{}^0A_3+2c\,{}^0A_4\,. \qquad (33)
\end{aligned}
$$

§ 5. Determination of the Circulation

Adopting the usual procedure for aerofoils possessing a sharp trailing edge we choose the circulation so that the flow leaves the trailing edge smoothly. The transformation (2) can always be chosen so that the trailing edge corresponds to the point $\zeta=-\pi$ in the ζ-plane. Thus, the condition for finite velocity at this point is

$$(dw/d\zeta)_{\zeta=-\pi}=0\,, \qquad (34)$$

which, together with (13) and (16), gives

$$A_0=i\sum_{n=1}^{\infty}(-1)^n n(D_n-\bar{D}_n)\,. \qquad (35)$$

If the expressions (17), (20), (21) for A_0 and D_n are substituted in (35), the resulting equation must be true for all values of b, so that, equating to zero the coefficients of each power of $1/b$, we obtain

$$
\left.
\begin{aligned}
&{}^0A_0=ic(\bar{a}_0-a_0)\,,\\
&{}^0A_1=i({}^1\bar{\gamma}_{-1}{}^1\bar{\alpha}_0-{}^1\gamma_{-1}{}^1\alpha_0)\,{}^0A_0\,,\\
&{}^0A_k=i\sum_{n=1}^{k}\sum_{m=n}^{k}(-1)^{n+1}n({}^m\bar{\gamma}_{-n}{}^m\bar{\alpha}_0\\
&\qquad\qquad-{}^m\gamma_{-n}{}^m\alpha_0)\,{}^0A_{k-m}\\
&\quad+i\sum_{n=1}^{k-1}\sum_{r=n}^{k-1}\sum_{m=n}^{r}(-1)^{n+1}\\
&\quad\times n({}^m\bar{\gamma}_{-n}{}^m\bar{\alpha}_{k-r}{}^{k-r}A_{r-m}\\
&\quad-{}^m\gamma_{-n}{}^m\alpha_{k-r}{}^{k-r}\bar{A}_{r-m})\,, \qquad (k\geqq 2)\,.
\end{aligned}
\right\}
\qquad (36)
$$

From these equations and (26), the circulation coefficients ${}^0A_k$ can be obtained successively and explicitly in terms of the constants a_n which define the aerofoil section. The first few of the coefficients ${}^0A_k$, which are necessary for our calculation, are

$${}^0A_1=\frac{1}{2}c(\bar{a}_0-a_0)^2, \qquad (37)$$

$$
\begin{aligned}
{}^0A_2=&\frac{1}{4}ic\{a_0\bar{a}_0(\bar{a}_2-a_2)+(\bar{a}_0-a_0)^2(a_1-\bar{a}_1)\\
&\qquad+3a_0\bar{a}_0(\bar{a}_0-a_0)\}\,, \qquad (38)
\end{aligned}
$$

$$
\begin{aligned}
{}^0A_3=&\frac{1}{8}c(\bar{a}_0-a_0)^2\{a_0\bar{a}_0-(a_1-\bar{a}_1)^2\}\\
&+\frac{1}{8}c(\bar{a}_0-a_0)(a_0{}^2a_2-\bar{a}_0{}^2\bar{a}_2)\\
&+\frac{1}{4}ca_0\bar{a}_0(\bar{a}_0-a_0)\{3(\bar{a}_1-a_1)+(\bar{a}_2-a_2)\}\\
&+\frac{1}{4}ca_0\bar{a}_0\{(\bar{a}_1-a_1)(\bar{a}_2-a_2)+(a_0a_2+\bar{a}_0\bar{a}_2)\\
&\qquad+(a_0a_3+\bar{a}_0\bar{a}_3)-2a_0\bar{a}_0\}\,, \qquad (39)
\end{aligned}
$$

$$
\begin{aligned}
{}^0A_4=&-\frac{1}{16}ic(\bar{a}_0-a_0)^3\{a_0\bar{a}_0+2(a_0a_2+\bar{a}_0\bar{a}_2)\}\\
&+\frac{1}{16}ic(\bar{a}_0-a_0)^2[(\bar{a}_1-a_1)^3+3(\bar{a}_1-a_1)\\
&\quad\times\{(a_0a_2+\bar{a}_0\bar{a}_2)-a_0\bar{a}_0\}-7a_0\bar{a}_0(\bar{a}_2-a_2)\\
&\quad-2(a_0{}^2a_2-\bar{a}_0{}^2\bar{a}_2)-(a_0{}^2a_3-\bar{a}_0{}^2\bar{a}_3)]\\
&-\frac{1}{16}ica_0\bar{a}_0(\bar{a}_0-a_0)\{9(\bar{a}_1-a_1)^2\\
&\quad+9(\bar{a}_1-a_1)(\bar{a}_2-a_2)+6(a_0+\bar{a}_0)(a_2+\bar{a}_2)\\
&\quad-4(a_0\bar{a}_0+a_2\bar{a}_2)+7(a_0a_3+\bar{a}_0\bar{a}_3)\}\\
&+\frac{1}{16}ica_0\bar{a}_0[a_0\bar{a}_0\{12(\bar{a}_1-a_1)+(\bar{a}_2-a_2)\\
&\quad-6(\bar{a}_3-a_3)\}-3(\bar{a}_1-a_1)^2(\bar{a}_2-a_2)\\
&\quad-6(\bar{a}_1-a_1)(a_0\bar{a}_2+\bar{a}_0a_2)\\
&\quad-6(\bar{a}_1-a_1)(a_0a_3+\bar{a}_0\bar{a}_3)+3(a_0a_2{}^2-\bar{a}_0\bar{a}_2{}^2)\\
&\quad+3(a_0{}^2a_4-\bar{a}_0{}^2\bar{a}_4)]. \qquad (40)
\end{aligned}
$$

Using these results, we obtain, from (29)—(33), the first five coefficients Y_0, Y_1, Y_2, Y_3, Y_4 in the expression (28) for the lift in the forms :

$$Y_0=2\pi i\rho c^2(\bar{a}_0-a_0)\,, \qquad (41)$$

$$\frac{Y_1}{Y_0}=i(a_0-\bar{a}_0)\,, \qquad (42)$$

$$
\begin{aligned}
\frac{Y_2}{Y_0}=&\frac{1}{2}(\bar{a}_0-a_0)(a_1-\bar{a}_1)-\frac{1}{2}(\bar{a}_0-a_0)^2\\
&+\frac{a_0\bar{a}_0(\bar{a}_2-a_2)}{4(\bar{a}_0-a_0)}+\frac{1}{4}(5a_0\bar{a}_0-a_0a_2-\bar{a}_0\bar{a}_2)\,,
\end{aligned}
\qquad (43)
$$

$$
\begin{aligned}
\frac{Y_3}{Y_0}=&\frac{i}{4}\,\frac{a_0\bar{a}_0}{\bar{a}_0-a_0}\,\{3a_0\bar{a}_0+a_2\bar{a}_2-2(a_0a_2+\bar{a}_0\bar{a}_2)\\
&-(a_0a_3+\bar{a}_0\bar{a}_3)-(\bar{a}_1-a_1)(\bar{a}_2-a_2)\}
\end{aligned}
$$

$$
\begin{aligned}
&+\frac{1}{8}i[2(\bar{a}_1-a_1)\{(a_0a_2+\bar{a}_0\bar{a}_2)-5a_0\bar{a}_0\}\\
&\quad-4a_0\bar{a}_0(\bar{a}_2-a_2)-(a_0{}^2a_2-\bar{a}_0{}^2\bar{a}_2)\\
&\quad-2(a_0{}^2a_3-\bar{a}_0{}^2\bar{a}_3)]\\
&+\frac{1}{8}i(\bar{a}_0-a_0)\{4(a_0a_2+\bar{a}_0\bar{a}_2)\\
&\quad+2(\bar{a}_1-a_1)^2-11a_0\bar{a}_0\}\\
&+\frac{1}{2}i(\bar{a}_0-a_0)^2(\bar{a}_1-a_1)+\frac{1}{8}i(\bar{a}_0-a_0)^3,
\end{aligned}
\tag{44}
$$

$$
\begin{aligned}
\frac{Y_4}{Y_0}=&\frac{1}{16}\frac{a_0\bar{a}_0}{\bar{a}_0-a_0}[6(\bar{a}_1-a_1)\{3a_0\bar{a}_0+a_2\bar{a}_2\\
&\quad-(a_0a_3+\bar{a}_0\bar{a}_3)-(a_0+\bar{a}_0)(a_2+\bar{a}_2)\}\\
&\quad-(\bar{a}_2-a_2)\{(a_0a_2+\bar{a}_0\bar{a}_2)-3a_0\bar{a}_0\}\\
&\quad-6a_0\bar{a}_0(\bar{a}_3-a_3)-3(\bar{a}_1-a_1)^2(\bar{a}_2-a_2)\\
&\quad+3(a_0a_2{}^2-\bar{a}_0\bar{a}_2{}^2)+6(a_0{}^2a_3-\bar{a}_0{}^2\bar{a}_3)\\
&\quad+3(a_0{}^2a_4-\bar{a}_0{}^2\bar{a}_4)+6(\bar{a}_0a_2\bar{a}_3-a_0\bar{a}_2a_3)]\\
&+\frac{1}{16}[8a_0{}^2\bar{a}_0{}^2-15a_0\bar{a}_0(\bar{a}_1-a_1)^2\\
&\quad+16a_0\bar{a}_0(a_0\bar{a}_0+a_2\bar{a}_2)\\
&\quad-11a_0\bar{a}_0(a_0a_3+\bar{a}_0\bar{a}_3)+3(a_0a_2+\bar{a}_0\bar{a}_2)^2\\
&\quad+(a_0a_2+\bar{a}_0\bar{a}_2)\{3(\bar{a}_1-a_1)^2-22a_0\bar{a}_0\}\\
&\quad-15a_0\bar{a}_0(\bar{a}_1-a_1)(\bar{a}_2-a_2)\\
&\quad-6(\bar{a}_1-a_1)(a_0{}^2a_3-\bar{a}_0{}^2\bar{a}_3)\\
&\quad+3(a_0{}^3a_4+\bar{a}_0{}^3\bar{a}_4)\\
&\quad-6a_0\bar{a}_0(\bar{a}_0+a_0)(\bar{a}_2+a_2)]\\
&+\frac{1}{16}(\bar{a}_0-a_0)[2(\bar{a}_1-a_1)^3+3(\bar{a}_1-a_1)\\
&\quad\times\{5(a_0a_2+\bar{a}_0\bar{a}_2)-11a_0\bar{a}_0\}\\
&\quad-13a_0\bar{a}_0(\bar{a}_2-a_2)-4(a_0{}^2a_2-\bar{a}_0{}^2\bar{a}_2)\\
&\quad-9(a_0{}^2a_3-\bar{a}_0{}^2\bar{a}_3)]\\
&+\frac{1}{16}(\bar{a}_0-a_0)^2\{4(a_0a_2+\bar{a}_0\bar{a}_2)\\
&\quad+6(\bar{a}_1-a_1)^2-13a_0\bar{a}_0\}\\
&+\frac{3}{16}(\bar{a}_0-a_0)^3(\bar{a}_1-a_1).
\end{aligned}
\tag{45}
$$

APPLICATION OF THE METHOD TO THE FLOW PAST SYMMETRICAL JOUKOWSKI AEROFOIL IN THE PRESENCE OF A WALL

§ 6. Case of Symmetrical Joukowski Aerofoil of Small Thickness

Applying Green's method so far described, we shall next calculate the lift on the symmetrical Joukowski aerofoil of small thickness placed at an angle of attack θ in the vicinity of a plane rigid wall. Neglecting the third and higher powers of ε, the chord length l of the aerofoil is given by

$$
l=4r(1+\varepsilon^2)\,. \tag{46}
$$

Thus, retaining only terms up to the order of ε^2, the coefficients a_n in the transformation (2) now become

$$
\left.
\begin{aligned}
a_0&=\frac{1}{4}l(1+\varepsilon-\varepsilon^2)e^{i\theta}\,,\\
a_1&=\frac{1}{4}l\varepsilon e^{i\theta}\,,\\
a_2&=\frac{1}{4}l(1-\varepsilon)e^{i\theta}\,,\\
a_3&=-\frac{1}{4}l\varepsilon(1-2\varepsilon)e^{i\theta}\,,\\
a_4&=\frac{1}{4}l\varepsilon^2e^{i\theta}\,,\\
a_n&=0\,,\quad(n\geqq 5)\,.
\end{aligned}
\right\}
\tag{47}
$$

Substituting these coefficients in the general expressions (41)—(45) we have

$$
\left.
\begin{aligned}
&Y_0=\pi\rho lc^2(1+\varepsilon-\varepsilon^2)\sin\theta\,,\\
&\frac{Y_1}{lY_0}=-\frac{1}{2}(1+\varepsilon-\varepsilon^2)\sin\theta\,,\\
&\frac{Y_2}{l^2Y_0}=\frac{1}{32}(5-3\cos 2\theta)\\
&\qquad+\frac{1}{32}\varepsilon(11-6\cos 2\theta)\\
&\qquad-\frac{1}{64}\varepsilon^2(7-4\cos 2\theta)\,,\\
&\frac{Y_3}{l^3Y_0}=-\frac{1}{256}\Big\{(26\sin\theta-6\sin 3\theta)\\
&\qquad+\varepsilon\left(\frac{3}{\sin\theta}+78\sin\theta-12\sin 3\theta\right)\\
&\qquad+\varepsilon^2\left(\frac{5}{\sin\theta}+14\sin\theta+5\sin 3\theta\right)\Big\}\,,\\
&\frac{Y_4}{l^4Y_0}=\frac{1}{2048}\{(47-70\cos 2\theta\\
&\qquad+11\cos 4\theta)\\
&\qquad+\varepsilon(206-228\cos 2\theta+25\cos 4\theta)\\
&\qquad+\varepsilon^2(195-50\cos 2\theta-15\cos 4\theta)\}\,.
\end{aligned}
\right\}
\tag{48}
$$

With these values of Y_0, Y_1, Y_2, Y_3, Y_4 the power-series expansion for the lift Y on the symmetrical Joukowski aerofoil is ultimately given by

$$
\begin{aligned}
\frac{Y}{Y_0}=1&+\frac{Y_1}{Y_0}\cdot\frac{1}{b}+\frac{Y_2}{Y_0}\cdot\frac{1}{b^2}\\
&+\frac{Y_3}{Y_0}\cdot\frac{1}{b^3}+\frac{Y_4}{Y_0}\cdot\frac{1}{b^4}\,.
\end{aligned}
\tag{49}
$$

It may not be superfluous to show here that if we put $\varepsilon=0$ in (49), we can obtain the well-known series expansion[3)] for the lift on a plane aerofoil of length l in the presence of a plane wall. In fact, we have

$$
\begin{aligned}
\frac{Y}{Y_0}=1&-\frac{1}{2}\sin\theta\frac{l}{b}+\frac{1}{16}(4-3\cos^2\theta)\left(\frac{l}{b}\right)^2\\
&-\frac{1}{32}\sin\theta(4-3\cos^2\theta)\left(\frac{l}{b}\right)^3
\end{aligned}
$$

$$+\frac{1}{512}(32-57\cos^2\theta+22\cos^4\theta)\left(\frac{l}{b}\right)^4, \tag{50}$$

b being now the distance of the mid-point of the plane aerofoil from the wall.

§ 7. Numerical Discussions

Values of the ratio Y/Y_0 have been calculated numerically in three cases in which the thickness parameter ε of the aerofoil takes the values 0, 0.1 and 0.2 respectively, the corresponding thickness ratios being 0, 0.118 and 0.215 respectively. The values of the angle of attack have been taken to be 5° and 10°.

The results are shown in Tables I and II, and curves of Y/Y_0 are plotted against l/b in Figs. 3 and 4.

Table I. ($\theta=5°$)

l/b	$\varepsilon=0$	$\varepsilon=0.1$	$\varepsilon=0.2$
0.1	0.9963	0.9960	0.9958
0.2	0.9938	0.9935	0.9933
0.3	0.9926	0.9923	0.9921
0.4	0.9925	0.9923	0.9921
0.5	0.9935	0.9933	0.9928
0.6	0.9955	0.9951	0.9941
0.7	0.9985	0.9976	0.9956
0.8	1.0023	1.0006	0.9971
0.9	1.0063	1.0038	—
1.0	1.0119	1.0071	—

Table II. ($\theta=10°$)

l/b	$\varepsilon=0$	$\varepsilon=0.1$	$\varepsilon=0.2$
0.1	0.9920	0.9914	0.9909
0.2	0.9853	0.9843	0.9826
0.3	0.9799	0.9787	0.9779
0.4	0.9757	0.9745	0.9737
0.5	0.9726	0.9714	0.9707
0.6	0.9705	0.9695	0.9687
0.7	0.9694	0.9684	0.9675
0.8	0.9691	0.9631	0.9670
0.9	0.9695	0.9683	0.9669
1.0	0.9704	0.9690	—

From these tables and figures it will readily be seen that when the symmetrical Joukowski aerofoil of small thickness is placed in the vicinity of a plane rigid wall at small angles of attack as used in practice, the wall effect on the lift is quite similar to that in the case of a plane aerofoil. Namely, as the symmetrical Joukowski aerofoil approaches the wall, the lift first decreases and then tends to increase to values which are greater than the corresponding values for the symmetrical Joukowski aerofoil in an unlimited stream, especially when the angle of attack is sufficiently small. Further it is found that in accordance with the prediction made by Tomotika *et al.*, the effect of thickness of the aerofoil is to decrease the value of the ratio Y/Y_0 even for small values of the angle of attack.

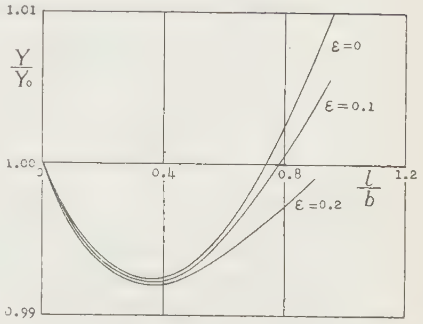

Fig. 3. ($\theta=5°$)

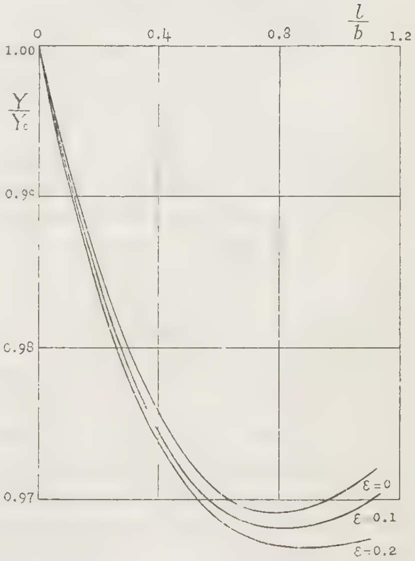

Fig. 4. ($\theta=10°$)

The present problem has been suggested by Professor S. Tomotika. The writer wishes to express his cordial thanks to him for his valuable advice and encouragement throughout the present investigation.

References

1) S. Tomotika, Z. Hasimoto and K. Urano: Quart. Journ. Mech. and Applied Math. **4** (1951) 289.
2) A. E. Green: Quart. Journ. Math., Oxford Series, **18** (1947) 167.
3) S. Tomotika, T. Nagamiya and Y. Takenouti: Report Aeron. Res. Inst., Tokyo Imp. Univ. No. **97** (1933).

JOURNAL OF THE PHYSICAL SOCIETY OF JAPAN Vol. 9, No. 2, MAR.—APR., 1954

Note on the Lift acting on a Circular-arc Aerofoil in a Stream bounded by a Plane Wall

By Hiroomi FUJIKAWA

Junior College of Engineering, Naniwa University

(Received June 1, 1953)

Being a continuation of the preceding paper, Green's new method, somewhat extended by the present writer, is applied to the evaluation of the lift acting on a circular-arc aerofoil in the presence of an infinite plane rigid wall. The expression for the lift is obtained in the form of a power series. By performing detailed numerical calculations, a discussion is made on the manner in which the ground-effect on the lift of an aerofoil is modified by its camber.

It is thus found that in accordance with the prediction made by Tomotika *et al.*, as the arc-aerofoil of sufficiently small camber approaches the wall, the lift first decreases and then tends to increase to values which are greater than the corresponding values for the same arc-aerofoil in an unlimited stream, especially when the angle of attack takes small values as used in practice. It is also found that the rate of increase in the lift becomes smaller as the camber of the aerofoil increases.

§ 1. Introduction and Summary

The lift and moment of a circular-arc aerofoil in the presence of an infinite plane rigid wall have been first evaluated by Green[1)] by employing suitable conformal transformations. Later, Tomotika, Tamada and Umemoto[2)] have reinvestigated the problem by using suitable conformal transformations, which are somewhat different from those used by Green. By carrying out detailed numerical calculations for three circular-arc aerofoils, the cambers of which are respectively 0.022, 0.053 and 0.097 approximately, the value of the angle of attack being taken to be 5° in all cases, Tomotika *et al.* have shown that when the camber is sufficiently small and the angle of attack is also fairly small, as in practice, the manner in which the lift and moment coefficients of a circular-arc aerofoil are affected by the presence of the wall is quite similar to that for the case of a plane aerofoil: namely, as the circular-arc aerofoil approaches the wall, the lift coefficient first decreases and then increases to values which are greater than the corresponding values for the arc-aerofoil in an unlimited stream. It has also been shown that similar results hold for the moment coefficient.

In the present note, a power-series expansion for the lift of a circular-arc aerofoil in a stream bounded by a plane wall is obtained, by applying Green's new method[3)] which has been somewhat extended by the present writer in the preceding paper[4)]. By performing detailed numerical calculations it is shown that in accordance with the results obtained by Tomotika *et al.*[2)], as the arc-aerofoil of sufficiently small camber approaches the wall, the lift first decreases and then tends to increase to values which are greater than the corresponding values for the same arc-aerofoil in an unbounded stream, especially when the angle of attack takes small values used in practice. It is also shown that the ground-effect on the lift of an aerofoil is greatly modified by its camber, and as predicted by Tomotika, the ground-effect on the lift becomes smaller as the camber of the aerofoi increases.

§ 2. The Conformal Transformations

We consider a steady irrotational continuous flow of an incompressible perfect fluid past a circular-arc aerofoil ABC which is placed at an angle of attack θ in the vicinity of an infinite plane rigid wall (Fig. 1). We take the plane of fluid motion, which is assumed to be two-dimensional, as the z-plane, and we take, with the mid-point B of the arc-aerofoil

ABC as the origin, the x-axis parallel to the wall. We assume that the fluid at infinity flows with a constant velocity c parallel to the wall in the negative direction of the x-axis.

Let 4α be the angle subtended by the arc ABC at the centre of its circle whose radius will be denoted by a. Then, the length l of the chord AC is given by $l=2a\sin 2\alpha$. It can be shown without difficulty that the equation:

$$\frac{z+ia(1-e^{2i\alpha})e^{i\theta}}{z+ia(1-e^{-2i\alpha})e^{i\theta}}=\left(\frac{1+e^{i\zeta}}{1-e^{i\zeta-2i\alpha}}\right)^2, \quad (\zeta=\xi+i\eta) \tag{1}$$

transforms the arc-aerofoil ABC in the z-plane into the straight line:

$$\eta=0\,, \qquad \xi=0\rightarrow-2\pi \tag{2}$$

in the ζ-plane.

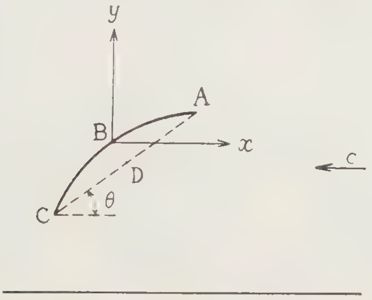

Fig. 1. z-plane.

As in the preceding paper, equation (1) can be expressed in the form:

$$z=e^{-i\zeta}\sum_{n=0}^{\infty}a_n e^{in\zeta}\,, \tag{3}$$

where the coefficients a_n are given by

$$\left.\begin{aligned} a_0&=ae^{i(\theta+\alpha)}\sin\alpha\,,\\ a_1&=-iae^{i\theta}\sin^2\alpha\,,\\ a_n&=-(-i)^n ae^{-i(n-1)\alpha}\\ &\quad\times e^{i\theta}\sin^{n-1}\alpha\cos^2\alpha\,. \qquad (n\geqq 2)\end{aligned}\right\} \tag{4}$$

§ 3. The Lift on the Circular-arc Aerofoil

The lift Y acting on the circular-arc aerofoil under discussion may be expressed as a power series in $1/b$, namely:

$$Y=\sum_{k=0}^{\infty}Y_k/b^k\,, \tag{5}$$

where b is the height of the mid-point B of the arc ABC above the boundary wall.

Substituting the values of the coefficients a_n given by (4) in the general expressions (41)—(45) in the preceding paper, the first five coefficients Y_0, Y_1, Y_2, Y_3, Y_4 in (5) become

$$Y_0=\pi\rho lc^2(\sin\theta+\cos\theta\tan\alpha)\,, \tag{6}$$

$$\frac{Y_1}{lY_0}=-\frac{1}{2}(\sin\theta+\cos\theta\tan\alpha), \tag{7}$$

$$\frac{Y_2}{l^2Y_0}=\frac{1}{64}\left\{2(4-3\cos 2\theta)+4\sin 2\theta\tan\alpha +5\tan^2\alpha+\frac{2\sin\theta}{\sin\theta+\cos\theta\tan\alpha}\right\}, \tag{8}$$

$$\begin{aligned}\frac{Y_3}{l^3Y_0}=&-\frac{1}{256}\{6(3\sin\theta-\sin 3\theta)-6\cos\theta\tan\alpha\\ &+(8\sin\theta-3\sin 3\theta)\tan^2\alpha\\ &-(2\cos\theta+\cos 3\theta)\tan^3\alpha\}\\ &-\frac{1}{512}\cdot\frac{8(1-\cos 2\theta)+8\tan^2\alpha+3\tan^4\alpha}{\sin\theta+\cos\theta\tan\alpha}\,,\end{aligned} \tag{9}$$

$$\begin{aligned}\frac{Y_4}{l^4Y_0}=\frac{1}{2048}\Big[&(35-50\cos 2\theta+11\cos 4\theta)\\ &-(48\sin 2\theta-11\sin 4\theta)\tan\alpha\\ &+(12-18\cos 2\theta+7\cos 4\theta)\tan^2\alpha\\ &-(5\sin 2\theta-\sin 4\theta)\tan^3\alpha\\ &+(1-\cos 2\theta+\cos 4\theta)\tan^4\alpha\\ &+\frac{\sin\theta}{\sin\theta+\cos\theta\tan\alpha}\{4(3-5\cos 2\theta)\\ &+3(17+4\cos 2\theta)\tan^2\alpha+9\tan^4\alpha\}\Big].\end{aligned} \tag{10}$$

If, in place of the height b of B above the wall, we use the height H of the mid-point D of the chord AC, which is related to b by the equation

$$b=H+\frac{1}{2}l\tan\alpha\cos\theta\,, \tag{11}$$

the lift ratio Y/Y_0 can be expressed as a power series in l/H in the form:

$$\frac{Y}{Y_0}=1+\sum_{k=1}^{\infty}\frac{Y_k'}{Y_0}\left(\frac{l}{H}\right)^k. \tag{12}$$

If we make use of the so-called camber σ of the arc-aerofoil, which is defined as usual by the ratio of its maximum height to the chord length so that $\sigma=1/2\tan\alpha$, the values of Y_0 and of the first four coefficients Y_k' become as follows:

$$Y_0=\pi\rho lc^2(\sin\theta+2\sigma\cos\theta)\,, \tag{13}$$

$$\frac{Y_1'}{Y_0}=-\frac{1}{2}(\sin\theta+2\sigma\cos\theta)\,, \tag{14}$$

$$\frac{Y_2'}{Y_0}=\frac{1}{32}\left\{(4-3\cos 2\theta)+12\sigma\sin 2\theta +2\sigma^2(13+8\cos 2\theta)+\frac{\sin\theta}{\sin\theta+2\sigma\cos\theta}\right\}, \tag{15}$$

$$\frac{Y_3'}{Y_0}=-\frac{1}{128}\{(13\sin\theta-3\sin 3\theta)$$
$$+2\sigma(7\cos\theta-6\cos 3\theta)$$
$$+2\sigma^2(24\sin\theta+13\sin 3\theta)$$
$$+28\sigma^3(6\cos\theta+\cos 3\theta)\}$$
$$-\frac{1}{32}\cdot\frac{2\sigma^2+3\sigma^4}{\sin\theta+2\sigma\cos\theta}, \tag{16}$$

$$\frac{Y_4'}{Y_0}=\frac{1}{2048}\Big[(59-74\cos 2\theta+11\cos 4\theta)$$
$$+2\sigma(48\sin 2\theta-25\sin 4\theta)$$
$$+4\sigma^2(84-30\cos 2\theta-29\cos 4\theta)$$
$$+8\sigma^3(105\sin 2\theta+23\sin 4\theta)$$
$$+16\sigma^4(115+105\cos 2\theta+11\cos 4\theta)$$
$$-\frac{4\sin\theta}{\sin\theta+2\,\sigma\cos\theta}\{(3-\cos 2\theta)$$
$$-3\sigma^2(1+4\cos 2\theta)+36\sigma^4\}\Big]. \tag{17}$$

It can easily be seen that if we put $\sigma=0$ in (13)—(17), these coefficients degenerate into those for a plane aerofoil⁵⁾.

§ 4. Numerical Discussions

The values of the ratio Y/Y_0 have been calculated numerically for three different circular-arc aerofoils, taking α to be equal to 2°30′, 6° and 11° respectively; these make the cambers, σ, of the aerofoils approximately equal to 0.022, 0.053 and 0.097 respectively. The values of the angle of attack θ have been taken to be 5° and 10° in all cases.

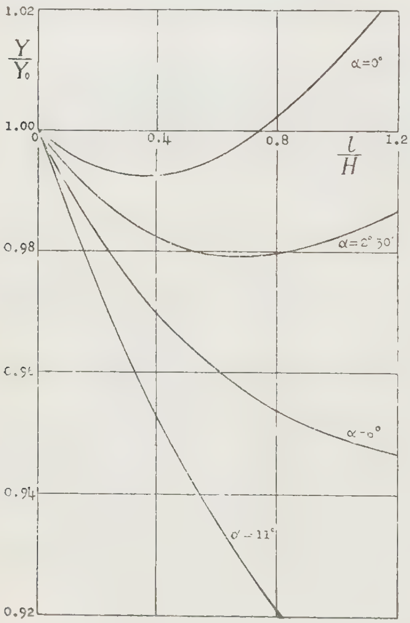

Fig. 2. ($\theta=5°$)

The values for the plane aerofoil ($\alpha=0°$, $\sigma=0$) have also been calculated for comparison.

The results are given in Tables I and II, and they are also shown graphically in Figs. 2 and 3.

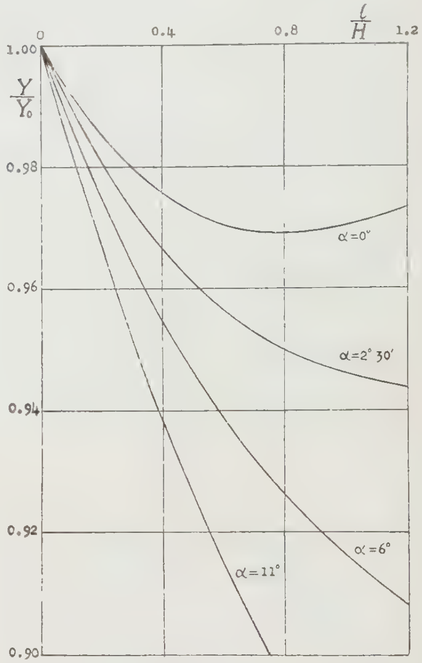

Fig. 3. ($\theta=10°$)

Table I. Values of Y/Y_0 when $\theta=5°$.

l/H	plane aerofoil ($\sigma=0$, $\alpha=0°$)	$\sigma=0.022$ ($\alpha=2°30'$)	$\sigma=0.053$ ($\alpha=6°$)	$\sigma=0.097$ ($\alpha=11°$)
0.1	0.9963	0.9940	0.9909	0.9866
0.2	0.9938	0.9891	0.9829	0.9743
0.3	0.9926	0.9853	0.9759	0.9631
0.4	0.9925	0.9824	0.9699	0.9530
0.5	0.9935	0.9805	0.9647	0.9438
0.6	0.9955	0.9795	0.9603	0.9355
0.7	0.9985	0.9793	0.9567	0.9281
0.8	1.0023	0.9798	0.9538	0.9213
0.9	1.0068	0.9809	0.9514	0.9152
1.0	1.0119	0.9824	0.9495	0.9096
1.1	1.0174	0.9844	0.9480	0.9044
1.2	1.0232	0.9867	0.9468	0.8996
1.3	1.0291	0.9890	0.9457	0.8950
1.4	1.0349	0.9913	0.9446	0.8904

As an addendum, the values of Y/Y_0 for some values of l/H have been compared in Tables III, IV and V with the corresponding exact values, denoted by $(Y/Y_0)_{\text{exact}}$ which have been obtained by Tomotika, Tamada and Umemoto²⁾.

From these tables and figures, it will

Table II. Values of Y/Y_0 when $\theta=10°$.

l/H	plane aerofoil ($\sigma=0$, $\alpha=0°$)	$\sigma=0.022$ ($\alpha=2°30'$)	$\sigma=0.053$ ($\alpha=6°$)	$\sigma=0.097$ ($\alpha=11°$)
0.1	0.9920	0.9898	0.9868	0.9825
0.2	0.9853	0.9809	0.9749	0.9665
0.3	0.9799	0.9732	0.9642	0.9518
0.4	0.9757	0.9666	0.9546	0.9383
0.5	0.9726	0.9611	0.9461	0.9261
0.6	0.9705	0.9565	0.9386	0.9149
0.7	0.9694	0.9529	0.9320	0.9047
0.8	0.9691	0.9500	0.9261	0.8954
0.9	0.9695	0.9478	0.9210	0.8868
1.0	0.9704	0.9461	0.9163	0.8789
1.1	0.9717	0.9448	0.9121	0.8715
1.2	0.9733	0.9438	0.9082	0.8645
1.3	0.9749	0.9429	0.9045	0.8578
1.4	0.9764	0.9419	0.9007	0.8512

Table III. Camber $\sigma=0.022$ ($\alpha=2°30'$), $\theta=5°$.

l/H	Y/Y_0	$(Y/Y_0)_{\text{exact}}$
0.0875	0.9947	0.9947
0.1756	0.9902	0.9902
0.8098	0.9798	0.9801
1.5925	0.9951	1.0048

Table IV. Camber $\sigma=0.053$ ($\alpha=6°$), $\theta=5°$.

l/H	Y/Y_0	$(Y/Y_0)_{\text{exact}}$
0.2106	0.9821	0.9821
0.4267	0.9684	0.9684
1.0014	0.9495	0.9503
1.5555	0.9425	0.9501

Table V. Camber $\sigma=0.097$ ($\alpha=11°$), $\theta=5°$.

l/H	Y/Y_0	$(Y/Y_0)_{\text{exact}}$
0.3895	0.9540	0.9540
0.8111	0.9206	0.9208

readily be seen that in accordance with the prediction made by Tomotika *et al.*[2], when the camber of the arc-aerofoil is sufficiently small and the angle of attack is also fairly small, as in practice, the manner in which the lift coefficient of the arc-aerofoil is affected by the presence of the wall is quite similar to that for the case of a plane aerofoil: namely, as the arc-aerofoil approaches the wall, the lift coefficient first decreases and then increases to values which are greater than the corresponding values for the arc-aerofoil in an unbounded stream. Also, it will be seen that the ground-effect on the lift of an aerofoil is greatly modified by its camber. Thus, for large distance of the aerofoil from the bounding wall the effect of the camber is to decrease the lift found for a plane aerofoil as compared with the lift in an unlimited stream. As the aerofoil gets nearer to the wall, the lift eventually increases, as previously mentioned, above the values for an unbounded stream, for small angles of attack, but the rate of increase in the lift is considerably decreased owing to the effect of the camber of the aerofoil.

The present problem has been suggested by Professor S. Tomotika. The writer wishes to express his cordial thanks to him for his valuable advice and kind guidance throughout the present investigation.

References

1) A. E. Green: Proc. London Math. Soc. **46** (1940) 19.

2) S. Tomotika, K. Tamada and H. Umemoto: Quart. Journ. Mech. and Applied Math. **4** (1951) 1.

3) A. E. Green: Quart. Journ. Math., Oxford Series, **18** (1947) 167.

4) H. Fujikawa: J. Phys. Soc. Japan **9** (1954) 233.

5) S. Tomotika, T. Nagamiya and Y. Takenouti: Report Aeron. Res. Inst., Tokyo Imp. Univ. No. **97** (1933).

Journal of the Physical Society of Japan Vol. 9, No. 2, Mar.—Apr., 1954

Experimental Studies on the Force exerted on a Disc placed in a Flow of Rarefied Gas

By Yoshikazu SUGIURA*

Physical Institute, Nagoya University, Nagoya, Japan

(Received October 15, 1953)

Uyeda has devised a *flow-meter* in vacuum technique [Uyeda & Sugiura, J. Phys. Soc. Japan **8** (1953) 99], whose principle is simply to measure the force on a disc placed in a pipe through which a rarefied gas flows. As a basic study of the meter, the force was measured under various conditions, namely, the pressure of the flowing gas, the diameter of the disc, and the position of the disc along the radius of the pipe being varied. The results of the measurement are shown in figures and expressed by empirical formula.

The results here obtained are in agreement with theoretical expectations for Knudsen and Poiseuille flow. In the Knudsen flow, it is confirmed that the assumption of diffuse reflection of molecules on the disc is adequate. In the intermediate flow case between Knudsen and Poiseuille flow, the force shows an anomalous behaviour which seems to have some correlation with the phenomena observed by Knudsen [Ann. d. Phys. **28** (1909) 75] and others.

§ 1. Introduction

Recently Uyeda[1)2)] showed that the force exerted by a flow of rarefied gas on a disc placed in a pipe is proportional to the so-called Q-value, $Q=PS$ (P means the pressure and S the pumping speed), in high vacua. He applied this fact to the design of his "flow-meter".

As a basic study of the meter, in the present experiments the forces were measured at pressures from 1 to 10^{-5} mmHg, on discs of various radii ; the variation of the force was also studied, when the disc was moved along the radial direction.

§ 2. Theory

When a rarefied gas is flowing through a circular pipe of radius a and a small circular disc of radius c is put in the pipe perpendicularly to its axis, and if $c \ll a$ and $a \ll \lambda$, λ being the mean free path of gas molecules, the force F exerted on the disc by the flow, calculated by the kinetic theory, is given by the formula[3)]:

$$F=3(\pi M/8RT)^{1/2}\gamma Q(c/a)^2 , \qquad (1)$$

where R is the gas constant per mol, M the molecular weight of the gas, T the absolute temperature, and γ a constant determined by the nature of reflection of molecules on the surface of the disc. This formula holds, when the flow velocity is much smaller than the thermal velocity and $c/a \ll 1$.

On the other hand, if $c \gg \lambda$, the force F is calculated by the hydrodynamics. If the fluid is extended infinitely, it is expressed as follows[4)]:

$$F=16\eta c u , \qquad (2)$$

where η is the coefficient of viscosity and u the flow velocity. When the fluid is limited in a pipe, the force F may be expressed by the following form :

$$F=\beta\eta c\bar{u} = \beta\eta c\frac{1}{\pi a^2}\frac{Q}{P} , \qquad (2')$$

where $\bar{u}$ is the mean flow velocity. Therefore, if Q and F are measured for Knudsen flow, γ can be obtained from Eq. (1), and if Q, P and F are measured for Poiseuille flow, β from Eq. (2').

Outside the regions of Knudsen and Poiseuille flow, the proportional constants γ and β may take apparent values, say γ' and β', which depend on the pressure P. The experimental values of γ' or β', which are determined by inserting the observed values

---

* Now at the Electrotechnical Laboratory, Ministry of Trade and Industry, Tokyo, Japan.

of F, Q, and P in (1) or (2′), depend not only on P but also on the radius c of the disc. Since these effects are too complicated to be treated theoretically, these dependencies were empirically taken into account, as will be described in IV *b* and *c*). The value of γ should be obtained as the limiting value of γ' for very small disc and very low pressure.

§ 3. Experiment

After a preliminary measurement[5] with a small glass pipe ($2a=22.5$ mm), a more accurate measurement was carried out, using a large brass pipe ($2a=57.2$ mm). The arrangement used is shown in Fig. 1 a. The air dried by P_2O_5 flowed through the pipe of about 1 meter in length. The force on the disc was measured by a torsion pendulum, as shown in Fig. 1 b. The disc is made of a mica leaf of about 4/100 mm thick and is suspended by a tungsten wire of about 15/1000 mm in diameter. The arm of the torsion balance is a tungsten wire of about 2/100 mm in diameter and the mica disc is fixed to the wire with a small amount of shellac. The torsion constant of the suspender was determined by the usual method ; *i.e.* by measuring the periods of the torsion balance, with and without an additional mass of a known moment of inertia. The deflection of the pendulum was read by a lamp and scale.

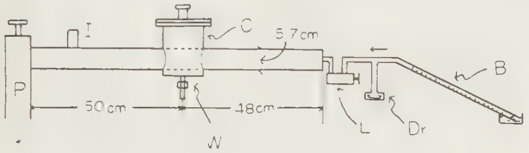

Fig. 1a.

P: Diffusion Pump, I: Ionization gauge,
C: Case of the pendulum (see Fig. 1b),
W: Window (see Fig. 1b),
L: Variable leak, Dr: Drying agent,
B: Burette.

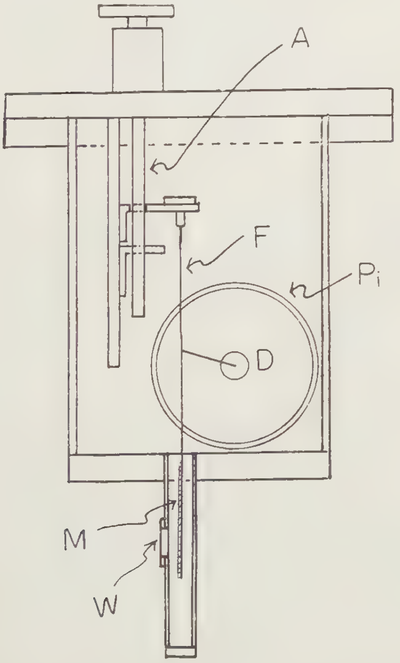

Fig. 1b.

D: Mica disc, F: Tungsten fiber,
Pi: Section of the pipe (shown by dotted lines in Fig. 1a),
M: Mirror, W: Window,
A: Device to adjust position of the disc.

The Q-value was measured by Dayton's Burette method[6] and the pressure by an ionization gauge at lower pressures and by an oil manometer at higher pressures.

To compute the value of the force F from the deflection D of the torsion balance, the formula

$$D=\text{const.}\, lF,$$

was assumed, where l is the length of the arm and the const. was determined from the torsion constant of the suspender and the distance between the scale and the mirror. The force exerted on the arm was, as a correction factor, taken into account in the computation of F. It was about 2% for the smallest disc. In the computation of γ' and β', the following numerical values were used:

$\eta=1.824\times10^{-4}-4.9\times10^{-7}(23°-t°)$*,

$M=29.0$ (molecular weight of dry air),

T=room temperature.

§ 4. Results and Discussions

a) γ'-P curve

An example of γ'-P curve is shown in Fig. 2a. As expected theoretically, γ' is constant in Knudsen flow and decreases linearly with $1/P$ in Poiseuille flow. The Fig. 2b shows the behaviour of γ' at the transition region from Knudsen flow to Poiseuille flow. It is

---

* from Landolt's table.

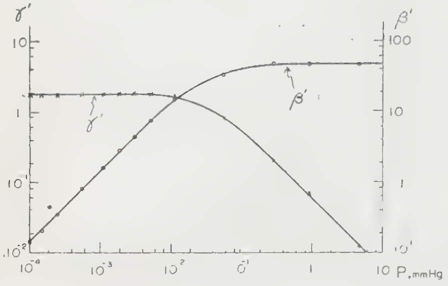

Fig. 2a.

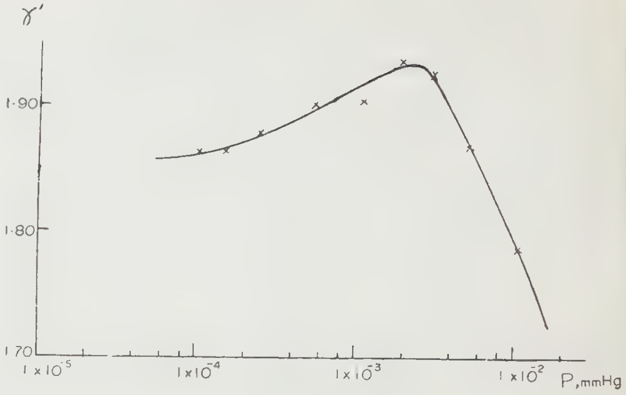

Fig. 2b.

Table I.

P mmHg	4.4×10^{-3}	3.1×10^{-3}	2.9×10^{-3}	2.2×10^{-3}
c cm	0.30	0.40	0.40	0.50
λ/c	3.7	4.0	4.3	4.4

worthy to be noted that γ' shows a maximum in this region. The value of γ' at the maximum exceeds that for the Knudsen flow by about 3.5%. The pressure at which the maximum appears is different for different value of c, but the corresponding value λ/c is almost constant as shown in Table I, using $\lambda=6.40\times10^{-6}$ cm at 760 mmHg and 15°C.

Knudsen, Gaede, and Azumi[7] measured the quantities of the flow through a glass capillary at various pressures and found that the quantity per unit pressure gradient had a minimum at the transition region. Knudsen reported that the minimum lay at $\lambda/c\approx5$ and its value was about 5% smaller than that in Knudsen flow.

The maximum observed in the present experiment and the minimum mentioned above may surely be a phenomenon characteristic of the transition region.

b) $\gamma'-(c/a)^2$ curve and γ

As mentioned in the preceding section, γ' is almost constant, independent of the pressure in Knudsen flow, but it depends on (c/a). The experimental curve of γ' *vs.* $(c/a)^2$ for Knudsen flow is shown in Fig. 3. In spite of this rather rough result, by the empirical formula obtained from the curve:

$$\gamma'=\gamma\{1+k(c/a)^2\}, \tag{3}$$

the values of constants

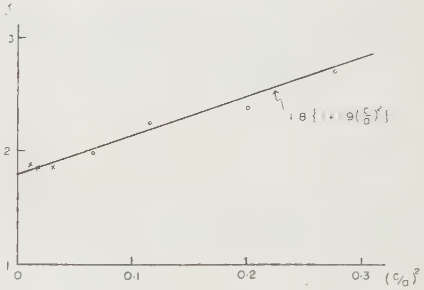

Fig. 3.

×: $a=2.86$ cm, ○: $a=1.13$ cm.

$$\gamma=1.8\,, \tag{4a}$$

and

$$k=1.9\,, \tag{4b}$$

are obtained.

We can calculate the theoretical value of γ after the method of Epstein[8] which was developed in relation to Millikan's oil drop experiment. According to his consideration, the molecules, which hit a surface of a sphere, reflect in the specular direction (1) or in the direction in accordance with the cosine-law (2). In the latter case, the following three cases are assumed: The reflected molecules run out with the conservation of velocity (2a), with the velocity corresponding to the surface temperature of the sphere which is assumed to be a thermal insulator (2b) or similarly as (2b) but the sphere assumed to be a thermal conductor (2c). The value of γ for a disc turns out respectively to be

(1) $\gamma=2$, (2a) $\gamma=1.89$, (2b) $\gamma=1.88$, and (2c) $\gamma=1.79$.

The present experimental result (4a) shows an agreement with the case (2c). Since, however, experimental errors of (4a) may amount to about 5%, both cases (2b) and (2c) are probable, so that we can state only that the molecules are reflected by the disc diffusely.

c) $\beta'-(c/a)$ curve

In the case of Poiseuille flow, β' is constant independent of the pressure, but depends on (c/a). The experimental values of β' in this region for various values of (c/a) are plotted in Fig. 4. From this figure, an empirical formula

$$\beta'=\beta\{1+k'(c/a)\} \tag{5}$$

with

$$\beta=32, \tag{6a}$$

$$k'=2.4, \tag{6b}$$

is obtained for small value of c/a $(0.1<c/a<0.3)$. The value 32 of β may be reasonable, because the coefficient 16 in Eq. (2) is doubled by the reason that the flow velocity u_0 at the center of a pipe is two times the mean flow velocity $\bar{u}$.

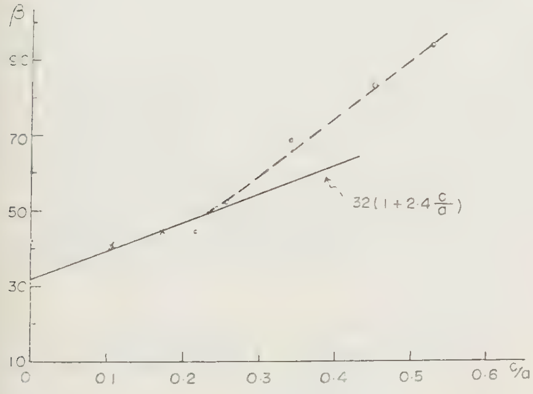

Fig. 4.
× : $a=2.86$ cm, ○ : $a=1.13$ cm.

The effect of finite size of the sphere or disc has been studied theoretically and experimentally[9]. In the case of small disc, Smiedel carried out an experiment and obtained the empirical formula of the type (5) with $k'=2.1$. The present result is in agreement with that of Smiedel for small (c/a), but not for larger value of (c/a).

d) Velocity distribution of flow in a pipe

The experimental result, when the disc was displaced from the center, is shown in Fig. 5. In this figure the abscissa is the square of (r/a), r being the distance between the center of the tube and that of the disc, and the ordinate is F/F_0, F and F_0 being the forces on the disc at r and at the center of the tube $(r=0)$ respectively. From this figure, it is easily seen that the force ratio is expressed by

$$F/F_0=1-A(r/a)^2, \tag{7}$$

where A is a constant which varies with the pressure. For the lowest pressure, A is almost 0.3 and it increases as the pressure becomes higher, but it does not exceed unity.

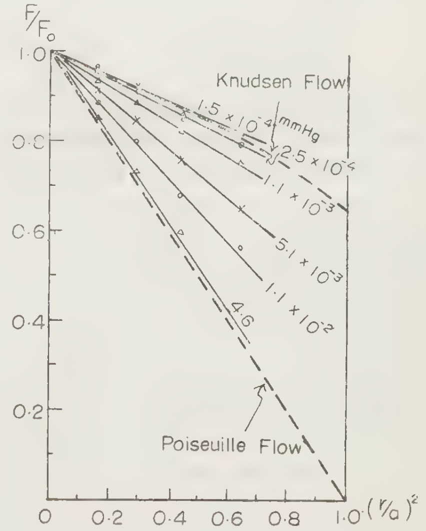

Fig. 5.
: Formula (7),
: Theoretical, Poiseuille and Knudsen flow,
○, △, × : Experiment,
$a=2.86$ cm, $c=0.50$ cm.

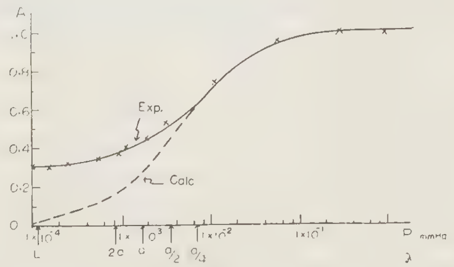

Fig. 6.

According to the hydrodynamics, the flow velocity in a pipe is given by

$$u=u_0(1-r^2/a^2) \tag{8}$$

for Poiseuille flow. As the pressure is reduced, (8) must be replaced by the formula for slip flow[10]:

$$u=u_0\left(1+\frac{2\zeta}{a}\right)\left(1-\frac{1}{1+2\zeta/a}\frac{r^2}{a^2}\right), \qquad (9)$$

where ζ is the coefficient of slip, and according to Zimiriazeff[11], $\zeta=6.8\times10^{-6}$ cm at the atmospheric pressure.

Since the force F is proportional to u in Poiseuille flow, as expressed in (2), comparison of (7) and (8) shows that $A=1$. If the same relation may also be assumed for slip flows, comparison of (7) and (9) predicts

$$A=\frac{1}{1+2\zeta/a}. \qquad (10)$$

The value of A is expressed as a function of p through ζ. $A-p$ curve calculated, by taking Zimiriazeff's value of ζ, is shown in Fig, 6. In this figure the experimental values of A are plotted. They lie very closely on the theoretical curve for pressure higher than 7×10^{-3} mmHg, which corresponds to $\lambda\approx a/4$. This result proves the formula (10) and Zimiriazeff's slip constant. At lower pressures, the plotts deviate from the curve. This may be due to the fact that the force is not proportional to the flow velocity, and also that the Eq. (9) does not hold for low pressures.

In the case of Knudsen flow, a calculation shows that the force is proportional to the number of molecules, N, which pass through the area of disc per unit time. The value of N is given by[12]

$$N=N_0E(r/a)$$
$$=N_0\left(1-\frac{1}{4}\frac{r^2}{a^2}-\frac{3}{64}\frac{r^4}{a^4}\cdots\cdots\right), \qquad (11)$$

where $(\pi/2)E(r/a)$ is the complete ellipti integral of the first kind. According to thi formula, the value of A should be 1/4, bu its experimental value is larger than 1/4. I may be due to the finite size of the disc, an to the finite length L of the pipe used.

In conclusion the author expresses hi sincere thanks to Prof. R. Uyeda for his guidance throughout the work.

This research was helped by researc grants of the Ministry of Education.

References

1) R. Uyeda: J. Appl. Phys. Japan **17** (1948 136. (in Japanese)

2) R. Uyeda & Y. Sugiura: J. Phys. Soc. Japan **8** (1953) 99.

3) R. Uyeda & N. Kato: J. Appl. Phys. Japan **17** (1948) 370. (in Japanese)

4) H. Lamb: Hydrodynamics (1932) p. 605.

5) Y. Sugiura: Vacuum Technique **1** (1950 No. 2, 7. (in Japanese)

6) B. B. Dayton: Ind. Eng. Chem. **40** (1948) 795.

7) M. Knudsen: Ann. d. Phys. **28** (1909) 75.
W. Goede: Ann. d. Phys. **41** (1913) 289.
H. Azumi: Bull. Chem. Soc. Japan **12** (1937) 292; **14** (1939) 343.

8) P. S. Epstein: Phys. Rev. **23** (1924) 710.

9) Hand. d. Experimental Physik, IV 2 teil 343.

10) E. H. Kennard: Kinetic Theory of Gases, (1938) p. 293.

11) E. H. Kennard: *loc. cit.* p. 298.

12) W. G. Pollard & P. D. Present: Phys. Rev. **73** (1948) 762.

JOURNAL OF THE PHYSICAL SOCIETY OF JAPAN Vol. 9, No. 2, MAR.—APR., 1954

On the Subsonic Flow behind the Bow Wave of a Finite Wedge

By Hakuro OGUCHI

Institute of Science and Technology, University of Tokyo

(Received October 20, 1953)

Recently K. Tamada analysed the subsonic flow over a finite wedge behind the attached shock wave by solving a linearized potential equation by an ingenious method. When the shock is not strong, the linearized potential equation may be applied with good approximation. But, when the shock is strong, the flow field behind the shock should be treated as an anisentropic and rotational one. For such an anisentropic flow Lighthill's equation will be more suitable. By the use of Lighthill's equation we obtained an analytical expression of the problem in a form analogous to Tamada's one. Futhermore, we also analysed the case for a finite wedge whose surface deviates slightly from a straight line.

§ 1. Introduction

Let us consider the flow past a symmetrical wedge of finite length. When the Mach number of the oncoming flow is high enough, it is well known that a shock front is attached to the tip of the wedge. If the flow behind the shock is still supersonic, the flow pattern can be completely determined by the theory of oblique shock wave. On the other hand, if the flow is subsonic, the flow field is non-uniform and the shock deviates from a straight line. K. Tamada (1) determined such a flow pattern by solving a linearized potential equation by an ingenious method. When the shock is not so strong, the linearized potential equation may be applied to the problem with good approximation, since the entropy variation normal to stream lines behind the shock is insignificant compared with the velocity variation. When the shock is strong, however, the entropy variation is of the same order of magnitude as the velocity variation. Hence the flow field considered should be treated as an anisentropic and rotational one. In this paper, we investigate such a flow field by the use of a method similar to Tamoda's one on the basis of Lighthill's linearized equation for anisentropic flow. Furthermore, we also investigate the case for a finite wedge whose surface deviates slightly from a straight line.

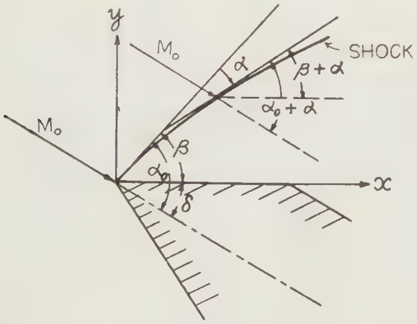

Fig. 1.

§ 2. Fundamental Equatoins

In the present paper, we consider the flow as steady, inviscid and adiabatic. Let (x, y) be the Cartesian coordinates with the origin at the tip of the wedge and x-axis parallel to the edge (Fig. 1).

For steady inviscid gas flow the velocity $\boldsymbol{q}$, density ρ and pressure p satisfy

$$\operatorname{div}(\rho\boldsymbol{q})=0, \quad \rho\boldsymbol{q}\cdot\nabla\boldsymbol{q}+\nabla p=0. \tag{1}$$

Let the velocity, density and pressure of the flow at the tip of the wedge be $(u_1, 0)$, ρ_1, p_1, respectively. Let the components of $\boldsymbol{q}$ be (u_1+u, v), then u and v will be regarded as small compared with u_1, since the flow in the subsonic region considered is nearly uniform. Hence, Eq. (1) become approximately

$$u_1\partial\rho/\partial x+\rho_1(\partial u/\partial x+\partial v/\partial y)=0\,, \tag{2}$$

$$\rho_1 u_1\partial u/\partial x+\partial p/\partial x=0\,, \tag{3}$$

$$\rho_1 u_1\partial v/\partial x+\partial p/\partial y=0\,. \tag{4}$$

The pressure, p, is a function of the density, ρ, and the entropy, s. Since the flow is adiabatic, the entropy behind the shock is constant on each stream line which is nearly parallel to the x-axis. Hence, the entropy, s, may be taken to be independent of x. Therefore,

$$\frac{\partial p}{\partial x}=\frac{\partial p}{\partial \rho}\frac{\partial \rho}{\partial x}+\frac{\partial p}{\partial s}\frac{\partial s}{\partial x}\simeq\left(\frac{\partial p}{\partial \rho}\right)_1\frac{\partial \rho}{\partial x}\ , \tag{5}$$

where $(\partial p/\partial \rho)_1{}^{-1/2}=a_1$ is the sound speed of the flow at the tip. Putting $u'=(p_1-p)/\rho_1 u_1$, Eq. 4 becomes

$$\partial u'/\partial y-\partial v/\partial x=0\ .$$

Thus the vector (u', v) is an irrotational one and therefore there exists a scalar ϕ such that

$$(p_1-p)/\rho_1 u_1=\partial\phi/\partial x\ ,\quad v=\partial\phi/\partial y\ . \tag{6}$$

Combining Eqs. (2), (3), (5) and (6), we obtain

$$\nabla^2\phi=M_1^2\partial^2\phi/\partial x^2,$$

where $M_1=u_1/a_1$ is the Mach number of the flow at the tip. This equation was first derived by M. J. Lighthill (**2**).

Further, by the transformation :

$$x=\xi\ ,\quad y=m^{-1}\eta\ , \tag{7}$$

where $m=(1-M_1^2)^{1/2}$, the above equation reduces to Laplace equation and Eqs. (6) become

$$(p_1-p)/\rho_1 u_1=\partial\phi/\partial\xi\ ,\quad v=m\partial\phi/\partial\eta\ . \tag{8}$$

Let us introduce a function, $W(z)$, defined by

$$W(z)=\partial\phi/\partial\eta+i\partial\phi/\partial\xi\ ,\quad z=\xi+i\eta\ . \tag{9}$$

Then, since ϕ is a harmonic function, our problem is to determine a regular function $W(z)$ compatible with appropriate boundary conditions.

§ 3. Boundary Conditions

In this paper, for brevity, the critical sound speed is taken as the unit of velocity and also the length of the edge of the wedge as the unit of length. Then, the condition that the edge of the wedge is a stream line gives $v=0$ on $1\geq x\geq 0$, $y=0$. According to Eqs. (7), (8) and (9), this condition becomes

$$\mathrm{Re}\ W(z)=0\quad \text{on}\quad 1\geq\xi\geq 0,\quad \eta=0\ . \tag{10}$$

Since, as predicted by A. Busemann (**3**), the sonic speed must be attained at the shoulder of the wedge, the pressure p_s there is given by

$$p_s/p_1=[2/(\gamma+1)]^{\gamma/(\gamma-1)}[(\gamma-1)M_1^2/2+1]^{\gamma/(\gamma-1)}, \tag{11}$$

where γ is the ratio of the specific heats. Hence, from Eqs. (7), (8) and (9), the condition at the shoulder is expressed as

$$\mathrm{Im}\ W(z)=(p_1-p_s)/\rho_1 u_1\ \text{at}\ \xi=1,\ \eta=0. \tag{12}$$

Next let us consider the condition along the shock. Let the shock angle with respect to the uniform flow ahead of the shock be $\alpha_0+\alpha$ where α_0 is the shock angle at the tip and α the perturbed shock angle (Fig. 1). Then the shock equations become as follows:

$$\rho_0 u_0 \sin(\alpha_0+\alpha)=\rho[(u_1+u)\sin(\beta+\alpha)\\ -v\cos(\beta+\alpha)]\ , \tag{13}$$

$$u_0\cos(\alpha_0+\alpha)=(u_1+u)\cos(\beta+\alpha)\\ +v\sin(\beta+\alpha)\ , \tag{14}$$

$$p_0+\rho_0 u_0^2\sin^2(\alpha_0+\alpha)=p+\rho[(u_1+u)\sin(\beta+\alpha)\\ -v\cos(\beta+\alpha)]^2, \tag{15}$$

$$u_0^2+[2\gamma/(\gamma-1)]p_0/\rho_0=(u_1+u)^2+v^2\\ +[(2\gamma/(\gamma-1)]p/\rho\ , \tag{16}$$

where suffix 0 signifies the quantity pertaining to the uniform flow ahead of the shock. From the first order terms of Eqs. (14), (15) and (16), we obtain

$$\alpha=[u_1(1-\rho_1/\rho_0)]^{-1}(\cot\beta\cdot u+v)\ , \tag{17}$$

$$p-p_1+2\rho_1 u_1\sin\beta(u\sin\beta-v\cos\beta)\\ +(\rho_1-\rho)u_1^2\sin^2\beta=0\ , \tag{18}$$

$$0=uu_1+\frac{\gamma}{\gamma-1}\left[\frac{p-p_1}{\rho_1}-\frac{p_1(\rho-\rho_1)}{\rho_1^2}\right]. \tag{19}$$

Further, from the first order terms of the well-known relation :

$$p[(\gamma+1)\rho_0-(\gamma-1)\rho]=p_0[(\gamma+1)\rho-(\gamma-1)\rho_0],$$

we have

$$\rho-\rho_1=\frac{(\gamma+1)\rho_0-(\gamma-1)\rho_1}{(\gamma+1)p_0+(\gamma-1)p_1}\cdot(p-p_1)\ . \tag{20}$$

From Eqs. (17)–(20) we obtain the linear relations between the perturbed quantities immediately behind the shock as follows (**2**) :

$$u=U(p_1-p)/\rho_1 u_1\ ,\quad v=V(p_1-p)\rho_1 u_1\ , \tag{21}$$

where, in terms of $y=p_1/p_0$ and M_0, the Mach number of the uniform flow ahead of the shock,

$$\left.\begin{aligned} U&=\frac{\gamma[\gamma(y+1)^2+(y-1)^2]}{\gamma^2(y+1)^2-(y-1)^2}\ ,\\ V&=-\frac{\gamma}{\gamma-1}\left[\frac{2\gamma M_1^2}{(\gamma+1)+(\gamma-1)y}-1\right]^{-1/2}\\ &\quad\times\left(y+\frac{\gamma+1}{\gamma-1}\right)^{-2}\left[-y^2-(2-M_0^2)y\right.\\ &\quad\left.+\left(\frac{3\gamma-1}{\gamma+1}M_0^2+\frac{3-\gamma}{\gamma+1}\right)\right],\\ M_1^2&=\frac{M_0^2[(\gamma+1)y+(\gamma-1)]-2(y^2-1)}{y[(\gamma+1)y+(\gamma-1)]}\ . \end{aligned}\right\} \tag{22}$$

By the use of Eq. (8) the second equation of Eqs. (21) is rewritten in terms of ϕ:

$$\partial\phi/\partial\eta = m^{-1}V\partial\phi/\partial\xi\,.$$

The location of the shock will be approximately on the line $y=\tan\beta\cdot x$ which is expressed in the z-plane as

$$\eta=\tan\beta'\cdot\xi\,,$$

where

$$\tan\beta'=m\tan\beta\,. \tag{23}$$

Hence, the condition on the shock is given by

$$\tan^{-1}[(\partial\phi/\partial\xi)/(\partial\phi/\partial\eta)]=\arg W(z)=K+n\pi,$$
$$(n=\ldots-1,\ 0,\ 1\ldots)\ \text{on}\ \eta=\tan\beta'\cdot\xi, \tag{24}$$

where

$$\tan K=m/V \tag{25}$$

and K takes the principal value.

Now we can show how the entropy variation depends on the value of U. From the hypothesis of isoenergetic flow,

$$(1/2)(u_1+u)^2+v^2+i=(1/2)u_1^2+i_1\,, \tag{26}$$

where i is the enthalpy per unit mass and i_1 is the enthalpy at the tip. Let $s=0$ and the temperature be T_1 at the tip, then the thermodynamical principle gives

$$i-i_1\simeq T_1s+(p-p_1)/\rho_1\,.$$

Hence Eq. (26) becomes

$$(p_1-p)/\rho_1u_1=u+T_1s/u_1\,.$$

Substituting the first equation of Eqs. (21) into the above equation, we have

$$[(1-U)/U]u=T_1s/u_1\,, \tag{27}$$

from which it follows that the entropy variation is of the same order of magnitude as the velocity variation except when $U\simeq1$ or, from Eq. (22), $p_1/p_0\simeq1$. When $p_1/p_0\simeq1$, in other words, the shock is weak, the entropy variation is insignificant compared with the velocity variation. For such a case the analytic expression derived by K. Tamada (**1**) on the basis of the linearized potential equation may be applied with good approximation. But, when the shock is not so weak, the entropy variation must be taken into consideration. As an example, for the wedge with the semi-vertex angle $\delta=20°$, the calculated value of U is shown in Fig. 2 as a function of M_0. In this case it follows from Eq. (27) that the entropy variation, T_1s/u_1, is about 25% of the velocity variation, u, for M_0 under consideration.

When the Mach number M_0 of the oncoming flow is equal to the extreme Mach number M_D, below which the shock is detached from the tip of the wedge, V in Eq. (21) vanishes. Therefore, the condition (24) reduces to a trivial one. Since, in this case, v is a small quantity of higher order compared with u or $(p_1-p)\rho_1u_1$, we must take into account the higher order terms in order to obtain a non-trivial condition on the shock. For this purpose it is more convenient to use the shock polar, as treated by K. Tamada (**1**).

The equation of the shock polar is written in the form:

$$(n-u_0\bar{u})\bar{v}^2=(u_0-\bar{u})^2(u_0\bar{u}-1)\,, \tag{28}$$

where

$$\left.\begin{aligned}
&n=1+2/(\gamma+1)\cdot u_0^2\,,\\
&\bar{u}=(u_1+u)\cos\delta-v\sin\delta\,,\\
&\bar{v}=(u_1+u)\sin\delta+v\cos\delta\,.
\end{aligned}\right\} \tag{29}$$

By substituting Eq. (29) into Eq. (28) and expanding in power series of u and v, the following relations are derived from the zero, the first and the higher order terms with respect to u:

$$\left.\begin{aligned}
&(n-u_0u_1\cos\delta)(u_1\sin\delta)^2\\
&\qquad=(u_0-u_1\cos\delta)^2(u_0u_1\cos\delta-1),\\
&u_1(2n-3u_1u_0\cos\delta)\sin^2\delta\\
&\qquad=(u_0-u_1\cos\delta)(u_0^2+2\\
&\qquad\quad-3u_0u_1\cos\delta)\cos\delta\,,\\
&v=Ru^2,
\end{aligned}\right\} \tag{30}$$

where

$$R=\frac{3u_0u_1\cos\delta-n+\gamma(1-n)\cos^2\delta}{u_0\sin\delta[2+u_0^2+u_1^2+2\gamma(1-n)u_1u_0^{-1}\cos\delta]}\,.$$

For any given value of δ, values of u_0 and u_1 can be determined from the first and second equations of Eqs. (30).

By the use of the first equation of Eqs. (21), the third equation of Eqs. (30) is rewritten as

$$v=RU^2[(p_1-p)/\rho_1u_1]^2.$$

Hence, from Eqs. (8) and (9), the condition on the shock for the extreme case $M_0=M_D$ becomes

$$\operatorname{Re}W(z)=m^{-1}RU^2[\operatorname{Im}W(z)]^2,\ \text{on}\ \eta=\tan\beta'\cdot\xi. \tag{31}$$

§ 4. Solution for Finite Wedge

A regular function $W(z)$ satisfying the conditions (10) and (24) is, in general, written in the form:

$$W(z)=i\sum_{n=1}^{\infty}A_n z^{(K+n\pi-\pi/2)/3'},$$

where A_n's are arbitrary constants.

Since, among the terms of the above series, the first one is most predominant, the actual solution will approximately be given by

$$W(z)=iA_1 z^{(K+\pi/2)/\beta'}. \tag{32}$$

From the condition (12),

$$A_1=(p_1-p_s)/\rho_1 u_1. \tag{33}$$

Putting $z=re^{i\theta}$ in Eq. (32), we have from Eqs. (8) and (9)

$$p_1-p=(p_1-p_s)r^{(K+\pi/2)/\beta'}\cos[(K+\pi/2)/\beta'\cdot\theta], \tag{34}$$

where r and θ are written in terms of x and y:

$$r=(x^2+m^2y^2)^{1/2}, \quad \theta=\tan^{-1}(my/x). \tag{35}$$

It follows from the above solution that the factor $(K+\pi/2)/\beta'$ is an important one characterizing the flow field. For the case when $(K+\pi/2)/\beta'=1$, the solution is no more singular even at the tip of the wedge. According to the definition, this case must correspond to the Crocco point.

Now we can show independently of the preceding analysis that $(K+\pi/2)/\beta'$ becomes unity at the Crocco point. Let a line element of the shock be $d\sigma$ and the angle between the flow direction and the x-axis ω, then the curvature, $(1/R)_1$, of the stream line at the tip is given by (4)

$$\left(\frac{1}{R}\right)_1=\left[\left(\frac{\partial\omega}{\partial\sigma}\right)_1\cos\beta+\frac{M_1^2-1}{\gamma M_1^2}\right.$$
$$\left.\times\sin\beta\left(\frac{\partial\log p}{\partial\sigma}\right)_1\right](1-M_1^2\sin^2\beta)^{-1}.$$

In our approximation,

$$\left(\frac{\partial\omega}{\partial\sigma}\right)_1 d\sigma\simeq\frac{v}{u_1}, \quad \left(\frac{\partial\log p}{\partial\sigma}\right)_1 d\sigma\simeq\frac{p_1-p}{p_1}.$$

Hence,

$$\left(\frac{1}{R}\right)_1=\left(\frac{v}{u_1}\cos\beta+\frac{M_1^2-1}{\gamma M_1^2}\sin\beta\cdot\frac{p-p_1}{p_1}\right)$$
$$\times(1-M_1^2\sin^2\beta)^{-1}(1/d\sigma).$$

Since the Crocco point is defined as the point where $(1/R)_1$ vanishes, the condition there is given by

$$(v/u_1)\cos\beta+[(M_1^2-1)\sin\beta/\gamma M_1^2](p-p_1)/p_1=0.$$

By the use of Eqs. (23) and (25) this equation is rewritten in the form:

$$\tan(K+\pi)=\tan(\beta'+\pi/2).$$

Hence, $(K+\pi/2)/\beta'=1$ at the Crocco point.

Next let us consider the extreme case $M_0=M_D$. A regular function $W(z)$ compatible with the conditions (10), (12) and (31) may be written in the form:

$$W(z)=-i(\log az^b)^{-1}, \tag{36}$$

where a and b are real constants.

From the condition (12),

$$\log a=-\rho_1 u_1/(p_1-p_s). \tag{37}$$

Putting $z=re^{i\theta}$ in Eq. (36),

$$W(z)=\frac{-b\theta-i\log ar^b}{(\log ar^b)^2+b^2\theta^2}.$$

If b is positive, $|\log ar^b|$ is a large quantity of the same or higher order of magnitude as $\rho_1 u_1/(p_1-p_s)$ in the domain considered. Then the above equation becomes approximately

$$W(z)=-b\theta(\log ar^b)^{-2}-i(\log ar^b)^{-1}. \tag{38}$$

Thus, we have from the condition (31)

$$b=-RU^2(m\beta')^{-1}. \tag{39}$$

It follows from the geometry of shock polar that b is positive. Therefore Eq. (38) represents the solution for the extreme case $M_0=M_D$ with good approximation. From Eqs. (8), (9) and (38) the pressure is given by

$$(p_1-p)/\rho_1 u_1=-(\log ar^b)^{-1}, \tag{40}$$

where a and b are given by Eqs. (37) and (39).

§ 5. Drag Coefficient, Shock Pattern and Comparison with Tamada's Results

From Eqs. (34) and (40) the pressure distribution on the wedge surface is given by

$$\left.\begin{aligned} p&=p_1-(p_1-p_s)x^{(K+\pi/2)/\beta'}, & M&>M_D\\ &p_1+\rho_1 u_1(\log ax^b)^{-1}. & M_0&=M_D \end{aligned}\right\} \tag{41}$$

Now we define, as usual, the drag coefficient C_D by

$$C_D=2\int_0^1 C_p\sin\delta dx\Big/2\sin\delta=\int_0^1 C_p dx, \tag{42}$$

where

$$C_p=2/(\gamma M_0^2)\cdot(p/p_0-1).$$

From Eqs. (41) and (42) we obtain after some calculations

$$C_D=(2/\gamma M_0^2)(Dp_1/p_0-1),$$

where

$$D=1-\beta'[(p_1-p_s)/p_1]/(K+\beta'+\pi/2), \quad M_0>M_D$$

$$1+(\gamma M_1^2/u_1)\int_0^1(\log ax^b)^{-1}dx. \qquad M_0=M_D$$

It should be noted that for both cases the pressure distribution on the surface and drag coefficient have a form similar to the results given by Tamada and characteristic factors $(K+\pi/2)/\beta'$ and b correspond to $\kappa-1$ and $-\mathcal{E}^{-1}$ in Tamada's solution, respectively. By the use of the notations in the present paper, $\kappa-1$ and $-\mathcal{E}^{-1}$ are written in the form :

$$\kappa-1=\pi/2+\tan^{-1}(Um/V),$$
$$-\mathcal{E}^{-1}=-R/(m\beta').$$

On the other hand, we have from Eqs. (23), (25) and (39)

$$(K+\pi/2)/\beta'=\pi/2+\tan^{-1}(m/V),$$
$$b=-RU^2/(m\beta').$$

Hence, if $U\simeq1$, $(K+\pi/2)/\beta'$ and b are almost equal to $\kappa-1$ and $-\mathcal{E}^{-1}$, respectively. Therefore, for the case when $U\simeq1$, in other words, when the shock is weak enough, the pressure distribution and drag coefficients have the same form as Tamada's one. But, when the shock is strong, $(K+\pi/2)/\beta'$ and b are fairly different from $\kappa-1$ and $-\mathcal{E}^{-1}$, respectively. For such a case our results deviate from Tamada's ones. The above description is also evident from the consideration with respect to the entropy variation, discussed before. As an example, for a wedge with a semi-vertex angle $\delta=20°$, $(K+\pi/2)\beta'$ and $\kappa-1$ are plotted as a function of M_0 in Fig. 2 and C_D is shown in Fig. 3.

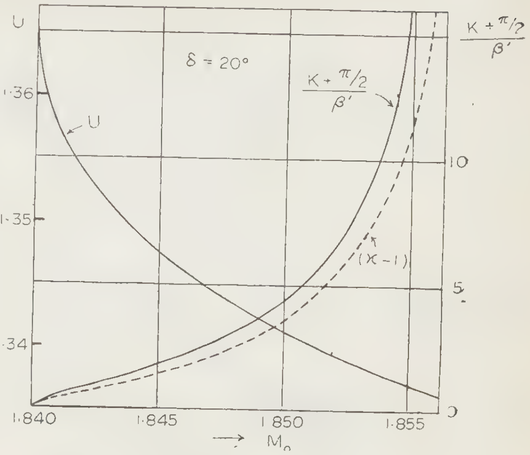

Fig. 2.

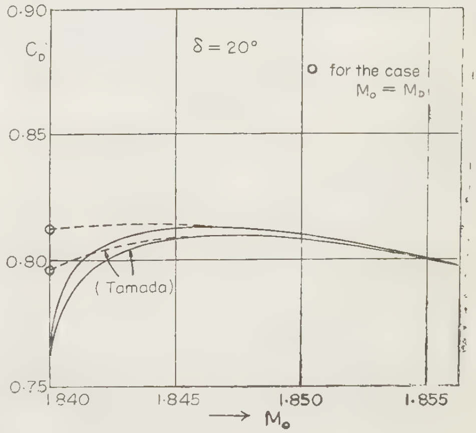

Fig. 3.

Next let us consider the shock pattern. The slope of the shock is given by

$$dy/dx=\tan(\beta+\alpha).$$

In our approximation, this equation becomes

$$dy/dx=\tan\beta+\sec^2\beta\cdot\alpha. \tag{43}$$

Since the lacation of shock in the z-plane is given by $\theta=\beta'$, we have from Eq. (35)

$$r=\sec\beta'\cdot x.$$

Substituting the above relation into Eq. (34), we obtain the pressure distribution on the shock as :

$$-p_1+p=(p_1-p_s)\sin K\cdot(\sec\beta'\cdot x)^{(K+\pi/2)/\beta'}.$$

From Eqs. (17) and (21)

$$\alpha=A(p_1-p)/\rho_1u_1,$$

where

$$A=[u_1(1-\rho_1/\rho_0)]^{-1}(\cot\beta\cdot U+V).$$

Substituting α from the above relations into Eq. (43) and integrating Eq. (43) with respect to x, we obtain the shock pattern in the form:

$$y=\tan\beta\cdot x+Sx^{(K+\pi/2)/\beta'+1},$$

where

$$S=\frac{(p_s-p_1)A\beta'\sin K(\sec\beta')^{(K+\pi/2)/\beta'}}{\rho_1u_1(K+\beta'+\pi/2)\cos^2\beta}.$$

By the same procedure we have the shock pattern for the case $M_0=M_D$ in the form :

$$y=\tan\beta\cdot x+S_D\int_0^x[\log a(\sec\beta'\cdot x)^b]^{-1}dx,$$

where

$$S_D=-A\sec^2\beta.$$

§ 6. Solution for a Wedge-Shaped Body

Suppose that a symmetrical wedge-shaped body which is slightly deformed from a finite wedge is placed in a supersonic flow (Fig. 4). As in the preceding analysis, the case when the flow behind the shock attached to the nose of the body is subsonic is of main interest to us.

Choose the x-axis along the edge of the basic wedge that will closely approximate the body and y-axis perpendicular to the x-axis (Fig. 4).

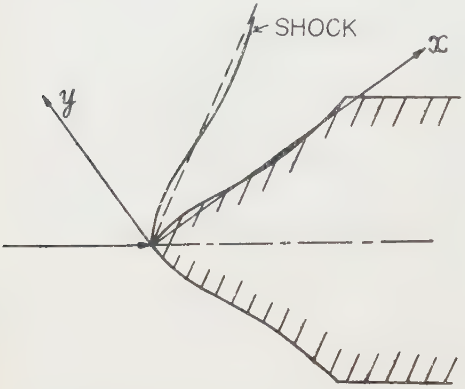

Fig. 4.

First let us consider the body whose edge is given by

$$y=\varepsilon x^{n+1}, \quad n>0$$

where ε is assumed to be a small quantity. Since, in this case, the surface of the basic wedge is tangential to the body at the nose, we may also consider the flow at the nose as the basic flow. Let the velocity component, density and pressure of the basic flow be $(u_1, 0)$, ρ_1 and p_1, respectively. In this case also, ϕ defined by Eq. (8) satisfies Laplace equation and therefore it is convenient to introduce a function, $W(z)$, defined by Eq. (9).

The condition that the edge be a stream line becomes

$$v/u_1 \simeq \varepsilon(n+1)x^n.$$

Since the edge is approximately coincident with the x-axis, we obtain the condition on the edge in the form:

$$\operatorname{Re} W(z)=m^{-1}\varepsilon(n+1)u_1\xi^n. \\ \text{on } 1\geq\xi\geq 0, \quad \eta=0.$$

Since the condition on the shock has exactly the same form as the condition (24), a regular function $W(z)$ satisfying these conditions may be written in the form:

$$W(z)=\frac{m^{-1}\varepsilon(n+1)u_1}{\cos(K+\pi-n\beta')}z^n e^{i(K+\pi-n\beta')} \\ +i\sum_{n=1}^{\infty} A_n z^{(K+n\pi-\pi/2)/\beta'},$$

where A_n's are arbitrary constant.

In the above solution the first term represents the contribution of the deformation of the body from the basic wedge and the second series the solution for the basic wedge. Therefore the case is of significance when the first term is not so small compared with the second series, in other words, when n is small or not so large compared with $(K+\pi/2)/\beta'$. In such a case the above solution may be written approximately

$$W(z)=\frac{m^{-1}\varepsilon(n+1)u_1}{\cos(K+\pi-n\beta')}z^n e^{i(K+\pi-n\beta')} \\ +iA_1 z^{(K+\pi/2)/\beta'}. \tag{44}$$

When the sonic speed is not attained anywhere on the edge except at the shoulder of the body, we may also apply the condition (12) that the sonic speed is attained just at the shoulder. Hence, A_1 can be determined as

$$A_1=\frac{p_1-p_s}{\rho_1 u_1}-m^{-1}\varepsilon(n+1)u_1\tan(K+\pi-n\beta').$$

Since $\tan(K+\pi-n\beta')$ rises to infinity when $K+\pi-n\beta'=\pi/2$ or $n=(K+\pi/2)/\beta'$, Eq. (44) is rewritten by the limiting process in the form:

$$W(z)=[m^{-1}\varepsilon(n+1)u_1(1+i\log z/\beta') \\ +i(p_1-p_s)/\rho_1 u_1]z^{(K+\pi/2)/\beta'}. \tag{45}$$

From Eqs. (44) and (45), the pressure distribution on the surface is given by

$$(p_1-p)/\rho_1 u_1=m^{-1}\varepsilon(n+1)u_1\tan(K+\pi-n\beta') \\ \times(x^n-x^{(K+\pi/2)/\beta'})+(p_1-p_s)/\rho_1 u_1\cdot x^{(K+\pi/2)/\beta'}, \\ n\neq(K+\pi/2)\beta'$$

$$[m^{-1}\varepsilon(n+1)u_1\log x/\beta'+(p_1-p_s)/\rho_1 u_1] \\ \times x^{(K+\pi/2)/\beta'}. \quad n=(K+\pi/2)/\beta'$$

If the flow is supersonic somewhere on the edge except at the shoulder of the body, the condition (12) is no longer applicable and hence A_1 remains undetermined. Therefore the preceding solution (45) is applicable only to the case when the condition:

$$(p_1-p)/\rho_1 u_1<(p_1-p_s)/\rho_1 u_1 \text{ on } 1>x\geq 0, \ y=0$$

is satisfied. Since, as mentioned before, the case when n is small or not so large compared with $(K+\pi/2)/\beta'$ is of significance, we may assume $(K+\pi)/\beta'>n$ or $\tan(K+\pi-n\beta')>0$. Then, if the edge is concave to the flow i.e. $\varepsilon>0$, it follows readily that the solution (45) always satisfies the above condition. On the other hand, if the edge is convex to the flow i.e. $\varepsilon<0$, the solution (45) satisfies the above condition for a given n only when $|\varepsilon|$ is less than the extremum $|\varepsilon|_{\text{ext.}}$:

$$|\varepsilon|_{\text{ext.}}=\begin{cases}\dfrac{m(K+\pi/2)(p_1-p_s)/(\rho_1 u_1^2)}{(n+1)(n\beta'-K+\pi/2)\tan(K+\pi-n\beta')}, & n\neq(K+\pi/2)/\beta'\\ m(n+1)^{-1}(K+\pi/2)(p_1-p_s)/(\rho_1 u_1^2). & n=(K+\pi/2)/\beta'\end{cases}$$

If $|\varepsilon|>|\varepsilon|_{\text{ext.}}$ for a given n, the flow will be supersonic somewhere on the edge except at the shoulder. As an example, the value of $|\varepsilon|_{\text{ext.}}$ for a body whose surface deviates from a wedge with $\delta=20°$ in a parabolic form $y=\varepsilon x^2$ is shown as a function of M_0 in Fig. 5.

For the case of a concave wedge, as readily seen from Eq. (45), a maximum occurs in the pressure distribution on the edge if $n>K+\pi/2$ and $\varepsilon(n+1)>m(p_1-p_s)/(\rho_1 u_1^2)\cdot\cot(K+\pi-n\beta')$ or else the pressure decreases monotonically from the nose to the shoulder. On the other hand, for the case of a convex wedge such that $|\varepsilon|<|\varepsilon|_{\text{ext.}}$, the pressure always decreases monotonically from the nose to the shoulder.

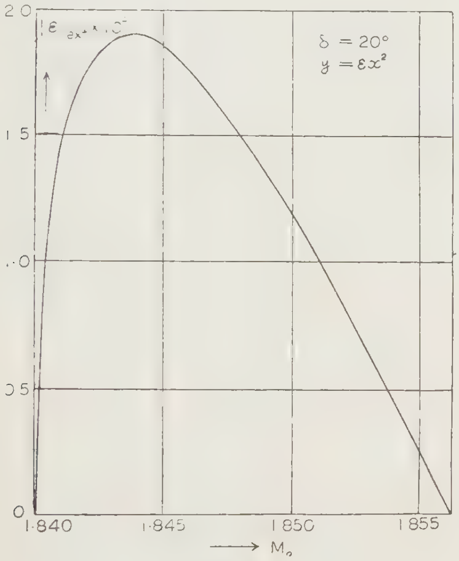

Fig. 5.

Lastly let us consider a symmetrical wedge-shaped body whose edge is given in the form of a power series:

$$y=\sum_{n=0}^{\infty} a_n x^{n+1}.$$

In this case the condition on the edge becomes

$$\text{Re}\, W(z)=\sum_{n=0}^{\infty} m^{-1}u_1(n+1)a_n\xi^n. \quad \text{on } 1\geq\xi\geq0,\ \eta=0 \tag{46}$$

The condition on the shock is also given by Eq. (24). A regular function $W(z)$ satisfying these conditions may be written in the form:

$$W(z)=m^{-1}u_1\sum\frac{(n+1)a_n}{\cos(K+\pi-n\beta')}z^n e^{i(K+\pi-n\beta')}+i\sum A_n z^{K+n\beta'},$$

where A_n's are real constants. By the same consideration as in the preceding analysis, we may take the function

$$W(z)=m^{-1}u_1\sum_{n=0}^{\infty}\frac{(n+1)a_n}{\cos(K+\pi-n\beta')}z^n e^{i(K+\pi-n\beta')}+iA_1 z^{(K+\pi/2)/\beta'} \tag{47}$$

as the main part of the above solution. If we assume that the condition at the shoulder is given by the condition (12), A_1 can be determined as

$$A_1=\frac{p_1-p_s}{\rho_1 u_1}-m^{-1}u_1\sum_{n=0}^{\infty}(n+1)a_n\tan(K+\pi-n\beta'),$$

It should also be noted that the solution (47) is applicable only to the case when the flow is subsonic everywhere on the edge except at the shoulder.

In conclusion, the author wishes to thank Dr. R. Kawamura for his suggestion and encouragement during the course of this investigation, and Prof. I. Imai for his advice and kind inspection of the manuscript.

References

1) K. Tamada: J. Phys. Soc. Japan **8** (1953).
2) M. J. Lighthill: Phil. Mag. **40** (1949).
3) A. Busemann: N.A.C.A. Tech. Note, No. 1858.
4) H. Melkus: Ing. Arch. **19** (1951).

JOURNAL OF THE PHYSICAL SOCIETY OF JAPAN Vol. 9, No. 2, MAR.—APR., 1954

On the Propagation and Structure of a Blast Wave, II

By Akira SAKURAI

Tokyo Electrical Engineering College

(Received December 11, 1953)

As a continuation of Part I (J. Phys. Soc. Japan **8** (1953) 662), the second approximation for the propagation and structure of a blast wave is now discussed. The solution for $\gamma=1.4$ is obtained by a numerical method, using the results of the first approximation obtained in Part I. By use of this solution, *U-R* curves, distance-time curves and the changing feature of distributions of velocity, pressure and density behind the shock front are discussed.

Further, the approximate solution of the equation is discussed by a refinement of the WKB method due to Imai.

§ 1. Eqations for the Second Approximation

In Part I of this series of papers (J. Phys. Soc. Japan 8 (1953) 662), we have attempted to construct the solution in power series of $(C/U)^2$ in the following forms:

$$u=U[f^{(0)}+(C/U)^2f^{(1)}+\cdots]\,,$$
$$p=p_0(U/C)^2[g^{(0)}+(C/U)^2g^{(1)}+\cdots]\,,$$
$$\rho=\rho_0[h^{(0)}+(C/U)^2h^{(1)}+\cdots]\,,$$
$$(C/U)^2(R_0/R)^{\alpha+1}=J_0[1+\lambda_1(C/U)^2+\cdots]\,.$$

Thereby, a procedure of successive determination of functions $f^{(0)}, g^{(0)}, h^{(0)}; f^{(1)}, g^{(1)}, h^{(1)}; \ldots$ (which are functions of $x=r/R$) and constants $J_0, \lambda_1, \lambda_2, \ldots$ was discussed; moreover the first approximation was discussed by a numerical as well as an approximate method.

Now, in this Part II, we shall develop the second approximation and determine $f^{(1)}, g^{(1)}, h^{(1)}$ and λ_1, for which we have the following system of equations as mentioned in Part I (Eqs. (18), (25), (27)):

$$\int_0^1\left(\gamma f^{(0)}h^{(0)}f^{(1)}+\frac{1}{\gamma-1}g^{(1)}+\frac{1}{2}f^{(0)2}h^{(1)}\right)x^\alpha dx$$
$$=\lambda_1J_0+\frac{1}{(\gamma-1)(\alpha+1)}\,,$$

$$h^{(0)}(f^{(0)}-x)f_x{}^{(1)}+g_x{}^{(1)}/\gamma$$
$$=-\{(\alpha+1)/2+f_x{}^{(0)}\}h^{(0)}f^{(1)}+\{(\alpha+1)f^{(0)}/2$$
$$+(x-f^{(0)})f_x{}^{(0)}\}h^{(1)}+(\alpha+1)\lambda_1f^{(0)}h^{(0)}/2\,,$$

$$h^{(0)}f_x{}^{(1)}+(f^{(0)}-x)h_x{}^{(1)}=-(h_x{}^{(0)}+\alpha h^{(0)}/x)f^{(1)}$$
$$-(f_x{}^{(0)}+\alpha f^{(0)}/x+\alpha+1)h^{(1)}\,,$$

$$\gamma g^{(0)}f_x{}^{(1)}+(f^{(0)}-x)g_x{}^{(1)}$$
$$=-(g_x{}^{(0)}+\alpha\gamma g^{(0)}/x)f^{(1)}$$
$$-\gamma(f_x{}^{(0)}+\alpha f^{(0)}/x)g^{(1)}+(\alpha+1)\lambda_1g^{(0)}\,,$$

$$f^{(1)}(1)=-2/(\gamma+1)\,,\quad g^{(1)}(1)=-(\gamma-1)/(\gamma+1)\,,$$
$$h^{(1)}(1)=-2(\gamma+1)/(\gamma-1)^2\,.$$

We introduce new dependent variables φ, ψ, χ as defined by

$$f^{(1)}=(x-f^{(0)})\varphi,\ g^{(1)}=g^{(0)}\psi,\ h^{(1)}=h^{(0)}\chi, \tag{1}$$

and use equations (24) and (26) in Part I concerning $f^{(0)}, g^{(0)}, h^{(0)}$; then the above system of equations is transformed into,

$$\int_0^1\left\{\gamma f^{(0)}(x-f^{(0)})h^{(0)}\varphi+\frac{g^{(0)}}{\gamma-1}\psi+\frac{\gamma}{2}f^{(0)2}h^{(0)}\chi\right\}$$
$$\times x^\alpha dx=\lambda_1J_0+\frac{1}{(\gamma-1)(\alpha+1)}\,, \tag{2}$$

$$-(x-f^{(0)})\varphi_x+\frac{1}{\gamma D}\psi_x=-\left(2f_x{}^{(0)}+\frac{\alpha-1}{2}\right)\varphi$$
$$+\left(f_x{}^{(0)}+\frac{\alpha+1}{2}\frac{f^{(0)}}{x-f^{(0)}}\right)(\chi-\psi)$$
$$+\frac{\alpha+1}{2}\frac{f^{(0)}}{x-f^{(0)}}\lambda_1\,, \tag{3}$$

$$(x-f^{(0)})(-\varphi_x+\chi_x)=(\alpha+1)(\varphi+\chi)\,, \tag{4}$$

$$(x-f^{(0)})(-\gamma\varphi_x+\psi_x)=(\alpha+1)\{(\gamma-1)\varphi+\psi-\lambda_1\}, \tag{5}$$

$$\varphi(1)=-2/(\gamma-1)\,,\quad \psi(1)=-(\gamma-1)/2\gamma\,,$$
$$\chi=-2/(\gamma-1)\,. \tag{6}$$

§ 2. An Integral Obtained from Eqs. (4) and (5)

As we have noted in Part I, (4) and (5) have an integral. If we perform the operation $(5)\times2-(4)\times(2\gamma-1)$, we have

$$(x-f^{(0)})\{-\varphi_x+2\psi_x-(2\gamma-1)\chi_x\}$$
$$=(\alpha+1)\{-\varphi+2\psi-(2\gamma-1)\chi-2\lambda_1\}\,.$$

Integrating this and inserting the condition (6) to determine the integration constant, we have a relation:

$$\varphi-2\psi+(2\gamma-1)\chi+2\lambda_1$$
$$=\left(2\lambda_1-\frac{3\gamma-1}{\gamma}\frac{\gamma+1}{\gamma-1}\right)\exp\left(\int_1^x\frac{\alpha+1}{x-f^{(0)}}dx\right). \tag{7}$$

Hereafter, we shall use (7) in place of (4) and consider (2), (3), (5), (6), (7) as a fundamental system of equations.

In this connection, it will be worth noticing that an integral of similar type to (7) always exists in each step of successive approximations. Thus, as will be shown in Appendix I, in the case of the $(i+1)$-th approximation $(i=2, 3, \dots)$ $\varphi^{(i)}, \psi^{(i)}, \chi^{(i)}$, we have

$$\varphi^{(i)}-(i+1)\psi^{(i)}+\{(i+1)\gamma-1\}\chi^{(i)}+(i+1)\lambda_i/i$$
$$=A_i \exp\left(i\int_1^x \frac{\alpha+1}{x-f^{(0)}}dx\right)$$
$$+(\text{function which can be derived from the relation up to the } i\text{-th approximation}), \qquad (8)$$

where A_i is a constant to be determined from the condition at $x=1$.

§ 3. Asymptotic Behaviour near $x=0$

Since $f^{(0)}\to x/\gamma$ as $x\to 0$*, we see from Eq. (36) in Part I that $D_x/D\to(\gamma+\alpha)/(\gamma-1)x$ as $x\to 0$, which can be integrated to give $D\to D_0x^{(\gamma+\alpha)/(\gamma-1)}$ where D_0 is the integration constant which can be determined from the result of the first approximation. Then, if we use the results:

$$x-f^{(0)}\to\frac{\gamma-1}{\gamma}x, \quad 2f_x^{(0)}+\frac{\alpha-1}{2}\to\frac{2}{\gamma}+\frac{\alpha+1}{2},$$
$$f_x^{(0)}+\frac{\alpha+1}{2}\frac{f^{(0)}}{x-f^{(0)}}\to\frac{1}{\gamma}+\frac{\alpha+1}{2}\frac{1}{\gamma-1},$$
$$\exp\left(\int_1^x\frac{\alpha+1}{x-f^{(0)}}dx\right)\to G_0x^{(\alpha+1)\gamma/(\gamma-1)},$$

where G_0 is a constant, (3), (5), (7) are reduced to the following forms;

$$-\frac{\gamma-1}{\gamma}x\varphi_x+\frac{1}{\gamma D_0}\cdot x^{-(\gamma+\alpha)/(\gamma-1)}\cdot\psi_x$$
$$=-\left(\frac{2}{\gamma}+\frac{\alpha-1}{2}\right)\varphi+\left(\frac{1}{\gamma}+\frac{\alpha+1}{2}\frac{1}{\gamma-1}\right)\times(\chi-\psi)+\frac{\alpha+1}{2}\frac{\lambda_1}{\gamma-1},$$
$$\{(\gamma-1)/\gamma\}x(-\gamma\varphi_x+\psi_x)=(\alpha+1)\{(\gamma-1)\varphi+\psi-\lambda_1\},$$
$$\varphi-2\psi+(2\gamma-1)\chi=-2\lambda_1+\{2\lambda_1-(3\gamma-1)\times(\gamma+1)/\gamma(\gamma-1)\}G_0x^{(\alpha+1)\gamma/(\gamma-1)}.$$

We put

$$\xi=x^\nu, \quad \nu=(\gamma+\alpha)/(\gamma-1)+1, \qquad (9)$$

then above three equations are reduced to

$$\frac{\gamma-1}{\gamma}\nu\left(-\xi\varphi_\xi+\frac{1}{\gamma-1}\frac{1}{D_0}\psi_\xi\right)=-\left(\frac{2}{\gamma}+\frac{\alpha-1}{2}\right)\varphi$$
$$+\left(\frac{1}{\gamma}+\frac{\alpha+1}{2}\frac{1}{\gamma-1}\right)(\chi-\psi)+\frac{\alpha+1}{2}\frac{\lambda_1}{\gamma-1}, \qquad (10)$$

$$\{(\gamma-1)/\gamma\}(-\gamma\xi\varphi_\xi+\xi\psi_\xi)=(\alpha+1)\{(\gamma-1)\varphi+\psi-\lambda_1\}, \qquad (11)$$

$$\varphi-2\psi+(2\gamma-1)\chi=-2\lambda_1+\{2\lambda_1-(3\gamma-1)(\gamma+1)/\gamma(\gamma-1)\}\times G_0\xi^{(\alpha+1)\gamma/(2\gamma+\alpha-1)}. \qquad (12)$$

We now proceed to determine the solutions of Eqs. (10), (11), (12). The particular solutions $\varphi_S, \psi_S, \chi_S$ can readily be obtained in the following forms:

$$\left.\begin{aligned}\varphi_S&=\varphi_0+\xi^{(\alpha+1)\gamma/(2\gamma+\alpha-1)}(C_{00}+C_{01}\xi+\dots),\\ \psi_S&=\psi_0+\xi^{(\alpha+1)\gamma/(2\gamma+\alpha-1)}(C_{11}\xi+\dots),\\ \chi_S&=\chi_0+\xi^{(\alpha+1)\gamma/(2\gamma+\alpha-1)}(C_{20}+C_{21}\xi+\dots),\end{aligned}\right\} \qquad (13)$$

where

$$\left.\begin{aligned}\varphi_0&=-\chi_0=-\left\{2+\frac{\gamma-1}{2}\gamma-(\gamma-2)\times\left(1+\frac{\alpha+1}{2}\frac{\gamma}{\gamma-1}\right)\right\}^{-1}\cdot\lambda_1,\\ \psi_0&=\lambda_1-(\gamma-1)\varphi_0,\\ c_{00}&=0,\quad c_{20}=\frac{G_0}{2\gamma-1}\left(2\lambda_1-\frac{3\gamma-1}{\gamma}\frac{\gamma+1}{\gamma-1}\right),\\ c_{11}&=\frac{(\gamma-1)D_0}{\gamma(\alpha+3)+\alpha-1}\left(1+\frac{\alpha+1}{2}\frac{\gamma}{\gamma-1}\right)c_{20}.\end{aligned}\right\} \qquad (14)$$

If we eliminate χ from the homogeneous parts of (10), (11), (12), we have

$$-(\gamma-1)\xi\varphi_\xi+\frac{1}{D_0}\psi_\xi$$
$$=-\frac{1}{\nu}\left\{2+\frac{\alpha-1}{2}\gamma+\frac{1}{2\gamma-1}\left(1+\frac{\alpha+1}{2}\frac{\gamma}{\gamma-1}\right)\right\}\varphi$$
$$+\frac{1}{\nu}\frac{3-2\gamma}{2\gamma-1}\left(1+\frac{\alpha+1}{2}\frac{\gamma}{\gamma-1}\right)\psi, \qquad (15)$$

$$-\gamma\xi\varphi_\xi+\xi\psi_\xi=\{\gamma(\alpha+1)/\nu\}\varphi+\{\gamma(\alpha+1)/\nu(\gamma-1)\}\psi, \qquad (16)$$

and assuming solutions of the forms:

$$\varphi=\xi^S(a_0+\xi a_1+\dots), \quad \psi=\xi^{S+1}(b_0+\xi b_1+\dots),$$

we get after some calculations, $S=-1$ or $-(\alpha+1)/\nu$ and

$$\left.\begin{aligned}\varphi&=A\xi^{-(\alpha+1)/\nu}(1+a_{11}\xi+\dots)+B(a_{20}+a_{21}\xi+\dots),\\ \psi&=A\xi^{-(\alpha+1)/\nu}(b_{10}+b_{11}\xi+\dots)+B(1+b_{21}\xi+\dots),\end{aligned}\right\} \qquad (17)$$

where A, B are arbitrary constants and

---

* This result was derived by G. I. Taylor in the case of $\alpha=2$: but the corresponding results for the cases of $\alpha=0$, 1 can also be derived in the same manner.

$$\left.\begin{aligned}
&a_{11}=-\frac{1}{\gamma^2}\left(\frac{2\gamma-1}{\gamma-1}n-\gamma\right)b_{10}\ ,\quad a_{20}=-\frac{1}{\gamma-1}\ ,\\
&\qquad a_{21}=-\frac{n-\gamma+1}{(\gamma-1)(n+\gamma)}b_{21}\ ,\\
&b_{10}=\frac{\gamma l+(\gamma-1)n}{n-\gamma}D_0\ ,\\
&b_{11}=\frac{D_0}{2\gamma-n}[\gamma m b_{10}-\{\gamma l-(\gamma-1)(\gamma-n)\}]a_{11}\ ,\\
&\qquad b_{21}=\left(m+\frac{l}{\gamma-1}\right)D_0\ ,\\
&l=\frac{1}{\nu}\left\{2+\frac{\alpha-1}{2}\gamma+\frac{1}{2\gamma-1}\left(1+\frac{\alpha+1}{2}\frac{\gamma}{\gamma-1}\right)\right\},\\
&m=\frac{1}{\nu}\frac{3-2\gamma}{2\gamma-1}\left(1+\frac{\alpha+1}{2}\frac{\gamma}{\gamma-1}\right),\\
&\qquad n=\frac{(\alpha+1)\gamma}{\nu}\ .
\end{aligned}\right\}\tag{18}$$

Accordingly, we can construct the general solutions of (10), (11), (12) by adding (13) and (17) together. Thus, returning to x by (9), we have

$$\begin{aligned}\varphi=\varphi_0&+x^{(\alpha+1)\gamma/(\gamma-1)}(c_{01}x^{\nu}+\dots)+Ax^{-(\alpha+1)}\\&\times(1+a_{11}x^{\nu}+\dots)+B(a_{20}+a_{21}x^{\nu}+\dots)\ ,\end{aligned}\tag{19}$$

$$\begin{aligned}\psi=\psi_0&+x^{(\alpha+1)\gamma/(\gamma-1)}(c_{11}x^{\nu}+\dots)+Ax^{\nu-(\alpha+1)}\\&\times(b_{10}+b_{11}x^{\nu}+\dots)+B(1+b_{21}x^{\nu}+\dots)\ ,\end{aligned}\tag{20}$$

$$\begin{aligned}\chi=[&-2\lambda_1+\{2\lambda_1-(3\gamma-1)(\gamma+1)/\gamma(\gamma-1)\}\\&\times G_0x^{(\alpha+1)\gamma/(\gamma-1)}-\varphi+2\psi]/(2\gamma-1)\ .\end{aligned}\tag{21}$$

Since ν and $(\alpha+1)\gamma/(\gamma-1)$ are both comparatively large numbers, it is readily seen that ψ approaches a constant ψ_0+B as $x\rightarrow 0$, while φ and χ tend to infinity for finite values of A.

§4. Numerical Solution for $\gamma=1.4$

As we have mentioned in §4, Part I, the system of equations (3), (5), (6), (7) cannot be integrated directly by the numerical method, since (3), (5), (7) contain an unknown constant λ_1.

Now, we split up φ, ψ, χ into two parts as

$$\varphi=\varphi_1+\lambda_1\varphi_2,\quad \psi=\psi_1+\lambda_1\psi_2,\quad \chi=\chi_1+\lambda_1\chi_2,\tag{22}$$

and substitute these in (3), (5), (7); then we have two systems of equations for $\varphi_1, \psi_1, \chi_1$ and $\varphi_2, \psi_2, \chi_2$ respectively. All these equations do no more contain λ_1. Moreover, substituting (22) in (6) we have

$$\begin{aligned}&\varphi_1(1)=-2/(\gamma-1)\ ,\quad \psi_1(1)=-(\gamma-1)/2\gamma\ ,\\&\qquad\chi_1(1)=-2/(\gamma-1)\ .\end{aligned}\tag{23}$$

$$\varphi_2(1)=\psi_2(1)=\chi_2(1)=0\ .\tag{24}$$

Starting from the initial values as given by (23) and (24), we can integrate the two systems of equations for $\varphi_1, \psi_1, \chi_1$ and $\varphi_2, \psi_2, \chi_2$ by a numerical step-by-step method. If we substitute the values of $\varphi_1, \psi_1, \chi_1; \varphi_2, \psi_2, \chi_2$ so obtained in the condition (2), we have the following equation for determining λ_1:

$$I_1+\lambda_1 I_2=\lambda_1 J_0+1/(\gamma-1)(\alpha+1)\ ,$$

from which we get

$$\lambda_1=\{I_1-1/(\gamma-1)(\alpha+1)\}/(J_0-I_2)\ ,\tag{25}$$

where

$$\begin{aligned}I_1=\int_0^1\Big\{&\gamma f^{(0)}(x-f^{(0)})h^{(0)}\varphi_1+\frac{g^{(0)}}{\gamma-1}\psi_1\\&+\frac{\gamma}{2}f^{(0)2}h^{(0)}\chi_1\Big\}x^{\alpha}dx\ ,\end{aligned}\tag{26}$$

$$\begin{aligned}I_2=\int_0^1\Big\{&\gamma f^{(0)}(x-f^{(0)})h^{(0)}\varphi_2+\frac{g^{(0)}}{\gamma-1}\psi_2\\&+\frac{\gamma}{2}f^{(0)2}h^{(0)}\chi_2\Big\}x^{\alpha}dx\ .\end{aligned}\tag{27}$$

With this value of λ_1, we can determine φ, ψ, χ by (22).

We shall carry out the above-mentioned procedure. After elimination of χ from (3), (7), we obtain the equations for φ, ψ as:

$$\left.\begin{aligned}&\psi_x=P_1\varphi+P_2\psi+P_3+P_4\cdot\lambda_1\ ,\\&\varphi_x=\psi_x/\gamma+P_5\{(\gamma-1)\varphi+\psi-\lambda_1\}\ ,\end{aligned}\right\}\tag{28}$$

where

$$\left.\begin{aligned}
P_1=&-\frac{D}{1-(x-f^{(0)})D}\Big\{2\gamma f_x{}^{(0)}+\frac{\alpha-1}{2}\gamma\\
&+\frac{\gamma}{2\gamma-1}\left(f_x{}^{(0}+\frac{\alpha+1}{2}\frac{f^{(0)}}{x-f^{(0)}}\right)\\
&\qquad+(\alpha+1)(\gamma-1)\Big\}\ ,\\
P_2=&\frac{D}{1-(x-f^{(0)})D}\Big\{\gamma\frac{3-2\gamma}{2\gamma-1}\Big(f_x{}^{(0)}+\frac{\alpha+1}{2}\\
&\qquad\times\frac{f^{(0)}}{x-f^{(0)}}\Big)-\alpha-1\Big\}\ ,\\
P_3=&-\frac{D}{1-(x-f^{(0)})D}\frac{3\gamma-1}{2\gamma-1}\cdot\frac{\gamma+1}{\gamma-1}\\
&\times\left(f_x{}^{(0)}+\frac{\alpha+1}{2}\frac{f^{(0)}}{x-f^{(0)}}\right)\\
&\qquad\times\exp\left(\int_1^x\frac{\alpha+1}{x-f^{(0)}}dx\right),\\
P_4=&\frac{D}{1-(x-f^{(0)})D}\Big[\frac{-2\gamma}{2\gamma-1}\Big(f_x{}^{(0)}+\frac{\alpha+1}{2}\\
&\times\frac{f^{(0)}}{x-f^{(0)}}\Big)\left\{1-\exp\left(\int_1^x\frac{\alpha+1}{x-f^{(0)}}dx\right)\right\}\\
&\qquad+\frac{\alpha+1}{2}\frac{\gamma f^{(0)}}{x-f^{(0)}}+\alpha+1\Big],\\
P_5=&-\frac{1}{\gamma}\frac{\alpha+1}{x-f^{(0)}}\ .
\end{aligned}\right\}\tag{29}$$

Table I.

$\alpha=2$

	φ_1, ψ_1			φ_2, ψ_2		
x	1.00–0.93	0.93–0.84	0.84–0.52	1.00–0.96	0.96–0.84	0.84–0.52
Δx	0.01	0.01	0.02	0.01	0.01	0.02
	R-K	L	L	R-K	L	L

$\alpha=1, 0$

x	1.00–0.02	0.92–0.40
Δx	0.02	0.02
	R-K	L

Δx: interval for one step of integration,
R-K: Runge-Kutta method,
L: Levy method.

These functions can be calculated from the first approximation, especially, from the values of $f^{(0)}, f_x^{(0)}, D$.

By (22) and (28), we have

$$\left.\begin{aligned} \psi_{1x} &= P_1\varphi_1+P_2\psi_1+P_3 , \\ \varphi_{1x} &= \psi_{1x}/\gamma+P_5\{(\gamma-1)\varphi_1+\psi_1\} ; \end{aligned}\right\} \quad (30)$$

$$\left.\begin{aligned} \psi_{2x} &= P_1\varphi_2+P_2\psi_2+P_4 , \\ \varphi_{2x} &= \psi_{2x}/\gamma+P_5\{(\gamma-1)\varphi_2+\psi_2-1\} . \end{aligned}\right\} \quad (31)$$

Numerical integrations of (30), (31) with the initial values (23), (24) have been carried out for $\gamma=1.4$. To this end, values of P_1, P_2, P_3, P_4, P_5 have been first calculated, using the numerical values of $f^{(0)}, f_x^{(0)}, D$ as obtained in Part I for the cases of $\alpha=0$ and 1. The corresponding values for the case of $\alpha=2$ had already been calculated by G. I. Taylor[1]. Since, however, more accuracy is required for our present purpose than that of Taylor's results, the calculation for $\alpha=2$ has also been carried out. The results are tabulated in Appendix II.

In the initial stage of integration, the Runge-Kutta method was used and the Levy method was then used. Details are presented in Table I.

In these integrations, rapid changes in ψ_1 near $x=1$ caused some difficulty; this was serious especially in the case of $\alpha=2$. Moreover, large values of φ_1, φ_2 as $x\to 0$ introduced a considerable absolute error in them.

Finally these integral curves were connected to the asymptotic formula (19), (20) by finding appropriate values for the constants A and B. This was done by use of the following formulae:

$$B=\{\psi-\psi_S-b_{10}x^{\nu}(\varphi-\varphi_S)\}\{1-(b_{21}-a_{20}b_{10})x^{\nu}\}^{-1},$$
$$A=(\varphi-\varphi_S-Ba_{20})x^{\alpha+1} .$$

The values of A, B so obtained produce the error of $O(x^{2\nu-\alpha-1})$ for ψ and $O(x^{\nu-\alpha-1})$ for φ. Since the absolute errors of φ_1, φ_2 are large compared with those of ψ_1, ψ_2, the above formulae are satisfactory for us.

Fig. 1 and Fig. 2 show respectively the results for φ_1, φ_2 and for ψ_1, ψ_2.

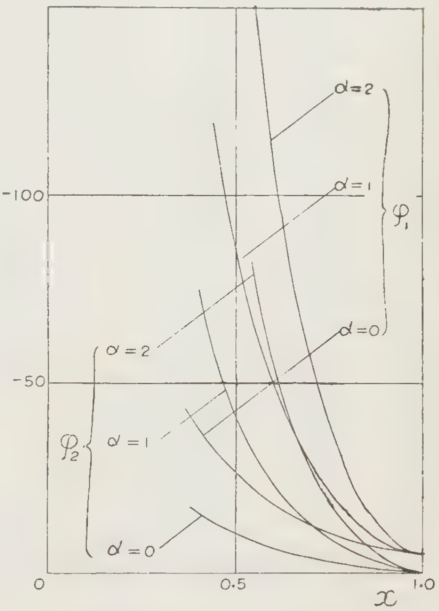

Fig. 1. φ_1, φ_2 for $\gamma=1.4$.

Using above values of $\varphi_1, \varphi_2; \psi_1, \psi_2$ and (7), the values of I_1, I_2 given by (26), (27) were calculated by Simpson's rule. Since the contribution of φ to the integral near $x=0$ is very little because of exceedingly small values of $h^{(0)}$, the error in φ_1, φ_2 near $x=0$ caused no difficulty. Then the values of λ_1 were determined by (25). Results are presented in Table II, where values of J_0 are also given for the sake of reference.

It is remarkable that λ_1 takes almost equal values for different values of α in contrast to J_0.

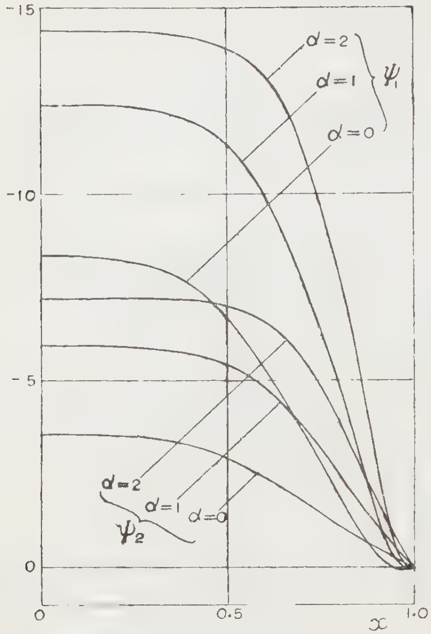

Fig. 2. ψ_1, ψ_2 for $\gamma=1.4$.

Table II.
λ_1, J_0 for $\gamma=1.4$.

α	2	1	0
λ_1	-1.918	-1.989	-2.138
J_0	0.596	0.877	1.696

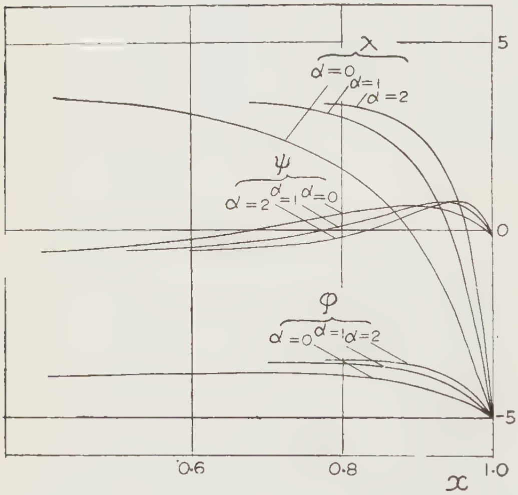

Fig. 3. Numerical solutions of φ, ψ, χ for $\gamma=1.4$.

Using the above values of λ_1, we can determine the final values of φ, ψ, χ by (22). The results obtained are given in Table III and plotted in Fig. 3.

An inspection of Table III and Fig. 3 shows that in each case φ tends to finite value as $x \to 0$, in spite of the fact that φ_1, φ_2 tend to infinity. Hence it will be seen that the particle velocity of gas at the centre of explosion remains zero, since

$$u=f^{(0)}+(x-f^{(0)})\varphi \text{ and } f^{(0)} \to x/\gamma \text{ as } x \to 0.$$

Moreover, it is remarkable that φ, ψ, χ have almost constant values outside the neighbourhood of $x=1$.

Using the finiteness and constancy of φ, we can determine the values of λ_1 by the formula $(\gamma-1)\varphi+\psi-\lambda_1=0$ or $(\gamma-1)\varphi_1+\psi_1+\{(\gamma-1)\varphi_2+\psi_2-1\}=0$, otherwise $\varphi_x \to -\infty$ with $P_5 \to -\infty$ as $x \to 0$ in the second equation of (28). Because of the constancy of φ, ψ, we can do this in the region not very far from $x=1$ where the error in the numerical integration is not yet large. λ_1 thus determined had the same values as those tabulated above, as had been expected. Thus, λ_1 itself could be determined with satisfactory accuracy, but the values of φ, ψ, χ near $x=0$ suffered from considerable diminishing of significant figures caused in the process of subtraction as we can see by comparing Figs. 1 and 2 with Fig. 3. Practically, this difficulty is not serious because of the fact that φ, ψ, χ are almost constant there. More precisely, we can see in Table III that φ for $\alpha=0$ has a slight maximum at about $x=0.69$. This is expected by the value of coefficients (18) of series expansion (19), (20) near $x=0$ as shown in Table IV, where a_{21} has a different character in each case; thus, if we increase x near $x=0$, φ increases for $\alpha=0$, remains constant for $\alpha=1$ and decreases for $\alpha=2$.

§ 5. Velocity-Distance Curves (U-R Curves) Time-Distance Curves

Inserting the values of λ_1, J_0 as given in Table II in the equation

$$\left(\frac{c}{U}\right)^2\left(\frac{R_0}{R}\right)^{\alpha+1}=J_0\left\{1+\lambda_1\left(\frac{c}{U}\right)^2\right\}, \quad (32)$$

velocity-distance curves are obtained as Fig. 4, where curves to the first approximation are also shown.

As expected, the curves tend to coincide with each other when R/R_0 becomes large. This fact corresponds to the values of λ_1 being almost equal values for various α.

Moreover, we can derive the relation between maximum pressure p_1 (the pressure at the shock front $x=1$) and R, utilizing (32)

Table III.

Numerical solutions of φ, ψ, χ for $\gamma=1.4$.

	$\alpha=2$			$\alpha=1$			$\alpha=0$		
x	φ	ψ	χ	φ	ψ	χ	φ	ψ	χ
1.00	−5.000	−0.143	−5.000	−5.000	−0.143	−5.000	−5.000	−0.143	−5.000
.99	−4.682	0.290	−3.123						
.98	−4.429	0.554	−1.702	−4.575	0.398	−2.592	−4.752	0.179	−3.665
.97	−4.229	0.702	−0.613						
.96	−4.039	0.768	0.227	−4.268	0.653	−0.935	−4.547	0.400	−2.566
.95	−3.941	0.779	0.879						
.94	−3.840	0.751	1.389	−4.047	0.743	0.236	−4.378	0.543	−1.659
.93	−3.761	0.700	1.793						
.92	−3.696	0.632	2.111	−3.889	0.729	1.068	−4.240	0.625	−0.905
.91	−3.645	0.556	2.365						
.90	−3.603	0.475	2.567	−3.778	0.659	1.674	−4.129	0.660	−0.274
.89	−3.571	0.395	2.732						
.88	−3.543	0.313	2.859	−3.694	0.554	2.111	−4.039	0.660	0.255
.87	−3.522	0.239	2.969						
.86	−3.506	0.159	3.048	−3.640	0.440	2.442	−3.969	0.632	0.700
.85	−3.490	0.102	3.131						
.84	−3.478	0.022	3.169	−3.595	0.316	2.680	−3.915	0.584	1.077
.82	−3.46	−0.09	3.25	−3.570	0.206	2.872	−3.873	0.522	1.399
.80	−3.45	−0.18	3.32	−3.542	0.092	3.002	−3.842	0.451	1.674
.78	−3.45	−0.27	3.34	−3.533	0.002	3.123	−3.820	0.374	1.912
.76		−0.32		−3.51	−0.093	3.192	−3·804	0.295	2.119
.74		−0.38		−3.51	−0.160	3.275	−3.795	0.215	2.300
.72		−0.42		−3.50	−0.237	3.306	−3.789	0.136	2.458
.70		−0.45		−3.50	−0.282	3.370	−3.787	0.060	2.598
.68		−0.47			−0.344	3.373	−3.787	−0.013	2.723
.66		−0.49			−0.370		−3.790	−0.081	2.836
.64		−0.50			−0.40		−3.792	−0.146	2.937
.62		−0.51			−0.42		−3.798	−0.205	3.028
.60		−0.51			−0.45		−3.803	−0.260	3.109
.58		−0.52			−0.47		−3.810	−0.309	3.187
.56		−0.52			−0.49		−3.816	−0.355	3.254
.54					−0.50		−3.824	−0.395	3.319
.52					−0.51		−3.830	−0.432	3.375
.50					−0.52		−3.838	−0.463	3.430
.48					−0.53		−3.842	−0.492	3.477
.46					−0.54		−3.853	−0.516	3.524
.44					−0.54		−3.858	−0.539	3.562
.42							−3.865	−0.556	3.602
.40							−3.869	−0.573	3.633
.00	−3.5	−0.53	3.5	−3.5	−0.56	3.5	−3.86	−0.617	3.86

Table IV.

α	0	1	2
B	1.812	1.56	1.51
a_{20}	−2.500	−2.50	−2.50
a_{21}	0.193	0.00	−1.17
b_{21}	1.484	2.15	2.04
A	0	0	0

and the Rankine-Hugoniot condition

$$p_1/p_0=\{2\gamma/(\gamma+1)\}(U/c)^2-(\gamma-1)/(\gamma+1)\ , \qquad \text{(Eq. (5), Part I)},$$

which is reduced to

$$(R_0/R)^{\alpha+1}=\{(\gamma+1)/2\gamma\}J_0\{2\gamma\lambda_1/(\gamma+1) +(\gamma-1)/(\gamma+1)+p_1/p_0\}\ .$$

For $\gamma=1.4$, using Table II, the above equation becomes

$$(p_1/p_0-2.07)(R/R_0)^3=1.96 \text{ for } \alpha=2\ , \quad (33)$$

$$(p_1/p_0-2.16)(R/R_0)^2=1.33 \text{ for } \alpha=1\ , \quad (34)$$

$$(p_1/p_0-2.33)(R/R_0)\ =0.69 \text{ for } \alpha=0\ , \quad (35)$$

respectively.

To compare the equation $p_1R^3=$const. with actual data, Taylor[1)] referred to an experiment about the explosion from a C.E. charge of 10 lb. which had been performed at Road Research Laboratory. The agreement between Taylor's theory and experiment was not very good; as he states, this is mainly due to a long cylindrical form of the charge.

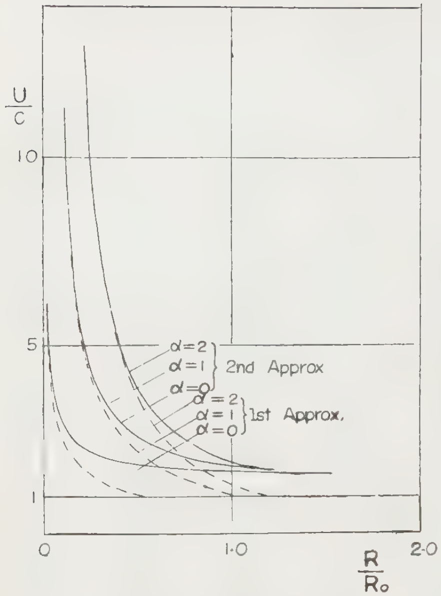

Fig. 4. U–R curves.

Now, we shall consider the relation $R^2(p_1/p_0-2.16)=\text{const.}$ derived from (34) in relation to the above data. It will be seen in Table V, where the case (33) is also presented for comparison, that there is a good agreement in this range, though the characteristic of a spherical wave can be seen at large R.

Table V.

Comparison with an experiment at Road Research Laboratory.

$R(ft)$	p_1/p_0	$(p_1/p_0-2.16)R^2$	$(p_1/p_0-2.07)R^3$
2	71.8	2.8×10^2	5.6×10^2
3	37.5	3.2	9.6
4	22.6	3.3	13
5	14.0	3.0	15
6	9.3	2.6	16
8	6.2	2.6	21

Morover, Taylor referred to Marley's experimental data which had been obtained from explosions of mixed charges of weight W made of T.N.T. and R.D.X. The comparison of these data with (33), (35) using a relation $W^{1/3}\propto R_0$ is shown in Table VI.

It is readily seen that (33) cannot be applied to the range near the charge where the wave behaves rather as a plane wave.

Table VI.

Comparison with Marley's experiment.

$R/W^{1/3}$ $\times(ft/lb^{1/3})$	p_1/p_0	$(R/W^{1/3})^3$ $\times(p_1/p_0-2.07)$	$(R/W^{1/3})$ $\times(p_1/p_0-2.33)$
0.5	198	0.25×10^2	99
1.0	117	1.2	110
1.5	68.3	2.2	100
2.0	42.0	3.2	80
2.5	25.1	3.6	57
3.0	15.4	3.6	45
3.5	10.5	3.6	20

Now, we shall consider the quantity λ defined in Part I as

$$\lambda=\frac{R}{y}\frac{dy}{dR} \quad \text{or using} \quad y=\left(\frac{c}{U}\right)^2,$$

$$\lambda=-\frac{2R}{U}\frac{dU}{dR},$$

which approximately corresponds to the decrement of U–R curve. In the second approximation now under discussion it becomes

$$\lambda=(\alpha+1)(1+\lambda_1 y).$$

Curves of λ derived from the experimental data quoted above seem to start from about $\lambda=1$ and approach to the curve $\lambda=3(1+\lambda_1 y)$ as shown in Fig. 5.

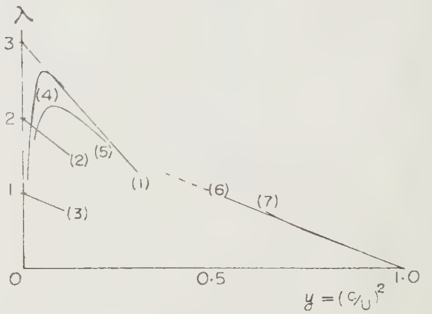

Fig. 5. (1) $\lambda=3(1-1.92y)$.
(2) $\lambda=2(1-1.99y)$.
(3) $\lambda=1-2.14y$.
(4) Marley's experiment.
(5) Experiment at Road Research Lab.
(6) Wolff's experimental formula $\lambda=2(1-y)$.
(7) Grime and Sheard's experiment.

On the other hand, for relatively small U, we have an experimental formula

$$U/c=\{1+(b/R)^2\}^{1/2}, \quad b=\text{const.},$$

given by Wolff[2], from which we have $\lambda=2(1-y)$. Grime and Sheard[3] give experimental data about explosions from cylindrical T.N.T./C.E. charges. Values of λ derived from them are also plotted in Fig. 5.

The theoretical λ curve in the case of an explosion from a point source may then be supposed to have a form of $\lambda=3(1+\lambda_1 y)$ in the initial stage and gradually approach to

$\lambda=2(1-y)$.

Distance-time relation can be obtained from an integration of (32), using the relation $U=dR/dt$. This gives

$$\left.\begin{aligned} \frac{ct}{R_0}&=\sqrt{J_0}\cdot K\,, \\ K&=\int_0^{R/R_0}\{z^{-(\alpha+1)}-J_0\lambda_1\}^{-1/2}dz\,. \end{aligned}\right\} \quad (35)$$

Hence

$$K=(-J_0\lambda_1)^{-3/2}\{\sqrt{v(1+v)}-\log(\sqrt{1+v}+\sqrt{v})\},$$
$$v=-J_0\lambda_1(R/R_0),\ (\alpha=0) \quad (36)$$

$$K=\{1-\sqrt{1-J_0\lambda_1(R/R_0)^2}\}/J_0\lambda_1,\quad (\alpha=1). \quad (37)$$

By using (36), (37) for $\alpha=0, 1$ and performing direct numerical computation for $\alpha=2$, distance-time curves are obtained, which are shown in Fig. 6, where the first approximation as given by

$$K=\{2/(\alpha+1)\}(R/R_0)^{(\alpha+3)/2}$$

is also presented.

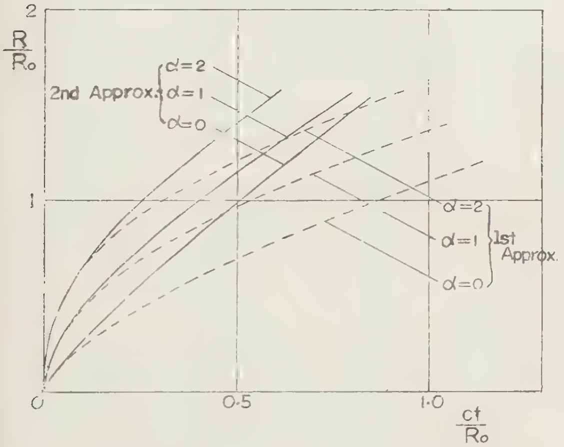

Fig. 6. Distance-time curves.

§ 6. Changing of Distributions of Velocity, Pressure and Density

To see the manner in which the distributions of velocity, pressure and density vary behind the shock front, values of

$$u/U=f=f^{(0)}+f^{(1)}(c/U)^2$$
$$=f^{(0)}+(x-f^{(0)})\varphi(c/U)^2\,,$$

$$p/p_0\cdot(c/U)^2=g=g^{(0)}+g^{(1)}(c/U)^2$$
$$=g^{(0)}\{1+\psi(c/U)^2\}\,,$$

$$\rho/\rho_0=h=h^{(0)}+h^{(1)}(c/U)^2=h^{(0)}\{1+\chi(c/U)^2\},$$

for various U/c are plotted in Figs. 7–15, Figs. 7–9 show f for $U/c=\infty, 5, 3, 2$, Figs. 10–12 show g for $U/c=\infty, 5, 3, 2$, and Figs. 13–15 give h for $U/c=\infty, 5, 3$. Values of R/R_0 corresponding to above values of U/c are shown in Table VII.

Table VII.
R/R_0

U/c \ α	0	1	2
∞	0	0	0
5	0.03	0.22	0.42
3	0.09	0.40	0.62
2	0.32	0.75	0.93

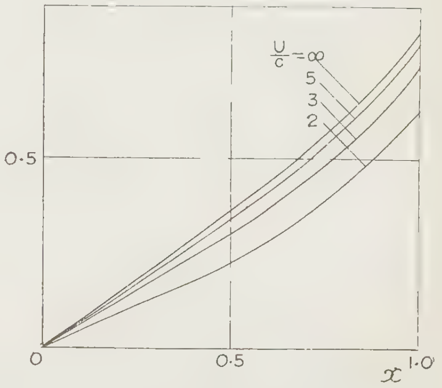

Fig. 7. f for $\alpha=2$.

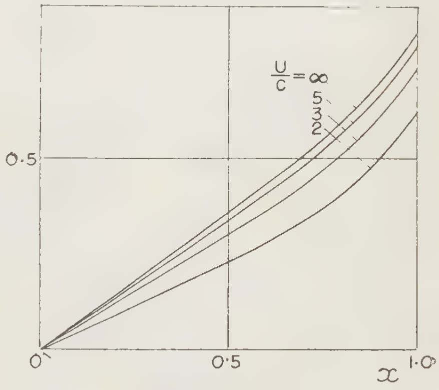

Fig. 8. f for $\alpha=0$.

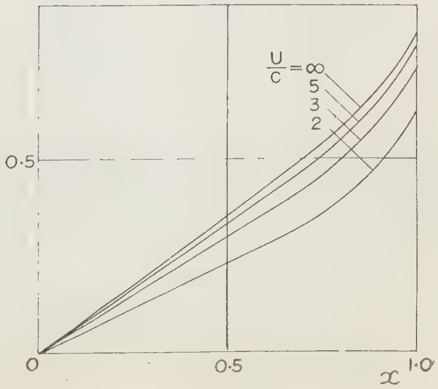

Fig. 9. f for $\alpha=1$.

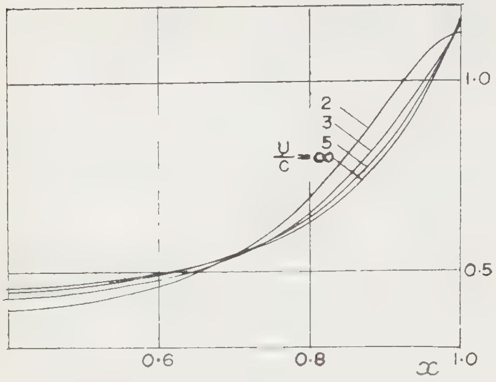

Fig. 10. g for $\alpha=0$.

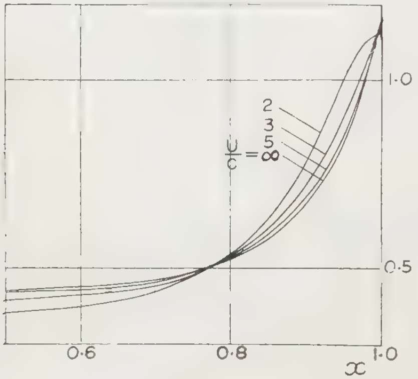

Fig. 11. g for $\alpha=1$.

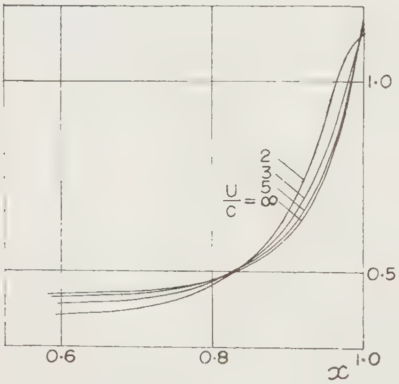

Fig. 12. g for $\alpha=2$.

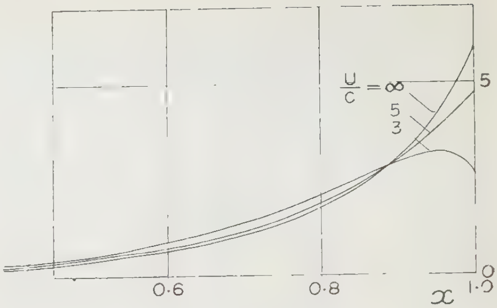

Fig. 13. h for $\alpha=0$.

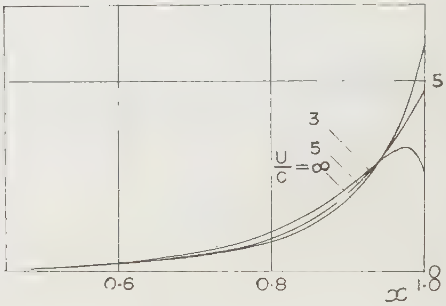

Fig. 14. h for $\alpha=1$.

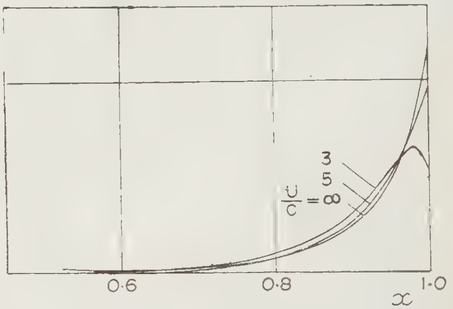

Fig. 15. h for $\alpha=2$.

According to the measurement on pressure distribution (cf. for example, the above-mentioned paper by Grime and Sheard[3]), pressure-gradient immediately behind the shock front becomes small and the curve becomes almost flat there, as the front goes far from the charge. Above curves for g show this tendency, although usual measurements are done at a fixed point and expressed as a function of time, while the above curve of g is concerned with the fixed time.

§ 7. Approximate Solution

The essential part of our problem is reduced to solving a problem of a linear differential equation of the second order derived from (3), (5), (7). Then, if we use a refinement of WKB method due to Imai[4),5)], we can obtain an approximate solution.

If we transform x to τ by

$$(x-f^{(0)})d/dx=-d/d\tau,\ x=1,\ \tau=0, \qquad (38)$$

Eqs. (3), (5), (7) are reduced to

$$\varphi_\tau-\psi_\tau/\gamma\Lambda=-Q\varphi+R(\chi-\psi)+P\lambda_1\,, \qquad (39)$$

$$\gamma\varphi_\tau-\psi_\tau=(\alpha+1)\{(\gamma-1)\varphi+\psi-\lambda_1\}\,, \qquad (40)$$

$$\varphi-2\psi+(2\gamma-1)\chi=S\,, \qquad (41)$$

where

$$\Lambda=(x-f^{(0)})D=\{f_x^{(0)}+\alpha f^{(0)}/x-(\alpha+1)/\gamma\}R\ ,$$
$$P=(\alpha+1)f^{(0)}/2(x-f^{(0)})\ ,$$
$$Q=2f_x^{(0)}+(\alpha-1)/2\ ,\quad R=f_x^{(0)}+P\ ,$$
$$S=\{2\lambda_1-(3\gamma-1)(\gamma+1)/\gamma(\gamma-1)\}e^{-(\alpha+1)\tau}-2\lambda_1\ ,$$

and then Λ, P, Q, R, S are all functions of $f^{(0)}/x, f_x^{(0)}$. This fact is useful because the approximate solution for $f^{(0)}$ derived in (39) in Part I is $f^{(0)}=x/\gamma+Ax^n$ and then $f^{(0)}/x$, $f_x^{(0)}$ are simple functions of $x^{n-1}=\eta$, say.

Now, we put

$$\gamma\varphi-\psi=We^Y\ ,$$

where

$$Y=\int_0^\tau Vd\tau$$
$$=\int_0^\tau\frac{(\gamma-1)(\alpha+1)/\gamma+\Lambda\{\alpha+1+Q+(\gamma-1)R\}}{2(1-\Lambda)}d\tau, \tag{42}$$

then (39)-(41) are reduced to

$$W_{\tau\tau}-J(\tau)W=-He^Y\ , \tag{43}$$

where

$$J=(\alpha+1)\{Q+(2-\gamma)R\}\Lambda(1-\Lambda)^{-1}-dV/d\tau+V^2,$$

and

$$H=H_1+\lambda_1H_2=(\alpha+1)[RS+\{(2\gamma-1)P-Q$$
$$-(\gamma-1)R\}\lambda_1]\Lambda(1-\Lambda)^{-1}\ .$$

Boundary conditions (6) are reduced to

$$\left.\begin{aligned}&(W)_{\tau=0}=(\gamma-1)/2\gamma-2\gamma/(\gamma-1),\\&(W_\tau)_{\tau=0}=-(\alpha+1)\{(5\gamma-1)2\gamma+\lambda_1\}\\&\qquad\qquad-(W\cdot V)_{\tau=0}.\end{aligned}\right\} \tag{44}$$

As mentioned above, V, J, H_1, H_2 can be considered to be functions of η; as an example, they are plotted in Fig. 16 for the case of $\alpha=2$, $\gamma=1.4$.

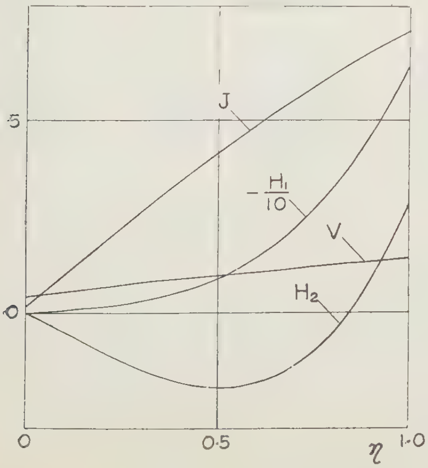

Fig. 16. V, J, H_0, H_2 as functions of η for $\alpha=2$, $\gamma=1.4$.

There is no turning point in J; thus we can get the approximate solution of (43), using the formula of the WKB method (cf. Eq. (4) of reference[5]) as follows:

$$W=\Big[A-\frac{1}{2}\int_0^\tau HJ^{-1/4}$$
$$\times\exp\left(-Y-z-\frac{1}{2}Q_1-\frac{1}{4}Q+\dots\right)d\tau\Big]J^{-1/4}$$
$$\times\exp\left(-z+\frac{1}{2}Q_1-\frac{1}{4}Q+\dots\right)$$
$$+\Big[B+\frac{1}{2}\int_0^\tau HJ^{-1/4}$$
$$\times\exp\left(-Y+z+\frac{1}{2}Q_1-\frac{1}{4}Q+\dots\right)d\tau\Big]J^{-1/4}$$
$$\times\exp\left(-z-\frac{1}{2}Q_1-\frac{1}{4}Q+\dots\right), \tag{45}$$

where

$$z=\int_0^\tau J^{1/2}d\tau\ ,\quad Q=-J^{-3/4}d^2/d\tau^2(J^{-1/4})\ ,$$
$$Q_1=\int_0^z Q(y)dy\ ,$$

and A, B are constants to be determined by (44).

Numerical calculations were performed for the case of $\gamma=1.4, \alpha=0, 2$ using the first approximation of (45) (where Q_1, Q were neglected), $\varphi_1, \varphi_2; \psi_1, \psi_2$ thus obtained were in good agreement with numerical solutions near $x=1$, but considerable deviations existed as $x\to0$, which were probably due to the neglect of Q_1, Q.

Values of λ_1 calculated from the above values of $\varphi_1, \varphi_2; \psi_1, \psi_2$ using (25) were -1.88 for $\alpha=2$ and -2.17 for $\alpha=0$. These values should be compared with the corresponding values shown in Table II, namely, -1.918 for $\alpha=2$ and -2.138 for $\alpha=0$.

Therefore, we may consider the present approximation to be very suitable for the determination of λ_1. This may be done more directly, utilizing the fact that the first term in (45) tends to infinity as $\tau\to\infty$ ($x\to0$ or $\eta\to0$), which is derived from $z\to\infty$ as $\tau\to\infty$, since $J^{1/2}\to$finite as $\eta\to0$. Because of the finiteness of φ as discussed in § 4, W must be finite; hence we have the condition for λ_1 as:

$$A-\frac{1}{2}\int_0^\infty HJ^{-1/4}\exp\Big(-Y-z-\frac{1}{2}Q_1$$
$$-\frac{1}{4}Q\dots\Big)d\tau=0\ ,$$

or if we put $A=A_1+\lambda_1 A_2$,

$$A_1-\frac{1}{2}\int_0^\infty H_1 J^{-1/4}\exp\left(-Y-z-\frac{1}{2}Q_1-\frac{1}{4}Q\ldots\right)d\tau$$
$$=\lambda_1\left\{A_2-\frac{1}{2}\int_0^\infty H_2 J^{-1/4}\times\exp\left(-Y-z-\frac{1}{2}Q_1-\frac{1}{4}Q\ldots\right)\right\}d\tau . \tag{46}$$

In conclusion the author wishes to express his sincere thanks to Professor I. Imai for his guidance and encouragement.

Appendix 1. Proof of the Equation (8)

We consider the second and the third equations of the fundamental equation (10) in Part I, namely :

$$\left.\begin{aligned}&(f-x)h_x+\lambda y h_y=-h(f_x+\alpha f/x)\ ,\\&-\lambda g+(f-x)g_x+\lambda y g_y=-\gamma g(f_x+\alpha f/x).\end{aligned}\right\}\ \text{(A1)}$$

Now, substituting the expressions

$$f=f^{(0)}+yf^{(0)}+\ldots\ ,$$
$$g=g^{(0)}+yg^{(1)}+\ldots\ ,$$
$$h=h^{(0)}+yh^{(1)}+\ldots\ ,$$
$$\lambda=(\alpha+1)(1+\lambda_1 y+\ldots)\ ,$$

in (A1) and considering the coefficients of the i-th powor of y, we get

$$\left.\begin{aligned}&(f^{(0)}-x)h_x^{(i)}+f^{(i)}h_x^{(0)}+(\alpha+1)ih^{(i)}\\&\quad+h^{(i)}(f_x^{(0)}+\alpha f^{(0)}/x)\\&\qquad+h^{(0)}(f_x^{(i)}+\alpha f^{(i)}/x)=\ldots\ ,\\&-(\alpha+1)\lambda_i g^{(0)}-(\alpha+1)g^{(i)}+(f^{(0)}-x)g_x^{(i)}\\&\quad+f^{(i)}g_x^{(0)}+(\alpha+1)ig^{(i)}\\&\quad+\gamma g^{(i)}(f_x^{(0)}+\alpha f^{(0)}/x)\\&\qquad+\gamma g^{(0)}(f_x^{(i)}+\alpha f^{(i)}/x)=\ldots\ ,\end{aligned}\right\}\tag{A2}$$

where the right-hand sides as shown as ... contain only the terms of $f^{(j)}, g^{(j)}, h^{(j)}, \lambda_j$ for $j<i$.

Introducing $\varphi^{(i)}, \psi^{(i)}, \chi^{(i)}$ as defined by $f^{(i)}=(x-f^{(0)})\varphi^{(i)}$, $g^{(i)}=g^{(0)}\psi^{(i)}$, $h^{(i)}=h^{(0)}\chi^{(i)}$ and using equations (24) in Part I for $f^{(0)}$, $g^{(0)}$, $h^{(0)}$, Eqs. (A2) are reduced to

$$(x-f^{(0)})(-\varphi_x^{(i)}+\chi_x^{(i)})-(\alpha+1)(\varphi^{(i)}+i\chi^{(i)})=\ldots\ , \tag{A3}$$

$$(x-f^{(0)})(-\gamma\varphi_x^{(i)}+\psi_x^{(i)})-(\alpha+1)\{(\gamma-1)\varphi^{(i)}+i\psi^{(i)}+\lambda_i\}=\ldots\ . \tag{A4}$$

If we make an operation

$$\text{(A3)}\times\{(i+1)\gamma-1\}-\text{(A4)}\times(i+1)\ ,$$

it results

$$(x-f^{(0)})d/dx[\varphi^{(i)}-(i+1)\psi^{(i)}+\{(i+1)\gamma-1\}\chi^{(i)}]$$
$$-(\alpha+1)i[\varphi^{(i)}-(i+1)\psi^{(i)}+\{(i+1)\gamma-1\}\chi^{(i)}+(i+1)\lambda_i/i]=\ldots\ .$$

This equation is readily integrated to give

$$\varphi^{(i)}-(i+1)\psi^{(i)}+\{(i+1)\gamma-1\}\chi^{(i)}+(i+1)\lambda_i/i=A_i\exp\left(i\int_1^x\frac{\alpha+1}{x-f^{(0)}}dx\right)+\ldots\ ,$$

where A_i is a constant.

Appendix 2. Numerical Values of $f^{(0)}, f_x^{(0)}$,
D for $\gamma=1\ 4$, $\alpha=2$

x	$f^{(0)}$	$f_x^{(0)}$	D
1.000	0.833333	1.805556	0.857143
.995	0.824387	1.772922	0.836304
.990	0.815605	1.739921	0.815245
.985	0.806988	1.706667	0.794012
.980	0.798538	1.673281	0.772652
.975	0.790255	1.639882	0.751212
.970	0.782139	1.606579	0.729738
.965	0.774189	1.573481	0.708275
.960	0.766404	1.540682	0.686869
.95	0.751320	1.47636	0.644388
.94	0.736869	1.41424	0.602614
.93	0.723026	1.35483	0.561828
.92	0.709762	1.29850	0.522267
.91	0.697045	1.24550	0.484136
.90	0.684841	1.19595	0.447583
.89	0.673115	1.14990	0.412736
.88	0.661831	1.10732	0.379662
.87	0.650957	1.06814	0.348426
.86	0.640457	1.03220	0.319025
.85	0.630303	0.99938	0.291485
.84	0.620459	0.96944	0.265737
.82	0.601610	0.91764	0.219549
.80	0.583695	0.87528	0.179981
.78	0.566547	0.84089	0.146426
.76	0.550016	0.81321	0.118261
.74	0.533982	0.79105	0.094793
.72	0.518345	0.77341	0.075421
.70	0.503021	0.75952	0.059576
.68	0.487943	0.74861	0.046681
.66	0.473061	0.74014	0.036319
.64	0.458323	0.73355	0.027960
.62	0.443711	0.72857	0.021462
.60	0.429169	0.72464	0.016081
.58	0.414724	0.72198	0.012399
.56	0.400275	0.71939	0.008504
.54	0.385965	0.71848	0.007423
.52	0.371495		0.002915

References

1) G. I. Taylor: Proc. Roy. Soc. London **A201** (1950) 159.

2) W. Wolff: Ann. d. Phys. **69** (1899) 329.

3) G. Grime & H. Sheard: Proc. Roy. Soc. London **A187** (1946) 357.

4) I. Imai: Phys. Rev. **74** (1948) 113.

5) I. Imai: Phys. Rev. **80** (1950) 1112.

JOURNAL OF THE PHYSICAL SOCIETY OF JAPAN Vol. 9, No. 2, MAR.—APR., 1954

Theory of the Visualization of Ultrasonic Waves

(I) Theory of the Schlieren Method for Visualizing Ultrasonic Waves*

By Otohiko NOMOTO

Kobayasi Institute of Physical Research, Kokubunzi, Tokyo

(Received September 24, 1953)

Intensity distribution of light in the image of the progressive ultrasonic waves obtained by the Schlieren method with stroboscopic illumination has been computed by the vector method. Pure phase-lattice is assumed in the plane of emergence of light out of the ultrasonic beam and the plane of focussing is assumed to be this plane. Several cases are to be distinguished according to the orders of light removed in obtaining the image. (a) In case the ultrasonic image is obtained by removing the zero order light, the visibility is good for small values of v, the amplitude of variation of the phase angle in the phase-lattice — corrugated wave — of light produced in the plane of emergence of light from the ultrasonic wave. The visibility vanishes, however, at zeros of the Bessel function $J_0(v)$ ($v=2.40$, $5.52, \ldots$); (b) In case the image is obtained by removing one of the two first order spectra, the visibility is zero for $v=0$, and for the other values of zeros of $J_1(v)$ ($v=3.83, \ldots$), having maximum between two neighbouring zeros. (c) The visibility of the image obtained by removing the zero order spectrum and one of the first order spectra is always better than that of the image obtained in case (b) and also better than the image obtained in case (a) except for small values of v ($v \leqq 1$). The visibility in the case (c) is comparatively insensitive to the values of v for wide range of v, being better than 75% for $v=1\sim6$. (d) The visibility of the image obtained by removing one of the first order spectra and part of the light of the zero order is improved in the region of small values of v as compared with the case (c), the visibility for greater values of v not much decreasing. For example, the visibility of the image obtained by removing 97.75% (in intensity) of the zero order light and one of the two first orders is more than 95% in the range $v=0.2\sim2$ and not less than 70% in the range $v=0.1\sim6$. In all cases, the ultrasonic images show fine structures as the value of v increases.

§ 1. Introduction

Various methods have been employed for the visualization of the ultrasonic waves (cf. Nomoto[1] for the classification of the methods). For visualizing the ultrasonic wave surfaces, the most commonly employed is the method of the secondary interferences (or the "Sichtbarmachungsmethode") and this method is thoroughly investigated already. The Schlieren method (method of striae) and the phase-shift method on the other hand, is not thoroughly investigated as yet.

The Schlieren method has hitherto been employed mainly for the visualization of the ultrasonic amplitude field and thoroughly investigated in this case, but not so widely employed for the visualization of the ultrasonic wave-surfaces, because in this case the method of the secondary interferences is the more convenient. Especially, the mechanism of the image formation in the Schlieren method in case of the visualization of the ultrasonic wave surfaces is almost unknown as yet.

For example, in usual experiments for visualizing the wave-surfaces of progressive ultrasonic waves employing stroboscopic (or instantaneous) light source, the zero order light or the central orders containing the zero order light are symmetrically stopped (cf. Tawil[2]), Rzevkin[3]), Kretschmer and Rzevkin[4)5]), Bergmann[6)7])), though the usual Toepler's Schlieren arrangement is also employed (cf. Oyama[8])). In order to obtain the image of the ultrasonic wave-surfaces, it is necessary to have two diffraction spectra at least, according to the theory of Abbe, and it is required to use both first orders in case of the visualization of the weak ultrasonic waves, where the higher order spectra are lacking. The usual arrangement removing the zero order spectrum, however, produce double periodicity as pointed out by Torikai and Negishi.[9]) Moreover, this method is not suitable for strong ultrasonic waves, as is to be shown later. Also in the experiments of Tawil[10]) and Pohlman[11]) for visualization of the stationary ultrasonic waves, the zero order spectrum or the central light including the zero order is stopped.

---

* Japanese text of this paper has been published partly in "Bulletin of the Kobayasi Institute of Physical Research, **3** (1953) 22" in a somewhat detailed form. The remaining part will be published there shortly.

This paper deals with the theoretical treatment of the visualization of ultrasonic wave-surfaces by the Schlieren method, restricting the problem to the visualization of the progressive ultrasonic waves by stroboscopic light source of the same frequency with that of sound. It is because of the fact that the image of the stationary ultrasonic wave is easily to be derived from this. At the same time, some new Schlieren arrangements have been discussed, which, though not hitherto employed as yet, are expected to give good images in some cases.

The schematical optical arrangement is indicated in Fig. 1, where the left part (I) represents an ultrasonic stroboscope employed in obtaining the stroboscopic illumination, and the right part (II) shows the apparatus for obtaining the Schlieren image. The figure shows the case when the +1st order spectrum is removed, but various arrangements are possible according to the order or orders of the spectra removed.

Generally speaking, it is true that among the images of the ultrasonic waves, the fundamental one is that obtained in case the progressive ultrasonic wave is observed with intermittent light source of the same frequency (high frequency stroboscope) with that of the ultrasonic wave, the ideal case, especially, being that of the instantaneous time of illumination. The stationary ultrasonic wave, too, produces the same image as the progressive ultrasonic wave, when observed with this ideal stroboscope. When the stationary ultrasonic wave is observed with stationary light source, the amplitude varies sinusoidally with respect to time, and produces an image given by a time average of the image of a progressive ultrasonic wave (by stroboscopic illumination) whose intensity varies sinusoidally with respect to time. The image of the amplitude field of an ultrasonic wave is given as the space average of the image of this progressive ultrasonic wave produced when observed with stroboscopic illumination.

The method employed in this paper is that of representing the amplitude and the phase of light with a vector, and also the analytical derivation of formulas are simplified by employing this method.

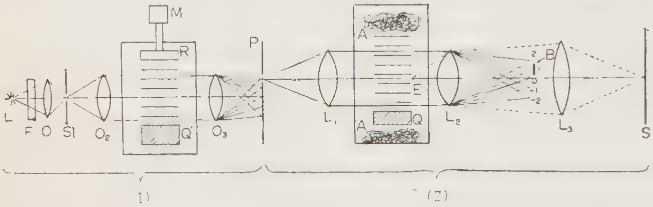

Fig. 1. Optical arrangement for the Schlieren method of visualizing the progressive ultrasonic wave (Schematical).

Part (I) Ultrasonic stroboscope for obtaining intermittent illumination. L: light source (mercury vapour lamp), F: filter for obtaining monochromatic light, O_1, O_2, O_3: lenses, Sl: slit, P: pinhole (or slit) to pass one of the diffraction spectra. Q′: quartz plate (half frequency as compared with Q), R: reflector, M: micrometer head to establish standing waves between Q′ and R.

Part (II) Schlieren arrangement. L_1, L_2, L_3: lenses, Q: quartz plate for producing ultrasonic wave, A, A: absorbers of sound, B: bar at the focal plane of L_2 to stop one or more of the orders of diffracted light. The numbers indicate the orders of the diffraction spectrum. The number is enumerated positively in the direction of propagation of the ultrasonic wave, and negatively in the opposite direction. S: screen at the image plane of the plane of emergence of light from the ultrasonic beam (E). We can dispense with the lens L_3 if the lens L_2 is placed apart from the plane E so that L_2E is larger than the focal length of L_2.

§ 2. Vector Representation of a Phase-Lattice of Light

In the following, it is assumed for the sake of simplicity that the ultrasonic wave constitutes a parallel beam of rectangular cross section emerging from the quartz plate, as is approximately the case in ordinary experiments of quantitative nature. The parallel beam of light after crossing this ultrasonic wave perpendicularly, has a corrugated wave front of the same periodicity with that of the ultrasonic wave-length, i.e., the phase angle of light is periodically modulated along the direction of propagation of the ultrasonic wave, the corrugation propagating with the velocity of sound. The amplitude of light along the wave-surface, or along the plane of emergence from the ultrasonic beam, is approximately constant, as long as the intensity of the ultrasonic wave is not very high and the width of the ultrasonic beam—length of path of the light across the ultrasonic beam—is not so great, as was pointed out by Raman and Nagendra Nath[12)] in their theory of the diffraction of light by ultrasonic waves.

If we take this amplitude for simplicity's sake as unity, then we have as the expression of the light amplitude (including phase) in the plane of emergence from the ultrasonic beam

$$\alpha = \cos\{\omega t - v \sin Kx\}\ , \qquad (2.1)$$

which represents a phase-lattice of light or the light wave with corrugated wave-surfaces. In this equation $\omega = 2\pi\nu$ (ν: frequency of light), x means the direction of propagation of the ultrasonic wave, $K = 2\pi/\Lambda$ (Λ: ultrasonic wavelength), v means the amplitude of phase modulation and is given by $v = 2\pi p = 2\pi\mu L/\lambda$ (L: width of the ultrasonic beam, i.e., length of path of the light across the ultrasonic beam, μ: amplitude of variation of the index of refraction of the medium produced by the ultrasonic wave).

The amplitude and the phase of the light at a fixed time ($t=0$) along the ultrasonic beam (on the plane of emergence of light from the ultrasonic beam, $y=0$) is to be represented by a vector CA of unit length in Fig. 2, rotating with C as center and with the tip A describing the arc of a unit circle in positive direction (counter-clockwise) from O to F through an angle $v = 2\pi p$ (or p rotations) while x increases from 0 to $\Lambda/4$, and then coming back along the same path from F to O in negative rotation while x increases from $\Lambda/4$ to $\Lambda/2$, and continuing the path from O to F′ in the negative direction while x increases from $\Lambda/2$ to $3\Lambda/4$, and finally describing the arc from F′ to O in positive rotation as x increases from $3\Lambda/4$ to Λ. This means the vector sweeps the sector from CF′ to CF to and from once for every period of the ultrasonic wavelength. The angular velocity is maximum at the middle point O, and zero at the two extremities, F, F′.

As we have the mathematical relations (identities)

$$\cos(v \sin\xi) = \sum_{n=-\infty}^{\infty} J_n(v) \cos n\xi\ ,$$

and

$$\sin(v \sin\xi) = \sum_{n=-\infty}^{\infty} J_n(v) \sin n\xi\ ,$$

where ξ means any quantity, and $J_n(v)$ means the Bessel functions of the n-th order we have from (2.1) as the expression of the amplitude of light in the plane of emergence from the ultrasonic wave

$$\alpha = \sum_{n=-\infty}^{\infty} J_n(v) \cos(\omega t - nKx)\ .$$

The component light wave with amplitude $J_n(v)$ propagates mainly in the y-direction, *i.e.* in the direction of propagation of the incident light, however with x-component of the propagation vector nK. If we assume the light velocity in the medium, and accordingly the propagation vector k, as independent of the direction of propagation, we have as the y-component of the propagation vector $\sqrt{k^2 - n^2K^2}$, where $k = 2\pi/\lambda$ (λ: wavelength of light in air), and we have as the expression of the light wave emergent from the ultrasonic beam

$$\alpha' = \sum_{n=-\infty}^{\infty} J_n(v) \cos\{\omega t - (nKx + \sqrt{k^2 - n^2K^2}\,y)\}\ . \qquad (2.2)$$

This means that the light with corrugated wave-surfaces as given in (2.1) is equivalent to the sum of plane waves of light given by (2.2), these plane waves being the diffraction spectra. The derivation of (2.2) from (2.1) here presented is only approximate, but the exact derivation by computation of the diffraction integral leads to the same result[12)].

The diffraction spectrum of the n-th order has amplitude $J_n(v)$. Especially, the zero order spectrum has amplitude $\alpha_0=J_0(v)$ and phase angle zero, and is to be represented by the vector $\overline{\mathrm{CS}}$, Fig. 3. In the following, we will consider the image produced by removing various orders of light from the diffraction spectra.

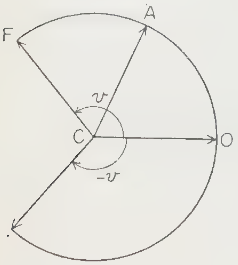

Fig. 2. Vector diagram representing the amplitude and the phase angle of light along a phase-lattice.

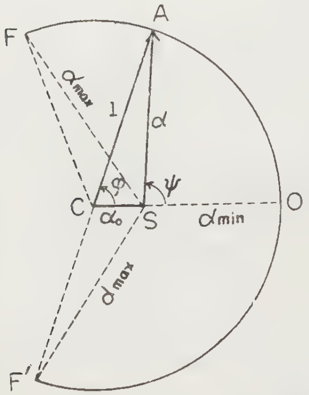

Fig. 3. Vector diagram representing the amplitude and the phase angle of light along the ultrasonic wave when the zero order light is removed from the phase-lattice.

§ 3. The Images Produced by Removing the Zero-Order Diffraction Spectrum

In case the zero order light is removed, the distribution of amplitude of light along the ultrasonic wave (and in the plane of emergence of light from the ultrasonic beam) is represented by the vector $\overline{\mathrm{SA}}$ in Fig. 3, as the point A describes the arc of a unit circle around C in pedulum motion. The amplitude α and the phase angle ψ at any point A on the phase-lattice with initial amplitude unity and with initial phase angle $\varphi=v\sin\theta$, $(\theta=2\pi x/\Lambda)$ now become $\alpha=\mathrm{SA}$ and $\psi=\angle\mathrm{ASO}$ respectively. The amplitude changes along the ultrasonic wave between the minimum value $\alpha_{\min}=\mathrm{SO}$ and the maximum value $\alpha_{\max}=\mathrm{SF}=\mathrm{SF}'$. (The figure represents the case when $\alpha_0>0$, i.e., $v<2.40$). In this case there are two equal maxima and two equal minima in a periodic length=ultrasonic wavelength) and the distribution of light intensity in the image is periodical with half wavelength of the ultrasonic wave.

The distribution of light amplitude along an ultrasonic wavelength can be obtained in this graphical manner. The light intensity is obtained from this as squares of the light amplitude. The intensity distribution curves given in the following have been obtained in this manner by employing large scale figures with diameters of the unit circles 10 cm or 15 cm. The accuracy of the graphical method here employed is larger than 1% of the incident light intensity and is sufficient for comparison with experiments.

Fig. 4 shows examples of the graphical construction for two values of v. Fig. 5 represents the intensity distribution of light along the ultrasonic waves obtained in this manner. Fig. 4 shows the half-period corresponding to $x=0\sim\Lambda/2$, the other half corresponding to $x=0\sim-\Lambda/2$ being symmetrical with the former with respect to the horizontal line. The figures along the circumference of the arc shows the values of $\theta=2\pi x/\Lambda$ and only the range of $\theta=0°$ to $90°$ is represented.

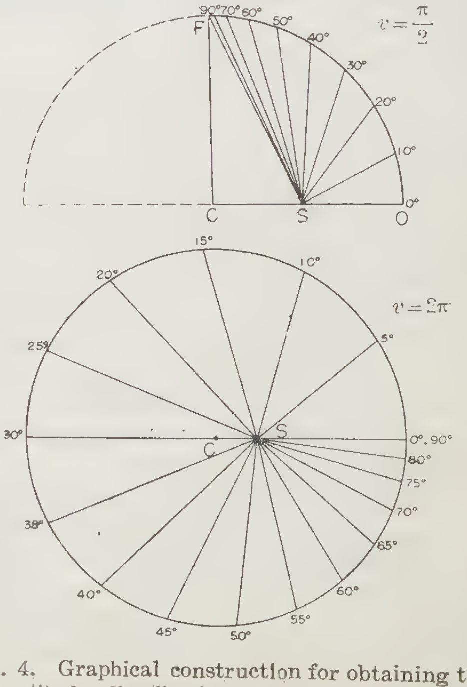

Fig. 4. Graphical construction for obtaining the amplitude distribution of light along the ultrasonic wave in the Schlieren method (in case the zero order spectrum is removed).

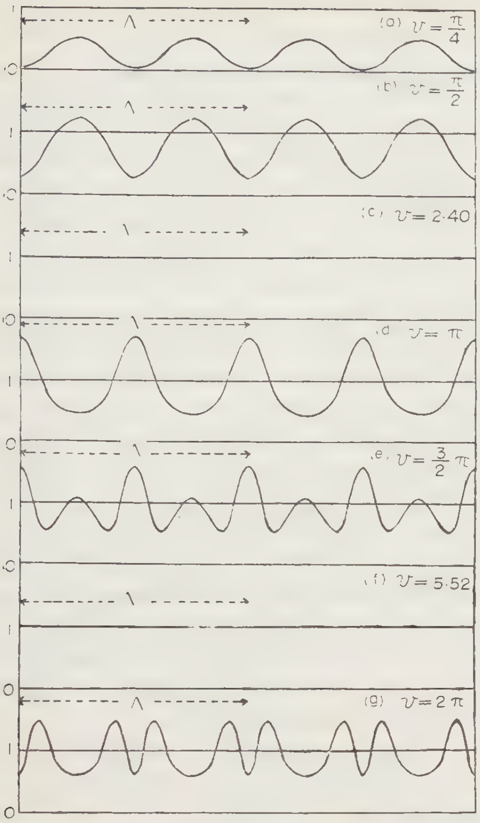

Fig. 5. Intensity distribution of light in the image of the progressive ultrasonic wave produced under ideal stroboscopic illumination by the Schlieren method (in case when the zero order spectrum is removed).

As $\varphi = v \sin\theta$, the angles θ and $\pi-\theta$ give the same value of φ. Thus $\theta = 100°, 110° \cdots$ overlap with $\theta = 80°, 70°, \cdots$ respectively.

As $\alpha_0 = J_0(v) = 0$ at $v = 2.40$, the image vanishes at this value of v (Fig. 5, (c)). When v increases beyond this value ($2.40 < v < \pi$), $\alpha_0 < 0$, and $\alpha_{\min} = \mathrm{SF}$ and $\alpha_{\max} = \mathrm{SO}$, and the peak and the valley of the light intensity distribution curve exchange (cf. Fig. 5, (d)).

In the range $\pi < v < 5.52$, the amplitude corresponding to the point O′, the other end of the diameter SO, becomes minimum, and SF now becomes a sub-maximum instead of a minimum. Thus the valley of the minimum now divides into two, enclosing a sub-maximum between them (cf. Fig. 5, (e)).

The image vanishes for the second time at $v = 5.52$, for which $J_0(v) = 0$ (cf. Fig. 5, (f)). For $v > 5.52$, the maximum and the minimum of the light intensity interchange, and there are four peaks for an ultrasonic wavelength (cf. Fig. 5, (g)). The distances between two neighbouring peaks are not equal, but the phenomenon repeats with half wavelength of sound as the periodic length. As the value of v increases further, the number of peaks and valleys increases, with increase of one peak per half wavelength as the value of v increases by π.

Also the analytical expression of the light intensity is easily to be obtained from Fig. 3. This becomes as follows.

(i) *In case when* $v < 2.40$

$$I = \alpha^2 = 1 + J_0^2(v) - 2J_0(v)\cos(v \sin Kx)\,, \tag{3.1}$$

with

$$I_{\max} = 1 + J_0^2(v) - 2J_0(v)\cos v\,,$$

and

$$I_{\min} = \{1 - J_0(v)\}^2\,. \tag{3.2}$$

If we define the visibility by

$$S = \frac{I_{\max} - I_{\min}}{I_{\max} + I_{\min}} \tag{3.3}$$

as usual, we have

$$S = \frac{(1-\cos v)J_0(v)}{1 + J_0^2(v) - 2(1+\cos v)J_0(v)} \tag{3.4}$$

in this case.

(ii) *In case* $2.40 < v < \pi (= 3.14)$

The expression

$$I = 1 + J_0^2(v) - 2J_0(v)\cos(v \sin Kx) \tag{3.1}$$

holds true also in this case, but the maximum and minimum interchange and become

$$\left.\begin{aligned} I_{\max} &= \{1 - J_0(v)\}^2\,, \\ I_{\min} &= 1 + J_0^2(v) - 2J_0(v)\cos v\,. \end{aligned}\right\} \tag{3.5}$$

The visibility is, therefore, given by

$$S = -\frac{(1-\cos v)J_0(v)}{1 + J_0^2(v) - 2J_0(v)(1+\cos v)}\,. \tag{3.6}$$

Thus we have as the expression of visibility applicable in the range $0 \leqq v \leqq \pi$,

$$S = \frac{(1-\cos v)|J_0(v)|}{1 + J_0^2(v) - 2J_0(v)(1+\cos v)}\,. \tag{3.7}$$

(iii) *In case when* $\pi < v$,

We have

$$\left.\begin{aligned} I_{\max} &= \{1 + |J_0(v)|\}^2\,, \\ I_{\min} &= \{1 - |J_0(v)|\}^2\,, \end{aligned}\right\} \tag{3.8}$$

and therefore,

$$S = \frac{2|J_0(v)|}{1 + J_0^2(v)}\,. \tag{3.9}$$

The curve (a) in Fig. 6 represents the visibility of the image obtained in the Schlieren method by removing the zero order light as function of v. In this case, the visibility is good for weak ultrasonic waves ($S=1$ at $v=0$), and decreases with increasing intensity of the ultrasonic wave, becomes zero at $v=2.40$, increases again, attains maximum and decreases till it vanishes at $v=5.52$ for the second time, and so on.

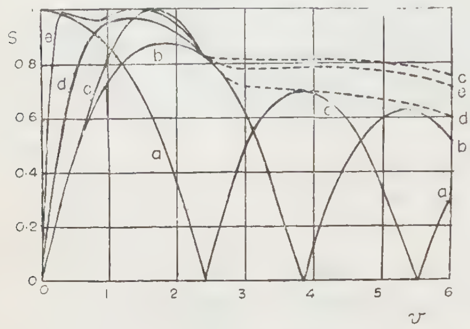

Fig. 6. Visibility of the image of the progressive ultrasonic waves obtained by the Schlieren method under ideal stroboscopic illumination. (a) in case when the zero order light is removed, (b) in case when one of the two first order spectra is removed, (c) in case when the zero order and one of the two first orders are removed. (d) In case when 75% (in intensity) of the zero order light and one of the first orders are removed, (e) in case when 97.75% (in intensity) of the zero order light and one of the first orders are removed.

§ 4. The Images Produced by Removing One of the Two First Order Spectra

As stated above, double periodicity occurs in the image of a progressive ultrasonic wave for one ultrasonic wavelength when the zero order light is removed. In obtaining a single periodicity for an ultrasonic wavelength, it is necessary to remove the light unsymmetrically with respect to the central order. The simplest method is to remove one of the two first order spectra as discussed below.

The first order spectrum has the amplitude $J_1(v)$ according to (2.2). (We will consider about the +1st order; the −1st order has the amplitude $J_{-1}(v)=-J_1(v)$, which means the same amplitude with the +1st order, but the opposite phase). The direction of propagation of the first order spectrum, however, is different from that of the zero order light, which propagates in the direction of the incident light, and the phase angle of the first order spectrum in the plane of emergence ($y=0$) varies periodically in the x direction, being 0 at $x=0$ and 2π at $x=\Lambda$.

Accordingly, the vector representing the +1st order becomes CE of Fig. 7, (a), with length $\mathrm{CE}=\alpha_1=J_1(v)$ and with the end-point E describing a circle around the point C with uniform angular velocity in the positive direction with increase in x, beginning from the point I corresponding to $x=0$ and describing the circle once for an ultrasonic wavelength.

The circumstance is similar also in case when the −1st order spectrum is removed. In this case, the vector representing the −1st order spectrum is CE′ with length −CE and the phase angle $\angle\mathrm{OCE}=-\theta$ (cf. Fig. 7 (b)). Thus the point E′ describes the circle once in negative direction as the value of x increases by an ultrasonic wavelength, beginning from the point I' corresponding to $x=0$.

As the value of φ, and accordingly the position of the point A, are the same for θ and $(\pi-\theta)$, we have as the light amplitude of the image the expression

$$\alpha(x)$$

in case the +1st order is removed and the expression

$$\alpha'(x)=\alpha(\Lambda/2-x)$$

in case the −1st order is removed. As the value of α does not change with change in sign of the parameter x, we have $\alpha(x)=\alpha(-x)$, and accordingly,

$$\alpha'(x)=\alpha(\Lambda/2+x)\ .$$

This indicates that the image produced by removing the −1st order is only displaced by an amount of half wavelength against the image produced by removing the +1st order spectrum, other points being the same.

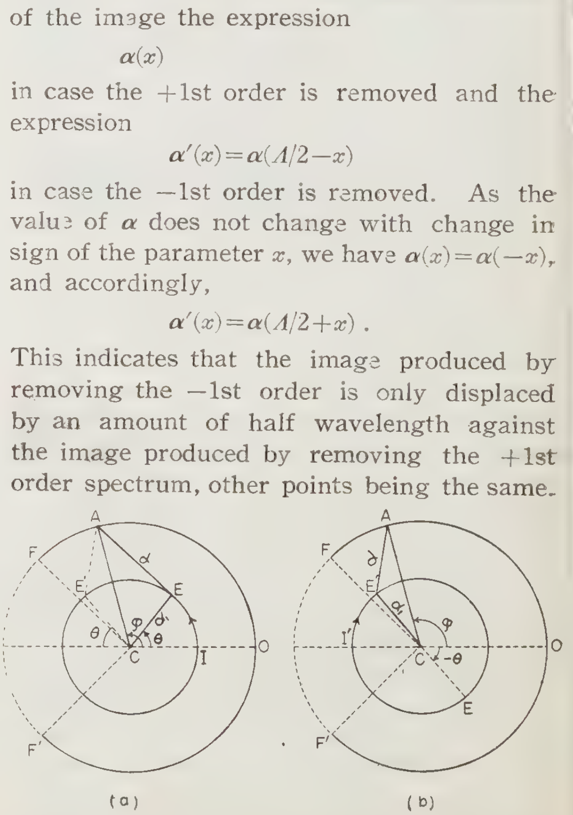

Fig. 7. Vector diagram representing the distribution of the amplitude and phase-angle of light along the image of the ultrasonic wave when (a) the +1st order or (b) the −1st order spectrum is removed from the phase-lattice.

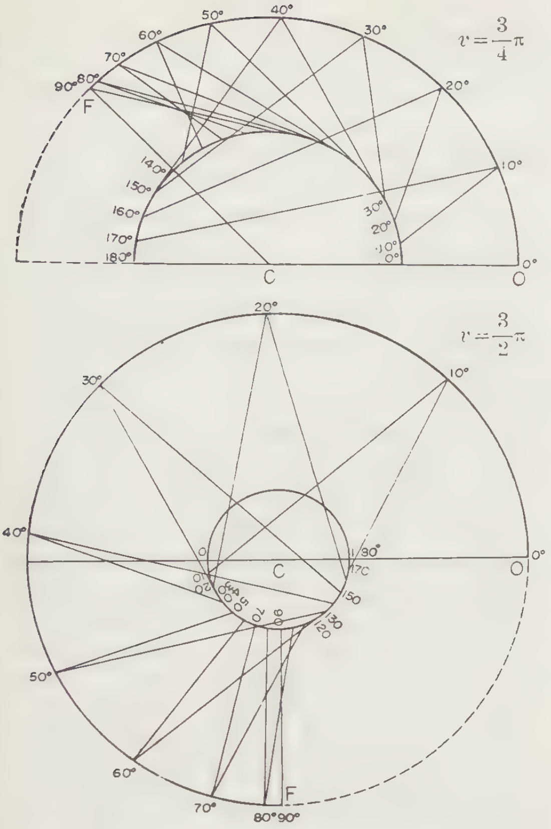

Fig. 8. Graphical construction for obtaining the amplitude distribution of light in the Schlieren method when the +1st order spectrum is removed.

Corresponding to any point A of the unit circle representing the phase-lattice (amplitude 1, and phase angle $\varphi=v\sin(2\pi x/\Lambda)$) there is a vector CE representing the 1st order diffracted light with amplitude $\alpha_1=J_1(v)$ and phase angle $\theta=2\pi x/\Lambda$. If, therefore, the first order light is removed, the vector EA = CA − CE gives the amplitude and the phase of the light at any point x along the direction of propagation of the ultrasonic wave, the magnitude of EA giving the amplitude.

Fig. 8 shows two examples of the graphical construction for obtaining the amplitude distribution of light in the image obtained by removing the +1st order spectra. The figures show the half-period corresponding to $x=0\sim\Lambda/2$, the other half corresponding to $x=0\sim-\Lambda/2$ being symmetrical with respect to the horizontal line.

Fig. 9 shows the intensity distributions of light of the images obtained by this method and at various ultrasonic intensities corres-

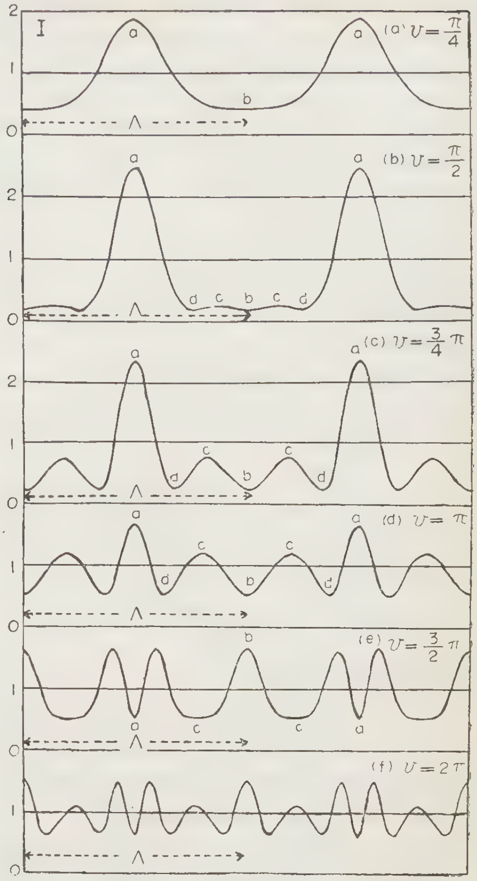

Fig. 9. Intensity distribution of light in the image of the progressive ultrasonic wave produced by the Schlieren method under ideal stroboscopic illumination (in case the +1st order spectrum is removed).

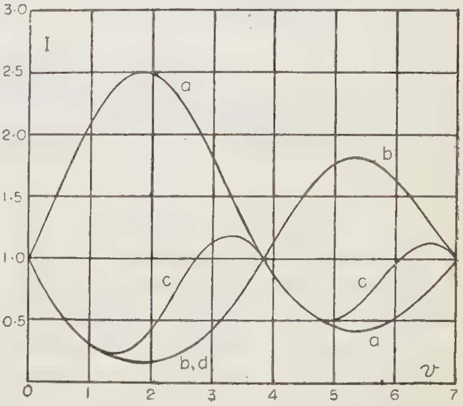

Fig. 10. Height of the peak and the valley of the distribution curve of light intensity along the ultrasonic image (previous method) in dependence on the value of v (Schlieren method, the case when the 1st order spectrum is removed)

ponding to various values of v. For smaller values of v ($v \leqq 1.2$) the visibility is poorer in this method than in the case of the image obtained by removing the zero order, though the difference of brightness (between maximum and minimum) is greater in this method because of the greater brightness. For greater values of v ($1.2 < v < 3.06$), both the visibility and the brightness is better in this case than in case when the zero order only is removed.

The analytical expression of the light intensity become as follows (cf. Fig. 7):

$$\left.\begin{array}{l} I = AE^2 = 1 + J_1^2(v) - 2J_1(v)\cos(v\sin\theta - \theta), \\ \text{where} \qquad \theta = 2\pi x/\Lambda\,. \end{array}\right\} \tag{4.1}$$

The maximum and minimum of intensity takes place for $\theta = 0°$ and $180°$ respectively and is given by

$$\left.\begin{array}{l} I_{\max} = 1 + |J_1(v)|^2\,, \\ I_{\min} = 1 - |J_1(v)|^2\,, \end{array}\right\} \tag{4.2}$$

and the visibility by

$$S = \frac{2J_1(v)}{1 + J_1^2(v)}\,. \tag{4.3}$$

The curve (b) in Fig. 6 represents the visibility in this case in dependence on v. The visibility increases at first with increase in v, beginning from zero visibility for $v = 0$ and attaining maximum at $v = 1.84$ (corresponding to the maximum of $J_1(v)$), but decreases afterwards and becomes zero at $v = 3.83$ (corresponding to $J_1(v) = 0$). The increase and the decrease in visibility is continued also hereafter but with the height of the maximum becoming smaller with increase in v.

The curves a and b in Fig. 10 show the light intensity at points a and b of the curve in Fig. 9 as functions of v. These are given by

$$\left.\begin{array}{l} I_a = \{1 + J_1(v)\}^2\,, \\ I_b = \{1 - J_1(v)\}^2\,, \end{array}\right\} \tag{4.4}$$

and the maximum and the minimum exchanges at $v = 3.83$. The curve c, Fig. 10, gives the intensity of the sub-maximum peak c in Fig. 9. The sub-maximum occurs at the maximum of $(v\sin\theta - \theta)$ as is to be seen from (4.1), or at

$$\cos\theta = 1/v\,, \tag{4.5}$$

so that it is required for the existence of the sub-maximum that $v > 1$. The magnitued of the sub-maximum is given by

$$I_c = 1 + J_1^2(v) - \frac{2J_1(v)}{v}\{\cos\sqrt{v^2-1} + \sqrt{(v^2-1)}\sin\sqrt{v^2-1}\}\,, \tag{4.6}$$

§ 5. The images produced by removing the zero order and the +1st order spectrum

The intensity distribution of light in the image of the progressive ultrasonic wave produced with stroboscopic light source by the Schlieren method in removing the zero order light and one of the two first orders can be obtained easily as in the previous cases.

The zero order spectrum is represented with a horizontal vector CS of length $\alpha_0 = J_0(v)$ in Fig. 11, (a), and the first order light (+1st order) is to be represented by a rotating vector SE with length $\alpha_1 = J_1(v)$ whose end describes a circle around S in positive direction once for an ultrasonic wavelength as the value of x increases, beginning from the point J corresponding to $x = 0$.

When the zero order and the +1st order are removed, the amplitude and the phase of the light at point A on the phase-lattice are now to be represented by the vector EA. ($\angle SCA = \varphi = v\sin(2\pi x/\Lambda)$ and $\angle OSE = \theta = 2\pi x/\Lambda$.

In case the zero order light and the −1st order light are removed, we have, Fig. 11, (b). The situation here is similar as in the case of Fig. 7, (b) and we have as the vector representing the −1st order spectrum $SE' = J_{-1}(v) = -J_1(v) = -SE$, and $\angle OSE = -\theta = -2\pi x/\Lambda$, so that the end point E' of the vector SE describes a circle around S in negative direction and once for an ultrasonic wavelength as the value of x increases, beginning from the point J' corresponding to $x = 0$.

As the point A is common for $\theta = \theta$ and $\theta = \pi - \theta$, i.e., for $x = x$ and $x = (\Lambda/2) - x$, the amplitude distribution of light of the image obtained by removing the zero order and the −1st order is given by

$$\begin{aligned} \alpha'(x) &= \alpha(\Lambda/2 - x) \\ &= \alpha(\Lambda/2 + x) \end{aligned}$$

and become identical with the amplitude distribution of light along the image obtained by removing the zero order and the +1st order if the coordinate axis is displaced by

$\Lambda/2$.

Fig. 12 shows two examples of the graphical constructions for obtaining the image in case the zero order and the +1st order are removed. Fig. 13 shows the intensity distributions of light along the images of the ultrasonic waves in this case. Comparing this figure with Fig. 9, we see that the difference of maximum and minimum brightness is smaller in this case than in the case of the image obtained by removing the first order

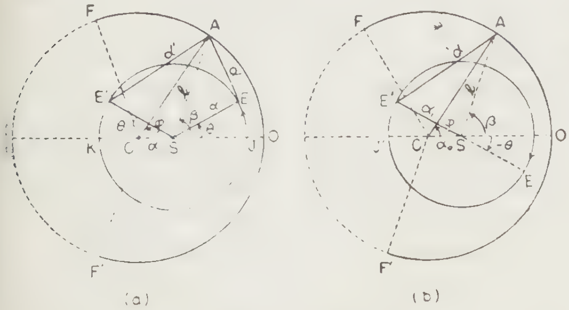

Fig. 11. Vector diagram representing the distribution of the amplitude and the phase-angle of light along the image of the ultrasonic wave when (a) the zero order and the +1st order, or (b) the zero order and the −1st order spectra are removed from light of the phase-lattice.

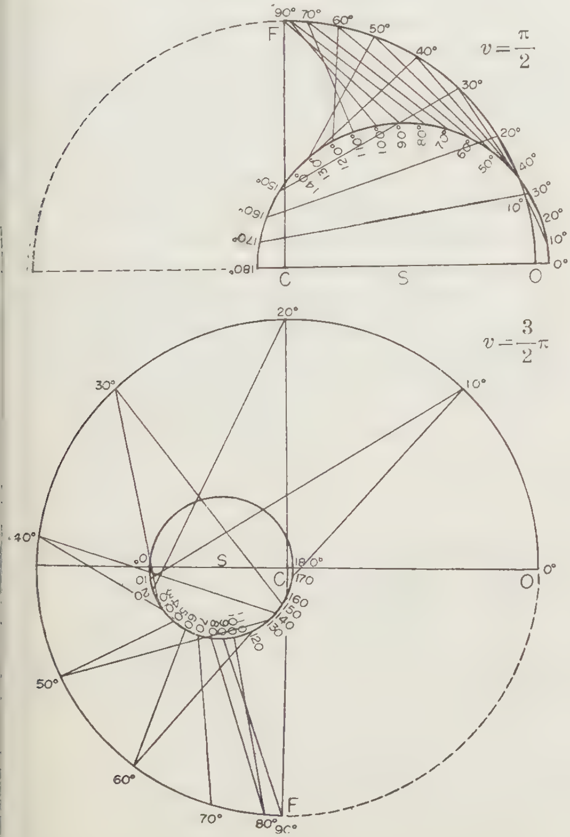

Fig. 12. Graphical construction for obtaining the amplitude distribution of light in the image of the ultrasonic wave obtained by the Schlieren method by removing the zero order and the +1st order spectra.

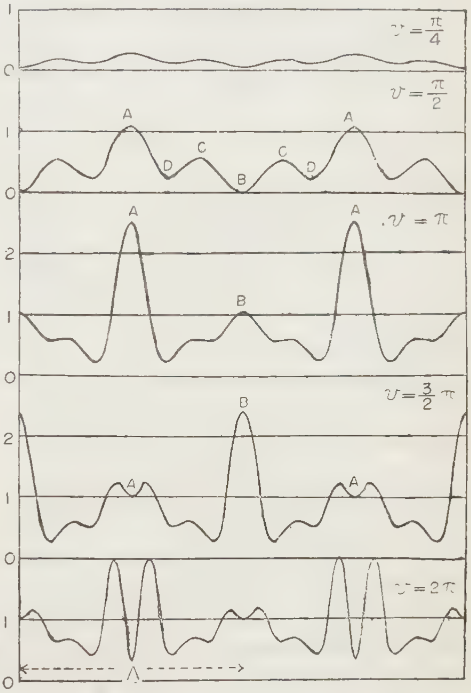

Fig. 13. Intensity distribution of light in the image of the progressive ultrasonic wave produced by the Schlieren method under ideal stroboscopic illumination (in case the zero order and the +1st order spectra are removed).

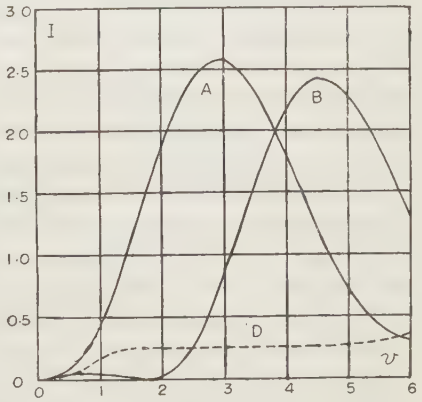

Fig. 14. Height of the peak and the valley of the distribution curve of light intensity (previous figure) in dependence on the value of v (Schlieren method, in case the zero order spectra and the +1st order are removed).

only, as long as the value of v is small ($v<2.5$), though the visibility is better in this case.

Fig. 14 shows the intensity of light at points A (peak at small values of v), B (valley at small values of v), and D (subminimum) in the curves of Fig. 13 as functions of v.

The analytical expression of the light intensity becomes as follows (cf. Fig. 11, (a)):

$$\left.\begin{aligned} &I=\alpha^2=l^2+J_1^2-2J_1 l\cos(\beta-\theta)\,, \\ &\text{where} \\ &l^2=1+J_0^2-2J_0\cos\varphi\,. \end{aligned}\right\} \quad (5.1)$$

We have, accordingly,

$$\left.\begin{aligned} &I=1+J_0^2+J_1^2-2J_0\cos\varphi \\ &\qquad -2J_1\cos(\varphi-\theta)+2J_0J_1\cos\theta\,, \\ &\text{where} \\ &\qquad \varphi=v\sin\theta\,. \end{aligned}\right\} \quad (5.2)$$

The light intensities at points A and B of Fig. 13 are given by (cf. Fig. 11)

$$\left.\begin{aligned} I_A&=\overline{OK}^2=\{1+J_1(v)-J_0(v)\}^2\,, \\ I_B&=\overline{OJ}^2=\{1-J_1(v)-J_0(v)\}^2\,, \end{aligned}\right\} \quad (5.3)$$

Accordingly, the visibility is given by

$$S=\frac{2J_1(1-J_0)}{J_1^2+(1-J_0)^2} \qquad (5.4)$$

as long as the value of v is small. The initial part—represented with real line—of the visibility curve (c) in Fig. 6 has been computed by this formula. When, however, the value of v become larger, I_A and I_B are no longer the principal maximum and minimum. In this case, the principal maximum and minimum have been obtained from the intensity distribution curves of Fig. 13. The visibility curve (c) in dotted line has been obtained in this manner.

It is to be seen from Fig. 6 that the visibility in this case is better than in case the first order alone is removed. The visibility is also better than that of the image obtained by removing the zero order if the value of v is greater than 1. The visibility does not decrease appreciably for greater values of v and does not vanish at zeros of $J_1(v)$ or $J_0(v)$ as in other cases.

§ 6. The Image Produced by Removing One of the 1st Order Spectra and Part of the Light of the Zero Order Spectrum

It is to be seen in Fig. 6, that the visibility of the images are not good for small values of v in case (b) when the first order only is removed, or in case (c) when the zero order and one of the first orders are removed, while we obtain images with good visibility in case (a) when the zero order is removed. The reason is that we have only the zero order and the two first orders when the ultrasonic intensity is small, so that in case (c) there is left only one of the first orders and we have no light to interfere with. The image in this case is produced by interference with the weak second orders and the field of sight is dark for small values of v. In case (b) on the other hand the strong zero order makes the background and the weak interference fringe with the first order is masked for small values of v, so that the field of sight is bright for small values of v. In case (a), however, the bright zero order is screened and the two first orders give fringes with good visibility at small values of v, though with double periodicity.

In removing, however, the light of one of the first orders and part of the light of the zero order in a suitable manner, it is possible to obtain images of good visibility at small values of v. It is always possible to make the visibility 100% if at one value of v. The brightness of the image is also increased as compared with the case (c).

The graphical construction is indicated in Fig. 15, where the light of the first order spectrum and a fraction of the light of the zero order are removed so as to fulfill the condition

$$kJ_0(v)+J_1(v)=1\,, \quad (k\leqq 1) \qquad (6.1)$$

i.e., to make

$$I_{\min}=0\,.$$

This is possible for the values of $v\leqq 1.65$ for which

$$J_0(v)+J_1(v)>1\,.$$

In this case the vector representing the amplitude of the removed part of the spectrum is (formally)

$$CS=kJ_0(v) \qquad (6.2)$$

and we have

$$CS+SE=1$$

and the circle representing the first order spectrum touches the unit circle representing the initial phase-lattice at point O. The intensity distribution in this case is represented in Fig. 16.

This does not mean, however, that the intensity of the removed light of the zero order in this arrangement is $k^2J_0^2(v)$. The vector diagram indicates that the amplitude of the zero order light must be diminished by the amount given in (6.2), i.e., fraction k. This means, therefore, that the amplitude of the remaining light of the zero order must be fraction $(1-k)$, or the intensity in fraction of $(1-k)^2$, so that the intensity of the zero order light to be removed is a fraction

$$f=1-(1-k)^2\,. \qquad (6.3)$$

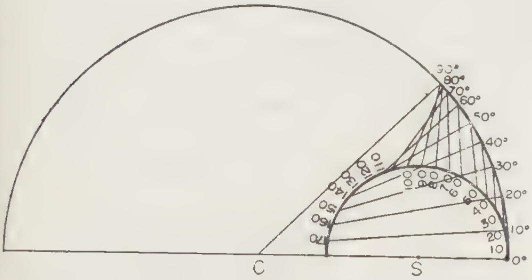

Fig. 15. Graphical construction for obtaining the ultrasonic image of 100% visibility by removing the light of the +1st order and part of the light of the zero order ($v=\pi/4$).

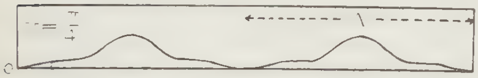

Fig. 16. Intensity distribution of light in the image of the progressive ultrasonic wave obtained by the Schlieren method under ideal stroboscopic illumination. (Image of 100% visibility obtained by removing the first order and part of the zero order light as indicated in the previous figure).

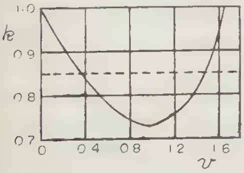

Fig. 17. Value of k satisfying the condition of 100% visibility as function of v.

The value of k satisfying (6.1), or

$$k=\{1-J_1(v)\}/J_0(v) \qquad (6.4)$$

has been computed as function of v and represented in Fig. 17. As is seen from the figure, the image with 100% visibility is to be obtained by selecting the value of k at suitable values between 1 and 0.73 when the value of v is smaller than 1.65. For obtaining the image with comparatively good visibility in this range, we have selected the value of k at 0.85 (as indicated with dotted line in Fig. 17) and obtained the intensity-distribution curves reproduced in Fig. 18. In this case the removed part of the zero order light is $f=97.75\%$ by (6.3), or 2.25% (in intensity) of the zero order light is employed for the image formation.

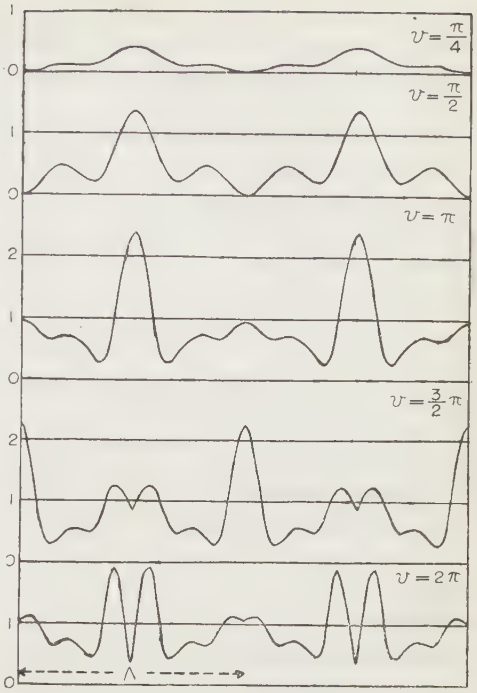

Fig. 18. Intensity distribution of light in the image of the progressive ultrasonic wave obtained by the Schlieren method under ideal stroboscopic illumination (in case the +1st order spectrum and 97.75% (in intensity) of the light of the zero order are removed).

The visibility of the images in this case are represented with curve (*e*) in Fig. 6. The visibility is improved for small values of v as compared with the case (*c*) when the zero order and the first order are removed, and the visibility does not decrease more than 5% also for greater values of v as compared with the case (*c*). The visibility is more than 95% for the range $v=0.2\sim2$ and not less than 70% for the range $v=0.1\sim6$.

The curve (*d*), Fig. 6, represents the visibility of the images obtained by removing 75% (in intensity) of the zero order light (i.e., $k=0.5$) and one of the first orders. The intensity distribution curves of light along the ultrasonic wave are not reproduced in this case because they are not so much different with that of the cases (*c*) and (*e*), though the fine-structures are not the same. Visibility of the images in case (*d*) is not better than that of (*e*) in the whole range of v investigated, though the visibility is better than in case (*c*) for small values of $v (v \leqq 1.35)$.

The analytical expression of the light intensity is to be obtained from Fig. 11 if we suppose $\alpha_0 = kJ_0(v)$ in this figure. We have in place of (5.1) the relations:

$$\left.\begin{aligned} &I = J_1^2 + l^2 - 2J_1 l \cos(\beta - \theta), \\ &\text{where} \\ &l^2 = 1 + (kJ_0)^2 - 2kJ_0 \cos\varphi, \\ &l \sin\beta = \sin\varphi, \\ &l \cos\beta = \cos\varphi - kJ_0. \end{aligned}\right\} \quad (6.4)$$

Accordingly, we have

$$\left.\begin{aligned} &I = 1 + k^2J_0^2 + J_1^2 - 2kJ_0 \cos\varphi \\ &\qquad - 2J_1 \cos(\varphi - \theta) + 2kJ_0J_1 \cos\theta. \\ &\text{where} \\ &\varphi = v \sin\theta. \end{aligned}\right\} \quad (6.5)$$

The light intensities at points A and B of Fig. 18 are given by

$$\left.\begin{aligned} &I_A = \{1 + J_1(v) - kJ_0(v)\}^2, \\ &\text{and} \\ &I_B = \{1 - J_1(v) - kJ_0(v)\}^2 \end{aligned}\right\} \quad (6.6)$$

respectively and the visibility for small values of v (as far as the I_A and I_B are the principal maximum and minimum) by

$$S = \frac{2J_1(1 - kJ_0)}{J_1^2 + (1 - kJ_0)^2}. \quad (6.7)$$

The parts of the visibility curves (*d*) and (*e*) in Fig. 6, represented in continuous lines have been computed by this formula, while the parts in dotted lines have been obtained from the distribution curves of light intensity.

Conclusion

Among the various possible arrangements for visualizing the progressive ultrasonic wave by the Schlieren method under stroboscopic light source, the arrangement giving images with high visibility for wide range of ultrasonic intensity is that of removing one of the first order spectra and 99.75% of the light of the zero order. The visibility of the images obtained by this arrangement is more than 95% in the range $v = 0.2 \sim 2$, and not less than 70% in the range $v = 0.1 \sim 6$. The visibility for very small ultrasonic intensity $(v \leqq 0.2)$ can be increased by increasing the fraction of the zero order light to be removed, though for very weak ultrasonic waves the arrangement with removal of the zero order only is the more preferable.

No experimental result is hitherto available which is to be compared with this theory, for the existing experiments are performed mainly by Schlieren arrangements by removing the zero order light or by the usual Schlieren arrangements. Moreover, no quantitative intensity distribution of light is hitherto obtained. The experiment to test this theory is to be performed in near future.

References

1) O. Nomoto: Classification of the methods of visualization of ultrasonic waves. to be published in J. Phys. Soc. Japan.

2) Edgar-Pierre Tawil: C. R. **191** (1930) 998.

3) S. T. Rzevkin: C. R. (Doklady) URSS. **16** (1937) 267.

4) S. Kretschmer and S. Rschevkin: Techn. Phys. URSS. **4** (1937) 1004.

5) S. I. Kretschmer and S. N. Rschevkin: C. R. (Doklady) URSS. **20** (1938) 17.

6) L. Bergmann: Sitz.-Ber. Schles. Ges. f. vaterl. Kultur, **108** (1936) 47.

7) L. Bergmann: "Ultraschall", 5. Aufl. (1949) 163.

8) H. Oyama: Denki-gakkaishi (J. Instn. Electr. Eng. Japan) **56** (1936) 743.

9) Y. Torikai and K. Negishi: J. Phys. Soc. Japan **8** (1953) 119. (see also J. Appl. Phys. Japan **21** (1952) 350.)

10) E.-P. Tawil: C. R. **191** (1930) 92, 163.

11) R. Pohlman: Naturwiss. **23** (1935) 511.

12) C. V. Raman and N. S. Nagendra Nath: Proc. Indian Acad. Sci. **2A** (1936) 406; 413; **3A** (1936) 75.

JOURNAL OF THE PHYSICAL SOCIETY OF JAPAN Vol. 9, No. 2, MAR.—APR., 1954

Theory of the Visualization of Ultrasonic Waves

(II) Theory of the Phase-shift Method for Visualizing Ultrasonic Waves

By Otohiko NOMOTO

Kobayasi Institute of Physical Research, Kokubunzi, Tokyo

(Received October, 9, 1953)

Intensity distribution of light in the image of the progressive ultrasonic wave obtained by the phase-shift method under stroboscopic illumination has been computed by the vector method. The phase-shift method applied to the zero order spectrum is particularly suitable for comparatively small values of $v(v<2\pi/3)$, where v means the amplitude of variation of the phase angle in the phase-lattice (corrugated wave) of light produced in the plane of emergence from the ultrasonic wave. Good visibility is to be obtained in the range of $v<2\pi/3$, with a phase-shift of $\delta=\pi/2$ and transmission unity ($g=1$), so long as the value of v is not so small. For small values of v the visibility is to be improved by reducing the transmission g. For values of $v\geqq 2\pi$, the phase-shift of $\delta=\pi$ is more suitable though in this case more satisfactory results are to be obtained by the Schlieren method, in which the first order spectrum and the zero order (or part of it) are removed. For values of v corresponding to the zero-point of $J_0(v)$, the phase-shift method gives, naturally, no image.

§ 1. Introduction

The application of the phase-shift method to the visualization of ultrasonic waves has been performed by Heinemann[1] and by Torikai and Negishi[2] independently. Heinemann observed the increase in visibility of the image produced by the Hiedemann's "Sichtbarmachungsmethode" by interposing a phase-plate at the focal plane of the objective lens and giving phase-shift and absorption to the zero-order diffraction spectrum. It is, however, not clear in his paper whether the images have been obtained by focussing in the plane of the phase-lattice (plane of emergence of light from the ultrasonic wave) or by focussing in the plane somewhat behind it (at a distance of $\Lambda^2/4\lambda$ for the stationary ultrasonic wave, where Λ means the ultrasonic wave-length and λ the wavelength of light in air) as in the case of the Hiedemann's "Sichtbarmachungsmethode."

Certainly, it is rightly recognized by Heinemann that the phase-shift method must be effective for ultrasonic waves because it acts as the phase-grating in first approximation, but the cause of the fact that in his experiments the phase-shift method has not been so effective as in the case of optics (phase-microscope) is erroneously attributed to the frequency-change of the diffraction spectra by the Doppler effect. The diffraction spectra with frequency shifts by the Doppler effect, however, are mutually coherent in case of the ultrasonic grating, producing the interference fringe or the image of the ultrasonic wave-surfaces under stroboscopic illumination. The image of the stationary ultrasonic wave (with stationary illumination) is to be obtained as the time average of the image of the progressive (or stationary) ultrasonic wave produced under stroboscopic illumination when the amplitude of sound varies sinusoidally with respect to time. It seems, therefore, that the cause has been in the inadequacy of the plane of focussing of the objective lens if the phase-shift method has not been so effective for ultrasonic waves in case of Heinemann's experiment.

Torikai and Negishi has discussed the intensity distribution of light and the visibility of the image of the progressive ultrasonic wave produced under stroboscopic illumination with sinusoidal illumination by giving phase-shift and absorption to the zero order spectrum and focussing on the phase-lattice plane. They have shown that for weak ultrasonic wave — when the amplitude v of the phase-change produced by the ultrasonic wave is small — the phase retardation of $\delta=\pi/2$ and a suitable transmission give image with 70% visibility and with light intensity far greater than in the case of the Schlieren method with removal of the zero order spectrum. This result has been also ascertained by experiment. As their calculation is made on the assumption of sinusoidal variation of the light intensity, more good visibility is to be expected if an instantaneous or ideal stroboscope is assumed. Experimentally, an approximately sinusoidal stroboscope is to be obtained by an ultrasonic stroboscope with stationary waves of half frequency and suitable ultrasonic intensity (corresponding to $v=2.4$) by employing the first order light or the zero order, while an approximately instantaneous or ideal stroboscope of short illumination is to be realized in an ultrasonic stroboscope of half frequency by employing one of the higher order diffraction spectra. It has recently been discussed by Torikai[3)] that the phase-method is also effective for the image in the Hiedemann's "Sichtbarmachungsmethode" (or the Fresnel diffraction image), though not so effective as in the case of the phase-lattice focussing.

It is desirable for the image of the ultrasonic waves to be of good visibility in wide range of the ultrasonic amplitude or the value of the amplitude v of the phase-lattice, to be of great brightness and to be able to show the change in ultrasonic intensity. (Here $v=2\pi\mu L/\lambda$, where λ means the wavelength of light in air, L the width of the ultrasonic beam, μ the amplitude of variation of the refractive index of the medium by the ultrasonic wave.)

This paper deals with the theoretical treatment of the characteristics of the image produced by the phase-shift method covering wide range of v and in comparison with the image produced by the Schlieren method. The method employed is the vector method as employed in the previous paper (Nomoto[4)]). The image of the progressive ultrasonic wave produced with stroboscopic light source of the same frequency with that of sound and with infinitesimal time of illumination has been treated as it is the most fundamental one, as discussed in the previous paper. The light emergent from the ultrasonic beam is assumed as the pure sinusoidal phase-lattice and the plane of focussing of the objective lens as the phase-lattice plane. Phase-plate is to be interposed on the focal plane of the objective lens and a suitable phase-shift and an absorption are to be given to the zero order light.

The optical arrangement is not so much different from Fig. 1 of the previous paper (I). The only difference is that we have to employ a phase-plate in place of the bar B in the previous figure. The phase method is applicable to any of the orders, but we restrict ourselves to the discussion of the case when the phase-shift is applied to the zero-order spectrum.

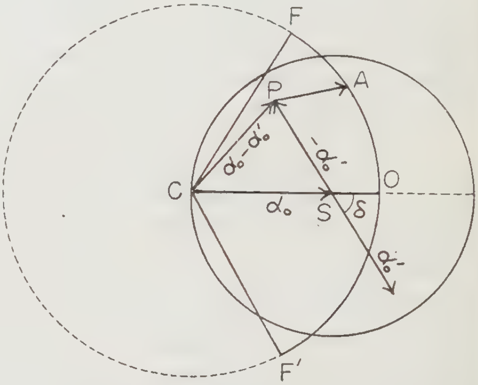

Fig. 1. Graphical construction for obtaining the distribution of the amplitude and the phase of light along the image of phase-lattice (in case when the phase-shift method is applied to the zero order spectrum).

§ 2. Vector Representation of the Image Produced by the Phase-shift Method

In the phase-shift method, a suitable phase-shift and a suitable absorption are to be given to one of the diffraction spectra. We will consider in the following that the zero order spectrum is submitted to phase-change and absorption. The plane of focussing of the image is considered to be the plane of the phase-lattice.

When a phase-shift (retardation) δ and an absorption (transmission coefficient of amplitude g) are given to the zero order light, the vector α_0 representating the zero order diffraction spectrum changes into α_0' (cf. Fig. 1). Here $|\alpha_0'|=g|\alpha_0|\leqq|\alpha_0|$.

In order to obtain the amplitude distribution of light in the image, it is necessary to subtract the vector α_0 from the vector representing the phase-lattice and add α_0', i.e,, to subtract $\alpha_0-\alpha_0'$.

The distribution of the amplitude and phase of light along the image of the ultrasonic wave is to be represented by the vector $\overline{PA}$ with the initial point P at the end of the vector $\alpha_0-\alpha_0'$ and with the end point A on the unit circle representing the phase-lattice. The initial point (or the working point) P of the vector $\overline{PA}$ can be selected at any point on the circumference (when $g=1$) or in the interior (when $g<1$) of the circle with center at S and radius α_0. Various cases are to be distinguished according to the magnitude of the quantity v proportional to the pressure amplitude of the ultrasonic wave.

§ 3. Intensity Distribution of Light in the Image of the Progressive Ultrasonic Wave produced by the Phase-shift Method under Ideal Stroboscopic Illumination

(a) the case when $v<0.9022$ ($=51.°692$)

Suppose that, as indicated in Fig. 2, the part of the unit circle representing the phase-lattice — arc $\widehat{FOF'}$ — is just enclosed in the circle of radius α_0 described around S, where $\overline{CS}=\alpha_0$. There is accordingly the relation $\angle SCF=v=\angle SFC$, and as

$\overline{CF}=1=2\overline{CS}\cos v=2J_0(v)\cos v$, we have

$$J_0(v)=1/(2\cos v)$$

or $v=0.9022=51.°692$.

When the value of v is smaller than this, arc $\widehat{FOF'}$ is completely enclosed in the circle S and $\overline{CF}$ does not meet with the circle S except at C.

(i) **Image F:** (the image with point F, Fig. 3, as the working point)

We have in this case

$$\left.\begin{aligned} I_{\max}&=\overline{FF'}^2=(2\sin v)^2=4\sin^2 v\,,\\ I_{\min}&=0\,,\\ S&=1\,,\end{aligned}\right\}\qquad(3.1)$$

and there is no submaximum and the visibility is 100%. The curve F in Fig. 4 represents the intensity distribution of light in the image obtained in this case. we have

$$\left.\begin{aligned} g&=\overline{SF}/\overline{CF}=(1+J_0^2(v)-2J_0(v)\cos v)^{1/2}/J_0(v),\\ \sin\delta&=\sin CSF=\sin v/gJ_0(v)\\ &=\sin v/(1+J_0^2(v)-2J_0(v)\cos v)^{1/2}.\end{aligned}\right\}$$
$$(3.2)$$

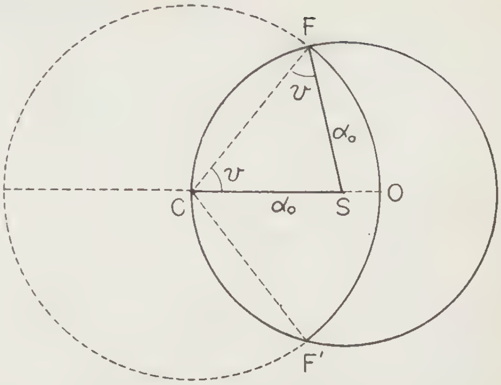

Fig. 2. The case when the arc of the unit circle representing the phase-lattice of light is just included in the circle around S, the working circle of the phase-shift method.

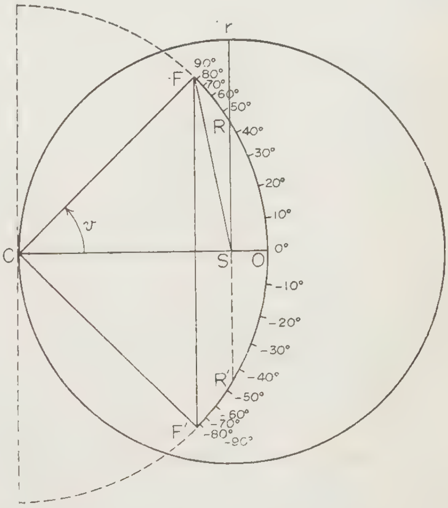

Fig. 3. Graphical construction for obtaining the amplitude distribution of light in the image of the ultrasonic wave by the phase-shift method ($v=\pi/4$).

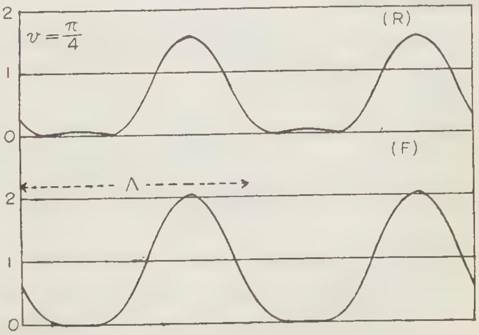

Fig. 4. Intensity distribution of light in the image of the progressive ultrasonic wave produced by the phase-shift method ($v=\pi/4$). (R) image R, (F) image F.

(ii) **Image R**: (the image with point R, Fig. 3, as the working point)

This image is obtained by taking $\delta=\pi/2$ and selecting the working point on the circumference of the unit circle. We have in this case

$$\left.\begin{aligned} &I_{\min}=0\ , \\ &I_{\max}=\overline{RF'}^2, \\ &I_{\text{sub-max}}=\overline{RF}^2, \end{aligned}\right\} \qquad (3.3)$$

and the intensity distribution of light is represented by curve R, Fig. 4. The brightness in this case is somewhat smaller than in the image (F), and there is a slight sub-maximum, but the visibility is 100% also in this case and there is no essential difference between the images (F) and (R),

As $\overline{SR}^2=1-J_0^2(v)$, we have

$$\left.\begin{aligned} &g=SR/CS=(1-J_0^2(v))^{1/2}/J_0(v), \\ &\delta=\pi/2\ . \end{aligned}\right\} \qquad (3.4)$$

Also the image (r) with $g=1$ and $\delta=\pi/2$ (cf. Fig. 3) is not so different from (R) and (F) so long as the value of v is not very small. The intensity distributions of light in the images (R') and (F') (cf. Fig. 3) are identical with those of the images (R) and (F) respectively but displaced by $\Lambda/2$.

(b) the case when $0.9022<v<1.52$

We have in this case $J_0(v)>1/2$, as $J_0(1.52)=1/2$. Accordingly the circle with α_0 described around S intercepts the unit circle in points Z and Z' (cf. Fig. 5). The tip of the vector α_0' (the working point) can be selected at any point on and inside the circle S. Various images are to be obtained according to the values of the phase-shift δ and the transmission g.

(i) **Image P**: (the image with the working point at P, Fig. 5)

This image has no sub-maximum. The condition for this is that the working point is on the crossing point of $\overline{CF}$ and the circle S. We have in this case

$$\left.\begin{aligned} &\delta=\pi-2v, \\ &\overline{CP}=\alpha_0-\alpha_0'=2J_0(v)\cos v, \\ &I_{\min}=\overline{PF}^2=(1-2J_0(v)\cos v)^2, \\ &I_{\max}=\overline{PF'}^2=1+(2J_0(v)\cos v)^2 \\ &\qquad -4J_0(v)\cos v\cos 2v\ , \end{aligned}\right\} \qquad (3.5)$$

and accordingly

$$S=\frac{2J_0(v)\cos v(1-\cos 2v)}{1+4J_0^2(v)\cos^2 v-2J_0(v)\cos v(1+\cos v)}\ , \qquad (3.6)$$

or

$$S=\frac{4J_0(v)\cos v\sin^2 v}{1+4J_0^2(v)\cos^2 v-4J_0(v)}\ . \qquad (3.7)$$

The curve (P), Fig. 6, represents the intensity distribution of light along the image in this case.

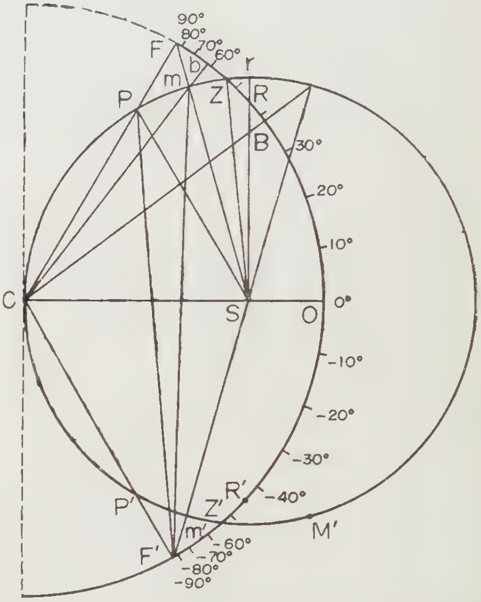

Fig. 5. Graphical construction for obtaining the amplitude distribution of light in the image of the ultrasonic wave produced by the phase-shift method ($v=\pi/3$).

(ii) **Image m**: (the image with smallest sub-maximum) (Working point at m, Fig. 5, and the intensity distribution curve (m), Fig. 6)

$$\begin{aligned} &I_{\min}=\overline{mb}^2, \\ &I_{\max}=\overline{mF'}^2, \\ &I_{\text{sub-max}}=\overline{mF}^2. \end{aligned}$$

(iii) **Image M**: (the image with greatest maximum) (Working point at M, Fig. 5, and the intensity distribution curve (M), Fig. 6).

$$I_{\max}=\overline{MF'}^2,\quad I_{\min}=\overline{MB}^2,\quad I_{\text{sub-max}}=\overline{MF}^2.$$

(iv) **Image Z**: (the image with zero-intensity minimum or 100% visibility) (Working point at Z, Fig. 5, and the intensity distribution curve Z, Fig. 6)

$$I_{\min}=0,\ \ I_{\max}=\overline{ZF'}^2,\ \ I_{\text{sub-max}}=\overline{ZF}^2,\ \ S=1.$$

(v) **Image R**: (the image with $\delta=\pi/2$ and 100% visibility) (Working point at R, Fig. 5,

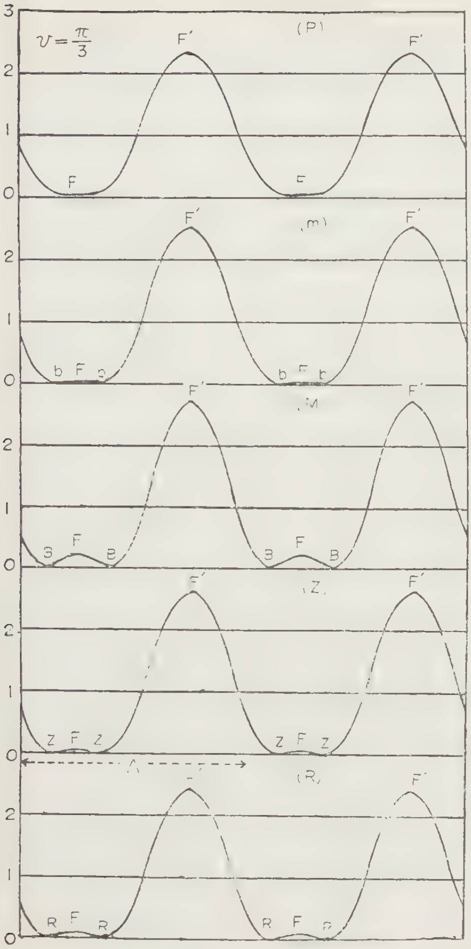

Fig. 6. Intensity distribution of light in the image of the progressive ultrasonic wave produced by the phase-shift method ($v=\pi/3$). (*P*) the image without submaximum, (*w*) the image with smallest sub-maximum, (*M*) the image with greatest maximum, (*Z*) the image with zero-intensity minimum (100% visibility), (*R*) the image with phase-shift $\delta=\pi/2$.

and the intensity distribution curve (*R*), Fig. 6).

$$\left.\begin{aligned} I_{\text{max}}&=\overline{RF'}^2=4\sin^2\tfrac{1}{2}\{v+\cos^{-1}J_0(v)\}\,,\\ I_{\text{sub-max}}&=\overline{RF}^2=4\sin^2\tfrac{1}{2}\{v-\cos^{-1}J_0(v)\},\\ {}_{\text{min}}&=0\,,\\ S&=1\,. \end{aligned}\right\}\tag{3.8}$$

We have in this case

$$\left.\begin{aligned} &\delta=\pi/2\\ \text{and}\qquad &g=(1-J_0^2(v))^{1/2}/J_0(v)\,. \end{aligned}\right\}\tag{3.9}$$

The result is nearly the same if we take $\delta=\pi/2$ and $g=1$ (working point *r*, Fig. 5). As is to be seen in Fig. 6, the images corresponding to various working points are not much different in this case and it is sufficient for ordinary purposes to make $\delta=\pi/2$.

(c) **the case when $1.52<v<2.40$**

We have

$$0<J_0(v)<1/2,$$

in this case and the working circles *S* is completely included in the unit eircle representing the phase-lattice (cf. Fig. 7 for $v=\pi/2$ and Fig. 9 for $v=2\pi/3$). Various images are to be obtained in this case according to the working points, though the image without sub-maximum (corresponding to the image *P* in case (b)) is not to be obtained in this case.

(i) **Image *R*:** (the image with $\delta=\pi/2$ and $g=1$) (Working point *R*, Fig. 7, intensity distribution curve (*R*), Fig. 8, when $v=\pi/2$, and working point *R*, Fig. 9, and intensity distribution curve Fig. 10, when $v=2\pi/3$).

As

$$I={}_{\text{max}}\overline{RF'}^2,$$

and

$$I_{\text{sub-max}}=\overline{RF}^2,$$

(cf. Fig. 10), we have

$$\begin{aligned} I_{\text{max}}-I_{\text{sub-max}}&=\overline{F'K}^2-\overline{FK}^2\\ &=4\sin v\cdot J_0(v), \end{aligned}$$

and the difference between I_{max} and $I_{\text{sub-max}}$ is greatest in this image as compared to other images.

When $v=\pi/2$, we have

$$\left.\begin{aligned} I_{\text{min}}&=\overline{Rt}^2=\{1-\sqrt{2}\,J_0(v)\}^2\\ &=1-2\sqrt{2}\,J_0(v)+2J_0^2(v)\,,\\ I_{\text{max}}&=\overline{RF'}^2=1+2J_0^2(v)-2\sqrt{2}\,J_0(v)\cos\tfrac{3}{4}\pi\\ &=1+2J_0(v)+2J_0^2(v)\,,\\ I_{\text{sub-max}}&=\overline{RF}^2=1+2J_0^2(v)-2\sqrt{2}\,J_0(v)\cos\tfrac{\pi}{4}\\ &=1-2J_0(v)+2J_0^2(v)\,,\\ S&=\frac{(1+\sqrt{2}\,)J_0(v)}{1+J_0^2(v)+(\sqrt{2}-1)J_0(v)}\,. \end{aligned}\right\}\tag{3.10}$$

More generally, we have

$$\left.\begin{aligned} I_{\text{min}}&=\overline{Rt}^2=1-2J_0(v)^2\\ &=1-2\sqrt{2}\,J_0(v)+2J_0^2(v)\,,\\ I_{\text{max}}&=\overline{RF'}^2=\overline{CF'}^2+\overline{CR}^2\\ &\qquad+2\,\overline{CF'}\cdot\overline{CR}\cos\left(v+\tfrac{\pi}{4}\right)\\ &=1+2J_0^2(v)-2J_0(v)\cos v+2J_0(v)\sin v,\\ I_{\text{sub-max}}&=1+2J_0^2(v)-2J_0(v)\cos v+2J_0(v)\sin v,\\ S&=\frac{(\sqrt{2}-1)J_0(v)\cos v+J_0(v)\sin v}{1+2J_0^2(v)-(\sqrt{2}+1)J_0(v)\cos v-J_0(v)\sin v}\,, \end{aligned}\right\}\tag{3.11}$$

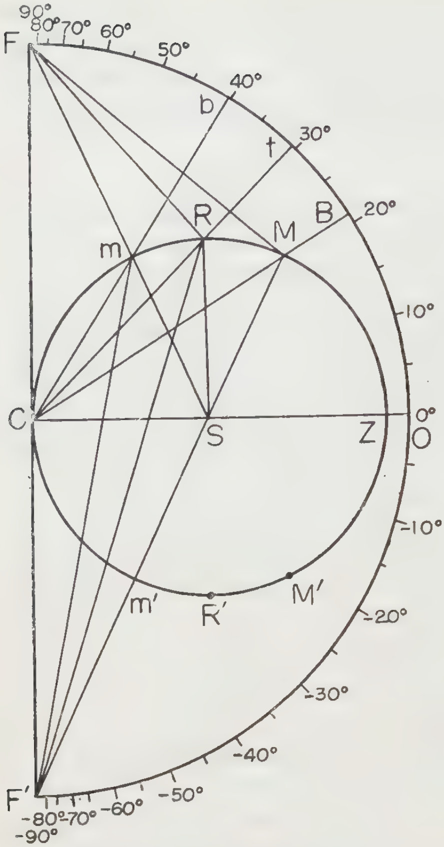

Fig. 7. Graphical construction for obtaining the amplitude distribution of light in the image of the ultrasonic wave produced by the phase-shift method ($v=\pi/2$).

The equations (3.11) remain valid also in the range $v<1.52$, where the working circle crosses with the unit circle, i.e., for the image r (cf. Fig. 3 and Fig. 5), if R is replaced with r in these equations.

(ii) **Image m:** (the image with smallest sub-maximum) (cf. curve m, Fig. 8).

As

$I_{\max}=\overline{mF'}^2$, $I_{\text{sub-max}}=\overline{mF}^2$, and $I_{\min}=\overline{mb}^2$,

in this case, we have for $v=\pi/2$,

$$\left.\begin{aligned}&\delta=\cot^{-1}J_0(v),\\&I_{\min}=[1-2\sin\tfrac{1}{2}\{\cot^{-1}J_0(v)\}]^2,\\&I_{\max}=1+4\sin^2(\delta/2)+4\sin(\delta/2)\cos(\delta/2)\\&\quad=1+2(1-\cos\delta)+2\sin\delta\\&\quad=1+2\left(1+\frac{1-J_0(v)}{1+J_0^2(v)}\right).\end{aligned}\right\}\tag{3.12}$$

More generally, as

$$\overline{FS}\cdot\sin\delta=\sin v\,,$$

and

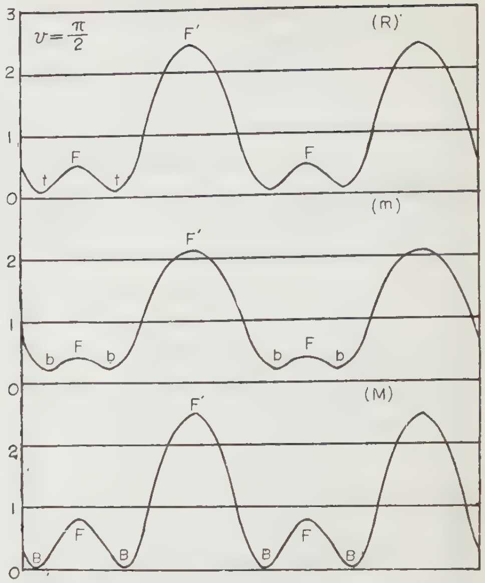

Fig. 8. Intensity distribution of light in the image of the progressive ultrasonic wave produced by the phase-shift method ($v=\pi/2$). (R) the image with maximum difference between the maximum and the sub-maximum, $\delta=\pi/2$, $g=1$, (m) the image with smallest sub-maximum, (M) the image with greatest maximum.

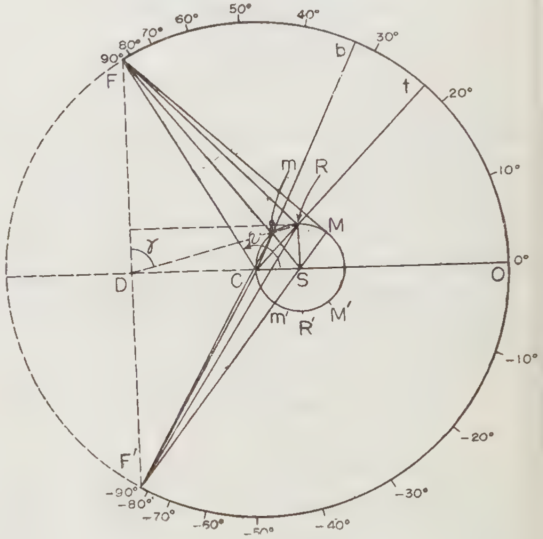

Fig. 9. Graphical construction for obtaining the amplitude distribution of light in the image of the ultrasonic wave produced by the phase-shift method ($v=2\pi/3$).

$$\overline{FS}\cdot\cos\delta=-\cos v+J_0(v)\,,$$

we have

$$\tan\delta=\frac{\sin v}{-\cos v+J_0(v)}\tag{3.13}$$

(and $g=1$).

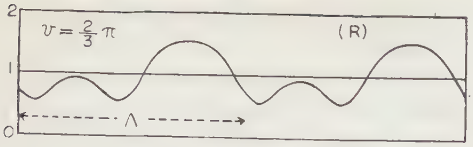

Fig. 10. Intensity distribution of light in the image of the progressive ultrasonic wave produced by the phase-shift method ($v=2\pi/3$). (R) the image with maximum difference between the maximum and the sub-maximum.

(iii) **Image M:** (the image with greatest maximum) (cf. curve M, Fig. 8).

We have in this case

$$I_{\max}=\overline{MF'}^2,\ I_{\text{sub-max}}=\overline{MF}^2, \text{ and } I_{\min}=\overline{MB}^2.$$

The images are mutually of small difference and it is simple for practical purposes to use the image with $g\cong 1$ and $\delta=\pi/2$. The phase method is, however, mainly effective in the range $v\leqq\pi/2$, and the visibility becomes somewhat bad at $v=2\pi/3$.

(d) **the case when $2.40<v<\pi$ ($=3.14$)**

The visibility of the image produced by the phase-shift method becomes zero at $v=2.40$ corresponding to $\alpha_0=J_0(v)=0$. For values of $v>2.40$, $J_0(v)<0$, and as v approaches π, the part of the unit circle representing the phase-lattice becomes nearly a closed circle and as the value of $J_0(v)$ is not so large in this range, the amerioration of visibility by the phase-shift method is not so great in this range (cf. Fig. 11).

The visibility is better in this case at the working point P corresponding to $\delta=\pi$ or at m near this point (where $I_{\min}=\overline{Fm}^2$ is the smallest) than at point R corresponding to $\delta=\pi/2$. The image is completely of double periodicity at point P and nearly so at point m. At point R, there are two maxima in a period, but the image is not of double periodicity (cf. Fig. 12).

(i) **Image R:** ($\delta=\pi/2$, $g=1$).

In this image we have

$$\begin{aligned}
I_{\max}&=\overline{Rt'}^2=(1-\sqrt{2}\,J_0(v))^2,\\
&=(1+\sqrt{2}\,|J_0(v)|)^2,\\
I_{\min}&=\overline{Rt}^2=(1+\sqrt{2}\,J_0(v))^2\\
&=(1-\sqrt{2}\,|J_0(v)|)^2,\\
I_{\text{sub-max}}&=\overline{RF}^2\\
&=1+2J_0^2(v)-2J_0(v)\cos v-2J_0(v)\sin v,\\
I_{\text{sub-min}}&=\overline{RF'}^2\\
&=1+2J_0^2(v)-2J_0(v)\cos v+2J_0(v)\sin v,\\
S&=2\sqrt{2}\,|J_0(v)|/(1+2J_0^2(v)).
\end{aligned}\tag{3.14}$$

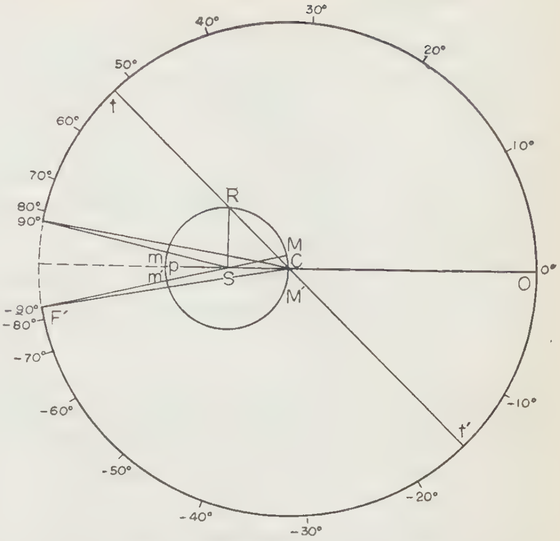

Fig. 11. Graphical construction for obtaining the amplitude distribution of light in the image of the ultrasonic wave produced by the phase-shift method ($v=17\pi/18$).

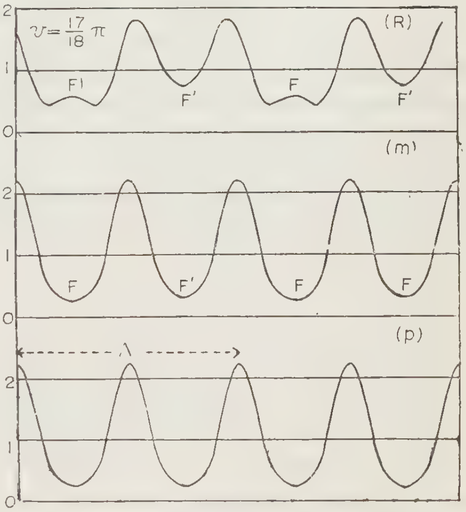

Fig. 12. Intensity distribution of light in the image of the progressive ultrasonic wave produced by the phase-shift method ($v=17\pi/18$). (R) the image with phase-shift $\delta=\pi/2$ and $g=1$, (m) the image with smallest minimum, (p) the image with double periodicity.

(ii) **Image P:** ($\delta=\pi$, $g=1$)

Here we have

$$\begin{aligned}
I_{\max}&=\overline{PO}^2=(1-2J_0(v))^2=(1+2|J_0(v)|)^2,\\
I_{\min}&=\overline{PF}^2=\overline{PF'}^2=1+4J_0^2(v)-4J_0(v)\cos v,\\
S&=\frac{-2J_0(v)(1+\cos v)}{1+4J_0^2(v)-4J_0(v)(1+\cos v)}\\
&=\frac{2|J_0(v)|(1-|\cos v|)}{1+4J_0^2(v)+4|J_0(v)|(1-|\cos v|)}.
\end{aligned}\tag{3.15}$$

§ 4. Conclusion

Ultrasonic images of comparatively good visibility are obtainable by the phase-shift method by giving a phase shift of $\delta=\pi/2$ to the zero order, as long as the value of the phase variation produced by the ultrasonic wave is not too large ($v<2\pi/3$). The visibility of the image vanishes, however, at $v=2.40$ and at other zero points of the function $J_0(v)$: a common fault with the Schlieren method in which the zero order alone is removed. The periodicity of the image is one ultrasonic wavelength when $\delta=\pi/2$. For obtaining images of good visibility, $\delta=\pi/2$ is suitable in the range $v=2\pi/3$, while $\delta=\pi$ is more preferable in the range $v>2\pi/3$. In the range $v>2\pi$, particularly, the images obtained by the phase-shift method with $\delta\doteq\pi$ are always of better visibility than the images obtained by the Schlieren method by removing the zero order only. The image in this case, however, is of double periodicity.

The phase-shift method is particularly excellent in the range of small values of v, where images of 100% visibility are to be obtained by making $\delta=\pi/2$ and selecting the transmission g at suitable values. The suitable values of g, however, decreases with decrease in the value of v, and this makes the image dark for small values of v. For visualization of the ultrasonic waves of variable intensity it is preferable to make $\delta=\pi/2$ and $g=1$. This method, however, is mainly useful in the range of $v=2\pi/3$, and the Schlieren methods with removal of the first order and the zero order or part of it become more effective for larger values of v.

No experiment has been hitherto performed which is comparable with this theory. Experiment to test this theory is to be performed in near future.

References

1) H. Heinemann: Optik, **9** (1952) 379.

2) Y. Torikai and K. Negishi: J. Phys. Soc. Japan **8** (1953) 119 (see also J. Appl. Phys. Japan (in Japanese) **21** (1952) 350).

3) Y. Torikai: J. Acous. Soc. Japan, in printing.

4) O. Nomoto: J. Phys. Soc. Japan **9** (1954) No. 2. (see also Bull Kobayasi Inst. Phys. Res. (in Japanese) **3** (1953) 22.

---

* Japanese text of this paper has been published in "Bulletin of the Kobayasi Institute of Physical Research, **3** (1953) 34.

JOURNAL OF THE PHYSICAL SOCIETY OF JAPAN Vol. 9, No. 2, MAR.—APR., 1954

On the Rate of Decomposition of Diffusion Pump Oil

By Chikara HAYASHI

Department of Physics, Tokyo University, Tokyo, Japan

(Received September 28, 1953)

The rate of decomposition of diffusion pump oil under the working condition seems to be an important quantity in reference to the vacuum. The following experiment was carried out to give an answer to the problems, " Whether various metals really catalyse the decomposition of diffusion pump oil? and " Will the gaseous components of the decomposition products limit the ultimate vacuum of an oil diffusion pump?"

The quantity of not condensing gaseous components of the decomposition products accumulated in a vessel in a given time was measured for the two typical oils, n-dioctylhexahydrophthalate and silicone DC-703, by using a flow meter designed by R. Ueda.

The results show that the rate of decomposition is of the order of 10^{-6} litre micron Hg per sec. per square centimeter of surface for both oil. The ester slightly suffered from catalitic decomposition, though the silicone had no indication. The measured rate of decomposition is so low that will never contribute more than 1×10^{-5} micron Hg to the ultimate vacuum of an oil diffusion pump.

§ 1. The Thermal Decomposition

The rates of the thermal decomposition of the two diffusion pump oils, n-dioctylhexahydrophthalate and silicone DC-703, were estimated by using the apparatus shown in Fig. 1. The gas flow meter was designed by R. Ueda[1] and has the construction shown in Fig. 2. The deflection on the scale is, in the region of molecular flow and the small angle of deflection, proportional to $\sqrt{M}\,Q$, where M is the molecular weight of the flowing molecule and Q is the so-called PV value of the flow rate. By using the mica vane of 1.5 cm × 1.5 cm and the tungsten fibre of 0.5 mil ϕ, the deflection of 1 mm per 6×10^{-3} litre micron per sec. was obtained on the scale 20 cm distant from the mirror.

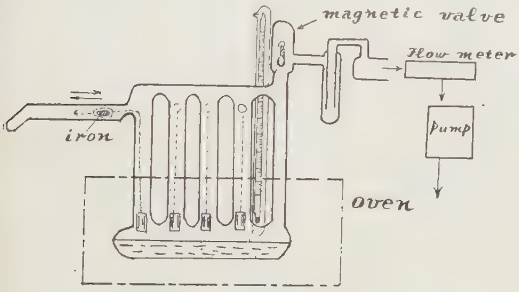

Fig. 1.

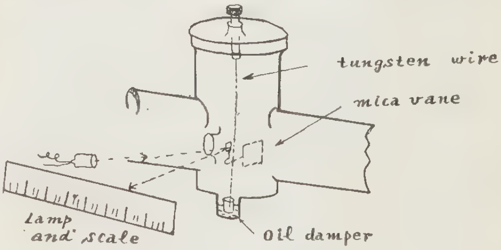

Fig. 2.

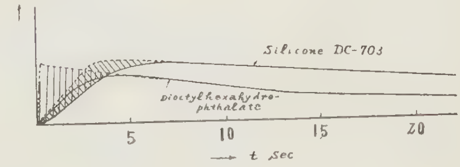

Fig. 3.

As the rate of the decomposition of the diffusion pump oil was small compared to the sensitivity of the flow meter, the decomposition products had to be accumulated for a given time T by closing the greaseless cock so as to give enough deflection on the scale of the flow meter at the time when the cock was reopened. The deflection of the flow meter was photographed on a rotating drum, which was driven by a synchronous motor.

The typical curves photographed are shown in Fig. 3. From such a curve is given the total quantity of the decomposition products by the integral $\int_0^\infty Q\,dt$. Practically, the deflection never tends to zero. This stationary deflection is, of course, due to the decomposition of the oil, but heavier and rather low vapour pressure components seem to be responsible for this. The value of this stationary deflection was chosen as the zero point of the deflection so as to get a definite value in the calculation of $\int_0^\infty Q\,dt$. In this manner, the heavier components having the vapour pressure less than 1×10^{-4} mmHg at room temperature are excluded in the values of the decomposition rate obtained from the following experiment. The limited sensitivity of the flow meter and the troublesome phenomena of intense adsorption prevent to get the knowledge about this heavier components.

Because of the relatively long period of the oscillation of the flow meter, the deflection shows retardation, which is particularly important in the build up region of the deflection. The true form of the $Q-t$ curves may be the one of dotted lines (see Fig. 3.), and the shadowed area must be included in the integral. The error comes from this is diminished by decreasing the ratio of the shadowed area to the total $\int_0^\infty Q\,dt$, which is achieved by decreasing the conductance from the vessel to the flow meter. The ratio was adjusted to be about 10% in our case, and the calculation was accomplished along the dotted line.

It must be noted here the remarkable difference in flow characteristics between the decomposition products of the phthalate and that of the silicone oil.

In the case of the phthalate the flow characteristics was fairly similar to that of gases evolved from the glass. About 4 seconds of retardation in the rise time of the deflection is consistent with the period of the flow meter, showing that non-adsorptive gases or vapours are predominant in the flow.

In the case of the silicone, however, the rise time of the deflection is 7 seconds, in which the excess of 3 seconds should be ascribed to the adsorptive property of the flowing vapours.[2] The $\log Q-t$ curves in Fig. 4 give far less decreasing coefficient for the decomposition products of silicone DC–703 compared to that of the phthalate. This also suggests the high adsorptive property and may also suggest the high molecular weight of the decomposition products of the silicone oil.

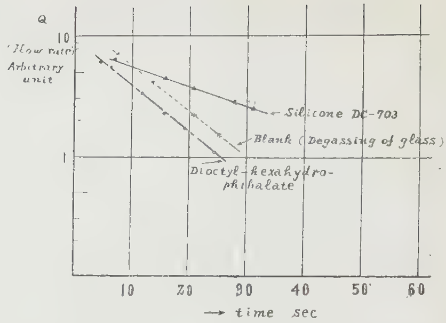

Fig. 4. $\log Q-t$ relation, showing different decreasing coefficient between the two oils.

Although the lack of quick response is the disadvantage of the flow meter, yet the advantage of getting rid of the additional decomposition by vacuum gauge, and of giving the direct reading of flow rate will prove the usefulness of the flow meter.

The furnace had the double wall construction. Heat was supplied by radiation from the wall of inner case consisting of aluminum plate, which in turn was heated by the nicrom wire set along the inner wall of the outer

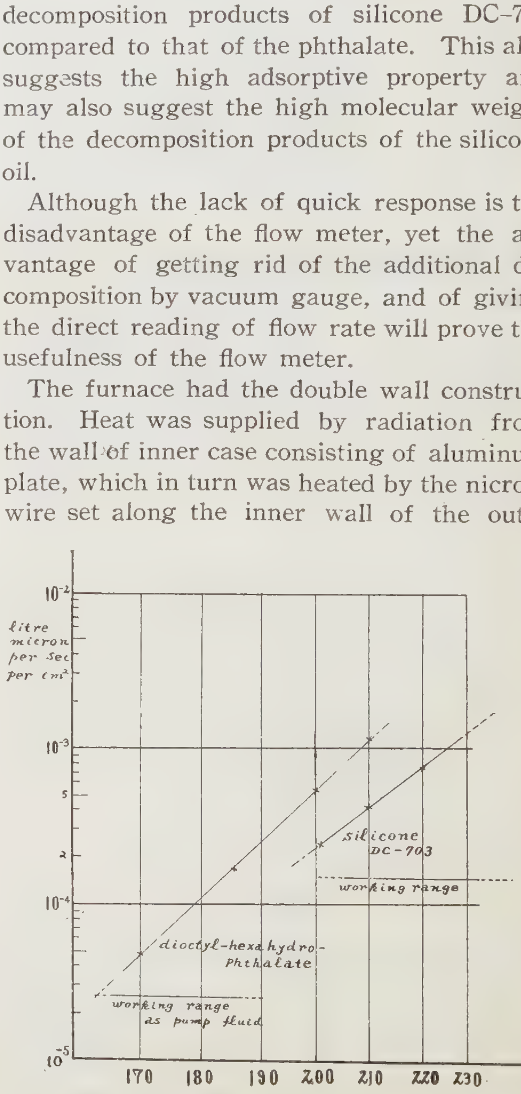

Fig. 5. The rate of decomposition of the two oils in a glass vessel, which has hot zone of about 250 cm³. The surface area of the hot zone is about 500 cm².

case. The temperature difference was thus maintained less than 1°C near the glass vessel.

In Figs. 5 and 6 are shown the rate of the thermal decomposition of the two oils. The total rate of thermal decomposition of 60 cm^3 of the oil, which evaporates and returns back to the boiler just like in a diffusion pump, is shown in Fig. 5. Both catalytic decomposition, if any, at the glass surface and the pure thermal decomposition are included in this case. The surface area and the volume of the hot portion in the vessel was estimated about 500 cm^2 and 250 cm^3 respectively.

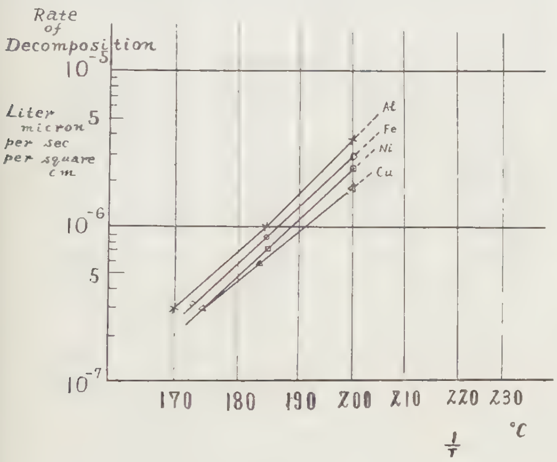

Fig. 6.

In the case of the metal plate positioned in the boiler, the additional decomposition will probably participate at the surface of the metal. This was realized, as shown in Fig, 6, by the phthalate, but the silicone oil in it working range seemed to be free from decomposition catalyzed by the metals, though the stability for the thermal decomposition of the oil seemed to be somewhat inferior to that of the phthalate. The rate of the decomposition at the glass surface in the case of the phthalate, if any, is calculated from Fig. 5 and the estimated glass surface, to be 1×10^{-6} litre micron per sec. per square centimeter at 200°C, which is about sixty percent of the value of copper.

The effect of cold trap for the decomposition products of the phthalate was estimated by using the trap of either liquid air or dry-ice-acetone. Only the non-trapped components of the decomposition products pass through the flow meter, and thus gave rise to the deflection of about one percent in the case of liquid air and about sixty percent in the case of dryice-acetone, of the original deflection.

After more than several days of initial conditioning of the oil at slightly elevated temperature than that in the measurements, the stationary state of the system was established in about 10 to 30 hours from the time when the value of the temperature of the system was changed. In these manner, the reproducibility of measurements was retained within about 10% during about four weeks run of each oil. The gas evolution from the wall was lowered to $\lesssim 1\times10^{-8}$ litre micron/sec.cm^2 by preliminary baking.

§ 2. The Decomposition induced by Gas Flow

The decomposition of n-dioctylhexahydrophthalate induced by flowing gases was estimated by using the apparatus shown in Fig. 7. A quantity of gas Q which is controlled by the variable leak flows through the side line L and is measured by the flow meter.

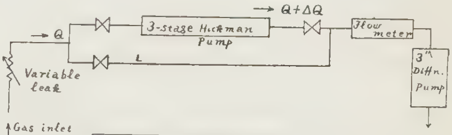

Q lit μ/s	ΔQ lit μ/sec			
	Air	O_2	H_2	H_2O
1.2×10^{-2}	nil	nil	nil	nil
2.5×10^{-1}	nil	nil	nil	nil
5×10^{-1}	less than 4×10^{-3}	less than 4×10^{-3}	nil	—

Fig. 7.

Next, the same gas flow is introduced to the three stage Hickman pump which is quite in its working condition. In this case the flow meter shows the deflection corresponding to the flow Q plus ΔQ which is produced in the Hickman pump. ΔQ should be the decomposition products induced by the flow Q in the pump.

The results obtained are shown in Table 1. The gas flow of H_2, O_2, air and H_2O through the pump gives no appreciable amount of additional flow ΔQ and thus we can see that no appreciable decomposition took place in the pump.

§ 3. Discussion

Although those experiments as described above will be, of course, influenced very much by constituents of oil, surface condition of metal and many other factors, yet we may have some interesting informations from the results obtained. Consider, for instance, the ultimate vacuum of an oil diffusion pump. Assume that n-dioctylhexahydrophthalate at 170°C act as pump fluid in 3 inch oil diffusion pump, which has the speed of 100 litres/sec. and the area of 1000 cm² of the hot chimney, the ultimate vacuum calculated as the balance of pump speed, which is assumed to be independent on pressure (3), and the rate of decomposition given in Figs. 5 and 6, will be less than 1×10^{-5} micron Hg. The decomposition products of higher molecular weight which was excluded in our ease, however, will contribute at room temperature and will give higher values to the ultimate vacuum. In the case of using the liquid air trap, however, the heavier components will certainly be excluded and the ultimate vacuum limited by the decomposition of pump oil is expected to be less than 1×10^{-7} micron Hg from our results. The higher pressure of ultimate vacuum usually experienced in spite of using the liquid air trap, should be ascribed to the gas evolution of construction material, the back diffusion at pump jet, the leakage and the permeability of gas through walls.

The author would like to express his gratitude to Dr. R. Sagane for his encouragement.

References

1) R. Uyeda: Oyobutsuri **17** (1948) 136. (in Japanese)
2) Ref.: P. Claussing: Ann. d. Phys. **7** (1930) 489.
3) Clifford E, Berry: R.S.I. **20** (1949) 835.

Short Notes

J. Phys. Soc. Japan **9** (1954) 290~291

A Measure for Approximation Degree of the Approximate TF Function for Free Neutral Atom

By Kwai Umeda

Department of Physics, Faculty of Science, Okayama University

(Received December 4, 1953)

There have been given the approximate solutions of the TF (Thomas-Fermi) equation for free neutral atom (denoted simply by AS) previously by Sommerfeld[1] and Rozental[2] as well as recently by March[3] and Kerner[4]. The comparison of these different ASs and the further derivation of prospective AS would be facilitated if there existed a measure for the approximation degree of any AS. For this measure we propose to employ the numerical value of the variational integral

$$I[\phi]\equiv\int_0^\infty\left[(\phi')^2+\frac{4}{5}\,\phi^{5/2}/x^{1/2}\right]dx\,, \qquad (1)$$

evaluated by putting the given AS in place of ϕ. Since the minimization of I is equivalent to the integration of the TF equation, the better AS should resultate the smaller numerical value of I, the value for the exact solution being the convergence limit. If the AS would contain some disposable parameters, the Ritz method for I enables us to find the best formula of the assumed type.

1. For Miranda's[5] exact solution, direct numerical quadrature of Eq. (1) gives the value

$$I=1.3625,$$

which should be of course the limiting minimum value of I.

2. As regards to Rozental's[2] AS consisting of two exponential terms, we observe its high degree of approximation in the value

$$I=1.3636.$$

3. For the AS of Sommerfeld type

$$\phi(x)=[1+(x/12^{2/3})^\lambda]^{-3/\lambda},$$

λ being considered as a disposable parameter, as was done by March[3], Eq. (1) can be analytically expressed as a function of λ

$$I=\frac{4}{5}12^{1/3}\frac{1}{\lambda}\Big[B\Big)\frac{1}{2\lambda}\,,\,\frac{7}{\lambda}\Big)+\frac{15}{16}B\Big(2-\frac{1}{\lambda}\,,\,\frac{7}{\lambda}\Big)\Big],$$

$B(p,\ q)$ being beta-function.

Table I. Approximation degrees of several ASs of Sommerfeld type.

Determination method of λ	Sommerfeld	March*	Umeda $dI/d\lambda=0$
λ	0.7722	0.8034	0.8371
I	1.4141	1.3779	1.3670

* The mean value method extended over the whole space, i.e.

$$\int_0^\infty(\phi''-\phi^{3/2}/x^{1/2})x^2dx=0.$$

From Table I we see that the well-known Sommerfeld[1] asymptotic formula is none the better AS because it has a sufficient foundation in regard to the asymptotic behavior, while the March[3] formula is obviously an improved AS, as seen also directly from his Table I.

4. For the AS of Kerner type

$$\phi(x)=1/(1+Cx),$$

C being considered as a disposable parameter, eq. (1) is reduced to a simple function of C

$$I=(1/3)[C+(16/5)/C^{1/2}].$$

Table II. Approximation degrees of several ASs of Kerner type.

Determination method of C	Kerner	least square method*	mean value method**	Umeda $dI/dC=0$
C	1.3501	1.2061	1.5874	1.3679
I	1.3680	1.3733	1.3757	1.3679

* Extended over the whole space, i.e.

$$\int_0^\infty(\phi''-\phi^{3/2}/x^{1/2})^2x^2dx=\text{min.}$$

** Extended over the whole radius, i.e.

$$\int_0^\infty(\phi''-\phi^{3/2}/x^{1/2})dx=0,$$

taking into consideration the divergence of the mean value extended over the whole space.

According to Table II the Kerner[4] formula seems to be capable of extensive application by virtue of its simplicity and higher degree of approximation.

This work was supported by the Ministry of Education Scientific Research Money grant to the Research Group for the Study of Atomic and Molecular Structure.

References

1) A. Sommerfeld: Z. Phys. **78** (1932) 283.
2) S. Rozental: Z. Phys. **93** (1935) 742.
3) N. H. March: Proc. Camb. Phil. Soc. **46** (1950) 356.
4) E. H. Kerner: Phys. Rev. **83** (1951) 71.
5) C. Miranda: Mem. R. Acad. d'Italia **5** (1934) 285.

J. Phys. Soc. Japan **9** (1954) 291~292

On the Approximate TF Function for Compressed Neutral Atom

By Kwai UMEDA

Department of Physics, Faculty of Science, Okayama University

(Received December 4, 1953)

Putting the TF (Thomas-Fermi) function for a compressed neutral atom with atomic radius x_0 measured in TF unit μ $\phi(x)\equiv\phi_0(x)+\delta(x)$, $\phi_0(x)$ being the TF function for the atom in free state, we have according to Fermi[1] the differential equation for $\delta(x)$

$$\delta''=(3/2)(\phi_0/x)^{1/2}\delta, \tag{1}$$

subject to the boundary conditions

$$\text{(i)}\quad \delta(0)=0, \tag{2}$$

and

$$\text{(ii)}\quad \phi'(x_0)=\phi(x_0)/x_0. \tag{3}$$

On the basis of the well-known Sommerfeld[2] asymptotic formula for $\phi_0(x)$, Sauvenier[3] previously gave the approximate formula

$$\phi(x)=\phi_0(x)\left[1+\frac{4z_0+1}{(\lambda_1-4)z_0-1}\left(\frac{1+z}{1+z_0}\right)^{\lambda_1/\lambda}\right], \tag{4}$$

from which follows the boundary value relation useful for the equation of state of metal

$$\phi(x_0)/\phi_0(x_0)=2.060\cdot z_0/(z_0-0.2651), \tag{5}$$

as the present author[4] has noticed. This relation has, however, several drawbacks, as follows.

1. For $0<z_0<0.2651$ $(0<x_0<0.9389)$, $\phi(x_0)<0$, while $\phi(x)$ must by nature be always positive.

2. At $z_0=0.2651$ $(x_0=0.9389)$ instead of origin, $\phi(x_0)=\infty$.

3. At $z_0=\infty$ $(x_0=\infty)$, $\phi(x_0)/\phi_0(x_0)=2.060$ instead of 1.

Now, it is to be reasoned, whether these drawbacks could be avoided, if for $\phi_0(x_0)$, the other approximate formulae would be adopted.

First, the March[5] approximate formula of Sommerfeld type comes into consideration. It only led, however, to the same boundary value relation as the above, Eq. (5).

Accordingly, we take the Kerner[6] approximate formula, $\phi_0(x)=1/(1+Cx)$, which is very simple and of such a relatively high degree of approximation as demonstrated in the preceding note by the present author. Eq. (1) becomes then asymptotically an equation of Bessel type

$$\delta''=\frac{3}{2}\frac{\delta}{[x(1+Cx)]^{1/2}}\approx\frac{3}{2}\frac{\delta}{C^{1/2}x}, \tag{6}$$

inasmuch as possible alternative simplifications as $Cx(1+Cx)\to(Cx+1)^2$ or $(Cx+0.5)^2$ bring about no essential improvement. Since $\delta(x)$ must be a monotonously increasing function with the boundary condition (i), the differential equation

(6) is satisfied by

$$\delta(x)=AXI_1(X),$$

where $X\equiv 6^{1/2}C^{-1/4}x^{1/2}$ and $I_n(x)=$Bessel function of purely imaginary argument. Determining the value of the disposable coefficient A by the boundary condition (ii), we obtain the approximate formula corresponding to Eq. (4),

$$\phi(x)=\phi_0(x)\left[1+4\left(\frac{x}{x_0}\right)^{1/2}\frac{I_1(X)}{X_0I_0(X_0)-2I_1(X_0)}\right], \tag{7}$$

from which follows in turn the boundary value relation corresponding to Eq. (5),

$$\phi(x_0)/\phi_0(x_0)=1+4/[X_0\{I_0(X_0)/I_1(X_0)\}-2]. \tag{8}$$

This formula is free from the drawbacks mentioned above, as follows.

1. At $x_0=0$. By virtue of the series expansions of $I_{0,1}(x)$ the boundary value Eq. (8) becomes

$$\phi(x_0)/\phi_0(x_0)=1+(16/X_0^2)[1+X_0^2/24+\cdots]\rightarrow\infty,$$

as it must necessarily be.

2. At $x_0=\infty$. By virtue of the asymptotic expansions of $I_{0,1}(x)$ the boundary value Eq. (8) becomes

$$\phi(x_0)/\phi_0(x_0)=1+4/X_0+\cdots\rightarrow 1,$$

as it also must necessarily be.

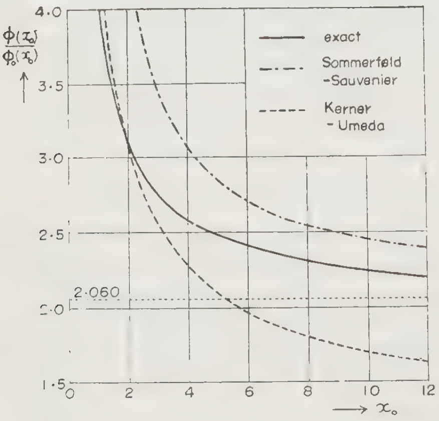

Fig. 1. Boundary values of the exact as well as approximate TF functions for compressed neutral atom as functions of the atomic radius, cf. eqs. (5) and (8).

In Fig. 1 the boundary values obtained from eqs. (5) and (8) are shown in comparison with these obtained from the exact numerical solution. Eq. (5) seems to be more favorable for larger values of x while eq. (8) for smaller values of x.

This work was supported by the Ministry of Education Scientific Research Money grant to the Research Group of the Mathematical Physics.

References

1) E. Fermi: Mem. R. Acad. d'Italia **1** (1930) 149.

2) A. Sommerfeld: Z. Phys. **78** (1932) 283.

3) H. Sauvenier: Bull. Soc. Roy. Liège **8** (1939) 313; P. Gombás: *Die statistische Theorie des Atoms und ihre Anwendungen* (Springer-Verlag, Wien, 1949) p. 53.

4) K. Umeda: Phys. Rev. **83** (1951) 651. I regret that I failed in this Letter to the Editor to refer to Sauvenier's work. Thanks are due Profs. Gombás and March for their calling of my attention to it.

5) N. H. March: Proc. Camb. Phil. Soc. **46** (1950) 356.

6) E. H. Kerner: Phys. Rev. **83** (1951) 71.

J. Phys. Soc. Japan **9** (1954) 292~293

Temperature Dependency of the Surface Recombination Velocity in Germanium

By Yasuo Kanai

The Electrical Communication Laboratory
Tokyo, Japan

(Read Oct. 20, 1953; Received December 8, 1953)

As is well known, the number of excess carriers in semiconductors returns to its thermal equilibrium value by the recombination processes in the bulk and at the surfaces of the semiconductors, and it seems quite important for the development of the transistor electronics to clarify the mechanism of these recombination process. The recombination process in bulk semiconductors has been investigated already1) and proved to be due to the recombination process via traps, but the recombination process at the surfaces of semicomductors has not been fully studied. This note will report some experimental results which will give some imformations about the mechanism of the surface recombination process.

To investigate the surface recombination process, we have measured the surface recombination velocity in n-type germanium by the Suhl's effect2) at weak magnetic field in the temperature range from about −30°C up to about +60°C. In this case the surface recombination velocity was calculated by the formula2):

$$p/p_0=1+\varphi(1+\sin 2\beta b/2\beta b)$$
$$\varphi=eE_2b/2kT$$
$$E_2=E_l\cdot 10^{-8}\cdot(\mu_e+\mu_h)H$$
$$v_sb/D=\beta b\cdot\tan\beta b\,,$$

where

p: hole density at the collector point

p_0: hole density at the collector point when the magnetic field absent

E_l: the longitudial electric field in volt/cm

μ_e, μ_h: the Hall mobility of electrons and holes in cm^2/volt. sec.

H: the magnetic field in gauss

$2b$: the width of the sample

v_s: surface recombination velocity.

In our experiment the hole density was measured by the zero voltage conductance at the collector point³⁾, and it was assumed that the electron and hole mobilities were proportional to $T^{-3/2}$, and the conductivity modulation due to the excess carriers was neglected to calculate the longitudinal electric field.

Our experimental result, which was given for the n-type germanium surfaces etched by the CP-4 solution, is shown in Fig. 1.

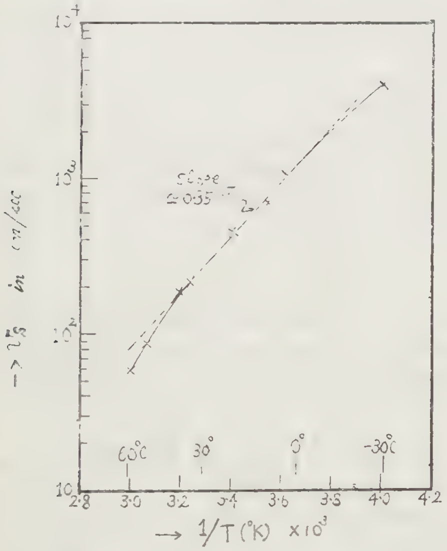

Fig. 1. Temperature dependency of the surface recombination velocity v_s.

Analysing their experimental data in the study of germanium surfaces, Brattain and Bardeen⁴⁾ proposed the surface recombination process via surface traps. Following their calculation the surface recombination velocity was given by the next formula⁴⁾

$$v_s = m\cdot S(kT/2\pi m^*)N_a/N_c\cdot\exp(E_c-E_a)/kT,$$

where

n: electron density in the interior of semiconductor at thermal equilibrium.

S: recombination cross-section for holes.

N_a: concentration of surface traps (no./cm^2).

N_c: state density of the lowest state of conduction band.

E_c-E_a: the energy difference between the trap state and the bottom of the conduction band.

If the recombination cross-section is assumed to be temperature insensitive, our results give about 0.35 ev. as the tentative value of the energy level of the surface trap below the bottom of the conduction band.

References

1) Hall: Phys. Rev. **87** (1952) 387.
2) Suhl and Shockley: Phys Rev. **75** (1949) 1617.
3) Shockley: "*Electrons and Holes in Semiconductors.*" (D. Van Nostrand Company, Inc., New York, 1950).
4) Brattain and Bardeen: B.S.T.J. **32** (1953) 1.

J. PHYS. SOC. JAPAN **9** (1954) 293~294

On the Dissociation Constant of Polyelectrolyte

By Shinji KATAOKA
Hitotsubashi University, Kunitachi, Tokyo

(Received December 21, 1953)

It is a well known fact that the dissociation constant of polyelectrolyte differs from that of its structural element,¹⁾,²⁾ (for example, monomer acid). In this short paper, we calculate the degree of dissociation of the polyelectrolyte as a solution of an integral equation which resembles Kirkwood-Riseman's³⁾,⁴⁾ equation in their papers on the theory of viscosity of the polymer solution.

For brevity, we think that the polyelectrolyte is a weak acid, for example polyacrylic acid and Z acid groups are attatched to the polyacid. As one dissociated group prevents others from dissociation by its electric potential, the dissociation constant of each acid group must be decided self-consistently to each other. The Bjerrum's formula, firstly, connects the electric potential $\psi(i)$ with the dissociation constant $\alpha(i)$ of an acid group, i,

$$\frac{\alpha(i)}{1-\alpha(i)}=\frac{K_0}{[H]}e^{\beta\varepsilon\psi(i)/kT}, \qquad (1)$$

where K_0 is the dissociation constant of a monomer acid, and $[H]$ the concentration of the hydrogen ion in the solution. The electric potential, on the other hand, can be written in terms of the dissociation constants as follows:

$$\psi(i)=-\sum_{\substack{j=-n\\ \neq i}}^{n}\frac{\beta\varepsilon}{Dr(i,j)}\alpha(i). \qquad (2)$$

where $r(i,j)$ is the distance between i and j-th segments, and D the dielectric constant of the solvent, and here the double layer effect of the free ions is neglected, and $-\beta\varepsilon$ is the smoothed charge per segment.

If we could solve these two equations correctly we would obtain exact values of $\alpha(i)$ and $\psi(i)$. Unfortunately these equations are non-linear and we can not yet solve them exactly, so we shall use the following approximation.

From (1),

$$\log\frac{\alpha(i)}{1-\alpha(i)}=\log\frac{K_0}{[H]}+\beta\varepsilon\psi(i)/kT\,. \tag{3}$$

Experimentally, $\alpha(i)$ is usually discussed to be about $\sim 1/2$. So putting

$$\alpha(i)=1+\delta(i)\,,\quad \delta\ll 1\,, \tag{4}$$

and substituting into (3), we have

$$\begin{aligned}\alpha(i)&=\alpha_0+(\beta\varepsilon/4kT)\psi(i)\\ \alpha_0&=\tfrac{1}{2}+\tfrac{1}{4}\log(K_0/[H]).\end{aligned} \tag{5}$$

From (5) and (2), we have the following equation:

$$\alpha(i)=\alpha_0-\frac{\beta^2\varepsilon^2}{4DkT}\sum_{\substack{j=-n\\ \neq i}}^{n}\frac{d(j)}{r(i,j)}\,. \tag{6}$$

This equation decides the dissociation constant $\alpha(i)$, and consequently the electric potential $\psi(i)$, self-consistently.

Then we must consider about $r(i,j)$ of the functional form of which determined by the form of polyacid, but we only know the functional form of $r(i,j)$ in the cases of rod like and random coil models. In these two cases $r(i,j)$ is equal to $1/b|i-j|$ and $(6/\pi)^{1/2}(1/b|i-j|^{1/2})$ respectively, and replacing the discontinuous variables i and j by continuous variables x and y, and the summation by an integration, quite analogously to Kirkwood-Riseman's treatments in their theories of viscosity of rod and random coil polymer. After some calculations we can obtain the following integral equations:

for the rod model

$$\alpha(x)=\alpha_0-\lambda_r\int_{-1}^{1}\frac{\alpha(y)}{|x-y|}dy, \tag{7}$$

for the random coil model,

$$\alpha(x)=\alpha_0-\lambda_c\int_{-1}^{1}\frac{\alpha(y)}{|x-y|^{1/2}}dy, \tag{8}$$

where

$$\lambda_r=\beta^2\varepsilon^2/4DkTb\,,\quad \lambda_c=\beta^2\varepsilon^2/4DkTb(6/\pi)^{1/2},$$
$$x=i/n\,,\qquad y=j/n\,.$$

These two equations were already solved by Kirkwood-Riseman elegantly, so we can use their results directly,

for rod

$$\alpha(x)=\frac{\alpha_0}{1-2\lambda_r\log(1/n)+2\lambda_r(\log 2-1)}+\sum_{\substack{k=-\infty\\ \neq 0}}^{\infty}\frac{\{\sin\pi k/\pi k-(\mu_k/\mu_0)\alpha_0\}e^{i\pi kx}}{1-2\lambda_r C_i(|k|\pi/n)}\,, \tag{9}$$

where

$$\mu_k=\frac{1}{2}\int_{-1}^{1}\{1-2\lambda_r\log(1/n)+\lambda_r\log(1-x^2)\}e^{-i\pi kx}dx,$$

$$C_i(x)=\int_0^x\frac{\cos t}{t}\,dt\,,$$

and for the coiled model

$$\alpha(x)=\frac{\alpha_0}{1+8\sqrt{2}\,\lambda_c/3}+\sum_{\substack{k=-\infty\\ \neq 0}}^{\infty}\frac{\sin\pi k/\pi k-(\mu_k/\mu_0)d_0}{1+\lambda_c(2/|k|)^{1/2}}\,e^{i\pi kx}\,, \tag{10}$$

where

$$\mu_k=\frac{1}{2}\int_{-1}^{1}[1+2\lambda_c(1+x)^{1/2}+2\lambda_c(1-x)^{1/2}]e^{-i\pi kx}dx.$$

Above treatment, however, is confined to the two extreme cases such as rod and random coil, but the real polyelectrolyte would have an intermediate form between them. By the data of light scattering, it seems that the polyelectrolyte has a considerably stretched form, not random coil. Then it is desirable to extend the above mentioned treatment to the general case, but mathematical diffiiculties make it impossible to do so. Although it is impossible to treat generally, an intuitive method can be devised as follows. If we put $1/r(i,j)$,

$$1/r(i,j)=1/b|i-j|^{\nu}, \tag{11}$$

where ν is a parameter which represents the order of stretching and takes a value between 1 and 1/2, then we can solve the integral equation, by utilizing the following relation:

$$\frac{1}{|x-y|^{\nu}}=\frac{1}{\Gamma(\nu)\nu}\int_0^\infty e^{-|x-y|Z^{1/\nu}}dZ\,. \tag{12}$$

To complete this theory the parameter α must be determined consistently with the free energy of the whole system which is minimized by this parameter. The full report will be given on the Journal of the Physical Society of Japan shortly.

References

1) Kuhn. Kuntzel, Katschalsky: J. Phys. Sci. **5** (1950) 283.

2) Katschalsky, Gillis: Rec. Trav. Chem. **68** (1949) 879.

3) Kirkwood, Riseman: J. Chem. Phys. **16** (1948) 565.

4) Riseman, Kirkwood: J. Chem. Phys. **18** (1950) 512.

J. PHYS. SOC. JAPAN **9** (1954) 295

Anomalous Structure of α-AgI

By Sadao HOSHINO

Department of Physics, Tokyo Institute of Technology, Tokyo, Japan

(Received December 21, 1953)

Silver iodide (AgI) has three phases α, β and γ. Concerning the α-phase in the temperature range from 146°C to the melting point 155°C, Strock proposed[1] the following structure in which iodine atoms are in body centered cubic lattice sites and silver atoms may be situated in 42 sites in the unit cell statistically. He considered that the behavior of the silver atoms may be almost liquid-like, in accordance with the well-known remarkably high ionic conductivity of this phase.

We have reexamined the structure of this substance and obtained results which differ from his conclusions.

If the silver atoms assume statistical positions, we can expect to observe, correspondingly, an X-ray diffuse scattering in the background of the Debye line. In order to examine this effect, we measured accurately X-ray intensities of the Debye lines and the background from a powder sample, by using a G-M X-ray spectrometer and the crystal monochromated CuKα radiation. For this purpose a rotating anode X-ray tube, having a fine focus, operated with electron current 50 mA and voltage 25 kV, was used.

In the measurement, we detected the diffuse scattering actually to exist, but found that its intensity relative to the integrated intensity of a Debye line is too weak in comparison with the theoretical value expected from the disordered structure such as Strock's model. Furthermore, the relative intensities of Debye lines are somewhat different from those calculated from Strock's structure (Fig. 1).

Let us imagine, now, two hypothetical structure of α-AgI, one is the perfectly ordered structure and the other the perfectly disordered one, then we can suppose that the actual structure of α-AgI is in intermediate of these two extremes. The perfectly ordered structure, then, should be such one which has a pseudocubic tetragonal symmetry, since there are no possible equivalent positions, with a cubic symmetry, for two Ag atoms in the body centered cubic lattice constructed from iodine atoms. While the perfectly disordered structure will be with cubic symmetry in the average, but it may be different from Strock's model. Concerning the tetragonal ordered structure, the following model is the most plausible: the axial ratio c/a is just unity, by chance, and the iodine and silver atoms are in the positions (0 0 0), (1/2 1/2 1/2) and (0 1/2 1/4), (1/2 0 3/4) respectively; the space group may be $D_{2d}{}^{9}-I_{\bar{4}m2}$. On the other hand, the cubic perfectly disordered structure may have the following averaged structure: the iodine atoms are in the same positions as in the ordered state whereas the two silver atoms are situated on the 12 sites (1/2 1/4 0 ◯), (0 3/4 1/2), (1/2 0 1/4 ◯), (0 1/2 3/4 ◯), statistically.

When we introduce a parameter S representing the degree of order just like that in the problem of alloys, and assume that there exists somewhat anharmonic thermal vibration for silver atoms, which is excessive especially towards every [110] direction, then the observed intensity of Debye lines and diffuse background at 200°C is explained fairly well by putting $S=0.8$ (Fig. 1).

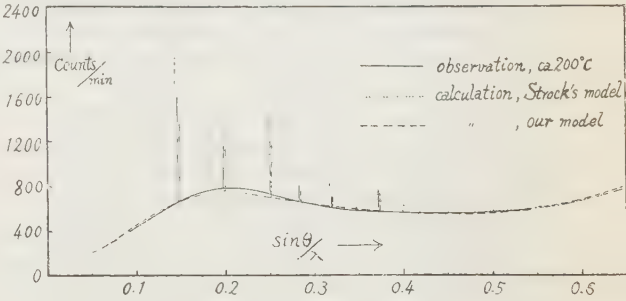

Fig. 1. Comparison of X-ray diffraction intensities between observation and calculation. The theoretical curves of diffuse background being drawn so as to coincide with the experimental curve at a position of high scattering angle. The length of vertical line represents the integrated intensity of Debye line.

It should be noticed, in this case, that the positions of Debye lines expected from the tetragonal ordered structure proposed above coincide completely with those for the cubic disordered one, and, therefore, there are no extra lines or superstructure lines as found in the case of alloys.

The S value of 0.8, which was found at 200°C, indicates that α-AgI has an almost ordered structure, being accompanied only by comparatively small disorder. But the higher the temperature, the smaller becomes the degree of order that may be epected. Regarding this point, investigation is now in progress. The further detailes will be published shortly.

The author wishes to express his sincere thanks to Prof. S. Miyake for his kind guidance in this work.

Reference

1) L. W. Strock: Z. Physik. Chem. **B25** (1934) 441; **B31** (1936) 132.

J. PHYS. SOC. JAPAN **9** (1954) 296~297

Asymptotic Expansions of Bessel Functions in the Transitional Resions

By Masahumi NAGASE
Department of Physics, Faculty of Liberal Arts, Saga University, Saga, Japan

(Received January 20, 1954)

The asymptotic expansion of Bessel functions are comparatively difficult to formulate, when the relation between the argument (z) and the order (ν) is in the transitional region, i.e. when $\gamma=0(z^{-1/3})$, where $\nu=z\cosh\gamma$. The formulas of the first approximation were investigated at an early date by Watson, who applied the method of steepest descents to Debye's integral[1]. The present author, carrying out Watson's analysis further, refined them to the second terms[2]. Imai also discussed the problem by tne so-called generalized W.K.B. method[3].

Recognizing the necessity of more accurate formulas in the study of the diffraction of waves by a sphere, the author has recently made a further investigation by using a method analogous to the perturbation method.

According to the author's work cited above, the approximate expressions for Bessel functions of the third kind are

$$H_\nu^{(1)}(z)=-3^{-1/2}\eta e^{(\pi/3)i}\Big\{\Big(1+\frac{1}{10}\eta^2\Big)H_{-1/3}^{(1)}(\xi)-\frac{3}{5}\eta^2\xi H_{2/3}^{(1)}(\xi)+0(\eta^4)\Big\},$$

$$H_\nu^{(2)}(z)=3^{-1/2}\eta e^{-(\pi/3)i}\Big\{\Big(1+\frac{1}{10}\eta^2\Big)H_{-1/3}^{(2)}(\xi)-\frac{3}{5}\eta^2\xi H_{2/3}^{(2)}(\xi)+0(\eta^4)\Big\},$$

where $\xi=i\nu/3\tanh^3\gamma$, $\eta=\tanh\gamma$, and z, ν are unrestricted complex numbers. Noticing these forms, we assume the following expansion with unknown coefficients

$$H_\nu^{(2)}(z)\sim 3^{-1/2}e^{-(\pi/3)i}\Big\{\eta H_{-1/3}^{(2)}(\xi)+\sum_{n=1}^{\infty}a_n(\xi)\eta^{2n+1}\Big\},$$

and substitute it into the differential equation for the Bessel function:

$$\frac{d^2}{dz^2}H_\nu^{(2)}(z)+\frac{1}{z}\frac{d}{dz}H_\nu^{(2)}(z)=-\Big(1-\frac{\nu^2}{z^2}\Big)H_\nu^{(2)}(z)$$
$$=\sinh^2\gamma H_\nu^{(2)}(z).$$

The equation becomes, after some rearrangements,

$$\sum_{n=1}^{\infty}\Big\{a_n''(\xi)+\frac{4n+3}{3\xi}a_n'(\xi)+\Big(1+\frac{4n^2-1}{9\xi^2}\Big)a_n(\xi)\Big\}\eta^{2n}$$
$$=-H_{-1/3}^{(2)}(\xi)\eta^2-\frac{2}{3\xi}H_{2/3}^{(2)}(\xi)\eta^2$$
$$-H_{-1/3}^{(2)}(\xi)\sum_{n=1}^{\infty}\eta^{2n}+\sum_{n=2}^{\infty}\Big\{a_{n-1}''(\xi)$$
$$+\frac{4n+1}{3\xi}a_{n-1}'(\xi)+\Big(-1+\frac{(2n-1)^2}{9\xi^2}\Big)a_{n-1}(\xi)\Big\}\eta^{2n}$$
$$-\sum_{n=3}^{\infty}\{a_{n-2}(\xi+a_{n-3}(\xi)+\cdots\cdots+a_1(\xi)\}\eta^{2n},$$

where the primes denote the derivatives with respect to ξ. Equating the coefficients of the same powers of η, we have the following system of differential equations:

$$a_1''(\xi)+\frac{7}{3\xi}a_1'(\xi)+\Big(1+\frac{1}{3\xi^2}\Big)a_1(\xi)$$
$$=-2H_{-1/3}^{(2)}(\xi)-\frac{2}{3\xi}H_{2/3}^{(2)}(\xi),$$

$$a_2''(\xi)+\frac{11}{3\xi}a_2'(\xi)+\Big(1+\frac{5}{3\xi^2}\Big)a_2(\xi)$$
$$=-H_{-1/3}^{(2)}(\xi)+a_1''(\xi)+\frac{3}{\xi}a_1'(\xi)+\Big(-1+\frac{1}{\xi^2}\Big)a_1(\xi),$$
$$=-3H_{-1/3}^{(2)}(\xi)-\frac{2}{3\xi}H_{2/3}^{(2)}(\xi)+\frac{2}{3\xi}a_1'(\xi)$$
$$+\Big(-2+\frac{2}{3\xi^2}\Big)a_1(\xi),$$

$$a_3''(\xi)+\frac{15}{3\xi}a_3'(\xi)+\Big(1+\frac{35}{9\xi^2}\Big)a_3(\xi)$$
$$=-H_{-1/3}^{(2)}(\xi)+a_2''(\xi)+\frac{13}{3\xi}a_2'(\xi)$$
$$+\Big(-1+\frac{25}{9\xi^2}\Big)a_2(\xi)-a_1(\xi),$$
$$=-4H_{-1/3}^{(2)}(\xi)-\frac{2}{3\xi}H_{2/3}^{(2)}(\xi)+\frac{2}{3\xi}a_2'(\xi)$$
$$+\Big(-2+\frac{10}{9\xi^2}\Big)a_2(\xi)+\frac{2}{3\xi}a_1'(\xi)+\Big(-3+\frac{2}{3\xi^2}\Big)a_1(\xi),$$

$$a_4''(\xi)+\frac{19}{3\xi}a_4'(\xi)+\Big(1+\frac{63}{9\xi^2}\Big)a_4(\xi)$$
$$=-H_{-1/3}^{(2)}(\xi)+a_3''(\xi)+\frac{17}{3\xi}a_3'(\xi)$$
$$+\Big(-1+\frac{49}{9\xi^2}\Big)a_3(\xi)-a_2(\xi)-a_1(\xi),$$
$$=-5H_{-1/3}^{(2)}(\xi)-\frac{2}{3\xi}H_{2/3}^{(2)}(\xi)+\frac{2}{3\xi}a_3'(\xi)$$
$$+\Big(-2+\frac{14}{9\xi^2}\Big)a_3(\xi)+\frac{2}{3\xi}a_2'(\xi)$$
$$+\Big(-3+\frac{10}{9\xi^2}\Big)a_2(\xi)+\frac{2}{3\xi}a_1'(\xi)+\Big(-4+\frac{2}{3\xi^2}\Big)a_1(\xi),$$

……………………………………

By successive intergrations we get

$$a_1(\xi)=\frac{1}{10}H_{-1/3}^{(2)}(\xi)-\frac{3}{5}\xi H_{2/3}^{(2)}(\xi),$$

$$a_2(\xi)=\Big(\frac{13}{280}-\frac{9}{50}\xi^2\Big)H_{-1/3}^{(2)}(\xi)+\Big(\frac{1}{210}-\frac{3}{7}\xi^2\Big)\frac{1}{\xi}\cdot H_{2/3}^{(2)}(\xi),$$

$$a_3(\xi)=\Big(\frac{803}{25200}-\frac{921}{3500}\xi^2\Big)H_{-1/3}^{(2)}(\xi)$$
$$+\Big(\frac{37}{18900}-\frac{197}{600}\xi^2+\frac{9}{250}\xi^4\Big)\frac{1}{\xi}\cdot H_{2/3}^{(2)}(\xi),$$

$$a_4(\xi)=\Big(-1.3959\frac{1}{\xi^2}+1.3329-0.61168\xi^2+0.0054\xi^4\Big)$$
$$\times H_{-1/3}^{(2)}(\xi)+(-2.0929+0.51938\xi^2-0.038541\xi^4)$$
$$\times\frac{1}{\xi}\cdot H_{2/3}^{(2)}(\xi).$$

The numerical coefficients in $a_4\ (\xi)$ are all but one rounded off to five significant figures.

Thus it follows, that

$$H_\nu{}^{(2)}(z)\sim 3^{-1/2}e^{-(\pi/3)i}\eta\Big[\Big\{1+\frac{1}{10}\eta^2+\Big(\frac{13}{280}-\frac{9}{50}\xi^2\Big)\eta^4$$
$$+\Big(\frac{803}{25200}-\frac{921}{3500}\xi^2\Big)\eta^6+\Big(-1.3959\frac{1}{\xi^2}+1.3329$$
$$-0.61168\,\xi^2+0.0054\,\xi^4\Big)\eta^8+\cdots\cdot\Big\}H_{-1/3}{}^{(2)}(\xi)$$
$$+\Big\{-\frac{3}{5}\xi^2\eta^2+\Big(\frac{1}{210}-\frac{3}{7}\xi^2\Big)\eta^4+\Big(\frac{37}{18900}-\frac{197}{600}\xi^2$$
$$+\frac{9}{250}\xi^4\Big)\eta^6+(-2.0929+0.51938\xi^2-0.038541\xi^4)$$
$$\times\eta^8+\cdots\cdot\Big\}\frac{1}{\xi}H_{2/3}{}^{(2)}(\xi)\Big].$$

Quite similarly

$$H_\nu{}^{(1)}\sim -3^{-1/2}e^{(\pi/3)i}\eta\Big[\Big\{1+\frac{1}{10}\eta^2+\Big(\frac{13}{280}-\frac{9}{50}\xi^2\Big)\eta^4$$
$$+\Big(\frac{803}{25200}-\frac{921}{3500}\xi^2\Big)\eta^6+\Big(-1.3959\frac{1}{\xi^2}+1.3329$$
$$-0.61168\,\xi^2+0.0054\,\xi^4\Big)\eta^8+\cdots\Big\}H_{-1/3}{}^{(1)}(\xi)$$
$$+\Big\{-\frac{3}{5}\xi^2\eta^2+\Big(\frac{1}{210}-\frac{3}{7}\xi^2\Big)\eta^4+\Big(\frac{37}{18900}-\frac{197}{600}\xi^2$$
$$+\frac{9}{250}\xi^4\Big)\eta^6+(-2.0929+0.51938\xi^2$$
$$-0.038541\xi^4)\eta^8+\cdots\cdot\Big\}\frac{1}{\xi}H_{2/3}{}^{(1)}(\xi)\Big].$$

References

1) G. N. Watson: Proc. Camb. Phil. Soc. **19** (1918) 96–110.

Theory of Bessel Functions (Cambridge University Press, London, 1922) 252.

2) M. Nagase: Journ. Phys. -Math. Soc. Japan **17** (1943) 552–556, in Japanese.

3) I. Imai: Phys. Rev. **80** (1950) 113.

J. Phys. Soc. Japan **9** (1954) 297~298

The Effect of Field Bump in A Strong Focusing Synchrotron

By Kazuo Huke and Giiti Iwata

Departmemt of Physics, University of Tokyo

(Received January 22, 1954)

Since the discovery of a strong focusing method[1], there have been added many papers that treat the method from various points of view. Here are calculated the effect due to the field bump and the form factor. The equation to the amplitude of a particle in the z-direction is written

$$\frac{d^2u}{d\theta^2}+p(\theta)u=\eta(\theta)$$
$$p(\theta)=\begin{cases} n & \text{for focusing sectors} \\ -n & \text{for defocusing sectors}\end{cases} \qquad (1)$$

where the nonhomogeneous term $\eta(\theta)$ arises from the field bump. $\eta(\theta)$ is taken to be periodic in θ, to have the mean value 0, the square mean value η^2, that is,

$$\eta(\theta+2\pi)=\eta(\theta),\ <\eta(\theta)>=0,\ <\eta(\theta)\eta(\theta')>=\eta^2\delta(\theta-\theta').$$

A periodic solution $u(\theta)$ to (1) is expressed as

$$u(\theta)=-\int_0^{2\pi}G(\theta,\theta')\eta(\theta')d\theta',$$

with the aid of Green's function $G(\theta,\theta')$ that is periodic and satisfies the equation

$$\Big(\frac{d^2}{d\theta^2}+p(\theta)\Big)G(\theta,\theta')=-\delta(\theta-\theta').$$

The root mean square of u, that is, $<u^2>^{1/2}$, is found to be under the condition

$$\sqrt{\frac{<u^2>}{\eta^2}}\leqq\frac{\sqrt{\pi}\,b}{4\sqrt{n}\ \sin 2\pi\mu\sin N\pi\mu}$$
$$\times\Big(1+\frac{2\sinh\phi\sin\phi}{b\phi}\Big)\Big\{1+\frac{1}{N}+\frac{1}{N}\Big|\frac{\sin(N-1)2\pi\mu}{\sin 2\pi\mu}\Big|\Big\}^{1/2}$$
$$b=\cosh\phi\sin\phi+\sinh\phi\cos\phi$$
$$\phi=\pi\sqrt{n}/N$$

N = the number of units

$\cos 2\pi\mu=\frac{1}{2}$ (the trace of characteristic matrix).

The form factor here is taken to be the square root of the ratio of the upper bound of u^2 to the mean value of u^2 for a solution u to the homogeneous equation (1) with the vanishing $\eta(\theta)$. Regardless of initial conditions, the ratio is found to be the under condition

$$\frac{\text{up bound of } u^2}{<u^2>}\equiv\beta^2\leqq\frac{4(\cosh\phi\sin\phi+\sinh\phi)}{b+(2\sinh\phi\sin\phi)/\phi}.$$

When free sectors are inserted between focusing and defocusing sectors, the condition takes the following form

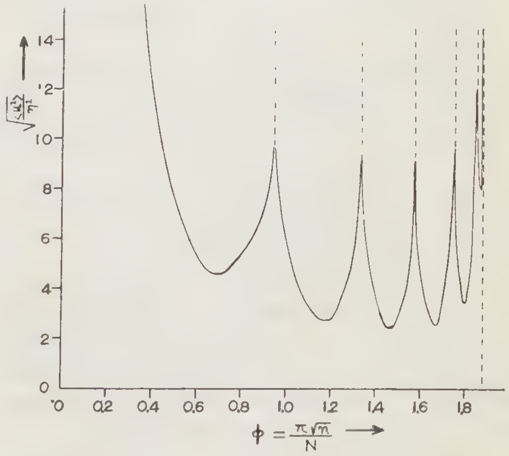

Fig. 1. $\sqrt{<u^2>/\eta^2}$ versus ϕ, the broken lines denoting the sites of resonance totaling $N/2$ $(=6)$.

$$\beta^2\leqq 4(1+\varepsilon)F(\phi)/G(\phi)$$
$$F(\phi)=\cosh\phi\sin\phi+\sinh\phi+\varepsilon\phi(\cosh\phi\cos\phi$$
$$+\sinh\phi\sin\phi+\cosh\phi)$$

$$+(1/2)\varepsilon^2\phi^2(\sinh\phi\cos\phi+\sinh\phi),$$

$$G(\phi)=b+(2\sinh\phi\sin\phi)/\phi+2\varepsilon\phi\cosh\phi\cos\phi$$
$$+(\varepsilon/2)^2\phi^2(\sinh\phi\cos\phi-\cosh\phi\sin\phi)$$
$$+\varepsilon(3b-\sinh^3\phi\cos\phi)+\varepsilon^2\phi(\sinh\phi\sin\phi$$
$$+4\cosh\phi\cos\phi)+\varepsilon^3\phi^2\{(4/3)(\sinh\phi\cos\phi$$
$$-\cosh\phi\sin\phi)-(1/2)\sinh^2\phi\cosh\phi\sin\phi\}$$
$$-(1/3)\varepsilon^4\phi^3\sinh\phi\sin\phi.$$

$$\varepsilon=\frac{\text{the length of a free sector}}{\text{the length of a focusing or defocusing sector}},$$

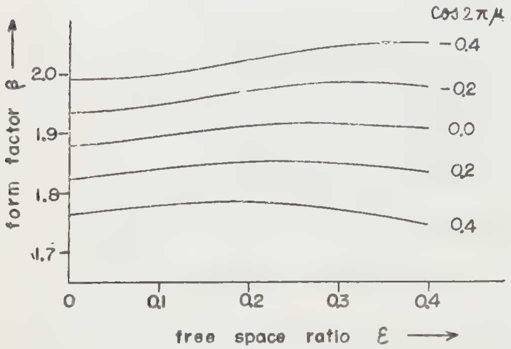

Fig. 2. The form factor β versus the free space ratio ε for some values of $\cos 2\pi\mu$.

The writers express sincere thanks to the cowerkers of Miyamoto Laboratory who suggested and urged these calculations.

Reference

1) Courant, Livingston, Snyder: Phys. Rev. **88** (1952) 1190.

J. Phys. Soc. Japan **9** (1954) 298~299

On the *g*-Factor and *Hi* of Nickel Ferrite-Aluminate

By Yosiharu Torizuka, Yuzo Kojima
and Tadao Fujimura

*Research Institute for Scientific Measurements,
Tohoku University*

(Received January 27, 1954)

The magnetic properties of nickel ferrite-aluminate have been studied by T. R. McGuire[1], Maxwell[2] et al. and R. K. Wangsness[3]. But the determination of g-factors was performed, being taken no notice of the internal field Hi.

From this point of view the present experiments were carried out to determine the true g-factor and Hi of these materials at the frequencies of 19230 MC and 28850 MC.

The chemical formula of nickel ferrite-aluminate is $NiFe_{2-x}Al_xO_4$, so that when x is increased from $x=0$ Fe^{3+} ions will be replaced by Al^{3+}.

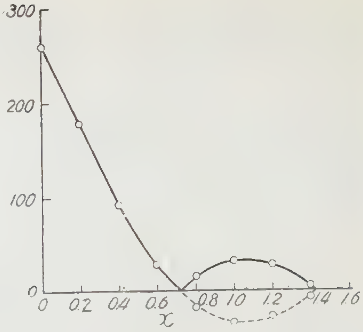

Fig. 1. The saturation magnetization of $NiFe_{2-x}Al_xO_4$ as a function of x at room temperature.

Fig. 1 shows the saturation magnetization of $NiFe_{2-x}Al_xO_4$ as a function of x at room temperature, measured in the field of 7500 Oe with a cylindrical specimen, and it suggests that the origin of magnetization of this system would be in 16c and 8f seits for $x<0.72$ and for $x<0.72$, respectively.

Fig. 2 gives an apparent g-factor of the spherical specimen of nickel ferrite-aluminate at 9384 MC, and the half line width ΔH at 19230 MC, extraporated to the zero diameter to eliminate the size effect.

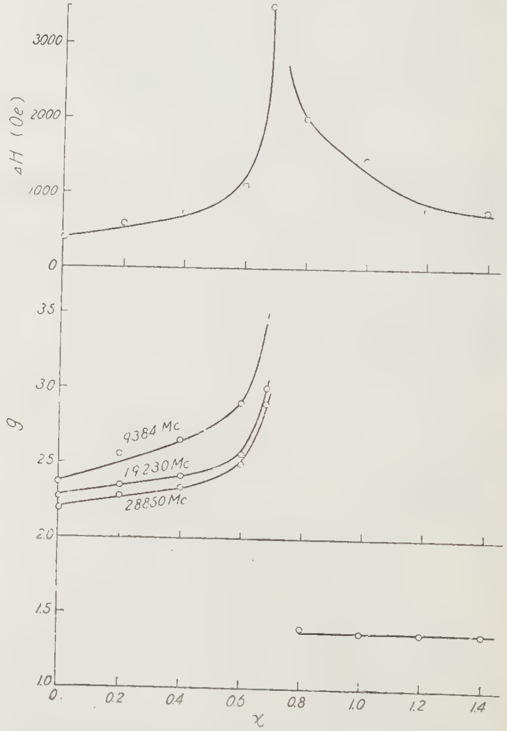

Fig. 2.

The above: the half line width ΔH versus x at 19230 MC.

The below: the apparent g-factor versus x for several frequencies.

Table. The true g-value and Hi of $NiFe_{2-x}Al_xO_4$ as a function of x, determined with the results at the frequencies of 19230 MC and 28850 MC.

x	0	0.2	0.4	0.6	0.68	0.8	1.0	1.2	1.1
g	2.16	2.20	2.29	2.45	2.80	1.40	1.37	1.37	1.37
Hi	280	370	320	240	310	0	0	0	0

The table gives the true g-value and Hi calculated from the following formula[4] using experi mental data of 19230 MC and of 28850 MC except the results at 9384 MC,

$$\omega=\gamma(H_z+Hi)\,.$$

For $x<0.72$, the changes in g-values are explained by the following equations due to Tuya[5] and Wangsness[3].

$$g=\frac{g_1S_1+g_2S_2}{S_1+S_2}\,,$$

where g_1 and g_2 are g-factors of Ni^{2+} and Fe_3^+ and S_1, S_2 are angular momentums corresponding to Ni^{2+} and Fe^{3+} in the present experiment. The large discrepancies from the above formula were found for $x>0.72$.

From the table, it is seen that the internal field Hi shows the values of 280∼370 Oe for $x<0.72$ but Hi is zero for $x>0.72$. This result would be very important in consideration of the origin of the internal field.

The authors expresss their thanks to Prof. T. Okamura for his discussion on this work. Details of this work will be published in the Science Report of RITU.

References

1) T. R. McGuire: Phys. Rev. **91** (1953) 206.

2) Maxwell, Pickart and Hall: Phys. Rev. **91** (1953) 206.

3) Roald K. Wangsness: Phys. Rev. **91** (1953) 1085.

4) T. Okamura, Y. Torizuka and Y. Kojima: Phys. Rev. 88 (1952) 1425. g-factor of $NiFe_2O_4$ in this paper don't agree with that of the present experiment, it may be caused from the difference of preparing methods for both the specimens; the value should be taken from the present paper.

5) N. Tuya: Prog. Theoret. Phys. **7** (1952) 263.

J. Phys. Soc. Japan **9** (1954) 299∼300

On the Radial Extent of Glow in Microwave Gas Discharge between Coaxial Cylinders

By Kenji Mitani

Yoshida College, University of Kyoto

(Received January 28, 1954)

When the microwave gas discharge takes place between coaxial cylinders, a bright luminous glow appears in the region of maximum electric field near the central wire, as shown schematically in Fig. 1. Thus the glow is limited within a volume whose radius is 1 or 2 mm and whose length along the wire is several millimeters. The length of glow having been already discussed by the author in the previous papers[1),2)], the present note is directed to the discussion of the radial extent of glow.

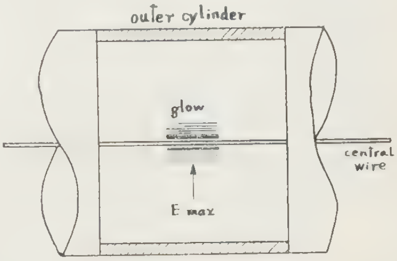

Fig. 1. Glow of the microwave gas discharge between coaxial cylinders.

First, it must be noted that the luminosity of glow depends directly neither on electron density n nor on electron current density potential ψ, but it depends upon the net production rate of electrons per unit volume, $n\nu$, where ν is the net production rate of electrons per one electron[3]. Although it is in general difficult to calculate $n\nu$, it will be shown in the following that the said quantity can be calculated rather easily in the case of the microwave gas discharge between coaxial cylinders.

According to the definition, the high frequency coefficient ζ is given by[4]

$$\zeta=\nu/(DE^2)\,, \qquad (1)$$

where D is the diffusion coefficient for electron and E the electric field intensity, and from this relation we can immediately obtain the following equation:

$$n\nu=(\zeta E^2)(Dn)=(\zeta E^2)\psi\,. \qquad (2)$$

Since, as is well known, the product Dn is the electron current density potential ψ. This equation enables us to calculate the values of $n\nu$ easily as follows.

ζ for various gases has been obtained by Herlin and Brown[5] as a function of E/p for uniform field, where p is the gas pressure. In the case of coaxial cylinders, they have put

$$\zeta E^2\simeq k^2(E/E_a)^\beta\,, \qquad (3)$$

and have assumed the radial electric field to be $E=(V/r)\ln(b/a)$, where V is the potential difference between the central wire ($r=a$) and the outer cylinder ($r=b$). Constants k, β and the electric field intensity E_a on the surface of the central wire can be determined by the method as used by Herlin and Brown. Thus, in order to determine ψ there remains undetermined only a constant contained therein[6]. However, such a constant has already been determined by the present author from the observation of the direct current associated with the microwave gas discharge[7]. In this way making use of equation (2) together with (3), we can calculate the values of $n\nu$ in the case of the microwave gas discharge between coaxial cylinders.

In the case of the author's experiment[7], $a=0.1$ mm, $b=12.5$ mm; $k=75.6$ cm, $\beta=2.13$; $V=1670$ volts/cm (gas-pressure $p=4.3$ mmHg, direct current $J=4.3\,\mu$A). ψ for this case is shown by a dotted-line curve in Fig. 2. By making use of these numerical data, the values of $n\nu$ have been calculated and are shown graphically by a solid-line curve in Fig. 2.

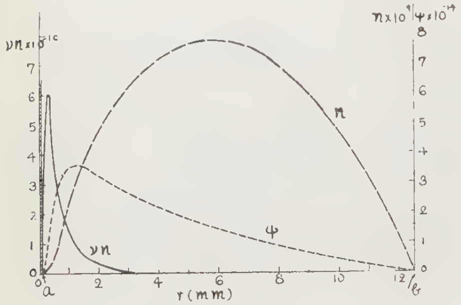

Fig. 2. Radial distributions of νn (electrons $\mathrm{cm}^{-3}\,\mathrm{sec}^{-1}$) = net production rate of electrons per unit volume (solid-line curve), $Dn=\psi$ ($\mathrm{cm}^{-1}\,\mathrm{sec}^{-1}$) = electron current density potential (dotted-line curve), and n (electrons cm^{-3}) = electron density.

As shown in this figure, the values of $n\nu$ are large only in the range near the central wire, and this range gives the radial extent of the glow, in almost coincidence with the author's observation. For reference, the electron density n is also shown by a broken-line curve, which is obtained by using the function ψ and the value of the diffusion coefficient D.

The author wishes to express his sincere thanks to Professor I. Takahashi for his kind guidance and encouragement throughout this work. Also, the author is indebted to Mr. H. Kubo for his assistance in carrying out the experiments.

References

1) K. Mitani: J. Phys. Soc. Japan **7** (1952) 637.
2) K. Mitani: J. Phys. Soc. Japan **7** (1952) 642.
3) W. P. Allis, S. C. Brown and E. Everhart: Phys. Rev. **84** (1951) 519.
4) M. A. Herlin and S. C. Brown: Phys. Rev. **74** (1948) 291.
5) S. C. Brown: Proc. I.R.E. **39** (1951) 1493.
6) M. A. Herlin and S. C. Brown: Phys. Rev. **74** (1948) 910.
7) K. Mitani: J. Phys. Soc. Japan **7** (1952) 634.

J. PHYS. SOC. JAPAN **9** (1954) 300~301

Electrical Resistivity of Polycrystalline Selenium at Higher Fields

Masahiro KUWAGATA, Eizo OTSUKA
and Masao TOMURA

Institute of Polytechnics, Osaka City University, Osaka

(Received February 5, 1954)

Among numerous semiconductors and insulators, whose resistivities under higher electric fields do not obey the Ohm's law, metallic selenium shows an interesting characteristic under such fields.[1] To interprete this phenomenon, Davydov[2] has suggested the space charge effect at the barrier layers in the polycrystal.

In our work, polycrystal specimens were annealed at 180°C~190°C during 5 to 30 minutes; and their resistivities were measured under strong elecctric fields up to 22 KV/cm., with the top flatted pulse voltage of 7 μsec. duration and 60 c.p.s., avoiding the Joule's heat. A typical result is shown in Fig. 1. The relation between resistivity and and field is seen to fit the Schottky plot at various temperatures and this shows that the circumstance is quite different in nature from the predictions of Davydov's theory. The Schottky effect, which occurs when the charge carriers jump over the grain boundary barriers, seems to be responsible for the non-Ohmic behavior of resistivity of selenium.

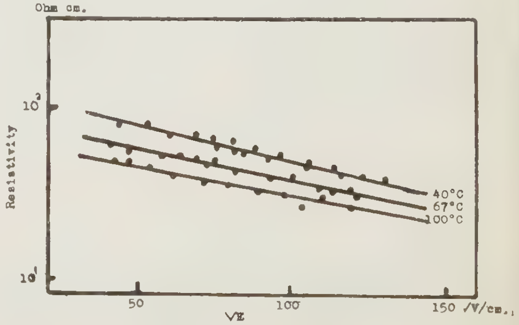

Fig. 1. The Schottky plot of resistivity *vs.* electric field strength. The resistivity in logarithmic scale linearly depends on the square root of the field strength E. The above result is obtained for a specimen which was annealed nearly 10 minutes at 180°C.

Since, according to the Schottky's formula, the slope of the line in the figure gives $-e^{3/2}/\kappa\surd kT$, we can obtain the dielectric constant κ. The results that κ were obtained as about 0.6 which is too small may mean the localization of the applied voltage over the barriers layers which exist at the crystal grain boundaries. Then E is not the applied field, but the one pressed over the thin barriers. (See Fig. 2.)

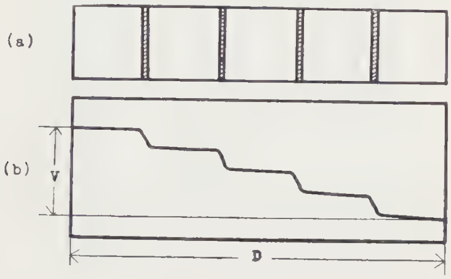

Fig. 2. (l) A supposed schematical one-dimensional structure and (b) the potential distribution within the polycrystalline selenium. The shaded parts in (a) are the grain boundary barriers where high electric fields exist, while the unshaded portions correspond to the crystal grains. In (b) V is the applied voltage and D is the sample thickness; the step line shows how the localization of the field occurs.

Next, the frequency characteristic of resistance was measured up to 20 MC. The result is shown in Fig. 3. The resistance decreases with increasing frequency, showing the existence of the barriers. Thus the apparent resistance of polycrystalline selenium is almost governed by the grain boundaries. These results just coincide with the Schottky effect mentioned above.

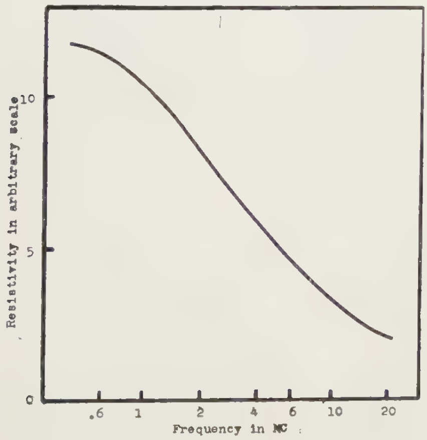

Fig. 3. Frequency response of the resistance of polycrystalline selenium.

By repeating heat treatment of a specimen, the slope of $\ln\rho$ *vs.* $\surd E$ line becomes steeper, indicating the decrease of the barrier thicknesses. On the other hand the activation energy, which was obtained from $1/T$ *vs.* non-field resistivity plot, was reduced from *ca* 0.40 eV. to *ca* 0.15 eV. in the course of repeated annealings, resulting the decrease of resistance.

Similar measurements were performed on the specimens containing less than 0.05% iodine. (Fig. 4.) In this case resistivities were reduced by the factor of 10^2 to 10^3 for each case of the annealing stages compared to the pure specimens. The Schottky effects were again observed, though less remarkable. This time the activation energy ranged from *ca* 0.30 eV. to *ca* 0.05 eV. in the course of annealings. These smaller values of the activation energy compared to those of the pure polycrystals would only be responsible for the reduction of resistivity, and are as well consistent with the less remarkable Schottky effect, which signifies the lower resistances at the grain boundary barriers.

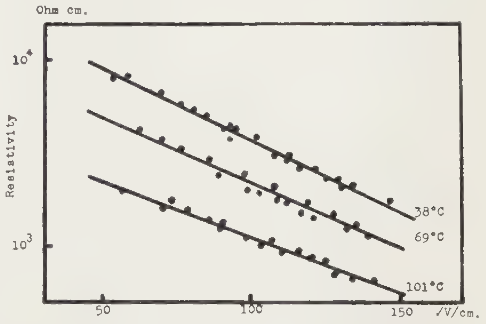

Fig. 4. The Schottky plot for the iodine-containing selenium. The above result was obtained for a specimen which underwent nearly the same degree of heat treatment as one quoted Fig. 1.

Plessner³⁾ measured the Hall constant of pure and iodine-containing polycrystalline selenium and observed that the carrier concentration was scarcely affected by the degree of heat treatment or by the amount of iodine concentration. From these results, we can suppose that the activation energy of the polycrystalline selenium is not related to the energy gap between the acceptor level and the filled band, but to the heights of the grain boundary barriers. Then, the process of annealing or adding iodine seems not to change the carrier concentration, but to change the above barrier heights.

References

1) A. V. Joffe and A. F. Joffe: Journ. Phys. **2** (1940) 283.
2) B. Davydov: Journ. Phys. **4** (1941) 335.
3) K. W. Plessner: Proc. Phys. Soc. (London), **B64** (1951) 681.

J. Phys. Soc. Japan **9** (1954) 302

An X-Ray Study of Thin evaporated Films of Metals

By Mitsuo Miwa and Shoichi Annaka
Physics Department,
Tokyo University of Education

(Received January 13, 1954)

The structure of thin evaporated films has been a favorite subject of electron diffraction study for a long time.1) Many interesting patterns with anomalous spots, streaks and haloes have been found to appear in metal films evaporated onto cleavage substrates. But owing to the very strong interaction between electrons and films it is not easy to investigate the anomalous patterns quantitative by electron diffraction. More quantitative information on the structure of thin films might be obtained by using X-rays. No such investigation seems to have been done owing to the weak interaction between X-rays and films.

The writers recently obtained with reasonable time exposures X-ray photographs of thin oriented films of silver, gold and aluminium which were evaporated onto heated rock-salt cleavage faces in vacuo. The evaporated films were removed from substrates by dipping them into water and streched across small holes perforated in thin mica plates and then subjected to Cu Kα-radiation monochromatised by a nickel filter.

1) Silver and gold. Strong normal spots of thin films of these metals (about 500Å thick) were obtained when Bragg conditions were satisfied for Cu *K*α-radiation. Twin spots well known in electron diffraction patterns were also observed, whose intensities, however, were about 1/5 or less of those of the normal spots. Besides these, very faint streaks were observed which run from the normal and twin spots to the nearest twin and normal spots respectively (Fig. 1). These patterns were explained by stacking faults (repeated twinning) on {111} planes.2)

Fig. 1. X-ray transmission photograph of thin silver film. The X-ray beam is parallel to the (100) plane and the angle between beam and (001) plane (film surface) is 68.7°.

2) Aluminium. Strong normal spots were observed when films were about 1000 Å thick. No anomalous patterns were observed in this case.

A further study is going on. The details of the results will be reported elsewhere.

The writers wish to express their sincere thanks to Mr. Keiei Kudo for his preparation of single crystals of rocksalt, and also to the Ministry of Education for financial aid.

References

1) O. Goche and H. Wilman: Proc. Phys. Soc. **51** (1939) 625.
L. Brú and M. K. Gharpurey: Proc. Phys. Soc. **A 64** (1951) 283.
H. Gottsche: Z. Phys. **134** (1953) 504.
2) M. S. Patterson: J. App. Phys. **23** (1952) 805.

Errata

On the Change of Density of Copper Single Crystals by Cold Working

By Sadabumi ISSIKI and Hiroshi KIMURA

J. PHYS. SOC. JAPAN **9** (1954) 139～140

Page		line			
140	left	−5	0.00011	should be read	±0.00011
			0.00018	〃	±0.00018
			0.00110	〃	±0.00110
		−2	0.00008	〃	±0.00008
			0.00038	〃	±0.00038
			0.00016	〃	±0.00016

Numerical Solution of the Navier-Stokes Equations for the Flow around a Circular Cylinder at Reynolds Number 40

By Mitutosi KAWAGUTI

J. PHYS. SOC. JAPAN **8** (1953) 747～757

Galelkin (P. 747, right column, line 1 from bottom; P. 748, left column, line 2; P. 750, right column, line 12 from bottom) should be read as Galerkin.

Following figure should be substituted for Fig. 8 (P. 753).

$R=40$ (P. 754, right column, line 25) should be read as $R>40$.

In Fig. 11 (P. 754), the abscissa R should be added.

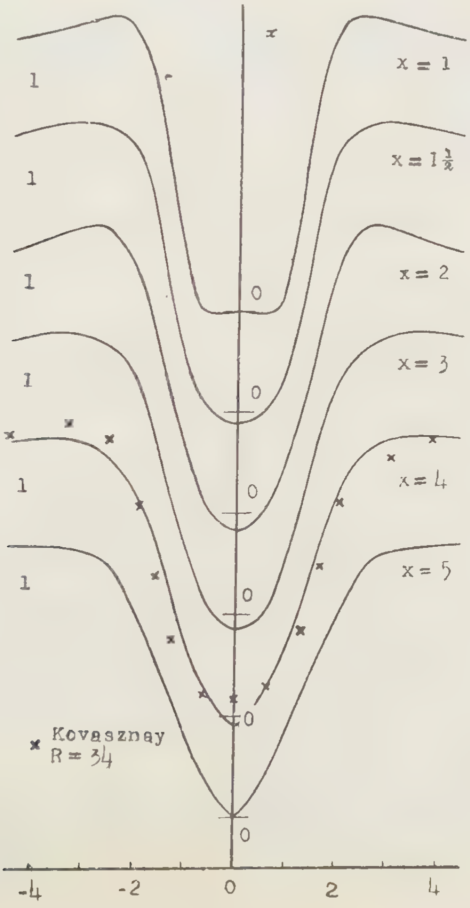

PROGRESS OF THEORETICAL PHYSICS

Published by
The Yukawa Hall
with the cooperation of
The Physical Society of Japan

Progress of Theoretical Physics Vol. 10, No. 3, 1953

Correction to the Beta-decay Nuclear Matrix Elements..Masami YAMADA....245
Theoretical Reinvestigation of the Beta-spectrum of RaE ....Masami YAMADA....252
On the Nuclear Saturation.........Syûzô OGAWA and Toshio MARUMORI....265
On the Interaction of Electrons with Lattice Vibration.Hideo KANAZAWA....275
On the Elastic Frequency Distribution Function of Simple Crystals ....Sigeru HUZINAGA and Tasuke HASINO....279
Spin-spin and Spin-other-orbit Interactions.................Hisashi Horie....296
Effect of Nucleon Excited State on Magnetic Moment Anomaly ....Tetuo HAMADA....309
Nuclear Forces in Pseudoscalar Meson Theory...............Iwao SATO....323

Letters to the Editor:

New Proposal on the Mass Spectrum of Elementary Particles ....S. YOSHIKAWA and T. HASEBE....359
On the Interaction Forms of the Beta-decay......Y. TANIKAWA....361
On the Electronic Structure of LiH Atomic Orbital Approach with Configurational Interaction..K. TOMITA and K. FUKUI....362
Interference Terms of Beta-ray Angular Correlations..M. MORITA....363
Note on Coexistence of Tensor and Axialvector Interactions in Beta-decay..........M. MORITA....364
On the Gauge Invariancy and the Structure of Elementary Particle..........Y. TAKAHASHI....366
On the State of Solid Hydrogen.....K. TOMITA and I. MANNARI....367
Errata..........369

Progress of Theoretical Physics Vol. 10, No. 4, 1953

On the Heisenberg Treatment of the Field Variables..Ichie WATANABE....371
A Remark on the Strong Coupling Approximation in Meson-nucleon Scattering....................Ziro MAKI and Masatomo SATO....386
Pion-nucleon Scattering and Nucleon Isobar ....Akira KANAZAWA and Masao SUGAWARA....399
Recoil Effects in the Strong Coupling Theory ....Toshiyuki TOYODA....415
On the Many-body Problem in the Intermediate Coupling Theory, I ....Takao TATI....421
A Generalization of Special Lorentz Transformation in de Sitter Space-time..........Hyôitirô TAKENO....431
On the Wave Theory of Light in General Relativity, I — *Path of Light* —..........Yoshio UENO....442
On the Spin of the μ-meson..........Kenzo IWATA....451
On the Baryon-meson-photon System..........A. PAIS....457

Letters to the Editor:

On the Universal Fermi Interaction ....O. HARA, T. MARUMORI, Y. OHNUKI and H. SHIMODAIRA....470
On the Radiative Interaction of Phonon Field with Electron ....H. KANAZAWA....471

Note on the Light Absorption in the Insulating Crystals .... T. Ohta....472
On the Atom-exciton Interaction........ T. Ohta....474
On the Radiation Damping and the Decay of an Excited State .... M. Namiki and N. Mugibayashi....474
A Test of Charge Independence by the Nuclear Reactions .... Y. Fujimoto and Y. Yamaguchi....476
Effect of Electromagnetic Radiation on Lamb Shift....I. Singh....476
Note on the Meson Theory of Nuclear Force .... S. Fujii, J. Iwadare, S. Otsuki, M. Taketani, S. Tani and W. Watari....478
Effect of Collective Motion on Beta Decay........ S. Suekane....480

Progress of Theoretical Physics Vol. 10, No. 5, 1953

On a Five Dimensional Representation of the Electromagnetic and Electron Field Equation in a Curved Space-time........ Mineo Ikeda....483
On the Fundamental Equation for the Nucleon...... Takeo Okabayashi....499
Note on a j-j Coupling Shell Model........ Minoru Umezawa....505
Static Spherically Symmetric Space-times in General Relativity .... Hyôitirô Takeno....509
Upper Bound of the Pseudoscalar Coupling Constant in Beta-decay .... Jun-ichi Fujita and Masami Yamada....518
Cerenkov Radiation and Supersonic Flows........ Tosiya Taniuti....525
Hamiltonian Formalism in Non-local Field Theories....Chusiro Hayashi....533
Many-body Problem in Quantum Field Theory...... Kazuhiko Nishijima....549

Letters to the Editor:

On the Inverse Power Expansion of the $S_{\rm vac}\,[\eta^*, \eta, J]$ and the Green-Functions........ S. Hori....575
The Second Virial Coefficient at Very Low Temperatures .... K. Hiroike....575
The Photon Self-energy Problem and Microscopic Space-time Structure........ T. Kimura....577
Analytical Representation of General Spin........ T. Yamamoto....579
On the Magnetic Structure of Manganese Antimonide .... K. Komatu....579
Charge Independence for V-particles .... T. Nakano and K. Nishijima....581
The Distribution Function of Degenerating Ensemble — *An Addition to "Generalization of Statistics"* —....... T. Okayama....583
An Interpretation of Asymmetric Fission .... T. Sasakawa and T. Sawada....585

Price $ 1.00 per copy
$ 12.00 per year (postage inclusive)
Annual dues for foreign members (individual subscribers)
$ 9.00 (postage inclusive)
" for foreign members of the Physical Society of Japan
$ 7.50 (postage inclusive)

Application for members, subscriptions and orders for back mumbers should be sent, directly or through book-dealers, to

The Publication Office
in
Yukawa Hall, Kyoto University, Kyoto, Japan

K. Honda

(1870~1954)

OBITUARY NOTICE OF PROFESSOR KŌTARO HONDA

Kōtaro Honda was born at Yasaku-Machi, Aichi Prefecture, on February 23, 1870. His father, Hyozaburo Honda, who was a land owner in that district and was engaged mainly in the reclamation of rice field, died when Kōtaro was ten years old. Kōtaro, the third son, was educated in a primary school of neighbouring village under the care of Kanzaburō, the eldest brother, and after graduation he stayed at home helping the firm work of his brother. In these days, without permission of his brother, he tried to go to Tokyo for the purpose of studying at that capital city, where his second elder brother, Asajiro, was studying in a higher middle school. After several trials, the permission was finally given to him to study at Tokyo, when Kotaro was eighteen years old.

At Tokyo, Kōtaro entered the preparatory course of the First Higher Middle School, and studied, among other things, mathematics, physics, chemistry and biology. At this period, he set his heart on a scientific career, and his interest was drawn to physics. In July 1894, he was matriculated in the Department of Physics, the College of Science, Tokyo Imperial University, and studied physics under Professors K. Yamakawa, A. Tanakadate and H. Nagaoka. In the last years of his university period, he commenced an investigation on the magnetostriction of ferromagnetic substances under Professor Nagaoka, and the results thus obtained was published in the Journal of the College of Science, Tokyo Imperial University, Vol. 9, (1895–1898), p. 355–391. Researches on magnetism in Japan had been started by J. A. Ewing, who spent five years from 1878 to 1883 in the Department of Physics as an invited professor to Tokyo Imperial University. It is well known that the hysteresis phenomenon in ferromagnetic substances was first discoverd by him during this period. After he left Japan, Nagaoka continued the researches on ferromagnetism, and the baton of Professor Ewing's is research was thus relayed to Honda through Nagaoka.

Graduated from the University in 1897, he took the postgraduate course and continued the research work on ferromagnetism under the guidance of Professor Nagaoka. In this year he married Kaneko, the younger sister of Vicount Masumichi Tani and the foster daughter of Shizuro Shibagaki. In 1901, he was appointed to a lecturer, and in 1903, the title of Rigakuhakushi was conferred on him. During this period, he published about twenty papers, dealing mainly with the properties of ferromagnetic substances, in the Journal of the College of

Science, Philosophical Magazine and Annalen der Physik. Rather remarkable is the fact that two papers were published on the subjects of geophysical field in collaboration with T. Terada, one on the geyser in Atami Hot Spring and the other on the secondary undulations of oceanic tide.

Early in 1907, he was recommended as a candidate for a professor of Tohoku Imperial University, which was then under planning to be founded at Sendai, and was sent abroad by the Government. First he visited Göttingen and studied under Professor Voigt on the magneto-optical effect of crystals, and then turned to Professor Tammann, under whose guidance he got the fundamental knowledge of metallography. In the last period of his sojourn in Germany, he transferred to the private laboratory of H. du Bois in Berlin and carried out a very elaborate measurement on the magnetic susceptibilities of various elements, 43 in number, at temperatures ranging from room temperature up to 1000°C. These data, thus obtained, together with the measurements made afterwards by H. Owen, showed their close relation with Mendeleff's periodic system of elements.

In February 1911, he came back to Japan and was appointed to the professor of Tohoku Imperial University. His investigations were directed mainly towards the magnetic properties of iron, steel and their alloys. As the most powerful weapon for attacking these problems, he used the method of magnetic analysis, in which a magnetometer was utilized to measure the intensity of magnetisation at various temperatures. He was deemed as one of the most distinguished pioneers in the world, who introduced the technics of experimental physics as a powerful tool for solving the metallurgical problems.

In 1914, because of the outbreak of the world war I, Japan confronted with a serious difficulty in obtaining iron and steel by importation from foreign countries. Considering the urgency for Japan to manufacture by herself the necessary metallic materials for industry, he planned to establish a research institute for iron and steel in order to carry out basic researches on these materials. With the financial support from Kichizaemon Sumitomo, he succeeded in establishing a governmental research institute attached to Tohoku Imperial University in 1916. Although this institute, thus established, was very small in scale at its initial stage, it made a remarkably rapid expansion. In May 1919, the name of this institute was changed to the Research Institute of Iron and Steel, and in August 1922, to the present well-known name: the Research Institute of Iron, Steel and Other Metals. From the very beginning of this institute, he was in charge of the Presidency up to May 1933, and conducted numerous investigations in the field of metals in collaboration with many able research workers, who were fully trained by himself.

During his life time, he published 188 papers and 8 books (excluding text-books). His research works can be devided into three groups; i.e. magnetism, physical metallurgy and geophysics. In the field of magnetism, 73 papers were published, among which the most outstanding would be those on the discovery of K. S. Magnet in 1917 (which was named after his financial supporter K. Sumitomo) and New K. S. Magnet in 1934, both were the best magnets throughout the world at the time of their discovery. Investigations on the anisotropy of ferromagnetic crystals, published during the period 1926 to 1930, gave important data for the development of present domain theory of ferromagnetic materials.

In the field of physical metallurgy, he invented and improved many experimental technics concerning magnetic analysis, thermo balance, dilatometer, electric resistance change, X-ray analysis, etc. In the study of the transformation of iron and steel, he first confirmed that the ferromagnetic transformation is accompanied only with energy change, but not with lattice transition. As to the A_4 transformation, he first reached the conclusion from the paramagnetic and dilatometric data, that this is inverse transition of A_3. His interest extended to the field of light alloys, where in collaboration with his students he set up a new theory concerning the mechanism of age hardning of quenched dulalmin.

He invented many usefully alloys, including the powerful permanent magnets, high permeable alloys, magneto-strictive alloys, etc. For his remarkable works, the Imperial Academy of Japan awarded him a prize in 1913, and the British Institute of Iron and Steel presented the Bessemer Medal in 1922. In 1931, the Franklin Institute awarded him Eliot Cresson Medal, and in 1933 he was elected to an Honorary Doctor of Science of Göttingen University. In recognition of his outstanding contributions to science, a Bunkakunsho (Order of Cultural Merit) was conferred on him in April 1937, when this order system was first established.

He gave much time not only to the scientific researches, but also to the bridging between science and its application. It was his great regret that the industry in Japan had no direct connection with the foundamental researches completed in universities or research institutes. As a result of his strong efforts towards paving a road between them, a new department providing large scale facilities was added to his institute, which, at present, is playing an important role along this line. He invited also to his institute several artisans in Kashiwazaki District, who were engaged in the manufacture of traditional Japanese tools, and gave them thoughtful training for quenching and tempering of carbon steels.

In the period from May 1931 to May 1940, he was the President of Tohoku Imperial University. During his tenure of office he showed very excellent ability for university administration, which was deeply appreciated by all the university staffs.

In May 1940, he retired from the President of the University, but because of the grave responsibility, which had fallen upon the Institute during the war time, he was in charge of the Acting President of the Institute from March 1944 to August 1947. After retiring from this post, he moved to Tokyo and enjoyed a quiet life with his wife. Even in these days, he was almost absorbed in accomplishing an investigation concerning the effect of hydrostatic pressure on the transformation temperature of metals. In April 1949, he was elected to the President of Tokyo College of Science. In 1950, his wife Kaneko died of an apopletic stroke. After almost one year of her death, a severe illness (cerebral softning) made him much weakened, which grew worse as the year progressed. On February 12, 1954, he died at the hospital of Tokyo University of a hypostatic pneumonia, which was added to cerebral softning and arachmoid homorrhage.

A funeral ceremony was held in Tsukiji-Honganji without any religious service on February 17 under the attendance of almost all the researchers of our country in the field of metals. In recognition of the most distinguished scientific contributions, which had never been made by a Japanese before him, the House of Councillors expressed his deep sorrow for the loss of this great scholar, and the Government conferred on him a Kyokujitsu Daijusho (Grand Order of Rising Sun), the highest order in this country.

Kōtaro Honda had two daughters, of which the elder married Ikusaku Amamiya, now the Emeritus Professor of Tokyo University, and the younger married Iwao Moriwake, the President of Steel Pipe Manufacturing Company. His grandson Ryukichi Amamiya became his adopted son, and is now studying on magnetism in the postgraduate course of Tokyo University.

——(*Seiji Kaya*)——

JOURNAL OF THE PHYSICAL SOCIETY OF JAPAN Vol. 9, No. 3, MAY—JUNE, 1954

Theory of Color Centers. III.
Continuum Models of F_2^+- and F_2-Centers*)

By Takeo NAGAMIYA and Noriko TATSUUMA

Department of Physics, Osaka University

(Received January 8, 1954)

The F_2^+- and F_2-centers, the molecule ion and molecule formed from two F-centers, are treated by the variational method developed by R. Kubo. The crystal is supposed to be a continuous medium with dielectric constants κ (static) and κ_0 (optical) and the two negative ion vacancies are considered as point charges. The polarization arising from ionic displacements is supposed to give a fixed field for the electronic motion. The electronic levels are calculated and compared with those obtained by Kubo for the F-center. A rough estimate of the dissociation energies are also given.

§ 1. Introduction

In recent years a number of new absorption bands have been found in colored alkali halides[1]. The majority of them are so far unidentified, although some of them, for instance the M-band, have been interpreted as corresponding to certain complex centers. The M-band, found by Molnar[2] at the red end of the visible spectrum, was investigated by Ueta[3] with an ingenious method of using polarized light and it was shown that his results could be interpreted in terms of a center which consists of two vacancies of negative ions and a vacancy of a positive ion, stacked together at right angles, and with an electron trapped there. This model was suggested earlier by Seitz[4]. Seitz also suggested that the R-bands, which are observed under certain conditions in a red region between the F-band and the M-band, might correspond to F_2 and F_2^+ centers, namely, the center composed of two F-centers stacked together and the center which one obtains by removing one of the two electrons from it. On the other hand, Uchida et. al.[5] interpreted the bands they found in the ultraviolet region in terms of these centers, although their bands might possibly arise from impurities. Under these circumstances it was felt to be of interest to carry out theoretical investigations on various complex centers, although we admit that it is very difficult to get accurate results for their absorption spectra.

In the present paper we shall attempt to treat the F_2^+ and F_2 centers with the approximation of a continuum model employed by Kubo[6] in his investigation of F and F′ centers. The crystal is supposed to be a continuous medium with a static dielectric constant κ and an optical dielectric constant κ_0. The two vacancies of negative ions are supposed to be two positive point charges. (Kubo treats also the case where the dielectric medium has a spherical cavity with a uniformly distributed surface charge.) This is of course too crude an approximation to afford accurate results for the absorption spectra due to these centers, but one can hope to get their positions relative to the F-band by comparing the results with Kubo's result for the F-center. In subsequent papers we shall make use of various other approximations.

§ 2. General Formulation

Before proceeding to the calculation, it is convenient to quote Kubo's method in a form simpler and more suitable to our application. Let a positive space charge of density ρ_+ and a negative space charge of density ρ_- be introduced into the dielectric medium, so that the total space charge is $\rho_+ + \rho_- = \rho$.

Then the space charge induced by dielectric polarization is $\rho/\kappa - \rho$. If the ions in the crystal were not displaced at all, so that only optical polarization could take place, the induced charge would be $\rho/\kappa_0 - \rho$. The difference between these is the polarization charge due to the displacements of the ions, reduced to $1/\kappa_0$ times its original value, ρ_i, owing to an accompanying optical polarization*. Thus

---

* Previous publication in Japanese: Busseiron Kenkyu **39** (1951) 68.

$$\left(\frac{\rho}{\kappa}-\rho\right)-\left(\frac{\rho}{\kappa_0}-\rho\right)=\frac{\rho_i}{\kappa_0}, \quad \rho_i=-\left(1-\frac{\kappa_0}{\kappa}\right)\rho . \tag{1}$$

We shall denote the electrostatic potential due to ρ_+, ρ_-, ρ_i, all imbedded in the dielectric medium with dielectric constant κ_0, as φ_+, φ_-, φ_i, respectively. Since ρ_i has been induced by $\rho_+ + \rho_-$, the interaction between these two is

$$\frac{1}{2}\int \varphi_i(\rho_+ + \rho_-)d\tau \quad \text{or} \quad \frac{1}{2}\int \rho_i(\varphi_+ + \varphi_-)d\tau . \tag{2}$$

The interaction energy between ρ_+ and ρ_- is obviously

$$\int \varphi_+\rho_- d\tau \qquad \text{or} \qquad \int \rho_+\varphi_- d\tau . \tag{3}$$

We shall specify ρ_- by assuming a wave function for the electron, ψ, as follows:

$$\rho_- = -e|\psi|^2. \tag{4}$$

At the same time, we shall assume ρ_+ as representing two point charges separated by a distance $2c$, that is, we assume that it behaves as a δ-function at these two points. The energy of the whole system, including the kinetic energy of the electron, is

$$E=-\frac{\hbar^2}{2m}\int \psi^* \Delta \psi \, d\tau + \frac{1}{2}\int \rho_i(\varphi_+ + \varphi_-)d\tau + \int \varphi_+\rho_- d\tau . \tag{5}$$

The final step in Kubo's method is to determine ψ from the condition of the minimum of the energy (5).

The preceding specialization applies to F_2^+. In the case of F_2, we have to add the interaction between the two electrons. Writing the wave function of the two-electron system as $\Psi(\boldsymbol{r}_1, \boldsymbol{r}_2)$, we have

$$\rho_- = -e\int |\Psi(\boldsymbol{r}, \boldsymbol{r}_2)|^2 d\tau_2 - e\int |\Psi(\boldsymbol{r}_1, \boldsymbol{r})|^2 d\tau_1 . \tag{6}$$

The total energy is

$$E=-\frac{\hbar^2}{2m}\iint \Psi^*(\boldsymbol{r}_1, \boldsymbol{r}_2)(\Delta_1+\Delta_2)\Psi(\boldsymbol{r}_1, \boldsymbol{r}_2)d\tau_1 d\tau_2 + \frac{1}{2}\int \rho_i(\varphi_+ + \varphi_-)d\tau + \int \varphi_+\rho_- d\tau + \frac{e^2}{\kappa_0}\iint \frac{1}{r_{12}}|\Psi(\boldsymbol{r}_1, \boldsymbol{r}_2)|^2 d\tau_1 d\tau_2 . \tag{7}$$

Ψ is determined by minimizing this expression.

It is of course difficult to solve the above problem exactly. We shall therefore try to find approximate solutions by assuming simple forms for the wave functions and determining the values of the parameters contained therein by the minimum principle.

§ 3. The Energy Levels of F_2^+

We shall assume the following simplest wave functions for the three electronic states which we are most interested in:

$1s\sigma$: $\psi = Ae^{-\alpha\xi/2}$
$2p\sigma$: $\psi = A\eta e^{-\alpha\xi/2}$
$2p\pi$: $\psi = A\sqrt{(\xi^2-1)(1-\eta^2)}\, e^{-\alpha\xi/2+i\varphi}$

where ξ, η are elliptic coordinates and φ is the azimuthal angle; A is the normalization constant and α is a parameter. In terms of the distance from the two centers, r_1 and r_2, the elliptic coordinates are expressed as

$$\xi=(1/2c)(r_1+r_2), \qquad \eta=(1/2c)(r_1-r_2).$$

It can be seen that

$$\varphi_+ = \frac{e^2}{\kappa_0}\left(\frac{1}{r_1}+\frac{1}{r_2}\right)=\frac{2e\xi}{\kappa_0 c(\xi^2-\eta^2)},$$

$$\varphi_- = -\frac{e}{\kappa_0}\int \frac{|\psi(\boldsymbol{r}')|^2}{|\boldsymbol{r}-\boldsymbol{r}'|}d\tau' .$$

In the second of these, $|\boldsymbol{r}-\boldsymbol{r}'|^{-1}$ may be expanded by the well-known Neumann's theorem into Legendre functions of the arguments ξ, ξ' and η, η' and trigonometrical functions of φ, φ'.

As an example, we take $2c=4.44$Å, $\kappa=4.68$, $\kappa_0=2.13$ which correspond to KCl. The results obtained are as follows:

$1s\sigma$: $\alpha=3.0$ $E=-1.96$ eV.
$2p\sigma$: $\alpha=2.0$ $E=-1.32$ eV.
$2p\pi$: $\alpha=2.0$ $E=-1.26$ eV.

Here α is expressed in units of the reciprocal Bohr radius of the hydrogen atom. That part of the interaction energy between ρ_+ and ρ_i which existed before introducing the elecron

---

* Strictly speaking, the optical part contained in $\rho/\kappa-\rho$ is not necessarily equal to $\rho/\kappa_0-\rho$, that is, the optical polarization in the case where ionic displacements are involved is not necessarily equal to that which one would have if they were not involved. We are therefore assuming that these two kinds of polarizations are taking place independently of each other. This assumption corresponds to taking $\gamma=0$ in *Mott and Gurney: Electronic Processes in Ionic Crystals* (1940), as is frequently shown there to be fairly valid.

(and which is actually infinite) was excluded from E.

The values of the energy obtained above represent the thermal equilibrium energies of the corresponding states. For the absorption of a light quantum by the center at its ground state, we have to take the energies of the excited states with the same value of ρ_i as that for the ground state. In this case we obtain the following results (we again obtain $\alpha=2$, though not very exactly):

$2p\sigma$: $\alpha=2$ $E=-1.08$ eV.,
therefore $1s\sigma \rightarrow 2p\sigma$: 0.88 eV.
$2p\pi$: $\alpha=2$ $E=-1.89$ eV.,
therefore $1s\sigma \rightarrow 2p\pi$: 1.09 eV.

We shall now compare these results with Kubo's result for the F-center. He assumed $\psi=Ae^{-\alpha r/2}$ for the $1s$-state of the F-center and $\psi=Ae^{-\alpha r/2}\cos\theta$ for the $2p$-state and obtained the result

$1s$: $E=-1.16$ eV.
$2p$: $E=-0.06$ eV. (optical),
therefore $1s\rightarrow 2p$: 1.10 eV.

Therefore, if it could be assumed that the errors involved in Kubo's calculation and in the present work are about the same, the absorption bands due to the $F_2{}^+$-center should come out on the red side of the F-band and we should have two bands for the former. These two bands should in principle be experimentally distinguishable, by observing at low temperatures or by using polarized light and measuring the dependency of the absorption intensity upon the relative orientation between the crystal and the plane of polarization. In actual crystals, the $F_2{}^+$-center does not possess the axial symmetry so that the state $2p\pi$ must split into two, giving rise to another absorption band.

§4. Energy Levels of F_2

We assume for the wave functions of the most interesting singlet states the following simplest forms:

$${}^1\Sigma_g(1s\sigma) \quad : \quad \Psi=Ae^{-\alpha\xi_1/2-\alpha\xi_2/2}$$

$${}^1\Sigma_u 1s\sigma 2p\sigma: \quad \Psi=A\{\eta_1 e^{-\beta\xi_1/2-\alpha\xi_2/2} + \eta_2 e^{-\beta\xi_2/2-\alpha\xi_1/2}\}$$

${}^1\Pi 1s\sigma 2p\pi$:

$$\Psi=A\{\sqrt{(\xi_1{}^2-1)(1-\eta_1{}^2)}\, e^{-\beta\xi_1/2-\alpha\xi_2/2+i\varphi_1} + \sqrt{(\xi_2{}^2-1)(1-\eta_2{}^2)}\, e^{-\beta\xi_2/2-\alpha\xi_1/2+i\varphi_2}\}\,.$$

The results are shown in Fig. 1 together with the results for $F_2{}^+$ and a part of Kubo's calculation for F. In particular, the optical transitions are

$(1s\sigma)^2 \rightarrow 1s\sigma 2p\sigma$: 1.07 eV.
$(1s\sigma)^2 \rightarrow 1s\sigma 2p\pi$: 1.63 eV.

The first of these comes out near the F-band on the side of longer wavelengths, while the second appears in the region of shorter wavelengths, if the position of the F-band could be represented by Kubo's calculation.

§5. The Dissociation Energies of $F_2{}^+$ and F_2

An $F_2{}^+$-center can be dissociated into one F-center and one negative ion vacancy within the crystal, and an F_2-center into two F-centers. The dissociation energy of the former can be calculated by adding the repulsive energy between the two point charges, namely $e^2/2c\kappa_0$, to E and subtracting from it the energy of the ground state of the F-center, which is, according to Kubo's result, equal to -1.16 eV. For the dissociation energy of the F_2-center, twice the latter is to be subtracted. Changing the sign in the final

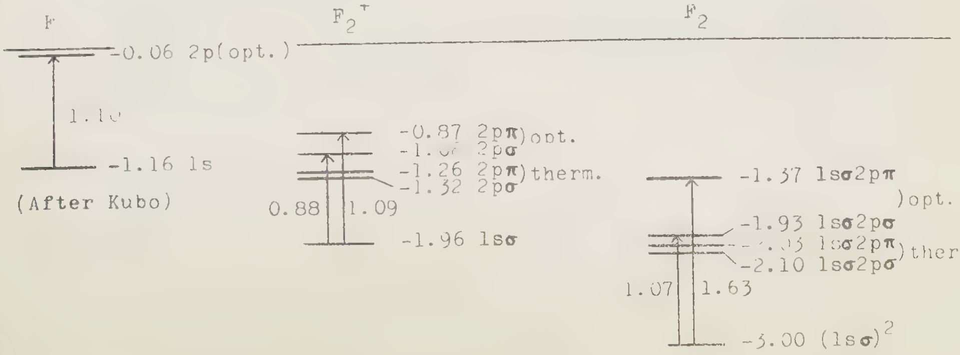

Fig. 1. The energy levels of F, $F_2{}^+$ and F_2 centers (eV.)

results, we have, as the dissociation energies of these centers,

$$F_2^+:\ 0.11\ \text{eV.},\qquad F_2:\ -0.01\ \text{eV.}$$

Therefore the F_2^+ is thermally stable and F_2 is unstable, although we cannot think that these results are very trustworthy.

Now, let N, n_1^+, n_1, n_2^+, n_2 be the numbers of negative ions, negative ion vacancies, F-centers, F_2^+-centers, F_2-centers, respectively, in the crystal. From the mass action law, it follows that

$$\frac{n_2^+}{N}=\frac{n_1^+}{N}\frac{n_1}{N}e^{w^+/kT},\qquad \frac{n_2}{N}=\left(\frac{n_1}{N}\right)^2 e^{w/kT},$$

where w^+ and w are the dissociation energies discussed above. In experiments on discoloring crystals in the neighborhood of 500°C, we usually get F-centers only; other centers are very few. If we take as a typical example $n_1^+/N=n_1/N=10^{-4}$ and $T=500°+273°$ in the formulas above, and n_2/n_1 to be smaller than 10^{-2} for instance, we have w^+ and $w<0.33$ eV., which is consistent with the values given above.

References

1) J. Molnar: Thesis (1940); F. Seitz: Rev. Mod. Phys. **18** (1946) 384; S. Petroff: Zeits. f. Phys. **127** (1950) 443; E. Burstein and J. J. Oberly: Phys. Rev. **76** (1949) 1254; A. B. Scott and L. P. Bupp: Phys. Rev. **79** (1950) 341; A. B. Scott, H. J. Hrostowski and L. P. Bupp: Phys. Rev. **79** (1950) 346; E. E. Schneider: "Fundamental Mechanisms of Photographic Sensitivity" (Edited by Mitchell, 1951), p. 13; etc. and many other works on V-centers.

2) J. Molnar: l.c., described in Seitz, l. c.

3) M. Ueta: J. Phys. Soc. Japan **7** (1952) 107.

4) F. Seitz: l.c.

5) Y. Uchida et. al.: J. Phys. Soc. Japan **4** (1947) 57; **6** (1951) 107.

6) R. Kubo: J. Phys. Soc. Japan **3** (1948) 254.

JOURNAL OF THE PHYSICAL SOCIETY OF JAPAN Vol. 9, No. 3, MAY—JUNE, 1954

Theory of Color Centers. IV. Energy Levels of Various Complex Centers

By Takeo NAGAMIYA, Tadanobu KOJIMA,
and Hisamoto KONDOH

Department of Physics, Osaka University

(Received January 8, 1954)

Several complex centers consisting of two or more negative and positive ion vacancies with one or two electrons trapped there are treated by an approximate method of taking for the electronic wave function a linear combination of the valence wave functions of the positive ions which surround the vacancies. The resonance integral between two neighboring positive ions is determined in the case of F-center by comparing theory with experiment and then it is used for other centers. Rough estimate of the dissociation energy of each center is also given.

§1. Introduction

The purpose of the present paper is to obtain theoretical information about the absorption bands due to various complex centers in crystals of alkali halides. We shall deal with F_2^+, F_2, M, and those other centers which contain one trapped electron. We use an approximation different from that employed in the preceding paper. Namely, the present calculation consists in taking a linear combination of the valence states of the positive ions which surround the vacancies. The resonance (or exchange) integral, which connects the valence states of a pair of neighbouring positive ions, is determined by comparing theory with experiment for the case of the

F-center and then used for other centers. The coefficients of the linear combination are determined by the principle of minimum energy. The most serious defect of the present calculation may perhaps lie in its rather arbitrary assumption as to the potential energy of the electron (or electrons) due to the vacancies. We assume that, when the electron is spending its time on a certain positive ion, its potential energy due to the vacancies other than that which is next to that positive ion (or other than one of those which are next to it, when there are two or more of them) is given in the form + or $-e^2/\kappa_0 r$, where κ_0 is the optical dielectric constant of the crystal and r is the distance between the center of that vacancy and the center of that positive ion. We shall investigate this point later by considering two extreme cases for the $F_2{}^+$-center, once by dropping κ_0 and then dropping this potential energy entirely. Another simplification in the present calculation is that we assume that all the ions surrounding the vacancies are at their normal lattice sites, or at least displaced, with respect to their mutual distances, in the same way as in the case of F-center. Therefore, the present calculation cannot be considered as giving more than a rough idea of the positions of the absorption spectra.

§ 2. The F-center

We shall begin with the F-center. There are six positive ions next to its missing negative ion. We shall denote the wave function of the lowest valence state of the i-th ion (4s in the case of K^+) as φ_i ($i=1, 2, \cdots, 6$). A stationary state of the electron in F-center may be approximately represented by a linear combination of these wave functions:

$$\varphi=\sum_{i=1}^{6} a_i\varphi_i \,. \qquad (1)$$

The energy of this state, in the approximation of Bloch's tight binding, is

$$\mathcal{E}=\text{const.}\ -\gamma \sum a_j{}^* a_i \,, \qquad (2)$$

$$-\gamma=\int \varphi_j{}^* v \varphi_i d\tau \,, \qquad (3)$$

where i, j represent a pair of nearest neighbors and v is the potential energy of the electron due to the vacancy and other part of the lattice. We neglect the non-orthogonality of the wave functions.

The extrema of (2) correspond to the following three kinds of states:

one 1s: all a_i's are equal to $1/\sqrt{6}$; $\mathcal{E}=-4\gamma$.

three 2p: a_i's of a pair of ions at the opposite sites are equal to $\pm 1/\sqrt{2}$, others are zero ; $\mathcal{E}=0$.

two 3d: four a_i's on one plane are alternatively + and $-1/\sqrt{4}$, others are zero; $\mathcal{E}=+2\gamma$.

We have dropped the const. of (2). The only possible optical transition from 1s in this approximation is therefore 1s→2p, which accounts roughly for the fact that the oscillator strength of the first excitation in the F-center is very near to 1.

In a more refined approximation, one might have to take into account the p and other states of the positive ion and also the valence states of the positive and negative ions other than the first six positive ions. It might be noted that the 4s–4p separation of an isolated K atom is 1.6 eV. which is not very large compared with the value of γ (0.5 eV.) given below. The neglection of the p-state of the positive ion, therefore, introduces another error into our calculation.

The value of 4γ will be put equal to the observed energy quantum for the maximum absorption intensity of the F-band:

NaCl: $4\gamma=h\nu=2.61$ eV.
KCl : $4\gamma=h\nu=2.09$ eV.

We shall make use of this γ in the following calculation.

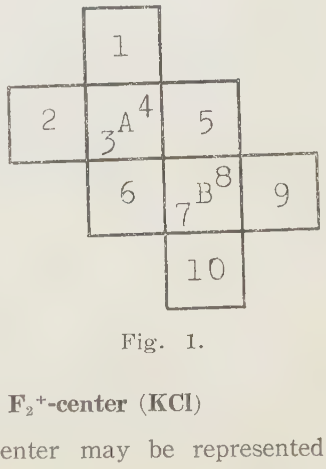

Fig. 1.

§ 3. The $F_2{}^+$-center (KCl)

This center may be represented by two vacancies A and B, ten positive ions surrounding them, and an electron trapped there.

These positive ions will be numbered in the way shown in Fig. 1, the ions 3 and 7 being above the plane of the paper and 4 and 8 below it.

We now take the following approximation as stated in the preceding section:

1. In calculating the diagonal elements of the Hamiltonian with respect to $\psi_1, \psi_2 \cdots, \psi_5$ (or $\psi_6, \psi_7, \cdots, \psi_{10}$), the potential energy of the electron due to the vacancy A (or B, respectively) is assumed to be the same as that of the F-center, and the potential energy due to B (or A) is assumed to be equal to $-e^2/\kappa_0 r_{iB}$ (or that in which B is replaced by A) where κ_0 is the optical dielectric constant of the crystal and r_{ib} (or r_{iA}) is the distance between the center of the positive ion i and the center of the vacancy B (or A).
2. The non-orthogonality of the wave functions ψ_i is neglected.
3. The resonance energy γ is assumed to be the same as in the case of the F-center.

The above assumption of the Coulomb potential screened by optical dielectric constant is a very crude approximation, especially for the ions $i=5$ and 6. Such a potential would be valid for ions far apart from the vacancies, provided all the ions are located at their normal lattice points. For ions which surround the vacancies the screening due to the electronic polarization may be imperfect, so that we have to take for them a smaller value of the optical dielectric constant, an effective value in some sense. At the same time, however, ionic displacements, which are surely present in such a way as to screen the charges of the vacancies, can be expected to compensate to a certain extent the mentioned imperfect screening by electronic polarization. It is obviously very difficult to estimate these effects, and here we want to content ourselves with the crude assumption stated above.

Proceding as before, we get

$$\mathcal{E}=\text{const.}-\sum_{i=1}^{5} a_i^2 \frac{e^2}{\kappa_0 r_{iB}}-\sum_{i=6}^{10} a_i^2 \frac{e^2}{\kappa_0 r_{iB}}-\gamma \sum a_i a_j \,. \tag{4}$$

Taking the extrema of this expression we have Table I and Fig. 2 KCl (const. in $\mathcal{E}$ being omitted). In this table we have used the notation $1s\sigma$, $2p\sigma$, $2p\pi_1$, and $2p\pi_2$ with the following meaning: $1s\sigma$ has no nodal plane, $2p\sigma$ has a nodal plane midway between the two vacancies, $2p\pi_1$ and $2p\pi_2$ have a nodal plane which contains the two vacancies but prependicular to the plane of Fig. 1 for the former and parallel for the latter.

At the beginning of our calculation, we did not use κ_0 in our Coulomb potential. The result for this case is included in Fig. 2. Also the case where this Coulomb potential is entirely omitted is included there for the sake of comparison.

Considering the nature of our approximation, we expect from Fig. 2 that the transition $1s\sigma \rightarrow 2p\sigma$ (which has the largest oscillator strength) is at the position of the F band or a little to the red side of it while the other two transitions appear to the violet side of it.

We made a similar calculation for another type of F_2^+-center shown in Fig. 3, two vacancies being separated by an intermediate positive ion. Using the Coulomb potential with κ_0, the result is as shown in Fig. 3. One absorption band is expected to appear in the near infrared region and the other in the violet side of the F-band.

The energy of dissociation of an F_2^+-center into an F-center and a negative ion vacancy could be calculated from the difference of the electronic energies of the F_2^+-center and F-center by adding the Coulomb repulsion energy between the two vacancies. If we care for the optical dielectric constant for the Culomb energy, we get 0.68 and 0.57 eV. for the dissociation energy of the two types of F_2^+-center considered here. The difference of the energies of polarization of the medium for the negative ion vacancy and for the F_2^+-center will diminish the above values, but it is difficult to estimate its amount.

§ 4. Two Negative and One Positive Ion Vacancies with an Electron Trapped There (KCl)

We shall drop out the positive ion $i=6$ of Fig. 1. The resulting one electron center is the model of the M-center suggested by Seitz[1]. A similar calculation as before was done and the results are shown in Table II and Fig. 4-a. In this figure the results for three other configurations of the vacancies are also given (b, c, d). For the first type (a), the transition $A_1 \rightarrow B_1$ with 1.31 eV. comes close to the observed M-absorption in KCl, namely, 1.45 eV., while the other is close to

Table I. F_2^+-center as shown in Fig. 1 and in the third column of Fig. 2. Energy ε is given in units of eV. a_i's are normalized so as $\sum a_i^2=1$.

level	ε	a_1	a_2	a_3	a_4	a_5	a_6	a_7	a_8	a_9	a_{10}
$1s\sigma$	−4.30	0.20	0.20	0.29	0.29	0.50	0.50	0.29	0.29	0.20	0.20
$2p\sigma$	−2.22	0.41	0.41	0.29	0.29	0	0	−0.29	−0.29	−0.41	−0.41
$2p\pi_1$	−1.98	0.22	−0.22	0	0	0.64	−0.64	0	0	0.22	−0.22
$2p\pi_2$	−1.76	0	0	0.5	−0.5	0	0	0.5	−0.5	0	0

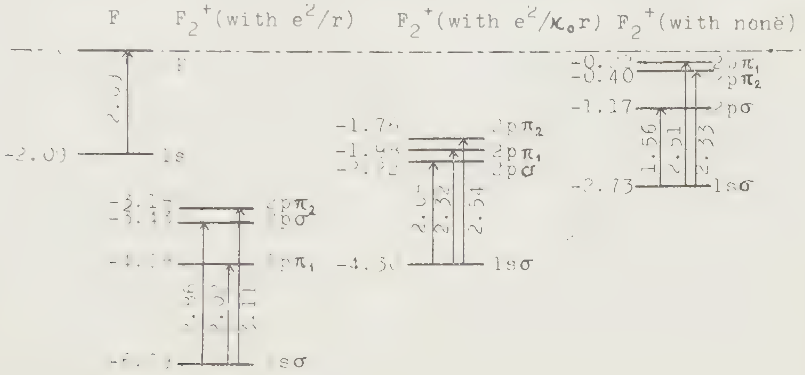

Fig. 2. Energy level scheme for F_2^+ (calc.) with three different approximations and that for F (obs.); KCl, energy measured in units of eV.

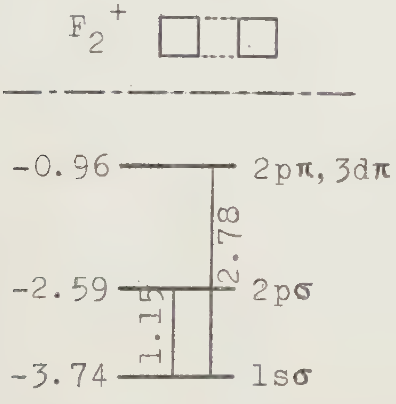

Fig. 3. Energy levels of another F_2^+-center.

the F-band. The type (b) is the most stable configuration when there is no electron trapped there, but when it contains an electron it is less stable than the other types. A rough estimate of the energy of dissociation of these centers into an F-center and a stacked pair of positive and negative vacancies can be made by taking into consideration the Coulomb interactions among the vacancies. Taking either $e^2/\kappa_0 r$ or $e^2/\kappa r$ for these Coulomb interactions we get:

Dissociations energy with κ_0 or κ:

Type	(a)	(b)	(c)	(d)
With κ_0	0.24	−0.30	0.04	−0.22 eV.
With κ	0.21	−0.57	0.50	0.39

§ 5. The F_2-center (KCl and NaCl)

We made a very rough calculation for this center in a way similar to the Heitler-London treatment of the hydrogen molecule. The basic atomic orbitals are assumed in the form:

$$\phi_A=a(\varphi_1+\varphi_2)+b(\varphi_3+\varphi_4)+c(\varphi_5+\varphi_6)\ ,$$
$$\phi_B=a(\varphi_{10}+\varphi_9)+b(\varphi_8+\varphi_7)+c(\varphi_6+\varphi_5)\ ,$$

where the numerical suffixes refer to Fig. 1 and a, b, c are the parameters to be determined by the minimum principle. The singlet ground state and the first excited state are respectively given as

$$\Psi_0=\frac{1}{\sqrt{2(1+S^2)}}[\phi_A(1)\phi_B(2)+\phi_A(2)\phi_B(1)]\ ,$$
$$\Psi_1=\frac{1}{\sqrt{2(1-S^2)}}[\phi_A(1)\phi_A(2)-\phi_B(1)\phi_B(2)]\ ,$$
$$S=\int\phi_A(1)\phi_B(1)d\tau_1\ .$$

The same resonance energy γ as that given before and the Coulomb potential of the form $-e^2/r_{iB}\kappa_0$ were used. There appears exchange integrals of the form

$$\iint (e^2/r_{12})\psi_i(1)\psi_{i'}(1)\psi_j(2)\psi_{j'}(2)d\tau_1 d\tau_2 .$$

In the case of $i=i'\neq j=j'$ they were put equal to e^2/r_{ij} where r_{ij} is the distance between the centers of the i-th and j-th ions. In the case of $i=i'=j=j'$ we put it equal to the electrostatic interaction energy between two superposed spherical electron clouds of a uniform density, and we assumed arbitrarily that the radius of the sphere is equal to the ionic distance (half the lattice constant). Other combinations of i, i', j, j' were neglected.

With this rather crude approximation we obtained the result of Table III. In this table the energy values of the electronic states are the difference between the energy of the two electrons in an F_2-center and that in two F-centers in the $2p$ state. The dissociation energy corresponds to the reaction F_2(ground state)→2F(ground state). The interaction between the two vacancies in the F_2-center is taken in the form $e^2/\kappa_0 r$.

§ 6. Discussion

The data obtained in this paper seem to support the intepretation of Seitz[1] that the M-center is that given by Fig. 4 (a) and R_1 and R_2-centers are F_2^+ and F_2, respectively. The present calculation shows that there are always two or three absorption bands associated with these centers. Inui, Uemura and Toyozawa[2] made a calculation on M-center along a line similar to that followed by this paper, and their results for NaCl and LiCl also agree with the corresponding observed M-bands. (Without any serious reason the publication of the present paper has been much delayed after it was presented at the Annual Meeting of the Physical Society of Japan in 1950, when they also announced their work.) Inui and his collaborators employed s and p orbitals and Coulomb potentials without dielectric screening, and calculated the resonance integral in a direct way, whereas we employed s orbital only, Coulomb poten-

Table II. The amplitudes for the center of the type (a) (Suffixes are as in Table I).

level	ε	a_1	a_2	a_3	a_4	a_5	a_7	a_8	a_9	a_{10}
A_1	−2.18	0.17	0.32	0.30	0.30	0.62	0.30	0.30	0.17	0.32
B_1	−0.87	0.37	0.48	0.26	0.26	0	−0.26	−0.26	−0.37	−0.48
B_2	−0.21	0	0	0.5	−0.5	0	0.5	−0.5	0	0

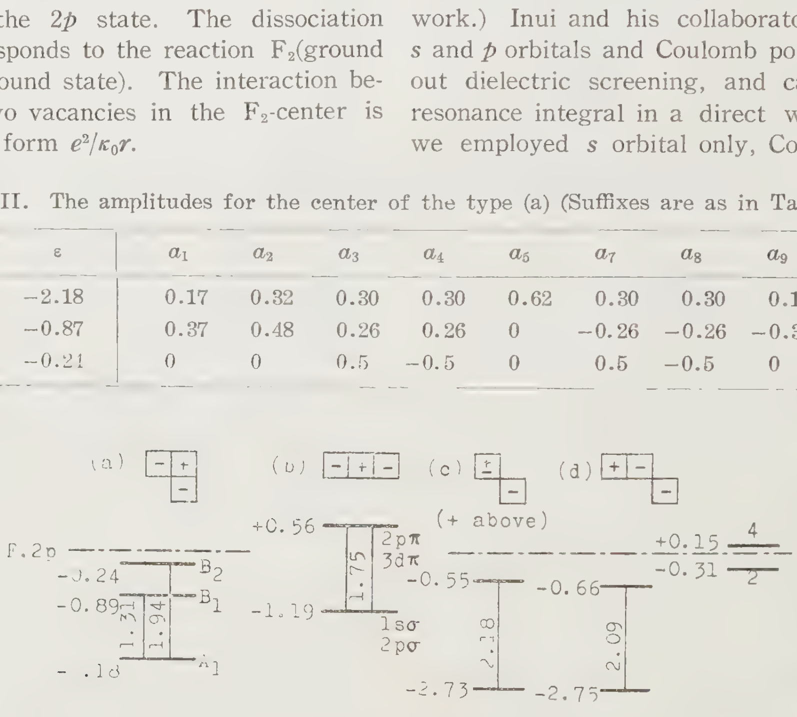

Fig. 4. Energy levels of four types of three-vacancy-centers with one trapped electron, KCl. Two levels on the right marked with 2 and 4 are the ground states of the electron trapped in a paired vacancies and a square quartet vacancies, respectively.

Table III. Energy values for the F_2-center of the form of Fig. 1, and those for the F_2-center of the form of Fig. 3 in ( ).

Crystal	Ground state $(1s\sigma)^2$	Excited state $(1s\sigma)(2p\sigma)$	Difference	Dissociation energy
KCl	−6.43 (−5.60)	−4.77 (−4.78)	1.66 (0.82)	0.72 (0.34)
NaCl	−7.64 (−6.60)	−5.80 (−5.82)	0.84 (0.84)	0.81 (0.30)

tials screened by optical dielectric constant, and the resonance integral derived from F-absorption band. The use of *p* orbital should lower the excited states while the use of pure Coulomb potential should lift them. The values of the resonance integrals calculated by them may have been higher than that employed in the present paper, because we neglected the *p* orbital also in the case of F-center. Such differences between their and our calculations appear to have cancelled among themselves in the final results.

Ueta[3] irradiated a crystal containing M-centers with a polarized monochromatic light at the M-band and observed the change of the concentration of M-centers after the irradiation, measuring again with a polarized light. He made his experiment at various temperatures and with various combinations of the planes of polarization of the two lights. The M-centers of certain orientations with respect to the crystal axes were observed to be destroyed by the first irradiation and to recover after a while, and it was shown that his results could be explained by Seitz' model. It could be expected, however, that the time required for one of the two negative vacancies to displace itself to a neighboring lattice site of the negative ion, that is, the time required for an M-center to change its orientation, is much smaller than a second at room temperature if one considers that the activation energy of the diffusion of paired vacancies is less than 0.5 eV.[1],[4], though the paired vacancies involved in the M-center might not be the same thing as the free paired vacancies, inasmuch as the M-center contains one electron. Actually Ueta observed that M-centers do not change their orientation appreciably at room temperature and that at 60°C the half life-time associated with their orientation is 20 minutes. This suggests either that the activation energy in the case of M-center, which involves the electronic energy, is higher than that for free paired vacancies, or that M-center is not a right-angled complex but a deformed one, or both. Alternatively, M-center could be interpreted in terms of F_2 (or F_2^+), which seems to be less probable. In fact, M-centers are produced at an early stage of X-ray irradiation where there are evidences for the creation of paired vacancies. These paired vacancies will combine with F-centers to become M-centers or combine with negative vacancies to form linear aggregates of three vacancies and then capture electrons to become M-centers. Petroff[5] irradiated additively colored KCl crystals at the F-band and found that M-centers develop to a maximum after an hour at room temperature and then decrease. He formed also that R_2-centers are formed with a speed proportional to the existing number of M-centers. These can be explained naturally if one assumes Seitz' model of M-center and considers that M-centers already existing capture photoelectrons and become F_2-centers by expelling positive vacancies.

According to our model, wherein the trapped electron or electrons are supposed to move on the positive ions surrounding the vacancies, the effect of thermal vibrations upon the breadth of absorption bands should be smaller for greater number of these positive ions, because the orbit of electron round about the vacancies is longer. In fact, the observed breadth is smaller for other centers than F-center.

References

1) F. Seitz: Rev. Mod. Phys. **18** (1946) 384.

2) T. Inui, Y. Uemura and Y. Toyozawa: Prog. Theor. Phys. **8** (1952) 355.

3) M. Ueta: J. Phys. Soc. Japan **7** (1952) 107.

4) J. G. Dienes: J. Chem. Phys. **16** (1948) 602

5) St. Petroff: Zeits. Phys. **127** (1950) 443.

Journal of the Physical Society of Japan Vol. 9, No. 3, May—June, 1954

A Mathematical Model for the Narrowing of Spectral Lines by Exchange or Motion*

By P. W. Anderson

Bell Telephone Laboratories, Inc.
Fulbright Lecturer, Tokyo University, 1953-54

(Received January 11, 1954)

In this paper a simplified mathematical model of exchange and motional narrowing, which we call the "random frequency-modulation model," is developed, and, to a certain extent, justified. A number of cases are treated. The one general conclusion which is common to all is that in the case of extreme narrowing the central part of the line is resonance-shaped while the wings fall off more steeply than the resonance shape; the half-width is always of order of magnitude of the mean square frequency breadth divided by the rate of motion or exchange.

In two cases the model makes some quantitative approach to realism: first, the case of a single dipolar-broadened line with exchange, where the "Gaussian" assumption can be made and the results have been fitted to Van Vleck's fourth moment calculation to give satisfactory numerical answers; and second, the case of narrowing by diffusion in solids, where the "Markoffian" assumption is valid. The problem of narrowing of hyperfine structure is considered, and on this model it is found that before merging the lines draw together, a result which is confirmed by experiments.

§ 1. Introduction

Magnetic resonance spectroscopy, the study of absorption and dispersion of electromagnetic radiation by atomic or nuclear magnetic moments precessing about an external magnetic field, remains an active branch of physics. This may at first seem surprising : the magnetic resonance spectrum of an isolated atomic or nuclear moment consists of a single line at the Larmor frequency $\omega=g\beta/\hbar H$, and apparently there is only one parameter, g, to be measured for each atomic or nuclear species. However, when these moments are assembled into a piece of matter, their interactions affect this line, causing it to be shifted, or split up into components, and spread into a practically continuous band. We can learn about these interactions by studying the shape and breadth of this band, or by studying the related phenomenon of relaxation. Among other experimental and theoretical reasons, this very simplicity of the unperturbed spectrum has caused the study of line breadths, line shapes, and relaxation to assume a greater importance in magnetic resonance than in any other branch of spectroscopy. From its beginnings, magnetic resonance work has been deeply concerned with the line shape problem, and from the very first it has made great contributions through its line shape studies to our knowledge of the interactions and motions of atoms in matter.

The phenomenon of "narrowing" is a unique feature of magnetic resonance line breadths, and one of the most interesting and useful ones. It takes two forms : "motional narrowing", which is caused by the motions of the atoms themselves in gases, liquids, and even some solids ; and "exchange narrowing", which is caused by exchange interactions (or exchange motions) of electronic magnetic moments. Exchange narrowing, although more complex, was apparently the first to be discussed, by Gorter and Van Vleck (1947)** and Van Vleck (1948), while motional narrowing was discussed by Bloembergen,

---

* Some of the work reported in this paper was also done independently by P. R. Weiss of Rutgers University, and discussions with Dr. Weiss have been most useful. A joint paper on this part has been published (Anderson and Weiss, 1953).

** References are found in a bibliography at the end of the paper, listed by year and author.

Purcell, and Pound (1948).

The mechanism is in principle the same in both motional and exchange narrowing. In order to understand this mechanism we must first have a clear understanding of what interactions can and cannot affect the magnetic resonance line directly. The line is a result of the precession of the magnetic moment of the sample, and therefore non-magnetic interactions cannot affect it directly. This is because these interactions (such as exchange, electric dipolar effects, etc.) are "unaware" of the direction of the magnetic moment, being magnetic scalars; in quantum language, they commute with the components of the magnetic moment and, by Heisenberg's equation of motion, cannot affect its motions. Only magnetic interactions, such as dipolar interactions, spin-orbit coupling, or hyperfine interactions of nuclei and electrons, can have a direct effect. These interactions, however, are themselves affected by non-magnetic interactions which cannot directly affect the line, and this produces the narrowing phenomenon.

Often the magnetic interactions are weak compared with the other interactions in the Hamiltonian. These other, non-magnetic interactions control the actual motions of electrons and atoms, and these motions may be quite rapid and completely independent of the magnetic phenomena. The magnetic interactions, since they depend on the positions of the electrons and atoms, will then vary in time in some way which is controlled by the electronic motions. It will be shown later that the magnetic resonance line experiences a time-averaged effect of the magnetic interactions. When the atomic or electronic motions are sufficiently rapid, this averaged effect may be much smaller than otherwise. Therefore the broadening effect of the magnetic interactions is reduced; the line is potentially narrowed and this is called the narrowing phenomenon.

The observed breadth of the line may contain two pieces of information: (1) the magnitude of the magnetic interactions; (2) the rate and magnitude of the motions of non-magnetic type. The second class of information may prove more interesting than the first. Unfortunately, while the breadth of the line in the absence of narrowing can be calculated in a rather rigorous manner (Van Vleck, 1948), no comparable treatment of the narrowing problem has appeared so far. There is a calculation of exchange narrowing by Van Vleck (1948) which, although perfectly rigorous, only shows that exchange narrowing occurs. At the same time it demonstrates that the actual line breadths and shapes are not calculable by the moment method.

Bloembergen, Purcell, and Pound (1948) attack the motional narrowing problem in a more physical way. They assume the basic mechanism explained above—that the broadening interactions vary in a random manner in time due to the non-magnetic interactions and motions—and estimate the line-breadth from this time variation. This estimate is very satisfactory. In the case of extreme narrowing (very rapid motions) it is

$$\Delta\omega \simeq \overline{\omega_p^2}/\omega_e\,, \tag{1}$$

where $\overline{\omega_p^2}$ is the mean squared breadth in the absence of narrowing, and ω_e is an average rate of change of the broadening interactions. ω_e is equal to $1/\tau_c$, where τ_c is the "correlation time" of the motions.

In this paper we attack the narrowing problem (of either kind) by a method very similar to that of Bloembergen, Purcell, and Pound, in that we use a mathematical model which is also based on the above physical picture of the process. The model assumes that the precessing moments give rise to a radiated electromagnetic wave which is undergoing frequency-modulation, because the magnetic interactions act to change the frequency of the precession. The frequency-modulation is changing in a random way in time due to the effect of the non-magnetic motions on the magnetic interactions.

Only a qualitative justification for the model can be presented. However, there are good reasons for putting forward this method in spite of this. Most important is the fact that its simplicity and definiteness makes it possible to make much more complete calculations than have as yet been possible, and to treat more complex situations. Some of the resulting advantages are the following:

(a) The mathematics of the problem can be worked out in sufficient detail to give line-shapes as well as breadths. In all the variations of our model the line has the same general form : a Lorentz (resonance) line in the center with a more rapid decrease of intensity (a "cutoff") on the extreme wings. The fact that this shape is observed experimentally is valuable in giving confidence in the model; at the same time, the shape has become a useful tool in understanding experimental situations.

(b) An attempt is made to justify the use of one form of the model for the exchange narrowing problem. Van Vleck's calculations give numerical answers for two of the moments of the line shape, which can also be calculated by our model. However, as we have pointed out, his calculations cannot for fundamental reasons give the line-shape or breadth. We use the two moments computed by Van Vleck to fix the two adjustable constants in our line-shape (which are essentially $\overline{\omega_p^2}$ and ω_e as defined above), and then the observable breadth of the central peak can be related quantitatively to the dipolar interactions and the exchange integral. Thus we have used our method in this case essentially as an extrapolation method for Van Vleck's computation, and have obtained rather good agreement with experiment. This work was reported in an earlier paper (Anderson and Weiss, 1953); further details and some justification are included here.

(c) A particular model for the case of hyperfine structure can also be worked out in detail. The result is a qualitative indication of how the hyperfine structure peaks merge, which seems to be verified by a number of experiments.

(d) An extension of this model can be shown to be a fair approximation to the motional narrowing problem under diffusion in a solid. Here the random modulation of the frequency is "Markoffian", since the atomic jumps are very rapid compared to the length of time between them. In principle this problem is solvable in general, especially if the simplifying assumption is made that the jumps lead to a completely randomized frequency distribution. In this paper we give certain preliminary results for this problem.

§ 2. A General Discussion of Motional and Exchange Narrowing

In this section the justification from basic principles which is possible for the random frequency-modulation model is given and discussed. It can be made plausible that the general type of line-shape to be expected is derivable with this model; however, certainly one can make no exact quantitative theory.

It can be shown in general that the spectrum of the radiation from any quantum-mechanical system is given by*

$$I(\omega)=\mathrm{Trace}\left|\int_{-\infty}^{\infty}\mu(t)e^{-i\omega t}dt\right|^2, \qquad (2)$$

where $\mu(t)$ is the radiating dipole moment matrix in the Heisenberg representation :

$$i\hbar\frac{d\mu}{dt}=H\mu-\mu H. \qquad (3)$$

H is the complete Hamiltonian.

Now in any problem involving the type of narrowing we deal with here the Hamiltonian may be split up into three parts :

$$H=H_0+H_p+H_m. \qquad (4)$$

These three parts are : first, H_0, the "unperturbed Hamiltonian" which causes the energy-differences which lead to the observed spectral lines whose shapes we wish to study. Second is H_p, the "perturbing Hamiltonian"—generally just the dipolar interactions between the moments, although it may also involve other interactions, such as hyperfine splitting —which does not commute with H_0 and thus can change the frequencies radiated by the system over some more or less known range. H_p causes the broadening of the sharp single lines due to H_0 into broader lines or a fine structure. Finally, there is H_m, the "motional Hamiltonian", whose characteristic is that it commutes with both H_0 and μ, and thus can have no direct effect upon the radiation emitted or absorbed by the system. On the other hand, H_m does not commute with H_p, and thus, by the relation

$$i\hbar\dot{H}_p=[H, H_p]=[H_0, H_p]+[H_m, H_p], \qquad (5)$$

H_m can cause a time-dependence of H_p. It is this time-dependence which "narrows out" the line-broadening which H_p otherwise would cause.

In the usual exchange narrowing case, H_0

---

* Anderson, 1949. A simple proof of equation (2) is given in Appendix I. The apparent lack of convergence is easily removed by convergence factors or by thinking of the integral as an average.

is the interaction of the magnetic moments μ of an assembly of atoms with the external field :

$$H_0=\sum_j \vec{\mu}_j\cdot\vec{H}=g\beta\sum_j \vec{S}_j\cdot\vec{H}\,. \qquad (6)$$

Here g is the Landé factor, β the Bohr magneton, $\vec{H}$ the external field, and $\vec{S}$ the spin.

H_p is the dipole-dipole interaction energy of the moments,

$$H_p=H_{dd}=g^2\beta^2\sum_{j,k}\frac{1}{r_{jk}{}^3}\left(\vec{S}_j\cdot\vec{S}_k-\frac{3(\vec{S}_j\cdot\vec{r}_{jk})(\vec{S}_k\cdot\vec{r}_{jk})}{r_{jk}{}^2}\right), \qquad (7)$$

which Van Vleck (1948) has shown can be simplified in some cases to

$$H_{dd}=g^2\beta^2\sum_{j,k}\frac{1}{r_{jk}{}^3}\left(\frac{3}{2}\cos^2\theta_{jk}-\frac{1}{2}\right)\times(\vec{S}_j\cdot\vec{S}_k-3S_{jz}S_{kz})\,. \qquad (8)$$

θ_{jk} is the angle between $\vec{r}_{jk}$ and the z-axis, along which we assume the external field to have been applied. It is assumed for the validity of (8) that $H_0 \gg H_p$; the terms omitted in (8) lead to the "satellite lines."

The "motional" Hamiltonian H_m in the exchange narrowing case is taken to be the Heisenberg exchange Hamiltonian,

$$H_m=H_{ex}=\sum_{j,k}J(\vec{r}_{jk})\vec{S}_j\cdot\vec{S}_k\,.$$

It can easily be shown that (9) commutes with the total spin vector of the system $\sum\vec{S}_j$, and thus both with its z-component, which is proportional to H_0 (6), and with its x or y component, which is the radiation dipole moment, $\mu(t)$, in (2). It does not commute with the dipole-dipole Hamiltonian H_{dd}, however.

In the case of motional narrowing H_0 and H_p ((6) and (7)) are of the same form as in exchange narrowing. Motion of the actual coordinates of the atoms can change H_{dd}, while neither H_0 nor $\mu=g\beta\sum_j S_{xj}$ are affected by physical motion, since they do not contain the spatial coordinates of the moments. In this case, H_m is the Hamiltonian of the translational and rotational motion of the molecules of the substance.

The random frequency-modulation picture of the narrowing process can be derived from the above physical assumptions :

(a) equation (2)

(b) equation (5)

(c) $H_m\mu-\mu H_m=0$

(d) $H_mH_0-H_0H_m=0$;

(e) and, in addition, the assumption that H_{dd} is small enough that it has no important matrix elements connecting different states $E_i{}^{(0)}$ and $E_j{}^{(0)}$ of the unperturbed energy H_0.

In any real substance assumption (e) will, of course, not be rigorously true, since there are many states of H_0 of equal energy (i.e. equal $S_z{}^{(0)}$) and therefore H_{dd} will obviously have important off-diagonal elements. However, we may look upon assumption (e) as an approximation—very like the "adiabatic approximation" of pressure broadening theory (Foley, 1946) which often, if carefully handled, leads to good quantitative results—which should not lead us too far astray. What is done is to use always a mean squared value of H_p which is computed without neglecting the off-diagonal elements, but to treat it as though it came only from diagonal ones. In other words, we do not neglect the magnitude of these elements but simply compute their effects non-rigorously whenever they are important.

Under assumptions (a–e), then, we wish to compute the spectral intensity (2). We realize first that we are only considering one spectral line, so that we only need to consider the element of $\mu(t)$ which connects two unperturbed levels of H_0, E_i and E_j. We can then say that for the spectral line under consideration,

$$I_{i\to j}(\omega)=\left|\int\mu_{ij}(t)e^{-i\omega t}dt\right|^2. \qquad (11)$$

Now we know part of the time-dependence of $\mu_{ij}(t)$, that due to the unperturbed Hamiltonian H_0. We express this fact by transforming to a new matrix element $\mu_{ij}'(t)$ which contains this time-dependence explicitly :

$$\mu_{ij}(t)=\mu_{ij}'(t)\exp(i\omega_{ij}{}^{(0)}t)\,, \qquad (12)$$

where

$$\hbar\omega_{ij}{}^{(0)}=E_i-E_j\,.$$

Now it is easily shown that the transformation (12) removes the terms of the time-equation (3) for μ which depend on H_0, so that now

$$i\hbar\frac{d\mu'}{dt}=[H_m+H_p,\mu]$$
$$=H_p\mu'-\mu'H_p\ , \qquad (13)$$

because of assumption (a).

Now, by the use of assumption (e) we can actually calculate $\mu_{ij}'(t)$, as follows :

$$i\hbar\dot{\mu}_{ij}'=[H_p\mu'-\mu'H_p]_{ij}$$
$$=(H_p)_{ii}\mu_{ij}'-\mu_{ij}'(H_p)_{jj}$$
$$\dot{\mu}_{ij}'(t)=i\Delta\omega_{ij}(t)\mu_{ij}'(t)\ . \qquad (14)$$

Here $\Delta\omega_{ij}(t)$ is defined as

$$\Delta\omega_{ij}(t)=\frac{H_p(t)_{ii}-H_p(t)_{jj}}{\hbar}\ . \qquad (15)$$

Equation (14) for the matrix element is easily integrated to give

$$\mu_{ij}'(t)=\mu_{ij}^{(0)}\exp\left(i\int_0^t\Delta\omega_{ij}(t')dt'\right). \qquad (16)$$

Inserting this into the intensity formula (11) gives us for the line shape (ignoring as usual constant or nearly constant factors since we wish only the shape function)

$$I_{ij}(\omega)\sim\left|\int_{-\infty}^{\infty}\exp\left(-i(\omega-\omega_{ij}^{(0)})t\right.\right.$$
$$\left.\left.-i\int_0^t\Delta\omega_{ij}(t')dt'\right)\right|^2. \qquad (17)$$

$\Delta\omega_{ij}(t)$ is a random function of time ; its value at any time depends on the values of the diagonal elements of H_p at that time, and these will change in a random way at a rate controlled by the motional Hamiltonian, H_m, as we see from the time equation (5) for H_p (there is no time dependence due to H_0 because these are diagonal elements) :

$$i\hbar\dot{H}_p=[H_m,H_p]\ . \qquad (18)$$

The reason for assuming randomness is that in the important cases the effect of H_p back on H_m can be neglected, so that the motions embodied in H_m appear to the magnetic quantities to be uncorrelated. Equation (17), and the idea of $\Delta\omega_{ij}(t)$ as a random function of time whose rate of change is controlled by H_m according to (18), are the basic ideas of the random frequency-modulation model of narrowing phenomena.

In general, we will have no rigorous basis for giving $\Delta\omega_{ij}(t)$ any particular form. In the first place, because of the inaccuracy of assumption (e) $\Delta\omega_{ij}(t)$ is simply a construct, a single function which is meant to embody all of the broadening effects, diagonal as well as off-diagonal, of H_p. In the second place, even if we actually had a true expression for $\Delta\omega_{ij}(t)$ as a random function, we could probably not handle it mathematically in the present state of the theory of random functions.

What we know about $\Delta\omega_{ij}(t)$, or can usually find, is at least a good approximation to its probability distribution : the probability that at a given time it has a given value. In many cases Van Vleck (1948) gives us at least the mean second and fourth moments of this probability distribution (which, fortunately, seldom has the peculiarity of anomalously large wings) ; in other cases (Anderson 1950) the entire distribution is available.

Finding the random time properties of $\Delta\omega_{ij}(t)$ is another problem. It is likely that the problem of finding the line-shape is hopeless unless this function falls into one of the two simple cases, the Markoffian or the Gaussian, of random functions. (See Wang and Uhlenbeck, 1945) Even if we knew the exact properties of $\Delta\omega_{ij}(t)$, it would therefore be necessary to assume the best Gaussian or Markoffian fit to the real function before proceeding farther. For each of these two simple cases a solution for the intensity distribution (17) will be given in a later section of this paper. We shall show that the exchange narrowing problem probably is closely represented by a particular type of Gaussian random function. The problem of narrowing under diffusion in solids is a very close fit to the exact Markoffian case. Other cases must be arbitrarily assigned certain types of random functions.

Before going on with these detailed considerations, let us take a general look at the structure of the problem embodied in equations (17) and (18). The appearance of equation (17) may be simplified in the following way : let us redefine ω as

$$\omega=\omega-\omega_{ij}^{(0)}\ ; \qquad (19)$$

this is the frequency deviation from the line center. Also, let us introduce the phase deviation $\eta(t)$, which is of course simply the integral of the frequency deviation :

$$\eta(t)=\int^t\Delta\omega_{ij}(t')dt'\ . \qquad (20)$$

Then (17) becomes

$$I(\omega)=\left|\int_{-\infty}^{\infty}e^{-(\omega t-\eta(t))}\,td\right|^2, \qquad (21)$$

a form which is familiar from the "adiabatic theory" of pressure broadening. (See Anderson, 1949, or Foley, 1946.)

We shall find it very convenient to use the correlation-function form of the Fourier integral. By a well-known transformation one can show that

$$\left.\begin{aligned} &I(\omega)=\int_{-\infty}^{\infty} d\tau e^{i\omega\tau}\int_{-\infty}^{\infty} dt' \\ &\qquad\qquad \times e^{-i(\eta(t'+\tau)-\eta(t'))} \\ &\text{or,} \\ &I(\omega)=\int_{-\infty}^{\infty} d\tau e^{i\omega\tau}\varphi(\tau)\,. \end{aligned}\right\} \qquad (23)$$

$\varphi(\tau)$ is called the "correlation (or autocorrelation) function" and can be written as:

$$\varphi(\tau)=\langle e^{i(\eta(t+\tau)-\eta(t))}\rangle \text{ave. over } t\,. \qquad (24)$$

In view of equation (16), this is just the same as

$$\varphi(\tau)=\langle \mu_{ij}'^{*}(t+\tau)\mu_{ij}(t)\rangle \text{ave. over } t\,.$$

This represents the averaged "memory" of the function μ_{ij}' at the time $t+\tau$ for what its state was at a time τ earlier.

This theorem as a method of finding the line-breadth is much less sensitive to the exact line-shape than the moment method. A number of simple theorems showing this are given in Appendix II; however, we need, for present purposes, only the familiar one that the product of the frequency width of the spectrum of a function with the time-extension of this function is always roughly unity: $\Delta\omega\Delta t\simeq 1$. Thus we know that if $\varphi(\tau)$ falls off appreciably, say to $1/e$ of its value at $\tau=0$, by the time T, then the breadth of $I(\omega)$, its Fourier transform, is roughly

$$\Delta\omega\cong 1/T\,. \qquad (25)$$

To find a rough estimate for T, let us go back to the definition (24) of $\varphi(\tau)$, remembering that η is given by (20).

Then

$$\varphi(\tau)=\langle\exp\left(i\int_t^{t+\tau}\Delta\omega_{ij}(t')dt'\right)\rangle\text{ave. over } t\,. \qquad (26)$$

If $\omega_{ij}^{(0)}$ (i.e. H_0) was correctly chosen, there will be no tendency for $\eta(t)$ to change other than randomly with time; its swings may become larger but its average is zero. Then the question to be answered becomes: when on the average will the integral of $\Delta\omega_{ij}(t)$ take on a value of order of magnitude unity? This will make the real part of (26) small, and the imaginary parts will cancel because η is equally often positive or negative. Let us consider two cases:

I. The variation of $\Delta\omega_{ij}(t)$ with time is very slow. Then, for any given time t, $\Delta\omega_{ij}$ will have a nearly constant random value of order of magnitude

$$\Delta\omega_{ij}\simeq\sqrt{\overline{\Delta\omega_{ij}^2}}=\omega_p\,,$$

where we define ω_p as this value. Thus η will become appreciable in a time T satisfying $\omega_p T\cong 1$, so that the linebreadth is given by

$$\Delta\omega\cong\omega_p\,. \qquad (27\text{–I})$$

Here we see that there has been no narrowing, as expected.

II. The time-rate of change of $\Delta\omega_{ij}(t)$ is greater than ω_p. In this case, although at any time $\Delta\omega_{ij}$ will be of roughly ω_p in magnitude, its value will change sign before the integral in (26) can become appreciable, and thus

$$\left.\begin{aligned} &T\gg 1/\omega_p \\ &\Delta\omega\ll\omega_p\,. \end{aligned}\right\} (27\text{–II})$$

Here we have narrowing, and we find that the criterion for "slow" vs. "rapid" motion is, correctly, that used by Bloembergen, Purcell and Pound (1948), namely a comparison with the line-breadth itself.

§ 3. The Spectrum for Gaussian Random Modulation; Exchange Narrowing

The case in which the random modulation of the frequency is Gaussian noise with an arbitrary spectrum is rather easily solved in general. The theorem which can be used in this case is the well-known one that any linear combination of values of a Gaussian random function is itself randomly distributed with a Gaussian probability curve. In the correlation function (26), the exponent

$$\int_t^{t+\tau}\Delta\omega_{ij}(t)dt=X(t,\tau) \qquad (28)$$

is just such a linear combination. Thus we know that the probability distribution of X is simply

$$P(X)=\frac{1}{\sqrt{2\pi\overline{X^2}}}\exp\left(-\frac{X^2}{2\overline{X^2}}\right). \qquad (29)$$

Now we see that if we can find $\overline{X^2}$ we can find $\varphi(\tau)$, since

$$\left.\begin{aligned} \varphi(\tau) &= \int_{-\infty}^{\infty} e^{iX} P(X)dX \\ \varphi(\tau) &= \exp(-\overline{X^2}/2)\left[\frac{1}{\sqrt{2\pi\overline{X^2}}}\int_{-\infty}^{\infty} dy \right. \\ &\quad \left. \times \exp(-y^2/2\overline{X^3}\right] = \exp(-\overline{X^2}/2) \, . \end{aligned}\right\} \quad (30)$$

Now if $\varDelta\omega_{ij}(t)$ is a Gaussian random function it is completely characterized, aside from its mean square magnitude, by either its spectrum or its correlation function

$$\varphi_{\Delta\omega}(T) = \frac{<\varDelta\omega_{ij}(t)\varDelta\omega_{ij}(t+\tau)>\text{ave.}}{\overline{\varDelta\omega_{ij}^2}} \, , \quad (31)$$

which are Fourier transforms of each other. Let

$$\omega_p^2 = \overline{\varDelta\omega_{ij}^2}$$

be substituted for the mean square magnitude of the perturbation, for the sake of brevity. $\overline{X^2}$ can be found most easily in terms of the correlation function for $\varDelta\omega_{ij}$:

$$\overline{X^2} = <\int_0^\tau dt \int_0^\tau dt' \varDelta\omega_{ij}(t)\varDelta\omega_{ij}(t')>\text{ave.}$$

$$= \omega_p^2 \int_0^\tau dt \int_0^\tau dt' \varphi_{\Delta\omega}(t'-t) \, ,$$

the average being taken by the use of (31). The substitution of

$$x = t' - t$$

$$y = t' + t$$

as new variables leads to

$$\overline{X^2} = 2\omega_p^2 \int_0^\tau dx(\tau - x)\varphi_{\Delta\omega}(x) \, .$$

This gives us

$$\varphi(\tau) = \exp\left(-\omega_p^2 \int_0^\tau dx(\tau-x)\varphi_{\Delta\omega}(x)\right) . \quad (32)$$

Two extreme cases are now of interest. The first one corresponds to little or no narrowing. Here we assume that $\varDelta\omega_{ij}$ does not change appreciably during the time (about $1/\omega_p$) in which $\varphi(\tau)$ falls to a relatively low value. Then we can set $\varphi_{\Delta\omega}(x) = 1$, so that

$$\varphi(\tau)_{\text{Case I}} = \exp(-\omega_p^2\tau^2/2) \, , \quad (33a)$$

and obviously the line shape is a Gaussian of second moment ω_p^2, which is of course precisely what we started out with. The more interesting case is Case II, in which we have a large narrowing. Then we can say that $\varphi_{\Delta\omega}(x)$ falls to a small fraction long before $\varphi(\tau)$ has changed appreciably. Let $1/\omega_e$ represent essentially the width of the $\varphi_{\Delta\omega}$ curve; this can be characterized by

$$\int_0^\infty \varphi_{\Delta\omega}(x)\,dx = \frac{1}{\omega_e} \, . \quad (34)$$

Then we can easily see that the contribution of the term in x in the integral is neglible, of order ω_p^2/ω_e^2, so that

$$\varphi(\tau) \cong \exp\left(-\omega_p^2 \int_0^\tau dx\, \varphi_{\Delta\omega}(x)\right)$$

which, since most values of τ of interest are much greater than ω_e, gives

$$\varphi(\tau)_{\text{Case II}} \cong \exp(-\omega_p^2/\omega_e \cdot \tau) \, . \quad (33b)$$

This exponential correlation function corresponds to a lineshape of the resonance type, as is well-known. Thus at least the central portion of the line is of resonance shape; the wings are determined by $\varphi(\tau)$ for small τ, as we show in Appendix II, so that for these we need more detailed considerations. Note that this result is completely independent of the detailed shape of the correlation function $\varphi_{\Delta\omega}(\tau)$, and thus of the detailed spectrum of the random function $\varDelta\omega_{ij}(t)$; this is so unless this function has a correlation which falls off only as $1/\tau$ or less. Such a function would have a spectrum divergent at zero frequency, a possibility which seems very unlikely.

We shall give two explicit examples of the function $\overline{X^2}$. The first numerical example is the case of the Markoffian Gaussian process. A Markoffian process is a random process which proceeds in jumps, the probability of a jump to a given value of the function being dependent only upon the value of the function immediately before the jump. Such a process can be made Gaussian by letting the jumps become infinitesimally small. (See Wang and Uhlenbeck 1945). In this case the correlation function is exponential:

$$(\varphi_{\Delta\omega})_{\text{Mark.}} = e^{-\omega_e\tau} \, . \quad (35)$$

Here ω_e is the inverse of the correlation time τ_c for the process. Now

$$\overline{X^2}_{\text{Mark.}} = 2\omega_p^2 \int_0^\tau dx(\tau-x)\exp(-\omega_e x)$$

$$= 2\omega_p^2\left[\frac{\tau}{\omega_e} - \frac{1}{\omega_e^2}(1-\exp(-\omega_e\tau))\right] .$$

This gives us for the correlation function

$$\varphi(\tau)_{\text{Mark.}} = \exp\left\{-\frac{\omega_p^2}{\omega_e}|\tau| + \frac{\omega_p^2}{\omega_e^2}(1-\exp(-\omega_e|\tau|))\right\} . \quad (36)$$

(We have inserted absolute value signs on τ because, of course, $\overline{X^2}$ is an even function of τ.) It can quickly be verified that our two limiting cases are true.

We should note that by either Theorem IV or V of the Appendix, the wings of the Gauss-Markoff spectrum fall off only as the fourth power of the frequency; it is easy to verify by those theorems, in fact, that the coefficient is

$$I(\omega)_{\omega\to\infty} \sim \frac{\omega_e \omega_p^2}{\omega^4} .$$

This means that, although it can be shown that in either limiting case the fourth power part is quite far on the wings, still it is true that the fourth moment is divergent. Van Vleck's calculations show that this is not a satisfactory model for exchange narrowing.

The second example we shall give is the Gaussian random noise with Gaussian spectrum. This should give results typical for the case in which the possible rate of change of frequency is severely limited. This is the situation one should expect to hold in exchange narrowing, where H_m can, after all, only change the frequency at a rate no greater than something of the order of $ZJ/\hbar$. Here we have a correlation function which is also Gaussian, and we define it as

$$\varphi_{\Delta\omega}(\tau) = \exp\left(-\frac{\pi}{4}\omega_e^2\tau^2\right) . \qquad (37)$$

With this definition of $\varphi_{\Delta\omega}$ it is easy to see that ω_e agrees with the definition (34), and that therefore the limiting equation (33b) will hold. It is easily shown that in this case

$$\varphi(\tau)_{\text{Gauss}} = \exp\left\{-\frac{\omega_p^2\tau}{\omega_e}\int_0^{\omega_e\tau} \exp\left(-\frac{\pi}{4}x^2\right)dx + \frac{2\omega_p^2}{\pi\omega_e^2}\left(1-\exp\left(-\frac{\pi}{4}\omega_e^2\tau^2\right)\right)\right\} . \qquad (38)$$

For this case we should also like to have the second and fourth moments. These are most easily obtained through the theorems of the Appendix. By Theorem II,

$$\overline{\omega^2} = \omega_p^2 . \qquad (39)$$

The fourth moment may be found either by Theorem I and taking the fourth derivative of (38), or by Theorem III of the Appendix. Using the latter method,

$$\omega^4 = \langle \varDelta\omega_{ij}^4 \rangle_{\text{ave.}} + \left\langle \left(\frac{d}{dt}\varDelta\omega_{ij}\right)^2 \right\rangle_{\text{ave.}} .$$

The first term is easily found, since $\varDelta\omega_{ij}$ is Gaussianly distributed; it is simply $3\omega_p^4$. A simple transformation based on the proof of theorem III given in the Appendix shows that

$$\left\langle \left(\frac{d}{dt}\varDelta\omega_{ij}\right)^2 \right\rangle_{\text{ave.}} = -\langle \varDelta\omega_{ij}^2 \rangle_{\text{ave.}} \left(\frac{d^2}{dt^2}\varphi_{\Delta\omega}(\tau)\right)_{\tau=0} = \frac{\pi}{2}\omega_p^2\omega_e^2 .$$

Then

$$\overline{\omega^4} = 3\omega_p^4 + \frac{\pi}{2}\omega_p^2\omega_e^2 . \qquad (40)$$

We see that now both moments (and in fact any further ones) are finite; the fourth moment, as discussed in Appendix III, has a form remarkably like that given by Van Vleck for the case of exchange narrowing.

For the comparisons with experiment which have as yet been made only these moments and the limiting cases of large and small narrowing are needed. The uncertainties caused by a number of experimental and theoretical complicating factors will make it hardly worthwhile, for these comparisons, to consider cases involving intermediate amounts of broadening. However, the line width has been computed approximately, for the sake of completeness, in the intermediate range where ω_p and ω_e are comparable. This material is therefore included in Appendix III.

The use of this Gaussian-Gaussian case as the model for exchange narrowing, and the comparison of its results with experiment, have been discussed in a previous paper (Anderson and Weiss, 1953). It is pointless to repeat this work here. The results are, in the main, very satisfactory, and indicate that the model is quite accurate and that no essentially new concepts need be introduced. The most interesting feature is the appearance of the "10/3 effect". The "satellite" (or non-secular) terms in the Hamiltonian (7) must be included when exchange is large, which can be understood from our model very easily.

§ 4. The Spectrum for Markoffian Random Modulation; Narrowing by Diffusion in Solids and Narrowing of Fine Structure

As has already been mentioned, the Markoffian is the second simple type of random function, and for this case too one can give a general method for finding the correlation function of the spectrum. The mathematics is considerably more complex than in the Gaussian case and in many cases the full solution cannot be carried out. We are, however, able to solve a few simple or limiting cases and get a general idea of the form of the solutions.

The problem is to find $\varphi(\tau)$ from equation (26)

$$\varphi(\tau) = \left\langle \exp\left(i \int_t^{t+\tau} \Delta\omega_{ij}(t')dt' \right) \right\rangle \text{ av. over } t \tag{26}$$

under the assumption that $\Delta\omega_{ij}(t)$ is Markoffian. A Markoffian function $f(t)$ may be defined in a number of ways (see Wang and Uhlenbeck, 1945); the simplest is that the probability of a given value f_1 at the time t, if the value was f_2 at $t-\Delta t$, is independent of the value of the function at any earlier time than $t-\Delta t$. Thus the probability depends only on the value of the function at the earlier time, not on its slope, past history, etc.

An example of such a function is one which can take on the values ±1, and whose probability of transition from one to the other in a given time interval dt is a constant, dt/τ. A more physical example is the momentum of a gas particle in a rarified gas of hard spheres. Collisions change the momentum by an amount independent of its earlier history, depending only on its present momentum.

The Markoffian process is characterized completely by its "second-order probabilities." In the case of a function of a continuous variable, the time, the second-order probabilities are written as

$$\left.\begin{array}{l}\text{Probability that value is } f_2 \textit{ if}\\ \text{value is } f_1\ \Delta t \text{ seconds earlier}\end{array}\right\} = W(f_1|f_2,\Delta t)\,. \tag{41}$$

If the function is not to vary in a senselessly rapid fashion it is known that W must be proportional to Δt for small Δt unless $f_1 = f_2$; in fact, W may be written as

$$W(f_1|f_2,\Delta t) = \delta(f_1,f_2) + \Pi(f_1,f_2)\Delta t\,, \tag{42}$$

where now Π is the probability per unit time of a transition from f_1 to f_2. The δ-symbol is Kronecker if the f's form a discrete set, Dirac if the f's are continuous. Finally, since*

$$\int W df_2 = 1\,,$$

(stating that the function must have some value at every time) we see that

$$\int \Pi\, df_2 = 0\,, \tag{43a}$$

so that, since the transitions to values of $f_2 \neq f_1$ must always have positive probabilities, we have

$$\Pi(f_1, f_2) = -\omega_e(f_1)(\delta(f_1, f_2) - P(f_1, f_2))\,, \tag{44}$$

where the presumably non-singular function P is normalized:

$$\int P(f_1, f_2) df_2 = 1\,, \tag{43b}$$

and ω_e represents the total probability of transitions from the value f_1.

A few more words on Markoffian functions: There is for the usual case of "stationary" functions a "static distribution" or intrinsic probability distribution, $W_1(f)$, which is the probability distribution of f one gets if the function is left alone, for an indefinite period. Such a distribution has to be self-perpetuating, which means that it must satisfy the Smoluchowski equation embodying the condition that if the distribution W_1 holds at t it must hold at $t+\Delta t$:

$$W_1(f_2) = \int df_1 W_1(f_1) W(f_1|f_2,\Delta t)\,, \tag{45}$$

or

$$0 = \int df_1 \Pi(f_1, f_2) W_1(f_1)\,, \tag{45a}$$

or, finally,

$$\omega_e(f_2) W_1(f_2) = \int df_1 P(f_1, f_2) W_1(f_1) \omega_e(f_1)\,. \tag{45b}$$

We see from comparing (45b) with (43b) that $P(f_1, f_2)$ is not symmetrical in its arguments. This could be avoided very easily by using instead the function $\omega_e(f_1)W_1(f_1)P(f_1, f_2)$ which is symmetrical, at least in all cases we consider. This corresponds to defining a second-order probability $W'(f_1|f_2,\Delta t)$ which is the probability that the value is f_1 at t and f_2 at $t+\Delta t$, which is symmetrical unless the process violates microscopic reversibility.

---

* All equations like the following can be written either as though f has a continuous range, in which case $\int df$ can be used, or as though f is discrete, in which case they are to be written as $\sum_f$. The one way of writing is generally obvious if the other is given, so that I shall not give both except where confusion might arise.

With this brief introduction to Markoffian theory, let us see what can be done with (26) if $\Delta\omega_{ij}(t)$ is our Markoffian function $f(t)$. A matrix method of solution is used* in which we consider the probabilities $W(f_1, f_2)$ or $P(f_1, f_2)$ as two-dimensional matrices connecting the sets of indices f_1 to f_2; thus possibly for the following the assumption that $\Delta\omega$ has a discrete set of values will be more convenient.

The average in (26) may be written in the following way. We divide the interval τ into n equally spaced steps, such that τ/n is very small compared with the rate of change of $\Delta\omega$; then (42) will hold. The averagand is

$$\exp\left(i\sum_{m=1}^{n}\frac{\tau}{n}\Delta\omega\left(t+m\frac{\tau}{n}\right)\right)$$
$$=\exp\left(i\int_t^{t+\tau}\Delta\omega(t')dt'\right). \qquad (46)$$

Now we want to know the probability that $\Delta\omega$ takes on a certain set of values at the various instants in equation (46): i.e., that

$$\Delta\omega\left(t+\frac{\tau}{n}\right)=\Delta\omega_1\,, \qquad \Delta\omega\left(t+2\frac{\tau}{n}\right)=\Delta\omega$$
$$\cdots\Delta\omega\left(t+\frac{m\tau}{n}\right)=\Delta\omega_m\,.$$

This is easily found (see, again, Wang and Uhlenbeck (1945)). The probability is

$$P(\Delta\omega_1\Delta\omega_2\cdots\Delta\omega_n)=W_1(\Delta\omega_1)\,W\left(\Delta\omega_1|\Delta\omega_2,\frac{\tau}{n}\right)$$
$$\times W\left(\Delta\omega_2|\Delta\omega_3,\frac{\tau}{n}\right)\times\cdots\times W\left(\Delta\omega_{n-1}|\Delta\omega_n,\frac{\tau}{n}\right). \qquad (47)$$

Now we can find (26) simply by summing the product of (46) and (47) over all the possible combinations of $\Delta\omega$'s, since these are respectively the value and the probability of a given averagand.

$$\varphi(\tau)=\sum_{\Delta\omega_1}\sum_{\Delta\omega_2}\sum_{\Delta\omega_3}\cdots\left(\exp\left(i\frac{\tau}{n}\sum_{m=1}^{n}\Delta\omega_m\right)\right)$$
$$\times W_1(\Delta\omega_1)\prod_{m=2}^{n}W\left(\Delta\omega_{m-1}|\Delta\omega_m,\frac{\tau}{n}\right). \quad (48)$$

$$\sum_{\Delta\omega_1}\sum_{\Delta\omega_2}\cdots\sum\prod_{m=1}^{n-1}\left(\exp\left(i\frac{\tau}{n}\Delta\omega_m\right)\right.$$
$$\left.\times W\left(\Delta\omega_m|\Delta\omega_{m+1},\frac{\tau}{n}\right)\right)\exp\left(i\Delta\omega_n\frac{\tau}{n}\right).$$

Now the central product has the form of a matrix product. It will have this form exactly if we define the diagonal matrix $\underline{\underline{\Delta\omega}}$:**

$$(\underline{\underline{\Delta\omega}})_{\Delta\omega_1\Delta\omega_2}=\delta(\Delta\omega_1, \Delta\omega_2)\times\Delta\omega_1 \qquad (49)$$

which has the effect in matrix multiplication simply of multiplying any matrix element $\underline{\underline{M}}_{\Delta\omega_1\Delta\omega_2}$ by $\Delta\omega_1$. The probability matrix has already been suggested:

$$\underline{\underline{W}}\left(\frac{\tau}{n}\right)_{\Delta\omega_1\Delta\omega_2}=W\left(\Delta\omega_1|\Delta\omega_2,\frac{\tau}{n}\right). \quad (50)$$

We also introduce $\underline{W_1}(\Delta\omega)$ as a row vector in $\Delta\omega$ space, and $\underline{1}\,(\Delta\omega)$, the vector all of whose components are unity, as a column vector.

Neglecting $\Delta\omega_n\cdot\tau/n$ at once compared to unity, we can write (48) as a matrix product multiplied on left and right by row and column vectors respectively:

$$\varphi(\tau)=\underline{W_1}\cdot\left(\exp\left(i\frac{\tau}{n}\underline{\underline{\Delta\omega}}\right)\underline{\underline{W}}\left(\frac{\tau}{n}\right)\right)^{n-1}\cdot\underline{1}\,. \qquad (48a)$$

Now, since $\tau/n\cdot\Delta\omega$ can be made as small as we like, it is permissible to let

$$\underline{\underline{\exp\left(i\frac{\tau}{n}\Delta\omega\right)}}=\underline{\underline{1}}+i\frac{\tau}{n}\underline{\underline{\Delta\omega}}$$

while from (42) we can rewrite the matrix W in terms of a matrix $\underline{\underline{\Pi}}$:

$$\underline{\underline{W}}\left(\frac{\tau}{n}\right)=\underline{\underline{1}}+\underline{\underline{\Pi}}\frac{\tau}{n}\,.$$

This gives us for the product in (48a)

$$\left(\underline{\underline{\exp\left(i\frac{\tau}{n}\right.}}\left.\Delta\omega\right)\underline{\underline{W\left(\frac{\tau}{n}\right)}}\right)^{n-1}$$
$$=\left(1+\frac{\tau}{n}(i\underline{\underline{\Delta\omega}}+\underline{\underline{\Pi}})\right)^{n-1}$$

which, letting, n go to infinity, is

$$\underline{\underline{\exp(\tau(i\Delta\omega+\Pi))}}$$

so that (48) becomes

$$\varphi(\tau)=\underline{W_1}\cdot\underline{\underline{\exp(\tau(i\Delta\omega+\Pi))}}\cdot\underline{1}$$

or,

---

* The method was suggested by the Kramers-Wannier (1941) method in statistical mechanics.

** We shall underline vectors once, matrices twice in this vector space, the coordinates of which are numbers referring to the various possible values of $\Delta\omega$.

$$\varphi(\tau)=\sum_{\Delta\omega_1,\Delta\omega_2}\underline{W_1}(\Delta\omega_1)\{\underline{\underline{\exp(\tau(i\Delta\omega+\Pi))}}\}\Delta\omega_1,\Delta\omega_2 \tag{49}$$

Equation (49) is the general solution of our problem. It expresses $\varphi(\tau)$ in terms of the known matrices $\underline{\underline{\Pi}}$, defining the Markoffian process, and $\underline{\underline{\Delta\omega}}$, and the function $\underline{W_1}(\Delta\omega_1)$ (actually derivable from $\underline{\underline{\Pi}}$ by the integral equation (45b).)

We see now the form which the solution to this problem will take. The basic problem will be to diagonalize the matrix $(\underline{\underline{i\Delta\omega+\Pi}})$ by means of a transformation matrix $\underline{\underline{T}}$:

$$\underline{\underline{T}}^{-1}(\underline{\underline{i\Delta\omega+\Pi}})\underline{\underline{T}}=\underline{\underline{\Lambda}}\ ,$$

where $\underline{\underline{\Lambda}}$ is a diagonal matrix. If we can find $\underline{\underline{\Lambda}}$ and $\underline{\underline{T}}$, we can transform the two vectors $\underline{W_1}$ and $\underline{1}$ by means of $\underline{\underline{T}}$ into the coordinate system in which $\underline{\underline{i\Delta\omega+\Pi}}$ is diagonal. $\varphi(\tau)$ will then be a sum of exponentials $e^{-\Lambda_i\tau}$ in the eigenvalues* whose coefficients will depend on the extent to which their individual eigenvectors are contained in $\underline{W_1}$ and $\underline{1}$. Fourier transformation then shows us that $I(\omega)$ is a sum of resonance (Laplacian) distributions, with central frequencies given by the imaginary parts of the Λ_i, and widths by the negative real parts. In explicit form, we label the eigenvalues of $\underline{\underline{\Lambda}}$ with the subscript α, β etc. and the various $\Delta\omega$'s as before, and

$$\begin{aligned}\varphi(\tau)&=\sum_{\Delta\omega_1,\Delta\omega_2}(\underline{W_1})_{\Delta\omega_1}[\underline{\underline{\exp(\tau(i\Delta\omega+\Pi))}}]_{\Delta\omega_1\Delta\omega_2}\\&=\sum_{\Delta\omega_1,\Delta\omega_2,\Delta\omega_3,\Delta\omega_4}\ \sum_{\alpha,\beta}(\underline{W_1})_{\Delta\omega_1}\underline{\underline{T}}_{\Delta\omega_1\alpha}\underline{\underline{T}}_{\alpha\Delta\omega_2}{}^{-1}\\&\quad\times[\underline{\underline{\exp(\tau(i\omega+\Pi))}}]_{\Delta\omega_2\Delta\omega_3}\underline{\underline{T}}_{\Delta\omega_3\beta}\underline{\underline{T}}_{\beta\Delta\omega_4}{}^{-1}\\&=\sum_{\Delta\omega_1,\Delta\omega_2,\alpha}(\underline{W_1})_{\Delta\omega1}\underline{\underline{T}}_{\Delta\omega_1\alpha}\exp(\Lambda_\alpha\tau)\underline{\underline{T}}_{\alpha\Delta\omega_2}{}^{-1}\end{aligned}\tag{50}$$

so that the coefficient going with $\exp(\Lambda_\alpha\tau)$ is

$$\sum_{\Delta\omega_1,\Delta\omega_2}(\underline{W_1})_{\Delta\omega_1}\underline{\underline{T}}_{\Delta\omega_1\alpha}\underline{\underline{T}}_{\alpha\Delta\omega_2}{}^{-1}\ .$$

The two limiting cases of extreme narrowing and no narrowing come out of this formalism very easily. For little narrowing, we should be able to neglect transitions relative to the frequency differences, so that $\underline{\underline{i\Delta\omega}}\gg\underline{\underline{\Pi}}$. Then the matrix $\underline{\underline{i\Delta\omega+\Pi}}$ is already diagonal so that there is no necessity for using T (i.e. $T_{\alpha\Delta\omega}=\delta_{\alpha\Delta\omega}$) and the eigenvalues of $\underline{\underline{i\Delta\omega+\Pi}}$ are just $i\Delta\omega$. Equation (50) becomes

$$\varphi(\tau)=\sum_{\Delta\omega}W_1(\Delta\omega)e^{i\Delta\omega\tau}$$

which transforms into the spectrum

$$I(\omega)=\sum_{\Delta\omega}W_1(\Delta\omega)\delta_{\omega,\Delta\omega}=W_1(\omega)\ ,$$

which is just the spectrum we started with (since W_1 represents the normal stationary distribution of frequencies).

In the case of extreme narrowing, on the other hand, we can at first neglect $\underline{\underline{i\Delta\omega}}$ relative to $\underline{\underline{\Pi}}$. Now we really know without further specification only one eigenvalue of $\underline{\underline{\Pi}}$: namely, the eigenvalue zero, which corresponds to the right eigenvector $\underline{1}$, the left eigenvector $\underline{W_1}$. This is easily seen from the equations (43a) and (45a), which in sum notation read

$$\sum_{\Delta\omega_1}\underline{W_1}(\Delta\omega_1)\underline{\underline{\Pi}}_{\Delta\omega_1\Delta\omega_2}=(\underline{W_1}\cdot\underline{\underline{\Pi}})_{\Delta\omega_2}=0\ ,$$

and

$$\sum_{\Delta\omega_2}\underline{\underline{\Pi}}_{\Delta\omega_1\Delta\omega_2}=(\underline{\underline{\Pi}}\cdot\underline{1})_{\Delta\omega_1}=0\ .$$

This is a fortunate situation: it shows us that the vectors we actually happen to have in (49) for this case are the eigenvectors of the only eigenvalue we know exactly, so that the transformation matrix $\underline{\underline{T}}$ has non-vanishing coefficients only for this one eigenvalue, and

$$\varphi(\tau)=1\ .$$

This of course gives us an infinitely sharp line at the central frequency: $I(\omega)=\delta(\omega)$.

Next we consider the effect of including $\underline{\underline{i\Delta\omega}}$ in the calculation to first or second order. In the first order, obviously all that happens is to change the eigenvalue by $\langle i\Delta\omega\rangle_{\text{ave.}}$: the center of our narrowed distribution is at the average frequency of the un-narrowed distribution. To second order, the other eigenvalues of $\underline{\underline{\Pi}}$ will begin to enter to some extent, but this is a minor effect, since the greater part of the line intensity will still be in the zero-eigenvalue line. This line, however, will also be affected, since the eigenvalue will be changed by an amount of order of magnitude $1/\Pi(i\Delta\omega)^2$. This can easily be shown to be a real negative contribution and means that the line has a breadth of order

---

* Note: For negative τ it may be easily verified that $\varphi(-\tau)=\varphi^*(\tau)$ so that, for negative τ, Λ_i must be replaced by $-\Lambda_i^*$. If this were not true the spectral intensity would take on complex values.

$(\Delta\omega)^2/\omega_e$, the usual "narrowed" breadth. Thus here again we see the basic features of the exchange narrowing phenomenon coming out.

It is of interest, both in clarifying the previous discussion and in bringing out further points, to actually work out some simple cases as far as possible. The simplest possible case is that in which we have only two possible frequency shifts, which we take (this is of course no specialization) to be $\pm\omega_0$, and these frequencies are equally probable so that $W_1(+\omega_0)=W_1(-\omega_0)$. The only possible "transition-matrix" $\underline{\underline{\Pi}}$ for this case is

$$\underline{\underline{\Pi}}=\begin{bmatrix} -\omega_e & \omega_e \\ \omega_e & -\omega_e \end{bmatrix}, \tag{51}$$

where ω_e is an adjustable parameter specifying the rate at which jumping takes place back and forth between the two frequencies. The matrix we wish to diagonalize is then

$$\underline{\underline{(i\Delta\omega+\Pi)}}=\begin{bmatrix} i\omega_0-\omega_e & \omega_e \\ \omega_e & i\omega_0-\omega_e \end{bmatrix}. \tag{52}$$

The secular equation is easily seen to be, (if λ is the eigenvalue)

$$(\omega_e+\lambda)^2+\omega_0{}^2-\omega_e{}^2=0\,,$$

or

$$\lambda=-\omega_e\pm\sqrt{\omega_e{}^2-\omega_0{}^2}\,. \tag{53}$$

Defining

$$x=\omega_0/\omega_e\,, \tag{54}$$

as the ratio of splitting to jump-rate,

$$\lambda=-\omega_e\ (1\pm\sqrt{1-x^2})\,. \tag{53a}$$

Equation (53a) already says a great deal about the spectrum, since it gives the center frequencies and the breadths of the two component lines. For $x>1$ (splitting predominant) (53) reads

$$\lambda=\pm i\sqrt{\omega_0{}^2-\omega_e{}^2}-\omega_e\,, \tag{53b}$$

which says that the two lines at $\pm\omega_0$ begin to draw together as the jump-rate increases but always have the breadth (half at half power) ω_e, given by the rate of jumping, so long as $x>1$. The breadth ω_e corresponds to the "exchange broadening" idea: lines separated by splittings large compared to the exchange frequency are broadened, not narrowed.

This tendency of the lines to draw closer together before being completely narrowed out seems to be experimentally confirmed by various measurements on hyperfine structure in dilute solutions of paramagnetic ions.* It seems to be a general property of the secular equations, although it can be less pronounced for larger numbers of lines, as we shall see.

In the case in which the jumping predominates, $x<1$, we have equation (53a), with no imaginary part of λ at all: both component lines are centered at the mean frequency. One line has a breadth of order of magnitude $2\omega_e$, the other a breadth (if $\omega_e\gg\omega_0$)

$$\Delta\omega=-\omega_e\left(1-\sqrt{1-\frac{\omega_0{}^2}{\omega_e{}^2}}\right)$$

$$\simeq\frac{\omega_0{}^2}{2\omega_e}\,,$$

which exhibits the usual exchange narrowing form. This is the line which predominates: we shall see that the effect of the other line is simply to introduce a cutoff in the wings so that these fall off as $1/\omega^4$ rather than $1/\omega^2$. (Note that the fourth moment is infinite, as is to be expected from the theorems of Appendix I.)

Proceeding with the calculations of the explicit line shape, we define the two roots as

$$\left.\begin{aligned} \lambda_1&=-\omega_e(1-\sqrt{1-x^2}) \\ \lambda_2&=-\omega_e(1+\sqrt{1-x^2}) \end{aligned}\right\} \tag{55}$$

The components of the transforming matrix $\underline{\underline{T}}$ must satisfy**:

$$\left.\begin{aligned} (i\omega_0-\omega_e-\lambda_1)T_{11}+\omega_e T_{21}&=0 \\ (i\omega_0-\omega_e-\lambda_2)T_{22}+\omega_e T_{12}&=0 \end{aligned}\right\} \tag{56}$$

Now the correlation function is

$$\varphi(\tau)=\sum_{\lambda=\lambda_1,\lambda_2}\ \sum_{\Delta\omega_1,\Delta\omega_2=\pm\omega_0}\underline{\underline{T}}_{\Delta\omega_1\lambda}e^{\lambda\tau}\underline{\underline{T}}_{\lambda\Delta\omega_2}{}^{-1} \tag{57}$$

so the coefficient of the λ_1 term, for instance, is

$$T_{11}T_{11}{}^{-1}+T_{21}T_{12}{}^{-1}+T_{21}T_{11}{}^{-1}+T_{11}T_{12}{}^{-1}.$$

We use the fact that $TT^{-1}=1$ to combine the first two terms, and using the orthogonality of T to effect further simplification it can eventually be shown that

---

* Schneider and England, 1951: they mention the effect on p. 225, and also it is evident in the 1N picture of their fig. 3. Garstens (1952) has also mentioned this effect.

** Note that this case involves a complex symmetric matrix $\underline{\underline{(i\Delta\omega+\Pi)}}$ so that a diagonalizing matrix can certainly be found. It can in fact be chosen to be a complex orthogonal matrix.

$$\left.\begin{aligned}\varphi(\tau)=&\exp\{-\omega_e\tau(1-\sqrt{1-x^2})\}\left(1+\frac{1}{\sqrt{1-x^2}}\right)\\&+\exp\{(-\omega_e\tau(1+\sqrt{1-x^2})\}\left(1-\frac{1}{\sqrt{1-x^2}}\right)\end{aligned}\right\} \tag{58}$$

To obtain the spectrum from (58), we must separate the two cases $x>1$ and $x<1$. For $x>1$ (splitting predominant) we get

$$\begin{aligned}I(\omega)=\int_0^\infty e^{-\omega_e\tau}\Big[&\cos(\omega+\omega_e\sqrt{x^2-1})\tau\\&+\frac{1}{\sqrt{x^2-1}}\sin(\omega+\omega_e\sqrt{x^2-1})\tau\\&+\cos(\omega-\omega_e\sqrt{x^2-1})\tau\\&-\frac{1}{\sqrt{x^2-1}}\sin(\omega-\omega_e\sqrt{x^2-1})\tau\Big]\end{aligned}$$

(the sine terms entering because, again, $\varphi(-\tau)=\varphi^*(\tau)$ so that the imaginary coefficients must change sign upon change of sign of τ.) This gives us

$$\begin{aligned}I(\omega)=2\Big[&\frac{2\omega_e+\omega/\sqrt{x^2-1}}{(\omega+\omega_e\sqrt{x^2-1})^2+\omega_e^2}\\&+\frac{2\omega_e-\omega/\sqrt{x^2-1}}{(\omega-\omega_e\sqrt{x^2-1})^2+\omega_e^2}\Big].\end{aligned} \tag{59a}$$

We note here that the spectrum is not exactly the sum of two resonance distributions, because of the imaginary terms which give us the odd terms in the numerator; but if $1\ll x$ or ω is not comparable with ω_0 (i.e. near the centers of the lines) the difference is small. However, as $x\to1$ these terms take on major importance in making the transition to the narrowed case, in which the signs of the two distributions are opposite. A summed form of (59a) will be of interest: It is

$$\begin{aligned}I(\omega)=&\frac{8\omega_e^3x^2}{\omega^4+2\omega^2\omega_e^2(2-x^2)+\omega_e^4x^4}\\&-\frac{8\omega_e\omega_0^2}{\omega^3+2\omega^2(2\omega_e^2-\omega_0^2)+\omega_0^4}.\end{aligned} \tag{59b}$$

This is the same as the expression which has been obtained by Archer (1953) by an entirely different method. It is rather interesting that this summed expression is identical in the two cases $x<1$ and $x>1$, in spite of the apparent discontinuity in λ_1 and λ_2 between the two cases.

For $x<1$ the same procedure can be followed, although here the mathematics is a little simpler.

$$\begin{aligned}I(\omega)=&2\int_0^\infty\cos\omega\tau e^{-\omega_e\tau}\Big(\exp(+\omega_e\sqrt{1-x^2}\tau)\\&\times\left(1+\frac{1}{\sqrt{1-x^2}}\right)+\exp(-\omega_e\sqrt{1-x^2}\tau)\\&\times\left(1-\frac{1}{\sqrt{1-x^2}}\right)\Big)\\=&\frac{2\omega_ex^2}{\sqrt{1-x^2}}\Big[\frac{1}{\omega^2+\omega_e^2(1-\sqrt{1-x^2})^2}\\&-\frac{1}{\omega^2+\omega_e^2(1+\sqrt{1-x^2})^2}\Big].\end{aligned} \tag{59c}$$

Note the behavior of (59c) when $x\ll1$. Then the first term will far overshadow the second until $\omega\sim\omega_e$; at this point the two begin to be approximately equal, and thus the wings of the line fall off more rapidly than $1/\omega^2$ beyond this point.

The two terms of (59c) can be added together:

$$\begin{aligned}I(\omega)=&\frac{2\omega_ex^2}{\sqrt{1-x^2}}\frac{(4\omega_e^2\sqrt{1-x^2})}{\omega^4+\omega_e^4(1+1-x^2)-2\omega_e^4\sqrt{1-x^2}}\\&\qquad\times(\omega^2+\omega_e^2(1+1-x^2)+2\omega_e^2\sqrt{1-x^2})\\=&\frac{8\omega_e^3x^2}{\omega^4+2\omega^2\omega_e^2(2-x^2)+\omega_e^4x^4}\end{aligned}$$

and we get (59b), again in agreement with Archer.

Archer's form can be used to show that the "two-line" formulas such as (53) must not be taken too seriously: the imaginary part of λ does not give exactly the frequency of the maxima of the spectrum, nor do these maxima come together exactly at $x=1$; it gives rather a way of dividing the spectrum into two "lines". The actual maxima occur at the minima of the denominator in (59b) which come at

$$\left.\begin{aligned}&\omega_{\max}=\pm\sqrt{\omega_0^2-2\omega_e^2}\qquad&x^2>2\\&\omega_{\max}=0&x^2<2\end{aligned}\right\} \tag{60}$$

In figures 1 and 2 are plotted some of these results. Figure 1a shows both the imaginary part of λ (the nominal frequency of the lines) and the maxima (60) plotted against x (we plot ω/ω_0 to show the effect of narrowing). Figure 1b gives the nominal half-breadth, λ_{real} (divided by ω_e), as a function of x. There is not much point in finding the true half-breadth from (59b) since the line shape is not even approximately resonance in the intermediate region where corrections are important. In figure 2 a few of the complete line shapes are plotted for the inter-

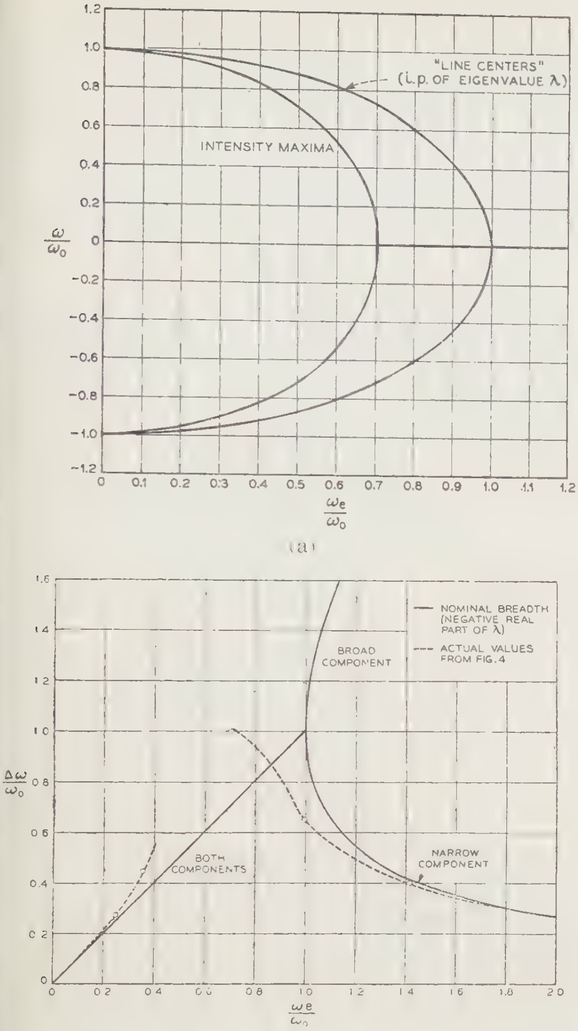

(b)

Fig. 1. Line breadths and frequencies for a pair of lines under exchange or motional narrowing.

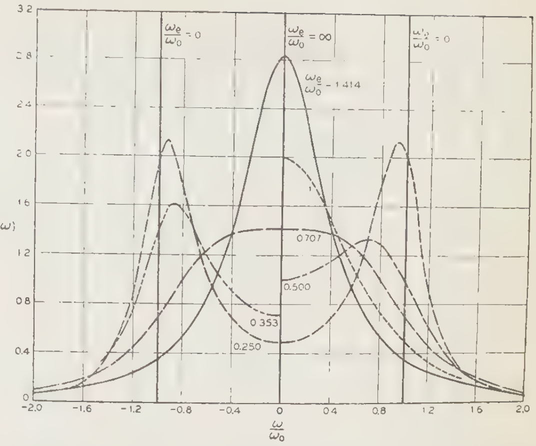

Fig. 2. Spectral intensity for a pair of lines with the ratio ω_e/ω_0 of jump-rate to splitting as parameter.

mediate region.

This very simple two-frequency case is the only one which is easily done exactly. It would be possible, but not very fruitful, to solve three- and four-line cases, which could of course be done in general. It seems to me more interesting to develop some fairly general perturbation methods for dealing with certain classes of cases involving many lines, so that we can get a rough idea of the behavior in the strong and weak narrowing regions.

The correct approach in the weak narrowing case is quite obvious: ordinary perturbation theory. Here the secular equation is nearly diagonal already, since we assume $i\Delta\omega \gg \Pi$. To first order, the j'th eigenvalue is just the j'th diagonal element:

$$\lambda_j^{(1)} = i\omega_j + \Pi_{jj} = i\omega_j - \omega_e(j) \,. \qquad (61)$$

This means that the individual lines are at first only broadened slightly by the frequency jumps. The second-order perturbation theory gives

$$\lambda_j^{(2)} = -\omega_e(j) + i\left(\omega_j - \sum_k \frac{\Pi_{jk}\Pi_{kj}}{\omega_j - \omega_k}\right). \qquad (62)$$

We see that there is a frequency-shift, of second order in Π (or ω_e) which, it is easily verified, is such as to shift the lines towards the center of the pattern. However, it is possible in some cases that the shift will not occur for all lines of a pattern, as we shall see, since it requires that there be more transition probability toward the center of the pattern than toward the edges *for each individual line,* which is not necessarily always the case.

We can give the expression for (62) for two simple cases which we shall consider as typical of two possible extremes. In each case we consider that the spectrum consists of a series of n equally spaced, equally strong lines, of frequencies

$$\omega_j = (n-1)i\omega_0,\ (n-3)i\omega_0 \cdots (-n+3)i\omega_0,$$
$$(-n+1)i\omega_0 \,. \qquad (63)$$

In case (a) we say that transitions are equally likely to all other lines of the spectrum (we assume a symmetrical Π-matrix) so that

$$\Pi_a=\left(\begin{array}{ccccccc} -\omega_e & \frac{\omega_e}{n-1} & \frac{\omega_e}{n-1} & - & - & - & \frac{\omega_e}{n-1} \\ \frac{\omega_e}{n-1} & -\omega_e & \frac{\omega_e}{n-1} & - & - & - & - \\ \frac{\omega_e}{n-1} & \frac{\omega_e}{n-1} & -\omega_e & - & - & - & - \\ \cdot & - & - & - & - & - & - \\ \cdot & - & - & - & - & - & - \\ \cdot & - & - & - & - & - & - \\ \frac{\omega_e}{n-1} & - & - & - & - & - & -\omega_e \end{array}\right) \tag{64}$$

The transition probability *from* each line is ω_e. In case (b) we say that transitions occur only to the nearest lines, and so except for the end lines each line must have a probability for transition from it of ω_e, to each of its neighbors of $\omega_e/2$. This gives

$$\Pi_b=\left(\begin{array}{cccccccc} -\frac{\omega_e}{2} & \frac{\omega_e}{2} & 0 & 0 & - & - & - & 0 \\ \frac{\omega_e}{2} & -\omega_e & \frac{\omega_e}{2} & - & - & - & - & - \\ 0 & \frac{\omega_e}{2} & -\omega_e & - & - & - & - & - \\ 0 & 0 & \frac{\omega_e}{2} & - & - & - & - & - \\ 0 & - & - & - & - & - & - & - \\ \cdot & - & - & - & - & - & \frac{\omega_e}{2} & 0 \\ \cdot & - & - & - & - & - & -\omega_e & \frac{\omega_e}{2} \\ 0 & - & - & - & - & 0 & \frac{\omega_e}{2} & -\frac{\omega_e}{2} \end{array}\right) \tag{65}$$

For case (a), (62) gives for the original line of frequency $m\omega_0$,

$$(\lambda_m)_a=-\omega_e+i\left(m\omega_0-\sum_{l=-n+1}^{n-1}{}' \omega_0\frac{\omega_e^2}{(n-1)^2}\times\frac{1}{m-k}\right).$$

(The prime, of course, means $k\neq m$). The pattern is symmetrical about 0, so pick $m>0$. Then

$$(\lambda_m)_a=-\omega_e+i\left(m\omega_0-\frac{\omega_e^2}{(n-1)^2\omega_0}\sum_{l=(n+1)-m}^{(n-1)+m}\frac{1}{l}\right). \tag{66}$$

(It must be remembered that all sums here are by steps of two.)

Case (b) is simpler. Clearly, all of the lines except the end ones are unshifted, as we suggested before could happen. The central lines have:

$$(\lambda_m)_b\big|_{|m|\neq n-1}=im\omega_0-\omega_e\,; \tag{67}$$

while the end lines obey

$$(\lambda_m)_b\big|_{m=\pm(n-1)}=-\frac{\omega_e}{2}+i\left((n-1)\omega_0-\frac{\omega_e^2}{8\omega_0}\right). \tag{68}$$

For the simple case of $n=4$ it might be useful to write down the various breadths and shifts, in Table I.

Table I

Line	Case a		Case b	
	breadth	shift	breadth	shift
$3\omega_e$	ω_e	$-\frac{11\,\omega_e^2}{108\,\omega_0}$	$\frac{\omega_e}{2}$	$-\frac{\omega_e^2}{8\,\omega_0}$
ω_0	ω_e	$-\frac{\omega_e^2}{36\,\omega_0}$	ω_e	0
$-\omega_0$	ω_e	$+\frac{\omega_e^2}{36\,\omega_0}$	ω_e	0
$-3\omega_0$	ω_e	$+\frac{11}{108}\frac{\omega_e^2}{\omega_0}$	$\frac{\omega_e}{2}$	$+\frac{\omega_e^2}{8\,\omega_0}$

It is interesting to note that the shifts are rather small, and also that the sum of the shifts of the two lines on one side of the center is roughly the same in the two cases. The smallness is checked by experiment, in that the lines seem to shift only a very little before they merge and begin to narrow as a group.

Finally, it has been checked, in connection with these formulas and with Table II, that the change in the amplitudes with which the various components enter is of still higher order in ω_e/ω_0 and will probably not be noticeable until the perturbation treatment breaks down entirely.

The approximation from the opposite end of the scale, large narrowing, ($\underline{\underline{\Pi}}\gg \underline{\underline{i\Delta\omega}}$) is based on the observation we have already made, that the line-shape at this end is determined by the one eigenvalue λ near zero; all others represent broad, weak components of the line and can be neglected. Thus we can set λ nearly equal to zero; this implies that the large terms in the secular equation are those with low powers of λ, which we now set out to compute.

The constant term in the secular equation is the determinant, $|i\Delta\omega+\Pi|$. We note that $|\Pi|=0$, and that if the pattern is symmetrical there must be no imaginary terms so that the first terms here are of order ω_0^2. The term in λ in the secular equation is made up of the product of the various subdeterminants times λ:

$$(-\lambda)\sum_j |i\Delta\omega+\Pi|^{jj}$$

where this denotes the determinant with the j'th row and column omitted. If $\sum_j |\Pi|^{jj}\neq 0$, it certainly will overwhelm $i\Delta\omega$, so that this term is of order $\lambda\Pi\sim\omega_0^2$, as we shall see. The next term must be of order $\lambda^2\sim\omega_0^4$, so we can omit it. We have then

$$-\lambda\sum_j|\Pi|^{jj}+|i\Delta\omega+\Pi|=0$$

$$\lambda=\frac{|i\Delta\omega+\Pi|_{\omega_0^2\text{terms}}}{\sum_j|\Pi|^{jj}}\,. \tag{69}$$

Examples will make this much clearer. We consider again the problems of Cases (a) and (b), defined by the transition matrices (64) and (65). In case (a)

$$\sum_j|\Pi|^{jj}=n\begin{array}{c|cccccc|l}
 & \multicolumn{6}{c}{n-1 \text{ columns}} & \\
 & -\omega_e & \frac{\omega_e}{n-1} & \frac{\omega_e}{n-1} & - & - & \frac{\omega_e}{n-1} & \\
 & \frac{\omega_e}{n-1} & -\omega_e & & & & \cdot & \\
 & \cdot & \cdot & & & & \cdot & n-1 \\
 & \cdot & \cdot & & & & \cdot & \text{rows} \\
 & \frac{\omega_e}{n-1} & - & - & - & - & -\omega_e &
\end{array}$$

This determinant can be evaluated to give

$$\sum_j|\Pi|^{jj}=\left(\frac{-n\omega_e}{n-1}\right)^{n-1}. \tag{70}$$

Now we want to compute the ω_0^2 terms in $|i\omega+\Pi|$.

$$|i\omega+\Pi|=\begin{vmatrix}
(n-1)i\omega_0-\omega_e & \frac{\omega_e}{n-1} & \frac{\omega_e}{n-1} & ---- & \frac{\omega_e}{n-1} \\
\frac{\omega_e}{n-1} & (n-3)i\omega_0-\omega_e & \frac{\omega_e}{n-1} & -------- & \\
\frac{\omega_e}{n-1} & \frac{\omega_e}{n-1} & (n-5)i\omega_0-\omega_e & ---- & \\
- & - & - & - &
\end{vmatrix}$$

The terms in $i\omega_0$, as already pointed out, vanish by cancellation between $+$ and $-\omega_j$. The terms in ω_0^2 can be picked out and are

$$|i\omega+\Pi|_{\omega_0^2}=\sum_{m<m'}(i\omega_0)^2mm'\left(\frac{\omega_e}{n-1}\right)^{n-2}$$
$$\times\begin{vmatrix}
1-n & 1 & 1 & 1 & \cdots & 1 \\
1 & 1-n & 1\ \cdots & 1 & \cdots & \\
1 & 1 & 1-n\ \cdots & & & \\
- & - & -\ \cdots & & &
\end{vmatrix}\begin{matrix}(n-2\\ \text{rows})\end{matrix} \tag{71}$$

This determinant and the sum are easily evaluated. The result is

$$|i\omega+\Pi|_{\omega_0^2}=\frac{n^2-1}{3}\,\omega_0^2\left(\frac{-n\omega_e}{n-1}\right)^{n-2} \tag{72}$$

and finally, the eigenvalue of interest is

$$\lambda=-\frac{\omega_0^2}{\omega_e}\,\frac{(n-1)^2(n+1)}{3n}\,. \tag{73}$$

Note that this expression (which is the breadth of the narrowed line in this case) represents roughly the ratio of the square of the breadth of the pattern ($n\omega_0$) to the rate at which the frequency changes (ω_e).

Case (b) can also be done in general. $\sum_j|\Pi|^{jj}$ can be seen to be the sum of all the possible partitions into pieces of form

$$\begin{array}{l|cccccc|}
 & \multicolumn{6}{c}{(m \text{ columns})} \\
 & -\omega_e & \frac{\omega_e}{2} & 0 & - & - & - \\
 & \frac{\omega_e}{2} & -\omega_e & \frac{\omega_e}{2} & & & - \\
m \text{ rows} & 0 & \frac{\omega_e}{2} & -\omega_e & & & - \\
 & & & & & -\omega_e & \frac{\omega_e}{2} \\
 & 0 & - & - & 0 & \frac{\omega_e}{2} & -\frac{\omega_e}{2}
\end{array}$$

$$=\left[-\left(\frac{\omega_e}{2}\right)\right]^m \tag{74}$$

by a simple computation. Adding the partitions together we get

$$\sum_j|\Pi|^{jj}=n\left(-\frac{\omega_e}{2}\right)^{n-1}. \tag{75}$$

Now we must find $|i\omega+\Pi|_{\omega_0^2\text{terms}}$. The determinant $|i\omega+\Pi|$ is

$$|i\Delta\omega+\Pi|=\left|\begin{array}{ccccc} (n-1)i\omega_0-\frac{\omega_e}{2} & \frac{\omega_e}{2} & 0 & 0 & \text{—} \\ \frac{\omega_e}{2} & (n-3)i\omega_0-\omega_e & \frac{\omega_e}{2} & 0 & \text{—} \\ 0 & \frac{\omega_e}{2} & (n-5)i\omega_0-\omega_e & \frac{\omega_e}{2} & 0 \\ 0 & 0 & \text{—} & \text{—} & \\ \cdot & \cdot & & & \frac{\omega_e}{2} \\ \cdot & \cdot & & & \\ \cdot & \cdot & & & \\ 0 & \text{—} & \text{—} & \frac{\omega_e}{2} & \left(-(n-1)i\omega_0\frac{-\omega_e}{2}\right) \end{array}\right| \qquad (76)$$

This may be broken up into a sum of terms containing $(im\omega_0)$ $(im'\omega_0)$ with $m>m'$. Multiplying these terms will be a product of three sub-determinants A, B, and C, with A being the part above $im\omega_0$. A and C will be of the form (74) with $(n-1-m)/2$ and $(n-1+m')/2$ rows and columns respectively.

$$A=\left(-\frac{\omega_e}{2}\right)^{((n-1)-m)/2}$$

$$C=\left(-\frac{\omega_e}{2}\right)^{(m'+(n-1))/2}.$$

The terms between $im\omega_0$ and $im'\omega_0$ give another type of determinant:

$$B=\left|\begin{array}{cccccc} -\omega_e & \frac{\omega_e}{2} & 0 & 0 & \text{—} & 0 \\ \frac{\omega_e}{2} & -\omega_e & \frac{\omega_e}{2} & & & \text{—} \\ 0 & \frac{\omega_e}{2} & -\omega_e & & & \text{—} \\ 0 & 0 & & & & \text{—} \\ \text{—} & & & -\omega_e & \frac{\omega_e}{2} & 0 \\ \text{—} & & & \frac{\omega_e}{2} & -\omega_e & \frac{\omega_e}{2} \\ 0 & \text{—} & \text{—} & 0 & \frac{\omega_e}{2} & -\omega_e \end{array}\right|$$

$$\times\left(\frac{m-m'}{2}-1 \text{ rows and columns}\right)$$

$$B=\left(\frac{\omega_e}{2}\right)^{(m-m')/2-1}\left(\frac{m-m'}{2}\right)(-1)^{(m-m')/2-1}$$

by another computation.

Thus, finally, we have

$$|i\Delta\omega+\Pi|_{\omega_0^2\text{terms}} = -\omega_0^2\left(\frac{-\omega_e}{2}\right)^{n-2}\sum_{m>m'} mm'\left(\frac{m-m'}{2}\right). \qquad (77)$$

The summation in (77) can be evaluated by straightforward application of the various summation formulas for powers of integers, and the final result is

$$|i\Delta\omega+\Pi|_{\omega_0^2\text{terms}}=\left(\frac{-\omega_e}{2}\right)^{n-2}\omega_0^2\,\frac{n(n^4-1)}{30} \qquad (78)$$

and

$$\lambda=-\frac{(n^4-1)}{15}\frac{\omega_0^2}{\omega_e}. \qquad (79)$$

The fact that n^4 instead of n^2 (as in 73) appears in (79) for large n is reasonable on the following basis. The total width of the original pattern is $\sim n\omega_0$. This means that for λ to remain reasonable as $n\to\infty$ $\omega_e\sim n^2$; but this is correct, because this is the condition that the rate of diffusion remains reasonable. That is, the expression (79) is still the square of the band-width divided by the effective rate of change of frequency, which in this case of only short jumps is ω_e/n^2.

For such an unrealistic model further detailed study of particular discrete cases is hardly important. The next logical step is to consider continuous distributions of ω and, particularly, to consider a relatively realistic model of the effect of solid diffusion on unclear resonance breadths, which has been observed experimentally by Norberg and Slichter (1951). Diffusion in solids usually proceeds by jumps, short compared to the time between jumps. It is also true that a given atom nearly completely changes its magnetic environment with each jump (if the system is not dilute; diffusion in such a system as H in Pd or Na in NH_3 is quite a different thing, since there the perturbers are relatively far away compared to the jump distance, and there will be long-term correlation). If this is the case, we may assume that the new frequency to which a given atom jumps is unrelated to its old frequency.

Such a Markoff system can be set up, and integral equations found for the eigenvalues and eigenvectors. We shall do this, although we have not been able to solve the system in general, because of certain irregularities. However, the interesting case of extreme narrowing can be solved.

In the continuous case, the matrix $\underline{\underline{\Delta\omega}}$ can be written

$$(\underline{\underline{\Delta\omega}})_{\omega_1,\omega_2}=\omega_1\delta(\omega_1-\omega_2)\,. \qquad (80)$$

We assume that the frequencies are distributed according to some probability function $P(\omega)$. $P(\omega)$ (which we take to be normalized) is then the line shape in case the jump rate is slow. In accordance with our physical idea of what happens in the diffusion process, we assume that the probability of jumping *from* a given frequency per unit time is constant, $=\omega_e$. The probability of jumping *to* a given frequency ω_2 we assume unrelated to the previous frequency, so it can only be proportional to $P(\omega_2)$. These two criteria are satisfied if we set

$$\underline{\underline{\Pi}}(\omega_1,\,\omega_2)=\omega_e(-\delta(\omega_1-\omega_2)+P(\omega_2))\,. \quad (81)$$

We could check that with $W_1(\omega)=P(\omega)$, the two Smoluchowski equations (43a) and (45a) are satisfied.

Now our problem is simply to diagonalize the matrix $(i\Delta\omega+\Pi)$, which gives us an integral eigenvalue equation. We introduce the eigenvector $\psi(\omega_2)$, and the integral equation is

$$\int d\omega_2(i\underline{\underline{\Delta}}\omega+\underline{\underline{\Pi}})(\omega_1,\,\omega_2)\underline{\psi}(\omega_2)=\lambda\underline{\psi}(\omega_1)\,. \qquad (82)$$

Equation (82) may be written out using (80) and (81), and we get

$$(\lambda+\omega_e-i\omega_1)\psi(\omega_1)=\omega_e\int P(\omega_2)\psi(\omega_2)d\omega_2\,. \quad (83)$$

(83) can be solved in the two limiting cases of $\omega_e\to0$ and $\omega_e\to\infty$. In case $\omega_e\to0$, obviously

$$\psi(\omega_1)=\delta(\omega-\omega_1)$$

and

$$\lambda=i\omega\,.$$

Here the distribution is, of course, unchanged. In case $\omega_e\to\infty$, we may for practical purposes neglect $i\omega$ on the left, and then there are two possibilities: $\psi(\omega_1)=$constant, $\lambda=0$ or $\psi(\omega_1)=$any function orthogonal to $P(\omega_1)$, in which case both sides are zero and $\lambda=-\omega_e$. This reflects the fact that any distribution which is not $P(\omega)$ will decay according to $\exp(-\omega_e t)$ into $P(\omega)$; the eigenvalue $\lambda=0$ belongs to the stationary distribution. $\lambda=0$ means an infinitely narrow line, of course.

Mathematical difficulties immediately attend any perturbation approach from the side of $\omega_e=0$, because of the singularity of the eigenvectors; one easily sees that the perturbation of the eigenvector is also singular.

On the other end, a fairly satisfactory treatment of the eigenvalue coming from $\lambda=0$ can be done, as follows. The right-hand side of (83) is just a constant if it does not identically vanish; call this constant $\alpha\omega_e$, and we get

$$\psi(\omega_1)=\frac{\alpha\omega_e}{\lambda+\omega_e-i\omega_1}\,. \qquad (84)$$

But this must integrate to give α back again, so that

$$\int P(\omega)\frac{\alpha\omega_e}{\lambda+\omega_e-i\omega}=\alpha$$

$$1=\omega_e\int_{-\infty}^{\infty}\frac{P(\omega)}{\lambda+\omega_e-i\omega}\,d\omega.$$

Now we assume λ real and $P(\omega)$ an even function of ω. Then we get

$$1=\omega_e\int_0^\infty P(\omega)d\omega\left(\frac{1}{\lambda+\omega_e-i\omega}+\frac{1}{\lambda+\omega_e+i\omega}\right)$$

$$=2\omega_e\int_0^\infty P(\omega)d\omega\,\frac{\lambda+\omega_e}{(\lambda+\omega_e)^2+\omega^2}\,. \qquad (85)$$

This is a rigorous integral equation for the eigenvalue λ which, in principle, could be directly integrated at any time if we had the distribution $P(\omega)$.

Notice, however, that (85) will cease to furnish a real eigenvalue when ω_e becomes too small. For instance, imagine that $P(\omega)$ is a flat-topped distribution of width $2\omega_p$, height $1/2\omega_p$. Then the most the integral in (85) can give is $\pi/4\omega_p$, so the right-hand side is always less than $(\pi/2)\omega_e/\omega_p$. If ω_p is too large, this cannot equal 1.

We are, then, concerned primarily with the case in which the breadth of $P(\omega)$ is fairly small relative to ω_e. We can expand the integral, then, and get

$$1=\frac{2\omega_e}{\lambda+\omega_e}\int P(\omega)d\omega\left(1-\frac{\omega^2}{(\lambda+\omega_e)^2}\right)$$

or,

$$\lambda+\omega_e=\omega_e-\frac{\langle\omega^2\rangle_{\text{ave}}\omega_e}{(\lambda+\omega_e)^2}\ .$$

If ω_e is not too small, we can assume $\lambda\ll\omega_e$, and

$$\lambda\simeq-\frac{\langle\omega^2\rangle_{\text{ave}}}{\omega_e}\ . \tag{86}$$

This is a very simple formula, and entirely in accordance with our expectations. It can be assumed that since all other eigenvectors will be approximately orthogonal to $P(\omega)$, only this eigenvalue will be important for large narrowing, and (86) may be taken to be the breadth of the line.

Further mathematical manipulations with the continuous case have not been successful, nor is it certain that they are of much help in solving problems. It would be of some interest to have a solution for the effect of correlation between the frequencies before and after a jump, but this has not been attempted. A sounder physical basis for the calculations in this section would also be desirable.

I am indebted to a number of my colleagues for helpful discussion, notably Drs. Lewis, Holden and Machlup. Professor Van Vleck kindly showed me Archer's results prior to publication.

Appendix I

Proof of the General Fourier Integral Equation for the Spectrum

The spectrum is given in more familiar form in the following way. We take the energy levels $E_1, \cdots E_m \cdots$ of the entire substance. The spectral intensity of the radiation or absorption of the substance, as it is most usually defined (we omit external factors) is given by

$$I(\omega)d\omega=\sum_{m,n}{}' \,|\mu_{mn}|^2\rho(m) \tag{a}$$

where the prime on the sum means that we sum only over levels such that

$$E_m-E_n=\hbar\omega \tag{b}$$

to within the interval $\hbar d\omega$. μ is the dipole moment matrix of the substance. $\rho(m)$ is essentially $\exp(-E_m/kT)$; it is practically constant in a paramagnet in normal circumstances and so will hereafter be omitted for brevity. The difficulty all comes from the restriction of the sum due to (b); but this can be avoided by the well-known trick of using the δ-function expansion

$$2\pi\delta(x)=\int_{-\infty}^{\infty}e^{ixt}dt\,. \tag{c}$$

Then we get

$$I(\omega)=\sum_{m,n}\left|\int_{-\infty}^{\infty}dt\exp\left(-i\left(\omega-\frac{E_m-E_n}{\hbar}\right)t\right)\mu_{mn}\right|^2$$

where now the sum is unlimited. But

$$\exp\left(i\frac{(E_m-E_n)t}{\hbar}\right)\mu_{mn}=(\mu(t))_{mn}\ ,$$

the time-dependent matrix element of the dipole moment, which satisfies equation (3) of the text. Thus we have,

$$I(\omega)=\sum_{m,n}\left|\int_{-\infty}^{\infty}dte^{-i\omega t}\mu(t)\right|^2_{mn}$$

$$=Tr\left|\int_{-\infty}^{\infty}dt\mu(t)e^{-i\omega t}\right|^2.$$

In case we want to include the density function $\rho(m)$, this can easily be done; the result is the more general formula given in the reference, Anderson (1949).

Appendix II

Some Useful Theorems About the Relationship Between $\varphi(\tau)$, $I(\omega)$ and $\Delta\omega_{ij}(t)$

Theorem I.

$$\frac{(-i)^n\left.\dfrac{d^n\varphi}{d\tau^n}\right|_{\tau=0}}{\varphi_{\tau=0}}=\frac{\displaystyle\int_{-\infty}^{\infty}d\omega\omega^nI(\omega)}{\displaystyle\int_{-\infty}^{\infty}d\omega I(\omega)}$$

or, if $\varphi(0)=1$ and $I(\omega)$ is normalized to unity,

$$(-i)^n\left.\frac{d^n\varphi}{d\tau^n}\right|_{\tau=0}=\int_{-\infty}^{\infty}d\omega\omega^nI(\omega)\,;$$

and conversely, the same theorem is true with $I(\omega)$ replaced by $\varphi(\tau)$ and vice versa, and the sign of i changed. The theorem is not new and is proved trivially by differentiating and setting $\tau=0$. The theorem means that the moments of $I(\omega)$ are determined by the behavior of $\varphi(\tau)$ very close to the origin, which may (as we shall see by the next theorem) have very little to do with its general course. On the other hand, we know intuitively that $I(\omega)$ will not be peculiar at the origin (unless it happens to have line structure, which case we shall ignore for the time being) so that we expect the moments of $\varphi(\tau)$ to be normal and manageable, and to be closely related to the line-breadth.

Theorem II.

The second moment of $I(\omega)$, in case it is of the form (21) of the text, is independent of whether or how $\Delta\omega_{ij}(t)$ changes in time, but depends only on the probability distribution of $\Delta\omega_{ij}(t)$; in fact, it is given by $\overline{(\Delta\omega_{ij})^2}$.

This is easily proved from the first theorem. Starting with

$$\frac{d\varphi}{d\tau}=\langle i\Delta\omega_{ij}(t+\tau)\exp\left(i\int_t^{t+\tau}\Delta\omega_{ij}dt'\right)\rangle_{\text{ave.}}$$

we may shift the origin by an amount τ, so long as we leave the points equivalent to t and $t+\tau$ in the same relationship to each other. (This trick is not really necessary here, but will be useful for theorem III.) Thus we may write

$$\frac{d\varphi}{d\tau}=i\langle\Delta\omega_{ij}(t)\exp\left(i\int_{t-\tau}^{t}\Delta\omega_{ij}(t')dt'\right)\rangle_{\text{ave.}};$$

$$\frac{d^2\varphi}{d\tau^2}=-\langle\Delta\omega_{ij}(t)\Delta\omega_{ij}(t-\tau)\times\exp\left(i\int_{t-\tau}^{t}\Delta\omega_{ij}(t')dt'\right)\rangle_{\text{ave.}}.$$

Clearly,

$$\left.\frac{d^2\varphi}{d\tau^2}\right|_{\tau=0}=-\langle(\Delta\omega_{ij}(t))^2\rangle_{\text{ave. over }t},$$

and by theorem I we get our theorem. This theorem shows one of the many close analogies between our model and the real narrowing problem. Van Vleck (1948) shows the above relation to be true for the exchange narrowing problem—i.e. exchange cannot change the mean squared breadth—and it also can be shown for the motional narrowing problem, since it depends only on the assumption (a) of section II of this paper.

Another theorem showing the similarity of the model to the real problem is the following:

Theorem III.

$$\overline{\omega^4}=\left.\frac{d^4\varphi}{d\tau^4}\right|_{\tau=0}=\langle\Delta\omega_{ij}^4\rangle_{\text{ave.}}+\langle\left(\frac{d}{dt}\Delta\omega_{ij}\right)^2\rangle_{\text{ave.}}.$$

This is easily proved starting from the expression for $d^2\varphi/d\tau^2$ above. We get

$$\frac{d^3\varphi}{d\tau^3}=-\langle\Delta\omega_{ij}(t)\left(\frac{d}{d\tau}\Delta\omega_{ij}(t+\tau)+i\Delta\omega_{ij}^2(t-\tau)\right)\exp\left(i\int_{t-\tau}^{t}\Delta\omega_{ij}(t')dt'\right)\rangle_{\text{ave.}}$$

and now shifting the averaging variable back again to the original one by a change of τ, we get

$$\frac{d^3\varphi}{d\tau^3}=\langle\Delta\omega_{ij}(t+\tau)\left(\frac{d}{dt}\Delta\omega_{ij}(t)-i\Delta\omega_{ij}^2(t)\right)\times\exp\left(i\int_{t}^{t+\tau}\Delta\omega_{ij}(t')dt'\right)\rangle_{\text{ave.}}$$

$$\frac{d^4\varphi}{d\tau^4}=\langle\left(\frac{d}{dt}\Delta\omega_{ij}(t+\tau)+i\Delta\omega_{ij}^2(t+\tau)\right)\times\left(\frac{d}{dt}\Delta\omega_{ij}(t)-i\Delta\omega_{ij}^2(t)\right)\times\exp\left(i\int_{t}^{t+\tau}\Delta\omega_{ij}(t')dt'\right)\rangle_{\text{ave.}}$$

$$\left.\frac{d^4\varphi}{d\tau^4}\right|_{\tau=0}=\overline{\omega^4}=\langle\Delta\omega_{ij}^4\rangle_{\text{ave.}}+\langle\left(\frac{d}{dt}\Delta\omega_{ij}\right)^2\rangle_{\text{ave.}}.$$

Now Van Vleck's result for $\overline{\omega^4}$ can be written in the following way;

$$\overline{\omega^4}=\langle[H,[H,\mu]]^2\rangle_{\text{ave.}}$$

which, in view of the facts that H_0 can be transformed out of all operators, and that H_m commutes with μ, gives us

$$\begin{aligned}\hbar^4\overline{\omega^4}&=\langle[H_p+H_m,[H_p,\mu]]^2\rangle_{\text{ave.}}\\&=\langle[H_p,[H_p,\mu]]^2\rangle_{\text{ave.}}\\&\quad+\langle[H_m,[H_a,\mu]]^2\rangle_{\text{ave.}}\\&\quad+2\langle[H_m,[H_p,\mu]][H_p,[H_p,\mu]]\rangle_{\text{ave.}}\end{aligned}$$

and he found that the last term on the right was always quite negligible. Thus he could write the fourth moment as the sum of the "normal" fourth moment, analogous to $\langle\Delta\omega_{ij}^4\rangle_{\text{ave.}}$, which comes entirely from H_p, and another term coming-from the time rate of change of $[H_p,\mu]$.

Theorem IV.

Under certain limitations, the expansion of the spectrum on the wings in inverse powers of the frequency:

$$I(\omega)\sim\frac{A}{\omega^2}+\frac{B}{\omega^4}+\cdots$$

is controlled by the values of the successive odd derivatives of $\varphi(\tau)$ at the origin:

$$A=-\left.\frac{d\varphi}{d\tau}\right|_{\tau=0},\quad B=\left.\frac{d^3\varphi}{d\tau^3}\right|_{\tau=0},\quad\text{etc.}$$

This theorem is very closely related to theorem I: clearly, a finite $(2n-1)$ derivative is a singularity of $\varphi(\tau)$ at the origin which may be approximated by letting the $(2n$-th) derivative become infinite there. (e.g. a finite first derivative means that $\varphi(\tau)$ goes down on each side of zero with finite slope, so that we need an infinitely sharp curvature at the origin.) Thus we suspect that the $(2n)$th moment will be infinite, so that the spectrum falls off at least as slowly as $1/\omega^{2n+1}$ and possibly slower.

Any real physical $\varphi(\tau)$ will not have real singularities at the origin, but may approximate them because some process—e.g. the jumps in diffusion, or collisions in a gas—occurs very much faster than other processes. Thus eventually any $I(\omega)$ will fall off exponentially rather than in inverse powers of ω. (See, for an example, Anderson (1949a)).

Proof of the theorem. This is done by successive partial integrations. If $\varphi(\tau)$ is real it must be even; we assume it is since we always treat this case only. Therefore

$$I(\omega)=\int_0^\infty \cos\omega\tau\varphi(\tau)d\tau\ .$$

By a partial integration

$$I(\omega)=\frac{\varphi(\tau)}{\omega}\sin\omega\tau\Big|_0^\infty-\frac{1}{\omega}\int_0^\infty\frac{d\varphi}{d\tau}\sin\omega\tau\,d\tau\ ;$$

φ and all its derivatives which we use must be assumed to vanish at infinity, and none of the derivatives to be infinite at the origin (except, of course, when the series is found to have a term, as explained above). Then by another partial integration, after observing that the first term above is zero,

$$I(\omega)=-\frac{1}{\omega^2}\frac{d\varphi}{d\tau}\Big|_{\tau=0}-\frac{1}{\omega^2}\int_0^\infty\cos\omega\tau\frac{d^2\varphi}{d\tau^2}d\tau\ .$$

Further integrations give us

$$I(\omega)=-\frac{1}{\omega^2}\frac{d\varphi}{d\tau}\Big|_{\tau=0}+\frac{1}{\omega^4}\frac{d^3\varphi}{d\tau^3}\Big|_{\tau=0}$$
$$-\frac{1}{\omega^6}\frac{d^5\varphi}{d\tau^5}\Big|_{\tau=0}+\frac{1}{\omega^7}\int_0^\infty\frac{d^7\varphi}{d\tau^7}\sin\omega\tau\,d\tau\ .$$

The process can be carried on until we find a nonvanishing term, so long as the derivatives are integrable and vanish at infinity. This proves the theorem.

Theorem V. If $\varphi_{\Delta\omega}(\tau)$—the correlation function of the random frequency modulation—has a finite first derivative at the origin, there is an inverse fourth power term in the expansion in theorem IV. This is easily proved from the expression for $d^3\varphi/d\tau^3$,

$$\frac{d^3\varphi}{d\tau^3}=\Big\langle\Delta\omega_{ij}(t+\tau)\Big(\frac{d}{dt}\Delta\omega_{ij}(t)-\Delta\omega_{ij}^2(t)\Big)$$
$$\times\exp\Big(i\int^{t+\tau}\Delta\omega_{ij}(t')dt'\Big)\Big\rangle_{\text{ave.}}$$

We let $\tau\to0$. $\overline{\Delta\omega_{ij}^3}$ is assumed to be zero; any term coming from this will be irrelevant to the theorem. The expression then becomes

$$\frac{d^3\varphi}{d\tau^3}\Big|_{\tau=0}=\Big\langle\Delta\omega_{ij}(t)\Big(\frac{d}{dt}\Delta\omega_{ij}(t)\Big)\Big\rangle_{\text{ave.}}$$

which is, in fact, just the same as

$$\frac{d}{d\tau}\overline{\Delta\omega_{ij}^2}\varphi_{\Delta\omega}(\tau)\Big|_{\tau=0}$$
$$=\frac{d}{d\tau}\langle\Delta\omega_{ij}(t)\Delta\omega_{ij}(t+\tau)\rangle_{\text{ave.}}\ .$$

From this we can easily prove that if

$$\varphi_{\Delta\omega}(\tau)=e^{-\omega_e\tau}$$

$I(\omega)\sim\omega_e\omega_p^2/\omega^4$, as stated in the text.

Appendix III

Exchange Narrowing (Gaussian Modulation with Gaussian Spectrum) in the Intermediate Case.

Equation (38) of the main part of the paper gives an exact expression for the correlation function in the Gaussian-Gaussian case which we have assumed to correspond to true exchange narrowing. This is

$$\varphi(\tau)=\exp\Big[-\frac{\omega_p^2\tau}{\omega_e}\int_0^{\omega_e\tau}\exp\Big(-\frac{\pi}{4}x^2\Big)dx$$
$$+\frac{2\omega_p^2}{\pi\omega_e^2}\Big\{1-\exp\Big(-\frac{\pi}{4}\omega_e^2\tau^2\Big)\Big\}\Big]\ . \tag{A III-1}$$

In this Appendix we use this to find out how the line shape varies in the intermediate case in which ω_p is comparable with ω_e.

The fact that this function can be computed and tabulated is of little use, because the Fourier integral required to get the line shape would still have to be evaluated numerically, at considerable labor. Thus an approximate procedure might as well be used from the first, and since we know the limiting behaviors both for large and for small ω_e/ω_p, it seems most sensible to try to find correction terms at both ends and then fit the two curves together by interpolation in the intermediate range. To do this we need no more than approximate values of $\varphi(\tau)$ in the two ranges (A) $\omega_e\tau \gg 1$, and (B) $\omega_e\tau \ll 1$. The following values are easily derived from (A III-1).

Range A: $\omega_e\tau \gg 1$

$$\varphi(\tau)=\exp\left[-\left(\frac{|\tau|}{\omega_e}-\frac{2}{\pi\omega_e^2}\right)\omega_p^2\right] \tag{A III-2}$$

Range B: $\omega_e\tau \ll 1$

$$\varphi(\tau)\simeq\exp\left[-\left(\frac{\omega_p^2\tau^2}{2}-\frac{\pi}{48}\omega_e^2\omega_p^2\tau^4\right)\right]. \tag{A III-3}$$

Let us for simplification use dimensionless ratios as our variables. We define these as:

$$\left.\begin{aligned} \omega_e/\omega_p &= y \\ \omega_e\tau &= x \\ \omega/\omega_p &= \nu\ . \end{aligned}\right\} \tag{A III-4}$$

In terms of these the two approximations for $\varphi(\tau)$ are:

$$\text{A}: \quad \varphi(\tau)=\exp\left[-\frac{1}{y^2}\left(|x|-\frac{2}{\pi}+\cdots\right)\right] \times y \gg 1 \tag{A III-2a}$$

$$\text{B}: \quad \varphi(\tau)=\exp\left[-\frac{1}{y^2}\left(\frac{x^2}{2}-\frac{\pi x^4}{48}+\cdots\right)\right] \times y \ll 1\ . \tag{A III-3a}$$

How well these two expressions fit together is shown in fig. A1, in which is plotted the true expression for the coefficient of $-1/y^2$ in the exponent of φ as a function of x, as well as the two approximations (A III-2a and 3a).

The Fourier integral becomes

$$I(\nu)=\int_{-\infty}^{\infty}\exp\left(i\frac{\nu x}{y}-\frac{1}{y^2}f(x)\right)dx \tag{A III-5}$$

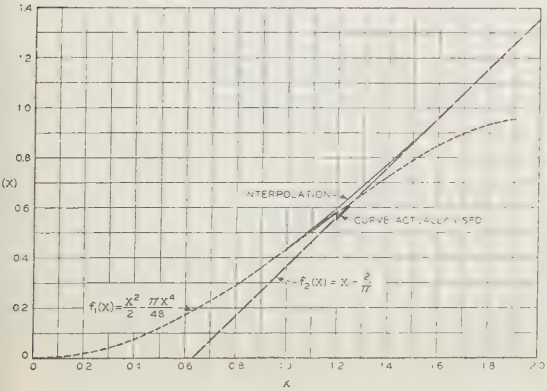

Fig. A-1. The function $f(x)$ from equation (A III-5).

where $f(x)$ is the function plotted in Fig. A1.

In computing line shapes, the easiest quantity to get is the central intensity, which, besides being of considerable experimental interest itself, is a fair measure of the line-breadth. This quantity, normalized on a scale of constant ω_p and varying $\omega_e/\omega_p=y$, is

$$I(0)=\frac{1}{y}\int_{-\infty}^{\infty}dx\exp\left(-\frac{1}{y^2}f(x)\right). \tag{A III-6}$$

This can rather easily be computed for the two limiting cases. For Case A we separate $f(x)$ into two parts:

$$f(x)=f_0+f_1=(x-2/\pi)+f_1(x) \tag{A III-7}$$

where

$$\begin{aligned} f_1(x)&=f(x)-\left(x-\frac{2}{\pi}\right) \\ &\simeq\frac{x^2}{2}-\frac{\pi x^4}{48}-\left(x-\frac{2}{\pi}\right) \quad x<1.2 \\ &\simeq 0 \qquad\qquad\qquad\qquad x>1.2 \end{aligned} \tag{A III-8}$$

f_1 is a function in any case which does not extend appreciably beyond $x=1$. This is a useful property.

Now,

$$\begin{aligned} I_A(0)&=\frac{2}{y}\int_0^{\infty}\exp\left(-\frac{f(x)}{y^2}\right)dx \\ &=\frac{2}{y}\int_0^{\infty}\exp\left(-\left(x-\frac{2}{\pi}\right)\frac{1}{y^2}\right)dx \\ &\qquad\times\exp\left(-\frac{f_1(x)}{y^2}\right) \end{aligned}$$

Changing variable,

$$I_A(0)=\exp(2/\pi y^2)(2y)\int_0^{\infty}e^{-u}du\exp(-f_1(y^2u)/y^2. \tag{A III-9}$$

This may be expanded into

$$I_A(0)=\exp(-2/\pi y^2)(2y)\int_0^{\infty}e^{-u}du \times\left(1-\frac{f_1(y^2u)}{y^2}+\cdots\right).$$

The appropriate approximation to the second term for large y is that unless u is very small $y^2u \gg 1$, so that e^{-u} is very close to unity. Thus

$$\begin{aligned} I_A(0)&\simeq 2y\exp(+2/\pi y^2)\left(1-\int_0^{\infty}\frac{f_1(y^2u)}{y^2}du\right) \\ &\simeq 2y\exp(+2/\pi y^2)\left(1-\frac{1}{y^4}\int_0^{\infty}f_1(x)dx\right). \end{aligned} \tag{A III-10}$$

Using the approximation A III-8 for $f_1(x)$, this gives

$$I_A(0)=2y\exp(+2/\pi y^2)\left(1-\frac{.299}{y^4}\right)$$

$$=2y\left(1+\frac{2}{\pi y^2}+\frac{.096}{y^4}\cdots\right). \qquad \text{(A III–11)}$$

The small y approximation (Case B) is more easily obtained. We get

$$I_B(0)=\frac{2}{y}\int_0^\infty \exp\left(-\frac{1}{y^2}\left(\frac{x^2}{2}-\frac{\pi x^4}{48}+\cdots\right)\right)dx$$

$$\cong\frac{2}{y}\int_0^\infty \exp(-x^2/2y^2)\,dx\left(1+\frac{\pi x^4}{48y^2}\right),$$

so

$$I_B(0)=2\sqrt{\frac{\pi}{2}}\left(1+\frac{\pi}{16}y^2\right). \qquad \text{(A III–12)}$$

(A III–11 and 12) as a function of y are plotted in figure A2, with an approximate interpolation drawn in to fit the two limiting cases together. This shows how the central intensity increases as a function of ω_e/ω_p, the "narrowing ratio".

The half-power width can also be estimated in a similar way. We start from the general expression for the ratio of intensity at a frequency ν to that at 0,

$$\frac{I(\nu)}{I(0)}=\frac{\int_0^\infty \cos\frac{\nu x}{y}\exp(-f(x)/y^2)\,dx}{\int_0^\infty \exp(-f(x)/y^2)\,dx}. \qquad \text{(A III–13)}$$

For the high narrowing case A we use (A III–7) for $f(x)$, and get

$$\frac{I(\nu)}{I(0)}=\frac{\int_0^\infty \cos\frac{\nu x}{y}\exp\left(-\frac{x}{y^2}-\frac{f_1(x)}{y^2}\right)dx}{\int_0^\infty \exp\left(-\frac{x}{y^2}-\frac{f_1(x)}{y^2}\right)dx}.$$

The half-width we assume to be close to that for the extreme case $y\rightarrow\infty$, which is $1/y$. Thus we set

$$\nu=\frac{1}{y}(1+\delta). \qquad \text{(A III–14)}$$

Then all quantities can be expanded, assuming as before that f_1/y^2 and δ are small. A straightforward calculation yields

$$\delta=-\frac{1}{2y^4}\frac{\int_0^\infty f_1(x)dx}{\int_0^\infty e^{-u}u\sin u\,du} \qquad \text{(A III–15)}$$

$$\cong-\frac{.299}{y^4}$$

$$(\varDelta\nu_{1/2})_A\cong\frac{1}{y}\left(1-\frac{.299}{y^4}\right). \qquad \text{(A III–16)}$$

Note that the order of the change in half-width is smaller than that in $I(0)$; tnis indicates that the line-shape is less sensitive than the total scale to decreasing y, an interesting fact experimentally.

The approximation from the other end goes again from (A III–13), but here we set

$$f(x)\cong\frac{x^2}{2}-\frac{\pi x^4}{48},$$

and get

$$\frac{I(\nu)}{I(0)}\cong\frac{\int_0^\infty \cos\frac{\nu x}{y}\exp\left(-\frac{x^2}{2y^2}+\frac{\pi}{48}\frac{x^4}{y^2}\right)dx}{\int_0^\infty \exp\left(-\frac{x^2}{2y^2}+\frac{\pi}{48}\frac{x^4}{y^2}\right)dx}.$$

Here again we expand as in the case of $I(0)$, assuming $(\pi/48)(x^4/y^2)$ small as well as the difference

$$\delta\nu=\nu-\sqrt{2\,ln\,2}$$

between the true half-width and the one for $y=0$. To second order in y^2 we get

$$(\varDelta\nu_{1/2})_B\cong\sqrt{2\,ln\,2}\left(1-\frac{\pi}{8}y^2\left(1-\frac{ln\,2}{3}\right)\right). \qquad \text{(A III–17)}$$

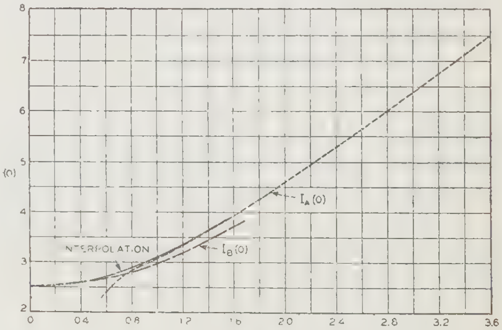

Fig. A–2. Central intensity I_0 in exchange narrowing as a function of the ratio $y=\omega_e/\omega_p$.

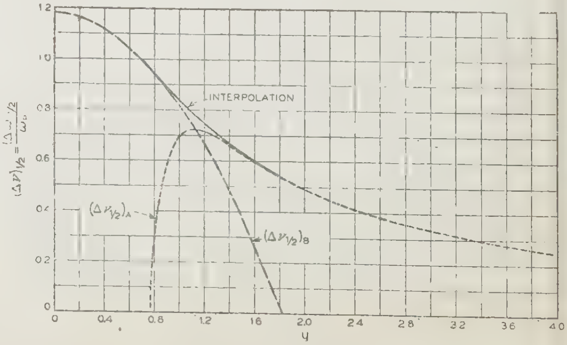

Fig. A–3. Half-power half-width (in units of ω_p) as a function of $y=\omega_e/\omega_p$.

The two approximations (A III-16 and 17) are plotted in figure A 3. It is seen that they fit fairly well together, and indicate an interpolation curve which one might well expect to be accurate to a few per cent. This curve then gives our best guess as to the half-width in the case of intermediate amounts of exchange narrowing.

Bibliography

1) 1941 H. A. Kramers and G. H. Wannier: Phys. Rev. **60**, 252.

2) 1945 M. C. Wang and G. E. Uhlenbeck: Rev. Mod. Phys. **17**, 323.

3) 1946 H. M. Foley: Phys. Rev. **69**, 616.

4) 1947 G. J. Gorter and J. H. Van Vleck: Phys. Rev. **72**, 1128.

5) 1948 Bloembergen, Purcell and Pound: Phys. Rev. **73**, 679.

6) 1948 J. H. Van Vleck: Phys. Rev. **74**, 1168.

7) 1949 P. W. Anderson, *Thesis*, Harvard: Phys. Rev. **76**, 647.

8) 1949 (a) P. W. Anderson: Phys. Rev. **76**, 471.

9) 1949 A. Wright: Phys. Rev. **76**, 471.

10) 1950 P. W. Anderson: Phys. Rev. **82**, 342.

11) 1951 T. S. England and E. E. Schneider: Physica **17**, 221.

12) 1951 A. F. Kip and M. Tinkham: Phys. Rev. **84**, 848; Res. Lab. Elect. (MIT) *Progress Report*, Oct. 17, p. 22.

13) 1951 Kumagai, Ono, Hayashi, Abe, Shono, Tachimori, Ibamoto, and Shimada: Phys. Rev. **82**, 954.

14) 1951 R. E. Norberg and C. P. Slichter: Phys. Rev. **83**, 1074.

15) 1952 M. A. Garstens, private communication.

16) 1953 P. W. Anderson and P. R. Weiss: Rev. Mod Phys. **25**, 269.

17) 1953 Archer, *Thesis*, Harvard.

JOURNAL OF THE PHYSICAL SOCIETY OF JAPAN Vol. 9, No. 3, MAY—JUNE, 1954

Theory of Superexchange Interaction in MnO Crystal

By Jiro YAMASHITA

Institute of Science and Technology, University of Tokyo

(Received January 23, 1954)

The mechanism of the superexchange interaction of MnO crystal is investigated qualitatively taking into consideration of the non-orthogonality of wave functions. The energy expression is obtained for both spin states, that is, the perfect parallel spin arrangement and the ordered antiparallel spin arrangement, by the method of Heitler-London-Lowdin. As a result we find the the energy of the ordered antiparallel spin arrangement may be lower than that of the perfect parallel spin arrangement mainly by the effect of the S-energy, which consists of several overlap-integrals.

§ 1. Introduction

The experiment of neutron diffraction reveals that in some substances there is a strong magnetic interaction between the ions, which are separated by intervening non-magnetic ions. The best example of this fact is MnO crystal. Anderson[1] has explained this interesting phenomenon in terms of superexchange interaction. Although his theory is very elegant and may be true in essence, he neglected the effect of the non-orthogonality of the wave functions, as Slater[2] has pointed out. Now it is well known that this effect is very important for explaining the mechanism of cohesion of ionic crystals[3], because the simplified theory, in which the charge-overlapping is neglected, can not explain this mechanism. As MnO crystal is supposed to be an ionic crystal, where the totally ionic state $Mn^{++}O^{--}$ may be predominant, and our present problem is after all the computation of the energy-difference between the two states of the ionic crystal, the one with parallel arrangement of spins and the other with antiparallel arrangement of spins, it does not seem unnecessary to consider the effect of the non-orthogonality of wave functions for the superexchange interaction.

Now we have a perfect quantitative theory for computing the cohesive energy of alkali-halide crystals[3] (we shall call it as the Heitler-London-Lowdin approximation). For the oxide crystals, however, we have no reliable computation of electronic structures[4] and many things are uncertain at present, but we assume here that the HLL approximation is well appliciable also to simple oxide crystals. Under this assumption we are able to formulate the interaction energy of MnO crystal for both of the spin states. In the following, we shall concern only with the qualitative nature of the superexchange interaction, because the quantative accuracy of the HLL approximation must be proved at first for the cohesive energy of the simpler oxide crystals, for example, MgO crystal.

§ 2. The Totally Ionic State

At first we assume that the ground state of MnO crystal is the totally ionic state Mn^{++} O^{--}. In the following we shall consider only two states of spin arrangement, the one being the fictitious state where spins of the neighbouring Mn ions are parallel, and the other being the state where spins are ordered antiparallel. It is well known that the later state is not the minimum-energy state, but we may suppose that this is an allowable approximation for the real state of MnO crystal at the absolute zero temperature.

Now let us seek for the energy of the totally ionic state. If we neglect the small direct magnetic interaction, we find the Hamiltonian of the system to be

$$H_{0p}=W+\sum_{i} H_i+\sum_{i,k}{}' G_{i,k}\ ,$$

with the abbreviations

$$\left\{\begin{aligned} W&=\frac{e^2}{2}\sum_{gg'}{}'\frac{Z_gZ_{g'}}{r_{gg'}}\\ H_i&=\frac{1}{2m}p_i{}^2-e^2\sum_{g}\frac{Z_g}{r_{ig}}\\ G_{ik}&=e^2/2r_{ik}\ . \end{aligned}\right.$$

Here e and m are the electronic charge and mass, Z_g is the atomic number of the nucleus at the point g, $r_{gg'}$ the distance between the points g and g', $r_{ig'}$ the distance between the electron i and the point g, r_{ik} the distance between the electron i and k, and p_i the momentum of the electron i. The wave function of the system is the Slater determiant constructed from the Hartree-Fock wave functions of the isolated Mn^{++} and O^{--} ions. Here we have the single configuration, because we take only the S-state $(2p)^6$ for oxygen ion and the ^6S-stare $(3d)^5$ for manganese ion. Let ϕ_u denote the atomic wave functions of oxygen ion and ψ_ν those of manganese ion;

$$\begin{aligned}\phi_\mu&=\phi(nlm|r\theta\varphi)\chi_j(\sigma)\\ &=k_{lm}\frac{f_{nl}(r)}{r}P_l{}^m(\cos\theta)e^{im\varphi}\chi_j(\sigma)\ ,\end{aligned}$$

$$\begin{aligned}\psi_\nu&=\psi(NLM|R\Theta\varphi)\chi_J(\sigma)\\ &=k_{LM}\frac{f_{NL}(R)}{R}P_L{}^M(\cos\Theta)e^{iM\varphi}\chi_J(\sigma),\end{aligned}$$

$$k_{lm}=\sqrt{\frac{2l+1}{4\pi}\frac{(l-m)!}{(l+m)!}}\ .$$

At the real ionic distance, $2p$ wave function of the oxygen ion overlaps to some extent with $3d$, $3p$ and $3s$ wave functions of the nearest neighbouring Mn ions. We define the overlap integrals as

$$S_{\mu\nu}=\int\phi_\mu\psi_\nu w\tau-\delta_{\mu\nu}\ ,$$

with $S_{\mu\mu}=0$. We follow the method of Lowdin; constructing the orthogonalized wave functions and matrix elements of the Hamiltonian operator with respect to the orthogonal wave function and expanding the total energy with respect to $S_{\mu\nu}$ up to the second order. then we obtain the total energy of the system as

$$E_g=E_1+E_2+E_{int}\ .$$

Here, E_1 and E_2 are the energy of isolated Mn^{++} and O^{--} ions respectively and E_{int} is the interaction energy,

$$E_{int}=E_{ele}+E_{exch}+E_s\ ,$$

where E_{ele} is the electrostatic energy, which consists of the Madelung energy and its correction terms, E_{exch} is the exchange energy and E_s is the so-called S-energy which is caused by the non-orthogonality of the wave functions. The explicit expressions of these terms are as follows:

$$E_{exch}=-\sum_{\mu}\sum_{\nu}{}^{\mu}(\mu\nu|G|\nu\mu)\ ,$$

$$E_s=-\sum_{\mu}\sum_{\nu}{}^{\mu}S_{\mu\nu}\{(\nu|H'|\mu)+2\sum_{\kappa}{}^{\mu}(\nu\kappa|G|\mu\kappa)$$
$$-2(\nu\nu|G|\nu\mu)\}+\sum_{\mu}\sum_{\nu}{}^{\mu}S_{\mu\nu}S_{\nu\mu}\{(\mu|H'|\mu)$$
$$+2\sum_{\kappa}{}^{\mu}(\mu\kappa|G|\mu\kappa)\}$$

with the abbreviations

$$(\mu\nu|G|\kappa\lambda)=e^2\int\frac{\phi_\mu(1)\phi_\nu(2)\psi_\kappa(1)\psi_\lambda(2)}{2r_{12}}d\tau_1 d\tau_2\ .$$

$$(\mu|H'|\nu)=-e^2\sum{}^{\mu}\int\frac{Z_g\phi_\mu(1)\psi_\nu(1)}{r_{1g}}d\tau_1\ .$$

The notation $\sum^{\mu}$ means that a summation is taken over all ions except for the ion to which the electron μ belongs. At first we consider E_{exch} in detail.

(1) The exchange energy

We assume that the exchange interaction is only effective between the nearest heighbouring ions. Then we obtain:

$$E_{exch}=N\sum_{+}\sum_{NL}\sum_{nl}\sum_{m}C(nlm|NL)$$
$$\times\sum_{Jj}\sum_{\sigma_1\sigma_2}\chi_J(\sigma_1)\chi_J(\sigma_2)\chi_j(\sigma_1)\chi_j(\sigma_2)\ ,$$

where N is the Avogadro's number, the notation $\sum_{+}$ being the summation taken over the six nearest neighbouring ions, and

$$C(nlm|NL)=-c^2\frac{2L+1}{4\pi}\int\frac{\varphi(nlm|\vec{r}_1)\varphi(nlm|\vec{r}_2)}{r_{12}}$$
$$\times\frac{f_{NL}(R_1)}{R_1}\frac{f_{NL}(R_2)}{R_2}P_L(\cos\alpha)d\tau_1 d\tau_2\ ,$$

where α is the angle between two vectors $(R_1\Theta_1\varphi_1)$ and $(R_2\Theta_2\varphi_2)$ and z-axis is taken along the joining line of Mn and O ions. When the two ions have the closed shell structure, the summation

$$\sum_{Jj}\sum_{\sigma_1\sigma_2}\chi_J(\sigma_1)\chi_J(\sigma_2)\chi_j(\sigma_1)\chi_j(\sigma_2)\ ,$$

becomes 2, whereas for the interaction between $(3d)^5$ and $(2p)^6$ of MnO it becomes one because of the wellknown relations

$$\chi_j(\sigma_i)=\delta_{j\sigma_i}\ (\sigma_i=1\text{ or }-1)$$

and $$\sum\chi_j(\sigma_i)\chi_{j'}(\sigma_i)=\delta_{jj'}\ .$$

These values do not depend on whether the spin of the Mn ion directs to $+z$-axis or $-z$-axis. Therefore, in the totally ionic state, the exchange energy is the same for the two states of the parallel and the antiparallel spin arrangement. Thus we find the exchange

$$E_{exch}=6N\sum_{NL}\sum_{nl}\sum_{m}C(nlm|NL)$$
$$=6N[2C(2p0|3S)+4C(2p1|3S)$$
$$+2C(2p0|3p)+4C(2p1|3p)]$$
$$+6N[C(2p0|3d)+2C(2p1|3d)]\ .$$

In the case of NaCl we know from Lowdin's computation that $C(3p0|2p)$ is much larger than $C(3p1|2p)$. From this fact, we may suppose that $C(2p0|3d)$ is also much larger than $C(2p1|3d)$ in the caso of MnO (Fig. 1).

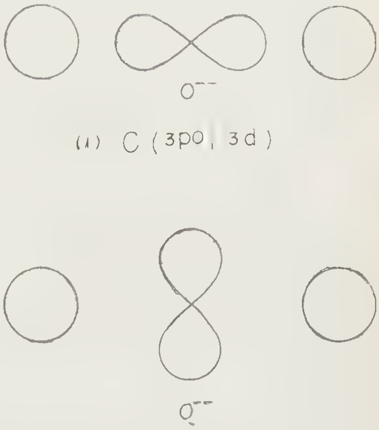

(1) C (3p0 | 3d)

(2) C (3p1 | 3d)

Fig. 1.

(2) S-energy

The overlap integral $S_{\mu\nu}$ vanishes for a pair of functions φ_μ and ψ_ν which are associated with opposite spin-directions and with different symmetries. Thue the important integrals of MnO may be $S(2p0|3d0)$, $S(2p0|3p0)$, $S(2p1|3d1)$ and $S(2p1|3p1)$. Since the integral $S(3p1|2p0)$ is much larger than $S(3p1|2p1)$ in the case of NaCl, we suppose that in the case of MnO $S(2p0|3d0)$ is much larger than $S(2p1|3d1)$. As the S-energy $E_s(\mu|\nu)$ is nearly proportional to the square of $S_{\mu\nu}$, $E_s(2p0|3d0)$ may be much larger than $E_s(2p1|3d1)$. From the above consideration and with the aid of

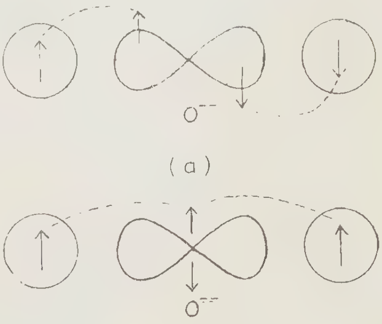

(a)

(b)

Fig. 2. (a) Antiparallel Arrangement.
(b) Parallel Arrangement.

Fig. 2, we find that the S-energy is given by following expression for both spin states:

$$E_s=6N[2B(2p0|3S)+2B(2p0|3p0)+4B(2p13p1)]$$
$$+6N[B(2p0|3d0)+2B(2p1|3d1)]\ .$$

Thus we see that the interaction energy is same for both states of spin in the totally ionic state. In the case of NaCl and other alkali-halide crystals, E_{exch} is negative, while E_s is positive and corresponds to the repulsive forces between the ions. We think that the same mechanism of the cohesion may be realized in MnO crystal, that is, $E_s>0$, $E_{exch}<0$ and $E_s>|E_{exch}|$. However, it is not quite certain if each part of E_s is larger than the corresponding part of E_{exch}, for example, $B(2p0|3d0)>|C(2p0|3d)|$.

The quantities $B(2p0|3d0)$ and $C(2p0|3d0)$ have been computed for Cu_2O by us and for Cu_2S by Kobayashi. The results showed that B is larger than C in both cases. Unfortunately the accuracy of these computations is not quite convincing, because the Slater type wave functions were used for negative ions instead of Hartree-Fock functions. We, however, suppose that the qualitative nature of these results may be preserved in more accurate computations.

§ 3. The State of the Parallel Spin Arrangement

At first we shall consider the state of the parallel spin arrangement. Here we take account of the excited state besides the totally ionic state. The excited state is one in which one electron has gone over from the $2p$-orbit of an O ion to one of the $3d$-orbit of its nearest neighbouring Mn ions. (Fig. 3). We construct the Slater determinant for this excited state after orthogonalizing the sets of wave functions of the isolated ions. These atomic functions contain one set of $(2p)^5$O state and $(3d)^6$Mn state. In this case, one of the oxygen ions has the incomplete shell structure, but in the case of the parallel spin arrangement we do not meet with the orthogonalization-difficulty5). In the following we shall denote determinantal function of the ground state by G and that of the excited state by A_p, and assume the wave function of the system to be a linear combination of these two states:

$$\Psi=gG+aA_p\ ,$$

where $g^2+a^2=1$ and we assume $g^2\gg a^2$. Using this wave function we find the energy of the system as

$$E(p)=g^2H_{gg}+a^2H_{aa}'+2gaH_{ga}$$
$$\doteqdot(1-a^2)H_{gg}+a^2H_{aa}'+2aH_{ga}\ ,$$

with the abbreviations

$$H_{gg}=[G|H|G]\ ,\qquad H_{aa}'=[A_p|H|A_p]$$

and

$$H_{ga}=[G|H|A_p]\ .$$

Here the notation [ ] means that the matrix element is refered to the orthogonalized AO, whereas the notation ( ) means that it is refered to the non-orthogonal AO. Now the constant a is determined by the condition $\partial E/\partial a=0$ as

$$a\doteqdot H_{ga}/(H_{gg}-H_{aa}')\ .$$

Then the energy becomes

$$E(p)=H_{gg}+H_{ga}^2/(H_{gg}-H_{aa}')\ .$$

For the purpose of the comparison of the magnitude of matrix elements it is convenient to return to the system of non-orthogonal AO and take account of the terms up to the second order of $S_{\mu\nu}$. The energy H_{gg} has been given in the previous chapter; $H_{gg}=H_g$. The main contribution to the energy difference between the ground state and the excited state ($H_{gg}-H_{aa}'<0$) comes from the intra-ionic energy change of the two ions, E(^6S-state of Mn^{++})$-E$(^5D-state of Mn^+) and E(^1S-state of O^{--})$-E$(^2P-state of O^-), and the Madelung energy $(4\alpha_M-1)e^2/a$. Another contribution comes from the change of the exchange energy and S-energy, which is much smaller than the intra-ionic energy change, but is important because it will depend on the spin arrangement. With the aid of Fig. 3 we can easily find the energy change due to E_{exch} and E_s. An additional enargy comes from the interaction of the electron (x) of Mn^+ ion (Fig. 3) with the nearest neighbouring six oxygen ions. We denote it as $\Delta(E_{exch}+E_s)_x$. It is nearly equal to $B(2p0|3d0)+C(2p1|3d1)$. Finally H_{ga} is the transition matrix element, which does not depend on the spin arrangement. By the consideration of the previous chapter, we see that the matrix element which corresponds to the transition, $2p0\rightarrow3d$, is much larger than that for $2p1\rightarrow3d$. This fact is very important to understand the directional nature of the superexchange interaction.

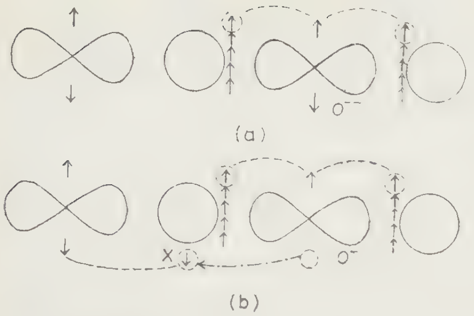

Fig. 3. (a) Ground State.
(b) Excited State.

§ 4. The State of the Ordered Antiparallel Spin Arrangement

Next we shall consider the state of the antiparallel spin arrangement. Here we have two excited states illustrated in Fig. 4, so that there are three possible configurations. We denote the Slater determinates of these states by G, A and B respectively. The wave function of the system is

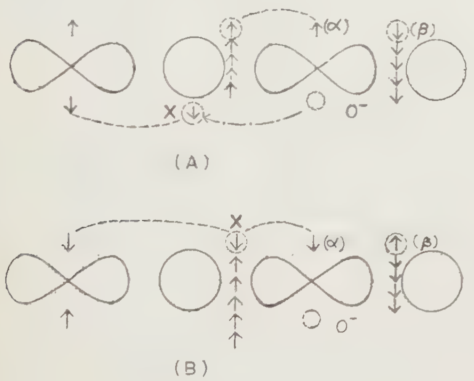

Fig. 4.

$$\Psi = gG + aA + bB \ .$$

Here we notice that we have used the orthogonalized $A0$ with respect to the electrons of the parallel spin. It is satisfactory in the case of the single configuration, where the electrons of the antiparallel spin are automatically orthogonal. But, we have to be more careful when the two configurations A and B are used, because then the non-orthogoral terms appear from the overlapping of the two electrons (α) and (β) of antiparallel spin (Fig. 4). We denote this by

$$\varDelta = \int \overline{\varphi}(2p0)\overline{\psi}(3d0)d\tau \ .$$

Using the above mentioned wave function with the normalization condition

$$g^2 + a^2 + b^2 + 2ab\varDelta^2 = 1 \ ,$$

we obtain the energy of the system as follows:

$$\begin{aligned} E(a) &= \frac{g^2 H_{gg} + a^2 H_{aa} + b^2 H_{bb} + 2ga H_{ga} + 2ab H_{ab}}{1 + 2ab\varDelta^2} \\ &= (1 - a^2 - b^2) H_{gg} + a^2 H_{aa} + b^2 H_{bb} + 2a H_{ga} \\ &\quad + 2ab(H_{ab} - H_{gg}\varDelta^2) \ , \end{aligned}$$

where the abbreviations are

$$H_{aa} = [A|H|A] \ , \qquad H_{ga} = [G|H|A] \ ,$$
$$H_{bb} = [B|H|B] \ ,$$

and

$$H_{ab} = \{A|H|B\}.$$

The notation $\{\quad\}$ means that the matrix element is refered to the AO functions which are orthogonalized except for the two electrons (α) and (β). The energy H_{bb} is larger than H_{aa} by the amount of the intra-ionic energy change of Mn ion due to the spin arrangement. Now the conditions $\partial E/\partial a = 0$ and $\partial E/\partial b = 0$ give the equations,

$$\begin{cases} (H_{gg} - H_{aa})a - (H_{ab} - H_{gg})b = H_{ga} \ , \\ (H_{ab} - H_{gg}\varDelta^2)a - (H_{gg} - H_{bb})b = 0 \ , \end{cases}$$

which yield the solution,

$$a = \frac{H_{ga}(H_{gg} - H_{bb})}{(H_{gg} - H_{aa})(H_{gg} - H_{bb}) - (H_{ab} - H_{gg}\varDelta^2)^2} \ ,$$
$$b = \frac{H_{ga}(H_{ab} - H_{gg}\varDelta^2)}{(H_{gg} - H_{aa})(H_{gg} - H_{bb}) - (H_{ab} - H_{gg}\varDelta^2)^2} \ .$$

Thus the energy becomes:

$$\begin{aligned} E(a) &= H_{gg} \\ &+ \frac{H_{ga}{}^2 (H_{gg} - H_{bb})^2 (H_{gg} - H_{aa})}{[(H_{gg} - H_{aa})(H_{gg} - H_{bb}) - (H_{ab} - H_{gg}\varDelta^2)^2]^2} \\ &- \frac{H_{ga}{}^2 (H_{gg} - H_{bb})(H_{ab} - H_{gg}\varDelta^2)}{[(H_{gg} - H_{aa})(H_{gg} - H_{bb}) - (H_{ab} - H_{gg}\varDelta^2)^2]^2} \ . \end{aligned}$$

If we assume $(H_{gg} - H_{aa})(H_{gg} - H_{bb}) \gg H_{ab}{}^2$, then $E(a)$ becomes;

$$\begin{aligned} E(a) = H_{gg} &+ \frac{H_{ga}{}^2}{H_{gg} - H_{aa}} \\ &+ \frac{H_{ga}{}^2 (H_{ab} - H_{gg}\varDelta^2)^2}{(H_{gg} - H_{aa})^2 (H_{gg} - H_{bb})} \ . \end{aligned}$$

The last terms is negative, so we see that the inclusion of the configuration B makes the energy lower. Thus we suppose that we must take much more configurations of the spin arrangement in order to obtain the minimum energy state, although the contribution from these states will be only a correction in order.

Now we shall examine the energy difference $H_{aa}' - H_{aa}$. With the aid of Fig. 3 and Fig. 4 we find easily that H_{aa}' contains one more interaction between the $2p$-electron of O ion and the $3d$-electron of Mn ion with parallel spins. Let us denote the energy difference by Q. Then Q is ;

$$Q \equiv H_{aa}' - H_{aa} = B(2p0|3d0) + 2B(2p1|3d1) + C(2p0|3d) + 2C(2p1|3d)\,.$$

If the Q is positive, then the state of the ordered antiparallel spin arrangement is more stable than the state of the parallel spin arrangement. In that case the energy difference is ;

$$E(p) - E(a) = \frac{H_{ga}{}^2 Q}{(H_{gg} - H_{aa})^2} + \frac{H_{ga}{}^2 (H_{ab} - H_{gg}\Delta^2)^2}{(H_{gg} - H_{aa})^2 (H_{bb} - H_{gg})}\,.$$

Is the quantity Q really positive ? At present we are not able to answer this question, because we have not yet had any reliable computation. We may imagine, however, that it is positive by the reason mentioned at the end of chapter 2.

From the expression of Q we have seen that in the straight line configuration Mn—O—Mn, the energy difference between two spin arrangements is mainly decided by $B(2p0|3d0)$, while in the right angle configuration $\begin{matrix} & \mathrm{Mn} \\ & | \\ \mathrm{Mn}\text{—} & \mathrm{O} \end{matrix}$ the energy difference is mainly decided by $B(2p1|3d1)$. As we have seen in chapter 2, the former is much larger than the latter. Therefore we can understand the directional nature of the superexchange interaction.

Hitherto we have assumed that one definite electron is in the excited state. As a matter of fact, any of $(2p)^6$ electrons of any O ion can go over to the $3d$-state of any one of the six nearest neighbouring Mn ions. This generalization is easily to be done, if we exclude the case where two excited electrons occupy the same excited state at the same time. As an example, we shall compute the energy of the state of the parallel spin arrangement. The wave function is ;

$$\Psi = gG + a \sum A_i\,, \qquad (\because\ a_i = a)$$

$$g^2 + 6Na^2 = N\,. \quad (\because\ [A_i|H|A_j] = 0,\ i \neq j).$$

Since the matrix elements $[A_i|H|A_i]$ and $[A_i|H|G]$ are independent of i, the energy of the total systen will be

$$E(p) = (1/N)[g^2 H_{gg} + 6a^2 N H_{aa}' + 12NgaH_{ga}] = (1-6a^2)H_{gg} + 6a^2 H_{aa}' + 12\sqrt{N} H_{ga}\,.$$

By the condition $\partial E/\partial a = 0$; we determine the parameter a and the energy ;

$$a = \frac{\sqrt{N} H_{ga}}{H_{gg} - H_{aa}'}\,, \quad E(p) = H_{gg} + \frac{6NH_{ga}{}^2}{H_{gg} - H_{aa}'}\,.$$

Thus we see that the energy difference is expressed as ;

$$E(p) - E(a) = \frac{6NH_{ga}{}^2}{(H_{gg} - H_{aa})^2} \times \left(Q + \frac{(H_{ab} - H_{gg}\Delta^2)^2}{H_{bb} - H_{gg}}\right).$$

The accurate computation of Q is a rather difficult problem, because it is almost certain that the state of electron (α) or (β) is not expressed by a single orbital but by superposion of many complex orbitals.

In the previous treatment we have assumed that the excited state has the configuration $(3d)_6\mathrm{Mn}(2p)^5\mathrm{O}$. On the other hand, we may also assume it to be $(3d)^5(4s)\mathrm{Mn}(2p)^5 0$. In this case we must assume with Anderson[1] that the s-state couples with the d-electron by some strong spin dependent interaction, which may be easily understood by the Hund's rule in our case. Our theory will also be applicable to this alternative model without any essential modification.

§ 5. Concluding Remarks

From the standpoint of the magnetism MnO is the typical antiferromagnetic substance and NaCl is the typical diamagnetic substance. On the other hand, from the standpoint of the electronic structure both are ionic crystals. But one thing is different. NaCl is constructed by two ions Na^+ and Cl^-, which have the closed shell structure, while MnO is constructed by O^{--} ion and by Mn^{++} ion, which has not the closed shell. In the case of NaCl the charge distribution around Na or Cl ions is almost spherically symmetric and the states are well expressed by $(2p)^6\mathrm{Na}$ and $(3p)^6\mathrm{Cl}$ of the Hartree-Fock functions of the free ions respectively. In the case of MnO, Mn ions have the ordered antiparallel arrangement. This fact has a important meaning, because the exchange interaction and the non-orthogonal interaction between ions are effective only between the electrons of parallel spins. Let us consider a oxygen ion which is situated at the center of two Mn ions. Then a $2p$-electron with certain spin direction may polarize in order to approach to one Mn ion, whose spin direction is opposite, and to go away from the other Mn ion, whose spin direction is parallel, because the increase of the kinetic energy due to the polarization may be compensated by the decrease of the interaction energy (S-energy) between the electrons of Mn($3d$) and O($2p$) with the same spin direclion. In this model we do not take into account the excited states considered in the previous treatment, but we suppose that the decrease of the energy due to the above mentioned polarization is also the origin of the superexchange interaction.

Finally we shall examine the validity of the spin-operator method; $V=-2J\vec{S}_i\vec{S}_j$. Although the condition of the appliciability of that method has heen discussed by Van Vleck⁶⁾, we shall review it here for convenienee. For example we consider the ground state of a hydrogen molecule. As well known the wave function of the molecule is expressed as the linear combination of two spin configurations with conventional notations;

$$\Psi=a\begin{matrix}\psi_a(1)\alpha(1), & \psi_b(1)\beta(1)\\ \psi_a(2)\alpha(2), & \psi_b(2)\beta(2)\end{matrix} - b\begin{matrix}\psi_a(1)\beta(1), & \psi_b(1)\alpha(1)\\ \psi_a(2)\beta(2), & \psi_b(2)\alpha(2)\end{matrix}.$$

If we assume that (1) the wave functions ψ_a and ψ_b are mutually orthogonal and (2) the probability of the two spin arrangements is equal ($a=b$), then the validity of the spin operator method can be proved. In the case of MnO, however, above two conditions are not reallized, then we see that the validity of the spin operator method is not self-evident. On the contrary we find that the S-energy caused by the non-orthogonality of the wave functions is very important for the origin of the superexchange interaction.

The author wishes to express his thanks to Prof. Muto, and Prof. Kubo for helpful discussions.

References

1) P. W. Anderson: Phys. Rev. **79** (1950) 350.

2) J. C. Slater: Revs. Modern Phys. **25** (1953) 199.

3) P. O. Lowdin: A Theoretical Investigation into some Properties of Ionic Crystals (thesis) Uppsala (1948).

4) J. Yamashita and M. Kojima: J. Phys. Soc. Japan **7** (1952) 261.

5) J. C. Slater: Jour. Chem. Phys. **19** (1951) 220.

6) Van Vleck: Revs. Modern Phys. **17** (1945) 27.

JOURNAL OF THE PHYSICAL SOCIETY OF JAPAN Vol. 9, No. 3, MAY—JUNE, 1954

Formation Energy of Superlattice in Ni_3Fe (II)

Kinetics of the Superlattice in the Stage of Local Ordering*

By Shūichi IIDA

Faculty of Science, University of Tokyo

(Received July 7, 1953)

The change of the internal energy of Ni_3Fe superlattice during cooling processes was studied by specific heat measurement for various rates of cooling. After eliminating the part of the internal energy due to magnetic transformation, it was shown that the formation of local order starts already at 600°C on cooling, and its rate attains a maximum at 520°C, decreasing to zero at about 400°C. The specific heat curves on cooling do not show any anomaly at 500°C, which is critical temperature for the long range order. The formation rate of local order at steady temperature annealing was also studied by keeping the specimen at 510°C and observing the heat of evolution directly. It was confirmed that the rate of local order formation is large enough to be observed at this temperature. It decreases monotonously and becomes zero after about five hours annealing. These data are all consistent with our previous assumption that one of the two steps' precesses of the formation of superlattice in Ni_3Fe at 490°C is the development of local order which has no critical temperature.

§ 1. Introduction

Iron-nickel alloys in the composition range from 40% to 100% nickel form a continuous series of solid solution having a face centered structure. It is well known that the superlattice Ni_3Fe exists in this series. A detailed study of this superlattice was carried out by S. Kaya by measuring the time change of the electric resistivity[1]. He showed that the superlattice has a typical A_3B type characteristic. The development of order begins abruptly at 490°C on cooling and the equilibrium state is attained by one week's annealing at this temperature. At the same time, it was also shown that the total change in resistivity at 490°C of about $9\mu\Omega$ cm was attained not by a single step but by two steps. This anomalous two-steps behaviour in the annealing at 490°C was studied in the previous paper by using the calorimetric methods.[2] It was confirmed that the variation of the internal energy at 490°C shows also the two-steps characteristic. Our tentative explanation for these facts was the following;

(i) The development of local order is well separated from that of the long range order. The former process requires a time of the order of hours at 490°C. It forms the first step of the process.

(ii) The long range order develops cooperatively, the ordering rate of which is very small at the beginning and it becomes appreciable after annealed more than five hours at 490°C.

The second postulate is standing on the following consideration. Though the state without long range order becomes unstable by passing over the critical temperature on cooling, the state will still have an equilibrium nature just like as the liquid in super cooling. Therefore, the first derivative of the free energy against the development of long range order will be zero. The situation will be seen by the following mathematical relations. We tentatively assume that the long range order parameter s and temperature T are independent variables. Then, we will be able to define the equilibrium state and its free energy $F(s, T)$ for fixed s and T. In reality, the state $s=0$ is realized at above the critical temperature Tc, and the state $s=s(T)\neq 0$ is realized at below Tc as true equilibrium states. We suppose the situation will be expressed mathematically as

---

* The experiments in this paper were carried out in 1950.

$$T>Tc \quad \left(\frac{\partial F}{\partial s}\right)_{s=0}=0, \quad \left(\frac{\partial^2 F}{\partial s^2}\right)_{s=0}>0,$$

$$T<Tc \quad \left(\frac{\partial F}{\partial s}\right)_{s=0}=0, \quad \left(\frac{\partial^2 F}{\partial s^2}\right)_{s=0}<0.$$

The concept of the cooperative formation of long range order would be important for our understanding of the mechanism of superlattice formation not only for this particular substance but also for many other alloys which are expected to have the same character. But, it has heen generally believed that in the usual A_3B type superlattice the development of long range order starts abruptly at the critical temperature on cooling. Therefore it seems very desirable to confirm the above two postulates by direct experimental evidences.

§ 2. Specific Heats During Cooling

In this situation, measurements of the specific heat during cooling will provide a effective proof. According to the current view of the superlattice, the formation of long range order will occur abruptly at the critical ordering temperature on cooling.1),3),4) Therefore, in the cooling procedure, critically anomalous specific heat will be observed at the critical ordering temperature. On the other hand, if our assumptions were true, there would be no discontinuous change of specific heat at the critical temperature as far as the rate of cooling is not so slow as to promote an appreciable development of long range order. Moreover, continuous increases of specific heat due to local ordering will be observed by changing the rate of cooling, even above the critical temperature.

The apparatus used and the specimen of Ni_3Fe were the same as the previous experiments.1) (74.59% Ni, 24.37% Fe, 0.71% Mn) A cylindrical specimen of 202,1 gr., the surrounding copper container, an outer heater, Pt–PtRh thermo-junction which was attached to the specimen, and chromel-alumel differential thermo-junction which was attached to the specimen and the copper container were the principal parts of the apparatus. The inner heater was removed in the cooling experiments.

The procedure of the cooling experiments was as follows: The specimen was heated by the outer heater to 850°C in vacuum, held for one hour and then cooled by lowering the temperature of the surrounding copper container. The temperature difference δT between the specimen and the surrounding wall was observed by the differential junction and controlled carefully to be constant by changing the current of the outer heater. Under these conditions, the temperature of the specimen, T, was observed continually at every constant time interval Δt. Then the specific heat C_p during the cooling will be given by the equation,

$$C_p=\frac{f(T)\cdot\Delta t}{\Delta T}.$$

where ΔT is the amount of decrease of temperature during the time interval Δt, and $f(T)$ is the energy radiated from the specimen per unit time and per gram atom. The function $f(T)$ was determined by an interpolation. That is, firstly, the specific heats during cooling were assumed to be equal to the specific heats during heating in two temperature ranges above 600°C and below 400°C; and secondly, the values of $f(T)$ in the intermediate region, 400°C∼600°C, were interpolated by a smooth

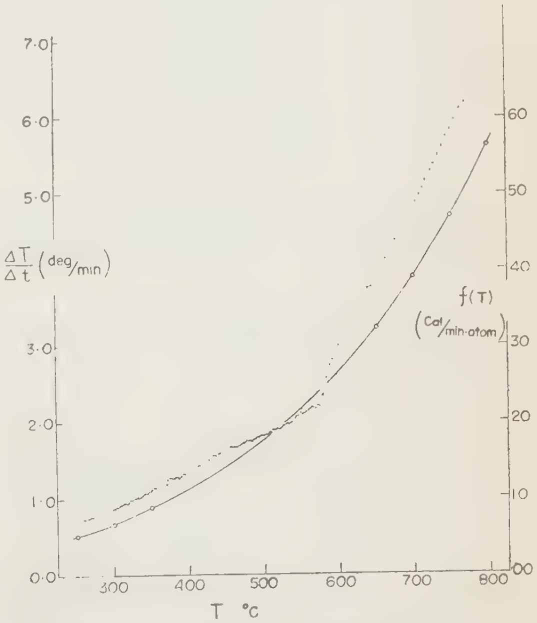

Fig. 1. An example for calculations of specific heat during cooling. Solid circles mean observed rates of temperature decreases of Ni_3Fe during cooling, and the solid line indicates the corresponding rate of heat loss of the specimen. Open circles indicate standard values of $f(T)$ evaluated from values of specific heat during heating.

curve. An example of such determination of $f(T)$ is shown in Fig. 1, where the rate of temperature decrease of the specimen $\Delta T/\Delta t$, and $f(T)$ are plotted. These are the original data of Fig. 2 (c). After that, the specimen is heated again and the corresponding specific heat during heating is observed.

Following these procedures, five observations of specific heat during cooling were carried out with various differences of temperature δT or various rates of cooling. These are shown in Fig. 2. In each figure, the upper scale indicates the time of cooling for each measurements.

In Fig. 3, the corresponding specific heat-temperature curves on heating observed after each measurement of cooling are plotted together with each corresponding specific heat curve during cooling. The two areas surrounded by the two curves of specific heat on heating and on cooling are nearly equal. It will show the reliability of our procedure. Here, the time interval between every two neighbouring points of the specific heat curves on heating is always two minutes.

The obtained curves of specific heat during cooling are very different from that of heating, showing the anomalous specific heat associated with the ferromagnetic transformation as their main characteristics. In addition to this magnetic part of the specific heat, there exists the anomalous specific heat, in the temperature range 600°C~400°C, which increases gradually as the rate of cooling is

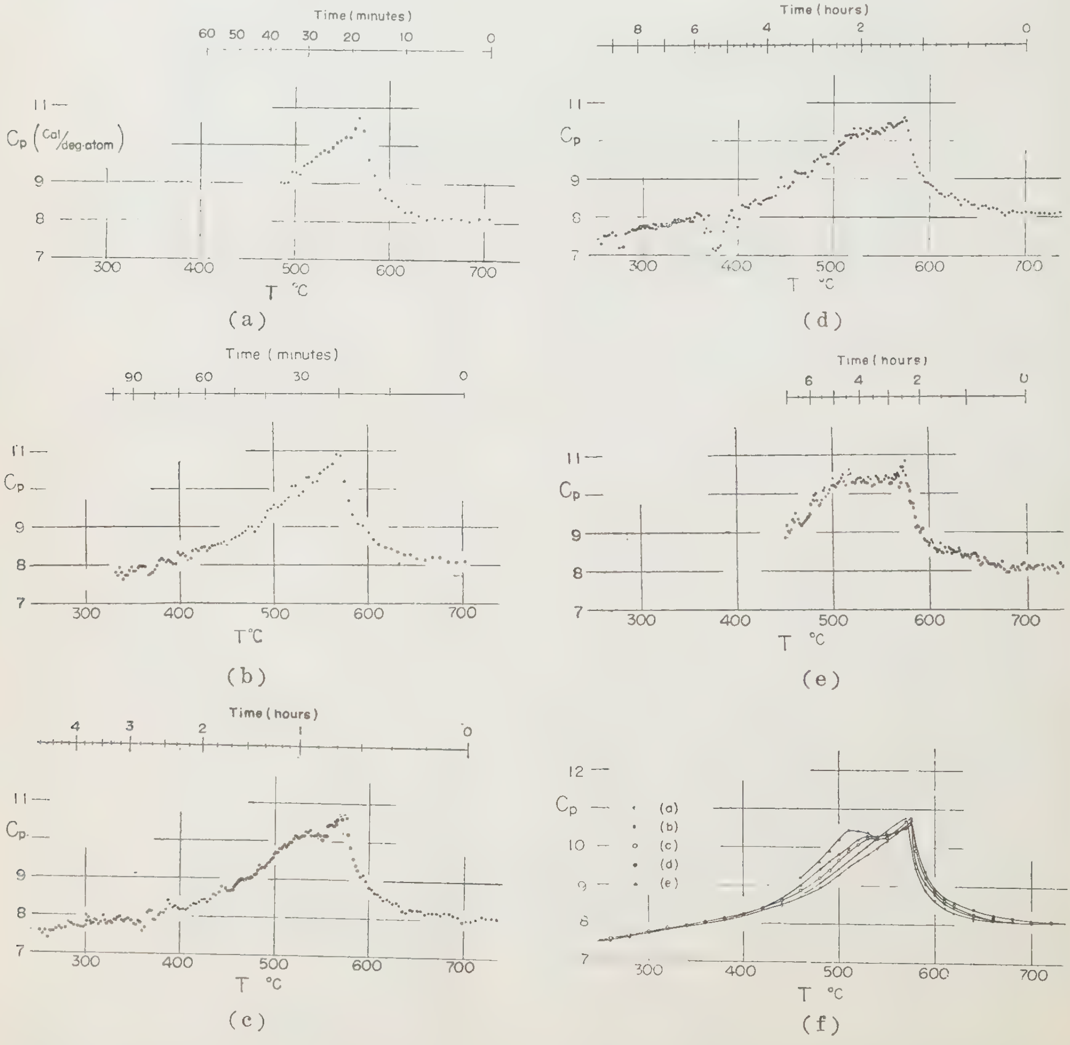

Fig. 2. Specific heats during cooling for various rates of cooling. The rates of cooling are; (a) 3.9, (b) 3.0, (c) 1.8, (d) 0.9, (e) 0.4 deg/min. at 500°C. In (f) all results are superposed.

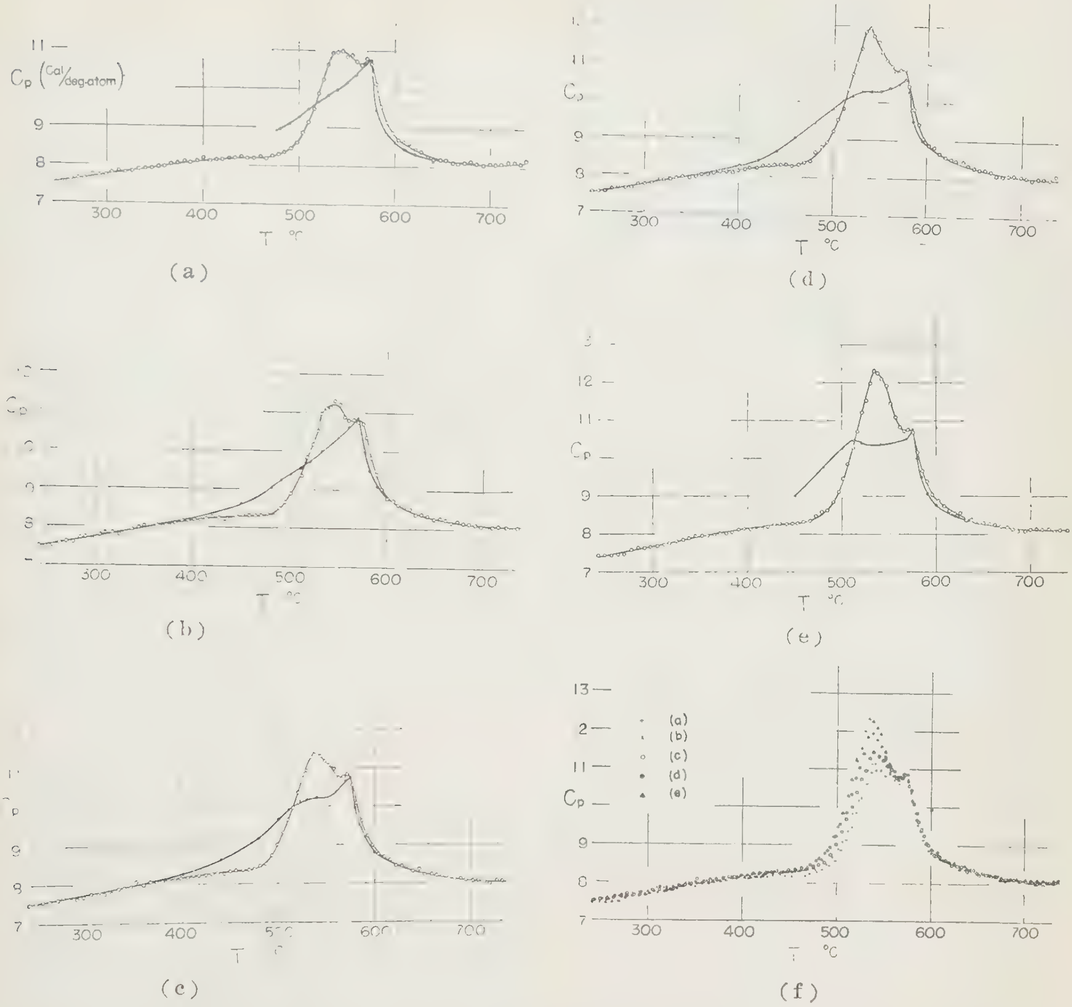

Fig. 3. Specific heats on heating for specimens cooled with various rates. In (a), (b), (c), (d), and (e), the corresponding specific heats during cooling are shown together, and in (f), all of the data are plotted.

lowered. The situation can easily be seen in Fig. 2 (f). The corresponding total amounts of internal energy decrease at room temperature compared with the specimen quenched from 600°C into water are calculated to 94, 113, 144, and 165 cal/atom for (a), (b), (c), (d), and (e) respectively. These are obtained by comparing the total energy supplied to the specimen from room temperature to 700°C in each measurement of specific heat on heating after each treatment.

There is no critical specific heat at 500°C even for the slowest cooling (e). In this observation, the duration about 500°C is considered to be sufficiently long to induce appreciable development of long range order, if it begins abruptly from 500°C. It can be said that our basic two postulates (i) and (ii) are proved.

§ 3. Further Analysis of the Cooling Experiments

Our previous results of the specific heat on cooling will be analyzed further. Firstly, we assume that the energy of lattice vibration and the energy of ferromagnetic transformation as functions of temperature are not influenced by the development of atomic order at least in the stage of local ordering such as studied in this paper. This assumption will be supported by a later study,[5] and the influence can be seen only after the sufficient development of long range order.

Then, the internal energy of the alloy $U(T)$ will be separated into two parts, $U^{re}(T)$ and $U^{ir}(T)$. Here, $U^{re}(T)$ consists mainly of the lattice vibration and ferromagnetic transformation, and is assumed to be reversible for the temperature variation of the order of rate used in the previous cooling experiments. On the other hand, $U^{ir}(T)$ is the part of energy associated with the atomic ordering and behave as irreversible for the rates of temperature variation used in our experiments. Therefore, we may put

$$U = U^{re} + U^{ir} ,$$

so that

$$\frac{dU}{dt} = \frac{dU^{re}}{dt} + \frac{dU^{ir}}{dt} .$$

Here, U will be a functional of the preceding temperature-time history of the specimen, but as far as we consider only the specific course of a experiment, it is a unique function of time or the temperature. Accordingly, we write

$$\frac{dU}{dt} = \frac{dU}{dT} \cdot \frac{dT}{dt} , \qquad \frac{dU^{re}}{dt} = \frac{dU^{re}}{dT} \cdot \frac{dT}{dt} ,$$

In our experiments of specific heat during cooling, $-dT/dt$ is the rate of cooling V, so that

$$-\frac{dU}{dT} \cdot V = -\frac{dU^{re}}{dT} V + \frac{dU^{ir}}{dt}$$

$$C_p = C_p^{re} + \left(-\frac{dU^{ir}}{dt} \right) \cdot \frac{1}{V} .$$

Thus the observed specific heat C_p is related to the reversible specific heat C_p^{re} and the rate of time change of the irreversible internal energy $-dU^{ir}/dt$.

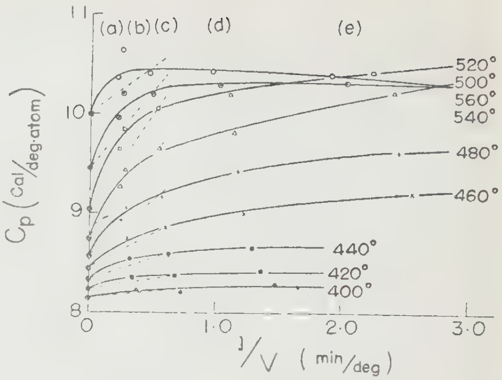

Fig. 4. Specific heats during cooling as functions of the reciprocal of the rate of cooling at each temperature.

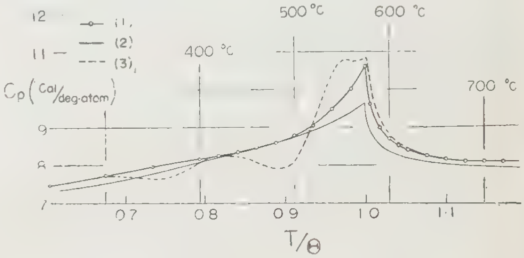

Fig. 5.

In Fig. 4, C_p were plotted against $1/V$, for nine temperatures from 560°C to 400°C, using the values of the previous five experiments of cooling. In this figure, the extrapolations of the constant temperature curves to the infinite rate of cooling $1/V = 0$, will give the reversible specific heats C_p^{re}. But, as we see in the figure, the data are not enough to allow a satisfactory extrapolation. Therefore, the extrapolations were carried out so as to give the same internal energy at room temperature as that of the specimen quenched into water from 600°C. In Fig. 5, (1) the reversible specific heats C_p^{re} thus obtained, (3) the specific heat curve on heating for the alloy quenched from 600°C into water, and (2) the specific heat curve for pure nickel measured by the same apparatus are plotted against reduced temperature scale, T/Θ. Considering the difference of magnetic energy of the two metals, it can be said that the anomalous part of C_p^{re} consists mainly of the energy associated with the magnetic transformation. Using this C_p^{re}, the rate of time change of the irreversible internal energy $-dU^{ir}/dt$ can be calculated by the equation,

$$-\frac{dU^{ir}}{dt} = (C_p - C_p^{re}) \cdot V .$$

Therefore, $-dU^{ir}/dt$ is equal to the inclination of the straight line connecting the origin of the curve and the point under consideration in Fig. 4. These straight lines are shown in the figure only in one case of the experiment (c) by dotted lines. In Fig. 6, the irreversible specific heats $C_p^{ir} = C_p - C_p^{re}$ and the rate of time change of the irreversible internal energy $-dU^{ir}/dt$ thus obtained are shown.

The figure shows the quantitative picture of the irreversible ordering process of Ni_3Fe during cooling in the stage of local ordering. The devlopment of local order starts at the

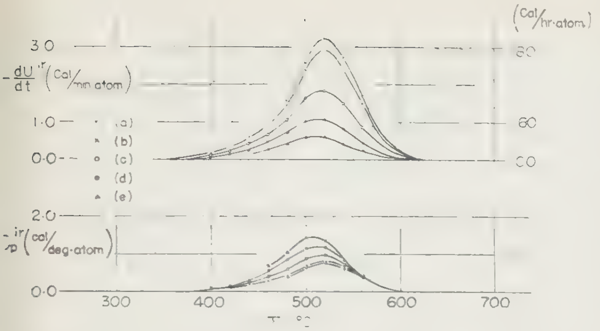

Fig. 6. The irreversible part of specific heat during cooling and the corresponding rate of time change of irreversible internal energy as functions of temperature. The notations (a), (b), (c), (d), and (e) correspond to these of Fig. 2 and Fig. 3.

temperature of about 600°C, then increases gradually to its maximum at about 520°C and decreases gradually to zero at about 400°C. Here even in this quantitative treatment, no anomalous behaviour is seen at the critical ordering temperature 500°C.

§ 4. The Development of Local Order at the Steady Temperature

The existence of short range ordering which had a relaxation time of hours was confirmed by the above cooling experiments. Moreover, Fig. 6 shows clearly that the equilibrium cooling was not obtained for our slowest cooling even in the temperature range above the critical temperature. In this situation, it will be possible to study the development of local order by measuring directly the rate of decrease of the internal energy. This method was used previously to observe the two steps' formation of superlattice at 490°C.²⁾

The specimen and the apparatus used were the same as the previous cooling experiments. The specimen in vacuum was heated to 850°C, held one hour, cooled to 600°C, held again for one hour and then cooled as rapid as possible to 510°C. At this temperature, the rate of decrease of the internal energy due to local order was observed. Then the temperature of the specimen was kept at 510°C as constant as possible, by controlling the outer heater and the differences of temperature δT between the specimen and the surrounding copper wall, which were indicated by the differential junction and galvanometer, were recorded continually. δT is considered to be proportional to the rates of the decrease of internal energy caused by the development of local order. After about half an hour at 510°C, the thermal equilibrium condition became enough to allow the observation. The observations continued for five hours until the difference of temperature δT became zero within the experimental error. Then, the specimen was cooled in furnace as rapid as possible to the room temperature. After that the specimen was heated again to observe the corresponding specific heat—temperature curve on heating.

To transform the observed differences of temperature δT into the rate of the internal energy, a proportional, constant k must be determined. However, in this case, the condition is different from that of the previous experiment.²⁾ Because, some unknown development of the local order would take place in the duration of cooling from 600°C to 510°C and annealing for half an hour at 510°C which was necessary to prepare the condition. This will have a great contribution to the total energy decreased in this experiment. Therefore, a certain complicated procedure was necessary to determine the total amount of energy decreased at 510°C.

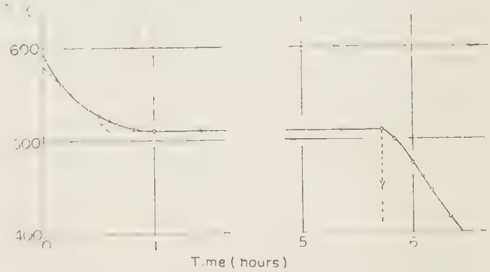

Fig. 7. Temperature-time history of the specimen in the experiment, by which the development of local order at 510°C was observed directly.

In Fig. 7, the temperature-time history of the specimen in this experiment is shown. The full line illustrates the actual history. We approximate the history to what is illustrated by the dotted lines. That is, (1), a cooling from 600°C to 510°C with the constant rate $\overline{V}=2.0$ deg/min, (2), an annealing for 30 minutes at 510°C, and (3), a quenching from 510°C to the room temperature. Then, the specific heats during cooling from 600°C to 510°C can be approximated to be equal to the values of the curves in Fig. 4, corresponding to $1/V=1/\overline{V}=0.50$ min/deg. at each temperature. The specific heats during cooling from 510°C to the room temperature after the measurements are also assumed to be equal to the reversible specific heats C_p^{re}. In Fig. 8, the specific heat during cooling estimated by the above procedures is shown together with the specific heat on heating observed after the cooling procedures. Here, the difference, 49 cal./atom, of the two areas surrounded by the two curves in the figure will give the total energy decreased by the annealing at 510°C. Moreover, the initial value of the rate of decrease of the internal energy at 510°C is assumed to be equal to the value $-dU^{ir}/dt$ of 1.7 cal/min. = 100 cal/hr. atom., corresponding to $1/V=1/\overline{V}=0.50$ min/deg. at 510°C in Fig. 4. Taking account of this initial value, the proportional constant k was determined.

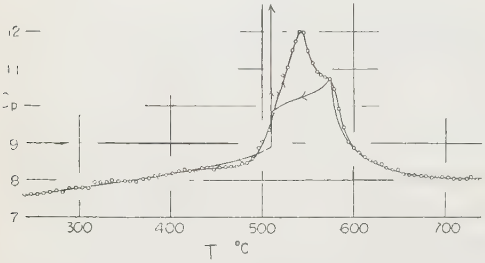

Fig. 8. Calculated specific heat curve during cooling in the experiment for the direct observation of local order at 510°C, and specific heats on heating of the specimen after the experiment.

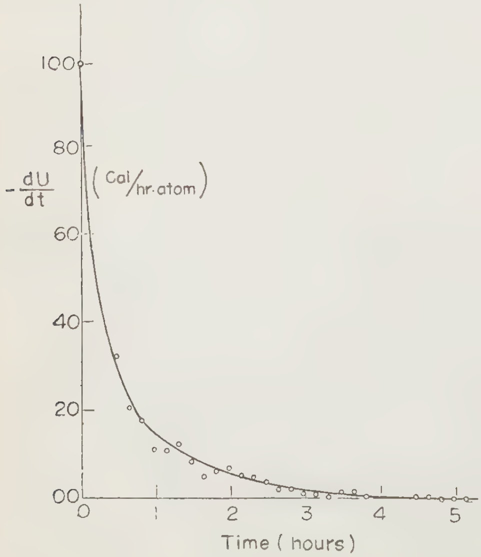

Fig. 9. The rate of decrease of the internal energy due to the development of local order at above the critical temperature. The abscissa indicates the times of annealing at 510°C.

The result is shown in Fig. 9. It can be said that the existence of the time dependent formation of local order above the critical temperature is confirmed quantitatively. It shows a simple type process which continues for about five hours at 510°C.

The study for the development of local order above the critical temperature is extended further by using the quenching treatment and by measuring the specific heat on heating. First the specimen was annealed for 15 hours at 510°C and quenched into the water, and next the specimen was annealed for 44 hours at 505°C and quenched into water. In both cases the measurements of specific heat on heating were carried out after each heat treatment. The results are shown in Fig. 10 and Fig. 11 with several previous curves for comparison. In Fig. 10 it can be seen that the excess energy of about 20 cal/atom. is required to heat the 15 hours annealed specimen from 500°C to 600°C, compared with the specimen of the previous experiment which had been annealed for 5 hours at 510°C. It seems probable that a further development of local order exists at 510°C after the five hours annealing. But in Fig. 11, the internal energy decreases further by the amount of about 23 cal/atom compared with that of the specimen annealed 15 hours at 510°C. Thus, it will be more adequate to

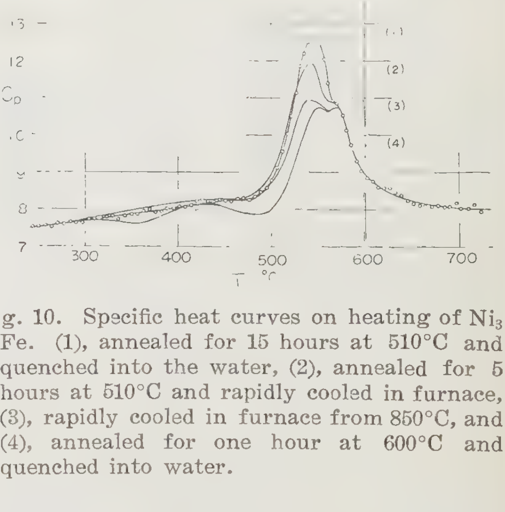

Fig. 10. Specific heat curves on heating of Ni_3Fe. (1), annealed for 15 hours at 510°C and quenched into the water, (2), annealed for 5 hours at 510°C and rapidly cooled in furnace, (3), rapidly cooled in furnace from 850°C, and (4), annealed for one hour at 600°C and quenched into water.

assume that the equilibrium energy of local order is very sensitive to the annealing temperature near the critical temperature, and the observed difference of energy between the five hours annealing and the fifteen hours annealing at 510°C is caused by the experimental error in the regulation of constant temperature at 510°C for the latter.

In Fig. 11, a specific heat curve of the specimen which has been annealed for 6 hours at 490°C[2] is also shown. It must be born in mind that although the total amounts of the internal energy decreased by the formation of superlattice are almost equal in the two cases of Fig. 11, the internal states of the specimen seem to be quite different, as we can see by the different positions of the anomaly. The curves indicate that the local order which developed at higher temperatures is more stable against the increase of temperature than the order which developed at lower temperatures. Here, the heating rates of the two measurements were almost equal.

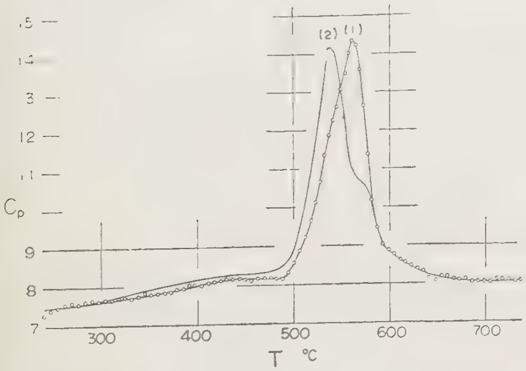

Fig. 11. Specific heat curves on heating of Ni_3Fe. (1), annealed for 44 hours at 505°C and quenched into water, (2), annealed for 6 hours at 490°C and quenched into water.

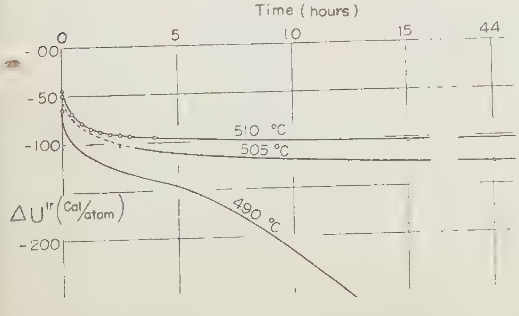

Fig. 12. Internal energy of Ni_3Fe as functions of the times of annealing at 510°C. The critical temperature is about 500°C.

In Fig. 12, the amount of the internal energy decrease are shown as functions of the time of annealing at 500°C, 505°C, and 490°C. The curves for 510°C and 505°C are infered from the data of the above measurements, and the curve for 490°C is taken from the previous paper.[2] Here, the zero points of the internal energy are chosen to the states having the internal energy consisting of only the reversible part of the internal energy. For example, in the direct observation at 510°C, the irreversible internal energy of about 45 cal/atom. has already been lost during the cooling from 600°C to 510°C.

§ 5. Discussions

The obtained curves for the development of local order shown in Fig. 12 are quite similar to the curve (1) of Fig. 10 of the previous paper.[2] Therefore, we believe that our postulates stated in the introduction were proved by direct experimental data.

The existence of local order above the critical temperature[6],[7],[8], is established both from theoretically and experimentally. The constant of atomic diffusion will not very different for the temperatures above and below the critical temperature, at least in the initial stage of ordering. Therefore, the difference between the characteristics of the time dependent formation of the atomic order above and below the critical temperature will be mainly due to (1) their different total amounts of ordering and (2) their different cooperation characteristics. Our unpublished theoretical treatment[9],[10] has shown that the difference of magnitude of their times of relaxation in the formation of atomic order between with and without long range order is not large. Therefore, for almost all superlattices which have a sufficiently long relaxation time for long range order, there will exist observable time dependent formation of the local order.

When we look at the well known heat treatment of permalloy, quenching from 600°C[11], from this point of view, it is the necessary and sufficient treatment for this alloy to suppress the development of local order. The situation can be seen in Fig. 6. Y. Tomono showed experimentally[12] that the effect of magnetic field cooling for this alloy is most efficient at temperatures about 520°C. This fact can be well understood by the assumption that the effect is caused by the development of the local order.[12),13),14)]

In the above analysis of the experiments, the coupling between the atomic ordering and the ferromagnetic spin ordering is neglected. This omission may be allowable in the approximation used in this paper. But there are several evidences about the existence of this coupling revealed in the characteristics of specific heat-temperature curves on heating observed for specimen annealed long below the critical temperature. They will be discussed in the next paper.[5)]

The writer wishes to express his sincere thanks to Professor Seiji Kaya for his fruitful suggestions and constant encouragements and to Dr. Sōshin Chikazumi for his discussions.

References

1) S. Kaya: J. Hokkaido Univ. **2** (1938) 29.
2) S. Iida: J. Phys. Soc. Japan **7** (1952) 373.
3) C. Sykes and H. Evans: J. Inst. Metals. **58** (1936) 255.
4) G. J. Diens: J. Appl. Phys. 22 (1951) 1020.
5) S. Iida: unpublished.
6) J. M. Cowley: J. Appl. Phys. **21** (1950) 24.
7) R. A. Oriani: J. Appl. Phys. **21** (1950) 1068.
8) C. H. Sutcliffe and F. E. Jaumot, Jr: Acta. metall. **1** (1953) 725.
9) S. Iida: unpublished.
10) Y. Takagi, T. Oguchi, and C. Shirane: Bull. Tokyo Inst. Tech. B. **3** (1950) 225.
11) G. W. Elmen: J. Frank, Inst. **107** (1929) 583.
12) Y. Tomono: J. Phys. Soc. Japan **4** (1949) 298.
13) S. Chikazumi: J. Phys. Sod. Japan **5** (1950) 227.
14) S. Iida: unpublished.
15) S. Kaya: Rev. Mod. Phys. **25** (1953) 49.

JOURNAL OF THE PHYSICAL SOCIETY OF JAPAN Vol. 9, No. 3, MAY—JUNE, 1954

X-Ray Study of Cold Work in Some Ordered Alloys

By Shoichi ANNAKA

Faculty of Science, Tokyo University of Education

(Received September 11, 1953)

The structure changes due to cold work on polycrystalline specimens of super-lattice alloys ($AuCu_3$, AuCu, AgCd and AgZn) were studied by X-rays. In $AuCu_3$ and AuCu, a small anti-phase domain and strain were found to be produced by cold work. In AgCd and AgZn, the ε and ζ phases both changed into the β' phases by cold work even at room temperature, and in the case of the ε phases severe slipping along the (001) plane as well as atomic diffusion took place during and after cold work.

§ 1. Introduction

Plastic deformation of metals due to cold work has previously studied by x-rays, by electron-microscope and by electric resistance measurement and it is known that slip and deformation bands, atomic diffusion, deformation twinning and structure changes are produced by cold work[1)]. These changes have significant importance in the explanation of the plastic deformation of metals. Among the methods of investigation mentioned above, the x-rays are of course the most convenient for the study of crystal structure change and many studies on cold work of metals and alloys have been carried out so far by this method. In polycrystalline material[2)], it is known that there occurs a broadening of the lines in the Debye-Scherrer photograph, accompained by a change in their intensities. The following two causes have been attributed to explain these facts: 1) reduction in crystal size, 2) uniform and non-uniform strain remaining in the crystal. In single crystals[3)], Laue asterism has been known to appear and is ascribed to deformation bands. On the other hand only few instances are found so far of studies on the cold work in super-lattice alloys, and the writer thought it shall be very usefull to develop this approach to the problem, since this method reveals even the changes in unit cells. Some recent findings by the author along this line have already elsewhere been reported elsewhere⁴⁾, and in this paper the writer will describe further experiments along the same lines and discuss the results. Four kinds of alloys, $AuCu_3$, AuCu, AgCd and AgZn have been taken up in the experiment, the former two differing from the latter two in their physical properties.

§ 2. Experimental Method

The x-ray powder patterns were studied by the photographic method and in some cases by the Geiger counter method. Care was taken to obtain monochromatic x-rays. In the case of the photographic method with CuKα-radiation, for example, a high tension of about 25,000 volts was employed and use was made of Ni filter. Cold work was effected by filing at room temperature, the average size of the grain obtained being of about 1/100∼2/100 mm. In the photographic method, the powder was mixed with a small quantity of paste and extruded from a glass tube. The wire-like sample (0.6 mm. diameter) thus obtained reveals no preferred orientation after cold work. In the counter method, the powder was fixed with aceton on a glass plate.

§ 3. Results and Discussion

1. $AuCu_3$, AuCu, AgCd(β') and AgZn(β').

It has been supposed mainly on the basis of electric resistance change, that cold work might be the cause of disordering in super-lattice alloys, but not in such cases as β-brass. To test this, we filed $AuCu_3$, AuCu, AgCd(β') and AgZn(β') in ordered states and studied them by an x-ray powder method.

We found that the super-lattice lines in these x-ray photographs had disappeared completely in $AuCu_3$ and AuCu, but not such change was observed in the cases of the AgCd and AgZn. We should be able to identify the nature of these changes by measuring the lattice constant, and the results of such an measurement are shown in Table I (though the atomic ratio of the components in these samples are not 25:75 or 50:50 precisely). And a diameter of camera was 24 cm. long (counter method). But owing to the broad Debye-Scherrer lines, the errors in absolute values were estimated as ±0.003 Å in the cases of $AuCu_3$ and AuCu. In these measurements no change of lattice constants was observed after cold work in the $AuCu_3$, AgCd and AgZn. In the AuCu, however, the crystal structure changed from the tetragonal to the cubic and the volume of unit cell increased.

Table I. The lattice parameters in Å unit. The error is estimated as ±0.003Å. ($AuCu_3$ and AuCu).

alloys	ordered state	filing sample	disordered state
AgCd (β')	3.330	3.330	
AgZn (β')	3.155	3.155	
$AuCu_3$	3.744	3.744	3.760
AuCu	$a=3.980$ $c/a=0.935$	3.881	3.888

The above experimental fact that the super-lattice lines disappear completly in the $AuCu_3$ is explained by thinking that ordered state of $AuCu_3$ becomes disordered state by atomic diffusion. But this phenomenon is also explained by thinking that the crystal is divided into a small anti-phase domains by slipping. This explanation is made in the following manner: Let us compare the peak hight of the (002) reflexion with fluctuation in the increased background of the counter record (Fig. 1a) or with the weak (111) reflexion due to Kβ-radiation. It may be supposed that the (002) reflexion would not be observed if the peak height of the (002) is reduced to about 1/20 or less, that is, when the integral breadth becomes about 1/20 or less. So if the apparent size of an anti-phase domain is about 1/20 or less of the coherent domain size, this explains the disappearance of the (001) super-lattice line⁵⁾, which has almost the same intensity as (002). The range of the anti-phase domain is hard to estimate since the super-lattice lines vanish entirely.

When we consider many experiments on plastic deformations¹⁾ it should be natural to think that the crystal is divided into small anti-phase domains by slipping. But the boundaries of these domains would be in disordered states. This latter idea is profitable for the result of the measurement of

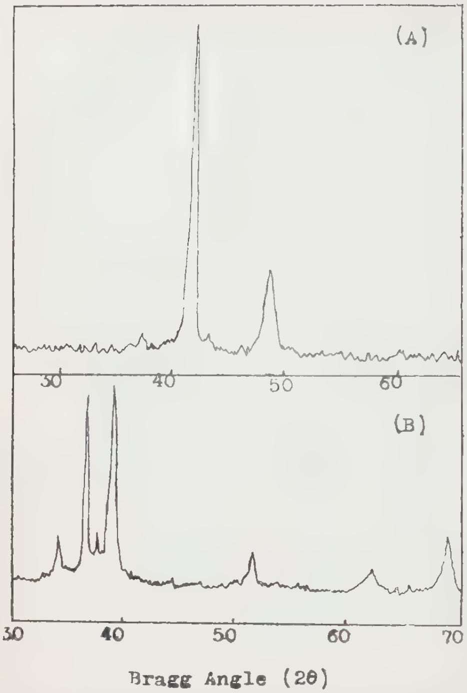

Fig. 1. The Geiger counter records of cold worked $AuCu_3$ (A) and ∊ phase of AgCd (B).

lattice constant although its error is large. In the AuCu, as may be supposed from the case of $AuCu_3$, we can not assume the occurrence of a disordered state of AuCu by filing. But the boundary of anti-phase domain must be in disorder by slipping. It should be natural to think that the tetragonal lattice changes into the cubic through depression of the cooperative phenomenon arising from the smallness of this domain and through the influence of the disordered boundary.

The order of the AgCd and AgZn did not change by cold work. In these cases the errors in lattice constants were estimated as ±0.001 Å or less because the lines were sharp. In the case of β-brass[6], ordering took place even at room temperature. So we may think that atomic diffusion instantly took place after cold work due to the low ordering energy of AgCd and AgZn and residual strain vanished.

The breadth of the fundamental lines became appreciably broader after cold work in the $AuCu_3$ and AuCu but to a minor extent in the AgCd and AgZn. One may determine the cause of line broadening if one knows whether the width of line is proportional to $\tan\theta$ or $\lambda\sec\theta$[7], where θ is Bragg angle and λ is wave length of x-rays. In this experiment, the next care was taken: 1) Correction for photometer curve. 2) Monochromatic x-rays were obtained as already mentioned. 3) Standard sample were used for the correction for spurious broadening due to apparatus.

The line profile was found to be well approximated by a curve $C/(1+k^2x^2)^2$, where C and k are constants[8]. The result obtained by this method differ in some cases by about 3% from those of the method of Stokes. Cr-, Fe-, Cu- and Mo-Kα-radiation were used. The breadth was nearly proportional to $\tan\theta$ as shown in Fig. 2. The proportionality against $\lambda\sec\theta$ was not so good as against $\tan\theta$. So it was concluded that main cause of the line broadening should be attributed to strain. In a case like this, the approximate coherent domain size is usually obtained in the following way: Line broadening (B) is given by the sum of strain broadening and particle size broadening, or approximately ($k\cdot\tan\theta+\lambda/D\cdot\sec\theta$), where k is constant and D is the range of the coherent domain. For constant λ, one may obtain two experimental values B_{111} and B_{222} for (111) and (222) lines respectively and these two points are connected by a curve ($k\cdot\tan\theta+\lambda/D$) an the graph of B versus θ. When θ is 0, the value of this curve is approximately λ/D. By this method, we calculated the average coherent domain size which was found to be 800±100 Å. In the AgCd and AgZn, the line broadening was very small.

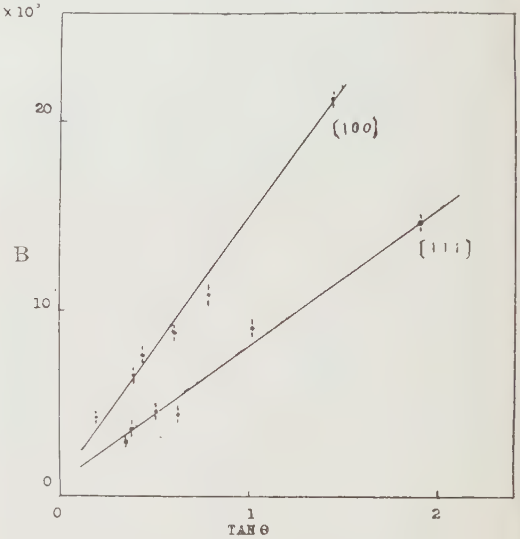

Fig. 2. The plots showing the variation of integral half intensity breadth (B) with tan θ.

The breadth of the (110) line of AgCd for CuKα for example was 1.3×10^{-3} radian.

2. AgCd(ε) and AgZn(ζ).

The ε and ζ phases are stable in the range of 258–450°C and below 283°C respectively[9]. It was found that the ε and ζ phases changed into the ordered β' by cold work at room temperature. The character of change is as follows: 1) The disordered state changes into the ordered. 2) The hexagonal lattice changes into the body-centered cubic. 3) The intermediate states, ($\varepsilon+\beta'$) and ($\zeta+\beta'$), are obtained by proper cold work. These intermediate states, however, change into the β' with the lapse of time. After light cold work, the ε phase is changed within about 20 hrs., but ζ phase is changed within about 3 months after heavy cold work. 4) The relative integral intensities of the x-ray reflexion lines of the ε and ζ phases change during the above intermediate states (Fig. 1b).

By studying these fact, one may expect to derive some knowledge of structural changes of metals by cold work. There is no room to doubt that a remarkable diffusion of atoms occurs in the AgCd and AgZn during and after cold work. This infers that diffusion must be the cause of order-disorder change in 1). The mechanism of these structural changes in 2) is not as yet clear, but the study of abnormal intensities of the intermediate states will be an approach to this problem. We considered the intermediate state of ($\varepsilon+\beta'$) because the ε phase had a simple crystal structure.

Table II. Effect of cold work on integrated intensities of x-ray diffraction lines for rod sample (AgCd ε). $K=\exp(-(8\pi^2/\lambda^2)\cdot\sin^2\theta_B\cdot\sin^2\phi\cdot2\langle\xi^2\rangle)$. $\longleftrightarrow$ indicates where cal. and obs. intensities matched.

($hk\cdot l$)	A cal.	A' obs.	B ($A\times K$)	C ($B\times0.86$)
(10·0)	12.7	6.5	9.8	8.4
(00.2)	15.0 ←	→15.0 ←	→15.0←	→15.0
(10·1)	62.4	38.0	50.0	43.0
(10.2)	12.7	7.0	9.9	8.5
(11.0)	19.5	10.0	9.7	9.7
(10·3)	24.1	19.0 ($\varepsilon+\beta'$)	19.0	16.3
(20·0)	3.7	—	1.4	1.2
(11·2)	28.1	13.0	12.7	12.7
(20·1)	21.1	5.5	7.5	6.5
(00·4)	4.4	4.5	4.4	4.4
(20·2)	6.1	—	2.2	1.9
(10·4)	5.5	3.0	4.0	3.4
(20·3)	16.7	5.4	6.6	5.7
(21·0)	50_6	—	—	—
(21·1)	33.9	6.6 ($\varepsilon+\beta'$)	7.0	6.1
(11·4)	23.8	13.4	11.8	11.8
(21·2) (10·5)	28.8	10.4	15.0	12.9

The x-ray intensities measured by photographic and counter methods are indicated in column A′ of Table II. These values differ from the theoretical (column A) in various respects. Firstly the reflexion lines from the planes inclining at a large angle to the (001) plane have weak intensities and their line breadths are a little larger than those of the planes inclining at a small angle. This abnormality suggests random displacement of atoms from lattice points in the (001) plane. Such a state is similar to that having an anisotropic thermal agitation parallel to the same plane. We therefore corrected the theoretical values in the following way: The theoretical values multiplied by $\exp((-8\pi^2/\lambda^2)\cdot\sin^2\theta_B\cdot\sin^2\phi\cdot2\langle\xi^2\rangle)$ are given in column B, where $\langle\xi^2\rangle$, the mean squre displacement of atoms in the (001) plane, is 0.04 Å, and ϕ is the inclining angle to the same plane. Comparing the column A with B, one will see that the agreement in the planes where $h-k=3n\pm1$ is not good. To explain these discrepancies, stacking disorder was assumed to be produced on the (001) plane. Let us consider simply that change of x-ray reflexion intensities due to stacking disorder. In the simple case of stacking disorder produced by slipping in one direction along the (001) plane, there will exist the following, (1) $A_1B_2A_1B_2A_1B_2\ldots\ C_1A_2C_1A_2C_1A_2\ldots\ B_1C_2B_1C_2B_1C_2\ldots\ A_1B_2A_1B_2A_1B_2\ldots$, (2) $A_1B_2A_1B_2A_1B_2\ldots\ A_1C_2B_1C_2B_1C_2\ldots\ B_1A_2C_1A_2C_1A_2\ldots\ C_1B_2A_1B_2A_1B_2\ldots$, where 1 and 2 indicate $z=0$ and 1/2, the height along the z direction in the unit cell and the structure of A, B and C planes are as shown in Fig. 3.

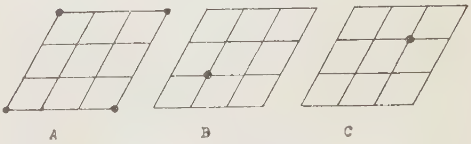

Fig. 3. The structure of planes A, B, and C.

If the sequence (1) exist in the crystal, the amplitude of the x-ray reflexion will be expressed by:

$$A_1=[\{1+\exp(2\pi i(\tfrac{1}{3}h+\tfrac{2}{3}k+\tfrac{1}{2}l))\}\sum_{n=0}^{n_0-1}\exp(2\pi inl)$$
$$+\{\exp(2\pi i(\tfrac{2}{3}h+\tfrac{1}{3}k))+\exp(2\pi i\cdot\tfrac{1}{2}l)\}$$

$$
\begin{aligned}
&\cdot\sum_{n=0}^{n_0-1} \exp(2\pi i(n_0+n)l) \\
&+\{\exp(2\pi i(\tfrac{1}{3}h+\tfrac{2}{3}k)) \\
&+\exp(2\pi i(\tfrac{2}{3}h+\tfrac{1}{3}k+\tfrac{1}{2}l))\} \\
&\cdot\sum_{n=0}^{n_0-1} \exp(2\pi i(n+2n_0)l)]\cdot \sum_{n'=0}^{N-1} e^{2\pi i(3n_0)n'l} \\
=&[(1-e^{2\pi i3Nn_0l})/(1-e^{2\pi i3n_0l})] \\
&\cdot[(1-e^{2\pi in_0l})/(1-e^{2\pi il})] \\
&\cdot\{1+\exp(2\pi i(\tfrac{1}{3}h+\tfrac{2}{3}k+\tfrac{1}{2}l)) \\
&+\exp(2\pi i(\tfrac{2}{3}h+\tfrac{1}{3}k+n_0l))+\exp(2\pi i(\tfrac{1}{2}+n_0)l \\
&+\exp(2\pi i(\tfrac{1}{3}h+\tfrac{2}{3}k+2n_0l) \\
&+\exp\{2\pi i(\tfrac{2}{3}h+\tfrac{1}{3}k+(2n_0+\tfrac{1}{2})l\}] \qquad (1)
\end{aligned}
$$

where it may be assumed that n_0 layers exist between faults, the number of faults being ($3N-1$). Each reflexion line satisfies one of following two conditions (a) or (b). The values of Eq. (1) give the answers for the cases where l is respectively even and odd.

(*a*) $h-k=3n$ (n: integer). When l is even, $A_1=6n_0N$. When l is odd, $A_1=0$.

(b) $h-k=3n\pm1$. In this case, let us consider the values of A_1^2.

$$
\begin{aligned}
A_1^2=&\frac{\sin^2\pi3Nn_0l}{\sin^2\pi3n_0l}\cdot\frac{\sin^2\pi n_0l}{\sin^2\pi l} \\
&\cdot[6+4\cos2\pi(\pm\tfrac{1}{3}+\tfrac{1}{2}l)+4\cos2\pi(\pm\tfrac{2}{3}+n_0l) \\
&+4\cos2\pi(\tfrac{1}{2}+n_0)l+4\cos2\pi(\pm\tfrac{1}{3}+2n_0l) \\
&+2\cos2\pi\{\pm\tfrac{2}{3}+(\tfrac{1}{2}+n_0)l\} \\
&+4\cos2\pi\{\pm\tfrac{1}{3}+(n_0-\tfrac{1}{2})l\} \\
&+4\cos2\pi(\pm\tfrac{1}{3}+2n_0l)+2\cos2\pi(2n_0-\tfrac{1}{2})l \\
&+2\cos2\pi(\pm\tfrac{2}{3}-\tfrac{1}{2}l)]\,. \qquad (2)
\end{aligned}
$$

We inserted the values of l into Eq. (2). The values of terms between square brackets are large in special cases as shown in Table III. If n_0 is large the term $\sin^2\pi n_0l/\sin^2\pi l$ has the values $n_0^2\times0.68$ and $n_0^2\times0.18$ when $l=1/3n_0$ and $2/3n_0$ respectively. Accordingly if the line profile is assumed to be nearly triangular the integral intensity is weakend by about 14%. The sequence (2) indicates nearly the same results. If n_0 is large, the sharpness of the line is little different from the case where no faults exist, and in our case line broadening due to strain is larger. The real crystal however has more complex structure of faults, but we corrected the values of B by 14% in the first approximation. The result is shown in column C, which is more likely to be observed.

Table III.

	l=even		l=odd	
$h-k$	$3n+1$	$3n-1$	$3n+1$	$3n-1$
1+0/3	0	0	0	0
1+1/3	9	0	27	0
1−1/3	0	9	0	27
1+2/3	0	9	0	27
1−2/3	9	0	27	0

§ 5. Conclusions

It is known that direct evidence for plastic deformation may be found in the slip and deformation bands found by the electron-microscope[1),10)], and this large slipping gives rise to reduction of dimension in the coherent domain.

In AuCu$_3$ and AuCu alloys, from the disappearance of the superlattice lines after cold work, we have concluded that small antidomains are produced by many elementary slips in the coherent domain. The measurement of the fundamental line width in AuCu$_3$ has shown that the main cause of line breadening is strain. Hence we have estimated the average dimension of the coherent domain to be about 800±100 Å in the [111] direction.

In AgCd and AgZn, the ε and ζ phases changed into the β' by cold work. The abnormal x-ray intensities in the intermediate phase (ε) suggests severe slipping along the (001) plane. In the ζ phase, the stable state (ζ) changed into the metastablestate (β') by cold work, so we must think that the lattice energy of the ζ phase increased at a moment as high as above 283°C by cold work.

In conclusion, the author wishes to express his sincere thanks to Prof. Mitsuo Miwa for his valuables discussion and to Mr. H. Suzuki of the Tohoku University for his helpful discussions. In the counter experiments, the author owes his gratitude to Prof. T. Ito. This work was supported by grants in aid for fundamental research dispensed by the Ministry of Education.

References

1) C. S. Barret: Structure of Metals, (McGraw Hill Book Co., Inc., New York, 1943.
2) B. L. Averbach and B. E. Warren: J. App. Phys. **20** (1949) 1066.
3) E. A. Calnan: Acta Cryst. **5** (1952) 557.
4) S. Annaka: J. Chem. Phys. **20** (1952) 1662.
5) A. J. C. Wilson: Proc. Roy. Soc. **181** (1943) 360.
6) R. R. Eggleston and F. E. Bowman: J. App. Phys. **24** (1953) 229.
7) C. S. Smith and E. F. Stickley: Phys. Rev. **64** (1943) 191.
8) F. R. L. Schoening, J. N. van Niekerk and R. A. W. Haul: Proc.P hys. Soc. B **391** (1952) 528.
9) S. Annaka and M. Yasumura: Nippon Kinzoku Gakkai-si, **17** (1953) 56.
10) R. D. Heidenreich and W. Schockley: J. App. Phys. **18** (1947) 1029.

JOURNAL OF THE PHYSICAL SOCIETY OF JAPAN Vol. 9, No. 3, MAY—JUNE, 1954

Electron-Diffraction Study of Liquid-Solid Transition of Thin Metal Films

By Mieko TAKAGI

Tokyo Institute of Technology, Tokyo

(Received January 9, 1954)

Structure changes of thin films of Pb, Sn and Bi at various temperatures has been studied by electron diffraction method. The films were prepared, in the electron diffraction camera by evaporating the metals, on cleavage surfaces of several kinds of crystals. The mean thickness of the films ranged from 10Å to 1000Å. The observed melting points are found to be lower than those of bulk metals. Anticipating this effect to be attributed to the small size of the crystal, the author has calculated the melting temperature as a function of crystal size. The observed values of the lowering of the melting point agree fairly well with the calculated values for the crystal sizes estimated from the mean thickness and the breadth of the Debye-Scherrer rings in diffraction patterns. On cooling, the films are supercooled down to considerablly lower temperatures which can be ascribed to the slowness of the rate of nucleation in a small crystal.

§ 1. Introduction

By means of the electron diffraction method, it has been revealed that thin films of some low melting-point metals show remarkable supercooling when cooled from temperatures above the melting point. Sayama[1] found that thin films of tin (melting point 231.8°C) evaporated on molybdenite cleavage surfaces show supercooling down to about 80°C. Miyake and the present author[2] have observed the same phenomenon also for lead films evaporated on cleavage surfaces of zincblende. Recently, Turnbull[3] has measured the solidifications temperature of small droplets, 50μ diameter of various metals under microscope, and confirmed a similar effect.

The present author has made observations on the structure change with temperature of thin films of lead, tin and bismuth, evaporated on crystal surfaces. In this experiment, besides the extreme supercooling as mentioned above, also the phenomenon of pre-melting, or the lowering of the melting point, has been noticed. Namely, when films are heated from temperatures below the melting point, diffraction patterns are found to change from solid to liquid patterns at temperatures lower than the melting point of the metal in bulk; these temperatures depend in general on the thicknesses of the films.

In this paper, the results of the observation on these phenomena, the pre-melting and the supercooling, will be reported, and explained in terms of existing theories.

§ 2. Experimental Procedure

The evaporation of metals, lead, tin and bismuth, on cleavage faces of single crystals of zincblende, galena, molybdenite and silicon carbide was performed in the electron diffraction camera[4,5]. The changes of diffraction patterns with temperature were observed on the fluorescent screen or by photographs.

The mean thickness of each film, which was calculated from the total mass of the evaporated metal, ranged from 10 to 1000Å.

In most cases, the temperature of films was measured by a thermocouple fixed close by the sample face. The temperature difference which may exist between the thermocouple and the cleavage face is estimated by the following method. As shown in Fig. 1, a piece of the metal (**m**) which is of the same kind to that to be evaporated on the base

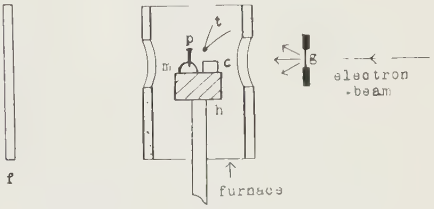

Fig. 1. Experimental Procedure.

crystal (**c**) is placed on the holder (**h**), close to (**c**); a small pin (**p**) is stuck on the top of the piece of metal (**m**). The electron beam is scattered by a golden foil (**g**) so as to produce a shadow of the sample holder on a fluorescent screen (**f**), then the melting of the metal piece is recognized by observing the fall-down of the pin in the shadow, and thus the temperature difference between the thermocouple and the metal piece at this moment can be determined. The difference was about 20°C, and the reading of the thermocouple was corrected by this value. The observation of the diffraction patterns from the metal films on the substrates (**c**) are done by removing the golden foil from the path of electrons.

§ 3. Experimental Results

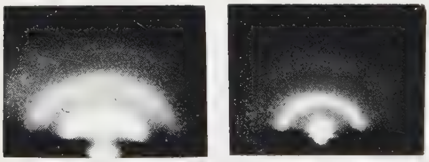
a. Pb b. Bi

Photo. 1. Diffraction pattern for liquid state.

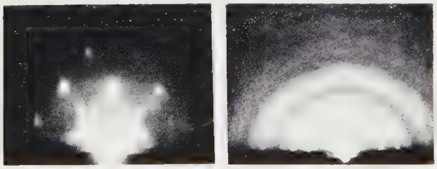
a. Pb b. Bi

Photo. 2. Diffraction pattern for solid state.

The diffraction patterns of thin films above melting point consist of liquid halos as are shown in Photos. 1a and 1b. When the films are cooled slowly, remarkable supercooling is observed; the halo patterns persist over a wide temperature range below the ordinary melting point of the bulk metal, but suddenly change into spotty (for Pb and Sn) or ring (for Bi) patterns as are shown in Photos. 2a and 2b.

Hereafter the observed solidification temperature on cooling will be denoted by T_s, and the melting point of the bulk metal by T_0. When these films are re-heated, the patterns change into halos, indicating the melting of the films. We denote the temperature corresponding to this change by T_r. The temperature T_r is lower than the bulk melting point T_0, but much higher than the solidification temperature T_s.

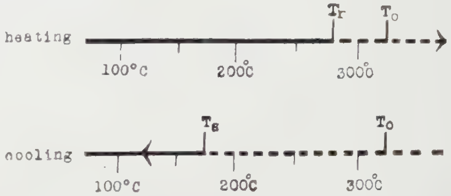

Fig. 2. Phase change of Pb film of 50 Å thick.
---- liquid region — — solid region
T_0 : melting point of bulk metal.
T_r : melting point of thin film.
T_s : solidification temperature of thin film.

An example of these phase changes for Pb films, 50Å thick, is illustrated in Fig. 2.

The observed values of T_r and T_s are given in Table I. These values depend upon the thickness of the films but the dependency upon the kind of base crystal was not remarkable. The temperature range of the

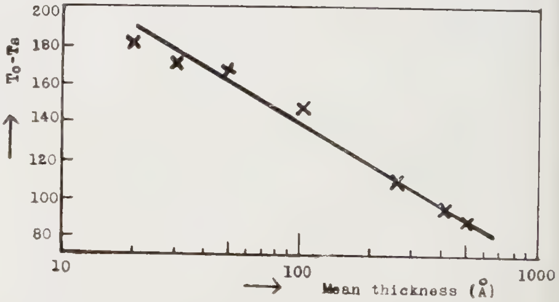

Fig. 3. (T_0-T_s) for various thickness of Pb films.

Table I.

Metal	T_0	Mean thickness (Å)	T_r	T_s	T_0-T_r	T_0-T_s	$T_0-\theta_s$	$2r$ (Å)
Pb	600	500	593	508	7	92	90	400
		50	559	443	41	157	109	72
Sn	505	50	475	313	30	192	136	86
Bi	544	50	521	397	23	147	121	78

supercooled state, (T_0-T_s), for various thickness of Pb films are shown in Fig. 3.

The lowering of the melting point of thin films of bismuth was reported also by Fujiki[6], but the temperatures observed by him do not agree with the values in our experiment. The reason of this discrepancy is not clear.

§ 4. The Theoretical Consideration on Pre-melting and Supercooling

By electron-microscopic observation, thin evaporated films of metal has been found to be the aggregation of small islands of metal crystals[7], so that, for simplicity, one may treat the film as the aggregation of spherical droplets of suitable size.

In this section, therefore, the effect of the drop size of metals on melting point and solidification temperature will be considered theoretically.

a. The melting point of small droplet

It has been known from a thermodynamical consideration[8] that the melting point of a solid having small size is lower than that of the solid in bulk. Suppose that a small sphere, r in radius, of a solid metal is in equilibrium with the surrounding uniform liquid at the equilibrium temperature θ_r. Let ΔU and ΔS denote respectively the change of internal energy and entropy per unit mass of the metal at melting. When dA denotes the decrease of the surface area of the solid sphere due to the melting of a mass dw into liquid at the equilibrium temperature, we have

$$\Delta U\cdot dw-\Delta S\cdot\theta_r\cdot dw-\sigma\cdot dA=0\ , \qquad (1)$$

where σ is the interfacial energy between liquid and solid. At the melting point, T_0, of the bulk metal,

$$\Delta U\cdot dw-\Delta S\cdot T_0\cdot dw=0\ , \qquad (2)$$

provided that ΔU and ΔS are independent of temperature. From (2) we obtain

$$\Delta U=\Delta S\cdot T_0\ , \qquad (3)$$

or

$$\Delta S=\Delta U/T_0=L/T_0\ , \qquad (4)$$

where L is the heat of fusion. Put (4) in (1), then

$$(T_0-\theta_r)/T_0=(\sigma/L)(dA/dw)\ , \qquad (5)$$

where $\Delta\theta=T_0-\theta_r$ means the lowering of the melting point. The Eq. (5) shows that $\Delta\theta=T_0-\theta_r$ is proportional to the decrease of the interfacial energy between solid and liquid due to melting, *viz.*, $\sigma\cdot dA/dw$.

If ρ is the density of the metal, we have

$$w=4/3\pi r^3\cdot\rho\ , \qquad A=4\pi r^2\ ,$$

and we obtain $dA/dw=2/\rho\cdot r$. Putting this in (5)

$$\Delta\theta/T_0=(T_0-\theta_r)/T_0=2\sigma/\rho\cdot L\cdot r\ , \qquad (6)$$

The lowering of the melting point $\Delta\theta$ is then proportional to $1/r$.

For the case of lead, for instance, $\sigma=33.3$ ergs/cm^2 (calculated by Turnbull[3]), therefore

$$\Delta\theta\sim1.5\times10^3/r \text{ (r in Å unit)},$$

which gives $\Delta\theta\sim15°\text{C}$ for $r=100$Å, and $\Delta\theta\sim150°\text{C}$ for $r=10$Å.

The relation (6) has been predicted theoretically since ago[8], but the direct experimental proof seems not to have been performed yet. In the present experiment, the films prepared are 10 to 1000Å in mean thickness, and since the order of the crystal size in films is considered not much different from the mean thickness of the film, $\Delta\theta$ may attain to one to ten times of the several degree.

In the above, the equilibrium temperature between the sphere of solid metal and surrounding uniform liquid has been considered. Though actually the thin film, being the aggregation of small crystals, is surrounded only by its vapor phase, the same result is obtained when we consider the equilibrium state after a small quantity of the outer part of the sphere has melted.

b. The solidification temperature of thin films

The theory of the formation of solid part in supercooled liquid has been treated by Turnbull and Fisher[9]; Turnbull[3] has compared the theory with the experimental observations for various metals. In the following paragraphs their results will be briefly outlined.

The formation of solid phase in supercooled liquid is usually thought of as the result of a sequence of two steps: nucleation and subsequent growth. The latter step occurs so rapid that the rate of formation of solid is mainly determined by the rate of nucleation. Since bulk metals are expected to contain sufficiently many accidental inclusions of external origin, effective as nuclei of crystallization, the supercooling is not usually observed. But when the volume of the metal is small, such inclusions may be seldom, because the probability of finding them in a isolated crystal is proportional to its volume. For such a case, the rate of the formation of solid parts having the critical size as defined below, developing in the liquid, will solely determine the solidification temperature.

As is shown in (6), a solid sphere of the radius r is in equilibrium with liquid phase at the temperature θ_r; and it melts away at higher temperatures. Therefore, at temperature θ_r, only the solid particles with radius larger than r given in (6) may act as nuclei for the subsequent crystallization. This size r is called as a critical size of crystal nucleus at temperature θ_r.

The nucleation rate, or the rate of the formation of the solid sphere with the critical size, in a supercooled liquid, calculated by Turnbull and Fisher, is given by

$$I=A\exp[-K\sigma^3/(\Delta F_v)^2\cdot k\theta],$$
$$A=n(kT/h)\exp[-\Delta F_A/k\theta], \qquad (7)$$

where I is the number of nuclei/sec.cm^3, n the number of atoms in unit mass of liquid, K a factor depending on the shape of the nucleus, σ the inferfacial energy/cm^2 between crystal and liquid, ΔF_v the difference in free energy/cm^3 between crystal and liquid phase of infinite volume and ΔF_A the free energy of activation for transporting an atom across the liquid-solid interface.

At the melting point of bulk metals the value of I is too small to give rise to nucleation, so that even bulk metals would be supercooled for wide temperature range if these were inclusion free. In my experiment, in which the volume v of the crystals is so small that the accidental inclusions are seldom, the crystallization begins practically at the temperature where the rate of nucleation I_v, given by

$$I_v=I\times v, \qquad (8)$$

becomes appreciable (for instance, I_v equals to $10^{-3}\sim10^{-4}$/sec.). This temperature will be called the theoretical solidification temperature θ_s.

§ 5. Comparison of Experimental Results with Theory. Discussions

a. The lowering of the melting point

When we identify the observed value of the lowering of the melting point, T_0-T_r, with the theoretical value θ_r in Eq. (6), the radius r can be estimated. If the shape of the islands are not spherical, r may be interpreted as the mean value of the radius of the curvature of islands. The calculated value $2r$ are shown in the last column in Table 1, in which the σ values calculated by Turnbull, 33.3 ergs/cm^2 for Pb, 54.4 ergs/cm^2 for Bi and 54.5 ergs/cm^2 for Sn were used. The calculated crystal size from the breadth of Debye-Scherrer rings in diffraction patterns of Pb of 50Å in the mean thickness is about 60Å, which also agrees well with the value above mentioned.

Electron-microscopic examination made by Levinstein⁷⁾ and Sennet & Scott¹⁰⁾ on thin films of low-melting point metals, evaporated at room temperature, has revealed that the size of the island crystals are nearly of the same order as the mean thickness, not all uniform in one film, showing moreover a greater tendency of aggregation at higher temperatures. While, the present experiment seems to show that the size of the islands are nearly uniform in a film since the change from crystal to halo pattern is always very abrupt, and that the crystal size remains in the order of the mean thickness even when the temperature of the substrates is high. These discrepancies may be due to the differences in the kind of substrate used, and the rate of evaporation.*

b. The solidification temperature

The solidification temperature θ_s can be calculated from Eqs. (8) and (7), by assuming appropriate values for I_v. In Table I, the value of $T_0-\theta_s$ is shown assuming the value of I_v as 10^{-4}/sec. In this calculation all the values of the other parameters are the same as those in Turnbull's calculation.

The calculated values agree rather well with the observed ones for the case of Pb of 500Å thick, but discrepancies are large for other cases. One of the reasons may be as follows: The solidification temperatures T_s are so low in these cases that, on calculation, the value of A in Eq. (8), which is related to the activation energy for transporting an atom across the liquid-solid interface, will be much smaller than that at higher temperatures.

---

* These also will be the cause of discrepancy between the observed values of the lowering of the melting point by the present author and that by Fujiki⁶⁾.

c. The effect of the artificial nuclei on the solidification temperatures

θ_s in (8) is calculated under the assumption that the thin metal films are inclusion free and the actual crystallization will not take place till the nucleation rate in the metal itself become of measureable order of magnitude. To examine this assumption directly, the author performed the following experiment. First, artificial centres for crystallization were made on the substrate by evaporating a small quantity of copper, then thin films of lead or bismuth were subsequently evaporated on the substrate. The range of the supercooled state, T_0-T_s, for these cases are given in Table II. The Table shows considerably smaller values of T_0-T_s than those in Table I. This result indicates that the supercooling range depends greatly on the existance of crystal nuclei.

Table II.

Metal	Mean thickness (Å)	T_r-T_s
Pb	50	96
Bi	50	53

In this experiment, though higher solidification temperatures are observed, considerably wide supercooling ranges do remain yet, which is interpreted as corresponding to the radius of the artificial centres. In bulk metals the size of the existing inclusions, effective as nuclei, may be somewhat large, while in the present case the artificial nuclei are so small as of the order of several Å in size, and several nuclei may probably be contained in a droplet of the liquid metal. The solidification will, then, begin from the places surrounding nuclei in the droplet and propagate outwards. Let the radius of the artifical nuclei and that of liquid droplet be r' and r respectively. Then the solidification temperature will be the equilibrium temperature $T_{r'}$ corresponding to the radius of artificial nuclei r', while on heating, the solid droplet will melt at the equilibrium temperature T_r, corresponding to the full size of the droplet. In any case, T_r is higher than $T_{r'}$ since $r>r'$.

d. On the twinning formed in lead films

In the case of lead films, twinning on (111) or (11$\bar{1}$) planes were formed as is shown in Photo. 2a. On cooling, only normal spots but no twin spots were observed at the beginning of the solidification; the twin spots begin to appear by cooling further. On heating, first the twin spots disappear and then soon afterwards all the other spots change into halos.

The above observation seems to show that the twinned crystals are formed in some extraordinary regions of the films, such as the boundaries of neighbouring crystals, or on some irregular places of the substrate. Moreover, the fact that the melting temperature of these twinned crystals are lower than that of normally oriented crystals seems to show that the radii of curvature of the twinned crystals are smaller than those of the normally oriented crystals, *viz.*, twinned crystals are more irregular in shape.

In conclusion, the author wishes to express her sincere thanks to Prof. S. Miyake for his important suggestions and kind advices, and also Prof. A. Harasima, for his discussions. The author's thanks are also due to Mr. S. Nagasaki of the Research Institute for Iron, Steel and other Metals, Tohoku University, Sendai for supply of sample metals, and also to Mr. S. Takagi for his advice throughout this investigation. The author is also indebted to the Ministry of Education for the research grant.

References

1) Y. Sayama: Proc. Phys.-Math. Soc. Japan **23** (1941) 869.

2) S. Miyake and M. Kubo (Takagi): At the annual meeting of the Physical Society of Japan (1946).

3) D. Turnbull: J. App. Phys. **21** (1950) 1022.

4) R. Uyeda: Proc. Phys.-Math. Soc. Japan **24** (1942) 809.

5) M. Kubo (Takagi) and S. Miyake: J. Phys. Soc. Japan **3** (1948) 115.

6) Y. Fujiki and R. Suganuma: J. Phys. Soc. Japan **8** (1953) 427.

7) H. Levinstein: J. App. Phys. **20** (1949) 306.

8) H. Freundlich: Kapillarchemie, Bd. 1 (Akademische Verlags Gesellschaft, Leipzig, 1930), S. 465.

9) D. Turnbull and J. C. Fisher: J. Chem. Phys. **17** (1949) 71.

10) R. S. Sennet and G. D. Scott: J. Opt. Soc. Am. **40** (1950) 203.

JOURNAL OF THE PHYSICAL SOCIETY OF JAPAN Vol. 9, No. 3, MAY—JUNE, 1954

Multiple Element Interferometer for Locating Sources of Solar Noise at 4,000 MC

By Haruo TANAKA and Takakiyo KAKINUMA

The Research Institute of Atmospherics, Nagoya University

(Received November 11, 1953)

With the intention of locating sources of radio noise from the disturbed sun at 4,000 MC, an interferometer with 5 aerials was constructed. Each aerial has a paraboloidal reflector of size 1.5 metre in diameter, which can be rotated equatorially. They are placed in E-W direction at 6 m intervals. The main lobes are 43′ apart and each lobe has a half power width of 7.8′. Each aerial is connected to the radiometer with waveguides and magic *T*. General design principles and the results of observations are described in this paper. Experimental record pattern, when the sun is quiet, do not agree with the calculated one corresponding to uniform distribution over the optical disk. From the eclipse observation, it is concluded that the radio disk is about 1.06 times larger than the optical disk. Record pattern is obtained if the outer region is about 2.5 times brighter than the optical disk of the uniform temperature about 1.9×10^4°K.

Photo. 1.

§ 1. Introduction

It is one of the important problems in the radio astronomy to observe the distribution of noise sources over the solar disk at various frequencies. The study in this field, however, has not yet been fully developed, as it is generally difficult to realize radio beams sharp enough to scan the sun directly.

The only means we can use is to apply the well-known interference method. The interferometer produces many lobes; but as the noise sources are restricted in a small region, each lobe can separately be used if no adjacent lobes do not lie on that area at a time. When a source extremely dominates the background radiation as is often the case at metre wavelengths, it can be located by two aerial interferometer with different aerial spacings. On the other hand, as the abnormal sources do not dominate the background radiation at decimetre or centimetre wavelengths, multiple element interferometer must be used to determine the complete distribution of noise sources over the solar disk. A needle beam interferometer is most desirable.

A 32-element interferometer for use at 21 cm has been constructed in Australia, and has also been reported that an auxiliary N-S aerial group is now under construction. On the other hand, a waveguide array for use at 10.3 cm has been constructed in Canada.

Prior to these informations, we have started to construct 5-element interferometer at 7.5 cm and finished in march, 1953. As the resolving power is insufficient, it is expected to be increased to 8-element in May, 1954.

Details of the equipment and the results of the observations are related in this paper. The calculations of the radio brightness distribution about the minimum quiet radiation at 4,000 MC are also given.

§ 2. Design and Construction

2.1 Number of aerials and aerial-spacings

Principles of the interferometer are the same as those of the optical diffraction gratings.

Assuming that the interferometer consists of m nondirective antennas, arranged in E–W direction at l metre intervals, its normalized power pattern is represented as follows:

$$P=\frac{1}{m^2}\frac{\sin^2(\pi lm\sin\theta/\lambda)}{\sin^2(\pi l\sin\theta/\lambda)}\,. \qquad (1)$$

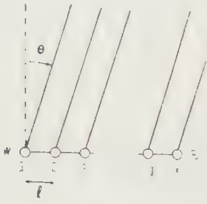

Fig. 1.

Denote that $\theta=\theta_p$ at maximum response and $\theta=\theta_q$ at $P=0$,

$$\left.\begin{aligned}&\sin\theta_p=p\lambda/l && p=0,\ 1,\ 2,\cdots\cdot\\ &\sin\theta_q=(p+q/m)\lambda/l && q=1,\ 2,\cdots(m-1)\end{aligned}\right\} \qquad (2)$$

As the sun passes through this pattern, it is scanned stripwise by each lobe in turn.

When the aerial is directive, Eq. (1) must be multiplied by its pattern. As each aerial must have a large gain, consequently a high directivity, at cm wavelengths, we can utilize only one or two beams with the fixed aerial system. Accordingly, aerials have to be constructed so as to be able to follow the sun.

As shown in Eq. (2), the wider the aerial-spacing, the smaller the angle between two beams and, consequently, each beam becomes sharp. But as the aerial-spacing must be so narrow that two beams do not scan the sun at the same time, one must increase the number of aerials in order to sharpen the beam.

If we use m aerials, we can devide the sun in m parts approximately.

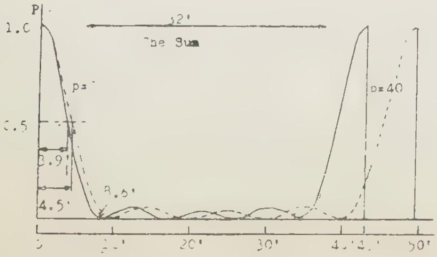

Fig. 2.

In the 5-element interferometer constructed, aerial-spacing is 6 m, the lobes are spaced 43′ and each lobe has a width of 7.76′ as shown in Fig. 2. It is preferable to use 8 aerials in all respects, but the financial condition compelled us to use 5 aerials for the time being.

2.2 How to combine the input signals and combination loss

We have combined the input signals two by two with the magic T. When a matched load is coupled to E-arm and two signals are fed to side arms respectively, the resultant signal comes out of H-arm. Unless the number of aerials is 2^n (n integer), the combination loss is produced, because the amplitude of each signal must be equal at the output of the last magic T. When m aerials are used, the coefficient of combination loss, L, is represented as follows:

$$L=m/2^{M+1}\,, \qquad (3)$$

where M is determined by $2^{M+1}\geqq m>2^M$. For example, when $m=5$, $L=5/8$. Moreover, as the signal is the noise of some bandwidth, each signal must be transmitted through the same course to the last magic T. Otherwise, we cannot obtain the pattern, as shown in Eq. (1), and besides cannot keep the correct phase relation for the thermal expansion of the transmission line, or the minute variation of the frequency of local oscillator.

The arrangement for minimizing the length of the transmission line is shown in Fig. 3.

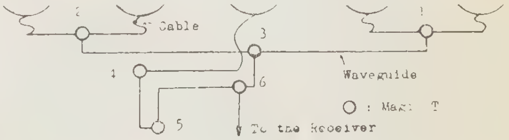

Fig. 3.

Each signal is transmitted through 1 m coaxial cable, 3 magic T, 2 H-bends and 15.9 m waveguide to the input of the receiver. In Fig. 3, two magic T (4^{th} and 5^{th}) are those to equalize losses by coupling the matched load to one side arm.

2.3 Size of one element

In order to determine the size of an aerial, maximum signal in equivalent antenna temperature at the input of radiometer (T_5) must be compared with that of each aerial (T_1).

When 5 aerials are used, gain increases by 5 times, but the received power decreases compared with an aerial with the same gain, because the interferometer has the sensitivity to only a part of the solar disk. A rate of decrease is about 0.3.

If the combination loss and the transmission losses are taken into account, T_5 is $0.7T_1$. From the view-point of S/N ratio, it is necessary that T_5 is about 200°K, consequently $T_1 = 290°K$. If T_1 is determined, antenna gain, i.e., the size of an antenna is easily calculated. At present, we use the antenna with the paraboloidal reflector of 1.5 m in diameter. Owing to the combination loss and the transmission losses, antenna equivalent temperature, when all aerials are directed towards the sky, increases by 160°K than the sky temperature (about 0°K at these frequencies). Accordingly, the receiving power oscillates between 160°K and 360°K approximately.

2.4 *Receiving bandwidth and hours of observation*

The output fluctuation of radiometer is proportional to $F/\sqrt{B}$, where F is the overall noise figure and B is the bandwidth of the receiver. Accordingly, in order to decrease the fluctuation it is preferable to choose the receiving bandwidth as wide as possible. As to the interferometer performance, it may be considered that for wider bandwidths the beam will become broad as θ increases, because the direction, in which the maximum response occurs, varies with frequency in the same way as in the optical grating.

We calculated the relation between the bandwidth and the beamwidth and concluded that this is not necessarily the case. Assume that the solar noise is Gaussian and the band shape of the receiver is rectangular and the bandwidth is B, the normalized power pattern is represented as follows:

$$P=\frac{1}{m^2}\left\{m+2\sum_{\nu=1}^{m-1}(m-\nu)k_\nu\cos 2\pi\nu f_0\tau\right\}, \quad (4)$$

where $\tau = l\sin\theta/c$,

$$k_\nu=\frac{\sin\pi\nu B\tau}{\pi\nu B\tau}.$$

If $k_\nu=1$, Eq. (4) agrees with Eq. (1). Within the limit $k_\nu \fallingdotseq 1$ or $B\tau \ll 1$, the change of beamwidth is negligible. In our case, in which $B=6$ MC, even the shape of 60th beam ($\theta \fallingdotseq 48°$) is almost unchanged though the amplitude decreases a little from the ideal case. The receiving bandwidth should rather be determined from the view-point of S/N ratio. Though the beamwidth is almost unaffected by the receiving bandwidth, it becomes essentially dull as θ (or p) increases (see Eq. (2) and Fig. 2.). Accordingly, the hours of observation are restricted to about one hour before and after the meridian passage. Were it allowed to confine the time of observation extremely short, we could receive two bands on both sides of the local oscillator frequency to improve the effective noise figure by about 3 db.

2.5 *Equipment*

The aerial system is shown in Photo. 1. 5 aerials are arranged in E–W direction at 6 m intervals. Each aerial has a paraboloidal reflector of size 1.5 m in diameter, which can be rotated equatorially. Motion about the declination axis is controlled by means of a hand-operated gear and motion about the polar axis is controlled by a common shaft which is driven by a synchronous motor. In order to keep input signals correctly in all seasons, each aerial must be installed accurately. Adjustment for equalizing the amplitude of each signal is easily performed by adjusting antenna gain. The phase relation is adjusted by varying the length of waveguide so that any interference pattern of two aerials, adjoining each other, has maximum response ($p=0$) at meridian passage. Resultant signal is fed to the radiometer and detected. Fundamental principles of this radiometer are the same as those of the modulation method developed by R. H. Dicke. A schematic diagram of the radiometer is shown in Fig. 4. Overall noise figure is 12 db, bandwidth is 6 MC and time const. is 1 sec. An example of the record is shown in Fig. 5. For a sun spot or bright

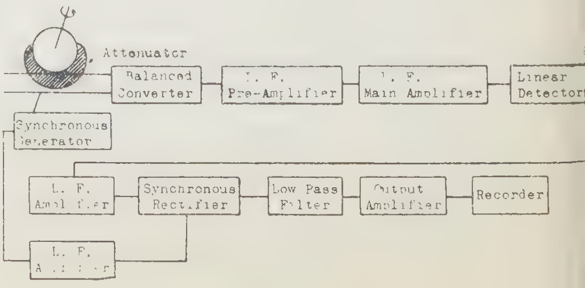

Fig. 4.

region, sensitivity of this interferometer is apparently 3 times as much as that for the quiet sun. Therefore we can detect considerably small sun spots.

It is to be noted that the scanning velocity varies with the declination and so the time from maximum to minimum of the record pattern varies every day remaining the resolving power constant.

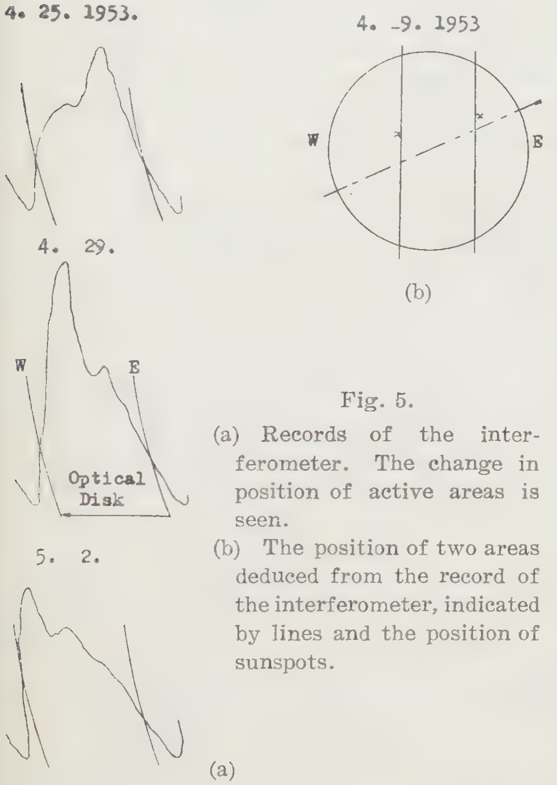

Fig. 5.

(a) Records of the interferometer. The change in position of active areas is seen.

(b) The position of two areas deduced from the record of the interferometer, indicated by lines and the position of sunspots.

§ 3. Distribution of Radio Brightness on the Quiet Solar Disk

3.1 Partial Eclipse

On Feb. 14, 1953, partial eclipse observation at 3,750MC was made at Toyokawa near Nagoya in Japan. The intensity variation of the solar radio noise during the eclipse is shown in Fig. 6, all times being Universal Time. It will be observed that; (1) the radio eclipse commenced about three minutes before the optical eclipse and ended after the same time, that is, the radio disk is larger than the optical disk. (2) the time of maximum obscuration does not agree with the time of minimum intensity. This result may be explained, assuming that there were some active zones on the sun, which were obscured at the earlier time. Daily observations of solar radiation have been made since Nov. 1951, at this frequency. Daily values during 6 months from Jan. to June, 1953, are shown in Fig. 7. Minimum intensity during this period is $0.375\times10^{-20}Wm^{-2}(c/s)^{-1}$ (May 11–15, 1953). The intensity at the time of the eclipse was $0.42\times10^{-20}Wm^{-2}(c/s)^{-1}$ and it is well supposed that there were some active zones at that time. The distribution of sun-spots on the solar disk on Feb. 14 is supposed to be as shown in Fig. 8. As it was cloudy on the day, it was based on the observation at the Tokyo Astronomical Observatory on Feb. 12. The distribution of radio brightness on the quiet solar disk could be determined from the later half of these observations, but it is too delicate to do so under these circumstances of eclipse. It may be concluded, however, that the radio disk is about 6% larger than the optical one.

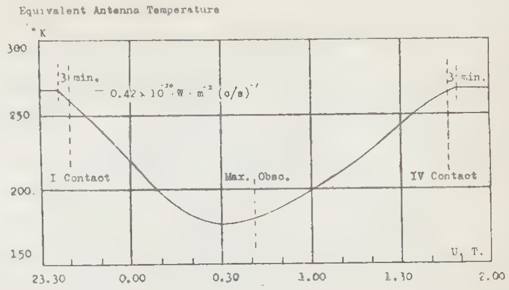

Fig. 6.

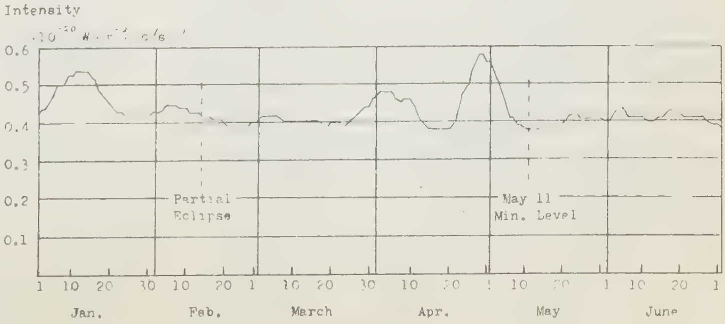

Fig. 7.

3.2 Record of the interferometer when the sun is quiet

In order to determine the distribution of radio brightness on the quiet solar disk, one had best wait until the sun becomes quiet.

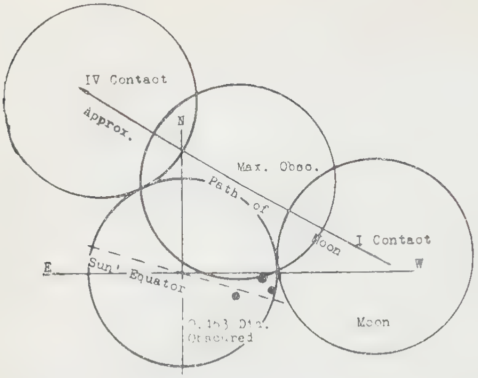

Fig. 8.

Fortunately, the records of the interferometer showed that the sun was almost quiet on May 11 and 12, that is, the records were almost the same and symmetrical. The intensity of radiation at 3,750 MC was also minimum on these days. So we use the average of some record patterns near meridian passage on these days. Assume that the distribution of the sun's equivalent temperature T is radially symmetrical, the receiving power N of 5-element interferometer can be represented approximately as follows:

$$N \propto \int_0^{\alpha} \int_0^{2\pi} \frac{\sin^2(5\pi l \sin\theta/\lambda)}{\sin^2(\pi l \sin\theta/\lambda)} T(r) r dr d\varphi . \quad (5)$$

where α is the radius of the radio-frequency disk, and we consider only the case when the sun passes near meridian. When the sun is in the direction of angle ϕ from meridian, $\theta \doteqdot \phi + r\cos\varphi$. Using Eq. (5), we calculated the theoretical record patterns for various distributions of equivalent temperature and compared them with the experimental record. The results are shown in Fig. 9. Curve (a) is the experimental curve, (b) corresponding to uniform distribution over the optical disk ($\alpha = 16'$) and (c) corresponding to uniform distribution over the disk, radius of which is 1.06 times larger than that of the optical disk. Experimental pattern is obtained if the radio-frequency disk is 1.06 times larger than the optical disk and excess region is about 2.5 times brighter than the optical disk of the uniform temperature (curve d). This assumption can also fully explain the variation of radio intensities in the later part of the eclipse. The experimental eclipse curve is shown as curve 1 in Fig. 10. Curve 2 is the theoretical curve corresponding to the above distribution (d). This theoretical curve does not agree with curve 1, but in curve 1 the effect of the active zone is contained. As shown in Fig. 8, it is considered that during a period from max. obscuration to IV contact none of the active zones was covered. Accordingly, if we subtract the amount increased by active zones from the observational values ($0.42 - 0.375 \times 10^{-20} Wm^{-2}(c/s)^{-1}$), we can obtain the curve 3 corresponding to the quiet sun. It agrees very closely with curve 2. Accordingly, a distribution of radiation consists of 23.6% from the limb and 76.4% from the uniform optical disk. The equivalent temperature of this uniform disk is calculated to be about 1.9×10^4 °K at 4,000 MC.

Acknowledgement

The authors wish to express their sincere thanks to Mr. S. Suzuki and Mr. K. Aoki (The Tokyo Astronomical Observatory) for their information about the astronomical data.

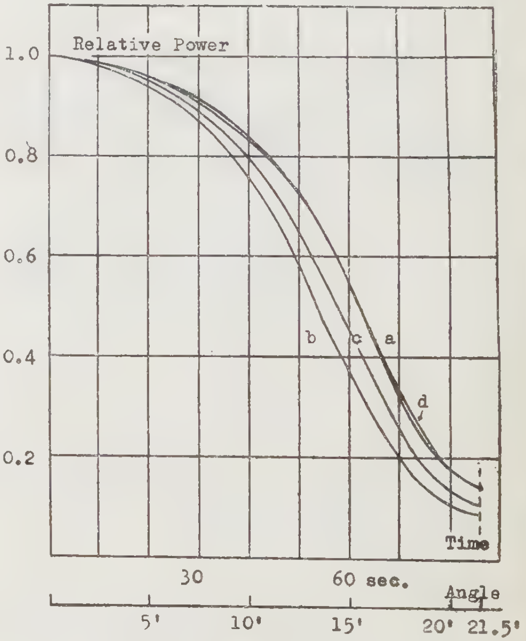

Fig. 9.

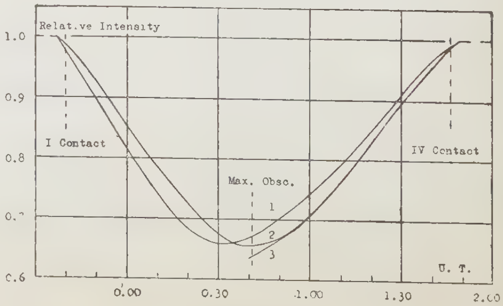

Fig. 10.

JOURNAL OF THE PHYSICAL SOCIETY OF JAPAN Vol. 9, No. 3, MAY—JUNE, 1954

On Line Widths of Paramagnetic Resonance Absorption

By H. KUMAGAI, K. ÔNO, I. HAYASHI, H. ABE, J. SHIMADA,
H. SHÔNO, H. IBAMOTO* and S. TACHIMORI**

Institute of Science and Technology, University of Tokyo

(Received November 17, 1953)

Paramagnetic resonance absorption of microwave (9970 MC) by thirteen salts containing manganese or copper ions was observed with special attention to obtain correct line shapes. The widths obtained were plotted against $1/a^3$, a being the lattice constant when the arrangement of ions are considered as simple cubic lattice. For smaller values of $1/a^3$, line shapes are near to gaussian type and the widths coincide with those by dipolar coupling calculated by Van Vleck. When $1/a^3$ is larger, that is, when ions come nearer, line shapes are near to resonance types and widths are in general smaller than those expected by dipolar coupling. This narrowing is caused by the existence of exchange coupling between magnetic ions. It is shown that the narrowing in salts of Mn^{++}, Fe^{+++} (S-state) and Cu^{++} can be related to the value of θ in the Curie-Weiss law of static susceptibility $\chi_s \backsim C/(T+\theta)$.

§ 1. Introduction

The resonance absorption of microwaves in paramagnetic salts was first observed by Zavoisky[1], and then many workers have developed wide researches in this field. The magnetic field for peak absorption H and the frequency of the microwave ν are related by the equation

$$h\nu = g\beta H\,, \tag{1}$$

where β is the Bohr magneton and g the Landé factor. In most cases, g-values are near to 2 as the orbital angular momentum L is quenched by crystalline electric field and the magnetic properties of ions are determined by almost free spins. Small departures of the g-value from 2 are caused by the (LS) coupling and the splitting of energy levels by the crystalline field. In this way, data on the position of the resonance peaks are useful for the study of crystalline field[2-8].

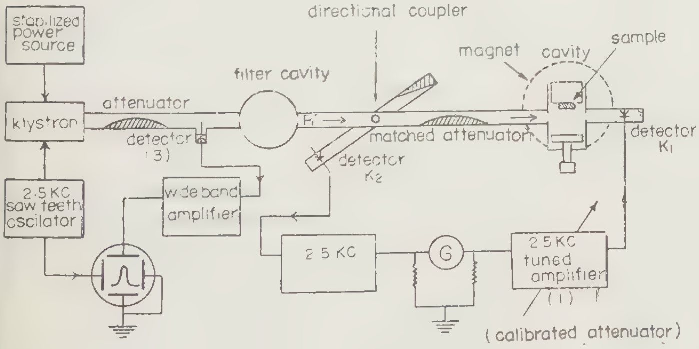

Fig. 1. Block diagram of the apparatus used.

In microwave resonance absorption, the line shapes can also be determined with significant accuracy. The line widths are caused by the coupling of the ion with neighbouring ions or interaction with the crystal lattice vibration. When the latter interaction is large, the line is very broad and hardly observed by microwave measurement at room temperature. Spins of Mn^{++} or Cu^{++} are loosely coupled to lattice vibrations.

We have two kinds of couplings between ions, one being the dipolar coupling, the other exchange coupling. Theoretical calculation for the widths of absorption lines has been given by Van Vleck[9]. According to his calculation and to many experimental results[2,5,6,7], line widths can not be explained by dipolar coupling only. In some kinds of salts, they are several times narrower than those expected by dipolar coupling due to the effect of exchange coupling.

---

* Department of Chemistry, Faculty of Sci., University of Ōsaka.

** Department of Physics, Faculty of Science University of Kanazawa.

We have observed resonance absorptions in thirteen kinds of salts containing manganese or copper ions, with special causions to obtain correct line shapes. Causions have been made in two points, one is the reliable chemical composition of salts, and the other is correct electrical measurements. Our preliminary results have been reported in Physical Review[10,11,12].

§ 2. Experimental Procedures

The block diagram of the measuring apparatus is shown in Fig. 1. Two points were aimed at in our apparatus, one being the accuracy in determining the line shape and absolute χ'' in the absorption and the other the compensation of output fluctuations of the oscillator, which was a demountable klystron continuously evacuated by an oil diffusion pump.

The frequency of the klystron is 9970 MC ($\lambda=3.01$ cm) which is modulated by a saw-teeth wave of 2.5 KC. The microwave is filtered by a cavity whose Q is about 10000, and passes, 2.5×10^3 times a second, into the resonant cavity for measurements of paramagnetic absorption. The power transmitted through this cavity is detected by the crystal rectifier K_1. To avoid the influence by output fluctuation of klystron on the value of transmission, the incident power is monitored by the directional coupler whose output crystal is K_2. Two outputs of crystals K_1 and K_2 are amplified by similar amplifiers tuned at 2.5 KC, whose outputs are rectified and compared by a galvanometer with small time constant. The amplifier attached to K_1 has a standard variable attenuator which is always adjusted so as the indication of the galvanometer is zero, then the change of transmission of the measuring cavity is read by the change of the attenuator reading. The microwave attenuator between the directional coupler and the measuring cavity has no reflection, and its object is to make the directional coupler more highly directional regarding the incident power of the cavity.

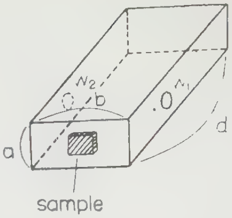

Fig. 2. The measuring cavity.

The construction of the measuring cavity is shown in Fig. 2. The cavity mode is H_{011} or H_{012} type and the paramagnetic salt was attached to one end of the cavity, the other end being a movable piston for tuning. The sample is placed at the centre of the gap of a electromagnet of 7 cm diameter. When the static magnetic field is near the absorption peak, variation of the resonance frequency of the cavity occurs, as the reactive part of susceptibility (χ') of the sample also changes. This is conpensated always during the course of measurements by adjusting the cavity piston to give maximum transmission at each static magnetic field.

When Q_0 and Q are Q-values of the cavity without and with static magnetic field respectively, Q_m, the Q-values of the magnetic absorption, is given by

$$\frac{1}{Q_m}=\frac{1}{Q}-\frac{1}{Q_0}=\frac{1}{Q_0}\left(\sqrt{\frac{T_0}{T}}-1\right), \qquad (2)$$

where T_0 and T are powers transmitted through the cavity without and with static magnetic field respectively. χ''_{ion} can be derived from Q_m by the following formula,

$$\chi''_{\text{ion}}=K\frac{V}{N}\frac{1}{4\pi}\frac{b^2+d^2}{2b^2}\cdot\frac{1}{Q_m}, \qquad (3)$$

$$\chi''_{\text{mol}}=L\chi''_{\text{ion}},$$

where V is the volume of the cavity, L the Avogadro number, N the number of paramagnetic ions in the sample, b and d dimentions of the cavity in Fig. 2, and K is a factor related to the position of the sample at the end of the cavity. K is unity when it is located uniformly all along the length of b and is one half when the sample is situated at the centre of the end wall. In our case, the thickness of the sample is thin enough.

When absolute value of x'' is required, we must know the absolute value of Q_0, which is obtained by the change of transmitted power of the cavity when the piston is displaced from resonance position. The same value of Q_0 was obtained by a separate observation of the transmitted power when the resonance frequency of the filter cavity is changed by a known amount.

Table I. Symmetry of used single crystals.

Crystals	Crystal Symmetry	Ratio of axes	Angle between Axes		
		$a : b : c$	α	β	γ
$Mn(NH_4)_2(SO_4)_2\cdot 6H_2O$	monoclinic	0.7360 : 1 : 0.4972	90°	107°2′	90°
$MnSO_4\cdot 5H_2O$	triclinic	0.5893 : 1 : 0.5691	81°37′	110°5′	104°59′
$MnSO_4\cdot 4H_2O$	monoclinic	0.4321 : 1 : 0.5820	90°	90°53′	90°
$Cu(NH_4)_2(SO_4)_2\cdot 6H_2O$	monoclinic	0.7433 : 1 : 0.4838	90°	106°6′	90°
$Cu(NH_4)_2\cdot Cl_4\cdot 2H_2O$	tetragonal	1 : 1 : 0.7417	90°	90°	90°
$CuK_2Cl_4\cdot 2H_2O$	tetragonal	1 : 1 : 0.7525	90°	90°	90°
$CuSO_4\cdot 5H_2O$	triclinic	0.5721 : 1 : 0.5554	82°5′	107°8′	102°41′
$CuCl_2\cdot 2H_2O$	rhombic	0.9179 : 1 : 0.4627	90°	90°	90°
$CuSO_4\cdot 4NH_3\cdot H_2O$	rhombic	0.5903 : 1 : 0.8892	90°	90°	90°

The static magnetic field is measured by the proton resonance method, the accuracy being 0.5∼1.0%.

Single crystals of paramagnetic salts used in our experiments are tabulated in Table I together with their crystal forms, most of them being prepared by one of us (H. I.) in R. Kiriyama's laboratory in Chemical Department, Faculty of Science, Ôsaka University. Their chemical compositions were checked by the agreement between actual crystal forms and those described by Groth[13)].

Some sorts of salts of lower hydration than those in Table I were used in polycrystal forms, which were derived from single crystals by dehydration. For example, $MnSO_4\cdot 4H_2O$ were crashed to powder and weighed, then kept in air at 60°∼70°C until the weight became constant by which we could know that its composition is $MnSO_4\cdot H_2O$. Some of these $MnSO_4\cdot H_2O$ powder was then kept at 200°∼250°C in air until the weight became constant, the resulting powder being $MnSO_4$. Samples of $CuSO_4\cdot H_2O$ and $CuSO_4$ were obtained from $CuSO_4\cdot 5H_2O$ in the same way as $MnSO_4$, but in $CuSO_4$ no microwave resonance absorption was observed.

In the case of diluted crystal of $Mn(NH_4)_2\cdot(SO_4)_2 6H_2O$, most of Mn^{++} ions were replaced by Zn^{++} without any change of crystal form. The ratio of Mn and Zn were determined by chemical analysis.

§ 3. Absorption Curves in Single Crystals

The problems concerning the shapes of resonance lines due to nuclear and atomic magnetic moments have been discussed by Van Vleck[9)]. When the absorption coefficient is $\chi''(\nu)$, the nth moment of absorption curve is given by

$$\int_0^\infty (\Delta\nu)^n \chi''(\nu)\,d\nu \Big/ \int_0^\infty \chi''(\nu)\,d\nu\,,$$

where $\Delta\nu$ is the frequency difference from the peak of the absorption line. In the case where the magnetic field is varied at constant microwave frequency, the moment is expressed by

$$\langle(\Delta\nu)^n\rangle_{\text{av}} = \left(\frac{g\beta}{h}\right)^n \int_0^\infty (\Delta H)^n \chi''(H)\,dH \Big/ \int_0^\infty \chi''(H)\,dH$$

using $h\nu = g\beta H$.

The second and fourth moments are obtained in Van Vleck's paper, which are determined by the arrangement of magnetic ions and the nature of interaction between ions. Although these moments are important for comparison of experimental results with theory, our experiments are not yet sufficiently accurate to obtain them. For this purpose, we must measure the absorption with accuracy at wings far from the centre of the line where the absorption is very small.

Although the half-widths of absorption lines are rather easily determined by experiment, the line shape and half-widths can not be calculated by the moment method. But, when we assume the line shape, half-widths can be calculated by Van Vleck's results. Assuming the line shape of gaussian form $e^{-\alpha^2(\Delta H)^2}$, the half-width $(\Delta H)_{1/2(\text{cal})}$ is given by

$$\begin{aligned}\Delta H_{1/2(\text{cal})} &= 2.35[\langle(\Delta H)^2\rangle_{\text{av}}]^{1/2}\\ &= 2.35 g\beta\{3S(S+1)\sum_k r_{jk}{}^{-6}\tfrac{1}{4}(3\cos^2\theta_{jk}-1)\}^{1/2},\end{aligned} \tag{4}$$

where S is the spin quantum number of the ion, r_{jk} is the distance between ions j and k, and θ_{jk} the angle between r_{jk} and static magnetic field. Although the second moment used in Eq. (4) is not affected by the existence of exchange coupling, Eq. (4) is valid in case that dipolar is the only one, because the line shape is not gaussian when exchange coupling exists. It is accepted experimentally that the line shapes are approximately gaussian in diluted salts, in which distances between magnetic ions are large. Our experiments on diluted salts also acertain these facts. Since the exchange coupling is very small at large distances between ions, it is probable that the line shape is gaussian when the interaction of magnetic ions is dipolar. In most cases of undiluted salts, the line shapes are not gaussian, but near to resonance curve $1/\{1+\alpha^2 \times(\Delta H)^2\}$. In these cases, the half-widths deviate from those given by Eq. (4). Such deviation of half-widths from Eq. (4) are treated in this paper as a measure of strength of exchange coupling.

In single crystals $(\Delta H)_{1/2(\mathrm{cal})}$ in Eq. (4) depends upon the orientation of static magnetic field. But it is often convenient to calculate the directional average of Eq. (4), which is given by

$$\Delta H_{1/2(\mathrm{cal})}=2.35g\beta\{(3/5)S(S+1)\sum_k r_{jk}{}^{-6}\}^{1/2}. \tag{5}$$

When the mean distance between ions is r, we have

$$\Delta H_{1/2(\mathrm{cal})} \backsim g\beta\sqrt{S(S+1)}\,r^{-3}\,. \tag{6}$$

Furthermore, we may treat, as a first step of approximation, the arrangement of ions as simple cubic, whose lattice constant a is given by

$$1/a^3=L\rho/M\,, \tag{7}$$

where L is the Avogadro number, ρ the density and M the molecular weight of the crystal. In this case r is proportional to a, and we have

$$\Delta H_{1/2(\mathrm{cal})} \backsim g\beta\sqrt{S(S+1)}\,a^{-3}\,. \tag{8}$$

We have checked the deviation of the half-widths calculated by Eq. (8) from those obtained by Eq. (4) for the correct arrangement of ions in $(NH_4)Fe(SO_4)_2$ because the crystal structure of this salt is known by x-ray analysis. The half-widths calculated by Eq. (8) are between 0.7 and 1.0 of those by Eq. (4). As the arrangement of magnetic ions are not much different from simple cubic lattice in many salts, calculation of half-widths by dipolar broadening using Eq. (8) may not have large error, the magnitude of error being shown by the example of $(NH_4)Fe(SO_4)_2$. In Table II, we show line shapes, range of variation of half-widths with orientation of the static magnetic field, and half-widths calculated by Eq. (8). The proportional constant in Eq. (8) is determined by Van Vleck's results in $CuSO_4\cdot5H_2O$ and $MnSO_4\cdot4H_2O$.

In Fig. 3, line shapes of $Cu(NH_4)_2(SO_4)_2\cdot6H_2O$, $MnSO_4\cdot4H_2O$ and $CuSO_4\cdot5H_2O$ are compared with gaussian and resonance curve. All curves are fitted at their peaks and half-widths. $CuSO_4\cdot5H_2O$ has line shapes very near to resonance curve, and that of $Cu(NH_4)_2\cdot(SO_4)_2\cdot6H_2O$ is near to gaussian. That of $MnSO_4\cdot4H_2O$ is intermediate between two types of curves. In diluted $Mn(NH_4)_2(SO_4)_2\cdot$

Table II. Line Shapes and Half-widths of single-crystals (9970 MC).

Single Crystals	Line Shapes	Range of Half Widths Oer.	Half Width $(\Delta H)_{1/2}$ (cal) by Eq. (8) Oer.	Range of g-value
$Mn(NH_4)_2(SO_4)\cdot6H_2O$ diluted (1/10)	Near to gaussian (many lines)	~70	~70	—
$MnSO_4\cdot5H_2O$	One peak intermediate of gaussian and resonance	—	—	—
$MnSO_4\cdot4H_2O$	The same as above	980—1500	1500	2.00—2.07
$Cu(NH_4)_2(SO_4)_2\cdot6H_2O$	Two peaks near to gaussian	~ 230	240	2.0 —2.3
$Cu(NH_4)_2\cdot Cl_4\cdot2H_2O$	One peak of resonance type	90— 230	380	2.05—2.20
$CuK_2Cl_4\cdot2H_2O$	The same as above	110— 250	390	2.05—2.20
$CuSO_4\cdot5H_2O$	The same as above	50— 220	480	2.04—2.24
$CuCl_2\cdot2H_2O$	The same as above	55— 70	680	2.03—2.23
$CuSO_4\cdot4NH_3\cdot H_2O$	The same as above	20— 30	350	2.04—2.19

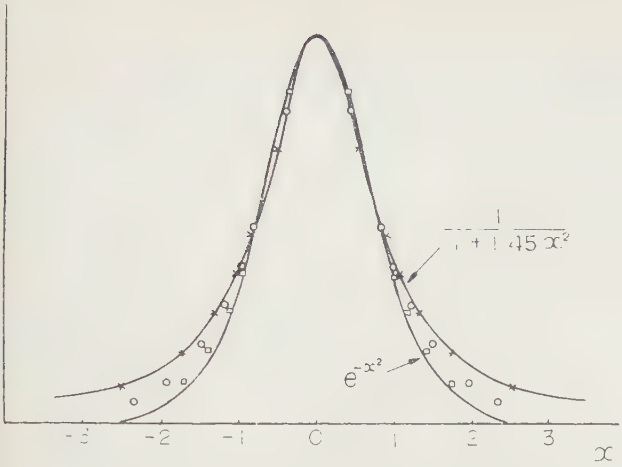

Fig. 3. Line shapes of resonance absorptions. × $CuSO_4 \cdot 5H_2O$, ○ $MnSO_4 \cdot 4H_2O$, □ $CuK_2(SO_4)_2 \cdot 6H_2O$.

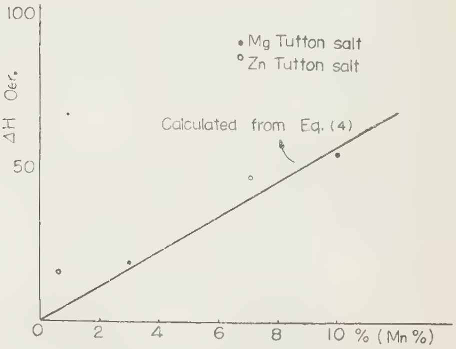

Fig. 4. Line widths of Mn Tutton salts diluted by Zn or Mg.

$6H_2O$, the observed half-widths coincide approximately with that given by Eq. (4) as shown in Fig. 4. In this case, the coupling is only dipolar and the line shape seems to be gaussian.

Half-width of $MnSO_4 \cdot 4H_2O$ is not much different from that calculated by Eq. (8), which shows that the exchange coupling in this salt is not large.

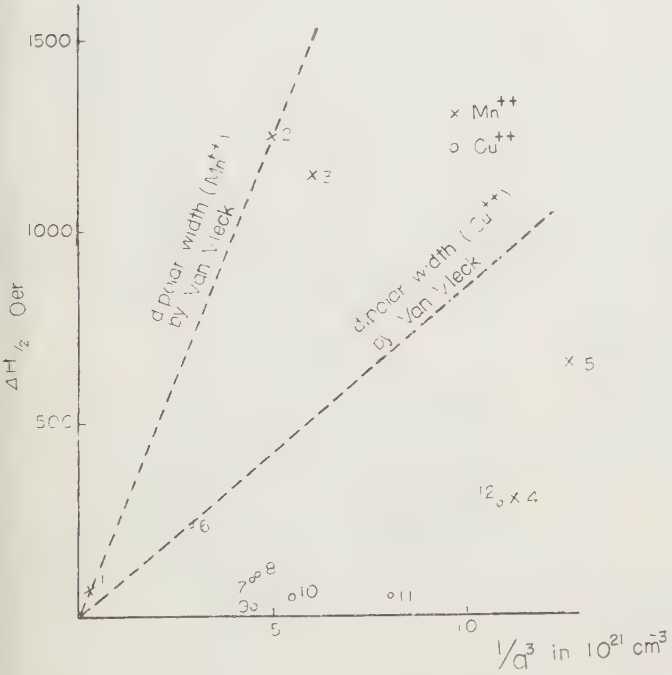

Fig. 5. Half width of salts of Mn^{++} and Cu^{++} and calculated dipolar width.

1. $Mn(NH_4)_2(SO_4)_2 \cdot 6H_2O$ diluted
2. $MnSO_4 \cdot 5H_2O$
3. $MnSO_4 \cdot 4H_2O$
4. $MnSO_4 \cdot H_2O$
5. $MnSO_4$
6. $Cu(NH_4)_2(SO_4)_2 \cdot 6H_2O$
7. $Cu(NH_4)_2Cl_4 \cdot 2H_2O$
8. $CuK_2Cl_4 \cdot 2H_2O$
9. $CuSO_4 4NH_3 \cdot H_2O$
10. $CuSO_4 \cdot 5H_2O$
11. $CuCl_2 \cdot 2H_2O$
12. $CuSO_4 \cdot H_2O$

In Fig. 5 the values of $(\Delta H)_{1/2}$ from Table II are plotted against $1/a^3$. The width indicated in the figure for Mn^{++}, for which the g-values are isotropic, are means of those in single crystals for different orientations. In the case of Cu^{++}, g-values are not isotropic (as shown in Table II) and only one resonance peak could be observed although more than one should be expected because these salts contain two or more dissimilar ions in each unit cell. This may be ascribed to the exchange coupling between dissimilar ions. In this case the variation of the line width with different crystal orientation depends on the difference in the precessional frequencies of dissimilar ions, and does not greatly depend on the dipolar coupling between neighbouring spins. On account of these circumstances we adopt the narrowest line width as $(\Delta H)_{1/2}$ for Cu^{++} in Fig. 4. It is probable that in $Cu(NH_4)_2(SO_4)_2 \cdot 6H_2O$, the observed half-widths are almost equal to those expected by Eq. (8) because there is no exchange coupling. In $CuSO_4 \cdot 5H_2O$, $CuCl_2 \cdot 2H_2O$, $Cu(NH_4)_2 Cl_4 \cdot 2H_2O$ and $CuK_2Cl_4 \cdot 2H_2O$, the observed widths are much smaller than those given by Eq. (8), showing the existence of very strong exchange coupling. Our observed widths in $CuSO_4 \cdot 5H_2O$ coincide well with data obtained by Bagguley and Griffiths[7].

As an example of the variation of observed half-width with orientation of static magnetic field, results in $MnSO_4 \cdot 4H_2O$ are shown in Fig. 6. This monolinic salt is very near to rhombic. The angular dependency of half-width is not near to rhombic, but clearly monoclinic.

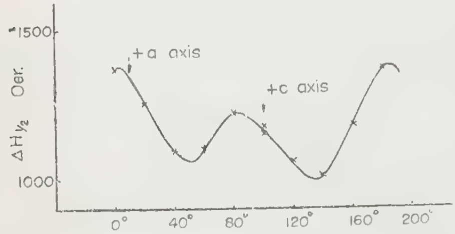

Fig. 6. Variation of width of $MnSO_4 \cdot 4H_2O$ with orientation for H in the a–c plane.

§ 4. Line Width under Strong Exchange Interaction

The absorption curves in polycrystals have no simple meanings when g-values are anisotropic, as the curves are superpositions of curves of different peak positions. But in the cases of Mn^{++} and Fe^{+++}, which are ions in S-state ($L=0$, $S=5/2$), g-values are isotropic, and absorption curves of polycrystals of these ions are superpositions of curves of the same peak positions, so that the half-widths of absorption curves in these cases can be compared with calculated half-widths in Eqs. (5), (6) and (8).

On the other hand, in Cu^{++} salts, we adopt as observed half-widths the narrowest ones of single crystals for which the g-values of two disimilar ions coincide.

Observed half-widths of polycrystals of two kinds of salts of Fe^{+++} ions and seven kinds of Mn^{++} ions, together with half-widths of single crystals of five kinds of Cu^{++} ions are shown in Table III. As data of x-ray analysis are not available in most cases, $(\Delta H)_{1/2(\mathrm{cal})}$ are calculated by Eq. (5) under the assumption that the lattice is simple cubic. The assumption of simple cubic has no significant influence on our rather qualitative discussions.

When we compare $(\Delta H)_{1/2(\mathrm{obs})}$ and $(\Delta H)_{1/2(\mathrm{cal})}$, they are nearly equal in some cases and in other cases, $(\Delta H)_{1/2(\mathrm{obs})}$ is smaller than $(\Delta H)_{1/2(\mathrm{cal})}$ due to the effect of exchange coupling between magnetic ions. The fifth column shows the value of θ in the Curie-Weiss formula for the static susceptibility, $\chi_s = C/(T+\theta)$. Generally θ is not zero by the exchange coupling between magnetic ions and by the splitting of electronic lebels of ions by crystalline field.

The influence is clear in Table III that when $(\Delta H)_{1/2(\mathrm{obs})}$ is smaller than $(\Delta H)_{1/2(\mathrm{cal})}$, θ is large. This circumstance can be treated quantitatively in order of magnitude, in the following way.

According to Van Vleck's considerations[9], $(\Delta\nu)_{1/2}$ under exchange coupling is given by $(\Delta\nu)_{1/2} \approx \tau_c \langle \Delta\nu^2 \rangle_{\mathrm{av}}$, where $\tau_c = h/2J$, J being the exchange integral. We tentatively equate the relations,

$$(\Delta\nu)_{1/2} = \tau_c \langle \Delta\nu^2 \rangle_{\mathrm{av}} = (h/2J) \langle \Delta\nu^2 \rangle_{\mathrm{av}}, \quad (9)$$

in which $(\Delta\nu)_{1/2} = (\Delta H)_{1/2(\mathrm{obs})} \cdot g\beta/h$.

In our cases of Mn^{++}, Fe^{+++} and Cu^{++}, it is probable that the effect by splitting of electronic levels upon θ is negligible and θ is only caused by exchange coupling[16]. In this case, θ is related with J by the following equation[17],

$$3k\theta = 2JzS(S+1), \quad (10)$$

where k is the Boltzmann constant, S is the spin quantum number (in Mn^{++}, Fe^{+++} $S=5/2$ and in Cu^{++} $S=1/2$), and z is the number of nearest neighbours in lattice.

Using Eqs. (4), (9) and (10), we can calculate $z_{(\mathrm{cal})}$ by

$$z_{(\mathrm{cal})} = \frac{3k\theta(2.35)^2(\Delta H)_{1/2(\mathrm{obs})}}{\{(\Delta H)_{1/2(\mathrm{cal})}\}^2 g\beta S(S+1)}, \quad (11)$$

the results being shown in the sixth column in Table III. In Fe^{+++} and Mn^{++}, values of $z_{(\mathrm{cal})}$ show no large divergencies from each other, but they are all several times larger than z deduced by real crystal structure. It must be noted that we neglect three sources of broadening due to the fine and hyperfine structure, spin-lattice relaxation and dipole coupling by neighbouring protons. These broadening effects are especially important in Cu^{++} ion because the line widths due to these effects are comparable to the observed line widths. Although further discussions have no value in our rather qualitative discussions, it is clear that line shapes of paramagnetic

Table III. Half-widths of paramagnetic microwave resonance absorption lines.

Polycrystals	Crystal symmetry	$(\Delta H)_{1/2}$ (obs) (oersteds)	$(\Delta H)_{1/2}$ (cal) (oersteds)	θ (°K)	z (calc)
$FeNH_4(SO_4)_2$	hexa.	580	1680	13[14]	38
$Fe_2(SO_4)_3$	hexa.	180	2300	70[14,15]	33
$MnCl_2$	hexa.	1250	2950	−16[14]	32
$MnCl_2 \cdot 2H_2O$	...	760	...	...	...
$MnCl_2 \cdot 4H_2O$	mono.	1340	1530	− 3(≈0)[16]	...
$MnSO_4$	mono.	655	3400	24[17]	19
$MnSO_4 \cdot H_2O$	mono.	305	2800	...	...
$MnSO_4 \cdot 4H_2O$	mono.	1140	1500	2(≈0)[16,17]	...
$MnSO_4 \cdot 5H_2O$	tric.	1250	1250	3(≈0)	...
$Cu(NH_4)_2(SO_4)_2 \cdot 6H_2O$	mono.	230	240	...	...
$CuSO_4 \cdot 5H_2O$	tric.	50	450	0.7	29
$K_2CuCl_4 \cdot 2H_2O$	tetra.	100	350	15	1500
$CuSO_4 \cdot 4NH_3 \cdot H_2O$	rhom.	20	350	13	300
$CuCl_2 \cdot 2H_2O$	rhom.	50	700	5	70

resonance lines of Mn^{++}, Fe^{+++} and Cu^{++} are closely connected with θ in Curie-Weiss formula.

After the present work was completed, a paper by Anderson and Weiss[18] has appeared, in which a relation more quantitative than Eq. (9) is deduced and better agrements between calculated z and real ones are found.

In conclusion, the author's thanks are due to Prof. T. Mutô and Prof. M. Kotani by cordial discussions. This research is partially supported by the grant for the promotion of science from the Ministry of Education and Yakuri-kenkyukai.

References

1) E. Zavoisky: J. Phys. U.S.S.R. **9** (1945) 211, 245, 447; **10** (1946) 170, 197.

2) R. L. Cummerow, D. Halliday and G. E. Moore: Phys. Rev. **72** (1947) 1233.

3) P. R. Weiss: Phys. Rev. **73** (1948) 470.

4) C. A. Whitmer, R. T. Weidner, J. S. Hsiang and P. R. Weiss: Phys. Rev. **74** (1948) 1478.

5) R. D. Arnold and A. F. Kip: Phys. Rev. **75** (1949) 1199.

6) J. Wheatley and D. Halliday: Phys. Rev. **75** (1949) 1412.

7) D. M. S. Bagguley and J. H. E. Griffiths: Proc. Roy. Soc. **201** (1950) 366.

8) D. M. S. Bagguley and J. H. E. Griffiths: Prof. Roy. Soc. **204** (1950) 188.

9) J. H. Van Vleck: Phys. Rev. **74** (1948) 1168.

10) H. Kumagai et al: Phys. Rev. **82** (1951) 954.

11) H. Kumagai et al: Phys. Rev. **83** (1951) 1077.

12) H. Kumagai et al: Phys. Rev. **85** (1952) 925.

13) P. Groth: Chem. Kryst. Teil 2.

14) T. Ishiwara: Sci. Rep. Tohoku University **3** (1914) 303.

15) P. Theodorides: J. de Phys. **3** (1922) 1.

16) J. H. Van Vleck and W. G. Penny: Phil. Mag. **17** (1934) 961.

17) J. H. Van Vleck: *The Theory of Electric and Magnetic Susceptibilities*, (1932) p. 332.

18) P. W. Anderson and P. R. Weiss: Rev. Mod. Phys. **25** (1953) 269.

JOURNAL OF THE PHYSICAL SOCIETY OF JAPAN Vol. 9, No. 3, MAY—JUNE, 1954

Absolute Values of Absorption Coefficients in Paramagnetic Resonance Absorption

By H. KUMAGAI, I. HAYASHI, K. ÔNO, H. ABE,
J. SHIMADA and H. SHÔNO
Institute of Science and Technology, University of Tokyo

(Received November 17, 1953)

As a special case of Kramers' equation, we have

$$\chi'(0)=\frac{2}{\pi}\int_0^\infty \frac{\chi''(H)}{H}\,dH,$$

where $\chi''(H)$ is the absorption coefficient in paramagnetic resonance absorption and $\chi'(0)$ is the static susceptibility. We have checked the equation in cases of paramagnetic resonance in powders of $MnSO_4$, $MnSO_4 \cdot H_2O$, $MnSO_4 \cdot 4H_2O$, $MnSO_4 \cdot 5H_2O$ and single crystals of $CuSO_4 \cdot 5H_2O$. It is found that the relation holds within errors of several percent.

§ 1. Kramers' Equation and Paramagnetic Resonance Absorption

General integral relations between the high frequency permeability χ' and absorption coefficient χ'' are established by Kramers and other physicists[1]. Recently Cummerow and others[2] have applied successfully these relations to paramagnetic resonance absorption in many salts in powdered forms.

When the magnetic susceptibility χ at frequency ν is expressed as

$$\chi(\nu)=\chi'(\nu)-i\chi''(\nu)\,. \tag{1}$$

Kramers' equation is written

$$\chi'(\omega)=\frac{2}{\pi}\int_0^\infty \frac{\nu'\chi'(\nu)}{\nu^2-\omega^2}\,d\nu\,. \tag{2}$$

In the special case $\omega=0$, we have

$$\chi'(0)=\frac{2}{\pi}\int_0^\infty \frac{\chi''(\nu)}{\nu}\,d\nu\,. \tag{3}$$

When we apply this equation to paramagnetic resonance, $\chi'(0)$ and $\chi''(\nu)$ must be measured under constant magnetic field H. But when we are concerned with one sharp resonance, we can obtain the integral of $\chi''(\nu)$ by experiments at constant frequency ν and varying magnetic field H. In this case, by the relation $h\nu=g\beta H$, we have

$$\chi'(0)=\frac{2}{\pi}\int_0^\infty \frac{\chi''(H)}{H}dH=\frac{2}{\pi}\,\frac{A}{H_m}\,, \tag{4}$$

in which, H in the integral is treated as approximately constant and substituted by H_m, the magnetic field at the maximum of absorption. A is the area

$$A=\int_0^\infty \chi''(H)dH.$$

Although $\chi'(0)$ in Eq. (4) is static susceptibility at magnetic field H_m, it is equal to that at any magnetic field by the linearity of magnetization. In cases where static susceptibility $\chi'(0)$ is measured by static measurements, calculated $\chi'(0)$ by Eq. (4) can be compared with measured $\chi'(0)$. Thus, Eq. (4) affords a useful method of testing the validity of results of paramagnetic microwave resonance absorption.

§ 2. Results obtained

The experimental procedures are the same with those in the preceding paper.

The results in powders of $MnSO_4 \cdot XH_2O$ are summarized in Table I. Calculated $\chi'(0)$ from Eq. (4) and observed $\chi'(0)$[3),4)] coincide within 5% in two cases and differ by 20% in one case. As the absorption by samples in Table I is strong, the amount of sample needed for experiment is small, so that the field distor-

Table I. Calculated and observed $\chi'(0)$ of powder of $MnSO_4 \cdot XH_2O$.

	$MnSO_4 \cdot 5H_2O$	$MnSO_4 \cdot 4H_2O$	$MnSO_4 \cdot H_2O$	$MnSO_4$
$\chi'(0)_{cal}$ (per mol in 10^{-2})	1.2_3	1.4_2	1.2_4	1.2_6
$\chi'(0)_{obs}$ (per mol in 10^{-2})	1.48	1.48	—	1.32

tion in the cavity can be neglected. In those cases, Eq. (3) in our preceding paper can be used without correction for field distortion.

Table II. Calculated and observed $\chi'(0)$ of single crystals of $CuSO_4 \cdot 5H_2O$.

	L_1-direction
$\chi'(0)_{cal}$ (per mol in 10^{-2})	0.14_4
$\chi'(0)_{obs}$ (per mol in 10^{-2})	0.1370

	$\chi'(0)_{L_3}/\chi'(0)_{L_1}$	$\chi'(0)_{L_2}/\chi'(0)_{L_3}$
cal	1.16	1.01
obs	1.20	1.00

angle definitions (by Bagguley and Griffiths⁵⁾)

L_2,L_4: tetragonal axes of crystalline field of two unequivalent copper ions in a unitcell.

L_1: perpendicular to L_2 and L_4.

L_3: bisector of exterior (or interior) angle between L_2 and L_4.

Table II shows results in $CuSO_4 \cdot 5H_2O$. Definitions of directions L_1, L_2 and L_3 are shown in the Table. In L_1-direction, calculated $\chi'(0)$ coincides with observed one⁶⁾ within 5%. In this case, small corrections by field distorsion by the sample were made roughly, but the coincidence may be better if the corrections were made exactly. Ratios of calculated $\chi'(0)$ are obtained in L_3:L_1 and L_2:L_3 directions. These ratios coincide well with those of observed $\chi'(0)$ as shown in the table.

As the calculated $\chi'(0)$ coincides with observed $\chi'(0)$ within 5% in most cases, it is probable that errors of our measurements of line shapes and widths are smaller than 5%.

In Table III, absolute values of χ'' at peaks of resonance are shown for powders of $MnSO_4 \cdot XH_2O$ and L_1-direction of single crystal of $CuSO_4 \cdot 5H_2O$. Cummerow and others²⁾ have obtained absolute χ'', which are shown in the table for comparison. In only one case of $MnSO_4 \cdot 4H_2O$, the data can be compared. But it is likely that Cummerow's sample was $MnSO_4 \cdot H_2O$, as $MnSO_4 \cdot 4H_2O$ is unstable in air and its power becomes $MnSO_4 \cdot H_2O$ in some time. If his sample is $MnSO_4 \cdot H_2O$, our data agree will with Cummerow's.

Table III. Absolute values χ'' at maximum absorption.

	$MnSO_4 \cdot 5H_2O$ powder	$MnSO_4 \cdot 4H_2O$ powder	$MnSO_4 \cdot H_2O$ powder	$MnSO_4$ powder	$CuSO_4 \cdot 5H_2O$ L_1-direction of single crystal
max χ'' (per mol in 10^{-2})	4.12	5.50	14.3	7.76	12.0
Cummerow and others' data	—	14.0	—	—	powder 1.73

References

1) H. Takahashi: Proc. Phys. Math. Japan **24** (1942) 63.

2) R. L. Cummerow, D. Halliday and G. E. Moore: Phys. Rev. **72** (1947) 1233.

3) H. K. Onnes and E. Oesterhuis: Leiden Comm. 132.ᵉ

4) L. C. Jackson: Proc. Roy. Soc. **140** (1933) 695.

5) D. M. S. Bagguley and J. H. E. Griffiths: Proc. Roy. Soc. **A 201** (1950) 366.

6) K. S. Krishnan and A. Mookherji: Phys. Rev. **54** (1938) 533, 841.

JOURNAL OF THE PHYSICAL SOCIETY OF JAPAN Vol. 9, No. 3, MAY—JUNE, 1954

Atomic Clocks and Frequency Standard on an Ammonia Line. I.

By Koichi SHIMODA

Department of Physics, Faculty of Science, University of Tokyo

(Received December 4, 1953)

Various causes of errors in an atomic clock utilizing the 3–3 line of ammonia are examined theoretically and experimentally. A brief description of a Stark modulation atomic clock designed for experimental purposes is given. It is shown that the fractional error will exceed 1 part in 10^{-8}, unless high degree of frequency-insensitive multiplier output and excellent matching of waveguide to generator and detector are achieved.

§ 1. Introduction

The present standard of time is the mean solar day, or more exactly the ephemeris time which is determined by astronomical observations. It has long been known that the length of the mean solar day is slowly increasing with fluctuations occurring at irregular intervals. The deviations from the average value are only severel parts in a hundred millions, but it has become important to obtain more constant and universal standards of time and frequency, because of the increase of accuracy in other physical measurements such as experiments on nuclear resonance, hyperfine splittings, determination of the velocity of light, and astronomical constants.

Clocks are based on some preiodic motions. The constancy of pace in pendulum clocks, chronometers, watches, quartz clocks and the like depends on the oscillation of a certain macroscopic matter which is subject to small changes and unpredictable perturbations. The advantages of the "atomic clock" have long been recognised. It is a clock controlled by some periodic phenomena in the atomic system which may be a free molecule, an atom, or a nucleus in crystal. It has become practicable by the recent discovery of spectral lines in the microwave region. Usable radio-frequency spectral lines are nuclear quadrupole absorption lines in crystals, molecular microwave spectral lines, and of hyperfine structure and other resonances detected by atomic or molecular beams.

The atomic standard, namely a spectral line standard is reproducible anywhere and at any time. Although the available spectral line in the microwave frequencies is not so sharp as an excellent quartz resonator, the center frequency is almost free from various disturbances and hence very accurate. Townes has shown that atomic clocks and time standards controlled by microwave absorption lines of ammonia or other resonances in atomic beams have potential accuracy of the order of 1 part in 10^{12} or better.[1] However, the practical atomic clock constructed for the first time at the National Bureau of Standards in 1949 was subject to much larger errors which amounted to 5 parts in 10^8, though the program for improving the atomic clock is now in good progress.[2] Improving the accuracy of time standards would contribute much to astronomy, geophysics, and other precise measurements.

Considerations about possible errors in the practical ammonia clock and experiments thereof by a Stark modulation ammonia clock are given in this article, and an attempt to reduce errors applying a magnetic field will be given in the following articles.

§ 2. Sources of Errors in an Ammonia Clock

There are three basic elements in an ammonia clock or an accurate time measuring equipment: (1) the source of microwaves, (2) the reference frequency standard, and (3) the discriminator or detector for comparing and correcting the operating frequency with the reference. The operating frequency of an ammonia clock employing 3–3 line is about 23,870 Mc/sec. Microwave power generated by a chain of multiplier or an oscillator with frequency measuring devices is fed to a waveguide absorption cell and detected after transmission. The frequency difference is detected by some change of the detector output due to variation of absorption with frequency. If the detector output change by other causes, there will be corresponding errors in frequency.

The spectral line is broadened by several causes which have been reported by many.1,3)

The width of the 3–3 line of ammonia filled in a waveguide at a pressure of several microns mercury at room temperature is measured to be about 0.2 Mc/sec.** which is nearly 10^{-5} of the center frequency, $\nu_0=23870.13$ Mc/sec. If it were possible to draw out the gas and refill it in a very short time, the maximum absorption would be easily detected irrespective of disturbances. The frequency for maximum absorption is practically insensitive to pressure changes and other disturbances as shown by Townes; but it is usually the minimum point of the output that we may find. The frequency for minimum output that is the apparent frequency is slightly different from the center frequency of the line because of various causes, which are considered as follows.

First the effect of frequency dependence of microwave input to the absorption cell is discussed. The shape of a microwave absorption line may be approximately given by*

$$y=y_0\frac{d^2(1+x)^2}{x^2+d^2}\,, \qquad (1)$$

putting

$$x=\frac{\nu-\nu_0}{\nu_0}, \quad \text{and} \quad d=\frac{\Delta\nu}{\nu_0}\,, \qquad (2)$$

where ν_0 is the center frequency and $\Delta\nu$ is the half line width. The frequency for maximum absorption is obtained from $dx/dx=0$. That is

$$x=d^2\ .$$

Because d^2 is of the order of 10^{-10} and hence negligible for the present, we may write instead of eq. (1)

$$y=y_0\frac{d^2}{x^2+d^2}\,, \quad \text{and} \quad \frac{dy}{dx}=-y_0\frac{2xd^2}{(x^2+d^2)^2}\ . \qquad (3)$$

If the input power to the waveguide cell were quite independent of the frequency, the point of minimum output through the cell would coincide with the point of maximum absorption. As a multiplier chain or an oscillator to be stabilized has some tuned circuits, it is more or less frequency-sensitive and brings about some errors of the atomic clock.

Assuming that the detector is frequency-insensitive, the apparent center of the absorption line is given by

$$\frac{d}{dx}(1-y)P=0\ ,$$

or

$$\frac{y'}{1-y}=\frac{P'}{P}\,, \qquad (4)$$

where P is the power input to the cell. Putting the fractional apparent frequency Δx and neglecting the higher orders of Δx and d, we may write approximately

$$\Delta x=\frac{1-y_0}{2y_0}\frac{P'}{P}d^2. \qquad (5)$$

If the frequency dependence of the generator is expressed by a single resonant circuit having a quality factor of Q,

$$\frac{P'}{P}=8Q^2x_0\ ,$$

where x_0 means the fractional shift of resonant frequency of the tuned circuit from the center of the spectral line.

In order to estimate the magnitude of error due to the power variation with frequency, we take $\Delta\nu=239$ kc/sec. or $d=10^{-5}$, and $y_0=0.5$***. And the deviation of apparent frequency from the center of the line is given in Table I. This table indicates that the detuning of

Table I. Shift of apparent frequency by a small detuning of generator with half power width of ν_0/Q.

Quality factor, Q	Frequently shift of tuned circuit, x_0 10^{-4}	10^{-3}	10^{-2}
1000	4×10^{-8}	4×10^{-7}	4×10^{-6}
500	1×10^{-8}	1×10^{-7}	1×10^{-6}
200	1.6×10^{-9}	1.6×10^{-8}	1.6×10^{-7}
100	4×10^{-10}	4×10^{-9}	4×10^{-8}

---

* Strictly speaking, doppler effect and collision with walls result in a little different line-shape which is not exactly known.

** G. Newell and R. H. Dicke: Phys. Rev. **83** (1951) 1064, and R. H. Johnson and M. W. P. Strandberg: Phys. Rev. **85** (1952) 503 have developed some methods of decreasing the doppler breadth of the line. But the gain of sharpness has been obtained by the loss of the intensity, and hence the theoretical limit of accuracy as a frequency standard cannot be improved.

*** This means that $\exp(-\alpha l)=0.5$, that is $\alpha=7\times10^{-4}\text{cm}^{-1}$ for $l=10^3$cm.

only one part in 10^3 will result in the appreciable error in frequency. The frequency sensitivity of the detector mount and other microwave components are also responsible for the error in detecting frequency of the line.

Secondly we consider the effect of mismatch in the microwave line upon the apparent frequency. It is impossible to eliminate reflections completely in the microwave line, because impedances of the generator and detector are unsettled and sensitive to temperature change and applied voltages. Let us assume that the waveguide absorption cell itself is reflectionless and reflection coefficient at both ends of the waveguide are r_1 and r_2 respectively, including reflections from windows, joints and terminations. As the waveguide is very long compared to the wavelength, the circuit resonance due to long line effect appears. It is expressed by

$$y_c = 1 + 2r \sin\left(\frac{4\pi l}{\lambda_g} x + \varphi\right), \qquad (6)$$

where $r = |r_1 r_2|$, l is the length of the cell, λ_g is the guide-wavelength, and φ is a constant depending on the phase of reflection coefficient. Then the variation of power into the detector with frequency is proportional to dy_c/dx. We obtain

$$\left|\frac{dy_c}{dx}\right| \leqq \frac{8\pi l}{\lambda_g} r . \qquad (7)$$

The circuit resonance may also become a source of error in the atomic clock. The minimum point of the detector output is given by

$$\frac{1}{1-y} \cdot \frac{dy}{dx} = \frac{dy_c}{dx} .$$

Thus the fractional error Δx_c caused by mismatches at the ends of a long waveguide cell is estimated.

$$|\Delta x_c| \leqq \frac{1-y_0}{2y_0} \cdot \frac{8\pi l d^2 r}{\lambda_g} , \qquad (8)$$

As a typical case, taking $l = 10^3$cm, $\lambda_g = 1.6$cm, $y_0 = 0.5$ and $d = 10^{-5}$, we obtain

$$|\Delta x_c| \leqq 8 \times 10^{-7} r .$$

For example, the reflection coefficient of a mica sheat of 0.1 mm thick will be arround 0.1. Though the reflection by mica window can be compensated for the most part, there remain reflections from generator and detector. Therefore, it is not so easy to reduce reflections beyond $r < 10^{-2}$. With $r = 10^{-2}$ we have the fractional error,

$$|\Delta x_c| \leqq 8 \times 10^{-9} .$$

If the phase of reflection were adjustable without changing the magnitude, we could reduce this error. In practice, however, it is very difficult to do so, because insertion of any phase shifter would be accompanied by some small reflections. We conclude therefore that considerable precautions and close adjustments must be done in order to reduce the error of an ammonia clock to less than a few parts in 10^8.

Distortions of the line shape due to small reflections may also affect the apparent frequency. This may be called the effect of circuit reactance and is discussed in § 4 with other sources of errors which are rather technical.

§ 3. Experimental Apparatus

So far as the variation of input power to the absorption cell with frequency is concerned, it may become unaffected by the use of Stark modulation which is familiar to the microwave spectroscopist. It is illustrated in Fig. 1 that the power variation with frequency does not shift the reference frequency, $\nu_0 + \Delta\nu_0$, where the output power at zero Stark field is equal to that at Stark field of $E \neq 0$.

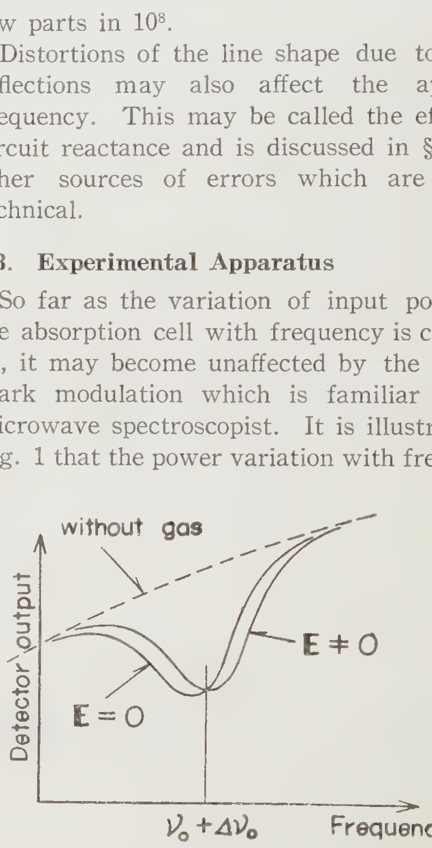

Fig. 1. Principle of Stark modulation method.

Another advantage employing Stark modulation is the reduction of low-frequency noise of the detector and generator. Accordingly, we can obtain enough signal even by the use of shorter waveguide cell.

Under a dc electric field parallel to the microwave field, 3–3 line of ammonia is split into nine components in the higher frequency

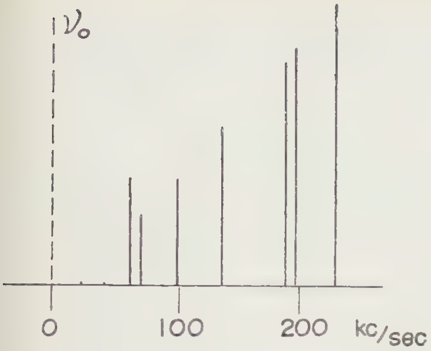

Fig. 2. Stark components of the 3–3 line of ammonia at weak field (E=100 volt/cm).

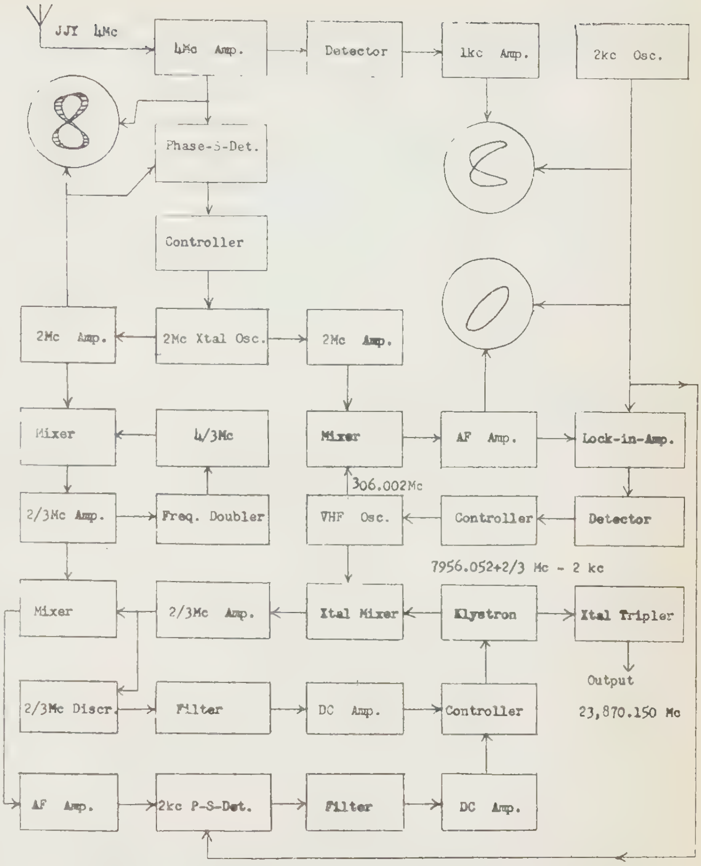

Fig. 3. Block diagram of an ammonia frequency comparater with Standard frequency broadcast or a sort of frequency multiplier.

side[4,5]. When the Stark field is less than 100 volt/cm, all Stark components lie within 250 kc/sec. and cannot be resolved usually, but observed as a single line at a little higher frequency being slightly broader and weaker than the original line. The reference frequency in this case is $\nu_0+\Delta\nu_0$, where $\Delta\nu_0$ is roughly one half the weighted average of all Stark shifts at the field. If the Stark field varies, $\Delta\nu_0$ and hence the reference frequency will vary. We have chosen it to be $\Delta\nu_0=23$ kc/sec. corresponding to the Stark field of E=48 volt/cm. Thus the variation of Stark field in 2 parts in 10^3 is responsible for the error in frequency and time of about 3 parts in 10^9, and the reference frequency, $\nu_0+\Delta\nu_0$=23,870.150 Mc/sec., may possess sufficient precision.

In order to reach the particular frequency above mentioned a method of automatic frequency control of a microwave oscillator as shown in Fig. 3 was devised and constructed. Because microwave multiplier tubes are not available in our country, an inexpensive method given in Fig. 3 was used instead of a multiplier chain. The use of multiplier chain would require many tuning circuits and result in the frequency-sensitive output with larger noises originating from lower frequency stages.

The operation of a sort of multiplier shown in Fig. 3 is as follows. For the purpose of frequency measurement or experimental use, 2 Mc/sec. output of the crystal oscillator is mixed with the received standard frequency broadcast, JJY, of 4 Mc/sec., followed by a phase-sensitive detector and controller. The controller is a small variable condenser which is connected in parallel to the quartz crystal and driven by a coil in a magnetic field. Adjusting a trimmer condenser, we can change the frequency in a small amount and easily lock the crystal oscillator into exactly half the frequency of the broadcasted 4 Mc/sec. This is shown by a Lissajous figure represented on a C.R.O. screen. Then a VHF oscillator is synchronized to the 153rd harmonics of the crystal oscillator with the difference frequency of exactly 2 kc/sec. The beat frequency is amplified by a lock-in amplifier, and controls the frequency of the VHF oscillator. Thus the VHF is kept exactly at 306.002 Mc/sec.

The frequency of a klystron is synchronized in a similar way, where double control-loops are used. This is because the self oscillation of a reflex klystron has considerable frequency-modulation noise and hence requires rapid and effective frequency control in order to establish precise microwave frequencies. For example, the 8000 Mc/sec. radiation from a klystron was found to have a frequency bandwidth of a few kilocycles, though it would be considerably reduced in favorable cases$^{6)}$. In the apparatus shown in Fig. 3 the output frequency of the klystron is controlled to be 7956.050+2/3 Mc/sec. by a 2/3 Mc/sec. discriminator and 2 kc/sec. phase-sensitive controller. The controlled frequency is tripled by a crystal multiplier to the desired frequency of 23,870.150 Mc/sec. Thus the microwave frequency to be compared to the 3–3 line of ammonia is controlled within the accuracy of ±1 c.p.s. on the basis of the standard frequency broadcast, JJY.

In the case of operating the apparatus as a servo clock the discriminator output of an absorption line is applied to the controller of the crystal oscillator, being out of control of the standard frequency broadcast.

The Stark waveguide cell used at first was an ordinary X-band cell of 2 meters in length. To obtain the Stark modulation voltage of good square waveform, lower modulation frequency of 30 kc/sec. was employed. The detected output of a crystal rectifier was amplified by a tuned 30 kc/sec. amplifier followed by a phase-sensitive detector to obtain the proper error signal (discriminator characteristics). The improved apparatus will be given in § 5.

§ 4. Discussions on Stark Modulation Ammonia Clock

The minimum detectable change of absorption coefficient employing a waveguide cell of l in length is given by equating the detector noise to the change of signal. We obtain

$$\varDelta\alpha_{\min}=\frac{\sqrt{4kT\varDelta f}}{lMP_t}e^{\alpha l}\,, \qquad (9a)$$

where P_t is the input power, M the figure of merit of the detector and $\varDelta f$ the effective bandwidth of the amplifier. The power output from the crystal tripler is several microwatts, which avoids excessive saturation effect*. Let us take $M=10$, $P_t=5\times10^{-6}$ watts, $T=300°\mathrm{K}$, $\varDelta f=1$ c.p.s., as a plausible case, then we have

$$\varDelta\alpha_{\min}=1.3\times10^{-8}\mathrm{cm}^{-1} \qquad (9b)$$

for the cell length of $l=200$ cm which is much shorter than the optimum length.

It is shown that the character of a crystal detector is nearly linear at higher power level and its sensitivity may be represented by a noise figure, F. Then the minimum detectable change in absorption is given by

$$\varDelta\alpha_{\min}=\frac{4}{l}\sqrt{\frac{FkT\varDelta f}{P_t}}e^{\alpha l}\,. \qquad (10a)$$

The value of F is rather large in our case, since the modulation frequency is low and the input power is small. Taking $F=100$, $l=200$ cm, and $\varDelta f=1$ c.p.s., we obtain from eq. (10a)

$$\varDelta\alpha_{\min}=1.8\times10^{-8}\mathrm{cm}^{-1}. \qquad (10b)$$

From eq. (3) we obtain in good approximation

$$\frac{d\alpha}{dx}=-\frac{2\alpha_0 xd^2}{(x^2+d^2)^2}\,. \qquad (11a)$$

Assuming $\varDelta\nu_0=23$ kc/sec., and taking the half line width of $\varDelta\nu=\nu_0 d=150$ kc/sec., we have

$$\frac{d\alpha}{dx}=13\ \mathrm{cm}^{-1}\,. \qquad (11b)$$

We conclude, therefore, from eqs. (9b) or (10b) and (11b) that the limit of detectable deviation of frequency, $\varDelta x_{\min}$, is around 1×10^{-9}. This is the noise limited accuracy of our ammonia clock with Stark cell of 2 meters in length. With longer cells and larger power we would have better accuracy.

Second, the optimum pressure and line width for the Stark modulation ammonia clock is considered. The doppler broadening is approximately given by

$$2\varDelta\nu_d=2\sqrt{2}\,\frac{\nu_0}{c}\sqrt{\frac{RT\log 2}{M}}\,, \qquad (12a)$$

where R is gas constant, M the molecular weight, and c the velocity of light. For ammonia we have

$$\varDelta\nu_d=3.58\times10^4\sqrt{\frac{T}{300}}\quad \text{c.p.s.} \qquad (12b)$$

Broadening by collision with cell walls is difficult to calculate. It was given by Johnson and Strandberg[7]. His result has been recently corrected by Danos and Geschwind[8]. It is approximately

---

* Townes has shown that the use of large enough power to saturate the absorption line is preferable in the theoretical limit of accuracy, but the sharpness of line is advantageous in the technical point of view, because there are many sources of errors other than thermal noises.$^{1)}$

$$\Delta\nu_w = 0.1\left(\frac{1}{a}+\frac{1}{b}\right)\sqrt{\frac{2RT}{M}} \tag{13}$$

where a and b are cross-sectional dimentions of the rectangular cell.

The pressure broadening has been well studied for ammonia, which shows[9]

$$\Delta\nu_p = 2.7\times 10^7 p\sqrt{\frac{300}{T}}, \tag{14}$$

where p is the pressure of ammonia in mmHg.

The saturation broadening is negligible, when

$$P_t \ll S\left(\frac{\Delta\nu}{\mu}\right)^2 \frac{3ch^2}{4\pi}, \tag{15}$$

where S is the cross-section of the cell. With the values of $\Delta\nu = 150$ kc/sec., $S = 2\,\mathrm{cm}^2$, and $\mu = 1.45$ D, the critical power to produce appreciable saturation effect is given by

$$S\left(\frac{\Delta\nu}{\mu}\right)^2 \frac{3ch^2}{4\pi} = 6\times 10^{-4}\ \text{watts}.$$

We may therefore neglect the effect of saturation in considering our ammonia clock, as the input power to the cell is much smaller than the above value.

Thus we can obtain the following values for 3–3 line of ammonia with $T = 300°\mathrm{K}$, $a = 2.28$ cm, and $b = 0.483$ cm.

$$\Delta\nu_d = 35.8\ \text{kc/sec.} \quad \Delta\nu_w = 13.9\ \text{kc/sec.}$$

and $\quad \Delta\nu_p = 2.7\times 10^4 p$ kc/sec.

If we assume for simplicity that the total line width is equal to the sum of above values, we can easily calculate the peak absorption coefficient, α_0, and line width, $\Delta\nu$, for optimum condition. Assuming

$$\Delta\nu = \Delta\nu_d + \Delta\nu_w + \Delta\nu_p, \tag{16a}$$

then

$$\alpha_0 = A\cdot\frac{p\theta}{1+p\theta}, \tag{17}$$

where A is approximately $7.2\times 10^{-4}\,\mathrm{cm}^{-1}$ at room temperature and

$$p\theta = \frac{\Delta\nu_p}{\Delta\nu_d + \Delta\nu_w} = 5.75\times 10^2 p.$$

The maximum sensitivity in the Stark modulation ammonia clock is obtained, when $d\alpha/dx$ becomes maximum at $x = \Delta\nu_0/\nu_0$.

$$\frac{\partial}{\partial p}\left(\frac{\partial\alpha}{\partial x}\right) = 0.$$

Assuming the line shape given by eq. (3) even with the doppler broadening and broadening by collision with cell walls, we obtain

$$2\Delta\nu_p = \Delta\nu_d + \Delta\nu_w \tag{18a}$$

as a first approximation* which is correct when $x \ll d$. Then the total line width is

$$\Delta\nu = 1.5(\Delta\nu_d + \Delta\nu_w) = 74.6\ \text{kc/sec.}$$

A successive approximation gives the following optimum condition for $\Delta\nu_0 = 23$ kc/sec. instead of eq. (18a)

$$\Delta\nu_p = 0.59(\Delta\nu_d + \Delta\nu_w).$$

This requires $p = 1.1\times 10^{-3}$ mmHg, $\alpha_0 = 2.7\times 10^{-4}\,\mathrm{cm}^{-1}$, and $\Delta\nu = 79$ kc/sec. Fig. 4 shows $d\alpha/dx$ at $x \doteqdot 0$, and α_0 as a function of pressure.

If we assume that the line width is given by

$$\Delta\nu = (\Delta\nu_d^2 + \Delta\nu_w^2 + \Delta\nu_p^2)^{1/2} \tag{16b}$$

which is supposed to be a better approximation than (16a), we obtain the optimum condition in the form

$$2\Delta\nu_p^2 = \Delta\nu_d^2 + \Delta\nu_w^2. \tag{18b}$$

This requires $p = 1\times 10^{-3}$ mmHg, $\Delta\nu_p = 27$ kc/sec. and $\Delta\nu = 47$ kc/sec.

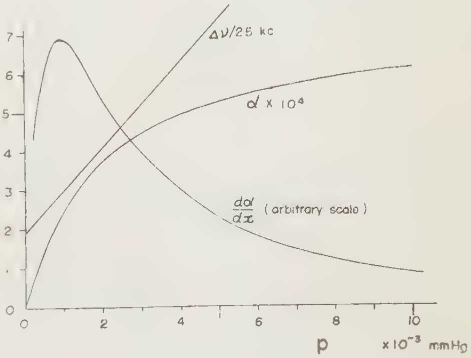

Fig. 4. Calculated maximum absorption coefficient, α_0, and sensitivity of weak field Stark modulation, $d\alpha/dx$, are plotted as a function of gas pressure, assuming $\Delta\nu = \Delta\nu_d + \Delta\nu_w + \Delta\nu_p$.

§ 5. Experimental Results and Discussions on Errors

The experimental apparatus of a Stark modulation ammonia clock is illustrated in Fig. 5, in which the detailed block diagram of the frequency multiplier was given in Fig. 3. This apparatus was found to have many defects in its operation.

---

* This is compared with the optimum condition of $\Delta\nu_p = \Delta\nu_d + \Delta\nu_w$ for video detection.

(1) On account of the non-limearity of phase sensitive detector, random noises could not be balanced out, but rectified spurious voltages were superposed on the output voltage. In order to eliminate this error due to rectified noise, Stark modulation was intermittently applied with equal interval and width of 1/50 sec., as shown in Fig. 6. The difference of output voltages with and without Stark modulation were obtained from a 25 c/s phase-sensitive detector so that it might be used as a frequency error signal. The noise limited value of minimum detectable freqnency deviation was measured to be nearly equal to the theoretically expected value given in § 4, but other errors not of random character were found to be appreciable.

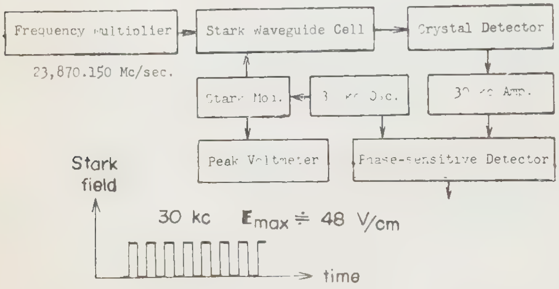

Fig. 5. Block diagram of Stark modulation atomic clock No. 1.

(2) The slightest distortion of either Stark modulation voltage or reference voltage to the phase-sensitive detector was found to bring about considerable errors. The apparent reference frequency was observed to vary within a few kilocycles or several parts in 10^8, as the frequency, phase, or width of the square pulse of modulation voltage was changed. This is explained as follows.

Because there are some finite rise-time and decay-time in the modulation waveform, the absorption by ammonia in the Stark cell does not instantly change between values corresponding to the Stark field of zero and $E \neq 0$. Then the rectified output from the crystal detector is not of a simple square wave-form, but accompanied by transient spikes, as illustrated in Fig. 7. The height of spikes may be of the order of 10^{-3} volts, and the width may be some fraction of microseconds which is nearly one percent of the square pulse width of applied Stark voltage.

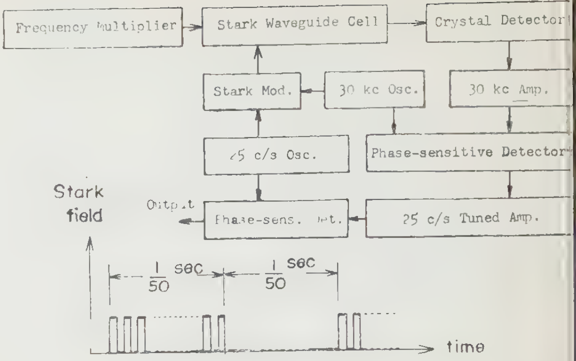

Fig. 6. Block diagram of Stark modulation atomic clock No. 2.

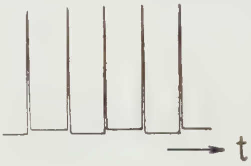

Fig. 7. Schematic wave-form of the detector out put.

On the other hand, signal voltage which is comparable to noise is of the order of 10^{-8} volts and hence much smaller than the spike voltage. Therefore, asymmetry of the modulation wave-form, non-linearity of the amplifier, and out of phase component of the reference voltage, even if they are small, will considerably deviate the apparent frequency of the line and bring about the error in frequency and time. For example, non-linearity of -40 db is responsible for the spurious signal of about 10^{-7} volts at the detector, which corresponds to the fractional error in frequency of several parts in 10^8.

(3) The distortion of line shape by circuit reactance due to reflections in waveguide components have also been found to have wrong effect on the apparent frequency of the absorption line. The dielectric constant of a gas, K, can be expressed in good approximation by

$$K=K_0-\frac{\lambda}{2\pi}\cdot\frac{\alpha_0 xd}{x^2+d^2}, \qquad (19)$$

where K_0 is insensitive to frequency near the absorption line and about unity. And the imaginary part, β, of the propagation constant is given by

$$\beta=\frac{2\pi}{\lambda_g}-\frac{\lambda_g}{\lambda}\cdot\frac{\alpha_0}{2}\cdot\frac{xd}{x^2+d^2}, \qquad (20)$$

where λ_g is the guide wavelength and λ the free space wavelength.

If there is some reactive component at the output and input of the waveguide cell caused by some reflection, the phase change due to dispersion by the gas will be converted to the amplitude change of the output, Let a certain fraction of change of β will be detected superposed on the absorption, α, then the detected line shape will be slightly distorted asymmetrically. Hence the apparent frequency, that is the frequency for maximum decrease of power, is given by the equation, neglecting other errors.

$$\frac{\partial}{\partial x}(f\beta+\alpha)=0\ . \tag{21}$$

We may obtain the apparent frequency, ν_{ap}, using eq. (20) and (21) for small values of f, in the form

$$\Delta x_a=\frac{\nu_{ap}-\nu_0}{\nu_0}=\frac{1}{4}\cdot\frac{\lambda_g}{\lambda}fd\ . \tag{22}$$

The absolute value of f is equal to or less than the magnitude of reflection coefficient.

For example, take $f=10^{-2}$, $d=6\times10^{-6}$, and $\lambda_g/\lambda=4/3$, then the fractional error caused by the line distortion is

$$|\Delta x_a|=2\times10^{-8}\ .$$

This is the same order of magnitude as the errors experimentally measured by purposely displacing tuners and plungers connected to the waveguide cell.

In order to accomplish detailed matching and to decrease the errors by circuit resonance and reactance, an experimental set shown in Fig. 8 was constructed. A K-band Stark waveguide of 76 cm in length tapered at the mica window was employed to avoid higher mode propagations in the absorption cell. The tuning adjustment on the generator side was performed while inserting a pad at the detector side, and tuning at the detector side was done while inserting a pad at the generator side. The presence of reflection in the microwave line could be seen by a standing wave pattern on a long-persistence cathode ray oscilloscope.

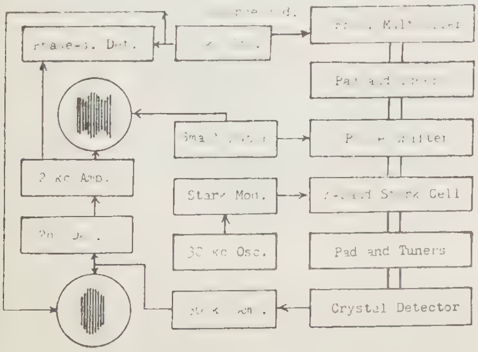

Fig. 8. Block diagram of Stark modulation atomic clock No. 3. For the operating frequency of $\nu_0+\Delta\nu_s=23{,}870.150$ Mc/sec. we use $E_{max}>10^3$, and $E_{min}=36$ volts/cm. And for the frequency of $\nu=\nu_0=23{,}870.127$ Mc/sec. we use $E_{max}>10^3$, and $E_{min}=0$.

We have used a large field Stark modulation ($E_{peak}>10^3$ volts/cm and $E_{min}<1$ volt/cm) so that it may remove spike voltage at the detector. A Stark field of more than 1000 volts/cm is sufficient to remove the absorption line almost perfectly from its original position. Source modulation has been employed together with Stark modulation in order to detect the deviation of frequency from the center of the line. If necessary, the reference frequency could be shifted a little from the center frequency by some dc bias field.

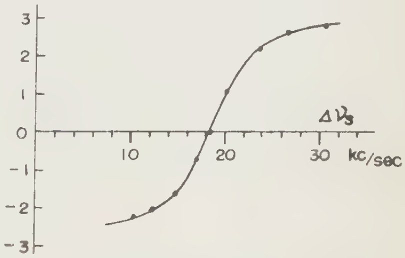

Fig. 9. Observed discriminator characteristics of the absorption line.

A typical observed result of the discriminator characteristics is shown in Fig. 9, where input frequency is constant and Stark bias voltage is changed. The saturation of the output voltage seen on the figure is not due to the absorption line, but the amplifier.

Even with the present cell length of 76 cm the noise limited accuracy of about 2×10^{-9} has been measured experimentally, but the precise matching by fine tuning could not be realised. Certainly, it requires exceedingly delicate tuning and good phase-sensitive detectors in order to decrease the error to a few parts in 10^9. Use of a longer absorption cell would improve the noise limited accuracy, but could not improve the accuracy caused by circuit mismatch, because the spurious effect of reflections at the ends of the cell is also proportional to the cell length.

There is a possibility to avoid the effect of reflections: if the imaginary part, β, of the propagation constant of the waveguide is adjusted to be independent of frequency, the output power of the cell being Stark modulation applied does only depend on α. The condition for the case is obtained using Eq. (20) by $d\beta/dx=0$ at $x=0$, and we have

$$\frac{d\beta}{dx}=\frac{2\pi\lambda_g}{\lambda}-\frac{\lambda_g}{\lambda}\frac{\alpha}{2d}=0 .$$

Therefore, if we have chosen α and d so as to be

$$\frac{\alpha}{d}=\frac{4\pi}{\lambda}, \tag{23}$$

then the error due to circuit reactance do not arise and we are able to get an accurate spectral frequency standard. For example, if we take $\lambda=1.25$ cm and $d=10^{-5}$, it requires $\alpha=1\times10^{-4}\text{cm}^{-1}$, which is smaller than the value for the 3–3 line of ammonia. But this condition can be satisfied by the use of 1–1 line ($\nu_0=23{,}694.49$ Mc/sec. and $\alpha_{\max}=1.4\times10^{-4}$ cm^{-1}), if we carefully control the pressure of the ammonia gas in the waveguide cell. It would be quite difficult and almost impossible, we suppose, to control the line width and peak absorption coefficient, say, within the accuracy of one percent.

We conclude therefore that, in order to construct a more accurate and reliable ammonia clock, we must realise either exquisite tuning devices, the line-width and intensity control, or any other new method such as will be described in the following part.

References

1) C. H. Townes: Journ. Appl. Phys. **22** (1951) 1365.

2) H. Lyons: Annals New York Acad. Sci. **55** (1952) 831.

3) W. Gordy: Rev. Mod. Phys. **20** (1948) 668.

4) J. M. Jauch: Phys. Rev. **72** (1947) 715.

5) D. K. Coles and W. E. Good: Phys. Rev. **82** (1951) 877.

6) K. Shimoda: Journ. Phys. Soc. Japan **8** (1953) 131.

7) R. H. Johnson and M. W. P. Strandberg: Phys. Rev. **86** (1952) 811.

8) N. Danos and S. Geschwind: Phys. Rev. **91** (1953) 1159.

9) B. Bleaney and R. P. Penrose: Proc. Phys. Soc. Lond. **59** (1947) 418.

JOURNAL OF THE PHYSICAL SOCIETY OF JAPAN Vol. 9, No. 3, MAY—JUNE, 1954

The Change of the Refractive Index of Some Germanium Films Irradiated by Intense Light

By Kozo ISHIGURO* and Toshiharu HAYASHI

Department of Physics, Faculty of General Education,
University of Tokyo, Komaba, Tokyo

(Received November 17, 1953)

A Rayleigh Löwe Interferometer has been modified to measure the changes of the refractive index of several germanium films when they are irradiated by the intense white light. The refractive index of the films was found to increase when the colour temperature of the irradiating light source was ca. 3000 K and to decrease when the temperature was ca. 1000 K. From the dispersion curves, it was suggested that the present effects were caused by the variation of the number of the bounded electrons and not of the free carriers.

§ 1. Introduction

When an intense light is focused on germanium films, some changes of refractive index can be observed by the use of the interference refractometers such as the Rayleigh-Löwe[1]. This effect which may be called "photo-refraction" will be used for the study of the behavior of the optical electrons (and perhaps of holes) in germanium films. When the wavelengths of the irradiating light are shorter than 1.8μ, the intrinsic absorption occurs and the density of the current carriers and at the same time the number of the bounded electrons will be changed and consequently the refractive index of the films will be affected by these changes. Recently an interesting influence of the change in the density of the current carriers to the absorption coefficient has been reported by A. F. Gibson[2]. But, on account of the fairly large time lag (order of several seconds) and the increase of the effect for the observation at the shorter wavelengths, the present photo-refraction effect may be related rather more closely to the electrons in the bounded states than to the free carriers not in accordance with the case of Gibson.

§ 2. Experiments

The interferometer had two auxiliary pairs of parallel slits, one pair being in the upper arm of the interferometer and the other in the lower arm[3),4)]. (Fig. 2.) This interferometer functioned as two independent double slit interferometers having their two fringe systems directly above each other. When the coated glass plate was inserted in the interferometer as in Fig. 1, both fringe systems were shifted horizontally by equal amounts but in opposite directions. By rotating a compensator inserted in the upper arm, the two sets of fringes could be brought into coincidence again. When the film was irradiated by intence light, some additional shift of the fringes was arisen and the magnitude of the difference in phase corresponding to this fringe shift was determined from the rotation angle of the calibrated compensator to bring into coincidence again the two sets of fringes.

A small piece of germanium of the resistivity of 1 ohm cm was placed in a tungsten coil and the films studied were evaporated from the coil on BK7 glass plates of good quality by the usual method of vacuum evaporation. Special heat treatments after the film formation were not tried this time.

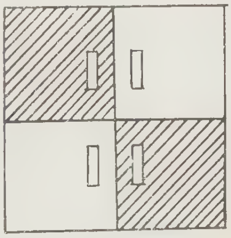

Fig. 1. The method of film deposition. The films are deposited only on the shadowed parts.

---

* They are also belonged to Institute of Science and Technology where the main parts of the present experiments have been obtained and the further developments are also in progress.

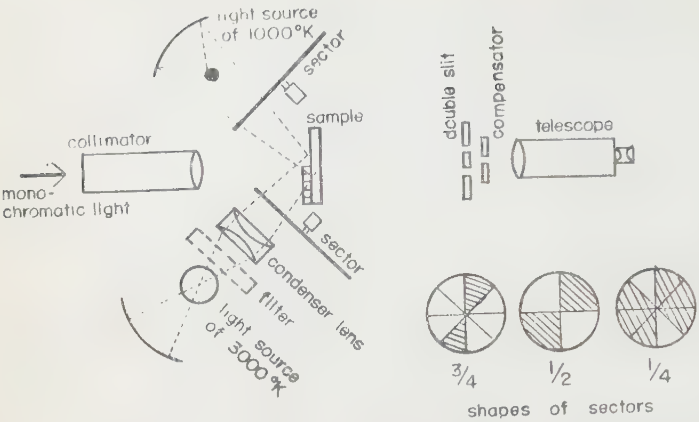

Fig. 2. The arrangements of the interferometer and the irradiating light sources. The shapes of the sectors are also shown in the figure.

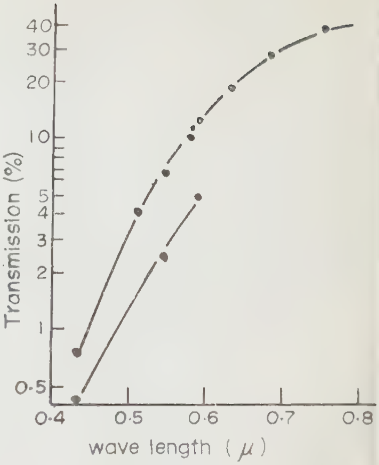

Fig. 3. The spectral transmissions of a germanium film.
Lower curve: soon after the preparation
Upper curve: after the repeated experiments during 3 months.

A specimen by which the principal results in the following section were obtained was a film evaporated on a glass plate of fairly complete constant thickness of 3 mm. The transmission of the specimen for $\lambda=0.59\mu$ was 5% soon after the preparation and 12% after the repeated measurements during 3 months. The final thickness of the film was 0.152μ by Tolansky's multiple beam interference method. The transmission spectrum of the film is given in Fig. 3.

As a supplemental experiment, a specimen evaporated on a glass plate of wedge form was also used for measurements. But the general tendencies of the phenomena in the following section were not changed from the results obtained using the former constant thickness plate specimen. If the deformation of the glass plate caused by the temperature rise by the irradiation of the intense light had some considerable influences on the present effects, this would not be same for the constant thickness plate and for the wedge form plate. Therefore, the fact that the observed results had the qualitatively same tendencies for both cases would give an assurence to the stand point that the observed phase shifts were not caused by the heat deformation of the glass substrate but were arisen from the more essential physical natures of germanium films.

The incident energies were determined from the temperature rise of the water of 50 cc in a glass beaker which was blackened by a drop of Japanese 'Sumi' or charcoal ink.

To change the intensity of the incident light, several sectors of the known ratios of the transparent parts to the intercepting parts were prepared and they were rotated to interrupt the irradiating light by a small motor with a sufficiently high velocity comparing with the time lag of the present effect.

The formula connecting the refractive index of a film and the observed phase change is given approximately by

$$l(n-1)=\lambda\Delta$$

or

$$l\delta n=\lambda\delta\Delta\ .$$

Here, n is the refractive index of the film and $\lambda\Delta$ the difference of the optical path length in the film and in the air layer of equal thickness, λ being the wave length in air, while δn and $\lambda\delta\Delta$ are their changes caused by the irradiation of light. l is the film thickness.

§ 3. Results

(1) *The effect caused by light from a tungsten lamp of 3000 K colour temperature*

When the light from a tungsten lamp of 1 K.W. was focused on the specimen from the film side, the interference fringes were shifted in the direction to indicate the increase of the refractive index of the film. The shift was increased almost linearly with the increase of the incident energy. (Fig. 4) The time lag of the effect seemed to be larger than several seconds.

When a water filter of 5 cm thickness was inserted in the light passage, the total energy was decreased to ca. 1/5 of the former case, but the decrease of the fringe shift was not so large comparing with this large change of the intensity, since the observed phase change of this case exceeded almost 3/4 of the former case. The spectral intensity distribution of the radiation from a black body of 3000K (with the consideration of the presence of the transparent glass plate in the light passage) is given in Fig. 5 and the effect of the water filter is also shown in the graph. The relatively small influence of the insertion of the water filter will indicate that the light of shorter wave lengths than 1μ are responsible chiefly for the present effect. Even when the light was projected from the glass plate side of the specimen, the general tendencies of the effect were not changed. To prevent the temperature rise of the specimen, it was effective to blow with a small hair drier. Though this disturbed the stability of the interference fringes a little, it was not so large to make difficult the observations.

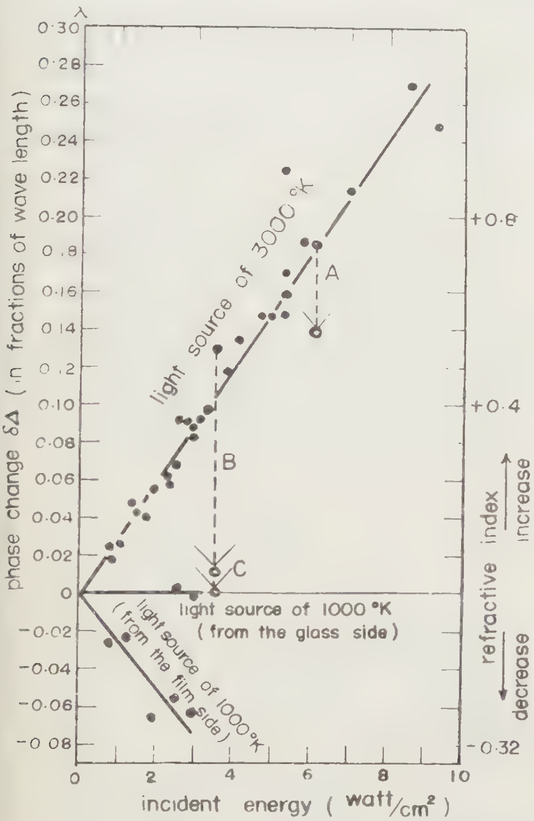

Fig. 4. The phase changes of a germanium film *versus* the intensities of the irradiating light.

The phase change of 0.1 λ for the present specimen corresponds to the change of the refractive index of ca. 0.4.

" A " shows the effect of the insertion of the water filter of 5 cm thickness.

" B " and " C " show the effects of the insertions of the dark glass filters which transmit only infra red light, where " C " is much darker than " B ".

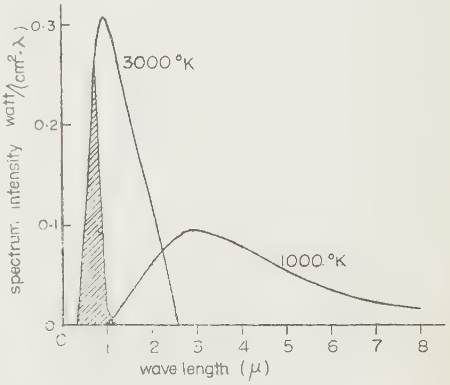

Fig. 5. Spectrum intensities of light from black bodies of 3000 K (with transparent glass filter) and 1000 K. The total energies are adjusted to be 1 watt per squ. cm on the surface of the specimen for both sources.

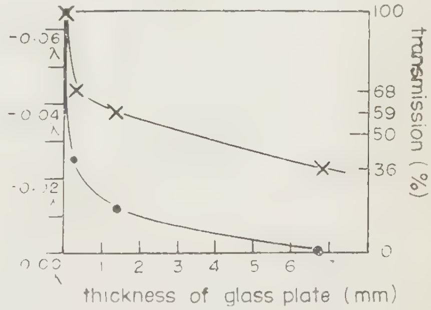

Fig. 6. Influences of the insertion of the glass filter for 1000 K source.

× : changes of the transmitted energy *versus* glass thicknesses.

● : changes of the phase shift *versus* glass thicknesses.

On the contrary when a glass filter which absorbed almost perfectly the visible light but transmitted fairly well the near infra red light was used instead of the water filter, the phase change was only 8% of the case without the filter in spite of the large transmission of ca. 47% comparing to 20% of the water filter for the present light source. This fact suggests also that the light of shorter wave lengths than 1μ are responsible chiefly for the present effect.

(2) *The effect caused by light from a heated carbon silicate rod of 1000K*

The light from a rod of carbon silicate was focused on the specimen from the film side by a large concave mirror of relatively short focal length. The insertions of any glass plates in the light passage were avoided. The most remarkable effect of the present case was the fact that the interference fringes were shifted in the direction indicating the decrease of the refractive index of the film, namely the opposite direction of the case of 3000K source. But linear response of the effect for the incident energy was also observed in this case. (Fig. 4) Furthermore, when the light was projected from the glass plate side of the film, the phase change was vanished utterly. To study this phenomenon more precisely, several glass plates of different thickness were inserted in turn in the light passage as filters when the light was projected from the film side of the specimen, the fringe shift was decreased more rapidly than the decreasing ratio of the transmission which was the function of the thickness of the glass plate filter. (Fig. 6).

The spectral intensity distribution of the radiation from a black body of 1000K is given in Fig. 5. The maximum intensity lies near 3μ. Since the insertion of the glass filter cuts off the longer wave lengths than ca. 2.6μ, the faster decrease of the fringe shift than the decrease of the total incident energy suggests that the light of longer wave lengths than ca. 3μ are chiefly responsible for the present effect.

The effect of the superposition of the irradiations of the both kinds of sources was algebraically additive, namely when the sole irradiation of the 3000K or 1000K light source caused the fringe shift of -0.088λ or $+0.047\lambda$ respectively, the superposed irradiation of the both sources caused the shift of -0.045λ.

(3) *The variation of the effect with the change of the observing wave length*

The above changes of the refractive index by the irradiation of white light were observed at $\lambda=0.59\mu$. However to make the present effects more clearly, the observations at the various wave lengths are desirable. But our visual method does not allow the variation of the observing wave length for the wide range and it was only possible to observe the effects between $\lambda=0.68\mu$ and 0.42μ under the constant irradiation of 3000K or 1000K light source. The results are given in Fig. 7. It is clear from the graph that the effects are large at the shorter wave length side for the both kinds of sources.

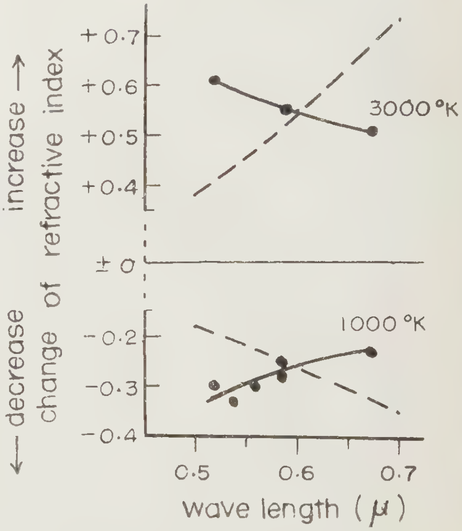

Fig. 7. Dispersion of the change of the refractive index.
The dotted curves are the calculated values under the assumption that conducting electrons are most effective for the present effects.

When the dispersion formula of Drude type is assumed as a first approximation, it is written as

$$n^2-1=\int_0^{\nu-\varepsilon}\frac{k_S d\nu_S}{\nu_S{}^2-\nu^2}+\int_{\nu+\varepsilon}^{\infty}\frac{k_L d\nu_L}{\nu_L{}^2-\nu^2}+\int_{\nu-\varepsilon}^{\nu+\varepsilon}\frac{k_N d\nu_N}{\nu_N{}^2-\nu^2+i\gamma\nu},$$

where, ν is the frequency to observe the refractive index, ν_S and ν_L are the resonounce frequencies in smaller and larger frequency regions than ν, and ν_N represents the resonounce frequency which lies very closely to

ν. k_S, k_L, k_N, γ and ε are the constants of which the physical meanings are not important in the present discussion.

If there is a most sensitive resonounce frequency ν_0 for the present photo-refraction effect, it is convenient to write the above formula as

$$n^2=k_{0}'(\nu_0^2-\nu^2)+A\,,$$

or

$$\delta n=\delta k_{0}'\{2n(\nu_0^2-\nu^2)\}\,.$$

Since δn increases with ν as is clear from Fig. 7, the wave length corresponding to ν_0 might lie in the shorter wave length region than 0.52μ if it were exist actually. When the variations of the number of the conducting carriers are directly responsible for the present phenomena, the dispersion curves ought to be the dotted curves in the graph. Therefore, the direct influence of the conducting carriers for the present phenomena will not be large as it might by thought at first.

§ 4. Summary

The influences of the irradiation of the intense white light on the pure germanium films are grouped in two classes. When the wave lengths of the irradiating light are shorter than 1μ, the refractive index of the films for $\lambda=0.59\mu$ increases linearly with the incident energy and when the wave lengths of the irradiating light are longer than 3μ, the refractive index of the films for $\lambda=0.59\mu$ decreases linearly with the increase of the incident energy and the light between 1μ and 3μ are inactive perhaps by the cancellation of the both effects. When the incident energy are constant, these photo-refractive effects are more prominent for the shorter wave lengths of the observation in the range of our experiments. Therefore, the most sensitive electrons for the present effects will be the bounded electrons rather than the free carriers.

The pure germanium samples were afforded by Dr. Hiroe Osahune of the Nihon Denki Co.. The writers appreciate his help heartily and also wish to thank Dr. Jiro Yamasita and Dr. Goro Kuwabara for the several valuable suggestions and encouragements.

References

1) K. Ishiguro: J. Phys. Soc. Japan **8** (1953) 269L.
2) A. F. Gibson: Proc. Phys. Soc. **66B** (1953) 588.
3) K. Ishiguro: J. Phys. Soc. Japan **5** (1950) 187.
4) K. Ishiguro and G. Kuwabara: J. Opt. Soc. Am. **43** (1953) 365.

JOURNAL OF THE PHYSICAL SOCIETY OF JAPAN Vol. 9, No. 3, MAY—JUNE, 1954

Quadrupole Moment of La^{139}

By Kiyoshi MURAKAWA

Institute of Science and Technology, Komaba-machi, Meguro-ku, Tokyo

(Received February 16, 1954)

Study of the hyperfine structure of the spectra of La I and La II yielded the result that the quadrupole moment of La^{139} is $(0.9\pm0.1)\times 10^{-24}$ cm^2. The construction of the light source (liquid-air cooled hollow cathode discharge tude) is described in detail.

§ 1. Introduction

No quadrupole moment of the odd-proton nuclei with Z between 53 and 57 has been studied, so in order to fill the gap La^{139} ($Z=57$) was studied. The purpose of the present paper is to describe the experimental arrangement and the result obtained. The abstract of the result has already appeared¹⁾.

§ 2. Experimental Arrangement

A hollow-cathode discharge tube cooled with liquid-air was used as a light source. The design of Arroe and Mack²⁾ was modified so as to be vacuum tight against any change of temperature of the cathode. In the present design (Fig. 1) no water.heating is necessary, so that the consumption of liquid air is very small. This is achieved by using a fernico-seal (or Kovar-seal as is also named in U.S.A.) as a glass to metal seal. Aluminum cannot be soldered to fernico, so that a copper cup is used outside the aluminum one.

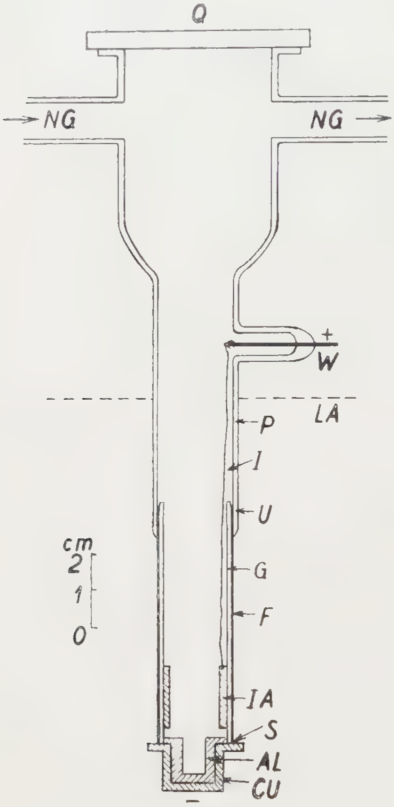

Fig. 1. Sketch of the liquid-air cooled hollow-cathode discharge tube.
Q: quartz window. NG: noble gas (helium, neon or argon). W: tungsten rod. LA: level of liquid-air. P: pyrex glass. I: iron wire. U: uranium glass. G: insulating glass. F: fernico hollow cylinder. IA: iron anode. S: soldered seal. AL: aluminum cup. CU: copper cup.

The sputtering of the sample within the hollow-cathode is also small. Thus a few milligrams of dysprosium, for example, is sufficient in order to maintain a bright spectrum of Dy I and Dy II for over one hundred hours. The sputtered sample can be returned by an appropriate chemical treatment of the anode and the inner surface of the insulating glass (named G in Fig. 1).

In order to resolve the hyperfine structure (hfs) a Fabry-Perot etalon was used. Fig. 2 shows some enlargements of the interference patterns of the spectra of La I and La II.

§ 3. Hfs of the Spectrum of La I.

The hfs of the spectrum of La I was studied by Anderson[3] who deduced the spin of La^{139} to be 7/2. However he detected no deviation from the cosine interval rule in any term of La I.

The deep terms of La I[4] are shown schematically in Fig. 3; the deepest term belongs to the configuration $5d6s^2$. The hfs splittings of $5d6s^2\ {}^2D_{3/2,5/2}$ are not sufficiently large to warrant accurate measurement. In the present work, therefore, study of these two levels was abandoned, and the configuration $5d^26s$ was studied. Crawford calculated the hfs formulas[5] for the $5d^26s$ configuration, and according to his investigation the term $5d^26s\ {}^4F$ is near an LS-coupling and ${}^4F_{3/2}$ is free from configuration perturbation.

In the present work the line

$$\lambda 5106\ [5d^26s\ {}^4F_{3/2} - 5d^2({}^3F)6p\ {}^4D_{1/2}]$$

was studied, the hfs being shown schematically in Fig. 4. The interval factor A and the quadrupole constant B of the final level are

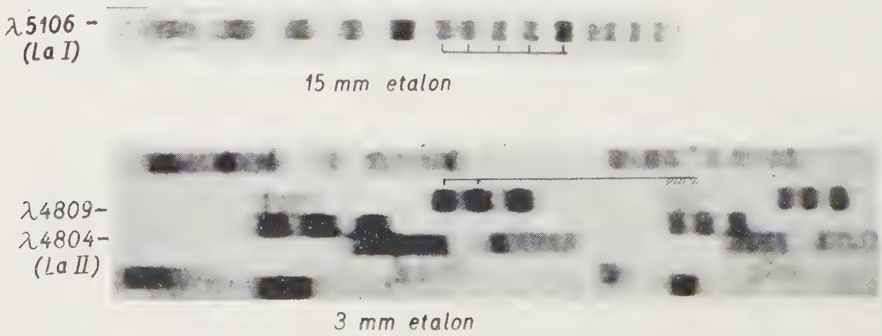

Fig. 2. Enlargements of the interference patterns of the spectra of La I and La II.

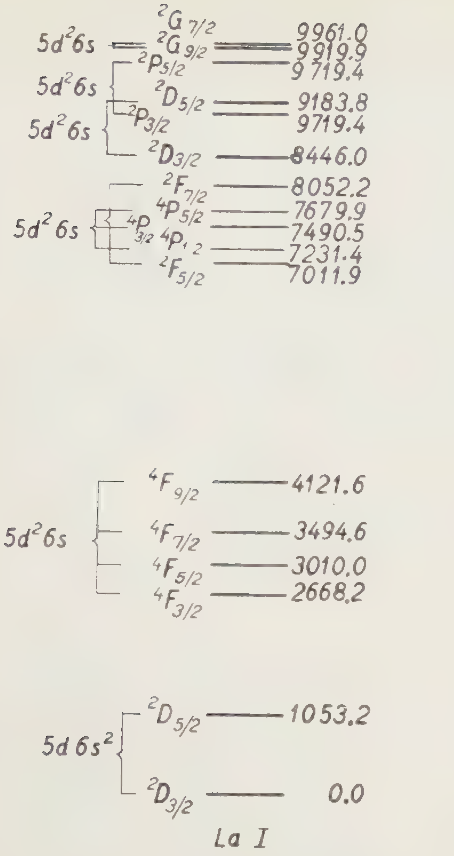

Fig. 3. Deep terms of the spectrum of La I.

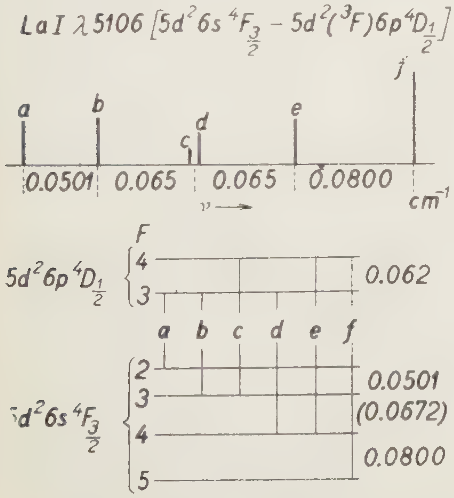
La I λ5106 $[5d^26s\,^4F_{\frac{3}{2}} - 5d^2(^3F)6p\,^4D_{\frac{1}{2}}]$
a
b
c
d
e
f
0.0501
0.065
0.065
0.0800
ν ⟶
cm^{-1}
F
$5d^26p\,^4D_{\frac{1}{2}}$
4
3
0.062
a b c d e f
2
3
4
5
$5d^26s\,^4F_{\frac{3}{2}}$
0.0501
(0.0672)
0.0800

Fig. 4. Hfs of La I λ5106.

calculated to be

$$A=-16.7\times10^{-3}\text{cm}^{-1}\,,\quad B=0.011\times10^{-3}\text{cm}^{-1}\,.$$

In order to calculate the quadrupole moment (Q), the value of $\overline{\sum(3\cos^2\theta-1)}$ must be calculated. This can be done most easily by using the (slm_sm_l)-representation, as was done by Schmidt[6] in the calculation of Q(Ta) under the assumption of an LS-coupling.

Since the fundamental formulas published by Schmidt contain serious misprints, they will be repeated here in a perfectly correct form.* The seventh column was corrected by Brown and Tomboulian[7]. The notation is the same as the book of Condon and Shortley[8].

$$(2^+|3\cos^2\theta-1|2^+)=(-2^-|3\cos^2\theta-1|-2^-)$$
$$=-\frac{4}{7}R_2'$$
$$(1^+|3\cos^2\theta-1|1^+)=(-1^-|3\cos^2\theta-1|-1^-)$$
$$=\frac{2}{175}(8R_2'-7R_2''+24S_2)$$
$$(2^-|3\cos^2\theta-1|2^-)=(-2^+|3\cos^2\theta-1|-2^+)$$
$$=\frac{4}{175}(R_2'-14R_2''-12S_2)$$
$$(0^+|3\cos^2\theta-1|0^+)=(0^-|3\cos^2\theta-1|0^-)$$
$$=\frac{4}{175}(12R_2'+7R_2''+6S_2)$$
$$(1^-|3\cos^2\theta-1|1^-)=(-1^+|3\cos^2\theta-1|-1^+)$$
$$=\frac{2}{175}(16R_2'+21R_2''-12S_2)$$
$$(1^+|3\cos^2\theta-1|2^-)=(-2^+|3\cos^2\theta-1|-1^-)$$
$$=\frac{4}{175}(2R_2'+7R_2''-9S_2)$$
$$(0^+|3\cos^2\theta-1|1^-)=(-1^+|3\cos^2\theta-1|0^-)$$
$$=\frac{2\sqrt{6}}{175}(8R_2'-7R_2''-S_2)$$

The wave functions in the LS coupling are first expressed by the wave functions in the (SLM_SM_L)-representation and then by the products of one-electron wave functions in the (s, l, m_s, m_l)-representation. For example the wave function for $^4F_{3/2}$ (of LS-coupling) is given by

$$^4F^{3/2}_{3/2}=\sqrt{\frac{1}{35}}[-(^4F,3/2,0)+2(^4F,1/2,1)$$
$$-\sqrt{10}(^4F,-1/2,2)+2\sqrt{5}(^4F,-3/2,3)]\,,$$

$$(^4F,3/2,0)=\frac{1}{\sqrt{5}}[2(1^+-1^+,+)+(2^+-2^+,+)]\,,$$

$$(^4F,1/2,1)=\frac{1}{\sqrt{30}}[\sqrt{6}(2^+-1^-,+)$$
$$+\sqrt{6}(2^--1^+,+)+\sqrt{6}(2^+-1^+,-)$$
$$+2(1^+0^-,+)2(1^-0^+,+)+2(1^+0^+,-)]\,,$$

$$(^4F,-1/2,2)=\frac{1}{\sqrt{3}}[(2^-0^-,+)+(2^+0^-,-)$$
$$+(2^-0^+,-)]\,,$$

---

* R', R'' and S are relativity correction factors in the notation of Casimir[9].

$$({}^4F, -3/2, 3) = (2^- 1^-, -)\ ,$$

in which the sign (+ or −) after comma refers to the spin of the 6*s*-electron. Putting these expressions in the above-mentioned formulas, we get

$$({}^4F_{3/2}|3\cos^2\theta-1|{}^4F_{3/2}) = \frac{8}{4375}(-7R_2'+28R_2''-96S_2)\ .$$

In the same way we get for the same electron-configuration:

$$({}^2D_{3/2}|3\cos^2\theta-1|{}^2D_{3/2}) = \frac{6}{875}(12R_2'+7R_2''+6S_2)$$

$$({}^4P_{3/2}|3\cos^2\theta-1|{}^4P_{3/2}) = -\frac{4}{1875}(104R_2'+34R_2''+27S_2)$$

$$({}^2P_{3/2}|3\cos^2\theta-1|{}^2P_{3/2}) = \frac{2}{375}(20R_2'+25R_2''+36S_2)\ .$$

According to Crawford[5)], the actual wave function (${}^4F_{3/2}'$) in intermediate coupling can be expressed in terms of wave functions in *LS*-coupling in the form:

$$ {}^4F_{3/2}' = K_1\,{}^4F_{3/2} + K_2\,{}^2D_{3/2} + K_3\,{}^4P_{3/2} + K_4\,{}^2P_{3/2}\ ,$$
$$K_1=0.9955,\ K_2=-0.0946,\ K_3=K_4=0.$$

We have therefore:

$$\begin{aligned}({}^4F_{3/2}'|3\cos^2\theta-1|{}^4F_{3/2}') &= K_1^2({}^4F_{3/2}|3\cos^2\theta-1|{}^4F_{3/2})\\ &\quad + K_2^2({}^2D_{3/2}|3\cos^2\theta-1|{}^2D_{3/2})\\ &\quad + 2K_1K_2({}^4F_{3/2}|3\cos^2\theta-1|{}^2D_{3/2})\ .\end{aligned}$$

We need, therefore, one more expression:

$$({}^4F_{3/2}|3\cos^2\theta-1|{}^2D_{3/2}) = \frac{8\sqrt{3}}{875\sqrt{5}}(2R_2'+7R_2''-9S_2)\ .$$

Putting these expressions in the fundamental formula

$$Q = -B\frac{Z^*H}{\zeta\sum(3\cos^2\theta-1)}I(2I-1) \times J(2J-1)\cdot 1{,}988\cdot 10^{-21}\ ,$$
$$(B \text{ and } \zeta \text{ in cm}^{-1})$$

and putting the values $\zeta_{5d}=400$ (according to Crawford), $B=0.011\times10^{-3}$, $Z^*=57-10=47$, $I=7/2$, $H=1{\cdot}01$, $R_2'=1.04$, $R_2''=1.15$, $S_2=1.04$ in the final formula, we get

$$Q(\text{La}^{139}) = (+0.95\pm0.20)\times10^{-24}\text{cm}^2\ .$$

§ 4. Hfs of the Spectrum of La II

The deep terms of La II are shown schematically in Fig. 5. The level $5d6s\,{}^3D_1$ should be the most suited for our purpose, so the line λ4809 ($5d6s\,{}^3D_1 - 5d4f\,{}^3P_0$) was studied and the result of measurement is shown in Fig. 6. Another line lies very close, so that it was only possible to use spacers thinner than 3.2 mm. The constants for $5d6s$ ${}^3D_1$ are:

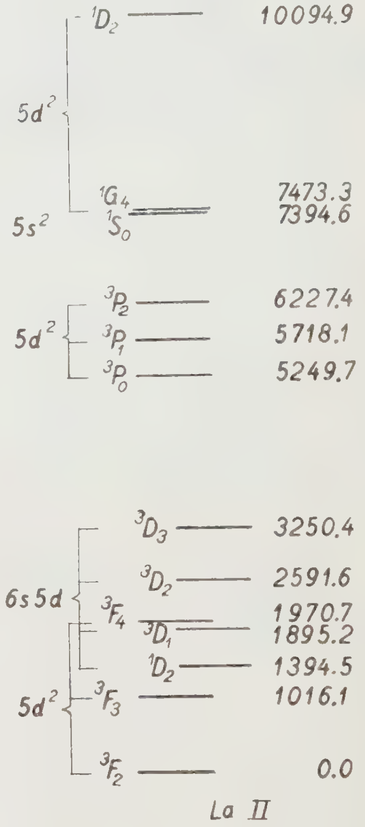

Fig. 5. Deep terms of the spectrum of La II.

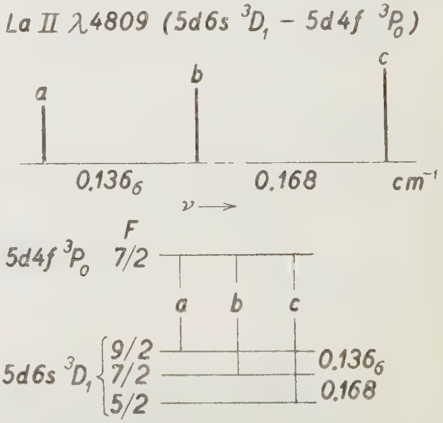

Fig. 6. Hfs of La II λ4809.

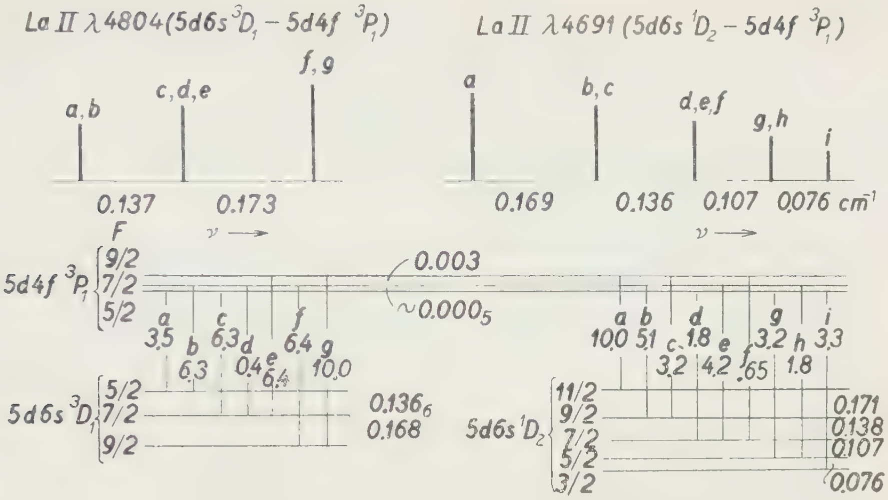

Fig. 7. Hfs of La II λ4804 and λ4691.

$$A=-38.1\times10^{-3}\,\mathrm{cm}^{-1}\,,\quad B=0.057\times10^{-3}\mathrm{cm}^{-1}.$$

Casimir's formula⁹⁾ gives

$$({}^3D_1\,|\,3\cos^2\theta-1\,|\,{}^3D_1)=-\frac{1}{5}R_2''\,.$$

Putting $\zeta_{5d}=542\,\mathrm{cm}^{-1}$, $R_2''=1.15$ and the value of B in the fundamental formula, we get

$$Q(\mathrm{La}^{139})=(0.91\pm0.10)\times10^{-24}\mathrm{cm}^2.$$

The splittings of the level $5d6s\,{}^1D_2$ can be determined via the hfs of λ4804 and λ4691 (see Fig. 7) only approximately. For this level we get

$$A=31.2\times10^{-3}\mathrm{cm}^{-1}\,,\quad B\approx0.011\times10^{-3}\mathrm{cm}^{-1}.$$

Starting from the formula

$$({}^1D_2'\,|\,3\cos^2\theta-1\,|\,{}^1D_2')$$
$$=-\left\{\frac{16}{35}R_2'c_1^2+\frac{2}{5}R_2''c_2^2-\frac{12}{35}\sqrt{\frac{2}{3}}\,S_2c_1c_2\right\}$$

$c_1=0.9501$, $c_2=-0.3115$ (determined from the multiplet structure),

we get

$$Q(\mathrm{La}^{139})=+0.4\times10^{-24}\mathrm{cm}^2.$$

This is a rough estimation and shows only that the sign of Q is positive.

Summarizing the results obtained from La I and La II, we can conclude that

$$Q(\mathrm{La}^{139})=(0.9\pm0.1)\times10^{-24}\mathrm{cm}^2.$$

Wageningen and de Boer¹⁰⁾ calculated theoretically the same moment and got $1.3\times10^{-24}\mathrm{cm}^2$. The order of magnitude of this prediction is in agreement with the above-mentioned experimental result.

References

1) K. Murakawa and T. Kamei: Phys. Rev. **92** (1953) 325.

2) O. H. Arroe and J. E. Mack: Jour. Opt. Soc. Am. **40** (1950) 386.

3) O. E. Anderson: Phys. Rev. **46** (1934) 473.

4) The classification of the spectra La I, La II and La III was published by H. N. Russell and W. F. Meggers, Jour. Res. Natl. Bur. Stand. **9** (1932) 625.

5) M. F. Crawford: Phys. Rev. **47** (1935) 768.

6) T. Schmidt: Zeits. f. Physik **121** (1943) 63.

7) B. M. Brown and D. H. Tomboulian: Phys. Rev. **88** (1952) 1158.

8) Condon and Shortley: *Theory of Atomic Spectra*. Cambridge (1935).

9) H. Casimir: Verh. Teylers Tweede Genootschap, Haarlem **11** (1936).

10) R. v. Wageningen and J. de Boer: Physica **18** (1952) 367.

JOURNAL OF THE PHYSICAL SOCIETY OF JAPAN Vol. 9, No. 3, MAY—JUNE, 1954

Contribution of the Change of Entropy to the Directions of Spines of Shock Polar

By Tōru KAWAMURA

Institute of Physics, Nara Women's University

(Received January 10, 1954)

The directions of spines of shock polar in two-dimensional iso-energetic flow of a compressible fluid are calculated and compared with approximated results as obtained by neglecting the variation of entropy change on the successive streamlines experienced at the shock wave surface. The series of numerical values of the spines show certain deviations, which would be due to the neglect of the entropy variations. The deviations are considered when the angle of inclination of the shock wave to the uniform stream is large, and the flow behind the shock wave is subsonic, which is the case of frequent occurrence in the study of the detached shock wave problem. Therefore, the present analysis indicates the necessity of computing the entropy variation in such a problem.

§ 1. Introduction

When a two-dimensional supersonic flow of a compressible fluid impinges upon an obstacle, there forms a sheet of stationary detached shock wave in front of it, provided certain conditions are satisfied. There is in general a subsonic region bounded by the shock wave, the surface of the obstacle and a pair of sonic lines starting from the sonic point on the body and extending to the shock wave surface. The flow in this region is completely determined by the conditions on these boundaries and the equations of motion, together with the equation of state of the fluid. If we transform the motion into the hodograph plane, the above conditions again determine the flow in the corresponding region. The initial directions of the streamlines in the hodograph plane as they start from the shock polar namely the directions of the so-called spines are, however, determined, for instance, by Rankine's shock wave relations and the equations of motion, together with the equation of state of the fluid. It should be noted here that the directions of spines are independent of the boundary conditions of the surface of the obstacle. Since the form of the shock polar is uniquely determined by the Mach number of the undisturbed flow and is independent of the special forms of the shock wave in the physical plane, the directions of spines are of a universal character and may be considered as an extended form of the well-known Rankine's shock wave relations.

The present analysis has been performed in order to obtain materials for studying the flow in the subsonic region, but, as will be seen in the subsequent analysis, the results obtained are also valid for the supersonic region behind the shock wave.

In the present analysis, the flow in front of the shock wave is assumed to be uniform, iso-energetic and iso-entropic. At an arbitrary point on the shock wave, Rankine's relations determine the pressure, density and velocity of the fluid immediately bedind the shock wave in terms of the undisturbed Mach number M_1 and the inclination α of the curved shock wave at that point[1].

The exact directions of spines have been calculated and compared with approximate results as obtained by neglecting the variations of entropy change on the successive streamlines experienced at the shock wave. The results of the present analysis show that the effect of the entropy change is considerable when α is large and the flow behind the shock wave is subsonic.

The present investigation is suggested by a review of Dr. Busemann[2] and a work of Dr. Guderley[3].

§ 2. Fundamental Relations

We shall consider a case of a uniform supersonic flow of a compressible fluid past an obstacle, in front of which there forms a sheet of a stationary curved shock wave. Let q, p, ρ, M, α and θ are velocity, pressure, density, Mach number, angle of inclination of the shock wave at an arbitrary point to the direction of the undisturbed stream and the inclination of the streamline to the same direction respectively. Suffices 0, 1, and 2 refer respectively to the quantities of the stagnation point corresponding to the state of the flow in front of the shock wave, the undisturbed stream and the flow immediately behind the shock wave. Further, u and v are the velocity components parallel and perpendicular to the uniform stream.

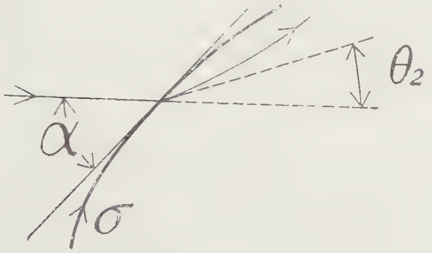

Fig. 1.

Rankine's shock wave relations are

$$\rho_1 q_1 \sin\alpha = \rho_2 q_2 \sin(\alpha-\theta), \tag{1}$$

$$p_1 + \rho_1 q_1^2 \sin^2\alpha = p_2 + \rho_2 q_2 \sin^2(\alpha-\theta), \tag{2}$$

and

$$q_1 \cos\alpha = q_2 \cos(\alpha-\theta). \tag{3}$$

Denoting the line-elements measured along the shock wave, along and perpendicular to a streamline by $d\sigma$, ds and dn respectively, the equations of motion are expressed in intrinsic forms as:

$$q\frac{\partial q}{\partial s} = -\frac{1}{\rho}\frac{\partial p}{\partial s}, \tag{4}$$

$$q^2\frac{\partial \theta}{\partial s} = -\frac{1}{\rho}\frac{\partial p}{\partial n}, \tag{5}$$

while the equation of continuity is given by

$$(1-M^2)\frac{1}{q}\frac{\partial q}{\partial s} + \frac{\partial \theta}{\partial n} = 0. \tag{6}$$

The components of velocity are

$$u_1 = q_1, \quad v_1 = 0, \quad u_2 = q_2 \cos\theta_2 \quad \text{and}$$
$$v_2 = q_2 \sin\theta_2, \tag{7}$$

Further, there is a geometrical relation at the shock wave, namely:

$$\frac{\partial}{\partial\sigma} = \frac{\partial}{\partial s}\cos(\alpha-\theta) + \frac{\partial}{\partial n}\sin(\alpha-\theta). \tag{8}$$

By means of the above relations, we have, after some calculations,

$$\frac{\partial \alpha}{\partial \sigma} = f_1(\alpha, M_1)\frac{\partial \theta}{\partial \sigma}, \tag{9}$$

where

$$f_1(\alpha, M_1) = \frac{4+\{4(\gamma-1)+(\gamma+1)^2 M_1^2\}M_1^2\sin^2\alpha - 4\gamma M_1^4 \sin^4\alpha}{2[2+(\gamma+1)M_1^2+\{(\gamma+1)M_1^2-4\}M_1^2\sin^2\alpha - 2\gamma M_1^4\sin^4\alpha]}.$$

Also, we have

$$\frac{1}{q_2}\left(\frac{\partial q}{\partial s}\right)_2 = f_3(\alpha, M_1)\left(\frac{\partial \theta}{\partial s}\right)_2, \tag{10}$$

where

$$f_3(\alpha, M_1) = \frac{\{4q_1^2 f_1(\alpha, M_1)\cos^2\alpha + (\gamma+1)q_2^2\}\rho_1\rho_2\tan\alpha}{4(1-M_2^2)f_1(\alpha, M_1)\rho_1^2 q_1^2 \sin^2\alpha - (\gamma+1)\rho_2^2 q_2^2}.$$

The direction of spine on the u, v-plane or hodograph plane is determined by

$$\tan\varphi = \left(\frac{dv}{du}\right)_2 = \frac{f_3(\alpha, M_1)\tan\theta_2 + 1}{f_3(\alpha, M_1) - \tan\theta_2}, \tag{11}$$

since the direction of spine is the initial direction of the streamline on the hodograph plane as it starts from the shock polar.

The Crocco point is determined by a relation

$$\tan\varphi = \tan\theta_2. \tag{12}$$

Values of α at the sonic point, the point of maximum deflection of the streamline behind the shock wave and the Crocco point are indicated by α_s, α_m and α_c respectively. The value of α_s is determined by the relation $M_2 = 1$, and after some calculations we have

$$2\gamma M_1^4 \sin^4\alpha_s - \{(\gamma-3) + (\gamma+1)M_1^2\}M_1^2\sin^2\alpha_s - 2 = 0. \tag{13}$$

The point of maximum deflection is defined by $\partial\theta/\partial\sigma = 0$ and an algebraic equation for determining α_m is derived from (9) as:

$$2\gamma M_1^4 \sin^4 \alpha_m - \{(\gamma+1)M_1^2-4\}M_1^2 \sin^2 \alpha_m \\ -2-(\gamma+1)M_1^2 = 0 \,. \qquad (14)$$

Further, an algebraic equation for determining α_c is derived from (10), (11) and (12) and we have

$$4\gamma(2\gamma-1)M_1^6 \sin^6 \alpha_c - 2(2\gamma-1)(\gamma+1)M_1^6 \sin^4 \alpha_c \\ -2(2\gamma^2-13\gamma+3)M_1^4 \sin^4 \alpha_c \\ -(\gamma^2+6\gamma+5)M_1^4 \sin^2 \alpha_c \\ -4(4\gamma-5)M_1^2 \sin^2 \alpha_c \\ +(\gamma^2-1)M_1^2+2(\gamma-5)=0 \,. \qquad (15)$$

Between the absolute values of α_s, α_m and α_c for given Mach number M_1, there holds an inequality:

$$\alpha_s < \alpha_c < \alpha_m \,.$$

At the extreme cases when $M_1=1$ and M_1 tends to infinity, however, these quantities assume one and the same value.

Further reductions give immediately

$$\frac{1}{q_2}\frac{(\partial q/\partial s)_2}{\partial\alpha/\partial\sigma} = \frac{f_3(\alpha,\ M_1)}{f_1(\alpha,\ M_1)}\frac{q_2}{q_1}\frac{1}{\cos\alpha} \\ \times\left\{1-(1-M_2^2)\frac{\rho_1}{\rho_2}f_3(\alpha,\ M_1)\tan\alpha\right\}^{-1} \\ \equiv f_4(\alpha,\ M_1)\,, \qquad (16)$$

and

$$\frac{\partial\theta/\partial s}{\partial\alpha/\partial\sigma} = \frac{f_4(\alpha,\ M_1)}{f_3(\alpha,\ M_1)} = f_5(\alpha,\ M_1)\,. \qquad (17)$$

A fluid particle moving along a streamline which passes through a point where a relation

$$f_4(\alpha,\ M_1)=0$$

is satisfied suffers no acceleration immediately behind the shock wave. We shall denote the angle of inclination of the shock wave at such a point by α_n, which is determined by the above relation through elementary calculations. The resulting algebraic equation for determining α_n is

$$2(2\gamma+1)M_1^4\sin^4\alpha_n - \{3(\gamma+1)M_1^2-4\}M_1^2\sin^2\alpha_n \\ -\{(\gamma+1)M_1^2+2\}=0\,. \qquad (18)$$

Numerical values of α_s, α_m, α_c and α_n can be calculated by means of (13), (14), (15) and (18) respectively.

The equation of the shock polar is given by

$$y^2\left(1+\frac{2}{\gamma+1}M^{*2}-M^*x\right)=(M^*-x)^2(M^*x-1), \qquad (19)$$

where $y=v/C^*$, $x=u/C^*$ and $M^*=q_1/C^*$, C^* being the critical velocity, namely:

$$C^*=\left\{\frac{2\gamma}{\gamma+1}\frac{p_0}{\rho_0}\right\}^{1/2}.$$

The Eq. (11) for determining the directions of spines is expressed in the notations of the present section, in the form:

$$\tan\varphi=\{(dy/dx)_\psi\}_2\,, \qquad (20)$$

where suffix ψ indicates that differentiation is taken along a streamline ψ=const.

The inclination of the shock polar is easily derived from (18) through differentiation, namely:

$$\left(\frac{dy}{dx}\right)_W = \frac{(M^*-x)(M^{*2}-3M^*x+2)+M^*y^2}{2y\{1+2M^*/(\gamma+1)-M^*x\}}\,.$$

Numerical values of this quantity have been calculated for the case when $M_1=2$ and $\gamma=1.4$ and are plotted in Fig. 2.

§ 3. Approximate Calculations

In the preceding sections the entropy change at the shock wave surface has been taken into account; entropy is different for different streamlines according to the inclinations of the shock wave at points where the streamlines pass through. No additional assumption is, however, made in the analysis. If we neglect the variations of entropy on the successive streamlines, or more practically, if we concentrate our attention to a streamline and its close neighbourhood, the variation of entropy may be small and may be neglected. Then we are able to develop an approximated analysis based upon the isentropic procedure, and the motion is irrotational in the narrow region under discussion. The above limitation allows us to use the Chaplygin's equation in the study of the flow in such a region. Here it must be remembered, however, that the present approximation does not assume a unique velocity potential valid for the whole region behind a shock wave, so that, it is different from the so-called Chaplygin's approximation.

Introducing a new variable4).

$$\bar\sigma=\bar\sigma_1+\int_q^{q_1}\frac{\rho}{\rho_0}\frac{dq}{q}\,, \qquad (21)$$

we have a set of differential equations for velocity potential and stream function, namely:

$$\frac{\partial\varphi}{\partial\theta}=-\frac{\partial\psi}{\partial\bar\sigma}\,, \qquad \frac{\partial\varphi}{\partial\bar\sigma}=K\frac{\partial\psi}{\partial\theta} \qquad (22)$$

with $K=(1-q^2/c^2)^2(\rho_0/\rho)^2$, c being the velocity of sound. These Eqs. (22) are used in the following study in place of (4) and (5) in the preceding exact analysis.

By means of (1) and (3), Frankle[5] has obtained the following relation along the shock polar, namely:

$$K\left(\frac{\partial\psi}{\partial\theta}\right)_W d\bar{\sigma}-\left(\frac{\partial\psi}{\partial\bar{\sigma}}\right)_W d\theta=\frac{\rho_0}{\rho_1}\cot\alpha\, d\psi\,, \tag{23}$$

where suffix W indicates the values at the shock wave surface. The directions of spines on the $\bar{\sigma}$, θ-plane are given by

$$\tan B=\left(\frac{d\theta}{d\bar{\sigma}}\right)_\psi .$$

There is also a geometrical relation along a streamline immediately behind the shock wave, which is given by

$$d\psi=\left(\frac{\partial\psi}{\partial\bar{\sigma}}\right)_W\cos B+\left(\frac{\partial\psi}{\partial\theta}\right)_W\sin B=0\,, \tag{24}$$

from which it follows immediately

$$\tan B=-(\partial\psi/\partial\bar{\sigma})_W/(\partial\psi/\partial\theta)_W\,. \tag{25}$$

Substituting (25) into (23), we have, after some calculations,

$$\left(\frac{\partial\theta}{\partial\bar{\sigma}}\right)_W=\frac{K+(\rho_0/\rho_1)\cot\alpha\tan B}{(\rho_0/\rho_1)\cot\alpha-\tan B}\,. \tag{26}$$

Solving (26) for $\tan B$ and taking account of the definition for the direction of spines, we have

$$\left(\frac{\partial\theta}{\partial\bar{\sigma}}\right)_\psi=\tan B=\frac{(\rho_0/\rho_1)\cot\alpha\,(\partial\theta/\partial\bar{\sigma})_W-K}{(\rho_0/\rho_1)\cot\alpha+(\partial\theta/\partial\bar{\sigma})_W}\,. \tag{27}$$

The similar equation is derived from the preceding exact analysis in the form:

$$\left(\frac{\partial\theta}{\partial\bar{\sigma}}\right)_\psi=-\frac{\rho_0}{\rho_2}\frac{1}{f_3}\,. \tag{28}$$

Next, we shall convert the above relations into those in the x, y-plane in order to compare them with the results of the preceding exact analysis. From (21) we have

$$dq=-\frac{\rho_0}{\rho}q\,d\bar{\sigma}\,,$$

and therefore

$$\frac{\partial\theta}{\partial q}=-\frac{1}{q}\frac{\partial\theta}{\partial\bar{\sigma}}\frac{\rho}{\rho_0}\,. \tag{29}$$

The direction of spine in the x, y-plane is given by

$$\tan\varphi_c=\left(\frac{dv}{du}\right)_\psi=\frac{\sin\theta_2+q_2\cos\theta_2(\partial\theta/\partial q)_\psi}{\cos\theta_2-q_2\sin\theta_2(\partial\theta/\partial q)_\psi}=\frac{\tan\theta_2+q_2(\partial\theta/\partial q)_\psi}{1-q_2\tan\theta_2(\partial\theta/\partial q)_\psi}\,,$$

where suffix c indicates the value of the present approximation. Substituting (29) into the above relation, we have

$$\tan\varphi_c=\frac{\tan\theta_2-(\rho_2/\rho_0)\tan B}{1+(\rho_2/\rho_0)\tan\theta_2\tan B}\,. \tag{30}$$

Comparing the results of the two analyses, it is readily seen that there are certain differences between the resulting equations. To illustrate the differences clearly, numerical values of the inclinations of spines have been calculated by (11) and (30) for the case when $M_1=2$ and $\gamma=1.4$, and the values are plotted in Fig. 2.

Following relations can easily be derived from Rankine's shock wave relations and the conservation of energy, and these have been used in the numerical calculations

$$\left.\begin{aligned}
&\frac{\rho_1}{\rho_2}=\frac{2+(\gamma-1)M_1^2\sin^2\alpha}{(\gamma+1)M_1^2\sin^2\alpha}\,,\\
&\frac{p_2}{p_1}=\frac{1}{\gamma+1}\{2\gamma M_1^2\sin^2\alpha-(\gamma-1)\}\,,\\
&\frac{q_2^2}{q_1^2}=\frac{\rho_1^2}{\rho_2^2}\sin^2\alpha+\cos^2\alpha\,,\\
&M_2^2=\\
&\frac{\{2+(\gamma-1)M_1^2\sin^2\alpha\}^2+(\gamma+1)^2M_1^4\sin^2\alpha\cos^2\alpha}{\{2+(\gamma-1)M_1^2\sin^2\alpha\}\{2\gamma M_1^2\sin^2\alpha-(\gamma-1)\}}\,,\\
&\tan\theta_2=\frac{2\cot\alpha\{M_1^2\sin^2\alpha-1\}}{(\gamma+1)M_1^2-2(M_1^2\sin^2\alpha-1)}\,.
\end{aligned}\right\}$$

Similar relations to those in (31) have also been derived by H. Melkus[6], but the above expressions seem to be simpler.

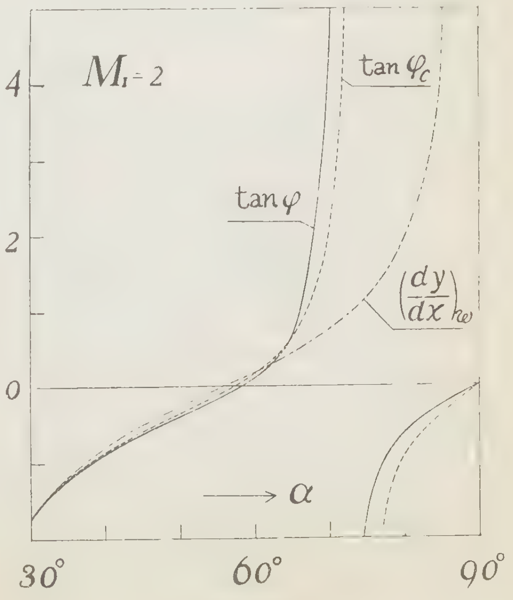

Fig. 2.

§ 4. Discussion of the Results

Comparing the two curves in Fig. 2, it will be seen that the isentropic curve as obtained from (30) coincides satisfactorily with the corresponding curve given by the exact formula (11) as long as the inclination α of the shock wave is sufficiently small and the flow behind the shock wave is supersonic. A marked difference is however seen for α greater than about 61°, since the sonic point for $M_1=2$ is between 61° and 62°. The two curves again assume the same value at $\alpha=90°$, at the normal portion of the shock wave. Therefore, a considerable deviation will be expected in the flow characteristics in the subsonic region except at the normal portion.

For the value of K in § 3 we have used its local values, so that no error will enter into the calculation and the deviations of the curves can only be explained as due to the neglect of entropy. Thus, the present analysis illustrates the effect of entropy changes on spines. The region where the deviations of the two curves are considerable corresponds to the region of most importance in the study of detached shock wave problems, and the present analysis show the necessity of computing the contributions of the change of entropy on the successive streamlines in such a region.

In conclusion, the writer expresses his cordial thanks to Prof. S. Tomotika of the University of Kyoto and Dr. E. R. C. Miles of the Johns Hopkins University for their continued interest throughout the work. The writer's thanks are also due to Dr. G. Guderley for his valuable discussions.

References

1) T. Kawamura: Mem. Coll. Sci. Kyoto Univ. A **26** (1950) 207.
2) A. Busemann: NACA TN 1858 (1949).
3) G. Guderley: Tech. Rep. No. F-TR-2168-ND, AAF, Air Material Command (1947).
4) D. Riabouchinski: Pub. Sci. Tech., Min. de l'Air, No. 108 (1937) 12.
5) F. Frankle: NACA TM 1155 (1947).
6) H. Melkus: Ing. Arch., **19** (1951) 208.

JOURNAL OF THE PHYSICAL SOCIETY OF JAPAN Vol. 9, No. 3, MAY—JUNE, 1954

Fog Formation due to Self Nucleation

By Hiromu WAKESHIMA
The Kobe University of Marcantile Marine

(Received November 2, 1953)

Discussing the fog formation in adiabatically expanded dust- and ion-free moist air, the relation between the droplet size, the time required for the growth of droplets and the rate of self-nucleation are derived, based on the assumption of a simple model process. These relations, when applied to the case of adiabatic expansion at the so-called cloud limit, give a plausible order of magnitude for these quantities. In particular, the discrepancy between the current theory of self-nucleation and the known critical expansion ratio 1.37 can be eliminated.

§ 1. Introduction

The theory of fog formation in a supersaturated vapour is not yet satisfactory at present, though the phenomenon itself is comparatively simple and also important among similar phenomena. The nature of the fog nuclei formed in an adiabatically expanded dust- and ion-free moist air has been clarified by the theory of nucleation developed by many authors such as M. Volmer and A. Weber[1], L. Farkas[2], R. Becker and W. Döring[3], J. C. Fisher and D. Turnbull[4], but the theoretical derivation of the critical expansion ratio 1.37 at the so-called cloud limit has yet been unsuccessful or unsatisfactory. M. Volmer and C. Tohmfor used the formula presented by R. Becker and W. Döring and calculated the critical expansion ratio to 1.27 for the case of supersaturated ion-free air. H. Oura⁵⁾ tried to derive the value 1.37 theoretically on the assumption that the embryos might be small crystals rather than super-cooled liquid drops. The crystalline nature of the embryos seems, however, to be hardly compatible with their spherical form which he assumed.

Up to present it has been generally assumed that the rate of nucleation, i. e. the number of nuclei formed in 1 cm^3 of the vapour per sec., is of the order of magnitude one. The present author being doubtful about the validity of this assumption, seeks the relations between the time required for the growth of fog droplets, the rate of nucleation, and the number of fog droplets. The last one can be determined by the total amount of liquid precipitated and the size of the droplets.

In this treatment, no assumption is made of the magnitude of nucleation rate and a simple calculation is carried out with an assumption of an idealized model process of fog formation in a supersaturated vapour.

These relations, when applied to the case of adiabatic expansion, of rate 1.37 of the air saturated with water vapour at 20°C, gives plausible results.

§ 2. Growth of a Fog Droplet

In elucidating the mechanism of fog formation, one must first consider in what way a nucleus develops itself spontaneously after passing over the free energy barrier.

In the following calculation, each droplet will be assumed to grow independently, i. e. the effect of its collision with other droplets and other mutual influences will not be taken into account.

The number of vapour molecules, captured by a droplet of radius r on its unit surface per unit time, is given by a gas kinetic consideration as $\beta=PN_r\sqrt{kT/2\pi m}$, where N_r is the number of vapour molecules per unit volume of the vapour in contact with the droplet of radius r, P the ratio of the captured molecules to those which collide with the droplet, k the Boltzmann constant, T the absolute temperature of the vapour and m the mass of a vapour molecule.

On the other hand, the number of vapour molecule librated from the unit surface of a droplet of radius r per unit time, which should be independent of the surrounding, can be shown to be given as

$$\alpha_r=PN_\infty e^{2\sigma v_B/rkT}\sqrt{kT/2\pi m}\,.$$

Here N_∞ is the number of the vapour molecules per unit volume of the vapour in equilibrium with a flat surface of the liquid, σ the surface tension of the liquid, v_B the molecular volume of the liquid. This relation can be derived from the condition of equilibrium between the molecules captured by and those librated from the surface of a droplet of radius r, for which the number of molecules $N_{r\cdot eq.}$ per unit volume of the surrounding vapour satisfies the modified Thomson's formula: $\log(N_{r\cdot eq}/N_\infty)=(2\sigma/r)v_B/kT$.

Therefore, the time rate of increase of the radius of the droplet, dr/dt, is

$$dr/dt=v_Bb(N_r-N_\infty e^{a/r})$$

with $a=2\sigma v_B/kT$ and $b=P\sqrt{kT/2\pi m}\,.$

In consequence of the capture of vapour molecules on the surface of a droplet, the number of molecules per unit volume diminishes in the vicinity of the surface and so there appears a gradient of the number density in the radial direction. If we assume the net capture of the molecules be steadily supplied by a stationary diffusion of the vapour in the radial direction, it is easy to get the relation $N-N_r=(r/D)b(N_r-N_\infty e^{a/r})$, where N denotes the number of vapour molecules per unit volume of the vapour at a great distance from the droplet and D the coefficient of diffusion of the vapour in the gas. In this case, the time rate of growth of a droplet can be written as

$$dr/dt=v_Bb(N-N_\infty e^{a/r})/(1+br/D) \qquad (1'')$$

The term $e^{a/r}$ is practically equal to 1 for water droplet of radius larger than 10^{-6} cm. For such droplet we have therefore an approximate relation

$$dr/dt=v_Bb(N-N_\infty)/(1+br/D). \qquad (1')$$

We have so far neglected the temperature gradient produced by the liberation of the latent heat due to condensation. If the heat librated on the surface of the droplet per 1 sec. is assumed to flow steadily outward, there appears a temperature drop ΔT, between the surface and a great distance, which satisfies

$\Delta T=(nm\lambda)/(4\pi r\kappa)$ where n is the net number of molecules captured on the surface of a droplet per 1 sec., λ the latent heat of condensation and κ the thermal conductivity of the gas around the droplet. Since $dr/dt=v_B n/(4\pi r^2)$, ΔT can be expressed as $r(dr/dt)\times(\rho_l\lambda/\kappa)$ where ρ_l is the density of the liquid. The number density N_∞ in (1′) corresponds to the temperature $T+\Delta T$ at the surface. Therefore, if we neglect the small influences of temperature difference ΔT on other quantities than N_∞, we get approximately

$$\frac{dr}{dt}=v_B\cdot b\left\{N-N_\infty-r\frac{\rho_l\lambda}{\kappa}\left(\frac{dN_\infty}{dT}\right)\frac{dr}{dt}\right\}\Big/\left(1+\frac{br}{D}\right)$$

whence

$$\frac{dr}{dt}=v_B\cdot b(N-N_\infty)\Big/\left[1+\frac{br}{D}\left\{1+\frac{D\lambda}{\kappa}\left(\frac{d\rho_s}{dT}\right)\right\}\right]$$
$$=v_B b\frac{N-N_\infty}{1+br/D_e}, \qquad (1)$$

with $D_e=D/\{1+(D\lambda/\kappa)(d\rho_s/dT)\}$, where ρ_s denotes the density of the saturated vapour. The effect of thermal diffusion can be neglected in this case.

§ 3. A Model Process of Fog Formation

Suppose a certain state of supersaturation be given at an instant and the embryos of condensation begin to pass over such a free energy barrier that they become nuclei. While a droplet grows from each nucleus, the degree of supersaturation decreases and the rate of nucleation diminishes so long as the vapour is not supplied from outside, and the rate will become practically zero after the lapse of a certain time interval. In the next stage the number of droplets will remain practically constant, though each of them will continue to grow further. Finally, they will practically cease to grow when the degree of supersaturation approaches 1. These behaviours might be the process of fog formation observed under ordinary conditions.

As a substitute for such a complicated actual process, the following simple idealized model process will be assumed.

(I) During the first stage of the process, the rate of self-nucleation will be assumed to remain constant and be given by the formula of the current theory corresponding to the temperature T of the vapour and the initial degree of supersaturation N_0/N_∞. We namely imagine in this stage that the consumption of vapour molecules due to the nucleation and the following growth of the nuclei is balanced by a fictive supply of vapour molecules.

This is an idealization of the process for the stage in which the decrease of the vapour molecules is not yet conspicuous but its influence on the nucleation is considerable.

(II) Next we assume that the vapour is suddenly decreased to its actual value and that the nucleation ceases. During this second stage of the process, the total number of droplets will therefore be assumed to be constant. We have only to consider the growth of the proplets and to persue it until they practically cease to develop owing to the vanishing of the supersaturation.

(III) The beginning of the second stage will be so chosen that the sudden decrease of vapour mentioned above, which could be calculated approximately by the assumed process in the first stage, corresponds to the decrease of the rate of self-nucleation to half its initial value.

The distribution of droplet size for the actual process at the end of the first stage and that of the second stage would presumably be something like the curve given in the accompanying figure, drawn with full line, while the model process would correspond to that drawn with broken line, the latter was obtained through the computation given in the next paragraph.

§ 4. Droplets Size, its Distribution Range and the Time of Fog Formation

The number of droplets whose radius lies between r and $r+dr$ may be expressed as

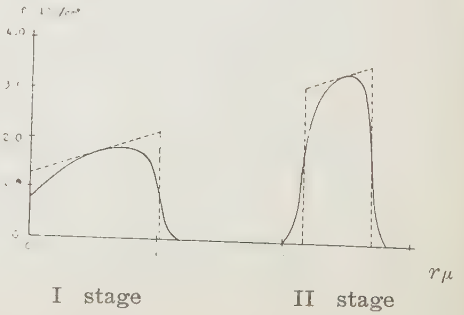

In drawing this figure a formula
$f=(\nu_0(1+br/D_e))/(v_B bN_0(1-N_\infty/N_0))$
and the following data for P=0.1 were used: $\delta_0=1.02\times10^{-4}$cm, $R=2.68\times10^{-4}$cm $R-\delta=2.16\times10^{-4}$cm (see next paragraph).

$f\cdot dr$ with f equal to $\nu(\partial\theta/\partial r)$, where ν is the rate of nucleation and θ the time required for a drop of radius r to grow from a nucleus. θ is in general a function of r and the degree of supersaturation which is a function of time t.

Now let us consider the first stage, where the degree of supersaturation remains constant. Then θ is a function of r only. Therefore, if the radius r of a droplet increases by dr in a time interval dt, $dt=(\partial\theta/\partial r)\cdot dr$ or

$$f=\nu\Big/\frac{dr}{dt}\,. \tag{2}$$

The decrease of the number of vapour molecules, imagined as being compensated by the supply of the vapour during the first stage (but actually not compensated) is shown from (1) and (2) to satisfy the relation $N_0-N_1=$

$$\frac{4\pi}{3v_B}\int_{r^*}^{\delta_0}r^3 f\,dr=\frac{\pi\nu_0}{3v_B{}^2b(N_0-N_\infty)}\times\delta_0{}^4(1+4b\delta_0/(5D_e))\,, \qquad (3')^*$$

where ν_0 is the constant rate of self-nucleation in the first stage and r^* and δ_0 the smallest and largest radii of droplets at the end of the first stage; N_0 and N_1 denote the numbers of vapour molecules in the unit volume of the vapour at the beginning and the end, respectively. If we put $N_0-N_1=(N_0-N_\infty)/Q$, Q can be derived from the condition (III) stated above, as follows: From Becker-Döring's formula of the rate of nucleation $\nu=AN^2e^{-Br^{*2}}$, where $A=2v_B\sqrt{\sigma/2\pi m}$, $B=4\pi\sigma/3kT$,* we get

$$d\nu/\nu=2(dN/N)-2Br^*\cdot dr^*\,.$$

Since $\quad r^*=a/\log(N/N_\infty)$,

$$\frac{d\nu}{\nu}=2\left(1+\frac{2\pi}{3v_B}r^{*3}\right)\frac{dN}{N}\,.$$

In the stage where the rate of nucleation has an appreciable value, the factor $2(1+(2\pi/3v_B)\cdot r^{*3})$ remains practically constant. So, in this stage, ν can approximately be expressed as

$$\frac{\nu}{\nu_0}=\left(\frac{N}{N_0}\right)^{2(1+(2\pi/3v_B)r_0{}^{*3})},$$

where $r_0{}^*$ denotes the initial critical radius. If we put, from the condition (III)

$$\frac{\nu_1}{\nu_0}=\frac{1}{2}=\left(\frac{N_1}{N_0}\right)^{2(1+(2\pi/3v_B)r_0{}^{*3})}$$

then we have

$$Q=\frac{N_0-N_\infty}{N_0-N_1}$$

$$=\left(1-\frac{N_\infty}{N_0}\right)\Bigg/\left\{1-\log_{10}^{-1}\frac{0.30103}{2(1+(2\pi/3v_B)r_0{}^{*3})}\right\}.$$

Solving the Eq. (3′), or

$$\frac{1}{Q}\left(1-\frac{N_\infty}{N_0}\right)^2=\frac{\pi\nu_0}{3v_B{}^2N_0{}^2b}\delta_0{}^4\left(1+\frac{4b}{5D_e}\delta_0\right), \tag{3}$$

we can get the value of δ_0 corresponding to the given initial state of supersaturation.

Furthermore, integrating (1), the time Θ_1 elapsed by the end of the first stage is

$$\Theta_1=\frac{\delta_0(1+b\delta_0/(2D_e))}{v_Bb(N_0-N_\infty)}\,. \tag{4}$$

The situation in the second stage is more complicated to handle; namely, with a further development of the droplets the width δ of the distribution range of droplet size and the distribution function $f(r,\ r_m)$ will change; here r_m means the largest radius at a given time and $r_m-r\leqslant\delta$. Using (1) for $r=r_m$ and $r=r_m-\delta$, we get

$$-\frac{d\delta}{dr_m}=\frac{d(r_m-\delta)}{dt}\Big/\frac{dr_m}{dt}-1=\delta\Big/\left(\frac{D_e}{b}+r_m-\delta\right),$$

which, after integration with the initial condition $r_m=\delta=\delta_0$, gives the relation

$$\delta^2-2\delta\left(r_m+\frac{D_e}{b}\right)+\delta_0\left(\delta_0+\frac{2D_e}{b}\right)=0\,, \tag{5}$$

δ can be computed from this equation.

The differential equation satisfied by the distribution function $f(r,\ r_m)$ is obtained as follows. From the constancy of the number of droplets in the second stage, we have

$$f(r,\ r_m)=f(r+dr,\ r_m+dr_m)\left\{1+\frac{\partial}{\partial r}\left(\frac{dr}{dr_m}\right)dr_m\right\},$$

if we denote by dr and dr_m the change of r and r_m in a time interval dt for the droplets of radii r and r_m. Neglecting small quantities we have

$$\frac{\partial f}{\partial r}\frac{dr}{dr_m}+\frac{\partial f}{\partial r_m}=-f\frac{\partial}{\partial r}\left(\frac{dr}{dr_m}\right)$$

and using (1)

$$\frac{\partial f}{\partial r_m}=-\frac{\partial}{\partial r}\left(f\cdot\frac{dr}{dt}\Big/\frac{dr_m}{dt}\right)$$

$$=f\frac{b(D_e+br_m)}{(D_e+br)^2}-\frac{\partial f}{\partial r}\frac{D_e+br_m}{D_e+br}\,. \tag{6}$$

This partial differential equation is generally

---

[*] r^* is of the order of magnitude 10^{-8} cm and can be neglected compared with δ_0.

[*] This expression of ν is essentially the same as that of Becker-Dörings. See Frenkel: Kinetic Theory of Liquid pp 397.

satisfied by

$$f=(D_e+br)/\Phi[(D_e+br_m)^2-(D_e+br)^2], \quad (7)$$

where Φ denotes an arbitrary function. Considering the initial condition that at $r_m=\delta_0$

$$f=\frac{\nu_0(D_e+br)}{D_e v_B b(N_0-N_\infty)},$$

we get for the distribution function in the second stage as

$$f=\frac{\nu_0(D_e+br)}{D_e v_B b(N_0-N_\infty)}. \quad (8)$$

Then in place of equations (3′) and (3) valid for the first stage, we now have

$$N_0-N=\frac{4\pi\nu_0}{3v_B{}^2 b(N_0-N_\infty)}\int_{r_m-\delta}^{r_m} r^3\left(1+\frac{br}{D_e}\right)dr, \quad (9')$$

or

$$\left(1-\frac{N_\infty}{N_0}\right)^2=\frac{\pi\nu_0}{3v_B{}^2 N_0{}^2 b}\times\left[R^4-(R-\delta)^4+\frac{4b}{5D_e}\{R^5-(R-\delta)^5\}\right], \quad (9)$$

where R denotes r_m at the end of the second stage.

From (3) and (9) we get

$$Q=\frac{R^4-(R-\delta)^4+(4b/5D_e)\{R^5-(R-\delta)^5\}}{\delta_0{}^4(1+4b/(5D_e)\delta_0)}. \quad (10)$$

This equation together with (5) gives R as well as δ.

To calculate the time $\Theta_{\rm II}$ required by the largest drop to grow in the second stage, we have to eliminate N from Eqs. (1) and (9′), replace δ by a function of r_m using (5), and carry out the integration of the equation $F(r_m, dr_m/dt)=0$ to be obtained in this way. But the computation is so involved that the author made the following simplified assumption. Namely, all the droplets are assumed to have the same radius $\bar{r}$ during the second stage of the process. Then, instead of (10), we have

$$Q=4\frac{R^3}{\delta_0{}^3}\frac{1+(b/2D_e)\delta_0}{1+(4b/5D_e)\delta_0}, \quad (10')$$

which gives R as a function of the state of supersaturation. As will be seen from the results given in the next paragraph, this simple assumption seems to be an admissible approximation. So we shall use this assumption in the estimation of the time $\Theta_{\rm II}$.

Eliminating N from (1) and the equation $N_0-N=(4\pi/3v_B)\nu_0\Theta_{\rm I}\bar{r}^3$ we get

$$\frac{3}{4\pi\nu_0\Theta_{\rm I}}\left(\frac{1}{b}+\frac{\bar{r}}{D_e}\right)\frac{d\bar{r}}{dt}=R^3-\bar{r}^3. \quad (11)$$

In these equations $\bar{r}_0$, the initial value of $\bar{r}$, satisfies

$$\bar{r}_0=\delta_0\left[\left(1+\frac{4b}{5D_e}\delta_0\right)\Big/4\left(1+\frac{b}{2D_e}\delta_0\right)\right]^{1/3}$$

as can be seen from (3′).

Integrating the Eq. (11), we have

$$\Theta_{\rm II}=\frac{D_e+Rb}{8\pi\nu_0\Theta_1 R^2 D_e b}\left[\log\left(\frac{1-(\bar{r}_0/R)}{1-(\bar{r}/R)}\right)^2 +\log\frac{1+\bar{r}/R+(\bar{r}/R)^2}{1+\bar{r}_0/R+(\bar{r}_0/R)^2}+2\sqrt{3}\frac{D_e-bR}{D_e+bR} \times\left(\tan^{-1}\frac{1+2(\bar{r}/R)}{\sqrt{3}}-\tan^{-1}\frac{1+2(\bar{r}_0/R)}{\sqrt{3}}\right)\right]. \quad (12)$$

$\Theta_{\rm II}$ tends to infinity as $\bar{r}/R$ approaches 1, but it will be shown in the next paragraph that it is not very large even for $\bar{r}/R=0.99$.

§ 5. Results of Numerical Computation and Discussion

Becker-Döring's formula as well as Fisher-Turnbull's one refer to the stationary state of nucleation, and a certain time interval, the so called incubation period, is necessary in order that the stationary state is established. But this time interval is of the order of 10^{-6} sec.[6] and need not be considered here. Deviation from the stationary state of diffusion and heat conduction assumed in the derivation of the Eq. (1) is of minor importance for small droplets considered here[7].

In the previous estimation of the temperature drop ΔT, between the surface of a droplet and a great distance there-from, we have neglected the change of temperature of a droplet. If we take the influence of this change upon ΔT into consideration, the factor $nm\lambda$ mentioned before should be modified to $nm\lambda-(4/3)\pi r^3\rho_l s(d(\Delta T)/dt))$. Therefore ΔT, instead of being $(\rho_l\lambda/\kappa)r(dr/dt)$ as before, is to be expressed as

$$\Delta T=\frac{\lambda\rho_l}{\kappa}r\frac{dr}{dt}\left\{1-\frac{sr}{3\lambda}\frac{d(\Delta T)}{dr}\right\}$$

where s denotes the specific heat of the liquid. But the second term in the bracket can be neglected as compared with 1, because $r(d(\Delta T)/dr)$ may be of the order of 10 at the largest, while $s/3\lambda$ is nearly equal to 0.5×10^{-3} for the case in question.

Now we make the numerical computation of the above relations for the state of supersaturation corresponding to the adiabatic expansion of ratio 1.28, of the air saturated with water vapour at 20°C, i.e. the state which, according to Becker and Döring, corresponds to the rate of nucleation of the order of 1. Then the following results are obtained:

ν_0	N_0/N_∞	r^*	R
2.4	4.76	8.0×10^{-8}cm	8.4×10^{-3}cm

δ_0	$\Theta_{\rm I}$
2.6×10^{-3}cm	1.8 sec.

In this calculation, the usual value of the surface tension of supercooled water was used: P in the quantity b was assumed arbitrarily to be 1. If smaller values are adopted, we obtain larger values for $\Theta_{\rm I}$. Such a large value of the nucleation period $\Theta_{\rm I}$ as that given in the above table would be impossible because of a rapid recovery to higher temperature after an adiabatic expansion of the air in the cloud chamber.[8] Moreover, the number of droplets per unit volume of the gas, $\nu_0\Theta_{\rm I}\simeq4$, is incredibly too small and the value of R too large. Therefore we suppose that the assumption $\nu_0\simeq1$ is neither compatible with the above theory nor with the known critical expansion ratio 1.37 for the cloud limit.

If we make the computation corresponding to the expansion of ratio 1.37, the results tabulated below are obtained.

$\nu_0=1.94\times10^8/\text{cm}^3.\ \text{sec. for } P=1,\qquad N_0/N_\infty=7.63,\qquad r^*=6.44\times10^{-8}\text{cm}$

P	R, 10^{-4}cm	δ_0, 10^{-5}cm	δ, 10^{-5}cm	$\Theta_{\rm I}$, 10^{-3}sec.	$\Theta=\Theta_{\rm I}+\Theta_{\rm II}$, 10^{-2}sec.
1	* 2.0 2.1	7.6	1.9	1.8	(a) 1.3 (b) 2.6
0.1	* 2.4 2.7	10.2	5.2	9.0	(a) 3.8 (b) 6.7
0.01	* 2.6 3.1	11.2	9.9	76.	(a) 22. (b) 34.

In this computation the rate of nucleation was calculated using Becker-Döring's formula modified by adding a factor P, i.e. $2v_B\sqrt{\sigma/2\pi m}\,N^2\times P\exp(-4\pi r^{*2}\sigma/3kT)$. It is natural to think that, in the first approximation, the same condensation coefficient P, as used for the calculation of growth of a larger droplet, can also be used, down to the embryos having sub-critical radius, for the calculation of the rate of nucleation and that the modification mentioned above may be necessary.

Concerning the coefficient P, we have only conflicting reports.[9] So values of $P=1$, 0.1, 0.01 are chosen arbitrarily. Values marked with * are obtained using (10′), and the values of Θ in the last column marked with (a) or (b) mean the values corresponding to $\bar{r}/R=0.9$ or $\bar{r}/R=0.99$, respectively.

As far as the author is aware of, there are no detailed experimental data to confirm or deny the theoretical results given above. It might be a questionable point that we have used the usual value of the surface free energy for so small droplets as those of radius 10^{-8} cm. Nevertheless, judging from the description of the phenomenon by many authors[10], the values of R and Θ obtained above seems to be of a reasonable order of magnitude. Therefore the present theory seems to be successful in avoiding such a discrepancy as that existing between the current theory of self nucleation and the critical expansion ratio at the cloud limit.

Now in this connection it would be worth while to investigate the influence of possible change of the surface free energy σ of small droplets upon the phenomenon in question.

According to Tolman[11] the surface tension σ of small droplets of radius r smaller than 10^{-6}cm is more or less smaller than the usual value σ_0 and can approximately be expressed as

$$\sigma \doteqdot \frac{\sigma_0}{1+(2\delta/r)}, \tag{13}$$

where δ denotes the distance between the Gibbs' surface of tension and a dividing surface which is so located as to make the so-called "superficial density" vanish when computed with respect thereto. In his theory r is also defined with reference to the surface of tension. As Tolman himself pointed out, there is much doubt about the validity of his theory when it is applied to so small droplets as those of the radius critical for embryo-nucleus transition. But it might be of some interest to consider what would be the results for the rate of nucleation when the above formula (13) is used.

In this case we have

$$\log \frac{N}{N_\infty}=\frac{2\sigma}{r}\frac{v_B}{kT}\left(1+\frac{1}{2}\frac{r}{\sigma}\frac{d\sigma}{dr}\right), \qquad (14)$$

in place of the Thomson's formula mentioned previously. When we put $d\sigma/dr$ from (13) into (14) and solve for r, we get

$$r=\frac{r_0}{2}\left(1-\frac{4\delta}{r_0}+\sqrt{1+\frac{4\delta}{r_0}}\right), \qquad (15)$$

where

$$r_0=\frac{2v_B\sigma}{kT}\left(\log\frac{N}{N_\infty}\right)^{-1}.$$

If we put, for example, $r_0=6.5$Å for the case considered before and $\delta=0.9$Å as extrapolated from Tolmans results for the same case, then r becomes $0.845\ r_0$. The maximum value of the free energy change $\Delta F_{\max}$ which we have when a liquid droplet of radius r^* is formed out of vapour molecules becomes

$$\Delta F_{\max}=\frac{4}{3}\pi r^{*2}\sigma\left(1-\frac{r^*}{\sigma}\frac{d\sigma}{dr}\right)$$
$$=\frac{4}{3}\pi r^{*2}\sigma\Big/\left(1+\frac{2\delta}{r^*}\right)^2.$$

Therefore, corresponding to $r_0^*=6.5$Å and $\delta=0.9$Å we have

$$\Delta F_{\max}=\frac{4}{3}\pi r_0^{*2}\sigma_0\times 0.44\,.$$

According to the theory mentioned in preceding paragraphs this results means that dense fog should appear at the expansion ratio, say, 1.25, even when there is no ion present in the moist air. This is in apparent contradiction to the experimental fact.

Bakker[12)] gave thermodynamic arguments to prove that the surface tension of droplets would be absolutely constant down to the smallest radii. Bakkers definitions of surface tension and of the radius of droplets seem to be more compatible with the derivation of the rate of nucleation by Volmer, Becker-Döring and others. And such a surface tension does not show a conspicuous change even for so small droplets as those of radius 10^{-8}cm.

The author expresses his deepest gratitude to Prof. T. Nagamiya of Osaka University for his kind criticism.

Thanks are also due to Prof. I. Uhara of Kobe University for his earnest discussion about the problem.

References

1) M. Volmer and A. Weber: Z. Phys. Chem. **119** (1926) 227.

2) L. Farkas: Z. Phys. Chem. **125** (1927) 236.

3) R. Becker and W. Döring: Ann. Phys. **24** (1935) 719.

4) D. Turnbull and J. C. Fisher: J. Chem. Phys. **17** (1941) 71.

5) H. Oura: Geophys. Mag. **23** (1952) 329.

6) R. F. Probstein: J. Chem. Phys. **19** (1951) 619.

7) cf.e.g. P. S. Epstein and M. S. Plesset: J. Chem. Phys. **18** (1950) 1505.

8) E. J. Williams: Proc. Camb. Phil. Soc. **35** (1939) 512.

9) T. Alty and C. A. Mackay: Proc. Roy. Soc. London (A) **149** (1935) 104.

J. Yoshida and H. Nakayama: Teion-kagaku (in Japanese) **2** (1949) 159.

10) cf.e.g. N. N. Das Gupta and S. K. Ghosh: Rev. Mod. Phys.

11) R. C. Tolman: J. Chem. Phys. **17** (1949) 333.

12) G. Bakker: Handbuch der Experimentalphysik (Akad. Verlag., Leibzig. 1928 Vol. 6, p. 434.)

JOURNAL OF THE PHYSICAL SOCIETY OF JAPAN Vol. 9, No. 3, MAY—JUNE, 1954

Fog Formation due to Self Nucleation (II)

By Hiromu WAKESHIMA

The Kobe University of Marcantile Marine

(Received December 2, 1953)

In the previous paper[1] a theory was presented by the author which concerns the fog formation due to self nucleation in adiabatically expanded dust- and ion-free moist air. In this theory the change of temperature of the air after expansion was not taken into account.

In this report the influence of the rise in temperature of the air after an initial cooling due to the heat transmission from outside of and the heat liberation inside the gas is treated in an approximate way and the results discussed.

§ 1. Introduction

The nature of the fog nuclei formed in an adiabatically expanded dust- and ion-free moist air has been clarified by the theory of nucleation developed by M. Volmer and A. Weber[2], R. Becker and W. Döring[3] and others, but the theoretical explanation of the whole process of fog formation was deficient until the writer tried in the previous report to establish possible relations between the time required for the growth of fog droplets, the rate of nucleation and the number of fog droplets under given initial conditions.

But in that theory, the temperature recovery of the air through heat transmission from outside after an initial cooling was ignored. This approximation is admissible when the cloud chamber is large enough and the rising of temperature after an expansion so slow that the whole process of fog formation is practically finished before the change of temperature becomes conspicuous. In actuality, the size of the expansion chamber is more or less limited and therefore, as will be seen later, the influence of the temperature recovery after an expansion, especially on the rate of self nucleation, is considerable.

In this report this effect is estimated. The influence of the warming of the air through the liberation of the latent heat of condensation is also considered and thus the previous theory improved. In view of the complexity of the process in question, we had to satisfy with only an approximate treatment.

§ 2. Approximate Expression of the Rate of Nucleation Containing the Time Explicitly

If we take the logarithm of the formula for the rate of nucleation used in the previous report

$$\nu=2v_B(\sigma/2\pi m)^{1/2}\cdot N^2 P\exp(-4\pi r^{*2}\sigma/3kT)\,, \qquad (1)$$

and differentiate the result, we get after rearrangement

$$\begin{aligned} d\nu/\nu=&2(1+2\pi r^{*3}/3v_B)dN/N\\ &+(1/2-4\pi r^{*2}\sigma/kT)d\sigma/\sigma\\ &+(4\pi r^{*2}\sigma/kT)(dT/T)\\ &-(4\pi r^{*3}/3v_B)(dN_\infty/N_\infty)\,. \end{aligned} \qquad (2)$$

Here the following notation is used: ν the rate of nucleation; v_B the molecular volume of the liquid; σ the surface free energy of the liquid; m the mass of the vapour molecule; N the number of the vapour molecules per 1 cm^3; N_∞ the number of the vapour molecules per 1 cm^3 of the vapour in equilibrium with a flat surface of the liquid; r^* the radius of droplet critical for embryo-nucleus transition; k Boltzmann constant; T the absolute temperature of the liquid droplet; P the condensation coefficient.

Assuming the relations $p_\infty=\alpha e^{-\beta/T}$, for the pressure p_∞ of the saturated vapour (α and β are material constants) and $p_\infty\propto N_\infty T$, we can transform (2) into

$$\begin{aligned} d\nu/\nu=&2(1+2\pi r^{*3}/3v_B)dN/N\\ &+[(T/2\sigma-4\pi r^{*2}\sigma/kT)d\sigma/dT\\ &+(4\pi r^{*2}/k)\{\sigma/T-(kr^*/3v_B)(\beta/T-1)\}]\\ &\times dT/T. \end{aligned} \qquad (2a)$$

During the period in which the rate of nucleation diminishes to a few percent of its initial value ν_0, the coefficient of dN/N, $2(1+2\pi r^{*3}/3v_B)$, as well as that of dT/T, $[(T/2\sigma-4\pi r^{*2}\sigma/kT)d\sigma/dT+(4\pi r^{*2}/k)\{\sigma/T-(kr^*/3v_B)(\beta/T-1)\}]$, do not change remarkably. So if we denote the initial values of them ϕ_{N_0} and $-\phi_{T_0}$ respectively, ν/ν_0 can approximately be expressed as

$$\nu/\nu_0 \doteqdot (N/N_0)^{\phi_{N_0}} \cdot (T/T_0)^{-\phi_{T_0}} \,. \qquad (3)$$

where N_0 and T_0 are the initial values of N and T respectively. The following figure (Fig. 1) shows to what extent this approximation is permissible. In A, $(\nu/\nu_0)_{T_0}$, the ratio of the rate of nucleation to its initial value, under constant initial temperature T_0, is computed for various values of N/N_0 using directly the Eq. (1) for an adiabatic expansion of the air saturated with water vapour at 20°C, the expansion ratio being 1.37. $(N/N_0)^{\phi_{N_0}}$ is given for comparison. In B, $(\nu/\nu_0)_{N_0}$, the ratio of the rate of nucleation to its initial value under constant number density of the vapour molecules N_0 but for various values of the ratio of temperature T/T_0, is calculated also using the Eq. (1); $(T/T_0)^{-\phi_{T_0}}$ is given for comparison. It will be seen from this figure that $(N/N_0)^{\phi_{N_0}} \cdot (T/T_0)^{-\phi_{T_0}}$ may be an admissible approximation to ν/ν_0.

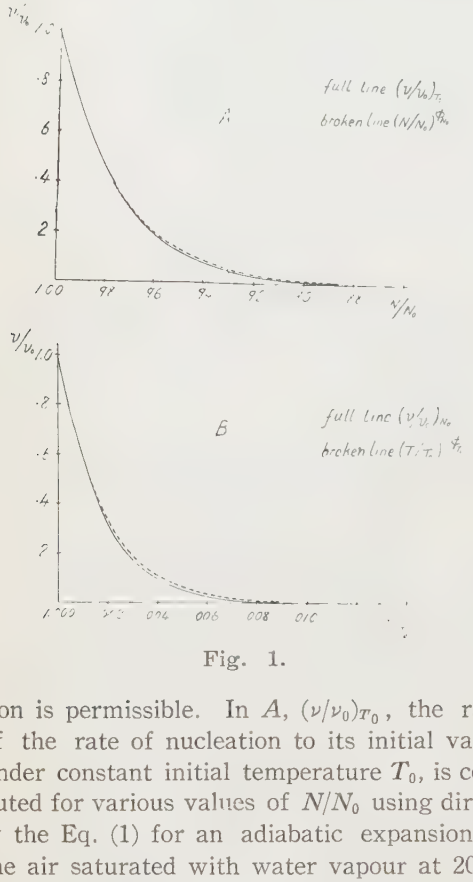

Fig. 1.

Using this expression for ν/ν_0, we can easily compute the temperature rise $\Delta T_{1/2}$ necessary for the reduction of the rate of nucleation ν to half its initial value, $(1/2)\nu_0$, when the number density of the vapour molecule is kept to a constant value N_0.

Now the rise in temperature of the gas occures in two ways; first, through heat transmission from the wall of the vessel into the gas, and second, through heat liberation inside the gas due to condensation of the vapour. The warming of the air due to these two causes will separately be considered here and superposed for the sake of simplicity.

In this and the following paragraphs let us consider the first effect only.

The mechanism of the warming of a gas in a vessel after an initial cooling is two-fold. Namely, the direct heating of the gas by conduction is confined to a layer of gas close to the walls whose thickness is small compared with the dimensions of the cloud chamber. But the expansion of the gas in this layer due to the rise in its temperature causes compression of the other part of the gas and makes it warm up. According to E. J. Williams[4] the rise in temperature of the gas due to such a cause is given by

$$\Delta_1 T = 2(\gamma-1)/\sqrt{\pi} \cdot \sqrt{\kappa/w} \cdot S/V \cdot (T_1-T_0)\sqrt{t} = K_0\sqrt{t} \,, \qquad (4)$$

with

$$K_0 = 2(\gamma-1)/\sqrt{\pi} \cdot \sqrt{\kappa/w} \cdot S/V \cdot (T_1-T_0),$$

where γ is the ratio of the specific heat of the gas, κ the thermal conductivity, w the heat capacity per unit volume under constant pressure, and S and V denote the surface area and the volume of the cloud chamber. T_1-T_0 means the temperature depression of the gas due to an adiabatic expansion; t the time elapsed since the expansion takes place.

From Eq. (4), we can get an expression explicit in t for

$$F_T(t) \equiv (T/T_0)^{-\phi_{T_0}} = (1+\Delta_1 T/T_0)^{-\phi_{T_0}}.$$

Namely in the following way.

$$\log F_T(t) = -\phi_{T_0} \log (1+\Delta_1 T/T_0),$$

as $\Delta_1 T/T_0 \ll 1$, we have

$$\log F_T(t) \doteqdot -\phi_{T_0} \Delta_1 T/T_0$$

or

$$F_T(t) \doteqdot \exp(-\phi_{T_0}\Delta_1 T/T_0) \,.$$

So if we define a constant ϕ such that $\phi = K_0\phi_{T_0}/T_0$ or from (4)

$$\phi = 2(\gamma-1)/\sqrt{\pi} \cdot \sqrt{\kappa/w} \cdot S/V \cdot (T_1-T_0)\phi_{T_0}/T_0 \,,$$

we have $F_T(t) = \exp(-\phi\sqrt{t}\,)$.

Using this formula, the time Θ_T, required for the reduction of the rate of nucleation ν to half its initial value when the number density of the vapour molecule remains constant, can easily be calculated. The following figure (Fig. 2) shows Θ_T and Θ_N in relation to the expansion ratio E. Here Θ_N denotes the time required for the reduction of the rate of nucleation ν to half its initial value, $1/2\cdot\nu_0$, when the temperature rise remains zero. (Θ_N can be calculated using (7) to be given later and is nearly equal to Θ_I of the preceding paper.)

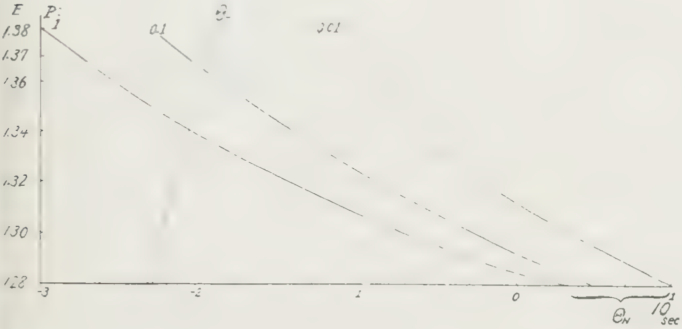

Fig. 2.

As for S/V, the value for a cloud chamber of cylindrical shape with a height and a radius of 10 cm each is arbitrarily assumed. From this figure we can see that a considerable influence is expected due to the rise in temperature of the gas after an adiabatic expansion, especially upon the rate of nucleation, and also that the results of measurement of the critical expansion ratio may vary more or less according to the apparatus used.

Now, in the stage where the rate of nucleation ν is of an appreciable value, the following formulae holds when warming of the gas is zero, as shown in the preceding paper.

$$dr_m/dt = v_B b(N_0-N_\infty)/(1+br_m/D_e), \qquad (5)$$

and also we make use of the same formula as before for the sake of simplicity

$$-dN/dt = 4\pi\nu_0(r_m^3/3v_B)\ , \qquad (6)$$

where r_m denotes the radius of the largest droplets ; $b=P(kT/2\pi m)^{1/2}$ and D_e the effective diffusivity of the vapour in the gas (cf. the preceding article). From (5) we have

$$r_m = (D_e/b)\{(1+(2b^2v_B/D_e)(N_0-N_\infty)t)^{1/2}-1\}$$

and putting this into (6) we get, on integration, the following formula for N/N_0

$$N/N_0 = 1-K_1\{(1+K_2t)^{3/2}(12/5K_2+(2/5)t) -t(4+3K_2t/2)-12/5K_2\}\ , \qquad (7)$$

with $K_1=(4\pi\nu_0/3v_BN_0)(D_e/b)^3$
and $K_2=(2b^2v_B/D_e)(N_0-N_\infty)$.

Using (7), we have

$$F_N'(t) \equiv (N/N_0)^{\phi_{N0}} = [1-K_1\{(1+K_2t)^{3/2} \times(12/5K_2+(2/5)t)-t(4+3K_2t/2)-12/5K_2\}]^{\phi_{N0}},$$

an approximate formula explicit in t. Thus the rate of nucleation ν as a function of the time t, elapsed after an expansion, can be expressed approximately as

$$\begin{aligned}\nu'(t) &= \nu_0F_N'(t)\cdot F_T(t)\\ &= \nu_0\left[1-K_1\left\{(1+K_2t)^{3/2}\left(\frac{12}{5K_2}+\frac{2}{5}t\right)\right.\right.\\ &\qquad \left.\left.-t\left(4+\frac{3K_2}{2}t\right)-\frac{12}{5K_2}\right\}\right]^{\phi_{N0}}\\ &\quad\times\exp\{-2(\gamma-1)/\sqrt{\pi}\cdot\sqrt{\kappa/w}\cdot S/V\\ &\quad\times(T_1-T_0)\phi_{T_0}/T_0\cdot\sqrt{t}\}\,.\end{aligned}$$

In (Fig. 3) $F_N'(t)$, $F_T(t)$ and $\nu'(t)$ etc. are shown in relation to t, for the expansion ratio 1.37 and $P=$ 0.01.

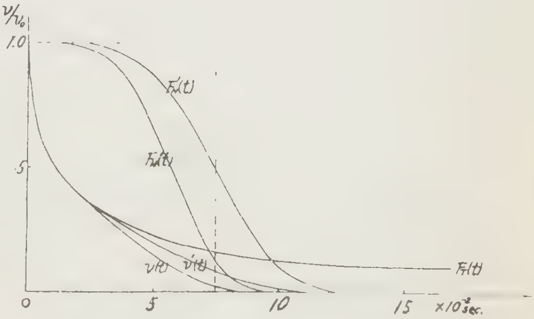

Fig. 3.

§ 3. The Number, the Average Size and the Time of Growth of Fog Droplets

The number of droplet n' per 1 cm³ of the gas,

$$n' = \int_0^\Theta \nu' dt = \nu_0\int_0^\Theta F_N'(t)F_T(t)dt\,. \qquad (8)$$

(here Θ denotes the time of growth of fog droplets and it is much larger than Θ_N) can be obtained through numerical or graphical integration of the above relation, but for the purpose of the approximate solution of the problem, the following simple treatment will suffice.

First we notice that

$$\int_0^\Theta F_N'(t)dt \fallingdotseq \Theta_N\,.$$

This relation shows that the model process chosen in the preceding article is adequate. Now we replace the function $F_N'(t)$ with a function which is 1 throughout the range from $t=0$ to $t=\Theta_N$ and is 0 thereafter. Then (8) becomes

$$n'\nu\doteqdot_0\int_0^{\Theta_N} F_T(t)\,dt=\nu_0\int_0^{\Theta_N}\exp\left(-\phi\sqrt{t}\right)dt$$
$$=2\nu_0/\phi^2\cdot\exp\left(-\phi\sqrt{\Theta_N}\right)$$
$$\times(\exp\phi\sqrt{\Theta_N})-\phi\sqrt{\Theta_N}-1)\,. \qquad \text{(8a)}$$

The next table shows an example of the comparison between Θ_N and $\Theta_N'\equiv\int_0^{\Theta} F'_N(t)dt$ as well as that of $\int_0^{\Theta_N} F_T(t)dt$ and $\int_0^{\Theta} F_N'(t)\,F_T(t)dt$.

Θ_N: 7.48×10^{-2} sec. $\int_0^{\Theta_N} F_T(t)dt$: 2.51×10^{-2}

Θ_N': 7.46×10^{-2} sec. $\int_0^{\Theta} F_N'(t)F_T(t)dt$: 2.42×10^{-2}

We see from this table that approximation mentioned above is admissible.

This replacement means that we adopt the following model process with two stages as in the preceding paper. Namely during the first stage of the process from $t=0$ to $t=\Theta_N$, the number density of the vapour molecules remains constant, i.e. N_0, whereas the temperature of the gas rises and the rate of nucleation diminishes. At the beginning of the next stage, the nucleation is assumed to cease suddenly; therefore the number of droplet remains constant during the second stage.

The influence of the heat transmission from outside upon the final size and the time of growth of the droplets is rather trifling. If we assume in the second stage of the process, for the average radius of droplet $\bar{r}$ satisfying

$$N_0-N=(4\pi/3v_B)n'\bar{r}^{-3}, \qquad (9)$$

the following relation

$$d\bar{r}/dt=v_B b(N-N_\infty)/(1+b\bar{r}/D_e)$$

which is similar to (5) or

$$N-N_\infty=(1/v_B)(1/b+\bar{r}/D_e)d\bar{r}/dt\,, \qquad (10)$$

then eliminating N from these equations we have

$$N_0-N_\infty=(1/v_B)(1/b+\bar{r}/D_e)d\bar{r}/dt+(4\pi/3v_B)n\bar{r}^3\,, \qquad (11)$$

But strictly speaking the left hand side of this equation cannot be replaced by $(4\pi/3v_B)\cdot nR^3$ (R denotes the final average radius of droplets) as it is the case in the preceding paper, because in this case N_∞ is a function of the time and N_∞ in Eq. (11) refers to the time $\bar{\theta}$ which corresponds to the average radius of the droplets equal to $\bar{r}$, whereas $(4\pi/3v_B)n'R^3=N_0-(N_\infty)_\Theta$, Here $(N_\infty)_\Theta$ means such N_∞ that refers to the time Θ of the growth of a droplet; therefore $(4\pi/3v_B)n'R^3$ is in general smaller than N_0-N_∞.

Now we replace the left hand side of (11) by $(4\pi/3v_B)n'R''^3$ and integrate the differential equation thus obtained

$$(3/4\pi n')(1/b+\bar{r}/D_e)d\bar{r}/dt=R''^3-\bar{r}^3\,, \qquad (12)$$

to get Θ'', as in the case of the preceding report. Here we suppose R'' which satisfies

$$4\pi n'R''^3/3v_B=N_0-(N_\infty)_{\Theta''}$$
$$=N_0-\{N_{\infty0}+K_0(dN_\infty/dT)_0\sqrt{\Theta''}\},$$

($N_{\infty0}$ being the initial value of N_∞). Then R'' becomes smaller than the actual value of the final radius of droplets.

On the other hand, the final radius of droplets R', satisfying $(4\pi/3v_B)n'R'^3=N_0-N_{\infty0}$, is of course larger than the actual one. It will be seen from the next table which shows the comparison between these two quantities R' and R'', that their difference is rather small and so R' can be considered as the final radius of droplets; consequently Θ' satisfying the relation

$$(3/4\pi n')(1/b+\bar{r}/D_e)d\bar{r}/dt=R'^3-\bar{r}^3, \qquad \text{(12a)}$$

can approximately be identified with the time of growth of the fog droplets.

E: 1.37, $\Theta'=0.59$ sec. , R' : 3.78×10^{-4}cm

P: 0.01, $n'=4.86\times10^4/\text{cm}^3$, R'': 3.75×10^{-4}cm

In computing R' and Θ' the initial limit of integration of the Eq. (12a), i.e. the initial average radius $\bar{r}_0$ in the second stage of the process is identified with δ_0, i.e. the largest radius of droplets at the beginning of the second stage which satisfies

$$\delta_0+b\delta_0^2/2D_e=v_B b\{(N_0-N_{\infty0})\Theta_N$$
$$-(2/3)(dN_\infty/dT)_0K_0\Theta_N^{3/2}\}\,,$$

or

$$\delta_0=(D_e/b)[\sqrt{1+(2v_Bb^2/D_e)\{(N_0-N_{\infty0})\Theta_N-(2/3)(dN_\infty/dT)_0K_0\Theta_N^{3/2}\}}-1]\,,$$

obtained through integration of (5). This approximation will be permissible from the following reasons 1) the influence of the error in $\overline{r_0}$ on R is rather small. 2) $\overline{r_0}/\delta_0$ is 70% or so even in the case treated in the preceding report where the rate of nucleation was assumed to be constant in the first stage. 3) the rate of nucleation decreases with time in the first stage and so the reduction of $\overline{r_0}$ from δ_0 due to the mixing of smaller droplet is smaller in this case than in the former.

§ 4. Influence of the Liberation of Heat Due to Condensation

When we assume an uniform warming of the air through liberation of the heat of condensation, we have, in place of the Eq. (4)

$$\Delta T = \Delta_1 T + \Delta_2 T = K_0\sqrt{t} + \lambda m(N_0 - N)/w\,, \tag{4a}$$

where λ denotes the heat of condensation (cf. next paragraph). Therefore $F_T(t)$ is to be replaced by

$$F_T'(t) = \exp(-\phi\sqrt{t})\exp(-\phi_{T_0}\lambda m(N_0 - N)/wT_0)$$

or $\nu'(t)$ by

$$\nu(t) = \nu_0(N/N_0)^{\phi_{N_0}}\exp\{-\phi_{T_0}mN_0(1-N/N_0)/wT_0\}$$
$$\times\exp(-\phi\sqrt{t})\,.$$

Now let

$$(N/N_0)^{\phi_{N_0}}\cdot\exp\{-\phi_{T_0}mN_0(1-N/N_0)/wT_0\}$$

be $F_N(t)$ and $F_N(\Theta_I)\equiv 1/2$, then we have approximately, as in the case treated before,

$$n \doteqdot \nu_0\int_0^{\Theta_I}\exp(-\phi\sqrt{t})dt$$
$$= (2\nu_0/\phi^2)\exp(-\phi\sqrt{\Theta_I})$$
$$\times(\exp(\phi\sqrt{\Theta_I}) - \phi\sqrt{\Theta_I} - 1)\,, \tag{8b}$$

where

$$n \equiv \nu_0\int_0^{\Theta} F_N(t)\cdot F_T(t)dt$$

replaces former n', the number of droplets per 1 cm³. Also in this case Θ_I is nearly equal to the time

$$\Theta' \equiv \int_0^{\Theta} F_N(t)dt.$$

These relations can be seen from the next table showing the comparison of Θ_I and Θ_I' as well as n computed using the Eq. (8b) and the defined.

Θ_I :	5.70×10^{-2} sec	n(8b)	4.08×10^4/cm³
Θ_I':	5.72×10^{-2} sec	n(def.)	4.02×10/cm³

We saw in the preceding paragraph that the warming of the air through heat transmission from the wall of the vessel has little influence on the final radius and the time of growth of droplets. So when we consider the effect of heating due to condensation we neglect this effect. We put namely $(4\pi/3v_B)\times nR^3 = N_0 - N_\infty$, where N_∞ refers to the temperature corresponding to the warming $\Delta_2 T$ due to condensation only, i.e.

$$\Delta_2 T = \lambda m(N_0 - N_\infty)/w\,.$$

Therefore from $N_\infty = N_{\infty 0} + (dN_\infty/dT)_0(\lambda m/w)N_0 - N_\infty = N_{\infty 0} + K_3(N_0 - N_\infty)$ with $K_3 = (dN_\infty/dT)_0\cdot\lambda m/w$, we have $N_\infty = (N_{\infty 0} + N_0K_3)/(1+K_3)$ and

$$(4\pi/3v_B)nR^3 = (N_0 - N_{\infty 0})/(1+K_3)\,. \tag{9a}$$

Now let us consider the time of growth of droplets in the second stage. Here we have

$$N_0 - N = (4\pi/3v_B)n\bar{r}^3\,, \tag{9b}$$

and $N - N_\infty = (1/v_B)(1/b + \bar{r}/D_e)d\bar{r}/dt$ as in the preceding paragraph. Since $N_\infty = N_{\infty 0} + K_3(N_0 - N)$ in this case, we have

$$N(1+K_3) - N_{\infty 0} - K_3N_0 = (1/v_B)(1/b + \bar{r}/D_e)d\bar{r}/dt.$$

Eliminating N between this equation and (9b), the following relation will be obtained:

$$N_0 - N_{\infty 0} = (1/v_B)(1/b + \bar{r}/D_e)d\bar{r}/dt$$
$$+ (1+K_3)(4\pi/3v_B)n\bar{r}^3\,,$$

or

$$(1+K_3)(4\pi/3v_B)nR^3 = (1/v_B)(1/b + \bar{r}/D_e)d\bar{r}/dt$$
$$+ (1+K_3)(4\pi/3v_B)n\bar{r}^3\,.$$

Therefore

$$(3/4\pi n(1+K_3))(1/b + \bar{r}/D_e)d\bar{r}/dt = R^3 - \bar{r}^3\,. \tag{12b}$$

This is similar to equation (11) of the preceding paper and can be integrated to give

$$\Theta_{II} = \frac{D_e + Rb}{8\pi n(1+K_3)R^3D_eb}\left[\log\frac{(1-\delta_0/R)^2}{(1-\bar{r}/R)^2}\right.$$
$$+\log\left\{1 + \frac{\bar{r}}{R} + \left(\frac{\bar{r}}{R}\right)^2\right\}^2\Big/\left\{1 + \frac{\delta_0}{R} + \left(\frac{\delta_0}{R}\right)^2\right\}$$
$$+ 2\sqrt{3}\frac{D_e - bR}{D_e + bR}\left\{\tan^{-1}\frac{1 + 2\bar{r}/R}{\sqrt{3}}\right.$$
$$\left.\left. - \tan^{-1}\frac{1 + 2\delta_0/R}{\sqrt{3}}\right\}\right].$$

§ 5. Results of Numerical Computation and Discussion

Considering the rise in temperature of the gas in a cloud chamber due to heat transmission from outside, we made use of the formula (4) given by E. J. Williams[4], as stated above. The validity of this formula is limited to the initial stage of the warming of the gas which follows the cooling by expansion. How long does this stage last will depend on the size and shape of the chamber, but at least during the period considered here for fog formation, it retains its validity.

More serious objection might arise for using the Eq. (4a) because the heat of condensation liberated from droplets is then doubly taken into account. Namely, on the one hand, the heat is assumed to make the temperature gradient around droplets, corresponding to a stationary heat flow; the equation like (5) for the growth of a droplet is derived on this assumption as stated in the preceding article. On the other hand, the liberation of heat due to condensation is assumed to warm the gas uniformly in a chamber, by an amount shown in the second term of the right hand side of the Eq. (4a). To what extent this reasoning is permissible? Consider a droplet of radius r, growing at the rate of dr/dt. If the temperature gradient around the droplet corresponding to a *stationary flow of heat* is assumed approximately, then ΔT_r, the difference between the temperature at the surface and that at a great distance therefrom, can be expressed as $\Delta T_r = r(dr/dt)\lambda/\kappa$, as shown in the previous report (here the density of the liquid is taken as 1). Therefore ΔT_ρ, the difference in temperature at a point of distance ρ from the centre of the droplet and that at a great distance, is $\Delta T_\rho = r^2(dr/dt)(\lambda/\kappa)(1/\rho)$.

Now the range ρ_m from the centre of the droplet over which the whole quantity of heat $(4/3)\pi r^3\lambda$, liberated through condensation on the droplet, distributes, can be roughly estimated from the following equation

$$(4\pi w r^2 dr/dt)(\lambda/\kappa)\int_r^{\rho_m} \rho d\rho = 4\pi r^3\lambda/3\,. \quad (14)$$

then we get

$$\rho_m{}^2/r^2 - 1 = (2\kappa/3w)(1/r\,dr/dt)$$
$$= (2\kappa/3w)(1/br + 1/D_e)/v_B N_\infty (N/N_\infty - 1)\,. \quad (15)$$

Take, for example, the case treated in the preceding paragraph, i.e. the case of the condensation coefficient $P=0.01$ and of expansion ratio $E=1.37$. Then at the end of the first stage of the process when $F_N'(t)$ or $F_N(t)=1/2$, the right hand side of the above Eq. (15) is of the order of 1×10^6 for larger droplets that are mainly responsible to the warming of the gas, namely for $r \simeq 10^{-4}$ cm and $N \doteqdot N_0$. This means that ρ_m is of the order of 1×10^{-1} cm, whereas the average distance between droplets is a few tenths of this quantity ($2.5\sim3\times10^{-2}$ cm or so). That is, only 10∼15% of the heat liberated by condensation is doubly accounted in the former estimation of the number of droplet. In the second stage of the process, this percentage becomes smaller, as the term $(N/N_\infty - 1)$ decreases more rapidly than $1/r$ increases. Therefore the formula given in paragraph (4a) can approximately be used in this case. When we consider the case where the condensation coefficient $P=1$, ρ_m will become of the order of 1×10^{-2} cm when $F_N'(t) \simeq 1/2$, that is, smaller than the average distance between droplets, and the Eq. (8a) will be valid. But in the final stage, ρ_m is always larger than the average distance of droplets and the Eq. (9a) can be used. Thus we are confronting to a rather complicated problem of judging what formula should be used in the estimation of the quantities mentioned. Fortunately the difference is not so large, as will be seen from the next table showing the comparison of these quantities, computed using the formulae given in paragraph 3 and 4, for the case of the condensation coefficient $P=0.01$ and of the expansion ratio $E=1.37$.

n': $4.86\times10^4/\text{cm}^3$ R': 3.78×10^{-4}cm
n : $4.08\times10^4/\text{cm}^3$ R : 3.20×10^{-4}cm
Θ': 5.16×10^{-1}sec.
Θ : 9.07×10^{-1}sec.

Finally, in the following table, some of the quantities given in the last table of the previous report are compared with the corresponding newly computed one (marked with *), using formulae given in paragraph 3 or 4. The time of fog development Θ is that corresponding to $\bar{r}/R=0.99$ (cf. the last paragraph of the preceding report).

$1.94\times10^8/\text{cm}^3\cdot\text{sec}$ for $P=1$, N_0/N_∞: 7.63, r^*: 6.44×10^{-8}cm

P	R 10^{-4}cm	δ_0 10^{-5}cm	Θ_I 10^{-3}sec	n $10^5/\text{cm}^3$	$\Theta=\Theta_I+\Theta_{II}$ 10^{-2}sec
1	2.1	7.6	1.8	3.4	2.6
	*1.9	7.5	Θ_N: 1.7	n': 2.8	3.2
0.1	2.7	10.2	9.0	1.8	6.7
	*2.8	7.8	6.5	0.89	10.8
0.01	3.1	11.2	76.	1.5	34.
	*3.2	8.0	55.	0.41	91.

We see from this table that the rise in temperature of the gas after an adiabatic expansion has the effect of diminishing the number density of fog droplet and of prolonging the time of development of fog, but has little influence upon the final size of fog droplet.

Comparison of the theoretical prediction given above with experimental observations has been undertaken in our laboratory and is now in progress. The results will be reported later when the experiment is completed.

In conclusion the author wishes to express his sincere thanks to Prof. T. Nagamiya for his kind advice. The author's thanks are also due to Dr. I. Syozi for his helpful discussion.

References

1) H. Wakeshima: J. Phys. Soc. Japan **9** (1954) 390.
2) M. Volmer and A. Weber: Z. Phys. Chem. **119** (1926) 227.
3) R. Becker and W. Döring: Ann. Phys. **24** (1935) 719.
4) E. J. Williams: Proc. Camb. Phil. Soc. **35** (1939) 512.

JOURNAL OF THE PHYSICAL SOCIETY OF JAPAN Vol. 9, No. 3, MAY—JUNE, 1954

Creep of Polymethyl Methacrylate at Low Temperature

By Koji SATO, Heinosuke NAKANE, Teruo HIDESHIMA
and Shigeo IWAYANAGI
Scientific Research Institute, Tokyo

(Received December 1, 1953)

In order to supplement the dynamical investigation of the secondary absorption region of polymethyl methacrylate, which appeared at 20°C in $\frac{1}{2}$ cps vibration measurement as described in the previous report, the torsional creep was observed at various temperatures from −50°C to 30°C. Assuming that this polymer is "thermorheologically simple", the master creep curve was constructed, and the activation energy of 30 kcal/mol was obtained.

§ 1. Introduction

In the previous papers,[1] two peaks were found in the elastic loss *vs* temperature curve of polymethyl methacrylate measured at a frequency of about 0.5 cps. One peak was at about 20°C which was lower and broader than the other at about 120°C, both shifting towards lower temperatures with the decrease of frequency. In view of the relaxational theory, as for the peak at 20°C, it may be expected that the anomaly of the creep curve will appear at a temperature much lower than 20°C, because the time-scale of the creep measurements is usually far larger than that of the dynamic measurements. Therefore, torsional creep measurement of polymethyl methacrylate was undertaken within the temperature range from −50°C to 30°C. As will be described later (§ 3), the anomaly of the creep was found at a temperature as low as −50°C when the time-scale was 10^4 sec or so.

§ 2. Experimental

A cylindrical specimen of polymethyl methacrylate was held horizontally at both ends by two chucks, one of which was clamped and the shaft of the other was connected through a ball bearing to a wheel to which a load was applied to twist the specimen. The specimen and the chucks including the ball-bearing were placed in a thermostat, the temperature of which was varied from −50°C to 30°C with less than 2°C fluctuations. Throughout the experiment the same cylindrical test piece, 0.425 cm in radius and 9.7 cm in effective length was used. The specimen was left at least for 1/2 hour at a desired temperature before measurements were made.

A load (the maximum shear stress corresponding to this load amounted to 5.4×10^7

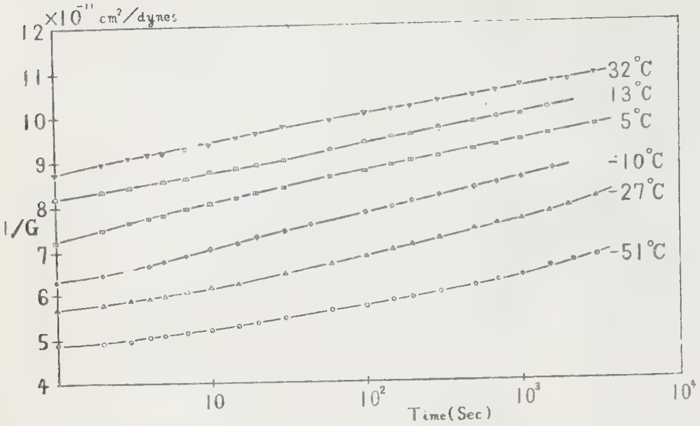

Fig. 1. Experimental creep curves (compliance as functions of time) at various temperatures.

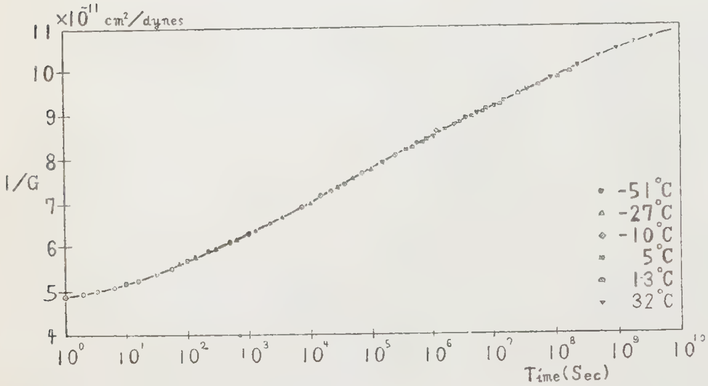

Fig. 2. The master creep curve at -51°C for polymethyl methacrylate.

dyn/cm^2) was then applied quickly and the consequent deformation was recorded on a photographic paper by an electromagnetic oscillograph camera for the first 1 minute, followed by successive direct readings of the position of the light spot on a scale for 60 minutes or so. Next, the load was removed and the recovery was observed in similar procedure. A typical example of this experiment is shown in Fig. 1. Both creep and recovery curves could be regarded identical within the experimental error.

§ 3. Discussion

These creep curves obtained at different temperatures could be made to one continuous curve designated at a certain temperature with the method already employed by several authors,[2)3)] its theoretical foundation being considered by F. Schwarzl and A. J. Staverman.[4)] The experimental creep curve at the lowest temperature (-51°C) was taken as the standard and the curve by the next higher temperature was shifted along the $\log t$ axis until it partially fell in which the standard curve. By transposing subsequent curves in similar manner, the master creep curve of Fig. 2 was obtained. This curve may be regarded as the creep curve at -51°C over a large time-scale from 1 to 10^{10} sec, if the assumption of "thermorheologically simple"[4)] is valid in the temperature range used. An inflection point is found at about 10^4 sec on this curve.

The activation energy E may be estimated by assuming the relation

$$E = R\frac{d \ln t_c}{d(1/T)}, \qquad (1)$$

where T is the absolute temperature, R the gas constant per mole and t_c the creep time in which the deformation reaches a constant value (in the present case, it is the value at the inflection point). This relation was used already by Tobolsky *et al*[5)] in the case of their stress relaxation measurements. Thus approximately the value of 30 kcal/mol was obtained as the activation energy for the elastic deformation of polymethyl methacrylate in the lower temperature range. Considering the value of 29 kcal/mol obtained from dynamical measurements described in the previous paper,[1)] the molecular mechanism of deformation in both cases should be the same. In contrast to this, creep measurements made within a temperature range from 70°C to 120°C (this experiment will be reported later) gave 150～200 kcal/mol, which is of the same order as the value obtained from stress relaxation measurements by Tobolsky *et al.*[3)] Dynamical measurements by Alexandrov and Lazurkin showed somewhat smaller value (75 kcal/mol).

There are two kinds of deformation mechanism with different values of activation energy evidenced by the two absorption peaks by dynamical measurement. The fact indicates that, in wide ranges of temperature and time-scale in which two anomalies appear, the polymer is not "thermorheologically simple" as was assumed by McLoughlin and Tobolsky[3].

The simplest model to represent main features of behaviour of the polymer would consists of at least three Maxwell elements connected in parallel (Fig. 3), if the model of Maxwell is preferred to that of Voigt. As shown in Fig. 3, the first element is degenerated to the spring G_1, the second element consists of the spring G_2 and the dashpot η_2, and the third the spring G_3 and the dashpot η_3. The relaxation times λ_2 and λ_3 of the latter two elements are defined by

$$\eta_2=G_2\lambda_2\ , \quad \eta_3=G_3\lambda_3\ . \tag{2}$$

The behaviour of this model is governed by the next four relations:—

$$\left.\begin{aligned} &f_1+f_2+f_3=f \\ &\frac{df_1}{dt}=G_1\frac{ds}{dt} \\ &\frac{df_2}{dt}=G_2\frac{ds}{dt}-\frac{f_2}{\lambda_2} \\ &\frac{df_3}{dt}=G_3\frac{ds}{dt}-\frac{f_3}{\lambda_3}\ , \end{aligned}\right\} \tag{3}$$

where f_1, f_2 and f_3 are stresses distributed among three elements, f is the total stress and s is the deformation which is assumed as common to three elements. These equations are easily solved for s, when f=const. Under the condition

$$\lambda_3 \ll \lambda_2\ , \tag{4}$$

this solution may be written as

$$s=\frac{f}{G_1+G_2+G_3}\left[1+\frac{G_2(G_1+G_2+G_3)}{G_1(G_1+G_2)}\right. \\ \left.\times\left\{1-e^{-t/\tau_3}\right\}+\frac{G_3}{G_1+G_2}\left\{1-e^{-t/\tau_3}\right\}\right], \tag{5}$$

where

$$\tau_2=\frac{G_1+G_2}{G_1}\lambda_2\ ,$$

and

$$\tau_3=\frac{G_1+G_2+G_3}{G_1+G_2}\lambda_3\ ,$$

and is shown schematically in Fig. 4.

Under a constant load, if the condition (4) is satisfied, the deformation takes place stepwise as is shown in Fig. 4. The Instantaneous deformation $f/(G_1+G_2+G_3)$ increases to $f/(G_1+G_2)$ by the first step (creep) which occurs in the neighbourhood of the time $t=\tau_3$, and the final stationary deformation f/G_1, is attained by the second step (creep) in the neighbourhood of the time $t=\tau_2$. If both steps (creeps) were observed on the same time-scale, the latter would appear within much higher temperature range (~100°C for polymethyl methacrylate) than the former.

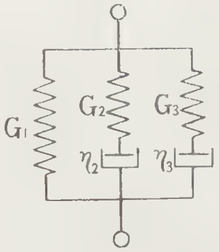

Fig. 3. A Maxwell model.

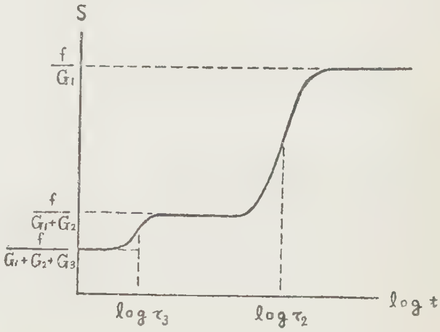

Fig. 4. The creep of the Maxwell model of Fig. 3 (schematic).

From the creep and vibrational data for polymethyl methacrylate, approximate values were assigned to the shear moduli G_1, G_2 and G_3* of the model as follows:—

$G_1=7.2\times10^6$ dyn/cm^2
$G_2=1.0\times10^{10}$ 〃
$G_3=1.0\times10^{10}$ 〃

where in estimating G_1 use was made of the tensile stress relaxation data by McLoughlin and Tobolsky.[3] At elevated temperatures, according to these authors, the stress due to G_1 would also gradually relax completely, for which reason it is impossible to omitt the dashpot η_1 from the first Maxwell element of the model shown in Fig. 3.

---

* G_2 & G_3 correspond respectively to G_1 & G_2 in the previous report.

Contrary to what was described above which was based upon the simple model, the experimental curve in Fig. 2 shows that the deformation under the constant load steadily increases, giving no well-defined instantaneous and stationary values of deformation (and therefore of elastic moduli G_2 and G_3). The stepwise increase of the deformation depicted in Fig. 4 is just recognizable as a slight anomaly in the monotanously increasing creep curve (Fig. 2). In order to explain such behaviour, the second and third elements of the above mentioned model must be replaced respectively by the groups of Maxwell elements whose relaxation times distribute broadly. Approximate feature of one of such distributions which corresponds to the third element may be inferred from the master creep curve** presented above.

In conclusion, the authors express their sincere appreciation to Dr. M. Kinoshita, the chief of the laboratory, for his encouragement throughout the study. They also wish to thank for financial help given by the Scientific Research Fund of the Ministry of Education.

References

1) S. Iwayanagi and T. Hideshima: J. Phys. Soc. Japan **8** (1953) 365, 368.

2) F. S. Conant, G. L. Hall and W. G. Lyons: J. Appl. Phys. **21** (1950) 499.

3) J. R. McLoughlin and A. V. Tobolsky: J. Polymer Sci. **8** (1952) 543; J. Colloid Sci. **7** (1952) 555.

4) F. Schwarzl and A. J. Staverman: J. Appl. Phys. **23** (1952) 838.

5) R. D. Andrews, H. Hofman-Bang and A. V. Tobolsky: J. Polymer Sci. **3** (1948) 669.

Note:—

After this paper was prepared, recent experimental results by K. Schmieder and K. Wolf (Kolloid-Zeitschrift 127 (1952) 89–) have been called to our attention. According to these German authors, the secondary absorption region of polymethyl methacrylate was found by using the method of torsional vibration and reported by K. Wolf as early as 1951. On the other hand our first and second papers of Reference (1) were read at the annual meeting of the Physical Society of Japan, April, 1951 and 1952 respectively.

** It is the distribution of retardation time that is derived directly from the master creep curve. The distribution of retardation times thus obtained can be transformed to that of relaxation times.

JOURNAL OF THE PHYSICAL SOCIETY OF JAPAN Vol. 9, No. 3, MAY—JUNE, 1954

On the Transitional Phenomena of Glass*

By Eizō KANAI

Research Laboratory, Asahi Glass Company Ltd., Yokohama, Japan

and Takesi SATOH

*Glass Laboratory, Tokyo Institute of Technology, Tokyo, Japan***

(Received December 24, 1953)

A new interpretation on the glassy state, which includes the explanation of the transitional phenomena, is proposed on the basis of the superposition of the two modes of motion, one of which is the network deformation and another is the vibration around the instantaneous configuration of network. To formulate this idea, a new parameter, that is the "network temperature". is introduced and the thermodynamical treatment is performed, with the independent derivation of the equation of motion. Finally, some experimental data are checked with this theory and its validity is discussed.

§ 1. Vitreous State

It is believed that the glass is in the frozen state of the supercooled liquid composed of various silicates. This description contains the two important concepts, namely, the 'supercooled liquid' and the 'frozen state'.

Actually we often experience that the silicate melts devitrify into crystals in the neighbourhood of their melting temperatures, when cooled down from higher temperatures. This means that the state of the melt below the melting temperature is not the true equilibrium state from the view point of the thermodynamics, but the unstable one containing some kinds of the relaxation mechanism. Usual soda-lime-silicate glasses have their devitrification region in the temperature range from 1000°C to 800°C. However, we can pass this region so quickly that the devitrification does not realize. Further, in the range of 600°C—750°C, we can obtain the unique properties of the glasses determined by their temperatures only, when they are held so long in those conditions. Hence, it becomes possible to treat glasses as if they are in the (conditional) equilibrium states, since the relaxation times for the crystalization are too long and the devitrification is practically forbidden. We need not, therefore, take account of the unstable character of glass caused by the 'supercooling', so long as we are interested in the glassy state under 700°C.

When we continue to cool these glasses, they solidify into the amorphous solids in the range of 500°C—600°C and change their physical properties in the various aspects, as well known experimentally. This transition constitutes the second content stated above, that is, the 'freezing phenomena'. And we shall try to study this transition succeedingly.

The freezing phenomena have the following features well known empirically. First, the freezing temperature is not a fixed constant, but has generally some extent of width. Second, the freezing range moves up and down according to the cooling conditions. Namely, it moves upward when cooled rapidly and downward when cooled slowly. Third, the freezing process by cooling and the releasing process by heating do not follow the same path. In other word, this phenomenon is the irreversible change. For example, Fig. 1, the expansion curve of the glass[1], shows this behavior schematically.

These facts suggest that above transition is not the true thermodynamical one, but the rate process accompanying some relaxation mechanisms. So, it becomes important to know the details of those relaxation mechanisms.

---

* The contents of this paper were read at the annual meeting of the physical society of Japan in 1951 by E. Kanai except some parts in § 5, whose remainder was added by T. Satoh in 1952. And both contents were independently written in the Japanese magazine, 'Bussei-ron Kenkyū'. With the mutual consultation, we decided to sum up these two papers and publish in this journal by English.

** Now at Physics Department, Safety Academy, Yokosuka, Japan.

We know the similar phenomena in the transition of the substances of organic high polymers which transform from the rubber state to the solid state. In those cases, it is probable that the suppression of micro-Brownian motion of the linear chains composing the high polymers is responsible for that transition. However, the silicate glass has not the rubber state between the fused and solid states, and does not posses the unit of motion like the chain, according to the X-ray investigation. Above the transition temperatures, the glass performs the Newtonian motion although the viscosity is very high, and below the transition region, it is an extremely hard and brittle solid.

On the other hand, the molecular structure of silicate glasses is fairly well studied in the solid state. Namely, their structure consists of the ramdom network composed of the unit tetrahedron each of which has a silicon atom in the center and four oxygen atoms at corners. And this network contains various metal ions in its inner holes. The strength of solid glass is able to be explained by the strong bonds of the network and the large value of viscosity of liquid glass is due to the difficulty of sliding motion between the layers of the network.

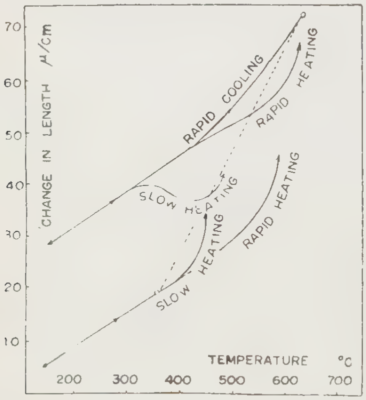

Fig. 1. Typical features of thermal expansion.

Considering from these facts, we may expect that the inner motion of glass is made up of the superposition of two kinds of motion. One is the network deformation from one configuration to other (which is typically seen in the flow of the glass), and another is the vibrational motion around the instantaneous configuration of the network. The latter motion exists not only in the solid state but also in the liquid state. But it is very probable that the network motion is suppressed as soon as the glass has been frozen. Further, the motion of network deformation is possibly the co-operative diffusion phenomenon of molecular groups from the microscopic standpoint. It is then naturally explained that the freezing phenomena are the rate processes as above stated.

Above idea is probably the most practical interpretation on the vitreous state, including the freezing phenomena. It is not easy, however, to treat successfully, on this standpoint, the complicated motion having so many degrees of freedom. In following sections, we shall describe one of simplified trials.

§ 2. Cocept of Network Temperature

Let us take up a glass sample having volume V at temperature T, and consider the pressure p as the atmospheric order. As mentioned above, the inner motion of the glass is divided into the network deformation and the vibration around the instantaneous network configuration. The latter exists commonly in both solid and liquid states. Moreover, we consider the vibrational motion exists always under the equilibrium condition and its behaviour is represented by the actual temperature T. If it were not so, it would be difficult to understand the temperature indicating the glassy state.

Now, we represent the vibrational energy by $E_{\text{vib}}\,(T,\,p\!:\!f_{\text{net}})$. Its definition is as follows: we assume that the network deformation be suddenly suppressed at the present time. Of course, the uniform expansion and contraction, and the small vibration are allowed. When this system was cooled down to the state of the absolute zero temperature, the system has only the potential energy designated by $E_{\text{net}}\,(p\!:\!f_{\text{net}})$ (which is possessed by the network). Then,

$$E_{\text{vib}}\,(T,\,p\!:\!f_{\text{net}})=E-E_{\text{net}}\,(p\!:\!f_{\text{net}})\,,$$

where E is the inner energy of the system concerned. That is, E_{vib} is the sum of the excess potential energy (compared with E_{net}) and the kinetic energy.

In order to treat exactly, the network motion should be properly described by the distribution function f_{net} with the aid of the statistical mechanics. But this procedure is practically impossible. So we try to reduce the network motion to the temperature scale and to introduce the "network temperature" τ. The way of introduction of τ is arbitrary to some extent. Here, we shall take up the following procedure.

If we wait the establishment of the thermal equilibrium of the total system including the network motion without limit of time, E_{net} must become a fixed function of T and p. So we borrow this functional form and pick up the temperature which gives the same network energy as the present E_{net}, and call this temperature as the network temperature τ. (c.f. Fig. 2)

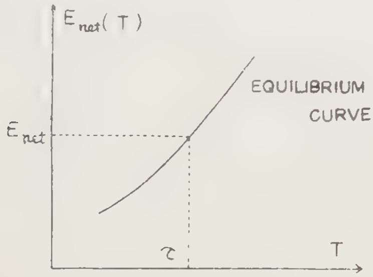

Fig. 2. A way of introduction of τ.

The network temperature τ is not always equal to the real temperature T. Only when we wait the fulfilment of the thermal equilibrium condition without limit of time, both temperatures will become equal:

$$\tau = T\,. \tag{2.1}$$

On the other extremity, when the network motion is forbidden by freezing, τ is fixed:

$$\tau = \text{const.} \tag{2.2}$$

Now we obtained three independent variables: p, T and τ. Other variables such as volume, inner energy etc. are the functions of these three variables:

$$\left.\begin{array}{l} V = V(p, T, \tau)\,, \\ E = E(p, T, \tau)\,. \end{array}\right\} \tag{2.3}$$

When the glass is still movable at the higher temperatures, the condition (2.1) is fairly easy to be satisfied. On the other hand, the condition (2.2) is satisfied at the lower temperatures. Hence E, V etc. turn to loss the continuous smoothness on the border of two temperature regions. It is the reason why the bends appeared on the expansion curve, the heat content curve etc.

The Eqs. (2.3) do not contain the time explicitly. But it is evident that τ must approach to T in the course of time. Hence, even at the constant p and T, the volume V continues to change according as τ changes. On the other hand, E, V etc. become the functions of p and T only, after τ has been fixed by freezing. That is, the glass below the transitional region has only the pressure p and the temperature T as state variables. Actually, at room temperature, the glass is a nearly complete elastic body and the various changes take place reversibly, which is the ordinary behaviour of the glass.

§ 3. Thermodynamical Treatment

In the last section, we introduced a new so-called 'concealed' parameter τ as well as the ordinary thermodynamical variables, p and T. In this section, we shall show that the discussions similar to the thermodynamics can be applied to our problem with the use of these variables.

It was already explained that the freezing phenomenon was the irreversible change. But it is right so long as we use the two variables p and T as state variables. If we add the new parameter τ to them, various quantities may be considered as the one-valued functions of p, T and τ, at least in the first approximation. Among them,

$$V = V(p, T, \tau) \tag{3.1}$$

corresponds to the equation of state of the glass, and

$$H = H(p, T, \tau) \tag{3.2}$$

may be used as the equation of thermal state, where H is the enthalpy of the system.

Of course, it is difficult to deduce the Eqs. (3.1) and (3.2) from the theoretical standpoint. It is, however, convenient to utilize the following empirical facts.

(i) Above the freezing range, V and H are both the functions of p and T alone which do not depend upon the past history of the glass sample.

(ii) Below the freezing range, the coefficient of thermal expansion and the specific heat do not depend on the thermal history experienced by the glass.

We henceforth take the pressure p as constant and ordinary. For, the data under the condition of high pressure are rare and out of our interest. The fact (i) is well-known and (ii) is approximately accepted[2].

From (i) and (ii), the following expressions are easily derived:

$$V(T,\tau)=V(T_0)\left\{1+\int_{T_0}^{T}\beta^* dT+\int_{T_0}^{\tau}(\beta-\beta^*)dT\right\}, \tag{3.3}$$

$$H(T,\tau)=H(T_0)+\int_{T_0}^{T}C_p^* dT+\int_{T_0}^{\tau}(C_p-C_p^*)dT, \tag{3.4}$$

where T_0 is a certain high temperature at which τ is equal to T, and β, C_p are the expansion coefficient and the specific heat under the equilibrim condition ($T=\tau$), β^*, C_p^* are the ones after freezing respectively.

In the ordinary cases, where β, β^*, C_p and C_p^* are nearly constants between 300°C—700°C, above equations can be represented as follows:

$$V(T,\tau)=V(T_0)\{1+\beta^*(T-T_0)+(\beta-\beta^*)(\tau-T_0)\}, \tag{3.3$'$}$$

$$H(T,\tau)=H(T_0)+C_p^*(T-T_0)+(C_p-C_p^*)(\tau-T_0). \tag{3.4$'$}$$

Further, if we are interested in the entropy of the system,

$$\Delta S'=(C_p^*/T)\Delta T$$

is the increment due to the vibrational motion, and

$$\Delta S''=\{(C_p-C_p^*)/\tau\}\Delta\tau$$

is the one due to the network deformation. Of course, the latter vanishes after freezing.

Above expressions refer apparently to the static relations between the variables. Independently of those relations, it is necessary to establish the equation which determines the behaviour for τ to approach to T.

§ 4. Equation of Motion

It is probably possible to treat the motion of the network by the method similar to the diffusion problem[3], since the deformation of network is microscopically constituted of the motion of the groups of several molecules, which translate step by step through the potential barriers.

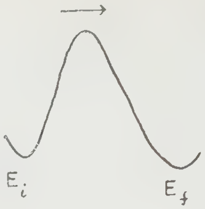

Fig. 3. Schematical reaction model.

Now, we shall pick up the rate-determining step of the network motion and consider the reaction model shown schematically in Fig. 3. Here we denote the energies before and behind the barrier by E_i and E_f, and the concentrations of the representative systems by C_i and C_f, respectively. Then,

$$\left.\begin{aligned}&C_i+C_f=1,\\&E_iC_i+E_fC_f=E_{\text{net}}(\tau).\end{aligned}\right\}$$

Further, we represent the reaction rate constant from the initial state to the final one by k and the one of the reverse reaction by k'. Then,

$$\left.\begin{aligned}\frac{dC_i}{dt}&=-kC_i+k'C_f,\\\frac{dC_f}{dt}&=\ \ kC_i-k'C_f.\end{aligned}\right\}$$

Hence

$$\frac{d}{dt}E_{\text{net}}(\tau)=E_i\frac{dC_i}{dt}+E_f\frac{dC_f}{dt}$$
$$=-k(E_i-E_f)C_i+k'(E_i-E_f)C_f.$$

Substituting the following relations to this equation,

$$\left.\begin{aligned}&(E_i-E_f)C_i=E_{\text{net}}(\tau)-E_f,\\&(E_i-E_f)C_f=E_i-E_{\text{net}}(\tau),\end{aligned}\right\}$$

above equation can be transformed into:

$$\frac{d}{dt}E_{\text{net}}(\tau)=(kE_f+k'E_i)-(k+k')E_{\text{net}}(\tau).$$

For the time being, we shall assume here that k and k' are the functions of the temperature T only. This means that the activation energies of k and k' are both independent of τ and in other word, the activation energy of viscosity is nearly constant in the transition region, as shown in the later section, which seems approximately to be satisfied in the case of usual soda-lime-silicate glasses[4].

Then, in the end of the isothermal reactions,

$$0=(kE_f+k'E_i)-(k+k')E_{\text{net}}(T).$$

Therefore, at last

$$\frac{d}{dt}E_{\text{net}}(\tau)=(k+k')\{E_{\text{net}}(T)-E_{\text{net}}(\tau)\}.$$

Especially, when $E_{\mathrm{net}}(\tau)$ is approximately represented by the linear function of τ, above expression becomes simply to the following equations:

$$\left.\begin{aligned} \frac{d\tau}{dt}&=\kappa(T-\tau)\,, \\ \kappa&=k(T)+k'(T)\,. \end{aligned}\right\} \tag{4.1}$$

This is the equation which describes the reaction for τ to approach to T. κ is the diffusion constant and has the next generalized form:

$$\kappa=\sum_i A_i \exp(-B_i/T)\,, \tag{4.2}$$

where T is shown as the absolute temperature of the system. We may often expect that one term in the summation symbol is predominant among others and then κ becomes written as follows,

$$\kappa \doteqdot A \exp(-B/T)\,. \tag{4.2$'$}$$

We can obtain more general expressions for the equation of motion. In the derivation of (4.1), we assumed that k and k' were both the functions of T only. But more generally, we can assume that

$$k(T,\tau)=K(T,\tau)R(T)\,,$$

and

$$k'(T,\tau)=K(T,\tau)R'(T)\,.$$

Speaking more concretely, it is the case in which the activation energies of k and k' are equal except the difference independent of τ, although the activation energies might be dependent on τ and T. Then, repeating the analogous procedure to the previous case, we reach, at last, the following equations,

$$\frac{d\tau}{dt}=\kappa(T-\tau), \tag{4.3}$$

$$\begin{aligned} \kappa&=k(T,\tau)+k'(T,\tau) \\ &\doteqdot A \exp\{-B(T,\tau)/T\}. \end{aligned} \tag{4.4}$$

Namely, we may consider the activation energy of the diffusion constant is the general function of T and τ.

Assuming, for example, that

$$B(T,\tau)=B_0-B_1\tau\,, \tag{4.5}$$

the Eq. (4.3) can be written as follows,

$$d\tau/dt=A(T-\tau)\exp\{B_1\tau-B_0)/T\}\,, \tag{4.6}$$

which is essentially the same form with the equation proposed by A. Q. Tool⁵⁾. His theory is rather of the empirical character, but we think that the essence of his theory consists in the assumption (4.5), which is reasonable in some cases.

We can further make another extension of the Eq. (4.1). The Eq. (4.1) shows that the reaction for τ to approach to T is drived by the force which is proportional to the difference $(T-\tau)$. Hence, for large $|T-\tau|$ (whose extent is different for each case), the Eq. (4.1) is to be transformed as follows:

$$d\tau/dt=\kappa' \sinh\{\varepsilon(T-\tau)\}\,, \tag{4.7}$$

$$\kappa'=A' \exp(-B'/T)\,, \tag{4.8}$$

from the analogy with the diffusion problem.

At any rate, the combination of Eq. (4.3) or (4.7) with Eqs. (3.3), (3.4) is sufficient to describe the change of the system. The next conclusions, however, are evident without computation. That is, $|T-\tau|$ is small at higher temperatures and $d\tau/dt$ is nearly equal to zero at lower temperatures, since κ or κ' is very large at higher temperatures and very small at lower temperatures. From the practical standpoint, $T=\tau$ [(2.1)] in former cases and $\tau=$const. [(2.2)] in latter cases.

§ 5. Comparison with Experiments

We will now apply our theory developed in the previous sections to the experimental data of thermal expansion and refractive index, and evaluate the rate constants of $\tau \to T$ reaction contained in both processes. The former used here is one made by A. Q. Tool⁵⁾, and the latter one by P. W. Collyer⁶⁾.

(*1*) *Thermal expansion*

Tool's sample is a kind of borosilicate crown glasses for a thermometer, and its chemical composition is not given. After a sample has been heated at 500°C during several weeks, it is cooled down rapidly to room temperature and then is reheated uniformly with a constant rate of 3°C per minute. The linear thermal expansion in this process has been observed by means of the interferometer method. His results are referred in Fig. 4. He has given another result with a sample cooled down quickly from a certain higher temperature. We suppose that this case will be certainly in the field of the Eq. (4.6) or (4.7) owing that $|T-\tau|$ is large, but we shall not take this case to check the theory, since unfortunately the necessary numerical values have not been given at detail.

Analizing the experimental result we can at the first place decide the values of linear

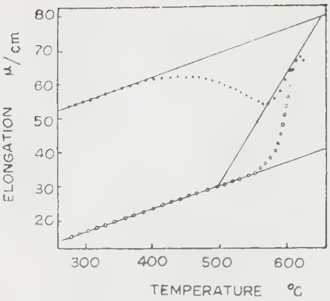

Fig. 4. Thermal expansion curves. (After cool)

coefficient of thermal expansion. From the slope of the straight line of rapid cooling and reheating below 500°C,

$$\alpha^*=0.066\ \mu/\text{cm}\ ^\circ\text{C},$$

and on the other hand from the curve at higher temperatures, referring with the data for chilled sample,

$$\alpha=0.317\ \mu/\text{cm}\ ^\circ\text{C}.$$

The changes below 500°C occur reversibly. Now if we take the time passing just at 500°C as an initial value zero, the following equation is derived from Eq. (3.3′).

$$\{l(T,\tau)-l_0\}/l_0=\alpha^*(T-T_0)+(\alpha-\alpha^*)(\tau-T_0)\,, \tag{5.1}$$

where l is the length of the sample, and the initial values of actual and network temperatures should be taken as 500°C in this case. Using the observed values of l, from the above equation we can evaluate the values of τ corresponding to each time. Taking $\tau\rightarrow T$ Eq. (4.1):

$$(d\tau/dT)(dT/dt)=\kappa(T-\tau)\,,$$

we can introduce following equations:

$$(d\tau/dT)/(T-\tau)=\kappa/u\,,$$

where $u\equiv dT/dt=3$°C/min., and then

$$\ln\left(\frac{d\tau/dT}{T-\tau}\right)=\ln\left(\frac{A}{u}\right)-\frac{B}{T}\,. \tag{5.2}$$

For the sake of simplicity we take an assumption (4.2′), namely $\kappa=A\exp(-B/T)$.

From the Eq. (5.2) we can expect that there will be a relationship of linearity between $\ln\{(d\tau/dT)/(T-\tau)\}$ and inverse of T. It is clear that this estimation is satisfied approximately as shown in Fig. 5. From the slope of this straight line the value of activation energy B is proved to be 140 Kcal/mol. The observed value of viscosity coefficient of this sample is not given, but the value of B is approximately of the same order as the activation energy of viscosity for ordinary soda-lime silica glasses at corresponding temperatures. It has resulted, therefore, from this argument that the activation energy of rate constant in this $\tau\rightarrow T$ process is of the same order with that of the activation energy of viscosity.

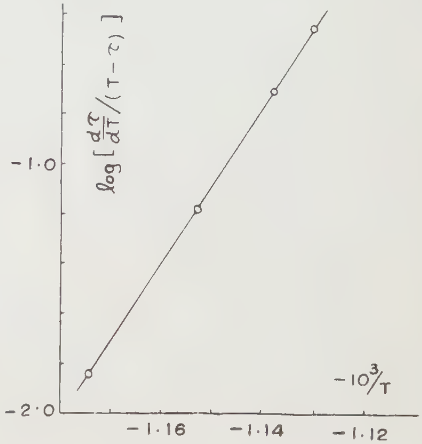

Fig. 5. $\log\left[\frac{d\tau}{dT}\Big/(T-\tau)\right]$ versus T^{-1}.

This is of course expectable. Because the change of τ with time is caused by the deformation of network, and on the other hand the mechanism of viscous flow is the continuous displacement of network. Namely the fundamental mechanisms involved in these two motions are entirely common.

(2) *Refractive index.*

The experimental data used here are those after P. W. Collyer with one of the borosilicate crown glasses, which is signed to be 517/645. The chemical composition of this glass is shown in Table I.

Table I. Chemical composition of BSC (517/645) glass (weight %).

SiO_2	68.6	Na_2O	3.9
B_2O_3	11.4	K_2O	10.0
ZnO	2.5	Sb_2O_3	1.3
BaO	1.8	R_2O_3	0.3

His samples are $8\times8\times2\ \text{mm}^3$ and are cooled rapidly from 852°K. Then they are reheated at a definite temperature in the annealing range. In these processes the change of the refractive index n with time is observed with a

Pulfrich refractometer keeping the temperature T to be constant. The fixed temperatures have been determined by the method of potentiometer. It is reported that the limits of errors of refractive indices and temperatures are 2 in the order of 10^{-5} and 2–3°F respectively. After the sufficient elapse of time ($t \to \infty$), the values of n saturate to the corresponding values of n_∞ which are determined as the function of temperature T. (Table II.) The initial value n_0 of refractive index is taken to be 1.51484 from a mean with six samples at room temperature.

Table II. Saturated values of refractive indices. (After Collyer)

T (°K)	n_∞
787	1.51825
795	780
803	721
823	624

Before examining our theoretical formulae, we have to decide the values of volume at a higher temperature T_0 and coefficients of thermal expansion, β and β^*. We will assume these values from the figures represented in the paper by L. Shartsis and S. Spinner⁷⁾:

$$\left.\begin{aligned} V(T_0=973) &= 0.4292\ , \\ \beta &= 153\times10^{-6}\ {}^\circ\mathrm{C}^{-1}, \\ \beta^* &= 25\times10^{-6}\ {}^\circ\mathrm{C}^{-1},^{**} \end{aligned}\right\}$$

where the value of V is determined from the density data during 1000°C–1300°C range by extraporation, and T_0 is taken to be 700°C arbitrarily.

Now when T=const., we can write the Eq. (3.3′) as follows:

$$V(\tau)=q\tau+r\ , \qquad (5.3)$$

or reversely

$$\tau=(V-r)/q\ , \qquad (5.3')$$

where

$$\left.\begin{aligned} q &= V(T_0)(\beta-\beta^*)\ , \\ r &= V(T_0)(1-\beta T_0+\beta^* T)\ . \end{aligned}\right\}$$

The differential Eq. (4.7) determining the rate of $\tau \to T$ reaction can be easily integrated in this case of constant temperature:

$$\mathcal{E}(T-\tau)/2=\tanh^{-1}[\tanh\{\mathcal{E}(T-\tau_0)/2\}\exp(-\mathcal{E}\kappa t)].$$

This is transformed as follows:

$$\ln\left[\frac{\tanh\{\mathcal{E}(T-\tau)/2\}}{\tanh\{\mathcal{E}(T-\tau_0)/2\}}\right]=-\mathcal{E}\kappa t\ , \qquad (5.4)$$

or when τ is written explicitely,

$$\tau=T-(2/\mathcal{E})\tanh^{-1}\{a\exp(-\mathcal{E}\kappa t)\}\ , \qquad (5.5)$$

where

$$a=\tanh\{\mathcal{E}(T-\tau_0)/2\}\ .$$

In this expression of a, τ_0 is an initial value of τ and taken to be 580°C in this experiment.

The relation between volume V and refractive index n is combined through the specific refractivity R. If we apply the Lorenz-Lorentz formula:

$$R=\frac{n^2-1}{n^2+2}V\ ,$$

the volume V is written by the use of refractive index, as follows:

$$V=R\frac{n^2+2}{n^2-1}\ . \qquad (5.6)$$

Now the quantity R is considered to be constant independently of the conditions. This

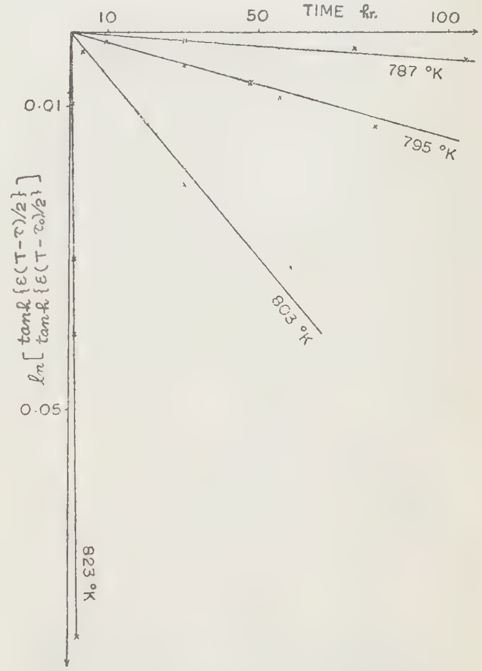

Fig. 6. Check of theory, assuming $\varepsilon=0.2$.

** After the beginning of our calculation, we have obtained the data of linear coefficients of thermal expansion of this glass by a private communication from Dr. N. M. Brandt (Mellon Institute, Univ. of Pittsburgh). Namely, $\alpha=50\times10^{-6}$ deg.$^{-1}$, $\alpha^*=8\times10^{-6}$ deg.$^{-1}$ and transition point $Tg=525$°C respectively. It has turned out that our estimations are precise exactly. In this opportunity we thank Dr. N. J. Kreidl (Bausch and Lomb Opt. Glass Co.) and Dr. N. M. Brandt for their sincere facility to our work.

consideration corresponds to that the polarizabilities of atoms or ions as constitutional elements are invariant during the annealing process. In practice, R is determined by the use of n_0 when (5.3) combined to (5.6). Then the values of $V(t)$ corresponding to the observed $n(t)$ is determined from Eq. (5.6), hence the values of $\tau(t)$ is able to be given by Eq. (5.3′). Therefore, when we substitute this $\tau(t)$ to the left-hand side of Eq. (5.4) and plot it versus time t, we would have a group of straight lines passing through the original point, provided that the Eq. (5.4) be satisfied. It will be recognized that Eq. (5.4) is nearly satisfied for any T, when the numerical value of unknown constant $\mathcal{E}$ is taken to be 0.2. It is shown in Fig. 6. Finally since the rate constants corresponding to parameter T can been determined from Fig. 6, [Table III], we shall try to plot $\ln\kappa$ versus the inverse of T. As seen in Fig. 7, the Eq. (4.2′) describing the rate constant κ as a function of temperature T is approximately satisfied. If we evaluate a value of activation energy B, from Fig. 7, it has resulted that B is decided to be 230 Kcal mol^{-1}, which is of the same order with that of thermal expansion obtained in the previous part (1). This result is considered to be quite reasonable, since the mechanism contained in this process comples to cause the continuous displacements of the network from one configuration to other—that is configurational readjustment in the internal structure. It is evident that the inner motions during the change of refractive index and the viscous flow are quite common. Further, starting from (5.5) we can obtain some kinds of approximate formulae representing the refractive index n as a function of time t, but we will not explain them in detail here.

Table III. Values of rate coefficients in the change of refractive index.

T	$T^{-1}\times10^3$	κ	$\ln\kappa$
787	1.27	0.000158	−8.75
795	1.26	0.000715	−7.24
803	1.25	0.0031	−5.78
823	1.22	0.17	−1.77

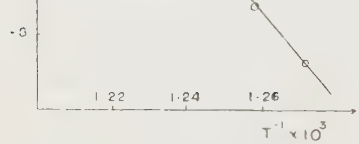

Fig. 7. $\ln\kappa$ versus T^{-1}.

Concluding from the comparisons with the above two examples of experiment, it can be regarded that our theoretical interpretation on the transitional phenomena of glass is probably valid. It is also considered that our theory will be able to be directly checked with the experimental results of the specific heat of glass. It is, however, unfortunate that hardly rare data on the specific heat have been known to us. We shall now state that the precise experiments on the specific heat during the annealing range have been undertaken and performed progressively by one of the authors, Kanai. Its results will be published elsewhere in the near future.

The authors wish to express our thanks to Dr. T. Moriya (Professor of glass technology, Tokyo Institute of Technology) and Dr. S. Suetoshi (Chief of Physics Department, Research Laboratory, Asahi Glass Co.) for their continuous encouragements.

We are also indebted to Dr. M. Mine (Professor of ceramics, University of Kyūsyū) and the staffs in both laboratories for their assistances and discussions.

References

1) A. Q. Tool, D. B. Doyd and G. E. Merrit: J. Amer. Ceram. Soc. **13** (1930) 632.

2) S. B. Thomas and G. S. Parks: J. Phys. Chem. **35** (1931) 2091.

3) Glasstone, Laidler and Eyring: 'The Theory of Rate Processes' (1941).

4) N. W. Taylor, E. P. Mc. Namara and J. Sherman: J. Soc. Glass Technol. **21** (1937) 61.

5) A. Q. Tool: J. Amer. Ceram. Soc. **29** (1946) 240.

6) P. W. Collyer: ibid. **30** (1947) 338.

7) L. Shartsis and S. Spinner: J. Res. Nat. Bur. Stand. **46** (1951) 176.

Short Notes

J. PHYS. SOC. JAPAN **9** (1954) 425

Electret

Chiyoe YAMANAKA
Faculty of Engineering, Osaka University
Japan

(Received January 17, 1954)

Since the experiment of Eguchi, many researches have been performed on the behaviors of electrets. But the mechanisms of electrets are still in ambiguity. I have carried out some experiments of Carnauba wax electret which was at about 60°C.

The experimental method was a usual one which was measured by a string electrometer and a capacitor.

From my experimental results, we can say the applied voltages themselves are important to determine the formation of electrets under a certain electric field. For instance, at the same field strength 7 KV/cm, under the applied voltage 1 KV, the electret was always charged as hetero which decayed with time. At the applied voltages between 1–3 KV, the electret was charged initially as hetero which decreased with time and then tended to homo. At the higher applied voltages, the electret was charged as homo from the first. This voltage depending effect seems to be caused by the distortion of the inner field of electrets. On account of space charges, the major portion of the applied voltages are imposed to the tip parts of electrets. Thus the applied voltages take a role to determine the ionization in electret which would supply the homo charges.

Homo charges in electrets also decayed with heating. During these processes, it was observed that the both surfaces of electrets showed temporarily the negative porality and then those charges decayed away. The difference of the mobility of positive and negative ions seems to be a reason of those behaviors.

To clarify the behaviors in boundary, we used the carnauba electret which was coated by the thin layer of paraffin, which is positively insensitive to electret phenomena. Those electrets also showed the ordinary variation from hetero to homo. When we took of the surface layer of paraffin by a grounded tool, the homo charges temporarily decayed. But they could recover to the same order of magnitude in a few days.

From the above three results, it can be concluded that the phenomena of electret depend upon the ionization of tip parts of wax as well as the ionization of interelectrode gaps.

References

F. Gutman: Rev. Mor. Phys. **20** (1948) 457.
M. Eguchi: Phil. Mag. **49** (1925) 178.
P. A. Thiessen, A. Winkel and K. Haerrman: Phys. Zeit. **37** (1938) 511.
B. Gross: British App. Phys. **1** (1950) 259.
Chem. Phys. **17** (1949) 10, 866.
Phys. Rev. **67** (1945) 253.
Phys. Rev. **66** (1944) 26.
W. F. G. Swann: Jour. Frank. Inst. **250** (1950) 219.
H. H. Wieder, Solkaufman: App. Phys. **24** (1953) 156. E. E. June (1953).

J. PHYS. SOC. JAPAN **9** (1954) 425∼426

Possible Mechanism of Ferroelectric Domain Boundary Movement

By Terutaro NAKAMURA
Department of Physics, Faculty of Science, University of Tokyo

(Received January 20, 1954)

It is probable that the 180° domain wall in barium titanate crystal is extremely thin, adjacent dipole planes being saturated in opposite directions without any transition layer, because calculations by Y. Takagi and W. Kinase[1] lead us to conclude that the energy for ferroelectric dipole arrangement is nearly equal to that for anti-ferroelectric one. Merz[2] observed hysteresis loops for the barium titanate crystal consisting of 180° domains exclusively, and found that the coercive field is very small (500 v/cm). It seems impossible for the extremely thin domain wall to move under such a small field. The purpose

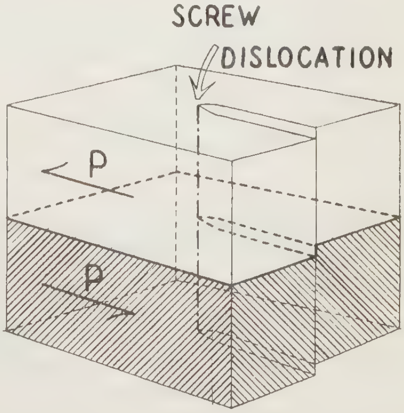

Fig. 1. Schematic picture of 180° domain boundary with a screw dislocation.

of the present paper is to suggest a possible mechanism of the domain boundary movement under a small electric field.

Assume that there exists a screw dislocation of Burgers' vector ***b*** perpendicular to the domain boundary, as shown in Fig. 1. Then the domain boundary must not be a plane but a helicoidal surface. From the intersection of the screw dislocation line with the domain boundary, a step of height b, which may be straight as well as bent, must extend to a free surface of the crystal or to another screw dislocation perpendicular to the domain boundary. This step forms a kind of "one dimentional imperfection" due to the displacement of ions. The amount of the ionic displacement is so small that this imperfection is very *weak* compared with the usual dislocations. When this step makes one revolution around the screw dislocation, the boundary surface moves by a distance equal to the step height, namely the magnitude of the Burgers' vector b of the screw dislocation. It will be seen that by repeated revolutions of the step the domain boundary can move smoothly. It will be readily understood that the movement of the helicoidal domain boundary by means of the revolutions of the step may take place by a very small electric field, whereas it would require a strong electric field for the domain boundary of a simple plane to displace without any imperfection.

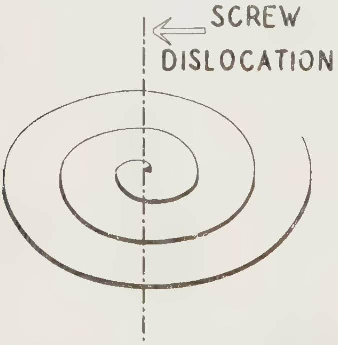

Fig. 2. Schematic picture of spiral step on the 180° domain boundary. (according to purely topological reasoning).

In the above discussion, it has been assumed that the step is possible to be a straight line. In reality, however, when it moves, it would not remain straight but would develop into a rotating spiral, owing to the higher angular velocity of the innermost portion (Fig. 2.). Successive closed loops of step will also be generated, when there are two screw dislocation lines of opposite signs passing through the boundary. These situations are closely analogous to those in the crystal growth[3].

In the case of 90° domain wall in barium titanate, the situation appears to be somewhat more complicated than the case of 180° domain wall, and 90° domain wall seems conceivable to be a little thicker, from a few to about ten lattice constant thick. The domain wall in rochelle salt may be also a little thicker, because the crystal in ferroelectric temperature range is always not far from its Curie point. In these cases, the simple displacement of the plane wall will take place by a small activation energy, and it will be unnecessary to take account of the mechanism presented in this paper.

In closing the discussion, another effect of dislocations on ferroelectric domains should be remaked briefly. Dislocations in ferroelectrics give rise to stress field around themselves, resulting in electric polarization. The stress Z_z in barium titanate crystal, and the stress Y_z in rochelle salt crystal, which affect the domain configuration, arise from edge dislocations parallel to a-axis in barium titanate, and screw dislocations parallel to b- and c-axes and edge dislocations parallel to a-axis in rochelle salt respectively. These dislocations, accordingly, have a tendency to fix the domains in the vicinity of them, where the stresses are very high. In the case of rochelle salt crystals, in which domain boundaries are perpendicular to b- and c-axes according to experiments, if the mechanism of domain boundary movement suggested in the present paper is the case, the situation is expected to be a little more complicated, because the screw dislocations perpendicular to the domain boundaries give rise to the effect of domain fixing.

The author wishes to express his gratitude to Prof. H. Takahasi for his invaluable advices and criticism, and to Prof. A. Ookawa for his advices and interests. This research has been supported in part by Grant in Aid for Fundamental Scientific Research from the Ministry of Education.

References

1) Y. Takagi: International Conference on Theoretical Physics, at Kyoto, Japan, Sep. 1953.
W. Kinase: ibid.
2) W. J. Merz: Phys. Rev. **91** (1953) 513.
3) F. C. Frank: Discussions of the Faraday Society, **5** (1949) 48 and 67.

J. Phys. Soc. Japan **9** (1954) 427~428

Hyperfine Structure of the Spectrum of Ruthenium. Part II

By Kiyoshi Murakawa
Institute of Science and Technology, Komaba-machi, Meguro-ku, Tokyo

(Received February 12, 1954)

In a previous work[1] the author studied the hyperfine structure (hfs) of the spectrum of Ru I, and found that some of the lines exhibit remarkable isotope shift and that the spins of the odd isotopes must be equal to 5/2 or larger. At that time impurity lines masked the genuine hfs of some important Ru I lines, but numerous plates showing no impurity lines have now been obtained. Fig. 1 shows the reproduction of some interference patterns of the Ru I spectrum. It shows especially that λ4361 is now not disturbed by other lines.

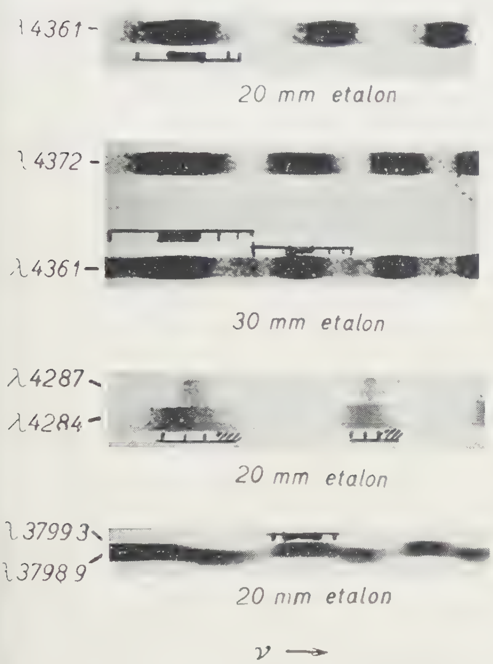

Fig. 1. Enlargement of some interference patterns of the spectrum of Ru I.

Measured hfs of some lines[2] are shown in Fig. 2. λ4361 was measured with special care, and the result shows that Ru^{101} and Ru^{99} must have equal spin and approximately equal magnetic moments. From the hfs of λ4361 and λ4171 the possibility of the spin being 9/2 or 7/2 is excluded and, therefore, both odd isotopes must have the spin 5/2. This conclusion is in agreement with that of Griffiths and Owen[3], who obtained the result by the method of paramagnetic resonance absorption. They obtained moreover $\mu^{101}/\mu^{99}=1.09\pm0.03$.

Measured hfs shown in Fig. 2 now allows us to calculate the magnetic moments (μ) of the odd isotopes. Necessary formulas* follow, all of them being calculated under the assumption of an *LS*-coupling.

$$A(4d^75p\,{}^3G_5)=\frac{11}{50}a_p+\frac{131}{210}a_d\ ,$$

$$A(4d^75s\,{}^3F_4)=-\frac{1}{16}a(s)+\frac{131}{168}a_d\ ,$$

$$A(4d^65s5p\,{}^5F_5)=\frac{1}{10}a(s)+\frac{17}{75}a_p+\frac{392}{1125}a_d\ ,$$

$$A(4d^65s5p\,{}^7P_4)=\frac{1}{8}a(s)+\frac{22}{35}a_d\ ,$$

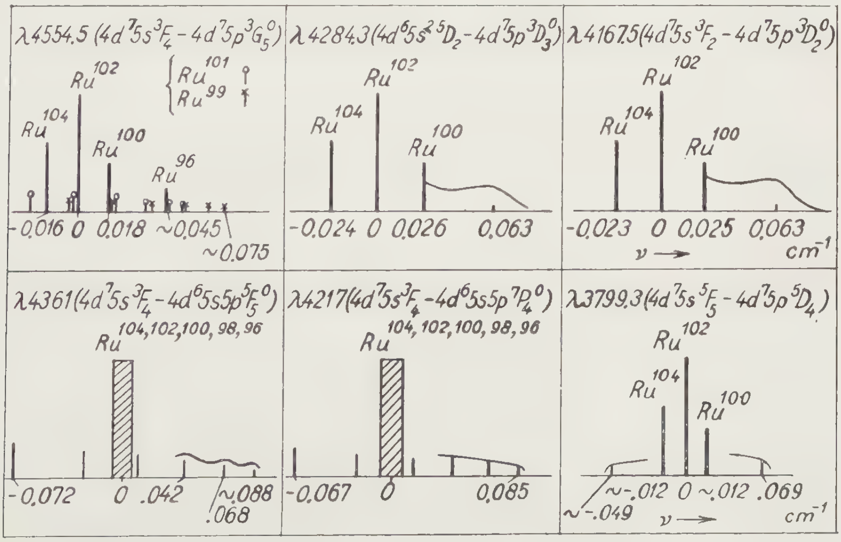

Fig. 2. Hyperfine structure of the spectrum of Ru I.

$$A(4d^75s\,{}^5F_5)=\frac{1}{10}a(s)+\frac{22}{35}a_d\ ,$$

$$A(4d^75p\,{}^5D_4)=-\frac{19}{105}a_p+\frac{508}{735}a_d\ ,$$

Putting the values $(dn^*/dn)/n_{5s}{}^{*3}=0.438$, $F=1.20$, $\zeta_{5p}\approx560\ \mathrm{cm}^{-1}$, $\zeta_{4d}=820\ \mathrm{cm}^{-1}$ and the observed values in the above formulas, we get

$$\mu(\mathrm{Ru}^{101})=-0.6\pm0.2\ \mathrm{n.m.}\quad \mu(\mathrm{Ru}^{99})=-0.6\pm0.2\ \mathrm{n.m.}$$

In each of the lines showing isotope shift, the position of the Ru^{96}-component is difficult to measure, owing to the disturbance of the odd isotope components (see, for example, $\lambda4554.5$). The ratio of the distances between neighboring even isotope components can, therefore, be given only approximately:

$$\Delta\nu(104-102):\Delta\nu(102-100):\Delta\nu(100-96)/2$$
$$=0.9\pm0.1:1:0.75\pm0.2.$$

Full account of the isotope shift in the spectrum of Ru I will be published in the future.

References

1) K. Murakawa: J. Phys. Soc. Japan **8** (1953) 535.

2) Classification of the Ru I spectrum was published by L. A. Sommer: Zeits. f. Phys. **37** (1926), 1 and W. F. Meggers and O. Laporte: Journ. Washington Acad. Scie. **16** (1926) 143 and G. R. Harrison and J. R. Mc Nally: Phys. Rev. **58** (1940) 703. In cases where no electron configuration was given, it was determined so as to be consistent with the measured hfs.

3) Griffiths and J. Owen: Proc. Phys. Soc. London **65** (1952) 951.

---

* Relativity corrections for the p and d electrons were neglected.

J. Phys. Soc. Japan **9** (1954) 428～430

Slip Bands in an α-Brass Crystal

By Hideji Suzuki and F. E. Fujita

*The Research Institute for Iron, Steel
and Other Metals, Tohoku University, Sendai*

(Received February 15, 1954)

In the course of the study of plastic deformation of α-brass crystals we have observed the surface structures of deformed crystals by means of an electron microscope using a high resolution replica technique, which has been employed by one of the authors[1]. One of these photographs seemed to show a very important character of the structure owing to its very favourable direction of the surface.

This photograph, shown here, reveals very fine structures parallel to the trace of the operative slip plane and also etching structures produced during the electro-polishing before the deformation. The etching structures have very low piramid shape with long edge in one direction which is nearly perpendicular to the trace of slip plane in the photograph. The most remarkable fact is that there are layers with considerable thickness as marked around the photograph, in which the long edges of the etch-pits are along to another direction. Fig. 2 represents the relation between pits before and after the deformation. We can, therefore, estimate the amount of shear from the angle between the directions of the edges of etch-pits before and after the deformation, knowing the angle between the operative slip plane and the free surface and also the angle between the slip direction and the surface. The orientations of the crystal and the surface were shown in Fig. 3. Assuming the initial direction of the edge of the etch-pits be parallel to the edges in zones in which these are nearly perpendicular to the slip plane, we obtain values from 1.0 to 1.3 as the net amount of shear in the deformed layer, which is nearly equal to that caused by the motion of dislocations situated in every atomic planes, one per one atomic plane.

One of the authors[2] has pointed out that Frank-Read sources multiplying dislocations in only one atomic plane, which has been proposed first by Frank and Read, seemed to be very rare compared with those multiplying in successive atomic planes, because the life time until the sources are swept out to the surface or annihilated in the crystal is considerably shorter in the case of the former type than the latter. And it was also pointed out that the surface structure of deformed pure crystals might be produced rather by the operation of the surface sources, which may be able to multiply dislocations in one atomic plane, than those in the interior because of greater length of surface sources than those of the interior.

However, on account of the locking force for the dislocation the operation of sources would depend scarcely on their length in these alloys, so the surface structures in α-brass seem to represent the situation in the crystal more accurately than in pure metals. The fine structure in the deformed zone may be caused by the disturbance in the disturibution of dislocations due to the interaction between sweeping dislocations and intersecting dislocations as noted in another paper[2].

Kuhlman-Wilsdorf and Wilsdorf[3] have observed the surface structures in cold worked polycry-

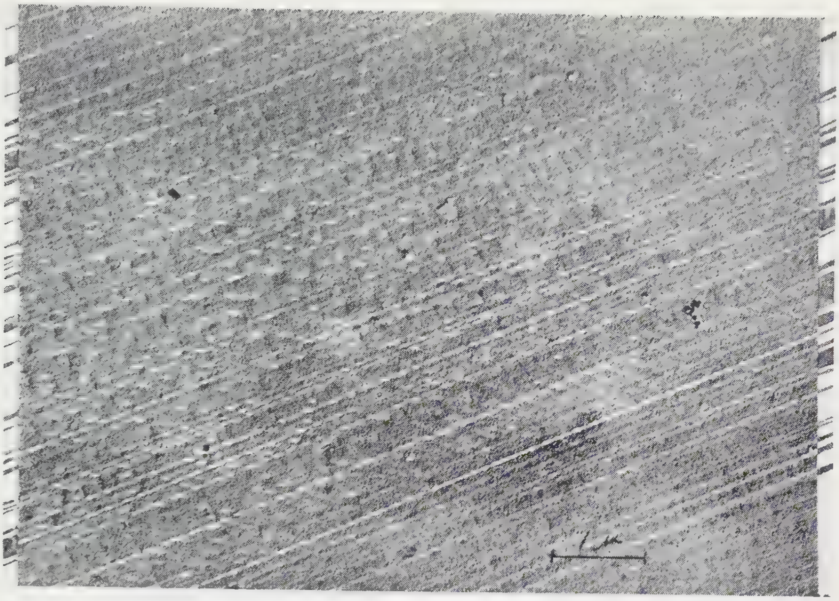

Fig. 1. ×12,000

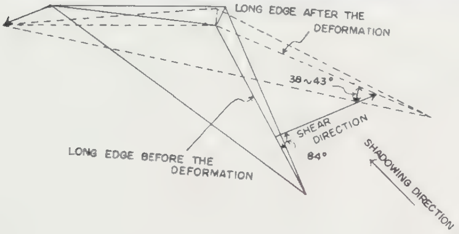
LONG EDGE AFTER THE DEFORMATION
38~43°
SHEAR DIRECTION
84°
SHADOWING DIRECTION
LONG EDGE BEFORE THE DEFORMATION

Fig. 2. Etch-pit before and after the deformation.

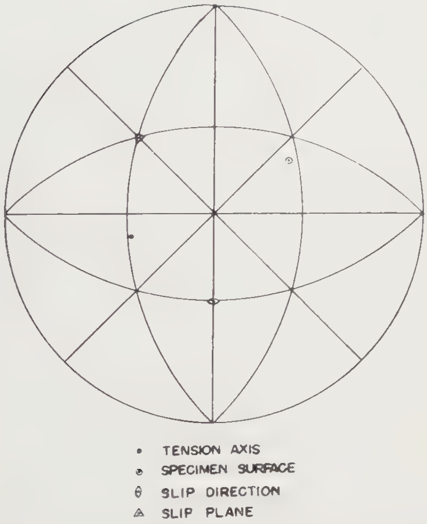

Fig. 3. Stereographic projection of the crystal orientation.

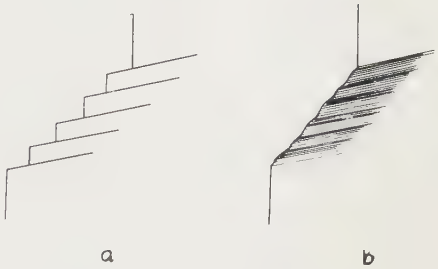

Fig. 4. Schematic representation of fine structure in a slip band due to the discrete and the gradual change in the distribution of slip amounts.

stalline α-brass and found large slip without any fine structure. Their observation, however, does not seem to be contradictory to our own. Because the fine structure in the large slip does not seem to correspond to the discrete distribution of elementary slip (Fig. 4a) but to the gradual change in distribution (Fig. 4b), and the observation from the slip direction could not be resolved the structure by the change in contrast. It is obvious that the width of a slip line could not be estimated in polycrystalline material. But the difference in blackning between parallel slip lines in their photographs, for example Plate IV Fig. 23, could not be explained without assuming a finite width of the slip lines.

References

1) F. E. Fujita, T. Suzuki and M. Yamamoto: To be published.

2) H. Suzuki: To be published; See also T. Suzuki and H. Suzuki: International Conference of Theoretical Physics held at Kyoto, September 1953, (to be published).

3) D. Kuhlman-Wilsdorf and H. Wilsdorf: Acta Metallurgica. **1** (1953) 394.

J. PHYS. SOC. JAPAN **9** (1954) 430~431

An Attempt to Treat the Interaction between Electrons and Lattice Vibrations

By Fumihiko TAKANO

Department of Physics, Tokyo University of Education

(Received February 22, 1954)

In his theory of superconductivity,[1] Bardeen has shown that the shift of the energy levels of the electron due to the interaction with lattice vibrations is given by

$$E_{\boldsymbol{k}}-\varepsilon_{\boldsymbol{k}}=\sum|M_{\boldsymbol{k}\boldsymbol{k}'}|^2/(E_{\boldsymbol{k}}-\varepsilon_{\boldsymbol{k}'}-\hbar\omega_{\boldsymbol{k}\boldsymbol{k}'}) , \qquad (1)$$

where $\varepsilon_{\boldsymbol{k}}$ is the energy level of the electron free from the interaction and $\omega_{\boldsymbol{k}\boldsymbol{k}'}$ is the angular frequency of lattice vibrations for the mode which connects the state $\boldsymbol{k}$ and $\boldsymbol{k}'$. $M_{\boldsymbol{k}\boldsymbol{k}'}$ is the usual matrix element of the interaction energy. But his procedure seems to be unsatisfactory in two points.

First, he treated only one electron as if it would interact with lattice vibrations independently with other electrons. Secondly, in his adiabatic approximation, he took a rather ambigous averaging over lattice coordinates. So we attempt to treat the problem along the line of Bardeen as rigorously as possible.

The Hamiltonian of the total system is taken as the usual form,

$$H=H_{\text{el}}+H_L+H_{\text{int.}} ,$$

$$H_{\text{el}}=\sum_i\left(\frac{1}{2m}\boldsymbol{p}_i^2+V_p(\boldsymbol{r}_i)\right) ,$$

$$H_L=\sum_q\sum_j\frac{1}{2}\hbar\omega_{qj}(a_{qj}^*a_{qj}+a_{qj}a_{qj}^*) ,$$

$$H_{\text{int.}}=-\sum_i\boldsymbol{u}(a_q,\boldsymbol{r}_i)\cdot\text{grad }V_p(\boldsymbol{r}_i) ,$$

$$\boldsymbol{u}(a_q,\boldsymbol{r})=\frac{1}{\sqrt{N}}\sum_q\sum_j\boldsymbol{e}_{qj}(a_{qj}e^{iqr}+a_{qj}^*e^{-iqr})\sqrt{\frac{\hbar}{2M\omega_{qj}}} , \qquad (2)$$

where the suffix j indicates the direction of polarization of lattice waves, and V_p is the periodic potential due to the ions in equilibrium positions. Adopting an adiabatic approximation like Bardeen, we take as the total wave function

$$\Psi(\boldsymbol{r}_i, a_q)=\Phi(\boldsymbol{r}_i, a_q)\Theta(a_q) .$$

We must solve the Schrödinger equation

$$H\Psi=E\Psi .$$

Multiplying Φ^* on both sides of this from the left and integrating over the electron coordinates, we obtain an equation

$$(\Phi, H\Phi)\Theta=E(\Phi,\Phi)\Theta . \qquad (3)$$

Regarding eq. (3) as an equation for Θ, we must solve it.

We assume the form of Φ to be

$$\Phi=\Phi\{n_{\boldsymbol{k}}^0\}+\sum_{\boldsymbol{k},q}b_{\boldsymbol{k},q}a_q\Phi\{n_{\boldsymbol{k}}^0\}-1_{\boldsymbol{k}}+1_{\boldsymbol{k}+q} , \qquad (4)$$

where $\Phi\{n_{\boldsymbol{k}}^0\}$ is the Slater determinant in which the occupation numbers of the levels are given by the set $\{n_{\boldsymbol{k}}^0\}\cdot\{n_{\boldsymbol{k}}^0\}-1_{\boldsymbol{k}}+1_{\boldsymbol{k}+q}$ expresses the state in which one electron is excited to a state $\boldsymbol{k}+\boldsymbol{q}$ from $\boldsymbol{k}$. $b_{\boldsymbol{k},q}$ are parameters to be determined later.

Substituting eq. (4) in eq. (3) we obtain an equation for Θ:

$$\begin{aligned}
&E\left[1+\frac{1}{2}\sum_{\boldsymbol{k},q}|b_{\boldsymbol{k},q}|^2(a_q^*a_q+a_q\cdot a_q^*)\right]\Theta\\
&=\Big[E_0+\sum_q\frac{1}{2}\hbar\omega_q(a_q^*a_q+a_qa_q^*)\\
&\quad+\frac{1}{2}\sum_{\boldsymbol{k},q}|b_{\boldsymbol{k},q}|^2\{E_0-\varepsilon_{\boldsymbol{k}}+\varepsilon_{\boldsymbol{k}+q}+\hbar\omega_q\}\\
&\quad\times n_{\boldsymbol{k}}^0(1-n_{\boldsymbol{k}+q}^0)(a_q^*a_q+a_qa_q^*)\\
&\quad+\left\{\frac{1}{2}\sum_{\boldsymbol{k},q}|b_{\boldsymbol{k},q}|^2n_{\boldsymbol{k}}^0(1-n_{\boldsymbol{k}+q}^0)(a_q^*a_q+a_qa_q^*)\right.\\
&\quad\times\left\{\sum_q\frac{1}{2}\hbar\omega_q(a_q^*a_q+a_qa_q^*)\right\}\\
&\quad-\frac{1}{\sqrt{N}}\sum_{\boldsymbol{k},q}\frac{1}{2}(b_{\boldsymbol{k},q}^*M_q^++b_{\boldsymbol{k},q}M_q^-)\\
&\quad\left.\times n_{\boldsymbol{k}}^0(1-n_{\boldsymbol{k}+q}^0)(a_q^*a_q+a_qa_q^*)\right\}\Theta , \qquad (5)
\end{aligned}$$

where we neglect the term in third power of a or a^*.

Setting

$$\langle a_q^*a_q\rangle=N_q \quad\text{and}\quad W=E-E_0-\sum_q\frac{1}{2}\hbar\omega_q ,$$

and minimizing W with respect to $b_{\boldsymbol{k},q}$, we obtain easily an equation for W,

$$W=\frac{1}{N}\sum_{\boldsymbol{k}}\sum_q\frac{|M_q|^2n_{\boldsymbol{k}}^0(1-n_{\boldsymbol{k}+q}^0)}{W+\varepsilon_{\boldsymbol{k}}-\varepsilon_{\boldsymbol{k}+q}-\hbar\omega_q}\left(N_q+\frac{1}{2}\right) . \qquad (6)$$

Eq. (6) resembles to eq. (1). Naturally, if we set $W=0$, $N_q=0$ in the right hand side of eq. (6), we get the Frohlich's expression[2] obtained by second order perturbation, from which he derived a shell distribution as a stable distribution of electrons.

It seems to us that one must treat the system as a whole and cannot treat only one electron to be influenced by the interaction with lattice waves. So Bardeen's expression (1) cannot be derived in a rigorous way.

Of course, for sufficiently strong interaction, it is not a good approximation to neglect the term in third power of a or a^*, but it seems certainly better than the perturbation method.

As the next step of calculation, it remains to solve eq. (6) for W, and then to determine the electron distribution $\{n_k^0\}$ giving the minimum value of E. The calculation is now being carried out, and the result will be published later.

References

1) J. Bardeen: Phys. Rev. **80** (1950) 567.
2) H. Fröhlich: Phys. Rev. **79** (1950) 845.

J. Phys. Soc. Japan **9** (1954) 431~432

On the Breakdown of Colored KCl

By Yoshio Inuishi and Tokuo Suita
Faculty of Engineering, Osaka University

(Received February 26, 1954)

The importance of space charge distortion of prebreakdown field in Alkali-Halides, were often stressed by von Hippel1)4) and by the authors.2) To obtain further information on this subject, the dielectric breakdown of X-ray colored KCl single crystal was worked, and the various interesting effects of space charge and initial electron injection upon the pheromena are concluded here.

Some of the well annealed KCl specimens were colored by X-ray irradiation at room temperature (1 hour, ½ hour), while the others were remained uncolored. Breakdown voltages of these colored and uncolored KCl specimen [(100) direction)], were obtained under various condition (wave form, temperature) with or without illumination of visible light (incandescent lamp).

The results obtained are tabulated in Table I, from which the following conclusions are derived together with the other experimental facts.

(1) D. C. breakdown voltage of colored KCl is found to decrease greatly with the illumination of visible light, while in the uncolored crystals no effect is observed. The low breakdown voltage in illuminated colored crystal does not depend on the temperature in the available range of temperatures of our observations.

(2) A. C. (60 C.P.S.) breakdown voltages of both colored and uncolored crystals are almost equal to each other and do not change by light illumination.

(3) Impulse breakdown voltages (0.1/100 μs) of colored and uncolored crystals are almost equal to each other and are not affected by light illumination, furthermore being independent of temperature.2)

(4) D. C. breakdown voltages of colored KCl decrease with both the intensity of visible light and the concentration of F centres.

5) At high temperatures ($>$100°C) the effects of coloration on the breakdown voltage disappear, corresponding to quick breaching. Detailed theoretical consideration of these "photo-breakdown" phenomena will need further data on time lag and conduction current measurements. The pure thermal mechanism, however seems to be excluded in our phenomena because of the above fact (2). The following mechanisms may be con-

Table I.

Wave form of voltage		D.C. kV		A.C. max kV (60 ∞)		impulse kV	
Sample thickness 0.5 mm	B.D. temperature	With * illumination	Without illumination	With * illumination	Without illumination	With * illumination	Without illumination
X-ray	100°C	40 kV	43 kV			21 kV	22 kV
Colored (½hr)	10	12	35	28 kV	25 kV	18	19
KCl	0	10	30	17	21	20	21
(0.5 mm)	− 20	8	23	17	17	21	21
Uncolored	100°C	43 kV	43 kV			21 kV	20 kV
	10	27	30	24 kV	24 kV	21	18
KCl	0	30	30	18	18	19	20
(0.5 mm)	− 20	25	25	17	17	21	21

* Ca 1000 lux at Specimen.

sidered to give rise to the various kinds of space charge effects reported by us. In KCl two types of space charge may be considered to take place according to the above mentioned experimental facts.

(a) trapped electrons in normally neutral imperfections (like coupled vacancies, ionically neutralized divalent impurities, and F′ centeres etc.). These negative space charges in front of the cathode play predominant role in suppressing electron injection (Fig. 1 (a)) and therefore, are responsible for the increase of D.C. & A.C. breakdown strength by interrupting collective avalanche cooperation as was suggested by A. von Hippel[1].

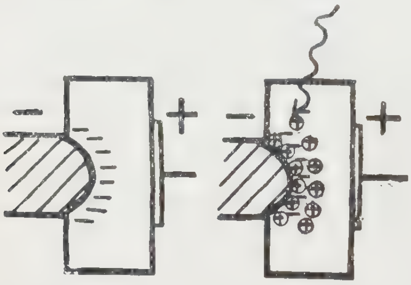

(a) (b)

Fig. 1.

(b) ionized F centeres. These positive space charge may be produced by the illumination of F band-light under the influence of electric field,[4] and then may be taken to neutralize negative space charge (a) to cause enhanced electron field emission from cathode[4]: Which situation consequently might lead to a sort of collective high energy electron breakdown of Fröhlich.[3] Relatively long relaxation time involved in these processes[4] may be considered to be responsible for the occurrence of "photo breakdown" only in D.C.

References

(1) von Hippel. et. al.: Phys. Rev. **76** (1949) 127.

2) Y. Inuishi and T. Suita: Jap. J. Phys. Soc. **8** (1953) 567; Tech. Rept. Osaka Univ. **3** (1953) 269.

3) H. Frödlich et. al.: Proc. Phys. Soc. A **63** (1950) 6.

4) Von Hippel. et. al: Phys. Rev. **91** (1953) 568.

J. Phys. Soc. Japan **9** (1954) 432~434

Temperature Dependence of Fluctuation of Sparking Voltages in a Gas Discharge Tube

By Makoto Hayashi

Laboratory of Physics, Department of General Education, Nagoya University

and Yasunori Miyoshi

Department of Electrical Engineering, Nagoya Institute of Technology

(Received February 12, 1954)

The sparking voltages of gas discharge tubes always fluctuate in the time lag, and the mechanism of this fluctuation seems to be very complicated. This fluctuation was investigated by the method of Zuber[1] and Tamagawa[2], and almost reproducible results were obtained depending on the temperature. The discharge tube used has tungsten electrodes and is filled with hydrogen. The gap length is about 0.6 mm and the pressure is about 20 mmHg.

Raising the voltage linearly at 30 volts per second, we measured the distribution of the sparking voltages. Several examples of the distribution are shown in Fig. 1. Every cross (×)

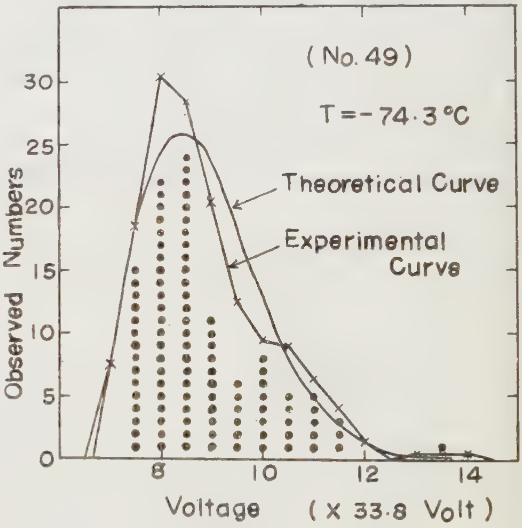

No. 49

$\overline{V}=8.84$	$\overline{v}$	V_s	
$\lvert\overline{\delta v}\rvert=0.935$	2.17	6.67	$k=3.08$
$\overline{\delta v^2}=1.391$	2.25	6.59	$V_s=225\text{V}$
$\lvert\overline{\varDelta}\rvert=1.263$	2.16	6.68	$f=33.1$
$\overline{\varDelta^2}=2.713$	2.23	6.61	
mean value	2.20	6.64	

(A)

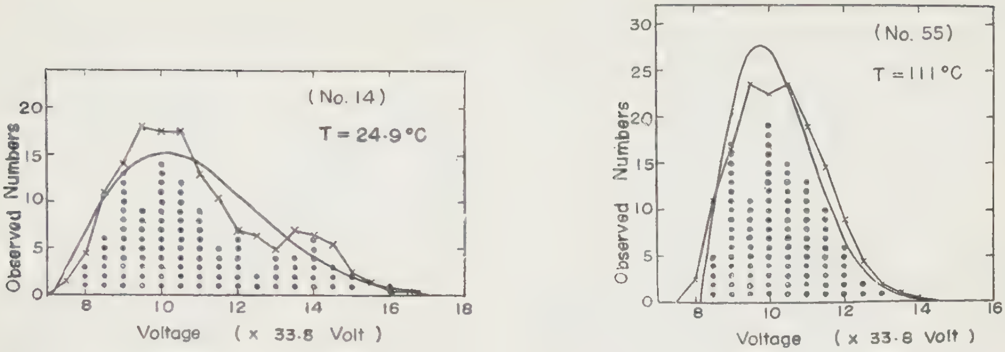

No. 14

$\overline{V}=10.89$	$\overline{v}$	V_s	
$\lvert\overline{\delta v}\rvert=1.54$	3.57	7.32	$k=8.88$
$\overline{\delta v^2}=3.54$	3.60	7.29	$V_s=242V$
$\lvert\overline{\Delta}\rvert=2.30$	3.93	6.96	$f=52.1$
$\overline{\Delta^2}=7.94$	3.81	7.08	
mean value	3.73	7.16	

(B)

No. 55

$\overline{V}=10.19$	$\overline{v}$	V_s	
$\lvert\overline{\delta v}\rvert=0.897$	2.08	8.11	$k=2.72$
$\overline{\delta v^2}=1.207$	2.10	8.09	$V_s=275V$
$\lvert\overline{\Delta}\rvert=1.200$	2.05	8.14	$f=25.4$
$\overline{\Delta^2}=2.250$	2.03	8.16	
mean value	2.07	8.13	

(C)

Fig. 1. The distribution of random sparking voltages at (A) −74.3°C, (B) 24.9°C, and (C) 111°C, and its calculated results. The raising rate of voltage is 30 V/sec and the mean rest time is 12 sec. constant. The symbols of the tables are as same as Tamagawa (see reference 2).

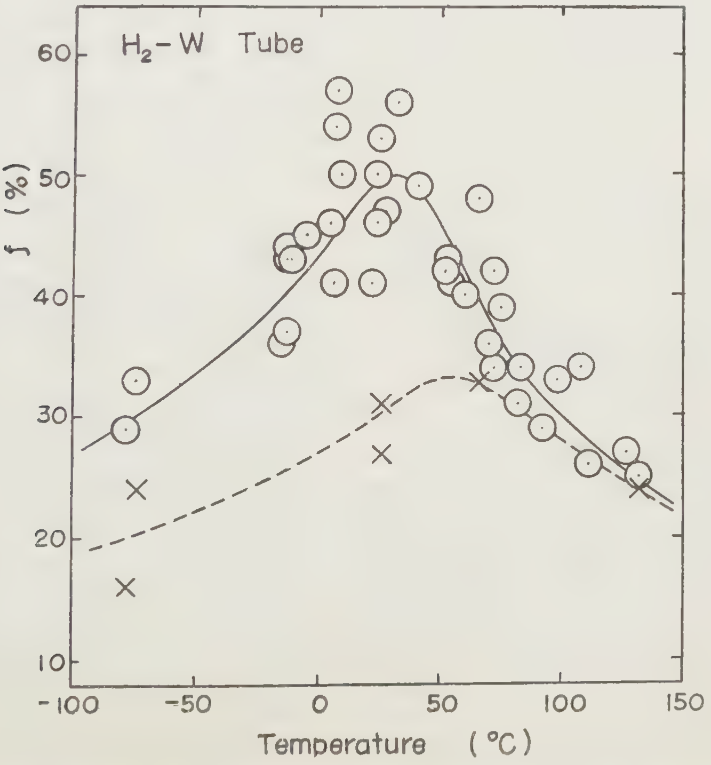

Fig. 2. The temperature dependence of the fluctuation f. Two runs show the exchange of the polarity of electrodes. Both electrodes have the same geometry.

on the experimental curves in Fig. 1 corresponds to a mean value of the number of three observations at V, $V-0.5$ and $V+0.5$.

These fluctuations satisfy fairly well, as Tamagawa pointed out, the equation

$$W(v)dv=\frac{v}{a\,k}\exp\left(-\frac{v^2}{2ak}\right)dv\,.$$

Here $v=V-V_s$, V is the random sparking voltage, V_s the static breakdown voltage, i.e. the sparking voltage when the raising rate of the voltage is very small, a the raising rate of voltage, and k the constant which depends mainly on the kind of gases and material of the electrode.

Each distribution was measured at a constant temperature between -78°C and 130°C and was obtained usually from one hundred measurements of the sparking potential. In order to show the degree of fluctuation quantitatively let us define

$$f=(\overline{V}-V_s)/V_s\times 100\ (\%),$$

where $\overline{V}$ is the average value of the sparking potential. The temperature dependence of the fluctuation f is shown in Fig. 2. The mean rest time $\bar{t}$ is a constant 12 seconds in Fig. 2, and the dependence on $\bar{t}$ is shown in Fig. 3 at a constant temperature. There was no effect of irradiation owing to the absorption of ultra-violet ray by the glass wall of the tube and to a high work function of the cathode material tungsten.

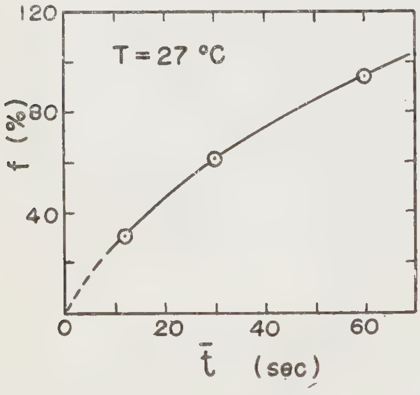

Fig. 3. The effect of mean rest time $\bar{t}$ at 27°C.

Fig. 2 shows a peak at about 40°C, and Fig. 3 indicates that $f\propto\sqrt{\bar{t}}$, and these characteristics are similar to those of gas adsorption on metal surfaces[3]. We consider, therefore, that the fluctuation may be due to the gas adsorption on the cathode.

The authors wish to express sincere thanks to Assistant Prof. Y. Mizuno for his encouragement, and Mr. H. Tamagawa for his kind advice and his lending of the discharge tube.

References

1) K. Zuber: Ann. d. Phys. **81** (1926) 205.

2) H. Tamadgawa: Electrotech. Papers, **2** (1950) 9 (in Japanese).

3) for example, C. J. Smithells: Gases and Metals (1937) 32 and 42.

J. PHYS. SOC. JAPAN **9** (1954) 434~435

Nuclear Quadrupole Interaction in Sodium Chlorate and Sodium Bromate

By Junkichi ITOH and Riichiro KUSAKA

Department of Physics, Osaka University, Osaka, Japan

(Received March 12, 1954)

The nuclear electric quadrupole spectrum of a nucleus of spin 3/2 consists of a single line, resulting from the transition between two levels with $m=\pm3/2$ and $m=\pm1/2$ [1)2)]. When a weak magnetic field is applied, this line shows the Zeemen effect and splits into four components[3]. In the case of sodium chlorate, the Zeeman effect of the nuclear quadrupole spectrum of the chlorine nucleus has been studied already[4]. Besides these lines, one more line is expected, which corresponds to the transition between two levels splitted from the level with $m=\pm1/2$ by the magnetic field. When $a\ (=e^2qQ/4)$ is much larger than $b\ (=\mu H/I)$, the energy of this line is calculated by a simple perturbation theory to be[3]

$$h\nu=b\sqrt{4\sin^2\theta+\cos^2\theta}\,, \qquad (1)$$

provided one assumes an axially symmetric gradient of the electric field at the nucleus; θ is the angle between the direction of the symmetry axis and the magnetic field. We measured this line for the bromine nuclei in a single crystal of sodium bromate. Fig. 1 shows the results of the experiment and the theoretical calculation, in which values of the resonance field are plotted against the orientation of the crystal, the frequency of the detector being maintained constant. The agreement between experiment and the theoretical formula (1) seems satisfactory[5].

When a is not very large compared with b, a further approximation is necessary in the calculation of the energy of this line. In the case of $\theta=90°$, the calculated energy up to the forth order power in b/a is given by[1)3)]

$$h\nu=2b\left\{1-\frac{3}{16}\left(\frac{b}{a}\right)^2+\frac{15}{256}\left(\frac{b}{a}\right)^4\right\}. \qquad (2)$$

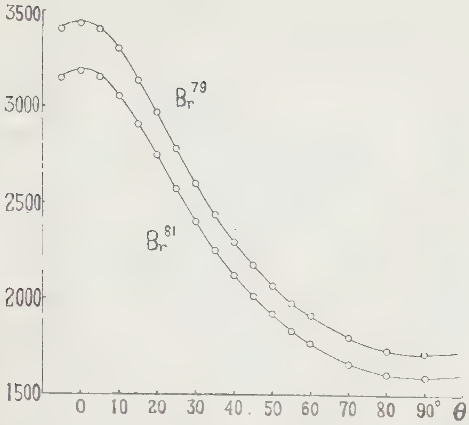

Fig. 1. The experimental and the theoretical results for the line corresponding to (1). Circular marks show the experimental result, while the curves are the calculated ones. The frequency which is kept constant, is 5.80 Mc/sec. The ordinate is the potentiometer reading which is proportional to the magnetic field strength, a value of 3000 of the ordinate corresponding to a field strength of 4720 gauss.

From the resonance frequency of this line and the Zeeman frequency of the nucleus at a fixed magnetic field, the value of a is obtainable1). We performed the experiment for Cl^{35} nucleus in a single crystal of sodium chlorate at about 7200 gauss. Taking the nuclear magnetic resonance frequency of Cl^- in LiCl aq. for b/h, the experimental value of $2b/h-\nu$ was found to be 40.8 ± 2 Kc/sec at $\nu=6.000$ Mc/sec. On the other hand, using the value, 29.920 Mc/sec, of $2a$ obtained from the pure quadrupole resonance6), $2b/h-\nu$ is calculated to be 45.6 Kc/sec by using (2). The difference is considered to be due to the chemical shift of the chlorine nucleus in sodium chlorate compared with that in Cl^-, amounting to $(8\pm3)\times10^{-4}$ in paramagnetic direction7). This value may be compared with the similar shift in $HClO_4$, 9×10^{-4} obtained by Proctor and Yu8). The rather large uncertainty in our measurement is caused by the difficulty in determining the true resonance position, since the intensity of the absorption is weak and the absorption line has a width of ~2 gauss, and, moreover, the magnetic field is slightly unstable. We have not yet performed the experiment to measure such shifts of Br nuclei in $NaBrO_3$.

We also performed the magnetic resonance experiment for the sodium nucleus in these crystals. In this case, the resonance lines corresponding to the electric quadrupole splitting of the nuclear magnetic resonance line1)9) were observed around ~5000 gauss at the frequency of 5.8 Mc/sec. The result of our experiment shows that the gradient of the electric field at the nucleus is also axially symmetric, and the direction of the symmetry axis coincides with that for the halogen nucleus. The value of e^2qQ for the sodium nucleus in sodium chlorate and sodium bromate is found to be 801 ± 8 and 864 ± 8 Kc/sec, respectively.

References

1) R. V. Pound: Phys. Rev. **79** (1950) 685.
2) H. G. Dehmelt and H. Kruger: Z. Physik **129** (1950) 401.
3) H. Kruger: Z. Physik **130** (1951) 321.
4) R. Livingston: Science **118** (1953) 61.
Y. Ting, E. Manring, and D. Williams: Phys. Rev. **92** (1953) 1581.
5) Since the frequency of the pure quadrupole resonance of Br^{79} in this crystal is 178 Mc/sec, the higher order term in (b/a) is less than 2×10^{-4} of (1) which is the same order of the experimental error in determining the resonance field.
6) Wang, Townes, Schawlow, and Holden: Phys. Rev. **86** (1952) 809.
7) T. Kanda and Y. Masuda (Kobe University) searched the magnetic resonance of the chlorine nucleus in the water solution of $NaClO_3$ to measure its chemical shift, but they could not observe the resonance.
8) W. G. Proctor and F. G. Yu: Phys. Rev. **81** (1951) 20.
9) G. Becker: Z. Physik **130** (1951) 415.

J. PHYS. SOC. JAPAN **9** (1954) 435~437

Cathodo-luminescence Study of (BaSr)O

By Kin-ichi NOGA and Koji NAKAMURA
Matsuda Research Laboratory,
Tokyo Shibaura Electric Co.
Kawasaki-shi, Kanagawa-ken, Japan

(Received March 17, 1954)

It has been concluded from the X-ray diffraction studies1)2)3)4) on the crystal structure of (BaSr)O that the homogeneous solid solution is formed by the heat treatment following to the decomposition of $(BaSr)CO_3$. On the other hand, Kawamura5) has suggested a coexistence of two separate phases of BaO and SrO from the cathodoluminescence studies on BaO, SrO and (BaSr)O containing a small quantity of samarium oxide. The luminescence of these specimens may be due to an inner shell transition in samarium ions, so the informations concerning the crystal structure obtained should be limited within a rather narrow region surrounding samarium ions. On the contrary, the X-ray method should give the result averaged over the wide coherent region, so our present studies on the cathodo-luminescence are of some meanings as an intermediate case.

The experimental apparatus consists of a vacuum tube furnished with an electron gun and a target on which the sample was sprayed in the form of carbonate. The carbonates were converted in to oxides by heating on the exhaust manifold. Precautions were taken so as to prevent the target from deposition of the getter and the cathode materials. The luminescence was excited by bombarding the sample with 250 volt electrons at a beam current of 2 mA. The samples were not heated deliberately, but they could not be free from some temperature rise due to the electron bombardment.

The emitted light was photographed by a Zeiss Drei Prismen spectrometer with a resolving power of 22Å per mm for D-line.

The luminescence spectra of BaO, SrO and (BaSr)O are shown in Fig. 1. (BaSr)O used here was an equimolar double oxide. All the samples were well activated thermionically before the luminescence measurements. All curves are normalized to the same height at the main peak lying in long wavelength region.

The wavelength of several bands identified from the curves are listed in Table I, in which the recent data on BaO by Stout⁶⁾ are also cited. The luminescence bands at 465, 595 and 650 mμ in his data are also found in our results. Furthermore, SrO and (BaSr)O show the luminescence spectra similar to that of BaO, having the corresponding bands as seen from Fig. 1. Each band in the luminescence spectrum of (BaSr)O is located just between the corresponding bands of BaO and SrO, and not the simple superposition of two individual spectra for BaO and SrO. It seems likely from this fact that the homogeneous

Table I. Peaks in luminescence spectra of BaO, SrO and (BaSr)O.

BaO				(BaSr)O		SrO	
by Stout		by authors					
mμ	(ev)	mμ	(ev)	mμ	(ev)	mμ	(ev)
345	(3.60)						
410	(3.02)						
465	(2.67)	465	(2.67)	440	(2.82)	430	(2.89)
		490	(2.54)	486	(2.56)	470	(2.65)
550	(2.25)	565	(2.20)				
595	(2.08)	600	(2.05)				
650	(1.91)	645	(1.93)	617	(2.02)	567	(2.19)
700	(1.71)						

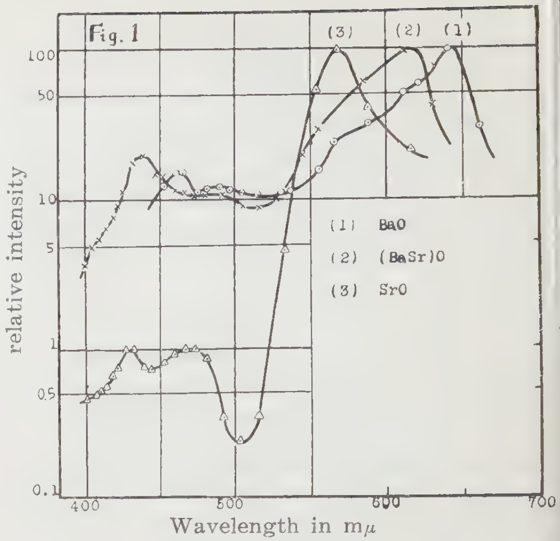

Fig. 1.

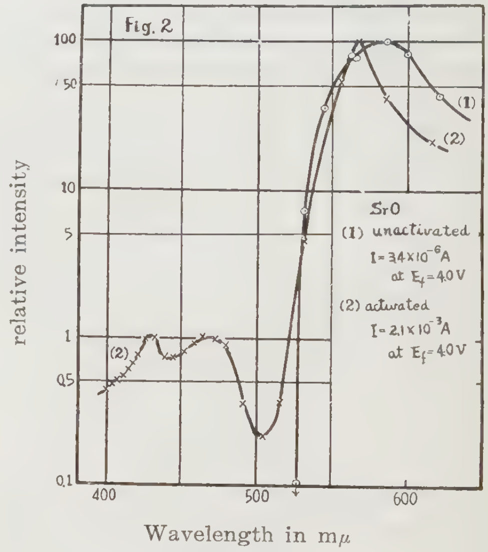

Fig. 2.

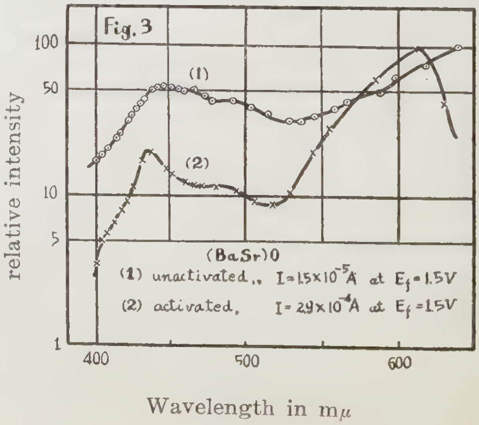

Fig. 3.

solid solution is formed in (BaSr)O as expected from the X-ray measurements.

The luminescence bands shifted towards shorter wavelength side with increasing thermionic activity. Figs. 2 and 3 show this in the case on SrO and (BaSr)O respectively. In these figures, the degree of activation is shown by the saturated thermionic emission current at a constant filament voltage E_f given in the figure. Result on BaO could not be obtained because a change in activity was induced by the prolonged electron bombardment during the exposure. No explanation for the shift of luminescence band with the thermionic activity is presented now.

The dependence of the luminescence intensity on the thermionic activity is difficult to investigate with photographic technique, but it seems to be sure that two bands at 430 mμ and 470 mμ in SrO appear only when the sample is well activated, suggesting the correlation of these bands with donor levels.

References

1) G. Burger: Z. f. Phys. **80** (1933) 352.
2) M. Benjamin and H. P. Rooksby: Phil. Mag. **15** (1933) 810; Phil. Mag. **16** (1933) 519.
3) M. Benjamin and R. O. Jenkins: Proc. Phys. Soc. **50** (1938) 345.
4) A. Eisenstein: Jour. Appl. Phys. **17** (1946) 434.
5) H. Kawomura: Matsuda Kenkyu-Jiho **16** (1941) 1 (in Japanese).
6) V. L. Stout: Phys. Rev. **89** (1953) 310.

J. PHYS. SOC. JAPAN **9** (1954) 437~438

A Note on Avoiding Scattered Electrons from the Spectrum Obtained by Magnetic Spectrometer

By Mitsuo SAKAI*

Department of Physics, Tokyo University

(Received March 26, 1954)

The present note stresses the energy selection characteristic of scintillation counter. If a G-M counter is used in a magnetic spectrometer, all the particles which pass the counter window may be counted. Among these particles there are of course many scattered particles, of which momentum does not correspond to that defined by the magnetic field. In this case if we replace G-M counter by scintillation counter, we can avoid the contribution of such particles to the spectrum by means of discriminator bias setting. And also the possibility is considered to avoid the effect of scattered γ rays.

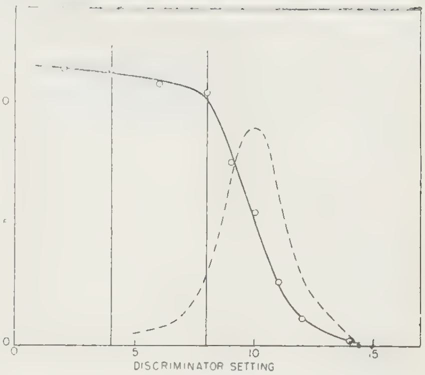

Fig. 1. Integral and differential pulse height distribution curve of 342 Kev internal conversion electrons of Pb^{206} measured by a 5819 photomultiplier tube and an anthracene crystal.

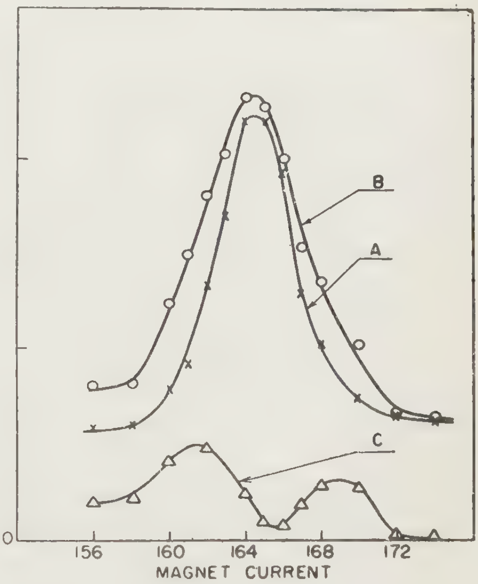

Fig. 2.

This is studied by a thin lens type magnetic spectrometer equipped by 5819 photomultiplier and an anthracene crystal. Fig. 1 is an integral pulse height distribution curve of K internal conversion electrons of 342 kev-γ ray emitted by Pb^{206}. When we set the discriminator diale—setting at points A and B (Fig. 1), the line spectra A and B are obtained as shown in Fig. 2. The curve C represents the difference between the counting rates of both curves, pointing out clearly the contribution of low energy scattered electrons to the spectrum. One characteristic feature of curve A is the sharp cut off of intensity at both sides of peak. This characteristic might be used for detecting the weak line masked by the foot of a strong line. This consideration was examined in the case of Cs^{137}. L internal conversion line of 661 Kev-γ ray is not separated clearly from K line in our experimental condition as shown in Fig. 3A. The discriminator dial setting is appropriately adjusted, then the L line clearly appeared as is shown in Fig. 3B.

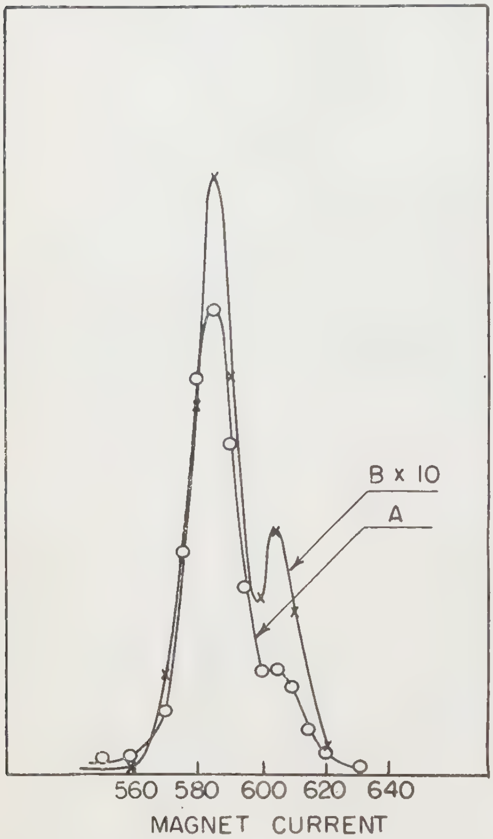

Fig. 3. Line spectrum of internal conversion electrons of Cs^{137}.

The author is indebted to Professor K. Siegbaln for his kindness to give the opportunity to study in his laboratory at Stockholm**.

---

* At present at Department of Physics and Astronomy, The Ohio State University, Columbus, Ohio.

** This work was done in winter time of 1953 at Stockholm.

J. PHYS. SOC. JAPAN **9** (1954) 438~439

On the Thickness Effect of Dielectric Breakdown of Mica and KCl

By Inseun RYU and Hazimu KAWAMURA

Faculty of Science and Engineering, Osaka City University

(Received March 26, 1954)

We can expect a remarkable thickness effect on breakdown strength, if the dielectric break down is brought about by a large single electron avalanche which arises at the cathode and grows up while drifting to the anode. Since the average size of the avalanches at the anode is given by $\exp(d/\lambda)$, where d is the thickness of the specimen and λ the average range for the ionization by collision, we must, in order to obtain the avalanche of the same size, assume that λ becomes smaller as the thickness is decreased. And since λ decreases with increasing field strength, the breakdown strength may increase as the thickness is decreased[1]. If the critical size of avalanche to cause the disruption is n_0, the breakdown strength F^* is given by[2]

$$\ln(d/F^*)=\alpha(F_H/F^*)+\ln[(e/m)\tau^2\ln(n_0)], \quad (1)$$

since λ is given by $F^*(e/m)\tau^2\exp(\alpha F_H/F^*)$,[3] where F_H is the breakdown field due to Hippel's low energy criterion, and $1/\tau$ the mean collision frequency of electrons with phonons. The above relation holds for various substances, if the thickness is less than 10^{-5}cm,[2][4][5] but it seems that F^* becomes independent of d for thicker specimens.

We have investigated this effect for mica (biotite) of $10^{-4}\sim10^{-3}$ cm thick and for KCl of $10^{-3}\sim10^{-2}$ cm. thick. In the case of mica, the electrodes were the aluminum films deposited in vacuum on both surfaces of the cleaved specimen. While in the case of KCl, aluminum deposited onto one of the cleaved surfaces and sticked to a brass rod with conductive sticking paste, and the other surface was etched with water-added alcohol, until the thickness is reduced to a desired one. Again, aluminum was deposited on this surface as an electrode. The thickness was determined from the electrical capacitance measured at 250 kc. The applied voltages were top flatted pulses of 30 μsec. with recurrence frequency of 100 sec^{-1}.. The pulse height could be varied continuously up to 10 kv. In dealing with mica the pulse height was raised very slowly, since the statistical time lag was as large as 10^{-3} sec. at 10% overvoltage.

The results are shown in Fig. 1. For mica we can in accordance with Eq. (1) draw a theoreti-

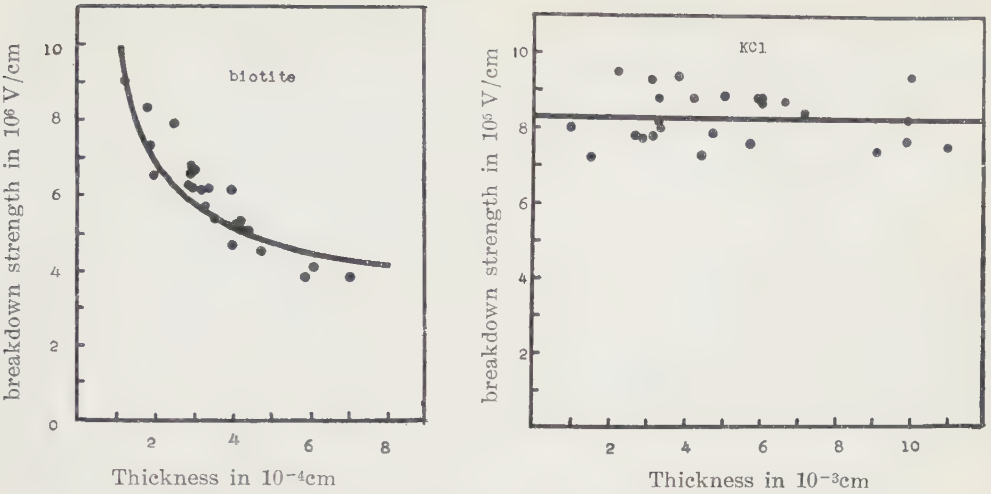

(a) (b)

Fig. 1. a) Breakdown strength v.s. thickness for mica. The line shows the theoretical curve obtained by assuming $\alpha F_H = 2.4\times10^7$ V/cm and $\tau = 4\times10^{-16}$ sec.
b) Breakdown strength v.s. thickness for KCl.

cal curve which fits fairly well with the experimental points, assuming that $\alpha F_H = 2.4\times10^7$V/cm and $\tau = 4\times10^{-16}$sec. as shown in Fig. 1-a. From this value of τ, we get 0.7 cm²/V.sec as the mobility of electron, $F_H = \sqrt{mk\Theta/e\tau} \sim 1.8\times10^7$ V/cm and, therefore, $\alpha \sim 1.3$, if we assume that $k\Theta = 1000°$K.

Since these values are resonable, the hypothesis that the breakdown is caused by a single large avalanche which has grown up during the drift from cathode to anode, is allowed in the case of mica. On the other hand, for KCl the breakdown strength is independent of d as shown in Fig. 1-b, and hence we get the histogram in Fig. 2, showing the distribution of breakdown strength, from which we have $F^* = (8.34\pm0.75)\times10^5$ V/cm. Therefore, we cannot apply the above hypothesis in this case and a different mechanism of breakdown is required. This is also confirmed through the facts that we can scarcely recognize both the statistical time lag and prebreakdown noise for KCl, in contrast to the case of mica. In the forthcoming paper it will be shown that these facts can be explained with the "collective mechanism" in which the interactions between electrons are taken into account.

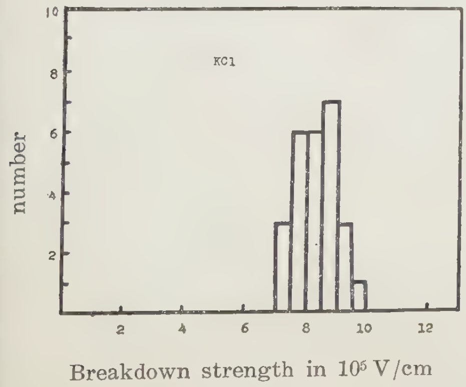

Fig. 2 Histogram showing the distribution of breakdown strength of KCl.

References

1) H. Froehlich: Proc. Roy. Soc. **A178** (1951) 493.
2) H. Kawamura and K. Azuma: J. Phys. Soc. Japan **8** (1953) 797.
3) F. Seitz: Phys. Rev. **76** (1949) 1376.
4) A. E. W. Austin and S. Whitehead: Proc. Roy. Soc. **A176** (1940) 33.
5) P. D. Lomer: Nature **166** (1950) 191.

J. Phys. Soc. Japan **9** (1954) 440

Diffusion on the Fermi-Surface and the Conductivity of Metals*

By F. J. Blatt

Department of Physics, University of Illinois, Urbana, Ill.

(Received April 8, 1954)

In a recent paper with the above title¹⁾, Toda has calculated the Lorentz number at low temperature for an ideal metal, using a method suggested by Koppe²⁾. Some of the approximations employed in T have been examined and were found to be invalid. The expression which Toda obtained is

$$L=L_\infty\left\{1+\frac{\alpha K^2}{2D}\right\}^{-1}, \qquad (1)$$

where

$$L_\infty=\frac{\pi^2}{3}\left(\frac{k}{e}\right)^2,$$

$$\alpha\simeq 2\pi\int_0^{q_0}B(q)N_q q^2dq\int_{-\infty}^{\infty}\frac{x}{\varepsilon}\,(I_{\varepsilon-x}-I'_{\varepsilon+x})d\varepsilon\,, \qquad (2)$$

and the various symbols appearing in Eqs. (1) and (2) are defined in T.

The ratio L/L_∞ was evaluated in T assuming $B(q)$ to be a constant and making a number of approximations by which the double integral expression for α, Eq. (2), was reduced to

$$\alpha\simeq 2\pi\left(\frac{T}{\theta}\right)^3 q_0^3\int_0^{\theta/T}\frac{B(q)x^3dx}{e^x-e^{-x}}\,. \qquad (3)$$

The resulting curve of L/L_∞ is curve A of Fig. 1. Also shown in Fig. 1 is the result of Sondheimer³⁾, curve B. Curve A is in much better agreement with experiment than curve B.

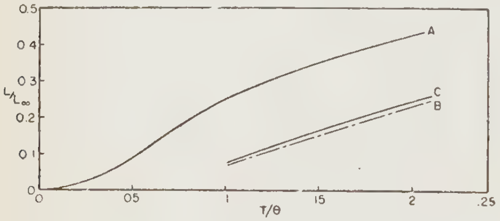

Fig. 1. L/L_∞; A—result obtained by Toda; B—result of Sondheimer; C—result of Toda's calculation using correct evaluation of the parameter α, Eq. (2).

However, examination of the approximations leading to Eq. (3) indicated that a more nearly correct approximate expression for α is

$$\alpha\simeq 2\pi\left(\frac{T}{\theta}\right)^3 q_0^3\int_0^{\theta/T}\frac{B(q)x^4dx}{e^x-e^{-x}}\,. \qquad (4)$$

If Eq. (4) is used in (1) the values of L/L_∞ fall slightly below curve *B*.

Rather than rely on the approximations leading to (4), the parameter α was evaluated by numerical integration for the range T/θ between 0.1 and 0.2. The curve of L/L_∞ so obtained is curve C is Fig. 1, which is seen to follow very closely the curve based on the Sondheimer calculation.

It appears, therefore, that the calculation of the Lorentz number by the method of Toda does not obviate the disagreement with experiment inherent in earlier calculations. Instead, the new method serves to substantiate the correctness of Sondheimer's work.

The writer wishes to thank Prof. J. Bardeen for drawing his attention to the calculation of Toda.

References

* Work supported by U. S. Department of Naval Research.

1) M. Toda: Journ. Phys. Soc. Japan **8** (1953) 339. Hereafter referred to as T.

2) H. Koppe: Zeits. f. Naturf. **7a** (1952) 17, 156.

3) E. H. Sondheimer: Proc. Roy. Soc. **A203** (1950) 75.

J. Phys. Soc. Japan **9** (1954) 440~441

Diffusion on the Fermi Surface

By Morikazu Toda

Department of Physics, Tokyo University of Education

(Received April 8, 1954)

The large discrepancy between theory and experiments on the thermal conductivity of metals is one of the most suspicious points for the current theory. The author tried to interprete the so-called Bloh's fundamental equation as that determines the diffusion processes on the Fermi surface¹⁾ for the distribution of electrons in the momentum space. The Lorentz's number $\kappa/\sigma T$ thus obtained was in better agreement with experiment than Sondheimer's numerical calculation²⁾. MacDonald, however, pointed out³⁾ that this result had a minimum of thermal conductivity which was not seen in experimental data. Sondheimer's result has also such a minimum, and this seems to be an essential weak point of Bloch's equation. In addition to this the author's computation had a over-simplification and led to incorrect results as was pointed out by Blatt⁴⁾. After revising the errors the result comes to a close agreement with Sondheimer's strict calculation.

We may say that the erroneous formula was accidentally in better agreement with experiments. It is, however, not for incorrectness of the method. As a matter of fact, the author started from the basic equation, Bloch's equation, as Sondheimer. The fact that these two have come to nearly the same results is nothing but a confirmation of the validity of the method of diffusion. The basic idea is therefore quite useful. It lies in that small distorsion of the distribution of electrons in momentum space can be resolved into two types which are subject to equations of diffusion type:

$$\partial F/\partial t = D\nabla^2 F, \quad \partial G/\partial t = D\nabla^2 G - \alpha G .$$

In the above equations F denotes the displacement of the Fermi surface in radial (normal) direction, and is connected with a net current and therefore with electric conductivity. G denotes the amount of change in the slope of the Fermi surface without net current and is connected with thermal conductivity.

The author also applied the same idea to the viscosity problem of Fermi gas.⁵⁾ Though the elementary process in this case is binary collision, it was shown that for a strongly degenerate Fermi gas the effect of collision of particles on a particle can be descrived by diffusion of the latter, if the distorsion of the Fermi surface is small. The diffusion coefficient is, in this case, given by

$$D = \frac{\pi^3 m^5 (kT)^2}{3h^3 P_0^2}\iint g^3 w(g, \theta)\sin^3\theta\, d\theta\, dg ,$$

where g denotes the relative velocity of colliding particles and $w(g, \theta)$ the scattering cross-section. For hard sphere of diameter σ we have

$$D = \frac{4\pi^3}{9h^3}(kT)^2 m P_0^2 \sigma^2 ,$$

(P_0: maximum momentum) and

$$\eta = \frac{1}{20\pi^2}\frac{P_0^5}{m^2 (kT)^2 \sigma^2} .$$

Thus the viscosity η of degenerate Fermi gas is inversely proportional to the square of the absolute temperature. This is in qualitative agreement with experiments on liquid He³.

References

1) M. Toda: Journ. Phys. Soc. Japan **8** (1953) 339.

2) E. H. Sondheimer: Proc. Roy. Soc. **A203** (1950) 75.

3) D. K. C. MacDonald: Private communication.

4) F. J. Blatt: This Journal.

5) M. Toda: Abstracts for Symposium on Liquid Helium, International Conference on Theoretical Physics (1953).

Errata

Simultaneous Excitation and Dissociation of Water Molecule by Hydrogen Canal Ray Impact

By Tadao HORIE and Masamoto OTSUKA

J. PHYS. SOC. JAPAN **9** (1954) 219

The photographs in Fig. 5 were wrongly arranged and the left and right ones must be interchanged as follows.

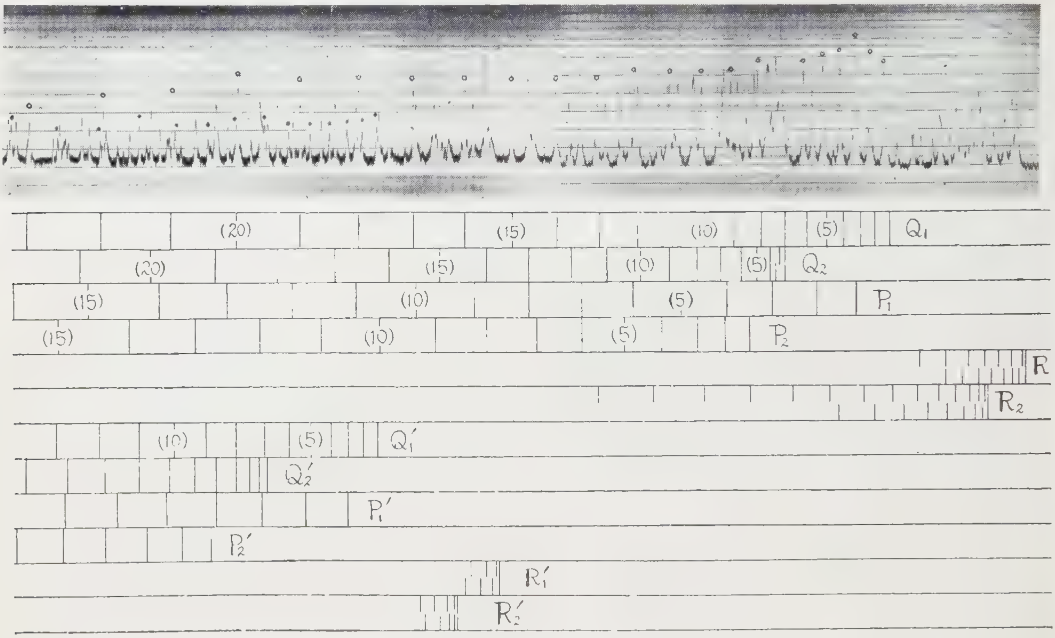

Electrical Resistivity of Polycrystalline Selenium at Higher Fields

By M. KUWAGATA, E. OTSUKA and M. TOMURA

J. PHYS. SOC. JAPAN **9** (1954) 300~301

Fig. 1 and Fig. 4 are interchanged.

JOURNAL OF THE PHYSICAL SOCIETY OF JAPAN Vol. 9, No. 4, JULY—AUGUST, 1954

K-Auger Electrons From Ba137

By Toshio AZUMA

Department of Physics, Naniwa University, Mozu, Sakai, Osaka

(Received February 5, 1954)

K-Auger electrons ejected from the L and M levels of Ba137 are studied by means of a double coil, magnetic lens beta-ray spectrometer with thin Zapon film G-M counter. The kinetic energies of those electrons observed were compared with the values evaluated from calculations by Slater's system of screening constants. The relative intensities K-LL : K-LM : K-MN are estimated to be 10 : 5.0±0.2 : 0.8±0.04 and the K fluorescence yield ω_K, 0.85±0.03.

§ 1. Introduction

In the decay of Cs137 nucleus, vacancies in the K electron shell are created by the internal conversion. The decay form of Cs137 and the values of the internal conversion coefficient are described by Waggoner[1]. This K vacancy is always filled by an electron from outer shells. The resulting energy can either be emitted as an electro-magnetic radiation, or be transfered to an electron in the other shell and eject it from the atom, resulting in an Auger electron.

In the theoretical treatment of the Auger effect which involves two electrons, for example, in the L shell when one electron makes a transition to the K shell and the other is ejected, the relativistic treatment will be necessary if the wave length of the K_α radiation ($L \rightarrow K$ transition) is of the order of the radius of the L orbit, as with the elements of atomic number $Z \gtrsim 50$. Relativistic calculations for the values of K fluorescence yield ω_K and for the probabilities of K–$L_I L_I$, K–$L_I L_{II}$, and K–$L_I L_{III}$ transitions are carried out for Au atom by Massay and Burhop[2]. But the values for K–LL, K–LM, and K–MM transitions are computed only by Pincherle[3] with non relativistic method. In his approximation the transition probabilities are independent of Z. The agreement between the observed and predicted relative intensities of various Auger electrons are qualitatively satisfactory, but more accurate experimental and theoretical values are needed[4].

Recently Burhop[4] has given a complete summary of the data of the Auger effect till 1950. Broyles *et.al.*[5], too made a similar summary and also measured the values of the K-Auger electron intensities of Sn113, Cs137, and Au198. The kinetic energies of the Auger electrons are computed theoretically by Ference[6] who analysed his own experimental result on the K–LL transitions from Ge atom. Without these estimations of the kinetic energies of the Auger electrons ejected from doubly ionized L, M, and N shells, the designation of the lines obtained and the evaluation of the effects of the electrons from N shells on the spectrum would be difficult. The discussions of Broyles *et.al.*[5] can not be considered as complete in so far as it does not takes account of the electrons ejected from the K–LN and K–MN transitions which are probably included in their observed spectrum.

We have tried to compute the kinetic energies of the Auger electrons ejected from Ba atom by the method of Slater's system of screening constants[7]. The procedure of calculations is the same as those of Ference[6]. We evaluated these values arising from doubly ionized shell of LL, LM, and MM, and corrected the effects of the electrons from the K–LN transitions, and compared with those observed.

§ 2. Experimental Procedure

A double coil, magnetic lens beta-ray spectrometer is used in these measurements. The experimental arrangement and the sources are the same as those which were reported previously[8]. The G–M counter used in the present work is the side window type, and the window of Zapon film which is maintained by the 50 mesh wire-netting is about 20 μg/cm^2 thickness. The counter is filled by Alcohol of 3 mmHg and Argon of 50 mmHg. The counter window has a diameter of 5 mm to

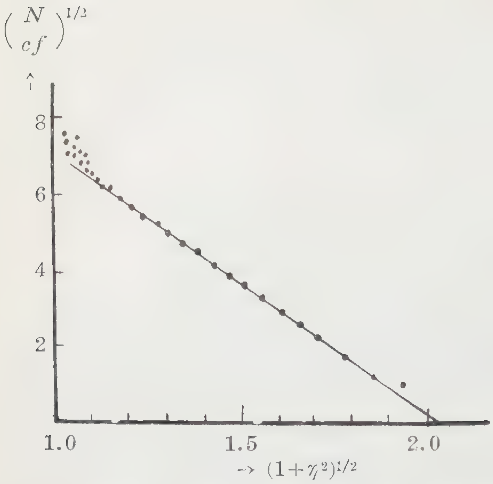

Fig. 1. Fermi plot of the 518 KeV beta-ray spectrum of Cs137, corrected with the correction factor C of first forbidden, where $C=(W^2-1)+(W_0-W)^2$.

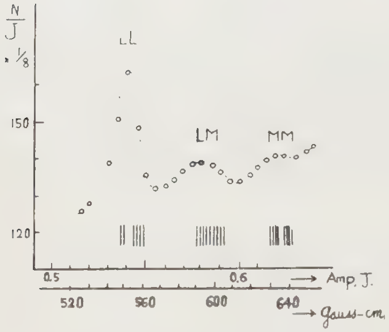

Fig. 2. Spectrum of K-Auger electrons from Ba atom designated as K-LL, K-LM, and K-MM transitions with the energy levels calculated.

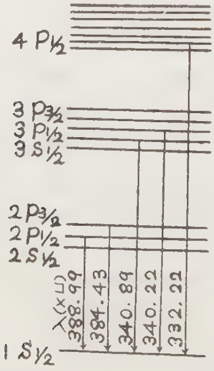

Fig. 3. X-ray energy diagram of Ba atom.

increase the number of counts per minute, but the resolution was reduced to 2.5 percent.

The momentum spectrum of the 518 KeV beta-ray radiated from the Cs137 nucleus can be measured correctly down to 5 KeV with this thin film *G-M* counter. The Fermi plot corrected with the correction factor of first forbidden[8)] are obtained as a straight line with the Auger lines at low energy side as shown in Fig. 1.

§ 3. Discussions of results

A typical data obtained in these measurements is shown in Fig. 2 with the lines of the Auger electrons calculated by the method of Slater's system of screening constants. The maximum energies of the Auger electrons designated as *K-LL*, *K-LM*, and *K-MM* transitions are 562±3, 610±3, and 654±3 gauss-cm respectively, which are in agreement with those calculated.

The qualitative x-ray energy diagram as shown in Fig. 3 must be remembered for the discussion of the results and the interpretation of the above curves obtained. The *K-LL*, *K-LM*, and *K-MM* levels arise from the configurations,

$$1s^2,\ 2sp^6,\ 3sp^8,\ 3d^{10},\ 4sp^8,\ 4d^{10},\ 5sp^6,\ 6s^2 \qquad \text{for } K\text{-}LL,$$

$$1s^2,\ 2sp^7,\left\{\begin{matrix} 3sp^7,\ 3d^{10}, \\ 3sp^8,\ 3d^9, \end{matrix}\right\} 4sp^8,\ 4d^{10},\ 5sp^6,\ 6s^2 \qquad \text{for } K\text{-}LM,$$

$$1s^2,\ 2sp^8,\left\{\begin{matrix} 3sp^6,\ 3d^{10}, \\ 3sp^7,\ 3d^9, \\ 3sp^8,\ 3d^8, \end{matrix}\right\} 4sp^8,\ 4d^{10},\ 5sp^6,\ 6s^2 \qquad \text{for } K\text{-}MM.$$

If we attempt to predict the kinetic energies of the Auger electrons from theoretical considerations, the energy levels of Ba atom which has lost two electrons from inner shells must be estimated. A comparatively rough method of Slater's system of screening constants has been used in these calculations, considering the low resolving power of the beta-ray spectrometer used in the present work. By this means the excess energy required to remove one *L* or *M* electron when one *L* or *M* electron is already missing has been obtained. In Table I the numerical details of the calculations about the energies of the normal Ba atom are summarised. Table II gives the energies of the Ba atom in different states of excitation.

If E_0 is the energy of the normal atom, $E_1{}^l$ the energy of the atom with one L electron missing, and $E_2{}^l$ the energy of the atom with two L electrons missing, then $E^l=E_0-E_1{}^l$ is the energy required to remove one L electron, and $E^{l\prime}=E_1{}^l-E_2{}^l$ is the energy required to remove the second L electron. The excess energy required to pull out one L electron when one L electron is already missing is $E^{l\prime}-E^l=157.03$ eV. The same considerations are applied to the electrons ejected from L level with one M electron missing and from M level with one L or M electron missing.

If we consider the levels arising from a doubly ionized shells LL, LM, and MM, their locations and the binding energies can be predicted with some confidence, assuming that these excess energies are sheared to each sub levels. The assignment of these sub levels is followed to the j-j coupling model. The binding energies of these levels calculated with these procedure are shown in Table III. Only the energy differences concerned with the K series x-rays, which can be obtained from Siegbahn's data[9], are needed in the present consideration. The probability of the appearance of the Auger electrons corresponding to the energy difference of forbidden transition will be small by a factor of about 1/10[10] compared with those of the allowed transition and may be neglected. The ultimately estimated energies of K-Auger electrons are shown in Table IV. There values are shown in Fig. 2 with those of observed spectrum. The fine structure of the Auger electrons ejected from the L_I, L_{II}, etc. sub levels are not resolved owing to the low resolution of the spectrometer used, which is rather characteristic for the lens type spectrometer.

The maximum energies of the Auger electrons ejected from the K–LL, K–LM, and K–MM transitions are in agreement with those calculated in the present work. Slater's method of calculations cannot be extended to the transitions concerning N shells, because of the errors which are about the same as those of the binding energies. But we can estimate the upper and lower bounds of energies within which the Auger electrons ejected from the K–LN and K–MN transitions lie. The lines designated as K–LN include the electrons arising from the transitions $L\rightarrow K$,

Table I. The numerical details of the calculations about the energies of normal Ba atom.

Electron shell	Effective quantum number n^*	Zeff.	(Zeff./n^*) in Rydberg unit
1s	1	55.70	3102.5
2s 2p	2	51.85	672.1
3s 3p	3	44.75	222.5
3d	3	34.85	134.9
4s 4p	3.7	28.25	58.3
4d	3.7	16.85	20.7
5s 5p	4.0	10.25	6.6
6s	4.2	2.90	4.8

Table II. The energies of Ba atom in different states of excitation.

Electron configurations	Energies in Rydberg unit	Designations
normal	−15439.5	E_0
missing one 2p electron	−15047.5	$E_1{}^l$
missing two 2p electrons	−14643.9	$E_2{}^l$
missing one 3p electron	−15384.4	$E_1{}^m$
missing two 3p electrons	−15317.3	$E_2{}^m$
missing one 2p and 3p electrons	−14989.4	E^{lm}

Table III. The binding energies of Ba atom in different states of excitation, in KeV unit.

Electron shell	Normal	Missing one L electron	Missing one M electron
2s	5.980	5.823	5.939
2p	5.614	5.457	5.574
2p	5.237	5.079	5.196
3s	1.293	1.131	1.253
3p	1.140	0.979	1.100
3p	1.066	0.904	1.025
3d	0.798	0.636	0.757
3d	0.814	0.620	0.741

Table IV. The energies of K-Auger electrons from Ba137 calculated, in KeV unit.

K–LL		K–LM	K–MN
25.912	29.917	30.778	34.725
26.278	30.035	30.848	34.843
26.644	30.282	30.961	34.877
26.656	30.400	30.978	34.952
27.022	30.482	30.994	34.995
	30.595	31.076	35.070
	30.660	31.344	35.220
	30.710	31.360	35.236
			35.338
			35.354

$N\to\infty$, and $N\to K$, $L\to\infty$, and its limit is estimated as 31.17$\sim$31.73 KeV from the binding energies of the normal atom. Those of *K–MN* transitions are estimated as 35.85$\sim$35.86 KeV. Electrons of such energies are not, however, detected in the present work. Present spectra obtained are, therefore, assumed to be the *K*-Auger electrons arissing from the transitions *K–LL*, *K–LM*, *K–LN*, and *K–MM*. The relative intensities of *K–LL* and *K–LN* lines can be obtained from the data of Steffen *et. al.*[10] as 1:0.21. This effect of *N* electrons must be subtracted from the spectrum of *K–LM* transitions obtained to get an estimation of the relative intensities of *K–LL*, *K–LM*, and *K–MM*. The final result obtained with the above correction is 10:5.0±0.2:0.8±0.04.

The *K* fluorescence yield ω_K is evaluated from the relation $\omega_K=1-\alpha_K$, where α_K is the *K*-Auger yield. α_K is obtained directly from the observed spectrum as the ratio of the *K*-Auger electrons to that of the *K* internal conversion electrons. The *K* fluorescence yield ω_K obtained in this way in the present work is 0.085±0.003. The error of the final result is estimated from the measured spectrum shown in Fig. 2, which is obtained within the error of 3 percent. It should be noted that differences in a absorption between the electrons arising from *K–LL*, *K–LM*, and *K–MM* transitions would be negligible owing to the extraordinary thiness of Ba137 sources and counter window.

For the Ba atom, the wave length of the κ_α radiation ($L\to K$ transition) is the order of 0.46Å and the radius of the *L* orbit is 0.16Å. Though these are of the same order of magnitude, the difference between the results which are obtained by the relativistic and non-relativistic procedure are small, and the data obtained by the spectrometer are not accurate enough to show these differences clearly.

In conclusion, the author express his sincere gratitude to Prof. K. Kimura of Kyoto University for his kind encouragements and discussions, and also to Dr. K. Shinohara for his kind discussions. Acknowledgement should also be made to Mr. K. Tsumori for his assistances during the operation of the spectrometer.

This work was financially supported by the special fund of the Ministry of Education.

References

1) M. A. Waggoner: Phys; Rev. **82** (1951) 906.
2) H. W. S. Massey and E. H. S. Burhop: Proc. Roy. Soc. (London) **153** (1936) 661.
3) L. Pincherle: Nuovo Cimento, **12** (1935) 81.
4) E. H. S. Burhop: "The Auger Effect" p 63, Camb. Univ. Press (1952).
5) C. D. Broyles, D. A. Thomas, and S. K. Hayness: Phys. Rev. **89** (1953) 715.
6) M. Ference: Phys. Rev. **51** (1937) 720.
7) J. C. Slater: Phys. Rev. **36** (1930) 57.
8) T. Azuma: J. Phys. Soc. Japan **9** (1954) 1.
9) M. Siegbahn: "Spectroskopy der Röntgenstrahlen" p 346, Julius Springer, Berlin (1931)
10) Steffen, Huber, and Humbel: Helv. Phys. Acta. **22** (1949) 167.

JOURNAL OF THE PHYSICAL SOCIETY OF JAPAN Vol. 9, No. 4, JULY—AUGUST, 1954

The Angular Distribution of Protons from the $C^{12}(d, p)C^{13}$ Reactions

By S. TAKEMOTO, T. DAZAI, R. CHIBA, S. ITO,
S. SUGANOMATA and Z. WATANABE
Department of Physics, Faculty of Science, Tohoku University

(Received February 26, 1954)

The angular distributions of protons from the $C^{12}(d, p)C^{13}$ reactions have been observed at three low bombarding energies, 0.52, 0.63 and 0.84 Mev, using nuclear emulsions at the proton detector. Some details of experimental equipments and procedure are described. The angular distributions observed were then expanded into series of Legendre polynomials. The expansion coefficients are tabulated and also plotted against the bombarding energy together with those reported by other authors. Large asymmetries have been found in the angular distribution curves at these low bombarding energies.

§ 1. Introduction

Numerous articles have ever been published about the nuclear reactions on carbon. They are all quite important not only for their theoretical interest, but also because carbon is always present as deposits or contaminations on every target surface. Among many reactions on carbon, the angular distributions of protons emitted from deuteron bombardment on C^{12} have been observed over the full angular range by G. C. Phillips[1] in the bombarding energy range of 0.75–1.32 Mev, together with the excitation functions, and by B. Koudijs et. al.[2] at an effective bombarding energy of 0.37 Mev.

Between these two measurements it seemed that there is an unexplored energy region, i.e. the angular distributions are quite different at 0.37 and 0.75 Mev. As a part of series of our investigations, therefore, we planned to measure the angular distributions and to investigate the behaviours of the expansion coefficients in this energy region. Measurements were performed at three bombarding energies of 0.52, 0.63 and 0.84 Mev.

§ 2. Apparatus and Procedure

In order to investigate the angular distributions of various nuclear reactions a multiple plate nuclear camera of usual design was constructed with a diameter of 20 cm and a depth of 7 cm, a photograph of which is shown in Fig. 1, where main components are easily seen. The chamber is made of brass and has four side tubes, two of which serving as the beam entrance and exist tubes and one of the other two as the vacuum line. The target support is a steel rod, which passes through a Wilson seal in the center of the bottom plate and allows smooth rotation and axial displacements. Great care was taken in constructing the chamber with the result that irregular displacements could be made negligible. In the beam entrance tube two collimating slits of 3 mm diameter were fixed, whose distances from the target were 9 cm and 18 cm. As the proton detector the Sakura nuclear emulsion plates were used. The plate holder is an iron ring with an outside diameter of 18 cm, inside diameter of 13 cm and a thick-

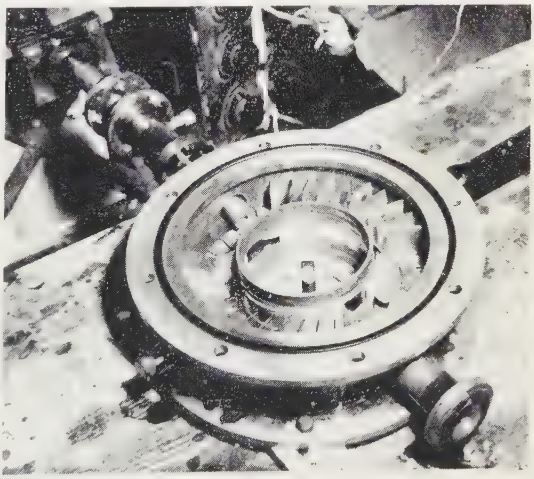

Fig. 1. Target chamber. Inside the chamber can be seen the nuclear plates and aluminum foil around the target, and also the slit system is in sight.

ness of 3 cm, on which are cut grooves to fix the angular positions of the plates making an angle of 20° with the center line. These grooves are divided into two groups, left and right, with respect to the beam; the inner edges of the former are at angular positions of 0°, 10°, etc., up to 180°. and those of the latter at 5°, 15°, etc., up to 175°.

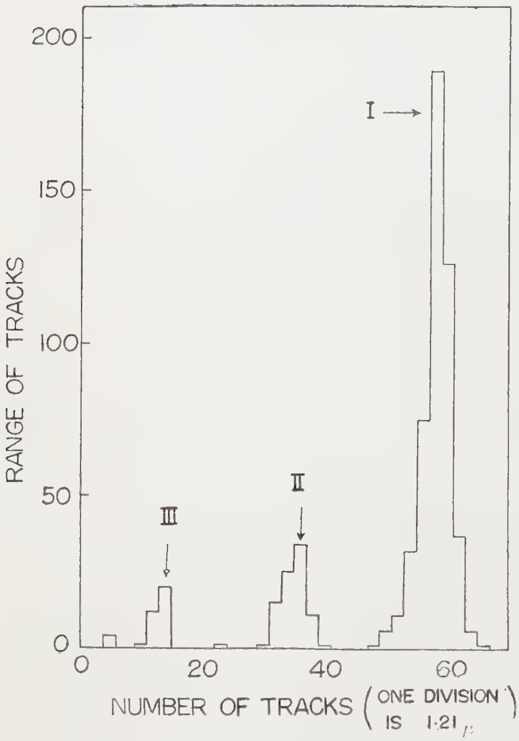

Fig. 2. Range spectrum of protons at an angle of observation of 60° from the deuteron bombardment of a target of purpurogalline at $E_d=0.63$ Mev. Arrows indicate a proton group of $C^{12}(d,p)C^{13}$ (I), $O^{16}(d,p)O^{17}$ (II) and $O^{16}(d,p)O^{17*}$ (III), respectively.

Between the target and the plate holder, there is a stopping-foil holder of special design. The stopping-foils serve to protect the emulsions from elastically scattered deuterons and from blackening due to the fluorescent light produced on the target during bombardment. They also reduce the ranges of protons to adequate lengths for scanning. In this work Al-foils with a thickness of 14 microns were used throughout. All metal parts were carefully machined.

After some trials, a good thin target of carbon was prepared by vacuum evaporation of purpurogalline³⁾ onto a silver backing leaf to a thickness of about 1 mg/cm². The silver leaf was supported by a fine iron frame, which was in turn fixed on the top of the target-supporting steel rod. In order to obtain angular distributions over the full angular range, 20 emulsion plates, cut to $1'' \times 1\frac{1}{2}''$ pieces, were loaded into the camera in one exposure, the forward group into grooves at 10°, 20°, etc., up to 100° and the backward group at 75°, 85°, etc., up to 165°, the emulsion side of the forward group facing backward and vice versa.

The homogeneous deuteron beam from the pressurized electrostatic generator at Tohoku University was, after being magnetically analysed, used to bombard the thin carbon target. The beam had negligible angular divergence. Before bombardment, when the target was held down and the plates were already loaded, the chamber was aligned with respect to the beam by watching the fluorescent light spot produced on the surface of a quartz disk at the end of the beam exit tube. During bombardment the chamber was continuously evacuated by a Hickmann type oil diffusion pump. The beam current and the target thickness were not measured precisely, so the absolute cross sections could not be obtained.

The emulsions were developed by the two-bath method⁴⁾ and the same areas at the same position on each plate were scanned under a biocular microscope at a magnification of 450. The lengths of detected tracks were recorded and, when numbers of tracks were plotted against their lengths, three proton groups were clearly resolved, as shown in Fig. 2, which is the result of scanning of the 60°-plate at the bombarding energy of 0.63 Mev and where the track numbers are plotted against their lengths (strictly speaking, their holizontal projections) at an interval of two divisions of the eye-piece scale (one division corresponding to 1.21 microns). These three groups were assigned to correspond to the $C^{12}(d,p)C^{13}$, $O^{16}(d,p)O^{17}$ and $O^{16}(d,p)O^{17*}$ reactions, respectively, with the aid of known Q-values⁵⁾ and stopping power of Al for protons. Some tracks of far larger ranges were also observed, but they were rejected because they could not be included in any of the groups, mentioned above. At lower bombarding energies the proton yield decreased considerably, so longer exposure time was needed and larger areas had to be scanned in order to obtain enough proton tracks.

§ 3. Results and Discussions

The numbers of proton tracks belonging to the $C^{12}(d,p)C^{13}$ reaction were plotted against the angular position of the small areas scanned, thus the angular distribution for each bombarding energy was obtained in the laboratory system. The angular distributions at three bombarding energies, thus obtained, were converted to the center-of-mass system according to the formulas

$$\sin(\theta-\theta_0)=\gamma\sin\theta$$

$$\sigma(\theta_0)\fallingdotseq\sigma(\theta)(1-2\gamma\cos\theta_0)$$

$$\text{and}\quad \gamma=\left(\frac{m_1m_3}{m_2m_4}\cdot\frac{E_d}{E_d+(1+m_1/m_2)Q}\right)^{1/2},$$

where θ and θ_0 are proton directions with respect to the incident deuterons in the laboratory and center-of-mass system, respectively. Usual notations are used for other quantities. The resulting distributions are shown in Fig. 3, where the ordinates are so normalized that the area under each curve is equal to 2, when the abscissa is transformed into $\cos\theta_0$ scale. The vertical lines through the experimental points represent the uncertainty calculated from the total number of tracks only. The overlapping of the data from the forward and the backward groups in the region around 90° was quite good, indicating no serious geometric errors. They were then expanded into series of Legendre polynomials up to P_4,

$$\sigma(\theta_0,E_d)\propto 1+\sum_{i=1}^{4}a_i(E_d)P_i(\theta_0)\,.$$

The coefficients are given in Table I and also plotted against the bombarding energy in Fig. 4 where those taken from references (1) and (2) are included. The curves in Fig. 3 represent the calculated most probable angular distributions.

Table I. The coefficients in Legendre polynomial series representation at three different deuteron energies.

E_d	0.52 Mev	0.63 Mev	0.84 Mev
a_1	0.20 ± 0.03	0.29 ± 0.03	0.09 ± 0.02
a_2	-0.39 ± 0.03	-0.39 ± 0.04	0.02 ± 0.03
a_3	-0.17 ± 0.04	-0.20 ± 0.05	-0.20 ± 0.04
a_4	-0.04 ± 0.05	-0.05 ± 0.05	-0.00 ± 0.04

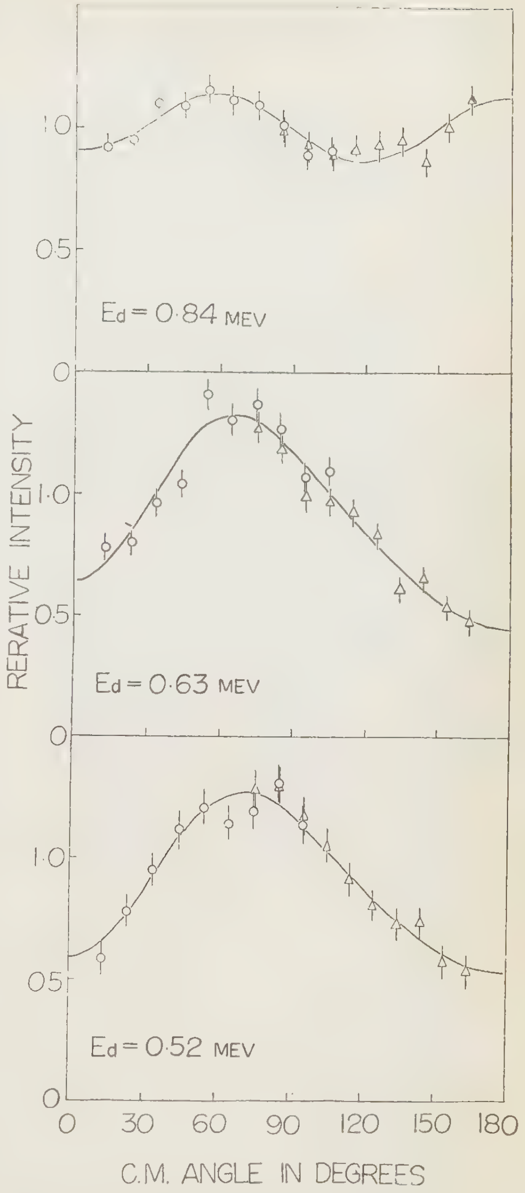

Fig. 3. The angular distributions of the protons from the reaction $C^{12}(d, p)C^{13}$ in C.M. coordinates at the deuteron bombarding energies indicated.

It is apparent that the angular distributions at these low energies are quite complex and vary markedly with energy. Fig. 4 shows this variation in terms of the expansion coefficients clearly. It seems that in this energy region not only resonances at 0.91 Mev and at higher energies, but also the contributions from lower levels in the compound nucleus, $C^{12}+d\rightarrow N^{14*}$, should, to some extent, be taken into account in estimating the angular distri-

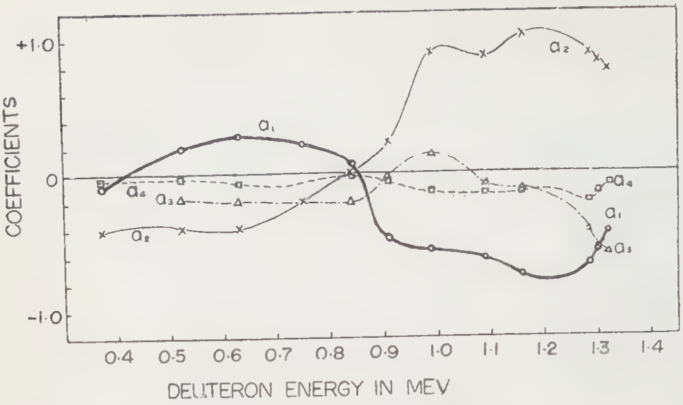

Fig. 4. The coefficients $a_i(E_d)$ in the expansion $\sigma(\theta_0, E_d) \propto 1 + \sum_{i=1}^{4} a_i(E_d) P_i(\theta_0)$, plotted against the deuteron bombarding energy. The points at $E_d = 0.52$, 0.63 and 0.84 Mev are from our data, and the others from references (1) and (2).

bution, though no definite evidence is present about this point. The presence of odd terms indicates large interference effects between levels of opposite parity of the compound nucleus and, accordingly, their theoretical interpretation would be quite a difficult matter. One conspicuous feature in the variation of the terms is the increase of a_2 with energy, which is in agreement with the Phillips' data.

The angular distributions of protons from the reactions on oxygen, obtained at the same time, will be published in the near future, (after proton tracks have been accumlated enough by further scanning.)

§ 4. Acknowledgement

It is a great pleasure to thank Prof. M. Kimura for his helpful discussions and encouragements. We are indebted to the Konishi-Roku Film Co. for supplying the emulsion plates and to the laboratory members of Prof. T. Nozoe for preparing purpurogalline.

References

1) G. C. Phillips: Phys. Rev. **80** (1950) 164.
2) B. Koudijs et. al.: Physica **18** (1952) 415.
3) Benzotropolone derivative, $C_{11}H_8O_5$.
4) M. Blau and J. A. DeFelice: Phys. Rev. **74** (1948) 1198.
5) K. F. Famularo and G. C. Phillips: Phys. Rev. **91** (1953) 1195.

JOURNAL OF THE PHYSICAL SOCIETY OF JAPAN Vol. 9, No. 4, JULY—AUGUST, 1954

Statistical Theory of Phase Transition. I

General Theory for Lattice Gas

By Ikuro SHIMOSE

Faculty of Literature and Science, Yamaguchi University

(Received October 30, 1953)

From the point of view of molecular clusters we physically interpret the statistical properties of phase transitions. Our results for a lattice gas are expected to be qualitatively correct, though these are approximate from the quantitative point of view. In Part **1** the partition function, the pressure and the density of a lattice gas are calculated in their general forms. Particularly, the discontinuity of the derivative of the isotherm in $P-v$ diagram is derived from our calculation of the partition function.

§ 1. Introduction

The existing exact theories, in which systems having strong interactions among molecules are dealt with by statistical mechanics, are classified into two types. One is the method of cluster integrals developed by Mayer,1) Kahn and Uhlenbeck,2) Born and Fuchs,3) and others. In this method there remain a doubt4) about the relation between phase transitions and singular points, and some difficulties in applying it to the condensed phase. The other is the matrix method elaborated by Onsager,5) Kaufman,6) Nambu,7) Yang,8) and others. In this method the exact solutions are obtained only for the case of no external magnetic field (an Ising system). For other cases many approximate theories9) have been proposed, but most of them do not give a proper statistical interpretation of the phase transition qualitatively as well as quantitatively.

Recently Katsura10) solved exactly the problem of small system (system containing only a few lattice points) for an Ising system or a lattice gas. Though he deduced, from these results, many properties of an infinitely large system (system containing an infinite number of lattice points), we believe that there may be properties peculiar to large system, the deduction of which is difficult if we start from small systems. On the other hand, Yang and Lee11) mathematically proved that the phase transition is possible at only one value of the activity for an Ising system or a lattice gas at the constant temperature, but they did not give the physical meaning.

In this paper we wish to make physically clear the statistical properties of the phase transition for an infinitely large system from the point of view of molecular clusters.

§ 2. Partition Function, Pressure and Density

We shall deal with a lattice gas composed of molecules interacting strongly. For simplicity, we confine ourselves to a two-dimensional case (square lattice type). However, the theory of the present paper will be applied also to three-dimensional systems of any lattice type as well as to two-dimensional systems of other types than the square lattice type.

In the first place, we shall assume the potential energy u between any two molecules to be of the following form; $u=+\infty$ if two molecules occupy the same lattice site, $u=-2\varepsilon$ ($\varepsilon>0$) if two molecules occupy adjacent sites, and $u=0$ otherwise. The partition function $\Omega(T, L, N)$ of the lattice gas (L lattice points, N molecules) at absolute temperature T is given by the following expression.

$$\Omega(T, L, N)=(2\pi mkT/h^2)^N\{\exp(4\varepsilon/kT)\}^N \times Q(T, L, N)\,, \tag{1}$$

$$Q(T, L, N)=\sum x^{N'}\,, \tag{2}$$

$$x=\exp(-\varepsilon/kT)\,, \quad (0\leqq x\leqq 1) \tag{3}$$

$$Q(T, L, L-N)=Q(T, L, N)\,, \tag{4}$$

where $\sum$ in Eq. (2) means the summation over all the possible cases in which N molecules are distributed among the lattice sites. N' is the number of the pairs of neighboring molecule and hole in one of the molecular configurations mentioned above. m, k, h have the usual meanings.

The pressure P and the (molecular number) density ρ of the system are given as follows:

$$P=\frac{kT}{\sigma}\cdot\frac{\partial}{\partial L}\log\Omega(T,L,N), \qquad (5)$$

$$\rho=N/L\sigma, \qquad (6)$$

where σ is the two-dimensional volume (or area) per lattice site.

§ 3. Calculation of Partition Function

In order to estimate the value of $Q(T,L,N)$, we shall call the group of molecules in which every molecule is connected with each other directly or indirectly a " molecular cluster ". By a direct connection of two molecules is meant that of molecules occupying the nearest sites and by an indirect connection that between two molecules which are not connected directly but joined from one of them to another by some molecules connected directly one by one. Similarly a hole cluster is defined for the cluster of holes connected with each other instead of molecules. Since from (4) we have the relation $Q(T,L,L-N)=Q(T,L,N)$, let us consider only the case in which the total number of molecules in question is smaller than or equal to $L/2$. Now we shall classify the configurations into the following two types:

(A) the configuration consisting of macro-molecular clusters and micro-molecular clusters,

(B) the configuration consisting of micro-molecular clusters only,

where macro-molecular clusters are those having molecules of order L (for example, $10^{12}\sim10^{16}$ when $L\sim10^{16}$) and micro-molecular clusters are those having molecules of order 1 (for example, $1\sim10^{4}$). Similarly macro- and micro-hole clusters are also defined. In A-type configuration micro-hole clusters lie sporadically over the macro-molecular cluster. In B-type configuration macro-hole clusters may exist naturally, butmacro-molecular clusters do not exist.

Then there may also exist intermediate (molecular and hole) clusters. However, we devide the contribution of any molecular configuration in an intermediate cluster to the value of $(1/L)\cdot\log Q(T,L,N)$ into those of two parts of micro- and intermediate-molecular configurations. Further, we devide the intermediate-molecular configurations into the intermediate configurations having no hole and the hole configurations in its cluster. In the former case, as the value of $(1/n)\cdot\log g(n)+h(n)\log x$ (as will be defined in § **3.1**) is of order $10^{-4}\sim10^{-7}$ when L is 10^{16}, its contribution to the value of $(1/L)\cdot\log Q(T,L,N)$ is neglected. In the later case, the hole configurations are added to those of macro-molecular clusters and the contribution of those to the value of $(1/L)\cdot\log Q(T,L,N)$ is calculated. Thus we think that intermediate clusters may be formally neglected without altering the statistical properties.

§ 3.1

Let us consider the case of A-type configuration composed of $(L/2)(1-q)$ molecules. We define the following quantities:

(a) in the group of micro-molecular clusters,

(n') cluster····the cluster containing n' molecules,

$(L/2)p'(n')$····the total number of molecules of (n') clusters,

$(L/2)p'(n')/n'$·····the number of (n') clusters,

$g(n')$····the number of all the possible configurations of a (n') cluster,

$h(n')$····the number of holes nearest to any molecule of a (n') cluster divided by the number of the molecules,

where $n'=1, 2, 3,\cdots, m'$,

(b) in the group of micro-hole clusters inside macro-molecular clusters,

(n'') cluster····the cluster containing n'' holes,

$(L/2)p''(n'')$····the total number of holes of (n'') clusters,

$(L/2)p''(n'')/n''$····the number of (n'') clusters,

$g(n'')$ and $h(n'')$ are defined in the same way as $g(n')$ and $h(n')$ respectively, interchanging the role of molecule and hole,

where $n''=1, 2, 3,\cdots, m''$.

We shall see that, by the approximate treatment (taking mean number) mentioned above for $h(n')$, $h(n'')$, the statistical properties of the system in question are not altered qualitatively, if we divide $g(n')$ (or $g(n'')$) into some groups so that the numbers of pairs of molecule-hole in the configurations belonging to the same group may be equal, and if we apply our theory to these.

From Eq. (2) the contribution of the molecular configuration mentioned above to the value of $Q_1(T, L, q)$ $(=Q(T, L, N))$ is given by

$$\begin{aligned}(Q_1(T, L, q))_{A;\,p'(n');\,p''(n'')} &= \prod_{n'=1}^{m'} \left\{ \frac{(L/2n')(1+q+p'(n')-p'')!}{(L/2n')p'(n')!\,(L/2n')(1+q-p'')!} \right. \\ &\quad \left. \times g(n')^{Lp'(n')/2n'} x^{h(n')Lp'(n')/2} \right\} \\ &\quad \times \prod_{n''=1}^{m''} \left\{ \frac{(L/2n'')(1-q+p''(n'')-p')!}{(L/2n'')p''(n'')!\,(L/2n'')(1-q-p')!} \right. \\ &\quad \left. \times g(n'')^{Lp''(n'')/2n''} x^{h(n'')Lp''(n'')/2} \right\}, \qquad (7)\end{aligned}$$

where

$$p' = \sum_{n'=1}^{m'} p'(n'), \qquad p'' = \sum_{n''=1}^{m''} p''(n'').$$

By using the Stirling formula for the logarithm of Eq. (7), we have

$$\begin{aligned}\log\,&(Q_1(T, L, q))_{A;\,p'(n');\,p''(n'')} \\ &= \frac{L}{2}\left[\sum_{n'=1}^{m'} \left\{ \frac{-p'(n')}{n'} \log p'(n') \right. \right. \\ &\quad + \frac{1+q+p'(n')-p''}{n'} \log(1+q+p'(n')-p'') \\ &\quad - \frac{1+q+p''}{n'} \log(1+q-p'') \\ &\quad \left. + \frac{p'(n')}{n'} \log g(n') + p'(n')h(n') \log x \right\} \\ &\quad + \sum_{n''=1}^{m''} \left\{ \frac{-p''(n'')}{n''} \log p''(n'') \right. \\ &\quad + \frac{1-q+p''(n'')-p'}{n'} \log(1-q+p''(n'')-p') \\ &\quad - \frac{1-q-p'}{n''} \log(1-q-p') \\ &\quad \left.\left. + \frac{p''(n'')}{n''} \log g(n'') + p''(n'')h(n'') \log x \right\} \right]. \qquad (8)\end{aligned}$$

We shall neglect the direct contribution of macro-molecular clusters to $\log(Q_1(T, L, q))_{A;\,p'(n');\,p''(n'')}$, because its absolute value is very small compared with that of micro-molecular clusters when L is of order 10^{16}. Then, if L is small ($L=1\sim100$), the values of $(1/n)\cdot\log g(n)+h(n)\log x$ are negative for the clusters of comparatively large n (having no hole, $n\leqq L/2$) and small values of x. Accordingly, the contributions of these clusters to the values of $\log(Q_1(T, L, q))_{A;\,p'(n');\,p''(n'')}$ are negative (not negligible generally). Therefore, in a small system we can not find any cluster corresponding to the macro-molecular one in an infinitely large system. Owing to this fact the properties of the phase transition of an infinitely large system may not be extrapolated from those of a small system.

As the formulas to determine $p'(n')$ and $p''(n'')$ which make $\log(Q_1(T, L, q))_{A;\,p'(n');\,p''(n'')}$ maximum under the condition that

$$q=\text{const.}, \quad p' = \sum_{n'=1}^{m'} p'(n'), \quad p'' = \sum_{n''=1}^{m''} p''(n''),$$

we have

$$\begin{aligned}&-\frac{1}{n'} \log p'(n') + \frac{1}{n'} \log(1+q+p'(n')-p'') \\ &+ \frac{1}{n'} \log g(n') + h(n') \log x \\ &+ \sum_{i=1}^{m'} p'(i) \left\{ \frac{1}{i} \frac{\partial}{\partial p'(n')} \log g(i) \right. \\ &\left. + \log x \frac{\partial}{\partial p'(n')} h(i) \right\} \\ &+ \sum_{n''=1}^{m''} \frac{1}{n''} \{-\log(1-q+p''(n'')-p') \\ &+ \log(1-q-p')\} = 0, \qquad (9) \\ &\qquad n'=1,\ 2,\ 3, \cdots,\ m',\end{aligned}$$

$$\begin{aligned}&-\frac{1}{n''} \log p''(n'') + \frac{1}{n''} \log(1-q+p''(n'')-p') \\ &+ \frac{1}{n''} \log g(n'') + h(n'') \log x \\ &+ \sum_{j=1}^{m''} p''(j) \left\{ \frac{1}{j} \frac{\partial}{\partial p''(n'')} \log g(j) \right. \\ &\left. + \log x \frac{\partial}{\partial p''(n'')} h(j) \right\} \\ &+ \sum_{n'=1}^{m'} \frac{1}{n'} \{-\log(1+q+p'(n')-p'') \\ &+ \log(1+q-p'')\} = 0, \qquad (10) \\ &\qquad n''=1,\ 2,\ 3, \cdots,\ m''.\end{aligned}$$

If we denote by p_0', $p_0'(n')$; p_0'', $p_0''(n'')$ respectively the values of p', $p'(n')$; p'', $p''(n'')$ for the case of $q=0$ which satisfy Eqs. (9) and (10), by using the symmetrical property, we have

$$\left.\begin{aligned} p_0' &= p_0'' \quad (=p_0), \\ p_0'(n) &= p_0''(n) \quad (=p_0(n)). \end{aligned}\right\} \qquad (11)$$

$$n=1,\ 2,\ 3, \cdots.$$

Then, for the maximum configuration (giving the maximum value of $\log (Q_1(T, L, q)_A)$, the number of molecules forming the macro-molecular clusters decreases when the value of q in creases from zero. We denote by q_1 the value of q corresponding to the disappearance of macro-molecular clusters. When we assume that $g(n')$, $h(n')$ are functions of n', x, $p'(n)/1+q+p'-p''$, and $g(n'')$, $h(n'')$ are functions of n'', x, $p''(n)/1-q+p''-p'$ $(n=1, 2, 3, \cdots)$, the solution of Eqs. (9) and (10) for $q=rq_1$ $(0\leqq r\leqq 1)$ is given by the following formulas as can be proved easily.

$$\left.\begin{aligned} &(1/2)(1-q_1)=p_0\ , \\ &p' =(1+r)p_0\ , \quad p'(n') =(1+r)p_0(n'), \\ &p''=(1-r)p_0\ , \quad p''(n'')=(1-r)p_0(n''), \end{aligned}\right\} \tag{12}$$
$$n',\ n''=1,\ 2,\ 3, \cdots .$$

Generally, the clusters contributing to the value of $\log Q_1(T, L, q)$ at the maximum rate are those of $n'=1$ (or $n''=1$), and when the value of n' (or n'') increases, its rate decreases. We determine the maximum value m' (or m'') of n' (or n'') from the maximum value of $\log (Q_1(T, L, q))_{A; p'(n'); p''(n'')}$. When $p_0(n)\ll 1$ and $g(n')$, $g(n'')$, $h(n')$, $h(n'')$ do not depend on $p'(n)$, $p''(n)$ $(n=1, 2, 3, \cdots)$, the formulas to determine the values of m', m'' are given from Eqs. (8), (9), (10), (11) and (12) by

$$m'=m'' \quad (=m_1), \tag{13}$$

$$\frac{1}{m_1}\{\log (1+p_0(m_1)-p_0)-\log (1-p_0)\} \geq \frac{p_0(m_1)}{(1-p_0)^2} \sum_{n=1}^{m_1} \frac{p_0(n)}{n}\ , \tag{14}$$

$$\frac{1}{m_1+1}\{\log (1+p_0(m_1+1)-p_0)-\log (1-p_0)\} < \frac{p_0(m_1+1)}{(1-p_0)^2} \sum_{n=1}^{m_1+1} \frac{p_0(n)}{n}\ . \tag{14$'$}$$

For the case where $p'(n')$ (or $p''(n'')$) are not very small compared with unity, one can also prove, that Eq. (13) holds and that the value of m_1 satisfying Eq. (13) does not depend on q $(0\leqq q\leqq q_1)$.

§ 3.2

We shall denote by a (∞) micro-molecular cluster the micro-cluster in which the number of molecules is so large that one may regard it as infinite. Similarly a (∞) micro-hole cluster is defined. In a (∞) micro-molecular cluster it is possible to realize all the possible molecular configurations in the cluster when the cluster is free from the surrounding ones. Contrary to the above the configurations of a macro-molecular cluster are realized only at an infinitesimal rate against all the possible ones in its cluster. The same holds for (∞) micro-hole and macro-hole clusters.

In the region of temperature T (or x) in which (∞) micro-clusters give an effective contribution to the partition function, one must add the following term to the right-hand side of Eq. (8).

$$\begin{aligned} &-(1/n_\infty)p'(n_\infty) \log p'(n_\infty) \\ &\quad +(1/n_\infty)(1+q+p'(n_\infty)-p'') \\ &\qquad \times\log (1+q+p'(n_\infty)-p'') \\ &\quad -(1/n_\infty)(1+q-p'') \log (1+q-p'') \\ &\quad +(1/n_\infty)p'(n_\infty) \log g(n_\infty)+p'(n_\infty)h(n_\infty) \log x \\ &\quad -(1/n_\infty)p''(n_\infty) \log p''(n_\infty) \\ &\quad +(1/n_\infty)(1-q+p''(n_\infty)-p') \\ &\qquad \times\log (1-q+p''(n_\infty)-p') \\ &\quad -(1/n_\infty)(1-q-p') \log (1-q-p') \\ &\quad +(1/n_\infty)p''(n_\infty) \log g(n_\infty) \\ &\quad +p''(n_\infty)h(n_\infty) \log x\ , \end{aligned} \tag{15}$$

where n_∞ is the number of molecules in a (∞) micro-cluster. As n_∞ is very large, the term (15) is given by

$$(p'(n_\infty)+p''(n_\infty))I_\infty(x)\ , \tag{15$'$}$$

where

$$I_\infty(x)=(1/n_\infty) \log g(n_\infty)+h(n_\infty) \log x\ .$$

In Eq. (8),

$$p'= \sum_{n'=1}^{m'} p'(n')+p'(n_\infty),\ p''= \sum_{n''=1}^{m''} p''(n'')+p''(n_\infty).$$

When the temperature is very low (or x is very small), $I_\infty(x)$ is generally negative and for the maximum configuration $p'(n_\infty)=p''(n_\infty)=0$ so that (∞) clusters do not at all contribute to the partition function. When the temperature becomes high (or x increases), $I_\infty(x)$ increases generally and becomes positive at a definite temperature. When $I_\infty(x)$ is larger than a definite value, (∞) micro-clusters contribute to the partition function in the value larger than those for (n) micro-clusters in which n is larger than a definite number m_2. Generally, the lower limit x_1 of x satisfying this condition is slightly less than the value x_c of x corresponding to the critical temperature. According to the numerical calculation which will be shown in Part **II**, x_1 is slightly larger than 0.41, where $x_c=\sqrt{2}-1=0.41421$.

When we assume that $g(n)$ and $h(n)$ do not depend on $p(i)$ $(i=1,\ 2,\cdots)$, we have the following formula to determine the value of m_2:

$$(1/m_2)\{\log(1+p_0(m_2)-p_0)-\log(1-p_0)\}\\ \geqq p_0(m_2)I_\infty(x)\ , \qquad (16)$$

$$(1/(m_2+1))\{\log(1+p_0(m_2+1)-p_0)-\log(1-p_0)\}\\ <p_0(m_2+1)I_\infty(x)\ . \qquad (16')$$

§ 3.3

Let us consider the case of B-type configuration composed of $(L/2)(1-q)$ molecules. We denote by $Lp(n)$ and $Lp(n)/n$ respectively the total number of molecules and the number of clusters belonging to (n) micro-molecular clusters $(n=1,\ 2,\ 3,\cdots,\ m)$. Similarly we denote by $Lp(n_\infty)$ the total number of molecules belonging to the group of (∞) micro-clusters.

From Eq. (2) the contribution of the molecular configuration mentioned above to the value of $Q_1(T, L, q)$ is given by

$$Q_1(T,L,q)_{B;\,p(n);\,p(n_\infty)}\\ =\prod_{n=1}^{m}\left\{\frac{(L/n)(1+p(n)-p)!}{(L/n)p(n)!\,(L/n)(1-p)!}\right.\\ \left.\times g(n)^{Lp(n)/n}\,x^{h(n)Lp(n)}\right\}\\ \times g(n_\infty)^{Lp(n_\infty)/n_\infty}\,x^{h(n_\infty)Lp(n_\infty)}\ , \qquad (17)$$

where $g(n)$ and $h(n)$ are defined in the same manner as those in § **3.1**, and

$$p=(1-q)/2=\sum_{n=1}^{m}p(n)+p(n_\infty)\ .$$

By using the Stirling formula for the logarithm of Eq. (17), we have

$$\log(Q_1(T,L;q))_{B;\,p(n);\,p(n_\infty)}\\ =L\left[\sum_{n=1}^{m}\left\{\frac{-p(n)}{n}\log p(n)\right.\right.\\ +\frac{1+p(n)-p}{n}\log(1+p(n)-p)\\ -\frac{1-p}{n}\log(1-p)+\frac{p(n)}{n}\log g(n)\\ \left.+p(n)h(n)\log x\right\}\\ \left.+p(n_\infty)\left(\frac{1}{n_\infty}\log g(n_\infty)+h(n_\infty)\log x\right)\right]. \qquad (18)$$

As the formulas to determine $p(n)$ and $p(n_\infty)$ which make $\log(Q_1(T, L, q)_{B;\ p(n);\ p(n_\infty)}$ maximum, we have

$$-(1/n)\log p(n)+(1/n)\log(1+p(n)-p)\\ +(1/n)\log g(n)+h(n)\log x\\ +\sum_{i=1}^{m}p(i)\{(1/i)(\partial/\partial p(n))\log g(i)\\ +\log x(\partial/\partial p(n))h(i)\}\\ +\sum_{i=1}^{m}(1/i)(-\log(1+p(i)-p)+\log(1-p))=0\\ n=1,\ 2,\ 3,\cdots,\ m, \qquad (19)$$

$$p(n_\infty)=(1-q)/2-\sum_{n=1}^{m}p(n)\ .$$

Then the value of m giving the maximum configuration is determined from Eqs. (16) and (16′) (from Eqs. (14) and (14′) if $p(n_\infty)=0$).

§ 3.4

The value of $Q_1(T, L, q)$ is given by the summation over the contributions of all the possible configurations (belonging to A-type and B-type). We denote by $Q_1(T, L, q))_m$ the maximum value of the contributions of all the possible configurations. This maximum configuration belongs to A-type or B-type. Then the number of possible configurations belonging to A-type and B-type is given by $(L(1-q)/2)^c$ from Eqs. (7) and (17), where c is of the order of the number of molecules of a (∞) micro-molecular cluster and hence is very small compared with L, but very large compared with unity. Therefore the relation

$$\log(Q_1(T,L,q))_m\leqq\log Q_1(T,L,q)\\ \leqq c\log(L(1-q)/2)+\log(Q_1(T,L,q))_m$$

holds. In Part II we shall see that the value of $\log(Q_1(T, L, q))_m$ is positive and of order L. Accordingly, if L is of order 10^{16}, the relation

$$\log Q_1(T,L,q)=\log(Q_1(T,L,q))_m \qquad (20)$$

holds correctly. Thus we can determine the value of $\log Q_1(T, L, q)$ by the contribution of configuration giving maximum value in ones given by Eqs. (8) and (18).

§ 3.5

As stated in § **3.1**, the maximum configuration may belong to A-type for $0\leqq|q|\leqq q_1$, but to B-type for $|q|\geqq q_1$. When q increases from zero, macro-molecular clusters disappear just at $q=q_1$. Then in the group of micro-molecular clusters, $g(n')$, $h(n')$, $I_\infty(x)$ are functions of n', x, $p'(n)/(1+q+p'-p'')$ $(n=1, 2, 3,\cdots)$ and in the group of micro-hole clusters inside macro-molecular clusters, $g(n'')$, $h(n'')$, $I_\infty(x)$ are functions of n'', x, $p''(n)/(1-q+p''-p')$ $(n=1, 2, 3,\cdots)$. Now, $(L/2)(1+q+p'-p'')$ is the number of lattice sites belonging to the group of micro-molecular clusters and $(L/2)(1-q+p''-p')$ that belonging to the group of micro-hole clusters inside macro-molecular clusters. Therefore, we can correctly prove from Eq. (8) by making use of Eqs. (12) and (13) that the value of $Q_1(T, L, q)$ is constant for $|q|\leqq q_1$.

§ 4. Equation of State

Since we can assume the relation

$$Q(T, L, N)=Q_1(T, L, q)=(\omega(T, q))^L, \quad (21)$$

for the large value of L (for example, $L\sim10^{16}$), the equation of state of the system is given by the following expression from Eqs. (5) and (6).

$$P=(kT/\sigma)\log\omega(T, q)+(kT(1-q)/\sigma)(\partial/\partial q)\times\log\omega(T, q), \quad (22)$$

and

$$v=1/\rho=L\sigma/N=2\sigma/(1-q), \quad (23)$$

where v is the specific volume per molecule. Particularly, as the value of $Q_1(T, L, q)$ (or $\omega(T, q)$) is constant from § **3.5** for $|q|\leqq q_1$, the isotherm has the portion parallel to v-axis for the above range of q.

§ 5. Conclusion

By the introduction of the idea of two types of molecular configurations, A- and B-types, we calculated the partition function of a lattice gas in the general form, in which we made clear the properties of phase transition physically. In Part II of this paper we shall numerically calculate the pressure and the densities (vapor and liquid) from the general form obtained above.

Acknowledgement

The author is greatly indebted to Professor A. Harasima, Tokyo Institute of Technology, for his kind suggestions and valuable discussions.

References

1) J. E. Mayer: J. Chem. Phys. **5** (1937) 67.
J. E. Mayer and Ph. G. Ackermann: J. Chem. Phys. **5** (1937) 74.
J. E. Mayer and S. F. Harrison: J. Chem. Phys. **6** (1938) 87.
S. F. Harrison and J. E. Mayer: J. Chem. Phys. **6** (1938) 101.
2) B. Kahn and G. E. Uhlenbeck: Physica **5** (1938) 399.
3) M. Born and K. Fuchs: Proc. Roy. Soc. **A 166** (1938) 391.
4) S. Katsura and H. Fujita: J. Chem. Phys. **19** (1951) 795; Prog. Theor. Phys. **6** (1951) 498.
S. Ono: Prog. Theor. Phys. **8** (1952) 1.
K. Ikeda: Busseiron Kenkyu (in Japanese) No. 57 (1952) 77; ibid. No. 65 (1953) 145; Abstract of Int. Conf. on Theor. Phys. Sec. **B** (1953) 38.
5) L. Onsager: Phys. Rev. **65** (1944) 117.
6) B. Kaufman: Phys. Rev. **76** (1949) 1232.
7) Y. Nambu: Prog. Theor. Phys. **5** (1950) 1.
8) C. N. Yang: Phys. Rev. **85** (1952) 808.
9) H. A. Bethe: Proc. Roy. Soc. **A 150** (1935) 552.
R. H. Fowler and E. A. Guggenheim: Proc. Roy. Soc. **A 174** (1940) 189.
Y. Takagi: Proc. Phys. Math. Soc. Japan **23** (1941) 44, 553; ibid. **24** (1942) 333; J. Phys. Soc. Japan **4** (1949) 99.
J. G. Kirkwood: J. Chem. Phys. **6** (1938) 70. etc.
10) S. Katsura: Busseiron Kenkyu (in Japanese) No. 64 (1953) 39; Abstract of Int. Conf. on Theor. Phys. Sec. **B** (1953) 34.
11) C. N. Yang and T. D. Lee: Phys. Rev. **87** (1952) 404.
T. D. Lee and C. N. Yang: Phys. Rev. **87** (1952) 410.

JOURNAL OF THE PHYSICAL SOCIETY OF JAPAN Vol. 9, No. 4, JULY—AUGUST. 1954

Statistical Theory of Phase Transition. II

Numerical Calculation for Lattice Gas

By Ikuro SHIMOSE

Faculty of Literature and Science, Yamaguchi University

(Received October 30, 1953)

Applying our theory derived in Part **1**, we numerically calculate, in this paper, the pressure and the densities (vapor and liquid) at the transition point of a lattice gas (having a square lattice type) for some ranges of temperature (or some values of x). Our values calculated from the molecular cluster method agree well with the exact values obtained by the matrix method. For small values of x (for example, $x=0.3$ or $T/T_c=0.7321$), the values of partition function are given as a function of q. The isotherm obtained from these values has the portion parallel to v-axis (corresponding to $P=$constant) and at both ends of this portion the derivatives of the isotherm are discontinuous. Furthermore, we show that the system in question has qualitatively the above properties also for larger values of x ($x<x_c$).

§ 1. Numerical Calculation of $g(n)$ and $h(n)$

Though $g(n)$ and $h(n)$ (defined in § **3.1** of Part **I**[1]) are generally functions of several variables as stated in § **3.5** of Part **I**, we shall regard these as functions of the variable n only, by which is meant that a (n) cluster in question is free from the surrounding ones. In the estimation in this section we shall assume that the central molecule of the cluster is fixed at a definite site. We denote by $g_0(n)$ and $h_0(n)$ respectively the values of $g(n)$ and $h(n)$ evaluated under the condition mentioned above. Though the numerical calculation of the values of $g_0(n)$ and $h_0(n)$ is generally difficult, for small values of n we can estimate these quantities by counting directly. We estimated the values of $g_0(n)$, $(1/n)\log g_0(n)$ and $h_0(n)$ for $n=1, 2, \cdots, 7$ by the above method. These values obtained are listed in Table I.

Table I

n	$g_0(n)$	$1/n\cdot\log g_0(n)$	$h_0(n)$
1	1	0	4
2	2	0.34657	3
3	6	0.59725	2.44444
4	19	0.73611	2.15789
5	63	0.82863	1.98095
6	212	0.89276	1.86478
7	710	0.93789	1.76419

From the values in Table I, we see that the values of $(1/n)\log g_0(n)$ and $h_0(n)$ are nearly linear for $1/n$ ($n=4, 5, 6, 7$). Therefore we obtained the following relations from these values by the method of least square.

$$(1/n)\log g_0(n)=1.20626-1.88228(1/n)\,, \quad (1)$$

$$h_0(n)=1.25361+3.62510(1/n)\,. \quad (2)$$

In the numerical calculations in § **3** we shall use the values of Table I for $(1/n)\log g(n)$ and $h(n)$ with $n=1, 2, \cdots, 7$ and use the values calculated from Eqs. (1) and (2) for those with n larger than 7.

§ 2. Exact Values of Pressure and Density at Transition Point

Onsager[2], Kaufman[3] and Yang[4] obtained the exact values of the free energy and the spontaneous magnetization of an Ising system (having a square lattice type) for the case of no external magnetic field (by using the matrix method). Applying the above method to a lattice gas (having a square lattice type), we have the following exact relations as derived by Yang and Lee[5].

$$\frac{(P)_t\sigma}{kT}=\log(1+x^2)+\frac{1}{2\pi}\int_0^\pi \log\left[\frac{1}{2}\{1+(1-k_1^2\sin^2\varphi)^{1/2}\}\right]d\varphi, \quad (3)$$

$$k_1=4x(1-x^2)(1+x^2)^{-2},$$

$$(\rho_g)_t+(\rho_l)_t=1/\sigma\,,$$

$$(\Delta\rho)_t=(\rho_l)_t-(\rho_g)_t$$
$$=\left(\frac{(1+x^2)(1-6x^2+x^4)^{1/2}}{(1-x^2)^2}\right)^{1/4}\frac{1}{\sigma}\,, \qquad (4)$$

where $(P)_t$, $(\rho_g)_t$, $(\rho_l)_t$ are respectively the values of pressure, densities of vapor and liquid phases at the transition point. In the subsequent section we shall denote by the term "exact value" the value calculated from Eq. (3) or (4).

§ 3. Numerical Calculation of Parition Function, Pressure and Density

(1) *Case of Small Value of x*

Let us treat the case of low temperature T $(T<T_c)$ or small value of x $(x<x_c)$. In this section we shall use $(1/n)\log g_0(n)$ and $h_0(n)$ for the values of $(1/n)\log g(n)$ and $h(n)$ respectively. In the maximum configuration $I_\infty(x)$ is not effective to $\omega(T,q)$ for small values of x so that we have $p'(n_\infty)=p''(n_\infty)=0$ in § **3.2** of Part **I** and $p(n_\infty)=0$ in Eq. (17) or (18) of Part **I**. By making use of the formulas derived in Part **I**, we evaluated the values of the pressure $(P)_t$ and the change of density $(\Delta\rho)_t$ on phase transition for $x=0.2$ $(T/T_c=0.5476)$ and $x=0.3$ $(T/T_c=0.7321)$, where from Eq. (23) in Part **I**

$$(\rho_g)_t=(1-q_1)/2\sigma\,, \qquad (5)$$

$$(\rho_l)_t=(1+q_1)/2\sigma\,, \qquad (6)$$

$$(\Delta\rho)_t=(\rho_e)_t-(\rho_g)_t=q_1/\sigma\,. \qquad (7)$$

These values obtained are listed in Table II.

Table II

x	T/T_c	$(P)_t\sigma/kT$	$(P)_{t,e}\sigma/kT$	$(\Delta\rho)_t\cdot\sigma$	$(\Delta\rho)_{t,e}\sigma$
0.2	0.5476	0.0017	0.0017	0.9964	0.9962
0.3	0.7321	0.0094	0.0099	0.9754	0.9741
0.41	0.9885	0.0453	0,0453	0.6907	0.6975

$(P)_t/kT$:—the value of P/kT calculated by Eq. (22) in Part **1** at the transition point,

$(P)_{t,e}/kT$:—the exact value of P/kT at the transition point,

$(\Delta\rho)_t$:—the value of the change of density calculated by Eq. (7) on phase transition,

$(\Delta\rho)_{t,e}$:—the exact value of the change of density on phase transition.

Our values agree well with the exact values. Further, for such small values of x the values of $p'(n')$, $p''(n'')$, $p(n)$ defined in § **3.1** and § **3.3** of Part **I** $(n', n'', n=1, 2, \cdots)$ are very small compared with unity. Therefore, by making use of the values of $(1/n)\log g(n)$ and $h(n)$ mentioned above, we shall be able to make clear, qualitatively at least, the proper statistical properties for small values of x. Accordingly we calculated, making use of the formulas derived in Part **I**, the values of $\omega(T,q)$, pressure P and density ρ (or specific volume $v=1/\rho$) as functions of q. For the case of $x=0.3$, the $\log\omega(T,q)$—q curve and the P—v diagram are given in Fig. 1 and Fig. 2 respectively. We see that, from the result of estimation, the type of configuration giving maximum contribution to $\omega(T,q)$ is A-type for $|q|\leqq q_1$, B-type for $|q|\geqq q_1$, and two maximum contributions for configurations of

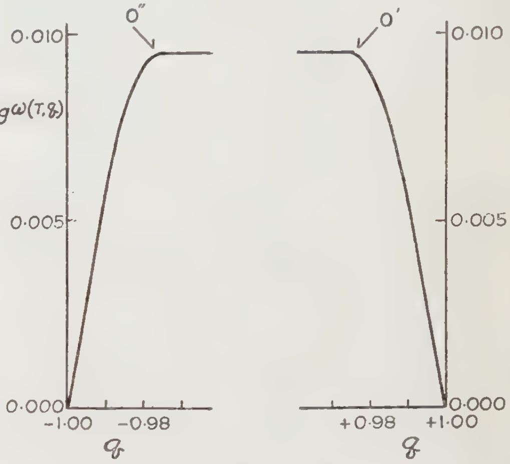

Fig. 1. $\log\omega(T,q)-q$ curve at $x=0.3$ $(T/T_c=0.7321)$
O': $\log\omega(T,q)=0.0094$, $q=+0.9754$,
O'': $\log\omega(T,q)=0.0094$, $q=-0.9754$.

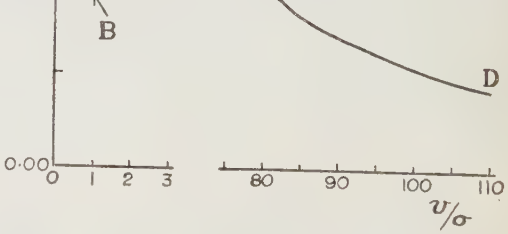

Fig. 2. $P/kT-v$ curve at $x=0.3$ $(T/T_c=0.7321)$
B: $P\sigma/kT=0.0094$, $v/\sigma=1.012$,
C: $P\sigma/kT=0.0094$, $v/\sigma=81.50$.

A- and B-types coincide with at $|q|=q_1$, where the calculated value of q_1 for $x=0.3$ is 0.9754. Further we see that the value of $\omega(T, q)$ is constant for $|q|\leq q_1$ and decreases when $|q|$ increases from q_1. As stated in § **3.5** of Part **I**, the relation of constancy of $\omega(T, q)$ for $|q|\leqq q_1$ holds independently of the approximate assumption for $(1/n)\log g(n)$ and $h(n)$. Therefore, we see from § **4** of Part **I** that the B—C part of the isotherm in Fig. 2 is parallel to v-axis (corresponding to $P=$ constant) and at two points B and C the derivatives of the isotherm are discontinuous.

(2) *Case of Large Value of* x

When x is large, it is not correct to assume that $(1/n)\log g(n)$ and $h(n)$ are functions of the variable n only, because each molecular (or hole) cluster is affected by the surrounding molecular (or hole) clusters. However, for simplicity, in this section we shall use for the values of $(1/n)\log g(n)$ and $h(n)$ those of $(1/n)(\log g_0(n)-(1/n)\log n)$ and $h_0(n)$ respectively. In Table II the values of $(P)_t/kT$, $(\Delta\rho)_t$ are given which were evaluated by making use of the above approximate values of $(1/n)\times\log g(n)$ and $h(n)$ for $x=0.41$. These values agree well with the exact values. Now we shall determine the value of $I_\infty(x)$ under the following conditions:

(i) $I_\infty(x)$ is linear for $\log x$,

(ii) $q_1=0$ for $x=x_c$ (using for x_c the exact value $\sqrt{2}-1=0.41421$) and $q_1>0$ for $x<x_c$,

(iii) for a definite value of x $(x>x_c)$ the pressure P calculated from Eq. (22) in Part **I** agrees with the exact value at $q=0$.

We can derive the following properties by assuming the above approximation. For $x\leqq x_c$, the same relations as those for small x given in § **3** (**1**) hold also for the case of large x. For $x\geq x_c$, the type of configuration giving maximum contribution to the value of $\omega(T, q)$ is B-type for every value of q, and the value of $\omega(T, q)$ increases when $|q|$ decreases from 1 to zero and becomes maximum at $q=0$. Therefore, a phase transition does not occur in $x>x_c$. Particularly, the property that the value of $\log\omega(T, q)$ is constant for $|q|\leqq q_1$, as stated in § **3.5** of Part **I**, hold independently of the approximate assumption for $(1/n)\log g(n)$ and $h(n)$. Accordingly, for large x $(x\leqq x_c)$ we can derive, qualitatively at least, the singularity of the equation of state from the value of partition function by making use of § **4** in Part **I**.

§ 4. Conclusion

By making use of the formulas derived in Part **I** from the point of view of molecular clusters, we numerically calculated the values of partition function as a function of q. Then the singularity of the equation of state was derived from the above values of partition function.

Acknowledgement

The author is greatly indebted to Professor A. Harasima, Tokyo Institute of Technology, for his kind suggestions and valuable discussions.

References

1) I. Shimose: J. Phys. Soc. Japan **9** (1954) 451.

2) L. Onsager: Phys. Rev. **65** (1944) 117.

3) B. Kaufman: Phys. Rev. **76** (1949) 1232.

4) C. N. Yang: Phys. Rev. **85** (1952) 808.

5) C. N. Yang and T. D. Lee: Phys. Rev. **87** (1952) 404.

T. D. Lee and C. N. Yang: Phys. Rev. **87** (1952) 410.

JOURNAL OF THE PHYSICAL SOCIETY OF JAPAN Vol. 9, No. 4, JULY—AUGUST, 1954

On the Variational Calculation of the Activation Energy of Dislocation

By Akira SUGIYAMA

Nagoya Technical College

(Received December 17, 1953)

The formulae of the activation energy of a dislocation trapped in potential trough are solved by variational method, which relates closely to usual Lagrangean form in analytical dynamics. To compare them with the approximate solution of Cottrel's, numerical calculations are carried out in the particular case where the anchored force is due to the interaction with Cottrel's atmosphere. Consequently, the elegant agreement between the observed and Cottrel's approximate solution is lost.

§ 1. Introduction

Cottrel and Bilby[1] regarded a yield phenomenon as the break-down of the anchored dislocation by the external stress supported by thermal fluctuation energy. The dislocation is anchored by imperfections in crystal, say, holes, impure atoms surrounding the dislocation (so-called Cottrel's atmosphere), the other dislocation, the assembly of the dislocations (grain boundary) etc. To develope this ground idea definitely, Cottrel and Bilby assumed as follow; first, the potential is the interaction energy of the Cottrel's atmosphere; secondly, this interaction can be calculated from the classical elastic theory, taking no account of the fact that strains round the dislocation are too large to be treated by it; thirdly self-energy of dislocation per unit length is constant in spite of the appearance of screw component; finally, the activation energy is calculated by the approximate methods to avoid the apparent difficulty of mathematics.

In spite of these approximation, the calculated activation energy agrees too good with the experimental curve of the dependency of the yield points of poly-crystalline iron on the temperature by McAdam and Mebs[2], then we have some questions whether the agreement is accidental, and are interested in how each stage of approximations effects on the results.

In this paper standing on the same ground idea as Cottrel's, the third and final approaches are examined by attempting to calculate on rigorous variational treatment and take account of the variations of self-energy of dislocation. To make the comparison clear, whole process is carried out in pararell to that of Cottrel.

This problem shows a typical feature of the activation energy, that is the suddle point energy (maximum point in minimum line).

§ 2. The Variational Calculus for the Activation Energy

As for a edge dislocation in rest under no external stress, we take z-axis along the dislocation line, x-axis the slip direction, therefore the origin is in potential rough (Fig. 1a). Now we assume that the interaction of dislocation with the imperfections is uniform along z-axis (this assumption may be valid in the case of uniform distribution of the impure atoms along z-axis—Cottrel's atmosphere—or pararell dislocations), then the potential energy of the dislocation per unit length is simply $V(x)$, where x is the position of centre of dislocation.

When the external stress σ is applied to this dislocation forward $+x$ direction, assuming that the active planes are inclined at $\pi/4$ to the external stress axis, we must add the interaction energy with this stress (it is clear that this is uniform type)

$$-\tfrac{1}{2}\lambda\sigma x\,, \tag{1}$$

where λ is the length of Burger's vector.

Then total potential energy of the dislocation per unit length is

$$F(x)=V(x)-\tfrac{1}{2}\lambda\sigma x\,. \qquad (2)$$

Then, the position of dislocation in rest moves into that of the quasi-stable x_1, where $F(x)$ takes the minimum. So the energy to translate the unit length of this dislocation rigidly from x_1 to x is

$$f(x)=F(x)-F(x_1)\,. \qquad (3)$$

With the increase of the value of x, first $f(x)$ increases, and soon reaches to the maximum value at x_m, then decreases for larger x (Fig. 1b). Usually, the energy corresponding to this potential barrier $f(x_m)$ is called as the activation energy, and a dislocation provided with enough energy to exceed this critical energy can move freely and cause the yield phenomenon. This energy, however, too great to be provided with the thermal energy, and Cottrel and Bilby showed the mechanism in which, taking the deformablity of dislocation into account, the dislocation provided with even much smaller energy can escape from this potential trough in the form of rather the appropriate looped shape than straight.

The excited energy $E(a)$ to bring the point of the dislocation to a given point on x-axis $x=a$, is the total energy difference between the looped form $x(z)$ and the straight form $x=x_1$. The energy difference of the element dz between the looped and the straight dislocation consists of two parts; the one is that of potential energy difference $f(x)dz$ mentioned above, the other is that of line energy as follows.

The variation of the line energy is also composed of two terms, the one is the increase of line length, the other is the diminission of the self-energy of dislocation due to the appearrance of the screw component. If the unit length of the edge dislocation becomes the composed dislocation with the angle φ to slip direction, the variation of the line energy per unit length $g(p)$ is

$$\begin{aligned} g(p)&=W(p)\sqrt{1+p^2}-W(0)\\ &=W(0)\{w(p)\sqrt{1+p^2}-1\}\,, \end{aligned} \qquad (4)$$

$$w(p)=W(p)/W(0)=1-\nu\cos^2\varphi\,, \qquad (5)$$

$$p=\frac{dx}{dz}=-\tan\left(\frac{\pi}{2}-\varphi\right), \qquad (6)$$

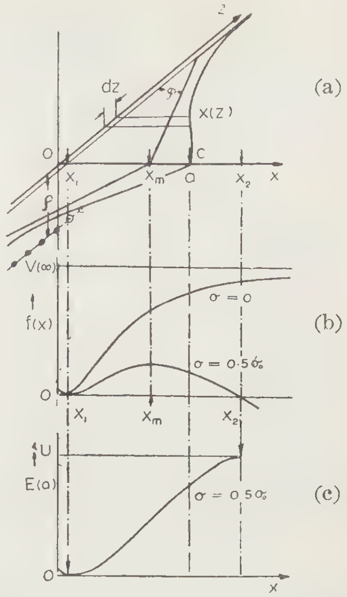

Fig. 1. a, b, c: (a); the shape of looped dislocation provided with excess energy. (b); the form of potential when $\sigma/\sigma_0=0$ and $\sigma/\sigma_0=0.5$. (c); total exited energy as function of parameter a when $\sigma/\sigma_0=0.5$.

where ν is Poisson ratio, $W(0)$, $W(p)$ are the self-energy of edge, composed dislocation, respectively.

Now, $E(a)$ is the integral

$$E(a)=\int_{-\infty}^{\infty}\{f(x)+g(p)\}dz\,, \qquad (7)$$

here, it is required that the looped form $x(z)$ should be chosen so as to minimize the $E(a)$ under the boundary condition that $z=0$, $x=a$; $z\to\pm\infty$, $x\to x_1$, $p\to 0$. Euler Equ. for this variational problem is easily integrated

$$p\cdot g'(p)-\{f(x)+g(p)\}=h\,, \qquad (8)$$

where the integral constant h is required to be zero by the boundary condition. It is noted that, for small values of p, $g(p)$ reduces to

$$g(p)=\tfrac{1}{2}W(0)(1-2\nu)p^2\,. \qquad (9)$$

In this case, variation of line energy is proportional to the square of the gradient, so corresponds to the kinetic energy in analytical dynamics regarding z as time t. Then Equs. (7), (8) correspond to Lagrangean function and energy integral, respectively.

From Equ. (8) we can determine the form $x(z)$ and energy

$$E(a)=\int_{-\infty}^{\infty} p\cdot g'(p)\cdot dz=2\int_{x_1}^{a}\{-g'(p)\}dx\,, \tag{10}$$

$$g'(p)=W(0)\cdot\frac{p}{\sqrt{1+p^2}}\cdot\left\{1-\nu\left(1+\frac{1}{1+p^2}\right)\right\}. \tag{11}$$

As a becomes larger, the value of $E(a)$ first becomes larger, but reaches to the maximum value U at $a=x_2$, and then decreases to negative value catastrophically (Fig. 1c). U is essentially the activation energy, namely minimum energy as for the form $x(z)$ and maximum value as for parameter a. Extreme values of $E(a)$ are obtained for the $a=x_1, x_2$, etc. where $g'(p)$, i.e. p, should be zero, so they are the roots of $f(x)=0$. From the definition, it is clear that x_1 is one of roots and in fact, x_1 gives the minimum of $E(x_1)$, say zero. Then, the next root x_2 gives the maximum,

$$U=E(x_2)=2\int_{x_1}^{x_2}\{-g'(p)\}dx\,, \tag{12}$$

where

$$f(x_1)=f(x_2)=\cdots=0\,. \qquad \cdots>x_2>x_1\,. \tag{13}$$

§ 3. The Particular Case: Cottre's Atmosphere

To carry out the calculation definitely, we take the $V(x)$ as the same form as the Cottrel's

$$V(x)=V_c(x)=-\frac{A}{\lambda}\frac{\rho}{x^2+\rho^2}\,, \tag{14}$$

where A is the constant which represents the strength of the interaction, and ρ is the distance between the row of the impure (carbon) atoms and the centres of the dislocation. In following, we assume the same values for A, $W(0)$, λ, ρ, etc. as Cottrel's. These values are given in Table I.

For convenience, we transform the variables to dimensionless quantities

$$\left.\begin{aligned}&\xi=\frac{x}{\rho}\,,\qquad \xi_1=\frac{x_1}{\rho}\,,\ \text{etc.}\quad Q=\frac{W(0)\lambda\rho}{A}\,,\\&\sigma_0=\frac{3\sqrt{3}}{\lambda^2\rho^2}A\,,\qquad U_0=\frac{2A}{\lambda}\,,\\&\beta=\frac{3\sqrt{3}}{8}\left(\frac{\sigma}{\sigma_0}\right).\end{aligned}\right\} \tag{15}$$

Now Equs. (12), (2) based on (14), and (4) are transformed to

$$U=E(\xi_2)=U_0\int_{\xi_1}^{\xi_2} Q\{-\bar{g}'(p)\}d\xi\,, \tag{16}$$

$$\begin{aligned}\bar{f}(\xi)&=\left\{\frac{1}{1+\xi_1^2}+\beta\xi_1\right\}-\left\{\frac{1}{1+\xi^2}+\beta\xi\right\}\\&=\frac{\beta}{(1+\xi_1^2)}\cdot\frac{(\xi-\xi_1)^2(\xi_2-\xi)}{1+\xi^2}\,,\end{aligned} \tag{17}$$

$$\bar{g}(p)=\frac{g(p)}{W(0)}=\left(1-\frac{\nu p^2}{1+p^2}\right)\sqrt{1+p^2}-1\,, \tag{18}$$

Then, we can calculate numerically in three cases;

i) $w(p)=1(\nu=0)$; this is the same as the Cottrel's third assumption. Here the solution,

$$\begin{aligned}U&=U_0\cdot\int_{\xi_1}^{\xi_2}\frac{-p}{\sqrt{1+p^2}}\,d\xi\\&=U_0\cdot\int_{\xi_1}^{\xi_2}\sqrt{\bar{f}(\xi)\{2Q-\bar{f}(\xi)\}}\,d\xi\\&=U_0\cdot I_1(\sigma/\sigma_0,Q)\,,\end{aligned} \tag{I}$$

Particularly, for the case $\bar{f}(\xi)/2Q\ll 1$ (allowable except the case 3 and the region for too small σ/σ_0), the integral in (I) is simplified to elliptic integral,

$$U=U_0\sqrt{2Q}\int_{\xi_1}^{\xi_2}\sqrt{\bar{f}(\xi)}\,d\xi=U_0\sqrt{2Q}\cdot I_0(\sigma/\sigma_0)\,. \tag{II}$$

Table I. The appropriate values of constants.
(borrowed from Cottrel and Bilby)

Case	1	2	3	4
$W(0)$ (e.v. per atomic plane)	5.0	5.0	1.0	1.0
A (erg. cm)	3.0×10^{-20}	3.0×10^{-21}	3.0×10^{-20}	3.0×10^{-21}
Q	5.333	53.33	1.0667	10.667
U_0 (e.v.)	1.51	0.151	1.51	0.151
σ_0 (dyne. cm^{-2})	15.84×10^{10}	1.584×10^{10}	15.84×10^{10}	1.584×10^{10}

In all cases, $\rho=2$ Å, $\lambda=2.48$ Å.

This is the same result as calculated from the approximate formula (9) for $g(p)$, then we can regard p as enough small to be approximated by (9) when $\overline{f}/2Q \ll 1$. The values of $I_0(\sigma/\sigma_0)$ are given in Table II.

Table II. The values of $I_0(\sigma/U_0)$.

σ/σ_0	$I_0(\sigma/\sigma_0)$
0.1	9.201
0.2	4.044
0.3	2.315
0.4	1.452
0.5	0.936
0.6	0.597
0.7	0.356
0.8	0.187
0.9	0.069
1.0	0.000

ii) Cottrel's approach; they approximated the loop by the triangle of which height is $x_m - x_1$ and angle φ is chosen to minimize the total energy (Fig. 1a), then obtained the solution $I_c(\sigma/\sigma_0, Q)$ (Fig. 4, 5).

iii) General case; $w(p) = 1 - \nu\cos^2\varphi (\nu = 0.3)$

$$U = U_0 \int_{\xi_1}^{\xi_2} Q[\sqrt{1-\alpha^2}\{1-\nu(1+\alpha^2)\}]d\xi$$
$$= U_0 \cdot I_2(\sigma/\sigma_0, Q, \nu),$$

where $$1 - \alpha - \nu(1-\alpha^2)\alpha = \frac{\overline{f}(\xi)}{Q}, \qquad \text{(III)}$$

also for $\overline{f}(\xi)/2Q \ll 1$, (III) reduces to

$$U = U_0 \sqrt{2Q(1-2\nu)} I_0(\sigma/\sigma_0). \qquad \text{(IV)}$$

Fig. 2 shows the ratios of the exact solutions (I) and (III) to simplified (II) and (IV), respectively, the full and dotted lines are the ratios $I_1(\sigma/\sigma_0, Q)/\sqrt{2Q}\, I_0(\sigma/\sigma_0)$ and $I_2(\sigma/\sigma_0, Q, \nu)/\sqrt{2Q(1-2\nu)} I_0(\sigma/\sigma_0)$. $Q = 1.066$, 10.66 are taken for the reason of the latter is case 4 that is considered as the most appropriate, the former is the case 3 where the approximation would be expected most wrong. We can concluded that (II) and (IV) are good approximation for cases except too small values of σ/σ_0.

Fig. 3 shows the absolute values of U in e.v., based on (III) for cases 1, 2, 3 and 4. In Fig. 4, curves 1, 2 and 3 are the activation energies calculated from (I), (III) and Cottrel's, respectively. Cottrell's is the smallest. This correspondence remains for all other cases 1, 2 and 3 in almost similar relation.

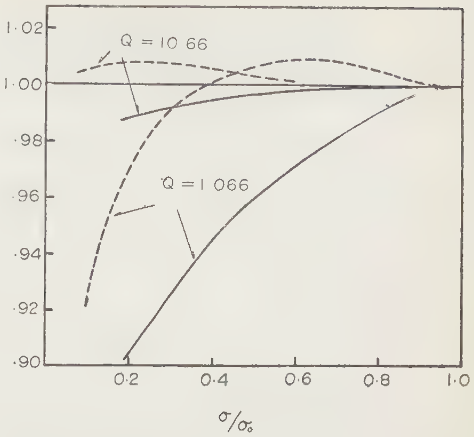

Fig. 2. Ratios of the exact solution to the approximate, the full and dotted lines are $I_1/\sqrt{2Q}I_0$, $I_2/\sqrt{2Q(1-2\nu)}I_0$, respectively, for $Q = 1.066$. 10.66 and $\nu = 0.3$.

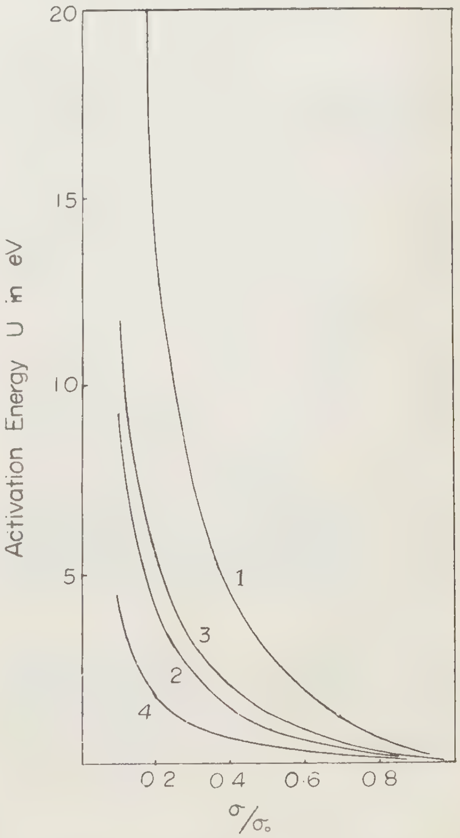

Fig. 3. Activation energies calculated from (III) for various cases 1, 2, 3 and 4, respectively.

Finally, Fig. 5 shows the experiments of yield points for various temperatures and the calculated activation energies so chosen as to be fitted at 195°K, curve 1 from the approximate solution of Cottrel's and curve 2 from

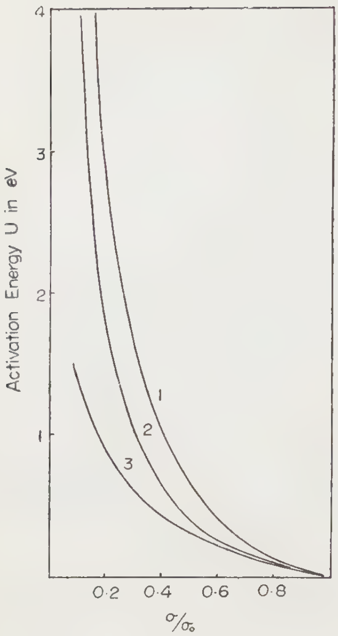

Fig. 4. Activation energies calculated from (I), (III) and Cottrel's, for curve 1, 2 and 3 respectively.

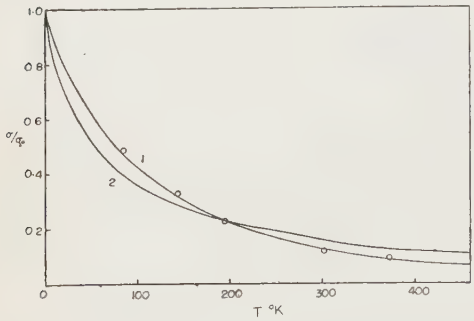

Fig. 5. Comparison with the experiments; the circles are obtained by McAdam and Mebs, curves 1, 2 are calculated from Cottrel's and variational method, respectively.

the more accurate solution (II). Then, the beautiful agreements of Cottrel's is lost for higher approximation. An attempt to take (IV) for more appropriate value of Q or the modulated curve by Yokobori's theory³⁾ of yield phenomenon from activation energy instead of (II) itself can not correct this large disagreement.

The reason why the higher approximation deviates from the experimental curve would be ; first, the form $V_e(x)$ is based on the elastic theory for too larger strains to be treated by it ; secondly, the experimental value are obtained for the poly-crystalline specimens where it is not certain whether the potential trough is caused by the impure (carbon) atoms or the grain boundary ; thirdly, the assumption that the potential trough is uniform, say $V=V(x)$, is also not certain⁴⁾, and the form of $V=V(x,z)$ would be more appropriate, then we lost the simplified integral of Euler's Equ. (8), where the problem corresponds to that of non-conservative in analytical dynamics.

The inverse problem that is to choose the appropriate form of $V(x)$ so as to agree with the given curve of activation energy is a kind of very difficult integral equations.

In conclusion, I wish to thank to Assist. Prof. R. R. Hashiguchi, in Tokyo Univ. for his encouragement in this work and to Mr. S. Inagaki and Mr. A. Iguchi for their assistance in numerical integration.

References

1) A. H. Cottrel and B. A. Bilby: Proc. Phys. Soc. **A 62** (1949) 49.

2) McAdam and R. W. Mebs: Trans. Amer. Soc. Test Mat. **43** (1943) 661.

3) T. Yokobori: J. Phys. Soc. Japan **7** (1952) 44.

4) A. H. Cottrel: Prog. Metal Phys. (1953) 240.

JOURNAL OF THE PHYSICAL SOCIETY OF JAPAN Vol. 9, No. 4, JULY—AUGUST, 1954

A Method of Treating the Zero-point Vibration of the Crystal of Lighter Molecules

By Akio YOSHIMORI
Department of Physics, Naniwa University,
and Takeo MATSUBARA
Department of Physics, Faculty of Science, Hokkaido University

(Received February 15, 1954)

A method of treating the zero point vibration of a molecular crystal of lighter elements, in which the vibrational amplitude is fairly large but the anharmonicity is small, is described. This consists of employing the Ritz variational method, assuming the wave function of the same form as that for an assembly of harmonic oscillators. The correlation between the positions of the molecules can be taken into account to some extent by this method. Two approximate methods are employed; one is essentially the usual method of supposing a harmonic vibrational potential and the other the method of supposing an anharmonic potential. Numerical calculations are carried out for solid neon, and reasonable results are obtained.

§ 1. Introduction

In the molecular crystal of lighter elements the zero-point vibration plays an important role. The usual method of treating the lattice vibrations as an assembly of harmonic oscillators is not adequate for instance for solid He, H_2 and D_2, since in these cases the mass of the molecules is small, their displacements are large, and hence the intermolecular potential cannot be considered as parabolic. This particularity has been considered by some authors[1)2)] by the method of the cage model for calculating the cohesive energy of these crystals. In the present paper, we shall develop another method of treating the zero-point vibration in which we take care to some extent of the correlation between the positions of the molecules. This method applies, however, only when the anharmonicity is small, as in the crystal of Ne.

Let us consider for a moment the ground state of an assembly of harmonic oscillators in order to investigate the correlation between the positions of the molecules. The ground state is described by the wave function

$\Psi \propto \exp\{-$(a quadratic form of the displacements of the molecules)$\}$.

In the case of one-dimension, the probability distribution function $|\Psi|^2$ contains in general a factor of the form $\exp(a\boldsymbol{u}_1\boldsymbol{u}_2)$, where a is a parameter (which we will assume to be positive) and $\boldsymbol{u}_1$ and $\boldsymbol{u}_2$ are the displacements of the first and second molecules respectively. This factor makes the motions of the neighbouring molecules into opposite directions unfavourable but those in the same direction favourable. In the present paper, we assume the same wave function as above but not necessarily assume a quadratic form for the potential energy. The calculation is performed by the Ritz variational method, assuming the coefficients of the above quadratic form as the variational parameters. An intermolecular potential of the central force type $\varphi(r)$ is assumed and two approximate methods are employed. The face-centered cubic lattice is treated, and the theory is applied to the crystal of neon.

§ 2. The Method

In the system of N molecules, the Hamiltonian H and the energy of the ground state E can be written as

$$\left.\begin{aligned} H&=\frac{1}{2m}\sum_{s=1}^{N}\boldsymbol{P}_s^2+\sum_{s>t}\varphi(|\boldsymbol{r}_s-\boldsymbol{r}_t|)\,,\\ E&=C^{-1}\int\cdots\int\Psi^*H\Psi\,d\boldsymbol{r}_1\cdots d\boldsymbol{r}_N\,,\\ C&=\int\cdots\int\Psi^*\Psi\,d\boldsymbol{r}_1\cdots d\boldsymbol{r}_N\,. \end{aligned}\right\} \tag{1}$$

Suppose that the s-th molecule vibrates in the neighbourhood of the lattice point $\boldsymbol{R}_s$. Writing its displacement from the lattice point $\boldsymbol{R}_s$ as $\boldsymbol{u}_s$ ($\boldsymbol{u}_s=\boldsymbol{r}_s-\boldsymbol{R}_s$), we have for Ψ

$$\Psi=\exp\{-\sum_{s,t}(\boldsymbol{u}_s\cdot\boldsymbol{A}_{st}\cdot\boldsymbol{u}_t)\}\,. \qquad (2)$$

$\boldsymbol{A}_{st}$'s are three-dimensional metrices which contain undetermined parameters. Assuming that $\boldsymbol{A}_{st}$ vanishes when s and t are not nearest neighbours and considering the symmetry of the crystal, the remaining $\boldsymbol{A}_{st}$'s are shown to be of the forms[3)]

$$\left.\begin{array}{l}
\boldsymbol{A}_0=\begin{pmatrix}\alpha&0&0\\0&\alpha&0\\0&0&\alpha\end{pmatrix}\\[2ex]
\left.\begin{array}{l}\boldsymbol{A}_1\\\boldsymbol{A}_7\end{array}\right\}=\begin{pmatrix}-\beta&0&0\\0&-\gamma&-\delta\\0&-\delta&-\gamma\end{pmatrix},\quad
\left.\begin{array}{l}\boldsymbol{A}_2\\\boldsymbol{A}_8\end{array}\right\}=\begin{pmatrix}-\beta&0&0\\0&-\gamma&\delta\\0&\delta&-\gamma\end{pmatrix},\quad
\left.\begin{array}{l}\boldsymbol{A}_3\\\boldsymbol{A}_9\end{array}\right\}=\begin{pmatrix}-\gamma&0&-\delta\\0&-\beta&0\\-\delta&0&-\gamma\end{pmatrix},\\[2ex]
\left.\begin{array}{l}\boldsymbol{A}_4\\\boldsymbol{A}_{10}\end{array}\right\}=\begin{pmatrix}-\gamma&0&\delta\\0&-\beta&0\\\delta&0&-\gamma\end{pmatrix},\quad
\left.\begin{array}{l}\boldsymbol{A}_5\\\boldsymbol{A}_{11}\end{array}\right\}=\begin{pmatrix}-\gamma&-\delta&0\\-\delta&-\gamma&0\\0&0&-\beta\end{pmatrix},\quad
\left.\begin{array}{l}\boldsymbol{A}_6\\\boldsymbol{A}_{12}\end{array}\right\}=\begin{pmatrix}-\gamma&\delta&0\\\delta&-\gamma&0\\0&0&-\beta\end{pmatrix},
\end{array}\right\} \qquad (3)$$

$\boldsymbol{A}_{ss}$ are the same irrespectively of s and are denoted as $\boldsymbol{A}_0$ and those $\boldsymbol{A}_{st}$ for which the relative positions between the s-th and t-th molecules are the same as those between the central and i-th molecules in Fig. 1 are put equal to $\boldsymbol{A}_i$ ($i=1, 2, \cdots, 12$) by a similar reason. We have therefore four parameters $\alpha, \beta, \gamma, \delta$.

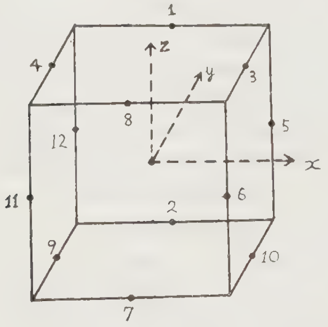

Fig. 1.

If we write as $\boldsymbol{A}$ the 3N-dimensional matrix whose elements consist of the elements of all the $\boldsymbol{A}_{st}$'s and as A the determinant of $\boldsymbol{A}$, we easily express the normalization constant and the kinetic energy as follows;

$$C=\int\cdots\int|\Psi|^2\,d\boldsymbol{u}_1\cdots d\boldsymbol{u}_N=(\pi/2)^{3N/2}A^{-1/2}\,, \qquad (4)$$

$$E_1=C^{-1}\int\cdots\int\Psi^*\Big\{-(\hbar^2/2m)\sum_s\frac{\partial^2}{\partial\boldsymbol{u}_s^{\,2}}\Big\}\Psi\,d\boldsymbol{u}_1\cdots d\boldsymbol{u}_N$$
$$=(\hbar^2/2m)\ \mathrm{trace}\ \boldsymbol{A}=(\hbar^2/2m)3N\alpha. \qquad (5)$$

In order to calculate the potential energy

$$E_2=C^{-1}\int\cdots\int\sum_{s>t}\varphi(|\boldsymbol{r}_s-\boldsymbol{r}_t|)|\Psi|^2\,d\boldsymbol{u}_1\cdots d\boldsymbol{u}_N\,, \qquad (6)$$

it is necessary to know the functional form of $\varphi(\boldsymbol{r})$. Two approximate methods will be considered for this purpose.

Method A. This method is essentially the same as the usual method of supposing harmonic oscillations and consists in expanding $U=\sum_{s>t}\varphi(|\boldsymbol{r}_s-\boldsymbol{r}_t|)$ into a power series of $\boldsymbol{u}$ in the neighbourhood of the position $\boldsymbol{u}=0$ and in neglecting the terms higher than the second power of $\boldsymbol{u}$. This does not necessarily mean that we are dealing with a small oscillation in the neighbourhood of the minimun of the total potential energy. We are assuming that the lattice constant is a given parameter and we shall later determine the equilibrium lattice constant by taking the minimum of total energy. Then we have

$$U=\sum_{s>t}\varphi(|\boldsymbol{r}_s-\boldsymbol{r}_t|)=\sum_{s>t}\varphi(|\boldsymbol{R}_s+\boldsymbol{u}_s-\boldsymbol{R}_t-\boldsymbol{u}_t|)$$
$$=\Phi_0+\frac{1}{2!}\sum_{s,t}(\boldsymbol{u}_s\cdot\boldsymbol{C}_{st}\cdot\boldsymbol{u}_t)\,. \qquad (7)$$

In the term quadratic in $\boldsymbol{u}_s$, the coeffecients $\boldsymbol{C}_{st}$'s have the same symmetry as $\boldsymbol{A}_{st}$'s and are given as

$$\left.\begin{aligned}
&\boldsymbol{C}_0=\begin{bmatrix} 4\left(\varphi''+2\frac{\varphi'}{r_0}\right) & 0 & 0 \\ 0 & 4\left(\varphi''+2\frac{\varphi'}{r_0}\right) & 0 \\ 0 & 0 & 4\left(\varphi''+2\frac{\varphi'}{r_0}\right) \end{bmatrix}, \quad
\left.\begin{matrix}\boldsymbol{C}_1\\ \boldsymbol{C}_7\end{matrix}\right\}=\begin{bmatrix} -\frac{\varphi'}{r_0} & 0 & 0 \\ 0 & -\frac{1}{2}\left(\varphi''+\frac{\varphi'}{r_0}\right) & -\frac{1}{2}\left(\varphi''-\frac{\varphi'}{r_0}\right) \\ 0 & -\frac{1}{2}\left(\varphi''-\frac{\varphi'}{r_0}\right) & -\frac{1}{2}\left(\varphi''+\frac{\varphi'}{r_0}\right) \end{bmatrix}, \\
&\left.\begin{matrix}\boldsymbol{C}_2\\ \boldsymbol{C}_8\end{matrix}\right\}=\begin{bmatrix} -\frac{\varphi'}{r_0} & 0 & 0 \\ 0 & \frac{1}{2}\left(\varphi''+\frac{\varphi'}{r_0}\right) & \frac{1}{2}\left(\varphi''-\frac{\varphi'}{r_0}\right) \\ 0 & \frac{1}{2}\left(\varphi''-\frac{\varphi'}{r_0}\right) & \frac{1}{2}\left(\varphi''+\frac{\varphi'}{r_0}\right) \end{bmatrix}, \quad \text{etc.}
\end{aligned}\right\} \tag{8}$$

Here the suffices 0, 1, 2, $\cdots$ 12 have the same meaning as in $\boldsymbol{A}_{st}$'s, and φ' and φ'' are the first and second derivatives of $\varphi(r)$ at $r=r_0$, r_0 being the distance between the nearest neighbours.

Using the expressions (7), E_2 becomes

$$E_2=\Phi_0+\frac{1}{4}\cdot\frac{1}{2!}\ \mathrm{trace}\,(\boldsymbol{C}\boldsymbol{A}^{-1})\,, \tag{9}$$

where $\boldsymbol{A}^{-1}$ is the inverse matrix of $\boldsymbol{A}$. In carrying out the calculation of trace$(\boldsymbol{C}\boldsymbol{A}^{-1})$, it is convenient to transform $\boldsymbol{C}$ and $\boldsymbol{A}$ into simpler forms by a unity matrix

$$\boldsymbol{S}=(\boldsymbol{S}_{ij})=\frac{\mathbf{1}}{\sqrt{N}}\ \exp\,(2\pi i\boldsymbol{\sigma}_i\cdot\boldsymbol{R}_j)\,,$$

where $\mathbf{1}$ is the three-dimensional unit matrix and $\boldsymbol{\sigma}_i(i=1, \cdots, N)$ the wave vectors contained in the first Brillouin zone that corresponds to the face-centered cubic lattice. We write

$$\boldsymbol{\Gamma}=\boldsymbol{S}^{-1}\boldsymbol{C}\boldsymbol{S}\,,\quad \boldsymbol{\Lambda}=\boldsymbol{S}^{-}\boldsymbol{A}\boldsymbol{S}\,.$$

The elements of $\boldsymbol{\Gamma}$ and $\boldsymbol{\Lambda}$ are zero except for the three-dimensional diagonal parts, i.e., $\boldsymbol{\Gamma}=(\boldsymbol{\Gamma}_{ij}\delta_{ij})$, $\boldsymbol{\Lambda}=(\boldsymbol{\Lambda}_{ij}\delta_{ij})$, where $\boldsymbol{\Gamma}_{ij}$ and $\boldsymbol{\Lambda}_{ij}$ are the three-dimensional matrices. Therefore we obtain

$$\begin{aligned}\mathrm{trace}\,(\boldsymbol{C}\boldsymbol{A}^{-1})&=\mathrm{trace}\,(\boldsymbol{\Gamma}\boldsymbol{\Lambda}^{-1})\\ &=\sum_{i=1}^{N}\mathrm{trace}\,(\boldsymbol{\Gamma}_{ii}\boldsymbol{\Lambda}_{ii}{}^{-1})\,.\end{aligned}$$

Accordingly; the calculation of the trace is reduced to a three-dimensional matrix calculus. The summation over i can be replaced by an integration over the first Brillouin zone. In this way we obtain trace$(\boldsymbol{C}\boldsymbol{A}^{-1})$ as a function of the variational parameters $\alpha, \beta, \gamma, \delta$. $\boldsymbol{\Gamma}_{ii}$ and $\boldsymbol{\Lambda}_{ii}$ are given as follows:

$$\boldsymbol{\Gamma}_{ii}=\begin{bmatrix}
4\left(\varphi''+2\frac{\varphi'}{r_0}\right)-2\frac{\varphi'}{r_0}K_1{}^{+}-\left(\varphi''+\frac{\varphi'}{r_0}\right)(K_2{}^{+}+K_3{}^{+}) & -\left(\varphi''-\frac{\varphi'}{r_0}\right)K_3{}^{-} & -\left(\varphi''-\frac{\varphi'}{r_0}\right)K_2{}^{-} \\
-\left(\varphi''-\frac{\varphi'}{r_0}\right)K_3{}^{-} & 4\left(\varphi''+2\frac{\varphi'}{r_0}\right)-2\frac{\varphi'}{r_0}K_2{}^{+}-\left(\varphi''+\frac{\varphi'}{r_0}\right)(K_3{}^{+}+K_1{}^{+}) & -\left(\varphi''-\frac{\varphi'}{r_0}\right)K_1{}^{-} \\
-\left(\varphi''-\frac{\varphi'}{r_0}\right)K_2{}^{-} & -\left(\varphi''-\frac{\varphi'}{r_0}\right)K_1{}^{-} & 4\left(\varphi''+2\frac{\varphi'}{r_0}\right)-2\frac{\varphi'}{r_0}K_3{}^{+}-\left(\varphi''+\frac{\varphi'}{r_0}\right)(K_1{}^{+}+K_2{}^{+})
\end{bmatrix}, \tag{10}$$

$$\boldsymbol{\Lambda}_{ii}=\begin{bmatrix}
\alpha-2\beta K_1{}^{+}-2\gamma(K_2{}^{+}+K_3{}^{+}) & -2\delta K_3{}^{-} & -2\delta K_2{}^{-} \\
-2\delta K_3{}^{-} & \alpha-2\beta K_2{}^{+}-2\gamma(K_3{}^{+}+K_1{}^{+}) & -2\delta K_1{}^{-} \\
-2\delta K_2{}^{-} & -2\delta K_1{}^{-} & \alpha-2\beta K_3{}^{+}-2\gamma(K_1{}^{+}+K_2{}^{+})
\end{bmatrix}, \tag{11}$$

$$K_1{}^{\pm}=\cos\left(2\pi\frac{l_1}{N_1}\right)\pm\cos\left\{2\pi\left(\frac{l_2}{N_2}-\frac{l_3}{N_3}\right)\right\}, \quad K_2{}^{\pm}=\cos\left(2\pi\frac{l_2}{N_2}\right)\pm\cos\left\{2\pi\left(\frac{l_3}{N_3}-\frac{l_1}{N_1}\right)\right\},$$

$$K_3{}^{\pm}=\cos\left(2\pi\frac{l_3}{N_3}\right)\pm\cos\left\{2\pi\left(\frac{l_1}{N_1}-\frac{l_2}{N_2}\right)\right\},$$

where

$$\boldsymbol{\sigma}_l=\sum_{k=1}^{3}\frac{l_k}{N_k}\boldsymbol{s}_k\,, \quad -\frac{N_k}{2}\leq l_k\leq\frac{N_k}{2}\,,$$

$$N_1N_2N_3=N$$

($\boldsymbol{s}_k$, $k=1,2,3$, are the reciprocal lattice vectors).

Method B. We express the function $\varphi(r)$ approximately in the form

$$C_1\exp(-\lambda r^2)-C_2\exp(-\mu r^2)\,.$$

For this potential the integration of (6) can be performed. The numerical values of C_1, C_2, λ and μ in Table I for neon gives in the range 2.8 A$\leq r\leq$4.5 A a good approximation to the potential determined by Kane from the heat of sublimation and the equilibrium lattice constant[4] (Fig. 2). Kane took in his calculation the zero-point vibration into account using the Debye model. A simple calculation gives the total potential energy in the form

Table I.

C_1 erg	C_2 erg	λ A^{-2}	μ A^{-2}
$2.358\cdot10^{-12}$	$1.805\cdot10^{-14}$	0.749	0.1235

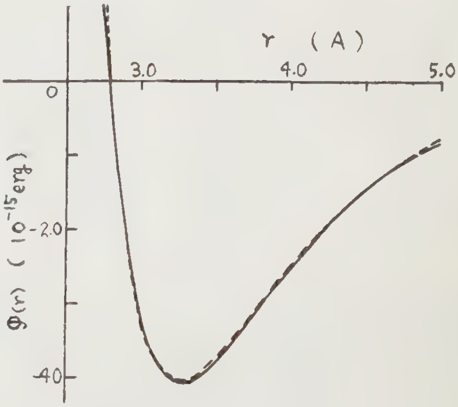

Fig. 2. Comparison of our approximate potential (----) with that determined by Kane (——).

$$E_2=\Phi_0-\frac{Nz}{2}\{C_1\exp(-\lambda r_0{}^2)-C_2\exp(-\mu r_0{}^2)\}+\frac{Nz}{2}\Bigg[C_1\left\{\frac{\rho_1\rho_2\rho_3}{(\rho_1+\lambda)(\rho_2+\lambda)(\rho_3+\lambda)}\right\}^{1/2}$$
$$\times\exp\{-\lambda r_0{}^2\rho_3/(\rho_3+\lambda)\}-C_2\left\{\frac{\rho_1\rho_2\rho_3}{(\rho_1+\mu)(\rho_2+\mu)(\rho_3+\mu)}\right\}^{1/2}\exp\{-\mu r_0{}^2\rho_3/(\rho_3+\mu)\}\Bigg] \qquad (12)$$

where we have neglected those terms which arise from the pairs of molecules separated by a distance greater than that between second neighbours. z is the number of the nearest neighbours ($z=12$), and ρ_1, ρ_2 and ρ_3 are connected with the elements of $\boldsymbol{\Lambda}^{-1}$ by

$$\rho_1=\frac{1}{Q-B}\,,\quad \rho_2=\frac{1}{Q-D+F}\,,\quad \rho_3=\frac{1}{Q-D-F}\,. \qquad (13)$$

Q; the xx-elements of $(\boldsymbol{\Lambda}^{-1})_0$,
D; the yy-elements of $(\boldsymbol{\Lambda}^{-1})_1$,
B; the xx-elements of $(\boldsymbol{\Lambda}^{-1})_1$.
F; the yz-elements of $(\boldsymbol{\Lambda}^{-1})_1$.

$Q, B, \cdots$ etc. can be calculated by use of $\boldsymbol{\Lambda}_{ll}$ defined by (11) to

$$\left.\begin{aligned}
Q&=\frac{1}{3N}\sum_{l=1}^{N}[(\boldsymbol{\Lambda}_{ll}{}^{-1})_{11}+(\boldsymbol{\Lambda}_{ll}{}^{-1})_{22}+(\boldsymbol{\Lambda}_{ll}{}^{-1})_{33}]\,,\\
B&=\frac{1}{6N}\sum_{l=1}^{N}[(\boldsymbol{\Lambda}_{ll}{}^{-1})_{11}K_1{}^{+}+(\boldsymbol{\Lambda}_{ll}{}^{-1})_{22}K_2{}^{+}\\
&\qquad\qquad+(\boldsymbol{\Lambda}_{ll}{}^{-1})_{33}K_3{}^{+}]\,,\\
D&=\frac{1}{12N}\sum_{l=1}^{N}[(\boldsymbol{\Lambda}_{ll}{}^{-1})_{11}(K_2{}^{+}+K_3{}^{+})\\
&\qquad\qquad+(\boldsymbol{\Lambda}_{ll}{}^{-1})_{22}(K_3{}^{+}+K_1{}^{+})\\
&\qquad\qquad+(\boldsymbol{\Lambda}_{ll}{}^{-1})_{33}(K_1{}^{+}+K_2{}^{+})]\,,\\
F&=\frac{1}{6N}\sum_{l=1}^{N}[(\boldsymbol{\Lambda}_{ll}{}^{-1})_{11}K_1{}^{-}+(\boldsymbol{\Lambda}_{ll}{}^{-1})_{22}K_2{}^{-}\\
&\qquad\qquad+(\boldsymbol{\Lambda}_{ll}{}^{-1})_{33}K_3{}^{-}]\,.
\end{aligned}\right\} \qquad (14)$$

The summations are taken over $\boldsymbol{\sigma}_l$ contained in the first Brillouin zone.

§ 3. Further Simplification and the Results for the Solid Neon

We apply the above results to the solid neon with certain further simplifying mathematical assumptions.

(i) *Method A.* We assume $\boldsymbol{A}_i \propto \boldsymbol{C}_i$ ($i=1, 2, \cdots, 12$). Then the parameters given by (3) are reduced to three α, β', γ' and $\boldsymbol{A}_i$'s are expressed as

$$\boldsymbol{A}_0=\begin{pmatrix}\alpha & 0 & 0\\ 0 & \alpha & 0\\ 0 & 0 & \alpha\end{pmatrix},$$

$$\left.\begin{matrix}\boldsymbol{A}_1\\ \boldsymbol{A}_7\end{matrix}\right\}=\frac{1}{2}\begin{pmatrix}-\beta' & 0 & 0\\ 0 & -\gamma' & -(\gamma'-\beta')\\ 0 & -(\gamma'-\beta') & -\gamma'\end{pmatrix},\quad \left.\begin{matrix}\boldsymbol{A}_2\\ \boldsymbol{A}_8\end{matrix}\right\}=\frac{1}{2}\begin{pmatrix}-\beta' & 0 & 0\\ 0 & -\gamma' & \gamma'-\beta'\\ 0 & \gamma'-\beta' & -\gamma'\end{pmatrix},\quad \left.\begin{matrix}\boldsymbol{A}_3\\ \boldsymbol{A}_9\end{matrix}\right\}=\frac{1}{2}\begin{pmatrix}-\gamma' & 0 & -(\gamma'-\beta')\\ 0 & -\beta' & 0\\ -(\gamma'-\beta') & 0 & -\gamma'\end{pmatrix},$$

$$\left.\begin{matrix}\boldsymbol{A}_4\\ \boldsymbol{A}_{10}\end{matrix}\right\}=\frac{1}{2}\begin{pmatrix}-\gamma' & 0 & \gamma'-\beta'\\ 0 & -\beta' & 0\\ \gamma'-\beta' & 0 & -\gamma'\end{pmatrix},\quad \left.\begin{matrix}\boldsymbol{A}_5\\ \boldsymbol{A}_{11}\end{matrix}\right\}=\frac{1}{2}\begin{pmatrix}-\gamma' & -(\gamma'-\beta') & 0\\ -(\gamma'-\beta') & -\gamma' & 0\\ 0 & 0 & -\beta'\end{pmatrix},\quad \left.\begin{matrix}\boldsymbol{A}_6\\ \boldsymbol{A}_{12}\end{matrix}\right\}=\frac{1}{2}\begin{pmatrix}-\gamma' & \gamma'-\beta' & 0\\ \gamma'-\beta' & -\gamma' & 0\\ 0 & 0 & -\beta'\end{pmatrix}. \tag{15}$$

Further, we expand trace$(\boldsymbol{\Gamma}_{ii}\boldsymbol{A}_{ii}^{-1})$ into a double power series of (β'/α) and (γ'/α) and neglect the terms higher than second order. In fact, the numerical values of (β'/α) and (γ'/α) turn out to be about 5×10^{-2} and 1×10^{-1}, respectively, in the case of neon at the equilibrium state. Finally, minimizing E with respect to α, β', γ', or solving $\partial E/\partial\alpha=0$, $\partial E/\partial\beta'=0$, $\partial E/\partial\gamma'=0$, we obtain

$$\left.\begin{aligned}
&E=\{\hbar^2/(2m)\}^{1/2}3N(G/2)^{1/2}+\Phi_0\,,\\
&G=4\left(\varphi''+2\frac{\varphi'}{r_0}\right)+\left(2\varphi''-4\frac{\varphi'}{r_0}\right)\left(\frac{\beta'}{\alpha}\right)_m-4\varphi''\left(\frac{\gamma'}{\alpha}\right)_m+\left(14\varphi''+22\frac{\varphi'}{r_0}\right)\left(\frac{\beta'}{\alpha}\right)_m^2\\
&\qquad-\left(24\varphi''+32\frac{\varphi'}{r_0}\right)\left(\frac{\beta'}{\alpha}\right)_m\left(\frac{\gamma'}{\alpha}\right)_m+\left(18\varphi''+26\frac{\varphi'}{r_0}\right)\left(\frac{\gamma'}{\alpha}\right)_m^2,\\
&\left(\frac{\beta'}{\alpha}\right)_m=\frac{4\varphi''\left(3\varphi''+4\frac{\varphi'}{r_0}\right)-\left(\varphi''-2\frac{\varphi'}{r_0}\right)\left(9\varphi''+13\frac{\varphi'}{r_0}\right)}{2\left(7\varphi''+11\frac{\varphi'}{r_0}\right)\left(9\varphi''+13\frac{\varphi'}{r_0}\right)-8\left(3\varphi''+4\frac{\varphi'}{r_0}\right)^2},\\
&\left(\frac{\gamma'}{\alpha}\right)_m=\frac{-\left(\varphi''-2\frac{\varphi'}{r_0}\right)\left(3\varphi''+4\frac{\varphi'}{r_0}\right)+\varphi''\left(7\varphi''+22\frac{\varphi'}{r_0}\right)}{\left(7\varphi''+11\frac{\varphi'}{r_0}\right)\left(9\varphi''+13\frac{\varphi'}{r_0}\right)-4\left(3\varphi''+4\frac{\varphi'}{r_0}\right)^2},
\end{aligned}\right\} \tag{16}$$

(ii) *Method B* We assume $\boldsymbol{A}\propto\boldsymbol{C}_{r_0=r_m}$ (r_m is defined by $\varphi'(r_m)=0$). Then, only one parameter α is left and we have

$$\left.\begin{aligned}
&\boldsymbol{A}_0=\begin{pmatrix}\alpha & 0 & 0\\ 0 & \alpha & 0\\ 0 & 0 & \alpha\end{pmatrix},\\
&\left.\begin{matrix}\boldsymbol{A}_1\\ \boldsymbol{A}_7\end{matrix}\right\}=\frac{1}{8}\begin{pmatrix}0 & 0 & 0\\ 0 & -\alpha & -\alpha\\ 0 & -\alpha & -\alpha\end{pmatrix};\quad \left.\begin{matrix}\boldsymbol{A}_2\\ \boldsymbol{A}_8\end{matrix}\right\}=\frac{1}{8}\begin{pmatrix}0 & 0 & 0\\ 0 & -\alpha & \alpha\\ 0 & \alpha & -\alpha\end{pmatrix},\quad \left.\begin{matrix}\boldsymbol{A}_3\\ \boldsymbol{A}_9\end{matrix}\right\}=\frac{1}{8}\begin{pmatrix}-\alpha & 0 & -\alpha\\ 0 & 0 & 0\\ -\alpha & 0 & -\alpha\end{pmatrix},\\
&\left.\begin{matrix}\boldsymbol{A}_4\\ \boldsymbol{A}_{10}\end{matrix}\right\}=\frac{1}{8}\begin{pmatrix}-\alpha & 0 & \alpha\\ 0 & 0 & 0\\ \alpha & 0 & -\alpha\end{pmatrix},\quad \left.\begin{matrix}\boldsymbol{A}_5\\ \boldsymbol{A}_{11}\end{matrix}\right\}=\frac{1}{8}\begin{pmatrix}-\alpha & -\alpha & 0\\ -\alpha & -\alpha & 0\\ 0 & 0 & 0\end{pmatrix},\quad \left.\begin{matrix}\boldsymbol{A}_6\\ \boldsymbol{A}_{12}\end{matrix}\right\}=\frac{1}{8}\begin{pmatrix}-\alpha & \alpha & 0\\ \alpha & -\alpha & 0\\ 0 & 0 & 0\end{pmatrix},
\end{aligned}\right\} \tag{17}$$

ρ_1, ρ_2 and ρ_3 are proportional to α, i.e.

$$\rho_1=\rho_1{}^0\alpha\,,\quad \rho_2=\rho_2{}^0\alpha\,,\quad \rho_3=\alpha \tag{18}$$

where $\rho_1{}^0$ and $\rho_2{}^0$ are numerical constant independent of α, as can be seen from (11), (13) and (14). In order to evaluate $\rho_1{}^0$ and $\rho_2{}^0$, the summations in (14) are replaced by integrations over the first Brillous zone which is replaced by the sphere of the same volume.

The integrands are expanded into surface harmonics of the cubic symmetry. In general, when a function $F(r, \theta, \varphi)$ has the cubic symmetry, it can be expanded as

$$F=F_0(r)+F_4(r)Y_4(\theta, \varphi)+F_6(r)Y_6(\theta, \varphi)+\cdots, \tag{19'}$$

where Y_4 and Y_6 have the cubic symmetry.

Neglecting higher terms, we have[5)]

$$\int_\Omega F d\omega \cong \frac{4\pi}{35}[10F(r, 0, 0)+16F(r, \pi/2, \pi/4) +9F(r, \cos^{-1}(1/\sqrt{3}), \pi/4)] , \tag{19}$$

where Ω is the whole solid angle. Therefore, if we replace the summation in

$$\alpha Q=\frac{1}{3N}\sum_i [\alpha(\boldsymbol{\Lambda}_{ii}{}^{-1})_{11}+\alpha(\boldsymbol{\Lambda}_{ii}{}^{-1})_{22}+\alpha(\boldsymbol{\Lambda}_{ii}{}^{-1})_{33}] =\frac{1}{N}\sum_i \alpha Q'(\boldsymbol{\sigma}_i) ,$$

by the corresponding integration over the sphere, we have

$$\begin{aligned}\alpha Q &= \int_\Omega\int_0^{\sigma_0} \alpha Q'(\sigma, \theta, \varphi)\sigma^2 d\sigma d\omega \\ &\simeq \frac{4\pi}{35}\Big[10\int_0^{\sigma_0} \alpha Q'(\sigma, 0, 0)\sigma^2 d\sigma \\ &\quad +16\int_0^{\sigma_0} \alpha Q'(\sigma, \pi/2, \pi/4)\, \sigma^2 d\sigma \\ &\quad +9\int_0^{\sigma_0} \alpha Q'(\sigma, \cos^{-1}(1/\sqrt{3}), \pi/4)\sigma^2 d\sigma\Big]\end{aligned} \tag{20}$$

αB, αD and αF can be treated in a similar manner. In this way, numerical values of $\rho_1{}^0$ and $\rho_2{}^0$ can be found, and the results are

$$\rho_1{}^0=0.7535 , \quad \rho_2{}^0=0.6924 .$$

Finally, we obtain from (5), (12), and (17).

$$\begin{aligned}E=&\{\hbar^2/(2m)\}3N\alpha+\Phi_0-(Nz/2)\{C_1 \exp(-\lambda r_0{}^2)-C_2 \exp(-\mu r_0{}^2)\} \\ &+\frac{Nz}{2}\Big[C_1\Big\{\frac{\rho_1{}^0\rho_2{}^0\alpha^3}{(\rho_1{}^0\alpha+\lambda)(\rho_2{}^0\alpha+\lambda)(\alpha+\lambda)}\Big\}^{1/2}\exp\{-\lambda r_0{}^2\alpha/(\alpha+\lambda)\} \\ &\qquad -C_2\Big\{\frac{\rho_1{}^0\rho_2{}^0\alpha^3}{(\rho_1{}^0\alpha+\mu)(\rho_2{}^0\alpha+\mu)(\alpha+\mu)}\Big\}^{1/2}\exp\{-\mu r_0{}^2\alpha/(\alpha+\mu)\}\Big] .\end{aligned} \tag{21}$$

Table II.

Potential	Method	r_0 A	$-E$ Rilo Joule/mol	Θ °K
(a)	A	3.12 (3.12)	1.87 (1.85)	57.4 (59)
(b)	A	3.16 (3.17)	1.90 (1.88)	53 (54)
	B	3.17 (3.19)	1.86 (1.85)	57 (56)
Experimental Value[4)]		3.2	1.87	64

In this method, we calculate the minimum value of E numerically at each given volume.

The intermolecular potential used is either

(a)[6)] $\varphi(r)=4\varepsilon[(r^*/r)^{12}-(r^*/r)^6]$,
$\varepsilon=48.82\cdot10^{-16}$ erg ,
$r^*=2.74$ A , (r in A)

or

(b)[4)] $\varphi(r)=(0.968\, e^{-r/0\cdot345} -0.1402/r^6)\cdot10^{-10}$ erg .

The corresponding Φ_0 is given by

(a)[6)] $\Phi_0=[1297/r^{12}-3.622/r^6]\cdot10^{13}$ erg

(b)[4)] $\Phi_0=[34.97 \exp(-r/0.345) \times(1+\frac{1}{2} \exp\{-(\sqrt{2}-1)r/0.345\} +2 \exp\{-(\sqrt{3}-1)r/0.345\} +\cdots)-6.105/r^6]\cdot10^{13}$ erg .

The results are shown in Fig. 3 and Table II.

In Table II the values enclosed by parentheses are those which are calculated by a further assumption that $\beta'=\gamma'=0$, or

$$\boldsymbol{A}_0=\begin{bmatrix}\alpha & 0 & 0\\ 0 & \alpha & 0\\ 0 & 0 & \alpha\end{bmatrix}, \quad \boldsymbol{A}_i=[0] \quad (i=1, \cdots, 12) . \tag{22}$$

This corresponds to assume Einstein's model, in which each molecule is supposed to vibrate independently of the others, r_0 in this table is the distance between the nearest neighbours at the minimum of the total energy, $-E$ the heat of sublimation, and Θ the Debye characteristic temperature calculated by assuming that the zero-point energy of the system (i.e., $E-\Phi_0$) is equal to that of the Debye model ($(9/8)R\Theta$).

The potential (b) was evaluated by Kane[4)] from the heat of sublimation and the lattice constant. The above results for $-E$ and r_0 agree well with those used by him in estimating $\varphi(r)$. In Table II values for Θ calculated from (b) lie below experimental one 64 K. Kane obtained also a lower value 52.7°K for Θ from the potential (b).

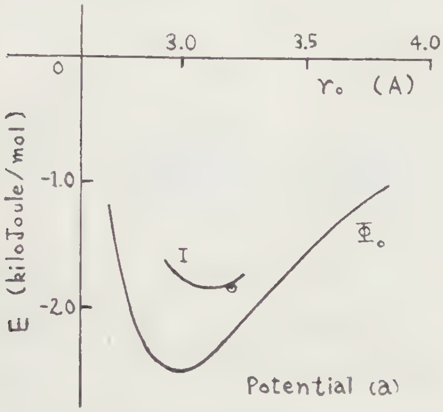

Fig. 3 (i). ◉ Experimental value,
I Calculated by the method A.

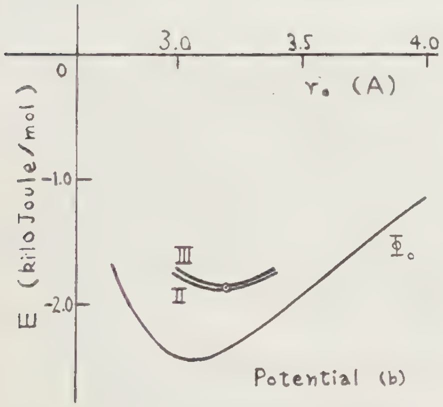

Fig. 3 (ii). ◉ Experimental value,
II Calculated by the method A,
III Calculated by the method B.

§ 4. Discussion

We may conclude that the zero-point vibration of the crystal of neon is almost describable by that of an assembly of harmonic oscillators. The difference between the calculated values of the total energy by the method A (essentially harmonic) and by the method B (including the anharmonicity) amounts only to about 2 per-cent of the total energy. Moreover, we see that the vibration is not far from that given by Einstein model. This make in particular the second simplification in the method A valid.

In general, if we suppose a quadratic form of the potential $(1/2)\sum_{s,t}(\boldsymbol{u}_s\cdot\boldsymbol{C}_{st}\cdot\boldsymbol{u}_t)$ and transform it to a diagonal matrix $\boldsymbol{D}$ by a unitary matrix $\boldsymbol{T}$.

$$\boldsymbol{D}=(D_i\delta_{ij})=\boldsymbol{T}^{-1}\boldsymbol{C}\boldsymbol{T}\ ,$$

then, we are easily led to

$$\boldsymbol{A}=\{m^{1/2}/(2\hbar)\}\boldsymbol{T}\boldsymbol{F}\boldsymbol{T}^{-1}\ , \tag{23}$$

where $\boldsymbol{F}$ is defined by $\boldsymbol{F}=(D_i^{1/2}\delta_{ij})$.

$$m^{1/2}D_i^{1/2}/(2\pi)$$

is the frequency of the i-th normal modes. Since, in our cases, we employed the variational method and did not necessarily suppose a quadratic form of the potential, the equation (23) is not necessarily valid. But it is plausible to use it in order to simplify $\boldsymbol{A}$, retaining adequate undetermined parameters in $\boldsymbol{C}_{st}$'s and calculating $\boldsymbol{F}$ approximately. From this point of view, our simplifications (16) and (17) correspond to assuming

$$\boldsymbol{F}=(D_i^{1/2}\delta_{ij})\cong\text{const.}(D_i\delta_{ij})\ ,$$

i.e.,

$$\boldsymbol{T}\boldsymbol{F}\boldsymbol{T}^{-1}\cong\text{const.}\boldsymbol{T}\boldsymbol{D}\boldsymbol{T}^{-1}=\text{const.}\boldsymbol{C}\ .$$

Since the exact equality in these equations holds only in Einstein's model in which all normal modes are supposed to have the same frequency, our simplified $\boldsymbol{A}$ can be of good approximate forms when the deviation from Einstein's model is small.

In the present method, the equilibrium lattice constant was determined by minimizing the total energy. By doing so, we could explain what may be called the expansion by the zero point vibration. Indeed, the zero point energy of the neon crystal occupies a considerably large part (ahout 27%) of the total energy and a considerable increase of r_0 as compared with that determined classically by minimizing Φ_0 was obtained (See Fig. 3).

The writers wish to express their cordial thanks to Prof. Nagamiya of Osaka University for his continual interest and helpful advices.

References

1) T. Nagamiya: Proc. Physico-Math. Soc. Japan, 3rd ser. **22** (1940) 492. The Zero-point energy of solid He is computed. The error comitted by him in applying the Margenau potential (the second replusive term was taken as positive instead of negative) is corrected for in his book *"Liquid Helium"* (in Japanese), 1946.

2) M. Toda: Proc. Physico-Math. Soc. Japan 3rd ser. **22** (1940) 503. The zero point energies of solid hydrogen and deuterium.

3) C. H. Begbie and M. Born: Proc. Roy. Soc. **A188** (1947) 189.

4) B. C. Kane: Jour. Chem. Phys. **7** (1939) 603.

5) W. V. Houston: Rev. Mod. Phys. **20** (1948) 161.

6) J. de Boer: Physica **14** (1948) 139.

JOURNAL OF THE PHYSICAL SOCIETY OF JAPAN Vol. 9, No. 4, JULY—AUGUST, 1954

Note on the Partition Function of a Free Rotator

By Tomoyasu TANAKA

Department of Physics, Faculty of Science,
Kyusyu University, Hukuoka

(Received March 8, 1954)

An integral representation of the density matrix of a free rotator is obtained by the use of the Fourier transformation. The general term of the high temperature expansion for the partition function is also obtained.

§ 1. Introduction

There are several methods in obtaining a high temperature expansion for the partition function of a rigid free rotator in connection with the rotational specific heats of diatomic molecules. One of them is to resort to the theorem of residues of a function of a complex variable.[1] Another is to use the Euler-MacLaurin summation formula.[2] In this article, integral representations of the density matrix, as well as the partion function, are obtained by the method of Fourier transformation, and the general term of a high temperature expansion for the partition function is obtained. As for the partition function the result is identical to that of Mulholland[1], however, the method adopted here is simpler than that of him, and also applicable to the density matrix.

§ 2. An Integral Representation

Apart from the electronic motions and nuclear spin a diatomic molecule can have no angular momentum about the axis through the two nuclei. Thus the correct model for its rotational motion is the rigid rotator without axial spin. The motion of the center of mass separates and can therefore, be ignored here.

Let A be the tranverse moment of inertia of the molecule, and θ, ϕ the ususal spherical polar coordinates of its axis. Then the conjugate momenta p_θ, p_ϕ are given by

$$p_\theta = a\dot{\theta}\,, \qquad p_\phi = A\sin^2\theta\dot{\phi}\,, \tag{2.1}$$

and the classical energy equation is

$$(2A)^{-1}(p_\theta{}^2 + p_\theta{}^2/\sin^2\theta) = \mathcal{E}\,. \tag{2.2}$$

The corresponding equation of Schrödinger is

$$\frac{1}{\sin\theta}\frac{\partial}{\partial\theta}\left(\sin\theta\frac{\partial\psi}{\partial\theta}\right) + \frac{1}{\sin^2\theta}\frac{\partial^2\psi}{\partial\phi^2} + \frac{8\pi^2 A}{h^2}\mathcal{E}\psi = 0\,. \tag{2.3}$$

The possible values of the energy are

$$\mathcal{E}_l = (h^2/8\pi^2 A)\,l\,(l+1)\,, \quad (l=0,\ 1,\ 2,\cdots\cdot), \tag{2.4}$$

and the corresponding eigen functions are the $2l+1$ spherical harmonics of order l:

$$\psi_{l,m}(\theta,\phi) = \left[\frac{2l+1}{4\pi}\cdot\frac{(l-|m|)!}{(l+|m|)!}\right]^{1/2} \times P_l{}^m(\cos\theta)e^{im\phi}\,, \quad m=-l,\ -l+1,\ \cdots\cdot l-1,\ l. \tag{2.5}$$

The density matrix of the rigid free rotator is thus given by

$$Z(\theta_0,\phi_0\,|\,\theta,\phi\,;\beta) = \sum_{l=0}^{\infty}\sum_{m=-l}^{l}\frac{2l+1}{4\pi}\frac{(l-|m|)!}{(l+|m|)!} \times P_l{}^m(\cos\theta_0)P_l{}^m(\cos\theta)e^{-im(\phi_0-\phi)} \times\exp\left[-\frac{\beta h^2 l(l+1)}{8\pi^2 A}\right], \tag{2.6}$$

where

$$\beta = 1/kT\,.$$

By use of the well known addition theorem for the spherical harmonics, the summation with respect to m can be carried out, and we have

$$Z(\theta_0,\phi_0\,|\,\theta,\phi\,;\beta) = \sum_{l=0}^{\infty}\frac{2l+1}{4\pi} \times\exp[-\sigma l(l+1)]P_l(\cos\gamma)\,, \tag{2.7}$$

where

$$\sigma = \beta h^2/8\pi^2 A\,,$$

and

$$\cos\gamma = \cos\theta_0\cos\theta + \sin\theta_0\sin\theta\cos(\phi-\phi_0)\,.$$

The partition function of the rotator is then given by putting $\theta=\theta_0$, $\phi=\phi_0$, i.e., $\gamma=0$, and intergrating over all possible θ and ϕ, and we have

$$Z(\sigma)=\int_0^{2\pi}\int_0^{\pi} Z(\theta,\phi\,|\,\theta,\phi\,;\beta)d\theta d\phi$$

$$=\sum_{l=0}^{\infty}(2l+1)e^{-\sigma l(l+1)}. \qquad (2.8)$$

In evaluating the integral (2.8) we paid no attention to symmetry with respect to the two nuclei. In molecules with two different nuclei (hetero-nuclear molecules), there is no need to do so. As is well known, in the case of molecules containing two identical nuclei (homonuclear molecules) on the other hand, it is necessary to calculate the following partition functions:

$$Z_e(\sigma)=\sum_{l=0,2,4,\cdots}(2l+1)e^{-\sigma l(l+1)}, \qquad (2.9)$$

$$Z_0(\sigma)=\sum_{l=1,3,5,\cdots}(2l+1)e^{-\sigma l(l+1)}. \qquad (2.10)$$

We shall mainly concern ourselves with a mathematical problem of evaluating the above given density matrix or the partition functions, at higher temperature, i.e., for smaller values of the parameter σ.

By noting well known property of a Fourier transformation of the normal distribution,[3] which is given by

$$e^{-x^2/2}=\frac{1}{\sqrt{2\pi}}\int_{-\infty}^{\infty}e^{-(u^2/2)+iux}du, \qquad (2.11)$$

we have

$$e^{-\sigma l(l+1)}=\frac{e^{\pi/4}}{\sqrt{\pi}}\int_{-\infty}^{\infty}$$
$$\exp[-u^2+i\sigma^{1/2}u+2i\sigma^{1/2}ul]du. \qquad (2.12)$$

If we define a function of a complex variable z (σ, l are both real and positive)

$$f(z)=\exp[-z^2+i\sigma^{1/2}z+2i\sigma^{1/2}zl], \qquad (2.13)$$

it has no singularities on the total complex plane, so it is easily shown that the path of integration can be changed as follows:*

$$e^{-\sigma l(l+1)}=\frac{e^{\sigma/4}}{\pi^{1/2}}\int_{-\infty+i\varepsilon}^{\infty+i\varepsilon}f(z)dz, \qquad (2.14)$$

where ε is any positive number. Thus the general term of the density matrix (2.7) can be represented as

$$(2l+1)e^{-\sigma l(l+1)}P_l(\cos\gamma)$$
$$=-\frac{1}{\sigma}\left[\frac{\partial}{\partial l}e^{-\sigma l(l+1)}\right]P_l(\cos\gamma)$$
$$=-\frac{1}{\sigma}\frac{e^{\sigma/4}}{\pi^{1/2}}\left[\frac{\partial}{\partial l}\int_{-\infty+i\varepsilon}^{\infty+i\varepsilon}f(z)dz\right]P_l(\cos\gamma)$$
$$=-\frac{2ie^{\sigma/4}}{(\pi\sigma)^{1/2}}\int_{-\infty+i\varepsilon}^{\infty+i\varepsilon}zf(z)P_l(\cos\gamma)dz. \qquad (2.15)$$

Substituting from (2.15) into (2.7), we have

$$Z(\sigma\,;\gamma)=-\frac{ie^{\sigma/4}}{2\pi^{3/2}\sigma^{1/2}}\int_{-\infty+i\varepsilon}^{\infty+i\varepsilon}z\exp(-z^2+i\sigma^{1/2}z)$$
$$\times\sum\exp(2i\sigma^{1/2}zl)P_l(\cos\gamma)dz, \qquad (2.16)$$

where the term by term integration is changed into an integral of an absolutely convergent series of continuous functions, since if we put

$$\exp(2i\sigma^{1/2}z)=t, \qquad (2.17)$$

then the absolute value of t is always less than unity on the total path of integration, because the number ε is a positive number. Actually, by the well known formula, we have

$$\sum_{l=0}^{\infty}t^lP_l(\cos\gamma)=(1-2t\cos\gamma+t^2)^{-1/2},\quad |t|<1. \qquad (2.18)$$

Introducing this into (2.16), we have an integral representation for the density matrix of a rigid free rotator

$$Z(\sigma\,;\gamma)=-\frac{ie^{\sigma/4}}{2\pi^{3/2}\sigma^{1/2}}\int_{-\infty+i\varepsilon}^{\infty+i\varepsilon}z\exp(-z^2+i\sigma^{1/2}z)$$
$$(1-2t\cos\gamma+t^2)^{-1/2}dz. \qquad (2.19)$$

§ 3. The High Temperature Expansion for the Partition Function

The partion function is obtained as the trace of the density matrix (2.19). Actually, we put $\gamma=0$, and integrate over all values of θ and ϕ, and we obtain

$$Z(\sigma)=\frac{e^{\sigma/4}}{\pi^{1/2}\sigma}\int_{-\infty+i\varepsilon}^{\infty+i\varepsilon}\frac{\sigma^{1/2}z\exp(-z^2)}{\sin(\sigma^{1/2}z)}dz. \qquad (3.1)$$

This is an integral representation for the partition function. Now we want to obtain a high temperature (small σ) expansion formula for the partition function. For this purpose we expand the function $u/\sin u$ into a power series of u as follows:[3]

---

* The author appreciates discussion with Mr. S. Nagata, as a result of which he noticed the necessity of the change of path of integration.

$$\frac{u}{\sin u}=1+2\sum_{n=1}^{\infty}\frac{(2^{2n-1}-1)}{(2n)!}B_n u^{2n}, \tag{3.2}$$

where B_n is the n-th Bernoulli number. Substituting from (3.2) into (3.1) and integrating term by term, we have

$$\begin{aligned}Z(\sigma)=&\frac{e^{\sigma/4}}{\pi^{1/2}\sigma}\int_{-\infty+i\varepsilon}^{\infty+i\varepsilon}\left[1+2\sum\frac{(2^{2n-1}-1)}{(2n)!}B_n\sigma^n z^{2n}\right]\\&\times\exp(-z^2)dz\\=&\frac{e^{\sigma/4}}{\sigma}\left[1+\sum_{n=1}^{\infty}\frac{(2^{2n-1}-1)}{2^{2n-1}\cdot n!}B_n\sigma^n\right].\end{aligned} \tag{3.3}$$

This is a high temperature expansion for the partition function of a rotator.

Similarly we can obtain the expressions for $Z_e(\sigma)$ and $Z_0(\sigma)$. From (2.14), we have

$$\begin{aligned}\exp-\sigma(4l^2+2l)=&\frac{e^{\sigma/4}}{(2\pi)^{1/2}}\int_{-\infty+i\varepsilon}^{\infty+i\varepsilon}\\&\times\exp[-z^2+i\sigma^{1/2}z+4i\sigma^{1/2}zl]dz\,.\end{aligned} \tag{3.4}$$

Then by the same procedure as above, we obtain

$$\begin{aligned}Z_e(\sigma)=&-\frac{e^{\sigma/4}}{2\sigma\pi^{1/2}}\cdot 4i\sigma^{1/2}\int_{-\infty+i\varepsilon}^{\infty+i\varepsilon}\\&\times\frac{z\exp(-z^2+i\sigma^{1/2}z)}{1-\exp(4i\rho^{1/2}z)}dz\,.\end{aligned} \tag{3.5}$$

Employing the method of partial fractions and discarding the integrands which are odd functions of z we obtain finally

$$\begin{aligned}Z_e(\sigma)=&\frac{1}{2}\frac{e^{\sigma/4}}{\sigma\pi^{1/2}}\int_{-\infty+i\varepsilon}^{\infty+i\varepsilon}\frac{\sigma^{1/2}z\exp(-z^2)}{\sin\sigma^{1/2}z}dz\\=&\frac{1}{2}Z(\sigma)\,.\end{aligned} \tag{3.6}$$

Therefore in the limit of small σ we have

$$Z_e(\sigma)=Z_0(\sigma)=(1/2)Z(\sigma)\,. \tag{3.7}$$

§ 4. Concluding Remark

A formula of the Fourier transformation of the normal distribution was applied to the evaluation of the partition function of a rigid rotator. In spite of its usefulness in the theory of the system of interacting diatomic molecules, the closed form of the density matrix of a free rotator is not yet obtained. To obtain such a formula the integral representation (2.19) seems to be useful.

References

1) H. P. Mulholland: Proc. Camb. Phil. Soc. **24** (1928) 280.

2) J. E. Mayer and M. G. Mayer: "*Statistical Mechanics*", John Willy and Sons. (1940) 151.

3) T. Takagi: "*Kaiseki Gairon*", Iwanami, p. 337.

4) K. Husimi: "*Kakurituron to Tokeiron*", Kawade, p. 161.

Journal of the Physical Society of Japan Vol. 9, No. 4, July—August, 1954

Electron Diffraction Study on the Ordered Alloy CuAu*

By Shiro Ogawa and Denjiro Watanabe

The Research Institute for Iron, Steel and Other Metals,
Tohoku University

(Received December 10, 1953)

The ordered state in the gold-copper alloy of the atomic ratio 1 to 1 was investigated by electron diffraction with well orientated thin films. Below 340°C the pattern corresponded with a tetragonal superlattice the c axis of which is distributed into three original cubic axes, while above 360°C sharp crosses appeared at some of the positions of superlattice reflection, being accompanied with subsidiary maxima, and at the same time regularly spaced satellites arose around normal reflections, especially, conspicuously around the incident beam position. The former phenomenon could be clearly interpreted by antiphase domains which occur in the tetragonal superlattice and which lead to the orthorhombic CuAu II structure, and the latter which was firstly found by this experiment proved that a definite expansion of lattice appears periodically in each boundary of antiphase domains, due to the asymmetrical distribution of gold and copper atoms at this place and to the tetragonality. Among the satellites around normal spots, only those around the direct spot are thought to be fundamental and those around the other normal spots arise from the secondary elastic scattering peculiar to electron diffraction and are the mere repetitions of the fundamental satellites. Thus, the lattice of CuAu II possesses the inherent defect of lattice which has hither-to been overlooked. The transitional region between CuAu II and the cubic phase in the equilibrium diagram was also studied, the composition of films being varied in the vicinity of 1 to 1, and it was concluded that the two phases surely coexist as in case of CoPt.

§ 1. Introduction

A gold-copper alloy of the atomic ratio 1 to 1 is of a tetragonal lattice in an ordered state, but at high temperatures below the critical point, an orthorhombic phase (CuAu II) appears as indicated in the X-ray study by Johansson and Linde[1]. According to them, this orthorhombic phase is nothing but the tetragonal lattice in which regularly spaced "out of step" arises at special atomic planes. An ordering manner in the alloy Cu_3Au has been investigated by various workers in Europe[2], U.S.A.[3] and Japan[4], theoretically or experimentally. Especially, Guinier and Griffoul[2-iv] found diffuse crosses at the positions of superlattice reflection in their X-ray photographs of incompletely ordered specimens of single crystal and attributed them to the "out-of-step" structure occurring at the {100} planes in the ordered regions. Raether[2-v] also studied the ordering process of Cu_3Au, especially by electron diffraction in thin, well orientated films, and inquired in detail into the dimension of the antiphase domain, with the results that this dimension is not definitely defined, and that, it increases as the temperature approaches to the critical point, so that crosses and doublets become indistinguishable from sharp spots.

We encounter, on the other hand, a different condition in the case of the ordered CuAu; i.e., antiphase domains of definite size exist in this alloy in an appropriate temperature range. If it is so and when we deal with single crystals, diffraction spots at the positions of superlattice reflection should be sharp and distinct, which may promise valuable informations about the ordering state. We already[5] studied, by electron diffraction, a new superlattice belonging to the gold-copper system, Au_3Cu, in the state of evaporated alloy film of polycrystal and proved such a study to be able to add some informations to the order-disorder problem of alloy. The first purpose of the present study is to carry out a detailed investigation on the ordered state of CuAu, especially on CuAu II, using well orientated alloy films, i.e., in a simpler crystalline state.

---

* A short note concerning this work has been published in Acta Crystallographica **5** (1952) 848.

The transitional region between the ordered and the disordered states near the atomic composition 1 to 1 in the equilibrium diagram is the second object of the examination, because the direct evidence of the coexistence of the two phases in the gold-copper system has not yet been given by X-ray studies, though Haughton and Payne[6] concluded it from the change in electrical resistance. Such a coexistence has been reported by Newkirk et al.[7] in their X-ray study of CoPt, which behaves itself almost like CuAu. From a thermodynamical viewpoint, it will be interesting to confirm such a coexistence in the latter alloy.

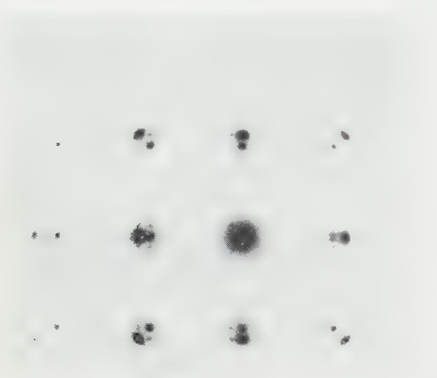

Fig. 1. The double film of gold and copper prepared by the method (a). Inner spots belong to the gold lattice, outer ones to the copper lattice respectively. Around each spot belonging to gold and also around the central spot are visible extra spots arising from the secondary diffraction due to the gold layer, into which beams diffracted initially by the copper layer enter as the incident ones.

We must be of course careful in applying the results obtained for thin films to the bulk metals and alloys, but examining former works of the same kind, we can know the fact that the electron diffraction study on thin films generally gives correct results, provided that attention was paid to peculiar properties of films, e.g. such as those concerning their submicroscopical, patchlike structure. It can give sometimes even a more precise information about problems of metals and alloys than X-rays.

§ 2. Experimental Method

(1) *Preparation of alloy films*

Alloy films are prepared usually by evaporation of alloys of a definite composition. In our study, however, different methods were used. They are itemized into the following three:

(a) A well orientated gold film was first formed by evaporation on a cloven surface of rocksalt heated at 400°C after preheated at 500°C, and copper was successively evaporated on it at room temperature. After being detached from the substratum, this composite film revealed, in its transmission pattern, the orientation of the copper layer following that of the underlying gold layer in a considerably precise manner (Fig. 1). This film was annealed at 320 or 330°C for several hours in order to be homogenized.

(b) Gold and copper were evaporated at the same time onto a cloven surface of rocksalt heated at 400°C, and the film was slowly cooled. This process was sufficient to make the diffusion, and consequently the homogenization, active, and an orientated, highly ordered alloy film was obtained without further heating process.

(c) The preparation of polycrystalline films was also required under a certain circumstance. Gold and copper were successively evaporated and condensed on cloven surfaces of rocksalt at room temperature. After detachment the homogenization was carried out at 500∼600°C.

In every case mentioned above, metals to be evaporated were fine wires (drawn into 0.1∼0.2 mm in dia.) which were laid in a small tungsten coil. The quantities of metals to be evaporated, known easily from the wire length, were determined so as to result in alloy films of proper thicknesses of 300∼400Å having required atomic compositions. The method (a) or (b) gave essentially the same results with respect to the ordering phenomena, though there was a slight difference in the crystallographical orientation due to the different thermal treatment. The former method was somewhat superior in elucidating the ordering process developing in an extended range of temperature.

(2) *Thermal treatment*

In the present work, the thermal treatment was carried out in a highly evacuated copper tube as described in Fig. 2. A film supporter of nickel C was fixed to a small copper holder B, and a thermocouple D was put close to C. B was tightly placed at the bottom of the copper tube A. As all diffraction patterns were recorded after quenching, the rapid quenching was very important and was carried out by pouring water rapidly onto the copper tube immediately after removal of an electric furnace. It is desirable that the observation of diffraction patterns at high temperatures is performed in a high temperature camera, but our results obtained by the above procedure seemed to be almost valid below the critical point, as they were self-consistent. Raether[2-v] also reported that, below about 400°C, results in Cu_3Au obtained by the quenching outside the camera were not different from those directly observed at high temperatures. The thermal treatment outside the diffraction chamber is excellent in that the temperature of specimen can be accurately measured because of a long region of uniform temperature. The heating duration was about 3 hr. at lower temperatures (up to 350°C), which seemed to be sufficient to attain the equilibrium state of ordering. Concerning the heating duration at higher temperatures, details will be described in § **3**-(*3*).

(3) *Determination of Composition*

The atomic composition of alloy films was determined from the lattice constant of the cubic phase (Fig. 3) quenched at the disordered state; the relation between the lattice constant and the composition in the gold-copper system[3] was used. In Fig. 3, some weak, diffuse superlattice reflections are visible, which unavoidably appear as a result of the very quick nuclear formation of the CuAu superlattice, but they did not seem to leave a serious influence in the estimation of composition. The determined compositions were in discord with those planned beforehand, i.e., the atomic percentage of the gold component was usually diminished by about 2 per cent. The discrepancy of such an order also existed in Cu_3Au films formed by evaporation of the alloy[2-v]. Our method of film preparation seemed to be more convenient than the usual method, as alloy films of different compositions can easily be formed without preparation of bulk alloys.

Under the following conditions the electron diffraction photographs were taken: the accelerating voltage for electron, 50 KV; the camera length, 505 mm; the standard specimen for measuring wave-length, an evaporated gold film.

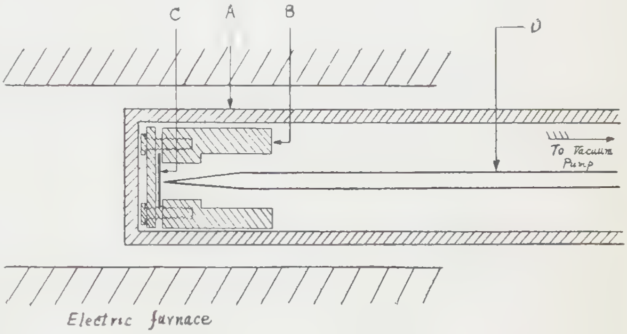

Fig. 2. The device for the heat-treatment. A: copper tube, B: copper holder, C: nickel supporter and D: thermocouple.

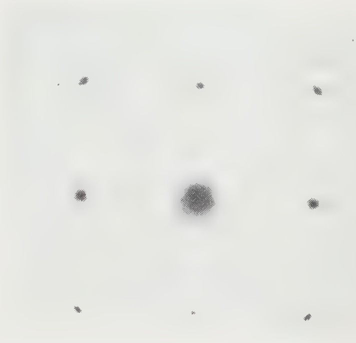

Fig. 3. The cubic phase quenched at the disordered state. (faint superlattice spots are visible.)

§ 3. Results and Discussions

Gold contents of examined alloy films ranged from 40 to 55 per cent. Various aspects of diffraction patterns of some films, which were heated up step by step from lower temperature to the critical point, and their interpretations will be described below.

(1) *Behaviour of the 50 per cent alloy film*

This film was prepared by the method (a) and exhibited the tetragonal symmetry ($c/a \sim 0.92$) immediately after being homogenized at

330°C. The pattern at 340°C is shown in Fig. 4. This figure is not so simple as it looks, because the *c* axis distributed in the three directions of the original cubic axes. At 350°C (Fig. 5) some of superlattice reflections became diffuse and spread, and at 360°C (Fig. 6) they were converted to crosses. At the same time appeared four new spots around the incident beam position and each of the normal reflections. The crosses at the superlattice reflection positions became sharp and intense at 370° as well as 380°C (Fig. 7), being accompanied with four satellites around each. The satellites around the central spot became intense and clearly visible at this stage and the four second satellites also ap-

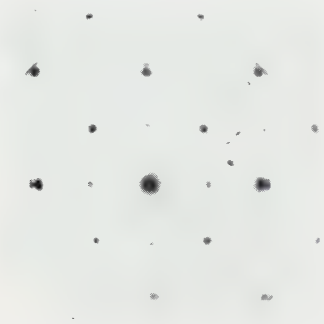

Fig. 4. The tetragonal phase quenched at 340°C (CuAu I).

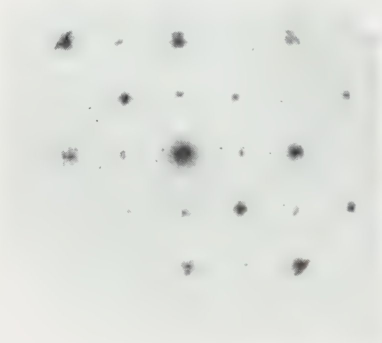

Fig. 5. The same sample as in Fig. 4 quenched at 350°C. $(110)_\perp$ spots become diffuse.

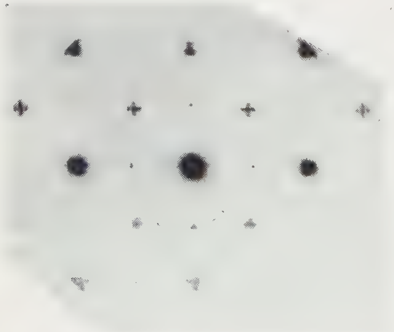

Fig. 6. The same sample as in Fig. 4 quenched at 360°C (CuAu I+CuAu II). Diffuse spots turn to clear crosses. (Satellites around the central spot and normal spots are unfortunately too faint to be reproduced in this figure.)

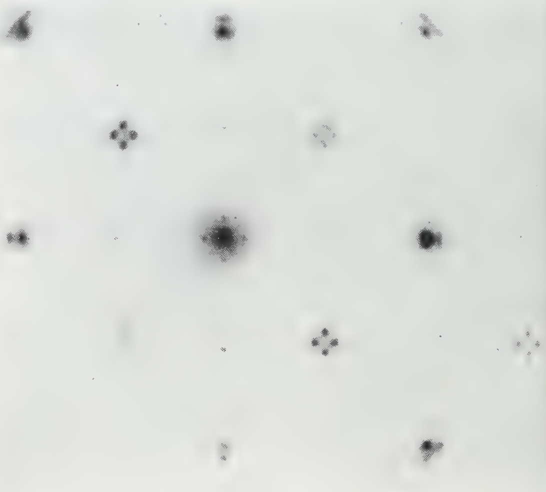

Fig. 7. The same sample as in Fig. 4 quenched at 380°C (CuAu II). Crosses consisting of four spots become sharp and strong, being accompanied with satellites. Satellites are visible around the normal spots, especially clearly around the central spot.

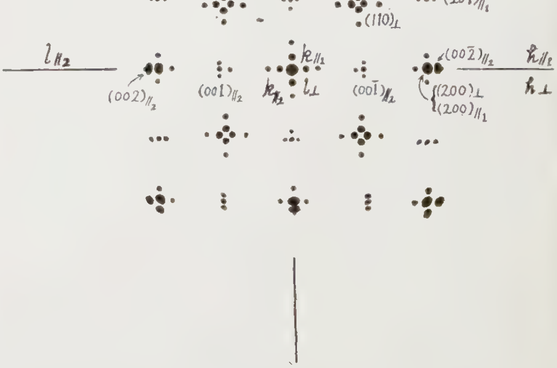

Fig. 8. The explanation of Fig. 7. The spots $(hkl)_\perp$ belong to a set in which the *c* axis is perpendicular to the film surface; the spots $(hkl)_{//_1}$, and $(hkl)_{//_2}$ belong to the other two sets in which the *c* axes are lying in this surface.

peared. At the latter temperature faded away the intensity of the central part of the crosses and, consequently, these become to consist of four clear spots. The aspect of the pattern did not almost change with the subsequent heating up to about 400°C, but the intensities of the superlattice reflections were somewhat diminished near the critical temperature, at which the crosses disappeared, though the weak, diffuse spots remained due to the incomplete quenching (Fig. 3). The satellites around the normal reflections also changed into diffuse, weak spots near the critical temperature and vanished when the phase changes to cubic.

Now, we shall elucidate the nature of the pattern, in which the crosses arose and in which the satellites appeared around different kinds of diffraction spot. For this purpose we will take Fig. 7 as a representative pattern, using Fig. 8 as an explanatory figure. First, in this figure should be watched three kinds of mark for the indices of diffraction spot, which suggest that the original uniform orientation of the cubic lattice splitted into three orientations of the tetragonal one, in one of them the *c* axis being perpendicular to the film surface (⊥ set) and in the other two the *c* axis lying in this surface (//1 and //2 set). Such a distributing manner of the *c* axis probably corresponds to that in Fig. 9 which Harker[9)] deduced from his microscopic as well as X-ray study. To minimize the local stress produced by the generation of nuclei of the tetragonal phase in the cubic lattice, the necessary condition seems to be that the new lattice appears with such thin (111) layers that the directions of the *c* axis in neighbouring regions must be perpendicular to each other as the tetragonal lattice is contracted along the direction of the *c* axis.

Next, the considerations will be put on the crosses and the satellites. The most intense crosses are seen in the {110} positions of the original cubic system and all crosses belong to the ⊥ set. The separation of two opposite spots in a cross is equal to the distance between one of them and its satellite. The central spot and its first and second satellites are spaced along one direction with an equal distance which is also equal to the separation in a cross (the same holds for the other normal reflections). Their separation value seems as if they arise from reflections due to planes having the spacing $5a$. Crosses similar to those obtained by us have been observed in the X-ray study of Cu$_3$Au by Guinier and Griffoul[2-iv)] as well as of CoPt by Newkirk et al.,[10)] and in the electron diffraction study of Cu$_3$Au by Raether[2-v)]. Among them, the observation by Newkirk et al. concerned the normal reflections and their crosses were considered to have an origin different from that in the present case. The interpretation for the origin of the crosses, as well as its separation, was given in Cu$_3$Au by Guinier and Griffoul and more exactly by Raether. We will subsequently explain the peculiar diffraction pattern of CuAu, i.e., the crosses and, especially, the satellites around normal reflections which have hitherto never been observed by electron diffraction, considering the existence of "out-of-step" in the ordered region. This was already concluded in the X-ray study of CuAu by Johansson and Linde and was treated theoretically by MacGillavry and Strijk[2-i)] and also by Wilson[2-ii)] in the problem of Cu$_3$Au.

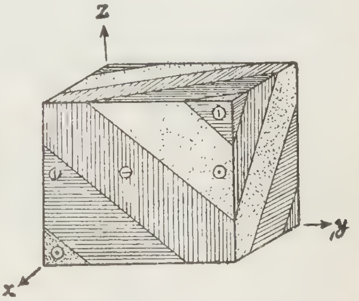

Fig. 9. The distributing manner of the *c* axis in the ordered CuAu. ⊙, ⦶ and ⊖ represent the directions of the *c* axis. (This figure is quoted from D. Harker's report[9)].)

(2) *Structure of CuAu II*

In the ordered lattice of CuAu, gold and copper atoms are distributed as illustrated in Fig. 10a. It is supposed that "out-of-step" occurs in the x direction with a period $L_x = Ma$. We assume that $N_x L_x$ is a total length of the coherent region in this direction. An asymmetrical distribution of gold and copper atoms exists in the "out-of-step" region. We shall consider the equilibrium of each atom in the atomic plane A in Fig. 10b. The forces exerted on it by the first nearest neighbours in the yz plane are balanced, but those in the xy and xz planes are not. If the attraction acts between the different kinds of atom and the repulsion between the same kind of atom, the resultant exerted by the first nearest neigbhours in the xy plane, f_1, points to the right, i.e., to the positive x direction. On the other hand, the resultant exerted by those in the xz plane, f_2, points to the negative x direction. In the present lattice c/a is about 0.92, and hence the first nearest neighbours in the xz plane are situated slightly nearer to the concerned atom than those in the xy plane, that is, the nearest neighbours are divided into two groups. Accordingly, $|f_2|$ may be slightly greater than $|f_1|$, so that the resultant pointing to the negative x direction may be exerted on each atom in the A plane. In the same way the resultant pointing to the positive x direction is exerted on each atom in the B plane. Thus, the repulsion acts between the two atomic planes. While, the second nearest neighbours, of which only those lying in the x direction should be considered, act to oppose to this repulsion. The distance between A and B may be expected to be elongated, as the first nearest neighbours have the larger influence than the second ones. Of course, this disturbance exists not only in AB but also in the neighbouring atomic distances. This is, however, neglected, because, e.g., if we consider each atom in the next atomic plane left of A, its first nearest neighbours distribute symmetrically and only the small resultant due to its second nearest neighbours remains there. The equilibrium position corresponding to AB$=a/2+\delta\cdot a$ must exist, because the repulsion due to the first nearest neighbours is greatly influenced by this elongation, whereas the attraction due to the second ones is less influenced owing to the larger distance. Thus, the lattice defect may possibly exist in each boundary of antiphase domains. The elongation $\delta\cdot a$ may be calculated if the expressions for the niteratomic forces corresponding to gold-gold, copper-copper and gold-copper are exactly given as a function of distance. The exact estimation of δ by means of such a calculation, however, seems to be difficult, because this value is expected to be considerably small. On the other hand, we can fortunately determine it from the pattern of electron and X-ray diffraction, as described below.

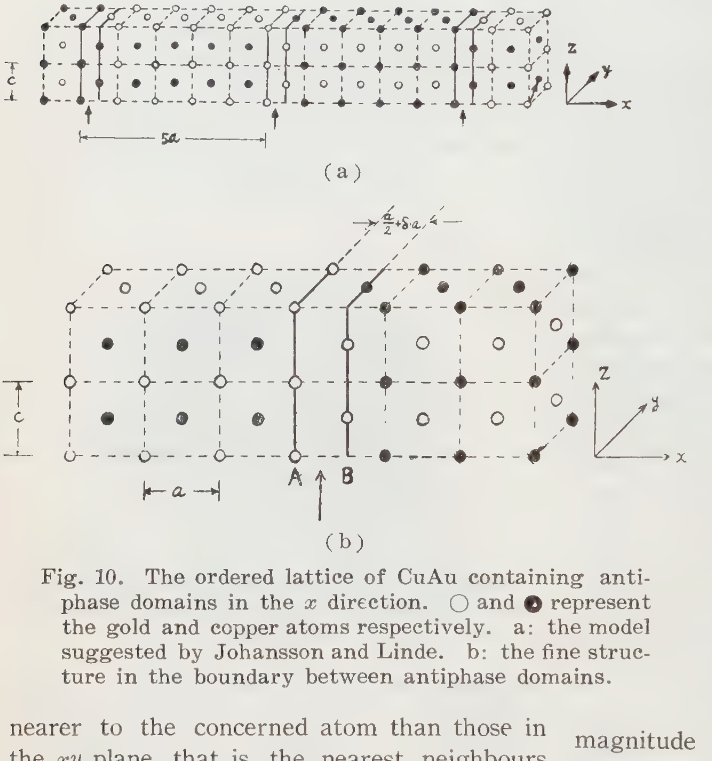

Fig. 10. The ordered lattice of CuAu containing antiphase domains in the x direction. ○ and ● represent the gold and copper atoms respectively. a: the model suggested by Johansson and Linde. b: the fine structure in the boundary between antiphase domains.

In the calculation of the structure amplitude we consider only such a lattice that N_xM unit cells of CuAu I are lined up in the x direction, "out-of-step" occurring in each distance Ma. The absolute magnitude of the structure amplitude for this lattice $|S|$ is

$$|S|=\Big|\{E_{Au}+E_{Au}\exp(\pi i(Ax+Ay)) +E_{Cu}\exp(\pi i(Ay+Az)) +E_{Cu}\exp(\pi i(Az+Ax))\} \cdot\underbrace{\frac{\sin\pi MAx}{\sin\pi Ax}}_{G_1}\cdot\underbrace{\frac{\sin\pi N_x\{(M+\delta)Ax-(Ay+Az)/2\}}{\sin\pi\{(M+\delta)Ax-(Ay+Az)/2\}}}_{G_1'}\Big|, \qquad (1)$$

where E is the atomic scattering factor for electron, Ax, Ay and Az are continuous variables in the reciprocal lattice, $(Ay+Az)/2$ is a phase difference produced by "out-of-step" and $M+\delta$ is a new period introduced due to the lattice defect. If N_x is far greater than M, positions of the maxima of the Laue function $G=G_1 \cdot G_1'$ is determined by those of G_1'. As G_1' has to be considered in the reciprocal lattice contracted in the x direction in proportion to $M/(M+\delta)$, each maximum of $|S|$ is situated as if it arises from a crystal lattice having an elongated lattice constant $a(1+\delta/M)$ in the x direction. According to the careful examination of positions of the normal spots $(202)_{//1}$ and $(20\bar{2})_{//2}$ in Fig. 7, belonging to the sets in which the c axes are lying in the film surface, they are situated slightly asymmetrically to each other, with respect to the direction passing through $(220)_{\perp}$ and the direct spot, which means that the direction in which antiphase domains are lined up is distributed in the film surface unequally in the two // sets. It was assumed that this direction lies in the surface for the one set and is perpendicular to the surface for the other set, and the measurement of these asymmetrical positions resulted roughly in $\delta/M=0.004\sim0.005$. This value should be calculated also from the width of the normal spot belonging to the $\perp$ set, e.g., $(220)_{\perp}$, which must show a slight elongation perpendicular to the radial direction due to the different a values. This width is, however, so small that the measurement gave no significant value. The lattice spacing can be, in general, more accurately measured in the X-ray method than in the electron diffraction method, and we found that δ/M had already been measured in the X-ray study by Johansson and Linde. They reported, on the basis of the slight break-up of some diffraction lines, that the true rhombic symmetry exists in the lattice of CuAu II and $a_x/a_y=1+\delta/M$ is 1.003. We shall adopt this value and apply it to the estimation of intensities of satellites, as described later.

Now, we shall examine in detail Eq. (1) for the following two cases.

i) Normal reflection. In this case h, k and l are unmixed, and if the positions $A_x=\{M/(M+\delta)\}h+\varepsilon_x$, $A_y=k$ and $A_z=l$ are considered, $(A_y+A_z)/2$ is an integer and $|S|$ becomes

$$|S|=\left|2(E_{Au}+E_{Cu})\cos\frac{\pi}{2}\left(\varepsilon_x-\frac{h\delta}{M+\delta}\right)\cdot\frac{\sin\pi MA_x}{\sin\pi A_x}\cdot\frac{\sin\pi N_x(M+\delta)A_x}{\sin\pi(M+\delta)A_x}\right|. \tag{2}$$

G_1' has its maxima at $A_x=(Mh+n)/(M+\delta)$, where n is 0, ±1, $\pm2,\cdots$, and if $N\gg M$, the same holds for $|S|$. Thus, we can easily understand the apparition of the satellites of normal reflection in the same way as "ghost" due to a periodic error in an optical grating.* The maximum values of $|S|$ at positions of satellites, neglecting $h\delta/(M+\delta)$ against $n/(M+\delta)$, are given by

$$|S|_{\max}\doteqdot\left|2N_x(E_{Au}+E_{Cu})\cos\frac{\pi n}{2M}\cdot\frac{\sin\pi(h+n/M)\delta}{\sin\pi(n/M)}\right| =\left|N_x(E_{Au}+E_{Cu})\frac{\sin\pi(h+n/M)\delta}{\sin(\pi n/2M)}\right|. \tag{3}$$

ii) Superlattice reflection. In this case h, k and l are mixed and it is easily known from Eq. (1) that $|S|$ vanishes if h and k are mixed. If h and k are unmixed, for the positions $A_x=\{M/(M+\delta)\}h+\varepsilon_x$, $A_y=k$ and $A_z=l$, A_y+A_z is an odd integer and $|S|$ becomes

$$|S|=\left|2(E_{Au}-E_{Cu})\cos\frac{\pi}{2}\left(\varepsilon_x-\frac{h\delta}{M+\delta}\right)\cdot\frac{\sin\pi MA_x}{\sin\pi A_x}\cdot\frac{\sin\pi N_x\{(M+\delta)A_x-1/2\}}{\sin\pi\{(M+\delta)A_x-1/2\}}\right|. \tag{4}$$

If $N\gg M$, $|S|$ has its maxima at $A_x=(Mh+m/2)/(M+\delta)$, where $m=\pm1$, $\pm3,\cdots$. If N is comparable with M, the maxima approach to the reciprocal lattice points. The maximum values of $|S|$ are

---

* Daniel and Lipson (Proc. Roy. Soc. **A 181** (1943), 368; **A 182** (1944), 378) have reported an unusual X-ray diffraction effect shown by the alloy Cu_4FeNi_3 when it is in the process of splitting up from one face-centred cubic structure into two. Before the formation of the intermediate tetragonal structures a state is formed in which each line of a powder photograph is accompanied by quite strong satellites. This effect was later confirmed by Hargreaves (Acta Cryst., **4** (1951) 301). The explanation by the above investigators was that the original cubic lattice is regularly deformed by the segregation of the different atoms in such a way that there occurs in the lattice the sinusoidally or rectangularly periodic variation in lattice parameter or atomic scattering factor. The satellites observed by us seem, however, to have a different origin from those observed by them for several reasons.

$$|S|_{\max} \fallingdotseq \left| 2N_x(E_{Au}-E_{Cu})\cos\frac{\pi m}{4M} \cdot \frac{\sin \pi(m/2)}{\sin \pi(h+m/2M)} \right| = \left| N_x(E_{Au}-E_{Cu})\frac{1}{\sin(\pi m/4M)} \right| . \tag{5}$$

Here, the influence of δ upon $|S|_{\max}$ is negligible. Thus a doublet accompanied by subsidiary maxima occurs in the x direction in the reciprocal lattice. The same holds for the y direction if antiphase domains are lined up in this direction in other parts of crystal, but not for the z direction, because in the ordered structure of CuAu the $(0\ 0\ l)$ planes are occupied alternately by gold and copper atoms and in the corresponding direction antiphase domains cannot exist.

Table I.

Atomic per cent of gold	Temperature (°C)	$M+\delta=\frac{m}{2\Delta A}$ (superlattice spots)	$M+\delta=\frac{n}{\Delta A}$ (normal spots)
40	310	5.8	
	320	5.8	
	330	5.8	
	340	5.6	
	345	5.6	
	350	5.6	
46.5	370	5.4	
	385	5.3	
	390	5.3	
	395	5.3	
~50	360	5.1	5.0
	370	5.1	5.0
	380	5.1	5.0
~50	370	5.4	5.3
	377	5.3	5.2
	390	5.2	
	400	5.1	5.1
55	340	5.4	
	350	5.4	
	360	5.4	
	370	5.3	
	380	5.3	

The crosses in Fig. 7 are sharp and intense and their satellites are also sharp, and, therefore, it is clear that N is considerably large and M is almost definite. Applying the formula to the case of large N, the measurement of the separation in the cross led to $M \fallingdotseq 5$ in case of 1 to 1 composition. This value was also obtained from the spacing of the satellites of normal reflection, including the position of incident beam. The detailed results in various compositions and temperatures are shown in Table I, in which the value of M tends to increase towards 6 as the gold content departs from 50 per cent. Johansson and Linde obtained $2M=11$ for alloys of 40 and 60 per cent gold. The value of $M+\delta$ in Table I seems to be somewhat larger than 5 in the 1 to 1 composition, but the measurement of small distances is so inaccurate, that the value of δ cannot be deduced from Table I. In Cu_3Au, the spacing of "out-of-step" is not definite as shown by the diffuseness of crosses[2-v], and M is 7~9 in average at about 300°C and increases between 300 and 380°C as the temperature rises. In CuAu (1 to 1), on the other hand, the value $M=5$ is almost constant between 360°C and the critical temperature. Therefore, we obtain $\delta=0.003 \cdot M = 0.015$. The expansion of lattice at the boundary between antiphase domains is, accordingly, about 0.06Å.

Now, we shall compare the calculated structure amplitude with the observed intensity, using

$$E=\frac{me^2}{2h^2}\frac{z-f}{(\sin\theta/\lambda)^2}, \tag{6}$$

where Ze is the nuclear charge and f is the atomic scattering factor for X-ray. For the satellites around the direct spot, Eq. (3) gives $|S|_{(\frac{1}{5}00)}=2.2Nx$ and $|S|_{(\frac{2}{5}00)}=1.2Nx$, $\sin\theta/\lambda$ being 0.026 for the former and 0.053 for the latter (we consider only the $\perp$ set). For the first satellites ($m=3$) of the cross, e.g., for $(1^3/_{10}\ 1\ 0)$, Eq. (5) gives $|S|_{(1^3/_{10}\,1\,0)}=8.4Nx$, $\sin\theta/\lambda$ being 0.21. The observed intensity of $(^1/_5\ 0\ 0)$ is, however, greater than that of $(1^3/_{10}\ 1\ 0)$. About the origin of this discrepancy may be thinkable the following: It is sure that E values at very small scattering angles are not correctly given by extrapolating the f values for neutral atom to such an angular range. There are the atomic cores of gold and copper atoms and the conduction electron cloud in the lattice of the concerned alloy. E for ions is, in general, thought to be considerably different from that for neutral atoms at $\sin\theta/\lambda<0.2$. If the conduction electron cloud is not so effective to the scattering factor, $E_{Au}+E_{Cu}$ might become much larger in the range of such a very small angle on account of the contribution of the positively ionized state of the atomic cores, than expected for free neutral atoms. Or, if such a distortion in the valence electron shell as found in zinc oxide by Yearian[11] and Lark-Horovitz[11] exists in the present alloy, it would produce a comparatively small effect on f, but cause E to increase in the range of scattering angle, where Z and f are comparable, i.e., at a very small value of $\sin\theta/\lambda$. In the following, we suppose that from some of reasons such as mentioned above the satellites around the direct spot have abnormally large intensities, which are, however, difficult to compute exactly. For the satellites around the normal spots other than the direct spot a completely different condition holds. They are considered theoretically to have the following three properties arising from Eq. (3).

i) First of all, their calculated intensities are far smaller than the actual ones. For example, the structure amplitude for $(1^4/_5\,0\,0)$ is $|S|_{(1^4/_5\,0\,0)}=3.1Nx$, using the E value due to Eq. (6) in which the f value for a neutral atom is applicable because of the larger $\sin\theta/\lambda$ (0,23) (we consider only the $\perp$ set). Accordingly, if the intensity I is proportional to $|S|^2$, $(I_{(1^4/_5\,0\,0)})/(I_{(1^3/_{10}\,1\,0)})\fallingdotseq 0.14$. The comparable intensities were, however, observed for both diffraction spots.

ii) The analysis for Eq. (3) results in that, in case of the line-up of antiphase domains in the x direction, the amplitudes of the satellites of $(h\,k\,l)$ $(h\neq 0)$ decrease as n increases, whereas those for the satellites of $(0\,k\,l)$ slowly increase with n, as the E value only slowly changes, except in the neighbourhood of the direct spot where E abruptly decreases with $\sin\theta/\lambda$. Therefore, the intensities of the satellites of $(0\,k\,l)$ or $(h\,0\,l)$ behave themselves differently in the two directions.

iii) The intensity ratio of the satellites to the relevant normal spot $(h\,k\,l)$ increases with h, if the antiphase domains are lined up in the x direction.

These properties contradict the observations except the last one. It could not be confirmed experimentally whether this was so or not. The satellites around $(200)_\perp$ and $(220)_\perp$ fall off in intensity both in the two directions as n increases, in the same way as in the neighbourhood of the direct spot. On these bases we will assert the following interpretation:

Owing to the small angles of Bragg reflection in electron diffraction and to the mosaic structure in evaporated films, the secondary elastic scattering occurred in our film, so that the satellites arose around the intense normal spots, which act as the secondary direct spots. Accordingly, among the satellites around the normal spots in Fig. 7 only those around the direct spot are fundamental and the others are nothing but the mere repetitions of the fundamental satellites, those which should arise there due to the primary elastic scattering being too faint to be observable. The secondary elastic scattering was observed also in our double film of gold and copper, as seen in Fig. 1, and Cowley, Rees and Spink[13] could fairly explain patterns from films of long-chain paraffins as due to the successive diffraction of electron from different single crystal regions and could accurately carry out the structure analysis, using intensities corrected by considering such an effect. The satellites around $(200)_\perp$ and $(220)_\perp$ in Fig. 7 can be clearly explained only by considering the secondary diffraction both in intensity and in appearing manner in the directions $(h\,0\,0)$ and $(0\,k\,0)$. As the secondary diffraction occurs around all intense spots, many spots have the superimposed intensities, but besides $\{^1/_5\,0\,0\}$ and $\{^2/_5\,0\,0\}$, those arising from the // sets occupy different positions owing to the c value, e.g., in Fig. 8 the secondary reflection $(0\,0\,1)_{//2}$ due to $(200)_\perp$ appears in the position slightly left to $(00\bar{1})_{//2}$. Thus, these weak spots slightly inside of $(001)_{//}$ and also the fine structure of $\{200\}$ could be just explained due to this effect, while no other explanation was successful. This effect may be possible to observe also in the polycrystalline state as Cowley et al. obtained "extra ring" envelopes due to many secondary rings, if the condition is favourable. In our polycrystalline films of CuAu II, however, the ring-envelopes corresponding to the satellites around the normal spots were too faint to be observable, and none was found in the neighbourhood of the rings $(200)_\perp$ and $(220)_\perp$, though the condition is somewhat better in the latter, because of such a preferred orientation that (111) is parallel to the film surface. The fact that there is no ring also around the direct spot is probably due to the increased background caused by the enhanced inelastic scattering in the polycrystalline state.

In the X-ray method the cirumstance is considerably changed. Applying the f value for a neutral atom to Eq. (3), we obtain $|S|_{(^1/_5\,0\,0)}=3.2Nx$ and $|S|_{(1^3/_{10}\,1\,0)}=96Nx$. The lowering of the f value at very small $\sin\theta/\lambda$, due to ions, has no serious influence on $|S|_{(^1/_5\,0\,0)}$. It is exceedingly difficult* to observe the spots or ring corresponding to ($^1/_5$ 0 0) by X-ray, without distinction of single-or polycrystal. The satellites of the other normal spots are in the similar condition. The successive diffraction effect is not observable in the X-ray pattern.

If antiphase domains were simultaneously lined up in the x and y directions, we should deal with a large tetragonal unit cell in place of the orthorhombic one. The Laue function for this lattice is, if the part refering to the z direction is neglected,

$$|G|=\left|\frac{\sin\pi MA_x}{\sin\pi A_x}\cdot\frac{\sin\pi N_x\{(M+\delta)A_x-(A_y+A_z)/2\}}{\sin\pi\{(M+\delta)A_x-(A_y+A_z)/2\}}\cdot\frac{\sin\pi MA_y}{\sin\pi A_y}\cdot\frac{\sin\pi N_y\{(M+\delta)A_y-(A_z+A_x)/2\}}{\sin\pi\{(M+\delta)A_y-(A_z+A_x)/2\}}\right|,$$

The following two phenomena would appear in this case.

i) Near the normal reflections ($A_x=\{M/(M+\delta)\}h+\varepsilon_x$, $A_y=\{M/(M+\delta)\}k+\varepsilon_y$ and $A_z=l$),

$$|G|=|G_1\cdot G_1'\cdot G_2\cdot G_2'|$$

$$=\left|\frac{\sin\pi MA_x}{\sin\pi A_x}\cdot\frac{\sin\pi N_x\left\{(M+\delta)\varepsilon_x-\dfrac{\varepsilon_y-\delta k/(M+\delta)}{2}\right\}}{\sin\pi\left\{(M+\delta)\varepsilon_x-\dfrac{\varepsilon_y-\delta k/(M+\delta)}{2}\right\}}\cdot\frac{\sin\pi MA_y}{\sin\pi A_y}\right.$$

$$\left.\cdot\frac{\sin\pi N_y\left\{(M+\delta)\varepsilon_y-\dfrac{\varepsilon_x-\delta h/(M+\delta)}{2}\right\}}{\sin\pi\left\{(M+\delta)\varepsilon_y-\dfrac{\varepsilon_x-\delta h/(M+\delta)}{2}\right\}}\right|.$$

At $\varepsilon_x=[2/\{4(M+\delta)^2-1\}]\{2(M+\delta)n_x+n_y\}$ and $\varepsilon_y=[2/\{4(M+\delta)^2-1\}]\{2(M+\delta)n_y+n_x\}$, where n_x and n_y are intergers, G_1' and G_2' have the maximum values N_x and N_y respectively. Here, the values of G_1 and G_2 are not negligible, and hence a cross-grating pattern of normal reflection satellites would be obtained, at least around the direct spot.

ii) Near the superlattice reflections ($A_x=\{M/(M+\delta)\}h+\varepsilon_x$, $A_y=\{M/(M+\delta)\}k$ and $A_z=l$),

$$|G|=|G_1\cdot G_1'\cdot G_2\cdot G_2'|$$

$$\doteqdot\left|\frac{\sin\pi M\varepsilon_x}{\sin\pi\varepsilon_x}\cdot\frac{\sin\pi N_x\{(M+\delta)\varepsilon_x-1/2\}}{\sin\pi\{(M+\delta)\varepsilon_x-1/2\}}\cdot M\cdot\frac{\sin\pi N_y\{(1+\varepsilon_x)/2\}}{\sin\pi\{(1+\varepsilon_x)/2\}}\right|.$$

At $\varepsilon_x=m/2(M+\delta)$, where G_1' has its maxima, G_2' has no appreciable value, therefore, $|G|$ has no maxima at places where the cross should arise if antiphase domains are lined up only in one direction. Thus all crosses and their satellites would vanish.

These both, however, completely contradict the observation, therefore antiphase domains are not simultaneously lined up in the two directions. The direction of line-up is changed from domain to domain, and it is not sure whether each (111) layer in Harker's figure is a coherent region having an uniform direction of line-up of antiphase domains or is divided into several regions.

Now, we shall add some informations, concerning the periodic elongation of lattice, δ. This quantity arises from the tetragonality

---

* The ratio of intensities of $\left(\frac{1}{5}\,0\,0\right)$, $\left(\frac{2}{5}\,0\,0\right)$, $\left(\frac{7}{10}\,1\,0\right)$, $\left(1\frac{3}{10}\,1\,0\right)$ and $\left(1\frac{4}{5}\,0\,0\right)$ rings in X-ray Debye-Scherrer pattern (CuK$_\alpha$) is calculated as follows, $I\propto p\dfrac{1+\cos^2 2\theta}{\sin^2\theta\cos\theta}|S|^2$ and the f values for a neutral atom being used.

$$I_{(\frac{1}{5}\,0\,0)}:I_{(\frac{2}{5}\,0\,0)}:I_{(\frac{7}{10}\,1\,0)}:I_{(1\frac{3}{10}\,0\,0)}:I_{(1\frac{4}{5}\,0\,0)}$$
$$=0.02:0.005:1:0.5:0.01\,.$$

The ring $\left(\frac{7}{10}\,1\,0\right)$ was very faintly observed in the photograph by Johansson and Linde.

without which no excessive force is produced at the boundary between antiphase domains, therefore, δ decreases with the approach of c/a to 1. In fact, the intensities of the normal reflection satellites became so weak at 55 per cent gold that they were scarcely visible except around the direct spot. As c/a is about 0.93 at this composition, δ seems to decrease very rapidly with the increase in c/a. Even if "out-of-step" occurred in the ordered alloy CoPt, δ would be negligible because c/a is about 0.98 in this alloy. δ is, on the other hand, considerable in CuAu II of the composition 1 to 1, and a coherent domain is by 0.3 per cent elongated in the direction of line-up of antiphase domains, and hence the expansion of total volume should be 0.3 per cent in the transition from CuAu I to II. M. Hirabayashi et al.[14] have measured the expansion coefficient of polycrystalline gold-copper alloys at various temperatures up to 500°C. According to them the expansion of volume at 49.3 per cent gold was about 0.6 per cent* in the transition from CuAu I to II. The coincidence between the result due to our model and the experimental datum is not good. However, there seems to be some change in the true lattice constants, which cannot be known from the data by Johansson and Linde, as they did not observe the dependence of the lattice constants upon temperature in the equilibrium state.

The aspect of the reciprocal lattice of the present alloy is depicted as in Fig. 11, the contribution of δ to the positions of lattice points being neglected. Such an intensity distribution as a cross-like platelet at the positions of superlattice reflection was well proved by observing, for example, the deformation and vanishing of crosses which occur when the film was rotated around various axes and tilted to the electron beam, as Raether did. When the beam is perpendicular to the film surface, the crosses can be observed only in the $\perp$ set and they transform to a line form in the other sets.

The structure in Fig. 10a has been accepted as an orthorhombic lattice, one axis of which has a length of $10a$ and which Jahansson and Linde concluded to be CuAu II in their polycrystalline specimen. It was, however, established by the present study, that this structure must be somewhat modified, that is, the inherent defect of lattice periodically exists in each boundary between antiphase domains.

The vanishing of the central intensity of the crosses at 380°C means that the CuAu I phase is completely destroyed, only the CuAu II phase predominating above this temperature. The behaviour of the crosses as well as the satellites near the critical point suggests that N_xL_x, the length of the coherent region, decreases and, probably, M becomes indistict, and, thus, the CuAu II phase begins to collapse.

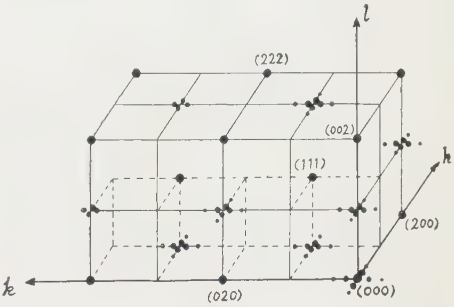

Fig. 11. The reciprocal lattice of CuAu II. Satellites around normal lattice points except the origin are not observable.

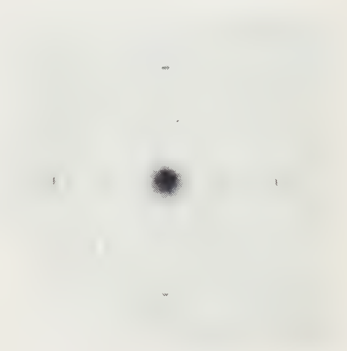

Fig. 12. The vanishing of the $\perp$ set.

After the film was once heated up to the disordered state, the $(110)_\perp$ and $(220)_\perp$ reflections often disappeared in the low temperature annealing, as shown in Fig. 12. This fact is due to the vanishing of the $\perp$ set. Therefore, the preparing manner of the film greatly influences the results. From this point of view, the preparing method (b) seems to be inadequate. In a polycrystalline specimen, crosses change to two Debye rings, as observed by Guinier and Griffoul. Such a break-up of a

* This value was privately communicated.

superlattice reflection arising from antiphase domains has previously been observed in the (110) ring of the polycrystalline Au_3Cu film[5] annealed at 200°C for 150 hr. This fact, however, was overlooked at that time. The width of the break-up gave the value $M \fallingdotseq 7$.

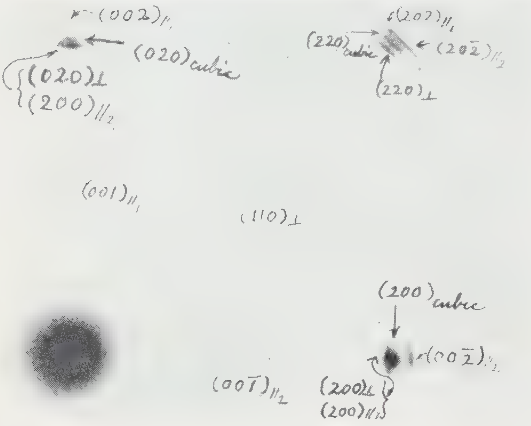

Fig. 13. The apparition of the spots belonging to the cubic lattice in the CuAu film containing 55 per cent gold, quenched at 370°C.

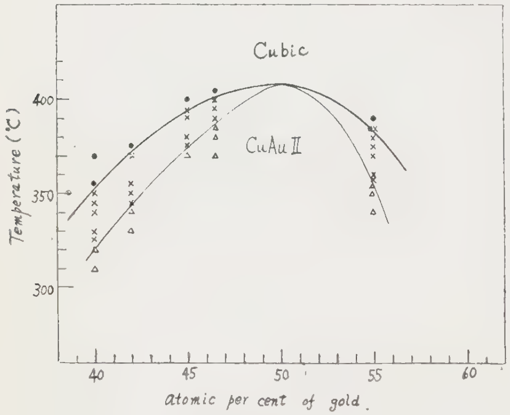

Fig. 14. The equilibrium diagram near the 1 to 1 composition. ●, △ and × represent the cubic state, CuAn II and the mixed state respectively.

(3) *Coexistence of CuAu II and the cubic phase**

In an alloy film containing 55 per cent of gold a mixed pattern of CuAu II and the cubic lattice was obtained at the temperature immediately below the critical point. The film was an orientated one prepared by the method (b) and was heated up step by step. At 357°C the spots (200) and (220) belonging to the cubic phase were associated with the ordered tetragonal pattern. They were faint at first but became strong gradually with the temperature rise and exceeded the ordered pattern in intensity at about 375°C. At 388°C remained only the f.c.c. pattern, in which, however, weak and diffuse spots belonging to the ordered phase were seen due to the incomplete quenching. Fig. 13 shows the aspect at 370°C. The above fact seems to indicate the coexistence of the two phases in the 55 per cent gold film at the temperature between 357 and 385°C. In order to examine systematically such a coexistence in the present system, several polycrystalline films containing 40, 42, 45 and 46.5 per cent of gold were prepared, the homogenization being carried out at 600°C for 30 min.~1 hr. The results obtained are shown in Fig. 14**. Against that this diagram reveals the coexistence of the two phases in the equilibrium state might be raised the following objections:

i) Incompleteness of the quenching.
ii) Unattainment to the equilibrium state.
iii) Inhomogeneity of composition.

The first item is thinkable to a certain extent, because, as often decribed, the quenching of the cubic phase was not complete. This objection is, however, not effective in the present case. If the sharp pattern of the ordered phase appeared in the course of quenching, this should also be the case at the quenching of the completely cubic state at higher temperature. It was, however, not so actually. The coexistence of the sharp patterns of both CuAu II and the cubic phase must be distinguished from the unavoidable apparition of the diffuse pattern of the ordered phase due

* Soon after we finished this work, J. B. Newkirk's X-ray work appeared in the Journal of Metals [**5** (1953) 823], which showed that in Cu-Au alloys near CuAu in composition there is a finite temperature range within which the ordered and disordered states can coexist in equilibrium. Our results are similar to his, and it seems to be worth while reporting that the similar results were obtained by electron diffraction with thin films.

** In this figure the boundary between the disordered and coexistence regions seems to be lowered by some degrees, compared with the preceding works. The source of this systematic error may be sought in the temperature difference between the specimen and the thermojunction, as the latter was covered with a thin glass tube. This error, however, has no effect on the catching of the essential nature of the present phenomenon.

to the incomplete quenching. To get rid of the second objection a sufficient care was taken. In each case, the film was gradually heated from lower temperature to a difinite temperature, at which it was kept for three hours. According to Borelius[15] and Hirabayashi[16], it was concluded, from the measurements by means of calorimetry, electrical resistance and X-rays, that the relaxation time for CuAu is the shortest at about 350°C and becomes larger as the temperature approaches the critical point. In order to examine whether the equilibrium state was attained or not, the prolonged annealing of twenty hours was made, which, however, had no influence on the diffraction pattern. Therefore, the equilibrium state seemed to be already attained by the 3 hr. annealing. Moreover, if we did not work with the equilibrium state, the amount of the disordered phase would become the less, the higher the temperature, for the same heating duration. The actual state was diametrically opposite as shown in Fig. 14. The grain size in our polycrystalline films was considerably small, compared with that in usual bulk metals. This fact may lead to a much smaller period of the relaxation time. According to Newkirk et al.[7] the ordering process in CoPt proceeded more rapidly in a surface layer, having smaller grains, than in an inside layer. The third objection, i.e., the inhomogeneity of composition can be dispelled by the sharpness of diffraction spots or rings. Especially, the fact, that the compositions of both CuAu II and the cubic lattice nearly coincide respectively with those of the phase boundaries in the two phase region at the concerned temperature, strongly supports the homogeneity of our films.

Concerning the ordered and disordered phases near the 1 to 1 atomic composition, the equilibrium diagram of the cobalt-platinum system is very similar to that of the gold-copper system. The coexistence of the disordered (f.c.c.) and the ordered (f.c. tetragonal) phases in the former system has been confirmed by Newkirk et al.[7] by X-ray studies associated with the measurements on electrical resistance as well as the microscopical observations. A similar coexistence of two phases in the magnesium-cadmium system was also observed[17][18].

(4) *Streaks emerging from the central spot*

Some films prepared by the method (b) often exhibited, in their patterns, streaks emerging from the incident beam position. The elongations were conspicuous in three directions, [100], [110] and [111], and they were also observed, though faintly, in other directions. In order to depict the detailed aspect of the original plate, Fig. 15 is shown, in which (a) reveals the intensity distribution in the (100) plane of the reciprocal lattice and (b) that in the (110) plane. This phenomenon has already been observed by Raether[19] in thin films of AuCu, $AuCu_3$ and gold-silver alloy of 50 atomic per cent of gold. In our case, streaks emerging from diffraction spots (normal-or superlattice) were also observed. As Raether described, these linear elongations can be observed not only in alloy films, but also in evaporated silver films as well as in electrodeposited nickel films. The phenomenon observed in orientated silver films resembles very much that in the present case, and, therefore, it will be sure that streaks arise

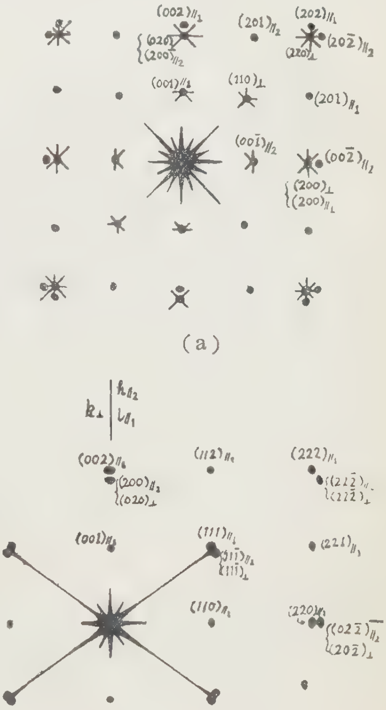

(a)

(b)

Fig. 15. Streaks emerging from tthe central spot. The electron beam is perpendicular to (100) in (a) and to (110) in (b).

from a lattice defect common to the orientated thin films formed by evaporation or by electrodeposition, but not from the alloy structure alone. At present, we do not engage in a detailed discussion on this topic, but it should be added that CuAu films prepared by the method (a) did not almost show such streaks, and, accordingly, the preparing method of films seems to be closely connected with the effect.

§ 4. Conclusion

As described in § 3, the main features in the structure of CuAu at various temperatures were elucidated by electron diffraction. Especially, the fact that the small elongation of lattice at every boundary between antiphase domains periodically exists in CuAu II caused the satellites to arise around the normal spots. On this occasion, those around the direct spot became conspicuous, probably, due to the larger atomic scattering factor for electron at a very small scattering angle than expected for free neutral atoms, and those around the other normal spots were merely the repetitions of those around the direct spot, due to the secondary elastic scattering.

Thus, the obtained results proved our method to be superior to the X-ray method in showing finely and easily the intensity distribution in the reciprocal lattice of the alloy. The structure of CuAu II was exactly known from the present study, but to the ordering process of CuAu I which starts from the quenched cubic state we cannot almost allude. The latter topic is interesting, being especially connected with Harker's study, and hence it is desirable to perform detailed investigations in the near future on thin films as well as bulk alloys by utilizing electron diffraction and also electron microscopy.

In conclusion we wish to express our sincere thanks to Dr. G. Honjo for his pertinent suggestions and kind discussions. Our thanks are also due to Dr. S. Shirai and Dr. Y. Takagi, for their useful suggestions. And, it should be added that ardent discussions by Mr. M. Hirabayashi and by several respected investigators in our institute contributed greatly to complete the present work. This has been supported partly by the fund of the Ministry of Education in Aid of Scientific Researches.

References

1) C. H. Johansson and J. O. Linde: Ann. Phys. **25** (1936) 1.

2) i) C. H. MacGillavry and B. Strijk: Physica **11** (1946) 369, **12** (1946) 129.

ii) A. J. C. Wilson: Proc. Roy. Soc. **A 81** (1943) 360, Nature **160** (1947) 305.

iii) I. G. Edmunds, R. M. Hinde and H. Lipson: Nature **160** (1947) 304.

iv) A. Guinier and R. Griffoul: Rev. de Métallurg. **14** (1948) 387.

v) H. Raether: Acta Crystallogr. **4** (1951) 70, Z. f. angew. Phys. **4** (1952) 53.

vi) I. G. Edmunds and R. M. Hinde: Proc. Phys. Soc. **B 65** (1952) 716.

3) J. M. Cowley: J. App. Phys. **21** (1950) 24.

4) T. Murakami: Busseiron Kenkyu (1952) No. 46, 69, J. Phys. Soc. Japan **8** (1953) 36.

5) S. Ogawa and D. Watanabe: J. App. Phys. **22** (1951) 1502, J. Phys. Soc. Japan **7** (1952) 36.

6) J. L. Haughton and R. J. M. Payne: J. Inst. Metals **46** (1931) 457.

7) J. B. Newkirk, R. Smoluchowski, A. H. Geisler and D. L. Martin: J. Appl. Phys. **22** (1951) 290.

8) L. Vegard and H. Dale: Z. Kristallogr. **67** (1928) 157.

9) D. Harker: Trans. A.S.M. **32** (1944) 210.

10) J. B. Newkirk, R. Smoluchowski, A. H. Geisler and D. L. Martin: Acta Crystallogr. **4** (1951) 507.

11) H. J. Yearian: Phys. Rev. **48** (1935) 631.

12) K. Lark-Horovitz: Thomson and Cochrane, Theory and Practice of Electron Diffraction, p. 96.

13) J. M. Cowley, A. L. G. Rees and J. A. Spink: Proc. Phys. Soc. **A 64** (1951) 609.

14) M. Hirabayashi, S. Nagasaki and H. Maniwa: J. Japan Inst. Metals **14** (1950), No. 3, 1.

15) G. Borelius: J. Inst. Metals **74** (1947) 17.

16) M. Hirabayashi: J. Japan Inst. Metals **B 15** (1951) 565.

17) D. A. Edwards, W. E. Wallace and R. S. Craig: J. Amer. Chem. Soc. **74** (1952) 5256.

18) M. Hirabayashi: unpublished.

19) H. Raether: Z. Naturforsch. **7a** (1952) 210.

JOURNAL OF THE PHYSICAL SOCIETY OF JAPAN Vol. 9, No. 4, JULY—AUGUST, 1954

Order-Disorder Transitions in A_2BC Ternary Alloys with the Plane Square or the Body-Centered Cubic Lattice

By Sukeaki HOSOYA

Institute of Physics, College of General Education, University of Tokyo

(Received December 24, 1953)

The statistics of the ternary alloy A_2BC in the plane square or the b.c.c. lattice is investigated with the same schematic model as used in the usual theories on binary alloys. The calculation is made at the level of the Bragg-Williams approximation. The behaviours of the system are determined by two quantities $v_1=V_{CA}/V_{BC}$ and $v_2=V_{AB}/V_{BC}$ and by the sign of V_{BC}, where $V_{ij}=(\varepsilon_{ii}+\varepsilon_{jj})/2-\varepsilon_{ij}$. ($i$ and j stand for A, B or C; ε_{ij} is the interaction energy between i- and j-atoms.) Four types of ordered states can appear: A(BC) type, (AB)(AC) type and other two intermediate types. They are all partly ordered states in which the Heusler type is not included, for only two sublattices can be distinguished under the present assumption. Which type appears is determined by v_1, v_2 values. The transition is always of the second kind. The contours of the transition temperature on the v_1-v_2 plane are parabolas, and those of the peak value of the specific heat are a pencil of the half infinite straight lines with the center at (3/4, 3/4). The latter contours have the maximum when $V_{BC}=0$, that is, when the system reduces to the AB binary alloy. The segregation temperatures are calculated, without taking the ordering effect into account, in order to show that the order-disorder transition cannot realize at least for some v_1, v_2 values, being covered by segregation.

§ 1. Introduction

Many statistical theories have been developed on binary alloys with success, and their applications to ternary alloys have been put into practice by several authors. In the early stage, T. Hirone and S. Matsuda[1] discussed this problem, chiefly on the A_2BC body-centered cubic alloy, considering only the Heusler type and neglecting A(BC) type. This is corrected by S. Matsuda[5] from the wider point of view, taking the effect of "the second nearest neighbours"* into account, though he investigated principally the conditions for various types to appear. T. Hirone and T. Katayama[2] investigated the stable constitution of ternary alloys in general, without considering the ordering effect, then they[3] discussed the influence of the third metal mixed in binary alloys. The former subject was dealt with by J. L. Meijering,[4] too. H. K. Hardy[6] tried to explain the actual behaviours of the Fe-(NiAl) alloy by assuming the effects of "the second nearest neighbours"*. In the present paper, the ternary alloy of the composition A_2BC in the plane square or the body-centered cubic lattice was theoretically investigated at the level of the Bragg-Williams approximation, the interaction among "the first nearest neighbours"* being assumed. Same assumptions as found in the usual theories on the binary alloy are made, though they may be less valid in the ternary alloy. For instance, we neglect the effect of lattice vibrations, the deformation of the lattice and the change of interaction energy values due to temperature and to ordering, and consider only the states in thermal equilibrium. Under these assumptions, the dependencies are investigated of their order-disorder transition temperatures and their peak values of the specific heat on the interaction energies. Moreover the segregation temperatures are also calculated, neglecting the ordering effects.

§ 2. Fundamental Equations

As shown in Fig.'s 1 and 2, lattice points are divided into four sites: 1-, 2-, 3- and 4-sites. Under the present assumptions, how-

---

* Those expressions in quotation marks are used for convenience sake, though not exact in the Bragg-Williams approximation.

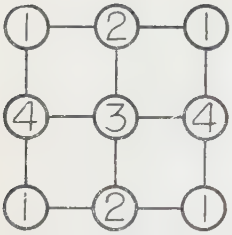

Fig. 1. The plane square lattice with four sublattices.

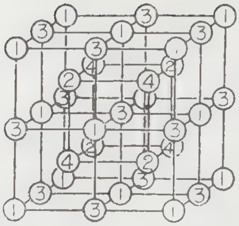

Fig. 2. The body-centered cubic lattice with four sublattices.

Under the first neighbour assumption 3- and 4-sites are equivalent to 1- and 2-sites respectively.

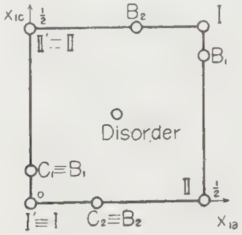

Fig. 3. All possible solutions are shown by the values of x_{1B} ane x_{1C}.

ever, 3- and 4-sites prove to be equivalent to 1- and 2-sites respectively. Therefore the type of Heusler alloy cannot be found among the present solutions. New let x_{ij} be the probability that an i-site is occupied by a j-atom, where i stands for 1 or 2 and j for A, B or C. Two x_{ij}'s out of six are independent, for there are four mutually independent and identical relations among them. Then let $\mathcal{E}_{mn}$ (m, n=A, B, C) represent the interaction energy between two neighbouring atoms, m and n. As seen afterwards, $\mathcal{E}_{mn}$'s appear in the equation only in such combined forms as $V_{mn}=(\mathcal{E}_{mm}+\mathcal{E}_{nn})/2-\mathcal{E}_{mn}$. Further, two ratios $v_1=V_{CA}/V_{BC}$ and $v_2=V_{AB}/V_{BC}$ are important. The temperature is measured by such an unit as $\tau=kT/V_{BC}$. So τ has the meaning only when τ is the same with V_{BC} in sign. Thus the internal energy of the system containing N atoms in total is expressed as follows:

$$U=(zN/8)\{(2\mathcal{E}_{AA}+\mathcal{E}_{BB}+\mathcal{E}_{CC})-2V_{BC}f(x_{1B},\ x_{1C})\}, \tag{2.1}$$

where

Table I. All possible solutions and the variable part of their internal energies.

Type	x_{1B}	x_{1C}	x_{2A}	f
Disordered state	1/4	1/4	1/2	$(1+2v_1+2v_2)/4$
I or A(BC)	1/2	1/2	1	v_1+v_2
II or (AB)(AC)	1/2	0	1/2	$(1+v_1+v_2)/2$
B_1	1/2	$(v_1-v_2+1)/8v_1$	$(5v_1-v_2+1)/8v_1$	$(7v_1^2+10v_1v_2-v_2^2+6v_1+2v_2-1)/16v_1$
B_2	$(v_1-v_2+1)/8v_2$	1/2	$(5v_2-v_1+1)/8v_2$	$(7v_2^2+10v_1v_2-v_1^2+6v_2+2v_1-1)/16v_2$

$$\begin{aligned}f(x_{1B},\ x_{1C})=&(x_{1B}+x_{1C})-4x_{1B}x_{1C}\\&+v_1\{(1-x_{1B}-3x_{1C})+4x_{1C}(x_{1B}+x_{1C})\}\\&+v_2\{(1-3x_{1B}-x_{1C})+4x_{1B}(x_{1B}+x_{1C})\}\ ,\end{aligned}$$

and z is the number of the nearest neighbouring atoms around any given atom, so it is four in the plane square lattice and eight in the body-centered cubic lattice. At the level of the Bragg-Williams approximation, the entropy of this system is obtained as follows, using the Stirling's formula.

$$S=-(kN/2)\sum_{6} x_{ij}\ln x_{ij}\ .$$

Fundamental equations are obtained in the following form by minimizing the free energy $F=U-TS$:

$$\begin{aligned}&2v_2(4x_{1B}-1)+(v_1+v_2-1)(4x_{1C}-1)\\&=(2\tau/z)\ln\{2x_{1B}(x_{1B}+x_{1C})/(1-2x_{1B})(1-x_{1B}-x_{1C})\},\end{aligned} \tag{2.2}$$

$$\begin{aligned}&2v_1(4x_{1C}-1)+(v_1+v_2-1)(4x_{1B}-1)\\&=(2\tau/z)\ln\{2x_{1C}(x_{1B}+x_{1C})/(1-2x_{1C})(1-x_{1B}-x_{1C})\}.\end{aligned} \tag{2.3}$$

§ 3. Various States at 0°K

At 0°K, U must take the minimum value, so $f(x_{1B},\ x_{1C})$ must take maximum or minimum according as V_{BC} is positive or negative. x_{1B} and x_{1C} can vary only in the next range:

$$0\leqq x_{1B}\leqq 1/2, \qquad 0\leqq x_{1C}\leqq 1/2. \tag{3.1}$$

$f(x_{1B},\ x_{1C})$ takes the extreme value on the point $x_{1B}=x_{1C}=1/4$ or on the boundary of the range (3.1). Several possible points are shown in Fig. 3. The type I is sometimes referred to as A(BC) type, and the type II as (AB)(AC) type. Their meanings will be understood by Table I, where all possible states are listed with their values of $f(x_{1B},\ _{1C})$. Types B_1 and B_2 lose any physical meaning in certain regions on the v_1-v_2 plane, because of the restrictions (3.1). The most stable type is determined, depending on the values of v_1 and v_2. The results are shown in Fig. 4. Further, the several solutions of another kind must be considered, that is, the ones in which the alloy segregate into two or three components. These are shown in Table II, where the lattice is considered to still hold its form and A_2B(ord), for instance, means such a type as the A-B pairs are found as many as possible. Thus the v_1-v_2 plane is divided into several regions as shown in Fig. 5. Types II, B_1 and B_2 are all covered by the segregating states.

§ 4. Solutions in the Ordered State

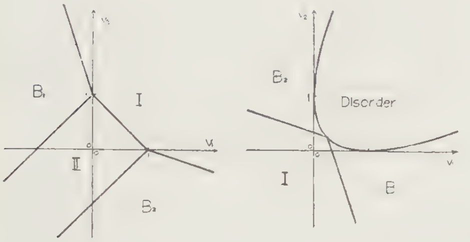

(a) The case $V_{BC}>0$. (b) The case $V_{BC}<0$.

Fig. 4. The most stable types of the states at 0°K neglecting the segregation.

Table II. The variable part of the internal energies of the segregating types.

Type	f
2A+B+C	0
2A+BC(ord)	1
2A+BC(disord)	1/2
$B+CA_2$(ord)	v_1
$B+CA_2$(disord)	$2v_1/3$
$C+A_2B$(ord)	v_2
$C+A_2B$(disord)	$2v_2/3$

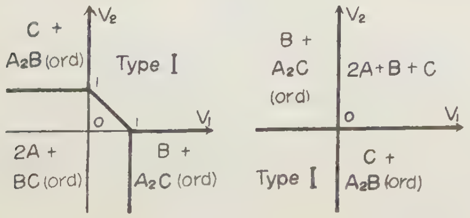

(a) The case $V_{BC}>0$. (b) The case $V_{BC}<0$.

Fig. 5. The most stable types of the states at 0°K taking the segregation into consideration.

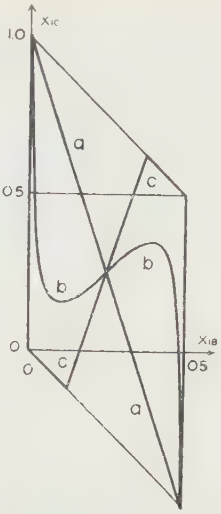

Fig. 6. The solutions (x_{1B}, x_{1C}) satisfying the equation (2.2). The straight line a shows the solution at the infinitely high temperature, whatever values v_1 and v_2 may take. The form of the curve depends upon the v_1 and v_2 values at the finite temperature. At 0°K, it reduces to such a zigzag line as c. Its form likes to the letter 2 when $V_{CA}+V_{AB}>V_{BC}$, but likes to the letter S as shown here, when $V_{CA}+V_{AB}<V_{BC}$.

The values of x_{1B} and x_{1C} which satisfy one Eq. (2.2) are on a curve inside the parallelogram shown in Fig. 6. Of course x_{1B} and x_{1C} have the physical meaning only inside the square limited by (3.1).

The situations are the same in the other Eq. (2.3), if only we interchange two sets of values, x_{1B}, x_{1C} and v_1, v_2. Then the solution (x_{1B}, x_{1C}) can be obtained as the crossing points of these two curves. One example is shown in Fig. 7. In this case the ordered solution appears in (a), then another ordered solution in (b) at the lower temperature. It is easily seen that the former solution is of A(BC) type and the latter is of B_1 or B_2 type. Moreover there are other solutions which suddenly appear without starting from the disordered solutions. These solutions are of B_2 or B_1, and II type in the present example. Thus, what type of solutions appear can be found. The results are summarized in Fig. 8 for the case $V_{BC}>0$. For the case $V_{BC}<0$, the transition temperature τ_c is always single-valued and the results are quite the same with those in Fig. 4(b). The ordered states which appear at the higher τ_c in Fig. 8 are the same with the states at 0°K shown in Fig. 4(a). Thus the various solutions in

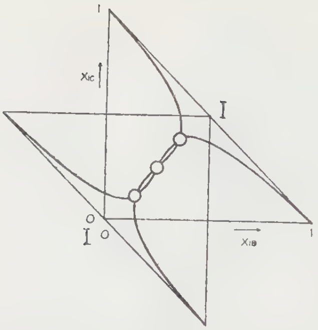

(a) A kind of ordered solution is shown at the certain temperature.

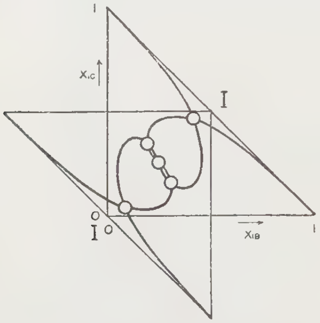

(b) The second ordered solution is shown at the lower temperature.

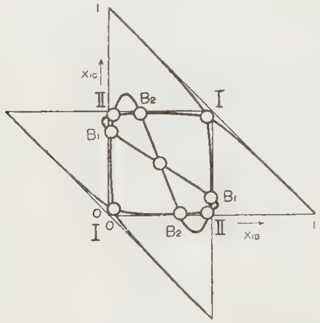

(c) Other kinds of ordered solutions appear at the further lower temperature without branching from the disordered solution.

Fig. 7. This shows how the several ordered solutions can appear in the case $V_{BC}>0$, $v_1+v_2>1$ and $|v_1-v_2|<1$.

Table I are all found again from the wider point of view. These facts indicate that the ordered states shown in Fig. 4 have possibilities to appear at the higher transition temperature, though Fig. 5 suggests that they must segregate at the lower temperature in some region of the v_1-v_2 plane.

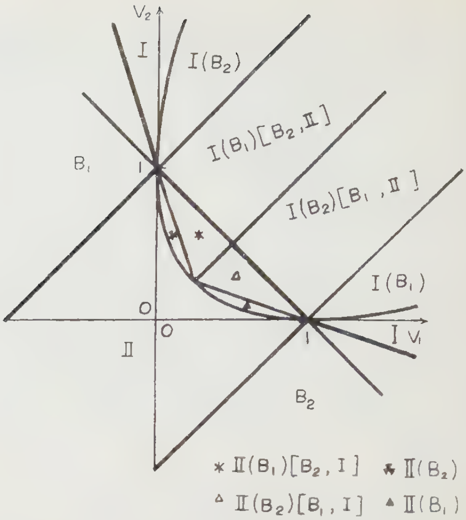

Fig. 8. All possible ordered states are shown for the case $V_{BC}>0$ on the v_1-v_2 plane. The results for the case $V_{BC}<0$ is quite the same with those in Fig. 4 (b). The ordered state written in ( ) is the solution which appear at the lower transition temperature, and the one in [ ] is the solution which appears without branching from the disordered state.

§ 5. The Transition Temperature

Variables x_{ij}'s can be expressed in such a general form as follows, using the parameters of the long range order, s_1 and s_2, which are 0 in the disordered state and approach 1 in any ordered state:

$$x_{1A}=(2-a_1s_1-a_2s_2)/4, \quad x_{1B}=(1+a_1s_1)/4,$$
$$x_{1C}=(1+a_2s_2)/4,$$
$$x_{2A}=(2+a_1s_1+a_2s_2)/4, \quad x_{2B}=(1-a_1s_1)/4,$$
$$x_{2C}=(1-a_2s_2)/4,$$

where a_1 and a_2 are the parameters given in Table III.

Table III.

Type	a_1	a_2
I	1	1
II	1	−1
B_1	1	$(1-v_1-v_2)/2v_1$
B_2	$(1-v_1-v_2)/2v_2$	1

The transition temperature is obtained by finding the temperature where two curves in Fig. 7 have the same value for dx_{1C}/dx_{1B} at $x_{1B}=x_{1C}=1/4$. It is determined by the following equation regardless of the ordered types:

$$2(4\tau_c/z)^2-\{2(v_1+v_2)+1\}(4\tau_c/z)+4v_1v_2 -(v_1+v_2-1)^2=0\,. \tag{5.1}$$

The contour of τ_c on the v_1-v_2 plane is generally a parabola which is symmetrical concerning

v_1 and v_2. It reduces to the line $v_1=v_2$ for $\tau_c=z/4$, as shown in Fig. 9. τ_c has two values for every point on the v_1-v_2 plane. Inside the parabola for $\tau_c=0$, there are two positive values for τ_c. Their meanings are quite clear if Fig. 8 is consulted, that is, two transition temperatures have relation to two different ordered states. The transition at the lower temperature cannot be realized being covered by the one at the higher temperature.

§ 6. The Peak Value of the Specific Heat

The peak value of the specific heat can be obtained in the following way[7]. Just below the transition temperature, s_1 and s_2 are very near to 0, and the ratio s_2/s_1 which can be equated to ds_2/ds_1, has the finite value. By expanding the right sides of (2.2) and (2.3) till the order of s_i^3, dividing them by s_1, equating the values s_2/s_1 in two equations and neglecting the higher terms of s_i, we get the expression for s_1^2. Differentiating this with respect to τ, and using (5.1), we get

$$\left(\frac{C}{R}\right)_{|\tau_c|-0}=\frac{6\{2\tau_c/z-(2v_1+2v_2+1)/8\}^2}{(3\tau_c/z-v_1)^2+(3\tau_c/z-v_2)^2+2(\tau_c/z-1/4)^2}\,. \tag{6.1}$$

This does not include a_i and is always positive. So the transition is always of the second kind regardless of the v_1, v_2 values or of the ordered types. The point $v_1=v_2=3/4$ is a singular point and the formula is changed into the simpler form, using (5.1) again, as

$$\left(\frac{C}{R}\right)_{|\tau_c|-0}=\frac{3(3k^2-2k+3)}{12(k^2-k+1)\pm|k+1|\sqrt{3k^2-2k+3}}\,, \tag{6.2}$$

where

$$k=(v_2-3/4)/(v_1-3/4)\,.$$

When $V_{BC}>0$, the positive sign must be taken for the point which lies in the same side with origin concerning the line $v_1+v_2=3/2$, and the negative sign must be taken for the point which lies in the opposite side, and, when $V_{BC}<0$, the sign in the above case must be reversed.

Thus as shown in Fig. 10, the contour of $(C/R)_{|\tau_c|-0}$ is a half infinite straight line starting from the point $v_1=v_2=3/4$, and its value is determined only by the direction coefficient k. If B atoms and C atoms are put to be identical, the system reduces to the AB binary alloy. Of course the results obtained by Bragg and Williams on the AB alloy are included in the results here, as the special case. In fact, at the points $v_1=v_2=\pm\infty$ ($V_{BC}\to\pm0$ respectively) which correspond to the AB alloy, the present alloy has 1.5 for the peak value of the specific heat.

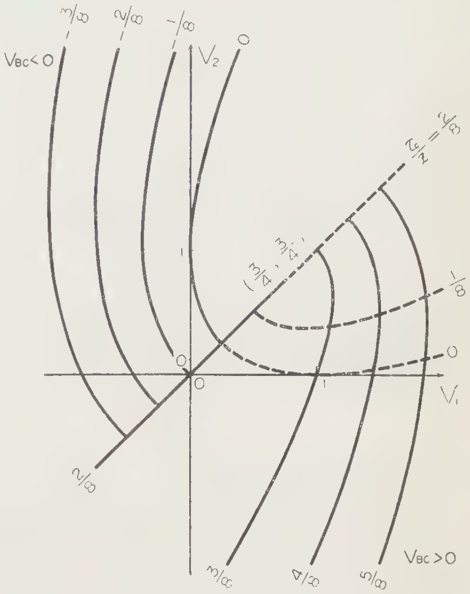

Fig. 9. The contours of τ_c on the v_1-v_2 plane. They are symmetrical concerning v_1 and v_2. Each half part shows the case $V_{BC}>0$ or $V_{BC}<0$ respectively.

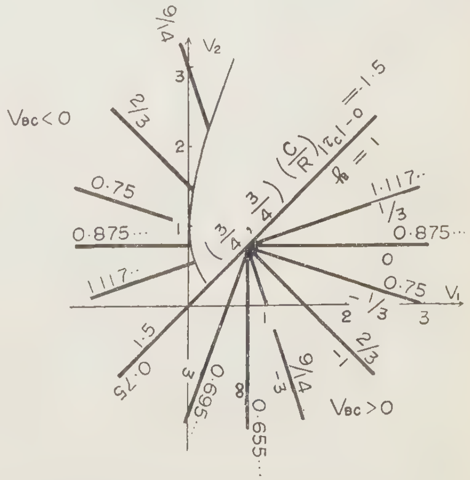

Fig. 10. The contours of $(C/R)_{|\tau_c|-0}$. They are symmetrical concerning v_1 and v_2, so each half part shows the case $V_{BC}>0$ or $V_{BC}<0$ respectively. The values of $(C/R)_{|\tau_c|-0}$ are symmetrical concerning the point $v_1=v_2=3/4$ in two cases. The maximum value is 1.5 and the minimum is 9/14.

§ 7. The Segregation Temperature

Segregation were so far neglected except in § 3, where the several segregating states were considered only at 0°K. It is desirable to think the stable constitution in the segregating states, taking the ordering effect into consideration. However, this investigation is too complicated to be dealt with, so here let us neglect the ordering effect. Then the phase diagram has such forms as shown in Fig. 11, for instance, in the case $V_{AB}>0$, $V_{BC}<0$, $V_{CA}>0$. The solubility curve moves upwards as the temperature decreases, and at the segregation temperature τ_s it passes the point P which corresponds to the constitution A_2BC. P′ is the conjugate point of P, that is, the point corresponding to the constitution of the alloy which can coexist with A_2BC. At the lower temperature than τ_s, the A_2BC alloy segregates into two alloys whose constitutions are given by the points Q and Q′.

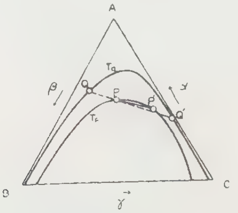

Fig. 11. The phase diagram of the ternary alloy in the case $V_{AB}>0$, $V_{BC}<0$, $V_{CA}>0$. The temperature T_P is higher than T_Q. P and P′ or Q and Q′ are a pair of conjugate points.

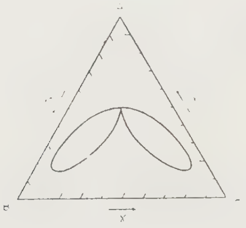

Fig. 12. The locus of the point P′. It means the point corresponding to the alloy which can coexist with the present A_2BC alloy.

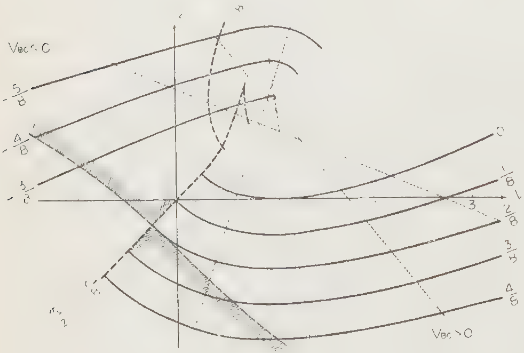

Fig. 13. The contours of the segregation temperature τ_s on the v_1-v_2 plane. They are symmetrical with v_1 and v_2, so each half part is shown for the case $V_{BC}>0$ or $V_{BC}<0$ respectively. τ_s distributes linearly on each dotted straight line. At least τ_c is covered by segregation on the hatched part.

The concentrations of the atoms, A, B and C will be denoted by α, β and γ respectively. The general condition that the two ternary alloys having the different concentrations can coexist is known.[2)4)] The concentrations (α, β, γ) of the alloy which can coexist with alloy A_2BC are given by the next three equations. Using the present notations,

$$\left.\begin{aligned}&\{(\beta+\gamma)\gamma-1/8\}v_1+\{(\beta+\gamma)\beta-1/8\}v_2\\&\qquad-(\tau_s/z)\ln 2(1-\beta-\gamma)=\beta\gamma-1/16\,,\\&(\gamma-1/4)v_1+(2\beta+\gamma-3/4)v_2\\&\qquad-(\tau_s/z)\ln\{(1-\beta-\gamma)/2\beta\}=\gamma-1/4,\\&(\beta+2\gamma-3/4)v_1+(\beta-1/4)v_2\\&\qquad-(\tau_s/z)\ln\{(1-\beta-\gamma)/2\gamma\}=\beta-1/4.\end{aligned}\right\}\tag{7.1}$$

Though β and γ cannot directly eliminated, the dependency of τ_s on the values (v_1, v_2) can be found as follows.

The coefficients of (7.1) have the next identical relation:

$$\begin{vmatrix}(\beta+\gamma)\gamma-1/8 & (\beta+\gamma)\beta-1/8 & \beta\gamma-1/16\\ \gamma-1/4 & 2\beta+\gamma-3/4 & \gamma-1/4\\ \beta+2\gamma-3/4 & \beta-1/4 & \beta-1/4\end{vmatrix}=0.$$

Therefore, β and γ can have only the limited values which satisfy the following equation:

$$\begin{vmatrix}(\beta+\gamma)\gamma-1/8 & (\beta+\gamma)\beta-1/8 & \ln 2(1-\beta-\gamma)\\ \gamma-1/4 & 2\beta+\gamma-3/4 & \ln\{(1-\beta-\gamma)/2\beta\}\\ \beta+2\gamma-3/4 & \beta-1/4 & \ln\{(1-\beta-\gamma)/2\gamma\}\end{vmatrix}=0.\tag{7.2}$$

This can be written as

$$(\beta+\gamma-1/2)^2\{(\alpha+1/2)\ln\alpha+(\beta+1/4)\ln\beta\\+(\gamma+1/4)\ln\gamma+(\beta+\gamma+5/2)\ln 2\}=0.\tag{7.3}$$

The first factor in (7.3) must be omitted, for it does not give any definite value to τ_s except 0. The second factor corresponds to two loops on the phase diagram as shown in Fig. 12. Each point on the loops gives a dotted straight line on the v_1-v_2 plane (Fig. 13) and on each line the τ_s value varies linearly, as seen from the form of (7.1), two of which are now independent. Thus the τ_s contours can be obtained on the v_1-v_2 plane. If the sign of τ_s is reversed, they resemble the τ_c contours in Fig. 9, but are not so simple especially in the region near $v_1=v_2=3/4$. Particularly the line $\tau_s=0$ is similar to the line $\tau_c=0$, and τ_s is equal to $-\tau_c$ on the line $v_1=v_2$. In some region τ_s has also two values with the same sign and their meanings are explained by the investigations by J. L. Meijering[4]. Here we have only to consider the larger τ_s in absolute value. On the broken curve in Fig. 13, which is approximated by the straight line $v_1+v_2=-1/2$, τ_c is equal to τ_s. At least on the hatched side, the alloy begins to segregate before undergoes the transition to the ordered state, so the contours of τ_c in Fig. 9 and of $(C/R)_{|\tau_c|-0}$ in Fig. 10 lose their practical meaning. The results in this section are valid as far as the constitution of alloy is A_2BC, without depending on the coordination number z or on the lattice type either.

§ 8. Conclusions and Discussions

The behaviours of the order-disorder transition of the ternary alloy A_2BC in the plane square lattice or the b.c.c. lattice can be summarized as follows. Any given ternary alloy has a corresponding point (v_1, v_2) on either of two v_1-v_2 planes according to the sign of V_{BC}. When the temperature of the alloy decreases from enough high temperature, it undergoes the order-disorder transition of the second kind. The values (v_1, v_2) decide the transition temperature τ_c according to Fig. 9, the ordered type according to Fig. 8 or Fig. 4(b) and the peak value of the specific heat according to Fig. 10. When the point (v_1, v_2) falls at least on the hatched side in Fig. 13, the alloy segregates before undergoes the transition to the ordered state, and finally gets to the state expressed in Fig. 5. More exactly the ordered segregating state must be considered, too, but it was neglected here for two reasons. The first reason is that the order-disorder problem in ternary alloys with arbitrary compositions is beyond our scope of this paper, and the second is that our model is too schematic to deal with such a problem, because for instance the lattice may not hold its form after segregation.

Such a real example as the Heusler type cannot be derived as far as only the interaction between the atoms on two sublattices is considered, without depending on the degree of the approximation. The practical calculation of various quantities may be complicated if the interaction among the atoms on 1- and 3-sites and 2- and 4-sites in Fig. 2 are taken into account. This is inferred from the paper by K. Adachi[8] on binary alloys and the paper by S. Matsuda[5]. Though the present model is very schematic, some results may be useful especially on the dependencies of the transition temperature and the peak value of the specific heat on the interaction energies. They are included as the special case of the small interaction among the atoms on the second nearest sites, if the various properties of the ternary alloy are calculated taking such effects into account.

The whole results can be applied also to the case where one component is a hole as found in Ag_2HgI_4 and other substances with the so-called average structure.

We are heartily thankful to Assistant Professor S. Takagi for his kind interests and encouragements.

References

1) T. Hirone and S. Matsuda: Rikagaku Kenkyujo Iho (Bulletin of the Physical and chemical Institute), **19** (1940) 931 (in Japanese).

2) T. Hirone and T. Katayama: Ibid. **19** (1940) 1419 (in Japanese).

3) T. Hirone and T. Katayama: Ibid. **21** (1942) 992 (in Japanese).

4) J. L. Meijering: Philips Res. Reports **5** (1950) 333 and **6** (1951) 183.

5) S. Matsuda: J. Phys. Soc. Japan **8** (1953) 20.

6) H. K. Hardy: Acta Metal. **1** (1953) 210.

7) R. Kikuchi: Busseiron-Kenkyu **24** (1950) 52, 65, **25** (1950) 41, **37** (1951) 1 (in Japanese) and Phys. Rev. **81** (1951) 988.

8) K. Adachi: Sci. Rep. Tôhoku Univ. Ser. I, **35** (1951) 30.

JOURNAL OF THE PHYSICAL SOCIETY OF JAPAN Vol. 9, No. 4, JULY—AUGUST, 1954

On the Ferrimagnetism of Iron Selenides*

By Tokutarō HIRONE, Seijirō MAEDA
The Research Institute for Iron, Steel and Other Metals
Tôhoku University, Sendai
and Noboru TSUYA
The Research Institute of Electrical Communication
Tôhoku University, Sendai

(Received February 1, 1954)

The thermomagnetic properties of iron selenides $FeSe_x$ with various selenium contents x were measured as functions of temperature. The thermomagnetic curves obtained belong to the ordinary Weiss type. It was also found that the magnetization at the boiling temperature of liquid nitrogen increases with the selenium content, reaches its maximum value, 35 gauss, at $x=1.23$, and then decreases again with further increase of x. The Néel temperature was approximately 150°C in the range of x from 1 to 1.26 whereas it decreases gradually with further increase of x and approaches to its lowest value 30°C at $x=1.35$. The origin of the magnetization of this substance was discussed based on the theory of ferrimagnetism.

§ 1. Introduction

It has been well known[1] that iron selenides as well as iron sulfides, nickel selenides, nickel tellurides and so forth with various anion contents x crystallize in the nickel arsenide structures, the lattice for iron or nickel atoms takes a simple hexagonal layer arrangement. In these substances the anions, such as sulfur, selenium, tellurium, are elements of chalcogen group, the electronegativity of which decreases in the order from sulfur to tellurium.

The magnetic properties of FeS_x have recently been investigated again in detail by several authors[2]. However, it is difficult to find the origin of magnetism of this substance. There are same explanations for the origin, but only from the data obtained with iron sulfides one can not make a proper choice of such possibilities. For this reason, it is desirable to perform a systematic study on the magnetic properties of this above mentioned series of these substances. If the electronegativity of anions decreases in such substances the transfer of the electrons from anions to cations become easy, so that the amount of super-exchange[3] which plays a great role in the magnetic properties of these substances is then increased. In such substances with various anion concentrations the crystal structure is the same as mentioned above, while the lattice constants a and c vary gradually with the concentration of anions. Hence, in these substances, the similar magnetic properties are expected with the gradual change of super-exchage interaction, which is important between the atoms in the nearest neighbours, the next-to-nearest and third neighbours, etc.

As the first step of the systematic investigations on the magnetism of these substances, the study of the thermomagnetic properties of iron selenides was undertaken. The purpose of this paper is to show the experimental results obtained on the magnetization in iron selenides with various selenium contents x ($1 \leq x \leq 1.35$) and to discuss the nature of magnetism in this substance. The reason why $FeSe_x$ was selected to be studied at first was that the crystal structure of this substance has been analyzed in detail[4] and that the magnetism of $FeSe_x$ is expected to be somewhat similar to that of FeS_x, because selenium is the next neighbor of sulfur in the periodic table.

§ 2. Preparation of Specimens

The method of preparation of the specimens was similar as that in the case of iron sulfides, which was described in detail in the previous paper[5]. Hence we shall describe the method

---

* This investigation was supported in part by the Grant-in-Aid of Fundamental Scientific Research of Ministry of Education.

of preparation very briefly. The selenium used was obtained by purifying the raw selenium by successive vacuum distillations repeated twice and it contained impurities less than 0.001%. The reduced iron powder, the purity of which was 99.99%, and the above mentioned selenium powder were mixed in proper compositions and the mixtures were heated in evacuated silica tubes at the temperature of about 1000°C for 12 hours or more; and thereafter the reaction products were cooled down slowly at the rate of 100°C per hour to the room temperature. Sometimes cracks were found on the wall of tubes during the cooling process of preparation of specimens with stoichiometric composition. However, by using fused silica for the reaction pipe no crack was found at all. In many cases we could obtain the samples in the form of single crystals and could find fine cleavage surfaces when the specimens were broken off. A part of the specimens prepared for the present study are listed in Table I.

The crystal structure of $FeSe_x$ was studied by Hägg and Kindström[4]; and the proposed phase diagram due to Hansen[6] for the system of $FeSe_x$ is shown in Fig. 1. Basing upon this diagram, all the specimens to be measured in the present case were reheated for 12 hours at 1100°C and quenched from 600°C in order to obtain the same $NiAs$ crystal structure for all substances. To prevent the oxidation during the measurements the specimens of about 20 mg were packed into evacuated capsules made of fused silica, 5 mm diameter, 10 mm length, and 0.1 mm thickness. The crystal structures of the present specimens were checked by X-ray photograph. The results are shown also in Table I. In the third column in Table I the crystal structures of the slowly cooled specimens are shown in order to compare the present results with those due to Hägg Kindström[4]. The fourth column shows those of the quenched specimens.

By the preparation of the samples, the selenium content x was chosen so as to lie between 1 and 1.35. Because, if selenium content x exceeds 1.35, the substance separates into two phases, namely the selenium phase and that of $FeSe_{1.35}$.

§ 3. Experimental Procedures and Results

The apparatus used for the susceptibility measurement was an automatically recording magnetic balance, which was already described in detail in another paper[7] by the present authors. The magnetic field used for the present measurements was 9,000 Oe. In order to measure the susceptibility under such a high field, the specimens were put at a position just above the center of truncated pole

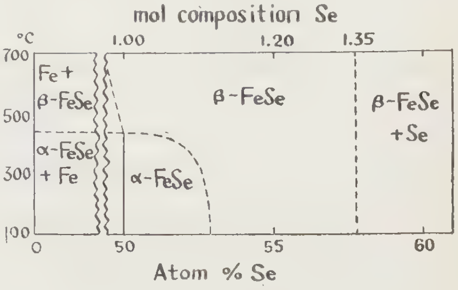

Fig. 1. The phase diagram of iron selenides due to Hansen.

Table I. The composition and crystal structure of the prepared specimen

Content of Se %	50.00	51.2	52.4	54.5	57.4
Content of Se x	1.00	1.05	1.10	1.20	1.35
Crystal structure slowly cooled	PbO	PbO	$NiAs$	$NiAs$	$NiAs+Se$
Crystal structure quenched	$NiAs$	$NiAs$	$NiAs$	$NiAs$	$NiAs+Se$

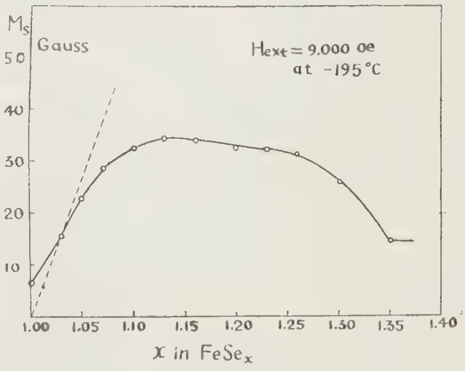

Fig. 2. The curve of saturation magnetization as a function of selenium contents x. The dotted line shows a corresponding values estimated from the simple application of ferrimagnetic theory with holes.

pieces of an electro-magnet, where the magnetic field was nearly at its maximum value and the field gradient in vertical direction was comparatively small.

In Fig. 2, the relations between selenium contents and the intensity of magnetization under 9,000 *Oe* at the boiling temperature of nitrogen are shown. The difference between the values of magnetization under 9,000 *Oe* and 12,500 *Oe* was so small that the values shown in Fig. 2 are regarded as the saturation magnetization of these substances. As Fig. 2 shows, the saturation magnetization increases with selenium contents and has a flat maximum in the range between $FeSe_{1.10}$ and $FeSe_{1.26}$ and it decreases again with further increase of selenium contents. The behaviour of magnetization of iron selenides is similar in some degree to that of iron sulfides[2) and the value is about one half of that in the case of FeS_x. The Néel point T_N is also shown in Fig. 3 as a function of selenium contents. As can be seen from the figure, the Néel temperature decreases gradually with increase of selenium content x in the range from 1 to 1.26 and the value is about 150°C. With further increase of x the Néel point decreases rather rapidly and reaches a value about 30°C at x=1.35. The forms of all the magnetization versus temperature curves under 9,000*Oe* belong to Weiss type as shown in Fig. 4. But in the case of specimens, in which selenium content is nearly 1.35, a hollow on the thermo-magnetic curve is found in the neighbourhood of Néel points, the origin of which is uncertain at the present stage**.

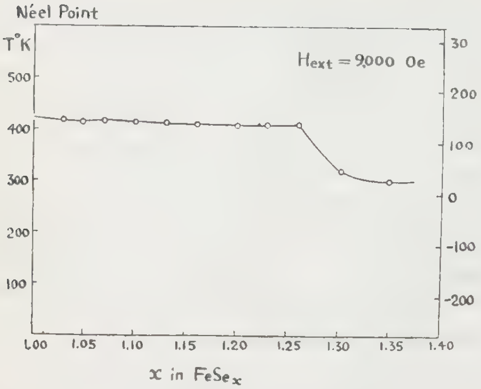

Fig. 3. The curve of Néel temperature T_N versus selenium contents.

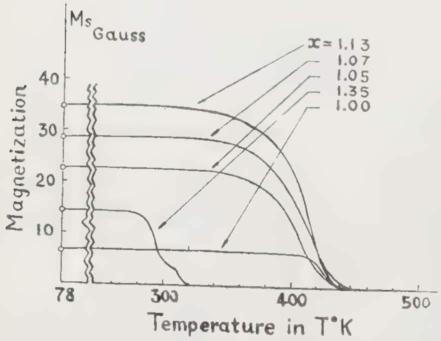

Fig. 4. The curves of magnetization versus temperature.

The temperature dependence of the paramagnetic susceptibility above the Néel point of these substances were also measured by the same apparatus. A result obtained is given in Fig. 5, which shows the inverse susceptibility as a function of temperature. As seen from the figure, hyperbolic dependence of the ferrimagnetic substances is obtained in the present case.

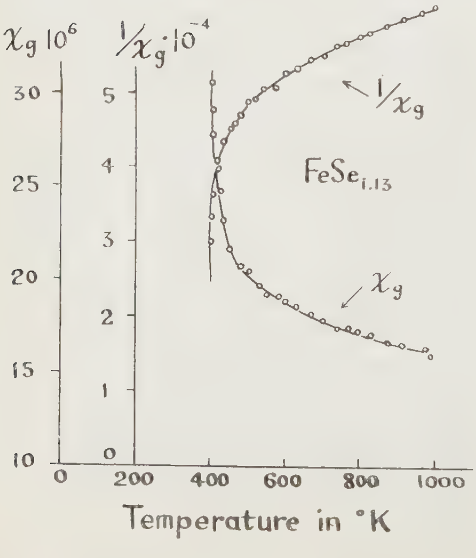

Fig. 5. The curve of inverse susceptibility of $FeSe_{1.13}$ as a function of temperature.

§ 4. Discussions

As the experimental results show, the magnetic properties of $FeSe_x$ $(1 \leq x \leq 1.11)$ are

---

** It may probably be caused by the change of anisotropy constant at such temperature range.

similar to those of FeS_x to some extent. It may be supposed that the magnetism of this substance is attributive to ferrimagnetism[8] just as in the case of iron sulfides. Such a conclusion is supported by the hyperbolic nature of the inverse susceptibility versus temperature curve in $FeSe_{1:14}$ as shown in Fig. 5. Here it should be expected basing upon the theory of ferrimagnetism that the apparent spontaneous magnetization will vanish at the stoichiometic composition due to the antiferromagnetic spin arrangement and it will increase linearly with the excess selenium content. Such an expected change is shown by the dotted line in Fig. 2. However, as the figure shows, curve of ferrimagnetization as a function of selenium content near the stoichiometic composition deviates from the expected line. Such a deviation is a marked difference in the magnetization of iron selenides and that of iron sulfides, in the latter case no spontaneous magnetization being found at the stoichiometric composition.

It might once be supposed that the above magnetism of iron selenide in stoichiometric composition were just an apparent one as one can suppose a similar shell structure as in the case of iron sulfide. In the rapidly cooled specimen of $FeSe_{1:00}$, which is used for the present measurement, an outer thin shell is composed of $FeSe_x$ with a little excess selenium content, whereas the inner part is $FeSe_{1.00}$ with a small amount of precipitated iron, and both iron and $FeSe_x$ ($x>1.00$) have ferro- or ferrimagnetization, However, only from such a shell structure, the observed magnetization in $FeSe$ can not be explained at all, since the observed magnetization is far greater than that what one will expect from this considerations. Moreover, we could not find any anomaly of the susceptibility at the temperature range including the Curie point of iron. Therefore the ferrimagnetization of $FeSe_{1.00}$ shown in Fig. 2 may be regarded as that of essential nature.

The observed magnetization of the iron selenides at the stoichiometric composition may be understood also by the ferrimagnetic mechanism. One possible model is the following: one can assume that the vacancies exist both in iron and selenium sites even at the stoichiometric composition. If the iron lattice can be devided into sublattices and further if the unbalance of the vacancy density or spin density exist between these sublattices, then ferrimagnetism will occur due to the antiferromagnetic spin arrangement in both sublattices.

The authors wish to express their thanks to Mr. Hiroshi Kato; student of physics department of Tōhoku University, who performed in part the present measurement.

References

1) R. W. G. Wyckoff: The Structure of Crystals, Second Ed. 1931.

2) H. Haraldsen: Z. Anorg. u. Allg. Chem. **246** (1941) 169, 195; F. Bertaut: Compt. Rend. **234** (1952) 1295; J. de Phys. **13** (1952) 372; Acta Cryst. **6** (1953) 557; R. Benoit: Compt. Rend. **234** (1952) 2175; L. Néel: Rev. Mod. Phys. **25** (1953) 58; S. Sidhu and O. Meneghetti: Phys. Rev. **91** (1953) 435; T. Hirone and N. Tsuya: Phys. Rev. **83** (1951) 1063; T. Hirone, S. Maeda and N. Tsuya: J. Phys. Soc. Japan **9** (1954) 496; T. Hirone, S. Maeda, S. Chiba and N. Tsuya: J. Phys. Soc. Japan **9** (1954) 500.

3) H. A. Kramers: Physica **1** (1934) 82; P. W. Anderson: Phys Rev. **79** (1950) 350, 705; M. Shimizu: Prog. Theoret. Phys. **8** (1952) 416; J. H. Vleck, J. de Phys. et Rad. **12** (1951) 262; L. Néel: Ann. de Phys. **3** (1948) 137.

4) F. Diacon: Compt. Rend. **130** (1900) 1100; L. Mosen u. E. Docter: Z. Anorg. u. Allg. Chem. **118** (1921) 285; G. Hägg u. A. L. Kindström: Z. Phys. Chem. **22** (1933) 453.

5) T. Hirone, S. Maeda, S. Chiba and N. Tsuya: J. Phys. Soc. Japan **9** (1954) 500.

6) M. Hansen: Der Aufbau der Zweistofflegierungen, 1936.

7) T. Hirone, S. Maeda and N. Tsuya: Sci. Rep. RITU, A-**6** (1954) 67.

8) L. Néel: Ann. de Phys. **3** (1948) 137.

JOURNAL OF THE PHYSICAL SOCIETY OF JAPAN Vol. 9, No. 4, JULY—AUGUST, 1954

Thermal Analysis of Iron Sulfides at the Temperature Range of β-transformation*

By Tokutarō HIRONE, Seijirō MAEDA, Shu CHIBA
The Research Institute for Iron, Steel and Other Metals, Tohoku University, Sendai
and Noboru TSUYA
The Research Institute of Electrical Communication Tohoku University, Sendai

(Received February 1, 1954)

The measurements of specific heat was performed at the temperature range of β-transformation in iron sulfides with various sulfur contents x ranging from $x=1$ to $x=1.12$. A peak in specific heat versus temperature curve is found at 315°C, and this temperature as well as the jump in specific heat, 0.05 cal gr.$^{-1}$ deg.$^{-1}$ in value, is almost independent of sulfur contents. The mechanism of transformation is discussed, based upon the theory of ferrimagnetism, and it is concluded that the present experimental results accord well with the theoretical ones.

§ 1. Introduction

In the previous paper,[1] a model concerning to the origin of magnetism in the iron sulfides with various sulfur contents is proposed. As reported by Haraldsen[2], when $FeS_{1.00}$ is cooled down from high temperature, the susceptibility χ increases gradually until the temperature reaches a certain point T_β (≈320°C), thereafter the susceptibility decrease more rapidly making an angular point at another temperature T_α. These anomalies were known as β-and α-transformation respectively.

For the mechanism of β-transformation Yoshida[3] and the present authors[1] consider that at temperature below T_β an antiferromagnetic ordering of spins occurs in the lattice of iron sites; the spins in a base plane perpendicular to c-axis line up in one direction, say parallel to a-axis, whereas the spins in the next upper and lower planes line up in the opposite direction, and so on. Then the direction of spines in the successive base planes are arranged oppositely. It is then proposed by these authors that the β-transformation is considered as the order-disorder change of such spin arrangements. To confirm the proposed mechanism of β-transformation, it is desirable to study the thermal properties of this transformation of iron-sulfides from the energetical point of view. Because, if such a ferrimagnetic mechanism is correct, the anomalous heat capacity to be measured should be coincide with that predicted theoretically from the model. Moreover it is expected that such a measurement also throws a light to clarify the mechanism of α-transformation.

§ 2. Preparation of Specimens

Specimens of iron sulfides FeS_x with various sulfur contents ($1.00 \leqq x \leqq 1.12$) were prepared by the direct reaction between powders of iron and sulfur at high temperature in a sealed silica tube. As the raw material of iron, the electrolytic iron was ground by a ball-mill to fine powder of 150 mesh, and then reduced by hydrogen stream at 800°C for 24 hours or more. The pure iron powder obtained by this method contained impurities less than 0.01% and was reserved in a evacuated vessel to prevent oxidation. The purification of sulfur was performed by vacuum distillations. After two times of successive repeating of vacuum distillations, the sulfur contained the impurities far less than 0.01%.

Powders of about 10 grs. of pure iron and the corresponding weight of sulfur above mentioned were weighed accurately by a micro-chemical balance and mixed in a silica tube of 2 cm diameter, 30 cm in length, with

---

* This investigation was supported in part by the Grant-in-Aid of Fundamental Scientific Research of Ministry of Education.

one end sealed. Then the silica tube was evacuated by a Hickman diffusion pump for 24 hours and the other end was sealed off by oxi-hydrogen flame. This sealed silica tube was put into a furnace to perform the reaction. The temperature of the furnace was raised at the rate of 100°C per hour up to 1000°C, and the sample was kept at this temperature for 24 hours, thereafter it was cooled slowly down to the room temperature with the same rate as in the case of raising. During the course of this heat treatment no breakdown of the tubes occurred. The specimens thus prepared are listed in Table I.

The compounds thus obtained were taken out from the silica tubes, then they were ground again in a mortar, and about 8 grs. of these substances were put into containers of telex glass for the measurements of specific heats, then evacuated by the diffusion pump for 24 hours and then sealed off.

§ 3. Experimental Arrangement and Procedures

The apparatus used for measuring the heat capacity was an automatically recording adiabatic calorimeter, whose detailed description was reported in the former paper[4]. The rate of temperature raising of the samples in the course of measurement was approximately 0.25°C per minute. The temperature fluctuation caused by this servo-system was of the order of 10^{-2} degree and the maximum deviation of temperature between specimen and the thermal shield was less than one tenth degree.

§ 4. Experimental Results

By this method above mentioned an anomaly of specific heat was found in FeS_x at the temperature range of β-transformation above mentioned and curves of anomalous specific heat versus temperature in such cases are shown in Fig. 1. As the figure shows these peaks take typical Λ-shape. The temperatures corresponding to the maxima of these curves are 315°C in all cases and this value accords with the temperature of magnetic transformation obtained experimentally by Haraldsen.

Table I

x in FeS_x	1.00	1.01	1.02	1.03	1.04	1.05
y in $Fe_{1-y}S$	0.00	0.010	0.020	0.029	0.038	0.048
z in $Fe_{100-z}S_z$	50.00	50.29	50.43	50.74	50.98	51.22
x in FeS_x	1.07	1.09	1.10	1.11	1.12	
y in $Fe_{1-y}S$	0.065	0.082	0.091	0.100	0.107	
z in $Fe_{100-z}S_z$	51.69	52.15	52.38	52.61	52.83	

Table of the prepared specimens of iron sulfides with various sulfur contents. x and z were used by Haraldsen, on the other hand y represents the concentration of holes among iron sites, hence $2y$ represents that of Fe^{3+} if these substances are assumed to be purely ionic crystals.

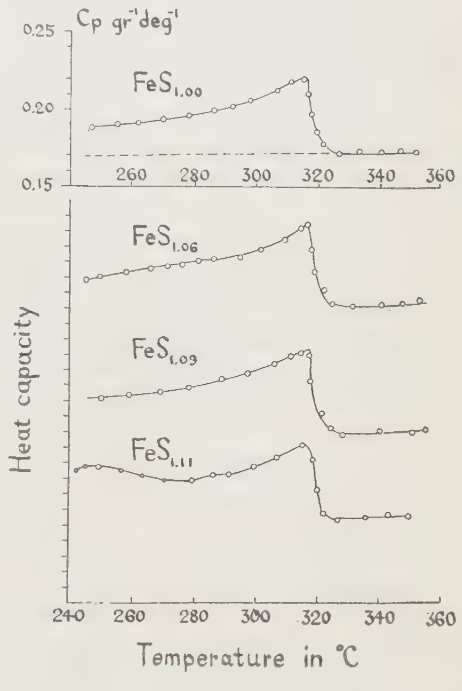

Fig. 1. The curves of specific heat vs. temperature at β-transformation of FeS_x for various sulfur contents x.

Here it should be noted that the behaviours of excess heat capacity for the compounds with various sulfur contents are the same with each other. The values of excess specific heat at T_β of the samples with various sulfur contents are also nearly equal with each other and are 0.05 cal gr.$^{-1}$ deg.$^{-1}$ in all cases. The estimation of anomalous heat absorption ΔQ_β at β-transformation is comparatively difficult, because the true range of β-transformation and the base line in the curve of anomalous specific heat are not decided certainly for the present cases. Then it may be estimated under the assumptions that the β-transformation already starts from low temperature and the base line of the specific heat is assumed to be the dotted curve in Fig. 1. The dotted curve is a extrapolation of the flat part at high temperature side in the curve of specific heat versus temperature. The estimated value of ΔQ_β by such a method is roughly 600 cal mol^{-1}. Since we neglect here the effect of short range order, the real value of ΔQ_β may be larger than that obtained.

§ 5. Discussion

As mentioned in the introduction, the origin of β-transformation in this substance is considered to be the order-disorder transformation of ferrimagnetic spin arrangement. In order to confirm this mechanism, the theoretically estimated values of ΔQ_β and ΔC_β based on this model must be compared with that of experimental ones. Since the true arrangement of the spins below T_β is not known, the theoretical calculation is performed using Bragg-Williams' approximation under some assumptions.

If the all magnetic ions in FeS_x have the same spin, S, the expression of anomalous heat absorption and the jump of specific heat ΔC_β at the Néel temperature T_β can be obtained from the theory proposed by Néel$^{5)}$ and Smart, et. al.$^{6)}$. The final formulas are given by

$$\Delta Q_\beta = \frac{3}{10}\,\frac{S^2+(1+S)^2}{(1+S)^2}\,T_\beta \Delta C_\beta\,, \qquad (1)$$

$$\Delta C_\beta = \frac{5S(S+1)}{S^2+(1+S)^2}\,R\,, \qquad (2)$$

where R is gas constant. If S is equal to 2, the theoretically estimated value of ΔC_β is 0.052 cal. gr.$^{-1}$ deg.$^{-1}$. This value of ΔC_β agrees very well with the experimental one 0.05 cal gr.$^{-1}$ deg.$^{-1}$.

Now we shall discuss the value of ΔQ_β using the formula (1) with the experimental values of ΔC_β and T_β under the assumption $S=2$. We get semi-empirically estimated value of ΔQ_β, the value obtained is 1,200 cal mol^{-1} which is different from that obtained in the previous section. Since the formulas cited above are based on Bragg-Williams' approximation then the present estimation may be certainly larger, about thirty or fourty per cent, namely the true value of ΔQ_β may be smaller about few hundreds than that calculated here. On the other hand, since we neglect the effect of short range order for the estimation of ΔQ_β experimentally as mentioned in the previous section, the value 600 cal mol^{-1} is surely smaller than the real one. Because, if the effect of short range order is taken into account, we should use a somewhat lower base line which differs from that in the former case of estimation. By this modification, few hundreds cal mol^{-1} should be added to the value of ΔQ_β mentioned above. Then we may conclude that there is no essential discrepancy between the theoretical and experimental values.

Such a ferrimagnetic nature of FeS_x mentioned above was also supported by another experiments; namely it was also known that hyperbolic inverse susceptibility as a function of temperature was found by Benoit$^{7)}$. Very recently, Sidhu$^{8)}$ and his collaborator found by the experimental studies of the neutron diffraction pattern that the spins in natural pyrrhotite are arranged antiferromagnetically.

References

1) T. Hirone and N. Tsuya: Phys. Rev. **83** (1951) 1063.

2) H. Haraldsen: Z. Anorg. u. Allg. Chem. **231** (1937) 78; **246** (1941) 169, 195.

3) K. Yoshida: Busseiron Kenkyu **35** (1951) 83 (in Japanese); Prog. Theoret. Phys. **6** (1951) 356; Physica **17** (1951) 794.

4) T. Hirone, S. Maeda, I. Tsubokawa and N. Tsuya: Sci. Rep. RITU, **A 5** (1953) 513.

5) L. Néel: Ann. Phys. **3** (1948) 137.

6) L. N. Howard and J. S. Smart: Phys. Rev. **90** (1953) 374; **91** (1953) 17.

7) R. Benoit: Compt. Rend. **234** (1952) 2175.

8) S. Sidhu and O. Meneghetti: Phys. Rev. **91** (1953) 435.

Journal of the Physical Society of Japan Vol. 9, No. 4, July—August, 1954

Thermal Analysis of Iron Sulfides at the Temperature Range of α-transformation*

By Tokutarō Hirone, Seijirō Maeda
The Research Institute for Iron, Steel and Other Metals, Tōhoku University, Sendai
and Noboru Tsuya
The Research Institute of Electrical Comunication Tōhoku University, Sendai

(Received February 1, 1954)

The specific heat of iron sulfides near stoichiometric composition from $FeS_{1.00}$ to $FeS_{1.07}$ at the temperature range of α-transformation was measured. It was found that the curves of specific heat versus temperature had a comparatively sharp Λ-shaped maximum. Both the temperature for such a maximum and the peak values of specific heat decreased with the increase of sulfur contents. It was also found that the heat absorption due to this transition also decreased with the increase of excess sulfur, its value being about 550 cal mol^{-1} at the stoichiometric compound, and vanishing at the composition $FeS_{1.07}$. The several possible models for the mechanism of this transition are discussed taking into account the above experimental results.

§ 1. Introduction

For the iron sulfides, near stoichiometric in composition, several transformations have been found above room temperature, one of which is called α-transformation. In connection with the α-transformation of iron sulfides, Haraldsen and others made some magnetic and Röntgenographic investigations[1][2]. The results are briefly summarized below: i) The susceptibility versus temperature curve in FeS_x shows a "knick" at a temperature T_α when the concentration x of sulfur in FeS_x lies between 1.00 and 1.08, ii) this transformation temperature T_α decreases with the increase of sulfur contents x, iii) in the temperature range below T_α a super-lattice structure is found which has the unit cell of 6 times $(\sqrt{3}a\times\sqrt{3}a\times 2c)$ as large as the original one, where a and c being the lattice constants in the hexagonal lattice, and this super-lattice structure is not found if the sulfur contents exceed 1.06; iv) the lattice constant c of $FeS_{1.00}$ contracts approximately 1 per cent during heating through T_α whereas almost no effect is found on a. Such an anomalous contraction of c due to the temperature change also decreases with the increases of sulfur contents; v) a definite range of temperature is required to finish such contraction in the lattice parameter c.

Several discussions on the origin of this transformation have been proposed, but owing to the lack of the experimental data, mainly concerning to the change of internal energy during the transformation, the validity of such considerations above mentioned is not yet completely accepted. Thus the measurements of specific heat change during the tramsformation for a wide range of sulfur contents are undertaken by the present authors, the results of which are described in the following pages.

§ 2. Experimental Procedure and the Specimen

The experimental apparatus, procedure[3] and preparing method[4] of specimens are the same with those mentioned in the former papers then the description of them are omitted here.

§ 3. Experimental Result

The experimental results on the change of heat capacities due to the temperature change for iron sulfides with various sulfur contents x are shown in Fig. 1. From this figure Λ-shaped peaks of the specific heat are found at the temperature range from 100°C to 135°C;

---

* This investigation was supported in part by the Grant-in-Aid of Fundamental Scientific Research of Ministry of Education.

the temperature of maximum specific heat will be denoted by T_α in the following pages. It is found further that both the peak of specific heat and the temperature T_α decrease with the increase of sulfur content x. The value of T_α agrees exactly with that of angular point on the susceptibility versus temperature curve obtained by Haraldsen. Fig. 2 also shows the temperature range of transition. This range corresponds just to the temperature range which is required for the change of lattice parameter c which is found by the X-ray studies.

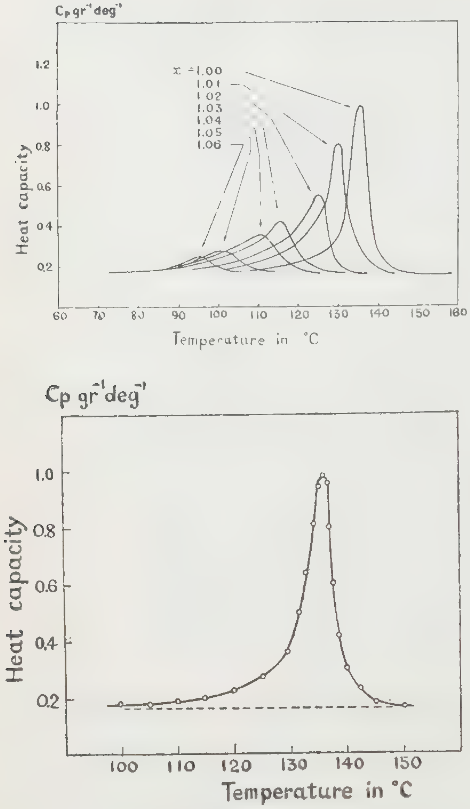

Fig. 1. Heat capacity vs. temperature curves in iron sulfides FeS_x with various sulfur contents x. In the figure the members stand for the sulfur contents x.

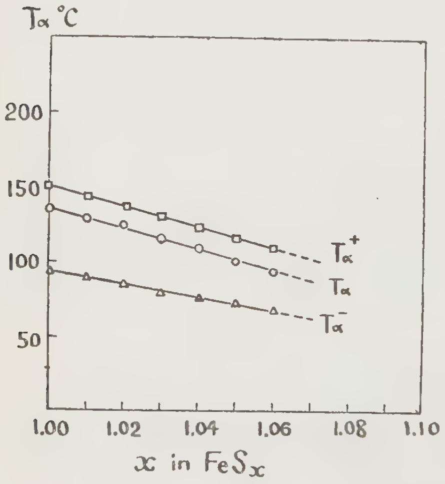

Fig. 2. α-transformation temperature T_α as a function of sulfur content x. In this figure T^- and T^+ are the temperatures corresponding to the initial and final point of α-transformation in FeS_x, namely the temperature range of α-transformation is considered as that from T^- to T^+.

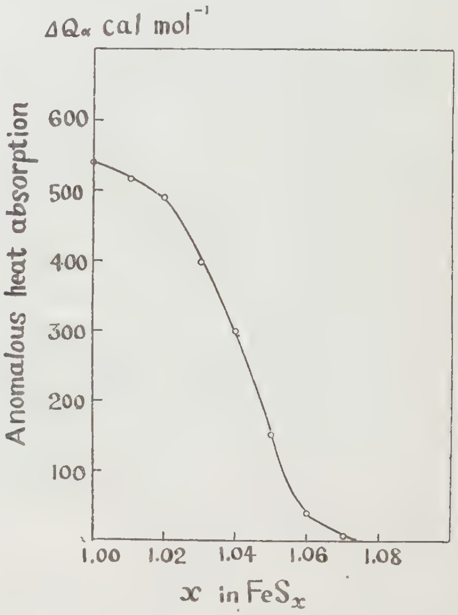

Fig. 3. Change of anomalous heat absorption ΔQ_α due to α-transformation as a function of sulfur content x in iron sulfides FeS_x.

Now if we assume that the specific heat due to the thermal vibration of the crystal lattice changes along the dotted lines with the rise of temperature as shown in Fig. 1a, we can estimate the absorption of heat ΔQ_α for this α-transformation. The result is plotted in Fig. 3. As it shows, such an anomalous heat absorption ΔQ_α takes a largest value (550 cal per mol) at the stoichiometric composition and decreases with the increase of sulfur content x and finally disappeares at $x = 1.06$. This vanishing concentration x of ΔQ_α just corresponds to the extinction concentration x of super-lattice lines in the Debye-Sherrer photograph obtained by Haraldsen¹⁾ and others²⁾.

§ 4. Discussions

For the origin of α-transformation, the following several kinds of mechanism have been considered. It has once been proposed an occurrence of the change of the nature of bonding⁵⁾, a transition from ionic to covalent binding between the base planes during this transformation. If such a transition would occur, the changes of other physical properties including the crystal structure at the transition point should be expected, but such changes could not be observed actually. We shall try to discuss other possibilities in the following pages.

1) Firstly the transformation may be supposed to be caused by the order-disorder transformation of the empty lattice points on the iron lattice sites. In this case the number of empty lattice points must be equal to the excess sulfur atoms. If such a mechanism were realized, the anomalous heat ΔQ_α and the transformation temperature T_α would increase monotonously with the excess sulfur contents. However as shown in Fig. 3, the anomalous heat ΔQ_α is greatest at stoichiometric composition and decreases with increasing sulfur content. This thermal behaviour contradicts clearly to the above postulation.

2) Secondly, if this tramsformation were attributed mainly to the change of sign of anisotropy energy similar to the case of transformation in α-$Fe_2O_3$⁶⁾ at slightly below the room temperature, the value of ΔQ_α should be small. Clearly, the present experimental facts do not support this mechanism.

3) Thirdly, we consider a magnetic structure transition⁷⁾ between two types of antiferromagnetic spin arrangements. For example, one arrangement is mentioned in the former report⁸⁾ and the other is something like an antiferromagnetic arrangement of spins in each base planes. In this case we may expect that the value ΔQ_α should be far smaller than that of ΔQ_β reported in the previous paper⁸⁾. Since this transition must be a transition of first order, the ordinary antiferromagnetic Curie point would be far higher than that observed. But from the experimental fact the value of ΔQ_α does not seem to be smaller than ΔQ_β, or at least, it is the same order in magnitude with ΔQ_β. Hence the experimental evidence conflicts with this model. Also the existence of super-structure above mentioned suggests that this mechanism is not the case, because in this magnetic structure transition, such a strong effect upon the X-ray photograph can not be expected.

4) Fourthly one can propose a different type⁹⁾ of ordering of holes in sulfur sites as well as in iron sites¹⁰⁾. Such a structure is expressed by $Fe_{11}LS_{11}L'$ in the case of $FeS_{1.00}$ where L and L' correspond to the holes in the definite lattice sites of iron and sulfur respectively. Since the observed volume of unit cell of the super-structure is 6 times as large as the original one, 12 molecules can be contained in a unit cell of super-lattice, hence we consider the above mentioned super structures as the lack of one molecule from 12 molecules in the unit cell. Here it may be supposed that if the sulfur content increases, the additional sulfur atoms find their sites at the holes of sulfur sites. If so, we can expect that the largest heat absorption ΔQ_α and the highest transformation temperature T_α are observed in the case of stoichiometic $FeS_{1.00}$ and are decreased by further addition of excess sulfur. By simple consideration based upon this model, it is further concluded that sulfur is soluble in the crystal lattice till $x=12/11=1.091$. Actually we can recognize the α-angular point on the susceptibility versus temperature curve in $FeS_{1.09}$. The anomaly in susceptibility at T_α may be attributed to the change of anisotropy constant owing to the contraction of lattice parameter c during the heating through T_α. Then we must consider the possibility of such ordered arrangements of holes in both ionic sites of iron and sulfur. We suppose, in this case, there are many holes in both iron and sulfur sites at high temperature and by cooling they are arranged at first in ordered form at T_α and by further cooling this ordered state of holes should be frozen, because the decrease of mobility of ions due to the decrease of temperature. So the crystal may be in the state of super structure of holes even at low temperatures.

However from this model the anomalous contraction of lattice constant c during the heating through T_α and the decrease of density with increasing excess sulfar content may be somewhat difficult to understood by the simple theoretical point of view.

Finally, it is concluded that all the properties of FeS_x in the temperature range of α-transformation might not be able to be explained completely by these models mentioned above so that true origin of α-transformation remains somewhat mysterious. However it seems that the mechanism of magnetic structure transition⁷⁾ including a slight displacement of some lattice points may describe the present transformation consistently.

The authors wish to express their thanks to Mr. Kimiyoshi Gotô, student of Physics Department of Tôhoku University, who performed in part the present measurements.

References

1) H. Haraldsen u. W. Klemm: Z. Anorg. u. Allg. Chem. **220** (1934) 138.
H. Häraldsen: Z. Anorg. u. Allg. Chem. **231** (1937) 78.
H. Haraldsen u. A. Neuber: Z. Anorg. u. Allg. Chem. **234** (1937) 337.
H. Haraldsen: Z. Anorg. u. Allg. **246** (1941) 169, 195.
2) R. Juza u. W. Biltz: Z. Anog. u. Allg. Chem. **205** (1932) 273.
G. Hägg u. I. Sucksdorff: Z. f. Phys. Chem. **22** (1933) 444.
R. Ueda, T. Ichinokawa and T. Mitsui: Busseiron Kenkyu **33** (1950) 55 (in Japanese).
3) T. Hirone, S. Maeda, I. Tsubokawa and N. Tsuya: Sci. Rep. RITU. **A 5** (1953) 513.
4) T. Hirone, S. Maeda, S. Chiba and N. Tsuya: J. Phys. Soc. Japan **9** (1954) 500.
5) H. Haraldsen: Z. f. Electrochem. **45** (1939) 370.
6) F. J. Morin: Phys. Rev. **78** (1950) 819; **83** (1951) 1256.
C. G. Shull and J. S. Smart: Phys. Rev. **76** (1951) 1256.
C. G. Shull, W. A. Strauser and E. O. Wollan: Phys. Rev. **83** (1951) 333.
7) J. S. Smart: Phys. Rev. **90** (1953) 55; Rev. Mod. Phys. **25** (1953) 326.
8) T. Hirone, S. Maeda, S. Chiba and N. Tsuy: J. Phys. Soc. Japan **9** (1954) 500.
9) T. Hirone and N. Tsuya: Phys. Rev. **83** (1951) 1063.
10) F. Bertaut: Compt. Rend. **234** (1952) 1295; J. de Phys. **13** (1952) 372; Acta Cryst. **6** (1953) 557.
R. Benoit: Compt. Rend. **234** (1952) 2175.
L. Néel: Rev. Mod. Phys. **25** (1953) 58.

JOURNAL OF THE PHYSICAL SOCIETY OF JAPAN Vol. 9, No. 4, JULY—AUGUST, 1954

The Magnetostriction Constants of Silicon Steel (I)

By Hideo TAKAKI and Yoji NAKAMURA

Faculty of Science, University of Kyoto

(Received March 17, 1954)

By use of long single crystal rods of 0.7% and 1.8% silicon steel, having various crystallographic orientations, prepared by strain-anneal method magnetization and magnetostriction were measured at room temperature by usual ballistic and optical methods respectively. It was found that in both materials Kaya's law with regard to the residual magnetization holds satisfactorily and on its basis their magnetostriction constants λ_{100} and λ_{111}, and also their crystal anisotropy constants K_1 were determined. Gradual decrease of these three constants with silicon content was confirmed.

§ 1. Introduction

Because of the close relation with the mechanism of magnetization of ferromagnetic materials, phenomena associated with magnetostriction have been investigated, both experimentally and theoretically, by many workers. By use of the array of magnetic dipole moments, Akulov1) and Becker2) have carried out classical calculation and reached a conclusion that the magnetostriction, thus obtained, is only one tenth of the experimental value, observed at iron crystals. Calculations conducted by Van Vleck,3) Vonsovsky4) and Katayama5) have shown that introduction of spin-orbit coupling will be able to account the crystal anisotropy of magnetization and magnetostriction, as well as their magnitudes to some extent.

On the other hand, so far as we know, only few precise measurements of the magnetostriction had been conducted, on account of the lack of perfect crystals of sufficient length. One of the authers has done a considerable amount of work on the change of magnetostriction constants of iron with temperature6) and stress,7) imposed upon them. The present work was carried out to examine the effect of other elements, which were added to iron; especially the effect of silicon on the magnetostriction canstants. Some early measurements by Heaps8) on silicon steel show that the magnetostriction depends markedly on crystal orientations. Shturkin9) measured the magnetostriction of single crystals of 3.5% silicon steel. Recently Carr and Smoluchowski10) published a paper on the magnetostriction of silicon steel from 2.5% to 8%, but the region within 0% to 2.5% has not been measured.

§ 2. Preparation of Specimens

Electrolytic iron, and metallic silicon were melted together in a crucible by a high frequency melting vacuum furnace.* In addition to these elements 0.5% calcium silicide was used as deoxidizer. Melted silicon steel ingots were cooled in vacuum, then forged and drawn until their diameter decreased to about 2 mm.

The travelling furnace method11) developed by Dr. T. Fujiwara was used to produce single crystal specimens. The specimens were annealed in the atomosphere of dry hydrogen at 850°C for 24 hrs in order to be decarbonized and also to be controlled to the adequate grain size. Then after a few percent elongation was added, the specimens were annealed in the travelling furnace, the maximum temperature of which is just below their A_3 points, and the travelling velocity of which is about 5 mm/hr. By this process, single crystal devloped from one end to the other and occupied the whole specimen.

In case of 0.7% silicon steel, according to Fujiwara's device, after a nucleus of crystal, about 2 cm in length, developed from one end of specimen—we call this part "the nucleus of single crystal"—the specimen was taken out from the furnace for the determination of the crystallographic orientation of the nucleus by the light-figure method12) developed by Dr. M. Yamamoto and others. After

---

* The high frequency vacuum melting furnace was employed at Tohoku Kinzoku Kogyo Kaisha, Ltd., through the kindness of Dr. T. Yamamoto.

Table I.

% Si	Sample number	Length (mm)	Demagnetizing factor	Direction cosines of rod-axis			$\left(\frac{I_r}{I_s}\right)_{\text{Obs.}}$	$\left(\frac{\delta l}{l}\right)_{\text{Sat.-Rem. Obs.}} \times 10^6$
				l	m	n		
0.7	1	144.3	0.00708	0.306	0.499	0.813	0.606	−10.06
0.7	2	142.4	0.00780	0.365	0.540	0.759	0.589	−12.27
0.7	3	140.6	0.00751	0.207	0.479	0.853	0.635	− 7.06
0.7	4	288.4	0.00218	0.497	0.527	0.690	0.571	−13.96
0.7	5	149.4	0.00728	0.031	0.310	0.950	0.751	0.00
0.7	6	212.2	0.00384	0.004	0.039	0.999	0.941	1.22
0.7	7	188.9	0.00479	0.183	0.206	0.961	0.730	2.43
0.7	8	134.0	0.00866	0.534	0.579	0.617	0.568	−14.86
0.7	9	198.6	0.00428	0.048	0.700	0.712	0.669	−10.77
1.8	1	223.5	0.00390	0.008	0.523	0.853	0.687	−45.90
1.8	2	166.0	0.00668	0.173	0.537	0.826	0.641	−45.30
1.8	3	147.1	0.00828	0.087	0.358	0.930	0.704	2.00
1.8	4	142.0	0.00886	0.026	0.442	0.897	0.693	−19.10
1.8	5	135.5	0.00967	0.243	0.367	0.898	0.642	−10.50
1.8	6	121.9	0.01144	0.181	0.387	0.906	0.643	−15.00
1.8	7	118.7	0.01213	0.151	0.494	0.856	0.639	−33.50
1.8	8	115.8	0.01239	0.049	0.406	0.913	0.696	− 9.00
1.8	9	113.4	0.01326	0.047	0.339	0.940	0.701	5.00
1.8	10	252.6	0.00311	0.065	0.253	0.956	0.768	19.80

Table II.

Charged silicon contents in %	Si (%)	C (%)	S (%)	Mn	P
1.0	0.73	0.043	0.001	trace	trace
2.0	1.79	0.008	0.001	trace	trace

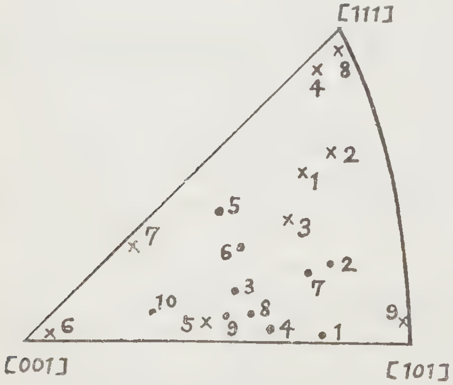

Fig. 1. Stereographic projection of the orientations of specimens.
×: 0.7% silicon •: 1.8% silicon.

bending the specimen so as to make its axis coincide with the desired crystallographic orientation annealing was further continued within the furnace travelling from the nucleus to the other end. Thus, repeating this process long single crystal rods with various crystallographic orientations were obtained. Unfortunately, because of the shortage of the specimens, we could not succeed to obtain the single crystals of 1.8% silicon steel with satisfactorily desired orientations. After being etched slightly by nitric acid solution, the crystallographic orientations of single crystals, thus obtained, were determined by the method mentioned above. The accuracy of orientation of single crystals is within ±1°. Fig. 1 shows the stereographic projection of the orientations of these rod-axes. The characteristic constans of the specimens are shown in Table I and their chemical analysis in Table II. These specimens were annealed in vacuum electric furnace for 2 hrs at 900°C for 0.7% silicon steel and at 950°C for 1.8% respectively, and then were slowly cooled in furnace up to 200°C, then rapidly cooled to room temperature by taking them out of the furnace.

§ 3. Experimental Results and Discussion

Fig. 2 and Fig. 3 show the magnetization *vs.* effecttive field for 0.7% and 1.8% silicon steel respectively measured by the ballistic method. The crystal anisotropy energy is given by the following relation:

$$E_k = K_0 + K_1(m^2n^2 + n^2l^2 + l^2m^2) + K_2 l^2m^2n^2, \quad (1)$$

where K_0, K_1 and K_2 are crystal anisotropy constants and l, m and n are the direction cosines of the rod axis with respect to the three cubic axes.

By measuring the area enclosed between the ordinate and the magnetization curves,

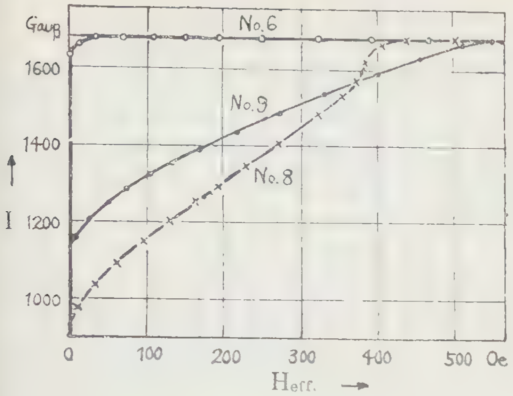

Fig. 2. Magnetization curves observed on single crystals of 0.7% silicon steel with various crystallographic orientations.

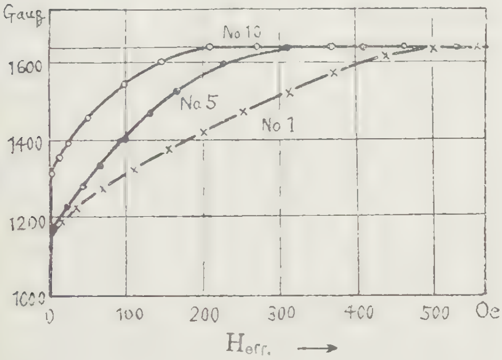

Fig. 3. Magnetization curves observed on single crystals of 1.8% silicon steels with various crystallographic orientations.

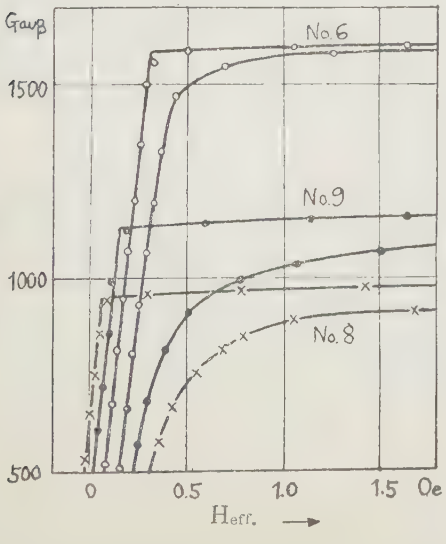

Fig. 4. Hysteresis curves of 0.7% silicon steel single crystals.

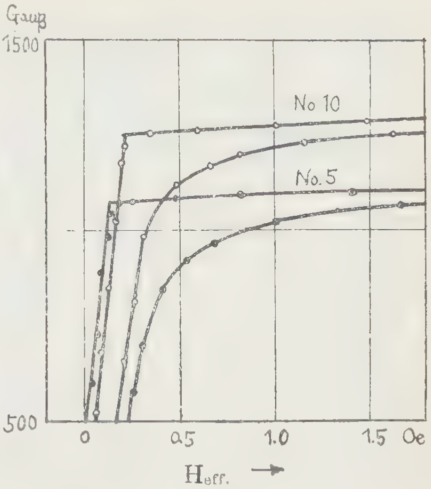

Fig. 5. Hysteresis curves of 1.8% silicon steel single crystals.

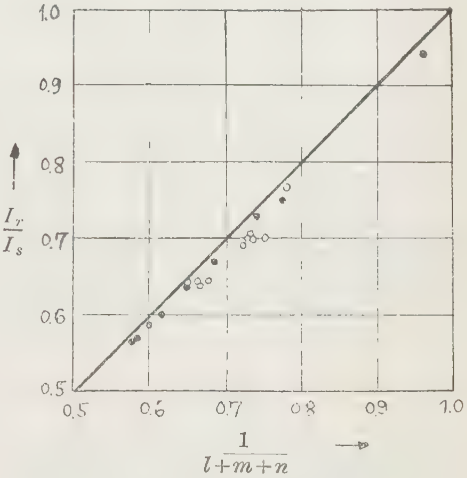

Fig. 6. I_r/I_s *vs.* $1/l+m+n$.
•: 0.7% silicon ∘: 1.8% silicon.

these constants can be determined. In case of 0.7% silicon steel, singl crystals, of which rod axes are quite near to [001] and [111], as shown in Fig. 1 or Table I, allowed us to evaluate easily the order of K_0 and K_2:

$$K_0 = 3\times10^2\ \text{ergs/cm}^3\ ,$$
$$K_2 = 1.0\times10^5\ \text{ergs/cm}^3\ .$$

In case of 1.8% silicon, because of lack of single crystal with the rod axis near any principal axis (see also Fig. 1 or Table I), we were in position only to determine K_1, assuming $K_0=0$ and $K_2=1.0\times10^5$ ergs/cm³. The obtained values of K_1 are

$$K_1 = 4.27\times10^5\ \text{ergs/cm}^3$$
for 0.7% silicon steel,

$$K_1 = 4.01 \times 10^5 \text{ ergs/cm}^3$$
$$\text{for } 1.8\% \text{ silicon steel.}$$

Next examination was made whether Kaya's law[13)] at the remanent magnetization holds or not. It states that magnetization I_r at the remanent point is given by the following relation:

$$\frac{I_r}{I_s} = \frac{1}{l+m+n}, \tag{2}$$

where I_s is the saturation magnetization. In this case the remanent magnetization is defined as the intensity of magnetization at the sharp corner near the point $H_{\text{eff.}}=0$, as shown in Fig. 4 and Fig. 5. As the calculated effective field corresponding to the remanent point shifts largely by the slight change of the demagnetizing factor of the specimen, the absolute value of the effective field itself has no important meaning. The observed values, $(I_r/I_s)_{\text{obs.}}$, are tabulated in Table I and the relation between $(I_r/I_s)_{\text{obs.}}$ and $1/l+m+n$ is shown in Fig. 6. As is seen in the figure, Kaya's law holds here satisfactorily. A closer inspection shows, that the experimental values are slightly lower than the theoretical one, about 1.5% for 0.7% silicon, about 3.0% for 1.8% in their mean values. These discrepancies can be ascribed to the disturbances of the domain distribution due to the unexpected local internal stress within the specimens.

The coercive forces of these samples are smaller than that of iron, and for 0.7% silicon they are from 0.028 Oe to 0.118 Oe depending upon their crystallographic orientations, and for 1.8% from 0.040 Oe to 0.118 Oe. Discussions on the coercive force will not be given in this paper.

Magnetostriction was measured at room temperature by the ordinary mechano-optical method. Fig. 7 and Fig. 8 show the change of length along the descending hysteresis loop for 0.7% silicon and 1.8% silicon respectively. As Kaya's law at the remanent magnetization holds, we can adopt this point as one of the standard point, at which the distribution of magnetic domains within the specimen is known.[13)] On the other hand, at saturation magnetization the distribution of magnetic domains is, of course, uniquely determined. So the difference of the length of the specimen between saturation and remanence can be expressed:

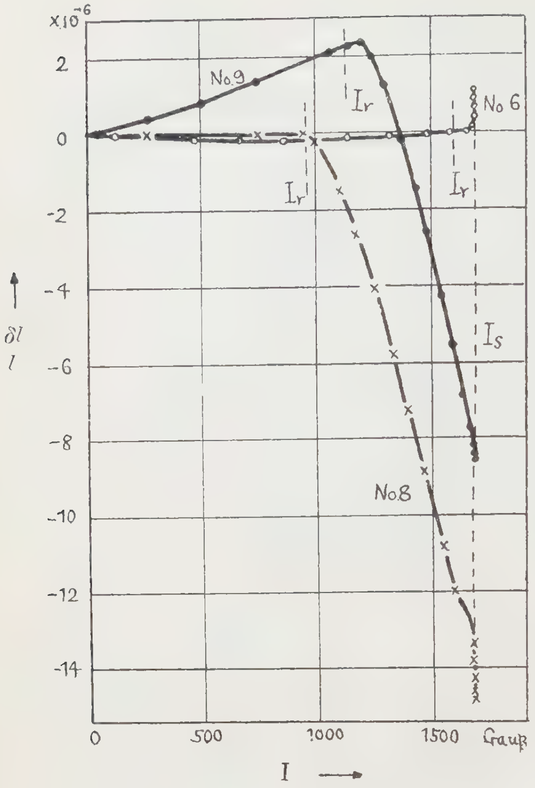

Fig. 7. The descending hysteresis curves of magnetostriction observed on 0.7% silicon steel single crystals with various crystallographic orientations.

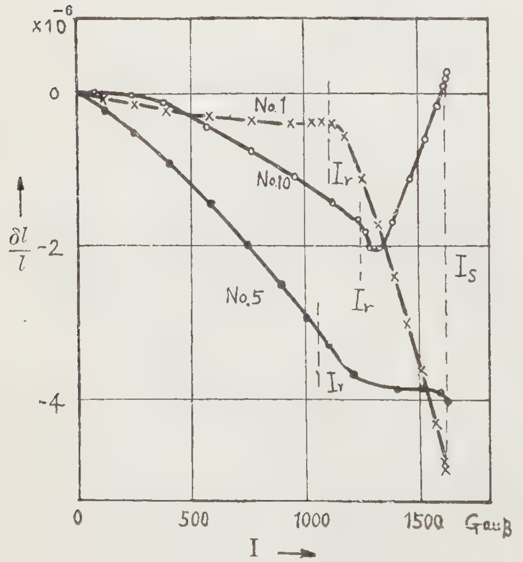

Fig. 8. The descending hystrersis curves of magnetostriction observed on 1.8% silicon steel single crystals with various crystallographic orientations.

$$\left(\frac{\delta l}{l}\right)_{\text{Sat.-Rem.}}=\left\{\frac{3}{2}\left(1-\frac{l^3+m^3+n^3}{l+m+n}\right)\right.$$
$$\left.-3(m^2n^2+n^2l^2+l^2m^2)\right\}\lambda_{100}$$
$$+3(m^2n^2+n^2l^2+l^2m^2)\lambda_{111}\,. \qquad (3)$$

Here the magnetostriction constants λ_{100} and λ_{111} are defined as the relative change in length during magnetization from the demagnetized state to saturation, when the former is assumed to have uniform distribution of domains in six easy axes.

Using the relation (3) and the observed values, $\left(\frac{\delta l}{l}\right)_{\text{Sat.-Rem. Obs.}}$, tabulated in Table I, we can determine λ_{100} and λ_{111} for 0.7% and 1.8%; they are:

% Si	$\lambda_{100}\times 10^6$	$\lambda_{111}\times 10^6$
0.7	18.82 ± 0.82	$-(15.41\pm0.17)$
1.8	16.05 ± 0.58	$-(9.42\pm0.23)$

Fig. 9 represents how the three constants λ_{100}, λ_{111} and K_1 change with silicon content. The constants λ_{100}, λ_{111} and K_1 for pure iron are taken from our previous paper¹⁴⁾; ($\lambda_{100}=25.6\times10^{-6}$, $\lambda_{111}=-18.9\times10^{-6}$ and $K_1=4.45\times10^5$ ergs/cm³). The decrease of λ_{111} and K_1 are proportional to silicon content but the decrease of λ_{100} seems to be not so, and to be rapid at low silicon content.

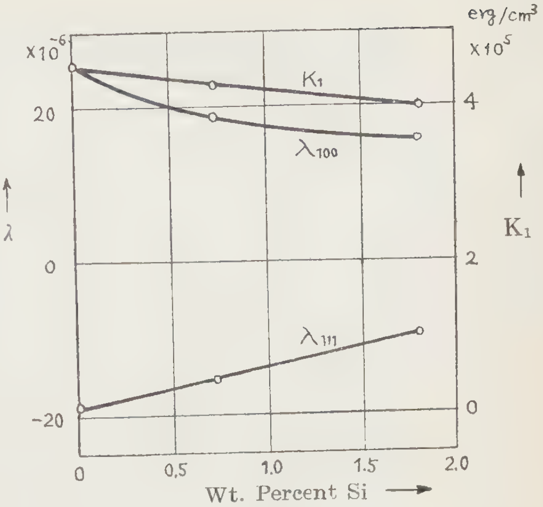

Fig. 9. Dependence of the three constants λ_{100}, λ_{111} and K₁ on the silicon content.

In case of 1.8% silicon steel, measurements were made both on magnetization and magnetostriction for the polycrystalline specimen. Under the assumption of uniform distribution of grain orientations, theoretical remanent magnetization for the polycrystalline specimen will be given by taking an average of (2):

$$\bar{I}_r=0.672\ I_s\,.$$

The observed value of remanent magnetization is just $0.672I_s$. Such an excellent agreement was also found in case of pure iron.¹³⁾ Calculation has been made for the magnetostriction of polycrystalline material:

$$\overline{\left(\frac{\delta l}{l}\right)}_{\text{Sat.-Rem.}}=\left\{\frac{3}{2}(1-0.489)-3\times\frac{1}{5}\right\}\lambda_{100}$$
$$+3\times\frac{1}{5}\lambda_{111}=-2.97\times10^{-6}\,.$$

The observed value is -1.76×10^{-6}. On the other hand, the crystal anisotropy of polycrystalline material is expressed:

$$\overline{E_k}=K_0+\frac{1}{5}K_1+\frac{1}{105}K_2=0.80\times10^5\ \text{ergs/cm}^3\,,$$

while observed value is only 0.67×10^5 ergs/cm³.

In conclusion the authors wish to express their sincere thanks to the late Dr. K. Honda, and professor S. Kaya of the University of Tokyo for his kind interest and encouragement throughout the work. The expense of this research has been partly defrayed by the Scientific Research Expenditure of the Educational Ministry.

References

1) N. S. Akulov: ZS. f. Phys. **52** (1928) 389.
2) R. Becker: ZS. f. Phys. **62** (1930) 253.
3) J. H. Van Vleck: Phys. Rev. **52** (1937) 1178.
4) S. V. Vonsovsky: J. Phys. (USSR) **3** (1940) 83.
5) T. Katayama: Sci. Rep. RITU, A **3** (1951) 341.
6) H. Takaki: ZS. f. Phys. **105** (1937) 92.
7) H. Takaki: Proc. Phys-Math. Soc. Japan **24** (1942) 875.
8) C. W. Heaps: Phys. Rev. **22** (1923) 649.
9) D. A. Shturkin: Compt. Rend. Acad. Sci. (USSR) **58** (1947) 581.
10) W. J. Carr and R. Smoluchowski: Phys. Rev. **83** (1951) 1236.
11) T. Fujiwara: J. Sci. Hiroshima Univ. **9** (1939) 227.
12) M. Yamamoto: Sci. Rep. Tohoku Univ. **29** (1940) 113 etc.
13) S. Kaya: ZS. f. Phys. **84** (1933) 705.
14) S. Kaya and H. Takaki: Sci. Rep. Tohoku Univ. (Honda) (1936) 314.

JOURNAL OF THE PHYSICAL SOCIETY OF JAPAN Vol. 9, No. 4, JULY—AUGUST, 1954

Study on the Crystallization Process of Polished Layers of Metals by Electron Diffraction and Microscopy*

By Kōzō NONAKA

Government Industrial Research Institute, Nagoya,
Nishishiga-chō, Kita-ku, Nagoya

and Kazutake KOHRA

Department of Physics, College of General Education,
University of Tokyo, Komaba, Meguro-ku, Tokyo

(Received March 18, 1954)

Polished layers, the so-called Beilby layers, of Cu, Ni and Au are heated in vacuum or, for Ni, in hydrogen atmosphere, and the process of crystal growth is studied by electron diffraction and electron microscopy. The crystallization curves at various temperatures are also obtained. Above a certain temperature, for each metal, the crystallization goes on pretty rapidly: for instance, polished surfaces of Cu, Ni and Au crystallize in one hour at 60°C, 250°C and below 200°C, respectively. The crystallized surfaces consist mostly of Cu_2O and of NiO for Cu and Ni surfaces respectively, and exclusively of metallic Au for Au surface. They are accompanied by weak fibre structures, which are more remarkable by the heating at lower temperatures. When the polished specimen of Ni is heated in hydrogen atmosphere, the number of the nuclei of crystallization is smaller than for specimens heated in vacuum.

§ 1. Introduction

It is well known that when a metallic surface is lapped with fine-grained abrasives or a chamois leather, the surface acquires a mirror-like appearance and gives the characteristic electron diffraction pattern composed of two diffuse haloes. Such a surface has been usually called the "Beilby layer"[2]. A considerable number of works[3] have been done on the Beilby layer by electron diffraction.

Two views have been proposed for the structure of the layer; one is that the layer consists of *extremely small crystal grains* and the alternative one is that the layer is, as Beilby first considered, *in amorphous state* or *liquid-like state.* Also there have been a question whether the layer, for usual metals except Au, are oxidised or not when polished in the air.

More recently Raether and his coworker[4] investigated the layer in detail by electron diffraction and also by electron microscopy in some cases. They supported the view of *small crystal grain,* saying that the size of the crystal grain near the surface is very small, and is as small as a few unit cell in length in the Beilby layer**. Also, they considered that the Beilby layer produced under the usual condition of polishing in the air is oxidised near the surface, while metallic in the deeper place.

However, the background in the halo pattern due to the incoherent scattering and the waviness of the surface is so strong that it is very difficult to carry out an quantitative analysis of the pattern in order to settle down the above mentioned problems. Moreover, the meaning of the crystal grain becomes obscure when the grain is so small as thought by Raether and coworkers, because the boundary region between the neibouring crystal grains, which is heavily distorted and might be considered rather as amorphous, cannot be neglected; it is doubtful that such small grains have the same atomic arrangement as that of an ideal crystal.

---

* This work was carried out at the Institute of Applied Science, Faculty of Engineering, Kyushu University, when the authors were the members of it. Some parts of the study were published in the other place[1].

** Following Beilby and others the term "Beilby layer" will be used also in this paper, though it does not mean to accept the *liquid-like* view. We mean by it the polished layer of metal which has a mirror-like appearance and gives a diffraction pattern of diffuse haloes.

There seems, however, to be some other points to be attacked by electron diffraction as well as by electron microscopy, from which a deeper insight into the nature of the Beilby layer would be obtained. The change in the state of the layer with heat-treatment might be one of them. Only a few, not much systematic investigations[5)] have hitherto been carried out along this line. Therefore, in this paper the changes in the state of polished surfaces of Cu, Ni and Au are studied in detail under various conditions of heat-treatment, and some considerations on the nature of the Beilby layer are given.

§ 2. Experimental Apparatus and Procedure

a. Polishing of the specimens.

The specimens of Cu and Ni (electrolytic nickel) were cut from blocks, and the ones of Au were cast. Their shapes are shown in Fig. 1.

All the specimens were annealed sufficiently before polishing to get rid of the effect of working. The automatic polishing apparatus as shown in Fig. 2 was used: the specimen holder is rotated around the holizontal axis, and is balanced by a weight at another end. During the polishing, the whole area of the specimen was pushed onto the surface of the rotating disk with an uniform pressure 25∼30 g/cm^2, which is adjusted by a weight on the holder. The polishing speed was 50∼60 m/min. All the specimens were first polished with the emery papers in sequence of 0, 00, 000, 0000. Then the Cu and Au specimens were polished with Al_2O_3 on a cloth, and the Ni specimen with Cr_2O_3, until the surface became glossy like a mirror (for about 10∼30 min.). Finally they were polished with a chamois leather dropping pure benzol for about 2.5, 3 and 4 hours, respectively for the three kinds of metals. Some specimens of Ni were polished longer, for about twenty hours.

b. Heat-treatment in vacuum.

The specimen for which the existence of the Beilby layer was confirmed by electron diffraction was fixed on the Ni holder and inserted into the furnace (Fig. 3). It was moved to the central part of a quartz tube by a small magnet outside the tube, and then was heated. After the heat-treatment, the specimen was brought to a brass tube connected to the quartz tube to be quenched to room temperature, and was immediately examined by electron diffraction.

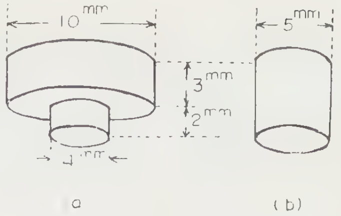

Fig. 1. Specimens. a) Cu and Ni b) Au.

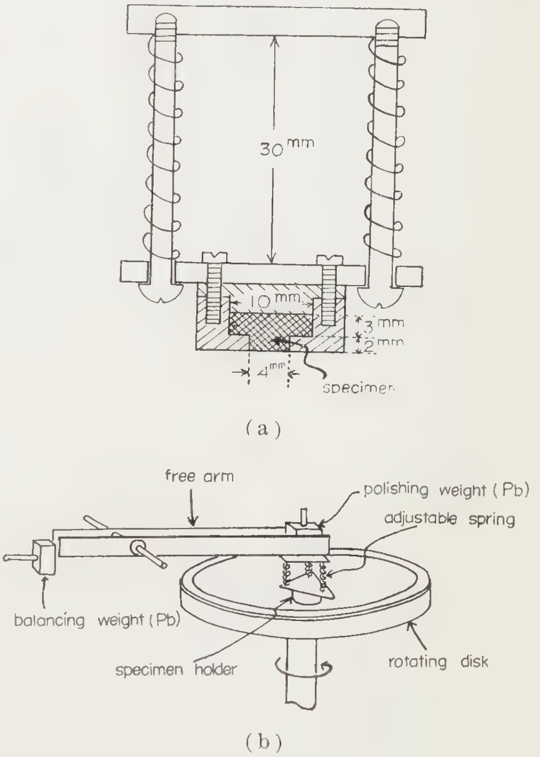

Fig. 2. (a) Specimen holder
(b) Polishing machine.

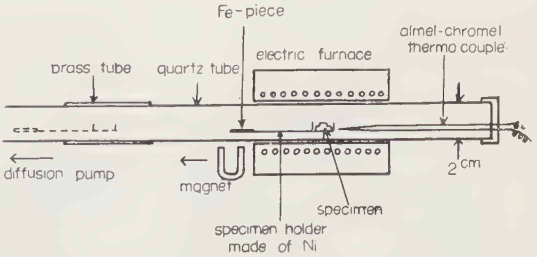

Fig. 3. Apparatus for heat-treatment in vacuum.

c. Heat-treatment of Ni *in the hydrogen atmosphere.*

Some specimens of Ni were also heat-treated in the hydrogen atmosphere. Activated hydrogen generated by electrolyzing the 30% aqueous solution of NaOH was passed through a solution of pyrogallol in NaOH and a P_2O_5 trap to absorb oxygen and water vapour. (Fig. 4). After the air was expelled from the furnace by filling it with water, the pure hydrogen gas of about one atmospheric pressure was introduced. The furnace was then pre-heated, and finally the Ni specimens was inserted in it.

§ 3. Experimental Results

The specimens polished and heat-treated were studied by electron diffraction and electron microscopy. In most cases the diffraction pattern was taken with the incident beam parallel or perpendicular to the direction of polishing. In electron microscopy, the method of methylmetaacryl alumina replica with shadowing by chromium at the angle of $\tan^{-1} 1/5$ was applied.

Table I.

Sabstances / Haloes	Cu	Ni	Au
1	4.0	3.86	4.1
2	2.26	2.23	2.25
3	1.25	1.26	1.24 (in Å)

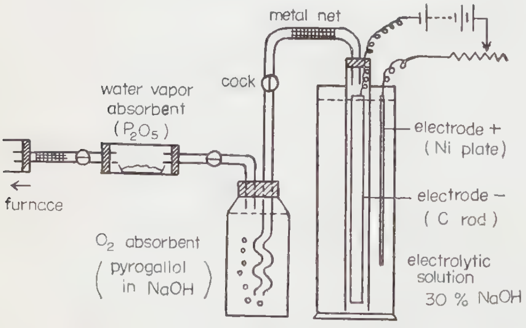
metal net
cock
water vapor absorbent (P_2O_5)
furnace
electrode + (Ni plate)
electrode − (C rod)
O_2 absorbent (pyrogallol in NaOH)
electrolytic solution 30 % NaOH

Fig. 4. Generator of hydrogen.

a. The diffraction pattern from the Beilby layer.

The diffraction patterns from Cu and Ni are shown in Photo 1 and 4. The spacings of haloes in these photographs are given in Table I. Besides the two haloes as usually observed (2 and 3 in the table), a low angle scattering was also observed which seemed to be bordered by another halo of a larger spacing (1 in the table). The spacings of the two outer haloes agree within error with those obtained by the previous workers. The new inner-most halo will be considered later.

b. Electron diffraction study of heat-treated specimens.

Cu) The specimens of Cu after polishing were kept at room temperature, 70° or 100°C in vacuum.

At room temperature, weak Cu_2O rings appeared after 20 hours. After 94 hours, the crystallization of the oxide was completed (Photo. 2) where the (200) and (220) rings showed arcing. The (111) rings also showed arcing after 142 hours.

At 100°C, several Cu_2O rings appeared after only 15 min., while the haloes still remained. After 30 min., about ten Cu_2O rings were observed, indicating that the crystal growth of the oxide proceeds to some degree (Photo. 3). After 1 hour, the crystallization of Cu_2O was almost completed although some diffuse rings still existed. After 6 hours, the diffuse rings disappeared and seven Cu_2O rings and some CuO rings were observed. The (111), (200) and (220) rings of Cu_2O showed slight arcing.

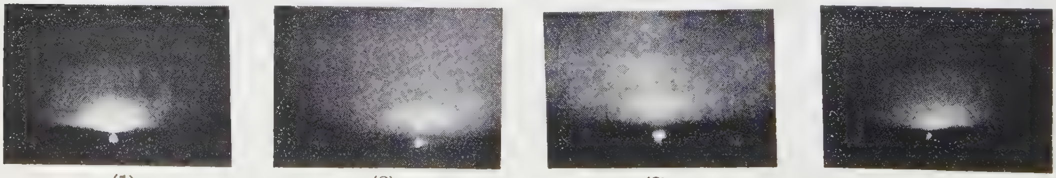

(1) (2) (3) (4)

Photo. 1–4. (1) Polished surface of Cu with chamois leather. (2) Cu surface kept at room temperature for 94 hours in vacuum after polishing. (Cu_2O.) (3) Cu surface heated at 100°C for 30 min. in vacuum after polishing. (Cu_2O.) (4) Polished surface of Ni with chamois leather.

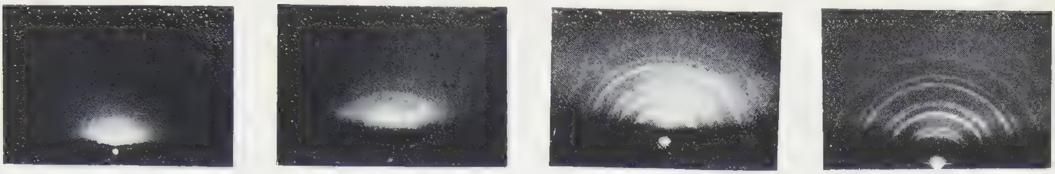

(5) (6) (7) (8)

Photo. 5–8. (5) Ni surface heated at 100°C for 6 hours in vacuum after polishing. (6) Ni surface heated at 300°C for 1 hour in vacuum after polishing. (NiO and Ni.) (7) Ni surface heated at 500°C for 10 hours in vacuum after polishing. (NiO.) (8) Ni surface heated at 700°C for 2 hours in vacuum after polishing. (NiO.)

Table II. Spacings of the diffraction rings from the crystallized surfaces of Ni

Heat-treatment in vacuum (10⁻⁴ mm Hg)				Heat-treatment in hydrogen atmosphere				X-ray diffraction data					
for 4 hrs at 300°C		for 16 hrs at 500°C		for 8 hrs at 300°C		for 4 hrs at 500°C		Ni			NiO		
d(Å)	Int.	d (Å)	Int.	d (Å)	Int.	d (Å)	Int.	(hkl)	d (Å)	Int.	(hkl)	d (Å)	Int.
						3.94	m						
2.90*	s												
						2.52*	m						
2.41*	m	2.39	s			2.40	m				(111)	2.40	s
		2.08*	s								(200)	2.08	v s
2.03	w			2.02	s	2.03*	w	(111)	2.03	v s			
1.82*	m			1.73	m	1.76*	s	(200)	1.76	s			
1.63*	m												
1.43	w	1.47	v s			1.49	v w				(220)	1.474	s
1.28	w					1.29	v w						
		1.26	s								(311)	1.258	m
1.21	w	1.20	m	1.23*	m	1.21	v w	(220)	1.24	m	(222)	1.203	w
1.08	m broad	1.05	w	1.05	m	1.07	m	(311)	1.061	m	(400)	1.042	v w
0.972	w diffuse between both	0.978	w	1.01	v w diffuse	0.975	w	(222)	1.017	v w	(331)	0.957	v w
0.89	w	0.948	s			0.931	v w				(420)	0.933	w
		0.852	m								(422)	0.852	v w
0.798	w	0.805	m	0.804	w	0.802	w	(400) (420)	0.808 0.778	w w	(333)	0.802	v w
0.746	w	0.737	w			0.730	w				(440)	0.737**	
				0.718	w			(422)	0.719	w			
0.709	v w	0.695	m	0.672	w	0.679	w				(442)	0.695	
0.658	w	0.658	m					(333)	0.678	w	(620)	0.659	
0.60	v w	0.626	m	0.603	w						(622)	0.628	
		0.575	m			0.588	v w				(640)	0.578	
		0.554	m	0.542	w						(624)	0.557	
		0.536	w								(553)	0.543	
		0.500	w								(733)	0.510	
		0.489	v w								(555)	0.482	
		0.448	v w								(646)	0.445	

* Shows the fibre structure. ** The spacings larger than this are obtained by the calculation.

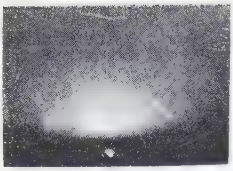

Photo. 9. Ni surface heated at 300°C for 8 hours in hydrogen atmosphere after polishing. (Ni.)

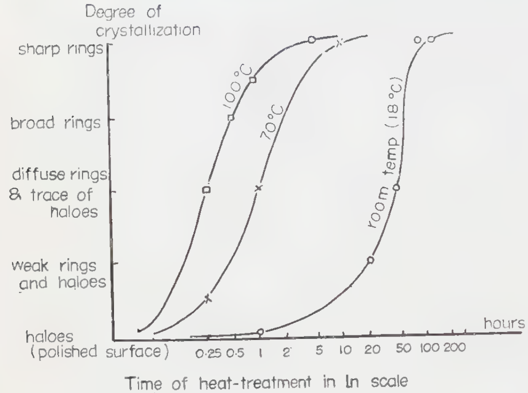

Fig. 5. Crystallization curves for the polished Cu surfaces heated in vacuum. Crystallized substance is Cu_2O.

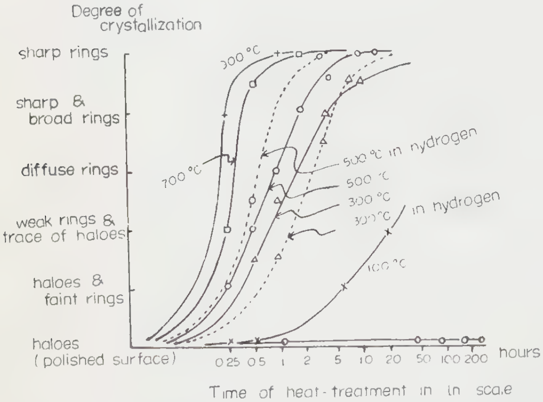

Fig. 6. Crystallization curves for the polished Ni surfaces heated in vacuum and hydrogen atmosphere. Crystallized substances are NiO in vacuum and Ni in hydrogen.

Ni) In the case of Ni kept at room temperature in vacuum, the change in the structure of the specimens was studied at temperatures, 100°, 300°, 500°, 700° and 900°C.

At 100°C, any sign of the change in the pattern did not appear before 5 hours, and afterwards, the ring pattern came to appear very slowly (Photo. 5). At 300°C, 12∼13 rings of NiO and a few weak rings of Ni were observed after 1 hour (Photo. 6), and after 4 hours, many NiO rings appeared additionally but the diffuse rings remained. At 500°C, the rings of NiO began to appear in only 15 min.. After 4 hours, the change proceeded considerablly, and after 10 hours, sharp twenty rings of NiO were observed (Photo. 7). No more change in the pattern was observed after further heating (16 hours). At 700°C, many sharp rings of NiO appeared in 30 min. without the diffuse pattern. The pattern was not changed with a further treatment (2 hours) (Photo. 8). In Table II, the spacings of the rings which appeared by the heat-treatment of some conditions are shown. When the ring pattern became strong, the arcing appeared in the (111), (200) and (220) rings of Ni as well as of NiO.

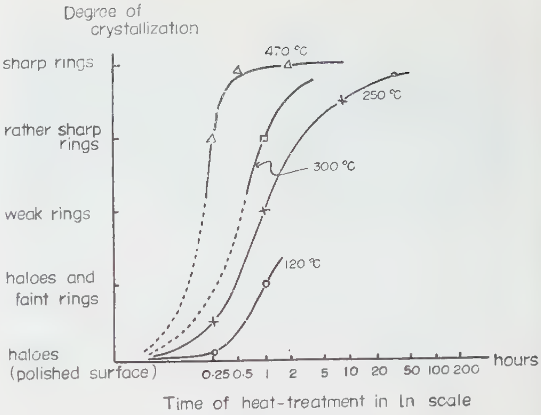

Fig. 7. Crystallization curves for the polished Au surfaces heated in vacuum.

When the polished specimens of Ni were heat-treated in hydrogen atmosphere instead of in vacuum, the process of the change was different from that observed when heated in vacuum. The rings obtained in hydrogen consisted mostly of Ni, the NiO rings being absent (at 300°C) (Photo. 9) or weak (at 500°C). The rings were generally sharp compared with those obtained in vacuum. The spacings of some of them are also given in Table II.

Some specimen polished with a chamois leather for a far longer time (about 20 hours) was also examined. The crystallization had been almost completed with the heat-treatment at 520°C for 3 hours, showing no essential difference from the ones polished for a shorter time.

Au) The polished specimens of Au were heat-treated at 120°, 250° and 470°C. At 120°C, the rings appeared after 1 hour, but the halo still existed. At 250°C, comparatively sharp rings appeared after 1 hour, in which

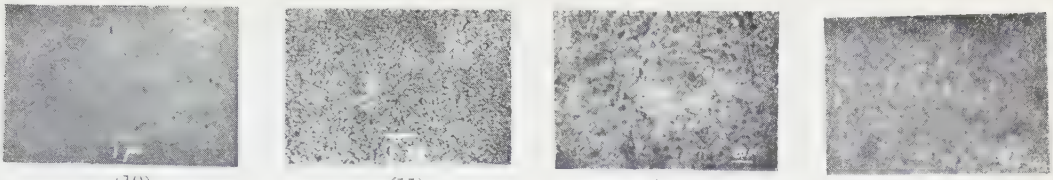

(10) (11) (12) (13)

Photo. 10–13. (10) Electron micrograph of polished surface of Ni with chamois leather. (Cr shadowing.) (11) Electron micrograph of Ni surface heated at 700°C for 2 hours in vacuum. (12) Photomicrograph of Ni surface heated at 300°C for 8 hours in hydrogen atmosphere. (13) Photomicrograph of Ni surface at 500°C for 4 hours in hydrogen atmosphere.

(111), (200) and (220) rings showed arcing. At 470°C, the crystallization proceeded to some extent in 15 min. and almost completed after 2 hours.

Crystallization Curves. The change from the halo pattern to the ring pattern indicates the crystallization of the substance composing the polished layer. However, the rings, especially those in the early stage, are too weak to measure quantitatively their intensity and width. Therefore, classifying the degree of crystallization into the only several stages by the type of the diffraction pattern, we obtained the crystallization curves for each metal as shown in Fig. 5, 6 and 7.

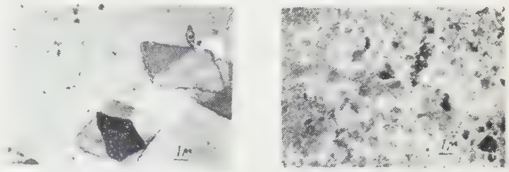

(14) (15)

Photo. 14–15. (14) Electron micrograph of the same surface as Fig. 12. (15) Electron micrograph of the same surface as Fig. 13.

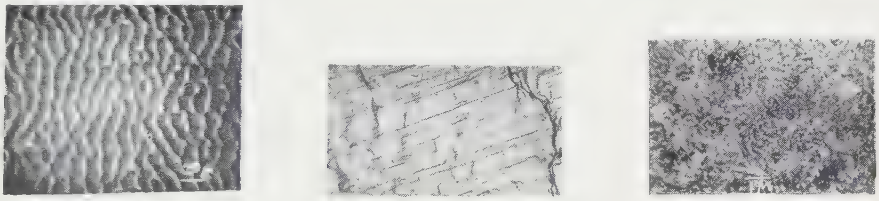

(16) (17) (18)

Photo. 16–18. (16) Photomicrograph of Au surface polished with alumina suspended in water. (17) Electron micrograph of the same gold surface as Fig. 16. (18) Electron micrograph of Au surface heated at 470°C for 2 hours in vacuum after polishing.

c. Osbervation by optical and electron microscope.

(i) The Beilby layer.

The surfaces of the polished specimens, for which the diffraction patterns of the haloes were obtained, were flat in the scale of electron microscope. An example of the nickel surface is shown in Photo. 10.

(ii) Ni specimens treated in vacuum and in hydrogen.

The electron micrograph of the polished specimen heated in vacuum at 700°C for 2 hours, is given in Photo. 11, which corresponds to the diffraction pattern of Photo. 8.

The optical and electron micrographs of the Ni specimens heat-treated in the hydrogen atmosphere are given in Photo. 12, 13, 14 and 15. By the heat-treatment at 300°C for 8 hours, pretty large grains (about 2∼4 μ), probably of Ni crystal, appeared in the flat matrix. By the heat-treatment at 500°C for 4 hours, the grains were far smaller in size but more in number than those at 300°C for 8 hours.

(iii) Au surface in the process of polishing.

The electron micrographs of the surface of Au, polished with Al_2O_3 suspended in water, on which the Beilby layer had not yet been observed, showed sometimes an interesting feature which was not seen in Cu and Ni. The optical and electron micrographs are shown in Photo. 16 and 17, respectively. There are seen major folds with a nearly constant spacing of about 20 μ, between which many minor folds were observed, both of them running nearly perpendicular to the direction of polishing. This peculiarity be attributed partly to the ease of deformation of Au, and partly to the fact that Au suffers no oxidation disturbing the deformation.

On the other hand, when the polished surface composing the Beilby layer was heat-treated at 470°C, the surface became considerably rough as if etched, as seen in Photo. 18.

§ 4. Considerations on the Results

a. The low angle scattering observed in the diffraction from the Beilby layer.

The low angle scattering in the diffraction from the Beilby layer, as mentioned in § **3**. *a*, has not yet been reported by any previous authors. To observe this, the incident angle was made as small as possible, and the background was lessen by setting a knife edge as close as possible to the surface.

The existence of the similar low angle scattering was reported in the *X*-ray diffraction from the cold worked Cu and Ni by Blin and Guinier[6] and was considered to result from the sub-microscopic cavities, the radius of gyration of which was about 7 Å. It may be conceived that the low angle scattering observed in the pattern from the Beilby layer is also caused by some imperfection within the crystal. However, for the moment, it is impossible to go further into this problem because of the qualitative nature of our observation.

b. The process of crystallization.

In this sub-section main features of the observations on the process of crystallization of the Beilby layer is mentioned. In the present paper the word crystallization means the process corresponding to the change from the halo pattern to the ring pattern, and it may actually be of complicated nature involving crystallization of pure metal and oxide in the layer.

(i) The initial stage of the crystallization.

At the initial stage of the heat-treatment, the diffuse halo pattern coexists with diffraction rings due to metal or oxide ; the latter becomes relatively stronger as the crystallization proceeds. This fact suggests that the crystallization, by the heat-treatment in hydrogen as well as in vacuum, develops gradually starting from some localized parts in the polished layer. This process is also supported by electron microscopy on Ni, for instance, annealed at 300°C in hydrogen.

(ii) The second stage of crystallization (especially the case of Ni).

For the Ni specimen heated in vacuum, the rings, mostly of NiO, remain broad even after the crystallization proceeds and the diffuse haloes have completely disappeared. On the other hand, when the Ni specimen is heated in hydrogen, the rings, mostly of Ni, become sharp even at the earlier stage (refer to § **3**. *b*). These facts suggest that in the case of the polished surface of Ni the existence of oxides disturbs the crystal growth or distorts the lattice of the grown crystal. The electron microscopic study seems also to support this view. As seen in Fig. 18, 20 and 22, the surface of the specimen heat-treated in vacuum is far uneven than that treated in hydrogen.

c. Fibre structures.

As mentioned in § **3**. *b*, fibre patterns are sometimes observed in the diffraction from the crystallized surfaces, as revealed by the arcing of the rings (111) and (222) etc. of Cu_2O, Ni, NiO and Au. The arcing becomes more prominent for the heat-treatment at lower temperatures. Although the accurate determination of the fibre axes cannot be made because the arc patterns are weak, it is likely that there exist independent fibre axes [100], [110] and [111].*

Lees[7] confirmed the existence of the [110] fibre structure in the region lying under the Beilby layers of Cu and Au. Takahashi[8] reported that lapped surfaces* of alloys with face-centered cubic structure such as α-brass and Al-bronze have the [111] and [100] fibre structures, both inclined about 8° towards the direction of polishing, and that when the surface of α-brass is polished by a chamois leather, the [110] fibre structure reaches to the depth of several μ. It is well known that, in the cold-worked metals in bulk with face-centered cubic structure, the [111] and [100] fibre axes appear parallel to the direction of force under tension, and the [110] fibre axis under compression[9].

---

* For example, when the polished Cu specimen was kept at room temeperature, the following diffraction pattern of Cu_2O is observed: when the incident beam is perpendicular to the direction of polishing, the arc in the (220) ring is seen in the direction normal to the shadow edge and the arcs in the (200) and (111) rings are respectively about 30° and 52° inclined to the normal on both sides, extending over the range of 13° and 17° respectively.

Considering the above facts, we may explain the generation of the fibre structure during the crystal growth as follows. Before the Beilby layer is formed, the region near the surface is divided into smaller crystal grains having fibre structures. From the results on the bulk metals, it is likely that the [111] and [100] fibre axes are produced by the tangential component of the force exerted and the [110] fibre axis by the normal component. Before the Beilby layer is formed, the fibre structure will have extended down to the region lying beneath the Beilby layer, and it may be possible that the trace of the fibre structure remains in the Beilby layer itself. These fibre structures may, then, be considered to be the origin of that appeared in the Beilby layer by the heat-treatment.

Whether the trace of fibre structure exists or not in the Beilby layer itself is an importan problem in order to decide between two views on the nature of the Beilby layer, the theories of "*small crystal grain*" and of "*liquid-like packing.*"** A few eleceron diffraction studies[10], carried out on the thin film of the Beilby layer stripped from the base, do not seem to observe the arcing in the diffraction rings. It is desirable to carry out further observations on this point.

d. *The temperature of crystallization.*

The crystallization curves in Fig. 5, 6 and 7 resemble the recrystallization curves of cold-worked metals in bulk. Because of the rough representation of the degree of crystallization, it is difficult to evaluate quantities such as activation energy of crystallization etc., but it is at least probable to say that the temperatures of crystallization are about 60°, 250° and below 200°C for Cu (actually Cu_2O), Ni (actually NiO) and Au, respectively. For Ni heated for one hour in hydrogen, this temperature is about 300°C, which is higher than that for treatment in vacuum. The oxides seem to make the crystallization temperature somewhat lower.

The results for Au and Ni treated in hydrogen are most important, since these cases are free, or almost free, from the influence of oxide. According to the data given by Seitz and Read[12], the recrystallization temperatures of heavily cold-worked polycrystalline Ni and Au in bulk are about 620° and 200°C, respectively, being higher than those for the Beilby layer. It is no wonder that there exists a difference in the behaviour of crystallization between the two cases, because the Beilby layer is far more heavily distorted than the metal in bulk cold worked in the usual way, although our present knowledge of the Beilby layer is too insufficient to make detailed comparison.

e. *The effect of prolonged polishing.*

According to the result mentioned in § **3**. *b*, the prolonged polishing (about 20 hours) does not change essentially the behaviour of the crystallization of the Beilby layer. This fact seems to mean that the state of polished layer (the degree of randomness in the atomic arrangement and the thickness of the layer) arrives at a certain limiting state in a certain time under a given pressure of polishing. This is in contrast to the case of metal in bulk for which the duration of cold-working has a great influence upon the state of strain and, accordingly, the rate of recrystallization.

f. *The oxides and the Beilby layer.*

Whether the Beilby layer is composed of oxides or not has been discussed by many authors. As mentioned before, Kranert and Raether[13] concluded that the surfaces of metals polished in the air are usually oxidised. We support their view from the reasonings mentioned below: (i) In the early stage of crystallization, the oxidation after polishing is improbable because the specimens were always kept in vacuum ($\sim 10^{-4}$ mm) or in benzol, and annealed in vacuum. (ii) In the cases of Ni as well as Cu, the oxide pattern is obtained from the surface when the polishing is underway. Especially, in the case of Cu, the surface sometimes becomes to bear a red tinge, showing the formation of Cu_2O.

---

* The surfaces, in this case, have not yet become the Beilby layer, but give the ring pattern.

** According to Prins[11], it seems to be that the fibre structure usually does not exist in the intrinsic amorphous state.

Notwithstanding, since the Beilby layer of Au is never oxidised, we may say that the existence of oxides takes generally no essential part on the formation of the Beilby layer, although it may lower the temperature of crystallization, or might hinder the growth of large crystal grains.

In conclusion, the authors with to express their sincere thanks to Prof. Futagami of Kyushu University for his generous guidance during the course of the study, and Prof. Suge of University of Tokyo for his interests and valuable advices, and also Messrs. J. Tasaki, T. Oda and T. Yoshii of the Department of Metallurgy, Kyushu University for their valuable discussions and affording the facilities to the experiments.

This work was indebted to the Scientific Research Expenditure of the Ministry of Education.

References

1) K. Nonaka and K. Kohra: Ōyōbutsuri (Jour. App. Phys. Japan, in Japanese), **21** (1952) 314.

2) G. T. Beilby: "Aggregation and Flow of Solids", London, (1921).

3) refer to

G. P. Thomson and W. Cochrane: "Theory and Practice of Electron Diffraction", London, (1939) Chap. XIII.

H. Raether: Erg. exakt. Naturwiss. XXIV (1951) IV, A and B.

P. S. Axon: Proc. Phys. Soc. **52** (1940) 312.

T. S. Rensema: Jour. App. Phys. **23** (1952) 1412.

4) W. Kranert and H. Raether: Ann. d. Physik **43** (1943) 520.

5) W. Cochrane: Proc. Roy. Soc. **A 166** (1938) 228.

H. Raether: Zeits. f. Phys. **126** (1949) 185.

6) J. Blin and A. Guinier: Compt. rend. **233** (1951) 1288.

7) C. S. Lees: Trans. Farad. Soc. **31** (1935) 1102.

8) N. Takahashi: Ōyōbutsuri (Jour. App. Phys. Japan, in Japanese) **21** (1952) 314.

9) For example,

R. Glocker: "Material Prüfung mit Röntgenstrahlen besondere Berücksichtung der Röntgenmetallkunde" (1936).

G. Sachs: "Praktische Metallkunde" Bd. 2, Berlin, (1934).

10) W. Cochrane: Proc. Roy. Soc. **A 166** (1938) 228.

E. Plessing: Phys. Zeits. **39** (1938) 618.

H. Raether: Zeits. f. Phys. **126** (1949) 185.

11) J. A. Prins: "Selected Topics in X-ray Crystallography", Amsterdam (1951) Part E. § 5.

12) F. Seitz and T. A. Read: Jour. App. Phys. **12** (1941) 170.

13) W. Kranert and H. Raether: refer to 3).

JOURNAL OF THE PHYSICAL SOCIETY OF JAPAN Vol. 9, No. 4, JULY—AUGUST, 1954

On Nickel Oxides of High Oxygen Content*

By Yasumitsu SHIMOMURA, Ichiro TSUBOKAWA
and Morio KOJIMA
Department of Physics, Naniwa University

(Received April 6, 1954)

Nickel oxides of high oxygen content formed by incomplete dissociation of nickel nitrate were investigated crystallographically and magnetically. The oxygen excess of these oxides ranges from zero to 0.2 gr. atom/mol., and their crystal structures are not essentially different from that of the ordinary nickel oxide. As they are not in a stable state, they have some curious but important behaviors. That is, with the degree of excess, they become to have a cubic structure the parameter of which is larger than that (a) of a rhombohedrally deformed one, and at sufficiently high oxygen contents they behave as something like a ferromagnetics. Such rather extraordinary phenomena may be considered to be originated from the fact that the oxygen excess in the specimens owes not only nickel vacancies but also the absolute excess of anions. In the measurements of susceptibility, the coincidency between the heating and cooling curves is very good for ferromagnetics-like oxides, while it is not for antiferromagnetic ones. There is also an evidence for the existence of antiferromagnetic cubic oxide at a temperature fairly lower than its Neél point.

§ 1. Introduction

The physical properties of nickel oxide is expected to change with the degree of oxygen excess. About this problem, few experiments have yet been performed, probably because of its very narrow range of oxygen concentration. In the stable state, the range has been generally accepted to be a fraction of one percent. According to a literature, however, incomplete dissociation of nickel nitrate may yield the oxides containing relatively high excess of oxygen, although they must not be stable. The present paper reports the results of crystallographic and magnetic observations on such oxides.

§ 2. Method of Experiments

The degree of oxygen excess in the samples were determined as follows. At first, a definite amount of nickel foil (0.06 mm. in thickness) of 98.95% purity was oxidized until no substratum remained. From the accurate measurement of the weight increase in this oxidation, the deviation from its stoichiometric composition was estimated to be 0.0033 gr. atom/mol. (deficient in nickel). And this composition was assumed to be valid when the oxide was stablely formed by high-temperature calcination of nitrate in air. Next, nickel oxides of various oxygen contents were obtained by heating nickel nitrate at various temperatures ranging from 550 to 1250°C. In order to estimate the degree of excess, the sample was heated again at 1250°C in a vessel of nickel oxide which had been prepared by oxidizing the nickel foil as mentioned above. By this means the sample will have dissociated completely without fears lest the sample should be contaminated by the vessel if the vessel were made of the other material. Consequently the weight decrease in this operation may be considered to be due to the excess oxygen leaving the sample and thus the degree of excess can be calculated.

The specific gravity was measured by the method analogous to the one which was employed by Hägg[1] in the determination of the crystal structure of magnesium nitride.** But the values thus obtained for the sample of stable oxide formed by the high temperature dissociation of nitrate were somewhat smaller than the calculated ones, the ratio of the latter to the former being 1.010. So the observed values were always corrected by multipling by this factor.

---

* The paper was read before the Osaka Meeting of this Society held in April, 1953.

** But in the present case, distilled water is employed, while Hägg employed benzol.

The X-ray and magnetic analyses were performed in the same way as in the previous reports.[2)3)]

§ 3. Results of Experiments

As is expected, the oxygen excess of the samples investigated increases with lowering the temperature of dissociation of nitrate (Table I)**, and the greater is the excess the smaller is the specific gravity (ρ) (Fig. 1).

Table I. Oxygen excess of the specimens.

Condition of dissociation		Oxgen excess
Temp. (°C)	Duration (hours)	(gr. atom./mol.)
1250	2	0.0033
850	2	0.02
800	2	0.05
650	2	0.09
550	2.5	0.20

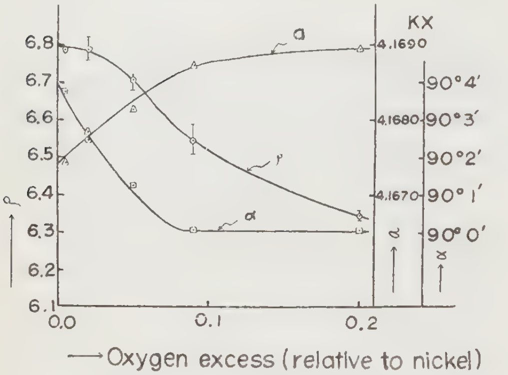

Fig. 1. Variations of specific gravity (ρ) and lattice constants with oxygen content.

Furthermore, their crystal structures are not any other than a rhombohedral (a slightly deformed rock-salt type) similar to the ordinary nickel oxide or than a rock-salt type similar to an oxide film. However, it is to be noted that their lattice constants, a and α, vary as in the corresponding curves in Fig. 1, which means that the unit cell expands and α approaches to 90° with the oxygen excess. Microphotometer plottings for {111}, {200} and {422} diffraction lines (Ni$K\alpha$) of the two kinds of oxides are reproduced in Fig. 2, where it is seen that the line broadening occurs in cubic oxide as in the case of oxide film on nickel.[4)]

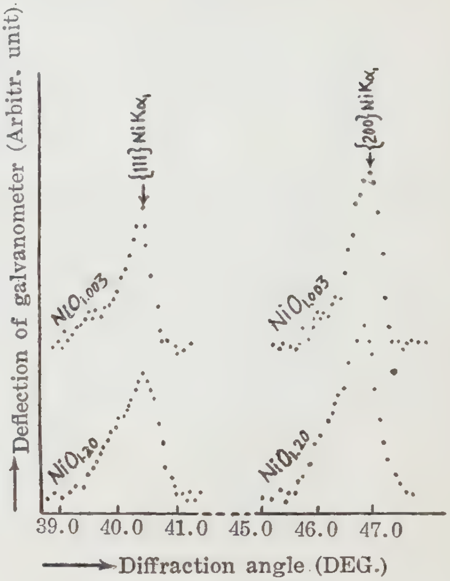

(a) {111} and {200}

(a)

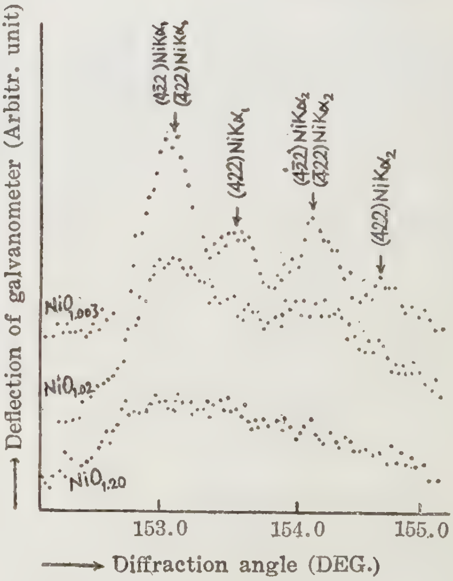

(b) {422}

(b)

Fig. 2. Microphotometer plottings of diffraction lines (NiK_α).

** The authors were doubtful if nitrogen remained in the sample formed by calcinating the nitrate at such a low temperature as 550°C. According to a chemical analysis, however, it amounted only to about 0.004%.

There is also an interesting change in the magnetic behavior with the oxygen content as illustrated in Fig. 3, which shows the susceptibility change with temperature for several specimens. The specimen formed by the complete dissociation of nitrate, of course, behaves as an antiferromagnetics (the curve for $NiO_{1.003}$), and the specimen of 0.09 oxygen excess still maintains the similar characteristic (the curve for $NiO_{1.09}$)*. But when the oxygen excess becomes as high as 0.20, the susceptibility increases in magnitude and becomes to have a negative temperature coefficient just like a ferromagnetics, though at sufficiently high temperatures it has a behavior analogous to that of the ordinary oxide (the curve for $NiO_{1.20}$). The former behavior cannot be ascribed to the contamination by ferromagnetic impurities, because there is no ferromagnetic substance with such a low Curie point and also no possibility to exist in the present specimen. Therefore, the behavior is considered to be due only to the high oxygen concentration. Actually the same specimen behaves as an antiferromagnetics when its oxygen contents is lowered by high-temperature calcination. To confirm the existence of such a ferromagnetics-like nickel oxide, several oxides from nitrate of higher purity were examined and even in this case the susceptibility decreased with temperature rise in the specimens with sufficiently high oxygen excess.

§ 4. Discussion

All the oxides treated here have compositions fairly deviating from the stoichiometric one (NiO), but in view of their crystal structures they must still belong to nickel oxide. And if their oxygen excess is caused only by the cation vacancies, the lattice is expected to contract and deform with the degree of excess. However, contrary to this expectation, it expands and does not deform with their oxygen content. So the excess must be originated not only from the cation vacancies but also from the absolute excess of anion. This can easily be demonstrated as follows. For convenience, their molecular formula is expressed as Ni_xO_y, where $y/x-1$ represents the degree of oxygen excess. Then x and y are calculated from the lattice constants and the density. The results are illustrated in Fig. 4, which shows that there exist more oxygen ions than their lattice points, though, of course, there are also nickel vacancies. Concerning such surplus oxygen ions, it can hardly be said at what positions in the lattice they are situated. Such a rather extraordinary structure perhaps comes from the metastable nature of the oxides formed by the incomplete dissociation of nitrate. And the change in the magnetic behaviors seems to be originated from these surplus oxygen ions.

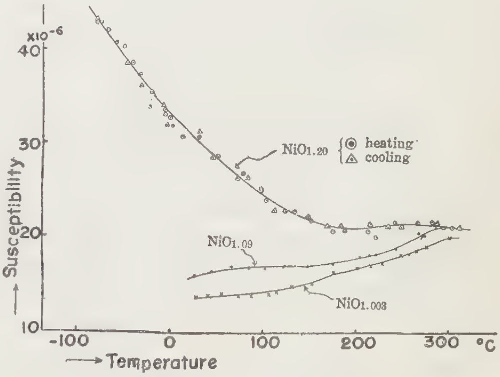

Fig. 3. Variation of susceptibility with temperature (1000 oersteds).

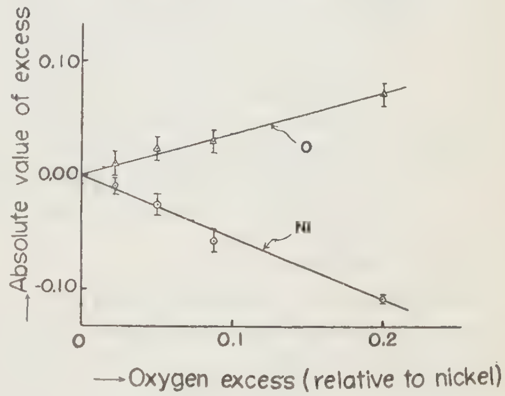

Fig. 4. Absolute excess of oxygen and absolute defficiency of nickel in nickel oxides.

It must be further noticed that in the measurement of susceptibility the heating and cooling curves well coincide with each other for the ferromagnetics-like oxide, while they do not for the antiferromagnetic one. Lastly the authors should like to point out the following fact. The specimen containing 0.09

---

* Both these two curves are of heating, and the cooling curves, which are omitted to avoid the complication of the figure, deviate considerably from the heating ones as in the previous reports.[3)]

excess oxygen has a cubic structure at room temperature, while its antiferromagnetic Curie point is as high as about 280°C. This shows that in some cases the nickel oxide lattice does not deform at temperatures fairly lower than its Neél point as previously reported.[3)5)]

References

1) G. Hägg: Zeits. Krist. **74** (1930) 95.

2) Y. Shimomura and Z. Nishiyama: Memoirs of the Institute of Scientific and Industrial Research, Osaka Univ. **6** (1948) 30.

3) Y. Shimomura and I. Tsubokawa: This journal **9** (1954) 19.

4) Y. Shimomura and Z. Nishiyama: J. Japan Inst. Metals **13** (1949) No. 4, p. 2.

5) Y. Shimoura: J. Japan Inst. Metals **17** (1953) 421.

Journal of the Physical Society of Japan Vol. 9, No. 4, July—August, 1954

On the Transition Temperature of Molecular Rotation in Long-Chain Compounds with the Discontinuous Model

By Sukeaki Hosoya

Institute of Physics, College of General Education, University of Tokyo

(Received August 25, 1953)

The rotational transition, which is found in some long-chain compounds, is discussed at the level of Bethe's approximation, assuming that the rigid molecules occupy the rigid two-dimensional triangular lattice points, and that they can take only three orientations around their axes. Four kinds of interaction energies must be considered. The calculations are made concerning what values of interaction energies make the transition to the paraffin-typed arrangement possible, and concerning how the transition temperature depends on these energy values. Some reasonable results are obtained. At the same time, another type of the ordered arrangement is also investigated, in which all molecules take the same orientation.

§ 1. Introduction

Some long-chain compounds such as normal hydrocarbons and alcohols have rotational phase transition, above which the molecules undergo the hindered rotation, and below which most of them arrange themselves in ordered states such as shown in Fig. 1.[1-8)] The crystal of such compounds changes its lattice form from the orthorhombic system to the hexagonal, when it goes over the transition point from the lower temperature. Experiments[9)] show that the interaction energy between molecules on the adjacent layers which are perpendicular to the c-axis is very weak when compared with the one among molecules on the same layer. So we can deal with this crystal always as a rigid two-dimensional triangular lattice above the transition point, if we neglect the thermal expansion of the lattice. This may also be assumed below the transition temperature, because the

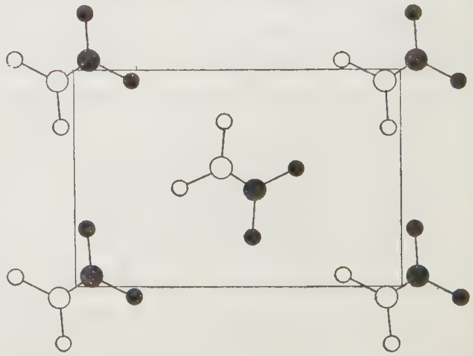

Fig. 1. The ordered molecular configuration of paraffins projected on the a-b plane. The smaller circles represent hydrogen atoms; the larger ones represent carbon atoms. The solid circles and the open ones are not on the same plane.

lattice deformation in the orthorhombic system from the hexagonal is small. Moreover, we consider only the interaction between the nearest neighbours, since this interaction may play a dominant part in the rotational transition.

Y. Kakiuchi10) developed his theory on the same subject in an analogous way to the theory of binary alloys, considering two possible orientations for each molecule above and below the transition point, because each molecule can rotate only cog-wheel-likely even above the transition point. However, it is desirable to assume six directions instead of two for the molecular orientation. In the present paper, we will make a certain plausible simplification; namely we consider three orientations for each molecule (Fig. 4) neglecting such distinctions as shown in Fig. 2 (a) and (b) or considering, as it were, only the projections of molecules on the *a*-*b* plane. Further, the thermal vibration of molecules around their axes is neglected, as it is usually done in this kind of theory. Then the system reduces to a ternary alloy consisting of nonscalar elements which vary in number, and its statistical problem can be solved at the level of Bethe's approximation.

§ 2. Fundamental Equations

To discuss our problem, the lattice points must be divided into four sublattices, which will be denoted by I, II, III and IV as shown in Fig. 3. It is assumed that each molecule can take three orientations 1, 2 and 3 shown in Fig. 4.

We introduce the following notations:

$\left[\frac{i}{\mathrm{p}}\right]\equiv\frac{N}{4}x_{\mathrm{p}i}$ (p=I, II, III, IV; i=1, 2, 3.): the number of p-sites occupied by any molecule with i-orientation.

$\left[\begin{matrix} i & j \\ \mathrm{p} & \mathrm{q}\end{matrix}\right]\equiv\frac{N}{2}y_{kij}$ (i, j=1, 2, 3; k refers to six kinds of pairs (p, q)): the number of pairs like $\begin{matrix} i & j \\ \mathrm{p} & \mathrm{q}\end{matrix}$, which means a pair of neighbours, a molecule i on a p-site and a molecule j on its neighbouring q-site.

Here N means the total number of molecules, so that $x_{\mathrm{p}i}$'s and y_{kij}'s are the parameters of long and short range order respectively. At the level of Bethe's approximation, the free energy of the system can be obtained by following Takagi's method11) as first used in his statistical theory of binary alloys. The free energy per molecule is

$$F/N=(1/2)\sum_{54}\varepsilon_n y_{kij}-kT\{(5/4)\sum_{12}x_{\mathrm{p}i}\ln x_{\mathrm{p}i}-(1/2)\sum_{54}y_{kij}\ln y_{kij}\},$$

where ε_n stands for one of the interaction energies, i.e. c, h, l and p shown in Fig. 5, according to the relative position to which y_{kij} refers.

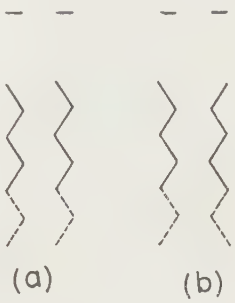

Fig. 2. The projections of C–C bonds on the *a*-*b* plane and on the plane parallel to the *c*-axis. (a) and (b) are different in the relative position but same in their projections on the *a*-*b* plane.

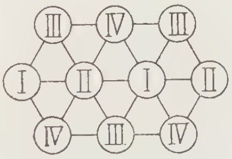

Fig. 3. Four sublattices in a two-dimensional triangular lattice.

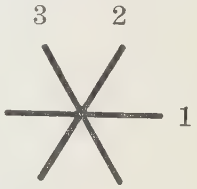

Fig. 4. Three possible orientations of each molecule.

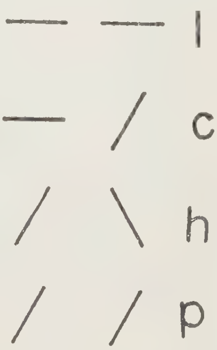

Fig. 5. Four kinds of relative positions of neighbouring molecules. Bars represent C–C bond projected on the *a*-*b* plane.

As referred above, we are not considering

Table I. The list of variables suitably chosen. $\sum$ shows the summation of each column or row. Each second suffix in y's shows the type of the relative position between the neighbouring molecules to which it refers.

$$x_{pi}\equiv\frac{4}{N}\left[\begin{array}{c} i \\ \hline \mathrm{p}\end{array}\right]$$

$i\diagdown \mathrm{p}$	I	II	III	IV
1	x_1	x_1	x_1	x_1
2	x_2	x_2	x_3	x_3
3	x_3	x_3	x_2	x_2
$\sum$	1	1	1	1

$$y_{kij}\equiv\frac{2}{N}\left[\begin{array}{cc} i & j \\ \hline \mathrm{I} & \mathrm{III}\end{array}\right] \text{ or } \frac{2}{N}\left[\begin{array}{cc} i & j \\ \hline \mathrm{II} & \mathrm{IV}\end{array}\right]$$

$i\diagdown j$	1	2	3	$\sum$
1	y_{2p1}	y_{2c3}	y_{2h1}	x_1
2	y_{2c4}	y_{2l}	y_{2c1}	x_2
3	y_{2h3}	y_{2c2}	y_{2p2}	x_3
$\sum$	x_1	x_3	x_2	

$$y_{kij}\equiv\frac{2}{N}\left[\begin{array}{cc} i & j \\ \hline \mathrm{I} & \mathrm{II}\end{array}\right]$$

$i\diagdown j$	1	2	3	$\sum$
1	y_{1l}	y_{1c3}	y_{1c2}	x_1
2	y_{1c3}	y_{1p2}	y_{1h}	x_2
3	y_{1c2}	y_{1h}	y_{1p3}	x_3
$\sum$	x_1	x_2	x_3	

$$y_{kij}\equiv\frac{2}{N}\left[\begin{array}{cc} i & j \\ \hline \mathrm{I} & \mathrm{IV}\end{array}\right] \text{ or } \frac{2}{N}\left[\begin{array}{cc} i & j \\ \hline \mathrm{II} & \mathrm{III}\end{array}\right]$$

$i\diagdown j$	1	2	3	$\sum$
1	y_{2p1}	y_{2h3}	y_{2c4}	x_1
2	y_{2h1}	y_{2p2}	y_{2c1}	x_2
3	y_{2c3}	y_{2c2}	y_{2l}	x_3
$\sum$	x_1	x_3	x_2	

$$y_{kij}\equiv\frac{2}{N}\left[\begin{array}{cc} i & j \\ \hline \mathrm{III} & \mathrm{IV}\end{array}\right]$$

$i\diagdown j$	1	2	3	$\sum$
1	y_{1l}	y_{1c2}	y_{1c3}	x_1
2	y_{1c2}	y_{1p3}	y_{1h}	x_3
3	y_{1c3}	y_{1h}	y_{1p2}	y_2
$\sum$	x_1	x_3	x_2	

Table II. The list of the independent and dependent variables.

Indep. \ Dep.	1	x_1-x_3 $\equiv\xi_1$	x_2-x_3 $\equiv\xi_2$	y_{1c2}	$y_{1c3}-y_{1c2}$ $\equiv\eta_{1c3}$	y_{1h}	$y_{2c1}-y_{1c2}$ $\equiv\eta_{2c1}$	$y_{2c2}-y_{2c1}$ $\equiv\eta_{2c2}$	$y_{2c3}-y_{2c1}$ $\equiv\eta_{2c3}$	$y_{2h1}-y_{1h}$ $\equiv\eta_{2h1}$
x_1	$\frac{1}{3}$	$\frac{2}{3}$	$-\frac{1}{3}$							
x_2	$\frac{1}{3}$	$-\frac{1}{3}$	$\frac{2}{3}$							
x_3	$\frac{1}{3}$	$-\frac{1}{3}$	$-\frac{1}{3}$							
y_{1l}	$\frac{1}{3}$	$\frac{2}{3}$	$-\frac{1}{3}$	-2	-1					
y_{1c3}				1	1					
y_{1p2}	$\frac{1}{3}$	$-\frac{1}{3}$	$\frac{2}{3}$	-1	-1	-1				
y_{1p3}	$\frac{1}{3}$	$-\frac{1}{3}$	$-\frac{1}{3}$	-1		-1				
y_{2l}	$\frac{1}{3}$	$-\frac{1}{3}$	$-\frac{1}{3}$	-2			-2	-1	-1	
y_{2c1}				1			1			
y_{2c2}				1			1	1		
y_{2c3}				1			1		1	
y_{2c4}			1	1			1	1	1	
y_{2h1}						1				1
y_{2h3}			-1			1		-1		1
y_{2p1}	$\frac{1}{3}$	$\frac{2}{3}$	$-\frac{1}{3}$	-1		-1	-1		-1	-1
y_{2p2}	$\frac{1}{3}$	$-\frac{1}{3}$	$\frac{2}{3}$	-1		-1	-1			-1

the arrangement in Fig. 1, but its projection on the *a-b* plane, which is later called the A type (Fig. 6) from a broader point of view. Here we reduce the number of variables by considering the symmetric characters of the A type arrangement. The list of variables suitably chosen, is shown in Table I, where the identical relations among x_{pi}'s and y_{kij}'s are shown together.

In the perfect ordered state of A type, $x_2 = y_{1p2} = y_{2c1} = 1$ or $x_3 = y_{1p3} = y_{2c2} = 1$ and others are all zero. These two arrangements are of course equivalent. For later convenience, nine independent variables such as shown in Table II are used. ξ's or η's are linear combinations of x's or y's and their definitions are also shown in Table II.

Nine fundamental equations are derived by minimizing the free energy with respect to the independent variables. After some simplification, they are written as follows:

$$(x_1/x_3)^5 = (y_{1l}/y_{2l})(y_{2c1}/y_{2c2})(y_{2p1}{}^2/y_{1p3}y_{2p2}), \tag{2.1}$$

$$(x_2/x_3)^5 = (y_{1p2}/y_{1p3})(y_{2c1}/y_{2c2})^2, \tag{2.2}$$

$$\exp[(l+p-2c)/kT] = y_{1c2}{}^2/y_{1l}y_{1p3}, \tag{2.3}$$

$$y_{1c2}{}^2/y_{1l}y_{1p3} = y_{1c3}{}^2/y_{1l}y_{1p2}, \tag{2.4}$$

$$y_{1c2}{}^2/y_{1l}y_{1p3} = y_{2c3}y_{2c4}/y_{2l}y_{2p1}, \tag{2.5}$$

$$\exp[2(p-h)/kT] = y_{1h}{}^2/y_{1p2}y_{1p3}, \tag{2.6}$$

$$y_{1h}{}^2/y_{1p2}y_{1p3} = (y_{2c1}y_{2h3}/y_{2c4}y_{2p2})^2, \tag{2.7}$$

$$y_{2c1}y_{2h3}/y_{2c4}y_{2p2} = y_{2c3}y_{2h3}/y_{2c2}y_{2p1}, \tag{2.8}$$

$$y_{2c1}y_{2h3}/y_{2c4}y_{2p2} = y_{2c2}y_{2h1}/y_{2c3}y_{2p2}. \tag{2.9}$$

In the disordered state, all x_i's are 1/3 and all y_{kij}'s are reduced to four variables y_c, y_h, y_l and y_p, the redundant suffixes being omitted. Only (2.3) and (2.6) are not identically satisfied, whcih give the following solutions:

$$\left.\begin{aligned} y_c &= (3-\sqrt{1+4\alpha})/6(2-\alpha), \\ y_p &= (1/3-y_c)/(1+\gamma), \\ y_l &= 1/3-2y_c, \\ y_h &= (1/3-y_c)\gamma/(1+\gamma), \end{aligned}\right\} \tag{2.10}$$

where

$$\alpha = \beta(1+1/\gamma), \quad \beta = \exp[(2c-h-l)/kT],$$
$$\gamma = \exp[(p-h)/kT].$$

§ 3. The State at 0°K

Because we divided the lattice points into four kinds of sites, six different types of arrangements shown in Fig. 6 can be distinguished. The internal energy of these perfect ordered states at 0°K are listed in Table III.

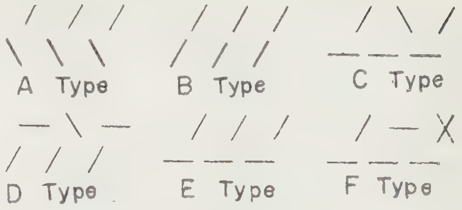

Fig. 6. Six types of the possible ordered states.

Table III. Internal energies per molecule in various types.

Type	U/N
A	$2c+p$
B	$l+2p$
C	$\frac{l}{2}+c+\frac{3h}{2}$
D	$2c+\frac{h}{2}+\frac{p}{2}$
E	$\frac{l}{2}+c+h+\frac{p}{2}$
F	$\frac{l}{2}+c+\frac{h}{2}+p$
Disordered State	$(l+4c+2h+2p)/3(\equiv 0)$

Now the zero level of the interaction energy U is chosen so as to make U zero in the perfect disordered state at the infinitely high temperature. This requires the relation:

$$-2p/l-2h/l-4c/l=1. \tag{3.1}$$

Therefore every set of values for c, h, l and p corresponds to one point on the plane, where the values $(-2p/l, -2h/l, -4c/l)$ are taken to be the trilinear coordinates. This plane is useful in the present theory and will be referred to as the *interaction energy plane*.

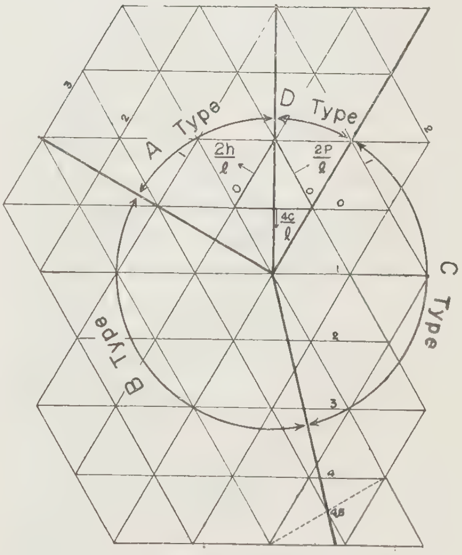

Fig. 7. The stable states at 0°K.

At 0°K, the most stable state, which has the lowest value of U, is easily found by comparing the values in Table III. Its type depends on the interaction energy as shown in Fig. 7. Here l is taken to be positive, because the molecular form and the lattice dimension indicate the very large value for l on account of the repulsive forces. So only positive values have meaning for the temperature variable τ ($\equiv kT/l$).

§ 4. Transition Temperatures

Transition temperatures are found in a similar way to that used by R. Kikuchi.[12] At and above the transition temperature τ_t ($\equiv kT_t/l$), two ξ's and five η's in Table II are zero. At τ_t, however, the ratios among their differential quotients with respect to τ are finite. We differentiate seven fundamental equations except (2.3) and (2.6) with respect to τ, then insert the conditions for the disordered state, that is, put $x_i=1/3$ ($i=1, 2, 3$) and express all the y_{kij}'s by y_c, y_h, y_l and y_p.

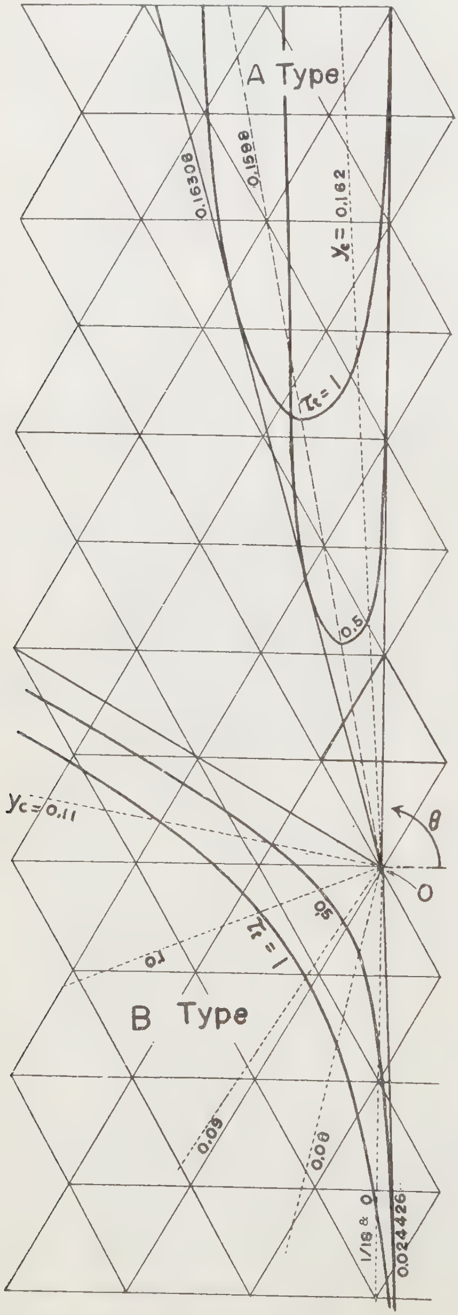

Fig. 8. Contours of τ_t on the *interaction energy plane.*

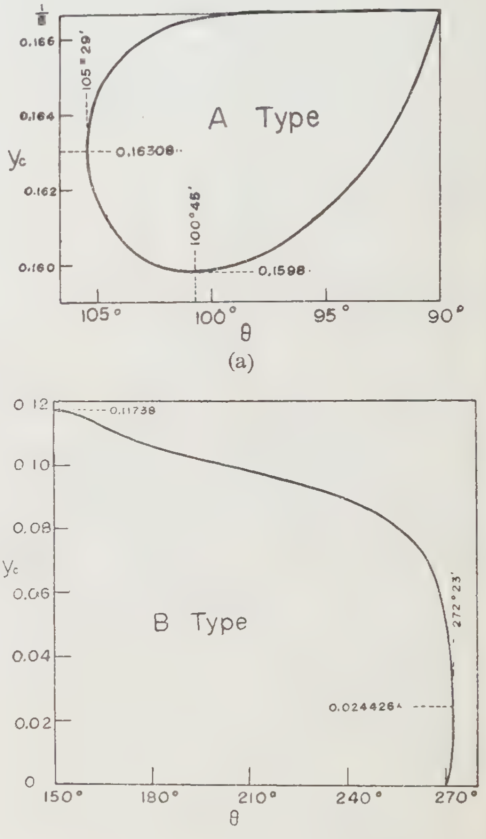

(a)

(b)

Fig. 9. The relation between y_c and θ in Fig. 8.

The determinant of coefficients in the seven equations thus obtained must be zero. This determines τ_t. The equation now splits into two factors, which can be expressed in the following way, using (2.10):

$$y_c(135y_c^2-108y_c+18)\gamma_t^2 -2(135y_c^3-99y_c^2+27y_c-2)\gamma_t +y_c(135y_c^2-90y_c+12)=0, \tag{4.1}$$

$$(810y_c^3-423y_c^2+84y_c-6)\gamma_t -(810y_c^3-639y_c^2+132y_c-8)=0, \tag{4.2}$$

where

$$\gamma_t=\exp[(p/l-h/l)/\tau_t].$$

Thus τ_t is determined by the interaction energies, though the actual calculation is in reverse order. The results show that the contours of a parameter, y_c, are a pencil of straight lines which pass the point $(2h/l=2p/l=-1)$ on the *interaction energy plane*. This point will be denoted by O. The value of τ_t varies linearly with the distance from O on each member of that pencil. So the contours of τ_t are a group of curves which have the point O as a common center of similitude, as shown in Fig. 8. The dependency of the parameter y_c on the angle θ shown in Fig. 8 can be seen in Fig. 9.

The τ_t contours determined by (4.1) and (4.2) are in the A and B type regions of Fig. 7 respectively. This can be seen beforehand, because (4.1) was derived from the condition that ξ_2, η_{1c3} and η_{2c2} have the branching point, and these variables characterize the transition to the A type. However, (4.2) can be derived even when we put $\xi_2=\eta_{1c3}=\eta_{2c2}=0$ from the very beginning, taking the orientations 2 and 3 as equivalent. It suggests that (4.2) gives the transition temperature to the B type.

In the A type region and in the small part of the B type region, τ_t is double-valued at each point. Considering the results obtained in § 3, we can guess that the higher τ_t is the transition point to the A and B types respectively. In the latter, it is directly proved by solving the equations at some point on the *interaction energy plane*. In this case, the variables decrease in number but it is still very laborious to solve the equations, since the double try and error calculations are inevitable. In this paper, we do not investigate what is meant by the lower τ_t.

§ 5. Summary

As far as our model is concerned, the behaviours of our crystal are determined by four interaction energy values among the molecules (Fig. 5) contained in it. Because the zero level of these energy values can be determined by satisfying the condition (3.1), any crystal with which we are concerned can be represented by a point on a plane as shown in Fig. 7 or 8. (How trilinear coordinates are to be taken is shown in Fig. 7.) The position on which a representative point of a crystal falls tells whether the crystal has a rotational transition to the A or B type, or has no transition. Moreover, the value of a transition temperature T_t $(=l\tau_t/k)$ can be obtained from the values of τ_t contours shown there. Thus most of the results obtained are concisely expressed in Fig. 8. In short, though not exact, the necessary condition for the A type to appear is c, $p<h$, l, and the larger their difference is, the higher the transition temperature becomes. These are the reasonable conclusions which can be foreseen qualitatively.

It remains now to determine whether the transition is of the first kind or of the second kind. If it is the transition of the first kind, the discontinuous change may occur at a more or less higher temperature than the higher τ_t obtained here. The rotational transition to the A and B types, however, are surely possible for such limited values of interaction energies as shown in Fig. 8.

§ 6. Discussions

Four kinds of interaction energies will be proportional to the carbon number n of the long-chain molecule, unless the end effects of the molecule are taken into account. As the value τ_t obtained in § 4 does not depend on n, the original transition temperature T_t in the absolute temperature scale is proportional to l, and therefore, to n. This conclusion may not change very much, even if the transition should be of the first kind. Now this contradicts the experimental results. One of the way to adapt the theory is to consider the entropy due to the molecular twisting as Y. Kakiuchi did.[10] The situation does not change even if the number of molecular orientations is six instead of three. The present model is too naive to be compared further with the experiments.

The statistical theory of the rotational transition has been developed by many authors since J. Kirkwood. These theories are very interesting, but mathematical difficulties make it hopeless to apply these theories to the long-chain compounds in which the molecular interactions are not simple. T. Oguchi[13] investigated the rotational phase transitions in the simple cubic dipolar molecular crystals with the continuous model and obtained the true transition point as the highest branching point of the integral equation. The lower τ_t in the present paper may correspond to the lower branching point found in his investigation. The present theory with the discontinuous model is far from being adequate, but may not be much different in its results from the theory with the continuous model, especially when energy valleys are so deep that the behaviours of molecules are almost determined by them.

There are some regions which belong to the A or the B type in Fig. 7 but which have no transition points in Fig. 8. In order to investigate the behaviour of our system in these peculiar regions, it seems that we must take various possibilities into consideration. For instance, only the perfect ordered states were investigated in § 3. However, partly ordered solutions may also be considered. These are the states where x_{pi}'s and y_{kij}'s can have some definite values other than 0 or 1 at 0°K. These definite values may depend upon the interaction energy values. It is possible that there are some partly ordered solutions and that they appear in Fig. 7. Moreover, it is conceivable that the transition point to the A type can not be realized being covered by the transition to such states. The lower τ_t already obtained seems to be the transition point to some partly ordered solution which can be expressed by the variables in Table I. If we want to calculate the transition point for other types, the variables must be reduced in such a way that the types may be characterized. However, these are beyond the scope of present investigation.

Here, a paper by J. D. Hoffman[14] must be referred to. He compared the experimental results with his theory which is at the level of Bragg-Williams' approximation, neglecting the short range order and using the discontinuous model. His assumption is interesting in that each molecule has one deep minimum and twelve other shallow minima in its potential around the axis, though the short range order must not be neglected in the rotational transition. An interesting report was published by R. J. Meakins and J. W. Mulley[15] on the dielectric absorptions of the long-chain acetates. They suggest a possible mechanism of dielectric loss, assuming the four positions for each molecule. Finally, a paper by H. Tompa[16] is also interesting from some point of view, because he investigated mixtures of oriented molecules with a simpler discontinuous model than ours.

Our thanks are due to Assistant Professor S. Takagi for his kind encouragements in the course of this work.

References

1) A. Müller: Proc. Roy. Soc. A **138** (1932) 514.

2) W. O. Baker and C. P. Smyth: J. Amer. Chem. Soc. **60** (1938) 1229.

3) K. Higashi and M. Kubo: Sci. Pap. I. P. C. R. **36** (1939) 4286.

4) J. D. Hoffman and C. P. Smyth: J. Amer. Chem. Soc. **71** (1949) 431.

5) K. Sano and Y. Kakiuchi: J. Phys. Soc. Japan **4** (1949) 178.

6) E. R. Andrew: J. Chem. Phys. **18** (1950) 607.

7) Y. Kakiuchi, T. Sakurai and T. Suzuki: J. Phys. Soc. Japan **5** (1950) 369.

8) Y. Kakiuchi, H. Komatsu and S. Kyoya: J. Phys. Soc. Japan **6** (1951) 321.

9) A. Müller: Proc. Roy. Soc. A **178** (1941) 227.

10) Y. Kakiuchi: J. Phys. Soc. Japan **6** (1951) 313.

11) Y. Takagi: Proc. Phys. Math. Soc. Japan **23** (1941) 44 and 553.

12) R. Kikuchi: Busseiron-Kenkyu **24** (1950) 52, 65, **25** (1950) 41, **37** (1951) 1 (in Japanese) and Phys. Rev. **81** (1951) 988.

13) T. Oguchi: J. Phys. Soc. Japan **8** (1953) 142.

14) J. D. Hoffman: J. Chem. Phys. **20** (1952) 541.

15) R. J. Meakins and J. W. Mulley: J. Chem. Phys. **21** (1953) 1934.

16) H. Tompa: J. Chem. Phys. **21** (1953) 250.

JOURNAL OF THE PHYSICAL SOCIETY OF JAPAN Vol. 9, No. 4, JULY—AUGUST, 1954

A Theory of the Formation of Slip Bands in Face-Centred Cubic Crystals

By Hideji SUZUKI

The Research Institute for Iron, Steel and Other Metals, Tohoku University, Sendai

(Received April 2, 1954)

A theory of slip band formation in a face-centred cubic crystal was given introducing three concepts, the one was a Frank-Read source multiplying dislocations in successive atomic planes, the second was the co-operative action of Frank-Read sources, the third was the different distribution of dislocations in the vicinity of the free surface than that in the interior of the crystal. By means of the former two, about one thousand dislocations could be multiplied from each source under the critical shear stress of the source without any dynamical effects. The third enables us to illustrate the difference in the surface structures between abraded and unabraded crystals.

§ 1. Introduction

Theoretical considerations on the formation of slip bands[1)][2)] have usually based on the assumptions that the amount of slip in a step observed first by Heidenreich and Shockley[3)] and examined by Brown[4)] took place in one atomic plane and that there are a sufficient number of Frank-Read sources multiplying dislocation loops in one atomic plane. Recent observations by Kuhlman-Wilsdorf and Wilsdorf[5)], Takamura[6)], and Fujita, T. Suzuki and Yamamoto[7)] indicate that the structure of slip bands is not so simple as Heidenreich and Shockly first described. Especially, Fujita, T. Suzuki and Yamamoto have shown that the step corresponding to the slip distance, 2000 Å, in mecanically polished surface of aluminium crystal was not parallel to the slip plane by revealing fine structures in the step using high resolution replica technique.

One the other hand, the theoretical considerations on the dislocation networks in an annealed crystal with the face-centred cubic lattice leads to the conclusion that the dislocation network with the longest life time is along {113} plane in which two edge and one screw dislocations meet at a node[8)]. This network does not multiply dislocations in one atomic plane, but in successive atomic planes, except the case in which the screw segment acts as the source in the slip plane belonging to the two lines parallel to the Burgers vectors of the two edge dislocations respectively.

The purpose of this paper is to give a semi-quantitative explanation of the observations of slip bands on the basis of the following three main concepts. The first is a Frank-Read source multiplying dislocations in successive atomic planes, the second is the co-operative action of Frank-Read sources, which was recently introduced by van Bueren[9)] for the sources in one atomic plane in rather a different way, the third is the difference of the distribution of dislocations in the vicinity of the free surface than in the interior of the crystal.

§ 2. Frank-Read Sources in a Sufficiently Annealed Face-centred Cubic Crystal.

Let us consider a part of a hexagonal network, which acts as a Frank-Read source, this network may notionally be dissociated into three dislocations, in which the operating dislocation segment is not dissociated as shown in Fig. 1. Each fashion of lines denotes a dislocation with each Burgers vector. Then the dislocation loop including the operative dislocation segment is just that proposed

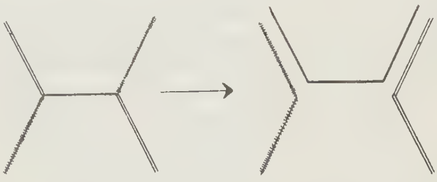

Fig. 1. Notional dissociation of a hexagonal network.

first by Frank and Read[10], which multiplies dislocations in one atomic plane. The other two dislocations, however, may change the state of affairs, namely, there are four cases; (i) If the Burgers vetors of the both pole dislocations are identically in the operative slip plane of the source, these dislocations do not change the original geometrical charactor of the slip plane. The slip plane, however, becomes a multivalued surface around the pole dislocations, if the Burgers vectors of the pole dislocations are not parallel to it, as shown in Fig. 2. (ii) When the components of both Burgers vectors normal to the slip plane are the same sign, the slip plane is deformed like *b* in the figure. (iii) If the one is of the opposit sign to the other, the plane becomes like *c*. (iv) At last if the Burgers vector of one of the pole dislocations is parallel to the operative slip plane and that of the other has a normal component, then the slip plane becomes a simple helicoidal plane round the latter pole dislocation as d^*.

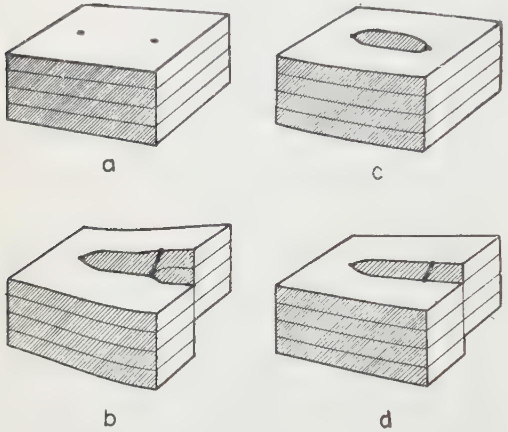

Fig. 2. Deformation of the operative slip plane of Frank-Read source, when it is an element of a hexagonal network.

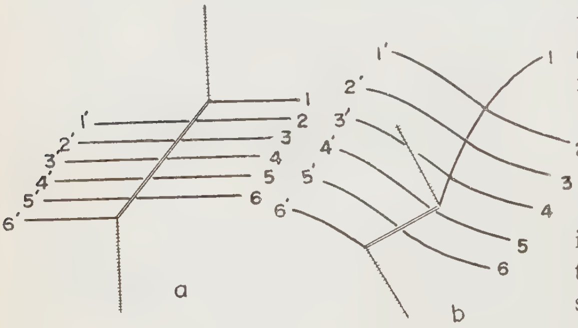

Fig. 3. Jog formation in a group of dislocations situated in every atomic plane when they cut an intersecting dislocation with Burgers vector crossing their slip plane. (a) View along the slip plane, (b) View along the the normal to the slip plane.

In the cases (ii), (iii) and (iv) the dislocation shifts successively to the neighbouring atomic plane at every revolution around the pole dislocation. In the case (ii) a jog with two atomic distance is produced after one revolution and in the case (iv) the amount of jump of the jog is one atomic distance, while in (iii) any jog is not formed.

On the other hand, since Burgers vectors of dislocations meeting at a node in a hexagonal network are in an octahedral plane, the case (i) is realized only if the operative slip plane is just the Burgers vector plane. Under this restriction the mechanical balance between the line tensions of three dislocations, however, could be established only in the two cases, the one being that the networks is in the Burgers vector plane, the other being that the operative dislocation is in screw type and the other two meeting at the node are in edge type forming $\{113\}$ network as already mentioned by T. Suzuki and the author[8]. The dislocation network lying in its Burgers vector plane, however, will disappear more easily than $\{113\}$ network, because the former is not required any vacancy generation during the coarsening of the mesh of the network. The screw dislocation in $\{113\}$ network would easily become shorter than edge dislocations during high temperature annealing, Frank-Read sources multiplying dislocation loops in one atomic plane, therefore, seems to be very rare in possible types of sources. When the edge dislocation in $\{113\}$ network operates as the source, the case (ii) is realized. Other cases (iii) and (iv) seem to be as rare as (i), because in these cases the network is not a regular hexagonal network, which means that the dislocation segments parallel to each other have the same Burgers vector[8)11], so the life time until it is annihilated is rather short.

We shall call the layer, in which dislocations propagate in every atomic plane, as slip layer in the following.

---

* I am indebted to Prof. Frank for this case.

Now we should note an important property of dislocations in every atomic plane concerning the jog formation when these cut through an intersecting dislocation with a Burgers vector crossing the operative slip plane. Let us suppose that the intersecting dislocation is fixed rigidly in the crystal, then a jog should be formed in a sweeping dislocation as cut through it, but either of the dislocation segments divided by the jog will interact with a segment of the next dislocation to eliminate the jog. The reaction takes place successively between dislocations in the neighbouring atomic planes. The process is schematically shown in Fig. 3. The jogs with jump amount of one atomic distance can be removed and only one large jog is left behind as shown in the figure. The large jog formed in this way may be considered rather reasonably as a segment of a network.

The both segments of a sweeping dislocation separated by the large jog can revolve around the intersecting dislocation when the jump amount of the jog increases beyond a critical distance, at which the both segments can move freely from each other under the applied stress. The regular elimination of jogs is then disturbed. The critical distance to cause such a disturbance is given by the expression, $Gb/[8\pi(1-\nu)\sigma]$, where G is the shear modulus, b the strength of the dislocation, ν the Poisson's ratio, σ the resolved shear stress[12]. It is, therefore, reasonable to suppose that the distribution of dislocations in a slip layer will lose its uniformity and result in dilute and dense lamellae alternately with the period of the thickness mentioned above. This period is nearly equal to the average spacing of the elementary slip calculated by Kuhlman-Wilsdorf, van der Merwe and Wilsdorf[13]. The fine structure in a large slip according to the above consideration, however, differs from the picture customarily accepted, as pointed out elswhere[13].

§ 3. Co-operative Action of Frank-Read Sources

Van Bueren[9] has pointed out that the back stress against a Frank-Read source due to dislocation loops multiplied from itself will considerably be decreased, if other sources situated in a thin layer including the initial source act simultaneously, extending the slip over the whole section of the specimen. Let us suppose that a dislocation loop is emitted from each source and its motion comes to an end forming a pair of screw dislocations with that emitted from the neighbouring source in the thin layer. The back stress against the action of the source is then

$$\frac{Gb}{2\pi}\frac{d^2}{L_1{}^3}\left(1+\frac{1}{3^3}+\frac{1}{5^3}+\cdots\right)$$

in a very crude approximation, where d is the separation between two slip planes in which the two neighbouring sources are situated, L_1 the distance between the source and the stopped dislocation pair and of the distance by which a screw dislocation propagates crossing the dislocation networks in the crystal. According to the consideration on the dislocation networks[8][15], L_1 may be assumed to be 5×10^{-3} cm and d is of the order of 3×10^{-5} cm in an aluminium crystal. Then the back stress caused by the first loop is about $10^{-10}G$.

On the other hand, according to the consideration in § 2, the shear stress required to continue the action of the source will decrease with the progression of multiplication on account of the increase of its length by its shift, provided that the crimb associated by vacancy flow does not take place. The shear stress required to continue the second revolution in an aluminium crystal is

$$\sigma_0\frac{l}{l+\Delta l}\simeq\sigma_0-10^{-3}G\,,$$

where σ_0 is the critical shear stress of the source, Δl the change of the source length after one revolution. From these estimations it is easily seen that the decrease of the required force to continue the multiplication is far greater than the back stress. It is, therefore, reasonable to suppose that the multiplication will continue until the increase of the length of the source comes to an end.

The length of the source increases until the operative dislocation reaches to the neighbouring node shifting over the screw dislocation in {113} networks. The direction cosine of the network plane to the operative slip plane is $\sqrt{3/11}$, and the length of the screw dislocation is supposed to be considerably shorter than the edge dislocations, so the distance of shift may be a fraction of

$\sqrt{3/11}\,l$. The number of dislocation loops emitted from each source is then about the order of one thousand in a very rough estimation, which agrees with the accepted value since Heidenreich and Shockley. The explanation of the observation by Heidenreich and Shockley[3] or by Brown[4], however, requires more detailed considerations, which will be found in § 4 and § 6.

§ 4. Role of Surface Sources

Hollomon[16] has pointed out that a source ending at the free surface will act as a source with the length of twice the real one, so the sources at the free surface will act under a smaller stress than in the interior of the crystal. On the other hand, it is reasonably supposed that the dislocations ending at the free surface are longer than those in the interior of the crystal in order to establish the mechanical balance between line tension of dislocations as follows.

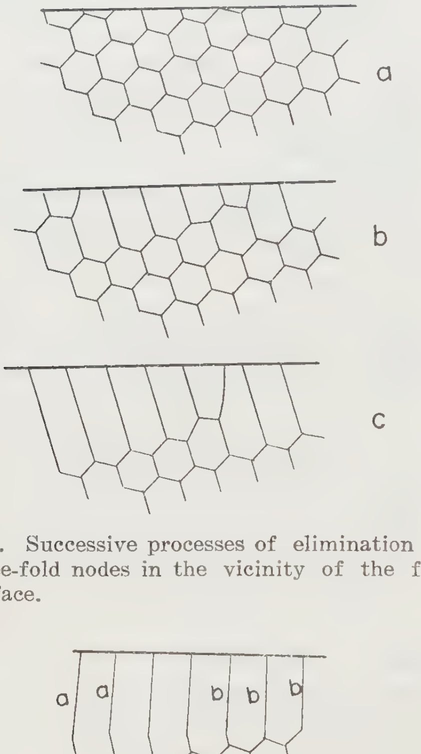

Fig. 4. Successive processes of elimination of three-fold nodes in the vicinity of the free surface.

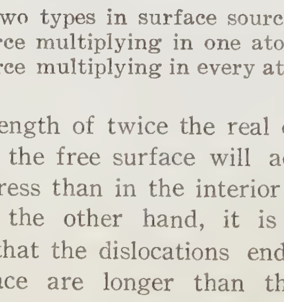

Fig. 5. Two types in surface sources.
a: Source multiplying in one atomic plane.
b: Source multiplying in every atomic plane.

The mechanical balance between line tensions of dislocations will be severly disturbed when a new free surface is appeared by electro-polish. The migration of a dislocation is not arrested by neither the anodic film nor the energy of the ledge in the metal surface because a metal ion will leave from the metal surface and occupy a suitable site in the anodic film to make the total energy of the system minimize during the electro-polish. The dislocations ending at the free surface therefore, tend to become perpendicular to the free surface. Three-fold nodes, in the sence of Thompson[11], in the vicinity of the free surface will then climb to the free surface as shown schematicall in Fig. 4. The process to eliminate the three-fold nodes resembles the unknitting in its propagating nature.

Since the decrease in the length of dislocation line is about l when a three-fold node is swept out to the free surface, the force acting on the node is about lT/R, where T is the line tension of the dislocation and R the distance between the node and the free surface before the unknitting, provided R be the order of l. This force is sufficiently large to make the node climb without any thermal activation until R reaches to a few times l. It seems, therefore, to be reasonable to suppose that a layer about 10 micron thick, in which a three-fold node cannot exist, is always developed in the surface of the crystal as it is subjected to electro-polish.

Frank-Read sources in the surface layer then have a different nature than those in the interior of the crystal. A source in this layer can multiply dislocations in one atomic plane, if it revolutes around its two-fold node, and it can multiply dislocations in successive atomic planes if the dislocation is directly connected to a three-fold node or the distance between the two-fold and the three-fold nodes is very small as shown in Fig. 5.

The co-operative action of sources will then differ in the vicinity of the free surface than in the interior of the crystal. The source at the surface will first act, but a source in the interior of the crystal could not act simultaneously, because the lengths of the sources differ markedly between these two regions.

The slip extending over the whole section of the crystal takes place rather irrespectively to the action of the surface sources. The majority of the surface sources produce microslip as already mentioned by Kuhlman-Wilsdorf et al[13], but some further considerations seem to be required as will be found in § 5. Very small number of the surface sources will continue a part of the slip extending over the whole section of the crystal.

In a mechanically polished surface, the mesh of the network becomes smaller than that in the interior and the layer free from three-fold nodes will become thinner than l, so the sources in the surface are not easier to act than that in the interior. The surface structure reveals then the situation of affairs in the interior more precisely than that in the carefully treated surface as already mentioned by Mott[1].

In a chemically etched surface, as employed by Heidenreich and Shockley[3] or by Yakutovitch, Yakovleva, Lerinman and Buinow[17], the surface layer free from three-fold nodes could not be developed, because a dislocation ending at the free surface is locked in a corner or in an edge of an etch pit during the etching process. The surface structure due to the deformation is then similar to that in abraded surface.

§ 5. Explanation of Observations by Optical Microscopes

1. *Orientation Dependence of Deformation Mechanism.*

Deformation mechanism of face-centred cubic crystals has been investigated by many workers especially on aluminium crystals with great details.[18][19][20][21][22][23][24] One of these results due to Igarashi, Okada and Hirakata[23] is shown in Fig. 6. The surface structure of a deformed crystal has close connection with the direction of the tension axis. The orientation dependence may be accounted for in terms of co-operative action of sources belonging to various slip systems as follows.

If all sources belong to only one slip system, parallel slip lines appear, and others do not. In a face-centred cubic crystal, however, there are many sources belonging to various slip systems. The local stress due to the dislocations belonging to the principal system may induce the action of a source belonging to another slip system, and the back stress will be released by the induced action of the source depending on the interaction between the principal and the drived system. Following Fujita et al we represent a slip system by the triangle in the stereographic projection of the tension axis, in which the slip system is the principal. The interaction between two parallel dislocations belonging to the principal slip system, a, and one of c, d, e, h, i, j, k and l systems is nearly equal to one half of a–a interaction, which is equal to a–f and a–g interactions, while there are no interactions between a–b and a–m systems using the notation in Fig. 7.

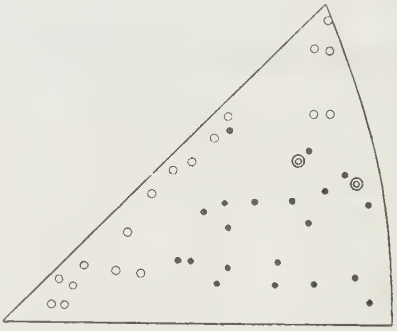

○ .... Clustered slip
● .... Deformation bands
◎ .... Unpredicted turst slip

Fig. 6. Orientation dependence of deformation mechanism. (After I. Igarashi, K. Okada and T. Hirakata[24].)

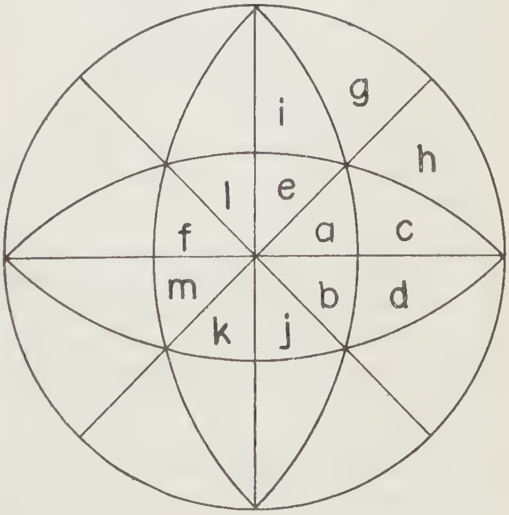

Fig. 7. Slip systems in a face-centred cubic crystal.

(*a*) *Cross Slip of the First Kind*

We shall call the kink in a slip layer accompanied by a distinct slip structure of the cross slip system as the cross slip of the second kind, and that accompanied by only the traces of the principal slip system as the cross slip of the first kind.

If the co-operative action takes place between sources belonging to the principal slip system, the back stress is decreased as mentioned in § 3. Since these sources are not situated in the same atomic plane, the slip layer is not exactly parallel to the operative slip plane, but has a stepped structure being composed of segments parallel to the slip plane. The stress due to the dislocations lined at the step depends on the direction of the dislocations, that is, screw dislocations lined at both boundaries of the slip layer will readily form pairs between dislocations on the both sides of the layer as shown in Fig. 8. The cross slip of the first kind is an inaccurate projection of the step in the slip layer in the interior of the crystal to the free surface through the action of surface sources.

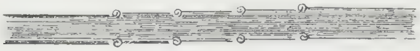

Fig. 8. Arrangement of screw dislocarions along the slip layer.

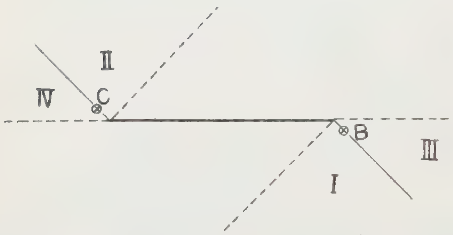

Fig. 9. Co-operative action between sources belonging to the principal and to one of *d*, *e*, *h*, *i*, *l*, *m* systems.

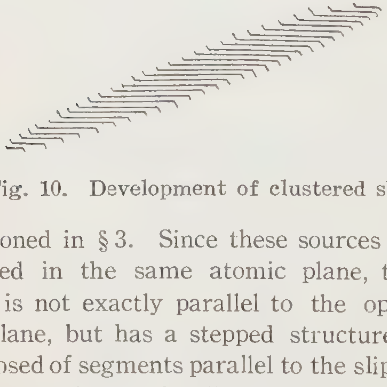

Fig. 10. Development of clustered slip.

(*b*) *Deformation Bands*

The step in the slip layer perpendicular to the slip direction becomes a nucleus of deformation band as already mentioned by Mott[25)1)] and Frank and Stroh[26)].

(*c*) *Clustered Slip*

Let us suppose that a source with a different Burgers vector than that of the principal slip system acts by the local stress due to the dislocations belonging to the principal, the back stress against the both sources decreases only to the half compared with the case of an isolated source. Mean- while, since the drived source is situated in the vicinity of the slip plane of the initial source, the multiplied dislocations from the drived source can move only by a small distance. The drived source, therefore, cannot multiply so many dislocations as discussed in § 3, and the slip of the principal system will come to an end when it drives the action of a source with a different Burgers vector than itself.

On account of the stress field of stopped dislocations the source belonging to the principal and situated in I and II in Fig. 9 could not act. The sources in III or IV could not multiply so many dislocations that mentioned in § 3, because the multiplied dislocations will be arrested interacting with dislocations produced from *B* or *C* source. The dislocations produced from sources situated in the regions except I, II, III and IV will be arrested by the stress field in I or II and tend to form stopped slip regions similar to the first one. The process seems to resemble the kinking as represented in Fig. 10. The so-called clustered slip seems to be developed by means of the above-mentioned mechanism.

The clustered slip will, therefore, be observed in the case of large resolved shear stress in *e*, *d*, *h*, *i*, *l*, *m*, systems. The orientation depence observed by Igarasi et al[23)] indicates qualitatively good argeement with this conclusion.

(*d*) *Cross Slip of the Second Kind*

When a source belonging to *f* or *g* slip system is induced to act by the local stress due to the dislocations of the principal system, the back stress against the initial and the drived sources can perfectly be removed by pair annihilation. The slip system, *f* or *g*, will, therefore, appear more easily than *e*, *b* systems even if the resolved shear stress is greater in *e* or *b* system than *f* or *g* system. The cross slip, however, is not so notable in the vicinity of {111} as in {100} owing to the more rapid decrease of the resolved shear stress of g system in the triangle a than that of f system.

Since the length of a surface source belonging to the cross slip system cannot become shorter than that belonging to the principal slip system, the sources belonging to the cross slip system are very rare in the surface layer. The cross slip of the second kind could, therefore, not be observed when the surface structure is produced only by the action of the surface sources.

2. *Slip Bands in an Alloy*

The threshold value for the action of sources in alloy does not depend on their length on account of locking force due to the heterogeneous distribution of solute atoms[27)28)], so the source can then continue the multiplication of dislocations more than in the case of pure metals as already mentioned by Mott[29)]. Then the local stress due to the group of dislocations multiplied from a source is very greater than in pure metals, so the sources belonging to another slip system with rather a low resolved shear stress may easily be activated. Moreover in the alloy once the action of the source begines, many dislocations can be multiplied if the dislocations do not pile up at the intersection of both slip planes of the principal and the drived systems. The cross slip, therefore, takes place more easily in α-brass than in pure copper.

The large group of dislocations can also pass over a local disturbance caused by the action of sources with a different Burgers vector than the principal. The clustered slip is, therefore, more difficult to take place in α-brass than in pure copper. The step in a slip layer cannot arrest the motion of dislocations in a different slip layer, so the deformation bands are not observed in an α-brass crystal.

Another difference between pure metals and alloys is caused from the difficulty in the formation of long surface sources, that is, the locking force of dislocations will resist the transmission of forces to make the node sweep out to the free surface. The surface sources, therefore, do not play special role in the formation of surface structure even in the later stages of deformation. The surface structure of a high alloy crystal thus represent the situation in the interior of the crystal more precisely than that of a pure metal.

§ 6. Explanations of Observations by Electron Microscopes

1. *Heidenreich and Shockley's Experiment*

In chemically etched specimens as used by Heidenreich and Shockley[3)] the surface sources do not play any special role during the deformation, and the step corresponding to the slip amount of 2000 Å will be produced by the cooperative action of sources situated in a thin layer parallel to the slip plane as already mentioned in § 3 and § 4.

The dislocation networks in the vicinity of the slip layer would severely be disturbed by collision with sweeping dislocations during the first co-operative action of sources and the length of dislocation segments along the slip plane will become to be short on account of climb of nodes. However, if the network recover to the initial form, next co-operation will preferentially take place near the first layer, because there are sufficient number of dislocations with the same sign lining on either side of the first layer, which may become the nucleus of the next co-operative action. The next action, however, does not take place in the same sources with the first one because the sources become to be short to establish the mechanical balance at the new positions. The dislocations multiplied by the next action, therefore, could not propagate through a layer with a finite thickness in which a dislocation is arrested by the local stress due to the lining dislocations in either side of the first slip layer. The thickness of the non-slip layer is nearly equal to $Gb/8\pi\sigma$ as mentioned in § 2, and this expression gives a value of the order of 200 Å in aluminium when $\sigma = 2\ \mathrm{kg/mm^2}$.

According to the above-mentioned picture the fine structure of a slip band should be represented by Fig. 11 b instead of Fig. 11 a.

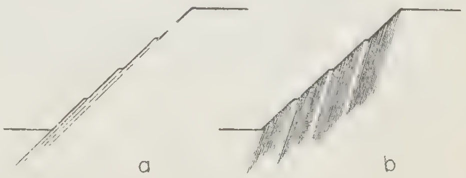

Fig. 11. Fine structure of a slip band. (a) The picture due to Heidenreich and Shockley. (b) The picture proposed in this paper.

The recent observation by Fujita et al[7] with high resolution replica technique succeeded in showing that the step corresponding to the slip amount about 2000 Å did not take place in one atomic plane.

The recovery of the hexagonal networks in the vicinity of the first layer, however, becomes difficult with decreasing temperature. The next slip layer then appears irrespectively to the first. The temperature dependence of the number of lamellae in a band observed by Brown[30] is thus explained in terms of recovery of hexagonal networks, as already suggested by Brown [31] and Mott[1] in rather an ambigious way.

2. *Interaction of slip lines with twin boundaries*

We shall deal only with the case in which the slip direction is parallel to the twin boundary.

Kuhlman-Wilsdorf and Wilsdorf[5] have observed two distinctly different types of interaction of slip lines with twin boundaries, the one being that a slip line crosses the twin boundary with change of direction, the other being a fan-shaped array of short slip lines. The former was found in α-brass and the latter was in pure metals.

Two cases may be possible when a group of dislocations meet with a twin boundary, the one being that the dislocations pass through the twin boundary and the other being that the dislocations do not pass through the twin boundary, but the slip layer continues through the boundary inducing the action of sources in the twinned material as in the case of cross slip of the second kind. Since the stress required to make a dislocation pass through a twin boundary is of the order of $G/50$, if a source at a suitable position in the twinned material acts before the local stress at the twin boundary reaches to this value, the dislocation does not pass through the boundary. If there are not suitable sources in the twinned material, the dislocation will pass through the boundary by means of stress concentration due to the piled up dislocations.

The average distance between the head of the piled up dislocations and a suitable source to continue the slip layer is

$$1/Ldn$$

where L is the length of the piled up dislocations along the twin boundary, d the thickness of a layer in which a suitable source should be situated, n the number of sources belonging to the slip system in a unit volume. The local stress acting on the source is of the order of $iGbLnd/2\pi$, where i is the number of the piled up dislocations required to pass through the twin bandary and $i=G/50\sigma$. Since in pure metals the surface structure is produced by the action of surface sources, L is about 10^{-3} cm, n is about $2\times10^{8}/\mathrm{cm}^3$, d is about 3×10^{-5} cm, and assuming σ is of the order of 1kg/mm^2 the local stress in pure aluminium is then about 5 g/mm^2. This magnitude of the local stress is not sufficient to induce the action of the source, so the dislocation should pass through the twin boundary in pure metals. Meanwhile in α-brass n is greater about one hundred times than in pure metals [8][16], and L is also large in α-brass and reasonably assumed to be about 10^{-2} cm. Then the local stress is about 5 kg/mm^2, which is sufficiently large to induce the action of the source. The dislocations, therefore, do not pass through the twin boundary in α-brass.

When a dislocation pass through the twin boundary, it must be of screw type, and also the both half dislocations in it should be unified. The dislocation then is not restricted in an octahedral plane and causes an uncrystallographic slip, in which the glide plane is decided according to the stress acting on the dislocation. The local stress due to the piled up dislocations at the twin boundary changes gradually as the dislocations pass through the boundary, so the fan-shaped slip takes place.

When sources in twinned material acts by the stress due to the piled up dislocations, the intersection of the both slip layers in the initial and twinned region is not usually in the twin boundary. The local disturbance in slip layer at the twin boundary found by Kuhlman-Wilsdorf and Wilsdorf is thus an evidence for the idea that the slip layer in the twinned material is caused by the action of sources in this region.

3. *Slip Bands in an α-brass Crystal*

Fujita and the author[14] have found slip layers in an α-brass crystal which have finite width from 100 Å to 1μ and the amount of shear in each layer being equal to that caused by the motion of a group of dislocations situated in every atomic plane. The photograph showed also fine structure in each slip layer at the spacing of a few hundred Angstrom. The fine structure may be attributed to the disturbance in the distribution of dislocations in a slip layer as discussed in § 3.

The slip cluster in α-brass crystals may be attributed to the difficulty to deform the dislocation network by the collision with the sweeping dislocations multiplied from sources in the first layer on account of the locking force, so the operation in the next layer can easily take place, because any recovery of networks mentioned in 1 or this section is not required.

4. *Microslip*

The mechanism of formation of microslip proposed by Kuhlman-Wilsdorf and Wilsdorf should be modified, because their explanation requires to assume a too high density of sources in the surface layer. According to the discussion in § 4 there are only two-fold nodes of dislocations in the surface layer about 10μ thick, and a segment between the free surface and the two-fold node act as a source. The two-fold node will be swept out to the free surface after the multiplication of small number of dislocations on account of the back stress, and new two-fold node is formed at a shifted position. If the shifting distance was smaller than $Gb/[8\pi(1-\nu)\sigma]$, the source cannot continue the next action under the applied force. A surface source, thus, produce many microslip with the average spacing of the order of $Gb/[8\pi(1-\nu)\sigma]$. Since the number of surface sources belonging to the operative slip system is about $n/6 \simeq 4 \times 10^5/\mathrm{cm}^2$, and assuming that the elementary lines have a length of 50μ, each surface source should be shifted by the distance about a few micron in order to cover the surface with microslip.

§ 7. Direct Evidences Indicating a Definite Width of a Slip Layer

The discussions in § 5 and § 6 support the view point that a slip layer has a definite width indirectly. It is, however, worth while to summerize the direct evidences indicating that elementary slip lines in the sence of Heidenreich and Shockley have a finite width.

1. *Difference of Blackening between Parallel Slip Lines Shadowed from a Definite Direction.*

Fujita, T. Suzuki and Yamamoto⁷⁾ have found parallel slip lines with different blackening in shadowed surface structure of deformed alminium crystals. It is obvious that, if the slip takes place only in one atomic plane, the blackening should identically the same. The difference indicates that a slip line has a finite width and the shear in each line is not identically the same. The photograph taken by Fujita et al may denotes that there are a few types of slip lines; the one is produced by the motion of dislocations belonging to the principal slip system situated in every atomic planes, the second corresponds to a similar homogeneous shear but belonging to another slip system common with the principal in the slip plane, the third is the usual one produced by the motion of dislocations in one atomic plane. These varaity of the slip lines, however, does not seem to correspond to the varaity of the sources in the crystal, but of the surface sources. The photograph taken by Kuhlman-Wilsdorf and Wilsdorf⁵⁾ shows also different blackening between parallel slip lines as already mentioned elswhere.¹⁴⁾.

2. *Different Blackening at the Intersection of two slip layers.*

When a slip line produced by the slip in one atomic plane intersects another slip line in any type, the blackening of the new slip line could not be changed at the intersection. Neither of the intersecting slip layers, however, has the same blackening with the intersections in many photographs already published, for example, Fig. 5 in Brown's paper³²⁾, Fig. 6 and Fig. 7 in Kuhlman-Wilsdorf and Wilsdorf's paper⁵⁾.

3. *Precipitates Along Slip Lines*

Castaing and Guinier³³⁾ have shown first an electron micrograph indicating selective precipitation in a slip band using 4 per cent copper aluminium copper alloy. The precipitates in their photograph were too large to know the real width of the layer in which selective precipitation took place. Recently Koda and Takeyama³⁴⁾ have succeeded in showing that each layer of selective precipitation has a finite width changing layer to layer by means of very fine precipitates in Al-Cu alloys.

4. *Slip Bands in an α-Brass Crystal*

See § 6, 3.

5. *Fine Structure in a Large Step in Mechanically Polished Surface.*

As already mentioned, Fujita et al⁷⁾ have found fine structure in a large step in mechanically polished surface which has not been resolved by Heidenreich and Shockley³⁾ and Brown⁴⁾. This fact indicates at least that it is not possible to produce so much as 700 dislocations in one atomic plane. The slip line found by Fujita et al seems to be accounted for by the mechanism mentioned in § 2.

The author wishes to express his thanks to Prof. Sakae Takeuchi for his interest and support, and to Prof. Taira Suzuki and Mr. F. E. Fujita for their valuable discussions on various subjects in the field of dislocation theory, especially, on their important unpublished results. He also expresses his thanks to Profs. N. F. Mott and F. C. Frank, of the University of Bristol, for their kind discussions during their visit to Japan, and to Prof. Shigeyasu Koda, of Hokkaido University, for allowing me to see his unpublished results.

References

1) N. F. Mott: Phil Mag. **43** (1952) 1151.

2) J. C. Fisher, E. W. Hart and R. H. Pry: Phys. Rev. **87** (1952) 958.

3) R. D. Heidenreich and W. Shockley: J. Appl. Phys. **18** (1947) 1029; The Strength of Solids (London, Phys. Soc., 1948) 57.

4) A. F. Brown: Nature **163** (1949) 961; Metallurgical Applications of the Electron Microscope (London, Institute of Metals, 1950) 103; Advances in Physics **1** (1952) 427.

5) D. Kuhlman-Wilsdorf and H. Wilsdorf: Acta Metallurgica **1** (1953) 394.

6) J. Takamura: Read at Nikko Symposium on Crystal Plasticity and Dislocation. (Sept. 1953)

7) F. E. Fujita, T. Suzuki and M. Yamamoto: To be published.

8) T. Suzuki and H. Suzuki: Read at Int. Nat. Conf. Theoretical Physics held at Kyoto on Sept. 1953.

9) H. G. van Bueren: Acta Metallurgica **1** (1953) 464.

10) F. C. Frank and W. T. Read: Rhys. Rev. **79** (1950) 722.

11) N. Thompson: Proc. Phys. Soc. London **66B** (1953) 481.

12) A. H. Cottrell: Progress in Metal Physics, **1** (London, Butterworths Scientific Publications, 1949), 77.

13) D. Kuhlmann-Wilsdorf, J. H. Van der Merwe, and H. Wilsdorf: Phil. Mag. **43** (1952) 632.

14) H. Suzuki and F. E. Fujita: J. Phys. Soc. Japan **9** (1954) 428.

15) H. Suzuki: To be published.

16) See N. F. Mott (1).

17) See A. F. Brown: Advances in Physics **1** (1952) 427.

18) R. W. K. Honeycombe: J. Inst. Metals **80** (1951) 45.

19) R. W. Cahn: J. Inst. Metals **79** (1951) 129.

20) N. K. Chen and C. H. Mathewson: J. Metals **3** (1951) 653.

24) A. Laloef and C. Crussard: Rev. Mét. **48** (1951) 461.

22) H. Nishimura and J. Takamura: Tech. Rep. Engineering Research Institute Kyoto University **2** (1952) 139.

23) I. Igarashi, K. Okada and T. Hirakata: J. Japan Inst. Metals, **16** (1952) 425. (in Japanese)

24) R. R. Hashiguchi: J. Metals **4** (1952) 528.

25) N. F. Mott: Proc. Phys. Soc. London: **64 B** (1951) 729.

26) F. C. Frank and A. N. Stroh: Proc. Phys. Soc. London **65 B** (1952) 811.

27) A. H. Cottrell: Strength of Solids (London, Phys. Soc., 1948), 30; A. H. Cottrell and B. A. Bilby: Proc. Phys. Soc. London **62 A** (1949) 49.

28) H. Suzuki: Sci. Rep. Research Institute Tohoku Univ. **4** (1952) 455.

29) N. F. Mott: Phil Mag. **44** (1953) 742.

30) A. F. Brown: Nature **163** (1949) 961.

31) A. F. Brown: J. Inst. Metals **80** (1951) 115.

32) A. F. Brown: Advances in Physics **1** (1952) 427.

33) R. Castaing and A. Guinier: Comptes Rendus, **228** (1949) 2033.

34) S. Koda and T. Takeyama: Private communication.

JOURNAL OF THE PHYSICAL SOCIETY OF JAPAN Vol. 9, No. 4, JULY—AUGUST, 1954

The Statistical Time Lag of the Dielectric Breakdown of Mica, Glass and KCl

By Hazimu KAWAMURA, Hiroshi OHKURA and Takeo KIKUCHI

Faculty of Science and Engineering, Osaka City University, Osaka

(Received February 8, 1954)

The statistical time lag of the dielectric breakdown were measured for mica, glass and KCl, applying the recurrent pulse voltage of $2\times10^{-8}\sim1\times10^{-7}$ sec width. For mica, the statistical time lag was as large as 10^{-4} sec at 10% over-voltage. On the other hand, it was at most less than 10^{-7} sec for glass and KCl at 10% over-voltage. Thus the "single avalanche mechanism" is favored for mica, since the occurrence of the extremely large avalanche which is responsible for the breakdown may rely on extreme fluctuation, and should be rare event at the threshold field. While, in the case of KCl as well as glass, we may conclude that the "collective mechanism" is favored, from the fact that the statistical time lag is very short. From a rough estimation, we can conclude that the avalanche electrons become collective when their density becomes larger than 10^{18} 1/cm³.

§ 1 Breakdown Mechanism and Statistical Time Lag

The importance of the statistical fluctuation in the consideration of the mechanism of dielectric breakdown was first pointed out by Fröhlich,[1] and the role of electrons, which extremely deviate from the average behavior, in the production of avalanche was deeply investigated by Seitz.[2] The free electron in an insulator has a chance to be accelerated to the ionization energy in the course of a single free path, even if the field is not strong enough to accelerate the average electrons. The probability of this chance is given by $\exp(\alpha F_0/F)$, where $\alpha=2\sim3$, F is the applied field strength and F_0 is the field strength required to accelerate the average electrons. Hence the mean range for the ionization by collision is given by

$$\lambda=E(e/m)\tau^2\exp(\alpha F_0/F)\,. \qquad (1)$$

If the solid is brought to disruption by the energy dissipation resulting from the drift of a single avalanche whose size is greater than a certain critical value n_0, the chance for the occurrence of the breakdown per second is given by[2]

$$\nu=\nu_0\exp(-n_0/\bar{n})\,. \qquad (2)$$

$\bar{n}$ is the mean avalanche size given by $\exp(L/\lambda)$, where L is the path length allowed for the avalanche to drift. ν_0 is the frequency with which the starting electrons are supplied. Hence the disruption does not occur just at the moment of the application of the field, but may delay for $1/\nu$ sec on the average. This delay time is called "statistical time lag" and is very long for mica according to our previous measurement.[3][4] On the other hand, if the disruption is caused by the energy gain of electron as a whole just as in the case of amorphous substance discussed by Fröhlich,[5] the delay time of the disruption has not the statistical nature and merely composed of a build-up time so-called "formative time lag" which is supposed to be less than 10^{-8} sec at 10% over-voltage.

§ 2. Experimental Method

The schematic diagram of our present equipment is shown in Fig. 1. The transient voltage of extremely short rise time less than 10^{-8} sec is generated by the spark discharge of three-electrodes trigger gap which is triggered by recurrent pulses of 10^{-6} sec applied to the center electrode with P.R.F. of 50 1/sec. This transient voltage is applied to the delay line through its characteristic impedance. If a point B on the delay line is connected to earth, the transient voltage is reflected back and absorbed by the characteristic impedance. Thus we have pulse voltage at point A, whose width is twice the delay time from A to B as shown in Fig. 2. The characteristics of the delay lines employed are as shown in the

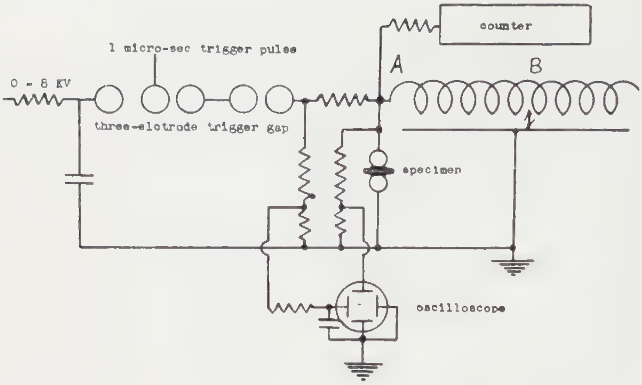

Fig. 1. Circuit diagram of 10^{-8} sec pulse generator.

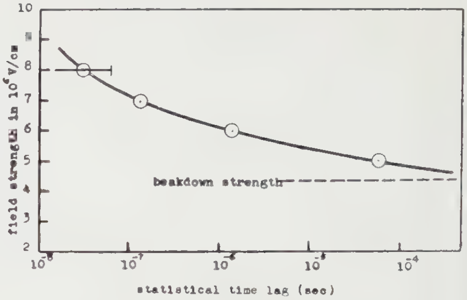

Fig. 4. Semi-log plot of statistical time lag of mica as a function of field strength: broken line indicates threshold breakdown field.

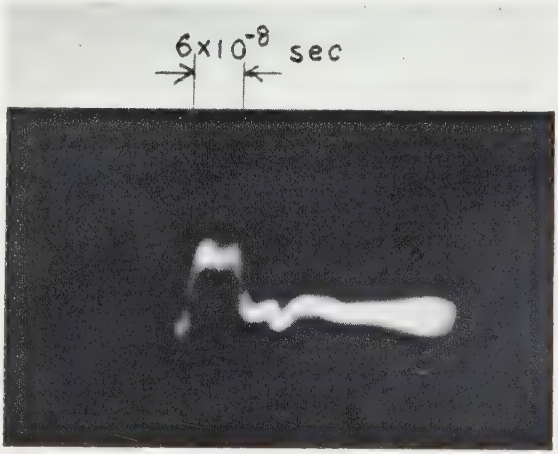

Fig. 2. Applied pulse voltage of 6×10^{-8} sec observed by oscilloscope.

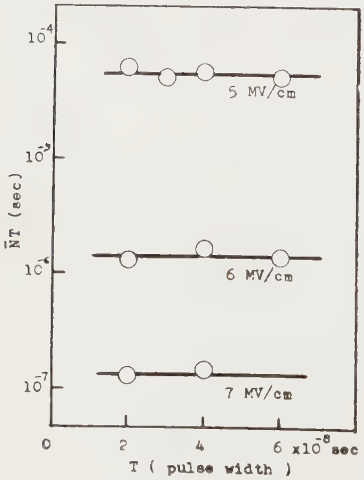

Fig. 3. Semi-log plot of time lag of breakdown (number of pulses × pulse width) of mica as a function of pulse width for various over-voltages.

following.

characteristic impedance	delay time
750 ohms	3.2×10^{-8} sec
910	1.46×10^{-7}

The height of the pulse was adjusted by changing the gap distance and the applied voltage, and was variable from 1 kv to 4 kv. Specimens were inserted between A and earth, and the recurrent pulses of a certain height were applied. The number of pulses applied before the breakdown occured were counted by a counter of scale 16 connected to A through a high resistance (1 MΩ). The time lag of the breakdown was obtained from (number of pulses)×(pulse width)

§ 3. Results

a) *Mica*

The specimens were biotite of $2.5\sim3.5\times10^{-4}$ cm thick on whose surfaces aluminium films were deposited by vacuum evaporation, and were inserted between steel balls which were used as electrodes. The thickness was determined from the electric capacitance measured at 100 kc. The breakdown strength of biotite was found previously⁶⁾ to be $4.32\pm0.12\times10^6$ volts/cm, employing recurrent pulse voltage of 7 μsec width.

We measured the number of pulses N applied before the breakdown occurred for various pulse widths and field strengths. Since time lags had random distributions, we determined the mean of N by Laue plot, and obtained the mean statistical time lag $\overline{N}T$, where T is the pulse width, for a certain pulse width and over-voltage. If the pulse width is longer than the formative time lag, $\overline{N}T$ may be constant and gives the statistical time lag, but if the pulse width becomes shorter than the formative time lag, N might increase rapidly, and we should be able to estimate the formative time lag from this pulse width. In Fig. 3 we plotted $\overline{N}T$ v.s. T for various over-voltage. We can see that the formative time lag is shorter than 2×10^{-8} sec.*

The statistical time lag $\overline{N}T$ is plotted against the field strength in Fig. 4. At 8×10^6 volts/cm, the disruption is brought about by a single pulse of 6×10^{-8} sec, and therefore, the statistical time lag is supposed to be less than 6×10^{-8} sec. The time lag increases as the field is decreased and amounts to longer than 10^{-4} sec at about 10% over voltage.

b) *Glass*

Soda-lime glass was blowed and made as thin as $2\sim3\times10^{-3}$ cm. The proccessing of the specimens was just as for mica. The measurements were done at elevated temperatures (150°C and 250°C), in order that the typical collective mechanism should be applied.[5] The breakdown strengths of many specimens were measured using the recurrent pulse voltage of 7 μ sec and of continuously variable height. The distributions of the strengths are shown in the histogram in Fig. 5a and Fig. 6a, from which the strengths were determined to be $2.41\pm0.06\times10^6$ volts/cm and $0.61\pm0.02\times10^6$ volts/cm respectively. Applying the pulse voltage of 3×10^{-8} sec whose height were ranging from 2.4 to 3.2×10^6 volts/cm for many specimens at 150°C, we counted the numbers of pulses required to cause the disruptions, and got the results as shown in Table I. We can see that the number of the events that the disruption is caused by a single pulse is overwhelmingly large compared to the other events which distribute rather widely and may be attributed to the errors resulting from the fluctuation of the pulse height or the lack of the accuracy in the measurements of the thickness etc.. The distribution of the field strength at which the single pulse disruptions are brought about is shown in the histogram in Fig. 5b. At 250°C we also made the similar experiment with the pulse of 3×10^{-7} sec at the field strength ranging from 0.5 to 0.7×10^6 volts/

Table I

Number of pulses	Number of events
1	11
2∼4	2
5∼30	3
30∼300	12
300∼3000	8
not disrupted	6

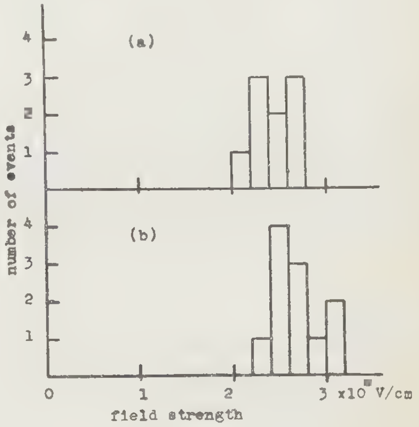

Fig. 5. Histogram showning the distribution of breakdown strength of glass at 150°C (a): distribution of field strength for single pulse disruption (b).

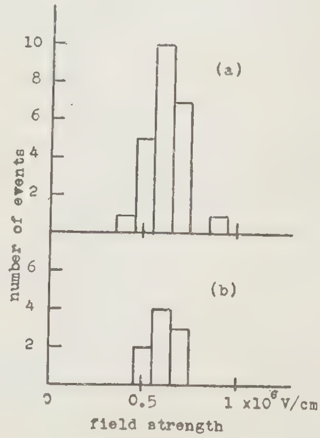

Fig. 6. Histogram showing the distribution of breakdown strength of glass at 250°C (a): distribution of field strength for single pulse disruption (b).

---

* In the previous paper, we reported that the formative time lag of biotite was in the range of 10^{-8}sec. We did not then pay a due care to the extremely large statistical time lag, and increased the pulse width too fast compared to the recurrence frequency of the pulses. The disruption should have occured at the width less than 10^{-8}sec, if a sufficient number of pulses had been applied.

cm, and obtained the results as shown in Table II. Clearly there is only two choices:

Table II

Number of pulses	Number of events
1	9
2	1
not disrupted	9

no disruption or single pulse disruption. The Fig. 6b is the histogram showing the distribution of the field strength under which the single pulse disruption occured. Thus it is shown that the statistical time lag does not exist or at least less than 3×10^{-7} sec at the neighborhood of the breakdown field, just as expected from the collective mechanism.

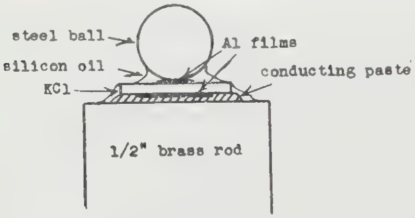

Fig. 7. Cross sectional diagram of specimen holder for the study of electric breakdown of KCl.

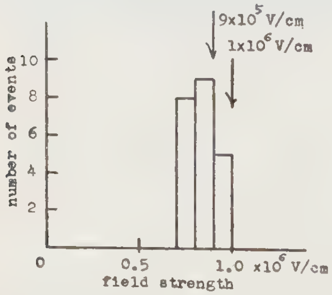

Fig. 8. Histogram showing the distribution of breakdown strength of KCl.

c) *Potassium Chloride*

Single crystals of potassium chloride were prepared by the Kylopoulus' methode from KCl powder containing divalent metals by less than 0.001%. The crystals were annealed at the neighborhood of the melting point. Aluminium was vacuum evaporated onto the cleaved surface and sticked to a brass rod by sticking paste containing graphite powder. The other surface was etched by the solution of alcohol and water until the thickness is reduced to $2.5\sim3.5\times10^{-3}$ cm. Again, aluminium was deposited on this surface as one electrode. The brass rod was employed as the other electrode. The specimen just prepared for the measurement was as shown in Fig. 7.

The breakdown strengths were measured increasing the pulse voltage of 3×10^{-8} sec by the step of 1×10^5 volts/cm for many specimens. The distribution of the breakdown strengths shown in Fig. 8, from which we obtained $8.4\pm0.6\times10^5$ volts/cm as the average breakdown strength. The number of pulses required to cause the disruption were counted at 9×10^5 volts/cm and 10^6 volts/cm with the pulse width of 3×10^{-8} sec. The results are listed on Table III. At 10^5 volts/cm the single pulse disruption amounts to 16 times out of the trials of 20 times. Therefore, we can conclude that the statistical time lag will be less than 3×10^{-8} sec under this field strength, even if it exists. Since at 9×10^5 volts/cm the single pulse disruption was not so doninant and the distribution was at-random, we could determine the mean statistical time lag from the Laue plot, and obtained 2.4×10^{-7} sec.

Table III

9×10^5 volts/cm

Number of pulses	Number of events
1	2
4	2
6	1
9	1
16	1
260	1

10^6 volts/cm

Number of pulses	Number of events
1	16
2	2
3	1
7	1

§ 4. Discussions

The fact that the time lag of the breakdown of KCl resembles to that of glass rather than to that of mica is unfavorable to the single avalanche mechanism for KCl. If the disruption is caused by a large single avalanche, the statistical time lag should be very large at the slight over-voltage as in the case of mica, since the occurrence of the large avalanche is resulting from the extreme fluctuation and hence the very rare event at the neighborhood of the breakdown field. The following facts also confirm the above feeling.

1) The pre-breakdown noise of KCl is supposed to be not resulting from the electron avalanches in solid,* since the applied voltage was higher than 5 kv in the experiment of Yamanaka and Suita.7) and there are some evidences that, if the applied voltage becomes higher than a few kv, we have the noise which is presumably the Schoenfeld type or resulting from corona discharge at the electrode.

2) If the single avalanche mechanism is correct, the breakdown strength must increase as the thickness of the specimen is decreased. In the case of mica we have confirmed this fact even for the specimens of as thick as 10^{-3} cm. But for KCl the strength is constant above 10^{-3} cm.9)10)

If the electron density of the avalanche becomes very high, we must consider, in addition to the electron-phonon interaction, the electron-electron interaction by which the fluctuations in the energy of electrons may be reduced. The rate of energy loss of an electron per unit distance resulting from the electron-electron interaction is roughly given by $\pi ne^4/\kappa_0\mathcal{E}$, where $\mathcal{E}$ is the energy of the electron, n the density of electrons and κ_0 the optical dielectric constant.11) If $\mathcal{E}$ is about ten times of the thermal energy and $n\sim10^{18}$ $1/\text{cm}^3$, we have $\sim10^5$ ev/cm. On the other hand, the rate of energy loss of the electron of velocity v resulting from the phonon excitation is given by $\hbar\omega_0/\tau v$, where ω_0 is the angular frequency of the longitudial lattice wave and $1/\tau$ is the electron-phonon collision frequency. In the case of KCl, we have 10^5 ev/cm for the electron whose energy is about ten times of the thermal energy, if we assume that $\tau\sim10^{-14}$ sec and $\hbar\omega_0\sim0.03$ ev. Thus the critical density at which the elecron-electron coupling would become comparable with the electron-phonon coupling may be about 10^{18} $1/\text{cm}^3$. The avalanche size required to cause disruption obtained by Seitz,2) under the assumption that the minute portion of the material where the avalanche drifts would be disrupted if each atom received as much as 10 ev, is about 10^{10} for KCl of 10^{-2} cm thick. The density of electron in this avalanche is about $10^{21}\sim10^{22}$,** since the diffusion radius of the avalanche is about 10^{-4} $\sim10^{-5}$ cm. This value is larger than the critical density obtained above by a factor of $10^3\sim10^4$. Therefore, the avalanche electrons become collective before they are multipled to the sufficient number to cause disruption. If the field is not so strong that the ionizations are resulting from the extreme fluctuations, the rate of growth of avalanche may be reduced, if the electron density of the avalanche becomes larger than the critical density. A stronger field is necessary to bring up the avalanche beyond this critical density. Under this strong field many electron avalanches may be produced at a time and this would cause the disruption to occur without any appreciable time delay. In the case of mica, if we assume that the collision frequency between electron and lattice is larger than that of KCl by the factor of 10, since the breakdown strength is larger by this factor, the critical density may be also larger by this factor. This might be the reason why the single avalanche mechanism is preferable in this case.

We wish to acknowledge the help by the Research Expenditure from the Ministry of Education.

References

1) H. Fröhlich: Phys. Rev. **56** (1939) 349.
2) F. Seitz: Phys. Rev. **76** (1949) 1376.
3) H. Kawamura, M. Onuki and H. Okura: J. Phys. Soc. Japan **7** (1952) 528.
4) H. Kawamura and M. Onuki: J. Phys. Soc. Japan **8** (1953) 731.
5) H. Fröhlich: Proc. Roy. Soc. **A 188** (1947) 532.
6) H. Kawamura and H. Okura: J. Phys. Soc. Japan **7** (1952) 540.
7) C. Yamanaka and T. Suita: J. Phys. Soc. Japan **6** (1951) 194.
8) A. von Hippel, E. P. Gross, J. G. Jelatis and M. Geller: Phys. Rev. **91** (1953) 568.
9) I. Ryu and H. Kawamura: J. Phys. Soc. Japan **9** (1954) 438.
10) J. H. Calderwood and R. Cooper: Proc. Phys. Soc. **B 66** (1953) 73.
11) A. J. Dekker and A. van der Ziel: Phys. Rev. **86** (1952) 755.

---

* von Hippel also has the opinion that the pre-breakdown noise is not resulting from the avalanche in the case of alkali halide8).

** We can not approve this value without some reservation, because the internal field due to the avalanche of this density is far greater than the breakdown field since the former is given by $(4\pi/3)\,rne/\kappa\sim10^9$ volts/cm, if we assume $r\sim10^{-5}$cm and $\kappa\sim5$.

JOURNAL OF THE PHYSICAL SOCIETY OF JAPAN Vol. 9, No. 4, JULY—AUGUST, 1954

Thermal Conductivity of Crystals and Liquids

By Sanchi MIZUSHIMA

Faculty of Engineering, Keio-gijuku University

(Read October 17, 1953, Received March 9, 1954)

Thermal conductivity of crystals without defects is calculated on the approximation that the mutual collisions of phonons of the normal type occur far more frequently than the Umklapp collisions. The conductivity K for crystals at temperatures not too low below the characteristic temperature and above is expressed as,

$$K \sim 0.1 \frac{qa(U/V)}{QT} ,$$

where q is the sound velocity, a the lattice constant, U/V the cohesive energy per unit volume, T the absolute temperature and Q is a number of the order of unity introduced to take into account of the difference of the crystal structure. This formula fits fairly well to observed values for ionic crystals having NaCl type lattice and furthermore applies equally to the conductivity of liquids. In the latter case it is shown that the above formula is approximately identical with the well known formula proposed by Bridgman.

§ 1. Introduction

In a non-conducting crystal, heat is carried in the form of flow of phonons. However, the thermal conductivity calculated from the continuum approximation of the crystal is known to become infinite. To get a finite value, the periodicity of the lattice has to be taken into account which enables the momentum transfer from the phonons to the lattice during a mutual collision of a certain number of phonons with the intervention of the lattice, known as Umklapp collisions. Collision process which is most effective for the hindrance of the heat flow against the temperature gradient in a perfect crystal is believed to be the three phonon collision one of this type in which one phonon is destroyed to create other two phonons or vice versa. This process arises from the nonlinearity of the vibration of the lattice. The exact calculation has been prevented by the lack of the knowledge on the forms and the frequencies of the normal modes in a given crystal as well as the ignorance of the explicit form of the nonlinearity of vibration.

In this paper we attempted to give the conductivity an expression applicable formally to every temperature range for perfect crystals and calculable from known physical constants. The calculation is based on the continuum approximation of the crystal and the periodicity of the lattice is introduced artificially as has been done by previous authors[1)2)]. The contribution from the optical modes which does not seem to have been taken into account explicity yet, is treated in two alternative ways. In the one approximation the optical modes are incorporated into the acoustical ones in the manner analogous to the method of Debye in the treatment of the specific heat of solids. In the other approximation a part of these is neglected at all which will be suitable when the optical modes have much higher frequencies than the acoustical ones and their group velocities are very small.

§ 2. Interaction Energy of Lattice Waves

In the harmonic approximation of the lattice vibration, the displacement D at point r is written as the sum of the amplitudes of the various modes of vibration.

$$D(r) = N^{-1/2} \sum_{\sigma} \xi_{\sigma} (a_{\sigma} e^{i\sigma r} + \bar{a}_{\sigma} e^{-i\sigma r}) , \quad (1)$$

where σ represents the wave propagation vector, ξ_σ is the unit polarization vector, N is the total number of atoms. a is the amplitude operator which is time-dependent, $\bar{a}$ its complex conjugate and the sum over σ means also the sum over the modes with different polarizations.

Mutual collision of lattice waves is the result of the existence of the nonlinear energy density in the Hamiltonian of the phonon system. Since the exact form is not known, we wish to use a simple form of the expansion in amplitudes.

$$U' = \lambda N^{-3/2} \sum_{1,2,3} \sigma_1\sigma_2\sigma_3 [a_1 a_2 a_3 \exp\{i(\sigma_1+\sigma_2+\sigma_3)r\} - a_1 a_2 \bar{a}_3 \exp\{i(\sigma_1+\sigma_2-\sigma_3)r\} + \cdots]. \quad (2)$$

This form of energy density has been chosen from consideration of the harmonic potential energy density

$$U = (\kappa/2)\Delta^2 + (n/2)\{2(\partial u/\partial x)^2 + 2(\partial v/\partial y)^2 + 2(\partial w/\partial z)^2 - (3/2)\Delta^2 + (\partial v/\partial z + \partial w/\partial y)^2 + (\partial w/\partial x + \partial u/\partial z)^2 + (\partial u/\partial y + \partial v/\partial x)^2\},$$

where κ and n are the volume elasticity and the rigidity respectively. u, v and w are the three components of the displacement D and

$$\Delta = \partial u/\partial x + \partial v/\partial y + \partial w/\partial z\,.$$

The first term of the right side which is the energy density for dilatation becomes by (1),

$$(\kappa/2N) \sum_{\text{(long. wave only)}} \sigma\sigma' \{-a_\sigma a_{\sigma'} \exp\{i(\sigma+\sigma')r\} + a_\sigma \bar{a}_{\sigma'} \exp\{i(\sigma-\sigma')r\} + \bar{a}_\sigma a_{\sigma'} \exp\{i(-\sigma+\sigma')r\} - \bar{a}_\sigma \bar{a}_{\sigma'} \exp\{i(-\sigma-\sigma')r\}\}\,,$$

and the second term representing the energy density for shear becomes,

$$(n/6N) \textstyle\sum_{\sigma,\sigma'} \{3(\xi_\sigma\cdot\xi_{\sigma'})(\sigma\cdot\sigma') + 3(\xi_\sigma\cdot\sigma')(\xi_{\sigma'}\cdot\sigma) - 2(\xi_\sigma\cdot\sigma)(\xi_{\sigma'}\cdot\sigma')\} \times \{\text{the same as the last factor of the former expression}\}.$$

Considering these expressions the simple form of (2) was adopted.

§ 3. Flows of Heat and Momentum

A flow of momentum in a crystal is accompanied by a flow of energy. The energy flow I defined as the energy passing through a unit cross section per second, is related to the momentum density p in that direction as,

$$I = q^2 p\,, \quad (3)$$

where q is the sound velocity. Apparently the collisions between phonons only cannot give a finite conductivity, since due to the conservation law of the total momentum of phonons these will not change p and therefore the energy flow will persist even when the temperature gradient is zero.

The finite conductivity of the actual solids results from the tendency of the phonon system to approach a Bose distribution, where the net momentum vanishes, with a certain rate characterized by some relaxation time by the aid of the intervention of the lattice periodicity in collisions.

When there is a steady temperature gradient, say in the x-direction, this tendency just balances to the rate of the increase of momentum in the same direction which is the difference between the momentum flowing in from high temperature region and that flowing out to low temperature region.

The relaxation time for the attainment of equilibrium in the absence of the temperature gradient of the phonon system is designated by τ. Then, $dp/dt = -p/\tau$. Though of course τ should depend on each form of the initial distribution of phonons, the approximation used in the next section permits the relaxation time to be uniquely determined.

In the steady state the net rate of the increase of the momentum in a small volume of unit cross-section and thickness δx is

$$\hbar q \delta x \textstyle\sum_\sigma (\partial n_\sigma/\partial x)(\sigma_x^2/\sigma)\,, \quad (4)$$

where the summation over σ is to be understood to be taken over those contained in unit volume, n_σ is the number of phonons belonging to σ. This increase is cancelled by the internal relaxation as,

$$\hbar q \textstyle\sum_\sigma (\partial n_\sigma/\partial x)(\sigma_x^2/\sigma) - p/\tau = 0\,. \quad (5)$$

Since n_σ differs little from the Bose distribution,

$$\partial n_\sigma/\partial x = \exp(\hbar\omega_\sigma/kT)\{\exp(\hbar\omega_\sigma/kT) - 1\}^{-2} \times (\hbar\omega_\sigma/kT^2)(dT/dx)\,,$$

where ω_σ is the frequency of σ and $\omega_\sigma = q\sigma$.

The summand in (4) becomes $e^u u^2 (e^u - 1)^{-2} \times \cos^2\theta$, where

$u = \hbar\omega_\sigma/kT$, θ = angle between x-axis and σ.

Accordingly (5) can be transformed as,

$$p = -(1/3)\tau c_v (dT/dx)\,, \quad (6)$$

where c_v is the heat capacity of unit volume.

Thermal conductivity K is therefore expressed by the relaxation time as,

$$K = (1/3) q^2 \tau c_v\,. \quad (7)$$

§ 4. The Most Probable Distribution of Phonons with a Definite Momentum

The approximation on which the following calculation is based is to regard the phonons belonging to the normal modes in each small volume remains at any instant in a most probable distribution under constant values of the densities of energy and momentum, the latter being assumed to be directed towards x-axis. This approximation will be satisfied when the normal collisions conserving momentum occurs far more frequently than Umklapp collisions which is accompanied by momentum change. Recently Klemens$^{3)}$ worked out calculations, with repeated use of approximations, on the roles played by these two types of collision and applied the results to the low temperature conductivity of crystals with defects. But the difference between both methods does not seem to be appreciable, since it becomes apparent that the normal collisions can occur more easily than the Umklapp collisions, the latter of which needs a certain kind of activation.

The determination of the most probable distribution of phonons is an easy task. The result is,

$$n_\sigma=\{\exp(\hbar\omega_\sigma/kT-\alpha\sigma_x)-1\}^{-1}, \qquad (8)$$

where α is related to the momentum density as,

$$\alpha=(3\hbar/2)q^2p/c_vkT^2. \qquad (9)$$

§ 5. Rate of Three-Phonon Collision

In crystals the 3-phonon collision is believed to provide the principal source for the limitation of the conductivity, since it comes from the lowest order perturbation and the observed temperature dependency of the conductivity is in accord with the theoretical conclusion based on that process.

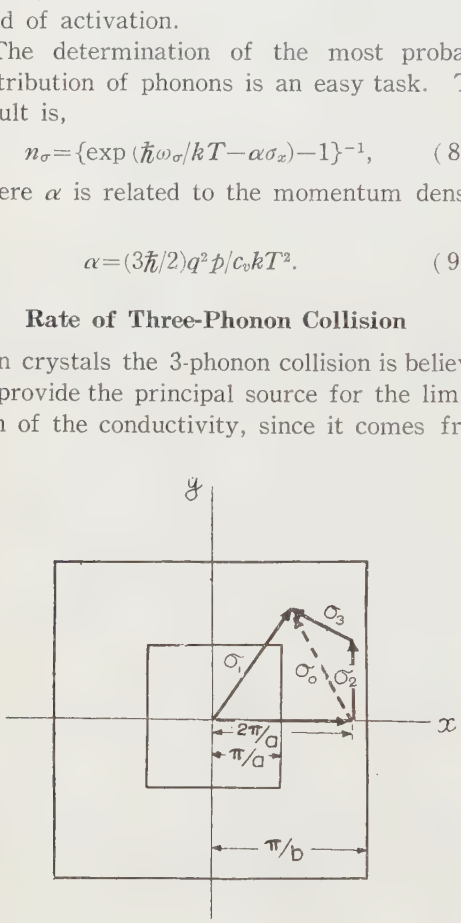

Fig. 1. Zone scheme for normal modes of vibration. a and b are the lattice constants of the original and virtual crystals respectively.

The occurence of this type of collision is rather restricted because of the difficulty of the simultaneous conservation of momentum and energy. For example, transitions in monatomic crystals with a simple cubic lattice are forbidden. Actually, it has been shown[4] empirically that the number of Umklapp collisions will increase with the mass difference between the constituent atoms in compound NaCl type crystals. Thus the cause of the occurence of thermal resistance is the existence of the optical modes.

The problem is to find some appropriate treatment of these modes for crystals with general lattice types, though an exact one is of course not possible.

Firstly, we take up the case where the constituents are the atoms or ions and suppose the crystal structure to be a cubic one. A virtual crystal is considered which has the same density as the original crystal and is composed of atoms(ions), which are arranged on the sites of a simple cubic lattice, having the mass equal to the mean value of the original atoms.

This replacement is analogous to that which was used by Debye in his theory on the specific heat of solids. The zone scheme for the normal modes of vibration becomes then a single-valued one in which the optical modes are replaced by acoustical modes, as it is to say. It is shown in Fig. 1 two-dimensionally. b is the lattice constant of the virtual crystal which is smaller than that of the original crystal a. If there are s atoms in a unit cell, then $b=s^{-1/3}a$: usually $b\sim a/2$.

To calculate the relaxation time for the decrease of momentum density we take this crystal of volume V held at temperature T. Let the phonon system be initially in a definite state which is designated by a state vector Ψ_0 having a given momentum P_0 in the x-direction.

Transitions to states with momenta other than P_0 take place in Umklapp collisions such as,

$$\Psi_0(\cdots n_1\cdots n_2\cdots n_3\cdots)\to\Psi(\cdots n_1-1\cdots n_2+1\cdots \cdots n_3+1\cdots),$$

$$\sigma_1=\sigma_2+\sigma_3+(2\pi/a)l,$$

$$l_x,\ l_y,\ l_z=0,\ \pm1,\ \cdots,\ \text{except } l_x=l_y=l_z=0,$$

where x-axis is taken to coincide with one of the lattice edge.

Collisions including the l's with components larger than unity may be excluded for the collisions considered here. We wish to calculate the transition rate for those with $l_x=\pm 1$, $l_y=l_z=0$, which is the most important case. This type of collision changes the momentum of the system by an amount of $(2\pi/a)\hbar$.

The rate R_1 of the transition $\sigma_1\rightarrow\sigma_2+\sigma_3+(2\pi/a)$, in which the system loses momentum is,

$$R_1=\{\lambda^2V^2\hbar^3/N^3(2m)^3q^3\}\sigma_1\sigma_2\sigma_3n_1(n_2+1)(n_3+1)\times\dot{\Omega}(E_f-E_i),$$

$$\Omega(x)=4\sin^2(xt/2\hbar)/x^2,\ E_f=\hbar(\omega_2+\omega_3),\ E_i=\hbar\omega_1, \tag{10}$$

where m refer to the virtual crystal and N is the number of total atoms in volume V.

Combining (10) with that for the reverse process in which the momentum is gained, we get the rate R_2 at which the system loses the momentum unit in the reaction $\sigma_1\rightleftarrows\sigma_2+\sigma_3+(2\pi/a)$ among these three modes.

$$R_2=L\sigma_1\sigma_2\sigma_3\{n_1(n_2+1)(n_3+1)-(n_1+1)n_2n_3\}\dot{\Omega}$$
$$=\alpha L(2\pi/a)e^{u_1}\prod_{i=1}^{3}\sigma_i(e^{u_i}-1)^{-1}\dot{\Omega},$$

$$L=\lambda^2V^2\hbar^3/2^3m^3N^3q^3,\ u_i=\hbar\omega_i/kT, \tag{11}$$

where α refers also to the virtual crystal and (8) was used.

Firstly we sum up the R_2's over the sets of σ_2 and σ_3 with σ_1 being fixed or the same thing for σ_0 (See Fig. 1).

$$\sum_{(\sigma_1\ \text{fixed})}R_2=\alpha L\frac{2\pi}{a}\frac{\sigma_1e^{u_1}}{e^{u_1}-1}\left\{\sum_{\sigma_2,\sigma_3}\frac{\sigma_2}{e^{u_2}-1}\frac{\sigma_3}{e^{u_3}-1}\dot{\Omega}\right\}. \tag{12}$$

Taking an ellipsoidal coordinate system we designate the coordinates by σ_ξ, σ_η and the angle ϕ,

$$\sigma_\xi=\sigma_2+\sigma_3,\quad \sigma_\eta=\sigma_2-\sigma_3.$$

The sum over σ_2 and σ_3 in (12) is replaced by an integral in the phase space as,

$$\frac{3^2V}{(2\pi)^3}\left\{\int\frac{(\sigma_\xi^2-\sigma_\eta^2)}{8\sigma_0}R_2d\sigma_\xi d\sigma_\eta d\phi\right\},$$

where the integrand except R_2 denotes the volume element in the momentum space divided by $\hbar^3$ and 3^2 in the first factor corresponds to the number of independent polarization vectors. Then the curly bracket of (12) becomes by the ordinary procedure,

$$\frac{2\pi}{\hbar}\frac{3^2V}{(2\pi)^2}\left[\frac{d\sigma_\xi}{dE_f}\int_{-\sigma_0}^{\sigma_0}\frac{(\sigma_\xi^2-\sigma_\eta^2)\sigma_2\sigma_3d\sigma_\eta}{8\sigma_0(e^{u_2}-1)(e^{u_3}-1)}\right]_{E_f=E_i}.$$

The integral is approximated as, since

$$[\sigma_\xi]_{E_f=E_i}=\sigma_1,$$

$$2^{-5}\int_{-\sigma_0}^{\sigma_0}\frac{(\sigma_1+\sigma_\eta)^2(\sigma_1-\sigma_\eta)^2d\sigma_\eta/\sigma_0}{\{\exp[(u_1+u_\eta)/2]-1\}\{\exp[(u_1-u_\eta)/2]-1\}}$$
$$\sim2^{-4}\frac{\sigma_1^4}{(e^{u_1/2}-1)^2},$$

where

$$u_\eta=\hbar\omega_\eta/kT,\quad \omega_\eta=q\sigma_\eta.$$

Therefore (12) becomes on substituting (9),

$$\sum_{(\sigma_1\ \text{fixed})}R_2=\frac{3^3\hbar^2\lambda^2p}{2^9\rho^3q^2ac_vkT^2}\frac{e^{u_1}\sigma_1^5}{(e^{u_1}-1)(e^{u_1/2}-1)^2}, \tag{13}$$

where $\rho=mN/V$.

The summation of (13) over the σ_1's is done by estimating the mean value of σ_1, where the limitation,

$$\pi/b>\sigma_{1x}>\pi/a, \tag{14}$$

for the reaction considered here, coming from the condition $\sigma_1>\sigma_0$, is to be considered. This mean value is written as π/d, where d is a length supposed to be near b, of the same order of the length corresponding to the wavelength which characterizes the Einstein frequency of the crystal. Correspondingly the u_1 in (13) is given a constant value $u\equiv\hbar\omega_d/kT$, where $\omega_d=q\pi/d$, which defines the characteristic temperature Θ for collision: $\Theta=\hbar\omega_d/k$.

For convenience we rewrite σ_1^5 as $(kT/\hbar q)^3\times u^3(\pi/d)^2$ and substituting we get in place of the right side of (13),

$$\frac{3^3\pi^2\lambda^2k^2Tf(u)}{2^9\hbar\rho^3q^5ad^2c_v},\quad f(u)=\frac{e^uu^3}{(e^u-1)(e^{u/2}-1)^2}$$
$$\left.\begin{aligned}&\sim2^2 \quad \text{for } u\rightarrow0\\&\sim u^3e^u \quad \text{for } u\rightarrow\infty.\end{aligned}\right\} \tag{15}$$

The number of σ_1's satisfying the condition (14) is $(3V/2b^3)(1-b/a)$, which varies from zero to $\sim3N/2$ with the increase of the number of the optical modes. On multiplying to (13) we get the rate R of the momentum decrease of the phonon system. But beforehand we have to double the calculated rate, because there remains another type of collision which is,

$$\sigma_1\rightleftarrows\sigma_2+\sigma_3-(2\pi/a),$$

giving exactly same rate as the above.

Thus,

$$\dot{P}=-\frac{3^4\pi^2\lambda^2k^2Tf(u)(1-b/a)}{2^9\hbar\rho^3q^5ad^2b^3c_v}P(2\pi/a)\hbar.$$

By the definition of the relaxation time we get,

$$\tau^{-1}=3^4\pi^3\lambda^2k^2Tf(u)(1-b/a)/2^8\rho^3q^5a^2d^2b^3. \tag{16}$$

From (7) and (16) the conductivity is given as,

$$K=2^8\rho^3q^7a^2d^2b^3c_v^2/3^5\pi^3\lambda^2k^2Tf(u)(1-b/a). \quad (17)$$

Now for ordinary crystals with several atoms in a unit cell,

$$b\sim d\sim a/2, \quad (18)$$

resulting to the approximate formula for the conductivity,

$$K\sim 0.002\{\rho^3q^7a^7c_v^2/\lambda^2k^2Tf(u)\}. \quad (19)$$

At high temperatures this becomes, since $c_v\to 3k/b^3$ and $f\to 2^2$,

$$K\sim 0.01(\rho^3q^7a/\lambda^2T), \quad (20)$$

showing the simple temperature dependency which is well known.

The condition (18) applies to cases where the number of atoms is about 8. When this number differs greatly from 8, it will be better to add another factor $(s/8)^{1/3}$ to the conductivity formula and the change of the factor $(1-b/a)$ in the denominator of (17) has to be taken into account.

Estimation of the nonlinearity constant λ is done as follows. The use is made of the Morse type potential energy supposed to apply to strained crystals.

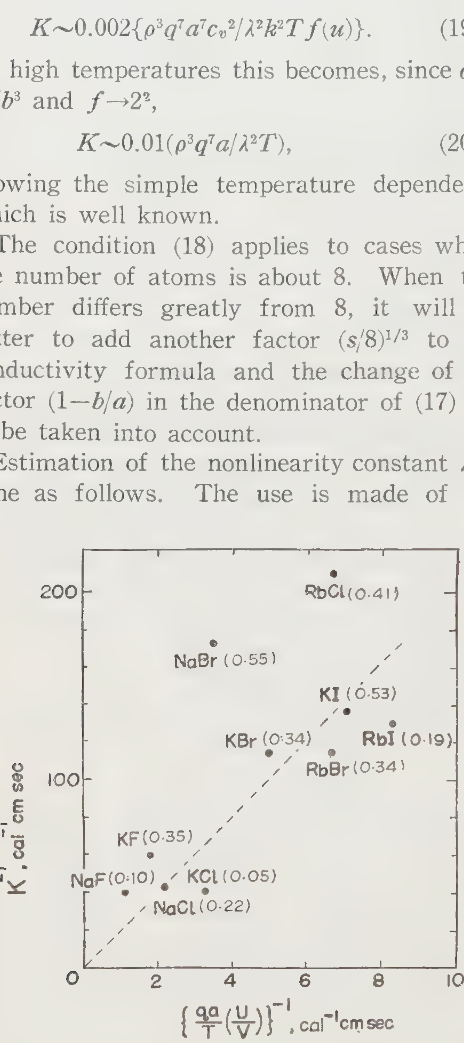

Fig. 2. Observed thermal resistances vs. calculated ones for ionic crystals at 0°C.

Let the following expression to hold for a crystal with volume V.

$$U=U_0(e^{-2\delta V/\beta V_0}-2e^{-\delta V/\beta V_0}),$$

where U_0 is the cohesive energy at the original unstrained volume V_0 and $\delta V=V-V_0$.

Then the volume elasticity κ and the nonlinearity constant for dilatation are expresse as,

$$\kappa=(2/\beta^2)(U_0/V_0),$$
$$\lambda=-(1/\beta^3)(U_0/V_0)=-(\kappa/2)^{3/2}(U_0/V_0)^{-1/2}. \quad (21)$$

We assume the λ given here to be just th same as the one introduced in (2). Meanwhil the sound velocity is roughly $(\kappa/\rho)^{1/2}$.

The thermal conductivity will therefore becomes,

$$K\sim 0.1\,qa(U_0/V_0)/QT, \quad (22)$$

at high temperatures, where the numerica factor Q of the order of unity was added t take into account of the difference of the crystal structure for various species of crystals and also the mass ratio of the componen atoms if the crystal is not monatomic. I any way, the numerical constant given as 0.1 above may be regarded as indicating only that it will not differ greatly from that order. Fortunately however, it will be seen that (22 fits fairly good to the experimental data.

§ 6. Ionic Crystals of NaCl Type Lattice

The results of the foregoing section will be compared with experimental values of the conductivity of ionic crystals having the NaC type lattice. In this case Q will depend o the relative mass difference of the componen ions. The number of ions in a unit cell is 8 here.

The comparison is made in Fig. 2 in which the ordinate is the observed thermal resistance which is the reciprocal of the conductivity at 0°C and the abscissa is the theoretical values calculated from (22) where the numerical factor and Q were temporarily set to unity. q was calculated by $(\kappa/\rho)^{1/2}$. The numerals added to each point represent the relative mass ratio of the component ions, $(m_1-m_2)/2(m_1+m_2)$, where m_1 and m_2 are the masses of the ions respectively.

In view of the fact that the experimental data are very scanty (they were taken from Landolt-Boerntein Tabellen), the proportionality between the formula and the experimental values may be regarded to be fairly good. The best fit is given by

$$K=0.05qaU_0/V_0T, \quad (23)$$

provided we set Q to be unity.

We shall be able to improve the agreement between theory and experiment by taking into account the mass difference of component ions in each crystal species, as it can be seen from the figure that in general the resistance comes high when the relative mass ratio is large, confirming the observation made by Blackman⁴⁾.

§ 7. Molecular Liquids

In 1935 Bridgman⁵⁾ proposed a simple formula for the conductivity of liquids.

$$K=3kq/\delta^2\,, \tag{24}$$

where δ is the mean distance between adjacent molecules. Its deduction is based on a simple model of the energy transfer that heat is carried from a molecule to an adjacent one with the speed of the sound velocity in liquids. But from the point of view of the quasi-crystalline structure of liquids the coincidence up to the numerical constant should not be regarded as a justification of the basic concept: the derivation of (24) might be classified as an example of the dimensional analysis.

Here also we wish to apply the previous discussions and show that the final expression is nearly coincident with the above equation accidentally. Molecules are assumed to be arranged on the sites of a closed packing lattice. The number of molecules per unit cell is then 4, which does not differ greatly from the above cases. Intermolecular motions are considered to be responsible for the transfer of heat, while the contribution from the intramolecular vibrations is neglected because of the large value of their frequencies and the low value of the group velocity. This approximation provides the alternative method for the treatment of a part of the optical vibrations. Since the characteristic temperature for the excitation of the intermolecular vibrations is very low, high temperature formula (22) may be used from low temperatures.

Now that U_0 is roughly the synonym of the heat of vaporization, (22) can be approximated by

$$K=CqL_v/a^2T, \quad C=\text{const.},$$

where L_v is the heat of vaporization per mole. Here the fact that $4/a^3$ is the number of molecules in unit volume is used. Furthermore, Trouton's rule says that $L_v\sim 20T_b$ where T_b is the boiling point. Thus the above expression becomes,

$$K\sim C'(q/a^2)(T_b/T), \quad C'=\text{const.} \tag{25}$$

Since liquids which had been compared with success with the Bridgman formula (24), such as water, carbon disulphide, ethanol, acetone and so forth have nearly same boiling temperatures, (25) is almost identical with (24) at a fixed temperature as far as these liquids are concerned.

K values calculated by the equation

$$K=0.12qa(U_0/V_0)T^{-1}, \tag{26}$$

where U_0/V_0 is the heat of vaporization per unit volume at room temperature, q is calculated by $(\kappa/\rho)^{1/2}$ and the numerical constant 0.12 was chosen to give the best fit, are listed in Table I in comparison with the observed values.

Table I.

Substance	Molecular shape	$K_{\text{calc.}}$ (cal. cm^{-1}sec^{-1})	K_{ob}
Carbon tetrachloride	spherical	0.00028	0.00026
Chloroform	〃	0.00027	0.00029
Benzene	disc-shaped	0.00035	0.00037
Aniline	〃	0.00053	0.00041
Toluene	〃	0.00036	0.00035
Carbon disulphide	rod-like	0.00031	0.00038
Acetone	〃	0.00034	0.00043
Hexane	〃	0.00020	0.00033
Heptane	〃	0.00023	0.00034
Octane	〃	0.00026	0.00036
Methanol	associated liquid	0.00054	0.00051
Ethanol	〃	0.00058	0.00044
Water	〃	0.00145	0.00143
Glycerol	〃	0.00162	0.00068

It is to be noted that the numerical factor comes into the same order as that for the ionic crystals. The fairly good coincidence is supposed due to the existence of a short range order in liquids: the mean free path in liquids will be short enough not to exceed the range of the ordered portions.

More detailed examination of that table reveals that for rodlike molecules the observed values are larger than the calculated ones, which seems to be indicating the increased contribution of the intramolecular vibrations.

§ 8. Temperature Dependency of the Conductivity

It has been known that the Eucken's law[6)] describes fairly well the observed temperature dependency of the conductivity of a certain number of ionic crystals. This law states that the conductivity is inversely proportional to the absolute temperature from well below the characteristic temperature.

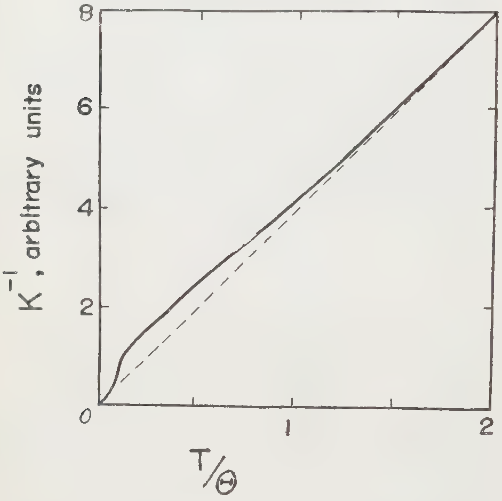

Fig. 3. Temperature dependency of calculated resistance.

The relation between the conductivity and the temperature in our calculation is given by $c_v^2/f(u)T$ in (19) and accordingly depends on the choise of the characteristic temperature Θ for Umklapp collisions. As can be seen from the foregoing calculations, this temperature does not need to coincide with that of specific heat. Any way, if we adopt such temperatures lying in the neighbourhood of Debye temperature, nearly straight proportionality of the thermal resistance against temperature results owing to the cancellation to some extent of the temperature dependencies of c_v^2 and $f(u)$ except in the region of very low temperatures. Fig. 3 is drawn to show this fact for the choise of $\Theta=\Theta_{\text{Debye}}$. At extremely low temperatures the functional dependency of (19) agrees with the existing theory that $K \infty T^{\nu} \exp(-\Theta/T)$ where ν is a constant, though of course not observed in reality due to the overlap of the scattering effects of the thermal waves by various kinds of imperfections which become dominant at very low temperatures.

Acknowledgement

I wish to thank to Prof. M. Mashima for his encouragement and guidance for the persecution of this work.

References

1) R. Peierls: Ann. Phys. **3** (1929) 1055.
2) I. Pomeranchuk: J. Phys. U. S. S. R. **4** (1941) 259.
3) P. G. Klemens: Proc. Roy. Soc. (London), **208** (1951) 108.
4) M. Blackman: Phil. Mag. **19** (1935) 989.
5) P. W. Bridgman: Rev. Mod. Phys. **7** (1935) 28.
6) International Critical Tables.

Journal of the Physical Society of Japan Vol. 9, No. 4, July—August, 1954

Tables of Integrals Useful for the Calculations of Molecular Energies. IV

By Masao Kotani,
Physics Department, Faculty of Science, University of Tokyo
Eiichi Ishiguro
Physics Department, Faculty of Science, Ochanomizu University
and Katsunori Hijikata
University of Electro-Communications

(Received April 1, 1954)

Coulomb, exchange, and ionic integrals as well as one-electron integrals involving $2s$ and $2p$ Slater type atomic orbitals have been calculated for homopolar diatomic molecules. This work is the extention of the table of the same title (J. Phys. Soc. Japan 8, No. 4, 463 (1953)) for $\delta R=7.50$, 8.00 and 8.50. The Coulomb and one-electron integrals have been calculated up to 11.50.

This table is the continuation of the works commenced by Kotani Amemiya and Simose on the calculation of molecular integrals including $1s$, $2s$ and $2p$ Slater type atomic orbitals[1)2)3)]. One of the authors has calculated the values of the auxiliary functions $W_\tau^\nu(m,n;\alpha)$ and $G_\tau^\nu(m;\alpha)$ for $\alpha=7.50$, 8.00 and 8.50[4)], which enable us to extend the previous tables for these arguments. Thus the exchange and ionic integrals for these arguments are tabulated. The Coulomb and one-electron integrals, the calculation of which is much easier, are tabulated to $\alpha=11.50$ with the interval of 0.50.

All the notations are the same as in the previous tables, but we duplicate them for the sake of convenience.

(1) Units. We shall use the following atomic units: lengths in units of the Bohr radius $a_0=0.5293$ A; energies in units of $e^2/a_0=27.204$ eV.

(2) Atomic orbitals. Let a_α, a_β, $\cdots\cdot$ be the atomic orbitals with their centers at A, and b_γ, b_δ, $\cdots\cdot$ be those with their centers at B. Their explicit forms are:

$$\begin{aligned}
&a_s(1)=(\delta^5/3\pi)^{1/2}\exp(-\delta r_{a1})r_{a1} && (2s\ \text{ orbital}),\\
&a_\sigma(1)=(\delta^5/\pi)^{1/2}\exp(-\delta r_{a1})r_{a1}\cos\theta_{a1} && (2p\sigma\ \text{orbital}),\\
&a_\pi(1)=(\delta^5/\pi)^{1/2}\exp(-\delta r_{a1})r_{a1}\sin\theta_{a1}\cos\varphi_1 && (2px\ \text{orbital}),\\
&a_{\pi'}(1)=(\delta^5/\pi)^{1/2}\exp(-\delta r_{a1})r_{a1}\sin\theta_{a1}\sin\varphi_1 && (2py\ \text{orbital}),\\
&a_+(1)=(\delta^5/2\pi)^{1/2}\exp(-\delta r_{a1})r_{a1}\sin\theta_{a1}\exp(i\varphi_1)=2^{-1/2}[a_\pi(1)+ia_{\pi'}(1)]\,,\\
&a_-(1)=(\delta^5/2\pi)^{1/2}\exp(-\delta r_{a1})r_{a1}\sin\theta_{a1}\exp(-i\varphi_1)=2^{-1/2}[a_\pi(1)-ia_{\pi'}(1)]\,.
\end{aligned}$$

In the above the coordinate system is chosen as follows: the position of the electron is denoted by P, $r_{a1}=\bar{\text{AP}}$, $r_{b1}=\bar{\text{BP}}$, $\theta_{a1}=\angle\text{BAP}$, $\theta_{b1}=\angle\text{ABP}$.

(3) Molecular integrals

Integrals	Notations	Roothaan-Rüdenberg's notations	Definitions
Overlap	$S_{\alpha\beta}$	$(\alpha_a\|\beta_b)$	$\int \alpha_\alpha(1)^* b_\beta(1)d\tau$.
Kinetic	$T_{\alpha\beta}$	$\left(\alpha_a\middle\|-\frac{1}{2}\varDelta\middle\|\beta_b\right)$	$\int a_\alpha(1)^*\left(-\frac{1}{2}\varDelta\right)b_\beta(1)d\tau$
Nuclear Attraction	$K_{\alpha\beta}$	$\left(\alpha_a\middle\|\frac{1}{r_b}\middle\|\beta_a\right)$	$\int a_\alpha(1)^*\left(\frac{1}{r_{b1}}\right)a_\beta(1)d\tau$

Resonance	$J_{\alpha\beta}$	$\left(\alpha_b \middle\| \frac{1}{r_b} \middle\| \beta_a\right)$	$\int b_a(1)^*\left(\frac{1}{r_{b1}}\right)a_\beta(1)d\tau$
Coulomb	$D_{\alpha\beta\gamma\delta}$	$(\alpha_a\gamma_a;\ \beta_b\delta_b)$	$\int \alpha_\alpha(1)^*a_\gamma(1)\left(\frac{1}{r_{12}}\right)b_\beta(2)^*b_\delta(2)d\tau_1 d\tau_2$
Exchange	$C_{\alpha\beta\gamma\delta}$	$(\alpha_a\gamma_b;\ \beta_b\delta_a)$	$\int \alpha_\alpha(1)^*b_\gamma(1)\left(\frac{1}{r_{12}}\right)b_\beta(2)^*a_\delta(2)d\tau_1 d\tau_2$
Ionic	$L_{\alpha\beta\gamma\bar{\delta}}$	$(\alpha_a\gamma_a;\ \beta_a\delta_b)$	$\int a_\alpha(1)^*a_\gamma(1)\left(\frac{1}{r_{12}}\right)\alpha_\beta(2)^*b_\delta(2)d\tau_1 d\tau_2$

The numerical values were checked by taking differences. In doing this, $e^{2\delta R}$ and $e^{\delta R}$ were multiplied beforehand in the cases of C and L, respectively. Throughout this procedure, several errors have been found in the previously published values of L, which together with the misprints, are listed in the Errata. Although we hope these errata are the final, we would gratefully acknowledge any information about errors and misprints in this series of tables.

In conclusion we are indebted to Miss Hama, Miss Sugawara, Miss Yuasa and Miss Mizushima for their assistance in numerical computations. For the financial support we owe to the members of Kotani Laboratory and the Research Grant of the Educationa Ministry. For the discovery of misprints we tnank Dr. Niira, Mr. Kimura, Mr. Nakamura and Mr. Ohno.

References

1) Kotani, Amemiya and Simose: Proc. Phys.- Math. Soc. Japan **20**, Extra No. 1 (1938).
2) Kotami and Amemiya: Proc. Phys.-Math. Soc. Japan **22**, Extra No. 1 (1940).
3) Kotani. Ishiguro, Hijikata, Nakamura and Amemiya: J. Phys. Soc. Japan **8** (1953) 463.
4) Hijikata: Reports of the University of Electro-Communications No. 5, p. 35 (1953).

			7.50	8.00	8.50	9.00	9.50	10.0	10.5	11.0	11.5
S	ss	$(s_a \mid s_b)$	0.08334 29	0.06217 99	0.04595 30	0.03366 62	0.02446 73	0.01765 05	0.01264 58	0.00900 26	0.00627 11
	$s\sigma$	$(s_a \mid \sigma_b)$	0.10896 91	0.08299 81	0.06245 72	0.04649 11	0.03426 72	0.02503 21	0.01813 70	0.01304 31	0.00931 54
	$\sigma\sigma$	$(\sigma_a \mid \sigma_b)$	0.13685 38	0.10719 15	0.08259 54	0.06274 15	0.04706 46	0.03491 25	0.02564 02	0.01866 14	0.01347 14
	$\pi\pi$	$(\pi_a \mid \pi_b)$	0.03270 11	0.02305 75	0.01614 35	0.01123 03	0.00776 65	0.00534 21	0.00365 62	0.00249 08	0.00168 96
J/δ	ss	$(s_b \mid 1/r_b \mid s_a)$	0.02222 71	0.01582 27	0.01117 52	0.00783 65	0.00545 95	0.00378 08	0.00260 39	0.00178 43	0.00121 69
	$s\sigma$	$(s_b \mid 1/r_b \mid \sigma_a)$	0.03263 09	0.02349 98	0.01676 68	0.01186 32	0.00833 07	0.00581 03	0.00402 72	0.00277 55	0.00190 29
	σs	$(\sigma_b \mid 1/r_b \mid s_a)$	0.02584 52	0.01885 15	0.01360 48	0.00972 57	0.00689 38	0.00484 92	0.00338 73	0.00235 12	0.00162 26
	$\sigma\sigma$	$(\sigma_b \mid 1/r_b \mid \sigma_a)$	0.03653 81	0.02711 66	0.01985 94	0.01437 72	0.01030 20	0.00731 70	0.00515 45	0.00360 48	0.00250 45
	$\pi\pi$	$(\pi_b \mid 1/r_b \mid \pi_a)$	0.00753 58	0.00508 78	0.00341 66	0.00228 31	0.00151 89	0.00100 64	0.00066 432	0.00043 702	0.00028 660
T/δ^2	ss	$(s_a \mid -\Delta/2 \mid s_b)$	-0.00569 79	-0.00522 20	-0.00453 72	-0.00379 28	-0.00307 78	-0.00243 90	-0.00189 53	-0.00144 86	-0.00109 16
	$s\sigma$	$(s_a \mid -\Delta/2 \mid \sigma_b)$	-0.00279 41	-0.00379 61	-0.00401 90	-0.00379 41	-0.00334 60	0.00281 78	-0.00229 39	-0.00181 91	-0.00141 24
	$\sigma\sigma$	$(\sigma_a \mid -\Delta/2 \mid \sigma_b)$	0.00464 94	0.00063 738	-0.00157 90	-0.00261 63	-0.00292 62	-0.00282 24	-0.00251 12	-0.00212 11	-0.00172 68
	$\pi\pi$	$(\pi_a \mid -\Delta/2 \mid \pi_b)$	-0.00127 90	-0.00135 30	-0.00123 86	-0.00104 90	-0.00084 551	-0.00065 832	-0.00049 944	-0.00037 133	-0.00027 161
K/δ	ss	$(s_a \mid 1/r_b \mid s_a)$	0.13332 480	0.12499 652	0.11764 564	0.11111 054	0.10526 293	0.09999 991	0.09523 806	0.09090 908	0.08695 652
	$s\sigma$	$(s_a \mid 1/r_b \mid \sigma_a)$	0.02564 510	0.02254 666	0.01997 505	0.01781 845	0.01599 268	0.01443 360	0.01309 178	0.01192 870	0.01091 298
	$\sigma\sigma$	$(\sigma_a \mid 1/r_b \mid \sigma_a)$	0.14041 835	0.13084 874	0.12252 774	0.11522 460	0.10876 151	0.10299 972	0.09782 950	0.09316 299	0.08892 905
	$\pi\pi$	$(\pi_a \mid 1/r_b \mid \pi_a)$	0.12977 803	0.12207 040	0.11520 459	0.10905 351	0.10351 364	0.09850 000	0.09394 233	0.08978 212	0.08597 025
D/δ	$ssss$	$(s_a s_a ; s_b s_b)$	0.13314 022	0.12490 500	0.11760 088	0.11108 892	0.10525 260	0.09999 503	0.09523 578	0.09090 802	0.08695 603
	σsss	$(s_a s_a ; s_b \sigma_b)$	0.02535 413	0.02240 154	0.01990 370	0.01778 383	0.01597 608	0.01442 572	0.01308 808	0.01192 698	0.01091 319
	$\sigma\sigma ss$	$(s_a \sigma_a ; s_b \sigma_b)$	0.00939 120	0.00789 704	0.00666 659	0.00565 837	0.00483 238	0.00415 367	0.00359 322	0.00312 764	0.00273 834
	$\sigma\sigma\sigma s$	$(s_a \sigma_a ; \sigma_b \sigma_b)$	0.02897 603	0.02533 158	0.02227 326	0.01970 583	0.01754 306	0.01571 147	0.01415 053	0.01281 131	0.01165 456
	$\pi s \pi s$	$(s_a s_a ; \pi_b \pi_b)$	0.12973 625	0.12205 072	0.11519 542	0.10904 928	0.10351 171	0.09849 913	0.09394 195	0.08978 194	0.08597 017
	$\pi\pi ss$	$(s_a \pi_a ; s_b \pi_b)$	0.00489 274	0.00404 817	0.00338 289	0.00285 352	0.00242 798	0.00208 248	0.00179 928	0.00156 507	0.00136 975
	$\pi\pi\sigma s$	$(s_a \pi_a ; \sigma_b \pi_b)$	0.00198 424	0.00155 419	0.00122 987	0.00098 344	0.00079 450	0.00064 820	0.00053 378	0.00044 337	0.00037 125
	$\pi\pi\sigma\sigma$	$(\sigma_a \pi_a ; \sigma_b \pi_b)$	0.00103 471	0.00077 631	0.00058 664	0.00044 728	0.00034 443	0.00026 798	0.00021 065	0.00016 725	0.00013 406
	$\pi\sigma\pi\sigma$	$(\sigma_a \sigma_a ; \pi_b \pi_b)$	0.13565 110	0.12705 774	0.11945 836	0.11270 088	0.10665 886	0.10122 777	0.09632 129	0.09186 796	0.08780 836
	$\sigma s \sigma s$	$(s_a s_a ; \sigma_b \sigma_b)$	0.13994 817	0.13061 355	0.12241 180	0.11516 819	0.10873 440	0.10298 683	0.09782 343	0.09316 016	0.08892 775
	$\pi\sigma\pi s$	$(s_a \sigma_a ; \pi_b \pi_b)$	0.02354 318	0.02093 653	0.01871 893	0.01682 283	0.01519 259	0.01378 285	0.01255 685	0.01148 481	0.01054 250
	$\sigma\sigma\sigma\sigma$	$(\sigma_a \sigma_a ; \sigma_b \sigma_b)$	0.14854 231	0.13772 519	0.12831 868	0.12010 279	0.11288 547	0.10650 496	0.10082 772	0.09574 457	0.09116 653
	$\pi\pi\pi\pi$	$(\pi_a \pi_a ; \pi_b \pi_b)$	0.12705 442	0.11974 941	0.11321 446	0.10733 710	0.10202 507	0.09720 219	0.09280 511	0.08878 083	0.08508 463
	$\pi\pi'\pi\pi'$	$(\pi_a \pi_a ; \pi_b' \pi_b')$	0.12650 322	0.11934 502	0.11291 345	0.10710 986	0.10185 119	0.09706 743	0.09269 944	0.08869 705	0.08501 753
	$\pi\pi\pi'\pi'$	$(\pi_a \pi_a' ; \pi_b \pi_b')$	0.00027 560	0.00020 220	0.00015 050	0.00011 362	0.00008 694	0.00006 738	0.00005 284	0.00004 189	0.00003 355
	$++++$	$(\pi_a^+ \pi_a^+ ; \pi_b^+ \pi_b^+)$	0.12677 882	0.11954 721	0.11306 396	0.10722 348	0.10193 813	0.09713 481	0.09275 228	0.08873 894	0.08505 108
	$+--+$	$(\pi_a^+ \pi_a^- ; \pi_b^- \pi_b^+)$	0.00055 120	0.00040 439	0.00030 101	0.00022 724	0.00017 388	0.00013 475	0.00010 567	0.00008 378	0.00006 710

			7.50	8.00	8.50
C/δ	$ssss$	$(s_as_b;\ s_bs_a)$	0.00207 04	0.00112 73	0.00060 23
	σsss	$(\sigma_as_b;\ s_bs_a)$	0.00284 94	0.00157 89	0.00085 65
	$\sigma\sigma ss$	$(\sigma_as_b;\ \sigma_bs_a)$	0.00390 02	0.00220 14	0.00121 34
	$\sigma s\sigma s$	$(\sigma_a\sigma_b;\ s_bs_a)$	0.00384 15	0.00217 50	0.00120 17
	$\sigma ss\sigma$	$(\sigma_as_b;\ s_b\sigma_a)$	0.00399 06	0.00224 48	0.00123 39
	$\sigma\sigma\sigma s$	$(\sigma_a\sigma_b;\ \sigma_bs_a)$	0.00536 35	0.00308 39	0.00172 70
	$\sigma\sigma\sigma\sigma$	$(\sigma_a\sigma_b;\ \sigma_b\sigma_a)$	0.00737 41	0.00431 79	0.00245 63
	$\pi\pi ss$	$(\pi_as_b;\ \pi_bs_a)$	0.00014 592	0.00007 406	0.00003 700
	$\pi s\pi s$	$(\pi_a\pi_b;\ s_bs_a)$	0.00072 061	0.00036 967	0.00018 663
	$\pi ss\pi$	$(\pi_as_b;\ s_b\pi_a)$	0.00016 375	0.00008 341	0.00004 182
	$\pi\pi\sigma\sigma$	$(\pi_a\sigma_b;\ \pi_b\sigma_a)$	0.00026 075	0.00013 697	0.00007 053
	$\pi\sigma\pi\sigma$	$(\pi_a\pi_b;\ \sigma_b\sigma_a)$	0.00129 696	0.00069 300	0.00036 233
	$\pi\sigma\sigma\pi$	$(\pi_a\sigma_b;\ \sigma_b\pi_a)$	0.00034 282	0.00017 882	0.00009 153
	$\pi\pi\sigma s$	$(\pi_a\sigma_b;\ \pi_bs_a)$	0.00019 654	0.00010 138	0.00005 138
	$\pi\sigma\pi s$	$(\pi_a\pi_b;\ \sigma_bs_a)$	0.00097 856	0.00051 116	0.00026 216
	$\pi\sigma s\pi$	$(\pi_as_b;\ \sigma_b\pi_a)$	0.00023 467	0.00012 111	0.00006 141
	$\pi\pi\pi\pi$	$(\pi_a\pi_b;\ \pi_b\pi_a)$	0.00027 797	0.00013 451	0.00006 423
	$\pi\pi\pi'\pi'$	$(\pi_a\pi_b';\ \pi_b\pi_a')$	0.00025 034	0.00012 124	0.00005 794
	$\pi\pi'\pi\pi'$	$(\pi_a\pi_b;\ \pi_b'\pi_a')$	0.00001 3814	0.00000 6637	0.00000 3147
	$++++$	$(\pi_a{}^+\pi_b{}^+;\ \pi_b{}^+\pi_a{}^+)$	0.00026 415	0.00012 788	0.00006 108
	$+--+$	$(\pi_a{}^+\pi_b{}^-;\ \pi_b{}^-\pi_a{}^+)$	0.00002 7627	0.00001 3274	0.00000 6294
L/δ	$sss\bar{s}$	$(s_as_a;\ s_as_b)$	0.01989 04	0.01428 66	0.01017 11
	$sss\bar{\sigma}$	$(s_as_a;\ s_a\sigma_b)$	0.02866 57	0.02088 64	0.01505 48
	$s\sigma s\bar{s}$	$(s_as_a;\ \sigma_as_b)$	0.02421 82	0.01776 81	0.01288 88
	$ss\sigma\bar{s}$	$(s_a\sigma_a;\ s_as_b)$	0.00446 75	0.00320 12	0.00226 77
	$s\sigma\sigma\bar{s}$	$(s_a\sigma_a;\ \sigma_as_b)$	0.00682 93	0.00489 07	0.00346 42
	$ss\sigma\bar{\sigma}$	$(s_a\sigma_a;\ s_a\sigma_b)$	0.00660 45	0.00481 05	0.00345 42
	$s\sigma s\bar{\sigma}$	$(s_as_b;\ \sigma_a\sigma_b)$	0.03378 97	0.02528 01	0.01864 21
	$\sigma s\sigma\bar{s}$	$(\sigma_a\sigma_a;\ s_as_b)$	0.02103 12	0.01510 68	0.01075 24
	$s\sigma\sigma\bar{\sigma}$	$(s_a\sigma_a;\ \sigma_a\sigma_b)$	0.01014 68	0.00737 79	0.00529 27
	$\sigma s\sigma\bar{\sigma}$	$(\sigma_a\sigma_a;\ s_a\sigma_b)$	0.03039 76	0.02215 18	0.01596 37
	$\sigma\sigma\sigma\bar{s}$	$(\sigma_a\sigma_a;\ \sigma_as_b)$	0.02624 24	0.01921 34	0.01390 77
	$\sigma\sigma\sigma\bar{\sigma}$	$(\sigma_a\sigma_a;\ \sigma_a\sigma_b)$	0.03688 39	0.02752 28	0.02024 25
	$s\pi s\bar{\pi}$	$(s_as_a;\ \pi_a\pi_b)$	0.00709 44	0.00481 55	0.00324 89
	$\pi s\pi\bar{s}$	$(\pi_a\pi_a;\ s_as_b)$	0.01932 01	0.01387 66	0.00988 04
	$s\pi\pi\bar{s}$	$(s_a\pi_a;\ \pi_as_b)$	0.00228 88	0.00156 64	0.00106 39
	$\pi ss\bar{\pi}$	$(s_a\pi_a;\ s_a\pi_b)$	0.00128 77	0.00085 30	0.00056 17
	$s\pi\sigma\bar{\pi}$	$(s_a\sigma_a;\ \pi_a\pi_b)$	0.00135 88	0.00091 57	0.00061 24
	$\pi\sigma\pi\bar{s}$	$(\pi_a\pi_a;\ \sigma_as_b)$	0.02320 61	0.01704 54	0.01237 93
	$\pi s\pi\bar{\sigma}$	$(\pi_a\pi_a;\ s_a\sigma_b)$	0.02779 97	0.02025 38	0.01460 04
	$s\pi\pi\bar{\sigma}$	$(s_a\pi_a;\ \pi_a\sigma_b)$	0.00354 78	0.00245 24	0.00168 00
	$\pi\sigma s\bar{\pi}$	$(s_a\pi_a;\ \sigma_a\pi_b)$	0.00135 88	0.00091 57	0.00061 24
	$\pi\pi\sigma\bar{s}$	$(\sigma_a\pi_a;\ \pi_as_b)$	0.00073 49	0.00051 03	0.00035 08
	$\sigma s\pi\bar{\pi}$	$(\sigma_a\pi_a;\ s_a\pi_b)$	0.00050 54	0.00033 42	0.00021 94
	$\sigma\pi\pi\bar{\sigma}$	$(\sigma_a\pi_a;\ \pi_a\sigma_b)$	0.00112 42	0.00079 16	0.00055 05
	$\pi\sigma\sigma\bar{\pi}$	$(\sigma_a\pi_a;\ \sigma_a\pi_b)$	0.00068 66	0.00045 46	0.00029 88
	$\pi\sigma\pi\bar{\sigma}$	$(\pi_a\pi_a;\ \sigma_a\sigma_b)$	0.03224 25	0.02415 87	0.01784 20
	$\sigma\pi\sigma\bar{\pi}$	$(\sigma_a\sigma_a;\ \pi_a\pi_b)$	0.00728 29	0.00494 53	0.00333 71
	$\pi\pi\pi\bar{\pi}$	$(\pi_a\pi_a;\ \pi_a\pi_b)$	0.00720 20	0.00488 06	0.00328 80
	$\pi\pi\pi'\bar{\pi}'$	$(\pi_a\pi_a';\ \pi_a\pi_b')$	0.00020 19	0.00013 00	0.00008 32
	$\pi\pi'\pi\bar{\pi}'$	$(\pi_a\pi_a;\ \pi_a'\pi_b')$	0.00679 82	0.00462 06	0.00312 15
	$++++$	$(\pi_a{}^+\pi^+{}_a;\ \pi_a{}^+\pi_b{}^+)$	0.00700 01	0.00475 06	0.00320 48
	$+--+$	$(\pi_a{}^+\pi^-{}_a;\ \pi_a{}^-\pi_b{}^+)$	0.00040 38	0.00025 99	0.00016 65

Errata

	page		
Part I	30	$-E_i(-2.50)$	0.0249 1491 7870 2*6*97 36
	70	line 26	$F_{1,10}$ (7.75, 5.75)
Part II	17	A_5 (6.00)	should be removed
	18	B_7 (11.5)	−5.*2*21 5849 331

Part III 472–475

	α	$\alpha\beta\gamma\bar{\delta}$	
L/δ	2.75	$sss\bar{\sigma}$	0.21200 *87*
		$\pi\sigma\sigma\bar{\pi}$	0.0*1588* *24*
	5.00	$s\sigma s\bar{s}$	0.09003 *73*
	5.50	$ss\sigma\bar{s}$	0.01453 *38*
		$\pi s\pi\bar{\sigma}$	0.0859*5* *05*
		$\sigma\pi\sigma\bar{\pi}$	0.0316*1* *28*
		$s\pi\pi\bar{\sigma}$	0.0137*8* *03*
	6.00	$sss\bar{s}$	0.05037 *50*
	6.50	$s\pi s\bar{\pi}$	0.0150*7* *40*
		$\pi\pi\pi\bar{\pi}$	0.01536 *37*
		$\pi\pi'\pi\bar{\pi}'$	0.01440 *65*
		++++	0.01488 *51*
	7.00	$sss\bar{s}$	0.0274*2* *19*
		$s\sigma\sigma\bar{\sigma}$	0.01*373* *79*
		$s\pi s\bar{\pi}$	0.0103*8* *09*
		$\pi\pi\pi\bar{\pi}$	0.0*1055* *80*
		$\pi\pi'\pi\bar{\pi}'$	0.00*993* *42*
		++++	0.0*1024* *61*

476

α		
2.25	$W_4^0(0,1)$	1.358 79
2.75	$W_4^2(0,0)$	4.336^{-3}
4.75	$-W_4^1(0,0)$	$1.291\ 0^{-6}$

JOURNAL OF THE PHYSICAL SOCIETY OF JAPAN Vol. 9, No. 4, JULY—AUGUST, 1954

Atomic Clocks and Frequency Standards on an Ammonia Line. II

By Koichi SHIMODA

Department of Physics, Faculty of Science, University of Tokyo

(Received December 28, 1953)

The practical accuracy of any atomic clock ever constructed has been much worse than theoretically expected. In this paper we examine the use of Zeeman and Faraday effects for the purpose of eliminating causes of errors discussed in article, I. The atomic or molecular system in a magnetic field violates the reciprocity theorem. A method is proposed and investigated to utilize the unreciprocal component of transmission characteristics of the absorption cell, though it proved to be not so useful as expected. And the character of a circular waveguide absorption cell in an axial magnetic field is treated in detail as an preparation for designing a high-precision atomic clock.

§ 1. Application of Zeeman and Faraday Effect on an Ammonia Clock

The ammonia molecule has a small rotational magnetic moment, coupled with the nuclear magnetic moment of N^{14} in the molecule. When the molecule is placed in a magnetic field, the inversion spectrum is split into two groups of Zeeman components¹⁾. These components are symmetrical to the centre frequency and the splitting is proportional to the intensity of magnetic field. Besides, in particular, the reciprocity relation which holds in usual electrical circuits should fail in the presence of magnetic field. Because the violation of reciprocity theorem will be found only near the spectral frequency, the use of unreciprocal component as a frequency standard might extremely improve the accuracy of the atomic clock.

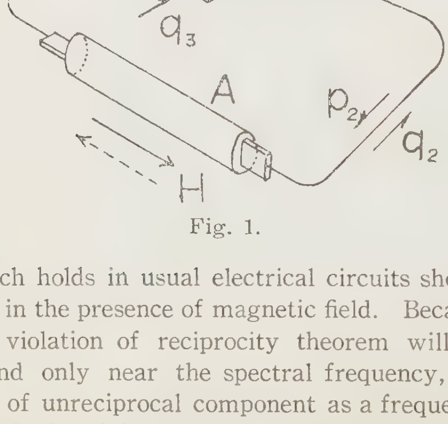

Fig. 1.

The reciprocity relation in a microwave circuit is expressed in terms of the characteristic matrix or scattering matrix, (S_{ik}), by the symmetry of matrix elements²⁾³⁾. We have usually

$$S_{ik}=S_{ki}\,. \tag{1.1}$$

On the contrary, when the magnetic moments in the circuit are placed in a magnetic field, the reciprocity relation does not hold and we have

$$S_{ik}\neq S_{ki}\,. \tag{1.2}$$

There are many devices to bring out the unreciprocal component, $S_{ik}-S_{ki}$. A microwave bridge employing a symmetrical six-arms waveguide junction may be used, although there are some difficulties, in its precise construction⁴⁾. Another device employing a magic tee is schematically illustrated in Fig. 1. A magic tee, B, and a circular waveguide absorption cell, A, are connected by two rectangular waveguides, (1) and (2). The characteristic matrix of the absorption cell in an axial magnetic field is given by

$$A=\begin{pmatrix} a_{11} & a_{12} \\ a_{21} & a_{22} \end{pmatrix}, \tag{1.3}$$

where a_{12} is not equal to a_{21}, and it is assumed that the rectangular waveguides allow to pass only one mode of waves.

The characteristic matrix of an ideal magic tee can be expressed in the form

$$B=\frac{1}{\sqrt{2}}\begin{pmatrix} 0 & 0 & 1 & -1 \\ 0 & 0 & 1 & 1 \\ 1 & 1 & 0 & 0 \\ -1 & 1 & 0 & 0 \end{pmatrix}, \tag{1.4}$$

where the phase reference planes in the waveguide arms are properly chosen. If not, the matrix elements should be multiplied by exp $(j\theta_{ik})$. Now, we consider a practical magic tee, the characteristic matrix of which is more or less different from Eq. (1.4) and has the form

$$B=\begin{pmatrix} b_{11} & b_{12} & b_{13} & b_{14} \\ b_{21} & b_{22} & b_{23} & b_{24} \\ b_{31} & b_{32} & b_{33} & b_{34} \\ b_{41} & b_{42} & b_{43} & b_{44} \end{pmatrix}. \qquad (1.5)$$

where

$$b_{ik}=b_{ki}, \quad \sum b_{ik}b_{kl}^*=\delta_{il}\ , \qquad (1.6)$$

and absolute values of b_{13}, b_{14}, b_{23}, b_{24} are nearly $1/\sqrt{2}$. Let q_1 and q_2 be the complex amplitudes of waves transmitting through waveguides (1) and (2) respectively from A to B; p_1 and p_2 be the amplitudes of waves transmitting in the reverse direction; q_3 and q_4 be respectively amplitudes of input waves in the arms (3) and (4) of the magic tee; and p_4 be the amplitude of output waves through arm (4) to the detector. Some reflection from the detector must be considered and we put

$$q_4=rp_4\ , \qquad (1.7)$$

in which r is the reflection coefficient. From the definition of the characteristic matrix we obtain

$$\left.\begin{aligned} q_1&=a_{11}p_1+a_{12}p_2 \\ q_2&=a_{21}p_1+a_{22}p_2 \\ p_1&=b_{11}q_1+b_{12}q_2+b_{13}q_3+b_{14}q_4 \\ p_2&=b_{21}q_1+b_{22}q_2+b_{23}q_3+b_{24}q_4 \\ p_4&=b_{41}q_1+b_{42}q_2+b_{43}q_3+b_{44}q_4\ . \end{aligned}\right\} \qquad (1.8)$$

Solving the set of linear equations, (1.6), (1.7), and (1.8), we can obtain the output, p_4.

$$\begin{aligned} p_4=\{q_3/(1-rG)D\}\{(&b_{31}b_{22}b_{14}+b_{31}b_{21}b_{24} \\ &-b_{32}b_{12}b_{14}-b_{32}b_{11}b_{21})(a_{11}a_{22}-a_{12}a_{21}) \\ &+b_{31}a_{11}b_{14}+b_{32}a_{22}b_{24}+b_{42}a_{21}b_{13}+b_{41}a_{12}b_{23}\}. \end{aligned} \qquad (1.9)$$

Here

$$D=\begin{vmatrix} -1 & 0 & a_{11} & a_{12} \\ 0 & -1 & a_{21} & a_{22} \\ b_{11} & b_{12} & -1 & 0 \\ b_{21} & b_{22} & 0 & -1 \end{vmatrix}, \qquad (1.10)$$

and

$$\begin{aligned} G=b_{44}+(1/D)\{&(b_{14}^2b_{22}-b_{24}^2b_{11})(a_{11}a_{22}-a_{21}a_{12}) \\ &+b_{14}^2a_{11}+b_{24}^2a_{22}+b_{14}b_{24}(a_{21}+a_{12})\}. \end{aligned} \qquad (1.11)$$

In the simplest case when the magic tee is ideal, we see from Eqs. (1.4) and (1.10) that $D=1$, and using Eq. (1.9), we obtain

$$p_4=(q_3/2)\{(a_{11}-a_{22})+(a_{21}-a_{12})\}e^{j\varphi}, \qquad (1.12)$$

assuming that $r=0$. From this equation we find that, if both coupling coefficients of waveguides to an absorption cell are made equal, $a_{11}=a_{22}$, then the output, p_4, will be proportional to $a_{21}-a_{12}$. Thus we can obtain the output which is proportional to the unreciprocal component, using a linear detector such as r.f. biased crystal detector.

Strictly speaking, however, we have small contributions of other terms appearing in Eq. (1.9) which are not proportional to $a_{21}-a_{12}$, since there must be some errors in machining and tuning. In order to eliminate these faulty effects we propose to reverse the direction of magnetic field at a low frequency and to obtain the difference of respective outputs by a phase-sensitive detector. This device is also effective in reducing gain-variation noises or errors due to slow changes of supply voltages.

Let the matrix element of A be $a_{ik}^{\pm}$ for the applied field of $\pm H$, then we may expect for a circular cylindrical waveguide cell that

$$a_{11}^{+}=a_{11}^{-},\ a_{22}^{+}=a_{22}^{-},\ \text{and}\ a_{12}^{\pm}=a_{21}^{\mp}.$$

Besides, $a_{12}^{\pm}+a_{21}^{\pm}$, $a_{12}^{\pm}\cdot a_{21}^{\pm}$, and hence D and G are independent on the sign of the magnetic field. Assuming a linear detection, we can obtain the output from the phase-sensitive detector proportional to

$$\begin{aligned} p_4^{+}-p_4^{-}=\{&q_3/(1-rG)D\}(b_{13}b_{24}-b_{23}b_{14}) \\ &\times(a_{21}^{+}-a_{12}^{+}). \end{aligned} \qquad (1.13)$$

This shows that the output signal will be proportional to $a_{21}-a_{12}$ even by the use of imperfect magic tee and absorption cell, and unmatched detector.

If there is any d.c. magnetic field such as terrestrial magnetic field, magnitudes of operating magnetic field of each direction will not always equal. The difference is probably less than one oersted and may be reduced to less than 0.1 oersted, if necessary. The inversion spectrum of ammonia is not so sensitive to magnetic field that we employ rather strong field, for example $H=200$ oersteds, which produces Zeeman shift of about 143 kc/sec. for 3–3 line. Therefore the effect of stray d.c. magnetic field will be small, and we may estimate the effect by considering a small correction proportional to Eq. (1.9). Eq. (1.9) itself is nearly equivalent to Eq. (1.13), when we use a good construction. Hence, the error due to d.c. field will be negligible.

In order to maximize $a_{21}-a_{12}$ the polarizations of two coupling waveguides should be orthogonal[5]. In this case, $a_{21}=a_{12}$ for $H=0$, and $a_{21}\neq a_{12}$ for $H\neq 0$. The absorption cell acts as a cavity resonator rather than a waveguide, because the crossed couplings are subject to large reflections at the junctions. The character of such an absorption cell is considered in the followings.

§ 2. Nearly Circular Waveguide Cell in a Magnetic Field

The characteristic matrix of an absorption cell in a magnetic field is calculated. First, we consider a circular cylindrical waveguide alone in an axial magnetic field. Since there are two orthogonal modes of TE_{11} waves in a circular waveguide, the characteristic matrix of the waveguide with two openings is expressed by a matrix with four columns and four rows.

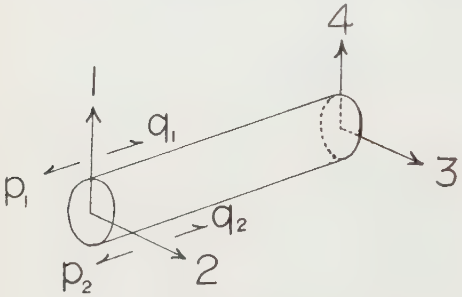

Fig. 2.

$$S=\begin{pmatrix} S_{11} & S_{12} & S_{13} & S_{14} \\ S_{21} & S_{22} & S_{23} & S_{24} \\ S_{31} & S_{32} & S_{33} & S_{34} \\ S_{41} & S_{42} & S_{43} & S_{44} \end{pmatrix}. \tag{2.1}$$

This matrix is unsymmetrical and not unitary in general.

Because it is impossible to have a perfect circular waveguide, let us consider a slightly deformed waveguide cell. When there is no magnetic field, the propagating TE_{11} waves in a nearly circular waveguide can be approximately expressed by a linear combination of two orthogonal modes whose propagation constants differ a little. Let the directions of polarizations of waves of normal modes be x and y, and the propagation constants be γ_x and γ_y respectively, then the characteristic matrix of the cell may be expressed in the form

$$\begin{pmatrix} 0 & 0 & 0 & e^{-\gamma_x l} \\ 0 & 0 & e^{-\gamma_y l} & 0 \\ 0 & e^{-\gamma_y l} & 0 & 0 \\ e^{-\gamma_x l} & 0 & 0 & 0 \end{pmatrix}, \tag{2.2}$$

where l is the cell length.

In a circular waveguide with axial magnetic field the polarization of propagating waves rotates, which may be considered as a superposition of two oppositely polarized circular waves having different propagation constants. Therefore we should use four propagation constants, γ_x^+, γ_y^+, γ_x^-, and γ_y^-, for a nearly circular waveguide in a magnetic field. Plus and minus sign denote the directions of circular polarization with respect to the right- and left-hand rotations about z-axis.

Let the amplitudes of two normal modes of outgoing (incoming) waves at the one opening (a) be p_1 and p_2 (q_1 and q_2), and at the other opening (b) be p_3 and p_4 (q_3 and q_4). Each linearly polarized waves can be expressed by a superposition of two circularly polarized waves. For example, let the circularly polarized components of q_1 be represented by q_1^+ and q_1^-, then we may write that

$$\left.\begin{aligned} q_1&=q_1^+ + q_1^- = 2q_1^+ = 2q_1^-, \\ q_2&=-jq_2^+ + jq_2^- = -2jq_2^+ = 2jq_2^-, \end{aligned}\right\} \tag{2.3}$$

in which the phase reference directions of circularly polarized waves are taken parallel to the direction of polarization of mode 1.

Instead of the linear polarization system we may use circular polarization system. Then we have amplitudes of component normal modes of circularly polarized waves in the form

$$\left.\begin{aligned} &p_a^{\pm}=p_1^{\pm}+p_2^{\pm}, \text{ and } p_b^{\pm}=p_3^{\pm}+p_4^{\pm}, \\ &\qquad\qquad\qquad\text{(outgoing)} \\ &q_a^{\pm}=q_1^{\pm}+q_2^{\pm}, \text{ and } q_b^{\pm}=q_3^{\pm}+q_4^{\pm}, \\ &\qquad\qquad\qquad\text{(incoming)} \end{aligned}\right\} \tag{2.4}$$

If the directions of polarizations of mode 1 and 4 are taken to be parallel to the x-direction, and mode 2 and 3 to the y-direction, we have

$$\begin{aligned} &p_1^{\pm}=q_4^{\pm}\exp(-\gamma_x^{\pm}l),\ \ p_2^{\pm}=q_3^{\pm}\exp(-\gamma_y^{\pm}l), \\ &p_3^{\pm}=q_2^{\pm}\exp(-\gamma_y^{\pm}l), \quad \text{and} \\ &p_4^{\pm}=q_1^{\pm}\exp(-\gamma_x^{\pm}l). \end{aligned} \tag{2.5}$$

From Eqs. (2.3) and (2.4) we obtain for the waves at the opening (a)

$$q_a^{\pm}=\tfrac{1}{2}(q_1+jq_2),$$

$$q_1^{+}=q_1^{-}=\tfrac{1}{2}(q_a^{+}+q_a^{-}),$$

and

$$q_2^{+}=-q_2^{-}=\tfrac{1}{2}(q_a^{+}-q_a^{-}).$$

Then, using Eqs. (2.4) and (2.5), we may write

$$\begin{aligned}p_b^{\pm}&=q_1^{\pm}\exp(-\gamma_x^{\pm}l)+q_2^{\pm}\exp(-\gamma_y^{\pm}l)\\&=\tfrac{1}{2}\{(q_a^{\pm}+q_b^{\mp})\exp(-\gamma_x^{\pm}l)\\&\quad-(q_a^{\pm}-q_b^{\mp})\exp(-\gamma_y^{\pm}l)\}.\end{aligned}\tag{2.6}$$

Thus we obtain the characteristic matrix of the absorption cell in the circular polarization system.

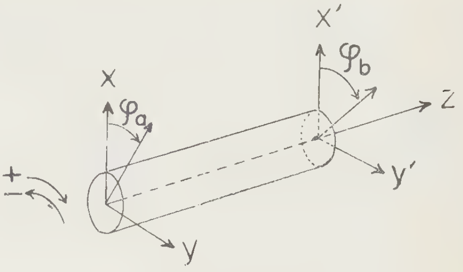

Fig. 3.

$$\begin{pmatrix}p_a^{+}\\p_a^{-}\\p_b^{-}\\p_b^{+}\end{pmatrix}=\tfrac{1}{2}\begin{pmatrix}0&0&r_x^{+}-r_y^{+}&r_x^{+}+r_y^{+}\\0&0&r_x^{-}+r_y^{-}&r_x^{-}-r_y^{-}\\r_x^{-}-r_y^{-}&r_x^{-}+r_y^{-}&0&0\\r_x^{+}+r_y^{+}&r_x^{+}-r_y^{+}&0&0\end{pmatrix}\begin{pmatrix}q_{a+}\\q_a^{-}\\q_b^{-}\\q_b^{+}\end{pmatrix},\tag{2.7}$$

where

$$r_x^{\pm}=\exp(-r_x^{\pm}l),\quad\text{and}\quad r_y^{\pm}=\exp(-r_y^{\pm}l).\tag{2.8}$$

If the phase reference directions are rotated by φ_a and φ_b at the two openings as shown in Fig. 3, the characteristic matrix of the waveguide cell is expressed by S_0 in the following form.

$$S_0=\tfrac{1}{2}\begin{pmatrix}0&0&(r_x-r_y)e^{-j(\varphi_a+\varphi_b)}&(r_x+r_y)e^{-j(\varphi_a-\varphi_b)}\\0&0&(r_x+r_y)e^{j(\varphi_a-\varphi_b)}&(r_x-r_y)e^{j(\varphi_a+\varphi_b)}\\(r_x-r_y)e^{j(\varphi_a+\varphi_b)}&(r_x+r_y)e^{-j(\varphi_a-\varphi_b)}&0&0\\(r_x+r_y)e^{j(\varphi_a-\varphi_b)}&(r_x-r_y)e^{-j(\varphi_a+\varphi_b)}&0&0\end{pmatrix}.\tag{2.9}$$

Transforming the above matrix into that of the linear polarization system by a transformation matrix, U, we obtain

$$S=US_0U^{-1},\tag{2.10}$$

where

$$U=\frac{1}{\sqrt{2}}\begin{pmatrix}1&1&0&0\\-j&j&0&0\\0&0&j&-j\\0&0&1&1\end{pmatrix}.\tag{2.11}$$

S is the characteristic matrix of a gas-filled nearly circular waveguide cell referred to the plane polarization system of arbitrary direction of the axes representated by φ_a and φ_b.

The matrix elements, S_{ik}, can be expressed in the form

$$\begin{aligned}&S_{11}=S_{22}=S_{33}=S_{44}=S_{12}=S_{21}=S_{34}=S_{43}=0\\&S_{42}=-F(r_x,r_y,\varphi_a,\varphi_b),\ S_{41}=F(r_x,r_y,\varphi_a+\pi/2,\varphi_b),\\&S_{24}=\ \ F(r_y,r_x,\varphi_a,\varphi_b),\ S_{14}=F(r_x,r_y,\varphi_b+\pi/2,\varphi_a),\\&S_{13}=\ \ F(r_x,r_y,\varphi_b,\varphi_a),\ S_{32}=F(r_y,r_x,\varphi_a+\pi/2,\varphi_b),\\&S_{31}=-F(r_y,r_x,\varphi_a,\varphi_b),\ S_{23}=F(r_y,r_x,\varphi_b+\pi/2,\varphi_a),\end{aligned}\tag{2.12}$$

where

$$\begin{aligned}&F(r_x,r_y,\varphi_a,\varphi_b)\\&\quad=\tfrac{1}{2}\{r_x^{+}\exp(-j\varphi_b)+r_x^{-}\exp(j\varphi_b)\}\sin\varphi_a\\&\qquad-j\{r_y^{+}\exp(-j\varphi_b)-r_y^{-}\exp(j\varphi_b)\}\cos\varphi_a\\&\quad=\tfrac{1}{4}\{-j\exp(\gamma_x^{+}l+j\varphi_a-j\varphi_b)\\&\qquad+j\exp(\gamma_x^{+}l-j\varphi_a-j\varphi_b)\\&\qquad-j\exp(\gamma_x^{-}l+j\varphi_a+j\varphi_b)\\&\qquad+j\exp(\gamma_x^{-}l-j\varphi_a+j\varphi_b)\\&\qquad+j\exp(\gamma_y^{-}l+j\varphi_a+j\varphi_b)\\&\qquad+j\exp(\gamma_y^{-}l-j\varphi_a+j\varphi_b)\\&\qquad-j\exp(\gamma_y^{+}l+j\varphi_a-j\varphi_b)\\&\qquad-j\exp(\gamma_y^{+}l-j\varphi_a-j\varphi_b)\}.\end{aligned}\tag{2.13}$$

§ 3. Cylindrical Cell Coupled with Rectangular Waveguides

The characteristic matrix of a nearly circular waveguide cell coupled with two rectangular waveguides is calculated. Let the absorption cell with two rectangular waveguides be divided into three parts, as shown in Fig. 4. T_a is a transformer between one of and rectangular waveguides and a circular opening of the cylindrical absorption cell, S. We assume that there is only one mode of waves in a rectangular waveguide denoted by 0, and there are two modes of waves in a circular waveguide denoted by 1 and 2. T_b is another transformer and the concerning three modes are denoted by 3, 4, and 5 as shown in Fig. 4. S is a nearly circular cylindrical cell with a certain absorptive gas pervaded in an axial magnetic field. The characteristic matrix of S is unsymmetrical and not unitary as already described in § 2.

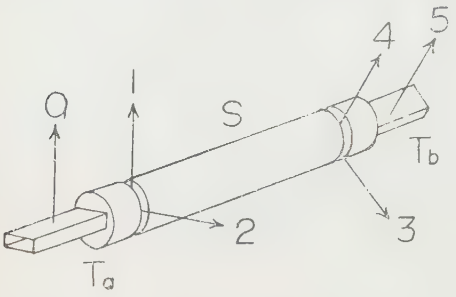

Fig. 4.

The characteristic matrix of a transformer, T_a, may be expressed by

$$T_a=\begin{pmatrix} T_{00} & T_{01} & T_{02} \\ T_{10} & T_{11} & T_{12} \\ T_{20} & T_{21} & T_{22} \end{pmatrix}, \tag{3.1}$$

where $T_{ik}=T_{ki}$ and $\sum_j T_{ij}T_{jk}^*=\delta_{ik}$, if we assume that it is lossless. Let us take the direction of polarization of mode 0 to be parallel to mode 1 and assume the symmetrical construction about that direction, then we find that

$$|T_{22}|=1,$$

$$\text{and} \qquad T_{21}=T_{12}=T_{20}=T_{02}=0. \tag{3.2}$$

When we choose the two phase-reference planes so as to make T_{22} real positive and $T_{00}=T_{12}$, the characteristic matrix of the transformer can be expressed in the form

$$T_a=\begin{pmatrix} T_1 & X_1 & 0 \\ X_1 & T_1 & 0 \\ 0 & 0 & 1 \end{pmatrix}, \tag{3.3}$$

where $|T_1|^2+|X_1|^2=1$, and $T_1X_1^*$ is a pure imaginary number. To avoid confusion a common phase-reference plane has been chosen for two modes of waves in a circular waveguide. If the transformer is matched, we shall have $T_1=0$ and $X_1=e^{j\varphi}$. Similarly, the characteristic matrix of T_b is given by

$$T_b=\begin{pmatrix} T_{33} & T_{34} & T_{35} \\ T_{43} & T_{44} & T_{45} \\ T_{53} & T_{54} & T_{55} \end{pmatrix}=\begin{pmatrix} 1 & 0 & 0 \\ 0 & T_4 & X_4 \\ 0 & X_4 & T_4 \end{pmatrix}, \tag{3.4}$$

where $|T_4|^2+|X_4|^2=1$ and $T_4X_4^*$ is a pure imaginary number.

Let the amplitudes of incoming waves to the cell through the opening (a) be q_1 and q_2, through the other opening (b) be q_3 and q_4, and outgoing waves be p_1, p_2, p_3, and p_4 respectively. The circuit as a whole has two openings of rectangular waveguides, the amplitudes of incoming waves through them are denoted by q_0 and q_5, and the outgoing waves by p_0 and p_5. As to the transformer T_a, its incoming waves are q_0, p_1 and p_2; and outgoing waves are p_0, q_1 and q_2. As to the transformer T_b, they are p_3, p_4 and q_5; and q_3, q_4 and p_5. Then the characteristic matrices of the two transformers may be combined into one matrix, (T_{ik}), in the following formulas.

$$\begin{pmatrix} p_0 \\ q_1 \\ q_2 \\ q_3 \\ q_4 \\ p_5 \end{pmatrix}=\begin{pmatrix} T_1 & X_1 & 0 & 0 & 0 & 0 \\ X_1 & T_1 & 0 & 0 & 0 & 0 \\ 0 & 0 & 1 & 0 & 0 & 0 \\ 0 & 0 & 0 & 1 & 0 & 0 \\ 0 & 0 & 0 & 0 & T_4 & X_4 \\ 0 & 0 & 0 & 0 & X_4 & T_4 \end{pmatrix}\begin{pmatrix} q_0 \\ p_1 \\ p_2 \\ p_3 \\ p_4 \\ q_5 \end{pmatrix}. \tag{3.5}$$

Using the characteristic matrix given by Eqs. (2.1) and (2.12), we may write

$$\begin{pmatrix} q_0 \\ p_1 \\ p_2 \\ p_3 \\ p_4 \\ q_5 \end{pmatrix}=\begin{pmatrix} 1 & 0 & 0 & 0 & 0 & 0 \\ 0 & 0 & 0 & S_{13} & S_{14} & 0 \\ 0 & 0 & 0 & S_{23} & S_{24} & 0 \\ 0 & S_{31} & S_{32} & 0 & 0 & 0 \\ 0 & S_{41} & S_{42} & 0 & 0 & 0 \\ 0 & 0 & 0 & 0 & 0 & 1 \end{pmatrix}\begin{pmatrix} q_0 \\ q_1 \\ q_2 \\ q_3 \\ q_4 \\ q_5 \end{pmatrix}. \tag{3.6}$$

From Eqs. (3.5) and (3.6) we can eliminate p_1, p_2, p_3 and p_4, and obtain

$$\begin{pmatrix} p_0 \\ q_1 \\ q_2 \\ q_3 \\ q_4 \\ p_5 \end{pmatrix}=\begin{pmatrix} T_1 & 0 & 0 & X_1S_{13} & X_1S_{14} & 0 \\ X_1 & 0 & 0 & T_1S_{13} & T_1S_{14} & 0 \\ 0 & 0 & 0 & S_{23} & S_{24} & 0 \\ 0 & S_{31} & S_{32} & 0 & 0 & 0 \\ 0 & T_4S_{41} & T_4S_{42} & 0 & 0 & X_4 \\ 0 & X_4S_{41} & X_4S_{42} & 0 & 0 & T_4 \end{pmatrix}\begin{pmatrix} q_0 \\ q_1 \\ q_2 \\ q_3 \\ q_4 \\ q_5 \end{pmatrix}. \tag{3.8}$$

This is a set of linear equations which is easily solved. Solving it, we obtain

$$\begin{aligned} q_1=(1/D)\{&X_1(1-S_{32}S_{23}-T_4S_{42}S_{24})q_0 \\ &+X_1(T_1S_{11}+T_1S_{13}S_{32}S_{31}-T_1S_{11}S_{32}S_{23})q_5\}, \end{aligned}$$

$$
\begin{aligned}
q_2=&(1/D)\{X_1(S_{31}S_{23}+T_4S_{41}S_{24})q_0\\
&+X_4(S_{24}+T_1S_{31}S_{14}S_{23}-T_1S_{24}S_{13}S_{31})q_5\},\\
q_3=&(1/D)\{X_1(S_{31}+T_4S_{32}S_{24}S_{41}-T_4S_{31}S_{42}S_{24})q_0\\
&+X_4(S_{32}S_{24}+T_1S_{14}S_{31})q_5\},\\
q_4=&(1/D)\{X_1(T_4S_{41}+T_4S_{42}S_{23}S_{31}\\
&-T_4S_{41}S_{23}S_{32})q_0\\
&+X_4(1-S_{32}S_{23}-T_1S_{13}S_{31})q_5\},
\end{aligned}
\qquad (3.8)
$$

where

$$
\begin{aligned}
D=1&-S_{32}S_{23}-T_1S_{31}S_{13}-T_4S_{42}S_{24}-T_1T_4S_{41}S_{14}\\
&+T_1T_4(S_{31}S_{13}S_{41}S_{14}+S_{42}S_{24}S_{32}S_{23}\\
&-S_{42}S_{23}S_{31}S_{14}-S_{13}S_{32}S_{24}S_{41}).
\end{aligned}
\qquad (3.9)
$$

Thus we have the following relations.

$$
\begin{aligned}
p_0&=a_{11}q_0+a_{12}q_5\,,\\
p_5&=a_{21}q_0+a_{22}q_5\,.
\end{aligned}
$$

The coefficients, a_{11}, a_{12}, a_{21} and a_{22}, are the same as used in § 1, and can be written in the form

$$
\begin{aligned}
a_{11}=&T_1-X_1^2/T_1\\
&+(X_1^2/T_1D)\{1-S_{23}S_{32}-T_4S_{42}S_{24}\},\\
a_{12}=&(X_1X_4/D)(S_{13}S_{32}S_{24}-S_{14}S_{32}S_{23}+S_{14}),\\
a_{21}=&(X_1X_4/D)(S_{42}S_{23}S_{31}-S_{41}S_{32}S_{23}+S_{41}),\\
a_{22}=&T_4-X_4^2/T_4\\
&+(X_4^2/T_4D)(1-S_{32}S_{23}-T_1S_{31}S_{13}).
\end{aligned}
\qquad (3.10)
$$

We see that, as expected, a_{12} is not equal to a_{21}, when $S_{ik}\neq S_{ki}$.

These matrix elements are calculated as a function of the propagation constants. Using Eqs. (2.12) and (2.13), we may rewrite Eq. (3.9) in the form

$$
\begin{aligned}
D=1&+T_1T_4\{4(\xi^2+\eta^2)^2-4(\Gamma^2+\Delta^2)\cos 2\varphi(\xi^2+\eta^2)\\
&+(\Gamma^2-\Delta^2)^2\cos^2 2\varphi+4\Gamma^2\Delta^2\}\\
&-(1/2)(1-T_1)(1-T_4)(\Gamma^2-\Delta^2)\cos 2\varphi\\
&+(1+T_1)(1+T_4)\{(3/2)\Gamma^2-(1/2)\Delta^2-2\xi\eta\}\\
&-\{(1-T_1)\xi-(1+T_1)\Gamma e^{j\varphi}\}\\
&\quad\times\{(1-T_4)\xi-(1+T_4)\Gamma e^{-j\varphi}\}\\
&-\{(1-T_1)\eta-(1+T_1)\Gamma e^{-j\varphi}\}\\
&\quad\times\{(1-T_4)\eta-(1+T_4)\Gamma e^{j\varphi}\},
\end{aligned}
\qquad (3.11)
$$

in which

$$
\left.
\begin{aligned}
\Gamma&=\tfrac{1}{4}(r_x{}^{+}+r_y{}^{+}+r_x{}^{-}+r_y{}^{-}),\\
\Delta&=\tfrac{1}{4}(r_x{}^{+}+r_y{}^{+}-r_x{}^{-}-r_y{}^{-}),\\
\xi&=\tfrac{1}{4}(r_x{}^{+}-r_y{}^{+})\exp(-j\varphi_a-j\varphi_b),\\
\eta&=\tfrac{1}{4}(r_x{}^{-}-r_y{}^{-})\exp(j\varphi_a+j\varphi_b),
\end{aligned}
\right\}
\qquad (3.12)
$$

and

$$\varphi=\varphi_a-\varphi_b.$$

When the cross-section of the waveguide cell is closely circular, we may neglect the higher order terms of ξ and η. We may take $\xi+\eta=\delta\cos\theta$, $\xi-\eta=j\delta\sin\theta$, and $\theta=\varphi_a+\varphi_b$. Then we obtain

$$
\begin{aligned}
D=1&-\tfrac{1}{2}(\Gamma^2+\Delta^2)(1+T_1)(1+T_4)\\
&-\tfrac{1}{2}(\Gamma^2-\Delta^2)(1-T_1)(1-T_4)\cos 2\varphi\\
&4\Gamma^2\Delta^2T_1T_4+(\Gamma^2-\Delta^2)^2T_1T_4\cos^2 2\varphi\\
&+2\delta\Gamma\{(1-T_1T_4)\cos\theta\cos\varphi\\
&-(T_1-T_4)\sin\theta\sin\varphi\}.
\end{aligned}
\qquad (3.13)
$$

Inserting Eqs. (3.13) and (3.12) into Eq. (3.10), we shall obtain a_{ik} in terms of $r_x{}^{\pm}$, $r_y{}^{\pm}$ and transformer constants. Simplified forms for the case of $r_x=r_y$ will be given in § 5.

§ 4. Effect of Magnetic Field on an Ammonia Line

Now we consider the interaction of microwaves and ammonia gas. Let the rotational quantum number of the ammonia molecule be J, nuclear spin of nitrogen be I, then the total angular momentum, F, is made up of J and I by the spin-rotation coupling under a weak magnetic field, H. And the magnetic components of F are given by

$$M=F,\ F-1,\cdots,\ -F.$$

Then energy levels are expressed in the form[1]

$$W=W_0(J,K,I,F)-M\mu_N H(\alpha_J g_{mol}+\alpha_I g_N), \qquad (4.1)$$

where

$$
\begin{aligned}
\alpha_J&=\{F(F+1)+J(J+1)-I(I+1)\}/2F(F+1),\\
\alpha_I&=\{F(F+1)+I(I+1)-J(J+1)\}/2F(F+1),
\end{aligned}
$$

and μ_N is the nuclear magneton, g_N the nuclear g-factor, and g_{mol} the molecular rotational g-factor. When the r.f. and d.c. field is perpendicular, the selection rules are:

$$\Delta J=0, \qquad \Delta M=\pm 1. \qquad (4.2)$$

Thus the Zeeman splitting, $\Delta\nu_0$, is given by

$$
\begin{aligned}
\Delta\nu_0=&(\mu_N H/h)[(g_{mol}+g_N)/2\\
&+\{(g_{mol}-g_N)/2\}\{J(J+1)-I(I+1)\}/F(F+1)].
\end{aligned}
\qquad (4.3)
$$

For the ammonia molecule, $N^{14}H_3$, we have $I=1$, $g_N=0.403$ and $g_{mol}=0.480$. Except for $I=1$ we have six Zeeman components, which are usually observed as partially resolved two lines. The splitting of the two lines at a field of $H=1000$ oersteds has been reported to be 0.718 Mc/sec.

Both the dispersion and absorption may be represented by the complex dielectric constant, $\varepsilon=\varepsilon'-j\varepsilon''$. But the dielectric constant of a gas in a magnetic field cannot be represented by a scalar but by a tensor. Let the molecular polarizability tensor be $\boldsymbol{\alpha}$ for the impressed r.f. field of $\boldsymbol{E}\exp(2\pi j\nu t)$, the average polarization of the molecule, $\boldsymbol{p}\exp(2\pi j\nu t)$, is given by

$$\boldsymbol{p}=\boldsymbol{\alpha}\boldsymbol{E}.$$

The dielectric constant of the gas with the number density of N is given by

$$\boldsymbol{\varepsilon}=\varepsilon_0+4\pi N\boldsymbol{\alpha}\,. \tag{4.4}$$

$\boldsymbol{\alpha}$ is a function of frequency, magnetic field, and quantum states of the molecule.

As for the sharp inversion lines of ammonia, symmetric and antisymmetric states of identical rotational states should be considered. Then we may write

$$\boldsymbol{\alpha}(J,K,I,F)=\boldsymbol{\alpha}_a(J,K,I,F)+\boldsymbol{\alpha}_s(J,K,I,F),$$

and the frequency is given by

$$h\nu_0=W_a-W_s\,.$$

As the Zeeman splittings for the transitions, $\Delta M=\pm1$, belonging to different F states differ little, the difference may be neglected. Then we may write for the transitions from symmetric to antisymmetric state

$$W_a-W_s=E_0\mp\kappa H,\quad \text{(absorption)}$$

and for the transitions from anti-symmetric to symmetric state

$$W_s-W_a=-E_0\mp\kappa H,\quad \text{(emission)}$$

Components of the dielectric constant under the magnetic field along z-axis,

$$\begin{matrix} \varepsilon_{xx}, & \varepsilon_{xy} & 0, \\ \varepsilon_{yx}, & \varepsilon_{yy}, & 0, \\ 0, & 0, & \varepsilon_{zz}, \end{matrix}$$

are calculated by the perturbation method. We obtain

$$\left.\begin{aligned} &\varepsilon_{xx}=\varepsilon_{yy}=\varepsilon_0+\varepsilon^{+}+\varepsilon^{-}, \\ &\varepsilon_{xy}=-\varepsilon_{yx}=j(\varepsilon^{+}-\varepsilon^{-}), \end{aligned}\right\} \tag{4.5}$$

where

$$\begin{aligned} \varepsilon^{\pm}&=4\pi N\alpha^{\pm} \\ &=4\pi N\sum_F\sum_M\frac{\mu^2}{Q_r}\frac{K^2}{J^2(J+1)^2} \\ &\quad\times\frac{\{F(F+1)-I(I+1)+J(J+1)\}^2}{4F^2(F+1)^2}g_i \\ &\quad\times\left\{\left(\frac{(F\mp M)(F\pm M+1)}{E_0-\kappa H+E}\right.\right. \\ &\quad+\left.\frac{(F\pm M)(F\mp M+1)}{E_0\pm\kappa H-E}\right)\exp(-W_s/kT) \\ &\quad+\left(\frac{(F\mp M)(F\pm M+1)}{-E_0\mp\kappa H+E}\right. \\ &\quad+\left.\left.\frac{(F\pm M)(F\mp M+1)}{-E_0\pm\kappa H-E}\right)\exp(-W_a/kT)\right\}, \end{aligned} \tag{4.6}$$

where μ is the dipole moment of the molecule, Q_r the rotational partition function, g_i the weight of the state. Since $E=h\nu$, $\sum g_i\exp(-W_i/kT)=3Q_r$, $\Delta\nu_0\ll\nu_0$ and $\exp(-W_s/kT)-\exp(-W_a/kT)\cong h\nu_0/kT$, we obtain

$$\begin{aligned} \varepsilon^{\pm}&=\frac{2\pi Ng_i}{3Q_rh}\frac{\mu^2K^2(2J+1)}{J(J+1)} \\ &\quad\times\left(1-\frac{4}{3J(J+1)}+\frac{2}{3J^2(J+1)^2}\right)\frac{h\nu_0}{kT} \\ &\quad\times\left(\frac{1}{\nu_0\pm\sigma H+\nu}+\frac{1}{\nu_0\mp\sigma H-\nu}\right), \end{aligned} \tag{4.7}$$

where $\sigma=\kappa/h$ and $g_i=2$, when $K=3n$, $g_i=1$, when $K\neq3n$.

When we take into account the line width, $2\Delta\nu$, according to Van Vleck and Weisskopf⁽⁶⁾, we obtain the following equation instead of Eq. (4.7).

$$\begin{aligned} \varepsilon^{\pm}&=\frac{2\pi Ng_i}{3Q_rkT}\frac{\mu^2K^2(2J+1)}{J(J+1)} \\ &\quad\times\left(1-\frac{4}{3J(J+1)}+\frac{2}{3J^2(J+1)^2}\right) \\ &\quad\times\frac{2\nu_0^2}{\nu_0^2-(\pm\sigma H+\nu)^2} \\ &\quad\times\left(1-\frac{(\nu_0\pm\sigma H+\nu)(\pm\sigma H+\nu)\Delta\nu}{2\nu_0^2\{\Delta\nu-j(\nu_0\mp\sigma H-\nu)\}}\right. \\ &\quad+\left.\frac{(\nu_0\mp\sigma H-\nu)(\pm\sigma H+\nu)\Delta\nu}{2\nu_0^2\{\Delta\nu+j(\nu_0\pm\sigma H+\nu)\}}\right). \end{aligned} \tag{4.8}$$

Thus the dispersion and absorption are given by $\mathrm{Re}(\varepsilon^{\pm})$ and $\mathrm{Im}(\varepsilon^{\pm})$. Because $\Delta\nu\ll\nu_0$, $\sigma H=\Delta\nu_0\ll\nu_0$, and

$$1-4/3J(J+1)+2/3J^2(J+1)^2\cong1,\ \text{when}\ J\geq3,$$

we may write

$$\begin{aligned} \mathrm{Re}(\varepsilon^{\pm})&\cong\mu^2\frac{K^2(2J+1)}{J(J+1)}\frac{2\pi Ng_i}{3kTQ_r} \\ &\quad\times\frac{\nu_0\mp\sigma H-\nu}{(\Delta\nu)^2+(\nu_0\mp\sigma H-\nu)^2}, \end{aligned} \tag{4.9}$$

$$\begin{aligned} -\mathrm{Im}(\varepsilon^{\pm})&\cong\mu^2\frac{K^2(2J+1)}{J(J+1)}\frac{4\pi Ng_i}{3kTQ_r}\frac{\nu^2}{\nu_0} \\ &\quad\times\frac{\Delta\nu}{(\Delta\nu)^2+(\nu_0\mp\sigma H-\nu)^2}. \end{aligned} \tag{4.10}$$

Since ε_{yx} is not equal to ε_{xy}, the propagation constants of right- and left-hand circularly polarized waves are not equal. With respect to the direction of magnetic field, which is parallel or antiparallel to the direction of propagation, let us represent the propagation constant of left-hand circular waves by γ^{+} and right-hand by γ^{-}. Then we obtain the propagation constant of plane waves in the form⁽⁷⁾

$$\gamma^{\pm}=(j\omega/c)\sqrt{\mu(\mathcal{E}_{xx}\pm j\mathcal{E}_{yx})}=(j\omega/c)\sqrt{\mu(\mathcal{E}_0+2\mathcal{E}^{\pm})}. \tag{4.11}$$

The problem for the propagation constants of quasi-TE_{11} waves in a circular waveguide was exactly solved by H. Gamo[8]. Using Eq. (30) in his paper and Eqs. (4.5) and (4.8), we shall be able to obtain the propagation constant of TE_{11} waves in the circular waveguide cell in an axial magnetic field. However, the propagation constant as a function of frequency may be calculated approximately as follows.

By differenciating $\gamma^2=k^2-\omega^2\mathcal{E}\mu$ with respect to frequency under the assumption that the cut-off wavelength constant, k, is constant, we obtain

$$d\gamma/d\mathcal{E}=-(\omega^2\mathcal{E}\mu/2\gamma)(1/\mathcal{E})\ .$$

Thus we can calculate the propagation constants of circularly polarized waves in good approximation.

$$\gamma^{\pm}=\gamma_0-j\pi(\lambda_g/\lambda^2)(\mathcal{E}^{\pm}/\mathcal{E}_0)\ .$$

Since $x=(\nu-\nu_0)/\nu_0$, $d=\Delta\nu/\nu_0$, $h=\Delta\nu_0/\nu_0=\sigma H/\nu_0$ are small compared to unity, using Eq. (4.8), we obtain

$$\gamma^{\pm}=\gamma_0-(j\lambda_g/2\lambda)\{\alpha d/(x\mp h-jd)\}, \tag{4.12}$$

where

$$\alpha=\frac{8\pi^2Ng_t}{3ckTQ_r}\ \frac{\mu^2K^2(2J+1)}{J(J+1)}\ \frac{\nu_0{}^2}{\Delta\nu} \tag{4.13}$$

is the peak absorption coefficient of the unsplit line.

Let us assume that $\alpha l\ll 1$ for simplicity of calculation. Practically, the solenoid coil is not so long that this condition can be satisfied. Then, Γ and Δ which have been defined in § 3 can be approximately given by

$$\Gamma=\tfrac{1}{2}\,e^{-\gamma_0 l}\{e^{-\gamma^+ l}+e^{-\gamma^- l}\}$$
$$=je^{-\gamma_0 l}\left\{1+j\,\frac{\lambda_g}{\lambda}\ \frac{\alpha ld(x-jd)}{x^2-2jxd-d^2-h^2}\right\}, \tag{4.14}$$

$$\Delta=\tfrac{1}{2}\,e^{-\gamma_0 l}\{e^{-\gamma^+ l}-e^{-\gamma^- l}\}$$
$$=je^{-\gamma_0 l}\,\frac{\lambda_g}{\lambda}\ \frac{\alpha lhd}{x^2-2jxd-d^2-h^2}\,. \tag{4.15}$$

$\Gamma e^{\gamma_0 l}$ and $\Delta e^{\gamma_0 l}$ are illustrated on the complex plane in Fig. 5. When the waveguide absorption cell is lossless, γ_0 is pure imaginary and it is $\gamma_0=2\pi j/\lambda_g$. Fig. 6 and Fig. 7 show respectively $|\Gamma|$ and $|\Delta|$ as a function of frequency.

§ 5. Discussions on Faraday Modulation Method

As was mentioned in § 1, nearly orthogonal coupling of two waveguides is desirable to utilize the unreciprocal component of the absorption cell. This corresponds to "crossed nicols" in the optical system. Neglecting the higher order terms of ξ and η which come

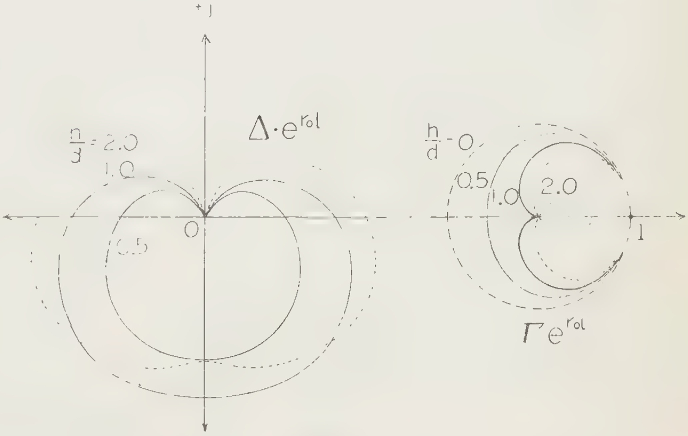

Fig. 5.

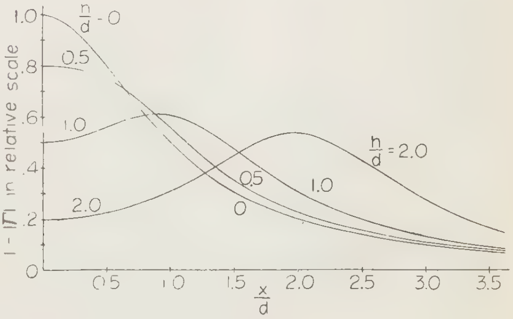

Fig. 6.

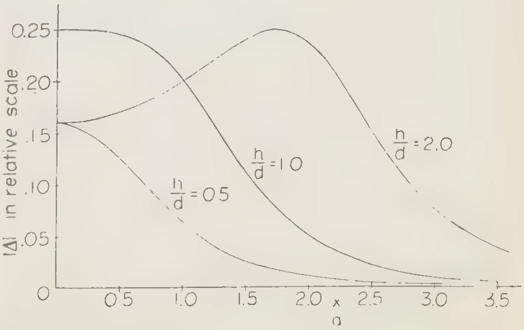

Fig. 7.

from circular cross-section, we can calculate the elements of the characteristic matrix of the absorption cell from Eqs. (2.12) and (3.10).

$$\begin{aligned}a_{12}&=j(X_1X_4/2D)\Delta(\Gamma^2+2\Delta^2)\{1+j(\xi+\eta)/D\},\\ a_{21}&=-j(X_1X_4/2D)\Delta(\Gamma^2+2\Delta^2)\{1-j(\xi+\eta)/D\},\end{aligned}\tag{5.1}$$

where

$$D=1-\Delta^2-(T_1+T_4)\Gamma^2+T_1T_4(\Gamma^4+2\Gamma^2\Delta^2-\Delta^2+\Delta^4).\tag{5.2}$$

a_{12} and a_{21} are odd functions of Δ, changing their sign with the direction of magnetic field. We obtain the unreciprocal component in the form

$$a_{12}-a_{21}=j(X_1X_4/D)\Delta(\Gamma^2+2\Delta^2).\tag{5.3}$$

This does not contain ξ and η in the first order so that it is practically independent upon the slight deviation from circular symmetry of the waveguide cell.

The output signal of the circuit shown in Fig. 1 will be more or less dependent upon $a_{11}-a_{22}$, even when the magic tee is ideal and Zeeman modulation is applied. Since $|X_1^2|+|T_1^2|=1$ and $X_1T_1^*$ is imaginary, we may write

$$\left.\begin{aligned}X_1&=je^{j\alpha_1}\cos\rho_1, & T_1&=e^{j\alpha_1}\sin\rho_1,\\ X_4&=je^{j\alpha_2}\cos\rho_2, & T_4&=e^{j\alpha_2}\sin\rho_2,\end{aligned}\right\}\tag{5.4}$$

and we have

$$X_1^2/T_1=T_1-1/T_1^*,\quad X_4^2/T_4=T_4-1/T_4^*.$$

Using Eqs. (2.12) and (3.10), we obtain $a_{11}-a_{22}$ for $\varphi=\pi/2$ after a little calculation.

$$\begin{aligned}a_{11}-a_{22}=1/T_1^*-1/T_4^*&+\{(1-\Delta^2)/D\}\\ &\times(T_1-T_4-1/T_1^*+1/T_4^*)\\ &+(\Gamma^2/D)(T_4/T_1^*-T_1/T_4^*)\\ &-(2\Gamma/D)\delta\sin\theta(T_4/T_1^*-T_1/T_4^*).\end{aligned}\tag{5.5}$$

Thus we find that $a_{11}-a_{22}$ will become zero, if $T_1=T_4$, as it is expected from symmetry consideration. If T_1 is not equal to T_4, however, we see that $a_{11}-a_{22}$ is not always small, even when the transformers are nearly matched.

When $T_1T_4\ll 1$, Eq. (5.5) can be approximately given by

$$\begin{aligned}a_{11}-a_{22}=(1/D)\{&(T_1-T_4)(1-\Delta^2)\\ &-(T_1/T_1^*-T_4/T_4^*)\Gamma^2\},\end{aligned}\tag{5.6}$$

where

$$D=1-\Delta^2(T_1+T_4)\Gamma^2.$$

For small absorptions in the cell, the above equation is reduced to

$$a_{11}-a_{22}\simeq 2je^{-2\gamma_0 l}e^{j(\alpha_1+\alpha_2)}\sin(\alpha_1-\alpha_2).\tag{5.7}$$

Hence we see that even with nearly matched transformers, where T_1, $T_4\ll 1$, $a_{11}-a_{22}$ is not small, if α_1 is not close to α_2. This is due to the fact that the crossed waveguide system is essentially reflective.

We conclude therefore that the output signal will be also dependent upon $a_{11}-a_{22}$, not only upon $a_{12}-a_{21}$, even by the use of Zeeman modulation, because the phase character of transformers cannot be made exactly equal and the magnetic field cannot be changed its sign without varying its magnitudes.

Finally, we investigate the character of the circular waveguide cell for arbitrary angles of polarization of the coupling, assuming that the waveguide cell has perfect circular symmetry. From the assumed symmetry we have $\gamma_x=\gamma_y$, and Eq. (2.12) can be reduced to

$$\left.\begin{aligned}S_{42}&=S_{31}=-\Gamma\sin\varphi+j\Delta\cos\varphi,\\ S_{24}&=S_{13}=-\Gamma\sin\varphi-j\Delta\cos\varphi,\\ S_{14}&=S_{23}=\Gamma\cos\varphi-j\Delta\sin\varphi,\\ S_{41}&=S_{32}=\Gamma\cos\varphi+j\Delta\sin\varphi.\end{aligned}\right\}\tag{5.8}$$

Substituting in Eq. (3.10), we obtain

$$\begin{aligned}a_{12}=(X_1X_4/2D)\{&-\Gamma^4(1+\cos 2\varphi)\cos 2\varphi\\ &+\Delta^4(1-\cos 2\varphi)\cos 2\varphi-2\Gamma^2\Delta^2(2-\cos^2 2\varphi)\\ &+2j\Gamma\Delta(\Gamma^2-\Delta^2)\sin 2\varphi+(\Gamma^2-\Delta^2)\cos 2\varphi\\ &+\Gamma^2+\Delta^2\}/(\Gamma\cos\varphi+j\Delta\sin\varphi),\\ a_{21}=(X_1X_4/2D)\{&-\Gamma^4(1+\cos 2\varphi)\cos 2\varphi\\ &+\Delta^4(1-\cos 2\varphi)\cos 2\varphi-2\Gamma^2\Delta^2(2-\cos^2 2\varphi)\\ &-2j\Gamma\Delta(\Gamma^2-\Delta^2)\sin 2\varphi+(\Gamma^2-\Delta^2)\cos 2\varphi\\ &+\Gamma^2+\Delta^2\}/(\Gamma\cos\varphi-j\Delta\sin\varphi)\end{aligned}\tag{5.9}$$

and

$$\begin{aligned}a_{11}-a_{22}=&(1/T_1^*-1/T_4^*)\\ &+(1/D)(T_1-T_4-1/T_1^*+1/T_4^*)\\ &\quad\times(1-\Gamma^2\cos^2\varphi-\Delta^2\sin^2\varphi)\\ &-(1/D)(T_4/T_1^*-T_1/T_4^*)\\ &\quad\times(\Gamma^2\sin^2\varphi+\Delta^2\cos^2\varphi),\end{aligned}$$

where

$$\begin{aligned}2D=2&-(1+T_1)(1+T_4)(\Gamma^2+\Delta^2)\\ &-(1-T_1)(1-T_4)(\Gamma^2-\Delta^2)\cos 2\varphi\\ &+2T_1T_4(\Gamma^2-\Delta^2)^2\cos^2 2\varphi+4\Gamma^2\Delta^2.\end{aligned}$$

Using these results, we can examine the character of the circular waveguide absorption cell for any angle of the waveguide coupling. The case for $\varphi=\pi/4$ seems to be a little promissing, but the calculation has shown that it is also improper in obtaining an accurate atomic frequency standard. Only when $\varphi=0$, we have a possibility to be free from transformer reflections, but the unreciprocal component will vanish at the same time, hence it will be unable to use it as a frequency standard.

We conclude, therefore, that it is difficult to construct a very accurate atomic clock by such a method as shown in Fig. 1, although it is very interesting. The dificulties are in constructing an extremely well-balanced magic tee and a circular waveguide cell of good symmetry, and in producing a discriminator characteristics by the unreciprocal component alone.

Another successful device to make the spectral frequency reference free from circuit reactances and other sources of errors by the use of a magnetic field will be described in article III with experimental results thereof.

References

1) C. K. Jen: Phys. Rev. **74** (1948) 1396.
2) S. Tomonaga: J. Phys. Soc. Japan **2** (1947) 158; **3** (1948) 93.
3) A. E. Pannenborg: Philips Res. Rep. **7** (1952) 131, 169, 270.
4) K. Shimoda: J. Phys. Soc. Japan **5** (1950) 255.
5) K. Shimoda and T. Nishikawa: J. Phys. Soc. Japan **6** (1951) 516.
6) J. H. Van Vleck and V. Weisskopf: Rev. Mod. Phys. **17** (1945) 277.
7) C. L. Hogan: Bell Syst. Tech. J. **31** (1952) 1.
8) H. Gamo: J. Phys. Soc. Japan **8** (1953) 176.

JOURNAL OF THE PHYSICAL SOCIETY OF JAPAN Vol. 9, No. 4, JULY—AUGUST, 1954

Atomic Clocks and Frequency Standards on an Ammonia Line. III

By Koichi SHIMODA

Department of Physics, Faculty of Science, University of Tokyo

(Received January 22, 1954)

In this paper the design and construction of a high precision atomic clock is described. The device effectively employs the Stark-, source- and Zeeman-modulation, and is free from the errors caused by reflections in the microwave line. The Zeeman splitting nearly equal to the line width is preferable. The preliminary result with one meter cell-length and an unsatisfactory Stark modulator has shown that the device is successful and the accuracy of 10^{-9} or better is obtainable. Measurements of the line width and the analysis are also given.

§ 1. Introduction

Atomic standards of time and frequency have become feasible by the development of coherent electronic oscillators for microwaves. Many usable spectral lines are found within the available range of frequency. Among them, the inversion lines of ammonia are the most favorable at present.(1) Serious difficulties in obtaining accurate standard frequency by these spectral lines come from the fact that they have finite line widths of the order of 100 kc/sec. at least. Some causes of errors were investigated by an experimental apparatus of a stark-modulation ammonia clock.(2) The author had an idea of utilizing the effect of magnetic field upon the spectral line, in order to decrease the errors of the apparent frequency. The use of Faraday effect was found to be unfavorable, though it is not hopeless.(3) However, the analytical treatment of the absorption cell in a magnetic field suggested the author another method for reducing errors caused by circuit reactances, modulation waveforms, and some frequency-sensitive components in the microwave circuit. The experiment has proved that the device described below is satisfactory.

§ 2. Source Modulation and Zeeman Effect

Because the output from the absorption cell will be minimum at the centre frequency of the absorption line, it is necessary to employ a sensing method or a so-called source modulation method in order to obtain a discriminator characteristics with the line. Applying the axial magnetic field, the absorption line of ammonia is split into two groups of Zeeman components. The transmission coefficient of the absorption cell, a_{12}, is optimum at the centre frequency, and hence the source modulation is needed. As was described in article II, a_{12} is nearly proportional to Γ (or Δ) which was illustrated in Fig. 6 (or Fig. 7) in article II.

When the microwave frequency is shifted a little (of the order of 10^{-6} or less) at a certain frequency, the detected signal at the same frequency will be approximately proportional to

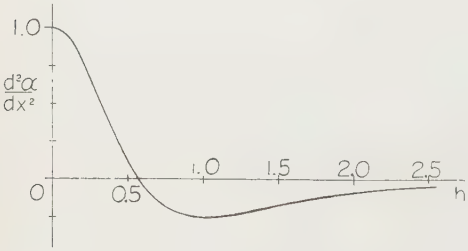

Fig. 1. $d^2\alpha/dx^2$ as a function of magnetic field.

$$\frac{dA}{dx}=\frac{d|a_{12}|^2}{dx},$$

assuming square-law detection. Here $x=(\nu-\nu_0)/\nu_0$, and ν_0 is the centre frequency of the line. Then the frequency sensitivity of the spectral line discriminator is given by d^2A/dx^2.

For the parallel polarizations of input and output waveguides, the sensitivity is approximately proportional to

$$\frac{d^2\alpha(x)}{dx^2}=2\alpha_0 d^2\frac{3h^2-d^2}{(d^2+h^2)^3}. \tag{2.1}$$

This is illustrated in Fig. 1 as a fuction of h.

If there is no circuit reactance or reflection in the absorption cell, dA/dx will be zero at $\nu=\nu_0$. And if there are some circuit reactances, the frequency for zero output will not coincide with the centre frequency of the line.

Now we consider the case of circular waveguide cell with parallel coupling, since the crossed coupling has been shown to be less useful in obtaining a precise frequency reference.$^{3)}$ Using Eq. (5.9) in II, we obtain for $\varphi=0$

$$a_{12}=a_{21}=\frac{X_1X_4}{D}(\Gamma-\Gamma^3-\Gamma\Delta^2), \tag{2.2}$$

where Γ and Δ are given by Eq. (4.14) and (4.15) in II, and

$$\begin{aligned}D&=1-(1+T_1T_4)\Gamma^2-(T_1+T_4)\Delta^2+T_1T_4\Gamma^4\\&=(1-\Gamma^2)(1-T_1T_4\Gamma^2)-(T_1+T_4)\Delta^2.\end{aligned}$$

As the cell length, l, is rather short because of the use of solenoid coil, αl is small, being of the order of 10^{-2} for the cell length of less than a few meters. Neglecting higher order terms of αl, the transmission coefficient is given by

$$A=|a_{12}|^2=\left|\frac{X_1X_4\Gamma}{1-T_1T_4\Gamma^2}\right|^2. \tag{2.3}$$

When the absorption cell is lossless, or when the loss is negligible, we may write $\gamma_0=j\beta=j\frac{2\pi}{\lambda_g}$. And we have

$$\begin{aligned}A&=\frac{X_1^2X_4^2\{1-2ud^2(x^2+d^2+h^2)\}}{1-2R\cos\theta\,\mathrm{Re}\,(\Gamma^2)-2jR\sin\theta\,\mathrm{Im}\,(\Gamma^2)+R\{1-4ud^2(x^2+d^2+h^2)\}}\\&=X_1^2X_4^2\{1-2ud^2(x^2+d^2+h^2)\}/\{1-2R\cos\psi+R^2\\&\quad+4ud^2(x^2+d^2+h^2)R\cos\psi-4ud(x^2+d^2-h^2)xR\sin\psi-4ud^2(x^2+d^2+h^2)R^2\},\end{aligned} \tag{2.4}$$

where $T_1T_4=Re^{j\theta}$, and $2\beta l-\theta=\psi$.

$$u=\frac{\lambda_g}{\lambda}\frac{\alpha l}{(x^2-d^2-h^2)^2+4d^2x^2}. \tag{2.5}$$

By differentiating Eq. (2.4) with respect to x, we obtain the output for source modulation, or the discriminator characteristics of the line. The apparent frequency of the line is given by $dA/dx=0$. After a little calculation we can obtain the apparent fractional frequency in the form

$$\delta x = \frac{R\sin\psi}{a}\,\frac{\dfrac{d\beta}{dx}(d^2+h^2-4ad^2)-\dfrac{ad(d^2-h^2)}{d^2+h^2}}{\dfrac{d^2(d^2-3h^2)}{(d^2+h^2)^2}(1-R^2)+\dfrac{2(d^2-h^2)}{d^2+h^2}\dfrac{d\beta}{dx}lRd\cos\psi}\,. \tag{2.6}$$

where $a=\dfrac{\lambda_g}{\lambda}\alpha$, and $d=\dfrac{\Delta\nu}{\nu_0}$, $h=\dfrac{\Delta\nu_0}{\nu_0}=\dfrac{\sigma H}{\nu_0}$.

The fractional error frequency, δx, will be zero when either

$$R=0\,,\qquad \sin\psi=0\,,$$

or

$$\frac{d\beta}{dx}(d^2+h^2-4ad^2)-\frac{ad(d^2-h^2)}{d^2+h^2}=0\,. \tag{2.7}$$

The third condition, Eq. (2.7), is essentially similar to that discussed in article I § 5. In order to satisfy this condition it is necessary to change peak absorption and line width, which would be difficult in practice, though there is a certain range of allowance to be controlled by the applied magnetic field. If Eq. (2.7) does not hold, the left-hand side of the equation is of the order of $\dfrac{d\beta}{dx}d^2$. Because $\dfrac{d\beta}{dx}=\dfrac{2\pi\lambda_g}{\lambda^2}$, the fractional error of the reference frequency may be

$$\delta x\approx\frac{d\beta}{dx}\frac{d^2}{a}R\sin\psi=\frac{2\pi d^2}{\lambda\alpha}R\sin\psi\,,$$

For example, taking $2\alpha=2\times10^{-4}\,\mathrm{cm}^{-1}$,* $d=5\times10^{-6}$ corresponding to $\Delta\nu=120$ kc/sec., we obtain

$$\delta x\approx10^{-4}R\sin\psi\,.$$

Consequently, when we want to get an accurary of 10^{-9}, $R\sin\psi$ is required to be less than 10^{-5}. Reduction of power reflection coefficient within 10^{-5} is prohibitively difficult, and the alternative, $\sin\psi<10^{-5}$, requires precise adjustment of cell length including electrical length of transformers within the accuracy of $10^{-5}/2\beta=10^{-4}$ cm, which is also nearly impossible. A most skilful technician would be able to reduce both R and $\sin\psi$ and obtain the accuracy of the order of 10^{-9}. But it would be very difficult to detect a small mismatch and to correct it.

§ 3. Stark- Source- and Zeeman-Modulation Ammonia Clock

One of the best devices in reducing errors due to reflections is to apply large field Stark modulation as was done in the Stark modulation ammonia clock No. 3 (Fig. 8 in I). The square wave modulation of strong Stark field will produce the output from the detecter at the modulation frequency proportional to the difference of output power with and without (that is, far shifted) absorption line. Moreover, this device is also effective in decreasing the error caused by frequency sensitivity of the multiplier and the detector.

The output signal from the absorption cell at the Stark modulation frequency is expressed by

$$P=P_i\{|a_{12}(\alpha)|^2-|a_{12}(0)|^2\}\,, \tag{3.1}$$

where P_i is the input power to the cell. Neglecting higher order terms of αl and R, the above equation may be rewritten in the form

$$\begin{aligned}P/P_i=&-2ud(x^2+d^2+h^2)(1+4R\cos\psi)\\&+4uxd(x^2+d^2-h^2)R\sin\psi\,,\end{aligned} \tag{3.2}$$

where the symbols are the same as already used.

Since the output becomes maximum or minimum about the centre of the line, it is necessary to employ source modulation of small amplitude in order to discriminate the centre of the line. The frequency of source modulation should be lower than that of Stark modulation. The output signal from the phase-detector at the source modulation frequency will be nearly proportional to dp/dx.

If we assume for the present that the input power, P_i, is insensitive to frequency, the apparent centre frequency of the line is given by

$$\frac{d}{dx}\left(\frac{P}{P_i}\right)=0\,.$$

And we obtain from Eq. (3.2), as $x\ll d$,

$$\frac{d}{dx}\left(\frac{P}{P_i}\right)=\frac{4al}{d^2+h^2}\left[\left\{\frac{d^2(d^2-3h^2)}{(d^2+h^2)^2}\right.\right.$$
$$\left.+2\frac{d^2-h^2}{d^2+h^2}\frac{d\beta}{dx}lRd\cos\psi\right\}x$$

---

* We have denoted the peak amplitude absorption coefficient by α, and power absorption coefficient by $\alpha_0(=2\alpha)$.

$$+\left\{\frac{d^2-h^2}{d^2+h^2}+4\frac{d\beta}{dx}ld\right\}Rd\sin\psi\Big]. \tag{3.3}$$

Thus we see that the fractional error will be zero, when we have

$$h^2=\frac{1+4\dfrac{d\beta}{dx}ld}{1-4\dfrac{d\beta}{dx}ld}\,d^2\,. \tag{3.4}$$

Because $\frac{d\beta}{dx}ld=\frac{2\pi\lambda_g}{\lambda^2}ld$ is about 10^{-2} for the cell length of a few meters, Eq. (3.4) may approximately be expressed by $h^2=d^2$. The reason why the effect of circuit reactance will vanish, when $h=d$, is the fact that the dispersion does not exist i.e. the imaginary part of the dielectric constant of the gas does not change near the centre of the line in this particular case. This can be seen from Fig. 5 in II by a cusp on the curve corresponding to $h=d$. Fortunately, the discriminator sensitivity by the absorption line becomes maximum at the same time as can be seen in Fig. 1.

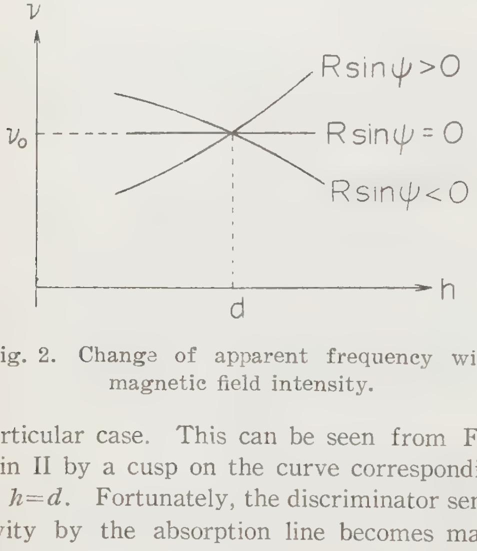

Fig. 2. Change of apparent frequency with magnetic field intensity.

Now we have a problem of how we may adjust the Zeeman splitting so as to satisfy Eq. (3.4). When $h\approx d$, the fractional error can be approximated from Eq. (3.3) by

$$\delta x=\left(\frac{h^2}{d^2}-1-8\frac{d\beta}{dx}ld\right)Rd\sin\psi\,,$$

as $\frac{d\beta}{dx}lRd\ll 1$. The apparent frequency of the line, $\nu=\nu_0(1+\delta x)$, will be independent of $Rd\sin\psi$, only when

$$h^2=\left(1+8\frac{d\beta}{dx}ld\right)d^2\,, \tag{3.4a}$$

and then it is exactly the same as the centre frequency, ν_0. Let us use a phase shifter or other waveguide components to vary the value $R\sin(2\beta l-\theta)$, and change the intensity of magnetic field so that the discriminator output may not vary with it. Then the condition, Eq. (3.4a), is satisfied and the fractional error will be practically negligible.

As the line width changes gradually, successive operation of the phase shifter and control of magnetic field are necessary. The process is so troublesome and difficult that it is better to superpose Zeeman modulation and automatically control the phase shifter so as to satisfy $\sin(2\beta l-\theta)=0$. The principle can be understood from Fig. 2. The discriminator output will vary with magnetic field intensity, if $R\sin\psi$ is not zero. Thus using an automatic control by the output of the phase-detector at the frequency of Zeeman modulation, we may make $R\sin\psi$ zero, and the error of the reference frequency may be made negligible, if $h\approx d$. We only have to adjust d.c. field at long intervals, according as the line width changes appreciably. The frequency of Zeeman modulation should be still lower than that of source modulation.

Finally we consider the effect of frequency sensitivities of the multiplier, detector and other components. The over-all characteristic may be represented by a function $P_i(x)$, and the output signal with Stark- and source-modulation can be given by

$$\frac{dP}{dx}=\frac{P}{P_i}\frac{dP_i}{dx}+P_i\frac{d}{dx}\left(\frac{P}{P_i}\right). \tag{3.5}$$

We have for $x\ll d$

$$\frac{P}{P_i}=\frac{2ald^2}{d^2+h^2}\,,$$

and we obtain approximately

$$\frac{dP}{dx}=\frac{2alP_i}{d^2+h^2}\Big[\frac{d^2}{P_i}\frac{dP_i}{dx}+\frac{2d^2(d^2-3h^2)}{(d^2+h^2)^2}x$$
$$+\left(2\frac{d^2-h^2}{d^2+h^2}+8\frac{d\beta}{dx}ld\right)Rd\sin\psi\Big], \tag{3.6}$$

where a term, $\frac{d\beta}{dx}lRd\cos\psi$, is neglected, since it may be less than 10^{-3} at most.

The output due to Zeeman modulation is approximately given by

$$\frac{d}{dh}\frac{dP}{dx}=2h\frac{d}{dh^2}\frac{dP}{dx}\,.$$

Differentiating Eq. (3.6) with respect to h^2, we obtain

$$\frac{d}{dh^2}\frac{dP}{dx}=-\frac{2alP_i}{(d^2+h^2)^2}\left[\frac{d^2}{P_i}\frac{dP_i}{dx}+8\frac{d^2(d^2-h^2)}{(d^2+h^2)^2}x+2\frac{3d^2-h^2}{d^2+h^2}Rd\sin\phi\right]. \qquad (3.7)$$

If either the phase shifter, tuners arround the transformers, or the detector is adjusted so that the output due to Zeeman modulation may be zero, then it requires

$$Rd\sin\phi=-4\frac{d^2(d^2-h^2)}{(d^2+h^2)(3d^2-h^2)}x-\frac{d^2(d^2+h^2)}{2(3d^2-h^2)}P_i\frac{dP_i}{dx}. \qquad (3.8)$$

At the same time the output of the phase-detector at the frequency of source modulation is fed back to the main crystal oscillator so as to control the operating frequency. Then the Eq. (3.6) will be equal to zero, and the fractional error of frequency, δx, is obtained, by substituting Eq. (3.8),

$$\delta x=\frac{d^2-2\frac{d\beta}{dx}ld(d^2+h^2)}{1+16\frac{d\beta}{dx}ld\frac{d^2-h^2}{d^2+h^2}}\frac{1}{P_i}\frac{dP_i}{dx}. \qquad (3.9)$$

As $\frac{d\beta}{dx}ld\ll 1$, we may write

$$\delta x \doteqdot \frac{d^2}{P_i}\frac{dP_i}{dx}. \qquad (3.10)$$

Only the noise-limited error will be found, if the detector output without the spectral line is frequency insensitive. If not, the error will change with square of the line width. Eqs. (3.9) and (3.10) show that the error is independent of the magnetic field intensity.

However, the case, $h\approx d$, is preferable as will be easily shown. When $h\approx d$, the output at the Zeeman modulation frequency, Eq. (3.7), is almost independent of x, but depends on $Rd\sin\phi$. On the other hand, the output at the source modulation frequency, Eq. (3.6), depends largely on x, but is almost independent of $Rd\sin\phi$. It is not necessary, therefore, to make Eq. (3.7) exactly vanish in order to reach the noice-limited accuracy of the reference frequency. Hence we have to only adjust the tuners at times so that the output of the phase-detector operating at the frequency of Zeeman modulation may be less than a certain limiting value, keeping the Zeeman splitting nearly equal to the half line width.

It is our regret that the effect of frequency sensitivity cannot be completely avoided even by the use of Zeeman mudulation and large field Stark modulation. But the simultaneous use of source- and Zeeman-modulation enables us to acquire the spectral frequency reference without errors caused by circuit mismatches and other faults.

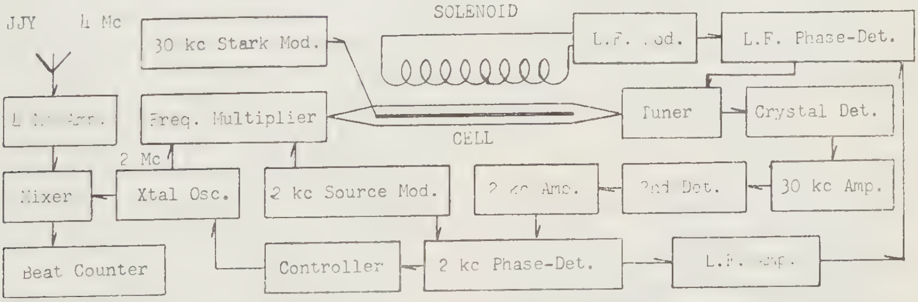

Fig. 3. Block diagram of a Stark- source- and Zeeman-modulation ammonia clock.

§ 4. Experimental Apparatus and Results

In order to study the validity of the reasoning described above and to realize a high precision atomic standard of time, an experimental apparatus has been constructed and tested. A block diagram of the Stark- source- and Zeeman-modulation ammonia clock is shown in Fig. 3. The frequency multiplier which was used in the experiment of Stark modulation clock is used. Because the operating frequency of the Zeeman modulation clock should be about 23,870.13 Mc/s, as compared to that of Stark modulation clock, 23,870.15 Mc/s, the main crystal oscillator is operated at a frequency a few c.p.s. lower than 2 Mc/s. The frequency of the crystal oscillator can be compared with the standard frequency broadcast of station, JJY, which is located about 20 km west of the University of Tokyo.

Modulators. Three types of modulators are employed on the grounds already described

The Stark modulator is required to generate a large square-wave voltage at a frequency of 30 kc/sec. The peak voltage of 400 volts has been obtained in good waveforms, but the amplitude has been found to be insufficient for the purpose of obtaining precise frequency standard. The construction of an improved Stark modulator capable of generating square-waves with peak voltage of about 1500 volts and with botom voltage of less than 1 volt is now in progress.

The operating microwave frequency is modulated at a frequency of 2 kc/sec. with the frequency shift or amplitude of about 10 kc/sec. The rectified signal from the crystal detector is amplified by a tuned amplifier at a frequency of 30 kc/sec., followed by a detector and 2 kc/sec. lock-in amplifier.

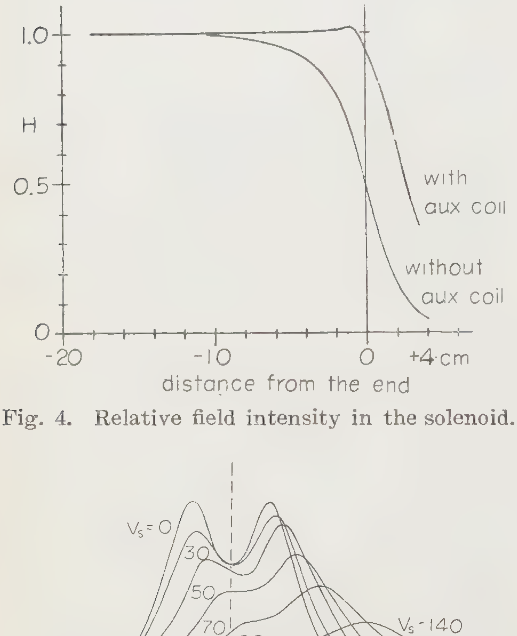

Fig. 4. Relative field intensity in the solenoid.

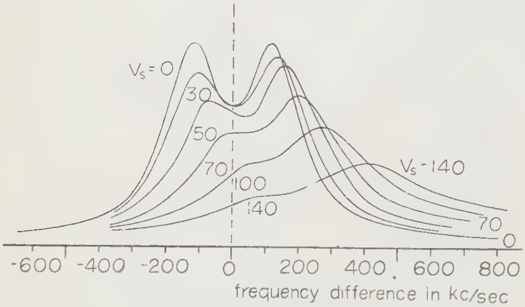

Fig. 5. Line shapes of 3–3 line of ammonia with Zeeman and Stark field. $H=340$ oersteds, $\Delta\nu=105$ kc/sec.

The magnetic field may be modulated at a low frequency, say, several c.p.s. However, the magnetic field modulation has been done in this preliminary work by the manual operation of a rheostat in the d.c. circuit.

Absorption cell. A cylindrical cell of 1 meter in length is used. The inner diameter is 10.2 mm and a Stark electrode of 0.8 mm in diameter is supported at the centre of the cylindrical waveguide by many triangulated mica spacers, arranged every several centimetres. One end of the cell is sealed by a mica window over which the circular to rectangular waveguide transformer of tapered junction type is connected. The polarization of the rectangular waveguide is rotatable with respect to the absorption cell. The other end of the cell has a transformer inside the vacuum seal which is placed in the rectangular waveguide. The lead to the Stark electrode is drawn out from the narrow face of the nearly rectangular waveguide between the cylindrical cell and the mica window. A vacuum outlet which is used as a gas inlet is connected on the broad face of the transformer near the lead of the Stark electrode. Hence the polarization is not rotatabe at this end with respect to the cylindrical cell.

The rotatable tranformer is connected to the detector mount through tuners, while the fixed end is connected to the frequency multiplier through phase-shifter, tuners and a filter.

Solenoid. The main coil of the solenoid is 1 meter in length, with 15,554 turns. The auxiliary coils of 2 cm long with 506 turns each are placed immediately outside the both ends of the main coil in order to make the intensity of magnetic field uniform near the ends. The inner diameter of the solenoid is 36 mm. The calculated field intensities with and without auxiliary coils are shown in Fig. 4. We are sure that the field is uniform within one percent.

Results (1). The line shapes of the absorption line were measured in detail, espetially with both Zeeman and Stark fields. As the Stark field is not uniform in the cell, it is too laborious for one to compute the line shape, which has been determined by experiment.

Applying the square-wave modulation with strong Stark field to the molecule, without magnetic field, the detected waveform has sharp large spikes at the higher frequency side as shown in article I, and no spikes at the lower frequency side. On the other hand, if there is such a magnetic field as to make the Zeeman splitting near equal to the line width, the detected signal has little or no spikes near the centre of the line. This is explained by the illustration of the observed line shapes in Fig. 5, where $\Delta\nu_0=1.16\Delta\nu$, and $\Delta\nu=105$ kc/sec. Though the crossing of curves for $V_s=0$ and $V_s=30$ volts can be seen in the centre frequency region, if the magnetic field is weaker so that $\Delta\nu_0\doteqdot\Delta\nu$, or the line width is narrower than this case, we hardly observe such crossings.

Because the line shape with finite Stark voltage is not symmetrical to the centre frequency, the detected signal with rounded square waveform of the Stark modulation will not be strictly symmetrical with respect to the centre frequency. But the effect can be practically negligible, when we use fairly good Stark waveform easily obtainable. In other words, the use of magnetic field will reduce the error due to spikes to much less than that of Stark modulation atomic clock No. 3 not to mention that of No. 1.

(2) Comparison of time of this atomic clock with quartz clocks can be performed by counting beats between the controlled crystal oscillator of nearly 2 Mc/sec. and the standard frequency broadcast, JJY, of 4 Mc/sec. which is considered to be accurate within 2×10^{-8}. The beat was counted by the visual observation of the Lissajous' figure in our preliminary work. It will be replaced by an electronic system in future.

Table I.

frequency 23,870 Mc/s+ kc/s	line width kc/s	estimated pressure 10^{-3} mmHg
130.67	111.3	1.68
130.99	109.2	1.60
130.93	109.2	1.60
131.29	101.9	1.28
130.99	101.9	1.28
131.04	98.0	1.12
130.87	90.6	0.80

mean value $\nu_0=23{,}870{,}130.97\pm0.10$ kc/sec.

The measured results may be expressed by the values of the spectral frequency with respect to the standard frequency broadcast. A set of values measured within two hours are shown in Table I. The pressure of ammonia was purposely changed in order to study the pressure dependence of the apparent frequency, which is given in Eq. (3.10). But the pressuer dependence cannot be seen from this result in this pressure range and accuracy of the frequency measurement.

The fluctuations of values in the table are considered to be chiefly caused by the short time fluctuation of the standard frequency broadcast which is estimated to be a few part in 10^9, and by the error of visual countings. The noise limited accuracy will be probably within one part in 10^9 for the band-width of about 0.1 c.p.s. Because the amplitude of Stark voltage used is not sufficient for the purpose, the error of about ±1 kc/sec. is estimated. Then the true centre of the 3–3 line of ammonia is tentatively determined to be

$$23{,}870{,}130.97\pm0.10\pm1 \text{ kc/sec.}$$

without any correction on the standard frequency broadcast.

§ 5. Analysis on the Line Width

Precise measurements of the line width are feasible by the experimental set of this atomic clock. The line width itself may be determined within the error of less than one percent. Because the absolute pressure of the gas in the absorption cell is very difficult to measure at the pressure of about 1×10^{-3} mm Hg, the relative intensities of the line and the line widths have been measured.

It was shown in article I that the line width might be given by either

$$\Delta\nu=\Delta\nu_P+\Delta\nu_W+\Delta\nu_d\ , \qquad (5.1a)$$

or

$$(\Delta\nu)^2=(\Delta\nu_P)^2+(\Delta\nu_W)^2+(\Delta\nu_d)^2\ . \qquad (5.1b)$$

However, the pressure broadening, $\Delta\nu_P$, and broadening by collision with cell walls, $\Delta\nu_W$, are both caused by sharp interruptions of the free paths of the molecules, and the doppler broadening is independent of the collision. It is more natural, therefore, to write the line width in the form

$$(\Delta\nu)^2=(\Delta\nu_P+\Delta\nu_W)^2+(\Delta\nu_d)^2\ . \qquad (5.1c)$$

Two other causes of broadening should be considered. The one is saturation and the other is the apparent broadening due to modulation. The saturation broadening has been well stodied theoretically and experimentally[4]. The line width broadened by saturation effect with input power, P_i, is approximately expressed by

$$\Delta\nu_s=\sqrt{1+\frac{P_i}{P_c}}\cdot\Delta\nu\ . \tag{5.2}$$

where

$$P_c=\frac{3ch^2}{4\pi}\cdot\frac{\Delta\nu(\Delta\nu_P+\Delta\nu_W)}{|\mu_M|^2}S\ , \tag{5.3}$$

and S is the cross-sectional area of the cell, μ_M the dipole matrix element for a typical or the most saturated Zeeman component. The saturation broadening is appreciable, when the line width is small and microwave radiation is intense.

It has been known that the apparent line is broadened and deformed, when modulation frequency is not considerably smaller than the line width. But the broadening of this type has never been evaluated as far as the author knows.* It will be given in the following.

Suppose that the square wave modulation is applied, then the molecule is subject to sharp disturbance every half period, $\frac{1}{2}T$, and kept in a constant condition only within a time of $\frac{1}{2}T$. The original line is assumed to be similar to that of the collision broadened line which is characterised by an effective average collision interval of $w=1/2\pi\Delta\nu$. Then the mean coherent length of absorbed waves is given by

$$\tau=\frac{\int_0^{T/2}\int_0^{T/2-\theta}te^{-t/w}dtd\theta+\int_0^{T/2}w\left(\frac{T}{2}-\theta\right)e^{-(T/2-\theta)/w}d\theta}{\int_0^{T/2}\int_0^{T/2-\theta}e^{-t/w}dtd\theta+\int_0^{T/2}we^{-(T/2-\theta)/w}d\theta}\ . \tag{5.4}$$

The second integrals in the numerator and denominator come from disturbances at every half period of the modulation. After a little calculation, we obtain

$$\tau=\frac{w}{\rho}(\rho-1+e^{-\rho})\ , \tag{5.5}$$

where

$$\rho=\frac{T}{2w}=\frac{\pi\Delta\nu}{f_m}\ .$$

Thus we obtain the apparent line width broadened by modulation, assuming $\Delta\nu_M=\frac{1}{2\pi\tau}$.

$$\Delta\nu_M=\frac{\rho\Delta\nu}{\rho-1+e^{-\rho}}\ . \tag{5.6}$$

If the modulation frequency, f_m , is lower than $0.6\Delta\nu$, the apparent width may be approximated by

$$\Delta\nu_m\doteqdot\frac{\rho}{\rho-1}\Delta\nu=\frac{\pi(\Delta\nu)^2}{\pi\Delta\nu-f_m}\ . \tag{5.7}$$

When we have $f_m\lesssim0.1\Delta\nu$, Eq. (5.7) may be simply written by

$$\Delta\nu_M\doteqdot\Delta\nu+\frac{f_m}{\pi}\ .$$

Now we can compute the line width of the 3–3 line of ammonia in the atomic clock. For the temperature of $T=290°K$ we obtain

$$\Delta\nu_d=35.2\ \text{kc/sec.}$$

and

$$\Delta\nu_P=27.5\times10^3p\ \text{kc/sec.}$$

Slightly modifying the result obtained by M. Danos and S. Geschwind[5], the broadening by collision with cell walls may be given by

$$\Delta\nu_W=\frac{0.1}{a-b}\sqrt{\frac{2RT}{M}}\ , \tag{5.8}$$

where a is the inner radius of the cylindrical cell and b is the radius of the Stark electrode. Taking $a=5.1$ mm and $b=0.4$ mm, we obtain for ammonia

$$\Delta\nu_W=11.2\ \text{kc/sec.}$$

Thus we can compute line width according to Eqs. (5.1a), (5.1b) and (5.1c). The microwave input power to the cell is rather difficult to measure. Assuming that the sensitivity of the crystal detector is about 0.4 μA/μ watts, we obtain the value of about 10 μ watts, as the rectified current was 4∼5 μA. The saturation broadened line width is calculated by Eq. (5.2), and the apparent broadening by Stark modulation with 30 kc/sec. is added to $\Delta\nu_S$, using Eq. (5.6) or (5.7). The results for $P_i=15\times10^{-6}$ watts and $|\mu_M|=1.2D$ are illustrated in Fig. 6 by dashed curves, a′ and c′ originating from Eq. (5.1a) and (5.1c) respectively. Though we use source modulation, its effect on the line width is negligible, as the modulation frequency, 2 kc/sec., is much smaller than the line width.

The exact calculation of the peak absorption coefficient, α_0 , is also too difficult to do, because it depends on the line shape. But the following simple calculation may not be so far from truth. Assuming that the over-all line shape is quite similar to that of pressure broadening, we can write

---

* He had missed a paper by R. Karplus, Phys. Rev. **73** (1948) 1027, when he wrote this.

$$\alpha_0 = A \frac{\Delta\nu_P}{\Delta\nu_{M.S}}, \qquad (5.9)$$

when $\Delta\nu_{M.S}$ is the over-all line width broadened by Stark modulation and saturation as well as doppler and collision broadenings. Curves, a, b, and c, in Fig. 6 show $\Delta\nu$ versus α_0 without saturation and modulation broadenings. Curves, a′, and c′, show $\Delta\nu_{M.S}$ versus α_0.

The observed values are shown in Fig. 7, where small circles indicate the results of directly measured values of line width and relative intensities, and crosses indicate those obtained from the line shape with magnetic field of a few hundred oersteds. The computed results for $P_i = 10\times10^{-6}$ watts are also given by full lines. Contrary to expectation, the observed results fit rather to an elementary assumption of Eq. (5.1a) than Eq. (5.1c).*

Conclusion

Although our preliminary apparatus is incomplete and a patch work, we have been assured that the Stark- source- and Zeeman-modulation ammonia clock is one of the best devices realizing the high precision atomic standard of time and frequency.

A rectangular Stark wave-guide cell might be used instead of cylindrical cell above mentioned. But the propagation of waves in a rectangular waveguide in a magnetic field is too difficult to calculate, and besides, the rotation of polarization of waves might cause some complex effect, which would result in decreasing the accuracy of the reference frequency.

The continual operation of the atomic clock needs many other problems to be solved. However, by the use of a good crystal oscillator and stabilized power supply this device will enable us to have an accuracy of the order of 10^{-9}. If we use a longer cell at a reduced temperature, it will not be so difficult to get an accuracy of better than 10^{-9}. The atomic clock is useful as a primary standard of time and frequency, since the accurate time and frequency is reproducible, even if it cannot be operated continuously.

The author expresses his thanks to the helps of the members of the laboratory, T. Nishikawa, Y. Saburi and others. He also wishes to thank Professor M. Miyaji at Tokyo Astronomical Observatory and Mr. K. Matsumoto at the station, JJY, for their encouragements.

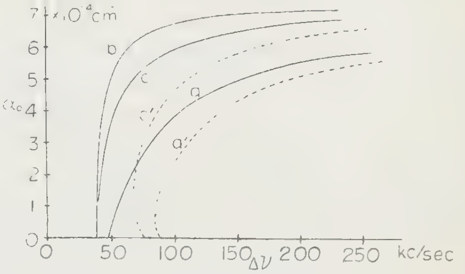

Fig. 6. Calculated line width versus absorption coefficient

——: no saturation, ...: with saturation effect for $P_i = 15\times10^{-6}$ watts.

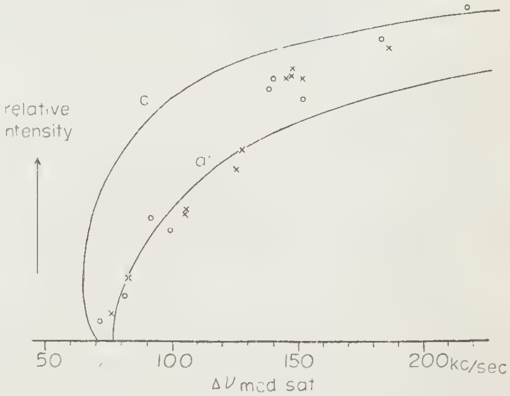

Fig. 7. Observed line width versus relative intensity

○: observed at $H=0$, ×: observed at $H=250\sim400$ oersteds. ——: calculated curves for $P_i = 10\times10^{-6}$ watts.

References

1) H. Lyons: Annals. N. Y. Acad. Sci. **55** (1952) 831, C. H. Townes, Journ. Appl. Phys. **22** (1951) 1365.

2) K. Shimoda: article I: Journ. Phys. Soc. Japan **9** (1954) 378.

3) K. Shimoda: article II.

4) C. H. Townes: Phys. Rev. **70** (1947) 665, J. S. Schwinger and R. Karplus: Phys. Rev. **73** (1948) 1020, R. L. Carter and W. V. Smith, Phys. Rev. **73** (1948) 1053.

5) M. Danos and S. Geschwind: Phys. Rev. **91** (1953) 1159.

Errata

article I **9** (1954) 386 left line 10
should read $2\pi\lambda_g/\lambda^2$ instead of $2\pi\lambda_g/\lambda$

---

* P. W. Anderson has noticed that Eq. (5.1a) should be a better approximation, when the doppler broadening is predominant, while Eq. (5.1b) should be a better one, when the collision broadening is predominant. This consideration agrees well with observed results in Fig. 7.

JOURNAL OF THE PHYSICAL SOCIETY OF JAPAN Vol. 9, No. 4, JULY—AUGUST, 1954

The Positive Joshi Effect in Oxygen under Electrodeless Discharge

By S. R. MOHANTY, J. JAYARAMAN and G. V. G. KRISHNA RAO

Physico-Chemical Laboratories, Banaras Hindu University, India

(Received March 13, 1954)

The Joshi effect $\pm\Delta i$ has been studied in oxygen, in the visible, as a function of the applied potential V under electrodeless 'sleeve' excitation. The positive *effect* $+\Delta i$ sets in well below the breakdown 'threshold potential' V_m, increases with V to a maximum at a limiting potential V_l near V_m, and decreases thereafter; it changes sign (to the negative *effect* $-\Delta i$) at an inversion potential V_i. Above V_i, $-\Delta i$ increases with V. The initial increase in $+\Delta i$ is the consequence of enhanced photoelectron emission due to diminution, under fields F, in the surface work function ϕ in proportion to $\sqrt{F}$. The subsequent diminution in $+\Delta i$ and inversion are due to simultaneous occurrence of $-\Delta i$ which sets in near V_m and increases rapidly with V.

§ 1. Introduction

Mohanty, *et al.*[1] have observed the negative Joshi effect[2] $-\Delta i$, *viz.*, the instantaneous and reversible photodiminution of the current i through gases and vapours under discharge, in oxygen over a wide range of the operative conditions, *e.g.*, applied potential[1][3] V, gas pressure[1][3] p, etc. Data on the positive Joshi effect $+\Delta i$, *i.e.*, the photoincrease in i, on the other hand, are scarce.[4] It was of interest therefore, to observe in the gas, under electrodeless 'sleeve' excitation, an appreciable $+\Delta i$, and the dependence of this last on, and its inversion to $-\Delta i$ with, V.

§ 2. Experimental

The general experimental arrangement and electric circuit employed are shown in Fig. 1.

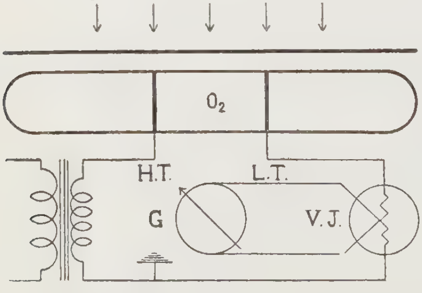

Fig. 1. Production of the Joshi effect in Oxygen under 'sleeve' excitation.

Oxygen, prepared and purified as described by Mohanty and Kamath[1], was contained at different (28–31 mm Hg, 30°C) p in cylindrical soft soda glass tubes (diameter: internal, 7.0–8.2 mm; external, 9.2–10.8 mm) provided with external 'sleeve' electrodes (3–5 cm apart). Each 'sleeve' consisted of a single turn of unoxidized copper wire (diameter *ca.* 1 mm). The gas was excited over 4–10 kV (rms) of 50 c/s frequency. The discharge current i was observed with a sensitive mirror galvanometer (G) actuated by a Cambridge vacuum thermocouple ('Vacuo-junction', V.J.) in dark (i_D) and when irradiated (i_L) with light (3700–7800Å) from a 300 watt, 200 volt, incandescent tungsten filament (in glass) lamp placed at a distance of 28 cm from the discharge tube(s). The heat radiations from the lamp were cut off with an appropriate filter. A representative set of results is contained in Table I, and shown graphically in Fig. 2. The net *effect* $\pm\Delta i$ is given by $i_L - i_D$, and the relative *effect* $\pm\%\Delta i$ by $(\pm\Delta i/i_D)\times 10^2$.

The structure of i at various V was observed with a DuMont cathode ray oscillograph. Input to this last was obtained from across 15 kΩ in the low tension (L.T.) circuit of the discharge tube. Fig. 3 contains a typical set of oscillograms, in dark and under light.

§ 3. Discussion

A. *The Breakdown 'Threshold Potential'*

That the 'threshold potential' V_m, which marks the transition from mainly capacitative to ohmic conduction brought about by the breakdown of the medium as a dielectric, is of fundamental importance to chemical and quasi-chemical changes in gaseous systems under electrical activation in general, and to the Joshi effect $\pm\Delta i$ in particular, has been emphasized by Joshi.[1][5] This V_m, as evident from Fig. 2, is characterized by a rapid increase in the current through (and the wattage dissipated in) the system; obtained by extrapolation, it is 6.27 kV in dark, and 4.80 kV under light.

Table I

Potential Dependence of the Joshi Effect, Positive and Negative, in Oxygen

pO_2 : 28 mm (30°C) Temperature : 31°C

Dimensions of the (glass) 'sleeve' tube : External diameter, 9.2 mm ; internal diameter, 7.0 mm ; inter-'sleeve' distance, 5.0 cm

V (kV, rms) 50∽	i_D	i_L	Δi	$\%\Delta i$
4.27	1.41	1.41	—	—
4.53	1.41	1.41	—	—
4.80	1.41	1.73	+0.32	+20.2
5.07	1.73	2.24	0.51	29.5
5.33	1.73	2.65	0.92	53.2
5.60	1.73	2.83	1.10	63.6
5.87	1.73	3.32	1.59	91.9
6.13	2.00	3.46	1.46	73.0
6.40	2.65	4.00	1.35	50.9
6.67	4.69	4.00	−0.69	−14.7
6.93	5.66	4.12	1.54	27.2
7.20	6.32	4.24	2.08	32.9
7.47	9.06	4.47	4.59	51.8
7.73	9.95	4.69	5.26	52.9
8.00	11.05	4.90	6.15	55.7
8.27	11.92	5.20	6.72	56.4
8.53	13.11	5.39	7.72	58.9
8.80	14.73	5.74	8.99	61.0
9.07	15.63	6.25	9.38	60.0

B. Potential Inversion of the Positive Joshi Effect

The V–i_D characteristic (Fig. 2) is intersected by the V–i_L curve at an inversion potential V_t (=6.6 kV), below which $i_D < i_L$ and the *effect* is positive, and above which $i_D > i_L$ and the *effect* is negative, at V_t, $i_D = i_L$ and $\pm\Delta i = 0$. It is significant that V_t is larger than V_m in dark.

The net positive *effect* $+\Delta i$ is zero at and below 4.53 kV, and increases with V to 1.59 at 5.87 kV (*cf.* Table I, Fig. 2) immediately below V_m. Beyond this V, $+\Delta i$ decreases and inverts to $-\Delta i$ at V_t; $-\Delta_i$ thereafter increases to 9.38 at 9.07 kV. The potential dependence of $\pm\%\Delta i$ is essentially similar, except for the fact that the latter diminution is comparatively more rapid. The transition $+\Delta i \rightleftarrows -\Delta i$ is potential reversible. Of a like nature are the findings of Joshi,[6] *et al.* in chlorine,[6][7] and iodine[8][9] and water vapour.[10]

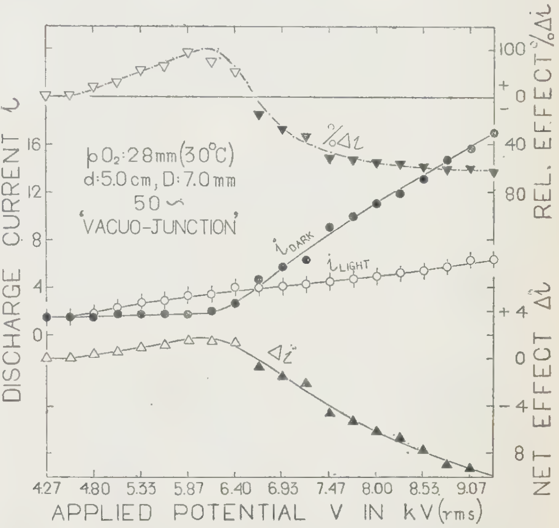

Fig. 2. Potential inversion of the positive Joshi effect (d: Inter- 'sleeve' distance; D: Internal diameter of 'sleeve' tube).

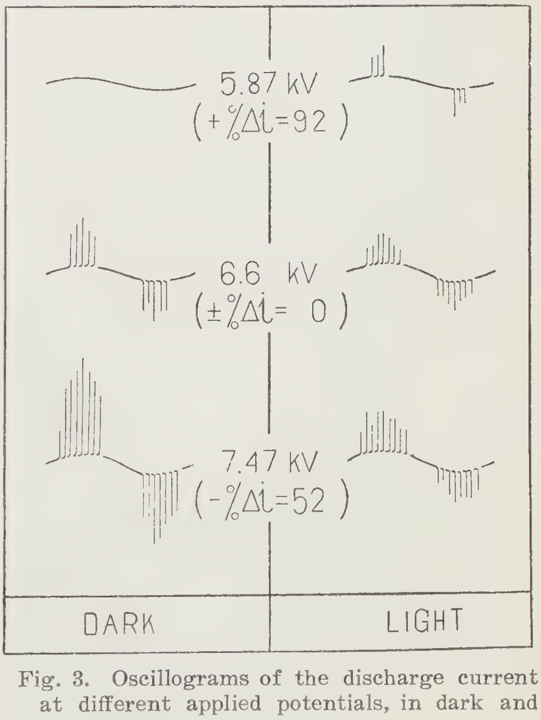

Fig. 3. Oscillograms of the discharge current at different applied potentials, in dark and under light.

Observed oscillographically (Fig. 3), $+\Delta i$ is characterized by the initiation of high frequency (h.f.) pulses on the otherwise smooth sinusoidal current trace (first pair). At V_t (middle pair), whilst there is no photovariation of i, the oscillograms reveal simultaneous occurrence of $-\Delta i$ and Δi, represented respectively by a decrease in the amplitudes of some h.f. pulses, and increase in their number. That at V_t, $\pm\Delta i=0$ (*vide supra*) is therefore due to the fact that $+\Delta i=-\Delta i$. This observation is in general agreement with Joshi's suggestion,[11] confirmed in other systems by Joshi,[11] Shukla,[7] Jatar[9] and Atchutaramaiah,[12] that depending upon the conditions, $+\Delta i$ and $-\Delta i$ co-occur, and that the detector shows the balance.

C. *The Harries and von Engel Mechanism*

According to Harries and von Engel,[13] the external irradiation is strongly absorbed by, and causes photodissociation of, molecules adsorbed on the electrodes into atoms. The secondary electrons released from the electrode walls, under discharge, are attached by these atoms, and therefore, no longer produce electron multiplication. Further, the negative ions formed have a negligible mobility compared with that of the electrons, and do not contribute to i. And hence, according to these authors, the negative *effect* $-\Delta i$.

The energy of dissociation of oxygen into normal atoms is 5.11 eV, corresponding to about 2400Å.[14] That $-\Delta i$ should occur in oxygen in the visible[15] (where the absorption[15] by the gas is negligible), including the extreme red, and in the near infrared,[16] shows that the above mechanism is not tennable. The secondary electron emission is the consequence of the γ and the $\eta\theta g$ processes.[17] Whilst electron attachment would diminish the extent to which these processes occur, their enhancement is independent of the external light. The observed $+\Delta i$ and its cooccurrence with $-\Delta i$ (*vide supra*) cannot therefore, be accounted for on the Harries and von Engel mechanism. These authors contend further[18] that photodissociation can occur above the threshold, especially with 'dense' wall-layers and large intensities of irradiation. This does not, however, appear probable in view of the large shift, from 2400 to *ca* 8000Å, involved. Furthermore, at temperatures much above the critical temperature in the case of gases, and at low relative pressures in the case of vapours, the formation of 'dense' multi-layers is excluded.

D. *The Joshi Theory*

For the occurrence of $\pm\Delta i$, Joshi[6][11][19] postulates that (*a*) an adsorption-like electrode layer[20] consisting of excited particles, ions and electrons is formed under discharge; (*b*) light releases electrons from this layer; (*c*) negative ion formation due to capture of the photoelectrons by excited neutral particles reduces i to give $-\Delta i$, mainly as a space charge effect;[21] and (*d*) uncaptured photoelectrons, and their secondaries produced under the applied fields, cause $+\Delta i$.

The observed influence on $\pm\Delta i$ of 'aging'[20] under discharge and electrode films[21] supports the postulate (*a*); furthermore, the marked increase of $\pm\Delta i$ with such films of photosensitive substances follows from (*b*).[22] A direct consequence of (*c*) is that the magnitude of $-\Delta i$ depends upon the electron affinity[1] of the excited media.

E. *Mechanism of the Positive Joshi Effect*

In the pruduction of $\pm\Delta i$, the photoelectric emission from the electrode layer takes place under fields F due to the applied V. The surface work function ϕ is therefore lowered,[23][24] as a Schottky consequence, to ϕ' according to the equation

$$\phi'=\phi-\sqrt{F}\ , \qquad (1)$$

the validity of which has been demonstrated by Lawrence and Linford.[25] If this value of ϕ' is substituted in the Richardson equation,

$$I=AT^2\exp\left(-e\phi'/kT\right)\ , \qquad (2)$$

there results

$$I=I_0\exp\left(eF^{1/2}/kT\right)\ , \qquad (3)$$

where I_0 is the current for zero external field. Experimental evidence for relationship (3) has been adduced by Pforte[26] and by de Bruyne.[27] As V on the discharge tube is progressively increased, emission occurs when, depending upon the nature of the photoactive surface and ϕ, the produced F is such that ϕ' is equal to or less than the energy of the incident light. This marks the onset of $+\Delta i$. With increase in V (and F), $1/\phi'$ and the emission, and therefore $+\Delta i$, increase. Below V_m, i_D is chiefly capacitative; $+\Delta i$ is thus the conductivity due to the photoelectrons released under F. Hence, the gas amplification being -relatively less important,

$$(+\Delta i)=(+\Delta i)_0\exp(eF^{1/2}/kT)\,, \qquad (4)$$

where $(+\Delta i)_0$ is the hypothetical $+\Delta i$ due to the primary photoelectron emission with zero external field. Since, for a given arrangement of electrodes, F is directly proportional to V, it follows from (4) that the plots of $\log(+\Delta i)$ against $\sqrt{V}$ should lie on a straight line. The fact, evident from Fig. 4, that this anticipation is realized experimentally for the potential enhancement of $+\Delta i$ (and $+\%\Delta i$) is in accord with the above deduction.[28] At a limiting potential V_l near V_m, the slope $d\log(+\Delta i, +\%\Delta i)/d\sqrt{V}$ changes sign; V_l marks the incipience of the co-occurrence of $+\Delta i$ and $-\Delta i$. As V is increased beyond V_l, $-\Delta i$ increases rapidly in magnitude. Consequently, the observed $+\Delta i$ decreases, and inverts at V_i.

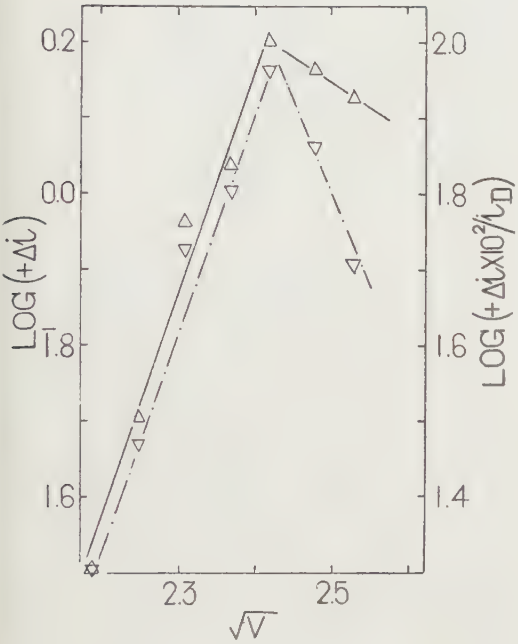

Fig. 4. The Schottky analogue in the potential enhancement of the positive Joshi effect.

§ 4. Acknowledgment

Grateful thanks of the authors are due to Prof. S. S. Joshi for his kind interest in the work, and encouragement.

References

1) S. R. Mohanty and G. S. Kamath: J. Indian Chem. Soc. **25** (1948) 405, *et seq.*

2) S. S. Joshi: Proc. Indian Sci. Congr., Presidential Address, Chem. Sec. (1943) 70–75.

3) S. R. Mohanty: J. Indian Chem. Soc. **26** (1949) 553.

4) S. R. Mohanty, T. D. Prasada Rao and R. Ramaiah: Communicated.

5) S. S. Joshi: Trans. Faraday Soc. **25** (1929) 118, 137; Current Sci. **8** (1939) 548; **15** (1946) 281; Proc. Indian Acad. Sci. **A 22** (1945) 389.

6) S. S. Joshi: Current Sci. **16** (1947) 19.

7) B. M. Shukla: J. Phys. and Coll. Chem. **53** (1949) 1239.

8) S. N. Tewari: Indian J. Phys. **22** (1948) 553. G. S. Deshmukh: Proc. Indian Acad. Sci. **A 29** (1949) 243. M. V. Ramanamurti: J. Sci. Res., Banaras Hindu University **2** (1951–52) 46.

9) D. P. Jatar: J. Sci. and Industr. Res. **B 9** (1950) 283.

10) N. Atchutaramaiah: J. Sci. Res., Banaras Hindu University **1** (1950–51) 91; **2** (1951–52) 1.

11) S. S. Joshi: Proc. Indian Sci. Congr., Part III, Phys. Sec. (1947) Abstr. 25.

12) N. Atchutaramaiah: J. Phys. Chem. **56** (1952) 218.

13) W. L. Harries and A. von Engel: J. Chem. Phys. **19** (1951) 514; Proc. Phys. Soc. **B 64** (1951) 916.

14) G. Herzberg: Z. Phys. Chem. **B 4** (1929) 223.

15) S. R. Mohanty and G. S. Kamath: J. Indian Chem. Soc. **25** (1948) 467.

16) S. R. Mohanty and Satya Prakash: Proc. Indian Sci. Congr., Part III, Phys. Sec. (1950) Abstr. 43.

17) L. B. Loeb: *Fundamental Processes of Electrical Discharge in Gases,* John Wiley and Sons, Inc., New York, 1939, p. 385.

18) W. L. Harries and A. von Engel: J. Chem. Phys. **20** (1952) 918.

19) S. S. Joshi: Proc. Indian Sci. Congr., Part III. Phys. Sec. (1946) Abstr. 26.

20) S. R. Mohanty: J. Indian Chem. Soc. **28** (1951) 487.

21) S. R. Mohanty: J. Phys. Chem. **58** (1954) 178.

22) B. M. Shukla: Proc. Indian Sci. Congr., Part III, Chem. Sec. (1949) Abstr. 34; B. M. Shukla, P. K. Tikkoo and K. N. Khare: Proc. Indian Sci. Congr., Part III, Phys. Sec. (1952) Abstr. 19.

23) W. Schottky: Zeits. f. Phys. **14** (1923) 63.

24) I. Langmuir and K. T. Compton: Rev. Mod. Phys. **2** (1930) 124.

25) E. O. Lawrence and L. B. Linford: Phys. Rev. **36** (1930) 482.

26) W. S. Pforte: Zeits. f. Phys. **49** (1928) 46.

27) N. A. de Bruyne: Proc. Roy. Soc. **120** (1928) 423.

28) H. J. Arnikar: Indian J. Phys. **25** (1951) 353.

JOURNAL OF THE PHYSICAL SOCIETY OF JAPAN Vol. 9, No. 4, JULY—AUGUST, 1954

On the Infrared-Sensitive Behaviors of Some Doubly Activated ZnS Phosphors

By Sumitada ASANO

Department of Physics, Faculty of Science, Okayama University

(Received October 9, 1953)

The quenching and stimulation of phosphoresent brightness under infrared irradiation, and their spectral sensitivities about some ZnS doubly activated phosphors, have been investigated as well as the photocurrents induced simultaneously. A model is proposed which contains two types of electron traps, namely traps associated with emission levels at the activator and isolated traps. Theoretical calculations based on this model are compared to the experimental results for nonstationary behavior. The comparison shows that non-radiative transitions from the conduction band to the filled band, and so-called infrared-sensitive "quasi-direct transitions" from the associated traps to the activators become negligible a few minutes after the ceasing of ultraviolet excitation, and then the proposed theory becomes available exactly.

§ 1. Introduction

The fact that sulfide phosphors show the stimulation and quenching of phosphorecence by infrared irradiation (abbreviated as ir), was early discovered by Lenard.[1] Recently Fonda,[2] Urbach[3] and others[4] have discovered that the sulfide and selenide phosphors show the remarkable stimulation of phosphorescence upon irradiation with ir light after natural phosphorescence has dropped to a negligible value.

The variations of photo-conductivity and phosphorescence under ir irradiation were quantitatively measured by Hardy[5], Ellickson[6], and Kallmann and Kramer[7].

The present paper deals with the stimulation and quenching of phosphorescence caused by ir light, their spectral sensitivities and the simultaneous induced photoconductivities about eight different doubly activated ZnS phosphors at room temperature.

§ 2. Preparation of Materials

Into aqueous solution of $ZnSO_47H_2O$ (Special class reagent, Katayama Chemical Works) were added small amounts of pure $FeCl_36H_2O$ and pure 30% H_2O_2, and pure NH_4OH enough to obtain zinc amine solution. After a few days the supernatant solution was decanted so that the $Fe(OH)_3$ precipitate (plus occluded hydroxides of strange metals) on the bottom of the vessel might be discarded. Further, the decanted solution was filtrated. From the filtrate we could deposit $Zn(OH)_2$ precipitate by heating. This process was repeated twice successively. The obtained $Zn(OH)_2$ precipitate was washed with hot distilled water by twenty or thirty decantations. Then, it was dissolved in 50% pure H_2SO_4, which was distilled twice in silica-stills. From the solution were recrystallized $ZnSO_47H_2O$ crystals. Further, they were fractionally recrystallized twice in aqueous solution. The purified crystals were dissolved in hot distilled water at the concentration about 150 g/l. The hot stirred solution was electrolysed with clean, pure, cylindrical Pt electrodes at 2.2 volts for several days. After the electrolysis, through the solution was passed H_2S gas, which was generated from FeS and HCl and washed through several washing-bottles containing HCl, $Ba(OH)_2$ and distilled water. The supernatant $ZnSO_4$ solution was fractionally decanted twice off the discarded ZnS precipitate (plus occluded low solibulity sulfides). The remaining $ZnSO_4$ solution was diluted to the concentration about 5 to 10 g of $ZnSO_4$ per litre. After the addition of 1 cc pure conc. H_2SO_4 per 1 l of the diluted solution, it was saturated with pure H_2S. The supernatant liquid was decanted and discarded. After decantations repeated several ten times with hot distilled water, the ZnS precipitate was collected by a glass-filter. Finally it was dried at 70°C in an electric drier. Thus was obtained the purely white, homogenious ZnS powder. In our case the average yield of the pure ZnS powder per 1 Kg of coase $ZnSO_4 \cdot 7H_2O$ was less than 10 g.

In order to investigate the purity of this material the following experiments were made. In each of four silica crucibles was put 25 g of the prepared ZnS. Previously into three of them had been added $10^{-4}\%$, $10^{-5}\%$, $10^{-6}\%$ copper ($CuSO_4 5H_2O$ purified by triple recrystallisation) respectively and into the remaining one no copper. Then the four phosphors were prepared at 1050°C for 15 min. in N_2 atomosphere. The spectral distribution of the pure ZnS phosphor (blue luminescent) compared with the results of the litteratures8)9) and the satisfactory agreement was recognized between them. The phosphor containing $10^{-4}\%$ copper showed the green, fairly persistent after-glow. Further, spectral analysis of the pure ZnS phosphor showed only trace of Ca. Cd and $<10^{-5}\%$ copper, which did not affect the optical and electric properties of the furnished phosphors.

Because it was difficult to detect the Cu impurity in our sample directly in use of our spectrographic equipment (Shimadzu QF–60), its amount was estimated by the following method. The analogous method has been already applied by several investigators10)11) for the detection of small Pb amount in minerals and sea-water.

20 g of the pure ZnS phosphor was dissolved bit by bit in 100 cc of pure hot conc. HNO_3 so that all the sample might be dissolved completely. The solution was filtrated off the deposited sulphur through a glass-filter, and the solution wetting the sulphur was washed down with distilled water, too. The filtrate was vaporized slowly in a porcelain basin on a sand-bath, until the deposited solids came to have the appearence of drying. Upon this solids about 15 cc of pure conc. H_2SO_4 was added and it was heated for long enough to change the deposited nitrates to sulphates. Then, all the contents in the basin was completely dissolved in 0.5 l of hot distilled water, and its acidity was made about 0.5 N by the addition of pure H_2SO_4. After the filtration, into this solution was added 40 mg of pure $AgNO_3$ (Schering-Khalbaum. Guaranteed reagent for analysis), in which no copper was detected by spectroscopic inspection. The solution was sufficiently saturated with pure H_2S. After one night the Ag_2S precipitate on the bottom of the vessel was collected and washed with distilled water saturated with H_2S. Finally it was dried at 110°C. The same process was applied for the three Cu-activated phosphors, too. In use of our spectrographic equipment the small amount of CuS, which could be occluded in Ag_2S and precipitated with it, was inspected. The precipitation-rate of Pb with CuS has been reported to be 60 to 70% by M. Isibasi et al.11) That of Cu with Ag_2S should be much larger. ($L_{PbS}=4.2\times10^{-28}$. $L_{CuS}=8.5\times10^{-45}$)

The dc source voltage of the carbon arc was 180 volts and its arc current was adjusted at 6 amp through a reostat. The impurities in the carbon electrodes (Shimadzu) were previously inspected by spectroscopic method. One sample was devided into nearly equal three parts and their photographs were superposed successively (Each exposure time: 40 sec. Plate: Fuji Panchro) so that all the sample might be consumed effectively. To avoid the scattering of the sample on the electrode, the arc current was increased gradually to the rated value. Among the strong, persistent lines Cu-3273.9Å and Cu-3247.5Å, the detection of the former was very difficult owing to the neighbouring intense Ag-3280.6Å line. Therefore, we used the latter as the characteristic line. According to our results, for $10^{-4}\%$ Cu that line was fairly distinct, for $10^{-5}\%$ Cu faintly recognizable but for $10^{-6}\%$ Cu and no additional Cu any trace of that line was not detected. In this manner the copper amount in the pure ZnS was estimated to be $<10^{-5}\%$. In order to avoid accidental errors, the same experiments were repeated twice and the same results were obtained.

Through all the chemical processes triply distilled water was used and all the glass vessels used in our experiments were of insoluble hard glass.

The preparing condition of all the doubly activated phosphors was kept at 1100°C for 15 min. in N_2 atomosphere. 0.05 mol of KCl per mol of ZnS was added as flux. Only core part of each batch was submitted to the experiments.

Table I. Composition, optical and electric characteristics of the prepared phosphors.

Phosphor	Composition (g atom per mol of ZnS)	Color of stimulated phosphorescence	Color of quenched Phosphorescence	Induced current by uv excitation	Max. induced current by ir irradiation (6 mW/cm^2)
No. 1	Pb 10^{-2} Cu 10^{-5}	Pale blue	Blue green	3×10^{-5} amp	4×10^{-7} amp
No. 2	Pb 10^{-2} Mn 10^{-3}	Nearly white	Pale yellow	3×10^{-5}	3×10^{-7}
No. 3	Mn 10^{-2} Cu 10^{-5}	Orange	Orange	6×10^{-5}	3×10^{-7}
No. 4	Mn 10^{-3} Cu 10^{-5}	Orange	Yellow	8×10^{-6}	3×10^{-7}
No. 5	Mn 10^{-4} Cu 10^{-5}	—	Yellow green	1×10^{-6}	9×10^{-8}
No. 6	Bi 10^{-2} Cu 10^{-5}	—	Yellow green	4×10^{-5}	2×10^{-7}
No. 7	Sn 10^{-3} Cu 10^{-5}	—	Blue green	2×10^{-6}	7×10^{-8}
No. 8	Sb 10^{-4} Cu 10^{-5}	—	Blue green	1×10^{-6}	6×10^{-8}

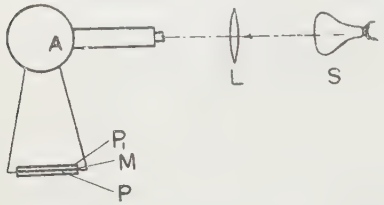

Fig. 1. Schematic diagram of sensitivity measuring apparatus.

A: Glass-spectrograph adjusted for ir region.
L: Convergent lens. S: Heating lamp.
P_1: Phosphorescent plate.
M: Weakening plat.
P: Photographic plate.

§ 3. Experimental Apparatus

(1) *Spectrographic Measurement*

Fig. 1 shows the experimental arrangement of the light sum measurements. The spectrograph was Shimadzu Type GW-30, whose slit was changed with a finely adjustable, bilateral one.

Fine, homogenious powder selected from the crushed phosphor by sedimentation was mixed with dilute amyl acetate solution of celluloid. The powder was spread over a glass-plate with uniform thickness about 0.3 mm by sedimentation. After sucking up the supernatant liquid, it was dried at 40°C. Thus was furnished a phosphorescent plate P_1.

Further, the gelatine films of several uniformly blackened plates (Fuji Process) of various density were striped with a knife-edge and they were steeped in very dilute HF solution for a while. The stripped gelatine ribbon-films (3×80 mm) were arranged on a thin glass-plate (0.5 mm thick) in order of density and pasted on it. A rectangular film (20×80 mm) stripped from the most transmissible plate was pasted on another glass-plate of same thickness, too. Thus were prepared a step-wedge W_s (5 steps) and a weakener W.

The plate P_1 was kept in darkness for t min. (20°C) after ultraviolet (abbreviated as uv) excitation (3650Å Hg) for three minutes and brought into contact with a photographic plate P. (Fuji Panchro.) The weakener W was inserted between them. Then, P_1 was irradiated by ir light for t_i minutes through the spectrograph equipped with a step-slit. (5 steps) The duration t was made enough long to diminish the blackening by natural phosphorescence to negligible value in the case of the stimulable phosphor. On the other hand, in the case of quenchable one P_1 was irradiated by ir light immediately after uv excitation, without being kept in darkness ($t=0$).

After the step-slit had been dismounted, the slit-width of the spectrograph was made equal to $B_{\max}$. (B: width of the step-slit) The same phosphorescent plate P_1 was brought into the same excited state again. Inserting the step-wedge W_s instead of W, we made it come in contact with another part of the plate P. Then, the similar process was repeated in the case of the stimulable phosphor. In the of case quenchable one, they were kept in darkness for t_i minutes without being irradiated by ir light. In this manner an intensity mark was made on the same plate P.

Measuring the distribution of ir irradiance I_λ incident upon P_1 and the density of the spectrograms on P obtained in use of the step-slit, we could determine the density D_λ for the light sum to be stimulated or diminished by an equal monochromatic photon density n incident upon P_1 by means of a graphical method. ($n=I_\lambda/h\nu=I_\lambda\lambda/hc$).

Further, plotting the density of each spectrogram obtained in use of the step-wedge W_s against log $(100T)$, we obtained a characteristic curve of the plate P. (T: Calibrated transmittance of W_s) In the case of the stimulable phosphor, it was made at the wavelength of maximum density about 0.8–0.9 μ. Interpolating the obtained D_λ to the characteristic curve, we determined the difference between the abscissas s_1, s_2 of two adjacent interpolated points. A diagram illustrating these processes is shown in Fig. 2.

In order to measure the light sum of phosphorescence by photographic method, some allowable assumptions were made. We assumed that phosphorescences stimulated or weakened by ir irradiation at two different points on P_1 have an identical spectral composition, and the their brilliances $i_1(t)$, $i_1(t)$ have the approximate relation

$$i_2(t)=ci_1(t)\ , \qquad (1)$$

in the case of stimulation, if the incident irradiance at the two points are comparable, or

$$i_2(t)=i_1(c't)\ , \qquad (2)$$

in the case of quenching, where c and c' are constants.

Further, one of the two phosphorescences may be replaced with natural phosphorescence in the latter case. Repeated visual observations showed that these assumptions were nearly allowable. Their reasonableness is expected from the consideration about mechanism of these phenomena, too. (§ 5.)

As t_i was enough long, $i_2(t)=i_1(c't)\fallingdotseq 0$ for $t>t_i$. If we assume Schwalzschild's relation for our emulsion, the ratio M of the light sums corresponding to the two interpolated points on the characteristic curve is given[12] by

$$M=L_2/L_1=Q\ , \qquad (3)$$

$$M=L_2/L_1=Q^{1/p}\ , \qquad (4)$$

for the case of Eq (1) or (2) respectively, where

$$L_1=\int_0^{ti} i_1(t)dt\ ,\quad L_2=\int_0^{ti} i_2(t)dt\ ,\quad s_2-s_1=\log Q.$$

p: Schwalzschild's constant of the emulsion.

The zero-line of stimulation or quenching was determined by the density of the non-blackened part or of the part blackened by natural phosphorescence respectively.

The stimulable light sum by a constant monochromatic irradiance was measured for various natural decay duration t in the similar manner, too.

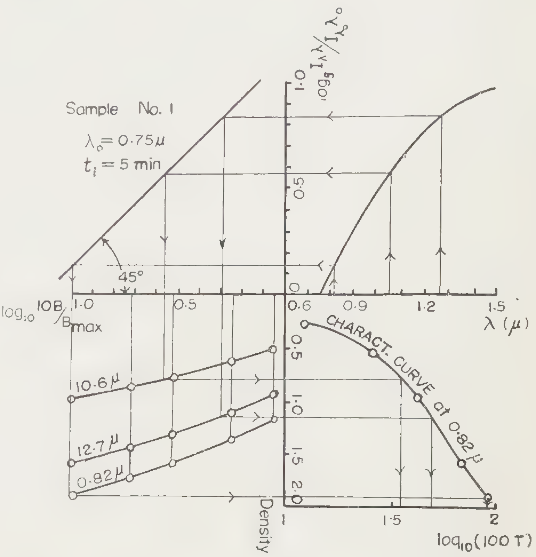

Fig. 2. Diagram illustrating graphical method.

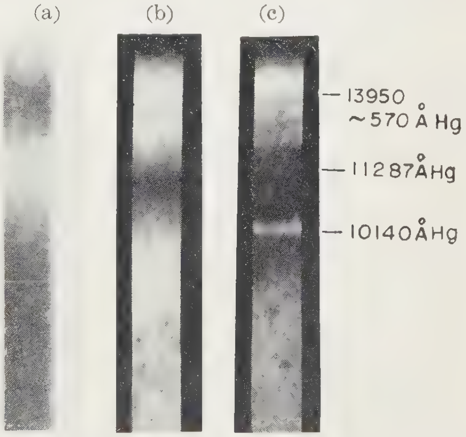

Fig. 3. Infra-red light-stimulation and -quenching spectra.
(a) Heating lamp (Sample No. 7).
(b) Heating lamp (Sample No. 1).
(c) High pressure mercury lamp (Sample No. 1).

For the calibration of wave-length the spectral lines from an Ar or Hg discharge tube in the range 0.7 to 1.5 μ were photographed in the above manner. Several photographs are shown in Fig. 3. The irradiance distribution was measured in use of a calibrated vacuum thermocouple* (Compensated type. Hutchins Alloys. 11.2 Ω. receiver area 3×0.5 mm) with a glass-window, which was connected to a high sensitivity galvanometer (Scient. Res. Inst. 5.3×10^{-8} V/mm. 18.4 Ω). A thin copper sheet with a rectangular aperture (4×1 mm) was pasted upon its window so that the radiation to be measured might be effectively incident upon one receiver alone without being hindered. It could be travelled along the position of P_1 by a micrometer-screw. The galvanometer deflection was read in use of a Shimadzu Galvoscale at 1 m distance. The window of the thermocouple was cut out of a glass-plate, which was similar to the base-plate of P_1 on quality and thickness (about 0.5 mm). Therefore, the monochromatic radiant energy incident upon the receiver through the window might be considered to be equal to that incident upon the phosphorescent layer of P_1 through the base-plate. The maximum irradiance about 1.5 μ was nearly 6×10^{-6} W/cm² for the minimum slit-width $B_{\min}$. The step-slit was calibrated by measuring the spectral irradiance through it in use of the thermocouple.

---

* This thermocouple was constructed at Osaka Industrial Research Laboratory (Ministry of Commercial and Industrial Affairs).

B. *Some Preliminary Calibrations*

First, we prepared two radiation sources; one for visible range, the other for ir range. The former was a Mazda Enlarging Lamp L_1 (100 V. 250 W. Color temperature: 2870°C), whose opal glass-bulb was covered by a diaphragm with a circular aperture R cm in radius in the manner such that its central axis coincided with the lamp-axis. The illuminance at the distance d cm from the lamp-top on the axis may be considered to be proportional to $1/(R^2+d^2)$ exactly. When $R=1.5$ cm, the illuminance measured in use of a Mazda Photoelectric Luxmeter was 2.59×10^{-2} lumen/cm² at $d=50$ cm.

The latter was a Mazda Heating Lamp L_2 (100 V. 250 W. S-type. Color temperature: 2060°C) equipped with a diaphragm in the similar manner. Its circular aperture could be covered with an opal glass-plate P_0. In order to calibrate the irradiance from L_2 without P_0, we used a Mazda Vacuum Thermocouple (Bi, Hutchins Alloy. 12.0 Ω. 1.02×10^{-1} mV/mW) sealed in a glass-bulb and a galvanometer (YEW. D3–D. 4.65×10^{-7} V/mm. 1.82×10^{-8} amp/mm. Coil resist. 10.5 Ω.) equipped with a compensated shunt suited to it. The sensitivity of the thermocouple had been calibrated for the standard radiation of similar spectral characteristics at Mazda-Institute. The irradiance corresponding to the galvanometer deflection at 1 m scale was calculated from the above constants and the multiplying power of the shunt. Further, measuring a known irradiance from L_2 without P_0 and an unknown irradiance from L_2 with P_0 at the same point on the axis in use of a thermopile without window (Eiko-Seiki Co. 14 elements. Manganin, Constantan. 17.4 Ω. 1.64×10^{-1} mV/mW), we could determine the latter from the ratio of the two responses at various distance. The measurements showed that the above proportionality was exactly available for the radiation from L_2 diffused by P_0, too. When $R=2$ cm, the irradiance at the distance 50 cm from P_0 was 6.4×10^{-4} W/cm². These lamps were lighted in use of a voltage stabulizer.

The step-wedge W_s was calibrated in the following method. The spectral transmittance at several points on each step was measured in use of a monochrometer (Shimadzu. GW-30) and a phototube (Mazda PT-25-V1 or PS-50.V), whose photocurrent was amplified by a dc amplifier connected to a galvanometer. According to our results, it was nearly nonselective in the visible range 700 to 400 mμ.

Inserting W_s between a photographic plate (Fuji Panchro.) and a ground glass-plate P_g, we set them in a light-tight container with a 10 cm aperture equipped with a shutter. Further, each one of ten diaphragms, which were cut out of thin sheet metal and had a similar rectangular aperture at shifted position to each other, was mounted one after another in front of P_g, being in close contact with it in the position such that the longitudinal azimuth of the aperture was perpendicular to that of W_s. Illuminating the different part on P_g through each aperture for an equal exposure time with an uniform colored light from L_1 at various distance, we made intensity marks on one plate successively. The color of illumination was made match that of the phosphorescence as nearly as possible in use of Mazda Glass Filters. From the obtained characteristic curves the transmittance T for the colored light was determined in use of Eq. (3). We could use them as that for the corresponding phosphorescence, because the difference between the transmittances of each step for the various colored illuminations was quite negligible.

Further, to investigate the deviation from the reciprocity law of our plate (Fuji Panchro.) the following experiments were made about some of them. Through the aperture of each diaphragm in the above set was thrown the colored uniform illumination of various intensity I from L_1 for the exposure time t, which was made inversely proportional to I. (t: 5 sec. to 5 min.) Then, fifty blackened squares could be obtained on one plate. Plotting the density of each square against $\log(100t/t_{\max})$, we obtained the five curves of equal light sum. Although slight falls appeared in the long exposure parts of each curves, they were nearly horizontal in the density range, within which the light sum measurements were made. Plotting the isopaque points in the $\log(100IT/I_{\max})$ versus $\log(100t/t_{\max})$ diagram by interpolation, we determine the Schwalzschild's constant p from the slopes of the curves connecting them. Although p was not rigorously constant even about one plate, it lay within 0.92 to 1.03 for all the colored illuminations in our density range. Therefore, we took for $p=1$ approximately. If we assume p to be slightly less than unity, M given by Eq (4) changes its value. Then, the peaks of the quenchability curves should become somewhat higher relatively owing to this correction.

The optical system of the microphotomer used in densitometry was of Shimazdu Reading Type and as a receiver we used a phototube (Mazda PS-50-V), whose current was amplified by a dc amplifier (Mazda UX-54. 1Q18: 1.2×10^8 Ω) connected to a galvanometer (YEW. D-2L. 5.18×10^{-8} amp/mm). The light beam from an auto lamp (8V. 50c.) lighted by storage batteries was incident upon the entrance slit of the receiver container covered with a red filter (Mazda VR3). Illuminating a side-aperture covered with a ground glass-plate by the lamp L_1 at various distance and focusing its image upon the entrance slit in use of a glass-lens and an Al-coated plane mirror, we repeatedly calibrated the galvanometer deflection during the measurement.

The compensated thermocouple was calibrated in the following process. For the radiation from L_2 with P_0 the transmittance of the glass-plate, of which the thermocouple's window had been cut out, was measured in use of the thermopile without window. Measuring a known irradiance from L_2 with P_0 in use of the compensated thermocouple connected to the high sensitivity galvanometer, we calibrated its response for the irradiance incident upon the receiver in the range 1 to 10×10^{-5} W/cm² from the transmittance of the window. As the calibrated points fell on a straight line passing through the origin in the response versus irradiance diagram, we could use it for the range $<1\times10^{-5}$ W/cm², too. The sensitivity calculated from the galvanometer constants was nearly 0.095 μV/μW cm$^{-2}\doteqdot$6.3 μV/μW. Setting the thermocouple to the spectrograph, we could determine the monochromatic radiant energy incident upon the receiver from the above calibration curve. In the above calibration the spectral absorptivity of the receivers coated with lamp-black in these radiometric instruments was assumed to be non-selective.

(2) **Photoconductivity and Phosphorescence Measurement**

Fig. 4 shows the electric circuit for the measurement of the current induced by ir stimulation. For the current measurements a high sensitivity galvanometer (YEW. D-3F. 1.3×10^{-10} amp/mm) was used. The electrode arrangement is shown in Fig. 5. On each one of sixteen rectangular, polished copper

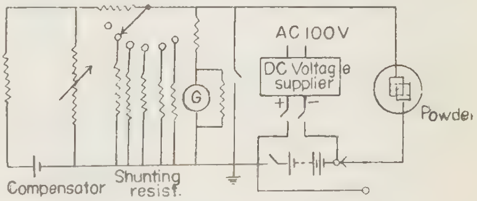

Fig. 4. Schematic diagram of current measuring apparatus.

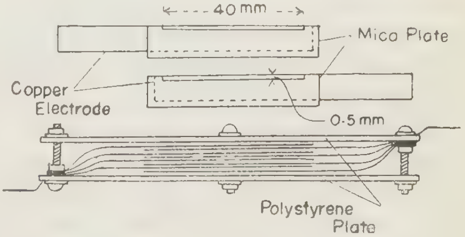

Fig. 5. Diagram illustrating electrode arrangement.

sheets (4×70 mm. 0.2 mm thick) was pasted a mica plate of 0.1 to 0.15 mm thickness with viscous solution of polystirol and they were left to dry. They were piled up each other and pressed between two polystyrene plates with screws slightly. Thus was built up a powder holder. The fine, homogenious powder was mixed with a small amount of dilute amyl acetate solution of Vinidine (Commercial binding cement). This mixture was inserted in the ditches of the holder and pressed with screws tightly so that the powder could be in good and stable contact with each other and electrodes, and make thin and homogenious layer. This set was enclosed in a glass-container with a quartz-window, and left to to dry at 60°C for several hours, being evacuated by a rotary pump. After the vacuum-drying had been finished, dried air was led into the container. The electrodes were polished and cleaned every time the powder was changed.

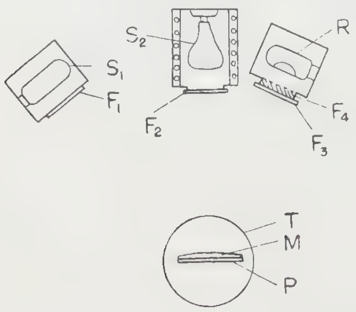

Fig. 6. Diagram illustrating radiation arrangement and brightness measurement.

S_1:	Mercury lamp	S_2:	Heating lamp
R:	Phototube	F_1:	uv filter
F_2:	ir filter	F_3:	Glass-filter
F_4:	Liquid filter	P:	Glass-plate
M:	Phosphor	T:	Rotative table.

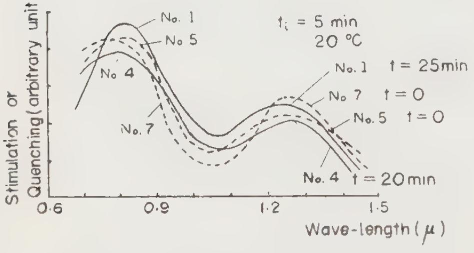

Fig. 7. Spectral stimulability and quenchability.

The experimental arrangement for phosphorescence measurement is shown schematicall in Fig. 6. The sample was a disk 3.5 cm i diameter and about 1 mm thick. It wa mounted on a rotative table. The light emitted from a phosphor was picked up by phototube (Mazd PT-25-V1) and it photocurren was amplified by Mazda UX-54 tube and high resistance tube (Mazda 1Q20: $2.0\times10^{10}\Omega$ in use of the Dubridge circuit[13]. The curren in the final stage was read on the galvanometer (1.3×10^{-10} amp/mm) equipped with a Ayrton shunt. Mazda Glass Filters and 4% solution of $CuCl_2 2H_2O$ (15 mm thick) were interposed between the phosphor and phototube, so that the ir light scattered on the surface of the sample was cut off and only the luminescent wave-length was effective The ir source was placed in a position such that the light fell on the sample at nearly normal incidence.

Placing a ground glass-plate in front of the aperture of the phototube container and illuminating it with the lamp L_1 at various distance, we ascertained the linear respondency of the galvanometer for various colored light.

The uv source used in our experiment was of high pressure mercury discharge type equipped with an uv filter (Mazda UVD-2). The ir source was a Mazda Heating Lamp (100V. 100W. R-type) enclosed in a light-tight, water-cooled container with 5 cm aperture and lighted in use of a voltage stabulizer. Through an ir filter (Mazda IRD-1) about 1 to 5 mW/cm² was incident upon the powder.

§4. Experiment Results

(1) Spectral Sensitivity

Fig. 7 shows the spectral stimulability or quenchability curves about some of the prepared phosphors, which were measured in the manner described in §3, (1). The most conspicuous behavior is that all the phosphors have their maximum sensitivity at 0.8 to 0.9 μ and about 1.3 μ. The general feature of the curves was completely similar about the eight stimulable or quenchable phosphors.

The second and third Columns of Table I give the observed color of the strongly stimulable and quenchable phosphorescence. It is remarkable that the Mn-activated phospoor changes its type corresponding to the change of its luminescent color with the increase of manganese concentration. This fact shows the existence of two sorts of Mn-activator[14], namely neutral Mn-atom and doubly ionized Mn-ion that substitutes a Zn-ion. Pb: Mn-activated phosphor showed a nearly white, bright emission caused by mixture of the two stimulated phosphorescences emitted from the both activators.

About the three stimulable phosphors the light sums of the stimulated phosphorescence were measured for various natural decay duration *t*. (Fig. 8) In the case of Pb-activated phosphors the stored light quanta by uv excitation were kept for a long time, and the stimulation could be observed even 20 or 30 hours after uv excitation.

(2) Induced Photoconductivity

The dc steady voltage supplied from a rectifying apparatus shown in Fig. 4 was raised slowly up to several hundred volts so that the applied field between the electrodes could be made greater than 15000 V/cm. Then, without making interruption, the voltage source was changed with accumlators supplying the same voltage. When the field was kept at this value, photoconductivity rose slowly to a constant saturated value under uv excitation during thirty minutes. Fig. 9 gives the curves of the natural decay and forced decay of photoconductivity after uv excitation has ceased. In the case of immediate ir irradiation after uv excitation, a retardation of decay rather than a stimulation was observed and noteceable quenching followed it (Fig. 9). A few minutes after the ceasing of uv excitation, the natural decay of conductivity became not so conspicuous and then a remarkably stimulated photocurrent by ir irradiation could be measured and a only slight quenching followed it. About the sample No. 3, the stimulated currents at two different ir intensities are shown in Fig. 10, and these of other several phosphors at ir intensity 6×10^{-3} W cm^{-2} are given in the same figure, too. General behaviours of the curves in Fig. 9 and Fig. 10 were throughly similar about all the prepared phosphors.

Absolute values of the currents were calculated from the sensitivity of the galvonometer and the shunting ratio of the resistor network. The reading when the decay of current ceased throughly after ir irradiation of several minutes, was taken as the zero-point of current. The steady photocurrents excited by uv and the observed maximum photocurrent induced by ir irradiation are given in the fourth and sixth Columns of Table I.

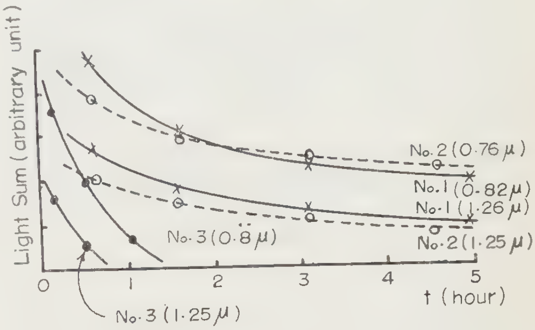

Fig. 8. Dependence of light sum as a function of natural decay duration.

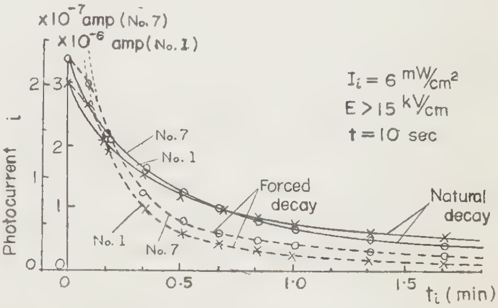

Fig. 9. Infra-red current-stimulation and -quenching 10 seconds after uv excitation had been interrupted.

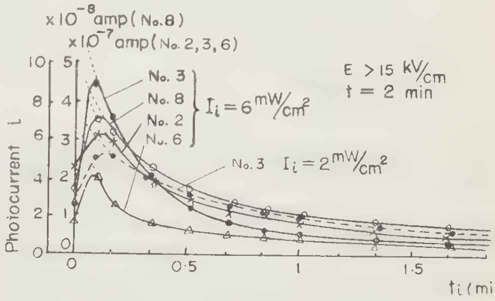

Fig. 10. Infra-red current-stimulation 2 minutes after uv excitation had been interrupted.

(3) Stimulation and Quenching of Phosphorescence

About the four quenchable phosphors the variations of phosphorescent brightness were measured immediately after the ceasing of uv exitation at two different ir intensities, and

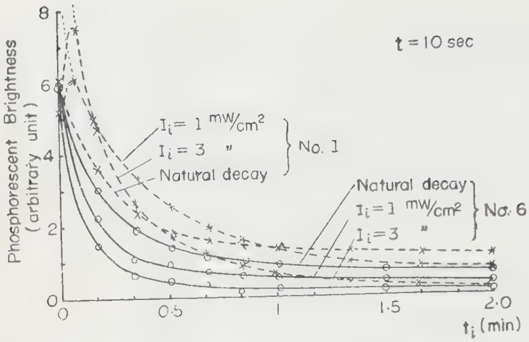

Fig. 11. Infra-red light-stimulation and -quenching 10 seconds after uv excitation had been interrupted.

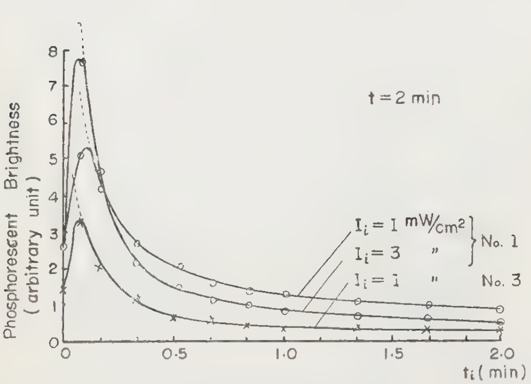

Fig. 12. Infra-red light-stimulation 2 minutes after uv excitation had been interrupted.

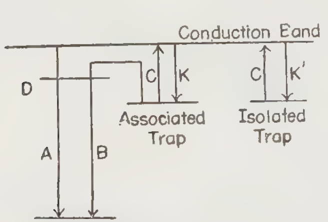

Fig. 13. Energy states of electron in phosphor.

compared with the natural decay. The quenching was accelerated with the increase of ir irradiating intensity. The results about one of these phosphors are given in Fig. 11.

The same experiments were repeated about the four stimulable phosphors. One of these results is shown in Fig. 11 also. In such an earlier irradiation only a slight rise of brightness was observed for comparatively low ir intensity as stated in the case of the induced carrent.

The conspicuous stimulation after natural phosphorescence has dropped, is shown in Fig 12 under different ir intensities. The genera features of the curves in Figs. 11 and 12 wer throughly similar for the other quenchabl and stimulable phosphors respectively.

§ 6. Theoretical Consideration

(1) Fundamental Equations

On the mechanism of ir-sensitive phosphor a simple theory has been presented by Herman et al[15], but it cannot explain the dependence of light sum on the ir intensity, and the quenching of natural phosphorescence. Recently, Kallmann and Kramer[7] have presented a more complicated mechanism which is available for the stationaly state, where an ir irratiation is added upon a constant uv excitation, too. But it is difficult to deduce any formulated mathematical conclusion about non-stationary state from their theory because of the complicacy of assumed mechanism. Here is presented a theory that covers the most important and general behaviors in non-stationary state and can be arranged mathematically.

According to the energy-band theory of solids, the spectrum of energy state of electrons in a phosphor may be represented as in Fig. 13. Electrons in the conduction band and associated traps fall into luminescence center via one of its upper state D. But the description of situation is simplified by considering only those electron transfer processes between the three states, namely, conduction band, trapping states and holes. This removes the difficulty of taking into account two possible transitions for an electron in the state D, namely, luminescent transitions to the normal state and thermal transitions to the conduction band in Kallmann and Kramer's theory. Further, for the sake of simplicity, it is assumed that the three states have only single multiplicity and isolated luminescence centers do not exist.

Let N_0, N_1, n_0, and n be the number of luminescence centres, isolated traps, vacant centres and conduction electrons per cm^3 respectively, and n_1, n_2 be the number of electrons per cm^3 in isolated and associated traps respectively. Now it is assumed that both the isolated and associated trapping states are at nearly equal energy ϵ_1 below the conduction band, because the spectral sensitivity curves of all the phosphor were throughly similar (Fig. 7) and these traps seem to be peculiar to ZnS crystal and to be caused pherhaps by omission defects.[16]

If $\epsilon_1 \gg kT$, then electron transfer processes that occur upon irradiation with ir light can be represented by the following set of differential equations.

$$dn_0/dt = -Ann_0 - (B/N_0)n_0 n_2\ , \qquad (1.1a)$$

$$dn/dt = -Ann_0 - Kn(N_0 - n_2) - K'n(N_1 - n_1) + c(n_2 + n_1)\ , \qquad (1.1b)$$

$$dn_1/dt = -cn_1 + K'n(N_1 - n_1)\ , \qquad (1.1c)$$

$$dn_2/dt = -cn_2 - (B/N_0)n_0 n_2 + Kn(N_0 - n_2)\ , \qquad (1.1d)$$

$$n_0 = n + n_1 + n_2\ , \qquad (1.1e)$$

where A is the probability that an electron in the conduction band recombines with an ionized luminescence centre or hole; K' and K are the probabilities that a conduction electron is captured into an isolated or associated trap respectively. The quantity c is given by

$$c = \sigma_p \cdot I_i / h\nu\ , \qquad (1.2)$$

where σ_p is the cross section of a trapped electron for a photon of energy $h\nu$, and I_i is the intensity of the ir light. σ_p is assumed to be common for traps of the both types.

The transition probability from an associated trapping state to a normal state of luminescence centre consists of the two transfer processes, namely, the transition to pass over or through a potential barrier and the normal spontaneous transition. In the former process an alternation of electron spin is required because the multiplicity of the intermediate state D is somewhat different from that of trapping state generally[17]. This spin alternation is to some extent forbidden, so that a low frequency factor results as observed in glow-curve experiments[18]. Therefore it is assumed that the probability for the former process is smaller than the normal light emission probability ($\simeq 10^{-8}\ \mathrm{sec}^{-1}$) and the probability for the whole process, consequently phosphorescent intensity by transition B, is controlled mainly by the former.

Then the specific rate constant B that an electron in an associated trap obtains the activation energy ϵ_2 and recombines with an ionized center or hole, is given by

$$B = s \exp(-\epsilon_2/kT)\ , \qquad (1.3)$$

where s is the frequency factor. Therefore, B is strongly temperature-dependent.

The number of electrons per $\mathrm{cm}^{-3}\ \mathrm{sec}^{-1}$ which have the possibility to pass over or through the potential barrier is Bn_2. Among these electrons, number of the electrons per $\mathrm{cm}^{-3}\ \mathrm{sec}^{-1}$ which are in the traps associated with the vacant centers and can realize the transition B, is $Bn_2 \cdot n_0/N_0$ statistically. The remaining electrons which correspond to the filled centers are excited to the conduction band by ir stimulation immediately. Therefore, B/N_0 means the probality that an electron in an associated trap falls into an ionized centre, when we consider the electron to have the possibility to recombine with arbitrary one of the vacant centres indifferently.

In this theory is neglected the probability of infrared-sensitive direct transition that an electron in an associated trap is excited to the upper state D by ir light without passing through the conduction band and falls into the normal state, because the excitation energy for this transition should depend on the sort of added activators and consequently spectral sensitivity curve should be influenced strongly by them, if it is comparable to the other infrared-sensitive transition probabilities.

Eqs. (1.1) can be stated in a more convenient form by following substitutions.

$$\xi \equiv n/N_0\ , \quad \eta \equiv n_0/N_0\ , \quad \zeta \equiv n_1/N_0\ , \quad \chi = n_2/N_0\ . \qquad (1.4)$$

Substisuting Eqs. (1.4) into Eqs. (1.1), we obtain

$$d\eta/d\tau = -\xi\eta - \beta\chi\eta\ , \qquad (1.5a)$$

$$d\xi/d\tau = -\xi\eta - \varepsilon\xi(1-\chi) - \varepsilon'\xi(l-\zeta) + \gamma(\chi+\zeta)\ , \qquad (1.5b)$$

$$d\zeta/d\tau = -\gamma\zeta + \varepsilon'\xi(l-\zeta)\ , \qquad (1.5c)$$

$$d\chi/d\tau = -\gamma\chi - \beta\chi\eta + \varepsilon\xi(1-\chi)\ , \qquad (1.5d)$$

and

$$\eta = \xi + \zeta + \chi \qquad (1.5e)$$

where

$$\tau \equiv at,\ \varepsilon \equiv K/A,\ \varepsilon' \equiv K'/A,\ \gamma \equiv c/AN_0$$
$$\beta \equiv B/AN_0\ ,\ a \equiv AN_0\ ,\ l = N_1/N_0\ .$$

Then phosphorescence brightnesses B_a and B_b caused by the transition A and B are expressed respectively by

$$\left.\begin{aligned} B_a &= p_a h\nu A n_0 n = p_a h\nu a N_0 \xi\eta \propto \xi\eta\ , \\ B_b &= p_b h\nu (B/N_0) n_0 n_2 = p_b h\nu a\beta N_0 \chi\eta \propto \chi\eta\ , \end{aligned}\right\} \qquad (1.6)$$

where p_a and p_b are the ratios of the radiative transition probability to the total transition probability for the transion A and B respectively. Therefore, they may be substituted approximately by the quantum yields of luminescence for these transitions.

Induced current density j is given by

$$j=newE=eEwN_0\xi\propto\xi\ , \qquad (1.7)$$

where w is the mobility of conduction electrons, e the absolute electron charge and E the applied field intensity.

If a phosphor is of stimulable type, p_a is fairly large ($\simeq 1$) and if it is of quenchable type, p_a is nearly equal to zero, in other words the transition A is non-radiative.

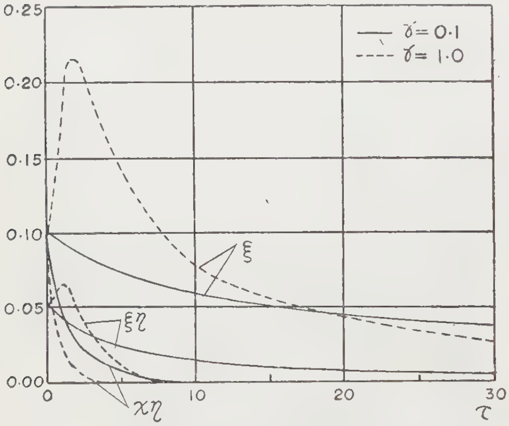

Fig. 14. Effect of varying γ on the time dependence of induced current, light-quenching and stimulation under ir irradiation for the case $\eta_0=0.5$, $\xi_0=0.1$, $\gamma_0=\zeta_0=0.2$ and for $\gamma=1.0,\ 0.1$.

Putting $\chi=\beta=\varepsilon=0$ in Eqs. (1.5), we obtain the Herman's simple equations.

(2) Special Solution for $\varepsilon=\varepsilon'=0$, $\beta=1$

If the retrapping probabilities are negligible compared to the recombination probability A, and the recombination probabity B/N_0 is comparable to it, $\varepsilon\equiv K/A=0$, $\varepsilon'\equiv K'/A=0$ and $A/BN_0\equiv\beta=1$. In this special case the Eqs. (1.5) can be solved exactly.

From Eqs. (1.5) we obtain

$$\zeta=\zeta_0\exp(-\gamma\tau)\ , \qquad (2.1)$$

and from Eqs. (1.5a), (1.5e)

$$d\eta/d\tau=-\eta(\eta-\zeta)\ . \qquad (2.2)$$

Further, combining (2.1) and (2.2), we obtain

$$\eta=(\eta_0 e^{y_0}/u)e^{-y}\ , \qquad (2.3)$$

where

$$u=1-(n_0e^{y_0}/\gamma)[\mathrm{Ei}(-y)-\mathrm{Ei}(-y_0)]\ ,$$
$$y=(\zeta_0/\gamma)\exp(-\gamma\tau)\ ,$$
$$-\mathrm{Ei}(-y)=\int_y^\infty \frac{e^{-t}}{t}\,dt\ .$$

ζ_0, η_0 and $y_0=$ the initial values of ζ, and y ($\tau=0$). From Eqs. (1.5c) (2.3) χ can be solved

$$\chi=(\chi_0/u)\exp(-\gamma\tau)\ , \qquad (2.4)$$

ξ is given necessarily from Eq. (1.5e)

$$\xi=(\eta_0e^{y_0}/u)e^{-y}-(\chi_0/\zeta_0u+1)\gamma y\ , \qquad (2.5)$$

where χ_0, ξ_0 are the values of χ, ξ at $\tau=0$.

In use of (2.3), (2.4) and (2.5) the decay curves of $\xi\eta$, $\chi\eta$ and ξ for the different two values of γ are plotted in Fig. 14. In the numerical calculation of the quantity u, tabulated values of the expotential integral $-$E $(-y)$ in the various references[19-21] were used

(3) Approximate Solution for large τ

Eqs. (1.5a), (1.5b), (1.5d) can be combined in the forms:

$$\frac{d\xi}{d\eta}=-\frac{\xi(\varepsilon\chi+\varepsilon'\zeta)}{\eta(\xi+\beta\chi)}+\frac{\xi}{\xi+\beta\chi}+\frac{(\varepsilon+\varepsilon' l)\xi-\gamma(\chi+\zeta)}{\eta(\xi+\beta\chi)} \qquad (3.1)$$

$$\frac{d\chi}{d\eta}=\frac{\varepsilon\xi\chi}{\eta(\xi+\beta\chi)}+\frac{\beta\chi}{\xi+\beta\chi}+\frac{\gamma\chi-\varepsilon\xi}{\eta(\xi+\beta\chi)}\ . \qquad (3.2)$$

If $\gamma\neq0$, ξ, η, ζ and χ vanish when $\tau\rightarrow\infty$ The physically important solutions are those for which $d\xi/d\eta$, $d\chi/d\eta$ are infinite when $\tau\rightarrow\infty$. In order that $d\xi/d\eta\rightarrow\infty$, $d\chi/d\eta\rightarrow\infty$ when $\tau\rightarrow\infty$, we have

$$\left.\begin{array}{r}(\varepsilon+\varepsilon' l)\xi-\gamma(\chi+\zeta)=0\ ,\\ \gamma\chi-\varepsilon\xi=0\ .\end{array}\right\} \qquad (3.3)$$

From Eqs. (1.5e), (3.3)

$$\xi=\frac{\gamma}{(\varepsilon+\varepsilon' l)+\gamma}\eta,\quad \chi=\frac{\gamma}{(\varepsilon+\varepsilon' l)+\gamma}\eta, \qquad (3.4)$$

and from Eqs. (1.5a), (3.4)

$$\eta=\frac{1}{k\tau+c}\ ,\quad \xi=\frac{P}{k\tau+c}\ ,\quad \chi=\frac{Q}{k\tau+c}\ ,$$

where

$$k=\frac{\gamma+\beta\varepsilon}{(\varepsilon+\varepsilon' l)+\gamma}\ ,\quad P=\frac{\gamma}{(\varepsilon+\varepsilon' l)+\gamma}\ ,$$
$$Q=\frac{\varepsilon}{(\varepsilon+\varepsilon' l)+\gamma}\ .$$

Consequently, B_a, B_b and j have the well known forms[22]:

$$B_a,\ B_b\propto[c_1\tau+c_2]^{-2},\quad j=[c_1\tau+c_2]^{-1}, \qquad (3.5)$$

Let L_a and L_b be light sums of stimulated and quenched phosphorescence respectively, then

$$\left.\begin{aligned} L_a &= \int_0^\infty B_a dt = p_a h\nu N_0 \eta_0 \cdot \gamma/(\gamma+\beta\varepsilon), \\ L_b &= \int_0^\infty B_b dt = p_b h\nu N_0 \eta_0 \cdot \beta/(\gamma+\beta\varepsilon). \end{aligned}\right\} \tag{3.6}$$

Combining (3.6) with (1.2)

$$1/L_a = c_1' + c_2' \cdot 1/I_i \quad 1/L_b = c_1'' + c_2'' I_i . \tag{3.7}$$

(4) Approximate Solution for $\beta \ll \gamma \ll \varepsilon \simeq \varepsilon'$

This case is of practical interest because ε and ε' lie between 0.5 and 1.0 for ZnS phosphors[18] and from Eq. (1.2) $\gamma \simeq 10^{-3}$ when $I_i \simeq 10^{-3}$ cm^{-2}, if $N^0 \simeq 10^{16}$ cm^{-2},[10)15)] $A \simeq 10^{-13}$ cm^3/sec,[15)] $\sigma_p \simeq 10^{-16}$ cm^2 [23)] and $\nu \simeq 10^{-4}$ cm. And $\beta \simeq 10^{-11}$, even if the probability B is of order of normal light emission probality ($\simeq 10^{-8}$/sec). Further, it is assumed that $n/N_0 = \xi \lesssim \gamma$, n/N_0 is of order 10^{-5}—10^{-7} with ordinary uv exciting intensity of 15—20 μW/cm^2,[10)] and this value becomes much smaller for the ir irradiation as shown in Table I. The assumption $\varepsilon \simeq \varepsilon'$ is allowable, because the formations of the traps of the both types seem to be attributed to an identical irregularity as described above.

Substituting $\varphi = \xi/\gamma$, $\varepsilon = \varepsilon'$ into Eqs. (3.1), (3.2), and neglecting γ for ε_1 we obtain

$$\frac{d\varphi}{d\eta} = \frac{\varphi[\varepsilon_1 + (1-\varepsilon)\eta] - \eta}{\gamma\eta[\varphi + (\beta/\gamma)\chi]} + \frac{\varepsilon\varphi^2}{\eta[\varphi + (\beta/\gamma)\chi]}, \tag{4.1}$$

$$\frac{d\chi}{d\eta} = \frac{\chi - \varepsilon\varphi + (\beta/\gamma)\eta\chi}{\eta[\varphi + (\beta/\gamma)\chi]} + \frac{\varepsilon\varphi\chi}{\eta[\varphi + (\beta/\gamma)\chi]}, \tag{4.2}$$

where

$$\varepsilon_1 = \varepsilon + \varepsilon l .$$

The state of a phosphors can be represented by a moving point P in the $\varphi\eta\chi$-space shown in Fig. 15. The point P is driven towards the origin along a curve by ir irradiation, and it tends to the origin when $\tau \to \infty$. If the point P is not on the surface

$$\varphi[\varepsilon_1 + (1-\varepsilon)\eta] - \eta = 0 . \tag{4.3}$$

$|d\varphi/d\eta|$ takes a very large value, because the denominator of the first term of Eq. (4.1) is very small quantity and the second term has a smaller value always. ($\varphi = \xi/\gamma \leq 1$) In this case the point P must be constrained in the plane $\eta = \eta_0$. On the other hand, the two terms of Eq. (4.2) do not become so large, because their denominators and numerators are of same order, even if the point P is not on the surface (4.3). Therefore, the point P moves on the straight line passing through the starting point P$_0$ (φ_0, η_0, χ_0), until it reaches the interaction with the surface (4.3) and then it tends to the origin along a curve C contained in the surface.

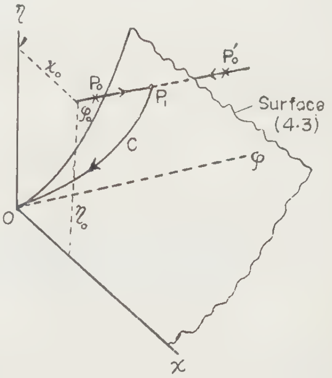

Fig. 15. Illustration of a path of a moving point P in the $\varphi\eta\chi$-space.

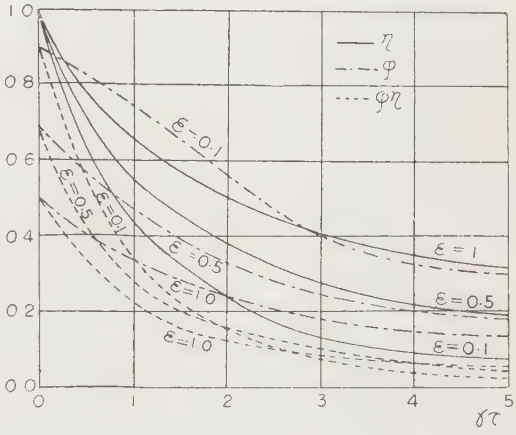

Fig. 16. Effect of varying ε on the time dependence of number of vacant centers, induced current and light-stimulation under ir irradiation for the case $\eta_0 = 1$ and for $\varepsilon = \varepsilon' = 0.1$, 0.5, 1.0.

According to the above order estimation, it can be assumed that $\varphi \gg \beta\chi/\gamma$. Then, neglecting $\beta\chi/\gamma$ for φ, we can write (4.2) in the form

$$d\chi/d\eta = (\chi/\eta)(1/\varphi + \varepsilon) - \varepsilon/\eta . \tag{4.4}$$

Combining (4.3) with (4.4), we obtain

$$d\chi/d\eta = (\chi/\eta)\{(\varepsilon_1 + \eta)/\eta\} - \varepsilon/\eta$$

$$\therefore \quad \chi = \eta\left\{\frac{\varepsilon}{\varepsilon_1} + \left(\frac{\chi_0}{\eta_0}\right)\exp\left[-\varepsilon_1\left(\frac{1}{\eta} - \frac{1}{\eta_0}\right)\right]\right\} . \tag{4.5}$$

This is the projection of the curve C on the $\chi\eta$-plane, and it has $\chi=\varepsilon\eta/\varepsilon_1$ as an asymptote, when $\eta\to 0$.

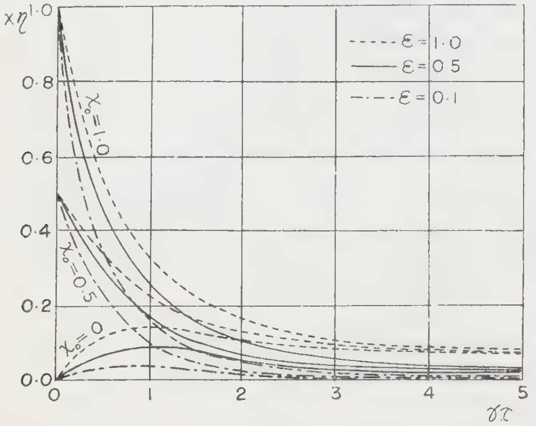

Fig. 17. Effect of varying ε on the time dependence of light-quenching under ir irradiation for the case $\eta_0=1$, $\chi_0=0$, 0.5, 1.0 and $\varepsilon=\varepsilon'=0.1$, 0.5, 1.0.

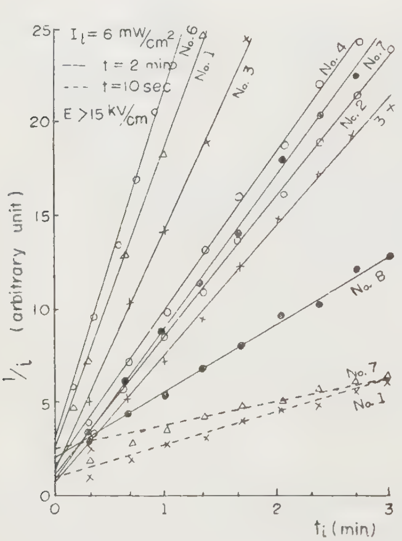

Fig. 18. Dependence of $1/i$ as a function of time under ir irradiation.

When $\eta_0=1$ specially,

$$\chi=\eta\left\{\frac{\varepsilon}{\varepsilon_1}+\left(\chi_0-\frac{\varepsilon}{\varepsilon_1}\right)\exp\left[-\varepsilon_1\left(\frac{1}{\eta}-1\right)\right]\right\}. \tag{4.6}$$

Using the relation $\varphi\gg\beta\chi/\gamma$ and substituting $\varphi=\xi/\gamma$ into Eq. (1.5a), we obtain

$$d\eta/d\tau=-\gamma\varphi\eta\ . \tag{4.7}$$

Further, from Eqs. (4.7), (4.3)

$$\gamma\tau=\varepsilon_1(1/\eta-1/\eta_0)-(1-\varepsilon')\ln(\eta/\eta_0)\ . \tag{4.8}$$

If $\eta_0=1$,

$$\gamma\tau=\varepsilon_1(1/\eta-1)-(1-\varepsilon')\ln\eta\ . \tag{4.9}$$

The curves of Eqs. (4.9) for $\varepsilon=\varepsilon'$, $l=1$, $\varepsilon_1=2\varepsilon$ are plotted in Fig 16. In use of those curves and (4.3), (4.6), $\varphi\eta$ and φ are plotted against $\gamma\tau$ in Fig. 16 and $\chi\eta$ in Fig. 17 respectively.

§ 6. Comparison between Experiments and Theory

The most general features about photoconductivity and phosphorescence shown in Figs. 9 to 12, are well covered by the theoretically calculated curves of Figs. 14, 16 and 17. In Fig. 17 the calculated $\chi\eta$-curves show a slight and slow rise for a very small value of χ_0. This cause is that the electrons in isolated traps are excited to the conduction band and retrapped into associated traps, when a large portion of trapped electrons is in isolated traps and associated traps are almost vacant at the initial state. Such an initial state can be realized only after the natural phosphorescence has dropped. But this rise of $\chi\eta$ is considered to negligible, if we assume the smaller value for ε or existence of isolated centres of considerable number. Also in the experiments any rise of phosphorescence by ir stimulation was not observed for the quenchable phosphors after natural phosphorescence had become negligible.

From Figs. 9 to 12 are obtained Figs. 18, 19 and 20. These results are in approximate agreement with the formulae (3.5). The behavior of induced photoconductivity curves along the earlier part of natural decay (Fig. 9) can be explained as follows. Although the trapped electrons are excited to the conduction band by ir irradiation, the process that the conduction electrons fall into vacant centers or traps, has more predominant effect in the earier stimulation. If the maximum value φ_m determined from the curves of Fig. 16 is smaller than the value of $\varphi_0=\xi_0/\gamma$ at this instance, not a remarkable rise but a retard of decay is observed. As γ increases abruptly by the ir stimulation, the conductivity decays more quickly than in the natural decay. (Fig. 16) This is the case that the moving point P starts from the point P_0, reaches the point P_1 and then tends towards the origin along the curve C. In order to rise the photocurrent in the earlier irradiation, a more intense radiation will be necessary so that the initial value ξ_0/γ becomes smaller than φ_m, and a more noticeable quenching will follow. This behavior is also similar about stimulation of brightness. (Fig. 12) The experimental values of the time required to reach the peak of photoconductivity and stimulated brightness seem to be somewhat larger than that expected theoretically. (Fig. 16) This discrepancy will be attributed to the thickness of the samples and the time lag of the galvanometer deflection for quick current change in the initial starting.

Therefore, the true peak values of induced current and brightness will be larger than the maximum values observed upon the deflections of the galvanometer as shown in Figs. 9 to 12 by dotted lines. The rise of phosphorescence was much more remarkable, compared with that of photoconductivity in earlier ir stimulation after the ceasing of uv excitation. (Figs. 9 and 11) This experimental result suggests the following possible explanation.

A large portion of conduction electrons has been excited from the filled band initially[24] and they return into it quickly after the ceasing of uv excitation, dissipating energy by phonon ejection.[25]

On the other hand, some of the electrons excited by ir stimulation to the conduction band from the traps, in whose vicinity vacant centers are abundant locally, pass through it only for a short time and immediately recombine with neighbouring vacant centers, giving negligible contribution to the electron density in the conduction band.[10] (quasi-direct transition)

A few minutes after uv excitation has been interupted, these processes become negligible and the presented theory may be available exactly.

Although the theory proposed here covers the same important behaviors of the results obtained in nonstationary state for all the prepared phosphors, it would be necessary to take into account more complicated electron transfer processes, in order to deal with the more detailed phenomena in nonstationary state.

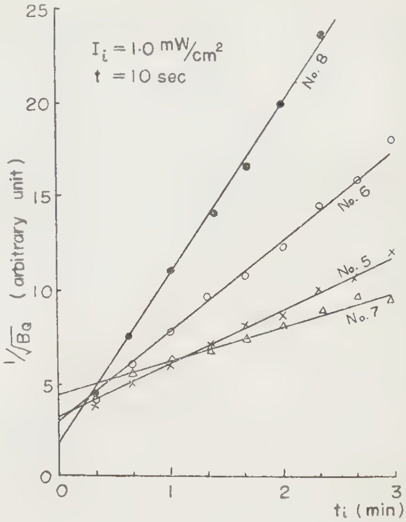

Fig. 19. Dependence of $1/\sqrt{B_Q}$ as a function of as a function of time under ir irradiation.

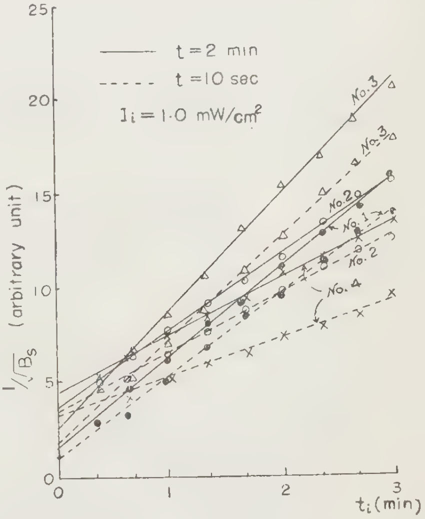

Fig. 20. Dependence of $1/\sqrt{B_S}$ as a function of time under ir irradiation.

§ 7. Acknowledgement

In conclusion, hearty thanks are due to Dr. Y. Uehara of Mazda-Institute (Tokyo-Sibaura Elec. Co.) for helpful consultation about the the preparation of materials and to Professor Dr. K. Umeda for valuable discussions throughout the work. Further, the writer is indebted to Mr. K. Toei and Mr. Y. Nakagawa of Department of Chemistry for their cooperation in purification and analysis of the materials and to Mr. M. Kazahaya and Mr. Kitayama for their assistance in the experiments.

References

1) P. Lenard: *Hd. Exp. Phys.* Bd. **23**, Tl. **2**. (1928) 786, 803.

2) G. R. Fonda: J. Opt. Soc. Am. **36** (1946) 382.

3) F. Urbach, D. Pearlman and H. Hemmendinger: J. Opt. Soc. Am. **36** (1946) 372.

4) H. Texin, H. Williams and P. Ward: J. Amer. Chem. Soc. **71** (1949) 2494.

5) A. E. Hardy: Trans. Electrochem. Soc. **87** (1945) 355.

9) P. T. Ellickson: J. Opt. Soc. Am. **36** (1946) 246.

7) H. Kallmann and B. Kramer: Phys. Rev. **87** (1952) 91.

8) N. Rhiel: Ann. d. Phys. **29** (1937) 637.

9) Y. Uehara: Bull. C. S. J. **15** (1940) 241; **16** (1941) 99.

10) G. v. Hevesy and K. Hobbie: Z. anal. Chem. **88** (1932) 1.

11) M. Isibasi, M. Tanaka and H. Hayakawa: J. Oceanog., Japan **2**. No. **3** (1943) 10.

12) P. Bauer: Zeits. f. Phys. **114** (1939) 245.

13) L. A. Dubridge and H. Brown: Rev. Scient. Instr. **4** (1933) 532.

14) F. A. Kroeger: Physica **6** (1939) 369.

15) R. C. Herman, C. F. Meyer and H. Hopfield: J. Opt. Soc. Am. **38** (1948) 999.

16) R. H. Bube: J. Chem. Phys. **20** (1952) 708.

17) F. E. Williams and H. Eyring: J. Chem. Phys. **15** (1947) 289.

18) J. T. Randall and H. L. Willkins: Proc. Roy. Soc. **A 184** (1945) 347, 366, 390.

19) T. Akahara: Sci. Pap. Inst. Phys. Chem. Res. Tokyo (June, 1929) Table No. 3, pp. 181~215.

20) E. Jahnke and F. Emde: *Funktionentafeln* (Leipzig-Berlin, 1933) pp. 83–85.

21) R. C. Herman and C. F. Meyer: J. Appl. Phys. **17** (1946) 743.

22) A. L. Reimann: Nature **140** (1937) 501.

23) A. Smakula: Zeits. f. Phys. **59** (1930) 603.

24) R. H. Bube: Phys. Rev. **83** (1951) 393.

25) C. F. J. Garlick and A. F. Gibson: J. Opt. Soc. Am. **39** (1949) 935.

JOURNAL OF THE PHYSICAL SOCIETY OF JAPAN Vol. 9, No. 4, JULY—AUGUST, 1954

Absorption Spectra of Dyes in Solution

By Yuzuru OOSHIKA

Kobayashi Institute of Physical Research, Kokubunji, Tokyo

(Received January 17, 1954)

A theory of absorption spectra of dyes in solution is presented. The wave-number shift of the absorption maximum is calculated by using the perturbation theory, where the distribution of solvent molecules is assumed to be uniform, and the shift is represented by experimentally convenient quantities, such as the dielectric constant, the refractive index, and the absorption wave-length of the solvent. The solvent effects are classified into several groups, and the theory can explain the various experimental facts successfully. Previous theories are criticized.

§ 1. Introduction

It has been well known that the absorption spectra of dyes vary from solvent to solvent both in intensities and in wavelengths. Since the effects of solvents are very complicated and various influences are superposed, there have been yet few theoretical studies concerning those effects. Sheppard has examined the experimental results extensively and found various sorts of solvent effects. From the theoretical point of view, it is convenient to classify those solvent effects into the following groups.

1. Dielectric effects, or, from the molecular point of view, the dipole interaction between solute and solvent molecules.

2. Short range specific interaction between solute and solvent molecules, or solvation effects, especially by hydrogen bonds and electron transfer.

3. Association effect between solute molecules. This effect changes with the solute

concentrations and may be neglected in dilute solutions.

4. Electrochemical effects, e.g., the change of the degree of dissociation of solute molecules, interactions between solute and added electrolytes.

5. Long range intermolecular resonance. Though this effect is important for the quenching phenomena of fluorescence, it may be rather unimportant for the light absorption.

In the present paper, we discuss the solute-solvent molecular interactions, neglecting the specific effect, in dilute solutions.

In discussing the effects of non-polar solvents, Chako1) derived a formula for the absorption intensity, based on the classical electromagnetic theory, but, according to the discussion by Jacobs and Platt2), the above formula does not hold in many cases and it should be regarded to be constant as average. This may mean that the intensity is very sensitive to the property of the solute and solvent interactions and it is not plausible to consider the solvent as an uniform dielectrics.

On the other hand, the influence on the wave-length of the absorption maximum has been investigated by several authors. In 1878, Kundt concluded for non-polar solvents that the absorption maximum is shifted towards the long wave-length side with increasing dispersion of the solvent Sheppard3) proposed the formula

$$\Delta\nu_m = a(1-1/K)\ ,$$

where $\Delta\nu_m$ is the increase of the wave number of the absorption maximum, K the dielectric constant of the solvent and a is a constant. In general, the dispersion increases with the refractive index and we may suppose that Kundt's rule means that the wave-length increases with increasing refractive index. Recently, Bayliss4) has proposed a theory that the wave-length shift is proportional to

$$\frac{2(n^2-1)}{2n^2+1}\cdot f\ ,$$

when n is the refractive index of the solvent and f is the f-value of the transition, considering the work for changing a dipole moment in dielectric medium.

If one investigates the effects of polar solvents, he will note that the circumstances are much more complicated, and, at first sight, the absorption maximum might seem to change its wave-length in no systematic way. On this point, Brooker5) found an interesting phenomenon for various merocyanine dyes, resently. In general, in merocyanines and other dyes, the absorption maximum is shifted towards the long wave-length side and the absorption intensity is increased with increasing dielectric constants. For example, the absorption wave number of the dye (I)

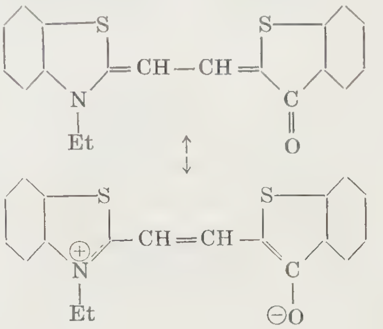

Ia

Ib

changes linearly with the dielectric constants of the solvents. On the other hand, λ_{max} (ε_{max}) of the dyes (II), (III)

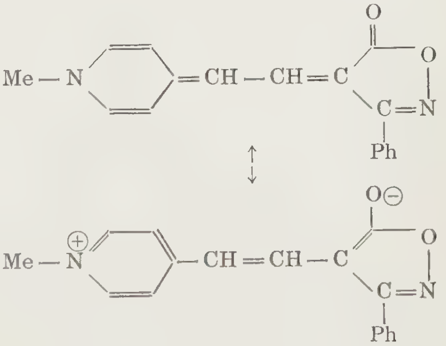

IIa

IIb

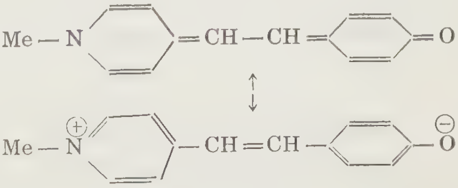

IIIa

IIIb

decrease with increasing dielectric constant of the solvent. However, the dye (IV)

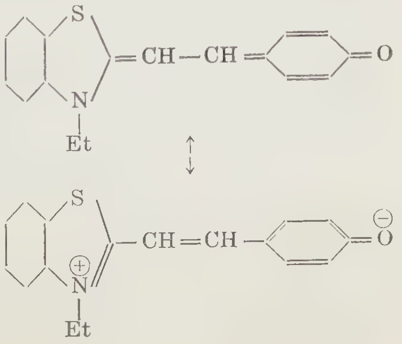

IVa

IVb

shows a strange behavior. The dye IV has $\lambda_{\max}$ at 5650Å ($\varepsilon_{\max}$ 9.7×10^4), in pyridine solution, but, as water is added, the absorption maximum is slightly shifted towards red and the absorption intensity is greatly increased, until the volume percent of pyridine becomes 92.5, $\lambda_{\max}$ is 5660Å ($\varepsilon_{\max}$ 12.9×10^4), and then the wave-length and the intensity are both decreased to $\lambda_{\max}$ 4900Å ($\varepsilon_{\max}$ 3.9×10^4) in water solution. The explanation of these phenomena by Brooker is as follows. In the case of the dye I, the non-polar resonance structure Ia is more important than the polar structure Ib for the ground state and the inverse for the excited state. Hence the stabilization by the solvent (as an uniform dielectrics) is larger in the excited state than in the ground state and the absorption is shifted towards the low energy side, i.e., towards red. On the other hand, in the case of II and III, the basicity of the left nucleus is very large and the contribution of the polar structure is larger to the ground state than to the excited state, and, therefore, the shift is towards blue, contrary to the case of the dye I. The dye IV has the intermediate property and IVa is more important for the ground state in pyridine solution, but IVb becomes more and more important with increasing water content until the contribution of IVb is equal to that of IVa at the maximum wave-lengh (isoenergetic point) and, after passing this point, the circumstances become the same with the case of the dyes II and III and the shift is towards blue. His suggestion will prove to be essentially correct by the present calculation, although there exist other influencing factors in his case.

W. T. Simpson[6] proposed a theory based on the valence bond method, assuming the energy for separating the electronic charges in a molecule to be proportional to $1/Dr$ ($D=$ the dielectric constant of the solvent, $r=$the distance between the charges.). But the result cannot explain the experiments. Further, from the theoretical point of view, the charges in a molecule are not burried in an uniform medium, but the molecule should be considered to exist in a cavity in a dielectric medium, and, therefore, the energy for sepa- rating charges is not proportional to $1/r$ and must be determined by an appropriate inner field.

Thus, Bayliss[7] found that the wave-length of the absorption maximum of the dye II and its homologs does not necessarily vary parallel to the dielectric constant of the solvent. In fact, the dielectric polarization of the solvent contains the part due to the orientation of the permanent dipoles of the solvent molecules and that due to the electronic polarizability The latter interacts with the motion of the electrons in the dye molecule and the former cannot follow the electronic motion and hence, it is obvious that the light absorption of dye molecules is not determined simply by the total dielectric constant of the solvent.

In this paper, the solvent effects are discussed in a general way, using the perturbation theory. The treatment is essentially based on the valence bond method.

§ 2. The Treatment by the Perturbation Method

Imagine a dye molecule surrounded by N solvent molecules. Fixing the dye molecule let the N molecular distribution function be

$$f(1,2,\cdots,N)=f_0+f_1\ , \qquad (1)$$

where f_0 is the hypothetical distribution function when the dipole moment of the dye molecule is assumed to be zero, and f_1 represents the orientation of solvent molecules by the dipole of the dye molecule in its ground state in the solution. The relaxation time for the orientation of the solvent molecules is much longer than the time required for the light absorption by a dye molecule, and hence the function f above does not change if the dye molecule is excited by light.

The electronic wave function of the solute molecule is given by

$$H_0\psi_m=\varepsilon_m\psi_m\ ,$$

and that of the solvent as a whole is

$$H\Psi_n=E_n\Psi_n\ , \qquad (2)$$

$$H=\sum_{i=1}^{N}H_i-\sum_i\sum_{j>i}\frac{\mu_i\mu_j}{r_{ij}^3}\Theta_{ij} \qquad (3)$$

$$\Theta_{ij}=2\cos\theta_i\cos\theta_j-\sin\theta_i\sin\theta_j\cos\varphi_{ij}\ , \qquad (4)$$

where n is a quantum number, H_i the hamiltonian operator of the i-th solvent molecule, μ_i its dipole moment operator, r_{ij} the distance between the i-th and the j-th solvent molecules and Θ_{ij} represents the mutual orientation between μ_i and μ_j. Since the hamiltonian H contains the interactions between solvent molecules, the wave function Ψ is not a simple product of the wave functions of particular molecules, but depends on the distribution of molecules. This interaction, however, may be assumed to be not so large. Then the perturbation operator by the interaction between the solute molecule and the solvent may be written

$$V=-\sum_i \frac{\mu_0\mu_i}{r_i^3}\Theta_i\ , \qquad (5)$$

where r_i and Θ_i are the distance and the mutual orientation between the dye and the i-th solvent molecule. Of course, when the distance between molecules are very small, the intermolecular interaction cannot be represented by such a simple dipole interaction, but such specific interaction is not considered in this paper.

Thus the problem reduces to discuss the energy change of the total system by the perturbation V, and to average that change over the disturtion of the solvent molecules f. In the following, we shall discuss the energy change by using several appropriate approximations, classify various solvent effects and relate the shift of absorption spectra of dyes to those quantities which are convenient to measure experimentally, for example, dielectric constant and refractive index.

The electronic wave function of the total system of the first order is approximately represented by

$$\Phi_{mn}=\phi_m\Psi_n\ . \qquad (6)$$

In the calculation below, we will assume that the solute molecule is in the state m and the solvent is in its ground state g. The excited states of the solvent are represented appromately by linear combinations of the states in which one solvent molecule is excited and hence they are almost N-fold degenerate. On the other hand, the probability distribution function of the solvent molecules is determined by the dipole moment of the solute molecule in the ground state in the solution ϕ_g and cannot follow the change by the light absorption.

1. *The first order perturbation*

The first order perturbation energy, ΔE_1, is the mean value of V in the state Φ_{mg}.

$$\Delta E_1=(\Phi_{mg}|V|\Phi_{mg})$$

$$=-\left(\Phi_{mg}\middle|\sum_i \frac{\mu_0\mu_i\Phi_i}{r_i^3}\middle|\Phi_{mg}\right)$$

$$=-(m|\mu_0|m)\sum_i \frac{(\Psi_g|\mu_i|\Psi_g)}{r_i^3}\Theta_i\ , \qquad (7)$$

where last Θ_i represents the mutual orientation between $(m|\mu_0|m)$ and $(\Psi_g|\mu_i|\Psi_g)$ and differs from that in hamiltonian operator. This is the same in the discussion below.

Averaging ΔE_1 over the molecular distribution, we shall write generally,

$$\int g(1,2,\cdots,N)f_l(1,2,\cdots,N)d\tau_1\cdots,d\tau_{N-k}$$

$$=\overline{g(N-k+1,\cdots,N)}^{l.k}\ f_l^{(k)}(N+k+1,\cdots,N),\quad l=0,1\ , \qquad (8)$$

where τ_i represents the position and orientation of the i-th solvent molecule and

$$f_l^{(k)}(1,\cdots,k)=\int f_l(1,2,\cdots,N)d\tau_{k+1}\cdots d\tau_N\ .$$

Now we assume that $f_0^{(1)}(i)$ is a function of r_i only and

$$\lim_{N\to\infty}\{Nf_0^{(1)}(i)\}=\begin{cases}1/v & \text{if } r_i\geqq a\\ 0 & \text{if } r_i<a\end{cases}\ , \qquad (9)$$

$$f_1^{(1)}(i)=f_1^{(1)}(\vec{r}_i,\ \omega_i)=-f_1^{(1)}(\vec{r}_i,\ -\omega_i)\ , \qquad (10)$$

where r_i and ω_i are the position vector of the i-th molecule and the solid angle representing its orientation. These assumptions are to be allowed in the range where the concept of the dielectric constant and refractive index is permissible. v is the molecular volume of the solvent.

$(\Psi_g|\mu_i|\Psi_g)$ is the dipole moment of the i-th solvent molecule in the solution, and, assuming $\overline{(\Psi_g|\mu_i|\Psi_g)}^{l.1}$ $(l=0,1)$ is independent on $\vec{r}_i$, it is reasonable to use the result obtained by Onsager

$$(\Psi_g|\mu_i|\Psi_g)=\frac{(2D+1)(n^2+2)}{3(2D+n^2)}\mu_{gas}=\mu\ , \qquad (11)$$

where D and n are the dielectric constant and the refractive index of the solvent, respectively.

Then

$$\int\frac{(\Psi_g|\mu_i|\Psi_g)\Theta_i}{r_i^3}f_0d\tau_1\cdots d\tau_N=0\ , \qquad (12)$$

and

$$\sum_i\int\frac{(\Psi_g|\mu_i|\Psi_g)\Theta_i}{r_i^3}f_1d\tau_1\cdots d\tau_N$$

$$=N\int\frac{\mu\Theta_1}{r_1^3}f_1^{(1)}(1)d\tau_1=F\cos\theta_{mm}\ . \qquad (13)$$

$F\cos\theta_{mm}$ is the component to the direction of $\vec{\mu}_m=(m|\vec{\mu}_0|m)$ of the so-called reaction field due to the orientation of the solvent molecules by the dipole moment μ_g' of the solute molecule in its ground state in the solution. θ_{mm} is the angle between $\vec{\mu}_g'$ and $(m|\vec{\mu}_0|n)$, and $\vec{\mu}_g'$ is not the dipole moment $\vec{\mu}_g=(g|\mu_0|g)$ of an isolated dye molecule, because of the polarization by the reaction field. In Onsager's approximation,

$$\vec{F}=\left\{\frac{2(D-1)}{2D+1}-\frac{2(n^2-1)}{2n^2+1)}\right\}\frac{\vec{\mu}_g'}{a^3}, \tag{14}$$

$$\vec{\mu}_g'=\vec{\mu}_g+\frac{2(D-1)}{2D+1}\frac{2}{a^3}\sum_{m\neq g}\frac{\vec{\mu}_g'\cdot(g|\vec{\mu}_0|m)(g|\vec{\mu}_0|m)}{\mathcal{E}_m-\mathcal{E}_g}$$

$$\simeq\vec{\mu}_g+\frac{2(D-1)}{2D+1}\frac{2}{a^3}\sum_{m\neq g}\frac{\vec{\mu}_g\cdot(g|\vec{\mu}_0|m)(g|\vec{\mu}_0|m)}{\mathcal{E}_m-\mathcal{E}_g},$$

in the second approximation. Thus we may write

$$\langle\varDelta E_1\rangle=-\left\{\frac{2(D-1)}{2D+1}-\frac{2(n^2-1)}{2n^2+1}\right\}\left\{\frac{\vec{\mu}_g\cdot\vec{\mu}_m}{a^3}\right.$$

$$\left.+\frac{2(D-1)}{2D+1}\frac{2}{a^6}\sum_{m'\neq g}\frac{\{\vec{\mu}_g(g|\vec{\mu}_0|m')\}\{\vec{\mu}_m(g|\vec{\mu}_0|m')\}}{\mathcal{E}_{m'}-\mathcal{E}_g}\right\}, \tag{16}$$

2. The second order perturbation is classified into three kinds of interactions

i) $\varPhi_{mg}-\varPhi_{mn}$ interaction

$$(\varPhi_{mg}|V|\varPhi_{mn})=-(m|\mu_0|m)\sum_i\frac{(\varPsi_g|\mu_i|\varPsi_n)\Theta_i}{r_i^3},$$

$$\varDelta E_{21}=\mu_m^2\sum_{n\neq g}\sum_{i.j}\frac{(\varPsi_g|\mu_i|\varPsi_n)(\varPsi_g|\mu_j|\varPsi_n)\,\Theta_i\Theta_j}{(E_g-E_g)r_i^3r_j^3}. \tag{17}$$

Firstly, averaging this energy over f_0,

$$\int\sum_j\sum_{n\neq g}\frac{(\varPsi_g|\mu_i|\varPsi_n)(\varPsi_g|\mu_j|\varPsi_n)\Theta_i\Theta_j}{(E_g-E_n)r_i^3r_j^3}$$
$$\times f_0\mu_m^2d\tau_1\cdots d\tau_{i-1}d\tau_{i+1}\cdots d\tau_N$$

$$=\sum_j\sum_{n\neq g}\overline{\frac{(\varPsi_g|\mu_i|\varPsi_n)(\varPsi_g|\mu_j|\varPsi_n)\,\Theta_i\Theta_j}{(E_g-E_n)r_i^3r_j^3}}^{0.1}f_0^{(1)}(i)\mu_m^2 \tag{18}$$

is the mean energy of the interaction between the dipole $\vec{\mu}_m$ of the solute molecule and the dipole induced on the i-th solvent molecule fixed at the position and the orientation in the solution by the field of $\vec{\mu}_m$. Thus

$$-\sum_i\int\overline{\sum_j\sum_{n\neq g}\frac{(\varPsi_g|\mu_i|\varPsi_n)(\varPsi_g|\mu_j|\varPsi_n)\Theta_i\Theta_j}{(E_g-E_n)r_i^3r_j^3}}^{0;1}$$
$$\times f_0^{(1)}(i)\mu_m d\tau_i$$

equals to

$$\frac{2(n^2-1)}{2n^2+1}\frac{\mu_m}{a^3}.$$

Then

$$\langle\varDelta E_{21}{}^0\rangle=-\frac{2(n^2-1)}{2n^2+1}\frac{\mu_m^2}{a^3}. \tag{19}$$

Further, assuming that the mean polarizability of the solvent molecule in the solution, i.e.,

$$-\sum_n\sum_j\overline{\frac{(\varPsi_g|\vec{\mu}_i|\varPsi_n)(\varPsi_g|\vec{\mu}_j|\varPsi_n)}{E_g-E_n}}^{i,1}$$

is isotropic, we can easily show that

$$\int\varDelta E_{21}f_1d\tau,\cdots d\tau_N=0$$

by using Eq. (10).

ii) $\varPhi_{ng}-\varPhi_{m'g}$ interaction

$$(\varPhi_{mg}|V|\varPhi_{m'g})=-(m|\mu_0|m')\sum_i\frac{(\varPsi_g|\mu_i|\varPsi_g)\Theta_i}{r_i^3},$$

$$\varDelta E_{22}=\sum_{m'\neq m}\sum_{i;j}\frac{\mu^2\Theta_i\Theta_j}{r_i^3r_j^3}\frac{(m|\mu_0|m')^2}{\mathcal{E}_m-\mathcal{E}_{m'}}. \tag{20}$$

When we average $\varDelta E_{22}$ over f_0, if we write

$$\int\sum_j\frac{\mu^2\Theta_i\Theta_j}{r_i^3r_j^3}f_0d\tau_1,\cdots d\tau_N$$
$$=\int\frac{\mu\mu_{eff}\Theta_i^2}{r_i^6}f_0^{(1)}(i)d\tau_i, \tag{21}$$

where

$$\frac{\mu_{eff}\Theta_i}{r_i^3}=\overline{\sum_j\frac{\mu\Theta_j}{r_j^3}}^{0}. \tag{22}$$

μ_{eff} represents effectively that, fixing the position and orientation of the i-th molecule, the other molecules are oriented and their dipoles can polarize the solute because of the correlation between the solvent molecules, when averaging over the distribution other than the i-th. It may, of course, be a function of the position and orientation of the i-th molecule. But, assuming that μ_{eff} is independent on the position of the i-th melecule, and that the solvent molecule is a point dipole at the center of a spherical cavity with a radius d $((4\pi/3)d^3=v)$, the apparent charges appearing on the surface of the cavity are just those which show the orientation of the medium due to the correlation between the solvent molecules and those apparent charges are equivalent to a dipole with a moment

$$-\frac{2(D-1)}{2D+1}\mu,$$

for the outer environment. Therefore,

$$\mu_{eff}=\mu-\frac{2(D-1)}{2D+1}\mu=\frac{3}{2D+1}\mu. \tag{23}$$

D in this formula involves the part due to the polarizability of the solvent molecules, while the Eq. (22) shows that μ_{eff} is only that part due to the permanent dipole of the solvent molecules, but in the discussion below, we include the former, which is of the higher order of magnitude, in μ_{eff}. Thus

$$\begin{aligned}\langle \varDelta E_{22}{}^{0}\rangle&=\int \varDelta E_{22}f_0 d\tau_1\cdots\cdots d\tau_N\\&=\sum_i\int\frac{\mu\mu_{eff}\Theta_i{}^2}{r_i{}^6}f_0'(i)d\tau_i\sum_{m'\neq m}\frac{(m|\mu_0|m')^2}{\mathcal{E}_m-\mathcal{E}_{m'}}\\&=\frac{2}{2D+1}\frac{\mu^2}{a^3d^3}\sum_{m'\neq m}\frac{(m|\mu_0|m')^2}{\mathcal{E}_m-\mathcal{E}_{m'}}.\end{aligned} \tag{24}$$

If we use the formula

$$\frac{\mu^2}{kT}=\frac{(2D+1)^2(D-n)}{3(2D+n^2)D}d^3, \tag{25}$$

we can eliminate the value of the dipole moment of a solvent molecule.

$$\langle \varDelta E_{22}{}^{0}\rangle=\frac{2(D+1)(D-n^2)}{3(2D+n^2)D}\frac{kT}{a^3}\sum_{m'\neq m}\frac{(m|\mu_0|m')^2}{\mathcal{E}_m-\mathcal{E}_{m'}}. \tag{26}$$

Next, we calculate the average over f_1.

$$\begin{aligned}\int\frac{\mu^2\Theta_i\Theta_j}{r_i{}^3r_j{}^3}f_1d\tau_1\cdots\cdots d\tau_N&=\int\frac{\mu^2\Theta_i\Theta_j}{r_i{}^3r_j{}^3}f_1{}^{(2)}d\tau_id\tau_j\\&\simeq\int\frac{\mu\Theta_i}{r_i{}^3}f_1{}^{(1)}(i)d\tau_i\int\frac{\mu\Theta_j}{r_j{}^3}f_1{}^{(1)}(j)d\tau_j.\end{aligned}$$

This approximation is not unimportant, because f_1 is a correction term and the neglected quantity is of higher order of magnitude. It is equivalent to that one puts the average of the square of the reaction field to be equal to the square of the average of the reaction field. Thus,

$$\begin{aligned}\langle \varDelta E_{22}{}^{1}\rangle&=\sum_{m'\neq m}\sum_{i,j}\int\frac{\mu\Theta_i}{r_i{}^3}f_1{}^{(1)}(i)d\tau_i\\&\quad\times\int\frac{\mu\Theta_j}{r_j{}^3}f_1{}^{(1)}(j)d\tau_j\frac{(m|\mu_0|m')^2}{\mathcal{E}_m-\mathcal{E}_{m'}}\\&=\sum_{m'\neq m}(F\cos\theta_{mm'})^2\frac{(m|\mu_0|m')^2}{\mathcal{E}_m-\mathcal{E}_{m'}}.\end{aligned}$$

This equation means that $\langle \varDelta E_{22}{}^{1}\rangle$ is the interaction energy between the reaction field due to the mutual orientation of the solvent molecules and the dipoles induced on the solute molecule by it. But, for convenience, we include in $\langle \varDelta E_{22}{}^{1}\rangle$ the energy due to the induced dipoles on the solvent molecules and write

$$\langle \varDelta E_{22}{}^{1}\rangle=\left\{\frac{2(D-1)}{2D+1}\right\}^2\frac{1}{a^6}\sum_{m'\neq m}\frac{\{\vec{\mu}_g(m|\vec{\mu}_0|m')\}^2}{\mathcal{E}_m-\mathcal{E}_{m'}}, \tag{27}$$

where the part of the reaction field due to the induced polarization of the reaction field due to the induced polarization of the solvent molecules is determined by μ_m, not by μ_g, but we neglect their difference.

iii) $\varPhi_{mg}$—$\varPhi_{m'n}$ interaction.

$$(\varPhi_{mg}|V|\varPhi_{m'n})=-(m|\mu_0|m')\sum_i\frac{(\varPsi_g|\mu_i|\varPsi_n)\Theta_i}{r_i{}^3},$$

$$\begin{aligned}\varDelta E_{23}&=\sum_{m'\neq m}\sum_{n\neq g}\sum_{i,j}(m|\mu_0|m')\\&\quad\times\frac{(\varPsi_g|\mu_i|\varPsi_n)(\varPsi_g|\mu_j|\varPsi_n)\Theta_i\Theta_j}{(\mathcal{E}_m-\mathcal{E}_{m'}+E_g-E_n)r_i{}^3r_j{}^3}.\end{aligned} \tag{28}$$

If we assume that the polarizability of a solvent molecule is isotropic, the average of E_{23} over f_1 vanishes as in 2, i, and we have to account only the average over f_0. Then

$$\begin{aligned}\langle \varDelta E_{23}\rangle&=\sum_{m'\neq m}\sum_{n\neq g}\\&\quad\times\int\sum_{i,j}\frac{(\varPsi_g|\mu_i|\varPsi_n)(\varPsi_g|\mu_j|\varPsi_n)\Theta_i\Theta_j}{(\mathcal{E}_m-\mathcal{E}_{m'}+E_g-E_n)r_i{}^3r_j{}^3}\\&\quad\times f_0d\tau_1\cdots\cdots d\tau_N\\&=\sum_{m'\neq m}\sum_i\\&\quad\times\int\sum_{n\neq g}\sum_j\frac{(\varPsi_g|\mu_i|\varPsi_n)(\varPsi_g|\mu_j|\varPsi_n)\Theta_i\Theta_j}{(\mathcal{E}_m-\mathcal{E}_{m'}+E_g-E_n)r_i{}^3r_j{}^3}\\&\quad f_{0)}{}^{1)}(i)d\tau_i,\end{aligned} \tag{29}$$

Considering that the excited states of the solvent are almost degenerate,

$$\begin{aligned}\langle \varDelta E_{23}\rangle&=\sum_{m'\neq m}\sum_i\\&\quad\times\int\sum_{n\neq g}\sum_j\overline{\frac{(\varPsi_g|\mu_i|\varPsi_n)(\varPsi_g|\mu_j|\varPsi_n)\Theta_i\Theta_j}{(E_g-E_n)r_i{}^3r_j{}^3}}^{0,1}\\&\quad\times f_0{}^{(1)}(i)\,d\tau_i\frac{(E_g-E_n)(m|\mu_0|m')}{\mathcal{E}_m-\mathcal{E}_{m'}+E_g-E_n}\\&=-\frac{2(n^2-1)}{2n^2+1}\frac{E_g-E_n}{a^3}\sum_{m'\neq m}\frac{(m|\mu_0|m')^2}{E_g-E_n+\mathcal{E}_m-\mathcal{E}_{m'}},\end{aligned} \tag{30}$$

by Eq. (19).

Ordinarily, as the light absorption of dye molecules occur at much longer wave-lengths than that of solvent molecules which are colorless,

$$|E_g-E_n|\gg|\mathcal{E}_m-\mathcal{E}_{m'}|,$$

Hence

$$\langle \varDelta E_{23}\rangle=-\frac{2(n^2-1)}{2n^2+1}\frac{1}{a^3}\sum_{m'\neq m}(m|\mu_0|m')^2\times\left\{1-\frac{\mathcal{E}_m-\mathcal{E}_{m'}}{E_g-E_n}\right\}. \tag{31}$$

In ordinary treatments, by the second order perturbation, the additivity holds for the induction energy and the dispersion energy. If we use it, we obtain $(n^2-1)(n^2+1)$ instead of $2(n^2-1)/(2n^2-1)$ in all equations above, which means that when the number of the molecule is very large, the total error cannot be always neglected, even if the particular error of each term is small, and that we cannot assume simply the additivity rule.

In the end, considering all the effects above we obtain for the energy change in the state m, and neglecting the term involving

$$\frac{2(D-1)}{2D+1}\frac{2(n^2-1)}{2n^2+1},$$

$$\begin{aligned}\langle \Delta E\rangle_m=&-\frac{2(D-1)}{2D+1}\frac{\vec{\mu}_g\vec{\mu}_m}{a^3}-\frac{2(n^2-1)}{2n^2+1}\frac{\mu_m{}^2-\vec{\mu}_g\vec{\mu}_m}{a^3}\\&+\frac{2(D-1)(D-n^2)}{3(2D+n^2)D}\frac{kT}{a^3}\sum_{m'\neq m}\frac{(m|\mu_0|m')^2}{\mathcal{E}_m-\mathcal{E}_{m'}}\\&+\left\{\frac{2(D-1)}{2D+1}\right\}^2\frac{1}{a^6}\left\{\sum_{m'\neq m}\frac{\{\vec{\mu}_g(m|\vec{\mu}_0|m')\}^2}{\mathcal{E}_m-\mathcal{E}_{m'}}\right.\\&\left.+2\sum_{m'\neq m}\frac{\{\vec{\mu}_g(g|\vec{\mu}_0|m')\}\{\vec{\mu}_m(g|\vec{\mu}_0|m')\}}{\mathcal{E}_g-\mathcal{E}_{m'}}\right\}\\&-\frac{2(n^2-1)}{2n^2+1}\frac{1}{a^3}\sum_{m'\neq m}(m|\mu_0|m')^2\\&\times\left\{1-\frac{\mathcal{E}_m-\mathcal{E}_{m'}}{E_g-E_n}\right\}.\end{aligned}\tag{32}$$

§ 3. Results

The shift of the wave-length of the absorption maximum is the difference between $\langle\Delta E\rangle$ for the ground state and that for the exited state,

$$\begin{aligned}&\langle\Delta E\rangle_e-\langle\Delta E\rangle_g\\&=\frac{2(D-1)}{2D+1}\frac{\mu_g{}^2-\mu_g\mu_e}{a^3}+\frac{2(n^2-1)}{2n^2+1}\frac{\mu_g\mu_e-\mu_e{}^2}{a^3}\\&+\frac{2(D+1)(D-n^2)}{3(2D+n^2)D}\frac{kT}{a^3}\left\{\sum_{m\neq g}\frac{(g|\mu_0|m)^2}{\mathcal{E}_m-\mathcal{E}_g}\right.\\&\left.-\sum_{m\neq e}\frac{(e|\mu_0|m)^2}{\mathcal{E}_m-\mathcal{E}_e}\right\}\\&+\left\{\frac{2(D-1)}{2D+1}\right\}^2\frac{1}{a^6}\left\{3\sum_{m\neq g}\frac{\{\vec{\mu}_g(g|\vec{\mu}_0|m)\}^2}{\mathcal{E}_m-\mathcal{E}_g}\right.\\&-\sum_{m\neq e}\frac{\{\vec{\mu}_g(e|\vec{\mu}_0|m)\}^2}{\mathcal{E}_m-\mathcal{E}_e}\\&\left.-2\sum_{m\neq g}\frac{\{\vec{\mu}_g(g|\vec{\mu}_0|m)\}\{\vec{\mu}_e(g|\vec{\mu}_0|m)\}}{\mathcal{E}_m-\mathcal{E}_g}\right\}\\&+\frac{2(n^2-1)}{2n^2+1}\frac{1}{a^3}\left\{\sum_{m\neq g}(g|\mu_0|m)^2\left(1-\frac{\mathcal{E}_m-\mathcal{E}_g}{E_n-E_g}\right)\right.\\&\left.-\sum_{m\neq e}(e|\mu_0|m)^2\left(1-\frac{\mathcal{E}_m-\mathcal{E}_e}{E_n-E_g}\right)\right\}.\end{aligned}$$

The first and the second terms may b either positive or negative according to th magnitudes and directions of $\vec{\mu}_g$ and $\vec{\mu}_e$ an we call them together the polarization effec The sign of the third and the fouth terms ar not constant, while the last term, which exist also for non-polar dyes in non-polar solvent is always negative (red shift). They may b named the induction effect, the polarizatio induction effect, and the dispersion effect, respectively.

Thus, we obtain the following formul which explains the shift of the wave-lengt of the absorption maximum of a dye in various solvents.

$$hc\Delta\sigma=\frac{2(D-1)}{2D+1}\alpha+\frac{2(n^2-1)}{2n^2+1}\left(\beta-\frac{\gamma}{\sigma_s}\right)+\left\{\frac{2(D-1)}{2D+1}\right\}^2\delta+\frac{(2D+1)(D-n^2)}{(2D+n^2)D}\varepsilon.\tag{33}$$

where

$$\alpha=\frac{\mu_g{}^2-\vec{\mu}_g\vec{\mu}_e}{a^3}.$$

$$\beta=\frac{\vec{\mu}_g\vec{\mu}_e-\mu_e{}^2}{a^3}+\frac{\sum_{m\neq g}(g|\mu_0|m)^2-\sum_{m\neq e}(e|\mu_0|m)^2}{a^3},$$

$$\begin{aligned}\gamma&=\frac{1}{hca^3}\left\{\sum_{m\neq g}(g|\mu_0|m)^2(\mathcal{E}_m-\mathcal{E}_g)\right.\\&\left.\qquad-\sum_{m\neq e}(e|\mu_0|m)^2(\mathcal{E}_m-\mathcal{E}_g)\right\}\\&\simeq\frac{2(g|\mu_0|e)^2\sigma_0}{a^3}>0,\quad\sigma_0=(\mathcal{E}_e-\mathcal{E}_g)/hc,\end{aligned}$$

$$\begin{aligned}\delta&=\frac{1}{a^6}\left\{3\sum_{m\neq g}\frac{\{\vec{\mu}_g(g|\vec{\mu}_0|m)\}^2}{\mathcal{E}_m-\mathcal{E}_g}\right.\\&\qquad-\sum_{m\neq e}\frac{\{\vec{\mu}_g(e|\vec{\mu}_0|m)\}^2}{\mathcal{E}_m-\mathcal{E}_e}\\&\qquad\left.-2\sum_{m\neq g}\frac{\{\vec{\mu}_g(g|\vec{\mu}_0|m)\}\{\vec{\mu}_e(g|\vec{\mu}_0|m)\}}{\mathcal{E}_m-\mathcal{E}_g}\right\}\\&\simeq\frac{2}{a^6}\frac{\{\vec{\mu}_g(g|\mu_0|e)\}\{(2\vec{\mu}_g-\vec{\mu}_e)(g|\vec{\mu}_0|e)\}}{\mathcal{E}_e-\mathcal{E}_g},\end{aligned}$$

$$\begin{aligned}\varepsilon&=\frac{2kT}{3a^3}\left\{\sum_{m\neq g}\frac{(g|\mu_0|m)^2}{\mathcal{E}_m-\mathcal{E}_g}-\sum_{m\neq e}\frac{(e|\mu_0|m)^2}{\mathcal{E}_m-\mathcal{E}_e}\right\}\\&\simeq\frac{4kT}{3a^3}\frac{(g|\mu_0|e)^2}{hc\sigma_0},\end{aligned}$$

$$\sigma_s=(E_n-E_g)/hc,\tag{35}$$

where h and c is Planck's constant and the light velocity and α, β, γ, δ and ε are estinated by the wave-length and the intensity of the intrinsic absorption of the dye. In the above equation, we used the approximation that the contributions from $(m|\mu_0|m')$ may be neglected except for that from $(e|\mu_0|g)$, if those terms have been divided by $\mathcal{E}_m-\mathcal{E}_{m'}$.

We can obtain various conclusions qualitatively from the above formula.

a. It is not only the dielectric constant D, but also the refractive index n and the absorption wave-number σ_s of the solvent that determines the shift $\Delta\sigma$. The fact that $\Delta\sigma$ is not always parallel to D is explained by this effect. The absorption maximum of the dye

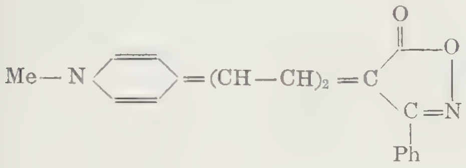

shifts towards blue with dielectric constants in the order of chloroform, pyridine and acetone, but in nitrobenzene, of which dielectric constant is larger than of acetone, the dye absorbs light at shorter wave-length than in acetone. This fact may be explained by the much larger refractive index and much longer absorption wave-length of nitrobenzene.

b. When the dielectric constant is small, it is the first and the second terms that produce the red shift, but, since the first term is predominant, the absorption maximum shifts towards red only if $\mu_g{}^2 < \vec{\mu}_g\vec{\mu}_e$. Ordinary dyes have a smaller dipole moment in the ground state, and hence the solvent effect is in general to produce the deeper color.

c. Even if the shift is towards red when D is small, it is possible that, with increasing dielectric constant, the absorption wave-length passes a maximum and then shifts towards blue. This is the case of the dye IV described previously, and the point where the wave-length is maximum is near the isoenergetic point as Brooker pointed out, but, since the present theory can be applied only when D is small, the detailed discussion will be presented in a later paper.

d. If the merocyanine has an abnormally acidic nucleus and an abnormally basic nucleus, the polar resonance structure may by more stable and $\mu_g{}^2$ may be more larger than $(\vec{\mu}_g\vec{\mu}_e)$. This corresponds to the case of the dyes II and III.

e. When $\mu_g \simeq 0$, the effect of the solvent is very small, even if a small dipole moment is produced by the interaction with the solvent, because the effect is proportional to μ_g. In contrast, if μ_g is large, the solvent effect is also large. This is in agreement with what Brooker has observed with the dye II and its homologs and is a special case of so called "Sensitivity rule".

Thus the solvent effect can be explained qualitatively by the present theory and no facts that are contrary to the theory have been found, so far as the author knows.

We will carry out the detailed calculation for actual dyes in a later paper, in which a discussion will be given without the perturbation theory, and, here, we content ourselves only with the discussion of the effect of non-polar solvents.

§ 4. Non-polar Solvents

In non-polar solvents, D equals n and the second power of $2(D-1)/(2D+1)$ may be neglected. Therefore,

$$hc\Delta\sigma = \frac{2(n^2-1)}{2n^2+1}\left(\alpha+\beta-\frac{\gamma}{\sigma_s}\right)$$

that is,

$$-\frac{2n^2+1}{2(n^2-1)}\Delta\sigma = a+b\lambda_s,$$
$$a,\ b>0.$$

If we plot $-\{(2n^2+1)/2(n^2-1)\}\Delta\sigma$ against λ_s, the absorption wave-length of the solvents, a straight line will be obtained. The following data are the ones for the dye I estimated by the author from the absorption curve in the paper of Sheppard.

solvent	in gas	n-hexane	CCl_4	C_6H_6	CS_2
n	—	1.38	1.46	1.50	1.62
λ_s(Å)	—	1,600	2,300	2,600	2,300
σ(cm^{-1})	21,300	19,700	19,000	18,600	18,300
$-\Delta\sigma=\sigma_0-\sigma$	—	1,600	2,300	2,700	3,000
$\frac{2n^2+1}{2(n^2-1)}\Delta\sigma$	—	4,260	5,360	5,940	5,760

The longest wave-length absorption of CS_2 is very weak, and we adopt the next absorption as λ_s. Fig. 1 shows $\{(2n^2+1)/2(n^2-1)\}\Delta\sigma$ as a function of λ_s, and it is seen that the four points lie on a straight line. Bayliss has thought that $\Delta\sigma$ was proportional to $2(n^2-1)/(2n^2+1)$, but the constant of proportion

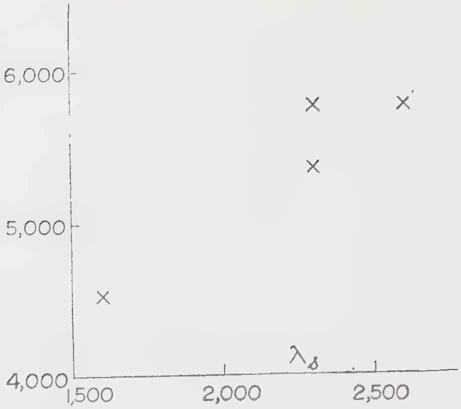

Fig. 1.

proves to be incorrect from the present theory, because it is

$$\frac{\mu_g^2-\mu_e^2}{a^3}+\frac{\sum_{m\neq g}(g|\mu_0|m)^2-\sum_{m\neq e}(e|\mu_0|m)^2}{a^3}$$

and the f-value of the transition vanishes.

This work has been done by the financi aid of the Ministry of Education in 1953.

References

1) N. Q. Chako: J. Chem. Phys. **2** (1934) 644

2) L. E. Jacobs and J. R. Platt: J. Chem Phys. **16** (1948) 1137.

3) S. E. Shppard: Rev. Mod. Phys. **14** (1942 303.

4) N. S. Bayliss: J. Chem. Phys. **18** (1950 292.

5) L. G. S. Brooker, G. H. Keyes, R. H. Sprague, R. H. Van Dyke, E. Van Laar, G. Van Zandt, F. L. White, H. W. J. Cressman and S. G. Dent: J. Am. Chem. Soc. **73** (1951) 5332.

6) W. T. Simpson: J. Am. Chem. Soc. **73** (1951) 5359.

7) N. S. Bayliss and E. G. Rae: J. Am. Chem. Soc. **74** (1952) 5803.

Journal of the Physical Society of Japan Vol. 9, No. 4, July—August, 1954

On the Wave Aberrations of the Decentred Lens System with the Finite Aperture

By Yukichi Ukita and Jumpei Tsujiuchi

The Government Mechanical Laboratory,
132 Sumiyoshi-cho, Suginami-ku, Tokyo, Japan

(Received April 8, 1954)

The authors calculated the wave aberrations of the slightly decentred lens system with the finite aperture. First a general formula was obtained for the wave aberrations of the decentred lens system, and then the problem was confined to the axial object point. In addition to the spherical aberration that had inherently existed before decentering, new aberrations were introduced. These new ones were the spherical aberration, coma and astigmatism, and of these three coma was the most effective, as the other two were the small quantities of higher order.

§ 1. Introduction

Generally speaking, when the axes of the lens elements composing a lens system are not at one with each other, the system is called as decentred, and the decentering deteriolates the lens performance seriously.

The problem of the decentred lens system has been studied by many investigators, and many interesting results have been reported.[1]

In the following we calculate the formula of the aberrations of the slightly decentred lens system with the finite aperture, by extending the André Maréchal's method.[2]

§ 2. General Theory

A centred lens system has a common optical axis both in the object and the image space. In Fig. 1 the optical axis crosses the entrance pupil Q and the exit pupil Q' at A and A′, the object plane O and the image plane I at C and C′, respectively.

In the polar coordinate with the origin at C in the object plane, an object point P is represented by y_1 and ψ_1, where y_1 is the height of the object point and ψ_1 is the azimuth measured from a certain standard meridional plane. A incident point H (h_1, ϕ_1) of a ray from P in the entrance pupil is also represented by the polar coordinate with the origin at A, where h_1 is the height of incidence and ϕ_1 is the azimuth measured from the same meridional plane.

If this lens system undergoes a slight decentering, a ray that emerges along A′C′ in the image space is no more on the original axis AC, but on the slightly displaced line BD. That is to say, the optical axis, observed from the image space, appear as if it had been removed from AC to BD after the decentering. The intersection points of the new axis with the object and the pupil plane are D (t, β) and B (s, α).

We transform the polar coordinates by changing the origins from C to D and from A to B in each plane. Then the object point P and the incident point H will be shown by P (y_2', ψ_2) and H (h_2', ϕ_2) respectively, and among these coordinates the following relations are found,

$$\left.\begin{aligned} y_1 \sin \psi_1 &= y_2' \sin \psi_2 + t \sin \beta\ , \\ y_1 \cos \psi_1 &= y_2' \cos \psi_2 + t \cos \beta\ , \\ h_1 \sin \phi_1 &= h_2' \sin \phi_2 + s \sin \alpha\ , \\ h_1 \cos \phi_1 &= h_2' \cos \phi_2 + s \cos \alpha\ . \end{aligned}\right\} \qquad (1)$$

Assuming the directions of the decentering elements are all the same, we get

$$\alpha = \beta\ . \qquad (2)$$

Let the inclination of the new and old axis be ε, then we have $s = fp + t$, where $p \equiv \sin \varepsilon$ and f is the object distance from the pupil. If the decentering is assumed to be small, then s, t and p are all small quantities of the same order.

As the axis inclines, the heights of the object and the pupil incidence must be corrected. The true heights y_2 and h_2 will be obtained from the vector products of the vector $\overrightarrow{\mathrm{DP}}$ or $\overrightarrow{\mathrm{BH}}$ and the unitary vector of the new axis.

Neglecting small quantities of the third and the higher order, we have the next expressions.

$$\left.\begin{aligned} y_2' &= y_2[1 + \tfrac{1}{2} p^2 \cos^2 (\psi_2 - \beta)] \\ h_2' &= h_2[1 + \tfrac{1}{2} p^2 \cos^2 (\phi_2 - \alpha)]\ , \end{aligned}\right\} \qquad (3)$$

Substituting (2) and (3) into (1), we get

$$\left.\begin{aligned} y_1 \sin \psi_1 &= y_2[1 + \tfrac{1}{2} p^2 \cos^2(\psi_2 - \alpha)] \sin \psi_2 + t \sin \alpha \\ y_1 \cos \psi_1 &= y_2[1 + \tfrac{1}{2} p^2 \cos^2(\psi_2 - \alpha)] \cos \psi_2 + t \cos \alpha \\ h_1 \sin \phi_1 &= h_2[1 + \tfrac{1}{2} p^2 \cos^2(\phi_2 - \alpha)] \sin \phi_2 + s \sin \alpha \\ h_1 \cos \phi_1 &= h_2[1 + \tfrac{1}{2} p^2 \cos^2(\phi_2 - \alpha)] \cos \phi_2 + s \cos \alpha . \end{aligned}\right\} \qquad (4)$$

By consideration of the rotational symmetry, the wave aberration of the lens system before decentering will be of the following type,

$$\Delta = f[y_1^2,\ h_1^2,\ y_1 h_1 \cos (\psi_1 - \phi_1)]\ . \qquad (5)$$

Owing to the slight decentration, the coordinates of the object and incident point turn into P (y_2, ψ_2), and H (h_2, ϕ_2), and the wave aberration Δ' after decentering will be shown as the sum of the following two terms, the term of the prism action, which contains as variables y_2, h_2, ψ_2, ϕ_2 instead of y_1, h_1, ψ_1, ϕ_1 and the term δ $(y_2, h_2, s, t, \psi_2, \phi_2, \alpha)$, which represents the small change of the aberration, i.e.

$$\begin{aligned} \Delta' = f&[y_2^2,\ h_2^2,\ y_2 h_2 \cos (\psi_2 - \phi_2)] \\ &+ \delta(y_2, h_2, s, t, \psi_2, \phi_2, \alpha) \end{aligned} \qquad (6)$$

The additional term introduced by decentering can be calculated by the total differentiation of the function f.

In general, Δ can be represented by

$$\begin{aligned} \Delta &= f[y^2,\ h^2,\ yh \cos (\psi - \phi)] \\ &= \sum {}_{2i+k}C_{2j+k \cdot k}\, y^{2i+k} h^{2j+k} \cos^k (\psi - \phi), \end{aligned} \qquad (7)$$

where ${}_{2i+k}C_{2j+k \cdot k}$ is the intrinsic constant about the lens system,[3)] and the order of the aberration term is defined as

$$n = i + j + k - 1\ .$$

We calculate the necessary quantities from (4) and (7), and substitute them into (6), then we obtain a following expression, the quantities of the third and the higher order being neglected,

$$\begin{aligned} \Delta' = \Delta &+ A + B \cos (\psi_2 - \alpha) + C \cos (\phi_2 - \alpha) \\ &+ D \cos^2 (\psi_2 - \alpha) + E \cos^2 (\phi_2 - \alpha) \\ &+ F \cos (\psi_2 - \alpha) \cos (\phi_2 - \alpha)\ , \end{aligned} \qquad (8)$$

where

$$\left.\begin{aligned}
\varDelta &= \sum {}_{2i+k}c_{2j+k\cdot k}y_2{}^{2i+k}h_2{}^{2j+k}\cos_k(\psi_2-\phi_2)\\
A &= \sum [(it^2h_2{}^2+js^2y_2{}^2)\cos(\psi_2-\phi_2)ksty_2h_2]_{2i+k}c_{2j+k\cdot k}y_2{}^{2i+k-2}h_2{}^{2j+k-2}\cos^{k-1}(\psi_2-\phi_2)\\
B &= \sum [2ith_2\cos(\psi_2-\phi_2)+ksy_2]_{2i+k}c_{2j+k\cdot k}y_2{}^{2i+k-1}h_2{}^{2j+k-1}\cos^{k-1}(\psi_2-\phi_2)\\
C &= \sum [2jsy_2\cos(\psi_2-\phi_2)+kth_2]_{2i+k}c_{2j+k\cdot k}y_2{}^{2i+k-1}h_2{}^{2j+k-1}\cos^{k-1}(\psi_2-\phi_2)\\
D &= \sum [2i(i-1)t^2h_2{}^2\cos^2(\psi_2-\phi_2)+2kisty_2h_2\cos(\psi_2-\phi_2)+\tfrac{1}{2}k(k-1)s^2y_2{}^2\\
&\quad +(i+k/2)p^2y_2{}^2h_2{}^2\cos^2(\psi_2-\phi_2)]_{2i+k}c_{2j+k\cdot k}y_2{}^{2i+k-2}h_2{}^{2j+k-2}\cos^{k-2}(\psi_2-\phi_2)\\
E &= \sum [2j(j-1)s^2y_2{}^2\cos^2(\psi_2-\phi_2)+2jksty_2h_2\cos(\psi_2-\phi_2)+\tfrac{1}{2}k(k-1)t^2h_2{}^2\\
&\quad +(j+k/2)p^2y_2{}^2h_2{}^2\cos^2(\psi_2-\phi_2)]_{2i+k}c_{2j+k\cdot k}y_2{}^{2i+k-2}h_2{}^{2j+k-2}\cos^{k-2}(\psi_2-\phi_2)\\
F &= \sum [4ijsty_2h_2\cos^2(\psi_2-\phi_2)+2(jks^2y_2{}^2+kit^2h_2{}^2)\cos(\psi_2-\phi_2)\\
&\quad +k(k-1)sty_2h_2]_{2i+k}c_{2j+k\cdot k}y_2{}^{2i+k-2}h_2{}^{2j+k-2}\cos^{k-2}(\psi_2-\phi_2)\,.
\end{aligned}\right\}\quad (9)$$

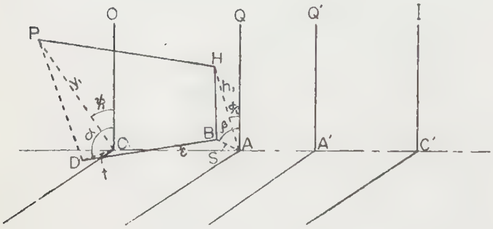

Fig. 1.

§ 3. Aberration for the Axial Object

In the special case, when the object point is on the axis, namely $y_2=0$, (8) becomes

$$\varDelta_0{}'=\varDelta_0+A_0+C_0\cos(\phi_2-\alpha)+E_0\cos^2(\phi_2-\alpha)\,, \tag{10}$$

and here

$$\left.\begin{aligned}
\varDelta_0 &= \sum_j {}_0c_{2j\cdot 0}h_2{}^{2j}\\
A_0 &= \sum [js^2{}_0c_{2j\cdot 0}+(st_1c_{2j+1\cdot 1}+t^2{}_2c_{2j\cdot 0})h_2{}^2]h^{2j-2}\\
C_0 &= \sum (2js_0c_{2j\cdot 0}+t_1c_{2j+1\cdot 1}h_2{}^2)h^{2j-1}\\
E_0 &= \sum [2j(j-1)s^2{}_0c_{2j\cdot 0}+2jst_1c_{2j+1\cdot 1}h_2{}^2\\
&\quad +t^2{}_2c_{2j+2\cdot 2}h_2{}^4+jp^2{}_0c_{2j\cdot 0}h_2{}^2]h_2{}^{2j-2}\,.
\end{aligned}\right\} \tag{11}$$

The first term of (10) is equal to the spherical aberration which is preserved constantly before and after decentering. The following terms correspond to the spherical aberration, coma and astigmatism, which have appeared by decentering. As s, t and p are small quantities of the same order, A_0 and E_0 are those of the second order.

For the usual lens systems of relatively wide aperture it is enough to take up to $n=2$ in the wave aberration formula,[4] and when we neglect the small quantities of the second order, we have from (10) and (11)

$$\varDelta'=({}_0c_{40}h_2{}^4+{}_0c_{60}h_2{}^6)+[(4s_0c_{40}+t_1c_{31})h_2{}^3+(6s_0c_{60}+t_1c_{51})h_2{}^5]\cos(\phi_2-\alpha)\,. \tag{12}$$

In this formula, ${}_0C_{40}$ and ${}_0C_{60}$ indicate the first and second order spherical aberrations and ${}_1C_{31}$ and ${}_1C_{51}$ indicate first and second order comas. Therefore, if one of them is not zero at least, the lens system will manifest coma for the axial object after decentering. After all for the axial object point the aberrations of the slightly decentred lens system are interpreted as the sum of the spherical aberration which had existed before decentering, and coma which appears after decentering.

The quantities s, t and p which appear by decentering are the small ones of the first order, and they can be calculated by paraxial ray tracing if the decentred values of the elements are known,[5] and then we can get the numerical values of the aberrations by these quantities.

§ 4. Acknowledgement

Finally, we desire to express our deep gratitude to Prof. H. Kubota for his kind and useful advices.

References

1) A. E. Conrady: M. N. Roy. Astr. Soc. **79** (1919) 384.

E. H. Linfoot: Proc. Phys. Soc. **58** (1946) 65.

A. Thomescheidt: Z. f. Inst-Kde **61** (1941) 201.

L. I. Epstein: J. O. S. A. **39** (1949) 847.

2) A. Maréchal: Comptes Rendus **228** (1949) 668.

A. Maréchal: Rev. d'Opt. **29** (1950) 1.

3) H. H. Hopkins: Wave Theory of Aberrations (1950) 50.

4) G. Tolardo di Francia: J. O. S. A. **43** (1953) 827.

5) F. Temmerman: Rev. d'Opt. **26** (1947) 423.

JOURNAL OF THE PHYSICAL SOCIETY OF JAPAN Vol. 9, No. 4, JULY—AUGUST, 1954

On the Subsonic Flow of a Compressible Fluid past an Axisymmetric Slender Body

By Ken-ichi KUSUKAWA

Department of Physics, Faculty of Science,
Tokyo Metropolitan University

(Read October 17, 1953; Received January 25, 1954)

Introducing new variables the fundamental equation for compressible fluid flow in the hodograph space is reduced to a form similar to that for incompressible fluid flow.

Safely neglecting the variation of the shape of an obstacle caused by the transformation, we can obtain the velocity distribution on the surface of the obstacle for the case of compressible fluid flow from the corresponding distribution on the surface of the same obstacle for the case of incompressible fluid flow (which is known theoretically or experimentally), with the aid of the following relations:

$$q_0=\frac{2}{(1+a)^{1/a}}\left(\frac{1+a\mu}{1-a\mu}\right)^{1/2a}\left(\frac{1-\mu}{1+\mu}\right)^{1/2},$$

$$\mu=(1-q^2/c^2)^{1/2}, \qquad a^2=(\gamma-1)/(\gamma+1),$$

where q_0, q, c and γ denote respectively the magnitudes of fluid velocity in incompressible and compressible fluid flows, the local speed of sound and the ratio of the specific heats.

As an example the velocity distributions on the surface of a prolate spheroid with thickness ratio $t=0.1$ are calculated for various Mach numbers and they are compared with the result obtained by the first approximation of the M^2-expansion method.

§ 1. Introduction

As is well known, the subsonic flow of a compressible fluid past an axisymmetric slender body can be easily dealt with by the linear theory, due originally to prandtl [1] and Glauert [2], which has been applied to the present problem by several writers [3], [4]. However, this method does not give a good approximation near the stagnation points where the perturbation velocity is not so small as to be negligible in comparison with the free stream velocity.

On the other hand, by using the successive approximations of the M^2-expansion method, due originally to Janzen [5] and Rayleigh [6], we can, in principle, approach the exact solution as closely as we want. In fact, this method is successfully used in the case of such low Mach numbers that even the first approximation can give a good result, but it is very laborious to obtain good approximation in the case of high Mach numbers where we need to take many terms of M^2-expansion because of the convergence of the series becoming very slow.

In this paper, the fundamental equation of compressible fluid flow in the hodograph space will be expressed in a simple form by the use of new variables, based on the assumption that the angle of inclination of the velocity is very small. This simple equation is formally equal to the hodograph equation for incompressible fluid flow. Thus we can obtain very easily the velocity distribution over the surface of an axisymmetric slender body, provided that numerical tables of new variables are prepared. In this connexion it will be of interest to mention here that an analogous procedure has been developed by Imai [7] for two-dimensional compressible flow and that the numerical table prepared by him can be immediately used in the present three-dimensional case.

§ 2. Fundamental Equations

We shall take the cylindrical coordinates 0-xy, where the x-axis is taken along the axis of revolution of the body and y denotes the distance from the axis. If we denote the velocity components along the x-and y-directions by u, v and the density of the fluid by ρ, the axisymmetric irrotational flow of a compressible inviscid fluid is governed by the equations:

$$\frac{\partial}{\partial x}(\rho y u)+\frac{\partial}{\partial y}(\rho y v)=0\,, \qquad (2.1)$$

$$\frac{\partial v}{\partial x}-\frac{\partial u}{\partial y}=0\,. \qquad (2.2)$$

If, instead of the velocity components u, v, we make use of the magnitude q and the angle of inclination θ of the velocity vector such that $u=q\cos\theta$, $v=q\sin\theta$, the above two equations become respectively

$$\begin{aligned} q\Big\{&\frac{\rho\sin\theta}{y}+\cos\theta\frac{\partial\rho}{\partial x}+\sin\theta\frac{\partial\rho}{\partial y} \\ &-\rho\sin\theta\frac{\partial\theta}{\partial x}+\rho\cos\theta\frac{\partial\theta}{\partial y}\Big\} \\ &+\rho\cos\theta\frac{\partial q}{\partial x}+\rho\sin\theta\frac{\partial q}{\partial y}=0, \qquad (2.3)\end{aligned}$$

$$\begin{aligned} q\Big\{\cos\theta\frac{\partial\theta}{\partial x}+\sin\theta\frac{\partial\theta}{\partial y}\Big\}+\sin\theta\frac{\partial q}{\partial x} \\ -\cos\theta\frac{\partial q}{\partial y}=0\,. \qquad (2.4)\end{aligned}$$

For a slender obstacle we may assume that (i) Except in the vicinity of the stagnation points, θ itself and spatial derivatives of q, θ and ρ are all very small so that the second and higher powers of these quantities can be neglected.

Thus, remembering that $\sin\theta\approx\theta$, $\cos\theta\approx 1$ when $q\neq 0$, Eqs. (2.3) and (2.4) become respectively

$$q\Big\{\frac{\rho\theta}{y}+\frac{\partial\rho}{\partial x}+\rho\frac{\partial\theta}{\partial y}\Big\}+\rho\frac{\partial q}{\partial x}=0\,, \qquad (2.5)$$

$$q\frac{\partial\theta}{\partial x}-\frac{\partial q}{\partial y}=0\,. \qquad (2.6)$$

(ii) At the stagnation points themselves we have $q=0$ and Eqs. (2.3) and (2.4) decome respectively

$$\cos\theta\frac{\partial q}{\partial x}+\sin\theta\frac{\partial q}{\partial y}=0\,, \qquad (2.7)$$

$$\sin\theta\frac{\partial q}{\partial x}-\cos\theta\frac{\partial q}{\partial y}=0\,. \qquad (2.8)$$

Hence we have

$$\partial q/\partial x=\partial q/\partial y=0\,. \qquad (2.9)$$

The same results can be obtained by putting $q=0$ in (2.5) and (2.6). Therefore we can conclude that Eqs. (2.5) and (2.6) can be used even at the stagnation points where the angle of inclination of the velocity is not always small.

We shall introduce the modified velocity potential φ satisfying (2.6) such that

$$\log q=\partial\varphi/\partial x\,, \qquad \theta=\partial\varphi/\partial y\,. \qquad (2.10)$$

Then using Bernoulli's theorem:

$$(c^2/\rho)d\rho+q\,dq=0\,, \qquad (2.11)$$

where $c=(dp/d\rho)^{1/2}$ is the local speed of sound, we obtain, from (2.5) and (2.10), the following fundamental equation:

$$\left(1-\frac{q^2}{c^2}\right)\frac{\partial^2\varphi}{\partial x^2}+\frac{\partial^2\varphi}{\partial y^2}+\frac{1}{y}\frac{\partial\varphi}{\partial y}=0\,. \qquad (2.12)$$

§ 3. Fundamental Equation in the Hodograph Space

Now we shall apply Legendre's transformation to (2.12). Thus putting

$$\left.\begin{aligned} &\partial\varphi/\partial x=\log q=Q\,, \qquad \partial\varphi/\partial y=\theta\,, \\ &x=\partial\omega/\partial Q\,, \qquad y=\partial\omega/\partial\theta\,, \\ &\omega=xQ+y\theta-\varphi\,, \end{aligned}\right\} \qquad (3.1)$$

we obtain the differential equation for determining the function ω with Q and θ as independent variables, namely:

$$\begin{aligned} &\left(1-\frac{q^2}{c^2}\right)\frac{\partial^2\omega}{\partial\theta^2}+\frac{\partial^2\omega}{\partial Q^2} \\ &+\left\{\frac{\partial^2\omega}{\partial Q^2}\frac{\partial^2\omega}{\partial\theta^2}-\left(\frac{\partial^2\omega}{\partial Q\partial\theta}\right)^2\right\}\frac{\theta}{\partial\omega/\partial\theta}=0\,. \qquad (3.2)\end{aligned}$$

§ 4. Approximations in the Hodograph Space

We shall consider the factor $K=1-q^2/c^2$ in the first term in (3.2). This K is of course a fixed function of q or Q. Thus, for the flow of gas obeying the adiabatic law $p\propto\rho^{\gamma}$, where γ is the ratio of the specific heats, we have

$$K=(1-q^2)/(1-a^2q^2)\,, \qquad a^2=(\gamma-1)/(\gamma+1).$$

If we introduce new variables τ and W such that

$$\left.\begin{aligned} &\tau=-\int K^{1/2}dQ=-\int\sqrt{1-q^2/c^2}\,dq/q\,, \\ &\omega=K^{-1/2}W\,, \end{aligned}\right\} \qquad (4.1)$$

then (3.2) becomes

$$\begin{aligned} &\frac{\partial^2 W}{\partial\theta^2}+\frac{\partial^2 W}{\partial\tau^2}+kW-n\frac{\partial W}{\partial\tau} \\ &\quad+\left[\left\{\frac{\partial^2 W}{\partial\tau^2}+kW-n\frac{\partial W}{\partial\tau}\right\}\frac{\partial^2 W}{\partial\theta^2}\right. \\ &\quad\left.-\left\{n\frac{\partial W}{\partial\theta}-\frac{\partial^2 W}{\partial\tau\partial\theta}\right\}^2\right]\frac{\theta}{\partial W/\partial\theta}=0\,, \qquad (4.2)\end{aligned}$$

where

$$k=K^{-1/2}\frac{d^2K^{-1/2}}{dQ^2}=\frac{(1-a^2)q^2}{(1-q^2)^3(1-a^2q^2)}\times\{2-(3a^2+5)q^2+6a^2q^4\}\ ,$$

$$n=\frac{dK^{-1/2}}{dQ}=\frac{(1-a^2)q^2}{(1-q^2)^{3/2}(1-a^2q^2)^{1/2}}\ .$$

We now discuss the orders of magnitude of various terms in Eq. (4.2). To do this, we note that

(i) In the vicinity of the stagnation points, all the terms kW, $n\partial W/\partial\tau$ and $n\partial W/\partial\theta$ can be neglected in comparison with other terms, since k and n are of the order of q^2.

(ii) Except in the vicinity of the stagnation points, the flow of gas is nearly parallel to the x-axis, so that $|W|$, $|\theta|$, and the spatial derivatives of q and θ are all very small.

On the other hand, following relations may exist:

$$\partial W/\partial\tau\sim O(x) \quad\text{and}\quad \partial W/\partial\theta\sim O(y)\ ,$$

and hence

$$\frac{\partial^2W}{\partial\tau^2}\sim O\left(q\frac{\partial x}{\partial q}\right),\quad \frac{\partial^2W}{\partial\tau\partial\theta}\sim O\left(q\frac{\partial y}{\partial q}\right),$$
$$\frac{\partial^2W}{\partial\theta^2}\sim O\left(\frac{\partial y}{\partial\theta}\right).$$

Thus, as in the vicinity of the stagnation points, all the terms kW, $n\partial W/\partial\tau$ and $n\partial W/\partial\theta$ can be neglected in comparison with other terms.

(iii) At a great distance from the obstacle, $\partial W/\partial\tau$ and $\partial W/\partial\theta$ may become very large, since they are of the same order of magnitude as x and y respectively. But, making use of the relations:

$$\lim_{x\to\infty} x\frac{\partial q}{\partial x}=0\ ,\quad \text{etc.},$$

it can be shown that the terms $\partial^2W/\partial\tau^2$, $\partial^2W/\partial\tau\partial\theta$ and $\partial^2W/\partial\theta^2$ become infinity of the order higher than $\partial W/\partial\tau$ and $\partial W/\partial\theta$.

Thus, finally Eq. (4.2) can be approximated very closely to

$$\frac{\partial^2W}{\partial\theta^2}+\frac{\partial^2W}{\partial\tau^2}+\left[\frac{\partial^2W}{\partial\tau^2}\frac{\partial^2W}{\partial\theta^2}-\left(\frac{\partial^2W}{\partial\tau\partial\theta}\right)^2\right]\frac{\theta}{\partial W/\partial\theta}=0\ . \qquad (4.3)$$

§ 5. Corresponding Incompressible Fluid Flow

In the case of incompressible fluid flow, we have the equations which correspond respectively to Eqs. (2.5) and (2.6) for compressible fluid flow, namely:

$$q_0\frac{\theta_0}{y}+q_0\frac{\partial\theta_0}{\partial y}+\frac{\partial q_0}{\partial x}=0\ , \qquad (5.1)$$

$$q_0\frac{\partial\theta_0}{\partial x}-\frac{\partial q_0}{\partial y}=0\ . \qquad (5.2)$$

Introducing the modified velocity potential φ_0 such that

$$\log q_0=\partial\varphi_0/\partial x\ ,\qquad \theta_0=\partial\varphi_0/\partial y\ , \quad (5.3)$$

we get from (5.1) and (5.2),

$$\frac{\partial^2\varphi_0}{\partial x^2}+\frac{\partial^2\varphi_0}{\partial y^2}+\frac{1}{y}\frac{\partial\varphi_0}{\partial y}=0\ . \qquad (5.4)$$

To this equation we apply Legendre's transformation. Thus, putting

$$\left.\begin{aligned}&\partial\varphi_0/\partial x=\log q_0=Q_0=-\tau_0\ ,\qquad \partial\varphi_0/\partial y=\theta_0\ ,\\ &x=\partial\omega_0/\partial Q_0\ ,\qquad y=\partial\omega_0/\partial\theta_0\ ,\\ &\omega_0=xQ_0+y\theta_0-\varphi_0\ ,\end{aligned}\right\} \qquad (5.5)$$

we obtain the differential equation for determining the function ω_0 with τ_0 and θ_0 as independent variables, namely:

$$\frac{\partial^2\omega_0}{\partial\theta_0^2}+\frac{\partial^2\omega_0}{\partial\tau_0^2}+\left[\frac{\partial^2\omega_0}{\partial\tau_0^2}\frac{\partial^2\omega_0}{\partial\theta_0^2}-\left(\frac{\partial^2\omega_0}{\partial\tau_0\partial\theta_0}\right)^2\right]\frac{\theta_0}{\partial\omega_0/\partial\theta_0}=0\ . \qquad (5.6)$$

It is of great importance to note that this equation is formally equal to the fundamental Eq. (4.3) for compressible fluid flow in the $\tau\theta$-space. Thus, if we know an incompressible flow pattern expressed by $\omega_0(\tau_0,\theta_0)$, we can immediately obtain a corresponding compressible flow pattern $\omega(\tau,\theta)$ by making use of the following relations between the variables:

$$\left.\begin{aligned}&\theta_0=\theta\ ,\\ &-\tau_0=Q_0=-\tau=\int^q\sqrt{1-q^2/c^2}\,dq/q\ .\end{aligned}\right\} \quad (5.7)$$

In the case of the adiabatic gas, the second equation becomes

$$\left.\begin{aligned}&q_0=e^{-\tau}=C\left(\frac{1+a\mu}{1-a\mu}\right)^{1/2a}\left(\frac{1-\mu}{1+\mu}\right)^{1/2},\\ &\mu=K^{1/2}=(1-q^2/c^2)^{1/2}\ ,\end{aligned}\right\} \quad (5.8)$$

where C is an arbitrary constant which can be conveniently determined by the requirement that $q_0\to q$ as $q\to 0$. We then have

$$C=2(1+a)^{-1/a}\ .$$

It may be of interest to remark here that the relation between q and q_0 as expressed by (5.8) is quite the same as the corresponding relation introduced by Imai [7], [8] in the case of two-dimensional irrotational flow.

§ 6. Boundary Conditions

We now consider the relation between the boundaries of compressible and incompressible fluid flows. In the case of compressible flow, the variables x and y can be expressed as functions of τ and θ in the forms:

$$\left.\begin{aligned} dx&=-\left(\frac{\partial^2 W}{\partial\tau^2}d\tau+\frac{\partial^2 W}{\partial\tau\partial\theta}d\theta\right), \\ dy&=K^{-1/2}(\tau)\left(\frac{\partial^2 W}{\partial\tau\partial\theta}d\tau+\frac{\partial^2 W}{\partial\theta^2}d\theta\right), \end{aligned}\right\} \quad (6.1)$$

while, in the case of incompressible flow we have

$$\left.\begin{aligned} dx_0&=-\left(\frac{\partial^2 \omega_0}{\partial\tau_0{}^2}d\tau_0+\frac{\partial^2 \omega_0}{\partial\tau_0\partial\theta_0}d\theta_0\right), \\ dy_0&=\frac{\partial^2 \omega_0}{\partial\tau_0\partial\theta_0}d\tau_0+\frac{\partial^2 \omega_0}{\partial\theta_0{}^2}d\theta_0 \,. \end{aligned}\right\} \quad (6.2)$$

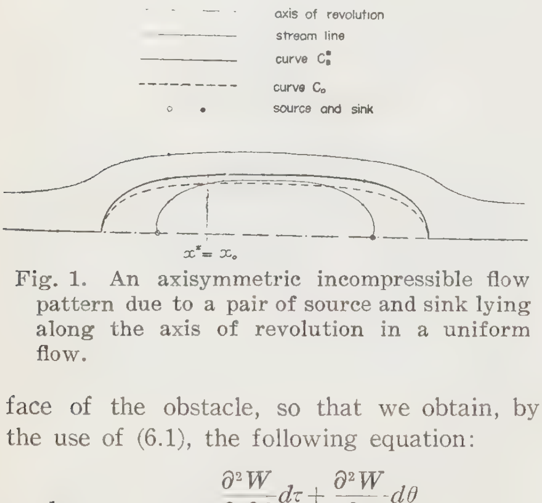

Fig. 1. An axisymmetric incompressible flow pattern due to a pair of source and sink lying along the axis of revolution in a uniform flow.

In the physical space of compressible flow, the gas must flow tangentially along the surface of the obstacle, so that we obtain, by the use of (6.1), the following equation:

$$\frac{dy}{dx}=-K^{-1/2}(\tau)\frac{\dfrac{\partial^2 W}{\partial\tau\partial\theta}d\tau+\dfrac{\partial^2 W}{\partial\theta^2}d\theta}{\dfrac{\partial^2 W}{\partial\tau^2}d\tau+\dfrac{\partial^2 W}{\partial\tau\partial\theta}d\theta}$$

$$=\tan\theta \quad \text{on } C_B\,, \qquad (6.3)$$

where C_B is the meridian curve of the obstacle. If we make use of (5.7) and (6.2), this equation becomes

$$\frac{dy}{dx}=-K^{-1/2}(\tau_0)\frac{\dfrac{\partial^2 \omega_0}{\partial\tau_0\partial\theta_0}d\tau_0+\dfrac{\partial^2 \omega_0}{\partial\theta_0{}^2}d\theta_0}{\dfrac{\partial^2 \omega_0}{\partial\tau_0{}^2}d\tau_0+\dfrac{\partial^2 \omega_0}{\partial\tau_0\partial\theta_0}d\theta_0}$$

$$=K^{-1/2}(\tau_0)\frac{dy_0}{dx_0}=\tan\theta_0\,. \qquad (6.4)$$

Hence $dy_0/dx_0=K^{1/2}(\tau_0)\tan\theta_0$ on curve C_0, say. (6.5)

The curve C_0 cannot be the boundary of the obstacle for incompressible fluid flow, since the gas does not flow tangentially along the curve C_0 but crosses it. (In fact, the condition that the gas flows tangentially along the curve C_0 should be expressed by $dy_0/dx_0=\tan\theta_0$.)

If we consider an axisymmetric incompressible flow pattern due to a certain distribution of sources and sinks along the axis of revolution in a uniform flow, it is recognized that the curve C_0 lies in the interior of the boundary of an obstacle denoted by a curve C_B^* on which the following condition is satisfied:

$$dy^*/dx^*=\tan\theta_0{}^* \quad \text{on } C_B^*\,, \qquad (6.6)$$

where (dx^*, dy^*) is the line element along the curve C_B^* and $\theta_0{}^*$ is the angle of inclination of the velocity at a point on C_B^* (cf. Fig. 1).

If an obstacle is slender, the flow is nearly parallel to the x-axis except near the stagnation points, while the value of $K^{1/2}(\tau_0)$ is almost equal to unity in the vicinity of the stagnation points. Hence we may safely assume that at the two points having the same abscissa $(x_0=x^*)$ on the curves C_0 and C_B^*, the inclinations of the velocity θ_0 and $\theta_0{}^*$ will take almost the same values. Thus, putting

$$\theta_0=\theta_0{}^* \quad \text{at} \quad x_0=x^*\,, \qquad (6.7)$$

Eq. (6.5) becomes

$$dy_0/dx_0=K^{1/2}(\tau_0)\tan\theta_0{}^*\,, \qquad (6.8)$$

which, by the use of (6.6), becomes

$$dy_0/dx_0=K^{1/2}(\tau_0)dy^*/dx^*\,. \qquad (6.9)$$

Comparing this with (6.4) we obtain

$$dy/dx=dy^*/dx^*\,, \qquad (6.10)$$

from which it will be seen that the shape of the boundary of an obstacle in compressible flow is quite the same as that of the corresponding obstacle in the correlated incompressible flow.

If this correspondence of the boundaries is used, we can find the magnitude q of the velocity of compressible flow on the surface of an obstacle with the aid of the relation (5.8), provided the magnitude of the velocity of incompressible flow on the surface of the same obstacle can be known theoretically or experimentally, and for this purpose we can conveniently use the numerical tables for the

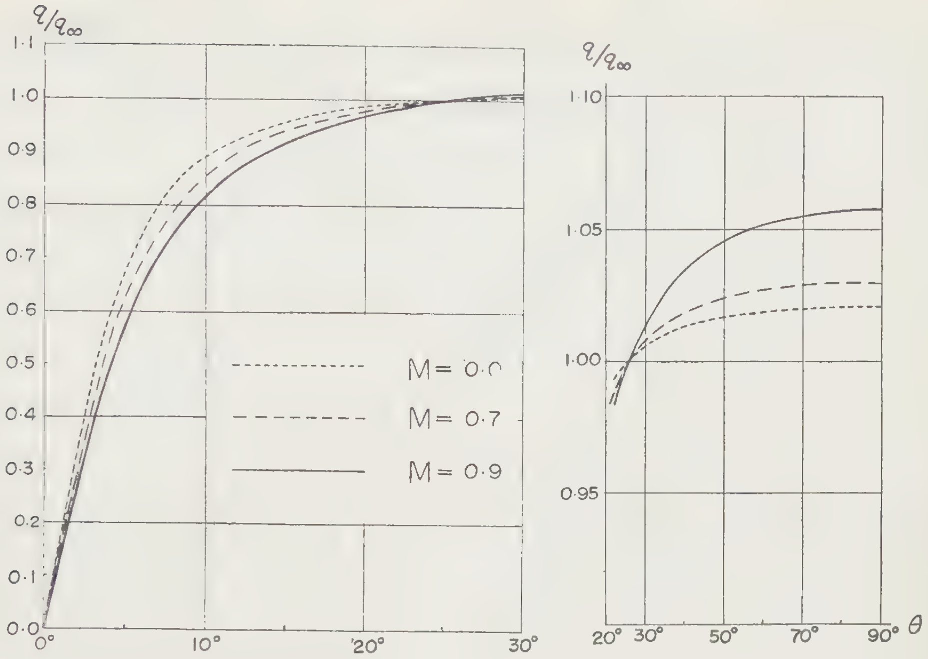

Fig. 2. Velocity distributions on the surface of a prolate spheroid with thickness ratio $t=0.1$ for $M=0$, 0.7 and 0.9.

relation (5.8). which has been given in Imai's papers [7], [9].

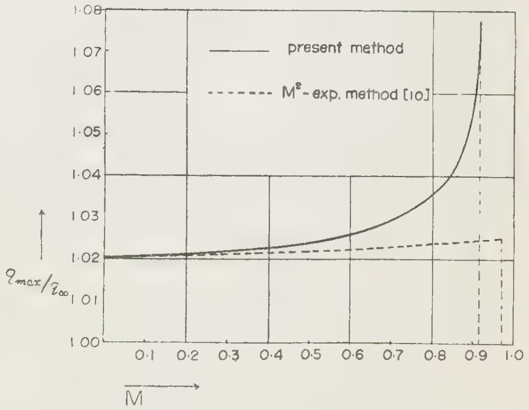

Fig. 3. Variation With the Mach number of the ratio of the maximum velocity occurring at the end of the minor axis of a prolate spheroid with thickness ratio $t=0.1$ to the free-stream velocity.

§ 7. A Numerical Example

As an example, we shall investigate the velocity distributions on the surface of a prolate spheroid of thickness ratio $t=0.1$ for several Mach numbers. As is well known, the magnitude of velocity of incompressible flow on the surface of a prolate spheroid is expressed by

$$\left.\begin{aligned} &q_0=Bq_{0\infty}\frac{\sin\theta}{\sqrt{1-e^2\cos^2\theta}}\,,\\ &B=e^2\Big/\left(1-\frac{1-e^2}{2e}\log\frac{1+e}{1-e}\right),\\ &t=c/a=\sqrt{1-e^2}\,,\\ &x=a\cos\theta\,,\qquad y=c\sin\theta\,,\end{aligned}\right\}\qquad(7.1)$$

where a, c and $q_{0\infty}$ are respectively the semi-major and semi-minor axes of the prolate spheroid and the free-stream velocity. If we take $t=0.1$ the value of B becomes 1.02071.

On the other hand, between the free-stream velocity q_∞ and the free-stream Mach number M in compressible flow there exists the relation:

$$q_\infty{}^2=\frac{\frac{1}{2}(\gamma+1)M^2}{1+\frac{1}{2}(\gamma-1)M^2}\,.\qquad(7.2)$$

Thus, starting from the incompressible flow velocity distribution as given by (7.1), we have calculated, with the aid of (5.8) and (7.2), the velocity distributions of compressible flow for $M=0.7$ and 0.9. The values of q/q_∞ thus calculated are shown in Fig. 2. The points on the surface at which $q=q_\infty$ are the same for all Mach numbers; this is due to the assumed simple correspondence between the boundaries of the obstacle in the physical and the hodograph planes.

Recently, Hida [10] has dealt with the present problem by the M^2-expansion method. He calculated the velocity distribution correct to the order of M^2 on the surface of the prolate spheroid with thickness ratio $t=0.9$. Because of the computational difficulty, however, he did not obtain the velocity distribution on the whole surface in the case of such a small thickness ratio as 0.1. But he has calculated the ratio of the maximum velocity occurring at the end of the minor axis to the free-stream velocity as a function of the Mach number, which can also be obtained by the present method.

Both results are shown in Fig. 3. It will be seen that at low Mach numbers both methods give almost the same values, but at high Mach numbers the values obtained by the present method become larger than those obtained by the first approximation of the M^2-expansion method. It may be expected, however, that if we proceed to calculate similar values correct to the order of M^4, M^6, ... by using the second and higher approximate solutions, they will approach to those obtained by the present method.

The critical Mach number at which the fluid velocity first becomes equal to the local speed of sound becomes 0.9153 by the present method, while it is 0.972 by the first approximation of the M^2-expansion method [10] and 0.962 by the linear theory. (This value 0.962 has been re-estimated by Hida from Sears's note [11].) Considering that the approximations of these three methods fail near the critical Mach number because of different reasons, this large difference among these three values of the critical Mach number is not surprising.

The writer wishes to express his heartiest gratitude to professor I. Imai for his many useful suggestions and kind advice on this work.

References

1) L. Prandtl: Handbuch der Physik, Band VII (1927) 340.
2) H. Glauert: Proc. Roy. Soc. **A 118** (1927) 113.
3) R. Sauer: Theoretische Einführung in die Gasdynamik (Springer, Berlin), (1943).
4) E. V. Laitone: Quart. Appl. Math. **5** (1947) 227.
5) O. Janzen: Phys. Zeits. **14** (1913) 639.
6) Lord Rayleigh: Phil. Mag. **32** (1916) 1.
7) I. Imai: Journ. Phys. Soc. Japan **3** (1948) 352.
8) I. Imai: Journ. Math. and Phys. **28** (1949) 173.
9) I. Imai and H. Hasimoto: Journ. Math. and Phys. **28** (1950) 205.
10) K. Hida: Journ. Phys. Soc. Japan **8** (1953) 257.
11) W. R. Sears: Quart. Appl. Math. **4** (1946) 89.

JOURNAL OF THE PHYSICAL SOCIETY OF JAPAN Vol. 9, No. 4, JULY—AUGUST, 1954

Rayleigh's Problem for a Cylinder of Arbitrary Shape

By Hidenori HASIMOTO

Department of Physics, Faculty of Science, University of Tokyo

(Received March 27, 1954)

The motion of an incompressible viscous fluid generated by a cylinder of arbitrary cross-sectional form which is started to move suddenly from rest with uniform velocity in the direction of its length is considered. By using Laplace transform and complex variables, asymptotic expansion formulae in powers of $a^2/(\nu t)$ are derived for the velocity distribution (valid in the vicinity of the cylinder) and for the frictional drag on the cylinder, correct to the order of $a^2/(\nu t)$, where a is the characteristic length of the cross section, ν is the kinematic viscosity, and t is the time. These formulae are given in terms of only the analytic function which maps conformally the region outside the cross section of the cylinder onto the region outside the unit circle, and of certain integrals $E_n{}^m(a/\sqrt{\nu t})$ which are common to any arbitrary cylinder. In particular, when $a/\sqrt{\nu t}$ is sufficiently small, the total frictional drag on the cylinder per unit length is expressed as $4\pi\mu W E_0(a/\sqrt{\nu t}) \sim 4\pi\mu W(\beta^{-1}-\gamma\beta^{-2}\cdots)$, irrespective of the cross-sectional form, where $\beta=-2[\gamma+\log(a/\sqrt{4\nu t})]$, and $\gamma=0.5772\cdots$ (Euler's constant).

§ 1. Introduction

In 1911 Rayleigh[12] considered the following problem: with Cartesian coordinates (x, y, z) an infinitely thin flat plate coincident with the plane $y=0$ is initially at rest surrounded by an incompressible viscous fluid also at rest: starting at time $t=0$ the plate is made to move uniformly with velocity W parallel to the z-axis, and we are required to determine the subsequent motion of the fluid.

The significance of this problem is great, especially from the point of view of the boundary-layer theory. The boundary-layer nature of the motion of the fluid is easily observed from the velocity distribution obtained,

$$w=W[1-\operatorname{erf} \tfrac{1}{2}y(\nu t)^{-1/2}]\,,$$

where ν is the kinematic viscosity. Also, replacing t by z/W in his unsteady flow solution, Rayleigh formed a qualitative picture of the Blasius problem of the steady flow past a semi-infinite plate $y=0$, $z\geqslant 0$, whose leading edge is normal to the direction of flow.

Recently, interest is developing in the three-dimensional boundary-layer theory. Howarth[5] appreciated the significance of 'Rayleigh's' problem, and treated the corresponding problem for a semi-infinite plate coincident with the half-plane $y=0$, $x\geqslant 0$, in order to throw some light on the flow past an infinite quarter-plate and on the edge effect on the boundary-layer growth. With a view to studying the corner effect, the author[3] discussed the problem for a bent flat plate of angle α; the same problem has also been discussed independently by Sowerby[14] and by Sowerby and Cooke[15]. Jaeger[8] also treated the corresponding heat conduction problem from a different point of view.

In these papers the width of the plate is infinite. The total skin friction D for a plate of finite breadth with corners and edges is given approximately by the formula

$$D=2\mu W[\overline{D}_R\times\Sigma L_i+\Sigma E_i]\,, \qquad (1.1)$$

where $\overline{D}_R=1/\sqrt{\pi\nu t}$ (Rayleigh's uniform friction per unit width for one side of an infinite flat plate), μ is the viscosity, ΣL_i is the total width of the plate, and ΣE_i is the sum of the so-called edge and corner correction constants. If $L_i/\sqrt{\nu t}$ is small the interference between edges and corners becomes so large that this approximation fails, and the effect of the curvature of the plate is also great. In a previous paper[4] the author studied the edge effect for a plate of finite breadth $2a$, using the Laplace transform and the integral equation for the vorticity distribution on the plate. As far as $a>\sqrt{\nu t}$ the approximation of (1.1) is good. On the other hand, the approximation is poor when $a<\sqrt{\nu t}$; however, the asymptotic solution in powers of $a^2/(\nu t)$ obtained by the author has been found to give a satisfactory result for this case and moreover give a smooth matching with (1.1) in the intermediate values of $a/\sqrt{\nu t}$, if the first two terms are taken and the terms higher than $a^2/(\nu t)$ are discarded.

In this paper the author discusses the problem from the most general point of view for the case of an infinitely long cylinder with an arbitrary cross-sectional form moving in the direction of its length.

Apart from the application to the boundary-layer theory, the solution is useful for the corresponding typical problem of heat conduction in solids and diffusion etc., because the defining equation is the same as the partial differential equation of heat conduction. Replacing velocity by temperature or concentration and ν by thermometric conductivity or diffusivity is only necessary.

In this connection we must mention the research work on heat conduction problem for a circular cylinder by several authors[1][2][8][9][10][11][13][16] and an elliptic cylinder and a plate of finite breadth by Tranter[17]. Although their treatment is rigorous, the numerical calculation seems to be very laborious. Especially with Tranter's solution, which is expressed as series of integrals of Mathieu functions, it would require prohibitive labour to proceed exactly ; in fact the numerical calculation is not carried out in his paper. Using the Laplace transform and complex variables, the author obtained the general asymptotic expansion formulae, in powers of $a^2/(\nu t)$, for the velocity distribution (valid in the vicinity of the cylinder) and for the frictional drag on the cylinder ; they are correct to the order of $O(a^2/\nu t)$, where a is the characteristic length of the cross section. They seem to give satisfactory approximation as far as $a/\sqrt{\nu t}<1$. For the actual evaluation it is only necessary to know the mapping function which maps conformally the region outside the cross section onto the region outside the unit circle, and the integrals $E_n{}^m(a/\sqrt{\nu t})$ which are common to any arbitrary cylinder. Values of $E_n{}^m$ have been calculated for some values of $a/\sqrt{\nu t}$ in Appendix and § 7. Application to cylinders of some cross-sectional form is made in § 7. The previous results obtained for a plate of finite breadth are derived as a special case.

§ 2. Fundamental Equations

The equations of motion and continuity possess a solution for which the velocity components parallel to the x- and y-axes vanish everywhere, provided w, the velocity component parallel to the z-axis, can be found as a function of x, y satisfying the equation

$$\frac{\partial w}{\partial t}=\nu\Delta w=\nu\left(\frac{\partial^2}{\partial x^2}+\frac{\partial^2}{\partial y^2}\right)w\ , \tag{2.1}$$

subject to the initial condition

$$\phi=w/W=0 \quad \text{when} \quad t=0\ , \tag{2.2}$$

and the boundary conditions when $t>0$

$\phi=w/W$

$=1$ at the surface of the cylinder: $\bar{S}$, (2.3)

$\to 0$ as $R^2=x^2+y^2\to\infty$. (2.4)

Multiplying (2.1) by e^{-pt}, integrating with respect to t from 0 to ∞, and using (2.2) we obtain

$$(\Delta-k^2)\phi^*=0\ , \tag{2.5}$$

for the Laplace transform of ϕ

$$\phi^*(x,\ y,\ p)=\int_0^\infty \phi(x,\ y,\ t)e^{-pt}dt\ , \tag{2.6}$$

where

$$k^2=p/\nu \qquad (\mathbf{Re}\ p>0). \tag{2.7}$$

From (2.3) and (2.4) we see that the boundary conditions on the function ϕ^* are

$$\phi^*=1/p \quad \text{on } \bar{S} \tag{2.8}$$

$$\phi^*\to 0 \quad \text{as} \quad R\to\infty. \tag{2.9}$$

The exact determination of ϕ^* is difficult for the general shape of cylinder, and the calculation of ϕ from ϕ^* by the inverse Laplace transform

$$\phi=\frac{1}{2\pi i}\int_{c-i\infty}^{c+i\infty} e^{pt}\phi^* dp \quad (c>0), \tag{2.10}$$

is laborious even in the case of a circular cylinder (radius a), where ϕ^* and ϕ are found to be

$$\phi^*=\frac{K_0(kr)}{pK_0(ka)}\ , \tag{2.11}$$

$$\phi=1+\frac{2}{\pi}\int_0^\infty e^{-\nu u^2 t}\,\frac{J_0(ur)Y_0(ua)-Y_0(ur)J_0(ua)}{J_0{}^2(ua)+Y_0{}^2(ua)}\,\frac{du}{u} \tag{2.12}$$

By consideration of dimensions, we know

that ψ has a similar functional form for cylinders having similar cross sections, if the value of

$$s=a/\sqrt{\nu t}\ , \qquad (2.13)$$

is the same, where a is any length defining the scale of the cross section (e.g. the radius a in the case of a circular cylinder). When a is small compared with $\sqrt{\nu t}$, i.e. when $s \ll 1$, we can find a general asymptotic solution for an arbitrary cross-sectional form, by investigating the behaviour of ψ^* when ka is small (see Appendix).

§ 3. Introduction of Complex Variables and Expansion in Powers of k^2a^2

Introducing complex variable ζ and its complex conjugate $\bar{\zeta}$

$$\zeta=x+iy\ , \quad \bar{\zeta}=x-iy\ , \qquad (3.1)$$

the region outside the cylinder: $\zeta=\zeta_p$ in the ζ-plane can be mapped conformally onto the region outside the unit circle: $Z=\exp(i\theta)$ in the Z-plane by means of analytic function $f(Z)$ of the form

$$\zeta=f(Z)=ag(Z)\ ,$$

$$g(Z)=Z+\sum_{n=1}^{\infty} C_n Z^{-n} \quad (Z>1), \qquad (3.3)$$

whose existence is asserted by the theory of functions, and which is easily found by the theory of arbitrary wing sections in aerodynamics[6)7)].

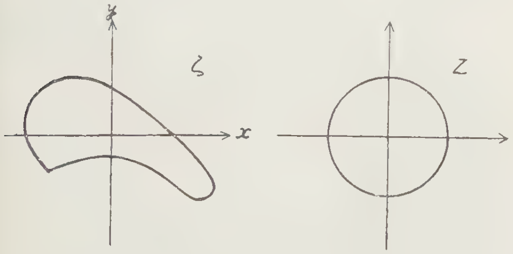

ζ-plane ; Z-plane.

Fig. 1.

Then (2.5) can be put in the form:

$$\frac{\partial^2}{\partial Z \partial \bar{Z}}\psi^*=\frac{k^2a^2}{4}g'\bar{g}'\psi^*\ , \qquad (3.4)$$

which must be solved with the boundary conditions:

i) ψ^* is one-valued, real and continuous in the field of flow, (3.5)

ii) $\psi^* \rightarrow 0$ as $|Z| \rightarrow \infty$, (3.6)

iii) $\psi^*=1/p$ on $\bar{S}$, accordingly at $Z\bar{Z}=1$, (3.7)

corresponding to (2.8) and (2.9). As far as the solution of (3.4) is concerned, we treat k and p as though they are real and positive.

The asymptotic solution of (2.1) when $a/\sqrt{\nu t} \ll 1$ corresponds to the solution of (3.4) when $ka \ll 1$. In the first approximation we may neglect the right-hand side of (3.4), in the vicinity of the cylinder. Physically speaking, when $a \ll \sqrt{\nu t}$ the flow becomes almost stationary ($w \sim W$) except in the region ($R \gtrsim \sqrt{\nu t}$) at a great distance from the cylinder.

Acting on an idea suggested by these considerations we assume that ψ^* can be expanded into

$$\psi^*=\sum_{n=0}^{\infty}\left(\frac{k^2a^2}{4}\right)^n \psi_n^*, \qquad (3.8)$$

in the vicinity of the cylinder.

Substituting (3.8) into (3.4) and equating the same powers of k^2a^2 we get

$$\frac{\partial^2 \psi_0}{\partial Z \partial Z}=0\ , \qquad (3.9)$$

$$\frac{\partial^2 \psi_1^*}{\partial Z \partial Z}=g'\bar{g}'\psi_0^*, \qquad (3.10)$$

$$\cdots\cdots \quad .$$

Integrating (3.9), (3.10) successively we obtain

$$\psi_0^*=F_0(Z)+c.c., \qquad (3.11)$$

$$\psi_1^*=[\bar{g}\int F_0 g' dZ+F_1(Z)]+c.c., \qquad (3.12)$$

$$\cdots\cdots \quad .$$

where $F_0(Z)$, $F_1(Z)$, $\cdots$ are the analytic functions of Z to be determined by the boundary conditions (3.5)–(3.7), and $c.c.$ denotes complex conjugate.

In order to match these solutions valid in the vicinity of cylinder with the condition (3.6) at infinity, the harmonic parts $F_n(Z)+\bar{F}_n(\bar{Z})$ must not be taken arbitrarily, but are obliged to obey some conditions.

§ 4. Harmonic Part of ψ^*

Using cylindrical coordinates $(R,\ \Theta)$

$$x=R\cos\Theta, \qquad y=R\sin\Theta, \qquad (4.1)$$

the fundamental solution of (2.5) satisfying the condition at infinity (2.4) is given by

$$\psi^*=\sum_{n=0}^{\infty}(A_n\cos n\Theta+B_n\sin n\Theta)K_n(kR)\ , \qquad (4.2)$$

where K_n denotes the modified Bessel function which vanishes exponentially at infinity. When $kR \ll 1$, by use of the expressions for $K_n(kR)$;

$$K_0(kR) \sim -\gamma - \log(kR/2)\,, \tag{4.3}$$

$$K_n(kR) \sim \frac{1}{2}\frac{(n-1)!}{(kR/2)^n}\,, \tag{4.4}$$

$$\gamma = 0.5772\cdots \text{ (Euler's constant)}\,, \tag{4.5}$$

ψ^* reduces to

$$\psi^* \sim A_0\left(-\gamma - \log\frac{kR}{2}\right) + \sum_{n=1}^{\infty} 2^{n-1}(n-1)! \times (A_n \cos n\Theta + B_n \sin n\Theta)(kR)^{-n}, \tag{4.6}$$

which is the only harmonic part in ψ^*, as has already been expected in (3.9).

In terms of complex variables $\zeta = Re^{i\Theta}$, $\bar{\zeta} = Re^{-i\Theta}$, (4.6) is the linear combination of

$$-\gamma - \log(k\zeta/2),\ \zeta^{-n} \text{ and their } c.c., \tag{4.7}$$

or, introducing (3.2), (3.3) into these expressions and using

$$\begin{aligned}\log\zeta &= \log a(Z + c_1 Z^{-1} + \cdots) \\ &= \log a + \log Z + c_1 Z^{-2} + \cdots,\end{aligned} \tag{4.8}$$

$$\begin{aligned}\zeta^{-n} &= a^{-n} Z^{-n}(1 + c_1 Z^{-2} + \cdots) \\ &= a^{-n}(Z^{-n} - c_1 Z^{-n-2} - \cdots), \\ &\qquad |Z| > 1,\end{aligned} \tag{4.9}$$

the harmonic parts in ψ^*, i.e. $F_n(Z)$ and $\bar{F}_n(\bar{Z})$ in (3.11) etc. must be expressed respectively by linear combination of

$$\begin{matrix} S - \log Z, & Z^{-n}, \\ S - \log \bar{Z}, & \bar{Z}^{-n}, \end{matrix} \quad (n = 1, 2, \cdots) \tag{4.10}$$

where

$$S = -\gamma - \log(ka/2)\,. \tag{4.11}$$

This is the condition mentioned in the last paragraph of § 3.

§ 5. Determination of ψ_0 and ψ_1

Using (4.10), (3.5), (3.7), and the fact that

$$\log Z\bar{Z} = 0 \text{ when } Z\bar{Z} = 1, \tag{5.1}$$

$F_0(Z)$ in (3.11) is easily seen to be

$$F_0(Z) = \frac{1}{2pS}(S - \log Z)\,. \tag{5.2}$$

The boundary condition to be satisfied by ψ_n^* at $\bar{S}$ becomes

$$\psi_n^* = 0 \text{ when } Z\bar{Z} = 1 \ (n > 1) \tag{5.3}$$

Introducing F_0 determined by (5.2) into (3.12) we obtain

$$\psi_1^* = \frac{1}{2pS}\left[g\bar{g}(S - \log Z) + \bar{g}\int g\,\frac{dZ}{Z}\right] + F_1(Z) + c.c., \tag{5.4}$$

where

$$\begin{aligned} g\bar{g} &= Z\bar{Z} + Z\sum_{n=1}^{\infty}\bar{c}_n\bar{Z}^{-n} + \bar{Z}\sum_{n=1}^{\infty} c_n Z^{-n} \\ &\quad + \sum_{m=1}^{\infty}\sum_{n=1}^{\infty} c_m\bar{c}_n Z^{-m}\bar{Z}^{-n}, \\ \bar{g}\int g\,\frac{dZ}{Z} &= Z\bar{Z} + Z\sum_{n=1}\bar{c}_n\bar{Z}^{-n} - \bar{Z}\sum_{n=1}^{\infty} n^{-1} c_n Z^{-n} \\ &\quad - \sum_{m=1}^{\infty}\sum_{n=1}^{\infty} m^{-1} c_m\bar{c}_n Z^{-m}\bar{Z}^{-n}\,. \end{aligned} \tag{5.5}$$

Taking account of (3.5), (3.7), (5.4), and (5.5) $F_1(Z)$ is determined as follows:

$$\begin{aligned} F_1(Z) = -\frac{1}{2pS}\Bigg[&(1 + \sum_{n=1}^{\infty} c_n\bar{c}_n)(S - \log Z) \\ &+ 2S\sum_{n=1}^{\infty} c_n Z^{-(n+1)} + 2S\sum_{m>n}^{\infty} c_m\bar{c}_n Z^{-(m-n)} \\ &+ \Bigg\{\frac{1}{S}\left(1 - \sum_{n=1}^{\infty} n^{-1} c_n\bar{c}_n\right)(S - \log Z) \\ &+ \sum_{n=1}^{\infty} c_n(1 - n^{-1}) Z^{-(n+1)} \\ &- \sum_{m>n}^{\infty}(m^{-1} + n^{-1}) c_m\bar{c}_n Z^{-(m-n)}\Bigg\}\Bigg]. \end{aligned} \tag{5.6}$$

In order to interpret $\psi^* = \psi_0^* + (a^2k^2/4)\psi_1^* \cdots$ by the formula (2.10), we need interpretation of $p^{-1}S^{-m}(ak)^{2n}$, which is given in Appendix. Then we have

$$w/W = \psi = \varphi_0 - (a^2/\nu t)\varphi_1 - O(a^4/\nu^2 t^2), \tag{5.7}$$

where

$$\varphi_0 = \psi_0 = 1 - E_0 \log Z\bar{Z}\,, \tag{5.8}$$

$$\begin{aligned} \varphi_1 = \frac{1}{4}E_1 \cdot \Bigg[&\bar{g}\int g\,\frac{dZ}{Z} - \left(1 - \sum_{n=1}^{\infty}\frac{1}{n} c_n\bar{c}_n\right) \\ &- \sum_{n=1}^{\infty} c_n\left(1 - \frac{1}{n}\right)\frac{1}{Z^{n+1}} + \sum_{m>n}^{\infty}\left(\frac{1}{m} + \frac{1}{n}\right) \\ &\times c_m\bar{c}_n\frac{1}{Z^{m-n}} - \left\{g\bar{g} - \left(1 + \sum_{n=1}^{\infty} c_n\bar{c}_n\right)\right\}\log Z\Bigg] \\ &+ E_1^1 \cdot \left(1 - \sum_{n=1}^{\infty}\frac{1}{n} c_n\bar{c}_n\right)\log Z \\ &+ c.c. \end{aligned} \tag{5.9}$$

The integrals

$$E_n^m\left(\frac{a}{\sqrt{\nu t}}\right)\int_0^{\infty}\frac{x^{n-1}(\beta - \log x)^m e^{-x}}{[(\beta - \log x)^2 + \pi^2]^{m+1}}\,dx\,, \tag{5.10}$$

$$\beta = -2\gamma - \log(a^2/4\nu t) = \log(4T) - 2\gamma,\quad T = \nu t/a^2$$

come from the interpretation of $p^{-1}S^{-(m+1)} \times (ak)^{2n}$. For the first approximation, making further expansion in the integral E_0, we obtain

$$w/W \sim \varphi_0 \sim 1 - (1/\beta)\log Z\bar{Z}, \quad \text{as } a/\sqrt{\nu t} \to 0. \tag{5.11}$$

§ 6. Skin Friction over the Cylinder

We now proceed to calculate the skin friction D_s per unit length over the cylinder.

This is connected with the vorticity distribution over the cylinder ω_s

$$\omega_s = -(\partial\omega/\partial n)_s \tag{6.1}$$

by the formula

$$D_s = \mu\omega_s\,, \tag{6.2}$$

where $\partial/\partial n$ denotes differentiation along the outward normal to the surface of the cylinder, which can be expressed by using complex variables as follows:

$$\frac{\partial}{\partial n} = \left|\frac{dz}{\partial Z}\right|^{-1}\left(Z\frac{\partial}{\partial Z}+\bar{Z}\frac{\partial}{\partial \bar{Z}}\right), \qquad Z\bar{Z}=1\,. \tag{6.3}$$

Thus, from (5.7)—(5.9) we obtain

$$\begin{aligned}\frac{D_s}{\mu W} = \frac{\omega_s}{W} = \left|\frac{dz}{dZ}\right|^{-1}\Bigg[2E_0 + \frac{a^2}{\nu t}\Bigg\{E_1\cdot\left(1+\sum_{n=1}^{\infty}c_n\bar{c}_n\right)\\ +2E_1{}^1\cdot\left(1-\sum_{n=1}^{\infty}\frac{1}{n}c_n\bar{c}_n\right)+E_1\\ \cdot\boldsymbol{Re}\left(\sum_{m>n}^{\infty}\frac{n}{m}c_m\bar{c}_n Z^{-(m-n)}-\sum_{n=1}^{\infty}\frac{1}{n}c_n Z^{-(n+1)}\right)\Bigg\}\Bigg].\end{aligned} \tag{6.4}$$

where, ***Re*** stands for "the real part of".

In particular, the total frictional drag D per unit length is given by

$$\begin{aligned}D &= \oint_{Z\bar{Z}=1} D_s|dz|\\ &= 2\pi\mu W\Bigg[2E_0+\frac{a^2}{\nu t}\Bigg\{E_1\cdot\left(1+\sum_{n=1}^{\infty}c_n\bar{c}_n\right)\\ &\quad +2E_1{}^1\cdot\left(1-\sum_{n=1}^{\infty}\frac{1}{n}c_n\bar{c}_n\right)\Bigg\}+O\left(\frac{a^4}{\nu^2t^2}\right)\Bigg].\end{aligned} \tag{6.5}$$

This shows the interesting similarity rule that: If $a/\sqrt{\nu t}$ is sufficiently small, the total frictional drag D is expressed by

$$4\pi\mu W E_0(a/\sqrt{\nu t}) \sim 2\pi\mu W/\{-\gamma-\log(a/\sqrt{4\nu t})\}, \tag{6.6}$$

irrespective of the shape of cylinder. Physically speaking, if $\sqrt{\nu t}$ is large compared with a, the boundary-layer thickness is large and the velocity of the fluid is almost stationary except in the region which forms the outer edge of the boundary layer. This vaguely defined region which surrounds the cylinder may be considered to have a nearly circular form as a result of diffusion of vorticity.

It may be noted that (6.4) and (6.5) can be also obtained directly from (5.4)—(5.6).

Instead of the series form $1+\sum_{n=1}^{\infty}c_n\bar{c}_n$ etc. given in (6.4), (6.5) and (5.6) we can use integral representations of them, which can be easily obtained by using the theorem of residues:

$$\begin{aligned}1+\sum_{n=1}^{\infty}c_n\bar{c}_n &= \frac{1}{2\pi i}\oint\frac{|g(\zeta)|^2}{\zeta}d\zeta\\ &= \frac{1}{2\pi}\int_0^{2\pi}|g(e^{i\theta})|^2 d\theta\,,\end{aligned} \tag{6.7}$$

$$\begin{aligned}1-\sum_{n=1}^{\infty}\frac{1}{n}c_n\bar{c}_n &= \frac{1}{2\pi i}\oint\frac{\bar{g}(\bar{\zeta})}{\zeta}d\zeta\int^{\zeta}\frac{g(\lambda)}{\lambda}d\lambda\\ &= \frac{1}{2\pi}\int_0^{2\pi}\bar{g}(e^{-i\theta})d\theta\int_0^{\theta}g(e^{i\omega})d\omega\,,\end{aligned} \tag{6.8}$$

$$\sum_{n=1}^{\infty}\frac{c_n}{n}Z^{-(n+1)} = \frac{1}{Z}\int_Z^{\infty}\frac{g(\lambda)-\lambda}{\lambda}d\lambda, \tag{6.9}$$

$$\begin{aligned}&\sum_{m>n}^{\infty}\frac{n}{m}c_m\bar{c}_n Z^{-(m-n)}\\ &\quad= \frac{1}{2\pi i}\oint\frac{g(\zeta)}{\zeta}\int^{1/\zeta}\frac{d\lambda}{1-\lambda z}[1-\bar{g}'(\lambda)],\end{aligned} \tag{6.10}$$

$$\begin{aligned}\sum_{m>n}^{\infty}\left(\frac{1}{m}+\frac{1}{n}\right)c_m\bar{c}_n Z^{-(m-n)} = \frac{1}{2\pi i}\Bigg[\oint\frac{g(\zeta)}{Z-\zeta}\\ \cdot d\zeta\int_{1/\zeta}^{\infty}\frac{\bar{g}(\lambda)-\lambda}{\lambda}d\lambda+\oint\frac{g(\zeta)}{\zeta}d\zeta\int_{1/\zeta}^{\infty}\frac{\bar{g}(\lambda)-\lambda}{\lambda(\lambda Z-1)}d\lambda\Bigg],\end{aligned} \tag{6.11}$$

where the path of contour integration $\oint$ is the unit circle $\zeta\bar{\zeta}=1$, and in (6.9), (6.10) and (6.11) we take $|Z|$ as though $|Z|>|\zeta|$. These formulae will be useful when the analytical expression for the mapping function $f(Z)=ag(Z)$ is known.

§ 7. Examples

i) *elliptic cylinder*

Using the function $f(Z)=ag(Z)$, where

$$g(Z)=Z+\sigma^2/Z\,, \tag{7.1}$$

i.e.

$$c_1=\sigma^2, \quad c_n=0 \quad (n>1)\,, \tag{7.2}$$

we can map the region outside the unit circle $Z=e^{i\theta}$ in the Z-plane onto the region outside an ellipse in the z-plane:

$$x=a(1+\sigma^2)\cos\theta, \quad y=a(1-\sigma^2)\sin\theta\,, \tag{7.3}$$

whose major and minor axes are respectively $2a(1+\sigma^2)$ and $2a(1-\sigma^2)$. Introducing (7.1) and (7.2) into (5.7), (6.4) and (6.5) we obtain

$$\begin{aligned}w/W &= 1-E_0\log Z\bar{Z}\\ &\quad -\frac{a^2}{\nu t}\Bigg\{\frac{E_1}{4}\Bigg[2\left(Z\bar{Z}-\frac{\sigma^4}{Z\bar{Z}}-1+\sigma^4\right)\\ &\quad -\left\{\left(Z+\frac{\sigma^2}{Z}\right)\left(\bar{Z}+\frac{\sigma^2}{\bar{Z}}\right)-(1+\sigma^4)\right\}\log(Z\bar{Z})\Bigg]\\ &\quad +E_1{}^1\cdot(1-\sigma^4)\log(Z\bar{Z})\Bigg\}+O\left(\frac{a^4}{\nu^2t^2}\right),\end{aligned} \tag{7.4}$$

$$|dz/dZ|_s^{-1}=|a(1-\sigma^2/Z^2)|^{-1}$$
$$=a^{-1}(1-2\sigma^2\cos 2\theta+\sigma^4)^{-1/2}, \qquad (7.5)$$

$$\frac{D_s}{\mu W}=\frac{1}{a\sqrt{1-2\sigma^2\cos 2\theta+\sigma^4}}\Bigg[2E_0+\frac{a^2}{\nu t}$$
$$\times\{(1+\sigma^4)E_1+2(1-\sigma^4)E_1^1-\sigma^2E_1\cos 2\theta\}+\cdots\Bigg], \qquad (7.6)$$

$$\frac{D}{2\pi\mu W}=2E_0+\frac{a^2}{\nu t}\{(1+\sigma^4)E_1+2(1-\sigma^4)E_1^1\}+\cdots. \qquad (7.7)$$

Taking $\sigma=0$ in (7.6) we get for the circular cylinder of radius a

$$D_s=\frac{2\mu W}{a}\Big[E_0+\frac{a^2}{2\nu t}(E_1+2E_1^1)+\cdots\Big]. \qquad (7.8)$$

Taking into account (I.13) in Appendix we see that the first term E_0 in the square brackets of (7.8) is in perfect accord with the formula § 127 (10) in Carslaw and Jaeger[1] to the order of $O(\beta^{-2})$.

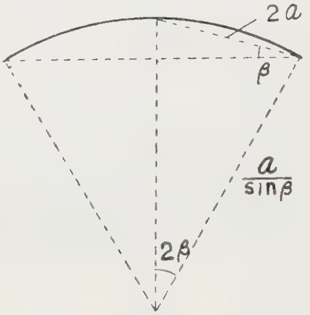

Fig. 2.

Replacing a by $a/2$ and σ by 1 in (7.7) and (7.8), we obtain for the flat plate of width $2a$

$$\frac{D_s}{\mu W}=\frac{1}{a\sin\theta}\Big[2\bar{E}_0+\frac{a^2}{2\nu t}\bar{E}_1\cdot\Big(1-\frac{1}{2}\cos 2\theta\Big)$$
$$+\cdots\Big], \qquad (7.9)$$

$$\frac{D}{2\pi\mu W}=2\bar{E}_0+\frac{a^2}{2\nu t}\bar{E}_1+\cdots. \qquad (7.10)$$

These are in accord with (3.14) and (3.15) of the previous paper[4] as far as $O(a^2/\nu t)$. Thus we know that the result in the previous paper can be derived as a special case.

ii) *Joukowski profile, especially circular arc* Consider

$$g(Z)=Z+\frac{b^2}{Z+q}, \quad |q|\leq 1, \quad b=\text{real}. \qquad (7.11)$$

This maps the region outside the unit circle $Z=e^{i\theta}$ in the Z-plane onto the region outsid a Joukowski profile in the z-plane. In thi case

$$c_n=b^2(-q)^{n-1}. \qquad (7.12)$$

Introducing (7.11) into (6.7)—(6.11), or makin summations directly by using (7.12) we obtai

$$1+\sum_{n=1}^{\infty}c_n\bar{c}_n=1+\frac{b^4}{1-q\bar{q}},$$
$$1-\sum_{n=1}^{\infty}\frac{1}{n}c_n\bar{c}_n=1+\frac{b^4}{q\bar{q}}\log(1-q\bar{q}),$$
$$\sum_{n=1}^{\infty}\frac{1}{n}c_nZ^{-(n+1)}=\frac{b^2}{qZ}\log\Big(1+\frac{q}{Z}\Big),$$
$$\sum_{m>n}^{\infty}\frac{n}{m}c_m\bar{c}_nZ^{-(m-n)}=b^4\Big\{\frac{-1}{1-q\bar{q}}\frac{1}{1+\bar{q}Z}$$
$$+\frac{1}{q}\frac{Z}{(1+\bar{q}Z)^2}\log\frac{Z+q}{Z(1-q\bar{q})}\Big\},$$
$$\sum_{m>n}^{\infty}\Big(\frac{1}{m}+\frac{1}{n}\Big)c_m\bar{c}_nZ^{-(m-n)}=b^4\Big[\frac{1}{q}\log(1-q\bar{q})$$
$$\times\Big\{\frac{1}{Z+q}+\frac{1}{q(1+\bar{q}Z)}\Big\}+\frac{Z}{1+\bar{q}Z}\log\Big(1+\frac{q}{Z}\Big)\Big] \qquad (7.13)$$

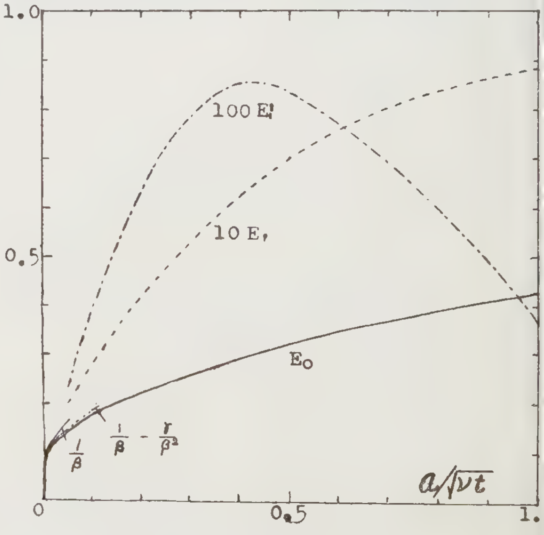

Fig. 3.

Especially when

$$b=\cos\beta, \qquad q=i\sin\beta, \qquad (7.14)$$

we obtain a circular arc as shown in Fig. 2 In this case D_s and D are respectively

$$\frac{D_s}{\mu W}=\frac{\Theta}{2a\sqrt{[1-\cos(\theta+\beta)][1+\cos(\theta-\beta)]}}$$
$$\times\Big[\bar{D}+\frac{a^2}{\nu t}E_1\cos^2\beta\Big\{-\frac{1+\sin\beta\sin\theta}{\Theta}$$
$$+\frac{\cos^2\beta}{\sin\beta\cdot\Theta^2}[\{\tfrac{1}{2}\log\Theta-\log\cos^2\beta\}$$
$$\times\{2\sin\beta+(1+\sin^2\beta)\sin\theta\}+\omega\cos^2\beta\cos\theta]$$

Table I

$a/\sqrt{\nu t}$	β	E_0	E_1	$E_1{}^1$	$1/\beta$	$1/\beta-\gamma/\beta^2$
0.000	∞	0.0000	0.0000	0.0000	0.0000	0.0000
0.005	10.828	0.0863	0.008*	0.0006*	0.0924	0.0874
0.010	9.442	0.0980	0.010*	0.0009*	0.1059	0.0994
0.025	7.610	0.1187	0.014*	0.0017*	0.1314	0.1214
0.050	6.223	0.1410	0.0189	0.00238	0.1607	0.1458
0.100	4.837	0.1726	0.0274	0.00391	0.2067	0.1807
0.250	3.004	0.2391	0.0474	0.00718		
0.500	1.618	0.3202	0.0698	0.00836		
0.750	0.807	0.3820	0.0821	0.00644		
1.000	0.232	0.4312	0.0881	0.00369		

* Approximate value calculated by (I. 12) and (I. 14).

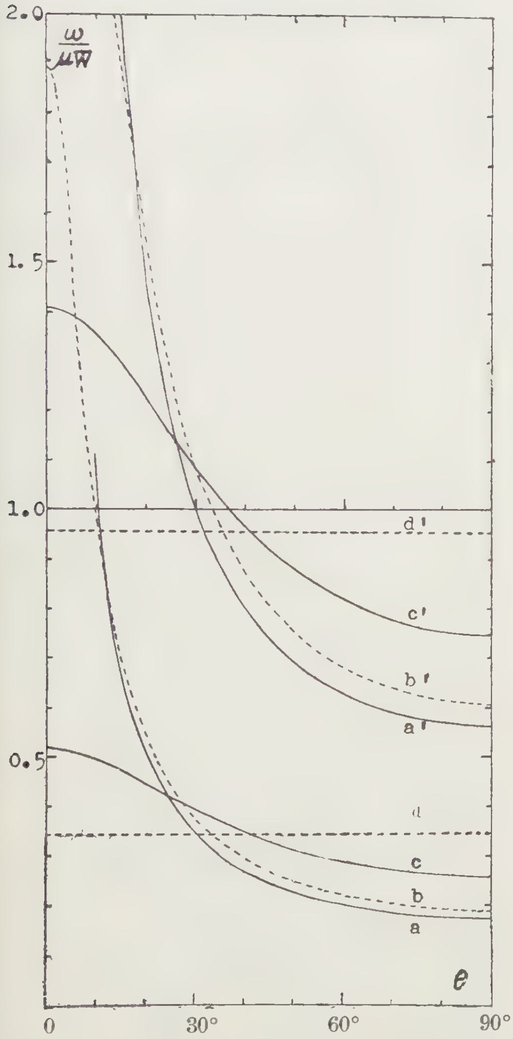

Fig. 4. Vorticity distribution on the cylinders. a, a'…flat plate; b, b'…elliptic cylinder ($\bar{t}=0.1$); c, c'…elliptic cylinder ($\bar{t}=0.5$); d, d'…circular cylinder: $a/\sqrt{\nu t}=0.1$ and 1.0. respectively.

$$+\frac{1}{2\sin\beta}(\sin\theta\log\Theta-2\omega\cos\theta)\Big\}\Big]+O\Big(\frac{a^4}{\nu^2t^2}\Big), \tag{7.15}$$

$$\Theta=1+\sin^2\beta+2\sin\beta\sin\theta\,,$$

$$\omega=\tan^{-1}\frac{\sin\beta\cos\theta}{1+\sin\beta\sin\theta}\,,$$

$$\overline{D}=\frac{D}{2\pi\mu W}=2E_0+\frac{a^2}{\nu t}[(1+\cos^2\beta)E_1+2(1+\cos^2\beta\cot^2\beta\log\cos^2\beta)E_1{}^1]+O\Big(\frac{a^4}{\nu^2t^2}\Big)\,. \tag{7.16}$$

Table I and Fig. 3 show the numerical values of the integral E_0, E_1, and $E_1{}^1$; and $1/\beta-\gamma/\beta^2$ as a further approximation to E_0 (see Appendix).

Fig. 4 shows the vorticity distribution on the cylinder with the same value of $a/\sqrt{\nu t}$ (0.1, 1.0) for a circular cylinder, a flat plate, and elliptic cylinders (thickness ratio $\bar{t}=1/2$ and 1/10) calculated by (7.6), taking respectively $\sigma^2=0$, 1, 1/3 and 9/11.

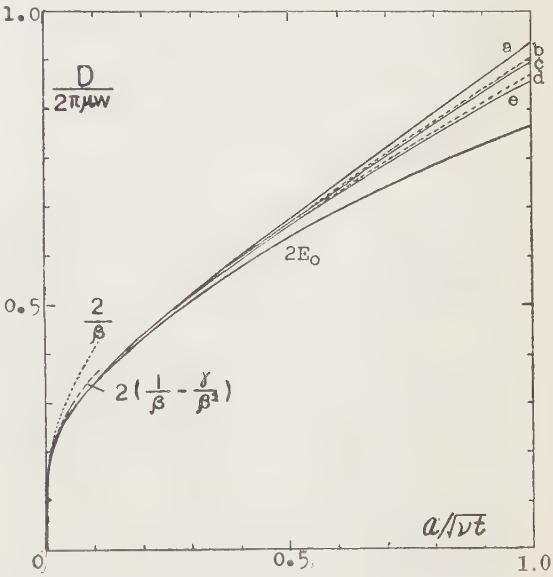

Fig. 5. Total frictional drag. a…flat plate (width $4a$), b…elliptic cylinder ($\bar{t}=0.1$, major axis $3.6\dot{6}\dot{3}\,a$), c…semicircle (radius $\sqrt{2}a$), d…elliptic cylinder ($\bar{t}=0.5$, major axis $2.\dot{6}\,a$), e…circular cylinder (radius a).

Fig. 5 shows the total frictional drag $\overline{D}$ on these cylinders. The value for a semicircle calculated by (7.16) ($\beta=\pi/4$) is added. The curve e for the circular cylinder corresponds to Fig. 32 of Carslaw and Jaeger,[1)] and is in accord with it as far as $a/\sqrt{\nu t}<1$. It is interesting to note that the values of the total frictional drag for a cylinder with complicated cross section are smaller than those for a circular cylinder if their peripheries are of equal length. This will be accounted for, by considering the interaction between the surface elements; the diffusion of vorticity is easy from the surface which is convex to the fluid, and is very difficult from the surface which is concave to the fluid.

In conclusion the author express his cordial thanks to Professor Isao Imai for his continual guidance.

Appendix Interpretation of ψ^*

In order to interpret ψ^* by use of the inversion formula for the Laplace transformation (2.10), we adopt the following procedure.

Taking into account the presence of $\log(ka)=\frac{1}{2}\log p+\cdots$ which makes ψ^* many-valued, we replace the path of integration by:

(1) the line $p=qe^{-i\pi}$ from $q=R$ to $q=\varepsilon$;

(2) the small circle $p=\varepsilon e^{i\theta}$ from $\theta=-\pi$ to $\theta=\pi$;

(3) the line $p=qe^{i\pi}$ from $q=\varepsilon$ to $q=R$.

Here the contribution from the large semicircle $Re^{i\theta}$ in the left half-plane tends to zero on account of (4.2) ($\psi^*\to 0$ as $|p|\to\infty$, $-\pi<\arg p<\pi$) and of Jordan's lemma. There may be some contribution from some poles (if exist) other than the origin in the left half-plane, but they should decay exponentially when $\nu t/a^2\to\infty$ in accordance with the diffusive nature of the problem. Thus, the main contribution to ψ is given by

$$\psi\sim\text{Residue of }\psi^*\text{ at }p=0$$
$$+\frac{1}{\pi}\boldsymbol{Im}\int_0^\infty e^{-qt}[\psi^*]_{p=q\exp(-i\pi)}dq, \tag{I.1}$$

corresponding to (1), (2), and (3); and on account of the factor $\exp(-qt)$ in the integrand, asymptotic solution when $\nu t/a^2\to\infty$ is obtained by introducing expansion (3.8) into (I.1), where ***Im*** stands for "the imaginary part of". The contribution from $\psi_{nm}{}^*=p^{-1}(ak)^{2n}S^{-m}$ can be calculated as follows;

$$\psi_{00}=1,\qquad \psi_{n0}=0\quad(n\neq 0), \tag{I.2}$$

$$\psi_{nm}=\frac{2^m(-1)^n}{\pi}\left(\frac{a^2}{\nu}\right)^n$$
$$\times\boldsymbol{Im}\int_0^\infty\frac{e^{-qt}q^n dq}{q[-2\gamma-2\log(a\sqrt{q/(4\nu)})-\pi i]^m}$$
$$=\frac{2^m(-1)^n}{\pi}\left(\frac{a^2}{\nu t}\right)^n\boldsymbol{Im}\int_0^\infty\frac{e^{-x}x^n dx}{x[\beta-\log x-\pi i]^m}, \tag{I.3}$$

where

$$\beta=-2\left(\gamma+\log\frac{a}{2\sqrt{\nu t}}\right), \tag{I.4}$$

using $k^2=p/\nu$ ((2.7)). Residue of ψ_{nm} $(m\neq 0$ at $p=0$ is zero. Differentiating the firs integral in (I.3) with respect to t we get

$$\psi_{nm}=\frac{a^2}{\nu}\frac{d}{dt}\psi_{n-1,m}=\cdots=\left(\frac{a^2}{\nu}\right)^n\frac{d^n}{dt^n}\psi_{0,m} \tag{I.5}$$

This corresponds to interpreting k^2a^2 formall as an operator $(a^2/\nu)(d/dt)$. Differentiatin the integral of (I.3) with respect to β we ge

$$t^n\psi_{nm}=\frac{-2}{m-1}\frac{d}{d\beta}[t^n\psi_{n,m-1}]$$
$$=\frac{(-2)^{m-1}}{(m-1)!}\frac{d^{m-1}}{d\beta^{m-1}}(t^n\psi_{n,1}). \tag{I.6}$$

In particular

$$\psi_{01}=\frac{2}{\pi}\boldsymbol{Im}\int_0^\infty\frac{e^{-x}dx}{x(\beta-\log x-\pi i)}=2E_0, \tag{I.7}$$

$$E_0=E_0{}^0=\int_0^\infty\frac{e^{-x}dx}{x[(\beta-\log x)^2+\pi^2]}, \tag{I.7$'$}$$

$$\psi_{11}=-\frac{2a^2}{\pi\nu t}\boldsymbol{Im}\int_0^\infty\frac{e^{-x}dx}{\beta-\log x-\pi i}=-\frac{2a^2}{\nu t}E_1, \tag{I.8}$$

$$E_1=E_1{}^0=\int_0^\infty\frac{e^{-x}dx}{(\beta-\log x)^2+\pi^2}, \tag{I.8$'$}$$

$$\psi_{12}=-\frac{4a^2}{\pi\nu t}\boldsymbol{Im}\int_0^\infty\frac{e^{-x}dx}{(\beta-\log x-\pi i)^2}=-\frac{8a^2}{\nu t}E_1{}^1, \tag{I.9}$$

$$E_1{}^1=\int_0^\infty\frac{(\beta-\log x)e^{-x}dx}{[(\beta-\log x)^2+\pi^2]^2}, \tag{I.9$'$}$$

$$\psi_{nm}\sim\frac{2^m(-1)^n}{\pi}\left(\frac{a^2}{\nu t}\right)^n$$
$$\times\int_0^\infty\frac{m\pi(\beta-\log x)^{m-1}e^{-x}x^n dx}{x[(\beta-\log x)^2+\pi^2]^m}$$
$$=2^m m(-1)^n\left(\frac{a^2}{\nu t}\right)^n E_n{}^{m-1}\quad(\beta\to\infty), \tag{I.10}$$

$$E_n{}^m=\int_0^\infty\frac{x^{n-1}(\beta-\log x)^m e^{-x}dx}{[(\beta-\log x)^2+\pi^2]^{m+1}}. \tag{I.10$'$}$$

A further expansion of E_1 as $\beta\to\infty$ is easily obtained by noting the relation

$$E_1=\frac{1}{\pi}\boldsymbol{Im}\int_0^\infty\frac{e^{-x}dx}{\beta-\log x-\pi i}\sim\frac{1}{\pi}\boldsymbol{Im}\int_0^\infty\sum_{n=0}^{N}\frac{e^{-}}{\beta^{n+}}$$
$$\times(\log x+\pi i)^n dx=\sum_{n=1}^{\infty}\frac{A_n}{\beta^{n+1}}, \tag{I.11}$$

where

$$A_n=\frac{1}{\pi}\,\boldsymbol{Im}\int_0^\infty e^{-x}(\log x+\pi i)^n dx,\ A_0=0,\ A_1=1,$$

$$A_2=2\int_0^\infty e^{-x}\log x\,dx=-2\gamma\ ,$$

as

$$E_1\sim\frac{1}{\beta^2}-\frac{2\gamma}{\beta^3}\ . \tag{I.12}$$

Using from (I.4) to (I.8) we get for E_0 and $E_1{}^1$

$$E_0=\frac{1}{2}\varphi_{01}=\frac{\nu}{2a^2}\int_\infty^t\varphi_{11}dt=-\int_\infty^t E_1\frac{dt}{t}$$

$$=-\int_\infty^\beta E_1 d\beta\sim\sum_{n=1}^N\frac{A_n}{n\,\beta^n}\sim\frac{1}{\beta}-\frac{\gamma}{\beta^2}\ , \tag{I.13}$$

$$E_1{}^1=-\frac{\nu t}{8a^2}\varphi_{12}=\frac{\nu}{4a^2}\frac{d}{d\beta}[t\varphi_{11}]=-\frac{1}{2}\frac{dE_1}{d\beta}$$

$$\sim\sum_{n=1}^N\frac{(n+1)A_n}{2\beta^{n+2}}\sim\frac{1}{\beta^3}-\frac{3\gamma}{\beta^4}\ . \tag{I.14}$$

Numerical values of E_0, E_1, $E_1{}^1$ have been obtained by numerical integration, using the formulae suited for this calculation:

$$E_0=\frac{1}{\pi}\tan^{-1}\frac{\pi}{\beta}-\int_0^1\frac{(1-e^{-x})dx}{x[(\beta-\log x)^2+\pi^2]}$$

$$+\int_0^1\frac{\exp(-1/x)}{x[(\beta+\log x)^2+\pi^2]}\ , \tag{I.15}$$

$$E_1=\int_0^1\frac{e^{-x}dx}{(\beta-\log x)^2+\pi^2}$$

$$+\int_0^1\frac{\exp(-1/x)}{x^2[(\beta+\log x)^2+\pi^2]}dx\ ,$$

$$E_1{}^1=\int_0^1\frac{(\beta-\log x)e^{-x}}{[(\beta-\log x)^2+\pi^2]^2}dx$$

$$+\int_0^1\frac{(\beta+\log x)\exp(-1/x)}{x^2[(\beta+\log x)^2+\pi^2]}dx\ ,$$

together with Simpson's rule. For very large values of β the approximate formulae (I.13), (I.12) and (I.14) are useful.

References

1) H. S. C. Carslaw and J. C. Jaeger: Proc. London Math. Soc. (2) **46** (1940) 361; or, Conduction of Heat in Solids (1947) 280.

2) S. Goldstein: Proc. London Math. Soc. (2) **34** (1932) 51.

3) H. Hasimoto: J. Phys. Soc. Japan **6** (1951) 400.

4) H. Hasimoto: Proc. 1st. Japan Nat. Congr. Appl. Mech. (1951) 447.

5) L. Howarth: Proc. Cambr. Phil. Soc. **46** (1950) 127.

6) I. Imai: J. Soc. Aeron. Sci. Japan **9** (1942) 865.

7) I. Imai and K. Sato: J. Aeron. Res. Inst. Tokyo Imp. Univ. **247** (1945) 91.

8) J. C. Jaeger: Phil. Mag. (7) **33** (1942) 527.

9) J. C. Jaeger: Proc. Roy. Soc. Eddinburgh **61** (1942) 223.

10) J. C. Jaeger and Clarke: ibid 229.

11) J. W. Nicholson: Proc. Roy. Soc. (A) **100** (1921) 226.

12) Lord Rayleigh: Phil. Mag. (6) **21** (1911) 697.

13) L. P. Smith: J. Appl. Phys. **8** (1937) 441.

14) L. Sowerby: Phil. Mag. (7) **42** (1951) 176.

15) L. Sowerby and J. C. Cooke: Quart. J. Mech. and Appl. Math. **6** (1953) 50.

16) E. C. Titchmarsh: Theory of Fourier Integrals

17) C. J. Tranter: Quart. J. Mech. and Appl. Math. **4** (1951) 461.

JOURNAL OF THE PHYSICAL SOCIETY OF JAPAN Vol. 9, No. 4, JULY—AUGUST, 1954

Absorption of Ultrasonic Waves in Organic Liquids (I)

Liquids with Positive Temperature Coefficients of Sound Absorption*

By Tadashi KISHIMOTO and Otohiko NOMOTO

Kobayasi Institute of Physical Research, Kokubunzi, Tokyo

(Received December 24, 1953)

Ultrasonic absorption coefficients have been determined for 12 organic liquids by the pulse technique in dependence of temperature (0°~40°C). The frequency employed was 8.25 Mc/sec, 14.5 Mc/sec or 20.0 Mc/sec. The "frequency-independent" absorption α/ν^2 (α: the absorption coefficient, ν: frequency) at 20°C are as follows (in units of 10^{-17} sec^2/cm): benzene 838 carbon tetrachloride 510, chloroform 406, cyclohexane 503, ethylene chloride 184, chlorobenzene 141, nitrobenzene 86, hexane 80, heptane 55, toluene 94, xylene 81, benzylchloride (13°C) 75. All these liquids proved to have positive temperature coefficient of ultrasonic absorption in the temperature range of 0°~40°C, the absorption increasing about 0.5~0.6% per degree. Toluene (1.06%/°C) and benzene (0.84%/°C) showed greater temperature coefficients of absorption and carbon tetrachloride and cyclohexane (ca. 0.27%/°C) showed lower values of temperature dependence than the other liquids. The chief mechanism of ultrasonic absorption in these liquids is attributed to the thermal relaxation of molecular vibrations, though the absorption due to viscosity amounts to 20% in some of the liquids. The relaxation times of vibrational energy have been computed for three of the liquids, giving $\beta=3.64\times10^{-10}$sec for benzene, 1.37×10^{-10}sec for carbon tetrachloride and 1.51×10^{-10}sec for chloroform at 20°C. The activation energy for the deactivation of molecular vibration are of the order of several hundred cal/mol at most for benzene, carbon tetrachloride and chloroform. The exact values of the relaxation time were not to be calculated for other liquids because of the lack of the molecular vibrational data, but they are of the order of 10^{-11}sec. The activation energy is presumably smaller than several hundred cal/mol.

§ 1. Introduction

Measurements of the ultrasonic absorption in organic liquids were performed by many authors and a great number of experimental results were published in these twenty years1). Many of the results, however, are rather fragmentary, and different from one another with respect to frequency, temperature, and the experimental techniques, and widely different from one another with respect to the values of the absorption coefficients. So we will consider the influence of various factors on the absorption coefficients, at first.

As to the techniques of measurements, there are various methods as the method of the diffraction of light by ultrasonic waves, the Schlieren method, the method of ultrasonic interferometry, the pulse technique, the method employing the torsion vane, the reverberation method, etc. There may be some sources of error in all of these methods, but the pulse technique developed in recent years seems to be the most reliable, giving absorption values which are mutually in good agreement.

As there is observed no velocity dispersion in ordinary organic liquids in the frequency range of usual ultrasonic experiments, except in a few cases as in acetic acid, carbon disulphide and highly viscous liquids such as glycerine and castor oil, the absorption coefficients obtained at different frequencies must be proportional to the square of the frequency in this case. The measurement of the absorption coefficient at various frequencies by a single method and on a single sample liquid, however, are required to test the constancy of the "frequency-independent absorption coefficient" α/ν^2, where α means the absorption coefficient and ν the frequency.

---

* The text in Japanese of this paper will be published in "Bulletin of the Kobayasi Institute of Physical Research, Vol. 3 (1953), No. 3."

The lack of systematic measurement of the absorption at various temperatures in many cases is certainly a more serious reason for the above-mentioned discrepancy, which makes difficult the comparison of the data obtained by various authors. Also the mechanism of the ultrasonic absorption in liquids must be carefully examined according to the results of the systematic measurements of the absorption coefficient and especially its temperature variation. There are various mechanisms of ultrasonic absorption in liquids as discussed by Pinkerton[2)] and others. The chief cause of the ultrasonic absorption in ordinary organic liquids are considered to be the molecular absorption. There is, however, the prevailing tendency that nearly all the liquids are classified as the liquids with molecular absorption as their chief absorption mechanism, without appropriate examination of the temperature dependence of the absorption coefficient. According to our measurements, there are also a number of liquids in which the sound absorption is mainly due to viscosity, though these liquids have hitherto been considered as liquids with molecular absorption as their chief absorption mechanism. The liquids in which the sound absorption decreases with temperature, naturally, have the viscosity as their chief absorption mechanism, while the liquids with strong molecular absorption have positive temperature coefficients of ultrasonic absorption.

The temperature coefficient of ultrasonic absorption in organic liquids are also of importance when they are used as solvents of high-molecular substances, the ultrasonic propagation in these solutions being investigated with much interest in resent years.

We have, therefore, performed the measurements of the ultrasonic absorption in ordinary organic liquids by the pulse technique at various temperatures and at frequencies 8.25 Mc/sec, 14.5 Mc/sec and 20.0 Mc/sec., although the three frequencies have been employed mainly for obtaining adequate absorption values for certain substances, and a systematic measurement with various frequencies was not performed for each substance. This first report describes of the result of measurements on the liquids, in which the sound absorption increased with increasing temperature. The chief mechanism of sound absorption in these liquids are supposed to be the molecular absorptian due to the thermal relaxation of molecular vibrations.

§ 2. Experimental Techniques

The apparatus and the methods of the measurement are nearly the same with those employed previously[3)] except a few alterations. The main difference is that a single quartz plate was used as the ultrasonic transducer both for generating and receiving the ultrasonic beam. The liquid vessel was of closed type and the temperature was obtained by a thermocouple inserted in the vessel. The total apparatus was immersed in a water bath to control the temperature. The quartz transducer was an *X*-cut plate 1 mm thick and 20 mm in diameter. The measurements were performed at frequencies corresponding to the 3rd, 5th and 7th harmonics of this plate, namely, at 8.25 Mc/sec, 14.5 Mc/sec and 20.0 Mc/sec. The oscillator worked only for the short interval of time when the pulse was impressed to the screen grid of the oscillator tube (6AG7). The received signal of pulse was amplified through a straight amplifier or a super-heterodyne amplifier and the absorption coefficient was determined from the plot of the reading of the attenuator attached before the amplifier against the reading of the distance of the reflector plate as the height of the received signal was maintained constant on the oscilloscope screen. The scattering of the measured absorption values seems to result in errors of the absorption coefficients of 2% or so, as indicated in the examples shown in the next paragraph.

The sample liquids were prepared from commercial pure liquids by fractional distillation under addition of suitable desiccation agents. The fraction with boiling point consistent with the table value was separated out and used. No chemical analysis was performed. Only the liquids hexane and heptane did not show the boiling points consistent with the table values, each exhibiting a rather wide range of boiling point.

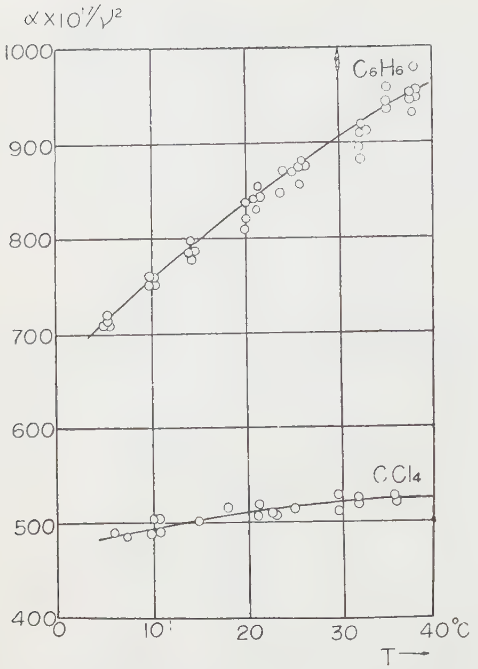

Fig. 1. Temperature dependence of ultrasonic absorption in benzene and carbon tetrachloride.

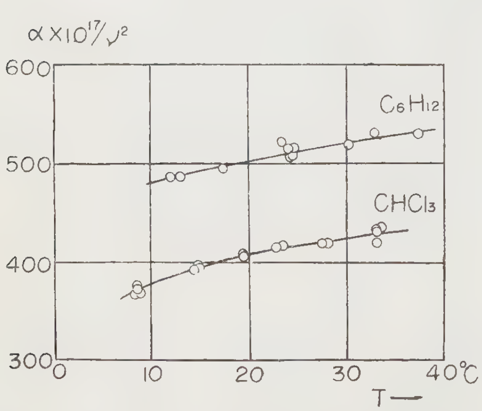

Fig. 2. Temperature dependence of ultrasonic absorption in cyclohexane and chloroform.

§ 3. Experimental Results

The results of the measurements are reproduced in Fig. 1 to 5. The values of the sound absorption are summarized in Table I. Fig. 1 and 2 (benzene, carbon tetrachloride, cyclohexane, and chloroform) indicate clearly the well-known property that the liquids with symmetric molecules are of high ultrasonic absorption coefficients.

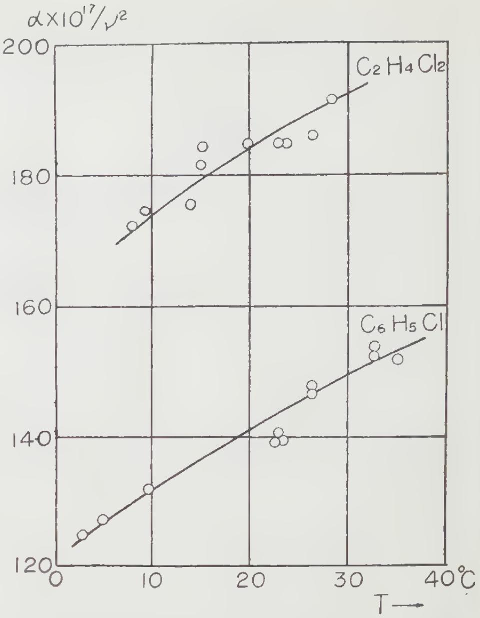

Fig. 3. Temperature dependence of ultrasonic absorption in ethylene chloride and chlorobenzene.

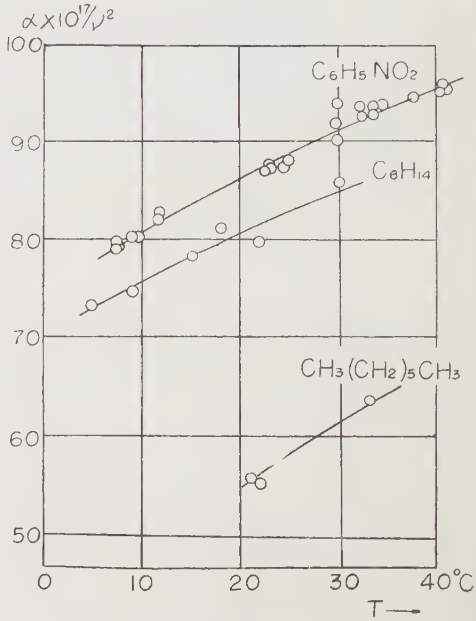

Fig. 4. Temperature dependence of ultrasonic absorption in nitrobenzene, hexane and heptane.

The liquids whose absorption coefficients are indicated in Fig. 3 to Fig. 5 (ethylenchoride, chlorobenzene, nitrobenzene, hexane, heptane, toluene, xylene) are of much smaller absorption than those reproduced in Fig. 1 and 2. These are mainly the liquids consisting of less symmetric molecules. The dirivatives of benzene, i.e., toluene, nitrobenzene, are of smaller sound absorption than benzene,

Table I. Temperature dependence of ultrasonic absorption in organic liquids $\left(\frac{\alpha}{\nu^2}\times 10^{17}\right)$.

liquids	ν (Mc/sec)	0°	5°	10°	15°	20°	25°	30°	35°	40°	$\frac{1}{\alpha}\left(\frac{d\alpha}{dT}\right)$
benzene	8.50		710	758	798	838	873	908	937	968	0.84%
carbon tetrachloride	8.50		482	492	501	510	517	521	527	530	0.27
chloroform	8.50		358	375	393	406	418	425	432	435	0.54
cyclohexane	14.5			489	496	503	510	517	523	528	0.26
ethylene chloride	14.5		168	174	180	184	188	191			0.51
chlorobenzene	14.5	123	128	132	136	141	145	149	153		0.61
nitrobenzene	14.5		77	80	83	86	89	91	93	95	0.60
hexane	20.0		73	76	78	80	82	84			0.55
heptane	14.5					55	58	61			(1.1)
toluene	14.5			83	89	94	99	103			1.06
xylene	14.5		72	75	78	81	84	86	89	91	0.67
benzyl chloride	20.0			75(13°C)							

not exceeding 20% of the absorption coefficient of benzene. The sound absorption coefficient of most of the liquids indicated in Fig. 3 to 5 does not exceed $\alpha/\nu^2=100\times10^{-17}$ cgs., except ethylenchloride and chlorobenzene.

The values of the temperature coefficient of the sound absorption are great for benzene and toluene, showing increases of about 30～40% absorption in the temperature range of 0°～40°C. Other liquids are of comparatively small temperature coefficient of sound absorption in this range (about 20% increase), and the increase in ultrasonic absorption of carbon tetrachloride and cyclohexane is only slight (about 10%) in this range of temperature.

As is well known, the classical sound absorption due to viscosity is given by the Stokes' formula

$$\alpha_{\text{class}}=\frac{2}{3}\frac{\eta}{\rho}\frac{\omega^2}{V^3}, \tag{1}$$

where $\omega=2\pi\nu$ (with ν the frequency), η the viscosity coefficient, ρ the density and V the sound velocity. Table II gives the classical part of sound absorption for some liquids, the values of ρ and V being taken from the paper of Freyer, Hubbard and Andrews[4]. The classical absorption, however, is small and amounts to only 1～4% of the total absorption shown in Fig. 1 and 2. It amounts to 10～20% of the observed absorption in other liquids in which the absorption coefficient is not so great as in these liquids.

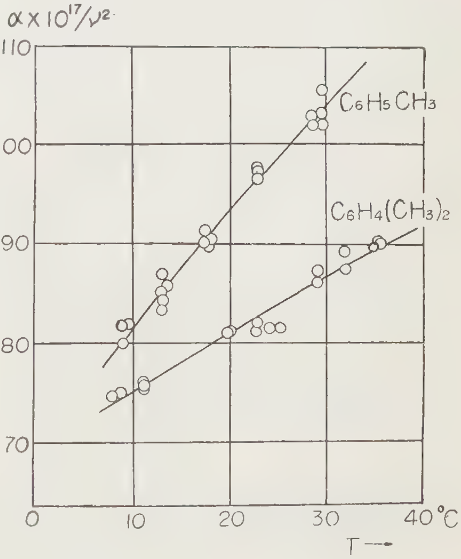

Fig. 5. Temperature dependence of ultrasonic absorption in toluene and xylene.

Table II. Classical sound absorption in liquids $\left(\frac{\alpha_{\text{class}}}{\nu^2}\times10^{17}\right)$.

T	benzene	carbon tetrachloride	chloroform
0°C		21.3	9.8
10	8.50	20.2	10.1
20	8.35	19.8	9.9
30	8.15	19.0	10.1
40	8.00	18.8	10.3

Thus the main part of sound absorption in the liquids here investigated are not the classical absorption due to viscosity. Also the fact that the total absorption increases with increasing temperature indicates that the most part of sound absorption in these liquids are due to molecular absorption or thermal relaxation mechanism.

The absorption coefficients here obtained are not necessarily in coincidence with the results of existing measurements, but are in comparatively good agreement with the results obtained by the pulse technique in resent years, for example, with those of Pellam and Galt[5].

As above stated, the sample liquids of hexane and heptane here employed were of somewhat different boiling points with those cited in the tables. This may account for the small absorption coefficient of heptane obtained in this research, 20% lower than the existing data.

The discrepancy of earlier measurements are presumably due to the defects of experimental techniques than to the scattering of the temperature of measurements, because the temperature coefficients of sound absorption proved to be not so great.

§ 4. Molecular Absorption of Sound

The nature of the molecular absorption of sound in liquids, constituting the main part of sound absorption in many of the organic liquids, became almost clear in recent years and the theoretical values of absorption are given by (cf. Kishimoto and Nomoto[3])

$$\frac{\alpha}{\nu^2}=\frac{2\pi^2}{V_0}\frac{C_iD}{C_{v0}C_{p\infty}}\frac{\tau}{1+\omega^2\tau^2}\,, \qquad (2)$$

where

$$\left.\begin{aligned} &D=C_{p0}-C_{v0}=C_{p\infty}-C_{v\infty}\,,\\ &\tau=\beta C_{p\infty}/C_{p0}\,,\\ &C_{p\infty}=C_{p0}-C_i\,, \qquad C_{v\infty}=C_{v0}-C_i\,, \end{aligned}\right\} \qquad (3)$$

and where V_0 means the sound velocity, C_i the internal specific heat of the molecule which is considered to contribute to the sound absorption, C_{p0} and C_{v0} the specific heats at constant pressure and at constant volume respectively at sufficiently low frequency, $C_{p\infty}$ and $C_{v\infty}$ the specific heats at sufficiently high frequency than the relaxation frequency, and β means the relaxation time or the period of adjustment of internal energy accompanying the volume change of the acoustic cycle.

The next step is to consider what degree of internal freedom will contribute to the sound absorption in our frequency range. There are various degrees of freedom of the molecules coestituting the liquid. The molecular rotation, however, is known to have very short relaxation times even in case of gases, due to the very close intervals between the energy levels. This presumably is true also for liquids, where the interaction between molecules is more strong than in gases. Thus we may treat the rotational energy of the molecule as external energy in this case. The electronic energy states, on the other hand, will afford only a negligible contribution to the specific heat, and therefore, also to the sound absorption. In experiments in the frequency range of 10^6 to 10^8 cycles/sec, therefore, we have to take into account only the influence of molecular vibration as the internal degree of freedom.

The results of existing experiments indicate that for most of the organic liquids the relaxation frequency is far higher than the frequency of our measurement, so that $\omega\tau\ll 1$. In this case Eq. (2) becomes simply as

$$\frac{\alpha}{\nu^2}=\frac{2\pi^2}{V_0}\frac{C_iD}{C_{v0}C_{p\infty}}\tau\,. \qquad (4)$$

As stated below, the values of the relaxation times obtained by employing this equation are found to be of the order of $10^{-10}\sim10^{-11}$ sec for all the liquids here examined. This indicates the adequacy of the assumption $\omega\tau\ll 1$.

We will assume that the relaxation times are the same for all the normal modes of vibration of the molecule[3]. Although there is left some doubt as to the general applicability of this assumption, it is not without reason considering from the result of absorption measurements in CS_2, and from the results of the dispersion and absorption of sound in various gases, and from theoretical considerations about them[6], although a few exceptional cases are also known. The relaxation times of various modes of vibrations of a single molecule are supposed at least to be of the same order of magnitude for most of the substances. We can obtain the vibrational or internal specific heat from the Planck-Einstein's formula

$$C_i=\sum_i\left(\frac{h\nu_i}{kT}\right)^2\frac{e^{-h\nu_i/kT}}{(1-e^{-h\nu_i/kT})^2}\,, \qquad (5)$$

based on the above assumption. Here ν_i means the frequencies of the normal modes of vibrations of the molecule, h the Planck's constant, k the Boltzmann's constant, and T

the absolute temperature.

If, therefore, all the normal vibration frequencies of the molecule are known for each substance, we can obtain the value of C_i, and calculate the value of the relaxation time from the absorption coefficient, at each temperature. This calculation was performed for benzene, carbon tetrachloride and chloroform for which the normal vibration frequencies are known. The result is indicated in Table III, where α' means the non-classical part of the sound absorption obtained by

$$\alpha' = \alpha - \alpha_{\text{class}} . \qquad (6)$$

The values of V, C_{p0}, γ and the values of C_{v0} obtained therefrom are taken from Freyer, Hubbard and Andrews' paper[4], the values of η from the "International Critical Tables" and the normal vibration frequencies (practically the wave-numbers) from Herzberg's book[7].

Table III. Molecular sound absorption and the relaxation time of vibrational energy in benzene, carbon tetrachloride and chloroform

T	benzene		carbon tetrachloride		chloroform	
	$\frac{\alpha'}{\nu^2}\times10^{17}$	$\beta\times10^{10}$	$\frac{\alpha'}{\nu^2}\times10^{17}$	$\beta\times10^{10}$	$\frac{\alpha'}{\nu^2}\times10^{17}$	$\beta\times10^{10}$
5°C	705	3.441	463	1.351	350	1.455
10	750	3.532	472	1.362	365	1.475
15	790	3.589	481	1.367	382	1.500
20	830	3.641	490	1.374	396	1.511
25	866	3.662	496	1.350	407	1.504
30	900	3.687	502	1.340	415	1.486
35	930	3.692	508	1.328	421	1.461
40	962	3.745	511	1.308	425	1.429

Table III indicates that the variation of the relaxation time β with temperature is comparatively small. There are observed some temperature regions where β increases with increase in temperature. It is, however, not certain whether this increase is real or merely the result of experimental errors of the absorption measurements, and especially because of the imperfection of the values of C_{p0} and C_{v0} given in tables.

We have stated above that the temperature coefficient of sound absorption is greater in benzene and toluene than in other liquids. It is known that the absorption of sound in toluene decreases at 1 Mc/sec (Moen[8]). It is, however, not certain whether the comparatively high temperature coefficient of sound absorption in toluene here obtained is the result of this low frequency relaxation. If the increase in temperature shifts the relaxation frequency to higher frequency, as is supposed to be the case in most of the liquids, the absorption coefficient on the high frequency side of the relaxation frequency will increase more rapidly with increase in temperature than on the low frequency side. The above result in toluene is consistent with this view at least qualitatively.

§ 5. Activation Energy for the Deactivation of Molecular Vibration and its Physical Interpretation

Assuming the temperature dependence of the relaxation time as $\beta = A(T)\exp(E/RT)$, or especially

$$\beta = B\exp(E/RT) , \qquad (7)$$

where B means a constant independent of (the absolute) temperature T, we have Fig. 6 as the plot of $\log\beta$ vs. $1/T$. In this figure, the curve for CS_2 is reproduced from the result of the previous paper[3].

The figure indicates that the result on CS_2 is fairly represented by a straight line of the form

$$\log_e\beta = \log_e B + E/RT . \qquad (8)$$

with an activation energy of $E \cong 1300$ cal/mole. On the other hand, the other three liquids do not obey this experimental formula so well. The figure indicates, however, that the activation energy is very small and not greater than several hundred cal/mol at most for these three liquids.

The physical significance of this small activation energy is that in liquids the exchange between the molecular vibrational energy and the translational energy of the molecule is very easy. This is also in accord with the small value of the relaxation time itself in the liquids.

In liquids other than indicated in Fig. 6, such as xylene, the complete set of the normal modes of vibrations was not available to us, and therefore, the value of the vibrational specific heat was not exactly to be computed, so that only an order of magnitude was estimated for the relaxation times. The β obtained in this manner is of the order of 10^{-11} sec for these liquids. The values of the activation energy will be too small to be determined exactly in these liquids if we assume emprical formulas of the type (7).

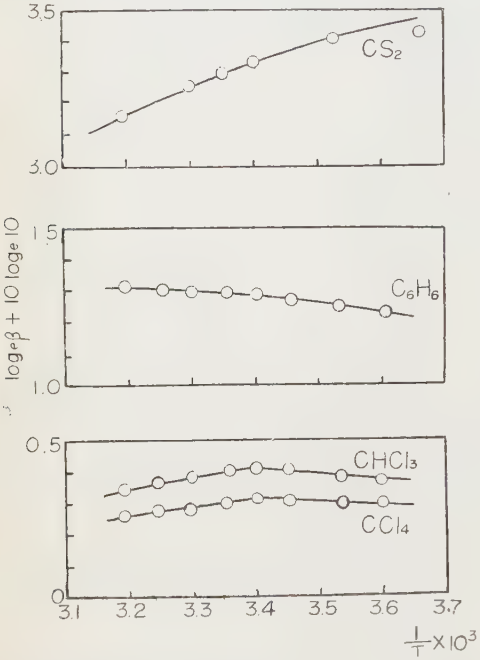

Fig. 6. $\log\beta$ *vs.* $1/T$ curves for carbon disulphide, benzene, chloroform and carbon tetrachloride.

As regards the rotational degrees of freedom, we may except a transition probability $10\sim10^2$ times higher than in the case of molecular vibration, so that we may expect the exchange between the rotational and the translational degrees of freedom by almost every molecular collision.

§ 6. Comparison with the Result of Experiperiments on the Scattering of Light by Elastic Heat Waves

Recently, Fabelinsky and Shustin[9] have reported of the result of emperiments on the scattering of light by elastic heat waves in benzene, carbon tetrachloride and toluene, in which a comparatively precise result has been obtained on the velocity of propagation of elastic waves of high frequency. After this work, the hypersonic velocity at 10^{10} cycles/sec is higher than the ultrasonic velocity by 10.4% in benzene and 16% in carbon tetrachloride, indicating the existence of dispersion between the ultrasonic and hypersonic frequency regions. Toluene has revealed no dispersion in this frequency range.

They used the theory of Mandelstam and Leontovich and formally employed the absorption formula due to the second viscosity

$$\alpha_{\eta'}=\frac{\omega^2}{2V_0^3\rho}\eta'=\frac{\omega^2\tau(V_\infty^2-V_0^2)}{2V_0^3(1+\omega^2\tau^2)}, \quad (9)$$

and explained the excess absorption and the dispersion by the relaxation phenomenon of the second viscosity. The interpretation of sound absorption by second viscosity, however, is permitted only in case when the sound absorption decreases with increasing temperature, as in the well-known case of water, for the second viscosity decreases with increasing temperature nearly in the same manner as the shear viscosity.

The second viscosity here considered, therefore, must correspond to the molecular absorption in its physical content, though the mathematical expressions of the absorption and dispersion formula coincide with those of the molecular absorption theory. As to the absorption coefficient, we have by substitution of

$$V_0^2=\frac{p}{\rho}\frac{C_{p0}}{C_{v0}}, \qquad V_\infty^2=\frac{p}{\rho}\frac{C_{p\infty}}{C_{v\infty}}, \quad (10)$$

(where ρ means the density and p the pressure,) in (8), the relation

$$\frac{\alpha_{\eta'}}{\nu^2}=\frac{2\pi^2}{V_0}\frac{D(C_{v0}-C_{v\infty})}{C_{p0}C_{v\infty}}\frac{\tau}{1+\omega^2\tau^2}, \quad (11)$$

which coincides with Eq. (2) of the molecular absorption theory within the order of approximation of the formula ($V=V_0$, or $C_{p0}C_{v\infty}=C_{p\infty}C_{v0}$).

The relaxation time τ is obtained from variation of the sound velocity as 2.44×10^{-10} sec for benzene and 6.7×10^{-11} sec for carbon tetrachloride. These values are in good agreement with the values to be obtained from our relaxation times β indicated in Table III, if an appropriate transformation $\tau=\beta C_{p\infty}/C_{p0}$ (cf. Eq. (3)) is performed. We have namely $\tau=2.32\sim2.37\times10^{-10}$ sec for benzene and $8.44\sim7.85\times10^{-11}$ sec for carbon tetrachloride.

Conclusion

Summarizing the results, we may conclude that the sound absorption increases in ordinary organic liquids with low viscosity (benzene, carbon tetrachloride, chloroform, cyclohexane, ethylen-chloride, chlorobenzene, nitrobenzene, hexane, heptane, toluene, xylene, and benzil chloride), though the temperature coefficient is not so great except in benzene and toluene, and that the chief mechanism of sound absorption in these liquids is the molecular absorption.

In conclusion, we express our sincere thanks to Mr. S. Okui, Ass. Prof., Institute of Pharmaceutics, Faculty of Medicine, Tokyo University, for his kind collaboration in distillation and desiccation of the sample liquids.

References

1) L. Bergmann: "Ultraschall," 5. Aufl. (1949).

2) J. M. M. Pinkerton: Proc. Phys. Soc. **62B** (1949) 129.

3) T. Kishimoto and O. Nomoto: Bull. Kobayasi Inst. Phys. Res. **2** (1952) 63.

4) E. B. Freyer, J. C. Hubbard, and D. W. Andrews: J. Amer. Chem. Soc. **51** (1929) 759.

5) J. R. Pellam and J. K. Galt: J. Chem. Phys. **14** (1946) 608.

6) K. Takayanagi: Progress theor. Phys. Jap. **8** (1952) 111.

7) K. Herzberg: "Molecular spectra and Molecular structure. II. Infrared and Raman Spectra," (1945).

8) C. J. Moen: J. Acous. Soc. Amer. **23** (1951) 62.

9) I. L. Fabelinsky and O. A. Shustin: C. R. (Doklady) URSS. **92** (1953) 285.

JOURNAL OF THE PHYSICAL SOCIETY OF JAPAN Vol. 9, No. 4, JULY—AUGUST, 1954

Crystal Habit of Magnesium Oxide Smokes

By Tadatosi HIBI and Takuji OGAWA*

Research Institute for Scientific Measurements,
Tohoku University, Sendai, Japan

(Received January 8, 1954)

Crystal habit of magnesium oxide smokes was observed by using a magnetic electron microscope. Interference fringes appearing in crystals and the contour forms of crystals in images were observed in order to determine the twin plane and the orientation of the crystals. As the results it was found that there existed many crystals having (111) twin beside normal cubic one. Extraordinary crystals having particular cut section were observed and it was known that their cut sections may be perhaps (111) planes. It was also found that there were many interesting modes of connection of cubic magnesium oxide crystals.

§ 1. Introduction

Electron microscopic studies on the crystal habit of metallic oxide smokes have scarcely been made up to present. After the study on the equal-thickness interference fringes due to Bragg reflection of electrons in magnesium oxide smoke by Heidenreich and Sturkey[1], one of the present authors, Kambe and Honjo[2] studied them electron-microscopically in detail, and found that magnesium oxide

---

* Now at Hitachi Laboratory, Hitachi Ltd., Hitachi, Japan.

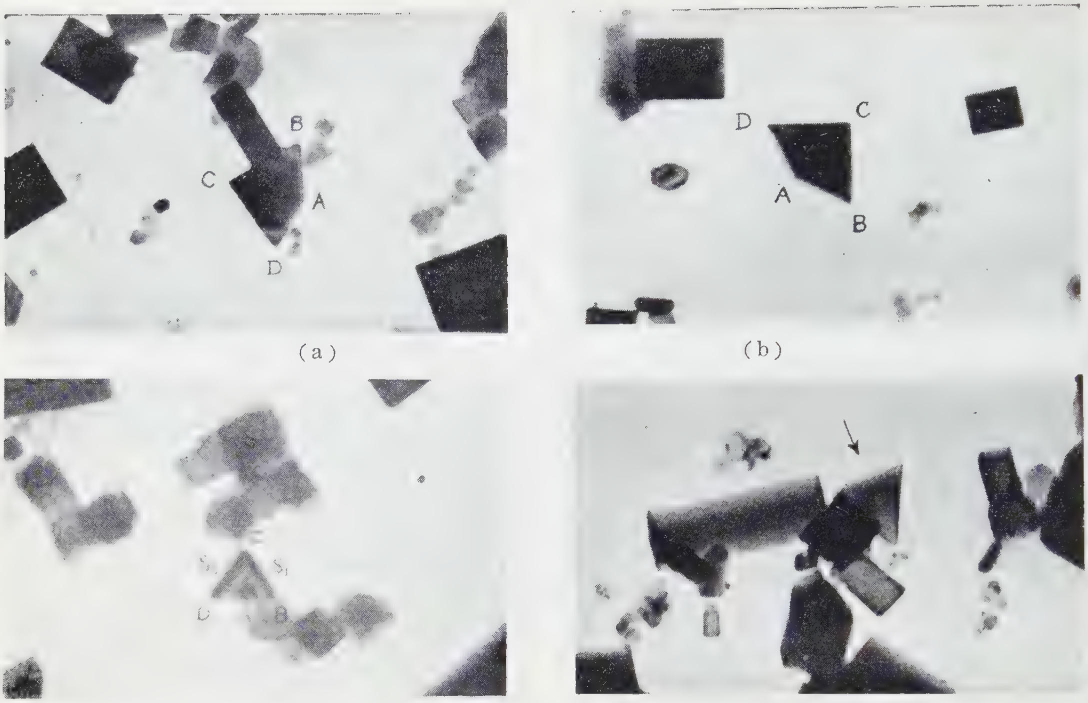

(a) (b) (c) (d)

Fig. 1. Crystals having (111) twin which can be explained by using the model in Fig. 2 (a). (a) and (b), 50,000 × ; (c), 100,000 × ; (d), 70,000 × .

crystal is sometimes twinned.

In the present study the crystal habit of magnesium oxide smokes was observed electron-microscopically in detail, and the existence of the (111) twin appearing in various manners was confirmed from the contour form of crystals in images and the interference fringes. The bare faces at the corners of crystals (we call it *cut section* in the present paper) and various modes of connection between crystals were also newly studied.

§ 2. Twin

Electron-microscopic photographs of magnesium oxide smokes were obtained by using a magnetic electron microscope with objective aperture of 0.078 mm and anode potential of 50 KV ($\lambda=0.054$Å). In order to determine the twin plane and the orientation of crystal, interference fringes appearing in the crystals were observed together with the contour forms of the crystals in image.

As already described in Hibi, Kambe and Honjo's paper[2], McGillavry[3] has developed the dynamical theory in the case of a plane-parallel plate, and has given the formulae which express the intensities of the transmitted and reflected waves as sinusoidal functions of the thickness of the crystal. Heidenreich and sturkey[1] used these formulae* to calculate the spacing of the fringes. By the equation[5] which Heidenreich derived from this conventional theory, the distance Z between the nodes of beat of electron wave travelling the crystal field is given as follows:

$$Z_{hkl}=(2\pi/|\boldsymbol{k}|)[(V_{hkl}/E)^2+(\Delta\theta)^2\sin^2 2\theta]^{-1/2},$$

where $(2\pi/|\boldsymbol{k}|)=\lambda$, λ is the wave length of incident electron beam, E the accelerating potential, θ the Bragg angle, $\Delta\theta$ the angular deviation from the Bragg angle, and V_{hkl} a Fourier term of the inner potential of crystal. In the case of applying this to a wedge-shaped part of the crystal, the spacing of the fringe is given by

---

* As the thickness varies rapidly in the case of magnesium oxide, this equation does not exactly hold. Generalized Bethe's theory to the case of a wedge-shaped crystal was treated by N. Kato[4]. However, in the present study the calculation on spacings of the fringes was made for the purpose of determining the twin or the cut section faces of crystals. So the equation in the case of planeparallel plate was used for simplicity.

$$S = f Z_{hkl} ,$$

where f is a function depending on the orientation of crystal and its shape. In this experiment the largest spacings of interference fringes were calculated, by using the values of Fourier terms of the inner potential of magnesium oxide crystal shown in Table I.**

Table I. Inner potential of MgO.

(hkl)	V_{hkl} (volts)	remark
(200)	7.42	(1)
(220)	5.37	(1)
(111)	1.56	(1)
(222)	4.30	(6)*

* The value introduced from calculated value of f (atomic structure factor for X-ray)

It was found from the observation and its discussion by Hibi, Kambe and Honjo[2] that the image shown in Fig. 1 (a) could easily be explained as a (111) twinned crystal corresponding to the model shown in Fig. 2 (a). In their work Fig. 1 (b) could also be explained from the same model. This is, namely, the case when (100) is perpendicular to the incident electron beam, and certain lattice plane of one or both crystals (*P*- and *Q*-crystal in (a) and *P*-crystal in (b)) of the twin satisfies the Bragg's condition. Fig. 1 (c) can also be explained from the same model; it is the case when (100) is parallel to the incident electron beam, [010] and [001] are in the direction making angle 45° to the incident beam, and one of the twinned crystals satisfies the Bragg's condition. However, as the observed value of the angle ∠B is not perfectly equal to observed ∠D as shown in Table II, it must be considered that the orientation of the crystal slightly rotates around [100] as compared with the ideal case. In this example (200) is the most probable reflecting plane for generation of fringes, as seen in Table II.

In some cases, crystals showing no striations but with triangular projections like Fig. 1 (d) are often observed.

The crystals having the (111) twin of other types are shown in Fig. 3 (a), (b), (c) and (d). These are expected to occur when one [100] (D D′ of the models shown in Fig. 2 (b) and (c)) is nearly parallel to the incident electron beam. Then, Fig. 3 (a) corresponds to the model in Fig. 2 (b), and Fig. 3 (b), (c) and (d) to the model in Fig. 2 (c). Fig. 3 (c) is a typical case among these and the inscribed letters A, B, C etc. are a projection corresponding to those in Fig. 2 (c). In the case when *P*-crystal of the model in Fig. 2 (c) has the base (CDE) either rectangle or regular square, a symmetric figure as Fig. 3 (b) or asymmetric

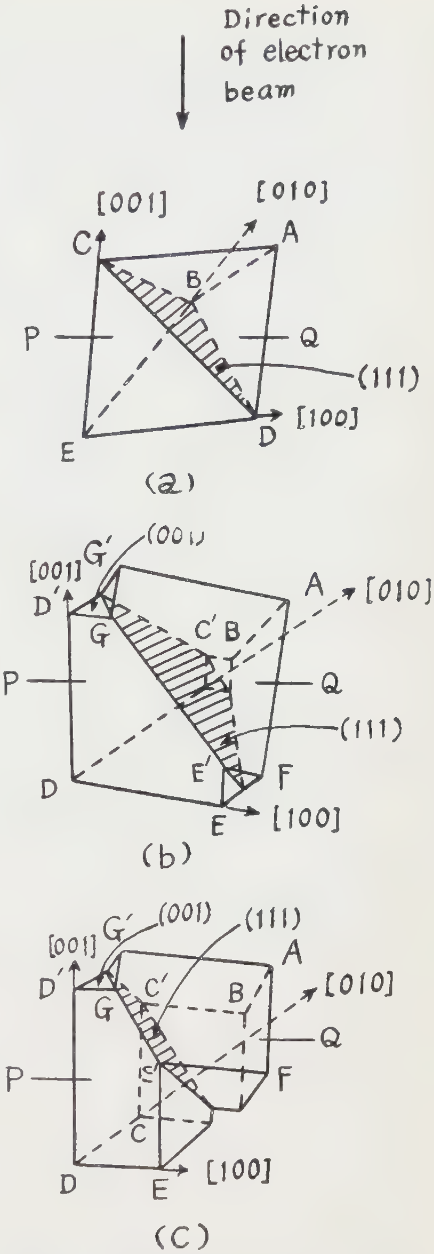

Fig. 2. Various models of crystals having (111) twin.

** In the case of using Mg^{++} and O^{--}, the values of V_{hkl} become larger a little than those in Table 1. See the reference (2).

Table II. Comparison of angles and spacings of the fringe between ideal and observed cases in the case of Fig. 1 (c).

case	∠B	∠C	∠D	spacing of fringe along BC-edge S_1 (200)	spacing of fringe along CD-edge S_2 (200)
ideal	54.7°	70.6°	54.7°	max 297 Å	max 297 Å
obs.	58	73	53	250	300

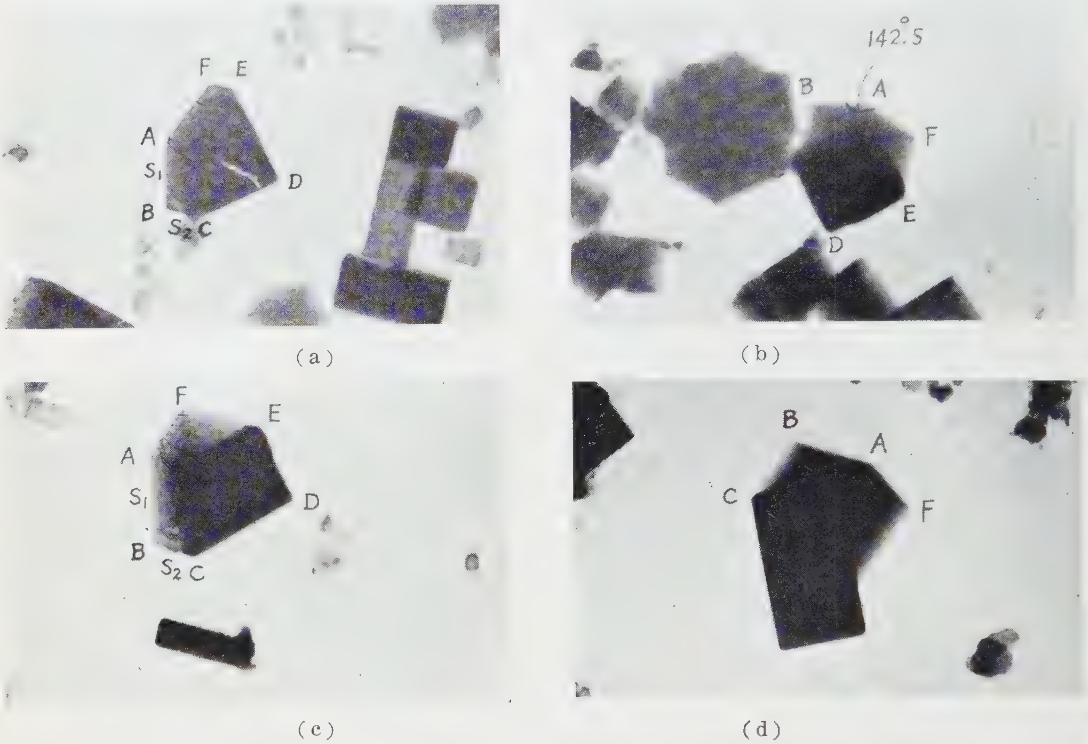

(a) (b)

(c) (d)

Fig. 3. Crystals having (111) twin which can be explained by using the models in Fig. 2 (b) and Fig. 2 (c). (a), (b), (c) and (d). 70,000×

Table III. Comparison of angles and spacings of the fringe between ideal and observed cases in the case of Fig. 3.

case	∠A	∠B	∠C	∠F	S_1 (220)	S_2 (220)
ideal	143.2°	108.6°	135°	108.6°	max 163 Å	max 252 Å
obs. a	142.5	108	135	109	130 126	230 259
〃 b	142.5		135			
〃 c	143	113	133	108	128 128	196 211
〃 d	145.5	111	133.5	108		

one as Fig. 3 (c) is obtained respectively. As (220) of Q-crystal is nearly parallel to the direction of the incident electron beam, this may be the reflection plane causing the interference fringes. The values of the corner angles and the spacing of fringes in the ideal case of this model, and those values observed are shown in Table III, and good agreement is seen between both values.

Crystals of apparently different type from previous ones are shown in Fig. 4 (a) and (b). These crystals can be, however, explained essentially from the model in Fig. 2 (c). These are the cases in which the model is

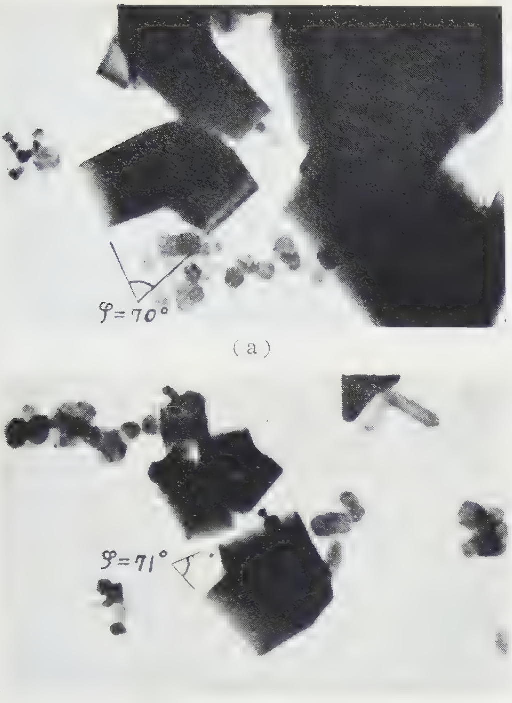

Fig. 4. Crystals of apparently different type from ones of Fig. 1 and Fig. 3. 70,000×

placed in such a manner that [001] axes of *P*- and *Q*-crystal are nearly perpendicular to the incident electron beam. Sizes of both crystals were nearly equal in our case. If [001] axes of both crystals are exactly perpendicular to the incident electron beam, φ indicated in Fig. 4 (a) and (b) should be 70.6°. In the cases (a) and (b), φ are 70° and 71° respectively, slightly deviating from the ideal case. In Fig. 4 apparently [100] slightly inclines to the plane perpendicular to the incident electron beam; but it is found by the calculation, that φ scarcely changes and has nearly a constant value of 70° even though [100] slightly inclines. Only in the case of (a), the striation is seen. This happens because only the right crystal satisfies the Bragg's condition. If (110) of this crystal is nearly parallel to the incident electron beam and the striation is caused by the reflection (220), the largest spacing of the fringe is 260Å corresponding to the observed value of 200Å.

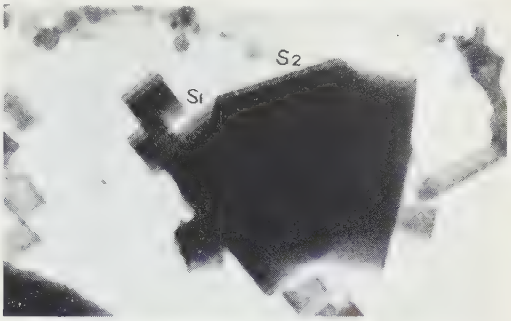

Fig. 5. Crystal which is essentially equal to Fig. 3 and Fig. 4. 70,000×

Fig. 5 is essentially similar to Fig. 3 and Fig. 4; it occurs when (100) (A B C′ G′-plane) of *Q*-crystal in the model of Fig. 2 (c) is nearly parallel to the incident electron beam whereas [100] (E E′) of *P*-crystal is perpendicular to the incident electron beam. In Fig. 6 (sketch of Fig. 5), S_1 is clearly due to the reflection (200) by *P*-crystal, and S_2 may also be considered to be due to *P*-crystal only. As no striations are seen at another part of *Q*-crystal, it is probable that only *P*-crystal satisfies the Bragg's condition. If the angle between (010) (E E′ G D′ D-plane in Fig. 2 (c)) of *P*-crystal and the incident electron beam is α, the spacing of the fringes S_2 is given by

$$S_2 = (\cos\alpha + \sin\alpha)\frac{\sin\alpha}{\sqrt{1+\sin^2\alpha}} Z_{200}\ .$$

Calculated value of S_2 in the case of $\varphi = 157.5°$ and observed one are shown in Table IV. From this, it can be seen that each calculated

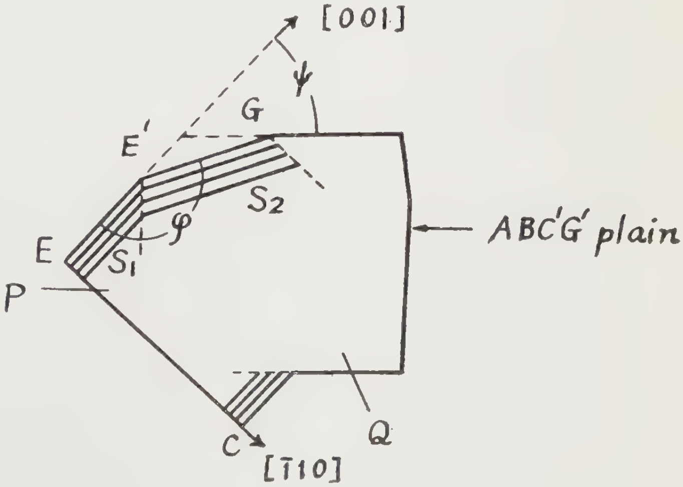

Fig. 6. Schema of Fig. 5.

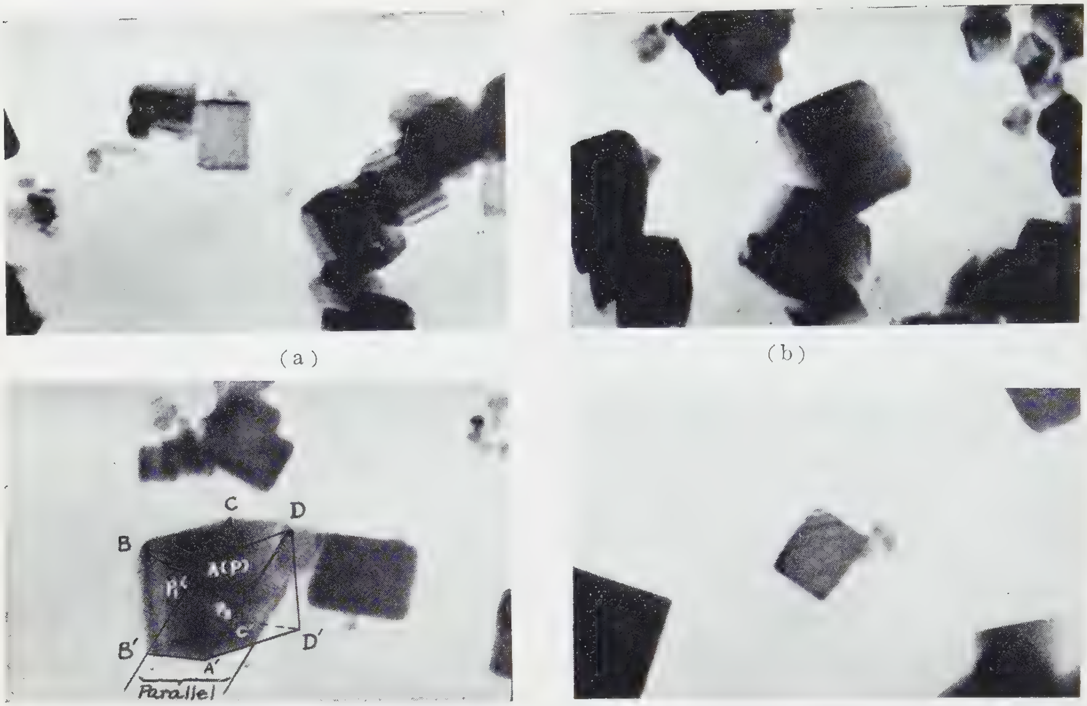

(a) (b)

(c) (d)

Fig. 7. Extraordinary crystals having particular cut section.
100,000×

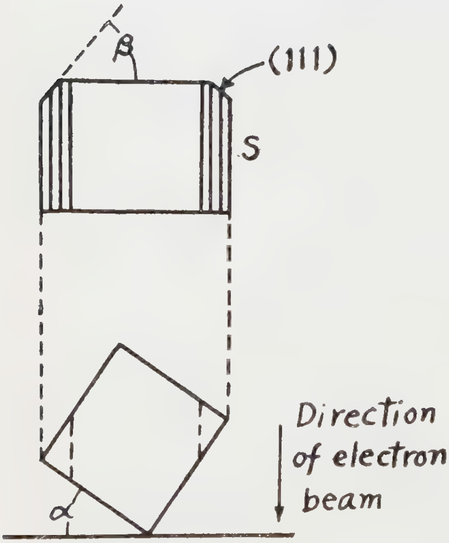

Fig. 8. Schema of Fig. 7 (a).

Table IV. Comparison between calculated and observed values on angles and spacings of the fringe in the case of Fig. 6.

case	φ	ϕ	γ *	S_1	S_2
calc.	157.5°	48.2°	88.5°	max 137 A	max 187 A
obs.	157.5	47.5	about 90	117	149

* γ is the angle between $A\ B\ C'\ G'$-plane and a plane perpendicular to the incident electron beam.

angle and spacing of the fringes are in good agreement with observed values. If the fringes S_1 and S_2 are due to the reflection at (200) of the same crystal, the values of the deviation $\Delta\theta$ from Bragg's angle, estimated from the fringes S_1 and S_2 neglecting the refraction effect, must agree to each other. We obtain from the equation by Heidenreich,

$$\Delta\theta(S_1)=0.0022 \quad \text{radian}$$

and

$$\Delta\theta(S_2)=0.0028 \quad \text{radian},$$

which are in a good agreement. This is very interesting because it proves the correctness of dynamical theory to some extent.

§ 3. Cut Section

Extraordinary crystals having particular cut section as shown in Fig. 7 (a) and (b) were often observed in crystals having the (111) twin. The striation appearing in such crystals is due to the reflexion on (200). Because of small cut section and distortion of image, errors easily enter into measurement of β (in

Fig. 8). The values of β in the right and left corners are considerably asymmetrical. The largest spacings $S_{\max}$ of the fringe due to theoretical calculation assuming the cubic crystal form are shown in Table V, which were calculated by using the mean value of β. In this table, $S_{\max}$ (111) and $S_{\max}$ (112) are respectively the spacings of the fringe in the cases when the cut sections (111) and (112) were assumed. Considering from this table, the cut section (111) is more probable than that of (112), but it cannot be concluded clearly to be so. If we assume the cut sections to be the {112} planes, there are two possible cases, namely; (A), the case of the cut section (112); (B), that of (121) or (211). By utilizing the calculated β—α curve and the $S_{\max}$—α curve given in Fig. 9, we can confirm, for the case of (A) the fact that the largest spacing of the fringe $S_{\max}$ (112) calculated from the observed angle β is smaller than the actually observed spacing, so that possibility of (A) is very small. For the case of (B), β obtained from observations can not exist theoretically, so that the possibility of (121) or (211) is none. Therefore, considering the fact that (111) has the largest atomic density except (100), it is concluded that cut section may be (111).

Table V. Comparison between calculated and observed values on spacings of the fringe in the case of Fig. 7 (a) and (b).

crystal	β		observed value of S		$S_{\max}$ (111)	$S_{\max}$ (112)
a	59°	52.3°	125 A	130 A	180 A	115 A
b	59.3 60.8	55.2	93	95	180	106
c	60	60			170	100
d	57.5	57.3	145	147	180	108
e	55.7	50.7	147	160	180	120
f	57.7		109	106	180	106
g	66.8		119	124	140	80
h	60.8		105		170	96

Fig. 7 (c) is another typical example. Crystals are nearly cubic and interference fringe due to the (222) reflexion is seen. In the figure, C, A and B′ are on a straight line and (111) is nearly parallel to the direction of the incident electron beam. The calculated values of ∠B and the spacings of fringe due to reflexion on (111) and (222) are shown in Table VI by assuming $AC/BP_1=0.64$.

Crystal shown in Fig. 7 (d) is imagined to be that with a cut section and a equal-thickness interference fringe due to Bragg reflexion of electrons. But, assuming that (100) is perpendicular to the direction of the electron beam and that (111) is the cut section, the largest spacing of the fringe become twofold larger than the observed value in both cases of (220)- and (200)-reflexion.

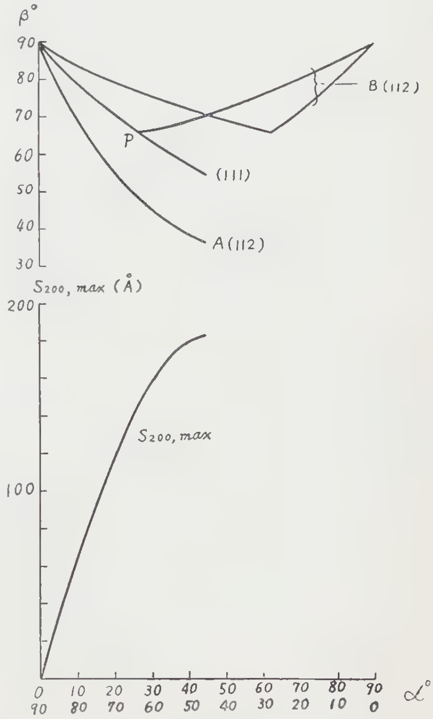

Fig. 9. $\beta-\alpha$ curve and $S_{\max}-\alpha$ curve. α and β are the angles defined in Fig. 8.

Table VI. Comparison between claculated and observed values on angle and spacings of the fringe in the case of Fig. 7 (c).

case	AC/BP_1	∠B	spacing of fringe	
			S (111)	S (222)
calc.	0.64	100.7°	max 940 A	max 270 A
obs.	0.60~0.64	100.5	290 A	

§ 4. Modes of Connection of Crystals

Various modes of connection of magnesium oxide cubic crystals are found in Fig. 10 (a) to (j). Modes of connection at edges ((c) and

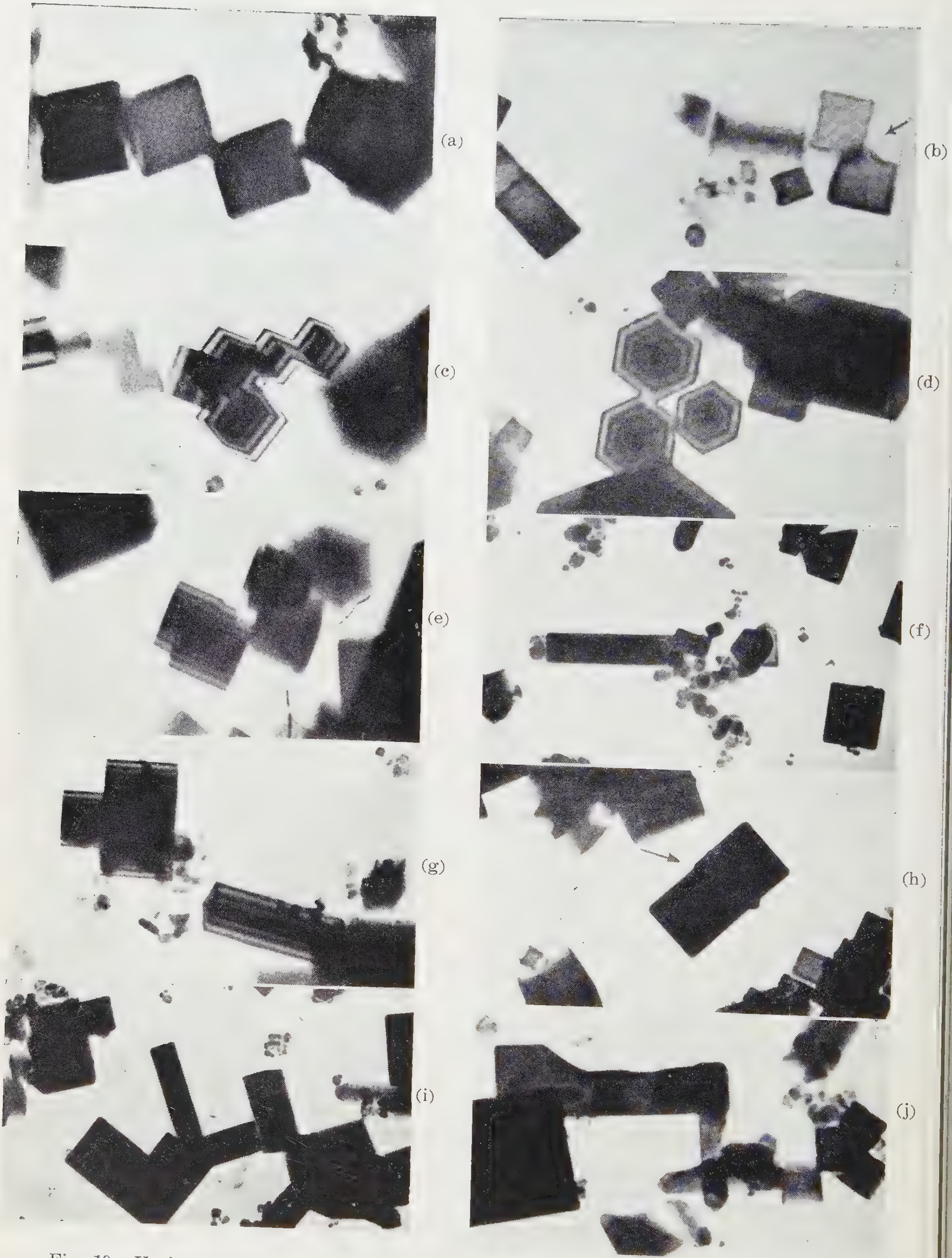

Fig. 10. Various modes of connection of MgO cubic crystal. (a), (b) and (e), 100,000× ; (c), (d), (g), (h) and (j), 70,000× ; (f) and (i), 50,000×.

(e)*), at corners ((a), (b) and (d)) and at (100) plane of crystal ((f) and (g)) are seen from this figure. (In the case of connection at edge there are crystals having uniform contrast as (a) and crystals having a part of weak contrast as (b)).

There also appears a considerably long crystal of rectangular parallelepiped, but it should be noted that the ratio of each side is not always integer, which suggests the fact that the crystal is one block, not a long chain of smaller cubic crystals.

Among crystals which are practically regarded as rectangular parallelepiped, there are crystals having not straight contour in their image such as (h), and also, crystals showing the manner of bridging over of a little contrast at connected part of (100) such as (b). Also, there is *L*-shaped crystals as shown in (i). And also there often appears a complicated crystal such as (j), though its origin cannot be explained at the present. From the appearance of crystals in which interference fringes are continuous as seen in (c), (d), (e) and (g), it can be concluded that all crystals have a common lattice.

§ 5. Conclusion

Considering from the above-mentioned results, it is clear that magnesium oxide smokes often produce the (111) twin. It is reasonable physically that the (111) plane, having the lowest index and the largest atomic density except (100), becomes the twin plane. It is also very interesting that there exist many crystals having the (111) cut section. Perhaps these may be produced by breaking off of twinned crystals at the twin plane. It was also found that there are many interesting modes of connection of crystals, and this will be an interesting problem to be studied in the future.

In conclusion the authors wish to express their appreciation to Prof. R. Uyeda and Prof. S. Miyake for their kind interests, to Dr. G. Honjo and Mr. K. Kambe for their kind discussions. They would also like to express their thanks to Mr. S. Takahashi for his helpful assistance.

References

1) R. D. Heidenreich and L. Sturkey: J. App. Phys. **16** (1945) 97.

2) T. Hibi, K. Kambe and G. Honjo: J. Phys. Soc. Japan, to be publish.

3) C. McGillavry: Physica **7** (1940) 334.

4) N. Kato: J. Phys. Soc. Japan **7** (1952) 397, J. Phys. Soc. Japan **8** (1953) 350.

5) R. D. Heidenreich: J. App. Phys. **20** (1949) 993.

6) R. W. James and G. W. Brindley: Phil. Mag. **12** (1931) 81.

---

* These micrographs were already shown in the paper by Hibi, Kambe and Honjo$^{2)}$.

JOURNAL OF THE PHYSICAL SOCIETY OF JAPAN Vol. 9, No. 4, JULY—AUGUST, 1954

On the Anomalous Absorption of X-rays by Crystals at the Setting of Bragg Reflection

By Hide YOSHIOKA

Physical Institute, Nagoya University, Nagoya, Japan

(Received March 30, 1954)

Intensities of X-rays transmitted through crystals of calcite, topaz and pyrite at the settings of Bragg reflections were studied using a double crystal spectrometer. In the case of MoKα, transmission patterns have minima at Bragg angles. However, an asymmetry is noted in the patterns. In the case of CuKα, the transmission pattern through calcite has a large maximum near the Bragg angle accompanying a small minimum on the side of large glancing angles.

§ 1. Introduction

G. Borrmann[1)] reported recently an interesting observation that when a thick crystal (2.71 mm in thickness) of calcite was exposed to a divergent CuKα X-ray, the photographic plate placed at the back of the crystal showed two kind of intensity maxima ; one was due to the reflected rays by the net planes, while the other appeared in the incident directions at which Bragg reflections take place. Subsequently Campbell[2)] measured intensities of transmitted CuKα X-rays through calcite using an X-ray spectrometer and found a sharp maximum at a setting of Bragg reflection.

These results are in contrast with those obtained previously by W. H. Bragg and W. L. Bragg, James and Bosanquet.[3)] These authors reported that the intensity of RhKα X-rays transmitted through diamond or NaCl crystal is decreased at Bragg angles. The difference of these results seems to imply that the transmitted intensity depends strongly on X-ray wave-length, crystal thickness and crystal perfectness. In order to study these dependences, the author carried out some experiments using MoKα and CuKα-rays and crystals of calcite, pyrite and topaz.

(Shortly after the experiments were finished Rogosa and others[4)] published a paper which is similar to this work).

§ 2. Experimental

The apparatus used in this work was a double crystal X-ray spectrometer. The first crystal was a calcite which was cloven carefully. The second crystal is a sample to be studied. The intensity of rays transmitted through or reflected by the sample was measured by a G. M. counter. The counter was a glass sealed type, the cathode was a brass cylinder *ca.* 2.5 cm in diameter and 12 cm long, and the anode a tungsten wire of 0.01 cm in diameter. An X-ray beam to be measured entered the counter through a window of thin mica (0.01 mm in thickness), and passed through the counter in its axial direction. The gas filled in the counter was a mixture of argon at 120 mmHg and C_2H_5OH vapour at 12 mmHg. Counter pulses were recorded by a 64 scale-down circuit and a mechanical register with resoluble time of 1/30 sec. Since the stabilization of the X-ray source was a difficult task, the intensity of the monochromatized X-ray was monitored before the sample by means of an ion chamber and an electrometer system. The ion chamber was filled with normal pressure of air mixed with a small amount of CH_3Br. The number of counter pulses was recorded for a period during which the electrometer gave a certain deflection.

§ 3. Results

(1) Experiments with MoKα.

Calcite. The sample was a plate parallel to the cleavage plane. Its thickness was reduced to 0.60 mm by grinding the surface with 800 mesh *Corrundum*. In order to remove the surface layer it was slightly etched with dil. HCl. The Bragg reflection studied was due to (112) plane (equivalent to the cleavage plane) which makes an angle of 74°55′ with the plate face. The paths of the transmitted and reflected rays are shown shematically in Fig. 7. Variations of the reflected intensity and the transmitted one with the glancing angle of incidence are shown in Fig. 1. It is noteworthy that the minimum of the transmission pattern coincides, within the experimental error, with the maximum of the reflection pattern. Moreover, the depth of the minimum of the transmission pattern is nearly equal to the peak height of the reflection pattern.

Topaz. The sample was a plate of thickness 1.57 mm parallel to (001) plane. The surface layer was not removed because no adequate etching reagent was available. The Bragg reflection by (120) plane was studied. The results are shown in Fig. 2.

Pyrite. The sample was a plate of thickness 0.26 mm parallel to a cube face. The surface was etched with boiled *aqua regia.* The measured reflection was due to (100) plane. The results are shown in Fig. 3.

In every case with MoKα it is noted that the transmission pattern is unsymmetrical with respect to its minimum, the transmitted intensity is slightly greater for small glancing angle side of the minimum than for the other side.

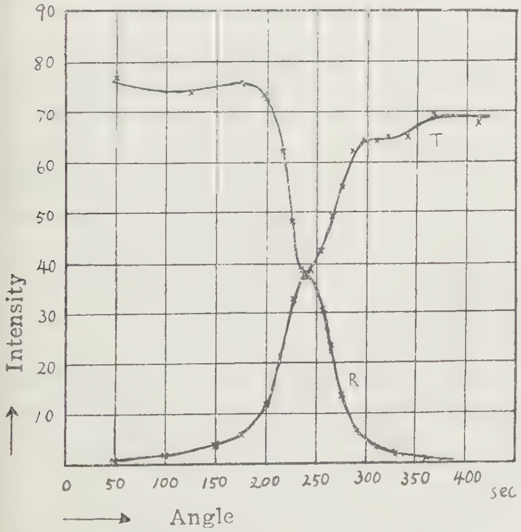

Fig. 1. Calcite, (112). thickness 0.60 mm, MoKα.

(2) Experiments with CuKα.

Samples used in these experiments were thin because the transmitted intensity through thick crystals such as used before became too weak to be measured by our apparatus. In the case of FeS_2 it was unable to prepare a sample thin enough to be used.

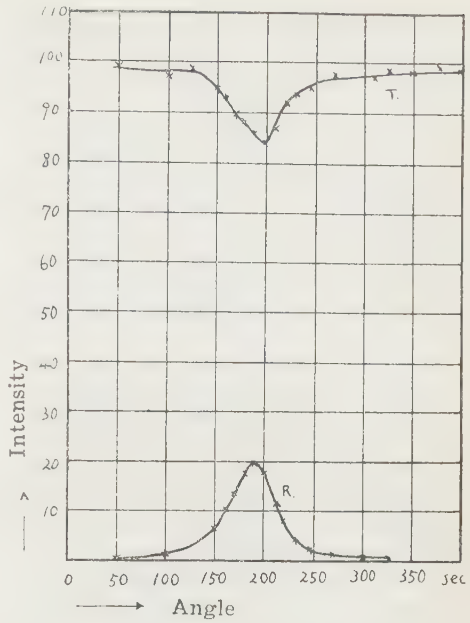

Fig. 2. Topaz, (120), thickness 1.59 mm, MoKα.

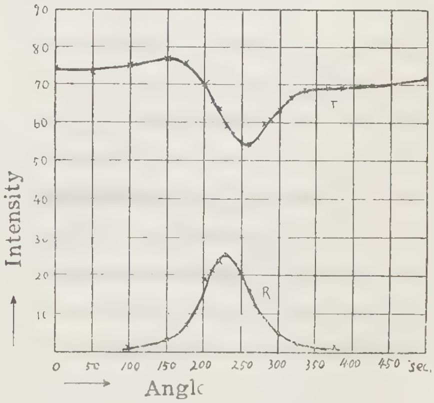

Fig. 3. Pyrite, (002), thickness 0.265 mm, MoKα.

Calcite. The results for a sample of thickness 0.33 mm is shown in Fig. 4. The transmission pattern has a large maximum accompanying a small minimum on its larger glancing angle side. The position of the maximum of the transmission pattern is slightly shifted to smaller angle from that of the maximum of the reflection pattern.

In the experiments described above (including the case of MoKα) reflection patterns had relatively large angular widths, which suggested the divergence of the beam incident upon the sample is large. This divergence seemed to cancel a large part of the minimum and maximum, and to flatten them. In order

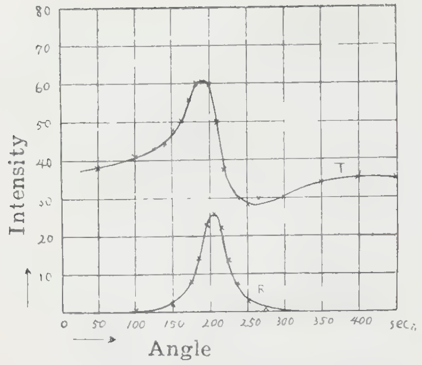

Fig. 4. Calcite, (112), thickness 0.33 mm, CuKα.

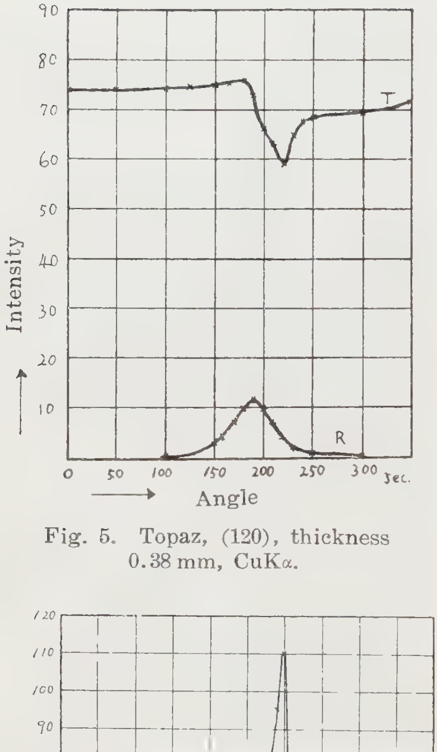

Fig. 5. Topaz, (120), thickness 0.38 mm, CuKα.

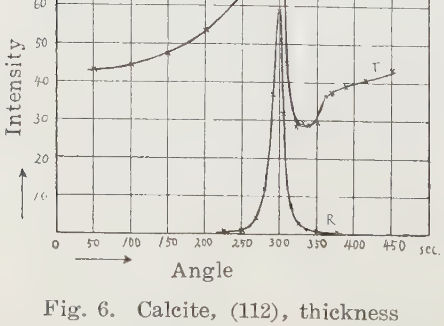

Fig. 6. Calcite, (112), thickness 0.285 mm, CuKα.

to reduce the divergence which is due to the imperfectness of the first crystal, only a small portion *ca* 2 mm in diameter of the first crystal is exposed to the X-ray beam. (At the same time the focus of the X-ray source was reduced to an area of 0.2 mm in diameter). A sample of 0.28 mm in thickness, was used and its exposed face was confined by a lead diaphram to a circle of 3 cm in diameter The results are shown in Fig. 6. The half angular width was reduced as expected, and it appeared to be only 17 seconds. It is remarkable that the maximum of the transmission pattern is now very sharp and the position of the maximum of the transmission pattern is very close to that of the maximum of the reflection pattern, the angle between them is the order of an experimental error 1 second.

Topaz. A sample of thickness 0.38 mm was used. The results are shown in Fig. 5 Though the maximum of the transmission pattern is not so marked as for the calcite the asymmetry of the pattern with respect to its minimum is strongly enhanced.

§ 4. Discussion

The transmission patterns of MoKα through calcite, topaz and pyrite show minima at Bragg angles as observed by James, Bragg and Bosanquet in the case of NaCl with RhKα X-ray. Recently Schwarz and Rogosa4) have observed a similar pattern for calcite 0.4 mm in thickness. They have also observed that a minimum in the pattern changes to a maximum when the thickness of the crystal is increased. In our experiments the transmission pattern in the case of CuKα X-rays through calcite crystal has a sharp maximum and a shallow minimum. This kind of pattern was also observed by Schwarz and Rogosa, and it is an intermediate pattern between that observed by James, Bragg and Bosaquet and that observed by Campbell and Borrmann.

The theory of the X-ray diffraction by absorbing perfect crystals was developed by G. Molière,5) v. Laue6) and recently by Hirsch.7) The calculated curves according to v. Laue's formula for the transmitted and reflected intensities for calcite in the case of CuKα are shown in Figs. 7, 8 and 9. The imaginary parts of Fourier coefficients of

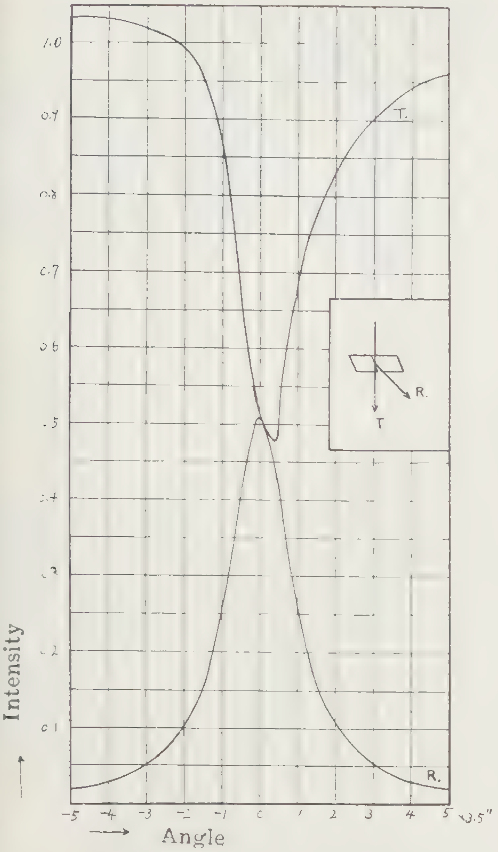

Fig. 7. Calcite, (112), thickness 0.01 mm, CuKα, calculated.

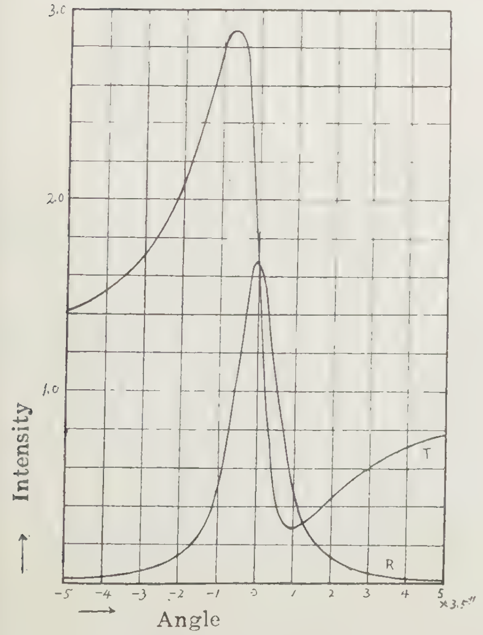

Fig. 8. Calcite, (112), thickness 0.10 mm, CuKα, calculated.

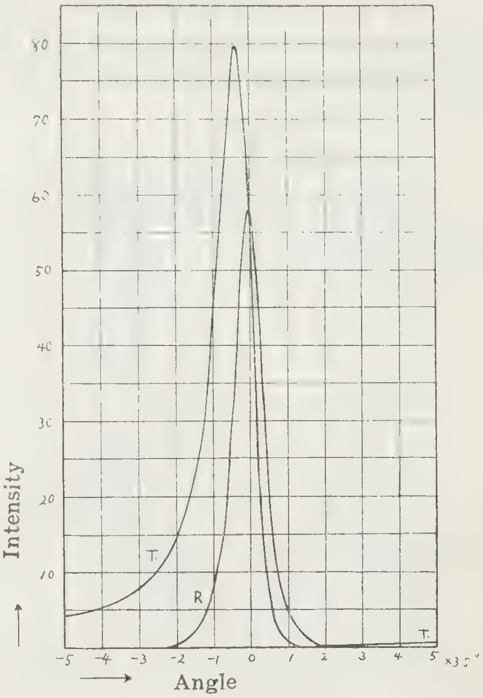

Fig. 9. Calcite, (112), thickness 0.285 mm, CuKα, calculated.

susceptibility χ_0'', χ_h'' in v. Laue's formula can be calculated from the value of complex scattering factors calculated by Hönl.[8] Amongst the calculated patterns for various thicknesses, that for 0.1 mm thickness (Fig. 8) has a similar form to the observed one for CuKα (Fig. 6) instead of that for 0.28 mm thickness (Fig. 9) This contradiction may be solved by assuming a mosaic structure for the sample crystal. However, a simple comparison of the observed and calculated curves is not adequate since there seems to exist an angular divergence of about 10 seconds in the incident X-ray. The difference of the maximum of reflection pattern and the minimum of the transmission pattern is calculated to be *ca* 1 second which is the order of an experimental error in our experiment.

The patterns for MoKα have similar forms to the calculated one for thin plate with CuKα. This is because the wavelength and the crystal thickness play similar roles in v. Laue's formula. The minimum of transmission pattern has much larger value than the maximum of the reflection pattern in the case of topaz and pyrite. This is not explained by v. Laue's formula and it seems to be due to the mosaic structure of the crystal.

The author would like to thank Prof. R. Uyeda for his interest in this work and many helpful discussions.

References

1) G. Borrmann: Phys. Z. **42** (1941) 157; Z. Phys. **127** (1950) 297.
2) H. N. Campbell: J. A. P. **22** (1951) 1139.
3) W. H. Bragg: Phil. Mag. **27** (1914) 881.
W. L. Bragg, R. W. James and C. H Bosanquet: Phil. Mag. **41** (1921) 309.
5) G. Molière: Ann. d. Phys. **35** (1939) 27 297.
6) M. v. Laue: Acta Cryst. **2** (1949) 106.
7) P. B. Hirsch: Acta Cryst. **5** (1952) 176.
8) cf. Zachariasen: Theory of X-ray Diffrac tion in Crystals, p. 144, (1945).

Short Notes

J. Phys. Soc. Japan **9** (1954) 640~641

The Use of Radioactive Isotope in a Study of Evolution of Strontium Oxide under Electron Bombardment

By Shigetomo Yoshida, Nagao Shibata
Yoshitaka Igarashi and
Hikaru Arata

Electrical Communication Laboratory,
Nippon Telegraph and Telephone Corporation,
Musashinoshi, Tokyo, Japan

(Read Oct. 17, 1953, Received Feb. 22, 1954)

The changes of thermionic emission of oxide-coated cathode caused by electron bombardment have been measured by the authors[1] to make clear the factors which determine the life of composite secondary emission surfaces such as barium, beryllium and magnesium oxides. The results obtained indicated that barium oxide decomposed into barium atoms and oxygen molecules by electron bombardment. From many experimental results,[2] it is certain that the oxygen molecules formed are liberated from the surface. There is, however, very few knowledge about the behaviour of barium atoms and, in general, of metal atoms. We, therefore, measured the quantities of strontium evolved during electron bombardment by using strontium oxide containing radioactive strontium 89.

The experimental tube is shown in Fig. 1. A is a nickel sleeve coated with strontium carbonate containing Sr^{89}. One gram of this strontium carbonate contained 0.36 mc of the radioactive isotope also as carbonate. F is the primary electron source and C is the nickel plate (2.5×1.5 cm) on which deposit strontium atoms evolved from A. In order to diminish the possibility of contaminating the collecting plate C by strontium radioactive isotope evaporated from A during evacuation, activation and aging processes, th circumference and the upper and lower sides c those electrodes are shielded by means of nick and mica plates respectively. The decompositio process of Sr-carbonate into oxide was carried ou at a pressure lower than 2.5×10^{-5} mm mercur S, in Fig. 1, is a movable shield to be remove only during the bombardment. The quantities c Sr^{89} deposited on C is measured by Nuclear In counter (1.4 mg/cm² mica window) which is shiel ed by 5 cm thickness of lead on all sides in orde to diminish natural counts.

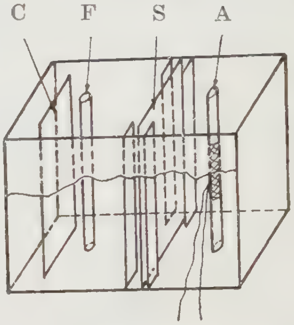

Fig. 1. Experimental tube.

The quantities of Sr^{89} and total mass of stro tium deposited on C under various bombardme conditions are shown respectively in Table I, as function of bombarding currents, times and vol ages. The factor (2.2×10^{-8} gr/cpm) which conver cpm into total mass of strontium is calculate from the counting rate of the standard specime As the temperature of strontium oxide depend on the input wattage (bombarding current×vo tage), the temperature is adjusted to be consta by means of backheater even though the bon barding current is varied at a given bombardme voltage. Fig. 2 gives an example of the curv showing the quantities of Sr^{89} deposited on C a a function of bombarding time.

Table I. The quantities of Sr^{89} and total mass of strontium deposited on C.

Bombardment conditions				c p m	Total mass of strontium
Voltage (volt)	Current (mA)	Temperature (°C)	Time (hour)		(10^7)gr
150	3.5	450	6†	26.4± 0.8	5.8±0.2
〃	〃	〃	6	26.8± 0.8	5.9±0.2
〃	〃	〃	34	95.1± 1.1	20.9±0.3
〃	〃	〃	57	222.2± 4.1	48.9±1.0
〃	〃	〃	100	141.9± 2.0	31.2±0.5
〃	〃	〃	110	415.1± 8.4	91.4±1.9
〃	〃	〃	140	637.2± 7.5	140.2±1.7
〃	〃	〃	150	627.8± 7.7	138.2±1.7
〃	〃	〃	180	682.1± 9.9	150.1±2.2
〃	2.5	400	6	11.4± 0.9	2.5±0.2
〃	〃	〃	150	233.6± 4.9	51.4±1.1
〃	〃	450*	43	230.6± 4.5	50.8±1.0
〃	〃	〃*	60	190.3± 7.0	41.9±1.5
〃	〃	〃*	128	412.5± 3.5	90.8±0.8
〃	〃	〃*	191.5	699.8±10.9	153.6±2.4
〃	1.0	260	21	0.2± 0.5	0.1±0.1
〃	〃	〃	122	1.3± 0.6	0.3±0.2
〃	〃	450*	21	17.7± 1.3	3.9±0.3
〃	〃	〃*	120	179.9± 3.3	39.6±0.8
500	〃	450	6	0± 0.6	0±0.2
〃	〃	〃	34	3.5± 0.6	0.8±0.2

† strontium oxide was heated at 800°C for 5 min after each bombardment which lasted for 10 min.

* temperature was adjusted using back heater.

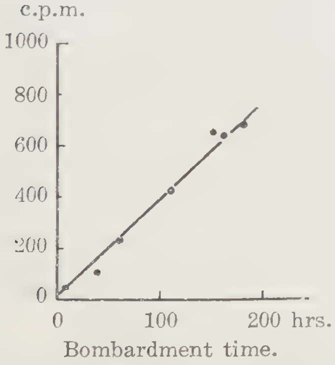

Fig. 2. The quantities of Sr^{89} deposited on C as a function of bombardment time.

Though there are some irregularities in the experimental results obtained, the following general conclusions may be drawn:

(1) When the voltage was kept at 150 volts and the current was varied as 1 mA, 2.5 mA and 3.5 mA, the rate of evolution increased linearly with the current provided the temperature of strontium oxide remained constant.

(2) The rate of evolution increased exponentially with the rise of the temperature between 250° and 450°C. The activation energy about 0.8 eV.

(3) When the input wattage is equal, the evolvement by 500 eV electrons is far less than by 150 eV electrons.

(4) The efficiency of the evolution, or the number of strontium atoms evolved per one primary electron, is around 1.5×10^{-5} at 150 eV and 3.5 mA primary electron current.

References

1) S. Yoshida, I. Takeda and H. Arata: J. Phys. Soc. Japan **7** (1952) 430.

2) J. Wood and D. A. Wright: British J. App. Phys. **4** (1953) 56.

3) K. Amakasu and T. Imai: J. App. Phys. **24** (1953) 107.

J. PHYS. SOC. JAPAN **9** (1954) 641~642

On the Relation Between Sound Velocity and Intermolecular Free Length of Liquids

By Yasaku WADA

Department of Applied Physics,
Faculty of Engineering,
University of Tokyo, Tokyo, Japan

(Received April 12, 1954)

Recently, B. Jacobson[1] has introduced the following experimental formula,

$$uLd^{1/2}=\text{constant}=K, \tag{1}$$

where u is the sound velocity (m/sec) in a liquid, L the intermolecular free length (Å) and d the density (gr/cm^3). The value K has been confirmed to be constant for a large class of liquids: 55 non-associated organic liquids and 5 series of liquid mixtures. The values of K at different temperatures have been given by Jacobson as listed in Table I. The procedures of computation of L have been given in another paper of the same author.[2)]

The relation (1) can be accounted for by the following simple consideration. According to the hard sphere model proposed by Kincaid and Eyring,[3)] the sound velocity in a liquid is related to the intermolecular free length by

$$u=u_0\cdot(D+L)/L\,, \qquad (2)$$

where u_0 is the sound velocity in the same substance in vapour phase and D is the diameter of the molecule. Using the perfect gas law, Eq. (2) reduces to

$$v=(\gamma RT/M)^{1/2}(D+L)/L\,, \qquad (3)$$

in familiar notations. The distance between the centres of adjacent molecules, $D+L$, is related to molal volume V approximately by

$$M/d=V=(\pi/6)N(D+L)^3. \qquad (4)$$

Substituting Eqs. (3) and (4) to (1), it follows

$$K=(6/\pi N)^{1/3}(\gamma RT)^{1/2}V^{-1/6}. \qquad (5)$$

Though γ, the ratio of specific heats in vapour phase, and V vary from liquid to liquid, $\gamma^{1/2}/V^{1/6}$ remains nearly constant for widely different kinds of liquids. As a consequence, it may be concluded from Eq. (5) that K is nearly independent of the substance.

Table I.

T (°K)	K	$K/T^{1/2}$
273	588	35.6
283	604	35.9
293	618	36.1
298	625	36.2
303	631	36.2
313	642	36.3
323	652	36.3

As for the temperature variation of K, it is easily seen from Eq. (5) that K is expected to be approximately proportional to $T^{1/2}$. In Table I the values of $K/T^{1/2}$ are calculated from Jacobson's data. The results are in agreement, at least approximately, with the above expectation.

Using numerical values of V and γ, e.g. $V=90$ cm^3/mole and $\gamma=1.2$, $K/T^{1/2}$ becomes 69 from Eq. (5), being larger than Jacobson's data by about a factor of 2. Anyhow, since the theory is only of a first approximation, it may be unreasonable to require a quantitative result.

References

1) B. Jacobson: J. Chem. Phys. **20** (1952) 92
2) B. Jacobson: Acta Chem. Scandinavica (1952) 1485.
3) J. F. Kincaid & H. Eyring: J. Chem. Phy **6** (1938) 620.

J. PHYS. SOC. JAPAN **9** (1954) 642~644

Transient Phenomena in the Backward Direction of Germanium Crystal Rectifiers

By Makoto KIKUCHI and Yasuo TARUI
Electrotechnical Lab. Tokyo, Japan

(Received April 16, 1954)

It has been found out that when certain vo tage was applied on a Ge point contact rectifie instantaneously in the backward direction, th current remained almost constant for first severa microseconds and it suddenly increased. Thi sudden increase of the current (called "*step* hereafter) observed on the oscilloscope is shown in Fig. 1. This *step*, whose rise time is of the order of 0.1~0.5 microsecond, is so sharp that it cannot be attributed to the self heating effect of the contact point such as proposed by Hunter and others[1)], since the variation of the contact temperature must be far more gradual. It seems, however, that some temperature effects must be responsible for this phenomena because the experimental results show that the time required for the *step* to occur after the application of the voltage (denoted by τ_s) is quite dependent on the value of the product of the voltage and the cur-

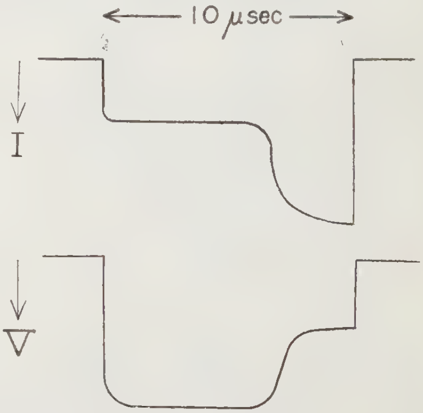

Fig. 1. The "step" observed on the oscilloscope. above ——— current, below ——— voltage. pulse width is 10 microseconds.

rent.

The experimental results of the relation between τ_s and the power (IV) is shown in Fig. 2.

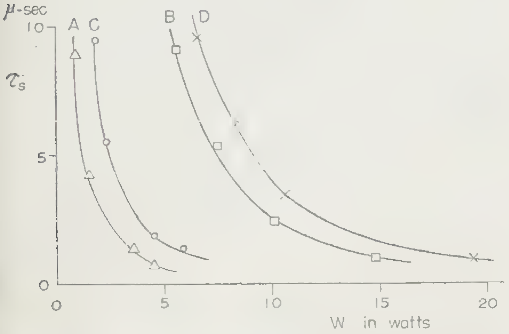

Fig. 2. Experimental results of τ_s-W relation.

We have analyzed this phenomena on the basis of the following physical picture.

(1) The temperatare of the contact point is increased after the application of the voltage.

(2) The strength of the heat source is proportional to the power dissipation.

(3) The heat source is concentrated just beneath the contact point.

(4) The *step* occurs just when the temperature of the contact point reaches a certain characteristic temperature Θ.

It must be noted that in this analysis the problems that "what is Θ?" and "what is the mechanism of the *step* itself?" are kept untouched.

Theoretical equations are derived for the contact temperature as a function of time as follows[2];

$$T=T_0+\alpha_0 W\{1-G^*(t)\}\ , \qquad (1)$$

where

$$G^*(t)=\exp(\pi\lambda^2 t)\left[1-\frac{2}{\sqrt{\pi}}\int_0^{\pi^{1/2}\lambda t^{1/2}}\exp(-S^2)dS^2\right]. \qquad (2)$$

T and T_0 are the temperature of the contact point and the ambient space, respectively, α_0, λ are the constants which depends only on the thermal constants of the materials used and the geometrical construction, and W is the power $V\times I$. Eq. (1) shows that when a voltage is applied on the diode in the backward direction, the temperature of the contact point increases with time and gradually saturates to certain finite value. From the assumption (4), the relation between Θ and W is obtained as follows;

$$\{(\Theta-T_0)/\alpha_0\}(1/W)=1-G^*(\tau_s)\ . \qquad (3)$$

This equation shows fair agreement with experimental results by the proper choice of the two constants. For example, comparison of the theoretical curve with experimental values on sample B is shown in Fig. 3.

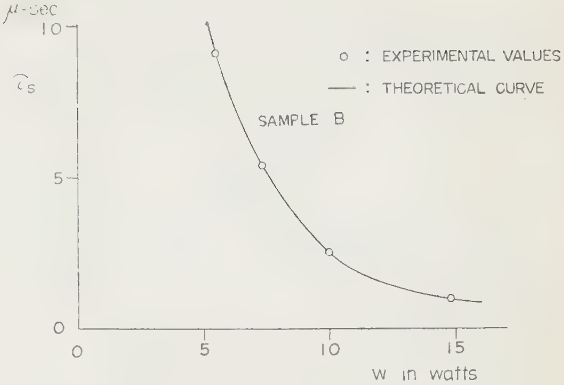

Fig. 3. τ_s-W relation.

As is shown in Eq. (3), $(\Theta-T_0)$ is linearly dependent on W for constant τ_s. This means that if we measure the power W which is necessary to make the *step* to occur just $\tau_s{}^0$ seconds after the application of the voltage as a function of the ambient temperature T_0, then it is expected for T_0-W relation to become a straight line cutting T_0 axis at Θ.

In fact, as is shown in Fig. 4, the experimental results have shown that the above expectation was a correct one. From these lines the values of Θ are determined as follows.

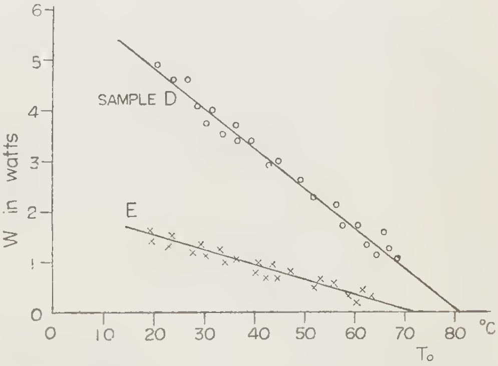

Fig. 4. Experimental results of W-T_0 relation. $\tau_s{}^0=10\mu$-sec.

sample	Θ
D	80°C
E	70°C

It is concluded, therefore, that sudden increase in the current as is shown in Fig. 1 occurs just when the contact temperature reaches to Θ, which is estimated to be about 80°C.

The meaning of the temperature Θ might be imagined in several ways. For instance, it may be the temperature at which the intrinsic conductivity initiates, or it may be the temperature necessary for the ionization of some kind of traps which offer minority carriers[3]. The definite conclusion on the mechanism of the *step* itself can not be given at present and some discussion will be given in some detail somewhere[4].

References

1) Hunter: Phys. Rev. **81** (1951) 152, Tillman: Phil. Mag. **44** (1953) 677, Armstrong: J. Appl. Phys. **24** (1953) 1332.

2) This equation was obtained by T. Iijima in this Laboratory.

3) Billig: Phys. Rev. **87** (1952) 1060.

4) To be published on Bulletin of the Electrotechnical Laboratory.

J. Phys. Soc. Japan **9** (1954) 644~645

On the Internal Field of the Microwave Resonance in Ferrites

By Noboru Tsuya

Research Institute of Electrical Communication, Tōhoku University, Sendai

(Received April 26, 1954)

From our experiments on resonance absorption in Ni-Cd ferrites anomalously large values of g-factors[1] were obtained when frequencies of microwave were comparatively low, e.g. 4,000 and 9,000 MC per sec.. Okamura[2] has proposed that the existence of an internal field H_i in addition to the observed resonance field H_{res}. In other words true values of g-factors, g_o, should be determined by the equation

$$h\nu = g_o\beta(H_{res}+H_i) ,$$

where β is the Bohr magneton, ν the frequency of microwave used, h the Plank constant, H_{res} the resonance field obtained experimentally using spherical samples with very small diameters so as to avoid the so-called size effects. The purpose of this note is to propose a possible mechanism which may cause such an additional internal field H_i, although we have not been able to determine its magnitude by mathematical calculations unfortunately.

According to a simple application of Kittel's formula[3] the effect of the anisotropy in polycrystalline case is not so large[4]. This internal field is also present even in the case of single crystals. Thus we do not consider here the anisotropy energy. The effect of ferrimagnetic coupling between spins is also small and moreover has an opposite sense in contradiction to experiments. Hence the true origin of this field H_i may most probably be attributed to the imperfectness o the specimen used. The real specimens of th ferrites have more or less low density[5] compare with that obtained by X-ray measurements. Thu there may be many holes, cracks, and other sort of imperfections within the specimens even in th case of single crystals, so that the most signif cant origin of H_i may be assumed as the spacia fluctuation of magnetic fields around the crack or cavities in the sample under test. This fluctuation of magnetic fields should come from th discontinuous disappearance and irreqularity[6] o the exchange energy at the surface of cracks o cavities and from the inhomogeneous magnetostrictive energy due to the change of stress fiel around the imperfections.

Now we shall discuss the effect of those imperfections more in detail. First we consider crack in a perfect crystal. If the magnetostati charge appears around cracks under the application of strong external field in z-direction, it i then easily concluded that the internal static fiel caused by the magnetostatic free charge result in a broadening of the resonance line but not in any shift. If we superpose the microwave fiel on the static field, there appear alternating fre charges on the surfaces which are parallel to th z-direction, though not on those which are parpendicular to it. These free charges behave very differently from the above mentioned static ones and can make additional demagnetizing field $H_{dx,y}$ such as expressed by

$$H_{dx,y} = Ni_{x,y}M_{x,y} .$$

Here it should be noticed that the effect of these additional fields will vanish if and only if al spins precess in the same phase and amplitude However the effective field fluctuates from place along the surfaces of cracks and cavities, so tha some spins may be in the states of reasonance and the remaining ones may be in advanced o retarted phases with smaller amplitudes and hence there should appear free charges at the surfaces of cavities. Generally, as we can easily understand, this demagnetizing effect does not vanish by the process of averaging over various shapes and orientations of cracks. Thus we obtain the internal field

$$H_i = \langle N_{ix,y}\rangle_{AV} M_z .$$

The author wishes to express his heartly thanks to Professors T. Hirone, T. Nagamiya and N. Bloembergen for their kind discussions and also to Professor T. Okamura, Dr. Y. Torizuka and Y. Kojima for their helpful discussions and for showing him their unpublished data on the internal field and the porosity of the specimens.

References

1) H. Watanabe, N. Tsuya and T. Takahasi: Sci. Rep. RITU, Tōhoku Univ. **A3** (1952) 62.

2) T. Okamura, Y. Torizuka and Y. Kojima: Phys. Rev. **88** (1953) 1425.

3) C. Kittel: Phys. Rev. **73** (1948) 155.

4) N. Tsuya: Talk at the meeting 1950 Nov.; M. Shimizu: read at the meeting 1953 April.

5) J. J. Went and H. P. J. Wijn: Physica **17** (1951) 976.

6) J. H. Van Vleck: Phys. Rev. **78** (1950) 266.

J. PHYS. SOC. JAPAN **9** (1954) 645~646

Chlorine Pure Quadrupole Spectra in Some Solid Compounds

By Kazuo TORIZUKA

Tokyo Gakugei University, Koganei, Tokyo

(Received May 11, 1954)

Using the frequency-modulated super-regenerative oscillator, which was already reported1), Cl^{35} pure quadrupole resonance spectra of some chlorine compounds have been observed at liquid oxygen, dry ice and room temperatures.

Frequencies were measured by superimposing the signal of a marker oscillator on the nuclear absorption pip on the oscilloscope screen. The marker oscillator was calibrated by crystal oscillator which in turn calibrated by JJY 4 mc/s standard signal. The error of measured frequencies was estimated ±40 kc/s and that of temperatures was ±2° at dry ice and liquid oxygen temperatures.

The results are listed in Table I.

Table I.

Molecule	Frequency, in mc/s 90°K	 210°K	 285°K
$CCl_3CH(OH)(OCH_3)$	38.59	38.06	37.65
	38.74	38.25	37.80
	38.83	38.33	37.99
$CCl_3CH(OH)(OC_2H_5)$	38.51	38.12	37.80
	38.70	38.35	38.02
	39.11	38.54	38.06
1-Chloro-2, 4-dinitrobenzene	37.75	37.54	37.34
$Ba(ClO_3)_2 \cdot H_2O$	29.93	29.62	29.38

Recently P. J. Bray and P. J. Ring2) also measured the chlorine quadrupole resonance of 1-chloro-2,4-dinitrobenzene, chloral alchoholate (ethyl) and $Ba(ClO_3)_2 \cdot H_2O$ at liquid nitrogen temperature. Present results are in agreement with them considering the temperature dependence and the error of measurements.

In Table I chloral compounds are methyl and ethyl substituents of a hydroxyl group hydrogen of chloral hydrate $CCl_3CH(OH)_2$. Chloral hydrate was reported by Kondo and Nitta3) to form intermolecular hydrogen bonds with chlorine atoms of adjacent molecules. Comparing the chloral hydrate chlorine quadrupole spectrum which was studied by Allen4) and the present results of chloral alchoholates, the following features are found.

(1) In alchoholates the separations of three lines which are due to three chlorine atoms in a molecule are small compared to hydrate. They are less than 600 kc/s and perhaps particular bonds of chlorine atom like inter- or intra-molecular hydrogen bond do not exist in alchoholates.

(2) Temperature dependence is larger in alchoholates than in hydrogen-bonded hydrate, and methyl substituent has larger value then ethyl. One of the chlorines of ethyl substituent has larger temperature dependence than the other two. This is compared to the particularly large temperature dependence of $CH_2ClCOOC_2H_5$ among the monochloroacetic acid derivatives.5)

Perhaps two chlorine atoms which are supposed to form hydrogen bonds would have higher quadrupole couplings of about 1.6 mc/s than the value of free molecules near the melting point. On the other hand non-hydrogen bonded chlorine would have lowered value about 0.8 mc/s. But more precise informations about the electronic structure of hydrogen-bonded chlorines will be obtained by Zeeman effect of quadrupole spectrum line using single crystal.

1-Chloro-2, 4-dinitrobenzene (m.p. 51.5°C) shows single line, so the chlorine positions in molecular crystal are not greately different in each molecule. Comparing it with the frequency of o-nitrochlorobenzene obtained by Dean and Pound6), NO_2 group at para position shifts the Cl resonance frequency about +0.7 mc/s and this is considered to be due to the electron withdrawal effect by NO_2 group from the benzene ring. Its temperature dependence is rather small compared with o-nitrochlorobenzene.

$Ba(ClO_3)_2 \cdot H_2O$, whose resonance frequency was already reported7), has resonance frequency between that of K and Na chlorates, and rather near to Na one. The order of their frequency Na: 30.01, Ba: 29.38 and K: 28.20 mc/s is the same as that of electronegativity Na: 0.9, Ba: 0.9 and K: 0.8. This parallelism between the quadrupole coupling and the electronegativity in chlorates is similar to bromates observed by Shimomura et al8).

The author wishes to express his sincere thanks to Prof. S. Kojima of the Tokyo University of

Education for his kind guidance and encouragement throughout this work.

This work is supported financially by the Ministry of Education.

References

1) K. Torizuka: Research Report of Tokyo Gakugei University (in Japanese) **5** (1953).
2) P. J. Bray and P. J. Ring: J. Chem. Phys. **21** (1953) 2226.
3) S. Kondo and I. Nitta: X-ray (in Japanese) **6** (1950) 53.
4) H. C. Allen: J. Phys. Chem. **57** (1953) 501.
5) H. C. Allen: J. Amer. Chem. Soc. **74** (1952) 6074.
6) C. Dean and R. V. Pound: J. Chem. Phys. **20** (1952) 195.
7) See: Summary of Symposium on Molecular Physics at Nikko, Japan (1953)
8) K. Shimomura, T. Kushida, N. Inoue and Y. Imaeda: J. Chem. Phys. **22** (1954) 350.

J. PHYS. SOC. JAPAN **9** (1954) 646~647

Internal Friction of Alpha-Iron Due to Boron Atoms

By Ryukiti Robert HASIGUTI
and Gen-ichi KAMOSHITA

Department of Metallurgy, Faculty of Engineering, University of Tokyo, Tokyo, Japan

(Received June 12, 1954)

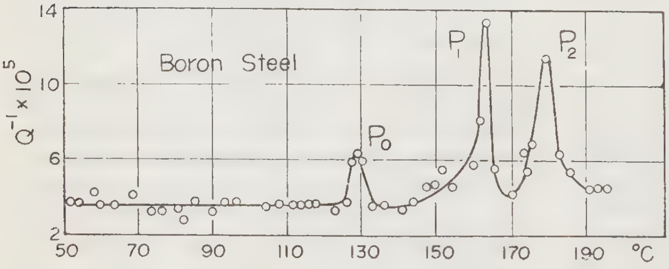

Fig. 1.

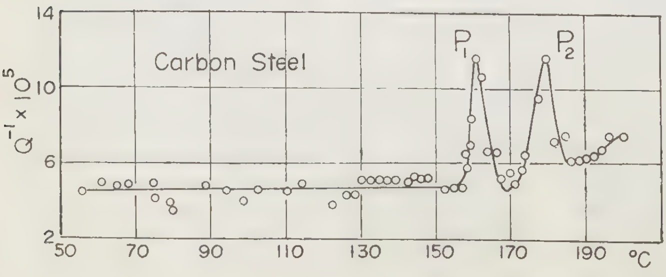

Fig. 2.

It has not been decided experimentally whether boron atoms dissolve in alpha-iron interstitially or substitutionally. A distinct evidence for the interstitial solution was found in our laboratory by means of internal friction measurements. Boron atom concentration in solid solution and diffusion coefficient of boron in alpha-iron were also determined.

Internal frictions at about 20 kilo-cycles per second of vibration were measured as a function of temperature. The results are shown in Figs. 1 to 3. Specimens are (1) boron steel containing 0.4% carbon and nominally 0.004% boron (Fig. 1), (2) carbon steel containing 0.4% carbon (Fig. 2), and (3) Armco iron. They were all annealed at 600°C for an hour.

Table I.

	Boron	Nitrogen	Carbon
Atomic per cent	1.4×10^{-5}	9.8×10^{-5}	9.8×10^{-5}
Weight per cent	2.6×10^{-6}	2.5×10^{-5}	2.1×10^{-5}
Diffusion coefficient cm²/sec.	2.9×10^{-12} at 128°C	3.0×10^{-12} at 163°C	3.0×10^{-12} at 177°C
Activation energy cal/mol.	17,900 (estimated)	19,500 (estimated)	20,100 (accepted value[2])

Three peaks of internal friction, P_0, P_1 and P_2 are found in boron steel as shown in Fig. 1. Two peaks at higher temperatures, P_1 and P_2, are found also in carbon steel and in Armco iron. P_1 is due to nitrogen atoms and P_2 is caused by carbon atoms. The peak at about 129°C is found only in boron steel, which means this is due to boron atoms. As the concentration of boron atoms is very small, their contribution to the internal friction peak is possible, only when they make interstitial solid solution in alpha-iron.

The concentrations and diffusion coefficients of boron, nitrogen and carbon were calculated from three peaks of Fig. 1 as tabulated in Table I.

Assuming a linear relation between absolute temperatures of peaks and activation energies of atomic jumps[1], we can estimate the activation energies for boron and nitrogen from the currently used value of activation energy of carbon[2]. These values are shown in Table I.

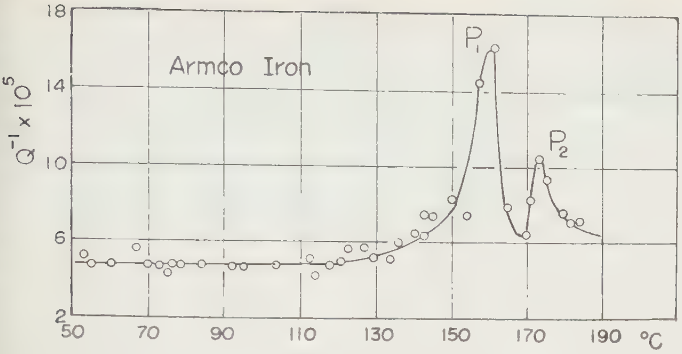

Fig. 3.

Figs. 1, 2 and 3. Internal friction as a function of temperature.

The authors would like to thank Mr. N. Igata for his kind cooperation and Mr. S. Ishii for his assistance in carrying out the experiments.

References

1) C. Wert and J. Marx: Acta Metallurgica, **1** (1953) 113.
2) A. S. Nowick: Internal Friction in Metals, Progress in Metal Physics, Vol. 4, 1953, p. 39.

J. PHYS. SOC. JAPAN **9** (1954) 647~648

On the Free Volume Theory of Liquid

By Kiyoshi ARAKAWA
Fuji Denki Seizo K.K. Material Laboratory
Kawasaki, Kanagawa

(Received June 19, 1954)

After the pioneering researches of Lennard-jones and Devonshire, and Eyring and his coworkers, not a few attempts have been made on the free volume theory of liquid, but with limited success. An approximation for the generalized free volume $j(\omega)$1) is proposed in this report. The total partition function of the whole assembly composed of N molecules distributed on L sites is, if it is assumed that a cell can be occupied by only one molocule and that the energy of interaction of two molecules is

$$E(r)=4\varepsilon\{(r_0/r)^{12}-(r_0/r)^6\}\ ,$$

$$Z=[2\pi mkT/h^2]^{3N/2}\sum\exp\{-z(N-X)E(0)/2kT\}\times\prod_i j(\omega_i)\ , \qquad (1)$$

where

$$j(\omega_i)=\int_{cell}\exp\{-(1-\omega_i)u_i/kT\}4\pi r^2dr$$

and

$$X=\sum_i\omega_i\ .$$

$E(0)$ is the energy of two molecules on neighbouring sites which from a face-centered cubic lattice, and u_i is the increase of the potential energy when the i-th molecule is at the distance r from the centre of the cell with all the neighboring cells occupied. We have assumed in (1) that $z\omega_i$ cells are vacant and $z(1-\omega_i)$ cells are occupied around the i-th molecule. We now propose the following approximation for $j(\omega)$:

$$\ln j(\omega)=\ln j(0)+\omega\{\partial\ln j(\omega)/\partial\omega\}_{\omega=0}\ . \qquad (2)$$

Then we have

$$\ln j(\omega)=\ln(2\pi r_0{}^3qg)+(q^{-4}\xi-2q^{-2}\eta)z\omega/\tau\ , \qquad (3)$$

q ; the reduced cell size
a ; the distance between two neighbouring lattice sites
$E(0)/kT$; $=(1/\tau)(q^{-4}-2q^{-2})$
τ ; the reduced temperature $=kT/\varepsilon$,
ξ ; g_l/g, $\eta=g_m/g$,

$$g=\int_0^{0.30554}y^{1/2}\exp\{-(z/\tau)(q^{-4}l(y)-2q^{-2}n(y)\}dy$$

$$gl=\int_0^{0.30544}y^{1/2}l(y)\exp\{-(z/\tau)(q^{-4}l(y)-2q^{-2}n(y)\}dy$$

$$g_m=\int_0^{0.30544}y^{1/2}n(y)\exp\{-(z/\tau)(q^{-4}l(y)-2q^{-2}n(y)\}dy$$

$$l(y)=(1+12y+25.2y^2+12y^3+y^4)(1-y)^{-10}-1,$$

$$n(y)=(1+y)(1-y)^{-4}-1\ .$$

Then, after the calculation by means of the quasi-chemical approximation, which is analogous to that of previous theories1)2)3), the following equations are obtained.

$$pv/nkT=-(1/x)\{\ln(1-x)+(z/2)\ln((\beta+1-2x)/(1-x)(1+\beta))\}\ , \qquad (4)$$

$$\beta=1-4x(1-x)[1-\exp\{-(1/\tau)\times\{(1+2\xi)q^{-4}-2(1+2\eta)q^{-2})\}]\ ,\quad x=N/L\ . \qquad (5)$$

The equation of state (4) has the same form as those of previous theories1)2)3), which results from various form of linear dependency of $\ln j(\omega)$ on ω, and the difference between our result and those of previous theories lies in the form of β. The second virial coefficient is

$$B=\tfrac{1}{2}Nr_0{}^3q[1+z\{1-\exp(-(1/\tau)((1+2\xi)q^{-4}-2(1+2\eta)q^{-2}))\}]\ . \qquad (6)$$

The value of B/b_0 ($b_0=2/3\pi r_0{}^3$) plotted against τ is shown in Fig. 1, together with those1) of other approximations and exact values4) for the Lennard-jones type intermolecular potential. Numerical calculations were made for $q=1.174$, the value which was used previously in the theory of Sato and Ono. The values of g, g_l, g_m are taken and interpolated from the tables of Wentorf, Buehler, Hirschfelder, and Curtiss6). The influence of the

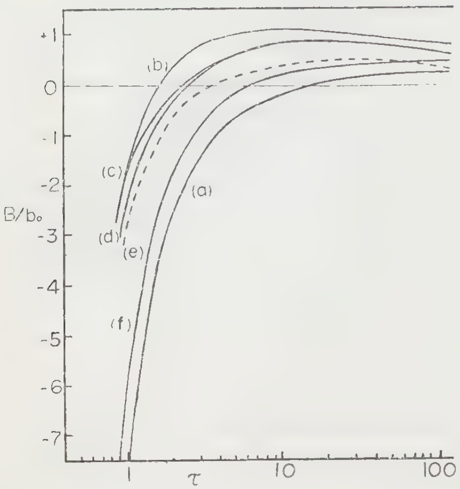

Fig. 1. The calculated second virial coefficient plotled aganst τ.
(a) Cernuschi and Eyring, (b) Ono, (c) Peek and Hill, (d) Rowlinson and Curtiss, (e) Exact values of Lennard-Jones, (f) this work.

second and third nearest neighbouring molecules is corrected by multiplying q term with 1.011 and 1.2045 respectively.

The critical constants are tabulated in the following and compared with those of other approximations[1]. (the values of Cernuschi and Eyring and those of Ono are calculated for $q=1.174$) τ_c is obtained by solving graphically the following equation.

$$(1/\tau_c)\{q^{-4}(1+2\xi)-2q^{-2}(1+2\eta)\}=-\ln\{z/(z-2)\}\ . \tag{7}$$

From the above results it is seen that this approximation is near to that of Cernuschi and Eyring, but is improved to some extent. In the latter the second term of the formulae (2) is dropped. Considering from the form of (2), this approximation is found to be useful at rather low values of ω, that is, at high density, and is not a good approximation at the values of ω near 1. Generally speaking, the state of liquid at the value of ω near 1 cannot be exactly treated by the cell model. In this approximation, the correlative effect of molecules between different cells is not considered, and, to improve the theory, it is necessary to consider the interaction of molecules between different cells, or to enlarge the cell so that each cell can be occupied by more than one molecule, as proposed recently.

Table I. Critical constants (including Boyle point).

critical constant	$(PV/NkT)_c$	τ_c	v_c/r_0^3	$\overline{\omega}$	Boyle point τ_b
mean experimental values for N, Ne, A	0.293	1.28	3.09	—	3.42
Lennard-jones and Devonshire	0.591	1.30	1.77	0.00	—
Peak and Hill	0.719	1.18	3.25	0.175	2.2
Cernuschi and Eyring	0.342	3.34	2.35	0.455	15.0
Ono	0.342	1.14	2.35	0.455	1.66
this work	0.342	2.42	2.35	0.455	6.00

References

1) J; Rowlinson and C. Curtiss: J. Chem. Phys. **19** (1951) 1519.

2) T. Sato and S. Ono: J. Phys. Soc. Japan **4** (1949) 103.

3) H. Peek and T. Hill: J. Chem. Phys. **18** (1950) 1252.

4) J. E. Lennard-jones: Proc. Roy. Soc. (London) **A106** (1924) 463.

5) F. Cernuschi and H. Eyring: J. Chem. Phys. **7** (1939) 547.

6) B. Wentorf, R. Buehler J. Hirschfelder, B. C. Curtiss: ibid, **18** (1950) 1484.

Lennard-jones and Devonshire: Proc. Roy. Soc. **A163** (1937) 53.

J. Phys. Soc. Japan **9** (1954) 648~650

Photoconductivity of In_2Te_3 and CdTe Single Crystals

By Hisao Miyasawa and Suezo Sugaike

Matsuda Research Laboratory,
Tokyo-Shibaura Electric Co.,
Kawasaki-shi, Kanagawa-ken

(Received July 2, 1954)

Recently, semiconducting properties of In_2Te_3 and CdTe were reported by Appel[1], who observed the electrical conductivity as a function of temperature and determined the values of their activation energies.

Artificial single crystals of these compounds have been grown and studied also in this laboratory[2], and here will briefly be given another evidence which may indicate the width of their forbidden energy band. The conclusion is deduced from the measurements of photoconductivity.

Usual photoconductive cells were prepared, consisting of a wafer of the single crystal cemented on a glass plate with Araldite resin and a pair of evaporated gold electrodes between which a cleavage surface of the crystal was exposed. These cells were fairly insulative in the dark and showed appreciable photoconductivity. Then, the voltage developed acoss a suitable load resistor connected in series with the cell and a battery was applied to a vacuum tube voltmeter through an amplifier. Monochromatic light directed upon these cells was interrupted at 140 cps by a rotating chopper disk, and the light intensity at each wavelength was measured which was required to give rise to a constant photoresponse.

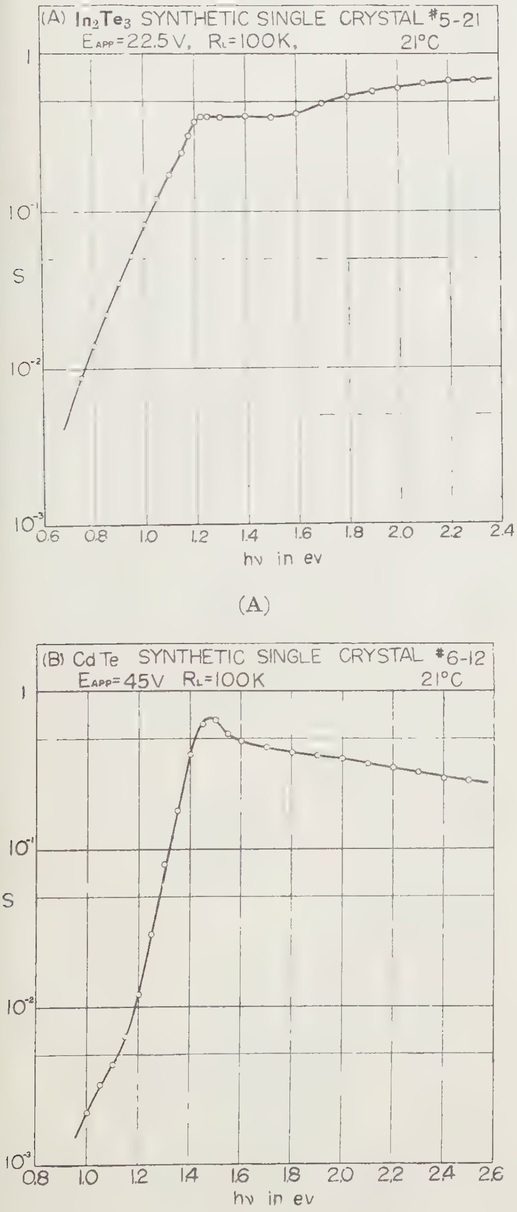

(A)

(B)

Fig. 1. Typical spectral sensitivity of the photoconductivity, (A) for In_2Te_3 and (B) for CdTe. S in the ordinate represents relative photoresponse per incident light quantum in logarithmic scale.

Typical results are shown in Fig. 1, where photocurrents passing through the electrodes per incident light quantum are plotted against the photon energy. In most semiconductors, sharp drop in the photoresponse may usually correspond to their fundamental optical absorption edge or their intrinsic energy gap, though there are several exceptions such as suitably activated lead sulphide films. Hence, it is tentatively believed that the values, 1.2 ev for In_2Te_3 and 1.47 ev for CdTe, respectively indicate the energy gap near room temperature of these compounds.

Meanwhile, isothermal values obtained by Appel have not been assigned to any electronic energy state. As compared with our data, however, 0.94 ev for In_2Te_3 and 1.48 ev for CdTe[3] may be regarded as intrinsic ones.

According to Frerichs[4], on the other hand, it is said that CdTe crystals show a maximum of photoconductivity corresponding to the absorption edge at 6200A or 2 ev. This does not agree with the data given here. The reason would be attributed to the difference in crystal structure; i.e., Frerichs' specimens presumably crystalize in the wurtzite structure, while those used by other workers are the zincblende type. In the former, interatomic distance between cadmium and tellurium is smaller than in the latter. In turn, this might cause the latter to have a smaller energy gap as is the case, because the lattice dilation in these type compounds tends to narrow the gap. It is plausible that an activation energy of 1.98 ev near 1000°K found by Appel, which is consistent with Frerichs' one, belongs to the wurtzite structure transformed at higher temperatures from the zincblende phase.

The authors wish to thank Dr. H. Inuzuka, Mr. Y. Uemura, and Mr. J. Okada for helpful discussions, Mr. M. Sugito for assistance with the experiments.

References

1) J. Appel: Zeits. f. Naturforschung **9a** (1954) 265.

2) Double furnace technique was always used for growing our crystals. As for the preparation and crystal structure of In_2Te_3, cf. H. Inuzuka and S. Sugaike: Proc. Japan Acad. **30** (1954) 383.

3) Value of the energy gap for CdTe, $\Delta E=1.5$ ev, is listed without detail or reference in the following paper: C. H. L. Goodman: Proc. Roy. Soc. **67B** (1954) 258.

4) R. Frerichs: Phys. Rev. **72** (1947) 594.
His crystals were produced by vapor method in contrast with the technique adopted by us and Appel.

J. Phys. Soc. Japan **9** (1954) 650

Some Electrical Properties of AlSb

By W. Sasaki, N. Sakamoto and M. Kuno
Electrotechnical Labolatory,
Nagatacho, Chiyodaku, Tokyo

(Received April 19, 1954)

An ingot of AlSb was prepared by stoichiometric fusion of Al and Sb, and purified by passing four molten zones in argon atmosphere. The ingot was composed of small crystals, each with about 1×1 mm area perpendicular to the axis of ingot and 5 mm length along the axis. Excess Al component, which was probably partly due to the evaporation of Sb during zone refining, is observed near the tail part of the ingot.

Specimens for electrical measurements were cut out, examined for electrical homogeniety, and resistivity, Hall constant, and thermoelectric power have been measured as functions of temperature.

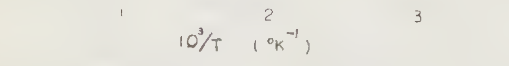

Fig. 1. Resistivity versus temperature plot for three specimens of AlSb.

Fig. 1 shows measured resistivity versus temperature curves of three specimens. Near room temperature the resistivity decreases slightly as the temperature is raised, then it increases to a maximum value at about 800°C, and decreases rapidly. The broken line shows the curve

$$\rho\propto T^{3/2},$$

which represents the expected resistivity versus temperature relation when the charge carrier produced by complete ionization of donors or a ceptors, are scattered by non-polar crystal vibr tions, and may be compared with the experiment curves.

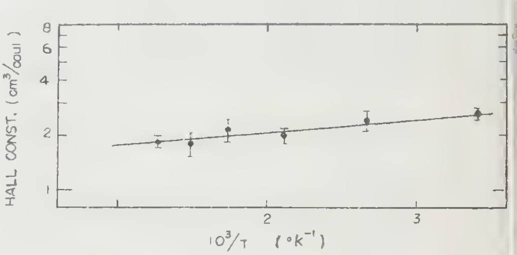

Fig. 2. The Hall constant of the specimen "C"

Fig. 2 shows the Hall constant measured on th specimen *C* in Fig. 1. The sign of the Hall con stant is that for conduction by holes. The Ha constant decreases slightly with increasing tem perature. The Hall mobility R/ρ is 40 cm²/v.sec at room temperature.

Thermoelectric power was measured on th specimen *C* over the temperature range fro 17°C to 89°C, and the result is shown in Fig. 3 We can calculate thermoelectric power from th Hall data when a model is proposed for the energ bands and the scattering process of the charg carriers of the semiconductor. The solid lines in Fig. 3 are such curves based on the following assumptions. (a) The *effective mass model* is ap plicable and the effective mass m^* is given by

$$(m^*/m)g^{2/3}=1.8,$$

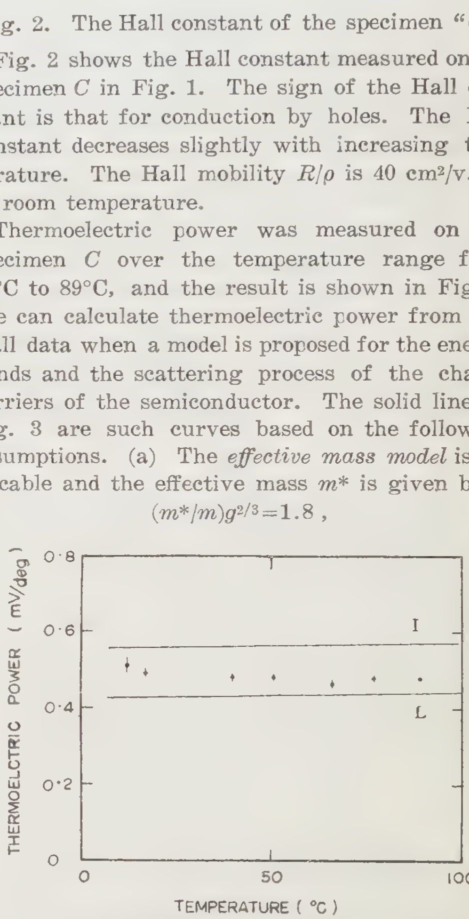

Fig. 3. The thermoelectric power of the specimen "*C*".

where m is the free electron mass, and g the degeneracy of the band edge except for spins. (b) The scattering is caused either by the lattice vibration, corresponding to the curve denoted by L, or by the ionized impurities, the curve denoted by I. Taking into account the experimental errors, the $(m^*/m)g^{2/3}$ value in the model described above is estimated to be 1.8 ± 0.8.

The authors wish to express their thanks to M. Hatoyama for his encouragements.

Errata

Hyperfine Structure of the Spectrum of Ruthenium. Part II

By Kiyoshi MURAKAWA

J. PHYS. SOC. JAPAN **9** (1954) 427~428

The last two lines of page 427 should read:

$$A(4d^6 5s5p^5 F_5)=\frac{7}{75}a(s)+\frac{23}{75}a_p+\frac{34}{75}a_d, \qquad A(4d^6 5s5p^7 P_4)=\frac{1}{8}a(s)-\frac{1}{16}a_p+\frac{13}{28}a_d.$$

$\sigma\pi$ Interaction in Benzene

By Kazuo NIIRA

J. PHYS. SOC. JAPAN **8** (1953) 630~642

Page				
633	Eq. (15.1a)	$1/3\,C_{\pi s s \pi}-\cdots+1/6\,C_{\pi\pi'\pi'\pi}$	should be read	$2\times(1/3\,C_{\pi s s \pi}-\cdots+1/6\,C_{\pi\pi'\pi'\pi}{}^{(2)})$
635	Table II, $^3E_{2g}$	10.9	〃	9.3
		(9.9)	〃	(8.5)
		9.0	〃	7.4
		(8.0)	〃	(6.6)
641	Table V, $^3E_{2g}$			
	for $\lambda=0.5$	−1.16	〃	−0.44
		2.92	〃	1.33
		(2.13)	〃	(0.73)
		1.76	〃	0.89
		(0.97)	〃	(0.29)
	for $\lambda=1$	−0.80	〃	−0.24
		2.96	〃	1.35
		(2.32)	〃	(0.87)
		2.16	〃	1.11
		(1.52)	〃	(0.63)

PROGRESS OF THEORETICAL PHYSICS

Published by
The Yukawa Hall
with the cooperation of
The Physical Society of Japan

Progress of Theoretical Physics Vol. 11, No. 2, 1954

Mass Spectrum of Elementary Particles, I
— Eigenvalue Problem in Space-time — ....Hiroshi ENATSU.... 125
Generalized Racah Coefficient and its Applications
.... Akito ARIMA, Hisashi HORIE and Yukito TANABE.... 143
On the Green-functions of Many-electron Problem ....Shinzo NAKAI.... 155
Bound States and S-matrix in Quantum Field Theory ....Shinzo NAKAI.... 179
Analysis of the Structure of Transformation Function in Quantum Mechanics .... Sumio TANI.... 190
On the Bose-Einstein Liquid Model for Liquid Helium, II
— Properties under High Pressures — .... Ziro MIKURA.... 207
An Invariance Theorem for Cross Sections of Meson-nucleon Scattering
....Shigeo MINAMI.... 213
β-γ Angular Correlation of Tm^{170}
..........Jun-ichi FUJITA, Masato MORITA and Masami YAMADA.... 219

Letters to the Editor:

On the Renormalization of Salpeter-Bethe Kernel of Meson-nucleon System in the State $T=1/2$..........T. YOSHIMURA.... 224
On Field Equations with Non-local Interaction......C. HAYASHI.... 226
On a Covariant Generalization of Tamm-Dancoff Approximation for Pion-nucleon Scattering.................... K. ITABASHI.... 227
Renormalization in Generalized Tamm-Dancoff Approximation for Pion-nucleon Scattering.................... K. ITABASHI.... 228

Progress of Theoretical Physics Vol. 11, No. 3, 1954

Anomalous Magnetic Moment of Nucleon and Nucleon Isobar
...................Akira KANAZAWA and Masao SUGAWARA.... 231
On the Bose-Einstein Liquid Model for Herium, III
— Further Considerations regarding Vapour Pressures of He^3-He^4 Mixtures —..........................Ziro MIKURA.... 244
On Gauge Invariance and the Structure of Elementary Particles
.... Yasushi TAKAHASHI.... 251
Reduced Widths from (d, p) Reactions
........Yoichi FUJIMOTO, Ken KIKUCHI and Shiro YOSHIDA.... 264
On the Structure of the Interaction of Elementary Particles, V
— Interaction of the Second Kind and Non-local Interaction —
.... Susumu KAMEFUCHI.... 273
On an Expression for the Total Cross Section..............L. I. SCHIFF.... 288
On the Construction of S-matrix in Lagrangian Formalism
...............Tsutomu IMAMURA, Shigenobu SUNAKAWA and Ryôyû UTIYAMA.... 291
Theory of Antiferromagnetic Resonance in $CuCl_2 \cdot 2H_2O$
....Takeo NAGAMIYA.... 309

Letters to the Editor:

A Note on the Generalized Statistics..F. FERRARI and C. VILLI.... 328
On the Weak Universal Boson-Fermion Interaction
.....................S. OGAWA, H. OKONOGI and S. ŌNEDA.... 330

Kinematical Studies of Pion-nucleon Interactions
..............S. HAYAKAWA, M. KAWAGUCHI and S. MINAMI.... 332
The Effect of the Mass Difference between Charged and Neutral
Pions on the Nuclear Force........................A. SUGIE.... 333
On the Neutron He^4 Scattering.....................T. TAMURA.... 335
On the Theory of Condensing Systems...............K. IKEDA.... 336

Progress of Theoretical Physics Vol. 11, No. 6, 1954

Interpretation of the Excitation of Gamma-rays by 10 Mev Neutrons
........................Satio HAYAKAWA and Ken KIKUCHI.... 513
A Method in Quantum Statistical Mechanics, III
— *Virial Expansion for the Quantum Gas* —
.... Hiroshi ICHIMURA.... 519
Statistical Mechanics of Surface Tension of Curved Interface, I
.... Ei TERAMOTO and Tomio SEGAWA.... 528
A Formulation of Field Theory in Hilbert Space .... Giiti IWATA.... 537
The Theory of Collisions between Two Diatomic Molecules
.... Kazuo TAKAYANAGI.... 557
Two Simple Stochastic Models of Cascade Multiplication
.... Alladi RAMAKRISHNAN and S. K. SRINIVASAN.... 595
Letters to the Editor:
Chain Configuration and Rubber Elasticity........E. TERAMOTO.... 604
On Fermi's Theory of High Energy Nucleon-nucleon Collisions
.... V. S. NANDA.... 605
A Remark on the Infinities due to the New Complex Poles of
Modified Propagators..........R. UTIYAMA and T. IMAMURA.... 606
Note on the Contribution of the Single Scattering to the
Lateral Structure of Cascade Showers
.... J. NISHIMURA and K. KAMATA.... 608
Some Generalization of the Theory of Scattering with Application
to Slow Electrons in Polar Crystals..............A. MORITA.... 609
Pion-nucleon Scattering by Tamm-Dancoff Method
.... K. ISHIDA and A. TAKAHASHI.... 611
The General Theory of Relativity and the Expanding Universe
....S. BHATTACHARYA.... 613

Price $ 1.25 per copy
$ 15.00 per year (postage inclusive)
Annual dues for foreign members (individual subscribers)
$ 12.00 (postage inclusive)
〃 for foreign members of the Physical Society of Japan
$ 10.00 (postage inclusive)

Application for members, subscriptions and orders for back mumbers should be sent, directly or through book-dealers, to

The Publication Office

in

Yukawa Hall, Kyoto University, Kyoto, Japan

JOURNAL OF THE PHYSICAL SOCIETY OF JAPAN

Vol. 9, No. 4, 1954

Single Copy $1.00. Yearly Rate $5.00. (Postage Covered).

日本物理學會歐字報告

第9巻 第4號 (昭和29年7~8月號)

編集兼發行者 茅誠司
東京都澁谷區青葉町 20

印刷者 笠井康頼
東京都千代田區富士見町 1の10

印刷所 株式會社 國際文献印刷社
東京都千代田區富士見町 1の10

發行所 社團法人 日本物理學會
東京都文京區本富士町 1 東京大學理學部內

昭和29年8月20日印刷・昭和29年8月25日發行

JOURNAL OF THE PHYSICAL SOCIETY OF JAPAN Vol. 9, No. 5, SEP.—OCT., 1954

On the Absorption of Cosmic Rays Underground

By S. HIGASHI, M. ODA, T. OSHIO, H. SHIBATA
and K. WATANABE

Physical Institute, Osaka City University

(Received May 21, 1954)

The local absorption in lead absorbers in a counter telescope has been measured at the depths of 20, 25.5 and 40 m.w.e., and compared them with the absorption produced by increasing the depth underground. It was found that the former agrees with the latter within the limit of the accuracy of the measurment. The results show that at least **98** percent of the cosmic rays underground consist of mu-mesons coming from the atmosphere, and that the remainder has short ranges and may be composed of electrons produced by mu-mesons in the ground. The cosmic rays underground created by unknown processes are probably very few.

§ 1. Introduction

A number of investigations[1-7] have made it clear that the penetrating particles detected underground are primarily *mu*-mesons, and that these particles penetrate through earth losing their energy mainly by the ionization processes and their ranges are accounted for by the energy loss of *mu*-mesons. It is also known that the *mu*-mesons are accompanied by a small amount of electrons and a smaller amount of N-components both of which are in equilibrium with the parent *mu*-mesons. Though the above view looks most reasonable, other possibilities may not be excluded, because the observed cross section for the large angle scattering of penetrating particles underground[8-11] seems to be larger than that expected and in this connection the hypothesis of K-mesons are suggested by Hayakawa[12]. If there were some charged penetrating particles produced locally in earth, the energy spectrum underground should slightly deviate from the expected from the intensity-depth relation and also the absorption in earth should be different from the absorption in matter placed between the counters by such an amount that are produced locally in earth. If the cosmic rays underground are wholly composed of *mu*-mesons which are created in the atmosphere, their absorption with increasing depths should agree with the local absorption, subtracting the absorption of electrons and also of the negligible amount of charged particles due to nuclear interactions.

An accurate absorption measurement was made by the Cornell group at a great depth of 1,600 m.w.e.[7], confirming the reasonable picture mentioned above. To see whether the anomalous absorption would take place at small depths or not, we carried out the absorption measurement at depths of 20, 25.5 and 40 m.w.e. in Isohama Tunnel*, Shizuoka, Japan (geomagnetic latitude; 24.5°N), from Oct. 1952 to June, 1953.

§ 2. Experimental Arrangement

We have constructed a counter telescope with attention to minimize following hazards;

1) If the absorption is as small as expected for *mu*-mesons and if the trajectories of the incident particles can not be traced clearly, spurious events may disturb results.

2) When the particles are scattered out by absorbers from the apparatus, the events are falsely interpreted as stopped in the absorbers.

3) As the rate of absorption is expected to be very small, it may be impossible to obtain the absorption with the statistical significance comparing the independent observations of penetrating and absorbed fluxes.

The arrangement of the counter telescope for measuring the absorption is shown in Fig. 1. The top of the telescope was separated from the ceiling of the tunnel by 60 cm. Earch counter was connected to a hodoscope circuit, and a master pulse was generated whenever one or more counters of every tray of A, B, C, D and E were discharged simultaneously. The photographic records show which counters have been discharged. Trays K, L, M and N indicated whether the master pulses of the hodoscope were made by a single particle or by two or more particles. Σ, Σ_1, Σ_2 and Σ_3 were lead absorbers, the thickness of which were occasionaly varied.

---

* The ground above the tunnel is composed of basalt and soil, and its mean density determined by gravity measurements, is found to be 1.6, 1.6 and 2.2 at the respective depths.

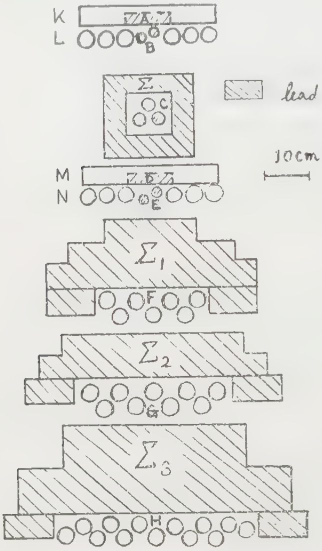

Fig. 1. Arrangement of counters and absorbers used to measure the absorption and the intensity of cosmic rays.

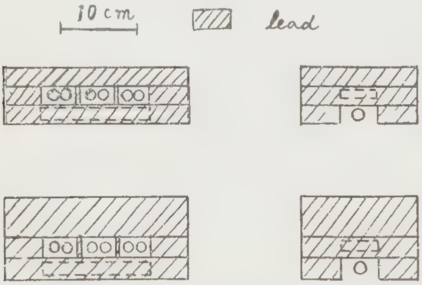

Fig. 2. Arrangement of counters and acsorbers used to measure the intensity of cosmic rays.

The intensity-depth relation was measured by the apparatus containing three sets of counter telescopes as shown in Fig. 2, in addition to the telescope shown in Fig. 1.

The coincidence resolving time of the apparatus was 15∼20 μ sec, and chance coincidences were completely negligible.

§ 3. Experimental Results

About 30 percent of photographic records obtained with the hodoscope shown in Fig. 1 at three depths concerned were the cases where two or three particles entered the apparatus, and about 9∼10 percent of records indicate four or more particles entering it and may be considered as coscade showers coming from earth. The former case is noted as A.P. (associated particle) and the latter as E.S. (earth shower). Relative frequency of A.P., E.S. per flux are shown in Fig. 3.

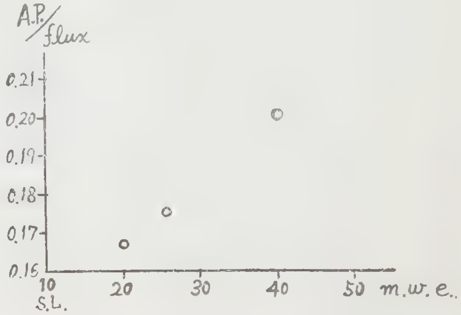

Fig. 3. (a) Relative frequency of A.P./flux.

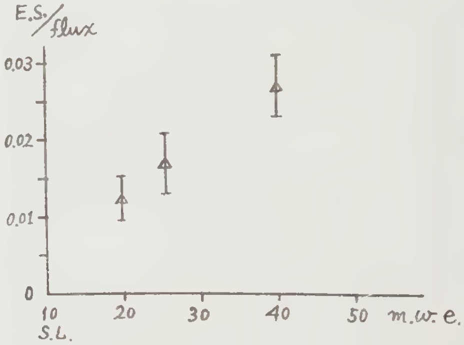

Fig. 3. (b) Relative frequency of E.S./flux.

About 60 percent of photographic records showed that the particles which entered into the apparatus were associated with no particle within the area of the apparatus. The trajectories of particles were traced, and a few of them were found to be scattered. The rates of absorption of the single particles in three layers of lead absorber were simultaneously obtained in each series of measurements. The observed curves are shown, for various depths, in Fig. 4 (a), (b), (c) and (d). As previously noted, when particles are scattered in the absorber and failed to discharge counter trays, they may erroneously be interpreted as absorbed. This was corrected on account of the observed rates of scattering, and was found to be completely negligible for trays F and G, but at most 2 percent or less for tray H.

In Fig. 4, the rate of local absorption was compared with the rate of absorption in earth. In this comparison, the integral range spectrum at depth h_0 is represented by the formula $I(h_0+\Delta h)=I(h_0)e^{-\alpha\Delta h}$, and hence the rates of absorption in earth f_{earth} and in lead f_{pb} are as follows:

$$f_{\text{earth}}=\frac{1}{I(h_0)}\{I(h_0)-I(h_0)e^{-\alpha\Delta h}\}\ ,$$

$$f_{pb}=\frac{1}{I(h_0)}\{I(h_0)-I(h_0)e^{-\alpha\cdot\eta\cdot\Delta h}\}\ ,$$

where I is the intensity of cosmic rays and η is a correction factor which comes from the difference in energy losses of mesons in lead and earth. In the energy range considered, the energy loss of mesons comes entirely from the ionization process and η was computed as 1.45 in reference to Halpern and Halls' calculations[13]. α is the gradient of the intensity-depth curve when it is plotted on the semi-log diagram and can easily be obtained graphically. As expected, the intensity-depth relation at 20 ~ 50 m.w.e. at 24°N geomagnetic latitude is consistent with that at high latitude within the limit of errors. α is estimated from a number of observations by various authors[14] including ours, and the relation f vs $\eta\Delta h$ is represented by the shaded regions in Fig. 4, on account of the errors in the estimate depths.

In Table I, α obtained from intensity-depth relation, absorption coefficient α_{local} computed from local absorption of the particles with ranges longer than 100 gr/cm² lead, and the discrepancy A coming from the particles which seem to have ranges shorter than 100 gr/cm² lead are listed.

§ 4. Discussions and Conclusions

In comparison of the local absorption curves with f-lines represented in Fig. 4, the slope of the local absorption curves is steeper than f-lines up to 100 gr/cm² lead and gradually

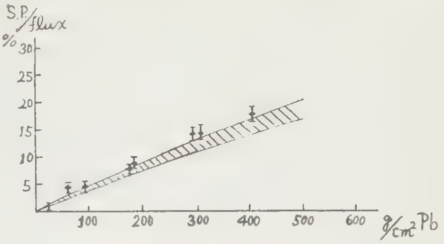

Fig. 4. (a) Absorption Curve at 20 m.w.e. $\Sigma=0$. (The shaded region indicates f-line)

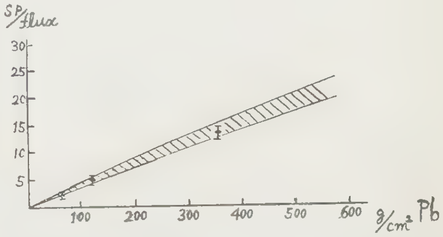

Fig. 4. (b) Absorption Curve at 20 m.w.e. $\Sigma=$ 10 cm Pb.

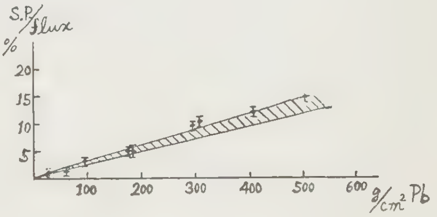

Fig. 4. (c) Absorption Curve at 25.5 m.w.e. $\Sigma=0$.

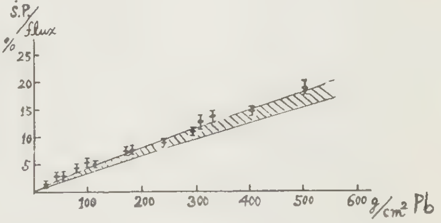

Fig. 4. (d) Absorption curve at 40m.w. e. $\Sigma=0$.

Table I.

	20 m.w.e.		22.5 m.w.e.	40 m.w.e.
	$\Sigma=0$	$\Sigma=10$ cm Pb	$\Sigma=0$	$\Sigma=0$
(/10 m.w.e.)	0.6 ~0.7	0.6 ~0.7	0.5 ~0.6	0.34~0.43
(/10 m.w.e.)	0.64±0.03	0.64±0.03	0.55±0.04	0.42±0.07
A (%)	1.0 ±0.7	−0.3 ±0.5	0.7 ±0.9	0.6 ±0.7

A; rates of short range particles per flux.

come to parallel. This fact indicates that some short range particles are produced in earth. The difference of two curves indicates the amount of particles produced in earth, and their rates per flux are listed in Table I. The short range particles, whose mean range seems to be shorter than 30 gr/cm^2 lead, may be almost electrons which are produced by *mu*-mesons in earth.

If the short range particles are produced by unknown neutral particles, the amounts of neutral particle should be less than $2 \cdot 10^{-4} I_\mu \cdot (\lambda/n)$, where λ is the mean range for neutral particles to produce charged particles in gr/cm^2, n is mean multiplicity and I_μ is the number of charged particles at the interesting depth.

If a few particles with the larger ranges are produced by some unknown processes, the difference between the local absorption and f-line should be scarcely detected.

The amount of charged particles due to unknown processes is estimated from the discrepancy between α and α_{local} must be less than 0.06 I_μ (I_μ: intensity of *mu*-mesons at the interesting depth).

However, Amaldi et al.$^{15),16)}$ had shown negative conclusion for the process following which charged particles are produced by K°-meson.

Even if all of the short range particles are slow *mu*-mesons, which are produced by some mechanisms, the amount of them should not be enough to explain anomalous scattering observed by many workers.

In Fig. 3, the rations of A.P./flux and E.S./flux increase with increasing depth. This fact is naturally recognized, if these events are considered as the electromagnetic interaction of *mu*-mesons, whose average energy increase with increasing depth.

The authors are greatly indepted to Professor Y. Watase for his suggestion and discussion, and to Messrs T. Kubozoe and I. Higashino for their useful help.

References

1) V. C. Wilson and D. J. Hughes: Phys. Rev. **63** (1943) 161.

2) O. L. Tiffany and W. E. Hazen: Phys. Rev. **77** (1950) 849.

3) E. P. George and J. Evans: Proc. Phys. Soc. **A 63** (1950) 1248.

4) M. Miesowicz, M. L. Jurkiewicz and J. M. Massalski: Phys. Rev. **77** (1950) 380.

5) D. E. Caro, J. K. Parry and H. D. Rathgeber: Nature, Lond. **165** (1950) 689.

6) C. A. Randall and W. E. Hazen: Phys. Rev. **81** (1951) 144.

7) P. H. Barrett, L. M. Bollinger, G. Cocconi, Y. Eisenberg and K. Greisen: Rev. Mod. Phys. **24** (1952) 133.

8) E. Amaldi and G. Fidecaro: Nuovo Cime. **7** (1950) 553.

9) E. P. George and P. T. Trent: Proc. Phys. Soc. **A 64** (1951) 1134.

10) Y. Watase et al: I. Phys. Soc. Japan **7** (1952) 436.

11) E. P. George: private comunication to Dr. Hayakawa.

12) S. Hayakawa: Proc. Phys. Soc. **A 65** (1952) 215.

13) O. Halpern and H. Hall: Phys. Rev. **73** (1948) 477.

14) J. G. Wilson: "Progress in Cosmic Ray Physics" 1952.

15) E. Amaldi, C. Castagnoli, A. Gigli and S. Sciuti: Nuovo Cimento **9** (1952) 453.

16) E. Amaldi, C. Castagnoli, A. Gigli and S. Sciuti: Nuovo Cimento **9** (1952) 969.

JOURNAL OF THE PHYSICAL SOCIETY OF JAPAN Vol. 9, No. 5, SEP.—OCT., 1954

On the Unstable Heavy Meson Decaying in Flight in the Photographic Emulsion Exposed at High Altitudes

By Kiyosi NIU

Cosmic Ray Laboratory, Physical Institute, Nagoya University

(Received June 22, 1954)

One decay event of the unstable heavy meson was found in the photographic plate exposed at high altitude. The unstable heavy meson was decayed in flight into single lighter charged meson and assumed to be κ particle on account of the energymomentum relation at the decay point. The possibility that this event occured due to a spurious distortion such as "wetting effect" will not be completely neglected, because the direction of motion of the emitted particle is very close to that of the parent. But it seems quite difficult to interprete whole event by the wetting effect.

§ 1. Introduction

During the last few years a number of examples[1)-4)] have been reported of heavy mesons which are usually referred as κ or χ particles. Each of those unstable heavy particles decays near the end of its range into single lighter charged meson and one or more neutral particles.

Recently, in our laboratory, a particle, which can not be identified as a proton or a π-meson and decays in flight into a lighter meson, has been found among star particles in a photographic plate exposed at high altitudes.

The plate in which this particle was found was one of those which were exposed and processed by Dr. V. Perterson.* They are 3 inches × 3 inches Ilford G-5 emulsions, originally 400 microns thick, and flown by means of free balloons** at Bismark, North Dakota (magnetic latitude 56°N) on August 3, 1951. The flight reached a minimum pressure of 1.2 m.m. Hg, and remained about 45 minutes above 50,000 feet. The plates were contained in a thin bakelite cylinder wrapped with rock-wool and suspended in a gondola of wire and cellophan. Prior to exposure these plates were eradicated of accumulated background tracks, and owing to this process the surface layer of the plate, about 80 microns thick, was not available for the investigation. The shrinkage factor of the plate was 2.2, and the grain density corresponding to minimum ionization tracks was about 25.7 grains/100 microns.

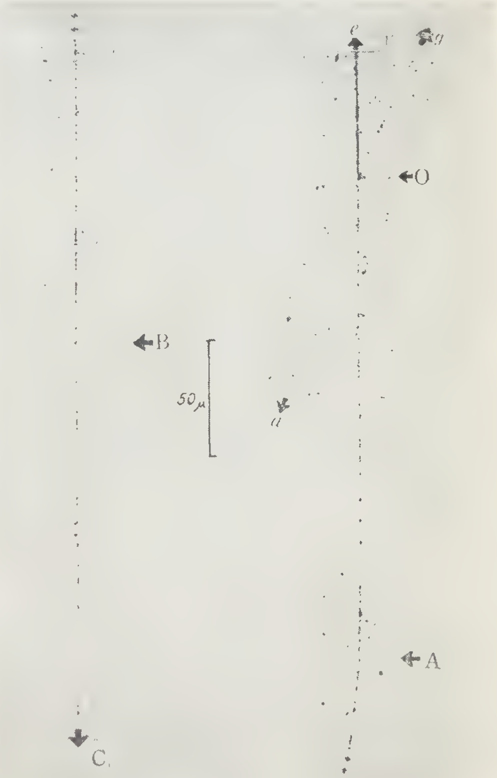

Photo 1. An unstable heavy meson (the grey track) emitted from the star O decayed in flight into a lighter meson at the point B after about 3500 μ flight. This event is possibly a κ-μ decay in flight.

---

* Dr. V. Perterson: California Institute of Technology.

** This balloon flight was financially supported by the "Office of Naval Reserrch U. S. Navy."

§ 2. General Description of the Event

The event in question is a simple star composed of two thin tracks, one grey track and one black track. Fig. 1 shows the projections of the star on the planes parallel and normal to the emulsion-glass plane. Photomicrographs of the event are shown in the Plate 1. Two thin tracks have very large dip angles as are shown in Fig. 1 (B), and the primary particle of this event cannot be identified. The grey track shows a sudden change of direction about 7° at the point A and further more abrupt decrehse of its grain density at the point B, and then enter into the surface layer at the point C. However, the direction change at the point B is very small, about 0.4° parallel and about 1.4° normal to the emulsion-glass plane. The length, grain densities, and mean scattering angles of each part of this track are shown in Table I. Before the interpretation of this unusual track, the distortion and the possible nonuniformity of the emulsion must be examined.

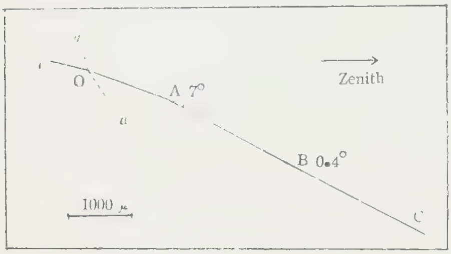

Fig. 1. (A) The projection of the star on the plane parallel to the emulsion-glass plane.
Oa: Thin track emerging to the surface, grain density 25/100 μ.
Og: Thin track emerging to the glass, grain density 34/100 μ.
Oe: Black track stopping in the emulsion, about 500 μ long.
OABC: Grey track.

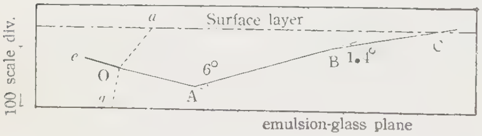

Fig. 1. (B) The projection of the star on the plane normal to the emulsion-glass plane.
Scale div. × Shrinkage factor (2.2) = Original thickness in μ.

Table I. The measured values of each part of the grey track.

	OA	AB	BC
Length in μ	1123	2379	2001
g.d. N/100μ	78.1	74.6	43.6
$\bar{\alpha}^\circ/(100\mu)^{\frac{1}{2}}$	0.180	0.197	0.336

Table II. The results after the correction for distortion on Table I.

	OA	AB	BC
Length in μ	1217	2326	1998
g.d. N/100μ	72.1	76·1	43.7
$\bar{\alpha}^\circ/(100\mu)^{\frac{1}{2}}$	0.195	0.195	0.336

§ 3. Correction for the Distorsion and the Examination of the Nonuniformity of the Emulsion

The star is created in the region near the edge of the plate as shown in Fig. 2. In this region, systematic C-shaped distortion of emulsion was found. Using some tracks which have large dip angles, it was found that the

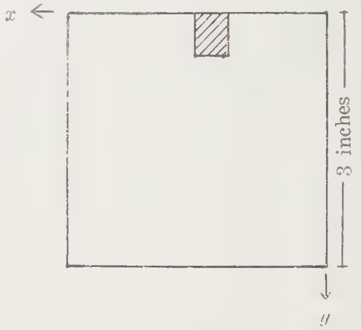

Fig. 2. The position of the region where the star was found (shaded region).

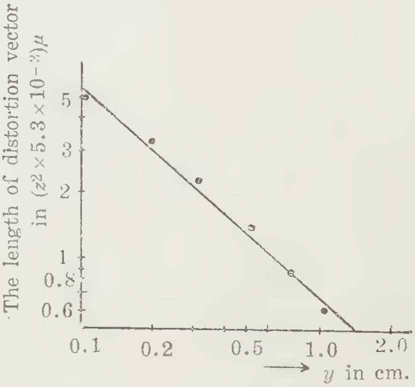

Fig. 3. The magnitude of distortion vector in the shaded region in Fig. 2, as a function of y-coordinate in Fig. 2.
z: The hight above the emulsion-glass plane in scale division.

distorsion vector had the direction parallel to the y-axis in Fig. 2, and its magnitude was given as a function of y-coordinates as shown in Fig. 3. The results corrected for this distorsion are shown in Table II. Possible local variation of grain densities was examined by means of neighboring tracks as seen in Fig. 4, and the result is shown in Fig. 5. No local variation of grain densities was found except the surface layer (80 μ). Still no local variation of background fogs was found except at the surface layer as shown in Fig. 6.

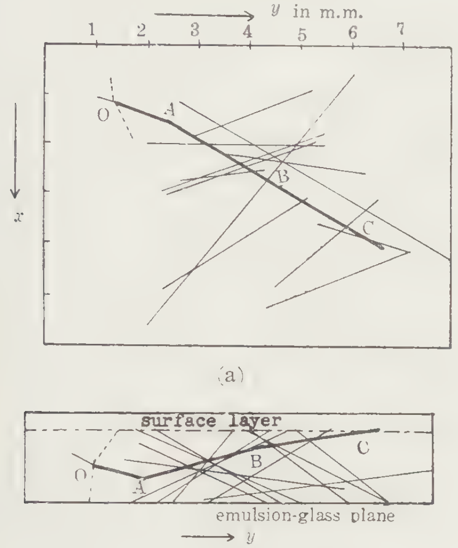

(b)

Fig. 4. The position of the neighbouring tracks examined the possible local variation of grain density.

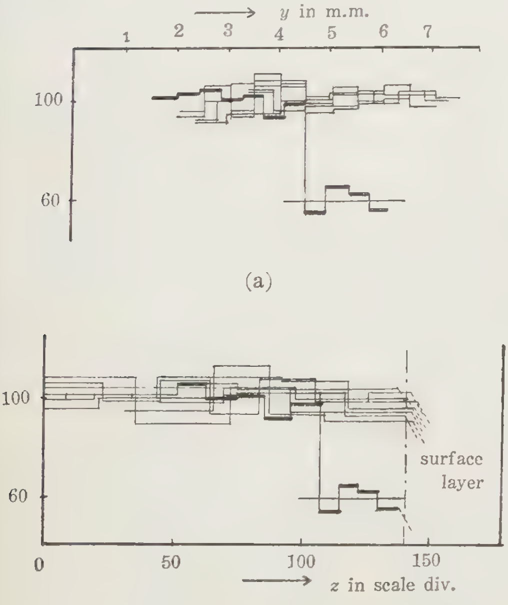

(b)

Fig. 5. The results of the examination of the possible local variation of grain density related to the y-coordinate (a), and related to the hight above the emulsion-glass plane (b). The grain density of each track is normalized by its mean value.

—: Naighbouring tracks.

━: The grey track.

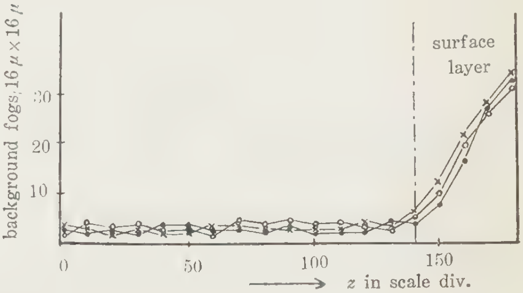

Fig. 6. The result of the examination of the possible local variation of background fogs.

-o-: y=5∼7 m.m. in the shaded region in Fig. 2.

×: y=2∼4 m.m. in the shaded region in Fig. 2.

-•-: The center region of the plate.

§ 4. Interpretation of the Event

Relations between the grain density and the scattering angles of the grey track (Table II) and those of other tracks in this plate are shown in Fig. 7. From this figure one can see that the particle which produced the grey

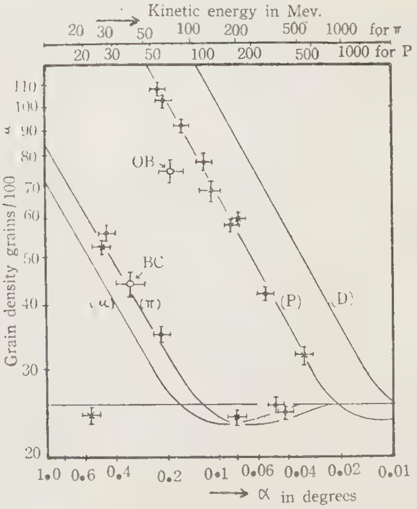

Fig. 7. Relation between the grain density and the scattering angle.

⊕: The grey track.

✚: The tracks related to stars in this plate.

✛: Single-tracks in this plate.

Table III. Difficultiness of the interpretation of the present event under the assumption that the particle in OB would be a proton

Assumption			The reason why the left side assumption cannot be held.
	OB	BC	
Particle	Proton (70 Mev)	meson (40 Mev)	
Direction of motion	O→B	B→C	A Proton whose kinetic energy is 70 Mev cannot produce meson at B.
	O→B	B←C	The probability which this event will happen is quite small.
	O→B O←B	B→C B←C	A proton whose kinetie energy is 70 Mev cannot produce a star which has two thin tracks.

track has the mass near the proton mass in the part OB and near the π-meson mass in the part BC respectively.

In the first place, one might assume that the particle in OB would be a proton and that in BC a π-meson. Then their kinetic energies should be about 70 Mev. and 40 Mev. respectively. This makes the interpretation of the whole event quite difficult under any assumption on the direction of motion of these particles as shown in Table III.

Next, let us assume that the particle in OB is one of the unstable heavy mesons, its mass (1160±170 me) being close to the proton mass but smaller than it. Then the event can be interpreted as follows. An unstable heavy particle was produced in the star and decayed in flight into a lighter meson (294±55 me) at the point B. Then the kinetic energy of the lighter meson in the rest system of the parent particle is about 7 Mev. This value is inconsistent with the current knowledge about the unstable heavy meson χ[5] which is considered to decay into one neutral particle and one charged π-meson with unique kinetic energy of about 110 Mev. If one assumes two particle decay mode, therefore, one should introduce another types of heavy mesons. Alternatively, however, if one assumes three particle decay mode, the present event can be interpreted as a κ-μ decay. Because the observed momentum value of secondary particle is not inconsistent with the expected one which ranges continuously from zero to the maximum value of about 220 Mev/c[3] provided that three particle decay mode (one charged μ-meson and two neutral particles) is assumed on the κ particle. The probability that the parent particle decays in the course OB is not so small, on account of the time of flight of 0.26×10^{-10} seconds. Thus it seems to be plausible that the present event is a $\kappa-\mu$ decay in flight.

§ 5. Discussion

Usually, the determination of such a event depends on the abrupt change in grain density at the given point and the direction change at the same soint. In the present event the crucial evidence is based only upon the abrupt change in the grain density at B, while the direction change at B is very small. Alternatively therefore we have to examine whether this event will occur due to a spurious distortion such as "wetting effect" (Appendix) or not. In the present case the wetting effect will not be completely neglected because of the facts that the direction of bending of the track at B is downward and that the distribution of the signs of the scattering angles in BC suggests a possibility of a different type of distorsion from that described in § 2. But, the order of the abrupt decrease in grain density at B seems quite larger than that expected from the wetting effect. Thus the very small direction change at B does not obstruct to explain this event as a decay, because in the decay process the angle between a parent particle and an emitted particle can take arbitrary value including zero. The different distribution of the scattering angle in BC may be explained as a statistical fluctuation. Moreover, it is presumed that the probability of observing this type of phenomena due to the wetting effect is very smaller than that observing this type of phenomena produced by the κ-μ decay (Appendix). After all, it seems to us most reasonable to explain this event as a κ-μ decay-in-flight.

Appendix

Wetting effect

The wetting effect is as follows. During the drying of the wet emulsion coated on the glass in the procedure of making up a photographic plate, a part of the emulsion may remain wet while the other part is already dry. One may therefore assume that just during this period a star was produced near the still wetting region and one of its prongs traversed there (Sse Fig. 8). In that case the sensitivity of the still wetting region is lower than that of the other part of the plate, and the grain density of the track in BC will be lower than that in OB. According to the later drying of that region the distorsion of the track in BC may be somewhat different from that in the other part. These effects, the decrease of grain densities and the possible difference in distortion may called as the wetting effect.

This effect may take place only in a limitted time interval, and almost all tracks are free from the wetting effect, for they are registered at high altitudes when the whole plate is completely dry. Even if all of the neighbouring tracks do not show any nonuniformity of the emulsion, therefore we cannot exclude the case in which this star prong alone suffered the wetting effect. In fact the direction change of this prong at B in the projection on the plane normal to the emulsion-glass plane is in such a direction as that which may be expected from the later drying of the still wetting region (See Fig. 9.) Though the examination of the neighbouring tracks show that there exists systematic C-shaped distortion in this part of the plate, the distribution of the sign of the scattering angles in BC is as if BC part of this prong was subjected by S shaped distorsion. (Of course it can also be explained as a statistical fluctuation.) Since it may be the case that this special event is produced by the wetting effect, the comparison was tried between the probability of detecting this type of phenomena produced by the wetting effect, P, and that of detecting it as produced by the κ-μ decay, P′, in the way shown in Table IV. Estimating the probability P and P′ by means of the above procedure following values were taken as N, T, V.—etc.

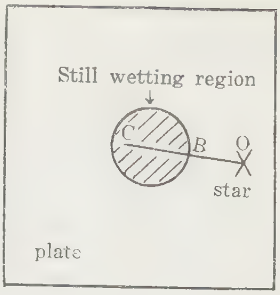

Fig. 8. The star which is produced near the "still wetting region".

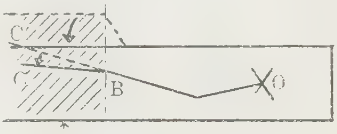

Fig. 9. The bending of a track expected from the later drying of the "still wetting region".

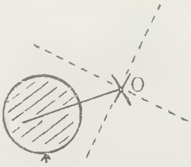

Fig. 10. The star-prong traversing the "still wetting region".

$N \sim 10^{-4}$ or 10^{-5} stars/hr. c.c. Based on the frequency of the star and the energy spectrum of N component at sea level. (7) (8)

$T \sim 1$ hr. Assumption.

$V \sim 10^{-2}$ C.C. Assumption. In the case of comparison between P and P′ this volume don't play any role, because $V = V'$.

$n \sim 1/40$/star Based on the experience.

$p_1 \sim 1/4$ Assumption. See Fig. 10.

$p_2 \sim X$ We have no information about the possibility that the ratio g.(BC)/g.(OB) ~ 0.6 will be explained as to be affected by the wetting effect. But $X \leqq 1$.

$p_3 \sim 1$ Expected from Fig. 9.

$N'T' \sim 40$ stars/c.c. The value on this plate.

$V' \sim 10^{-2}$ C.C. Equal to V.

$n' \sim 10^{-3}$ or 10^{-4}/star Assumption. But this value is not inconsistent with the frequency of K-particles coming to rest in the emulsion 6/140 c.c. hr., observed by Crussard et. al.[3].

$p_1' \sim 10^{-1}$ Based on the time of flight of this K-meson 0.26×10^{-10} sec.

Table IV. Comparison between the probability detecting this type of phenomena in the case of the wetting effect and that in the case of the $\kappa-\mu$ decay.

This event.	Type of phenomena	Probability of observing this type of phenomena in the case of the wetting effect. $P=NTVnp_1p_2p_3\cdots$		Probability of observing this type of phenomena in the case of the $\kappa-\mu$ decay. $P=N'T'V'n'p'_1p'_2p'_3\cdots$	
A star involving 2 thin tracks.	Production of high energy star	Frequency of high energy star at sea level.	N stars/hr, c.c.	Frequency of high energy star at high altitude.	N' stars/hr, c.c.
		Still wetting time.	T hr.	Exposure time.	T' hr
		Emulsion volume in question. (volume neighbouring around the still wetting region)	V c.c.	Emulsion volume in question.	V' c.c. $=V$
Length OC 5500μ g.d. OB $=74.7\pm1.2$ $\bar{\alpha}$ OB $=0.195\pm0.028$	Emission of heavy grey particle from the star.	Frequency of emission of grey proton in the direction nearly parallel to the emulsion-glass plane.	n/star	Frequency identifying low energy κ meson among the prongs of the high energy stars.	n'/star
$\frac{\text{g.d. BC}}{\text{g.d. OB}}\sim0.6$	Abrupt change in grain density of the grey prong at a point a few m.m. distant from the star.	Probability with which the prong, emitted from the star in the volume V nearly parallel to the emulsion-glass plane, traverses the still wetting region.	p_1	Probability of decay-in-flight of meson in the volume V.	p'_1
		Probability with which the abrupt change in grain density at the entrance of the still wetting region is so large as in this case.	p_2	Probability of abrupt change in grain density at the decay point.	$p'_2=1$
Direction change at B is very small. $0.4°\sim1.4°$	Very small or negligible direction change at the point of abrupt change in grain density.	Probability of direction change at the entrance of the still wetting region.	p_3	Probability of direction change (including zero) at the decay point.	$p'_3=1$

$p_2'\sim 1$ The ratio g(BC)/g(OB)$\sim$0.6 can be explained by the decay.

$p_3'\sim 1$ In the case of the decay the secondary particle can be emitted into any direction.

Applying above values, to N, T, V,$\cdots$etc., P and P$'$ are estimated as follows.

$$P \sim (0.6\times 10^{-8} \text{ or } 10^{-9})\times X,$$
$$P'\sim (0.4\times 10^{-4} \text{ or } 10^{-5}).$$

Therefore the probability of observing this type of phenomena produced by the wetting effect seems to be much smaller than that of observing it as produced by the κ-μ decay.

Acknowledgements

The author wishes to express his appreciation to Dr. V. Perterson, who exposed and processed these plates, for his kindness of providing these valuable plates to our laboratory. He is also indebted to Prof. Y. Sekido, Prof. I. Miura, Mr. Y. Tuzuki and Mr. J. Nisimura for many helpful discussions.

References

1) C. Oceallaigh: Phil. Mag. **42** (1951) 1032.

2) Mevi-Setti and Tomasini: Nuovo Cimento IX, (1952) 1224.

3) J. Crussard, L. Leprince-Ringuet, D. Morellet, A. Orkin-Lecourtois and J. Trembley: Phys. Rev. **90** (1953) 1127.

4) N. Isachsen, V. Vangen and S. O. Sörensen: Phil. Mag. **44** (1953) 224.

5) M. G. K. Menon: International Conference on Cosmic Radiations Bagneres de Bigorre, France (1953).

6) H. Yagoda: *Radioactive Measurements with Nuclear Emulsions.*

7) J. G. Willson: *Progress In Cosmic Ray Physics* (I).

JOURNAL OF THE PHYSICAL SOCIETY OF JAPAN Vol. 9, No. 5, SEP.—OCT., 1954

Long Period Effects in Germanium Crystal Rectifiers

By Makoto KIKUCHI

Electrotechnical Laboratory, Tokyo

(Received October 9, 1953)

Long period phenomena in germanium diodes, i.e. the "creep" and the "creep of photocurrent", have been observed. These phenomena have close connection with the "photoaftereffect" which we have reported in our previous paper[1].

It is proposed to take the trapping levels into account to explain these three related phenomena consistently. Although the time constants observed in these experiments, as long as 30-50 sec. or 200-300 sec., may seem to be too large to be attributed to the traps, we believe that this model is the most reasonable one to treat such long period effects in crystal rectifiers hereafter.

§ 1. Introduction

We have found out that when a germanium diode is illuminated for one minute or two, the resistance of the rectifier decreases to 1/2 —1/5 of the initial value, and the effect decays away in 5–10 minutes after the light is turned off. We have reported on the experimental results of this "photoaftereffect" and have proposed to consider trapping levels in the forbiddenband.[1]

Recently, we have examined about 50 samples of 1N34 germanium diodes furnished by Sylvania Electric Co., and found out that they can be classified into two groups.

About 60–70% of them constitute one group which show following three phenomena, i.e.

(1) photoaftereffect,

(2) creep,

(3) creep of photocurrent.

The remaining 30–40% constitute the other group which show none of these effects. It must be noted that there is no sample which shows only one or two of these phenomena.

The purpose of this paper is to present the experimental results of "creep" and "creep of photocurrent", and to discuss the physical model underlying the above mentioned three phenomena.

§ 2. Experimental Procedure

In performing the experiments of these effects, we must avoid any creeping effects coming from the measuring operation itself. For instance, in measuring the recovery of the backward current after few minutes' application of certain large voltage, we cannot apply low (measuring) valtage continuously during the recovery period, since it will cause undesirable creep effect in the measurement. Therefore, a single pulse method such as suggested by Ono2) is most preferable but, as it is too troublesome in its preparation, we adopted a pendulum method which is commonly used in the experiments of physiology.

The circuit is shown in Fig. 1. S_A, S_B are the switches coupled in the pendulum and are closed initially. When the pendulum is set free it first opens S_A and then opens S_B. The time interval is about 1/50 sec. Using the galvanometer ballistically, we can measure the value of the current with a proper calibration.

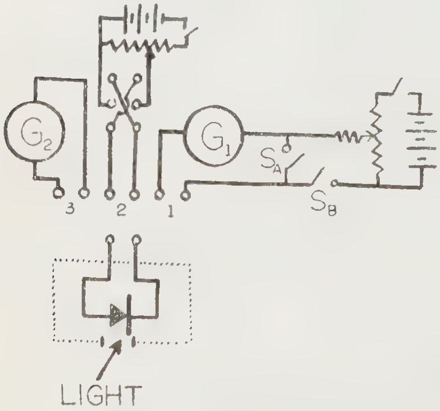

Fig. 1. The circuits used in the experiment.

The terminal 2 in the figure is to apply certain voltage in either easy or hard direction to cause the creep phenomena (we use the symbol V_C for this voltage in this paper), and the terminal 3 is to measure the variation of the photocurrent with time. The voltage V_C is interrupted for about 1/3 sec. for a measurement when the variation of the current under the application of V_C is studied.

A tungsten lamp for a microscope was utilized as the light source.

§ 3. Creep and the Static Characteristics

We have intended to find out some correlations between the creep phenomena and the static characteristics. This is only a phenomenological treatment, but as for the creep phenomena we have few knowledge about its substantial nature at present.

We can define several quantities from the static characteristics, i.e.,

(1) R_B; the resistance of the linear part of the backward characteristic,

(2) I_S; so called saturation current of the backward characteristic,

(3) R_0; so called low level resistance.

On the other hand, as a measure of the creep, we define the ratio r as a ratio of Δi to i_0 where Δi is the increase of the current observed at 2 volts reverse voltage after the application of certain voltage of V_c, and i_0 is the initial value.

As a result, we could not find out any correlation between r and the quantities, R_B, I_S, R_O, I_S/R_O, R_B/R_O. Namely, we could not get any information about the creep phenomena from the static characteristics.

§ 4. Creep Phenomena

It has been intended by several authors to observe the creep phenomena as a variation of the voltage across the rectifier fixing the current flow constant. We observed, however, the variation of the current under constant voltage. The main reason is as follows; we are going to find out some substantial knowledge about the barrier layer, so it is perferable to use the energy diagram as is shown in Fig. 2 fixing the difference of Fermi levels of the metal and the semiconductor, and to find the causes of the variation of the current in this model, (e.g., the variation of the shape of the barrier, the traps in the forbidden band, etc.), rather than to find out the causes of the variation of the difference of Fermi levels.

We have observed the variation of the current at 2 volts reverse voltage throughout these experiments.

Fig. 3 shows the variation of the current when 2 volts reverse voltage is applied on Sample No. 5. As is shown, the current first increases rapidly and the increase becomes very slow after 200 sec., but showing no evidence of saturation in the time range of the observation. The time constant of the first part of this curve is about 40 sec.

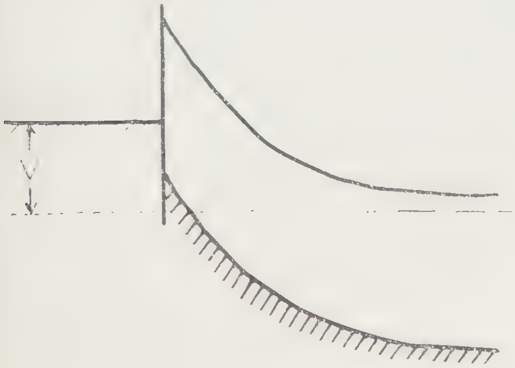

Fig. 2. A energy diagram of the barrier.

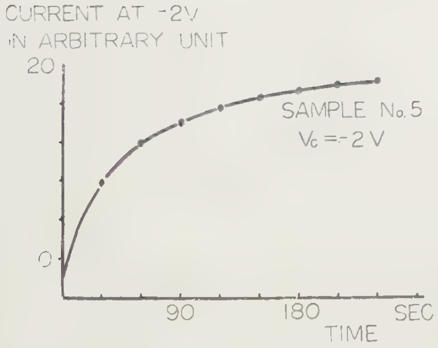

Fig. 3. Variation of the current at volts reverse voltage under the application of $V_c = 2V$ reverse voltage. (somple No. 5)

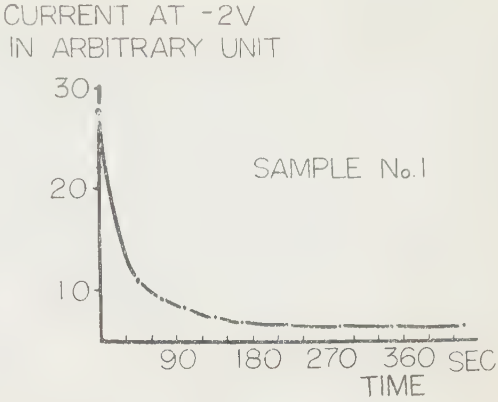

Fig. 4. The variation of the current at 2V reverse voltage after 1 minute's application of 2V reverse voltage. (Sample No. 1)

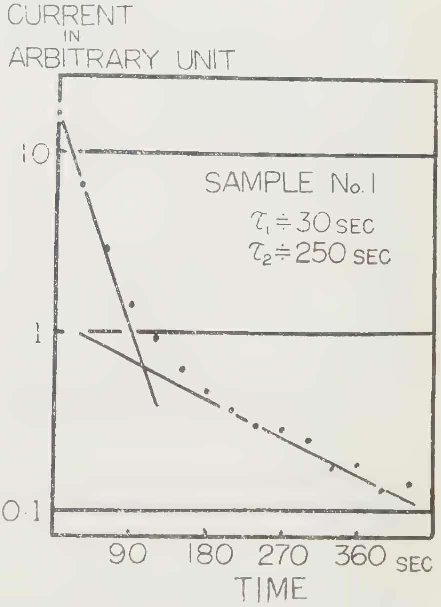

Fig. 5. Semi-log plot the curve of Fig. 4.

Fig. 4 shows the variation of the current in the recovery period after 1 minute's applicacation of 2V reverse voltage on Sample No. 1. It must be noted that this typical decay curve of the creep phenomena is quite similar to that observed on the photoaftereffect, namely it first decays rapidly and then slowly to the initial value. When this curve is replotted on the semi-log paper (Fig. 5) it does not plot a straight line, but it might be explained by two time constants, τ_1 and τ_2, where

$$\tau_1 = 30 \text{ sec.}$$

$$\tau_2 = 250 \text{ sec.}.$$

We did not try to pick up two different time constants from such a curve as shown in Fig. 5 in the previous paper for some reasons, but we have tried the analysis here because informations about the decay constants were obtained from some other experiments. It will be discussed later in some detail.

The time constants τ_1 and τ_2 determined in this way in 7 samples are

$$\tau_1 = 30-50 \text{ sec.}$$

$$\tau_2 = 200-300 \text{ sec.}.$$

It must be noted that one sample out of 8 samples showed the decay curve which was a simple exponential curve with the time constant of 105 sec..

Fig. 6 shows the variation of the current when the voltage V_C is applied successively. Namely, Curve A is the first run of the creep. After the first run, the same voltage is applied before the effect of the first run does not completely decay away. The variation of the current under this condition is shown by the Curve B. At first we expected that Curve B would come to coincide with Curve A by just shifting it to the right, but the Curves B and C did not coincide with A by such an operation.

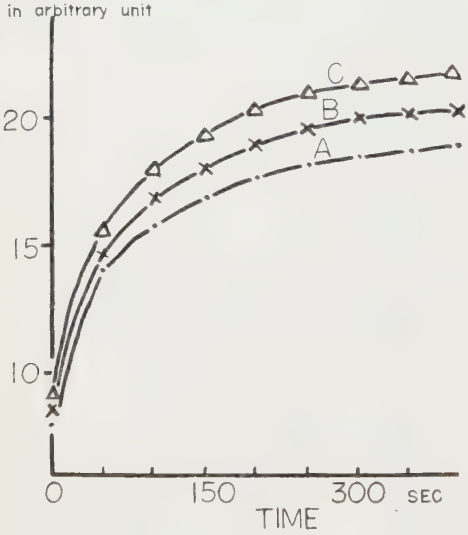

Fig. 6. The creep phenomena when the voltage V_c is applied before the former effect does not decay completely.

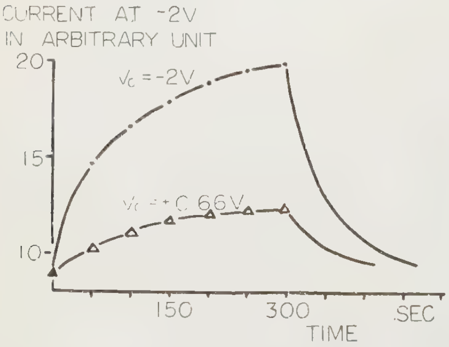

Fig. 7. Dependence of the creep on the voltage V_c. (Sample No. 5)

It has been found that the ratio $r = \Delta i/i_0$ (whose definition is given before,) depends on the value and the direction of the voltage V_C. An example for sample No. 5 is shown in Fig. 7. In this case the amount of the cree by the application of 2V reverse is larger tha that by the application of 0.66V forward, an also this figure shows that the ratio r is positive both for positive and negative V_C.

Figs. 8 and 9 show the dependence of r o V_C for three samples. As is shown in thes figures, there is no definite tendency of the dependence of r on V_C, namely r is larger i the positive V_c than in negative V_c in the case of No. 4, while, in the case of No. 7 r becomes negative for positive V_c. It should be noted that this peculiar characteristic of No. 7 has no correlation with the fact that the decay curve of this sample can be expressed by a simple expotential law, since the

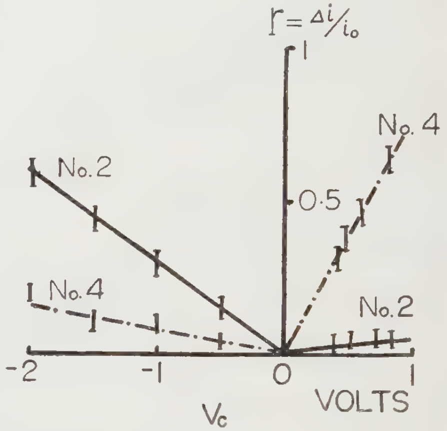

Fig. 8. Dependence of r on V_c. (Samples No. 2 and No. 4)

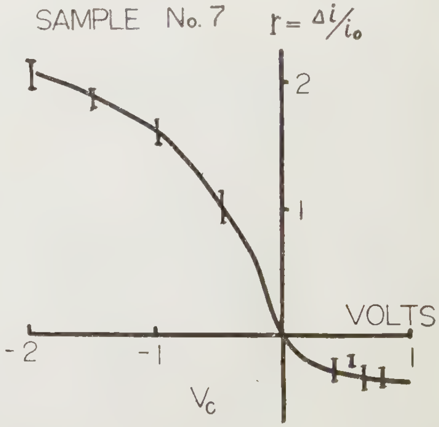

Fig. 9. Dependence of r on V_c. (Sample No. 7)

$r - V_c$ characteristic similar to that shown in Fig. 9 can also be found in other samples whose decay curves consist of two time constants.

These results seem to show that the creep phenomena can not be explained simply by the temperature rise or impurity migration.

§ 5. Creep of the Photocurrent

In close connection with the photoaftereffect, we have observed the variation of the short-circuited photocurrent with time. It first increases with a time constant of 30–50 sec., and then very slowly without showing an evidence of saturation in as long as 5 minutes or so. (Fig. 10). This effect is also quite well reproducible. The accuracy of this effect is relatively low because the absolute value of the variation of the photocurrent is small, but presumably the time constants of the recovery process are nearly the same with those observed in the other two phenomena.

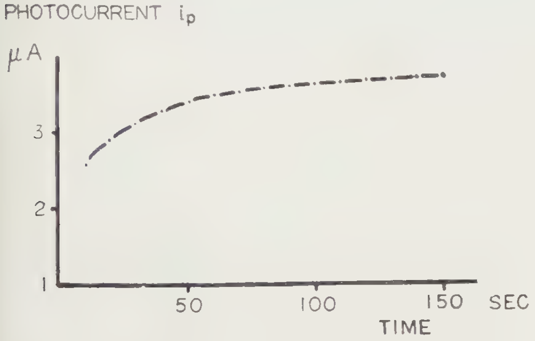

Fig. 10. Variation of the photocurrent with time.

§ 6. Discussions

We have pointed out in the previous paper1) that the photoaftereffect is due to neither the temperature rise during the illustration nor the impurity migration. We have also rejected the possibility of being due to the humidity.

The model which we have proposed in that paper is also applicable to the above mentioned phenomena, but we shall first examine other possible factor briefly.

In the case of the creep, the heat dissipation at the contact point may cause some temperature rise but the observed variation of the current can not be attributed to this effect, since in some cases the ratio r is negative for positive V_c as shown in Fig. 9. If we want to explain this result by the temperature effect, we must introduce the Peltier effect. It seems, however, too sophisticated to take such an effect into consideration, and moreover, the creep must be expected to occur in every sample if it is caused only by the temperature rise.

It is also quite unlikely that the creep might be due to the impurity migration by the application of the voltage V_c, since in many samples the ratio r is positive for both positive and negative V_c as shown in Fig. 8.

Now, first we shall discuss the case of the creep of photocurrent. The photocurrent i_p can be given by

$$i_p=(Je/h\nu)\alpha A(o)\,, \qquad (1)$$

where

$$A(o)=\left[1+\frac{kT}{eF_0\mu}\right]^{-1}-\exp(-d/\mu), \qquad (2)$$

as deduced by Lehovec3). The symbols are used as follows;

J = intensity of incident light,
α = number of electrons released by a photon,
F_0 = electric field strength at the metal-semiconductor interface without applied voltage,
d = effective thickness of the barrier layer,
μ = absorption length.

We must integrate this formula with frequency if the experiment is performed using white light.

In short, the increase of i_p may be attributed to either the increase in

(1) the number of electrons released, or
(2) the electric field which sweeps the created carriers.

The first case may be explained by the "trap" model. If there are several trapping levels in the forbidden band, the electrons will be excited from the filled band to the conduction band stepwise through these levels

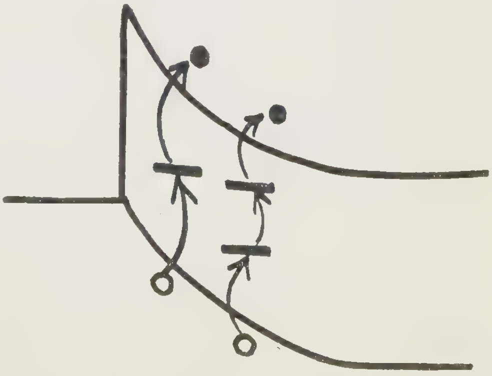

Fig. 11. Energy diagram of the barrier with trapping levels.

(Fig. 11) by the photons having an energy

$$h\nu < E_G \qquad (3)$$

where E_G is the width of the forbidden band. The time constants of this phenomenon may be attributed to that of the trapping and releasing processes of the traps. We should like to point out that the creep of photocurrent and the photoaftereffect may also be observed using the light whose wave-length satisfies the Eq. (3).

Considering that the excitation of carriers might take place due to the electric field in the barrier, it seems reasonable to apply the trap model to the creep phenomena. The result as shown in Fig. 9 is expected from this model, but as for the case of Fig. 8 in which r is positive in both posite and negative V_c, further modification with some other factors might be necessary.

There still remains a possibility that the creep phenomena might be explained by *combining* the temperature effect and the impurity migration. The photoaftereffect and the creep of photocurrent can not, however, be explained even if they are combined, while the trap model meet with only one difficulty in explaining these three phenomena consistently. Moreover, according to Tillman and Henderson⁶⁾, the time constant coming from the temperature effect connot exceed several micro-seconds.

Hence, we propose that,

(1) three related phenomena are caused by the same or at least similar mechanism, and

(2) the substance which is responsible for these phenomena is the "traps".

Recently, Haynes and Hornbeck⁴⁾ have reported the decay time canstant of 260 sec. of the photoconductivity of Si and Ge bulk, and explained it to be due to the deep traps. This result seems to support our conclusion.

There are some comments on the creep phenomena and the nature of the traps: i.e.,

(1) The traps are not essentially localized only on the surface but may be distributed in the bulk.

(2) It is probable that such traps become a kind of surface states when they exist at the surface.

(3) It is likely that the traps might be produced by the electrical forming, but it is not the only possible way to produce them.

(4) According to Osahune⁵⁾, there are some correlations between the bulk resistivity and the creep, e.g., the creep phenomena can be observed only on the Ge whose resistivity is higher than several ohm-cm.

§ 7. Conclusion

We have observed three related phenomena on 1N34 Ge diodes and proposed the trap model to explain them. Our discussion of the trap model is qualitative and not exactly quantitative, but as for the investigation of the surface phenomena of Si and Ge, we think, it is necessary to discuss about the physical model of the barrier layer qualitatively or semi-quantitatively since the accuracy of the experiments is not high enough at present to treat the results quantitatively.

Of course our model is not the only possible one but it seems to be most reasonable for us.

References

1) To be published on the Journ. Phys. Soc. Japan. See also Kikuchi and Onishi: Bull. Electrotechnical Lab. Vol. 17. No. 8, 1953 (in Japanese) for the discussion in detail.

2) M. Ono: presented at the meeting of the Phys. Soc. Japan April 1952.

3) Lehovec: Phys. Rev. **74** (1948) 463.

4) Haynes and Hornbeck: Phys. Rev. **90** (1953) 152.

5) Private communication.

6) Tillman and Henderson: Phil. Mag. **44** (1953) 677.

JOURNAL OF THE PHYSICAL SOCIETY OF JAPAN Vol. 9, No. 5, SEP.—OCT., 1954

Hall Effect and Electrical Conductivity of Lead Selenide

By Eiji HIRAHARA and Miyuki MURAKAMI
Department of Applied Physics, Faculty of Engineering,
Hiroshima University

(Received March 12, 1954)

Electrical conductivity and Hall constant of both P-type and N-type specimens were measured all over the range of temperatures from 500°C to −180°C. The complicated properties of P-type specimens were fairly well analysed by taking into consideration the scattering from both lattice and impurity centers and the temperature dependence of Fermi energy. The agreement between the calculated and measured values of conductivity and Hall constant at any temperature was satisfactory. The Fermi energies of impurity semiconductors in which both electrons and holes act as current carriers were calculated, and the errors in the approximate calculation of Fermi energy were discussed.

§ 1. Introduction

The electrical properties of lead selenide have been studied by K. Bauer1), and L. Eisenmann2), but there is a leak of the detailed reports about the conducting electrons and holes in this material. The authors have performed the experimental measurements of conductivity and Hall effect, and discussed the conduction mechanism of the material.

The samples used in this study are polycrystalline ones containing excess selenium or excess lead as impurity. Selenium excess samples were P-type and lead excess samples, N-type. A remarkable impurity scattering was observed on the samples containing rather large amounts of impurity.

At first, the experimental results on these samples were analysed by the semi-empirical formula. And then the exact analysis taking account of the temperature effects on the Fermi levels was carried out. In the semi-empirical analysis it was found that the energy gap between conduction and filled bands was considerably narrow. In these narrow gap semiconductors (similar to the case of germanium and silicon) the thermal transitions of electrons from filled band to conduction band would be observed above room temperatures.

Therefore, it is necessary for computing the Fermi energy that the electron and hole distributions over both conduction and filled bands should be taken into account. This computation generally yields the equation of the fourth degree with respect to $\eta(\eta=\exp \zeta/kT$, ζ is Fermi energy), the solution of which is complicated and laborious to be worked out.

In this paper, by using some method of approximation the equation of the third degree with respect to η has been delt with, the errors of which have been estimated for the case of our materials.

§ 2. Samples and Experimental Procedures

Lead Selenide used in our experiment are prepared as follows; the suitable quantities of powders mixed of pure selenium and pure lead are heated about 600°C in a quartz or pyrex vacuum tube, and the lumps of the compound prepared are then grinded into powder, and are sintered in a iron mould under a pressure of 100 Kg/cm. The specimens used in this measurements were made rectangular in shape, approximately 1 mm × 3 mm × 10 mm. Metallic electrodes and Hall sonde contacts were fixed on the specimen by the spattering of gold in a vacuum jar. The specimen holder was bedded in a wolfram wire furnace of dimensions 20 mm in diameter, 10 cm in length. These holder and furnace were put in a pyrex tube (25 mm in diameter) and set them into the refrigerant bath (Dewar Vessel), situated between the pole faces of magnet which diameter is of 150 mm. The measurements were carried out over the range from 500°C to −180°C; using the wolfram wire furnace in atmosphere of pure nitrogen gas at high temperature measurements and the liquid-air refrigerant bath at low temperature measurements. The magnetic field strength, produced at between pole faces of 50 mm in distance, was chosen about 8000 Gauss for most of the measurements of Hall effect.

Our measurements of conductivities, Hall voltages and thermo electric powers of thermocouple were made by using a K-type potentiometer.

§ 3. Experimental Results

Results of the measurements on many samples have clearly shown that the samples containing selenium as impurity were of P-type, whereas the ones containing lead as impurity were of N-type. The typical results only in many measurements are picked up and shown in Figs. 1∼4. In these figures, the solid and open circles represent the measured points of conductivity and Hall constant.

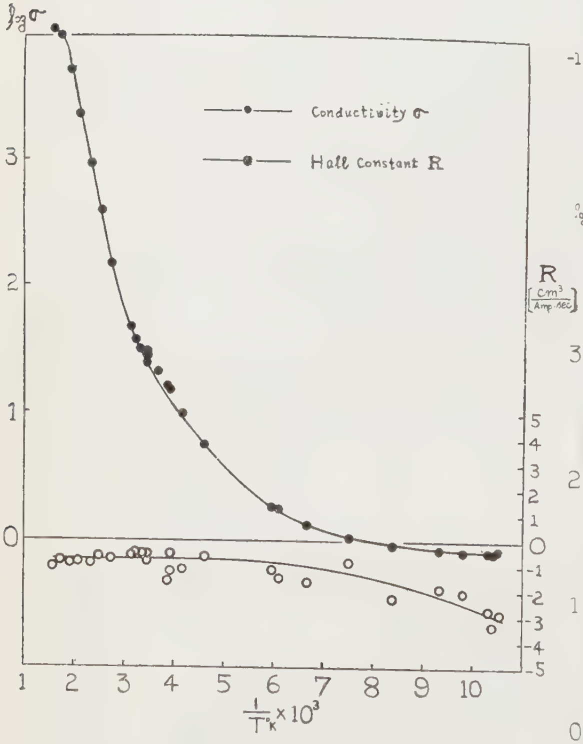

Fig. 1. PbSe, Specimen, No. 16.

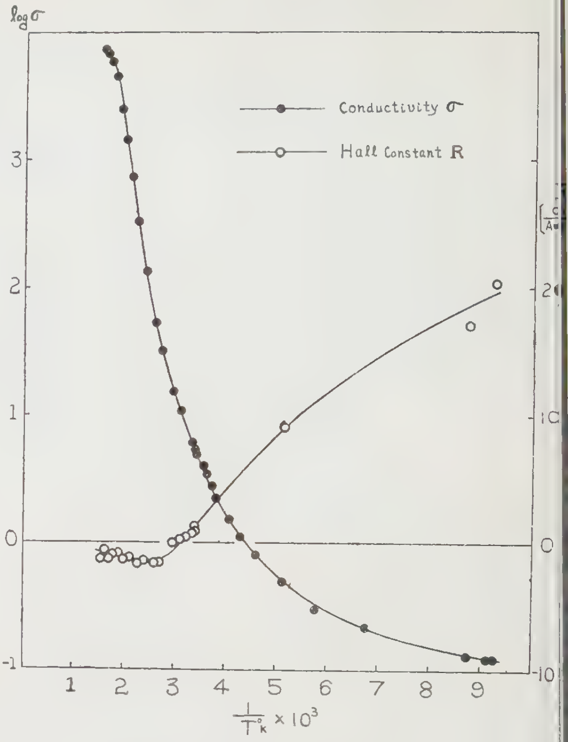

Fig. 2. PbSe, Specimen, No. 10.

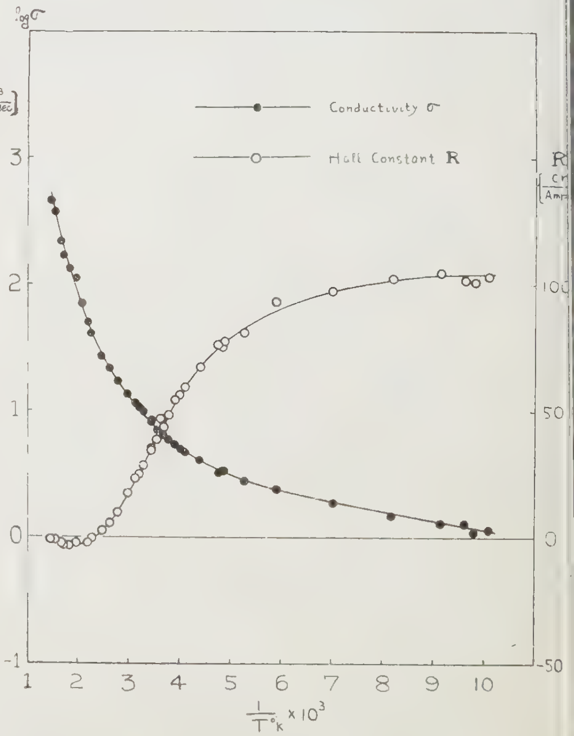

Fig. 3. PbSe, Specimen, No. 11.

The specimen of No. 16 (Fig. 1) is the sample containing a small quantity of lead as impurity (probably less than 0.1%) and shows N-type behaviour. The specimen of No. 10 (Fig. 2) and No. 11 (Fig. 3) are the samples containing excess selenium of 0.5% and 1% respectively and show P-type behaviour, that is, at low temperatures the Hall constants are positive and decrease with increasing temperature and then show negative values above room temperature after passing zero value. The fact that the Hall constant changes to negative from positive values will correspond to the fact that the appreciable numbers of electrons in filled band are activated thermally to conduction band at high temperatures. The specimen of No. 6 (Fig. 4) containing excess selenium of 3% shows rather complicated behaviour in conductivity, in this sample its values at low temperature are larger than those of the last three specimens and decrease with increasing temperatures and pass minimum value at about 150°C before the rapid increase with temperature. The increment of conductivity at higher temperatures as well as the change in sign of the Hall constant will be ascribed to the thermal transition of the electrons in filled band to the conduction band.

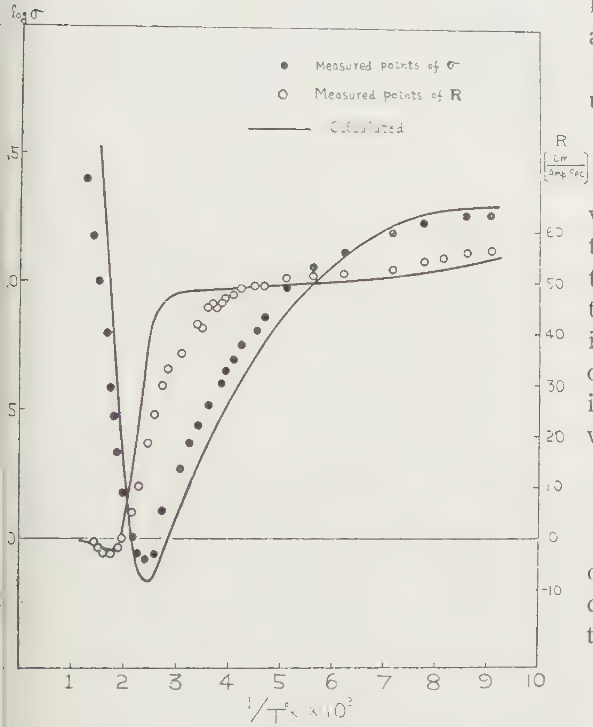

Fig. 4. PbSe, Specimen, No. 6.

The qualitative analysis of the mentioned results shall be described in the next section.

§ 4. Analysis of the Experimental Results

The temperature dependence of conductivity of specimens Nos. 16, 10 and 11 are so monotonous that they may be easily analysed in the two ranges of temperatures, that is, the impurity range at low temperatures and the intrinsic range at high temperatures. But, as seen later, the specimen of No. 6 is found to have important and essential properties. Therefore, the results of No. 6 will be delt with at first and the results of other specimens will be discussed later on.

§ 4.1. Lattice and Impurity Scattering

The drop of the conductivity in the specimen of No. 6 in the range from low temperatures to room temperatures may be interpreted by the scattering due to the lattice vibrations and impurity centers.

A mobility of electrons (or electron holes) under a thermal lattice scattering is³⁾

$$\mu_a=\frac{2\sqrt{2\pi}}{3}\,\frac{\hbar^4\cdot C_{ll}\cdot e}{\mathcal{E}^2\cdot m_e^{5/2}\cdot k^{3/2}}\cdot T^{-3/2}\,, \tag{1}$$

where C_{ll} is the elastic constant for [110] longitudial acoustical waves, $\mathcal{E}$ the energy relating to the deformation energy of the lattice, and m_e the effective mass of electrons. Now, if m_e is assumed as a free electron mass, $\mathcal{E}$, oder of 1 ev, and C_{ll}, oder of 10^{11} dyne/cm² and μ is expressed in cm²/volt·sec in the following way

$$\mu_a=3\times10^6\cdot T^{-3/2} \text{ or } 1/\mu_a=0.3\times10^{-6}\cdot T^{3/2}. \tag{2}$$

In a polar crystal, a scattering by the optical vibration of the lattice also should be considered. A mobility due to an optical lattice scattering is⁴⁾

$$\mu_0=2\sqrt{\frac{3}{\pi mk\Theta}}\cdot\frac{\kappa-\kappa_0+1}{\kappa-\kappa_0}\cdot e\cdot a_0(e^{\Theta/T}-1)\,, \tag{3}$$

where κ and κ_0 are the dielectric constants for static fields and high frequency fields respectively, a_0 the Bohr radius of hydrogen atom, e electronic charge and Θ the characteristic temperature defined by $k\Theta=h\nu_0$ for polar lattice vibrations ν_0.

Since Θ for polar crystals may be between 300°K and 800°K, the insertion of numerical values in μ_0 leads to

$$\mu_0=C(e^{\Theta/T}-1),\quad C\approx1.6\sim2.6. \tag{4}$$

A mobility due to the scattering by the ionized impurity centers is⁵⁾

$$\frac{1}{\mu_I}=\frac{N_I\cdot\pi^{3/2}\cdot e^3\cdot m^{1/2}}{2^{7/2}\cdot\kappa^2\cdot(kT)^{3/2}}\cdot\log(1+x^2)\,,$$
$$x=6\kappa\cdot d\cdot kT/e^2\,, \tag{5}$$

where N_I is the concentration of impurity centers, d the average distance, which is assumed to be the average distance between neighbouring ions, since the field of any one ion extends on the electrons or holes.

If $N_I \approx 10^{17}$, $\kappa=8$ and $d=0.5\cdot N^{-1/3}$, we have

$$1/\mu_I=0.47\cdot T^{-3/2}. \qquad (6)$$

Finally, a mobility due to the scattering by the neutral impurity centers becomes[5)]

$$\begin{aligned}1/\mu_n&=(m/e)\cdot N_n\cdot v\cdot A\ ,\\ A&=124\cdot\pi\cdot\kappa^2\cdot A_0\cdot\alpha(T)\ , \qquad (7)\end{aligned}$$

where N_n is the concentration of neutral impurities, v an average thermal velocity for the carrier, and $\alpha(T)$ a numerical factor less than unity.

Using the numerical values, $1/\mu_n$ is of the oder of $2.9\times10^{-22}\cdot T^{1/2}\cdot N_n\cdot\alpha(T)$ which is negligiblly small compared with $1/\mu_I$.

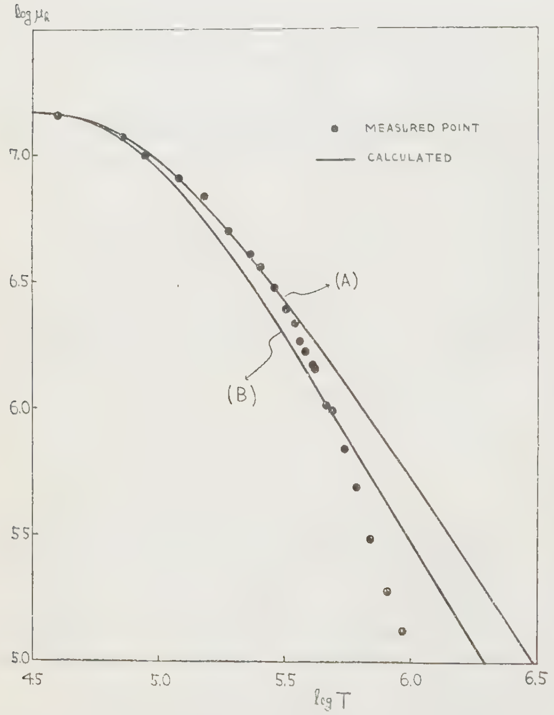

Fig. 5. The fall of mobility by the scatterings.

As seen later, the activation energy for an impurity level is very small so that almost all the impurity ions are found to be become ionized centers. Because of the above situations, the ionized impurity center will take a main part in the impurity-scattering in our case.

The total mobility, therefore, may be expressed, all over the temperature range, approximately by an expression of the form

$$\begin{aligned}1/\mu&=1/\mu_I+1/\mu_a+1/\mu_0\\ &=a\cdot T^{-3/2}+b\cdot T^{3/2}+c(e^{\Theta/T-1})^{-1}, \qquad (8)\end{aligned}$$

which is used in the analysis of the conductivity behaviour for the specimen of No. 6 In our actual procedure, coefficients a, b an c in Eq. (8) are determined by fitting th equation to the observed mobilities and the they are compared with Eqs. (5), (2) and (4 respectively.

Since the conduction phenomena in the lo temperatures ranges are nearly ascrived to th hole-carrier, the following expression for th mobility of non-degenerate carriers is considered to be valid approximately,

$$\mu=(8/3\pi)\cdot\sigma\cdot\boldsymbol{R}=0.85\cdot\sigma\cdot\boldsymbol{R}, \qquad (9)$$

where σ is the conductivity and $\boldsymbol{R}$ the Ha constant.

Using the best fitted values of a, b and c Eq. (8) for the holes becomes

$$\begin{aligned}1/\mu_h=0.38\cdot T^{-3/2}&+4\times10^{-7}\cdot T^{3/2}\\ &+5.8\times10^{-3}(e^{\Theta/T}-1)\ , \qquad (10)\end{aligned}$$

with $\Theta=800°\mathrm{K}$.

The values for a and b in Eq. (10) are i qualitative agreements with the theoretica ones in Eqs. (6) and (2), but the value for is smaller by a factor of 10^{-2} in compariso with Eq. (4), which discrepancy become larger for the smaller values of Θ than 800°K suggesting the negligible contribution from μ

The actual situation of the fitting procedu is shown in Fig. 5, in which the curve (A does not contain the term of scattering due to the optical modes but the curve (B) contains them. If the ratio of electron mobilit μ_e/μ_h is assumed to be constant all over th temperature ranges, the μ_e may be obtaine from Eq. (10) multiplied by the factor $s=$ μ_e/μ_h.

§ 4.2. Calculations of Fermi Energy

For the detailed analysis of both conductivit and Hall constant, the Fermi energy is require to be calculated as a function of temperature and its temperature-dependence for sem conductors has been studied by many worker Shifrin[6)], Putley[7)], Lehovec and Kedesdy[8 and Blakemore[9)].

In the high temperature range, our exper mental data suggest us the appreciab number of both electrons and holes in the conduction and filled bands respectively. In the calculations of Fermi energy, therefore, we must take account of the electron distribution over conduction-, filled-bands and impurity levels. Our model of P-type impurity semiconductor is shown in Fig. 6 in which E_1, E_2 and E_3 are the energies of the top of filled band, of impurity levels and of the bottom of conduction band respectively. N_A is the concentration of impurity states.

We assume that n_e, n_h and n_i are the concentrations of the electrons in conduction band, of the holes in filled band, and of the electrons in impurity levels respectively. Thus we have

$$\begin{aligned} n_e &= 2\int_{E_3}^{\infty} f(E)\cdot D(E)\cdot dE\,, \\ n_h &= 2\int_{-\infty}^{E_1} \{1-f(E)\}\cdot D(E)\cdot dE\,, \\ n_i &= N_A\cdot f(E)\,, \end{aligned} \tag{11}$$

where $f(E)$ is Fermi distribution function, $f(E)=[1+\exp\{(E-\zeta)/kT\}]$, ζ the Fermi energy and $D(E)$ the state density near the band edges which is given by

$$D(E)=(1/4\pi^2)(8\pi m'/h^2)^{3/2}\cdot(E-E')^{1/2}, \tag{12}$$

m' is an effective mass and E' the energy at the band edges.

At any temperature the hole concentration in the filled band is equal to the sum of the electron concentrations in the conduction band and in the impurity levels. Then, we get

$$\begin{aligned} &2\int_{-\infty}^{E_1} \{1-f(E)\}\cdot D(E)\cdot dE \\ &\quad = N_A\cdot f(E)+2\int_{E_3}^{\infty} f(E)\cdot D(E)\cdot dE. \end{aligned} \tag{13}$$

In case $E_3 \gg \zeta$, the Fermi distribution function in the conduction band may be approximately replaced by the Maxwell distribution function, which leads to

$$\begin{aligned} n_e &= 2\int_{E_3}^{\infty} f(E)\cdot D(E)\cdot dE \\ &= 2\frac{1}{4\pi^2}\left(\frac{8\pi^2 m_e}{h^2}\right)^{3/2} \\ &\quad \cdot\int_{E_3}^{\infty}\frac{(E-E_3)^{1/2}}{1+\exp\{(E-\zeta)/kT\}}\cdot dE \\ &\doteqdot 2\cdot\left(\frac{2\pi m_e\cdot kT}{h^2}\right)^{3/2}\cdot\exp\left(-\frac{E_3-\zeta}{kT}\right) \\ &= \alpha_e\cdot\exp\left(-\frac{E_3-\zeta}{kT}\right), \end{aligned} \tag{14}$$

and

$$\alpha_e = 2\cdot\left(\frac{2\pi m_e\cdot kT}{h^2}\right)^{3/2},$$

where m_e is the effective mass of electrons in the conduction band.

Similarly, the concentration of holes in the filled band,

$$\begin{aligned} n_h &= 2\int_{-\infty}^{E_1} \{1-f(E)\}\cdot D(E)\cdot dE \\ &= \frac{1}{2\pi^2}\left(\frac{8\pi m_h}{h^2}\right)^{3/2}\cdot\int_{-\infty}^{E_1}\frac{\exp\{(E-\zeta)/kT\}}{1+\exp\{(E-\zeta)/kT\}} \\ &\quad \cdot(E_1-E)^{1/2}\cdot dE\,, \end{aligned} \tag{15}$$

is simplified approximately into

$$\begin{aligned} n_h &\doteqdot \frac{1}{2\pi^2}\left(\frac{8\pi^2\cdot m_h}{h^2}\right)^{3/2}\cdot\int_{-\infty}^{E_1}\exp\left(-\frac{\zeta-E}{kT}\right) \\ &\quad \cdot(E_1-E)^{1/2}\cdot dE \\ &= 2\cdot\left(\frac{2\pi m_h\cdot kT}{h^2}\right)^{3/2}\cdot\exp\left(-\frac{\zeta-E_1}{kT}\right) \\ &= \alpha_h\cdot\exp\left(-\frac{\zeta-E_1}{kT}\right), \end{aligned} \tag{16}$$

and

$$\alpha_h = 2\left(\frac{2\pi m_h\cdot kT}{h^2}\right)^{3/2},$$

for the case $E_1 \ll \zeta$.

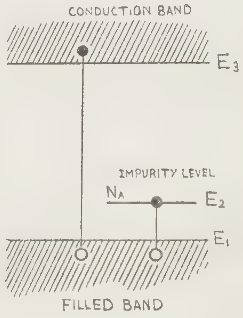

Fig. 6. Energy diagram of P-type.

The above approximation does not hold for $E_1 \sim \zeta$, which case shall be discussed in the later section (§ 6).

The substitution of Eqs. (14), (16) into Eq. (13) leads to

$$\begin{aligned} \alpha_h\cdot e^{E_1/kT}\cdot e^{-\zeta/kT} &= N_A\cdot\left\{1+\exp\frac{E_2-\zeta}{kT}\right\}^{-1} \\ &\quad +\alpha_e\cdot e^{-E_3/kT}\cdot e^{\zeta/kT}\,. \end{aligned} \tag{17}$$

At low temperatures range in which $E_3 \gg kT$, the electrons in the conduction band, activated from filled band and iupurity levels, may be taken to be negligibly small in number.

Thus, Eq. (17) reduces to a quadratic equation for $\exp(-\zeta/kT)$,

$$\alpha_h \cdot e^{(E_1+E_2)/kT} \cdot e^{-2\zeta/kT} + \alpha_h \cdot e^{E_1/kT} \cdot e^{-\zeta/kT} = N_A. \tag{18}$$

from which $\exp(-\zeta/kT)$ may easily be solved. Putting the solution of Eq. (18) into Eq. (16), we obtain for the concentration of holes in filled band,

$$n_h = \alpha_h \cdot e^{-(\zeta-E_1)/kT} = \tfrac{1}{2} \cdot \alpha_h \cdot e^{-(E_2-E_1)/kT} \cdot \left\{\sqrt{1+\frac{4\cdot N_A}{\alpha_h \cdot \exp\{-(E_2-E_1)/kT\}}}-1\right\}. \tag{19}$$

Replacing n_h and α_h by n_t and α_e, we would have a usual expression for the electron concentration of impurity level at low temperatures.

From Eqs. (14) and (16), we have the well-known relation

$$n_e \cdot n_h = 4\left(\frac{2\pi kT}{h^2}\right)^3 (m_e \cdot m_h)^{3/2} \cdot e^{-(E_3-E_1)/kT}. \tag{20}$$

This relation will be of use to obtain the energy gap (E_3-E_1) from the slope of the curve relating $n_e n_h/T^3$ to $1/T$.

Now, the Eq. (17) becomes of the thied degree with respect to $\exp(-\zeta/kT)$,

$$e^{-3\zeta/kT} + e^{-E_2/kT} \cdot e^{-2\zeta/kT} - \left[\frac{\alpha_e}{\alpha_h} \cdot e^{-(E_1+E_3)/kT} + \frac{N_A}{\alpha_h} \cdot e^{-(E_1+E_2)/kT}\right] \cdot e^{-\zeta/kT} - \frac{\alpha_e}{\alpha_h} \cdot e^{-(E_1+E_2+E_3)/kT} = 0, \tag{21}$$

which is easily solved by the well-known theorem in algebra.

If put

$$A = \frac{1}{3} e^{-E_3/kT},$$

$$B = \frac{1}{3}\left[\frac{\alpha_e}{\alpha_h} \cdot e^{-(E_1+E_3)/kT} + \frac{N_A}{\alpha_h} \cdot e^{-(E_1+E_2)/kT}\right],$$

$$C = \frac{1}{2} \cdot \frac{\alpha_e}{\alpha_h} \cdot e^{-(E_1+E_2+E_3)/kT},$$

$$x = e^{-\zeta/kT} + A.$$

Eq. (21) is transformed into

$$x^3 - 3(A^2+2B)x + 2(A^3+3A\cdot B-C) = 0, \tag{22}$$

which solution are

$$x_1 = \sqrt[3]{-q+\sqrt{q^2-p^3}} + \sqrt[3]{-q-\sqrt{q^2-p^3}},$$

$$x_2 = w\sqrt[3]{-q+\sqrt{q^2-p^3}} + w^3\sqrt[3]{-q-\sqrt{q^2-p^3}},$$

$$x_3 = w^2\sqrt[3]{-q-\sqrt{q^2-p^3}} + w\sqrt[3]{-q-\sqrt{q^2-p^3}},$$

where

$$p = A^2+2B, \qquad q = A^3+3A\cdot B-C,$$

$$w = \frac{-1+\sqrt{-3}}{2}, \quad w = \frac{-1-\sqrt{-3}}{2}.$$

As shown in "Appendix", we have $q^2-p^3 > 0$, in which case the solutions are easily expressed through a new variable φ in the following way.

$$x_1 = 2\sqrt{p} \cdot \cos\frac{\varphi}{3}, \quad x_2 = -2\sqrt{p} \cdot \cos\frac{\pi-\varphi}{3},$$

$$x_3 = -2\sqrt{p} \cdot \cos\frac{\pi+\varphi}{3}, \tag{23}$$

where

$$\cos\varphi = -q/\sqrt{p^3}, \qquad \pi \leq \varphi \leq 0.$$

In view of x being always positive by its definition, the admissible solution of Eq. (22) is clearly seen to become x_1 only.

The application of the above formula to the actual case shall be shown in the next section.

§ 4.3. Calculation of σ and R

The expressions of conductivity and Hall constant for the case of both electrons and holes contributing to current carriers are as follows.

$$\sigma = e(n_e \cdot \mu_e + n_h \cdot \mu_h),$$

$$R = \frac{-n_e \cdot \mu_e^2 + n_h \cdot \mu_h^2}{e(n_e \cdot \mu_e + n_h \cdot \mu_h)^2} \tag{24}$$

For the calculation of σ and R we must compute n_e and n_h for all temperatures in addition to the expressions Eq. (10) for μ_e and μ_h.

Furthermore, for the computations of n_e and n_h, N_A, E_1, E_2, E_3 and α_e, α_h should be estimated for the measured sample, and Fermi energy should be computed as a function of temperature as mentioned in the last section.

The analysis of the experimental results for the specimen of No. 6, P-type impurity semiconductor have been proceeded as follows.

[i]. *Impurity level distance E_t, and concentration of impurity level N_A.*

At low temperatures it may be assumed that the concentration of electrons in the conduction band is negligibly small compared with that of holes, and then the concentration of electrons in impurity levels is nearly equal to the one of holes in the filled band. In such case, Hall constant R thus will become

$$R = 1/en_h = 1/en_i\,. \qquad (25)$$

On the other hand, at low temperatures n_i may be given from Eq. (19) replacing n_h by n_i,

$$n_i = \frac{1}{2}\,\alpha_h\cdot e^{(E_1-E_2)/kT} \cdot\left\{\sqrt{1+\frac{4N_A}{\alpha_h\cdot\exp\{(E_1-E_2)/kT\}}}-1\right\}. \qquad (19')$$

By fitting a temperature dependence of n_i calculated through Eq. (25) by the use of the observed R to the theoretical formula (19′), both the impurity level distance $E_i = E_2 - E_1$ and the concentration of impurity levels N_A will be obtained. In such procedure it will be assumed approximately that the effective mass of holes m_h in α_h is equal to free electron mass.

[ii]. *E_0, energy gap between conduction and filled bands.*

At high temperatures, in which the electronic transition to the conduction band becomes appreciable, we have

$$n_h = n_i + n_e\,,$$

and

$$\sigma = e(n_e\cdot\mu_e + n_h\cdot\mu_h) = e(1+s)n_e\cdot\mu_h + en_i\cdot\mu_h\,, \qquad (26)$$

where

$$s = \mu_e/\mu_h\,.$$

The hole mobility μ_h is given by Eq. (10), but the third term in the right hand of Eq. (10) may be neglected compared with other terms as mentioned above.

At high temperatures of the intrinsic range now in consideration the Fermi level will locate near the middle of the energy gap between conduction and filled bands, and then $(E_3-E_2)/2$ may be used for $(E_3-\zeta)$ in Eq. (14). Therefore,

$$\begin{aligned} n_e &= 2\left(\frac{2\pi m_e\cdot kT}{h^2}\right)^{3/2}\cdot e^{(\zeta-E_3)/kT} \\ &\doteqdot 2\left(\frac{2\pi m_e\cdot k}{h^2}\right)^{3/2}\cdot T^{3/2}\cdot e^{-E_0/2kT} \\ &= n_0\cdot T^{3/2}\cdot e^{-E_0/kT}\,, \end{aligned} \qquad (27)$$

where $E_0 = E_3 - E_1$ the energy gap between conduction and filled bands and n_0 is nearly constant.

Putting Eq. (27) into Eq. (26), the estimation of the first term (designated σ') in the right hand of Eq. (26) is graphically obtained by subtracing $(e\cdot h_i\cdot\mu_h)$ from the measured values of σ. And then a plot of the obtained result on $\log\sigma' : 1/T$ will be used, as usual, to determine E_0, i.e., the energy gap between the conduction and filled bands.

[iii]. *Constant n_0 and mobility rotio s.*

The expression of R in Eq. (24) becomes

$$R = \frac{-n_e\cdot\mu_e^2 + n_h\cdot\mu_h^2}{e(n_e\cdot\mu_e + n_h\cdot\mu_h)^2} = \frac{-n_e(s^2-1)+n_i}{e[n_e(s+1)+n_i]^2}\,, \qquad (28)$$

which will have unknown parameters n_0 and s, since n_i (Eq. 19′) and n_e (Eq. 27) have been estimated already. Making use of the measured values of R at high temperatures, therefore, Eq. (28) will yield the values of n_0 and s.

The above mentioned analysis of the specimen of No. 6 has been found to give the following result,

$E_i = 0.014$ ev, $N_A = 1.54\times10^{17}$, $E_0 = 0.48$ ev, $n_0 = 2.89\times10^{15}$,

and $s = 1.43$.

[iv]. *Effective mass m_e and m_h.*

At high temperatures the lattice scattering may be assumed to predominate compared with the other scattering mechanisms, in which case we have

$$s = \mu_e/\mu_h \doteqdot (m_h/m_e)^{5/2}.$$

By making use of the above relation and $s = 1.43$, we have $m_h/m_e = 1.15$, and

$$\left.\begin{aligned} \alpha_e &= 2\cdot\left(\frac{2\pi m_e\cdot kT}{h^2}\right)^{3/2} = 2\cdot\left(\frac{m_e}{m}\right)^{3/2} \\ &\qquad\times 2.42\times10^{15}\times T^{3/2}, \\ \alpha_h &= 2\cdot\left(\frac{2\pi m_h\cdot kT}{h^2}\right)^{3/2} = 2\cdot\left(\frac{m_h}{m}\right)^{3/2} \\ &\qquad\times 2.42\times10^{15}\times T^{3/2}, \end{aligned}\right\} \qquad (30)$$

where m is the free electron mass.

From the numerical value of n_0 obtained in [iii] and the expression of Eq. (27)

$$n_0 = 2\cdot\left(\frac{m_e}{m}\right)^{3/2}\times 2.42\times10^{15} = 2.89\times10^{15},$$

$m_e/m = 0.71$ is obtained, and using $m_h/m_e = 1.15$, we have $m_h/m = 0.82\,m$, from which α_e and α_h may be numerically estimated.

[v]. *Fermi energy*

Using the numerical values obtained above, A, B, and C in Eq. (22) are computed and finally the Fermi energy is obtained as a function of temperatures as mentioned in § 4.2. In the calculations of Fermi energy the origin of energy is conveniently chosen to be the top of the filled band, i.e. $E_1=0$. The temperature dependence of Fermi energy for specimen of No. 6 is shown in Fig. 7.

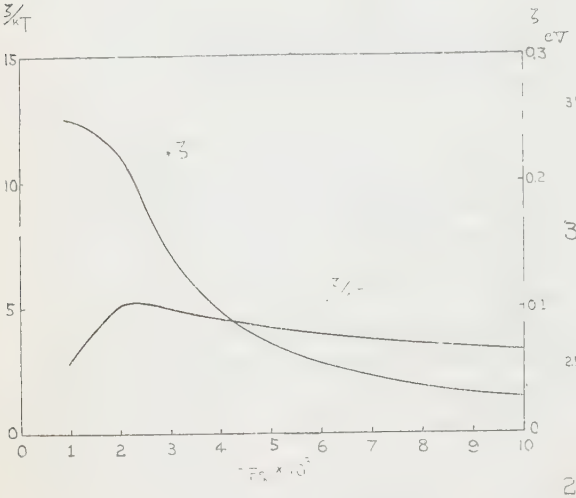

Fig. 7. ζ and ζ/kT for Specimen, No. 6.

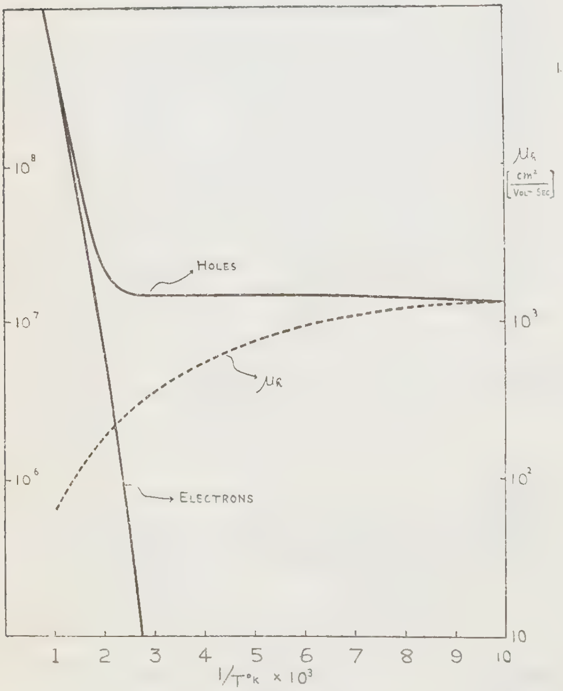

Fig. 8. Carrier Concentrations and u_h for Specimen No. 6.

[vi]. *Carrier concentrations* n_e *and* n_h, *conductivity* σ *and Hall constant* $\boldsymbol{R}$.

From the values of ζ obtained above and Eqs. (14), (16) the temperature dependences of n_e and n_h were computed as shown in Fig. (8).

Using these n_e and n_h we can calculate σ and $\boldsymbol{R}$ in Eq. (24) at any temperature. The results calculated are shown in Fig. 9, in which open and solid circles are respectively the measured values of Hall constant and conductivity.

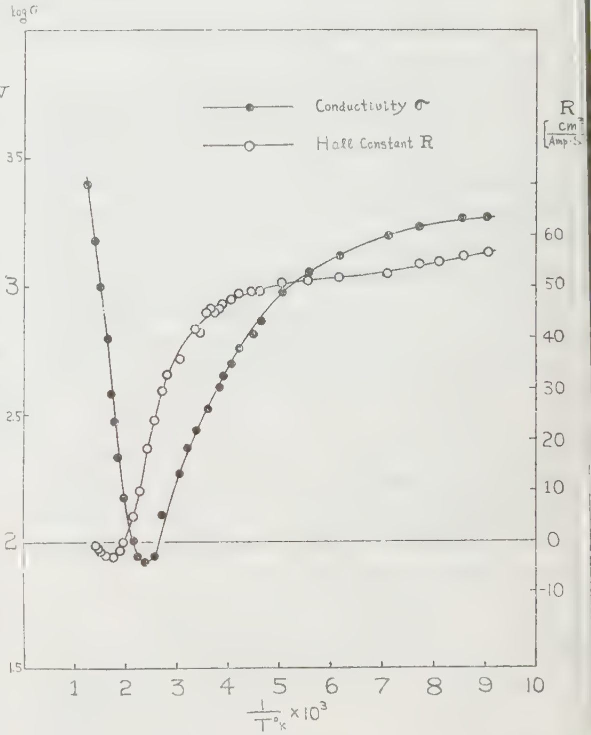

Fig. 9. Comparison between measured and calculated values of σ and R for Specimen, No. 6.

§ 5. Discussions of the Results for other Samples

On the specimens of No. 16, No. 10 and No. 11, which show rather monotonous behaviours, there are some troublesome problems which are hardly soluved at present.

That is, the plotting of $\log \sigma$ to $1/T$ are not necessarily straight lines but curved like bows as seen in Fig. 10, in which the conductivities of No. 10, and No. 16 are represented approximately by $\sigma=\exp(T/200)$ and that of No. 11, $\sigma=\exp(T/120)$, and such behaviours seem not be explained by the usual simple formula for semiconductors.

Although the definite conclusion about the mentioned anomalous behaviour has not yet been obtained, these bending might be due to the scattering by some inhomogeneity at the grain boundary[10)] or to the some temperature shift of energy gap between the conduction and filled bands.

Another difficult problem is that Hall constants of these specimens except No. 6 are considerably smaller than expected from their conductivities, which situation leads to the considerably small mobilities compared with that of No. 6 specimen by using Eq. (9), as shown in Table I.

Table I. Mobilities of specimens. (at −150°C)

Specimens.	No. 16,	No. 10,	No. 11,	No. 6
Mobility. (cm²/volt. sec.)	1.65	5.87	106.2	1151.

In particular, in view of the extremely small values of Hall constant for specimen of No. 16, there might be some mixtures of N-type and P-type in the non-equilibrium state of such specimen, in which negative values of N-type are reduced by positive values of P-type.

Anyhow, no matter that it may be, in order to solve these troublesome problems, it will be necessary that the further detailed measurements be made on the poly- and single-crystalline samples.

§ 6. Errors of the Approximation

In § 4.2 it was mentioned that the approximate calculation of n_h replacing Fermi function by Maxwell function, introduced some amounts of errors.

In this section the errors will be estimated. The exact expression for hole concentration, i.e., Eq. (15) is

$$n_h{}^0 = \frac{1}{2\pi^2} \cdot \left(\frac{8\pi^2 m_h}{h^2}\right)^{3/2} \cdot \int_{-\infty}^{E_1} \frac{\exp\{(E-\zeta)/kT\}}{1+\exp\{(E-\zeta)/kT\}} \cdot (E_1-E)^{1/2} \cdot dE$$
$$= \frac{1}{\pi^2}\left(\frac{8\pi^2 \cdot m_h \cdot kT}{h^2}\right)^{3/2} \cdot \eta \cdot \int_0^\infty \frac{x^2 \cdot e^{-x^2}}{1+\eta \cdot e^{-x^2}} \cdot dx$$
$$= \alpha_h{}^0 \cdot \eta \,, \tag{31}$$

where

$$x = \left(\frac{E_1 - E}{kT}\right)^{1/2}, \qquad \eta = \exp\left(-\frac{\zeta - E_1}{kT}\right),$$
$$\alpha_h{}^0 = \frac{1}{\pi^2} \cdot \left(\frac{8\pi^2 \cdot m_h \cdot kT}{h^2}\right)^{3/2} \cdot \int_0^\infty \frac{x^2 \cdot e^{-x^2}}{1+\eta \cdot e^{-x^2}} \cdot dx.$$

The approximate expression of Eq. (16) is written as

$$n_h = \frac{1}{\pi^2}\left(\frac{8\pi^2 \cdot m_h \cdot kT}{h^2}\right)^{3/2} \cdot \eta \cdot \int_0^\infty x^2 \cdot e^{-x^2} \cdot dx$$
$$= 2 \cdot \left(\frac{2\pi m_h \cdot kT}{h^2}\right)^{3/2} \eta = \alpha_h \cdot \eta. \tag{32}$$

It must be noticed that $\alpha_h{}^0$ contains η but α_h does not.

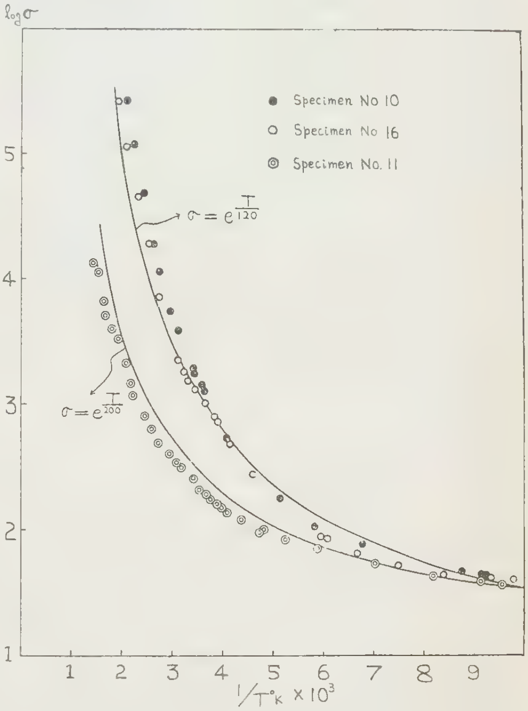

Fig. 10. Conductivities of Specimens, Nos. 16, 10, 11.

The exact equation for η (or ζ), therefore, becomes

$$\eta^3 + Q \cdot \eta^2 - Q \cdot \eta/\alpha_h{}^0 - R \cdot 1/\alpha_h{}^0 = 0 \,, \tag{33}$$

where

$$P = e^{-E_2/kT}, \quad Q = (\alpha_e \cdot e^{-E_3/kT} + N_A \cdot e^{-E_2/kT}),$$
$$R = \alpha_e \cdot e^{-(E_2+E_3)/kT}.$$

In this equation the energy is measured from the top of the filled band as before.

If α_h is replaced for $\alpha_h{}^0$, Eq. (33) is clearly seen to be reduced to Eq. (21). We must examine the variations of η when $\alpha_h{}^0$ changes into α_h.

For this purpose, therefore, η is expanded into the Tayler series.

$$\eta(\alpha_h) = \eta(\alpha_h{}^0 + \Delta\alpha_h) = \eta(\alpha_h{}^0) + \frac{\partial\eta}{\partial\alpha_h{}^0} \cdot \Delta\alpha_h$$
$$+ \frac{1}{2} \cdot \left(\frac{\partial^2\eta}{\partial\alpha_h{}^{02}}\right) \cdot (\Delta\alpha_h)^2 + \cdots,$$

and then

$$\begin{aligned}\varDelta\eta &= \frac{\partial\eta}{\partial\alpha_h{}^0}\cdot\varDelta\alpha_h+\frac{1}{2}\left(\frac{\partial^2\eta}{\partial\alpha_h{}^{02}}\right)\cdot(\varDelta\alpha_h)^2+\cdots\cdot\\ &=\frac{\partial\eta}{\partial\alpha_h{}^0}\cdot\alpha_h{}^0\cdot\left(\frac{\varDelta\alpha_h}{\alpha_h{}^0}\right)\\ &+\frac{1}{2}\left(\frac{\partial^2\eta}{\partial\alpha_h{}^{02}}\right)\cdot\alpha_h{}^{02}\left(\frac{\varDelta\alpha_h}{\alpha_h{}^0}\right)^2+\cdots\cdot . \end{aligned}\tag{34}$$

The numerical calculations of this series have been carried out by the following method of approximations.

At first, we must know $\varDelta\alpha_h$ $(=\alpha_h-\alpha_h{}^0)$ as a function of η. From $\alpha_h{}^0$ and α_h in Eqs. (31) and (32), we have

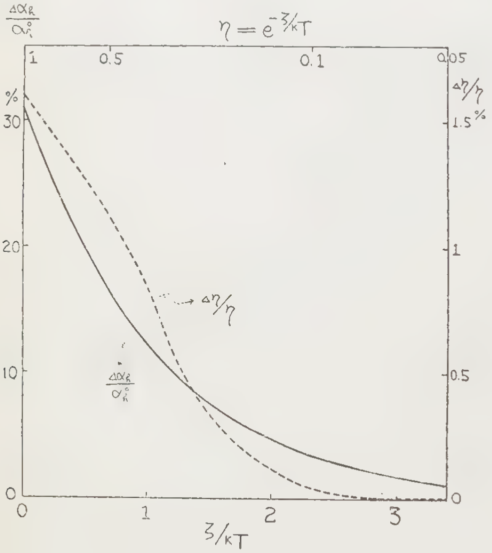

Fig. 11. $\Delta\eta/\eta$ and $\Delta\alpha_h/\alpha_h{}^0$ versus ζ/kT, and η.

$$\frac{\varDelta\alpha_h}{\alpha_h{}^0}=\frac{\alpha_h-\alpha_h{}^0}{\alpha_h{}^0}=\frac{\displaystyle\int_0^\infty x^2\cdot e^{-x^2}\cdot dx-\int_0^\infty\frac{x^2\cdot e^{-x^2}}{1+\eta\cdot e^{-x^2}}\cdot dx}{\displaystyle\int_0^\infty\frac{x^2\cdot e^{-x^2}}{1+\eta\cdot e^{-x^2}}\cdot dx},$$

which was numerically evaluated with the parameter η the result of which is shown in Fig. 11. It will be found that at one limiting case $\log\eta=1$ (or $(\zeta-E_1)/kT=0$), the deviation of $\alpha_h{}^0$ will become a largest value of 31%.

Secondly, we have to calculate the coefficients of $(\varDelta\alpha_h/\alpha_i{}^0)$ and its powers. Eq. (33) gives, for constants P, Q and R,

$$3\eta^2\cdot\frac{\partial\eta}{\partial\alpha_h{}^0}+3P\cdot\eta\cdot\frac{\partial\eta}{\partial\alpha_h{}^0}+Q\frac{\eta}{\alpha_h{}^{02}}-\frac{Q}{\alpha_h{}^0}\cdot\frac{\partial\eta}{\partial\alpha_h{}^0}+R\frac{1}{\alpha_h{}^{02}}=0\,,$$

and than we get

$$\left(\frac{\partial\eta}{\partial\alpha_h{}^0}\right)\cdot\alpha_h{}^0=-\frac{(Q/\alpha_h{}^0)\cdot\eta+R/\alpha_h{}^0}{3\eta^2+2P\cdot\eta-Q/\alpha_h{}^0}\,,\tag{35}$$

Similarly, it follows

$$\begin{aligned}\alpha_h{}^{02}\cdot\left(\frac{\partial^2\eta}{\partial\alpha_h{}^{02}}\right)=-&\frac{2\alpha_h{}^{02}}{3\eta^2+2P\cdot\eta-Q/\alpha_h{}^0}\\ &\cdot\left\{\left(\frac{\partial\eta}{\partial\alpha_h{}^0}\right)^2(3\eta+P)+\frac{Q}{\alpha_h{}^{02}}\left(\frac{\partial\eta}{\partial\alpha_h{}^0}\right)\right.\\ &\left.-\left(\frac{Q}{\alpha_h{}^{03}}\cdot\eta+\frac{R}{\alpha_h{}^{03}}\right)\right\}\,,\end{aligned}\tag{36}$$

We may compute the numerical values of Eqs. (35) and (36) at any value of η for a given semiconductor, in which E_2, E_3, E_A and m_e, m_h, (even approximate values they are !) are known and also the values of $(\varDelta\alpha_h/\alpha_h{}^0)$ may be estimated on Fig. 11.

From these values computed above and Eq. (34), we are able to calculate $\varDelta\eta$ at any value of η.

The calculations mentioned above have been carried out for the specimen of No. 6. The case of $\eta=1$ will be expected to give rise to the largest error, the second term in Eq. (34) being taken into consideration, in the cases of $\eta=0.5$, 0.1 and 0.05 the only first term is sufficient for our estimation.

The values of $\varDelta\eta$ and $\varDelta\eta/\eta$ for each value of η are given in Table II, and the plotting of $\varDelta\eta/\eta$ versus η is shown by dotted line in Fig. 11.

Table II.

η	1	0.5	0.1	0.05
$\Delta\eta$	0.16	0.061	0.0034	0.0009
$\Delta\eta/\eta$	0.16	0.12	0.034	0.018

The variations of ζ/kT with respect to $1/T$, for the specimen of No. 6 are described in Fig. 7. In the temperature range of our measurements, ζ/kT is found to be larger than 3 as shown in Fig. 7, and for these values of ζ/kT the errors of $\varDelta\eta/\eta$ are smaller than 2% at most.

In conclusion, the authors wish to express their sincere thanks to Prof. Dr. T. Muto and Dr. J. Yamashita, University of Tokyo for their kind discussions.

Appendix

The expressions of A, B and C are given in § 4.2, and as far as $q^2-p^3<0$, the second term of B will be safely neglected because of its positive value. Hence, then

$$
\begin{aligned}
q^2-p^3 &= \frac{1}{4}\left(\frac{\alpha_e}{\alpha_h}\right)^2\cdot e^{-2(E_1+E_2+E_3)/kT} \\
&\quad -\left[\frac{1}{27}\left(\frac{\alpha_e}{\alpha_h}\right)\cdot e^{-(E_1+4E_2+E_3)/kT}\right. \\
&\quad +\frac{19}{108}\left(\frac{\alpha_e}{\alpha_h}\right)^2\cdot e^{-2(E_1+E_2+E_3)/kT} \\
&\quad \left.+\frac{1}{27}\left(\frac{\alpha_e}{\alpha_h}\right)^3\cdot e^{-3(E_1+E_3)/kT}\right] \\
&= \frac{8}{108}\left(\frac{\alpha_e}{\alpha_h}\right)\cdot e^{-2(E_1+E_2+E_3)/kT} \\
&\quad +\frac{4}{108}\left(\frac{\alpha_e}{\alpha_h}\right)^2\cdot e^{-(E_1+4E_2+E_3)/kT} \\
&\quad -\frac{4}{108}\cdot\left(\frac{\alpha_e}{\alpha_h}\right)\cdot e^{-3(E_1+E_3)/kT} \\
&= \frac{-4}{108}\left(\frac{\alpha_e}{\alpha_h}\right)\left[\left(\frac{\alpha_e}{\alpha_h}\right)\cdot e^{-3(E_1+E_3)/2kT}\right. \\
&\quad \left.-e^{-(E_1+4E_2+E_3)/2kT}\right]^2 < 0\,.
\end{aligned}
$$

References

1) K. Bauer: Ann. d. Phys. **38** (1940) 84.

2) L. Eisenmann: Ann. d. Phys. **38** (1940) 121.

3) W. Shockley: Electrons and Holes in Semiconductors. (D. Van Norstrand Co. Inc. New York. 1950.) p. 278.

4). N. F. Mott and R. W. Gurney: Electronic Processes in Ionic Crystals. 2nd. Ed. (Oxford Press. 1950.) p. 107.

5) G. L. Pearson and J. Bardeen: Phys. Rev. **75** (1949) 865.

6) K. Shifrin: J. Phys. U.S.S.R. **8** (1944) 242.

7) E. H. Putley: Proc. Phys. Soc. (London) A. **62** (1949) 284.

8) K. Lehovec and H. Kedesdy: J. Appl. Phys. **22** (1951) 65.

9) J. S. Blakemore: Electrical Communication, June, (1952) 131.

10) H. K. Henisch: Phil. Mag. **42** (1951) 734.

JOURNAL OF THE PHYSICAL SOCIETY OF JAPAN Vol. 9, No. 5, SEP.—OCT., 1954

Statistics of Two-Dimensional Lattices with Many Components

By Taro KIHARA, Yukio MIDZUNO and Toshio SHIZUME

Department of Physics, Faculty of Science, University of Tokyo

(Received April 15, 1954)

The statistics of the two-dimensional Ising lattice, for which each lattice site may take one of two states, has been partly generalized to the following model: each lattice site may take one of s states and each pair of neighboring sites in different states has a common excess energy, J, compared with a pair of neighboring sites in a same state. The partition function for the square lattice has a temperature symmetry and the Curie temperature, T_c, is given by

$$(s-1)\exp(-2J/kT_c)+2\exp(-J/kT_c)-1=0\,,$$

(k is the Boltzmann constant). Although the partition function itself has only been obtained in the form of power series valid at low and high temperature regions, it is highly probable that for any finite s the specific heat is infinite at the Curie temperature. The transition is not the normal phase transition of the first order which the Bragg-Williams approximation predicts for our lattice with $s\geqq 3$.

§ 1. Introduction

Recently Ookawa[1] treated the solid-liquid transition considering the liquid phase as a mosaic of crystal fragments as shown in Fig. 1 (a). Making use of several assumptions and approximations he concluded that he could explain, by means of this mosaic model of liquids, the normal phase transition of the first order between liquid and solid. (Here "normal" means that the specific heat remains finite at the transition temperature.) The conclusion, however, is doubtful since his model is not clearly defined and his statistical calculation is not rigorous. The present authors want to criticize such an approximate treatment of phase transition by means of a clearly defined model which is as follows.

Each mosaic domain is composed of one or several unit cells and may take one of s possible orientations as shown in Fig. 1 (b). the boundary surface of a mosaic domain has an excess energy proportional to its area.

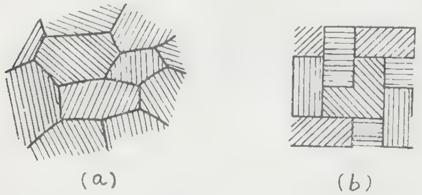

Fig. 1.

If we apply the Bragg-Williams approximation to our model with $s \geqq 3$, we shall come to the conclusion that there should exist a normal phase transition of the first order (§ 5). In reality, however, we can show below that the transition is not normal phase transition.

Our model is equivalent to a lattice composed of many equivalent lattice sites, each of which may take one of s different states; each pair of neighboring sites in different states has a common excess energy compared with a pair of neighboring sites in a same state. We shall treat two-dimensional case for the sake of mathematical simplicity. In the particular case of $s=2$, our lattice reduces to the Ising lattice which has been playing an important role as a typical model of phase transition of the second order[2)3)].

§ 2. Dual Transformation

Let us formulate our problem as follows. Consider a lattice composed of N equivalent lattice sites, each of which possesses an internal coordinate μ which may take s values e_1, $e_2, \cdots$, e_s corresponding to s different states, where

$$e_l e_m = \begin{cases} 1 & \text{for} \quad l=m \\ 0 & \text{for} \quad l \neq m. \end{cases} \qquad (2.1)$$

Then the interaction energy of the system takes the form

$$E = -\frac{1}{2} J \sum_{\langle i,k \rangle} (2\mu_i \mu_k - 1) \, . \qquad (2.2)$$

Here J is the energy gained when a pair of unlike neighbors changes to a pair of like neighbors; $\sum\limits_{\langle i,k \rangle}$ means the summation carried out over all pairs $\langle i, k \rangle$ of neighbors. The partition function of this system is

$$f(T) = \sum_{\mu_i = e_1, \cdots, e_s} \exp\left[K \sum_{\langle i,k \rangle} (2\mu_i \mu_k - 1)\right], \quad (2.3)$$

where

$$K = J/2kT\,, \qquad (2.4)$$

and $\sum\limits_{\mu_i = e_1, \cdots, e_s}$ denotes the summation extending over all possible states of the system; i.e. it would have to be written explicitly as

$$\sum_{\mu_i = e_1, \cdots, e_s} \sim \sum_{\mu_1 = e_1, \cdots, e_s} \sum_{\mu_2 = e_1 \cdots, e_s} \cdots\cdots\cdot \sum_{\mu_N = e_1, \cdots, e_s} .$$

Eq. (2.3) is a sum of terms each of which is a product of factors of the type $\exp[K(2\mu\mu' - 1)]$ where μ and μ' are the internal coordinates of direct neighbors. Each factor $\exp[K(2\mu\mu' - 1)]$ can be replaced at will by some other expression, provided it yields the same two values e^{K} and e^{-K}. We, therefore, introduce the following "dual transformation"

$$e^{K(2\mu\mu'-1)} = F_s(K)[e^{K^*} + (s\mu\mu' - 1)e^{-K^*}]\,. \quad (2.5)$$

Here K^* and $F_s(K)$ are determined by

$$e^{-K} = F_s(K)[e^{K^*} - e^{-K^*}]\,,$$
$$e^{K} = F_s(K)[e^{K^*} + (s-1)e^{-K^*}]\,.$$

From these two relations can be derived the expressions

$$(s-1)e^{-2K}e^{-2K^*} + e^{-2K} + e^{-2K^*} - 1 = 0\,, \quad (2.6)$$

and

$$[F_s(K)]^2 = \frac{1}{s} \frac{e^{2K} + (s-1)e^{-2K}}{e^{2K^*} + (s-1)e^{-2K^*}}\,, \qquad (2.2)$$

which will be used later. Inserting (2.5) into (2.3) we have

$$f(T) = [F_s(K)]^M \sum_{\mu_i = e_1, \cdots, e_s} \prod_{r=1}^{M} [e^{K^*} + (s\mu_r \mu_r' - 1)e^{-K^*}].$$

Here the product over r extends over all connecting rods in our lattice, and M denotes the total number of such connections. (For example, $M=2N$ in the case of the square lattice, $M=3N$ in the case of the simple cubic lattice.)

In developing the product, we get a sum of products of e^{K^*} and $(s\mu_r \mu_r' - 1)k^{-K^*}$, each product of which can be characterized in our lattice by a polygon (not necessarily closed) running along the connecting rods. The exponential factor of each term is such that every connecting rod not included in the polygon contributes a factor e^{K^*} to it, and every connecting rod included in the polygon a factor e^{-K^*}. Then we get

$$f(T)=[F_s(K)]^M \sum_{\mu_i=e_1,\cdots,e_s} \sum_{\text{polygon}} \prod_{r=1}^{l}{}_{(\Gamma)} \times(s\mu_r\mu_r'-1)e^{(M-2l)K^*}$$
$$=[F_s(K)]^M \sum_{\text{polygon}} \gamma(\Gamma)e^{(M-2l)K^*}. \qquad (2.8)$$

Here l is the number of connecting rods included in the polygon Γ; $\prod_{r=1}^{l}{}_{(\Gamma)}$ means the product extending over all connecting rods of the polygon Γ; $\sum_{\text{polygon}}$ indicates the sum over all possible polygons; and we have denoted for brevity

$$\gamma(\Gamma)=\sum_{\mu_i=e_1,\cdots,e_s} \prod_{r=1}^{l}{}_{(\Gamma)}(s\mu_r\mu_r'-1). \qquad (2.9)$$

In the product development (2.8), $\gamma(\Gamma)$ vanishes when the polygon is not closed. In fact, if the polygon Γ consists of two polygons Γ' and Γ'' which possess only one common lattice site, holds the relation

$$(1/s^N)\gamma(\Gamma)=(1/s^N)\gamma(\Gamma')\times(1/s^N)\gamma(\Gamma''), \quad (2.10)$$

and for an isolated rod

$$\sum_{\mu_1=e^1,\cdots,e_s} \sum_{\mu_2=e_1,\cdots,e_s} (s\mu_1\mu_2-1)=s\times s-s^2=0.$$

Hence only closed polygons (with bridges in general) give a non-zero contribution. Thus we have

$$f(T)=[F_s(K)]^M \sum_{\text{closed polygon}} \gamma(\Gamma)e^{(M-2l)K^*}. \qquad (2.11)$$

§ 3. Temperature Symmetry

In 1941, Krammers and Wannier[4] proved that the partition function for the usual Ising square net has a temperature symmetry and succeeded first to locate the Curie temperature. A more general relation of the temperature symmetry will be derived in this section.

We start from Eq. (2.11) in the previous section. For a lattice on a simply connected surface, every closed polygon divides the surface into several regions. We can, therefore, characterized every term in our product development by such an arrangement of s states $\nu_i=e_1, e_2, \cdots, e_s$ in the dual net, that all the lattice sites in a region are in a same state and two sites in neighboring regions are in different states. (see Fig. 3). If $(\nu_1^0, \cdots, \nu_{N_*}^0; \Gamma)$ is one of such arrangements corresponding to the polygon Γ, we can write

$$e^{(M-2l)K^*}=\exp\left[\sum_{r=1}^{M} K^*(2\nu_r^0\,\nu_r^{0\prime}-1)\right]. \qquad (3.1)$$

Furthermore, we shall show in Appendix the relation

$$\gamma(\Gamma)=s^{N-1}p(\Gamma), \qquad (3.2)$$

where $p(\Gamma)$ is the number of different ways to paint by s different colors (states) a map which has the boundary lines corresponding to the polygon Γ.

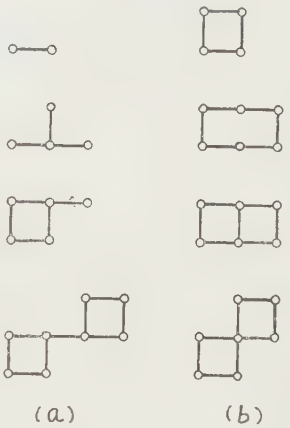

Fig. 2. (a): Examples of noncontributing polygons.
(b): Examples of contributing or "closed" polygons.

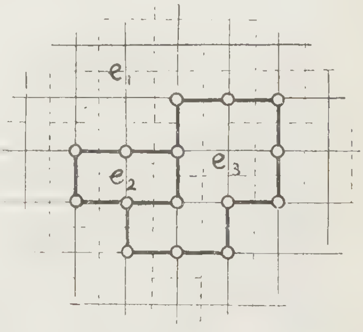

Fig. 3.

Hence we get from Eq. (2.11)

$$f(T)=[F_s(K)]^M \sum_{\text{closed polygon}} s^{N-1}p(\Gamma)$$
$$\times\exp\left[\sum_r K^*(2\nu_r^0\nu_r^{0\prime}-1)\right]$$
$$=[F_s(K)]^M s^{N-1} \sum_{\nu_i=e_1,\cdots,e_s}$$
$$\times\exp\left[\sum_r K^*(2\nu_r\nu_r'-1)\right]$$
$$=[F_s(K)]^M s^{N-1} f^*(T^*), \qquad (3.3)$$

where $f^*(T)$ means the partition function for the dual net, and T^* is the "dual" temperature given by $K^*=J/2kT^*$.

Inserting (2.7) into (3.3) we obtain finally

$$\frac{f(T)}{s^{N/2}[e^{2K}+(s-1)e^{-2K}]^{M/2}} = \frac{f^*(T^*)}{s^{N^*/2}[e^{2K^*}+(s-1)e^{-2K^*}]^{M/2}}, \tag{3.4}$$

where N^* is the total number of lattice sites of the dual net, and $N+N^*=M+2$ (Euler's theorem) has been used.

In particular, for the square net

$$f^*(T)=f(T), \quad N^*=N, \quad M=2N,$$

and we have

$$\frac{f(T)}{[e^{2K}+(s-1)e^{-2K}]^N}=\frac{f(T^*)}{[e^{2K^*}+(s-1)e^{-2K^*}]^N}. \tag{3.5}$$

This is the generalized form of Krammers-Wannier's relation⁵⁾ of the temperature symmetry for the square net.*

With use of the function

$$\chi(K)=\frac{f(T)^{1/N}}{e^{2K}+(s-1)e^{-2K}}, \tag{3.6}$$

for which

$$\chi(K)=\chi(K^*), \tag{3.7}$$

the energy and the specific heat of the system are given by

$$E(K)=-NJ\left[\frac{e^{2K}-(s-1)e^{-2K}}{e^{2K}+(s-1)e^{-2K}} + \frac{1}{2}\frac{d}{dK}\ln\chi(K)\right], \tag{3.8}$$

$$C(K)=NkK^2\left[\frac{16(s-1)}{[e^{2K}+(s-1)e^{-2K}]^2} + \frac{d^2}{dK^2}\ln\chi(K)\right]. \tag{3.9}$$

From (3.7), we see that if $\chi(K)$ has a singular point at a certain temperature T_0, then it must also have a singular point at the temperature $T_0{}^*$ "dual" to T_0. Accordingly if there exists only one singular point of $\chi(K)$, it is located at the temperature T_c for which $K^*=K$. From (2.6) the temperature is given by

$$(s-1)e^{-4K_c}+2e^{-2K_c}-1=0, \tag{3.10}$$

or

$$e^{2K_c}=1+\sqrt{s}, \tag{3.11}$$

where

$$K_c=J/2kT_c.$$

Thus the Eq. (3.10) gives the transition temperature (which henceforth we shall call "the Curie temperature") of the system under the assumption that there exists only one. (This assumption will be confirmed to some extent in the following section.)

At the Curie temperature, we can derive the following relations: from (2.6)

$$\left(\frac{dK^*}{dK}\right)_{K=K_c}=-1, \quad \left(\frac{d^2K^*}{dK^2}\right)_{K=K_c}=\frac{4}{\sqrt{s}}, \tag{3.12}$$

and therefore from (3.7)

$$\left(\frac{d\chi}{dK}\right)_{K_c+0}+\left(\frac{d\chi}{dK}\right)_{K_c-0}=0, \tag{3.13}$$

$$\left(\frac{d^2\chi}{dK^2}\right)_{K_c+0}-\left(\frac{d^2\chi}{dK^2}\right)_{K_c-0} = -\frac{2}{\sqrt{s}}\left[\left(\frac{d\chi}{dK}\right)_{K_c+0}-\left(\frac{d\chi}{dK}\right)_{K_c-0}\right]. \tag{3.14}$$

Using (3.8) and (3.13) we see that the arithmetical mean of $E(K_c+0)$ and $E(K_c-0)$ is given by

$$E(K_c)=-N\frac{J}{\sqrt{s}}, \tag{3.15}$$

When the energy is continuous at the Curie temperature, this $E(K_c)$ is equal to the energy of the system itself. It is also concluded from (3.8), (3.9) and (3.14) that if the energy is continuous at the Curie temperature, then the specific heat is either continuous or infinite. It will be shown in the next section that the latter case is highly probable.

§ 4. Partition Function for the Square Lattice

We evaluate the partition function for the square lattice by the method of power series expansion used by Kramers and Wannier⁶⁾ and several other authors in the case of the Ising lattice.

The partition function (2.3) can be expressed in the form

---

* For the special case $s=4$, a relation equivalent to this was obtained by Ashkin and Teller in 1943. See reference 5.

$$f(T)=\sum_i g_i \exp(-E_i/kT)\ .$$

Here g_i is the number of states of the system at the energy level E_i; $\sum_i$ means the summation over all energy levels.

At low temperatures terms corresponding to low energy levels predominate. At the lowest level all the lattice sites are in a state so that $E_0=NJ$ and $g_0=s$. At the first excited level a single site is in another state so that $E_1=NJ+4J$ and $g_1=N(s-1)s$. Proceeding in this way, we find a power series expansion valid at low temperatures

$$f(T)=x^{-N}[s+N(s-1)sx^4+2N(N-1)sx^6+\cdots],$$

with

$$x\equiv e^{-J/kT}.$$

Taking Nth root we have

$$[f(T)/s]^{1/N}=x^{-1}P(x)\ ,$$

$$P(x)=1+(s-1)x^4+2(s-1)x^6+\cdots$$

$$=1+(s-1)\sum_{i=4}^{\infty} a_i x_i\ , \qquad (4.1)$$

where the coefficients a_i for $i\geqq 4$ are given in Table I.

Table I.

i	a_i
4	1
5	0
6	2
7	$2(s-2)$
8	$-2s+9$
9	$12(s-2)$
10	$2(3s^2-16s+27)$
11	$2(s-2)(-5s+32)$
12	$s^3+55s^2-243s+302$
13	$2(s-2)(9s^2-71s+180)$
14	$-37s^3+561s^2-1802s+1808$
15	$2(s-2)(4s^3+130s^2-704s+1189)$
16	$58s^4-998s^3+6269s^2-15162s+12870$

By virtue of the symmetry relation (3.5) the high temperature expansion is shortly obtained from the low temperature expansion:

$$f(T)^{1/N}=\frac{s}{(1-u)(1+(s-1)u)}P(u)\ , \qquad (4.2)$$

where

$$u\equiv\frac{1-x}{1+(s-1)x}\ ,$$

and $P(u)$ is the same as in (4.1).

From these two expansions the energy per site

$$\frac{E}{N}=kT^2\frac{\partial}{\partial T}[\ln f(T)^{1/N}]\ ,$$

and the specific heat per site

$$\frac{C_v}{N}=\frac{1}{N}\frac{\partial E}{\partial T}\ .$$

can be calculated.

Fig. 4 shows the specific heat for several values of s. (The curve for $s=2$ is taken from Onsager's solution[7].) It is highly probable that for any finite s the specific heat is infinite at the Curie temperature T_c given by (3.11).

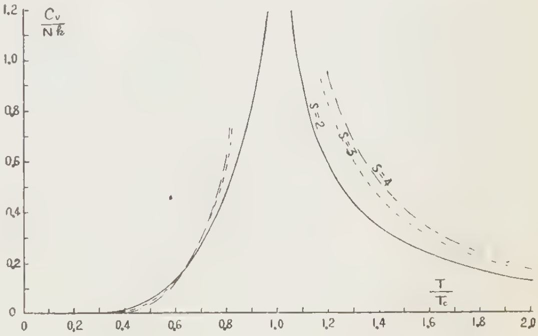

Fig. 4. Specific heat curves for the square lattice.

§ 5. A Criticism of the Bragg-Williams Approximation

It may be instructive to compare our result with the Bragg-Williams approximation applied to our lattice. Let $N_i\equiv Nx_i$ be the number of sites in the ith state $(x_1+x_2+\cdots\cdot+x_s=1)$; let z be the number of direct neighbors of a site.

The Bragg-Williams approximation is characterized by the assumptions that the energy of the system is

$$E=\frac{Nz}{4}J[1-2(x_1{}^2+x_2{}^2+\cdots\cdot+x_s{}^2)]\ , \qquad (5.1)$$

and that the entropy of the system is given by the entropy of the random mixing

$$S=-kN[x_1\ln x_1+x_2\ln x_2+\cdots\cdot+x_s\ln x_s]. \qquad (5.2)$$

Then the free energy becomes

$$F/N=(E-TS)/N$$
$$=zJ/4-(zJ/2)(x_1{}^2+x_2{}^2+\cdots\cdot+x_s{}^2)$$
$$+kT(x_1\ln x_1+\cdots\cdot+x_s\ln x_s). \qquad (5.3)$$

The equilibrium values $\bar{x}_i$'s of x_i's are determined by the minimum of the free energy under the subsidiary condition

$$x_1+x_2+\cdots\cdot+x_s=1.$$

Namely, with the Lagrange multiplier λ, $\bar{x}_i$'s are given by

$$-zJ\bar{x}_i+kT(\ln\bar{x}_i+1)+\lambda=0 \quad i=1, 2,\cdots, s, \qquad (5.4a)$$

and

$$\bar{x}_1+\bar{x}_2+\cdots\cdot+\bar{x}_s=1\ . \qquad (5.4b)$$

Eq. (5.4a), as an equation for $\bar{x}_i$, has at most two roots, α and β. Thus, we can assume $\bar{x}_1=\cdots\cdot=\bar{x}_j=\alpha$, $\bar{x}_{j+1}=\cdots\cdot=\bar{x}_s=\beta$. It can be shown that only the state corresponding to $j=1$ can be stable, and other states are always metastable.

For our purpose, therefore, sufficient is the investigation in the special case

$$x_1-\sigma=x_2=x_3=\cdots\cdot=x_s\ ,$$

namely

$$x_1=\frac{1}{s}+\frac{s-1}{s}\sigma\ ,$$

$$x_2=x_3=\cdots\cdot=x_s=\frac{1}{s}-\frac{1}{s}\sigma\ , \qquad (5.5)$$

$$\frac{F(\sigma)}{N}=\frac{z}{4}J-\frac{zJ}{2}\cdot\frac{1}{s}[1+(s-1)\sigma^2]$$
$$+\frac{kT}{s}\Big[-s\ln s+\ln[1+(s-1)\sigma]+(s-1)\ln(1-\sigma)$$
$$+(s-1)\sigma\ln\frac{1+(s-1)\sigma}{1-\sigma}\Big]. \qquad (5.6)$$

The disordered phase corresponds to $\sigma=0$ and an ordered phase to $\sigma\neq 0$.

The transition temperature, T_c, and the value of σ of the ordered phase at the transition temperature, σ_c, are determined by the relations

$$[F]_{\sigma=\sigma_c}=[F]_{\sigma=0}\ ,$$

and

$$\left[\frac{\partial F}{\partial\sigma}\right]_{\sigma=\sigma_c}=0\ , \qquad (5.7)$$

the result being

$$T_c=\frac{zJ}{2k\ln(s-1)}\frac{s-2}{s-1}\ ,\qquad \sigma_c=\frac{s-2}{s-1}\ . \qquad (5.8)$$

The latent heat of transition is calculated to be

$$\frac{\varDelta E}{N}=\frac{1}{N}\{[E]_{\sigma=0}-[E]_{\sigma=\sigma_c}\}=\frac{z}{2}J\frac{(s-2)^2}{s(s-1)}\ . \qquad (5.9)$$

In the case of $s\geqq 3$ the calculated latent heat is non-vanishing and the specific heat remains finite at the transition temperature. Thus the Bragg-Williams approximation leads to a normal phase transition of the first order for $s\geqq 3$, the result being far from the reality.

Appendix

Proof of $\gamma(\Gamma)=s^{N-1}p(\Gamma)$.

We shall begin with mentioning some features of $p(\Gamma)$ which will be used later. Let us define Γ_1, Γ_2, $\cdots\cdot$, Γ_k as the closed polygons which are obtained by erasing some of the rods constituting the closed polygon Γ, and Γ_0 as that obtained by erasing all rods (see Fig. 5). Then we see that

$$p(\Gamma)+p(\Gamma_1)+\cdots\cdot+p(\Gamma_k)+p(\Gamma_0)=s^f\ . \qquad (A.1)$$

(f is the number of regions divided by Γ), because the sum on the left-hand side is equal to the number of different ways to paint by s colors a map corresponding to the closed polygon Γ allowing the appearance of pairs of neighboring regions in a same color.

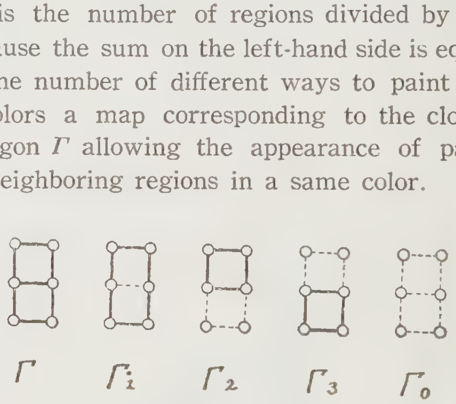

Fig. 5.

Returning to the proof, the following relation is obvious.

$$\gamma(\Gamma_0)=s^{N-1}p(\Gamma_0)\ , \qquad (A.2)$$

because

$$\gamma(\Gamma_0)=\sum_{\mu_i=e_1,\cdots,e_s}1=s^N,\quad p(\Gamma_0)=s.$$

Let us assume that $\gamma(\bar{\Gamma})=s^{N-1}p(\bar{\Gamma})$ has been proved for every closed polygon $\bar{\Gamma}$ including $\bar{l}(<l)$ connecting rods and consider $\gamma(\Gamma)$ for the closed polygon Γ with l connecting rods.

When Γ consists of two isolated closed polygons Γ' and Γ'', we can easily verify that

$$p(\Gamma)=\frac{1}{s}\,p(\Gamma')\,p(\Gamma'')\ ,$$

$$\frac{1}{s^N}\gamma(\Gamma)=\frac{1}{s^N}\gamma(\Gamma')\times\frac{1}{s^N}\gamma(\Gamma'')\ .$$

Hence using the assumption $\gamma(\Gamma')=s^{N-1}p(\Gamma')$, $\gamma(\Gamma'')=s^{N-1}p(\Gamma'')$, we get the result we wanted to prove

$$\gamma(\Gamma)=s^{N-1}p(\Gamma)\ . \tag{A.3}$$

When Γ is a single closed polygon, the following topological relation can be easily shown from Euler's theorem:

$$n+f=l+2\ , \tag{A.4}$$

where n is the number of lattice sites on Γ. Then with the help of this relation (A.4) and the argument in the last paragraph of § 2, we get

$$\begin{aligned}
&\gamma(\Gamma)+\gamma(\Gamma_1)+\cdots\cdots+\gamma(\Gamma_k)+\gamma(\Gamma_0)\\
&\quad=\sum_{\mu_i=\epsilon_1,\cdots,\epsilon_s}\Big\{\prod_{r=1}^{l}{}_{(\Gamma)}(s\mu_r\mu_r'-1)\\
&\qquad+\prod_{r=1}^{l_1}{}_{(\Gamma_1)}(s\mu_r\mu_r'-1)+\cdots\\
&\qquad+\prod^{l_k}{}_{(\Gamma_k)}(s\mu_r\mu_r'-1)+1\Big\}\\
&\quad=\sum_{\mu_i=\epsilon_1,\cdots,\epsilon_s}\prod_{r=1}^{l}{}_{(\Gamma)}\{(s\mu_r\mu_r'-1)+1\}\\
&\quad=s^l\sum_{\mu_i=\epsilon_1,\cdots,\epsilon_s}\prod_{r=1}^{l}{}_{(\Gamma)}\mu_r\mu_r'\\
&\quad=s^{l+N-n+1}\\
&\quad=s^{N-1}s^f\ .
\end{aligned} \tag{A.5}$$

Comparing this equation with (A.1), we get

$$\gamma(\Gamma)=s^{N-1}p(\Gamma)\ . \tag{A.6}$$

The mathematical induction completes the proof.

References

1) A. Ookawa: J. Phys. Soc. Japan **2** (1947) 108, **3** (1948) 295, **4** (1949) 14, **7** (1952) 543; Bull. Kobayasi Inst. Phys. Res. **2** (1952) 45.

2) G. H. Wannier: Rev. Mod. Phys. **17** (1945) 50.

3) G. F. Newell and E. W. Montroll: Rev. Mod. Phys. **25** (1953) 353.

4) H. A. Kramers and G. H. Wannier: Phys. Rev. **60** (1941) 252.

5) J. Ashkin and E. Teller: Phys. Rev. **64** (1943) 178.

6) H. A. Kramers and G. H. Wannier: Phys. Rev. **60** (1941) 263.

7) L. Onsager: Phys. Rev. **65** (1944) 117.

JOURNAL OF THE PHYSICAL SOCIETY OF JAPAN Vol. 9, No. 5, SEP.—OCT., 1954

Second Virial Coefficient between Unlike Molecules

By Taro KIHARA and Saburo KOBA

Department of Physics, Faculty of Science, University of Tokyo

(Received April 15, 1954)

By means of the core model of molecules introduced by Kihara in Revs. Modern Phys. **25** (1953) potentials between unlike molecules in nonpolar gases have been determined from the second virial coefficients. The intermolecular potential U_{AB} for the pair of molecules (A, B) is assumed to be a function of the shortest distance ρ between the cores of the molecules, and furthermore

$$U_{AB}(\rho)=U_{0AB}\left[\left(\frac{\rho_{0AB}}{\rho}\right)\right]^{12}-2\left(\frac{\rho_{0AB}}{\rho}\right)^{6}\Bigg] .$$

Here U_{0AB} and ρ_{0AB} are constants which have been determined. Regarding these model constants the following relations have been verified:

$$\rho_{0AB}=\tfrac{1}{2}(\rho_{0AA}+\rho_{0BB}) ,$$
$$U_{0AB}=(U_{0AA}\,U_{0BB})^{1/2} .$$

One of the present authors[1] introduced a model of nonspherical molecules in gases by use of which the second virial coefficient can be integrated easily. He assumes, namely, an appropriate convex body called core inside each molecule and defines the intermolecular distance ρ as the shortest distance between two cores. The intermolecular potential U_{AB} for the pair (A, B) is assumed to be a function of ρ only: $U_{AB}=U_{AB}(\rho)$.

Making use of this "core model" he determined the potential between like molecules from the second virial coefficient of pure gases. The object of the present article is to determine the potential between unlike molecules from the virial coefficient of two-component gases.

The equation of state of two-component gases may be expressed in the form

$$\frac{p}{kT}=\frac{1}{V}(N_A+N_B)+\frac{1}{V^2}(B_{AA}N_A^2+2B_{AB}N_AN_B+B_{BB}N_B^2)+\cdots\cdots.$$

Here p is the pressure; T is the absolute temperature; k is the Boltzmann constant; N_A and N_B are the numbers of molecules of the species A and B, respectively, in the volume V. The coefficient B_{AB}, which is a function of the temperature, is called the second virial coefficient for the molecular pair (A, B).

By mean of the core model of molecules, the second virial coefficient is given by

$$B_{AB}=\int_{\rho=0}^{\rho=\infty}\left[1-\exp\frac{-U_{AB}(\rho)}{kT}\right]db_{AB}(\rho)+b_{AB}(0) ,$$

where

$$b_{AB}(\rho)=\frac{V_A+V_B}{2}+\frac{M_BS_A+M_AS_B}{8\pi} ,$$
$$M_A=2\pi\rho+M_{0A} ,$$
$$S_A=\pi\rho^2+M_{0A}\rho+S_{0A} ,$$
$$V_A=\frac{\pi}{6}\rho^3+\frac{1}{4}M_{0A}\rho^2+\frac{1}{2}S_{0A}\rho+V_{0A} ,$$

and similar relations as regards the species B. Here V_{0A}, S_{0A} and M_{0A} are, respectively, the volume, the surface area and the mean curvature integrated over the whole surface of the convex core of the molecule A. The function $b_{AB}(\rho)$ may also be expressed in the form

$$b_{AB}(\rho)=\frac{2\pi}{3}\rho^3+\frac{M_{0A}+M_{0B}}{2}\rho^2+\left(\frac{S_{0A}+S_{0B}}{2}+\frac{M_{0A}M_{0B}}{4\pi}\right)\rho+\frac{V_{0A}+V_{0B}}{2}+\frac{M_{0B}S_{0A}+M_{0A}S_{0B}}{8\pi} .$$

In particular, when the potential $U_{AB}(\rho)$ is the Lennard-Jones function,

$$U_{AB}(\rho)=U_{0AB}\left[\left(\frac{\rho_{0AB}}{\rho}\right)^{12}-2\left(\frac{\rho_{0AB}}{\rho}\right)^{6}\right],$$

the second virial coefficient B_{AB} is expressed by a power series with respect to

$$z_{AB}{}^{1/2}\equiv(U_{0AB}/kT)^{1/2} ,$$

that is

Table I. The second virial coefficient between unlike molecules.

(A, B)	T°K	B_{AB}A^3	Reference
A, H_2	298	13.6	a
	323	15.4	
	348	18.3	
	373	20.8	
	398	22.9	
	423	24.7	
	447	26.2	
H_2, N_2	273	20.4	a
	293	22.7	
N_2, O_2	273	−32.4	a
	323	−13.4	
	373	− 2.5	
	423	5.6	
	473	12.8	
O_2, C_2H_4	298	−70	b
C_2H_4, A	298	−72	b
O_2, O_2	273	−36.9	c
	323	−15.4	
	373	− 4.3	

a. E. A. Guggenheim, *Mixtures* (University Press, Oxford, England, 1952) p. 160.

b. Calculated from the data by L. Masson and L. G. F. Dolley: Proc. Roy. Soc. London **A103** (1923) 524.

c: L. Holborn and J. Otto: Zeits. Phys. **10** (1922) 367.

$$B_{AB}=\frac{2\pi}{3}\rho_{0AB}{}^3F_3(z_{AB})$$
$$+\frac{M_{0A}+M_{0B}}{2}\rho_{0AB}{}^2F_2(z_{AB})$$
$$+\left(\frac{S_{0A}+S_{0B}}{2}+\frac{M_{0A}M_{0B}}{4\pi}\right)\rho_{0AB}F_1(z_{AB})$$
$$+\frac{V_{0A}+V_{0B}}{2}+\frac{M_{0B}S_{0A}+M_{0A}S_{0B}}{8\pi},$$

where

$$F_s(z)=-\frac{s}{12}\sum_{t=0}^{\infty}\frac{1}{t!}\Gamma\left(\frac{6t-s}{12}\right)2^t z^{(6t+s)/12},$$
$$(s=1,\ 2,\ 3)$$

the table of which is given in reference 1.

The potential constants U_{0AB} and ρ_{0AB} between unlike molecules, which are determined from the second virial coefficient given in Table I, are shown in Table II. The Table contains also the model constants between like molecules for comparison. (Our cores of molecules are given in reference 1 except for oxygen. The core of oxygen O_2 has been chosen as a thin rod connecting two O's with length 1.10A, so that $V_0=0$, $S_0=0$ and $M_0=$ 3.45A. The core of argon is, of course, a point.)

From the results shown in Table II we may conclude as follows. (1) Within the limits of experimental accuracy, ρ_{0AB} is equal to the arithmetical mean of ρ_{0AA} and ρ_{0BB}. In fact we have assumed $\frac{1}{2}(\rho_{0AA}+\rho_{0BB})$ as ρ_{0AB} in cases of oxygen-ethylene and argon-ethylene mixtures for which the number of observed values is not sufficient for the determination of the two parameters U_0 and ρ_0. (2) Within the limits of experimental accuracy, U_{0AB} is equal to the geometrical mean of U_{0AA} and U_{0BB}. These are similar to the relation which Beattie and Stockmayer[2)] verified on the spherical approximation of nonspherical molecules.

Table II. The model constants determined from the second virial coefficient.

(A, B)	ρ_{0AB}A	$\frac{2\rho_{0AB}}{\rho_{0AA}+\rho_{0BB}}-1$	$\frac{U_{0AB}}{k}$ °K	$\frac{U_{0AB}}{(U_{0AA}U_{0BB})^{1/2}}-1$
A, A	3.83		119	
A, H_2	3.42	0.03	74.1	0.08
H_2, H_2	2.81		39.4	
H_2, N_2	3.14	0.00	66.8	−0.04
N_2, N_2	3.47		124	
N_2, O_2	3.20	−0.03	149	0.08
O_2, O_2	3.14		153	
O_2, C_2H_4	2.8	0, assumed	250	−0.07
C_2H_4, C_2H_4	2.5		470	
C_2H_4, A	3.2	0, assumed	220	−0.06

References

1) T. Kihara: Revs. Modern Phys. **25** (1953) 831.

2) J. A. Beattie and W. H. Stockmayer: J. Chem. Phys. **10** (1942) 473.

JOURNAL OF THE PHYSICAL SOCIETY OF JAPAN Vol. 9, No. 5, SEP.—OCT., 1954

Simultaneous Reflexion in Electron Diffraction as a Cause of the Failure of Friedel's Law

By Kazutake KOHRA
Institute of Physics, College of General Education, University of Tokyo, Komaba, Meguro-ku, Tokyo

(Received April 24, 1954)

Miyake and Uyeda found a remarkable phenomenon: that an asymmetry occurs in the intensities of a pair of reflexions (hhl) and $(hh\bar{l})$ when an electron beam impinges upon a cleavage face (100) of a zincblende crystal in the $[\bar{1}10]$ azimuth, which violates Friedel's law. In the present paper this phenomenon is studied in detail by applying the dynamical theory. Assuming the intensities of only the twor eflexions (hhl) and $(hh\bar{l})$ to be large and neglecting all other reflexions, we find that asymmetry occurs for an odd index when the selective reflexion takes place in the Bragg case, and does not for an even index. By numerical calculation, (331) has one peak and $(33\bar{1})$ has two peaks, with the integrated intensity of (331) larger than that of $(33\bar{1})$. These results are in accordance with the general trend of experimental observations. Detailed features of experimental observations which are inconsistent with this theory may be explained qualitatively by taking into account the effect of weak reflexions or additional simultaneous reflexions.

The present work proves that Friedel's law fails in the dynamical theory. It must be emphasized that the failure is not caused by the effect of absorption or dispersion, but is due to a dynamical interaction between simultaneously excited reflexion.

§ 1. Introduction

According to Friedel's law in X-ray crystallography, even for non-centrosymmetrical crystals, the intensities of (hkl) and $(\bar{h}\bar{k}\bar{l})$ reflexions are equal to each other.[2] By this law, senses of polar axes can be determined not alone by diffraction patterns. This law fails when an anomalous dispersion of X-rays takes place in atoms of one kind within the composition of the crystal. Nishikawa and Matsukawa[3] and other workers[4] comfirmed this phenomen by experiment using zincblende crystal.

Although Friedel's law is usually considered to hold also in electron diffraction, the following two observations seem to violate it. Thiessen and Molière[5] reported an anomaly that the diffraction patterns produced by the natural (111) and $(\bar{1}\bar{1}\bar{1})$ surfaces of zincblende give different values for apparent mean inner potential. Molière[6] studied the effect of absorption on apparent mean inner potential by applying the dynamical theory; but found the effect too small to explain quantitatively the above phenomenon. He then suggested that the anomaly might be due to a certain difference in surface states.

Later, Miyake and Uyeda[7] reported as follows: When an electron beam impings on a cleavage surface (110) of a zincblende crystal in the $[\bar{1}10]$ or $[1\bar{1}0]$ azimuth so as to excite simultaneously the (hhl) and $(hh\bar{l})$ reflexions, the diffraction pattern shows an asymmetry across the plane of incidence. (The principal features of their experiments are described in § 5.) Although the asymmetry is concerned with the intensities of the (hhl) and $(hh\bar{l})$ reflexions, and not of (hhl) and $(\bar{h}\bar{h}\bar{l})$, the experimental result can be considered to violate Friedel's law in a broad sense, because $(\bar{h}\bar{h}\bar{l})$ is equivalent crystallographically to $(hh\bar{l})$ in zincblende and because the senses of polar axes of the crystal can be determined by the observed asymmetry. It is to be noted that, in their experiment, the both reflected waves leave the crystal from the same surface so that the complicated factor encountered in the experiment of Thiessen and Molière is absent. Accordingly the observation by Miyake and Uyeda may be compared less ambiguously with the theory than the one by Thiessen and Molière.

---

* A short communication was given in Acta Crystallographica.[1]

In the present paper the asymmetry observed by Miyake and Uyeda is studied. Previously Miyake and Uyeda considered, on the basis of the kinematical theory, three causes for the asymmetry: (1) the displacement of ions at the extreme surface (as previously discussed by Lennard-Jones[8]); (2) the effect of strong absorption resulting in two-dimensional diffraction on the uppermost layer; (3) the phase change of scattered waves expected from the collision problem. In submitting these possible causes. they failed to give any satisfactory explanations. Using the dynamicel theory, the present author calculated the effect of absorption on the (*hhl*) and (*hh$\bar{l}$*) reflexions by assuming periodic inner potential in a way similar to Molière. The numerical calculation, however, gave too slight an asymmetry to explain the experiment (see Appendices).

Now we should notice that because, under the experimental condition of Miyake and Uyeda, the (*hhl*) and (*hh$\bar{l}$*) reflexions take place simultaneously, a strong dynamical interaction between both reflexions must be inevitable. It is most probable that the failures of the previous considerations are attributed to the neglect of this state of affairs. In the present paper, in the hope of explaining their experiment, we calculate the intensities of both reflexions on the basis of the dynamical theory taking into account the occurrence of simultaneous reflexion.

§ 2. The Dynamical Treatment of Simultaneous Reflexion

The general procedure of the dynamical theory was given by Bethe.[9] Some special cases of simultaneous reflexion were treated by Shinohara[10] and Heidenreich[11]. An outline of the treatment will be given below.

(i) *Derivation of the reduced fundamental equations.*

Suppose that the incident wave with the energy eE impinges on the surface of a crystal slab of infinite area and of thickness H and that two strong reflexions simultaneously emerge from the crystal. The two boundary surfaces will be called hereafter the upper and lower surfaces, upon the former of which the incident wave impinges. The two free spaces divided by the slab are called the upper and lower free spaces. The wave function in the crystal satisfies the Schrödinger equation:

$$\varDelta\psi+\frac{8\pi^2 me}{h^2}(E+V)\psi=0\,, \tag{1}$$

where all the notations have the usual meanings. The periodic potential V can be expanded into Fourier series as follows:

$$\frac{2me}{h^2}V=\sum_g v_g \exp(2\pi i\boldsymbol{gr})\,, \tag{2}$$

where $\boldsymbol{g}$ is a vector representing a reciprocal-lattice point,

$$\boldsymbol{g}=g_1\boldsymbol{b}_1+g_2\boldsymbol{b}_2+g_3\boldsymbol{b}_3\,, \tag{3}$$

and the suffix g means $(g_1g_2g_3)$. The wave function ψ can be expanded into a form

$$\psi=\sum_g \psi_g \exp(2\pi i\boldsymbol{k}_g\boldsymbol{r})\,, \tag{4}$$

where

$$\boldsymbol{k}_g=\boldsymbol{k}_0+\boldsymbol{g}\,. \tag{5}$$

From (1), (2) and (4), we have an infinite set of linear homogeneous equations,

$$(\boldsymbol{K}_0{}^2+v_0-\boldsymbol{k}_h{}^2)\psi_h+\sum{}' v_{h-g}\psi_g=0\,, \tag{6}$$

where $K_0{}^2=2meE/h^2$ is the square of the magnitude of the incident wave vector $\boldsymbol{K}_0$ and $\sum'$ the summation over g except for $g=h$. Let us assume that only the amplitudes of three waves ψ_0, ψ_m and ψ_n, primary and two diffracted waves, are large compared with the others, ψ_g's. Then we have the reduced fundamental wave equations in the approximation neglecting the weak waves:

$$\begin{pmatrix} \boldsymbol{K}_0{}^2+v_0-\boldsymbol{k}_0{}^2 & v_{-m} & v_{-n} \\ v_m & K_0{}^2+v_0-\boldsymbol{k}_m{}^2 & v_{m-n} \\ v_n & v_{n-m} & K_0{}^2+v_0-\boldsymbol{k}_n{}^2 \end{pmatrix}\begin{pmatrix}\psi_0\\ \psi_m\\ \psi_n\end{pmatrix}=0\,. \tag{7}$$

In order that (6) has the finite solution, the equation

$$\begin{vmatrix} \boldsymbol{K}_0{}^2+v_0-\boldsymbol{k}_0{}^2 & v_{-m} & v_{-n} \\ v_m & K^2+v_0-\boldsymbol{k}_m{}^2 & v_{m-n} \\ v_n & v_{n-m} & K^2+v_0-\boldsymbol{k}_n{}^2 \end{vmatrix}=0\,, \tag{8}$$

must be satisfied. For the vectors $\boldsymbol{k}_0$, $\boldsymbol{k}_m$ and $\boldsymbol{k}_n$ satisfying (8), we obtain from (7) the following relations:

$$\psi_m=\frac{v_{m-n}v_n-v_mQ_n}{Q_mQ_n-v_{m-n}\,v_{n-m}}\psi_0=c_m\psi_0\ , \qquad (9a)$$

and

$$\psi_n=\frac{v_{n-m}v_m-v_nQ_m}{Q_mQ_n-v_{m-n}\,v_{n-m}}\psi_0=c_n\psi_0\ , \qquad (9b)$$

where

$$\left.\begin{aligned} Q_m&=\boldsymbol{K}_0^2+v_0-\boldsymbol{k}_m^2\ ,\\ \text{and}\qquad Q_n&=\boldsymbol{K}_0^2+v_0-\boldsymbol{k}_n^2\ . \end{aligned}\right\} \qquad (10)$$

(ii) *Determination of the wave vectors and the general solution.*

When the incident wave is given, the wave vectors, $\boldsymbol{k}_0$, $\boldsymbol{k}_m$ and $\boldsymbol{k}_n$ are determined by the secular equation (8) and the condition of tangential continuity of wave vectors. Namely, the wave points in the reciprocal space are given as the intersections of the dispersion surface determined by (8) and a line (ν-normal) normal to the surface of the crystal and at a distance from the origin of this space equal to the tangential component of $\boldsymbol{K}_0$. We denote the wave vectors of the two diffracted waves in the free space by $\boldsymbol{K}_m$ and $\boldsymbol{K}_n$, where their tangential components are equal to those of $\boldsymbol{k}_m$ and $\boldsymbol{k}_n$ respectively according to the condition of tangential continuity. We also denote the components of $\boldsymbol{k}_0$, $\boldsymbol{k}_m$ and $\boldsymbol{k}_n$ along the normal to the upper surface directing downwards by γ_0, γ_m and γ_n, and the magnitudes of the normal components of $\boldsymbol{K}_0$, $\boldsymbol{K}_m$ and $\boldsymbol{K}_n$ by Γ_0, Γ_m and Γ_n respectively. From the relation $|\boldsymbol{K}_0|=|\boldsymbol{K}_m|=|\boldsymbol{K}_n|$ and the condition of tangential continuity, the diagonal terms of (8) are rewritten as follows:

$$\left.\begin{aligned} Q_0^2=\Gamma_0^2+v_0-\gamma_0^2,\quad Q_m^2&=\Gamma_m^2+v_0-\gamma_m^2\ ,\\ \text{and}\qquad Q_n^2&=\Gamma_n^2+v_0-\gamma_n^2\ . \end{aligned}\right\} \qquad (11)$$

Since γ_m and γ_n can be written in terms of γ_0 by (5), and Γ_m and Γ_n in terms of Γ_0 as will be given by (33), γ_0 is determined as a function of Γ_0 from (8) and (11).

The Eq. (8) gives six roots of γ_0. We adopt, as usually done, only three roots of them, $\gamma_0^{(s)}$ ($s=1$, 2 and 3), which make all the diagonal terms to be nearly zero, in accordance with the assumption that the amplitudes of the three waves are large. Corresponding to these roots, (9a) and (9b) are written as follows:

$$\psi_m^{(s)}=c_m^{(s)}\psi_0^{(s)} \text{ and } \psi_n^{(s)}=c_n^{(s)}\psi_0^{(s)}. \quad (12)$$

The remaining three solutions are neglected because they would be proved to have only small contributions to the amplitudes of di fracted waves in vacuum. (A rigorous cor sideration taking into account all of the root was given by Lamla.[12])

Then the general solution of the wav function in the crystal is given by

$$\psi=\sum_s^{1,2,3}\sum_g^{0,m,n}\psi_g^{(s)}\exp\left(2\pi i\boldsymbol{k}_g^{(s)}\boldsymbol{r}\right). \qquad (13)$$

(iii) *Determination of the amplitudds of th waves by boundary conditions.*

The wave function ψ in the crystal shoul be joined to those in the upper and lowe space, Ψ and Φ, respectively, so as to satisf the conditions of equality of the amplitude and their normal derivatives at the boundar surface. These conditions are written sepa rately for each set of plane waves in an outside the crystal which have a common tan gential component of wave vectors. For ex ample, corresponding to the index m, there ar possible waves as follows: $\psi_m^{(s)}\exp(2\pi i\boldsymbol{k}_m^{(s)}\boldsymbol{r}$ ($s=1$, 2 and 3) within the crystal, $\Psi_m^{(u)}$ ex $(2\pi i\boldsymbol{K}_m^{(u)}\boldsymbol{r})$ and $\Psi_m^{(d)}\exp(2\pi i\boldsymbol{K}_m^{(d)}\boldsymbol{r})$ in th upper free space, $\Phi_m^{(u)}{}_m\exp(2\pi i\boldsymbol{K}_m^{(u)}\boldsymbol{r})$ an $\Phi_m^{(d)}\exp(2\pi i\boldsymbol{K}_m^{(d)}\boldsymbol{r})$ in the lower free epace where the superfices (u) and (d) are referre to waves travelling upwards and downward respectively (Fig. 1.). The symbols used before

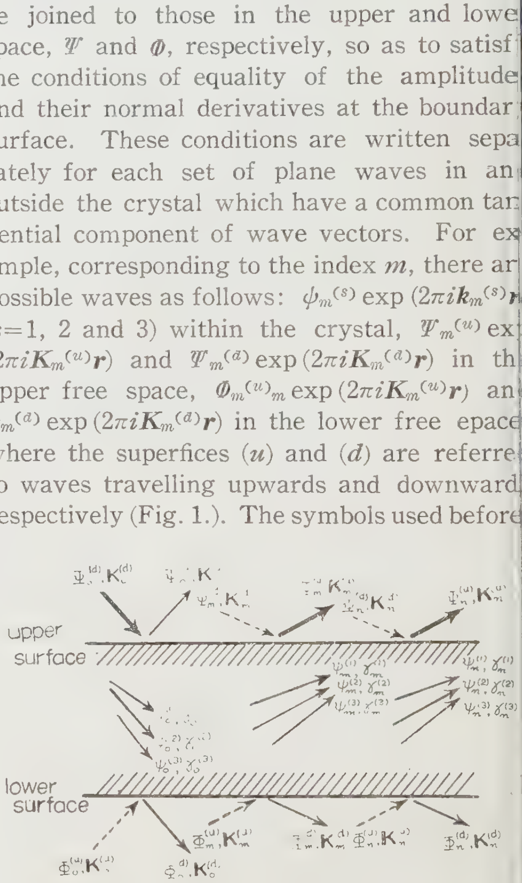

$\Psi_0^{(d)}, \boldsymbol{K}_0^{(d)}$
$\Psi_m^{(1)}, \boldsymbol{K}_m^{(1)}$
$\Psi_n^{(d)}, \boldsymbol{K}_n^{(d)}$
$\Psi_n^{(u)}, \boldsymbol{K}_n^{(u)}$
upper surface
$\psi_m^{(1)}, \gamma_m^{(1)}$
$\psi_m^{(2)}, \gamma_m^{(2)}$
$\psi_m^{(3)}, \gamma_m^{(3)}$
$\psi_n^{(1)}, \gamma_n^{(1)}$
$\psi_n^{(2)}, \gamma_n^{(2)}$
$\psi_n^{(3)}, \gamma_n^{(3)}$
$\psi_0^{(3)}, \gamma_0^{(3)}$
lower surface
$\Phi_m^{(u)}, \boldsymbol{K}_m^{(u)}$
$\Phi_n^{(u)}, \boldsymbol{K}_n^{(u)}$
$\Phi_n^{(d)}, \boldsymbol{K}_n^{(d)}$
$\Phi_0^{(u)}, \boldsymbol{K}_0^{(u)}$
$\Phi_0^{(d)}, \boldsymbol{K}_0^{(d)}$

Fig. 1. Waves in vacuum and crystal.

$\boldsymbol{K}_0$, $\boldsymbol{K}_m$ $\boldsymbol{K}_n$ are rewritten $\boldsymbol{K}_0^{(d)}$, $\boldsymbol{K}_m^{(u)}$ an $\boldsymbol{K}_n^{(u)}$ respectively according to the presen notation. Let us assume that the coordinat origin is taken at a certain point in the uppe surface, then the boundary conditions for thes waves at the two surfaces are given by

$$\begin{aligned} \Psi_m^{(u)}+\Psi_m^{(d)}&=\sum_s\psi_m^{(s)}\\ \text{and}\qquad \Gamma_m(-\Psi_m^{(u)}+\Psi_m^{(d)})&=\sum_s\gamma_m^{(s)}\psi_m^{(s)} \end{aligned} \qquad (14)$$

for the upper surface, and

$$\left.\begin{aligned} &\varPhi_m{}^{(u)}\exp(-2\pi i\Gamma'_m H)+\varPhi_m{}^{(d)}\exp(2\pi i\Gamma'_m H)\\ &\qquad=\sum\psi_m{}^{(s)}\exp(2\pi i\gamma_m{}^{(s)}H),\\ &\text{and}\\ &\Gamma_m\{-\varPhi_m{}^{(u)}\exp(-2\pi i\Gamma_m H)\\ &\qquad\qquad+\varPhi_m{}^{(d)}\exp(2\pi i\Gamma'_m H)\}\\ &\qquad=\sum\gamma_m{}^{(s)}\psi_m{}^{(s)}\exp(2\pi i\gamma_m{}^{(s)}H)\end{aligned}\right\}\tag{15}$$

for the lower surface. Similar equations are obtained for other sets of waves corresponding to the indices 0 and n.

Now let us calculate the amplitudes of the two strong diffracted waves for the case in which these emerge from the crystal through the upper surface, corresponding to the experiment of Miyake and Uyeda. By the analogy with the case of single reflexion we call hereafter such a case the Bragg case, and the case where the diffracted waves emerge from he crystal through the lower surface the Laue case. The quantities in the boundary equations, $\varPsi_m{}^{(d)}$, $\varPsi_n{}^{(d)}$, $\varPhi_0{}^{(u)}$, $\varPhi_m{}^{(u)}$ and $\varPhi_n{}^{(u)}$ should de actually zero because there are no waves entering the crystal besides the incident wave, but in the present calculation three among them must be assumed to have finite values, in order to make the number of the unknown quantities to be equal to that of the boundary equations. This inadequacy comes from neglected half the roots of the secular equation (8). In the present treatment (the Bragg case), $\varPsi_m{}^{(d)}$, $\varPsi_n{}^{(d)}$ and $\varPhi_0{}^{(u)}$ are assumed to have finite values, but they are usually so small that such an assamption does not have any serious influence on the amplitudes of the stronger waves $\varPsi_m{}^{(u)}$ and $\varPsi_n{}^{(u)}$ (see Appencices). Then from (12) and the boundary equations (15), (16) and similar equations, we can determine the ratios of the amplitudes of all waves to that of the incident wave. The amplitudes of the diffracted waves emerging from the upper surface are given by

$$\varPsi_m{}^{(u)}=\frac{\Gamma_0\prod\limits_{s}^{1,2,3}(\Gamma_m+\gamma_m{}^{(s)})\sum\limits^{(1,2,3)}[c_m{}^{(1)}(c_m{}^{(2)}c_n{}^{(3)}-c_m{}^{(3)}c_n{}^{(2)})\exp\{2\pi i(\gamma_m{}^{(2)}+\gamma_n{}^{(3)})H\}]}{\Gamma_m\sum\limits^{(1,2,3)}[(\Gamma_0+\gamma_0{}^{(1)})(\Gamma_m+\gamma_m{}^{(2)})(\Gamma_n+\gamma_n{}^{(3)})(c_m{}^{(2)}c_n{}^{(3)}-c_m{}^{(3)}c_n{}^{(2)})\exp\{2\pi i(\gamma_m{}^{(2)}+\gamma_n{}^{(3)})H\}]}\times\varPsi_0{}^{(d)}\tag{16a}$$

and

$$\varPsi_n{}^{(u)}=\frac{\Gamma_0\prod\limits_{s}^{1,2,3}(\Gamma_n+\gamma_n{}^{(s)})\sum\limits^{(1,3,3)}[c_m{}^{(1)}(c_n{}^{(2)}c_m{}^{(3)}-c_n{}^{(3)}c_m{}^{(2)})\exp\{2\pi i(\gamma_n{}^{(2)}+\gamma_m{}^{(3)})H\}]}{\Gamma_n\sum\limits^{(1,2,3)}[(\Gamma_n+\gamma_0{}^{(1)})(\Gamma_n+\gamma_n{}^{(2)})(\Gamma_m+\gamma_m{}^{(3)})(c_n{}^{(2)}c_m{}^{(3)}-c_n{}^{(3)}c_m{}^{(2)})\exp\{2\pi i(\gamma_n{}^{(2)}+\gamma_m{}^{(3)})H\}]}\times\varPsi_0{}^{(d)},\tag{16b}$$

where $\sum\limits^{(1,2,3}$ means the summation over three terms which are obtained by changing cyclically the super fices (1), (2) and (3), and $\varPsi_0{}^{(d)}$ means the amplitude of the incident wave.

(iv) *Intensity fluxes of the diffradted waves in the selectiv region.*

Since the form of the matrix in (8) is hermitian, the roots $\gamma_0{}^{(s)}$ (accordingly $\gamma_m{}^{(s)}$ and $\gamma_n{}^{(s)}$) are either all real or one of them is real and the remaining two are complex and conjugate to each other. The former case takes place only in the Bragg case when the Laue condition is nearly satisfied (§ 3 (iii)), whereas it cannot be expected to take place in the Laue case. The angular region of the incident beam for which the roots, $\gamma_0{}^{(1)}$ and $\gamma_0{}^{(2)}$, have the complex values or the selective reflexion takes place, will be called hereafter the selective region. Let the imaginary parts of $\gamma_0{}^{(1)}$ and $\gamma_0{}^{(2)}$ be positive and negative respectively, then $\gamma_0{}^{(1)}$, $\gamma_0{}^{(2)}$ and the real root $\gamma_0{}^{(3)}$ correspond to exponentially decreasing, increasing and periodic waves respectively.

In the present case (the Bragg case) there exists the selective region. Inside the region each of three terms in the denominators and parentheses of (16a) and (16b) show monotonous increase or decrease or oscillation with increasing H. When H is sufficiently large, only one of three terms corresponding to the decreasing wave remains, and (16a) and (16b) are reduced to

$$\varPsi_m{}^{(u)}=\frac{\Gamma_0(\Gamma_m+\gamma_m{}^{(1)})}{\Gamma_m(\Gamma_0+\gamma_0{}^{(1)})}c_m{}^{(1)}\varPsi_0{}^{(d)},\tag{17a}$$

and

$$\Psi_n^{(u)}=\frac{\Gamma_0(\Gamma_n+\gamma_n^{(1)})}{\Gamma_n(\Gamma_0+\gamma_0^{(1)})}\,c_n^{(1)}\Psi_0^{(d)}. \tag{17b}$$

The ratios of the intensity fluxes (intensities multiplied by the cross section of electron beam) of the diffracted waves to that of the incident wave, or the reflexion powers, are given by the use of (9a), (9b), (17a) and (17b) as follows:

$$P_m=\frac{\Gamma_m|\Psi_m^{(u)}|^2}{\Gamma_0|\Psi_0^{(d)}|^2}$$
$$=\frac{\Gamma_0|\Gamma_m+\gamma_m^{(1)}|^2|v_{m-n}v_n-v_mQ_n^{(1)}|^2}{\Gamma_m|\Gamma_0+\gamma_0^{(1)}|^2|Q_m^{(1)}Q_n^{(1)}-v_{m-n}v_{n-m}|^2}, \tag{18a}$$

and

$$P_n=\frac{\Gamma_n|\Psi_n^{(u)}|^2}{\Gamma_0|\Psi_0^{(d)}|^2}$$
$$=\frac{\Gamma_0|\Gamma_n+\gamma_n^{(1)}|^2|v_{n-m}v_m-v_nQ_m^{(1)}|^2}{\Gamma_n|\Gamma_0+\gamma_0^{(1)}|^2\,|Q_m^{(1)}Q_n^{(1)}-v_{m-n}v_{n-m}|^2}. \tag{18b}$$

Since the calculation is much simpler inside the selective region than outside and moreover, the reflexion is expected to be strong only inside the region, we shall be concerned hereafter solely with the reflexion inside the region.

§ 3. Calculation of the Reflexion Powers

In this section, we carry out a calculation for the (hhl) and $(hh\bar{l})$ reflexions by assuming that the incident beam impinging upon the cleavage (110) in the [$\bar{1}$10] azimuth (Fig. 2) as in the experiment of Miyake and Uyeda.

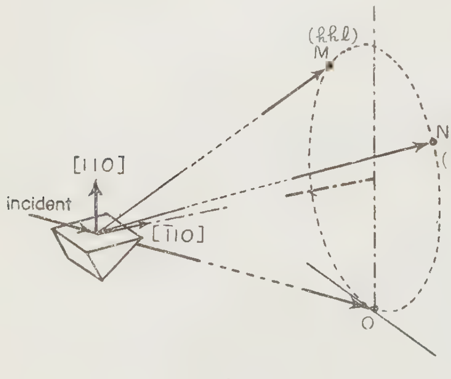

Fig. 2.

(i) *Relations among the Fourier coefficients.*

The values of the Fourier coefcients v_g's are given by

$$v_g=\sum_{(w)} v_g^{(w)}\exp(2\pi i\boldsymbol{g}\boldsymbol{R}^{(w)}), \tag{19}$$

where $\boldsymbol{R}^{(w)}$ is the position vector for the w-th ion in the unit cell, $\sum_{(w)}$ means the summatio over all the ions in the unit cell, and

$$v_g^{(w)}=(8\pi me/h^2g^2a)(Z^{(w)}-f_g^{(w)}), \tag{20}$$

where $Z^{(w)}$ and $f_g^{(w)}$ mean the atomi number and the structure factor of the w-th ion in the unit cell respectively. The origi of the unit cell is taken on a zinc atom s that the coordinates of the other ions in th unit cell are given by (see Fig. 3)

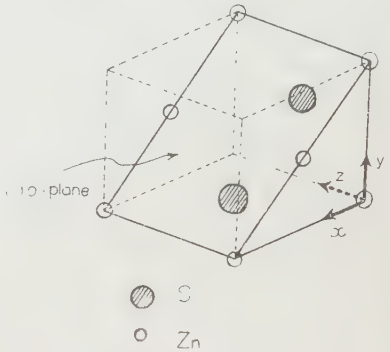

Fig. 3.

Zn^{++}: (0 0 0), (0 1/2 1/2), (1/2 0 1/2),
(1/2 1/2 0) and
S^{--}: (1/4 1/4 1/4), (1/4 3/4 3/4), (3/4 1/4 3/4)
(3/4 3/4 1/4).

Then v_g's are zero for mixed indeces and

$$v_g=4(v_g^{(Zn)}+(-i)^{(h+k+l)}v_g^{(S)}), \tag{21}$$

for all even or all odd indices. For $m=(hhl$ and $n=(hh\bar{l})$, we have

$$v_m=v_{-m}^*=v_{-n}=v_n^*. \tag{22}$$

For even indices, these are real and

$$v_m=v_{-m}=v_{-n}=v_n. \tag{23}$$

Since $m-n=(0\ 0\ 2l)$, both v_{m-n} and v_{n-m} ar always real and

$$v_{m-n}=v_{n-m}. \tag{24}$$

(ii) *Comparison of the reflexion powers o* *(hhl) and $(hh\bar{l})$.*

Now we calculate the difference betwee the reflexion powers for (hhl) and $(hh\bar{l})$ insid the selective region by the expressions (18a and (18b). Since, under the assumed condi tion, both the reflexions are geometricall symmetrical with respect to the (001) plan we have

$$\Gamma_m=\Gamma_n,\ \gamma_m^{(s)}=\gamma_n^{(s)}\ \text{and}\ Q_m^{(s)}=Q_n^{(s)}. \tag{25}$$

From (18a), (18b) and (25), we obtain

$$\Delta P=P_m-P_n=\frac{\Gamma_0|\Gamma_m+\gamma_m^{(1)}|^2(|v_{m-n}v_n-v_mQ_n^{(1)}|^2-|v_{n-m}v_m-v_nQ_m^{(1)}|^2)}{\Gamma_m|\Gamma_0+\gamma_0^{(1)}|^2|Q_m^{(1)}Q_n^{(1)}-v_{m-n}v_{n-m}|^2},$$

and from (22) and (24),

$$\begin{aligned}\Delta P&=\frac{4\Gamma_0|\Gamma_m+\gamma_m^{(1)}|^2}{\Gamma_m|\Gamma_0+\gamma_0^{(1)}|^2|Q_m^{(1)}Q_n^{(1)}-v_{m-n}^2|^2}(Q_m^{(1)}-Q_m^{*(1)})(v_m^{*2}v_{m-n}-v_m^2v_{m-n}^*)\\&=\frac{4\Gamma_0|\Gamma_m+\gamma_m^{(1)}|^2}{\Gamma_m|\Gamma_0+\gamma_0^{(1)}|^2|Q_m^{(1)}Q_n^{(1)}-v_{m-n}|^2}\cdot v_{m-n}I(Q_n^{(1)})I(v_{-m}^2)\,,\end{aligned}\tag{26}$$

where $I(\ \ )$ means the imaginary part of the expression in the bracket. When $\gamma_m^{(1)}$ which corresponds to the decreasing wave is written down in a form

$$\gamma_m^{(1)}=\alpha+i\beta\,. \tag{27}$$

with real α and β, we have $\alpha<0$ and $\beta>0$. It is seen from (11) that

$$I(Q_m^{(1)})=I(\gamma_m^{(1)2})=-2\alpha\beta>0\,, \tag{28}$$

and from (21) that

$$\left.\begin{aligned}I(v_{-m}^2)&=0 &&\text{for } l=4\mu \text{ or } 4\mu+2,\\&=32v_{-m}^{(Z_n)}v_{-m}^{(S)} &&\quad=4\mu+1,\\&=-32a_{-m}^{(Z_n)}v_{-n}^{(S)} &&\quad=4\mu+3,\end{aligned}\right\}\tag{29}$$

where μ is positive or negative integer. When m and n are odd indices, we have

$$v_{m-n}=v_{002l}^{(Z_n)}-v_{002l}^{(S)}>0\,. \tag{30}$$

Substituting (28), (29) and (30) into (26), we obtain

$$\left.\begin{aligned}\Delta P=P_{hhl}-P_{hh\bar{l}}&=0 &&\text{for } l=4\mu \text{ or } 4+2,\\&<0 &&\quad=4\mu+1,\\&>0 &&\quad=4\mu+3.\end{aligned}\right\}\tag{31}$$

This result means that the asymmetry in intensity is observed only in the reflexions of odd indices, but not of even indices.

In the present calculation, it is assumed that the coordinate origin lies on the upper surface (§ 2 (iii)) and further is taken at the centre of a certain zinc atom (§ 3 (i)). This implies that the upper halves of all the atoms in the uppermost layer are cut off by the boundary surface. This apparent inadequacy however, is trivial since the the results (26) and (31) are independent of the choice of the origin from the following reason: when the origin is displaced by $\boldsymbol{R}_0$, the reflexion powers are calculated to be $P_m'=P_m|\exp(-2\pi i\boldsymbol{R}_0\boldsymbol{m})|^2$ and $P_n'=P_n|\exp(-2\pi i\boldsymbol{R}_0\boldsymbol{n})|^2$ $P_m'=P_m$ and $P_n'=P_n$.

(iii) *Numerical calculation on the (331) and (33$\bar{1}$) reflexions.*

Now we carry out a numerical calculation for the (331) and (33$\bar{1}$) reflexions in which the asymmetry is observed especially conspicuous. We have to solve γ_0 (accordingly γ_m and γ_n) as the function of Γ_0 from the Eq. (8) under the boundary requirement. For this purpose we rewrite them in terms of new parameters by the use of the Ewald construction (Fig. 4). For a given incident vector $\boldsymbol{K}_0$, ν-normal is determined on which a point L (Laue point) is taken so that $\overline{LO}=\sqrt{K_0^2+v_0}$. For a certain $\boldsymbol{K}_0$, we have a special point L' which satisfies the Laue condition, $\overline{L'O}=\overline{L'M}=\overline{L'N}$ where M and N mean the reciprocal-latticep oints (hhl) and ($hh\bar{l}$) respectively. We put $(\overrightarrow{L'O})_\nu=p$ and introduce a quantity ζ (resonannce error) defined by

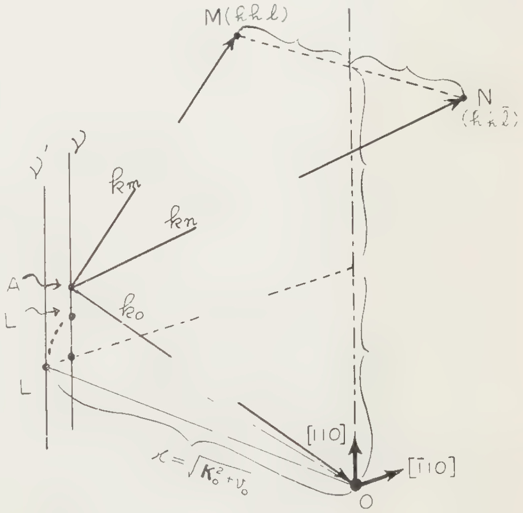

Fig. 4. Wave vectors in reciprocal spaɔe.

$$\zeta=(\overrightarrow{LO})_\nu-(\overrightarrow{L'O})_\nu=\sqrt{\Gamma_0^2+v_0}-p\,, \tag{32}$$

where $(\ \ )_\nu$ means the component of the vector in the bracket along the normal directing downwards. ζ gives a measure of the deviation from the Laue condition. As earsily seen, Γ_0, Γ_m and Γ_n are respectively given by

$$\Gamma_0=\sqrt{(p+\zeta)^2-v_0}$$

and $\Gamma_m=\sqrt{(p+\zeta)^2-v_0-(l/a)^2}=\Gamma_n\ ,\qquad(33)$

where a is the length of the edge of the unit cell. We introduce another quantity δ (anpassung) which gives the distance from the Laue point L to the wave point A ($\delta=\overrightarrow{LA}$). Then γ_0, γ_m and γ_n are rewritten as follows:

$$\gamma_0=(\overrightarrow{OA})_\nu=p+\zeta+\delta$$

and $\qquad\gamma_m=\gamma_n=(\boldsymbol{m})_\nu-(p+\zeta+\delta)\ .\qquad(34)$

where $(\boldsymbol{m})_\nu$ stands for the normal component of $\boldsymbol{m}$, the reciprocal-lattice vector of M.

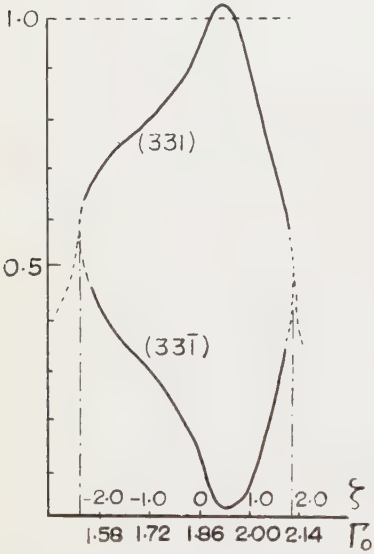

Fig. 5. Reflexıonpowers of (331) and (331) reflexions. Vertical lines indicate the selective region.

We substitute (11), (33), (34) into (8) and neglect terms higher than third-degree of ζ and δ since ζ and δ are small quantities inside the selective region. Then we obtain the third-degree equation of δ with parameter ζ as follows:

$$\begin{aligned}&8pq^2\delta^3+16p(p+q)q\zeta\delta^2+\{8p(p+q)^2\\&\quad-2pv_{m-n}{}^2+4qv_mv_m{}^*\}\\&\quad+\{4v_mv_m{}^*(p+q)\zeta-(v_m{}^2+v_m{}^{*2})v_{m-n}\}=0,\end{aligned}\qquad(35)$$

where $q=(\boldsymbol{m})_\nu-p$ and, in the present case, $(\boldsymbol{m})_\nu=h/a$. For a practical calculation, the following numerical values are used: $p=0.414$, $q=0.368$ (in A^{-1}) and $v_0=3.28$, $v_{m-n}=v_{002}=0.64$ and $v_m=v_{331}=0.57+0.331i$ (in A^{-2}); p and q are values in accordance with the lattice constant of zincblende $a=5.42$ A; v_0 corresponds to the mean inner potential 12.5 volts of zincblende which is the average of the values measured by various workers[13]; v_{m-n} and v_m are calculated by (20) and (21) using the f-factors for S^{--} and Zn^{++} given by the table of James and Brindley[14] or its extrapolation.*

Substituting δ, calculated numerically as the function of ζ by (35), into (18a) and (18b), the reflexion powers P_{hhl} and $P_{hh\bar{l}}$ are given as the function of ζ or by (32) as the function of Γ_0. The result is shown in Fig. 5. The dotted curve outside the selective region is drawn by extrapolation because the above calculation covers only this region. In this figure it is noticed that the sum of the both reflexion powers are not constant and exceeds unity. This inadequacy is a result of simplification of boundary condition which will be discussed in Appendices.

§ 4. Comparison of the Experiment with the Theory

(i) *The (331) and (33$\bar{1}$) reflexions.*

In the experiment of Miyake and Uyeda, the asymmetry of the (hhl) and $(hh\bar{l})$ reflexions appeared not only in integrated intensity but also in profile of the intensity distributions (Photo 1 and refer to Fig. 4 of

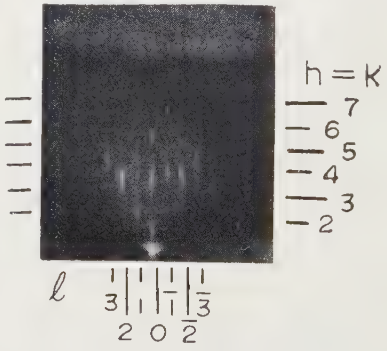

Photo. 1.** Reflexion spectra from (110) surface of a ZnS crystal. (Incident azimuth: [$\bar{1}$10])

---

* The present values are corrected by the Debye factor corresponding to the Debye temperature 250°K, although this is not based on any theoretical ground in the dynamical theory, and is not essential to the present problem.

** For Photo 1 we are indebted to Prof. R. Uyeda.

Miyake and Uyeda's paper). The difference was especially conspicuous for the intense reflexions such as (331) and ($33\bar{1}$). Namely, the integrated intensity of (331) is considerably larger than that of ($33\bar{1}$) and moreover, the intensity curve of the latter splits, showing a minimum at the angle for which the former shows a maximum. We see that these features of the observation are reproduced to some extent by the theoretical curve shown in Fig. 5 where the (331) reflexion has a single stronger peak while the ($33\bar{1}$) reflexion splits into two weaker peaks at the both ends of the selective region, although the observed intensity distribution is more complicated.

(ii) *The effects of weak reflexions and additional simultaneous reflexion.*

In spite of the agreement between the theory and observation in the case of the (331) and ($33\bar{1}$) reflexions, the general result (31) fails in explaining the following experimental observations: (i) the asymmetry is also observed for the reflexions of the even index such as (442) and ($44\bar{2}$) or (222) and ($22\bar{2}$), and (ii) the (hhl) reflexion is more intense than ($hh\bar{l}$) for lower order reflexions although this is not always the case with higher order reflexions, for instance, (553) is more intense than ($55\bar{3}$) in opposition to (31). Such discrepancies, however, are interpreted in the following way.

In the above calculation, the influence of all weak waves other than the assumed strong waves are neglected. In electron diffraction, this influence is usually not so small but is pretty large when the incident direction is nearly parallel to a simple zone axis, as in the condition of Miyake and Uyeda, where many reciprocal-lattiec points ($g_1\,g_2\,g_3$) with $g_1=g_2$ lie close to the Ewald sphere. The influence of weak waves can be taken into account following the method of Bethe. From (6) the amplitude of the weak wave is given in terms of ψ_0, ψ_m and ψ_n as follows:

$$\psi_g=-\frac{v_g\psi_0+v_{g-m}\psi_m+v_{g-n}\psi_n}{K_0^2+v_0-\boldsymbol{k}_g^2}\,. \tag{36}$$

Substituting (36) into (6), we have the following reduced fundamental equation in place of (7):

$$\begin{pmatrix} \boldsymbol{K}_0^2-\boldsymbol{k}_0^2+V_{00} & V_{0m} & V_0 \\ V_{m0} & \boldsymbol{K}_0^2-\boldsymbol{k}_m^2+V_{mm} & V_{mn} \\ V_{n0} & V_{nm} & \boldsymbol{K}_0^2-\boldsymbol{k}_n^2+V_{nn} \end{pmatrix}\begin{pmatrix}\psi_0\\ \psi_m\\ \psi_n\end{pmatrix}=0\,, \tag{37}$$

where

$$\left.\begin{aligned}
&V_{00}=v_0-\sum{}''' \frac{v_{-g}v_g}{\kappa^2-\boldsymbol{k}_g^2}\,, \quad V_{0m}=v_{-m}-\sum{}''' \frac{v_{-g}v_{g-m}}{\kappa^2-\boldsymbol{k}_g^2}\,, \quad V_{0n}=v_{-n}-\sum{}''' \frac{v_{-g}v_{g-n}}{\kappa^2-\boldsymbol{k}_g^2}\,,\\
&V_{m0}=v_m-\sum{}''' \frac{v_{m-g}v_g}{\kappa^2-\boldsymbol{k}_g^2}\,, \quad V_{mm}=v_0-\sum{}''' \frac{v_{m-g}v_{g-m}}{\kappa^2-\boldsymbol{k}_g^2}\,, \quad V_{mn}=v_{m-n}-\sum{}''' \frac{v_{m-g}v_{g-n}}{\kappa^2-\boldsymbol{k}_g^2}\,,\\
&V_{n0}=v_n-\sum{}''' \frac{v_{n-g}v_g}{\kappa^2-\boldsymbol{k}_g^2}\,, \quad V_{nm}=v_{n-m}-\sum{}''' \frac{v_{n-g}v_{g-m}}{\kappa^2-\boldsymbol{k}_g^2}\,, \quad V_{nn}=v_0-\sum{}''' \frac{v_{n-g}v_{g-n}}{\kappa^2-\boldsymbol{k}_g^2}\,,
\end{aligned}\right\} \tag{38}$$

where $\kappa^2=\boldsymbol{k}_0^2+v_0$ and $\sum{}'''$ means the summation over g excluding $g=0$, m and n.

Each denominator in the summation terms is written as $\kappa^2-\boldsymbol{k}_g^2=\Gamma_g^2+v_0-\gamma_g^2$ and finally in terms of ζ and δ. But these quantities are so small that we can neglect them so long as they are contained in the summation terms which are correction terms. Then V_{ij}'s become constant and relations corresponding to (9a), (9b), (11), (16a), (16b), (18a) and (18b) are obtained by replacing only v_{i-j} by V_{ij}. Corresponding to the expression (26) we obtain

$$\begin{aligned}\Delta P&=P_{hhl}-P_{hh\bar{l}}\\ &=\frac{4\Gamma_0|\Gamma_m+\gamma_m^{(1)}|^2}{\Gamma_m|\Gamma_0+\gamma_0^{(1)}|^2|Q_m^{(1)}Q_n^{(1)}-V_{mn}^2|}\\ &\quad\times I(Q_m^{(1)})I(V_{0m}^2V_{mn}^*).\end{aligned} \tag{39}$$

V_{0m} and V_{mn}^* are always complex not only for odd indices but also for even indices, because complex Fourier terms (with odd indices) are without fail contained in the summation. Accordingly for the selective region, that is, for $I(Q_m^{(1)})\neq0$, we have in general $\Delta P\neq0$ for even indices as well as odd indices. Thus the discrepancy (i) between the theory and observation might be explained. Another discrepancy (ii) must be reexamined by calculating practically values of V_{ij}'s. However, it seems to be not worthy to practised because of the circumstances mentioned below.

In the above treatment it is assumed that only the two reflexions (hhl) and $(hh\bar{l})$ are strong although the effect of other weak reflexions are taken into account. However, we must notice the situation that other strong simultaneous reflexions take place additionally under the experimental condition of Miyake and Uyeda. For instance, the Ewald sphere passing the reciprocal-lattice points (331) and $(33\bar{1})$ runs very closely to the points (222) and $(22\bar{2})$, and the value of Γ_0 satisfying the Laue condition for the simultaneous reflexion of (222) and $(22\bar{2})$ lies well inside the selective region for (331) and $(33\bar{1})$ as seen in Fig. 6. This means that the (222) and (222) reflexions practically occur simultaneously with (331) and $(33\bar{1})$ reflexions. Similar additional simultaneous reflexions seem to take place almost always in other cases, for instance, a pair of (442) and $(44\bar{2})$ is accompanied by another pair of (333) and $(33\bar{3})$. It is beyond doubt that such additional simultaneous reflexions, if exist, will have a greater influence upon the asymmetry between the two reflexions concerned than the weak ones above mentioned. Thus it is very likely that the discrepancies between the theory given in the preceding sections and the observation are caused by the effects of the additional simultaneous reflexions and weak other reflexions, although it is very difficult to carry out a calculation taking into account them.

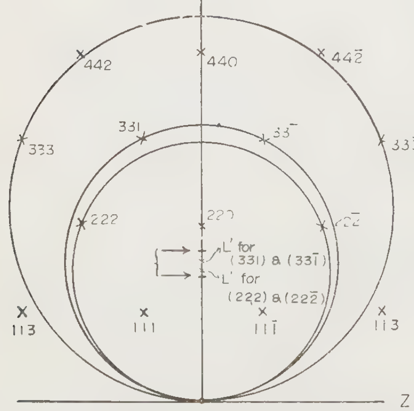

Fig. 6. Intersections of Ewald spheres and (110) plane in reciprocal sapce.
Horizontal arrows indicate the selective region for $(33\bar{1})$ and (331) reflexions.

§ 5. Discussions

In the previous sections the asymmetry observed by Miyake and Uyeda is explained theoretically. According to (26) or (39), the asymmetry occurs theoretically when the coeffecient v_{m-n} or V_{m-n} which correlates the (hhl) and $(hh\bar{l})$ reflexions does not vanish and, at the same time, Q_m or the wave vector in the crystal is complex. In other words, as seen from (26), the asymmetry is caused by the fact that effect of the (hhl) reflexion upon the $(hh\bar{l})$ reflexion is different from the effect of the latter upon the former when the selective reflexion takes place in the Bragg case. In short, we can say that the dynamical inter-correlation between the symultaneous reflexions is the cause of the asymmetry. All the other possible causes of the asymmetry as mentioned in § 1 could not explain the experiment so succesfully as the present theory.

Recently Schoemaker and Glauber[15] suggested that the difference in the phase shifts of the scattered wave for Zn and S ions is a possible cause of the asymmetry. Since the phase shift discussed by them is expected only for the scattered wave by each individual atom, it has some effect upon the diffraction in the kinematical theory, but it is meaningless to consider the effect in the dynamical theory: in the latter case, the resultant scattered waves by all the atoms in the crystal is considered. So far as the kinematical theory is adopted, the phase shift, as considered previously by Miyake and Uyeda, whould not cause any asymmetry more remarkable than the one caused by the effect of absorption. At least it is not a principal cause for the asymmetry observed.

According to the present theory, the asymmetry occurs only in the Bragg case and does not in the Laue case. This result is in agreement with the experimental result by Uyeda, Takagi and Hagihara[16]. They observed the diffraction pattern from the etched surface (110) of zincblende crystal under the same geometrical condition as in the experiment of

Miyake and Uyeda, and they observed no asymmetry as far as the integrated intensities are concerned. Since the etched surface gives the transmission pattern, the Laue case occurs and the asymmetry should not appear according to the present theory. If some of other causes mentioned in § 1 has a predominant effect on the occurrence of asymmetry, the asymmetry would be expected in the Laue case as well as in the Bragg case. Therefore the disappearance of the asymmetry in transmission pattern gives a strong support to the present theory.

The present theory shows that Friedel's law fails in the dynamical theory of electron diffraction even when the anomalous dispersion or absorption does not exist. Since the formalism of the dynamical theory is the same for X-ray, electron and neutron diffractions the failure of Friedel's law should occur in general in the dynamical theory. This result contradicts to the generally accepted views[17] that the law holds in the dynamical theory as well as in the kinematical theory. This contradiction is discussed in detail by Miyake and Uyeda[18].

The asymmetry similar as the observed by Miyake and Uyeda should also be observed in X-ray diffraction by zincblende under suitable conditions, even if the dispersion is not utilized. The actual observation of the asymmetry, however, may be most difficult, because the dynamical effect is far smaller in X-ray diffraction than in electron diffraction.

In conclusion the author wishes to express his hearty thanks to Professors R. Uyeda and S. Miyake who suggested this problem and gave valuable discussions. He is also indebted to the Ministry of Education for its research grant.

Appendices

(1) The Effect of Absorption in the Case of Single Reflexion

In oder to take into account the effect of absorption, we add the imaginary potential to the usual one in the Schrödinger equation as done by previous authors:[19]

$$\Delta\psi+(8\pi^2 me/h^2)(E+V+iV')\psi=0\,, \qquad \text{(a.1)}$$

where V' is supposed to be a periodic function like the real potential, the Fourier expansion of which is given by

$$(2me/h^2)V'=\sum_g v_g'\exp(2\pi i\boldsymbol{gr}).^* \qquad \text{(a.2)}$$

Basing on the Eq. (a.1), the amplitude and reflexion power of the diffracted wave for a single reflexion with the index h are expressed by

$$\Psi_h=-\frac{\Gamma_0(\Gamma_h+\gamma_h^{(1)})}{\Gamma_h(\Gamma_0+\gamma_0^{(1)})}\frac{(v_h+iv_h')}{(\Gamma_h^2+v_0+iv_0'-\gamma_h^2)}\,, \qquad \text{(a.3)}$$

and

$$P_h=(\Gamma_h/\Gamma_0)|\Psi_h|^2. \qquad \text{(a.4)}$$

Let us consider the reflexions of (hhl) and $(hh\bar{l})$ separately. Suppose that, in each case, the direction of incidence deviates a little from $[\bar{1}10]$ azimuth so as to excite only one reflexion but not the other simultaneously, and that the incident directions in both cases are symmetrical to each other with respect to (100) so that the normal components of the corresponding wave vectors are equal. We carry out numerical calculations on the reflexion powers for the (331) and $(33\bar{1})$ reflexions where, for the sake of simplicity in calculation, we suppose that the incident direction in each case changes in such a way that Γ_0 is equal to Γ_h. This condition is satisfied only approximately in the usual rotation photograph and exactly realized by varying the incident azimuth and angle at the same time in a suitable way. The procedure of calculation is similar to that in § **3**. As the values of the Fourier terms of potential, the following values are used: $v_0=3.28$, $v_{331}=0.67+0.38i$, $v_{33\bar{1}}=0.67-0.38i$, $v_0'=0.4$ and $v_{331}'=v_{33\bar{1}}'=0.33$. The values of v_0 is the same with that in § 3, and the values of v_{331} and $v_{33\bar{1}}$ are a little different from those in § 3, only because the structure factors used this time is not corrected by the Debye factor. $v_0=0.4$ corresponds to the path-length $l=250$A in which a wave travelling in a medium with an uniform potential v_0+iv_0' decreases in intensity $1/e$ times of the initial value.** The values of v_{331}' and $v_{33\bar{1}}'$ are assumed in such that $v_g'=v_0'(|v_g|/|v_0|)$ following Molière.

---

* According to the theory of Yoshioka[20], the effect of absorption cannot be introduced in such a simple way. However, in order to see the general tendency of the effect of absorption, we follow the conventional way.

The intensity curves of the (331) and $(33\bar{1})$ reflexions for various cases are shown in Fig. 7. The curve ***a*** shows the one for no absorption, the curve ***b*** the one for uniform absorption (iv_0'), and the curves ***c*** and ***c***$'$ the ones for periodic absorption $(iv_0'+iv_h')$. As seen in Fig. 7, there is no difference between both reflexions for the case of uniform absorption as well as for the case of no absorption. For the case of periodic absorption, the positions of the maxima remain almost constant, although a slight difference can be observed. From these results we see that the absorption cannot be the principal cause for the asymmetry observed in the experiment by Miyake and Uyeda.

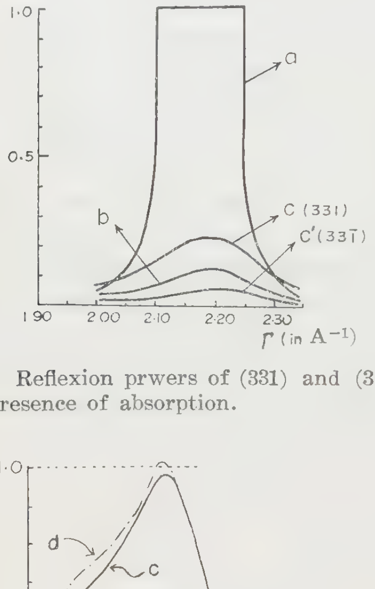

Fig. 7. Reflexion prwers of (331) and $(33\bar{1})$ in the presence of absorption.

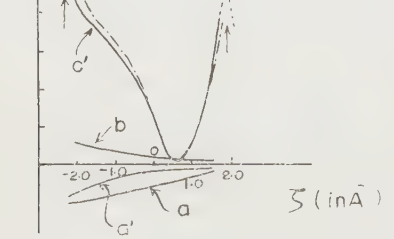

Fig. 8. Intensiry fluxes of various curves.

a: $\frac{\Gamma_m}{\Gamma_0}|\Psi_m{}^{(d)}|^2$, ***a***$'$: $\frac{\Gamma_n}{\Gamma_0}|\Psi_n{}^{(d)}|^2$, ***b***: $|\Psi_0{}^{(u)}|^2$,

c: $\frac{|\gamma_m{}^{(1)}|}{\Gamma^0}|\psi_m{}^{(1)}|^2$, ***c***$'$: $\frac{|\gamma_m{}^{(1)}|}{\Gamma_0}|\psi_m{}^{(1)}|^2$,

d, ***d***$'$: the same curves as in Fig. 5. ***c*** and ***c***$'$ are the intensity fluxes of the diffracted waves in the crystal.

(2) On the Apparent Excess of the Intensity Fluxes of the Diffracted Waves over that of the Incident Wave.

As pointed out in § **3**, the sum of the intensity fluxes of the (331) and $(33\bar{1})$ reflexions exceeds the value of the flux of the incident wave (Fig. 5). This difficulty is met by a following consideration. In the treatment of the boundary condition (§ **2** (iii)), the amplitudes of the specular reflexion and two suprious entering waves, $\Psi_0{}^{(u)}$, $\Psi_m{}^{(d)}$ and $\Psi_n{}^{(d)}$ are supposed to be finite in the upper free space besides those of the incident and two diffracted waves. In order to insure formally the equalness of the intensity fluxes of the entering and emerging waves, the above mentioned three waves must be taken into account. The intensity fluxes $|\Psi_0{}^{(u)}|^2$, $(\Gamma_m/\Gamma_0)\times|\Psi_m{}^{(d)}|^2$ and $(\Gamma_n/\Gamma_0)|\Psi_n{}^{(d)}|^2$ are evaluated and shown in Fig. 8. When we take into account these fluxes it is seen that the sum of the intensity fluxes of entering waves is equal to that of emerging waves within the error of calculation.

If six roots are taken on solving the secular equation in § **2** (ii), the boundary conditions are rigrously solved without assuming the existence of the above mentioned suprious waves, and the entering intensity flux would be equal to the emerging one. The calculation would be pretty complicated, but the essential feature of the intensity curves of the (331) and $(33\bar{1})$ reflexions would not be changed.

** When a wave, which has a wave vector K_0 in vacuum, travels in a medium with an unform potential of v_0+iv_0', the wave vector within the crystal is given by $\boldsymbol{k}_0=\sqrt{K_0{}^2+v_0+iv_0'}\,\boldsymbol{s}_0$ and the damping coefficient of the intensity by

$$\exp\left(-\frac{v_0'}{\sqrt{K_0{}^2+v_0}}s_0\boldsymbol{r}\right), \qquad (a.5)$$

where $\boldsymbol{s}_0$ means the unit vector in the direction of travelling of the wave. From (a.5), l is given by $l=\frac{\sqrt{K_0{}^2+v_0}}{v_0'}$ and for the accerelating voltage of 40 kv, we have approximately

$$v_0'=\frac{400}{l}, \quad (l \text{ in } A). \qquad (a.6)$$

References

1) K. Kohra, R. Uyeda and S. Miyake: Acta Cryst. **3** (1950) 479.

2) G. Friedel: Compt. rend. **157** (1913) 1533.

3) S. Nishikawa and K. Matsukawa: Proc. Imp. Acad. **4** (1928) 96.

4) C. Coster, K. Knol and J. A. Prins: Zeits. f. Phys. **63** (1930) 45.

I. G. Geib and K. Lark-Horovitz: Phys. Rev. **42** (1932) 908.

5) P. A. Thiessen and K. Molière: Ann. Physik **34** (1939) 449.

6) K. Molière: Ann. Physik **34** (1939) 461.

7) S. Miyake and R. Uyeda: Acta Cryst. **3** (1950) 461.

8) J. E. Lennard-Jones: Zeits. f. Krist. **75** (1930) 215.

9) H. Bethe: Ann. Phys. **87** (1928) 55.

10) K. Shinohara: Sci. Pap. Inst. P. C. Res. **20** (1932) 39.

11) R. D. Heidenreich: Phys. Rev. **77** (1950) 271.

12) E. Lamla: Ann. Physik **32** (1938) 178 and 225; Jour. f. reine u. angew. Math. **179** (1938) 134. Also,

M. v. Laue: "Materiewellen u. ihre Interferenzen" (Leipzig, Akademische Verlag, 1944) § 19, § 21.

13) S. Miyake: Proc. Phys. Math. Soc. Japan **22** (1940) 666.

14) W. James and W. Brindley: Zeits. f. Krist. **78** (1931) 740.

15) V. Shoemaker and R. Glauber: Nature **170** (1952) 290, Phys. Rev. **89** (1953) 667-671.

16) R. Uyeda, S. Takagi and H. Hagihara: Proc. Phys. Math. Soc. Japan **23** (1941) 1049.

17) For example, P. P. Ewald: Physica **5** (1925) 368.

M. v. Laue: refer to (12) (§ 19.).

M. v. Laue: "Röntgeninterfenzen" (Leipzig, Akademishce Verlag, 1948) § 17.

18) S. Miyake and R. Uyeda: to be published.

19) J. C. Slater: Phys. Rev. **51** (1937) 840.

K. Molière: refer to (6).

K. Kohara: J. Phys. Soc. Japan **5** (1950) 272.

20) H. Yoshioka: Busseiron Kenkyu **69** (1953) 118. (in Japanese).

Journal of the Physical Society of Japan Vol. 9, No. 5, Sep.—Oct., 1954

X-ray Studies on the Structures of Solid Solutions NaCl-CaCl2

I. Main Results and General Considerations

By Shizuo Miyake and Kazuo Suzuki

Tokyo Institute of Technology, Oh-Okayama, Meguro, Tokyo

(Received June 26, 1954)

Stationary X-ray diffraction patterns from transparent single crystals of solid solutions of NaCl dissolved with a few per cent of $CaCl_2$ show a number of diffuse spots. Their displacements with the change of the direction of incident X-rays reveal the existence of several kinds of rods in reciprocal space. Among them, the rods running along ⟨111⟩ and ⟨310⟩ rows are most remarkable. The appearance of these rods are considered as the result of the formation of thin plate-like precipitates in the matrix because of the homogeneous solid solutions being unstable at room temperatures. The precipitates may be the places where Ca^{++} ions replacing Na^{+} ions, and vacancies of Na^{+} sites, are locally concentrated. It was shown, by a general consideration, that the plate-like precipitate responsible for ⟨111⟩ or ⟨310⟩ rods is likely composed of an assembly of anti-phase domains of super structures.

§ 1. Introduction

Although X-ray studies on structures of metallic solid solutions are numerous, similar studies on ionic salts have hitherto been reported only very rarely. Wasastjerna1)2) studied the solid solutions of the system KCl-KBr and KCl-RbCl mainly by the powder method, and concluded irregular displacements of ions from the normal lattice sites due to different sizes of corresponding ions in the component salts.

The present authors have intended a systematic X-ray investigation of solid solutions of metallic halides by using single crystals. Such a study seems to be worthy to be performed not only because it deals with the formerly neglected field, but because it appears to be interesting from the following points of view. Firstly, we can expect that it might bring informations on behaviours of imperfections in ionic crystals, since the solid solutions of ionic salts are regarded as crystals containing many artificially made imperfections. Secondly, some valuable suggestions on the mechanism of the precipitation of new phases in alloys by aging or other heat treatments might be obtained from the observation of the similar phenomenon in ionic salts.

As was reported first by Preston3) and Guinier4) and afterwards by Barrett & Geisler5) and Geisler & Hill6), some alloys such as Cu-Be, Al-Cu, Al-Ag and Al-Mg-Si etc. give characteristic diffuse diffraction patterns in certain stages of the precipitation hardening. Some of these patterns, which are explained in terms of a rod-like distribution of the intensity weight in reciprocal space, has been ascribed to the precipitation of small plate-like structures in the homogeneous matrices. There are, however, some controversies concerning the detailed structure of the precipitates.

In the course of our studies, in which single crystals of the solid solutions such as NaCl-KCl, NaCl-AgCl, NaCl-$BaCl_2$, NaCl-$CaCl_2$ KCl-KBr, and KCl-$SrCl_2$ were dealt with, it was found that the system NaCl-$CaCl_2$ containing a few moles per cent of $CaCl_2$ gives diffuse diffraction patterns resembling those observed in the above mentioned alloys. This result suggested an intimate analogy to exist between the phenomena in the solid solutions of metals and of ionic salts. Though it is anticipated that the phenomenon in ionic salts would be more complicated than in alloys, we can expect that the comparative study of the both kinds of solid solutions would be fruitful.

The details of the study of solid solutions NaCl-$CaCl_2$ will be published in a few separate papers. In the present paper, Part I, the main experimental results and the general considerations on the observed diffuse pattern are reported.

§ 2. Experimental Method

a) *Preparation of samples*

Single crystals of solid solutions NaCl-CaCl$_2$ were prepared from the melt. The mixture of NaCl and $CaCl_2 \cdot 2H_2O$ which were finely ground and mixed uniformly in a desired ratio was put in a ceramic crucible suspended in an electric furnace, and heated to temperatures above the melting point. The crucible was then downed gradually to cooler portions in the furnace so as to solidify the melt from its bottom. After the solidifications was finished, the crucible was cooled slowly to room temperature with the cooling rate of about 1-2°/min. Single crystals of the size of about 1 cm^3 were obtained by the above procedure when the content of CaCl$_2$ did not much exceed 10 moles per cent. When this content was less than 4 moles per cent, almost all parts of the crystals were transparent. For higher contents, the part corresponding to the later stage of the solidification became perfectly opaque.

The phase diagram of the system NaCl-CaCl$_2$ was reported by Menge[7)] and also by Sato & Amano[8)]. Fig. 1 is a reproduction of the result of Sato & Amano. Though Menge suggested the existence of an inter-salt compound in the range near 20 moles per cent of CaCl$_2$, Sato & Amano could detect no such evidence. Unfortunately Sato & Amano failed in determining the exact phase boundaries for the range of low CaCl$_2$. The boundaries shown by the broken curves in Fig. 1 which were presumed by Sato & Amano seems, however, to be reasonable in main, because they were found to be in general accordance with the results of the present study (see § 3 and § 4). These boundaries can be refined a little further by assuming the maximum solubility of CaCl$_2$ in NaCl, which occurs at the eutectic temperature, is about 4–5 moles per cent of CaCl$_2$, the fact which is suggested from the limit of CaCl$_2$ proportion (about 4 moles per cent) to prepare wholly transparent crystals. We can believe, then, that the phase diagram in the range in question is approximately given by that shown in Fig. 2.

As is clear from Fig. 2, the concentration of CaCl$_2$ in a single crystal prepared can not be uniform, varying over a wide range with different stages of the progress of crystallization. Consequently, it is difficult to mention exactly the concentration of CaCl$_2$ in each specimen subjected to the X-ray examination. Different specimens, which correspond to tiny portions of the single crystals, are hereafter discriminated by the composition of CaCl$_2$ by the preparation of the mother crystal, but this value indicates only the possible upper limit of the CaC$_2$l concentration in the specimen concerned. (The fact that the CaCl$_2$ concentration for transparent crystals is in any case less than 4-5 per cent (the solubility limit) should also be remembered.)

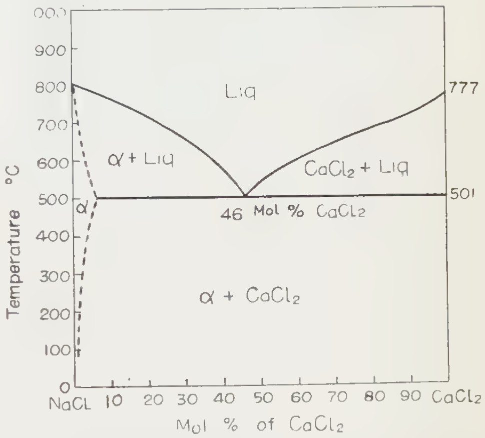

Fig. 1. Phase diagram for NaCl-CaCl$_2$ system. (Sato and Amano)

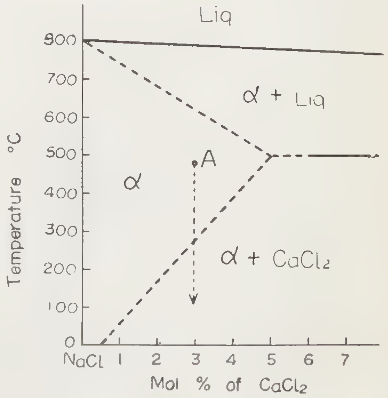

Fig. 2. Phase diagram for NaCl-CaCl$_2$ system at lower CaCl$_2$ compositions.

b) *Heat treatment*

There is nothing to be especially mentioned with respect to annealing, slow cooling or heating. The quenching was made by placing suddenly the heated specimen on a copper plate kept at room temperature. By this method we could avoid cracks resulting from thermal stresses.

c) *X-ray examination*

The specimens used in the X-ray study were thin plates parallel to a cube face, say (010), about 0.1 mm in thickness and about 3×4 mm^2 in area. We took series of stationary-crystal X-ray photographs by keeping either [001] or [101] direction of the specimen vertical and varying successively the azimuthal angle around the vertical axis. Cylindrical or flat films were used: the specimen-to-film distance was 4 cm in either cases. The X-ray scattering by air is minimized by putting a small stop just behind the specimen.

In most cases nickel-filtered Cu radiation or Mo radiation were used. In some cases a pure monochromatic Cu $K\alpha$ radiation, generated in a rotating X-ray tube and crystal-reflected, was applied. In all cases the focal area of electrons on the anode surface was about 6×0.3–0.5 mm^2, which was adjusted by bias voltage applied to a Wehnelt cylinder of the electron gun. Examples of the exposure time are: with filtered Cu radiation (not crystal-monochromated), 10 mA, 40 kV, 5–10 hours; with crystal-monochromated Cu $K\alpha$ radiation (using a pentaerythritol crystal), 80 mA, 40 kV, 2 hours.

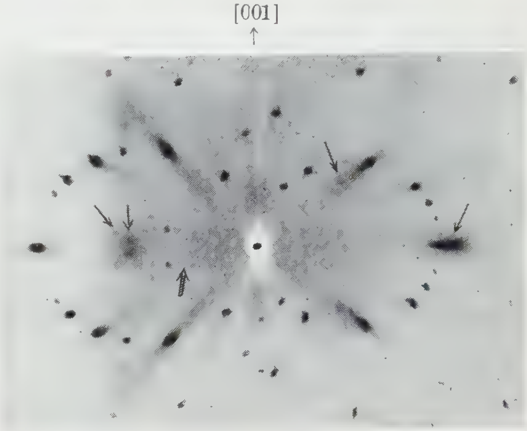

Fig. 3. Stationary-crystal X-ray photograph for NaCl-CaCl$_2$ solid solution containing 2% CaCl$_2$. $\varphi=24°$. Filtered Cu radiation, 40 kV, 10 mA, 10 h. Flat film. Diffuse spots and streaks are indicated by $\longrightarrow$ and $\Longrightarrow$ respectively.

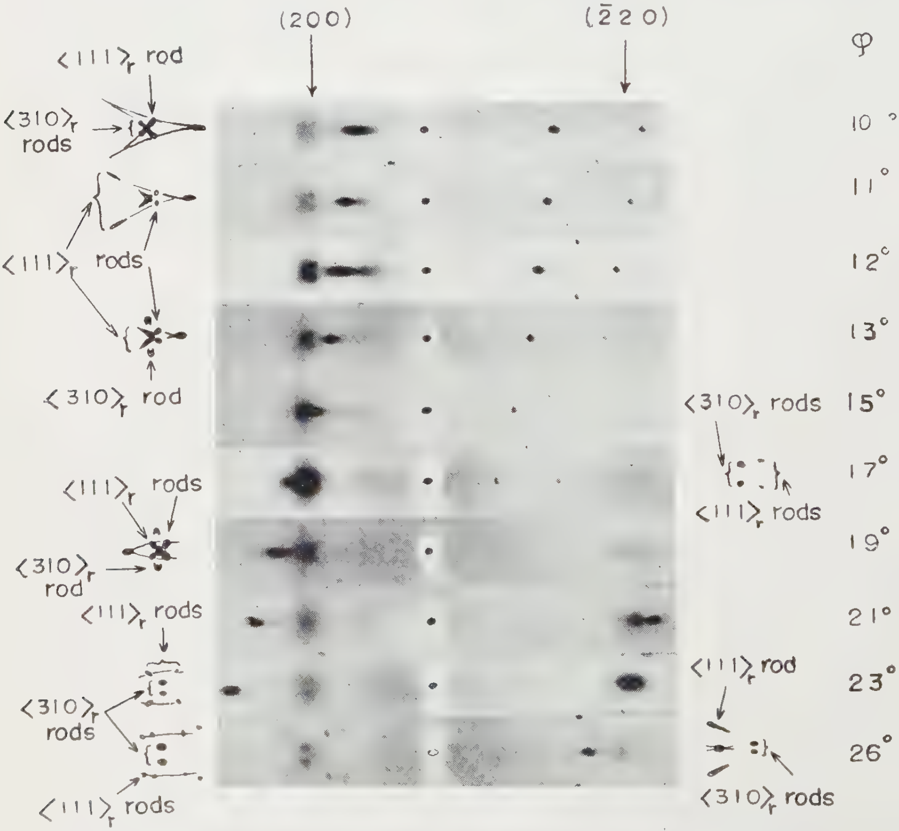

Fig. 4. Series of stationary-crystal X-ray photographs for NaCl-CaCl$_2$ solid solution containing 2% CaCl$_2$. Crystal was rotated around [001]. Flat film.

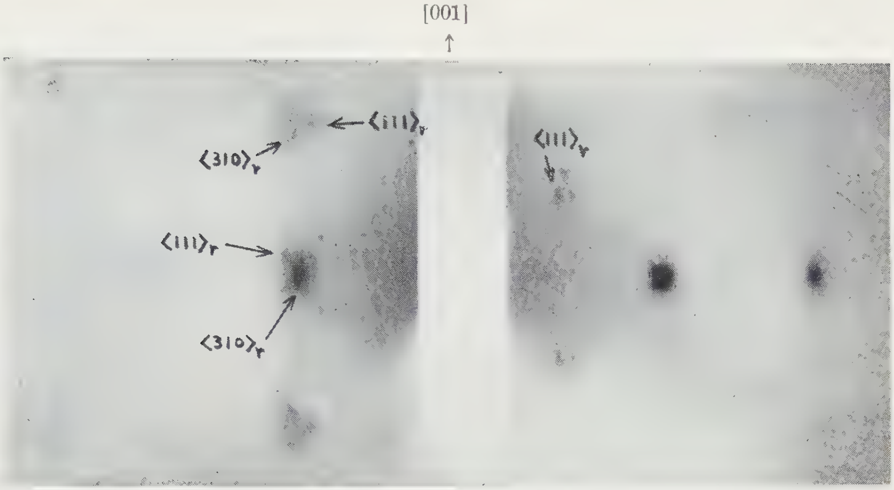

Fig. 5. Stationary-crystal X-ray photograph for NaCl-CaCl$_2$ solid solution containing 2% CaCl$_2$, taken with monochromatic Cu Kα radiation reflected by pentaerythritol crystal. $\varphi=24°$, 40 kV, 80 mA, 2 h. Cylindrical film.

§ 3. Experimental Result

a) *General features of diffraction patterns*

Fig. 3 shows an example of the stationary-crystal photograph for a transparent crystal of CaCl$_2$ content 2 moles per cent, with the [001] axis vertical. Fig. 4 is a series of stationary-crystal photographs for the same sample rotated successively around the same axis. φ is the angle between the incident X-rays and the horizontal $[0\bar{1}0]$ axis. In these photographs one may see many Laue spots and, in addition, the extra diffuse reflexions composed of streaks and spots. Similar diffuse patterns were observed on specimens which were cut from transparent parts of the mother single crystals of various CaCl$_2$ contents (from 0.5 to 10 moles per cent), not being subjected to any heat treatment. The larger was the CaCl$_2$ content by the preparation of the crystals, the stronger the intensity of diffuse patterns. For CaCl$_2$ content less than 0.5 moles per cent, the patterns became indiscernible.

The positions of diffuse spots moved with changing φ, from which we could deduce the corresponding distribution of intensity weight in reciprocal space. It was found that there are a number of rod-like distributions of intensity weight in reciprocal space. Among them, the two kinds of rods parallel respectively to the reciprocal rows $\langle 111\rangle_r$ and $\langle 310\rangle_r$[*] are most remarkable; they pass through reciprocal lattice points and are most intense about these points. Diffuse spots due to other kinds of rods were also observed (e.g., see the photographs for $\varphi=23°\sim24°$ in Fig. 3, or Fig. 4). These rods, however, are in general short, and located at positions independent of the reciprocal lattice points due to the matrix. We found, besides, weak rods about $\{\frac{1}{2}\frac{1}{2}\frac{1}{2}\}$ reciprocal lattice points. The directions of these rods, however, correspond to neither $\langle 111\rangle_r$ nor $\langle 310\rangle_r$.

On the other hand, the streaks in the diffraction patterns seemed to suggest the presence of planar distribution of the intensity weight in reciprocal space. However, in photographs taken with the crystal-monochromated radiation, almost all streaks disappeared, leaving only faint short arcs passing through certain diffuse spots (Fig. 5), hence it is clear that most of the streaks in the photographs taken with the filtered radiation are due to the continuous X-rays. As was discussed by Geisler & Hill[6)], a rod in reciprocal space produces an apparent planar distribution of intensity weight by the presence of continuous

---

[*] In the present paper, the lattice planes in real lattice and the corresponding reciprocal-lattice points are denoted by (hkl) or {hkl}. On the other hand, the lattice planes in reciprocal space are denoted by $(hkl)_r$, or $\{hkl\}_r$ and the lattice rows by $[hkl]_r$ or $\langle hkl\rangle_r$. In previous works (e.g. by Guinier[9)] and Geisler and Hill[6)]) the lattice planes and rows in reciprocal space are denoted by the same symbols as those for real lattice, which, however, would result in confusion if the lattice were of lower symmetry.

X-rays.

b) *Influence of heat treatment*

The diffraction patterns changed when the specimens were subjected to heat treatments. The results obtained are a little complicated, so, only typical examples are reported here.

The diffuse spots (or rods in reciprocal space) given by a transparent specimen (10 moles per cent $CaCl_2$) disappeared after heating up to 400°C and subsequent quenching to a room temperature. The rods, especially the $\langle 111\rangle_r$ and $\langle 310\rangle_r$ rods, reappeared gradually within a month when the specimen was kept at the room temperature. Recovery of the $\langle 111\rangle_r$ and $\langle 310\rangle_r$ rods to similar extent occured when the quenched specimen was kept at 100°C for 1 hour, though there were some differences between this case and that at room temperature. For instance, intensities of $\langle 111\rangle_r$ rods were generally stronger than those of $\langle 310\rangle_r$ rods for the specimens kept at 100°C, while it was opposite for the specimens kept at room temperature.

When the specimen annealed at 100°C was kept at 250°C for 1 hour, the diffuse spots changed to a more spotty pattern. This pattern disappeared at 400°C by reheating.

§4. Assumption of Plate-Zones. Distribution of the $\langle 111\rangle_r$ and $\langle 310\rangle_r$ Rods in Reciprocal Space

As mentioned in introduction, there is a close analogy between the diffuse patterns from the NaCl-$CaCl_2$ solid solutions and those from certain alloys in early stages of the precipitation. Also, the phase diagrams for these cases bear a common characteristic in concentration ranges concerned. On the ground of these similarities the origin of the rods in the case of the NaCl-$CaCl_2$ solid solutions may be presumed as follows: At higher temperatures where the solubility of $CaCl_2$ in NaCl is large, the specimen containing a few moles per cent of $CaCl_2$ may assume a homogeneous structure (the α-phase in Fig. 2). When such a specimen (in a state, say, A in Fig. 2) is brought to lower temperatures, the homogeneous structure becomes unstable and the precipitation of new phase (the β-phase) may begin to be motivated. In its initial stage, a number of small thin plate-like zones (or simply *plate-zones*) with certain structures may be transiently formed in the interior of the matrix, which give rise to the rods in reciprocal space along the directions perpendicular to the plates.

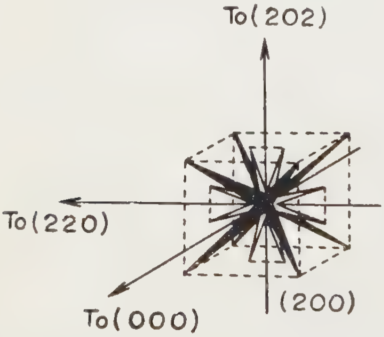

Fig. 6. Distribution of rods about (200) reciprocal-lattice point.

The phase diagram Fig. 2 seems to be in general accordance with the above presumed process. For instance, the disappearance of the rods by heating to 400°C for the specimen of $CaCl_2$ content about 10 moles per cent ((b) in § 3) is explained reasonably by the solubility curve in the diagram. (On the other hand, the solubility limit of about 0.5 per cent at room temperature shown in the same diagram has been determined by taking account of the minimum $CaCl_2$ content to give rise to rods ((a) in § 3)).

Let us concern ourselves, from now on, only with the diffuse spots due to the $\langle 111\rangle_r$ and $\langle 310\rangle_r$ rods, because they are most noticeable and their origin is conceived to be independent of other kinds of spots. Then, according to the presumption of plate-zones these rods are interpreted as indicating the presence of the two kinds of plate-zones respectively parallel to $\{111\}$ and $\{310\}$ planes of the matrix lattice. There exist a number of rods around each reciprocal-lattice point: for instance the rods along $[111]_r$, $[\bar{1}11]_r$, $[1\bar{1}1]_r$ and $[11\bar{1}]_r$ and $[031]_r$ $[013]_r$. $[0\bar{3}1]_r$ and $[0\bar{1}3]_r$ were found around the (200) reciprocal-lattice point (Fig. 6). Analysing sets of such rods, resulting from a superposition of contributions from the zones of different orientations, we can obtain the rod distribution due to the zones corresponding to a single orientation. Fig. 7a & b, show the rod distributions near the reciprocal-space origin due to the $(11\bar{1})$ and (031) plate-zones respectively: the change of intensity along rods is indicated qualitatively by the thickness of stripes, which run perpendicular to

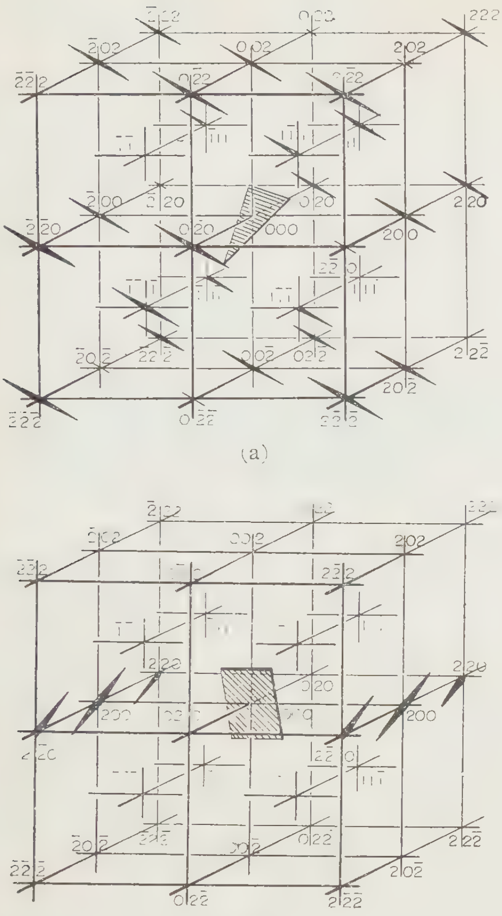

(a)

(b)

Fig. 7. Distribution of rods for a single plate orientation. (a) for the $(11\bar{1})$ plate; (b) for (031) plate. The hatched planes at (000) indicate orientations of the plates concerned.

the corresponding plate. The rod distributions for other orientations of plate zones are obtained by symmetrical relation. From Fig. 7 we know the following facts:

(a) For both $[11\bar{1}]_r$ and $[031]_r$ rods:

(i) The rods appear only about normal reciprocal-lattice points.

(ii) There is no rod accompanying the reciprocal origin.

(b) For $[11\bar{1}]_r$ rods:

(i) There is no rod accompanying the reciprocal-lattice points $(11\bar{1})$, $(\bar{1}\bar{1}1)$, $(22\bar{2})$ and $(\bar{2}\bar{2}2)$.

(ii) The rods accompanying some of the {220} points, e.g. (202) and (022), are less noticeable than (220).

(iii) The intensity distribution of most of rods is symmetrical with respect to the reciprocal-lattice point concerned, but asymmetry is noted for the rods accompanying the point $(\bar{1}11)$, (111), $(1\bar{1}\bar{1})$ and $(\bar{1}1\bar{1})$.

(c) For $[031]_r$ rods:

(i) The rods are present only about the points (200), $(\bar{2}00)$, (220), $(2\bar{2}0)$, $(\bar{2}20)$ and $(\bar{2}\bar{2}0)$. Other reciprocal-lattice points, so far as observed, seems to be wanting rods.

(ii) Asymmetry of the intensity distribution of rod is noted at the {220} points.

The length and thickness of rods may supposedly be related to the dimention of external shape of the plate-zones. The thickness and lateral length of the presumed zones estimated from the usual theory of the size-effect of small crystals are respectively about 10–20Å and about 100–200Å.

§ 5. General Consideration on the Nature of {111} and {310} Plate-Zones

Let us now proceed on general considerations on the structure of the presumed {111} and {310} plate-zones. The atomic process of the formation of plate-zones in the NaCl-CaCl$_2$ solutions may be conceived as follows. When calcium chloride is dissolved in a sodium chloride crystal, a Na$^+$ ion at a lattice site may be replaced by a Ca^{++} ion and, at the same time, another Na$^+$ ion may be removed from the crystal to satisfy the requirement of the neutrality of electric charge, leaving a positive ion vacancy. When the CaCl$_2$ composition increases, Ca^{++} ions and positive ion vacancies will begin to concentrate locally to certain regions in the matrix lattice, whereat plate-zones may be formed. The zone, being supposedly the earliest product of the process of the precipitation, may be made of Ca^{++}, vacancies and other ions (Na$^+$ and Cl$^-$) in a certain way.

A theory of X-ray scattering from a crystal including internally a small foreign structure of arbitrary kind was given by Guinier⁹⁾ (1952). The scattering amplitude F due to a crystal including a plate-zone is expressed by

$$F=\Sigma_0+\Sigma_r'-\Sigma_r\,, \tag{1}$$

$$\left.\begin{aligned}\Sigma_0&=\sum_{\substack{n\text{ in}\\ \text{whole volume}}} f_n\exp(2\pi i\boldsymbol{hr}_n)\,,\\ \Sigma_r&=\sum_{\substack{n\text{ in}\\ \text{plate-zone}}} f_n\exp(2\pi i\boldsymbol{hr}_n)\,,\\ \Sigma_r'&=\sum_{\substack{N\text{ in}\\ \text{plate-zone}}} f_N\exp(2\pi i\boldsymbol{hr}_N)\,,\end{aligned}\right\} \tag{2}$$

where $\boldsymbol{h}=(\boldsymbol{s}-\boldsymbol{s}_0)/\lambda$ ($\boldsymbol{s}_0$ and $\boldsymbol{s}$ being the unit vector of the directions of incident and scattered X-rays, and λ the wave length of X-rays), and f_n and $\boldsymbol{r}_n$ are respectively the scattering factor and position vector of the n-th atom in the original matrix crystal, and f_N' and $\boldsymbol{r}_N$ those of the N-th atom in the structure of the plate-zone. When the crystal is sufficiently large, $\sum_0$ is a diffraction function for ordinary crystals which shows sharp maxima only at reciprocal-lattice points, so that the contribution to the diffuse scattering comes solely from

$$F'=\sum_r'-\sum_r\,. \qquad (3)$$

On the other hand, the scattered waves from different plate-zones are assumed to be incoherent with each other.

By applying the above considerations to the results of the present experiments, we reach the following conclusions concerning the structure of the plate-zones:

(a) The absence of any rod about the origin of reciprocal space (Fig. 7a & b) is in accordance with the presumption that a positive ion vacancy is produced for every Ca^{++} ion introduced into the matrix. For, the scattered waves from atoms in the crystal superpose in phase, or nearly in phase, towards the directions ahead of the incident beam, for which (3) assumes the form

$$F'=n_{Ca^{++}}(Z_{Ca^{++}}-2Z_{Na^{+}})=-n_{Ca^{++}}\cdot 2\,, \qquad (4)$$

where $Z_{Ca^{++}}$ and $Z_{Na^{+}}$ are the number of electrons in Ca^{++} and Na^{+} ions respectively, and $n_{Ca^{++}}$ the total number of Ca^{++} ions included in the plate-zone. Since the factor 2 in the right-hand side of (4) is very small, corresponding only to the scattering power of a helium atom, rods with appreciable intensity are not expected to appear about the reciprocal origin, as is actually the case.

(b) Let us assume, for a moment, that all the atoms in the plate-zone succeed the atomic sites of the original matrix, which are given by

$$\boldsymbol{r}_n=n_1(\boldsymbol{a}_1/2)+n_2(\boldsymbol{a}_2/2)+n_3(\boldsymbol{a}_3/2)\,, \qquad (5)$$

where $\boldsymbol{a}_1$, $\boldsymbol{a}_2$ and $\boldsymbol{a}_3$ are the axes of the cubic cell of NaCl lattice, and n_1, n_1 and n_3 integers. Then (3) is written

$$F'=\sum_{n\text{ in plate-zone}}(f_n'-f_n)\exp(2\pi i\boldsymbol{h}\boldsymbol{r}_n), \qquad (6)$$

where f_n' is the scattering factor corresponding to the atom assuming the n-th site in the plate-zone. This atom may be Ca^{++}, Na^{+}, Cl^{-} or vacancy (for which $f_n'=0$). $(f_n'-f_n)$ corresponds to the *effective* scattering factor for the diffuse scattering due to the n-th lattice site in the plate-zone. Since F' in (6) is a periodic function in the reciprocal space with periods of the reciprocal lattice corresponding to the space lattice given by (5) when the monotonous change of f_n and f_n' is disregarded, the actually observed strong intensities of the rods accompanying the reciprocal lattice points of even indices, e.g. (200), (220), (222) etc., can not be compatible with the absence of the both kinds of rods about the reciprocal origin. (Fig. 7a & b) This contradiction can never be removed unless displacements of atoms in the plate-zones from the lattice sites of the matrix are taken into account.

(c) The fact that the rods are present only around the normal reciprocal-lattice points (Fig. 7a & b) seems to indicate that the structure of the plate-zone (responsible for the first term in (3)) would be a periodic pattern with the lattice period equal to that of the matrix lattice. However, such is not possible so far as the plate zone is presumed to be the place whereto the Ca^{++} ions concentrate. For, what kind of periodic structure it may be, its primitive cell should contain at least three particles, one Ca^{++} ion associated with two negative particles (Cl^{-} ions or positive ion vacancies), to satisfy the condition of neutrality of electric charge; whereas the volume of the primitive cell of matrix, containing one Na^{+} and one Cl^{-} in full, is too small to accommodate even the above three. That is to say: if the plate-zone have a periodic structure, it must possess a larger primitive cell than that of the NaCl lattice so that it must give rise to rods at non-integral positions in reciprocal space, in contradiction to the observation. Accordingly, the structure of the plate-zone having a coherent periodic pattern should be discarded. This result represents a serious difficulty in interpreting the nature of plate-zone, since structures having no any crystalline character are least conceivable concerning the precipitation product.

§ 6. Structure of the Plate-Zones as Assemblies of Smaller Units

In the present section, we propose a possible model for the structure of {111} or {310} plate-zones avoiding the lastly mentioned difficulty. Let us assume that the plate-zone is an assemblage of a number of smaller units, each of which possess a crystalline pattern developed to a certain extent. Though there may be several species of structures in these units, they are presumed to have unit cells of a common size, which is a few multiple of that of the matrix lattice, namely being a super unit cell. The external shape of each unit is arbitrary, but since a thin plate-like form is most conceivable, we call them "platelets".

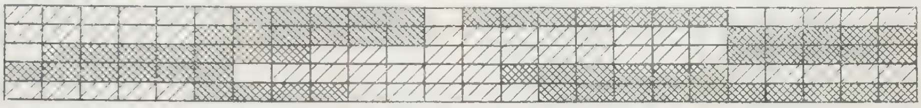

Fig. 8. Plate-zone registered by S-lattice. ▨ and ▩ indicate respectively the platelets for which $p=1$ and $p=2$ (only two kinds of platelets being considered).

Let us consider fictitiously a lattice, having a super lattice period as mentioned above, extending over the whole space of the plate-zone (Fig. 8), and call it the S-lattice, (whereas the lattice of matrix is called the O-lattice). The structure contained in each unit cell of the S-lattice may be in general various, not only because of different kinds of platelets, but also of the possibility of different coordinations of platelets relative to the S-lattice (see later paragraphs). Correspondingly, we may have several — presumably not too numerous — species of the structure amplitude (related to the structure in each unit cell of the S-lattice) effective to the diffuse scattering. We denote them by

$$F_p(\boldsymbol{h}), \qquad p=1,\ 2,\ \cdots\cdots.$$

Let us then classify the lattice points of S-lattice to groups $p=1,\ 2,\ \cdots\cdots$ according to the species of the structure amplitude of the cell concerned, and denote the position of the n-th lattice point of the p-group by $\boldsymbol{R}_{pn}$. The S-lattice points with the index pn may be distributed over different platelets, even with fixed p. p is constant within a single platelet.

The scattering amplitude due to a plate-zone as a whole is given by

$$F' = \sum_p F_p(\boldsymbol{h}) \sum_n \exp(2\pi i \boldsymbol{h}\boldsymbol{R}_{pn}). \tag{7}$$

We assume now that the crystalline structure of each platelet is developed at least to such degree that the corresponding scattering amplitude is appreciable either only in the neighbourhood of the S-reciprocal-lattice points, or only along reciprocal-lattice rows perpendicular to the plane of the platelets. Then $\sum_n \exp(2\pi i \boldsymbol{h}\boldsymbol{R}_{pn})$, the sum for lattice points in different platelets corresponding to a common p, may also be appreciable only in the neighbourhood of the S-reciprocal-lattice points, or, at most, along the reciprocal-lattice rows. Furthermore, since the location of the relevant S-lattice points is, according to our presumption, confined only to the thin layer of the plate-zone, it is safe to say that $\sum_n \exp(2\pi i \boldsymbol{h}\boldsymbol{R}_{pn})$ will really give a rod at every S-reciprocal-lattice point.

We can show now the fact that, in certain cases the assembly of platelets may give rods only about the O-reciprocal-lattice points, notwithstanding individual platelet has the super lattice. For example, let us assume that there are only two groups $p=1$ and 2, and that:

(I) The two groups of S-lattice points $p=1$ and 2 on a lattice plane parallel to the surface of the plate-zone are always equal to each other in their total numbers.

(II) (a) $F_1(\boldsymbol{h})=F_2(\boldsymbol{h})$ (8)
in the neighbourhood of the S-reciprocal-lattice points coinciding with O-reciprocal-lattice points;

(b) $F_1(\boldsymbol{h})=-F_2(\boldsymbol{h})$ (9)
in the neighbourhood of the other S-reciprocal-lattice points.

Let us treat the cases (a) and (b) separately.

(a) *Region around the S-reciprocal-lattice points coinciding with O-reciprocal-lattice points.* (7) is written, with (8), as

$$F' = F_1(\boldsymbol{h}) \sum_p \sum_n \exp(2\pi i \boldsymbol{h}\boldsymbol{R}_{pn}). \tag{10}$$

The right-hand side of (10) is the summation taken over the S-lattice cells occupied by the platelets. Since all of them are confined to the thin layer of the plate-zone, it is sure that (10) gives rods about the reciprocal-lattice points concerned. When, especially, the space of the plate-zone is filled with the platelets densely, (10) becomes

$$F' \sim F_1(\boldsymbol{h}) \sum_P \exp(2\pi i \boldsymbol{h}\boldsymbol{R}_P) \,, \qquad (11)$$

where $\sum_P$ is the summation taken over all S-lattice points $\boldsymbol{R}_P$ (indexed by P) in the plate-zone. In this case, the rods possess such an extension as expected from the whole size of the plate-zone according to the usual theory of the crystal-size effect, since $\sum_P$ is the diffraction function for a crystal having the same size. In other cases, the extension of the rods might be larger than expected from the size of the plate-zone.

(b) *Region around the S-reciprocal-lattice points not coinciding with O-reciprocal-lattice points.* (7), with (9), is written as

$$F' = F_1(\boldsymbol{h})\Big\{(\sum_{\substack{n\\p=1}} \exp(2\pi i \boldsymbol{h}\boldsymbol{R}_{pn}) - \sum_{\substack{n\\p=2}} \exp(2\pi i \boldsymbol{h}\boldsymbol{R}_{pn})\Big\} \,, \qquad (12)$$

Since, as we have shown, the both summations in (12) are appreciable only along the rods passing through S-reciprocal-lattice points, we consider exclusively the value of F' along the rods. Let us put

$$\boldsymbol{h} = \boldsymbol{H}_s + \boldsymbol{t} \,, \qquad (13)$$

where $\boldsymbol{H}_s$ is the vector of the S-reciprocal-lattice point concerned, and $\boldsymbol{t}$ is the vector which starts from this point along the direction of a rod. Let $\boldsymbol{a}_1'$ and $\boldsymbol{a}_2'$ (which are respectively parallel to the axes $\boldsymbol{a}_1$ and $\boldsymbol{a}_2$ of the O-lattice) be the axes of the S-lattice lying in the lattice planes parallel to the surface of the plate-zone, and $\boldsymbol{a}_3'$ (parallel to $\boldsymbol{a}_3$) the third axis, then $\boldsymbol{a}_1'$ and $\boldsymbol{a}_2'$ are perpendicular to $\boldsymbol{t}$, and $\exp(2\pi i \boldsymbol{a}_i' \boldsymbol{H}_s) = 1$ for $i = 1, 2, 3$. Let m_3 be the index specifying the S-lattice plane in the plate-zone parallel to the plate surface, n_{1m_3} and n_{2m_3} be the number of the S-lattice points for two groups $p=1$ and 2 on the m_3-th lattice plane. We carry out the summation in (12) first on lattice points on each lattice plane m_3, and then on different lattice planes in the plate-zone. Then, as readily proved, (12) becomes

$$F' = F(\boldsymbol{h})\Big(\sum_{m_3} \exp(2\pi i \boldsymbol{t}\cdot m_3 \boldsymbol{a}_3')\Big)(n_{1m_3} - n_{2m_3}) \,. \qquad (14)$$

Thus, we obtain $F' = 0$ by virtue of the condition (I), or $n_{1m_3} = n_{2m_3}$. Namely, the rod does not appear about the S-reciprocal-lattice points not coinciding with O-reciprocal-lattice points.

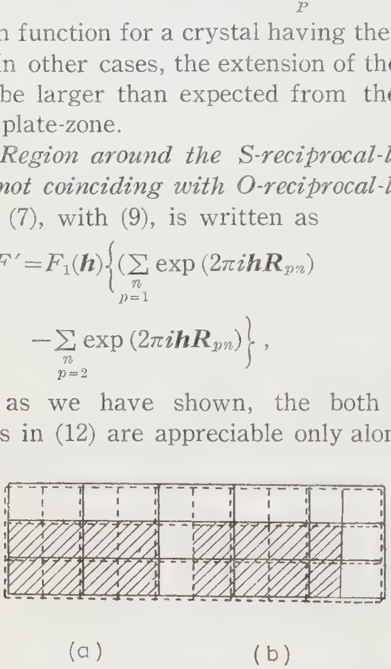

Fig. 9. Formation of domains with anti-phase relation. Solid lines indicate S-lattice, and broken lines O-lattice.

We must mention here an important circumstance as follows. The different species of the structure amplitudes $F_p(\boldsymbol{h})$ result not only from the different species of the platelets, but also from the property of the super lattice itself even when we have only one kind of the platelet. This circumstance is similar to the case of super structure alloys, e.g. Cu_3Au,[10] in which the formation of domains accompanied by the anti-phase (or out-of-step) relation among them has been well known. For example when $\boldsymbol{a}_1' = 2\boldsymbol{a}_1$, $\boldsymbol{a}_2' = \boldsymbol{a}_2$, $\boldsymbol{a}_3' = \boldsymbol{a}_3$, the formation of the super structure in the matrix lattice may occur in the alternative ways as shown schematically in Fig. 9a and b. The modes of the formation of both structures are equivarent with respect to the O-lattice (which is shown by broken lines), but differ from each other with respect to the S-lattice (shown by solid lines). Let the structure amplitude for the structures (a) and (b) in Fig. 9 be $F_1(\boldsymbol{h})$ and $F_2(\boldsymbol{h})$ respectively, then

$$F_2(\boldsymbol{h}) = F_1(\boldsymbol{h}) \exp\{2\pi i \boldsymbol{h}(\boldsymbol{a}_1'/2)\} \,, \qquad (15)$$

and they satisfy just the relation (8) and (9), and the assembly of platelets of this kind gives rods only about the normal reciprocal-lattice points, when provided with the condition (I).

For the super structure $\boldsymbol{a}_1' = 3\boldsymbol{a}_1$, $\boldsymbol{a}_2' = \boldsymbol{a}_2$, $\boldsymbol{a}_3' = \boldsymbol{a}_3$, we have three kinds of the structure amplitudes $F_1(\boldsymbol{h})$, $F_2(\boldsymbol{h})$ and $F_3(\boldsymbol{h})$ such that

$$\left.\begin{aligned} F_2(\boldsymbol{h}) &= F_1(\boldsymbol{h}) \exp\{2\pi i \boldsymbol{h}(\boldsymbol{a}_1'/3)\}, \\ F_3(\boldsymbol{h}) &= F_1(\boldsymbol{h}) \exp\{2\pi i \boldsymbol{h}(2\boldsymbol{a}_1'/3)\}. \end{aligned}\right\} \qquad (16)$$

In this case it holds:

(a) $F_1(\boldsymbol{h})=F_2(\boldsymbol{h})=F_3(\boldsymbol{h})$ (17)

for the S-reciprocal-lattice points coinciding with O-reciprocal lattice points;

(b) $F_1(\boldsymbol{h})+F_2(\boldsymbol{h})+F_3(\boldsymbol{h})=0$ (18)

for the other S-reciprocal-lattice points.

Replacing the condition (8) and (9) by (17) and (18) and with an assumption a little modified from (I), we reach the same result as in the previous example.

The above mentioned examples can be extended to more complicated cases. In more general cases, the intrinsically different species of platelets, not due to the out-of-step relations among them, may also take place.

§ 7. Discussion

According to the general consideration in the sections § 5 and § 6 it became most probable that the presumed {111} or {310} plate-zone in the NaCl-CaCl$_2$ solid solutions is composed of a number of platelets having a super cell. As was already noticed, the external size of the plate-zones may be larger than that estimated from the extension of the rods according to the theory of crystal size effect. Therefore, their lateral dimension might be considerably larger than the formerly mentioned value of about 100–200Å. On the other hand, its thickness can not be much larger than the former values 10–20Å, because the small thickness of the plate-zone is one of the essential assumptions in the foregoing theory. However, the formation of a thicker plate by piling-up of a number of plate-zones incoherently with each other might be possible.

It may be interesting to compare here the structure of the {111} and {310} plate-zone presumed for the NaCl-CaCl$_2$ solid solutions with those for alloys. Geisler and Hill⁶⁾ considered that precipitates formed in certain stages of the precipitation process in the alloys such as Al-Ag, Al-Mg-Si, etc. are small thin plates having concrete crystalline patterns, which give rise to rods in reciprocal space as the result of the crystal size effect. On the other hand, according to Guinier⁹⁾ the same precipitates have structures which are not simply small crystals of the final products, but they are of a transient character accompanied by irregularities, being in more or less coherent relations with the matrix crystal. Though there is no exact similarity between the cases of NaCl-CaCl$_2$ solid solutions and above mentioned alloys, the structures of the presumed plate-zones in NaCl-CaCl$_2$ seems to akin to the model by Guinier rather than by Geisler and Hill, in the sence that the plate-zone in NaCl-CaCl$_2$ is considered to be a transient structure, not being a uniform periodic pattern. Guinier proposed that the precipitate formed in Al-Ag (20 wt%Ag) aged at temperatures $<150°$C is composed of a pile of thin *plaquettes* (as shown by Fig. 5 in his paper). Our consideration in the previous section (§ 6) may be applied to it when these *plaquettes* are incoherent to each other, and, moreover, each of them is divided by antiphase domains of a super structure. (His *plaquette* then corresponds to our plate-zone. Piling-up or scattered distribution of plate-zones can not be discriminated from the diffraction pattern alone.)

Since the intensities of the rods depend on the structures of platelets, it is now required to propose their detailed structures explaining the observed distribution of the $\langle 111\rangle_r$ and $\langle 310\rangle_r$ rods given by Fig. 7a and b. Though the conclusive determination of these structures seems to be not easy, we can suppose that they may be at least as follows: (i) positions of atoms in the platelets are in general displaced from the original matrix lattice sites (§ 5, paragraph (c)); (ii) the packing of ions in the platelets is compatible with the NaCl lattice surrounding them; (iii) the neutrality of electric charge is fulfilled; (iv) the arrangement of ions around a Ca^{++} ion may bear some resemblance to that in the crystal structure of CaCl$_2$. In a subsequent paper (Part II), the structures of platelets in the {111} and {310} plate-zones will be respectively discussed by proposing plausible detailed models. It is to be mentioned here only the fact that these models could explain not only the relative intensities of rods qualitatively, but also their absolute intensities in order of magnitude.

Throughout the foregoing consideration on the $\langle 111\rangle_r$ and $\langle 310\rangle_r$ rods, we have assumed the existence of thin plate-zones by the analogy with the phenomenon in alloys, but it must be mentioned that this is not the unique assumption in order to interprete the presence of rods in reciprocal space. Generally speaking, the rods may result also from the stacking disorder of some kind, or certain lattice distorsion, spreading over more extended volume than that of the plate-zones. However, the consideration taking account of all of possible causes is postponed to avoid complication. Also, the discussion on the nature of rods other than the $\langle 111\rangle_r$ and $\langle 310\rangle_r$ rods is entrusted to the future study.

This work was supported by the research grant from the Ministry of Education.

References

1) J. A. Wasastjerna: Acta Soc. Sci. Fennicae, A, III, No. **8** (1944).

2) J. A. Wasastjerna: Soc. Scient. Fenn., Comment. Phys.—Math. XIII, **5** (1945).

3) G. D. Preston: Proc. Roy. Soc. **A 167** (1938) 526.

4) A. Guinier: Compt. Rend. **206** (1938) 1641.
A. Guinier: Rev. de Métallurgie, **16** (1944) 1.

5) C. S. Barrett and A. H. Geisler: J. App. Phys. **11** (1940) 733.

6) A. H. Geisler and J. K. Hill: Acta Cryst. **1** (1948) 238.

7) O. Menge: Z. anorg. Chem. **72** (1911) 162.

8) T. Sato and T. Amano: Kinzoku no Kenkyu (Metal Research, in Japanese) **11** (1934) 305.

9) A. Guinier: Acta Cryst. **5** (1952) 121.

10) F. W. Jones and C. Sykes: Proc. Roy. Soc. **A 166** (1938) 376.

JOURNAL OF THE PHYSICAL SOCIETY OF JAPAN Vol. 9, No. 5, SEP.—OCT., 1954

The Magnetic Properties and their Temperature Dependence of Ferromagnetic Alloys with an Order-disorder Transformation. I. Ni_3Fe

By Tadami TAOKA and Taiichiro OHTSUKA

Institute of Science and Technology, University of Tokyo

(Received April 24, 1954)

The temperature dependence of magnetic properties of Ni_3Fe have been measured at a fixed state of order. Ni_3Fe is a characteristic example of the A_3B type ferromagnetic alloy undergoing an order-disorder transformation. Particular stress was placed on the change of magnetic properties at the order-disorder transformation temperature 490°C. Magnetization was measured with an astatic magnetometer equipped with an electric vacuum furnace enabling rapid heating of the sample. Magnetostriction was measured by a new apparatus designed to simplify manipulation of the sample at high temperatures. At a fixed state of order, the saturation magnetostriction was seen to decrease monotonically with temperature, whereas at a fixed temperature it was seen to increase with the formation of order. In particular, λ_s increases by 200%, from below $2\cdot10^{-6}$ at the disordered state to $5.8\cdot10^{-6}$ at the ordered state at the order-disorder transformation point.

§1. Introduction

The effect of the formation of a superlattice in a ferromagnetic alloy on its non-magnetic and magnetic properties is diverse, depending on the type of lattice, composition and the elements involved. For instance, although Ni_3Fe⁽¹⁾, Ni_3Mn⁽²⁾ and Fe_3Al⁽³⁾ being to the same A_3B type, the ferromagnetic Curie point rises with the increase of order in some cases (e.g. Ni_3Mn) and falls in others (e.g. Fe_3Al). Also the rate of the order-disorder transformation itself varies considerably from alloy to alloy. Complications are due mainly to the fact that two different cooperative phenomena, i.e. the formation of the superlattice and the alignment of the spin moments, are taking place simultaneously interacting with each other in an intricate manner depending on the elements and the composition of the alloy in question. A thorough treatment of this problem from the atomic point of view encounters seemingly unsurmountable difficulties in calculation. However, statistical treatments have been made by Sato⁴⁾ on the basis of the Bragg-Williams approximation⁵⁾, and by Muto⁶⁾ using the Bethe approximation⁷⁾. Although the approximation is more coarse, Sato's method involves simpler calculations and yet enables one to explain at least qualitatively the observed diversity of the phenomenon. However he introduces a certain number of adjustable parameters which affect the results to a considerable extent. Hence it is doubtful whether a quantitative comparison with experiment would have much significance. It seems that the interaction between the two cooperative phenomena is too complex to be dealt with by such a simple model.

Therefore it was thought desirable to see if we could get any further information by studying the behavior of some quantity with the other quantities fixed, e.g. the temperature dependence of saturation magnetization at a fixed degree of order. One encounters difficulties, however, due to the fact that it is impossible to maintain an ideally fixed degree of order at appreciably high temperatures. On the other hand, it is known that the relaxation time for the rearrangement of atoms is much longer than that of the magnetic moments. Thus by utilizing this large difference in relaxation times it is possible to achieve the desired measurements to a satisfactory extent.

Our experiments were conducted essentially along this line. By appropriate heat treatments, various degrees of order were formed and the effect of the formation of the superlattice on the ferromagnetic Curie point, saturation magnetization and magnetostriction along with the temperature dependence of some of these properties at a fixed degree of order were measured. Particular attention was focused on the behaviour near the order-disorder trans- formation point. We shall first report the results obtained on Ni_3Fe.

§ 2. Apparatus

§ 2.1. *Astatic Magnetometer*

The astatic magnetometer developed by F. Kohlrausch and L. Holborn⁸⁾ is most convenient for measuring the temperature dependence of magnetic properties. Fig. 1 illustrates the magnetometer we constructed for this purpose. The two small magnets I and II have the same magnetic moments. They are fixed antiparallel to each other at a distance 80 cm apart by a thin glass rod. The system is suspended by a thin Pt-Ir filament. The small magnet II compensates external magnetic disturbances. The Pt-Ir filament consists of two parts, I and II, with different thicknesses. The sensibility can be decreased by clamping the suspension at the junction of filament I and II. The whole system is then suspended by filament II only. Important dimensions and properties of our meter are listed in Table I. An electric furnace wound with Molybdenum wire (diameter 0.8 mm) is placed inside coil I. The heat capacity of the furnace is made small so that the sample can be heated up to 600°C at the rate of 50°C per minute. The change in the magnetic properties at this heating rate can be followed sufficiently by the magnetometer.

Table I.

Magnet		Filament (90% Pt-Ir) dia.	Filament (90% Pt-Ir) length	Period	Sensibility*
M.D. Steel	I	0.049 mm	585 mm	21.1 sec	0.02764
3 mm by 50 mm	II	0.10 mm	105.5 mm	3.4 sec	0.778
Kohlrausch & Holborn					0.2928

* Kohlrausch and Holborn⁸⁾, Eq. (5).

§ 2.2. *Magnetostriction Apparatus*

The conventional method for measuring magnetostriction at room temperature is to utilize the rotation of a small roller. This method has been used by Takagi⁹⁾ to measure magnetostriction at high temperatures. However, various difficulties, e.g. setting of the sample, etc., are encountered when this method is used at elevated temperatures. Therefore, an apparatus illustrated in Fig. 2 was built for the purpose of our experiment. The schematic diagram (b) shows the principle of the apparatus. The contraction or expansion of the sample is transferred through *A* to point *p* of lever L_1. The displacement is thus enlarged by a factor of about five at point *r* which rotates the mirror *M* supported by a knife edge *s*. The rotation of the mirror is observed by the telescope and light method. When $\overline{rs}=2.0$ mm, the system exhibits the same sensibility of a roller $2.0/5=0.4$ mm in diameter. The actual procedure for measurement is as follows (cf. Fig. 2 (a)): (1) During the process of raising or lowering the temperature, the sample and its supporting rod *D* are left free to expand or contract on rollers R_4, R_5 (Fig. 2b) and R_1, R_2, R_3 (Fig. 2(a)) without transferring its displacement to the lever. (2) After a sufficiently constant temperature has been attained, part *B*, which supports the lever L_1 by the action of a spring, is moved by a worm gear *W* until *A* and *P*, *r* and *M* come into contact with each other, (3) the mirror is then adjusted by lever L_2 with screw S_1 so that an appropriate portion of the scale comes into the field of view of the telescope, (4) due to displacements caused by temperature fluctuation, etc. the scale will fluctuate for some time. When it is seen that these effects have disappeared or become sufficiently small, the field is applied and the magnetostriction measured. As the whole system is enclosed in a vacuum chamber, the various adjustments, i.e. the rotation of screws and gears are conducted *via* tombac bellows. The sensibility of the system, calibrated with a precision micrometer, is such that when a sample 200 mm long changes its length by 10^{-6}, the deflection observed on the scale set 2 meters apart is 1.74 mm. Reproducibility was checked by making test runs on a suitable sample and was found to be satisfactory.

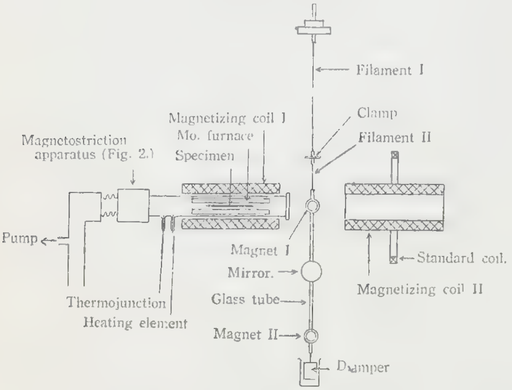

Fig. 1. Astatic magnetometer.

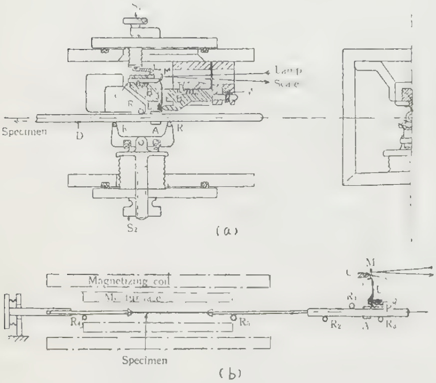

Fig. 2. Magnetostriction apparatus.

The characteristics of our apparatus as compared to the conventional roller method can be described as follows: a) Sensibility is of the same order, b) difficulties due to slipping of the sample on the roller and external vibration are removed, c) sample can be readily set at identical conditions from outside of the vacuum chamber, d) measurements at high temperature can be easily performed. The power for the furnace was supplied from a battery of large capacity in order to maintain the current as constant as possible.

§ 3. Sample and the Experimental Procedure

Electrolytic nickel, electrolytic iron and manganese (0.5% of the entire weight) was melted in vacuum and drawn to a rod 1.5 mm in diameter and 250 mm in length. Upon analysis the sample was found to contain 25.1% Fe which is slightly iron rich as compared with the stoichiometric composition of Ni_3Fe (24.2% Fe). The superlattice was formed according to the heat treatment prescribed by Kaya[10]. Various degrees of order were obtained by lowering the temperature from 1000°C to the order-disorder transformation point (490°C) and holding it there for certain lengths of time. A sample held at 490°C for 100 hrs., cooled to 450°C in 6 days, and then slowly cooled in the furnace to room temperature was defined to be in a perfectly ordered state. Measurements on electrical resistance, hardness, etc. made by Kaya *et al.*[11] show that the formation of the superlattice at

490°C takes place in three stages. The annealing procedure for forming the superlattice was reduced from the the results of these measurements.

The magnetization curve at various temperatures were measured by the astatic magnetometer described in § 2.1. The temperature dependence of magnetization at a fixed degree of order was performed by applying a constant field and heating the sample from room temperature to about 600°C at a rate of over 50°C per minute. The temperature of specimen was measured by *Pt-PtRh* thermojunction with diameter 0.4 mm which was in tight contact with the specimen by means of a thin *Pt* wire. It is doubtful whether the temperature observed by the junction would be the temperature of specimen itself in our case. This uncertainty must be considered in some degree on the discussion in later section.

§ 4. Experimental Results

§ 4.1 *Properties at Room Temperature*

The specific electrical resistance and the magnetic properties at room temperature are shown in Table II for various degrees of order. The magnetization curves are shown in Fig. 3. The general tendency of the results agrees with the measurements made by Kaya[10),11)] and Chikazumi*[12)]. The formation of the superlattice appears as a decrease in electrical resistance. The maximum permeability decreases abruptly in the first stage of superlattice formation, reaches a minimum value at the second stage and recovers slightly in the third stage. The magnetization at 150 Oe, which can be considered approximately as the saturation magnetization, increases by about 4% in going from the disordered to the ordered state. This is in agreement with the results obtained by Grabbe[13)], although the manganese content has essential effect upon this change. The susceptibilities obtained by the magnetometer yielded smaller values than those obtained by other authors by the ballistic method.

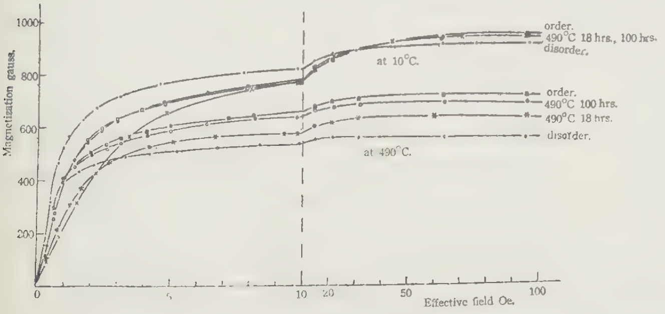

Fig. 3. Magnetization curves at 10°C and 490°C for various states of order.

§ 4.2. *Temperature Dependence of the Magnetic Properties*

The magnetization curve of samples with a fixed degree of order were measured at various temperatures extending up to the Curie temperature. The temperature dependence of the maximum susceptibility and the magnetization at 150 Oe are shown in Figs. 4 and 5. Up to 400°C the samples were maintained at the respective temperatures for about an hour after which various measurements were made. The time maintained at the order-disorder transformation point (490°C) are listed in Table IV. For the disordered state, the maximum susceptibility remains sensibly constant up to 300°C and decreases abruptly near the transformation point, tending to zero at the Curie point**. At other degrees of order, it increases gradually with the increase of temperature. As seen in Fig. 4, the susceptibility at the order-disorder transformation point becomes larger for the ordered states than for the disordered state. This behavior is also inferred from the magnetization curves at 490°C shown in Fig. 3.

To determine the saturation magnetization, several experimental formulas related to the field strength have been proposed. Unfortunately, we could not determine the saturation magnetization from our experiment shown in Fig. 3, because of the accuracy and the magnetic field range of our measurement. The magnetization at 150 Oe could not be regarded as the saturation magnetization, especially for the specimen which has high magnetic anisotropy or at the elevated temperatures. But the strength of magnetization are constant over the range of field from 80 Oe to 160 Oe within the experimental error (1∼2%), therefore we shall regard the

---

* Chikazumi's sample consists of 21.5% Fe.

** The tail near zero is perhaps due to the nonuniformity of temperature along the sample.

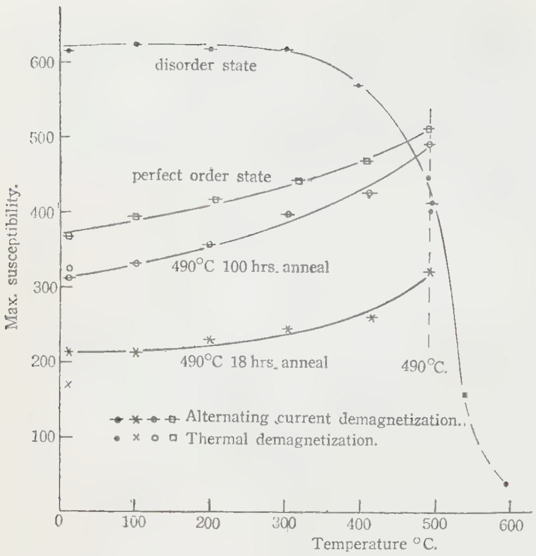

Fig. 4. Temperature dependence of maximum susceptibility for various states of order.

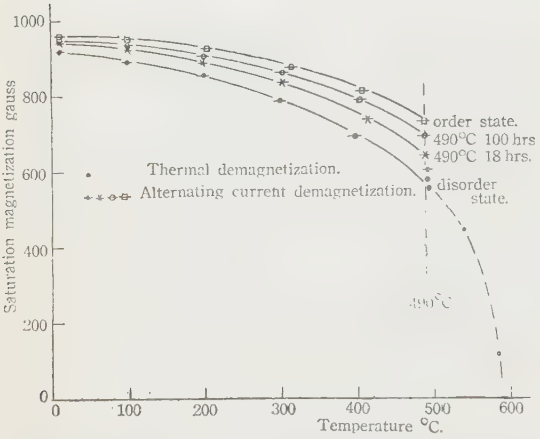

Fig. 5. Temperature dependence of magnetization at 150 Oe. for various states of order.

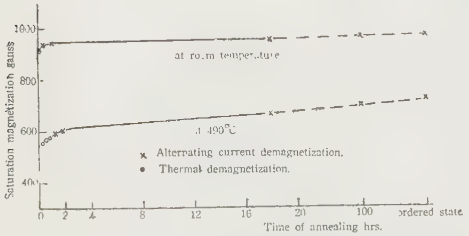

Fig. 6. Change of saturation magnetization with annealing time.

magnetization at 150 Oe as the saturation magnetization in the following.

On the whole, the saturation magnetization decreases with increasing temperature in a normal fashion. However, it is seen in Fig. 5 that the difference in values of saturation magnetization for various states of order increases as the temperature becomes higher. This behavior is more clearly exhibited in Fig. 6 where the saturation magnetization at room temperature and 490°C has been plotted against the annealing time. It is seen that the saturation magnetization at 490°C increases by over 30% from the disordered to the ordered state, whereas we have already seen that the increase amounts to only 4% at room temperature.

The saturation magnetization-temperature curve for the disordered state agrees fairly well with the curve obtained by Weiss and Forrer on Nickel*. The ferromagnetic Curie point lies at about 585°C. A large deviation from the Weiss curve is seen for the ordered states if the Curie point is assumed to remain constant. We shall next look into the effect of superlattice formation on the Curie point.

§ 4.3. *Variation of the Ferromagnetic Curie Point*

According to Kaya's measurements[14] on the temperature hysteresis of electrical resistance of Ni_3Fe, we can expect the sample to maintain its degree of order to an appreciable extent even after surpassing the transformation temperature if the heating rate is made sufficiently large. We have made use of this sluggishness of the order-disorder transformation in determining the change in the ferromagnetic Curie point with order. An external field of 50 Oe was applied and the magnetization measured while heating the sample at the rate of over 50°C per minute. The results are shown in Fig. 7. The curve for the disordered state coincides with the Weiss curve. On the other hand, the curves for the various ordered states show an abrupt decrease at temperatures over 550°C. The point of disappearance of ferromagnetism increases, however, from 585°C to 620°C. The increase in the separation of the curves at higher temperatures can be considered as due to the difference in Curie temperature. It must be noted, however, that the increase in the anisotropy energy with order (Grabbe[15]) will produce a similar effect if the sample is insufficiently saturated at lower temperatures.

---

* Henceforth this will be called the Weiss curve.

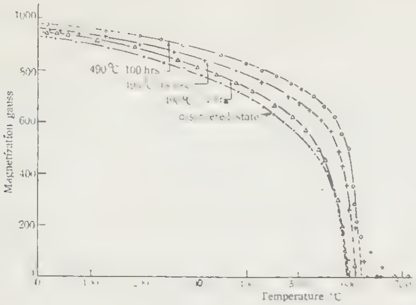

Fig. 7. Temperature dependence of magnetization at 50 Oe. for various states of order.

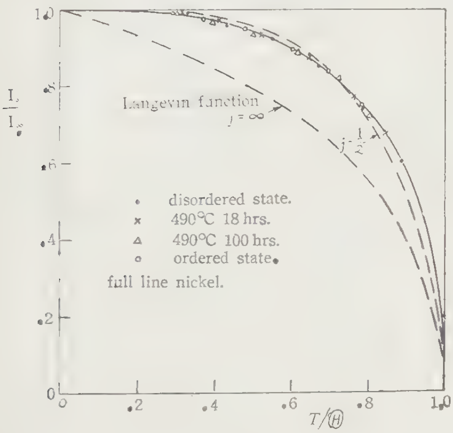

Fig. 8. Weiss curve: Temperature dependence of saturation magnetization of Ni_3Fe for various states of order and nickel as compeared with theory.

The effect may appear to a certain extent in our case because of the relatively low external field (50 Oe) used*. The abrupt descent at temperature above 550°C can be regarded as due to the destruction of order. As the curve for the disordered state which suffers on effect due to the destruction of order agrees well with the Weiss curve, it is plausible to assume that the curves for the ordered states will also fit the Weiss curve if the order could be maintained ideally up to the Curie point. Therefore, in order to determine the true Curie point, the values for the saturation magnetization between 10°C and 490°C were normalized with the value for the Curie point and the saturation magnetization at 0°K so chosen that the best fitting with the Weiss curve was obtained (cf. Fig. 8). The Curie point thus obtained are listed in Table III. Up to now, no attempt had been made to measure the change of the Curie point with order due to the fact that the Curie point lies above the transformation point. Therefore, Ni_3Fe has been so far regarded as a case in which the Curie point does not change remarkably with the formation of the superlattice. As the value of saturation magnetization were replaced by the magnetization at 150 Oe, as noted at § 4.2, we can not discuss the details of this point. Our results, however, show that it increases by about 20% from the disordered to the ordered state. We feel it more reasonable to take this effect into account when considering other effects in Ni_3Fe.

Table II. The Electric and Magnetic Properties of Ni_3Fe at Room Temperature.

Degree of order	Specific electrical resistance $\mu\Omega$	Initial suscepti-bility χ_0	Maximum suscepti-bility χ_m	Coersive force H_cOe	Saturation magnetization in Gauss
Disorder	16.1	235	612	0.19	919
490° C 10 min.	15.5	150	370	0.31	939
490° C 1 hr.	15.2	100	260	0.42	942
490° C 18 hrs.	14.0	65	212	0.44	945
490° C 100 hrs.	12.5		325	0.33	955
Perfect order	11.1		368		960

Table III. Saturation Magnetization and the Ferromagnetic Curie Point of Ni_3Fe for various States of Order.

State of order	Saturation magnetization at 0°K	Curie point °C
Disorder	927	585
490°C 18 hrs.	949	630
490°C 100 hrs.	964	680
Perfect order	972	710

§ 4.4. *Magnetostriction*

Magnetostoriction was measured at various temperature on samples in different states of

---

* Higher fields could not be used because of difficulties encountered in the manipulation of the astatic magnetometer.

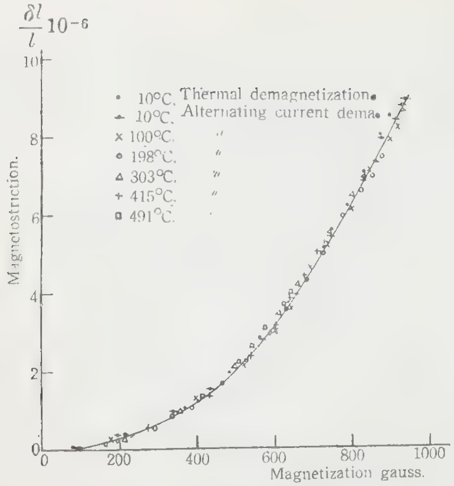

Fig. 9. Magnetostriction—magnetization curve for the state annealed at 490°C for 18 hrs.

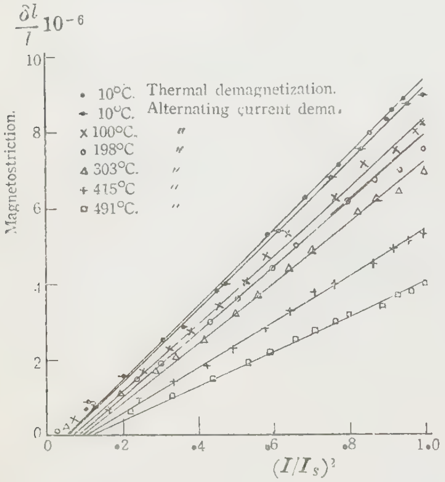

Fig. 10. Relation of $(\delta l/l)$ and $(I/I_s)^2$ for the state annealed at 490°C for 18 hrs.

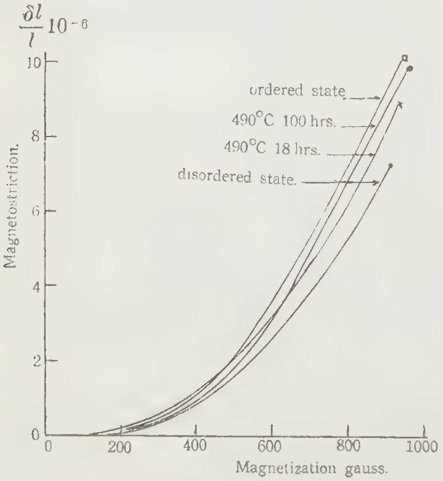

Fig. 11. Magnetostriction—magnetization curves for various states of order.

order. The apparatus and the experimental procedure has been described in § 2.2. The magnetization curve was measured immediately following the magnetization measurement under similar conditions. As is well known, the magnetization of a polycrystal is affected by the domain distribution in the initial demagnetized state. In a long thin sample an anisotropy in the distribution of the domains is produced when the sample is demagnetized by alternating current. When demagnetized thermally, the domain distribution can be regarded as to be nearly isotropic. In our case, the magnetostriction at room temperature for the two alternative methods of demagnetization coincided with each other within experimental uncertainties. Therefore the alternating current method was used up to 490°C and the thermal method from there on. The reason for not using the simpler alternating current method over and in the vicinity of 490°C is because the application of a magnetic field in this region is known to result in the fixation of the domains in the direction of the applied magnetic field. Figs. 9 and 10 show representative curves obtained. The curves correspond to a sample annealed at 490°C for 18 hours. The form of the curves for other states of order are similar. It is seen in Fig. 9 that the points for all temperatures fall on the same line satisfying the relation

$$\delta l/l = C(I^2 - I_0^2)\ , \tag{1}$$

where C and I_0 are constant. The relation is more explicitly presented in Fig. 10 where $\delta l/l$ has been plotted against $(I/I_s)^2$. Here I_s is the saturation magnetization at the temperature in question. The slope C remains unvaried with temperature but depends on a degree of order. I_0/I_s also remains sensibly constant with a slight tendency to increase with temperature. Fig. 11 shows the variation in $\delta l/l - I$ curves with the change in order, and Fig. 12 the corresponding $\delta l/l - I/I_s)^2$ curves. It is seen that the simple quadratic relation (1) tends to break down in the initial stage of magnetization as the order increases. The point near saturation, however, fall on a straight line. The extrapolation of the line shows that the slope C increases and I_0 decreases with increasing order. The values of magnetostriction approach constants,

Table IV.

Degree of order	Temp. °C	Demagnetization	$\lambda_s 10^{-6}$	I_s Gauss	$\frac{\lambda_s}{I_s^2} 10^{-12}$	* $C\,10^{-12}$	Time at** 490°C, min.
Disorder	10	T.D.	7.2	918	8.5	10.2	
	10	A.D.	7.1	919	8.4	10.1	
	100	A.D.	6.4	889	8.1	10.4	
	200	A.D.	6.1	853	8.2	10.3	
	300	A.D.	4.8	786	7.8	9.9	
	398	A.D.	3.8	690	8.0	9.7	
	493	A.D.	3.1	600	8.6	11.1	100
	492	T.D.	2.9	575	8.7	10.5	40
	495	T.D.	2.2	555			15
	540	T.D.	1.2	443			
	585	T.D.	0.6	118			
490°C 18 hrs.	10	T.D.	8.9	943	10.0	11.3	
	10	A.D.	8.9	945	10.0	10.9	
	100	A.D.	8.2	926	9.6	10.3	
	198	A.D.	7.4	886	9.4	11.0	
	303	A.D.	6.9	833	9.9	11.5	
	415	A.D.	5.3	731	9.9	11.4	
	491	A.D.	4.0	640	9.8	11.2	30
	492	T.D.	2.8	574	8.5		25
490°C 100 hrs.	10	T.D.	9.9	952	10.9	14.0	
	10	A.D.	9.8	955	10.8	13.5	
	100	A.D.	9.4	935	10.7	13.1	
	200	A.D.	8.5	905	10.4	13.0	
	304	A.D.	7.6	863	10.2	13.8	
	410	A.D.	6.2	790	9.9	14.1	
	490	A.D.	5.3	692	11.2	14.8	160
	495	T.D.	1.7	555			15
Perfect order	11	T.D.	10.1	960	11.0		
	11	A.D.	10.1	960	11.0		
	100	A.D.	9.7	953	10.9		
	207	A.D.	9.3	921	11.0		
	315	A.D.	7.9	869	10.5		
	407	A.D.	6.7	808	10.3		
	489	A.D.	5.8	727	11.0		55

T.D. Thermal Demagnetization
A.D. Alternating Current Demagnetization
* C in Eq. (1)
** Time spent at 490°C until measurements were made

the saturation magnetostriction, before the field strength reaches 150 Oe.

The temperature dependency of the saturation magnetostriction is shown in Fig. 13. All states of order show a similar monotonic decrease with increasing temperature. Points measured at temperatures over 490°C by the method previously described fall on the extension of the curve for the disordered state. Large fluctuations in the measurements at 490°C for the disordered state is due to the fact that in the course of waiting for the system to reach thermal equilibrium, the formation of the superlattice inevitably takes place.

The variation of saturation magnetostriction with the annealing time at 490°C has been measured both at room temperature and at 490°C and the results are shown in Fig. 14. Both curves show an abrupt initial rise taper-

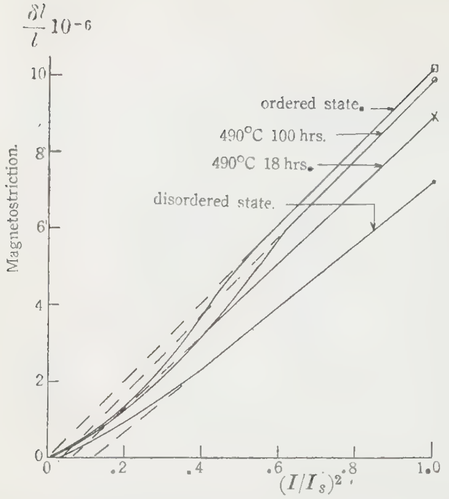

Fig. 12. Relation of $(\delta l/l)$ and $(I/I_s)^2$ for various states of order at room temperature.

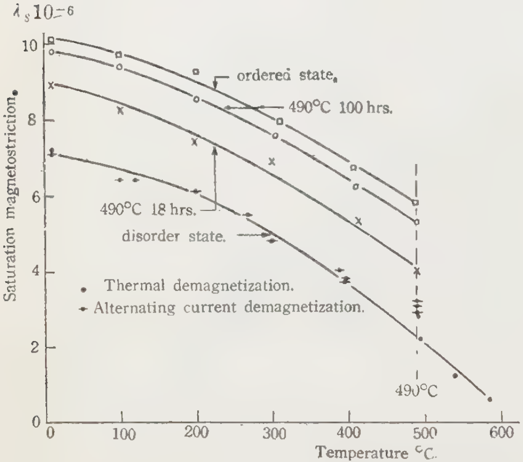

Fig. 13. Change of saturation magnetostriction with temperature for various states of order.

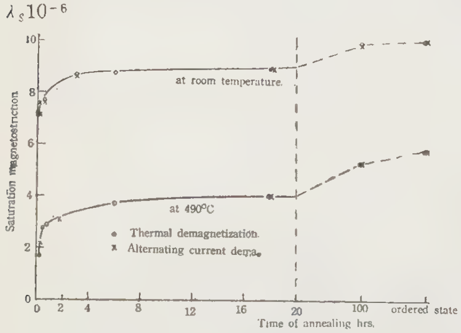

Fig. 14. Change of saturation magnetostriction with time of annealing at 490°C. measured at room temperature and at 490°C.

ing off to a gradual monotonic increase. The saturation magnetostriction for the disordered state at room temperature is $7.1 \cdot 10^{-6}$. At the perfectly ordered state, the value increases to $10.1 \cdot 10^{-6}$. The increase thus amounts to 30%. At 490°C, the percentage increase is much larger amounting to 200%, the saturation magnetostriction for the ordered and disordered states being $5.8 \cdot 10^{-6}$, and below $2.0 \cdot 10^{-6}$, respectively. Results for various state of order are listed in Table IV.

§ 5. Discussion

The results of our experiment show that in Ni_3Fe, the ferromagnetic Curie point, saturation magnetization and magnetostriction all increase with the formation of the superlattice. Up to now it had been tentatively assumed that the Curie point does not change remarkably with order from consideration of other factors. Recently Josso[16)] found that in a Ni-Fe alloy containing 77% Ni and 3.6% Mo, the Curie point increases from 475°C for samples quenched from high temperatures to 520°C for samples annealed at 450°C for 50 hours. The addition of Mo is known to inhibit the formation or destruction of the superlattice, thus making direct observations of the change in Curie point easier. His results suggest that the Curie point of Ni_3Fe will also increase with the degree order in agreement with our results*.

The increase in the saturation magnetization from the disordered to the ordered state is about 4% at room temperature in agreement with the results obtained by Grabbe and other people. The fact that the corresponding increase becomes over 30% at the transformation temperature, 490°C, can be understood if the increase in the Curie temperature is taken into account. It is noted that the tendency in the increase of saturation magnetization at 490°C closely resembles the manner with which the electrical resistance decreases. Smoluchowski[17)] has attempted to explain the change of magnetization with order on the basis of the band theory. He assumes that the magnetic moments of the superlattice alloy is determined by the local electron density and then calculates the effect of superlattice formation by considering the change in the local electron density due to the change in the type of the nearest and second nearest neighbours. The electron density is related to the magnetic moment by Pauling's relation[18]. His results are compared with the experimental values obtained by Goldman et al.[19] The theory can not be adapted to our results, however, because the conditions required by the theory fail to be satisfied in cases such as Ni_3Fe where changes in length amounting to about $5\cdot10^{-4}$ occur with the formation of the superlattice.

---

* More recently, Wakelin and Yates have observed the same tendency for the Ni-Fe alloy containing no Mn, but do not give the details of the heat treatment, experimental method and the determination of the Curie point concerning the formation and destruction of the superlattice during the measurements.

We shall next consider the results of the magnetostriction measurements. Until recently, no particular effect of heat treatment had been observed on the magnetostriction of Ni-Fe alloys, even for those with compositions known to possess an order-disorder transformation[20]. In recent years, however, it has been found that the saturation magnetostriction for alloys such as Fe-Co[21], Fe-Si (11% Si)[22], and Fe-Ni[23] show an increase of 40%, 100% and 100%, respectively, with the formation of the superlattice. Our results show the same tendency. In particular, we have made measurements not only on the value of the saturation magnetostriction, but on the relation of magnetostriction and magnetization at various degrees of order and temperatures, with special attention paid to the behaviour at the transformation temperature. As was seen, our results can be expressed by Eq. (1). Eq. (1) can be deduced from the domain theory if it is assumed that the magnetostriction is isotropic and that the magnetization takes place by discontinuous rotation of magnetic moments towards the easy axis lying nearest to the direction of the applied field up to I_0 and by continuous rotation from there on. It is interesting to note that the ΔR effect measured by Gerlach[24] on single crystals of Fe, Ni and Fe-Ni alloys can also be expressed by the same equation. The deviation from Eq. (1) suggests that the discontinuous and continuous rotations are taking place simultaneously. The fact that the points for the ordered state lie lower than the straight line (Fig. 12) cannot be explained unless anisotropic features are taken into consideration. In Eq. (1), $(I_0/I_s)^2$ should be equal to 1/3[25] if the anisotropy energy is predominant. The fact that this value decreases with order indicates that there happen some other factor which may control the distribution of domains, for instance the appearance of uniaxial anisotropy. The manner in which the saturation magnetostriction λ_s increases with order at room temperature and at 490°C is similar to the increase of saturation magnetization and the decrease in going from the disordered to the ordered state 30% at room temperature, whereas the increase at 490°C exceeds 200%.

Bozorth and Walter[26] have recently measured the magnetostriction of a Ni_3Fe single crystal at room temperature. The values corresponding to a polycrystal can be calculated from their results assuming random grain distribution. They are $10.2\cdot10^{-6}$ for the disordered state and $12.6\cdot10^{-6}$ for the ordered state. The result for the ordered state agrees fairly well with our values. However, the change in saturation magnetostriction from the disordered to the ordered state amounts to 24% in their measurements whereas it is as large as 30% in our case. This may be due to the difference in heat treatment.

At present there is no satisfactory theory concerning the phenomenon of magnetostriction. Assuming dipolar interaction between magnetic moments and considering the condition of equilibrium for the magnetic plus the elastic energy, R. Becker[27] has derived an expression of magnetostriction as a function of saturation magnetization, elastic constant and crystallographical orientation. His result agrees qualitatively with the magnetostriction of body centered cubic Fe at room temperature but fails for the face centered Ni, the sign coming out to be the opposite. Smoluchowski[28] has extended this theory to alloys by considering different interaction energies for pairs of like and unlike atoms. He succeeds to some extent in explaining the change of magnetostriction in Fe-Co. However, his result fails, as in Becker's case, to give satisfactory explanation for the face centered cubic crystals. When $\lambda_{(100)}$ of Ni_3Fe is calculated from Smoluchowski's result, the sign becomes negative and the value decreases by 1/4 from the disordered to the ordered state. In view of this present lack of theory, we can only hope that our results may provide a clue for future theories concerning the mechanism of magnetostriction.

Magnetization curves of Ni_3Fe at room temperature has been thoroughly discussed by

Kaya and others. According to Chikazumi[29] and Nagashima[30], the change in the magnetization curve with order can be explained by assuming the internal stress* σ_i, which is almost zero for the disordered state, to increase with order, reaching a maximum value at the second stage of superlattice formation and decreasing again in the third stage. At the intermediate state of order, the energy of the internal stress becomes larger than the anisotropy energy whereby the distribution of the spontaneous magnetization at the demagnetized state will be determined by the randomly distributed internal stress. The expression for the initial susceptibility derived by Becker[25] for the case of large internal stress is

$$\chi_0 = \frac{2}{g} \frac{I_s^2}{\lambda \sigma_i} . \qquad (2)$$

Eq. (2) can also be thought of as a qualitative expression of the maximum susceptibility from considerations of the factors influencing it. As seen in Table IV, the factor I_s^2/λ appearing in Eq. (2) decrease with order. This effect plays an auxiliary role in explaining the change in the magnetization curve. The temperature dependence of the maximum susceptibility is completely different at the ordered and disordered states. Now if it is assumed that Eq. (2) holds for the ordered state, Fig. 4 can be considered as the inverse curve of the dependence of σ_i as I_s^2/λ is practically temperature independent. In his experiment, Chikazumi has obtained σ_i but unfortunately our values cannot be compared directly due to the difference in composition of the samples used. However, the temperature dependence of λ_s he derives from his observed values of σ_i and I_s agrees very well with the curve obtained by the authors through direct observation. This implies that we are not too much in error in interpreting the $\chi_m - T$ curve as the inverse of the $\sigma_i - T$ curve.

§ 6. Conclusion and Acknowledgements

Measurements made on the changes in the ferromagnetic Curie point, saturation magnetization, susceptibility and magnetostriction of Ni_3Fe with the formation of order has been reported. Particular attention has been focused on the behavior of these properties at the order-disorder transformation temperature.

The authors wish to express their hearty thanks to Prof. S. Kaya for his kind guidance and stimulating discussions throughout the course of this research. We also wish to thank Mr. Tsuji of the Inst. of Science and Technology for the construction of the magnetometer and the magnetostriction apparatus. Part of this research was supported by the Scientific Research Fund granted by the Ministry of Education.

References

1) S. Kaya: Butsurigaku Kōen-shu (2) 1942 (in Japanese).

2) S. Kaya and M. Nakayama: Proc. Phys. Math. Soc. Japan **22** (1940) 126.
N. Thompson: Proc. Phys. Soc. **52** (1940) 217.

3) C. S. Sykes, O. F. Inst and H. Evans: J. Iron and Steel Inst. **131** (1935) 225.

4) H. Sato: Nihon Butsuri Gakkai-shi Vol. **3** (1948) No. 1–2 (in Japanese), Sci. Rep. Res. Inst. Tōhoku Univ. **1** (1949) 71.

5) W. L. Bragg and E. J. Williams: Proc. Roy. Soc. London **145** (1934) 699 ibid. **151** (1935) 540.

6) T. Muto, T. Eguchi and M. Shibuya: J. Phys. Soc. Japan **3** (1948) 277, 284.

7) H. A. Bethe: Proc. Roy. Soc. London **150** (1935) 552.

8) F. Kohlrausch and L. Holborn: Ann. der Phys. u. Chem. **287** (1903) 10.

9) H. Takagi: Zeit. f. Phys. **105** (1937) 92.

10) S. Kaya: J. Faculty of Sci., Hokkaido Univ. Ser. II, **2** (1938) 29.

11) S. Kaya, H. Sato and K. Kumasaka: Nihon Kinzoku Gakkai-shi **6** (1941) 188 (in Japanese).

12) S. Chikazumi: J. Phys. Soc. Japan, **5** (1950) 327, 333.

13) M. Grabbe: Phys. Rev. **57** (1940) 728.

14) S. Kaya: loc. cit. (10).

15) M. Grabbe: loc. cit. (13).

16) E. Josso: J. Phys. Rad. **12** (1951) 399.

17) R. Smoluchowski: J. Phys. Rad. **12** (1951) 389.

18) L. Pauling: Phys. Rev. **54** (1938) 899.

19) R. Smoluchowski: loc. cit. (17).
J. E. Goldman and R. Shull: Phys. Rev. **75** (1949) 310.
J. E. Goldman: J. App. Phys. **20** (1949) 1131.

20) H. J. Williams, R. M. Bozorth and R. Christensen: Phys. Rev. **59** (1941) 1005, S. Kaya: loc. cit. (10).

21) J. E. Goldman and R. Smoluchowski: Phys. Rev. **75** (1949) 140.

22) J. Carr: Carnegie Inst. of Tech. Thesis 1950.

23) J. E. Goldman: Phys. Rev. **76** (1949) 471.

24) W. Gerlach: Ann. Phys. **12** (1932) 849.

25) R. Becker und W. Döring: Ferromagnetismus, J. Springer (1939) p. 287.

26) R. M. Bozorth and T. Walter: Phys. Rev. **89** (1953) 624.

27) R. Becker: Zeit. f. Phys. **62** (1930) 253.

28) R. Smoluchowski: loc. cit. (17), (21).

29) S. Chimazumi: loc. cit. (12).

30) T. Nagashima: Ōyō-Butsuri **19** (1950) 53 (in Japanese).

---

* The word "internal stress" should be understood as an unidirectional magnetic anisotropy that fixes the direction of the domain. It would perhaps be more appropriate to write it in a form $3/2\lambda\sigma_i = K$. However, we shall continue to use the word as matter of convenience of terminology.

JOURNAL OF THE PHYSICAL SOCIETY OF JAPAN Vol. 9, No. 5, SEP.—OCT., 1954

The Magnetic Properties and their Temperature Dependence of Ferromagnetic Alloys with an Order-disorder Tsansformation. II Ni_3Mn

By Tadami TAOKA and Taiichiro OHTSUKA

Institute of Science and Technology, University of Tokyo

(Received April 24, 1954)

Measurements on the change of magnetic properties with the formation of the superlattice and their temperature dependency at a fixed state of order has been carried out on the ferromagnetic alloy Ni_3Mn which shows characteristic properties different from the same A_3B type Ni_3Fe. Measurements were made by the apparatus described in Report I. Ni_3Mn is known to undergo an order-disorder transformation in the temperature range 600°C to 300°C. Major results obtained are; (1) the ferromagnetic Curie point increases from below room temperature at the disordered state to over 490°C at the ordered state, (2) saturation magnetostriction is very small and the temperature dependence complicated, (3) large and long magnetic after-effects were found at the intermediate states of order.

§ 1. Introduction

As mentioned in our previous report on Ni_3Fe, Ni_3Mn has two characteristic features as a ferromagnetic alloy with an order-disorder transformation. Firstly, it has no definite transformation point which is characteristic of the A_3B type alloy. The transformation takes place over a wide range of temperature extending from 300°C to 600°C. As for the magnetic properties, the alloy is paramagnetic at the disordered state (room temperature) with ferromagnetism appearing with the formation of the superlattice. Previous experiments have placed particular stress on the investigation of the above mentioned characters. The discussions have been mainly pointed towards the questions, (1) in what manner can the electrical resistance-temperature equilibrium curve (Kaya and Nakayama[1]), Thompson[2])) be explained from the point of view of superlattice formation, and (2) how do the magnetic properties, in particular, the saturation magnetization and the Curie point change with order ? In view of the fact that X-ray analysis has not been able to detect a superlattice line in Ni_3Mn and from considerations of properties such as the absence of hysteresis in the electrical resistance-temperature curve, the form of the anomalous specific heat, and various magnetic properties, Kaya, in his second paper[3]), suggested that probably no long range order was formed in this alloy and that only short range order was being formed in the temperature range 300°C to 600°C. On the other hand, Thompson sets 510°C as the transformation point by considering his results on measurements of saturation magnetization made on samples quenched from various temperatures. In his calculations, Sato[4]) concludes that it is perhaps more appropriate to consider the existence of long range order at least below 480°C ($1/\chi$ vanishes at 480°C).

As for question (2), Kaya concludes that the Curie point for the disordered state is below room temperature and increases with the formation of the superlattice, rising to over 480°C at the ordered state, whereas Thompson estimates the Curie point of the ordered state to be 460°C. Both authors, however, did not make direct observations on the change of the Curie point.

The factors influencing such phenomenon are very complicated, the two cooperative phenomena interacting with each other in an intricate fashion. We have attempted to simplify matters by approaching the problem in a manner discussed in the previous report, i.e. by measuring the magnetic properties and their temperature dependence at a fixed state of order, with hope that the results will present a clearer insight in the underlying mechanism.

In contrast with the case of Ni_3Fe, very few measurements have been made on the magnetic properties of Ni_3Mn. To the author's knowledge, no detailed investigations on the magnetic properties outside of the saturation magnetization have been reported. Therefore we shall first report some supplementary data obtained. During the course of experiment, a hitherto unknown effect, namely an anomalous magnetic after-effect was found to be present at the intermediate states of order. Preliminary measurements on this anomaly will also be reported.

§ 2. Sample and Experimental Procedure

Samples prepared by Kaya[5] in form of a rod 220 mm long and 1.5mm in diameter were used. The composition was 24.7% Mn, 74.3% Ni, with about 1% richer in Mn as compared to the stoichimetric composition of Ni_3Mn (23.8% Mn).

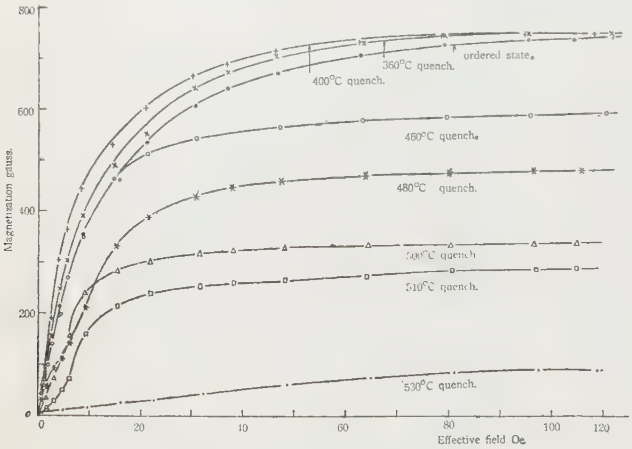

Fig. 1. Magnetization curve for various state of order of Ni_3Mn at room temperature.

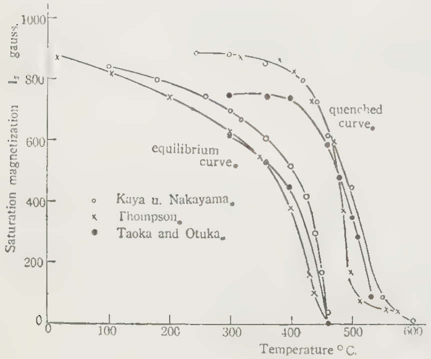

Fig. 2. Change of saturation magnetization with quenching temperature.
quenched curve: measured at room temperature.
equilibrium curve: measured at respective temperature.

The heat treatment for superlattice formation was performed according to the method prescribed by Kaya. A sample annealed at 1000°C for 1 hour, cooled slowly to 700°C, held at 700°C for another one hour, then cooled from 700°C to 500°C at the rate of 20°C per 30 min., from 500°C to 480°C at the rate of 10°C per 30 min., from 480°C to 300°C at the rate of 20°C per day, and finally cooled in the furnace very slowly down to room temperature was defined as to be in a state of perfect order. Intermediate degrees of order were formed by leaving the sample at a certain temperature (under 700°C) for 1 hour and then quenching it in air to room temperature.

The magnetic properties were measured by the apparatus described in the first report. Three samples with practically identical electric and magnetic properties were annealed simultaneously. One of them was used for the measurement of electric properties and the other two for the measurement of magnetic properties at weak and high fields, respectively. The temperature dependence of the magnetic properties were measured by the method described in Report I. The magnetic after-effect was measured by the ballistic method. A system was constructed so as to enable the search coil to be pulled out from the central portion of the specimen automatically at a certain time after the application or removal of the external field. With this system it was possible to measure the magnetization from 0.3 sec. up to several days after the application, removal or change of the external field.

§ 3. Experimental Results

§ 3.1 *Properties at Room temperature*

Fig. 1 show the magnetization curve for various states of order at room temperature. The saturation magnetization increases abruptly from the 530°C quenched sample, and continues to increase up to the 400°C quenched sample. Samples quenched from under 400°C maintain approximately the same value. The results are plotted in Fig. 2 (quenched curve). The discrepancy from the results obtained by Kaya *et al.* is perhaps due to insufficient saturation because of the relatively low external field employed in our experiments (100 Oe)*. The magnetization curves become steeper with the increase of saturation magnetization. The saturation magnetization stays approximately constant after the 400°C quenched state is passed and the magnetization curve shows a slight decrease in slope. Although the change involved is small, the later stage closely resembles the case of Ni_3Fe. However, for the discussion of the change in slope of the magnetization curves to have any significance, the effect of the change in saturation magnetization has to be taken into account. When this is considered, it is seen that the slope reaches a maximum at the 460°C quenched state. The irregular behavior of the magnetization curve at weak fields is due to the magnetic after-effect and will be discussed later. It must be noted here that the entire magnetization curve was measured in a relatively short length of time (15 minutes). We shall see later that all the irregularities tend to disappear if the time for measurement is taken longer. Fig. 3 shows the change in initial susceptibility with order. The initial susceptibility was unaffected by the time for measurement. It increases rapidly with order, reaching a maximum at the 400°C quenched state. Taking into account the change in saturation magnetization measured by Kaya, the initial permeability shows a sharper maximum at the 460°C quenched state. Fig. 4 shows the change in coecive force with order. As there is a time effect, measurements were all made at 100 seconds after the application of the field. It is seen that there is a sharp maximum for the 500°C quenched state. Further details of the time effect will be discussed later.

§ 3.2 *Temperature Dependence of the Magnetic Properties*

The specific heat-temperature curve measured by Kaya *et. al.*[5)] and Thompson show that transformation of order-disorder takes place over a wide range of temperature extending from 300°C. Therefore it is impossible to measure the temperature dependence of magnetic properties of an ideally fixed state of order up to the Curie temperature. However, the presence of temperature hysteresis[6)] in the electrical resistance-temperature curve measured at the rate of 2°C per minute and the fact that it takes several hours for the electrical resistance to reach an equilibrium value[7)] imply that if the temperature were to be raised at a sufficiently rapid rate, the degree of order can be maintained to an appreciable extent up to higher temperatures. Fig. 5 shows the temperature dependence of magnetization at 98 Oe for various state of order measured with a heating rate of over 50°C per minute. The temperature at which ferromagnetism disappears increases with order from 360°C for the 510°C quenched state to about 480°C for the perfectly ordered state. The temperature at which ferromagnetism disappears is plotted against the quench-

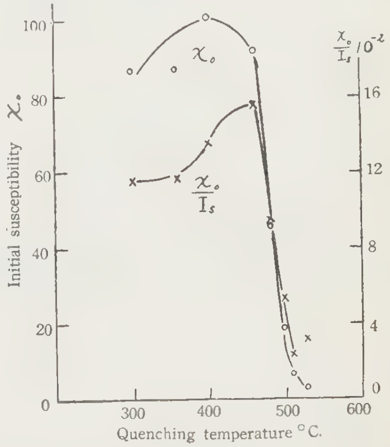

Fig. 3. Change of initial susceptibility with quenching temperature at room temperature.

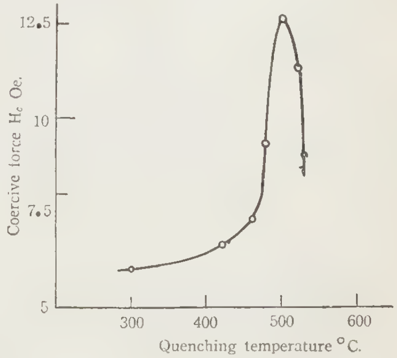

Fig. 4. Change of coercive force with quenching temperature.

---

* Thompson does not give absolute values. His curve was plotted by making an arbitray fit of the scale.

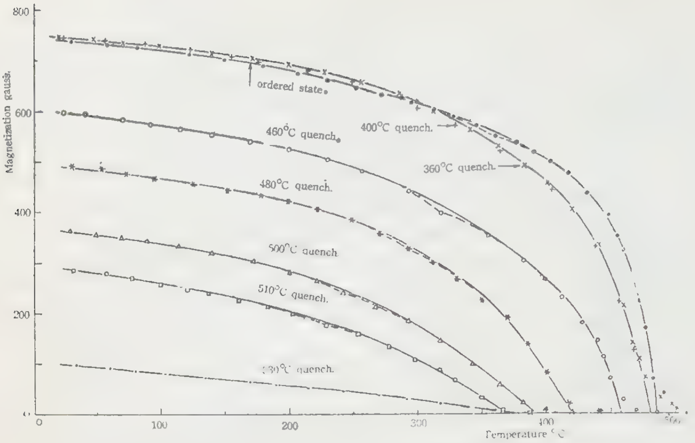

Fig. 5. Temperature dependence of magnetization at 98 Oe. for various states of order.

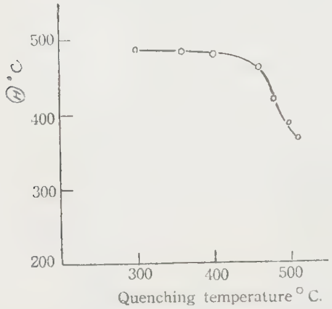

Fig. 6. Change of temperature at which ferromagnetism disappears with quenching temperature.

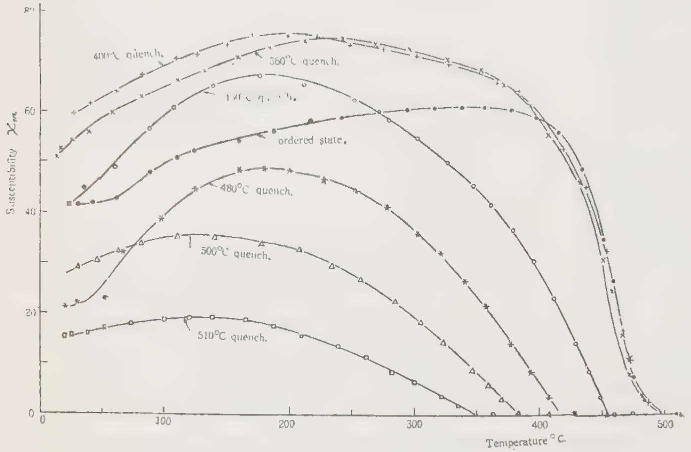

Fig. 7. Temperature dependence of susceptibility at 8.16 Oe. for variovs states of order.

ing temperature in Fig. 6. The slope is steep down to the 460°C quenched state and becomes nearely horizontal from there on. It is noted that in the magnetization-temperature curve (Fig. 5) for the various ordered state, there exists an anomaly indicated by the dotted lines. Although the effect is not very clear there are reasons to believe that this anomaly may be due to the existence of two phases with different Curie points.

Fig. 7 shows the temperature dependence of susceptibility at an applied field of 8.16 Oe. The irregularities in the curves under 200°C for the intermediate states of order arise from the previously mentioned time effect*.

§ 3.3 *Magnetostriction*

The magnetostriction-magnetization curve at various temperatures for the perfect ordered state is shown in Fig. 8. The values are very small, barely exceeding 10^{-6} at the most. Thus it is very difficult to establish any quantitative relations. It is clear, however, that the magnetostriction changes sign from negative to positive as the temperature increases. Fig. 9 shows the temperatre dependence of saturation magnetostriction λ_s at various states of order. The saturation magnetization was measured as fast as possible at temperatures over 400°C where the destruction or formation of the superlattice is accelerated. For the ordered state, λ_s starts $-1.0\cdot10^{-6}$ at room temperature, becomes zero at about 110°C, reaches a maximum of $1.5\cdot10^{-6}$ at 300°C and then decreases to zero at the Curie point. The general form of the curve is the same for all states of order. It is seen that the value at maximum shifts to higher temperatures as the order increases. In order words, there is a contraction at room temperature and expansion at 300°C which increase as the order increases. λ_s for various states of order coincide at about 200°C. The behavior as a whole is very complicated but systematic.

---

* It is noted that this time effect does not appear for high external fields so the values for saturation magnetization are unaffected.

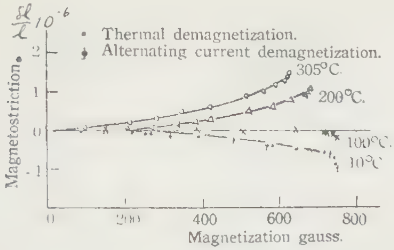

Fig. 8. Magnetostriction—magnetization curves at various temperatures for a perfect ordered state.

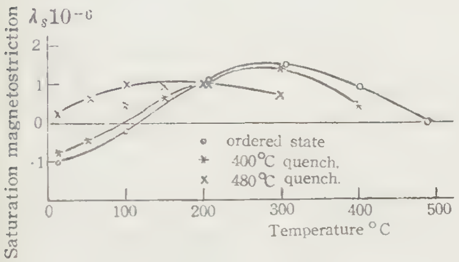

Fig. 9. Temperature dependence of saturation magnetostriction for various states of order.

§ 3.4 *Magnetic After-Effect*

In the course of our experiment, a large magnetic after-effect which could be measured over a duration as long as a weak was found to exist in samples at intermediate states of order, namely those quenched from 500°C~480°C. We shall, as an example, describe the 500°C quenched case. The magnetization curves shown in Fig. 10 were plotted by applying a field and measuring the magnetization after various time intervals as indicated in the figure. In order to express the amount of after-effect on the virgin curve, we introduce a quantity γ defined as

$$\gamma=(I_{1000}-I_1)/I_1 ,$$

where I_1 and I_{1000} are the values of magnetization at 1 sec. and 1000 sec. after the application of the field. The quantity for the descending branch of the hysteresis curve is defined as

$$\gamma'=(I_{1000}-I_1)/(I_s-I_1) ,$$

where I_s the saturation magnetization. Fig. 11 shows γ and γ' for different values of the applied field. A sharp maximum is seen on both the virgin and the descending hysteresis curves at points corresponding to the maximum reversible susceptibility. Both γ and γ' reach a value of 140% at the maximum. The major portion of the magnetization *versus* time curve can be expressed by the relation,

$I=I_0+\alpha \log t$ virgin curve

$I=I_0+\beta \log t$ descending branch of the hysteresis curve.

The dependence of α and β on the applied field is shown in Fig. 12. The curves resemble those of γ and γ'.

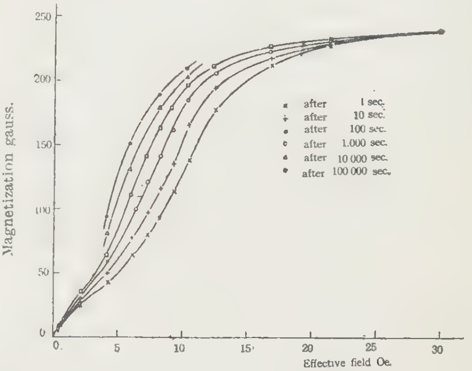

Fig. 10. Time effect on magnetization curve for a 500°C quenched specimen.

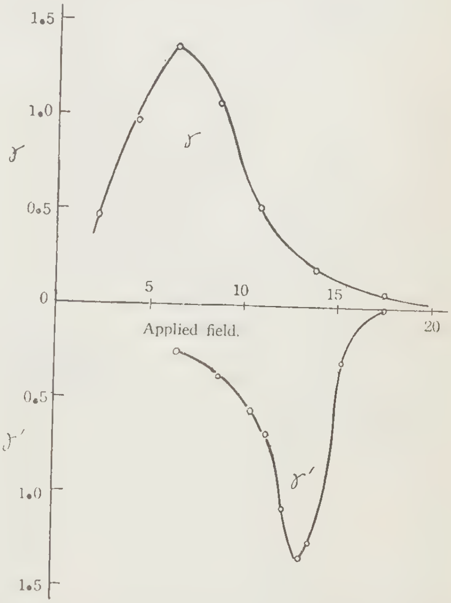

Fig. 11. Variation of γ and γ' with an applied field strength.

Due to the presence of the after-effect, the coercive force H_c is also a function of time. The influence of the after-effect on the coercive force is shown in Fig. 13. It is seen that the value of H_c decreases logarithmically with time for all states of order. The relation between $\alpha_{\max}/I_s$ and H_c (after 100 sec.) is shown in Fig. 14. The figure shows the

Table I. Electric and Magnetic Properties of Ni_3Mn at Room Temperature.

State of order	Specific Resistance $\mu\Omega$ at 20°C	Magnetization at 100 Oe	Magnetic Curie Point °C	Initial Susceptibility	Saturation Magnetostriction 10^{-6}
Disorder	73.8				
530°C q.	69.1	90		3	
510°C q.	63.7	287	363	7	
500°C q.	60.8	335	383	19	
480°C q.	50.8	347	415	46	0.2
460°C q.	44.4	583	458	92	
400°C q.	28.1	743	476	101	−0.8
360°C q.	25.0	745	488	87	
order	22.2	745	486	87	−1.0

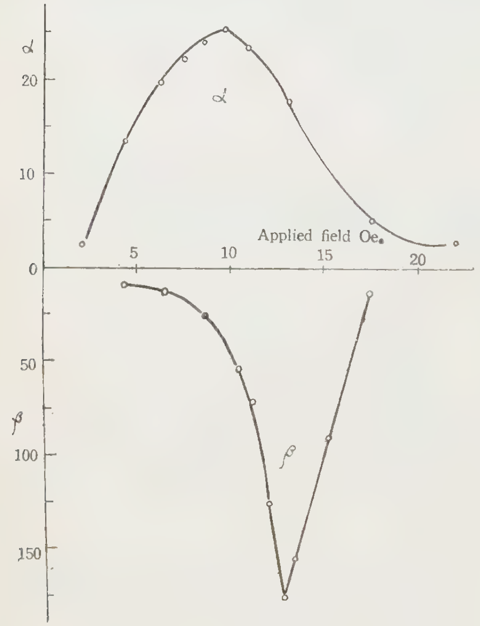

Fig. 12. Variation of α and β (gauss) with an applied field strength.

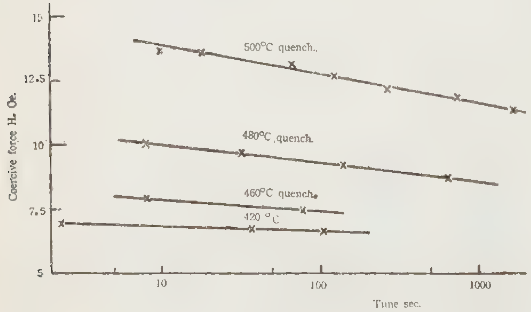

Fig. 13. Change of coercive force with time.

straight line in agreement with the measurement for Alnico V[8])

Various properties of Ni_3Mn at room temperature are listed in Table I.

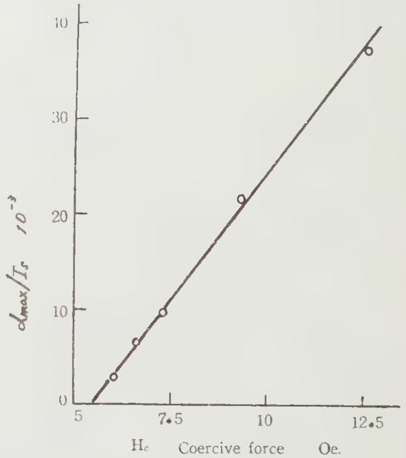

Fig. 14. Relation of $\alpha\, max/I_s$ and H_c.

§ 4. Discussion

First of all, the change in saturation magnetization with order is, in agreement with previous measurements, rapidly increasing at the initial stage of order formation. The increase above the 400°C quenched state is very small and of comparable order with the entire change in the case of Ni_3Fe.

The temperature at which ferromagnetism disappears was seen to increase with the increase of order. These points, however, cannot be immediately regarded as the ferromagnetic Curie point because even with a heating rate of over 50°C per minute, the destruction or formation of the superlattice cannot be neglected. Thus the true curve for the dependence of the Curie point on order must be more exaggerated than the curve shown in Fig. 6. In short, our results lead us to the conclusion that the Curie point actually increases with the formation of the superlattice in contrast with Thompson's argument which sets the Curie point at 460°C regardless of the state of order.

The behaviour of the highly ordered states namely the small increase in saturation magnetization and Curie point, decrease of the susceptivelity, increase in the magnitudes of magnetostriction is quite similar to the changes encountered in the second stage (1 hr. to 20 hrs. at 490°C) of superlattice formation in Ni_3Fe (refer previous report). This infers that the mechanism of order formation and the interaction with the alignment of spin moments is similar for the two alloys at the respective regions of superlattice formation.

Thus the apparently intricate influence of order on the magnetic properties is to some extent made more clear. However not much can be said from our results as to how the formation of the superlattice takes place. Shull⁹⁾ has recently shown by neutron diffraction that long range order does indeed exist in the ordered state of Ni_3Mn.

Although the apparent change in magnetostriction with order and temperature is quite complicated, the behavior as a whole is systematic. It is difficult, however, to interpret the results along Smoluchowski's line¹⁰⁾ discussed in the previous report.

The anomalous magnetic after-effect which was seen to be closely related with the state of order is a very interesting problem. The measurements reported here are of preliminary nature. We hope to report further measurements concerning this effect to throw light upon the mechanism in our next report.

§ 5. Conclusion and Acknowledgement

The rise of the Curie point, changes in the magnetization curve and magnetostriction with the formation of order and the temperature dependence of some of these properties at a fixed state of order has been reported. An abnormally large and long magnetic aftereffect was found to exist at intermediate states of order.

The authors wish to express their hearty thanks to Prof. Seiji Kaya for his kind guidance throughout the course of this research. We also wish to thank Mr. R. Fujita of the Osaka Technical School for his assistance in making the magnetostriction measurements. Part of this research was supported by the Scientific Research Fund granted by the Ministry of Education.

References

1) S. Kaya and M. Nakayama: Proc. Phys. Math. Soc. Japan **22** (1940) 126.

2) N. Thompson: Proc. Phys. Soc. **52** (1940) 217.

3) S. Kaya, M. Nakayama and H. Sato: Proc. Phys. Math. Soc. Japan **25** (1943) 179.

4) H. Sato: Nihon Butsuri Gakkai-shi **3** (1948) No. 1–2.

H. Sato: Sci. Rep. of Res. Inst. Tohoku Univ. **1** (1949) 71.

5) S. Kaya: loc. cit (1)

6) S. Kaya: loc. cit (1)

7) N. Thompson: loc. cit. (2)

L. R. Aronin: J. App. Phys. **23** (1952) 642.

8) R. Street, J. C. Wooley, Jr and P. B. Smith: Proc. Phys. Soc. **B 65** (1952) 461.

9) C. G. Shull and S. Siegel: Phys. Rev. **75** (1949) 1008.

10) J. E. Goldman and R. Smoluchowski: Phys. Rev. **75** (1949) 140.

JOURNAL OF THE PHYSICAL SOCIETY OF JAPAN Vol. 9, No. 5, SEP.—OCT., 1954

On the Solid Solubility of Silver in Aluminium

By Ken-ichi HIRANO and Yutaka TAKAGI

Department of Physics, Tokyo Institute of Technology,
Oh-okayama, Meguro-ku, Tokyo

(Received April 24, 1954)

Heating the specimens of aluminium-silver alloy which are in thermal equilibrium, from the room temperature to above the two phase boundary, the changes of specific heat and electrical resistance have been examined: from the characteristic changes of them due to the resolution of precipitated phase, the solid solubility curve or "solvus" of silver in aluminium has been determined.

A remarkable change in the direction of the solvus at about 20 atomic percentage of silver and at 526°C which was for the first time observed by Raynor and Wakeman through their micrographic examination, has been reconfirmed.

Besides, the energy of solid solution and accompanied entropy change have been determined and shown plotted against silver content from 1.3 to 50 atomic %. Both curves show a bending which is probably attributable to the effect of the electronic band structure of pure aluminium metal.

The energy of valence electrons in the solid solutions has been calculated by means of the state density curve due to Matyáš, Axon and Hume-Rothery. It was found: In order to explain the observed increasing of the energy of alloys, it seems that aluminium must have 2.5 electrons per atom but not three.

§ 1. Introduction

In the course of studies on the mechanism of precipitation phenomena in aluminium rich aluminium-silver alloys, it became necessary to know the complete solid solubility curve. Hitherto an abnormally extensive solubility of silver in aluminium has been reported by several investigators1)−5).

Recently Raynor and Wakeman6) have examined the solvus from 2.7 up to 27.3 atomic % of silver and obtained a result very much different from all of the previous workers. They have used micrographic technique and materials of very high purity. The wide divergences in the results of earlier workers, they say, should be attributable to the impure materials.

Subsequently to them, Rotherham and Larke7) have redetermined the solvus for the alloys of lower silver content from 0.3 to 2.1 atomic % by electrical resistance and X-ray measurements. They have shown that their solvus can be linked with that of Raynor and Wakeman by a smooth curve.

Now having examined the temperature dependence of the specific heat and the electrical resistance with sufficiently aged specimens, we have also obtained the solvus curve which is in precise agreement with the Raynor and Wakeman's. And at the same time we have obtained the energy and entropy of solid solutions as a function of silver concentration.

Raynor and Wakeman have suggested that the characteristic kink of the solvus curve is possibly attributable to the irregular hump of the free energy curve which they have expected to be present at about 2.6 electrons per atom.

Now that we have actually obtained the energy curves, it should be our task to see whether this energy curve should be explained by the electronic energy band, and if so, how much electrons the aluminium metal must have.

§ 2. Materials Used, Heat Treatment

The alloys containing from 1.3 to 50 atomic % of silver were prepared from assay silver (99.99% pure) and superpure aluminium (99.99 % pure). The metals were melted in a graphite crucible, well stirred with graphite rod, cast into a chill mould, cold worked and then annealed to remove the casting structures.

The specimens used for the specific heat measurements were cylinders, 2 cm in diameter and 3 cm high; those used for the electrical resistance measurements were square bars, having dimension of 0.2 cm thick, 0.3 cm wide and 10.0 cm long.

After a long enough annealing had been given at a temperature in one phase region, the alloys were cooled down to the room temperature very slowly. The time elapsed for the cooling was 80~100 hours, which was sufficiently slow to get the two phase state, for no trace of supersaturation could be detected anymore.

§ 3. Experimental Methods

The specific heat measurements were carried out from room temperature to above the solvus by the adiabatic high temperature calorimeter of the Nagasaki-Takagi type[8], which seems to be suitable for the present work because of its sensitivity to small energetic changes prior to any sign of the transformation detectable by means of X-ray or micrographic technique.

The heating rate used most often was about 2°C per minute, although the same results were also obtained by other heating rates; 1°, 2.5° or 4°C per minute.

The electrical resistance has been measured by a potentiometer method. Four silver contactors were pressed to the specimen. Two of them were for the current leads and the other two were pressed at a distance 5 cm apart for the potential leads.

The apparatus was set in vacuum to prevent oxidation. The heating rate was the same as used in the specific heat measurements.

§ 4. Experimental Results

The results obtained are shown in Figs. 1 and 2. In Fig. 1 three dimensional relation among the specific heat, the silver content and the temperature is illustrated.

The ordinary part of the specific heat due to the lattice vibrations is here disregarded because of its insignificance for the present purpose.

Three typical humps of heat absorption are clearly distinguishable in Fig. 1, which are shown separately in Fig. 2 above those of the electrical resistance.

Fig. 2(a) is a normal type curve which is characteristic with the alloys containing less than 16.4 atomic % of silver. The temperature denoted by **A**, where the heat absorption attains its maximum and above which the curve falls down almost vertically to the normal value, corresponds to the two phase boundary. It was observed that the slower the heating rate is, the sharper the peak of heat absorption curve becomes, but, nevertheless, the heating rate does not affect appreciably the position of the temperature **A**.

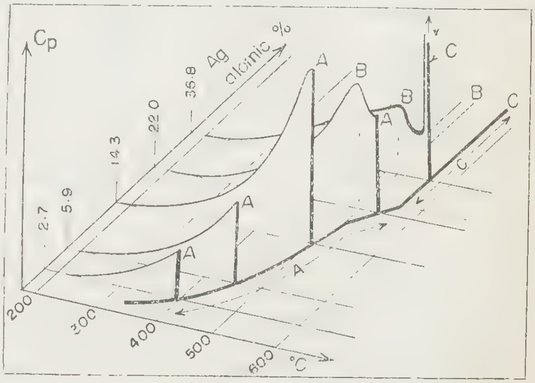

Fig. 1. Relation among specific heat, silver content and temperature.

On the other hand, 20.0, 21.3, 22.0 and 23.4 atomic % alloys show Fig. 2(b) type, in which two inflexion points denoted by **A** and **B** shall be observed. Whereas the temperature of the point **A** depends upon the silver content just as so in the case of (a), the temperature of the inflexion point **B** is entirely independent of the silver content; it is recognized for all alloys at a constant temperature, 526°C.

With 27.3, 36.8 and 50.0 atomic % alloys, Fig.2 (c) type is observed. The characteristic heat absorption denoted by **C** occurs at 566° ~568°C. It is clearly due to the eutectic reaction. And here also the inflexion point denoted by **B** is recognized at the constant temperature 526°C for all alloys regardless of their concentrations, just as so in the case of (b).

As shown in Figs. 2(a′), (b′) and (c′) the change of electrical resistance corresponds exactly to the change of the specific heat.

The silver content dependence of the three temperatures **A**, **B** and **C** was shown in Fig. 1 as a projected trace on the temperature-silver content plane.

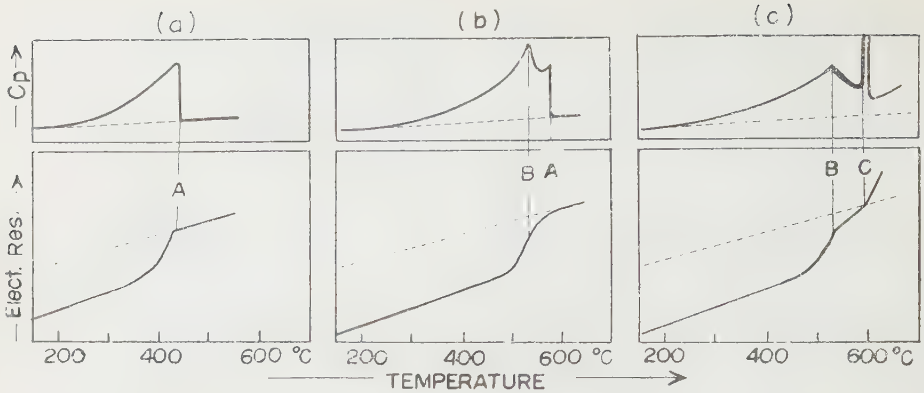

Fig. 2. Three typical shapes of Specific heat and Electrical resistance curves.

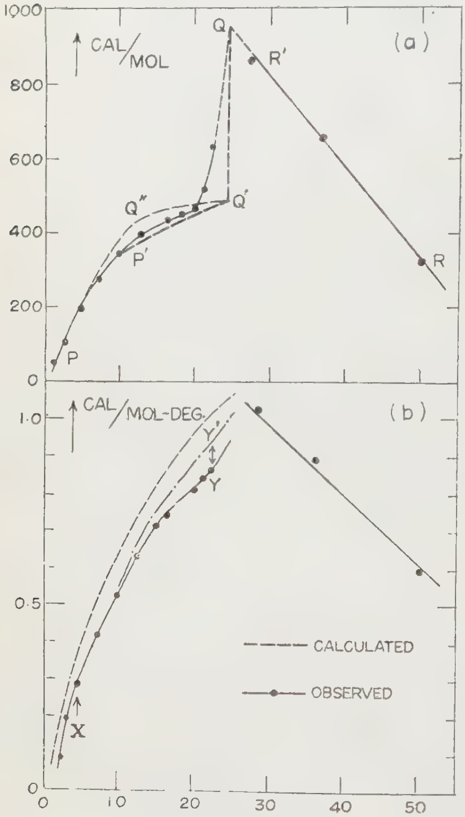

Fig. 3. (a) Energy of solid solution, (b) Entropy of solid solution.

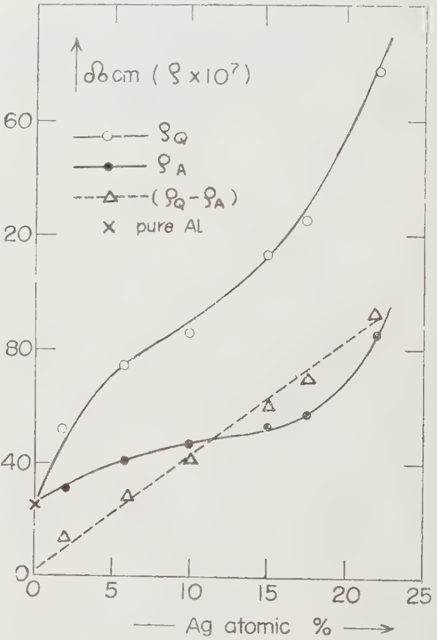

Fig. 4. Electrical resistance.
ρ_Q: Specific resistance of quenched alloys,
ρ_A: Specific resistance of annealed alloys.

From the heat absorption curves we have calculated the energy of solid solution, and plotted them against the silver content in Fig. 3(a). Above 10 atomic % the curve decreases gradually its slope but again a steeply increasing portion is reached. At a point denoted by **Q**, the extrapolation of the lower content portion crosses the straight line, **RR′**, given by the alloys with higher silver contents. The point **Q** represents the maximum energy point and is at 23.8 atomic %.

Fig. 3(b) represents the entropy changes in the formation of solid solutions, derived from the heat absorption curves obtained above. It should be compared with the dashed curve, which represents the ideal mixing entropy,

$$-R\{\theta\log\theta+(1-\theta)\log(1-\theta)\},$$

where R is the gas constant and θ is the mole fraction of silver.

In Fig. 4, the dependence of the specific electrical resistance upon the silver content are shown for two states; the one is attained after quenching from 560°C to water and the other after slow-cooling in the furnace from 560°C to room temperature at a rate of 2∼5°C per hour. The former is denoted by ρ_Q and the later by ρ_A; the difference between them, $\rho_Q-\rho_A$, is shown by a dashed line.

§ 5. Interpretation of the Results and Discussions

As shown in Fig. 1, the projected trace of the point **A** is the solvus curve in the phase diagram. Let us show it again in Fig. 5 in comparison with that of Hansen[3]. Our curve overlaps exactly that of Raynor and Wakeman, the two can not be separated in the figure. As was expected from Figs. 2(b) and (c) where the inflexion point **B** at 526°C occurs independently of the silver content, a marked change in direction at about 20 atomic % and 526°C was thus reconfirmed.

The heat absorption curves cannot be due to some transformation in the phase with which the solid solution is in contact. Raynor and Wakeman have illustrated the log S versus $1/T$ curve, where S is atomic % of soluble silver at the absolute temperature T, and indicated that the form of the curve is not typical of systems in which the change in the direction of the solvus is due to some transformation in the phase with which the primary solid solution is in equilibrium.

As shown in Fig. 4, we obtained a straight line by plotting $(\rho_Q-\rho_A)$ against the silver content, though both ρ_Q and ρ_A curves show the characteristic inclination which seems just corresponding to the solvus. Then the decrease in the electrical resistance due to the precipitation is proportional to the silver content of the alloy.

From Fig. 2(c) it was recognized that the eutectic temperature lies between 566° and 568°C, which is in good agreement with the temperatures 567°, 568°, and 566°∼568.5° reported respectively by Petrenko[1], Crepaz[4], and Raynor-Wakeman[9].

The point **Q** in Fig. 3(a) shows that the maximum solid solubility is 23.8 atomic % at the eutectic temperature, and the energy of solid solution for this maximum concentration is about 970 cal. per mol. The straight line **RR′Q** given at higher silver content is a typical one for the alloys with the eutectic reactions.

If the solvus were to have a normal form as shown by the dashed curve in Fig. 5, then the energy of solid solution should also have a normal form as represented by the curve **PP′Q′**, whereas dashed curve **PQ′′Q′** represents the one which must be obtained if the solvus is deflected as in the present case. Then it is obvious that the abnormal great increase of solid solution energy, as **P′Q**, can not be associated with the deflection on the solvus itself.

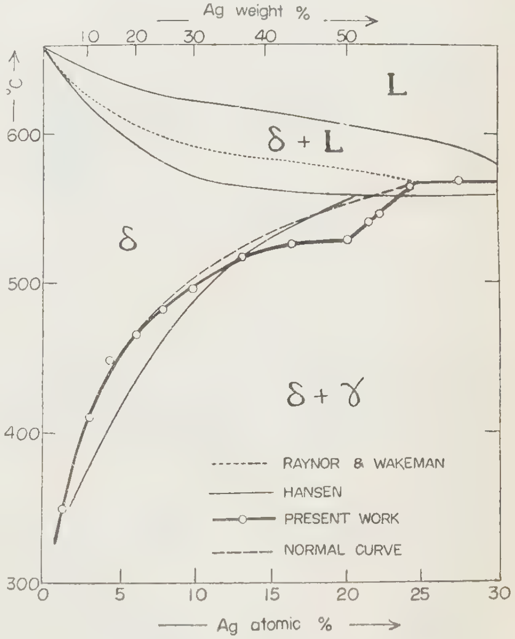

Fig. 5. Solvus Curve.

The conceivable origin is the effect of the electronic energy caused by the electronic band structure of aluminium metal. For the estimation of this effect with sufficient certainty it is desired to know the detailed distribution of the electronic energy states in aluminium.

We have referred to the $N(E)$ curve which has been given by Axon and Hume-Rothery[13], based on the theoretical work of Matyáš[14]. (Fig. 6) The curve is defined such that $N(E)dE$ gives the number of electronic states per atom with energies between E and $E+dE$. From this we have calculated the mean energy per electron,

$$\overline{E}=\sum_{E=0}^{E} N(E)\cdot E\Big/\sum_{E=0}^{E} N(E)\,,$$

and have plotted it against the number of electrons, $\sum_{E=0}^{E} N(E)$ per atom. (Fig. 7)

No abnormality can be predicted in the region of 2.6 electrons per atom, where Raynor and Wakeman have expected the occurrence of some irregularity to affect the free energy composition curve, but the deviations from the normal smooth curve have in fact been found at two positions **AB** and **CD**; the former upward deviation is related to 2.2～1.9, and the latter downward deviation is related to 1.4～0.6 electrons per atom. The **CD** deviation seems to be insignificant for the present work because of its too small electron: atom ratio.

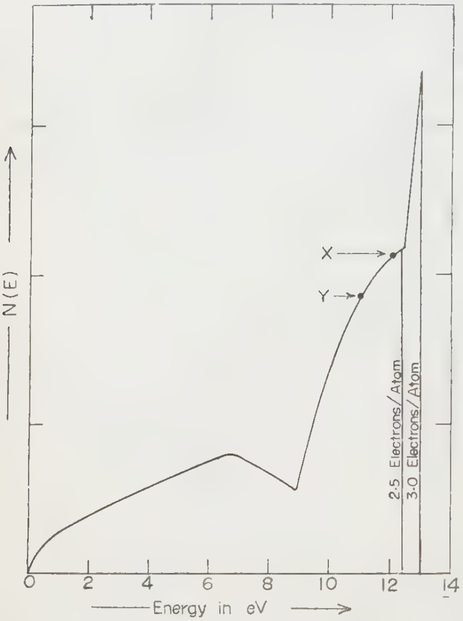

Fig. 6. Distribution of the Electronic Energy State in Aluminium, *after* Axon and Hume-Rothery.

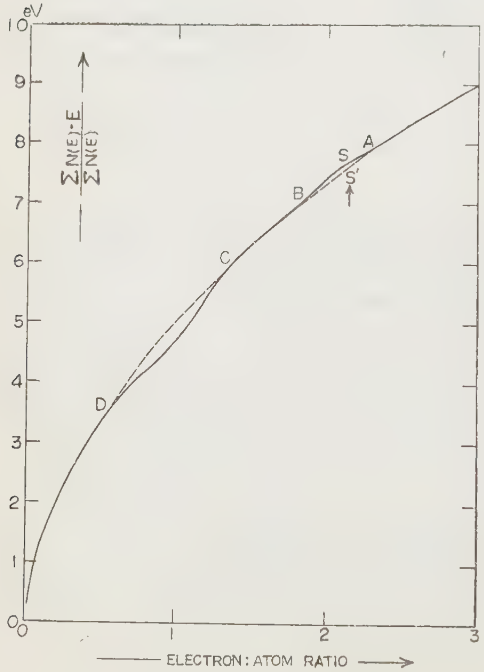

Fig. 7. $\overline{E}$ *versus* $\sum_{E=0}^{E} N(E)$ curve, Numerically calculated from Fig. 6.

As a matter of record, many properties suggest that the number of bonding electrons in metallic aluminium is less than three. Recently Dorn and his coworkers[9)10)] have suggested that, in order to get a systematized relation of the effect of alloying elements on the plastic properties of aluminium alloys, it is necessary to assume two rather than three bonding electrons per atom. Furthermore they[11)] examined the effect of additional elements, Cu, Zn, Ge, Ag, Cd, and Mg, on the electrical resistance of aluminium and applying the Norbury rule[12)], suggested that the effective vaelnce of aluminium must approximately be 2.5. If we adopt this value, themaximum solid solubility limit and the kink point of the solvus correspond respectively to about 2.16 and 2.20 electrons per atom as shown in Fig. 8. As shown in Fig. 7 by an arrow the deviation **AB** attains it maximum at the point of maximum solubility. The point **A** where the deviation begins corresponds to the point of inflexion on the solvus. The maximum deviation **SS′** in Fig. 7 seems to cause the maximum abnormal increase in the energy of solid solution, **QQ′** in Fig. 3(a). **SS′** is evaluated as 600～700 cal/mol., and is in satisfactory agreement with the experimental result of **QQ′**=500 cal/mol.

In contrast to the increasing tendency of solid solution energy, the entropy change accompanied with them shows rather an inclination of decreasing sense as shown in Fig, 3(b), where the observed entropy change runs nearly parallel with the entropy of ideal mixing at lower silver content, but above 15 atomic % the former begins to deviate downward. The entropy of valence electrons can be written[15)],

$$S=N(\pi^2/3)k^2T\,, \tag{1}$$

where N is the state density at the Fermi surface of the electron band, k the Boltzmann constant and T the absolute temperature. Then the higher the state density at the Fermi surface of the electron band is, the higher the electronic entropy is. In the present case, the downward deviation **YY′** in Fig. 3(b) seems to be caused by decreasing state density at the Fermi surface. In Fig. 6, the points **X** and **Y** correspond respectively to **X** and **Y** in Fig. 3(b). Inserting the values obtained from Fig. 6 into the Eq. (1), we have computed the difference of entropy between **X** and **Y** and obtained 0.06 cal/mol.deg. which is in good agreement with the experimental result as shown in Fig. 3(b), for **YY′** is about 0.05 cal/mol.deg.

Moreover, if we assume 2.5 valance electrons per aluminium atom, we can obtain further interesting results. This shall be illustrated in Fig. 8, where the two solvus curves of Al-Ag and Al-Zn[19)] systems are plotted in terms of the electron:atom ratio. It seems that the same factor may be responsible for the anomalous form of the solubitity relations in both systems. The correlation demonstrated in Fig. 7 implies that the portions of the maximum solid solubility limit of the two solvus curves occur approximately at the same electron:atom ratio. And at the same time this correlation may add another powerful evidence for the assumption of 2.5 electrons per atom of aluminium.

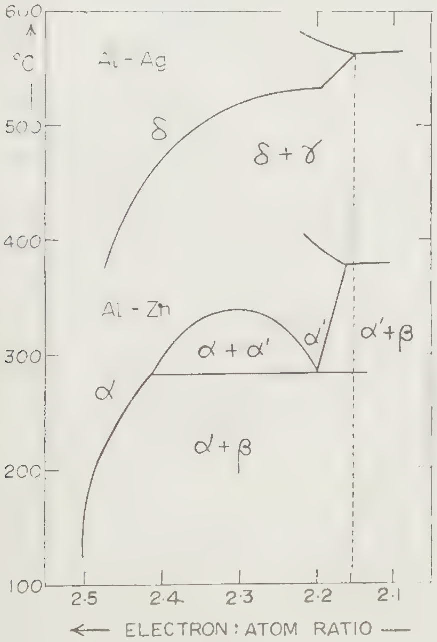

Fig. 8. Comparison of solvus curves of Al-Ag and Al-Zn systems.

This will not at all be unreasonable, because the electron:atom ratio must play the most important role in both systems where the atomic size factor are favourable for solid solution. To get more informations, it is desired to determine the solvus curve for ternary cases of suitable compositions intermediate between Al-Ag and Al-Zn systems.

§ 6. Acknowledgements

The authors wish to express sincere thanks to Mr. H. Sakai who kindly carried out numerical integration of Fig. 6 independently of us, and gave a useful check to our Fig. 7., and also to Mr. H. Maniwa for his helpful discussions.

References

1) G. T. Petrenko: Z. Anorg. Chem. **46** (1905) 49.
2) M. Tasaki: Kinzoku no Kenkyu **4** (1927) 35.
3) M. Hansen: Z. Metallkde. **20** (1928) 217.
4) E. Crepaz: Atti. III Congr. Chim. Pure Appl., Firenze e Toscana, (1929) 371.
5) W. Guertler: Metallwirtschaft **19** (1940) 432.
6) G. V. Raynor, D. W. Wakeman: Phil. Mag. **40** (1949) 404.
7) L. Rotherham, L. W. Larke: Jr. Inst. Met. **81** (1952) 67.
8) S. Nagasaki, Y. Takagi: Jr. Appl. Phys. Japan **17** (1948) 104.
9) J. E. Dorn, P. Pietrolowsky, T. E. Tietz: Jr. of Metals, July (1950) 933.
10) J. E. Dorn, P. Pietrolowsky, T. E. Tietz: 5th Tech. Rep. to N.R., N7-ONR-295 (1949).
11) A. T. Robinson, J. E. Dorn: Jr. of Metals, June (1951) 457.
12) A. L. Norbury: Trans. Faraday Soc. **16** (1921) 570.
13) H. J. Axon, W. Hume-Rothery: Proc. Roy. Soc. **A 193** (1948) 1.
14) R. Matyáš: Phil. Mag. **39** (1948) 429.
15) See for instance, J. C. Slater: Introduction to Chemical Physics, p. 79.
16) G. V. Raynor: Inst. Metals (London) Annoted Equilib. Diag. Series, No. 1, 1943.

JOURNAL OF THE PHYSICAL SOCIETY OF JAPAN Vol. 9, No. 5, SEP.—OCT., 1954

On the Λ-shaped Ferrimagnetism of $FeS_{1.10}$*

By Tokutarō HIRONE, Seijirō MAEDA
Research Institute for Iron, Steel and Other Metals, Tōhoku University,
and Noboru TSUYA
Research Institute of Electrical Communication, Tōhoku University

(Received April 26, 1954)

A Λ-shaped change in the thermomagnetic curve in iron sulfide $FeS_{1.10}$ (γ-transformation) was investigated experimentally. It was found that the height of peak was increased by decreasing the heating speed of the specimen. Temperature hysteresis in the thermomagnetic curves were also found at the low temperature side of the peak. Excess specific heat corresponding to the thermomagnetic anomaly was observed; the amount of anomalous heat absorption during the transformation was of the order of 100 cal/mol. It was concluded that the change of magnetism at the transformation is due to the ferrimagnetic distribution of ferrous and ferric ions and the change of vacant site distribution at the transformation.

§ 1. Introduction

The magnetism of iron sulfides FeS_x with comparatively high sulfur content x ($x \lessdot 1.12$) has been considered[1] as a sort of ferrimagnetism[2]. Namely in these substance magnetism is considered to arise from the difference of the net magnetic moments between the two interpenetrating sublattices, one of which contains the vacancies in the iron sites in the ordered arrangement[3] whereas the other does not. According to Haraldsen[4], the magnetization of FeS_x with $x \approx 1.12$ appears to be of the normal Weiss form. On the other hand, when $x \approx 1.11$ there appears a Λ-type anomaly superposed on the ordinary Weiss curve. When x decreases to 1.10 the magnetization versus temperature curve becomes entirely of the Λ-type. In other words, when the temperature is raised from room temperature the magnetization of $FeS_{1.10}$ is at first very small whereas above a certain temperature ($\approx$200°C), the magnetization increases very rapidly and soon reaches its maximum value and them decreases along the normal Weiss curve. The temperature at which the magnetization vanishes is slightly lower than T_β, the Curie point of antiferromagnetic spin arrangement.

On the other hand the curve[4] of susceptibility as a function of temperature of an antiferromagnetic FeS_x with comparatively small excess sulfur content x($1.06 \leqq x \leqq 1.09$) has a peak between the temperatures T_α[5] and T_β[6]. When x reaches 1.10 this peak (which is designated by γ) transfers to the Λ-type spontaneous magnetization mentioned above. To obtain more information about the Λ-type curve we have tried to measure the susceptibility of these substances. The purpose of this report is to present some experimental evidences concerning the above behaviours and to discuss the mechanism of this peculiar magnetism.

§ 2. Specimens and the Experimental Apparatus

The details on the preparation of the sample used and the apparatus for measuring the susceptibility, an automatic type of magnetic balance, have been reported in other papers[6][7]. The apparatus for the heat capacity measurement was also the same as that described in the previous report[8]. Hence the description on these apparatus will be omitted.

For the measurement of magnetic susceptibility χ as a function of temperature, the spceimen to be measured was packed into an evacuated thin capsul made of fused silica. The diameter, length and thickness of the

---

* This investigation was supported in part by the Grant-in-Aid of Fundamental Scientific Research of Ministry of Education.

capsul were about 5 mm, 20 mm and 0.5 mm respectively. The weight of the specimen used was about 20 mg.

§ 3. Experimental Procedures and Results

Before each measurement the specimen was heated at 1000°C for a sufficiently long time, then cooled down to 300°C per hour. The heating circuit of the electric furnace was then opened and the specimen was left to cool down in the furnace to room temperature at very slow rate.

The susceptibility as a function of temperature for $FeS_{1.00}$ at the various rates of temperature change are shown in Figs. 1, 2 and 3. The rate of temperature change in the course of susceptibility measurements corresponding to Figs. 1, 2 and 3 were 300°/hour, 100°/hour and 30°/hour, respectively. The arrows in these figures show the direction of temperature change. Curve 1 in Fig. 1 shows the change of susceptibility with increasing temperature and curve 2 the change with decreasing temperature. Curve 3 in the same figure shows the change of susceptibility when the specimen was reheated immediately after the second run corresponding to curve 2. The curves in Fig. 2 also show similar results of susceptibility measunements as shown in Fig. 1 but the rate of temperature change was about one third of the corresponding cases. It can be seen from Figs. 1 and 2 that cooling and reheating are accompanied by a thermal hysteresis. It was also confirmed that these thermal hysteresis observed reproducible. When similar measurements were performed with a slower temperature change, the largest value of Λ-shaped susceptibility and no thermal hysteresis were observed. (Fig. 3).

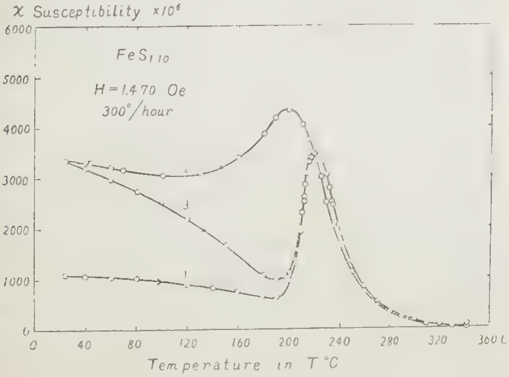

Fig. 1. The change of susceptibility of $FeS_{1.10}$ with temperature change at rate of 300°C per hour under the applied magnetic field of 1470 Oe.

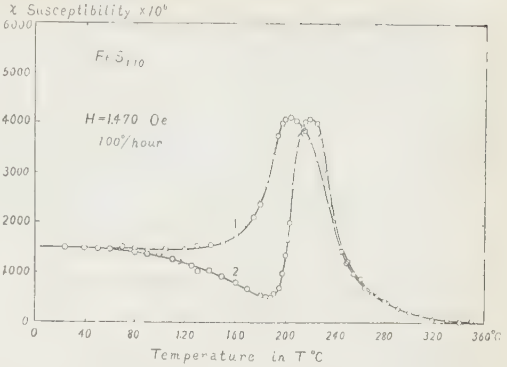

Fig. 2. The change of susceptibility of $FeS_{1.10}$ with temperature change at rate of 100°C per hour.

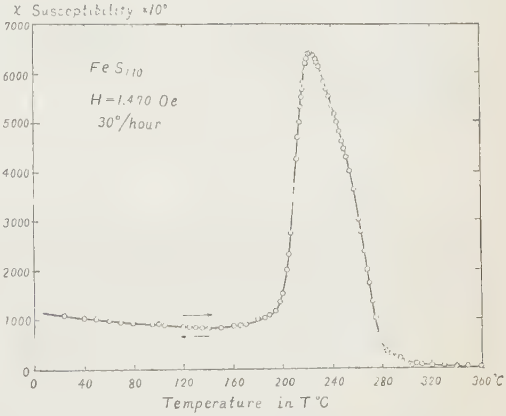

Fig. 3. The change of susceptibility of $FeS_{1.10}$ with temperature change at a rate of 30° per hour.

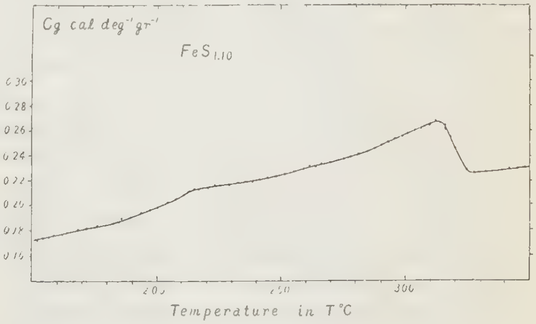

Fig. 4. The heat capacity of $FeS_{1.10}$ as a function of temperature.

These figures infer that the magnetization may be considered as a sum of two parts, one of which is a Λ-shaped ferrimagnetism and the other of the ordinary Weiss type. The former increases whereas the latter decreases with decrease of the rate of temperature change. It should be noted here that the apparent magnetic Curie point T_s remains unchanged and equal to 280°C whereas the T_s' of discontinuous rise of this Λ-shaped magnetism (about 200°C) is slightly shifted to lower temperatures with the increase of cooling rate. The specific heat of this specimen was measured in the same temperature range as that of susceptibility measurements. A broad hump of specific heat was found in the temperature of γ-transformation, T_γ, for the specimen of $FeS_{1.10}$ as shown in Fig. 4*. The rate of temperature increase was 0.3°C per minute. As shown in Fig. 4 there are two anomalies in the specific heat at temperatures of about 220°C and 315°C. The anomalous heat absorption at the latter temperature correspond to the β-transformation mentioned in the previous paper⁶⁾.

§ 4. Discussions

In the previous paper¹⁾, we tried to explain the Λ-shaped ferrimagnetism by the occurrence of two types of electronic ordered states. We will try to modify this mechanism taking into account the ordered arrangement of holes which was proposed firstly by Benoit and Bertaut³⁾.

By similar considerations as mentioned in the previous paper¹⁾, we can explain the origin of this Λ-shaped spontaneous magneti zation as follows: When the substance $FeS_{1.00}$ is cooled from sufficiently high temperature it becomes antiferromagnetic at the temperature T_β ($\approx$320°C), and when the temperature reaches T_s ($\approx$280°C) an ordered arrangement of holes (superlattice I) occurs among the iron lattice sites as in the case of Fe_7S_8 at 560°C. Consequently an unbalance of the net spin moment of the two sublattices occurs. Therefore this magnetism must be considered as a sort of ferrimagnetism. At lower temperatures it is assumed that there another type of superlattice (superlattice II) of the holes. In the superlattice II, however, the density of ions in the two magnetic sublattices is assumed to be just equal with each other. Thus, in this state, the unbalance of net spins between the two magnetic sublattices disappears completely and the substance becomes antiferromagnetic. Hence if the superlattice II is more stable than the superlattice I, then the ferrimagnetic state which occurred at 280°C should transform into the antiferromagnetic state at low temperatures. As mentioned in the previous section the anomalous heat obsorption was actually found. The anomaly which appears at about 220°C may correspond to the two changes of the holes mentioned above. The peak at 315°C corresponds to the order-dis-order transformation of spin arrangement at the Curie temperature T_β.

The thermal hysteresis observed in the susceptibility measurements under fairly rapid temperature change may be explained as follows; If there is a finite relaxation time, which is necessary for the change of arrangement of holes between superlattices I and II, the formation of superlattice II is not completed in the case of rapid cooling and superlattice I is partially frozen in. Then the ferrimagnetization due to the superlattice I is not destroyed completely as shown by the curve 1 in Fig. 1. During the reheating course the transformation of the remaining superlattice I is promoted and hence the magnetization is decreased as shown by the curve 3 in Fig. 1. These thermal hysteresis in the susceptibility showed decrease with decreasing rate of temperature change as observed in the present measurements.

Acknowledgements

It is a pleasure for the present authors to express their thanks to Professor Y. Watanabe, the director of the Research Institute of Electrical Communication for his helpful support in the course of this work. A part of the present investigation was carried out by Messrs Yasuo Uehara and Yoshimitsu Sugita, students of the Faculty of Science of Tōhoku University.

References

1) T. Hirone and N. Tsuya: Phys. Rev. **83** (1951) 1063.

2) K. Yoshida: Physica **17** (1951) 794, Prog. Theoret. Phys. **6** (1951) 691.; L. Néel: Ann. d. Phys. **3** (1948) 137; Proc. Phys. Soc. **A 65** (1952)

---

* The complete report on the specific heat measurement in the region of γ-transformation for various sulfur contents will be published shortly by T. Hirone, S. Maeda, S. Chiba and N. Tsuya.

869, Rev. Mod. Phys. **25** (1953) 58, S. S. Sidhu and O. Meneghetti: Phys. Rev. **91** (1953) 435; J. S. Smart: Phys. Rev. **90** (1953) 55.

3) R. Benoit: Compt. Rend. **254** (1952) 2174; F. Bertaut: Compt. Rend. **234** (1952) 1295, J. Phys. Radium **13** (1952), 372, 499, Acta, Cryst. **6** (1953) 557.

4) H. Haraldsen: Z. Anorg. Allgem. Chem. **246** (1941) 169, 195.

5) T. Hirone, S. Maeda and N. Tsuya: J. Phys. Soc. Japan **9** (1954) 503.

6) T. Hirone, S. Maeda, S. Chiba and N. Tsuya: J. Phys. Soc. Japan **9** (1954) 500.

7) T. Hirone, S. Maeda and N. Tsuya: Sci. Rep. RITU **A 6** (1954) 67.

8) T. Hirone, S. Maeda, I. Tsubokawa and N. Tsuya: Sci. Rep. RITU **A 5** (1953) 513.

JOURNAL OF THE PHYSICAL SOCIETY OF JAPAN Vol. 9, No. 5, SEP.—OCT., 1954

The Crystallographic Aspect of the Mechanical Twinning in Metals

By Hiroshi KIHÔ

Department of Physics, Yoshida College, Kyoto University

(Received May 11, 1954)

In order to investigate twinning dislocations of metals, a simple crystallographical calculation is done, assuming that atomic movements are periodic as the twinning plane moves, that there is no diffusion, and that atoms come to new twin lattice sites from the most neighbouring original lattice sites of them. The shear strain S, Burgers vector $\boldsymbol{b}_t$ and its associated atomic movements $\boldsymbol{U}$, and the structure of twin boundary are obtained for any crystallographic plane. It is shown that $\boldsymbol{U}$ may be easily demonstrated by using a "modified lattice" in which $\boldsymbol{b}_t$ diminishes to zero.

Compared with various twinning planes, the observed twinning planes have the following characteristic: their S is the smallest, but their $|\boldsymbol{b}_t|$ and $|\boldsymbol{U}|$ are not. And when their S is equal to others, the twinning planes which have smaller $|\boldsymbol{b}_t|$ are liable to twin. There are several twinning planes, which are possible to twin, e.g. $\{431\}$ of β-Sn, and $\{100\}$, $\{531\}$, $\{221\}$ of Bi type. In $\{10\bar{1}1\}$ of Mg, $S=0.353$, and K_2 plane is such a one as $(1\bar{3}20)$ which is somewhat rotated around the axis normal to $(10\bar{1}1)$.

§ 1. Introduction

The process of mechanical twinning (deformation twin) has been studied by many authors and the results were summarized by E. Schmid and W. Boas⁽¹⁾, C. F. Elam⁽²⁾, F. Seitz⁽³⁾, and R. Clark and G. B. Craig⁽⁴⁾. In those papers they described many phenomena of twinning. On the other hand, on other sorts of twins, i.e. annealing twin and natural twin, many crystallographists, including I. Schracke⁽⁵⁾ and others, have made the crystallographical classification of twin planes. Very recently, A. H. Cottrell and B. A. Billy⁽⁶⁾ explained the mechanism of twinning for cubic lattices, using the pole mechanism of crystal growth by F. C. Frank. But, it seems impossible to apply it directly to other lattice systems, because the formulation of dislocations has not yet been done.

However, if we neglect the mechanism of the production of twinning dislocations and the relation between twinning ones and others, e.g. slip dislocations, twinning dislocations can be exactly determined from the crystallographic aspect. In this paper, a simple crystallographic calculation is done for some crystal systems. The shear strain S produced by twinning process, Burgers vector $\boldsymbol{b}_t$ and its associated atomic movements $\boldsymbol{U}$, and accordingly the structure of twin boundaries and twinning dislocations are obtained for various crystallographic planes. Here we use the assumptions which are considered profitable from the physical standpoint.

The shear strain S has been already estimated by the experimental observation or calculated by the consideration of K_2 plane[1]. But such a calculation has failed when no crystallographic plane could be regarded as K_2 plane. In this paper S can be generally calculated only by using twinning plane, i.e. K_1 plane. Next, the structure of twin boundaries, including $\boldsymbol{b}_t$ and $\boldsymbol{U}$, has been suggested for some twinning planes[1,7,8,9,], but they are only trials in simple cases. Here it will be treated systematically and it is explained that there are three types of twinning boundary and no other types, according to the assumptions used.

§ 2. Calculation

We consider the case when a twin nucleus has already grown and the twin bounds the original part with a twinning plane (hkl), which moves with the passage of a twinning dislocation on it. Here we discuss in the *reference lattice,* so that all the positions of atoms are represented geometrically by

$$\boldsymbol{R}_i = m_i\boldsymbol{a} + n_i\boldsymbol{b} + p_i\boldsymbol{c}\,, \qquad (1)$$

where $\boldsymbol{a}$, $\boldsymbol{b}$, $\boldsymbol{c}$ are vectors which construct a unit cell, and $(m_in_ip_i)$ denote the ith lattice point. Also for the twin part, primed respectively,

$$\boldsymbol{R}_i = m_i'\boldsymbol{a}' + n_i'\boldsymbol{b}' + p_i'\boldsymbol{c}' + \boldsymbol{r}_i'\,, \qquad (2)$$

where $\boldsymbol{r}_i'$ is a vector which joins the both origins, and it varies with the motion of the twin boundary, on which the lattice point $(m'n'p')$ lies, for the crystal shears by Burgers vector. It should be noticed that the orientations of $\boldsymbol{a}'$, $\boldsymbol{b}'$, and $\boldsymbol{c}'$ are mirror images of those of $\boldsymbol{a}$, $\boldsymbol{b}$. and $\boldsymbol{c}$, respectively, across the (hkl) plane, so that $(\boldsymbol{a}'\boldsymbol{b}'\boldsymbol{c}')$ is the left-handed coordinate-system, when $(\boldsymbol{abc})$ is the right-handed coordinate-system (as shown in Fig. 1).

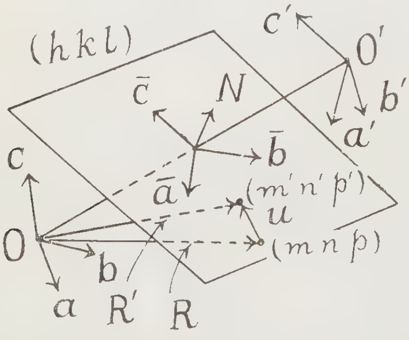

Fig. 1. The relations among the coordinate-systems and the twinning plane.

When d denotes the plane distance of (hkl) of simple space-lattice, $\boldsymbol{N}$ is the unit vector normal to (hkl), and $\bar{\boldsymbol{a}}$, $\bar{\boldsymbol{b}}$, $\bar{\boldsymbol{c}}$ denote respectively the components of $\boldsymbol{a}$, $\boldsymbol{b}$, $\boldsymbol{c}$ parallel to (hkl) (as shown in Fig. 1), using the following notations:

$$m_i\bar{\boldsymbol{a}} + n_i\bar{\boldsymbol{b}} + p_i\bar{\boldsymbol{c}} = \boldsymbol{T}_i\,,$$
$$m_ih + n_ik + p_il = N_i\,,$$

we can reduce (1) and (2) to

$$\boldsymbol{R}_i = \boldsymbol{T}_i + N_id\boldsymbol{N}\,, \qquad (1')$$

and

$$\boldsymbol{R}_i' = \boldsymbol{T}_i' - N_i'd\boldsymbol{N} + \boldsymbol{r}_i'\,. \qquad (2')$$

In (1′) and (2′) the first terms on the right-hand sides represent the components of $\boldsymbol{R}$ and $\boldsymbol{R}'$ parallel to (hkl), while the second terms represent their normal components.

In order to determine atomic movements of twin boundary, such two lattice points are extended all over the whole crystal. When the distance from an original lattice site $(m_in_ip_i)$ to a twin one $(m_i'n_i'p_i')$ is represented by a vector:

$$\boldsymbol{U}(m_i'n_i'p_i' : m_in_ip_i) = \boldsymbol{R}_i' - \boldsymbol{R}_i$$
$$= \boldsymbol{r}_i' + \boldsymbol{T}_i' - \boldsymbol{T}_i - (N_i + N_i')d\boldsymbol{N}\,, \qquad (3)$$

(3) denotes the atomic movement from $(m_in_ip_i)$ to $(m_i'n_i'p_i')$. But it is not determined uniquely to which one of the twin lattice sites an atom jumps from some definite original lattice site (mnp). That is, it is not determined uniquely which one of $(m'n'p')$ must be joined with some (mnp). Hence, unless some physically profitable assumption is made, we cannot discuss the atomic movements of (3).

Assumption I. There are a few sorts of $\boldsymbol{U}$, which, when the twin boundary moves, only appear periodically. It is obvious by the periodicity of crystals.

Assumption II. The atom which comes into some twin crystal lattice site $(m_i'n_i'p_i')$, is at the nearest original crystal lattice site

Table I. The values of I. ($m=0$ or integer)

f. c. c. Bi Type and Hg		b. c. c.		h. c. p.		β−Sn	
(hkl)	I	(hkl)	I	(hkl)	I	(hkl)	I
h, k, l;		$h+k+l$;		$h+2k=3m$,		l; odd	
all odd	1	even	1	l; even	1	h, k; odd and even	1
odd and even	$\frac{1}{2}$	odd	$\frac{1}{2}$	l; odd	$\frac{1}{2}$	h, k; all odd and all even	$1/4$
				$h+2k \neq 3\mathrm{m}$	1		
						$l=4m+2$;	
						h, k; all odd	1
						h, k; odd and even	$\frac{1}{2}$
						$l=4m$	$\frac{1}{2}$

of it (mnp), i.e. the distance between (mnp) and ($m'n'p'$) which form U is the nearest one, when the twin boundary passes there.

Assumption III. The whole crystal does not displace but S, i.e. the average of atomic movements becomes Burgers vector. It is sure of the nature of the reference lattice.

By *Assumption I*, we shall consider only a narrow band limited by its priodicity. Let the two origins of twin and original crystal lattices attach to the both sides of this band. Then these two origins have the same U. Now, when ($m_0n_0p_0$) is joined with the twin origin ($0'0'0'$), and ($m_0'n_0'p_0'$) with the original origin (000), we have, without any limitation,

$$(m_0n_0p_0)=(m_0'n_0'p_0') .$$

Then,

$$\left.\begin{aligned} \boldsymbol{U}(m_0n_0p_0:000)&=\boldsymbol{r}(m_0n_0p_0)+\boldsymbol{T}_0-N_0d\boldsymbol{N} , \\ \boldsymbol{U}(000:m_0n_0p_0)&=\boldsymbol{r}(000)-\boldsymbol{T}_0-N_0d\boldsymbol{N} . \end{aligned}\right\} \tag{4}$$

$\boldsymbol{r}$, however, varies by the shear strain S, which is parallel to the (hkl). Therefore,

$$\left.\begin{aligned} \boldsymbol{r}(000)&=\boldsymbol{r}_0 && \text{for } \boldsymbol{U}(000:m_0n_0p_0) , \\ \boldsymbol{r}(m_0n_0p_0)&=\boldsymbol{r}_0+N_0d\boldsymbol{S} && \text{for } \boldsymbol{U}(m_0n_0p_0:000) , \end{aligned}\right\} \tag{5}$$

where $\boldsymbol{r}_0$ is an arbitrary constant to be determined in each case by *Assumption III*, and $\boldsymbol{S}$ is the vector representation of the shear strain S. From (4) and (5) we obtain

$$\boldsymbol{S}=-(2/N_0d)\boldsymbol{T}_0 , \tag{6}$$

and Burgers vector $\boldsymbol{b}_t$ of a twinning dislocation which produces the shear S has the following expression, taking the number of (hkl) planes (on which twinning dislocations pass) from (000) to ($m_0n_0p_0$) as q,

$$\boldsymbol{b}_t=-(2/q)T_0 . \tag{7}$$

By the use of q, N_0 may be represented as:

$$N_0=qI , \tag{8}$$

where I is a simple number which depends on h, k, and l, and is determined by the method analogous to the structure factor of X-ray analysis. It is tabulated in Table I.

Using analytical expression for $\boldsymbol{T}_0$,

$$\begin{aligned} |\boldsymbol{T}_0|^2&=\boldsymbol{R}_0{}^2-N_0{}^2d^2 \\ &=m_0{}^2s_{11}+n_0{}^2s_{22}+p_0{}^2s_{33}+2m_0n_0s_{12} \\ &\quad+2n_0p_0s_{23}+2p_0m_0s_{13}-N_0{}^2d^2 , \end{aligned} \tag{9}$$

where s_{ij} are Eisenstein's indices of the normal lattice. The orientations of $\boldsymbol{S}$ and $\boldsymbol{b}_t$ can be represented by using the zone axis, $[uvw]$,

$$\left.\begin{aligned} u&=K\left\{\begin{vmatrix} h & s_{12} & s_{13} \\ k & s_{22} & s_{23} \\ l & s_{23} & s_{33} \end{vmatrix}\frac{N_0d^2}{V^2}-m_0\right\} \\ v&=K\left\{\begin{vmatrix} s_{11} & h & s_{13} \\ s_{12} & k & s_{23} \\ s_{13} & l & s_{33} \end{vmatrix}\frac{N_0d^2}{V^2}-n_0\right\} \\ w&=K\left\{\begin{vmatrix} s_{11} & s_{12} & h \\ s_{12} & s_{22} & k \\ s_{13} & s_{23} & l \end{vmatrix}\frac{N_0d^2}{V^2}-p_0\right\} , \end{aligned}\right. \tag{10}$$

where V is the volume of a unit cell, and K is a certain positive number which makes all the values of u, v, and w integral. The indices ($h_2k_2l_2$) of K_2 plane can be represented as follows:

$$h_2:k_2:l_2=\begin{vmatrix} \boldsymbol{R}_0{}^2 & m_0s_{11}+n_0s_{12}+p_0s_{13} \\ N_0 & h \end{vmatrix}:\begin{vmatrix} \boldsymbol{R}_0{}^2 & m_0s_{12}+n_0s_{22}+p_0s_{23} \\ N_0 & k \end{vmatrix}:\begin{vmatrix} \boldsymbol{R}_0{}^2 & m_0s_{13}+n_0s_{23}+p_0s_{33} \\ N_0 & l \end{vmatrix} .$$

If we select the profitable ($m_0n_0p_0$) for a definite (hkl) plane, S can be exactly determined, and moreover, by knowing q, $\boldsymbol{b}_t$ also can be determined.

Then, in order to decide $(m_0 n_0 p_0)$ and q, and to investigate further the atomic movements, we deform the crystal virtually and remove the effects of Burgers vector. Hence, we regard s_{ij} as variable in Eq. (9). The condition that $\boldsymbol{S}=\boldsymbol{b}_t=0$ is represented by

$$\frac{m_0 s_{11}+n_0 s_{12}+p_0 s_{13}}{h}=\frac{m_0 s_{12}+n_0 s_{22}+p_0 s_{23}}{k}$$
$$=\frac{m_0 s_{13}+n_0 s_{23}+p_0 s_{33}}{l}=N_0 d^2\,. \qquad (11)$$

This equation cannot determine s_{ij} uniquely, but it is sufficient to determine s_{ij}, if only the vast change of crystal symmetry can be avoided. We take such a crystal lattice as satisfying Eq. (11) and call it the '*modified lattice*'. For the modified lattice, of course,

$$\boldsymbol{S}=\boldsymbol{b}_t=\boldsymbol{T}_0=0\,. \qquad (12)$$

A. Type I. At first, when there is only one kind of U, which is caused by $\boldsymbol{b}_t$, each $\boldsymbol{U}$ is equal to (4). Then, using (12),

$$U^{\mathrm{mod}}(m'n'p':mnp)=\boldsymbol{r}_0-N_0 d\boldsymbol{N}\,,$$

where U^{mod} denotes an atomic movement in the modified lattice. Because $\boldsymbol{r}_0$ is an arbitrary constant, we can take

$$\boldsymbol{r}_0=N_0 d\boldsymbol{N}\,.$$

Therefore,

$$U^{\mathrm{mod}}(m'n'p':mnp)=0\,. \qquad (13.1)$$

This means that in the modfiied lattice there are no atomic movements. We must know the condition under which each lattice point has the same U.

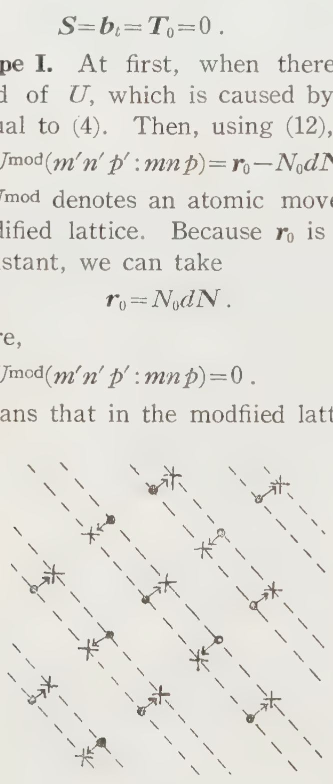

Fig. 2. U^{mod} of Type II, in the cross section perpendicular to the (hkl) plane.
· the original lattice site;
× the twin lattice site;
---- the (hkl) plane.

It can be proved briefly that each lattice point lying on the same (hkl) plane must have the same U^{mod}. Consequently, the state of atomic movements is determined with each (hkl) plane. Also it can be shown that if there is (hkl) plane apart by $\frac{1}{2}N_0$ from the origin, the lattice points on it also have the same U^{mod} as (000) and $(m_0 n_0 p_0)$, and other planes generally have not. Therefore, if the distances among (hkl) planes are all equal, all U^{mod} can be equal, and $(m_0 n_0 p_0)$ lies in the first or the second (hkl) plane from the origin. But the case in which $(m_0 n_0 p_0)$ lies in the first plane can be reduced to the case of $(m_0 n_0 p_0)$ in the second plane. So it requires the following relation:

$$q=2\,. \qquad (14)$$

Then turning to the usual lattice,

$$\boldsymbol{U}=\boldsymbol{b}_t=-\boldsymbol{T}_0\,. \qquad (15.1)$$

B. Type II. When the condition of $U^{\mathrm{mod}}=0$ is not satisfied, i.e. the distances among (hkl) planes are not equal, $U^{\mathrm{mod}}(000:m_0 n_0 p_0)$ will have a small value:

$$U^{\mathrm{mod}}(000:m_0 n_0 p_0)=\boldsymbol{e}+\eta d\boldsymbol{N}\,.$$

And by (4) and (12),

$$\boldsymbol{r}_0=\boldsymbol{e}+(N_0+\eta)d\boldsymbol{N}\,.$$

It is assumed that the distances among (hkl) planes have only two values, fd and $(1-f)d$, $(f<\frac{1}{2})$. This condition is satisfied in the crystal systems of nearly all metals.* In this case, $(m_f n_f p_f)$ on the (hkl) plane apart by fd from $(m_0 n_0 p_0)$ has, by *Assumption II*, the following atomic movement:

$$U^{\mathrm{mod}}(m_f-m_0,\ n_f-n_0,\ p_f-p_0;\ m_f n_f p_f)$$
$$=(\eta-2f)d\boldsymbol{N}+\boldsymbol{e}\,.$$

By *Assumption III*, $\boldsymbol{e}=0$, and $\eta=f$. Therefore,

$$U_{\perp}{}^{\mathrm{mod}}=\pm f d\boldsymbol{N}\,. \qquad (13.2)$$

Then, U^{mod} consists of two kinds, having adverse directions each other (as shown in Fig. 2).

As is evident from the above atomic movements, (hkl) planes apart by fd from each other interchange their atoms. Therefore, when a twinning dislocation passes on that twin boundary, both planes apart by fd contribute simultaneously to it. That is, the twin boundary on which a twinning dislocation passes is not a single plane but double planes. Except for this point, the twinning of this type agrees with the type I. Then $(m_0 n_0 p_0)$ must exist on the second (hkl) double planes, and $q=2$. And turning to the usual lattice,

---

* For the crystal systems which do not satisfy the above condition, e.g. Se, a similar calculation can be made. But such crystals have no tendency to twin and there is no experimental evidence.

$$\left.\begin{array}{l} \boldsymbol{U}_{\perp}=\boldsymbol{b}_t \pm f d \boldsymbol{N} \\ \boldsymbol{b}_t=-\boldsymbol{T}_0\,. \end{array}\right\} \qquad (15.2)$$

C. Type III. When we return to the usual lattice constant from the modified lattice, it happens that the *Assumption II* does not hold. Hence,

$$|\boldsymbol{T}_f| < |\boldsymbol{U}_{\perp}|, \qquad (16)$$

where $(m_f n_f p_f)$ is on the (hkl) plane which is apart by fd from $(m_0 n_0 p_0)$. In this case, by *Assumption II* the atom at $(m_0 n_0 p_0)$ cannot come to this usual new twin lattice site, but the atom at $(m_f n_f p_f)$ should come to it. Because $(m_f n_f p_f)$ and (000) cannot have the same $\boldsymbol{U}^{\mathrm{mod}}$, the period of atomic movements must be twice, and $(m_0 n_0 p_0)$ must be taken apart by twice from (000). Then it lies on the fourth (hkl) double planes from the origin. That is,

$$q=4\,. \qquad (14')$$

With the lattice points on the first (hkl) double planes from (000), the twin lattice points on the third (hkl) double planes are joinned, and this $\boldsymbol{U}^{\mathrm{mod}}$ may be the above $\boldsymbol{T}_f^{\mathrm{mod}}$ (as shown in Fig. 3).

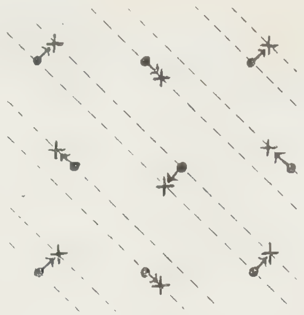

Fig. 3. $\boldsymbol{U}^{\mathrm{mod}}$ of Type III, in the cross section perpendicular to the (hkl) plane.

· the original lattice site;
× the twin lattice site;
---- the (hkl) plane.

$$\left.\begin{array}{l} \boldsymbol{U}_{\perp}{}^{\mathrm{mod}}=\pm f d \boldsymbol{N}\,, \\ \boldsymbol{U}_{\parallel}{}^{\mathrm{mod}}=\pm \boldsymbol{T}_f{}^{\mathrm{mod}}\,. \end{array}\right\} \qquad (13.3)$$

Then $\boldsymbol{U}$ in the usual crystal lattice are

$$\left.\begin{array}{l} \boldsymbol{U}_{\perp}=\boldsymbol{b}_t \pm f d \boldsymbol{N}\,, \\ \boldsymbol{U}_{\parallel}=\boldsymbol{b}_t \pm (\boldsymbol{T}_f+\boldsymbol{b}_t)\,, \\ \boldsymbol{b}_t=-\tfrac{1}{2}\boldsymbol{T}_0\,. \end{array}\right\} \qquad (15.3)$$

The method for determining m_0, n_0, and p_0

Table II. S and $\boldsymbol{b}_t$ in cubic lattices.

r_0: The distance between the most neighbours.
(hkl) *: The observed twinning plane.

Crys. Sys.	(hkl)	Type	$(m_0 n_0 p_0)$	S	$\lvert b_t\rvert/r_0$	$[uvw]$	K_2
b. c. c.	(112)*	I	$(\frac{1}{2}\ \frac{1}{2}\ \frac{1}{2})$	$1/\sqrt{2}$	1/3	$[1\bar{1}1]$	$(\bar{1}\bar{1}2)$
	(310)	I	$(\frac{1}{2}\ \frac{1}{2}\ \frac{1}{2})$	$\sqrt{7/2}$	$\sqrt{7/15}$	$[13\bar{5}]$	$(5\bar{1}\bar{4})$
f. c. c.	(111)*	I	$(1\ \frac{1}{2}\ \frac{1}{2})$	$1/\sqrt{2}$	$1/\sqrt{3}$	$[\bar{2}11]$	$(\bar{1}11)$
	(113)	I	$(\frac{1}{2}\ 0\ \frac{1}{2})$	$\sqrt{3/2}$	$\sqrt{3/11}$	$[\bar{7}41]$	$(\bar{1}11)$

Table III. S, $\boldsymbol{b}_t$ and $\boldsymbol{U}$ in β-Sn. Axial ratio$=0.541$.

(hkl)	Type	$(m_0 n_0 p_0)$	$(m_f n_f p_f)$	S	$\frac{\lvert\boldsymbol{b}_t\rvert}{r_0}$	$[uvw]$	K_2	$\frac{\lvert\boldsymbol{U}_{\perp}\rvert}{r_0}$	$\frac{\lvert\boldsymbol{U}_{\parallel}\rvert}{r_0}$	
(110)	I	$(\frac{1}{2}\ \frac{1}{2}\ \frac{1}{2})$		0.765	.522	$[00\bar{1}]$	$(11\bar{2})$			
(210)	I	$(\frac{1}{2}\ 0\ \frac{1}{4})$		1.17	.507	$[64\bar{5}]$	$\div(18\bar{2})$			
(112)	I	$(0\ 0\ 1)$		0.765	.373	$[11\bar{1}]$	(110)			
(312)	I	$(\frac{1}{2}\ 0\ \frac{1}{4})$		1.53	.608	$\div[\bar{3}14]$	$\div(\bar{2}2\bar{3})$			
(211)	II	$(\frac{1}{2}\ \frac{1}{2}\ \frac{1}{2})$		0.909	.605	$\div[0\bar{1}1]$	$\div(1\bar{3}\bar{2})$	.637		
(101)*	III	$(1\ 0\ 3)$	$(\frac{1}{2}\ 0\ {}^{5}/_{4})$	0.113	.104	$[\bar{1}01]$	$(\bar{3}01)$	.252	.228	.021
(301)*	III	$(1\ 0\ 1)$	$(\frac{1}{2}\ 0\ {}^{5}/_{4})$	0.113	.062	$[\bar{1}03]$	$(10\bar{1})$	.150	.284	.161
(321)	III	$(\frac{1}{2}\ \frac{1}{2}\ 1\frac{1}{2})$	$(\frac{1}{2}\ 0\ \frac{1}{4})$	0.869	.414	$\div[10\bar{3}]$	$\div(1\bar{2}\bar{4})$	.431	.630	.923
(431)	III	$(\frac{1}{2}\ \frac{1}{2}\ \frac{1}{2})$	$(\frac{1}{2}\ 0\ \frac{1}{4})$	0.268	.097	$\div[3\bar{4}0]$	$\div(1\bar{1}0)$	.133	.313	.414
(323)	III	$(\frac{1}{2}\ \frac{1}{2}\ \frac{1}{2})$	$(\frac{1}{2}\ 0\ \frac{1}{4})$	1.506	.440	$\div[\bar{2}\bar{3}4]$	$\div(\bar{1}\bar{3}4)$	.445	.754	.860

Table IV. S, $\boldsymbol{b}_t$ and U in Bi type and Hg.

$\frac{1}{2}-p\approx s/2$ is used and s of higher orders are neglected.
$|\boldsymbol{b}_t|=|\boldsymbol{U}_\perp|$ in this approximation, for {311}, {210} and {221}.

(hkl)	Type	$(m_0n_0p_0)$	$(m_fn_fp_f)$	$[uvw]$	K_2		Bi	Sb	As	Hg
						s	.0456	.0566	.0942	-0.142
(100)	II	(1 0 0)		$[0\bar{1}\bar{1}]$	(011)	S	0.13	0.16	0.25	0.42
						$\boldsymbol{b}_t/r_0$	0.13	0.17	0.28	0.33
						$\boldsymbol{U}_\perp/r_0$	0.14	0.18	0.30	
(110)*	II	$(\frac{1}{2}\ \frac{1}{2}\ 0)$		$[00\bar{1}]$	(001)	S	0.13	0.16	0.25	0.42
						$\boldsymbol{b}_t/r_0$	0.10	0.12	0.21	0.22
						$\boldsymbol{U}_\perp/r_0$	0.12	0.15	0.26	
(311)	II	$(\frac{1}{2}\ \frac{1}{2}\ 0)$		$\div[1\bar{7}4]$	$\div(1\bar{1}1)$	S	1.20	1.19	1.17	1.32
						$\boldsymbol{b}_t/r_0$	0.74	0.79	0.82	0.46
$(31\bar{1})$	II	$(\frac{1}{2}\ 0\ \overline{\tfrac{1}{2}})$		[147]	(111)	S	1.14	1.12	1.05	1.49
						$\boldsymbol{b}_t/r_0$	0.72	0.71	0.70	0.60
$(3\bar{1}\bar{1})$	II	$(\frac{1}{2}\ \overline{\tfrac{1}{2}}\ 0)$		$\div[17\bar{4}]$	$(11\bar{1})$	S	1.22	1.21	1.21	1.25
						$\boldsymbol{b}_t/r_0$	0.74	0.75	0.77	0.52
(210)	III	(1 0 0)	$(p\ \ p-\frac{1}{2}\ \ p-\frac{1}{2})$	$\div[\bar{1}20]$	$\div(010)$	S	0.91	0.89	0.81	
						$\boldsymbol{b}_t$	0.44	0.43	0.42	
						$\boldsymbol{U}_\parallel/r_0$	0.42	0.41	0.38	
						$\boldsymbol{U}_\parallel/r_0$	0.46	0.46	0.46	
$(2\bar{1}0)$	III	(1 0 0)	$(p\ \ p-\frac{1}{2}\ \ p-\frac{1}{2})$	$\div[\bar{1}\bar{2}0]$	$\div(010)$	S	1.09	1.11	1.19	
						$\boldsymbol{b}_t/r_0$	0.50	0.51	0.56	
						$\boldsymbol{U}_\parallel/r_0$	0·56	0.59	0.68	
						$\boldsymbol{U}_\parallel/r_0$	0.52	0.54	0.60	
(221)	III	$(\frac{1}{2}\ \frac{1}{2}\ 0)$	$(p\ \ p-\frac{1}{2}\ \ p-\frac{1}{2})$	$\div[\bar{1}\bar{1}4]$	(001)	S	0.59	0.57	0.47	
						$\boldsymbol{b}_t/r_0$	0.22	0.21	0.20	
						$\boldsymbol{U}_\parallel/r_0$	0.75	0.75	0.75	
						$\boldsymbol{U}_\parallel/r_0$	0.76	0.77	0.78	
$(2\bar{2}1)$	III	$(\frac{1}{2}\ \overline{\tfrac{1}{2}}\ 0)$	$(p\ \ p-\frac{1}{2}\ \ p-\frac{1}{2})$	$\div[\bar{1}14]$	(001)	S	0.69	0.69	0.67	
						$\boldsymbol{b}_t/r_0$	0.23	0.22	0.22	
						$\boldsymbol{U}_\parallel/r_0$	0.75	0.75	0.75	
						$\boldsymbol{U}_\parallel/r_0$	0.78	0.78	0.80	
$(22\bar{1})$	III	$(\frac{1}{2}\ \frac{1}{2}\ 0)$	$(p\ \ p-\frac{1}{2}\ \ p-\frac{1}{2})$	$[\bar{1}14]$	(001)	S	0.85	0.89	1.01	
						$\boldsymbol{b}_t/r_0$	0.30	0.31	0.36	
						$\boldsymbol{U}_\parallel/r_0$	0.73	0.72	0.70	
						$\boldsymbol{U}_\parallel/r_0$	0.80	0.81	0.86	
(111)	III	$(1\ 1\frac{1}{2}\ 1\frac{1}{2})$	$(p\ \ p\ \ p)$	$[2\bar{1}\bar{1}]$	$\div(\bar{3}11)$	S	0.33	0.32	0.30	
						$\boldsymbol{b}_t/r_0$	0.42	0.42	0.43	
						$\boldsymbol{U}_\perp/r_0$	0.82	0.85	0.94	
						$\boldsymbol{U}_\parallel/r_0$	0	0	0	
						$\boldsymbol{U}_\parallel/r_0$	0.83	0.84	0.85	
$(11\bar{1})$	III	$(1\ 1\frac{1}{2}\ \overline{1\tfrac{1}{2}})$	$(p\ \ p\ \ p-1)$	$\div[2\bar{1}1]$	$\div(31\bar{1})$	S	0.38	0.38	0.40	
						$\boldsymbol{b}_t/r_0$	0.42	0.42	0.43	
						$\boldsymbol{U}_\perp/r_0$	0.75	0.76	0.94	
						$\boldsymbol{U}_\parallel/r_0$	0	0	0	
						$\boldsymbol{U}_\parallel/r_0$	0.75	0.73	0.67	
(531)	III	$(\frac{1}{2}\ \frac{1}{2}\ 0)$	$(p\ \ p-\frac{1}{2}\ \ p-\frac{1}{2})$	$\div[5\bar{1}\bar{1}8]$	$\div(1\bar{1}1)$	S	0.56	0.55	0.51	
						$\boldsymbol{b}_t/r_0$	0.21	0.21	0.19	
						$\boldsymbol{U}_\perp/r_0$	0.23	0.22	0.19	
						$\boldsymbol{U}_\parallel/r_0$	0.29	0.29	0.30	
						$\boldsymbol{U}_\parallel/r_0$	0.78	0.79	0.82	
$(5\bar{3}1)$	III	$(\frac{1}{2}\ \overline{\tfrac{1}{2}}\ 0)$	$(p\ \ p-\frac{1}{2}\ \ p-\frac{1}{2})$	[5118]	(111)	S	0.57	0.56	0.53	
						$\boldsymbol{b}_t/r_0$	0.20	0.20	0.19	
						$\boldsymbol{U}_\perp/r_0$	0.25	0.25	0.23	
						$\boldsymbol{U}_\parallel/r_0$	0.29	0.29	0.28	
						$\boldsymbol{U}_\parallel/r_0$	0.72	0.72	0.71	
$(\bar{5}31)$	III	$(\frac{1}{2}\ \overline{\tfrac{1}{2}}\ 0)$	$(p-\frac{1}{2}\ \ p\ \ p-\frac{1}{2})$	$[\bar{5}\bar{1}\bar{1}8]$	$(11\bar{1})$	S	0.61	0.61	0.60	
						$\boldsymbol{b}_t/r_0$	0.21	0.21	0.21	
						$\boldsymbol{U}_\perp/r_0$	0.27	0.27	0.27	
						$\boldsymbol{U}_\parallel/r_0$	0.28	0.27	0.27	
						$\boldsymbol{U}_\parallel/r_0$	0.70	0.69	0.65	
$(53\bar{1})$	III	$(\frac{1}{2}\ \frac{1}{2}\ 0)$	$(p\ \ p-\frac{1}{2}\ \ p-\frac{1}{2})$	$[5\bar{1}\bar{1}\bar{8}]$	$\div(\bar{1}11)$	S	0.71	0.73	0.81	
						$\boldsymbol{b}_t/r_0$	0.25	0.27	0.30	
						$\boldsymbol{U}_\perp/r_0$	0.27	0.27	0.30	
						$\boldsymbol{U}_\parallel/r_0$	0.29	0.29	0.30	
						$\boldsymbol{U}_\parallel/r_0$	0.79	0.81	0.85	

Table V. S, $\boldsymbol{b}_t$ and $\boldsymbol{U}$ in h. c. p.

(hkl)	Type	$(m_0 n_0 p_0)$	$(m_f n_f p_f)$	$[uvw]$	K_2	Axial Ratio
(112)	I	(1 1 0)		$[\bar{1}\bar{1}1]$	(001)	$>\sqrt{8/3}$
		$(\frac{1}{3}\ \frac{2}{3}\ \frac{1}{2})$		$\doteqdot[20\bar{1}]$	$(30\bar{2})$	$<\sqrt{8/3}$
(201)	II	(1 0 0)		$\doteqdot[\bar{1}82]$	$(0\bar{1}1)$	
(203)	II	(1 0 0)		$\doteqdot[\bar{3}\bar{3}2]$	$(0\bar{1}3)$	
(101)*	III	(3 1 1)	$(\frac{4}{3}\ \frac{2}{3}\ \frac{1}{2})$	$\doteqdot[15\bar{1}]$	$\doteqdot(1\bar{3}0)$	
(102)*	III	(2 1 1)	$(\frac{4}{3}\ \frac{2}{3}\ \frac{1}{2})$	$[21\bar{1}]$	$(10\bar{2})$	$>\sqrt{3}$
				$[\bar{2}\bar{1}1]$		$<\sqrt{3}$
(103)	III	(1 0 1)	$(\frac{1}{3}\ \overline{\tfrac{1}{3}}\ \frac{1}{2})$	$\doteqdot[39\bar{1}]$	$\doteqdot(010)$	
(104)	III	(0 0 1)	$(\frac{1}{3}\ \frac{2}{3}\ \frac{1}{2})$	$[42\bar{1}]$	(100)	

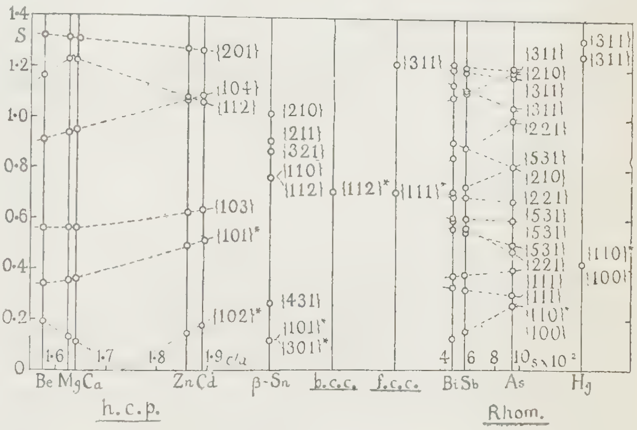

Fig. 4. The values of S.
(hkl)*: The observed twinning plane.

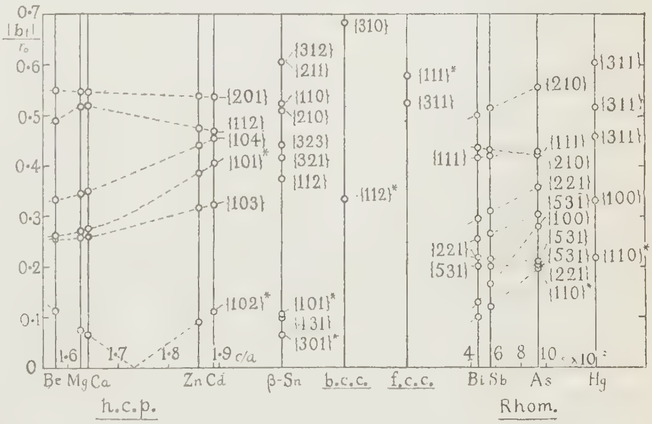

Fig. 5. The values of $|\boldsymbol{b}_t|/r_0$.
(hkl)*: The observed twinning plane.

has not been explained up to this time. It is as follows; besides (8), (14) and (14′), we take by *Assumption II* as:

$$|\boldsymbol{R}_0|:\text{minimum}. \qquad (17)$$

Thus even if we take any (hkl) for twin plane we can know uniquely by this method how the twin dislocation and the twin boundary are to exist.

§ 3. Application and Discussion

It is the first problem how h, k, l are selected from all integers as a twinning plane. In accordance with (7), S increases with h, k, l for a definite N_0 and $(m_0 n_0 p_0)$. And by *Assumption II,* in order that the distance from $(m_0 n_0 p_0)$ to the twin origin is smaller than that from the origin to $(m_0 n_0 p_0)$, $S<2$. Because (m_0, n_0, p_0) have a lower limit which is the nearest neighbour of the origin and N_0 is determined by q and I, (hkl) which satisfy $S<2$ are not the higher order but the lower. It is sufficient that the calculation is done until S exceeds 2 for a definite N_0 and $(m_0 n_0 p_0)$.

Next, we decide $(m_0 n_0 p_0)$ by (8), (14) and (17) for any (hkl) plane, and so twinning dislocations of Type I and II can be obtained. In Type II, however, there are such (hkl) planes that the condition (16) is fulfilled. Hence, they become to the ones of Type III, and $(m_0 n_0 p_0)$ is decided by (8), (14′) and (17). Then S can be obtained by (6) and $\boldsymbol{b}_t$ and $\boldsymbol{U}$ also can be obtained by (10) and (15). S and $|\boldsymbol{b}_t|$ for possible twinning planes are summarized in Figs. 4 and 5. And Tables II, III and IV show the values of S, $|\boldsymbol{b}_t|$, $|\boldsymbol{U}|$, and etc., for cubic, β-Sn and rhombohedral lattice. respectively. Table V and Fig. 6 show partly them for h.c.p. lattice. The discussion of these figures and tables will be described in the following lines. In those the experimentally observed twinning planes are indicated with *.

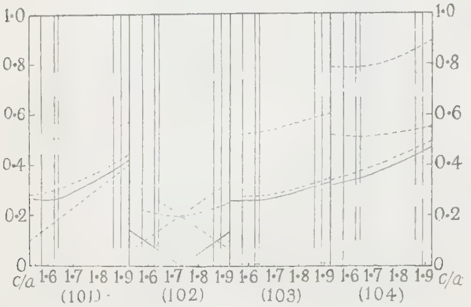

Fig. 6. $|\boldsymbol{b}_t|/r_0$ and $|\boldsymbol{U}|/r_0$ in h.c.p.; the full line represents $|\boldsymbol{b}_t|$ and the dotted line $|\boldsymbol{U}|$.

In the following, the obtained results will be discussed.

(1) It seems that the differences between the already obtained shears and the corresponding ones now calculated are due to the difference of the lattice constants which are used.

(2) The internal structure of twinning dislocations and twinning boundaries is simple for Type I, but is more complicated for Types II and III. In the {110} of Bi lattice our result agrees with Boas's one and in the $\{10\bar{1}2\}$ of h.c.p. it does not agree with Gough's one but agrees with Mathewson's and Barrett's[10], when they are somewhat modified, i.e. by uniform displacement of twin to normal direction of the (*hkl*) plane. Also, in the (301) of β-Sn it agrees with Hirokawa's[8] but not with Chalmers'[9].

(3) It is important to see which is more essential for the twinning process among $\boldsymbol{S}$, $\boldsymbol{b}_t$ and $\boldsymbol{U}$. In Fig. 4, the observed twinning planes have the smallest shear strain S, in order. But, their $\boldsymbol{b}_t$, as shown in Fig. 5, is out of this order and $\boldsymbol{U}$'s of one dislocation are far apart from each other and migle with those of other, and there is no evident conclusion. It seems therefore that the shear S is more essential for the twinning process than $\boldsymbol{b}_t$ and U. The shear S of {101} and of {301} of β-Sn are equal, and that of the {110} and of the {100} of Bi type are equal, too. Therefore, when the shear S of two twinning planes are equal to each other, the one having the smaller $\boldsymbol{b}_t$ is liable to twin.

Those relations can be proved by the consideration of the energy of twinning dislocations. The energy of a twinning dislocation depends on the shear stress produced around it, the core energy and the surface energy of twin boundary. The first factor can be related to the modulus of the Burgers vector[11] and the elastic constants of the substance. The other two factors are probably determined by the shear strain S rather than by Burgers vector. The reason is that the effect of atomic movements to the core energy and the surface energy depends on not only their magnitude but also on the distance among the atomic layers in which they lie, i.e. the larger the distance, the smaller the force which acts upon them. Compared with core energy and stress energy, the former is much larger than the latter. Then, the shear S is predominant and next Burgers vector is effective.

After all the following condition for twinning process is needed. To twin on any crystallographic plane, it is necessary that the shear S produced by twinning is small and secondarily Burgers vector is small. Those relations correspond to Chalmers' one[12] for slip dislocations.

(4) S of the $\{10\bar{1}1\}$ in Mg has not been determined because of the indistinctness of K_2 plane, but by this method it is determined exactly $S=0.353$. K_2 plane of the $(10\bar{1}1)$ twin is not a simple crystallographical plane, but is one that the $(13\bar{2}0)$ plane is somewhat rotated around the axis normal to the $(10\bar{1}1)$ plane. This is caused by the fact that the direction of $\boldsymbol{b}_t$ is not a crystallographic direction. Moreover, some such twinning planes are possible.

Clark and Claig throw doubt on the existence of the $\{10\bar{1}1\}$ twin[4], because the recent experiments[13,14] show only the $\{10\bar{1}2\}$ twin. The experiment of Barrett and Haller[13], however, is the case where the direction of the compression is nearly parallel to the basal plane, and in this orientation of the crystal, the $\{10\bar{1}1\}$ twin cannot occur. Thus it is no wonder that the $\{10\bar{1}1\}$ twin has not found. Though the more investigations are demanded, the existence of the $(10\bar{1}1)$ twin will be reliable by the earlier experiments.

(5) In 1934 the $(7\bar{5}1)$ twin of Bi was shortly

reported[15]. The reasons for the occurrence of the $(7\bar{5}1)$ twin are the following: (a) "The change in shape and size of the crystal is much bigger than that due to a (110) twin". and (b) from the (111) cleavage experiment, "The atoms of the (111) planes therefore remain atoms of the (111) plane in the twin. Thus one is able to find the position of the twinning plane. —"' which means that the (111) plane is K_2 plane. But, in our treatment the $(7\bar{5}1)$ twin cannot occur, and from Fig. 4 the twins which rank next to the (110) twins are {111}, $\{1\bar{1}1\}$, {531}, $\{5\bar{3}1\}$, {221} and so on. And the twinning planes of which the (111) plane is K_2 plane are the $\{5\bar{3}1\}$ and $\{3\bar{1}1\}$ twins. The $\{5\bar{3}1\}$ twin has smaller S_t and $\boldsymbol{b}_t$ than the $\{31\bar{1}\}$ twin and will be reliable to twin. The angle between the $\{5\bar{3}1\}$ plane and the $\{7\bar{5}1\}$ plane is less than 3°, then the above $\{7\bar{5}1\}$ twin may be really the $\{5\bar{3}1\}$ twinning plane. But, the certain conclusion must not be made.

(6) Accoding the conclusion in (3), the {101} twinning of β-Sn also seems to occur. Investigating the surface of shocked crystal by microscope, we observed fine twins along the {101} plane[16]. T. Hirokawa[17] studied it in detail, independently. He restrained a single crystal so as to avoid the {301} twinning and to stimulate the {101} twin, and compressed nearly parallel to the *a-b* plane. And he obtained the wide band of {101} twin and confirmed it by X-ray measurement.

(7) From Figs. 4 and 5, the new crystallographic planes which satisfy the above condition are liable to twin. They are the {431} twin of β-Sn and the {100} twin of Bi type, etc. The reason why these twins are not observed will be that they are covered with slip process and the already observed twinning process, or that this treatment points out only the necessary condition for twinning. In either case it remains doubtful whether they will really twin. Experiment for those twinning planes is necessary and desirable.

The author expresses his cordial thanks to Professor Kenzo Tanaka, Kyoto University, for his valuable suggestions and also to Mr. Ken-ichiro Ishii, Nagoya Industrial University, for many valuable discussions.

References

1) E. Schmid and W. Boas: Kristallplastizität (1935).

2) C. F. Elam: Distortion of metal crystals (1935).

3) F. Seitz and W. T. Read: J. Appl. Phys. **12** (1941) 470.

4) R. Clark and G. B. Craig: Progress in Metal Physics, (1952).

5) I. Schaacke: Zeits. für Kristallog. **98** (1938) 143, 211, 281.

6) A. H. Cottrell and B. A. Bilby: Phil. Mag. **42** (1951) 573.

7) H. J. Gough and H. T. Cox: Proc. Roy. Soc. A **127** (1930) 453.

8) T. Hirokawa: Read at the Annual Meeting of the Physical Society of Japan, Kyoto, 1952.

9) B. Chalmers: Proc. Phys. Soc. **47** (1935) 733.

10) G. S. Barrett: Symp. on Cold Working of Metals, Amer. Soc. Met., 1948.

11) J. S; Koehler: Phys. Rev. **60** (1941) .

12) B. Chalmers and U. Martius: Nature **167** (1951) 681.

13) H. S. Barrett and Haller: Trans. A.I.M. (M). E. **171** (1947) 246.

14) Bakarian and Mathewson: Trans. A.I.M. (M). E. **152** (1943).

15) W. F. Berg: Nature **134** (1934) 143.

16) K. Tanaka, K. Ishii, and H. Kihô: Read at the First Meeting of the crystallographical Society of Japan, Tokyo, 1950.

17) T. Hirokawa: Read at the Annual Meeting of the Physical Society of Japan, Tokyo, 1953.

JOURNAL OF THE PHYSICAL SOCIETY OF JAPAN Vol. 9, No. 5, SEP.—OCT., 1954

The Magnetostriction Constants of Silicon Steel (II)

By Hideo TAKAKI and Yoji NAKAMURA

Faculty of Science, University of Kyoto

(Received June 10, 1954)

By use of long cylindrical single crystal rods of 2.6%, 3.2% and 4.0% silicon steel with various crystallographic orientations, prepared by the Bridgman method, magnetization and magnetostriction were measured at room temperature. It was found that Kaya's law with regard to the remanent magnetization holds for these specimens and on the basis of the law their magnetostriction constants λ_{100} and λ_{111}, and also their crystal anisotropy constants K_1 were determined. Together with our previous results, λ_{111} and K_1 decrease almost linearly with silicon content. On the other hand, λ_{100} decreases more rapidly at low silicon content, then suddenly increases at about two percent silicon and shows no considerable change up to four percent silicon.

§ 1. Introduction

In our previous paper[1] we have investigated the magnetic properties of 0.7% and 1.8% silicon steel and found that the magnetostriction constants λ_{100} and λ_{111} and the crystal anisotropy constant K_1 decrease with silicon content. Carr and Smoluchowski[2] found both λ_{100} and λ_{111} dependent on silicon concentration from 2.5% to 8%. Comparing our previous results with theirs, the change of λ_{111} with silicon content is connected smoothly. However, it is not the case with λ_{100} and the value of λ_{100} at 2.5% silicon by Carr and Smoluchowski is about one and three quarter times larger than the one at 1.8% silicon by us. This paper deals with the investigation of the magnetostriction of silicon steel, containing silicon from 2.6% to 4.0%, done by the same method as in our previous paper.

§ 2. Preparation of Specimens

By means of a modified form from the Bridgman method we were able to obtain long cylindrical single crystals of 2.6%, 3.2% and 4.0% silicon steel having various crystallographic orientations. The precise description of this method has been published in this *Journal* recently[3], so only a brief description will be given of the method used by us.

Materials used to prepare single crystals are commercial silicon steel whose chemical analyses are tabulated in Table I. These strips were decarbonized by annealing in a wet hydrogen atomosphere at 750°C for 3 hr. In the following procedures we used the Tammann furnace which was set in a vacuum chamber to aboid the oxidation of the specimens. In the first procedure a "seed" with any orientation is prepared by the usual Bridgman method. The seed thus obtained is cut off to a rod of about 2 cm length and its crystal axes were determined by the back reflection Laue patterns. Then the second procedure is to obtain the rod of seed with a desired orientation with respect to the crystal axes. A cylindrical crucible with sectorial solid part is used and is perforated through the sectorial part which makes an adequate angle with the axis of its upper straight tube. Then the crucible is filled with the seed in the sectorial part with a proper position and with a polycrystalline wire in the upper straight tube. After the crucible is hung in the furnace in such a manner that the upper

Table I.

Si (%)	C (%)	Mn (%)	P (%)	Cr (%)	Cu (%)	S (%)	Ni (%)
* 2.62	0.058	0.080	0.020	0.043	0.32	0.008	—
** 3.2	—	0.019	—	Trace	—	—	0.045
* 4.03	0.08	0.07	0.02	0.026	0.31	0.007	0.031

*: All elements were analysed before annealing. **: Analyses were made after annealing.

Table II.

% Si	Sample Number	Length in mm.	Demagnet. Factor	Direction Cosines l	m	n	$\left(\frac{I_r}{I_s}\right)_{\text{Obs.}}$	$\left(\frac{\delta l}{l}\right)\times 10^6$ Sat.-Rem. Obs.	Velocity of Crystal Growth in mm/min *
2.6	10	206.7	0.00666	0.024	0.046	0.999	0.910	45.2	1.1
	11	188.8	0.00722	0.046	0.658	0.751	0.656	−47.5	0.8
	13	211.0	0.00550	0.174	0.254	0.952	0.736	65.3	1.1
	14	198.0	0.00672	0.034	0.207	0.978	0.795	47.9	0.5
	20	210.0	0.00652	0.019	0.121	0.993	0.879	62.1	1.1
	27	162.9	0.00828	0.481	0.610	0.630	0.584	−73.4	0.6
3.2	1	251.2	0.00821	0.054	0.086	0.995	0.889	40.6	7.0
	2	227.1	0.00713	0.077	0.298	0.951	0.747	64.2	5.5
	4	218.8	0.00826	0.015	0.053	0.998	0.912	35.9	7.7
	13	197.3	0.01241	0.123	0.438	0.891	0.694	27.8	4.7
	19	209.9	0.01060	0.183	0.664	0.725	0.639	−14.7	4.5
	39	171.7	0.01059	0.436	0.615	0.657	0.550	−58.6	0.4
	42	213.6	0.00777	0.048	0.669	0.742	0.677	−17.1	1.1
	49	226.7	0.00461	0.561	0.567	0.603	0.556	−63.7	0.4
	50	234.4	0.00682	0.108	0.134	0.985	0.803	72.2	2.8
4.0	16	268.8	0.00489	0.057	0.282	0.958	0.745	74.2	4.3
	21	258.6	0.00494	0.083	0.348	0.934	0.716	50.3	3.5
	23	196.8	0.00810	0.013	0.391	0.920	0.690	60.3	1.7
	25	265.3	0.00511	0.520	0.572	0.635	0.548	−27.2	0.7
	28	267.6	0.00467	0.198	0.369	0.908	0.668	69.8	3.0
	30	233.6	0.00672	0.492	0.592	0.638	0.565	−21.8	0.6
	35	267.0	0.00500	0.029	0.084	0.996	0.881	55.8	0.8
	36	263.8	0.00547	0.042	0.699	0.711	0.709	−14.7	0.7

* These values are not maximum velocities for crystal growth.

half of seed would just melt, it is lowered at an appropriate velocity. Thus the seed with a desired orientation is obtained. Then the third procedure is to obtain a long single crystal rod using a long straight tube and the seed, and the procedure is similar to the second one. In all the three procedures the crucible should be lowered smoothly through the furnace at the appropriate velocity for the growth of a single crystal. The appropriate velocity depends upon the crystal orientation, and is given in Table II for each of our specimens. The obtained single crystals are long cylindrical rods, 3 mm in diameter, and Fig. 1 shows the stereographic projection of the orientations of the specimens and the characteristic constants of the specimens are represented in Table II.

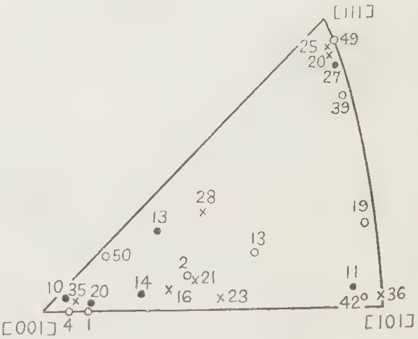

Fig. 1. Stereographic projection of the orientations of specimens. ●: 2.6% silicon steel, ○: 3.2% silicon steel. ×: 4.0% silicon steel.

§ 3. Experimental Results and Discussion

Before measuring the magnetic properties, the specimens were annealed in a vacuum electric furnace at 1000°C for 2 hr in order to remove the internal stress. After being annealed they were slowly cooled in furnace down to 250°C, and then rapidly cooled to room temperature by taking them out of the furnace. Magnetization curves were measured

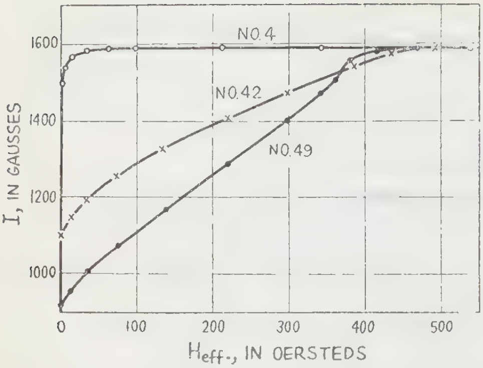

Fig. 2. Magnetization curves in single crystals of 3.2% silicon steel with various crystallographic orientations.

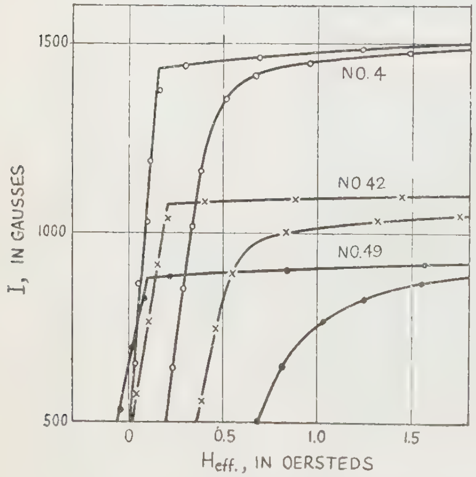

Fig. 3. Hysteresis loops of single crystals of 3.2% silicon steel with a sharp corner near the remanent magnetization.

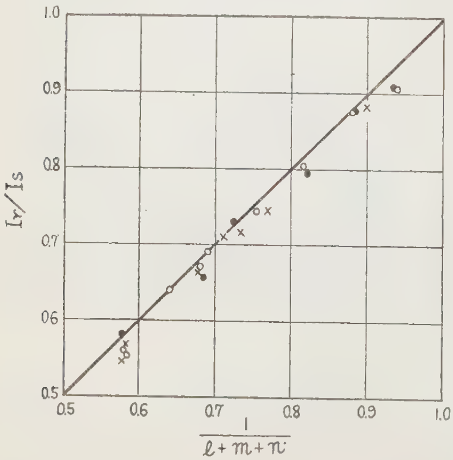

Fig. 4. I_r/I_s vs. $1/l+m+n$.
●: 2.6% silicon steel, ○: 3.2% silicon steel, ×: 4.0% silicon steel.

by the conventional ballistic method, and those of 3.2% silicon steel for the three principal directions are shown in Fig. 2. The curves of 2.6% and 4.0% silicon are similar to that of 3.2%, except that abnormal behavior which appears near saturation in [111] direction decreases with silicon content.

By measuring the areas enclosed between the ordinate and the magnetization curves, one can obtain the crystal anisotropy constants K_0, K_1 and K_2 from the following theoretical relation:

$$E_K = K_0 + K_1(m^2n^2 + n^2l^2 + l^2m^2) + K_2 l^2m^2n^2. \qquad (1)$$

where E_K is the crystal anisotropy energy, and l, m and n are the direction cosines of the rod axis with respect to the crystal axes. The values of K_0 is negligibly small compared with K_1 and the obtained values of K_1 are as follows:

3.65×10^5 ergs/cm^3	for 2.6% silicon,
3.50×10^5 ergs/cm^3	for 3.2% silicon,
2.95×10^5 ergs/cm^3	for 4.0% silicon.

On account of the shortage of samples with a sufficiently large coefficient of K_2, its value could not be determined exactly.

The descending hysteresis curves of these specimens show a sharp corner near the point $H_{eff.}=0$, as shown, for example, in Fig. 3 in case of 3.2% silicon, so the magnetization intensity corresponding to this point is defined as the remanent magnetization I_r. Now we shall discuss the applicability of Kaya's law[4] at the remanence. According to Kaya the remanent magnetization I_r can be expressed as

$$I_r/I_s = 1/(l+m+n)\,, \qquad (2)$$

where I_s is the saturation magnetization. Table II and Fig. 4 show that this law holds for these specimens as in the previous paper[1]. A closer inspection shows that the experimental values are slightly lower than the theoretical ones. However, these discrepancies can be ascribed to the disturbance of the domain distribution due to the unexpected local internal stress and due to the surface of the specimen.

The coercive forces of these specimens are larger than that of low silicon content. It would be mainly attributed to the difference of their impurity contents. For 2.6% silicon

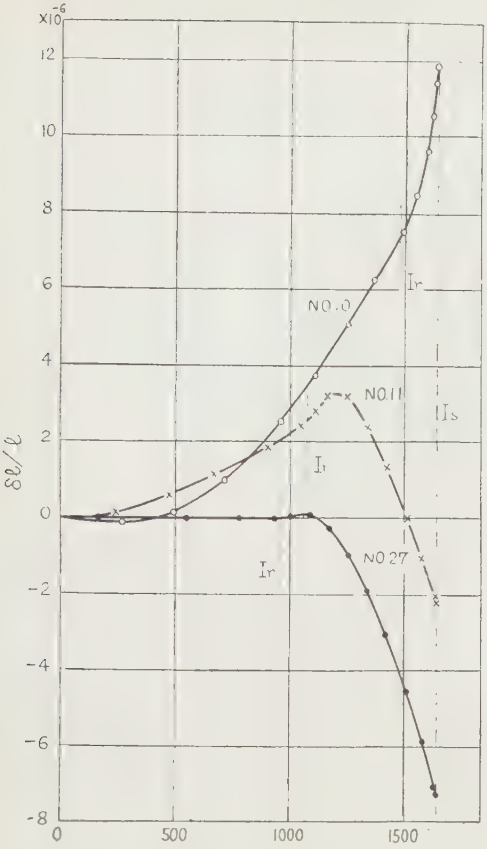

Fig. 5. Magnetostriction curves along the descending hysteresis in single crystals of 2.6% silicon steel with various crystallographic orientations.

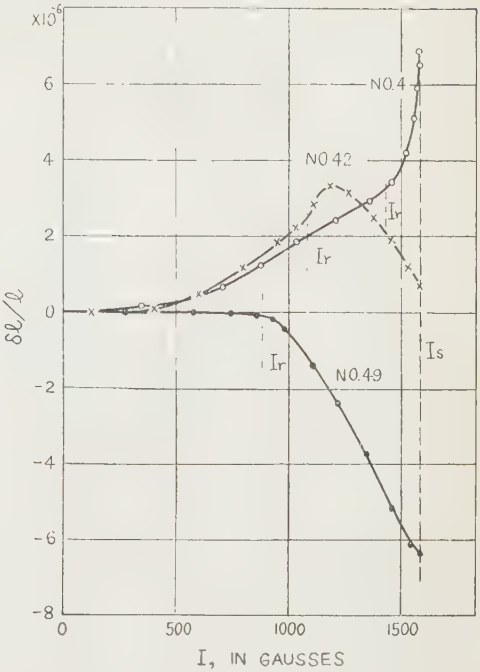

Fig. 6. Magnetostriction curves along the descending hysteresis in single crystals of 3.2% silicon steel with various crystallographic orientations.

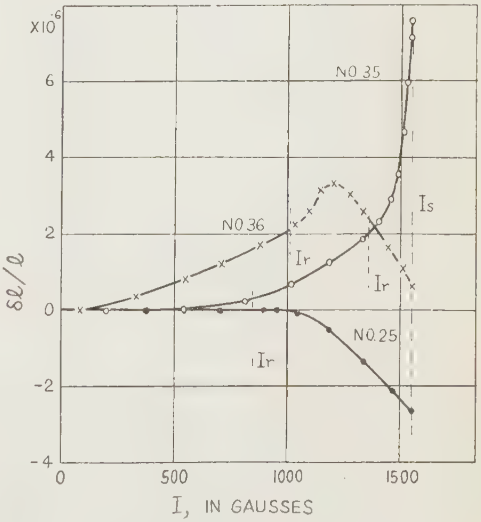

Fig. 7. Magnetostriction curves along the descending hysteresis in single crystals of 4.0% silicon steel with various crystallographic orientations.

the coercive forces are from 0.078 Oe to 0.237 Oe depending upon their crystallographic orientations, and for 3.2% silicon from 0.078 Oe to 0.319 Oe and for 4.0% silicon from 0.057 Oe to 0.265 Oe.

Magnetostriction was measured at room temperature by the usual mechano-optical method. Fig. 5, Fig. 6 and Fig. 7 represent the change of length along the descending hysteresis loop for 2.6%, 3.2% and 4.0% silicon respectively. By taking the remanent point and the saturation as two standard points at which the distribution of magnetic domains is uniquely determined, the difference of magnetostriction between at saturation and at remanence can be represented by the following relation:

$$\left(\frac{\delta l}{l}\right)_{\text{Sat.-Rem.}}=\left\{\frac{3}{2}\left(1-\frac{l^3+m^3+n^3}{l+m+n}\right)-3(m^2n^2+n^2l^2+l^2m^2)\right\}\lambda_{100}$$

$$-3(m^2n^2+n^2l^2+l^2m^2)\lambda_{111}\,, \qquad (3)$$

where λ_{100} and λ_{111} are the magnetostriction constants. Using the relation (3) and the observed values $(\delta l/l)_{\text{Sat.-Rem.Obs.}}$, tabulated in

Table II, we can determine magnetostriction constants as follows:

% Si	$\lambda_{100} \times 10^6$	$\lambda_{111} \times 10^6$
2.6	36.0±2.3	−(7.9±0.7)
3.2	32.0±1.8	−(5.6±0.4)
4.0	35.3±1.8	−(2.8±0.5)

Fig. 8 shows the dependency of magnetostriction constants λ_{100} and λ_{111} and crystal anisotropy constant K_1 on the silicon content, together with the results of our previous paper. As can be seen, λ_{111} and K_1 decrease almost linearly with silicon content. However, λ_{100} decreases more rapidly at low silicon content, and then suddenly increases at about two percent silicon and has no considerable change up to four percent silicon. Dr. Imai[5] pointed out that the changes of the lattice parameter and the Curie point with silicon content show slight but sharp discontinuities near the silicon concentration corresponding to the abrupt change of λ_{100}. Yensen[6] showed that the plastic properties have an abrupt change near this silicon content. These anomalies might have some relation with each other. For comparison, the data by Carr and Smoluchowski and others are also given in Fig. 8. Carr and Smoluchowski[2] measured λ_{100} and λ_{111} on the samples of disk form, 1 in. in diameter and 0.1 in. in thickness, by means of resistance strain gauges and an electromagnet, supplying the field of 3,300 Oe, in which the crystal was rotated through various angles. Our data of λ_{111} are connected smoothly with the data by Carr and Smoluchowski and the values of K_1 agree with that of Tarasov[7] and others. However, our values of λ_{100} are larger than that of Carr and Smoluchowski.

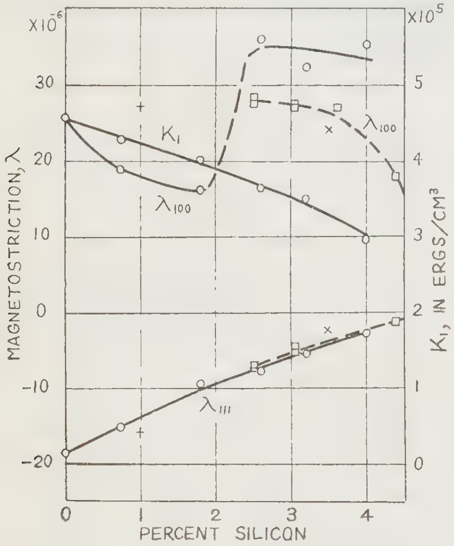

Fig. 8. Dependency of three constants, λ_{100}, λ_{111} and K_1, on silicon content. —○—: authors, --□--: Carr and Smoluchowski, ×: Shturkin[8], +: Tatsumoto[9].

In conclusion the authors wish to express their sincere thanks to Professor S. Kaya of the University of Tokyo for his kind interest and encouragement throughout the work and also to express their thanks to Mr. S. Nakamura and Mr. Y. Deguchi for their helpful assistances in preparation of single crystal specimens. The expense of this research has been partly defrayed by the Scientific Research Expenditure of the Ministry of Education.

References

1) H. Takaki and Y. Nakamura: J. Phys. Soc. Japan **9** (1954) 507.

2) W. J. Carr and R. Smoluchowski: Phys. Rev. **83** (1951) 1236.

3) H. Takaki, S. Nakamura, Y. Nakamura, J. Hayashi, K. Furukawa and M. Aso: J. Phys. Soc. Japan **9** (1954) 204.

4) S. Kaya: ZS. f. Phys. **84** (1933) 705.

5) M. Imai: The thesis for Doctor of Engineering, Tohoku Univ.

6) T. D. Yensen: Trans. Am. Inst. Elect. Engrs. **34** (1915) 2601.

7) L. P. Tarasov: Phys. Rev. **56** (1939) 1231.

8) D. A. Shturkin: Compt. Rend. Acad. Sci. (USSR) **58** (1947) 581.

9) E. Tatsumoto: J. Sci. Hiroshima Univ. **A 17** (1953) 229.

JOURNAL OF THE PHYSICAL SOCIETY OF JAPAN Vol. 9, No. 5, SEP.—OCT., 1954

On the Absorption Spectra of Complex Ions. I

By Yukito TANABE
Department of Physics, University of Tokyo
and Satoru SUGANO
Institute of Broadcasting, N. H. K.

(Recieved June 11, 1954)

In order to explain the origin of both absorption bands and lines of the octahedral normal complex ions in which the central metal ions belong to iron group elements, the crystalline field approximation interpreted in somewhat generalized sense is adopted. For this purpose the calculation of the energy matrix elements for d^n ($n=1, 2, \ldots, 9$) electron configuration in cubic field is performed by means of Racah's method. Comparison of the results with experiments will be made in the following paper.

§ 1. Introduction

Much work, both theoretical and experimental, has been done about the ground states of the normal complex ions of the type $[XY_6]^{3+}$, $[XY_6]^{2+}$, where X represents an iron group element and Y represents a ligand such as H_2O, NH_3, ethylenediamine, etc.. Especially owing to recent investigations by the method of the paramagnetic resonance absorption, rather detailed knowledge of them has been obtained. As to the excited states, however, little is known of these normal complex ions, and, it seems, there remain many problems to be investigated further from the theoretical point of view.

The optical absorption of both crystals and solutions (aqueous in many cases) containing these complex ions have been studied since the days of Werner by many physicists and chemists, and it is known that the absorption spectra of solutions are quite similar (although the width and the intensity of bands are slightly different) to those of crystals containing the same complex ion as the solutions except for an intense edge absorption ($\log \varepsilon_{\max} \sim 4$) in the ultra violet region which does not appear in the latter, so that they are considered to be due mainly to the absorption of the complex ion as a whole. The absorption spectra of these complex ions are characterized by the presence of several (one to three) bands in the near infrared, visible and ultra violet region (8000 cm^{-1} to 40000 cm^{-1}). Some of them show several sharp absorption lines besides these broad bands (e.g. Chrome Alum).

There have been several explanations of the origin of these spectra, but many of them are only of qualitative nature and it is not yet certain which is the correct one. Only two of them shall be quoted here, because they bear close relation to our calculation. Finkelstein and Van Vleck[1] treated the doublet lines of Chrome Alum at 6700 Å and obtained quantitative agreement between theory and experiment using the crystalline field approximation, but they left the origin of the broad bands unanswered. Recently, Hartmann and Schlaefer et al.[2] treated the problem of broad bands also from the same standing point. They maintained that these absorption bands were due to the transitions between the Stark components of the ground multiplet of the central metal ion, and showed that the number of broad bands (which are observed in the region up to 33000 cm^{-1}) could be reasonably explained on this assumption at least in case the central metal ion has no more than five d-electrons. But they made no mention of the line spectra at all. Though these explanations seem to be resonable, it is not clear why some of the transitions correspond to the broad bands and the others to the sharp lines. It seems necessary to examine if such an assignment should give the order of magnitude of the observed intensity and the band width theoretically, and if the calculation could predict the position of the absorption maxima satisfactorily.

In order to study to what degree the crystalline field approximation succeeds in explaining the absorption spectra of these complex ions including both the lines and bands, the energy matrix elements for the electron configuration d^n in cubic field are calculated in this paper.

§ 2. The Crystalline Field Approximation

These complex ions are known to be of the octahedral shape, and the central ion X is considered to be exposed to the cubic electric field (crystalline field) due to the octahedrally coordinated ligands Y.*

In the case of the rare earth salts, the crystalline field is relatively weak because of the screening effect of the electrons in the outer shells, so that, when one wants to study the electronic structure of the rare earth ions it is generally allowed to treat each SL multiplet separately and to consider the splittings of these multiplets due to the crystalline field. In our case of the iron group complex ions, however, the following treatment** will be more adequate, because here d-electrons are exposed directly to the strong crystalline field. In Cubic field the d-level splits into two levels, i.e., triply degenerate $d\varepsilon$ and doubly degenerate $d\gamma$ ($d\varepsilon$ is lower than the original d-level by $-4Dq$, and $d\gamma$ higher by $6Dq$, where Dq is the crystalline field parameter usually used.) and the electrons are accomodated in these two levels. For those complexes where the free $X^{3,2+}$ ion has the electrons configuration d^N, we now take the configurations $d\varepsilon^n d\gamma^{N-n}$ ($n=0$ to N) as the starting point.

If the crystalline field is sufficiently strong, we may neglect the interaction between these configurations. Then the problem is to find the positions of the $S\Gamma$ multiplets arising from each configuration mentioned above, but unfortunately the crystalline field is not so strong as to permit us to neglect the configuration interaction entirely and we must take it into account for some of the levels.

As is easily seen, in the calculation under the scheme which we mentioned to be suited for the weak field case, if the interaction between the Stark components of different SL multiplets is fully taken into account as in Finkelstein and Van Vleck's one, the results are of course the same as those calculated in our way, when we construct $d\varepsilon$, $d\gamma$ wave function there by proper linear combinations of the d-wave function.

It is here necessary to consider the meaning of the "crystalline field." Recently Kleiner[4)] has calculated the strength of the crystalline field Dq of Chrome Alum semi-classically taking the overlapping of the charge cloud of the Cr^{3+} ion and that of H_2O into account, and found that the calculated value was by far smaller (the sign was wrong) than the value estimated from the magnetic susceptibility data, though his model seemed more reasonable than the point-dipole or -charge model[5),6)] which can give the resonable values of Dq in many cases. This is unfortunate, but this may not be so serious. It seems to us that, as far as Dq is considered as an empirical parameter, the validity of the crystalline field approximation is not so limited as one might suppose from his results, since this approximation can be interpreted in a generalized sense as follows.

That is, we consider $[XY_6]^{3,2+}$ complex ion as a single molecule whose filled orbitals with lower energies correspond to the inner shells or closed shells of the central ion and ligands in the free states which may be deformed in the complex ion, and whose next higher orbitals are f_2 and e (which correspond to $d\varepsilon$ and $d\gamma$ respectively) belonging to the irreducible representations F_{2g} and E_g of O_h group. This is just the model which corresponds to the crystalline field approximation. f_2 and e orbitals will not have the pure d-character in general, and may be approximated by the linear combinations of d-orbitals and the ligand orbitals. For $d\gamma$ this departure from the atomic d-character will be large, but also for $d\varepsilon$ such deformation would exist as Stevens has recently pointed out[7)]. Thus in this generalized crystalline field formalism, Dq is now defined through the relation $\epsilon_e - \epsilon_{f_2} = 10Dq$ where ϵ_e and ϵ_{f_2} denote the orbital energies of e and f_2 orbitals. Futhermore in this molecular treatment, the integrals appearing in the calculation may be different from those in the usual crystalline field approximation, where they are expressed in terms of the Slater integrals for the free ions.

If we go further in this way there is no reason why only two levels f_2 and e should be taken into account. But when we include further configurations the calculation would become somewhat tedious and the empirical treatment such as adopted in the following paper would become impossible. Thus we assume with a hope that the generalized crystalline field model will well approximate the reality, and carry out the calculation under this assumption.

---

* Throughout this and the following paper the Jahn-Teller effect is neglected.

** Similar calculations along this line has already been done by Kotani for the case of d^2 and by Kambe and Usui for d^3 [3)].

In the next section, however, we calculate the energy matrix elements using the atomic $d\varepsilon$ and $d\gamma$, and express them in terms of A, B, C and Dq (A, B, C are the linear combinations of Slater integrals introduced by Racah). Thus, the effect of deformation appears only through the change of B, C from those for the free ions. This was done only to avoid the complexity caused by many unknown parameters which appear when e and f_2 are considered not to be pure $d\varepsilon$ and $d\gamma$, although the method of calculation is also applicable when the crystalline field approximation is taken in a generalized sence.

§ 3. The Calculation of Energy Matrices and the Results

When we adopt the scheme stated in § 2 and confine ourselves to the states which come from the configurations $d\varepsilon^n d\gamma^{N-n}(n=0,\ldots,N)$, the orthonormal basic functions to construct the energy matrix of symmetry species $S\Gamma$ are $\Psi(d\varepsilon^n(S_1\Gamma_1)d\gamma^{N-n}(S_2\Gamma_2)S\Gamma)$. The matrix elements of the scalar (cubic scalar in this case) operator $G_N=\sum_{i>j}^{N} g_{ij}$ between these states can be calculated by means of the following recurrence formula, which is a generalization of the formula (1) of R IV[8]:

$$
\begin{aligned}
&(\gamma_1^n(S_1\Gamma_1)\gamma_2^{N-n}(S_2\Gamma_2)S\Gamma|G_N|\gamma_1^{n'}(S_3\Gamma_3)\gamma_2^{N-n'}(S_4\Gamma_4)S\Gamma)\\
&\quad=\sqrt{nn'}/(N-2)\sum_{S'S''\bar{S}\Gamma'\Gamma''\bar{\Gamma}}(\gamma_1^n S_1\Gamma_1\{|\gamma_1,\gamma_1^{n-1}(S'\Gamma')S_1\Gamma_1)(\gamma_1 S'\Gamma'(S_1\Gamma_1)S_2\Gamma_2 S\Gamma|\\
&\qquad\qquad\gamma_1,S'\Gamma'S_2\Gamma_2(\overline{S\Gamma})S\Gamma)(\gamma_1^{n-1}(S'\Gamma')\gamma_2^{N-n}(S_2\Gamma_2)\overline{S\Gamma}|G_{N-1}|\gamma_1^{n'-1}(S''\Gamma'')\gamma_2^{N-n'}(S_4\Gamma_4)\overline{S\Gamma})\\
&\qquad\qquad\times(\gamma_1,S''\Gamma''S_4\Gamma_4(\overline{S\Gamma})S\Gamma|\gamma_1 S''\Gamma''(S_3\Gamma_3)S_4\Gamma_4 S\Gamma)(\gamma_1\gamma_1^{n'-1}(S''\Gamma'')S_3\Gamma_3|\}\gamma_1^{n'}S_3\Gamma_3)\\
&\quad+\sqrt{(N-n)(N-n')}/(N-2)\sum_{S'S''\bar{S}\Gamma'\Gamma''\bar{\Gamma}}(\gamma_2^{N-n}S_2\Gamma_2\{|\gamma_2^{N-n-1}(S'\Gamma')\gamma_2 S_2\Gamma_2)\\
&\qquad\qquad\times(S_1\Gamma_1,S'\Gamma'\gamma_2(S_2\Gamma_2)S\Gamma|S_1\Gamma_1 S'\Gamma'(\overline{S\Gamma})\gamma_2 S\Gamma)\\
&\qquad\qquad\times(\gamma_1^n(S_1\Gamma_1)\gamma_2^{N-n-1}(S'\Gamma')\overline{S\Gamma}|G_{N-1}|\gamma_1^{n'}(S_3\Gamma_3)\gamma_2^{N-n'-1}(S''\Gamma'')\overline{S\Gamma})\\
&\qquad\qquad\times(S_3\Gamma_3 S''\Gamma''(\overline{S\Gamma})\gamma_2 S\Gamma|S_3\Gamma_3,S''\Gamma''\gamma_2(S_4\Gamma_4)S\Gamma)\\
&\qquad\qquad\times(\gamma_2^{N-n'-1}(S''\Gamma'')\gamma_2 S_4\Gamma_4|\}\gamma_2^{N-n'}S_4\Gamma_4)\,. \qquad (3.1)
\end{aligned}
$$

Although γ_1, γ_2 and Γ's here are the symbols for the irreducible representations of the octahedral group (γ_1, γ_2 being E and F_2 respectively), this formula is generally valid for any other group.

In order to calculate this matrix element for the N electron system, it is necessary to know the transformation matrices $(S'\Gamma'S''\Gamma''(\overline{S\Gamma}),S'''\Gamma'''S\Gamma|S'\Gamma',S''\Gamma''S'''\Gamma'''(\underline{S\Gamma})S\Gamma)$ and the coefficients of the fractional parentage $(\gamma^n S\Gamma\{|\gamma^{n-1}(S'\Gamma')\gamma S\Gamma)$ (c.f.p.) besides the matrix elements for the $N-1$ electron system.

The transformation matrices were simply calculated according to the definition (3) of R III[8], and the Clebsch-Gordan coefficients thereby used are given in Table I.

The c.f.p. for n-electrons are obtained solving the following linear equations which are (11) of R III, assuming that we know those for $n-1$ electrons and the transformation matrices of the type $(S''\Gamma'',\gamma\gamma(S'''\Gamma''')S\Gamma|S''\Gamma''\gamma(S'\Gamma')\gamma S\Gamma)$:

$$
\begin{aligned}
&\sum_{S'\Gamma'}(S''\Gamma'',\gamma\gamma(S'''\Gamma''')S\Gamma|S''\Gamma''\gamma(S'\Gamma')\gamma S\Gamma)\\
&\qquad\times(\gamma^{n-2}(S''\Gamma'')\gamma S'\Gamma'|\}\gamma^{n-1}S'\Gamma')\\
&\qquad\times(\gamma^{n-1}(S'\Gamma')\gamma S\Gamma|\}\gamma^n S\Gamma)=0\,. \qquad (3.2)
\end{aligned}
$$

Here $S'''\Gamma'''$'s denote the "forbidden states" for the configuration γ^2. For instance, in the case of $\gamma=d\varepsilon$ they are ${}^3A_1$, ${}^3E$, ${}^1F_1$ and ${}^3F_2$. c.f.p. calculated in this way are given at the end of this paper (Table II), together with the c.f.p. of the type $(\gamma^{n-2}(S'\Gamma')\gamma^2(S''\Gamma'')S\Gamma|\}\gamma^n S\Gamma)$ which were calculated according to (32) of R III and useful in some cases (see below).

Further relation analogous to Eq. (29) of R III was also used:

$$\begin{aligned}(\gamma, \gamma^{n-1}(S'\Gamma')S\Gamma|\}\gamma^n S\Gamma) \\ =(-)^{S'+1/2-S+f(\gamma\Gamma'\Gamma)+n+1} \\ \times(\gamma^{n-1}(S'\Gamma')\gamma S\Gamma|\}\gamma^n S\Gamma)\,,\end{aligned} \tag{3.3}$$

where

$$\begin{aligned} f(\gamma\Gamma'\Gamma)&=1 \quad \text{for} \quad (\gamma\Gamma'\Gamma)=(EEA_2)\,, \\ &\qquad\qquad\qquad\qquad\quad (F_1F_1F_1)\,, \\ &\qquad\qquad\qquad\qquad\quad (F_2F_2F_1)\,, \\ &=0 \quad \text{otherwise.}\end{aligned}$$

The formula (3.1) is rather complicated and the calculation becomes somewhat tedious when one uses this formula as it is. But it is often not necessary to cary out both summations and the labor is greatly reduced especially when one of the two sums becomes simple owing to the restriction on the summation parameters.

This fact applies to the calculation of the non-diagonal elements.

Without loss of generality we may assume $n'+3>n\geq n'$. When $n-n'=2$, applying (3.1) successively we see that this type of matrix elements has a single ancestor of the type $(\gamma_1{}^2S\Gamma|g|\gamma_2{}^2S\Gamma)$, and in this case, it can be shown (Appendix) that the ratio of two sums is a constant which depends only N, n, n', and therefore it is sufficient to calculate the simpler sum. When $n-n'=1$, we have two ancestors for this type of elements, i.e., $(\gamma_1\gamma_2S\Gamma|g|\gamma_2{}^2S\Gamma)$ and $(\gamma_1{}^2S\Gamma|g|\gamma_1\gamma_2S\Gamma)$ so that no simplification can be obtained. But in our case fortunately there is no ancestor of the type $(d\varepsilon d\gamma S\Gamma|g|d\gamma^2S\Gamma)$, because configurations $d\varepsilon d\gamma$ and $d\gamma^2$ have no common state $S\Gamma$, and we can simplify the formula (3.1) in a similar way as was made in the case $n-n'=2$. In the last case, i.e., when $n=n'$, there are three ancestors, namely $(\gamma_1{}^2S\Gamma|g|\gamma_1{}^2S\Gamma)$, $(\gamma_2{}^2S\Gamma|g|\gamma_2{}^2S\Gamma)$ and $(\gamma_1\gamma_2S\Gamma|g|\gamma_1\gamma_2S\Gamma)$. The non-diagonal elements in this case are, however, seen to originate only from the last type of the three ancestors mentioned above, i.e., $(\gamma_1\gamma_2S\Gamma|g|\gamma_1\gamma_2S\Gamma)$, so also in this case the same simplification is achieved in the calculation of these elements.

In some of the last cases the matrix elements of G_N are calculated more easily from those of G_{N-2} or from an ancestor directly by making use of the c.f.p. of the type

$$(\gamma^{n-2}(S'\Gamma')\gamma^2(S''\Gamma'')S\Gamma|\}\gamma^n S\Gamma)$$

than from those of G_{N-1}. The recurrence formulae of this type are easily obtained in a way analogous to (3.1) and some of these are already given in (33) of R III.

The matrix elements of the electrostatic interaction for two electron system are easily calculated and the results are given below. Here (u,v) and (ξ,η,ζ) denote the real orbitals which belong to the irreducible representations E_g and F_{2g} respectively of the octahedral group.

$$\left.\begin{array}{ll}
n-n'=0 & (d\varepsilon^2S\Gamma|g|d\varepsilon^2S\Gamma) \\
 & S\Gamma={}^1A_1:\ (\xi\xi|g|\xi\xi)+2K(\zeta\eta)=(A+10B+5C)\,, \\
 & \qquad {}^1E\ :\ (\xi\xi|g|\xi\xi)-K(\zeta\eta)=(A+B+2C)\,, \\
 & \qquad {}^3F_1:\ J(\zeta\eta)-K(\zeta\eta)=(A-5B)\,, \\
 & \qquad {}^1F_2:\ J(\zeta\eta)+K(\zeta\eta)=(A+B+2C)\,, \\
 & \qquad (d\varepsilon d\gamma S\Gamma|g|d\varepsilon d\gamma S\Gamma) \\
 & S\Gamma={}^1F_1:\ J(\zeta v)+K(\zeta v)=(A+4B+2C)\,, \\
 & \qquad {}^3F_1:\ J(\zeta v)-K(\zeta v)=(A+4B)\,, \\
 & \qquad {}^1F_2:\ J(\zeta u)+K(\zeta u)=(A+2C)\,, \\
 & \qquad {}^3F_2:\ J(\zeta u)-K(\zeta u)=(A-8B)\,, \\
 & \qquad (d\gamma^2S\Gamma|g|d\gamma^2S\Gamma) \\
 & S\Gamma={}^1A_1:2(uu|g|uu)-J(uv)-K(uv)=(A+8B+4C)\,, \\
 & \qquad {}^3A_2:\ J(uv)-K(uv)=(A-8B)\,, \\
 & \qquad {}^1E\ :\ J(uv)+K(uv)=(A+2C)\,, \\
n-n'=1 & (d\varepsilon^2S\Gamma|g|d\varepsilon d\gamma S\Gamma) \\
 & S\Gamma={}^3F_1:2(\eta\xi|g|v\zeta)=(6B), \\
 & \qquad {}^1F_2:2(\eta\xi|g|u\zeta)=(2\sqrt{3}B)\,, \\
n-n'=2 & (d\varepsilon^2S\Gamma|g|d\gamma^2S\Gamma) \\
 & S\Gamma={}^1A_1:\sqrt{3/2}\{K(\xi u)+K(\xi v)\}=(\sqrt{6}(2B+C))\,,
\end{array}\right\} \tag{3.4}$$

$$ {}^1E : \sqrt{3} \quad \{K(\xi u)-K(\xi v)\}=(-2\sqrt{3}B) , $$

where

$$ J(ab)=(ab|g|ab) , \qquad K(ab)=(ab|g|ba) . $$

To obtain these results the following relations were used, which come from the transformation properties of the basic orbitals ;

$$ \left.\begin{aligned} &(\xi\xi|g|\xi\xi)=(\eta\eta|g|\eta\eta)=(\zeta\zeta|g|\zeta\zeta) , \\ &(\xi\xi|g|\eta\eta)=(\eta\eta|g|\zeta\zeta)=(\zeta\zeta|g|\xi\xi) , \\ &(uu|g|uu)=(vv|g|vv) , \\ &(uu|g|vv)=(uu|g|uu)-J(uv)-K(uv) , \\ &(\eta\xi|g|v\zeta)=-(\eta\xi|g|\zeta v) , \\ &(\eta\xi|g|u\zeta)=(\eta\xi|g|\zeta u) , \\ &(\xi\xi|g|uu)=(\eta\eta|g|uu) , \\ &(\xi\xi|g|vv)=(\eta\eta|g|vv) , \\ &(\xi\xi|g|uu)-(\xi\xi|g|vv)=2/\sqrt{3}(\xi\xi|g|uv) , \\ &(\zeta\zeta|g|uu)=-1/2(\eta\eta|g|uu)+3/2(\eta\eta|g|vv) , \\ &(\zeta\zeta|g|vv)=3/2(\eta\eta|g|uu)-1/2(\eta\eta|g|vv) , \end{aligned}\right\} \tag{3.5} $$

and from their reality ;

$$ \left.\begin{aligned} &(\zeta\zeta|g|\eta\eta)=K(\zeta\eta) , \qquad &(uu|g|vv)=K(uv) , \\ &(\zeta\zeta|g|uu)=K(\zeta u) , \qquad &(\zeta\zeta|g|vv)=K(\zeta v) , \\ &(\xi\xi|g|uu)=K(\xi u) , \qquad &(\xi\xi|g|vv)=K(\xi v) . \end{aligned}\right\} \tag{3.6} $$

Using these matrix elements of $G_2=1/r_{12}$, we can now proceed to calculate the matrix elements of $G_N=\sum_{i>j}^{N} 1/r_{ij}$. The complete energy matrix is obtained adding the orbital (crystalline field) energies to its diagonal elements.

As was mentioned at the end of § 2, we now return to the crystalline field approximation in normal sense, and assume the orbitals (u, v) and (ξ, η, ζ) are pure $d\gamma$ and $d\varepsilon$ respectively, namely, of the form ;

$$ \left.\begin{aligned} u&=R(r)Y_{20}(\theta\varphi), \\ v&=1/\sqrt{2}\ R(r)\{Y_{22}(\theta\varphi)+Y_{2-2}(\theta\varphi)\} , \\ \xi&=-i/\sqrt{2}\ R(r)\{Y_{21}(\theta\varphi)+Y_{2-1}(\theta\varphi)\} , \\ \eta&=-1/\sqrt{2}\ R(r)\{Y_{21}(\theta\varphi)-Y_{2-1}(\theta\varphi)\} , \\ \zeta&=i/\sqrt{2}\ R(r)\{Y_{22}(\theta\varphi)-Y_{2-2}(\theta\varphi)\} . \end{aligned}\right\} \tag{3.7} $$

The matrix elements (3.4) are accordingly expressed in terms of Racah's parameters A, B, C as are shown at the right hand side of (3.4) in parenthesis.

The orbital energy for the configuration $d\varepsilon^n d\gamma^{N-n}$ is given by $(6N-10n)Dq$.

The results thus obtained are given in Table III, where the term $N(N-1)/2\cdot A$ in the diagonal elements is omitted. They were checked by examining whether they gave the energies of the free state when Dq was set equal to zero, or not.

Conjugation is simple in this case, that is, we can obtain the energy matrices for d^{10-N} from those for d^N merely changing the sign of Dq[1]. Conjugate states are given at the top of the columns of each matrix in Table III.

Table I. Tables of the clebsch-gordan coefficients. $(\Gamma_1\gamma_1\Gamma_2\gamma_2|\Gamma_1\Gamma_2\Gamma\gamma)$

$A_2 \times A_2$

	Γ	A_1
	γ	e_1
γ_1	γ_2	
e_2	e_2	-1

$A_2 \times E$

	Γ	E	
	γ	u	v
γ_1	γ_2		
e_2	u		-1
	v	1	

$A_2 \times F_1$

	Γ	F_2		
	γ	ξ	η	ζ
γ_1	γ_2			
	α	1		
e_2	β		1	
	γ			1

$A_2 \times F_2$

	Γ	F_1		
	γ	α	β	γ
γ_1	γ_2			
	ξ	-1		
e_2	η		-1	
	ζ			-1

$E \times E$

	Γ	A_1	A_2	E	
	γ	e_1	e_2	u	v
γ_1	γ_2				
u	u	$1/\sqrt{2}$		$-1/\sqrt{2}$	
	v		$1/\sqrt{2}$		$1/\sqrt{2}$
v	u		$-1/\sqrt{2}$		$1/\sqrt{2}$
	v	$1/\sqrt{2}$		$1/\sqrt{2}$	

Table I. (continued)

$E\times F_1$

	Γ	F_1			F_2		
γ_1	γ_2 \ γ	α	β	γ	ξ	η	ζ
	α	$-1/2$			$\sqrt{3}/2$		
u	β		$-1/2$			$-\sqrt{3}/2$	
	γ			1			
	α	$\sqrt{3}/2$			$1/2$		
v	β		$-\sqrt{3}/2$			$1/2$	
	γ						-1

$E\times F_2$

	Γ	F_1			F_2		
γ_1	γ_2 \ γ	α	β	γ	ξ	η	ζ
	ξ	$-\sqrt{3}/2$			$-1/2$		
u	η		$\sqrt{3}/2$			$-1/2$	
	ζ						1
	ξ	$-1/2$			$\sqrt{3}/2$		
v	η		$-1/2$			$-\sqrt{3}/2$	
	ζ			1			

$F_1\times F_1$

	Γ	A_1	E		F_1			F_2		
γ_1	γ_2 \ γ	e_1	u	v	α	β	γ	ξ	η	ζ
	α	$-1/\sqrt{3}$	$1/\sqrt{6}$	$-1/\sqrt{2}$						
α	β						$-1/\sqrt{2}$			$-1/\sqrt{2}$
	γ					$1/\sqrt{2}$			$-1/\sqrt{2}$	
	α						$1/\sqrt{2}$			$-1/\sqrt{2}$
β	β	$-1/\sqrt{3}$	$1/\sqrt{6}$	$1/\sqrt{1}$						
	γ				$-1/\sqrt{2}$			$-1/\sqrt{2}$		
	α					$-1/\sqrt{2}$			$-1/\sqrt{2}$	
γ	β				$1/\sqrt{2}$			$-1/\sqrt{2}$		
	γ	$-1/\sqrt{3}$	$-2/\sqrt{6}$							

$F_1\times F_2$

	Γ	A_2	E		F_1			F_2		
γ_1	γ_2 \ γ	e_2	u	v	α	β	γ	ξ	η	ζ
	ξ	$-1/\sqrt{3}$	$-1/\sqrt{2}$	$-1/\sqrt{6}$						
α	η						$1/\sqrt{2}$			$-1/\sqrt{2}$
	ζ					$1/\sqrt{2}$			$1/\sqrt{2}$	
	ξ						$1/\sqrt{2}$			$1/\sqrt{2}$
β	η	$-1/\sqrt{3}$	$1/\sqrt{2}$	$-1/\sqrt{6}$						
	ζ				$1/\sqrt{2}$			$-1/\sqrt{2}$		
	ξ					$1/\sqrt{2}$			$-1/\sqrt{2}$	
γ	η				$1/\sqrt{2}$			$1/\sqrt{2}$		
	ζ	$-1/\sqrt{3}$		$2/\sqrt{6}$						

Table I. (continued)

$F_2 \times F_2$

	Γ	A_1	E		F_1			F_2		
	γ	e_1	u	v	α	β	γ	ξ	η	ζ
γ_1	γ_2									
ξ	ξ	$1/\sqrt{3}$	$-1/\sqrt{6}$	$1/\sqrt{2}$						
	η						$1/\sqrt{2}$			$1/\sqrt{2}$
	ζ					$-1/\sqrt{2}$			$1/\sqrt{2}$	
η	ξ						$-1/\sqrt{2}$			$1/\sqrt{2}$
	η	$1/\sqrt{3}$	$-1/\sqrt{6}$	$-1/\sqrt{2}$						
	ζ				$1/\sqrt{2}$			$1/\sqrt{2}$		
ζ	ξ					$1/\sqrt{2}$			$1/\sqrt{2}$	
	η				$-1/\sqrt{2}$			$1/\sqrt{2}$		
	ζ	$1/\sqrt{3}$	$2/\sqrt{6}$							

Table II.

Tables of the C. F. P. $(\gamma^{n-1}(S'\Gamma')\gamma\, S\Gamma|\}\gamma^n S\Gamma)$.

$(d\varepsilon^{n-1}(S'\Gamma')d\varepsilon\, S\Gamma|\}d\varepsilon^n S\Gamma)$

$n=3$

$S\Gamma$ \ $S'\Gamma'$	$^1A_1$	$^3F_1$	^1E	$^1F_2$
$^4A_2$		1		
$^2F_1$		$1/\sqrt{2}$	$1/\sqrt{3}$	$1/\sqrt{6}$
^2E		$1/\sqrt{2}$		$1/\sqrt{2}$
$^2F_2$	$\sqrt{2}/3$	$1/\sqrt{2}$	$-1/3$	$-1/\sqrt{6}$

$n=4$

$S\Gamma$ \ $S'\Gamma'$	$^4A_2$	$^2F_1$	^2E	$^2F_2$
$^1A_1$				1
$^3F_1$	$1/\sqrt{3}$	$-1/2$	$-1/\sqrt{6}$	$1/2$
^1E		$\sqrt{3}/2$		$1/2$
$^1F_2$		$1/2$	$1/\sqrt{2}$	$1/2$

$n=5$

$S\Gamma$ \ $S'\Gamma'$	$^1A_1$	$^3F_1$	^1E	$^1F_2$
$^2F_2$	$1/\sqrt{15}$	$\sqrt{3}/\sqrt{5}$	$-\sqrt{2}/\sqrt{15}$	$-1/\sqrt{5}$

$(d\gamma^2(S'\Gamma')d\gamma\, {}^2E|\}d\gamma^3\, {}^2E)$

$S\Gamma$ \ $S'\Gamma'$	$^1A_1$	^1E	$^3A_2$
^2E	$1/\sqrt{6}$	$-1/\sqrt{3}$	$1/\sqrt{2}$

Tables of the C. F. P. $(\gamma^{n-2}(S_1\Gamma_1)\gamma^2(S_2\Gamma_2)S\Gamma|\}\gamma^n S\Gamma)$

$(d\varepsilon^{n-2}(S_1\Gamma_1)d\varepsilon^2(S_2\Gamma_2)S\Gamma|\}d\varepsilon^n S\Gamma)$

$n=4$

$S\Gamma={}^1A_1$

$S_1\Gamma_1$ \ $S_2\Gamma_2$	$^1A_1$	$^3F_1$	^1E	$^1F_2$
$^1A_1$	$\sqrt{2}/3$			
$^3F_1$		$1/\sqrt{2}$		
^1E			$-1/3$	
$^1F_2$				$-1/\sqrt{6}$

$S\Gamma={}^3F_1$

$S_1\Gamma_1$ \ $S_2\Gamma_2$	$^1A_1$	$^3F_1$	^1E	$^1F_2$
$^1A_1$		$1/3\sqrt{2}$		
$^3F_1$	$1/3\sqrt{2}$	$1/\sqrt{3}$	$1/3$	$1/\sqrt{6}$
^1E		$1/3$		
$^1F_2$		$1/\sqrt{6}$		

$S\Gamma={}^1E$

$S_1\Gamma_1$ \ $S_2\Gamma_2$	$^1A_1$	$^3F_1$	^1E	$^1F_2$
$^1A_1$			$1/3\sqrt{2}$	
$^3F_1$		$-1/\sqrt{2}$		
^1E	$1/3\sqrt{2}$		$\sqrt{2}/3$	
$^1F_2$				$1/\sqrt{6}$

$S\Gamma={}^1F_2$

$S_1\Gamma_1$ \ $S_2\Gamma_2$	$^1A_1$	$^3F_1$	^1E	$^1F_2$
$^1A_1$				$1/3\sqrt{2}$
$^3F_1$		$-1/\sqrt{2}$		
^1E				$1/3$
$^1F_2$	$1/3\sqrt{2}$		$1/3$	$-1/\sqrt{6}$

Table II. (continued)

$n=5$
$S\Gamma={}^2F_2$

$(d\gamma^2(S_1\Gamma_1)d\gamma^2(S_2\Gamma_2)\,{}^1A_1|\}\,d\gamma^4\,{}^1A_1)$

$S_1\Gamma_1$ \ $S_2\Gamma_2$	${}^1A_1$	${}^3F_1$	${}^1E$	${}_1F_2$
${}^4A_2$		$1/\sqrt{5}$		
${}^2F_1$		$\sqrt{3}/2\sqrt{5}$	$1/\sqrt{10}$	$1/2\sqrt{5}$
${}^2E$		$1/\sqrt{10}$		$-1/\sqrt{10}$
${}^2F_2$	$1/\sqrt{15}$	$-\sqrt{3}/2\sqrt{5}$	$-1/\sqrt{30}$	$-1/2\sqrt{5}$

$S_1\Gamma_1$ \ $S_2\Gamma_2$	${}^1A_1$	${}^1E$	${}^3A_2$
${}^1A_1$	$1/\sqrt{6}$		
${}^1E$		$-1/\sqrt{3}$	
${}^3A_2$			$1/\sqrt{2}$

Table III.

Energy Matrices

d^3

${}^2F_2\ (a\,{}^2D,\ b\,{}^2D,\ {}^2F,\ {}^2G,\ {}^2H)$

	$d\varepsilon^3({}^2F_2)d\gamma^4$	$d\varepsilon^4({}^3F_1)d\gamma^3$	$d\varepsilon^4({}^1F_2)d\gamma^3$	$d\varepsilon^5 d\gamma^2({}^1A_1)$	$d\varepsilon^5 d\gamma^2({}^1E)$
$d\varepsilon^3$	$-12Dq+5C$	$-3\sqrt{3}B$	$-5\sqrt{3}B$	$4B+2C$	$2B$
	$d\varepsilon^2({}^3F_1)d\gamma$	$-2Dq-6B+3C$	$3B$	$-3\sqrt{3}B$	$-3\sqrt{3}B$
		$d\varepsilon^2({}^1F_2)d\gamma$	$-2Dq+4B+3C$	$-\sqrt{3}B$	$\sqrt{3}B$
			$d\varepsilon\ d\gamma^2({}^1A_1)$	$8Dq+6B+5C$	$10B$
				$d\varepsilon\ d\gamma^2({}^1E)$	$8Dq-2B+3C$

${}^2F_1\ ({}^2P,\ {}^2F,\ {}^2G,\ {}^2H)$

	$d\varepsilon^3({}^2F_1)d\gamma^4$	$d\varepsilon^4({}^3F_1)d\gamma^3$	$d\varepsilon^4({}^1F_2)d\gamma^3$	$d\varepsilon^5 d\gamma^2({}^3A_2)$	$d\varepsilon^5 d\gamma^2({}^1E)$
$d\varepsilon^3$	$-12Dq-6B+3C$	$-3B$	$3B$	0	$-2\sqrt{3}B$
	$d\varepsilon^2({}^3F_1)d\gamma$	$-2Dq+3C$	$-3B$	$3B$	$3\sqrt{3}B$
		$d\varepsilon^2({}^1F_2)d\gamma$	$-2Dq-6B+3C$	$-3B$	$-\sqrt{3}B$
			$d\varepsilon d\gamma^2({}^3A_2)$	$8Dq-6B+3C$	$2\sqrt{3}B$
				$d\varepsilon d\gamma^2({}^1E)$	$8Dq-2B+3C$

${}^2E\ (a\,{}^2D,\ b\,{}^2D,\ {}^2G,\ {}^2H)$

	$d\varepsilon^3({}^2E)d\gamma^4$	$d\varepsilon^4({}^1A_1)d\gamma^3$	$d\varepsilon^4({}^1E)d\gamma^3$	$d\varepsilon^6 d\gamma$
$d\varepsilon^3$	$-12Dq-6B+3B$	$-6\sqrt{2}B$	$-3\sqrt{2}B$	0
	$d\varepsilon^2({}^1A_1)d\gamma$	$-2Dq+8B+6C$	$10B$	$\sqrt{3}(2B+C)$
		$d\varepsilon^2({}^1E)d\gamma$	$-2Dq-B+3C$	$2\sqrt{3}B$
			$d\gamma^3$	$18Dq-8B+4C$

Table III. (continued)

$^4F_4$ (^4P, ^4F)

	$d\varepsilon^4(^3F_1)d\gamma^3$	$d\varepsilon^5 d\gamma^2(^3A_2)$
$d\varepsilon^2(^3F_1)d\gamma$	$-2Dq-3B$	$6B$
	$d\varepsilon\, d\gamma^2(^3A_2)$	$8Dq-12B$

$^4A_2$ (^4F)	$d\varepsilon^3$	$-12Dq-15B$	$d\varepsilon^3(^4A_2)d\gamma^4$
$^4F_2$ (^4F)	$d\varepsilon^2(^3F_1)d\gamma$	$-2Dq-15B$	$d\varepsilon^4(^3F_1)d\gamma^3$
$^2A_1$ (^2G)	$d\varepsilon^2(^1E)d\gamma^3$	$-2Dq-11B+3C$	$d\varepsilon^4(^1E)d\gamma^3$
$^2A_2$ (^2F)	$d\varepsilon^2(^1E)d\gamma$	$-2Dq+9B+3C$	$d\varepsilon^4(^1E)d\gamma^3$

d^4

$^3F_1$ ($a\,^3P$, $b\,^3P$, $a\,^3F$, $b\,^3F$, ^3G, ^3H)

	$d\varepsilon^2(^3F_1)d\gamma^4$	$d\varepsilon^3(^2F_1)d\gamma^3$	$d\varepsilon^3(^2F_2)d\gamma^3$	$d\varepsilon^4(^3F_1)d\gamma^2(^1A_1)$	$d\varepsilon^4(^3F_1)d\gamma^2(^1E)$	$d\varepsilon^4(^1F_2)d\gamma^2(^3A_2)$	$d\varepsilon^5 d\gamma$
$d\varepsilon^4$	$-16Dq-15B+5C$	$-\sqrt{6}B$	$-3\sqrt{2}B$	$\sqrt{2}(2B+C)$	$-2\sqrt{2}B$	0	0
	$d\varepsilon^3(^2F_1)d\gamma$	$-6Dq-11B+4C$	$5\sqrt{3}B$	$\sqrt{3}B$	$-\sqrt{3}B$	$3B$	$\sqrt{6}B$
		$d\varepsilon^3(^2F_2)d\gamma$	$-6Dq-3B+6C$	$-3B$	$-3B$	$5\sqrt{3}B$	$\sqrt{2}(B+C)$
			$d\varepsilon^2(^3F_1)d\gamma^2(^1A_1)$	$4Dq-B+6C$	$-10B$	0	$3\sqrt{2}B$
				$d\varepsilon^2(^3F_1)d\gamma^2(^1E)$	$4Dq-9B+4C$	$-2\sqrt{3}B$	$-3\sqrt{2}B$
					$d\varepsilon^2(^1F_2)d\gamma^2(^3A_2)$	$4Dq-11B+4C$	$\sqrt{6}B$
						$d\varepsilon\, d\gamma^3$	$14Dq-16B+5C$

$^1F_2$ ($a\,^1D$, $b\,^1D$, $a\,^1G$, $b\,^1G$, ^1F, ^1I)

	$d\varepsilon^2(^1F_2)d\gamma^4$	$d\varepsilon^3(^2F_1)d\gamma^3$	$d\varepsilon^3(^2F_2)d\gamma^3$	$d\varepsilon^4(^3F_1)d\gamma^2(^3A_2)$	$d\varepsilon^4(^1F_2)d\gamma^2(^1E)$	$d\varepsilon^4(^1F_2)d\gamma^2(^1A_1)$	$d\varepsilon^5 d\gamma$
$d\varepsilon^4$	$-16Dq-9B+7C$	$3\sqrt{2}B$	$-5\sqrt{6}B$	0	$-2\sqrt{2}B$	$\sqrt{2}(2B+C)$	0
	$d\varepsilon^3(^2F_1)d\gamma$	$-6Dq-9B+6C$	$-5\sqrt{3}B$	$3B$	$-3B$	$-3B$	$-\sqrt{6}B$
		$d\varepsilon^3(^2F_2)d\gamma$	$-6Dq+3B+8C$	$-3\sqrt{3}B$	$5\sqrt{3}B$	$-5\sqrt{3}B$	$\sqrt{2}(3B+C)$
			$d\varepsilon^2(^3F_1)d\gamma^2(^3A_2)$	$4Dq-9B+6C$	$-6B$	0	$-3\sqrt{6}B$
				$d\varepsilon^2(^1F_2)d\gamma^2(^1E)$	$4Dq-3B+6C$	$-10B$	$\sqrt{6}B$
					$d\varepsilon^2(^1F_2)d\gamma^2(^1A_1)$	$4Dq+5B+8C$	$\sqrt{6}B$
						$d\varepsilon\, d\gamma^3$	$14Dq+7C$

$^1A_1$ ($a\,^1S$, $b\,^1S$, $a\,^1G$, $b\,^1G$, ^1I)

	$d\varepsilon^2(^1A_1)d\gamma^4$	$d\varepsilon^3(^2E)d\gamma^3$	$d\varepsilon^4(^1A_1)d\gamma^2(^1A_1)$	$d\varepsilon^4(^1E)d\gamma^2(^1E)$	$d\varepsilon^6$
$d\varepsilon^4$	$-16Dq+10C$	$-12\sqrt{2}B$	$\sqrt{2}(4B+2C)$	$2\sqrt{2}B$	0
	$d\varepsilon^3(^2E)d\gamma$	$-6Dq+6C$	$-12B$	$-6B$	0
		$d\varepsilon^2(^1A_1)d\gamma^2(^1A_1)$	$4Dq+14B+11C$	$20B$	$\sqrt{6}(2B+C)$
			$d\varepsilon^2(^1E)d\gamma^2(^1E)$	$4Dq-3B+6C$	$2\sqrt{6}B$
				$d\gamma^4$	$24Dq-16B+8C$

Table III. (continued)

d^4

${}^1E$ ($a\,{}^1D$, $b\,{}^1D$, $a\,{}^1G$, $b\,{}^1G$, ${}^1I$)

	$d\varepsilon^2({}^1E)d\gamma^1$	$d\varepsilon^3({}^2E)d\gamma^3$	$d\varepsilon^1({}^1E)d\gamma^2({}^1A_1)$	$d\varepsilon^4({}^1A_1)d\gamma^2({}^1E)$	$d\varepsilon^4({}^1E)d\gamma^2({}^1E)$
$d\varepsilon^4$	$-16Dq$ $-9B+7C$	$6B$	$\sqrt{2}(2B+C)$	$-2B$	$-4B$
$d\varepsilon^3({}^2E)d\gamma$		$-6Dq$ $-6B+6C$	$-3\sqrt{2}B$	$-12B$	0
$d\varepsilon^2({}^1E)d\gamma^2({}^1A_1)$			$4Dq$ $+5B+8C$	$10\sqrt{2}B$	$-10\sqrt{2}B$
$d\varepsilon^2({}^1A_1)d\gamma^2({}^1E)$				$4Dq$ $+6B+9C$	0
$d\varepsilon^2({}^1E)d\gamma^2({}^1E)$					$4Dq$ $-3B+6C$

${}^3F_2$ (${}^3D$, $a\,{}^3F$, $b\,{}^3F$, ${}^3G$, ${}^3H$)

	$d\varepsilon^3({}^2F_1)d\gamma^3$	$d\varepsilon^3({}^2F_2)d\gamma^3$	$d\varepsilon^4({}^3F_1)d\gamma^2({}^3A_2)$	$d\varepsilon^4({}^3F_1)d\gamma^2({}^1E)$	$d\varepsilon^5d\gamma$
$d\varepsilon^3({}^2F_1)d\gamma$	$-6Dq$ $-9B+4C$	$-5\sqrt{3}B$	$\sqrt{6}B$	$\sqrt{3}B$	$-\sqrt{6}B$
$d\varepsilon^3({}^2F_2)d\gamma$		$-6Dq$ $-5B+6C$	$-3\sqrt{2}B$	$3B$	$\sqrt{2}(3B+C)$
$d\varepsilon^2({}^3F_1)d\gamma^2({}^3A_2)$			$4Dq$ $-13B+4C$	$-2\sqrt{2}B$	$-6B$
$d\varepsilon^2({}^3F_1)d\gamma^2({}^1E)$				$4Dq$ $-9B+4C$	$3\sqrt{2}B$
$d\varepsilon d\gamma^3$					$14Dq$ $-8B+5C$

${}^1F_1$ (${}^1F$, $a\,{}^1G$, $b\,{}^1G$, ${}^1I$)

	$d\varepsilon^3({}^2F_1)d\gamma^3$	$d\varepsilon^3({}^2F_2)d\gamma^3$	$d\varepsilon^4({}^1F_2)d\gamma^2({}^1E)$	$d\varepsilon^5d\gamma$
$d\varepsilon^3({}^2F_1)d\gamma$	$-6Dq$ $-3B+6C$	$5\sqrt{3}B$	$3B$	$\sqrt{6}B$
$d\varepsilon^3({}^2F_2)d\gamma$		$-6Dq$ $-3B+8C$	$-5\sqrt{3}B$	$\sqrt{2}(B+C)$
$d\varepsilon^2({}^1F_2)d\gamma^2({}^1E)$			$4Dq$ $-3B+6C$	$-\sqrt{6}B$
$d\varepsilon d\gamma^3$				$14Dq$ $-16B+7C$

${}^3E$ (${}^3D$, ${}^3G$, ${}^3H$)

	$d\varepsilon^3({}^4A_2)d\gamma^3$	$d\varepsilon^3({}^2E)d\gamma^3$	$d\varepsilon^4({}^1E)d\gamma^2({}^3A_2)$
$d\varepsilon^3({}^4A_2)d\gamma$	$-6Dq$ $-13B+4C$	$-4B$	0
$d\varepsilon^3({}^2E)d\gamma$		$-6Dq$ $-10B+4C$	$-3\sqrt{2}B$
$d\varepsilon^2({}^1E)d\gamma^2({}^3A_2)$			$4Dq$ $-11B+4C$

${}^3A_2$ ($a\,{}^3F$, $b\,{}^3F$)

	$d\varepsilon^3({}^2E)d\gamma^3$	$d\varepsilon^4({}^1A_1)d\gamma^2({}^3A_2)$
$d\varepsilon^3({}^2E)d\gamma$	$-6Dq$ $-8B+4C$	$-12B$
$d\varepsilon^2({}^1A_1)d\gamma^2({}^3A_2)$		$4Dq$ $-2B+7C$

${}^1A_2$ (${}^1F$, ${}^1I$)

	$d\varepsilon^3({}^2E)d\gamma^3$	$d\varepsilon^4({}^1E)d\gamma^2({}^1E)$
$d\varepsilon^3({}^2E)d\gamma$	$-6Dq$ $-12B+6C$	$6B$
$d\varepsilon^2({}^1E)d\gamma^2({}^1E)$		$4Dq$ $-3B+6C$

${}^5E$	(${}^5D$)	$d\varepsilon^3({}^4A_2)d\gamma$	$-6Dq-21B$	$d\varepsilon^3({}^4A_2)d\gamma^3$
${}^5F_2$	(${}^5D$)	$d\varepsilon^2({}^3F_1)d\gamma^2({}^3A_2)$	$4Dq-21B$	$d\varepsilon^4({}^3F_1)d\gamma^2({}^3A_2)$
${}^3A_1$	(${}^3G$)	$d\varepsilon^3({}^2E)d\gamma$	$-6Dq-12B+4C$	$d\varepsilon^3({}^2E)d\gamma^3$

Table III. (continued)

d^5

$^2F_2$ ($a\,^2F$, $b\,^2F$, $a\,^2G$, $b\,^2G$, ^2H, ^2I, $a\,^2D$, $b\,^2D$, $c\,^2D$)

$d\varepsilon^5$	$-20Dq$ $-20B+10C$	$3\sqrt{6}B$	$\sqrt{6}B$	0	$-2\sqrt{3}B$	$4B+2C$	$2B$	0	0	0
$d\varepsilon^4(^3F_1)d\gamma$		$-10Dq$ $-8B+9C$	$3B$	$\sqrt{6}/2B$	$-3\sqrt{2}/2B$	$3\sqrt{6}/2B$	$3\sqrt{6}/2B$	0	$4B+C$	0
$d\varepsilon^4(^1F_2)d\gamma$			$-10Dq$ $-18B+9C$	$3\sqrt{6}/2B$	$-3\sqrt{2}/2B$	$5\sqrt{6}/2B$	$-5\sqrt{6}/2B$	C	0	0
$d\varepsilon^3(^2F_1)d\gamma^2(^3A_2)$				$-16B+8C$	$2\sqrt{3}B$	0	0	$-3\sqrt{6}/2B$	$-\sqrt{6}/2B$	0
$d\varepsilon^3(^2F_1)d\gamma^2(^1E)$					$-12B+8C$	$-10\sqrt{3}B$	0	$3\sqrt{2}/2B$	$3\sqrt{2}/2B$	$-2\sqrt{3}B$
$d\varepsilon^3(^2F_2)d\gamma^2(^1A_1)$						$2B+12C$	0	$-5\sqrt{6}/2B$	$-3\sqrt{6}/2B$	$4B+2C$
$d\varepsilon^3(^2F_2)d\gamma^2(^1E)$							$-6B+10C$	$-5\sqrt{6}/2B$	$3\sqrt{6}/2B$	$-2B$
$d\varepsilon^2(^1F_2)d\gamma^3(^2E)$								$10Dq$ $-18B+9C$	$3B$	$-\sqrt{6}B$
$d\varepsilon^2(^3F_1)d\gamma^3(^2E)$									$10Dq$ $-8B+9C$	$-3\sqrt{6}B$
$d\varepsilon\, d\gamma^4$										$20Dq$ $-20B+10C$

$^2F_1$ (^2P, $a\,^2F$, $b\,^2F$, $a\,^2G$, $b\,^2G$, ^2H, ^2I)

$d\varepsilon^4(^3F_1)d\gamma$	$-10Dq$ $-22B+9C$	$-3B$	$-3\sqrt{2}/2B$	$3\sqrt{2}/2B$	$-3\sqrt{2}/2B$	$-3\sqrt{6}/2B$	0	C
$d\varepsilon^4(^1F_2)d\gamma$		$-10Dq$ $-8B+9C$	$3\sqrt{2}/2B$	$3\sqrt{2}/2B$	$15\sqrt{2}/2B$	$5\sqrt{6}/2B$	$4B+C$	0
$d\varepsilon^3(^2F_1)d\gamma^2(^1A_1)$			$-4B+10C$	0	0	$10\sqrt{3}B$	$3\sqrt{2}/2B$	$-3\sqrt{2}/2B$
$d\varepsilon^3(^2F_1)d\gamma^2(^1E)$				$-12B+8C$	0	0	$-3\sqrt{2}/2B$	$-3\sqrt{2}/2B$
$d\varepsilon^3(^2F_2)d\gamma^2(^3A_2)$					$-10B+10C$	$2\sqrt{3}B$	$15\sqrt{2}/2B$	$-3\sqrt{2}/2B$
$d\varepsilon^3(^2F_2)d\gamma^2(^1E)$						$-6B+10C$	$5\sqrt{6}/2B$	$-3\sqrt{6}/2B$
$d\varepsilon^2(^1F_2)d\gamma^3$							$10Dq$ $-8B+9C$	$-3B$
$d\varepsilon^2(^3F_1)d\gamma^3$								$10Dq$ $-22B+9C$

Table III. (continued)

d^5

${}^2E$ ($a\,{}^2D$, $b\,{}^2D$, $c\,{}^2D$, $a\,{}^2G$, $b\,{}^2G$, ${}^2H$, ${}^2I$)

$d\varepsilon^4({}^1A_1)d\gamma$	$-10Dq$ $-4B+12C$	$10B$	$6B$	$6\sqrt{3}B$	$6\sqrt{2}B$	$-2B$	$4B+2C$
$d\varepsilon^4({}^1E)d\gamma$		$-10Dq$ $-13B+9C$	$-3B$	$3\sqrt{3}B$	0	$2B+C$	$2B$
$d\varepsilon^3({}^2E)d\gamma^2({}^1A_1)$			$-4B+10C$	0	0	$-3B$	$-6B$
$d\varepsilon^3({}^2E)d\gamma^2({}^3A_2)$				$-16B+8C$	$2\sqrt{6}B$	$-3\sqrt{3}B$	$6\sqrt{3}B$
$d\varepsilon^3({}^2E)d\gamma^2({}^1E)$					$-12B+8C$	0	$6\sqrt{2}B$
$d\varepsilon^2({}^1E)d\gamma^3$						$10Dq$ $-13B+9C$	$-10B$
$d\varepsilon^2({}^1A_1)d\gamma^3$							$10Dq$ $-4B+12C$

${}^2A_1$ (${}^2S$, $a\,{}^2G$, $b\,{}^2G$, ${}^2I$)

$d\varepsilon^4({}^1E)d\gamma$	$-10Dq$ $-3B+9C$	$-3\sqrt{2}B$	0	$6B+C$
$d\varepsilon^3({}^2E)d\gamma^2({}^1E)$		$-12B+8C$	$-4\sqrt{3}B$	$3\sqrt{2}B$
$d\varepsilon^3({}^4A_2)d\gamma^2({}^3A_2)$			$-19B+8C$	0
$d\varepsilon^2({}^1E)d\gamma^3$				$10Dq$ $-3B+9C$

${}^2A_2$ ($a\,{}^2F$, $b\,{}^2F$, ${}^2I$)

$d\varepsilon^4({}^1E)d\gamma$	$-10Dq$ $-23B+9C$	$3\sqrt{2}B$	$-2B+C$
$d\varepsilon^3({}^2E)d\gamma^2({}^1E)$		$-12B+8C$	$-3\sqrt{2}B$
$d\varepsilon^2({}^1E)d\gamma^3$			$10Dq$ $-23B+9C$

${}^4F_1$ (${}^4P$, ${}^4F$, ${}^4G$)

$d\varepsilon^4({}^3F_1)d\gamma$	$-10Dq$ $-25B+6C$	$-3\sqrt{2}B$	C
$d\varepsilon^3({}^2F_2)d\gamma^2({}^3A_2)$		$-16B+7C$	$-3\sqrt{2}B$
$d\varepsilon^2({}^3F_1)d\gamma^3$			$10Dq$ $-25B+6C$

${}^4F_2$ (${}^4F$, ${}^4G$, ${}^4D$)

$d\varepsilon^4({}^3F_1)d\gamma$	$-10Dq$ $-17B+6C$	$\sqrt{6}B$	$4B+C$
$d\varepsilon^3({}^2F_1)d\gamma^2({}^3A_2)$		$-22B+5C$	$-\sqrt{6}B$
$d\varepsilon^2({}^3F_1)d\gamma^3$			$10Dq$ $-17B+6C$

${}^4E$ (${}^4D$, ${}^4G$)

$d\varepsilon^3({}^2E)d\gamma^2({}^3A_2)$	$-22B+5C$	$-2\sqrt{3}B$
$d\varepsilon^3({}^4A_2)d\gamma^2({}^1E)$		$-21B+5C$

${}^6A_1$	(${}^6S$)	$d\varepsilon^3({}^4A_2)d\gamma^2({}^3A_2)$	$-35B$
${}^4A_1$	(${}^4G$)	$d\varepsilon^3({}^4A_2)d\gamma^2({}^3A_2)$	$-25B+5C$
${}^4A_2$	(${}^4F$)	$d\varepsilon^3({}^4A_2)d\gamma^2({}^1A_1)$	$-13B+7C$

Appendix

Here we will show by induction that the following relation holds between the first and second sum in (3.1) in certain cases:

$$\begin{gathered}\text{(the first sum in (3.1)}\\ \text{for } N \text{ electron system)}\end{gathered} = A(N{:}nn')\begin{gathered}\text{(the second sum in (3.1)}\\ \text{for } N \text{ electron system)}\end{gathered}\,, \tag{A.1}$$

with

$$A(N{:}nn')=\{1+A(N-1{:}n-1,n'-1)\}/\{1+A^{-1}(N-1{:}n,n')\}\,. \tag{A.2}$$

$A(N{:}nn')$ is a constant (including zero) depending only on N, n and n'. (When the sum on the right hand side of (A.1) is zero, we consider A^{-1} to be zero.)

For this purpose we assume similar relation for $N-1$ electron system, namely

$$\begin{array}{l}\text{(the first sum in (3.1)}\\ \quad\text{for } N-1 \text{ electron system)}\end{array} = A(N-1{:}nn')\begin{array}{l}\text{(the second sum in (3.1)}\\ \qquad\text{for } N-1 \text{ electron system)}\,.\end{array} \tag{A.3}$$

To verify the relation (A.1), we express

$$(\gamma_1{}^{n-1}(S'\Gamma')\gamma_2{}^{N-n}(S_2\Gamma_2)\overline{S}\overline{\Gamma}|G_{N-1}|\gamma_1{}^{n'-1}(S''\Gamma'')\gamma_2{}^{N-n'}(S_4\Gamma_4)\overline{S}\overline{\Gamma})$$

and

$$(\gamma_1{}^{n}(S_1\Gamma_1)\gamma_2{}^{N-n-1}(S'\Gamma')\overline{S}\overline{\Gamma}|G_{N-1}|\gamma_1{}^{n'}(S_3\Gamma_3)\gamma_2{}^{N-n'-1}(S''\Gamma'')\overline{S}\overline{\Gamma})$$

in (A.1) by

$$(\gamma_1{}^{n-1}(S'\Gamma')\gamma_2{}^{N-n-1}(S_0'\Gamma_0')\overline{S}_0\overline{\Gamma}_0|G_{N-2}|\gamma_1{}^{n'-1}(S''\Gamma'')\gamma_2{}^{N-n'-1}(S_0''\Gamma_0'')\overline{S}_0\overline{\Gamma}_0)$$

using both the recurrence formula and the assumed relation (A.3), and apply the following relation for the transformation matrices;

$$\begin{aligned}&\sum_{\overline{\Gamma}}(\Gamma^1,\Gamma_3\Gamma_4(\Gamma^2)\Gamma|\Gamma^1\Gamma_3(\overline{\Gamma}),\Gamma_4\Gamma)\\ &\quad(\Gamma_1\Gamma_2(\Gamma^1),\Gamma_3\overline{\Gamma}|\Gamma_1,\Gamma_2\Gamma_3(\Gamma'')\overline{\Gamma})\\ &\quad(\Gamma_1,\overline{\Gamma}_2\overline{\Gamma}_3(\Gamma'')\overline{\Gamma}|\Gamma_1\overline{\Gamma}_2(\Gamma^3),\overline{\Gamma}_3\overline{\Gamma})\\ &\quad(\Gamma^3\overline{\Gamma}_3(\overline{\Gamma}),\Gamma_4\Gamma|\Gamma^3,\overline{\Gamma}_3\Gamma_4(\Gamma^4)\Gamma)\end{aligned} = \begin{aligned}&\sum_{\overline{\Gamma}}(\Gamma_1\Gamma_2(\Gamma^1),\Gamma^2\Gamma|\Gamma_1,\Gamma_2\Gamma^2(\overline{\Gamma})\Gamma)\\ &\quad(\Gamma_2,\Gamma_3\Gamma_4(\Gamma^2)\overline{\Gamma}|\Gamma_2\Gamma_3(\Gamma''),\Gamma_4\overline{\Gamma})\\ &\quad(\overline{\Gamma}_2\overline{\Gamma}_3(\Gamma''),\Gamma_4\overline{\Gamma}|\overline{\Gamma}_2,\overline{\Gamma}_3\Gamma_4(\Gamma^4)\overline{\Gamma})\\ &\quad(\Gamma_1,\overline{\Gamma}_2\Gamma^4(\overline{\Gamma})\Gamma|\Gamma_1\overline{\Gamma}_2(\Gamma^3),\Gamma^4\Gamma)\,.\end{aligned} \tag{A.4}$$

(A.4) can be proved in the following way:

$$\begin{aligned}&\text{the left hand side}\\ &=\sum_{\overline{\Gamma}}(\Gamma_1\Gamma_2(\Gamma^1),\Gamma_3\Gamma_4(\Gamma^2)\Gamma|\Gamma_1,\Gamma_2\Gamma_3(\Gamma'')(\overline{\Gamma})\Gamma_4\Gamma)\\ &\qquad(\Gamma_1,\overline{\Gamma}_2\overline{\Gamma}_3(\Gamma'')(\overline{\Gamma})\Gamma_4\Gamma|\Gamma_1\overline{\Gamma}_2(\Gamma^3)\overline{\Gamma}_3\Gamma_4(\Gamma^4)\Gamma)\\ &=\sum_{\overline{\Gamma}}(\Gamma_1\Gamma_2(\Gamma^1),\Gamma_3\Gamma_4(\Gamma^2)\Gamma|\Gamma_1,\Gamma_2\Gamma_3(\Gamma'')\Gamma_4(\overline{\Gamma})\Gamma)\\ &\qquad(\Gamma_1,\overline{\Gamma}_2\overline{\Gamma}_3(\Gamma'')\Gamma_4(\overline{\Gamma})\Gamma|\Gamma_1\overline{\Gamma}_2(\Gamma^3)\overline{\Gamma}_3\Gamma_4(\Gamma^4)\Gamma)\\ &=\text{the right hand side,}\end{aligned}$$

because

$$\sum_{\underline{\Gamma}}(\Gamma_1\Gamma''(\overline{\Gamma})\Gamma_4\Gamma|\Gamma_1,\Gamma''\Gamma_4(\underline{\Gamma})\Gamma)(\Gamma_1,\Gamma''\Gamma_4(\underline{\Gamma})\Gamma|\Gamma_1\Gamma''(\overline{\Gamma}')\Gamma_4\Gamma)=\delta(\overline{\Gamma},\overline{\Gamma}')\,.$$

To complete the proof for the simplification of the recurrence formula for non-diagonal elements described in § 3, it is necessary to show that the relation (A.3) holds for 4 electron system. This is possible only when a single ancestor exists and so the value of $A(3{:}nn')$ or $A^{-1}(3{:}nn')$ is equal to zero.

For the case of $n-n'=2$, where the ancestor of the type $(\gamma_1{}^2S\Gamma|g|\gamma_2{}^2S\Gamma)$ and the constants $A(3{:}2,0)$ and $A(3{:}3,1)$ are zero, we obtain the value of $A(4{:}3,1)$ as unity and so on, using the relation (A.2). $A(N{:}N,N-2)$ and $A(N{:}2,0)$ are always zero, because we have only one sum in the recurrence formula for these configurations. The general expression for $A(N{:}nn')$ in this case is

$$A(N{:}n,n-2)=(n-2)/(N-n)\,. \tag{A.7}$$

As was mentioned in § 3, there is only one ancestor of the type $(\gamma_1{}^2S\Gamma|g|\gamma_1\gamma_2S\Gamma)$ for the case of $n-n'=1$ in our special problem of the octahedral group, and the constant A is given by

$$A(N{:}n,n-1)=(n-2)/(N-n)\,. \tag{A.8}$$

For the non-diagonal elements in the case of $n-n'=0$, we see that A takes the following values:

$$A(N{:}n,n)=(n-1)/(N-n-1)\,. \tag{A.9}$$

References

1) R. Finkelstein and J. H. Van Vleck: J. Chem. Phys. **8** (1940) 790.

2) F. E. Ilse and H. Hartmann: Zs. f. phys. Chem. **197** (1951) 239.
H. Hartmann and H. L. Schlaefer: *ibid.* **197** (1951) 115.
H. Hartmann and H. L. Schlaefer: Zs. f. Naturforschg. **6a** (1951) 751, 754, 760.

3) M. Kotani: unpublished.
K. Kambe and T. Usui: unpublished.

4) W. H. Kleiner: J. Chem. Phys. **20** (1952) 1784.

5) D. Polder: Physica **IX** (1942) 709.

6) J. H. Van Vleck: J. Chem. Phys. **7** (1939) 72.

7) K. W. H. Stevens: Proc. Roy. Soc. **A219** (1953) 542.

8) G. Racah: Phys. Rev. **63** (1943) 367; Phys. Rev. **76** (1949) 1352, cited as R III and R IV respectively.

JOURNAL OF THE PHYSICAL SOCIETY OF JAPAN Vol. 9, No. 5, SEP.—OCT., 1954

On the Absorption Spectra of Complex Ions II

By Yukito TANABE
Physics Department, Tokyo University
and Satoru SUGANO
Institute of Broadcating N.H.K.

(Received June 11, 1954)

The secular determinants obtained in the previous paper are solved for the energy levels which are important in the absorption spectra of the normal complex ions, leaving the crystalline field strength as a parameter. The values of B and C (Racah's parameters) there needed are determined from the observed spectra of free ions or in some cases by extrapolation.

The f-values of the transitions which connect the energy levels calculated are estimated and compared with the observed intensities. The difference of the spectral width among absorption bands and lines is also considered using the energy diagram obtained. Following the assignments determined by the above considerations, the calculated positions of lines and bands are rather in good agreement with the experimental data in divalent ions $[MX_6]^{2+}$ (M=Cr, Mn, Fe, Co, Ni), when we adjust the crystalline field parameter Dq suitably. In trivalent ions $[MX_6]^{3+}$ (M=Ti, V, Cr, Mn, Fe), it is necessary besides the adjustment of Dq to use smaller values of B and C than those of the free ions to obtain better agreement with experiments. The values of Dq thus determined are of reasonable magnitude close to those obtained in other ways. The decrease of B and C compared with those of the free ions might be connected with the recent Stevens' suggestion. It is interesting that, though the agreement is poor about $[Co(H_2O)_6]^{3+}$ and $[Co(NH_3)_6]^{3+}$ whose bindings are usually considered covalent, the qualitative explanation of their spectra is found possible in the crystalline field approximation.

§ Introduction

It has already been mentioned in the previous paper (1) that the complex ions under consideration show several forms of the absorption spectra, namely the relatively intense band, the weak band and the sharp line. No quantitative consideration, however, has been made to explain the origin of these differences.

We shall therefore investigate the nature of the transitions due to the optical absorption in these complexes in § 3. Then the comparison with the experimental data will be given in § 4 using the energy level diagram obtained in § 2.

§ 2. Determination of *B*, *C* and the Resulting Energy Level Diagram

Because most of the spectra of the free ions of the iron group elements are not yet completely known, in order to make the extrapolation possible, the values of *B* and *C* for the doubly or triply ionized states were estimated in the following way.

Since the term values of the elements in the d^2-isoelectronic sequence, i.e., Ti III, V IV, Cr V, Mn VI and Fe VII are experimentally known[1)], we have determined the values of *B* and *C* so that they will give the observed values for ^3F, ^3P and ^1G. When we plot these values of *B* and *C* against the atomic number *Z*[2)], they approximately fall on a straight line: $B=145\ (Z-s)\ \mathrm{cm}^{-1}$. $C=705\ (Z-s)\ \mathrm{cm}^{-1}$ (compare with $B=129.5\ (Z-s)\ \mathrm{cm}^{-1}$, $C=514.5\ (Z-s)\ \mathrm{cm}^{-1}$ which one obtains using the Slater type wave function with $n^*=3$).

To obtain *B* and *C* in the d^3-isoelectronic sequence, we calculate $\Delta B=B(d^3)-B(d^2)$, $\Delta C=C(d^3)-C(d^2)$ using the observed value of the parent ion after Meshkov[3)] (for the term value of $^1S(d^2)$ we adopt the calculated value, since the observed values are lacking), so that they give term values of ^4F, ^4P and ^2H correctly. In Table I, the column (diff. (I)) gives the differences between the values calculated in this way and the observed ones, and the column (diff. (II)) gives differences between the observed values and the values calculated in the usual way using the values of *B* and *C* determined so as to give ^4F, ^4P and ^2H correctly. The values of $B(d^3)$, $C(d^3)$ thus obtained also fall on a straight line parallel to the line for d^2 determined previously.

For d^n-isoelectronic sequences ($n \geq 4$) where we have few observed term values, this method cannot be applied, and the values of *B* and *C* were determined roughly from the observed three levels suitably chosen. Then they were adjusted so that they fall on straight lines which are parallel to the lines of d^2- and d^3-isoelectronic sequences and equally spaced with the distance between the d^2- and d^3-lines.

In Fig. 1 and 2 the points marked by × indicate the values thus determined for d^2 and d^3. But for d^4 *B*-values are not plotted,

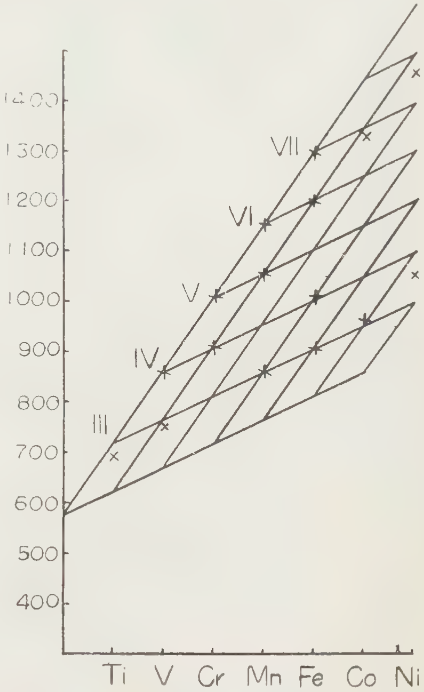

Fig. 1. *B*-values for various *Z* and ionicities.

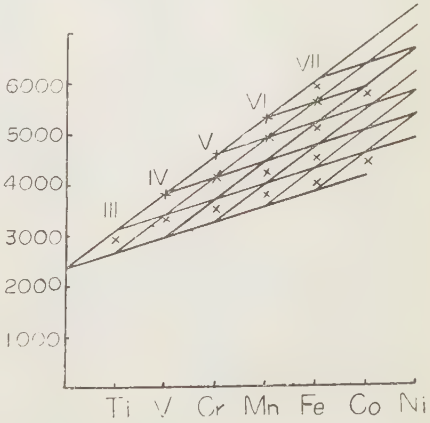

Fig. 2. *C*-values for various *Z* and ionicities.

since if they were determined from ^5D, ^3H, ^3G we have far smaller values than those expected (smaller about by 130 cm^{-1}). *C*-values for d^4 determined from ^5D, ^{3}H, ^3G fall on the points expected from the graph. For d^5 *B*, *C*-values are the average of the two determined from ^6S, ^4G, ^4D and ^4P, ^4F respectively. For d^6 they were determined from ^5D,

Table I. The deviations of the calculated term values from those of the observed. (obs.—calc.) (Values are given in cm^{-1})

d^2

V IV		Diff.	Cr V		Diff.	Mn VI		Diff.	Fe VII		Diff.
^3F	419		^3F	662		^3F	964		^3F	1346	
^1D	10960	−1397	^1D	13200	−1764	^1D	15336	−2065	^1D	17475	−2335
^3P	13344		^3P	15868		^3P	18344		^3P	20855	
^1G	18389		^1G	22060		^1G	25511		^1G	28915	
$B=862$			$B=1014$			$B=1159$			$B=1301$		
$C=3815$			$C=4617$			$C=5322$			$C=5981$		

d^3

V III		Diff. (I)	Diff. (II)	Cr IV		Diff. (I)	Diff. (II)	Mn V		Diff. (I)	Diff. (II)	Fe VI		Diff. (I)	Diff. (II)
^4F	336			^4F	554			^4F	813			^4F	813		
^2P	11327	−3484	−5579	^4P	14324			^4P	16781			^4P	19235		
^4P	11668			^2P	14229	−4341	−6985	^2G	18158	−195	−1670	^2G	20996	−292	−1961
^2G	12089	−43	−1040	^2G	15258	−106	−1366	^2P	22961	908	−2190	^2P	26297	820	−2685
^2D	16317	−590	−2443	^2D	20487	−788	−3652	^2D	24626	−661	−3172	^2D	28524	−686	−3516
^2H	16907			^2H	21214			^2H	25150			^2H	28981		
$B=755$				^2F	36735	2506	1751	$B=1065$				$B=1205$			
$C=3257$				$B=918$				$C=4919$				$C=5659$			
				$C=4133$											

Table II. The values of B, C* and γ determined in the way described in § 2. (cm^{-1})

	B	C	C/B		B	C	C/B
Ti III	694.6	2910.4	4.190				
V	755.4	3257.2	4.312	V IV	861.6	3814.9	4.428
Cr	810.	3565.	4.401	Cr	918.	4132.7	4.502
Mn	860.	3850.	4.477	Mn	965.	4450.	4.611
Fe	917.	4040.	4.406	Fe	1015.	4800.	4.729
Co	971.	4497.	4.633	Co	1065.	5120.	4.808
Ni	1030.	4850.	4.709	Ni	1115.	5450.	4.888

* These B-values are not greatly different from those values recommended by Catalan et al.[5] after our calculation has been performed, and the value determined by Meshkov[4] for V III.

^3H, ^3G, and for d^7 B's were determined from ^4F, ^4P, ^2G and C's are the average of the two determined from ^4F, ^4P, ^2G and ^4P, ^2G, ^2H respectively. For d^8 B and C were determined from ^3F, ^3P.

The calculated term values using these B, C do not show so good agreement with the observed ones which were not used in the determination of these values ($\Delta E \simeq 2000$–$3000\,\mathrm{cm}^{-1}$ except some particular terms for which the error is even larger), so that we may expect that error of the same order would occur for the element, for example Co IV, for which spectral terms are not known yet. These errors are much larger than the errors that occur when one uses the values B, C determined by the least square method. But as our calculations are for molecular ions, we consider that the accuracy of such degree is sufficient for our purpose, judging from the nature of the crystalline field approximation. Values we adopt here are given in Table II. $\gamma = C/B$ is nearly constant for all elements and is about 4∼5, while, if we adopt the Slater type wave function, $\gamma = 3.97$ and is independent of the effective nuclear charge.

With these values we solved the secular determinants including the interaction between configurations, and obtained the lowest eigenvalues among those belonging to the same $S\Gamma$. The results are shown in the energy diagrams in full line (Fig. 3–9). The other interesting levels were also solved neglecting the interaction between different configurations and are given in broken lines in the range $\Delta = Dq/B \geq 2$. Both the level energy (ordinate) which are measured always from the ground level and the strength of the crystalline field (abscissa) are scaled by B as unit. The values of γ and B used in the calculation of the level energy are also given. The observed term values and the lowest level of $d^{N-1}s$ configuration in the free state of the ion are indicated there.

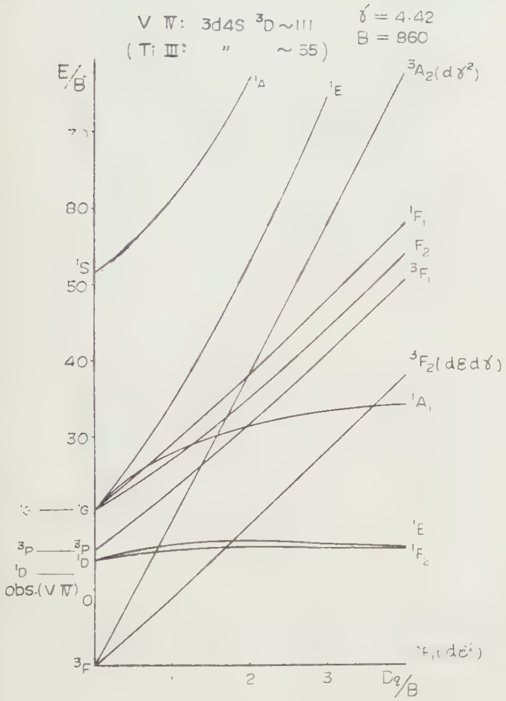

Fig. 3. The energy diagram for d².

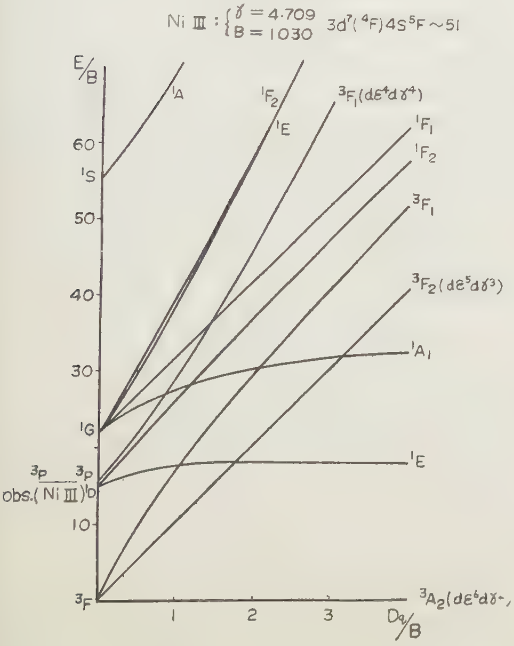

Fig. 4. The energy diagram for d⁸.

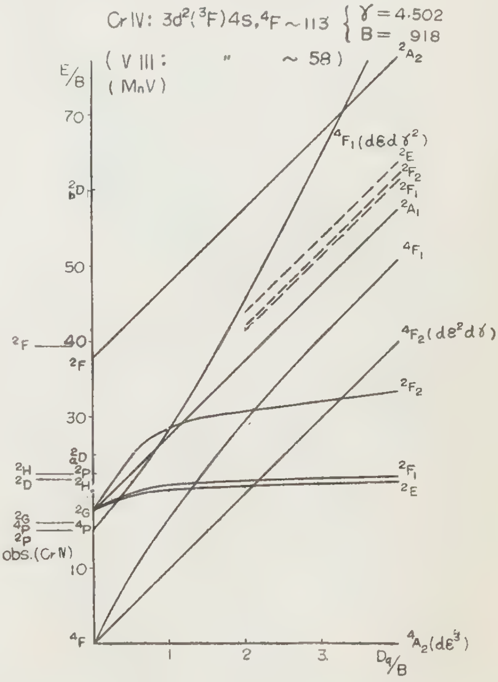

Fig. 5. The energy diagram for d³.

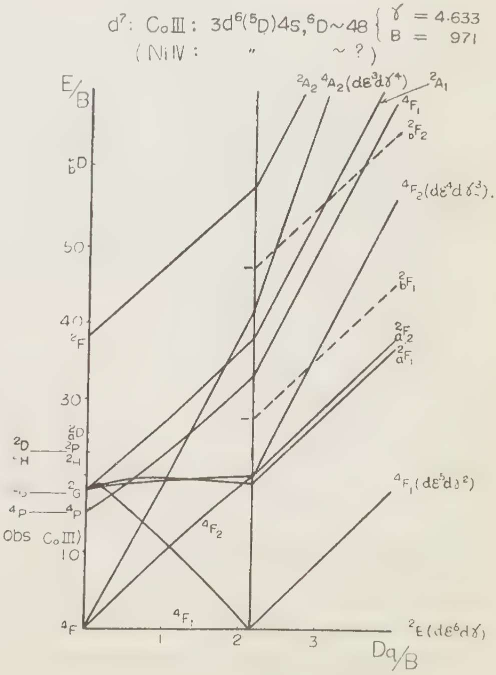

Fig. 6. The energy diagram for d⁷.

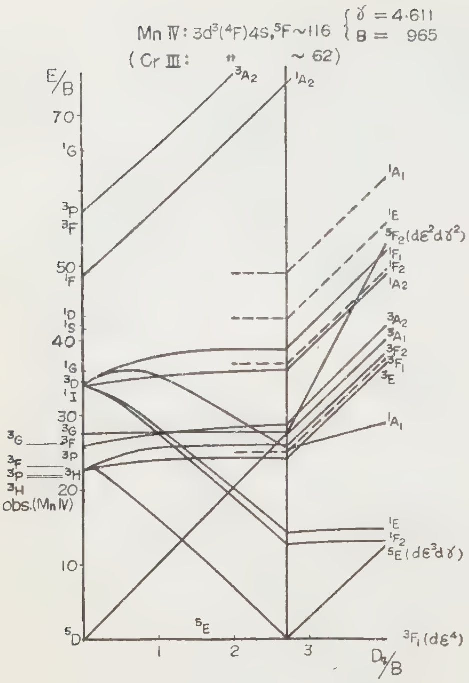

Fig. 7. The energy diagram for d^4.

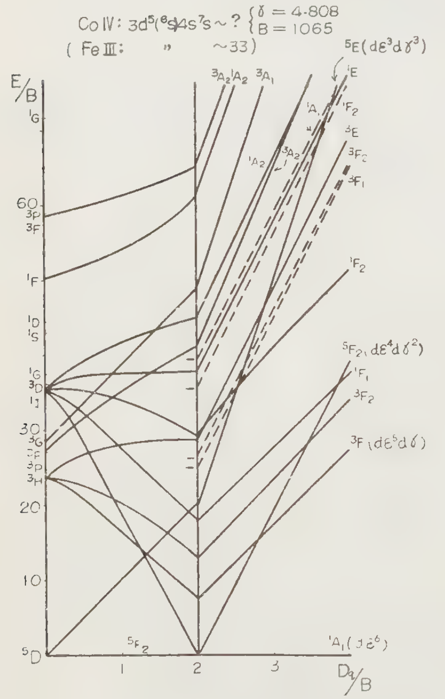

Fig. 8. The energy diagram for d^6.

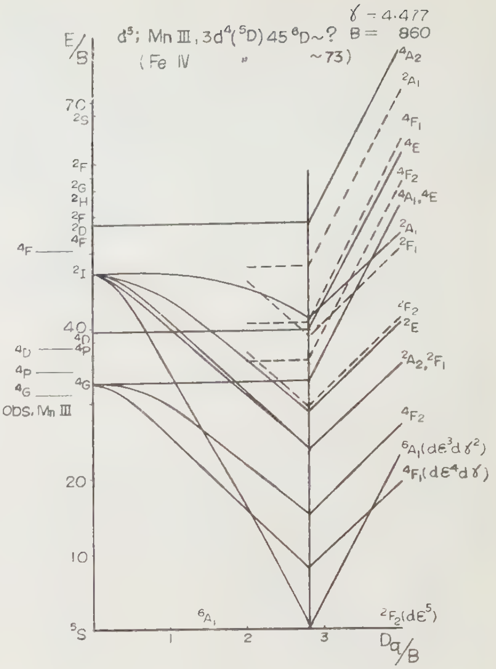

Fig. 9. The energy diagram for d^5.

§ 3. Nature of the Transitions

In this section we shall consider the intensity of transitions, selection rules and the problem of the width of the observed absorption, in order to obtain some theoretical foundations for the interpretation of the observed spectra.

The relation between the absorption coefficient $k(\nu)$ and the oscillator strength f is given by the relation

$$f = \frac{mc}{\pi N e^2}\int k(\nu)d\nu\ , \qquad (3.1)$$

where N is the number of the absorption centres per cubic centimeter, and ν the frequency measured in sec^{-1}. For solutions, the intensity of the absorption is ordinarily given in terms of the extinction coefficient ε defined through the relation $I = I_0 10^{-\varepsilon c_0 x}$ where x is the thickness of the solution in cm and c_0 is the concentration in mol per litre, so that correspondingly to (3.1) we have

$$f = \frac{2.3\times 10^3}{N_{\mathrm{Avog}}}\cdot\frac{mc}{\pi N e^2}\int \varepsilon(\nu)d\nu\ , \qquad (3.2)$$

where N_{Avog} is the Avogadro number. For a rough estimation of f, we can replace the integral in (3.1) or (3.2) with $2.5\times k_{\max}\Delta\nu$ or $2.5\times\varepsilon_{\max}\Delta\nu$ in which $\Delta\nu$ represents the half width, assuming the absorption curve to be gaussian.

Experimentally it is known that in solutions all the bands in question have the values of $\log\varepsilon \simeq 1\sim 2$, $\Delta\nu \simeq 10^{14}\,\mathrm{sec}^{-1}$ ($3000\,\mathrm{cm}^{-1}$) except for the case of $[\mathrm{Fe(H_2O)_6}]^{3+}$, whose bands observed at 14300 cm^{-1} and 18200 cm^{-1} have rather small intensity $\log \mathcal{E} \simeq -1$ and the width $\Delta\nu \simeq 2\times10^{14}$ sec^{-1}. Therefore, for the broad bands observed in solutions f-value can be estimated to be of the order of 2×10^{-4} if we take $\log \mathcal{E}=1$ (according to Sauer's measurement[6] for the bands of chrome alum, f is of the order of 10^{-3}), but for the weak bands of $[\mathrm{Fe(H_2O)_6}]^{3+}$ it is about 4×10^{-6}.

On the other hand, the doublet lines of the chrome alums have the oscillator strength $f \simeq 3\times10^{-8}$ according to Sauer's results. The line (though it is rather broad, the reason why we regard it as a line will be given later in § 4.) observed at 24600 cm^{-1} at room temperature has the values $\log \mathcal{E} \simeq -1$, $\Delta\nu \simeq 4\times10^{13}$ sec^{-1}, so that its f-value becomes to be of the order of 10^{-6}.

All the observed absorption in question are thus considered to be due to forbidden transitions. This fact supports the interpretation that they are the transitions between the levels arising from the d^n-configuration, since all the levels then have the same parity so that the transitions between them are forbidden.

Among the forbidden transitions between the states with the same parity, the following transitions are able to have non-vanishing intensity; 1) the electric-dipole transition coupled with the vibration, 2) the electric-quadrupole transition and 3) the magnetic-dipole transition. Electric-dipole radiation due to naturally unsymmetric fields can be treated in a similar way to 1) and its transition probability may be of the same order of magnitude as those of 1), but we do not thuch it here because of its uncertainly. (See Van Vleck[7][8].)

We now estimate the f-values of those transitions in the same way as Van Vleck has done on the spectra of the rare earth salts.

For the intrasystem transition which connects the two states with the same multiplicity, the transition probability of the type 1) is given by

$$\sigma_{\mathrm{I}} \simeq \sigma_{\mathrm{allow}} (V_{\mathrm{hem}}/h\nu')^2 , \qquad (3.3)$$

where V_{hem} is a matrix element of the hemihedral part of the crystalline field, and ν' is the frequency interval separating the state in question from the excited states of the opposite parity, which are not limited to the excited states of the central metal ion but include those of the complex as a whole.

To obtain V_{hem} we expand the crystalline field $V(x,Q)$ in power series of Q where x denotes the electron coordinate and Q is the normal coordinates of the vibrational displacements

$$V(x,Q) = V_0(x) + \sum V_q^{(k)} Q_q^{(k)} + \tfrac{1}{2} \sum V_{qq'}^{(kk')} Q_q^{(k)} Q_{q'}^{(k')} , \qquad (3.4)$$

where $V_0(x)$ represents the crystalline field at the equilibrium position of the nuclei. We see that $V_q^{(k)}$ and $Q_q^{(k)}$ or $V_{qq'}^{(kk')}$ and $Q_q^{(k)}Q_{q'}^{(k)}$ have the same transformation properties, since the crystalline field has the properties

$$V(x,Q) = V(Rx, RQ) , \qquad (3.5)$$

where R denotes the symmetry operation. Now V_{hem} originates from the vibrational displacement with odd inversion symmetry F_{1u} and F_{2u}, that is, the main contribution to V_{hem} comes from $V_q(F_{1u})Q_q(F_{1u})$ and $V_q(F_{2u})Q_q(F_{2u})$ of the second term in (3.4). The order of magnitude of the second term is seen to be $(Q/r)V_0$. so that we can estimate V_{hem} using the relation

$$V_{\mathrm{hem}} \simeq (\delta R/\bar{r}) V_0 , \qquad (3.6)$$

where δR is the zero-point amplitude of the vibration and $\bar{r}$ is the average of r. The amplitude δR is estimated from

$$2\pi^2 \mu \nu_0^2 (\delta R)^2 = \tfrac{1}{2} h\nu_0 ,$$

where ν_0 is the fundamental frequency of the vibration and μ is the effective mass for the vibrating complex. For the numerical value of ν_0, we adopt 10^{13} sec^{-1} which may be compared with the infrared absorption at 2.4×10^{13} sec^{-1} and 4×10^{13} sec^{-1} of the cobalt complex recently found by Hill and Rosenberg[9]. For the value of μ, we take the mass of the central ion, $\mu \sim 4\times10^{-23}$ gr., as μ does not seem to differ from the mass of the central ion so much. Then we obtain the zero point amplitude to be of the order of 10^{-9} cm. Assuming the value $\bar{r} \simeq 10^{-8}$ cm, $V_0 \simeq 10^4$ cm^{-1}, we have $V_{\mathrm{hem}} \simeq 10^3$ cm^{-1}. With this and $\nu' \simeq 10^5$ cm^{-1}, we finally obtain

$$\sigma_{\mathrm{I}} \simeq 10^{-4} \cdot \sigma_{\mathrm{allow}} . \qquad (3.7)$$

The f-value of the allowed transition can be estimated from the relation

$$f \simeq \frac{8\pi^2 m}{3h} \nu \bar{r}^2 , \qquad (3.8)$$

where m is the electron mass and the frequency ν is assumed to be $6\times10^{14}\,\mathrm{sec}^{-1}$, so that the f-value of the allowed transition may be considered to be of the order of unity. The f-value of the case 1) thus would be of the order of

$$f_{\mathrm{I}}\simeq10^{-4}\,. \tag{3.9}$$

The transition probabilities of the case 2) and 3) for the intrasystem combinations are estimated from the relation

$$\text{for 2)} \quad \sigma_{\mathrm{II}}=32\pi^6\nu^5e^2Q^2/5hc^5\,, \tag{3.10}$$

$$\text{for 3)} \quad \sigma_{\mathrm{III}}=64\pi^4\nu^3M^2/3hc^3\,. \tag{3.11}$$

Here Q is the "quadrupole amplitude" which can be estimated from the relation $Q\simeq\bar{r}^2$, and M is the matrix element of the magnetic moment connecting the states in question and considered of the order of the Bohr magneton. Then the corresponding f-values are

$$\text{for 2)} \quad f_{\mathrm{II}}\simeq2\times10^{-7}\,, \tag{3.12}$$

$$\text{for 3)} \quad f_{\mathrm{III}}\simeq4\times10^{-6}\,. \tag{3.13}$$

So that, for the intrasystem combinations, it seems to us that the electric-dipole transition coupled with the vibration predominates over the other two cases in our problem, though the intensity of the magnetic-dipole transition has the possibility to become comparable with that of the case 1) as our estimates may be in error by a factor of 10 or 100.

For the intersystem combinations we must take the spin-orbit interaction into account. We thus consider the contamination of the state with different multiplicity due to the spin-orbit interaction as follows[10)]

$$\Psi(\alpha_0\Gamma_T)=a\Psi(\alpha S\Gamma,\Gamma_T)+b\Psi(\alpha' S'\Gamma',\Gamma_T)\,, \tag{3.14}$$

where Γ_T is the irreducible representation of $S\times\Gamma$ and contamination occurs only among the states with the same Γ_T. Here it may generally be assumed that the coefficient a is nearly equal to unity, and b is of the order of magnitude $\Delta\nu/\nu$ where $\Delta\nu$ is the multiplet width and ν is the interval between different multiplets. Then the f-values of 1), 2) and 3) for the intersystem combinations are estimated from (3.9), (3.12) and (3.13) multiplying the factor b^2 respectively. Assuming the value of b as 3×10^{-2} which is estimated to be a little smaller than that of the rare earth salts, f-values thus obtained are

$$\left.\begin{aligned} &\text{for 1)} && \bar{f}_{\mathrm{I}}\simeq10^{-7}\,,\\ &\text{for 2)} && \bar{f}_{\mathrm{II}}\simeq2\times10^{-10}\,,\\ &\text{for 3)} && \bar{f}_{\mathrm{III}}\simeq4\times10^{-9}\,. \end{aligned}\right\} \tag{3.15}$$

From these considerations we now have some theoretical ground to say that, to the relatively strong absorption bands, the intrasystem transitions may be assigned in which electric-dipole transitions coupled with vibrations probably predominates, whose estimated f-value 10^{-4} should be compared with the observed ones $10^{-3}\sim10^{-4}$, and that, to the weak bands of $[\mathrm{Fe(H_2O)_6}]^{3+}$ or to the lines, the intersystem transitions may correspond, where estimated f-value $\simeq10^{-7}$ is not so different from those observed $10^{-6}\sim10^{-8}$.

We shall briefly consider the fact that the absorption bands of the triply ionized complex show always a larger intensity than those of the doubly ionized one by a factor 10 in ε. This difference of the absorption intensity between the doubly and the triply ionized complexes is thought to come from the difference in the strength of the crystalline field and from that in ν', because the factor σ_{allow} does not differ greatly in both cases. The crystalline field is generally stronger in the triply ionized complex ions as will be seen later. Further ν' in the latter may be smaller than that of the former since the excited states with the odd parity likely exist at relatively lower positions in the more tightly bound triply ionized complexes owing to their departure from the atomic character. This supposition will be only justified when it is tested by a more thorough treatment of the complex as a molecule.

The selection rules were examined on the individual cases 1), 2) and 3) in each complexes. All assignment adopted in the following section do not break such selection rules. In our problem of the perfect cubic field, difference of the absorption due to the polarization of the incident light does not, of course, occur, but if we introduce the field of the lower symmetry that may really exist in crystals, or if some of the ligands are replaced with other atoms or molecules, i.e., in $[\mathrm{M\ X}_n\ \mathrm{Y}_{6-n}]^{2+,3+}$ complexes, this occurs and further investigation on the selection rules in these cases will give more precise information as to the nature of the absorption.

The coexistence of broad bands and lines in iron group complexes is an interesting phenomenon. In the energy diagrams (Fig. 3→Fig. 9), we can see that the energy intervals between the levels belonging to the same configuration $d\varepsilon^n d\gamma^{N-n}$ becomes to be almost independent of the strength of the crystalline field in the region where Dq is $\gtrsim 2B$ (this is really what happens in the iron group complexes), in other words, in this region interactions between configurations are negligible. But those belonging to different configurations are strongly dependent of the field strength, so that we are led to assign the transitions which connect the levels belonging to the same configurations to the lines and those belonging to different configurations to broad bands. Thus, we consider that the strong crystalline field in the iron group complexes is the cause of such a phenomenon. In rare earth salts where the crystalline field is much weaker than that of the iron group salts by a factor of 10^2, the broad bands has not been observed in the visible region as far as we know. (The broad bands observed in the ultraviolet region in Ce^{3+} 11) or Yb^{3+} 12) salts seem to be somewhat different from those of the iron group complex in their origin.)

The observed half width $3000\,cm^{-1}$ of the broad bands would be explained from this view-point, since the crystalline field could fluctuate with the amplitude of $V_{hem} \simeq 1000\,cm^{-1}$ even by the zero-point vibration of the system, coupled with which electric-dipole transitions are allowed to have non-vanishing intensities.

§ 4. Comparison with Experiments

We now compare our results with the experimental data in accordance with the considerations in the previous section, and determine Dq and, redetermine, if necessary, B and C which may be somewhat different from those determined previously from data for free ions, so as to give good agreement with the observation.

Measurements on these absorption spectra have been performed by many experimentalists, but the numbers of observed lines and bands available in the individual complex are often not so rich that the arbitrariness of the values of these parameters will exist in some cases.

$3d$: In the case of a single d-electron or hole, only a single absorption band is allowed to appear in our treatment. According to Hartmann an Schläfer13), $[Ti(H_2O)_6]^{3+}$ has a single band with intensity $\log \varepsilon \simeq 0.6$ and its absorption maximum is at $20300\,cm^{-1}$, which can be assigned to $(d\varepsilon)^2F_2 \to (d\gamma)^2E$ transition; the value of Dq thus determined is $Dq = 2030\,cm^{-1}$.

$3d^9$: Dreisch14) found a single band on $Cu^{2+}{}_{aq.}$; its absorption maximum is at $12200\,cm^{-1}$, which can be assigned to $(d\varepsilon^6 d\gamma^3)^2E \to (d\varepsilon^5 d\gamma^4)^2F_2$ transition. Then Dq is given as $1220\,cm^{-1}$.

$3d^2$: Hartmann and Schläfer15) found two bands in the $[V(H_2O)_6]^{3+}$ complex ion at room temperature:

	abs. max.	$\log \varepsilon$
$V(ClO_4)_3$ in $HClO_4$	$17.3 \times 10^3\,cm^{-1}$	0.74
	25.0	0.92
$NH_4V(SO_4)_2 \cdot 12H_2O_{aq.}$	17.8	0.54
	25.6	0.81
$CsV(SO_4)_2 \cdot 12H_2O_{aq.}$	17.8	0.65
	25.6	0.81

We assign these two bands to $(d\varepsilon^2)^3F_1 \to (d\varepsilon d\gamma)^3F_2$, $(d\varepsilon^2)^3F_1 \to (d\varepsilon d\gamma)^3F_1$ transitions respectively. Calculated values are $17300\,cm^{-1}$ for ${}^3F_1 \to {}^3F_2$ and $25400\,cm^{-1}$ for ${}^3F_1 \to {}^3F_1$, when we take the value of B as $640\,cm^{-1}$ which is determined using the fact that the energy interval between ${}^3F_2$ and ${}^3F_1$ should be approximately equal to $12B$. (In our treatment γ is always assumed not to be changed from those of the free ion.) The corresponding Dq is about $1860\,cm^{-1}$. It must be remarked here that our assignment of the second band is different from that adopted by Hartmann et al.,15) namely the second band in their treatment corresponds to $(d\varepsilon^2)^3F_1 \to (d\gamma^2)^3A_2$ transition in our case, which is considered to be strongly forbidden even if the coupling with vibrations were taken into account, for it corresponds to a two electron jump. Further, besides this broad band just mentioned, our treatment leads to the expectation that lines must be found corresponding to the transitions $(d\varepsilon^2)^3F_1 \to (d\varepsilon^2)^1E, {}^1F_2$ and $(d\varepsilon^2)^3F_1 \to (d\varepsilon^2)^1A_1$ at $9600\,cm^{-1}$ and $21000\,cm^{-1}$ respectively, which will be of course very weak.

$3d^8$: A. v. Kiss et al.16) measured the absorption spectra of the $[Ni(H_2O)_6]^{2+}$ complex ion, and obtained the following results:

	abs. max.	log. $\mathcal{E}$
$[Ni(H_2O)_6]SO_{4\,aq.}$	$\left(\begin{array}{l}13.9\times10^3\ cm^{-1}\\15.2\end{array}\right.$	$\left(\begin{array}{l}0.32\\0.27\end{array}\right.$
	25.3	0.76
$[Ni(H_2O)_6]Cl_{2aq.}$	8.5	0.35
	$\left(\begin{array}{l}13.9\\15.2\end{array}\right.$	$\left(\begin{array}{l}0.36\\0.27\end{array}\right.$

But Dreisch and Trommer[17)] reported the existence of three bands at 8400, 14100 and 25000 cm^{-1} respectively for this complex ion $NiSO_{4\,aq.}$, and Houston, Bose and Mookherji[18)] also observed these three bands. So that we will take these values as the absorption maxima of the three bands.

Our assignment and calculated values are as follows:

transition	calc. val.	obs. max.
$(d\varepsilon^6 d\gamma^2)^3A_2\rightarrow(d\varepsilon^5 d\gamma^3)^3F_2$	$8.2\times10^3\ cm^{-1}$	8.4
$\rightarrow(d\varepsilon^5 d\gamma^3)^3F_1$	13.9	14.1
$\rightarrow(d\varepsilon^4 d\gamma^4)^3F_1$	26.3	25.0

$$Dq=824\ cm^{-1}\ ,$$

where we have used the same values of B and C as those of the free ion. Here again the third band corresponds to a two electron jump. However in this case, because of the smallness of Dq, the mixing of the two configurations $d\varepsilon^5 d\gamma^3$, $d\varepsilon^4 d\gamma^4$ occurs for the $^3F_1$ level and the intensity of the third band is thus considered to be stolen from that of the second band, while in the case of vanadium complex there was no counter-part of the state $d\gamma^2\ {}^3A_2$. For the first two bands of Ni tutton salts, the same assignment has been done by Griffth and Owen[19)], using the value of the crystalline field parameter determined from their experimental data on the paramagnetic resonance absorption of Ni tutton salts. We have no resonable explanation as to the origin of the double maxima at 13900 and 15200 cm^{-1} found by A. v. Kiss at the position corresponding to the second band (14100 cm^{-1}).

For the optical absorption of $[Ni(NH_3)_6]^{2+}$, measurements are performed by Sone[20)], Dreisch and Trommer[17)], Bose and Mookherji[19)] and for $[Ni(en)_3]Cl_{2\,aq.}$ by Sone[20)]. Our results are the foliowing, where the same assignments, the same B, C values were adopted as for $[Ni(H_2O)_6]^{2+}$:

$[Ni(NH_3)_6]^{2+}$	calc. val.	obs. max.	obs. log $\mathcal{E}$	
	$10.3\times10^3\ cm^{-1}$	10.6	0.92	Dreisch and Trommer
	17.0	17.5	0.75	Sone
	29.3	27.6	0.92	
		$Dq=1030\ cm^{-1}$		
$[Ni(en)_3]^{2+}$	10.8	—	—	
	17.5	18.4	0.84	
	29.9	28.9	0.93	
		$Dq=1080\ cm^{-1}$		

The first band must be found in the near infrared region for $[Ni(en)_3]^{2+}$ too. Further, a line due to the transition $(d\varepsilon^6 d\gamma^2)^3A_2\rightarrow{}^1E$ must be found at 17500 cm^{-1} for the $[Ni(H_2O)_6]^{2+}$ complex ion (for the other two complexes, it will be masked by the broad bands). Actually Gielessen[21)] reported the existence of the line in the region 17300–20500 cm^{-1} in the solid $[Ni(H_2O)_6]Cl_2$ at −189°C.

$3d^3$: For $[Cr(H_2O)_6]Cl_{3\,aq.}$, Tsuchida and Kobayashi[22)] found two bands at 17500 cm^{-1} ($\log\mathcal{E}=1.02$) and 24500 cm^{-1} ($\log\mathcal{E}=1.20$) respectively, and later found one more absorption maximum at 36600 cm^{-1} ($\log\mathcal{E}=0.5$)[23)]. This maximum is also found in the solution of $KCr(SO_4)_2\cdot12H_2O$, but its presence is obscured by the existence of the intense edge absorption. In solid states of chromic salts, however, it is clearly observed.

It is well known that the spectra of the chromic salts show sharp lines in many cases; Sauer[6)], Joos and Schnetzler[24)] have reported the existence of the lines in the crystals of $[Cr(H_2O)_6]Cl_3$ (14800 cm^{-1}, 14900 cm^{-1}), $[Cr(NH_3)_6]Cl_3\cdot H_2O$ (15200 cm^{-1}, 15400 cm^{-1}) and $[Cr(en)_3]Br_3$ (14900 cm^{-1}, 15400 cm^{-1}) at −180°C, and Spedding[25)] further found a sharp absorption (21000 cm^{-1}) between the two bands. The same lines are also observed in the solution containing $[Cr(NH_3)_6]^{3+}$ or $[Cr(en)_3]^{3+}$ ion.

To compare our results with the observed spectra of $[Cr(H_2O)_6]^{3+}$, we will take the observed values of $KCr(SO_4)_2 \cdot 12H_2O$ crystal. The results are as follows;*

$[Cr(H_2O)_6]^{3+}{}_{\text{crys.}}$

	transition	calc. val.	obs. max.	obs. log α	
$(d\varepsilon^3)^4A_2$	$\rightarrow(d\varepsilon^2d\gamma)^4F_2$	$17.2\times10^3\ \text{cm}^{-1}$	18.0	0.5	
(bands)	$\rightarrow(d\varepsilon^2d\gamma)^4F_1$	24.6	24.6	0.6	Tauchida at room temp.
	$\rightarrow(d\varepsilon d\gamma^2)^4F_1$	38.2	36.6	0.2	
	$\rightarrow(d\varepsilon^3)^2E$	14.9	14.9		
(lines)	$\rightarrow(d\varepsilon^3)^2F_1$	15.3	15.1		Sauer at −190°C
	$\rightarrow(d\varepsilon^3)^2F_2$	21.8	21.0		Spedding at liq. hydrg. temp.

$$Dq=1720\ \text{cm}^{-1}$$

Here we changed the values of B and C from those of the free ion in the following way: The values of B and C of the free ion are determined previously to give the term values of ^4F, ^4P and ^2H correctly, so that if we use these B, C the agreement of the calculated term value of ^2G is not so good. This is unfortunate because as we see the lines originate from ^2G of the free ion in our treatment. So we replace γ so as to give the correct term value ^2G of the free ion (resulting γ being 4.0). But on comparing the result thus calculated with the observation we found that we further had to adjust the value of B, C in order to give the right positions of the lines. The value of B to be used here was 765 cm⁻¹ (γ being the same as above 4.0) which is much smaller than those of the free ion 918 cm⁻¹. We cannot get better agreement with the observed spectra by adjusting only the parameter Dq as Finkelstein and Van Vleck[26)] claimed in their paper on a similar calculation of the position of the doublet line of the chrome alum, since the energy interval between the states of the same configuration is almost independent of the crystalline field.

The third absorption band corresponds to the two electron excitation and the same consideration applies to this case as was mentioned for the two electron jump in the case of Ni complex. In this case, however Dq is rather large so that the degree of contamination may be small and consequently there remain doubts about our assignment of the observed third band to this transition. If this assignment were correct, this band would be nearly twice as broad as the first and second bands according to the considerations given at the end of § 3. The third band really seems rather broad, but it may be safe not to draw any definite conclusisn as to the origin of this third band.

It is doubtful whether the observed two lines do correspond to the transitions to ^2E and $^2F_1$ respectively or not. To make this clear, it would be necessary to take the deviation from the perfect cubic symmetry due to the Jahn-Teller effect[8)] or to the trigonal field[27)] exerted by the ions outside the complex ion in question, and the influence of the spin-orbit interaction into consideration. Moreover, if we consider the deformation of the $d\varepsilon$ orbital from the atomic d-character, the excited states ^2E and $^2F_1$ have no necessity to lie so close together. (Though the deformation of orbits may be taken into account in some degree in the adopted B, C values which is different from those of the free ion, we cannot include in this way the deformation that will remove the accidental degeneracy of ^2E and $^2F_1$ levels occurred in the strong crystalline field limit.)

For $[Cr(NH_3)_6]^{3+}$ complex ion, assuming the same assignment and the B, C values redetermined above to be correct, the comparison is as follows:

---

* These data were used here with Tsuchida's which was obtained at room temperature, because for these lines the temperature shift is small. According to Sauer's experiments the doublet line at 14900 cm⁻¹ shifts only about 20Å towards the longer wave leugth side when the temperature is changed from −190° to 18°C, while the bands shift as much as 150 Å.

$[Cr(NH_3)_6]^{3+}$		calc. val.	obs. max.	obs. log ε	
(bands)		$21.4\times10^3\ \mathrm{cm}^{-1}$	21.5	1.62	Linhard[28]
		29.4	28.5	1.57	
		46.6	—	—	
(lines)		14.9	15.2		Joos and Schnetzler[24]
		15.3	15.4		
		21.8	—		

$$Dq=2140\ \mathrm{cm}^{-1}$$

For $[Cr(en)_3]^{3+}$, we shall omit the discussion, since its spectra are almost identical (though a slight decrease of the intensity is found) with those of $[Cr(NH_3)_6]^{3+}$.

$3d^7$: On the $[Co(H_2O)_6]Cl_2$ complex ion, many observations have been made (Houston[18], Dreisch[14], Dreisch and Trommer[17], Datta and Deb[29], Gielessen[21]) and, though there exist slight differences among them, the existence of the following the bands is generally accepted. The comparison is as follows.

trans.	calc. val.	obs. max.	obs. log ε	
$(d\varepsilon^5d\gamma^2)^4F_1\rightarrow(d\varepsilon^4d\gamma^3)^4F_2$	$8.1\times10^3\ \mathrm{cm}^{-1}$	8.13	0.56	
$\rightarrow(d\varepsilon^4d\gamma^3)^4F_1$	20.6	19.6	0.62	Dreisch and Trommer[17]

$$Dq=840\ \mathrm{cm}^{-1}$$

If we assume the value of Dq as above, the absorption lines to which the transitions $(d\varepsilon^5d\gamma^2)^4F_1\rightarrow(d\varepsilon^5d\gamma^2)a^2F_1$, a^2F_2 and $^4F_1\rightarrow b^2F_1$ have to be assigned must appear near 18000 cm^{-1} and $\sim$24000 cm^{-1} respectively. These positions of the lines, however, do not seem to be compatible with the line observed by Gielessen in the crystals at -189°C.

Transition $(d\varepsilon^5d\gamma^2)^4F_1\rightarrow(d\varepsilon^6d\gamma)^2E$ may give rise to a broad band with much weaker intensity, and, if it could actually be found, it would be very interesting because the dependence of its excitation energy on the strength of the crystalline field is different from those hitherto discussed. That is, this band is considered to have a different temperature shift (Fig. 6), if the magnitude of the temperature shift of the absorption maximum is predominantly due to the increase of the atomic distance caused by the thermal expansion. The absorption maximum of this band will then shift towards shorter wave length side when temperature is increased (Dq becomes smaller), while those of hitherto discussed will shift towards longer side as is often experimentally observed.

$3d^4$: For $[Mn(H_2O)_6]^{3+}$, Hartmann and Schläfer measured the absorption spectra of $CsMn(SO_4)_2\cdot12H_2O$[30], and found only one band at 21000 cm^{-1}. This band will correspond to the transition $(d\varepsilon^3d\gamma)^5E\rightarrow(d\varepsilon^2d\gamma^2)^5F_2$. If we determine Dq to be 2100 cm^{-1}, our calculation predicts the existence of the lines near 24000 cm^{-1} corresponding to the transitions to ^3E, $^3F_2$ etc.

Recently the absorption spectra of the aqueous solution of $CrSO_4\cdot7H_2O$ was measured by Tsuchida et al.*. According to their measurement, $[Cr(H_2O)_6]^{2+}$ shows a single band at 13900 cm^{-1} (log $\varepsilon\simeq0.8$). In this complex ion, we can also adopt the same assignment as above, and Dq value thus determined is 1390 cm^{-1}.

$3d^6$: The binding property of the $[Co(NH_3)_6]^{3+}$ complex ion has been considered to be covalent by the reasons that it has the diamagnetic normal state and that the atomic distance between the central ion and one of the ligands is relatively small. The same argument will apply for the $[Co(H_2O)_6]^{3+}$ complex, because a recent measurement on the susceptibility of this complex shows that this is also diamagnetic[31].

But an alternative explanation is possible in the ionic model that the small atomic distance means the strong crystalline field and at such strong field the change of the ground state could occur, i.e., the ground state could become singlet (Fig. 8)[32]. In our treatment we shall adopt the latter explanation, and assume that the ionic structure will predominate over the covalent structure, so that the latter can be neglected.

---

* This was reported at the meeting of the Chemical Society of Japan held in April, 1954.

For $[Co(H_2O)_6]^{3+}$, our assignment is as follows:

trans.	calc. val.	obs. max.	obs. log ε	
$(d\varepsilon^6)^1A_1\rightarrow(d\varepsilon^5d\gamma)^1F_1$	$16.0\times10^3\ \mathrm{cm}^{-1}$	16.3	1.62	Topp[33]
$(d\varepsilon^5d\gamma)^1F_2$	28.1	25.0	1.70	

$$Dq=1920\ \mathrm{cm}^{-1}\ ,$$

where we use a little smaller value of γ, so that the ground state is singlet when the value of Dq is determined to give the position of the first band correctly. The B value was not changed from that for the free ion. Assuming the parameter values to be as above, the third band corresponding to the transition $(d\varepsilon^6)^1A_1\rightarrow(d\varepsilon^4d\gamma^2)^1F_2$ must appear (which might be masked by an intense edge absorption in solution) and, moreover, according to our energy diagram a weak band due to the transition $^1A_1\rightarrow{}^3F_1$ and $^1A_1\rightarrow{}^3F_2$ must be found at the long wave length side of the first band.

In a similar way, the comparison of our results with observations for the $[Co(NH_3)_6]^{3+}$ complex ion is

$[Co(NH_3)_6]^{3+}{}_{aq.}$	calc. val.	obs. max.	obs. log ε	
	$20.4\times10^3\ \mathrm{cm}^{-1}$	21.1	1.78	
	33.6	29.5	1.74	Linhard[28]

$$Dq=2260\ \mathrm{cm}^{-1}\ ,$$

and for the $[Co(NH_3)_6]Cl_3$ crystal

$[Co(NH_3)_6]Cl_3\ {}_{crys.}$	calc. val.	obs. max.	obs. log ε	
	19.2	21.6	1.35	
	32.0	28.6	1.29	Tsuchida[34]
$(d\varepsilon^6)^1A_1\rightarrow(d\varepsilon^4d\gamma^2)^1F_2$	39.4	35.4	1.25	

$$Dq=2260\ \mathrm{cm}^{-1}\ ,$$

where the third band is observed. However, as was mentioned earlier, the third band is considered to have an intensity much smaller than the first two bands, because Dq is also here rather large. So that the assignment for the third band is doubtful, judging from the comparative intensity of this band with the first two bands.

Calculated values do not show so good agreement with those of the observed as is seen above. When we adjust the value of B to give the relative positions of the bands correctly, the calculate absolute positions shift far from those of the observed values towards the longer wave length side. These facts perhaps mean that for this complex ion the approximation that assumes this complex as completely ionic is not so good as to give a quantitative agreement. But it suggests the possibility that this complex could be treated successfully starting from the ionic model and then taking the covalent structure into account. From this point of view, it is very interesting that the absorption band of relatively low intensity has recently been found* at the longer wave length side of the first band which seems to be due to the transition $^1A_1\rightarrow{}^3F_1$ or $^1A_1\rightarrow{}^3F_2$ in our ionic model.

For $[Fe(H_2O)_6]^{2+}$, only one band is observed by Dreisch and Kallscheuer[35] at $10300\ \mathrm{cm}^{-1}$ in the near infrared region. (Though Dreisch reports two maxima for $FeCl_2{}_{aq.}$ at $9300\ \mathrm{cm}^{-1}$ ($\varepsilon=1.74$) and $10500\ \mathrm{cm}^{-1}$ ($\varepsilon=1.86$), we suspect that these two maxima would correspond to the vibrational structure of the band peaked at $10300\ \mathrm{cm}^{-1}$.) Our energy diagram gives the observed value if we assign the transition $(d\varepsilon^4d\gamma^2)^5F_2\rightarrow(d\varepsilon^3d\gamma^3)^5E$ to the observed band and use the value of Dq as $1030\ \mathrm{cm}^{-1}$.

$3d^5$ Absorption spectra of the complex ion $[Fe(H_2O)_6]^{3+}{}_{aq.}$ has been measured by Rabinowitch and Stockmayer[36] and A. v. Kiss[37], who found the same results, though the complex $[Fe(H_2O)_6]^{3+}$ is rather unstable and their results may possibly contain some error in details. Absorption spectra in $[Fe(H_2O)_6]^{3+}{}_{aq.}$

---

* Private communication from Dr. Y. Kondo.

found by them consist of two weak bands and a relatively sharp one. Though the latter is broader than the lines found in other complexes, it is sharper than the bands which ordinarily appear, and we will therefore treat it as a line taking the possible error of the experiments into consideration. The results are as follows:

$[Fe(H_2O)_6]^{3+}{}_{aq.}$	trans.	calc. val.	obs. max.	obs. log ε
$(d\varepsilon^3 d\gamma^2)^6A_1$	$\rightarrow(d\varepsilon^4 d\gamma)\ {}^4F_1$	14.3	14.3	−1.21
(bands)	$\rightarrow(d\varepsilon^4 d\gamma)\ {}^4F_2$	18.8	18.2	−1.00
(lines)	$\rightarrow(d\varepsilon^4 d\gamma^2)^4A_1, {}^4E$	25.0	24.6	−0.48

$Dq=1350\ \text{cm}^{-1}$,

where we recalculated the value of γ to give the term value of ^4G of the free ion correctly in the same way as was done for the chromium complexes, and adjusted the value of B to be 820 cm^{-1}—a value a little smaller than that of the free ion.

According to this assignment, just as was seen in the case of the transition $(d\varepsilon^5 d\gamma^2)^4F_1 \rightarrow (d\varepsilon^6 d\gamma)^2E$ in $3d^7$, the excitation energies of the two absorptions at 14300 cm^{-1} and 18200 cm^{-1}, show the opposite dependence on the crystalline field strength to the usual absorptions (Fig. 9), while a relatively sharp absorption found at 2400 cm^{-1} is insensitive to the crystalline field. Experimental study of this difference in temperature dependence will be interesting as was mentioned at the case of $3d^7$.

For $[Mn(H_2O)_6]^{2+}$, Kato[38] observed a band at 19600 cm^{-1} in $MnCl_{2\,aq.}$. Gielessen's measurement on $MnCl_2\cdot 6H_2O$ crystal[21] shows that this has also line spectra near 25000 cm^{-1}. The comparison is as follows:

$[Mn(H_2O)_6]^{2+}$	trans.	calc. val.	obs. max.
(band)	$^6A_1 \rightarrow {}^4F_2$	19.6×10^3 cm^{-1}	19.6
(line)	$\rightarrow {}^4A_1, {}^4E$	26.2	25.0

$Dq=1230\ \text{cm}^{-1}$,

where the value of γ was adjusted as before, but the B-value was assumed to be that of the free ion. This assignment leads to the existence of the weak band at 14600 cm^{-1} corresponding to the transition $^6A_1 \rightarrow {}^4F_1$ which is not reported yet.

§ 5. Conclusion

Though absorption spectra of many iron group complexes could be identified with our calculated energy diagram choosing the values of the parameters suitably and their observed behaviours were explained fairly well from the view-point of the crystalline field approximation, we do not feel the ground for justifying our treatment settled perfectly because of the shortage of available absorption data in the individual complex. In the following, however, we shall survey the results to show that the values of the parameters thus determined empirically are resonable ones and the arbitrariness of their values is not so large as one might suppose at first.

The calculated positions of lines and bands are rather in fair agreement with the experimental data in divalent ions, if we adjust only the crystalline field parameter Dq suitably. In trivalent ions, it was necessary, besides the adjustment of Dq, to use smaller values of B and C than those of the free ions to obtain better agreement with experiments. The values of B and Dq determined in this way are summarized below, where the corresponding values of B in free states are parenthesized. The values of C are not tabulated there because γ are not altered from those of the free ions.

	Ti^{3+}	V^{3+}	Cr^{3+}	Mn^{3+}	Fe^{3+}	Co^{3+}	
Dq (cm^{-1})	2030	1860	1720	2100	1350	1920?	
B (cm^{-1})		642	765	?	820	?	
		(862)	(918)	(965)	(1015)	(1065)	
			Cr^{2+}	Mn^{2+}	Fe^{2+}	Co^{2+}	Ni^{2+}
Dq (cm^{-1})			1390	1230	1030	840	820
B (cm^{-1})			810	860	917	971	1030
			(810)	(860)	(917)	(971)	(1030)

These values of Dq are of resonable magnitude, being close to those obtained in other ways, for instance, those obtained from the paramagnetic suceptibilities or the paramagnetic resonance absorption data. It is to be noticed that the values of Dq in trivalent complex ions are always larger than those of corresponding divalent complexes, and that in each isovalent complexes the Dq-value has a tendency to decrease as the atomic number Z increases. The Dq-value of Co^{3+} remarked by ? will have possibly a large error because of the particular binding property of Co^{3+} compiex ion as was mentioned in § 4.

We suppose that the decrease of B and C compared with those of free ions will be connected with Stevens' recent suggestion[39)] on the interpretation of the paramagnetic resonance absorption, and a further theoretical investigation on B and C and Dq would be necessary.

Experimentally more detailed observation on the behavior of the absorption in the individual complex ions is highly desirable; particularly the detection of weak bands and lines which are usually obscured by relatively intense and broad bands; the measurement of the temperature shift of the absorption maxima or the temperature dependence of their intensities and all that will give the keys to these puzzles. Especially for Co^{3+} complexes, the absorption spectra of $[CoF_6]^{3-}$ will be interesting, since it has the paramagnetic normal state and its spectra may be identified with our energy level diagram where the value of Dq we must adopt is smaller than those at which the alteration of the ground state occur.

Acknowledgement

We should like to express our gratitude to Prof. M. Kotani for his much instructive advice and continual encouragement during the course of this work. Particularly we are greatly indebted to Dr. Y. Kondo of Chemical Department, Tokyo Institute of Technology, for his helpful information about the experimental data and to Dr. K. Itoh of Nagoya University for his kind discussion on this problem. Appreciation is also due to the members of Prof. Kotani's Laboratory.

References

1) Atomic Energy Levels (*National Bureau of Standard*, 1952)
2) W. M. Cady: Phys. Rev. **43** (1933) 322.
3) S. Meshkov: Phys. Rev. **91** (1953) 871.
4) S. Meshkov: Phys. Rev. **93** (1954) 270.
5) M. A. Catalan: F. Rohrlich and A. G. Shenstone: Proc. Roy. Soc. **A 221** (1954) 421.
6) H. Sauer: Ann. d. Phys. **87** (1928) 197.
7) J. H. Van Vleck: J. Phys. Chem. **41** (1937) 67.
8) J. H. Van Vleck: J. Chem. Phys. **7** (1939) 72.
9) D. G. Hill and A. F. Rosenberg: J. Chem. Phys. **22** (1954) 148.
10) E. U. Condon and G. H. Shortley: The Theory of Atomic Spectra (*Cambridge University press*), 1935.
11) S. Freed: Phys. Rev. **38** (1931) 2122.
12) S. Freed and R. J. Mesirow: J. Chem. Phys. **5** (1937) 22.
13) H. Hartmann and H. L. Schläfer: Zs. f. Phys. Chem. **197** (1951) 115.
14) T. Dreisch: Zs. f. Phys. **40** (1927) 714.
15) H. Hartmann and H. L. Schläfer: Zs. f. Naturforschg. **6a** (1951) 754.
16) A. v. Kiss et al.: Z. anorg. allg. Chem. **245** (1941) 356.
17) T. Dreisch and W. Trommer: Z. Phys. Chem. **B 45** (1939) 37, *ibid.* **B 45** (1940) 19.
18) D. M. Bose and P. C. Mookherji: Phil. Mag. **26** (1938) 757.
A. G. Houston: Proc. Roy. Soc. Edinburgh **31** (1910) 530.
19) J. H. E. Griffth and J. Owen: Proc. Roy. Soc. **A 213** (1952) 459.
20) K. Sone: J. Chem. Soc. Japan **71** (1950) 271.
21) J. Gielessen: Ann. d. Phys. **22** (1935) 537.
22) R. Tsuchida and M. Kobayashi: Bull. Chem. Soc. Japan **13** (1938) 47, J. Chem. Soc. Japan **64** (1943) 1268.
23) R. Tsuchida: Chemistry (in Japanese) No. **6** (1951) 4.
24) G. Joos and K. Schnetzler: Z. Phys. Chem. **B 20** (1933) 1.
25) F. H. Spedding and G. C. Nutting: J. Chem. Phys. **2** (1934) 421.
26) R. Finkelstein and Van Vleck: J. Chem. Phys. **8** (1940) 790.
27) J. H. Van Vleck: J. Chem. Phys. **7** (1939) 61.
28) M. Linhard: Z. f. Elektrochem. **50** (1944) 224.
29) S. Datta and M. Deb: Phil. Mag. **20** (1935) 1121.
30) H. Hartmann and H. L. Schläfer: Zs. f. Naturforschg. **6a** (1951) 760.
31) H. L. Friedman aud J. P. Hunt: J. Amer. Chem. Soc. **73** (1951) 4028.
32) J. H. Van Vleck: J. Chem. Phys. **3** (1935) 807.
33) J. Topp: Dissert. Münst. (1928).
34) R. Tsuchida: The Structure and The Color of Complex Salts (in Japanese).
35) T. Dreisch and O. Kallscheuer: Zs. f. Elektrochem. **50** (1944) 224.
36) E. Rabinowitch and W. H. Stockmeyer: J. Amer. Chem. Soc. **64** (1942) 335.
37) A. v. Kiss et al.: Z. anorg. allg. Chem. **244** (1940) 99.
38) S. Kato: Sci. Pap. Inst. Phys. Chem. Reserch, Tokyo **13** (1930) 49.
39) K. W. H. Stevens: Proc. Roy. Soc. **A 219** (1953) 542.

Journal of the Physical Society of Japan Vol. 9, No. 5, Sep.—Oct., 1954

Statistical Mechanics of Flexible Linear Polymers

I. Moments of End-to-End Distance of a Polymer

By Nobuhiko Saitô*

Department of Applied Physics, Faculty of Science and Engineering, Waseda University, Tokyo

(Received June 22, 1954)

A statistical mechanical theory of the configuration of long flexible linear polymers is developed with pearl-necklace model. The "volume effect" is taken into account, the potential between two non-neighboring structural units being assumed to be of rigid sphere type. Using the method of coupling parameter and the technique of Laplace transform, we obtained the moments of end-to-end distance of polymers. Especially the average square of end-to-end distance is given by

$$\langle r^2\rangle \simeq Nb^2\left[1+\frac{4}{3}\sqrt{\frac{6}{\pi}}\left(\frac{a}{b}\right)^3\left(1+\frac{1}{5}\left(\frac{a}{b}\right)^2+\cdots\right)\sqrt{N}\right]$$

where N_1 a and b are respectively number of structural units or beads of a polymer, diameter of a bead and bond length.

§ 1. Introduction

The theory of the statistical configuration of a polymer chain is of fundamental importance in the studies of properties of macromolecules. Earlier theories, which may be called random flight theory, are treated from the point of view that a linear polymer is regarded as constructed from vectors of definite length connected successively one after another and the "volume effect" or the interaction of non-neighboring structural units is not taken into account. In the language of probability theory, a polymer chain is assumed to be built up by a Markoff process. One of the most successful theories along this line may be that of Kubo[1]. However the theory as a Markoff process has been criticized by several authors, especially by Flory[2], who pointed out that the volume effect of segment can never be neglected in the statistical configuration and other related properties of polymers in solution. Recently Teramoto and Yamamoto[3] developed two independent theories, the one by the method of Ursell development and the other by a more intuitive way and showed that the average square of end-to-end distance of a linear polymer is proportional to 3/2th power of the number of segments of the polymer, i.e.,

$$\langle r^2\rangle \simeq Nb^2\left[1+\frac{1}{2}\left(\frac{a}{b}\right)^2 + \frac{4}{3}\sqrt{\frac{6}{\pi}}\left(\frac{a}{b}\right)^3\sqrt{N}\right],$$

where b is the bond length, a is the diameter of a segment, and N is the number of segments.

On the other hand, various theories[4][5] are developed to estimate this volume effect, but the results obtained are rather at variance.

In the following, a statistical mechanical theory of the interaction of segments is developed, which is different from those due to Teramoto et al. and which leads to the same result obtained by them.

§ 2. Integro-Differential Equation for Distribution Function

The method adopted here is that of coupling parameter invented by Kirkwood[6]. For the sake of simplicity a polymer molecule is assumed to be represented by a pearl-necklace model with bond length b, diameter of a pearl or a segment a and free rotation around each segment, were it not for the volume effect. The pearls or segments are numbered from 0 to N, and the position of i-th segment is denoted by $\boldsymbol{r}_i$. Let the interaction energy between two segments i and j be $\mathcal{E}(r_{ij})$, $(r_{ij}=|\boldsymbol{r}_{ij}|=|\boldsymbol{r}_i-\boldsymbol{r}_j|)$, then the distribution function for $\boldsymbol{r}_0$ and $\boldsymbol{r}_N$ irrespective of the positions of other segments is given by

$$\rho(\boldsymbol{r}_0,\boldsymbol{r}_N;\xi)=\underset{\boldsymbol{r}_{0N}=\text{const.}}{\int\cdots\cdots\int}\exp[-\beta E(\xi)]\prod_{i=1}^{N-1}d\boldsymbol{r}_i/Q\,, \tag{1}$$

---

* Research member of Kobayasi Institute of Physical Research, Kokubunzi, Tokyo.

$$Q=\frac{1}{V}\int\cdots\int\exp\left[-\beta E(\xi)\right]\prod_{i=0}^{N}d\mathbf{r}_i\ , \quad (2)$$

$$E(\xi)=\xi\sum\mathcal{E}(r_{ij})\ ,\qquad \beta=1/kT\ ,$$

where ξ is the coupling parameter and V is the total volume. The integrals involved here are performed under the consideration that the segments are connected by bonds with definite length b. The case $\xi=1$ corresponds to a real system, and $\xi=0$ to an ideal case without " volume effect " which can be treated by Markoff process. By differentiating (1) with respect to ξ, we obtain

$$\frac{1}{\rho}\,\frac{\partial\rho(\mathbf{r}_0,\mathbf{r}_N;\xi)}{\partial\xi}=-\,\beta I-\frac{1}{Q}\,\frac{\partial Q}{\partial\xi}\ , \quad (3)$$

$$\begin{aligned}I&=\sum_{0\leq i<k\leq N}\int\mathcal{E}(\mathbf{r}_i-\mathbf{r}_k)\exp\left[-\beta E(\xi)\right]\prod_{j=1}^{N-1}d\mathbf{r}_j/Q\rho\\&=\sum_{0\leq i<k\leq N}\int\mathcal{E}(\mathbf{r}_i-\mathbf{r}_k)\rho(\mathbf{r}_0,\mathbf{r}_i,\mathbf{r}_k,\mathbf{r}_N;\xi)\\&\qquad\times d\mathbf{r}_i d\mathbf{r}_k/\rho(\mathbf{r}_0,\mathbf{r}_N;\xi)\ , \quad (4)\end{aligned}$$

$$\begin{aligned}\frac{1}{Q}\,\frac{\partial Q}{\partial\xi}&=-\,\frac{\beta}{QV}\sum_{0\leq i<k\leq N}\\&\qquad\times\int\mathcal{E}(\mathbf{r}_i-\mathbf{r}_k)\exp\left[-\beta E(\xi)\right]\prod_{j=0}^{N}d\mathbf{r}_j\\&=-\frac{\beta}{V}\sum_{0<i<k\leq N}\\&\qquad\times\int\mathcal{E}(\mathbf{r}_i-\mathbf{r}_k)\rho(\mathbf{r}_i,\mathbf{r}_k;\xi)d\mathbf{r}_i d\mathbf{r}_k\ , \quad (5)\end{aligned}$$

where $\rho(\mathbf{r}_0,\mathbf{r}_i,\mathbf{r}_k,\mathbf{r}_N;\xi)$ is the distribution function for $\mathbf{r}_0,\mathbf{r}_i,\mathbf{r}_k,\mathbf{r}_N$ irrespective of the positions of other segments, and in the case $i=0$ or $k=N$, it is implied to be the distribution function for three or two segments.

We make the following assumptions,

(i) $\rho(\mathbf{r}_0,\mathbf{r}_i,\mathbf{r}_k,\mathbf{r}_N;\xi)$
$=\rho(\mathbf{r}_0,\mathbf{r}_i;\xi)\rho(\mathbf{r}_i,\mathbf{r}_k;\xi)\rho(\mathbf{r}_k,\mathbf{r}_N;\xi)$,

(ii) $\rho(\mathbf{r}_i,\mathbf{r}_k;\xi)$ is the function of only the distance and the number of segments between i-th and k-th segments, i.e., $\rho(\mathbf{r}_i,\mathbf{r}_k;\xi)=\rho(\mathbf{r}_{ik},k-i;\xi)$,

(iii) The sums over i and k can be replaced by integrals.

The assumptions (i) and (ii) are correct in case $\xi=0$. Then Eqs. (3), (4), and (5) can be written as

$$\begin{aligned}\frac{\partial\rho(\mathbf{r}_{0N};\xi)}{\partial\xi}&=-\,\beta\int_0^N dk\int_0^k di\iint\mathcal{E}(r_{ik})\rho(\mathbf{r}_{0i},i;\xi)\\&\qquad\times\rho(\mathbf{r}_{ik},k-i;\xi)\rho(\mathbf{r}_{kN},N-k;\xi)d\mathbf{r}_i d\mathbf{r}_k\\&\quad+\beta\rho\int_0^N[N-(k-i)]d(k-i)\\&\qquad\times\int\mathcal{E}(r_{ik})\rho(\mathbf{r}_{ik},k-i;\xi)d\mathbf{r}_{ik}\ . \quad (6)\end{aligned}$$

Now we introduce the Laplace transforms,

$$l(\mathbf{s},k;\xi)=\int_V\rho(\mathbf{r},k,\xi)\exp(-\mathbf{rs})d\mathbf{r})\ , \quad (7)$$

$$e(\mathbf{s},k;\xi)=\int_V\mathcal{E}(\mathbf{r})\rho(\mathbf{r},k,\xi)\exp(-\mathbf{rs})d\mathbf{r}\ , \quad (8)$$

$$L(\mathbf{s},t;\xi)=\int_0^\infty(\mathbf{s},k;\xi)\exp(-kt)dk\ , \quad (9)$$

$$E(\mathbf{s},t;\xi)=\int_0^\infty e(\mathbf{s},k;\xi)\exp(-kt)dk\ , \quad (10)$$

and obtain

$$\frac{\partial L}{\partial\xi}=-\beta L^2(\mathbf{s},t;\xi)E(\mathbf{s},t;\xi)+\beta F\ , \quad (11)$$

$$\begin{aligned}F&=\int_0^\infty e^{-Nt}dN\int d\mathbf{r}_{0N}\exp(-\mathbf{r}_{0N}\mathbf{s})\rho(\mathbf{r}_{0N},N;\xi)\\&\qquad\times\int_0^N d(k-i)[N-(k-i)]e(0,k-i;\xi)\\&=\int_0^\infty e^{-Nt}dN\,l(\mathbf{s},N;\xi)\\&\qquad\times\int_0^N d(k-i)[N-(k-i)]e(0,k-i;\xi)\\&=\int_0^\infty e(0,n;\xi)e^{-nt}dn\\&\qquad\times\int_0^\infty ml(s,n+m,\xi)e^{-mt}dm\ . \quad (12)\end{aligned}$$

In this the last line follows by putting $k-i=n$, $N=n+m$ and interchanging the order of integrations. On the other hand, the assumptions (i) and (ii) give

$$\rho(\mathbf{r},n+m;\xi)=\int\rho(\mathbf{r},n;\xi)\rho(\mathbf{r}-\mathbf{r}',m;\xi)d\mathbf{r}'\ ,$$

and its Laplace transform yields

$$l(s,n+m;\xi)=l(\mathbf{s},n;\xi)l(\mathbf{s},m;\xi)\ ,$$

therefore finally we obtain,

$$\begin{aligned}F&=\int_0^\infty e(0,n;\xi)l(\mathbf{s},n;\xi)e^{-nt}dn\\&\qquad\times\int_0^\infty ml(\mathbf{s},m;\xi)e^{-mt}dm\\&=-\frac{\partial L(\mathbf{s},t;\xi)}{dt}\int_0^\infty e(0,n;\xi)l(\mathbf{s},n;\xi)e^{-nt}dn\ , \quad (13)\end{aligned}$$

and

$$\begin{aligned}\frac{\partial L}{\partial\xi}&=-\beta L^2(s,t;\xi)E(\mathbf{s},t;\xi)\\&\qquad-\beta\frac{\partial L}{\partial t}\int_0^\infty e(0,n;\xi)l(\mathbf{s},n;\xi)e^{-nt}dn\ . \quad (14)\end{aligned}$$

In order to solve this integro-differential equation, we must know the functions E and e, and for this purpose, it is necessary to know the function $\rho(\boldsymbol{r},k;\xi)$ for $\boldsymbol{r}$ where $\mathcal{E}(\boldsymbol{r})$ is not substantially equal to zero. Then we assume further;

$$\text{(iv)}\qquad \rho(\boldsymbol{r},k;\xi)=\int\rho(\boldsymbol{r}-\boldsymbol{b}_k,k-1;\xi)\times c(\boldsymbol{r}-\boldsymbol{b}_k)\varphi(\boldsymbol{b}_k)\exp[-\xi\beta\mathcal{E}(\boldsymbol{r})]d\boldsymbol{b}_k\,, \tag{15}$$

where $\boldsymbol{b}_k$ is the vector from $k-1$-th segment to k-th segment ($|\boldsymbol{b}_k|=b$), $\varphi(\boldsymbol{b}_k)$ is the orientational probability of the vector $\boldsymbol{b}_k$ and is equal to $1/4\pi$ in our model, that is, $\varphi(\boldsymbol{b}_k)\exp[-\xi\beta\mathcal{E}(\boldsymbol{r})]$ is the orientational probability of vector $\boldsymbol{b}_k$ under the influence of the intermolecular force of the segment situated at the origin and c is the normalization constant

$$1/c=\int_{\boldsymbol{r}-\boldsymbol{b}_k=\text{const.}}\varphi(\boldsymbol{b}_k)\exp[-\xi\beta\mathcal{E}(\boldsymbol{r})]d\boldsymbol{b}_k\,. \tag{16}$$

The assumption (iv) is in contradiction to the assumption (ii), but where $\boldsymbol{r}$ is a little large, $\mathcal{E}(\boldsymbol{r})\simeq 0$, therefore the assumption (ii) holds almost everywhere.

If we assume for the intermolecular force the potential of the rigid sphere type,

$$\left.\begin{aligned}\mathcal{E}(\boldsymbol{r})&=\infty \qquad |\boldsymbol{r}|<a\,,\\ &=0 \qquad |\boldsymbol{r}|\geq a\,,\end{aligned}\right\} \tag{17}$$

we have

$$\left.\begin{aligned}c&=\frac{4br_{k-1}}{(r_{k-1}+b)^2-a^2} \qquad |r_{k-1}-b|<a\,,\\ &=1 \qquad |r_{k-1}-b|\geq a\,,\end{aligned}\right\} \tag{18}$$

and from the assumption (iv)

$$\left.\begin{aligned}\mathcal{E}(\boldsymbol{r})\rho(\boldsymbol{r},k;\xi)&=0 \qquad |\boldsymbol{r}|\geq a\,,\\ &=\frac{\delta(\xi)b}{\beta\pi}\int\frac{r_{k-1}}{(r_{k-1}+b)^2-a^2}\\ &\quad\times\rho(\boldsymbol{r}-\boldsymbol{b}_k,k-1,\xi)d\boldsymbol{b}_k \qquad |\boldsymbol{r}|<a\,,\end{aligned}\right\} \tag{19}$$

which is derived from the consideration that

$$\lim_{\mathcal{E}\to\infty}\int_0^1\mathcal{E}\exp[-\xi\beta\mathcal{E}]d\xi=\frac{1}{\beta}\,,$$

therefore

$$\lim\mathcal{E}\exp[-\xi\beta\mathcal{E}]=\delta(\xi)/\beta\,,$$

where $\delta(\xi)$ is a function defined by

$$\begin{aligned}\delta(\xi)&=0\,,\qquad \xi\neq 0\,,\\ &=\infty\,,\qquad \xi=0\,,\\ \int_0^1\delta(\xi)d\xi&=1\,.\end{aligned}$$

The right-hand side of Eq. (19) contains $\delta(\xi)$, and the function ρ in the integrand can be replaced by ρ at $\xi=0$. For $\xi=0$, the distribution function can be obtained by theories of Markoff process (see Appendix I).

Then Eq. (19) is transformed into

$$\mathcal{E}(\boldsymbol{r})\rho(\boldsymbol{r},k;\xi)=\frac{\delta(\xi)}{\beta}\frac{2}{r}\left(\frac{3}{2\pi b^2k}\right)^{3/2}\times\int_{b-r}^{b+r}\exp\left(-\frac{3}{2}\frac{y^2}{b^2k}\right)\frac{y^2}{(y+b)^2-a^2}dy\,, \tag{20}$$

The Laplace transforms of Eq. (20), i.e. functions $e(\boldsymbol{s},k;\xi)$ and $E(\boldsymbol{s},t;\xi)$ are given by

$$e(\boldsymbol{s},k;\xi)=\frac{\delta(\xi)}{\beta}\phi(s,k)\,, \tag{21}$$

$$E(\boldsymbol{s},t;\xi)=\frac{\delta(\xi)}{\beta}\int_0^\infty\phi(s,k)\exp(-kt)dk\,, \tag{22}$$

where $\phi(s,k)$ is defined by

$$\phi(s,k)=\int_{|\boldsymbol{r}|\leq a}\exp(-\boldsymbol{rs})d\boldsymbol{r}\times\int\frac{c}{4\pi}\rho(\boldsymbol{r}-\boldsymbol{b}_k,k-1;0)d\boldsymbol{b}_k\,. \tag{23}$$

Furthermore we have

$$\int_0^\infty e(0,k;\xi)l(\boldsymbol{s},k;\xi)\exp(-kt)dk=\frac{\delta(\xi)}{\beta}\int_0^\infty\phi(0,k)l(s,k;0)\exp(-kt)dk\,. \tag{24}$$

Integrating Eq. (14) from 0 to 1 with respect to ξ, we have

$$L(1)-L_0=-L_0{}^2(s,t)\int_0^\infty\phi(s,k)\exp(-kt)dk-\frac{\partial L_0}{\partial t}\int_0^\infty\phi(0,k)l(s,k;0)\exp(-kt)dk\,, \tag{25}$$

where $L(1)$ and L_0 mean the values of L at $\xi=1$ and $\xi=0$. In what follows, the argument ξ will not be written explicity in the functions for $\xi=1$, i.e., for real system. $l(s,k;0)$ and $L_0(s,t)$ can be calculated by random flight theory (Appendix I);

$$\left.\begin{aligned}l_0(s,k)&=l(s,k;0)=\exp(s^2b^2k/6)\,,\\ L_0&=\left(t-\frac{s^2b^2}{6}\right)^{-1}\,,\end{aligned}\right\} \tag{26}$$

and $\phi(s,k)$ is expressed in power series of s (see Appendix II),

$$\phi(s,k)=\sum_{m=0}^{\infty}q_m(k)s^{2m}\,. \tag{27}$$

Putting

$$\left.\begin{aligned}\int_0^\infty q_m(k)\exp(-kt)dk&=\alpha_m(t)\,,\\ \int_0^\infty q_0(k)k^m\exp(-kt)dk&=\beta_m(t)\,,\end{aligned}\right\} \tag{28}$$

we have

$$\left.\begin{aligned} L-L_0&=-\left(\frac{6}{b^2x^2}\right)^2\sum_{p=0}^{\infty}\sum_{\substack{m,n\\ m+n=p}}\frac{n+1}{x^{2m}}\\ &\quad\times\left(\alpha_m-\frac{1}{m!}\left(\frac{b^2}{6}\right)^m\beta_m\right)s^{2p},\\ x&=\sqrt{6t}/b\,. \end{aligned}\right\}\tag{29}$$

§ 3. Mean Square and Higher Moments of End-To-End Distance

By definition we have

$$\begin{aligned} l(s,N)&=\int\rho(\boldsymbol{r},N)\exp(-\boldsymbol{rs})d\boldsymbol{r}\\ &=1+\frac{1}{3!}<r^2>s^2+\cdots\cdots\\ &\quad+\frac{<r^{2p}>}{(2p+1)!}s^{2p}+\cdots\cdots\,, \end{aligned}\tag{30}$$

Hence Mellin inverse transform of Eq. (29) as a power series of s gives immediately various moments of end-to-end distance. The result is the following (Appendix III):

$$\begin{aligned} l(s,N)&=l_0(s,N)+\sum_p s^{2p}\left(\frac{b^2}{6}\right)^{p-3/2}\frac{D_pN^{p+1/2}}{(p+1/2)!}\\ &\quad\times\int_{b-a}^{b+a}\frac{x^2}{(y+b)^2-a^2}\{a^2-(b-y)^2\}dy\,, \end{aligned}\tag{31}$$

where

$$D_p=\sum_{\substack{m+n=p\\ m\neq 0}}\frac{(n+1)}{2^m m!}1\cdot3\cdot5\cdot\ldots\ldots(2m-3)\,.\tag{32}$$

The definite integral involved in (31) is shown to be

$$\begin{aligned} &\int_{b-a}^{b+a}\frac{y^2}{(y+b)^2-a^2}\{a^2-(b-y)^2\}dy\\ &=-\frac{2}{3}a^3-10ab^2+\frac{2b(b-a)^3}{a}\log\left(1-\frac{a}{b}\right)\\ &\quad+\frac{2b(b+a)^3}{a}\log\left(1+\frac{a}{b}\right)\\ &\simeq\frac{a^3}{3}\left[1+\frac{1}{5}\left(\frac{a}{b}\right)^2+\text{higher order of }(a/b)\right]. \end{aligned}\tag{33}$$

Then we finally obtain

$$\begin{aligned} <r^{2p}>&\simeq(Nb^2)^p\frac{(2p+1)!}{p!\,6^p}\\ &\quad\times\left[1+2\sqrt{6}\left(\frac{a}{b}\right)^3\left(1+\frac{1}{5}\left(\frac{a}{b}\right)^2+\cdots\right)\right.\\ &\quad\left.\times\frac{D_p p!^{\,2}}{(p+1/2)!}\sqrt{N}\right]. \end{aligned}\tag{34}$$

In particular when $p=1$, we have

$$\begin{aligned} <r^2>&=b^2N\left[1+\frac{4}{3}\sqrt{\frac{6}{\pi}}\left(\frac{a}{b}\right)^3\right.\\ &\quad\left.\times\left(1+\frac{1}{5}\left(\frac{a}{b}\right)^2+\cdots\right)\sqrt{N}\right], \end{aligned}\tag{35}$$

which is identical with the results by Teramoto and Yamamoto* and those recently obtained by Grimley and Bueche5) if we neglect higher terms of $(a/b)^2$ compared with unity.

The applications of this method to the angular distribution of the intensity in the light scattering and to the distribution function of end-to-end distance will be given in the next paper in near fnture.

In conclusion we wish to thank Messrs. Teramoto and Yamamoto for their stimulating discussions.

Appendix I. Some Results in the Random Flight Theory

The distribution function of end-to-end distance of a linear polymer in random flight theory is given by

$$\rho_0(\boldsymbol{r},N)=\left(\frac{3}{2\pi b^2N}\right)^{3/2}\exp\left(-\frac{3}{2}\frac{r^2}{Nb^2}\right),\tag{A1}$$

and its Laplace transforms are

$$\begin{aligned} l_0(\boldsymbol{s},N)&=\int\rho_0(\boldsymbol{r},N)\exp(-\boldsymbol{rs})d\boldsymbol{r}\\ &=\exp(s^2b^2N/6)\,, \end{aligned}\tag{A2}$$

and

$$\begin{aligned} L_0(\boldsymbol{s},t)&=\int l_0(\boldsymbol{s},N)\exp(-Nt)dN\\ &=\left\{t-\frac{s^2b^2}{6}\right\}^{-1}. \end{aligned}\tag{A3}$$

Appendix II. Calculations of $\phi(s,k)$, α_m and β_m

By definition (23) we have

$$\begin{aligned} \phi(s,k)&=\int_{|\boldsymbol{r}|\leq a}\exp(-\boldsymbol{rs})d\boldsymbol{r}\\ &\quad\times\int_{|\boldsymbol{b}_2|=b}\frac{c}{2\pi}\rho_0(\boldsymbol{r}-\boldsymbol{b}_k,k-1)d\boldsymbol{b}_k \end{aligned}$$

---

* The results of Teramoto and Yamamoto contain a term $(a^2/2b^2)N$ proportional to N. They obtained it by giving special consideration upon the neighboring structural unit. Indeed, chains with small numbers of structural units are not Gaussian even in the ideal case of neglecting volume effect. However in our calculation this is not taken into account.

$$
\begin{aligned}
&= \frac{4\pi}{s}\left(\frac{3}{2\pi b^2 k}\right)^{3/2}\int_0^a (e^{rs}-e^{-rs})dr \\
&\quad\times\int_{b-r}^{b+r}\exp\left(-\frac{3y^2}{2b^2k}\right)\frac{y^2}{(y+b)^2-a^2}dy \\
&=4\pi\left(\frac{3}{2\pi b^2k}\right)^{3/2}\int_{b-a}^{b+a}\exp\left(-\frac{3y^2}{2b^2k}\right) \\
&\quad\times\frac{y^2}{(y+b)^2-a^2}dy\int_{y-b}^{a}\frac{e^{rs}-e^{-rs}}{s}dr \,. \qquad \text{(A4)}
\end{aligned}
$$

Expanding (A4) in power series of s, we have for the coefficient $q_m(k)$ of s^{2m} in $\phi(s,k)$

$$
\begin{aligned}
q_m(k)=&\frac{8\pi}{(2m+2)!}\left(\frac{3}{2\pi b^2k}\right)^{3/2}\int_{b-a}^{b+a}\exp\left(-\frac{3y^2}{2b^2k}\right) \\
&\times\frac{y^2}{(y+b)^2-a^2}\{a^{2m+2}-(b-y)^{2m+2}\}dy \,, \qquad \text{(A5)}
\end{aligned}
$$

and

$$
\begin{aligned}
E(s,t;\xi)&=\frac{\delta(\xi)}{\beta}\int_0^\infty \phi(s,\,k)\exp(-kt)dk \\
&=\frac{\delta(\xi)}{\beta}\sum_{m=0}^{\infty} s^{2m}\int_0^\infty q_m\exp(-kt)dk \\
&=\frac{\delta(\xi)}{\beta}\sum_{m=0}^{\infty}\alpha_m s^{2m} \,, \qquad \text{(A6)}
\end{aligned}
$$

$$
\begin{aligned}
&\int_0^\infty e(0,k;\xi)l(s,k;\xi)\exp(-kt)dk \\
&\quad=\frac{\delta(\xi)}{\beta}\int_0^\infty\phi(0,k)l_0(s,k)\exp(-kt)dt \\
&\quad=\frac{\delta(\xi)}{\beta}\int_0^\infty q_0 l_0(s,k)\exp(-kt)dk \\
&\quad=\frac{\delta(\xi)}{\beta}\sum_{m=0}^{\infty}\left(\frac{s^2b^2k}{6}\right)^m\frac{\beta_m}{m!} \,, \qquad \text{(A7)}
\end{aligned}
$$

where α_m and β_m are defined by Eqs. (28)

$$
\begin{aligned}
\alpha_m(t)&=\int_0^\infty q_m(k)\exp(-kt)dk \\
&=\frac{12}{(2m+2)!\,b^2}\int_{b-a}^{b+a}\exp(-xy) \\
&\quad\times\frac{y\{a^{2m+2}-(b-y)^{2m+2}\}}{(y+b)^2-a^2}dy \,, \qquad \text{(A8)}
\end{aligned}
$$

$$
\begin{aligned}
\beta_m(t)&=\int_0^\infty q_0(k)k^m e^{-kt}dk \\
&=\frac{1\cdot3\cdot5\cdot\cdots\cdot(2m-3)}{2^m x^{2m-1}}\left(\frac{6}{b^2}\right)^{2m+1} \\
&\quad\times\int_{b-a}^{b+a}e^{-xy}\frac{y^2}{(y+b)^2-a^2}\{a^2-(b-y)^2\}dy \\
&\quad+\text{lower order of } (1/x) \,, \qquad m\geq 1 \,, \qquad \text{(A9)}
\end{aligned}
$$

$$
\beta_0=\alpha_0 \,, \qquad x=\sqrt{6t}\,/b \,. \qquad \text{(A10)}
$$

Appendix III. Mellin Transform of Eq. (29)

Eq. (29) is rewritten as

$$
L(1)=L_0-\left(\frac{6}{b^2}\right)^2\sum_{p=0}^{\infty}c_p s^{2p} \,, \qquad \text{(A11)}
$$

$$
c_p=\sum_{\substack{m,n=0\\ m+n=p}}^{p}\frac{n+1}{x^{2n+4}}\left\{\alpha_m-\frac{1}{m!}\left(\frac{b^2}{6}\right)^m\beta_m\right\} \,, \qquad x=\sqrt{6t}\,/b \,, \qquad \text{(A12)}
$$

and its inverse transform is given by

$$
\begin{aligned}
l(s,N)=&\,l_0(s,N)-\left(\frac{6}{b^2}\right)^2\sum_{p=0}^{\infty}s^{2p} \\
&\times\frac{1}{2\pi i}\int_C c_p\exp(Nt)dt \,. \qquad \text{(A13)}
\end{aligned}
$$

Since α_m and β_m are given by Eqs. (A8, 9, 10), we must evaluate the integrals of the following type.

$$
I=\frac{1}{2\pi i}\int_C\frac{\exp(-\gamma\sqrt{t}+Nt)}{t^{m/2}}dt \,. \qquad \text{(A14)}
$$

The path C of this integral is along a line from $t^*-i\infty$ to $t^*+i\infty$ ($t^*>0$) at the right side of the imaginary axis. The integrand has a branch point at $t=0$, and we make a cut from $-\infty$ to zero along the negative real axis. Then it is shown that the path C of this integral is equivalent to the path C' starting from $-\infty$ below the cut, rounding the origin counter-clockwise and reaching again to $-\infty$ over the cut. Putting $Nt=\zeta$, and ex-expanding $\exp(-\gamma\sqrt{\zeta/N})$ in power series of $\sqrt{\zeta}$, we obtain after termwise integration,*

$$
\begin{aligned}
I=&\frac{N^{m/2-1}}{2\pi i}\int_{C'}\frac{\exp\zeta}{\zeta^{m/2}}\left\{1-\frac{\gamma\sqrt{\zeta}}{\sqrt{N}}+\frac{\gamma^2\zeta^2}{2N}+\cdots\right\}d\zeta \\
=&N^{m/2-1}\left[\frac{1}{\Gamma(m/2)}-\frac{\gamma}{\sqrt{N}}\frac{1}{\Gamma((m-1)/2)}\right. \\
&\left.+\cdots+\frac{(-)^n\gamma^n}{n!\,N^{n/2}}\frac{1}{\Gamma((m-n)/2)}+\cdots\right]. \qquad \text{(A15)**}
\end{aligned}
$$

However as β_m is higher about the order of $1/x$ than α_m when $m\geq1$, from Eq. (A15) we have only to deal with the integral arising from β_m when N is sufficiently large.

$$
\begin{aligned}
c_p=&\sum_{\substack{m\geq1\\ m+n=p}}\frac{n+1}{x^{2n+4}}\left[-\frac{1}{m!}\frac{1\cdot3\cdot5\cdot\cdots\cdot(2m-3)}{2^m x^{2m-1}}\frac{6}{b^2}\right. \\
&\times\int_{b-a}^{b+a}\exp(-xy)\frac{y^2\{a^2-(b-y)^2\}}{(y+b)^2-a^2}dy
\end{aligned}
$$

---

* For the validity of this procedure, see Bromwich: *An Introduction to the Theory of Infinite Series*, London, 1931, p. 499.

** N. W. McLachlan, *Complex Variable and Operational Calculus with Technical Applications*, Cambridge, 1939, p. 78.

$$+\text{lower order of } (1/x)\Big]$$

$$=-\frac{1}{x^{2p+3}}\left(\frac{6}{b^2}\right)D_p$$

$$\times\int_{b-a}^{b+a}\exp(-xy)\frac{y^2\{a^2-(b-y)^2\}}{(y+b)^2-a^2}dy$$

$$+\text{lower order of } (1/x)\,, \tag{A16}$$

where

$$D_p=\sum_{\substack{m\geq 1\\ m+n=p}}\frac{(n+1)}{2^m m!}1\cdot 3\cdot 5\cdot\cdots\cdot(2m-3)\,. \tag{A17}$$

The integral

$$\frac{1}{2\pi i}\int_C\frac{\exp(-xy+Nt)}{x^{2p+3}}dt\,,\qquad x=\sqrt{6t}/b\,,$$

is evaluated by Eq. (A15) to be

$$=\left(\frac{b^2}{6}\right)^{p+3/2}\left[\frac{N^{p+1/2}}{\Gamma(p+3/2)}-\frac{N^p\sqrt{6}\,y}{b}\frac{1}{\Gamma(p+1)}+\cdots\cdots\right], \tag{A18}$$

and finally we obtain

$$l(s,N)=l_0(s,N)+\Bigg[\sum s^{2p}\left\{D_p\left(\frac{b^2}{6}\right)^{p-3/2}\times\frac{N^{p+1/2}}{(p+1/2)!}+\text{lower order of } N\right\}\Bigg]$$

$$\times\int_{b-a}^{b+a}\exp(-xy)\frac{y^2\{a^2-(b-y)^2\}}{(y+b)^2-a^2}dy\,. \tag{A19}$$

By the way I want to make mention of the method of steepest descent for the integration of Eq. (A14). Putting

$$\left.\begin{aligned}I&=\frac{1}{2\pi i}\int_C\exp(\phi(t))dt)\,,\\ \phi(t)&=-\gamma\sqrt{t}-(m/2)\log t+Nt\,,\end{aligned}\right\} \tag{A20}$$

and determining t^* by the condition $\phi'(t^*)=0$, we obtain the following result after a formal application of the method of steepest descent,

$$I\simeq\frac{1}{2\pi}\exp[\phi(t^*)]\sqrt{\frac{2\pi}{\phi''(t^*)}}\,,$$

$$\frac{1}{\sqrt{t^*}}=\sqrt{\frac{\gamma^2}{4}+2mN}-\frac{\gamma}{2m}\,,$$

$$\simeq\sqrt{\frac{m}{4\pi}}\left(\frac{2e}{m}\right)^{m/2}N^{m/2-1}\,. \tag{A21}$$

Using Stirling approximation

$$\Gamma(m+1)=\sqrt{2\pi m}\,(m/e)^m\,,$$

we have

$$I\simeq\frac{m/2}{\Gamma(m/2+1)}N^{m/2-1}=\frac{N^{m/2-1}}{\Gamma(m/2)}\,, \tag{A22}$$

in agreement with the previous result (A15). However in this calculation the neglected terms in the formal application of the method of steepest descent are of the order of $N^{m/2-1}$, therefore there is some doubt about this estimation. The first method is preferable in analytical point. We wish to thank Prof. Koizumi and Mr. Namiki for their discussions on these mathematical points.

References

1) R. Kubo: J. Phys. Soc. Japan **2** (1947) 47, 51, 84; **3** (1948) 119; **4** (1949) 319.

2) P. J. Flory: J. Chem. Phys. **17** (1949) 303.

3) E. Teramoto: Busseiron Kenkyu **39** (1951) 1; **40** (1951) 18; **41** (1951) 14; **42** (1951) 24.

M. Yamamoto: Busseiron Kenkyu **44** (1951) 36.

M. Yamamoto, E. Teramoto: Busseiron Kenkyu **47** (1952) 18. (in Japanese.)

4) E. Montroll: J. Chem. Phys. **18** (1950) 734.

H. Frisch, F. C. Collins, B. Friedman: J. Chem. Phys. **19** (1951), 1402.

T. B. Grimley: Proc. Roy. Soc. A **212** (1952) 339.

H. Hadwiger: Makromol. Chem. **5** (1951) 148.

J. J. Hermans: Rec. trav. Chim. **69** (1950) 220.

J. J. Hermans, M. S. Klamkin, R. Ullman: J. Chem. Phys. **20** (1952) 1360.

R. Ullman, J. J. Hermans: J. Polymer Sci. **10** (1953) 559.

5) R. J. Rubin: J. Chem. Phys. **20** (1952) 1940.

T. B. Grimley: J. Chem. Phys. **21** (1953) 185.

F. Bueche: J. Chem. Phys. **21** (1953) 205.

6) J. G. Kirkwood: J. Chem. Phys. **3** (1935) 300.

JOURNAL OF THE PHYSICAL SOCIETY OF JAPAN Vol. 9, No. 5, SEP.—OCT., 1954

The Relation between Dynamic Elastic Modulus, Internal Friction, Creep and Stress Relaxation in Polymethyl Methacrylate

By Eiichi FUKADA

Kobayasi Institute of Physical Research, Kokubunji, Tokyo

(Received June 29, 1954)

The dynamic Young's modulus and the internal friction of polymethyl methacrylate have been measured over a frequency range of 100–2000 c.p.s. by the lateral vibration. The dynamic rigidity modulus and the internal friction have been measured over a frequency range of 0.2–1 c.p.s. by the torsional vibration. The creep and stress relaxation have been also measured in a time range of 1–50 minuites. It was found that both creep and relaxation function are proportional to the logarithm of time. By making use of this creep function and assuming only the superposition principle, the dynamic elastic modulus and the internal friction were calculated as functions of frequency. Any assumption about the distribution function of relaxation time was not used. The agreement between calculated curves and the measured values is considerably good when the parameter C is taken to be 0.09, where C represents the ratio of the slope of creep function against logarithm of time to the instantaneous strain. While the experimentally observed C is 0.065. Stress relaxation function was calculated over a broader time range from the above curves and was found not to be linear to the logarithm of time in the very early time after loading. But it was linear after about 1 minuite and gave a reasonable agreement with the measured values.

§ 1. Introduction

In the previous paper[1] the relationship between the dynamic Young's modulus and internal friction and the static creep were investigated over a frequency range of 100–2000 c.p.s. Afterwards the dynamic rigidity modulus and associated internal friction have been measured over a frequency range of 0.2–1 c.p.s. The creep and stress relaxation have been also measured of the same sample as used in the dynamical studies. The general transformation method of these quantities assuming the superposition principle was applied over a broader range of frequency making use of these experimental results.

The creep of polymethyl methacrylate at room temperature can be represented fairly well by the following equation:

$$y(t)=a+b\log_e(t+\theta)\,, \qquad (1)$$

where y denotes the strain as the function of time t, a and b the constants depending on stress, and θ the unknown parameter which can be determined by the experiment.

Applying the general transformation theory of Gross[2] to this equation, the dynamic elastic modulus E and the internal friction $\tan\delta$ are represented by the following equations:

$$E=E_0(1+CA)/[(1+CA)^2+(CB)^2]\,, \qquad (2)$$

$$\tan\delta=CA/(1+CA)\,, \qquad (3)$$

where E_0 is the instantaneous elastic modulus and C is the ratio of the slope of creep against $\log_e t$ to the instantaneous strain, and

$$A=\int\frac{\cos\omega t}{\theta+t}dt\,, \qquad (4)$$

$$B=\int\frac{\sin\omega t}{\theta+t}dt\,. \qquad (5)$$

When the two parameters C and θ are determined in the experiment of creep, E and $\tan\delta$ can be numerically calculated as functions of angular frequency ω.

§ 2. Experiment

The measurement of dynamic Young's modulus and associated internal friction using thelateral vibration of plate were already described in the previous paper[1][3]. The same material were cut to a square bar about 10

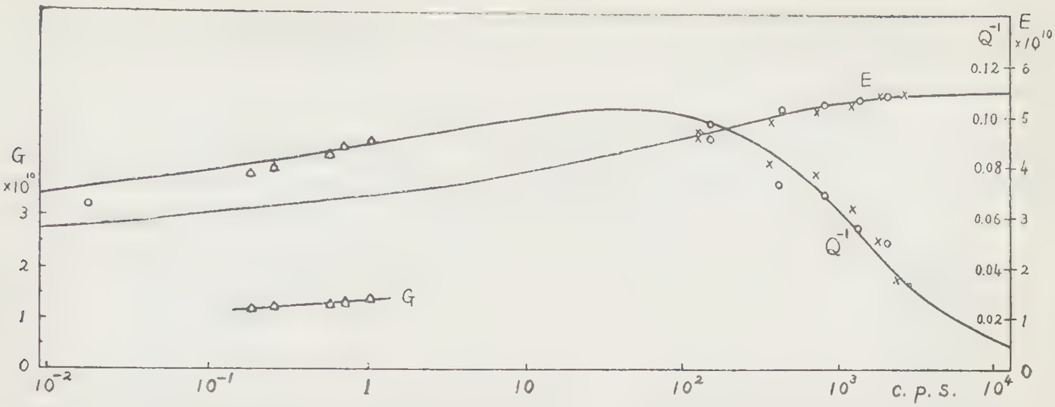

Fig. 1. Frequency dependence of the dynamic elastic modulus and the internal friction. Circles and crosses are the observed values by the lateral vibration of plate, triangles are by the torsional vibration of square bar. Solid lines are the calculated curves assuming $C=0.09$ and $\theta=1.2\times10^{-4}$.

cm long and about 0.2 cm wide. A brass bar with the suitable moment of inertia was attached on this specimen and the free torsional vibration was observed by means of the mirror and the scale[4]. The dynamic rigidity can be derived from the natural frequency of the coupled oscillator and the internal friction can be directly obtained from the attenuation of amplitude. The data at 0.2-1 c.p.s. are shown by the triangles in Fig. 1. The maximum shear in the specimen is $1.5\times10^{-4}-1.5\times10^{-3}$ and the maximum shearing stress is 2—20 kg/cm².

The bending creep of polymethyl methacrylate was measured by the same specimen as used in the lateral vibration. One end of the rectangular plate is clamped and on the other end the stress is applied by hanging the weight. The deflection of the edge is measured by the cathetometer at the interval of 1 minute. The effective length of specimen is 9.85 cm, width 2 cm, thickness 0.14 cm. For the measured time range from 1 to 30 minuites, the strain increased linearly with the logarithm of time. Fig. 2 shows the strain (y_1) at 1 minuite after applying stress and the slope of creep (k) against logarithm of time as functions of applied stress. The abscissa represents the maximum tensile stress at the clamped edge of specimen. The average maximum internal stress may be one forth of this value.

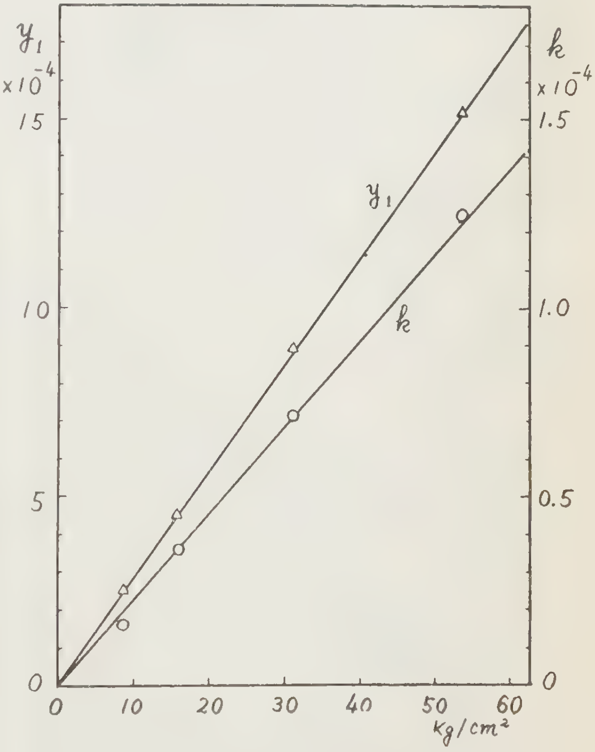

Fig. 2. y_1: strain at 1 minute after loading, k: tangent of bending creep against $\log_{10}t$.

As described in § 3, by comparing the calculation and the dynamical data alone the parameter C and θ are determined and we get $\theta=1.2\times10^{-4}$. Then extraporating the creep function to $t=0$, the instantaneous strain y_0 is given by the next equation:

$$y_0=y_1-k\log_{10}(60+\theta)/\theta\ . \qquad (6)$$

Thus $C=0.434k/y_0$ can be calculated and the result is $C=0.065$. The extreme left point of Young's modulus in Fig. 1 shows one derived from the bending strain 1 minute after applying stress.

The stress relaxation was measured by the bending of the same sample. Fig. 3 represents the apparatus. The free edge of the sample is pulled down by a piano wire, 0.13 mm diameter, and fixed giving a constant deflection of the specimen. The electromagnetic coils are placed close to the wire as shown in Fig. 3. The a.c. voltage is applyed in one coil to excite the lateral vibration of wire, the amplitude of which is picked up by the other coil and the resonant frequency of piano wire is determined. With the stress relaxation in the specimen the tension of wire relaxes with time, and the natural frequency f is proportional to the square root of tension. So the resonant frequency f, which is f_1 at 1 minuite after applying stress, decreases gradually with stress relaxation in the sample. The percentage of relaxed stress is, therefore given by $2\Delta f/f_1$.

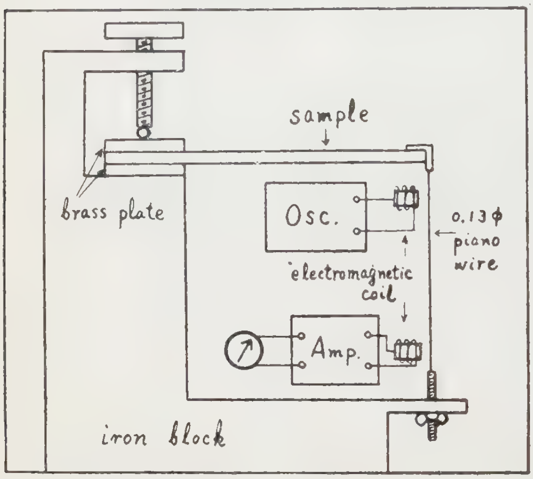

Fig. 3. Apparatus for the measurement of stress relaxation by bending.

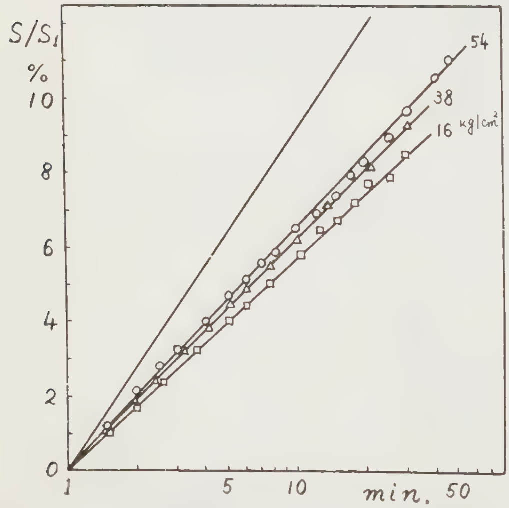

Fig. 4. Bending stress relaxation. Solid line is a part of the calculated curve in Fig. 5.

Fig. 4. shows the percentage of relaxed stress for the stress at 1 minuite after apply stress as a function of time. Over the measurable time range, 1–50 minuites, the following equation is valid,

$$S(t)=a'+b'\log_{10}(\theta'+t)\,, \qquad (7)$$

where $S(t)$ is the relaxed stress, a', b' and θ' are the constant respectively. The slope of the plotted lines are almost constant for the different fixed strain and b'/S_1 is found to be about 0.028, where S_1 is the stress at 1 minuite after applying stress and is determined from the deflection of the edge of sample.

§ 3. Comparison between Experiment and Calculation

If we take the creep function like Eq. (1), we can calculate E and $\tan\delta$ as functions of frequency f as described in § 1. Over the whole frequency range including the lateral and torsional vibration, the fit of calculated curves to the observed data is best when $C=0.09$ and $\theta=1.2\times10^{-4}$ are adopted. Obviously the value of rigidity modulus is smaller than that of Young's modulus but the frequency dependence is similar. C determined from the bending creep experiment using $\theta=1.2\times10^{-4}$ is 0.065, which is some 70% of the predicted value.

When we assume the stress relaxation follows Eq. (7) in the broader time range and calculate E and $\tan\delta$ from this equation in the similar way as the case of creep, the fit to the experimental values is unsatisfactory, especially in the lower frequency range. It might be wrong to extrapolate the relaxation function in Eq. (7) over the earlier time range.

According to the Gross's theory²⁾ we can derive mathematically the relaxation function $\overline{\psi}(t)$ from A and B in Eqs. (4), (5). One convenient formula is as follows:

$$\overline{\psi}(t)=\frac{2}{\pi}\int_0^\infty \overline{A}(\omega)\frac{\sin\omega\tau}{\omega}\,d\omega\,, \qquad (8)$$

where,

$$\overline{A}=\frac{CA(1+CA)+(CB)^2}{(1+CA)^2+(CB)^2}\,. \qquad (9)$$

Using these equations and taking the value of

A, B and C which lead to the theoretical curves in Fig. 1, we calculated numerically the stress relaxation function $\bar{\psi}(t)$ as a function of time t. The results is shown in Fig. 4. The proportionality to $\log_{10} t$ is valid only after about 1 second after loading. The ratio $\bar{\psi}(t)$ to the $\bar{\psi}$ at 60 seconds after loading is shown as a straight line in Fig. 4, the slope of which is about 0.040. The observed slope is about 0.028 and 70% of the above value.

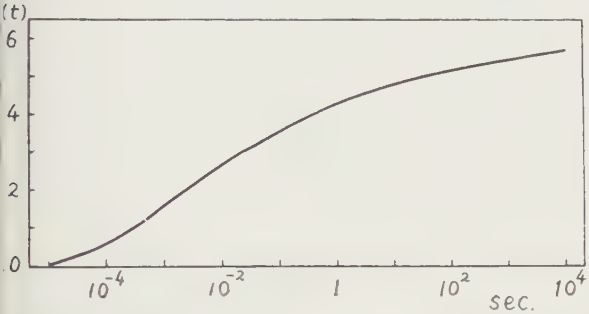

Fig. 5. Calculated stress relaxation function.

§ 4. Discussion

The comparison between the dynamic and static properties of high polymers has been already studied by several authors[5-10]. There the concept of distribution function of relaxation time is often used. But when the creep or relaxation function can be represented by a simple analytical form, the application of general transformation theory of Gross is convenient. As described above in the case of polymethyl methacrylate we could get a considerably good agreement between the calculation and experiment. When the creep or relaxation function can not be represented by an analytical form, the calculation would be very difficult. But the transformation by this method is always possible in principle without any assumption of the distribution function of relaxation time.

In order to make comparison between the dynamic and static experiment, the time scale and the magnitude of strain must be in the same range. The maximum internal strain was about 6×10^{-5} in the lateral vibration, 10^{-3}—10^{-4} in the torsional vibration, and 10^{-3}–10^{-4} in the creep and stress relaxation. The frequency range for the vibration was 0.2–2000 c.p.s., while the time range for the creep and relaxation was 1–50 minuites.

It is seen that the strain amplitude of lateral vibration is rather smaller than that of static experiment. Recently we have devised an apparatus to measure the creep at the strain in the order of 10^{-5} and in the time range 1–100 seconds. In this range the creep function was also found to be proportional to $\log t$ and C in the similar value as given in this paper. The static experiment in the time range smaller than 1 second is now desirable.

The author expresses his hearty thanks to Dr. Kawai for his helpful suggestions in this work. The research fund was defrayed from the Ministry of Education.

References

1) E. Fukada: J. Phys. Soc. Japan **6** (1951) 254.

2) B. Gross: J. App. Phys. **18** (1947) 212; **19** (1948) 257.

3) E. Fukada: J. Phys. Soc. Japan **5** (1950) 321.

4) T. S. Ke: Phys. Rev. **71** (1947) 533.

5) W. Kuhn, O. Künzle and A. Preissmann: Helv. Chim. Acta. **30** (1947) 307, 464, 839.

6) S. Iwayanagi, T. Hideshima and K. Shibata: Rep. Sci. Res. Inst. **26** (1950) 41, 44, 133; **28** (1952) 168. (in Japanese)

7) W. Lethersich: B. J. App. Phys. **1** (1950) 294.

8) A. V. Tobolsky, B. A. Dunell and R. D. Andrews: Tex. Res. J. **6** (1951) 404.

9) R. D. Andrews and A. V. Tobolsky: J. Poly. Sci. **7** (1951) 221.

10) E. Catsiff and A. V. Tobolsky: J. App. Phys. **25** (1954) 145.

JOURNAL OF THE PHYSICAL SOCIETY OF JAPAN Vol. 9, No. 5, SEP.—OCT., 1954

Paramagnetic Resonance Absorption in Manganese Fluosilicate Diluted with Magnesium Ions*

By Taiji ARAKAWA

Department of General Education, Nagoya University

(Received April 9, 1954)

Studies on fine and hyperfine structures of paramagnetic resonance absorption spectra in single crystals of manganese fluosilicate $MnSiF_6 \cdot 6H_2O$ diluted with Mg^{++} ions in several ratios of Mn:Mg=(1:20) ~(1:150) are reported. This crystal, in undiluted state, has one ion in the unit cell. Measurements were made at room temperature and at the wavelength of 3.2 cm. It is concluded that in these diluted crystals, the unit cell contains six inequivalent Mn^{++} ions, the surrounding crystalline fields having different orientations respectively, and that each field has the rhombic symmetry ($D=-294$ oe., $|E|=32$ oe.). It should be pointed out that this field is measurably different from that of the crystal diluted with Zn^{++} ions, in which the field has the axially symmetry.

§ 1. Introduction

The method of paramagnetic resonance absorption provides informations on the ground state of paramagnetic ions in a salt. The ground electronic state of a free Mn^{++} ion is $(3d)^5\ {}^6S_{5/2}$. In a magnetically diluted crystal under the influence of the external magnetic field, its spin degeneracy is split according to the approximate spin Hamiltonian of a Mn^{++} ion[1][2],

$$\mathfrak{H}=g\beta \boldsymbol{H}\cdot \boldsymbol{S}+D\{S_z^2-\tfrac{1}{3}S(S+1)\}+E(S_x^2-S_y^2) +F(a)+AS_zI_z+B(S_xI_x+S_yI_y)\,, \qquad (1)$$

where g is the spectroscopic splitting factor, β the Bohr magneton, $\boldsymbol{H}$ the external (magnetic) field, $\boldsymbol{S}$ ($S=5/2$) the total electron spin operator, and $\boldsymbol{I}$ ($I=5/2$) the nuclear spin operator. The first term is the Zeeman term. The following three terms represent the fine structure terms due to the combined action of the crystalline field and the spin-spin interaction between electrons in a Mn^{++} ion. The D term arises from the axially symmetric component, the E term from the rhombic component and $F(a)$ from the cubic component of the crystalline field. The last two terms—A and B terms—are the hyperfine structure terms due to the magnetic interaction between electronic and nuclear spins of a Mn^{++} ion. In the strong external field of the order of 3000 oe., the Zeeman term is the most dominant and the direction of quantization is along the field. If M and m denote the components of electronic and nuclear spins along this direction respectively, the selection rules for main transitions between splitted levels induced by the radio frequency field perpendicular to the external field are given by $\Delta M=\pm 1$ and $\Delta m=0$. Therefore, in a magnetically diluted crystal containing one Mn^{++} ion per unit cell, the main spectrum may be generally expected to consist of thirty lines because of six values allowed for M as well as m. When microwaves of 3 cm-wavelength are used, the main spectrum is centered on a field of about 3000 oe. For a crystal with the dominant axially symmetric crystalline field, the energy levels are given approximately by the following formula, neglecting the E term, $F(a)$ and the slight anisotropy B–A in the formula (1)[1]

$$Mg\beta H+\frac{1}{2}\left(M^2-\frac{35}{12}\right)(3\cos^2\Theta-1)D+A\cdot M\cdot m$$

where Θ is the angle between the external field and the z axis—the axially symmetric axis of the crystalline field. The external field corresponding to the transition $(M\cdot m)\longleftrightarrow(M-1,\ m)$ is

$$H=H_0-(D/2)(2M-1)(3\cos^2\Theta-1)-A\cdot m, \qquad (2)$$

here $H_0=h\nu/g\beta$. (ν: microwave frequency, h: Planck's constant). $M=5/2, 3/2, \cdots, -3/2$. $m=5/2, 3/2, \cdots, -5/2$ and D, A are expressed in oe. From this formula, we can see that the main spectrum of such a crystal has a fine structure which consists of five groups each possessing six hyperfine lines of equal seperation $|A|$.

---

* This work was carried out during the author's visit for study in Kumagai Laboratory, Institute of Science and Technology, University of Tokyo.

In order to observe these fine and hyperfine structures it is usual to dilute Mn^{++} ions with diamagnetic ions for the purpose of making the interactions between neighbouring Mn^{++} ions negligible. In the research of manganese fluosilicate $MnSiF_6 \cdot 6H_2O$ which is trigonal symmetric and has one Mn^{++} ion per unit cell, Bleaney and Ingram diluted the single crystal with Zn^{++} ions, observing the spectra consisting of thirty lines[2]. The spectrum in the external field parallel to the trigonal axis of the crystal is sketched in Fig. 1 (a). They determined the constants in the formnla (1) as follows:

$$D=-179\times10^{-4}\,\mathrm{cm}^{-1}\ (192\ \mathrm{oe.}),$$
$$E=0,\quad a=+7\times10^{-4}\,\mathrm{cm}^{-1}\ (7{,}5\ \mathrm{oe.}),$$
$$A=-96.1\times10^{-4}\,\mathrm{cm}^{-1}\ (103\ \mathrm{oe.}),$$
$$B=-93.3\times10^{-4}\,\mathrm{cm}^{-1}\ (100\ \mathrm{oe.}),$$

at 290°K; and confirmed the z axis to be parallel to the trigonal axis.

In the experiment on the spectra of undiluted $MnSiF_6 \cdot 6H_2O$, the author concluded that this value of D for the crystal diluted with Zn^{++} ions may differ measurably from that for the undiluted, and that the constant D may vary with the kind of diamagnetic ions used for dilution[3]. It implies that the crystalline field by the distorted octahedron which consists of six water molecules surrounding a M^{++} ion may be different in various fluosilicates $MSiF_6 \cdot 6H_2O$ (M being a divalent ion). So, the paramagnetic resonance absorption spectra of diluted salts may give also suggestive informations on the crystal structure and the crystalline field of diamagnetic salts used for dilution. In the present paper the author has analysed the spectra of single crystals of $MnSiF_6 \cdot 6H_2O$ diluted with Mg^{++} ions.

§ 2. Crystallography and Experimental Method

It is known that the fluosilicates of the form $MSiF_6 \cdot 6H_2O$ (M being a divalent ion) crystallize as rhombohedra (having a trigonal symmetric axis) with the angle α which is given as 112°30′, 112°10′, and 112°9′ for M= Mn, Zn and Mg respectively[4]. According to the x-ray analysis, their atomic arrangements for M=Mn and Zn show rhombohedral crystal structures with one molecule per unit cell. The $M^{++} \cdot 6H_2O$ ion and the $(SiF_6)^{--}$ ion are situated at the corner and the center of the rhombohedral unit cell respectively.

As for $MgSiF_6 \cdot 6H_2O$, however, the one molecule rhombohedral unit is not compatible with x-ray diffraction data and the more thorough examination of it has been desired[5].

The crystalline field acting on a M^{++} ion is mainly due to the slightly distorted octahedron of six water molecules surrounding it.

Single crystals of $MnSiF_6 \cdot 6H_2O$ diluted with Mg^{++} ions in several ratios of Mn:Mg =1/20, 1/30, 1/40, 1/80 and 1/150 (mainly 1/40) were prepared. We shall denote them by $Mg(1/20Mn)SiF_6 \cdot 6H_2O$, $Mg(1/30Mn)SiF_6 \cdot 6H_2O$ etc. They had developed faces with indices $(1\bar{1}0)$ and (100) relative to the three axes with α of about 112°.

Crystals were mounted rotatably on one of the plungers of a rectangular microwave resonant cavity which is operated in the H_{011} mode. The cavity was situated between the pole faces of an electromagnet which was operated by direct current through the main coil and modulating current at a frequency of 50 c/sec. through the auxiliary coil. The external magnetic field by the electromagnet was normal to the microwave magnetic field to insure transverse absorption. The measurements were carried out at room temperature and a wavelength of 3.2 cm. The microwave power from a reflex klystron was divided at a magic T into its two arms. One of them was terminated by the cavity and the other by a matched load which was adjusted to make no power flow out of the fourth arm of the magic T when there exists no magnetic absorption. When it occurred, the power flowed out of the fourth arm and was mixed at a crystal detector with the power from another reflex klystron whose frequency was stabilized to differ from that of the former klystron by 10 Mc/sec. The crystal detector was followed by a 10 Mc/sec. amplifier, a detector, an audio amplifier and the vertical plate of an oscillograph. Its horizontal plate was swept at a frequency of 50 c/sec. to observe absorption lines on the oscillograph. All the spectral lines appearing successively with the increase of the external field were traced. The external field was calibrated by

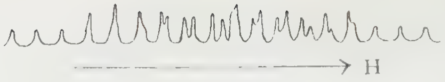

Fig. 1. (a)

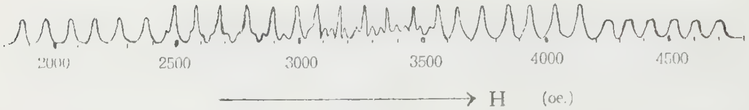

Fig. 1. (b)

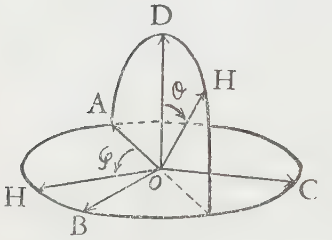

Fig. 2.

(AOD) plane: $(1\bar{1}0)$ BOD) plane: $(10\bar{1})$
(COD) 〃 : $(01\bar{1})$ (ABC) 〃 : (111)
OD: trigonal axis
H : external fields in two cases—Fig. 3 and Fig. 5.

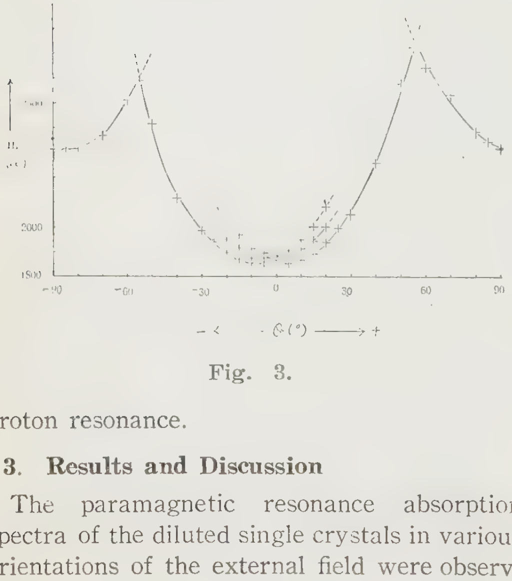

Fig. 3.

proton resonance.

§ 3. Results and Discussion

The paramagnetic resonance absorption spectra of the diluted single crystals in various orientations of the external field were observed. The spectrum for the external field parallel to the trigonal axis of the crystal Mg(1/40Mn)$SiF_6 \cdot 6H_2O$, for instance, is sketched in Fig. 1 (b). This spectrum should be compared with that in the case of dilution with Zn^{++} ions shown in Fig. 1 (a). Fig. 1 (a) shows the characteristics of one Mn^{++} ion per unit cell as explained in § 1. On the other hand, Fig. 1 (b) has different features and the absorption consists of more than thirty lines. Such features were observed in every cases of dilution with Mg^{++} ions examined. So it follows that these crystals contain more than one Mn^{++} ion per unit cell.

We shall keep our eyes on the first line of these spectral lines—the line which appears first with the increase of the external field—, and denote the field corresponding to it by H_1. In Fig. 3, the values of H_1 for various orientations θ (Fig. 2) of the field in the $(1\bar{1}0)$ plane are shown, which varied from 0° to ±90° relative to the trigonal axis. The behaviors of superposed line splitting in the neighbourhood of $\theta=0°$ are also illustrated. We can see that the angular dependence of H_1 varies roughly as $|3\cos^2\theta-1|$; the seperation of the first line from the central line ($|H_1-H_0|$) shows a minimum near $\theta=55°$ and a main or subsidiary maximum near $\theta=0°$ or $90°$. These are main features for the axially symmetric crystalline field (as seen in § 1). The crystalline field of inequivalent ions of lower symmetry than cubic can be approximately regarded as being axially symmetric with an axis parallel to the trigonal axis.

Though the spectrum at $\theta=0°$ (shown in Fig. 1 (b)) is composed of more than thirty lines, it can be approximated to consist of five fine structure groups each possessing six hyperfine lines. Then, we can determine the approximate values of the constants D, a and A in (1) according to the analysis of Bleaney and Ingram[2)], and they are tabulated in Table I, where the signs are reasonably assumed.

Table I. Fine and hyperfine structure constants in oe.

	D	a	A	$\|E\|$
Mg(1/30 Mn)$SiF_6 \cdot 6H_2O$	−293	+7	−99	32
Mg(1/40 Mn)$SiF_6 \cdot 6H_2O$	−294	+7	−99	33
Mg(1/80 Mn)$SiF_6 \cdot 6H_2O$	−294	+8	−98	30
mean	−294	+7	−99	32

It must be noted that this value of D is about one and a half times of that ($D=-192$ oe) in the case of dilution with Zn ions[3].

As expected, it results that the value of D determined by the method of paramagnetic resonance absorption varies with the kind of diamagnetic ions used for dilution. Next, the spectra for various orientations of the external field in the (111) plane perpendicular to the trigonal axis were observed. Some spectral lines of the crystal $Mg(1/40Mn)SiF_6 \cdot 6H_2O$ appearing first with the increase of the external field for the direction $\varphi=105°$ are sketched in Fig. 4. φ is the angle between the field and a straight line (OA) along which the $(1\bar{1}0)$ plane cuts the (111) plane (Fig. 2). In this spectrum we find the first, second and third lines at the fields of 2303 oe., 2393 oe. and 2425 oe. respectively. This first line must be one of thirty spectral lines belonging to one of inequivalent Mn^{++} ions. We shall call this ion the first ion and denote the fields for its thirty lines by H_{11}, H_{12}, H_{13} etc. in the sequence of magnitude. As we know the hyperfine lines appearing successively in nearly equal seperation $|B| \approx |A| \approx 99$ oe., the line for H_{12} may be expected to appear near the field of 2400 oe. Hence we can regard the second line at 2393 oe. as one composed of two lines—the line for H_{12} and the first line belonging to the second ion of inequivalent ions i.e. the line for H_{21}—, if we pay attention to its intensity and width. The third line at 2425 oe. may belong to the third ion, which is denoted by H_{31}. The fourth line at 2482 oe. may be one composed of two lines—the line for H_{13} and the second line of the second ion i.e. the line for H_{22}. The fifth line at 2513 oe. may be the line for H_{32}.

In such a way, we can plot the external fields for the first spectral lines belonging to inequivalent ions, i.e. H_{i1} $(i=1, 2, \cdots)$, for values of φ. (Fig. 5). We find that these points H_{i1} $(i=1, 2, \cdots)$ can be situated on either of six similar sine curves in the form $C \sin(2\varphi+\delta)+2505$ oe., the phase δ shifting each other. When diluted with Zn^{++}, the spectrum in the (111) plane is independent of φ and we have $H_{11}=H_{21}=H_{31}$ etc. Such features were observed in every cases of dilution with Mg^{++} ions examined. It follows that these crystals contain six inequivalent Mn^{++} ions per unit cell. The variation of H_{i1} with φ should be ascribed to the effect of the crystalline field. Because of the approximate equivalence of these sine curves except their phases, the crystalline field surrounding each of six ions can be considered to be nearly equivalent except orientation. The possible cases are as follows:

Each field is axially symmetric.

Each axially symmetric axis (z axis) is orientated differently in six ions and makes a small angle with the trigonal axis.

In this case, the angle Θ between the external field and the z axis changes slightly around $\Theta=90°$, with the rotation of the field in the (111) plane. From (2) and Fig. 3, we can expect that H_{i1} is minimized at the field perpendicular to each z axis. This minimum value H_w should be given by the following formula (3). This formula can be derived using $\Theta=\pi/2$, $M=+5/2$ or $-3/2$, $m=+5/2$ or $-5/2$ in (2) and also adding the second order perturbation term of the D term.

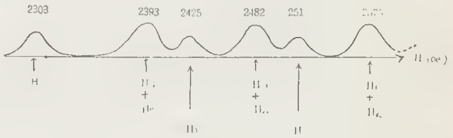

Fig. 4.

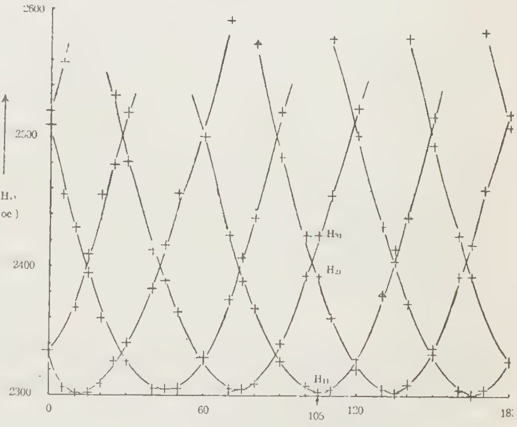

Fig. 5.

$$H_w=H_0-2|D|+D^2/H_0-(5/2)|A|. \qquad (3)$$

The spectral line corresponds to the transition $(M=+5/2 \longleftrightarrow +3/2)$ assuming the negative sign of D.

Using the data: $H_0=3310$ oe. (determined by the observation of the resonance peak of α-diphenyl β-picryl hydrazyl), $|D|=294$ oe. $|A|=99$ oe. (in Table I), we get $H_w=2498$ oe.

from (3), while its observed value in Fig. 5 is about 2303 oe. This discrepancy is beyond the experimental error. This conclusion cannot be upset by considering the $F(a)$ term, which contributes to (3) by $2pa$, where $a=+7$ oe. and $p=-1/4$ (assumed)[2], and also the slight anisotropy $B-A$. So the above case is not correct.

If it is noticed that the calculated field $H_{\omega}=2498$ oe. gives roughly the position of the common central line of six sine curves in Fig. 5, we must attribute the angular variation of H_{i1} to the existence of the rhombic component superposed on the axially symmetric component. The following case can be regarded approximately as the probable one.

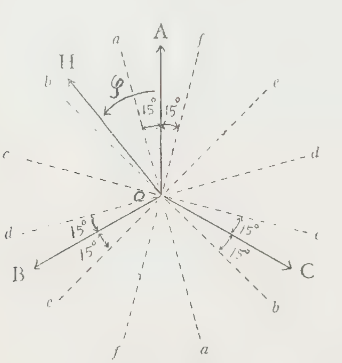

Fig. 6.

$aa//x_6$ axis, y_1 axis $bb//x_5$ axis, y_2 axis
$cc//x_3$ 〃 , y_4 〃 $dd//x_1$ 〃 , y_6 〃
$ee//x_2$ 〃 , y_5 〃 $ff//x_4$ 〃 , y_3 〃
OA, OB, OC: see Fig. 2
H: external field
The x_i and y_i axes belong to the i th Mn ion in the unit cell.

> Each field has a small rhombic component superposed on the axially symmetric component. The latter axis (z axis) is parallel to the trigonal axis commonly in six ions, while the directions of the two rhombic axes in the (111) plane—x and y axes—are different in six ions.

Taking consideration of the rhombic term $E(S_x^2-S_y^2)$ (omitted above) in the Hamiltonian (1), the formula for H_{i1} is given by the following equation[6]

$$H_{i1}=H_0-2|D-3E\cos 2\psi| +\{(D+E\cos 2\psi)^2-32E^2\sin^2 2\psi\}/H_0 -(5/2)|A|. \qquad (4)$$

Here ψ is the angle between the external field and the x axis of the i-th ion, and is equal to φ plus constant. The x axis can be prefered so as to make the sign of E positive. Ascribing the angular variation of H_{i1} centered on the field of 2505 oe. mainly to $6E\cos 2\psi$ in (4), Fig. 5 yields the results that the value of E is about 33 oe. and that the x axis (along which the field H_{i1} is minimized because of $D<0$ and $E>0$) makes an angle of 15° with the straight line (OA, OB or OC) along which one of $(1\bar{1}0)$, $(10\bar{1})$ and $(01\bar{1})$ planes cuts the (111) planes. The six sets of the x- and y-axes are shown in Fig. 6. These directions do not depend on the degrees of dilution (1/20 ~1/150). The values of E are tabulated in the fourth colomn in Table I. We can neglect the effect of this rhombic component on the behaviors of the spectral lines near $\theta=0°$ in Fig. 3. The directions of six z axes are not accurately along the trigonal axis, but differ slightly one auother. The observation of the spectra in some planes through the trigonal axis shows that the angle between each z axis and the trigonal axis is about 7°. It is not easy to determine these accurate directions because of the complicated spectrum. Thus, the directions of x and y axes shown in Fig. 5 are also approximate.

The author wishes to express his sincere thanks to Prof. H. Kumagai for his kind guidance and also to I. Hayashi and K. Ono for their kind advices. This work has been supported by the Research Grant from the Education.

References

1) A. Abragam and M. H. L. Pryce: Proc. Roy. Soc. (London) **A 205** (1951) 135.

2) B. Bleaney and D. J. E. Ingram: Proc. Roy. Soc. (London) **A 205** (1951) 336.

3) T. Arakawa: to be published.

4) P. Groth: Chemische Crystallographie 1 teil, p. 550.

5) R. W. G. Wyckoff: The structure of crystals second edition (1931) p. 311.

6) H. Kumagai, K. Ono, I. Hayashi and K. Kambe: Phys. Rev. **87** (1952) 374.

JOURNAL OF THE PHYSICAL SOCIETY OF JAPAN Vol. 9, No. 5, SEP.—OCT., 1954

Zeeman Splitting of Nuclear Quadrupole Resonance Line of Bromine

By Shoji KOJIMA, Kineo TSUKADA, Akira SHIMAUCHI
and Yasushi HINAGA

*Department of Physics, Tokyo University of Education,
Otsuka, Tokyo*

(Received April 16, 1954)

With a single crystal of about 35 g, which was prepared by the method of the pointed-bottom crucible, Zeeman patterns of the pure quadrupole spectrum of bromine were studied. The observations were carried out in the following orientations of the magnetic fields: (1) parallel to the b axis of the crystal, (2) parallel to the c axis and (3) about 43° from the b axis in the a plane. The pattern at the b axis, where the magnetic field was perpendicular to all molecular bonds, consisted of four lines. This indicated the existence of asymmetry in the field gradient tensor. The asymmetry parameter η was determined as 20 percent. This large value was discussed from the standpoint of resonance switching of auxiliary bonds.

§ 1. Introduction

The pure quadrupole spectrum of crystalline iodine was first studied by Dehmelt[1]. The two resonance frequencies of the iodine nucleus indicated that the asymmetry parameter of the field gradient, η, was 15 percent. This large value was explained by Townes and Dailey[2] with the idea of the resonance switching bonds. A study of a similar crystal of bromine seems to be also interesting. The asymmetry parameter of bromine, however, has not yet been measured by the fact that at the nucleus with a spin of three-halves only one resonance line is observed. The frequency of the line is given by

$$\nu_0=\frac{1}{2h}\,eQq_{zz}\sqrt{1+\frac{1}{3}\eta^2}\ , \qquad (1)$$

where eQq_{zz} is the coupling constant of the nuclear electric quadrupole interaction and h is Planck's constant*. For the determination of the two quantities, eQq_{zz} and η, the measurement of one resonance frequency is not sufficient. Dean[3] showed in the study on dichlorobenzene that these two quantities could be measured through the Zeeman effect. We have carried out observations of Zeeman patterns in a single crystal of bromine and determined the asymmetry parameter.

§ 2. Theory of the Zeeman Effect

In the case of a spin of three halves the Hamiltonian for the interaction between a nuclear quadrupole moment and molecular electric field plus external magnetic field is given by the expression[4]:

$$H=\frac{1}{12}\,eQq_{zz}\{3\boldsymbol{I}_z^2-\boldsymbol{I}^2+\eta(\boldsymbol{I}_x^2-\boldsymbol{I}_y^2)\}$$
$$-\frac{2}{3}\,\mu(H_x\boldsymbol{I}_x+H_y\boldsymbol{I}_y+H_z\boldsymbol{I}_z)\ , \qquad (2)$$

where

$\eta=(q_{xx}-q_{yy})/q_{zz}$,

Q = quadrupole moment of nucleus,

μ = magnetic moment of nucleus,

q_{xx}, q_{yy}, q_{zz} = components of the field gradient tensor, being x, y, z as the principal axis system, whose z axis usually so chosen that q_{zz} is the largest of the three components,

H_x, H_y, H_z = components of magnetic field,

$\boldsymbol{I}$ = angular momentum operator divided by $\hbar$.

The first-order Zeeman effect for any spin was solved by Bersohn[5] when η is small enough so that the term second order in η is a sufficient approximation to the energy level. In the case of a spin 3/2 the energies calculated by him reduce to the expressions

---

* Plancks constant h is usually omitted when eQq is expressed in frequency unit.

$$\left.\begin{aligned}\epsilon_{3/2,\pm}&=\sqrt{1+\frac{1}{3}\eta^2}\mp\sqrt{\frac{9}{4}\gamma^2+\frac{1}{4}\eta^2\left(\alpha^2+\beta^2-\frac{1}{2}\gamma^2\right)}\ ,\\ \epsilon_{1/2,\pm}&=-\sqrt{1+\frac{1}{3}\eta^2}\mp\sqrt{\alpha^2+\beta^2+\frac{1}{4}\gamma^2-\eta(\alpha^2-\beta^2)+\frac{1}{4}\eta^2\left(\alpha^2+\beta^2-\frac{1}{2}\gamma^2\right)}\ ,\end{aligned}\right\}\tag{3}$$

where

$$\epsilon=\frac{E}{(1/4)eQq_{zz}}\ ,\qquad (\alpha,\beta,\gamma)=\frac{(2/3)\mu}{(1/4)eQq_{zz}}(H_x,H_y,H_z)\ .\tag{4}$$

The states laveled for convenience by $m,+$ or $m,-$ become $+m$ or $-m$ states respectively when H_x, H_y and η vanish adiabatically. Between these four levels transitions take place.* The resonance frequencies for the following transitions between the levels:

$$\text{(I)}\ \frac{1}{2}+\longleftrightarrow\frac{3}{2}-\ ,\quad \text{(II)}\ \frac{1}{2}-\longleftrightarrow\frac{3}{2}+\ ,\quad \text{(III)}\ \frac{1}{2}-\longleftrightarrow\frac{3}{2}-\quad\text{and}\quad \text{(IV)}\ \frac{1}{2}+\longleftrightarrow\frac{3}{2}+\ ,$$

are expressed by

$$\nu_{\mathrm{I,\,II}}=\nu_0\pm\tfrac{1}{2}S\qquad\text{and}\qquad \nu_{\mathrm{III,\,IV}}=\nu_0\pm\tfrac{1}{2}s\ ,\tag{5}$$

respectively, where ν_0 is given by Eq. (1) and

$$\left.\begin{matrix}S\\ s\end{matrix}\right\}=\frac{eQq_{zz}}{4h}\left\{\sqrt{9\gamma^2+\eta^2\left(\alpha^2+\beta^2-\frac{1}{2}\gamma^2\right)}\pm\sqrt{4(\alpha^2+\beta^2)+\gamma^2-4\eta(\alpha^2-\beta^2)+\eta^2\left(\alpha^2+\beta^2-\frac{1}{2}\gamma^2\right)}\right\}\ .\tag{6}$$

The effect of the asymmetry parameter is most sensitive when the magnetic field is perpendicular to the z axis which coincides usually with the molecular axis. When the magnetic field is parallel to the x axis, the four resonance frequencies are given by

$$\nu_{\mathrm{I,II}}=\nu_0\pm(|\eta\alpha|+2\alpha-\eta\alpha)eQq_{zz}/8h\ ,$$
$$\nu_{\mathrm{III,IV}}=\nu_0\pm(|\eta\alpha|-2\alpha+\eta\alpha)eQq_{zz}/8h\ .$$

For $\eta>0$,

$$\nu_{\mathrm{I,II}}=\nu_0\pm\frac{2}{3}\frac{\mu H_x}{h}\ ,\qquad \nu_{\mathrm{III,IV}}=\nu_0\mp\frac{2}{3}\frac{\mu H_x}{h}(1-\eta)\ ,\tag{7}$$

For $\eta<0$,

$$\nu_{\mathrm{I,II}}=\nu_0\pm\frac{2}{3}\frac{\mu H_x}{h}(1+|\eta|)\ ,\qquad \nu_{\mathrm{III,IV}}=\nu_0\mp\frac{2}{3}\frac{\mu H_x}{h}\ .\tag{8}$$

The energy values given by Eq. (3) were calculated by the first order perturvation theory. To obtain more acculate values we have tried to solve directly. The Hamiltonian (2) is written in the representation, that diagonalizes $\boldsymbol{I}_z$, by the following matrix form:

$$\boldsymbol{H}=\frac{eQq_{zz}}{4}\begin{pmatrix}1-\frac{3}{2}\gamma & -\frac{\sqrt{3}}{2}(\alpha-i\beta) & \frac{1}{\sqrt{3}}\eta & 0\\ -\frac{\sqrt{3}}{2}(\alpha+i\beta) & -1-\frac{1}{2}\gamma & -(\alpha-i\beta) & \frac{1}{\sqrt{3}}\eta\\ \frac{1}{\sqrt{3}}\eta & -(\alpha+i\beta) & -1+\frac{1}{2}\gamma & -\frac{\sqrt{3}}{2}(\alpha-i\beta)\\ 0 & \frac{1}{\sqrt{3}}\eta & -\frac{\sqrt{3}}{2}(\alpha+i\beta) & 1+\frac{3}{2}\gamma\end{pmatrix}.\tag{9}$$

The secular equation was reduced to

$$\left\{(\epsilon^2-1)-\frac{3}{4}(\alpha^2+\beta^2+\gamma^2)-\frac{1}{3}\eta^2\right\}^2=\alpha^2(\epsilon-1+\eta)^2+\beta^2(\epsilon-1-\eta)^2+\gamma^2(\epsilon+2)^2\ .\tag{10}$$

In the case of $\beta=\gamma=0$ this was solved exactly:

---

* The transitions between the levels $\frac{1}{2},\pm$ and between $\frac{3}{2},\pm$ are also possible. But, when η is not large, the probability is small because of the small mixing of level of the different $|m_z|$.

$$\left.\begin{aligned}\epsilon_{3/2,\pm}&=\sqrt{(1\pm\alpha+\alpha^2)\mp\alpha\eta+\frac{1}{3}\eta^2}\mp\frac{\alpha}{2}\,,\\ \epsilon_{1/2,\pm}&=-\sqrt{(1\pm\alpha+\alpha^2)\mp\alpha\eta+\frac{1}{3}\eta^2}\mp\frac{\alpha}{2}\,.\end{aligned}\right\}\tag{11}$$

When α is small, an approximate calculation of the second order in α shows that all the frequencies given by Eq. (8) are only added on term $\frac{3}{4}\alpha^2\frac{eQq_{zz}}{4h}$.

The Eq. (10) can be solved exactly when

$$2\gamma^2=\alpha^2(1-\eta)+\beta^2(1+\eta)\,.\tag{12}$$

The energies in this case are

$$\begin{aligned}\epsilon_{3/2,\pm}&=\left\{\left(1+\frac{5}{4}k^2+\frac{1}{3}\eta^2\right)\mp\sqrt{3k^2-3\eta(\alpha^2-\beta^2)+k^2\eta^2+\frac{1}{3}\eta^3(\alpha^2-\beta^2)+k^4}\right\}^{1/2},\\ \epsilon_{1/2,\pm}&=-\epsilon_{3/2,\mp}\,,\end{aligned}\tag{13}$$

where $k^2=\alpha^2+\beta^2+\gamma^2$.

Since the resonance frequencies are expressed by Eq. (5) with $s=0$, the lines ν_{III} and ν_{IV} coincide with each other. The exact value of the separation S of the lines ν_I and ν_{II}, is easily calculable. For the following experiment, however, an approximate expression is sufficient for the use. It is

$$S=\frac{4\sqrt{3}}{3}\left(1-\eta\frac{\alpha^2-\beta^2}{2k^2}\right)\frac{\mu H}{h}\,.\tag{14}$$

§ 3. Calculation of Zeeman Patterns on a Single Crystal of Bromine

Bromine forms a orthorhombic crystal of a layer-like structure similar to iodine. The position of the atoms are shematically shown in Fig. 1, which was calculated with parameters of the structure at −150°C described in the book by Wyckoff[6]. The bonds of all molecules are perpendicular to the b axis. Half of them orientate with +31°25′ from the c axis and the other half with −31°25′. When a magnetic field is applied, Zeeman patterns consist of eight lines generally. However, when the direction of the magnetic field lay in the a plane or the b plane, they appeared four lines because of the equalness of the angle between the field and the bond for all molecules.

The principal axis system x, y, z of the field gradient tensor could be so chosen that the x axis fit on the b axis and the z axis on one of the molecular bonds. When the auxiliary bonds were taken into account, the z axis would be slightly different from the molecular bond. When the direction of the magnetic field lay on the a plane, the frequen-

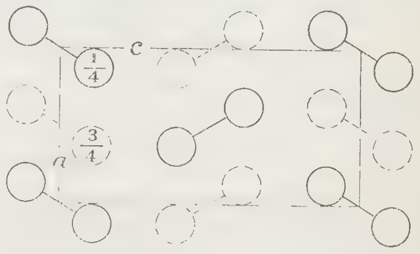

Fig. 1. Crystal structure of bromine. A unit cell contains four bromine molecules. All molecules are perpendicular to the b axis. The parameters at −150°C are a=4.48A, b=6.67A, c=8.72A. The angle between the molecular bonds and the c axis is 31°25′.

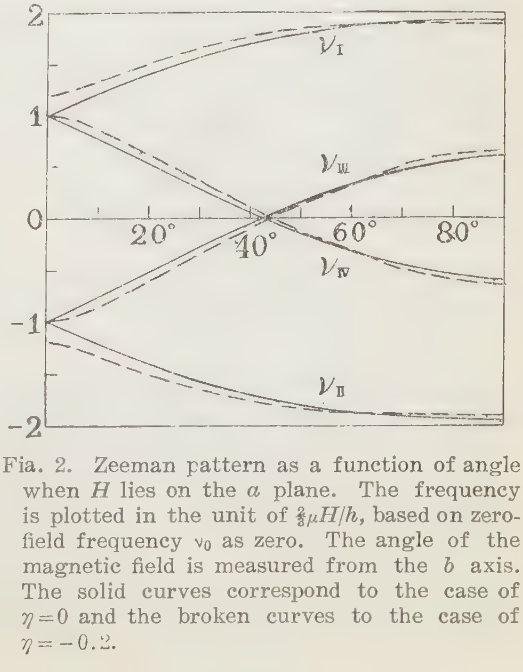

Fia. 2. Zeeman pattern as a function of angle when H lies on the a plane. The frequency is plotted in the unit of $\frac{2}{3}\mu H/h$, based on zero-field frequency ν_0 as zero. The angle of the magnetic field is measured from the b axis. The solid curves correspond to the case of $\eta=0$ and the broken curves to the case of $\eta=-0.2$.

cies of the four resonance lines were calculated from Eq. (6) by putting

$$\left.\begin{array}{ll} H_x = H\cos\theta\ , & H_y = H\sin\theta\sin 31°25'\ , \\ H_z = H\sin\theta\cos 31°25'\ , & \end{array}\right\} \tag{15}$$

where θ was the angle of the magnetic field from the b axis. The Zeeman pattern calculated as a function of θ is reproduced in Fig. 2. The solid curves show the resonance frequencies when η vanishes. In this case the intensity of line was estimated by the equation[7]:

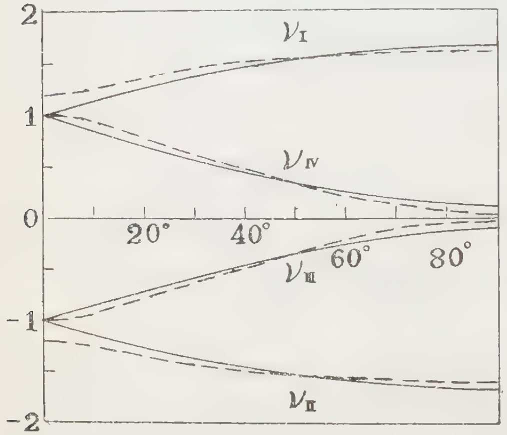

Fig. 3. Zeeman pattern as a function of angle when H lies on the c plane. The notations are same as Fig. 2.

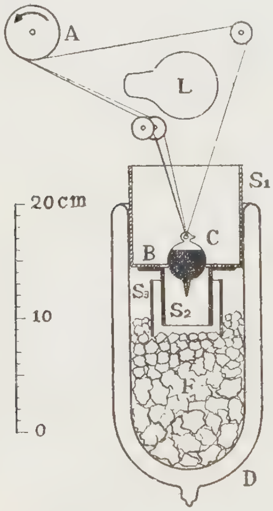

Fig. 4. Apparatus for the production of a single crystal. A: rotating dram, B: baffle, C: crucible, D: Dewer vessel, F: solid carbon-dioxide, L: lamp for heating, S_1: paper cylinder, S_2: metal cylinder fixed to the baffle, S_3: metal cylinder floating on freezing matter.

$$J_{\mathrm{I,II}} = \frac{1}{2}\,\frac{1}{1+F}\ ,\qquad J_{\mathrm{III,IV}} = \frac{1}{2}\,\frac{F}{1+F}\ , \tag{16}$$

where

$$F = \{\gamma + \sqrt{4(\alpha^2+\beta^2)+\gamma^2}\}^2/4(\alpha^2+\beta^2)\ .$$

The intensity ratio between the lines ν_{I} and ν_{III} is 1 at the b axis and about 1:4 at the c axis. The broken curves show the effect of η. The curves indicate that two resonance frequencies, ν_{III} and ν_{IV}, fit exactly and the Zeeman pattern forms a triplet at the angle of about 43°. The exact position of triplet is given from Eq. (12) as

$$\tan\theta = 0.916\ (1-0.39\,\eta)\ . \tag{17}$$

The Zeeman pattern when the magnetic field lay on the c plane was also calculated. It is reproduced in Fig. 3.

§ 4. Apparatus and Procedure of Experiments

Single crystals of bromine, whose melting point, −7.2°C, was below the room temperature, were produced by the method of "pointed-bottom crucible." The glass crucible, diameter of 3.0 cm, contained about 35 g of liquid bromine was slowly fallen in a cold place which was cooled by solid carbon dioxide. The apparatus is shown in Fig. 4 shematically. For the production of a good crystal we took care in the following conditions: (1) The shape of the pointed bottom was sharp, (2) the temperature gradient in vertical direction was large, and (3) the isothermal surfaces were horizontal.

The lamp shown in Fig. 4 worked as a heater which produced a large temperature gradient. The speed of falling was about 1.1 cm/hour. At first, commercial bromine was used. But to obtain strong absorption lines we had to purify it, taking the fraction which has boiling point between 58.5°C and 59.5°C by distillation.* The sample was cooled at −20°C through the experiment by carbon-tetra-chloride and solid carbon-dioxide.

The magnetic field was produced by a Helmholtz coil of diameter of 16 cm with a simple equipment of water cooling. In place of the rotation of the sample the magnet was orientated. The magnet yielded 600 gauss at 10 amp.

---

* The procedure of distillation was owing to Mr. R. Harada, whom we wish to express our thanks.

The spectrometer used was a super regenerative type. The block diagram including the circuit of the super regenerative detector is shown in Fig. 5. The super regenerative detector was same as Dehmelt's circuit¹⁾ in principle, but with slight modifications in practice. A push pull oscillator with a transmission line tuned circuit was quenched by a oscillator of about 500 kc, whose frequency was chosen so that the sensitivity of the detection might be maximum. The signal was picked up through the anode resistance and then amplified by two stage audio-amplifier. One end of the transmission line was connected to a coil of two turns, which contained a sample to be seached, and the other end was made a short circuit with a movable reflecting disk. The frequency was changed from 250 Mc to 320 Mc by displacing the disk. The transmission line in the cathode circuit served as a choking impedance, which was not so sensitive for the frequency of oscillation. A frequency modulation was made by changing a capacity with a vibrating metal foil which was attached to the membrane of a dynamic speaker. The super regenerative detector was put in a shielding box. The reflecting disk and the vibrator, which was kept a constant distance from the disk, were controled from the outside of the box. The sweep of the oscilloscope was synchronized to the frequency modulation. Therefore the horizontal axis of the scope could be marked by the frequency. The measurements of frequency were made as following: The resonance absorption of the sample was supperposed by a signal of a oscillator of 310 Mc, which was calibrated by a crystal oscillator. A frequency of the test oscillator was detected accompanying by many side bands with the interval of quenching frequency. By changing the quenching frequency the coincidence of one of the side bands, usually 9th or 10th, with the resonance frequency was searched. A small separation of lines was determined only by the measurement of quenching frequency. The crystal axis was determined not by inspection, but by a study of the Zeeman patterns with the help of the relation mentioned in § 3. From the patterns the triplet points, the *a* plane and the *b* plane were searched and then the *b* axis and the *c* axis were determined.

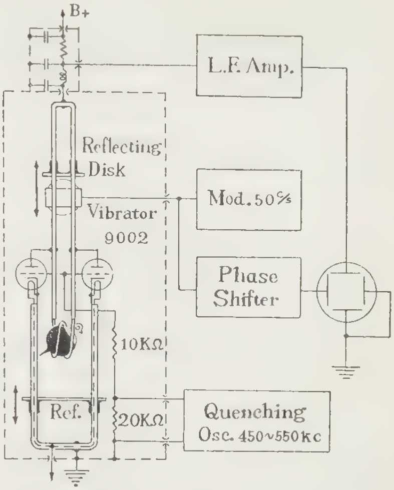

Fig. 5. Spectrometer block diagram with the circuit of the super regenerative detector.

§ 5. The Results of Experiments

The Zeeman patterns were studied precisely at three orientations of magnetic field. All measurements were made for Br^{81} of about 315 Mc.

(1) Magnetic field parallel to the *c* axis. The observed Zeeman pattern was composed of four lines, in which the two outer lines were weak and the two inner lines strong, having the intensity ratio of about 1:4. The separation between the strong lines, *s*, was measured as 143±5 kc at 94.5 gauss. The separation between the weak lines, *S*, could not be measured accurately. The rough value was about 415 kc. The frequencies of the lines were calculated from the theory by putting $\theta=90°$ in Eq. (15) and using Eq. (6).

$$\left.\begin{aligned}\nu_{\mathrm{I,II}}&=\nu_0\pm\frac{2}{3}\frac{\mu H}{h}(1.95+0.20\eta)\,,\\ \nu_{\mathrm{III,IV}}&=\nu_0\mp\frac{2}{3}\frac{\mu H}{h}(0.61-0.20\eta)\,.\end{aligned}\right\}\quad(18)$$

In our case that $H=94.5$ gauss and $(\mu)\mathrm{Br}^{81}=2.27$ nuclear magneton⁷⁾, Eq. (18) yielded the separation between the inner lines as

$$s=(1-0.33\eta)132\ \mathrm{kc}.$$

Comparing this equation with the observed value we obtained

$$\eta=-0.25\pm0.10\,.$$

(2) The pattern of triplet was observed when the magnetic field was applied to the direction of about 44° from the *b* axis in the *a* plane, Eq. (17) indicated that θ took the values of $40°10'$, $42°30'$ and $44°40'$ when η was equal

to +0.2, zero and −0.2 respectively. The observation showed a negative η. The outer two lines of the triplet had equall intensity, which was about 1/4 of the intensity of the central line. The separation between the outer lines, S, was 390±20 kc at 94.5 gauss. The expected value from Eq. (14) was

$$S=(1-0.19\eta)376\text{ kc}.$$

This yielded $\eta=-0.20\pm0.28$.

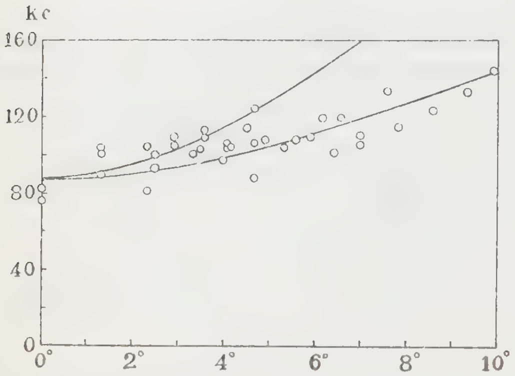

Fig. 6. The frequency difference between ν_{II} and ν_{III} as a function of angle from the b axis. The upper curve represents the theoretical value with $\eta=-0.2$ when the magnetic field lies in the a plane and the lower curve when it lies in the c plane.

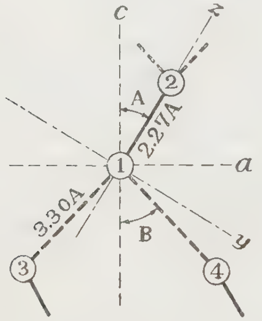

Fig. 7. Positions of bromine nuclei. $A=31°25'$ $B=42°45'$. Solid lines correspond to molecular bonds and broken lines to auxiliary bonds. The crystal axes are represented by a and c. The z and y axes represent the principal axes of the field gradient tensor when auxiliary bonds vanish.

(3) Magnetic field parallel to the b axis. When the orientation of the magnetic field was brought close to the b axis, the pair of lines ν_{II} and ν_{III} approached each other. The separation between these lines was observed at 380 gauss in various orientations of the magnet in neighbourhood of the b axis. The results were plotted against to the angle between the magnetic field and the b axis. Since the b axis had been determined by the Zeeman patterns as previously mentioned, it remained inaccuracy of ±2°. The measurement of the frequency also had some in accuracy due to the line broadning. Then the observed points were distributed. The plot is reproduced in Fig. 6. The separation corresponding exactly to the b axis was inspected as 87±10 kc. Theoretically the frequency difference between ν_{II} and ν_{III} was given from Eq. (8),

$$|\eta|(3/2)(\mu H/h)=|\eta|437\text{ kc}.$$

This yielded $|\eta|=0.20$. Using this value and the sign determined from the measurements described (1) and (2)* we determined

$$\eta=-(20\pm2)\quad\%.$$

The curves in Fig. 6 were drawn with this value for the cases where the magnetic field lay in the a plane (the lower curve) and in c plane (the upper curve).

§6. Discussion of Results

The observed asymmetry parameter of bromine is considerably large. We have tried to interpret this by the resonance switching of bonds as the case of iodine crystal which was studied by Townes and Dailey[2].

We consider the two auxiliary bonds, as shown in Fig. 7, with the resonance switching of a fractional importance of f.

On the bromine nucleus 1 the field gradient tensor comes from the molecular bond with the fractional importance $(1-2f)$, and from two auxiliary bonds with f. The components of the tensor for each bond, on the coordinate system referred to itself, are $q_{\xi\xi}=-\frac{1}{2}q$, $q_{\eta\eta}=-\frac{1}{2}q$ and $q_{\zeta\zeta}=q$ where q is the field gradient tensor when auxiliary bond vanishes. If we write the resultant tensor with the coordinate system refered to the molecular bond as shown in Fig. 7, one obtains

---

* If we examined which of ν_{III} or ν_{II} agreed with ν_0+437 kc, we would determine the sign of η. We have not obtained an accurate value, though a rough measurement yielded ν_0+380 kc for ν_{III}.

$$\left.\begin{aligned} q_{xx} &= -\frac{1}{2}q\,, \\ q_{yy} &= -\frac{1}{2}q + \frac{3}{2}fq(1-\cos 2A\cos 2B)\,, \\ q_{zz} &= q - \frac{3}{2}fq(1-\cos 2A\cos 2B)\,, \\ q_{yz} &= q_{zy} = \frac{3}{2}fq\sin 2A\cos 2B\,, \\ q_{xy} &= q_{yx} = q_{xz} = q_{zx} = 0\,, \end{aligned}\right\} \tag{17}$$

where the angles, A and B,. are shown in the figure. The principal axis system x', y', z' of the tensor are related to the x, y, z system such that $x=x'$, and y' and z' are rotated with an angle Θ from y and z around the x axis. Where Θ is given by expression:

$$\tan 2\Theta = \frac{2q_{yz}}{q_{yy}-q_{zz}} = \frac{2f\sin 2A\cos 2B}{1-2f(1-\cos 2A\cos 2B)}\,. \tag{18}$$

For the case of bromine crystal the angle between the auxiliary bonds, $2B$, is 85°30′ which is very close to 90°. Therefore the angle Θ becomes so small that an approximation of the second order in $\tan 2\Theta$ is possible. In this approximation the components of tensor referred to the principal axis system, x', y', z' can be written,

$$\left.\begin{aligned} q_{x'x'} &= q_{xx}\,, \\ q_{y'y'} &= q_{yy} + \frac{1}{2}q_{yz}\tan 2\Theta\,, \\ q_{z'z'} &= q_{zz} - \frac{1}{2}q_{yz}\tan 2\Theta\,. \end{aligned}\right\} \tag{19}$$

Then

$$\begin{aligned} \eta &= \frac{q_{x'x'}-q_{y'y'}}{q_{z'z'}} \approx \frac{q_{xx}-q_{yy}}{q_{zz}} \\ &= -\frac{3}{2}f(1-\cos 2A\cos 2B)\left(1+\frac{3}{2}f\right). \end{aligned} \tag{20}$$

Putting $\eta=-0.2$ we obtain $f=0.11$. For this value, the angle Θ is calculated as 0°33′.

Finally we estimate the coupling constant of eQq. The observed resonance frequency ν_0, 315 Mc, gives $(eQq_{zz})_{\mathrm{Br}^{81}}$ as 630 Mc. From the definition of η, $q_{xx}=-(1-\eta/2)q_{zz}$. On the other hand Eq. (17) indicates that $q_{xx}=-(1/2)q$ then

$$q=(1-\eta)q_{zz}\,. \tag{21}$$

Putting $\eta=-0.2$, we obtain,

$$(eQq)_{\mathrm{Br}^{81}} = 756\ \mathrm{Mc},$$

This corresponds to 900 Mc for Br^{79}. This value is about 17 percent larger than the quadrupole coupling for a single *p*-electron, which was obtained as 769.6 by King and Jaccarino⁹⁾. The discrepancy corresponding to iodine crystal is about 9 percent, if one use the quadrupole coupling for *p*-electron of 2292 Mc which was obtained recently by Jaccarino, King and Stroke. Townes¹⁰⁾ interpretes this discrepancy by assuming that some *d*-hybridization of the iodine bond is present. Our result may indicate that *d*-hybridization is also important in bromine.

We wish to thank Professor C. H. Townes of Columbia University for discussions on *d*-hybridization. This study was supported by the Scientific Research Expenditure of the Ministry of Education.

References

1) H. G. Dehmelt: Z. Physik **130** (1951) 356.

2) C. H. Townes and B. P. Dailey: J. Chem. Phys. **20** (1952) 35.

3) C. Dean: Phys. Rev. **86** (1952) 607 (abstract at meeting).

4) H. Krüger: Z. Physik **130** (1951) 371.

5) R. Bersohn: J. Chem. Phys. **20** (1952) 1505.

6) R. W. G. Wyckoff: "Crystal Structures", Interscience Publishers, Inc., New York, (1948).

7) H. Krüger and Meyer-Berkhout: Z. Physik **132** (1952) 221.

8) W. Gordy, W. V. Smith and R. F. Trambarulo: "Microwave Spectroscopy", J. Wiley and Sons, Inc., New York (1953).

9) ibid. Table 7.1.

10) C. H. Townes: Private communication.

Journal of the Physical Society of Japan Vol. 9, No. 5, Sep.—Oct., 1954

Noise of Gas Discharge Plasma

By Shoji Kojima, Kazuo Takayama* and Akira Shimauchi

Tokyo University of Education, Otsuka, Tokyo

(Received May 4, 1954)

The noise of a "quiet" plasma has been studied in the frequency range between 1 Mc and 10 Mc. The observed noise consisted of the thermal noise and the current noise. The thermal noise was constant through the frequency region. The electron temperature determined from the noise agreed with the temperature measured by the method of double probes. The current noise had the frequency dependency expressed by the law of $1/f$. These results show that the noise of plasma is similar to the noise of semiconductor.

§ 1. Introduction

Gas discharges generate often large noises, which depend on the state of discharge. When these large noises vanish in a suitable condition, there remains a small noise. As reported previously¹⁾, this small noise depended on the electron temperature of the plasma and corresponded to the thermal noise. In the analogy with the noise of semiconductor, the current noise should exist when a current pass through the plasma. We have studied these noises in the frequency range between 1 Mc and 10 Mc.

§ 2. Apparatus and Procedure of Experiments

The discharge tube used, of which the diameter was 4 cm and the length 45 cm, was filled with argon and mercury vapour at about 2 mm Hg. The electrodes were constructed in the same way as the fluorescent lamp. The discharge was maintained at the anode current of 60 mA. The noise of plasma was taken up by means of a probe which was inserted into the plasma at the position of 24 cm from the anode. The measuring apparatus used was a superheterodyne amplifier, whose output was read by a square-law detector and simultaneously observed by a cathode-ray oscillosoope. The block diagram of the apparatus and the circuit diagram of its input circuit are shown in Figs. 1 and 2 respectively.

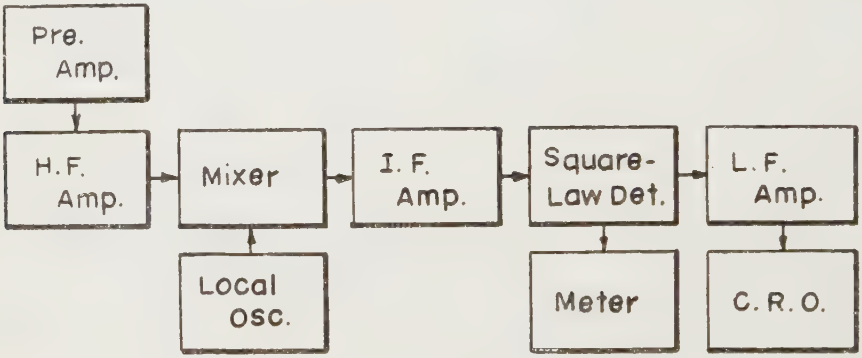

Fig. 1. Block diagram of the apparatus.

The noise generated between the probe and the anode was measured by comparing to the shot noise of a temperature limited diode. The comparison, however, could not be made directly because the diode was different from the plasma on the internal resistance. We took the following method: First the noise of plasma alone was read with the square-law detector and then the noise of the diode was superposed on it in such a way that deflection of the meter of the detector became twice. Since the apparatus had a linear character for the mean square noise, the noise of this diode $\langle i_d^2\rangle_{Av}$ had to be equal to the noise of plasma $\langle i^2\rangle_{Av}$. Therefore the noise of plasma was expressed by the formula of the temperature limited diode:

---

* Present address: The Electrical Communication Laboratory, Musashino, Tokyo.

$$\langle i^2\rangle_{Av}=\langle i_d^2\rangle_{Av}=2eI_d df\ , \qquad (1)$$

where e is the charge of electron, I_d is the anode current of the diode and df is the frequency band of the amplifier.

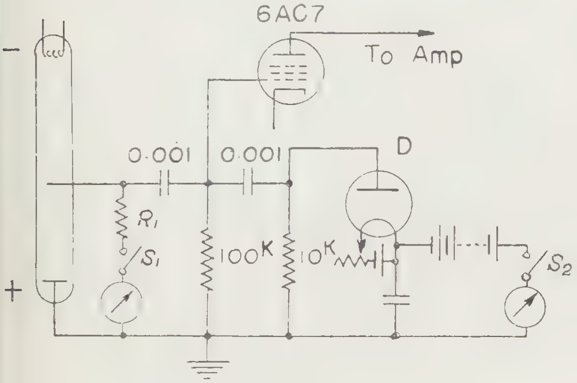

Fig. 2. Diagram of the input circuit. D: The diode for the shot noise. The current of the diode is changed with the heating current of the cathode.

The thermal noise was measured at the condition that the switch S_1 was open as shown in Fig. 2. When the switch was closed, a current flowed into the plasma through the probe. The current was restricted by the resister R_1. It was 83 μA and 220 μA for the resistor of 500 kΩ and 200 kΩ respectively. The current noise was measured in these two cases.

§ 3. The Thermal Noise

The results of the measurement are reproduced in Fig. 3, where the mean square of the noise current $\langle i^2\rangle_{Av}$ is expressed by the equivalent diode current I_d given by Eq. (1). The thermal noise is shown by the horizontal line I, which indicates the independency of the frequency. The thermal noise is expressed by

$$\langle i_{th}^2\rangle_{Av}=\frac{4kT}{R}df\ , \qquad (2)$$

where k is Boltzmann constant, T is electron temperature and R is the internal resistance between the probe and the anode. The resistance R was estimated with the help of the noise in the following way: First the resultant noise of the plasma and the diode, which generated the equal noise, was measured. Then the discharge tube was replaced by a resistor which did not generate any noises. When the mean square value of the noise in this case was just a half of the former case, the resistance of the resistor should be equal to the internal resistance of the plasma. By this method we have estimated the value of R as 2.0 kΩ at 5 Mc. With this value the electron temperature was obtained as 9300°K. The electron temperature was also measured by the double-probe method[2]. The obtained value was 9800°K. The agreement was well.

In the previous report we pointed out that the noise depending on the electron temperature existed in the plasma. The accurate determination of the electron temperature from the noise, however, was not tried because of lack of the data of h.f. resistance of R. The value of temperature estimated by using the d.c. resistance, which was calculated from the static character, was somewhat larger than the value obtained by the double-probe method. The agreement given in the present experiment indicates that the discrepancy in the previous experiment came from the evaluation of resistance.

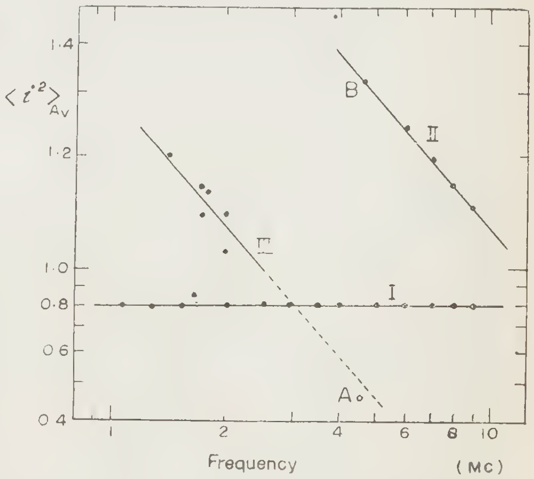

Fig. 3. The noise *vs.* the frequency. The ordinate is expressed by the equivalent diode current in mA. The line I represents the thermal noise. The lines II and III, represent the current noises corresponding to the current of 220 μA and 83 μA respectively.

Mumford studied the noise of the fluorescent lamp at 3000 Mc.[3] He obtained 11400°K as the electron temperature, provided that the noise was due to the thermal noise. Furthermore Easeley and Mumford carried out the determination of the electron temperature with the method of single probe[4]. Their result was 11300°K at the tube temperature of 40°C. We have reported independently the determination of the electron temperature of fluorescent lamps of the same type by means of the double probe method[5]. The obtained temperatures were in the range between 11000°K and 12000°K. The agreement between the temperatures determined from the noise and from the probe method indicates that the measured noise was the thermal noise.

§4. The Current Noise

The current noise, which was obtained from the measured noise by subtracting the thermal noise, is shown by the lines II and III in Fig. 3. Both lines indicate that the mean square of the current noise is proportional to $f^{-1.15}$. Therefore we can say that the current noise is inversely proportional to the frequency.

The point A shown in Fig. 3 is calculated from the measured point B on the line II by multiplying the factor $(83/220)^2$. The fact that the point A lies on the line III indicates the current noise to be proportional to the square of the current.

Parzen and Goldstein derived a theoretical formula for the noise of plasma[6], it is expressed by

$$<i^2>_{Av} = \left\{ \frac{4kT}{R} + 4 \frac{I^2}{N} \frac{z(4\pi^2 f^2 + 3z^2)}{(4\pi^2 f^2 + z^2)^2} \right\} df\,, \tag{3}$$

where N is the total number of electrons which carry the current I and z is the collision frequency. The collission frequency in the present experiment is estimated as about 10^{10} sec^{-1} from the electron temperature and the mean free path. Since this value is much larger than the frequency f, the current noise expressed in the second term of the Eq. (3) shows to be independent on the frequency. This fact contradicts to the observed frequency character, whereas the proportionality to the square of the current I is in accord with the observation.

Van der Ziel pointed out that z had to be considered as the reciprocal of the lifetime of electrons when the collision frequency was much larger than f.[7] This consideration takes the theory closer to the experimental result. The observed frequency character, however, could not be explained completely. The situation is the same for the semiconductor, where the law of $1/f$ is not derived from a simple theory.

References

1) S. Kojima and K. Takayama: Phys. Rev. **80** (1950) 907.

2) E. O. Johnson and L. Malter: Phys. Rev. **80** (1950) 58.

3) W. W. Mumford: Bell Syst. Tech. J. **28** (1949) 608.

4) M. A. Easley and W. W. Mumford: J. Appl. Phys. **22** (1951) 846.

5) S. Kojima, K. Takayama and A. Shimauchi: Rep. Microwave Res. Com. **3** (1952) 3.

6) P. Parzen and L. Goldstein: Phys. Rev. **79** (1950) 190, Phys. Rev. **82** (1951) 724.

7) A. van der Ziel: J. Appl. Phys. **24** (1953) 223.

JOURNAL OF THE PHYSICAL SOCIETY OF JAPAN Vol. 9, No. 5, SEP.—OCT., 1954

Nuclear Quadrupole Resonances in Arsenic Tribromide and Arsenic Tri-iodide

By Shoji KOJIMA, Kineo TSUKADA, Shizuko OGAWA,
Akira SHIMAUCHI and Yoshihito ABE
Tokyo University of Education, Otsuka, Tokyo

(Received June 8, 1954)

The pure quadrupole spectra of As^{75}, Br^{79} and Br^{81} in $AsBr_3$, and of I^{127} in AsI_3 have been studied by the method of superregenerative detection. The observed resonance frequencies yielded the following couplings: 127 Mc, 415 Mc and 1328 Mc for As^{75}, Br^{79} and I^{127} respectively. The spectrum of bromine in arsenic tribromide was a triplet. Above 90°C, the iodine in arsenic tri-iodide also showed a triplet, whereas below that temperature it had a single line. The asymmetry parameter on iodine was determined from the resonance frequencies. The result was 18.4% at the liquid air temperature and 14.5% at the room temperature. The low couplings and the high asymmetry of iodine in arsenic tri-iodide were interpreted by the mechanism of resonance switching of the bond.

§ 1. Introduction

The crystal structure of arsenic tri-iodide is well known.[1] The arrangement of the atoms is shown in Fig. 1, where an arsenic atom is neighbouring six iodine atoms and each iodine atom neighbouring two arsenic atoms. Then arsenic tri-iodide forms a layer-like macromolecule. We have attempted to study the nuclear quadrupole resonances in arsenic tri-iodide and arsenic tribromide which seems to be similar in crystal structure.

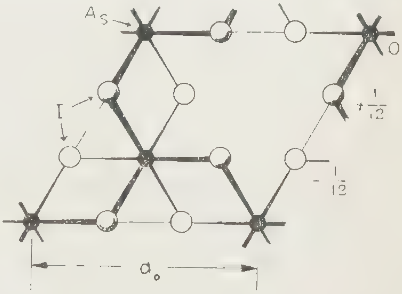

Fig. 1. Arrangement of the atoms in the crystal of AsI_3. The bond length of As–I is 2.98 A and the angle of As–I–As is about 88°. ($a_0=7.187$ A, $c_0=21.39$ A)

§ 2. Experimental Procedure and Results

The method of the superregenerative detection and oscilloscope was employed for the experiment.[2] Three superregenerative oscillators were prepared in response to the three frequency ranges between 45 Mc and 100 Mc, between 150 Mc and 350 Mc, and between 350 Mc and 700 Mc. The first oscillator was made of a single miniature tube 9002 with *LC* tuning circuit. The second was a push-pull oscillator of tubes 9002 with transmission line tuning circuit. The third was similar to the second, but the miniature tube were replaced by light house tubes 2C43. The frequency of the resonance was measured by comparing it with a test oscillator which was calibrated with the standard waves.

The experiments below the room temperature were performed with cooling materials of the mixture of dry ice and carbon tetrachloride, the mixture of dry ice and chloroform, and the liquid air.

(*a*) *Arsenic Tribromide*

The resonance frequencies of the arsenic isotope, As^{75}, and the bromine isotopes, Br^{79} and Br^{81}, were observed. Since these isotopes have a spin of 3/2, a single resonance line was expected for each of them. The bromine isotopes, however, showed a triplet structure which was caused by nonequivalent positions in the crystal. The measured resonance frequencies are listed in Table I, where the values on Br^{81} were omitted, because the ratio between the frequencies of Br^{79} and Br^{81} was agreed with the previous experiment.[3]

The resonance frequency of the arsenic isotope was plotted as a function of temperature, which is reproduced in Fig. 2a. The similar curves on the triplet lines of the bromine isotope are also shown in Fig. 2b.

Table I.

a. Resonance Frequencies of As^{75} in $AsBr_3$.

Frequency (Mc)	Temperature (K°)
63.569 ±0.003	83
62.417 ±0.003	202
61.946 ±0.001	248
61.315 ±0.001	291

b. Resonance Frequencies of Br^{79} in $AsBr_3$.

Frequency (Mc)			Temperature
ν_{I}	ν_{II}	ν_{III}	(°K)
205.758	207.384	207.940	83
203.566	204.933	205.655	214
202.750	203.987	204.772	249
201.731	202.822	203.626	291

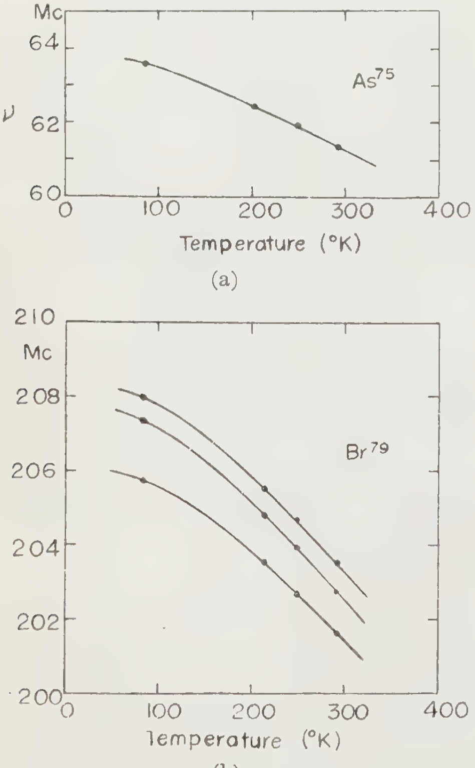

(a)

(b)

Fig. 2. (a) The resonance frequency of As^{75} in $AsBr_3$ *v.s.* temperature.
(b) The resonance frequencies of Br^{79} in $AsBr_3$ *v.s.* temperature.

The resonance frequency, ν, is expressed by[4)5)]

$$\nu=\frac{1}{2}\frac{eQq_{zz}}{h}\sqrt{1+\frac{1}{3}\eta^2}\,, \tag{1}$$

where eQq_{zz} is the coupling constant and η is the asymmetry parameter of the field gradient tensor. Without knowing the asymmetry parameter, one can not determine the coupling constant. However, its approximate value is obtained by doubling the frequency.

(*b*) *Arsenic Tri-iodide*

The iodine isotope I^{127}, whose spin is 5/2, has two resonance frequencies ν_1 and ν_2 corresponding to the transitions $m_z=\pm 1/2\longleftrightarrow\pm 3/2$ and $m_z\pm 3/2\longleftrightarrow\pm 5/2$. These frequencies are expressed by[4)5)]

$$\left.\begin{aligned}\nu_1&=\frac{3}{20}\frac{eQq_{zz}}{h}\left(1+\frac{59}{54}\eta^2\right),\\ \nu_2&=\frac{3}{10}\frac{eQq_{zz}}{h}\left(1-\frac{11}{54}\eta^2\right).\end{aligned}\right\} \tag{2}$$

We have measured both resonance frequencies of the iodine isotope in the temperature range between the liquid air and 110°C, and determined the quadrupole coupling constant and the asymmetry parameter by the help of Eqs. (2). The results are listed in Table II. A part of the results was already reported in the letter to the editor of the Journal of Chemical Physics.[6)]

Table II. The resonance frequencies of I^{127} in AsI_3.

ν_1 (Mc)	ν_2 (Mc)	eQq_{zz} (Mc)	η (%)	T(°K)
207.011	395.78	1328.24	18.4	83
206.76	400.02	1340.10	15.8	218
206.69	400.70	1341.48	15.4	250
206.54	401.80	1344.93	14.5	300
206.20	403.16	1348.53	13.1	383
208.45	406.96	1361.48	13.5	
211.74	412.46	1380.50	14.1	

The spectrum at 110°C showed a triplet structure. The critical temperature, above which the triplet exhibited, was about 90°C. This suggests that a phase transition occurs at this temperature and that above this temperature the crystal structure of arsenic triiodide is similar to that of arsenic tribromide which shows a triplet spectrum at any temperature.

The temperature dependencies of both frequencies, ν_1 and ν_2, and both constants, eQq_{zz} and η, are shown in Fig. 3. In this figure the scale of frequency of ν_2 is taken to be just twice of the scale of ν_1. If there were no asymmetry field, both curves of ν_1 and ν_2

would coincide. The separation of these curves indicates nonvanishing asymmetry parameter. The resonance frequency of the line ν_1 was almost constant in the range from the liquid air temperature to the room temperature, whereas the other quantities changed. The constancy of this resonance frequency comes from the fact that the increase of the coupling constant is cancelled out by the decrease of the asymmetry parameter.

The resonance absorption of the arsenic isotope in arsenic tri-iodide was unsuccessfully searched in the frequency range from 45 Mc to 100 Mc. The reason seems to be the inhomogeneity of the crystal, which was indicated by broadness of the absorption line of iodine isotope compared to that of bromine isotope in arsenic tribromide.

§ 3. Discussion of Results

(a) *Arsenic Tri-iodide*

The quadrupole coupling constant of iodine in solid arsenic tri-iodide, 1328 Mc, at the liquid air temperature, is considerably smaller than 2153 Mc of solid iodine. This discrepancy is too large to be explained by the ionic character, which is estimated as about 6 percent from the difference of electronegativity. Moreover the observed asymmetry parameter of 18.4 percent is so high that it can not be understood by the double bond character in the iodine bond. For the interpretation of these features, we consider the interaction of neighbor molecules through resonance switching.5) As shown in Fig. 1 an iodine atom has two nearest arsenic atoms at the same distance of 2.98A, one being molecular partner and the other belonging to the neighbor molecules. Since neighbors of other atoms are larger than 4.14A, we take into account only two arsenic atoms as neighbors. This picture is shown in Fig. 4, where the angle As-I-As is about 88°. If the covalent bond from a given iodine atom resonates between these two arsenic atoms with fractional importance of fifty percent, the principal axes of the field gradient tensor are as follows: the x axis is the internal bisector of the angle As-I-As and the z axis is the perpendicular to the plane of As-I-As as shown in Fig. 4. In respect to this principal axis system, the nonvanishing components of the field gradient tensor are

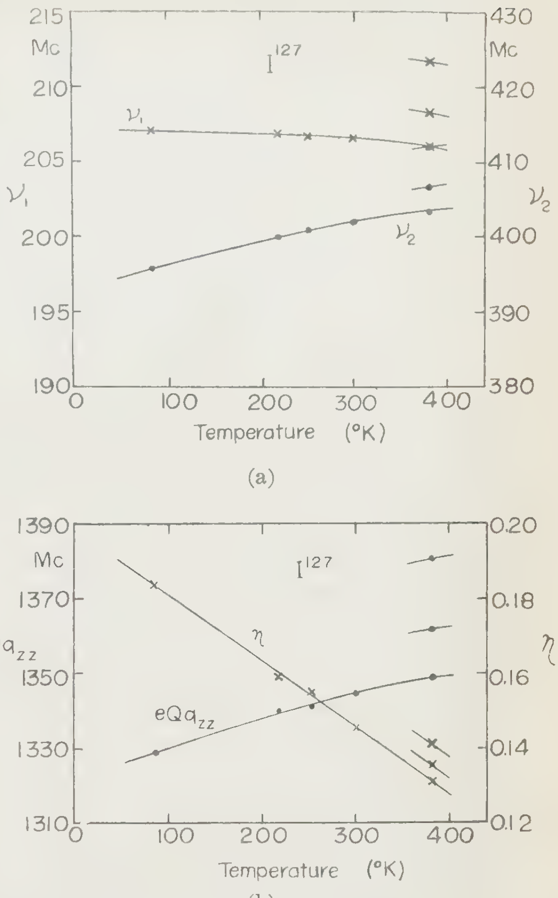

(a)

(b)

Fig. 3. (a) The resonance frequency of I^{127} in AsI_3 *v.s.* temperature.
(b) The coupling constant and the asymmetry parameter of I^{127} in AsI_3 *v.s.* temperature.

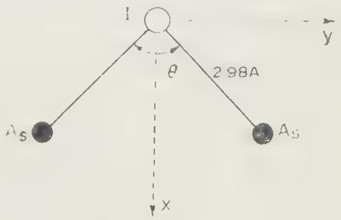

Fig. 4.

$$q_{xx} = (1/4)(1-3\cos\theta)q\,, \qquad (3)$$

$$q_{yy} = (1/4)(1+3\cos\theta)q\,, \qquad (4)$$

$$q_{zz} = -(1/2)q\,, \qquad (5)$$

where θ is the angle of As-I-As and q is the field gradient component of the iodine bond in a free molecule. Then the asymmetry parameter is expressed by

$$\eta = (q_{xx} - q_{yy})/q_{zz} = 3\cos\theta. \qquad (6)$$

The observed asymmetry parameter at the liquid air temperature gives the angle of 86°30′ and the value at the room temperature yields 87°14′, which agrees well with the value determined from the crystal structure. The quadrupole coupling constant for the iodine bond of a free molecule, eQq, is obtained by doubling the observed coupling constant eQq_{zz}, as given by Eq. 5. The result at the liquid air temperature yields eQq of 2656 Mc. Since by Pauling's formula of electronegativity, the As-I bond has partial ionic character of 6 percent, the coupling constant of iodine in a pure covalent bond would be 2815 Mc. This value is about 23 percent larger than the generally accepted value of 2292 Mc, which was determined by the atomic beam method.⁷⁾ The latter value, however, is calculated simply by doubling the coupling constant of the atom without taking into consideration the effect of overlapping of atomic orbitals. If it is taken into account, the value of 2292 Mc must be increased about 10 percent.⁸⁾ This correction being done, there still remains a discrepancy of about 12 percent. This may be interpreted by assuming a small amount of d-hydridization in the iodine bond.

Recently Robinson, Dehmelt and Gordy⁹⁾ reported that the resonance frequencies of iodine in arsenic tri-iodide, which were measured by employing the molecular addition compounds, $AsI_3 \cdot 3S_8$, gave the coupling constant of 1517 Mc and the asymmetry parameter of 0.9 percent at the liquid nitrogen temperature. These results are different from those obtained with pure arsenic tri-iodide.

(*b*) *Arsenic Tribromide*

If we can apply the same discussion on arsenic tribromide as the previous case the coupling constant for the bromine bond of a free molecule, is obtained by doubling the observed coupling constant. It yields $(eQq)_{Br^{79}}=$ 810 Mc. This is only five percent higher than the value of 770 Mc, which was determined by the atomic beam method. However, in this case the ionic character is estimated as 15 percent from the difference of the electronegativity. Then the discrepancy is almost same as in the previous case.

The coupling constant of arsenic in the symmetric top molecule of $AsBr_3$ would vanish, if the angles between bonds ∠Br-As-Br were just 90°. A simple calculation shows that the coupling constant depends on this bond angle, θ, by the following expression

$$(eQq_{zz})_{As}=3\cos\theta(eQq)_{As}(1+2\beta), \qquad (7)$$

where $(eQq)_{As}$ is the coupling constant of pure covalent arsenic bond. The factor, $1+2\beta$, represents the effect of ionic character where β is the ionic fraction.¹⁰⁾

The coupling constant of pure covalent bond of arsenic was estimated to be 600 Mc by Schüler and Marketu with the method of hyperfine structure of atomic spectra.¹¹⁾ Applying this value for $(eQq)_{As}$ and putting 0.15 for β, we have estimated the angle θ from the observed coupling constant. The result was 87° or 93°.

References

1) R. W. G. Wyckoff: *"Crystal Structures"*, Interscience Publishers, Inc., New York, (1948).

2) S. Kojima, K. Tsukada, A. Shimauchi and Y. Hinaga: J. Phys. Soc. Japan, **9** (1954) 795.

3) S. Kojima, K. Tsukada, S. Ogawa and A. Shimauchi: J. Chem. Phys. **21** (1953) 1415.

4) H. Krüger: Z. Physik **130** (1951) 371.

5) C. H. Townes and B. P. Dailey, J. Chem. Phys. **20** (1952) 35.

6) S. Kojima, K. Tsukada, S. Ogawa and A. Shimauchi: J. Chem. Phys. **21** (1953) 2237.

7) Jaccarino, King and Stroke: See reference 9) and 10).

8) K. Tsukada: **9** (1954) 872.

9) H. Robinson, H. G. Dehmelt and W. Gordy: J. Chem. Phys. **22** (1954) 511.

10) W. Gordy, W. V. Smith and R. F. Trambarulo: *"Microwave Spectroscopy"* John Wiley, Inc., New York (1953).

11) H. Schüler and M. Marketu: Z. Physik **102** (1936) 703.

Journal of the Physical Society of Japan Vol. 9, No. 5, Sep.—Oct., 1954

Zeeman Splitting of Nuclear Quadrupole Spectra of $NaBrO_3$

By Toshimoto KUSHIDA
Department of Physics, Hiroshima University
Yoshitaka KOI and Yoshiro IMAEDA
Faculty of Technology, Tokushima University

(Received May 29, 1954)

The Zeeman effect of nuclear quadrupole resonance line in a single crystal of sodium bromate is observed in the magnetic field of 3760 gauss. The Zeeman patterns for various crystallographic orientations are investigated and they are compared with the theoretical patterns. From the observed splitting the nuclear magnetic moment of Br^{79} is calculated. The value obtained is 2.1033 ± 0.0052 nuclear magnetons.

§ 1. Introduction

A nuclear quadrupole resonance line of a single crystal specimen splits into many lines when the homogeneous magnetic field is applied to the specimen. The effect, called the Zeeman effect of quadrupole spectra, has been observed by several workers in several specimens, namely para-dichloro benzene[1]), stannic iodide[2]), arsenic oxide[3]), iodine[4]), and sodium chlorate[5,6]).

The magnitude of the splitting depends on the strength of the applied field and the angle between the direction of the magnetic field and crystallographic axes. This problem has been considered by Bersohn[4]), et al. The precise comparison between the experimental splitting and the calculated one is attempted in rather a strong magnetic field with respect to the quadrupole line of Br^{79} in a single crystal of sodium bromate which has sharp and strong resonance lines and whose crystallographic structure is simple. The similar attempt has been found to be in progress in the Ohio State University with the Cl-resonance line in a single crystal of sodium chlorate[7]) by Yu Ting, et al. As the resonance frequency in our case lies in a sub-microwave region while in case of $NaClO_3$ the frequency lies in a short-wave region (about 30 Mc/sec.), our oscillator may be a little different from theirs.

§ 2. Apparatus and Experimental Procedure

The spectrograph used is an ordinary super-regenerative oscillator with 955 acorn tubes, and the frequency of the oscillator is swept slowly with a small condenser. The oscillator is frequency-modulated with a piece of metal plate which is being vibrated by a dynamic speaker. The signals are amplified with a lock-in amplifier and recorded with a recording milli-ammeter. This method is similar to the one which is often used to detect the weak nuclear magnetic resonance lines, though the magnetic field modulation is usually adopted in case of nuclear magnetic resonance absorption. The single crystal of sodium bromate, the size of which is about $20 \times 13 \times 13$ mm, is inserted into the four-turns oscillator coil, 20 mm in length and 15 mm in diameter.

Such a crystal holder is used to rotate the crystal around the axis which is perpendicular to the magnetic field that the direction of this rotating axis will become perpendicular exactly to the magnetic field direction and the direction of the crystal with respect to this axis can be changed arbitrarily while the absorption lines are being viewed on an oscilloscope screen. The very fine adjustment of the direction of the crystal is necessary because the patterns of Zeeman splitting in this specimen are very sensitive to the crystal direction. The magnetic field is applied to the specimen with an electro-magnet whose pole piece is 12 cm in diameter. The field strength is measured by means of proton magnetic resonance, and this strength is usually adjusted to such value that the proton resonance whose frequency is equal to 16 Mc/sec. exactly, is just observed in this field. Then the field strength in 3757.8 gauss. The exciting current of the electro-magnet is measured with a K-2 type potentiometer, and this value of current is kept constant during the observation of Zeeman splitting. This calibration of the magnetic field is done every day before observation of the Zeeman effect. As the preliminary experiment, it is very convenient to observe the Zeeman splitting in a weak magnetic field to see a general feature of the resonance line. This weak field is easily applied with a Helmholtz coil, and it is convenient to make the field so weak that the Zeeman splitting of the central line of the super-regenerative spectroscope does not overlap with the splittings of the side-band lines. All the Zeeman components are displayed on the recorder in 30 minutes or so by sweeping the frequency of the oscillator with a clock-motor. The separations of the observed lines are easily calculated by comparing these separations with those of the side-band lines, but the values of separations thus measured are less accurate, because these values are not so larger than the line breadth of the component lines. But the rough adjustment of the crystal direction and semi-quantitative comparison of the Zeeman splitting with the theoretical one are made conveniently by this method, before the tedious frequency measurement of each component line in the strong magnetic field.

The crystal structure of sodium bromate is cubic and a distorted NaCl type⁹⁾ in which there are four molecules in a unit cell. Each BrO_3^- ion in the unit cell has a pyramidal configuration with a three-fold axis of symmetry, and these axes lie along the directions of the four body-diagonals of the cube. In this pyramid of BrO_3^- ion, the bromine and the oxygens are bound covalently, that is to say, the bromine, after having given its two 4p electrons to the oxygens, forms a trigonal-pyramid bonding. On the other hand, the three oxygens, having accepted two electrons from the bromine and one electron from the Na^+ ion, make single bonds respectively. Of course, some double-bond structure may resonate with this structure. Speaking more precisely, the three 4p orbitals at bromine make a spherically symmetric charge distribution around the bromine nucleus, and so this type of configuration can not produce at the nucleus electric field gradient which is responsible for the pure quadrupole resonance absorption. But if these 4p orbitals are hybridized with an s orbital, these s-p hybridized orbitals produce the asymmetric charge distribution, and consequently, the electric field gradient¹⁰⁾. This type of hybridized orbitals explains the fact that pretty large quadrupole coupling exists in this salt and the O-Br-O angle in this BrO_3^- ion is larger than 90°, a value which should be expected in case of pure p orbitals. In fact the observed O-Br-O angle, 112°, is compatible with the observed magnitude of quadrupole coupling constant. But details of such a consideration will be published elsewhere.

The angle between the direction of the magnetic field and the rotation axis of the crystal holder and the angles of the crystal axis with respect to the axis of rotation are adjusted precisely to desired value by the following method.

As will be shown later on, each resonance line splits generally into four lines in the magnetic field. Though sixteen Zeeman lines might be observed generally in this specimen when the field is applied, because there are four independent directions of BrO_3^- ions in a unit cell, only twelve lines are observed in this experiment because the crystal is now so mounted as the magnetic field always lies in the (011) plane of this crystal. If the crystal and the crystal holder are mounted in the desired manner, only three lines should be observed when the field lies along [100] direction and six lines should be observed at $[01\bar{1}]$ direction, as will be shown later. This fact is used to mount the crystal. In the first place, after the crystal axis is determined by means of x-ray, it is cemented to the rod of the crystal holder as precisely as possible. Here the directions of the surface planes of the single crystal can be used to good advantage. But, in general, a small error in the mounting can not be avoided, especially the error in the direction of the rotation axis with respect to the field direction can not be avoided by any means. Then the crystal holder with the crystal mounted is so set in the magnetic field as the field direction lies nearly along [100] direction of the crystal and the center line of the expected triplet Zeeman lines is viewed in the oscilloscope screen. Not a single line but complex lines will be observed there, because the line structures vary very sensitively with the angle of the crystal. Error in the angle of the crystal mounting less than one twentieth degree is sufficient to split the desired single line into multiplet ones. The angle of the crystal with respect to the *holder* is so adjusted as the multiplet lines in the oscilloscope screen become a single line. And then more precise adjustment is done by means of the lock-in amplifier and recording meter method. Now the crystal is rotated around the axis of the crystal holder by 180°. If the axis of rotation of the holder were really perpendicular to the magnetic field, a single line would be observed again in this direction of the crystal (180° direction).

If the lines observed do not become a single line, though the crystal is rotated around the rotation axis of the holder in the neighbourhood of this angle, *both the direction of the crystal* with respect to the holder and *the rotation axis of the holder* with respect to the magnetic field direction are varied until the lines converge into a single line. This process is repeated until the single line is observed when the magnetic field lies along both 0° and 180° directions. Then the crystal is rotated by 90°. The accuracy of this angle 90° is precisely confirmed by observing the fact that the 7 or 6 line in Fig. 3 becomes a single one respectively. Now the direction of the crystal is so adjusted that the 8 or 9 line converges into single one. Thus, *the axis of rotation of the crystal* becomes exactly perpendicular to *the field direction* and parallel to *the* [011] *direction of the crystal*. The frequencies of the Zeeman component lines are measured by a heterodyne frequency-meter which is calibrated at the time of each measurement with a 100 kc-marker-signal generator. The center of each line is found on the recorded line shape in the recording meter. If the center frequency is just reached, when the frequency is swept very slowly, the frequency sweeper is stopped sweeping then, and the frequency is measured quickly. It is necessary to keep the temperature of the specimen constant, while each component of a set of the Zeeman lines is measured, for the center of gravity of a set of these lines depends on the temperature of the specimen, that is to say, if this specimen, is cooled from the room temperature to the dry-ice temperature, the resonance frequency without field increases by about 1 Mc/sec. The center of gravity of these lines is equal in frequency to the resonance line without field, and so depends on the temperature, but the magnitude of the Zeeman splitting is independent of the temperature if the asymmetric parameter $\mathcal{E}$ is zero.

§ 3. Result Obtained and Discussion

The interaction-energy levels between a nuclear quadrupole and the static crystalline field split into the following levels in the magnetic field:

$$\left.\begin{aligned} E_1&=\frac{eQ\varphi_{zz}}{4I(2I-1)}\{3(\tfrac{1}{2})^2-I(I+1)\}\\ &\quad+\frac{1}{2}\frac{\mu}{I}H\sqrt{(I+\tfrac{1}{2})^2\sin^2\theta+\cos^2\theta}\ ,\\ E_2&=\frac{eQ\varphi_{zz}}{4I(2I-1)}\{3(\tfrac{1}{2})^2-I(I+1)\}\\ &\quad-\frac{1}{2}\frac{\mu}{I}H\sqrt{(I+\tfrac{1}{2})^2\sin^2\theta+\cos^2\theta}\ ,\\ E_{\pm mz}&=\frac{eQ\varphi_{zz}}{4I(2I-1)}\{3m_z^2-I(I+1)\}\\ &\quad\pm m_z\frac{\mu}{I}H\cos\theta \qquad m_z>\tfrac{1}{2}\ , \end{aligned}\right\} \tag{1}$$

where the usual notation is used; E_1 and E_2 are the energy levels which reduce to ±1/2 levels when the applied field is removed, and θ is the angle between the direction of the magnetic field and that of the maximum electric field gradient. The fact that the asymmetric parameter $\mathcal{E}(=\varphi_{xx}-\varphi_{yy}/\varphi_{zz})$ is zero in this specimen is used when the Eqs. (1) are derived. As the spin of the observed nucleus Br^{79} in this specimen is 3/2, four lines should be observed in the magnetic field, corresponding to the transitions $\pm 3/2 \rightleftarrows 1, 2$, but these lines reduce to a single line, when the magnetic field is removed. The values of this Zeeman splitting, namely, the separations of these four lines from the frequency of the line which should be observed when the field is not applied, are:

$$\left.\begin{aligned} h\nu_1&=\frac{1}{2}\frac{\mu}{I}(\sqrt{4\sin^2\theta+\cos^2\theta}-3\cos\theta)\ ,\\ h\nu_2&=\frac{1}{2}\frac{\mu}{I}H(\sqrt{4\sin^2\theta+\cos^2\theta}+3\cos\theta)\ ,\\ h\nu_3&=\frac{1}{2}\frac{\mu}{I}H(-\sqrt{4\sin^2\theta+\cos^2\theta}-3\cos\theta)\ ,\\ h\nu_4&=\frac{1}{2}\frac{\mu}{I}H(-\sqrt{4\sin^2\theta+\cos^2\theta}+3\cos\theta)\ . \end{aligned}\right\} \tag{2}$$

These separations are shown in Fig. 1.

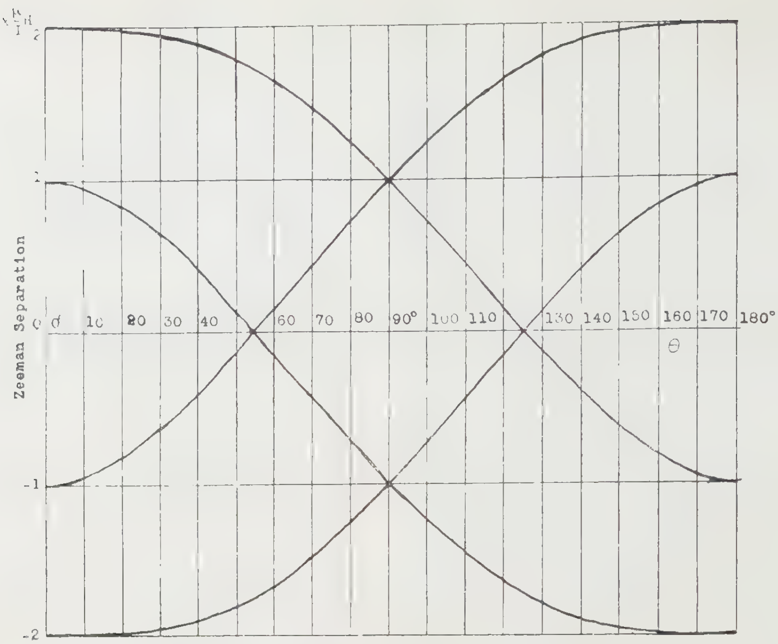

Fig. 1. The Zeeman separation of pure quadrupole resonance line in the case of spin 3/2. θ: the angle between the direction of the maximum electric field gradient and that of the applied magnetic field.

The relative intensities of these lines are also calculated easily, because these are proportional to the squares of the matrix elements of I_x concerning to the initial and final states, $(\psi_{1,2}|I_x|\psi_{\pm 3/2})^2$. These values are also shown in Fig. 2.

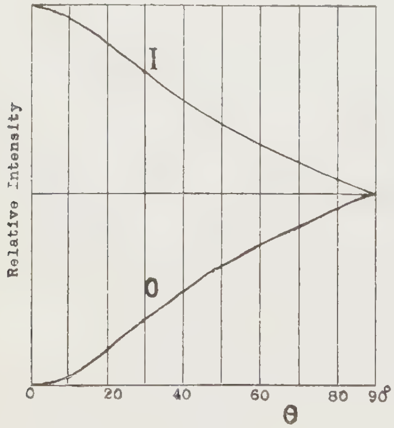

Fig. 2. The relative intensity of the Zeeman components. I and 0 are the intensity for the inner and the outer lines respectively in Fig. 1.

As there are four independent directions of φ_{zz} in this specimen as stated in § 2, namely $[1\bar{1}1]$, $[111]$, $[1\bar{1}\bar{1}]$, and $[11\bar{1}]$, and the direction of the rotation axis of the crystal is along $[011]$ which is perpendicular to the magnetic field, the field direction lies in (011) plane which contains both φ_{zz} along $[1\bar{1}1]$, α and φ_{zz} along $[11\bar{1}]$, γ. The φ_{zz}'s along $[111]$ and $[1\bar{1}\bar{1}]$, β and β' behave equally during the rotation of the crystal. If the origin of the rotation angle Θ is chosen $[1\bar{1}1]$, the separations between each pair of lines shown (2) are:

$$\left.\begin{aligned} h\Delta\nu_{\alpha} &= \frac{1}{2}\frac{\mu}{I}H\{\sqrt{4-(\cos\Theta-\sqrt{2}\sin\Theta)^2} \\ &\quad \pm\sqrt{3}(\cos\Theta-\sqrt{2}\sin\Theta)\}\,, \\ h\Delta\nu_{\beta,\beta'} &= \frac{1}{2}\frac{\mu}{I}H\{\sqrt{4-\cos^2\Theta} \\ &\quad \pm\sqrt{3}\cos\Theta\}\,, \\ h\Delta\nu_{\gamma} &= \frac{1}{2}\frac{\mu}{I}H\{\sqrt{4-(\cos\Theta+\sqrt{2}\sin\Theta)^2} \\ &\quad \pm\sqrt{3}(\cos\Theta+\sqrt{2}\sin\Theta)\}\,, \end{aligned}\right\} \tag{3}$$

where $\Delta\nu_{\alpha}$ is the separations due to φ_{zz} along α and so on. These values and observed values are shown in Fig. 3, where the dots with numbers 1, 2,.... indicate the observed values, and the symbols Δ show the values which are obtained by the preliminary experiment in the Helmholtz coil and are converted

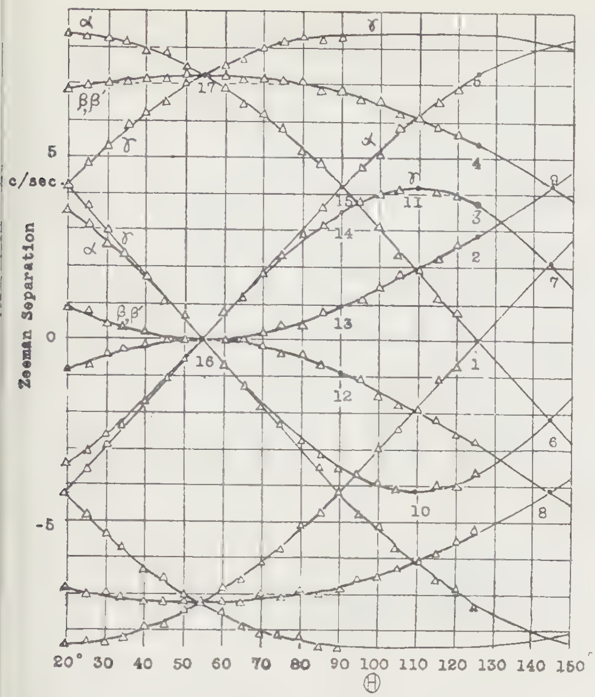

Fig. 3. The Zeeman separation of Br^{79} in the single crystal of $NaBrO_3$. The field strength is 3757.8 gauss which is measured by means of proton resonance. The axis of rotation of the crystal lies along [011] which is perpendicular to the magnetic field direction. Θ is the angle between the direction of the magnetic field and that of $[1\bar{1}1]$. α, β, β', and γ denote the lines due to $\varphi_{zz}{}^{\alpha}$, $\varphi_{zz}{}^{\beta}$, $\varphi_{zz}{}^{\beta'}$, and $\varphi_{zz}{}^{\gamma}$ respectively.

△: the values obtained by the less-accurate preliminary experiment.

· : the values obtained in the strong field, and these values are used to calculate the magnetic moment of Br^{79}.

to the values in the stronger magnetic field in which the values of dots are observed.

From the values shown by the dots, the nuclear magnetic moment of Br^{79} is calculated:

$$\mu = 2.1033 \pm 0.0052 \quad \text{(nuclear magnetons)}.$$

This result is in excellent agreement with the value 2.10576±0.00037 obtained by means of magnetic resonance. The outer components of α lines and γ lines can not be observed in the neighbourhood of $\Theta = 54°44' \times 2$. This fact is expected from the calculated transition probabilities. (Fig. 2)

It is a pleasure to express our indebtedness to Professor Hideo Tazaki for the stimulating interest he has taken in the progress of this work. This work has been done by the financial aid of the Educational Ministry.

References

1) C. Dean: Phys. Rev. **86** (1952) 607.
2) H. G. Dehmelt: Z. Physik **130** (1951) 356.
3) H. Krüger and U. Meyer-Berkhout: Z. Physik **132** (1952) 221.
4) R. Bersohn: J. Chem. Phys. **20** (1952) 1505.
5) K. Shimomura and T. Kushida: to be published.
6) R. Livingston: Science **118** (1953) 61.
7) Y. Ting, E. Maning, and D. Williams: Phys. Rev. **92** (1953) 1581.
8) H. Krüger: Z. Physik **130** (1951) 371.
9) R. W. G. Wyckoff: *Crystal Structure*, vol. 1 (1951). Interscience Pub. N. Y.
10) W. Gordy, W. V. Smith, and R. F. Trambarulo: *Microwave Spectroscopy*, (1953) 281. John Wiley and Sons, Inc. N. Y.

Journal of the Physical Society of Japan Vol. 9, No. 5, Sep.—Oct., 1954

Paramagnetic Resonance Absorption in $K_2CuCl_4 \cdot 2H_2O$

By H. Abe, K. Ôno, I. Hayashi, J. Shimada
and K. Iwanaga

Institute of Science and Technology, University of Tokyo

(Received June 21, 1954)

Single crystals of $K_2CuCl_4 \cdot 2H_2O$ and $(NH_4)_2CuCl_4 \cdot 2H_2O$ were examined at 7 different frequencies of microwaves (from 5.4 mm to 6.2 cm wave-lengths). If there were no exchange coupling, two absorption peaks would be expected corresponding to different g-values of two dissimilar Cu^{++} ions in unit cell. Experimentally, however, only one peak can be observed at longer wave-lengths, though the line width remarkably increases with decreasing wavelengths. At the wave-length of 5.4 mm two isolated peaks can be observed. These facts can be interpreted in terms of exchange interaction between dissimilar ions. The exchange energy estimated from these data is greater than $0.1\,\mathrm{cm}^{-1}$. On the other hand, the width for the c-axis, where the situations of two Cu^{++} groups are identical, decreases with decreasing wavelengths to aboutthe value 1/4 of that at long enough wave-length. According to the treatment by Anderson and Weiss, this result may be explained by their "10/3" effect.

§ 1. Introduction

After the first experiment by Zavoisky[1], many experiments on paramagnetic microwave resonance absorption have been achieved to study the behaviours of paramagnetic ions in crystals. These works can be roughly divided into following two groups. The first is the works with the aim of clarifying the nature of interactions between magnetic ions and between the ions and the surrounding atoms[2],[3],[4],[5]. The second is the works related to the nuclear hyperfine structure, measured in magnetically diluted crystals[6],[7]. The present work belongs to the former. Single crystals of the potassium cupric chloride dihydrate $K_2CuCl_4 \cdot 2H_2O$ and ammonium cupric chloride dihydrate $(NH_4)_2CuCl_4 \cdot 2H_2O$ are examined with special attention to obtain correct line shapes and line widths, in order to study the influence of the exchange coupling between ions on the shape of resonance absorption line.

When a crystal containing paramagnetic ions is placed in a magnetic field H_s, it absorbs the microwave energy having the frequency ν with the relation

$$h\nu = g\beta H\,, \qquad (1)$$

where h is the Planck constant, β the Bohr magneton, H the strength of magnetic field H_s, and g is the Landé factor usually called g-value. This relation means that the absorption occurs when the Larmor frequency of spinning electron under the static magnetic field H_s coincides with the microwave frequency used. The g-value for Cu^{++} ion is slightly different from that of free electron, 2.00, on account of spin-orbit coupling and crystalline electric field acting on the ion. The g-value has a tensor charactor whose axes are attached to the crystalline field.

Generally, if unit cell of the crystal contains more than one paramagnetic ions and these ions have inequivalent g-tensors in space, then, more than one absorption lines would be expected corresponding to the number of inequivalent ions in the unit cell. But, in actual case, only one line can be observed at lower frequencies by the existence of the exchange coupling between paramagnetic ions, as in the cases of $CuCl_2 \cdot 2H_2O$[8] and $CuSO_4 \cdot 5H_2O$[9]. As the result of the unifying effect of the exchange coupling, we can not observe the individual lines but only one line at about the mean position of them. When sufficiently high frequency is available, however, the individual lines corresponding to the dissimilar Cu^{++} ions can be observed separately. These facts have, for the first time, been proved experimentally by Bagguley and Griffiths in $CuSO_4 \cdot 5H_2O$[9].

Absorption lines have widths spreading over both sides of the peak given by Eq. (1). These widths are originated or modified by the followings. (1) The dipole-dipole interaction, the influence on the magnetic moment of ions by the magnetic field produced by the surrounding magnetic ions. (2) The spin-lattice relaxation, namely the coupling between the paramagnetic ions and thermal lattice vibration. (3) The fine and the nuclear hyperfine structure. (4) The exchange coupling between ions which brings out either "exchange narrowing" or "exchange broadening." In the present paper the term width means twice the deviation in magnetic field measured from the central peak, for which the absorption has dropped to half its maximum.

The preliminary data of this work have been already reported[10),11)]. The measurement on the same crystal at longer wave-length has been performed at Itoh's laboratory in Osaka University[8)].

§ 2. Experimental Methods and Techniques

Our measurements have been performed in the following order in wave-lengths; $\lambda=3.01$ cm, 16.5 mm, 7.7 mm, 5.4 mm, 6.2 cm, and then 6.5 mm and 11 mm. The methods adopted for the absorption measurements were not always quite the same for these wave-lengths. But, throughout this work, the main microwave circuit was always the transmitting cavity method and special attention was paid to put a microwave attenuator in front of the sample cavity to secure the correct shape of absorption line. Brief notes will be given in the followings concerning the apparatus for different wave-length.

$\lambda=3$ cm : The detailed description of this apparatus has been given elsewhere[12)].

$\lambda=16$, 11 and 7.7 mm : The block diagram of the apparatus for these wave-lengths is shown in Fig. 1. From second to fourth harmonics of the fundamental oscillation ($\lambda=3$ cm) from the 2K25-type klystron K were obtained by the aid of harmonics multiplier H using a silicon crystal diode. As to the multiplier crystal and detecter D for these frequencies, it is essentially required that the crystal should be constructed with a silicon wafer and a tungsten "cat-whisker" within each wave guide. The cross-section of multiplier H is shown in Fig. 2.

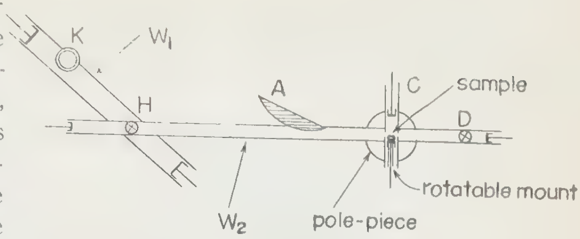

Fig. 1. Block diagram of the apparatus for $\lambda=16\sim8$ mm.

K =2K25-type klystron
H =harmonics multiplier
W_1=waveguide for $\lambda=3$ cm
W_2=waveguide for harmonics
A =attenuator
C =measuring cavity
D =detector

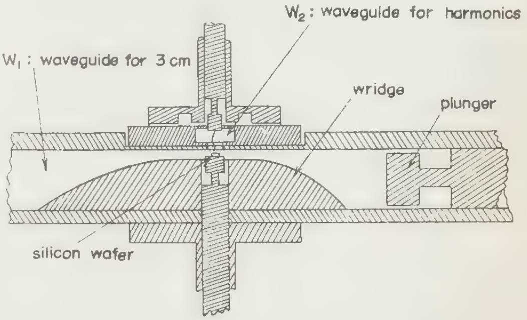

Fig. 2. Schematic cross-section of harmonics multiplier.

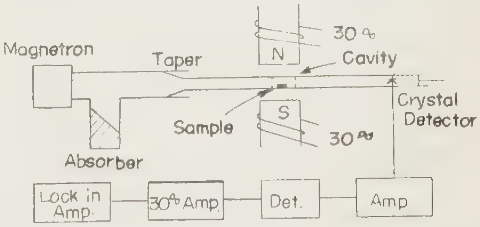

Fig. 3. Schematic diagram of apparatus at $\lambda=5.4$ and 6.5 mm employing magnetron harmonics.

$\lambda=6.5$ mm and 5.4 mm : The block diagram for these wave-lengths is shown in Fig. 3. The high power pulse magnetron M (peak power 50 KW) of wave-length 3 cm emits harmonics besides the fundamental oscillation[13)]. We can use each harmonics up to the sixth. The magnetron is operatated with a pulse length about one micro-second and a repetition rate of about 1000 per second. The detector is a demountable one just as that for $\lambda=16\sim8$ mm.

$\lambda=6.2$ cm : The oscillater is an ordinary 2K55-

type klystron. The output current of the crystal detector is measured by a micro-ammeter. As the absorption is weak at such longer wave-length, the cavity for this frequency is specially constructed as shown in Fig. 4; with this cavity, we can perform the experiment with samples of the same size as in $\lambda=3$ cm.

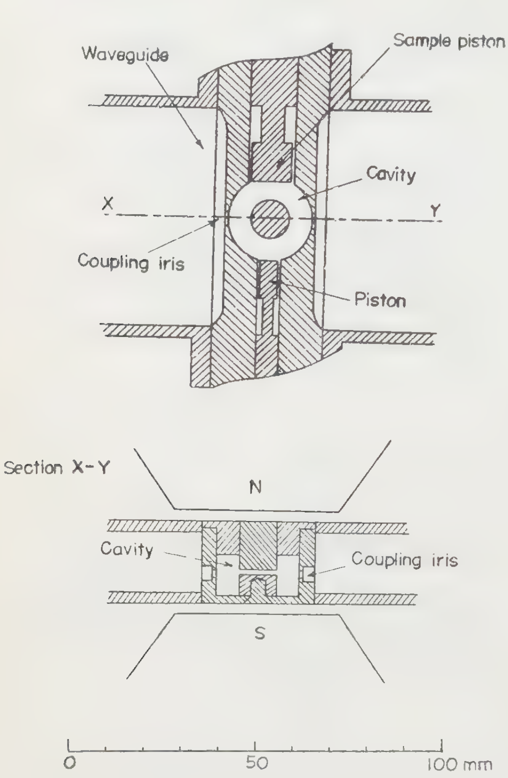

Fig. 4. Cavity resonator for 6.2 cm wave.

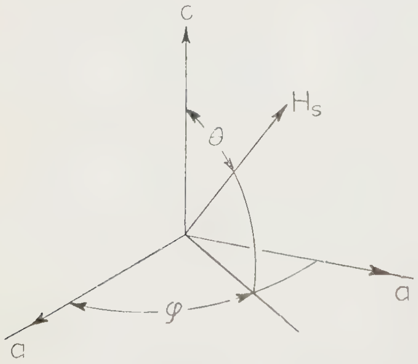

Fig. 5. Definition of θ and φ.

In all of these cases, the microwave magnetic field is perpendicular to the static one. The sample crystal attached to the mount in the end plunger of the measuring cavity is always rotated in the plane of the static and micro-wave magnetic fields.

The static magnetic field is produced by electromagnets. Their *H-I* curves, *i.e.* the relations between the strength of magnetic field and the exciting current, were determined either by the proton resonance method directly or by a fluxmeter calibrated by the proton resonance.

The determination of g-values was performed by comparing the magnetic field for absorption peak of the sample to that of $MnSO_4 \cdot H_2O$ powder ($g=2.0$, $\Delta H=305$ oer.)[14] in earlier experiments but, now, α-diphenyl β-picryl hydrazyl ($g=2.00$, $\Delta H=$several oer.) is used as the measure $g=2.0$. The chief origin of errors of g-values is the error in reading fluxmeter when the *H-I* curve of the electromagnet was measured, the curve being not quite linear. So the error in the g-value is smaller when the g-value is near to 2.00.

§ 3. Results and Discussions

1. *On the Sample*

The potassium copper chloride dihydrate $K_2CuCl_4 \cdot 2H_2O$ is the double salt of $CuCl_2$ and KCl, and $(NH_4)_2CuCl_4 \cdot 2H_2O$ is that of $CuCl_2$ and $(NH_4)Cl$. The single crystals of them can be obtained from the mixed solution of their component substances. Their suitable ratio is determined by the mode curve. The former is of light green and the latter light blue. The crystal symmetry of these two salts is tetragonal[15] and their *X*-ray data were given by Chrobak[16],[17],[18]. Frequently, these crystals grow in twins. Used samples were all optically checked and were found to be free from twins. Terms "*crystal axes*" in this report are identical with the crystallographic ones used by Chrobak but not the morphological ones by Groth[15] which are rotated by 45° about the *c*-axis from our axes. The direction of static magnetic field is expressed by θ and φ, where θ is the angle between the *c*-axis and the static field H_s and φ the azimuthal angle of H_s from an *a*-axis, as shown in Fig. 5. In this report the bisecter of the angle between the two *a*-axes is labelled as γ-direction for convenience.

The *X*-ray analysis[16],[18] shows that each unit cell ($a=7.45$ Å, $c=7.88$ Å for potassium salt and $a=7.58$ Å, $c=7.95$ Å for ammonium salt) contains two Cu^{++} ions as shown in

Fig. 6. One Cu^{++} ion is at the origin (0, 0, 0) and the other at the body centre (1/2, 1/2, 1/2). Each ion is surrounded by four chlorine atoms forming a rhomb in the *aa*-plane and by two water molecules located on the normal of this plane passing the ion.

Then the Cu^{++} ion may be acted by a crystalline electric field of rhombic symmetry and its *g*-tensor must be also rhombic. Each unit cell contains two rhombs of chlorines. One of these rhombs has its major diagonal in the γ-direction namely (110) direction, and can be derived from the other by a rotation of 90° about the *c*-axis accompanied by a translation, as shown in Figs. 7 and 8.

2. *On the Moments of Absorption Lines*

In order to compare our results to Van Vleck's theory[19] of dipolar broadening in the moment expression, some trials were made at $\lambda=3$ cm and 1.6 cm. The *n*-th moment of an absorption line is defined by

$$\langle (H-H_0)^n\rangle_{AV}=\frac{\int_0^\infty A(H-H_0)^n dH}{\int_0^\infty A\,dH}, \qquad (2)$$

where A is the absorption coefficient at the magnetic field H and H_0 is the field of the peak. From experimental point of view, it is very difficult to obtain these quantities in micro-wave measurements for usual paramagnetic crystals, because, for this purpose, very accurate measurements of weak absorption coefficients at the wings are necessary rather than measurements of strong ones near the peak. Small experimental errors at the absorption wings caused by the fluctuation of

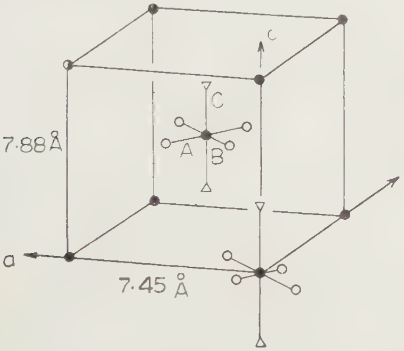

Fig. 6. Atomic arrangement of $K_2CuCl_4\cdot 2H_2O$ (Positions of K atoms are omitted for simplicity).

• =Cu $A=2.95$Å
o =Cl $B=2.32$Å
△=O $C=1.97$Å

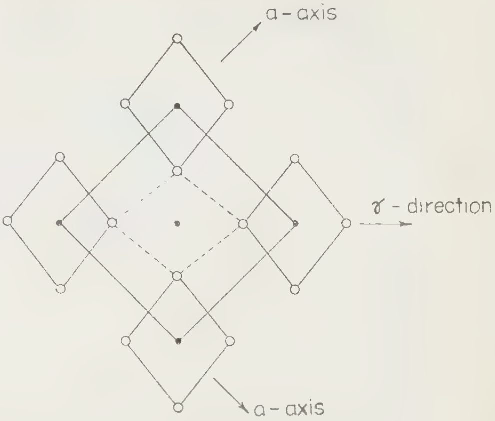

Fig. 7. Atomic arrangement projected on an *aa*-plane. Rhomb shown by dotted line lies in the upper plane by 1/2 *c*-unit.

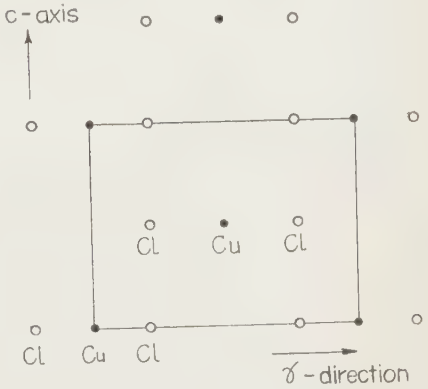

Fig. 8. Atomic arrangement within $c\gamma$-plane.

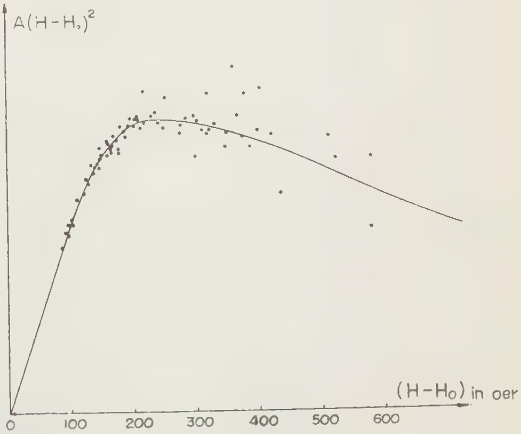

Fig. 9. One of results obtained attempting to determine the second moment.

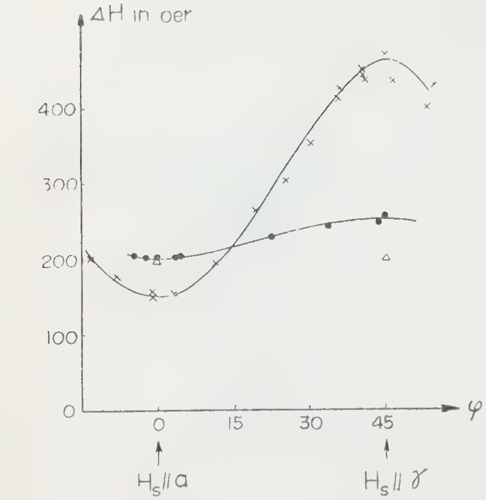

Fig. 10. Variation of line width in the aa-plane.
(△···λ=10 cm, ●···λ=3 cm, ×···λ=16 mm)

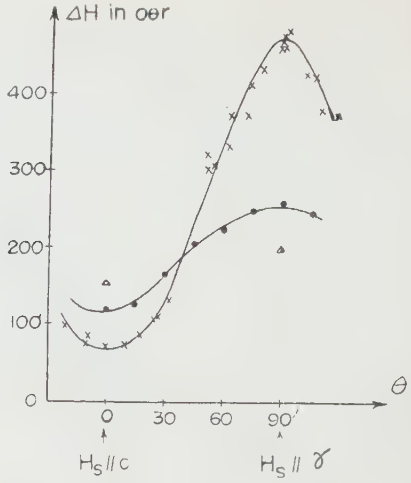

Fig. 12. Variation of line width in the γc-plane.
(△···λ=10 cm, ●···λ=3 cm, ×···λ=16 mm)

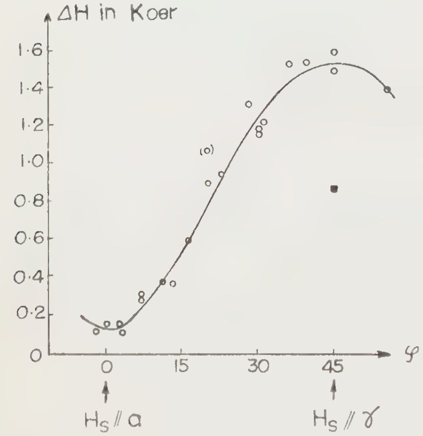

Fig. 11. Variation of line width in the aa-plane.
(■···λ=11 mm, ○···λ=8 mm)

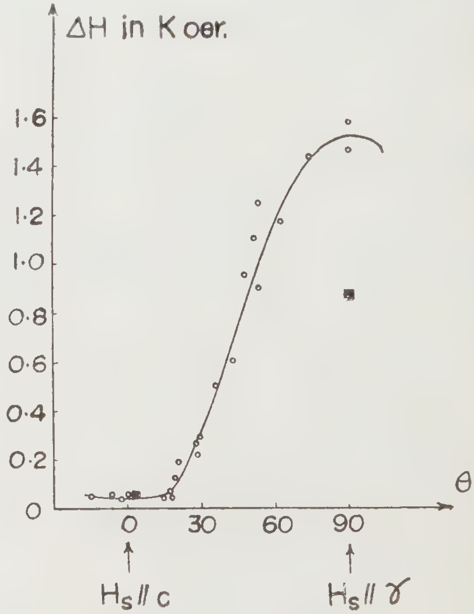

Fig. 13. Variation of line width in the γc-plane.
(■···λ=11 mm, ○···λ=8 mm)

the apparatus will greatly change the final result and, in some cases, will make it diverge. For example, one of the results for the second moment is shown in Fig. 9, where the static field is in the a-axis of this crystal and the wave-length is 16.5 mm. In the figure, the ordinate is the integrand $A(H-H_0)^2$ in the numerator of Eq. (2), and the abscissa is $(H-H_0)$. In these results, we could not find any clear tendency that the integrand comes to zero and so the integral converges to some value within the measured range of H. A conclusion which we can deduce from these data is that the line shape in this sample agrees well, within the experimental errors, with the Lorentzian type or the resonance type expressed as

$$A \propto \frac{1}{1+a(H-H_0)^2}\,, \tag{3}$$

in the measurable region, so far as the wave-lengths 3 cm and 1.6 cm are used, because A in Eq. (3) is inversely proportional to $(H-H_0)^2$, at large $(H-H_0)$, and $A(H-H_0)^2$ is independent of $(H-H_0)$.

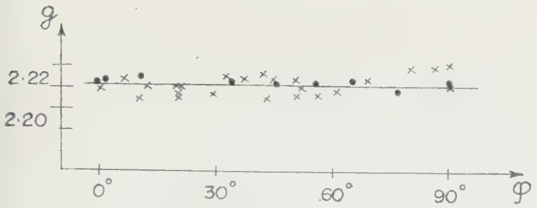

Fig. 14a. Observed g-values in the aa-plane.
(● ··· $\lambda = 3$ cm, × ··· $\lambda = 16$ mm)

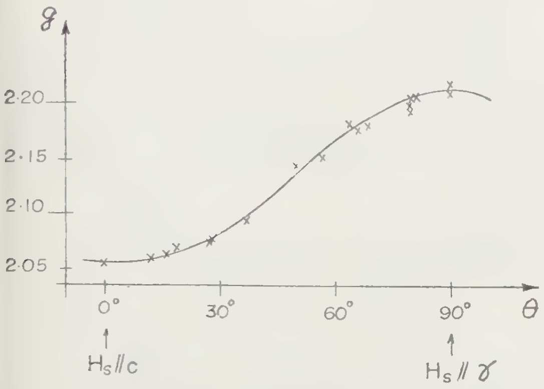

Fig. 14b. Observed g-values in the γc-plane.
($\lambda = 16$ mm)

On the other hand, as a rough measure of dipolar contribution to the width, the "dipolar width" of this crystal were tentatively estimated using the relation[19] derived under the assumption that the line shape is Gaussian, though the observed line shape is not actually Gaussian. The calculated results are 250 oer. for H_s in c-axis, 290 oer. in a-axis and 380 oer. in γ-direction, and they are shown in Table I for comparison with experimental widths.

3. *Observed Line-Widths*

We could obtain only one peak at $\lambda = 10$ cm[8] and $\lambda = 6.2$, 3.0, 1.6[10], 1.1 and 0.8 cm[11] with a remarkable frequency dependence of line-widths. This may be ascribed to the exchange coupling between the dissimilar ions. The observed line-widths at these frequencies in the aa-plane are shown in Figs. 10 and 11 and those in the γc-plane in Figs. 12 and 13. In Fig. 14 the observed g-values are also plotted which give $g = 2.06$ in the c-direction and $g = 2.22$ in any directions perpendicular to the c-axis independent of the azimuthal angle φ. The g-values are independent of the frequency used within the experimental errors.*

4. *Discussion on Line-Widths in the γ-Direction*

The width is the broadest when the H_s is in the γ-direction where the difference between the two Zeeman energies is the largest. The results of repeated measurements in this direction are listed in Table I and plotted in Fig. 15 which increase rapidly with decreasing wave-length.

Table I. The line widths of $K_2CuCl_4 \cdot 2H_2O$ at various wave-lengths used.

λ in cm	ΔH with H_s along γ-direction	ΔH with H_s along c-axis
10 *	200	150
6.23	240 ± 10	175 ± 10
3.01	250 ± 10	115 ± 5
1.65	470 ± 25	80 ± 10
1.09	870 ± 100	65 ± 10
0.77	1500 ± 100	40 ± 10
0.65	~1900	40 ± 10
0.54	two maxima ~1000	40 ± 10
calculated dipolar width**	380	250

* See ref. 20.
** See § 3.2 in the text.

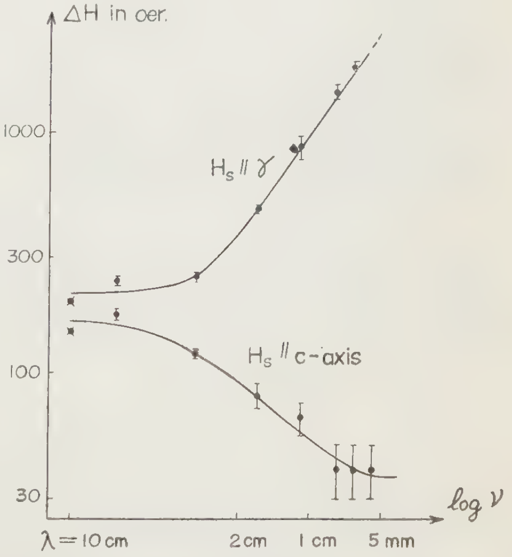

Fig. 15. Frequency dependence of line widths ΔH in $K_2CuCl_4 \cdot 2H_2O$ resonance absorption.

---

* In our earlier note[10] the g-values obtained in the aa-plane at $\lambda = 16.5$ mm were reported as about 1% higher than the present results, but it was a mistake originated from a rough calibration of the magnetic field.

When the wave-length is further reduced, we obtain separated peaks at $\lambda=5.4$ mm. Even at $\lambda=7.7$ mm, there exist some indications of two peaks, since the top of the absorption curve is very flat. The absorption curves at $\lambda=7.7$ mm, 6.5 mm and 5.4 mm are shown in Fig. 16.

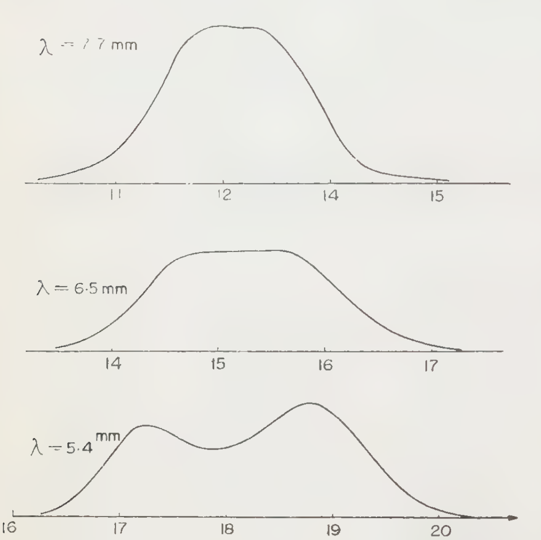

Fig. 16. Absorption curves of $K_2CuCl_4 \cdot 2H_2O$ in γ-direction at $\lambda=7.7$, 6.5 and 5.4 mm.

If there is no exchange coupling between ions, two resonance peaks should be observed separately at ω_1 and ω_2 with the fixed magnetic field H, corresponding to the two types of ions with different g-values, g_1 and g_2 respectively, under the following relations,

$$\left.\begin{aligned}\hbar\omega_1&=g_1\beta H\,,\\ \hbar\omega_2&=g_2\beta H\,,\end{aligned}\right\} \qquad (4)$$

according to Eq. (1). The difference in the Zeeman energies of these ions ΔW_z is expressed by

$$\Delta W_z=(\Delta g)\beta H\,, \qquad (5)$$

where

$$\Delta g=|g_1-g_2|\,. \qquad (6)$$

It is expected that the observed line shape will depend on whether the exchange energy $2J$ is greater or smaller than the difference ΔW_z between the Zeeman energies of two dissimilar ions. In the former case, where $2J>\Delta W_z$, only one peak is expected because of the unifying effect of the exchange coupling. In the latter case, where $2J<\Delta W_z$, namely the energy corresponding to the beat frequency between the Larmor frequencies of dissimila ions is larger than the exchange energy, tw separated peaks should be expected. For sufficiently high frequencies, two observed peaks should show the individual g-values, g_1 and g_2.

Since there is some indication of separated peaks at $\lambda=7.7$ mm, let us assume that ΔW_z for this frequency equals to the exchange energy.

Then,

$$2J\approx(\Delta W_z)_{\lambda=7.7\,\mathrm{mm}}\,. \qquad (7)$$

For the evaluation of this (ΔW_z) with Eq. (5), we shall use the difference of g-values obtained from the experimental result in the γ-direction at $\lambda=5.4$ mm, though it may be smaller than the true Δg which may be obtained at sufficiently high frequencies. Therefore,

$$\begin{aligned}2J&\gtrapprox(\Delta g)_{\lambda=5.4\,\mathrm{mm}}\cdot\beta\cdot(H)_{\lambda=7.7\,\mathrm{mm}}\\ &=(\Delta g)_{\lambda=5.4\,\mathrm{mm}}\;(h\nu/g_m)_{\lambda=7.7\,\mathrm{mm}}\,,\end{aligned} \qquad (8)$$

where g_m is the mean of g-values. Since $g_1=2.30_0$ and $g_2=2.10_5$ were obtained at $\lambda=5.4$ mm, we have $\Delta g=0.19$, $g_m=2.20$ and $h\nu=1.3\ \mathrm{cm}^{-1}$. Using these values, we can estimate the exchange energy as follows

$$2J\gtrapprox0.1\ \mathrm{cm}^{-1}\,. \qquad (9)$$

From the results of the static susceptibility measurements by Guha[21] at the temperature range from 290°K to 85°K, the Curie temperature Θ of $(NH_4)_2CuCl_4\cdot 2H_2O$, whose behavior in the paramagnetic resonance absorption is almost the same as the potassium salt, is obtained to be 16°∼18°K after an extraporation. A rough estimation of the exchange energy, $2J$, may be given by the relation[22]

$$3k\Theta\simeq2J\cdot zS(S+1)\,, \qquad (10)$$

which, in the case of Cu^{++} ion ($S=1/2$), reduces to

$$k\Theta\simeq(1/2)Jz\,, \qquad (11)$$

where z means the number of the nearest neighbours. In our case z is assumed to be 8, then we have

$$2J\simeq10\ \mathrm{cm}^{-1}\,, \qquad (12)$$

which is much larger than our result.

There may be some different circumstances from the case of the copper sulphate pentahydrate $CuSO_4\cdot5H_2O$. Bagguley and Griffiths[8] were themselves able to estimate, in this crystal, the exchange energy from the frequency at which they could resolve certain lines owing to the two dissimilar Cu^{++} ions in unit cell. This estimated value well agrees with the exchange energy estimated from Curie temperature within 15%.

In the case of resolved peaks obtained at $\lambda=5.4$ mm, there are two notable facts. One is that the two resolved peaks are not remarkably different in width (~900 oer. for the lower field peak and ~1140 oer. for the upper.) The other is that the resolved lines have rather broader line widths than that expected. This may be ascribed to the effect of exchange broadening between dissimilar ions.

5. *Discussions on Line-Widths in the c-Direction*

The frequency dependence of line widths with H_s along the c-axis is also given in Table I and in Fig. 15. It must be noted that the Larmor frequencies of two ions belonging to the different groups just coincide in this case and that the measured width decreases slowly with increasing frequency.

Recently, Anderson and Weiss[23] published a new theory on the line shape of the paramagnetic resonance absorption which is useful to account for the behavior of the observed line-widths under the influence of exchange coupling. They discussed their conclusion in connection with experimental results of many powdered crystals and of the single crystal of $CuSO_4 \cdot 5H_2O$. By their theory, the above mentioned narrowing may be attributed to their "10/3 effect." When the exchange frequency ω_e (about $J/\hbar$) is larger enough than the resonance frequency ω_0, both being larger than the dipolar frequency ω_p (about dipolar interaction divided by $\hbar$), namely $\omega_e \gg \omega_0 \gg \omega_p$, the exchange interaction introduces a new effect. It makes the line-width larger by a factor of roughly 10/3, under the assumption of cubic lattice, than that expected to be observed with the higher frequency satisfying the condition $\omega_0 \gg \omega_e$. Here the broadening by the fine and hyperfine splittings is not taken into account.

The width obtained in the c-direction is 150 oer. at the wave-length of 10 cm and about 40±10 oer. at 5.4 mm, which bring the ratio of 3~5. The agreement of this ratio with the above-mentioned theoretical value, 10/3, is fairly satisfactory, since they assumed the cubic lattice and neglected the hyperfine effect etc.* This narrowing phenomenon in this crystal is more remarkable than that of $CuSO_4 \cdot 5H_2O$[7),24)] where the observed ratio is about 3/2.

Another result of their theory is that the expected line shape in case of $\omega_e \gg \omega_p$ is of the Lorentzian type as far as the neibourhood of the central peak is concerned, which is also in good agreement with our experimental results.**

Recently an equivalent theory in another mathematical expression was developed by Kubo and Tomita[25]. Tomita[26] applied their theory to this narrowing phenomenon, taking the atomic structure of this crystal into account and tried to explain the frequency dependence of widths in c-direction giving the value of 0.09 cm^{-1} as the exchange energy $2J$, which is contained in their expression as an adjustable parameter. This exchange energy agrees well with 0.1 cm^{-1} obtained in our experiments in γ-direction, but this agreement is rather accidental, because in his computaticn both the tensor character of g and the hyperfine structure are neglected.

6. *Other Remarks*

As for the broadening from the hyperfine structure effect, we have no reliable knowledge to discuss. As the usual experimental procedure to study the nuclear hyperfine structure by microwaves, "diluted" crystals are used. For example, in case of Cu^{++} ion in $CuK_2(SO_4)_2 \cdot 6H_2O$, a part of Zn^{++} ions in its isomorphous crystal $ZnK_2(SO_4)_2 \cdot 6H_2O$ is replaced by Cu^{++}. Since the distances between Cu^{++} ions in this "diluted" crystal are very large and the dipole-depole interaction becomes neglegible, observed discrete lines bring us the knowledge about the hyperfine structure. But, unfortunately, our samples can not be "diluted," because there is no isomorphous crystal of them.

The broadening from spin-lattice relaxation should be also responsible to the observed width. In this crystal, however, it may not be considered to affect greatly the frequency dependence of widths in γ-direction, since the minimum width in the c-direction is 40 oer. So the measurements in lower temperature, if they were performed, would only slightly change our results on the frequency dependence of widths in the γ-direction.

---

* The fine structure vanishes in this case of Cu^{++} ion which has an electron spin of 1/2.

** *Note added in proof*: After this paper was prepared, Anderson's more detailed article was published, in which he discussed the line shape and its narrowing under exchange coupling.

P. W. Anderson: Jour. Phys. Soc. Japan **9** (1954) 316.

Acknowledgements

The authors wish to express their sincere thanks to Professor Hiroo Kumagai for his continuous guidance. They wish to thank Professor R. Kiriyama and his coworkers at the Osaka University for their preparation of the samples used. They also express their thanks to Mr. H. Osafune of the Nippon Electric Co., Ltd. who supplied a part of silicon wafers, to Mr. Y. Yasuoka and coworkers of the Japan Radio Co., Ltd. for the pulse-type magnetrons and to Professor R. D. Myers of the University of Maryland for offering us α-diphenyl β-picryl hydrazyl as the marker.

References

1) E. Zavoisky: J. Phys. (U.S.S.R.) **10** (1946) 170, 197.

2) B. Bleaney, R. P. Penrose and B. I. Plumpton: Proc. Roy. Soc. London A **198** (1949) 406.

3) P. R. Weiss: Phys. Rev. **73** (1948) 470.

4) R. D. Arnold and A. F. Kip: Phys. Rev. **75** (1949) 1199.

5) D. M. S. Bagguley and J. H. E. Griffiths: Proc. Phys. Soc. **65** (1952) 594.

6) B. Bleaney: Physica **17** (1951) 175.

7) A. Abragam and M. H. L. Pryce: Proc. Roy. Soc. **205** (1951) 135.

8) J. Itoh, M. Fujimoto and H. Ibamoto: Phys. Rev. **83** (1951) 852.

9) D. M. S. Bagguley and J. H. E. Griffiths Proc. Roy. Soc. London A **206** (1950) 366.

10) H. Kumagai, H. Abe, J. Shimada, I. Hayash K. Ono and H. Ibamoto: Jour. Phys. Soc. Japa **7** (1952) 535.

11) K. Ono, H. Abe and J. Shimada: Phys Rev. **92** (1953) 551.

12) H. Kumagai, K. Ono, I. Hayashi, H. Abe J. Shimada, H. Shôno, H. Ibamoto and S Tachimori: Jour. Phys. Soc. Japan **9** (1954) 369

13) J. A. Klein, J. H. N. Loubser, A. H Nethercot, Jr., and C. H. Townes: Rev. Sci Inst. **23** (1952) 78.

14) H. Kumagai, K. Ono, I. Hayashi, H. Abe H. Shôno, S. Tachimori, H. Ibamoto and J. Shimada: Phys. Rev. **82** (1951) 954.

15) P. Groth, Chemische Krystallographie (Leipzig 1906) Vol. I, p. 355.

16) L. Chrobak: Z. Krist. **88** (1934) 35.

17) D. Harker: Z. Krist. **93** (1936) 136.

18) R. W. G. Wyckoff: Crystal Structures (New York, 1951) Vol. II, Table XB, 1 (2).

19) J. H. Van Vleck: Phys. Rev. **74** (1948) 1168.

20) J. Itoh et al.: Private communication. Data obtained by the galvanometer reading which are a little different from their published values[8].

21) B. C. Guha: Proc. Roy. Soc. London A **206** (1951) 353.

22) J. H. Van Vleck: Electric and Magnetic Susceptibilities, (Clarendon Press, Oxford, 1932).

23) P. W. Anderson and P. R. Weiss: Rev. Mod. Phys. **25** (1953) 269.

24) K. Iwanaga: to be published.

25) R. Kubo and K. Tomita: Lecture at International Conference on Theoretical Physics (Kyoto, 1953) in press.

26) K. Tomita: Lecture at International Conference on Theoretical Physics (Kyoto, 1953) in press.

JOURNAL OF THE PHYSICAL SOCIETY OF JAPAN Vol. 9, No. 5, SEP.—OCT., 1954

Optical Behaviours of Multi-domain Single Crystal of $BaTiO_3$ in Dependence on Temperature

By Tadao HORIE, Kazuo KAWABE
Faculty of Science, Osaka University
and Shozo SAWADA
Institute of Science and Technology, Tokyo University

(Read November 1, 1952, Received April 19, 1954)

Apparent absorption edge, transmissivity and true characteristic absorption edge of multi-domain single crystal of barium titanate have been measured in dependence on temperature covering the three transition points, −70°C, 5°C and 120°C. The true characteristic absorption edge shifts linearly with the temperature coefficient quite close to that in ionic crystals which has so far been well known. Both the apparent absorption edge and the transmissivity exhibit quite steep hysteresis curves especially near −70°C. It may be due to the domain structure which is expected to develope when the lattice changes from orthorhombic to rhombohedral near this transition point.

One of the authors attempted to grow single crystals of $BaTiO_3$ in a kryptol furnace by the help of Na_2CO_3 as flux. The method has already been reported in detail[1]. Among the crystals obtained, there are many single-domain ones, but they are not always thin enough to insure optical observations. For the present purpose, therefore, the restriction to single-domain was given up. The samples used were picked out from crystals prepared as above. Most of them are about 20μ in thickness. One of the microscopic photographs of the samples inserted between crossed Polaroids is shown in Fig. 1.

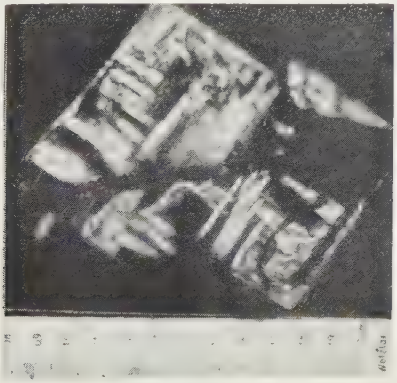

Fig. 1.

First, it has been studied how their optical absorption edge shifts along with gradual variation of temperature. A zirconium lamp[2] was used as a continuous light source. In Fig. 2, *c* is the continuous spectrum due to the light source itself and *a* the absorption spectrum of a thin crystal at room-temperature. The absorption seems to be complete at shorter wave-lengths than about 4,000Å. This optical absorption edge shifts towards longer wave-lengths when the temperature of crystal is raised up to 200°C, as shown in *b*. The wave-length of the edge was measured in dependence on temperature, ranging from −120°C to 150°C and the result for a sample 25μ thick is shown in Fig. 3.

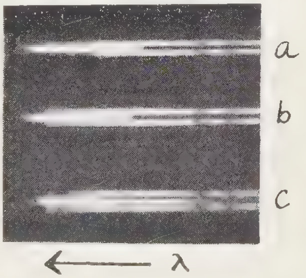

Fig. 2.

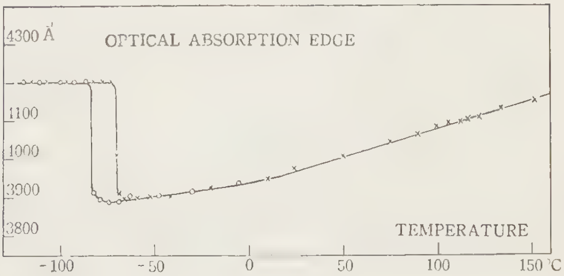

Fig. 3.

There is hardly any anormaly at all near the transition point at 120°C. There may be nothing more than a slight change in slope of the curve near the transition point at 5°C. Near −70°C, however, an extremely abrupt change was found to appear. The amount of jump in wave-length and the width of loop in temperature scale seem to be more or less variable with the sample used. It might be due to change in thickness of crystal. It seems to be certain that a sufficiently thin crystal exhibits a hysteresis loop independent of which sample is used. Fig. 4 shows how a sudden shift in absorption edge to occur near −70°C. The hysteresis curve for a sample 18μ thick is rather steep and the width of loop is about fifteen degrees in Centigrade as shown in Fig. 5.

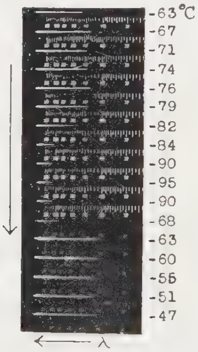

Fig. 4.

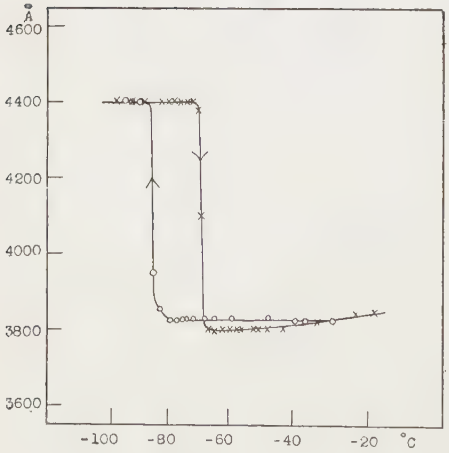

Fig. 5.

Next, the transmissivity of thin crystals has also been studied in dependence on temperature. Under constant illumination, the intensity of light with wave-length ranging from 4,000 to 4,500Å transmitted through a crystal was measured by means of a combination of a multiplier phototube, a d.c. amplifier and a micro-ammeter. The transmissivity for a sample 18μ thick was also found to exhibit a quite steep hysteresis loop near −70°C as shown in Fig. 6. In order to prevent a crystal from condensation of water vapour on its surface, it was mounted in vacuum as long as measurements were undertaken. According to these results, among the three transition points of the crystal used it looks as though the one at −70°C might be rather different optically from the other two.

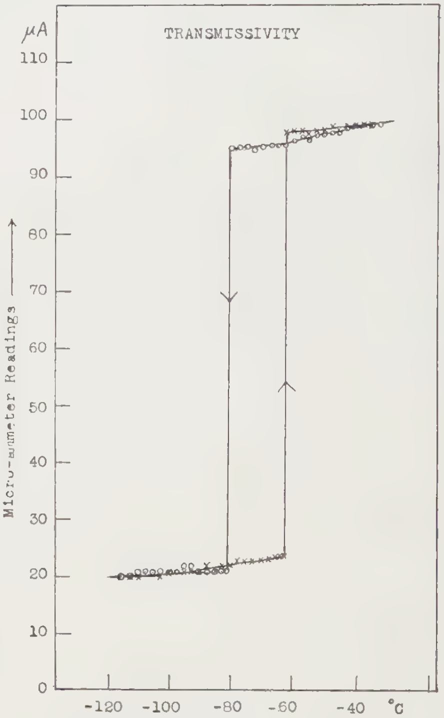

Fig. 6.

When over-exposures were made in taking photographs of absorption spectra, the edge did not exhibit any sudden shift mentioned above even below −70°C. And now the intrinsic absorption edge shifts linearly towards ultraviolet with decreasing temperature as shown in Fig. 7. The temperature coefficient is about 1 Å/degree, being close to the value which has so far been well known in ionic crystals[3]. A linear shift of absorption edge in temperature change like this has recently been studied theoretically[4]. It is interpreted by the interactions between the lattice vibration and the electron in crystal. Fig. 7

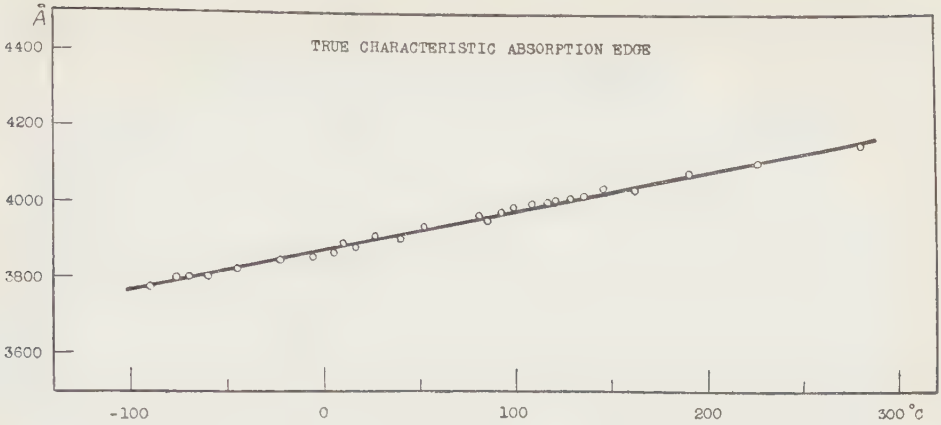

Fig. 7.

may be considered to express the temperature dependence of the *true* characteristic absorption edge of the crystal studied.

Near −70°C, the lattice changes from orthorhombic to rhombohedral and therefore much more complicated and fine domain structures may be expected to develope than near 5°C and 120°C[5]. Plenty of these fine domain may absorb especially in the shorter wave-lengths. The absorption by this fine domain structure may play an important role in the hysteresis curves of apparent absorption edge and transmissivity as shown in Figs. 5 and 6. Investigations are in progress which the authors hope will lead to a more detailed discussion on the relation between the absorption and the domain structure.

References

1) S. Sawada, S. Nomura and S. Fujii: Rep. Inst. Sci. Tech., Univ. Tokyo **5** (1951) 6.

2) W. D. Buckingham and C. R. Deibert: J.O.S.A. **36** (1946) 245.

3) H. Fesefeldt: Z.f.P. **64** (1930) 627, 741.

4) T. Muto and Ôyama: Prog. Theor. Phys. **5** (1950) 833.

5) P. W. Forsbergh, Jr: Phys. Rev. **76** (1949) 1187.

H. D. Megaw: Acta Cryst. **5** (1952) 739.

JOURNAL OF THE PHYSICAL SOCIETY OF JAPAN Vol. 9, No. 5, SEP.—OCT., 1954

On the Zeros of Certain Transcendental Functions related to Hankel Functions. Part I

By Masahumi NAGASE

Department of Physics, Faculty of Liberal Arts,
Saga University, Saga, Japan

(Received March 27, 1954)

The aim of this paper is to determine the zeros of the form

$$f_1(\nu)\equiv\varphi_1(\nu^2, a)H_\nu^{(2)}(a)+\varphi_2(\nu^2, a)dH_\nu^{(2)}(a)/da$$

qua function of ν, where $H_\nu^{(2)}(a)$ denotes a Hankel function of order ν and φ_1, φ_2 are given functions, a being real positive. By studying the analytical behavior of $d\log H_\nu^{(2)}(a)/da$ the regions where the zeros looked for may exist can be determined. If $|\varphi_1(\nu^2, a)|\lesssim|\varphi_2(\nu^2, a)|$, these regions are shown to be a narrow strip, extending from $\nu=a$ to $-\infty i$, and that obtained by the inversion about the origin, where $d\log H_\nu^{(2)}(a)/da$ changes its value infinite times from zero to infinity. The method of estimating these zeros is established by employing the asymptotic expansions of $H_\nu^{(2)}(a)$, and is discussed in detail especially for the zeros near a. As an example the following form is treated,

$$dH_\nu^{(2)}(a)/da+(n/a)H_\nu^{(2)}(a)\ ,$$

which occurs actually in the case of the diffraction of waves by a sphere. The first several zeros are shown to be given by

$$\nu=a\Big[1+\frac{1}{2}\Big(\frac{3\rho}{a}\Big)^{2/3}\exp\Big(\frac{5}{3}\pi i\Big)+\Big(\frac{1}{120}-\frac{5n-1}{45\rho^2}\Big)\Big(\frac{3\rho}{a}\Big)^{4/3}\exp\Big(\frac{4}{3}\pi i\Big)$$
$$+\Big\{\frac{1}{2800}-\frac{5n-2}{450\rho^2}+\frac{(5n-1)^2}{(45\rho^2)^2}\Big\}\Big(\frac{3\rho}{a}\Big)^2+\cdots\Big]\ ,$$

where ρ denotes one of the following values,

0.6853843, 3.9027676, 7.0549300, 10.2006884, 13.3445027, $\cdots$.

§ 1. Introduction

In various problems of mathematical physics, we often find it necessary to determine the zeros of certain types of transcendental functions, which are homogeneous with respect to Hankel functions and their derivatives, qua functions of the order, taken as a complex variable. The aim of this work is to discuss the existence of the zeros and to show how to evaluate them.

In Part I we shall deal exclusively with the case of linear homogeneous forms. We shall first show in § 2 that the problem can then be reduced to that concerning the zeros of the linear forms of logarithmic derivative of the Hankel function and, having discussed in § 3–3.3 the analytical behavior of this derivative, we shall determine the regions of the complex order in which the zeros of these forms may exist. By using the asymptotic expansions of the Hankel function in forms adequate to the regions concerned and others, discussed in § 4–4.6, we shall locate them approximately in § 5. In § 6 we shall apply this method to an example, which occurs actually in the case of the diffraction of waves by a sphere.

In Part II we apply the above-stated method to bilinear forms of Hankel functions of different arguments and their derivatives, to show how its application can be extended to those higher than linear. An example, which occurs in the case of the diffraction of elastic waves, will be treated.

§ 2. General Considerations

We take as the linear form to be considered

$$f_1(\nu)\equiv\varphi_1(\nu^2, a)H_\nu^{(2)}(a)+\varphi_2(\nu^2, a)H_\nu^{(2)\prime}(a)\ , \tag{2.1}$$

where $H_\nu^{(2)}(a)$ and $H_\nu^{(2)\prime}(a)$ are the Hankel function of argument a and order ν and its derivative with respect to a, $\varphi_1(\nu^2, a)$ and $\varphi_2(\nu^2, a)$ being any given functions of ν^2 and a, with suitable conditions, if necessary. We assume here, for simplicity of treatment, a to be real positive, without losing the generality of our consideration since this is always the case in practice. Also the assumption of the dependence of φ_1 and φ_2 on ν^2, not on ν, is not an essential but only convenient one, which makes the problem much easier and has never conflicted with the actual situation. Instead of $H_\nu^{(2)}(a)$ we may also consider $H_\nu^{(2)}(a)$ *mutatis mutandis.*

Since it is clear from the theorem concerning the Wronskian of Bessel's differential equation, that $H_\nu^{(2)}(a)$ and $H_\nu^{(2)\prime}(a)$ never vanish for the same a and ν, the zeros of (2.1) are equivalent to those of

$$f_1(\nu)/[\varphi_2(\nu^2, a)H_\nu^{(2)}(a)] \equiv \varphi_1(\nu^2, a)/\varphi_2(\nu^2, a) + H_\nu^{(2)\prime}(a)/H_\nu^{(2)}(a), \qquad (2.2)$$

if we exclude such a case that some zeros of $H_\nu^{(2)}(a)$ should accidentally coincident with those of $\varphi_2(\nu^2, a)$. Let us therefore, take as the form to be considered the following one anew, instead of the previous one,

$$f_1(\nu) \equiv F(\nu, a) + \varphi(\nu^2, a)\,, \qquad (2.3)$$

where

$$F(\nu, a) \equiv H_\nu^{(2)\prime}(a)/H_\nu^{(2)}(a) = d \log H_\nu^{(2)}(a)/da\,. \qquad (2.4)$$

As to the excluded case we have to investigate in each particular problem whether this is the case or not.

we shall observe some simple properties of $f_1(\nu)$.

(a) $f_1(\nu)$ is an even function of ν. Since $F(\nu, a)$ is an even function of ν, owing to the relations

$$\left.\begin{aligned} H_{-\nu}^{(2)}(a) &= e^{-\nu\pi i} H_\nu^{(2)}(a), \\ H_{-\nu}^{(2)\prime}(a) &= e^{-\nu\pi i} H_\nu^{(2)\prime}(a), \end{aligned}\right\} \qquad (2.5)$$

$f_1(\nu)$ also is even with respect to ν. Accordingly it is sufficient to consider a half of the ν-plane, say, the right half plane bounded by the imaginary axis. Therefore we shall henceforth confine our discussion to this region.

(b) $f_1(\nu)$ never vanishes for real and purely imaginary values of ν, provided that $\varphi(\nu^2, a)$ does not contain i explicitly.

For, let us suppose $f_1(\nu)$ vanishes on the real axis, i.e.

$$f_1(\nu) = F(\nu, a) + \varphi(\nu^2, a) = 0 \qquad (2.6)$$

for real ν; then its conjugate complex also will vanish, i.e.

$$\overline{f_1(\nu)} = \overline{F(\nu, a)} + \varphi(\nu^2, a) = 0 \qquad (2.7)$$

for such ν, and therefore

$$f_1(\nu) - f_1(\nu) = F(\nu, a) - F(\nu, a) = 0. \qquad (2.8)$$

Since for real values of ν

$$\overline{H_\nu^{(2)}(a)} = H_\nu^{(1)}(a)\,, \qquad (2.9)$$

(2.8) becomes

$$\frac{H_\nu^{(2)\prime}(a)H_\nu^{(1)}(a) - H_\nu^{(1)\prime}(a)H_\nu^{(2)}(a)}{H_\nu^{(1)}(a)H_\nu^{(2)}(a)} = 0, \qquad (2.10)$$

which may be transformed into

$$-4i/\{\pi a |H_\nu^{(2)}(a)|^2\} = 0\,, \qquad (2.11)$$

in virtue of the value of the Wronskian

$$W\{H_\nu^{(1)}(a), H_\nu^{(2)}(a)\} = -4i/(\pi a)\,; \qquad (2.12)$$

the Eq. (2.11) will conflict with the fact that $H_\nu^{(2)}(a)$ has no poles in the finite region of a.

Secondly, since for purely imaginary values of ν $(=\mu i)$

$$H_{\mu i}^{(2)}(a) = H_{-\mu i}^{(2)}(a) = e^{-\mu\pi} H_{\mu i}^{(1)}(a)\,, \qquad (2.13)$$

we obtain

$$\{\overline{H_{\mu i}^{(2)\prime}(a)/H_{\mu i}^{(2)}(a)}\} = H_{\mu i}^{(1)\prime}(a)/H_{\mu i}^{(1)}(a).$$

If $f_1(\nu)$ and therefore $\overline{f_1(\nu)}$ also vanished for a purely imaginary value of ν, i.e.

$$f_1(\nu) = F(\mu_i, a) + \varphi(-\mu^2, a) = 0\,, \qquad (2.15)$$

$$\overline{f_1(\nu)} = H_{\mu i}^{(1)\prime}(a)/H_{\mu i}^{(2)}(a) + \varphi(-\mu^2, a) = 0\,. \qquad (2.16)$$

then we should obtain

$$\begin{aligned} f_1(\nu) - \overline{f_1(\nu)} &= F(\nu, a) - \overline{F(\nu, a)} \\ &= W\{H_\nu^{(1)}(a),\ H_\nu^{(2)}(a)\}/\{H_\nu^{(1)}(a)\cdot H_\nu^{(2)}(a)\} \\ &= 0, \end{aligned}$$

or

$$-4i/\{\pi a e^{\mu\pi} |H_\nu^{(2)}(a)|^2\} = 0, \qquad (2.17)$$

which never occurs, as stated above.

§ 3. Analytical Behavior of $F(\nu, a)$ qua Function of ν.

To investigate the general analytical behavior of $F(\nu, a)$ we shall transform it into another expression, more easily accessible to intuition, though not necessarily convenient for closer evaluation.

We first take up the following relation in connection with Nicholson's integral [(1) p. 441], valid for any complex ν and $\operatorname{Re} a > 0$,

$$\begin{aligned} H_\nu^{(1)}(a)H_\nu^{(2)}(a) &= J_\nu(a)^2 + Y_\nu(a)^2 \\ &= (8/\pi^2)\int_0^\infty K_0(2a \sinh \xi) \cosh 2\nu\xi\, d\xi\,, \end{aligned} \qquad (3.1)$$

where J_ν and Y_ν are Bessel functions of the first and the second kind of order ν and K_0 is Bessel function of imaginary argument of order 0. By differentiating both sides of (3.1) with respect to a we have

$$H_\nu^{(1)}(a)H_\nu^{(2)\prime}(a)+H_\nu^{(1)\prime}(a)H_\nu^{(2)}(a)$$
$$=-(16/\pi^2)\int_0^\infty K_1(2a\sinh\xi)\sinh\xi\cosh 2\nu\xi d\xi\,; \tag{3.2}$$

the legitimacy of the differentiation under the integral sign is secured, as in the domain: $\xi\geqq 0$, $a\geqq\delta>0$, $K_1(2a\sinh\xi)\sinh\xi\cosh 2\nu\xi$ is continuous and the integral on the right of (3.2) converges uniformly.

By dividing (3.2) by (3.1) we therefore obtain

$$H_\nu^{(2)\prime}(a)/H_\nu^{(2)}(a)+H_\nu^{(1)\prime}(a)/H_\nu^{(1)}(a)$$
$$=-2\int_0^\infty K_1(2a\sinh\xi)\sinh\xi\cosh 2\nu\,\xi d\xi\Big/\int_0^\infty K_0(2a\sinh\xi)\cosh 2\nu\xi\,d\xi\,. \tag{3.3}$$

Secondly by dividing (2.12) by (3.1) we have

$$H_\nu^{(2)\prime}(a)/H_\nu^{(2)}(a)-H_\nu^{(1)\prime}(a)/H_\nu^{(1)}(a)=-(\pi i/2a)\Big/\int_0^\infty K_0(2a\sinh\xi)\cosh 2\nu\xi\,d\xi. \tag{3.4}$$

It follows from (3.3) and (3.4) that

$$F(\nu,a)=H_\nu^{(2)\prime}(a)/H_\nu^{(2)}(a)$$
$$=-\left\{\int_0^\infty K_1(2a\sinh\xi)\sinh\xi\cosh 2\nu\xi\,d\xi+(\pi i/4a)\right\}\Big/\int_0^\infty K_0(2a\sinh\xi)\cosh 2\nu\xi\,d\xi\,, \tag{3.5}$$

or by partial integration

$$F(\nu,a)=-(\nu/a)\left\{\int_0^\infty K_1(2a\sinh\xi)\cosh 2\nu\xi\sinh\xi\,d\xi\Big/\int_0^\infty K_1(2a\sinh\xi)\sinh 2\nu\xi\cosh\xi\,d\xi\right\}$$
$$-(\pi i/4a)\left\{1\Big/\int_0^\infty K_0(2a\sinh\xi)\cosh 2\nu\xi\,d\xi\right\}. \tag{3.6}$$

We shall then estimate $F(\nu,a)$ for the values of ν classified as follows.

3.1 *Real positive values of* ν

When ν is real positive $=\lambda$, then we obtain from (3.5) and (3.6) respectively

$$F(\lambda,a)=\left\{-\int_0^\infty K_1(2a\sinh\xi)\cosh 2\lambda\xi\sinh\xi\,d\xi-(\pi i/4a)\right\}\Big/\int_0^\infty K_0(2a\sinh\xi)\cosh 2\lambda\xi\,d\xi\,, \tag{3.7}$$

and

$$F(\lambda,a)=-(\lambda/a)\left\{\int_0^\infty K_1(2a\sinh\xi)\cosh 2\lambda\xi\sinh\xi\,d\xi\Big/\int_0^\infty K_1(2a\sinh\xi)\sinh 2\lambda\xi\cosh\xi\,d\xi\right\}$$
$$-(\pi i/4a)\left\{1\Big/\int_0^\infty K_0(2a\sinh\xi)\cosh 2\lambda\xi\,d\xi\right\}. \tag{3.8}$$

In the evaluation of the above integrals we shall assume a to be considerably large, without biasing the general tendency of their dependency on a and λ except in the case of a being very small, since they are of non-oscillatory character with increasing a, owing to the fact that both of $K_0(2a\sinh\xi)$ and $K_1(2a\sinh\xi)$ are positive and monotonously decreasing functions of a as well as of ξ, and we shall use, if necessary, asymptotic expansions for large a. In the further discussion, as occasion demands, we shall also assume it tacitly, if there is no fear of misunderstanding.

(a) When $\lambda\ll 1$, the Eq. (3.8) becomes

$$F(\lambda,a)=-(1/2a)\left\{\int_0^\infty K_1(2a\sinh\xi)\sinh\xi\,d\xi\Big/\int_0^\infty K_1(2a\sinh\xi)\xi\cosh\xi\,d\xi\right\}$$
$$\times\Bigg[1+2\lambda^2\left\{\int_0^\infty K_1(2a\sinh\xi)\xi^2\sinh\xi\,d\xi\Big/\int_0^\infty K_1(2a\sinh\xi)\sinh\xi\,d\xi\right.$$
$$\left.-(1/3)\int_0^\infty K_1(2a\sinh\xi)\xi^3\cosh\xi\,d\xi\Big/\int_0^\infty K_1(2a\sinh\xi)\xi\cosh\xi\,d\xi\right\}+O(\lambda^4)\Bigg]$$

$$-(\pi i/4a)\left\{1\Big/\int_0^\infty K_0(2a\sinh\xi)d\xi\right\}\Big[1-2\lambda^2\left\{\int_0^\infty K_0(2a\sinh\xi)\xi^2\,d\xi\Big/\int_0^\infty K_0(2a\sinh\xi)d\xi\right\}$$
$$+O(\lambda^4)\Big], \tag{3.9}$$

which may be transformed into

$$F(\lambda,a)=-\{(1/2a)(1+(\lambda^2/a^2))+i(1-(\lambda^2/2a^2))\}\{1+O(a^{-2})+O(\lambda^4)\}, \tag{3.10}$$

in view of the relations

$$\int_0^\infty K_1(2a\sinh\xi)\sinh\xi\,d\xi=(1/4a^2)\int_0^\infty K_1(t)tdt\{1+(t/2a)^2\}^{-1/2}=(\pi/8a^2)\{1+O(a^{-2})\}, \tag{3.11}$$

$$\int_0^\infty K_1(2a\sinh\xi)\xi\cosh\xi\,d\xi=(1/2a)\int_0^\infty K_1(t)\sinh^{-1}(t/2a)dt=(\pi/8a^2)\{1+O(a^{-2})\}, \tag{3.12}$$

$$\int_0^\infty K_1(2a\sinh\xi)\xi^3\cosh\xi\,d\xi=(3\pi/32a^4)\{1+O(a^{-2})\}, \tag{3.13}$$

and others which are derived from the formula

$$\int_0^\infty K_\nu(t)t^{\mu-1}dt=2^{\mu-2}\Gamma\{(\mu-\nu)/2\}\Gamma\{(\mu+\nu)/2\}, \tag{3.14}$$

[(1) p. 388].

(b) When $\lambda\simeq1/2$, we have the relations

$$\operatorname{Re}F(\lambda,a)\gtreqless-\lambda/a \quad \text{for} \quad \lambda\gtreqless1/2, \tag{3.15}$$
$$\operatorname{Im}F(\lambda,a)\gtreqless-1 \quad \text{for} \quad \lambda\gtreqless1/2, \tag{3.16}$$

considering

$$\operatorname{Re}F(\lambda,a)=-\lambda/a+(\lambda/a)\int_0^\infty K_1(2a\sinh\xi)\sinh(2\lambda-1)\xi\,d\xi\Big/\int_0^\infty K_1(2a\sinh\xi)\sinh2\lambda\xi\cosh\xi\,d\xi, \tag{3.17}$$

$$\operatorname{Im}F(\lambda,a)=-1+\int_0^\infty K_0(2a\sinh\xi)(\cosh2\lambda\xi-\cosh\xi)d\xi\Big/\int_0^\infty K_0(2a\sinh\xi)\cosh2\lambda\xi\,d\xi. \tag{3.18}$$

(c) Fer $\lambda\gtrsim a$, we shall first evaluate the integrals contained in (3.7) and (3.8), i.e.

$$\int_0^\infty K_1(2a\sinh\xi)\cosh2\lambda\xi\sinh\xi\,d\xi,$$
$$\int_0^\infty K_1(2a\sinh\xi)\sinh2\lambda\xi\cosh\xi\,d\xi,$$
$$\int_0^\infty K_0(2a\sinh\xi)\cosh2\lambda\xi\,d\xi.$$

The integrand of the first integral tends to $1/(2a)$ with a horizontal tangent as $\xi\to O$, and for $\lambda<a$ it decreases monotonously with increasing ξ, while for $\lambda>a$ it once increases to a maximum and then monotonously decreases to zero; in the latter case the value of the integrand near the maximum contributes the most to the integral.

The approximate value of the integrand for not small ξ is

$$(1/4)(\pi/a)^{1/2}(\sinh\xi)^{1/2}\exp(-2a\sinh\xi+2\lambda\xi), \tag{3.19}$$

if we use the asymptotic expression of K_1 of large argument

$$K_1(2a\sinh\xi)=(1/2)(\pi/a)^{1/2}(\sinh\xi)^{-1/2}\exp(-2a\sinh\xi)\{1+O(a^{-1})\}. \tag{3.20}$$

We are, therefore, able to evaluate the integral by a method analogous to the method of steepest descents, expanding the integrand about the stationary point of the exponential function. If we denote by ξ_0 the value of ξ giving the maximum of

$$-2a\sinh\xi+2\lambda\xi,$$

i.e.

$$\xi_0=\cosh^{-1}(\lambda/a), \tag{3.21}$$

which exists only when $\lambda>a$, then

$$-2a\sinh\xi+2\lambda\xi=-2a\sinh\xi_0+2\lambda\xi_0-a\sinh\xi_0(\xi-\xi_0)^2+\cdots\cdots,$$

and

$$\sinh\xi=\sinh\xi_0+\cosh\xi_0(\xi-\xi_0)+(1/2)\sinh\xi_0(\xi-\xi_0)^2+\cdots\cdots.$$

Hence the first integral will be evaluated as follows:

$$\begin{aligned}\int_0^\infty K_1(2a\sinh\xi)\cosh 2\lambda\xi\sinh\xi\,d\xi&=(1/4)(\pi/a)^{1/2}(\sinh\xi_0)^{1/2}\exp(-2a\sinh\xi_0+2\lambda\xi_0)\\&\quad\times\int_0^\infty\exp(-a\sinh\xi_0t^2)\{1+(1/4-(1/8)\coth^2\xi_0)t^2\}dt\\&=(\pi/4a)\exp\{2a(\xi_0\cosh\xi_0-\sinh\xi^0\}\{1+O(a^{-1})\}.\end{aligned} \tag{3.22}$$

Similarly, as to the second and third integrals, we have

$$\int_0^\infty K_1(2a\sinh\xi)\sinh 2\lambda\xi\cosh\xi\,d\xi=(\pi/4a)\coth\xi_0\exp\{2a(\xi_0\cosh\xi_0-\sinh\xi_0)\}\{1+O(a^{-1})\}. \tag{3.23}$$

$$\int_0^\infty K_0(2a\sinh\xi)\cosh 2\lambda\xi\,d\xi=(\pi/4a\sinh\xi_0)\exp\{2a(\xi_0\cosh\xi_0-\sinh\xi_0)\}\{1+O(a^{-1})\}. \tag{3.24}$$

Accordingly it follows that

$$\operatorname{Re}F(\lambda, a)=-\sinh\xi_0\{1+O(a^{-1})\}, \tag{3.25}$$

or

$$\operatorname{Re}F(\lambda, a)=-(\lambda^2/a^2-1)^{1/2}\{1+O(a^{-1})\}, \tag{3.26}$$

and

$$\operatorname{Im}F(\lambda, a)=-\sinh\xi_0\exp\{-2a(\xi_0\cosh\xi_0-\sinh\xi_0)\}\{1+O(a^{-1})\}. \tag{3.27}$$

(d) In view of the non-oscillatory character of $F(\lambda, a)$ we may, joining its behaviors in the above-mentioned cases, imagine as $F(\lambda, a)$ such function whose real and imaginary parts are illustrated schematically in Fig. 1.

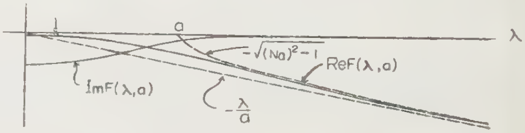

Fig. 1.

3.2 *Purely imaginary* ν

When ν is purely imaginary $=\mu i$, (3.5) and (3.6) are written in the forms

$$\begin{aligned}F(\mu i, a)=&-\int_0^\infty K_1(2a\sinh\xi)\sinh\xi\cos 2\mu\xi\,d\xi\Big/\int_0^\infty K_0(2a\sinh\xi)\cos 2\mu\xi\,d\xi\\&-(\pi i/4a)\cdot 1\Big/\int_0^\infty K_0(2a\sinh\xi)\cos 2\mu\xi\,d\xi.\end{aligned} \tag{3.28}$$

$$\begin{aligned}F(\mu i, a)=&-(\mu/a)\int_0^\infty K_1(2a\sinh\xi)\sinh\xi\cos 2\mu\xi\,d\xi\Big/\int_0^\infty K_1(2a\sinh\xi)\sinh\xi\sin 2\mu\xi\,d\xi\\&-(\pi i/4a)\cdot 1\Big/\int_0^\infty K_0(2a\sinh\xi)\cos 2\mu\xi\,d\xi.\end{aligned} \tag{3.29}$$

Since $F(\nu, a)$ is even with respect to ν, we have only to consider positive values of μ.

(a) For $\mu\ll 1$ we have

$$\begin{aligned}\operatorname{Re}F(\nu, a)=&-\left\{\int_0^\infty K_1(2a\sinh\xi)\sinh\xi\,d\xi\Big/\int_0^\infty K_0(2a\sinh\xi)d\xi\right\}\\&\times\left[1-2\mu^2\left\{\int_0^\infty K_1(2a\sinh\xi)\xi^2\sinh\xi\,d\xi\Big/\int_0^\infty K_1(2a\sinh\xi)\sinh\xi\,d\xi\right.\right.\\&\left.\left.-\int_0^\infty K_0(2a\sinh\xi)\xi^2\,d\xi\Big/\int_0^\infty K_0(2a\sinh\xi)\,d\xi\right\}+O(\mu^4)\right]\\=&-(1/2a)\{1-\mu^2/a^2+O(\mu^4)\}\{1+O(a^{-2})\},\end{aligned} \tag{3.30}$$

and

$$\operatorname{Im} F(\nu, a) = -(\pi/4a)\left\{ 1\Big/\int_0^\infty K_0(2a \sinh \xi) d\xi \right\}\left\{1+2\mu^2\right.$$
$$\left. \times\left(\int_0^\infty K_0(2a \sinh \xi)\xi^2\, d\xi \Big/ \int_0^\infty K_0(2a \sinh \xi) d\xi\right)+O(\mu^4)\right\}$$
$$= -\{1+(\mu^2/(2a^2)+O(\mu^4)\}\{1+O(a^{-2})\}\ . \tag{3.31}$$

(b) For $\mu = O(a) \gg 1$, we have

$$F(\nu, a) = -\{(1/2)a/(a^2+\mu^2)+i(a^2+\mu^2)^{1/2}/a\}\{1+O(a^{-2})\}\ , \tag{3.32}$$

since

$$\int_0^\infty K_0(2a \sinh \xi) \cos 2\mu\xi\, d\xi = \int_0^\infty K_0(t) \frac{1}{2a}\left\{1+\left(\frac{t}{2a}\right)^2\right\}^{-1/2} \cos\left[2\mu \log\left\{\frac{t}{2a}\right.\right.$$
$$\left.\left. +\sqrt{1+\left(\frac{t}{2a}\right)^2}\right\}\right] dt,$$
$$= \int_0^\infty K_0(2at) \cos 2\mu t\, dt\{1+O(a^{-2})\},$$
$$= (\pi/4)(a^2+\mu^2)^{-1/2}\{1+O(a^{-2})\}\ , \tag{3.33}$$

and

$$\int_0^\infty K_1(2a \sinh \xi) \cos 2\mu\xi \sinh \xi\, d\xi = \int_0^\infty K_1(2at) \cos 2\mu t \cdot t\, dt\{1+O(a^{-2})\}$$
$$= (\pi/8)a(a^2+\mu^2)^{-3/2}\{1+O(a^{-2})\}\ ; \tag{3.34}$$

as to the evaluation of the integral on the right of (3.33) see the reference (1) p. 388. By differentiating it with respect to a we obtain the evaluation of the right of (3.34).

(c) For the values of μ much greater than a we must first prove the following formulas:

$$\int_0^\infty \cos 2\mu\xi\, K_0(2a \sinh \xi) d\xi = (\pi/4\mu)\{1-a^2/\mu^2+O(\nu^{-4})\}\ , \tag{3.35}$$

$$\int_0^\infty \cos 2\mu\xi \sinh \xi\, K_1(2a \sinh \xi) d\xi = (\pi a/8\mu^3)\{1+O(\mu^{-2})\}, \tag{3.36}$$

valid for large μ and any positive a.

Since it is shown that

$$2\mu\int_0^\infty \cos 2\mu\xi\, K_0(2a \sinh \xi) d\xi = 2a\int_0^\infty \sin 2\mu\xi \cosh \xi\, K_1(2a \sinh \xi) d\xi, \tag{3.37}$$

by partial integration, it is obvious that

$$2\mu\int_0^\infty \cos 2\mu\xi\, K_0(2a \sinh \xi) d\xi \to \pi/2,$$

as $\mu \to \infty$, in virtue of $2aK_1(2a \sinh \xi)$ tending to $1/\xi$ with decreasing ξ. Further, since we obtain

$$\mu^3\left[\int_0^\infty \cos 2\mu\xi\, K_0(2a \sinh \xi) d\xi - (1/2\mu)\int_0^\infty \sin 2\mu\xi\, d\xi/\xi\ \right] = -(1/2)\int_0^\infty \sin 2\mu\xi$$
$$\times\{-4a^2 \cosh \xi \sinh \xi\, K_0(2a \sinh \xi)+4a^3 \cosh^3 \xi\, K_1(2a \sinh \xi)$$
$$+2a \cosh \xi\, (\sinh \xi)^{-2} K_1(2a \sinh \xi)+2a^2 \cosh \xi\, (\sinh \xi)^{-1} K_0(2a \sinh \xi)-\xi^3\} d\xi\ , \tag{3.38}$$

by repeated partial integrations, it is easily seen that

$$\mu^3\left[\int_0^\infty \cos 2\mu\xi\, K_0(2a \sinh \xi) d\xi - \pi/(4\mu)\right] = -(\pi a^2/4)\{1+O(\mu^{-2})\},$$

as $\mu \to \infty$, by considering the expression in the bracket { } on the right of (3.38) tending to $a^2\xi^{-1}$ as $\xi \to 0$.

Secondly, as we see by partial integrations,

$$8\mu^3\int_0^\infty \cos 2\mu\xi \sinh \xi\, K_1(2a\sinh \xi)d\xi = -\int_0^\infty \sin 2\mu\xi\,\{8a\cosh \xi \sin \xi\, K_0(2a\sinh \xi)$$
$$-4a^2(2\cosh^2 \xi - 1)K_1(2a\sinh \xi)\cosh \xi + 8a^3 \sinh \xi \cosh^3 \xi\, K_0(2a\sinh \xi)$$
$$-8a^2\sinh^2 \xi \cosh \xi\, K_1(2a\sinh \xi)\}d\xi, \tag{3.39}$$

where the expression in the bracket { } tends to $-2a\xi^{-1}$ as $\xi \to +O$, and therefore we obtain the relation to be proved

$$8\mu^3\int_0^\infty \cos 2\mu\xi \sinh \xi\, K_1(2a\sinh \xi)d\xi = \pi a\{1+O(\mu^{-2})\},$$

as $\mu \to O$.

Consequently we have

$$F(\nu, a) = -\{(1/2)(a/\mu^2) + i\mu/a)\}\{1+O(\mu^{-2})\}. \tag{3.40}$$

(d) Joining the above-stated cases, we have for all values of μ

$$F(\nu, a) = -\{(1/2)a(a^2+\mu^2)^{-1} + i(a^2+\mu^2)^{1/2}/a\}\{1+O(a^{-2})\}, \tag{3.41}$$

whose real and imaginary parts are illustrated in Fig. 2.

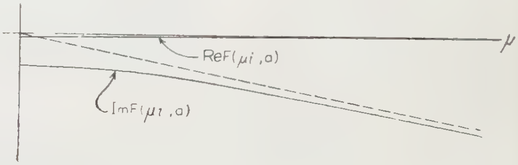

Fig. 2.

3.3 *Any complex* $\nu = \lambda + \mu i$ $(\lambda > O)$

In order to estimate the value of $F(\nu, a)$, referring to (3.5), we shall evaluate the two integrals constituting its important parts, i.e.

$$J_1 \equiv \int_0^\infty K_0(2a\sinh \xi)\cosh 2\nu\xi\, d\xi,$$
$$= \int_0^\infty K_0(2a\sinh \xi)\cosh 2\lambda\xi \cos 2\mu\xi\, d\xi + i\int_0^\infty K_0(2a\sinh \xi)\sinh 2\lambda\xi \sin 2\mu\xi\, d\xi, \tag{3.42}$$

$$J_2 \equiv \int_0^\infty K_1(2a\sinh \xi)\cos 2\nu\xi \sinh \xi\, d\xi,$$
$$= \int_0^\infty K_1(2a\sinh \xi)\sinh \xi \cosh 2\lambda\xi \cos 2\mu\xi\, d\xi + i\int_0^\infty K_1(2a\sinh \xi)\sinh \xi \sinh 2\lambda\xi \sin 2\mu\xi\, d\xi. \tag{3.43}$$

(a) For $\lambda \ll 1$ we have

$$\mathrm{Re}\, J_1 = \int_0^\infty K_0(2at)\{1+2\lambda^2\sinh^{-1} t + O(\lambda^4)\}\cos(2\nu\sinh^{-1} t)(1+t^2)^{-1/2}dt,$$
$$= \int_0^\infty K_0(2at)\{1-(1/2-2\lambda^2)t^2+\cdots\}\cos 2\mu t\, dt - \int_0^\infty K_0(2at)(t^3+\cdots)\sin 2\mu t\, dt$$
$$= (\pi/4)(a^2+\mu^2)^{-1/2}[1-\{(1/2-2\lambda^2)/4\}(a^2-2\mu^2)(a^2+\mu^2)^{-2}]\{1+O(a^{-4})+O(\mu^4)\}, \tag{3.44}$$

$$\mathrm{Im}\, J_1 = (\pi/4)\lambda(a^2+\mu^2)^{-3/2}\{\mu+(\lambda^2/2)(3a^2-2\mu^2)(a^2+\mu^2)^{-2}\}\{1+O(a^{-4})+O(\mu^3)\}, \tag{3.45}$$

considering the relation

$$\int_0^\infty \cos 2\mu t\, K_0(2at)\, dt = (\pi/4)(a^2+\mu^2)^{-1/2}, \tag{3.46}$$

and those, which are derivable from it by differentiations.

(b) For $\lambda > a$, by using the same method as employed in the deduction of (3.22) and (3.23), we obtain

$$\mathrm{Re}\, J_1 = (1/4)(\pi/a)^{1/2}\cos 2\mu\xi_0 (\sin \xi_0)^{-1/2}\exp(-2a\sinh \xi_0 + 2\lambda\xi_0)$$
$$\times\int_{-\infty}^\infty \exp(-a\sinh \xi_0 \cdot t^2)\cos 2\mu t\cdot dt\{1+O(a^{-1})\},$$
$$= (\pi/4a)(\sinh \xi_0)^{-1}\exp\{2a(\xi_0\cosh \xi_0 - \sinh \xi_0) - \mu^2/(a\sinh \xi_0)\}\cos 2\mu\xi_0\{1+O(a^{-1})\}, \tag{3.47}$$

and

$$\operatorname{Im} J_1=(\pi/4a)(\sinh \xi_0)^{-1} \exp\{2a(\xi_0 \cosh \xi_0-\sinh \xi_0)-\mu^2/(a \sinh \xi_0)\} \sin 2\mu\xi_0\{1+O(a^{-1})\}, \tag{3.48}$$

where

$$\xi_0=\cosh^{-1}(\lambda/a).$$

The behaviors of $\operatorname{Re} J_1$ and $\operatorname{Im} J_1$ are made accessible to intuition by the schematic relieves in Fig. 3 and 4. The chain lines denote the intersections of the relieves and the horizontal plane of the height O.

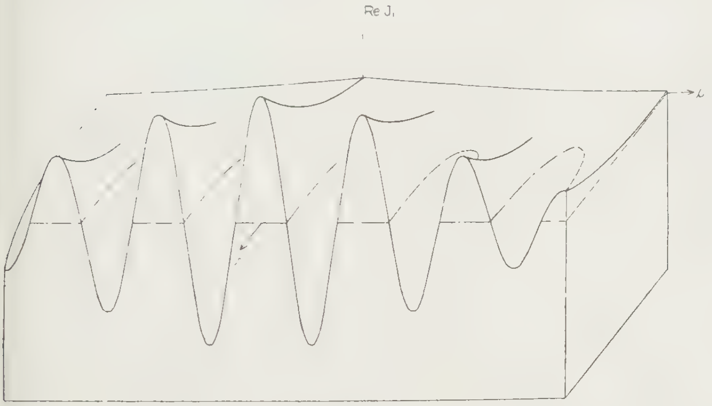

Fig. 3.

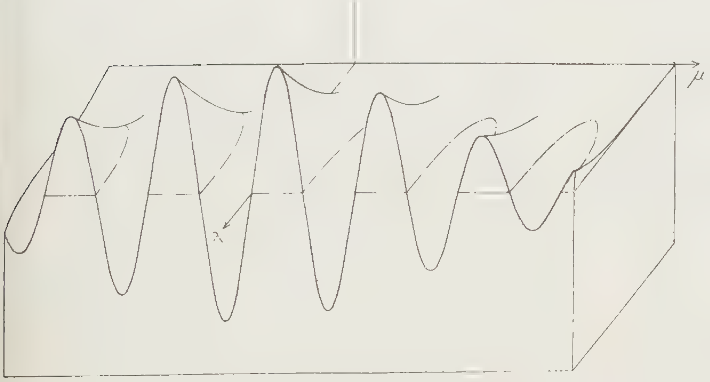

Fig. 4.

The zeros of J_1 are given by the crossing points of the curves on which

$$\operatorname{Re} J_1=0 \quad \text{and} \quad \operatorname{Im} J_1=0,$$

respectively. Since these curves certainly cross each other in pairs, as is easily seen in Fig. 5, drawn extremely schematically in view of Figs. 3 and 4, and are expressed approximately by

$$2\mu\xi_0=(m+1/2)\pi \quad \text{and} \quad 2\mu\xi_0=m\pi,$$

respectively, where m is any positive integer, or by

$$\lambda/a=\cosh\{(m+1/2)\pi/2\mu\}$$

and $$\lambda/a=\cosh(m\pi/2\mu),$$

respectively. There are an infinite number of zeros, as one may infer from the illustration, placed in order, the real part of their values being of the order of a and the imaginary part tending to $\pm\infty i$. As to the closer location of these zeros we shall see later.

We shall further deal with J_2. J_2 is also expressed on similar discussions as follows:

$$J_2=(\pi/8)a(a^2+\mu^2)^{-3/2} \cdot\{1+O(a^{-2})\} \text{ for } \lambda\ll 1, \tag{3.49}$$

$$\begin{aligned} J_2=(\pi/4a) &\times\exp\{2a(\xi_0 \cosh \xi_0-\sinh \xi_0) \\ &-\mu^2/(a \sinh \xi_0)\} \\ &\times(\cos 2\mu\xi_0+i \sin 2\mu\xi_0) \\ &\times\{1+O(a^{-1})\} \quad \text{for} \quad \lambda>a. \end{aligned} \tag{3.50}$$

It is therefore clear, that for $\lambda>a$ J_2 is approximately same as J_1 multiplied by $\sinh \xi_0$ and that one can discuss the zeros of J_2 in the same way as those of J_1.

Summing up the above-mentioned results, we shall estimate $F(\nu, a)$. Since

$$\begin{aligned} F(\nu, a) &= -\{J_2+\pi i/4a\}/J_1 \\ &= -[\operatorname{Re} J_2+i\{\operatorname{Im} J_2+\pi/4a\}] \\ &\quad /(\operatorname{Re} J_1+i\operatorname{Im} J_1). \end{aligned} \tag{3.51}$$

$F(\nu, a)$ becomes infinite at each zero of J_1 and vanishes at each zero of $J_2+i\pi/4a$, which is given by the intersection of

$$\operatorname{Re} J_2=0 \quad \text{and} \quad \operatorname{Im} J_2+\pi/4a=0,$$

if none of the zeros of the numerator coincides with those of the denominator. The zeros of $J_2+i\pi/4a$ are indicated by the symbolx in Fig. 6, drawn referring to the relieves of J_2, which can be constructed in the same way as J_1.

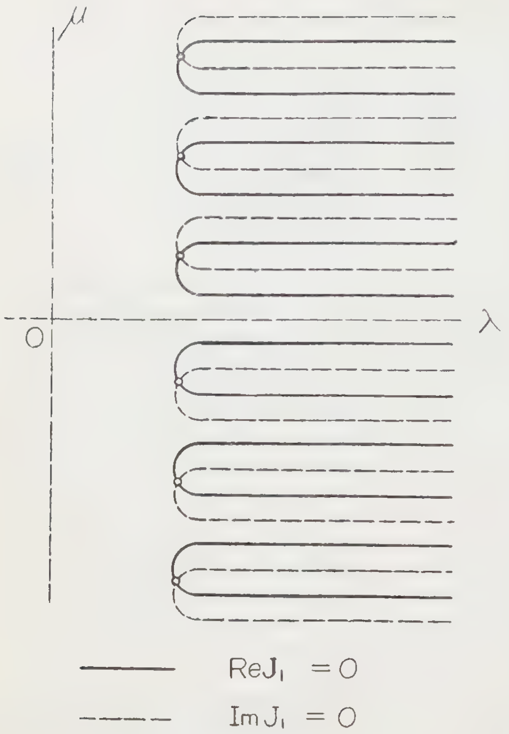

Fig. 5.

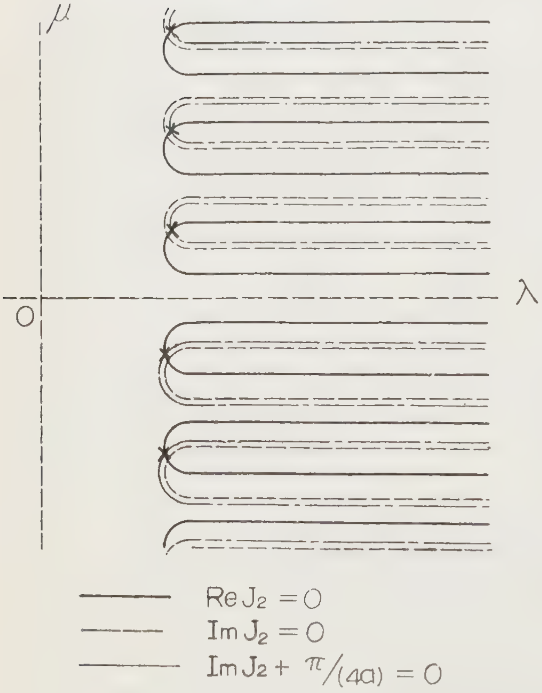

Fig. 6.

It is to be noted here that all the points indicated by ○ are not poles of $F(\nu, a)$ and that the points indicated by × not always zeros of $F(\nu, a)$. Since by (3.1) and (3.42)

$$J_1=(\pi^2/8)H_\nu^{(1)}(a)H_\nu^{(2)}(a)\ ,$$

the zeros of J_1, the points indicated by symbol ○ in Fig. 5, comprise not only the zeros of $H_\nu^{(2)}(a)$ but also those of $H_\nu^{(1)}(a)$, their values being complex comjugate of one another because of the relation

$$\overline{H_\nu^{(1)}(a)}=H_{\bar{\nu}}^{(2)}(a)\ ,$$

for real a.

Further, anticipating the results of the later discussions, that $H_\nu^{(2)}(a)$ does not vanish in the first quadrant but in the fourth and as to $H_\nu^{(1)}(a)$ the reverse is true, we can conclude that the upper series of zeros belong to $H_\nu^{(1)}(a)$ and the lower one to $H_\nu^{(2)}(a)$. Now, since $F(\nu, a)$ becomes infinite at every zero of $H_\nu^{(2)}(a)$, and only there, owing to the fact that $H_\nu^{(2)}(a)$ and $H_\nu^{(2)\prime}(a)$ do not vanish simultaneously, it is easily seen that the upper series of zeros of $J_2+\pi i/4a$, indicated by ×, and the upper series of those of J_1, indicated by ○, just coincide; in other words, the zeros of $F(\nu, a)$ are the lower series of the points indicated by × and the poles of $F(\nu, a)$ are the lower series of those indicated by ○. Hence it becomes clear that $F(\nu, a)$ has an infinite number of zeros and poles of the first order within a relatively narrow region extending from $\nu=a$ to $-\infty i$; we shall henceforth refer to this region as the *oscillatory* region.

Combining (3.49), (3.50) and (3.51) we have

$$F(\nu, a)=-(1+\mu^2/a^2)^{1/2}\{1+O(a^{-1})\}\ \text{for}\ \lambda\ll 1\ ,$$

and

$$F(\nu, a)=-\sinh\xi_0\{1+O(a^{-1})\}$$
$$=-(\lambda^2/a^2-1)^{1/2}\{1+O(a^{-1})\}\ \text{for}\ \lambda>a,$$

where $\nu=\lambda+\mu i.$, hence we may express $F(\nu, a)$ for the whole ν-plane except the oscillatory regions as

$$F(\nu, a)=-(\nu^2/a^2-1)^{1/2}\{1+O(a^{-1})\}.$$

Here, referring to such a Riemann surface as shown in Fig. 7, which has in the right half plane a cut from a to $-\infty i$ within the oscillatory region, we assume as the argument of $(\quad)^{1/2}$ such one as vanishes when ν tends to $+\infty+i\varepsilon$. This estimation may seem at first sight to be too bold but its legitimacy will be soon shown. Further it is to be added that $|F(\nu, a)|\gtrsim 1$ except in the oscillatory regions.

Thus the analytical behavior of $F(\nu, a)$ has been made intuitive, though roughly. To determine the zeros of $f_1(\nu)$, however, we must have a closer estimate of $F(\nu, a)$ and closer location of its zeros and poles; such a problem will be dealt with in the following section. The reason why we have consumed so much space without going straightforwardly to the next section will become clear in Part II, where we shall encounter such a problem as soluble only by employing the results of the discussions here.

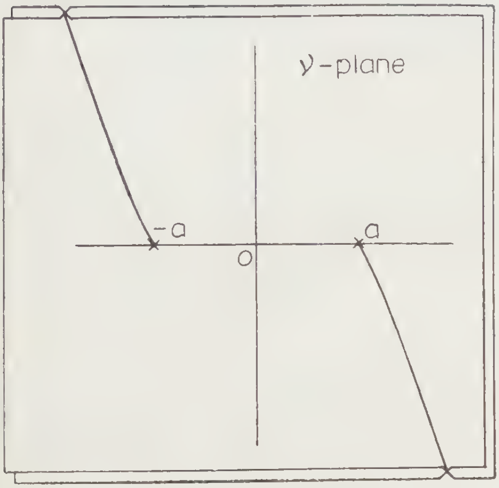

Fig. 7.

§ 4. Closer Evaluation of $F(\nu, a)$

In order to obtain a closer estimate of $F(\nu, a)$ we shall approximate $H_\nu{}^{(2)}(a)$ and $H_\nu{}^{(2)\prime}(a)$, which constitute the denominator and numerator of $F(\nu, a)$, by using the asymptotic expansions for large a and ν. The asymptotic expansions give a qualitatively correct account of the behavior of the functions even for not so large a and ν.

4.1 Asymptotic expansion of $H_\nu{}^{(2)}$ for large and a

We shall only recapitulate the result of the study of Watson and others, so far as necessary to the following discussions.

If we assume

$$\nu = a\cosh\gamma = a\cosh(\alpha + i\beta),$$

where $O < \beta < \pi$ and α any real number, then we can express $H_\nu{}^{(1)}(a)$ and $H_\nu{}^{(2)}(a)$ as

$$\left.\begin{aligned} H_\nu{}^{(1)}(a) &= \frac{1}{\pi i}\int_{-\infty}^{\infty+\pi i} e^{-af(w)}dw\,, \\ H_\nu{}^{(2)}(a) &= \frac{1}{\pi i}\int_{-\infty}^{\infty-\pi i} e^{-af(w)}dw \\ &= -\frac{1}{\pi i}\int_{-\infty+\pi i}^{\infty} e^{af(w)}dw\,, \end{aligned}\right\} \tag{4.1}$$

where

$$f(w) \equiv w\cosh\gamma - \sinh w\,.$$

It is to be noted that the Riemann surface here is different from that in § *3.3* and therefore one must scrutinize the arguments of many valued functions when applying the formulas. The coexistence of two different Riemann surfaces in our discussions does not mean any confusion but rather these two ways of treatment are complementary to one another, as one may recognize later.

To evaluate the above integrals, we choose such contours as correspond to the steepest descent through the stationary point of the integrand $w = \gamma$, i.e. the curve whose equation is $\operatorname{Im} f(w) = \operatorname{Im} f(\gamma)$. There are two branches through $w = \gamma$, their slopes there being

$$\pm(1/4)\pi + (1/2)\tan^{-1}(\tanh\alpha\cot\beta),$$

where the $\tan^{-1}$ denotes acute angle. The integrals along these branches (i) and (ii) are respectively denoted by

$$S_\nu{}^{(1)}(a) = \frac{1}{\pi i}\int_{(i)} e^{-af(w)}dw\,,$$

$$S_\nu{}^{(2)}(a) = -\frac{1}{\pi i}\int_{(ii)} e^{af(w)}dw\,,$$

whose asymptotic expansions are

$$\left.\begin{aligned} S_\nu{}^{(1)}(a) &\sim \left(-\frac{1}{2}\nu\pi i\tanh\gamma\right)^{-1/2}\exp\left\{\nu(\tanh\gamma-\gamma)-\frac{1}{4}\pi i\right\}\sum_{m=0}^{\infty}\frac{\Gamma(m+\frac{1}{2})}{\Gamma(\frac{1}{2})}A_m\left(\frac{1}{2}\nu\tanh\gamma\right)^{-m}, \\ S_\nu{}^{(2)}(a) &\sim \left(-\frac{1}{2}\nu\pi i\tanh\gamma\right)^{-1/2}\exp\left\{-\nu(\tanh\gamma-\gamma)+\frac{1}{4}\pi i\right\}\sum_{m=0}^{\infty}\frac{\Gamma(m+\frac{1}{2})}{\Gamma(\frac{1}{2})}A_m\left(-\frac{1}{2}\nu\tanh\gamma\right)^{-m}, \end{aligned}\right\} \tag{4.2}$$

where

$$\arg\{-(1/2)\nu\pi i\tanh\gamma) = \arg(-i\sinh\gamma)$$

and the value of $\arg(-i\sinh\gamma)$ which lies between $-(1/2)\pi$ and $(1/2)\pi$ is to be taken; the values of A_1, A_2, ····· are

$$A_0=1,\quad A_1=1/8-(5/24)\coth^2\gamma,\quad A_2=3/128-(77/576)\coth^2\gamma+(385/3456)\coth^4\gamma,\ \cdots\cdots .$$

These asymptotic expansions are invalid for such values of ν as correspond to small γ, this case being to be dealt with in another way.

Since $S_\nu^{(1)}(a)$ and $S_\nu^{(2)}(a)$ are solutions of Bessel's differential equation, they are plainly to be represented as linear combinations of $H_\nu^{(1)}(a)$ and $H_\nu^{(2)}(a)$, the coefficients being to be determined by considering the terminal points of the above contours, which vary correspondingly to various values of γ, or to those of ν. Here we shall rewrite Watson's table of $H_\nu^{(1)}(a)$ and $H_\nu^{(2)}(a)$ for various values of ν in a form suitable for the following discussion, together with Figs. 8 and 9, indicating the corresponding regions of ν and γ respectively.

Table I.

Regions	$H_\nu^{(1)}(a)$	$H_\nu^{(2)}(a)$
1	$S_\nu^{(1)}(a)$	$S_\nu^{(2)}(a)$
2	$S_\nu^{(1)}(a)-S_\nu^{(2)}(a)$	$S_\nu^{(2)}(a)$
3	$S_\nu^{(1)}(a)$	$S_\nu^{(2)}(a)-S_\nu^{(1)}(a)$
4	$S_\nu^{(1)}(a)$	$S_\nu^{(2)}(a)-e^{2\nu\pi i}S_\nu^{(1)}(a)$
5	$S_\nu^{(1)}(a)-e^{-2\nu\pi i}S_\nu^{(2)}(a)$	$S_\nu^{(2)}(a)$
6a	$\dfrac{\sin(M+1)\nu\pi}{\sin\nu\pi}e^{M\nu\pi i}S_\nu^{(1)}(a)-S_\nu^{(2)}(a)$	$S_\nu^{(2)}(a)-\dfrac{\sin M\nu\pi}{\sin\nu\pi}e^{(M+1)\nu\pi i}S_\nu^{(1)}(a)$
6b	$S_\nu^{(1)}(a)-\dfrac{\sin N\nu\pi}{\sin\nu\pi}e^{(N-1)\nu\pi i}S_\nu^{(2)}(a)$	$\dfrac{\sin(N+1)\nu\pi}{\sin\nu\pi}e^{N\nu\pi i}S_\nu^{(2)}(a)-e^{2\nu\pi i}S_\nu^{(1)}(a)$
7a	$S_\nu^{(1)}(a)-\dfrac{\sin M\nu\pi}{\sin\nu\pi}e^{-(M+1)\nu\pi i}S_\nu^{(2)}(a)$	$\dfrac{\sin(M+1)\nu\pi}{\sin\nu\pi}e^{-M\nu\pi i}S_\nu^{(2)}(a)-S_\nu^{(1)}(a)$
7b	$\dfrac{\sin(N+1)\nu\pi}{\sin\nu\pi}e^{-N\nu\pi i}S_\nu^{(1)}(a)-e^{-2\nu\pi i}S_\nu^{(2)}(a)$	$S_\nu^{(2)}(a)-\dfrac{\sin N\nu\pi}{\sin\nu\pi}e^{-(N-1)\nu\pi i}S_\nu^{(1)}(a)$

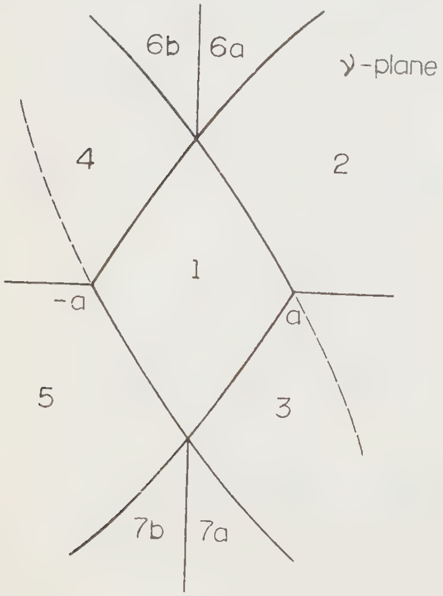

Fig. 8.

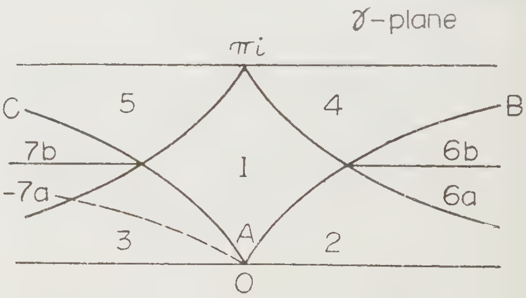

Fig. 9.

In the figures the curves AB, AC correspond to

$$1-\beta\cot\beta-\alpha\tanh\alpha=0,$$

and in the table M denotes the smallest integer for which

$$1-\alpha\tanh\alpha+\{(M+1)\pi-\beta\}\cot\beta>0,\quad \text{when}\quad \cot\beta>0,$$

and N the smallest integer for which

$$1-\alpha\tanh\alpha-(N\pi+\beta)\cot\beta>0,\ \text{when}\ \cot\beta<0.$$

4.2 *Asymptotic expansion of $H_\nu^{(2)\prime}(a)$.*

The values of $H_\nu^{(2)\prime}(a)$ corresponding to various values of ν are obtained, when in the above table $S_\nu^{(1)}(a)$ and $S_\nu^{(2)}(a)$ are replaced by $S_\nu^{(1)\prime}(a)$ and $S_\nu^{(2)\prime}(a)$. The asymptotic expansions of $S_\nu^{(1)\prime}(a)$ and $S_\nu^{(2)\prime}(a)$ are given by differentiation of the above expressions of $S_\nu^{(1)}(a)$ and $S_\nu^{(2)}(a)$ as follows:

$$\left.\begin{aligned}S_\nu^{(1)\prime}(a)&\sim\{-(1/2)\nu\pi i\tanh\gamma\}^{-1/2}\sinh\gamma\cdot\exp\{\nu(\tanh\gamma-\gamma)-(1/4)\pi i\}\{1+(-3/8+(7/24)\coth^2\gamma)\\&\quad\times(\nu\tanh\gamma)^{-1}+\{-15/128+(33/64)\coth^2\gamma-(455/1152)\coth^4\gamma)(\nu\tanh\gamma)^{-2}+\cdots\cdot\},\\S_\nu^{(2)\prime}(a)&\sim-(-(1/2)\nu\pi i\tanh\gamma)^{-1/2}\sinh\gamma\cdot\exp\{-\nu(\tanh\gamma-\gamma)+(1/4)\pi i\}\{1-(-3/8\\&\quad+((7/24)\coth^2\gamma)(\nu\tanh\gamma)^{-1}+(-15/128+(33/64)\coth^2\gamma-(455/1152)\coth^4\gamma)(\nu\tanh\gamma)^{-2}+\cdots\cdot\}.\end{aligned}\right\}\tag{4.3}$$

4.4 *Asymptotic expansions of $H_\nu^{(2)}(a)$ and $H_\nu^{(2)\prime}(a)$ for $\gamma\ll 1$.*

As mentioned above, the asymptotic expansions in the preceeding sections are invalid for such values of ν as correspond to small values of γ. Such cases have already been studied by the present author [2].

Thus we have

$$\begin{aligned}H_\nu^{(2)}(a)&\sim 3^{-1/2}e^{-(1/3)\pi i}\eta[\{1+(1/10)\eta^2+(13/280-(9/50)\xi^2)\eta^4+(803/25200-921/3500)\xi^2)\eta^6\\&\quad+(-1{\cdot}3959\,\xi^{-2}+1{\cdot}3329-0{\cdot}61168\,\xi^2+0{\cdot}0054\,\xi^4)\eta^8+\cdots\cdot\}H_{-1/3}^{(2)}(\xi)+\{-(3/5)\xi^2\eta^2\\&\quad+(1/210-(3/7)\xi^2)\eta^4+(37/18900-(197/600)\xi^2+(9/250)\xi^4)\eta^6+(-2{\cdot}0929+0{\cdot}51938\xi^2\\&\quad-0{\cdot}038541\xi^4)\eta^8+\cdots\cdot\}\xi^{-1}H_{2/3}^{(2)}(\xi)],\end{aligned}\tag{4.4}$$

where

$$\xi=(i\nu/3)\tanh^3\gamma\,,\quad \eta=\tanh\gamma\,,$$

and, by differentiation with respect to a,

$$\begin{aligned}H_\nu^{(2)\prime}(a)&\sim-i3^{-1/2}e^{-(1/3)\pi i}\eta^2(\cosh\gamma)^{-1}[\{(1/15-(3/5)\xi^2)\eta^2+(1/15-(36/35)\xi^2)\eta^4+\cdots\cdot\}\xi^{-1}H_{-1/3}^{(2)}(\xi)\\&\quad+\{-1-(9/10)\eta^2+(-253/280+(9/50)\xi^2)\eta^4+\cdots\cdot\}H_{2/3}^{(2)}(\xi)].\end{aligned}\tag{4.5}$$

4.4 *Location of the poles of $F(\nu, a)$*

The estimate of $F(\nu, a)$ are simply given by the ratio of the above expressions of $H_\nu^{(2)\prime}(a)$ and of $H_\nu^{(2)}(a)$ respectively, for any ν corresponding to various regions of the ν-plane. Since it is necessary to study its behavior in the oscillatory region, we shall consider closely the poles of $F(\nu, a)$, i.e. the zeros of $H_\nu^{(2)}(a)$, and the zeros of $F(\nu, a)$, i.e. those of $H_\nu^{(2)\prime}(a)$. We shall first deal with the poles of $F(\nu, a)$, or the zeros of $H_\nu^{(2)}(a)$.

Now $S_\nu^{(1)}(a)$ and $S_\nu^{(2)}(a)$ never vanish themselves, since in the expressions

$$\begin{aligned}S_\nu^{(1)}(a)&=\frac{1}{\pi i}e^{-a\,\mathrm{Im}f(\gamma)}\int_{(i)}e^{-a\,\mathrm{Re}f(w)}dw\\&=\frac{1}{\pi i}e^{-a\,\mathrm{Im}f(\gamma)}\left\{\int_{(i)}e^{-a\mathrm{Re}f(w)}du\right.\\&\qquad\left.+i\int_{(i)}e^{-a\mathrm{Re}f(w)}dv\right\},\\S_\nu^{(2)}(a)&=-\frac{1}{\pi i}e^{a\,\mathrm{Im}f(\gamma)}\left\{\int_{(ii)}e^{a\mathrm{Re}f(w)}du\right.\\&\qquad\left.+i\int_{(ii)}e^{a\,\mathrm{Re}f(w)}dv\right\},\end{aligned}$$

derived by using the property of the integration contour, the contours, as the figures in the treatise of Watson show [(1) pp. 264–266], are not such that both du and dv change their sign in the intervals contributing to the integrals; in the case of γ being finite it is also deducible from the expansion form (4.2). Hence $H_\nu^{(2)}(a)$ never vanishes in the regions 1, 2, 5, where $H_\nu^{(2)}(a)$ is equal to $S_\nu^{(2)}(a)$.

Considering the order of magnitude of $e^{\nu\pi i}$, it is clear that $H_\nu^{(2)}(a)$ never vanishes in the region 6a and 7b, but vanishes only in a part of the regions 3,7a and 4,6b, where $S_\nu^{(2)}(a)$, $S_\nu^{(1)}(a)$ are of the same order.

In view of the expansion forms of $S_\nu^{(1)}(a)$ and $S_\nu^{(2)}(a)$ the zeros of $H_\nu^{(2)}(a)$ are given by such values of ν as corresponding to γ satisfying

$$a(\gamma\cosh\gamma-\sinh\gamma)=i(m\pi-\pi/4)\{1+O(a^{-1})\}\,,\tag{4.6}$$

for not small γ, where m denotes any positive integer; in other words, the zeros of $H_\nu^{(2)}(a)$ lie close to the curve

$$\mathrm{Re}\,(\gamma\cosh\gamma-\sinh\gamma)=0,$$

or

$$\alpha\coth\alpha-\beta\tan\beta-1=0,$$

which starts from the point $\nu=a$, forming an angle $-\pi/3$ with the real axis, passes through the medium part of the region 3 and goes off to $-\infty i$, as shown by the dotted lines in Figs. 8, 9.

To obtain the closer estimate of the zeros we have only to take as the first-approximate values of γ such $\gamma_m^{(0)}$ as satisfy

$$\operatorname{Im}(\gamma_m^{(0)}\cosh\gamma_m^{(0)}-\sinh\gamma_m^{(0)})=(m-1/4)\pi;$$

such values always exist once for any integral m, since $\operatorname{Im}(\gamma\cosh\gamma-\sinh\gamma)$ increases monotonously on the curve under consideration from zero to infinity as γ varies from O to $-\infty+(\pi/2)i$. Assuming such an expansion with unknown coefficients as

$$\gamma=\gamma_m^{(0)}(1+a_1a^{-1}+a_2a^{-2}+\cdots\cdot),$$

and the corresponding expansion of ν, we substitute them in the expansions of $S_\nu^{(1)}(a)$ and $S_\nu^{(2)}(a)$. Them we determine the coefficients $a_1, a_2, \cdots\cdot$ by equating all the coefficients of the powers of a^{-1} in the expression of $S_\nu^{(2)}(a)-S_\nu^{(1)}(a)$ to zero.

For large m it is easily seen that

$$\nu\simeq-(m-1/4)\pi i/\log m. \qquad (4.8)$$

For such values of ν as close to a, with which we are most concerned, we must discuss in another way.

4.5 Poles of $F(\nu, a)$ close to a

The relation (4.4) suggests to us that the zeros of $H_\nu^{(2)}(a)$ near a are, in the first approximation, given by those corresponding to such values of ξ as satisfy

$$H_{-1/3}^{(2)}(\xi)=0. \qquad (4.9)$$

Now, according to the study of Macdonald [(1) p. 551] the zeros of $H_{-1/3}^{(2)}(\xi)$, $H_{2/3}^{(2)}(\xi)$ are situated on the axis with $\arg\xi=\pi$. By putting

$$\xi=\rho e^{\pi i},$$

we have

$$H_{-1/2}^{(2)}(\xi)=(\sqrt{3}/2-i/2)\{\sqrt{3}J_{1/3}(\rho)-Y_{1/3}(\rho)\}; \qquad (4.10)$$

the zeros of the right-hand side are computed numerically, by using a table, say, that of Watson [(1) p. 714]. First several values are

2·3834466, 5·5101956, 8·6473577,
11·7868429, 14·9272068, ……·.

We shall take as the first-approximate values of γ those which correspond to these values of ρ, that is,

$$\gamma^{(0)}=(3\rho/a)^{1/3}e^{(5/6)\pi i}, \qquad (4.11)$$

choosing among three possible arguments of γ such one as compatible with the previous discussion. If we assume the following expansion with unknown coefficients

$$\gamma=\gamma^{(0)}(1+a_1\gamma^{(0)2}+a^2\gamma^{(0)4}+\cdots\cdot) \qquad (4.12)$$

then we have

$$\left.\begin{aligned}
\nu&=a\cosh\gamma=a\left\{1+\frac{1}{2}\gamma^{(0)^2}+\left(a_1+\frac{1}{4!}\right)\gamma^{(0)^2}+\left(\frac{1}{2}a_1^2+a_2+\frac{1}{3!}a_1+\frac{1}{6!}\right)\gamma^{(0)^6}+\cdots\cdot\right\},\\
\eta&=\gamma^{(0)}\left\{1+\left(a_1-\frac{1}{3}\right)\gamma^{(0)^2}+\left(a_2-a_1+\frac{2}{15}\right)\gamma^{(0)^4}+\cdots\cdot\right\},\\
\xi&=\rho e^{\pi i}\left\{1+\left(3a_1-\frac{1}{2}\right)\gamma^{(0)^2}+\left(3a_2+3a_1^2-\frac{5}{2}a_1+\frac{11}{40}\right)\gamma^{(0)^4}+\cdots\cdot\right\},\\
H_{-1/3}^{(2)}(\xi)&=H_{2/3}^{(2)}(\rho e^{\pi i})\gamma^{(0)^2}\left[\rho\left(3a_1-\frac{1}{2}\right)+\left\{\rho\left(3a_2+3a_1^2-\frac{5}{2}a_1+\frac{33}{120}\right)\right.\right.\\
&\qquad\left.\left.-\frac{\rho}{2}\left(3a_2-\frac{1}{2}\right)^2\right\}\gamma^{(0)^2}+\cdots\cdot\right],\\
H_{2/3}^{(2)}(\xi)&=H_{2/3}^{(2)}(\rho e^{\pi i})\left[1-\frac{2}{3}\left(3a_1-\frac{1}{2}\right)\gamma^{(0)^2}+\cdots\cdot\right],
\end{aligned}\right\} \qquad (4.13)$$

by expanding $H_{-1/3}^{(2)}(\xi)$ and $H_{2/3}^{(2)}(\xi)$ about $\xi=\rho e^{\pi i}$. Having substituted these expressions in the right of (4.4) and arranged all the terms in a form of expansion with respect to $\gamma^{(0)}$, we equate each coefficient to zero, and obtain

$$a_1=-1/30, \qquad a_2=41/12600+1/630\rho^2, \cdots\cdots.$$

Thus the zeros of $H_\nu^{(2)}(a)$ required are

$$\nu=a\left[1+\frac{1}{2}\left(\frac{3\rho}{a}\right)^{2/3}e^{(3/5)\pi i}+\frac{1}{120}\left(\frac{3\rho}{a}\right)^{4/3}e^{(4/3)\pi i}-\left(\frac{-1}{2800}+\frac{1}{630\rho^2}\right)\left(\frac{3\rho^2}{a}\right)^2+\cdots\cdot\right], \qquad (4.14)$$

where

$\rho=$2·3834466, 5·5101956, 8·6473577, 11·7868429, 14·9272068. ……·.

4.6. *Location of the zeros of $F(\nu, a)$*

The zeros of $F(\nu, a)$, or those of $H_\nu^{(2)\prime}(a)$ can be dealt with in a similar way; they are situated in the fourth quadrant and approximately given by the equation

$$S_\nu^{(2)\prime}(a)-S_\nu^{(1)\prime}(a)\simeq-\sinh\gamma\{S_\nu^{(2)}(a)+S_\nu^{(2)}(a)\}=0\,; \qquad (4.15)$$

reserving $\sinh\gamma=0$, which belong to the region of the expansions being invalid, they are approximately given by

$$a(\gamma\cosh\gamma-\sinh\gamma)=\{(2m+1)/2-1/4\}\pi i\,,$$

m being any positive integer. Thus it becomes plain, that the poles and zeros of $F(\nu, a)$ are situated alternately along the curve stated above.

For large m we have

$$\nu\simeq-(m+1/4)\pi i/\log m. \qquad (4.16)$$

For such zeros as close to a we must consider (4.5), which shows that they are approximately given by the values corresponding to such ξ as satisfy

$$H_{2/3}^{(2)}(\xi)=0. \qquad (4.17)$$

The first several roots of this equation are represented by $\rho e^{\pi i}$, where

$$\rho=0{\cdot}6853843,\quad 3{\cdot}9027676,\quad 7{\cdot}0549300,\quad 10{\cdot}2006884,\quad 13{\cdot}3445027,\quad \cdots\cdots,$$

by employing the tables of Hankel function of order 1/3 and of their derivative [3] and others. The first-approximate values of γ are $(3\rho/a)^{1/3}e^{(5/6)\pi i}=\gamma^{(0)}$.

Assuming the expansion

$$\gamma=\gamma^{(0)}\{1+a_1\gamma^{(0)^2}+a_2\gamma^{(0)^4}+\cdots\cdots\}\,, \qquad (4.18)$$

and the therefore

$$\left.\begin{aligned}H_{-1/3}^{(2)}(\xi)&=H_{-1/3}^{(2)}(\rho e^{\pi i})\cdot\{1-(a_1-1/6)\gamma^{(0)^2}+\cdots\cdot\}\\ H_{2/3}^{(2)}(\xi)&=H_{-1/3}^{(2)}(\rho e^{\pi i})\gamma^{(0)^2}\{-\rho(3a_1-1/2)\\&\quad-\rho(3a_2-(3/2)a_1^2-a_1+3/20)\gamma^{(0)^2}+\cdots\cdot\}\,,\end{aligned}\right\} \qquad (4.19)$$

we obtain, after substituting in (4.5) and equating to zere,

$$a_1=(1/45\rho^2)-1/30,$$
$$a_2=(1/1350\rho^4)-(1/135\rho^2)+41/1260,\quad\cdots\cdots,$$

Thus we have as the zeros of $F(\nu, a)$

$$\nu=a\left[1+\frac{1}{2}\left(\frac{3\rho}{a}\right)^{2/3}e^{(5/3)\pi i}+\left(\frac{1}{45\rho^2}+\frac{1}{120}\right)\cdot\left(\frac{3\rho}{a}\right)^{4/3}e^{(4/3)\pi i}+\left(\frac{1}{2025\rho^4}+\frac{1}{225\rho^4}+\frac{1}{2800}\right)\cdot\left(\frac{3\rho}{a}\right)^2+\cdots\cdots\right], \qquad (4.20)$$

with the above-mentioned values of ρ.

§ 5. Zeros of $f_1(\nu)$

On the basis of the preceeding discussions we shall now consider how to find out the zeros of $f_1(\nu)$, that is, the solutions of the equation

$$F(\nu, a)+\varphi(\nu^2, a)=0. \qquad (5.1)$$

We shall deal with it, separating the half ν-plane into two regions specified as follows.

(a) In the oscillatory region an infinite number of the zeros and poles, of the first order, of $F(\nu, a)$ are placed alternately near the curve whose equation is

$$\mathrm{Re}\,(\gamma\cosh\gamma-\sinh\lambda)=0\,.$$

Therefore, $F(\nu, a)$ assumes any assigned complex value once and only once in the vicinity of each pair of one of its zeros and the neighboring pole, at the intersection of one of the equal-modulus contours of $F(\nu, a)$ between them and one of the equal-argument contours joining them, and hence one and only one solution of the Eq. (5.1) exists for such a pair, provided that $\varphi(\nu^2, a)$ varies gradually there. By the use of (4.3) and Table I, this is approximately given by

$$\exp\{2a(\gamma\cosh\gamma-\sinh\lambda)+\tfrac{1}{2}\pi i\}=-\frac{\sinh\gamma-\varphi(a^2\cosh^2\gamma, a)}{\sinh\gamma+\varphi(a^2\cosh^2\gamma, a)}\,, \qquad (5.2)$$

If

$$|\sinh\gamma|\gg|\varphi(a^2\cosh^2\gamma, a)|$$

or

$$|\sinh\gamma|\ll|\varphi(a^2\cosh^2\gamma, a)|,$$

then the zeros are given by the values of ν corresponding to

$$2a(\gamma\cosh\gamma-\sinh\gamma)+\pi i/2\simeq(2m+1)\pi i\,,$$

or

$$2a(\gamma\cosh\gamma-\sinh\gamma)+\pi i/2\simeq2m\pi i\,,$$

where m is any positive integer; if $\sinh\gamma$ and $\varphi(a^2\cosh^2\gamma, a)$ are of the same order of magnitude, we have to solve (5.2) numerically, whose solutions must lie in the intermediate positions.

For higher m they are of the order of

$$-m\pi i/\log m.$$

For such zeros as close to a, the Eq. (5.1) becomes

$$-i\eta(\cosh\gamma)^{-1}\Big[\Big\{\Big(\frac{1}{15}-\frac{3}{5}\xi^2\Big)\eta^2+\Big(\frac{1}{15}-\frac{36}{35}\xi^2\Big)\eta^4+\cdots\cdots\Big\}\xi^{-1}H_{-1/3}{}^{(2)}(\xi)+\Big\{-1-\frac{9}{10}\eta^2$$
$$+\Big(-\frac{253}{280}+\frac{9}{50}\xi^2\Big)\eta^4+\cdots\cdots\Big\}H_{2/3}{}^{(2)}(\xi)\Big]\Big/\Big[\Big\{1+\frac{1}{10}\eta^2+\Big(\frac{13}{280}-\frac{9}{50}\xi^4\Big)\eta^4+\cdots\cdots\Big\}H_{-1/3}{}^{(2)}(\xi)$$
$$+\Big\{-\frac{3}{5}\xi^2\eta^3+\Big(\frac{1}{210}-\frac{3}{7}\xi^2\Big)\eta^4+\cdots\cdots\Big\}\xi^{-1}H_{2,3}{}^{(2)}(\xi)\Big]+\varphi(a^2\cosh^2\gamma, a)=0, \qquad (5.3)$$

considering the asymptotic expansions of $H_\nu{}^{(2)}(a)$ and $H_\nu{}^{(2)\prime}(a)$ for small γ (4.4), (4.5), so we may take as first-approximate values of γ such values as correspond to

$$H_{2/3}{}^{(2)}(\xi)=0\ ,$$

if $\varphi(a^2, a)<\eta$, and such values as correspond to

$$H_{-1/3}{}^{(2)}(\xi)=0,$$

if $\varphi(a^2, a)>\eta$; further calculation is quite similar to that concerning the zeros of $H_\nu{}^{(2)}$ and $H_\nu{}^{(2)\prime}(a)$.

(b) In the remaining region of the ν-plane

$$F(\nu, a)\simeq-\{(\nu/a)^2-1\}^{1/2},$$

as shown in § 3.3; hence we have only to solve

$$-\{(\nu/a)^2-1\}^{1/2}+\varphi(\nu^2, a)=0, \qquad (5.4)$$

in order to obtain the first-approximate values.

Especially if $|\varphi(\nu, a)|<1$ for any value of ν, no such values of ν exist, since alway $|F(\nu, a)|\gtrsim 1$ in this region, as evident from the results in § 3.3.

If $\varphi(\nu^2, a)$ is real whatever value ν may assume, we can conclude that no zeros of (5.1) exist here, since, while $\{(\nu/a)-1\}^{1/2}\}$ becomes real only when ν is real, greater than a, we have already proved in § 2.1 that no such zeros exist.

If we have obtained any solutions of (5.4), $\nu^{(0)}$, then, in order to obtain closer estimates of the zeros, we have only to substitute the expansion of ν with unknown coefficients

$$\nu=\nu^{(0)}(1+a_1a^{-1}+a_2a^{-2}+\cdots\cdots),$$

and those which are derived from it in the asymptotic expansions of $H_\nu{}^{(2)}(a)$ and $H_\nu{}^{(2)\prime}(a)$ and in $\varphi(\nu^2, a)$ on the left-hand side of (5.1), and to determine the coefficients a_1, a_2, $\cdots\cdots$ by equating the coefficients of the powers of a^{-1} to zero.

Since asymptotic expansions for large a are involved in this procedure of calculating the zeros of $f_1(\nu)$, we cannot get rid of considerable error, if we are to apply it to the case of $a\lesssim 1$, although the asymptotic expansions still give a qualitatively correct account of the behavior of the functions. Then it is desirable, if necessary, to compute them numerically by interpolation from the values of $H_\nu{}^{(2)}(a)$, $H_\nu{}^{(2)\prime}(a)$ and $\varphi(\nu^2, a)$ corresponding to several such values of ν as enclosing the approximate values determined by this method. Fortunately the series defining $H_\nu{}^{(2)}$(a) are rapidly convergent for $a\lesssim 1$.

§ 6. Example

As an example we shall deal with the solution of

$$H_\nu{}^{(2)\prime}(a)+(n/a)H_\nu{}^{(2)}(a)=0\ , \qquad (6.1)$$

the equation occuring actually in the case of the diffraction of waves by a sphere; n is a real constant.

Since $\varphi(\nu^2, a)=n/a$ is real, the zeros lie only in the oscillatory region of ν-plane. In actual n/a is almost always less than unity.

(a) For $\gamma\geqq O(1)$, the values of γ corresponding to the zeros satisfy

$$\exp\{2a(\gamma\cosh\gamma-\sinh\gamma)+\pi i/2\}$$
$$=-(\sinh\gamma-n/a)/(\sinh\gamma+n/a)\{O(a^{-1})\}\ ,$$
$$=-1+O(a^{-1}).$$

Therefore

$$2a(\gamma\cosh\gamma-\sinh\gamma)=(2m+1/2)\pi i\{1+O(a^{-1})\}, \qquad (6.2)$$

where m denotes a positive integer.

(b) For $|\gamma|\gg 1$, we obtain as the zeros

$$\nu\simeq-(m+1/4)\pi i/\log m\ ,$$

m being a higher integer.

(c) For $|\gamma|\ll 1$, we shall estimate them, employing as the first-approximative values those corresponding to

$$H_{2/3}{}^{(2)}(\xi)=0\ , \qquad (4.17)$$

whose solutions are given by $\xi=\rho e^{\pi i}$, where

$$\rho=0{\cdot}6853843,\quad 3{\cdot}9027676,\quad 7{\cdot}0549300,$$
$$10{\cdot}2006884,\ 13{\cdot}3445027,\ \cdots\cdots.$$

If we suppose the following with unknown coefficients,

$$\gamma=\gamma^{(0)}(1+a_1\gamma^{(0)2}+a_2\gamma^{(0)4}+\cdots\cdots)\ , \qquad (6.4)$$

where

$$\gamma^{(0)}=(3\rho/a)^{1/3}e^{(5/6)\pi i},$$

then we have the expantion formulas (4.13). Substituting these expressions in the Eq. (5.3) with $\varphi(\nu^2, a)$ replaced by n/a, we equate the coefficients of the powers of $\gamma^{(0)}$ to zero and obtain

$$\left.\begin{aligned} &a_1=-1/30-(5n-1)/45\rho^2\,, \\ &a_2=41/12600-(1/\rho^2)(11/1350-n/30+n^2/54)\,, \\ &\quad\cdots\cdots\cdots. \end{aligned}\right\} \tag{6.5}$$

Thus we have as the solutions of (5.1)

$$\begin{aligned}\nu=a\Big[\,&1+\frac{1}{2}\left(\frac{3\rho}{a}\right)^{2/4}e^{(5/3)\pi i} \\ &+\left(\frac{1}{120}-\frac{5n-1}{45\rho^2}\right)\left(\frac{3\rho}{a}\right)^{4/3}e^{(4/3)\pi i} \\ &+\left\{\frac{1}{2800}-\frac{5n-2}{450\rho^2}+\left(\frac{5n-1}{45\rho^2}\right)^2\right\}\left(\frac{3\rho}{a}\right)^2 \\ &+\cdots\cdots\Big],\end{aligned} \tag{6.6}$$

with the above-mentioned values of ρ.

Acknowledgement

The author is sincerely grateful to Professor Isao Imai for his continued encouragement and useful advice out of friendship and also to Dr. Hisamitu Nisi, the President of Saga University, and Dr. Tatudiro Sasaki, the Director of the Numerical Computation Bureau, who have given all kinds of facilities for the research.

References

1) G. N. Watson: Theory of Bessel Functions, Cambridge University Press, London, 1922.

2) M. Nagase: Journ. Phys. Soc., Japan **9** (1954) 296–297.

3) Staff of the Computation Laboratory: Tables of the Modified Hankel Functions of Order One-third and of their Derivatives, Harvard University Press, Cambridge, Mass., 1945.

JOURNAL OF THE PHYSICAL SOCIETY OF JAPAN Vol. 9, No. 5, SEP.—OCT., 1954

On the Zeros of Certain Transcendental Funcitons related to Hankel Functions. Part II

By Masahumi NAGASE

Department of Physics, Faculty of Liberal Arts,
Saga University, Saga, Japan

(Received March 27, 1954)

The aim of this paper is to show that the methods discussed in Part I to estimate the zeros of linear homogeneous forms with respect to Hankel function and its derivative is applicable also to the case of higher than linear forms. As a typical form we take the bilinear form

$$f_2(\nu)\equiv\varphi_1(\nu^2, a, m)H_\nu^{(2)}(a)H_\nu^{(2)}(ma)+\varphi_2(\nu^2, a, m)dH_\nu^{(2)}(a)/da\cdot H_\nu^{(2)}(ma)$$
$$+\varphi_3(\nu^2, a, m)H_\nu^{(2)}(a)dH_\nu^{(2)}(ma)/d(ma)$$
$$+\varphi_4(\nu^2, a, m)dH_\nu^{(2)}(a)/da\cdot dH_\nu^{(2)}(ma)/d(ma)$$

qua function of ν. As an example we discuss in detail the form such that

$$\varphi_1\equiv 1-\frac{4\nu^2}{a^2}+\frac{4\nu^2(\nu^2-9/4)}{a^4}, \qquad \varphi_2\equiv\frac{2}{a}\left(1+\frac{\nu^2-9/4}{a^2}\right),$$
$$\varphi_3\equiv\frac{4m}{a}\left(1-\frac{\nu^2-9/4}{2a^2}\right), \qquad \varphi_4\equiv-\frac{4m}{a^2}\left(\nu^2-\frac{9}{4}\right)$$

with $m<1/\sqrt{2}$, which appears actually in the case of the diffraction of elastic waves by a sphere. This is shown to have as zeros, besides the one whose real part is somewhat greater than a and imaginary part $=-O(ae^{-a})$, those such as

$$\nu=a\Big[1+\left(\frac{3\rho}{a}\right)^{2/3}\exp\left(\frac{5}{3}\pi i\right)+\frac{4}{3\rho}\sqrt{1-m^2}\frac{3\rho}{a}+\frac{1}{120}\left(\frac{3\rho}{a}\right)^{4/3}\exp\left(\frac{4}{3}\pi i\right)$$
$$-\left\{-\frac{17}{6}+\frac{1}{2}\frac{1}{1-m^2}+\frac{16}{3}(1-m^2)\right\}\frac{4}{3\rho}\sqrt{1-m^2}\left(\frac{3\rho}{a}\right)^{5/3}\exp\left(\frac{2}{3}\pi i\right)$$
$$+\left\{\frac{1}{2800}+\frac{171}{70\rho^2}-\frac{80}{9\rho_2}(1-m^2)-\frac{2}{9\rho^2}\frac{1}{1-m^2}+\frac{128}{9\rho^2}(1-m^2)^2\right\}\left(\frac{3\rho}{a}\right)^2+\cdots\Big]$$

and

$$\nu=ma\Big[1+\frac{1}{2}\left(\frac{3\rho}{ma}\right)^{2/3}\exp\left(\frac{5}{3}\pi i\right)-\frac{4m^3}{3\rho}\frac{(1-m^2)^{1/2}}{(2m^2-1)^2}\left(\frac{3\rho}{ma}\right)\exp\left(\frac{\pi}{2}i\right)$$
$$+\frac{1}{120}\left(\frac{3\rho}{ma}\right)^{4/3}\exp\left(\frac{4}{3}\pi i\right)-\left\{\frac{1}{6}-\frac{2m^2+1}{2m^2-1}-\frac{1}{2}\frac{m^2}{1-m^2}\right.$$
$$\left.-\frac{16m^2}{3}\frac{(1-m^2)}{(2m^2-1)^4}\right\}\frac{4m^3}{3\rho}\frac{(1-m^2)^{1/2}}{(2m^2-1)^2}\left(\frac{3\rho}{ma}\right)^{5/3}\exp\left(\frac{\pi}{6}i\right)$$
$$+\left\{\frac{1}{2800}-\frac{1}{630\rho^2}-\left(\frac{1}{2}-2\cdot\frac{2m^2+1}{2m^2-1}-\frac{m^2}{1-m^2}-\frac{1}{m^2}+\frac{1}{8m^4}\right.\right.$$
$$\left.\left.+\frac{1}{2m^4}\cdot\frac{(m^2-1/2)^2}{(m^2-1)^2}\right)\frac{16m^6}{9\rho^2}\cdot\frac{1-m^2}{(2m^2-1)^4}+\frac{128m^{12}(1-m^2)^2}{9\rho^2(2m^2-1)^8}\right\}\left(\frac{3\rho}{ma}\right)^2+\cdots\Big],$$

where ρ denotes one of the following values:

2.3834466, 5.5101956, 8.6473577, 11.7868429, 14.9272068, $\cdots$.

§ 1. General Considerations

We discussed in Part I concerning the zeros of

$$f_1(\nu)\equiv\varphi_1(\nu^2, a)H\nu^{(2)}(a)+\varphi_2(\nu^2, a)H\nu^{(2)\prime}(a) \tag{1.1}$$

qua function of complex ν. We shall here show how the method described there can be applied to the case of higher than linear forms. We shall choose here as a typical form the function

$$\begin{aligned} f_2(\nu) \equiv & \varphi_1(\nu^2, a, m) H\nu^{(2)}(a) H\nu^{(2)}(ma) \\ & + \varphi_2(\nu^2, a, m) H\nu^{(2)\prime}(a) H\nu^{(2)}(ma) \\ & + \varphi_5(\nu^2, a, m) H\nu^{(2)}(a) H\nu^{(2)\prime}(ma) \\ & + \varphi_4(\nu^2, a, m) H\nu^{(2)}(a) H\nu^{(2)\prime}(ma), \end{aligned} \tag{1.2}$$

where φ_1, φ_2, φ_3, and φ_4 are any given functions of ν^2, a, and m, satisfying suitable conditions, if necessary, m being a positive parameter, which we assume less than unity without losing the generality, since if $m=1$ we can reduce this case to that of linear forms by breaking up $f_2(\nu)$ into factors of the form of $f_1(\nu)$ and for $m>1$ we may take $ma=a'$ a new parameter. Any presumptions and definitions not specified here are to be interpreted as those in Part. I. It will be easily seen from our procedure that this method is also applicable to the higher than bilinear forms.

Since any two of $H\nu^{(2)}(a)$, $H\nu^{(2)}(ma)$, $H\nu^{(2)\prime}(a)$ and $H\nu^{(2)\prime}(ma)$ do not vanish simultaneously qua functions of ν, the zeros of f_2 are equivalent to those of

$$\frac{f_2(\nu)}{\varphi_4 \cdot H\nu^{(2)}(a) H\nu^{(2)}(ma)} = \frac{\varphi_1}{\varphi_4} + \frac{\varphi_2}{\varphi_4} \cdot \frac{H\nu^{(2)\prime}(a)}{H\nu^{(2)}(a)} + \frac{\varphi_3}{\varphi_4} \cdot \frac{H\nu^{(2)\prime}(ma)}{H\nu^{(2)}(ma)} + \frac{H\nu^{(2)\prime}(a)}{H\nu^{(2)}(a)} \cdot \frac{H\nu^{(2)\prime}(ma)}{H\nu^{(2)}(ma)}, \tag{1.3}$$

except for such an accidental case that φ_4, φ_ν and $H\nu^{(2)}(a)$ or φ_4, φ_3 and $H\nu^{(2)}(ma)$ have any common zeros. We may therefore consider the form

$$\begin{aligned} f_2(\nu) = & F(\nu, a) \cdot F(\nu, ma) + \varphi_1(\nu^2, a, m) F(\nu, ma) \\ & + \varphi_2(\nu^2, a, m) F(\nu, a,) + \varphi_3(\nu^2, a, m) \end{aligned} \tag{1.4}$$

anew instead of the previous one, where $F(\nu, a)$ denotes $H\nu^{(2)\prime}(a)/H\nu^{(2)}(a)$. As to the exceptinal cases specific consideration is needed in each particular case. In such a case we have only to consider

$$\frac{f_2(\nu)}{\varphi_1 H\nu^{(2)\prime}(a) H\nu^{(2)\prime}(ma)} = \frac{1}{F(\nu, a) F(\nu, ma)} + \frac{\varphi_2}{\varphi_1} \cdot \frac{1}{F(\nu, ma)} + \frac{\varphi_3}{\varphi_1} \cdot \frac{1}{F(\nu, a)} + \frac{\varphi_4}{\varphi_1}. \tag{1.5}$$

Moreover $f_2(\nu)$ can be transformed into

$$\left. \begin{aligned} f_2(\nu) = & \{F(\nu, a) + \varphi_1(\nu^2, a, m)\}\{F(\nu, ma) \\ & + \varphi_2(\nu^2, a, m\} + \psi(\nu^2, a, m) \\ \psi(\nu^2, a, m) \equiv & \varphi_3(\nu^2, a, m) \\ & - \varphi_1(\nu^2, a, m) \varphi_2(\nu^2, a, m) \end{aligned} \right\} \tag{1.6}$$

By relatively simple considerations the following properties of $f_2(\nu)$ will become obvious.

(a) $f_2(\nu)$ is an even function of ν, since $F(\nu, a)$ is even, as shown in § 2 of Part I, so it is sufficient to deal with a semi-infinite ν-plane, say, the right half-plane.

(b) If ν is real or purely imaginary, $f_2(\nu)$ does not vanish for arbitrary values of a and m, provided φ_1, φ_2, $\cdots$ do not contain i explicitly; especialy, if $\psi(\nu^2, a, m) \leqq 0$, $f_2(\nu)$ never vanishes for any values of a, m. For, suppose $f_2(\nu)=0$ for some values of ν, i.e.

$$\left. \begin{aligned} & \{\mathrm{Re} F(\nu, a) + \varphi_1(\nu^2, a, m)\}\{\mathrm{Re} F(\nu, ma) \\ & \quad + \varphi_2(\nu^2, a, m)\} - \mathrm{Im} F(\nu, a) \mathrm{Im} F(\nu, ma) \\ & \quad + \psi(\nu^2, a, m) = 0 \\ & \mathrm{Im} F(\nu, a)\{\mathrm{Re} F(\nu, ma) + \varphi_2(\nu^2, a, m)\} \\ & \quad + \mathrm{Im} F(\nu, ma)\{\mathrm{Re} F(\nu, a) \\ & \quad + \varphi_1(\nu^2, a, m)\} = 0 \end{aligned} \right\} \tag{1.7}$$

By eliminating ν from these equations, the left sides of which never vanish identically, it is evident that there must be a relation between a and m. Further from these equations we can deduce

$$\begin{aligned} & [\{\mathrm{Re} F(\nu, a) + \varphi_1(\nu^2, m)\}^2 \\ & \quad + \{\mathrm{Im} F(\nu, a)\}^2] \mathrm{Im} F(\nu, ma) / \mathrm{Im} F(\nu, a) \\ & = \psi(\nu^2, a, m). \end{aligned}$$

Now, since $\mathrm{Im} F(\nu, a) < 0$, $\mathrm{Im} F(\nu, ma) < 0$ for the values of ν under consideration, as shown in § 3–3.2 of Part I, this relation is not valid so far as $\psi(\nu^2, a, m) \leqq 0$.

§ 2. Zeros of $f_2(\nu)$

To find out the zeros of $f_2(\nu)$ we shall consider the whole ν-plane as separated into two oscillatory regions [(1) § 3.3], where the respective values of $F(\nu, a)$ and $F(\nu, ma)$ oscillate infinite times from 0 to infinity, and the remaining region.

(a) In the oscillatory region (i) including the curve, which, starting from $\nu=a$ and going off to $-\infty i$, satisfies

$$\mathrm{Re}(\gamma \cosh \gamma - \sinh \gamma) = 0 \qquad [\nu = a \cosh \gamma],$$

an infinite number of zeros and poles of $F(\nu, a) + \varphi_1(\nu^2, a, m)$ lie alternately in order nearly along this curve, provided that $\varphi_1(\nu^2, a, m)$ varies gradually, as shown in § 5 of Part I. If we consider in place of $f_2(\nu)$

$$\begin{aligned} & f_2(\nu) / \{F(\nu, ma) + \varphi_2(\nu^2, a, m)\} \\ & \quad \equiv F(\nu, a) + \varphi_1(\nu^2, a, m) \\ & \qquad + \psi(\nu^2, a, m) / \{F(\nu, ma) + \varphi_2(\nu^2, a, m)\} \end{aligned} \tag{2.1}$$

in view of $F(\nu, ma) + \varphi_2(\nu^2, a, m)$ having here no zeros of such a kind, the problem will be reduced to that of the linear form, treated in Part I, with $\varphi(\nu^2, a)$ replaced by

$\varphi_1(\nu^2, a, m)+\psi(\nu^2, a, m)/\{F(\nu, ma)+\varphi_2(\nu^2, a, m)\}$;

but it is necessary to examine whether or not $F(\nu, ma)+\varphi_2(\nu^2, a, m)$ accidentally vanishes here.

(b) In the oscillatory region (ii) including the curve which, starting from $\nu=ma$ and passing off to $-\infty i$, satisfies

$$\mathrm{Re}(\gamma^* \cosh \gamma^* - \sinh \gamma^*)=0 \quad [\nu=ma \cosh \gamma^*],$$

the problem is similarly reducible to that of the linear case with

$$F(\nu, ma)+\varphi_2(\nu^2, a, m) + \psi(\nu^2, a, m)/\{F(\nu, a)+\varphi_1(\nu^2, a, m)\}.$$

(c) In the remining region we can find out the values of the zeros, if exist, approximately by solving the equation

$$[-\{(\nu/a)^2-1\}^{1/2}+\varphi_1(\nu^2, a, m)]\cdot[-\{(\nu/ma)^2-1\}^{1/2} + \varphi_2(\nu^2, a, m)]+\psi(\nu^2, a, m)=0. \tag{2.2}$$

In order to avoid any confusion in the argument of the many-valued function we shall here set up such Riemann surface as illustrated in Fig. 1, with cuts starting respectively from $\nu=a$ and ma, which are in reality excluded from the region under consideration; $\arg\{(\nu/a)^2-1\}^{1/2}$ and $\arg\{\nu/ma)^2-1\}^{1/2}$ are assumed to become 0 as ν tends to $+\infty+i\varepsilon$.

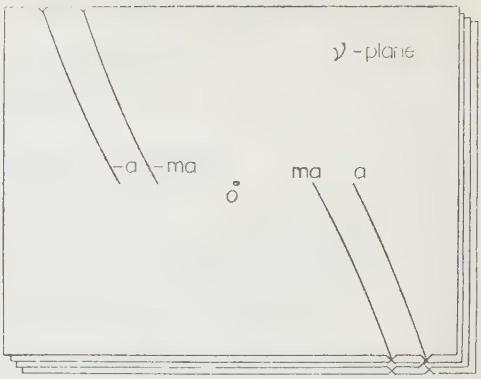

Fig. 1.

Once such values are found out, we can obtain a closer estimate in the same manner as that in Part I. Thus, assuming an expansion of ν in powers of a^{-1} with unknown coefficients and substituting it in (1.6) with $H\nu^{(2)}(a)$, $H\nu^{(2)}(ma)$ replaced by their asymptotic expansions, we are to determine these unknown coefficients such that (1.6) vanishes.

§ 3. Example

We shall explain the above outlined procedure more concretely by applying it to an example, which occurs actually in the case of the diffraction of elastic waves by a spherical canity; the form to be dealt with is

$$f_2(\nu)=\left\{1-\frac{4\nu^2}{a^2}+\frac{4\nu^2(\nu^2-9/4)}{a^4}\right\}H\nu^{(2)}(ma)H\nu^{(2)}(a)+\frac{4m}{a}\left(1-\frac{\nu^2-9/4}{2a^2}\right)H\nu^{(2)\prime}(ma)H\nu^{(2)}(a)$$
$$+\frac{2}{a}\left(1+\frac{\nu^2-9/4}{a^2}\right)H\nu^{(2)}(ma)H\nu^{(2)\prime}(a)-\frac{4m}{a^2}\left(\nu^2-\frac{9}{4}\right)H\nu^{(2)\prime}(ma)H\nu^{(2)\prime}(a), \tag{3.1}$$

where m denotes the ratio of the propagation velocity of two elastic waves and is less than $1/\sqrt{2}$.

Since $H\nu^{(2)}(a)$, $H\nu^{(2)}(ma)$ and $\varphi_4=-4(m/a^2)(\nu^2-9/4)$ have no common zeros, the zeros of $f_2(\nu)$ are the same as those of $f_2(\nu)/\varphi_4\cdot H\nu^{(2)}(ma)$, the latter being to be taken anew as $f_2(\nu)$.

Furthermore $f_2(\nu)$ can be written as

$$f_2(\nu)=\left\{F(\nu, ma)-\frac{1}{2ma}\left(1+\frac{a^2}{\nu^2-9/4}\right)\right\}\left\{F(\nu, a)+\frac{1}{2a}\left(1-\frac{2a^2}{\nu^2-9/4}\right)\right\}-\frac{\nu^2-1/4}{ma^2}\left\{1-\frac{a^2}{2(\nu^2-9/4)}\right\}^2. \tag{3.2}$$

3.1. $f_2(\nu)$ *on the real axis.*

We shall investigate whether or not $f_2(\nu)$ vanishes for real values of $\nu=\lambda>0$.

(a) For values of $\lambda\geqq 1/2$ obviously $f_2(\nu)$ does not vanish, since the last term of (3.2) is negative for such λ, as shown in § 1, (b).

(b) For values of $\lambda<1/2$, we shall observe $\mathrm{Im} f_2(\nu)$; this is

$$\operatorname{Im} f_2(\nu)=\Big[\Big\{-\int_0^\infty K_0(2ma\sinh\xi)\cosh 2\lambda\xi\sinh\xi d\xi-\frac{1}{2ma}\Big(1-\frac{a^2}{9/4-\lambda^2}\Big)$$
$$\cdot\int_0^\infty K_0(2ma\sinh\xi)\cosh 2\lambda\xi d\xi\Big\}\Big(-\frac{\pi}{4a}\Big)+\Big\{-\int_0^\infty K_1(2a\sinh\xi)\cosh 2\lambda\xi\sinh\xi d\xi$$
$$+\frac{1}{2a}\Big(1+\frac{2a^2}{9/4-\lambda^2}\Big)\int_0^\infty K_0(2a\sinh\xi)\cosh 2\lambda\xi d\xi\Big\}\Big(-\frac{\pi}{4ma}\Big)\Big]\Big/$$
$$\cdot\int_0^\infty K_0(2ma\sinh\xi)\cosh 2\lambda\xi d\xi\int_0^\infty K_0(2a\sinh\xi)\cosh 2\lambda\xi d\xi\,. \tag{3.3}$$

The numerator of $\operatorname{Im} f_2(\nu)$ is, after partial integration,

$$-\frac{\pi}{4ma}\Big[-m\int_0^\infty K_1(2ma\sinh\xi)\cosh 2\lambda\xi\sinh\xi d\xi-\frac{1}{2a}\Big(1-\frac{a^2}{9/4-\lambda^2}\Big)\frac{ma}{\lambda}$$
$$\cdot\int_0^\infty K_1(2ma\sinh\xi)\cosh\xi\sinh\xi d\xi-\int_0^\infty K_1(2a\sinh\xi)\cosh 2\lambda\xi\sinh\xi d\xi$$
$$+\frac{1}{2a}\Big(1+\frac{2a^2}{9/4-\lambda^2}\Big)\frac{a}{\lambda}\int_0^\infty K_1(2a\sinh\xi)\cosh\xi\sinh 2\lambda\xi d\xi\Big]\,.$$

The expression in the bracket [ ] can be written as

$$\Big[\quad\Big]=\frac{m}{2\lambda}\int_0^\infty K_1(2ma\sinh\xi)\cosh 2\lambda\xi\cosh\xi\Big\{\frac{a^2}{9/4-\lambda^2}\tanh 2\lambda\xi-2\lambda\tanh\xi\Big\}d\xi$$
$$+\int_0^\infty K_1(2at)\Big\{\frac{2a^2}{9/4-\lambda^2}\sinh(2\lambda\sinh^{-1}t)-\sinh\Big(2\lambda\sinh^{-1}\frac{t}{m}\Big)\Big\}dt$$
$$+\frac{1}{2\lambda}\int_0^\infty K_1(2a\sinh\xi)\cosh 2\lambda\xi\cdot\cosh\xi\{\tanh 2\lambda\xi-2\lambda\tanh\xi\}d\xi\,. \tag{3.4}$$

Since the above expression does not vanish for $\lambda<1/2$, considering

$$\tanh 2\lambda\xi>2\lambda\tanh\xi \qquad \text{for}\quad \lambda<1/2\,, \tag{3.5}$$

so far as

$$a^2/(9/4)\gtrsim 1/m>1\,, \tag{3.6}$$

t is obvious that $\operatorname{Im} f_2(\lambda)$ and therefore $f_2(\lambda)$ do not vanish for $\lambda<1/2$, at least so far as $a\gtrsim\sqrt{2}/\sqrt{m}$.

3.2. *$f_2(\nu)$ on the imaginary axis.*

We shall examine whether $f_2(\nu)$ vanishes for purely imaginary values of $\nu=\mu i(\mu>0)$ or not. Then we have

$$\operatorname{Im} f_2(\mu i)=-\frac{\pi}{4ma}\cdot\Big\{-m\int_0^\infty K_1(2ma\sinh\xi)\sinh\xi\cos 2\mu\xi d\xi-\frac{1}{2a}\Big(1-\frac{a^2}{\mu^2+9/4}\Big)$$
$$\cdot\int_0^\infty K_0(2ma\sinh\xi)\cos 2\mu\xi d\xi-\int_0^\infty K_1(2a\sinh\xi)\cos 2\mu\xi\sinh\xi d\xi+\Big(1+\frac{2a^2}{\mu^2+9/4}\Big)\frac{1}{2a}$$
$$\cdot\int_0^\infty K_0(2a\sinh\xi)\cos 2\mu\xi d\xi\Big\}\Big/\Big\{\int_0^\infty K_0(2a\sinh\xi)\cos 2\mu\xi d\xi\int_0^\infty K_0(2ma\sinh\xi)\cos 2\mu\xi d\xi\Big\}\,. \tag{3.7}$$

By using the formulas (3.33), (3.34) in § 3.2 of Part I, useful for any μ, it becomes

$$\operatorname{Im} f_2(\mu i)=\Big[\frac{-1}{2m}\frac{(1-m^2)\mu^2+m^2(a^2-9/4)}{(9/4+\mu^2)(m^2a^2+\mu^2)}\cdot(a^2+\mu^2)^{1/2}-\frac{1}{2m}\frac{a^2-9/4}{(9/4+\mu^2)(a^2+\mu^2)}(m^2a^2+\mu^2)^{1/2}$$
$$-\frac{1}{2ma^2}\cdot\frac{1}{9/4+\mu^2}\cdot\Big\{-(9/4+\mu^2)(a^2+\mu^2)^{1/2}+(9/4+\mu^2+a^2)(m^2a^2+\mu^2)^{1/2}\Big\}\Big]\{1+0(a^{-2})\}\,. \tag{3.8}$$

The last term in the bracket [ ], suitably rationalized,

$$(9/4+\mu^2+a^2)^2(m^2a^2+\mu^2)-(9/4+\mu^2)^2(a^2+\mu^2)$$

will be transformed into

$$a^2(1+m^2)(9/4+\mu^2)^2+a^2\{a^2(1+2m^2)-9/2\}(9/4+\mu^2)+a^4(m^2a^2-9/4)$$
$$=a^2(1+m^2)\left\{\left(\mu^2+\frac{a^2(1+2m^2)+9/2m^2}{2(1+m^2)}\right)^2-\frac{1}{4}\frac{(a^2-9/2)^2+9a^2(1-m^2)}{(1+m^2)^2}\right\}.$$

It is sufficient for this expression to be positive for any values of μ that

$$\left(\frac{a^2(1+2m^2)+9/2\cdot m^2}{2(1+m^2)}\right)^2>\frac{1}{4}\frac{(a^2-9/2)^2+9a^2(1-m^2)}{(1+m^2)^2},$$

which reduces to

$$(a^2+9/4)^2-(81/16)(1+m^4)/\{m^2(1+m^2)\}>0.$$

Thus, since $m<1$, it is sufficient that

$$a^2+9/4>9/(4m)$$

or

$$a^2>(9/4)(1-m)/m.$$

Hence by considering the sign of the terms in (3.8) one may easily see that $\mathrm{Im}\, f_2(\mu i)$ is always negative so far as $a^2 \geqq (9/4)(1-m)/m$ or $a^2>9/4$ for such values of $m \leqq 1/2$ or $>1/2$ and that consequently $f_2(\nu)$ never vanishes on the imaginary axis at least under the above-mentioned condition.

3.3 $f_2(\nu)$ *in the oscillatory region* (*i*).

We shall here consider the roots of the equation

$$F(\nu, a)=-\frac{1}{2a}\left(1-\frac{2a^2}{\nu^2-9/4}\right)+\frac{\nu^2-1/4}{ma^2}\left(1-\frac{a^2}{2(\nu^2-9/4)}\right)^2\Big/\left\{F(\nu, ma)-\frac{1}{2ma}\left(1+\frac{a^2}{\nu^2-9/4}\right)\right\}. \quad (3.9)$$

The value of the left-hand side oscillates in this region infinite times from zero to infinity, while the right one varies its value gradually, so the solution lie in order, passing off to $-\infty i$ as described in § 2. The most interesting zeros are those near a.

The right-hand side of (3.9) will be transformed for ν close to a into

$$-\frac{1}{2a}\left(1-\frac{2}{\cosh^2\gamma}\right)+\frac{1}{m}\cosh^2\gamma\left(1-\frac{1}{2}\cdot\frac{1}{\cosh^2\gamma}\right)^2\frac{1}{\sinh\gamma^*}\left\{1-\frac{1}{\sinh\gamma_*}\left(\frac{m^2}{\cosh^2\gamma-m^2}\right.\right.$$
$$\left.\left.-1-\frac{1}{\cosh^2\gamma}\right)\frac{1}{2ma}\right\}\times(1+0(a^{-2}))\}$$
$$=-\left\{\cosh^2\gamma-1+\frac{1}{4}(\cosh\gamma)^{-2}\right\}(\cosh^2\gamma-m^2)^{-1/2}-\frac{1}{2a}\left\{-1-\frac{3}{4}\cdot\frac{1}{1-m^2}+\frac{1}{4}\frac{1}{(1-m^2)^2}\right\}+0(\gamma^5), \quad (3.10)$$

by means of the asymptotic expansion of

$$F(\nu, ma)=S\nu^{(1)\prime}(ma)/S\nu^{(1)}(ma)\sim\sinh\gamma^*(1+(\sinh\gamma^*)^{-3}(2ma)^{-1}+\cdots\cdot);$$

in this derivation, considering the position of ν relative to ma in Fig. 8 of Part I, we have taken the corresponding expressions for $H\nu^{(2)}(a)$ and $H\nu^{(2)\prime}(a)$. [Refer to (1) § 4]. It is also to be noticed that $\mathrm{Re}\sinh\gamma^*<0$.

Now $F(\nu, a)$ has for such values of ν the following asymptotic expansion:

$$F(\nu, a)\sim-i\eta(\cosh\gamma)^{-1}\left[\left\{\left(\frac{1}{15}-\frac{3}{5}\xi^2\right)\eta^2+\left(\frac{1}{15}-\frac{36}{35}\xi^2\right)\eta^4+\cdots\cdot\right\}\xi^{-1}H^{(2)}{}_{-1/3}(\xi)+\left\{-1-\frac{9}{10}\eta^2\right.\right.$$
$$\left.\left.+\left(-\frac{253}{280}+\frac{9}{50}\xi^2\right)\eta^4+\cdots\cdot\right\}H^{(2)}{}_{2/3}(\xi)\right]\Big/\left[\left\{1+\frac{1}{10}\eta^2+\left(\frac{13}{280}-\frac{9}{50}\xi^2\right)\eta^4+\cdots\cdot\right\}H^{(2)}{}_{-1/3}(\xi)\right.$$
$$\left.+\left\{-\frac{3}{5}\xi^2\eta^2+\left(\frac{1}{210}-\frac{3}{7}\xi^2\right)\eta^4+\cdots\cdot\right\}\xi^{-1}H^{(2)}{}_{2/3}(\xi)\right], \quad (3.11)$$

where $\xi=(i\nu/3)\tanh^3\gamma$, $\eta=\tanh\gamma$ [(2)]. By assuming the expansion of γ with unknown coefficients

$$\left.\begin{aligned}&\gamma=\gamma^{(0)}\{1+a_1\gamma^{(0)}+a_2\gamma^{(0)2}+a_3\gamma^{(0)3}+a_4\gamma^{(0)4}+\cdots\cdot\},\\&\gamma^{(0)}=\left(\frac{3\rho}{a}\right)^{1/3}\exp\left(\frac{5}{6}\pi i\right),\end{aligned}\right\}\tag{3.12}$$

where ρ is one of such real positive values as satisfy

$$H^{(2)}{}_{-1/3}(\rho e^{\pi i})=0$$

[(1) 4.5], we shall determine a_1, a_2, $\cdots\cdot$ so that (3.9) is satisfied. Thus

$$\left.\begin{aligned}\nu/a&=1+(1/2)\gamma^2+(1/4!)\gamma^4+(1/6!)\gamma^6+\cdots\cdot,\\&=1+(1/2)\gamma^{(0)2}+a_1\gamma^{(0)3}+(a_2+(1/2)a^2{}_1+1/24)\gamma^{(0)4}+(a_3+a_1a_2+(1/6)a_1)\gamma^{(0)5}\\&\quad+(a_4+a_1a_3+(1/2)a^2{}_2+(1/6)a_2+(1/4)a^2{}_1+(1/6!)\gamma^{(0)6}+\cdots\cdot,\\\eta&=\gamma^{(0)}\{1+a_1\gamma^{(0)}+(a_2-1/3)\gamma^{(0)2}+(a_3-a_1)\gamma^{(0)3}+(a_4-a_2-a^2{}_1+2/15)\gamma^{(0)}+\cdots\cdot\},\\\xi&=\rho e^{\pi i}-\rho\gamma^{(0)}\{3a_1+(3a_2+3a^2{}_1-1/2)\gamma^{(0)}+(3a^3-(5/2)a_1+6a_1a_2+a^3{}_1)\gamma^{(0)2}\\&\quad+(3a_4-(5/2)a_2-5a^2{}_1+6a_1a_3+3a^2{}_2+3a^2{}_1a_2+11/40)\gamma^{(0)3}+\cdots\cdot\},\\H^{(2)}{}_{-1/3}(\xi)&=\rho H^{(0)}{}_{2/3}(\rho e^{\pi i})\gamma^{(0)}\{3a_1+(3a_2-(3/2)a^2{}_1-1/2)\gamma^{(0)}+(3a_3-a_1+(3/2)a^3{}_1-3a_1a_2\\&\quad-(9/2)\rho^2a^3{}_1)\gamma^{(0)2}+(3a_4-a_2-(3/4)a^2{}_1-3a_1a_3-(3/2)a^2{}_2+(9/2)a_1{}^2a_2+(3/20)\\&\quad-(3/2)a^4{}_1-(27/2)a^2{}_1a_2\rho^2-(27/4)\rho^2a^4{}_1+(9/4)\rho^2a^2{}_1)\gamma^{(0)3}+\cdots\cdot\},\\H^{(2)}{}_{2/3}(\xi)&=H^{(2)}{}_{2/3}(\rho e^{\pi i})\{1-2a_1\gamma^{(0)}+(-2a_2+3a^2{}_1-(9/2)\rho^2a^2{}_1+1/3)\gamma^{(0)2}+(-2a_3-4a^3{}_1\\&\quad+6a_1a_2-9\rho^2a_1a_2-(3/2)\rho^2a^3{}_1+(3/2)\rho^2a_1)\gamma^{(0)}+\cdots\cdot\}.\end{aligned}\right\}\tag{3.13}$$

Substituting these values in (3.9) in view of (3.10), (3.11), we obtain

$$\left.\begin{aligned}a_1&=-(4/3)i(1-m^2)^{1/2}/\rho,\\a_2&=(8/9\rho^2)\cdot(1-m^2)-1/30,\\a_3&=-(4/3)i(1-m^2)^{1/2}/\rho\cdot\left\{\frac{71}{30}+\frac{1}{2}\cdot\frac{1}{1-m^2}-\frac{16}{3}m^2-\frac{8}{9}\,\frac{1-m^2}{\rho^2}\right\},\\a_4&=\frac{532}{135\rho^2}(1-m^2)+\frac{41}{12600}-\frac{160}{81\rho^4}(1-m^2)^2-\frac{128}{27\rho^2}(1-m^2)^2+\frac{1}{630\rho^2}-\frac{14}{9\rho^2}+\frac{4}{9\rho^2}\cdot\frac{1}{1-m^2}\end{aligned}\right\}\tag{3.14}$$

Thus we have as the first several zeros of (3.9)

$$\begin{aligned}\nu=a\Bigg[1&+\frac{1}{2}\left(\frac{3\rho}{a}\right)^{2/3}e^{5/3\pi i}+\frac{4}{3\rho}(1-m^2)^{1/2}\left(\frac{3\rho}{a}\right)+\frac{1}{120}\left(\frac{3\rho}{a}\right)^{4/3}e^{4/3\pi i}\\&-\left\{-\frac{17}{6}+\frac{1}{2}\cdot\frac{1}{1-m^2}+\frac{16}{3}(1-m^2)\right\}\frac{4}{3\rho}(1-m^2)^{1/2}\left(\frac{3\rho}{a}\right)^{5/3}e^{2/3\pi i}+\left\{\frac{1}{2800}-\frac{171}{70\rho^2}\right.\\&\left.-\frac{80}{9\rho^2}(1-m^2)-\frac{2}{9\rho^2}\cdot\frac{1}{1-m^2}+\frac{128}{9\rho^2}(1-m^2)^2\right\}\left(\frac{3\rho}{a}\right)^2+\cdots\cdot\Bigg],\end{aligned}\tag{3.15}$$

where ρ denotes one of the following values:

2.3834466, 5.5101956, 8.6473577, 11.7868429, 14.9272068, $\cdots\cdot\cdot$

3.4. $f_2(\nu)$ *in the oscillatory region* (*ii*).

We shall here consider the roots of

$$F(\nu,ma)=\frac{1}{2ma}\left(1+\frac{a^2}{\nu^2-9/4}\right)+\frac{\nu^2-1/4}{ma^2}\left(1-\frac{a^2}{2(\nu^2-9/4)}\right)^2\Bigg/\left\{F(\nu,a)+\frac{1}{2a}\left(1-\frac{2a^2}{\nu^2-9/4}\right)\right\}.\tag{3.16}$$

The situation here is quite the same as in the preceeding section, so we shall confine ourselves to the determination of zeros near ma.

For values of ν close to ma we have

$$F(\nu,a)=S^{(2)\prime}{}_\nu(a)/S^{(2)}{}_\nu(a)=-\sinh\gamma+\frac{1}{2a\sinh^2\gamma}+0(a^{-2}),$$

$$\sinh\gamma\simeq i(1-m^2)^{1/2}$$

[(1) § 4], and therefore

$$\frac{1}{2ma}\left(1+\frac{a^2}{\nu^2-9/4}\right)+\frac{\nu^2-1/4}{ma^2}\left(1-\frac{a^2}{2(\nu^2-9/4)}\right)^2\Big/\left\{F(\nu, a)+\frac{1}{2a}\left(1-\frac{2a^2}{\nu^2-9/4}\right)\right\}$$

$$=i\frac{m\cosh^2\gamma^*}{(1-m^2\cosh^2\gamma^*)^{1/2}}\left(1-\frac{1}{2m^2\cosh^2\gamma^*}\right)^2$$

$$-\frac{1}{2ma}\left\{\frac{1}{m^4}\left(m^2-\frac{1}{2}\right)^2\left(1+\frac{1}{(m^2-1)^2}\right)-\frac{1+m^2}{m^2}\right\}+0(\gamma^{*5}). \qquad (3.17)$$

Now we have for ν close to ma

$$F(\nu, ma)\sim -i\eta^*(\cosh\gamma^*)^{-1}\left[\left\{\left(\frac{1}{15}-\frac{3}{5}\xi^{*2}\right)\eta^{*3}+\left(\frac{1}{15}-\frac{36}{35}\xi^{*2}\right)\eta^{*2}+\cdots\right\}\xi^{*-1}H^{(2)}{}_{-1/3}(\xi)\right.$$

$$\left.+\left\{-1-\frac{9}{10}\eta^{*2}+\left(-\frac{253}{280}+\frac{9}{50}\xi^{*2}\right)\eta^{*4}+\cdots\right\}H^{(2)}{}_{2/3}(\xi)\right]\Big/\left[\left\{1+\frac{1}{10}\eta^{*2}\right.\right.$$

$$\left.\left.+\left(\frac{13}{280}-\frac{9}{50}\xi^{*2}\right)\eta^{*4}+\cdots\right\}H^{(2)}{}_{-1/3}(\xi)+\left\{-\frac{3}{5}\xi^{*2}\eta^{*2}+\left(\frac{1}{210}-\frac{3}{7}\xi^{*2}\right)\eta^{*4}+\cdots\right\}\xi^{*-1}H^{(2)}{}_{2/3}(\xi)\right], \qquad (3.18)$$

where $\xi^*=(i\nu/3)\tanh^3\gamma^*$, $\eta^*=\tanh\gamma^*$. Then by putting

$$\gamma^*=\gamma^{*(0)}\{1+a_1\gamma^{*(0)}+a_2\gamma^{*(0)2}+a_3\gamma^{*(0)3}+a_4\gamma^{*(0)4}+\cdots\cdot\},$$

where $\gamma^{*(0)}=(3\rho/ma)^{1/3}e^{(5/6)\pi i}$, ρ being one of the roots of

$$H^{(2)}{}_{-1/3}(\rho e^{\pi i})=0,$$

and by substituting it and the similar expressions for ν, ξ^{*4} η^* in the equation (3.16) transformed by (3.17), (3.18) have

$$\left.\begin{aligned}
a_1&=-\frac{4}{3}\frac{(1-m^2)^{1/2}}{m\rho}\frac{m^4}{(2m^2-1)^2},\\
a_2&=-\frac{1}{2}a^2{}_1-\frac{1}{30},\\
a_3&=a_1\left\{\frac{1}{30}-\frac{2m^2+1}{2m^2-1}-\frac{1}{2}\frac{m^2}{1-m^2}+\left(\frac{1}{2}--3\rho^2\right)a^2{}_1\right\},\\
a_4&=\frac{41}{12600}+\frac{1}{630\rho^2}+\left[\frac{17}{60}-\frac{2m^2+1}{2m^2-1}-\frac{1}{2}\frac{m^2}{1-m^2}+\frac{1}{2m^4}\left\{\left(m^2-\frac{1}{2}\right)^2\left(1+\frac{1}{(m^2-1)^2}\right)\right.\right.\\
&\quad\left.\left.-m^2(m^2+1)\right\}\right]a^2{}_1-\left(\frac{5}{8}+\frac{3}{2}\rho^2\right)a^4{}_1
\end{aligned}\right\} \qquad (3.19)$$

Consequently we obtain

$$\nu=ma\left[1+\frac{1}{2}\left(\frac{3\rho}{ma}\right)^{2/3}e^{(5/3)\pi i}-\frac{4m^3}{3\rho}\frac{(1-m^2)^{1/2}}{(2m^2-1)^2}\left(\frac{3\rho}{ma}\right)e^{(\pi/2)i}+\frac{1}{120}\left(\frac{3\rho}{ma}\right)^{4/3}e^{(4/3)\pi i}-\left\{\frac{1}{6}-\frac{2m^2+1}{2m^2-1}\right.\right.$$

$$\left.-\frac{1}{2}\cdot\frac{m^2}{1-m^2}-\frac{16m^6}{3}\frac{(1-m^2)}{(2m^2-1)^4}\right\}\frac{4m^3}{3\rho}\frac{(1-m^2)^{1/2}}{(2m^2-1)^2}\left(\frac{3\rho}{ma}\right)^{5/3}e^{(\pi/6)i}+\left\{\frac{1}{2800}-\frac{1}{630\rho^2}\right.$$

$$-\left(\frac{1}{2}-2\cdot\frac{2m^2+1}{2m^2-1}-\frac{m^2}{1-m^2}-\frac{1}{m^2}+\frac{1}{8m^4}+\frac{1}{2m^4}\cdot\frac{(m^2-1/2)^2}{(m^2-1)^2}\right)\frac{16m^6}{9\rho^2}\cdot\frac{1-m^2}{(2m^2-1)^4}$$

$$\left.\left.+\frac{128m^{12}}{9\rho^2}\cdot\frac{(1-m^2)^2}{(2m^2-1)^8}\right\}\left(\frac{3\rho}{ma}\right)^2+\cdots\cdot\right], \qquad 3.20)$$

where ρ is one of the values

2.383466, 5.5101956, 8.6473577, 11.7868429, 14.9272068, $\cdots\cdot$

3.5. $f_2(\nu)$ *in the region of* ν *with large negative imaginary part.*

As ν tends to $-\infty i$, two above-stated regions approach to each other, the condition, to which the previous discussion is subject, fails to be satisfied, so it is necessary to consider in another way.

Since there are valid the relations

$$\mathrm{Re}\,(\gamma\cosh\gamma-\sinh\gamma)\simeq 0\,,$$
$$\mathrm{Re}\,(\gamma^*\cosh\gamma^*-\sinh\gamma^*)\simeq 0\,,$$

in view of the asymptotic expansions of

$$H^{(2)}{}_\nu(a)=S^{(2)}{}_\nu(a)-S^{(1)}{}_\nu(a)\,,$$
$$H^{(2)}{}_\nu(ma)=S^{(2)}{}_\nu(ma)-S^{(2)}(ma)$$

and of their derivatives, we take

$$F(\nu, a)+\frac{1}{2a}\left(1-\frac{2a^2}{\nu^2-9/4}\right)=-\sinh\gamma\cdot\cosh\Big\{\nu(\gamma-\tanh\gamma)+\frac{\pi}{4}i+\left(\frac{7}{8}-\frac{7}{24}\coth^2\gamma-\tanh^2\gamma\right)\Big/$$
$$(a\sinh\gamma)\Big\}\times\mathrm{cosech}\,\Big\{\nu(\gamma-\tanh\gamma)+\frac{\pi}{4}i-\left(\frac{1}{8}-\frac{5}{24}\coth^2\gamma\right)\Big/(a\sinh\gamma)\Big\}\{1+0(a^{-2})\}\,,\quad(3.21)$$

and

$$F(\nu, ma)-\frac{1}{2ma}\left(1+\frac{a^2}{\nu^2-9/4}\right)=-\sinh\gamma^*\cosh\Big\{\nu(\gamma^*-\tanh\gamma^*)+\frac{\pi}{4}i$$
$$+\left(\frac{11}{8}-\frac{7}{24}\coth^2\gamma^*-\frac{1}{2}\tanh^2\gamma^*\right)\Big/(ma\sinh\gamma^*)\Big\}\,\mathrm{cosech}\,\Big\{\nu(\gamma^*-\tanh\gamma^*)+\frac{\pi}{4}i$$
$$-\left(\frac{1}{8}-\frac{5}{24}\coth^2\gamma^*\right)\Big/(ma\sinh\gamma^*)\Big\}\times\{1+0(a^{-2})\}\,.\qquad(3.22)$$

By substituting these expressions in (3.2) we shall see that the zeros looked for are given approximately by the solutions of

$$\sinh\gamma\cdot\sinh\gamma^*\cosh\Big\{\nu(\gamma-\tanh\gamma)+\frac{\pi}{4}i+\left(\frac{7}{8}-\frac{7}{24}\coth^2\gamma-\tanh^2\gamma\right)\Big/$$
$$(a\sinh\gamma)\Big\}\cdot\cosh\Big\{\nu(\gamma^*-\tanh\gamma^*)+\frac{\pi}{4}i+\left(\frac{11}{8}-\frac{7}{24}\coth\gamma^*-\frac{1}{2}\tanh^2\gamma^*\right)\Big/$$
$$(ma\sinh\gamma^*)\Big\}\cdot\mathrm{cosech}\,\Big\{\nu(\gamma-\tanh\gamma)+\frac{\pi}{4}i-\left(\frac{1}{8}-\frac{5}{24}\coth^2\gamma\right)\Big/(a\sinh\gamma)\Big\}\,\mathrm{cosech}\,\Big\{\nu(\gamma^*$$
$$-\tanh\gamma^*)+\frac{\pi}{4}i-\left(\frac{1}{8}-\frac{5}{24}\coth^2\gamma^*\right)\Big/(ma\sinh\gamma^*)\Big\}=\cosh\gamma\cdot\cosh\gamma^*\left(1-\frac{1}{2\cosh^2\gamma}\right)^2.$$
$$(3.23)$$

When $\alpha\to\infty$, $\beta\to\pi/2-\varepsilon$ we have

$$\nu=a\cosh\gamma=a\cosh\alpha\cos\beta+ia\sinh\alpha\sin\beta\to-i\infty\,,$$
$$\sinh\gamma=\sinh\alpha\cos\beta+i\cosh\alpha\sin\beta\to+i\infty\,,$$
$$\tanh\gamma\qquad\qquad\to-1$$

and similar relations for γ^*. Hence the roots of (2.23) for large γ, γ^* are given approximately by those of

$$\cot\{|\mu|(\cosh^{-1}(|\mu|/a)-1)+\pi/4\}=-\tan\{|\mu|(\cosh^{-1}(|\mu|/(ma))-1)+\pi/4\}\,,\qquad(3.24)$$

or

$$|\mu|\cdot\{\cosh^{-1}(|\mu|/a)-\cosh^{-1}|\mu|/(ma))\}=(n-1/2)\pi\,,$$

when n is a large positive integer. Such values of $|\mu|$ are given approximately by

$$|\mu|\simeq(n-1/2)\pi\log(1/m)\,,$$

Consequently we take as the values of the large zeros

$$\nu\simeq-(n-1/2)\pi\log(1/m)\cdot i$$

3.6. $f_2(\nu)$ *in the remaining region.*

We shall investigate on the scheme of § 2 (c).

3.6.1. First approximation.

Remembering (2.2), we have in this case

$$f_2(\nu)=\left[-\surd\{(\nu/a)^2-1\}\{1+0(a^{-1})\}+\frac{1}{2a}\left(1-\frac{2a^2}{\nu^2-9/4}\right)\right]\cdot\left[-\surd\}(\nu/ma)^2-1\}\cdot\{1+0(a^{-1})\}\right.$$

$$\left.-\frac{1}{2ma}\left(1+\frac{a^2}{\nu^2-9/4}\right)\right]-\frac{\nu^2-1/4}{ma^2}\left\{1-\frac{a^2}{2(\nu^2-9/4)}\right\}^2,$$

$$=[\{(\nu/a)^2-1\}^{1/2}\{(\nu/a)^2-m^2\}^{1/2}-\nu^2/a^2\cdot\{1-a^2/(2\nu^2)\}^2]\cdot(1/m)\{1+0(a^{-1})\}\,, \tag{3.26}$$

the zeros of $f_2(\nu)$ in this region are approximately given by the solutions of

$$\zeta(\zeta-1)^{1/2}(\zeta-m^2)^{1/2}-(\zeta-1/2)^2=0\,, \tag{3.27}$$

if we put $(\nu/a)^2=\zeta$. To find out the solutions of this equation we first consider, instead of (3.27), the rationalized one, obtained by multiplying (3.27) by

$$\zeta(\zeta-1)^{1/2}(\zeta-m^2)^{1/2}+(\zeta-1/2)^2\,,$$

i.e.

$$\zeta^2(\zeta-1)(\zeta-m^2)-(\zeta-1/2)^4=0\,,$$

or

$$(1-m^2)\zeta^3-(3/2-m^2)\zeta^2+(1/2)\zeta-1/16=0\,. \tag{3.28}$$

We are already informed by the well-known discussion on Rayleigh waves that this equation has a real root ζ_0 greater than unity and two conjugate complex roots ζ_1, $\bar{\zeta}_1$ [(3) p. 9]. Since

$$\zeta_0+\zeta_1+\bar{\zeta}_1=(3/2-m^2)/(1-m^2)\,,$$
$$\operatorname{Re}\zeta_1=1/\{4(1-m^2)\}+1/2-\zeta_0/2\,,$$

and therefore

$$\operatorname{Re}\zeta_1<1/\{4(1-m^2)\}<1/2\,,$$

in view of

$$m^2<1/2\,.$$

We shall then investigate whether or not ζ_0, ζ_1, $\bar{\zeta}_1$ satisfy the original Eq. (3.27).

Since for ζ_0 both $\arg\zeta_0(\zeta_0-1)^{1/2}(\zeta_0-m^2)^{1/2}$ and $\arg(\zeta_0-1/2)^2$ are zero, ζ_0 satisfies undoubtedly this equation.

In order for ζ_1 and $\bar{\zeta}_1$ to be solutions of (3.27) the following relation must be satisfied:

$$\arg\zeta_1+\arg(\zeta_1-1)^{1/2}+\arg(\zeta_1-m^2)^{1/2}=2\arg(\zeta_1-1/2)\,,$$

which can be interpreted, if one considers the discussion on the arguments of $(\zeta_1-1)^{1/2}$ and $(\zeta_1-m^2)^{1/2})$ in § 2 (c), as

$$\theta_4+1/2\cdot\theta_1+1/2\cdot\theta_3=2\theta_2\,,$$

where θ_1, θ_2, $\cdots$ are the angles illustrated in Fig. 2, or, in view of

$$\theta_1=\theta_3+(\alpha_1+\alpha_2+\alpha_3)\,,$$
$$\theta_2=\theta_4+(\alpha_2+\alpha_3)\,,$$
$$\theta_3=\theta_4+\alpha_3\,,$$

the relation

$$\alpha_1=3\alpha_2+2\alpha_3$$

must be satisfied. Now, since $\operatorname{Re}\zeta_1<1/2$, α_1 is less than $\alpha_2+\alpha_3$, as shown in the illustration, so that ζ_1 and $\bar{\zeta}_1$ do not satisfy (3.27). By closer observation it becomes clear that ζ_1 and $\bar{\zeta}_1$ are the solution of

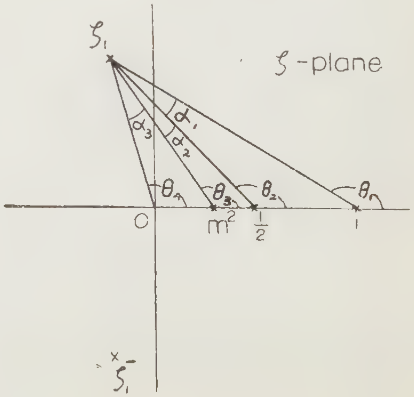

Fig. 2.

$$\zeta(\zeta-1)^{1/2}(\zeta-m^2)^{1/2}+(\zeta-1/2)^2=0\,,$$

or the solutions of (3.27) placed on such a ζ-plane as corresponding to the lower sheet of the Riemann surface in Fig. 1, where either $(\zeta-1)^{1/2}$ or $(\zeta-m^2)^{1/2}$ changes its sign. This Riemann surface, however, is not really characteristic of $F(\nu,a)=H^{(2)\prime}{}_{\nu}(a)/H^{(2)}{}_{\nu}(a)$, which is a one-valued function of ν, but was introduced on approximating $F(\nu,a)$; in fact, the cuts are never passed over, since, as one approaches them $F(\nu,a)$ will take quite a different expression. Hence only the uppermost sheet is relevant to our problem. Thus we can conclude that $\nu_0=a\zeta_0^{1/2}$ is the unique solution.

The xalue of ν_0 is dependent on m and, for example, is $1.0723557\cdots a$ for $m=1/2$.

3.6.2. IMAGINARY PART OF ν_0.

The above-determined value of ν_0 seems to contradict with the result in 3.1, where we showed that no real zeros exist. It comes from the imperfection of the approximation of $F(\nu,a)$.

In the expression of $F(\nu,a)$ discussed in § 3 of Part I

$$F(\nu,a)=-\left\{\int_0^\infty K_1(2a\sinh\xi)\sinh\xi\cosh 2\nu\xi d\xi+\pi i/(4a)\right\}\Big/\int_0^\infty K_0(2a\sinh\xi)\cosh 2\nu\xi d\xi\ ,$$

and in that of $F(\nu,ma)$, if we neglect the second term of the numerator, then $F(\nu,a)$, $F(\nu,ma)$ and therefore $f_2(\nu)$ do not contain i explicitly, so, with every value of ν satisfying

$$f_2(\nu)=0\ ,$$

its complex conjugate also satisfies

$$f_2(\bar{\nu})=0\ .$$

Thus it is obvious that the value of ν considered here remains real, to however high approximations we may proceed, so far as the above-mentioned term is neglected.

We shall here estimate the imaginary part of ν_0, leaving the higher approximation of the real part in the next section. By using the approximation formulas discussed in 3.3 of Part I, we have

$$f_2(\nu_0)\sim\left[-\left(\frac{\nu_0^2}{a^2}-1\right)^{1/2}-\frac{\pi i}{4a}\left\{\int_0^\infty K_0(2a\sinh\xi)\cosh 2\nu\xi d\xi\right\}^{-1}\right]\left[-\left(\frac{\nu_0^2}{m^2a^2}-1\right)^{1/2}-\frac{\pi i}{4ma}\right.$$
$$\left.\left\{\int_0^\infty K_0(2ma\sinh\xi)\cosh 2\nu\xi d\xi\right\}^{-1}\right]-\frac{\nu_0^2}{ma^2}\left(1-\frac{a^2}{2\nu_0^2}\right)^2\simeq\frac{1}{m}\left(\frac{\nu_0^2}{a^2}-1\right)^{1/2}\left(\frac{\nu_0^2}{m^2a^2}-1\right)^{1/2}$$
$$\left[1+i\exp\left\{-2a\left(\frac{\nu_0}{a}\cosh^{-1}\frac{\nu_0}{a}-\left(\frac{\nu_0^2}{a^2}-1\right)^{1/2}\right)\right\}\right]\cdot\left[1+i\exp\left\{-2ma\left(\frac{\nu_0}{ma}\right.\right.\right.$$
$$\left.\left.\left.\times\cosh^{-1}\frac{\nu_0}{ma}-\left(\frac{\nu_0^2}{m^2a^2}-1\right)^{1/2}\right)\right\}\right]-\frac{\nu_0^2}{ma^2}\left(1-\frac{a^2}{2\nu_0^2}\right)^2=0\ . \tag{3.29}$$

The substitution

$$\nu_0=\nu_0^{(0)}+i\mu^{(0)}$$

transforms (3.29) into

$$\left(\frac{\nu_0^{(0)2}}{a^2}-1\right)^{1/2}\left(\frac{\nu_0^{(0)2}}{a^2}-m\right)^{1/2}\left[1+i\frac{\nu_0^{(0)}\mu^{(0)}}{a^2}\left(\frac{1}{\dfrac{\nu_0^{(0)2}}{a^2}-1}+\frac{1}{\dfrac{\nu_0^{(0)2}}{a^2}-m^2}\right)\right.$$
$$+i\exp\left\{-2a\left(\frac{\nu_0^{(0)}}{a}\cosh^{-1}\frac{\nu_0^{(0)}}{a}-\left(\frac{\nu_0^{(0)2}}{a^2}-1\right)^{1/2}\right\}+i\exp\left\{-2a\left(\frac{\nu_0^{(0)}}{a}\cosh^{-1}\frac{\nu_0^{(0)}}{ma}\right.\right.$$
$$\left.\left.\left.-\left(\frac{\nu_0^{(0)2}}{a^2}-m^2\right)^{1/2}\right)\right\}\right]-\frac{a^2}{\nu_0^{(0)2}}\left(\frac{\nu_0^{(0)2}}{a^2}-\frac{1}{2}\right)^2\cdot\left\{1+\left(\frac{4}{\dfrac{\nu_0^{(0)2}}{a^2}-\dfrac{1}{2}}-\frac{2a^2}{\nu_0^{(0)2}}\right)\frac{\nu_0^{(0)}\mu^{(0)}}{a^2}i\right\}=0\ ,$$

where, under the assumption $|\mu^{(0)}|\ll\nu_0^{(0)}$, the higher powers of $\mu^{(0)}/a$ have been neglected. Thus we have, in view of (3.27),

$$\mu^{(0)}=-\frac{a^2}{\nu_0{}^{(0)}}\Bigg[\exp\left\{-2a\left(\frac{\nu_0{}^{(0)}}{a}\cosh^{-1}\frac{\nu_0{}^{(0)}}{a}-\left[\left(\frac{\nu_0}{a}\right)^2-1\right]^{1/2}\right)\right\}+\exp\left\{-2a\left(\frac{\nu_0{}^{(0)}}{a}\cosh^{-1}\frac{\nu_0{}^{(0)}}{ma}\right.\right.$$
$$\left.\left.-\left[\left(\frac{\nu_0{}^{(0)}}{a}\right)^2-m^2\right]^{1/2}\right\}\right]\Bigg/\left[\left(\left\{\left(\frac{\nu_0{}^{(0)}}{a}\right)^2-1\right\}^{1/2}-\left\{\left(\frac{\nu_0{}^{(0)}}{a}\right)^2-m^2\right\}^{-1/2}\right)^2\right.$$
$$\left.+\frac{1}{2}\left(\frac{\nu_0{}^{(0)}}{a}\right)^{-2}\left\{\left(\frac{\nu_0{}^{(0)}}{a}\right)^2-\frac{1}{2}\right\}^{-2}\right]. \tag{3.30}$$

Consequently we see that the imaginary part of $\mu^{(0)}$ is negative and of the order of $O(a\varepsilon^{-a})$, or that this zero lies in the fourth quadrant of the ν-plane, very close to the real axis.

3.6.3. CLOSER LOCATION OF THE ZEROS.

Taking as the first approximate value of ν the value $\nu_0{}^{(0)}$, we shall find out its closer estimate.

We express the corresponding value of γ as

$$\gamma=\gamma^{(0)}+p_1a^{-1}+p_2a^{-2}+\cdots\cdot \tag{3.31}$$

where $\gamma^{(0)}=\cosh^{-1}\nu_0{}^{(0)}/a$, p_1, p_2, $\cdots$ being unknown coefficients. Then we have

$$\nu=a\cosh\gamma^{(0)}+p_1\,\mathrm{sihh}\,\gamma^{(0)}+\left(\frac{1}{2}p_1{}^2\cosh\gamma^{(0)}+p_2\sinh\gamma^{(0)}\right)a^{-1}+\cdots\cdot \tag{3.32}$$

and

$$\gamma^*=\gamma^{*(0)}+p_1{}^*(ma)^{-1}+p_2{}^*(ma)^{-2}+\cdots\cdot$$

where

$$p^*=(\sinh\gamma^{(0)}/\sinh\gamma^{*(0)})p_1\,,$$
$$\sinh\gamma^{*(0)}p_2{}^*=(m/2)(1-m^2)\cosh\gamma^{(0)}(\cosh^2\gamma^{(0)}-m^2)^{-1}p_1{}^2+m\sinh{}^{(0)}p_2,\ \cdots\cdot.$$

By employing the asymptotic expansions of Hankel function and its derivative corresponding to the position of ν_0 in the ν-plane [(1) § 4], we obtain

$$F(\nu,a)\sim\sinh\gamma\{1+(1/2)(\sinh\gamma)^{-3}a^{-1}+(1/8)\cdot(1-5\coth^2\gamma)(\sinh\gamma)^{-4}a^{-2}+\cdots\cdot\}\,,$$
$$\sim\sinh\gamma^{(0)}\Bigg[1+\{p_1\coth\gamma^{(0)}+1/2\cdot(\sinh\gamma^{(0)})^{-3}\}a^{-1}+\left\{\frac{1}{2}p_1{}^2+p_2\cosh\gamma^{(0)}(\sinh\gamma^{(0)})^{-1}\right.$$
$$\left.-p_1\cosh\gamma^{(0)}(\sinh\gamma^{(0)})^{-4}+\frac{1}{8}(1-5\coth^2\gamma^{(0)})(\sinh\gamma^{(0)})^{-4}\right\}a^{-2}+\cdots\cdot\Bigg], \tag{3.33}$$

and for $F(\nu, ma)$ the same expression with a and $\gamma^{(0)}$ replaced by ma and $\gamma^{*(0)}$. Substituting these expressions in

$$f_2(\nu)=0\,,$$

and evuating the coefficients of powers of a^{-1} to zero, we obtain

$$\left.\begin{aligned}
p_1&=\frac{2(2-m^2)\cosh^8\gamma^{(0)}-(21/2)\cosh^6\gamma^{(0)}+\{7+(17/2)m^2\}\cosh^4\gamma^0-(1+7m^2)\cosh^2\gamma^{(0)}+m^2}{\cosh\gamma^{(0)}(\cosh^2\gamma^{(0)}-1)(2\cosh^2\gamma^{(0)}-1)\{2(m^2-1)\cosh^4\gamma^{(0)}-m^2\cosh^2\gamma^{(0)}-2m^2\}}\\
p_2&=\Bigg[p_1{}^2\Bigg\{-\frac{m^2}{\cosh^2\gamma^{(0)}-m^2}-\frac{m^2(1-m^2)}{2(\cosh^2\gamma^{(0)}-m^2)^2}-\frac{3}{\cosh^2\gamma^{(0)}}-\frac{4}{(2\cosh^2\gamma^{(0)}-1)^2}\\
&\quad+\frac{8}{2\cosh^2\gamma^{(0)}-1}\Bigg\}+p_1\cosh\gamma^{(0)}\Bigg\{\frac{1}{\sinh^4\gamma^{(0)}}-\frac{2}{\cosh^4\gamma^{(0)}}+\frac{5-1/m^2}{\cosh^2\gamma^{(0)}}+\frac{10}{(2\cosh^2\gamma^{(0)}-1)^2}\\
&\quad-\frac{13+2m^2/(1-2m^2)}{2\cosh^2\gamma^{(0)}-1}+\frac{m^2}{(\cosh^2\gamma^{(0)}-m^2)^2}-\frac{m^2}{(\cosh^2\gamma^{(0)}-m^2)^2(2\cosh^2\gamma^{(0)}-1)^2}\\
&\quad-\frac{1}{2(1-m^2)}\cdot\frac{1}{\sinh^2\gamma^{(0)}}+\left(\frac{m^2}{2(1-m^2)}+\frac{1}{m^2}+\frac{m^2}{1-2m^2}\right)\frac{1}{\cosh^2\gamma^{(0)}-m^2}\\
&\quad-\frac{2m^2}{(2\cosh^2\gamma^{(0)}-1)^2(\cosh^2\gamma^{(0)}-m^2)}\Bigg\}+\frac{1}{2}\cdot\frac{1}{(\cosh^2\gamma^{(0)}-1)^2}+\frac{5}{8}\,\frac{1}{(\cosh^2\gamma^{(0)}-3)^3}
\end{aligned}\right\}$$

$$+\frac{m^2}{2}\cdot\frac{1}{(\cosh^2\gamma^{(0)}-m^2)^2}+\frac{5}{8}\frac{m^2}{(\cosh^2\gamma^{(0)}-m^2)^3}-\frac{1}{2}\left(\frac{1}{2\cosh^2\gamma^{(0)}-1}+\frac{1}{(2\cosh^2\gamma^{(0)}-1)^2}\right)$$
$$\left(\frac{1}{\cosh^2\gamma^{(0)}-1}+1-\frac{2}{\cosh^2\gamma^{(0)}}\right)\left(\frac{m^2}{\cosh^2\gamma^{(0)}-m^2}-1-\frac{1}{\cosh^2\gamma^{(0)}}\right)+\frac{17}{4}\frac{1}{\cosh^2\gamma^{(0)}}$$
$$\left.-\frac{9}{2\cosh^2\gamma^{(0)}-1}\right]\frac{\cosh\gamma^{(0)}}{\sinh\gamma^{(0)}}\bigg/\left(\frac{m^2}{\cosh^2\gamma^{(0)}-m^2}-\frac{4}{2\cosh^2\gamma^{(4)}-1}+\frac{1}{\cosh^2\gamma^{(0)}-1}\right)\Bigg) \quad (3.34)$$

Putting these values of p_1, p_2 $\cdots$ into (3.32), we obtain the closer estimate of the position of the zero.

References

1) M. Nagase: On the zeros of certain transcendental functions related to Hankel functions-Part I, J. Phys. Soc. Japan **9** (1954) 826.

2) M. Nagase: Journ. Phys. Soc. Japan, **9** (1954) 296–297.

3) T. Sakai: Geophys. Mag., **8** (1934) 1–71.

JOURNAL OF THE PHYSICAL SOCIETY OF JAPAN Vol. 9, No. 5, SEP.—OCT., 1954

On the Curved Shock Wave due to an Infinite Wedge placed in a Supersonic Uniform Flow

By Kinzo HIDA

Department of Applied Physics, Faculty of Engineering,
Naniwa University

(Received May 10, 1954)

This paper gives detailed discussions on a problem dealt with briefly by the writer in a recent short note with the same title.[1)]

It will be shown with the aid of analysis in the hodograph plane that besides the well-known two shock configurations, two more shock configurations are possible to occur due to an infinite wedge placed in a supersonic uniform flow. These two shocks are both curved waves; one is an attached shock which turns from weak shock at the vertex of the wedge to strong one at infinity as we move out along the shock, while the other is a detached shock which is normal shock at the nose of the body and becomes strong one at infinity.

Numerical calculations are carried out for the case when $M_1=1.50$ and $\theta_0=11°45'$ where M_1 and θ_0 are respectively the Mach number at infinity upstream and the semi-vertical angle of the wedge.

§ 1. Introduction and Summary

This paper gives detailed discussions on a problem dealt with briefly in the writer's recent short note in Reader's Forum of the Journal of the Aeronautical Sciences under the title: "On the Curved Shock Wave due to an Infinite Wedge."[1)]

It is well known that when an infinite wedge is placed in a supersonic uniform flow, two shock configurations are possible provided that the vertical angle of the wedge, $2\theta_0$, is smaller than a certain critical value. They are both attached shock waves and are called "strong-shock" and" weak-shock" respectively.

In the present paper it will be shown with the aid of analysis in the hodograph plane that two more shock configurations are possible to occur. They are both curved shock waves ; one is an attached shock which turns from weak-shock at the vertex of the wedge to strong one at infinity as we move out along the shock, while the other is a detached shock at the nose of the body and becomes strong one at infinity. Bearing these properties in mind we shall call them briefly "weak-strong-shock" and "normal-strong-shock" respectively.

In the hodograph plane (i.e. velocity plane), not only the magnitude and direction of the velocity, which is attained when the flow passes through a shock, are given by a shock polar, but also the initial curvature of a stream line immediately behind a shock is shown by shock-spines[2] (see Fig. 1).

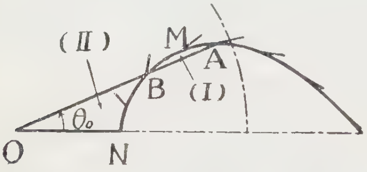

Fig. 1. Shock polar and spines.

As shown in Fig. 1, let a straight line be drawn through the origin O making the angle θ_0 with ON, and let A and B be the points of intersection of this straight line with the shock polar. Then, these two points correspond respectively to the weak-shock and the strong-shock.

In case where the point A lies in the supersonic region, it is likely that one possible shock configuration will die out, because the line AB cuts the sonic line in the directicn of the characteristics and generally some singularity may appear in the physical plane. Therefore, confining ourselves to the case when the point A lies in the subsonic region, we shall seek for solutions in the region AMB and OBN, which correspond to "weak-strong-shock" and "normal-strong-shock" respectively.

For the sake of simplicity we take the Laplace equation, $\varDelta\varPsi=0$, as the fundamental equation for the stream function $\varPsi$ in each region by the extension of Kármán-Tsien's method[3),4)]. and the solution of this Laplace equation having the singularity of doublet type at B will be sought, which necessarily makes a finite region in the hodograph plane to correspond to a semi-infinite region behind the shock in the physical plane.

Numerical computations are carried out for the case when $M_1=1.50$ and $\theta_0=11°45'$, where M_1 is the Mach number at infinity upstream and θ_0 is, as before, the semi-vertical angle of the wedge. Since an infinite wedge has evidently no characteristic length, we cannot settle uniquely the shock wave in the physical plane, but rather we obtain an infinite system of similar flow patterns. Fig. 7 shows configurations of newly found two possible shocks, together with those of two straight shocks hitherto well-known.

§ 2. Fundamental Equations and Boundary Conditions

We assume that the vorticity in the flow field behind the shock wave may safely be neglected. Then, if we neglect the heat conductivity and the viscosity of the fluid, the velocity potential $\varPhi$ and the stream function $\varPsi$ for a two-dimensional irrotational flow of a compressible fluid are governed by the equations:

$$\varPhi_q=q\frac{d}{dq}\left(\frac{\rho_0}{\rho q}\right)\varPsi_\theta\,,\qquad \varPhi_\theta=q^2\left(\frac{\rho_0}{\rho q}\right)\varPsi_q\,, \tag{1}$$

where q and θ are the magnitude and direction of the fluid velocity at any point in the flow and ρ and ρ_0 denote the density of the fluid at any point and at the stagnation point respectively.

If, as suggested by Kármán and Tsien[3),4)], we use the reduced velocity defined as:

$$q'=\frac{2q}{\sqrt{1+(q/c_0)^2}+1}\,,\qquad \theta'=\theta\,, \tag{2}$$

Eqs. (1) can be reduced to

$$\left.\begin{aligned}&\varDelta\varPhi=0\,,\qquad \varDelta\varPsi=0\,,\\ &\text{with}\\ &\varDelta\equiv\frac{d^2}{dq'^2}+\frac{1}{q'}\frac{d}{dq'}+\frac{1}{q'^2}\frac{d^2}{d\theta'^2}\,,\end{aligned}\right\} \tag{3}$$

where c_0 is the sonic speed at the stagnation point. Here, the gas is assumed to have the relations of the following forms between the sonic speed, the fluid velocity and the density, namely:

$$c^2-q^2=\text{const}=c_0^2\,, \tag{4}$$

$$\rho^2c^2=\text{const}=\rho_0^2c_0^2\,. \tag{5}$$

If we write q_*' for the value of q' corresponding to a certain value q_* of q, it follows from Eqs. (2) and (4) that

$$\frac{(q'/q_*')}{(q/q_*)}=\varLambda=\frac{\sqrt{1+\lambda}+1}{\sqrt{1+\lambda(q/q_*)^2}+1} \tag{6}$$

with

$$\lambda=q_*^2/c_0^2=q_*^2/(c_s^2-q_s^2)\,, \tag{7}$$

where the suffix s refers to the value at a suitably chosen standard point.

Since in the flow of the hypothetical gas used originally by Kármán and Tsien a supersonic velocity cannot occur on account of Eq. (4), we make the following three assumptions in order to extend the method to the case now under consideration.

(i) q_* stands for the critical velocity, i.e. the velocity when the local Mach number is equal to unity.

(ii) If q/q_* is transformed, by Eq. (6), into the corresponding reduced velocity, q'/q_*', the shock polar and spines for the hypothetical gas are the same as those for the gas obeying the adiabatic law.

(iii) The adiabatic law is also used in estimating the constant λ in the conversion factor Λ of Eq. (6).

Thus, if, as usual, we denote the adiabatic exponent by γ, we have

$$\lambda=\frac{2}{(\gamma+1)(1-M_{*s}^2)}\,,\qquad M_{*s}=q_s/q_*\,,\qquad (7')$$

Although these assumptions are rather bold, they may be justifiable by the reason that they will have no essential influence upon the general nature of the field of flow.

Now, we shall introduce non-dimensional velocity components (ξ, η) in place of the rectangular components of velocity (u, v) by the relations:

$$\left.\begin{aligned}\xi&=u/q_*=(q/q_*)\cos\theta=M_*\cos\theta\,,\\ \eta&=v/q_*=M_*\sin\theta\,.\end{aligned}\right\}\qquad (8)$$

Then the equation for the shock polar takes the form:

$$\eta^2\left(1+\frac{2}{\gamma+1}M_{*1}^2-M_{*1}\xi\right)=(M_{*1}-\xi)^2(M_{*1}\xi-1)\,,\qquad (9)$$

where the suffix 1 refers to the state upstream of the shock wave.

Further, the direction of spine, i.e. the initial curvature of a stream line, β, as measured from the radius vector passing through the point under consideration, is expressed by

$$\tan\beta=\frac{q(\partial\theta/\partial s)}{\partial q/\partial s}=\frac{-\cot 2(\alpha-\theta)+(\gamma+1)/4\cdot(\sin 2\theta/\sin 2\alpha)-M^2\sin^2(\alpha-\theta)}{\cos 2(\alpha-\theta)-(\gamma+1)/4\cdot(\sin 2\theta/\sin 2\alpha)+1}\cot(\alpha-\theta)\,.\qquad (10)$$

Here, s denotes the curve length along a stream line and M is the Mach number which is related with M_* as defined in (8) in the form:

$$M_*^2=\frac{(\gamma+1)M^2}{(\gamma-1)M^2+2}\,.\qquad (11)$$

Moreover, the angle of a shock wave, α, made with the direction of the undisturbed flow is found from the geometrical properties of the shock polar to be

$$\tan\alpha=(M_{*1}-\xi)/\eta\,.\qquad (12)$$

Next, by Eq. (6) we transform the hodograph plane into the reduced hodograph plane and we denote quantities in the latter plane by means of primes. Then, in place of Eqs. (9) and (10) we have

$$\frac{\eta'^2}{\Lambda^2}\left(1+\frac{2}{\gamma+1}M_{*1}^2-M_{*1}\frac{\xi'}{\Lambda}\right)=\left(M_{*1}-\frac{\xi'}{\Lambda}\right)^2\times\left(M_{*1}\frac{\xi'}{\Lambda}-1\right),\qquad (13)$$

$$\tan\beta'=\frac{(\Lambda q)(\partial\theta/\partial s)}{\partial(\Lambda q)/\partial s}=\sqrt{1+\lambda M_*^2}\tan\beta\,,\qquad (14)$$

where use has been made of Eq. (6) in obtaining the latter equation.

Also, the slope of the shock polar, δ', in the reduced hodograph plane can be easily evaluated as:

$$\tan\delta'=d\eta'/d\xi'=N/D\,,\qquad (15)$$

with abbrevations:

$$\left.\begin{aligned}N=\eta'[&\xi'(1-\sqrt{1+\lambda})(M_{*1}-\xi')\\ &\times\{2(M_{*1}^2+1)\xi'-3M_{*1}\Lambda\}\\ &+(M_{*1}\Lambda-\xi')\{(M_{*1}^2+2)\Lambda-3M_{*1}\xi'\}\\ &-\eta'^2\{(1-\sqrt{1+\lambda})\\ &\times(1+2M_{*1}^2/(\gamma+1))\xi'-M_{*1}\}]\,,\\ D=2&(M_{*1}\Lambda-\xi')^2(M_{*1}\xi'-\Lambda)\\ &-\eta'^2(1-\sqrt{1+\lambda})(M_{*1}\Lambda-\xi')\\ &\times\{2(M_{*1}^2+1)\xi'-3M_{*1}\Lambda\}\\ &+\eta'^4(1-\sqrt{1+\lambda})\{1+2M_{*1}^2/(\gamma+1)\}\,.\end{aligned}\right\}\qquad (15a)$$

Our problem is now formulated as follows: It is required to find the solution of the Laplace equation $\Delta\Psi=0$ in the region A′B′M′ (denoted simply as the region I) or in the region B′N′O′ (denoted as the region II), which has a singularity of doublet type at B′ and satisfies the following boundary conditions:

$$\text{(i)}\quad \Psi=0\begin{cases}\text{on B}'\text{A}' & \text{(for the region I)},\\ \text{on O}'\text{B}'\text{ and O}'\text{N}' & \text{(for the region II)};\end{cases}$$

(ii) The initial direction of every stream line should be coincident with the direction of spine at each point on the shock polar.

By placing the singularity at B′, the finite region in the hodograph plane corresponds to the semi-infinite region behind the shock wave in the physical plane in the reverse order, which is consistent with the condition that the Jacobian of transformation should be negative in the subsonic region. In the actual calculation, the second boundary condition (ii) is made to be satisfied at a few points suitably chosen in the boundary.

To proceed further in the analysis, the two cases will be discussed separately.

§ 3. Weak-strong-shock

In the first place we shall find the solution for the region A′B′M′.

We shall replace the second boundary conditions in the previous section by that at M′ corresponding to the point of maximum deflection. For the notations used in the following lines, reference should be made to Fig. 2. $\bar{\beta}$ and $\bar{\delta}$ are connected with various quantities in § 2 by the relations:

$$\bar{\beta}=\beta'+\theta'-\theta_0\,,\qquad \bar{\delta}=\delta'-\theta_0\,,\qquad (16)$$

and can be calculated by taking Eqs. (10)–(15) into account.

Thus, the boundary conditions are given in the forms:

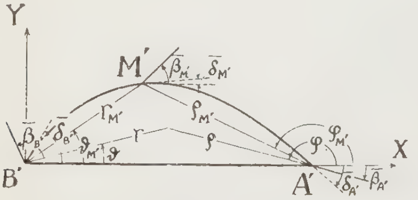

Fig. 2.

$$\left.\begin{array}{lll}\text{(i)} & \Psi=0 & \text{along B}'\text{A}',\\ \text{(ii)} & \displaystyle\lim_{\varphi=\bar{\delta}_{A'},\ \rho\to 0}\left(\frac{dY}{dX}\right)_{\Psi=\text{const}}=\tan(\bar{\beta}_{A'}+\pi) & \\ & & \text{at A}',\\ \text{(iii)} & \displaystyle\lim_{\vartheta=\bar{\delta}_{B'},\ r\to 0}\left(\frac{dY}{dX}\right)_{\Psi=\text{const}}=\tan\bar{\beta}_{B'} & \\ & & \text{at B}',\\ \text{(iv)} & \displaystyle\left(\frac{dY}{dX}\right)_{\Psi=\text{const}}=\tan\bar{\beta}_{M'} & \text{at M}'.\end{array}\right\}\qquad (17)$$

We now take the stream function Ψ satisfying the Laplace equation of the form:

$$\frac{\Psi}{C}=\frac{D}{r^n}\sin n\vartheta+\rho^m\sin m(\pi-\varphi)\,,\qquad (18)$$

where C and D are constants to be determined appropriately. Then it can be easily confirmed that this function has a singularity at the point B′ ($r=0$) and also satisfies the first condition (i) in (17). The indices n and m can be determined in such a way that the second and third conditions (ii) and (iii) in (17) are satisfied by the above Ψ. We then have

$$n=\bar{\beta}_{B'}/\bar{\delta}_{B'}-1\,,\quad m=1-\bar{\beta}_{A'}/\bar{\delta}_{A'}\,.\qquad (19)$$

The constant D is to be determined by the fourth condition (iv) in (17). For this purpose it is convenient to expand the right-hand side of (18) in the vicinity of M′. Referring to the polar coordinates (R, Θ) with the origin at M′ and the initial line parallel to the line B′A′, the equation for the stream line passing throuth M′ is easily obtained, after some reductions, in the form:

$$\begin{aligned}&DnRr_{M'}{}^{-(n+1)}\sin\{\Theta-(n+1)\vartheta_{M'}\}\\&\quad-mR\rho_{M'}{}^{m-1}\sin\{m(\varphi_{M'}-\pi)+\Theta-\varphi_{M'}\}\\&\quad+O\left\{\left(\frac{R}{\rho_{M'}}\right)^2,\left(\frac{R}{r_{M'}}\right)^2\right\}=0\,.\end{aligned}\qquad (20)$$

Then the condition (iv) can be put in an alternative form as:

(iv′) $\Theta\to\bar{\beta}_{M'}$ as $R\to 0$. (for the stream line through M′)

Thus, the constant D can be determined as:

$$D=\frac{mr_{M'}{}^{n+1}\sin[m(\varphi_{M'}-\pi)+\bar{\beta}_{M'}-\varphi_{M'}]}{n\rho_{M'}{}^{1-m}\sin[\bar{\beta}_{M'}-(n+1)\vartheta_{M'}]}\,.\qquad (21)$$

The constant C remains undetermined, since there is no characteristic length in the case of infinite wedge. This evidently results in indeterminacy of flow patterns, all of which are similar to each other in the physical plane.

We next proceed to the determination of the shape of the shock wave in the physical plane. In accordance with the continuity of every stream line passing across a shock, we have the relation valid on a shock wave in the form:

$$y=\frac{\rho_0}{\rho_1}\frac{\Psi}{q_1}=\frac{\rho_0}{\rho_s}\frac{\rho_s}{\rho_1}\frac{\Psi}{q_1}\,,\qquad (22)$$

where the suffix s has the same meaning as in Eq. (7).

In Kármán-Tsien's approximation used here, the ratio of the density at the stagnation point to that at any arbitrary point is given by

$$\frac{\rho_0}{\rho}=\frac{4c_0{}^2+q'^2}{4c_0{}^2-q'^2}=\frac{(1+\sqrt{1+\lambda})^2+\lambda M_*'^2}{(1+\sqrt{1+\lambda})^2-\lambda M_*'^2}\,. \tag{23}$$

In deriving the equation, use has been made of Eqs. (2), (4), (5) and (7). It should be noted that in accordance with the assumptions made in deriving (7′), this relation can be used only in the subsonic region.

Then, substituting ρ_0/ρ_s as obtained from (23), Eq. (22) can ultimately be written in the form:

$$y=\frac{(1+\sqrt{1+\lambda})^2+\lambda M_{*s}'^2}{(1+\sqrt{1+\lambda})^2-\lambda M_{*s}'^2}\frac{1}{M_{*1}}\left(\frac{\rho_s}{\rho_1}\right)\frac{\Psi}{q_*}\,, \tag{24}$$

where ρ_s/ρ_1 should take the value as determined from the exact shock relations.

y is evidently proportional to Ψ, while the slope of the shock wave can be calculated by Eq. (12). Therefore we can draw graphically the shape of the shock in the physical plane by taking a suitable value for the constant C.

§ 4. Normal-strong-shock

We next proceed to seek for the solution for the region O′B′N′. Here the boundary condition (ii) in § 2 is made to be satisfied at the two points B′ and N′. Taking the two polar coordinates (r, ϑ) and (ρ, φ) with the origins at O′ and B′ respectively as shown in Fig. 3 and measuring the angles $\bar{\beta}$ and $\bar{\delta}$ from the positive direction of the ξ-axis, we have the relations between these quantities and those defined in § 2 as:

$$\left.\begin{aligned}\bar{\beta}&=\beta'+\theta', & \bar{\delta}&=\delta',\\ r&=M_*', & \vartheta&=\theta'=\theta\,.\end{aligned}\right\} \tag{25}$$

Then, the boundary conditions are expressed in the forms:

(i) $\Psi=0$ along N′O′ and O′B′,

(ii) $\lim\limits_{\varphi=\bar{\delta}_{B'}+\pi,\,\rho\to0}\left(\dfrac{d\eta}{d\xi}\right)_{\Psi=\text{const}}=\tan\bar{\beta}_{B'}$ at B′,

(iii) $\left(\dfrac{d\eta}{d\xi}\right)_{\Psi=\text{const}}=\tan\bar{\beta}_{N'}=0$ at N′, (26)

in which the condition (iii) is redundant, because it is satisfied automatically when the condition (i) is satisfied.

In accordance with the condition (i), we take a harmonic function of the form:

$$\Psi=-\Im\frac{C}{(\zeta^n+b^n)^m}\,, \tag{27}$$

which can be easily obtained by means of the conformal transformation. Here, b denotes the magnitude of O′B′, i.e. $M_{*B'}'$ and ζ is the complex coordinates in the (ξ, η)-plane defined as:

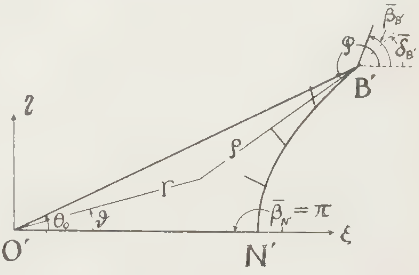

Fig. 3.

$$\zeta=re^{i\vartheta}=\xi+i\eta\,, \tag{28}$$

and C is an arbitrary constant. Also, the indices n and m can be determined by the conditions (i) and (ii) as follows:

$$n=\frac{\pi}{\theta_0}\,,\qquad m=\frac{\bar{\beta}_{B'}-\bar{\delta}_{B'}}{\pi+\bar{\delta}_{B'}-\theta_0}\,. \tag{29}$$

In the flow pattern in the physical plane corresponding to the stream function given by (27), there occurs a detached shock wave which should be determined uniquely by the position of the nose of the shock. Taking rectangular axes (x, y) with the origin at the nose N of the detached shock wave as shown in Fig. 4, the relation between the physical and the hodograph plane in Kármán-Tsien's method is given by

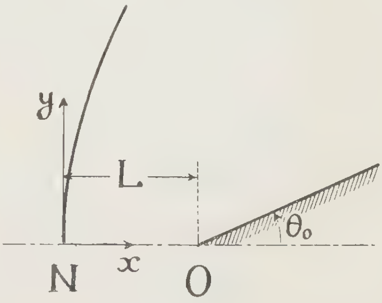

Fig. 4. Physical plane.

$$dz=dx+idy=\frac{df}{V}-\frac{Vd\bar{f}}{4c_0{}^2} \tag{30}$$

with

$$\left.\begin{aligned} f(\overline{V})&=\Phi+i\Psi\,, & \overline{f}(V)&=\Phi-i\Psi\,,\\ \overline{V}&=q'e^{-i\theta}\,, & V&=q'e^{i\theta}\,. \end{aligned}\right\} \tag{31}$$

Since $y=\Psi=\theta=0$ on the segment between the nose N of the shock and the nose O of the body, it follows from Eqs. (30), (31), (7) and (2) that

$$\begin{aligned} dx &= \frac{d\Phi}{q'}\left(1-\frac{q'^2}{4c_0{}^2}\right)\\ &= \frac{d\Phi}{q_*}\frac{\{(1+\sqrt{1+\lambda})^2-\lambda M_*'^2\}}{2(1+\sqrt{1+\lambda})M_*'}\,. \end{aligned} \tag{32}$$

The velocity potential Φ, which is conjugate to Ψ as given in (27), takes the following form on ON:

$$\Phi=\left[\Re\frac{C}{(\zeta^n+b^n)^m}\right]_{\theta=0}=\frac{C}{(r^n+b^n)^m}\,. \tag{33}$$

Integrating Eq. (32) with the value for Φ as given in (33), the distance, L say, from the vertex of the wedge to the nose of the shock is obtained as:

$$\begin{aligned} L\left(\frac{q_*}{C}\right)&=\frac{mn}{2(1+\sqrt{1+\lambda})}\\ &\times\int_0^{M_{*N'}'} r^{n-2}\frac{\{(1+\sqrt{1+\lambda})^2-\lambda r^2\}}{(r^n+b^n)^{m+1}}dr\equiv J\,. \end{aligned} \tag{34}$$

On the other hand, the y-coordinate on the shock is given by (24), while for the normal shock we have the well-known formula:

$$\frac{\rho_s}{\rho_1}=\frac{(\gamma+1)M_1{}^2}{2+(\gamma-1)M_1{}^2}=M_{*1}{}^2.$$

Thus, when we take the nose of the shock as a standard point, Eq. (24) becomes

$$y\left(\frac{q_*}{C}\right)=K\left(\frac{\Psi}{C}\right), \tag{35}$$

with

$$K=\frac{(1+\sqrt{1+\lambda})^2+\lambda M_{*N'}'^2}{(1+\sqrt{1+\lambda})^2-\lambda M_{*N'}'^2}M_{*1}\,. \tag{36}$$

In the calculation of K, use has been made of Eq. (11).

Combining (35) with (34) we have

$$\frac{y}{L}=\left(\frac{K}{J}\right)\left(\frac{\Psi}{C}\right). \tag{37}$$

Since, as easily seen from Eqs. (34) and (36), the ratio K/J is constant, we can find the shock wave in the physical plane except for an indeterminate length L in the same way as in the case of an attached shock.

§ 5. Numerical Computation

Numerical computation has been made for the case when

$$M_1=1.50, \qquad \theta_0=11°45',$$

where M_1 and θ_0 are respectively the Mach number of the undisturbed flow at infinity upstream and the semi-vertical angle of the infinite wedge. The value of the adiabatic exponent γ has been taken to be equal to 1.4 for air.

In Table I are shown the Mach number referred to the critical speed, M_*, the inclination of stream line, θ, and the slope of the shock, α, for the points A, M, B and N in Fig. 1, which correspond respectively to the weak shock, the point of maximum deflection, the strong shock and the normal shock.

Table I.

Points	M_*	θ	α
A	0.9951	11°45′	62°34′
M	0.9331	12° 7′	66°35′
B	0.8771	11°45′	70°31′
N	0.7328	0° 0′	90° 0′

(a) Weak-strong-shock

In this case the point of maximum deflection is taken as a standard point so as to simplify the fundamental equation in a manner as mentioned in § 2.

From Eqs. (6) and (7), the conversion factor from the hodograph plane to the reduced hodograph plane is given by

$$\Lambda=\frac{(q'/q_*')}{(q/q_*)}=\frac{3.72868}{1+\sqrt{1+6.44571M_*{}^2}}\,.$$

In Fig. 5 the reduced hodograph plane is drawn passing through the five points A′, M′, B′, C′ and D′, the last two of which correspond to $\theta=12°$. It should be noted that in this figure the ordinates are enlarged as twice as the abcissae for the sake of convenience. Numerical values of various quantities at each of these five points are given in Table II

Table II.

Points	X	Y	$\overline{\delta}$	$\overline{\beta}$
A′	4.752×10^{-2}	0	−27°46′	−7°47′
C′	3.686 〃	4.309×10^{-3}	−15°55′	−2°55′
M′	2.351 〃	6.169 〃	2° 3′	28°56′
D′	1.031 〃	4.193 〃	16°20′	55°58′
B′	0	0	27°34′	70°47′

with the notation shown in Fig. 2.

Following the analysis in § 3, we can calculate the stream function as

$$\frac{\Psi}{C}=\frac{3.290\times10^{-4}}{r^{1.568}}\sin(1.568\vartheta)$$
$$+\rho^{0.7196}\sin(0.7196\pi-\varphi)\,.$$

By plotting Ψ/C against Y for various constant values of X and making the interpolation graphically, we can obtain a number of stream lines in the reduced hodograph plane, some of which are shown in Fig. 5.

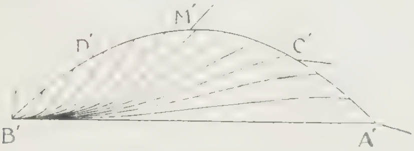

Fig. 5. Reduced hodograph plane.

Table III.

$\Psi/C\times10^3$	α	$\Psi/C\times10^3$	α
0	62°34′	73.4	67°10′
8.2	63° 9′	107.2	67°51′
15.8	63°50′	173.9	68°30′
23.0	64°30′	338.5	69°10′
31.0	65° 9′	1025	69°51′
41.3	65°49′	∞	70°31′
54.4	66°30′		

Although the coincidence of the direction of a stream line with that of shock spine is not so good in the vicinity of C′, yet it may be improved by making the boundary condition (ii) to be satisfied at more points.

In order to find the shape of shock wave in the physical plane, it is sufficient to know the value of Ψ on the shock as well as the angle of inclination of the shock, α, which are given in Table III.

As mentioned already, the constant C remains indeterminate so that the flow pattern is not determined uniquely. All the flow patterns are however similar to that given in Fig. 7, where the well-known two configurations of shock wave, namely a weak shock and a strong shock, are also shown for comparison.

(b) Normal-strong-shock

In this case the point N′ is taken as a standard point. The factor of transformation into the reduced hodograph plane is

$$A=\frac{2.67332}{1+\sqrt{1+1.8M_*^2}}\,.$$

In Fig. 6 the reduced hodograph plane is shown by letting a shock polar pass through the three points P′, Q′ and R′ corresponding to $\theta=3°$, 6° and 9° respectively, as well as the two points B′ and N′. For convenience's sake, the ordinates of this figure are also enlarged as twice as the abcissae. With the notation used in Fig. 3, the corresponding values for each point are shown in Table IV.

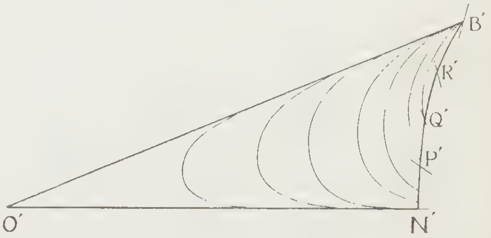

Fig. 6. Reduced hodograph plane.

Table IV.

Points	ξ	η	$\overline{\delta}$	$\overline{\beta}$
N′	0.8155	0	90° 0′	180° 0′
P′	0.8186	0.0429	81°49′	161°47′
Q′	0.8287	0.0871	72°42′	142° 9′
R′	0.8502	0.1347	58°34′	117°57′
B′	0.9027	0.1877	37°48′	61° 9′

The velocity potential Φ and the stream function Ψ can be calculated from the formulae in § 4 as follows:

$$\Phi-i\Psi=\bar{f}(V)=\frac{C}{(\zeta^{15.319}+0.28812)^{0.11328}}\,.$$

Taking the imaginary part of both sides, the stream function becomes

$$\Psi/C=(R^2+I^2)^{-0.05664}\sin(0.11328\Theta)$$

with

$$R=q^{15.319}\cos(15.319\theta)+0.28812\,,$$
$$I=q^{15.319}\sin(15.319\theta),$$
$$\tan\Theta=I/R.$$

Proceeding in the same manner as in the preceding case (a), we can find typical stream lines as shown in Fig. 6. The direction of stream lines differs from that of spines to slightly larger extent than in the preceding case (a), but this discrepancy may be reduced by adding the appropriate regular solutions to that used here so as to satisfy the boundary condition at more points on the shock polar.

The values of J and K as defined in § 4 are

$$J=2.7815\times10^{-2},$$
$$K=1.9137.$$

In evaluating the value of J, use has been made of Simpson's rule by dividing the integration range into 10 suitable sub-ranges.

Table V.

$\Psi/C\times10^3$	α	$\Psi/C\times10^3$	α
0	90° 0′	34.0	80°32′
6.4	88°22′	41.1	78° 0′
13.7	86°29′	53.9	74°12′
20.7	84°36′	90.6	71° 1′
27.4	82°40′	∞	70°31′

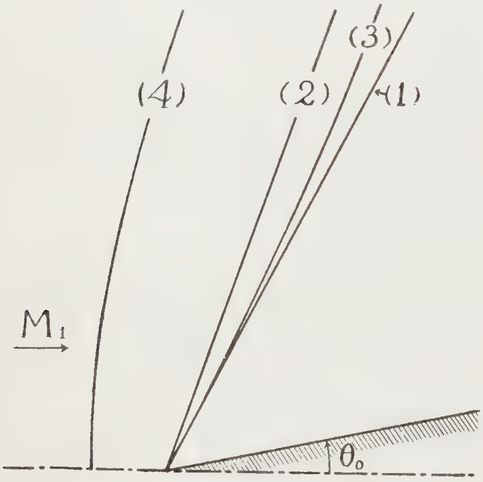

Fig. 7. Various shock configurations.
(1) Weak-shock (2) Strong-shock
(3) Weak-strong-shock (4) Normal-strong-shock

With these numerical values Eq. (37) becomes

$$y/L=6.8801\times10^1(\Psi/C)$$

and in Table V are given the values of Ψ/C and the corresponding values of the inclination, α, of the shock at the same point. (They are however not necessarily related with each stream line in Fig. 6.)

The shape of the shock wave is not determined uniquely on account of the indeterminate length L. One example is shown in Fig. 7. All the flow patterns expressed by the same function are similar to each other.

Acknowledgements

In conclusion, the writer wishes to express his cordial thanks to Professor S. Tomotika not only for his continual encouragement but also for his kind inspection of the manuscript. The writer's thanks are also due to Dr. K. Tamada for his suggestion of this problem and for many valuable discussions. For the calculation of shock spines in § 2, the writer is much indebted to Dr. T. Kawamura, who kindly showed him his unpublished paper.

This work has been supported partly by a grant-in-aid for fundamental scientific research of the Ministry of Education in 1953.

References

1) K. Hida: J. Aero. Sci. **21** (1954) 214.
2) A. Busemann: N.A.C.A. T.N. No. 1858 (1949).
3) Th. von Kármán: J. Aero. Sci. **8** (1941) 337.
4) H. S. Tsien: J. Aero. Sci. **6** (1939) 399.

JOURNAL OF THE PHYSICAL SOCIETY OF JAPAN Vol. 9, No. 5, SEP.—OCT., 1954

On the Attached Curved Shock in Front of an Open-Nosed Axially Symmetrical Body

By Hakuro OGUCHI

Institute of Science and Technology, University of Tokyo, Japan

(Received June 22, 1954)

The flow near the nose over an open-nosed axially symmetrical body placed in a uniform flow of sufficiently high Mach number is considered. The equation valid near the nose is derived by employing a method of perturbation. From the solution of this equation, the flow near the nose can be determined and further a formula relating the initial curvature K_W of the shock to the curvature K_S of the body surface in a meridian plane is derived in the form

$$\frac{K_W}{K_S}=\left(\frac{K_W}{K_S}\right)_p\left[1-\frac{\tan(\alpha-\omega)\sin\omega}{1-(U^2/a_0^2-1)\tan^2(\alpha-\omega)}\frac{K_N}{K_S}\right],$$

where $(K_W/K_S)_p$ is the corresponding ratio for the cylindrical body having the same profile as that of the body of revolution, α the angle of inclination of the shock to the uniform flow, ω the initial slope of the body, K_N the curvature of the nose in the plane perpendicular to the axis of symmetry and U/a_0 the Mach number of the flow immediately behind the shock at the nose. In this formula the curvature K_W is positive for the shock which is concave upwards and the curvature K_S of the surface also is positive under this condition.

Finally the conical shock and the attached shock of a sharp-nosed body are discussed on the basis of this formula. In the axially symmetrical case it is pointed out that the curvature of the shock exhibits a singular behaviour at the Crocco point as in the two dimensional case.

§ 1. Introduction

When an open-nosed body of revolution is placed in a uniform flow of sufficiently high Mach number, a curved attached shock wave emerges from the nose (Fig. 1). In the present paper we investigate the flow immediately behind the shock near the nose and discuss the relation between the initial curvature of the shock and of the body.

The curved shock in two dimensions was first treated by L. Crocco¹⁾ and later by various authors²⁾³⁾⁴⁾; in particular, Lin and Rubinov indicated that their analysis would be applicable to the case of axial symmetry. However, the Cartesian coordinates used in their analysis are not suitable to the present problem because the nose does not lie on the axis. Therefore, in the present paper, a different approach should be adopted.

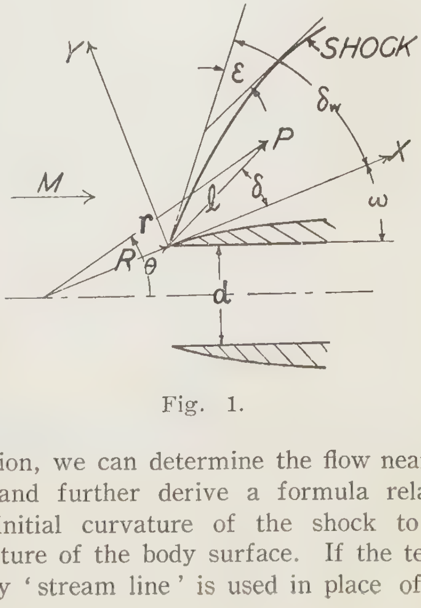

Fig. 1.

The equations of fluid motion are described in polar coordinates (r, θ) whose origin is chosen to coincide with the point of intersection of the axis and the tangent at the nose (Fig. 1). Since the flow may be assumed to be non singular at the nose, the method of perturbation starting from the state pertaining to the nose is employed to derive a linearized equation valid near the nose. By solving this equation, we can determine the flow near the nose and further derive a formula relating the initial curvature of the shock to the curvature of the body surface. If the terminology 'stream line' is used in place of the body surface, the formula may be reinterpreted as the relation between the curvature of the axially symmetrical shock and of the stream line at any point on the shock except on the axis of symmetry. From this formula it can be shown that, when a shock is straight in a meridian plane, the flow immediately behind the shock is conical and that the attached shock of finite curvature may emerge for a sharp-nosed body of revolution only when the flow is conical at the nose.

§ 2. Fundamental Equation

Let the velocity components in the r- and θ-directions, pressure and density be u, v, p, ρ, respectively.

The equations governing the axially symmetric flow are

$$u\frac{\partial u}{\partial r}+\frac{v}{r}\frac{\partial u}{\partial\theta}-\frac{v^2}{r}=-\frac{1}{\rho}\frac{\partial p}{\partial r}\,, \tag{1}$$

$$u\frac{\partial v}{\partial r}+\frac{v}{r}\frac{\partial v}{\partial\theta}+\frac{uv}{r}=-\frac{1}{\rho}\frac{\partial p}{r\partial\theta}\,. \tag{2}$$

The equation of continuity is

$$\frac{\partial}{\partial r}(\rho u)+\frac{\partial}{r\partial\theta}(\rho v)+2\frac{\rho u}{r}+\frac{\rho v}{r}\cot\theta=0\,. \tag{3}$$

Let the velocity components in the r- and θ-directions, pressure and density at the nose be U, 0, p_0, ρ_0, respectively and let the coordinates of the nose be (R, ω). Referring to Fig. 1, ω is considered to be the deflection angle of the stream line through the shock. Here let us introduce the new polar coordinates (l, δ) whose origin and axis coincide with the nose and the line $\theta=\omega$, respectively, then they are related to the coordinates (r, θ) as follows:

$$\left.\begin{aligned} r\cos(\theta-\omega)-R&=l\cos\delta,\\ r\sin(\theta-\omega)&=l\sin\delta\,. \end{aligned}\right\} \tag{4}$$

In the immediate neighbourhood of the nose, it suffices to retain the lowest power of l/R. Hence,

$$\left.\begin{aligned} r-R&=l\cos\delta+O(l^2/R^2)\,,\\ \theta-\omega&=(l\sin\delta)/R+O(l^2/R^2)\,, \end{aligned}\right\} \tag{5}$$

or

$$\left.\begin{aligned} r-R&=x+O(l^2/R^2),\\ \theta-\omega&=y/R+O(l^2/R^2), \end{aligned}\right\} \tag{6}$$

where (x, y) are the Cartesian coordinates with the nose as the origin, and the x-axis is coincident with the line $\theta=\omega$ and the y-axis perpendicular to it in a meridian plane (Fig. 1).

Since the perturbations $u-U$, v, $p-p_0$, $\rho-\rho_0$ tend to zero as the nose is approached and these quantities may be assumed to be regular at the nose, these quantities will be expressed in the form

$$\left.\begin{aligned} u-U&=\sum_{n=1}^{\infty}(l/R)^n u_n(\delta)\,,\\ v&=\sum_{n=1}^{\infty}(l/R)^n v_n(\delta)\,,\\ p-p_0&=\sum_{n=1}^{\infty}(l/R)^n p_n(\delta)\,,\\ \rho-\rho_0&=\sum_{n=1}^{\infty}(l/R)^n \rho_n(\delta)\,, \end{aligned}\right\} \tag{7}$$

where $u_n(\delta)$, $v_n(\delta)$, $p_n(\delta)$, $\rho_n(\delta)$ depend only on δ.

Let the x- and y-components of the velocity be $\bar{u}$, $\bar{v}$, respectively, then

$$\left.\begin{aligned} \bar{u}&=u\cos(\theta-\omega)-v\sin(\theta-\omega)\,,\\ \bar{v}&=u\sin(\theta-\omega)+v\cos(\theta-\omega)\,. \end{aligned}\right\} \tag{8}$$

In view of Eqs. (6) and (7), Eqs. (8) become

$$\left.\begin{aligned} \bar{u}&=u+O(l^2/R^2),\\ \bar{v}&=Uy/R+v+O(l^2/R^2). \end{aligned}\right\} \tag{9}$$

By the transformations (6) and (9), Eqs. (1)–(3) are rewritten in the xy-system as

$$U(\partial\bar{u}/\partial x)=-(1/\rho_0)(\partial p/\partial x)+O(l/R)\,, \tag{10}$$

$$U(\partial\bar{v}/\partial x)=-(1/\rho_0)(\partial p/\partial y)+O(l/R)\,, \tag{11}$$

$$\rho_0(\partial\bar{u}/\partial x+\partial\bar{v}/\partial y)+U(\partial\rho/\partial x)=-\rho_0 U/R+O(l/R), \tag{12}$$

respectively.

The entropy s must be constant along each stream line downstream of the shock. In the neighbourhood of the nose the stream line may be assumed to be nearly coincident with the x-axis. Hence,

$$\begin{aligned} \frac{\partial\rho}{\partial x}&=\left(\frac{\partial\rho}{\partial p}\right)\frac{\partial p}{\partial x}+\left(\frac{\partial\rho}{\partial s}\right)\frac{\partial s}{\partial x}\simeq\left(\frac{\partial\rho}{\partial p}\right)_0\frac{\partial p}{\partial x}\\ &=a_0^{-2}\frac{\partial p}{\partial x}\,, \end{aligned} \tag{13}$$

where a_0 is the sound speed at the nose.

In view of Eq. (11), it is convenient to introduce a scalar ϕ as follows:

$$\bar{v}=\partial\phi/\partial y\,,\quad -(p-p_0)/\rho_0 U=\partial\phi/\partial x\,, \tag{14}$$

Ignoring the higher order terms in Eqs. (10)–(13) and combining these equations with Eq. (14), we have

$$(1-U^2/a_0^2)(\partial^2\phi/\partial x^2)+\partial^2\phi/\partial y^2+U/R=0\,. \tag{15}$$

§ 3. Boundary Conditions

Let the curvature of the body surface at the nose be K_S, then the surface is represented by the equation

$$y=K_S x^2/2+\text{higher order terms.}$$

Since the surface is a stream line, the condition at the surface becomes approximately

$$\bar{v}/U=K_S x \quad \text{at} \quad y=0$$

or, in terms of ϕ,

$$\partial\phi/\partial y=UK_S x \quad \text{at} \quad y=0. \tag{16}$$

Next let us consider the condition on the shock. Let the variation of the angle of inclination of the shock from that of the shock at the nose be ε (Fig. 1); then it follows from the Rankine-Hugoniot shock conditions that, to the first order with respect to the perturbations, the following linear relations hold on the shock

$$\bar{v}=V(p_0-p)/\rho_0 U\,, \quad \varepsilon=W(p_0-p)/\rho_0 U\,, \tag{17}$$

where V and W are given as the functions of quantities at the nose as follows:

$$V=-\frac{\gamma(\gamma+1)}{(\gamma-1)^2}\tan\delta_W\cdot\left(\frac{\gamma+1}{\gamma-1}+k\right)^{-2} \cdot\left[-k^2+(M^2-2)k+\left\{\frac{3\gamma-1}{\gamma+1}M^2+\frac{3-\gamma}{\gamma+1}\right\}\right], \tag{18}$$

$$W=-\frac{\gamma+1}{2}(U\sin 2\delta_W)^{-1},$$

where M is the Mach number of the uniform flow ahead of the shock, δ_W is the angle between the x-axis and the shock at the nose, γ is the ratio of specific heats and k is the ratio of the pressure immediately behind the shock at the nose to that of the uniform flow. Since the shock lies nearly on the tangent to the shock at the nose, Eqs. (14) and (17) are combined to yield the condition on the shock

$$\frac{\partial\phi/\partial y}{\partial\phi/\partial x}=V \quad \text{on the line} \quad y=\tan\delta_W\cdot x\,. \tag{19}$$

§4. Specialization for the Subsonic Case

The cases when the entire field behind the shock is subsonic or supersonic will be designated as 'subsonic' or 'supersonic case', respectively.

In this section the subsonic case is considered. By the transformation

$$x=\xi, \qquad y=\eta/m, \tag{20}$$

where

$$m=(1-U^2/a_0^2)^{1/2}, \tag{21}$$

Eq. (15) becomes

$$\partial^2\phi/\partial\xi^2+\partial^2\phi/\partial\eta^2+U/m^2R=0\,.$$

The solution of this equation is written in the form

$$\phi=\Psi-(U/4m^2R)(\xi^2+\eta^2)\,, \tag{22}$$

where Ψ represents a harmonic function.

It is more convenient to introduce the new variables (l', δ') defined by

$$\xi=l'\cos\delta', \qquad \eta=l'\sin\delta'. \tag{23}$$

In view of Eqs. (20) and (23), the condition (19) becomes

$$\frac{\partial\phi/\partial l'}{\partial\phi/l'\partial\delta'}=V' \quad \text{on the line} \quad \delta'=\delta_W', \tag{24}$$

where

$$V'=\frac{m\cos\delta_W'+V\sin\delta_W'}{V\cos\delta_W'-m\sin\delta_W'}\,,$$
$$\delta_W'=\tan^{-1}(m\tan\delta_W). \tag{25}$$

The condition (16) also becomes

$$\partial\phi/l'\partial\delta'=UK_S l'/m \quad \text{on the line} \quad \delta'=0. \tag{26}$$

According to Eq. (22), the function ϕ compatible with the above conditions may be written in the form

$$\phi=(A\cos 2\delta'+B\sin 2\delta')l'^2-(U/4m^2R)l'^2,$$

or, in view of Eqs. (20) and (23),

$$\phi=[A\cos\{2\tan^{-1}(my/x)\}+B\sin\{2\tan^{-1}(my/x)\}](x^2+m^2y^2)-(U/4m^2R)(x^2+m^2y^2). \tag{27}$$

From the conditions (24) and (26), the constants A and B are determined as follows:

$$\left.\begin{aligned} A&=\frac{(V'\cos 2\delta_W'-\sin 2\delta_W')UK_S/(2m)+U/(4m^2R)}{\cos 2\delta_W'+V'\sin 2\delta_W'}\,,\\ B&=(U/2m)K_S\,. \end{aligned}\right\} \tag{28}$$

Thus, by use of Eqs. (14), (27) and (28), the flow over an open-nosed body of revolution can be determined for the subsonic case. As an example, the pressure distributions are given by

on the surface

$$(p_0-p)/\rho_0 U=(2A-U/2m^2R)x\,, \tag{29}$$

on the shock

$$(p_0-p)/\rho_0 U=2(A\cos\delta_W'+B\sin\delta_W')\sec\delta_W'\cdot x-(U/2m^2R)\cdot x\,, \tag{30}$$

where A and B are given by Eqs. (28).

It should be noted that the preceding analysis is not applicable to the case when the field is not purely subsonic, for in this case the condition on the other boundary, i.e. the sonic line must be taken into account.

§ 5. Specialization for the Supersonic Case

In this section the supersonic case is considered. For abbreviation, we put

$$U^2/a_0^2-1=\mu^2. \tag{31}$$

Then the general solution of Eq. (15) may be written in the form,

$$\phi=f(x-\mu y)+g(x+\mu y)+(U/4\mu^2R)(x^2-\mu^2y^2), \tag{32}$$

where f and g are arbitrary functions of the indicated arguments and represent the incident and reflected waves, respectively. Since ϕ is assumed to be regular at the nose, f and g can be expanded in power series of the argument. Hence, it follows that ϕ compatible with the conditions (16) and (19) should be written in the form

$$\phi=C(x-\mu y)^2+D(x+\mu y)^2+(U/4\mu^2R)(x^2-\mu^2y^2). \tag{33}$$

From the conditions (16) and (19), fhe constants C and D are determined as follows:

$$\left.\begin{aligned}C=&\{1/4\mu(V-\mu^2\tan\delta_W)\}[(1+\mu\tan\delta_W)\\&\cdot(\mu-V)UK_S-(U/2\mu R)(V+\mu^2\tan\delta_W)],\\D=&\{1/4\mu(V-\mu^2\tan\delta_W)\}[(1-\mu\tan\delta_W)\\&\cdot(V+\mu)UK_S-(U/2\mu R)(V+\mu^2\tan\delta_W)].\end{aligned}\right\} \tag{34}$$

Thus, by use of Eqs. (14), (33) and (34), the flow over an open-nosed body of revolution can be determined for the supersonic case. As an example, the pressure distributions are given as follows:

on the surface

$$(p_0-p)/\rho_0U=(2C+2D+U/2\mu^2R)x,$$

on the shock

$$\begin{aligned}(p_0-p)/\rho_0U=&2C(1-\mu\tan\delta_W)x\\&+2D(1+\mu\tan\delta_W)x+(U/2\mu^2R)x,\end{aligned} \tag{35}$$

where C and D are given by Eqs. (34).

§ 6. The Relation between the Initial Curvature of the Shock and of the Body

Let the line length along the shock be σ, then the curvature K_W of the shock is written as

$$K_W=d\varepsilon/d\sigma, \tag{36}$$

where K_W is positive when the shock is concave upwards. In the neighbourhood of the nose, Eq. (36) becomes approximately

$$K_W=(d\varepsilon/dx)\cos\delta_W.$$

From the second equation of Eqs. (17), this equation becomes

$$K_W=W\cos\alpha\,(d/dx)\{(p_0-p_W)/\rho_0U\},$$

where p_W is the pressure immediately behind the shock. Substituting $(p_0-p_W)/\rho_0U$ from Eqs. (30), (35) into the above equation, we obtain

for the subsonic case

$$\begin{aligned}K_W=UW\cos\delta_W\Big[&\frac{\sec\delta_W'\cdot K_S}{V\cos\delta_W'+m\sin\delta_W'}\\&-\frac{\sin\delta_W'}{(V\cos\delta_W'+m\sin\delta_W')R}\Big],\end{aligned} \tag{37}$$

for the supersonic case

$$\begin{aligned}K_W=UW\cos\delta_W\Big[&\frac{1-\mu^2\tan\delta_W}{V-\mu^2\tan\delta_W}K_S\\&-\frac{\tan\delta_W}{(V-\mu^2\tan\delta_W)R}\Big],\end{aligned} \tag{38}$$

respectively.

Since $\tan\delta_W'=m\tan\delta_W$, it is easily verified that Eq. (37) is identical with Eq. (38). Hence Eq. (38) can be applied either for the subsonic or supersonic case and, although the sonic case when $U/a_0=1$ has been excluded in the preceding analysis, the relation between the initial curvature of the body and of the shock can be given by the limiting form of Eq. (38) as $\mu\to0$. Here it is worth noting that at the nose Eq. (38) yields the exact formula because Eq. (38) holds independently of x.

Let the diameter of the nose be d and the curvature of the body in the plane perpendicular to the axis of symmetry at the nose be K_N, then

$$K_N=2/d,\quad R=d/2\sin\omega=1/K_N\sin\omega. \tag{39}$$

Thus Eq. (38) becomes

$$\begin{aligned}K_W=\frac{UW\cos\delta_W}{V-\mu^2\tan\delta_W}&[(1-\mu^2\tan^2\delta_W)K_S\\&-\tan\delta_W\sin\omega\cdot K_N].\end{aligned} \tag{40}$$

As $K_N\to0$, Eq. (40) reduces to the relation

$$K_W=UW\cos\delta_W\left[\frac{1-\mu^2\tan^2\delta_W}{V-\mu^2\tan\delta_W}\right]K_S. \tag{41}$$

It can be readily shown that this relation is exactly the same as that in the two-dimensional case given by many authors. This is also obvious from the fact that in the limiting case $K_N\to0$ the nose is located infinitely far from the axis. Let $(K_W/K_S)_p$ represent the ratio corresponding to a cylindrical body which has the same cross-sectional form as the open-nosed body of revolution under consideration, then $(K_W/K_S)_p$ is given by Eq. (41), and Eq. (40) is rewritten in the form

$$\frac{K_W}{K_S}=\left(\frac{K_W}{K_S}\right)_p\left[1-\frac{\tan\delta_W\sin\omega}{1-\mu^2\tan^2\delta_W}\frac{K_N}{K_S}\right]. \tag{42}$$

The value of $(K_W/K_S)_p$ can be evaluated by substituting V, W from Eqs. (18) into Eq. (41). The values of $(K_W/K_S)_p$ versus the initial inclination α of the shock to the uniform flow are tabulated in detail in Reference 5) for the various Mach number of the uniform flow. Thus, when an open-nosed body of revolution is placed in a uniform supersonic flow, the ratio of the initial curvature of the shock to that of the body surface can be easily evaluated from Eq. (42). As an example, the values of $[(K_W/K_S)_p-K_W/K_S]K_S/K_N$ are shown as a function of α for $M=1.35$, 2.12, 3.24 in Figs. 2, 3, 4, respectively.

If we consider the body surface in the preceding analysis as a stream line, Eq. (42) can be reinterpreted to be the formula relating the curvature of the shock to the curvature of the stream line at any point on the shock except on the axis of symmetry. It follows from Eq. (41) that the ratio $(K_W/K_S)_p$ increases to infinity at the Crocco point since $V-\mu^2\cdot\tan\delta_W$ vanishes there, and that the attached shock of finite curvature emerges for a plane body with straight sides. On the other hand, in the case of axial symmetry, the shock also exhibits a singular behaviour at the Crocco point. In this case, however, the attached shock of infinite curvature emerges even for an open-nosed body of revolution with straight sides. Indeed, the difference in the ratio of curvatures in the two cases rises to infinity at the Crocco point, as shown in Figs. 2–4.

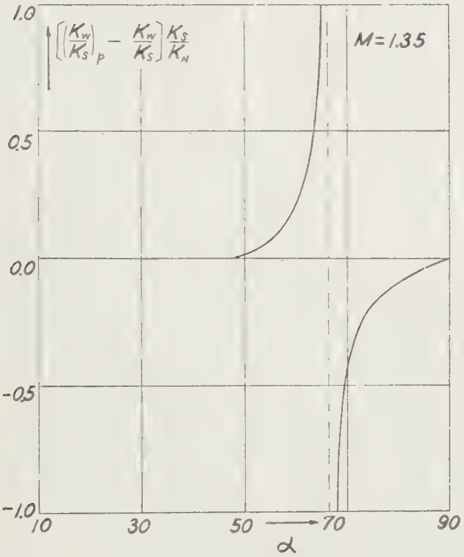

Fig. 2.

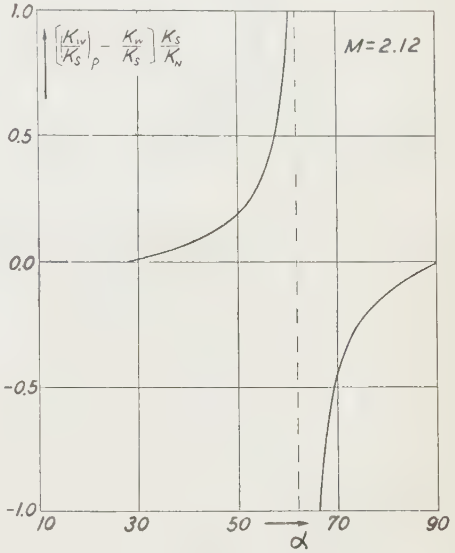

Fig. 3.

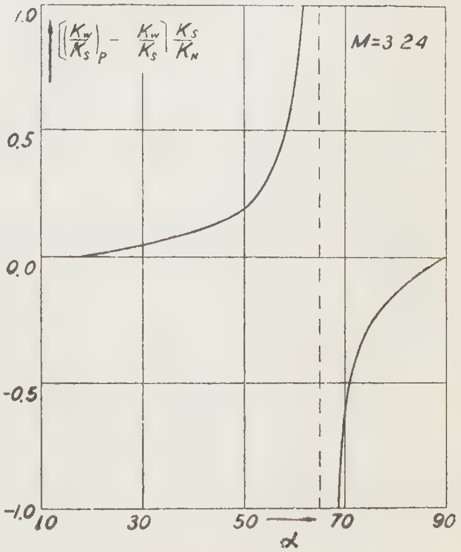

Fig. 4.

Let us consider the conical shock which is an interesting case of axially symmetrical shock. Since the conical shock is straight in a meridian plane, i.e. $K_W=0$, we have from Eq. (42)

$$K_S=\{\tan\delta_W\cdot\sin\omega/(1-\mu^2\tan^2\delta_W)\}K_N. \tag{43}$$

This equation yields the curvature of the stream line immediately behind the conical shock in a meridian plane. Here it is worth noting that at the Crocco point there exists no conical shock even for the case that the relation (43) is satisfied, for $(K_W/K_S)_p$ becomes infinity there and therefore the value of K_W given by Eq. (42) remains finite. Since μ, δ_W are constant along a straight shock, Eq. (43) means that the ratio K_S/K_N also is constant along the shock. Hence the flow field immediately behind the shock straight in a meridian plane must be locally conical.

Finally we consider the case of a sharp-nosed body of revolution as the limiting case $d \rightarrow 0$ in the preceding analysis. If the flow approaches a conical one as the nose is approached, as assumed in Shen and Lins' analysis[6)7)], both K_N and K_S increase to infinity while K_N/K_S tends to the finite value given by Eq. (43) and $(K_W/K_S)_p$ also tends to the finite value except at the Crocco point. Hence, from Eq. (42), the curvature of the shock may remain finite at the nose and exhibits a singular behaviour at the Crocco point, as in the two-dimensional case. On the other hand, in the case when the flow does not approach a conical one as the nose is approached, the curvature of the shock at the nose becomes infinite even if the body is of regular shape, for in Eq. (42) the terms in the square bracket tend to infinity as K_S tends to a finite value.

In conclusion, the author wishes to thank Dr. R. Kawamura for his help and encouragement during the course of this investigation. He also wishes to thank Prof. I. Imai for his advice and kind inspection of the manuscript.

References

1) L. Crocco: L'Aerotecnica **17** (1937) 519.

2) T. Y. Thomas: J. Math. Phys. **26** (1947) 62.

3) C. C. Lin and S. I. Rubinov: J. Math. Phys. **27** (1948) 105.

4) H. Melkus: Ing. Arch. **19** (1951) 208.

5) T. Y. Thomas: J. Math. Phys. **27** (1948) 279.

6) S. F. Shen and C. C. Lin: NACA TN No. 2505 (1951).

7) M. D. Van Dyke: J. Aero. Sci. **21** (1954) 179.

Journal of the Physical Society of Japan Vol. 9, No. 5, Sep.—Oct., 1954

The Relaxation of Stress in Undrawn Amilan

By Hiroshi Fujita and Akira Kishimoto
Department of Fisheries, Faculty of Agriculture,
Kyoto University, Maizuru

(Received May 6, 1954)

Stress relaxation data for undrawn Amilan monofilaments (Thin fineness is about 800 deniers and viscosity-average molecular weight is 10,600,) are obtained as functions of draw ratio and heat-treatment temperature. The relaxation curves obtained are all fitted satisfactorily by an empirical equation derived in our previous study for a commercial drawn Amilan yarn. Increasing cold-drawing is shown to decrease over-all rates of stress relaxation in such a manner that a rather rapid fall of these rates appears in the neighborhood of draw ratio 3.0. Both the elastic modulus and the elongation at break also exhibit a characteristic change in this region of draw ratio.

Comparison with the data for the drawn sample of the previous study indicates an interesting similarity in stress relaxation behavior of the drawn sample at enough high temperature and of the unstretched sample at room temperature.

It is shown that the length of cooling period after heattreatment has a pronounced effect upon the initial stress (or modulus) as well as the subsequent stress relaxation curve. This is found to be attributable to the absorption of vapor occurring during the course of cooling. Measurements of stress relaxation are made for samples which were allowed to reach sorption equilibrium after heat-treating at various temperatures, and the results are discussed as providing the true heat-treatment effect on the behavior in question.

§ 1. Introduction

The dependences of the stress relaxation behavior of drawn Amilan (polycapramide) multifilaments (yarn) on temperature, elongation, and heat-treatment have been reported in a previous communication[1]. In the present paper, the results of stress relaxation measurements carried out for undrawn Amilan monofilaments with particular interest in changes in stress relaxation behavior brought about by "cold-drawing" and heat-treatment are presented. The structural changes occurring in undrawn synthetic fibers due to various mechanical conditionings such as drawing or heat-treatment have been extensively investigated by means of x-ray diffraction methods (see, for example, an excellent review article by Susich[2]). However, information is still few in the literature about the fashion in which the viscoelastic behavior of undrawn synthetic fibers is controlled by such mechanical conditionings. The main purpose of the present study is to inspect a part of such fashion from stress relaxation measurements of undrawn Amilan monofilaments.

§ 2. Material and Method

Samples of undrawn Amilan monofilaments of different deniers and different degrees of polymerization were kindly furnished to us by Professor H. Kawai of the Department of Textile-Chemistry, Faculy of Engineering, Kyoto University. Most of the present experiments, however, were carried out for the sample whose denier was about 800 and whose viscosity-average molecular weight was 10,600. Although some additional experiments were conducted with samples of other molecular weights to get information about the molecular weight effect, we shall here give only the data obtained with the main sample for the lack of space.

The relaxometer used was identical with that employed in our previous studies[1][3], details of which are described in reference (3). All the present relaxation measurements were conducted, keeping the temperature, relative humidity, and elongation constant (these are, respectively, 30°C., 65%, and 10%), and varying the draw ratio and the heat-treatment temperature over a range of interest within the limits of our experimental arrangement.

Cold-drawing of the given unstretched fiber was made manually under room conditions, the rate of extension used being about 10% strain per sec. Before beginning a particular relaxation run, the stretched specimen was allowed to stand for at least 24 hours so that it might reach mechanical equilibrium.

Heat-treatment of the given sample was made according to the similar procedure as used before for drawn Amilan multifilaments. However, since it was found that the length of the cooling period had a pronounced effect upon the subsequent stress relaxation behavior, as will be shown below, some detailed considerations on this effect were undertaken.

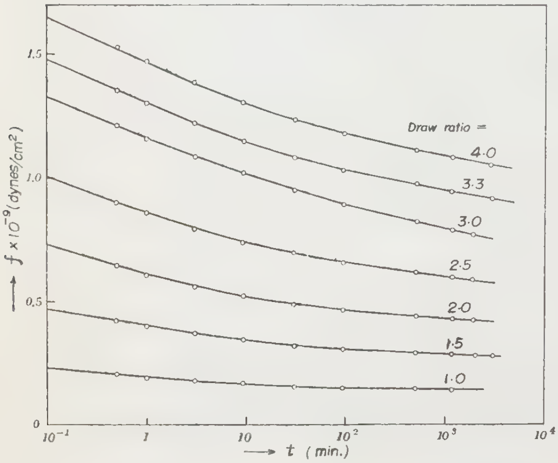

Fig. 1. Stress relaxation for undrawn Amilan at various draw ratios. 10% elongation, 30°C., and 65% R. H.

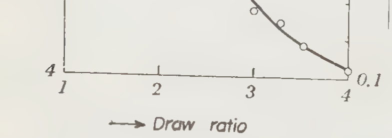

Fig. 2. Factors a, b and c in Eq. (1) as functions of draw ratio.

§ 3. Results and Discussion

1. Effect of drawing. Fig. 1 shows a family of experimental stress relaxation curves for untreated undrawn Amilan as a function of the draw ratio. The general trend of these curves is almost identical with that for the drawn Amilan dealt with in the previous study. It is noted from the figure that the slope of the curves in the part of large t (time in min.) changes rather definitely in the range of draw ratio from 3.0 to 3.3. This range of draw ratio was found to be in accordance with the part of the load-elongation curve of the sample where the so-called necking was terminated. In reference (1) it was shown that the relaxation process of drawn Amilan multifilaments can be well represented over wide ranges of temperature and elongation by an empirical equation of the form:

$$f = f_0[1 - a - b \log t + c \log (1 + \alpha/t)], \quad (1)$$

where f_0 is the stress value at $t=0.1$ min., and a, b, c, and α constants. Specifically, b represents the slope of the stress vs. the logarithm of time curve at sufficiently large t, while c gives the rate of relaxation at the initial stage of the same curve. It was found that this empirical equation can also be fitted satisfactorily to all of the present relaxation data plotted in Fig. 1 as well as in the other similar figures shown below. In fact, the smooth curves drawn in Fig. 1 are the computed curves from Eq. (1) with suitable choice of the parameters involved. The values of a, b, and c determined in this way are plotted against the draw ratio in Fig. 2. Each of these parameters decreases following a sigmoidal curve as the draw ratio is increased and appears to tend to a constant value at draw ratios higher than 4. Of particular interest is the finding that these sigmoidal curves have commonly a point of inflection at a draw ratio near 3.0, where, as noted above, the necking of the specimen is also terminated. The monotonic decreases in b and c indicate that the overall rate of stress relaxation decreases with increasing the degree of stretching. This might be expected because stretching of an undrawn fiber results in a gradual rearrangement of the long chain molecules in the direction of the fiber from their unoriented, random arrangement to a well-oriented, fiber-like one. Kinoshita, Mukoyama, and Oka$^{4)}$ reported that birefringence and dynamic elastic modulus of an undrawn Amilan monofilament measured as a function of draw ratio show a characteristic break in the neighborhood of draw ratio 3.0. A similar trend of the static elastic modulus can also be obtained from our data plotted in Fig. 1. An apparent static elastic modulus, E, may be computed from the stress value which can be obtained by extrapolating the stress relaxation curve back to $t=0.1$ min. In Fig. 3, the values of E obtained in this way from Fig. 1 are plotted against the draw ratio by open circles. In the same figure, the elongations at break obtained at various praw ratios are also plotted by solid circles. It is observed that not only E but also the elongation at break shows a rather sharp change in the vicinity of the draw ratio in question. From these findings it is *supposed* that the concentration of hydrogen bondings between the chain molecules of Amilan, which are lined up side by side, parallelized, and brought close together with increasing the degree of stretching, may increase rather abruptly when passing through the draw ratio 3.0. This may, however, not necessarily imply a sudden crystallization of the structure which may occur when the filament is stretched more than three times the original length. As shown by Susich²⁾ for undrawn Dacron polyester samples, the specimens extened below and above the draw ratio where this material also exhibited in its load-elongation curve a similar characteristic break as found above for undrawn Amilan have essentially identical x-ray diagrams. Although it may be somewhat critical to apply this finding on Dacron directly to our case of Amilan, this evidence from x-ray diffraction studies on Dacron deserves attention in considering the characteristic mechanical behavior of Amilan in the neighborhood of draw ratio 3.0.

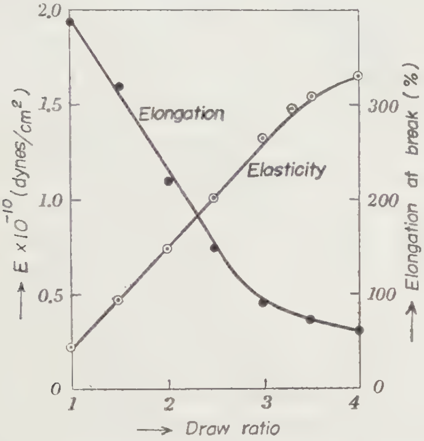

Fig. 3. Apparent elastic modulus (calculated from stress at 10% strain) and elongation at break for undrawn Amilan as functions of draw ratio.

The molecular weight of the undrawn Amilan used in the present work is approximately the same as that of the drawn Amilan used in the previous study. It is, therefore, permissible to examine the extent to which the stress relaxation behavior as well as the elastic modulus of the undrawn sample approach those of the drawn sample as the degree of drawing is increased toward that to which the previous commercial drawn sample had been subjected. However, the strict comparison was impossible because the drawn sample used before would have been subjected to a certain heat-treatment (unknown to us) before coming in our hands, while the undrawn sample of the present study was apparently free from any previous heat-treatment. In Table I, the values of the parameters a, b, c, and α, which characterize the stress relaxation behavior of undrawn Amilan and of drawn Amilan as well, and the values

Table I.

Sample	Temp. of Experiment (°C.)	a	$b\times10^2$	c	α (min.)	$E\times10^{-10}$ (dynes/cm².)
(1) Undrawn Amilan monofilament	30	0.23	6.5	0.17	0.8	0.22
(2) Undrawn monofilament extended 300%.	30	0.17	5.5	0.10	1.1	1.65
(3) Drawn multifilament (commercial)	30	0.21	3.8	0.10	4.8	1.35
(4) Drawn multifilament reheat-treated at 110°C.	120	0.16	7.3	0.11	0.5	0.52

of the apparent elastic mudulus, E, computed in the way explained above are listed for (1) undrawn Amilan monofilament, (2) undrawn monofilament extended 300%, (3) drawn multifilament, and (4) drawn multifilament re-heat-treated at 110°C. The data for the latter two cases are taken from reference (1). It should be noted here that the data for (4) are those at 120°C., while the remaining three are those equally at the same temperature, 30°C. The reason for the inclusion of these high temperature data will be undestood below.

It is seen from the table, though not so decidedly, that the stress relaxation behavior of the undrawn sample tends to approach that of the drawn sample as the degree of stretching is increased. This appears to be the case with the elastic modulus, although it is somewhat peculiar that the elastic modulus of the sample extended 300% exceeded that of the commercial yarn. Comparing the first and fourth columns, it is realized that both the stress relaxation behavior and the elastic modulus of the heat-treated drawn sample at high temperature have a resemblance to those of the non-heat-treated unstretched sample. In other words, there is a tendency for the mechanical behavior of the drawn sample that it is reduced back to the behavior of the original undrawn sample when measured at high temperatures. To confirm this better, use of the data for non-heat-treated but fully stretched samples at much higher temperatures than used here is preferable, but, since such data were not considered necessary at the time when the previous study was made, we must, in this place, be satisfied with a tentative comparison as illustrated above The tendency as found here may be interpreted in terms of the disordering or melting of crystallites involved in the heat-treated, drawn sample which may occur when the material is exposed to high temperatures. The x-ray diagram of a fully stretched sample of Amilan is known to have a resemblance to that of the unstretched sample when measured at sufficiently high temperatures. This fact in part supports our finding on a similarity in mechanical behavior of the drawn sample at high temperature and of the undrawn sample.

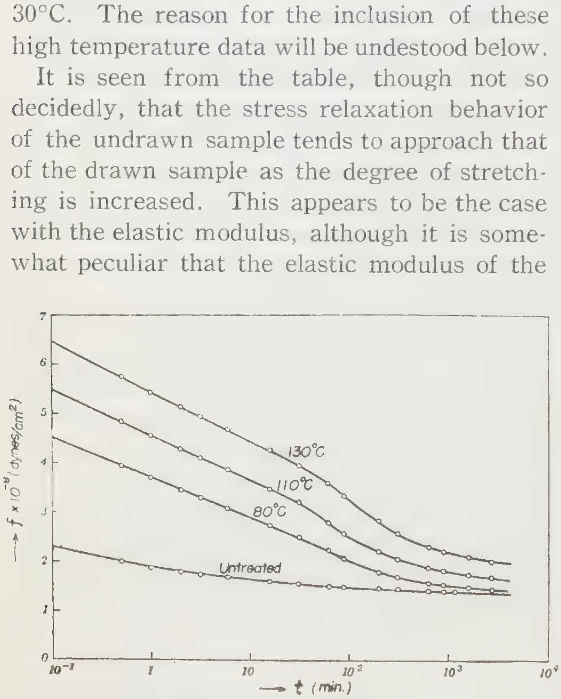

Fig. 4. Stress relaxation for heat-treated undrawn Amilan exposed for one hour to various temperatures.

2. **Effect of heat-treatment**. The effect of heat-treatment on the stress relaxation behavior of the undrawn sample was first studied according to the following procedure. The given unstretched sample was heated in an air oven to the desired temperature at a rate of 1.5°C./min., and then cooled for one hour in a still air regulated at 30°C. and 65% R. H. The specimen was then quickly introduced into the relaxometer and a particular relaxation run was started. The temperatures, used for the heat-treatment were 60°, 80° 110°, and 130°C. Fig. 4 shows the results of stress relaxation measurements for these heat-treated samples. Here, the curve for the original, untreated sample is also plotted for comparison. A marked influence of the heat-treatment is here evident not only on the initial stress value, f_0, but also on the shape of the subsequent relaxation curve. With increasing the temperature of heat-treatment, f_0 is increased considerably, resulting in a high elasticity, and, at the same time, the shape of the relaxation curve is markedly modified from that for the untreated sample. It should be noted, however, that, while the relaxation rate in the initial stage is appreciably influenced and enhanced by the heat-treatment, this rapid process is followed after some interval of time by an ordinary slow process which is observed for the untreated sample. Such an extraordinary relaxation process as found here for heat-treated undrawn Amilan might be an interesting subject worthy of further investigation if it were truly produced by the structural changes brought about by the present heat-treatment. However, after some interpretative experiments, it was realized that this unusal

relaxation behavior and the unusal increase of the initial stress were only an apparent one produced as a result that the sample dried by heat-treatment absorbed vapor from the surrounding air during the course of a stress relaxation measurement. Fig. 5 shows the results obtained on a series of samples which had been lnitially heated to the same temperature (110°C.) and then cooled for different hours under the same conditions of temperature and humidity. The results show that as the cooling period is prolonged the sample get softer and its stress relaxation behavior becomes as normal as may be compared with that of the untreated sample. A separate experiment on the sorption of vapor by a heat-treated undrawn sample indicated that the vapor gain followed a change similar to that in the initial stress and that the cooling period of 71 hours was enough so that the sample might reach the sorption equilibrium under the given condition. Based on these evidences it may be regarded that the curve with the index "71 hours" in Fig. 5 represents the true form of stress relaxation for the sample which was heat-treated at 110°C. according to the procedure described above. In passing, it may be remarked that the modulus of undrawn Amilan is first increased by heat-treatment and then decreases as the time of standing is extended has already been reported by Nagai and Sagane[5]. They also interpreted this behavior in terms of the vapor absorption during the course of standing, the same opinion as ours given above.

In view of the above-mentioned findings, it proved that to examine the effect of heat-treatment only such samples must be used for the measurements that which have been made to attain the sorption equilibrium before beginning a particular stress relaxation run. Fig. 6 shows the results of the relaxation measurements carried out with such a precaution in mind for samples heated initially to three different temperatures. It is seen from the figure that the initial stress increases regularly (but not so markedly as in Fig. 4) with increasing the temperature of heat-treatment, while the shape of the stress relaxation curve is hardly affected by the heat-treatment, thus retaining a similarity to that of the untreated sample. The application of Eq. (1) to these curves results in the values listed in Table II. In this table, the corresponding values of the

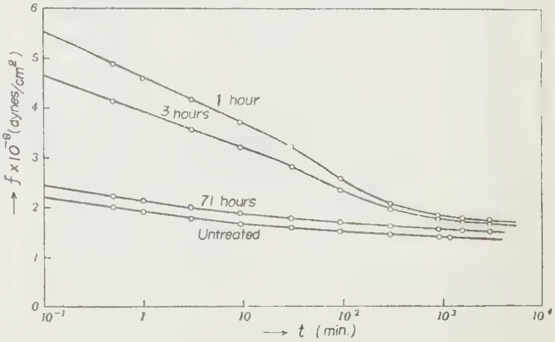

Fig. 5. Stress relaxation for undrawn Amilan heated at 110°C. and then exposed to air for various times.

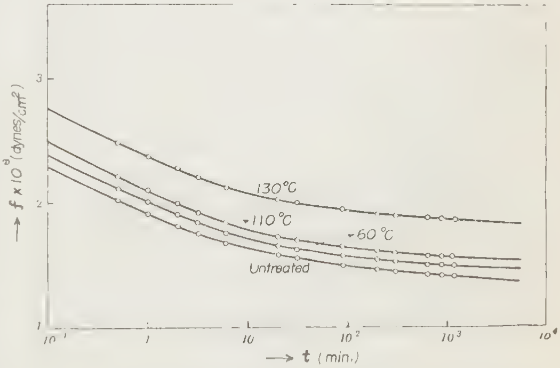

Fig. 6. Stress relaxation for heat-treated undrawn Amilan as a function of heating temperature.

Table II.

Temp. treated (°C.)	a	$b \times 10^2$	c	α (min.)	$E \times 10^{-10}$ (dynes/cm^2.)
Untreated	0.23	6.5	0.17	0.8	0.22
60	0.23	5.3	0.16	1.2	0.24
80	0.23	5.0	0.15	1.4	0.24
110	0.22	4.8	0.15	1.5	0.25
130	0.22	4.1	0.14	1.7	0.28
Drawn multifilament (commercial)	0.21	3.8	0.10	4.8	1.35

drawn multifilament at 30°C. are reproduced from (1). A tendency is here observed that the values of a, b, and c decrease systematically and approach the corresponding ones for the drawn sample as the temperature of heat-treatment is elevated. Contrary to this, both the values of α and E (particularly, E) are too low compared with those for the drawn sample, even when the undrawn sample is heat-treated at 130°C. This latter result suggests that, at least, as regards the elastic modulus, the same degree of mechanical conditioning as obtainable in cold drawing can not be expected by such a relatively low temperature heat-treatment as attempted in this work. If, as pointed out by Nagai and Sagane[5], enough high concentrations of hydrogen bondings between the chain molecules of Amilan for making the cold-drawing of the material impossible cannot be produced till the temperature of heat-treatment is not raised to 160°C. or higher, data for undrawn samples heat-treated at such degrees of high temperatures are certainly determined. This problem, however, will be considered in our future publication.

The authors wish to express their thanks to Professor H. Kawai of the Department of Textile-Chemistry, Faculty of Engineering, Kyoto University, who kindly supplied them with the undrawn Amilan samples used in the present study. This work was supported in part by the Scientific Research Expenditure from the Ministry of Education.

References

1) H. Fujita and A. Kishimoto: J. Phys. Soc. Japan, in press; also, A. Kishimoto: J. Soc. Textile and Cellulose Ind. Japan **9** (1953) 621.

2) G. Susich: Textile Research J. **23** (1953) 545.

3) H. Fujita and A. Kishimoto: J. Soc. Textile and Cellulose Ind. Japan **9** (1953) 74.

4) Y. Kinoshita, E. Mukōyama and E. Oka: Paper read at the VIth Annual Meeting of the Chemical Society of Japan, Kyoto, April, 1953.

5) E. Nagail and N. Sagane: J. Soc. Textile and Cellulose Ind. Japan **8** (1952) 165.

Short Notes

J. PHYS. SOC. JAPAN **9** (1954) 872~873

Contribution of Overlap Integral to Nuclear Quadrupole Coupling

By Kineo TSUKADA

Department of Physics, Tokyo University of Education

(Received June 8, 1954)

When one calculates the nuclear quadrupole coupling constant in a molecule from the data on an atom, overlap integral must be taken into account as pointed out by Towes and Dailey[1]. However, the results of pure quadrupole experiments are often compared with those of atomic beam experiments without this consideration. This note describes the estimation of contribution of overlap integral for the molecules of Cl_2, Br_2 and I_2.

In table I, the coupling constants for the pure covalent bond, which were derived from the observed data by using the model of resonance switching of bonds[2] and by using the model of macromolecule[3], are compared with the double of the values obtained by the atomic beam method. As shown in the table, there are some dis-

Table I.

Molecule	$\lvert(eQq)_{obs}\rvert$(Mc)	$\lvert(eQq)^{res}_{mole}\rvert$(Mc)	$\lvert(eQq)^{mac}_{mole}\rvert$(Mc)	$2\lvert(eQq)_{atom}\rvert$(Mc)
$Cl_2{}^{35}$	109.0[5]	—	—	109.7[4]
$Br_2{}^{79}$	760.4[6,7]	900[7]	811	769.6[8]
$I_2{}^{127}$	2,153[9]	2,480[2]	2,280[3]	2,292[10]

$(eQq)_{obs}$: observed coupling constant.

$(eQq)^{res}_{mole}$: coupling of a molecule by the resonance switching model

$(eQq)^{mac}_{mole}$: coupling of a molecule by the macromolecule model.

Table II.

Molecule	Δ_{res}	Δ_{mac}	S^2	q_s/q
$Cl_2{}^{35}$	—	—	0.120	-10×10^{-4}
$Br_2{}^{79}$	0.170	0.054	0.096	-3×10^{-4}
$I_2{}^{127}$	0.082	−0.005	0.091	-1×10^{-4}

Δ_{res}: Δ calculated by using the resonance switching model.

Δ_{mac}: Δ calculated by using the macromolecule model.

crepancies between these constants.

Neglecting hybridization and ionic character, the coupling constant of a halogen molecule is approximately expressed by¹⁾

$$|(eQq)_{\mathrm{mole}}|=2|(eQq)_{\mathrm{atom}}|(1+S^2-2Sq_s/q)\,, \quad (1)$$

where

$$S=\int\psi_1{}^*\psi_2 d\tau\,,\quad q_s=\int\psi_1{}^*(3\cos^2\theta-1)/r^3\psi_2 d\tau\,,$$

$q=\int\psi_1{}^*(3\cos^2\theta-1)/r^3\psi_1 d\tau$, ψ_1 is atomic wave function of a halogen atom and ψ_2 is that of an atom bonded to the halogen. To see the effect of the overlap integral S, we shall use the quantity defined by

Table III.

Molecule	$X-X$ gas (A)	$X-X$ solid (A)	nearest intermolecular (A)	Van der Waals radii $\times 2$ (A)
Cl_2	1.989	2.02	2.52	3.60
Br_2	2.284	2.27	3.30	3.90
I_2	2.667	2.70	3.54	4.30

$$\Delta=\{|(eQq)_{\mathrm{mole}}|-2|(eQq)_{\mathrm{atom}}|\}/\{2|(eQq)_{\mathrm{atom}}|\}\,.$$

This quantity was calculated from the data given in table I. On the other hand, Δ is approximately equal to S^2 by Eq. (1), because of smallness of Sq_s/q. In table II, these Δ and S^2 are compared. The overlap integral was calculated by using Slater AO's and the Mulliken's table¹¹⁾. For solid I_2, the result by using the resonance switching model agrees well with S^2. For solid Br_2, however, the calculated S^2 lies between Δ_{res} and Δ_{mac}. For solid Cl_2, the asymmetry parameter has not yet been measured, but, as shown in table II¹²⁾¹³⁾, auxiliary bonds with rather large fractional importance seem to exist. Though $|(eQq)_{\mathrm{obs}}|$ of Cl_2 agrees with $2|(eQq)_{\mathrm{atom}}|$ as shown in table I, this agreement may be accidental, because the contribution of overlap integral to $|(eQq)_{\mathrm{obs}}|$ cancels the decrease of $|(eQq)_{\mathrm{obs}}|$ due to existence of auxiliary bonds.

Temperature dependence of overlap integral will influence temperature coefficient of the coupling constant. This effect due to overlap integral for halogens is roughly estimated to be about -2×10^{-5} per degree and observed values are about -1×10^{-4} per degree.

Values of q_s/q in table II, calculated by using hydrogenic wave function for ψ_1 and by using Slater AO for ψ_2, are very small, as is neglected at above discussions.

In conclusion, I should like to thank Prof. S. Kojima for his deep interest and many helpful discussions.

References

Writing this note, I found the letter by P. N. Schatz. He discussed relation between overlap integral and hybridization for solid Cl_2. J. Chem. Phys. **22** (1954) 755L.

1) C. H. Townes and B. P. Dailey: J. Chem. Phys. **17** (1949) 782.
2) C. H. Townes and B. P. Dailey: J. Chem. Phys. **20** (1952) 35.
3) H. Robinson, H. G. Dehmelt and W. Gordy: J. Chem. Phys. **22** (1954) 511.
4) V. Jaccarino and J. G. King: Phys. Rev. **83** (1951) 471.
5) R. Livingston: J. Chem. Phys. **19** (1951) 1434.
6) H. G. Dehmelt: Z. Physik. **130** (1951) 480.
7) S. Kojima, K. Tsukada, A. Schmauchi and Y. Hinaga: J. Phys. Soc. Japan **9** (1954) 795.
8) J. C. King and V. Jaccarino: see reference 3).
9) H. G. Dehmelt: Z. Physik **130** (1951) 356.
10) Jaccarino, King and Stroke: see reference 3).
11) R. S. Mulliken, C. A. Rieke, D. Orloff and H. Orloff: J. Chem. Phys. **17** (1949) 248.
12) R. W. G. Wyckoff: "*Crystal Structures*", (1948).
13) R. L. Collin: Acta Cryst. **5** (1952) 431.

J. PHYS. SOC. JAPAN **9** (1954) 873~874

Powder Density Measurement by Gas Burette

By Atsuo NISHIOKA and Kyozo SEKIKAWA
Electrical Communication Laboratory

(Read at the annual meeting of the Society, October 19th, 1953)
(Received July 10, 1954)

To measure the density of fine particles of about few microns in diameter, we used a gas burette in place of picnometer and measured directly the volume of the specimen, resulting in fairly accurate values in comparison with that of usual method.

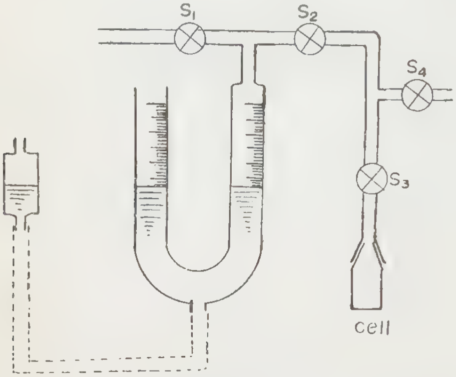

Fig. 1.

As shown in Fig. 1 we at first open all the cocks and set the level of mercury in the gas burette at lower position. Then all the cocks are closed except S_4 and the dead space enclosed by S_2, S_3 and S_4 is evacuated. After evacuation, S_4 is closed, S_2 opened. By the change of the pressure in the right branch of the burette, the level of mercury globe is raised slowly so that both levels of the burette become equall again. So the volume difference is clearly equall to that of the dead space.

By the similar operation in the case of S_3 opened, we obtain the sum of the dead space and the cell volume. So the cell volume is easily obtained by the difference. Thus after the third operation of similar manner for the case of cell containing a specimen, the volume of the specimen is easily obtained.

In our experiment we used the gas burette, about 13 c.c. in volume, 8 mm in diameter, 0.05 c.c. in one scale. The volume of the cell is about 8 c.c. and that of the dead space is 0.64 c.c.. To find the equivalence of level, we read the scale at the two positions near it by the travelling microscope and calculate by interpolation method.

Table I.

Diameter in microns (Weight Average)	Volume of specimen (c.c.)	Density	Reference value
3	1.542 ± 0.011	7.26 ± 0.05	7.3~7.4
5	1.622 ± 0.025	7.80 ± 0.12	7.79
8	1.644 ± 0.014	7.73 ± 0.07	7.77
10	1.477 ± 0.033	7.90 ± 0.18	7.86
20	1.422 ± 0.030	7.90 ± 0.17	7.85

The accuracy of this method is mainly determined by the volume of specimens, and the larger the volume, the better. In the case of empty cell it is about 0.01 c.c. and when the cell contains a specimen it is about 0.03 c.c.. The overall accuracy of density is about 1~2% in the case of specimens about 1~2 c.c., but becomes lower in the case of smaller volume. Our results are shown in the following table 1 in the case of carbonyl iron powders.

The accuracy is shown in the reliable limit of the mean value in the reliability of 95%.

Also we obtained very good consistent results in the case of pure metal blocks such as aluminium, copper, and zinc, but in the case of a strong adsorptive fine powder such as carbon black, the final equilibrium is not easily attained, so that the reliable results cannot be obtained.

J. PHYS. SOC. JAPAN **9** (1954) 874~876

An Evaluation of Plasma-ion Temperature

By Osamu SHIMADA

Faculty of Education, Yamagata University

(Received July 12, 1954)

For the study on the structure of plasma in low pressure gas-discharge-tubes, it is necessary to determine the physical quantities: density, velocity and temperature of electrons, of ions and of neutral molecules. Recently, the double-probe method has been introduced[1] to evaluate the electron temperature of high frequency discharges. Therefore if we can evaluate the ion temperature we know other quantities in plasma because densities or velocities are joind to the ion temperature by well-known equations. I have tried to measure the ion temperature by the following three methods, where r_C, r_F are the radii of probe and sheath respectively, the other notations are the same as in Loeb's book.[2]

First method.* The potential of floating probe inserted in plasma is expressed by

$$V_w = -\frac{kT_-}{e} \ln \left(\frac{r_C}{r_F} \sqrt{\frac{T_- M_+}{T_+ M_-}} \right) . \quad ^{3)} \tag{1}$$

The saturation current per unit length of a cylindrical probe is

$$i_+ = \frac{2}{9} \sqrt{\frac{2e}{M_+}} \cdot \frac{|V_w|^{3/2}}{r_C \beta^2} . \quad ^{4)} \tag{2}$$

Here β represents Langmuir's series,[5] which is a function of r_F/r_C. If we assume the value of r_F, a measurement i_+ yields V_w by the aid of Eq. (2). Therefore, measuring T_- and putting

---

* This method was suggested by S. Kojima, K. Takayama and A. Shimauchi (unpublished).

	V_p, i_p of main oscillator	Wall potential V_w	Thickness of ion sheath $\gamma_F - r_C$	Electron temperature T_-	Ion temperature T_+	Ion density N_+	Mean velocity $\bar{c}_+$	Dielectric constant ε
I	500 V 70 mA	V −9.2	mm 0.75	°K 21,800	°K 1,670	1/cm³ 2.5×10^{10}	cm/sec 10.9×10^4	−5.5
II	550 V 80 mA	−8.8	0.48	19,600	1,390	5.0×10^{10}	7.4×10^4	−12.1
III	600 V 100 mA	−9.5	0.45	21,700	2,050	5.2×10^{10}	9.0×10^4	−12.8
IV	650 V 110 mA	−9.8	0.42	22,000	1,760	6.4×10^{10}	7.2×10^4	−16.2

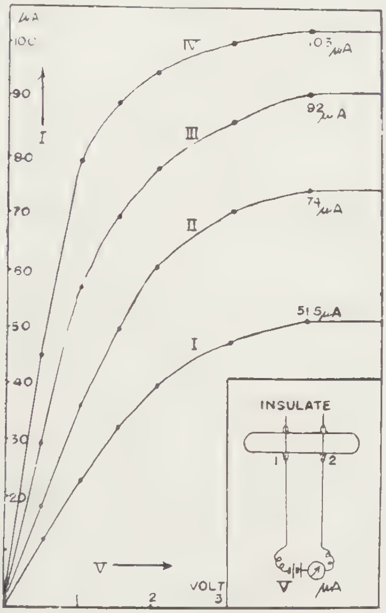

Fig. 1. Diagram and characteristics of the doubleprobe for saturation current.

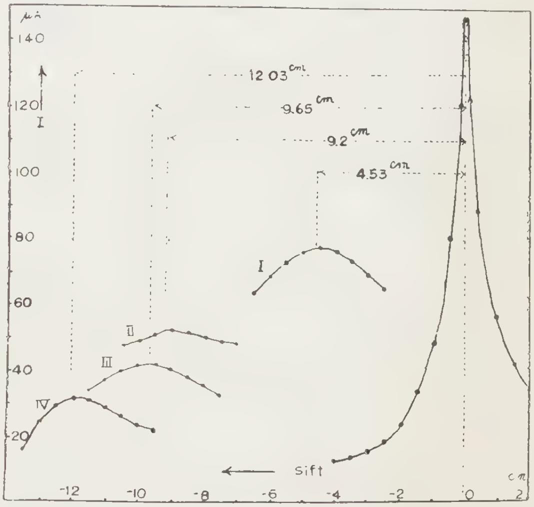

Fig. 2. Detected current vs. shift of shorting plate.

these values into Eq. (1) we can evaluate T_+.

Second method. Joining the well-known relations,

$$\left.\begin{array}{l} \varepsilon = 1 - \omega_0^2/\omega^2, \quad \varepsilon = 1 + \text{shift}/S,^{6)} \\ \omega_0^2 = 4\pi N e^2/M_-, \\ I_+ = eN_+\bar{c}_+F/4, \quad \bar{c}_+ = \sqrt{8kT_+/\pi M_+}, \end{array}\right\} \quad (3)$$

we get

$$T_+ = \frac{2M_+e^2S^2\lambda^4}{kM_-{}^2\pi C^4(2\pi r_F l)^2} \cdot \frac{I_+{}^2}{(\text{shift})^2}$$

$$= D \cdot \frac{I_+{}^2}{r_F{}^2(\text{shift})^2} . \quad (4)$$

Here '*shift*' means the value of the difference between resonance point of Lecher system feeding another high frequency wave for measurement into h.f. plasma and that of non-plasma. Again, if we assume the value of r_F, by measuring I_+ and *shift*, we can evaluate T_+ from Eq. (4). The details of this method was reported in the previous paper.[7)]

Third method. Owing to the fact that evaluation of the thickness of sheathes is not very simple, the writer tried the following method. Namely, considering Eqs. (1), (2) and (4) as simultaneous equations for T_+, V_w, r_F, we know β from (2); and from the Langmuir's table we can determine r_F, and so T_+; consequently N_+, $\bar{c}_+$ can be evaluated.

The h.f. plasma used in this experiment was made by feeding power from a push-pull oscillator of T-310 ($\lambda = 172$ cm) through a Lecher system into a cylindrical discharge-tube, filled with argon of pressure 3 mmHg, whose geometry is 5 cm in diameter and 0.7 cm in thicknes, two tungsten probes of 1 mm in diameter passing through the tube. The shift curve was measured by an apparatus similar to that used by Kojima et al. to measure the microwave dispersion;[8)] the used h.f. wave length was 96 cm. Double-probe method was applied for measuring T_-. Figs. 1, 2 and a following table show a result.

The reliability of these values is not very high, because Eqs. (1)~(3) have their own applicable conditions. Especially $\varepsilon=1-\omega_0^2/\omega^2$ does not hold in the plasma oscillation or near the dispersion point of ε. Besides, the error of T_+ amounts to about 40%, since the errors of l, S, r_F, and the *shift* are 14%, 12%, 8% and 6% respectively.

The writer wishes to express his sincere thanks to Dr. S. Kojima for his discussion and to Dr. K. Honda for his encouragement. The writer is also indebted to the Ministry of Education for the research grant.

References

1) S. Kojima and K. Takayama: J. Phys. Soc. Japan **4** (1949) 349, **5** (1950) 357.
E. O. Johnson and L. Malter: Phys. Rev. **76** (1949) 1411.
2), 3), 4) L. B. Loeb: *"Fundamentai Processes of Electrical Discharge in Gases."* John Wiley and Sons, Inc. 1939, Chap. V. B. 4; p. 242 Eq. (10); p. 238 Eq. (3).
5) I. Langmuir: Phys. Rev. **22** (1923) 347.
6) R. King: Rev. Sci. Inst. **8** (1937) 201.
7) O. Shimada: Bull. Yamagata Univ. **2** (1952) 77.
8) S. Kojima and K. Takayama: Proc. Phys. Soc. Japan **5** (1950) 211 (in Japanese).

J. PHYS. SOC. JAPAN **9** (1954) 876~877

Isotope Shift in the Spectra of Tin and Lead

By Kiyoshi MURAKAWA

Institute of Scinece and Technology,
Komaba-machi, Meguro-ku, Tokyo

(Received July 22, 1954)

§1. Isotope Shift in the Spectrum of Sn II.

Since the proton number of tin is 50, a magic number, it would be reasonable to assume that the nuclear intrinsic deformations of the even isotopes of Sn are relatively small compared with the even isotopes of neighboring elements. Investigation of the isotope shift in the Sn spectrum would therefore be interesting and would offer some basis for testing the theory proposed by Wilets, Hill and Ford[1] concerning the isotope shift.

The Sn spectrum was excited by a liquid-air cooled hollow cathode discharge tube, the discharge current being less than twenty milliamperes. The hyperfine structure (hfs) was examined with a Fabry-Perot etalon. Of the strong lines only Sn II λ5799 and λ5589 were found to exhibit measurable isotope shift. It was not possible to get Sn II λ3994 ($sp^2\,{}^4P_{3/2}-6\,{}^2P_{1/2}$) and λ3705 ($sp^2\,{}^4P_{1/2}-6\,{}^2P_{1/2}$) and λ3587 ($sp^2\,{}^4P_{1/2}-6\,{}^2P_{3/2}$) with strong intensity.

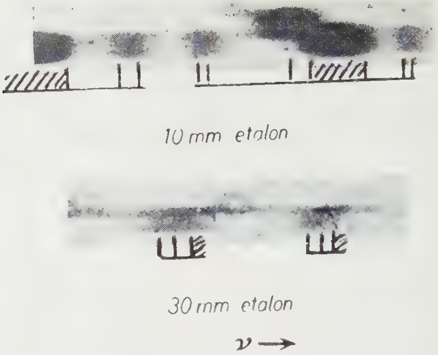

Fig. 1. Interference patterns of Sn II λ5799.

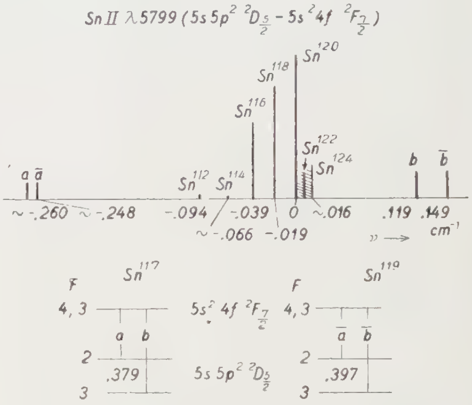

Fig. 2. Hfs of Sn II λ5799.

Some of the interference patterns of λ5799 is reproduced in Fig. 1, and the essential finding concerning the hfs of λ5799 is presented in Fig. 2. Sn II λ5799 was classified by McCormick and Sawyer[2] as $5\,{}^2D_{5/2}-4\,{}^2F_{7/2}$. However a simple calculation based on the nuclear magnetic moments[3] of Sn 117 and Sn119 and the hfs splittings of the final level in these odd isotopes shows that at least 70% of $5s5p^2\,{}^2D_{5/2}$ is contained in the wave function of the final level, which is therefore named $5s5p^2\,{}^2D_{5/2}$ in the present work. Tolansky[4] also found that the central strong components of λ5799 and λ5589 are diffuse and he attributed this fact to an isotope displacement effect.

From Fig. 2, we find

$$\Delta\nu(N62-N66)/2\Delta\nu(N66-N68)=1.37$$

for Sn, where N represents the neutron number. For Cd, we find[5] $\Delta\nu(N62-N66)/2\Delta\nu(N66-N68)=1.43$. These two are qualitatively equal, as is expected from the regularity in isotope shifts in other heavy elements. On the other hand we find $2\Delta\nu(N68-N70)/\Delta\nu(N70-N74)\approx 2.38$ for Sn, and 0.83 for Te⁶⁾. Inequality of these two are remarkable and show that neutron number alone does not determine the main feature of the isotope shift.

§ 2. Isotope Shift in the Spectrum of Pb I.

In the work on the Sn spectrum some Pb lines appeared as impurity lines, and the hfs of Pb I λ2613.7 was obtained without self-reversal. Although the measurement is not so accurate, the hfs is given in Fig. 3. It shows that Pb^{207} has a splitting of about $-0.150\,\mathrm{cm}^{-1}$ in $6p6d\,{}^3D_1$ and requires a revision of the interpretation of λ4062 published previously by the author⁷⁾. The component *b* in Fig. 8 in ref. 7 appears only when zinc is used as the hollow cathode that contains lead as an impurity, and should be discarded from the hfs scheme. The non-existence of this component was kindly pointed out to the author by Drs. Blaise and Chantrel who used a photo-electric device⁸⁾ and a Fabry-Perot etalon coated with dielectric multilayers. Their excellent intensity measurement shows that the intensity ratio of *a* to *c* of λ4062 (Fig. 3) is just 9:5. The isotope shift anomaly for λ4062 reported in ref. 7 now disappears, but from the numerical values given in Fig. 3 (λ4062) it would seem that the c.g. of Pb^{207} in $6d\,{}^3D_1$ is slightly attracted (instead of showing repulsion) towards $6d\,{}^3F_2$. Investigation to test whether this attraction is genuine within the error of measurement is still in progress.

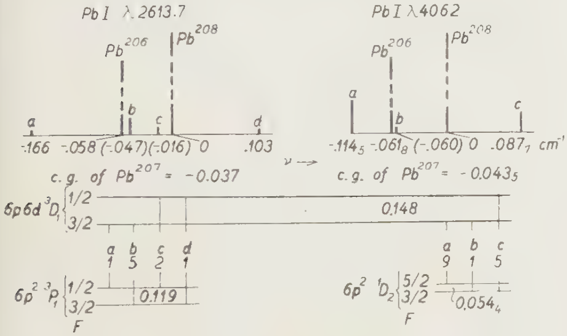

Fig. 3. Hfs of Pb I λ2613.7 and Pb I λ4062.

References

1) L. Wilets, D. L. Hill and K. W. Ford: Phys. Rev. **91** (1953) 1488.

2) W. W. McCormick and R. A. Sawyer: Phys. Rev. **54** (1938) 71.

3) J. E. Mack: Rev. Mod. Phys. **22** (1950) 64; P. F. A. Klinkenberg: Rev. Mod. Phys. **24** (1952) 63; K. Murakawa and T. Kamei: Rep. Inst. Sci. Tech. Univ. Tokyo **7** (1953) 219.

4) S. Tolansky: Proc. Roy. Soc. London **144** (1934) 574.

5) K. Murakawa: Phys. Rev. **93** (1954) 1232.

6) J. S. Ross and K. Murakawa: Phys. Rev. **85** (1952) 559.

7) K. Murakawa: Jour. Phys. Soc. Japan **8** (1953) 382.

8) J. Brochard, R. Chabbal, H. Chantrel et P. Jacquinot: Jour. Physique Rad. **13** (1952) 29.

Note added in proof. After the manuscript was sent for publication, we received the article of W. R. Hindmarsh, H. Kuhn and S. A. Ramsden, Proc. Phys. Soc. London **117** (1954) 478. The shift of the even isotopes of Sn in the line Sn II λ6454 was studied by them with the aid of separated isotopes.

J. PHYS. SOC. JAPAN **9** (1954) 877~878

On the External Cathode Proportional Counter

By Isao KUMABE and Masateru SONODA

Department of Physics, Faculty of Science, University of Kyoto

(Received July 29, 1954)

An external cathode proportional counter is very simple in its construction and has a very long life-time as compared with an ordinary proportional counter. It was described by a few workers,¹⁾²⁾ but its characteristics are not yet decidedly known. We therefore studied some properties of such a counter and found it quite satisfactory for use.

The counter used is shown in Fig. 1. The envelope is of an ordinary soda-glass and 1 mm in thickness. A thin layer of aquadag is coated on its outer surface and used as a cathode. The varnish is painted on the glass surface between the cathode and the central wire in order to avoid the large electric leakage, and the aquadag ring coated in the varnish layer was used as a guard electrode. Observations were made for the pressures of 40 and 57 cmHg of the tank methane by introducing a collimated beam of Po α-particles. The Po source on the iron piece was sealed in a small tube connected coaxially to the counter, which could be put forward or backward by a magnet from the outside of the counter.

The characteristic curves are shown in Fig. 2. Except for the region of low counter voltage, the gas multiplication factor is represented by a straight line in the semi-logarithmic scale and its slope is such that the gas multiplication factor increases by 1.7 times when the counter voltage is increased by one hundred volts. This slope seems to be the same as that of the ordinary

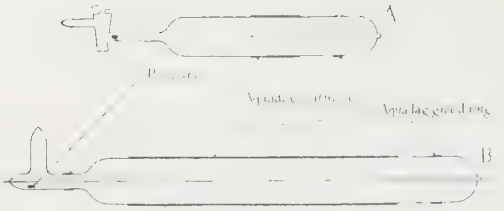

Fig. 1.
Counter A: outer diameter 20 mm, central wire diameter 0.1 mm.
Counter B: outer diameter 23 mm, central wire diameter 0.1 mm.

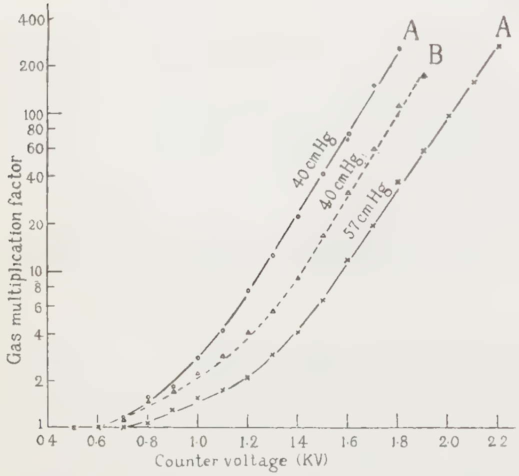

Fig. 2. Gas multiplication factor plotted against counter voltage for pressures of 40 and 57 cm Hg respectively. Solid- and dotted-line curves represent the experimental curves for counter A and counter B respectively.

proportional counter. Moreover, no change of the pulse height was found, after the operation at large counting rate (5000 counts per minutes) for about one hour. When the counter voltage was increased to higher values, the counter became sensitive to β-rays and γ-rays.

Thus, our counter seems to have the similar characteristics to those of the ordinary proportional counter and be quite useful in nuclear studies.

References

1) R. Maze: J. Phys. Radium, **6** (1946) 164.
2) D. West and Miss P. Rothwell: Phil. Mag., **41** (1950) 873.

J. Phys. Soc. Japan **9** (1954) 578~579

The Electrode Surface-Gas Interface as the Seat of the Joshi Effect under Silent Electric Discharge

By S. R. Mohanty
Physico-Chemical Laboratories, Banaras Hindu University, India

(Received August 10, 1954)

Harries and von Engel,1) and Khastgir2) found that the Joshi effect $\pm\Delta i$, the instantaneous and reversible photovariation (diminution $-\Delta i$ and enhancement $+\Delta i$) in the discharge current i through gases (and vapours) due to an exciting potential V, is associated with the electrode surface-gas interface. Agashe,3) on the other hand, emphasises the rôle of the positive column in the production of the *effect*. In view of this nonconcurrence of existing results, it was desirable to study in some detail $\pm\Delta i$ in different parts of the discharge.

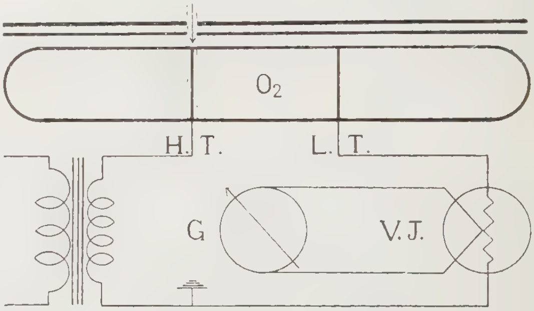

Fig. 1. Production of the Joshi effect in oxygen under 'Sleeve' excitation.
[H.T., the high tension electrode; L.T., the low tension electrode; V.J., Cambridge vacuum thermocouple ('Vacuo-junction'); G, galvanometer]

The discharge was produced at different V(4–11 kV rms, 50 cycles/second) in pure oxygen (28–31 mm Hg, 29–30°C) contained in cylindrical glass tubes (7.0–8.2 mm internal diameter) with external 'sleeve' electrodes. Each 'sleeve' was formed of a single turn of bright copper wire (diameter 0.48 mm). The current i was observed on a Cambridge vacuum thermocouple ('Vacuo-junction', V.J.)—galvanometer (G) system (Fig. 1) in dark (i_D), and when different parts of the discharge were irradiated (i_L) with a 2.5 mm wide intense light (3700–7800Å) beam. This last was obtained from a 500 watt, 200 volt, incandescent tungsten filament lamp, and an appropriate slit and lens assembly. A representative set of results is contained in Table I, and shown graphically in Fig. 2. The i values are in square roots of the

Table I. The Joshi Effect in Different Regions of the 'Sleeve' Discharge.
$p^0{}_2$: 28 mm Hg (30°C). Internal diameter of tube: 7.0 mm.

Distance from H.T. (mm)	6.4 kV(rms); $i_D=1.00$			10.66 kV(rms); $i_D=13.64$		
	i_L	$+\Delta i$	$+\%\Delta i$	i_L	$-\Delta i$	$-\%\Delta i$
−20	1.00	—	—	13.64	—	—
10	2.65	1.65	165	12.49	1.15	8.4
0 (H.T.)	7.21	6.21	621	12.21	1.43	10.5
+10	4.69	3.69	369	13.23	0.41	3.0
20	2.00	1.00	100	13.64	—	—
25	1.00	—	—	13.64	—	—
30	2.00	1.00	100	13.64	—	—
40	2.45	1.45	145	13.23	0.41	3.0
50 (L.T.)	3.74	2.74	274	12.96	0.68	5
60	2.00	1.00	100	13.27	0.37	2.7
70	1.00	—	—	13.64	—	—

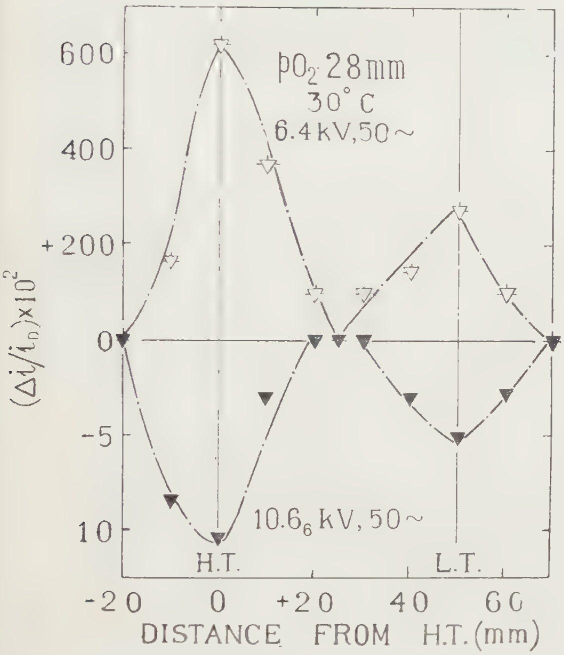

Fig. 2.

corresponding galvanometer deflections. The net *effect* $\pm\Delta i$ is given by $i_D \sim i_L$, and the relative *effect* $\pm\%\Delta i$ by $(\pm\Delta i/i_D)\times 10^2$.

It will be evident from Table I (*cf.* Fig. 2) that $\pm\Delta i$ is maximum at the two electrodes, and diminishes rapidly on either side; the *effect* is either absent or inappreciably small in the middle regions of the discharge. Furthermore, there is dissimilarity between the high tension (H.T.) and the earth connected low tension (L.T.) electrodes as regards $\pm\Delta i$; the magnitude of this last is generally larger at the H.T. than at the L.T. The *effect* $\pm\Delta i$ observed on either side of the electrodes is attributable to unavoidable diffused light reaching the electrodes from the irradiated parts of the discharge tube. There is indeed sufficient experimental evidence now for the surface origin of the *effect*.[4)5)6)7)]

References

1) W. L. Harries and A. von Engel: J. Chem. Phys. **19** (1951) 514; Proc. Phys. Soc. (London) **64B** (1951) 916.

2) S. R. Khastgir: J. Chem. Phys. **20** (1952) 1052.

3) V. V. Agashe: J. Chem. Phys. **19** (1951) 8, 1002.

4) S. S. Joshi: Proc. Indian Sci. Congr., Presidential Address, Chem. Sec. (1943).

5) K. V. Rao: Proc. Indian Acad. Sci. **27A** (1948) 72.

6) N. A. Ramaiah, P. V. Ratnam and K. P. Devi: J. Sci. Industr. Res. **11B** (1952) 524.

7) S. R. Mohanty: J. Phys. Chem. **58** (1954) 178.

J. PHYS. SOC. JAPAN **9** (1954) 879~880

Sur la Résistance à la Rupture du Verre à la Basse Pression*

Par Nobuzo TERAO

Institut de Physique, Faculté des Sciences, Université de Tokyo

(reçu le 27 août 1954)

Nous avons étudié jusqu'ici la résistance à la rupture du verre au point de vue statistique en introduisant la probabilité de rupture μ. D'après les résultats obtenus, les influences de la tension[1)], de la vitesse de la charge[2)], de la température[3)] et de l'humidité[4)] permettent d'exprimer μ par la formule

$$\mu = a\exp\left(-\frac{E_0-\beta f}{kT}\right) \qquad (1)$$

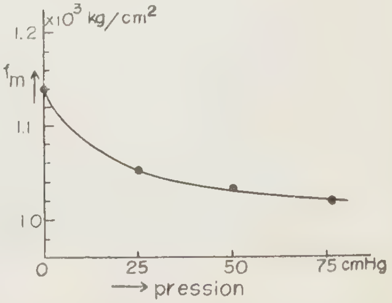

Fig. 1: Résistance moyenne à la rupture.

où E_0 représente l'énergie d'excitation de rupture, f la tension, βf l'énergie apportée par la force extérieure, k la constante de Boltzmann et T la température absolue.

On sait déjà que la résistance à la rupture du verre augmente dans le vide[5]. Pour établir à quelle variation de E_0 et de β correspond cette augmentation, nous avons mesuré la résistance à la rupture du verre à la basse pression.

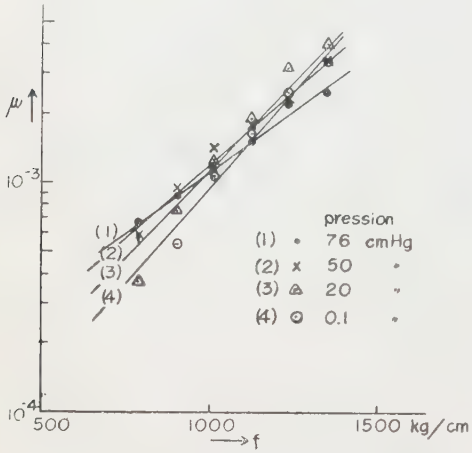

Fig. 2. Relation entre log μ et la tension f.

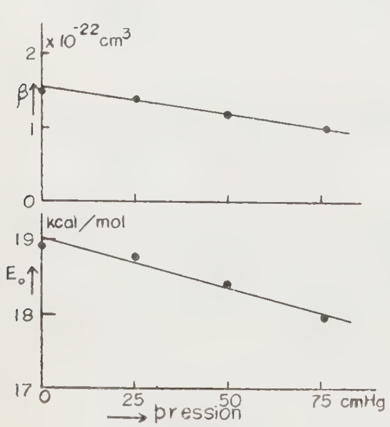

Fig. 3. β et l'énergie d'excitation. E_0.

On dispose un échantillon de verre au Sodium-Calcium d'une largeur de 10,0 mm et d'une épaisseur de 1,75 mm, horizontalement. sur deux appuis cunéiformes placés à un intervalle de 100 mm dans une cloche à vide où la pression est maintenue à une certaine valeur et on impose au point central de l'échantillon une charge qui augmente proportionnellement au temps grâce à un appareil de rupture à electro-aimant de même type que celui qu'employaient autrefois MM. F. W. Preston et T. C. Baker[6]. La vitesse de la charge était de 23,0 g/sec, la température d'environ 8°C. Nous avons ainsi mesuré la distribution de la résistance à la rupture dans les cas où la pression atmosphérique était respéctivement de 76 (l'humidité relative était de 70%), 50, 25 et 0,1 cm Hg.

La résistance moyenne f_m augmente dans l'air à basse pression comme on le voit sur la Fig. 1. La Fig. 2 montre la relation entre log μ et la tension f exprimée par l'effort maximum de tension au point central de l'échantillon. La Fig. 3 montre la variation de β et l'énergie d'excitation de rupture E_0 dans le cas où l'on suppose que $a=10^{10}$ sec^{-1}.

Nous nous sommes ensuite assuré que la relation suivante obtenue précédemment[7][4] entre la grandeur moyenne $\bar{l}$ du foyer d'éclatement de la cassure du verre et la tension f, est bien vérifiée:—

$$\bar{l}-l_0=C\exp\left(-\frac{\alpha}{2}f\right) \qquad (2)$$

où l_0 exprime la grandeur la plus petite du foyer d'éclatement, C et α des constantes.

Je remercie très vivement M. le Professeur M. Hirata d'avoir bien voulu m'encourager à poursuivre la présente étude et m'aider de ses conseils. Ce travail a pu être réalisé grâce à une allocation du Ministère de l'Instruction Publique que je remercie également.

Bibliographie

1) M. Hirata: Bull. Math. Stat. **3** (1949) 57; *Kikai no Kenkyû*. **1** (1949) 182, 231; *Ôyô Tôkeigaku*. (1949) 11.01.

2) M. Hirata and N. Terao: J. Appl. Phys. Japan **20** (1951) 234.

3) N. Terao: J. Phys. Soc. Japan **7** (1952) 627.

4) N. Terao: J. Phys. Soc. Japan **8** (1953) 550.

5) T. C. Baker and F. W. Preston: J. Appl. Phys. **17** (1946) 179.

6) T. C. Baker and F. W. Preston: J. Appl. Phys. **17** (1946) 162.

7) N. Terao: J. Phys. Soc. Japan **8** (1953) 545.

---

* *Séance du* 8 *avril* 1954.

Errata

On the Subsonic Flow of a Compressible Fluid past an Axisymmetric Slender Body

By Ken-ichi KUSUKAWA

J. Phys. Soc. Japan **9** (1954) 605–610

Page	line				
605	17	in q_0	$\frac{2}{(1+a)^{1/a}}$	should be read	$\frac{2(1-a^2)^{(1-a)/2a}}{(1+a)^{1/a}}$
607	− 5 right	in C	$2(1+a)^{-1/a}$	,,	$2(1+a)^{-1/a}(1-a^2)^{(1-a)/2a}$

PROGRESS OF THEORETICAL PHYSICS

Published by

The Yukawa Hall

with the cooperation of

The Physical Society of Japan

Progress of Theoretical Physics Vol. 11, Nos. 4–5, 1954

The Formulation of Quantum Mechanics in terms of Ensemble in Phase Space ....Takehiko TAKABAYASHI....341
A Method in Quantum Statistical Mechanics, I
— *General Theory* —........................Hiroshi ICHIMURA....374
A Method in Quantum Statistical Mechanics, II
— *The Degenerate Fermi-Dirac Assemlly* —
....Hiroshi ICHIMURA....385
The Problem of Many Bodies and the Superposition of Spherically Symmetric Space-times in General Relativity....Hyôitirô TAKENO....392
Tentative Theory of Λ-particles
— *Theory of 4-dimensional τ-space* —
.... Tadao NAKANO and Ryôyû UTIYAMA....411
On the Magnetic Anisotropy Energy of FeF_2
.... Kazuo NIIRA and Takehiko OGUCHI....425
Conservation Laws in Classical and Quantum Physics
.... Eugene P. WIGNER....437
On the Group of Transformations in Six-dimensional Space, II
— *Conformal Group in Physics* — .... Yasuhisa MURAI....441
Note on the Slow Electrons in a Polar Crystal.............Eijiro HAGA....449
The Generalization of Stueckelberg Formalism in the Theory of Quantized Field .... Minoru HAMAGUCHI....461
On the Theory of Cooperative Phenomena.......... Shigetoshi KATSURA....476
Letters to the Editor
A Variation Principle in Deuteron Problem .... T. KIKUTA....493
Renormalization in the Covariant Treatment of Pion-nucleon Scattering .... S. CHIBA....494
Further Comments on the Proposed Mass Spectrum
.... S. YOSHIKAWA and T. HASEBE....496
On the χ-μ Decay-in-flight in the Photographic Emulsion exposed at High Alititude .... K. NIU....499

Covariant Subtraction of "Overlapping Divergences" appearing in the Pion-nucleon Scattering ...... D. ITO and H. TANAKA....501
Further Considerations regarding Liquid Helium II at High Pressures..Z. MIKURA....503
On the Thermal Rayleigh Disk in Liquid Helium containing He^3 .... Z. MIKURA....504
Composite States of Two Fermions through Fermi-type Interaction .... H. KATSUMORI....505
Configuration Mixing and Magnetic Moments of Nuclei ....A. ARIMA and H. HORIE....509

Progress of Theoretical Physics Vol. 12, No. 1, 1954

On the Spin Wave Field Theory and its Application to the Microwave Resonance ....Noboru TSUYA.... 1
Super-stationary Variational Method ....Takashi KIKUTA.... 10
On Static Solutions of Einstein's Generalized Theory of Gravitation, I .... Mineo IKEDA.... 17
The Classical Equations of Motion of a Point Particle in a Symmetric Meson Field....R. C. MAJUMDAR, S. GUPTA and S. K. TREHAN.... 31
On a Treatment of Many-particle Systems in Quantum Field Theory.. .... Hiroshi SUURA.... 49
Some Remarks on the Charge Conjugation..................Shō TANAKA.... 72
Theoretical Analysis of Pion-nucleon Scattering .... Nobuyuki FUKUDA, Shigeo GOTO, Susumu OKUBO and Katsuro SAWADA.... 79
On the Effective Hamiltonian for Pseudoscalar Meson with Pseudoscalar Coupling with Nucleon..Tomoya AKIBA and Katsuro SAWADA.... 94

Letters to the Editor:

High Energy Nucleon Scattering by Nuclei ....O. KAWAGUCHI, M. KAWAY, Y. NISHIDA, M. SANO and H. UI.... 99
Electromagnetic Properties of Deuteron ..I. SATO and K. ITABASHI....100
Diagonalisation of Hamiltonian ....S. ÔKUBO....102
Reformulation of Brueckner-Watson Method by means of Canonical Transformations ....S. TANI....104
On the Variational Solution of Bethe-Salpeter Equation in Pion-nucleon Scattering .... D. ITO and H. TANAKA....105
Some Remarks on the Even-odd Rule ....K. NISHIJIMA....107
Damping Effect in the Gamma-decay of a Neutral Pion........ .... J. IWADARE and K. NISHIJIMA....108
A Remark on Neutron-proton Mass Difference................. .... Y. OISHI and H. KATSUMORI....109
A Note on Photon-nucleon Scattering ....Y. YAMAGUCHI....111

Price $ 1.25 per copy
$ 15.00 per year (postage inclusive)
Annual dues for foreign members (individual subscribers)
$ 12.00 (postage inclusive)
〃 for foreign members of the Physical Society of Japan
$ 10.00 (postage inclusive)

Application for members, subscriptions and orders for back mumbers should be sent, directly or through book-dealers, to

The Publication Office
in
Yukawa Hall, Kyoto University, Kyoto, Japan

JOURNAL OF THE PHYSICAL SOCIETY OF JAPAN Vol. 9, No. 6, NOV.—DEC., 1954

A Study of Shower Curves with the Multiplate Cloud Chamber

K. HINOTANI, K. SUGA and Y. TANAKA
Department of Physics, Osaka University, Osaka

(Received July 14, 1954)

With the multiplate cloud-chamber, cosmic-ray cascade showers up to 800 Mev were examined with respect to the shower curves and fluctuation. The form of the shower curve is in good agreement with the Wilson's Monte Carlo curve. And the fluctuation in the number of shower particles seems to be of the Poisson type. From the Shapiro's experiment and the authors', Wilson's results seem to be most reliable in both the absolute value and the form of the shower curve at least up to 800 Mev.

§ 1. Introduction

When the cloud-chamber photographs of the cosmic-ray mixed showers are analysed, it will become very important to find the energy of the associated cascade showers. For this purpose, comparing the observed shower development with the theoretical shower curves, the energy of the cascade showers may be estimated. In this case, it must be considered whether the theoretical shower curves are true or not, and how much the electron numbers fluctuate in the cascade showers.

Hitherto, the shower theories have been developed by many authors[1),6)] but their results are considerably different from each other in both the shower curves and fluctuation, corresponding to the approximations and the methods of calculation used. And there have been a few experimental studies[7)8)9)] on the features of the cascade development, but they have been limited up to a few hundred Mev.

Therefore, it is important to examine the reliability of the shower theories in higher energy region. For this purpose an experiment by cosmic-ray showers was carried out with a multiplate cloud-chamber.

§ 2. Apparatus

The arrangement of the apparatus used in this work is shown schematically in Fig. 1. The apparatus was placed at sea level. The chamber is of rear-illumination and lateral-expansion type. Its size is 60×60×40 cm and its ceiling is made of 1 cm Fe.

Shower producer Σ (3 cm Fe) was located above the chamber. The chamber contained seven lead plates of 1 cm thickness (2 radiation lengths).

To avoid the ambiguity due to the bias for selection of cascade showers in counter-controlled cloud chamber experiment, it is desirable to observe the cascades associated with the hard showers. Therefore, the chamber was operated by hard shower coincidence $A(\geqq 2)+B(\geqq 2)+C(\geqq 1)$, and was photographed stereoscopically with two cameras.

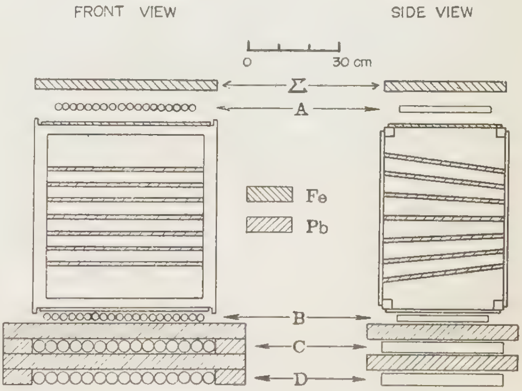

Fig. 1. Schematic View of the Apparatus.

§ 3. Analysis

About 500 photographs were taken during this experiment. But on the examination of the transition curve of the cascade showers, one should be careful of the selection of data. With the triggering master mentioned above, one expects to observe in the cloud chamber photographs; (1) penetrating showers and mixed showers produced in Σ or chamber ceiling or Pb plates (2) cascade showers originated from the electronic components of high energies (3) knock-on showers by μ-mesons. To minimize the bias in favour of the showers of slow development or of fast extinction, and to pick up the photon initiated showers, the following criteria were required,

(1) Cascade showers must be associated with penetrating showers, and be confirmed not to contribute to the coincidence. (Or shower must be random cascade shower and of photon origin.)

(2) The axis of the shower and whole of the shower particles must fall on Pb plate, in other words, shower must not escape half way out of the chamber.

(3) Shower must be absorbed entirely in the chamber; that is, there must be no shower particle in one or more successive gas spaces at the tail of the shower. Therefore none of the shower particles is not to be observed at least in the lowest space.

In the transition curve obtained by these data, slightly higher absorption should be expected than in truth, because there can be the case of missing-link development under the cloud chamber. But this probability is considered to be very small.

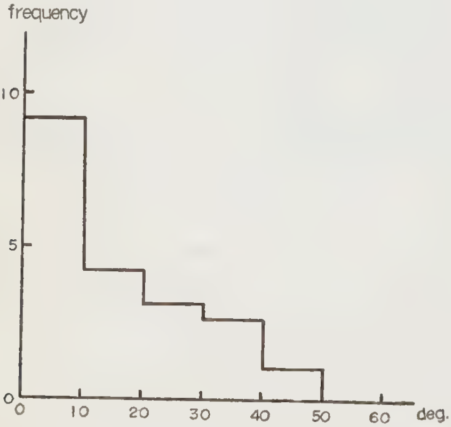

Fig. 2. The Distribution of the Projected Zenith Angles of the Shower Axes.

In this manner, 35 showers were selected. Among these, about 90% are cascades associated with hard showers and 10% are of random nature. Each of them was examined with respect to the following points:–

(1) the origin at which the shower initiating particles were produced.

(2) the number of electrons observed in each space between lead plates.

(3) projected zenith angle of the shower axis.

Thus the shower initiating particles of the cascade showers were mostly created in the Fe producer (Σ). For those showers 2 r.l. were added to the lead absorber thickness traversed. (Fe producer 1.5 r.l. and Fe chamber ceiling 0.5 r.l.).

It is necessary to classify the showers with respect to their energies. The sum of the electron number N in each space was taken for each shower, and the total number of electrons $\sum N$ was considered to be fairly proportional to the primary energy E_0. All showers observed were classified with respect to $\sum N$ as shown in Table I.

Table I. Classification of Observed Showers

Class	$\sum N$	No. of Showers Observed	Average Energy Estimated, Using Wilson's Monte Carlo Results
1	7～12	9	250 (Mev)
2	12～17	11	350
3	17～22	9	450
4	20～30	10	500
5	30～40	7	800 (see §4)

The distribution of the projected zenith angle of the shower axis is shown in Fig. 2. Average angle obtained from this distribution was 15°, and the correction to the absorber thickness (about 10%) was neglected.

§4. Shower Curves and Comparison with Theories

To compare the theoretical shower curves with the experimental, average number of electrons $\overline{N}$ was taken at 2, 4, 6, 8, 10, 12 and 14 r.l., for each class mentioned above. The results are shown in Fig. 3 (a)–(e). The errors attached to the experimental values are the ordinary standard errors.

These results were compared with the theoretical curves corresponding to the photon initiated showers*. The curves of Snyder and Wilson are shown in Fig. 3 as the typical ones. Snyder's4) curve calculated under approximation B is normalized so that $\int_0^\infty N(t)\,dt$ is equal to E_0/β. So, for convenience,

---

* The position of experimental shower maximum is close to that of the photon initiated shower in Snyder's theory as well as Wilson's. And it seems to be reasonable from the present criteria for selection of the cascades.

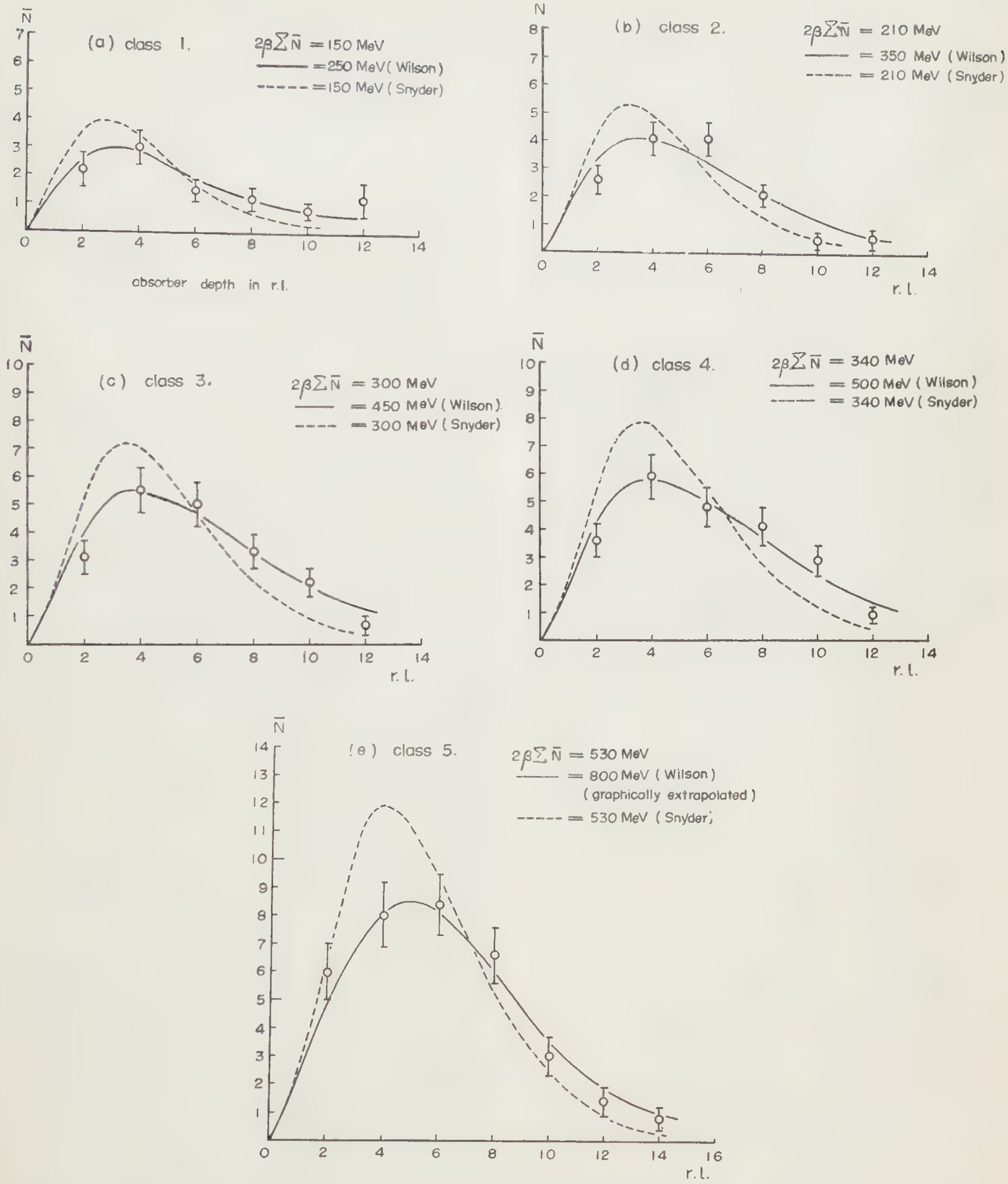

Fig. 3. Experimental results in comparison with the theoretical curves. (The full curves show the Wilson's Monte Carlo curves, and the dashed ones are Snyder's curves. The energies are shown in the figures.)

curves which satisfied the relation $E_0/\beta=2\sum\overline{N}$ (experimental) as an approximation of $\int_0^\infty N(t)\times dt$ were taken for comparison. β is the ionization loss per radiation length and was assumed to be 7.5 Mev. Another curve in Fig. 3 is Wilson's6) Monte Carlo curve which includes the effect of multiple scattering in lead. It was chosen so that $\int_0^\infty n_c dt=2\sum N$. n_c is the number of observed electrons of all energies.

Now, comparing the forms of the shower curves with the experimental results, Wilson's curves seem to be in good agreement with the experimental points within the limit of errors. The error-bars shown in Fig. 3 are the standard errors, assuming that the distribution of electron numbers at any thickness is of Poisson type. (see section 5) Therefore, it might be necessary to consider that the errors may be slightly larger. But in any way the agreement with Wilson's curves seems to be very satisfactory.

On the other hand, Snyder's curves deviate considerably from the experimental points. In Fig. 3 it is clearly seen that (1) the shower maximum appears at slight smaller absorber depths, (2) electron number at shower maximum is much greater, and (3) electrons are absorbed much more rapidly, in comparison with the experimental results. Therefore, the use of complete screening cross sections for radiation and pair production may not be good in the case of lead, and it is necesssry to take into consideration the effect of change of cross sections with energy.

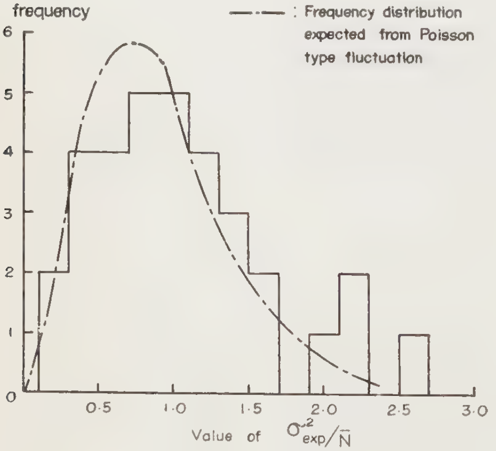

Fig. 4. Distribution of Experimental Values of $\langle(N-\bar{N})^2\rangle_{Av}/N$.

The effect of multiple scattering must be taken into account when the energy of the incident particle is concerned. The value $2\beta\sum N \simeq \int_0^\infty n_c\,\beta dt$ corresponds to the ionization loss of the counted electrons when they are assumed to go straight-forward along the shower axis. Therefore, by considering the effect of multiple scattering, the total ionization loss becomes naturally greater than $\int_0^\infty n_c\beta dt$, hence $E_0 > \int_0^\infty n_c\beta dt$. The effect of multiple scattering was not examined in this experiment. But the electrons off the shower axis by more than 30° were observed rather frequently. For these electrons of low energy, the correction for the multiple scattering effect cannot be neglected. In fact, according to Wilson, $\int_0^\infty n_c\beta dt$ amounts to only 60∼70% of total ionization loss, or E_0.

§ 5. Fluctuation

To find the fluctuation in the number of shower electrons from the average number $\bar{N}$ in each energy class and at each thickness, the mean square deviations divided by $\bar{N}$, $\sigma^2\,\text{exp.}/\bar{N} = \langle(N-\bar{N})^2\rangle A_v.\,\text{exp.}/\bar{N}$, were calculated. And it is desirable to find dependency of $\sigma^2/\bar{N}$ value at each thickness on the primary energy. But because of the poor statistics in this study, it could not be recognized. So, all the values $\sigma^2\,\text{exp.}/\bar{N}$ calculated at each absorber thickness in each energy class are shown together in the histogram form (Fig. 4). From Fig. 4, the $\sigma^2/\bar{N}$ values extend from 0.2 to 2.6 but their distribution is very near to the theoretical curves expected from Poisson type fluctuation.

However, one should be careful in discussing the type of fluctuation (Poisson, Furry, Pólya, etc.) In the first place, sufficient number of data must be taken for such statistical problems. In the second place, primary energies are not unique in the present case. Though the fluctuation in the value $\sum N$ as energy indicator is not yet known even in the case of unique energy, the range of $\sum N$ taken as the energy class in this study might be too narrow. Therefore the extended width in $\sum N$ was taken and $\sigma^2/\bar{N}$ was obtained for it, and the deviations due to different primary energies were subtracted. But this value of $\sigma^2/\bar{N}$ did not change essentially.

Accordingly, it may be true that the fluctuation of the number of electrons is rather close to the Poisson type in the present energy region and absorber thicknesses. But the Pólya type fluctuation in the case of small b

can not be excluded,** for the poor statistics in this study. It must be noted that the distribution obtained by the Monte Carlo method⁶⁾ is different from the Poisson distribution in small number of electrons but the values of $\sigma^2/\bar{N}$ are 1.2∼1.5 at small thicknesses and low energies.

§ 6. Conclusion

It was shown by this experiment that the Wilson's Monte Carlo curves are correct at least in the 'form' up to high energies, say 800 Mev, although the energies of the incident particles could not be found experimentally.

Shapiro⁸⁾ used a multi-plate cloud chamber and examined the showers with 200 Mev. electrons incident, and it was reported⁶⁾ that his results were in very good agreement with the Monte Carlo ones including multiple scattering.

Therefore, from the Shapiro's experiment and the present one, it may be concluded that at least up to 800 Mev. Wilson's results are most reliable.

In the end, the authors wish to express their heartfelt thanks to Prof. Y. Watase for his very helpful discussions and advice.

Thanks are due to Prof. W. E. Hazen of University of Michigan and Prof. R. R. Wilson of Cornell University for their kind letters, in which they have given precious criticisms and instructions. Finally the authors wish to express their gratitude to Mr. Tomizo Shiota for financial support given to this work.

References

1) B. Rossi and K. Greisen: Rev. Mod. Phys. **13** (1941) 240.
2) Niels Arley; On the Theory of Stochastic Processes and their Application to the Theory of Cosmic Radiation (1943 and 1949).
3) H. J. Bhabha and S. K. Chakrabarty: Phys. Rev. **74** (1948) 1352.
4) H. S. Snyder: Phys. Rev. **76** (1949) 1563.
5) I. B. Bernstein: Phys. Rev. **80** (1950) 995.
6) R. R. Wilson: Phys. Rev. **86** (1952) 261.
7) Salva Nassar and W. E. Hazen: Phys. Rev. **69** (1946) 298.
8) A. M. Shapiro: Phys. Rev. **82** (1951) 307.
9) W. Blockner, R. W. Kenney and W. K. H. Panofsky: Phys. Rev. **79** (1950) 419.

** $\sigma^2/\bar{N}$ $=1$ Poisson
$=\bar{N}-1$ Furry
$=1+b\bar{N}$ Pólya[2]

JOURNAL OF THE PHYSICAL SOCIETY OF JAPAN Vol. 9, No. 6, NOV.—DEC., 1954

A General Theory of Magnetic Resonance Absorption*

By Ryogo KUBO
Department of Physics, University of Tokyo
and Kazuhisa TOMITA
Department of Physics, Kyoto University

(Received June 26, 1954)

A general expression for the frequency-dependent susceptibility of a magnetic system is derived by a quantum-statistical method based on the linear theory of irreversible process. This fundamental equation provides a physical ground for the so-called Fourier transform method for computing the resonance line contour. The auto-correlation function, or the relaxation function of the magnetic moment, that is the Fourier transform of the absorption intensity distribution, can be expanded in terms of the perturbation energy, which is assumed to be responsible for changes of the resonance spectrum from the unperturbed distribution. A general method is shown how to choose from the expansion terms those which contribute to a particular line of interest. This is a generalization of the method of using projection operators. The customary moment method is examined from this point of view. Introducing a further assumption, we propose a method for computing the contour of resonance lines from the obtained expansion. This may be regarded as the quantum-mechanical formulation of the idea employed by Anderson and Weiss for the exchange narrowing problem of paramagnetic resonance. The problem of motional effect on the broadening is treated from this general point of view. Particular applications of the theory to the motional effect of the dipolar broadening in nuclear magnetic resonance and to the exchange effect in paramagnetic cases are also discussed in detail. Some basic equations such as used by Bloembergen, Purcell and Pound for nuclear magnetic case are reexamined and corrected.

§ 1. Introduction

In recent years, a great progress has been achieved in the field of the magnetic resonance method. For the nuclear magnetism, the new field of the nuclear induction method and the nuclear magnetic resonance absorption was opened by Bloch, Purcell, and their collaborators1),2). An extensive study was made by Bloembergen, Purcell and Pound on the nuclear magnetic resonance absorption in condensed phases3). Since then, a great number of papers have appeared concerning with the magnetic resonance spectroscopy of nuclear magnetism, paramagnetism, ferromagnetism, and also of antiferromagnetism.

One of the most important and interesting things coming out of these investigations is the fact that the observed resonance spectra reveal the mechanism of interactions existing between the resonating magnetic moments and their surrounding. Thus, for instance, the shift and split of some paramagnetic resonance lines may enable us to analyse the crystalline fields and the hyperfine interactions acting on the magnetic ions. The broadening of the spectral lines and the relaxation effects may provide us important indications to the mechanism of interactions and the dynamical behaviour of the interacting degrees of freedom such as the atomic motion in the nuclear magnetic case and the spin motion due to the exchange coupling in the paramagnetic cases.

From the theoretical point of view, the problem is relatively simple if the fields on each of the magnetic moments are independent. The spectra of certain paramagnetic materials are determined by the crystalline field due to the surrounding ions and by the hyperfine interaction with the nucleus of the paramagnetic ion. Theoretical analysis becomes more complicated when the magnetic moments are coupled together directly or indirectly and the fields on these moments are correlated. Typical examples of this kind of interaction are the dipolar and the exchange interactions.

---

* A part of this study was presented to the International Conference on Theoretical Physics held at Kyoto, September 1953.

The effect of dipolar interactions was first treated by Waller[4)] and later by Broer[5)] and Van Vleck[6)]. For the nuclear magnetic resonance absorption, Bloembergen, Purcell and Pound[3)] made beautiful analysis of their experiments on the basis of these theories. In particular, they showed most clearly the effect of the nuclear motion on the dipolar broadening, which was treated as a sort of random modulation of dipolar field owing to the Brownian motion of the atomic nuclei. An effect essentially similar to this motional narrowing was predicted by Van Vleck and Gorter[7)] for the paramagnetic resonance absorption in the presence of exchange coupling between the paramagnetic spins, which was proved later by experiments. More recently, Anderson and Weiss[8)] presented a theory which treats the motion of spins induced by the exchange interaction as a stochastic process and makes it possible to describe the line shapes in a fairly reasonable way. This stochastic theory has been developed further by Anderson[9)]. This method goes a step further than the moment method, which was employed by Van Vleck for the same problem, and gives under certain conditions, more detailed description of the narrowing process. As a matter of fact, the stochastic method may also be regarded as a direct extension of the theory of Bloembergen, Purcell and Pound for the motional narrowing of the nuclear magnetic cases. It is, however, to be admitted that the quantum-mechanical grounds of these theories have not been made very clear, in contrast to the moment method for which a rigorous formulation is accessible from quantum-mechanical principles.

The purpose of the present paper is, therefore, to give a more satisfactory formulation of the general theory of the magnetic resonance phenomenon. We begin in Part A with a quantum-mechanical theory of frequency-dependent susceptibilities of magnetic systems, which is beyond the scope of the statistical-thermodynamic theory of equilibrium states and so necessarily is related to the statistical mechanics of non-equilibrium states or the theory of irreversible processes in quantum-mechanical systems. We shall not, however, go so far into the complication of general treatments of irreversible processes, but shall confine ourselves to the simple case of the linear theory, which assumes that the external disturbance is always small and the response of the system to it is linear. It will be shown there that the frequency-dependent susceptibilities are essentially the Fourier transforms of auto-moments of the magnetization vectors, which may be called the relaxation function of the magnetization. This is the physical basis of the Fourier-transform method applied for this particular case of magnetic resonance phenomenon.

Part B deals with quantum-mechanical calculation of the relaxation function. Our fundamental assumption is that the motion of the magnetic system is described by an unperturbed Hamiltonian $\mathcal{H}_0$ and a small perturbation $\mathcal{H}'$. The separation of $\mathcal{H}_0$ and $\mathcal{H}'$ must be chosen in such a way that the unperturbed Hamiltonian $\mathcal{H}_0$ will give a reasonable approximation to the observed structure of the resonance curve which is modified by the perturbation $\mathcal{H}'$. Thus we make use of a perturbation calculation and expand the relaxation function into a power series of $\mathcal{H}'$. This is most conveniently done by taking the interaction representation in which the motion of the magnetization is now looked from a reference system moving with the unperturbed motion of the system. With this technique we can find a natural way to separate the expansion terms into groups each of which is correlated to a particular line of the unperturbed resonance spectra. This is a generalization of the method of projection operators used by Pryce and Stevens[10)] to pick up those matrix elements which are needed to calculate the moments of a particular line of interest. The most essential assumption of our method is discussed in § 4. Namely, we assume that each part of the relaxation function associated with each of the unperturbed resonance lines can be approximated by an exponential function, the exponent of which can be calculated with the use of the expanded series of the relaxation function. This is, in fact, mathematically equivalent, or at least similar to those assumptions adopted by Anderson and Weiss for their stochastic treatment, and enables us to predict the line shapes of resonance lines in a certain approximation. Our assumption relies upon the validity of perturbation calculation and on the belief of the success of the quantum-mechanical theory of irreversible process. Relations of the present method and the moment method will be discussed in § 5, where some remarks will also be made on the so-called adiabatic approximation.

Our method will be applied in § 6 to a general treatment of the motional effects, that is the motional narrowing of the width and an additional broadening effect due to the non-secular perturbation, in the second order approximation. This is based on the model that the unperturbed motion of the system consists of two kinds of modes, one of which gives rise to an organized motion of the magnetization vector and the other affects the resonance spectrum indirectly through its influence on the perturbation $\mathscr{H}'$, modifying thus the pattern of the distortion of the spectrum due to $\mathscr{H}'$. The non-secular broadening effect is naturally related to the so-called spin-lattice relaxation effect though not quite the same. Rigorous relations of these two will be examined there in detail.

Last two sections, § 7 and § 8 will be devoted to the applications of our theory to the motional effect in the nuclear magnetic resonance absorption and the exchange effect in the paramagnetic resonance. Some results of former investigations will be corrected.

Part A. Fundamental Equation of the Magnetic Dispersion and Absorption.

§ 1. Relaxation Function and Susceptibility

First, we shall discuss the general theory of magnetic dispersion and absorption phenomena and derive fundamental equations to correlate the susceptibility and the relaxation function to the dynamical properties of the system we are concerned with. This will be done on the basis of quantum statistics and in the limitation of the linear theory, which means that the response of our system to the external disturbance is treated only in the first order of perturbation theory. Thus, our treatment corresponds to the so-called linear theory of irreversible processes. As we shall see later, the relaxation function is essentially the Fourier transform of the frequency-dependent susceptibility, so that we may obtain here some deeper insights into the logical relation of the general theory of irreversible processes and the Fourier-transform theory of spectral lines.

Let us consider a sample of a certain magnetic material in an oscillating magnetic field,

$$\boldsymbol{H}_1(t)=\boldsymbol{H}_1\cos\omega t\,, \qquad (1.1)$$

with the wave-length very large compared to the dimension of the sample. Then the induced magnetic moment of the sample will be expressed as

$$\begin{aligned}\boldsymbol{M}_{\text{ind}}(t)&=\mathrm{Re}(\chi'-i\chi'')\boldsymbol{H}_1\exp(iwt)V\\&=(\chi'\cos\omega t+\chi''\sin\omega t)\boldsymbol{H}_1V\,,\end{aligned} \qquad (1.2)$$

where V is the volume of the sample and

$$\chi=\chi'-i\chi''\,, \qquad (1.3)$$

is the complex susceptibility.*
Since we confine ourselves to the linear theory as incorporated in the assumed linearity of $\boldsymbol{M}_{\text{ind}}$ and $\boldsymbol{H}_1$ in Eq. (1.2), our problem is now to calculate the magnetic response of the system in the first order of the external field $\boldsymbol{H}_1$. This kind of problem can generally be solved by a first order perturbation method. We can apply here two approaches, the one of which might be called the relaxation function method, and the other the more direct application of the ordinary perturbation method. Leaving the discussion of the second to the Appendix, we shall adopt here the first method.

The relaxation function is the function which describes the time change of the response after the external disturbance is cut down to zero. Thus, we now suppose a constant magnetic field $\boldsymbol{H}_1$ is applied from $t=-\infty$ to $t=t_0$, when it is suddenly removed. We may then assume a canonical distribution,

$$\rho'=\frac{\exp\{-\beta(\mathscr{H}-\boldsymbol{H}_1\boldsymbol{M})\}}{\mathrm{Tr}\exp\{-\beta(\mathscr{H}-\boldsymbol{H}_1\boldsymbol{M})\}}\,, \qquad (1.4)$$

for $t=-\infty$ to $t=t_0$. Here $\mathscr{H}$ is the Hamiltonian which describes the dynamical nature of the magnetic system in the absence of the disturbing field $\boldsymbol{H}_1$, and $\boldsymbol{M}$ is the magnetic moment operator. For $t>t_0$, the density matrix will follow the equation of motion,

---

* It must be noted that χ' and χ'' defined by Eq. (1.2) are not necessarily material constants, but may depend on the shape of the sample if the effect of the demagnetization field is taken into account. But, keeping this in mind, we use in the following these conventional susceptibilities.

$$i\hbar\dot{\rho}=\mathcal{H}\rho-\rho\mathcal{H}\,, \qquad (1.5)$$

so that at the time t the time dependent density matrix is given by

$$\rho(t)=\exp(-i(t-t_0)\mathcal{H}/\hbar)\rho'\exp(i(t-t_0)\mathcal{H}/\hbar)\,. \qquad (1.6)$$

Therefore, the expectation value of the magnetic moment operator $\boldsymbol{M}$ will be

$$\begin{aligned}\overline{\boldsymbol{M}}(t)&=\mathrm{Tr}\,\rho(t)\boldsymbol{M}\\ &=\mathrm{Tr}\,\{\exp(-i(t-t_0)\mathcal{H}/\hbar)\rho'\exp(i(t-t_0)\mathcal{H}/\hbar)\boldsymbol{M}\}\\ &=\mathrm{Tr}\,\rho'\boldsymbol{M}(t)\,, \qquad (1.7)\end{aligned}$$

where

$$\boldsymbol{M}(t)=\exp(i(t-t_0)\mathcal{H}/\hbar)\boldsymbol{M}\exp(-i(t-t_0)\mathcal{H}/\hbar)\,, \qquad (1.8)$$

is the Heisenberg representation of the magnetic moment following the equation of motion

$$i\hbar\dot{\boldsymbol{M}}(t)=\boldsymbol{M}(t)\mathcal{H}-\mathcal{H}\boldsymbol{M}(t)\,, \qquad (1.9)$$

with the initial condition

$$\boldsymbol{M}(t_0)=\boldsymbol{M}\,. \qquad (1.10)$$

Now, using the expansion,

$$\begin{aligned}&\exp(-\beta(A+B))\\ &=\exp(-\beta A)\Big\{1-\int_0^\beta d\lambda\exp(\lambda A)B\exp(-\lambda A)\\ &+\int_0^\beta d\lambda_1\int_0^{\lambda_1}d\lambda_2\exp(\lambda_1 A)B\exp(-(\lambda_1-\lambda_2)A)\\ &\qquad\times B\exp(-\lambda_2 A)+\cdots\Big\}\,,\end{aligned}$$

which is easily obtained from the identity

$$\begin{aligned}&\exp(\beta A)\exp(-\beta(A+B))\\ &=1-\int_0^\beta d\lambda\exp(\lambda A)B\exp(-\lambda(A+B)\,,\end{aligned}$$

we find the first order approximation of ρ', Eq. (1.4), to be

$$\begin{aligned}\rho'=&\{\exp(-\beta\mathcal{H})/\mathrm{Tr}\exp(-\beta\mathcal{H})\}\\ &\times\Big\{1+\int_0^\beta d\lambda\exp(\lambda\mathcal{H})\,\boldsymbol{H}_1(\boldsymbol{M}-\overline{\boldsymbol{M}}_0)\\ &\times\exp(-\lambda\mathcal{H})\Big\}+O(H_1^2)\,.\end{aligned}$$

Thus, retaining only the first order of H_1, the last expression of Eq. (1.7) is written as

$$\begin{aligned}\overline{\boldsymbol{M}}(t)=&\overline{\boldsymbol{M}}_0+\int_0^\beta d\lambda\\ &\times\mathrm{Tr}\,\rho_0\exp(\lambda\mathcal{H})\boldsymbol{H}_1(\boldsymbol{M}-\overline{\boldsymbol{M}}_0)\\ &\times\exp(-\lambda\mathcal{H})\boldsymbol{M}(t-t_0)+O(\boldsymbol{H}_1^2)\,, \qquad (1.11)\end{aligned}$$

with

$$\rho_0=\exp(-\beta\mathcal{H})/\mathrm{Tr}\exp(-\beta\mathcal{H})\,, \qquad (1.12)$$

and

$$\overline{\boldsymbol{M}}_0=\mathrm{Tr}\,\rho_0\boldsymbol{M}\,, \qquad (1.13)$$

which is the magnetic moment of the system with the unperturbed Hamiltonian $\mathcal{H}$. Hence, in the linear theory, the relaxation function $\tilde{\phi}$ as a tensor defined by

$$\overline{\boldsymbol{M}}(t)-\overline{\boldsymbol{M}}_0=\boldsymbol{H}_1\tilde{\phi}(t-t_0)\,, \qquad (1.14)$$

is expressed by

$$\begin{aligned}&\tilde{\phi}(t-t_0)\\ &=\int_0^\beta\langle\exp(\lambda\mathcal{H})(\boldsymbol{M}-\overline{\boldsymbol{M}}_0)\exp(-\lambda\mathcal{H})\boldsymbol{M}(t-t_0)\rangle d\lambda\\ &=\int_0^\beta\langle\boldsymbol{M}\boldsymbol{M}(t-t_0+i\hbar\lambda)\rangle d\lambda-\beta\boldsymbol{M}_0\boldsymbol{M}_0)\,, \qquad (1.15)\end{aligned}$$

and the transposed tensor of $\tilde{\phi}$, defined by

$$\overline{\boldsymbol{M}}(t)-\overline{\boldsymbol{M}}_0=\phi(t-t_0)\boldsymbol{H}_1\,, \qquad (1.14a)$$

is given by

$$\begin{aligned}&\phi_{xy}(t-t_0)\\ &=\int_0^\beta d\lambda\langle M_yM_x(t-t_0+i\hbar\lambda)\rangle-\beta\overline{M}_{0y}\overline{M}_{0x}\,, \qquad (1.15a)\\ &=\int_0^\beta d\lambda\langle\exp(\lambda\mathcal{H})M_x(t-t_0)\exp(-\lambda\mathcal{H})M_y\rangle\\ &\qquad-\beta\overline{M}_{0x}\overline{M}_{0y}\\ &=\int_0^\beta d\lambda\langle M_x(t-t_0-i\hbar\lambda)M_y\rangle-\beta\overline{M}_{0x}\overline{M}_{0y}\,. \qquad (1.15b)\end{aligned}$$

In these expressions and in the following, the averages are defined by

$$\langle A\rangle=\mathrm{Tr}\,\rho_0 A\,. \qquad (1.16)$$

The expression (1.15b) is obtained from (1.15a) by changing the integration variable λ to $\beta-\lambda$.

Eqs. (1.14)–(1.15a) are straightforward generalizations of Takahashi's theory[11] for classical systems to quantum-mechanical systems. In the classical limit, $\hbar\to0$, Eqs. (1.15) and (1.15a) become

$$\left.\begin{aligned}\tilde{\phi}(t-t_0)&=\beta\{\langle \boldsymbol{M}\boldsymbol{M}(t-t_0)\rangle-\overline{\boldsymbol{M}}_0\overline{\boldsymbol{M}}_0\}\,,\\ \phi(t-t_0)&=\beta\{\langle \boldsymbol{M})t-t_0)\boldsymbol{M}\rangle-\overline{\boldsymbol{M}}_0\overline{\boldsymbol{M}}_0\}\,.\end{aligned}\right\} \tag{1.15c}$$

we shall see in the next section that Eq. (1.15c) holds also in quantum-mechanical cases under a certain condition.

The quantum-mechanical expression for $\boldsymbol{M}(t)$ for an arbitrary function $\boldsymbol{H}_1(t)$ is obtained easily from our relaxation function. Assuming that

$$\boldsymbol{H}_1(-\infty)=0\,,\qquad \rho(-\infty)=\rho_0\,, \tag{1.17}$$

that is to say, assuming that our system has been in equilibrium at $t=-\infty$ with the unperturbed Hamiltonian $\mathscr{H}$ and that the perturbing field $H_1(t)$ has been switched on adiabatically at $t=-\infty$ and applied up to $t=t'$, we see that the expectation of $\boldsymbol{M}$ at the time t is

$$\overline{\boldsymbol{M}}(t)-\overline{\boldsymbol{M}}_0=\int_{-\infty}^{t}\left\{\frac{d}{dt'}\phi(t-t')\right\}\boldsymbol{H}_1(t')dt' \tag{1.18}$$

$$=\phi(0)\boldsymbol{H}_1(t)-\int_{-\infty}^{t}\phi(t-t')\frac{d\boldsymbol{H}_1(t')}{dt'}dt'\,, \tag{1.18a}$$

because $d\phi(t-t')/dt'$ represents the response of the system for $t>t'$ when a δ-type disturbance is applied at t'. Inserting Eq. (1.15b), we have

$$\frac{d\phi(t-t')}{dt'}=-\frac{d\phi(t-t')}{dt}$$

$$=\int_0^\beta d\lambda\,\langle\exp(\lambda\mathscr{H})\left\{-\frac{d}{dt}\boldsymbol{M}(t-t')\right\}$$

$$\times\exp(-\lambda\mathscr{H})\boldsymbol{M}\rangle$$

$$=\int_0^\beta d\lambda\frac{i}{\hbar}\langle\exp(\lambda\mathscr{H})[\boldsymbol{M},\mathscr{H}]\exp(-\lambda\mathscr{H})\boldsymbol{M}\rangle\,, \tag{1.19}$$

for this response to a pulse. Writing the expression explicitly in the representation diagonalizing $\mathscr{H}$, we observe that Eq. (1.19) is equivalent to

$$-\frac{d}{dt}\phi_{xy}(t-t')=\frac{i}{\hbar}\langle[M_x(t-t'),M_y]\rangle\,, \tag{1.19a}$$

which is a direct consequence of the application of the usual perturbation method as will be discussed in the Appendix. Usui and Kambe have made use of equations which are essentially equivalent to (1.19a) in their treatment of temperature effect of paramagnetic resonance[12].

The expressions for the susceptibility is obtained from (1.18) and (1.18a) in the following forms:

$$\left.\begin{aligned}\chi'&=\chi_0-\frac{\omega}{V}\int_0^\infty\phi(\tau)\sin\omega\tau d\tau\,,\\ \chi''&=\frac{\omega}{V}\int_0^\infty\phi(t)\cos\omega\tau d\tau\,,\end{aligned}\right\} \tag{1.20}$$

or in brief

$$\chi^*=\chi'-i\chi''=\chi_0-\frac{i\omega}{V}\int_0^\infty\phi(\tau)\exp(-i\omega\tau)d\tau\,, \tag{1.21}$$

where χ_0 is the static susceptibility

$$\chi_0=\frac{\phi(0)}{V}$$

$$=\frac{1}{V}\left\{\int_0^\beta\langle\exp(\lambda\mathscr{H})\boldsymbol{M}\exp(-\lambda\mathscr{H})\boldsymbol{M}\rangle d\lambda\right.$$

$$\left.-\beta\overline{\boldsymbol{M}}_0\overline{\boldsymbol{M}}_0\right\}\,, \tag{1.22}$$

and $\phi(\tau)$ is given by Eq. (1.15a) or (1.15b). If one likes, one may also express χ^* as

$$\chi^*=-\frac{1}{V}\int_0^\infty\frac{d\phi(\tau)}{d\tau}\exp(-i\omega\tau)d\tau\,, \tag{1.23}$$

with $d\phi/d\tau$ given by Eq. (1.19) or (1.19a). Eq. (1.21) or (1.23) is the most general formula to correlate the relaxation function to the complex susceptibility. Naturally one can easily derive the inverse relations of these equations. Evidently $\chi'(\omega)$ and $\chi''(\omega)$ are mutually connected by the Kramers-Kronig relations[13]. For practical calculations, Eq. (1.23) is more convenient than Eq. (1.21).

§ 2. General Properties of the Relaxation Tensor and the Susceptibility

Now, we shall show some general properties of the relaxation function defined by Eq. (1.15a) or (1.15b). First, $\phi(t)$ must be real as required by its physical meaning, and as indeed has been assumed in our derivation of Eq. (1.20). This is seen from Eqs. (1.15a) and (1.15b) since these two expressions are really conjugates;

$$\overline{\phi_{xy}}(t)=\phi_{xy}(t)\,. \tag{2.1}$$

Secondly, an important property of the relaxation function is

$$\lim_{t\to\infty}\phi(t)=0\ , \qquad (2.2)$$

which is also naturally required from physical reasons, because it means the eventual approach of the system to the thermal equilibrium. This limiting property of ϕ is, however, rather difficult to prove rigorously. In fact, a logical justification is the most essential point of any rigorous theory of irreversible processes, which is beyond of the scope of this article.

The third important property of ϕ is its symmetry as a tensor. By Eq. (1.15a) and (1.15b), we have primarily defined $\phi(t)$ for $t>0$. Generalizing the definition to $t<0$ by the same equation, we first observe that

$$\phi(-t)=\tilde{\phi}(t) \quad \text{or} \quad \phi_{xy}(-t)=\phi_{yx}(t)\ . \qquad (2.3)$$

Now let us suppose that a constant magnetic field $\boldsymbol{H}_c$ is continually applied to our system, so that the unperturbed Hamiltonian $\mathscr{H}$ does actually involve this magnetic field $\boldsymbol{H}_c$. We find immediately that the unperturbed motion of the system and also the density matrix itself are invariant to the simultaneous change of signs of $\boldsymbol{H}_c$, $\boldsymbol{M}$, and t. This is actually the microscopic or dynamical reversibility of our system[14]. Thus we see that

$$\phi(t,H_c)=\phi(-t,-H_c)\ . \qquad (2.4)$$

Combining with (1.26), we obtain the reciprocal relation of Onsager[14],

$$\phi(t,\boldsymbol{H}_c)=\tilde{\phi}(t,-\boldsymbol{H}_c), \quad \text{or} \quad \phi_{xy}(t,\boldsymbol{H}_c)=\phi_{yx}(t,-\boldsymbol{H}_c), \qquad (2.5)$$

and accordingly,

$$\chi(\omega,\boldsymbol{H}_c)=\tilde{\chi}^*(\omega,-\boldsymbol{H}_c)\ . \qquad (2.6)$$

Evidently, both the real and the imaginary parts of the susceptibility tensor can be asymmetric if we have a constant field $\boldsymbol{H}_c$. This will never be of importance for us if we are concerned only with the absorption of energy for a linearly polarized radiation. We then have to deal with only the symmetric part of the χ'' tensor. But for other cases the antisymmetric parts can also be observed.

We have mentioned in the previous section that the relaxation functions are simplified to Eq. (1.15c) for the classical cases. It is very important to notice that this simplification does not necessarily require that the dynamical motion is classical, but requires only that the energy differences E_m-E_n of the various levels of the system connected by matrix elements of $\boldsymbol{M}$ should be much smaller than kT, i.e.,

$$|E_m-E_n|=\hbar\omega_{nm}\ll kT\ . \qquad (2.7)$$

This is easily seen if one writes down the explicit form of Eq. (1.15b) in the representation diagonalizing $\mathscr{H}$ in the following way:

$$\begin{aligned}
&\phi_{xy}(t)+\beta\overline{\boldsymbol{M}}_{0x}\overline{\boldsymbol{M}}_{0x}\\
&\quad=\int_0^\beta d\lambda\sum_n\sum_m \exp(-\beta E_n)\exp(\lambda(E_n-E_m))\\
&\qquad\times(\boldsymbol{n}|\boldsymbol{M}_x(\boldsymbol{t})|\boldsymbol{m})(\boldsymbol{m}|\boldsymbol{M}_y|\boldsymbol{n})/\sum_n\exp(-\beta E_n)\\
&\quad=\sum_n\sum_m\exp(-\beta E_n)\frac{\exp(\beta(E_n-E_m))-1}{E_n-E_m}\\
&\qquad\times(\boldsymbol{n}|\boldsymbol{M}_x(\boldsymbol{t})|\boldsymbol{m})(\boldsymbol{m}|\boldsymbol{M}_y|\boldsymbol{n})/\sum_n\exp(-\beta E_n)\\
&\quad=\beta\sum_n\sum_m\exp(-\beta E_n)(\boldsymbol{n}|\boldsymbol{M}_x(t)|\boldsymbol{m})\\
&\qquad\times(\boldsymbol{m}|\boldsymbol{M}_y|\boldsymbol{n})/\sum\exp(-\beta E_n)\ .
\end{aligned}$$

Or, one may use the expansion

$$\begin{aligned}
M_x(t+i\hbar\lambda)&=M_x(t)+i\hbar\lambda\dot{M}_x(t)\\
&\qquad+\tfrac{1}{2}(i\hbar\lambda)^2\ddot{M}_x(t)+\cdots\ ,
\end{aligned}$$

to insert into Eqs. (1.15a) and (1.15b). We then get

$$\begin{aligned}
&\phi_{xy}(t)+\beta\overline{\boldsymbol{M}}_{0x}\overline{\boldsymbol{M}}_{0y}\\
&\quad=\beta\langle M_x(t)M_y\rangle+\tfrac{1}{2}i\hbar\beta^2\langle\dot{M}_x(t)M_y\rangle+\cdots\\
&\quad=\beta\langle M_yM_x(t)\rangle-\tfrac{1}{2}i\hbar\beta^2\langle M_y\dot{M}_x(t)\rangle+\cdots\ .
\end{aligned} \qquad (2.8)$$

In both expressions, the first term of the expansion provides a good approximation if the condition (2.7) is satisfied. But it is more convenient and more reasonable to use

$$\phi_{xy}(t)=\beta[\langle\{M_x(t)M_y\}\rangle-\overline{M}_{0x}\overline{M}_{0y}]\ , \qquad (2.9)$$

as the approximation in the first order of $\beta\hbar\omega_{nm}$. In this equation, $\{M_x(t)M_y\}$ on the right hand side is the symmetrized product of $M_x(t)$ and M_y, which, of course, is the quantum-mechanical counterpart of the classical product. The expression (2.9) satisfies the conditions (2.1), (2.3) and (2.5). Thus, if we have only low frequency levels such as are assumed in the usual derivation of the Langevin-Debye formula of paramagnetism[15], or if we make some approximation to cut off the contributions from high frequency levels, Eq. (2.9) may well be used for quantum-mechanical calculations. This is always so for the important applications of the theory to radio- and micro-wave experiments.

The function

$$\langle M_x(t+\tau)M_y(\tau)\rangle=\langle M_x(t)M_y(0)\rangle\ , \quad (2.10)$$

represents the correlation of $M_x(t+\tau)$ and $M_y(t)$. We may call this the x-y component of the *correlation tensor* of magnetic moment at the time interval t. Thus, in the low frequency cases, the relaxation function, Eq. (2.9) is simply proportional to the correlation tensor of the magnetic moment, and by Eq. (1.21) the frequency-dependent susceptibility is essentially the Fourier-transform of the correlation tensor.

§ 3. Symmetric and Antisymmetric Tensors. Energy Absorption

The symmetric and antisymmetric parts of the relaxation tensor are defined by

$$\left.\begin{aligned}\phi_{xy}{}^s(t)&=\tfrac{1}{2}(\phi_{xy}(t)+\phi_{yx}(t))=\tfrac{1}{2}(\phi_{xy}(t)+\tilde{\phi}_{xy}(t))\ ,\\ \phi_{xy}{}^a(t)&=\tfrac{1}{2}(\phi_{xy}(t)-\phi_{yx}(t))=\tfrac{1}{2}(\phi_{xy}(t)-\tilde{\phi}_{xy}(t))\ ,\end{aligned}\right\} \quad (3.1)$$

which are explicitly given by

$$\begin{aligned}&\phi_{xy}{}^s(t)\\ &=\int_0^\beta \tfrac{1}{2}\langle M_x(t-i\hbar\lambda)M_y+M_x(-t-i\hbar\lambda)M_y\rangle d\lambda\\ &\qquad\qquad -\beta\overline{M}_{0x}\overline{M}_{0y}\\ &=\int_0^\beta \tfrac{1}{2}\langle M_y(t-i\hbar\lambda)M_x+M_y(-t-i\hbar\lambda)M_x\rangle d\lambda\\ &\qquad\qquad -\beta\overline{M}_{0x}\overline{M}_{0y}\ , \quad (3.2)\end{aligned}$$

and

$$\begin{aligned}&\phi_{xy}{}^a(t)\\ &=\int_0^\beta \tfrac{1}{2}\langle M_x(t-i\hbar\lambda)M_y-M_x(-t-i\hbar\lambda)M_y\rangle d\lambda\\ &=\int_0^\beta \tfrac{1}{2}\langle -M_y(t-i\hbar\lambda)M_x+M_y(-t-i\hbar\lambda)M_x\rangle d\lambda\ .\end{aligned} \quad (3.3)$$

By Eq. (2.3), $\phi_{xy}{}^s(t)$ is real and even in t, while $\phi_{xy}{}^a(t)$ is odd in t. If we have only low-frequency levels, these expressions are simplified to

$$\begin{aligned}\phi_{xy}{}^s(t)&=\tfrac{1}{2}\beta\langle\{M_x(t)M_y\}+\{M_x(-t)M_y\}\rangle\\ &\qquad -\beta\overline{M}_{0x}\overline{M}_{0y}\\ &=\tfrac{1}{2}\beta\langle\{M_xM_y(t)\}+\{M_xM_y(-t)\}\rangle\\ &\qquad -\beta\overline{M}_{0x}\overline{M}_{0y}\ , \quad (3.4)\end{aligned}$$

and

$$\begin{aligned}\phi_{xy}{}^a(t)&=\tfrac{1}{2}\beta\langle\{M_x(t)M_y\}-\{M_x(-t)M_y\}\rangle\\ &=\tfrac{1}{2}\beta\langle-\{M_xM_y(t)\}+\{M_xM_y(-t)\}\rangle\ .\end{aligned} \quad (3.5)$$

The symmetric and antisymmetric parts of the susceptibility tensor are calculated by

$$\left.\begin{aligned}\chi_s{}^*&=\chi_0-\frac{i\omega}{V}\int_0^\infty \phi^s(t)\exp(-i\omega t)dt\ ,\\ \chi_a{}^*&=-\frac{i\omega}{V}\int_0^\infty \phi^a(t)\exp(-i\omega t)dt\ .\end{aligned}\right\} \quad (3.6)$$

In particular we have

$$\chi''_s=\frac{\omega}{2V}\int_{-\infty}^\infty \phi^s(t)\exp(-i\omega t)dt\ , \quad (3.7)$$

because ϕ^s is even in t. This is again simplified to

$$\begin{aligned}\chi''_{sxy}=\frac{\omega\beta}{4V}\int_{-\infty}^\infty &[\langle\{M_x(-t)M_y\}+\{M_x(-t)M_y\}\rangle\\ &-2\overline{M}_{0x}\overline{M}_{0y}]\exp(-i\omega t)dt\ , \quad (3.8)\end{aligned}$$

for low-frequency cases where the absorption is appreciable only for those frequencies satisfying

$$\hbar\omega\ll kT=1/\beta\ . \quad (3.9)$$

For linearly polarized radiation, Eq. (1.1), the rate of energy absorption by the magnetic system is given by

$$Q=(\pi\nu\boldsymbol{H}_1\chi''\boldsymbol{H}_1)V=(\pi\nu\boldsymbol{H}_1\chi_s''\boldsymbol{H}_1)V\ . \quad (3.10)$$

This is obtained with the use of Eq. (1.2) from a phenomenological point of view. Naturally the same result is to be derived by a quantum-mechanical treatment calculating the transition probability by the ordinary perturbation method. This equivalence is also shown in the Appendix.

Similarly to (3.7), we have for the antisymmetric part

$$\chi_a'=\frac{i\omega}{2V}\int_{-\infty}^\infty \phi^a(t)\exp(-i\omega t)dt\ . \quad (3.11)$$

This is also related to the energy absorption. For circularly polarized radiation, e.g.,

$$\boldsymbol{H}_1(t)=(H_1\cos\omega t, H_1\sin\omega t, 0)\ , \quad (3.12)$$

the rate of energy absorption is given by

$$Q=\pi\nu H_1{}^2(\chi'_{xy}-\chi'_{yx}+\chi''_{xx}+\chi''_{yy})V\ . \quad (3.13)$$

Now let us consider a little further the absorption of radiation linearly polarized in the x-direction by a system with low-frequency levels. Then, from Eqs. (1.20), (2.19) and (3.10) we see that the absorption coefficient,

$$A(\omega)=\nu\chi''_{xx}(\omega)\ , \tag{3.14}$$

is given by

$$\begin{aligned}&A(\omega)\\&=\frac{\omega^2\beta}{2\pi V}\int_{-\infty}^{\infty}[\langle\{M_x(t)M_x\}\rangle-\overline{M}_{0x}{}^2]\exp(i\omega t)dt\\&=\frac{\omega^2\beta}{2\pi V}\int_{-\infty}^{\infty}G(t)\exp(-i\omega t)dt\ .\end{aligned} \tag{3.15}$$

Thus $A(\omega)$ is essentially the Fourier transform of the "*auto-moment*" of $M_x(t)$,

$$\begin{aligned}G(t)&=\langle\{M_k(t)M_x\}\rangle-\overline{M}_{0x}{}^2\\&=\langle\{M_x(t+\tau)M_x(\tau)\}\rangle-\overline{M}_{0x}{}^2\ ,\end{aligned} \tag{3.16}$$

and conversely the auto-moment, $G(t)$, is the Fourier tranform of $A(\omega)/\omega^2$:

$$G(t)=\frac{V}{\beta}\int_{-\infty}^{\infty}\frac{A(\omega)}{\omega^2}\exp(i\omega t)d\omega\ , \tag{3.17}$$

where $A(\omega)$ is understood as an even function of ω.

In fact, $M_x(t)$ can be considered to represent a stochastic process, the second moment of which is $G(t)$. Following the usual terminology used in the theory of stochastic process, the spectral density of this process will be defined by [16)]

$$\begin{aligned}I(\omega)=\lim_{T\to\infty}\frac{T}{2}\Big\langle\Big|\frac{1}{T}\int_0^T&\{M_x(t)-\overline{M}_{0x}\}\\&\times\exp(-i\omega t)dt\Big|^2\Big\rangle\ .\end{aligned} \tag{3.18}$$

Interpreting the product of the two integrals on the right hand side as a symmetrized product, we see easily that

$$\begin{aligned}I(\omega)&=\int_0^{\infty}G(t)\cos\omega t\,dt\\&=\tfrac{1}{2}\int_{-\infty}^{\infty}G(t)\exp(-i\omega t)dt\ ,\end{aligned} \tag{3.19}$$

because $G(t)$ is even in t. The inversion of Eq. (3.19) gives

$$\begin{aligned}G(t)&=\frac{2}{\pi}\int_0^{\infty}I(\omega)\cos\omega t\,d\omega\\&=\frac{1}{\pi}\int_{-\infty}^{\infty}I(\omega)\exp(i\omega t)d\omega\ .\end{aligned} \tag{3.20}$$

The auto-correlation of $M_x(t)$ is $G(t)/G(0)$. Therefore, the distribution of $A(\omega)/\omega^2$ is the spectral density of the stochastic variation of $M_x(t)$, or the Fourier transform of the autocorrelation function.

Part B. General Treatment of Resonance Absorption

§ 4. Expansion Formulae for the Automoment $G(t)$

In this section, we shall develop a method for calculating the relaxation function (2.9), which, as we have seen in the preceding sections, will allow us to obtain the susceptibilities and in particular the spectral intensity of absorbed energy. We shall, however, discuss only the auto-moment of $M_x(t)$, that is

$$\begin{aligned}G(t)&=\langle\{M_x(t+\tau)M_x(\tau)\}\rangle\\&=\tfrac{1}{2}[\langle M_x(t)M_x\rangle+\text{conjugate complex}]\ ,\end{aligned} \tag{4.1 *}$$

because we want to apply the theory, in later sections, particularly to the resonance absorption of linearly polarized radiation, and also because the generalization of the following method to the calculation of general components of the relaxation tensor is obvious.

The assumptions of our development are the following:

a) The system under consideration is described in terms of the Hamiltonian

$$\mathscr{H}=\mathscr{H}_0+\mathscr{H}'\ , \tag{4.2}$$

where the unperturbed Hamiltonian $\mathscr{H}_0$ is supposed to be such that it will give rise to sharp resonance lines well separated from one another. The perturbation $\mathscr{H}'$ will change this skeleton structure of resonance spectrum causing shifts and broadening of the main lines and the appearance of satellite lines, but it is not too strong so that the actual resonance lines are still well separated. This means that a reasonable approximation may be obtained with the use of perturbation calculation.

b) The intensity distribution of each of the perturbed resonance lines is better described by the *semi-invariants* of the distribution function rather than the *moments*. Or rather we may say that the logarithm of the Fourier transform of the intensity distribution function of each line, which as we shall show later will be separated out from the Fourier-transform of the whole spectrum, is a well-behaved function of the perturbation parameter and accordingly may be calculated by the perturbation method.

---

* The equilibrium value of $\overline{M}_x$, i.e. M_{0x}, is assumed to be zero and is omitted in Eq. (4.1).

c) The frequency range of our interest is low, that is,

$$\hbar\omega \ll kT\ . \qquad (4.3)$$

d) The perturbation $\mathcal{H}'$ has only negligible effects on the quantum-mechanical distribution function at the temperature of interest.

Let us suppose that the perturbation $\mathcal{H}'$ is proportional to an interaction constant ε, which represents, for instance, the dipolar coupling constant of two magnetic spins if $\mathcal{H}'$ is the dipolar interaction. In the limit of $\varepsilon=0$, $A(\omega)$, or $I(\omega)$, Eq. (3.14) or (3.19), is composed of a set of δ-functions according to the assumption a), and therefore $G(t)$, Eq. (4.1), is a sum of simple exponential functions:

$$\lim_{\varepsilon\to 0} G(t)=\sum_{\alpha} G_{\alpha} \exp(i\omega_{\alpha}t)\ . \qquad (4.4)$$

In the presence of the perturbation $\mathcal{H}'$, we may assume generally that the coefficients of the exponential functions on the right hand side of Eq. (4.4) become functions of t:

$$G(\varepsilon,t)=\sum_{\alpha} G_{\alpha}(\varepsilon,t) \exp(i\omega_{\alpha}t)\ , \qquad (4.5)$$

which have the limits

$$\lim_{\varepsilon\to 0} G_{\alpha}(\varepsilon,t)=G_{\alpha} \text{ (independent of } t).$$

As we shall see later, the perturbation calculation gives a natural way to expand $G(t)$ in the form of (4.5). Then each term $G_{\alpha}(\varepsilon,t)$ can be considered as the Fourier transform of the absorption peak originally centered at $\omega=\omega_{\alpha}$.

The resonance lines with finite strength ($G_{\alpha}\neq 0$) for $\varepsilon=0$, that is the absorptions appearing for the unperturbed system, will be called the *main lines*, or the resonance lines or zero-th order. The perturbation will give rise to shifts and the broadening of these lines, and also cause the appearance of other lines, called the *satellites* or the resonance lines of higher order, for which

$$\lim_{\varepsilon\to\infty} G_{\alpha}(\varepsilon,t)=0\ .$$

The decomposition of the whole expression for $G(\varepsilon,t)$ into such a sum as (4.5) is not unique. But there will be a most natural way to choose the frequencies ω_{α} and to separate the Hamiltonian into $\mathcal{H}_0$ and $\mathcal{H}'$. For instance, if the spectrum has a resolved hyperfine structure, $\mathcal{H}_0$ should contain the nuclear interaction, and, if not, this should be put into $\mathcal{H}'$.

By a proper choice of $\mathcal{H}_0$ and $\mathcal{H}'$, we may expect $G_{\alpha}(\varepsilon,t)$ to be regular in ε at least for small values of ε. The assumption b) means further that the functions $\psi_{\alpha}(\varepsilon,t)$ defined by the equation

$$G_{\alpha}(\varepsilon,t)=G_{\alpha}(\varepsilon,0)\exp\psi_{\alpha}(\varepsilon,t)\ , \qquad (4.6)$$

are regular in ε and can be calculated in power series of ε from the expansions of $G_{\alpha}(\varepsilon,t)$ obtained by a perturbation method. Then the intensity distribution of absorption lines will be calculated from

$$A(\omega)=\frac{\omega^2\beta}{2\pi V}\sum_{\alpha} G_{\alpha}(\varepsilon,0) \times\int_{-\infty}^{\infty} \exp\{\psi_{\alpha}(\varepsilon,t)-i\omega t\}dt\ , \qquad (4.7)$$

as one sees by Eq. (3.15). If we stop the perturbation calculation at some stage, the obtained approximation of $\psi_{\alpha}(\varepsilon,t)$ will give, by Eq. (4.7), a certain approximation to the intensity distribution or the line shape. Generally speaking, we cannot decide off hand how close this approximation is to reality, without referring to the detailed nature of the system in question. From a mathematical point of view, we may give a criterion of the approximation by calculating the semi-invariants of the distribution, that is the coefficients of the powers of t in the expansion of $\psi_{\alpha}(\varepsilon,t)$ in t. Namely, the approximation is good enough if the corrections to the semi-invariants from higher order perturbation are negligible compared to those obtained in that approximation. It is, however, quite remarkable that the second approximation in this line, that is the approximation to ε^2 in $\psi_{\alpha}(\varepsilon,t)$, reveals most of the interesting features of the motional narrowing in the nuclear magnetic and paramagnetic resonance absorptions, in *condensed phases*, which will be discussed in later parts of this article.

The most convenient way to obtain the expansion of $G(t)$ is to solve the equation of motion, Eq. (1.9),

$$i\hbar\dot{M}_x(t)=[M_x(t),\mathscr{H}]=[M_x(t),\mathscr{H}_0+\mathscr{H}'] \ , \tag{4.8}$$

by an expansion in $\mathscr{H}'$, which is found to be

$$M_x(t)=M_x{}^0(t)+M_x{}'(t)+\cdots+M_x{}^{(n)}(t)+\cdots \ , \tag{4.9}$$

with the general term of the form

$$M_x{}^{(n)}(t)=(i\hbar)^{-n}\int_0^t dt_1\int_0^{t_1}dt_2\cdots\int_0^{t_{n-1}}dt_n \times[M_x{}^0(t);\mathscr{H}'(t_1),\cdots,\mathscr{H}'(t_n)] \ , \tag{4.10}$$

where

$$M_x{}^0(t)=\exp(it\mathscr{H}_0/\hbar)M_x\exp(-it\mathscr{H}_0/\hbar) \ , \tag{4.12}$$

$$\mathscr{H}'(t)=\exp(it\mathscr{H}_0/\hbar)\mathscr{H}'\exp(-it\mathscr{H}_0/\hbar) \ , \tag{4.12}$$

and we have used the notation

$$[A;B,C,\cdots,K]=[\cdots[A,B]C]\cdots]K] \ , \tag{4.13}$$

for convenience. The expansion (4.9) is easily obtained in the following way. Taking the so-called interaction representation, we transform $M_x(t)$ by

$$M_x(t)=\exp(it\mathscr{H}_0/\hbar)M_x{}^*(t)\exp(-it\mathscr{H}_0/\hbar) \ . \tag{4.14}$$

Then Eq. (4.8) becomes

$$i\hbar M_x{}^*(t)=[M_x{}^*(t),\mathscr{H}'(-t)] \ . \tag{4.15}$$

Integrating both sides of this equation with the initial condition $M_x{}^*(0)=M_x$, we get

$$M_x{}^*(t)=M_x+(1/i\hbar)\int_0^t[M_x{}^*(t'),\mathscr{H}(-t')]dt' \ ,$$

which is solved by iteration to give

$$M_x{}^*(t) =M_x+\sum_{n=1}^{\infty}(i\hbar)^{-n}\int_0^t dt_n\int_0^{t_n}dt_{n-1}\cdots\int_0^{t_2}dt_1 \times[M_x;\mathscr{H}'(-t_1),\cdots,\mathscr{H}'(-t_n)] \ .$$

Inserting this into (4.14), Eq. (4.9) is proved.

The transformation from M_x to $M_x{}^*(t)$, Eq. (4.14), is the change of our representation to that which moves together with the motion described by $\mathscr{H}_0$. Thus, without the perturbation $\mathscr{H}'$ the magnetic moment M_x would be at rest in this interaction representation, which corresponds to an organized motion of the system giving rise to sharp resonance lines. The effect of the perturbation is to give a sort of randomness to the motion of the moment, which reveals itself as the broadening of the resonance. Inserting Eqs. (4.9) and (4.10) into Eq. (4.1), we get

$$G(t)=G_0(t)+G_1(t)+G_2(t)+\cdots \ , \tag{4.16}$$

where

$$G_n(t)=(i\hbar)^{-n}\int_0^t dt_1\int_0^{t_1}dt_2\cdots\int_0^{t_{n-1}}dt_n \times\langle\{[M_x{}^0(t);\mathscr{H}'(t_1),\cdots,\mathscr{H}(t_n)]M_x\}\rangle \ . \tag{4.17}$$

The general way of evaluating this expression would be as follows. First we observe that the unperturbed motion of M_x, that is $M_x{}^0(t)$, can be expanded in a Fourier series of the form,

$$M_x{}^0(t)=\sum_{\alpha}M_x(\omega_\alpha)\exp(i\omega_\alpha t) \ , \tag{4.18}$$

Similarly, the interaction representation of $\mathscr{H}'$, $\mathscr{H}'(t)$, will also be developed into a Fourier series

$$\mathscr{H}'(t)=\sum_{\alpha}\mathscr{H}'(\omega_\alpha)\exp(i\omega_\alpha t) \ , \tag{4.19}$$

if the spectrum of $\mathscr{H}'(t)$ is discrete. More generally, it is represented by a Fourier integral

$$\mathscr{H}'(t)=\int_{-\infty}^{\infty}\mathscr{H}'(\omega)\exp(i\omega t)d\omega \ , \tag{4.19a}$$

with the Fourier coefficient

$$\mathscr{H}'(\omega)=\frac{1}{2\pi}\int_{-\infty}^{\infty}\mathscr{H}'(t)\exp(-i\omega t)dt \ , \tag{4.20}$$

which reduces to

$$\mathscr{H}'(\omega)=\sum_{\alpha}\mathscr{H}'(\omega_\alpha)\delta(\omega-\omega_\alpha) \ , \tag{4.20a}$$

for the discrete cases. Since $M_x(t)$ is hermitian, $M_x(\omega_\alpha)$ and $M_x(-\omega_\alpha)$ are mutually hermite-conjugates, and the same is true for $\mathscr{H}'(\omega)$ and $\mathscr{H}'(-\omega)$. From Eqs. (4.18) and (4.19), we find at once that

$$\left.\begin{aligned}&\exp(it\mathscr{H}_0/\hbar)M_x(\omega_\alpha)\exp(-it\mathscr{H}_0/\hbar)\\&\qquad=\exp(i\omega_\alpha t)M_x(\omega_\alpha) \ ,\\&\exp(it\mathscr{H}_0/\hbar)\mathscr{H}'(\omega)\exp(-it\mathscr{H}_0/\hbar)\\&\qquad=\exp(i\omega t)\mathscr{H}'(\omega) \ ,\end{aligned}\right\} \tag{4.21a}$$

and

$$\left.\begin{aligned}&[\mathscr{H}_0,M_x(\omega_\alpha)]=\hbar\omega_\alpha M_x(\omega_\alpha) \ ,\\&[\mathscr{H}_0,\mathscr{H}'(\omega)]=\hbar\omega\mathscr{H}'(\omega) \ .\end{aligned}\right\} \tag{4.21b}$$

Using these Fourier components, $G_n(t)$, Eq. (4.17), can be expressed as

$$G_n(t)=\sum_\alpha i^{-n}\exp(i\omega_\alpha t)\int_{-\infty}^{\infty}d\omega_1\cdots\int_{-\infty}^{\infty}d\omega_n$$
$$\times g_n(t;\omega_1,\cdots,\omega_n)F_n(\omega_\alpha;\omega_1,\cdots,\omega_n), \tag{4.22}$$

where

$$F_n(\omega_\alpha;\omega_1,\cdots,\omega_n)$$
$$=\hbar^{-n}\langle\{[M_x(\omega_\alpha);\mathscr{H}'(\omega_1),\cdots,\mathscr{H}'(\omega_n)]M_x\}\rangle, \tag{4.23}$$

and

$$g_n(t;\omega_1,\cdots,\omega_n)$$
$$=\frac{1}{2\pi i}\int_{-i\infty}^{i\infty}e^{pt}[p(p-i\omega_1)(p-i\omega_1-i\omega_2)$$
$$\cdots(p-i\sum_{l=1}^{n}\omega_l)]^{-1}dp, \tag{4.24}$$

which is a Bromwitch integral commonly used in operational calculus.

Eq. (4.24) is proved as follows. The integral over the time variables in (4.17) is transformed as

$$\int_0^t dt_1\int_0^{t_1}dt_2\cdots\int_0^{t_{n-1}}dt_n\exp(i\sum_1^n\omega_l t_l)$$
$$=\int_0^t dt_1\int_0^{t_1}dt_2\cdots\int_0^{t_{n-1}}dt_n\exp[i(t_1-t_2)\omega_1$$
$$+i(t_2-t_3)(\omega_1+\omega_2)+\cdots$$
$$+i(t_{n-1}-t_n)\sum_1^{n-1}\omega_l+it_n\sum_1^n t_l]g_n(t;\omega_1,\cdots,\omega_n),$$

because the second expressions is the convolution of the functions, 1, $\exp(i\omega_1 t)$, $\exp i(\omega_1+\omega_2)t,\cdots$, and $\exp i\sum_1^n\omega_l t$. The integral representation of g_n, Eq. (4.24) is convenient for calculation. Explicit forms of these functions can be obtained from the residues at the poles of the integrand. Sometimes it proves more convenient to write g_n as a certain convolution or to simplify it by approximating the integrand of (4.24). Examples of such calculations will be shown in later sections.

Now let us examine further the structure of F_n, Eq. (4.23), and find simplifications with use of the assumptions c) and d). Using the relation

$$M_x=\sum M_x(\omega_\alpha), \tag{4.25}$$

which is seen from (4.18), we may write F_n as

$$F_n(\omega_\alpha;\omega_1,\cdots,\omega_n)=\sum_\beta F_n{}^*(\omega_\alpha,\omega_\beta;\omega_1,\cdots,\omega_n), \tag{4.26}$$

where

$$F_n{}^*(\omega_\alpha,\omega_\beta;\omega_1,\cdots,\omega_n)$$
$$=\hbar^{-n}\langle\{[M_x(\omega_\alpha);\mathscr{H}'(\omega_1),\cdots,\mathscr{H}'(\omega_n)]M_x(\omega_\beta)\}\rangle. \tag{4.26a}$$

At high temperatures, we may ignore the perturbation $\mathscr{H}'$ in the expression for the density matrix, Eq. (1.12), as has been mentioned in the assumption d), and replace it by the density matrix for the unperturbed Hamiltonian, that is

$$\rho_0\cong\exp(-\beta\mathscr{H}_0)/\mathrm{Tr}\exp(-\beta\mathscr{H}_0). \tag{4.27}$$

Then the function $F_n{}^*$, Eq. (4.26a), has an important property, that is,

$$F_n{}^*(\omega_\alpha,\omega_\beta;\omega_1,\cdots,\omega_n)=0,$$

if

$$\omega_\alpha+\omega_\beta+\omega_1+\omega_2+\cdots\cdot+\omega_n\neq0. \tag{4.28}$$

This means that the perturbation diagram connecting unperturbed levels by the matrix elements of M_x and $\mathscr{H}'$ must be closed in order to result in a non-vanishing contribution to $G(t)$. Mathematically, this is proved as follows. Nothing that the trace operation is invariant under any canonical transformation, we transform every operator, including the density matrix, (4.27), in the expression of (4.26a) by

$$A\to\exp(it'\mathscr{H}_0/\hbar)A\exp(-it'\mathscr{H}_0/\hbar).$$

Then the expression on the right hand side of (4.26a) is multiplied by

$$\exp i(\omega_\alpha+\omega_\beta+\sum_1^n\omega_l)t',$$

because of Eq. (4.21a). Since $F_n{}^*$ itself is independent of t', we must have the condition

$$\omega_\alpha+\omega_\beta+\sum_1^n\omega_l=0, \tag{4.28a}$$

in order that the function $F_n{}^*$ does not vanish.

The approximation (4.27) also shows that

$$\langle[M_x(\omega_\alpha);\mathscr{H}'(\omega_1),\cdots,\mathscr{H}'(\omega_n)]M_x(\omega_\beta)\rangle$$
$$=\exp(\hbar\omega_\beta/kT)$$
$$\times\langle M_x(\omega_\beta)[M_x(\omega_\alpha);\mathscr{H}'(\omega_1),\cdots,\mathscr{H}'(\omega_n)]\rangle, \tag{4.29}$$

owing to the relation

$$\exp(\beta\mathscr{H}_0)M_n(\omega_\gamma)\exp(-\beta\mathscr{H}_0)$$
$$=\exp(\beta\hbar\omega_\gamma)M_x(\omega_\gamma). \tag{4.30}$$

Thus we can put

$$F_n^*(\omega_\alpha,\omega_\beta;\omega_1,\cdots,\omega_n)$$
$$\simeq\hbar^{-n}\langle[M_x(\omega_\alpha);\mathscr{H}'(\omega_1),\cdots,\mathscr{H}'(\omega_n)]M_x(\omega_\beta)\rangle, \tag{4.31}$$

if $\hbar\omega_\beta\ll kT$. We remark further that

$$F_n^*(\omega_\alpha,\omega_\beta;\omega_1,\cdots,\omega_n)$$
$$=(-)^{n-k}\hbar^{-n}\langle[M_x(\omega_\alpha);\mathscr{H}'(\omega_1),\cdots,\mathscr{H}'(\omega_k)]$$
$$\times[M_x(\omega_\beta);\mathscr{H}'(\omega_n),\cdots,\mathscr{H}'(\omega_{k+1})]\rangle, \tag{4.32}$$

if ω_{k+1}, ω_{k+2}, $\cdots$ and ω_n are all low frequencies. If some of these frequencies are high, which can happen even if the temperature is high enough to allow the approximation (4.31), the relation (4.32) is no longer true.

These high frequency components, however, will produce only small effects on the low frequency parts of the auto-moment of M_x, because Eq. (4.24) shows that their contribution is in the order of the ratio of the low frequency to the high frequency. Therefore, if the high frequency components of $\mathscr{H}'(t)$ are definitely separated from its low frequency parts, we can, at least to first approximation, neglect those high frequency components in the calculation of $G(t)$ by Eq. (4.22). Or, if the amplitudes of the high frequency components of $\mathscr{H}'(t)$ is small enough, we may use Eq. (4.32) for the calculation of the low frequency parts of $G(t)$. In other cases, one has to be careful about the approximations, (4.31) and (4.32).

§ 5. The Moment Method. The Secular and Non-Secular Perturbation

The moment method, introduced by Broer[5], Van Vleck[6] and Pryce and Stevens[10], is the most common and basic method used so far for the discussions of the line shapes of magnetic resonance absorption. The moment expansion is essentially an expansion of the auto-moment, $G(t)$, in powers of t, because the expansion coefficients give, by Eq. (3.15), the moments of the distribution of the absorption intensity. Using the expansion,

$$\left.\begin{aligned}
M_x(t)&=M_x(0)+t\dot{M}_x(0)+\cdots\\
&\qquad+\frac{t^n}{n!}\left(\frac{d^n}{dt^n}M_x\right)_0+\cdots\\
\dot{M}_x(0)&=(i\hbar)^{-1}[M_x,\mathscr{H}],\\
\left(\frac{d^n}{dt^n}M_x\right)&=(i\hbar)^{-n}[M_x;\mathscr{H},\cdots,\mathscr{H}],
\end{aligned}\right\} \tag{5.1}$$

we have

$$G(t)=\sum_n\frac{t^n}{n!}\left\langle\left\{\left(\frac{d^n}{dt^n}M_x\right)_0M_x\right\}\right\rangle. \tag{5.2}$$

Therefore

$$\mu_n=\left\langle\left\{\left(\frac{d^n}{dt^n}M_x\right)_0M_x\right\}\right\rangle, \tag{5.3}$$

is the n-th moment of the intensity distribution.

As is well known, the moment method is more complicated than is implied by simple formulae like (5.3). As a matter of fact, we are not interested in such moments as (5.3), which are the moments of the whole spectrum. On the contrary, our interest is usually limited to a certain line, or a certain group of lines which are observed experimentally. Thus, we want to calculate the moments of the intensity distribution associated with this particular absorption. This, of course, assumes that the absorption lines of our interest are well separated from other parts of the spectrum (assumption a, § 4). The contributions from the latter have to be carefully eliminated in the calculation of the moments. This has been particularly emphasized by Van Vleck[5] for the case of dipolar broadening, and formulated more generally by Pryce and Stevens[10].

Our expansion method, developed in the preceding section, is primarily an expansion in the perturbation, and not an expansion in t. Nevertheless, it is essentially a moment expansions around the resonance lines, provided that the spectrum of the perturbation, (4.20), is discrete Eq. (4.20a). This fact is to be seen from Eqs. (4.22) and (4.24), because the function $g_n(t;\omega_1,\cdots,\omega_n)$ is then of the form

$$g_n=\sum_k\sum_m^n c_{k,m}t^m\exp(i\omega_k t), \tag{5.4}$$

and the integration over the frequencies in Eq. (4.22) is replaced by the sum over the discrete spectrum of $\mathscr{H}'(t)$. Therefore, $G(\varepsilon,t)$ in Eq. (4.5) will be a power series in t, the highest powers of t being n or smaller if the expansion (4.16) is terminated at n-th order of $\mathscr{H}'$. Thus, we obtain the moment expansion of each of the resonance lines by picking up the particular terms with the desired exponent from the function $G(t)$. The exponential functions in (5.4) are used as the indicators to collect the right terms.

The component $\mathcal{H}(0)$, in Eq. (4.20a), is called the *secular* or the *semi-diagonal* part of the perturbation, and commutes with the unperturbed Hamiltonian $\mathcal{H}_0$. Other components $\mathcal{H}'(\omega_\alpha)(\omega_\alpha \neq 0)$ are the *non-secular* parts of the perturbation. Explicit forms of these terms will be found either directly from the expression of the perturbation, or will be expressed with the use of certain projecting operators.

In this article, we shall only discuss some general aspects of the moment method, without going into any particular or detailed applications. First, we note that there are general relations between the orders of the moments, of the resonance lines, and of the perturbation.

An obvious example is that the term in the order $\mathcal{E}^n$ in the n-th moment of zero-th order resonance line comes only from the secular part of the perturbation. This is because $t^n/n!$ appears in g_n, Eq. (4.24), if and only if $\omega_1=\omega_2=\cdots=\omega_n=0$.

Similarly, the t^{n-1} term will appear in g_n, if and only if it has the form

$$\begin{aligned} g_n(t) &= \frac{1}{2\pi i}\int_{-i\infty}^{i\infty} \exp(pt)p^{-n}(p-i\omega_\gamma)^{-1}dp \\ &= \int_0^t \frac{1}{(n-1)!}(t-t')^{n-1}\exp(i\omega_\gamma t')dt' \\ &= \frac{\exp(i\omega_\gamma t)}{(i\omega_\gamma)^n} - \sum_{m=0}^{n-1}\frac{t^{n-1-m}}{(n-1-m)!(i\omega_\gamma)^{m+1}}, \end{aligned} \tag{5.5}$$

or

$$\begin{aligned} g_n(t) &= \frac{1}{2\pi i}\int_{-i\infty}^{i\infty} \exp(pt)p^{-1}(p-i\omega_\gamma)^{-n}dp \\ &= \int_0^t \frac{1}{(n-1)!}(t-t')^{n-1}\exp(i\omega_\gamma(t-t'))dt' \\ &= (-i\omega_\gamma)^{-n} - \exp(i\omega_\gamma t) \\ &\quad \times \sum_{m=0}^{n-1}\frac{t^{n-1-m}}{(n-1-m)!(-i\omega_\gamma)^{m+1}}. \end{aligned} \tag{5.6}$$

Considering Eqs. (4.22), (4.26), and the condition (4.28a), one sees at once that the type of term in Eq. (5.5) occurs for the following combinations of the secular and non-secular perturbations;

1. $\omega_\alpha+\omega_\beta=0$:

$$\left.\begin{aligned} &\omega_1=-\omega_2=\omega_\gamma, \omega_3=\cdots\cdots=\omega_n=0, \\ &\omega_1=0, \omega_2=-\omega_3=\omega_\gamma, \omega_4\cdots\cdots=\omega_n=0 \\ &\cdots\cdots \\ &\omega_1=\cdots\cdots=\omega_{n-2}=0, \quad \omega_{n-1}=-\omega_n=\omega_\gamma. \end{aligned}\right\} \tag{5.5a}$$

2. $\omega_\alpha+\omega_\beta+\omega_\gamma=0$:

$$\omega_1=\cdots\cdots=\omega_{n-2}=0, \quad \omega_{n-1}=-\omega_n=\omega_\gamma, \tag{5.5b}$$

and similarly the type of (5.6) for

$$\left.\begin{aligned} &\omega_\alpha+\omega_\beta+\omega_\gamma=0, \quad \omega_1=\omega_\gamma\neq 0, \\ &\omega_2=\cdots\cdots=\omega_n=0. \end{aligned}\right\} \tag{5.6a}$$

Eq. (5.5) shows that the non-secular perturbation $\mathcal{H}'(\omega_\gamma)(\omega_\gamma\neq 0)$ contributes, in these combinations with the secular perturbation, to the $(n-r)$-th moment of the main lines in the order of $\mathcal{E}^n$, in proportion to $|\omega_\gamma|^{-r}$. At the same time, according to Eq. (5.6), it gives the same effect to the satellite at $\omega_\alpha+\omega_\gamma$ if there exists a frequency ω_β of M_x satisfying the condition $\omega_\alpha+\omega_\beta+\omega_\gamma=0$. For example, the non-secular perturbation comes into the first order calculation ($n=1$) only in the form of (5.6a). The example of the second order calculation will be given in the following.

One may proceed in this way to see how the non-secular perturbation will give effects to the moments in higher order combinations with the secular part. Consideration of this kind is useful in general to find out particular types of perturbation contributing to the moment one wants to calculate in a certain approximation. But we shall not go further into details.

Perhaps it would be instructive to examine a little further the first and the second approximations. The first order perturbation term of $G(t)$, (4.5), is easily found to be

$$\begin{aligned} G_1(t) = \sum_\alpha \exp(i\omega_\alpha t)\Big\{ &-itF_1^*(\omega_\alpha, -\omega_\alpha; 0) \\ &-\sum_\beta \frac{1}{\omega_\alpha+\omega_\beta}\Big[F_1^*(\omega_\alpha, \omega_\beta; -\omega_\alpha-\omega_\beta) \\ &+F_1^*(-\omega_\beta, -\omega_\alpha; \omega_\alpha+\omega_\beta)\Big]\Big\}, \end{aligned} \tag{5.7}$$

where

$$\begin{aligned} &F_1^*(\omega_\alpha, -\omega_\alpha; 0) \\ &\quad = \hbar^{-1}\langle\{[M_x(\omega_\alpha), \mathcal{H}'(0)]M_x(-\omega_\alpha)\}\rangle \\ &\quad \cong \hbar^{-1}\langle\mathcal{H}'(0)[M_x(-\omega_\alpha), M_x(\omega_\alpha)]\rangle, \end{aligned} \tag{5.8}$$

and

$$\begin{aligned} &F_1^*(\omega_\alpha, \omega_\beta; -\omega_\alpha-\omega_\beta)+F_1^*(-\omega_\beta, -\omega_\alpha; \omega_\alpha+\omega_\beta) \\ &\quad \cong \hbar^{-1}\langle\mathcal{H}(-\omega_\alpha-\omega_\beta)[M_x(\omega_\beta), M_x(\omega_\alpha)] \\ &\qquad + [M_x(-\omega_\alpha), M_x(-\omega_\beta)]\mathcal{H}'(\omega_\alpha+\omega_\beta)\rangle, \end{aligned} \tag{5.8a}$$

are real numbers as they ought to be. Obviously, the first order perturbation never gives rise to satellite lines. Its effect is shifts due to the secular part and a modification of intensities of main lines by the non-secular part.

Similarly the second order perturbation term,

$$G_2(t)=\sum_{\alpha}\sum_{\beta}\sum_{\omega_\alpha+\omega_\beta+\omega_\gamma+\omega_\delta=0} i^{-2}\exp(i\omega_\alpha t)g_2(t;\omega_\gamma,\omega_\delta)F_2{}^*(\omega_\alpha,\omega_\beta;\omega_\gamma,\omega_\delta)\ , \tag{5.9}$$

is shown to give

$$\begin{aligned}G_2(t)=&-\sum_{\alpha}\exp(i\omega_\alpha t)\Bigg[\tfrac{1}{2}t^2F_2{}^*(\omega_\alpha,-\omega_\alpha;0,0)+\sum_{\omega_\gamma\neq0}\left(\frac{1}{\omega_\gamma{}^2}+\frac{it}{\omega_\gamma}\right)F_2{}^*(\omega_\alpha,-\omega_\alpha;\omega_\gamma,-\omega_\gamma)\\&+\sum_{\omega_\beta\neq\omega_\alpha}\frac{1}{(\omega_\alpha+\omega_\beta)^2}\Big\{-F_2{}^*(\omega_\alpha,\omega_\beta;-\omega_\alpha-{}_\beta,0)+F_2{}^*(\omega_\alpha,\omega_\beta;0,-\omega_\alpha-\omega_\beta)\\&\qquad-F_2(-\omega_\beta,-\omega_\alpha;0,\omega_\alpha+\omega_\beta)+F_2{}^*(-\omega_\beta,-\omega_\alpha;\omega_\alpha+\omega_\beta,0)\Big\}\\&+\sum_{\omega_\beta\neq-\omega_\alpha}\sum_{\omega_\gamma\neq0}\frac{1}{\omega_\gamma(\omega_\alpha+\omega_\beta)}\Big\{F_2{}^*(\omega_\alpha,\omega_\beta;\omega_\gamma,-\omega_\alpha-\omega_\beta-\omega_\gamma)\\&\qquad+F_2{}^*(-\omega_\beta,\omega_\alpha;\omega+{}_\alpha\omega_\beta+\omega_\gamma,-\omega_\gamma)\Big\}\\&-it\sum_{\omega_\beta\neq\omega_\alpha}\frac{1}{\omega_\alpha+\omega_\beta}\Big\{F_2{}^*(\omega_\alpha,\omega_\beta;0,-\omega_\alpha-\omega_\beta)+F_2{}^*(-\omega_\beta,-\omega_\alpha;\omega_\alpha+\omega_\beta,0)\Big\}\Bigg]\\&+\sum_{\alpha}\sum_{\omega_\gamma\neq0}\exp(i(\omega_\alpha+\omega_\gamma)t)\Big\{\frac{1}{\omega_\gamma{}^2}F_2{}^*(\omega_\alpha,-\omega_\alpha;\omega_\gamma,-\omega_\gamma)\\&+\sum_{\omega_\beta\neq-\omega_\alpha}\frac{1}{\omega_\gamma(\omega_\alpha+\omega_\beta+\omega_\gamma)}F_2{}^*(\omega_\alpha,\omega_\beta;\omega_\gamma,-\omega_\alpha-\omega_\beta-\omega_\gamma)\Big\}\ .\end{aligned}\tag{5.10}$$

We observe that the coefficients of it and t^2 in the expressions multiplying the exponential functions are all real, because of the relation

$$\overline{F_2{}^*(\omega_\alpha,\omega_\beta;\omega_\gamma,\omega_\delta)}=F_2{}^*(-\omega_\beta,-\omega_\alpha;-\omega_\delta,-\omega_\gamma)\ ,$$

which holds in the approximatiom of (4.31). Eq. (5.10) shows that the second order perturbation gives the second moment from the secular part of the perturbation and the corrections to the first moment (shift) and the zero-th moment (integrated intensity) for the main lines from the non-secular parts, which contributes nothing to the second moments. The non-secular perturbation also gives rise to satellites lines at $\omega_\alpha+\omega_\gamma$, the intensities of which are inversely proportional to the second power of the frequency difference of the satellite and the main line, if we neglect the last term of (5.10).

The expression, (5.10), is pretty complicated because of the cross terms with unsymmetrical combinations of frequencies ($\omega_\alpha+\omega_\beta\neq0$). Under most circumstances, however, these terms will vanish because of the symmetries of the perturbation and of the structure of the system. This is actually so, for instance, in nuclear magnetic and paramagnetic cases when the distribution of spins is completely random, or highly symmetric with regard to the direction of the applied constant magnetic field. If we omit these unsymmetrical terms from the expression of (5.10), the second order terms of $G(t)$ is simplified to

$$\begin{aligned}G(t)=&\sum_{\alpha}\langle|M_x(\omega_\alpha)|^2\rangle\Big\{1-\sum_{\omega_\gamma\neq0}\sigma_{\alpha\gamma}{}^2\\&\times\left(\frac{1}{\omega_\gamma{}^2}+\frac{it}{\omega_\gamma}\right)-\tfrac{1}{2}\sigma_{\alpha0}{}^2t^2\Big\}\exp(i\omega_\alpha t)\\&+\sum_{\alpha}\sum_{\omega_\gamma\neq0}\langle|M_x(\omega_\alpha)|^2\rangle\\&\times\frac{\sigma_{\alpha\gamma}{}^2}{\omega_\gamma{}^2}\exp(i(\omega_\alpha+\omega_\gamma)t)\ ,\end{aligned}\tag{5.11}$$

where

$$\begin{aligned}\sigma_{\alpha0}{}^2=&F_2{}^*(\omega_\alpha,-\omega_\alpha,;0,0)/\langle\{M_x(\omega_\alpha)M_x(-\omega_\alpha)\}\rangle\\&\simeq\hbar^{-2}\langle|[M_x(\omega_\alpha),\mathscr{H}'(0)]|^2\rangle/\langle|M_x(\omega_\alpha)^2|\rangle\ ,\end{aligned}\tag{5.12}$$

and

$$\begin{aligned}&\sigma_{\alpha\gamma}{}^2\\&=F_2{}^*(\omega_\alpha,-\omega_\alpha;\omega_\gamma,-\omega_\gamma)/\langle\{M_x(\omega_\alpha)M_x(-\omega_\alpha)\}\rangle\\&\simeq\hbar^{-2}\langle|[M_x(\omega_\alpha),\mathscr{H}'(\omega_\gamma)]|^2\rangle/\langle|M_x(\omega_\alpha)|^2\rangle\ ,\end{aligned}\tag{5.12}$$

are both positive. If the intensity is calculated with the use of Eq. (4.7) inserting $\psi_\alpha(\mathcal{E},t)$ obtained from (5.11), it will be

$$
\begin{aligned}
&A(\omega)\\
&=\sum_{\alpha}\omega^{2}\frac{\langle|M_{x}(\omega_{\alpha})|^{2}\rangle}{VkT}\left(1-\sum_{\omega_{\gamma}\neq 0}\frac{\sigma_{\alpha\gamma}{}^{2}}{\omega_{\gamma}{}^{2}}\right)\frac{1}{\sqrt{2\pi}\sigma_{\alpha 0}}\\
&\qquad\times\exp\left\{-\frac{1}{2\sigma_{0\alpha}{}^{2}}\left(\omega-\omega_{\alpha}+\sum_{\omega_{\gamma}\neq 0}\frac{\sigma_{\alpha\gamma}{}^{2}}{\omega_{\gamma}}\right)^{2}\right\}\\
&+\sum_{\alpha}\sum_{\omega_{\gamma}\neq 0}\frac{\omega^{2}\langle|M_{x}(\omega_{\alpha})|^{2}\rangle}{VkT}\frac{\sigma_{\alpha\gamma}{}^{2}}{\omega_{\gamma}{}^{2}}\delta(\omega-\omega_{\alpha}-\omega_{\gamma})\,. \qquad (5.13)
\end{aligned}
$$

Namely the spectrum is the Gaussian lines shifted by $\sum_{\gamma}\sigma_{\alpha\gamma}{}^{2}/\omega_{\gamma}$ from the original centers ω_{α} and broadened to the breadth $\sigma_{\alpha 0}$ and satellite lines with the relative intensities $\sigma_{\alpha\gamma}{}^{2}/\omega_{\gamma}{}^{2}$ at $\omega_{\alpha}+\omega_{\gamma}$. The appearance of a satellite line is thus connected with a shifts of the main line as though it repels the latter. This is easily understood remembering that the total intensity and the first moment are invariant, if the satellite contributions are included. It is well known that in simple cases of nuclear magnetic and paramagnetic resonance the satellite at the double frequency is caused by the dipolar interactions with an intensity inversely proportional to the square of the Larmor frequency. The above statements are just generalizations of this fact.

The perturbation calculation will break down if there exist one or more satellites close to a main line, because, then, the correction due to the perturbation will become very large. Reasonable measures of the criterion for the break would be

$$\omega_{\gamma}\lesssim\sigma_{\alpha\gamma}\,,\qquad\text{or}\qquad\omega_{\gamma}\lesssim\sigma_{\alpha 0}\,. \qquad (5.14)$$

Then, the perturbation $\mathscr{H}'(\omega_{\gamma})$ should be considered as nearly secular rather than non-secular. It would be more realistic to treat the main line ω_{α} and the satellites near by as a whole. Mathematically this means that the function $g_{2}(t,\omega_{\gamma},-\omega_{\gamma})$ in Eq. (5.9) is evaluated by taking ω_{γ} very small. Thus we simply attribute the second moment $\sigma_{\alpha 0}{}^{2}+\sigma_{\alpha\gamma}{}^{2}$ to this mixture.

As we have seen, the most important terms in the moments of a main line are from the secular perturbation, provided that none of the frequencies belonging to the non-secular perturbations is too small. The intensity distribution of main lines, then, could be reproduced by these dominant terms of the moments as a certain approximation, which we may call the *secular* or the *adiabatic* approximation. It is easy to show that the auto-moment $G(t)$ in this approximation is simply given by

$$
\begin{aligned}
&G(t)\sim G^{0}(t)\\
&\quad=\langle\exp(it\mathscr{H}'(0)/\hbar)M_{x}{}^{0}(t)\exp(-it\mathscr{H}'(0)/\hbar)M_{x}\rangle\\
&\quad=\sum_{\alpha}\langle\{\exp(it\mathscr{H}'(0)/\hbar)M_{x}(\omega_{\alpha})\\
&\qquad\times\exp(-it\mathscr{H}'(0)/\hbar\cdot M_{x}(-\omega_{\alpha})\}\rangle\exp(i\omega_{\alpha}t)\,. \qquad (5.15)
\end{aligned}
$$

Unfortunately, however, exact calculations of this are not always easy, although the calculation of low order moments would be practical. It will be important, by the condition (5.14), to check the secular assumption by comparing the relative magnitudes of the square roots of the second moments and the frequencies of the non-secular perturbation.

The next step of approximation would be to take account of non-secular perturbations appearing in the combinations of (5.5a, b) and (5.6a). All of these contributions can be summed up to give a correction to (5.15). The explicit formula is fairly complicated and will be omitted here.

§ 6. Motional Narrowing

6a) General Formulation of the Problem

It is well known that the dipolar broadening in nuclear magnetic and paramagnetic resonance lines is affected by the presence of other modes of motion of the system. The thermal motion of the nuclei in the nuclear magnetic case, and the stirring of paramagnetic spins due to their exchange coupling will result in the averaging out of the dipolar interaction, and consequently in a decrease of the width. This narrowing process will be generally accompanied by another effect, which causes an increase of the width. This is called the spin-lattice relaxation, or the 10/3 effect. In the following, we shall treat this kind of resonance phenomenon from a somewhat general point of view, without referring to any specified type of system. It is helpful to understand the universal nature of the motional effect in resonance absorption. Particular applications will be discussed in later sections.

As a general model of a system, which shows the motional effect, we assume the unperturbed Hamiltonian can be divided into two parts:

$$\mathscr{H}_{0}=\mathscr{H}_{1}+\mathscr{H}_{2}\,, \qquad (6.1)$$

which satisfy the conditions

$$[\mathscr{H}_1,\mathscr{H}_2]=0\ , \qquad (6.1a)$$

$$[\mathscr{H}_2,M_x]=0\ . \qquad (6.1b)$$

In other words, the unperturbed motion of the system essentially consists of two kinds of modes. The first mode, represented by $\mathscr{H}_1$, is assumed to be not commutable with the moment operator M_x, so that it causes a motion of the moment, giving rise to the resonance lines in zero-th order. The second mode of motion, represented by $\mathscr{H}_2$, has in itself no effect on the motion of M_x and also is separated from the first mode. The resonance lines are distorted by the perturbation $\mathscr{H}'$, resulting in shifts, broadening the appearance of satellites and so forth. Naturally, this distortion will be influenced by $\mathscr{H}_2$, which is the motional effect of the resonance to be discussed here.

According to our assumptions, (6.1), the Fourier decomposition of the unperturbed motion of M_x and $\mathscr{H}'(t)$, Eqs. (4.18) and (4.19), can be written as follows. The unperturbed motion of the moment M_x is expanded as

$$\begin{aligned}M_x(t)&=\exp(it\mathscr{H}_0/\hbar)M_x\exp(-it\mathscr{H}_0/\hbar)\\&=\exp(it\mathscr{H}_1/\hbar)M_x\exp(-it\mathscr{H}_1/\hbar)\\&=\sum_\alpha M_x(\omega_\alpha)\exp(i\omega_\alpha t)\ ,\end{aligned} \qquad (6.2)$$

where the Fourier component $M_x(\omega_\alpha)$ satisfy the relations;

$$\left.\begin{aligned}&[\mathscr{H}_1,M_x(\omega_\alpha)]=\hbar\omega_\alpha M_x(\omega_\alpha)\ ,\\&\exp(it\mathscr{H}_1/\hbar)M_x(\omega_\alpha)\exp(-it\mathscr{H}_1/\hbar)\\&\qquad=\exp(i\omega_\alpha t)M_x(\omega_\alpha)\ ,\\&[\mathscr{H}_2,M_x(\omega_\alpha)]=0\ .\end{aligned}\right\} \qquad (6.3)$$

Similarly

$$\begin{aligned}\mathscr{H}'(t)&=\exp(it\mathscr{H}_0/\hbar)\mathscr{H}'\exp(-it\mathscr{H}_0/\hbar)\\&=\exp(it\mathscr{H}_2/\hbar)(\exp(it\mathscr{H}_1/\hbar)\mathscr{H}'\\&\quad\times\exp(-it\mathscr{H}_1/\hbar))\exp(-it\mathscr{H}_2/\hbar)\\&=\sum_\alpha\exp(i\omega_\alpha t)\mathscr{H}_\alpha'(t)\ ,\end{aligned} \qquad (6.4)$$

where we have put

$$\exp(it\mathscr{H}_1/\hbar)\mathscr{H}'\exp(-it\mathscr{H}_1/\hbar)=\sum\mathscr{H}_\alpha'\exp(i\omega_\alpha t)\ , \qquad (6.4a)$$

and

$$\exp(it\mathscr{H}_2/\hbar)\mathscr{H}_\alpha'\exp(-it\mathscr{H}_2/\hbar)=\mathscr{H}_\alpha'(t)\ . \qquad (6.4b)$$

We see that

$$\mathscr{H}'=\sum_\alpha\mathscr{H}_\alpha'\ , \qquad (6.5)$$

is the decomposition of $\mathscr{H}'$ referred to the mode $\mathscr{H}_1$, and $\mathscr{H}'(t)$, Eq. (6.4b), represents the development of $\mathscr{H}_\alpha'$ in time caused by the mode $\mathscr{H}_2$.

Now we shall calculate the expansion terms of $G(t)$ up to the second, with the assumptions mentioned at the beginning of § 4. The general term of the expansion is

$$\begin{aligned}G_n(t)=&\sum_\alpha\sum_\beta\exp(i\omega_\alpha t)\int_0^t dt_1\int_0^{t_1}dt_2\cdots\int_0^{t_{n-1}}dt_n\\&\times(i\hbar)^{-n}\sum_{\gamma,\cdots\nu}\exp(i(\omega_\gamma t_1+\cdots+\omega_\nu t_n))\\&\times\langle\{[M_x(\omega_\alpha);\mathscr{H}_\gamma'(t_1),\cdots,\mathscr{H}_\nu'(t_n)]M_x(\omega_\beta)\}\rangle\ .\end{aligned} \qquad (6.6)$$

By the relations (6.3), we see that each term vanishes after averaging unless the condition

$$\omega_\alpha+\omega_\beta+\omega_\gamma+\cdots+\omega_\nu=0\ , \qquad (6.7)$$

is satisfied. This is seen by a reasoning similar to that we used for the condition (4.28a). With this condition, the integrand of (6.6) is invariant to a simultaneous addition of arbitrary constant t_0. This invariance is used in the following calculations.

Thus we find at once the zero-th order term to be

$$\begin{aligned}G_0(t)&=\sum_\alpha\exp(i\omega_\alpha t)\langle\{M_x(\omega)_\alpha M_x(-\omega_\alpha)\}\rangle\\&=\sum_\alpha\exp(i\omega_\alpha t)\langle|M_x(\omega_\alpha)|^2\rangle\ .\end{aligned} \qquad (6.8)$$

The first order term is

$$\begin{aligned}G_1(t)=&\sum_\alpha\sum_\beta\exp(i\omega_\alpha t)\int_0^t dt_1\\&\times\exp(-i(\omega_\alpha+\omega_\beta)t)(i\hbar)^{-1}\\&\times\langle\{[M_x(\omega_\alpha),\mathscr{H}'_{-\alpha-\beta}(0)]\cdot M_x(\omega_\beta)\}\rangle\ ,\end{aligned} \qquad (6.9)$$

which is idential with (5.7) after integration. The motional effect does not come into the first order perturbation.

The second order term is now

$$\begin{aligned}G_2(t)=&\sum_{\omega_\alpha+\omega_\beta+\omega_\gamma+\omega_\delta=0}\sum\sum\exp(i\omega_\alpha t)\\&\times\int_0^t dt_1\int_0^{t_1}dt_2\exp(i(\omega_\gamma t_1+\omega_\delta t_2)(i\hbar)^{-2}\\&\times\langle\{[M_x(\omega_\alpha);\mathscr{H}_\gamma'(t_1-t_2),\mathscr{H}_\delta'(0)]\cdot M_x(\omega_\beta)\}\rangle\ ,\end{aligned} \qquad (6.10)$$

which contains various combinations of ω_α, ω_β, ω_γ, and ω_δ, exactly in the same way as Eq. (5.10). For simplicity we neglect here terms other than the combinations of the type

$(\omega_\alpha, -\omega_\alpha, \omega_\gamma, -\omega_\gamma)$, because the other terms are negligible for most cases. Then the second order term (6.10) has the form

$$\begin{aligned} &G_2(t) \\ &=\sum_\alpha\sum_\gamma \exp(i\omega_\alpha t)\int_0^t dt_1\int_0^{t_1} dt_2 \\ &\qquad\qquad\times\exp(i\omega_\gamma(t_1-t_2))(i\hbar)^{-2} \\ &\quad\times\langle\{[M_x(\omega_\alpha);\mathscr{H}_\gamma'(t_1-t_2),\mathscr{H}_{-\gamma}'(0)]\cdot M_x(-\omega_\alpha)\}\rangle \\ &=\sum_\alpha\sum_\gamma \exp(i\omega_\alpha t)\int_0^t (t-\tau)\exp(t\omega_\gamma\tau)d\tau(i\hbar)^{-2} \\ &\quad\times\langle\{[M_x(\omega_\alpha);\mathscr{H}_\gamma'(\tau),\mathscr{H}_{-\gamma}'(0)]\cdot M_x(-\omega_\alpha)\}\rangle\,. \end{aligned} \tag{6.11}$$

Now we define the relaxation functions $\overline{f_{\alpha\gamma}}(\tau)$ by

$$\begin{aligned} &\sigma_{\alpha\gamma}^2 f_{\alpha\gamma}(\tau) \\ &=\frac{\langle\{[M_x(\omega_\alpha);\mathscr{H}_\gamma'(\tau),\mathscr{H}_{-\gamma}'(0)]M_x(-\omega_\alpha)\}\rangle}{\hbar^2\langle\{M_x(\omega_\alpha)M_x(-\omega_\alpha)\}\rangle}\,, \end{aligned} \tag{6.12}$$

where $\sigma_{\alpha\gamma}^2$ are the same quantities as are introduced by Eqs. (5.12) and (5.12a). Then Eq. (6.11) is written as

$$\begin{aligned} G_2(t)=&-\sum_\alpha\sum_\gamma \exp(i\omega_\alpha t)\langle|M_x(\omega_\alpha)|^2\rangle \\ &\times\int_0^t (t-\tau)\exp(i\omega_\gamma\tau)d\tau\,\sigma_{\alpha\gamma}^2 f_{\alpha\gamma}(\tau)\,. \end{aligned} \tag{6.13}$$

This is the equation we want to use for the discussion of the motional effect.

Neglecting the effect of the high frequency components of $\mathscr{H}_\gamma'(t)$, we may write (6.12) as

$$\begin{aligned} &f_{\alpha\gamma}(\tau) \\ &\quad=\frac{\langle\{[M^x(\omega_\alpha),\mathscr{H}_\gamma'(\tau)]\,[\mathscr{H}_{-\gamma}'(0),M_x(-\omega_\alpha)]\}\rangle}{\langle|[M_x(\omega_\alpha),\mathscr{H}_\gamma'(0)]|^2\rangle}\,, \end{aligned} \tag{6.14}$$

which shows the symmetrical properties of $f_{\alpha\gamma}(\tau)$;

$$\overline{f_{\alpha\gamma}(\tau)}=f_{-\alpha,-\gamma}(\tau)=f_{\alpha\gamma}(-\tau)\,. \tag{6.15}$$

Hence we can divide $f_{\alpha\gamma}(\tau)$ into its real and imaginary parts;

$$\left.\begin{aligned} &f_{\alpha\gamma}(\tau)=\mathrm{Re}\,f_{\alpha\gamma}(\tau)+i\,\mathrm{Im}\,f_{\alpha\gamma}(\tau)\,, \\ &\mathrm{Re}\,f_{\alpha\gamma}(\tau)=\tfrac{1}{2}(f_{\alpha\gamma}(\tau)+f_{\alpha\gamma}(-\tau))\,, \\ &\mathrm{Im}\,f_{\alpha\gamma}(\tau)=1/2i(f_{\alpha\gamma}(\tau)-f_{\alpha\gamma}(-\tau))\,, \end{aligned}\right\} \tag{6.16}$$

where the real part is even in τ, and the imaginary part is odd in τ.

The contribution from the secular perturbation ($\omega_\gamma=0$) to $G_2(t)$ and that from the non-secular perturbation ($\omega_\gamma\neq0$) may be called the *secular* effect and the *non-secular* effect respectively. They are often called also the *adiabatic* and *non-adiabatic* effects. In the static case ($\mathscr{H}_2=0$, $f_{\alpha\gamma}(\tau)=$constant) the secular effect is the broadening of the main line ω_α giving the second moment $\sigma_{\alpha0}^2$ while the non-secular effect is the shift and intensity decrease of the main lines and the appearance of satellites (see Eq. (5.13)).

6b) The Secular Effect

Since the first order perturbation, (6.9), is responsible only for a shift of the main lines, we may omit it from our consideration, and we concentrate our attention on the second order perturbation effect. Then, according to our method described in § 4, the secular effect is now expressed by the generating function,

$$\begin{aligned} \phi_{\alpha0}(t)&=\exp\psi_{\alpha0}(t) \\ &=\exp\left\{-\sigma_{\alpha0}^2\int_0^t(t-\tau)f_{\alpha0}(\tau)d\tau\right\}\,, \end{aligned} \tag{6.17}$$

which gives

$$\mathrm{I}_{\alpha0}(\omega)=\frac{1}{2\pi}\int_{-\infty}^{\infty}\exp(\psi_{\alpha0}(t)-i\omega t)dt\,, \tag{6.17a}$$

for the line contour of the main line affected by the adiabatic motional effect.

The expansion of $\psi_{\alpha0}(t)$ in powers of t provides us the semi-invariants of the distribution, which are defined as the coefficients of the expansion. It should be noticed that the semi-invariants are proportional to $\sigma_{\alpha0}^2$, that is to say, they are of the second order with respect to the perturbation $\mathscr{H}'$. Thus, if the perturbation is actually small, the generating function $\phi_{\alpha0}(t)$, (6.17), can be regarded as a good approximation. The even order semi-invariants are determined by Re $f_{\alpha0}(\tau)$, and the odd order semi-invariants by Im $f_{\alpha0}(\tau)$. The existence of the semi-invariants or the moments higher than the second is not necessarily assured. Namely, if $f_{\alpha0}(\tau)$ is not analytical around $\tau=0$, they cannot be defined.

If $f_{\alpha0}(\tau)$ is analytic and is developed as

$$f_{\alpha0}(\tau)=1+\sum_{n=1}^{\infty}\frac{c_{2n}\tau^{2n}}{(2n)!}+i\sum_{n=0}^{\infty}\frac{c_{2n+1}\tau^{2n+1}}{(2n+1)!}\,, \tag{6.18}$$

we find the semi-invariants

$$\kappa_2=\sigma_{\alpha0}^2\,,\quad \kappa_{2n+2}=\sigma_{\alpha0}^2c_{2n}\,,\quad \kappa_{2n+3}=\sigma_{\alpha0}^2c_{2n+1}\,. \tag{6.19}$$

In particular, the second moment is the same as that in the static case, thus uninfluenced by the motional effect. This fact is not dependent on the analytic property of $f_{\alpha 0}(\tau)$. The fourth moment and the coefficient of excess are given by

$$m_4 = 3\sigma_{\alpha 0}{}^4 - \sigma_{\alpha 0}{}^2 c_2 \ , \qquad (6.20)$$

and

$$\text{coef. of excess} \equiv m_4/m_2{}^2 - 3 = -c_2/\sigma_{\alpha 0}{}^2 \ . \qquad (6.20\text{a})$$

The latter is positive, if $c_2 < 0$, which would be expected in most cases, since $f_{\alpha 0}(\tau)$ will decrease in time. This means, of course, that the shape is narrowed. The best example of this case is the exchange narrowing in paramagnetic resonance.

The line shape in the neighborhood of the center is mainly determined by the asymptotic behaviour of $\psi_{\alpha 0}(t)$ as $t \to \infty$, which is represented by

$$\psi_{\alpha 0}(t) \sim -\sigma_{\alpha 0}{}^2(\tau_{\alpha 0}{}' |t| + i\tau_{\alpha 0}{}'' t) \ , \qquad (6.21)$$

with $\tau_{\alpha 0}{}'$ and $\tau_{\alpha 0}{}''$ defined by

$$\left.\begin{aligned} \tau_{\alpha 0}{}' &= \int_0^\infty \mathrm{Re}\, f_{\alpha 0}(\tau) d\tau \ , \\ \tau_{\alpha 0}{}'' &= \int_0^8 \mathrm{Im}\, f_{\alpha 0}(\tau) d\tau \ , \end{aligned}\right\} \qquad (6.22)$$

or

$$\tau_{\alpha 0}{}' + i\tau_{\alpha 0}{}'' = \int_0^\infty f_{\alpha 0}(\tau) d\tau \ , \qquad (6.22\text{a})$$

provided that the infinite integrals are convergent. Therefore, the line contour around the center is approximated by a Lorentzian function

$$\mathrm{L}_{\alpha 0}(\omega) = \frac{1}{\pi} \frac{\sigma_{\alpha 0}{}^2 \tau_{\alpha 0}{}'}{\sigma_{\alpha 0}{}^4 \tau'_{\alpha 0}{}^2 + (\omega - \omega_\alpha + \sigma_{\alpha 0}{}^2 \tau_{\alpha 0}{}'')^2} \ , \qquad (6.23)$$

that is, by a resonance curve of damped oscillator type with the half width

$$1/T_2{}' \equiv \varDelta\omega_{1/2} = \sigma_{\alpha 0}{}^2 \tau_{\alpha 0}{}' \ , \qquad (6.23\text{a})$$

and the shift

$$\delta_{\alpha 0} = -\sigma_{\alpha 0}{}^2 \tau_{\alpha 0}{}'' \ , \qquad (6.23\text{b})$$

to the lower side of the unperturbed frequency ω_α. This kind of shift is to be distinguished from that caused by the non-adiabatic effect to be discussed later.

The Lorentzian approximation (6.23) is poor at the wings, where the true intensity distribution must decrease faster than the Lorentzian curve, because the existence of the second moment is always assured by the fact that $f_{\alpha 0}(0)$ is equal to 1. If the functional form of $f_{\alpha 0}(t)$ allows the existence of higher moments, the true distribution decreases still faster on the wings. This fact has been recognized and emphasized by Anderson and Weiss for the particular case of exchange narrowing⁸⁾.

The width of the Lorentzian distribution, (6.23), increases indefinitely as the relaxation time $\tau_{\alpha 0}{}'$ increases. The approximation becomes certainly meaningless if $\sigma_{\alpha 0}{}^2 \tau_{\alpha 0}{}' \gg \sigma_{\alpha 0}$. On the other hand, the observed curve will be practically Lorentzian if $\sigma_{\alpha 0}{}^2 \tau_{\alpha 0}{}' \ll \sigma_{\alpha 0}$, the deviations being only in the far wings. Therefore, we can say that the general condition for an effective narrowing is

$$\sigma_{\alpha 0} \tau_{\alpha 0}{}' \lesssim 1 \ , \qquad (6.24)$$

and that the width of the narrowed peak is approximately equal to (6.23a), which holds exactly for the strong narrowing $\sigma_{\alpha 0} \tau_{\alpha 0}{}' \ll 1$, as far as the secular effect is concerned. This has been pointed out by Bloembergen, Purcell and Pound³⁾ for the case of diffusion narrowing of nuclear magnetic resonance, and by Van Vleck and Gorter⁷⁾ for the exchange narrowing of paramagnetic resonance.

The condition for the validity of the Lorentzian approximation can be proved to be necessary in a more rigorous way. For simplicity, we may neglect the shift and assume that the distribution has only one peak. Then for every $k > 0$, we must have

$$\int_{-k\sigma_{\alpha 0}}^{k\sigma_{\alpha 0}} L_{\alpha 0}(\omega) d\omega = \frac{2}{\pi} \tan^{-1} \frac{k}{\sigma_{\alpha 0} \tau_{\alpha 0}{}'} \geqq 1 - \frac{4}{9k^2} \ ,$$

in order that the Lorentzian function, in the region $(\omega_\alpha - k\sigma_{\alpha 0}, \omega_\alpha + k\sigma_{\alpha 0})$, is consistent with the existence of the second moment $\sigma_{\alpha 0}{}^2$. This inequality is due to Gauss and is a more exact form of the famous Bienayme-Tchebycheff inequality for an unimodal distribution¹⁷⁾. Thus

$$\sigma_{\alpha 0} \tau_{\alpha 0}{}' \leqq k \left[\tan \frac{\pi}{2} \left(1 - \frac{4}{9k^2} \right) \right]^{-1} \ ,$$

is required for (6.23) to be valid in the interval $2k\sigma_{\alpha 0}$ around the center distribution.

If the functional form of $f_{\alpha 0}(\tau)$ is known, the line shape is calculated from (6.17). In the reverse way, it might also be possible in principle to determine the relaxation function $f_{\alpha 0}(\tau)$ from the observed line shape if the measurements were accurate enough. However, the experimental accuracy is not sufficient for such an analysis.

For a particular assumption as to the relaxation function,

$$f_{\alpha 0}(\tau)=\exp(-|\tau|/\tau_0)\,, \qquad (6.25)$$

which was adopted by Bloembergen, Purcell and Pound[3] as the correlation function representing the stochastic motion of nuclei, we have

$$\psi_{\alpha 0}(t)=-\sigma_{\alpha 0}{}^2\tau_0{}^2\{\exp(-|t|/\tau_0)-1+|t|/\tau_0\}\,. \qquad (6.25a)$$

Then the line shape around the center is shown to be

$$I(\omega)=\frac{\exp(\sigma_{\alpha 0}\tau_0)^2}{2\pi\sigma_{\alpha 0}}\sum_{n=0}^{\infty}\frac{(-)^n}{n!}(\sigma_{\alpha 0}\tau_0)^{2n} \times\frac{\sigma_{\alpha 0}\tau_0+(n/\sigma_{\alpha 0}\tau_0)}{(\sigma_{\alpha 0}\tau_0+n/\sigma_{\alpha 0}\tau_0)^2+(\omega/\sigma_{\alpha 0})^2}\,, \qquad (6.26)$$

which converges rather rapidly for $\sigma_{\alpha 0}\tau_0<1$. This first term is the Lorentzian distribution for extreme narrowing. For $\sigma_{\alpha 0}\tau_0\to\infty$, the distribution goes into a Gaussian distribution with the dispersion $\sigma_{\alpha 0}$, which was the starting point of our second approximation for the rigid limit. Some examples of the distribution (6.26) are shown in Fig. 1. Fig. 2. shows the behaviour of the half width $\Delta\omega_{1/2}$ as a function of $\sigma_{\alpha 0}\tau_0$.

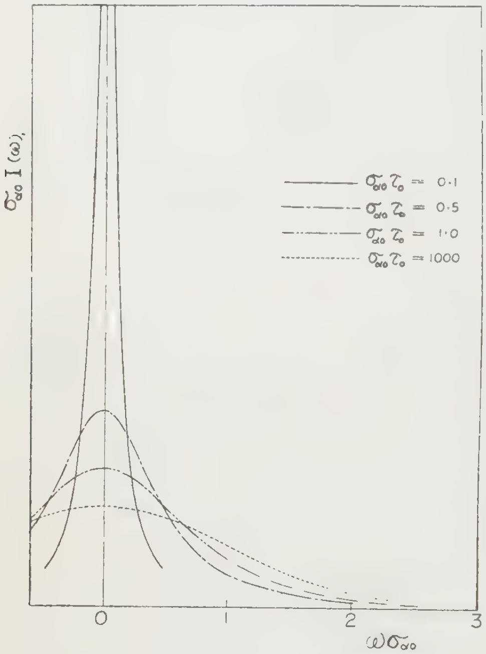

Fig. 1. Examples of narrowed resonance lines, calculated from Eq. (6.26).

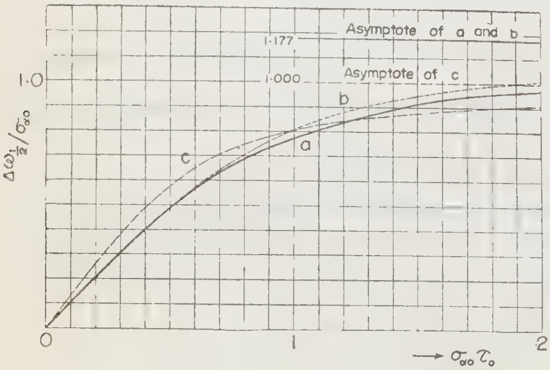

Fig. 2. Change of the secular half width with the relaxation rate of the correlation of local fields. Curve a is calculated from Eq. (6.26). Curve c is the solution of BPP equation, (6.27). The modified BPP equation, (6.27a), gives the curve b.

Naturally, the general trend of the change of the half width is in good agreement with what one predicts from the famous equation due to Bloembergen, Purcell and Pound[3]

$$\left(\frac{1}{T_2{}'}\right)^2=\left(\frac{2}{T_2{}''}\right)^2\frac{2}{\pi}\tan^{-1}\frac{2\tau_0}{T_2{}'}\,, \qquad (6.27)$$

where $1/T_2{}''$ stand for the breadth $\sigma_{\alpha 0}$ for the rigid case ($f_{\alpha 0}(\tau)$=const.) and $1/T_2{}'$ for the breadth with the narrowing. Eq. (6.27) is derived in an intuitive way assuming that the Fourier spectrum of the relaxation function (6.25) in the range of the frequencies lower than the width to be observed is to be regarded as secular, the other parts being cut off as inactive in producing a fluctuating local field. To be rigorous, however, Eq. (6.27) is not correct for quantitative purposes, although quite satisfactory for order of magnitude work. The numerical calculation proves that the half width for the model (6.25) is well represented by the solution of a modified form of (6.27);

$$\left(\frac{1}{T_2{}'}\right)^2=\frac{4\log 2}{\pi}\sigma_{\alpha 0}{}^2\tan^{-1}\left\{\frac{\pi\tau_0}{(4\log 2)T_2{}'}\right\}\,. \qquad (6.27a)$$

(See Fig. 2).

6c) The Non-Secular Effect and the Spin-Lattice Relaxation

Next, we turn to the discussion of the non-adiabatic effect, which is given by the terms with $\omega_\gamma \neq 0$ in Eq. (6.13). Similarly to Eq. (6.21), the contribution of the non-adiabatic motional effect to the main line is determined by the asymptotic behaviour of the integrals involved in the right hand side of Eq. (6.13). Thus, the generating function to describe the contribution to the main line ω_α from the non-secular perturbation ω_γ is given by

$$\phi_{\alpha\gamma}(t) = \exp \psi_{\alpha\gamma}(t) , \qquad (6.28)$$

with

$$\psi_{\alpha\gamma}(t) = -\sigma_{\alpha\gamma}{}^2 t \int_0^{\pm\infty} \exp(i\omega_\gamma\tau) f_{\alpha\gamma}(\tau) d\tau ,$$
$$= -\sigma_{\alpha\gamma}{}^2 (\tau_{\alpha\gamma}{}' |t| + i\tau_{\alpha\gamma}{}'' t) , \qquad (6.28a)^*$$

where

$$\tau_{\alpha\gamma}{}' + i\tau_{\alpha\gamma}{}'' = \int_0^\infty \exp(i\omega_\gamma\tau) f_{\alpha\gamma}(\tau) d\tau . \qquad (6.28b)$$

Considering the relation (6.16), we may write this as

$$\tau_{\alpha\gamma}{}' = \tfrac{1}{2} \int_{-\infty}^\infty \exp(i\omega_\gamma\tau) f_{\alpha\gamma}(\tau) d\tau = \pi \overline{f}_{\alpha\gamma}(-\omega_\gamma) , \qquad (6.28c)$$

$$\tau_{\alpha\gamma}{}'' = \frac{1}{2i} \int_{-\infty}^\infty \exp(i\omega_\gamma\tau) f_{\alpha\gamma}(\tau) \operatorname{sign}\tau d\tau$$
$$= -\frac{1}{2\pi} \mathrm{P} \int_{-\infty}^\infty d\omega' \int_{-\infty}^\infty d\tau \times \frac{\exp(i(\omega_\gamma + \omega')\tau)}{\omega'} f_{\alpha\gamma}(\tau)$$
$$= \mathrm{P} \int_{-\infty}^\infty \frac{\overline{f}_{\alpha\gamma}(\omega)}{\omega + \omega_\gamma} d\omega . \qquad (6.28d)$$

In this transformation we used the formula

$$\frac{\mathrm{P}}{\pi i} \int_{-\infty}^\infty \exp(i\omega t) \frac{d\omega}{\omega} = \operatorname{sign}\tau .$$

P forebe the integration means to take the Cauchy's principal value of the following integral, and $\overline{f}_{\alpha\gamma}(\omega)$ is the Fourier transform of $f_{\alpha\gamma}(t)$. Thus, the non-secular motional effect is to fold on the distribution $I_{\alpha 0}(\omega)$ Eq. (6.17a), the Lorentzian distribution

$$\mathrm{L}_{\alpha\gamma}(\omega) = \frac{1}{\pi} \frac{\Delta\omega_{\alpha\gamma}}{\Delta\omega_{\alpha\gamma}{}^2 + (\omega - \omega_\alpha - \delta_{\alpha\gamma})^2} , \qquad (6.29)$$

with the half width

$$\Delta\omega_{\alpha\gamma} = \sigma_{\alpha\gamma}{}^2 \tau_{\alpha\gamma}{}' , \qquad (6.29a)$$

and the shift

$$\delta_{\alpha\gamma} = -\sigma_{\alpha\gamma}{}^2 \tau_{\alpha\gamma}{}'' , \qquad (6.29b)$$

for every non-secular perturbation ω_γ. In the case of strong narrowing, the secular effect also gives approximately a Lorentzian curve, so that the convoluted distribution is a Lorentzian function with the half width

$$\Delta\omega_\alpha = 1/T_{2\alpha} = \textstyle\sum_\gamma \sigma_{\alpha\gamma}{}^2 \tau_{\alpha\gamma}{}' , \qquad (6.30)$$

and the shift

$$\delta_\alpha = -\textstyle\sum \sigma_{\alpha\gamma}{}^2 \tau_{\alpha\gamma}{}'' . \qquad (6.30a)$$

The notation $T_{2\alpha}$ is employed here in analogy to T_2 used by Bloch[1)] to designate *transverse relaxation time*. Thus, $T_{2\alpha}$ will be called the transverse relaxation time belonging to the resonance mode ω_α. The non-secular part of $T_{2\alpha}$ will be denoted by $T_{1\alpha}{}'$, namely

$$1/T_{1\alpha}{}' = \sum_{\omega_\gamma \neq 0} \sigma_{\alpha\gamma}{}^2 \tau_{\alpha\gamma}{}' . \qquad (6.31)$$

The suffix 1 is meant to show that $T_{1\alpha}{}'$ is related to the *longitudinal relaxation time* T_1, which will be discussed later.

If the relaxation function $f_{\alpha\gamma}(\tau)$ is assumed to be a simple exponential decay of the type

$$f_{\alpha\gamma}(\tau) = \exp(-|\tau|/\tau_{\alpha\gamma}) , \qquad (6.32)$$

as in Eq. (6.25), one gets from Eq. (6.28b)

$$\left.\begin{aligned} \tau_{\alpha\gamma}{}' &= \frac{\tau_{\alpha\gamma}}{1 + \omega_\gamma{}^2 \tau_{\alpha\gamma}{}^2} , \\ \tau_{\alpha\gamma}{}'' &= \frac{\tau_{\alpha\gamma}{}^2 \omega_\gamma}{1 + \omega_\gamma{}^2 \tau_{\alpha\gamma}{}^2} . \end{aligned}\right\} \qquad (6.32a)$$

This particular assumption has been commonly used since the pioneer work of Bloembergen, Purcell and Pound. Usually, $\tau_{\alpha\gamma}$ is assumed to be identical to τ_0, so that the single relaxation time,

$$\tau_0 = \tau_{\alpha\gamma} = \tau_c ,$$

is used for the analysis of experimental data.

In experiments in which ω_γ is kept constant and the relaxation time (or the correlation time) is changed by, for instance, temperature variation, the non-secular broadening becomes considerable only when $1/\tau_c$ is nearly equal to ω_γ. It is negligible compared to the secular broadening unless $\omega_\gamma \tau_{\alpha\gamma} \lesssim 1$. If τ_c is kept constant, the broadening decreases when ω_γ increases. Such behaviour of the non-secular broadening is generally expected if $f_{\alpha\gamma}(\tau)$ shows monotonous relaxation.

---

* Note the difference between Eq. (6.17) and (6.28a). For the non-adiabatic effect, we should use the asymptotic forms like (6.28a) in order to pick up the contributions to the main lines. This can be seen more directly from Eq. (6.37a).

Thus, the non-secular effect is to be observed when the secular effect is already in the region of strong narrowing. This is easily seen if $\tau_{\alpha0}$ and $\tau_{\alpha\nu}$ are of the same order of magnitude. Then we expect

$$\tau_{\alpha0}\sim\tau_{\alpha\gamma}\lesssim 1/\omega_\gamma \ll 1/\sigma_{\alpha0}\ ,$$

provided that the satellite $\omega_\alpha+\omega_\gamma$ is far apart from the main line ω_α. Therefore, the width of the resonande ω_α will be of the order of $\sigma_{\alpha0}{}^2\tau_{\alpha0}'(\sim\sigma_{\alpha\gamma}{}^2\tau_{\alpha\gamma}')$, and the non-secular shift (6.29a) of the order of $-\sigma_{\alpha\gamma}{}^2/\omega_\gamma$. Although this shift is very small in the usual experimental conditions, it is, in fact, of the same order of magnitude as the width itself. Hence, it could be observed by experiments, and also it should be considered in careful analysis of experimental data.

The non-secular effect is usually connected with the relaxation process of the system by which it attains equilibrium when the incident radiation is cut off. In our general formulation, this relaxation is concerned with the energy transfer between the modes 1 and 2. Regarding $\mathscr{H}'$ as the perturbation responsible for this energy exchange, the rate of energy transfer from the mode 1 to the mode 2 is given by the basic formula,

$$-\frac{dE_1}{dt}=\frac{1}{\hbar^2}\int_{-\infty}^{\infty}dt\,\frac{\mathrm{Tr}\,\{\exp(-\beta_1\mathscr{H}_1-\beta_2\mathscr{H}_2)\exp(it(\mathscr{H}_1+\mathscr{H}_2)/\hbar)[\mathscr{H}_1,\mathscr{H}']\exp(-it(\mathscr{H}_1+\mathscr{H}_2)/\hbar)\mathscr{H}'\}}{\mathrm{Tr}\exp(-\beta_1\mathscr{H}_1-\beta_2\mathscr{H}_2)}\ , \tag{6.33}$$

where we assumed that the modes 1 and 2 are themselves in internal thermal equilibrium with the temperatures, $T_1=1/k\beta_1$ and $T_2=1/k\beta_2$ respectively. Except for this assumption, the invariant form (6.33) is simply the result of the usual perturbation theory. The rate is seen to be zero, as it should be, when the temperatures T_1 and T_2 are equal. Assuming now that the temperature difference is small, we put

$$\beta_1=\beta_2+\Delta\beta\ ,$$

and calculate the first order term in $\Delta\beta$, which turns out to be

$$\begin{aligned}\frac{dE_1}{dt}&=\frac{\Delta\beta}{\hbar^2}\int_{-\infty}^{\infty}\langle[\mathscr{H}_1,\mathscr{H}'(t)]\mathscr{H}'\mathscr{H}_1\rangle dt\\&=\frac{\Delta\beta}{\hbar^2}\int_{-\infty}^{\infty}\langle\mathscr{H}_1\mathscr{H}'[\mathscr{H}'(t)\mathscr{H}_1]\rangle dt\ .\end{aligned}$$

Using Eq. (6.4) and the assumption of low frequency, the above expression is shown to be

$$\begin{aligned}\frac{dE_1}{dt}=\frac{\Delta\beta}{2\hbar^2}&\int_{-\infty}^{\infty}\exp(i\omega_\gamma t)dt\\&\times\sum_{\omega_\gamma\neq0}\langle[\mathscr{H}_1,\mathscr{H}_\gamma'(t)][\mathscr{H}_{-\gamma}'(0),\mathscr{H}_1]\rangle\ ,\end{aligned} \tag{6.34}$$

where the summation over γ excludes $\omega_\gamma=0$, because it does not cause any energy transfer.

If the temperature is high enough, the average energy of the mode 1 is

$$E_1=-\beta\langle\mathscr{H}_1{}^2\rangle\ .$$

Thus we obtain

$$\begin{aligned}\frac{1}{T_1}=\frac{1}{2\hbar^2}&\sum_{\omega_\gamma\neq0}\int_{-\infty}^{\infty}\exp(i\omega_\gamma t)dt\\&\times\frac{\langle[\mathscr{H}_1\mathscr{H}_\gamma'(t)][\mathscr{H}_{-\gamma}'(0)\mathscr{H}_1]\rangle}{\langle\mathscr{H}_1{}^2\rangle}\ ,\end{aligned} \tag{6.35}$$

for the relaxation time T_1 to establish the equilibrium of the energy partition between the modes 1 and 2.

On the other hand, the non-secular width (6.31) is, in its explicit form

$$\begin{aligned}\frac{1}{T_{1\alpha}'}=\frac{1}{2\hbar^2}&\sum_{\omega_\gamma\neq0}\int_{-\infty}^{\infty}\exp(i\omega_\gamma t)dt\\&\times\frac{\langle\{[M_x(\omega_\alpha),\mathscr{H}_\gamma'(t)][\mathscr{H}_{-\gamma}'(0),M_x(-\omega_\alpha)]\}\rangle}{\langle|M_x(\omega_\alpha)|^2\rangle}\ ,\end{aligned} \tag{6.36}$$

as seen from Eqs. (6.12) and (6.28c). Both expressions (6.35) and (6.36) are quite similar, and presumably of the same order of magnitude, but they are not exactly equal. An example of this will be discussed in the next section. This difference between T_1 and $T_{1\alpha}'$ is also to be considered in a quantitative analysis of experiments. Physically, only a part of $1/T_{1\alpha}'$ is to be attributed to the finite life time of the initial and final states of the transition $\hbar\omega_\gamma$, perturbed by $\mathscr{H}'$. Actually, there is a complication due to an interference effect of the interplay of $M_x(\omega_\alpha)$, $M_x(-\omega_\gamma)$,

$\mathscr{H}_\gamma'$ and $\mathscr{H}_{-\gamma}'$, so that generally $1/T_{1\alpha}'$ cannot be interpreted in a simple way. This is one reason for the difference of T_1 and $T_{1\alpha}'$.

An obvious, still important point to be noticed here is that non-secular broadening occurs if and only if there exists the spectral component of $\mathscr{H}_\gamma'(t)$ at the frequency ω which satisfies the energy conservation law

$$\hbar\omega+\hbar\omega_\gamma=0\ ,$$

and does not commute with $M_x(\omega_\alpha)$. In other words, the non-secular broadening never occurs if the mode $\mathscr{H}_2$ cannot emit or absorb the energy quantum $\hbar\omega_\gamma$ by the perturbation $\mathscr{H}_\gamma'$. Naturally, then, both $1/T_1$ and $1/T_{1\alpha}'$ will vanish simultaneously. This is seen at once from Eq. (6.28c).

Or, we can also go back to the expression

$$G_{2\alpha\gamma}(t)=-\langle|M_x(\omega_\alpha)|^2\rangle\exp(i\omega_\alpha t)\times\int_0^t(t-\tau)\exp(i\omega_\gamma\tau)\sigma_{\alpha\gamma}^2 f_{\alpha\gamma}(\tau)d\tau\ ,\tag{6.37}$$

in Eq. (6.13), which describes the non-secular effect connected with the satellite $\omega_\alpha+\omega_\gamma$. Introducing the Fourier spectrum of $f_{\alpha\gamma}(\tau)$, we may write Eq. (6.37) as

$$\begin{aligned}&G_{2\alpha\gamma}(t)\\&=\langle|M_x(\omega_\alpha)|^2\rangle\sigma_{\alpha\gamma}^2\exp(i\omega_\alpha t)\\&\times\int_{-\infty}^{\infty}d\omega\,\frac{\exp(i(\omega+\omega_\gamma)t)-1-i(\omega+\omega_\gamma)t}{(\omega+\omega_\gamma)^2}\bar{f}_{\alpha\gamma}(\omega)\ .\end{aligned}\tag{6.37a}$$

Thus, we may take

$$G_{2\alpha\gamma}'(t)=\langle|M_x(\omega_\alpha)|^2\rangle\sigma_{\alpha\gamma}^2\times\int_{-\infty}^{\infty}\frac{\exp(i(\omega+\omega_\alpha+\omega_\gamma)t)}{(\omega+\omega_\gamma)^2}\bar{f}_{\alpha\gamma}(\omega)d\omega\ ,$$

as the generating function to describe the *intensity distribution* of the *satellite* centered at $\omega_\alpha+\omega_\gamma$. The same result is, of course, obtained by customary perturbation calculation. The satellite intensity distributes, therefore, as

$$I(\omega+\omega_\alpha+\omega_\gamma)\propto\sigma_{\alpha\gamma}^2\frac{\bar{f}_{\alpha\gamma}(\omega)}{(\omega+\omega_\gamma)^2}\ .\tag{6.38}$$

It should be noticed that in this case the second order calculation can give this information about the satellites, whereas it can give only the integrated intensity for the rigid lattices. Eq. (6.38) also means that the intensity distribution of satellite lines becomes infinite at the position of the main line ω_α, if $\bar{f}_{\alpha\gamma}(-\omega_\gamma)$ is not zero. This divergence is, of course, only spurious, because there the other terms in (6.27a) come into play to cancel the infinity. The net effect is described by (6.28a) as far as the satellite $\omega_\alpha+\omega_\gamma$ is not too close to ω_α.

Finally, some remarks should be made about minor corrections due to the terms we have disregarded in the above treatment. In the first place, we have neglected constant terms which are to be added to $\psi_{\alpha0}(t)$ and $\psi_{\alpha\gamma}(t)$ Eqs. (6.21) and (6.28a). They come in from the term

$$\lim_{|t|\to\infty}\left\{-\sigma_{\alpha\gamma}^2\int_0^t\exp(i\omega_\gamma\tau)\tau f_{\alpha\gamma}(\tau)d\tau\right\}\ ,\tag{6.39}$$

in Eq. (6.13). Similarly to (6.28b), this limit is shown to be expressed as

$$\begin{aligned}&\rho_{\alpha\gamma}'-i\rho_{\alpha\gamma}''\qquad\text{for}\qquad t\to\infty\\&\rho_{\alpha\gamma}'+i\rho_{\alpha\gamma}''\qquad\text{for}\qquad t\to-\infty\end{aligned}$$

with

$$\rho_{\alpha\gamma}'=\sigma_{\alpha\gamma}^2\,\mathrm{P}\int_{-\infty}^{\infty}\frac{\bar{f}_{\alpha\gamma}(\omega)}{\omega+\omega_\gamma}d\omega\ ,$$

$$\rho_{\alpha\gamma}''=\pi\sigma_{\alpha\gamma}^2\bar{f}_{\alpha\gamma}'(-\omega_\gamma)\ ,$$

The effect of this constant term is to replace the Lorentzian function (6.29) by

$$\frac{1}{\pi}\exp(\rho_{\alpha\gamma}')\times\frac{\varDelta\omega_{\alpha\gamma}\cos\rho_{\alpha\gamma}''-(\omega-\omega_\alpha+\delta_{\alpha\gamma})\sin\rho_{\alpha\gamma}''}{(\varDelta\omega_{\alpha\gamma})^2+(\omega-\omega_\alpha+\delta_{\alpha\gamma})^2}\ ,$$

which, however, differs very little from the Lorentzian function in the region which is physically important.

Another point is concerned with those terms with $\omega_\alpha+\omega_\beta\neq0$ in the complete expression of $G_2(t)$, Eq. (6.10). As we have noticed in connection with Eq. (5.10), they can be neglected if the system is highly symmetric, but we can also see that these terms are not important for the discussion of line shape, because their effect is similar to that we have just mentioned.

Part C. Simple Applications to Nuclear Magnetic and Paramagnetic Resonance.

§ 7. Dipolar Broadening of Nuclear Magnetic Resonance

To illustrate our method, we shall consider in this part the applications of the general theory to simple examples of dipolar broadening of nuclear magnetic resonance absorption and the exchange narrowing problem in paramagnetic resonance. The nuclear magnetic resonance has been treated by Bloembergen, Purcell and Pound[3] both from experimental and theoretical sides. The reason why this problem is again taken up here is to reconsider this from a rigorous basis of quantum mechanics and to correct some of their results.

We assume the unperturbed Hamiltonian to be the sum of the Zeeman energy $\mathcal{H}_z$ of nuclear spins in a constant magnetic field H_z and the energy of nuclear motion, $\mathcal{H}_L$, namely

$$\mathcal{H}_0=\mathcal{H}_z+\mathcal{H}_L=-\hbar\omega_z\sum I_{jz}+\mathcal{H}_L\ , \qquad (7.1)$$

where

$$\hbar\omega_z=\hbar\gamma H_z=\mu_0 H_z\ , \qquad (7.1a)$$

is the Zeeman splitting, γ being the nuclear gyromagnetic ratio. The perturbation responsible for the broadening is now assumed to be the dipolar interaction of the nuclear magnetic moments,

$$\begin{aligned}\mathcal{H}'&=\sum_{j>k}\mathcal{H}_{jk}\\ &=\mu_0^2\sum_{j>k}r_{jk}^{-3}\left(\boldsymbol{I}_j\boldsymbol{I}_k-3\boldsymbol{I}_j\frac{\boldsymbol{r}_{jk}\boldsymbol{r}_{jk}}{r_{jk}^2}\boldsymbol{I}_k\right)\ ,\end{aligned} \qquad (7.2)$$

which is conveniently decomposed as

$$\begin{aligned}\mathcal{H}'&=\sum_{\alpha=-2}^{2}\mathcal{H}_\alpha'\ ,\\ \mathcal{H}_\alpha'&=\sum_{jk}\mathcal{H}_{\alpha jk}'=\sum_{jk}\Phi_{jk}^{-\alpha}\{jk_\alpha\}\ ,\end{aligned} \qquad (7.3)$$

where the abreviations are

$$\begin{aligned}\{jk\}_2\ &=I_j^+I_k^+\ ,\\ \{jk\}_1\ &=I_j^+I_{kz}+I_{jz}I_k^+\ ,\\ \{jk\}_0\ &=I_{jz}I_{kz}-\tfrac{1}{4}(I_j^+I_k^-+I_j^-I_k^+)\ ,\\ \{jk\}_{-1}&=I_j^-I_{kz}+I_{jz}I_k^-\ ,\\ \{jk\}_{-2}&=I_j^-I_k^-\ ,\end{aligned} \qquad (7.4)$$

and

$$\begin{aligned}\Phi_{jk}^{\pm2}&=-(3/4)\mu_0^2 r_{jk}^{-5}(x_{jk}\pm iy_{jk})^2\ ,\\ \Phi_{jk}^{\pm1}&=-(3/2)\mu_0^2 r_{jk}^{-5}z_{jk}(x_{jk}\pm iy_{jk})\ ,\\ \Phi_{0jk}&=-\mu_0^2 r_{jk}^{-5}(3z_{jk}^2-r_{jk}^2)\ .\end{aligned} \qquad (7.5)$$

In these expressions r_{jk}, etc., denote relative coordinates of the nuclei.

The magnetic moment M_x, which represents the interaction of the system with the radiation field, is written as

$$M_x=M_++M_-\ , \qquad (7.6)$$

where

$$M_+=\tfrac{1}{2}\mu_0\sum_j I_j^+,\quad M_-=\tfrac{1}{2}\mu_0\sum_j I_j^-. \qquad (7.6a)$$

The unperturbed motion of each component of M_x is simply

$$\begin{aligned}M_\pm(t)&=\exp(it\mathcal{H}_z/\hbar)M_\pm\exp(-it\mathcal{H}_z/\hbar)\\ &=\exp(\mp i\omega_z t)M_\pm\ .\end{aligned} \qquad (7.7)$$

Similarly, we have

$$\begin{aligned}\mathcal{H}_\alpha'(t)&=\exp(it\mathcal{H}_z/\hbar)\mathcal{H}_\alpha'\exp(-it\mathcal{H}_z/\hbar)\\ &=\exp(-i\alpha\omega_z t)\mathcal{H}_\alpha'\ .\end{aligned} \qquad (7.8)$$

Further we define

$$\Phi_{jk}^\alpha(t)=\exp(it\mathcal{H}_L/\hbar)\Phi_{jk}^\alpha\exp(-it\mathcal{H}_L/\hbar)\ , \qquad (7.9)$$

to describe the time change of dipolar coefficients induced by the nuclear motion.

Since the nuclear magnetic moments are very small, we may safely assume the density matrix to be approximated by

$$\rho=\exp(-\beta\mathcal{H}_L)/\mathrm{Tr}\exp(-\beta\mathcal{H}_L)\ ,$$

which is used for the average of any quantity we may be concerned with. Thus the average procedure for the spin variables is simply the trace operation divided by the trace of the unity in the spin space.

Then Eq. (6.8) becomes

$$\begin{aligned}G_0(t)&=\langle M_x^0(t)M_x\rangle\\ &=(N/6)\mu_0^2I(I+1)\\ &\qquad\times\exp(i\omega_z t)+\exp(-i\omega_z t)\ ,\end{aligned} \qquad (7.10)$$

and Eq. (6.9) reduces to

$$G_1(t)=0\ .$$

The general expression for the second order perturbation, Eq. (6.10) is now

$$\begin{aligned}G_2(t)=&-\sum\sum_{\alpha+\beta+\gamma+\delta=0}\sum\exp(-i\alpha\omega_z t)\int_0^t dt_1\int_0^{t_1}dt_2\\ &\times\exp\{-i(\gamma t_1+\delta t_2)\omega_z\}\\ &\times\hbar^{-2}\langle\{[M,\mathcal{H}_{\alpha\gamma}'(t_1)][\mathcal{H}_\delta'(t_2)M_\beta]\}\rangle.\end{aligned} \qquad (7.11)$$

The perturbation $\mathcal{H}_\alpha'$ are spherical harmonics of second order with regard to the angular dependence of position vectors of nuclei, so that the cross terms involving $\mathcal{H}_\gamma'(\tau)\mathcal{H}_\delta'(0)$ with $\gamma+\delta\neq0$ are zero for $\tau=0$ on average over the distribution of atomic nuclei, if the distribution is highly symmetric. For $\tau\neq0$, these averages are not zero, but they are neglected in the following on the ground discussed in the previous sections. Thus, we have only two combinations, $\alpha=-1$, $\beta=1$ and $\alpha=1$, $\beta=-1$, corresponding to the time factors $\exp\{\pm i\omega_z t\}$ in front of the integral on the right hand side of Eq. (7.11). We need only to write down the term with $\alpha=-\beta=-1$, the other part being obviously the conjugate complex. Thus the subscript α may be omitted, leaving only the subscript γ to specify the type of the perturbation $\mathscr{H}_{-\gamma}$ and $\mathscr{H}_\gamma$.

For our calculation, the following formulae are useful;

$$\left.\begin{aligned}&[(I_j^-+I_k^-),\ \{jk\}_{-\gamma}]=c_\gamma\{jk\}_{-\gamma-1}\ ,\\&[(I_j^++I_k^+),\ \{jk\}_\gamma]=-c_\gamma\{jk\}_{\gamma+1}\ ,\\&\langle\{jk\}_\gamma\{jk\}_{-\gamma}\rangle=K_\gamma I^2(I+1)^2\ ,\end{aligned}\right\}\tag{7.12}$$

where the numerical coefficients are shown in Table I.

Table I. Coefficients for Eq. (7.12)

	-2	-1	0	1	2
c_γ	-2	-4	$3/2$	2	0
K_γ	$4/9$	$4/9$	$1/6$	$4/9$	$4/9$
$c_\gamma^2K_{\gamma+1}$	$16/9$	$8/3$	1	$16/9$	0

Corresponding to Eq. (6.12), we define the static moments σ_γ^2 and the correlation functions $f_\gamma(\tau)$ for $\gamma=0, \pm1, \pm2$, by the following equations;

$$\begin{aligned}&\hbar^2\langle M_-M_+\rangle\sigma_{-\gamma}^2 f_{-\gamma}(\tau)\\&=\langle\{[M_-,\ \mathscr{H}_{-\gamma}'(\tau)][\mathscr{H}_\gamma'(0),\ M_+]\}\rangle\\&=\sum_{jk}\sum_{lm}\langle[M_-\{jk\}_{-\gamma}][\{lm\}_\gamma M_+]\rangle\\&\qquad\times\langle\{\Phi_{jk}^\gamma(\tau)\Phi_{lm}^{-\gamma}(0)\}\rangle\\&=\tfrac{1}{4}\mu_0^2I^2(I+1)^2c_\gamma^2K_{\gamma+1}\sum_{jk}\langle\{\Phi_{jk}^\gamma(\tau)\Phi_{jk}^{-\gamma}(0)\}\rangle,\end{aligned}\tag{7.13}$$

where we used Eqs. (7.12). Thus we get

$$\hbar\sigma_{-\gamma}^2=(3/4)c_\gamma^2K_{\gamma+1}I(I+1)\sum_k\langle|\Phi_{jk}^\gamma(0)|^2\rangle\ ,\tag{7.13a}$$

and

$$f_{-\gamma}(\tau)=\frac{\sum_k\langle\{\Phi_{jk}^\gamma(\tau)\Phi_{jk}^{-\gamma}(0)\}\rangle}{\sum_k\langle\{\Phi_{jk}^\gamma(0)\Phi_{jk}^{-\gamma}(0)\}\rangle}\ ,\tag{7.13b}$$

For brevity, we introduce the notations:

$$\hbar\sigma_p^2=I(I+1)\mu_0^4b^{-6}\ ,\tag{7.14}$$

and

$$\begin{aligned}F_{jk}^0\ &=b^3r_{jk}^{-3}(1-3\cos^2\theta_{jk})\ ,\\F_{jk}^{\pm1}&=b^3r_{jk}^{-3}\cos\theta_{jk}\sin\theta_{jk}\exp(\pm i\varphi_{jk})\ ,\\F_{jk}^{\pm2}&=b^3r_{jk}^{-3}\sin^2\theta_{jk}\exp(\pm2i\varphi_{jk})\ ,\end{aligned}\tag{7.15}$$

where b is a natural unit for the length. Hence, σ_p is a natural unit for the frequency associated with the dipolar interaction, and F_{jk}^α are dimensionless quantities representing the nuclear arrangement around a nucleus.

With these notations, we can write the moments as

$$\begin{aligned}\hbar^2\sigma_0^2\ &=(3/4)\hbar^2\sigma_p^2\sum_k\langle(F_{jk}^0)^2\rangle\ ,\\\hbar^2\sigma_1^2\ &=(9/2)\hbar^2\sigma_p^2\sum_k\langle|F_{jk}^1|^2\rangle\ ,\\\hbar^2\sigma_{-1}^2&=3\hbar^2\sigma_p^2\sum_k\langle|F_{jk}^1|^2\rangle\ ,\\\hbar^2\sigma_2^2\ &=(3/4)\hbar^2\sigma_p^2\sum_k\langle|F_{jk}^2|^2\rangle\ ,\end{aligned}\tag{7.16}$$

which are associated with the perturbations $\mathscr{H}_{-\gamma}'$, $\mathscr{H}_\gamma'$). If the nuclear arrangement around each nucleus is isotropic on the average, or regularly symmetric, these moments are expressed by the following simple formulae;

$$\sigma_0^2=\sigma_1^2=(3/5)\sigma_p^2B,\quad \sigma_{-1}^2=\sigma_2^2=(2/5)\sigma_p^2B\ ,\tag{7.17}$$

where B is a dimensionless lattice sum,

$$B=\sum_k(b/r_{jk})^6.\tag{7.17a}$$

Of course, σ_0^2 is the dipolar breadth of the main line for the rigid lattice, which has been given by Van Vleck⁶⁾. The total sum of the moments

$$\sigma_w^2=\sigma_0^2+\sigma_1^2+\sigma_{-1}^2+\sigma_2^2=2\sigma_p^2B\ ,\tag{7.18}$$

is the total second moment including the satellite contributions, which was calculated by Waller⁴⁾. The ratio of the moment σ_0^2, associated with the main line, to the total moment σ_w^2 is the famous 3/10, which holds only for isotropic or regularly symmetric cases.

The correlation functions $f_\gamma(\tau)$ which correspond to the moments σ_γ^2 are expressed by

$$f_\gamma(\tau)=\sum_k\langle\{F_{jk}^{-\gamma}(\tau)F_{jk}^\gamma(0)\}\rangle/\sum_k\langle|F_{jk}^\gamma|^2\rangle\ ,\tag{7.19}$$

The motional effect due to the time decay of these correlation functions were already discussed in the previous section. For $\sigma_0\tau_0\lesssim1$, the secular breadth of the main line is narrowed approximately as

$$(\varDelta\omega_{\frac{1}{2}})_0\sim\sigma_0^2\tau_0\ .$$

which holds exactly for the half width of the Lorentizian curve in strongly narrowed limit. More detailed shape of the narrowed line is to be determined by the function $f_0(\tau)$. If the simple exponential decay is assumed for $f_0(\tau)$, the function (6.26) can be used. Or one may use the modified form of BPP equation, (6.27a), for an approximate evaluation of the width. For these analysis, one needs, of course, to be careful about the assumption of the Gaussian shape for the limit of rigid case. As is well known, this is approximately true in condensed phases, where the number of interacting neighbors is large enough to allow the approximate validity of the central limit theorem (see Van Vleck[6]).

Another point to be noticed with regard to the secular effect in the present problem is that the correlation function $f_0(\tau)$ is real, namely

$$f_0(\tau)=f_0(-\tau)=\overline{f_0(\tau)}\,, \qquad (7.20)$$

which means that the secular shift, Eq. (6.23b), is now zero.

The non-secular broadening, Eq. (6.30) is explicitly given by

$$\begin{aligned}(\varDelta\omega_{1/2})_{\text{nonsec.}}&\equiv 1/T'\\ &=\pi\,[\sigma_{-1}^2 f_{-1}(-\omega_z)+\sigma_1^2 f_1(\omega_z)+\sigma_2^2 f_2(2\omega_z)]\\ &=\pi\,[(5/3)\sigma_1^2 f_1(\omega_z)+\sigma_2^2 f_2(2\omega_z)]\\ &=(5/3)\sigma_1^2\tau_1'+\sigma_2^2\tau_2'\,, \qquad (7.21)\end{aligned}$$

because σ_1^2 is $2\sigma_{-1}^2/3$ by Eq. (7.16) and $f_{-1}(\tau)$ is the complex conjugate of $f_1(\tau)$. By Eqs. (6.28c) and (7.16), the above equation can also be written as

$$\begin{aligned}&1/T_1'\\ &=\sigma_p^2\Big[\frac{15}{4}\int_{-\infty}^{\infty}\sum_k\langle\{F_{jk}^{-1}(\tau)F_{jk}^{1}(0)\}\rangle\exp(i\omega_z\tau)d\tau\\ &\quad+\frac{3}{8}\int_{-\infty}^{\infty}\sum_k\langle\{F_{jk}^{-2}(\tau)F_{jk}^{2}(0)\}\rangle\exp(2i\omega_z\tau)d\tau\Big]\,, \qquad (7.21\text{a})\end{aligned}$$

or as

$$1/T_1'=\sigma_p^2\Big[\frac{15}{4}J_1(\nu_0)+\frac{3}{8}J_2(2\nu_0)\Big]\,, \qquad (7.21\text{b})$$

where

$$J_\gamma(\nu)=\int_{-\infty}^{\infty}\sum_k\langle\{F_{jk}^{-\gamma}(t)F_{jk}^{\gamma}(0)\}\rangle\exp(-2\pi i\nu t)dt, \qquad (7.22)$$

are the local field spectra which were introduced by Bloembergen, Purcell and Pound[3] (their Eq. (26)).

On the other hand, the spin-lattice relaxation time, Eq. (6.35) is calculated as

$$\begin{aligned}1/T_1&=(1/2\hbar^2)\sum_{\gamma\neq0}\int_{-\infty}^{\infty}\gamma^2\hbar^2\omega_z^2\frac{\langle\mathcal{H}_{-\gamma}'(t)\mathcal{H}_\gamma(0)\rangle}{\langle\mathcal{H}_z^2\rangle}\\ &\qquad\times\exp(i\gamma\omega_z t)dt\\ &=\frac{3}{4}\sum_{\gamma\neq0}\gamma^2K_\gamma I(I+1)\hbar^{-2}\int_{-\infty}^{\infty}\sum_k\langle\varPhi_{jk}^{\gamma}(t)\varPhi_{jk}^{-\gamma}(0)\rangle\\ &\qquad\times\exp(i\gamma\omega_z t)dt\\ &=\frac{3}{2}\sum_{\gamma=1,2}\gamma^2K_\gamma I(I+1)\hbar^{-2}\int_{-\infty}^{\infty}\sum_k\langle\varPhi_{jk}^{-\gamma}(t)\varPhi_{jk}^{\gamma}(0)\rangle\\ &\qquad\times\exp(-i\gamma\omega_z t)dt\\ &=\frac{3}{2}\sigma_p^2[J_1(\nu_0)+J_2(2\nu_0)]\,. \qquad (7.23)\end{aligned}$$

Therefore, if we divide $1/T_1$ into two parts,

$$\frac{1}{T_1}=\Big(\frac{1}{T_1}\Big)_{\nu_0}+\Big(\frac{1}{T_1}\Big)_{2\nu_0}\,,$$

corresponding to the single spin- and double spin-inversion processes, each part is expressed as

$$\Big(\frac{1}{T_1}\Big)_{\nu_0}=\frac{3}{2}J_1(\nu_0)=\frac{2}{3}\sigma_1^2\tau_1'\,, \qquad (7.24)$$

and

$$\Big(\frac{1}{T_1}\Big)_{2\nu_0}=\frac{3}{2}J_2(2\nu_0)=4\sigma_2^2\tau_2'\,, \qquad (7.24\text{a})$$

so that we have

$$1/T_1=(2/3)\sigma_1^2\tau_1'+4\sigma_2^2\tau_2'\,. \qquad (7.25)$$

With these notations, Eq. (7.21) is written as

$$1/T_1'=\frac{5}{2}\Big(\frac{1}{T_1}\Big)_{\nu_0}+\frac{1}{4}\Big(\frac{1}{T_1}\Big)_{2\nu_0}\,. \qquad (7.26)$$

In the ideal case of isotropic nuclear arrangements, these equations reduce to

$$\begin{aligned}1/T_1'&=\sigma_p^2B\{\tau_1'+(2/5)\tau_2'\}\,,\\ 1/T_1&=\sigma_p^2B\{(2/5)\tau_1'+(8/5)\tau_2'\}\,, \qquad (7.27)\end{aligned}$$

by Eq. (7.17). Thus, the two kinds of spin inversion processes have different weights for the spin-lattice relaxation and the non-secular broadening effect, so that $1/T_1$ and $1/T_1'$ are not identical in contradiction to what has been assumed by Bloembergen, Purcell and Pound,[3] who used the equation

$$1/T_1=(3/2)\sigma_p^2[J_1(\nu_0)+\tfrac{1}{2}J_2(2\nu_0)]\,.$$

The double spin inversion is obviously more efficient for the energy transfer than for the broadening. The broadening effect is partly determined by the life time of energy levels, for which the single spin inversion is more important. Actually the broadening is a more complicated effect than to be interpreted simply in terms of the life time.

As we have seen in the previous section, the non-secular broadening becomes important only when the time constants (which we shall briefly call τ_c) of the correlation functions $f_1(\tau)$ and $f_2(\tau)$ become comparable to or smaller than $1/\omega_z$. In the limit of very rapid decrease of the correlations, the secular width is, of course, strongly narrowed, and the non-secular broadening is also small ($1/\sigma_0 \gg 1/\omega_z \gg \tau_c$). In this limit, the total width, Eq. (6.30),

$$\begin{aligned} 1/T_2 &= \sigma_0^2\tau_0 + 1/T_1' \\ &= \sigma_0^2\int_0^\infty f_0(t)dt + \frac{5}{3}\,\sigma_1^2\,\mathrm{Re}\int_0^\infty f_1(t)\exp(-i\omega_z t)dt \\ &\quad + \sigma_2^2\,\mathrm{Re}\int_0^\infty f_2(t)\exp(-2i\omega_z t)dt\,, \end{aligned} \tag{7.28}$$

tends to

$$\begin{aligned} 1/T_2 \to \sigma_0^2\int_0^\infty f_0(t)dt + \frac{5}{3}\,\sigma_1^2\int_0^\infty f_1(t)dt \\ + \sigma_2^2\int_0^\infty f_2(t)dt\,, \end{aligned} \tag{7.28a}$$

which is independent of ω_z. The integrals define the relaxation times of correlations. If these are assumed to be τ_c, the same for the three, and if the nuclear arrangement is isotropic, then we have

$$1/T_2 \to 2\sigma_p^2 B\tau_c = (10/3)\sigma_0^2\tau_c\,. \tag{7.29}$$

This is the so-called the 10/3 effect. Namely, for extreme narrowing, the width is just 10/3 of that would be expected only from the secular effect, the excess of the 7/3 part coming from the *non-secular* effect. The ratio, 10/3, is the same as that for the total second moment σ_w^2 to the secular second moment σ_0^2. This ratio depends, first, on the symmetry of atomic arrangement, and second, on the assumption that the correlation functions behave in the same way.* If these assumptions are not satisfied, the value 10/3 has to be changed, depending on the symmetry, the direction of magnetic fields, and the magnitudes of the relaxation times of all kinds.

In the intermediate cases, where the secular breadth is already narrowed, but the non-secular width shows a frequency-dependence ($1/\sigma_0 \gg \tau_c \sim 1/\omega_z$), the relative contribution of the non-secular width has to be calculated from detailed expression of the correlation functions, $f_1(\tau)$ and $f_2(\tau)$.

For the non-secular shift, the relative weights of single spin- and double spin-inversion process are again different. From Eqs. (6.28d) and (6.30a), we find

$$\begin{aligned} -\delta &= \sigma_{-1}^2\tau_{-1}'' + \sigma_1^2\tau_1'' + \sigma_2^2\tau_2'' \\ &= (1/3)\sigma_1^2\tau_1'' + \sigma_2^2\tau_2'' \\ &= \frac{1}{3}\,\sigma_1^2\,\mathrm{P}\int\frac{f_1(\omega)d\omega}{\omega-\omega_z} + \rho_2^2\,\mathrm{P}\int\frac{f_2(\omega)d\omega}{\omega-2\omega_z} \\ &= \sigma_p^2\,\mathrm{Im}\left\{\frac{3}{2}\int_0^\infty \exp(-i\omega_z t)\right. \\ &\qquad\qquad \times\sum_k \langle\{F_{jk}^{-1}(t)F_{jk}^{1}(0)\}\rangle dt \\ &\quad \left. + \frac{3}{4}\int_0^\infty \exp(-2i\omega_z t)\sum_k \langle\{F_{jk}^{-2}(t)F_{jk}^{2}(0)\}\rangle\right\}, \end{aligned} \tag{7.30}$$

because $\tau_{-1}'' = -\tau_1''$. Thus, the single spin inversion process is less effective for the shift than for the width. Naturally, the shift vanishes for extremely narrowed case. It increases in magnitude just when the non-secular broadening reaches at the maximum, and approaches to the value for the static case as the relaxation time increases to infinity. Generally, the relation of the shift and the broadening of the non-secular effect is essentially similar to that between the dispersion and the absorption.

To illustrate the general features of the motional effect discussed above, let us now take the simple example with isotropic arrangement of atoms and with a single relaxation time τ_c, and draw the curves of the secular and the non-secular widths, the total width, the spin-lattice relaxation time and the

---

* The following is particularly to be noticed here. The conditions which give the 10/3 effect brings out the remarkable result, $T_2 = T_1$, at the limit of extreme narrowing ($1/\sigma_0 \gg 1/\omega_z \gg \tau_c$). This is seen from (7.28a), (7.24), (7.24a), (7.25) and (7.17) (see also (7.31) and (7.32)). Thus, for this limiting case, T_1 and T_2 appearing in Bloch's equation need not be distinguished. Like the 10/3 effect, this equality of T_2 and T_1 depends on the two assumptions mentioned in the text. If the first assumption about the atomic arrangement is discarded, the limiting ratio of T_2 and T_1 becomes.

$$T_2/T_1 = \sum_j 2(1-\overline{\cos^2\theta_{ij}})/\sum_j (1+\overline{\cos^2\theta_{ij}})\,,$$

where θ_{ij} is the angle between the radius vector r_{ij} connecting neighboring atoms and the direction of the constant field. Generally anisotropy is to be expected for both T_1 and T_2.

shift as functions of τ_c or ω_z. The secular width $(\Delta\omega)_{\text{sec}}$ is determined by Eq. (6.26) or by the approximate Eq. (6.28).

Theoretical expressions for this model are summarized below:

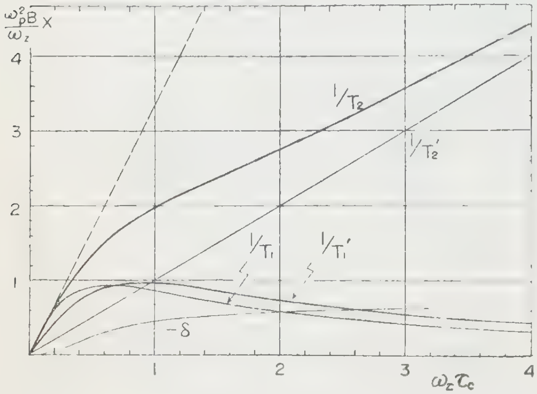

Fig. 3. Change of the width, the shift and the spinlattice relaxation time with the correlation time, τ_c of the local fields. The secular width $1/T_2'$ is here strongly narrowed. The non-secular width $1/T_1'$ is added to $1/T'_2$ to give the half width $1/T_2$ of the absorption line narrowed by the motional effect and broadened by the non-secular perturbation. T_1 is the spin-lattice relaxation time. The dotted line is the asymptote of $1/T_2$ and $1/T_1$ for $\tau_c\to 0$ (or $\omega_z\to 0$). δ is the nonsecular shift. ($\omega_p^2=(3/5)\sigma_p^2 B$ is the secular second moment).

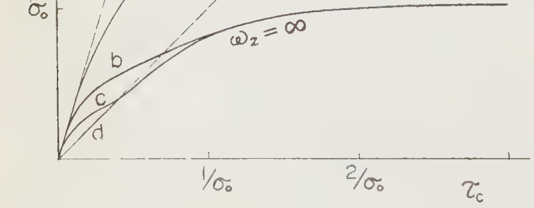

Fig. 4. A schematic disgram showing the width as a function of ω_z and τ_c. Curve a is the asymptote for $\omega_z\to 0$, including the whole contribution from the satellites. Curve d is another asymptote for $\omega_z\to\infty$, thus including only the secular width. Intermediate curves b and c show the widths for intermediate Zeeman frequencies, for which both the secular and non-secular perturbations contribute to the width. For a fixed τ_c the width decreases with increase of ω_z.

$$\begin{aligned}\Delta\omega_{1/2}&=(\Delta\omega)_{\text{sec}}+(\Delta\omega)_{\text{nonsec}}=1/T_2\\&=1/T_2'+1/T_1',\\1/T_1'&=\sigma_p^2B\left\{\frac{\tau_c}{1+\omega_z^2\tau_c^2}+\frac{2}{5}\frac{\tau_c}{1+4\omega_z^2\tau_c^2}\right\},\\1/T_1&=\sigma_p^2B\left\{\frac{2}{5}\frac{\tau_c}{1+\omega_z^2\tau_c^2}+\frac{8}{5}\frac{\tau_c}{1+4\omega_z^2\tau_c^2}\right\},\\-\delta&=\sigma_p^2B\left\{\frac{1}{5}\frac{\omega_z\tau_c^2}{1+\omega_z^2\tau_c^2}+\frac{4}{5}\frac{\omega_z\tau_c^2}{1+4\omega_z^2\tau_c^2}\right\},\end{aligned}\tag{7.31}$$

Note that these formulae are based on the assumption that the main line is far apart from the satellites. In other words, the condition

$$\sigma_0=\sqrt{\frac{3}{5}}\,B\,\sigma_p\ll\omega_z,$$

is necessary in order that Eq. (7.31) is valid. The secular width is well approximated by

$$1/T_2'=(3/5)\sigma_p^2B\tau_c, \tag{7.32}$$

in the region where the non-secular effect becomes important. In Fig. 3, $1/T_1$, $1/T_1'$, $1/T_2$, $1/T_2'$ and δ are plotted against τ_c, for the region of strong narrowing. Fig. 4 shows schematically the general nature of shape dependence on ω_z and τ_c. In the limit of $\tau_c\to 0$ and $\omega_z\to 0$, the resonance line emerges into the natural resonance, which is a half Gaussian curve in our approximation with the second moment σ_w^2. (This may not be of physical interest for the nuclear magnetic cases, but we mention this here because the physics is quite the same for paramagnetic cases, for which the natural resonance can be observed.) This natural resonance will also be narrowed to a half-Lorentzian resonance when the correlation time τ_c decreases to zero. The effective narrowing sets in for τ_c determined by

$$\tau_c\sim 1/\sigma_w=(3/10)^{1/2}/\sigma_0,$$

and the width for smaller τ_c will be approximately

$$\sigma_w^2\tau_c=(10/3)\sigma_0^2\tau_c.$$

Thus, the asymptotic curve for $\omega_z\to 0$ is such as shown in Fig. 4. At $\tau_c\approx 0$, every curve for $\omega_z\neq 0$ starts along this asymmetric curve, and emerges into another asymptote $1/T_2'$, which is the limit for $\omega_2\to\infty$. If σ_0 and ω_z are comparable, the situation is much more complicated. In such cases, the resonance lines at 0, ω_z, $2\omega_z$ $\cdots$ are too close to be separated, and the actual resonance is continuous from $\omega=0$ to infinity.

The non-secular shift δ will be observable only in the cases where $\omega_z \sim 1/\tau_c$. Then it becomes of the same order of magnitude as the width.

Finally, we note that the structures of correlation functions $f_\gamma(\tau)$ are essentially similar to that of the relaxation function of the magnetic moment itself (see Eqs. (7.13b) and (2.9).) Thus, in principle, we may employ here the same technique of calculation as we developed in § 4. We can perhaps discriminate two cases. The first is that the energy levels of the nuclear motion make a quasi-continuum with a fairly large density. The second case is that the nuclear motion has groups of energy levels, the energy difference of different groups being large compared to $\hbar\sigma_0$. In the second case, the high frequency elements of $\Phi_{jk}{}^\gamma(t)$, Eq. (7.9), can be omitted, and the nuclear motion may be regarded as consisting of completely separate modes with proper Boltzmann weights. The correlation functions are to be calculated for each of the groups. This actually occurs in systems which involves some kind of molecular rotation. In the first case, we may calculate the expansion of $f_\gamma(t)$ in powers of t to obtain an approximation of $\log f_\gamma(t)$. Generally, however, the nuclear motion in this case can be regarded as highly classical, so that some classical approximation would be reasonably applied.

§ 8. Exchange Narrowing in Paramagnetic Resonance

Exchange narrowing in paramagnetic resonance absorption is another typical example of the motional effect, as has been pointed out by Gorter, Van Vleck[7] and others. This phenomena will be treated here completely in parallel to the motional effect of the nuclear magnetic resonance discussed in the preceding section. Now the stirring motion of the resonating spins is due to the exchange interaction of the spins, or more generally due to any kind of isotropic interaction of the spins which is stronger than the dipolar coupling. Thus, the unperturbed Hamiltonian of the spin system is assumed to be

$$\mathscr{H}_0=\mathscr{H}_z+\mathscr{H}_{ex}\ . \tag{8.1}$$

Our assumption is that the exchange energy commutes with the Zeeman energy and the total magnetic moment in x-directoin, namely

$$[\mathscr{H}_{ex},\ \mathscr{H}_z]=0,\quad [\mathscr{H}_{ex},\ M_x]=0\ . \tag{8.2}$$

The perturbation is the dipolar interaction:

$$\begin{aligned}\mathscr{H}'=\sum_\gamma \mathscr{H}_\gamma{}'&=\sum_\gamma\sum_{jk}\mathscr{H}_{\gamma,jk}{}'\\ &=\sum_\gamma\sum_{jk}\Phi_{jk}{}^{-\gamma}\{jk\}_\gamma\ ,\end{aligned} \tag{8.3}$$

where the notations are the same as Eqs-(7.2)–(7.5).

Furthermore, we assume the temperature to be so high that no long range ordering is appreciable either by the applied magnetic field or by the exchange coupling. This means that the density matrix (4.27) may be replaced simply by unity. On the other hand, if the temperature is low compared to the exchange coupling energy, a complication enters because of the long order effect, which actually happens when we deal with the ferromagnetic or antiferromagnetic resonance. These are, however, beyond the scope of the present work.

Therefore, most of the basic formulae of the preceding section can be directly applied to the present problem with minor modifications. In particular, Eq. (7.13) now reads as

$$\begin{aligned}&\hbar^2\langle M_-M_+\rangle\sigma_\gamma{}^2 f_\gamma(\tau)\\ &=\langle[M_-,\ \exp(i\tau\mathscr{H}_{ex}/\hbar)\mathscr{H}_{-\gamma}\exp(-i\tau\mathscr{H}_{ex}/\hbar)]\\ &\qquad\qquad\times[\mathscr{H}_\gamma{}',M_+]\rangle\\ &=\langle\exp(i\tau\mathscr{H}_{ex}/\hbar)[M_-,\mathscr{H}_{-\gamma}]\exp(-i\tau\mathscr{H}_{ex}/\hbar)\\ &\qquad\qquad\times[\mathscr{H}_\gamma{}',M_+]\rangle\ ,\end{aligned} \tag{8.4}$$

and Eq. (7.13a) as

$$\hbar^2\sigma_\gamma{}^2=(3/4)c_\gamma{}^2K_{\gamma+1}S(S+1)\sum_k|\Phi_{jk}{}^\gamma|^2, \tag{8.4a}$$

where S is the magnitude of the spin, and $\sigma_\gamma{}^2$ is the second moment associated with the dipolar interaction γ running from -1 to 2. The secular component $\sigma_0{}^2$ is the second moment of the main line.

According to the general theory developed in § 6, our problem is now to calculate the correlation functions $f_\gamma(t)$ for each part of the perturbation. A rigorous calculation is prohibitively difficult and we are forced to take an approximate way, which is given in the following.

The right hand side of Eq. (8.4) can be expanded in powers of τ as

$$\begin{aligned}&\langle\exp(i\tau\mathscr{H}_{ex}/\hbar)[M_-,\mathscr{H}_{-\gamma}']\exp(-i\tau\mathscr{H}_{ex}/\hbar)[\mathscr{H}_\gamma' M]\rangle\\ &\quad=\langle[M_-\mathscr{H}_{-\gamma}'][\mathscr{H}_\gamma' M_+]\rangle\\ &\qquad+(i\tau/\hbar)\langle[\mathscr{H}_{ex}[M_-\mathscr{H}_{-\gamma}']][\mathscr{H}_\gamma' M^+]\rangle\\ &\qquad+\tfrac{1}{2}(i\tau/\hbar)^2\langle[\mathscr{H}_{ex}[\mathscr{H}_{ex}[M_-\mathscr{H}^-{}_\gamma']]][\mathscr{H}_\gamma' M]\rangle\\ &\qquad+\cdots\cdots.\end{aligned}\tag{8.5}$$

The first order term of this expansion is easily proved to be zero. The successive terms are, in principle, to be calculated in elementary manner. But, of course, calculations of higher terms are very tedious. Thus, avoiding such complications, we assume that

$$f_\gamma(\tau)=\exp\{-\tfrac{1}{2}\omega_{e\gamma}{}^2\tau^2\}\ ,\tag{8.6}$$

where $\omega_{e\gamma}$ is defined by

$$\omega_{e\gamma}{}^2=\frac{\langle[\mathscr{H}_{ex}[M_-\mathscr{H}_{-\gamma}']][[\mathscr{H}_\gamma',\ M_+]\mathscr{H}_{ex}]\rangle}{\hbar^2\langle[M_-\mathscr{H}_{-\gamma}'][\mathscr{H}_\gamma' M_+]\rangle}\ .\tag{8.7}$$

The assumption (8.6) is analogous to our basic approximation method (4.6). It is also equivalent to the Gaussian assumption of random frequency modulation adopted by Anderson and Weiss[8] in their theory of exchange narrowing. It should be admitted that the assumption is by no means rigorous, but it is highly probable that it affords a good approximation to reality. Here we use this only because it is simple and makes the calculation accessible.

Therefore, our description of the exchange narrowing of the secular broadening is quite the same as that of Anderson and Weiss. That is,

$$\phi_0(t)=\exp\left[-\sigma_0{}^2\int_0^t(t-\tau)\exp(-\omega_{e0}{}^2\tau^2/2)\,d\tau\right],\tag{8.8}$$

(see Eq. (6.17a)) is the generating function of the intensity distribution of the main line broadened by the secular part of dipolar interaction and narrowed by the exchange effect. Expanding $\phi_0(t)$ in powers of t, we obtain

$$\phi_0(t)=1-\tfrac{1}{2}\sigma_0{}^2t^2+(1/24)\sigma_0{}^2\omega_{e0}{}^2t^4+(1/8)\sigma_0{}^4t^4+\cdots.$$

Thus we see at once that

$$\varDelta\omega^4-3(\overline{\varDelta\omega^2})^2=\sigma_0{}^2\omega_{e0}{}^2\ ,\tag{8.9}$$

is just the excess of the fourth moment over its normal value $3\sigma_0{}^4$. Anderson Weiss have made use of Van Vleck's calculation[6] of the fourth moment to determine $\omega_{e0}{}^2$ (which they wrote as $(\pi/4)\omega_e{}^2$).

In our approximation, the line shape of the main line is represented by

$$I_0(\omega)=\int_{-\infty}^{\infty}\exp\left\{-\sigma_0{}^2\int_0^t(t-\tau)\exp(-\omega_{e0}{}^2\tau^2/2)d\tau-i\omega t\right\}dt\ .\tag{8.10}$$

This reduces, in the case of strong narrowing, to a Lorentzian distribution with the half width,

$$(\varDelta\omega)_{\rm sec}=\sigma_0{}^2\tau_0'\ ,\tag{8.11}$$

where

$$\tau_0'=\int_0^\infty\exp(-\omega_{e0}{}^2\tau^2/2)d\tau=\sqrt{\frac{\pi}{2}}\Big/\omega_{e0}\ .\tag{8.11a}$$

The secular shift is zero in this approximation.

In stead of carrying out a numerical integration of (8.10), we shall content ourselved with an approximate estimation of the half width by a modified BPP equation similar to Eq. (6.27a), which is replaced by

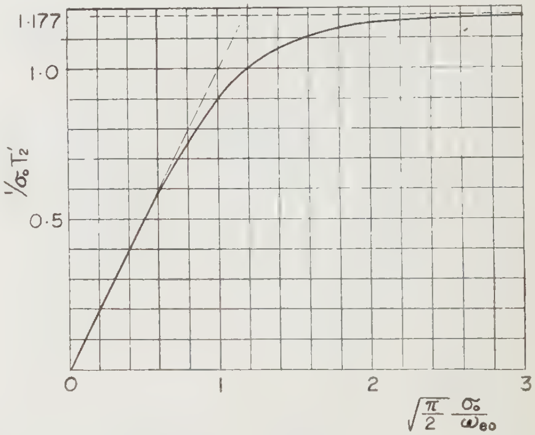

Fig. 5. The secular half width calculated by Eq. (8.12) showing the exchange narrowing.

$$\begin{aligned}\left(\frac{1}{T_2'}\right)^2&=(2\log2)\sigma_0{}^2\int_{-4\log2/T_2'}^{4\log2/T_2'}\frac{1}{\sqrt{2\pi}\,\omega_{e0}}\\ &\qquad\times\exp(-\omega^2/2\omega_{e0}{}^2)d\omega\\ &=(2\log2)\,\sigma_0{}^2\,\varPhi\left(\frac{\pi}{4\sqrt{2}\log2}\,\frac{1}{\omega_{e0}T_2'}\right),\end{aligned}\tag{8.12}$$

where the first integrand is the spectrum of the correlation function $\exp(-\omega_{e0}{}^2\tau^2/2)$ and the function $\varPhi(x)$ is the error integral,

$$\varPhi(x)=\frac{2}{\sqrt{\pi}}\int_0^x e^{-t^2}dt\ .$$

Fig. 5 shows the half width calculated from

(8.12) against $\sqrt{\pi/2}\,\sigma_0/\omega_{e0}$. Naturally, the change of the secular width with the exchange parameter is very similar to that for Eq. (6.27a).

The non-secular width and shift are given by (see Eqs. (6.28) and (6.29))

$$(\varDelta\omega)_\gamma=\sigma_\gamma^2\tau_\gamma'\,,\quad \delta_\gamma=-\sigma_\gamma^2\tau_\gamma''\,, \tag{8.13}$$

where

$$\tau_\gamma'=\mathrm{Re}\int_0^\infty \exp(-i\gamma\omega_z\tau)-\tfrac{1}{2}\omega_{e\gamma}^2\tau^2 d\tau$$

$$=\sqrt{\frac{\pi}{2}}\,\frac{1}{\omega_{e\gamma}}\exp(-\tfrac{1}{2}\gamma^2\omega_z^2/\omega_{e\gamma}^2)\,, \tag{8.13a}$$

and

$$\tau_\gamma''=\mathrm{Im}\int_0^\infty \exp(-i\gamma\omega_z\tau-\tfrac{1}{2}\omega_{e\gamma}^2\tau^2)d\tau$$

$$=\frac{1}{\omega_{e\gamma}}\exp(-\gamma^2\omega_z^2/2\omega_{e\gamma}^2)$$

$$\times\int_0^{\gamma\omega_z/\omega_{e\gamma}} \exp(u^2/2)du\,. \tag{8.13b}$$

For the numerical computation of the expression, (8.13b), we refer a table given by Terazawa[18]. The behaviour of τ_γ' and τ_γ'' are again qualitatively similar to the case of single exponential correlation (6.32a).

As we have discussed in § 6, the non-secular broadening becomes important when the Zeeman frequency is comparable to the frequency of the exchange interaction. In this region, a frequency dependence of the width is generally to be expected. If a strong exchange effect is assumed, the half width,

$$\omega_{1/2}=\varDelta\omega_{\mathrm{sec}}+\varDelta\omega_{\mathrm{nonsec}}\,,$$

may be expressed by

$$\varDelta\omega_{1/2}=\sqrt{\frac{\pi}{2}}\left[\frac{\sigma_0^2}{\omega_{e0}}+\frac{\sigma_{-1}^2+\sigma_1^2}{\omega_{e1}}\exp(-\omega_z^2/2\omega_{e1}^2)\right.$$

$$\left.+\frac{\sigma_2^2}{\omega_{e2}}\exp(-2\omega_z^2/\omega_{e2}^2)\right], \tag{8.14}$$

Thus, the width becomes smaller for shorter waves (i.e. for stronger fields) because of the disappearance of the non-secular broadening. The ratio of the widths at low freuency and at high frequency limits is

$$\frac{\varDelta\omega_{\text{low freq.}}}{\varDelta\omega_{\text{high freq.}}}=1+\frac{\omega_{e0}}{\omega_{e1}}\frac{\sigma_{-1}^2+\sigma_1^2}{\sigma_0^2}+\frac{\omega_{e0}}{\omega_{e2}}\frac{\sigma_2^2}{\sigma_0^2}\,. \tag{8.15}$$

This reduces to 10/3 for ideal cases where the atomic arrangement is isotropic or regularly symmetric and the characteristic frequencies, ω_{e0}, ω_{e1} and ω_{e2} are all identical. Otherwise, this ratio should depend on the crystal structure as well as on the orientation of the constant and oscillating magnetic fields.

Eq. (8.14) is a refined expression of the 10/3 effect which was discussed by Anderson and Weiss[8] in connection with the breadth of resonance absorption in some paramagnetic salts like $Fe_2(SO_4)_3$, $Fe(NH_4)(SO_4)_2$, $MnSO_4$, and $MnCl_2$. They showed that the nonadiabatic broadening, which they called the 10/3 effect, can account for the excess of the widths in these salts over the narrowed widths as one expects from Eq. (8.11). More recently, Ono *et al*[19] have observed a frequency dependence of the width of paramagnetic resonance in $K_2CuCl_4\cdot 2H_2O$. As a matter of fact, there are two inequivalent copper ions in an unit cell of this crystal and these ions have anisotropic *h*-factors. Thus the situation is rather complicated. But, when the field is applied along the (001) direction, the *g*-factors of the two ions are both equal to 2.23, which allows us to apply the present theory. Preliminary calculations[20] showed a reasonable agreement between the theoretical analysis and their experimental data.

In actual paramagnetic substances, there may exist, besides the dipolar interaction, other causes for the broadening, for example, the hyperfine structure effect. Eq. (8.14) has, of course, to be modified to include such effects. It should be also remembered that the non-secular broadening effect is always accompanied by a shift of the peak,

$$\delta=-\sum\sigma_\gamma^2\tau_\gamma''\,,$$

(see Eqs. (6.30a) and (8.13b)).

Further theoretical developments on this topic of paramagnetic resonance absorption is out of space here, so that they will be given in another article.

§ 9. Summary

In our formulation of the general theory of magnetic resonance, our particular intention was to construct the theory on a clear basis of quantum mechanics. We saw in Part A that the Fourier transform method is logically connected with a general treatment of irreversible processes. The most general expression of the relaxation function, Eq. (1.19) was shown to be reasonably replaced by a simpler expression (2.9) for most of practical cases where the low-frequency approximation is correct. In Part B, we showed a formal expansion method to calculate the relaxation on the basis of perturbation theory. The magnetic moment and the perturbation are decomposed into Fourier components according to their characteristic frequencies in reference to the unperturbed motion of the system. This general consideration gives a natural way to separate the whole spectrum into the main lines and the satellites, and it also shows how we can select a particular part of the relaxation function to obtain the generating function in the form of Eq. (4.6) to describe the intensity distribution of a line of our interest. The logical relation of the method to the customary moment was discussed in § 5. In § 6 we treated the motional effect from a most general point of view. This gives a satisfactory formulation of the theoriee of the narrowing of the secular width, the additional broadening due to the non-secular perturbation, and the shifts which accompany to the secular and non-secular perturbation. Also it was pointed out that the non-secular broadening and the so-called spin-lattice relaxation are different things though very closely related to each other. Examples of the motional effect, that is the motional effect in the nuclear magnetic resonance absorption and the exchange effect in the paramagnetic resonance, were discussed further in § 7 and § 8. Explicit expressions were derived in § 7 for the simple case of dipolar broadening in nuclear magnetic case assuming the correlation functions of the nuclear motion as exponentially decaying type. Our treatment of the exchange effect in paramagnetic resonance, which was developed in § 8, includes approximate equations for calculating the narrowing of the secular width and the additional broadening due to the so-called 10/3 effect.

Acknowledgements

We would like to express appreciation to Dr. P. W. Anderson for much valuable discussions, and to Mr. Y. Obata and Mr. H. Hasegawa for their help in some numerical computations. This study was partially financed by the Scientific Research Fund of the Ministry of Education.

Appendix

Here we shall briefly sketch a perturbation calculation to derive Eqs. (1.19a) and (3.15). We start from the equation of motion for the density matrix,

$$i\hbar\dot{\rho}(t)=\overline{\mathscr{H}}\rho-\rho\overline{\mathscr{H}}\ , \qquad \text{(A.1)}$$

where

$$\overline{\mathscr{H}}=\mathscr{H}-\boldsymbol{H}_1(t)\boldsymbol{M}\ , \qquad \text{(A.2)}$$

$\boldsymbol{H}_1(t)$ being the applied magnetic field and $\boldsymbol{M}$ the magnetic moment of the system. Transforming Eq. (A.1) into the interaction representation,

$$\rho(t)=\exp(-it\mathscr{H}/\hbar)\rho'(t)\exp(i\mathscr{H}t/\hbar)\ , \qquad \text{(A.3)}$$

we get

$$ih\dot{\rho}'(t)=[\rho'(t),\ \boldsymbol{M}(t)]\boldsymbol{H}_1(t)\ , \qquad \text{(A.4)}$$

where $\boldsymbol{M}(t)$ is defined by

$$\boldsymbol{M}(t)=\exp(it\mathscr{H}/\hbar)\boldsymbol{M}\exp(-it\mathscr{H}/\hbar)\ . \qquad \text{(A.5)}$$

Thus we integrate Eq. (A.4) to the first order of $H_1(t)$ to obtain

$$\rho'(t)=\rho'(-\infty)+(i\hbar)^{-1}\int_{-\infty}^{t}[\rho'(-\infty),\ \boldsymbol{M}(t')]\times\boldsymbol{H}_1(t')dt'+0(\boldsymbol{H}_1{}^2)\ ,$$

or, going back to $\rho(t)$, Eq. (A.3),

$$\rho(t)=\rho_0+(i\hbar)^{-1}\int_{-\infty}^{t}[\rho_0,\boldsymbol{M}(t'-t)]\boldsymbol{H}_1(t)dt'+0(\boldsymbol{H}_1{}^2)\ , \qquad \text{(A.6)}$$

where ρ_0 means

$$\rho_0=\exp(-it\mathscr{H}/\hbar)\rho'(-\infty)\exp(it\mathscr{H}/\hbar)\ .$$

We assume that the field $\boldsymbol{H}_1(t)$ has been adiabatically inserted at $t=-\infty$, so that the density matrix ρ_0 is a function of $\mathscr{H}$ which represents a statistical equilibrium in the absence of $\boldsymbol{H}_1$. Accordingly ρ_0 and $\rho'(-\infty)$ are both commutable with $\mathscr{H}$. Now the expectation value of the magnetization at the time t is

$$\begin{aligned}\langle\boldsymbol{M}(t)\rangle&=Tr\rho(t)\boldsymbol{M}\\&=\overline{\boldsymbol{M}}_0+(i\hbar)^{-1}\int_{-\infty}^{t}Tr\{[\rho_0\boldsymbol{M}(t'-t)]\boldsymbol{H}_1(t')\boldsymbol{M}\}dt'\\&\qquad+0(H_1{}^2)\ ,\end{aligned} \qquad \text{(A.7)}$$

which can be written in the form of Eq. (1.18) with the relaxation tensor ϕ defined by

$$(d/dt')\phi_{xy}(t-t')=(i/\hbar)Tr\rho_0[M_x(t-t'),\ M_y]\,.$$

This proves Eq. (1.19a), which may also be written as Eq. (1.19), if the density matrix ρ_0 is assumed to be canonical.

If the magnetic field $\boldsymbol{H}_1(t)$ is assumed to be harmonic, i.e.,

$$\boldsymbol{H}_1(t)=\boldsymbol{H}_1\cos\omega t\ .$$

Eq. (A.7) is transformed as follows.

$$\begin{aligned}
&\langle M_x(t)\rangle-\langle M_0\rangle_x\\
&=\frac{i}{\hbar}\sum_y\int_{-\infty}^{t} Tr\rho_0[M_x(t-t')M_y]H_{1y}(t')dt'\\
&=\frac{i}{\hbar}\sum_y\sum_j\sum_k \rho(E_j)\int_0^{\infty}[(j|M_x|k)(k|M_y|j)\\
&\qquad\times\exp(i(E_j-E_k)\tau/\hbar)-(j|M_y|k)(k|M_x|j)\\
&\qquad\times\exp(i(E_k-E_j)\tau/\hbar]H_{1y}\cos\omega(t-\tau)d\tau\\
&=\frac{i}{2}\sum_y\sum_j\sum_k \rho(E_j)\Big[(j|M_x|k)(k|M_y|j)\\
&\qquad\times\Big\{\Big(\pi\delta(E_j-E_k-\hbar\omega)+i\frac{1}{E_j-E_k-\hbar\omega}\Big)e^{i\omega t}\\
&\quad+\Big(\pi\delta(E_j-E_k+\hbar\omega)+i\frac{1}{E_j-E_k-\hbar\omega}\Big)e^{-i\omega t}\Big\}\\
&\quad-(j|M_y|k)(k|M_x|j)\\
&\qquad\times\Big\{\Big(\pi\delta(E_k-E_j-\hbar\omega+1\frac{1}{E_k-E_j-\hbar\omega}\Big)e^{i\omega t}\\
&\quad+\Big(\pi\delta(E_k-E_j+\hbar\omega)+i\frac{1}{E_k-E_j+\hbar\omega}\Big)e^{-i\omega t}\Big\}\Big],
\end{aligned}\tag{A.8}$$

where we have made use of the relation

$$\int_0^{\infty}e^{ixt}dt=\pi\delta(x)+iP(1/x).$$

Comparing the above expression with

$$\begin{aligned}\langle M_x(t)\rangle-\bar{M}_x^0=\sum_y\{\chi_{xy}'H_{1y}\cos\omega t\\
+\chi_{xy}''H_{1y}\sin\omega t\}V\ ,\end{aligned}$$

we get explicit formulae for the susceptibility components. In particular, one finds easily

$$\begin{aligned}V\chi_{xx}'=\sum_j\sum_k\rho(E_j)|(j|M_x|k)|^2\\
\times\Big(\frac{1}{E_k-E_j-\hbar\omega}+\frac{1}{E_k-E_j+\hbar\omega}\Big),\end{aligned}\tag{A.9}$$

and

$$\begin{aligned}V\chi_{xx}''=\pi\sum_j\sum_k\{\rho(E_j)-\rho(E_k)\}\ |(j|M_x|k)|^2\\
\times\delta(E_k-E_j-\hbar\omega)\ ,\end{aligned}\tag{A.10}$$

Eq. (A.9) is the well known dispersion formula (see, for instance, reference 21). Eq. (A.10) and Eq. (3.10) give the rate of energy absorption

$$\begin{aligned}Q=H_{1x}^2V\frac{\pi}{2\hbar}h\nu\sum_j\sum_k\{\rho(E_j)-\rho(E_k)\}\\
\times|(j|M_x|k)|^2\delta(E_k-E_j-\hbar\omega)\ ,\end{aligned}$$

which is a direct consequence of ordinary calculation of transition probability. One can also see quite easily that

$$Q=H_{1x}^2V\frac{\pi\nu}{2\hbar}\int_{-\infty}^{\infty}\langle[M_x(\tau),\ M_x]\rangle e^{i\omega\tau}d\tau\ .$$

Similar consideration apply to other cases than the linearly polarized radiation, for instance, to Eq. (3.13).

References

1) F. Bloch: Phys. Rev. **70** (1946), 460.

2) E. M. Purcell, H. C. Torrey, and R. V. Pound: Phys. Rev. **69** (1946) 37.

3) N. Bloembergen, E. M. Purcell and R. V. Pound: Phys. Rev. **73** (1948), 679.

4) I. Waller: Zeits. f. Physik, **79** (1932) 370.

5) L. J. Broer: Physica, **10** (1943), 801.

6) J. H. Van Vleck: Phys. Rev. **74** (1948), 1168.

7) C. J. Gorter and J. H. Van Vleck: Phys. Rev. **72** (1947) 1128.

8) P. W. Anderson and P. R. Weiss: Rev. Mod. Phys. **25** (1953) 269.

9) P. W. Anderson: J. Phys. Soc. Japan, **9** (1954), 316.

10) M. H. L. Pryce and K. W. H. Stevens: Proc. Phys. Soc. **A 63** (1951) 36.

11) H. Takahashi: J. Phys. Soc. Japan **7** (1952) 439.

12) T. Usui and H. Kambe: Prog. Theor. Phys. **8** (1952) 302.

13) H. A. Kramers: Atti Congr. Fis., Como (1927) 545; R. Kronig: J. Opt. Soc. Amer. **12** (1926) 547.

14) L. Onsager: Phys. Rev. **37** (1931) 405; **38** (1931) 2265.

15) J. H. Van Vleck: *The Theory of Electric and Magnetic Susceptibilities* (1931), Chapter VII.

16) M. C. Wang and C. F. Uhlenbeck: Rev. Mod. Phys. **17** (1945) 323.

17) H. Cramer: *Mathematical Methods of Statistics* (1946) p. 183.

18) K. Terazawa: Sci. Rep. Tohoku Imp. Univ. 1st Ser. 1917, 169.

19) K. Ono, H. Abe and J. Shimada: Phys. Rev. **92** (1953) 551; H. Abe, K. Ono, I. Hayashi, J. Shimada, and K. Iwanaga: J. Phys. Soc. Japan, to appear.

20) T. Tomita: Proc. International Conference on Theoretical Physics, 1953.

21) G. Placzek: Handbuch der Radiologie, Bd VI, Teil ii, p. 211.

JOURNAL OF THE PHYSICAL SOCIETY OF JAPAN Vol. 9, No. 6, NOV.—DEC., 1954

On the Velocity Analysis of Electrons Scattered by Thin Foils

By Hiroshi WATANABE

Hitachi Central Research Lab. Kokubunji-machi,
Kitatama-gun, Tokyo

(Received July 1, 1954)

Results of measurement on the energy loss of 22 kev electrons after passing through various substances—metals, metal oxides, NaCl, $Ca(OH)_2$ and collodion—are given. The apparatus used was an electron velocity analyzer of Möllenstedt type. The design and construction of the analyzer is briefly described and some discussions are given on the results obtained.

§ 1. Introduction

It was early recognized that the measurement of the velocity distribution of electrons after passing through materials was interesting and important from various standpoints and a number of such experiments have already been carried out.1)*

G. Ruthemann2) has experimented with 5～8 kev electrons and obtained the energy spectra of electrons passed through foils of collodion, Al, Be, etc. He used a semi-circular magnetic deflector of Dempster type. In the case of Al and Be he reported that the energy spectra of electrons after passing through the foils had a remarkably characteristic feature, vig. the existence of several peaks of energy losses with equal intervals. G. Möllenstedt1),3) has also performed a similar experiment on various substances. He analysed the electron velocities by deflecting the electrons with an electrostatic cylindrical lens which had a large chromatic aberration constant. The resolving power of his instrument was so high that the detectable energy loss was 1 ev for 35 kev electrons.

Since the velocity retardation of electrons in materials may be caused by the transition of electronic states, these experimental results would give some informations on the electronic structure of the materials. Y. Cauchois4) compared the energy loss of electrons reported by Ruthemann with her own experimental results on the K-absorption edge of X-rays in Al. D. Pines5) explained the same experimental results on Al and Be from his theoretical standpoint, and considered that the energy loss would be caused by the excitation of a plasma oscillation of electron gas in metal.

These experimental results on electron retardation have attracted much attentions of electron microscopists, since the retarded electrons in specimens have considerable effects upon the image of electron microscope. Furthermore, the detailed knowledge of energy spectra may be useful for the understanding of electron diffraction phenomena such as Kikuchi-patterns.6)

The author has constructed an electron velocity analyzer of Möllenstedt type and performed some experiments on the energy loss of electrons in passage through metals, metal oxides and alkali-halide etc. This velocity analyzer has no original feature in regard to the operating principles, but is designed so that the analyzer unit can be easily attached to an ordinary electron mictroscope or to an electron diffraction camera.

§ 2. Instrument

Fig. 1 shows the instrument used in this experiment. Only an electrostatic lens of a unipotential type is inserted between the objective and the projection lenses of an ordinary electron microscope. The electron source is a usual gun with a self-biased Wehnelt cylinder. The electron beam is converged on a specimen by a condenser lens, and after passing through the specimen the beam is appropriately diverged by an objective lens, (the latter is a comparatively strong lens). Each of these lenses can be moved horizontally and can be inclined with adjusting screws.

The width and the horizontal position of the fine slit above the cylindrical lens are adjustable from the outside of the vacuum column; it is usually several microns wide. On the plane of the fine slit the electron pencil is about 2 mm in its diameter.

---

* On the way of preparing this manuscript Marton's letter was published in Phys. Rev. **94** (1954) 203.

The beam, after being scattered in the specimen elastically and inelastically, enters into a cylindrical unipotential lens situated below the fine slit. The longer axis of the cylindrical lens aperture and of the fine slit are parallel to each other. Because the cylindrical lens has only a transverse refracting power, the image of the fine slit formed on the screen becomes a straight line. This straightness of the image is of great advantage in obtaining the energy spectra of scattered electrons. It enables us to get an ordinary energy spectrum. Since the cylindrical lens has a chromatic aberration similar to an ordinary lens, a difference of the energy of electrons gives rise to a shift of the image of fine slit; the image shift is perpendicular to the length of the image as mentioned above.

The amount of the image shift Δu_b caused by a difference of the energy of electrons is proportional to the chromatic aberration constant in magnification of the analyzer lens, C_{Fm}, to the distance of the beam from the lens axis, r, and lastly to the ratio of the energy lost by the impact to its initial energy, $\Delta\phi/\phi$. It is therefore,

$$\Delta u_b = M\cdot C_{Fm}\cdot r\cdot \Delta\phi/\phi\ , \qquad (1)$$

where M is the magnification of the lens.

Fig. 2 shows the path of the beam in the analyzer lens under the operating condition in the present experiment. Since the electrostatic field in the lens is remarkably strong, the lens has a large chromatic aberration constant.* M is nearly equal to 1 in this case, and r is assumed to be only 1/2 mm. Because of the large distance between the fine slit and the analyzer lens, the exact value of r is not measurable. Under the usual operating condition of the instrument $MC_{Fm}r=3.4\times10^3$ mm as is shown below. Thus Δu_b takes a sufficiently large value to be detectable on a photographic plate, although $\Delta\phi/\phi$ is usually small; for example $\Delta\phi$ is 5∼20 ev and ϕ is 22 kv in the present instrument, i.e. $\Delta\phi/\phi$ is $2.5\times10^{-4}\sim10^{-3}$, then the corresponding image shift Δu_b is 0.85∼3.4 mm on the plate.

The projection lens of relatively large di-

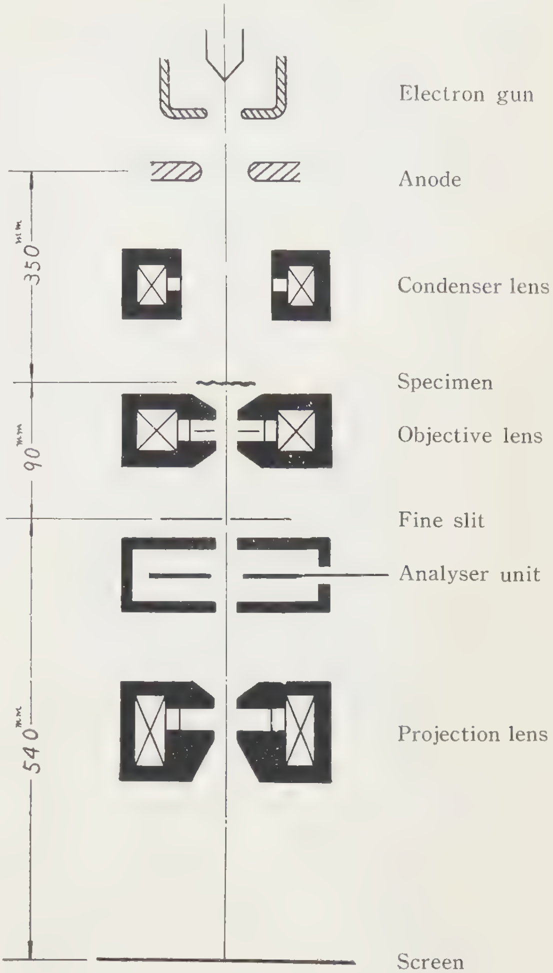

Fig. 1. Schematic diagram of the instrument.

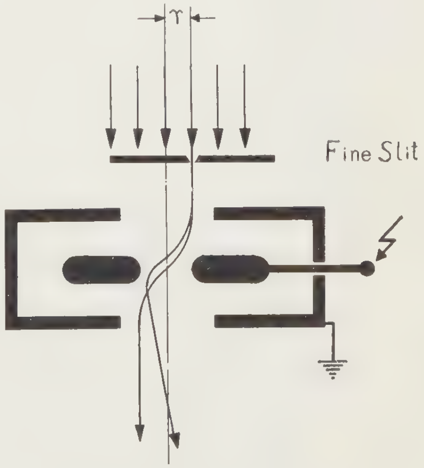

Fig. 2. Schematic diagram of the ray path in the analyzer lens.

---

* The author has ascertained experimentally that the stronger the lens is, the larger the chromatic aberration coefficient becomes,

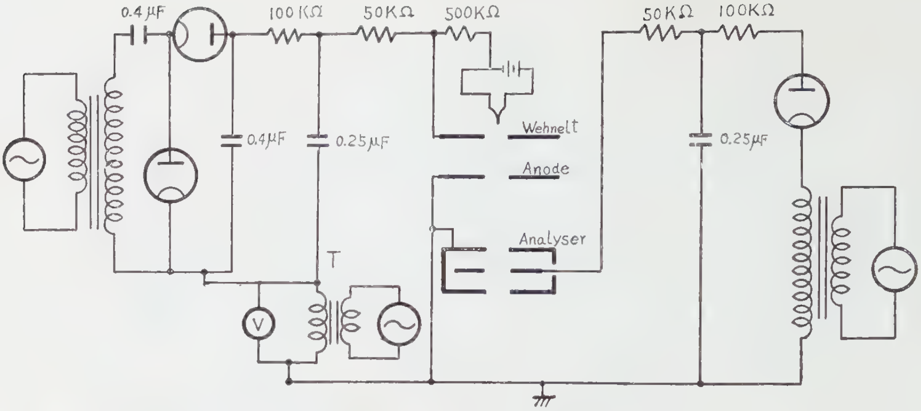

Fig. 3. Circuit diagram of the high voltage.

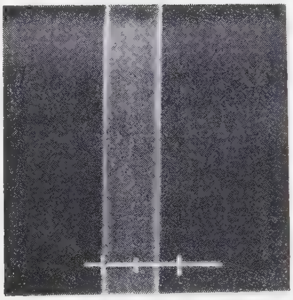

Fig. 4. The movement of the image of fine slit caused by a sinusoidally alternating variation of acceleration voltage. V=10 V, ϕ=22 KV.

ameter is used to make it possible to obtain an enlarged electron micrograph of the specimen, when it is necessary. This procedure was used very advantageously to know the state of specimen. It is, of course, more desirable for the instrument to have an intermediate lens which enables us to take an electron diffraction pattern of the specimen situated at the ordinary specimen position in the electron microscope. The addition of such an intermediate lens to the instrument is now being planned.

Final image of the fine slit or the energy spectrum of the scattered electrons is photographed on a plate, the camera box being an ordinary one of an electron microscope.

Fig. 3 shows the circuit of the high voltage. In order to obtain an energy scale a small transformer T is connected to the earth side of the filter condensers. Because of the high impedance of the main transformer the output of T will be superposed on the high voltage. When a sinusoidal wave of effective voltage V is superposed on the accelerating voltage ϕ through this circuit, the maximum voltage variation ratio is $2\sqrt{2}\,V/\phi$. This voltage variation causes a sinusoidal motion of the image of the fine slit; its amplitude corresponds to the definite voltage variation and is available as an energy scale.

Fig. 4 is a photograph of a fluctuating image of fine slit when a sinusoidally alternating voltage (50 cycles) of the effective value of 10 volts is superposed on the accelerating voltage of 22 kv. The width of this image corresponds to the variation ratio of accelerating voltage, viz. 28.3/22000. From the measurement of this width it was concluded that $MC_{Fm}r$ in Eq. (1) is equal to 3.4×10^3 mm. On the other hand the least width of the final image of the fine slit was about 0.3 mm on the photographic plate. Therefore, the resolving power of this velocity analyzer is nearly equal to 1/10000, and the detectable energy loss of 22 kev electrons is 2 ev.

The resolving power of the electron velocity analyzer of this type[7] depends mainly upon the width of the fine slit and also upon the opening defects such as the spherical aberration in an ordinary lens. It also depends on the collimation of the electron beam to be analysed. It may be possible to obtain the resolving power of 1/50000 by making use of another cylindrical lens which makes the effective width of the electron beam narrower and finer without any loss of the beam intensity.

§ 3. Experimental Results

After ascertaining a sufficient resolving power of the instrument and a linearlity between the image shift and the variation of the accelerating voltage, the energy losses

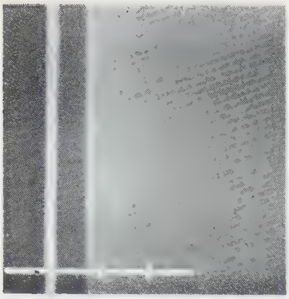

Fig. 5. The energy distribution of electrons after passing through an Al foil, the scale is 20 eV.

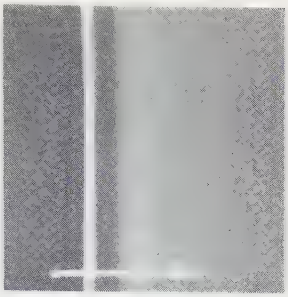

Fig. 6. Al_2O_3. The scale is 20 eV.

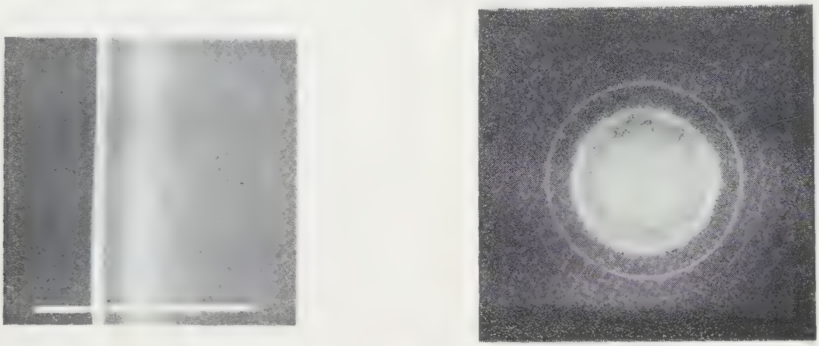

Fig. 7. The energy distribution and electron diffraction of an Sn foil.

of electrons after passing through various metal and oxide foils have been measured. The accelerating voltage was 22 kv throughout this study.

(a) Al & Al_2O_3

An Al foil was prepared by evaporating the metal of 99.99% purity on a collodion substratum in high vacuum and then dissolving the collodion base in appropriate solvents. The thickness of the foil was about 200 Å and it has a sufficient transparency for 22 kev electrons. Fig. 5 shows the energy distribution of electrons after passing through this Al foil; one can see several peaks, viz. at 6.5, 14.8, 23 and 29.5 ev. The main peak corresponds to the electrons transmitted without loss of energy. The first peak at 6.5 ev is a comparatively feeble one, and the peak at 14.8 ev is the most intense and sharp. There is a broad and intense peak at 23 ev. The peak at 29.5 ev which is the last one to be detectable on this plate is very weak, but its sharpness is nearly equal to the one at 14.8 ev. The second and the forth peaks were reported by Ruthemann[2)], and the three peaks discovered in Möllenstedt's experiment[1)] may correspond to the first, the second and the third peak in Fig. 5. Peaks of larger energy loss could not be observed because of the existence of the continuous background and the weakness of the intensity of such peaks. Lang[8)] reported an increase of the number of detectable peaks with the increase of the thickness of Al foil. The author was also able to ascertain this fact qualitatively.

The Al_2O_3 film was prepared by electrolytic etching of Al metal in a dilute solution of borax and ammonia. Fig. 6 shows the result of the velocity analysis of the electrons after passing through this Al_2O_3 film. Except a very feeble peak near the main one, only a broad peak at 22.5 ev is clearly observable, though a weak but broad peak seems to exist at ca. 46 ev.

(b) Sn & SnO_2

An evaporated Sn foil which was prepared by a usual method from the chemical pure Sn metal was mounted in the instrument. Fig. 7 shows the result of the velocity analysis and also the electron diffraction pattern of this foil. There are seen three peaks of energy losses at 6.3, 13 and 19.5 ev; the last one is

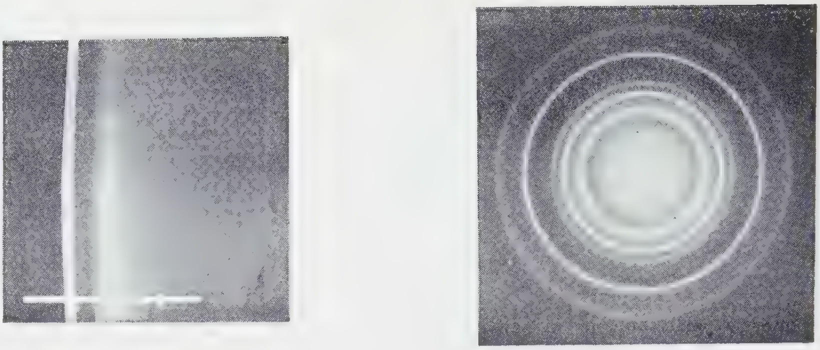

Fig. 8. The energy distribution and electron diffraction from an SnO_2 foil.

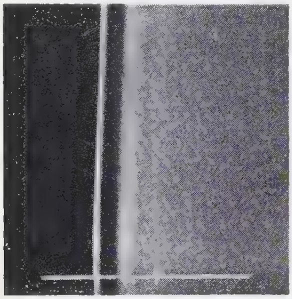

Fig. 9. Be. The scale is 20 eV.

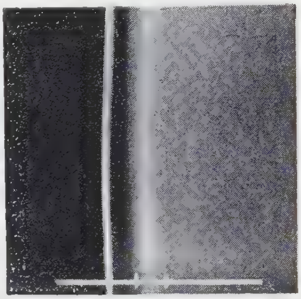

Fig. 10. BeO. The scale is 20 eV.

very broad.

An SnO_2 foil was prepared by heating the Sn foil in an open air at 400°C, for two hours. The electron diffraction patterns proved that the Sn foil converted completely into SnO_2. The diffraction pattern and the energy distribution of electrons after passing through this SnO_2 foil are shown in Fig. 8.

The feature of this energy distribution is not so different from that of Sn foil in spite of the remarkable differences in their diffraction patterns; only the peak at 36 and 63 ev have newly appeared in this case.

(c) Be & BeO

A Be foil of about 300 Å thick was used as a specimen. The energy distribution of electrons passing through this foil is shown in Fig. 9. There are seen two peaks at 19 and 38 ev. In the remoter part of the energy distribution there seem to exist very feeble peaks corresponding to ca. 57 and 76 ev. It was reported by Ruthemann[2)] that the energy distribution of electrons in this case had a similar feature to that of Al.

After the Be foil was heated in an O_2 flow at 500°C, for two hours, the foil converted completely into BeO as was ascertained by electron diffraction. Fig. 10 shows the energy loss of electrons passing through this specimen. In this case it is remarkable that there are several sharp peaks which are not seen in the case of Be metal. The peaks are situated at 5.7, 16.5, 28 and 57 ev.

(d) MgO*

It was difficult to obtain a thin Mg foil by reason of the rapid oxidation of this metal foil especially under the relatively heavy electron bombardment. Thus only the measurement on an MgO foil was carried out. The MgO foil was prepared by leaving an Mg foil supported on a sheet mesh in an O_2 filled desiccator for 2∼3 days at room temperature. The thickness of the Mg foil was about 200 Å. Electron diffraction patterns proved that the foil converted into MgO.

The formation of the hydroxide was prevented by use of a desiccator and prompt mounting in the vacuum column of the instrument at pressures of 10^{-4} mm Hg or less.

Fig. 11 is the energy distribution of electrons after passing through this specimen, and Fig. 12 shows the microphotometer record along the arrow in Fig. 11. One can see there a small peak at 5.5 ev, a sharp one at

---

* Partly reported in Phys. Rev. **95** (1954) 1684.

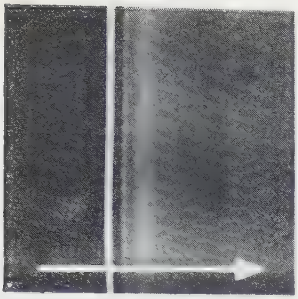

Fig. 11. MgO.

11.4 ev, and somewhat broad one at 25 ev.

(e) Other Metals

The energy losses of electrons passing through various foils such as Ni, Cu, etc. are tabulated in Table I. Most of these values of energy losses coincide with the experimental results obtained by Ruthemann[2] or Mölleestedt[1]. However, in the case of Au the energy distribution has a different feature from that of Möllenstedt. Although Möllenstedt reported peaks at 15, 30, 45 and 60 ev, peaks observed in the present experiment were at 6.5, 17.5, 25, 34 and ca. 50 ev. No difference in the energy loss could be observed between the electrons scattered by an ordinary evaporated Au foil and those by extremely thin gold-leaf prepared by etching in 5% KCN.

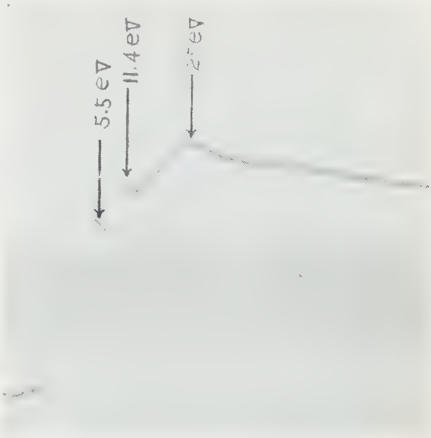

Fig. 12. The microphotometric record along the the arrow in Fig. 11.

Table I. The experimental results on the energy losses of electrons after passing through various materials.

		Energy Losses (eV)	
Specimens	eV 10 20 30 40 50 60	Present Author	Möllenstedt (Ruthemann, Lang)
Al	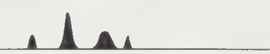	6.5, 14.8, 23, 29.5,	7, 15, 22, (14.72, 29.59, 44.34,)
Al_2O_3	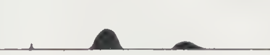	22.5, 46,	22.5, (22.31, 45.52)
Ag	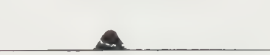	22,	(22.56, 45.31,)
Au	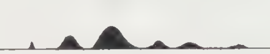	6.5, 17.5, 25, 34, 49	15, 30, 45, 60,
Be	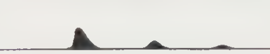	19, 38, 56,	(18.97, 38.11, 57.31,)
BeO	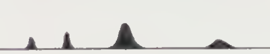	5.7, 16.5, 28, 57,	
* Ca(OH)$_2$	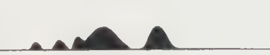	7.5, 12, 15, 22, 37,	
Cr	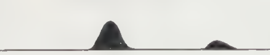	26, 54,	
Cu	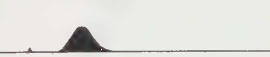	7, 19.5,	(19.1)
Ge	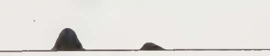	17, 34,	
MgO	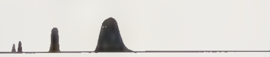	4.5, 5.5, 11.4, 25,	
NaCl	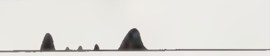	14.5, 20, 24, 29, 32,	
Ni	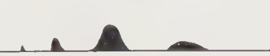	6.5, 12, 22.5, 45,	22.6, 65, (24.2)
Sb	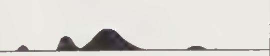	6.5, 18, 24.5, 46,	15, 20, 31,
Sn	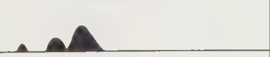	6.3, 13, 19.5,	
SnO_2	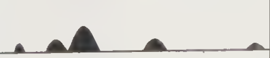	5.5, 12.5, 19.5, 35, 63,	
Collodion	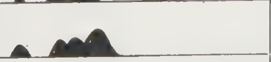	7, 13, 18, 21.2,	[illegible], 21, (21.3)
Residual gas in Vacuum	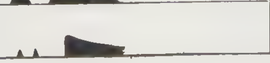	6, 9, 13.5,.	3.5, 7, 12, 66,

(f) Hydroxides & Alkali Halides

In the cases of Ca(OH)$_2$ and NaCl the results are as shown in Fig. 13 and Fig. 14. There are seen in both figures several

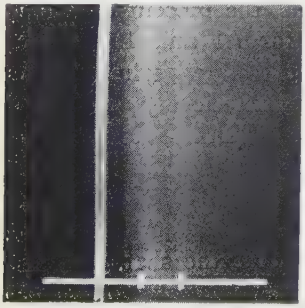

Fig. 13. Ca(OH)$_2$.
The scale is 20 eV.

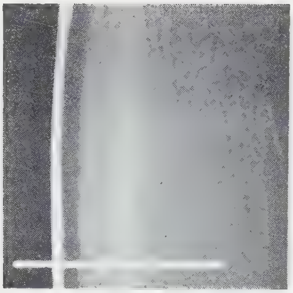

Fig. 14. NaCl. The scale is 20 eV.

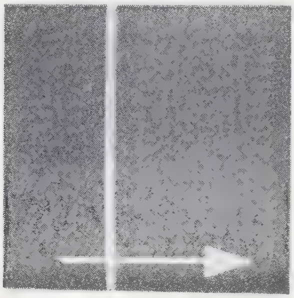

Fig. 15. Residual gas in the vacuum of 10^{-3}mmHg.

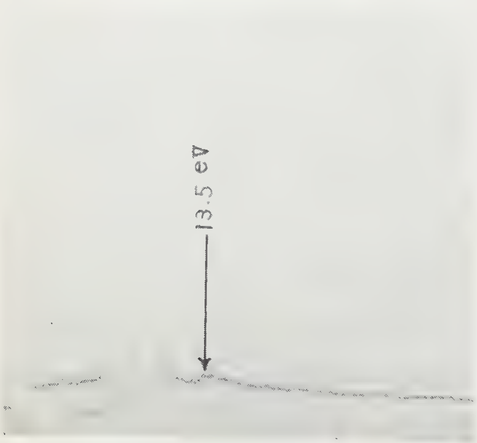

Fig. 16. The microphotometric record along the arrow in Fig. 11.

sharp peaks; particularly in the case of NaCl very fine lines are observed between the peaks at 14.5 and 32 ev. Since the substratum of collodion has a large contribution to the energy spectrum of scattered electrons in the case of $Ca(OH)_2$, the values of energy losses can not be measured with sufficient accuracy.

(g) Residual Gases in the Vacuum of 10^{-3} mm Hg

When the pressure in the vacuum column is less than 10^{-4} mmHg the blank test with no specimen has given nothing but the main peak on the plates. However, at a poorer vacuum of about 10^{-3} mmHg the similar test has given a few peaks as shown in Fig. 15. The microphotometric record of the plate takes a sudden jump at 13.5 ev. This jump may correspond to the ionization energy of N or O; the ionization energy of the former is 14.5 ev and that of the latter is 13.5 ev. Perhaps these two peaks of energy losses were not separated on the plate. There seems to exist also two feeble peaks at 6 and 9 ev.

§ 4. Discussions

In table 1 there are tabulated all of the results which were hitherto obtained. The relative intensities are estimated only by visual inspection and are not so accurate.

(a) Metals

Most of the metals have several peaks which correspond to the energy losses of integral multiples of a basic quantum of 15~25 ev. Möllenstedt has interpreted these peaks as the results of multiple collisions of electrons, without refering to the origin of the basic quanta. In order to go further in this interpretation of the multiple peaks, it seems necessary to make clear the relation between the intensity distribution of retarded electrons and the specimen thickness. However as the intensity measurement is very difficult at the present stage, the discussions on the Möllenstedt's interpretation will be left as a future problem.

On the other hand Pines⁵⁾ has considered that these peaks would be the result of the excitation of a plasma oscillation of electron gas in metal, particularly in the cases of Al and Be. His calculated values of the basic quantum of the energy losses were 15.9 ev for Al and 18.8 ev for Be under the assumption that all the valence electrons are free. These values agree well with Ruthemann's results as well as the present experimental data, i.e. 14.8 ev for Al and 19 ev for Be. It is hard in the present experiment to decide which of these interpretations, by Möllenstedt's and Pines', is more suitable to explain the experimental data in the case of metals. At any rate, there are observed many peaks which could not be attributed to the plasma oscillations, if we take the sharpness and the non-multiplicity of such peaks into consideration; for example the peaks at 6.5 and 23 ev of Al, and also those of Sn, etc.

The basic quanta of the energy loss and the other peaks which can not be explained by plasma oscillation may be considered to correspond to the transitions of the electronic state. Thus the comparison with the data on the fine structure of *K*- or *L*-absorption edge of *X*-rays which are considered to correspond to the excited electronic states of solids may be valuable for the interpretation of the peaks in the present experiment. Cauchois[4] compared the peaks of energy losses in Ruthemann's experiment with her own experimental results on the *K*-absorption edge of Al. She compared the peaks of the energy losses with the maxima of the microphotometric record of absorption spectrum. The peaks of the energy losses, however, should be compared with the valleys of absorption spectrum, because in the case of metals there is an empty level just above the Fermi level. Table II shows the comparison of the peaks of Al in the present experiment with the valleys of *K*- and *L*-absorption edges obtained by Cauchois and Johnston[9] respectively. The peaks of energy losses 6.5 and 14.8 ev may correspond to the fine structures of *K*-absorption edge, and the peak at 23 ev to a valley of *L*-absorption edge. An energy loss of 29.5 ev may be considered as the result of dual collisions, losing the energy of 14.8 ev in each inelastic collision process.

Table II. The comparison of the peaks of Al in the present experiment with the valleys of K- and L-absorption edges of X-rays. (see reference (4), (9))

Valleys of K-abs. edge (eV)	Valleys of L-abs. edge (eV)	Peaks in present experi.
6.1	(3.8)	6.5
14.0	(10)	14.8
	23.0	23
		29.5
37	39	
55	54	

In the case of Be, Sn etc. the similar consideration would be applicable, although the author has no suitable data to be compared with the present experimental results.

(b) Metal oxides and Alkali halides

In the case of metal oxides multiple peaks are also observed, for example, for Al_2O_3, BeO, SnO_2 etc. In this case the plasma oscillation can not be excited, thus all of the basic quanta and the other peaks may be caused by the transitions of the electronic states, and the multiple peaks are considered to be attributable to multiple collisions.

MgO has a sharp peak at 11.4 ev in the energy spectrum. This sharp peak is reasonablly interpreted as a threshold of the first forbidden band above the full band; the width of the forbidden band is assumed to be 10～15 ev by soft *X*-rays measurements[10]. On the other hand Townsend's experiment[11] on *L*-absorption edge of MgO shows that a nearly forbidden range of energies is present at 12 ev above the lowest empty level. If the sharp peak at 11.4 ev in the present experiment is considered to correspond to the lowest empty level, the broad peak at 25 ev of this specimen is also reasonablly interpreted as a threshold of such a nearly forbidden band; in this case the width of the latter is estimated as 13.6 ev. The small peaks near the main peak of MgO suggest the existence of localized levels in the forbidden band. It is evident that the energy transitions of a few electron volts measured by photoconductivity correspond to the localized levels above the valence band. Measurements of the spectral distribution of photoconductivity in MgO show that the electronic transitions are possible at 1.2, 2.1, 3.7 and 4.8 ev, and the additive coloration experiments of Weber[12] have identified the absorption bands at 4.3 and 5.6 ev with excess oxygen. Thus the present small peaks near the main peak are considered to be corresponding to the localized leveles.

By analogy with the case of MgO, the sharp peak of BeO at 16.5 ev could be interpreted as a threshold of the first forbidden band, and the feeble peak at 5.7 ev as a localized level in the forbidden band. In this case the author has no suitable data to compare with the broad peak at 28 ev. The broad one at 57 ev can be considered as the result of dual collision.

The experiment on energy loss of electrons in NaCl gives also several fine peaks which are considered to correspond to the transition of the electronic states.

Although no discussions on the intensities of peaks are given in this paper, it is obvious that the measurement of the intensities of scattered electrons will be an important problem in future along with the problem of obtaining the more accurate data on the energy retardation of electrons.

Acknowledgement

The author wishes to express his heartfelt thanks to Dr. N. Kato of Kobayasi Institute of Physical Research for his helpful discussions. The author is also gratetul to Dr. B. Tadano and Mr. N. Morito of his laboratory for their encouragements throughout this study.

References

1) See for example,
G. Möllenstedt: Optik **5** (1949) 499.
2) G. Ruthemann: Ann. d. Phys. **2** (1948) 113.
3) G. Möllenstedt: Optik **9** (1952) 473.
4) Y. Cauchois: Acta. Cryst. **5** (1952) 351.
5) D. Pines and D. Bohms: Phys. Rev. **85** (1952) 338.
D. Pines: Phys. Rev. **92** (1953) 626.
6) H. Boersch: Optik **5** (1949) 436.
7) F. Lenz: Optik **10** (1953) 439.
8) W. Lang: Optik **3** (1948) 233.
9) J. E. Johnston: Proc. Camb. Phil. Soc. **35** (1939) 108.
10) Mott and Gurney: Electronic Processes in Ionic Crystals. (Oxford)
11) J. R. Townsend: Phys. Rev. **92** (1953) 556.
12) H. Weber: Zeits. f. Phys. **130** (1951) 392.

JOURNAL OF THE PHYSICAL SOCIETY OF JAPAN Vol. 9, No. 6, NOV.—DEC., 1954

On the V-centers in Alkali Iodide Crystals

By Yōichi UCHIDA and Yoshio NAKAI

Department of Physics, Faculty of Science, Kyoto University

(Received July 5, 1954)

The properties of V-center were investigated in the alkali iodide crystals (KI and NaI) containing excess iodine. In KI, the absorption spectrum was similar to that obtained by Mollwo, but for details, there were some difference. It was pointed out that the V-band in KI can be understood as superposition of three bell-shaped bands **I**, **II**, and **III**. Of these, both band **I** and **II** can be safely assigned to V_2-band. As for band **III**, however, explanation is not possible at present though it seems to have fairly close relation to the other two bands.

Some proposals were made in regard to the mechanism of the coloring with the pointed electrode and the explanation of the doublet structure of V_2-band in KI.

§ 1. Introduction

Most of the recent investigations on the V-center in alkali halide crystals have been carried out on the crystal colored by X-ray irradiation.[1] In this case, since the generation of V-centers is inevitably accompanied by that of F-centers causing thermal instabilities of both centers, the interpretation of experimental facts becomes considerably difficult. Therefore, it seems necessary to pay some attention to experiments on the V-centers produced by the presence of the stoichiometric excess of the halogen component in the crystal.[2] Moreover, although F-centers show generally a similar absorption spectrum regardless of variety of the ways of coloration, i.e. the X-ray coloring and pointed cathode coloring, this relation is not yet ascertained in the case of V-centers at present (cf. reference (1) especially the paper by Casler, Pringsheim, and Yuster). The present study is concerned with some properties of V-bands in the additively colored* alkali iodide crystals

---

* "the V-bands in the additively colored crystal" means the V-bands produced by heating the crystal in the atmosphere of the halogen gas. This should not be confused with the F-band in the additively colored crystal nor with the V-center produced by the pointed anode coloring (see § 2 (ii) in this paper).

(KI and NaI) especially their behavior on the process of heat and light bleaching.

§ 2. On the Production of V-center

(i) Additive coloring

The technique of additive coloring does not differ appreciably from that employed to produce F-center.[3],[2] A piece of alkali iodide crystal, ~10×10×20 mm in size, and some solid iodine distilled in vacuum were sealed in a quartz tube, the former being put in the upper part of the tube and the latter in the lower. The two parts of the tube were heated by two separate furnaces, temperatures of which could be regulated independently. The pressure of iodine around the crystal specimen was known as the saturating vapor pressure at the temperature of the lower furnace.

In Fig. 1, the curve A shows the absorption spectrum of V-center in KI colored by this method, the temperature of the crystal being held at 530°C and the pressure of I_2 at 1.3 atm. press. Curve C shows absorption of the original blank KI crystal. Measurements were done at room temperature with a Beckman DU spectrophotometer using air as blank. Mollwo's data[2] is also shown by curve B for comparison.

Curve A differs from B in the following respects: (1) B has the second maximum to the short wave-length side of its principal maximum, but A has not. A has only a curve of knee shape in the same region. (2) The wave-length of the principal maximum is longer, though a little, in A than in B. (3) B seems to have some other component to the long wave-length side of its principal maximum but A does not.

We believe curve A to be more reliable from the following reasons: (1) In our case the absorption measurement was possible at any wave-length but it was not possible for Mollwo presumably because the continuous light source was not used in his absorption measurements.[2] (2) The absorption spectrum of original uncolored crystal obtained in our laboratory has no remarkable hump* (having absorption coefficient>0.1 cm^{-1}) at least within the range from the long wave-length side of the fundamental band to 1000 mμ. (see curve C in Fig. 1) (3) A crystal of KI which does not satisfy the condition described in (2) was colored by the method of the pointed anode (to be described in next section), and it was found that just the same absorption spectrum as Mollow's is obtained. (cf. Fig. 2) (4) It was reported by Mollow that some heat treatments were indispensable to obtain his typical V-bands in KI, but curve A was obtained without any special heat treatment.

(ii) Coloring with the pointed anode

It was shown previously[4]** that the production of V-centers is also possible, at least in alkali iodide, when the crystal is colored by the pointed anode at elevated temperature. This process seems to be just the inverse of the well-known method of producing F-centers with the pointed cathode. The absorption spectrum of KI colored by this process was found to be *exactly the same**** as that obtained by heating the crystal in the atmosphere of the halogen gas provided that the crystal has such blank absorption as shown

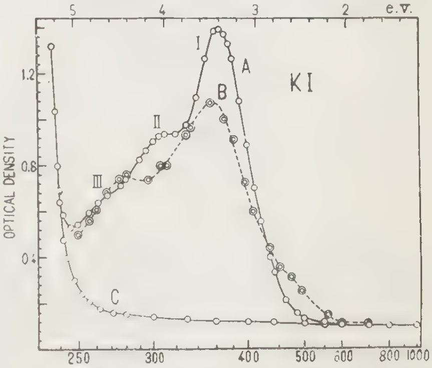

Fig. 1. Absorption curve of KI colored in iodine vapor. (measured at room temperature)
A: colored at 530°C in iodine vapor of 1.35 atm. press.
B: after Mollwo.
C: original blank KI crystal.

---

* It is considerably difficult to obtain those crystals which satisfy this condition.

** The possibility of V-coloration by this method was pointed out by Moll wo, cf. Mollwo: Nachr. Gött. math-phys. Kl. (1943) 89. But this paper was not available for us.

*** In our previous report, (cf. the Fig. 2 in reference 4), there were some differences between the absorption spectra in the short wave length region. But later experiments showed that these differences can be attributed to some disturbance, perhaps, caused by the lack of sufficient annealing for the original crystal used in the case of coloring with the pointed anode. A complete absorption spectrum of KI colored with pointed anode is shown by curve A in Fig. 9 in the present paper.

by curve C in Fig. 1. However, as was described in (**i**), when the KI crystals having a small hump at λ 287 mμ in its absorption spectrum is colored by this method, a similar spectrum as Mollwo's is obtained. This is shown in Fig. 2 with Mollwo's curve.

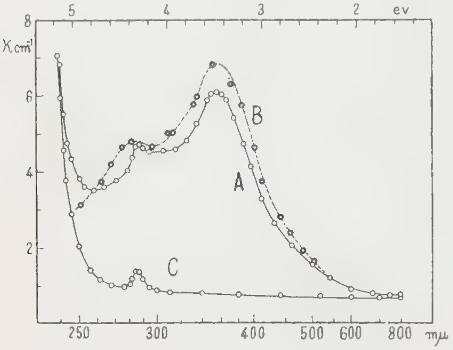

Fig. 2. When the KI crystals having a small hump at λ 287 mμ in its blank absorption (curve C) is colored with a pointed anode, the absorption curve A is obtained. Curve A is very similar to Mollwo's curve (curve B).

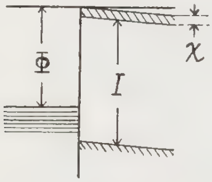

Fig. 3. Proposed energy diagram at the moment of contact between metal and alkali halide crystal. Energy scale is fitted to that of platinum and KI. Double layer is formed with charge produced by the displacement of electrons from crystal to metal.

Although, at present, the quantitative explanation of these coloring process is not available, we may suppose that V-centers were originated by the positive holes introduced into the crystal from the pointed anode, just as F-centers by electrons from the pointed cathode. So far investigated, the V-centers can be produced only when platinum is used as the pointed anode contrary to F-centers which can be produced as well by using other metals such as Fe, Ni and Cu as the pointed cathode.

These facts may be explained as follows. In order to produce V-centers, holes must be introduced from the anode into the crystal, in a meaning that electrons are carried from the top of the filled band of the crystal up to the Fermi level of the anode metal. Fig. 3 shows the relation of these energy levels at the point of contact. Then if Φ is the work function of the metal, χ the crystal affinity and I the energy gap between the bottom of conduction band and the top of the filled band of the crystal, the smaller is the value $(\chi+I)-\Phi$, the easier will be the process. Now it is known that among ordinary metals, this condition is best satisfied with platinum of which $\Phi=5.32$ ev. Using the energy of the second fundamental absorption maximum (6.58 ev) as the value of I in KI, and assuming $\chi=0.5$ ev, we obtain $(\chi+I)-\Phi=(0.5+6.58)-5.32=1.76$ ev for the energy required to raise a electron up to the Fermi level of platinum. However the actual value will be smaller than this since I for KI should be smaller than 6.58 ev because of the fact that the direct optical transition is forbidden between the top of filled band and the bottom of conduction band.*

In the case of F-coloring, since the electron has to be carried from the Fermi-level of metal to the bottom of conduction band of crystal, $\Phi-\chi$ must be as small as possible in order to facilitate F-coloration.[5] However, the mechanism of electrolytic coloration has been studied by some workers,[6] and it is reported that the growth of F-cloud can be understood as being generated from the alkali metal which has been deposited at the surface of cathode by the flow of electrolytic currents. Thus it seems natural to suppose that these alkali metals, having a small value of Φ and hence of $\Phi-\chi$, play a role of a new cathode to supply electrons into the crystal during the process of F-coloration. Therefore the initial choice of cathode metal is unessential.

(iii) The resolution of V-bands

After reducing to the same thickness of specimen, curve A in Fig. 1 was corrected for the general absorption by subtracting curve C. The curve abtained in this way can be resolved into three bell-shaped bands **I**, **II**, and **III** as shown in Fig. 4. The band maximum and the half-breadth at room temperature are shown for each band in the figure. These are the mean values of seven cases under various coloring conditions. The resolution was performed under the assumption of no overlapping in the long wave-length side of the principal maximum and a symmetrical shape of each band. Band **I** was separated out at first, then, the rest was resolved into two constituent bands **II** and **III**.

---

* The effect of surface state was assumed not so important in these phenomena, because the behavior of V-coloration did not seem independent of the choice of anode metal. Density of the surface levels, if any, may be supposed so low in KI that the major part of the processes is not effected by these levels. In fact it was found that a tungsten anode, which has a considerably large value of Φ, produced also the V-coloration in KI though the degree of coloration was lower than a platinum anode under the same conditions.

(iv) On the V-band in NaI

Although only qualitatively, V-center was found to be producible also in the crystal of NaI by both coloring methods mentioned above. Fig. 5 shows the V-band in NaI colored by heating the crystal at 550°C in the presence of iodine gas at 1.5 atm. press. However, in this case, it was noticed that the coloration was fairly dense only immediately after the removal of crystal from the electric furnace and most part of the coloration was lost while the temperature of crystal was lowered to room temperature. This fact seems to suggest that V-center in NaI is stable only at room temperature or below, so that curve A in Fig. 5 is supposed to show the absorption due to those V-centers in NaI still remaing after the bleaching mentioned above. A similar phenomenon was experienced also in the case of coloration with the pointed anode. Further, the absorption measurement in NaI crystal were greatly disturbed-by its very hygroscopic nature. This causes a considerable increase of error in the absorption measurement towards the short wavelength region of the spectrum (see curve A and B in Fig. 5), so that the correction and the resolution of the absorption curves could not be made in this case. However, at any rate, two bands which seem undoubtedly to correspond to band **I** and **II** in the case of KI are recognizable in this case, too. Hence it would be natural to assign curve A in Fig. 5 to the absorption spectrum of V-center in NaI.

§ 3. Properties of V-bands in KI

(i) On the relative intensity of V-bands

Mollwo found that the concentration of excess halogen in colored KI and KBr crystals varies with the first power of the pressure of the surrounding diatomic halogen gas. However, the concentration of halogen was determined by measuring the total charges in excess of the purely electrolytic charges which flow when the color centers are removed from the crytsal with the use of an electrostatic field at high temperature. Accordingly one could not obtain information concerning the behavior of V-band during the variation of the halogen pressure. We have studied the variation of V-bands in KI colored at 530°C with various pressure of iodine gas. The results are shown in Fig. 6.

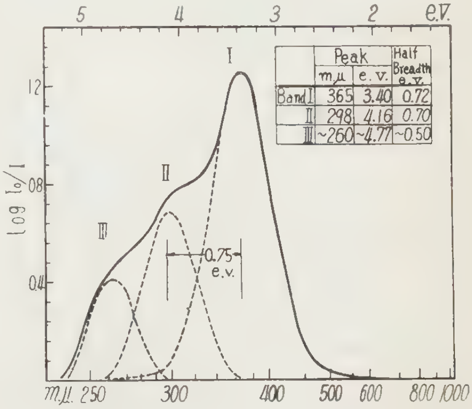

Fig. 4. Resolution into three bands **I**, **II** and **III**.

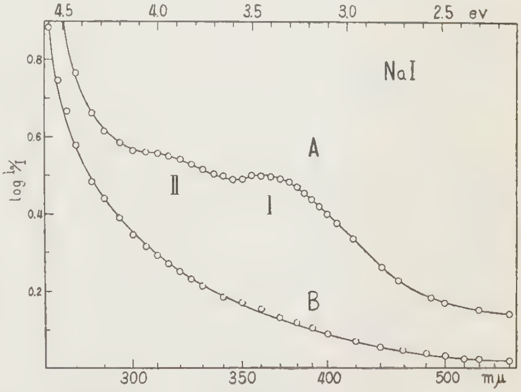

Fig. 5. Absorption curve ot NaI crystal containing excess iodine.

A: coloring at 530°C in iodine vapor of 3.5 atm. pressure.

B: original blank NaI crystal.

The scale of the optical density is arbitrary, and can not be common for two curves.

In Fig. 7, the height of each band, which is obtained by the analysis described in § 2 (**iii**), is plotted in cm^{-1} *vs* the pressure of iodine gas. One can see that the linear relation is established between the band height and the pressure of iodine for each of band **I** and **II**, but is not for band **III**. This suggests that bands **I** and **II** may be attributed to centers having diatomic nature. Moreover it is seen from Fig. 7 (b) that the relative intensity of bands **I** and **II** does not depend on the pressure, namely the ratio close to 2:1 is always obtained. This ratio is not altered even when the temperature is varied at which the crystal is colored. The highest and the lowest value of this ratio which have ever been obtained were 0.55 and 0.48 respectively.

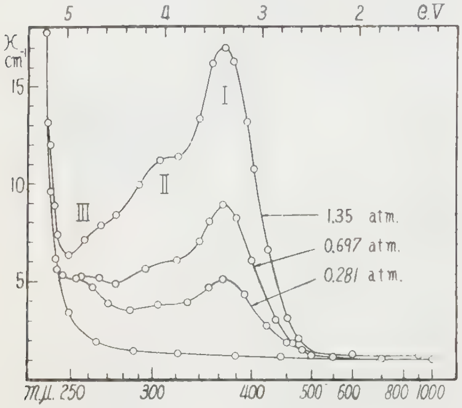

Fig. 6. Changes in the absorption coefficients in KI, additively colored at 530°C, with the pressure of iodine vapor. The height of band **I** and **II** are proportional to the pressure of I_2 vapor.

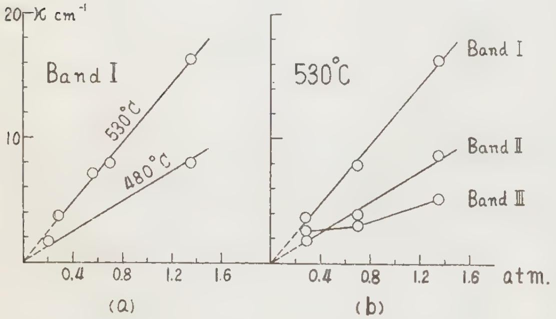

(a) (b)

Fig. 7. The relation between the intensity of V-band in KI (in cm^{-1}) and the pressure of iodine vapor around the crystal (in atm. press).

(a) Intensity of band **I** *vs* iodine pressure. Coloring temperatures are 530°C and 480°C.

(b) Intensity of each band *vs* iodine pressure. Coloring temperature is 530°C. The linear relation is satisfied for band **I** and **II**, but not for band **III**.

(**ii**) **Thermal bleaching**

When the crystal of KI containing V-centers was heated above 300°C, bands **I** and **II** were reduced gradually, but **III** was somewhat enhanced.

In Fig. 8 is shown the behaviours of these bands during the thermal bleaching at 310°C. The absorption were measured at room temperature on each step of 20, 110, and 430 minutes after the initiation of heating as illustrated. It is seen that band **III** ceases its growth as soon as the perfect vanishing of bands **I** and **II** is attained.

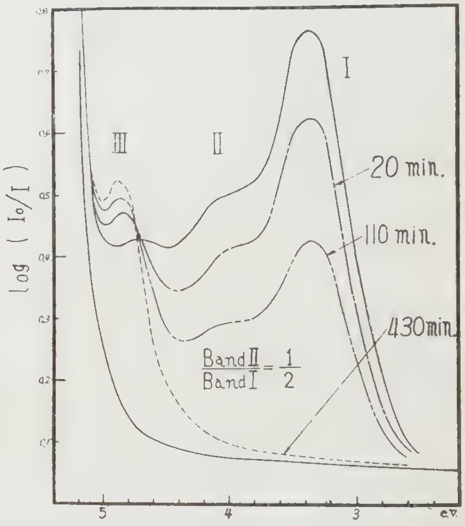

Fig. 8. Thermal bleaching of V bands in KI for various time intervals at 310°C. The ratio of heights is maintained constantly in band **I** and **II**.

Further continuation of heating can alter the shape of absorption spectrum no more, the fact suggesting strongly that band **III** is related essentially to bands **I** and **II**, and accordingly to be assigned to one of the V-type bands.

Attention should be given here again to the relative intensities of bands **I** and **II**. The ratio near 0.5 was found to be maintained also during the course of thermal bleaching. We can suppose therefore that these two bands issue from a single kind of center.

In this connection, it should be noted that the perfect disappearance of bands **I** and **II** produces no other changes of spectrum than a small increase in band **III** at least within the range of our measurements (from λλ 235 to 1000 mμ). Thus it may be concluded that the aggregates of higher order, i.e. larger cluster of excess halogen, are not formed during the annealing process at 310°C. This fact may be contrasted with the formation of colloidal particles in the case of additively F-colored crystal.[7]

(iii) Light bleaching

V-bands in KI were bleached by irradiating with ultra-violet light. In this experiments, the crystal containing V-centers was irradiated at room temperature with a light from filtered Hg-arc ($\lambda\lambda$ 365 and 312 mμ). These two lines nearly coincide with maximum absorptions of bands **I** and **II** respectively. It is seen from Fig. 9 that a saturation is reached by the irradiation for a sufficiently long time. This saturation state is indicated by a persisting curve D. A typical restoration phenomenon was observed concerning this saturation state; that is, if the crystal in the saturation state is heated for 20 minutes at 210°C, the original shapes of the V-bands are reestablished to a great extent as shown by curve E in Fig. 9. Since the broad band D grows during the course of light bleaching of bands **I** and **II**, the above-mentioned constant intensity ratio between latters is not recognizable except at the earlier stages of bleaching.

§ 4. Discussion

Recently, many detailed experiments were carried out on the V-center[1] produced by irradiating the crystals such as NaCl, KCl, and KBr with X-rays. On the other hand the V-center produced by the additive coloring was investigated by Mollwo[2] about twenty years ago on KI and KBr. However the correspondence of the V-band produced by X-raying and the one produced by additive coloring does not seem to be clear with the exception of V_2- and V_3-band of KBr. In KBr these bands obtained by X-ray irradiation can correspond, though not completely, to the V-bands found by Mollwo in the same crystal colored additively.

As to the models of V-center,[8],[9],[10] it has been suggested that V_2-center consists of two positive-ion vacancies and two holes, and V_3-center of two positive-ion vacancies and a single hole. These suppositions are based mainly on the fact that the V-center produced in the additively colored crystal seems to have a diatomic structure[8],[9] and that the V_3-center has a great stability under conditions in which free electrons are produced in the lattice.[10] Our results concerning band **I** and **II** in KI suggest that both bands can be attributed to V_2-center.

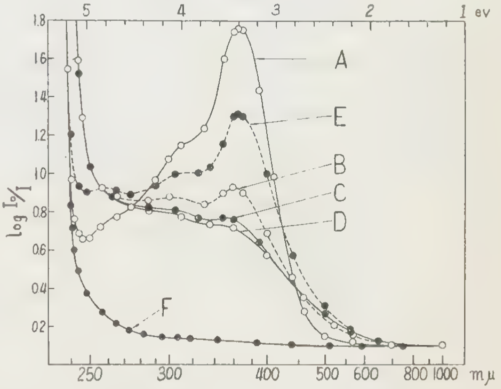

Fig. 9. Bleaching of V-bands in KI by the irradiation of ultraviolet light.

A: initial state. This curve shows the absorption of the crystal colored with the platinum pointed anode at 520°C.
B: after the irrad. of 12.5 hrs.
C: after the further irrad. of 7.5 hrs.
D: after the further irrad. of 7.5 hrs.
E: after heating the crystal in state D at 210°C for 20 minutes.
F: original blank crystal.

On the other hand, it was proposed by Mollwo that the separation of two peaks obtained in his spectrum of V-band in KI (see curve B in Fig. 1) can be attributed to the doublet separation in the normal state of free iodine atom. The same idea was proposed again by Alexander and Schneider[11] to understand the doublet structure of their V-bands obtained in KBr colored with X-rays. But their proposals seems to be derived from somewhat inadequate ground since it was pointed out by Casler, Pringsheim, and Yuster[12] that the relative intensities of these two peaks varies with changing the conditions of coloring. Moreover, at present, these two peaks have been assigned to V_2- and V_3-band in KBr. Taking these affairs into consideration, we would like to apply once more the above-mentioned idea to explain the separation between bands **I** and **II** in KI. Band **I** and **II** show the separation of 0.75 ev as shown in Fig. 4, and the ratio of the height of band **II** to that of band **I** is always nearly 0.5. These facts can be explained if one assumes that the atomic nature of iodine appears strongly at least in the excited state of V_2-center. If most part of the doublet structure in the excited state of V_2-center could be attributed to the separation of the doublet in the ground state of iodine atom, i.e. to ${}^2P_{3/2}-{}^2P_{1/2}$, the intensity of band **I** will be twice as large as that of band **II** because the intensity of absorption may be proportional to $(2J+1)$-value of two upper levels. Fig. 10 shows our proposed interpretation of bands **I** and **II** as arising from the excitation of a positive hole in the V_2-center.

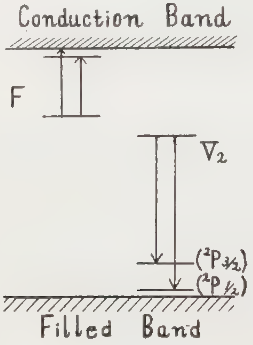

Fig. 10. Energy level scheme of F- and V_2-center in KI. Larger energy is required to produce the halogen atom in ${}^2P_{1/2}$ state than in ${}^2P_{3/2}$ state.

This explanation seems merely speculative unless similar facts can be confirmed also in other crystal such as KBr and KCl. However it should be noted here that the magnitude of separation of the two bands is nearly equal to that of half-breadth of each band in the case of KI. This fact means that the resolution of V_2-band will be very difficult in the case of KBr even when the absorption measurements were made at low temperature, since it may be estimated that the separation will be less than 0.35*, whereas according to Dorendorf[13] the half-breadth of V_2-band at −180°C in KBr irradiated with X-rays is 0.6 ev. Hence it seems possible to occur that the V_2-band is observed as a single band without any structure in KBr even at low temperatures. A fairly complicated behaviors, as reported by Casler, Pringsheim, and Yuster,[12] of V_2- and V_3-band in KBr colored with X-rays might be partly caused by these circumstances.

References

1) J. Alexander and E. E. Schneider: Nature **164** (1949) 653. R. Casler, P. Pringsheim and P. Yuster: J. Chem. Phys. **18** (1950) 887, 1564. H. Dorendorf: Zeits. Phys. **129** (1951) 317. D. Dutton and R. Maurer: Phys. Rev. **90** (1953) 126.

2) E. Mollwo: Gött. Nachr. Math. Nat. Kl. N.F. **1** (1935) 215, Ann. Phys. (5) **29** (1937) 397.

3) H. Rögener: Ann. Phys. (5) **29** (1937) 386.

4) Y. Uchida and Y. Nakai: J. Phys. Soc. Japan **8** (1953) 795.

5) N. F. Mott and R. W. Gurney: Electronic Processes in Ionic Crystals (1948) 168.

6) G. Heiland: Zeits. Phys. **127** (1950) 144. R. Hilsch and R. W. Pohl: Zeits. Phys. **111** (1938) 399.

7) A. B. Scott: J. Phys. Chem. **57** (1953) 757.

8) F. Seitz: Phys. Rev. **79** (1950) 529.

9) T. Nagamiya: J. Phys. Soc. Japan **7** (1952) 358.

10) F. Seitz: Rev. Phys. **26** (1954) 7.

11) J. Alexander and E. E. Schneider: cf. reference (1).

12) Casler, Pringsheim and Yuster: J. Chem. Phys. **18** (1950) 1564.

13) H. Dorendorf: cf. reference (1).

---

* Since the separation in free I atom (0.94 ev) is reduced to 0.75 ev in the crystal, the separation in free Br atom (0.44 ev) may also be reduced to $0.44\times0.75/0.94=0.35$ ev in the crystal.

Journal of the Physical Society of Japan Vol. 9, No. 6, Nov.—Dec., 1954

Note on the Stochastic Theory of Resonance Absorption

By Ryogo Kubo

Department of Physics, University of Tokyo

(Received July 16, 1954)

The stochastic theory of magnetic resonance absorption developed recently by P. W. Anderson is examined here further in some details. The fundamental idea of the theory is that the resonating units suffer transitions among their possible states each of which is characterized by a proper frequency of the magnetic moment. The transition is assumed to be described by a Markoffian process. The fundamental equation for the auto-moment or the auto-correlation of the magnetic moment is rederived and transformed. Some general properties of the absorption spectrum are discussed on the basis of this equation. In particular, the narrowed spectrum for the case of rapid transition is proved to be Lorentzian with a half width determined by the equilibrium distribution of the units and the transition matrix of the Markoffian jumps. If the relaxation time of the transition is assumed to be completely degenerate, the resonance spectrum is given by

$$I(\omega)=\frac{1}{\pi}\mathrm{Re}\int\frac{P(\omega')d\omega'}{\omega_e+i(\omega-\omega')}\Big/\left\{1-\int\frac{\omega_e P(\omega')d\omega'}{\omega_e+i(\omega-\omega')}\right\}$$

where $P(\omega)$ is the intensity distribution in the limit of slow relaxation, $1/\omega_e$ being the relaxation time. Although this idealization is not quite physical, the result is useful for qualitative understanding of the changes in line shapes due to the motional effect. The limit of Gaussian-Markoff case is also discussed.

§ 1. Introduction

Recently P. W. Anderson[1)] presented an interesting theory of the motional effect in magnetic resonance absorption. His model is that the resonance frequency is modulated randomly as a stochastic process. More specifically it is assumed that the resonating units make transitions between various states each of which has a characteristic resonance frequency. The transition process is assumed to be described as a Markoffian process. If the transition process is sufficiently slow, the observed spectrum of the resonance must be the set of those proper frequencies weighted by the relative probability of finding an unit in each of the frequencies. On the other hand, if the transition is extremely rapid, then the system will give rise to a sharp line the frequency of which is a certain average of the proper frequencies. Thus, the observed resonance spectrum will change between these two extremes as the transition rate varies. On this model, Anderson has developed a mathematical theory which affords at least qualitative understanding of such physical phenomena as the motional narrowing in nuclear magnetic resonance or the exchange effect in paramagnetic resonance absorption. The purpose of this note is to examine a little further some mathematical aspects of this model and to discuss certain problems which were left unsolved or untouched in Anderson's treatment.

§ 2. Fundamental Equations

Let us suppose that the possible states of the resonating unit are finite and numbered as $E_1, E_2\cdots E_r$. Our fundamental assumption is that the process in which the unit realizes in the course of time the various states is Markoffian, so that it is determined by the transition probabilities $P_{jk}(t)$. It is assumed further that this stochastic process is stationary, which means that the transition probabilities depend only on the time interval t. Furthermore, the following conditions are assumed[2)].

1) $$P_{jj}(t)=1-c_jt+o(t)\,, \tag{2.1}$$

2) $$P_{jk}(t)=c_jp_{jk}t+o(t)\,, \tag{2.2}$$

where

$$p_{jj}=0,\ \text{and}\ \sum_k p_{jk}=1\,. \tag{2.3}$$

If the number of the states is infinite, we must assume that (2.2) holds uniformly with respect to j for every fixed k[3].

Under these assumptions, the Chapman-Kolmogorov equation

$$P_{jk}(t)=\sum_m P_{jm}(t-h)P_{mk}(h) \qquad 0<h<t,$$

can be transformed into the differential equations

$$\dot{P}_{jk}(t)=-c_kP_{jk}(t)+\sum_m P_{jm}(t)c_m p_{mk}\,, \qquad (2.4)$$

which is the so-called forward equation. This is a set of r equations for a fixed i. We may conveniently write this as

$$\varphi_j(t)=-\varphi_j D\,,$$

where φ_j is the row vector

$$\varphi_j=(P_{j1},\ P_{j2},\ \cdots\ P_{jr})\,, \qquad (2.5a)$$

and D the matrix

$$D_{mk}=c_k\delta_{km}-c_m p_{mk}\,. \qquad (2.5b)$$

Eq. (2.5) determines the matrix of transition probability $(P_{jk}(t))$ with the initial condition

$$P_{jk}(0)=\delta_{jk}. \qquad (2.6)$$

The adjoint equation of (2.5) is

$$\psi(t)=-D\psi(t)\,, \qquad (2.7)$$

which corresponds to the backward equation, ψ being a column vector. Eq. (2.7) has an obvious solution

$$\psi_0=\begin{pmatrix}1\\1\\\cdot\\\cdot\\1\end{pmatrix}, \qquad D\psi_0=0\,, \qquad (2.8)$$

as one seems from the condition (2.3). Correspondingly Eq. (2.5) must have a stationary solution φ_0 which satisfies

$$\varphi_0 D=0\,. \qquad (2.8a)$$

The eigenvector φ_0 must be unique and independent of j provided that our Markoffian process is ergodic, which we assume throughout the following treatment. The components of the eigenvector φ_0 are the stationary distribution or the equilibrium distribution to which the ensemble of our system must approach starting from any arbitrary distribution. The normalization of this equilibrium distribution is expressed by

$$\varphi_0\psi_0=1\,, \qquad (2.9)$$

which is

$$\sum_k P_k^0=1\,,$$

where P_k^0 are the components of φ_0,

$$\varphi_0=(P_1^0,\ P_2^0,\cdots\cdots,\ P_r^0). \qquad (2.8b)$$

Now let the proper frequency of the resonating unit be denoted by ω_j in the state E_j. Thus the moment $M(t)$ of the resonating unit is assumed to be given by

$$M(t)=M(0)\exp i\int\omega(t')dt', \qquad (2.10)$$

where $\omega(t)$ is a stochastic variable assuming various values $\omega_1,\ \omega_2,\cdots\cdots,\ \omega_r$, as the unit jumps to and fro according to the basic process described by Eq. (2.4). Here we have neglected other possible complications coming from the variations in amplitudes and phases. It is also possible to construct a theory taking account of these, but we shall here employ the assumption (2.10) for the sake of simplicity. The problem we have now to solve is the calculation of the auto-moment of $M(t)$, which is the Fourier transform of the intensity distribution of the resonance absorption.

We shall here adopt a formulation which is a little different from that used by Anderson to derive the fundamental equation. Let us introduce a function $Q_{jk}(t)$ which is defined as the average of

$$\mu(t)=\exp i\int\omega(t')dt', \qquad (2.10a)$$

on the condition that the unit is in the state E_j at the time $t=0$ and is found in the state E_k at the time t. This definition yields, corresponding to the Chapman-Kolmogorov equation of $P_{jk}(t)$,

$$Q_{jk}(t+h)=\sum_m Q_{jm}(t)Q_{mk}(h)\,. \qquad (2.11)$$

We now see from the assumptions (2.1) and (1.2) that

$$Q_{jj}(h)=(1-c_jh)\,e^{ih\omega_j}+o(h)\,,$$

$$Q_{jk}(h)=c_jp_{jk}h+o(h)\,.$$

Therefore, going to the limit of $h\to 0$ in Eq. (2.11), we obtain the equation

$$\dot{Q}_{jk}(t)=(i\omega_k-c_k)Q_{jk}(t)+\sum_m Q_{jm}(t)c_m p_{mk}\,, \qquad (2.12)$$

which may be written as

$$\dot{Q}(t)=iQ\Omega-QD\ , \qquad (2.13)$$

if we denote the matrix (Q_{jk}) by Q and the diagonal matrix $\omega_k\delta_{jk}$ by Ω. Eq. (2.12) has to be solved with the initial condition,

$$Q_{jk}(0)=\delta_{jk}\ .$$

The auto-moment of $M(t)$, Eq. (2.10), or that of $\mu(t)$, Eq. (2.10a) is now given from the fundamental solution of Eq. (2.13). Namely we first take the average of $Q_{jk}(t)$ with respect to the initial states distributed with the equilibrium probability (2.8b) and then sum up over all of the possible final states. Thus the auto-momemt of $\mu(t)$, or the correlation function of $M(t)$ is

$$g(t)=\varphi_0 Q(t)\psi_0\ . \qquad (2.14)$$

Or, defining the vector function

$$u(t)=\varphi_0 Q(t)\ , \qquad (2.15)$$

we may write (2.14) as

$$g(t)=u(t)\psi_0\ . \qquad (2.14a)$$

For the function $u(t)$ we can set up the equation

$$u(t)=iu(t)\Omega-u(t)D\ , \qquad (2.16)$$

which is imposed by the initial condition,

$$u(0)=\varphi_0\ . \qquad (2.17)$$

Eq. (2.16) is the fundamental equation of our treatment.

The formal solution of (2.16) is

$$u(t)=\varphi_0 \exp\{-(D-i\Omega)t\}\ , \qquad (2.18)$$

which gives

$$g(t)=\varphi_0 \exp\{-(D-i\Omega)t\}\psi_0\ . \qquad (2.19)$$

This is, of course, identical with the basic formula derived by Anderson[1)].

Since simultaneous addition of ω_0 to all of the frequencies $\omega_1, \omega_2, \cdots, \omega_r$, gives to $u(t)$ only an extra factor $\exp i\omega_0 t$ we can choose the frequencies in such a way that

$$\sum_j P_j^0\omega_j=0 \qquad (2.20)$$

or

$$\varphi_0\Omega\psi_0=0\ . \qquad (2.20a)$$

This means that we are dealing with the spectrum the center of which is now arbitrarily chosen to zero. This particular choice is useful to simplify the calculation, so that we shall assume (2.20) in the following treatment.

§ 3. Some Direct Consequences of the Fundamental Equation

The auto-correlation, $g(t)$, and the normalized intensity distribution, $I(\omega)$, are mutually connected by the Fourer transforms,

$$g(t)=\int_{-\infty}^{\infty} I(\omega)e^{i\omega t}d\omega\ . \qquad (3.1)$$

and

$$I(\omega)=\frac{1}{2\pi}\int_{-\infty}^{\infty} g(t)e^{-i\omega t}dt \qquad (3.2)$$

Thus we must have

$$g(-t)=g(t)\ . \qquad (3.3)$$

Now the moments of the distribution $I(\omega)$ are generally given by the derivatives of $g(t)$ at $t=0$ provided that those derivatives uniquely exist. It is easy to see that the assumption of Markoffian process forbids the existence of the moments higher than the second. Expanding Eq. (2.29) one gets

$$\begin{aligned} g^{(n)}(+0)&=\varphi_0(\Omega+iD)^n\psi_0 \\ &=\varphi_0\Omega(\Omega+sD)^{n-2}\Omega\psi_0, \end{aligned} \qquad (3.4)$$

where we made the use of Eqs. (2.8) and (2.8a). Thus the second moment is

$$m_2=\varphi_0\Omega^2\psi_0=\sum_j P_j^0\omega_j^2, \qquad (3.5)$$

whereas Eq. (3.3) and (3.4) show that the third derivative of $g(t)$ at $t=0$ cannot be uniquely defined, the right and left limits being generally different except when

$$\varphi_0\Omega D\Omega\psi_0=\sum P_j^0\omega_j D_{jk}\omega_k=0\ .$$

Thus, the third moment of $I(\omega)$ will not be convergent and the distribution falls off at infinity to allow only the existence the second moment, (3.5), which is independent of D, namely of the relaxation process. It is, however, to be remembered that the non-existence of higher moments just mentioned is utterly a mathematical consequence of our Markoffian assumption, which will certainly break down for very small time interval if our system is really a physical one. The dynamical coherence is always dominant for small time interval either in classical or quantum-mechanical systems so that the correlation function $g(t)$ must behave quite regularly in the neighborhood of $t=0$. Therefore, the Markoffian theory as a physical theory is doomed to fail to describe correctly the wings of the resonance curves. But it is correct near the center and can give valuable conclusions if it covers the most of the frequency range which is practically important. The criterion of the validity or the usefulness of the Markoffian theory is actually pretty complicated depending on the dynamical nature of physical system of interest. Thus more detailed discussion of this point is beyond the scope of the present article.

The extreme limits of very slow and very rapid relaxation are, of course, to be seen at once from Eq. (2.19). If D is negligible, we have

$$g(t)=\sum_j P_j{}^0 e^{i\omega_j t} . \tag{3.6}$$

Thus, the spectrum is simply

$$I(\omega)=\sum_j P_j{}^0\delta(\omega-\omega_j) , \tag{3.7}$$

as it ought to be. On the other hand, when D is so large that Ω can be neglected, Eqs. (2.19) and (2.8) or (2.8a) shows that $g(t)=1$, which gives

$$I(\omega)=\delta(\omega) . \tag{3.8}$$

The approximation from the side of weak relaxation can be made with the aid of perturbation method, which has been discussed by Anderson.

The approximation from the other side, that is from the limit of strong relaxation, needs somewhat more careful investigation. For this purpose and also for a general treatment of the problem, we may conveniently rewrite Eq. (2.16) as we shall see in the following section.

§ 4. Method of Solution of the Fndamental Equation

Noticing that the operator D has the particular eigenvalue zero, we now want to elimithis particular eigen-space R_0 and set up the equation for the rest of the whole vector space. Let us put the solution $u(t)$ of Eq. (2.16) in the form

$$u(t)=c_0(t)\varphi_0+v(t) , \tag{4.1}$$

where $v(t)$ is orthogonal to the zero-eigenvector of D, namely,

$$v(t)\psi_0-\sum_j v_j(t)=0 . \tag{4.2}$$

Inserting (4.2) into Eq. (2.16) we get

$$\dot{c}_0(t)\varphi_0+\dot{v}(t)=ic_0(t)\varphi_0\Omega+iv(t)\Omega-v(t)D , \tag{4.3}$$

which can be separated into two equations:

$$c_0(t)=iv(t)\Omega\psi_0 , \tag{4.4a}$$

$$v(t)=ic_0\varphi_0\Omega+i(v\Omega-v\Omega R_0)-vD , \tag{4.4b}$$

where R_0 is the projection operator defined by

$$R_0=\psi_0\varphi_0 . \tag{4.5}$$

This is easily seen by making scalar product of the vector Eq. (4.3) with the eigen vector ψ_0 from the right. It gives Eq. (4.4a) by virtue of Eqs. (2.8), (2.9), and (2.20a). Eq. (4.4b) is obtained by subtracting (4.4a) from (4.3).

The most convenient way of treating Eq. (4.4) is the method of Laplace transformation. The Laplace transforms of $c_0(t)$ and $v(t)$ are defined as

$$C_0(s)=\int_0^\infty c_0(t)e^{-st}dt, \tag{4.6a}$$

$$V(s)=\int_0^\infty v(t)e^{-st}dt. \tag{4.6b}$$

Then Eqs. (4.4a) and (4.4b) are transformed into

$$sC_0(s)-1=iV(s)\Omega\psi_0 , \tag{4.7a}$$

$$sV(s)=iC_0(s)\varphi_0\Omega+iV(s)\Omega(1-R_0)-V(s)D , \tag{4.7b}$$

because, by the initial condition (2.17), we have

$$c_0(0)=1, \quad \text{and} \quad v(0)=0 .$$

Eliminating C_0 from Ex. (4.7a) we arrive at

$$V(s)\{s^2+sD-is\Omega(1-R_0)+\Omega R_0\Omega\}=i\varphi_0\Omega . \tag{4.8}$$

Since $V(s)$ and $i\varphi_0\Omega$ belong to the space $1-R_0$, we may write (4.8) in the form,

$$V(s)(1-R_0)\{s^2+sD-is\Omega(1-R_0)+\Omega R_0\Omega\} =i\varphi_0\Omega , \tag{4.8a}$$

using the relations,

$$R_0D=R_0=R_0\Omega R_0=0 .$$

The operators appearing on the left hand side of Eq. (4.8a) are essentially matrices in the spase $1-R_0$ with $r-1$ dimensions. Eq. (4.8) can also be written as

$$V(s)(s-i\Omega)[s(1-R_0)+(s-i\Omega)^{-1}sD+iR_0\Omega]$$
$$=i\varphi_0\Omega\ , \qquad (4.8\text{b})$$

or as

$$V(s)(1-R_0)(s-i\Omega)[s(1-R_0)+(s-i\Omega)^{-1}sD$$
$$+iR_0\Omega]=i\varphi_0\Omega\ , \qquad (4.8\text{c})$$

since

$$R_0(s-i\Omega)[s(1-R_0)+(s-i\Omega)^{-1}sD+iR_0\Omega]=0.$$

From Eq. (4.8c) we see easily that, in the limit of vanishing D, the solution of (4.8) becomes

$$V(s)=\varphi_0(s-i\Omega)^{-1}(1-R_0)\ , \qquad (4.9)$$

as it must be.

If Eq. (4.8) is solved after $V(s)$, Eq. (4.7a) gives $C_0(s)$ which is nothing but the Laplace transform of $g(t)$, i.e.,

$$C_0(s)=\int_0^\infty g(t)e^{-st}dt\ , \qquad (4.10)$$

because Eqs. (4.1) and (2.14a) give

$$g(t)=c_0(t)\ ,$$

by virtue of (4.2). But the required intensity distribution is

$$I(\omega)=\frac{1}{2\pi}\int_{-\infty}^{\infty}g(t)e^{-i\omega t}dt$$
$$=\frac{1}{\pi}\ \text{Re}\int_{-\infty}^{\infty}g(t)e^{-i\omega t}dt$$
$$=\frac{1}{\pi}\ \text{Re}\,[C_0(s)]_{s=i\omega}\ . \qquad (4.11)$$

Therefore our problem is generally reduced to the solution of Eq. (4.8) or (4.8a) in the space $1-R_0$. With the obtained solution $V(s)$ the intensity distribution is given explicitly by

$$I(\omega)=(1/\pi)\,\text{Re}\,(1+iV(i\omega)\Omega\psi_0)/(i\omega)\ . \qquad (4.12)$$

Perhaps it should be noticed here that the function $C_0(s)$ has no pole at $s=0$. This can be seen from Eq. (4.8), because for $s=0$ it becomes

$$V(s)\Omega\psi_0\varphi_0\Omega=i\varphi_0\Omega\ ,$$

which gives $V(0)\Omega\psi_0=i$. Thus

$$[1+iV(s)\Omega\psi_0]_{s\to 0}=0\ .$$

§ 5. Narrowing for Rapid Relaxation

Eq. (4.8) can easily solved for the limit of strong narrowing, that is for the case where the relaxation effect is overwhelming. Let us denote the orders of magnitudes of D and Ω by τ_r^{-1} and ω_a. Then the orders of magnitudes of the four terms in the bracket on the left hand side of Eq. (4.8) are

$$\omega^2,\ \omega/\tau_r,\ \omega\omega_a,\ \text{and}\ \omega_a^2 \quad (s=i\omega)$$

respectively. Therefore, if we are interested in the frequencies satisfying the condition

$$\omega\lesssim\omega_a^2\tau_r\ , \qquad (5.1)$$

and if we assume that

$$\omega_a\tau_r\ll 1\ , \qquad (5.2)$$

the first and the third terms can be neglected, so that Eq. (4.8) becomes approximately

$$V(s)[sD+\Omega R_0\Omega]=i\varphi_0\Omega\ , \qquad (5.3)$$

or

$$V(s)D=s^{-1}\varphi_0\Omega(i-V\Omega\psi_0)\ . \qquad (5.4)$$

Here D is understood as $(1-R_0)D(1-R_0)$, which is an operator in the space $1-R_0$ and has no zero-eigenvalue. Thus the inverse D^{-1} of D can be defined in the space $1-R_0$. Eq. (5.4) now gives

$$V(s)\Omega\psi_0=s^{-1}\varphi_0\Omega D^{-1}\Omega\psi_0(i-V\Omega\psi_0)\ .$$

Hence we get

$$V\Omega\psi_0=\frac{is^{-1}\varphi_0\Omega D^{-1}\Omega\psi_0}{1+s^{-1}\varphi_0\Omega D^{-1}\Omega\psi_0}\ ,$$

Inserting this into Eq. (4.12) we find

$$I(\omega)=\text{Re}\,\frac{1}{\pi}\,\frac{1}{i\omega+\varphi_0\Omega D^{-1}\Omega\psi_0}\ , \qquad (5.5)$$

where both $\varphi_0\Omega$ and $\Omega\psi_0$ are vectors in the space $1-R_0$ so that the quantity $\varphi_0\Omega D^{-1}\Omega\psi_0$ has a definite meaning. If the eigenvalues of D in the space $1-R_0$ are all degenerate (see the next section), that is, if the relaxation time of the system is single, we have

$$D^{-1}=(1-R_0)\tau_r(1-R_0)\ ,$$

and

$$\varphi_0\Omega D^{-1}\Omega\psi_0=\sum_j P_j{}^0\omega_j{}^2\tau_r=\overline{\omega^2}\tau_r\ . \qquad (5.6)$$

More generally we may write

$$\varphi_0\Omega D^{-1}\Omega\psi_0=\int_0^\infty\varphi_0\Omega e^{-Dt}\Omega\psi_0 dt$$
$$=\overline{\omega^2}\tau_{\text{eff}}\ , \qquad (5.7)$$

and express the intensity distribution as

$$I(\omega)=\frac{1}{\pi}\,\frac{\overline{\omega^2}\tau_{\text{eff}}}{\omega^2+(\overline{\omega^2}\tau_{\text{eff}})^2}\ . \qquad (5.8)$$

Thus the narrowed spectrum is generally a Lorentzian curve centered at the average frequency of the proper frequendies each of which is weighted by the equilibrium probability. The width of this Lorentzian curve is given by Eq. (5.7).

§ 6. Simple Relaxation

An interesting example which allows exact treatment is provided by the system with a single relaxation time. This is defined by a particular assumption for the elements of stochastic matrix involved in Eq. (2.2) such that

$$c_j = \omega_e(1-P_j^0)\ , \qquad (6.1a)$$

and

$$p_{jk} = P_k^0(1-P_j^0)^{-1}, \quad p_{jj}=0\ . \qquad (6.1b)$$

with the condition

$$\sum_j P_j^0 = 1\ . \qquad (6.2)$$

Thus the explicit form of D is

$$D_{jk} = \omega_e\delta_{jk} - \omega_e P_k^0\ . \qquad (6.3)$$

With this matrix D one finds at once that any deviation from the equilibrium distribution (2.8b) relaxes as $\exp(-\omega_e t)$. This example was discussed by Anderson[1], but he did not give the complete solution of the problem. Although the model is not quite physical, it can still give qualitative understanding of the changes of line shapes as the rate of relaxation varies. Hence an exact solution of this model is not without physical interest.

For the sake of generality we shall consider here continuous cases rather than the discrete cases. Corresponding to Eq. (6.3) we may write the kernel of D as

$$D(\omega, \omega') = \omega_e\delta(\omega_e-\omega') - \omega_e P^0(\omega')\ , \qquad (6.3a)$$

for continuous cases. In this expression $P^0(\omega)$ is normalized as

$$\int P^0(\omega)d\omega = 1\ . \qquad (6.2a)$$

More rigorously we may write

$$\varphi D \equiv \int \varphi(\omega)d\omega D(\omega, \omega')$$
$$= \omega_e\left\{\varphi(\omega') - P^0(\omega')\int\varphi(\omega)d\omega\right\}\ , \qquad (6.4a)$$

$$D\psi \equiv \int D(\omega, \omega')d\omega'\psi(\omega')$$
$$= \omega_e\left\{\psi(\omega) - \int P^0(\omega')d\omega'\psi(\omega')\right\}\ , \qquad (6.4b)$$

The equilibrium solution for D is provided by $P^0(\omega)$, that is

$$\int P^0(\omega)D(\omega, \omega')d\omega = 0$$

and

$$\int D(\omega, \omega')\times\text{const.}\ d\omega' = 0\ ,$$

Any function $f(\omega)$ which is orthogonal to the stationary solution, that is

$$\int f(\omega)d\omega = 0\ ,$$

satisfies

$$fD = \omega_e f, \qquad (6.5)$$

which means that any deviation from the equilibrium distribution decays with the relaxation time $1/\omega_e$.

Now the fundamental Eq. (2.16) is

$$(\dot{u}\omega, t) = i\omega u(\omega, t) - \omega_e u(\omega, t)$$
$$+ P^0(\omega)\int u(\omega', t)d\omega'\ . \qquad (6.6)$$

Eqs. (4.4a) and (4.4b) are explicity written as

$$sC_0(s) - 1 = i\int\omega V(\omega, s)d\omega\ , \qquad (6.7a)$$

and

$$(s+\omega_e-i\omega)V(\omega, s)$$
$$= iP^0(\omega)C_0(s) - \{sC_0(s)-1\}P^0(\omega)\ . \qquad (6.7b)$$

The latter equation gives

$$V(\omega, s)$$
$$= \{(i\omega-s)P^0(\omega)C_0(\omega)P^0(\omega)\}/(s+\omega_e-i\omega)$$
$$= -P^0(\omega)C_0(s) + \frac{\omega_e P^0(\omega)C_0(s)}{s+\omega_e-i\omega} + \frac{P^0(\omega)}{s+\omega_e-i\omega}\ . \qquad (6.8)$$

Hence we get from Eq. (6.7b)

$$C_0(s) = \frac{1+\int\dfrac{i\omega P_0(\omega)d\omega}{s+\omega_e-i\omega}}{s-i\omega_e\int\dfrac{\omega P_0(\omega)d\omega}{s+\omega_e-i\omega}}\ . \qquad (6.9)$$

We define the characteristic function of $P^0(\omega)$ by

$$Q^0(t) \equiv \int_{-\infty}^{\infty} P^0(\omega) e^{i\omega t} d\omega \,, \qquad (6.10)$$

from which we find

$$R(s) \equiv \int_0^{\infty} Q^0(t) \exp\{-(\omega_e+s)t\} dt$$
$$= \int_{-\infty}^{\infty} \frac{P^0(\omega) d\omega}{s+\omega_e-i\omega} \,, \qquad (6.11)$$

and

$$\int_0^{\infty} \frac{d}{dt} Q^0(t) \exp\{-(\omega_e+s)t\} dt$$
$$= \int \frac{i\omega P^0(\omega) d\omega}{s+\omega_e-i\omega}$$
$$= Q^0(t) \exp\{-(\omega_e+s)t\} \Big]_0^{\infty}$$
$$+ (\omega_e+s) \int_0^{\infty} Q^0(t) \exp\{-(\omega_e+s)t\} dt$$
$$= -1 + (\omega_e+s) R(s) \,. \qquad (6.12)$$

Thus Eq. (6.9) can be written as

$$C_0(s) = \frac{R(s)}{1-\omega_e R(s)} \,. \qquad (6.13)$$

This assures that the function $v(\omega, t)$ or $V(\omega, s)$ is zero when integrated over ω, because we get Eq. (6.13) from Eq. (6.8) if we integrate both sides of (6.8) over ω. Therefore Eq. (6.13) is the exact solution of our problem, from which we can find the spectrum $I(\omega)$ using Eq. (4.11):

$$I(\omega) = \mathrm{Re} \frac{1}{\pi} \frac{\displaystyle\int \frac{P^0(\omega') d\omega'}{\omega_e + i(\omega-\omega')}}{1-\omega_e \displaystyle\int \frac{P^0(\omega') d\omega'}{\omega_e + i(\omega-\omega')}} \,. \qquad (6.14)$$

It is interesting to note here that the relaxation has no effect if the original distribution $P^0(\omega)$ is Lorentzian. Namely, a Lorentzian function

$$P^0(\omega) = (1/\pi) b/(\omega^2+b^2) \,,$$

will give

$$Q^0(t) = \exp(-b|t|) \,,$$

and

$$R(s) = 1/(s+\omega_e+b) \,,$$

which leads to

$$C_0(s) = (s+b)^{-1} \,, \quad \text{and} \quad I(\omega) = P^0(\omega).$$

Thus the spectrum remains unchanged.

General expansion formulae of Eq. (6.14) for small ω_e and large ω_e can be derived as follows. For large ω_e, we expand $Q^0(t)\exp(-st)$ in power series of t to obtain

$$R(s) = \sum_n \int_0^t \frac{t^n}{n!} \left[\frac{d^n}{dt^n} \{e^{-st} Q^0(t)\} \right] \exp(-\omega_e t) dt$$
$$= \sum_n \frac{1}{\omega_e^{n+1}} \left[\left(\frac{d}{dt} - s \right)^n Q^0(t) \right]_{t=0}$$
$$= \sum (\omega_e)^{-n-1} (i\omega' - s)^n \,. \qquad (6.15)$$

Inserting this into (6.13) an explicit expression of $I(\omega)$ can be obtained. Thus we have

$$R(i\omega) = \frac{1}{\omega_e} - i \frac{\omega}{\omega_e^2} - \frac{\overline{\omega^2} - \omega^2}{\omega_e^3} + \cdots \,,$$

so that

$$I(\omega) = \frac{1}{\pi} \mathrm{Re} \frac{R(i\omega)}{1-\omega_e R(i\omega)}$$
$$= \frac{1}{\pi} \frac{\omega_e \overline{\omega^2} + \cdots}{(\omega^2 + \omega^2)^2 + \omega^2 \omega_e^2 + \cdots} \,,$$

which is simplified to

$$I(\omega) \simeq \frac{1}{\pi} \frac{\overline{\omega^2}/\omega_e}{\omega^2 + (\overline{\omega^2}/\omega_e)^2} \,, \qquad (6.16)$$

in accord to Eq. (5.8) for practically important frequencies

$$\omega \sim \overline{\omega^2}/\omega_e \,.$$

Next we shall derive an approximation for small ω_e assuming the distribution $P^0(\omega)$ to be continuous. Noticing that

$$R(i\omega) = \int_0^{\infty} Q^0(t) \, \mathrm{ext} \{-i(\omega - i\omega_e)t\} dt \,,$$

(Eq. 6.11), we introduce

$$\int_0^{\infty} Q^0(t) e^{-i\omega t} dt = \pi(\chi_0''(\omega) - i\chi_0'(\omega)) \,, \qquad (6.17)$$

which means that

$$\chi_0''(\omega) = \mathrm{Re} \frac{1}{\pi} \int_0^{\infty} Q^0(t) e^{-i\omega t} dt = P^0(\omega),$$

and

$$\chi_0'(\omega) = \frac{1}{\pi} \mathrm{HW} \cdot \int \frac{P^0(\omega') d\omega'}{\omega' - \omega} \,,$$

are the absorption and dispersion for the limiting case where $\omega_e = 0$. Therefore we may write

$$R(i\omega) = \pi\{\chi_0''(\omega - i\omega_e) - i\chi_0'(\omega - i\omega_e)\} \,, \qquad (6.18)$$

where we have assumed that the functions χ_0'' and χ_0' can be analytically continued to complex values of the argument. These two functions are mutually connected by the Kramers-Kronig relations, so that the knowledge of $P^0(\omega)$, for instance, allows us to construct its complementary part $\chi_0'(\omega)$. By the assumption of the regularity, we can then expand $R(i\omega)$ in powers of ω_e. Thus the intensity $I(\omega)$ can be calculated in power series of ω_e provided tha $\chi_0''(\omega)$ and $\chi_0'(\omega)$ are continuous and differentiable. To the first order of ω_e, we get

$$I(\omega)=P^0(\omega)$$
$$+\omega_e\left[-\frac{d\chi_0'(\omega)}{d\omega}+\pi\{P^0(\omega)^2-\chi_0'(\omega)^2\}\right]+\cdots\cdots. \tag{6.19}$$

One finds easily that this first order term vanishes if $P^0(\omega)$ is Lorentzian. It would be interesting to examine the condition that the relaxation will result in the narrowing, or more roughly, in the enhancement of the peak. For this, let us assume the particular case where $P^0(\omega)$ has a single maximum at $\omega=0$ (which is the center of the gravity of the distribution $P^0(\omega)$) and further that $\chi_0'(0)=0$. Then

$$\omega_e\left[-\left\{\frac{d\chi_0'(\omega)}{d\omega}\right\}_{\omega=0}+\pi P^0(0)^2\right]$$
$$=\frac{\omega_e}{\pi}\left\{\left[\int_0^\infty Q^0(t)\,dt\right]^2-\int_0^\infty tQ^0(t)dt\right\}, \tag{6.20}$$

is the first order change of the intensity at the peak. Evidently, this is equal to zero for the Lorentzian case, $Q^0(t)=\exp(-b|t|)$. If the decrease of $Q^0(t)$ is slower than the simple exponential decay for small values of t and faster for large t, then we may expect

$$\left\{\int_0^\infty Q^0(t)\,dt\right\}^2>\int_0^\infty tQ^0(t)dt\,,$$

and the narrowing will take place as the result of the relaxation. If $Q^0(t)$ behaves in the opposite way, then we may except broadening rather than narrowing at least in the first order of ω_e. Thus, in a sense, the Lorentzian form is a stable distribution against the effect of random modulation of the resonating frequencies, which seems certainly of some physical interest.

§ 7. Remark on the Gaussian-Markoffian Limit

As we mentioned in § 2, the resonance frequency ω of a resonating unit is considered as a stochastic variable. If the random variable $\omega(t_1)$, $\omega(t_2)$, $\cdots\cdot$ $\omega(t_n)$ for any set of arbitrarily chosen n time points (n being arbitrary) are distributed with a Gaussian (normal) distribution function (naturally we assume here every $\omega(t)$ realizes continuous values),

$$f(\omega(t_1),\,\omega(t_2),\cdots\cdot,\,\omega(t_n))$$
$$=C\exp\left\{-\frac{1}{2}\sum_j\sum_k a_{jk}\omega(t_j)\omega(t_k)\right\},$$
$$\left(\int_{-\infty}^{\infty}\cdots\cdot\int_{-\infty}^{\infty}f(\omega(t_1),\cdots\cdot\omega(t_n))d\omega(t_1)\cdots\cdot d\omega(t_n)=1\right),$$

then the stochastic process of $\omega(t)$ is called a *Gaussian process*[3]. If the stochastic process $\omega(t)$, which is stationary, is Gaussian, it is easy to see that

$$\varphi(t)=\exp\left\{-\int_0^t(t-\tau)\langle\omega(t'+\tau)\omega(t')\rangle d\tau\right\}, \tag{7.1}$$

as has been pointed out by Anderson and Weiss[4].

Now we shall remark here that under a certain conditions Markoffian process we have assumed in the above treatment approaches to a Gaussian-Markoffian process. Let us suppose that the resonance frequency of the resonating unit in each of its states is constructed from a number of small contributions. i.e.,

$$\omega(t)=\sum_n^N \varDelta\omega_n(t)\,. \tag{7.2}$$

For instance, the resonance frequency of an unit can be conceived as determined by a local fied which is the resultant of small disturbances exerted by a number of surrounding atoms. The state of an unit is now characterized by the states of the surrounding atoms which are specified by set of numbers $(j_1, j_2, \cdots\cdot j_N)$. For simplicity we further assume that each of these atoms will realize its various states independently of the others. The stochastic process of the component $\varDelta\omega_n(t)$ is thus assumed to be Markoffian which is due to random jumps of the n-th atom. Corresponding to our treatment in § 2, we describe this by the matrices D_n and $\varDelta\Omega_n$. The zero-eigenvectors of D_n will be denoted by φ_{0n} and ψ_{0n}. Then we see at once that the correlation function $g(t)$ for a resonating unit is given by

$$g(t)=\prod_{n=1}^{N} g_n(t)\ , \qquad (7.3)$$

where

$$g_n(t)=\varphi_{0n}\exp\{-(D_n-i\varDelta\Omega_n)t\}\psi_{0n}\ , \qquad (7.4)$$

is the correlation function for the component $\varDelta\omega_n(t)$. Now we expect there exists a generalization of the central limit theorem of probability theory which states that under some conditions the stochastic process of $\omega(t)$, (7.2), becomes Gaussian. A rigorous examination of this assertion is out of space, but we may say that if

$$\lim_{N\to\infty}\sum_{n=1}^{N}\langle(\varDelta\omega_n-\langle\varDelta\omega_n\rangle)^2\rangle=\lim_{N\to\infty}\sum_{n=1}^{N}\varphi_{0n}(\varDelta\Omega_n)^2\psi_{0n}$$
$$=\omega_p{}^2\ , \qquad (7.5)$$

exists and if the distribution of every $\varDelta\omega_n$ satisfies a certain condition such as the Lindeberg condition to prevent too wide a spread of its distribution function, the correlation function, (7.3) approaches to the form (7.1), for which we now have

$$\langle\omega(t'+\tau)\omega(t')\rangle=\lim_{n\to\infty}\sum_{n=1}^{N}\varphi_{0n}\varDelta\Omega_n e^{-D_n\tau}\varDelta\Omega_n\psi_{0n}$$
$$=\lim_{N\to\infty}\varphi_0\Omega e^{-D\tau}\Omega\psi_0\ , \qquad (7.6)$$

where Ω, D, φ_0 and ψ_0 now refer to the whole configuration space for all of the components.

With the use of the expansion formula for an exponential operator function,

$$e^{a+b}=e^a+\int_0^1 e^{(1-s)a}be^{sa}ds$$
$$+\int_0^1\int_0^s e^{(1-s)a}be^{(s-s')a}be^{s'a}dsds'+\cdots,$$

we get

$$g_n(t)=\varphi_{0n}\Big[e^{-D_nt}+\int_0^t e^{-D_n(t-t_1)}i\varDelta\Omega_n e^{-D_nt_1}dt_1$$
$$+\int_0^t\int_0^{t_1} e^{-D_n(t-t_1)}i\varDelta\Omega_n e^{-D_n(t_1-t_2)}i\varDelta\Omega_n e^{-D_nt_2}$$
$$\times\, dt_1dt_2+o(\varDelta\omega^2)\Big]\psi_{0n}$$
$$=1+it\varphi_{0n}\varDelta\Omega_n\psi_{0n}-\int_0^t(t-\tau)\varphi_{0n}\varDelta\Omega_n e^{-D_n\tau}$$
$$\times\,\varDelta\Omega_n\psi_{0n}d\tau+o(\varDelta\omega^2)$$
$$=\exp\left\{-\int_0^t(t-\tau)\langle\varDelta\omega_n(\tau)\varDelta\omega_n(0)\rangle d\tau+o(\varDelta\omega^2)\right\}\ ,$$

where

$$\langle\varDelta\omega_n\rangle=\varphi_{0n}\varDelta\Omega_n\psi_{0n}=0\ ,$$

can be assumed without loss of generality.

Inserting the above expression into (7.3) and omitting the sum of the residual terms, we get

$$g(t)=\exp\left[-\int_0^t(t-\tau)\langle\omega(\tau)\omega(0)\rangle d\tau\right], \qquad (7.7)$$

where $\langle\omega(\tau)\omega(0)\rangle$ is identical with (7.6). The correlation function (7.7) or (7.1) is equivalent to the Fourier transform of the absorption spectrum derived by Kubo and Tomita⁵⁾ with the use of second order perturbation theory. In particular, the strongly narrowed width of the spectrum is determined by

$$\int_0^\infty\langle\omega(\tau)\omega(0)\rangle d\tau=\int_0^\infty\varphi_0\Omega e^{-D\tau}\Omega\psi_0 d\tau\ ,$$

in agreement with Eq. (5.7). It should be noticed that this limit of strong narrowing is independent of the Gaussian assumption.

If the relaxation times or the eigenvalues of D (except the zero eigenvalue) are all degenerate (see § 6), we may write Eq. (7.7) as

$$g(t)=\exp\left[-\omega_p{}^2\int_0^\infty\exp(-\omega_e\tau)\,(t-\tau)d\tau\right]$$
$$=\exp\left[-\omega_p{}^2(\exp(-\omega_et)-1+\omega_et)\right]. \qquad (7.8)$$

This should be compared with Eq. (7.25a) of Kubo and Tomita's paper. As was discussed by these authors (7.8) is a typical function to describe the narrowing process of a Gaussian spectrum with the second moment $\omega_p{}^2$ in the presence of a Markoffian motion characterized by the relaxation time $1/\omega_e$. This is the basis of the theory of motional narrowing of adiabatic broadening in nuclear magnetic resonance spectrum first discussed by Bloembergen, Purcell and Pound⁶⁾.

A particularly simple example of Eq. (7.8) is the case where every $\varDelta\omega_n$ takes only two values ω_1 and $-\omega_1$ and the stochastic matrix of each component is

$$D_1=\begin{pmatrix}\frac{1}{2}\omega_e & -\frac{1}{2}\omega_e\\ -\frac{1}{2}\omega_e & \frac{1}{2}\omega_e\end{pmatrix}.$$

Then $g_1(t)$ is easily calculated to be

$$g_1(t)=\frac{1}{2\omega'}\left[\left(\frac{\omega_e}{2}+\omega'\right)\exp\left\{-\left(\frac{\omega_e}{2}-\omega'\right)t\right\}\right.$$
$$\left.-\left(\frac{\omega_e}{2}-\omega'\right)\exp\left\{-\left(\frac{\omega_e}{2}+\omega'\right)t\right\}\right],$$

$(\omega'^2=\omega_e^2/4-\omega_1^2)$.

Taking the limit of $N\omega_1^2\rightarrow\omega_p^2$ as N increases indefinitely, it is easy prove directly Eq. (7.8).

Acknowledgement

The author wishes to thank Dr. P. W. Anderson for much valuable discussions. This study was partially financed by the Scientific Research Fund of the Ministry of Education.

References

1) P. W. Anderson: J. Phys. Soc. Japan **9** (1954) 316.

2) W. Feller: *An Introduction to Probability Theory and its Applications.* Vol. 1. 1950 (John Wiley and Sons) p. 386 ff.

3) M. C. Wang and C. E. Uhlenbeck: Rev. Mod. Phys. **17** (1945) 323.

4) P. W. Anderson and P. R. Weiss: Rev. Mod. Phys. **25** (1953), 269. See also L. A. Zadeh: Proc. I. R. E. **39** (1951) 425, and Z. Kiyasu: Inst. Electrical communication Eng. Japan, **34** (1951) 605.

5) R. Kubo and K. Tomita: J. Phys. Soc. Japan **9** (1954) 888.

6) N. Bloembergen, E. M. Purcell and R. V. Pound: Phys. Rev. **73** (1948) 679.

JOURNAL OF THE PHYSICAL SOCIETY OF JAPAN Vol. 9, No. 6, NOV.—DEC., 1954

Formation Energy of Lattice Defect in Simple Oxide Crystals

By Jiro YAMASHITA and Tatumi KUROSAWA

Institute of Science and Technology, University of Tokyo

(Received July 17, 1954)

Determining the inter-ionic potentials in MgO, CaO and SrO crystals phenomenologically, we have found that the affinity of the O^{--} ion has different value in each crystal. Using these potentials we have computed the formation energy of the Schottky defect in these crystals and found that the results are reasonable. Finally we tried to explain the deviation from Cauchy-relations in MgO by Lowdin's many-body forces.

§ 1. Introduction

Fifteen years have passed since Mott and Gurney wrote their famous book " The Electronic Processes in Ionic Crystals ". Since then many good works have been published in this research field. However there is no accurate theoretical work which makes clear the electronic structure of oxide crystals, while there are vast experimental observations regarding the various kinds of physical properties of oxide crystals. Thus it is highly desirable to compute the electronic structure of simple oxide crystals on the basis of the quantum theory of solids. Nevertheless it seems to be useful at present to develop the phenomenological theory of oxide crystals, in order to find the unified model for them as far as possible. Of course, we can not expect to deduce any decisive conclusions from such a phenomenological theory, but we can hope that it helps us to grasp the direction for further researches.

In the following we shall treat simple oxide crystals, MgO, CaO and SrO, under the assumption of the totally ionic state which consists of (metal ions)$^{++}$ and O^{--} ions. The appropriateness of this assumption has not been well established theoretically, but it seems to us that many of the experimental facts are explained at least qualitatively by this assumption. So we think that the stable existence of the doubly-charged negative oxygen ions within such crystals may be considered to be a useful presupposition in order to clarify the many physical properties of the crystals, in spite of the well known fact that the doubly-charged negative oxygen ions have not been observed in gaseous phase. If a doubly-charged negative ion is stable in oxide crystals by the effect of the surrounding ions, the wave-function of the O^{--} ion should not be equal in all oxide crystals, but has a proper character in each crystal so as to minimize the total energy of that crystal in the proper crystalline field, though the electronic state of that ion approximately corresponds to the $(1s)^2(2s)^2(2p)^6$ configuration of free ions. Thus we expect that it leads to different values of the electronic affinity of the O^{--} ion in different crystals. We shall later confirm this fact from our analysis.

In the following we shall determine the interaction potentials between ions phenomenologically (§ 2), discuss the polarizability of an oxygen ion in crystals (§ 3) and properties of the elastic constants in MgO (§ 4) and finally compute the formation energy of the Schottky defect in MgO, CaO and SrO crystals (§ 5).

§ 2. Determination of Interaction Potentials

In the following we shall determine interaction potentials between various ions in MgO, CaO and SrO crystals. We assume that the interaction potential between a positive ion and an oxygen ion separated by a distance r is given by

$$U_0 = -4e^2/r + be^{-\rho r} , \qquad (1)$$

and between a pair of oxygen ions by

$$V_0 = 4e^2/r + c\exp(-\sigma r/\sqrt{2}) . \qquad (2)$$

The so-called Van der Waals energy is included approximately in the short range part of the above potentials. In order to determine four constants b, ρ, c and σ phenomenologically, we must have four relations which contain these constants. These relations are as follows:

(a) lattice energy E

The short range forces fall off so quickly that only ions which are nearest neighbours and next nearest neighbours need be taken into account. Then the lattice energy is given by

$$-e^2Z^2\alpha_M/a + x + y = -E, \quad E > 0 . \qquad (\mathrm{I})$$

where (a) is the distance between the nearest neighbouring ions in equilibrium state, α_M is the Madelung constant, Z is the valency of the ions ($Z=2$),

$$x = 6be^{-\rho a} \quad \text{and} \quad y = 6ce^{-\sigma a} . \qquad (3)$$

(b) lattice constant $2a$.

The condition that the lattice has a equilibrium state with the lattice constant $2a$ is expressed as

$$\rho x + \sigma y = e^2Z^2\alpha_M/a^2 = 0 . \qquad (\mathrm{II})$$

(c) compressibility β.

The compressibility is expressed as

$$\rho^2x + \sigma^2y - 2e^2Z^2\alpha_M/a^3 = 18a/\beta . \qquad (\mathrm{III})$$

(d) the fourth relation

The above three relations are common in the Born theory of ionic crystals and were applied to oxide crystals by Mayer.3) We, however, need one more relation for our analysis. Now, we introduce a new relation between force constants and dielectric properties. As well known, when the ions are displaced in an electrostatic field, the change of the energy of the crystal per ion pair is given by8)

$$e^2Cd^2 = 4be^{-\rho a}(\rho^2 - 2\rho/a)d^2 = \tfrac{2}{3}x\rho(\rho - 2/a) , \qquad (4)$$

where $2d$ is the relative displacement. Recently Szigeti1) has derived a relation between C and dielectric properties:

$$e^2C = 2\frac{\kappa+2}{\kappa_0+2}m\omega_t^2 , \qquad (5)$$

where κ is the dielectric constant in static field, κ_0 is the dielectric constant in optical frequency, ω_t is the Reststrahlenfrequenz and m is the reduced mass of the ions. Moreover, if we assume that the short range force is central and effective only between the nearest neighbours, we have the following relation,

$$e^2C = 12a/\beta . \qquad (6)$$

From Eqs. (5) and (6) we obtain a relation:

$$1/\beta = \{(\kappa+2)/6(\kappa_0+2)\}(m\omega_t^2/a). \qquad (7)$$

Szigeti has found that the above relation holds very well for many alkali-halide crystals but does not hold for MgO, which means that the above assumptions are not valid for MgO. Although we do not know at present which of these assumptions is the true origin of the failure, we assume here that the discrepancy is caused by the existence of the short range interaction between a pair of oxygen ions. In this case Eq. (6) is no longer valid, since C depends only on forces between the nearest neighbours, while compressibility depends on forces between a pair of oxygen ions besides forces between the nearest neighbours. On the other hand, one of the authors has derived a similar relation under the assumption that the energy change by the electric field is expressed by a quadratic form of two kinds of dipole moment, dipoles due to the displacement of ions and dipoles due to the deformation of ions respectively:

$$e^2C_k=2\frac{\kappa+2}{\kappa_0+2}m\omega_t{}^2+\frac{4\pi}{3}\frac{e^2Z^2}{a^3}\frac{\kappa_0+2}{\kappa_0-1}\times\left(1-\frac{e^*}{e}\right)^2, \qquad \text{(IV)}$$

where the effective charge e^* is defined by Szigeti[2] as

$$e^{*2}=\frac{9m\omega_t{}^2a^3}{2\pi Z^2}\cdot\frac{\kappa-\kappa_0}{(\kappa_0+2)^2}, \qquad (8)$$

In general, the difference of these two equations is small as shown in Table I (in atomic units), because the second term of (IV) is rather small compared with the first term. In the following we shall use the relation (IV) as the fourth relation of our analysis. Thus, we use six observed quantities E, a, β, κ, κ_0, and ω_t in our analysis instead of three in the previous one. Among the six quantities the value of the lattice energy is not accurate, since one has no direct means to measure the affinity of doubly-charged negative oxygen ions. Thus, it is better at first to consider the lattice energy as a adjustable parameter and then to try to limit its value in the certain reasonable region.

Table I.

	C_S	C_K
MgO	0.578	0.588
CaO	0.311	0.325
SrO	0.137	0.195

Table II.

	$E_0\frac{\text{Kcal}}{\text{mol}}$	$I\frac{\text{Kcal}}{\text{mol}}$	$a(A)$	β	$\omega_t(\text{sec}^{-1})$
MgO	238	521	2.10	0.59×10^{-12}	10.89×10^{13}
CaO	254	412	2.40	—	6.88×10^{13}
SrO	238	384	2.58	—	4.01×10^{13}

	κ	κ_0	e^*/e	$A\frac{\text{Kcal}}{\text{mol}}$	$\alpha(+)$ (cm³)
MgO	9.8	2.95	0.88	E—759	0.10×10^{-24}
CaO	11.8	3.28	0.76	E—666	0.47×10^{-24}
SrO	13.3	3.31	0.58	E—622	0.86×10^{-21}

Before beginning our analysis, we find it convenient to tabulate the data which are necessary for us. In Table II, E_0 means the cohesive energy of crystals relative to the monoatomic gases of the constituents, while E means the cohesive energy of crystals relative to constituent ions.[3] The relation of the two is:

$$E=E_0+I+A, \qquad (9)$$

where I is the ionization energy of the metal ions and A is the affinity of the oxygen ion.

(1) Now we begin with MgO. A set of equations to be solved are:

$$\left\{\begin{aligned} &x+y=1.7476-E, \\ &\rho x+\sigma y=0.4369, \\ &\rho^2x+\sigma^2y=0.6346, \\ &\rho x(\rho-\tfrac{1}{2})=0.8820. \end{aligned}\right.$$

The values of four constants which are determined for various values of E are listed in Table III (in atomic units). From Table III we see that the force acting between a pair of oxygen ions is attractive and its magnitude becomes smaller when the cohesive energy becomes larger. But in the case of (f) the value of σ is unreasonably large and in cases (a) and (b) the ratio $|y|/x$ becomes too large to be compatible with our usual crystal model. Thus our analysis shows that the value of the affinity of the oxygen ion in MgO crystals lies within the range of $A=-180\pm20$ Kcal/mol.

Table III. MgO

	E	x	y	ρ	$\sigma/\sqrt{2}$
a	1.4300	0.5864	−0.2688	1.520	1.123
b	1.4620	0.4203	−0.1347	1.720	1.501
c	1.4820	0.3260	−0.0604	1.919	2.209
d	1.5020	0.2795	−0.0339	2.044	2.698
e	1.5220	0.2408	−0.0152	2.180	4.093
f	1.5420	0.2107	−0.0051	2.311	6.946

b	$-c$	$\|y\|/x$	$A\frac{\text{Kcal}}{\text{mol}}$
42.71	25.70	0.458	−133
68.13	109.3	0.320	−153
117.1	2672	0.185	−165
165.5	2.39×10^4	0.121	−178
245.7	2.86×10^7	0.063	−190
363.1	9.83×10^{13}	0.024	−203

(2) Next we proceed to CaO. Unfortunately the compressibility of the single crystal has not been observed and the lack of it prevents us from determining the four potential-constants empirically as before. Then, we are compelled to use the following less satisfactory method. At first we give a set of values for two constants, and then determine the remaining two using the relations (II) and (IV). Then we obtain the lattice energy E from Eq. (I) as listed in Table IV. The values of x and ρ in rows (b) and (c) are determined by the assumption that the interaction constants between a pair of oxygen ions are given by (d) and (c) of Table III respectively. The values of x and y in rows (a), (d) and (e) are determined by giving the denoted values of ρ and σ. Since the mutual distance between a pair of oxygen ions in CaO is larger than that of MgO, we may expect that values of y is also smaller than that of MgO. Then we estimate the affinity of the oxygen ion in CaO as $A=-165\pm 25$ Kcal/mol.

Table IV. CaO.

	ρ	x	$\sigma/\sqrt{2}$	y	$\lvert y\rvert/x$	E	$A\,\frac{\text{Kcal}}{\text{mol}}$
a	2.00	0.1557	3.000	0.0095	0.006	1.3763	−192
b	1.81	0.1970	2.698	−0.0044	0.022	1.3488	−175
c	1.74	0.2155	2.209	−0.0113	0.052	1.3372	−168
d	1.60	0.2629	1.767	−0.0323	0.123	1.3054	−151
e	1.50	0.3070	1.500	−0.0569	0.185	1.2913	−141

Table V. SrO.

	ρ	x	σ	y	$\lvert y\rvert/x$	E	$A\,\frac{\text{Kcal}}{\text{mol}}$
a	1.40	0.2091	—	0	0	1.2242	−141
b	1.30	0.2530	2.0	−0.0175	0.069	1.1978	−127
c	1.20	0.3086	2.0	−0.0382	0.123	1.1629	−105
d	1.60	0.1536	2.0	+0.0240	0.156	1.2557	−163

(3) For SrO the same method as CaO is employed. If we put $y=0$, we obtain the results listed in the row (a) of Table V, and values of other rows are determined by giving the values of ρ and σ. In the case of SrO we may expect that the short range interaction between a pair of oxygen ions is very small, since the mutual distance of oxygen ions (3.65A) is much larger than twice of the Goldschmidt's ionic radius of the oxygen ion (1.32A). On the other hand, if we compute the Van der Waals energy between neighbouring oxygen ions by the conventional formula, we find the value 0.00574 (3.6 Kcal/mol). Thus, we think that the possibility of (c) and (d) of Table V is excluded and the affinity of the oxygen ion in SrO lies near-(130∼140) Kcal/mol. From these results we see that the affinity of oxygen ions in MgO is different from that in SrO. Is it caused by the error of our analysis or has it real meaning? Really our analysis has many ambiguous points, but we think that the very existence of the difference of the affinity-values has real meaning, if our fundamental assumptions mentioned previously be approximately allowable.

§ 3. The Optical Dielectric Constant

Recently Shockley[4] has published the interesting result of his analysis about the electronic polarizability of ions in many ionic crystals. It was shown that the additivity of the polarizability of each ion is well established for alkali-halide crystals, but not for oxide crystals. The polarizability of the oxygen ion seems to increase with the molar volume per oxygen ion. Moreover, he has shown that if one plots the polarizability of the oxygen ion as a function of the volume per oxygen ion for several compounds (BeO, MgO, CaO, SrO and BaO), the values of the polarizability fall near one line. We think that these phenomena may be well interpreted by the assumption that the state of the oxygen ion is variable according to the crystalline field in each crystal. As mentioned previously, the electronic state of the oxygen ion is different in each crystal and the absolute values of the affinity become smaller, when the charge distribution of the oxygen ion is more spread. Since the polarizability is roughly proportional to $(\overline{r^2})^2$, there may be a close relation between the polarizability and the affinity in various crystals. As we have computed the affinity only for three crystals, so we can not deduce any decisive conclusions, but the above three examples seem to support our speculation (Table VI). Several years ago we computed the $(2p)^6$ wave function of the O^{--} ion in MgO crystal[5] by a variational method. The trial function was assumed to be:

$$\phi = Ar^2\{\exp(-\alpha_0 r) + B\exp(-\beta_0 r)\}, \qquad (10)$$

where α_0, β_0 and B are variational parameters. We found that the energy of $(2p)^6$ configuration of at O^{--} ion was higher than the energy of $(2p)^5$ of an O^- ion. Thus, we found that the O^{--} ion was unstable in the free state but became stable in MgO crystal owing to the Madelung energy, exchange energy and S-energy. We determined three parameters so as to minimize the total energy of MgO crystal. The results are:

$\alpha_0 = 2.9$, $\beta_0 = 1.1$, $B = 0.15$, $(\overline{r^2})^2 = 7.2$,
the affinity of the 2nd electron $= -11.8$ ev.

The usual value of the affinity of the oxygen ion is the sum of the affinity of the second electron of an O^{--} ion and the affinity of a neutral oxygen, which was measured by Lozier[6] as 2.2 ev. Then the computed value of the affinity of the oxygen ion becomes 224 Kcal/mol. Next, if we choose parameters as $\alpha_0 = 2.9$, $\beta_0 = 1.1$ and $B = 0.20$, we find the affinity $= 160$ Kcal/mol and $(\overline{r^2})^2 = 8.6$. Thus, we see that the theoretical result gives roughly the same order of magnitude for the relation between the affinity and the magnitude of $(\overline{r^2})^2$. Unfortunately the accuracy of our computation was not high, so we can not deduce any quantitative conclusions from it. We think, however, that our computation seems to support our speculation.

Table VI.

	$\alpha\ (O^{--})$	$A\ \frac{\text{Kcal}}{\text{mol}}$
O^{--} in MgO	1.77×10^{-24}	~ -180
O^{--} in CaO	2.35×10^{-24}	~ -165
O^{--} in SrO	$2.7\ \times 10^{-24}$	~ -140

§ 4. The Elastic Constants

In the preceding chapters it was assumed that the ions interacted with spherically symmetric forces. If this assumption were correct, the elastic constants c_{12} and c_{44} in MgO should satisfy the Cauchy-Poisson relation: $c_{12} = c_{44}$. Measurements, however, show that this relation is not valid even for alkali-halide crystals and become much worse for MgO as shown in Table VII. It follows that the deviation from the Cauchy relation occurs, because there should be some non-central forces in these ionic crystals. Previously one might have thought that there was some degree of homopolar binding even in alkali-halide crystals and it brought forth the non-central interaction. However, Lowdin[7] has shown that the S-energy in ionic crystals depends on the distances between the nuclei of three and more ions and corresponds to many-body forces. Considering them he really computed the elastic constants of some alkali-halide crystals quantum-mechanically with success.

According to Lowdin there are two non-central energies $E(B)$ and $E(D)$. These are with some approximations:

$$E(B) = 2e^2 \sum_{g_\nu}^{(+)} \sum_{g_\mu}^{(-)} F_0(a_{\mu\nu}) \sum_g{}' \frac{Z_g}{r_{gg_\nu}}, \qquad (11)$$

and

$$E(D) = -e^2 \sum_{g_\nu}^{(+)} \sum_{g_\mu}^{(-)} F_0(a_{\mu\nu}) \left\{ \sum_g{}' \frac{Z_g}{r_{gg_\mu}} + \sum_g{}' \frac{Z_g}{r_{gg_\nu}} \right\}, \qquad (12)$$

where

$$F_0 = \overset{\text{(one pair)}}{\sum_\nu \sum_\mu} S_{\mu\nu}{}^2,$$

$$S_{\mu\nu} = \int \psi_\mu{}^*(1)\psi_\nu(1)d\tau - \delta_{\mu\nu}, \qquad (13)$$

and $a_{\mu\nu}$ is the distance between the lattice point g_μ and g_ν. The notations $\overset{(+)}{\sum}$, $\overset{(-)}{\sum}$ mean that the summation is carried over + ions and − ions respectively and the notation $\overset{\text{(one pair)}}{\sum\sum}$ means that the summation is taken over one pair of ions.

Here we note that $E(D)$ is zero in a usual equilibrium state or even in a homogeneously strained crystal, because the two lattice sums in the second factor of expression (12) have the same absolute value, but different signs.

Now, as for MgO crystals we do not know whether the large deviation from the Cauchy-relation is caused by the same origin. We, however, shall apply the Lowdin theory to the elastic constants c_{12} and c_{44} of MgO. Then, we devide the short range potential energy in two parts;

$$E=E_1(\text{central})+E_2(\text{non-central}),$$

where E_1(central) is assumed to be given by the sum of ordinary exponential functions:

$$E_1=\sum_{\mu}^{(+)}\sum_{\nu}^{(-)}A\exp(-\rho a_{\mu\nu})$$
$$+\tfrac{1}{2}\sum_{\mu}^{(-)}\sum_{\nu}^{(-)}C\exp\left(-\frac{\sigma}{\sqrt{2}}a_{\mu\nu}\right), \tag{14}$$

while E_2(non-central) is given by

$$E_2=-(12e^2Z\alpha_M/a)F_0\ , \tag{15}$$

according to Lowdin. Here we must notice that Eq. (15) contains the non-central interaction of the nearest neighbouring ions only. Then, the difference of the elastic constants c_{12} and c_{44} is expressed as follows (Lowdin's first approximation):

$$c_{44}-c_{12}=-(18e^2Z/a^4)\{0.1295a(dF_0/da)\}\ . \tag{16}$$

The values of adF_0/da for some alkali-halides computed by Lowdin are listed in Table VII. Now, if we insert the observed value of $c_{12}-c_{44}$ and a of MgO into Eq. (16), we obtain the value -0.1288 for adF_0/da. We see that this value is the same order of magnitude as compared with that of the alkali-halide crystals, although the value of $c_{12}-c_{44}$ of MgO is much larger than that of alkali-halides. At a glance this would seem to be a rather surprising success, but we must not overlook the fact that we considered the non-central potential only between the nearest neighbouring ions. On the other hand, we have found that the effect of the oxygen-oxygen interaction is by no means negligible for the compressibility of MgO. Thus, there may be no reason to expect that the effect of the oxygen-oxygen interaction is negligibly small for $c_{12}-c_{44}$. If we want to consider these effects also, we unfortunately have too many arbitrary constants to be manageable in such a phenomenological treatment. At any rate we believe from our results that the deviation from the Cauchy-relation does not mean grave difficulties about the cohesive mechanism of MgO crystals.

Table VII.

	c_{12}	c_{44}	$c_{44}-c_{12}$	adF_0/da
LiF	4.04×10^{11}	5.54×10^{11}	$1.50\ \times10^{11}$	
NaCl	1.10×10^{11}	1.34×10^{11}	$0.24\ \times10^{11}$	-0.0801
KCl	$0.6\ \times10^{11}$	0.069×10^{11}	0.009×10^{11}	-0.1835
MgO	8.57×10^{11}	15.67×10^{11}	$7.10\ \times10^{11}$	-0.1288

Now, we must inquire whether our fundamental equations are correct or not, when we consider many-body-forces. If we newly assume the equivalent interaction potential between a Mg^{++} ion and an O^{--} ion as follows:

$$U(r)=-\frac{4e^2}{r}+Ae^{-\rho r}-\frac{2e^2Z\alpha_M}{r}F_0$$
$$=-\frac{4e^2}{r}+Ae^{-\rho r}-\frac{2e^2Z\alpha_M}{r}\Gamma e^{-\rho r}$$
$$=-\frac{4e^2}{r}+\left(A-\frac{2e^2Z\alpha_M}{r}\Gamma\right)e^{-\rho r}$$
$$=-\frac{4e^2}{r}+be^{-\rho r}, \tag{17}$$

there is no need of modifying Eqs. (I), (II) and (III). On the other hand, we must treat Eq. (IV) more carefully. When an external electric field is applied, $E(B)$ becomes

$$E(B)=12Ne^2\Gamma e^{-\rho a}(e^{\rho d}+e^{-\rho d})$$
$$\times\left[-\frac{Z\alpha_M}{a}-\frac{4\pi}{3}Pd\right], \tag{18}$$

where d is the relative displacement of a positive and a negative ion and P is the polarization of the medium. Thus the extra term

$$-12Ne^2\Gamma e^{-\rho a}(e^{\rho d}+e^{-\rho d})(4\pi/3)Pd\ , \tag{19}$$

appears owing to the polarization., Fortunately, however, this extra term is cancelled out by the contribution from $E(D)$, because $E(D)$ is no longer zero under the homogeneous electrostatic force $-4\pi P/3$, but will be

$$12Ne^2\Gamma e^{-\rho a}(e^{\rho d}+e^{-\rho d})(4\pi/3)Pd\ . \tag{20}$$

Thus we see that the introduction of the non-central potential does not bring any change to the basic equations of our analysis, if it be allowed to consider only the totally ionic state of MgO and to explain the deviation from the Cauchy-relation by the Lowdin theory. Although the appropriateness of the assumptions is by no means obvious, we see that our analysis is self-consistent.

§ 5. The Formation Energy of the Schottky Defect in MgO, CaO and SrO

(*a*) *Method*

In this chapter we shall compute the formation energy of the Schottky defect in MgO, CaO and SrO by the method of Mott and Littleton.[8] We take as unknown the displacements x and the electronic dipoles μ of the six nearest neighbours and compute the dipoles of all the other ions from the continuous model. Let us denote the polarization due to displacement of ions and due to electronic dipoles of a positive ion and a negative ion by $p_d = Zed$, $p(+)$ and $p(-)$ respectively. Further we introduce three non-dimentional quantities M_+, M_- and M for convenience. These are defined by:

$$d = Ma^3/r^2, \quad p(+)+p_d = 2a^3eM_+/r^2$$

and

$$p(-)+p_d = 2a^3eM_-/r^2 \ ,$$

where r is the distance from the centre of the hole. These values are determined by the continuous model, in which the polarization per unit volume is given by

$$P = (eZ/4\pi r^2)(1-1/\kappa) \ . \tag{21}$$

These are:

$$\left.\begin{aligned} M_+ &= \frac{(2/4\pi)(1-1/\kappa)[p_d+p(+)]}{[2p_d+p(+)+p(-)]} \ , \\ M_- &= \frac{(2/4\pi)(1-1/\kappa)[p_d+p(-)]}{[2p_d+p(+)+p(-)]} \ , \\ M &= \frac{(2/4\pi)(1-1/\kappa)p_d}{[2p_d+p(+)+p(-)]} \ . \end{aligned}\right\} \tag{22}$$

As for MgO we know the ratio of dipoles from our previous work ;

$$2p_d : p(-) : p(+) = 48.24 : 42.09 : 2.37 \ ,$$

and for CaO and SrO we use the following relations for that purpose

$$(p(+)+p(-))/2p_d = \kappa_0/(\kappa-\kappa_0)$$

and

$$p(+)/p(-) = \alpha(+)/\alpha(-).$$

Using these relations and α-values from Table II and Table VI the values of M's are determined as listed in Table VIII.

As for x and μ, Mott and Littleton determined them by the following set of equations:

$$\left\{\begin{aligned} F_e+F_r &= 0 \ , \\ \alpha F_e &= \mu \ , \end{aligned}\right. \tag{23}$$

where F_e is the electrostatic force and F_r is the repulsive force at the position of the nearest neighbouring ions. When an ion is removed from the lattice point, ions being adjacent to the hole are pushed outwards by F_e. On the other hand, the field of the short range forces has not the cubic symmetry there, and then the repulsive force works so as to push back the ions towards the hole. The two kinds of forces are in equilibrium at a certain configuration of ions. In the second equation α is the polarizability of the ions being adjacent to the hole. In the case of alkali-halides Mott used the usual values of the ionic polarizability for it and the results justified such an approximation. For oxygen ions, however, such an approximation will be very poor, because the electronic state of the oxygen ion adjacent to the hole must be different from the oxygen ion at the usual lattice points. We think that this is a characteristic feature of the O^{--} ion, since the electronic state of it is determined by the surrounding conditions. Owing to the lack of an ion at the centre of the hole the overlap-energy will be reduced, when the ion-cloud is polarized towards the hole[10], while the electrostatic energy increases then. Thus, at the lattice point adjacent to the hole there may be a overlap-repulsive force which works to hinder the polarization of the ion-core against the action of the electrostatic field. Then we suppose that the polarizability of the oxygen ion may be somewhat reduced at the lattice point adjacent to the hole. In fact the situation must not be so simple there and a detailed quantum theoretical investigation is required in order to clarify the electronic structure of ions there. We, however, are content at present to treat it phenomenologically by introducing one more parameter $\mathcal{E}$ to characterize the polarizability of the oxygen ion there, which is denoted by $\alpha^* = \mathcal{E}\alpha$.

(*b*) *Results*

In the following we shall write down the

Table VIII.

	M_+	M_-	M
MgO	0.04084	0.1020	0.03718
CaO	0.05930	0.08626	0.0526
SrO	0.05872	0.07603	0.0506

results of computations. Since many notations are used, it is convenient to summarize them in the beginning.

W: the formation energy of the Schottky defect

W_+: work necessary to remove a positive ion from the normal lattice point to infinity

W_-: work necessary to remove a negative ion from the normal lattice point to infinity

E: lattice energy per ion pair

$$W=W_+ + W_- - E\,,$$

$V(+)$: potential energy due to the polarization of the medium surrounding the positive vacant lattice point

$V(-)$: potential energy due to the polarization of medium surrounding the negative vacant lattice point

$V_0(\pm)$: $V(\pm)$ computed by the continuous model (zero order app.)

$V_1(\pm)$: $V(\pm)$ computed by the above mentioned method (first approximation of Mott and Littleton)

$w(r)=b\exp(-\rho r)$: the short range repulsive potential between a pair of ions of unlike sign

$\mu=Zam$ and $x=\xi a$.

Then the work necessary to remove an ion consists of the following terms:

(1) that due to the electrostatic forces, namely

$$Z^2\alpha_M e^2/a-(Z/2)eV\,.$$

(2) that due to the overlap forces; consider the work done to bring back the ion into the hole; if we keep the ions displaced the work done is

$$6w(a+x)\,.$$

We then move the ions back to their original positions, the force opposing this motion is initially $w'(a+x)$, so the total work is, per neighbour,

$$\tfrac{1}{2}xw'(a+x)\,.$$

Thus the contribution of the overlap forces to the work to remove an ion is

$$-6[w(a+x)-\tfrac{1}{2}xw'(a+x)]\equiv\chi(x)\,.$$

Thus we find:

$$W_\pm=\frac{Z^2\alpha_M e^2}{a}-\frac{Z}{2}eV_1(\pm)$$
$$-6[w(a+x)-\tfrac{1}{2}xw'(a+x)]\,.$$

The results of the computation are listed in

Table IX. MgO.

(−) ion vacancy.

	ξ	m	V_1	$-\chi$	W_-	E
c	0.060	0.0112	0.6085	0.2530	0.8861	1.4820
d	0.063	0.0110	0.6174	0.2111	0.9191	1.5020

(+) ion vacancy.

	ε	ξ	m	V_1	$-\chi$	W_+	W
c	0.5	0.0455	0.112	0.7817	0.2701	0.6958	0.100
	0.4	0.0486	0.0907	0.7303	0.2664	0.7509	0.155
	0.3	0.0517	0.0692	0.6785	0.2626	0.8065	0.210
d	1	0.039	0.168	0.9231	0.2457	0.5778	−0.004
	0.6	0.064	0.100	0.8324	0.2122	0.7030	0.120
	0.5	0.067	0.0813	0.7889	0.2102	0.7485	0.165
	0.4	0.062	0.062	0.7461	0.2070	0.7945	0.211

$V_0(+)=0.6494$, $V_0(-)=0.5313$.

Table X. CaO.

(−) ion vacancy.

	ξ	m	V_1	$-\chi$	W_-	E
b	0.074	0.0336	0.6101	0.1400	0.7913	1.3488
c	0.072	0.034	0.6072	0.1568	0.7774	1.3372

(+) ion vacancy.

	ε	ξ	m	V_1	$-\chi$	W_+	W
b	1.0	0.0567	0.148	0.8178	0.1525	0.5711	0.0136
	0.5	0.0670	0.0796	0.6765	0.1448	0.7201	0.163
	0.4	0.0691	0.0647	0.6479	0.1434	0.7501	0.192
	0.3	0.0715	0.0492	0.6155	0.1416	0.7843	0.227
c	0.5	0.0654	0.0812	0.6773	0.1618	0.7024	0.142
	0.4	0.0676	0.0660	0.6460	0.1601	0.7353	0.175
	0.3	0.0700	0.0503	0.6146	0.1591	0.7677	0.208

$V_0(+)=0.5535$, $V_0(-)=0.5076$

Table XI. SrO.

(−) ion vacancy.

	ξ	m	V_1	$-\chi$	W_-	E
a	0.096	0.0436	0.6033	0.1442	0.6858	1.2242
b	0.093	0.0448	0.6001	0.1821	0.6521	1.1978

(+) ion vacancy.

	ε	ξ	m	V_1	$-\chi$	W_+	W
a	1.0	0.0877	0.129	0.7497	0.1491	0.5345	−0.004
	0.5	0.0972	0.0686	0.6416	0.1434	0.6483	0.110
	0.4	0.0993	0.0556	0.6189	0.1420	0.6724	0.134
	0.3	0.101	0.0422	0.5947	0.1412	0.6974	0.159
b	0.5	0.0891	0.0678	0.6252	0.1844	0.6237	0.078
	0.4	0.0911	0.0553	0.6031	0.1831	0.6471	0.101
	0.3	0.0933	0.0420	0.5798	0.1815	0.6820	0.136

$V_0(+)=0.4704$, $V_0(-)=0.4429$

Tables IX, X and XI, in which the notation (b) and (c) corresponds to the same notation in Tables III, IV and V. Unfortunately the formation energy of the Schottky defect of those crystals have not been observed, so we must estimate them indirectly. Since the melting point of those oxide crystals is much higher than that of NaCl, we suppose that the formation energy of oxide crystals is also much larger than that of NaCl (about 2 ev.). Thus, we estimate them as follows: MgO, 4∼6 ev.; CaO, 3∼5 ev., SrO, 3∼5 ev. The facts that the ionic current is scarcely observed in MgO and the number of defect-points is very small may support the above estimation.

As seen from Tables the lattice formation would be impossible at room temperature under the assumption of $\varepsilon=1$. At first sight this result is ridiculous, but we have already mentioned the reason. Now, if we consider ε as a variable parameter, we are able to obtain the resonable result at suitable values of ε. The plausible values of ε may be 0.3∼

0.5 for MgO, 0.4∼0.5 for CaO and 0.3∼0.4 for SrO, although these values are somewhat different according to the choice of the interaction potentials. If the plausible values of $\mathcal{E}$ were widely different for different crystals, the idea of the effective polarizability would have been entirely meaningless, but our analysis shows that is not the case.

Finally we wish to express our sincere thanks to Prof. T. Muto for helpful discussions and to Prof. N. F. Mott for his suggestion of the problem.

References

1) B. Szigeti: Proc. Roy. Soc. **204** (1950) 51.
2) B. Szigeti: Trans. Faraday Soc. **45** (1949) 155.
3) J. E. Mayer and M McC Maltbie: Zeits. f. Phys. **75** (1932) 748.
4) J. R. Tessman, A. H. Kahn and W. Shockley: Phys. Rev. **92** (1953) 890.
5) J. Yamashita: Jour. Phys. Soc. Japan **7** (1952) 261.
6) W. W. Lozier: Phys. Rev. **46** (1934) 268.
7) P. O. Lowdin: A Theoretical Investigation into Some Properties of Ionic Crystals (thesis) 1948)
8) N. F. Mott and M. J. Littleton: Trans. Faraday Soc. **34** (1938) 485.
9) J. Yamashita and T. Kurosawa: Soon published in Prog. Theor. Phys.
10) J. Yamashita: Prog. Theor. Phys. **8** (1952) 280.

JOURNAL OF THE PHYSICAL SOCIETY OF JAPAN Vol. 9, No. 6, NOV.—DEC., 1954

The Exchange Effects on the Absorption Spectrum by the Paramagnetic Crystal with Anisotropic *g*-factors

By Mario YOKOTA
Department of Physics, Faculty of Science, University of Tokyo
and Shoichiro KOIDE
Institute of Physics, College of General Education, University of Tokyo

(Received July 28, 1954)

Using the Fourier transform method developed by Kubo and Tomita, the effects of the exchange interaction have been studied for the absorption spectrum of the paramagnetic crystal containing two kinds of unequivalent ions with different anisotropic g-factors. The analysis has been made for the two extreme cases: (i) The exchange interaction is weak and the spectrum consists of two peaks, (ii) The exchange interaction is so strong that the two lines fuse into a single peak. Comparing with the experimental data, the values of the exchange parameters are estimated for $CuSO_4 \cdot 5H_2O$ and $K_2CuCl_4 \cdot 2H_2O$, and reasonable results have been obtained.

§ 1. Introduction

It is well known that the exchange coupling between the paramagnetic ions gives the narrowing effect on the width of the absorption line in the case of equivalent ions. However, the effects of the exchange interaction are not so simple in general. In the absorption spectrum by a substance whose unit cell contains two paramagnetic ions with different anisotropy of the Landé g-factors, the exchange interaction seems to play some interesting roles. This phenomenon was first investigated by Bagguley and Griffiths for copper sulphate pentahydrate¹⁾, and thereafter similar observations have been made by several authors²⁾. When the interaction between the ions does not exist, the absorption spectrum consists of two lines corresponding to the two different

g-factors. The exchange interaction gives two effects on this spectrum, i.e. the broadening of each line and the closing of these two peaks. In the case of sufficiently strong interaction, the latter effect makes the two lines fuse into a single peak.

Pryce made preliminary discussions for this phenomenon in 1948³⁾, and one of the present authors (S.K.) has tried to investigate the dependence of the line width on the orientation of the static magnetic field by means of the moment method⁴⁾.

Validity of the moment method is, however, quite restricted, because in this method we must pick up the so-called semi-diagonal parts out of the Hamiltonian, so the influences of the non-adiabatic terms (off-diagonal elements) cannot be included. Hence we cannot handle the shift of the spectral lines due to the interactions by this method. It is also impossible to treat the frequency dependence of the line width.*

Anderson has recently discussed the spectrum with two peaks on the basis of random modulation⁵⁾. His theory is very interesting physically, but, since it does not account for the effects of the non-adiabatic terms explicitly, it is not appropriate to discuss the frequency dependence of the line width.

Recently, Kubo and Tomita have also developed a theory of line shape⁶⁾, which includes the influences of the non-adiabatic terms quite automatically. Using this method, Tomita has studied the frequency dependence of the line width for $K_2CuCl_4\cdot 2H_2O$. Since he ignores the anisotropy of the g-factors, his treatment is limited to the case that the static magnetic field is applied in such directions that the positions of the two lines coincide.

It seems, therefore, to be interesting to study these spectra more fundamentally by the use of the Kubo's method. We shall discuss here the effects of the exchange interaction on the structure of the spectrum taking account of the anisotropy of the g-factors as far as possible. For the sake of simplicity, the dipolar interaction between the ions will be neglected, because it does not play any essential role in our problem.

§ 2. General Theory

In this section, we shall briefly summarize the general theory of the magnetic resonance absorption spectra given by Kubo and Tomita⁶⁾. They show that the intensity distribution of the spectral line is given by the Fourier transform of a function $G(t)$ which is closely connected with the auto-correlation function of the dipole moment M. Assuming that the absorption energy $\hbar\omega$ associated with the observed spectrum is much smaller than the thermal energy, i.e. $\hbar\omega \ll kT$, they defined the function $g(t)$ by

$$g(t)=\frac{\mathrm{Tr}\,(M\exp(it\mathscr{H}/\hbar)M\exp(-it\mathscr{H}/\hbar))}{\mathrm{Tr}\,(1)} =\langle MM_t\rangle\,. \qquad (1)$$

If we pick up the terms of $g(t)$ containing the factor $\exp(i\alpha t)$ with positive α, we can get the function $G(t)$.

In order to calculate the function $g(t)$, they develop M_t in a series of the parameter, $\mathcal{E}$, of the perturbation as follows:

$$\begin{aligned} M_t&=\exp(it\mathscr{H}/\hbar)M\exp(-it\mathscr{H}/\hbar)\\ &=M_t^{(0)}+\mathcal{E}M_t^{(1)}+\mathcal{E}^2M_t^{(2)}+\cdots\,, \end{aligned} \qquad (2)$$

where

$$M_t^{(n)}=(-1)^n\int_0^t idt_1\int_0^{t_1}idt_2\cdots\int_0^{t_{n-1}}idt_n \times[[\cdots[[M_t^{(0)},\mathscr{H}'(t_1)]\mathscr{H}'(t_2)]\cdots]\mathscr{H}'(t_n)]\,,$$

with (3)

$$\mathscr{H}'(t)=\exp(it\mathscr{H}_0/\hbar)\mathscr{H}'\exp(-it\mathscr{H}_0/\hbar)\,.$$

$\mathscr{H}_0$ and $\mathcal{E}\mathscr{H}'$ denote the unperturbed and perturbing Hamiltonian respectively. Considering this expansion as the expanded form of an exponential function, they reconstruct $G(t)$ in a closed form.

We can divide the total Hamiltonian $\mathscr{H}$ into $\mathscr{H}_0$ and $\mathcal{E}\mathscr{H}'$ in the most appropriate way for the problem in question. In § 3, we shall treat the exchange interaction as the perturbation. This treatment is suitable for the case that the static field is so strong that the two peaks are observed separately. The case of strong exchange interaction will be discussed in § 4.

§ 3. The Case of Strong Field

Let us distinguish the quantities corresponding to the two kinds of unequivalent ions with prime and double prime. Then, since the g'

---

* It might be possible to treat the shift by the moment method if we appropriately take account of the non-secular parts.

and $\boldsymbol{g}''$ should be considered as tensors, the directions of $\boldsymbol{g}'\boldsymbol{H}$ and $\boldsymbol{g}''\boldsymbol{H}$ do not generally coincide with that of the applied field $\boldsymbol{H}$. We may, therefore, take the axes of quantization, z' and z'', to be parallel to the directions of $\boldsymbol{g}'\boldsymbol{H}$ and $\boldsymbol{g}''\boldsymbol{H}$ respectively, and define the x'- and x''-directions so as to coincide with each other and to be perpendicular to the $z'-z''$ plane.

Using the above choice of the coordinate axes, the Zeeman energy of the system is given by

$$\mathscr{H}_z=\beta|\boldsymbol{g}'\boldsymbol{H}|S'_{z'}+\beta|\boldsymbol{g}''\boldsymbol{H}|S''_{z''}\,, \qquad (4)$$

where $\boldsymbol{S}'=\sum_i{}'\boldsymbol{S}_i$ and $\boldsymbol{S}''=\sum_i{}''\boldsymbol{S}_i$ are the resultant spin moment of each group respectively.

The exchange interaction may be considered to be present only between the nearest neighbor ions, which are assumed to belong to the different groups, i.e. to the primed and the doubly primed ones. Then the exchange energy of the total system can be expressed as

$$\begin{aligned}\sum_{j>k}\sum A_{jk}(\boldsymbol{S}_j\boldsymbol{S}_k)&=J\sum_{j-k}{}'\sum{}''\{\tfrac{1}{4}(1-\cos\theta)(S'_{j+}S''_{k+}+S'_{j-}S''_{k-})\\&+\tfrac{1}{4}(1+\cos\theta)(S'_{j+}S''_{k-}+S'_{j-}S''_{k+})\\&+\tfrac{1}{2}i\sin\theta(S'_{j+}S''_{kz''}-S'_{jz'}S''_{k+}\\&-S'_{j-}S''_{kz''}+S'_{jz'}S''_{k-})+\cos\theta\,S'_{jz'}S''_{kz''}\},\end{aligned} \qquad (5)$$

where θ indicates the angle between the z' and z'' directions, and the summation should be taken over all pairs of the nearest neighboring j (belonging to the primed group) and k (belonging to the doubly primed group).

Let the direction of the oscillating magnetic field which causes the transition be denoted by ξ. Then the operating dipole moment M is given by the ξ-component of the total moment vector $\beta(\boldsymbol{g}'\boldsymbol{S}'+\boldsymbol{g}''\boldsymbol{S}'')$, i.e.

$$\begin{aligned}M&=\beta(g'_{\xi x'}S'_{x'}+g'_{\xi y'}S'_{y'}+g'_{\xi z'}S'_{z'}\\&\quad+g''_{\xi x''}S''_{x''}+g''_{\xi y''}S''_{y''}+g''_{\xi z''}S''_{z''})\\&\equiv\lambda'S'_{+}+\mu'S'_{-}+\nu'S'_{z'}\\&\quad+\lambda''S''_{+}+\mu''S''_{-}+\nu''S''_{z''}\,.\end{aligned} \qquad (6)$$

Now, taking the Zeeman energy (4) as the unperturbed term $\mathscr{H}_0$ and the exchange energy as the perturbation, we shall calculate the function $g(t)$ by the use of Eq. (2). In our case, $M_t^{(0)}$ is given by

$$\begin{aligned}M_t^{(0)}&=\exp(i\omega't)\lambda'S'_{+}+\exp(-i\omega't)\mu'S'_{-}\\&+\nu'S'_{z'}+\exp(i\omega''t)\lambda''S''_{+}\\&+\exp(-i\omega''t)\mu''S''_{-}+\nu''S''_{z''}\,,\end{aligned} \qquad (7)$$

where ω' and ω'' are equal to $|\beta\boldsymbol{g}'\boldsymbol{H}/\hbar|$ and $|\beta\boldsymbol{g}''\boldsymbol{H}/\hbar|$ respectively. Thus we obtain for the zero-th term

$$\begin{aligned}&\langle MM_t^{(0)}\rangle\\&=\tfrac{1}{3}S(S+1)N\{(\exp(i\omega't)+\exp(-i\omega't))2\lambda'\mu'+\nu'^2\\&+(\exp(i\omega''t)+\exp(-i\omega''t))2\lambda''\mu''+\nu''^2\}\,,\end{aligned} \qquad (8)$$

where $2N$ represents the total number of the paramagnetic ions. This is the correlation function of the dipole moment of the unperturbed system and corresponds to the two sharp absorption lines at the frequencies of ω' and ω''. It can be easily shown that the first order term gives no contribution to the function $g(t)$, that is

$$\langle MM_t^{(1)}\rangle=0\,. \qquad (9)$$

The exact calculation of the second order term is fairly complicated. So we may neglect the small terms of order $o(\theta^2)$. Then, after some manipulations, we obtain the expression of $\langle MM_t^{(2)}\rangle$, which, together with (8) and (9), gives

$$\begin{aligned}G(t)&\doteqdot\tfrac{2}{3}\lambda'\mu'S(S+1)N\exp(i\omega't)\\&\quad\times\left\{1-(\delta\omega')it-\frac{J^2Z}{6\hbar^2}S(S+1)\cos^2\theta\cdot t^2\right\}\\&+\tfrac{2}{3}\lambda''\mu''S(S+1)N\exp(i\omega''t)\\&\quad\times\left\{1+(\delta\omega'')it-\frac{J^2Z}{6\hbar^2}S(S+1)\cos^2\theta\cdot t^2\right\}\,,\end{aligned} \qquad (10)$$

where

$$\left.\begin{aligned}\delta\omega'&=\frac{J^2ZS(S+1)}{12\hbar^2(\omega'-\omega'')}\left\{2\left(\frac{\lambda''}{\lambda'}+\frac{\mu''}{\mu'}\right)\right.\\&\qquad\left.\times(1+\cos\theta)\cos\theta-(1+\cos\theta)^2\right\}\\\delta\omega''&=\frac{J^2ZS(S+1)}{12\hbar^2(\omega'-\omega'')}\left\{2\left(\frac{\lambda'}{\lambda''}+\frac{\mu'}{\mu''}\right)\right.\\&\qquad\left.\times(1+\cos\theta)\cos\theta-(1+\cos\theta)^2\right\}\,.\end{aligned}\right\} \qquad (11)$$

Each of the terms of (10) corresponds to the absorption line by the ions of each group. $\delta\omega'$ and $\delta\omega''$ represent the shift of the resonance lines by the exchange interaction, and the third terms in the braces of Eq. (10), being half the second moment of the corresponding lines, express the broadening of the lines. If the line shape is gaussian, the half width is related to the second moment by

$$\varDelta\omega_{1/2}=2.35\sqrt{\langle\varDelta\omega^2\rangle_{\mathrm{AV}}}\,. \tag{12}$$

In our case, however, the line shape is not secured to be gaussian. In order to guess the line shape, we may estimate the fourth moment of each line by the use of the Van Vleck's formula

$$\hbar^4\langle\omega^4\rangle_{\mathrm{AV}'}=\frac{\mathrm{Tr}\,[\mathscr{H}[\mathscr{H}M']]^2}{\mathrm{Tr}\,(M')^2}$$

and

$$\hbar^4\langle\omega^4\rangle_{\mathrm{AV}''}=\frac{\mathrm{Tr}\,[\mathscr{H}[\mathscr{H}M'']]^2}{\mathrm{Tr}\,(M'')^2}\,,$$

where M' and M'' indicate the parts of M corresponding to primed and doubly primed system. Ignoring the tensor character of the g-tensors, these give us the approximate expression of the mean fourth deviation of each line as

$$\hbar^4\langle\varDelta\omega^4\rangle_{\mathrm{AV}'}\simeq\hbar^4\langle\varDelta\omega^3\rangle_{\mathrm{AV}''}\simeq(4/3)J^4Z^2S^2(S+1)^2\,. \tag{13}$$

So the ratio of the fourth moment and the square of the second moment is approximately

$$\frac{\langle\varDelta\omega^2\rangle^2{}_{\mathrm{AV}'}}{\langle\varDelta\omega^4\rangle_{\mathrm{AV}'}}\simeq\frac{\langle\varDelta\omega^2\rangle^2{}_{\mathrm{AV}''}}{\langle\varDelta\omega^4\rangle_{\mathrm{AV}''}}\simeq\frac{1}{12}\,.$$

This ratio should be equal to 1/3 in the case of the gaussian shape. The above value shows that our lines have somewhat long tails compared with the gaussian. We may therefore adopt as the approximate relation between the half width and the second moment the following expression:

$$\varDelta\omega_{1/2}\simeq(2.35/2)\sqrt{\langle\varDelta\omega^2\rangle_{\mathrm{AV}}}\,. \tag{14}$$

After all, we know that our spectrum consists of the two peaks with their maxima at

$$\omega'-\frac{J^2ZS(S+1)}{12\hbar^2(\omega'-\omega'')}\left\{2\left(\frac{\lambda''}{\lambda'}+\frac{\mu''}{\mu'}\right)\right.$$
$$\left.\times(1+\cos\theta)\cos\theta-(1+\cos\theta)^2\right\}, \tag{15a}$$

and

$$\omega''+\frac{J^2ZS(S+1)}{12\hbar^2(\omega'-\omega'')}\left\{2\left(\frac{\lambda'}{\lambda''}+\frac{\mu'}{\mu''}\right)\right.$$
$$\left.\times(1+\cos\theta)\cos\theta-(1+\cos\theta)^2\right\}, \tag{15b}$$

having the half widths of

$$(\varDelta\omega_{1/2})'=(\varDelta\omega_{1/2})''$$
$$\simeq1.2/\hbar\{J^2ZS(S+1)/3\}^{1/2}\cos\theta\,. \tag{16}$$

The intensities of the two peaks are proportional to $\lambda'\mu'$ and $\lambda''\mu''$ respectively, and are not equal in general. This difference comes from the inequality of the effective moments of the two unequivalent sublattices with respect to the oscillating magnetic field.

Bagguley and Griffiths measured the absorption curves for copper sulphate pentahydrate[1], and further observations have been performed by Arnold & Kip[2] and by K. Ono[7] for the same substance. The unit cell of this crystal contains two unequivalent cupric ions surrounded by the octahedral arrangements consisting of four water molecules and two oxygen atoms. The crystalline field acting on the cupric ion has an approximately tetragonal symmetry and this results in the same symmetry of the g-tensors. The angle between the two tetragonal axes corresponding to the two unequivalent ions are reported to be ca. 82°, and the principal values of the g-tensors are $g_{\parallel}=2.47$ and $g_{\perp}=2.06$[1]. Bagguley and Griffiths show the absorption curve of this substance for the static field along one of the tetragonal axes at the wavelength of 0.85 cm. The spectrum consists of two peaks at 10600 oer and 11850 oer with the half widths of about 900 oer. The expected resonance fields without exchange are 10200 oer and 12190 oer for this wave length and for this orientation of the static field. Therefore, the observed shifts of the two peaks due to the excharge interaction are

$$(\delta H')_{\mathrm{Obs}}\simeq400\ \mathrm{oer}\,,\quad\text{and}\quad(\delta H'')_{\mathrm{Obs}}\simeq340\ \mathrm{oer}\,,$$

respectively.

Using the Eqs. (15) and (16) and considering J^2Z as an adjustable parameter, the theoretical values of the shifts and the widths translated in the unit of oersted are calculated so as to get the good agreement with the above values. A good agreement is obtained by assuming $J^2Z=0.031\ \mathrm{cm}^{-2}$:

$$(\delta H')_{\mathrm{Theor}}\simeq400\ \mathrm{oer}\,,\qquad(\delta H'')_{\mathrm{Theor}}\simeq300\ \mathrm{oer}\,,$$

and

$$(\varDelta H_{1/2})'_{\mathrm{Theor}}\simeq970\ \mathrm{oer}\,,\quad(\varDelta H_{1/2})''_{\mathrm{Theor}}\simeq870\ \mathrm{oer}.$$

Similar analyses are made for the data obtained by K. Ōno[7]. The results concerning the shifts are shown in Fig. 1. The best agreement is obtained by assuming $J^2Z=0.045$ cm^{-2}, which shows good coincidence with the above value. The observed half widths are about 700 oer and the calculated ones are about 1200 oer. This discrepancy is not so serious on account of our rough approximation.

Another typical example of this type of substances is potassium cupric chloride dihydrate ($K_2CuCl_4 \cdot 2H_2O$). Its absorption spectra have been observed by Itoh et al and Kumagai and his collaborators for various frequencies²⁾,⁸⁾. The crystal structure is shown in Fig. 2. Each cupric ion has the g-factor of rhombic symmetry with the principal axes parallel to the X, Y and Z directions shown in the figure. The principal values are⁸⁾

$$\tfrac{1}{2}(g_1+g_2)=2.23 \qquad \text{and} \qquad g_3=2.06\,,$$

where

$$g_1=g'_{XX}=g''_{YY}\,, \qquad g_2=g'_{YY}=g''_{XX}$$

and

$$g_3=g'_{ZZ}=g''_{ZZ}\,.$$

The two peaks are observed separately for the wave lengths shorter than ca. 6 mm. To determine the values of J and of g_1 and g_2 separately, we have utilized the spectrum obtained for the static field in the X-axis, and for the wavelength of 0.54 cm. A good agreement can be obtained by assuming $J=0.06$ cm^{-1} and $\frac{1}{2}(g_1-g_2)=0.17$:

the half widths: $(\Delta H_{1/2})'_{\mathrm{Theor}}=950$ oer ,
$(\Delta H_{1/2})''_{\mathrm{Theor}}=1040$ oer ,
(observed: 900 oer, 1100 oer)

the positions of the maxima:
17.3 k oer, 18.9 k oer
(observed: 17.3 k oor, 18.8 k oer).

Since we have used somewhat arbitrary assumption for the determination of the half width from the mean square deviation and the mean fourth deviation, these values of parameters cannot be expected to be decisive.

§ 4. The Case of Strong Exchange Interaction

As has been reported by several authors, the absorption spectrum of the paramagnetic substances with two kinds of unequivalent ions has sometimes only a single peak instead of two lines corresponding to the g' and g''. This phenomenon occurs when the exchange interaction between the ions is sufficiently strong compared with the difference between the absorption energies $\hbar\omega'$ and $\hbar\omega''$. In this case the treatment developed in the preceding section is not available. In this section, therefore, we shall take the part of the Hamiltonian which gives rise to the single peak in the spectrum as the unperturbed part, and the terms which originate in the anisotropies of

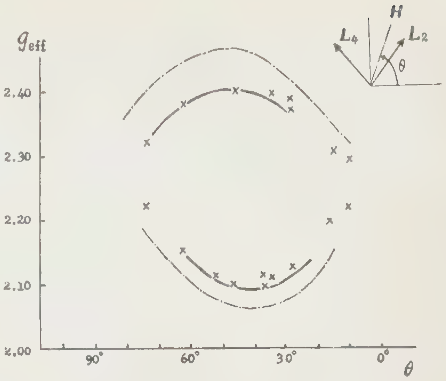

Fig. 1. The position of the two peaks expressed by the effective g-values ($g_{\mathrm{eff}}=\hbar\omega/\beta H$). The static field lies in the plane determined by the two tetragonal axes (L_2 and L_4) and the oscillating field with the wave length of 0.54 cm is also in this plane and perpendicular to the static one. The solid curve represents the theoretical values obtained by assuming $J^2Z=0.045$ cm^{-2}, the broken lines show the expected position of the two peaks in the case of $J=0$, and the experimental values are those obtained by K. Ōno.⁷⁾

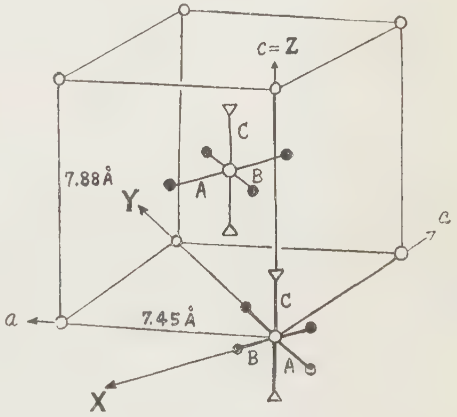

Fig. 2. Crystal structure of $K_2CuCl_4 \cdot 2H_2O$.

○ = Cu $A=2.95$ Å
● = Cl $B=2.26$ Å
▽ = O $C=2.52$ Å

the $\boldsymbol{g}'$ and $\boldsymbol{g}''$ as the perturbations. The exchange interaction should be included in the former rather than in the perturbation. This treatment was first suggested by Pryce[3)].

We take the z-axis in the direction of $\frac{1}{2}(\boldsymbol{g}'+\boldsymbol{g}'')\cdot\boldsymbol{H}$ and x-axis to lie in the plane containing the directions of $\boldsymbol{g}'\boldsymbol{H}$ and $\boldsymbol{g}''\boldsymbol{H}$. Then

$$(\boldsymbol{g}'\boldsymbol{H})_y=(\boldsymbol{g}''\boldsymbol{H})_y=0\,, \quad \text{and} \quad (\boldsymbol{g}'\boldsymbol{H})_x=-(\boldsymbol{g}''\boldsymbol{H})_x\,.$$

So the Zeeman energy and the exchange energy of our system can be written as

$$\begin{aligned}\mathscr{H}_z=\tfrac{1}{2}\beta|(\boldsymbol{g}'+\boldsymbol{g}'')\cdot\boldsymbol{H}|S_z+\beta(\boldsymbol{g}'\boldsymbol{H})_x(S_x'-S_x'')\\ +\tfrac{1}{2}\beta\{(\boldsymbol{g}'-\boldsymbol{g}'')\cdot\boldsymbol{H}\}_z(S_z'-S_z'')\,, \qquad (17)\end{aligned}$$

and

$$\mathscr{H}_{\mathrm{ex}}=J\sum_{i-j}{}'\sum{}''(\boldsymbol{S}_i\boldsymbol{S}_j)\,. \qquad (18)$$

We construct the unperturbed Hamiltonian with the first term of the Zeeman energy and of the exchange energy, i.e.

$$\mathscr{H}_0=\tfrac{1}{2}\beta|(\boldsymbol{g}'+\boldsymbol{g}'')\cdot\boldsymbol{H}|S_z+J\sum_{i-j}{}'\sum{}''(\boldsymbol{S}_i\boldsymbol{S}_j)\,, \qquad (19)$$

and the perturbing Hamiltonian with the remainders;

$$\begin{aligned}\mathscr{H}'=\tfrac{1}{2}\beta\{(\boldsymbol{g}'-\boldsymbol{g}'')\cdot\boldsymbol{H}\}_z(S_z'-S_z'')\\ +\beta(\boldsymbol{g}'\boldsymbol{H})_x(S_x'-S_x'')\,. \qquad (20)\end{aligned}$$

We may partly neglect the anisotropy effects for the magnetic moment associated with the oscillating field applied in the ξ-direction, which is, as usual, assumed to be perpendicular to the static field, thus

$$\begin{aligned}M=\tfrac{1}{2}\beta(g_{\xi x}'-ig_{\xi y}')S_+'+\tfrac{1}{2}\beta(g_{\xi x}'+ig_{\xi y}')S_-'\\ +\tfrac{1}{2}\beta(g_{\xi x}''-ig_{\xi y}'')S_+''\\ +\tfrac{1}{2}\beta(g_{\xi x}''+ig_{\xi y}'')S_-''\,, \qquad (21)\end{aligned}$$

so

$$\begin{aligned}M_t^{(0)}=\tfrac{1}{2}\beta(g_{\xi x}'-ig_{\xi y}')\exp(i\omega_0t)S_+'\\ +\tfrac{1}{2}\beta(g_{\xi x}'+ig_{\xi y}')\exp(-i\omega_0t)S_-'\\ +\tfrac{1}{2}\beta(g_{\xi x}''-ig_{\xi y}'')\exp(i\omega_0t)S_+''\\ +\tfrac{1}{2}\beta(g_{\xi x}''+ig_{\xi y}'')\exp(-i\omega_0t)S_-''\,, \qquad (22)\end{aligned}$$

where ω_0 denotes the angular frequency of the center of the peak:

$$\omega_0=(1/2\hbar)\beta|(\boldsymbol{g}'+\boldsymbol{g}'')\cdot\boldsymbol{H}|\,. \qquad (23)$$

Since $\mathscr{H}'$ does not commute with the exchange term, we have to make the following expansion

$$\begin{aligned}\mathscr{H}'(t)=\exp(it\mathscr{H}_0/\hbar)\mathscr{H}'\exp(-it\mathscr{H}_0/\hbar)\\ =\mathscr{H}'+\frac{it}{\hbar}[\mathscr{H}_0\mathscr{H}']+\frac{(it)^2}{2\hbar^2}[\mathscr{H}_0[\mathscr{H}_0\mathscr{H}']]+\cdots\,. \qquad (24)\end{aligned}$$

Using these approximations we get

$$\begin{aligned}\langle MM_t^{(0)}\rangle\\ =\tfrac{1}{3}S(S+1)Ng^2(\exp(i\omega_0t)+\exp(-i\omega_0t))\,, \qquad (25)\end{aligned}$$

where

$$\begin{aligned}g^2=\tfrac{1}{2}(g_{\xi x}'^2+g_{\xi y}'^2+g_{\xi y}''^2-g_{\xi y}''^2)\\ \simeq\tfrac{1}{2}(g_{\xi\xi}'^2+g_{\xi\xi}''^2)\,. \qquad (26)\end{aligned}$$

The first order term $\langle MM_t^{(1)}\rangle$ vanishes in our approximations. The second order term gives

$$\begin{aligned}\langle MM_t^{(2)}\rangle=-\tfrac{1}{3}NS(S+1)\\ \times\int_0^t d\tau[\tfrac{1}{4}\beta^2\{(\boldsymbol{g}'\boldsymbol{H})_z-(\boldsymbol{g}''\boldsymbol{H})_z\}^2g^2(t-\tau)\\ \times(\exp(i\omega_0t)+\exp(-i\omega_0t))+\tfrac{1}{2}\beta^2(\boldsymbol{g}'\boldsymbol{H})_x^2g^2(t-\tau)\\ \times\{\exp(i\omega_0(t-\tau))+\exp(-i\omega_0(t-\tau))\}]\\ \times\exp(-(2/3\hbar^2)S(S+1)J^2Z\tau^2)]\,. \qquad (27)\end{aligned}$$

As a result of the expansion (24), each term of the correlation function is expressed as an ascending power series of iJt. Considering this as the expansion of a exponential function, we obtain the last factor

$$\exp(-(2/3\hbar^2)S(S+1)J^2Z\tau^2)\,,$$

in (27).* As is pointed out by Anderson[5)] and Kubo[6)], the exchange coupling is considered to act as a modulation to the Larmor precessions. It would he, therefore, not so unreasonable to assume the gaussian form the dependence of the correlation function of the angular frequency on the exchange effects.

In order to get the function $G(t)$ in a closed form, we have further to make the following approximations under the condition of strong exchange:

$$\begin{aligned}\mathrm{Re}\int_0^t d\tau(t-\tau)\\ \times\exp(-\tfrac{2}{3}S(S+1)J^2Z\tau^2)\exp(-i\omega_0\tau)\\ \simeq t\,\mathrm{Re}\int_0^\infty\exp(-\tfrac{2}{3}S(S+1)J^2Z\tau^2)\\ \times\exp(-i\omega_0\tau)d\tau\\ \simeq\frac{t}{2J}\sqrt{\frac{3\pi}{2S(S+1)Z}}\exp\left\{-\frac{3\hbar^2\omega_0^2}{8S(S+1)ZJ^2}\right\}.\end{aligned}$$

---

* See the Eqs. (8.4) and (8.5) of the reference 6.

Then the final form of $G(t)$ is

$$G(t)=\frac{\beta^2}{3}NS(S+1)g^2\exp\Big\{i\omega_0 t-\frac{1}{8J}\sqrt{\frac{3\pi}{2S(S+1)Z}}\cdot\beta^2\Big[\{(\boldsymbol{g}'\boldsymbol{H})_z-(\boldsymbol{g}''\boldsymbol{H})_z\}^2+2(\boldsymbol{g}'\boldsymbol{H})_x{}^2\exp\Big(\frac{-3\hbar^2\omega_0{}^2}{8S(S+1)ZJ^2}\Big)\Big]t\Big\}\,. \tag{28}$$

The Fourier transform of this expression is a Lorentzian curve with its center at ω_0 and with the half width of

$$\hbar\Delta\omega_{1/2}=\frac{\beta^2}{4J}\sqrt{\frac{3\pi}{2S(S+1)Z}}\Big[\{(\boldsymbol{g}'\boldsymbol{H})_z-(\boldsymbol{g}''\boldsymbol{H})_z\}^2+2(\boldsymbol{g}'\boldsymbol{H})_x{}^2\exp\Big(\frac{3\hbar^2\omega_0{}^2}{8S(S+1)ZJ^2}\Big)\Big]\,. \tag{29}$$

The first term in the square brackets represents the width due to the difference of the effective moments in the direction of quantization, and the second term comes from the difference of the directions of the effective fields. The latter represents the contribution from the non-adiabatic effects and corresponds to the so-called 10/3 effect in the case of dipolar broadening.

Using (29), the directional dependence of the line width has been analyzed for the data obtained by Bagguley and Griffiths at the wavelength of 3.04 cm. The contridution from the non-adiabatic term seems to be negligibly small in this case, and, if we attribute the remaining width to the contribution from the dipolar interaction, the directional variation can be explained by the first term of the Eq. (29) for the value of $J^2Z=0.013\,\text{cm}^{-2}$. The proportionality of the line width (except for the dipolar contribution) to the square of $\{(\boldsymbol{g}'\boldsymbol{H})_z-(\boldsymbol{g}''\boldsymbol{H})_z\}$ is the result of the exchange narrowing.

§ 5. Discussion

A merit of the Kubo's method is that it can give the terms corresponding to all the absorption lines simultaneously. Therefore we can treat the spectrum with several lines quite artlessly by this method. Thus we have been able to derive the expression (10) and get the formulas (11) giving the magnitudes of the shifts. The shift phenomenon can be considered as the pulling of the two peaks towards each other, and the magnitude of the shift of one line depends on the magnetic moment of the other sublattice with respect to the oscillating field. This situation is expressed it the Eq. (11). According to the approximation adopted § 3, i.e. the perturbation treatment for the exchange interaction, our results are valid only for the case of small exchange energy compared with $|\hbar(\omega'-\omega'')|$. If the exchange interaction is not so small, (11) may give somewhat larger magnitudes for the values of the shifts than the actual ones. So our estimation of J in the case of $K_2CuCl_4\cdot 2H_2O$ may be an underestimation, because the exchange interaction is fairly large for this substance. However, our expressions of the shifts can be thought to give a good approximation in the case of weak exchange and of sufficiently large separation of the two peaks.

In the calculation of a single peak spectrum, we have neglected the anisotropy effect for the magnetic moment associated with the oscillating field. The effect, however, contributes to the second moment by the amount of

$$\frac{2S(S+1)\{(g_{\xi x}'-g_{\xi x}'')^2+(g_{\xi y}'-g_{\xi y}'')^2\}}{3(g_{\xi x}'^2+g_{\xi x}''^2+g_{\xi y}'^2+g_{\xi y}''^2)}J^2Z\,. \tag{30}$$

As a result of the neglection of this term, our estimation of J in § 4 may be also an underestimation. Since the expression (30) depends on the direction of the oscillating field ξ, we cannot estimate this without knowing the direction ξ.

In order to avoid unessential complication, we have ignord the dipolar interaction. In the case of a two peak spectrum, the most part of the broadening of each peak can be considered to come from the exchange interaction. In the case of the narrowed single peak, however, the half width is proportional to the second moment, and, in the approximation of neglecting the anisotropy effect for M, the dipolar interaction contributes to the second moment additively to the effect of (20). Therefore, the calculation of the dipolar effect is necessary to compare the calculated width with the experimental data in more detail.

Finally, we shall discuss the effects of the exchange interaction between similar ions. For the case of a two peak spectrum, this interaction affects as the narrowing of each lines in the sence of the ordinary "exchange narrowing." In the case of a single peak spectrum, however, the exchange interaction between the similar ions $\mathscr{H}_{ex}{}^{sim}$ does not contribute up to the fourth monent,* hence its effect is not so important for this case.

In conclusion, the authors express their sincere thanks to Prof. R. Kubo and Prof. K. Yosida for their valuable suggestions and discussions, to Prof. T. Usui for his continuous encouragement, and to Mr. A. Ikushima for his help in numerical computations. Thanks are also due to Drs. K. Ōno and H. Abe, who very kindly supplied the experimental data obtained in their laboratory.

References

1) D. H. S. Bagguley and J. H. E. Griffiths: Nature **162** (1948) 538; Proc. Roy. Soc. **A 201** (1950) 366.

2) R. D. Arnold and A. F. Kip: Phys. Rev. **75** (1949) 1199.

J. Itoh, M. Fujimoto and H. Ibamoto: Phys. Rev. **83** (1951) 852.

Kumagai, Abe, Shimada, Hayashi, Ōno and Ibamoto: J. Phys. Soc. Japan **7** (1952) 535.

3) M. H. L. Pryce: Nature **162** (1948) 538.

4) K. Kambe, S. Koide and T. Usui: unpublished calculation.

5) P. W. Anderson: J. Phys. Soc. Japan **9** (1954) 316.

6) R. Kubo and K. Tomita: J. Phys. Soc. Japan **9** (1954) 888.

7) K. Ōno: unpublished data.

8) Kumagai et al: J. Phys. Soc. Japan (to be published).

---

* It is easily seen that $[M, \mathscr{H}_{\mathrm{ex}}^{\mathrm{dis}}]=[M, \mathscr{H}_{\mathrm{ex}}^{\mathrm{sim}}]=0$, where $\mathscr{H}_{\mathrm{ex}}^{\mathrm{dis}}$ is the exchange Hamiltonian between dissimilar ions which has been denoted as $\mathscr{H}_{\mathrm{ex}}$ in §4. Hence $[M, \mathscr{H}]=[M, \mathscr{H}']$, which has the form $\sum_{\gamma=x,y,z}(\alpha'_\gamma S'_\gamma+\alpha''_\gamma S''_\gamma)$ and commutes with $\mathscr{H}_{\mathrm{ex}}^{\mathrm{sim}}$: $[\mathscr{H}_{\mathrm{ex}}^{\mathrm{sim}}[M, \mathscr{H}']]=0$. The contribution of $\mathscr{H}_{\mathrm{ex}}^{\mathrm{sim}}$ to the fourth moment is proportional to $[\mathscr{H}_{\mathrm{ex}}^{\mathrm{sim}}[M, \mathscr{H}']]^2$, so it vanishes.

JOURNAL OF THE PHYSICAL SOCIETY OF JAPAN Vol. 9, No. 6, NOV.—DEC., 1954

Dependence of the Intermetallic Diffusion Coefficient upon Concentration

By Joji MIZUNO, Shiro OGAWA and Tokutaro HIRONE

The Research Institute for Iron, Steel and Other Metals, Tohoku University, Sendai

(Received June 11, 1954)

A new method to determine the intermetallic diffusion coefficient is proposed. A thin layer of one metal was electrodeposited on a surface of another metal, and the surface concentration was examined by the X-ray back-reflection method during the process of diffusion. From the surface concentration vs. time curves the diffusion coefficient was given as a function of concentration. This method was applied to the measurement of intermetallic diffusion coefficient for nickel copper system at the temperature 800, 900, and 1000°C respectively. A discrepancy was found between the diffusion coefficients obtained from the nickel-deposited copper plates and from copper-deposited nickel plates. This is considered to originate from porosities formed near the diffusion interface due to the vacancy flow and from some properties of electrodeposited layer.

§ 1. Introduction

The intermetallic diffusion in alloys, in which concentration gradients of the components exist, have been investigated by various authors. If we denote the diffusion coefficient by D and if the concentration gradient occurs along the x direction only, then the concentration change is given by

$$\frac{\partial c}{\partial t}=\frac{\partial}{\partial x}\left(D\frac{\partial c}{\partial x}\right). \qquad (1)$$

The coefficient D depends, in general, upon concentration. A solution of Eq. (1) has already been given by Boltzmann[1)] on the assumption that the concentration is a function of $\lambda=x/\sqrt{t}$ only. The validity of Boltzmann's assumption was proved experimentally by Matano,[2)] who applied this method to the analysis of the diffusion data for the nickel-copper system obtained by Grube and Jedele[3)] and successfully found a pronounced variation of D with concentration. In the usual study for determining the intermetallic diffusion coefficient, the concentration at various parts is determined by chemical analysis, after the specimen has been kept for a definite duration at a suitable fixed temperature. However, no essential change takes place in the mathematical treatment in deriving D, if we work under reverse condition, that is, at definite x and variable t. The object of the present investigation is to examine the applicability of this new method in the determination of D. The experimental treatment is comparatively simple by this method and the specimen remains undestroyed, as described later.

§ 2. Theoretical Consideration

On the basis of the solution obtained for Eq. (1), the diffusion coefficient D is expressed by

$$D=\frac{1}{2t}\,\frac{dx}{dc}\int_c^1 x\,dc\ , \qquad (2)$$

where $\int_0^1 x\,dc=0$. This solution is obtained under the following conditions:

$c=0$ for $t=0$ and $x<0$,
$\partial c/\partial x=0$ for $x=\pm\infty$.

If the different metallic plates are brought in contact and the mutual diffusion is caused by heating during a certain period t, and if the concentration distribution of the both metallic elements is obtained, then D can be calculated from (2). This is the method which Matano adopted for the determination of D between nickel and copper. For the same purpose we tried to obtain, by the X-ray method, C as a function of t at a given x, i.e., at a surface in the present case, and to calculate D by the following procedure. For this case the boundary conditions are shown in Fig. 1, that is,

$$\begin{aligned} &\text{at } t=0 \quad c=0 \quad \text{for} \quad 0<x<h \\ &\qquad\qquad c=1 \quad \text{for} \quad 0>x, \text{ and} \\ &\text{at } x=h \text{ and } x=-\infty, \ \partial c/\partial x=0, \end{aligned}$$

where h means the thickness of the deposited layer. This circumstance fits a metal surface covered with another metal layer which is, for example, electrodeposited. The Eq. (1) can be transformed into (3) by introducing the variable $\lambda=x/\sqrt{t}$

$$-\frac{\lambda}{2}\frac{dc}{d\lambda}=\frac{d}{d\lambda}\left(D\frac{dc}{d\lambda}\right). \tag{3}$$

Fixing the value of x to be h and integrating both sides of this equation with respect to λ from $\lambda=\infty$ to $\lambda=\rho=h/\sqrt{\theta}$, we obtain

$$-\frac{1}{2}\int_0^{C(\theta)}\lambda_h dc_h=\left(D\frac{dc}{d\lambda}\right)_{\lambda=\rho}-\left(D\frac{dc}{d\lambda}\right)_{\lambda=\infty}. \tag{4}$$

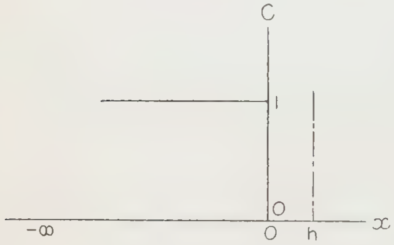

Fig. 1.

On the other hand,

$$\frac{dc}{d\lambda}=\frac{\partial c}{\partial x}\sqrt{t}-\frac{\partial c}{\partial t}\cdot 2t^{3/2}/x. \tag{5}$$

As $dc/d\lambda$ and $\partial c/\partial x$ vanish at $\lambda=\infty$ and at $x=h$ respectively, Eq. (4) can be transformed into

$$\begin{aligned} -\frac{1}{2}\int_0^{C(\theta)}\lambda_h dC_h&=-\frac{1}{2}\int_0^{C(\theta)}ht^{-1/2}dC_h \\ &=-D(C_h)\cdot 2t^{3/2}\cdot h^{-1}(\partial c/\partial t)_h. \end{aligned} \tag{6}$$

Hence for D the following type of expression is obtained:

$$D(C_h)=\frac{h^2}{4t^{3/2}}\cdot\frac{1}{(\partial c/\partial t)_h}\int\frac{dc}{t^{1/2}}. \tag{7}$$

If the change of surface concentration of the element in the deposited layer due to annealing is obtained as a function of the annealing period t, then $D(C_h)$ is calculated according to (7).

§ 3. Experimental Method

For the present experiment we chose nickel and copper as a diffusion pair. The nickel-copper system forms the solid solution with all proportion of both components: hence no metallographical difficulties exist in the analysis of the data obtained in this case. A thin nickel (or copper) layer was electrodeposited at room temperature on the surface of a copper (or nickel) specimen which was about 7 mm×7 mm×1 mm in size. The following electrolytic solutions were used: for nickel plating, 200 gr of $NiSO_4\cdot 7H_2O$, 20 gr NH_4Cl and 15 gr of H_3BO_2 in *1l* of water; for copper plating 50 gr of $CuCN$, 60 gr of $NaCN$, 24 gr of Na_2CO_3 and 0.3 gr of $Na_2S_2O_3\cdot 5H_2O$ in *1l* of water. The used electrolytic current density was 1 A/dm² for nickel plating and 0.3–0.5 A/dm² for copper plating. The thickness of the layer was calculated the weight difference before and after plating. The smoothness of metal surface to be electroplated was required in order that the exact application of the boundary condition might be possible. The substrata were, therefore, electropolished after being mechanically polished with emery (4—0) and the highly smoothed surfaces were obtained. The following solutions were used for electropolishing; for nickel, 700 cc of H_3PO_3, 200 cc of H_2SO_4 and 50–100 gr of Cr_2O_3 in 100 cc of water; for copper, 400–500 cc/l of H_3PO_4.

Each specimen thus electroplated was heated, in a highly evacuated silica tube, at a fixed temperature for a definite period. To make the diffusion period exact, the temperature rise and drop in a specimen were carried out as quickly as possible. In heating in vacuum at high temperature the surface evaporation is quite probable, and this was prevented by the following procedure; two specimens electroplated in almost equal thickness were brought into contact with the electroplated surfaces inside. In one series of experiments, several annealings at the same temperature were given successively on the specimen. Each time after one period of diffusion was finished, the surface concentration was measured by X-ray in the following way and the total duration of diffusion at a fixed temperature was calculated by summing up each period. The X-ray procedure was the usual one, i.e., the lattice constant in a central part (circle about 3 mm in diameter) of each specimen plate was measured by the back-reflection method, a camera of Gayler-Preston type being used. As Vegard's law holds almost exactly in the nickel-copper system, the atomic concentration is easily known from the lattice constant of the alloy. We can use the atomic concentration in place of C in Eq. (7) which means the number of atoms in unit volume, since the difference between the lattice constants of both metals in question is quite little.

§ 4. Experimental Results

Diffusion tests were carried out at 800, 900 and 1000°C. A very long period of heating was required with only one deposit of optimum thickness even at these temperatures in order that the surface concentration might be changed considerably, and it was necessary to measure the concentration *vs.* time curve as exactly as possible. Hence, D as a function of concentration covering the wide range was obtained by connecting the curves corresponding to several specimens with different thicknesses of deposition. If two specimens 1 and 2 with the deposits of different thickness h_1 and h_2 were chosen for the test, then for the former case

$$D(C_1)=\frac{h_1^2}{4t^{3/2}}\frac{1}{(\partial C_1/\partial t)_1}\int_0^C \frac{dC_1}{t^{1/2}}\,, \qquad (8)$$

and for the latter

$$D(C_2)=\frac{h_2^2}{4t^{3/2}}\frac{1}{(\partial C_2/\partial t)_2}\int_0^C \frac{dC_2}{t^{1/2}}\,. \qquad (9)$$

If the surface concentration is measured from 0 to C^* (from $t=0$ to $t=t_1$) for specimen "1" and above C^* ($t \geq t_2$) for "2", we shall obtain the following equation by equating (8) and (9) at $C=C^*$,

$$\int_0^{C^*}\frac{dC_2}{t^{1/2}}=\left(\frac{h_1}{h_2}\right)^2\left(\frac{t_2}{t_1}\right)^{3/2}\cdot\left\{\left(\frac{\partial C_2}{\partial t}\right)_2\Big/\left(\frac{\partial C_1}{\partial t}\right)_1\right\} \times\int_0^{C^*}\frac{dC_1}{t^{1/2}}\,. \qquad (10)$$

Hence, for $C>C^*$

$$D(C)=\frac{h_2^2}{4t^{3/2}}\frac{1}{(\partial C/\partial t)} \times\left[\left\{\left(\frac{h_1}{h_2}\right)^2\left(\frac{t_2}{t_1}\right)^{3/2}\left(\frac{\partial C_2}{\partial t}\right)_2\Big/\left(\frac{\partial C_1}{\partial t}\right)_1\right\} \times\int_0^{C^*}\frac{dC_1}{t^{1/2}}+\int_{C^*}^{C}\frac{dC_2}{t^{1/2}}\right]. \qquad (11)$$

Thus, the integration at $h=h_1$ can be converted into that at $h=h_2$. Fig. 2 and Fig. 3 show the C *vs.* t curves obtained from nickel on copper at 1000°C and from copper on nickel at 900°C respectively. In the latter case the value of D was obtained for $0<C\leq 0.15$ from the curve at $h_1=36.7\,\mu$, for $0.15\leq C\leq 0.50$ from the curve at $h_2=9.7\,\mu$, converting

$$\int_0^{0.15} dC_1/t^{1/2} \text{ into } \int_0^{0.15} dC_2/t^{1/2}\,,$$

and for $0.50\leq C\leq 0.80$ from the curve $h=4.3\mu$, by going through the similar procedure. Our purpose was to determine the value of D over the whole range of concentration, and even the procedure mentioned above was insufficient for this purpose, because the C *vs.* t curve became so flat with the duration of time, especially in a thin deposition, that an exact value of $\partial C/\partial t$ was very difficult to obtain as the surface concentration approached that of

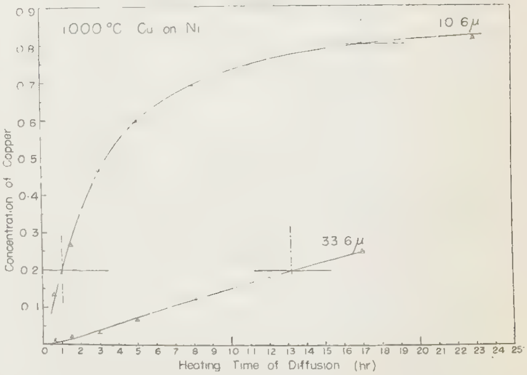

Fig. 2. $C-t$ curves at 1000°C, obtained from surfaces of copper layers deposited on nickel plates.

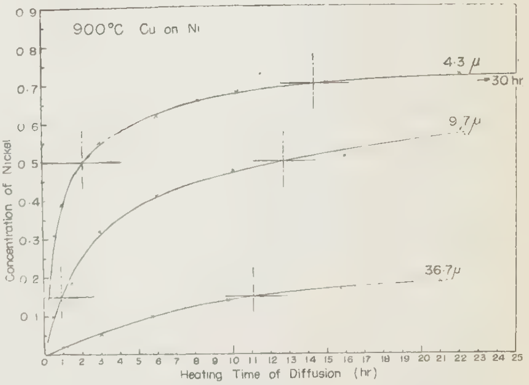

Fig. 3. $C-t$ curves at 900°C, obtained from surfaces of nickel layers deposited on copper plates.

Table I. (deposited layer: Ni)

heating temperature	thickness of deposited layer (μ)	assigned range of concentration (C_{Cu})	heating duration corresponding to the highest concentration (*hr.*)
1000°C	33.6	0 —0.2	13.25
	10.6	0.2 —0.8	17.13
900°C	29.9	0 —0.13	25.04
	9.2	0.13—0.3	3.15
	4.2	0.3 —0.8	16.75
800°C	25.3	0 —0.1	15.95
	3.0	0.1 —0.7	6.85

Table II. deposited layer: Cu)

heating temperature	thickness of deposited layer (μ)	assigned range of concentration (C_{Ni})	heating duration corresponding to the highest concentration (*hr.*)
1000°C	51.2	0 —0.2	12.02
	13.7	0.2 —0.5	9.89
	8.2	0.5 —0.65	12.84
900°C	36.7	0 —0.15	16.06
	9.7	.015—0.5	12.73
	4.3	0.5 —0.7	14.35
800°C	29.6	0 —0.13	20.10
	9.0	0.13—0.35	7.76
	5.9	0.35—0.5	8.40
	2.3	0.5 —0.75	18.96

the substratum. *D* on the nickel side was, therefore, determined, by using nickel-deposited copper specimens, and *D* on the copper side vice versa, under the supposition that both measurements would be fairly connected with each other. The data concerning the used specimens are shown in Tables I and II. The *D* values thus obtained are plotted for the whole range of concentration in Figs. 4, 5, and 6, corresponding to 800, 900 and 1000°C respectively. For each curve, due to the nickel-deposited copper specimen, *D* abruptly descends with increase in copper concentration initially, then slowly at about $C_{Cu}=0.1$ and becomes almost flat for $C_{Cu}>0.3$. The curve corresponding to 1000°C, however, shows a tendency of ascent of D at about $C_{Cu}=0.65$. For each curve, due to the copper-deposited nickel specimen, *D* descends monotonously with increase in nickel concentration abruptly initially and slowly thereafter. In these figures the following three points should be noted:

(1) In each case no datum was obtained in the neighbourhood of terminal concentration

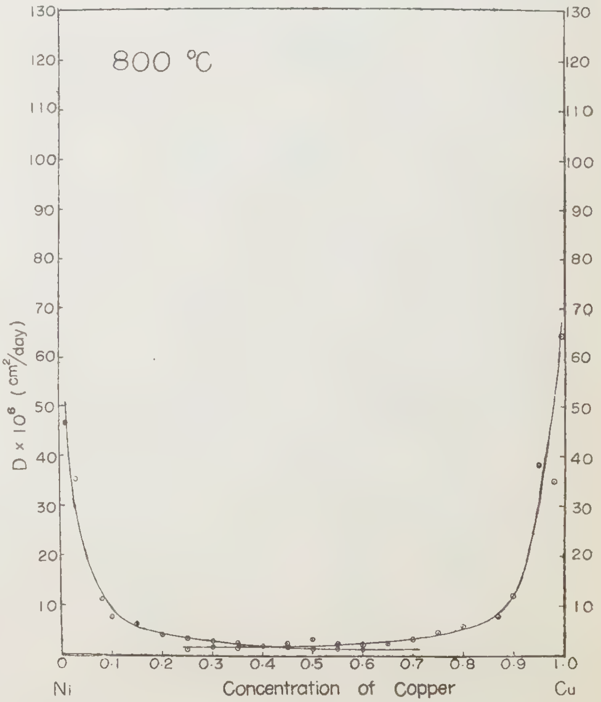

Fig. 4. *D*−*C* curves at 800°C.

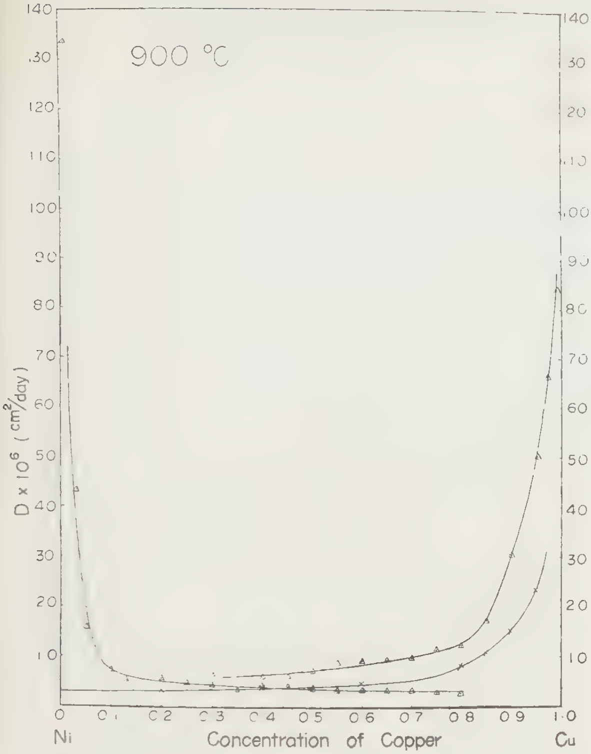

Fig. 5. $D-C$ curves at 900°C. △ represents our result and × the result by Da Silva & Mehl (at 947°C. total time of diffusion: 362 hrs. in vacuum, specimen: B 38).

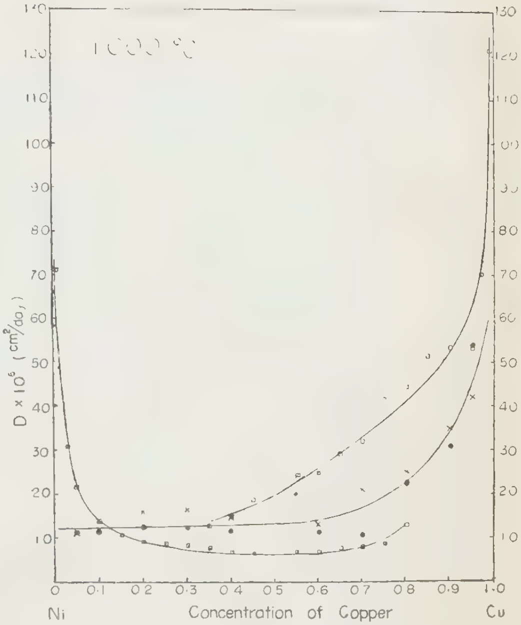

Fig. 6. $D-C$ curves at 1000°C. ⊡ represents our result and × (33 hr. at 1000°C) and • (3 days at 1025°C) represent Matano's result calculated from the data by Glube and Jedele.

($0.8<C_{Cu}<1$ and $0.7<C_{Ni}<1$). We tried to obtain D value in these regions, using thin deposited layers 2–3 μ thick, but failed to determine exactly the values of $\partial C/\partial t$, as the measurements became erroneous in the concerned regions for the reason already described. Thus, we could not determine D values in the whole range of concentration, by using one kind of deposition.

(2) As seen obviously from each figure, the values of D from nickel and copper side do not coincide with each other, which is especially pronounced in Figs. 5 and 6. We shall have some discussions upon this topic in § 5.

(3) In Figs. 5 and 6 are also shown respectively the results obtained by da Silva and Mehl at 947°C and those whice Matano obtained from the experimental data at 1000 and 1025°C by Grube and Jedele. Comparing the data from chemical analysis with those obtained by us, we notice the discrepancy between them for $C_{Cu}<0.1$. Measurements under definite t and variable x gave the result that D was constant in this region, but the lack of the data for very small content of copper should be noted. On the other hand, measurements under variable t and definite x showed it to decrease remarkably from the high initial value to the one which almost coincided with the constant value obtained by the other method, as C_{Cu} increased. The order of magnitude of the diffusion coefficient, however, generally coincide with each other in both cases.

§ 5. Discussions

The unfitness of D from nickel and copper side seems to be not an essential nature of matter, because we deal with the chemical diffusion coefficient in the present experiment. In experiments hitherto performed, the influence of change in the boundary condition during heating was averaged and masked in appearance, and D was determined after spacial examination of the terminal state. In the present experiment, on the other hand, it directly influenced each value of D as the measurements were carried out at variable time. We supposed initially the interface of two metals to be a plane, which might, however, be deformed with the lapse of time during diffusion.

Kirkendall effect has recently become an important key in the intermetallic diffusion mechanism since Smigelskas and Kirkendall[4] found it in the copper-brass system. It was confirmed also in many other systems, e.g., in copper-aluminium, copper-tin, copper-gold, silver-gold[5] and copper-nickel.[6] Now, Kirkendall effect is explained by the vacancy theory as follows: a net flow of vacancy takes place toward the copper side in the copper-nickel system, and therefore, the accumulation of vacancy results in the formation of voids which are lined up on the copper-rich side near the original interface and accordingly, the original interface shifts to this side as the contraction occurs here.[7][8][9]

In usual experiments, voids which are observable under microscope seem to be formed after about 100–200 hours. Also in the present experiment, although the heating duration was here far short as compared with usual one, a fairly large number of small voids is considered to exist on the copper-rich side. The diffusion interface is deformed, therefore, from an initial flat form to a more complicated one, and so diffusion may be difficult to take place at the final stage. This circumstance may cause D value to decrease seemingly with the change in concentration in the deposited layer, i.e., with the duration of diffusion. The above explanation is, however, not sufficient with the present problem, because the higher D values were always obtained, for a definite composition, from the surface copper-deposited initially, the comparison being made at the diffusing duration of almost the same grade. It is probable that the structure of the electro-deposited thin layer plays an important role, but we cannot give a consistent explanation to this problem at the present stage.

Next, we should note the abrupt decrease of D in the highest concentration of nickel which has never been observed. The reliability of D values depends upon the accuracy in measuring $\partial C/\partial t$ and $\int_0^C dC/t^{1/2}$ in our case and dx/dC and $\int_C^1 x dC$ in the usual case. In every case it is considerably difficult to determine exactly the inclination in the flat part on the C *vs.* t or C *vs.* x curve, and considering it, we carried out measurements as carefully as possible. Though we cannot say that the constancy of D in the highest concentration of nickel in measurements which have so far been made is erroneous, there seems, at least, to be some doubt about it.

After all, we did not succeed, at the present stage, in realizing the anticipation that D is fairly determined in all concentration, due to the occurrence of the unexpected circumstances. These may, however, give many suggestions to measurements of the intermetallic chemical diffusion coefficient, as voids or porosities formed by the vacancy flow probably always exist in the intermetallic diffusion.

In conclusion, we wish to express our sincere thanks to Mr. N. Kunitomi for his kind and useful discussion. The present investigation has been supported partly by the funds from the ministry of Education in Aid of Scientific Researches.

References

1) L. Boltzmann: Ann. Phys. Lpz. **53** (1894) 959.

2) C. Matano: Japan J. Phys. **8** (1933) 109.

3) G. Grube and A. Jedele: Z. f. Electrochem. **38** (1932) 799.

4) A. D. Smigelskas and E. O. Kirkendall: Trans. AIME **170** (1947) 130.

5) L. C. C. Da Siva and R. F. Mehl: Trans. AIME **191** (1951) 155.

6) D. E. Thomas and C. E. Birchenall: J. Metals **4** (1952) 867.

7) R. S. Barnes: Proc. Phys. Soc. **B95** (1952) 512.

8) W. Seith and A. Kottmann: Naturwiss. **39** (1952) 40.

9) R. W. Balluffi and B. H. Alexander: J. Appl. Phys. **23** (1952) 1237.

JOURNAL OF THE PHYSICAL SOCIETY OF JAPAN Vol. 9, No. 6, NOV.—DEC., 1954

Magneto-thermoelectric Powers of Nickel Single Crystals

By Nahonori MIYATA and Zenya FUNATOGAWA

Yokohama National University

(Received July 2, 1954)

The magneto-thermoelectric power (change of thermoelectric power due to magnetization of ferromagnetic substances) and its temperature dependency of nickel single crystals are measured. The $(E_m)_{100}$ and $(E_m)_{111}$, which specify the characteristic property along the directions [100] and [111] respectively, are calculated under some reasonable approximations. The true magneto-thermoelectric power depends on the orientations of the crystal and is always positive, except that in the neighbourhood of the Curie point which is negative and is due to additive magnetizations proportional to the external magnetic fields, and represents a maximum value near the room temperature and tends to zero at 0°K and also at the Curie point respectively.

§ 1. Introduction

Since the discovery by W. Thomson in 1856 that a thermocouple could be made of a magnetized ferromagnetic substance and another unmagnetized same one, many investigations[1] concerning the properties of this thermocouple have been performed with complicate and sometimes conflicting results, because the effect had been studied under the conditions with wide temperature difference, i.e., 100°C or more and also the samples used were polycrystals. One of the authors defined anew, as described in previous papers[2], the "magneto-thermoelectric force per degree" or the "magneto-thermoelectric power" at given temperature t as a mean value of the e.m.f. of the couple between $t-\Delta t/2$ and $t+\Delta t/2$, and studied the magnetothermoelectric power of iron single crystals and its temperature dependency.

This time we study the magneto-thermoelectric power of nickel single crystals by using the same methods described in the previous papers.

The magneto-thermoelectric power of a single magnetic domain that is magnetized to the saturation corresponding to the given temperature, is given from the symmetry of the cubic crystal such as iron and nickel as follows:—

$$(E_m)_{\alpha\beta\gamma}=-a_1/3+a_1\sum\alpha_i^2\beta_i\gamma_i+2a_2\sum_{i\neq j}\alpha_i\beta_i\alpha_j\gamma_j \qquad i,j=1,2,3. \qquad (1)$$

where $(E_m)_{\alpha\beta\gamma}$ is the magneto-thermoelectric power induced along a direction with the direction cosines β_1, β_2 and β_3 with respect to the principal axes of the cubic crystal, when the directions of the magnetization and of the temperature gradient are $\alpha_1, \alpha_2, \alpha_3$ and $\gamma_1, \gamma_2, \gamma_3$ respectively. a_1 and a_2 in Eq. (1) are so-called anisotropic constants of the sample at given temperature. In our case $\beta_i=\gamma_i$, and then we get

$$(E_m)_{\alpha\beta}=-a_1/3+a_1\sum\alpha_i^2\beta_i^2+2a_2\sum_{i\neq j}\alpha_i\alpha_j\beta_i\beta_j\,. \qquad (2)$$

If (E_m) in the above equation is substituted by $(\Delta l/l)$ we get the well-known magnetostrictive formula derived from the crystal symmetry. $(E_m)_{100}$ and $(E_m)_{111}$ which are the magneto-thermoelectric powers along the directions [100] and [111] are given by

$$(E_m)_{100}=2a_1/3\,;\quad (E_m)_{111}=2a_2/3\,, \qquad (3)$$

respectively.

In order to determine the constants a_1 and a_2 by using real crystal rods, we must select two standard distributions of magnetic domains in the crystal, because they do not distribute equally in the directions of the easiest magnetization even when the rod as a whole is in the state of demagnetization as pointed out by S. Kaya and H. Takaki and also one of the authors in the case of iron. They found that at the breaking point corresponding to the residual magnetization of the descending hysteresis curve the domain magnetizations were distributed along the directions of the easiest magnetization near the external magnetic field, proportional to the cosines of the angles between the directions of the easiest magnetization and that of the external magnetic field to reduce as much as possible the normal component, $J_\perp$, of magnetization perpendicular to the bar axis and to minimize the magneto static energy $2\pi J_\perp^2$. It is, therefore, reasonable to adopt the breaking point of the descending hysteresis curve as one of the standard states. Another state, of course, is saturation where the crystal consists of one domain as a whole. From these considerations, one of the authors determined the constants a_1 and a_2 of iron by measuring the magnitude of the magneto-thermoelectric power between the saturation and residual magnetization. In the case of iron crystal rods the residual magnetization $J_{\text{r. calc.}}$ is given by the Kaya's formula

$$J_{\text{r. calc.}}=J_\infty/(\beta_1+\beta_2+\beta_3)\ , \qquad (4)$$

where J_∞ is the saturation value of magnetization.

In the case of nickel we can not use the Kaya's formula. If V_1, V_2, V_3 and V_4 are the volumes of magnetic domains distributed among the directions [111], $[1\bar{1}1]$, $[1\bar{1}\bar{1}]$ and $[11\bar{1}]$ of a nickel crystal, viz., the directions of the easiest magnetizatin at room temperature, then the total volume V of the crystal is given by $V=V_1+V_2+V_3+V_4$ and the components M_x, M_y and M_z along the [100], [010] and [001] of the total magnetic moment M of the crystal are given, respectively, by

$$\begin{aligned} M_x=J_xV&=J_\infty(V_1+V_2+V_3+V_4)/\sqrt{3}\\ &=J_\infty V/\sqrt{3}\ , \end{aligned} \qquad (5)$$

$$M_y=J_yV=J_\infty(V_1-V_2-V_3+V_4)/\sqrt{3}\ , \qquad (6)$$

$$M_z=J_zV=J_\infty(V_1+V_2-V_3-V_4)/\sqrt{3}\ . \qquad (7)$$

If the direction of the residual magnetization coincides with the direction β_1, β_2 and β_3, viz., the bar axis, then the next relation must be held;

$$\begin{aligned} \frac{J_\infty(V_1+V_2+V_3+V_4)}{\sqrt{3}\,\beta_1}&=\frac{J_\infty(V_1-V_2-V_3+V_4)}{\sqrt{3}\,\beta_2}\\ &=\frac{J_\infty(V_1+V_2-V_3-V_4)}{\sqrt{3}\,\beta_3}\ , \end{aligned} \qquad (8)$$

and from these equations we get

$$\begin{aligned} V_1-V_2-V_3+V_4&=\beta_2V/\beta_1\ ,\\ V_1+V_2-V_3-V_4&=\beta_3V/\beta_1\ . \end{aligned} \qquad (9)$$

The residual magnetization $J_{\text{r. calc.}}$ is given by

$$J_{\text{r. calc.}}=(M_x\beta_1+M_y\beta_2+M_z\beta_3)/V=J_\infty/\sqrt{3}\,\beta_1\ , \qquad (10)$$

and also the saturation value $(E_m)_{\text{sat.}}$ and the remanent value $(E_m)_{\text{rem.}}$ of the magneto thermoelectric power of the descending hysteresis curve are given by

$$\begin{aligned} (E_m)_{\text{sat.}}=&\,a_1(\beta_1^4+\beta_2^4+\beta_3^4-1/3)\\ &+2a_2(\beta_1^2\beta_2^2+\beta_2^2\beta_3^2+\beta_3^2\beta_1^2)\ , \end{aligned} \qquad (11)$$

$$\begin{aligned} (E_m)_{\text{rem.}}=&\,2a_2[\beta_1\beta_2+\beta_2\beta_3+\beta_3\beta_1)V_1/V\\ &+(-\beta_1\beta_2-\beta_2\beta_3+\beta_3\beta_1)V_2/V\\ &+(-\beta_1\beta_2+\beta_2\beta_3-\beta_3\beta_1)V_3/V\\ &+(\beta_1\beta_2-\beta_2\beta_3-\beta_3\beta_1)V_4/V]/3\\ =&\,2a_2[\beta_2^2+\beta_3^2+\beta_2\beta_3(p-q+r-s)]/3\ , \end{aligned} \qquad (12)$$

where p, q, r and s are fractions of the volumes V_1, V_2, V_3 and V_4 with respect to the total volume V, respectively.

§ 2. Samples, Experimental Method and Results

(1). Samples The samples are cylindrical rods made by the Bridgeman's method in the vacuum Tammann's furnace (No. 1 and No. 2) or in the vacuum molybdenum furnace (No. 3, No. 4 and No. 5) and annealed at 950°C

Table I.

sample	bar axis	length (cm)	diameter (cm)	direction cosines			$J_{\text{r. calc.}}$	$J_{\text{r. obs.}}$	H_c
				β_1	β_2	β_3			
No. 1	[111]	17.80	0.283	0.633	0.576	0.518	456	460	0.50
No. 2	[110]	19.70	0.289	0.795	0.602	0.073	363	375	0.25
No. 3	[100]	20.03	0.277	0.996	0.091	0.000	289	287	0.96
No. 4	[511]	20.90	0.275	0.958	0.223	0.178	301	300	0.98
No. 5	[210]	19.10	0.275	0.883	0.467	0.052	327	330	0.76
polycry.	—	20.00	0.201	—	—	—	—	—	0.45

for 2 hours in the ordinary nichrome furnace. The purity of the samples is 99.2% or more and impurities detected by spectoscopic analysis are Si, Mn and Mg and trace Co. The constants of the samples are shown in the Table 1.

$J_{r.calc.}$, $J_{r.obs.}$ and H_c in the table are calculated values by Eq. (10) and observed values of residual magnetization and coercive forces at room temperature respectively.

(2). Experimental method. In order to make measurement of the magneto-thermoelectric power, a nickel (sample)-copper thermocouple was constructed by connecting each end of the specimen rod with copper wires. The hot junction (one side of the specimen) of the couple was always kept 5°C∼10°C higher than the cold junction (the other side of the specimen) by a small non-inductive nichrome furnace when the middle point of the specimen was kept at t°C by another non-inductive nichrome furnace or by liquid air, dry ice or other suitable freezing mixtures. The ordinary thermoelectric force set up from the couple was nearly balanced as usual by connecting the copper wires, lead from the specimen, with a potentiometer. The magneto-thermoelectric force ΔE set up in consequence of magnetization by a magnetizing coil surrounding the specimen was determined by noting a deflection of a sensitive galvanometer through the potentiometer circuits. The magneto-thermoelectric power at given temperature t°C was obtained from the ΔE and the temperature difference Δt by $E_m = \Delta E/\Delta t$.

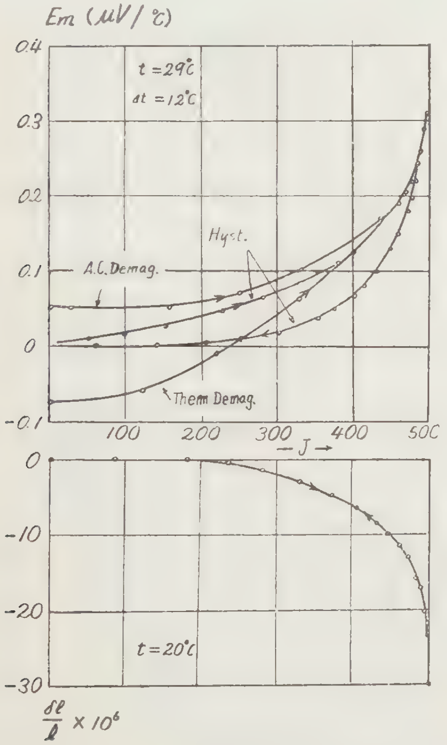

Fig. 1. Magneto-thermoelectric power and magnetostriction of No. 1, trigonal crystal [111].

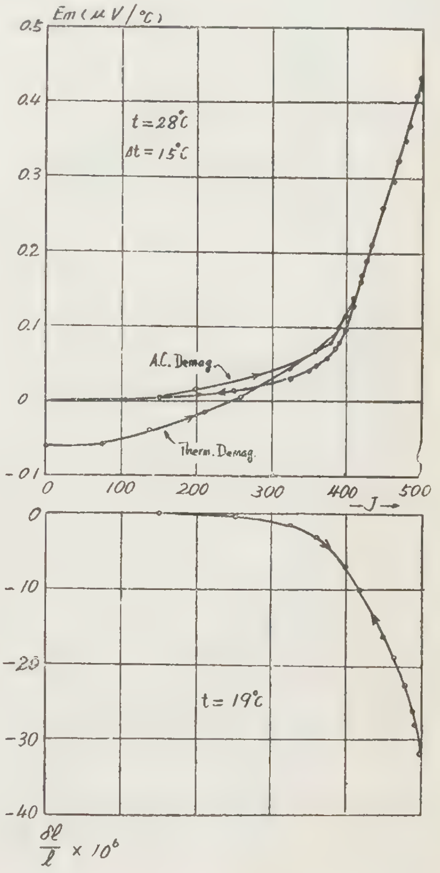

Fig. 2. Magneto-thermoelectric power and magnetostriction of No. 2, diagonal crystal [110].

(3). Results at room temperature. The magneto-thermoelectric powers and magnetostrictions of No. 1, No. 2 and No. 3, bar axes ofw hich nearly coincide with trigonal-axis [111], diagonai-axis [110] and tetragonal-axis [100] respectively, are shown in Fig. 1, Fig. 2 and Fig. 3 and the magneto-thermoelectric powers of No. 4 and No. 5 in Fig. 4 and Fig. 5. In the case of the polycrystal they are shown in Fig. 6.

The magneto-thermoelectric powers occurring in the region of the steep parts of magnetization curves, that is to say, in the discontinuous parts of magnetization are very small and most of them occur in the region of high magnetic fields, namely in the rotational part of magnetizations, similiar to the magnetostrictions; especially in the case of No. 3, [100], the change can not be observed practically between the demagnetization state and the residual magnetization $J=287$, but occurs between the states of the residual magnetization and of the saturation. The saturation value of the magneto-thermoelectric power of each sample is changed definitely by demagnetization methods such as A.C.-or thermal-method as shown in the figures. The greatest effect of this change can be seen in the case of No. 1, next in No. 2, and barely in No. 3. The difference or non-coincidence of the magneto-thermoelectric power of each sample between the descending and ascending hysteresis curves can be seen more distinctly than that in the case of the corresponding magnetostriction. General styles of the curves of the magneto-thermoelectric powers and of the magneto-strictions of each sample are similar except No. 3; the origin of this exception may be due to the

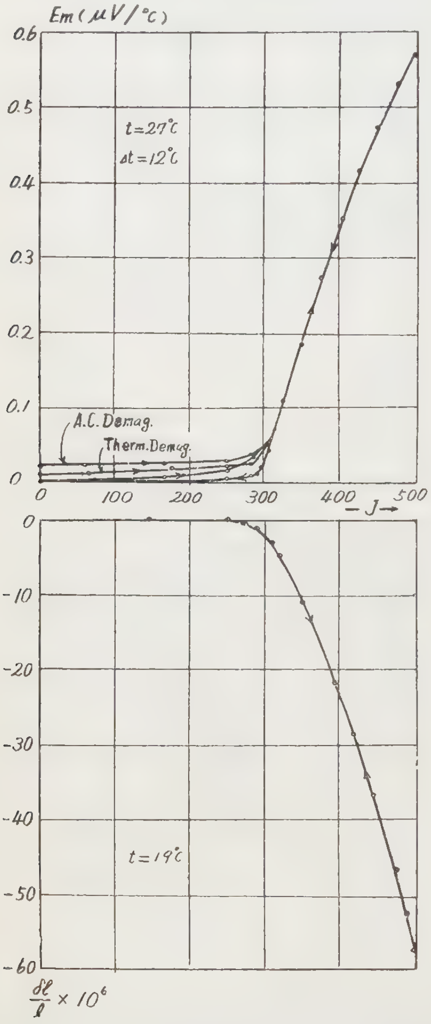

Fig. 3. Magneto-thermoelectric power and magnetostriction of No. 3, tetragonal crystal [100].

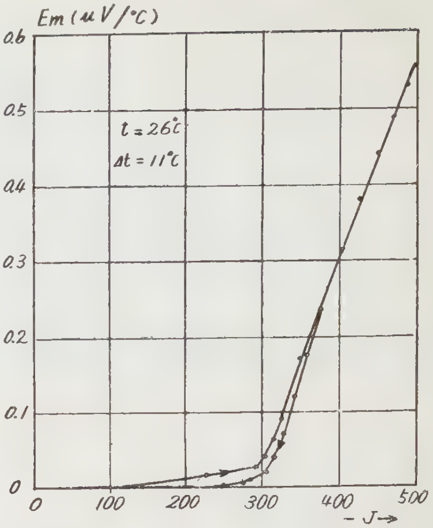

Fig. 4. Magneto-thermoelectric power of No. 4, [511].

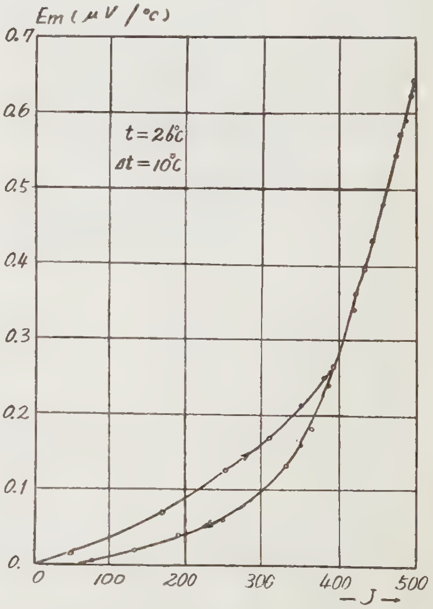

Fig. 5. Magneto-thermoelectric power of No. 5, [210].

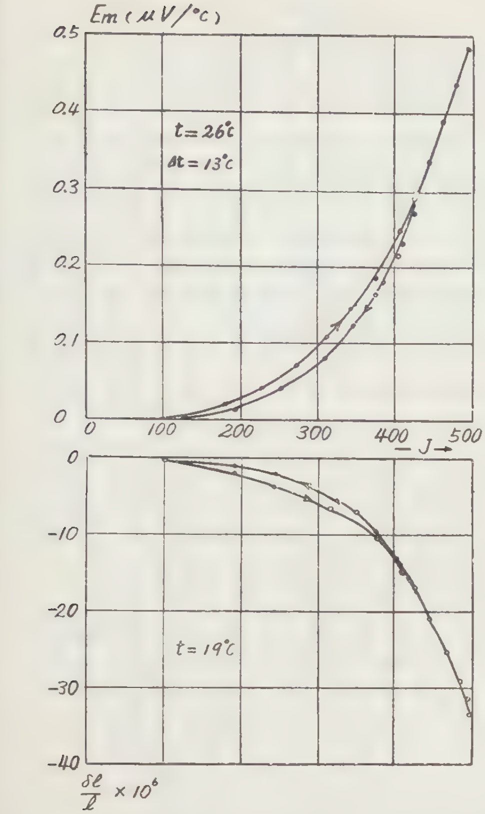

Fig. 6. Magneto-thermoelectric power and magnetostriction of the polycrystal.

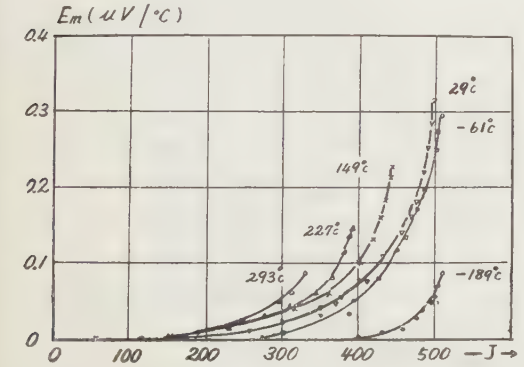

Fig. 7. Magneto-thermoelectric power of the trigonal crystal, No. 1 [111], at various temperatures.

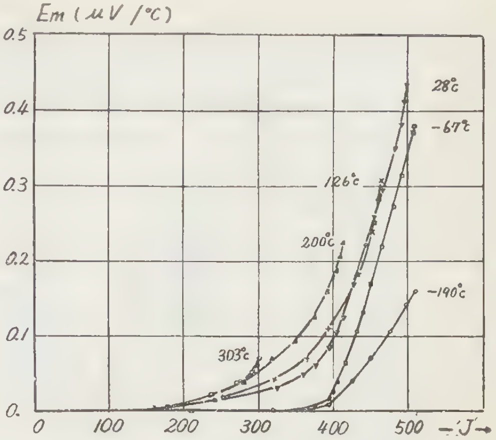

Fig. 8. Magneto-thermoelectric power of the diagonal crystal, No. 2 [110], at various temperatures.

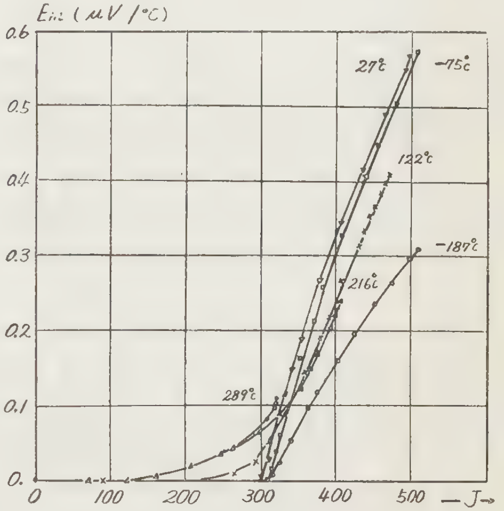

Fig. 9. Magneto-thermoelectric power of the tetragonal crystal, No. 3 [100], at various temperatures.

sensitive temperature dependency of the magnetization curve, because in the former the temperature of the sample is not uniform contrary to the case of the latter.

(4). Temperature dependency. The temperature dependencies of magneto-thermoelectric powers of No. 1, [111], No. 2 [110], and No. 3, [100] on their descending hysteresis curves are shown in Fig. 7, Fig. 8 and Fig. 9 respectively. The saturation values (as described already, they are not so important) at various temperatures are plotted in Fig. 10, each curve showing a maximum value in the neighbourhood of the room temperature, for instance, at −30°C in the case of No. 3, [100], and tending to zero on both sides. The magneto-thermoelectric power in the neighbourhood of the Curie point is easily saturated by a weak magnetic field and then decreases linearly with increasing field. It is reasonable to separate it into two parts by the extrapolation method; one of which is due to the rotation of magnetizations of magnetic domains and the other is due to the growth of

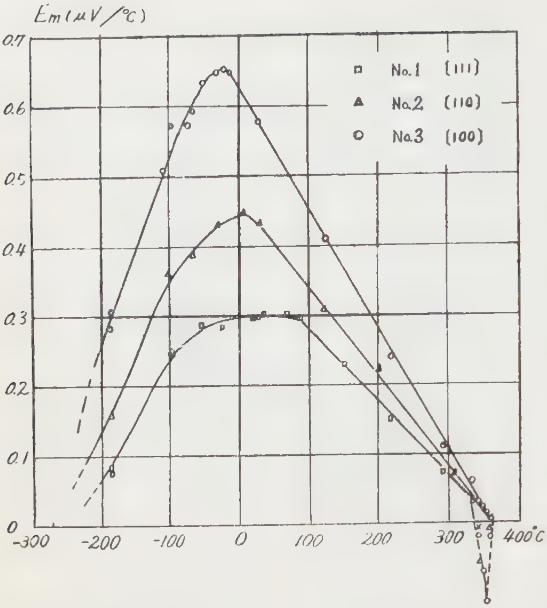

Fig. 10. Saturated values of magneto-thermoelectric power of the crystals (differences between the two states; J_∞ and $J=0$ on the descending hysteresis curves). The dotted line in the neighbourhood of the Curie point, a part of which is due to the magneto-caloric effect, is attributed to the additive magnetization proportional to the external magnetic field and is shown in the case of 700 Oerstead.

spontaneous magnetization by external magnetic field; the former is positive sign shown in the figure as full lines and the latter is negative shown as dotted lines in the case of 700 oerstead. It is known from our previous experiments that the magneto-thermoelectric power in the neighbourhood of the Curie point contains some small parts, which is not corrected in the figure, due to the magneto-caloric effect.[3)]

§ 3. Discussion

An absolute thermoelectric power of nickel is always negative and shows an abrupt decrease of its magnitude at the Curie point by the appearance of spontaneous magnetizations, as explained by N. F. Mott from the standpoint of the modern theory of metals, and is independent of the crystal orientation. The negative magneto-thermoelectric power in the neighbourhood of the Curie point corresponds to the decrease of the absolute thermoelectric power. The positive magneto-thermoelectric power depends on the directions of the magnetization in domains. It is not, at present, certain whether the positive magneto-thermoelectric powers are directly related to ferromagnetism, for instance $3d$- and $4s$-electron interactions or only indirectly related —through the magnetostrictive lattice distortion. Our previous experiments in the case of iron-nickel alloys show that the magneto-thermoelectric power is not intimately related to magnetostrictive lattice distortion.

Because the distributions of magnetic domains in each sample in the demagnetized state are affected by demagnetization methods, the saturation values of the magneto-thermoelectric power are not so important but the distributions of magnetic domains at the residual magnetization on the descending hysteresis curve are significant, if the fractions p, q, r and s are uniquely decided and hence the differences between the saturation and the remanence are always constant in spite of the different demagnetization methods as shown in Table II at room temperature.

The expression of these differences of the magneto-thermoelectric powers is obtained from Eq. (11) and Eq. (12) as follows:-

$$(E_m)_{\text{srt.}}-(E_m)_{\text{rem.}}=a_1(\beta_1{}^4+\beta_2{}^4+\beta_3{}^4-\tfrac{1}{3})$$
$$+2a_2[(\beta_1{}^2\beta_2{}^2+\beta_2{}^2\beta_3{}^2+\beta_3{}^3\beta_1{}^2)$$
$$-\tfrac{1}{3}\{(\beta_2{}^2+\beta_3{}^2)+\beta_2\beta_3(p-q\pm r-s)\}]\,, \tag{13}$$

and we get next equations of each sample

$$\text{No. 1}\quad 0.01a_1+(0.26-0.20t)a_2=0.16, \tag{14}$$

$$\text{No. 2}\quad 0.20a_1+(0.22-0.30t)a_2=0.38, \tag{15}$$

Table II.

sample	$(E_m)_{\text{sat.}}$ $\mu V/°C$	$(E_m)_{\text{rem}}$ $\mu V/°C$	$(E_m)_{\text{sat.-rem}}$ $\mu V/°C$	$\left(\frac{\Delta l}{l}\right)_{\text{sat.}}\times10^6$	$\left(\frac{\Delta l}{l}\right)_{\text{rem}}\times10^6$	$\left(\frac{\Delta l}{l}\right)_{\text{sat.-rem}}\times10^6$
No. 1	0.31	0.15	0.16	−23.3	−11.8	−11.5
No. 2	0.44	0.06	0.38	−32.0	− 3.6	−28.4
No. 3	0.57	0.00	0.57	−58.0	− 0.5	−57.5
No. 4	0.55	0.02	0.53	−49.0	− 0.5	−48.5
No. 5	0.65	0.14	0.51	−38.8	− 4.9	−33.9

No. 3 $0.65a_1+(0.01-0.00t)a_2=0.57,$ (16)

No. 4 $0.51a_1+(0.10-0.03t)a_2=0.53,$ (17)

No. 5 $0.32a_1+(0.20-0.01t)a_2=0.51,$ (18)

where $t=p-q\pm r-s$, and $-r$ must be chosen when the angle between the [$1\bar{1}\bar{1}$] and magnetic field is greater than that between the [$\bar{1}11$] and the field. If we assume that $p \doteqdot s$ and $q \doteqdot r$ from the crystal symmetry, that is $t=0$, in No. 2, 3 and 5, then the constants a_1 and a_2 at room temperature can be determined as follows:—

$$a_1=0.86\ \mu\text{V}/^\circ\text{C}\ ,$$
$$a_2=1.03\ \mu\text{V}/^\circ\text{C}\ .$$

If we put the values of a_1 and a_2 in Eq. (14), No. 1 [111], then we get $t=0.5$ and therefore $p=0.75$, $q=0.05$, $r=0.1$ and $s=0.1$, each of which coincides nearly with that calculated from the magnetostrictive data. Fig. 11 shows the temperature variation of the a_1 and a_2 below 100°C, because the anisotropic constants of magnetic energy change their signs and hence the directions of the easiest magnetization change from ⟨111⟩ to another at about 100°C, so that the calculation to obtain the a_1 and a_2 must be selected from other methods. As expected from the previous papers, the a_1 and a_2 show maximum values at −30°C and 20°C respectively and both of them tend to zero at 0°K.

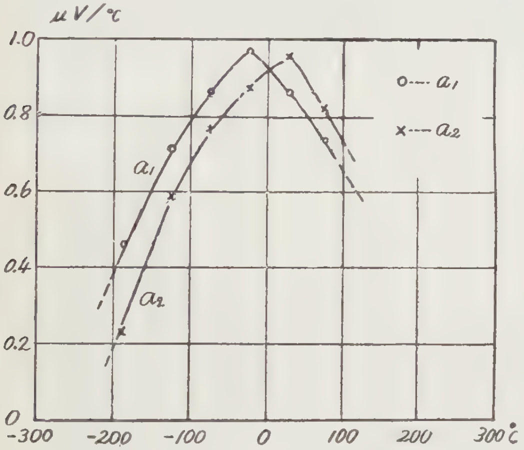

Fig. 11. Temperature dependency of the anisotropic constants a_1 and a_2.

§ 4. Summary

The magneto-thermoelectric power and its temperature dependency of nickel single crystals are measured and then the constants a_1 and a_2, which specify the characteristic properties, are calculated.

(1). The magneto-thermoelectric power depends on the orientation of the crystal and is always positive except that in the neighbourhood of the Curie point.

(2). $(E_m)_{100}=2a_1/3=0.57\ \mu\text{V}/^\circ\text{C}$,
$(E_m)_{111}=2a_2/3=0.69\ \mu\text{V}/^\circ\text{C}$
at room temperature.

(3). The magneto-thermoelectric powers ($(E_m)_{100}$ and $(E_m)_{111}$ or a_1 and a_2) represent maximum values in the neighbourhood of the room temperatures (−30°C and 20°C, respectively) and tend to zero toward 0°K and the Curie point.

(4). The negative parts of the magneto-thermoelectric powers in the neighbourhood of the Curie point in strong magnetic fields are due to the additive magnetization proportional to the magnetic fields.

In conclusion, the authors wish to express their thanks to Prof. H. Takaki and his collabolators of the University of Kyoto and Mr. Y. Gondō in our laboratory for the preparation of the samples.

References

1) F. E. Lawrence and F. W. Constant: Phys. Rev. **48** (1935) 257.
H. Broili: Ann. d. Phys. **14** (1932) 259.

2) Z. Funatogawa: J. Phys. Soc. Japan **5** (1950) 311; **6** (1951) 256.
Y. Gondo and Z. Funatogawa: J. Phys. Soc. Japan **7** (1952) 589.

3) N. Miyata and Z. Funatogawa: Sci. Rep. Yokohama National Univ. **3** (1954) 14.

JOURNAL OF THE PHYSICAL SOCIETY OF JAPAN Vol. 9, No. 6, Nov.—Dec., 1954

Microwave Spectrum of Methylamine

By Koichi SHIMODA, Tetsuji NISHIKAWA
and Takashi ITOH

Department of Physics, Faculty of Science,
University of Tokyo, Tokyo, Japan

(Received July 16, 1954)

Microwave spectrum of methylamine molecule has been studied in the frequency range between 7 and 30 kMc/sec. More than two hundred lines and their Stark effects have been measured. These lines are divided into three kinds: (1) $\Delta J=0$, $\Delta K=\pm 1$, (2) $\Delta J=\pm 1$, $\Delta K=\mp 1$, and (3) $\Delta J=0$, $\Delta K=0$. Lines of $\Delta J=0$ and $\Delta K=\pm 1$ form seven well-defined series, p_1, p_2, q_1, q_2, r_1, r_2, and s_1. Among them, lines of p series show first-order Stark effects and the others show second-order Stark effects. With theoretical considerations we have assigned these series. From this assignment, the height of the potential barrier for the hindered internal rotation has been determined to be about 680 cm^{-1}. Inversion doubling and its effect on the over-all and hindered rotations are studied. Lines belonging to the classes (2) and (3) are also analyzed. But the determination of molecular constants from the observed data is deferred to a forthcoming paper.

§ 1. Introduction

The methylamine molecule is an asymmetric rotor, the amino group of which is rotatable around the axis of the methyl group in a manner like the methylalcohol molecule. Besides, this molecule may invert itself about nitrogen in a manner like the well-known inversion of ammonia.

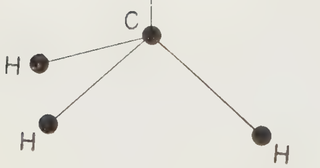

Fig. 1. Structure of methylamine.

As to the hindered rotation, Dennison and others[1),2),3)] developed a theory in order to analyze the spectrum of methylalcohol. And it will also be applied to the spectrum of methylamine. We assume a sinusoidal form of hindering potential,

$$V=\tfrac{1}{2}H(1-\cos 3x)\ ,$$

where x is the angle of mutual rotation of the two groups and H is the height of the potential barrier.

Aston and others determined the barrier height of methylamine to be 1000 cm^{-1} from the calorimetric data[4)] on the one hand, and to be 530 cm^{-1} from the infrared data[5)] on the other hand. Lassettre and Dean estimated the barrier height to be 740 cm^{-1} by a semi-empirical theory[6)]. From the rough value of barrier height, we expected several series of lines in the microwave range corresponding to the hindered rotation.

As to the inversion, experimental evidence had been found only in ammonia molecule, until we found the inversion doubling in the spectrum of methylamine, the magnitude being of the order of 10 kMc/sec*. The theory of inversion doubling which has been developed for ammonia by Dennison and Uhlenbeck[7)] has to be considerably modified on account of coupling between inversion and hindered rotation. This modification has been performed mostly by one of us (T. I.), and will be discussed in 5.

Some lines of the spectrum have first been found by Hershberger and Turkevitch[8)] in the region between 22 and 26 kMc/sec. Shimoda and Nishikawa have remeasured the frequencies of these lines more accurately with reference to the standard frequency broadcast JJY and also found many other lines in the range between 15 and 27 kMc/sec.⁹⁾ Since then, the observed range has been extended down to 7 kMc/sec and up to 30 kMc/sec, and the Stark effects of the lines were investigated over the whole frequency range.

---

* For this value, the authors owe greatly to the guess by Prof. D. M. Dennison.

The spectrum is, however, very complicated by the coupling of inversion and hindered rotation as well as over-all rotation of the molecule. A careful study of the Stark pattern of each line is of much help with theoretical considerations to assign the corresponding transition and to determine the height of potential barrier and rotational constants.

Lide is also studying the spectrum of methylamine and his results are is good agreements with ours. He has assigned three rotational lines of the transition $\Delta J=\pm 1$, and determined three moments of inertia of the molecule¹⁰⁾. However these values of rotational constants must be revised taking account of inversion and hindered rotation.

§ 2. Theoretical

1. Hindered Rotation

The theory of hindered rotation of a slightly asymmetric rotor molecule developed by Dennison and others¹⁾,²⁾,³⁾ is also applicable to methylamine. According to the earlier theory¹⁾, in which both rotatable groups of the molecule are assumed to be symmetric rotors, the energy levels including both overall and hindered rotations are described by the quantum numbers J, K, τ, and n. J and K are the quantum numbers corresponding to the total angular momentum and its component along the figure axis of the molecule. n is the quantum number of torsional oscillation, and τ is related to the tunneling of the hydrogen atoms in the amino group from one of the potential minimum to another. Since the hindering potential has three-fold symmetry, τ may take three values 1, 2, or 3.

The rotational energy can be written as the sum of two terms,

$$E=E_\alpha+E_\beta\,, \tag{1}$$

where E_β is the usual rotational energy of a symmetric rotor and is a function of J and K; E_α represents the contribution of hindered rotation which depends on the quantum numbers K, τ, and n, but not on J. E_α becomes $(n+\frac{1}{2})h\nu_t$ in the limiting case of very high potential barrier where ν_t is the torsional frequency. As the height of the potential barrier decreases, each level splits into three sublevels designated by $\tau=1$, 2, and 3 with increasing separations.

Burkhard and Dennison²⁾ refined this theory by taking account of the asymmetry of the molecule. Their method is adopted in this paper for the analysis of the microwave spectrum of methylamine. Then we treat the problem of hindered rotation using a model which consists of a rigid amino and a rigid methyl group, where the CNH angle is assumed to be constant during the hindered rotation. According to this refined theory, K, τ, and n are no longer good quantum numbers, but they are still used approximately, since the effect of asymmetry is very small in methylamine.

The rotational energy can also be written in the form of Eq. (1) neglecting a relatively small correction term, $\mathcal{E}$, arising from the asymmetry effect. In this case overall rotational energy E_β is given by

$$E_\beta=\frac{h^2}{16\pi^2}\left(\frac{1}{A}+\frac{C_1}{BC_1-D^2}\right)(J^2+J-K^2)+\frac{h^2}{8\pi^2}\frac{1}{C}K^2\,, \tag{2}$$

where A, B, C are moments of inertia of the molecule about ξ, η, and ζ axes and D is the product of inertia with respect to the η, ζ axes. The ξ, η, ζ axes are chosen in the following way: ζ axis is parallel to the symmetry axis of the methyl group, and η axis is perpendicular to the ζ axis and comprised in the bisecting plane of the HNH angle, the origin of the coordinate system being taken at the center of gravity of the molecule. C_1 is defined by $C_1=C-C_2$, where C_2 is the moment of inertia of the methyl group about its own symmetry axis.

Hindered rotational energy E_α is the eigenvalue of the secular problem

$$\left[\frac{h^2}{8\pi^2}\frac{C}{C_1C_2}\left(\frac{1}{i}\frac{d}{dx}-\frac{C_1}{C}K\right)^2+V(x)\right]P(x)=E_\alpha P(x)\,, \tag{3}$$

where $V(x)=H/2(1-\cos 3x)$, and $P(x)$ is the eigenfunction of hindered rotation. The Eq. (3) can be solved by expanding $P(x)$ in a

Fourier series in the form

$$P(x)=\sum_m a_m e^{imx} . \qquad (4)$$

On account of the three-fold symmetry of $V(x)$, m takes every third integral value in Eq. (4): that is, $m=\cdots, -6, -3, 0, 3, 6, \cdots$ for $\tau=1$; $m=\cdots, -4, -1, 2, 5, \cdots$ for $\tau=2$; and $m=\cdots, -5, -2, 1, 4, \cdots$ for $\tau=3$.

The small term $\mathcal{E}$, which represents the effect of asymmetry of the molecule, can be calculated by a perturbation method. The calcuiation is complicated and in any case this term is not large for lower values of J, so that the simplified expression, Eq. (1) with Eq. (2) and Eq. (3) is satisfactorily used to find the general nature of the energy levels. For large values of J, however, the term $\mathcal{E}$ becomes very large (10∼100 kMc/sec). Particularly the effect of K-type doubling becomes so predominant that it must be taken into consideration.

2. Selection Rules and Classification of Lines

The selection rules for the asymmetric hindered rotor have been investigated in detail by Ivash and Dennison[3]. However, the approximation of a symmetric rotor assumed by Koehler and Dennison is sufficient for practical purposes, since the effect of asymmetry is very small for methylamine. Then, the allowed transitions are those for which $\Delta J=0, \pm 1$, $\Delta K=0, \pm 1$, $\Delta(K+\tau)=0$ (mod. 3), and $\Delta n=0, \pm 1, \pm 2, \cdots$. The change of τ is always associated with the change of K by the above relation. The frequencies corresponding to the transitions $\Delta n=\pm 1, \pm 2, \cdots$ fall into the infrared region, and only the transitions $\Delta n=0$ into the microwave region. n may be 0, 1, or even 2 for the microwave transitions, since these levels are considerably populated at room temperature.

All the transitions in the microwave region are divided into four classes (1) $\Delta J=0$, $\Delta K=\pm 1$, (2) $\Delta J=\pm 1$, $\Delta K=\pm 1$, (3) $\Delta J=0$, $\Delta K=0$ (transition between the levels separated by the asymmetric K-type doubling), and (4) $\Delta J=\pm 1$, $\Delta K=0$. The transitions $\Delta K=0$ will be very weak, as the component of the dipole moment of the molecule along the figure axis, $\mu_{\parallel}$, is very small, being about a quarter of the perpendicular component, $\mu_{\perp}$. Accordingly, most of the observed lines are probably due to the transitions $\Delta K=\pm 1$. But some of the weaker lines may correspond to the transitions $\Delta J=0$, $\Delta K=0$, and other weaker lines may correspond to the transitions in which K changes by more than one. No lines of the class (4) fall in the observed range.*

The lines of $\Delta J=\pm 1$, $\Delta K=\pm 1$ are irregularly spaced in the microwave region, and most of them are due to the transitions in which J and K changes in opposite directions. The transitions in which J and K change in the same direction fall in tne higher frequency range.

The frequencies of the transitions $\Delta J=0$, $\Delta K=\pm 1$ are independent of J, as far as the approximate expressions (1) for the rotational energy is used. However, when the effect of asymmetry is taken into account, this type of transition gives rise to a series of lines corresponding to $J=K$, $K+1$, $K+2, \cdots$. Several series may appear superposed in the microwave region. Furthermore, each series may be doubled by the inversion doubling, which will be discussed in later sections.

3. Frequencies of the Series Lines

Since the analysis of series lines is the most important, a theoretical calculation of the frequencies is given in the following. The frequency of the transitions $\Delta J=0$, $\Delta K=\pm 1$ is the difference of two large terms arising from E_α and E_β in Eq. (1). E_β, which is concerned with the over-all rotation, is a function of moments and products of inertia of the molecule. Since the molecular dimensions are fairly well known from electron diffraction and infrared data, we can estimate it at least very roughly. On the other hand, E_α, which is concerned with the hindered rotation, depends considerably on the height of potential barrier. Since the height of potential is not yet known decisively, it is necessary to plot the frequencies of the transitions as functions of H.

In carrying out the calculation, we must assume molecular dimensions. We assume that the structure of the CH_3 group is the same as in methane, that is, $d_{CH}=1.093$ A, ∠HCH=109°28′. Likewise, the structure of

---

* Edwards, Gilliam, and Gordy have assigned the $J=0\to 1$, $K=0\to 0$ line in 50 kMc/sec region, but their assignment has not yet been confirmed (private communication).

NH_2 group is assumed to be the same as in ammonia, that is, $d_{NH}=1.014$ A, ∠HNH$=106°47'$. The C-N distance is known from the electron diffraction data to be 1.47 A. The C-N direction may not coincide with the symmetry axis of the methyl group,* and we take the angle of the discrepancy equal to 3° as a plausible value. We also assume that the CNH angle is 110°, somewhat larger than the HNH angle in ammonia.

In order to look over the general trend of the frequency versus potential curves, it will be convenient to use an approximate formula for E_α. As has been mentioned by Dennison and others, E_α is a periodic function of $\gamma=2\pi/3((C_1/C)K+\tau-1)$, and to a good approximation it can be expressed by

$$E_\alpha=\alpha_n-\beta_n\cos\gamma\ , \qquad (5)$$

where α_n and β_n are numerical constants depending on the height of the hindering potential and the quantum number n. β_n can be determined by solving the secular equation, (3), for two arbitrary values of γ, and then we can readily calculate E_α for any value of γ from Eq. (5). In this way, we can pick out such transitions that may appear in the microwave region for the probable value of H.

The next step is to calculate the frequencies of the picked out transitions more precisely. By rigorously determining E_α from Eq. (3), we obtain the frequencies of the transitions versus potential curves as illustrated in Fig. 2. The order of Stark effect, which will be discussed in the next section, is also shown in parentheses.

Each transition gives a series of lines corresponding to the values of J equal to or greater than the larger K involved. The curves of Fig. 2 show the origins of the series, or the frequencies of the lines of the smallest J. For larger J values, however, the frequencies deviate considerably from these values. Besides, the effect of K-type doubling has to be considered for the transitions with smaller K, as described in the following section.

4. *K*-type Doubling

Although methylamine is an asymmetric rotor molecule, not all of the rotational levels undergoes the K-type splitting. According to the theory of Bunkhard and Dennison, only one third of the levels are split into doublets, and the degeneracies of the other levels are not removed by the asymmetry. The coupling between over-all and hindered rotations brings about certain essential double degeneracies. This is the reason why some lines of the methylamine exhibit first-order Stark effects while other lines do second-order Stark effects, in contrast to the spectra of other rigid asymmetric rotor molecules.

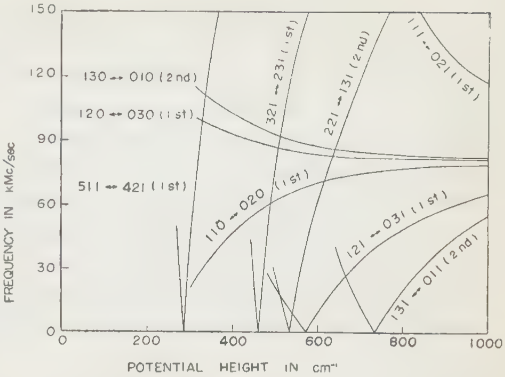

Fig. 2. Frequencies of K, τ, $n\leftarrow\rightarrow K-1$, $\tau+1$, n transitions for $n=0$ and $n=1$. The order of Stark effect is indicated in parentheses.

The general structure of energy levels has been illustrated by Ivash and Dennison in Fig. 1 of their paper. The levels with $K+\tau-1$ divisible by 3 are split into doublets by the effect of asymmetry, while the levels with $K+\tau-1$ not divisible by 3 remain degenerate. Therefore, the lines arising from transitions between levels whose $K+\tau-1$ are divisible by 3 give rise to second-order Stark effects, and the other lines give rise to first-order Stark effects.

In some cases when apparent degeneracies may take place, the lines will also exhibit first-order Stark effects. Such a close degeneracy will be caused when the K-type doubling is sufficiently small. Since K-type doubling for the slightly asymmetric hindered rotor is roughly the same as for the rigid rotor, the magnitude of the K-type doubling may be estimated by the Wang's formula[11)]

$$\Delta E=\frac{c-a}{2}\,\frac{(J+K)!}{(J-K)!(K-1)!(K-1)!}\times\frac{\delta^K}{16^{K+1}(1-\frac{1}{2}\delta)^{K-1}}\ , \qquad (6)$$

---

* Dennison and others have pointed out a similar discrepancy as to methyl alcohol.

where $a=h^2/8\pi^2 A$, $b=h^2/8\pi^2 B$, $c=h^2/8\pi^2 C$, and $\delta=(a-b)/(c-a)$. In the case of methylamine molecule, the K-type doubling of each rotational level with $K\geq 5$ is expected to have the separation less than 0.5 Mc/sec because of the small asymmetry parameter, $\delta\approx 0.01$. Transitions between levels with $K\geq 5$, therefore, show first-order Stark effects, even when $K+\tau-1$ is divisible by 3.

On the other hand, the magnitude of K-type doubling may be quite large for smaller values of K. For example, when we take $K=1$, Eq. (5) reduces to $\Delta E=(a-b)J(J+1)/2$. Since the value of $a-b$ is nearly 900 Mc/sec, we have $\Delta E\approx 50{,}000$ Mc/sec for $J=10$. Of course, the above estimation must be corrected, taking into account the effect of hindered rotation as described in the paper by Ivash and Dennison. However, the order of magnitude of the K-type doubling will be unchanged.

We conclude therefore that the frequencies for such transitions which show second-order Stark effects with $K=1$ and $K+\tau-1=3m$ will deviate greatly from the original values described in 3 with increasing values of J. Accordingly, we can expect that frequencies of lines of the series of $n=0$, whose original frequency lies around 80,000 Mc/sec in Fig. 2, may descend down to less than 30,000 Mc/sec for larger J values.

Besides, the transitions between the levels of K-type doublet may be observed in the microwave range when $K=1$, $\tau=3$ (and $J\geq 4$). They will also form a series corresponding to different J values. Discussions on the observed spectrum will be given in § 4.

5. Inversion Doubling

Up to this day, ammonia and deuterated ammonia are the only molecules for which the phenomenon of inversion doubling has been observed. Since methylamine can be obtained by replacing one hydrogen of the ammonia with the methyl group, it may exhibit an observable inversion. In methylamine the inversion motion will take place in such a way that the heavy group NCH_3 remains almost at rest while the two hydrogen atoms of the NH_2 group turn over from one side to the other. Then, if the hydrogen atoms in NH_2 are initially at the bottom of the hindering potential, they will be at the top of the potential hill at the end of the inversion. Thereafter, they must rotate by an angle of 60° to arrive at the minimum position. Thus each inversion motion must be followed by a mutual rotation of NH_2 and CH_3 groups by 60°. This implies a complicated coupling between inversion and hindered rotation. For this reason, the magnitude of inversion doubling may be strongly dependent on the rotational quantum numbers.

As a first approximation, the order of magnitude of the inversion doubling may be theoretically or semi-emplically estimated using the formula of Dennison and Uhlebeck⁷⁾, which has been applied successfully for ammonia and deuterated ammonia¹²⁾. We assume that the potential for inversion is the same as in ammonia, and take the reduced mass proportional to the inverse square of the frequency of the NH_2 wagging vibration ν_1. The inversion splitting Δ_0 of the ground vibrational state is given by

$$\frac{\Delta_0}{\nu_1}=\frac{2\alpha}{\pi^{1/2}}\exp\left[-\alpha^2-2(x_0-\alpha)(\alpha^2-1)^{1/2}\right], \tag{7}$$

where $x_0=(4\pi^2\mu\nu_1/h)^{1/2}q$, $V_t=\alpha^2 h\nu_1/2$, $q=$ height of the ammonia pyramid $=0.38$ A, $V_t=$height of the inversion potential$=1793.36$ cm^{-1}. The calculated result is shown in Table I with the values for ammonia and deuterated ammonia for comparison. From this result we may conclude that the inversion doubling for methylamine is observable in the microwave spectrum. However, since Δ_0 is a very sensitive function of molecular parameters, we must consider various correction factors to obtain a more reliable result.

Table I. Inversion splittings for ammonia, deuterated ammonia, and methylamine calculated from Dennison and Uhlenbeck's formula.

	NH_3	NH_2D	NHD_2	ND_3	CH_3NH_2
Δ_0(cm^{-1})	0.7935	0.402	0.172	0.068	0.110
ν_1(cm^{-1})	950.16	884	813	747.3	780
μ (amu)	2.47	2.87	3.385	4.20	3.66

In the first place, the CNH angle of methylamine is expected to be somewhat larger than the HNH angle of ammonia, as mentioned in the previous section. This corresponds to a smaller distance between two minima of the inversion potential, and it will result in a three or four times larger inversion splitting than that estimated above.

The second correction is introduced by the coupling between inversion and hindered rotation mentioned before. The potential of the internal motions of the molecule can not be written as a simple sum of the potential of inversion and that of hindered rotation, but it will be a rather complicated function. Climbing the potnetial of hindered rotation will mean at the same time climbing the potential of the inversion. For this reason, the effective potential of the inversion will be relatively lowered for the excited torsional state $n=1$ than for the ground state $n=0$. Therefore the magnitude of inversion splitting for the state $n=1$ may be somewhat larger than that for the state $n=0$.

Thirdly, it must be noted that the inversion motion for the state $n=0$ does not always take place in the way described at the beginning of this section (inversion followed by a 60° internal rotation), but in some cases one of the hydrogen atom remains at rest during the inversion process, while the other hydrogen atom moves from one potential well to the other. This is the probable case when the hydrogen atoms in the amino group are tightly bound to the potential well. If we take account of this new path on the two dimensional potential surface, the frequency of inversion for $n=0$ will be increased, and the inversion splitting will become larger.

In view of all the above considerations, we conclude that the inversion doubling for methylamine may be as large as 10,000 Mc/sec or more. For a more quantitative discussion, we must consider the dependence of the inversion doubling on the rotational quantum numbers.

Being unable to solve the complicated two dimensional wave equation for the internal motions of the molecule, we must resort here to a simple semi-classical consideration. Since the potential minimum and maximum of the hindered rotation are exchanged by inversion, the wave functions of the hindered rotation at the beginning and at the end of the inversion will be given by $P(x)$ and $P(x-\pi)$ respectively.* The tunneling probability is proportional to the overlap integral

$$\int P^*(x)P(x-\pi)dx \ ,$$

and this probability is expected to be proportional to the magnitude of inversion splitting. Then we obtain the following formula for the inversion splitting:

$$\Delta=\Delta_0\int P^*(x)P(x-\pi)dx \ , \qquad (8)$$

where Δ_0 means the hypothetical inversion splitting when the coupling between inversion and hindered rotation is absent.

From the periodic property of $P(x)$, we can show that the integral in the Eq. (8) is a periodic function of

$$\gamma'=-\frac{\pi}{3}\frac{C_1}{C}K+\frac{2\pi}{3}(\tau-1)\,.$$

In the practical computation, it was found that a simple sinusoidal function gives a good approximation. We may write

$$\Delta=\Delta_0 s_n \cos\gamma' \ , \qquad (9)$$

where s_n is a constant depending on n. For the estimated value of the hindering potential 680 cm^{-1}, we obtain $s_0=0.21$ and $s_1=-0.75$. The value of Δ_0 may be determined by fitting the calculated result to the observed data.

The above expression is not expected to give the inversion splitting of the rotational states accurately. Nevertheless, it indicates clearly the strong dependence of Δ on the quantum numbers K, τ, and n. This point must be considered in the detailed understanding of the observed spectrum.

Finally, some remarks on the nuclear statistical weight of the sublevels of the inversion doubling should be noted. As is easily understood, one of the two levels of the inversion doublet is symmetric and the other is antisymmetric with respect to the exchange between the coordinates of two protons in the amino group. According to Pauli's principle these levels correspond to the singlet and triplet nuclear spin state of the two protons. The ratio of nuclear statistical weight of these levels is 1:3. Then the intensity of the two components of the rotational lines must be about 1:3. The magnitude of the inversion splitting of the rotational line is the difference of the inversion splittings of the upper and lower rotational levels.

§ 3. Experimental Results

6. Experimental Procedure

The block diagram of the Stark modulation

---

* We take the angle $\pi=180°$ instead of $\pi/3=60°$, since these two values are equivalent for $P(x)$ because of its three-fold symmetry.

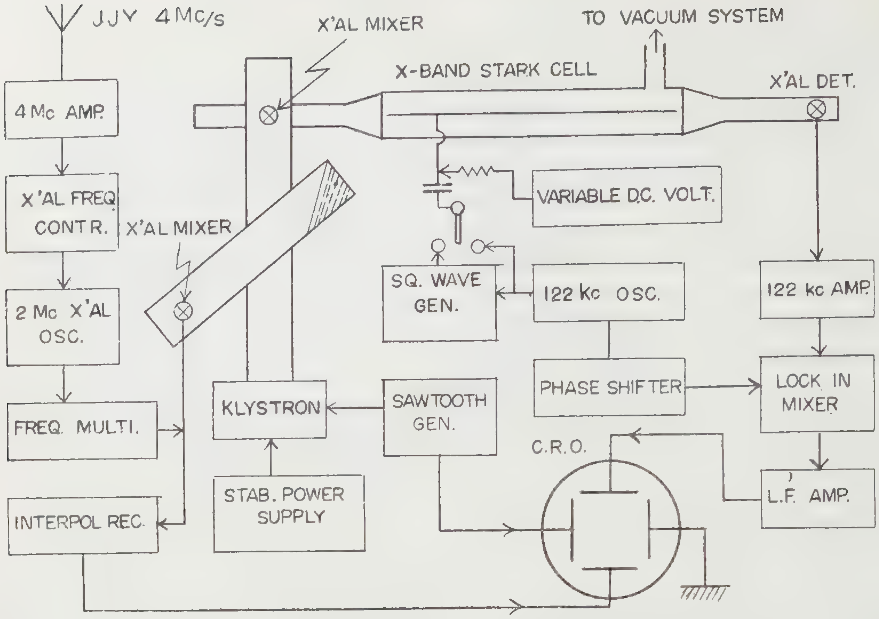

Fig. 3. Block diagram of Stark modulation spectrograph.

microwave spectrograph used is shown in Fig. 3. The frequency range between 7 and 30 kMc/sec has been covered by crystal doublers and triplers driven by klystrons, 2K25, 2K26, and 2K22. An ordinary *X*-band Stark waveguide cell of three meters in length was employed. The attenuation was measured to be about 1.2 db/m (0.4 db/ft) at 24 kMc/sec. Sine wave Stark modulation of 122 kc/sec is applied to the central electrode with d.c. bias voltage which is variable from zero up to 1500 volts. After transmission through the cell, the microwave power is rectified by a crystal detector, 1N26, the output of which is fed to a tuned amplifier and a lock-in mixer followed by a video amplifier.

In order to resolve the precise structures of the Stark patterns we have also used square wave modulation method. To avoid difficulties in generating square wave of variable amplitude, a constant amplitude (ca 1,000 V/cm) square wave modulation and variable d.c. bias were used.

Frequencies of the absorption lines were measured by means of a sort of multiplier controlled by standard frequency broadcast, JJY, and an interpolating receiver, halicrafter model SX-28. The width of the marker signal represented on the oscilloscope screen has been narrower than 5 kc/sec.

The sample of methylamine was prepared by adding sodium hydroxide into methylamine hydrochloride. Although possible impurities such as ammonia, di-methyl amine, tri-methyl amine and others were removed by repeated recrystallizations from commercial methylamine hydrochloride and by fractionation of methylamine in a vacuum system, a small quantity of ammonia still remained in the sample. This became a little troublesome, but it was more or less useful for rough estimations of intensities and frequencies.

7. Observed Spectrum

More thah two hundred lines and their Stark effects have been observed. The mea-

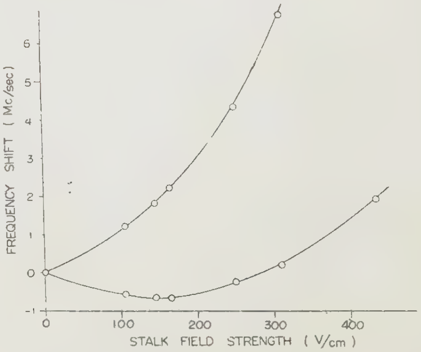

Fig. 4. Field dependence of the frequencies of two groups of Stark components of a line ($\nu_0=$ 17302.03 Mc/sec) showing typical (1→2) Stark effect.

Table II. Observed Lines of the Methylamine Spectrum.

	Frequency in Mc/sec.	Intensity	Stark-effect
q_2	6894.81	MS	1→2
	6939.82	WW	1(i)?
	7000.71	WW	1(i)?
p_1	7115.14	W	1(o)
	7213.43	W	2(+)
r_2	7253.64	MW	2(+)
	7718.11	WW	1(i)?
q_2	7727.74	MS	1→2
	7757.18	W	1(i)
	7896.89	WW	2(+)
s_1	7911.49	MS	2(+)
p_1	8131.59	MW	1(o)
r_1	8201.65	MS	2(+)
	8233.22	W	2(−)?
r_2	8268.99	MW	2(+)
	8411.94	M	1(i)
q_2	8684.29	S	1→2
	8813.22	MW	2(+)
r_2	8884.29	M	2(+)
	8950.90	W	2(+)?
q_1	9057.85	S	1→2
s_1	9079.39	MS	2(+)
s_1	9127.61	S	2(+)
s_1	9128.14	S	2(+)
p_1	9223.83	MW	1(o)
	9285.77	WW	1(i)?
	9452.63	WW	2(−)
	9453.06	W	2(−)
	9459.96	WW	2(+)
r_2	9584.09	MW	2(+)
	9706.10	MW	1(i)
q_2	9779.33	S	1→2
r_1	9938.95	MS	2(+)
	10108.45	MW	2(+)
	10109.61	MW	2(+)
	10178.86	MW	2(−)
s_1	10240.48	MS	2(+)
	10262.41	WW	1(i)?
r_2	10379.79	MW	2(+)
p_1	10381.21	MW	1(o)
r_1	11878.90	MS	2(+)
	11961.29	W	1(i)?
	12061.92	W	2(+)
	12162.44	MW	1(i)
	12238.84	W	1(i)
	12258.96	W	1(i)
p_2	12271.51	WW	1(o)
r_2	12306.86	M	2(+)
q_2	12444.04	S	1→2
s_1	12482.96	S	2(+)
s_1	12484.56	S	2(+)
	12592.65	WW	1(i)?
q_1	12744.25	S	1→2
p_1	12841.24	M	1(o)
p_2	12903.16	WW	1(o)
	13050.32	W	1(i)
	13242.99	WW	2(+)
	13336.58	WW	2(+)
	13390.07	WW	1(i)
╫	13415.33	MW	2(+)
╫	13416.57	MW	2(−)
r_2	13464.76	M	2(+)
s_1	13528.26	MS	2(+)
p_2	13592.68	WW	1(o)
	13799.79	W	1(i)
	13897.60	W	1(i)
s_1	13932.46	MS	2(+)
r_1	14033.54	S	2(+)
q_2	14044.39	S	1→2)
	14098.16	W	1(i)
p_1	14115.35	M	1(o)
	14215.99	MW	1(i)
p_2	14339.06	WW	1(o)
	14437.75	M	1(i)
s_1	14494.64	S	2(+)
r_2	14771.22	M	2(+)
q_1	14910.71	MS	1→2
	15047.43	W	1(i)
	15094.56	WW	1(i)?
	15109.45	W	1(i)
p_2	15141.72	W	1(o)
s_1	15146.16	S	2(+)
	15252.52	W	2(+)?
s_1	15357.69	S	2(+)
p_1	15397.72	MS	1(o)
q_2	15842.14	S	1→2
	15907.61	M	1(i)
p_2	15999.68	W	1(o)
s_1	16088.98	S	2(+)
s_1	16089.84	S	2(+)
r_2	16240.64	MW	2(+)
r_1	16410.63	S	2(+)
s_1	16661.73	S	2(+)
p_1	16670.02	MS	1(o)
	16681.80	MW	1(i)
s_1	16742.98	S	2(+)
p_2	16911.46	W	1(o)
	16947.65	W	1(i)
s_1	17042.46	MS	2(+)
s_1	17108.99	MS	2(+)
s_1	17200.97	MS	2(+)
	17228.32	WW	2(+)
	17237.77	WW	2?
	17238.04	WW	2?
	17263.86	WW	1?
q_1	17302.03	MS	1→2
	17345.10	W	2(+)
	17345.70	W	2(+)
	17360.58	W	2(+)
	17361.10	WW	2(+)
	17475.66	MW	2(+)
	17476.28	MW	2(+)
	17585.33	WW	2(+)
	17660.45	WW	1(i)
q_2	17849.46	S	1→2
p_2	17874.52	W	1(o)
r_2	17887.20	M	2(+)
p_1	17913.74	MS	1(o)
	18023.18	W	2(+)
	18562.40	W	1(i)
	18680.50	MW	2(+)
p_2	18884.52	WW	1(o)
r_1	19013.55	MS	2(+)
p_1	19110.66	S	1(o)
r_2	19724.62	MS	2(+)
	19776.40	W	1?
	19776.66	WW	1?
	19776.84	W	1?
q_1	19919.56	MS	1→2
p_2	19933.82	W	1(o)

Table II. (Continued)

Frequency in Mc/sec.	Intensity	Stark-effect
q_2 20076.00	S	1→2
p_1 20243.54	MS	1(o)
20325.82	W	1(i)
20547.17	MS	1(i)
20831.28	MS	1(i)
20911.74	WW	1(i?)
20947.05	WW	1(i?)
+ 20971.70	W	2(+)
+ 20973.15	W	2(−)
p_2 21013.62	W	1(o)
21019.17	MW	1(i)
♯ 21027.06	WW	2(+)
♯ 21035.13	WW	2(−)
21051.62	MW	1(i)
21244.56	WW	1(i?)
p_1 21297.12	MS	1(o)
21477.62	WW	2(+)
21614.33	W	1(i)
21712.65	MW	1(i)
r_2 21765.23	M	2(+)
r_1 21842.31	MS	2(+)
21930.00	MW	1(i)
21931.48	MW	1(i)
p_2 22112.46	W	1(o)
p_1 22258.35	MS	1(o)
q_2 22527.93	MS	1→2
q_2 22528.21	MS	1→2
22581.49	M	1(i)
22588.42	W	1(o?)
22722.62	S	1(i)
q_1 22759.22	MS	1→2
q_1 22759.63	M	1→2
22765.62	WW	1?
22980.95	M	2(+)
22981.60	M	2(+)
p_1 23119.06	MS	1(o)
p_2 23219.21	MW	1(o)
* 23300.79	W	2(+)
* 23311.31	W	2(−)
23315.55	MW	1(i)
23340.67	MS	2(+) $5_{14}\to4_{22}$
23341.31	M	2(+) $5_{14}\to4_{22}$
23409.16	M	1(i)
23424.70	WW	1(i)?
23429.42	M	1(i)
23432.84	WW	2?
23449.39	M	2(−) $5_{23}\to6_{15}$
23449.65	W	2(−) $5_{23}\to6_{15}$
23450.17	M	2(−) $5_{23}\to6_{15}$
23683.17	M	1(i)
23861.40	MS	1(i)
p_1 23873.61	MS	1(o)
r_2 24019.01	M	2(+)
24078.75	M	1(i)
p_2 24320.57	MW	1(o)
24382.16	WW	2(+)
p_1 24520.75	M	1(o)
r_1 24889.42	MS	2(+)
r_1 24889.80	M	2(+)
24993.76	WW	?
p_1 25063.65	MS	1(o)
q_2 25206.62	MS	1→2
p_2 25401.99	W	1(o)
p_1 25507.61	M	1(o)
q_1 25810.49	M	1→2
q_1 25810.96	MW	1→2
p_1 25861.23	M	1(o)
p_1 26134.72	M	1(o)
p_1 26339.57	M	1(o)
p_2 26448.15	W	1(o)
p_1 26487.00	M	1(o)
r_2 26493.54	M	2(+)
r_2 26493.82	MW	2(+)
p_1 26588.65	MW	1(o)
p_1 26654.86	M	1(o)
p_1 26695.43	M	1(o)
p_1 26717.89	MW	1(o)
p_1 26728.77	W	1(o)
p_1 26733·54	WW	1(o?)
27323.13	W	2(+)
p_2 27445.47	MW	1(o)
27504.75	W	1(o?)
27758.40	W	1(i?)
q_2 28107.75	MS	1→2
r_1 28142.85	MS	2(+)
28183.46	W	2(+)
28186.02	W	2(+)?
p_2 38380.93	M	1(o)
28515.45	M	1(i)
28533.92	WW	1?
q_1 29055.20	M	1→2
29138.85	W	1(i)
29147.37	W	1(i)
r_2 29191.47	MW	2(+)
p_2 29244.20	W	1(o)

sured frequencies and intensities are listed in Table II. The estimated maximum errors of measurements must lie within ±0.10 Mc/sec for weaker lines (W) and within ±0.04 Mc/sec or better for stronger lines (MS, S).

The absolute intensities of lines have not been measured, because we have no calibrated attenuator. And the observed relative intensities are given by S, MS, M, MW, W, and WW in order of strength. The peak absorption coefficient has been estimated for S lines, $\alpha > 1\sim2\times10^{-6}\,\text{cm}^{-1}$; for M lines, $1\sim2\times10^{-6}\,\text{cm}^{-1} > \alpha > 1\sim2\times10^{-7}\,\text{cm}^{-1}$; and for W lines, $\alpha < 1\sim2\times10^{-7}\,\text{cm}^{-1}$. The minimum detectable absorption lines have intensities less than $3\times10^{-8}\,\text{cm}^{-1}$ throughout the whole frequency range.

The observed lines are classified into five kinds according to their Stark effects, though the Stark components of most lines are not

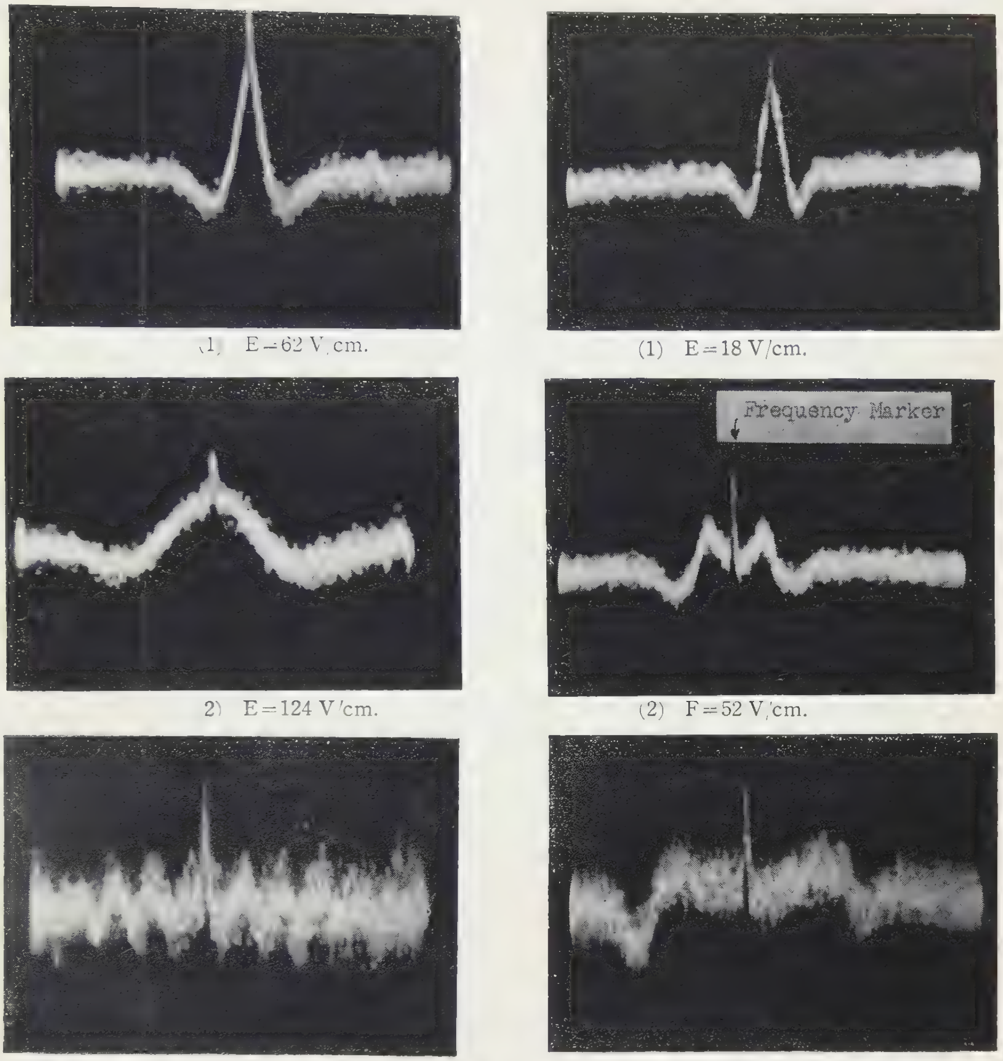

(1) E=62 V/cm.

(2) E=124 V/cm.

(3) E=414 V/cm.

(a)

(1) E=18 V/cm.

(2) E=52 V/cm.

(3) E=104 V/cm.

(b)

Fig. 5. CRO pictures of first-order Stark patterns. (a) 15907.61 Mc/sec line showing 1(i) Stark effect, (b) 17913.74 Mc/sec line showing 1(o) Stark effect.

perfectly resolved. The lines which show first-order Stark effects are denoted by 1(i) or 1(o), according as the inner or outer Stark components are stronger. The lines which show second-order Stark effects are denoted by 2(+) or 2(−), according as the components shift to higher or lower frequency side with increasing Stark field. The remaining lines denoted by (1→2) show some peculiar Stark effects. The Stark components split into two main groups: at weaker Stark field ($E \lesssim 50$ V/cm) one group shifts to the higher frequency side and the other to the lower frequency side showing a first-order Stark effect, while at stronger Stark field both shift to higher frequency side roughly proportional to the square of the Stark field, showing a second-order Stark effect. A typical example of the Stark splitting of two main components of such a line (1→2) is illustrated in Fig. 4 as a function of the applied field.

8. Stark Patterns

Fig. 5 shows typical CRO pictures of first-order Stark patterns of lines. (a) is an example of the line denoted by 1(i) and (b) is that denoted by 1(o). Fig. 6 and Fig. 7 show the field dependence of the Stark patterns of

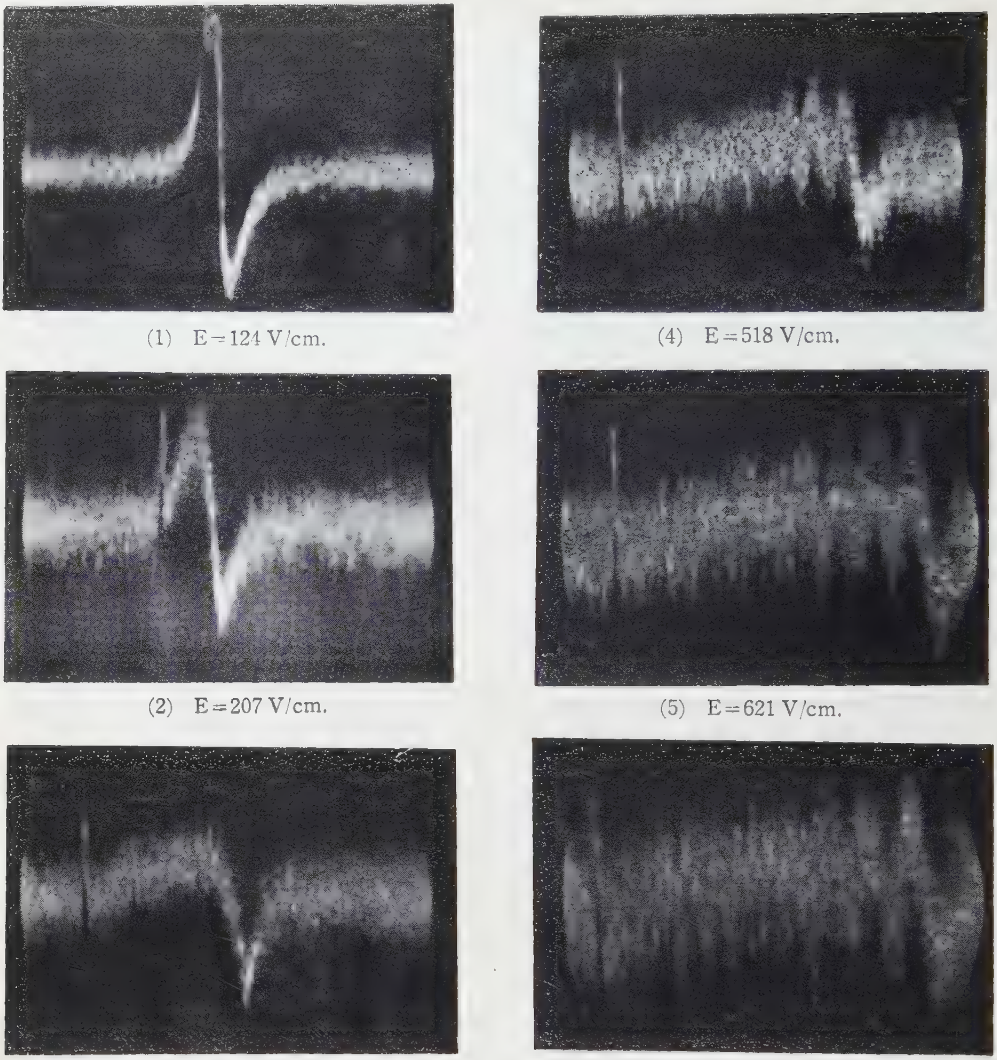

(1) E=124 V/cm.

(2) E=207 V/cm.

(3) E=414 V/cm.

(4) E=518 V/cm.

(5) E=621 V/cm.

(6) E=745 V/cm.

Fig. 6. CRO picture of a 2(+) line (ν_0=17200.97 Mc/sec).

2(+) and (1→2) lines respectively. The frequency marker pip on each picture indicates position of the line when the Stark field is not applied. Because we have used small sine wave modulation with a phase sensitive detector, the first derivative of the line shape is observed on the CRO screen for the line which shows second-order Stark effect. As to the line which show first-order Stark effect, the Stark pattern is symmetrical about the original frequency and it resembles the second derivative of the line shape at small Stark field.

There are several sets of paired lines, denoted by ∗, +, ‡, and ♯ in Table II, which form mirror images respectively. The Stark components of the lower frequency lines move towards higher frequency side with increasing Stark field (2(+)), and the higher frequency lines towards lower frequency side (2(−)). The strongest image pair found around 23 kMc/sec is shown in Fig. 8. We can see another line of 1(i) at the right hand side of the same picture. With increasing Stark voltage, the Stark effects of paird lines become approximately first-order. This is because the forbidden lines appear with increasing Stark field and their Stark components merge with those of allowed lines. Similar Stark effects have also been found in the spectrum of methylalcohol by Hughes, Good, and Coles[13], and they were ascribed to the

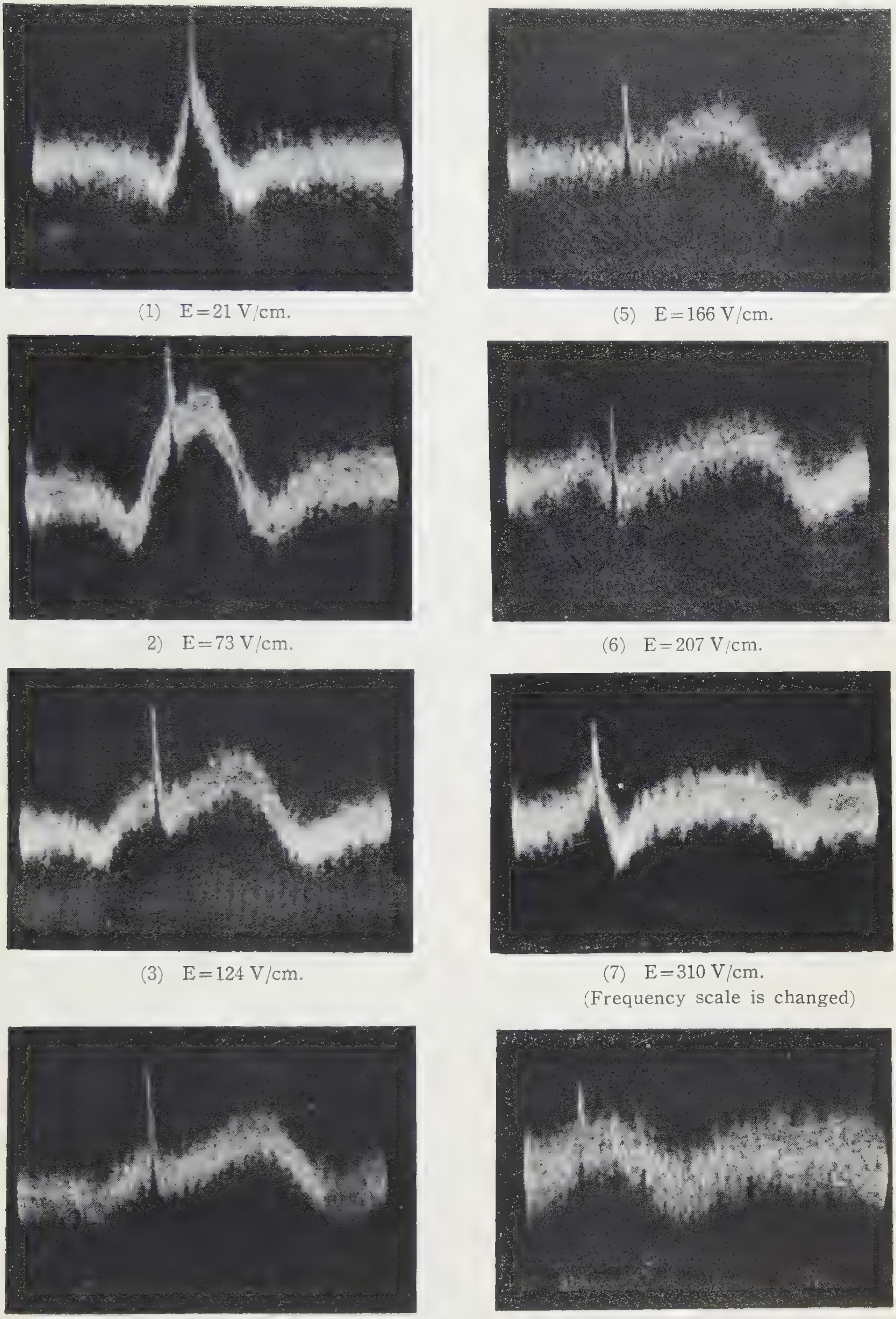

(1) E=21 V/cm.

(2) E=73 V/cm.

(3) E=124 V/cm.

(4) E=145 V/cm.

(5) E=166 V/cm.

(6) E=207 V/cm.

(7) E=310 V/cm.
(Frequency scale is changed)

(8) E=435 V/cm.

Fig. 7. CRO picture of a (1→2) line (ν_0=17302.03 Mc/sec).

K-type doublings of $\Delta J=\pm1$, $\Delta K=\mp1$ lines.

As to the Stark effect of the asymmetric rotor, Golden and Wilson have shown that the intensities of the Stark components are proportional to M^2 for the transitions $\Delta J=0$ and to $J^{*2}-M^2$ for the transitions $\Delta J=\pm1$,

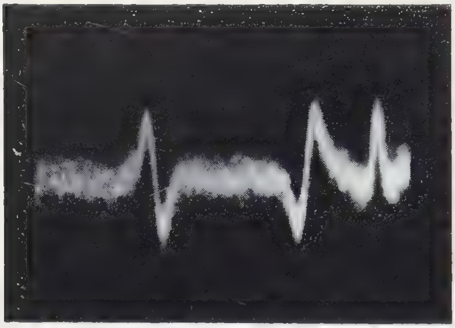

E=100 V/cm.

Fig. 8. CRO picture of image pair lines (ν_0= 23300.79 and 23311.31 Mc/sec).

where J^* is the larger value of J of the levels concerned. In the case of a first-order Stark effect the component lines are symmetrically arranged about the frequency of the original line according to the formula, $\Delta\nu=BME$. Intensities of inner components are stronger when $\Delta J=\pm1$, and outer components are stronger when $\Delta J=0$. The lines denoted by 1(i) in Table II is, therefore, ascribed to the transition $\Delta J=\pm1$, while the lines denoted by 1(o) to the transition $\Delta J=0$.

In the case of a second-order Stark effect, the displacement of each component is given by $\Delta\nu=(C+DM^2)E^2$, so that the stronger components are more closely spaced than the weaker components, when $\Delta J=\pm1$, while they are more separately spaced, when $\Delta J=0$. However, Stark components were not completely resolved except for a few lines, so that it has not been determined whether $\Delta J=\pm1$ or $\Delta J=0$ for most lines denoted by 2(+).

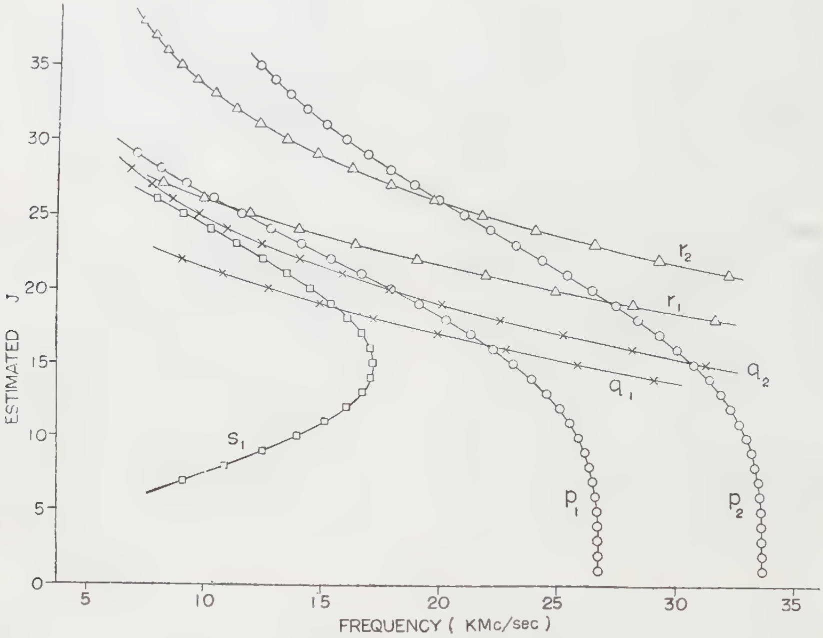

Fig. 9. Frequencies of series of lines arranged according to their estimated rotational quantum number, J.

Table III. Coefficients of the powers of $J(J+1)$ in the expression (10) for the frequencies of the the lines of p_1 and p_2 series (in Mc/sec).

	p_1	p_2
ν_0	26734.98	33638.93
a	-0.5769	-0.9637
b	-0.071173	-0.051535
c	0.4982×10^{-4}	-0.1896×10^{-4}
d	-0.1243×10^{-6}	0.2368×10^{-6}

The above values were determined from the first five alternate lines.

The peculiar Stark effect (1→2) may be explained by an intermediate coupling between the nuclear quadrupole effect and Stark effect. Somewhat similar effects have been found in the inversion spectrum of ammonia by Coles, Good, and others[14]. Thus Stark effect of a line of (1→2) should be second-order, if there were no quadrupole coupling. However,

Table IV. Lines of p series.

a) p_1 series

Frequency in Mc/sec.	1st Difference	2nd Difference	3rd Difference	4th Difference
26733.54				
	4.77			
26728.77		−6.11		
	10.88		5.47	
26717.89		−11.58		−1.06
	22.46		6.53	
26695.43		−18.11		−1.00
	40.57		7.53	
26654.86		−25.64		−2.27
	66.21		9.80	
26588.65		−35.44		−0.54
	101.65		10.34	
26487.00		−45.78		−1.30
	147.43		11.64	
26339.57		−57.42		0.42
	204.85		11.22	
26134.72		−68.64		−0.27
	273.49		11.49	
25861.23		−80.13		1.28
	353.62		10.21	
25507.61		−90.34		1.61
	443.96		8.60	
25063.65		−98.94		3.30
	542.90		5.30	
24520.75		−104.24		2.13
	647.14		3.17	
23873.61		−107.41		4.42
	754.55		−1.25	
23119.06		−106.16		4.39
	860.71		−5.64	
22258.35		−100.52		2.53
	961.23		−8.17	
21297.12		−92.35		4.88
	1053.58		−13.05	
20243.54		−79.30		2.21
	1132.88		−15.26	
19110.66		−64.04		1.98
	1196.92		−17.24	
17913.74		−46.80		0.98
	1243.72		−18.22	
16670.02		−28.58		0.29
	1272.30		−18.51	
15397.72		−10.07		−0.18
	1282.37		−18.33	
14115.35		8.26		(−2.17)
	1274.11		(−16.16)	
12841.24		(24.42)		(−1.23)
	(1249.69)		(−14.93)	
(11591.55)		(39.35)		(−1.32)
	(1210.34)		(−13.61)	
10381.21		(52.96)		(−1.43)
	1157.38		(−12.18)	
9223.83		65.14		(−1.53)
	1092.24		−10.65	
8131.59		75.79		
	1016.45			
7115.14				

b) p_2 series

Frequency in Mc/sec.	1st Difference	2nd Difference	3rd Difference	4th Difference
33636.8				
	5.3			
33631.50		−6.3		
	11.58		2.9	
33619.92		−9.24		−2.8
	20.82		5.72	
33599.10		−14.96		−0.05
	35.78		5.77	
33563.31		−20.73		−1.45
	56.51		7.22	
33506.81		−27.95		−0.68
	84.46		7.90	
33422.35		−35.85		−1.50
	120.31		9.40	
33302.04		−45.25		0.56
	165.56		8.84	
33136.48		−54.09		−0.06
	219.65		8.90	
32916.83		−62.99		0.21
	282.64		8.69	
32634.19		−71.68		0.97
	354.32		7.72	
32297.87		−79.40		2.65
	433.72		5.07	
31846.15		−84.47		1.11
	518.19		3.96	
31327.96		−88.43		2.54
	606.62		0.42	
30721.34		−88.85		3.07
	695.47		−2.65	
30025.87		−86.20		1.95
	781.67		−4.60	
29224.20		−81.60		4.81
	863.27		−9.41	
28380.93		−72.19		0.92
	935.46		−10.33	
27445.47		−61.86		2.69
	997.32		−13.02	
26448.15		−48.84		0.56
	1046.16		−13.58	
25401.99		−35.26		1.74
	1081.42		−15.32	
24320.57		−19.94		−0.77
	1101.36		−14.55	
23219.21		−5.39		−1.25
	1106.75		−13.30	
22112.46		7.91		−2.17
	1098.84		−11.13	
21013.62		19.04		0.33
	1079.80		−11.46	
19933.82		30.50		−2.66
	1049.30		−8.80	
18884.52		39.30		−1.16
	1010.00		−7.64	
17874.52		46.94		−3.30
	963.06		−4.34	
16911.46		51.28		−1.80
	911.78		−2.54	
15999.68		53.82		−1.06
	857.96		−1.48	
15141.72		55.30		−0.50
	802.66		−0.98	
14339.06		56.28		−0.40
	746.38		−0.58	
13592.68		56.86		0.43
	689.52		−1.01	
12903.16		57.87		
	631.65			
12271.51				

Table V. Lines of q series.

a) q_1 series

Frequency in Mc/sec.	1st Difference	2nd Difference	3rd Difference	4th Difference
29055.20				
	3244.55			
25810.65		193.26		
	3051.29		−18.23	
22759.36		211.49		−7.45
	2839.80		−10.78	
19919.56		222.27		−6.84
	2617.53		−3.94	
17302.03		226.21		−5.29
	2391.32		1.35	
14910.71		224.86		(−4.60)
	2166.46		(5.95)	
12744.25		(218.91)		(−4.26)
	(1947.55)		(0.21)	
(10796.70)		(208.70)		
	(1738.85)			
9057.85				

b) q_2 series

Frequency in Mc/sec.	1st Difference	2nd Difference	3rd Difference	4th Difference
31221.00				
	3113.25			
28107.75		212.12		
	2901.13		−10.46	
25206.62		222.58		−6.56
	2678.55		−3.90	
22528.07		226.48		−4.85
	2452.07		0.95	
20076.00		225.53		−5.36
	2226.54		6.31	
17849.46		219.22		−3.34
	2007.32		9.65	
15842.14		209.57		−2.52
	1797.75		12.17	
14044.39		197.40		(−1.47)
	1600.35		(13.64)	
12444.04		(183.76)		(−1.65)
	(1416.59)		(15.29)	
(11027.45)		(168.47)		(−0.10)
	(1248.12)		(15.39)	
9779.33		(153.08)		(0.80)
	1095.04		(14.59)	
8684.29		138.49		(−0.28)
	956.55		14.87	
7727.74		123.62		
	832.93			
6894.81				

Table VI. Lines of r series.

a) r_1 series

Frequency in Mc/sec.	1st Difference	2nd Difference	3rd Difference	4th Difference
31583.64				
	3440.79			
28142.85		187.49		
	3253.30		−18.57	
24889.55		206.06		−6.15
	3047.24		−12.42	
21842·31		218.48		−5.06
	2828.76		−7.36	
19013.55		225.84		−7.37
	2602.92		0.01	
16410.63		225.83		−3.37
	2377.09		3.38	
14033.54		222.45		−4.38
	2154.64		7.76	
11878.90		214.69		−4.28
	1939.95		12.04	
9938.95		202.65		
	1737.30			
8201.65				

b) r_2 series

Frequency in Mc/sec.	1st Difference	2nd Difference	3rd Difference	4th Difference
32112.71	2921.24			
29191.47	2697.84	223.40	0.18	
26493.63	2474.62	223.22	2.38	−2.20
24019.01	2253.78	220.84	7.67	−5.29
21765.23	2040.61	213.17	9.98	−2.31
19724.62	1837.42	203.19	12.33	−2.35
17887.20	1646.56	190.86	13.72	−1.39
16240.64	1469.42	177.14	14.18	−0.46
14771.22	1306.46	162.96	14.40	−0.22
13464.76	1157.90	148.56	(14.32)	(0.08)
12306.86	(1023.66)	(134.24)	(13.99)	(0.33)
(11283.20)	(903.41)	(120.25)	(12.54)	(1.45)
10379.79	795.70	(107.71)	(11.81)	(0.73)
9584.09	699.80	95.90	11.40	(0.41)
8884.29	615.30	84.50	(10.39)	(1.01)
8268.99	(541.19)	(74.11)	(7.08)	(3.31)
*(7727.80)	(474.16)	(67.03)		
7253.64				

* This line is accidentally in coinsidence with the strong line of q_2 series.

Table VII. Lines of s_1 series.

Frequency in Mc/sec.	1st Difference	2nd Difference	3rd Difference	4th Difference
9127.88	(−1730.17)			
(10858.05)	(−1626.51)	(−103.66)	(74.95)	
12484.56	−1447.90	(−178.61)	(55.59)	(19.36)
13932.46	−1213.70	−234.20	36.68	(18.91)
15146.16	−942.82	−270.88	17.94	18.74
16088.98	−654.00	−288.82	−0.83	18.77
16742.98	−366.01	−287.99	−13.96	13.13
17108.99	− 91.98	−274.03	−23.54	9.58
17200.97	158.51	−250.49	−28.27	4.73
17044.46	380.73	−222.22	−31.06	2.79
16661.73	571.89	−191.16	−30.90	−0.16
16089.84	732.15	−160.26	−29.36	−1.54
15357.69	863.05	−130.90	−27.57	−1.79
14494.64	966.38	−103.33	−24.41	−3.16
13528.26	1045.30	−78.92	(−21.86)	(−2.55)
12482.96	(1102.36)	(−57.06)	(−19.30)	(−2.56)
(11380.60)	(1140.12)	(−37.76)	(−16.79)	(−2.51)
10240.48	1161.09	(−20.97)	(−14.16)	(−2.63)
9079.39	1167.90	−6.81		
7911.49				

Table VIII. Assignment of series.

Series	Assignment	Frequency of the Initial Line		Nuclear Statistical Weight	Magnitude of Inversion Doubling	
	$K,\tau,n\rightarrow K',\tau',n'$	Observed (Mc/sec)	Calculated (Mc/sec)		Observed (Mc/sec)	Calculated (Mc/sec)
p_1	0,3,1→1,2,1	26,733.54	(26,700)	3	6,903.3	(6,900)
p_2	0,3,1→1,2,1	33,636.8	(33,600)	1		
q_1	0,1,0→1,3,0		79,000	3	~5,000	10,000
q_2	0,1,0→1,3,0		89,000	1		
r_1	1,3,1→2,2,1		102,000	3	~10,000	20,000
r_2	1,3,1→2,2,1		122,000	1		
s_1	1,3,1→0,1,1	~0	0	3	≳30,000	35,000
s_2	1,3,1→0,1,1		35,000	1		

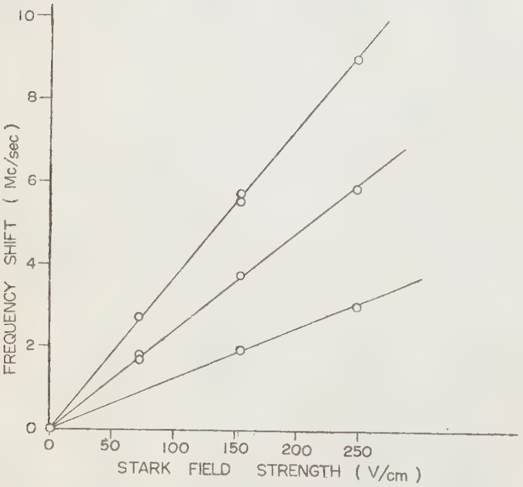

Fig. 10. Stark patterns of the third line of p_1 series (ν_0=26717.89 Mc/sec).

at intermediate external field where the Stark energy and the quadrupole energy are the same order of magnitudes, Stark pattern of the line is appreciably distorted and shows a peculiar effects. At zero external field, these lines show doublet structures by the nuclear quadrupole effect as can be seen in Table II, though some of them could not be resolved.

§ 4. Analysis and Assignment

Observed lines are divided into three classes of transitions as follows.

9. Lines of $\Delta J=0$, $\Delta K=\pm 1$

Lines showing first-order Stark effects, 1(o) correspond to the transitions, $\Delta J=0$, $\Delta K=\pm 1$, and $\Delta(K+\tau)=0$. Their frequencies form two well-defined series* which are denoted by p_1 and p_2 in Table II. The frequencies of the lines in each series can be expressed by a power series expansion in $J(J+1)$ as follows.

$$\nu=\nu_0+aJ(J+1)+bJ^2(J+1)^2+cJ^3(J+1)^3+\cdots . \qquad (10)$$

This is in good agreement with the theoretical consideration on the transitions $\Delta J=0$, $\Delta K=\pm 1$. The values of the coefficients are given in Table III.

We have found five other series in the observed range. Three of them have second order Stark effects 2(+) and the others have (1→2). The formers are denoted by r_1, r_2, and s_1, while the latters are denoted by q_1 and q_2 in Table II. These series also correspond undoubtedly to the transitions $\Delta J=0$, $\Delta K=\pm 1$, as well as p series. Frequencies of the lines belonging to each series are regularly spaced as can be seen by taking the successive differences. They are shown in Tables IV, V, VI, and VII.**

Frequencies of lines belonging to seven series are plotted in Fig. 9 against estimated J values. The starting points of q, r, and s series are out of the observed range, while those of p series fall in the range.

From these Tables and Fig. 9, it may be infered that each of the pairs p_1-p_2, q_1-q_2, and r_1-r_2 is the pair of transitions associated with inversion doubling, because the successive differences or expansion coefficients in the form, Eq. (10), have close resemblance between the partners of each pair. The partner of s_1 series, however, could not be found in the observed range.

Now we must assign quantum numbers J, K, τ, and n to each pair of series.

First, we have examined the precise pattern of Stark effect on the third line of p_1 series, which is shown in Fig. 10. Measurements were done only on the lower frequency side, because the Stark components on the higher frequency side were obscured by the disturbance of another line components. J values of this line is determined as 3 from Fig. 10, so that the first line of the series must have $J=1$ and the K-transition must be $0\rightleftarrows 1$ for this series.

From Fig. 2 of 3, we know that within the acceptable value of the potential height H the first-order series of the ground vibrational state $n=0$ can not be found in the observed range. Therefore, p series is assigned to be $K, \tau, n = 0, 3, 1 \rightleftarrows 1, 2, 1$ definitely. If we take the transitions $K, \tau, n = 0, 3, 1 \to 1, 2, 1$, the height of the potential barrier will be about 680 cm^{-1}, while if the transitions are in the reverse direction, $K, \tau, n = 0, 3, 1 \leftarrow 1, 2, 1$, it will be about 500 cm^{-1}. If the former is true the lower frequency partner of the inversion pair must be three times stronger than the higher frequency one, and vice versa for the latter case according to the discussion of 5. Intensity measurements show that p_1 series is roughly three times stronger than p_2 series. Then it is concluded that the transitions for p series must be $K, \tau, n = 0, 3, 1 \to 1, 2, 1$ and that the height of the potential barrier is about 680 cm^{-1}.

Secondly, the second-order series q, r, and s are to be discussed. Among them the q series show a very peculiar Stark effect (1→2) and seem to be more or less stronger than the others and about twice as strong as p series. The starting points of q series seem to fall in the higher frequency region than we have studied. Thus, we may assign them to $n=0$ with second-order Stark effect, corresponding to the transitions $K=0\to 1$, $\tau=1\to 3$. Although the starting points of these series may be in 80 kMc/sec region, the frequencies of the lines may be remarkably lowered with increasing J values by the large K-type doubling effects. This is confirmed by the rather large value of spacings of the lines of these series, Rough estimations of K-type splittings indicate that the J values of observed lines are from about 15 to 30. But this is not verified by experiment because the Stark patterns were not completely resolved for these lines.

If these assignments are correct, r and s series have to be allotted to the first excited state $n=1$. Because the arrangements of r series are somewhat similar to those of q series, their starting positions must also lie in the higher frequency region. This pair of series, therefore, are determined to correspond to the transitions, $K, \tau, n = 1, 3, 1 \to 2, 2, 1$. r_1 series is stronger than r_2 series confirming the intensity consideration on the inversion pair belonging to these transitions.

---

* p_1 series was first found by D. R. Lide.

** Recently, Lide followed these series up to 34 kMc/sec range, where the starting point of p_2 series was found, and his results are also quoted in these Tables. Some lines of series, q, r and s could not be observed by want of microwave source in the frequency range between 10,300 and 11,800 Mc/sec. Their frequencies, however, can be estimated from those of adjacent lines and are listed with parentheses in these Tables.

Lastly, the starting point of s_1 series seems to lie in the lower frequency region. As the barely resolved Stark pattern of the lowest J line indicates seven or eight components, J values of the observed members are probably from 7 or 8 to 25 or 26. By a extrapolation of frequencies up to the line of $J=1$ the starting point of the series is estimated to be nearly zero. Transitions for this series, therefore, are obviously assigned to K. τ, n = 1, 3, 1→0, 1, 1. As to the weaker partner of inversion, which could not be found in the observed range, semi-empirical estimation show that the magnitude of the doubling of s series is considerably large ($\sim$35 kMc/sec) so that the partner may be out of the observed range.

Our assignments of the series are listed in Table VIII. The calculated values for the starting points and magnitudes of inversion doubling assuming the values in parentheses for p series are also listed in the Table VIII. Estimated experimental values are also given for comparison. The theoretical expectation that the magnitudes of inversion doubling should depend considerably on the quantum numbers, K, τ, and n, is confirmed so far as the order of magnitude is concerned. The experimental estimations of J have some uncertainties and the theory is very crude, and the agreement seems to be satisfactory.

There remains a little possibility that one of the r series is a partner of s_1 series. In order to confirm our assignments it is necessary to study the spectrum in the millimeter wave region.

10. Lines of $\Delta J=\pm1$, $\Delta K=\mp1$

Lines which belong to the transitions $\Delta J=\pm1$, $\Delta K=\mp1$ may be divided into two cases.

(1) When the value of $K+\tau-1$ is not divisible by three, there is an intrinsic degeneracy of the two rotational levels with the same J. Then the line shows a first-order Stark effect 1(i). Several stronger and lower J lines, the Stark pattern of which have been partially resolved, are expected to belong to this case.

(2) When the value of $K+\tau-1$ is divisible by three, the K-type degeneracy is removed and the line is split into image pair of lines. The Stark effects of the doublet show the second-order Stark effects 2(+) and 2(−) for the partner in the lower and higher frequency respectively. Lide assigned three transitions of this kind, $5_{1,4}\rightarrow4_{2,2}(\tau=3\rightarrow2,\ n=0)$, $5_{1,5}\rightarrow4_{2,3}(\tau=3\rightarrow2, n=0\rightarrow0)$, and $5_{2,3}\rightarrow6_{1,5}(\tau=2\rightarrow3, n=0\rightarrow0)$, two of which were found in our frequency range and confirmed. He determined the rotational constants of methylamine from these lines, assuming that the molecule is a rigid rotor, though the other rotational lines are inconsistent with his results. We could not find any lines predicted from his constants in the observed range, while about ten lines of other image pairs have been observed. This inconsistency may be explained if we consider the effect of inversion doubling and hindered rotation. But the quantitative discussion is obliged to be deferred till the inversion partner of the assigned lines will be observed. We suppose that they lie in the slightly higher frequency region than the observed range.

The separation of an image pair depends predominantly on the lower K value of the levels concerned. Because the asymmetry parameter is very small for the molecule, the separation decreases rapidly with increasing K. Rough estimation from Wrang's formula shows that the separation is less than about 0.5 Mc/sec when $K\geq5$. On account of such close degeneracy, the lines of case (2) with higher K values show also the first-order Stark effects 1(i), which are hardly distinguished from those of case (1).

11. Lines of $\Delta J=0$, $\Delta K=0$

We have found some lines which probably correspond to the transitions between the levels of K-type doublets. These lines are listed in the first column of Table IX. We have tentatively assigned them to $K=1$ and $J=4\sim7$. Their intensities are so weak and the spacings are so large that the above assignment is ambiguous. Observed frequencies

Table IX. Lines corresponding to the K-type transitions.

Observed frequency in Mc/sec.	Frequency estimated from Wang's formula in Mc/sec.	J
8813.22	9000	4
13242.99	13500	5
18680.50	18900	6
24993.76	25200	7

are compared with the values estimated from the Wang's formula (6) which are shown in the second column of Table IX.

The effects of inversion doubling on these lines are expected to be too small to be observed.

§ 5. Conclusion

Seven series of lines belonging to the transitions $\Delta J=0$, $\Delta K=\pm 1$ have been analyzed and assigned, and from this assignment the height of potential barrier hindering internal rotation was determined to be about 680 cm^{-1}. This value is about twice as large as that in methylalcohol, consistent with the simple view that the hindering potential may be given by a sum of the contributions from two NH bonds, each being nearly equal to that of the OH bond in methylalcohol.

Inversion doublings were observed for the series of lines, and their magnitudes were found to depend on the rotational quantum numbers in agreement with the theoretical considerations.

Expansion coefficients in Eq. (10) for the frequencies of the lines of p_1 and p_2 series which are given in Table III are in good agreement with the values calculated theoretically using trial values for molecular constants. It is possible to determine the molecular constants of methylamine from these coefficients. The calculations are now being carried out.

Stark effect coefficients for the p_1 series is also in fair agreement with theoretical values calculated from estimated electric dipole moment.

Nuclear quadrupole effect was observed for some of the lines. The splittings of the lines corresponding to the transitions which involve the levels with $K=\pm 1$ and $K+\tau-1=3m$ were found to be larger than those of other lines. This can be explained by the effect of off-diagonal $K=-1\rightarrow 1$ matrix elements of the quadrupole hamiltonian which are non-vanishing since $\partial^2 V/\partial\xi^2 \not\fallingdotseq \partial^2 V/\partial\eta^2$. The peculiar Stark effect of q series may also be explained by the quadrbpole energy of the levels concerned.

Quadrupole coupling constants have been determined from the hyperfine structure of two lines $5_{1,4}\rightarrow 4_{2,2}$ and $5_{2,3}\rightarrow 6_{1,5}$. The results are $eQ\partial^2 V/\partial\zeta^2=2.2$ Mc/sec and $eQ(\partial^2 V/\eta^2-\partial^2 V/\partial\xi^2)=-5.6$ Mc/sec. These values are consistent with the splittings of other lines and also with the theoretical values calculated by assuming that the electronic structure around the nitrogen atom is similar to that in ammonia.

Most lines except the lines with Stark effect 1(i) have been assigned or examined. Only a strong doublet with quadrupole separation of 0.7 Mc/sec near 22,980 Mc/sec, showing second-order Stark effect could not been assigned. This doublet seems to belong to $\Delta J=\pm 1$, $\Delta K=\mp 1$ involving $K=1$, though the proper assignment has not yet been done. Other some ten weaker lines with the second-order Stark effects have also remained unassigned. They may correspond to the excited vibrational stae $n=2$ or higher rotational states or some others.

In order to avoid the ambiguity of the analysis and assignment it is desirable to trace the q and r series up to their starting points and to find the partner lines of inversion doubling and hindered rotation tripling of the lines of $\Delta J=\pm 1$. Therefore, we are now planning to study the spectrum in millimeter wave region.

Acknowledgement

We wish to express our hearty thanks to Prof. M. Kotani and Prof. D. M. Dennison for the continued interest in this work, and to Dr. D. R. Lide for sending his unpublished work. This work was financially supported by grants in aid for Fundamental Scientific Research of the Ministry of Education.

References

1) J. S. Koehler and D. M. Dennison: Phys. Rev. **57** (1940) 1006.

2) D. G. Burkhard and D. M. Dennison: Phys. Rev. **84** (1951) 408.

3) E. V. Ivash and D. M. Dennison: J. Chem. Phys. **21** (1953) 1804.

4) J. G. Aston, C. W. Siller and G. H. Messerly: J. Am. Chem. Soc. **59** (1937) 1743.

5) J. G. Aston and P. M. Doty: J. Chem. Phys. **8** (1940) 743.

6) E. N. Lassettre and L. B. Dean, Jr.: J. Chem. Phys. **17** (1949) 317.

7) D. M. Dennison and G. E. Uhlenbeck: Phys. Rev. **41** (1932) 313.

8) W. D. Hershberger and J. Turkevitch: Phys. Rev. **71** (1947) 554.

9) K. Shimoda and T. Nishikawa: J. Phys. Soc. Japan **8** (1953) 133, 425.

10) D. R. Lide, Jr.: J. Chem. Phys. **20** (1952) 1812; **21** (1953) 571.

11) S. C. Wang: Phys. Rev. **34** (1929) 243.

12) M. T. Weiss and M. W. P.Strandberg: Phys. Rev. **83** (1951) 567.

13) R. H. Hughes, W. E. Good and D. K. Coles: Phys. Rev. **84** (1951) 418.

14) D. K. Coles, W. E. Good, J. K. Bragg and A. H. Sharbaugh: Phys. Rev. **82** (1951) 877.

JOURNAL OF THE PHYSICAL SOCIETY OF JAPAN Vol. 9, No. 6, NOV.—DEC., 1954

Optical Properties of Cadmium Sulfide in Glass

By Goro KUWABARA

Department of Physics, Faculty of Science, University of Tokyo

(Received July 9, 1954)

The optical properties of glasses containing CdS were measured for a few specimens of different heat treatment. The absorption edge shifts towards longer wavelengths as the reheating progresses. However, its shape and temperature dependence are similar to those of the single crystal. The maximum wave lengths of luminescent and excitation spectra also shift according with the absorption edge and the linear relation exists between those wavenumbers. From these results, it may be infered that the optical properties of these glasses are due to CdS crystals, and their changes show that the energy gap between the filled and the conduction band in the crystals decreases with reheating, which is probably caused by the change in the lattice constants of the crystal.

§ 1. Introduction

Gadmium sulfide, which has been studied as a luminescent material has recently attracted much attention as an useful radiation detector because of its large photoresponse, and many results have been reported. As to the optical properties, though there is a slight difference according to the specimens, it is granted that cadmium sulfide, whether it is a single crystal or an evaporated film shows a strong and structureless absorption in shorter wavelengths than ca. 510 mμ, which is assumed to correspond to the electronic transition from the filled to the conduction band.[1] While, when cadmium sulfide powder is precipitated from the sulphate solution, the colour of the powder varies from light yellow to orange according to the conditions in precipitation. The similar phenomenon occurs for many substances; especially in antimony-trisulfide, the colour changes from orange to black. These great differences in colour can not be explained only as an apparent phenomenon caused by the variation in the size or the form of the powder, that is, the change in the ratio of the transmitted to the reflected light, and it may be inferred that they are due to the change in the electronic structure. While, the yellow glass, that is the soda-lime silicate glass containing CdS, shows no absorption in the visible range when quenched from the melt, it shows visible colour when reheated above 500°C~600°C and cooled slowly. According to the time or temperature of reheating, the colour of the glass varies from light to deep yellow, and moreover glasses show visible luminescence when irradiatee by the near-ultraviolet light. The luminescence of the powder or the single crystal of CdS ordinarily lies in the infrared region. These phenomena were described or discussed by Jaeckel[2] and Weyl[3] but the detailed study has not been reported. Although it is uncertain whether the colour change in CdS glass and in the precipitated powder occurs from the same origin, it seems to us that the detailed measurement of these phenomena is useful for the understanding of the effect of the size or the state of the crystal on the optical properties or the energy structure of insulators or semiconductors.

In this paper, the results of measurements on optical properties of four kinds of CdS glasses, which were taken from the same melt but were reheated to various degrees are described. The specimen No. 1 was quenched from the melting point and the reheating progressed in the order of No. 2, 3, and 4.*

§ 2. Optical Absorptions

The optical absorption were measured for these 4 specimens. The results were shown in Fig. 1. The absorption of No. 1 is almost the same as the glass without CdS and shows no absorption in the visible range. The absorption edge moves towards longer wave length without changing its shape as the reheating progresses, and lies at ca. 430, 460, and 485 mμ for Nos. 2, 3, and 4, respectively.

---

* The specimens used in the experiment were kindly furnished by Hoya Crystal Co. Tokyo.

By decreasing the temperatures, the absorption edge moves towards shorter wavelengths. The shift of the absorption edge is about -2.7×10^{-4} ev/°K between the room and the liquid air temperature, which is slightly smaller than that obtained for the single crystal. The temperature dependence of the absorption edge of this type indicates the broadening of the energy level by lattice vibrations or the existence of the electron-lattice interaction.[4] The variation of extinction coefficient is larger at shorter wavelengths than at the longer wavelengths.

§ 3. Luminescence

These glasses show bright luminescence when irradiated by violet or near ultra-violet lights. The spectral distribution of fluorescence and the excitation spectrum were shown in Fig. 3. The fluorescence, excited by the light of mainly 365 mμ, that is, the light from the high pressure mercury lamp combined with the filter containing NiO, was dispersed by a double monochromator and the spectral distribution was measured with the photomultiplier tube 1P22, whose spectral response was calibrated with the light from the tungsten filament of known brightness temperature. In Fig. 3, the relative height of the luminescent maximum for these specimens were obtained under the excitation light of the same intensity. The excitation spectrum was obtained by exciting the specimens with monochromatized light from the tungsten lamp through the monochrometor and the fluorescent light was measured by the photomultiplier tube combined with the suitable filters which cut off the scattered exciting light. The specimen No. 1 shows no fluorescence, and even the brightest fluorescence of No. 2 is far weaker than those of ordinary fluorescent materials. The spectral distributions show the broad band of a bell shape with the maxima at ca. 660, 720, and 770 mμ for Nos. 2, 3, and 4, respectively. The intensity of the luminescent lighe decreases with increased reheating. The excitation spectrum has a maximum near the absorption edge, which shifts towards longer wavelengths as the reheating progresses. The efficiency of luminescence decreases on the shorter wavelengths side. This feature resembles to that for the edge emission of CdS crystals at low

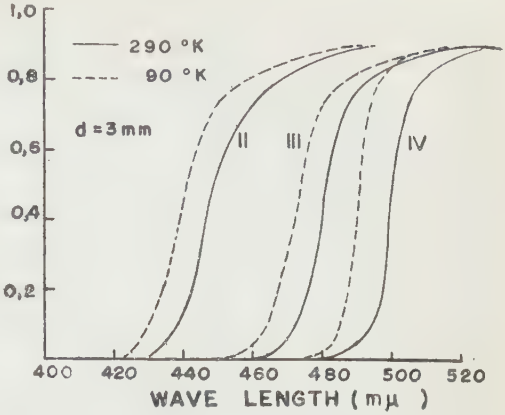

Fig. 1. Optical absorption of CdS glasses.

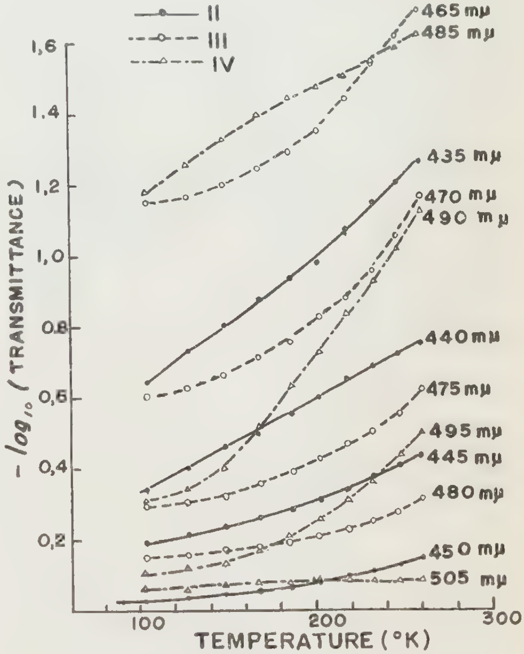

Fig. 2. Temperature dependence of extinction coefficients.

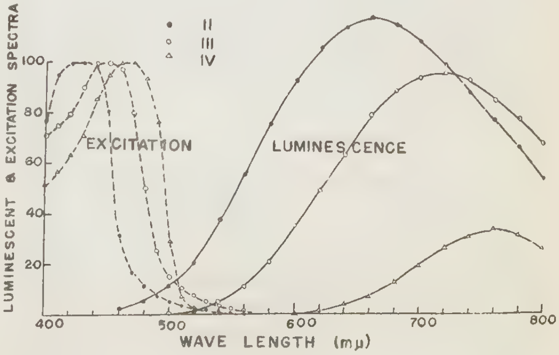

Fig. 3. Excitation (dotted lines) and luminescent spectra (full lines).

temperature.5) The luminescent intensity was measured as a function of excitation intensity, which was changed by a known amount with a calibrated diaphragm, and was found strictly linear to the excitation intensity within the intensity range of 100:1 for the light of 365 mμ. By decreasing the temperatures, the luminescent intensity increases but the spectral distribution remains unchanged. There may be a slight shift of the maximum wavelength towards shorter wavelengths, which can not be detected because of the wide slit width used in the experiment. In order to detect the fine structure or the weak band in luminescence, the spectrogram was taken with the spectrograph of high dispersion, but there was neither a fine structure nor a new band, which has been reported as "edge emission",5) even at the liquid air temperature.

To obtain the insight into the mechanism of luminescence, the luminescent intensity was measured as a function of temperature between −190°C and 200°C. The results were shown in Fig. 4. At −190°C, the intensity increases as much as three or four times of that at the room temperature and approaches to the saturated value. By increasing the temperature, the intensity decreasing monotonically, attains, at ca. 150°C, to one-tenth of that at the room temperature. The relation between the luminescent intensity and the temperature can be expressed by the following equation.

$$I=\frac{I_0}{1+b_1\exp(-E_1/kT)+b_2\exp(-E_2/kT)}\,. \tag{1}$$

The constants in the equation are listed in Table 1. The intensity does not perfectly saturate even at −190°C and the quenching range is relatively long, which may be the characteristics of the luminescence in amorophous substances. Equation 1 shows that there are two processes of radiationless transition, and the frequency factor of the term with small activation energy is far less than that in the ordinary case.

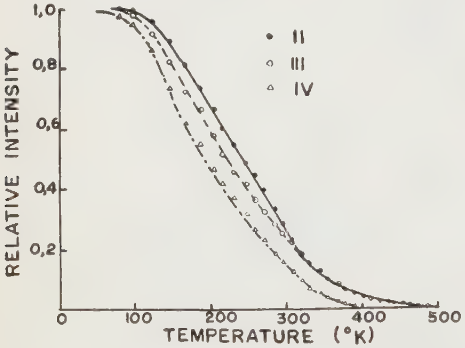

Fig. 4. Temperature dependence of luminescent intensity. Lines were obtained by Eq. 1 with constants in Table 1 and points show experimental values.

§4. Summary and Discussions

The main results were shown in Table 1. From these it can be said that the cadmium sulfide plays a main role in the optical properties of reheated CdS glass. In a quenched state cadmium sulfide is dissolved as separate ions and shows no visible absorption.2) By reheating, cadmium and sulphur aggregate to form tiny crystals and show yellow colour. In these glasses neither the precipitated particles nor the Tyndal light could be perceived by an optical microscope. Therefore, the particles of precipitated CdS is far smaller than the wave length. While, the shape of the absorption curve and the temperature dependence of the absorption edge, which is assumed to be caused by the electron-lattice interaction, resembling to those of films or single crystals and not to those of the isolated molecules, it may be infered that even in specimen No. 2, there is CdS which can be

Table I.

Specimen	Absorption Edge		Luminescent Peak		Peak of Excitation		Temperature dependence			
	(ev.)	cm^{-1}	(ev.)	cm^{-1}	(ev.)	cm^{-1}	E_1 (ev.)	E_2 (ev.)	b_1	b_2
1	no visible absorption		non		—		—	—	—	—
2	2.85	23100	1.86	15200	2.86	23200	0.28	0.06	7.02×10^4	15.6
3	2.66	21800	1.71	13900	2.75	22200	0.29	0.06	7.71×10^4	20.7
4	2.53	20600	1.60	13000	2.61	21200	0.36	0.06	2.28×10^6	28.4

regarded as a crystalline state rather than isolated molecules, and as reheating progresses, the crystals grow larger. Accordingly, the shift of the absorption edge with reheating corresponds to the variation of the energy gap between the filled and the conduction band, and as the particles grow larger, the width of the gap becomes narrower to approach to that of the ordinary CdS crystals.

The maximum of the luminescent spectrum also shifts towards longer wavelengths in the order of Nos. 2, 3, and 4, and there exists a linear relation between the wave-numbers of luminescent maxima and those of the absorption edges. This indicates that the energy gap between the ground and the excited level of luminescent centers varies proportionally to that of the forbidden zone. While, there are little differences in the constants in Eq. (1) for these three specimens, it may be infered that there are little differences in the relative positions of the adiabatic potential curves corresponding to the ground and the excited levels of the luminescent center. These features are very similar to the case of the mixed crystal of ZnS-CdS, in which the absorption edge and the maximum wavelengths of luminescent spectra shift according to the molar percent of the two components. From the fact that the optical absorption edge, which is to be structure insensitive, varies regularly with reheating, it can be concluded that there must be a change as a whole, not the local, in the properties of CdS crystals in the glass. Therefore the change in the optical properties caused by reheating may be explained by the hypothesis that the lattice constants of CdS crystals which precipitate in the early stage of reheating is smaller than those of the ordinary crystal, and with further reheating the crystals growing larger, the lattice constants approach to the ordinary value. In order to confirm this hypothesis, the specimens were investigated by X-ray diffraction. With the monochromatized X-ray, a few faint and broad lines were obtained between halos corresponding to the glass structure. However, the lines are too faint to detect the minute change in the lattice constants which are supposed to be a few percent of the ordinary value. Another method of X-ray investigation is now under progress. If this hypothesis fails to explain the observed phenomena, the effect of the crystal size on the energy structure or the effect of other ions as crystal constituents will have to be taken into consideration.

The excitation spectrum shows that the fundamental absorption is effective for luminescence, especially the light near the absorption edge being of high efficiency. It is ordinarily assumed that owing to the bimolecular recombination process the efficiency of luminescence decreases at the shorter wavelengths side of the absorption edge. In this case, however, the strictly linear relation exists between the excitation and the luminescent intensity even when excited by the light of 365 mμ. Therefore, the ordinary bimolecular recombination argument is inadequate, and a more fundamental explanation should be sought for the high efficiency near the absorption edge. The low quantum yield on the shorter wavelengths side should be explained either by some mechanisms that allow the high probability of energy dissipation into heat in the case of high energy photons or by the hypothesis that the very weak absorption by luminescent centers corresponding to the excitation spectrum overlaps to the fundamental absorption edge. This anomaly in the absorption edge also appears in the spectral response of photoconductivity, and the nature of electronic transition corresponding to the absorption edge of insulators or semiconductors should be reexamined experimentally and theoretically.

As to the mechanism of luminescence, no definite explanation can be given at present. However, the decrease of luminescent intensity for ultraviolet excitation with progressed reheating may be partly ascribed to the shift of the excitation spectra. The glass used in the experiment has many components, and in order to simplify the condition it is desirable to form CdS crystals of various states in a more simple medium and, if possible, without heat treatment.

§ 5. Acknowledgements

The author wishes to express his sincere thanks to Dr. M. Takagi for the X-ray analysis, to Professors S. Makishima and K. Ishiguro for their suggestions and instructions, and to Professor Z. Koana for his encouragement throughout the work.

References

1) R. Frerichs: Phys. Rev. **72** (1947) 594.
G. Kuwabara: J. Phys. Soc. Japan **9** (1954) 97.

2) G. Jaeckel: Zs. tech. Phys. **7** (1926) 301.

3) J. K. Inman, A. M. Mraz and W. A. Weyl: Solid Luminescent Material: Cornell Symposium, 182. John Wiley and Son. Inc. New York, 1948.
W. A. Weyl: Coloured Glass; The Society of Glass Technology, Sheffield 1951.

4) A. Radkowsky: Phys. Rev. **73** (1948) 749.
H. Y. Fan: ibid. **82** (1951) 900.
T. Muto and S. Oyama: Prog. Theor. Phys. **5** (1950) 833; **6** (1951) 81.
I. C. Cheeseman: Proc. Phys. Soc. **A 65** (1952) 25.

5) C. C. Klick: Phys. Rev. **89** (1953) 274.

JOURNAL OF THE PHYSICAL SOCIETY OF JAPAN Vol. 9, No. 6, NOV.—DEC., 1954

On the Optical Absorption of Thin BaO Film in the Ultraviolet Region

By Kazunori TAKAZAWA and Tosiro TOMOTIKA

Physical Institute, Faculty of Science, University of Kyoto

(Received June 10, 1954)

By measuring the optical transmittance of evaporated BaO film in vacuum, it has been found that the threshold for absorption occurs at 3200 Å and the second rapid rise in absorption begins at 2500 Å approximately. Two absorption bands have been observed in the region ranging from 2500 Å to 3200 Å: one has a maximum at 2800 Å and the other has a maximum at about 3000 Å. The latter absorption hand is new and has not been observed so far by the method of optical transmittance, though its presence has been suggested by the photoconduction of BaO single crystal.

The influence of oxygen vapour upon the absorption bands has also been investigated, and it has been observed that when thin BaO film was exposed to oxygen, the absorption bands in the region 2500 Å—3200 Å vanished out suddenly and the film became transparent in the region of wavelengths longer than 2500 Å.

§ 1. Introduction

Barium oxide (BaO) has long been an important material used in practice as low temperature source of electrons in a vacuum tube, and several experimenters have so far investigated its thermionic emission as well as its activity. But, the mechanism of electron emission is not yet well understood. One method to approach an understanding of the said mechanism is to study the energy bands in pure BaO and impurity levels contained in them. Recently, the results of measurements of the optical absorption in BaO have been reported by some investigators. Thus, Tyler[1] has found that the edge of optical absorption of evaporated BaO films lies at 3.8 e.v. and a second increase in the absorption constant occurs at 4.8 e.v. approximately. By measuring the photoelectric emission from very thin metallic films deposited on the surface of BaO layers, Taft and others[2],[3] have confirmed that the edge of optical absorption in BaO is located at 3.8 e.v. Also, the optical absorption and photoconductivity were measured by Tyler and Sproull[4] in the case of BaO single crystals, and the threshold photon energy for both processes has been found to be 3.8 e.v. Tyler assumes that the first absorption band whose threshold is at 3.8 e.v. may be due to the production of excitons in BaO lattice.

In our laboratory, the optical properties of a group of divalent alkaline earth oxides have been investigated so far, and in connexion with the production of BaO single crystals, the optical absorption in thin BaO films was measured under various conditions in order to see the condition of evaporation of BaO. In this paper will be reported the results of observation on the index of refraction of thin BaO films as well as on the influence of oxygen vapour upon the absorption bands in the region ranging from 3.8 e.v. to 4.2 e.v. Such thin BaO films used in the measurements were evaporated from a filament coated with BaO. The filament itself was coated initially with $BaCO_3$ using nitrocellulose-amylacetate solution as a 'binder' and then $BaCO_3$ was converted to BaO. However, great care should be taken in using the nitrocellulose-amylacetate binder.

§ 2. Experiment

Fig. 1 shows schematically the evaporation vacuum chamber used in the present experiment at earlier stages. The space in the glass chamber was separated by a shutter S into two parts, and the filament F made of coil of tungsten wire of 0.2 mm diameter was set in one part and was coated with $BaCO_3$ (Merk Ultra Pure) which was pasted in the nitrocellulose-amylacetate binder or in water. Initially the quartz plate Q was laid in the other part of the chamber as shown in Fig. 1 (a). After exhausting, $BaCO_3$ was converted to BaO by heating the filament slowly to 1000°C approximately, the heating having been continued until gas evolution has substantially ceased. After this procedure the quartz plate was moved and placed just below the coated filament. The temperature of the coated filament was measured by an optical pyrometer and was found to be in the range 700°C–1200°C in most of the present experiment. During the course of evaporation, the thickness of thin BaO film evaporated onto the quartz plate was estimated by observing interference patterns. It was noted that such interference patterns had very deep colour, indicating that the index of refraction of thin BaO film is fairly large. In order to examine the structure of absorption spectrum, evaporation of BaO onto the quartz plate had to be continued until the interference patterns could not be observed any more. After finishing evaporation, thin BaO film evaporated onto the quartz plate was held in a dry box desicated by porous BaO or $CaCl_2$ or P_2O_5. In this case, therefore, thin BaO film was exposed to the vapour of dry oxygen.

The measurements of absorption of light by thin BaO film as prepared by the abovementioned method were made by a D.U. monochrometer. As shown by curve A in Fig. 2, the absorption was not appreciable for the light in the range from 4000 Å to 2500 Å, but the absorption became appreciable quite abruptly at about 2500 Å and the transmission cut-off was very sharp. The maximum of this absorption band could not be detected by D.U. monochrometer, since wavelengths smaller than 2000 Å cannot be measured by such an instrument. It seems however that the maximum is located at a wavelength just below 2000 Å. In case when the nitrocellulose-amylacetate binder was used to paste $BaCO_3$, two more small bands were often

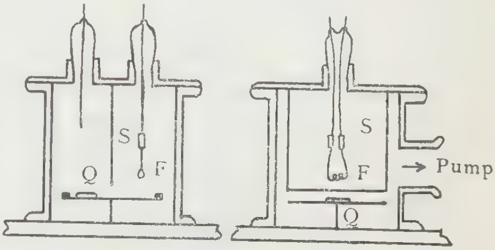

(a) (b)

Fig. 1. Evaporation chamber.

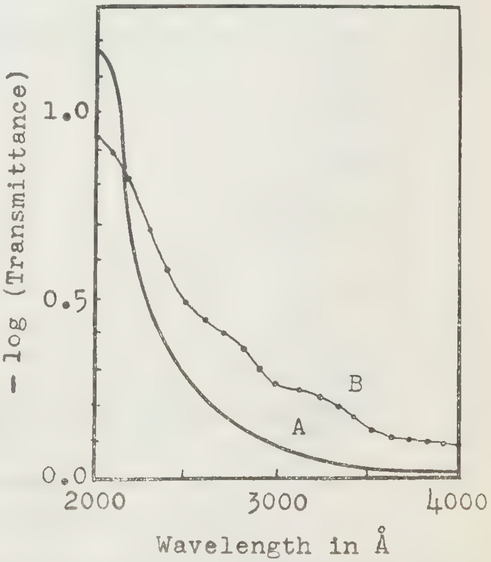

Fig. 2. The absorption spectrum of thin BaO film in oxygen vapour.

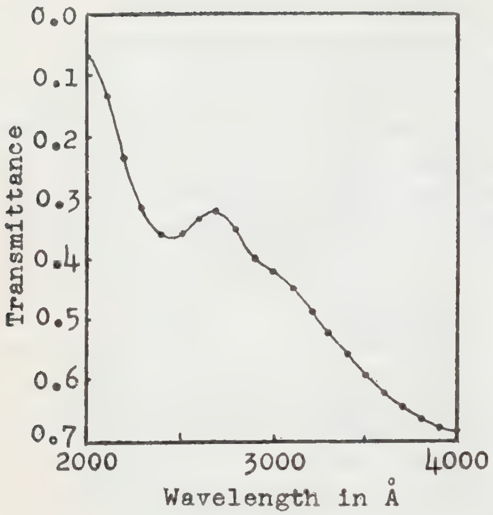

Fig. 3. Curve of optical transmittance *versus* wavelength for thin BaO film, in dry oxygen containing some impurities.

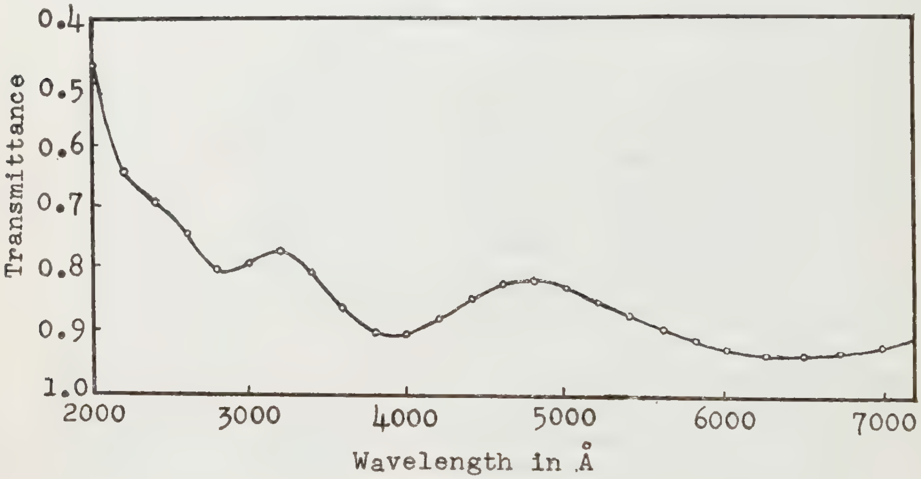

Fig. 4. Transmittance spectrum of thin BaO film showing interference patterns.

observed in the region ranging from 2500 Å to 3500 Å as shown by curve B in Fig. 2; namely, one in the region 2500 Å—3000 Å and the other in the region 3000 Å—3500 Å. To clarify the matter, $BaCO_3$ was pasted in very concentrated nitrocellulose-amylacetate solution and the tungsten filament was coated with it. In raising the temperature of the filament, the outgasing followed as the result of decomposition of $BaCO_3$ and a black substance was produced on the surface of the filament. Occasionally such a black substance evaporated out for long heating and the colour of the coated filament became white, indicating that the filament was coated with the mixture of $BaCO_3$ and BaO. In some cases, however, aggregates of some black substances did not remove from the filament. The colour of thin film evaporated onto the quartz plate became then brown, and in this case we obtained the absorption spectrum as shown in Fig. 3.

From this figure it will readily be seen that as we proceed from the visible region to the ultraviolet one, the curve rises rather slowly till a wavelength of 2700 Å where it attains a first maximum and a second rise of the curve begins at about 2500 Å. Colouring in the visible region is probably due to the absorption band having the maximum at 2700 Å, which is believed to be due to some impurities contained in thin BaO film used. Since the curve B in Fig. 2 has the similar appearance to the curve in Fig. 3, it may be concluded that the same impurities were contained in BaO films in both cases. Judged from the fact observed in vacuum tube technique that filaments coated with $BaCO_3$ become sometimes black on heating, possibly due to the existence of carbon, we may consider that a thin BaO film showing an absorption curve similar to the curve B in Fig. 2 contains carbon as impurities.*

During the course of evaporation of thin BaO film onto the quartz plate, the interference pattern was observed, which was due to the interference of the light reflected from the surface of the thin BaO film with the light reflected from the upper surface of the quartz plate. The evaporation was stopped when the interference pattern became uniform in colour and the thin BaO film was then exposed to dry oxygen. No detectable change in the interference pattern was observed either when the thin film was placed in vacuum or when it was exposed to dry oxygen. The typical curve of optical transmittance of thin BaO film showing interference patterns is given in Fig. 4.

---

* Private communication by Dr. S. Narita of the Technical Department, Kobe Kogyo Corporation.

If we obtain such a transmittance curve for the system consisting of air, thin film, quartz plate and air in this order, we can calculate the thickness, d, as well as the index of refraction, n, of the thin film. In case when the light is not absorbed either in the thin film or in the quartz plate, it can be shown, by starting from Brattin-Brigg's equation[5], that the maximum and minimum values of the transmittance for the case of normal incidence are given respectively by the formulae:

$$R_{\mathrm{max}}=1-\left(\frac{n_0-1}{n_0+1}\right)^2 \quad \text{for} \quad nd=2m\frac{\lambda}{4},$$

$$R_{\mathrm{min}}=1-\left(\frac{n^2-n_0}{n^2+n_0}\right) \quad \text{for} \quad nd=(2m+1)\frac{\lambda}{4},$$

where n_0 is the refractive index of the quartz and $m+1$ denotes the order of interference.

Thus, if we find the values of R_{max} and R_{min} from the transmittance curve as shown in Fig. 4, we can determine the refractive index of thin BaO film evaporated onto the quartz plate. It was found that the refractive index thus determined of thin BaO film exposed to dry oxygen was about 1.9 in the visible region.

As mentioned already, the evaporated thin BaO film was always exposed to dry oxygen in the experiment so far made. It has been reported, however, that the oxide coated cathode is very sensitive to the presence of oxygen vapour. In order to measure the transmittance in thin BaO film in vacuum, therefore, some vacuum tubes were used. Fig. 5 shows schematically one of the vacuum tubes used in our experiment. It was made almost entirely of fused quartz and the filament was set at its upper space so that the transmittance measurement was capable of being made through the lower part of the quartz envelope. To this evaporation tube was connected another small tube as shown in Fig. 5, which was used as the oxygen source to fill up the evaporation tube with oxygen when necessary. When the evaporation was over, the system was sealed off.

The spectral distributions obtained in vacuum differ appreciably from those obtained in case when thin BaO film was exposed to dry oxygen. The optical transmittance of thin BaO film in vacuum is shown by curve (1) in Fig. 6, from which it will be seen that the threshold of absorption is located at about 3200 Å and the absorption constant rises rapidly in the region from 3200 Å to 3000 Å and then it rises rather slowly up to a maximum at about 2800 Å. Also it is seen that the second rise in the absorption constant starts from about 2500 Å. Tyler's measurements of the transmittance also indicate that the strong absorption starts at about 3200 Å and the transmittance curve obtained by him is of the form similar to curve (1) in fig. 6. But we have observed a new band with the absorption maximum at about 3000 Å, which has not yet been observed so far by optical measurement. This new band is coincident with the first maximum of photoconductivity in BaO single crystal. Further, it is found in curve (1) in Fig. 6 that there is another

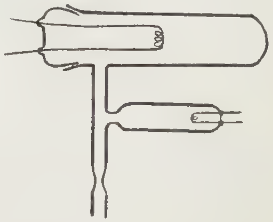

Fig. 5. A vacuum tube for absorption measurement in vacuum. The left small tube was used as oxygen source when necessary.

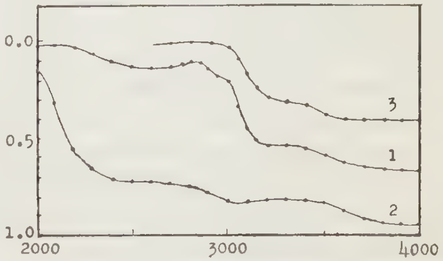

Fig. 6. Curve of optical transmittance *versus* wavelength for thin BaO film evaporated onto the quartz tube as shown in Fig. 5.

absorption band at a wavelength larger than 3200 Å, and this band is considered to be due to some impurities contained in thin BaO film.

After the measurement in vacuum was carried out, the evaporation tube was filled up with oxygen and the measurement of transmittance was again made. The result is shown by curve (2) in Fig. 6. It will readily be seen that this curve (2) is of similar form to curve B in Fig. 2, and this seems to suggest that thin BaO film evaporated onto the inner surface of the evaporation tube contained some impurities, the greater part of which was carbon.

If in the procedure of evaporation, the temperature of filament was raised up to about 1250°C, the inner surface of the tube near the filament became dark in colour, indicating that a certain substance has deposited there. Judged from the fact that when exposed to oxygen, the darkening vanished out and the deposited substance became white in colour, it may be said that the substance was not carbon. The absorption curve in this case is shown by curve (3) in Fig. 6. It is seen that the effect of darkening is revealed in the region ranging from 3200 Å to 4000 Å where the absorption curve is shifted uniformly upwards. Although it is not yet certain what sort of substance was evaporated from the filament coated with BaO, it is of great interest to note that the absorption band ranging from 3200 Å to 2500 Å and its darkening are both sensitive, to the same extent, to the presence of oxygen.

§ 3. Summary and Conclusion

By measuring the optical transmittance of evaporated BaO film in vacuum, it has been found that the threshold for absorption occurs at 3200 Å and the second rapid rise in absorption begins at 2500 Å approximately. Two absorption bands have been observed in the region ranging from 2500 Å to 3200 Å: one has a maximum at 2800 Å and the other has a maximum at about 3000 Å. The former absorption band has already been observed by Tyler, but the latter absorption band is new and has not been observed so far by the method of optical transmittance, though its presence has been suggested by the photoconduction of BaO single crystal. When thin BaO film was exposed to oxygen, the absorption bands in the region 2500 Å—3200 Å vanished out suddenly and the film became transparent in the region of wavelengths longer than 2500 Å. Tyler has assumed that the onset of absorption at 3200 Å is due to the production of excitons, with the accompanying photoconductivity of excitons or exciton ionization of impurity centres. According to our experiment, however, the absorption bands in the region from 2500 Å to 3200 Å were seriously affected by the presence of oxygen vapour, and this fact seems to suggest that these absorption bands are not inherent in the BaO lattice itself, but are due to imperfection of the lattice, and that the absorption band beginning at 2500 Å is rather inherent in the BaO lattice. Tyler found that when water came in contact with thin BaO film, the film became transparent throughout the visible and ultraviolet regions up to 2000 Å. Although the absorption band beginning at 2500 Å does not seem to be due to the film of hydrate of BaO, yet more careful examination on the effect of water is necessary, since the water vapour comes out from the surface of the quartz envelope on heating.

The writers wish to express their sincere thanks to Professor Y. Uchida for his kind guidance and helpful suggestion. The writer's thanks are also due to Dr. M. Ueta for his encouragement.

References

1) W. W. Tyler: Phys. Rev. **76** (1949) 1886.

2) E. A. Taft and J. E. Dickey: Phys. Rev. **78** (1950) 625.

3) H. B. DeVore and J. W. Dewdney: Phys. Rev. **82** (1951) 805.

4) W. W. Tyler and R. L. Sproull: Phys. Rev. **83** (1951) 548.

5) W. H. Brattin and H. B. Briggs: Phys. Rev. **75** (1949) 1705.

JOURNAL OF THE PHYSICAL SOCIETY OF JAPAN Vol. 9, No. 6, Nov.—Dec., 1954

Feed-back Resonance Amplifier for the Infrared Spectrometry Part III

By Hisamitu YOSIMURA and Kuniya FUKUDA*

Department of Physics, Faculty of Science, Kyoto University

(Received July 20, 1954)

In succesion to Part I and II some important properties of the feed-back resonance amplifier, espescially its response time and noise, are discussed in detail so that the working condition of amplifier may be deduced. Furthermore, it is shown how the working condition is related to scanning rate and resolving power in automatic absorption measurements.

§ 1. Introduction

In Parts I and II[1] the feed-back resonance amplifier, in which a feed-back device was applied on an amplifying galvanometer system, was introduced and its characteristic properties were computed by theoretical analysis with good agreement to experimental results. But there remained some important properties of amplifier undiscussed, response time and noises. In this paper we shall treat them in detail.

In § 2 it will be proved that the response time of amplifier is determined by the time constant of primary galvanometer, which can be easily estimated by solving numerically the equation of motion of the galvanometer for a shock signal. In § 3 noises and working condition are treated. The noises of amplifier result from the following various causes; Brownian motion of galvanometer mirror, Johnson current in thermocouple circuit, temperature variation in zero point of thermocouple, induction of electromagnetic wave in air, and mechanical vibrations. The latter three can be eliminated in our instrument as shown in the previous papers and so Brownian and Johnson noises are discussed in this section. As the results of our theoretical computations the noise level of amplifier is determined by Johnson noise rather than Brownian one. This fact makes it possible to use the amplifier under an extremely high sensitivity (up to the order of 1×10^{-10} volt). The working condition of amplifier is prescribed by sensitivity, response time, and noise level, but in our system only by the former two because of its very small noises. Accordingly the best working condition must be determined so as to make a response time as short as possible under a high sensitivity. Our amplifier has this condition at a period near 5 sec. In the last section it will be theoretically discussed how to determine scanning speed and resolving power in automatic spectroscopic measurements and the results will be compaired with the experimental data.

§ 2. Response Time of Amplifier

The response time of amplifier can be derived from the transient behaviour of secondary galvanometer deflections for a shock change of incident radiation, but in this behaviour will take part the following three time constants: those of thermocouple, primary galvanometer, and secondary one.

Provided that a shock signal in radiation has unit amplitude for $t<0$ and is zero for $t>0$, the change in emf. of thermocouple will obey to $e^{-\alpha t}$ for $t>0$, where $1/\alpha$ is its time constant. Accordingly the signal current to the primary galvanometer may be set equal to $i_0e^{-\alpha t}$. Since feed-back resonance was realized in experiments for a negligible small value of resistance R_2, the equation of motion of the primary galvanometer can be written in the following form*;

$$I_1\ddot{\phi}_1+P_1\dot{\phi}_1+D_1\phi_1+\frac{B_1n\chi}{1+A(d/dt)}\frac{\phi_1}{R+R_1}=B_1i(t), \tag{1}$$

under the abbreviation $A=RR_1C/(R+R_1)$. In Part I the particular solution of this equation was derived for a sinusoidal signal current and in Part II it was experimentally proved that under suitable values of amplifier circuit constants the solution corresponded to the steady state of motion called "feed-back resonance". Now we must solve Eq. (1) for the shock signal $i(t)=i_0e^{-\alpha t}$; that is,

---

* Present adress, Institute of Physics, Department of Science and Engineering, Ritsumeikan University.

* See Appendix of Part I.

$$I_1\ddot{\phi}_1+P_1\dot{\phi}_1+D_1\phi_1+\frac{B_1n\chi}{1+d/dt}\frac{\phi_1}{R+R_1}=B_1i_0e^{-\alpha t}, \tag{2}$$

For this purpose we use Laplace transformation under the initial conditions $\ddot{\phi}_1=\phi_1=0$ at $t=0$. These initial conditions can be easily brought about in practice by means of shutting off radiation at the moment when the rotating sector covers the entrance slit, because the deflection of primary galvanometer ϕ_1 has phase delay $\pi/2$ to signal under the resonance condition.* Thus we obtain the following solution;

$$\varphi_1=Fe^{-\alpha t}+Ge^{-\beta t}+He^{-(\gamma+i\omega)t}+\overline{H}e^{-(\gamma-i\omega)t}, \tag*{(2–1)**}$$

where all coefficients are constants determined by amplifier conditions and $\overline{H}$ is conjugate to H. $-\beta$ and $-\gamma\pm i\omega$ are roots of the third order equation** derived from Eq. (2) and under resonance conditions all β, γ, and ω becomes positive real, which gives, of course, a convergence to ϕ_1. For the above deflection of primary galvanometer ϕ_1 the output current i_2 is obtained from the expression (6) of Part I. For this current the deflection of the secondary galvanometer can be easily obtained as**

$$\begin{aligned}\phi_2=&Ie^{-\varepsilon t}+Jte^{-\varepsilon t}+Ke^{-\alpha t}+Le^{-\beta t}\\&+We^{-\gamma t}\sin(\omega t+\rho),\end{aligned} \tag{2–2}$$

where all coefficients are also constants determined by amplifier conditions. ε is the time constant of the secondary galvanometer and becomes natural frequency under critical damping. Our galvanometer has ε of 0.8 sec^{-1}. Thus the expression of the transient behaviour of secondary galvanometer (accordingly of amplifier) has been obtained for the shock signal, but it is not necessary to take into account all terms of the above expression. In our case, as described above, $1/\alpha$ and $1/\varepsilon$ are about 1 sec., whereas $1/\beta$ can be estimated as of order 1/10 sec. and $1/\gamma$ as from 10 sec. to 30 sec. from numerical calculations. Hence the expression (2–2) can be simplified in good approximation as following;

$$\phi_2=We^{-\gamma t}\sin(\omega t+\rho). \tag{3}$$

It follows that the response time of amplifier is given by the time constant $1/\gamma$ of primary galvanometer. We found that under various resonance conditions the experimental γ-values fairly well coincided with the calculated ones within experimental errors.

§ 3. Noise and Working Condition of Amplifier

The working condition of amplifier can be prescribed by sensitivity, response time, and noise level and so the best condition must be determined so as to give compromise among them. In this section we shall first discuss the noises of amplifier and then seek for the best working condition.

The Brownian noise results from random motion of primary galvanometer mirror caused by collision of air molecules and consequently has an effect on the deflection of secondary galvanometer directly through the photo-voltage

$$E=\chi\phi_1=\chi\sum_k\phi_{1k}, \tag{4}$$

where ϕ_{1k} is a Fourier component of the Brownian deflection of primary galvanometer. It should be noted, here, that for both ϕ_1 and the following $M(t)$ the interval $2T$ in Fourier expansion must be taken as much greater than $2\pi/\omega_f$.²⁾ As easily seen from the expression (11) in Part I, the m.s. of Brownian current in output becomes

$$i_{2B}{}^2=\frac{\chi^2}{R^2}\sum_k\frac{A^2\omega_k{}^2}{1+A^2\omega_k{}^2}\phi_{1k}{}^2. \tag{5}$$

If $M(t)$ is the fluctuation torque caused by Brownian motion, the m.s. of the Brownian deflection of primary galvanometer can be expressed by²⁾

$$\phi_1{}^2=\sum\phi_{1k}{}^2=\sum_k\frac{\frac{2}{T}\overline{M}^2\Delta t}{\left\{-\omega_k{}^2I_1+D_1+\frac{B_1n\chi/(R+R_1)}{1+A^2\omega_k{}^2}\right\}^2+\omega_k{}^2\left\{P_1-\frac{B_1n\chi A/(R+R_1)}{1+A^2\omega_k{}^2}\right\}^2},$$

because of the expression (8) in Part I. $\overline{M}^2$ is the m.s. of the mean fluctuation torque in a physically infinitesimal time element Δt, within which many collisions occur. It holds only for $\omega_k = 2\pi k/T \ll 1/\Delta t$ that the each square amplitude of Fourier components of $M(t)$ is replaced by $(2/T)\overline{M^2}\Delta t$, but it does not for $\omega_k \gg 1/\Delta t$. However, the same expression of $\overline{\phi_{1k}^2}$ may be allowed even for the latter case, since then its denominator becomes sufficiently large. For a resonance frequency ω_f the expressions (8–1) and (8–2) of Part I hold and l is considered to be small and comparable with resisting torque (f_1) due to mechanical resistance. Hence, the above expression of $\overline{\phi_1^2}$ can be rewritten in good approximation as

---

* See the expression (9) in Part I.

** See Appendix in this paper.

$$\overline{\phi_1^2} = \sum_k \overline{\phi_{1k}^2} = \frac{\overline{M^2}}{I_1^2} \frac{2\Delta t}{T} \sum_k \frac{1}{(\omega_k^2 - \omega_f^2)^2 + \omega_k^2 \Gamma^2},$$

under the abbreviation $\Gamma = l/I_1$ and then this formula becomes Schottky integral[3)] for integration in place of summation. By using this formula the expression (5) becomes

$$\overline{i_{2B}^2} = \frac{\chi^2}{R^2} \frac{\overline{M^2}\Delta t}{I_1^2 \pi} \int_0^\infty \frac{A^2\omega^2}{1 + A^2\omega^2} \frac{d\omega}{(\omega^2 - \omega_f^2)^2 + \omega^2\Gamma^2}.$$

The first factor in integrand can be replaced on an average by its value $c(\omega_f)$ at the resonance frequency ω_f, since it is a monotonously increasing function of ω_k contrary to the second factor having a sharp resonance character, and accordingly the integration may be carried out only for the latter. Thus, using Schottky integral, we obtain

$$\overline{i_{2B}^2} = c(\omega_f) \frac{\chi^2}{R^2} \frac{\overline{M^2}}{I_1^2} \Delta t \frac{1}{2\omega_f^2 \Gamma},$$

where, as described above, Γ $(\equiv l/I_1)$ is nearly equal to f_1/I_1. $\overline{M^2}$ and f_1 can be estimated according to Uhlenbeck and Goudsmidt formula[2)] in rarefied gas; that is,

$$\overline{M^2}\Delta t = \frac{4m\bar{c}p}{\rho} \quad \text{and} \quad f_1 = \frac{2m\bar{c}pI_1}{\rho kT},$$

where m is mass of gas molecule, $\bar{c}$ its mean velocity, p pressure of surrounding gas, ρ mass of mirror per cm², k Boltzman constant, and T absolute temperature. By substituting these formulae into the expression of $\overline{i_{2B}^2}$, the m.s. of Brownian output current can be expressed by

$$i_{2B}^2 = c(\omega_f) \frac{\chi^2}{R^2} \frac{kT}{\omega_f^2 I_1}. \qquad (6)^*$$

The Johnson noise arises from the thermal motion of electrons in the thermocouple-primary galvanometer circuit and is defined by Nyquist formula[4)] as

$$\overline{i_J^2} = \frac{4kT}{r} \quad \text{per cycle,}$$

where r is the total resistance of circuit. From the expression (11) in Part I the output current caused by Johnson noise is given as following;

$$\overline{i_{2J}^2} = \frac{\chi^2}{R^2} \frac{2kT}{\pi r} \int_0^\infty \frac{B_1^2}{\left\{-\omega^2 I_1 + D_1 + \frac{B_1 n\chi/(R+R_1)}{1+A^2\omega^2}\right\}^2 + \omega^2 \left\{P_1 - \frac{B_1 n\chi A/(R+R_1)}{1+A^2\omega^2}\right\}^2} \frac{A^2\omega^2}{1+A^2\omega^2} d\omega.$$

Table I. The variation of amplifier properties under a fixed l-value (2×10^{-10}) for various resonance frequencies.

T in sec.	ω in sec⁻¹	R in kΩ	$(S_{1,f})_{\omega f}$ in 10^5 rad/amp	$(S_{2,f})_{\omega f}$ in 10^5 rad/amp	$(S_{1,f})_{drift}$ in 10^5 rad/amp	E_B in 10^{-9} volt	E_J in 10^{-9} volt	Resp. time in sec.	C_{lower} in μf
7.1	0.88	33	11.6	95	0.58	1.8	4.5	33	40
6	1.05	18	9.7	110	0.56	2.5	1.9	25	25
5	1.25	10.5	8.2	120	0.48	3.1	8.0	23	19
4	1.57	6.5	6.5	90	0.38	3.3	8.3	20	15
3	2.09	3.5	4.9	65	0.25	3.7	9.2	16	13

In the same approximation as for Brownian noise, we obtain

---

* The validity of the approximation in § 4 Part I has been proved here.

$$\overline{i_{2J}^2} = c(\omega_f) \frac{\chi^2}{R^2} \frac{kT}{\gamma \omega_f^2 \Gamma} \frac{B^2_1}{I_1^2}, \qquad (7)$$

for Johnson output current.

Thus the ratio of Johnson current to Brownian one becomes

$$\overline{i_{2J}^2} / \overline{i_{2B}^2} = \frac{1}{\gamma} \frac{B_1^2}{I_1} \frac{1}{\Gamma} = \frac{P_1 - f_1}{l}.$$

Under the usual working conditions of amplifier this ratio is about 10 as shown in Table I and II. Brownian noise of galvanometer is, in general, greater than Johnson one and for an ideal, but seldom realized, case both are in the same order of magnitude⁵⁾, whereas in our amplifier the relation is inverse and the noise level may be always determined by Johnson noise. Consequently it is expected that in our amplifying system the sensitivity of detector is available in full.

Being combined with the results in Parts I and II, the above discussions of response time and noise will enable us to estimate the working condition of amplifier. For this purpose circuit constants, sensitivity, resonanse time, and noises were calculated for a fixed l-value (2×10^{-10})* in the range of resonance period from 7.1 sec. to 3 sec. (from 0.88 sec^{-1} to 2.09 sec^{-1} in frequency) and listed in Table I; response time (τ) is, of course, the time constant $1/\gamma$ of primary galvanometer calculated by the method in § 2 and Brownian and Johnson noise voltages (E_B and E_J) are the net voltages impressed onto the secondary galvanometer by the currents (6) and (7) respectively. As shown in Table I, when resonance (or signal) period is varied from 7.1 sec. to 3 sec., zero drift ($(S_1)_{drift}$) and response time decrease, but noise voltages (E_B and E_J) increase. On the other hand the sensitivity of amplifier ($(S_{2,f})\omega_f$) shows a maximum value at the resonance perion 5 sec. Such a behaviour of sensitivity is also easily presumed from its expression**

$$\frac{\delta(\phi_{2f})_{\omega f}}{\delta i_0} = \frac{\chi}{R} \frac{A\omega_f}{\sqrt{1 + A^2 \omega_f^2}} \frac{\omega_0^2}{\omega_0^2 + \omega_f^2} \frac{B_1}{\omega_f l}.$$

In our problem now concerned, however, zero drift and noise do not matter. Because zero drift changes little under variation of resonance period and besides because the above two noise voltages are of no importance in practice due to their magnitudes extremely small compared with the sensitivity 1×10^{-7} volt/mm of our secondary galvanometer. Hence from the tendency of response time and sensitivity we can predict to some extent the existence of the best working condition of amplifier at the resonance period of 5 sec. This is, furthermore, confirmed by taking into consideration Table II and the following data: $(S_{2f})_{\omega f} = 80 \times 10^5$ rad/amp, $\tau = 13$ sec. for $l = 3 \times 10^{-10}$ at $T = 5$ sec. and $(S_{2f})_{\omega f} = 130 \times 10^5$ rad/amp, $\tau = 33$ sec. for $l = 1 \times 10^{-10}$ at $T = 3$ sec. For the exact determination of the best condition it is necessary to carry out troublesome numerical calculations, but unnecessary in practice.

The last column of Table I, C_{lower}, indicates lower limit of the condenser C, below which the feed-back resonance cannot be realized. It may be desirable for the condenser to have a considerably large capacity above the lower limit so that a high sensitivity of amplifier can be brought about.

Table II. The properties of amplifier at the resonance period of 3.8 sec.

l in 10^{-10}	R in kΩ	$(S_{1,f})_{\omega f}$ in 10^5 rad/amp	$(S_{2,f})_{\omega f}$ in 10^5 rad/amp	$(S_{2,f})_{\omega f}$ in 10^{-9} volt	$(S_{1,f})_{drift}$ in 10^5 rad/amp	E_B in 10^{-9} volt	E_J in 10^{-9} volt	Resp. time in sec.
1	6	12.4	160	0.9	0.34	3.5	13	33
2	5.5	6.2	86	1.7	0.35	3.5	9.2	20
3	5.5	4.1	54	2.7	0.36	3.5	7.3	15
4	5	3.1	42	3.5	0.37	3.5	6.4	10
5	4.5	2.5	35	4.2	0.39	3.5	5.7	8

§ 4. Spectroscopic Works with Amplifier (scanning rate and resolving power)

The whole system of our automatic recording spectrophotometer is schematically depicted in Fig. 1, the construction of which was described in Part II. In this section we shall discuss the relation between scanning rate and resolving power.

---

* The unit of l is the same as P_1 and now defined in practical unit.

** See Part I and II.

Since an absorption curve can be expanded into Fourier series, we shall now think only one of its components with any wavelength period $2D$. Assuming that it has unit amplitude, we may express this component absorption by $F(\lambda)=\sin(\pi\lambda/D)$ at any wavelength λ. In measurements with the same finite slit width S of both entrance and exit slits it is weakened as following ;[6)]

$$G(\lambda)=\left(\frac{\sin\{(\pi/2)(\Delta/D)\}}{(\pi/2)(\Delta/D)}\right)^2\sin(\pi\lambda/D)$$

$$\equiv g\cdot\sin(\pi\lambda/D),$$

where Δ is spectral slit width and defined by

$$\Delta=S\cdot(1/B),$$

and

$$B=-\frac{dn}{d\lambda}f\frac{4\sin(\varphi/2)}{\sqrt{1-n^2\sin^2(\varphi/2)}},$$

for focal length of collimator mirror f, apex angle of prism φ, and its refractive index n. g is deformation factor by slit width. In scanning speed v, since $v=d\lambda/dt$,

$$G(\lambda)=g\cdot\sin(\pi vt/D+\delta)\equiv g\cdot\sin(\sigma t+\delta).$$

and accordingly the amplitude of signal current from thermocouple will be modulated with the frequency σ $(\equiv\pi v/D)$ of absorption curve.

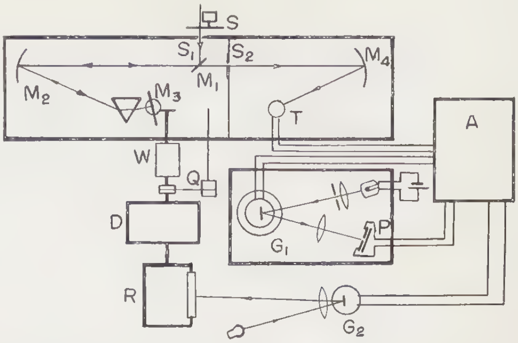

Fig. 1. The whole diagram of the automatic recording spectrometer.

A: Amplifier circuit.
D: Driving motor and connection gear system.
G_1: Primary galvanometer on Julius hunger.
G_2: Secondary galvanometer.
M_1: Plane mirror.
M_2 and M_4: Spherical mirrors ($F=10$ for M_2 and $F=2$ for M_4).
M_3: Littrow mirror.
P: Photovolataic cell.
Q: Coupling reel, by which slits are coupled with wavelength drum.
R: Recording drum.
S: Rotating sector.
S_1 and S_2: Entrance and exit slits, which are driven simultaneously by gears.
W: Wavelength drum.
T: Thermocouple.

When a signal current with unit amplitude is so modulated, that is, when it is given by $i(t)=\sin\sigma t\cdot\sin\omega_f t$, the output current, which will suffer also the amplitude modulation corresponding to the absorption curve, can be easily obtained by solving Eq. (1) for this signal and substituting the solution into the expression of i_2.* Then the amplitude of amplified absorption curve is approximately expressed by**

$$I_\pm=\frac{\chi}{R}\sqrt{c(\omega_f)}\cdot S_\pm$$

$$S_\pm=\frac{B_1}{\sqrt{\left\{-I_1(\omega_f\pm\sigma)^2+D_1+\dfrac{B_1n\chi/(R+R_1)}{1+A^2(\omega_f\pm\sigma)^2}\right\}^2+(\omega_f\pm\sigma)^2\left\{P_1-\dfrac{B_1n\chi A/(R+R_1)}{1+A^2(\omega_f\pm\sigma)^2}\right\}^2}}.$$

On the other hand, for the measurements over an infinite time at each wavelength the absorption curve is exactly traced and its amplitude in output is, of course, written by***

---

* See Part I.

** The exact expression of output current i_2 is

$$i_2=\frac{1}{2}\frac{\chi}{R}\left[\sqrt{c(\omega_f-\sigma)}S_-\cos(\omega_f t-\sigma t-\tan^{-1}\theta_{\omega f-\sigma})-\sqrt{c(\omega_f+\sigma)}S_+\cos(\omega_f t+\sigma t-\tan^{-1}\theta_{\omega f+\sigma})\right].$$

When $\sigma\gg\omega_f$, the relations, $c(\omega_f\pm\sigma)\doteqdot c(\omega_f)$, $S_+\doteqdot S_-$, and $\tan^{-1}\theta_{\omega f\pm\sigma}=\frac{\pi}{2}\pm\Delta$ hold and then

$$i_2\doteqdot\frac{\chi}{R}c(\omega_f)I_\pm\sin(\sigma t\pm\Delta)\sin(\omega_f t-\pi/2)$$

(see also Part I).

*** In this case it should be noted that the observation is to be carried out in an infinitely long time at each wavelength point λ.

$$I=(\chi/R)\sqrt{c(\omega_f)}(B_1/\omega_f l)\ .$$

Hence, the rate of deformation in absorption curve, caused through the amplifier in scanning, can be expressed in the same approximation as that of the last section as following;

$$F=\frac{I_\pm}{I}$$
$$=\frac{\omega_f\Gamma}{\sqrt{\{\omega_f{}^2-(\omega_f\pm\pi v/D)^2\}^2+(\omega_f\pm\pi v/D)^2\Gamma^2}}\ . \qquad (8)$$

Thus it has been proved out that the total deformation rate in absorption curve with period $2D$ is defined by g.F.

Next we shall examine the noise-to-signal ratio in our amplifying system. Since Brownian noise is several times as small as Johnson one, we may take only the latter for the noise level; that is, from (7),

$$i_n\equiv\sqrt{\overline{i_{2J}{}^2}}=W_0\frac{1}{\sqrt{\Gamma}}$$

and $$W_0{}^2=\frac{\chi^2}{R^2}c(\omega_f)\frac{B_1{}^2}{I_1{}^2}\frac{kT}{r\omega_f{}^2}\ .$$

On the other hand the output signal current is given by

$$i_s=S^2\cdot i_2{}^* \quad \text{and} \quad i_2{}^*=\frac{\chi}{R}\frac{\sqrt{c(\omega_f)}}{I_f\omega_f\Gamma}i_0{}^*\ ,$$

where $i_0{}^*$ is the signal current from thermocouple per unit slit width * and $i_2{}^*$ the corresponding output current. Then the noise-to-signal ratio is

$$\frac{i_n}{i_s}=\frac{1}{i_0{}^*S^2}\sqrt{\frac{kT}{r}}\cdot\sqrt{\Gamma}=\frac{i_J}{i_0{}^*B^2\Delta^2}\sqrt{\frac{\Gamma}{2}}\ , \qquad (9)$$

where $i_J/(i_0{}^*B^2\Delta^2)$ is the input n/s ratio. It follows that n/s ratio is proportional to square root of Γ.**

The just obtained two formulae, (8) and (9), prescribe the observed data as well as the working conditions in automatic spectrophotometric measurements. For example, under a fixed condition of amplifier, accordingly fixed Γ- and ω_f-values, a value of spectral slit width Δ will be determined from the condition (9) for a required noise-to-signal ratio. For this Δ-value the condition (8), or g.F, will give the relation between resolving power and scanning rate; that is, from the condition (8) we can determine a scanning speed satisfying the requirment for resolving power, that the two absorptions at interval of $2D$ in wavelength are to be observed at the rate of g.F percent.

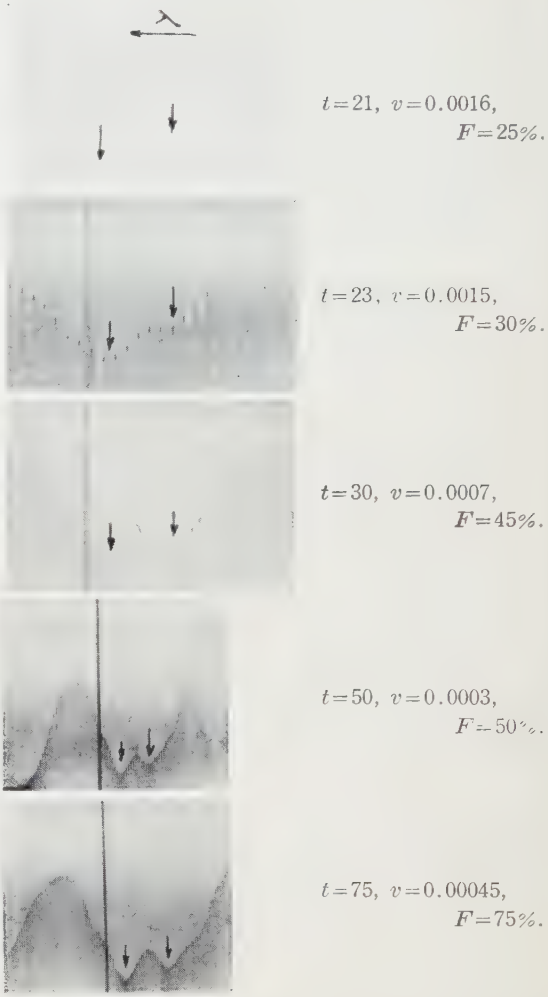

Fig. 2. The shapes of polystirene absorption bands at 3.269μ and 3.303μ for various scanning speeds.

In our experiments, taking aside the condition (9) for a moment, we have examined the variation in shape of absorption for various scanning speeds to compare it with the variation in calculated F-value. The absorption bands of polystirene at 3.269 μ and 3.303 μ were taken as the standard absorptions and measured by using quartz prism for the slit width 0.05 cm under the amplifier condition $l=3\times10^{-10}$, $\omega_f=1.65\ \text{sec}^{-1}$ (3.8 sec in period), and response time $\tau=1/\gamma=15$ sec. (see Table II). The variation of these absorptions were photographed for various scanning speeds as shown in Fig. 2. The values in the left column of this figure correspond to those of Table III, where t is scanning time in the interval $2D=0.034\ \mu=30\ \text{cm}^{-1}$, v scanning speed, and F the rate of deformation by scanning. In this case g is the deformation rate by slit width and equal to 90%. From the contour shown in Fig. 2 the recorded absorption curve may be analyzed into two curves far different in frequency; the one is the ground curve having small frequency (curve II in Fig. 3 (a)) and the other the sinusoidal curve having the frequency $\sigma=\pi v/D$ corresponding to the wavelength period $2D$ (curve III in Fig. 3 (a)). Hence, the amplitude of the standard absorption may be approximately taken as half the length AB in Fig. 3 (a). By measuring this amplitude for each scanning speed in Fig. 2 we can examine the validity in the calculation method of F-value. It was found that experimental and theoretical results were in good coincidence within the experimental error.*

---

* $i_0{}^*$ is essentially related to the sensitivity of thermocouple.

** Γ is approximately the halfwidth of resonance curve in amplifier under sharp tuning. The Eq. (9) is the same as the n/s ratio of the electronic amplifier, assuming Γ^{-1} equal to the time constants. (See Zwinden[6])

Table III. The values of rate of deformation for various scanning speeds in standard absorptions of polystirene 3.303μ and 3.269μ.

t in sec.	v in μ/sec.	σ in sec^{-1}	F in %	$g\cdot F$ in %
21	0.0016	0.30	25	23
23	0.0015	0.27	30	27
30	0.0011	0.20	40	36
50	0.0007	0.13	50	45
75	0.00045	0.08	75	68

$\omega_f=1.65$ sec, (3.8 sec in period), $l=3\times10^{-10}$:
$\Gamma=0.19$ $2D=30\ \text{cm}^{-1}=0.034\mu$, $S=0.05$ cm
$\sigma=\pi v/D$, $\Delta=5\ \text{cm}^{-1}$, $v=2D/t$

There is another way to determine scanning rate and resolving power by analyzing an absorption curve into step functions. In this case the resolving power $d\lambda$ is defined by

$$d\lambda \geqq (\Delta\lambda/\Delta t)\tau\ , \tag{10}$$

where $\Delta\lambda$ is scanning wavelength range and Δt is scanning time in this range. We shall set forth below that this method also indicates the deformation rate in absorption. The standard absorptions in our experiments can be replaced by the step function as shown in Fig. 3 (b). For the sake of simplicity of estimation we take the case ($t=30$ sec. in $2D$) corresponding to the case 3 in Fig. 2. Then, since the wavelength interval D is covered in the time (15 sec.) equal to the response time τ, the absorption amplitude decreases to $1/e$ per one step interval and so the deformation rate becomes about 40% as shown in Fig. 3 (c), where the abcissa is taken in t. This value of deformation fairly well coincides with the corresponding F-value. Although the deformation rate is obtainable by the step function method, the definition (10) for resolving power is not convenient in practice, because it does not directly supply the quantitative information in amplitude deformation.

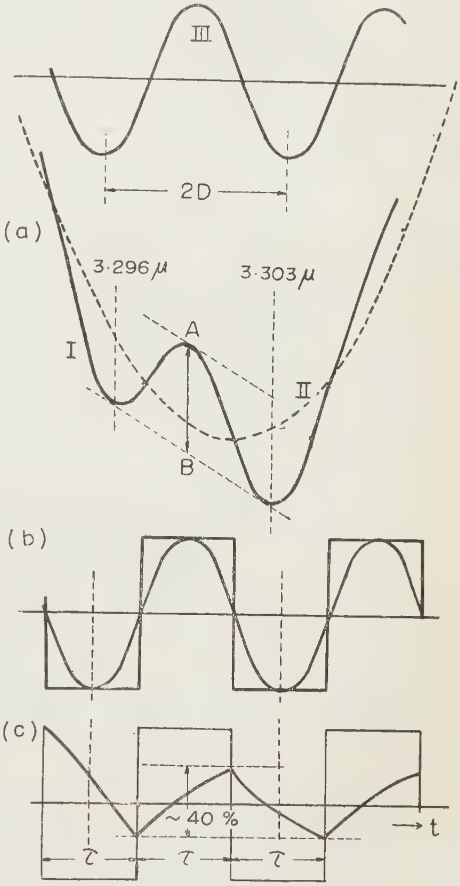

Fig. 3. The schematic representations of polystirene bands in sinusoidal and step functions.

---

[*] The experimental error was considered as of the order of Johnson noise 1×10^{-8} volt in secondary galvanometer.

§ 5. Conclusion

Examining the response time and the noises, we could explain the various characteristics of the amplifier. It has the disadvantage of a long time constant, and consequently somewhat long scanning time is required in continuous measuremeuts, but, as is known from the analysis, this can be shortened by using a lower sensitive first galvanometer (with larger torsion constant and shorter period) and a higher sensitive photocell (with large χ); that is, we can easily see that the last constant term $B_1 n\chi/(R+R_1)+D_1$ has large contribution to the time constant $1/\gamma$ and the characteristic features of the amplifier are as following; it has simple construction, steadiness for long time, which results from keeping the first galvanometer without zero drift by the feed-back method, and higher sensitivity, by which it is allowed for the amplifier to approach easily to the natural limit of the noises. Since Brownian noise becomes comparatively small with the Johnson noise of the detector, we can utilize effectively the response of detector and consequently obtain a higher resolving power in infrared spectrophotometry. Moreover, from the quantitative estimation of deformation rate we can inform of the true absorption intensity. Thus our method of amplification adapted for low resistance detector such as thermocouple will find other various applications in other fields than in infrared spectroscopy.

The authors wish to express their sincere thanks to Prof. Uchida for his continual interest and direction in this research.

Appendix

From the Eq. (2)

$$AI_1\dddot{\phi}_1+(I_1+AP_1)\ddot{\phi}_1+(P_1+D_1A)\dot{\phi}_1 +\left(\frac{B_1n\chi}{R+R_1}+D_1\right)\phi_1=B_1i_0(1-\alpha A)e^{-\alpha t} . \tag{2'}$$

By Laplace transformation on both sides under the initial conditions $\ddot{\phi}_1(0)=\phi_1(0)=0$, we obtain

$$L(\phi_1)= \frac{[AI_1p+(I_1+AP_1)]\dot{\phi}_1(0)+B_1i_0(1-\alpha A)/(\alpha+p)}{AI_1(p+\beta)(p+\kappa)(p+\mathcal{E})} , \tag{I}$$

where $L(\phi_1)=\int_0^p \phi_1 e^{-pt}dt$ and $-\beta$, $-\kappa$ and $-\mathcal{E}$ are the roots of the third order equation;

$$f(p)\equiv A_1I_1p^3+(I_1+AP_1)p^2+(P_1+D_1A)p +\left(\frac{B_1n\chi}{R+R_1}+D_1\right)=0 . \tag{II}$$

Thus by inverse Laplace transformation,

$$\phi_1=\frac{1}{2\pi i}\int_{-i\infty}^{+i\infty}\frac{(Mp+N)(p+\alpha)+B_1i_0(1-\alpha A)}{AI_1(p+\alpha)(p+\beta)(p+\kappa)(p+\mathcal{E})} \times e^{pt}dp , \tag{III}$$

under the abbreviation $M=AI_1\dot{\phi}_1(0)$ and $N=(I_1+AP_1)\dot{\phi}_1(0)$. For the values of the amplifier constants, under which the feed-back resonance is realized as a final steady state, we have one negative real root $(-\beta)$ and two complex conjugates ones $(-\gamma\pm i\omega$ with $\gamma>0)$. Thus we obtain Eq. (2–1) in this paper from (III); in order to give the coefficients of Eq. (2–1), we have only to substitute $-\alpha$, $-\beta$, and $-\gamma\pm i\omega$ for p of the integrand. We can find the numerical values of β, γ and ω from the relation between the roots and the coefficients of $f(p)=0$. For each condition of feed-back resonance (listed in Tables of this paper) β is much larger than γ and does not affect the responce time of amplifier. The values of ω always become nearly equal to the resonance frequency.

Now, substituting (2–1) into i_2 expression of Appendix of part II through $E=\chi\phi_1$, we obtain Eq. (2–2). Since the secondary galvanometer (with the moment of damping P_2, the moment of inertia I_2, the torsion constant D_2, and the moment of displacement B_2) is under the critical damping condition, its behaviour under the signal $i_0'e^{-\eta t}$ is shown by following differential equation

$$I_2\ddot{\phi}_2+P_2\dot{\phi}_2+D_2\phi_2=B_2i_0'e^{-\eta t} ,$$

where $P_2=2(I_2D_2)^{1/2}$. Solving this equation by the previous meteod, we obtain

$$\phi_2=(a+bt)e^{-\mathcal{E}t}+ce^{-\eta t} ,$$

where $\mathcal{E}=P/2I$ and a, b, and c are constant coefficients. Accordingly, in our case the expression (2–2) can be obtained.

References

1) K. Fukuda: Jour. Phys. Soc. Japan **9** (1954) 115 and 123.

2) G. E. Uhlenbeck and S. Goudsmidt: Phys. Rev. **34** (1929) 145.

3) W. Schottky: Ann. d. Physik **68** (1922) 157.

4) H. Nyquist: Phys. Rev. **32** (1928) 110.

5) J. Strong: Rev. Mod. Phys. **20** (1948) 180.

6) R. Zwinden and E. Baldinger: Helv. Phys. Acta. XXVI (1953) 111.

JOURNAL OF THE PHYSICAL SOCIETY OF JAPAN Vol. 9, No. 6, NOV.—DEC., 1954

On a Refinement of the Transonic Approximation Theory

By Isao IMAI

Department of Physics, Faculty of Science, University of Tokyo

(Received July 30, 1954)

In this paper it is proposed that the basic equation for the two-dimensional transonic flow of a compressible fluid should be

$$\frac{\partial^2\psi}{\partial\tau^2}+\frac{\partial^2\psi}{\partial\theta^2}=-\frac{5}{36}\frac{1}{\tau^2}\psi \tag{A}$$

rather than the commonly used one

$$\frac{\partial^2\Psi}{\partial\eta^2}-\eta\frac{\partial^2\Psi}{\partial\theta^2}=0\,,\qquad \eta=(\gamma+1)^{1/3}\frac{q-q_*}{q_*} \tag{B}$$

or its equivalent. Here $\tau=-\int\mu q^{-1}dq$, $\mu=(1-M^2)^{1/2}$, $K=(\mu\rho_0/\rho)^2$, and $\Psi=K^{-1/4}\psi$ is the stream function, (q,θ) are the magnitude and direction of the velocity, q_* the critical velocity, M the local Mach number, ρ the density, ρ_0 the stagnation density, and γ the ratio of specific heats.

A set of fundamental solutions of (A), which have singularity at the point $(\tau=\tau_1,\ \theta=0)$, is obtained in a natural and elementary way in the form

$$\psi_m=\tau^m\sin^m\alpha\{C_1Q^m{}_{-1/6}(\cos\alpha)+C_2Q^m{}_{-5/6}(\cos\alpha)\}\,,$$

where $\tau_1-i\theta=\tau\cos\alpha$, $Q_n{}^m$ being the associated Legendre function. In particular, flow through a Laval nozzle and past a lenticular-shaped body can be constructed by employing the solutions with $m=\pm1/2$. Finally, discussion is given on the advantage of (A) over (B) as the fundamental equation for the transonic flow.

§ 1. Introduction

The object of the present paper is two-fold; first, to give an elementary and natural approach to the transonic-approximation theory, and second, to widen the scope of the usual transonic approximation so as to cover the transonic flow around moderately thick profiles where the fluid velocity is not necessarily confined to the neighbourhood of the sonic velocity.

It is well known that the two-dimensional irrotational flow of a compressible fluid can be exactly dealt with by the hodograph method. Thus, assuming the adiabatic law, uniform flow of gases past obstacles has been studied by a number of investigators, among whom we may mention especially Bergman [1], Tsien and Kuo [9, 14], Lighthill [10], and Cherry [2]. But the mathematical difficulty involved is so great, that the numerical discussions on the flow patterns based on the exact hodograph method have hitherto been very scanty [3, 9, 14]. For practical purposes, therefore, we are compelled to have recourse to some approximate method.

In a recent paper [6] the present author has expressed the hodograph equations in terms of variables suggested by the WKB method as

$$\partial^2\psi/\partial\tau^2+\partial^2\psi/\partial\theta^2=k(\tau)\psi\,, \tag{1.1}$$

and developed an approximate method for treating subsonic flows, based on the consideration that $k\psi$ can be safely neglected in comparison with $\partial^2\psi/\partial\tau^2+\partial^2\psi/\partial\theta^2$. It should be noted that the method can be applied to gas flows obeying any arbitrary pressure-density relation. As examples of application of the method, the author has treated, in conjunction with Hasimoto, the subsonic flow of air (obeying the adiabatic law) past a circular cylinder and an elliptic cylinder of thickness ratio 1/10 as well as the discontinuous flow past a flat plate accompanied with a dead air region [7].

Though very accurate for purely subsonic flow, the method is expected to be less satisfactory for transonic flow having both subsonic and supersonic local speeds. In this paper, a method of treating transonic flow will be developed by the approximation of replacing $k(\tau)$ in (1.1) by $-(5/36)\tau^{-2}$.

Now, it may be said that recent progress in transonic-flow theory has been achieved mainly on the basis of von Kármán's transonic similarity [8]. For example, Guderley and Yoshihara's research may be mentioned [4]. Tomotika and Tamada [13] have also introduced a hypothetical gas which represents the real gas sufficiently accurately near the sonic velocity, and obtained valuable informations concerning the characteristic features of transonic flow. The hypothetical gas is characterized by the property that it satisfies exactly the approximate equation proposed by von Kármán. Thus, the Tricomi equation plays a fundamental role in Tomotika and Tamada's paper just as in the usual transonic-approximation theory.

It will be seen that the analysis presented in this paper bears a close resemblance to the usual transonic approximation based on the Tricomi equation. However, in contrast to the fact that the usual transonic approximation is only applicable to such flows that the velocity is very near to the local sound velocity throughout the field of flow, our method is believed to be free from such restrictions. Indeed, it may be applied with success to transonic flow past moderately thick profiles where large velocity variation occurs. In this respect it is parallel to the exact treatment of the original hodograph equation. Its drawback of being approximate seems to be well compensated by the simplicity of procedure, both analytical and numerical. Moreover, the exact treatment is usually only concerned with the adiabatic gas flow, and cannot give information about the behaviour of gas flow when deviations occur from the adiabatic law. Though approximate in nature, our method can be equally well applied to any gas with any arbitrary pressure-density relation; in particular, it is exact for the hypothetical gas proposed by Tomotika and Tamada.

In this paper, first, an approximation $k(\tau)=-(5/36)\tau^{-2}$ is introduced in the modified hodograph equation (1.1). To obtain the flow past obstacles we must find the so-called fundamental solutions, which have singularity of the nature of a pole or branch point. In view of the mathematical complication of the existing transonic-flow theory, it will be desirable to proceed in as elementary a way as possible. With this in mind, starting from a typical solution for an incompressible fluid and using analogy considerations, we shall obtain a particular solution for a compressible fluid in a very natural and elementary way. Then, suggested by the form of the particular solution thus obtained, new variables are introduced, in terms of which a class of fundamental solutions will be obtained in closed forms using the Legendre functions. It will be seen that the Legendre functions fortunately reduce to elementary functions in the important case of flow past obstacles, where the singularity of the nature of a branch point of degree of a half odd integer is required.

These solutions are then investigated in some detail concerning their transonic as well as singularity properties. It will then be shown that the flow through a Laval nozzle or around a lenticular-shaped body can be obtained by taking one or two such fundamental solutions respectively.

Finally, the general nature of our approximate method will be discussed in comparison with other existing methods, such as the von Kármán-Tsien method and the transonic-approximation method based on von Kármán's similarity law.

Detailed numerical discussions on the flow through a type of Laval nozzle as well as the flow around lenticular-shaped bodies, with special attention to the appearance of limiting-lines and branch-lines have been made with the cooperation of H. Hasimoto. These will form the subject of a forthcoming paper.

§ 2. Fundamental Equations

According to the previous investigation [6], the fundamental equation for the irrotational motion of a compressible fluid can be expressed in the form

$$\partial^2\psi/\partial\tau^2+\partial^2\psi/\partial\theta^2=k\psi\,, \qquad (2.1)$$

where ψ is the reduced stream function such that

$$\Psi=K^{-1/4}\psi\,, \qquad (2.2)$$

$$\tau=-\int_1^q\left(1-\frac{q^2}{c^2}\right)^{1/2}\frac{dq}{q}\,, \qquad (2.3)$$

$$K=(1-q^2/c^2)(\rho_0/\rho)^2\,, \qquad (2.4)$$

$$k=K^{-1/4}d^2K^{1/4}/d\tau^2\,. \qquad (2.5)$$

Here q and θ are the magnitude and direction of the velocity, Ψ the stream function, ρ the density, ρ_0 the stagnation density, and c the local velocity of sound.

For purely subsonic flow $k\psi$ can be safely neglected in comparison with $\partial^2\psi/\partial\tau^2+\partial^2\psi/\partial\theta^2$ in (2.1). But this will not be the case for transonic flow. Indeed, if, for example, we consider the case of adiabatic flow, we have

$$\left.\begin{aligned} k&=-\frac{1-a^2}{4}q^4\frac{8-2(1+3a^2)q^2-(1-a^2)q^4}{(1-q^2)^3(1-a^2q^2)} \\ a^2&=\frac{\gamma-1}{\gamma+1} \end{aligned}\right\} \tag{2.6}$$

and, hence, in the transonic region: $q\doteqdot 1$, k is very great and it can even become infinite for $q=1$. Thus it will be natural to suppose that the approximation based on the neglect of $k\psi$ would be unsatisfactory for the transonic flow.

Now, for the adiabatic flow, we have

$$\mu=\left(1-\frac{q^2}{c^2}\right)^{1/2}=\left(\frac{1-q^2}{1-a^2q^2}\right)^{1/2}, \tag{2.7}$$

$$\tau=\tanh^{-1}\mu-a^{-1}\tanh^{-1}a\mu \tag{2.8}$$

$$=\frac{1}{3}(1-a^2)\mu^3\left\{1+\frac{3}{5}(1+a^2)\mu^2+O(\mu^4)\right\}, \tag{2.9}$$

$$k=-\frac{5}{4}(1-a^2)^{-2}\mu^{-6}\times\left\{1-\frac{6}{5}(1+a^2)\mu^2+O(\mu^4)\right\}, \tag{2.10}$$

in the neighbourhood of $q=1$. Hence we have

$$k=-\frac{5}{36}\frac{1}{\tau^2}+O(\tau^{-2/3}). \tag{2.11}$$

It may be interesting to note that, as may be shown without difficulty, the relation (2.11) holds not only for the real isentropic gas but also for any gas provided only that $K(q)$, regarded as a function of q, has a simple zero at $q=1$, the pressure being of course assumed to be a function of the density only.

In this paper, we shall approximate to the exact gas characteristic by the expression

$$k=-(5/36)\tau^{-2}. \tag{2.12}$$

For air, we have calculated k as a function of q, by employing (2.6) and taking $\gamma=1.4$. We have also calculated $-(5/36)\tau^{-2}$ by the use of (2.8). They are graphically shown in Fig. 1. It will be seen that (2.12) provides a very good approximation to the reality for any value of q, either sub- or supersonic, except near the maximum velocity:

$$q_m=\{(\gamma+1)/(\gamma-1)\}^{1/2}.$$

More detailed discussions concerning the accuracy of the assumption (2.12), especially in comparison with some other existing methods of approximation, will be given in later sections.

§ 3. Particular Solutions

We have now to deal with the equation

$$\frac{\partial^2\psi}{\partial\tau^2}+\frac{\partial^2\psi}{\partial\theta^2}=-\frac{5}{36}\frac{1}{\tau^2}\psi. \tag{3.1}$$

A set of particular solutions to (3.1) can be obtained as usual in the form

$$\psi=W_n(\tau)e^{ni\theta}, \tag{3.2}$$

where $W_n(\tau)$ is the solution of the ordinary second-order differential equation

$$\frac{d^2W_n}{d\tau^2}+\left(-n^2+\frac{5}{36}\frac{1}{\tau^2}\right)W_n=0,$$

so that

$$W_n=\tau^{1/2}Z_{1/3}(ni\tau), \tag{3.3}$$

where $Z_{1/3}$ is the Bessel function of order 1/3.

We can obtain a general solution of (3.1), by taking a linear combination of (3.2) with different n. Thus

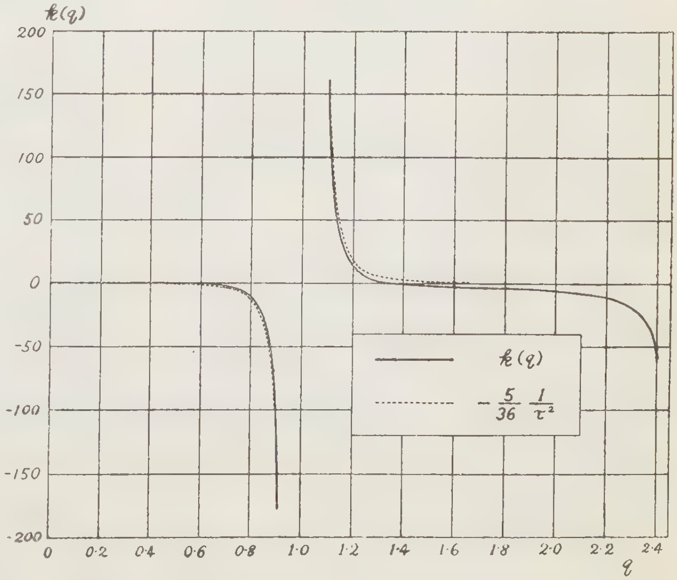

Fig. 1. $k(q)$-curves, exact and approximate, for a real gas with $\gamma=1.4$.

$$\psi=\sum C_n W_n(\tau)e^{ni\theta}\,,\quad \int f(n)W_n(\tau)e^{ni\theta}dn\,. \tag{3.4}$$

We shall next seek for the solution of (3.1) giving the compressible flow past an obstacle. For this purpose, we shall start from the corresponding solution for the incompressible flow.

§ 4. Incompressible Flow past a Circular Cylinder

As is well known, the uniform flow of an incompressible fluid with velocity U past a circular cylinder of radius unity is given by the complex velocity potential

$$f(z)=U(z+z^{-1})\,,\qquad z=x+iy\,. \tag{4.1}$$

Hence, putting

$$w=\frac{1}{U}\frac{df}{dz}=\frac{q}{U}e^{-i\theta}\,, \tag{4.2}$$

we have

$$w=1-z^{-2}\,. \tag{4.3}$$

Hence (4.1) becomes

$$f=U\{(1-w)^{-1/2}+(1-w)^{1/2}\}\,. \tag{4.4}$$

We shall attempt to express (4.4) in a form similar to (3.4). First, noting that $w=1$ is a branch point, we have

$$\begin{aligned}(1-w)^{-1/2}&=\pm\sum_{n=0}^{\infty}(-\tfrac{1}{2},n)(-w)^n\,,\quad |w|<1\,, \quad (4.5)\\&=\pm\sum_{n=0}^{\infty}(-\tfrac{1}{2},n)(-w)^{-n-1/2}\,,\quad |w|>1\,,\end{aligned} \tag{4.6}$$

with

$$(-\tfrac{1}{2},n)\equiv\frac{(-\frac{1}{2})!}{n!(-\frac{1}{2}-n)!}=\frac{(-1)^n}{\pi^{1/2}}\frac{(n-\frac{1}{2})!}{n!}\,, \tag{4.7}$$

where $x!$ stands for $\Gamma(x+1)$.

Now, we can construct, in various ways, analytic functions of w for which $w=1$ is a singularity of the same nature as for $(1-w)^{-1/2}$. For this purpose, we notice that the nature of a singularity of a power series $\sum c_n z^n$ is completely determined by the asymptotic behaviour of the coefficients c_n as $n\to\infty$ (Titchmarsh [12], p. 224).

By Stirling's formula we have

$$(-\tfrac{1}{2},n)\sim(-1)^n(\pi n)^{-1/2}\sim(-1)^n[\pi(n+\tfrac{1}{2})]^{-1/2}\,. \tag{4.8}$$

For convenience, we first consider the series (4.6). The series (4.5) will be considered later. Remembering (4.8) we have

$$\begin{aligned}(1-w)^{-1/2}&\sim(-\pi)^{-1/2}\sum^{\infty}(n+\tfrac{1}{2})^{-1/2}w^{-(n+1/2)}\\&\sim(-\pi)^{-1/2}\int^{\infty}w^{-\nu}\nu^{-1/2}d\nu\,,\end{aligned} \tag{4.9}$$

where the symbol $\sim$ denotes that the functions on both sides of it have a singularity of the same nature. The last member has been obtained by putting $\nu=n+\frac{1}{2}$ and noting that the summation and integration will give asymptotically equal results. In fact, since we are concerned with a divergent series, we are only interested in the coefficient c_n for $n\to\infty$, and thus any finite number of c_n can be replaced by arbitrary values without affecting the nature of the singularity under consideration. Accordingly the lower limit of the infinite integral can be given any arbitrary value. For the present purpose it is convenient to take the lower limit as zero. Thus, by the definition of the Γ-function, we have

$$\begin{aligned}\int_0^{\infty}w^{-\nu}\nu^{-1/2}d\nu&=\int_0^{\infty}e^{-\nu\log w}\nu^{-1/2}d\nu\\&=\pi^{1/2}(\log w)^{-1/2}\,.\end{aligned}$$

Hence

$$(1-w)^{-1/2}\sim(-\log w)^{-1/2}\,. \tag{4.10}$$

It may be remarked here that we should have immediately arrived at the result, if we noticed that in the neighbourhood of $w=1$

$$\begin{aligned}\log w&=-\log\{1-(1-w)\}\\&=(1-w)+\tfrac{1}{2}(1-w)^2+\cdots\,.\end{aligned}$$

§ 5. Fundamental Solutions

In order to deal with a compressible flow past an obstacle, it is clear that we should find, at least, a solution of the equation (3.1) which has a singularity at $w=1$ (corresponding to $\tau=\tau_1$, $\theta=0$) of the same nature as (4.4). Let us call a solution possessing a certain singularity at a point $(\tau=\tau_1\,,\ \theta=0)$ a fundamental solution.

We shall now find a fundamental solution of the same nature as $(1-w)^{-1/2}$ by using the procedure suggested in the preceding section. First, we write (4.9) in the form

$$(1-w)^{-1/2}\sim(-\pi)^{-1/2}\int^{\infty}n^{-1/2}\left(\frac{q}{U}\right)^{-n}e^{ni\theta}dn\,. \tag{5.1}$$

Now, it may be expected that the solution of (3.1) can in general be expressed as (3.4), so that, remembering (3.3), we have

$$\phi=\int^{\infty} f(n)\tau^{1/2}Z_{1/3}(ni\tau)e^{ni\theta}dn\ . \qquad (5.2)$$

But, by the use of the asymptotic expansions of the Bessel functions, we have for $n\to\infty$

$$(n\pi/2)^{1/2}e^{-n\tau_1}i^{-1/3}\tau^{1/2}H_{1/3}^{(2)}(ni\tau)e^{ni\theta} \sim e^{n[(\tau-\tau_1)+i\theta]}\ . \qquad (5.3)$$

If we assume that the velocity at infinity, $q=U$, corresponds to $\tau=\tau_1$, then $U<q<1$ will correspond to $\tau_1>\tau>0$. Hence, noting that $|\exp n[(\tau-\tau_1)+i\theta]|=\exp n(\tau-\tau_1)<1$, we may take

$$\begin{aligned}F&=(-\pi)^{-1/2}\int_0^{\infty} dn\cdot n^{-1/2}\left(\frac{n\pi}{2}\right)^{1/2} \\ &\qquad\times e^{-n\tau_1}i^{-1/3}\tau^{1/2}H_{1/3}^{(2)}(ni\tau)e^{ni\theta} \\ &=2^{-1/2}i^{-3/4}\tau^{1/2}\int_0^{\infty} H_{1/3}^{(2)}(ni\tau)e^{-n(\tau_1-i\theta)}dn\ ,\end{aligned} \qquad (5.4)$$

as a candidate for the fundamental solution looked for. In fact, F has the form (5.2) and, moreover, the asymptotic behaviour of its integrand as $n\to\infty$ is quite similar to that of (5.1).

Now we have (Watson [15], p. 74)

$$H_\nu^{(2)}(z)=(i\sin\nu\pi)^{-1}[e^{i\nu\pi}J_\nu(z)-J_{-\nu}(z)]\ . \qquad (5.5)$$

Also we have (Watson [15], p. 386)

$$\int_0^{\infty} e^{-at}J_\nu(bt)dt=\frac{\{(a^2+b^2)^{1/2}-a\}^\nu}{b^\nu(a^2+b^2)^{1/2}}\ , \qquad (5.6)$$

if $\mathrm{Re}\,(a+ib)>0$, $\mathrm{Re}\,(\nu)>-1$, where such branch of $(a^2+b^2)^{1/2}$ should be taken that $|(a^2+b^2)^{1/2}-a|<|b|$.

In (5.6) we can put $a=\tau_1-i\theta$, $b=i\tau$, $\nu=1/3$, since

$$\mathrm{Re}\,(a\pm ib)=\mathrm{Re}\,(\tau_1-i\theta\pm\tau)=\tau_1\pm\tau>0\ ,$$
$$\mathrm{Re}\,(\pm1/3)>-1\ .$$

Then, by (5.5), we find

$$\int_0^{\infty} H_{1/3}^{(2)}(ni\tau)e^{-n(\tau_1-i\theta)}dn =\frac{\tau^{-1/3}\{(\sigma^2-\tau^2)^{1/2}-\sigma\}^{1/3}-\tau^{1/3}\{\sigma^2-\tau^2)^{1/2}-\sigma\}^{-1/3}}{i^{2/3}\sin(\pi/3)(\sigma^2-\tau^2)^{1/2}}\ , \qquad (5.7)$$

with $\sigma=\tau_1-i\theta$.

Next, to simplify the various formulae, let us put $a=-ib\cos\alpha$. Then (5.6) reduces to

$$\int_0^{\infty} e^{-at}J_\nu(bt)dt=\mp\frac{i^\nu e^{\pm i\nu\alpha}}{b\sin\alpha}\ , \qquad \mathrm{Im}\,\alpha\gtrless0\ , \qquad (5.8)$$

where $\mathrm{Re}\,(a\pm ib)>0$, $a=-ib\cos\alpha$.

In particular, putting $a=\tau_1-i\theta$, $b=i\tau$, we have in place of (5.7)

$$\int_0^{\infty} H_\nu^{(2)}(ni\tau)e^{-n(\tau_1-i\theta)}dn =\mp\frac{2i^{\nu-1}\sin\nu(\pi\pm\alpha)}{\tau\sin\nu\pi\sin\alpha}\ , \qquad \mathrm{Im}\,\alpha\gtrless0\ . \qquad (5.9)$$

Inserting (5.9) with $\nu=1/3$ in (5.4), we have finally

$$F=\left(\frac{8}{3\tau}\right)^{1/2}\frac{\sin\frac{1}{3}(\pi+\alpha)}{\sin\alpha}\ , \qquad (5.10)$$

where

$$\tau_1-i\theta=\tau\cos\alpha\ , \quad \alpha=\xi+i\eta\ , \quad \eta>0\ . \qquad (5.11)$$

Now it is quite easy to show directly that the function F, as given by (5.10), has in fact the singularity required. For this purpose, let us put

$$\omega=\tau-\tau_1+i\theta\ . \qquad (5.12)$$

Then, by (5.11) we have

$$\omega=\tau(1-\cos\alpha)=2\tau\sin^2(\alpha/2)\ , \qquad (5.13)$$

whence

$$\sin(\alpha/2)=(\omega/2\tau)^{1/2}\ ; \qquad (5.14)$$

consequently, in the neighbourhood of $\tau=\tau_1$, $\theta=0$, i.e., $\omega=0$, we have $\alpha\to(2\omega/\tau)^{1/2}$. Therefore, as $\omega\to0$ (5.10) becomes

$$F\to(8/3\tau)^{1/2}\alpha^{-1}\sin(\pi/3)\to\omega^{-1/2}\ .$$

Thus it is confirmed that F has a singularity at $\tau=\tau_1$, $\theta=0$ which is of the same nature as the singularity of $(1-w)^{-1/2}$.

§ 6. Another Method of Obtaining a Fundamental Solution

We can also obtain a fundamental solution for compressible flow, starting from the infinite series (4.5) for incompressible flow. Thus, we have, for $q<U$,

$$(1-w)^{-1/2}=\sum_{n=0}^{\infty}(-\tfrac{1}{2},n)(-w)^n \sim\pi^{-1/2}\int_0^{\infty} n^{-1/2}\left(\frac{q}{U}\right)^n e^{-ni\theta}dn\ . \qquad (6.1)$$

Then we introduce

$$F=2^{-1/2}i^{4/3}\tau^{1/2}\int_0^{\infty} H_{1/3}^{(1)}(ni\tau)e^{n(\tau_1-i\theta)}dn\ . \qquad (6.2)$$

Now, we can show that[*]

---

[*] This can be proved just as (5.9) by assuming $\tau_1<-\tau$. The result is then extended to the actual case $\tau_1>0$ by analytic continuation,

$$\int_0^\infty H_\nu^{(1)}(ni\tau)e^{n(\tau_1-i\theta)}dn$$
$$=-\frac{2i^{-\nu-1}\sin\nu(\pi+\alpha)}{\tau\sin\nu\pi\sin\alpha}\,,\qquad \mathrm{Im}\,\alpha>0\,, \tag{6.3}$$

where $$\tau_1-i\theta=\tau\cos\alpha\,. \tag{6.4}$$

Therefore (6.2) becomes

$$F=-\left(\frac{8}{3\tau}\right)^{1/2}\frac{\sin\frac{1}{3}(\pi+\alpha)}{\sin\alpha}\,, \tag{6.5}$$

which is just the same as (5.10) except for the sign.

§ 7. Introduction of New Variables

It is to be noted that the fundamental solution (5.10) or (6.5) for compressible flow is expressed in a simple form in terms of variables τ, α. This suggests us to introduce τ, α as independent variables, in place of τ, θ, in order to integrate the fundamental equation (3.1).

Thus, from

$$\tau_1-i\theta=\tau\cos\alpha\,, \tag{7.1}$$

where α is of course complex, we have the transformation formulae

$$\frac{\partial}{\partial\tau}=\frac{\partial}{\partial\tau}+\frac{\cot\alpha}{\tau}\frac{\partial}{\partial\alpha}\,,\qquad \frac{\partial}{\partial\theta}=\frac{i}{\tau\sin\alpha}\frac{\partial}{\partial\alpha}\,. \tag{7.2}$$

Hence (2.1) becomes

$$\left(\frac{\partial^2}{\partial\tau^2}-\frac{1}{\tau^2}\frac{\partial^2}{\partial\alpha^2}+\frac{2}{\tau}\cot\alpha\frac{\partial^2}{\partial\tau\partial\alpha}-\frac{1}{\tau^2}\cot\alpha\frac{\partial}{\partial\alpha}\right)\psi=k\psi\,. \tag{7.3}$$

Let us assume here

$$k(\tau)=-b\tau^{-2}\,,\qquad b=\text{const}\,. \tag{7.4}$$

In our case $b=5/36$, but we can deal with the general case of an arbitrary value of b just in the same way.

It will readily be seen that (7.3) has a particular solution

$$\psi=\tau^m A(\alpha)\,,\qquad m=\text{const}\,, \tag{7.5}$$

where $A(\alpha)$ has to satisfy

$$A''-(2m-1)\cot\alpha\,A'-\{b+m(m-1)\}A=0, \tag{7.6}$$

dashes denoting differentiation with respect to α. If, in particular, $m=1/2$, (7.6) reduces to

$$A''+\kappa^2A=0\,,\qquad \kappa^2=\tfrac{1}{4}-b\,. \tag{7.7}$$

Hence $A=e^{\pm i\kappa\alpha}$, and consequently

$$\psi_{1/2}=\tau^{1/2}e^{\pm i\kappa\alpha} \tag{7.8}$$

is a particular solution of (7.3).

Now it is obvious from the original equation (2.1) that if ψ is a solution, then $\partial\psi/\partial\theta$ is also a solution. Therefore, starting from $\psi_{1/2}$, we can obtain a series of particular solutions $\partial\psi_{1/2}/\partial\theta$, $\partial^2\psi_{1/2}/\partial\theta^2,\ldots$ Accordingly, remembering (7.2), we find that

$$\psi_{1/2-n}=\frac{\partial^n}{\partial\theta^n}\psi_{1/2}=\left(\frac{i}{\tau\sin\alpha}\frac{\partial}{\partial\alpha}\right)^n\tau^{1/2}e^{\pm i\kappa\alpha}$$
$$=i^n\tau^{1/2-n}\left(\frac{1}{\sin\alpha}\frac{d}{d\alpha}\right)^n e^{\pm i\kappa\alpha} \tag{7.9}$$

(where $n=0,1,\ldots$) are particular solutions of (6.3). It will be obvious that (7.9) are nothing other than the solutions (7.5) which correspond to $m=\frac{1}{2}-n$.

In our problem $b=5/36$ and hence, by (7.7), $\kappa=1/3$.

In particular, putting $n=1$, we have from (7.9)

$$\psi_{-1/2}=\mp\tau^{-1/2}\frac{e^{\pm i\alpha/3}}{3\sin\alpha}\,. \tag{7.10}$$

It will readily be seen that the previous result (5.10) or (6.5) can be obtained as a linear combination of (7.10), as should naturally be expected.

§ 8. General Solution of (7.3)

It can be shown without difficulty that the general solution of (7.6) is given by

$$A=\sin^m\alpha\{C_1P_n^m(\cos\alpha)+C_2Q_n^m(\cos\alpha)\}\,, \tag{8.1}$$

where P_n^m and Q_n^m are the associated Legendre functions, and

$$n=-\tfrac{1}{2}+\kappa=-\tfrac{1}{2}+(\tfrac{1}{4}-b)^{1/2}\,. \tag{8.2}$$

Hence, by (7.5), we find that

$$\psi_m=\tau^m\sin^m\alpha\{C_1P_n^m(\cos\alpha)+C_2Q_n^m(\cos\alpha)\} \tag{8.3}$$

is a solution of (7.3).

Now we have (Hobson [5], p. 204)

$$P_n^m(\mu)=e^{-m\pi i}\times$$
$$\times\frac{Q_n^m(\mu)\sin(n+m)\pi-Q_{-n-1}^m(\mu)\sin(n-m)\pi}{\pi\cos n\pi}\,. \tag{8.4}$$

Therefore we can also write (8.3) in the form

$$\psi_m=\tau^m\sin^m\alpha\{C_1Q_n^m(\cos\alpha)$$
$$+C_2Q_{-n-1}^m(\cos\alpha)\}\,, \tag{8.5}$$

C_1, C_2 being arbitrary. Further, it is immediately seen from Hobson [5], p. 286, that

$$Q_n{}^m(\cos\alpha)$$
$$=\left(\frac{\pi}{2}\right)^{1/2}\frac{(n+m)!}{(n+\frac{1}{2})!}\frac{\exp[(m+\frac{1}{4})\pi+(n+\frac{1}{2})\alpha]i}{\sin^{1/2}\alpha}$$
$$\times F(m+\tfrac{1}{2},-m+\tfrac{1}{2},n+3/2;(1-e^{2i\alpha})^{-1}), \tag{8.6}$$

$$Q_{-n-1}{}^m(\cos\alpha)$$
$$=\left(\frac{\pi}{2}\right)^{1/2}\frac{(m-n-1)!}{(-n-\frac{1}{2})!}\frac{\exp[(m+\frac{1}{4})\pi-(n+\frac{1}{2})\alpha]i}{\sin^{1/2}\alpha}$$
$$\times F(m+\tfrac{1}{2},-m+\tfrac{1}{2},-n+\tfrac{1}{2};(1-e^{2i\alpha})^{-1}), \tag{8.7}$$

$F(a,b,c;x)$ being the hypergeometric series. In view of the fact that each one of the above hypergeometric series reduces to a finite sum when m is a half odd integer, either positive or negative, the solution ψ_m, as given by (8.5), is then expressible in terms of elementary functions of τ and α. For example, we have, for $m=1/2$,

$$Q_n{}^{1/2}(\cos\alpha)=(\pi/2)^{1/2}e^{3\pi i/4}e^{i\kappa\alpha}\sin^{-1/2}\alpha,$$
$$Q_{-n-1}{}^{1/2}(\cos\alpha)=(\pi/2)^{1/2}e^{3\pi i/4}e^{-i\kappa\alpha}\sin^{-1/2}\alpha.$$

Substituting these into (8.5), we obtain

$$\psi_{1/2}=\tau^{1/2}(c_1e^{i\kappa\alpha}+c_2e^{-i\kappa\alpha}),$$

which is the same as the previous result (7.8).

§ 9. Transonic Property of Fundamental Solutions

Let us now show that each one of the particular solutions obtained above can represent a transonic flow which contains both sub- and supersonic regions.

From (2.2) we have

$$\Psi=K^{-1/4}\psi=R\tau^{-1/6}\psi, \tag{9.1}$$

where

$$R=K^{-1/4}\tau^{1/6}. \tag{9.2}$$

R is easily seen to be an anlytic function of $\tau^{2/3}$, and hence, of $q-1$. On the other hand, we have from (8.5)

$$\tau^{-1/6}\psi_m=\tau^{m-1/6}\sin^m\alpha\{C_1Q_n{}^m(\cos\alpha)$$
$$+C_2Q_{-n-1}{}^m(\cos\alpha)\}. \tag{9.3}$$

Now we have for $|\mu|>1$ (Hobson [5], p. 195)

$$Q_n{}^m(\mu)=\frac{e^{m\pi i}}{2^{n+1}}\frac{(-\frac{1}{2})!\,(n+m)!}{(n+\frac{1}{2})!}(\mu^2-1)^{m/2}\mu^{-(n+m+1)}$$
$$\times F\left(\frac{n+m+2}{2},\ \frac{n+m+1}{2},\ n+\frac{3}{2};\ \frac{1}{\mu^2}\right). \tag{9.4}$$

But, putting $\mu=\cos\alpha$, we have, in virtue of (7.1),

$$\mu^2=\cos^2\alpha=\tau^{-2}(\tau_1-i\theta)^2,$$
$$\sin^2\alpha=1-\mu^2=\tau^{-2}\{\tau^2-(\tau_1-i\theta)^2\}.$$

Hence (9.3) can be rewritten as

$$\tau^{-1/6}\psi_m$$
$$=C_1'\tau^{n+5/6}\{\tau^2-(\tau_1-i\theta)^2\}^m(\tau_1-i\theta)^{-(n+m+1)}$$
$$\times F\left(\frac{m+n+2}{2},\ \frac{m+n+1}{2},\ n+\frac{3}{2};\ \frac{\tau^2}{(\tau_1-i\theta)^2}\right)$$
$$+C_2'\tau^{-n-1/6}\{\tau^2-(\tau_1-i\theta)^2\}^m(\tau_1-i\theta)^{n-m}$$
$$\times F\left(\frac{m-n+1}{2},\ \frac{m-n}{2},\ \frac{1}{2}-n;\ \frac{\tau^2}{(\tau_1-i\theta)^2}\right), \tag{9.5}$$

C_1', C_2' being certain arbitrary constants related to C_1 and C_2. In our case $n=-1/6$, so that $\tau^{n+5/6}=\tau^{2/3}$, $\tau^{-n-1/6}=1$. Therefore $\tau^{1/6}\psi_m$ and hence Ψ, as given by (9.1), is analytic as a function of $\tau^{2/3}$ near $\tau=0$, that is, of $q-1$ near $q=1$. Thus Ψ represents transonic flow such that the subsonic region is smoothly continued to the supersonic region.

§ 10. Nature of Sigularity of Fundamental Solutions

Next we shall study the nature of the singularity possessed by the particular solutions (8.5).

According to Hobson [5], p. 205, we have

$$Q_n{}^m(\mu)=C_1[(\mu-1)/(\mu+1)]^{m/2}$$
$$\times F(-n,\ n+1,\ 1+m;\ \tfrac{1}{2}(1-\mu))$$
$$+C_2[(\mu-1)/(\mu+1)]^{-m/2}$$
$$\times F(-n,\ n+1,\ 1-m;\ \tfrac{1}{2}(1-\mu)), \tag{10.1}$$

C_1, C_2 being certain constants. It will be obvious that $Q_{-n-1}{}^m$ has quite a similar expression as above.

Putting $\mu=\cos\alpha$ and remembering (5.14) we get

$$\tfrac{1}{2}(1-\mu)=\sin^2\tfrac{1}{2}\alpha=\omega/2\tau, \qquad \omega=\tau-\tau_1+i\theta,$$
$$-(\mu-1)/(\mu+1)=\tan^2\tfrac{1}{2}\alpha=\omega/(2\tau-\omega).$$

Hence (8.5) can be expressed in the form

$$\psi_m=A\omega^mF(-n,\ n+1,\ 1+m;\ \omega/2\tau)$$
$$+B(2\tau-\omega)^mF(-n,\ n+1,\ 1-m;\ \omega/2\tau), \tag{10.2}$$

A, B being certain constants. (10.2) shows clearly that ψ_m has, at $\omega=0$ or $\omega=2\tau$, a zero of order m, which is a branch point if m is not an integer. In the subsonic case τ is real and positive, so that, according as τ_1 is positive or negative, either $\omega=0$ or $\omega=2\tau$ can take place corresponding to $(\tau=\tau_1,\ \theta=0)$ or $(\tau=-\tau_1,\ \theta=0)$ respectively. Thus it may naturally be expected that ψ_m will play, in the theory of compressible flow, a role similar to that $(1-w)^m$ plays in the theory of incompressible flow.

In the supersonic case, however, τ is purely imaginary, and hence $\omega=0$ and $\omega=2\tau$ correspond to

$$|\tau|+\theta=0 \quad \text{and} \quad |\tau|-\theta=0\ , \qquad (10.3)$$

respectively, τ_1 being necessarily zero in both cases. Thus, in the supersonic case, the singularity (with $\tau_1=0$) is not isolated as in the subsonic case, but, so to speak, it extends over a particular pair of characteristic curves passing through the origin $(\tau=0,\ \theta=0)$, i.e. $|\tau|\pm\theta=0$, which may suitably be called branch lines.

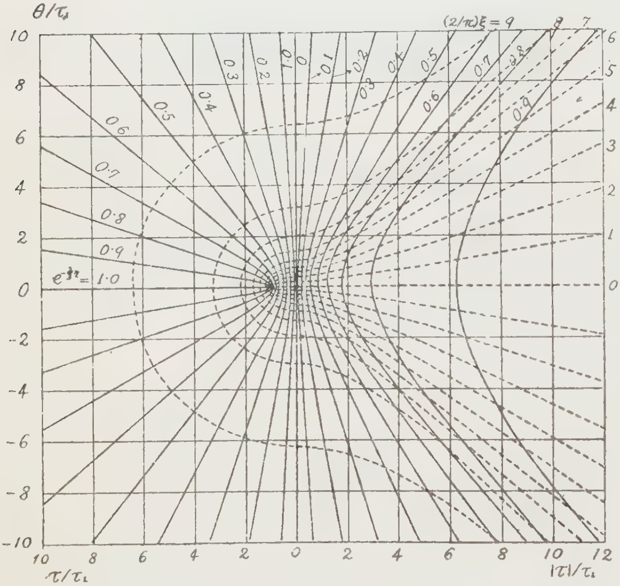

Fig. 2. Curvilinear coordinates (ξ,η) in the $\tau\theta$-plane.

§ 11. Curvilinear Coordinates (ξ,η)

Let us consider the curvilinear coordinates (ξ,η) given by (5.11):

$$\tau_1-i\theta=\tau\cos\alpha\ , \qquad \alpha=\xi+i\eta\ . \qquad (11.1)$$

In the subsonic case $q<c$, τ is real and positive. Hence, separating real and imaginary parts of (11.1), we get

$$\tau=\tau_1\sec\xi\ \mathrm{sech}\,\eta\ , \qquad \theta=\tau_1\tan\xi\tanh\eta\ . \qquad (11.2)$$

It may readily be seen that one-to-one correspondence exists between the domain $\tau>0$, $-\infty<\theta<\infty$ and the domain

$$-\pi/2<\xi<\pi/2\ ,\ \eta>0 \quad \text{if} \quad \tau_1>0\ , \qquad (11.3)$$

or

$$\pi/2<\xi<3\pi/2\ ,\ \eta>0 \quad \text{if} \quad \tau_1<0\ . \qquad (11.4)$$

Eliminating η or ξ from (11.2) we get respectively

$$\tau^2\cos^2\xi+\theta^2\cot^2\xi=\tau_1^2\ , \qquad (11.5)$$

$$\tau^2\cosh^2\eta-\theta^2\coth^2\eta=\tau_1^2\ . \qquad (11.6)$$

Thus $\xi=$const are a system of confocal ellipses with foci at $(\tau_1,0)$, $(-\tau_1,0)$ and $\eta=$const are a system of confocal hyperbolas with the same foci.

Next we consider the supersonic case $q>c$. Then we have to put $\tau=i^{-3}|\tau|$, so that

$$\tau\cosh\eta=|\tau|\sinh(\eta-(3/2)\pi i)\ ,$$
$$\tau\sinh\eta=|\tau|\cosh(\eta-(3/2)\pi i)\ .$$

Accordingly, if we formally make the transformations

$$\tau\to i^{-3}|\tau|\ , \quad \eta\to\eta+(3/2)\pi i\ , \qquad (11.7)$$

the relations (11.2) will be expressed in terms of the real variables ξ,η as

$$|\tau|=\tau_1\sec\xi\ \mathrm{cosech}\,\eta\ ,$$
$$\theta=\tau_1\tan\xi\coth\eta\ . \qquad (11.8)$$

The domain of the variables ξ,η are again given by (11.3) or (11.4) according as $\tau_1>0$ or $\tau_1<0$.

Eliminating η or ξ from (11.8) we get respectively

$$|\tau|^2\cos^2\xi-\theta^2\cot^2\xi=-\tau_1^2\ , \qquad (11.9)$$

$$|\tau|^2\sinh^2\eta-\theta^2\tanh^2\eta=\tau_1^2\ . \qquad (11.10)$$

Thus $\xi=$const and $\eta=$const are both systems of hyperbolas.

Fig. 2 shows the curvilinear net $\xi=$const, $\eta=$const as given by (11.5), (11.6), (11.9), and (11.10).

Finally it should be remarked that, when considering the supersonic case, $\alpha=\xi+i\eta$ should be replaced by $\alpha-(3/2)\pi$ in the expression for ψ in accordance with the formal transformations (11.7).

§ 12. Flow Represented by $\psi_{1/2}$. Flow in a Channel

Let us consider the flow pattern represented by the particular solution $\psi_{1/2}$. By (7.8) we have

$$\psi_{1/2}=\tau^{1/2}e^{\pm i\kappa\alpha}\ , \qquad \kappa=1/3\ . \qquad (12.1)$$

Putting $\alpha=\xi+i\eta$ and separating real and imaginary parts, we obtain

$$\psi_{1/2}=\tau^{1/2}e^{\pm\kappa\eta}\cos\kappa\xi\ ,\quad \tau^{1/2}e^{\pm\kappa\eta}\sin\kappa\xi\ . \tag{12.2}$$

Further, forming linear combinations, we may also find that

$$\psi_{1/2}=\tau^{1/2}(A\cos\kappa\xi+B\sin\kappa\xi)\times(C\cosh\kappa\eta+D\sinh\kappa\eta) \tag{12.3}$$

is a solution, where A, B, C, D are arbitrary constants.

In particular, taking $B=C=0$ and remembering (9.2), we have

$$\Psi_{1/2}=R\tau^{1/3}\cos\kappa\xi\sinh\kappa\eta\ . \tag{12.4}$$

It can readily be seen that (12.4) represents a flow in a channel (two-dimensional Laval nozzle) which is symmetrical with respect to both x- and y-axes. For, remembering (11.2) and (11.8), we can easily find that the stream lines $\Psi=$const in the $\tau\theta$-plane are such as shown in Fig. 3. Hence the physical plane should be as shown in Fig. 4.

Similarly we may also find that

$$\Psi=R\tau^{1/3}(A\cos\kappa\xi+B\sin\kappa\xi)\times(C\cosh\kappa\eta+D\sinh\kappa\eta) \tag{12.5}$$

represents the flow in a channel which is in general unsymmetrical with respect to both x- and y-axes. But, if $B=0$, the channel is symmetrical with respect to the y-axis; and if $C=0$, it is symmetrical with respect to the x-axis.

The expression (12.5) is appropriate to the subsonic case. For the supersonic case we should make the substitution: $\tau\to i^{-3}|\tau|$, $\xi\to\xi$, $\eta\to\eta+(3/2)\pi i$ and hence

$$\Psi=R|\tau|^{1/3}(A\cos\kappa\xi+B\sin\kappa\xi)\times(C\sinh\kappa\eta+D\cosh\kappa\eta) \tag{12.6}$$

is the analytic continuation of (12.5). It should be remembered that (ξ,η) in (12.5) are related to (τ,θ) by (11.2) while those in (12.6) by (11.8).

Finally it may be added that some numerical calculations have been carried out in the case of symmetrical channels in collaboration with H. Hasimoto. Also it has been found that in the case of $\tau_1=0$ the analysis can be simplified considerably and some informations can be obtained concerning the transition from symmetrical to unsymmetrical flow patterns in a Laval nozzle with increasing Mach number. These will be reported in a forthcoming paper*.

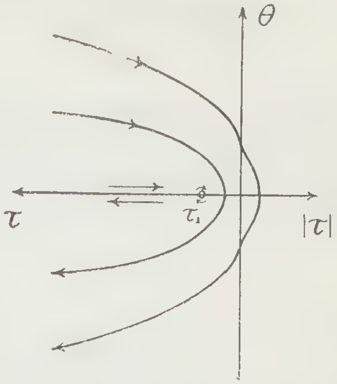

Fig. 3. Flow in a channel. Flow pattern in the $\tau\theta$-plane.

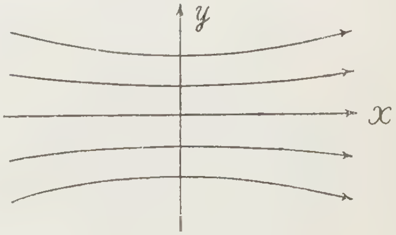

Fig. 4. Flow in a channel. Fow pattern in the physical plane.

§ 13. Flow Represented by $\psi_{-1/2}$. Flow around a Lenticular-Shaped Body

Putting $m=-1/2$ in (8.6) and (8.7) we have respectively

$$Q_n{}^{-1/2}(\cos\alpha)=(\pi/2)^{1/2}\kappa^{-1}e^{-\pi i/4+i\kappa\alpha}\sin^{-1/2}\alpha\ ,$$
$$Q_{-n-1}{}^{-1/2}(\cos\alpha)=-(\pi/2)^{1/2}\kappa^{-1}e^{-\pi i/4-i\kappa\alpha}\sin^{-1/2}\alpha\ .$$

Substituting these in (8.5) we have

$$\psi_{-1/2}=\tau^{-1/2}e^{\pm i\kappa\alpha}/\sin\alpha\ , \tag{13.1}$$

which is nothing other than the already obtained result (7.10).

Putting $\alpha=\xi+i\eta$ in (13.1) and separating real and imaginary parts we get

$$\psi_{-1/2}=\begin{cases}\tau^{-1/2}D^{-1}\{e^{(1\mp\kappa)\eta}\sin(1\pm\kappa)\xi\\ \qquad+e^{-(1\pm\kappa)\eta}\sin(1\mp\kappa)\xi\}\ ,\\ \tau^{-1/2}D^{-1}\{e^{(1\mp\kappa)\eta}\cos(1\pm\kappa)\xi\\ \qquad-e^{-(1\pm\kappa)\eta}\cos(1\mp\kappa)\xi\}\ ,\end{cases} \tag{13.2}$$

where

$$D=\cosh 2\eta-\cos 2\xi\ . \tag{13.3}$$

---

* Tomotika and Tamada [13] have studied the transition from symmetrical (Taylor's type) to unsymmetrical (Meyer's type) flow pattern in an unsymmetrical Laval nozzle. It will be seen that this type of flow corresponds to a particular selection of values of A, B, C, D in (12.5).

Forming a linear combination of (13.2), we have

$$\psi_{-1/2}=\tau^{-1/2}D^{-1}\times$$
$$\times[C_1(\sin\kappa_1\xi\cosh\kappa_2\eta+\sin\kappa_2\xi\cosh\kappa_1\eta)$$
$$+C_2(\sin\kappa_1\xi\cosh\kappa_2\eta-\sin\kappa_2\xi\sinh\kappa_1\eta)$$
$$+C_3(\cos\kappa_1\xi\cosh\kappa_2\eta-\cos\kappa_2\xi\cosh\kappa_1\eta)$$
$$+C_4(\cos\kappa_1\xi\sinh\kappa_2\eta+\cos\kappa_2\xi\sinh\kappa_1\eta)]\,,$$
$$(\kappa_1=1+\kappa\,,\quad \kappa_2=1-\kappa)\,, \qquad (13.4)$$

C_1, C_2, C_3, C_4 being arbitrary constants. The term with the coefficient C_4 in (13.4) is even with respect to ξ and odd with respect to η. Therefore $\psi_{-1/2}$ with $C_1=C_2=C_3=0$ will represent a flow symmetrical with respect to both x- and y-axes. Then combining with $\Psi_{1/2}$ given by (12.4), we have

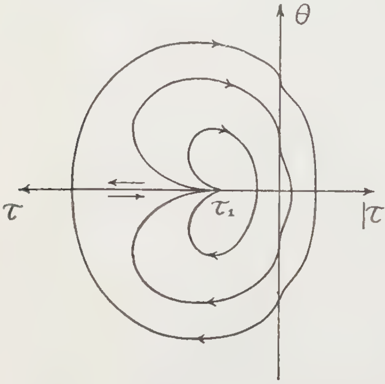

Fig. 5. Flow around a lenticular-shaped body. Flow pattern in the $\tau\theta$-plane.

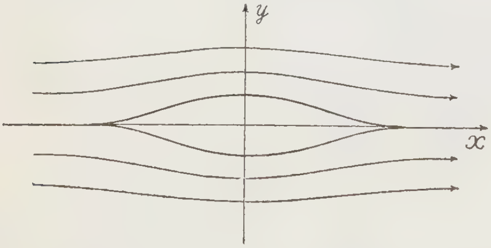

Fig. 6. Flow around a lenticular-shaped body. Flow pattern in the physical plane.

$$\Psi=R\tau^{1/3}[\cos\kappa\xi\sinh\kappa\eta$$
$$-A\tau^{-1}D^{-1}\{\cos(1+\kappa)\xi\sinh(1-\kappa)\eta$$
$$+\cos(1-\kappa)\xi\sinh(1+\kappa)\eta\}]\,, \quad (13.5)$$

or

$$\Psi=R|\tau|^{1/3}[\cos\kappa\xi\cosh\kappa\eta$$
$$+A|\tau|^{-1}D_1^{-1}\{\cos(1+\kappa)\xi\sinh(1-\kappa)\eta$$
$$-\cos(1-\kappa)\xi\sinh(1+\kappa)\eta\}]\,, \quad (13.6)$$

corresponding to the subsonic or supersonic case respectively. Here A is an arbitrary constant and

$$D_1=\cosh 2\eta+\cos 2\xi\,. \qquad (13.7)$$

The stream function Ψ given by (13.5) and (13.6) represents in the modified hodograph plane (τ, θ) such flow patterns as shown in Fig. 5, and thus in the physical plane a flow past a lenticular-shaped body with double symmetry as shown in Fig. 6. The results of numerical calculation will be reported in a forthcoming paper.

Further, it may be added that the flow past unsymmetrical lenticular bodies would be obtained by taking a linear combination of $\psi_{-1/2}$ and $\psi_{1/2}$ as given by (13.4) and (12.3) respectively.

§ 14. Discussions of the Assumption: $k=-(5/36)\tau^{-2}$

We have adopted in this paper the simplifying assumption

$$k=-(5/36)\tau^{-2}\,. \qquad (14.1)$$

We shall now consider the accuracy of the assumption.

In a recent paper von Mises and Schiffer [11] have studied in detail the physical relations corresponding to the assumption

$$k=-b\tau^{-2}\,, \qquad (14.2)$$

so that it will be sufficient here to give some additional discussions of the physical behaviour of the hypothetical gas.

From (2.5) and (14.2), we have

$$\frac{d^2K^{1/4}}{d\tau^2}+\frac{b}{\tau^2}K^{1/4}=0\,, \qquad (14.3)$$

which on integration gives

$$K^{1/4}=\tau^{1/2}(A\tau^{\kappa}+B\tau^{-\kappa})\,,\quad \kappa^2=\tfrac{1}{4}-b\,, \qquad (14.4)$$

where A and B are arbitrary constants.

(14.4) can also be written in the form

$$K^{1/2}=\rho_0 c_1\tau(\tau^{\kappa}+c_2\tau^{-\kappa})^2\,, \qquad (14.5)$$

c_1 and c_2 being arbitrary constants.

From (2.3) and (2.4) we have

$$d\tau=-K^{1/2}(\rho/\rho_0)q^{-1}dq\,. \qquad (14.6)$$

But, from the Bernoulli equation, we have

$$dp=-\rho q dq\,, \qquad (14.7)$$

whence

$$c^2=\frac{dp}{d\rho}=-\rho q\frac{dq}{d\rho}\,. \qquad (14.8)$$

Combining this with (2.4), we obtain

$$\frac{dq}{q}=\frac{d\rho}{\rho[K(\rho/\rho_0)^2-1]}\,, \qquad (14.9)$$

which, in conjunction with (14.6), gives

$$d(\rho/\rho_0)=[K^{-1}-(\rho/\rho_0)^2]K^{1/2}d\tau\ . \qquad (14.10)$$

Remembering (14.5), we can integrate (14.10) in the form

$$\tau=f_1(c_1\rho\,;\,c_2\,,\,c_3)\ , \qquad (14.11)$$

where c_3 is an arbitrary constant of integration and f_1 is a certain definite function. Substituting from (14.5) and (14.11) in (14.9) and integrating, we obtain

$$q=c_4 f_2(c_1\rho\,;\,c_2\,,\,c_3)\ , \qquad (14.12)$$

where c_4 is an arbitrary constant and f_2 is a definite function. Furthere, from (14.7), we shall find

$$p=c_5+c_1{}^{-1}c_4{}^2 f_3(c_1\rho\,;\,c_2\,,\,c_3)\ , \qquad (14.13)$$

c_5 being another arbitrary constant and f_3 a definite function.

Thus the p-ρ relation of the hypothetical gas has 7 parameters κ, ρ_0, $c_1,\ldots,c_5$, which may be so chosen as to obtain good agreement with the real gas. (In our determination $\kappa=1/3$, and 6 parameters remain to be chosen appropriately.)

Now, von Kármán-Tsien's hypothetical gas corresponds to the assumption $K=1$, so that $\kappa=-1/2$, $c_1=\rho_0{}^{-1}$, $c_2=0$. Thus 4 parameters remain to be determined. Our hypothetical gas ($\kappa=1/3$) has, therefore, two more degrees of freedom than von Kármán-Tsien's gas, and thus it would be expected to afford better agreement with the real gas.

Up to this point the discussion on the merit of our hypothetical gas is quite similar to the discussion given by von Mises and Schiffer [11]. But, the present author believes that the essential advantage of our method should be found in the following procedure. Thus, in actual calculations, we should not use the hypothetical gas relations $K(\rho)$, $\tau(\rho)$, $q(\rho)$, $p(\rho)$ as given by (14.5), (14.11), (14.12), (14.13), but instead always use the real gas relations such as given by (2.6), (2.7) and (2.8). Accordingly, approximation lies only in using approximate functional form for the stream function Ψ, e.g. $K^{-1/4}\tau^{1/2}Z_{1/3}(ni\tau)e^{ni\theta}$ in place of

$$q^nF(a_n,\,b_n,\,n+1\,;\,q^2/2\beta c_0{}^2)e^{ni\theta}\ ,$$

where $\beta=(\gamma-1)^{-1}$ and

$$a_n,\,b_n=\tfrac{1}{2}[(n-\beta)\pm\{(1+2\beta)n^2+\beta^2\}^{1/2}]\ ,$$

while keeping to the exact values for the argument $\tau(q)$. Such a prescription is indeed familiar in the usual application of the WKB method.

In the previous paper [7] we have calculated several cases of subsonic flow past obstacles by employing the approximation $k(\tau)=0$, with the same prescription as above, and obtained remarkably good results. This fact may be considered to show that our prescription is founded on a sound basis.

§ 15. Comparison with the Usual Transonic Approximation

It is well known that the hodograph equation can be written in the form

$$\frac{\partial^2\Psi}{\partial t^2}+K\frac{\partial^2\Psi}{\partial\theta^2}=0\ , \qquad (15.1)$$

where

$$t=\int\frac{\rho}{\rho_0}\frac{dq}{q}\ , \qquad (15.2)$$

and K is given by (2.4). In the neighbourhood of $q=1$, K can be approximated by

$$K=-bt\ , \qquad (15.3)$$

neglecting second and higher powers of t. Here $b=-(dK/dt)_{t=0}$; and, in particular, for the adiabatic flow we have

$$b=(\gamma+1)(\rho_0/\rho_*)^3=(\gamma+1)[\tfrac{1}{2}(\gamma+1)]^{3/(\gamma-1)}\ , \qquad (15.4)$$

ρ_* being the density pertaining to the critical state $q=q_*(=1)$. Usual transonic approximation (as well as Tomotika and Tamada's assumption) consists in adopting (15.3) as a substitute for (2.4); thus (15.1) reduces to the Tricomi equation

$$\partial^2\Psi/\partial\eta^2-\eta\partial^2\Psi/\partial\theta^2=0\ , \qquad (15.5)$$

with $\eta=b^{1/3}t$.

In the usual transonic approximation (15.2) is further approximated by

$$t=(\rho_*/\rho_0)(q/q_*-1)\ , \qquad (15.6)$$

so that

$$\eta=(\gamma+1)^{1/3}(\rho_0/\rho_*)t=(\gamma+1)^{1/3}(q-q_*)/q_*\ , \qquad (15.7)$$

and η immediately represents the magnitude of velocity on a suitable scale [4].

Now we have [6]

$$d\tau=-K^{1/2}dt\ , \qquad (15.8)$$

whence, by (15.3),

$$\tau=(2/3)b^{1/2}(-t)^{3/2}\ , \qquad (15.9)$$

so that

$$K=(3/2)^{2/3}b^{-4/3}\tau^{2/3}\ . \qquad (15.10)$$

Inserting this into (2.5), we have finally

$$k=-(5/36)\tau^{-2}\ , \qquad (15.11)$$

which is nothing but the assumption forming the basis of our method. Accordingly, the assumption (15.3), on which the usual transonic approximation is based, is found to be more restrictive than our assumption (15.11). This may also be seen from the fact that (15.10) is a special case of (14.5) such that $c_2=0$. Further, it may be interesting to note that we have only to put $\tau=(2/3)b^{1/2}(-t)^{2/3}$ in our various formulae in order to obtain the corresponding formulae for the usual transonic approximation.

Moreover, it should be emphasized that the usual transonic approximation is only applicable to the flow in which the fluid velocity is everwhere not very different from the critical velocity $q=q_*(=1)$. It might seem at first sight that our approximation method would also suffer from this restriction, in view of the very similar appearance of the various formulae to those of the above-mentioned approximation. But this is not the case; indeed our adoption of the WKB variables enables us to widen the region of applicability so as to cover the region near the stagnation point as well. This will be made plausible by referring to Fig. 1, where the hypothetical k-τ relation is compared with the real adiabatic gas relation.*

On the other hand, it is easy to show that the basic equation (3.1) can be reduced to the Tricomi equation (15.5), by putting

$$\psi=\eta^{1/4}\Psi\ , \qquad \tau=(2/3)(-\eta)^{3/2}\ . \qquad (15.12)$$

Consequently, if a specific problem is already solved in the usual transonic approximation (in which η is defined by (15.7)), we can immediately obtain the solution in the WKB approximation proposed in this paper by the substitution (15.12); the velocity q in the final result is, of course, to be calculated from τ by means of the relation (2.3).

As a concluding remark, it may be suggested that the existing results of the usual transonic-approximation theory based on the Tricomi equation would be materially improved by reconsidering them from the viewpoint of the WKB method.

References

1) S. Bergman: Amer. J. Math. **70** (1948) 856. This paper gives references to his earlier papers.

2) T. M. Cherry: Proc. Roy. Soc. London A **192** (1947) 45; **196** (1949) 1.

3) T. M. Cherry: Proc. Roy. Soc. London A **196** (1949) 32.

4) G. Guderley and H. Yoshihara: J. Aero. Sci. **17** (1950) 723.

5) E. W. Hobson: *The theory of spherical and ellipsoidal harmonics.* Cambridge Univ. Press (1931).

6) I. Imai: J. Math. Phys. **28** (1949) 173.

7) I. Imai and H. Hasimoto: J. Math. Phys. **28** (1950) 205.

8) Th. von Kármán: J. Math. Phys. **26** (1947) 182.

9) Y. H. Kuo: NACA Tech. Note **1445** (1948).

10) M. J. Lighthill: Quart. J. Mech. Appl. Math. **1** (1948) 442. This paper gives references to his earlier papers.

11) R. von Mises and M. Schiffer: *Advances in applied mechanics.* Vol. **1** (1948) 249.

12) E. C. Titchmarsh: *The theory of functions.* Oxford (1932).

13) S. Tomotika and K. Tamada: Quart. Appl. Math. **7** (1950) 381; **8** (1950) 127; **9** (1951) 133.

14) H. S. Tsien and Y. H. Kuo: NACA Tech. Note **995** (1946).

15) G. N. Watson: *A treatise on the theory of Bessel functions.* Cambridge Univ. Press (1922).

---

* Another justification of our approximation method may be obtained by considering the nature of the WKB method. It is concerned with the ordinary second-order differential equation

$$d^2y/dx^2+k^2P(x)y=0\ , \qquad (1)$$

where $P(x)$ has a zero at $x=0$ such that

$$P(x)=a_1x+a_2x^2+\cdots, \quad a_1\neq 0. \qquad (2)$$

The solution is asymptotically given, for $k\to\infty$, by

$$y=P^{-1/4}z^{1/2}Z_{1/3}(kz)\ , \qquad (3)$$

where $z=\int_0^x P^{1/2}dx$ and $Z_{1/3}$ is the Bessel function of the order 1/3. (See, e.g. I. Imai: Phys. Rev. **74** (1948) 113.)

If $P(x)$ were approximated by $P(x)=a_1x$ as in the transonic approximation, the solution would be given by

$$y=x^{1/2}Z_{1/3}(\tfrac{2}{3}a_1{}^{1/2}x^{3/2})\ , \qquad (4)$$

which furnishes a very good approximation to the exact solution near $x=0$, but for moderate values of x, the approximation is less accurate. On the other hand, the solution (3) reduces to (4) near $x=0$ and moreover

$$y=P^{-1/4}(Ae^{ikz}+Be^{-ikz}) \qquad (5)$$

for $P(x)\neq 0$, by means of the asymptotic expansion of the Bessel function. (5) is nothing other than the well-known formula of the usual WKB approximation. Thus (3) represents a very good approximation for all values of x, in spite of its resemblance to (4).

JOURNAL OF THE PHYSICAL SOCIETY OF JAPAN Vol. 9, No. 6, NOV.—DEC., 1954

Absorption of Ultrasonic Waves in Organic Liquids (II)

Liquids with Negative Temperature Coefficient of Sound Absorption (a) Glycols, Cyclohexanol and Cresol*

By Tadashi KISHIMOTO and Otohiko NOMOTO

Kobayasi Institute of Physical Research, Kokubunzi, Tokyo

(Received July 21, 1954)

Ultrasonic absorption coefficients (at about 8 Mc/sec) were determined by the pulse technique in glycols, cyclohexanol and *m*-cresol in dependence of the temperature. Also the ultrasonic velocity (at 1.43 Mc/sec) in these liquids was determined by the ultrasonic interferometry. The experimental absorption coefficient α_{exp} in these liquids decreased with increasing temperature quite in a similar manner as the classical sound absorption due to viscosity α_{vis}. In most of the liquids investigated, however, α_{exp} was higher than α_{vis}, and the excess absorption was attributed to the bulk viscosity due to the hydrogen bond association in these liquids. The ratio $\alpha_{\text{exp}}/\alpha_{\text{vis}}$ was nearly independent of the temperature for all these liquids, the mean values of this ratio being given by: ethylene glycol 4.88; diethylene glycol 2.23; triethylene glycol 0.98; polyethylene glycol 0.89; propylene glycol 1.46; cyclohexanol 1.14; and *m*-cresol 1.32. The low value of this ratio for polyethylene glycol is considered to be due to the experimental errors, especially those of the determination of the static viscosity. The activation energyies of the shear and the bulk viscosity were determined from the temperature dependence of the shear viscosity, and that of the bulk viscosity, the latter being calculated from the excess absorption. The two activation energies are nearly the same for the same liquid, being of the order of 8～10 kcal/mole for most of the liquids here investigated, though slightly lower for ethylene glycol and much higher for *m*-cresol. The molecular sound absorption, if present, is small, and presumably less than $\alpha_{\text{mol}}/\nu^2=30\sim60\times10^{-17}$ (α_{mol}=absorption coefficient due to this mechanism, ν=frequency) for most of the liquids investigated. Also ultrasonic absorption (at 24 Mc/sec) in water was determined and was found to be in good agreement with the existing results.

§ 1. Introduction

In the first part of this research[1] we reported of the measurements of the ultrasonic absorption in 12 organic liquids. All these liquids proved to have positive temperature coefficients of sound absorption, the absorption coefficients being far greater than the classical theoretical values, and it was concluded that the chief mechanism of sound absorption in these liquids are the molecular absorption. In this second part, we will report of the results of the measurements of ultrasonic absorption in some other liquids, which proved to have negative temperature coefficients of sound absorption.

As was noticed in the first part of this paper, most of the organic liquids have been considered hitherto as liquids with the molecular sound absorption as the chief mechanism of sound absorption, when the sound absorption in these liquids are higher than the classical theoretical values. This, however, requires a close reexamination, especially when the temperature coefficient of sound absorption is negative.

It is known that the sound absorption in monoatomic liquids Hg, liquid Ar, and liquid He I (except in the very neighbourhood of the λ-transition point) can be accounted for by the classical absorption mechanism due to viscosity and heat conduction. Highly viscous liquids as castor oil[2),3)] and glycerine at low temperatures[4)-6)] exhibit relaxation phenomenon of viscosity, the "frequency independent absorption" α/ν^2 decreasing with increase in frequency and exhibiting lower values than the classical theoretical values. Here α means the absorption coefficient and ν the frequency. (The glycerine at ordinary temperature exhibits higher absorption than the classical viscosity absorption due to the existence of the bulk viscosity).

---

* The text in Japanese of this paper will be published in "Bulletin of the Kobayasi Institute of Physical Research, Vol. 4 (1954)".

Associated liquids as water7)−10) and alcohols11)−13) on the other hand, have sound absorption coefficients 1.5∼3 times the viscosity absorption, the excess part being attributed to the bulk viscosity due to the formation of associated molecules by the hydrogen bonds. These liquids have negative temperature coefficients of sound absorption and the temperature dependence is nearly the same as in the case of the classical absorption due to viscosity. This indicates that the activation energy for shear motion of the liquid is nearly the same with the activation energy for compression, because both the shear motion and the compression requires the breaking of hydrogen bonds.

The ultrasonic absorption in most of the other liquids have hitherto been attributed to the molecular absorption.

The classification of the liquids into four classes according to the ultrasonic absorption, i.e., the normal liquids (monoatomic liquids), normal liquids with relaxation phenomenon of viscosity (highly viscous liquids), abnormal liquids with bulk viscosity (water and alcohols), and abnormal liquids with molecular absorption (non-associated organic liquids) have proposed by Pinkerton13) (cf. also Verma14) and Herzfeld for other classifications). This however, is only schematical. There may exist some intermediate or combined cases as well, in which two or more mechanisms cooperate in nearly the same weights. Moreover, there are presumably not a small number of liquids with comparatively low values of ultrasonic absorption which are erroneously considered to be the liquids with the molecular absorption as the chief absorption mechanism.

It is the purpose of this paper and the next paper to elucidate the mechanism of sound absorption in some of the liquids which exhibited negative temperature coefficients of sound absorption. We treat glycols, cyclohexanol and *m*-cresol in this paper, and some other liquids in the following paper (part III).

§ 2. Experimentals

Measurements of ultrasonic absorption and velocity were performed in water, some glycols (ethylene glycol, diethylene glycol, triethylene glycol, polyethylene glycol, propylene glycol), and two phenol derivatives (cyclohexanol and *m*-cresol). The absorption coefficients were obtained by the pulse technique and the method was the same as was employed in the first part of this paper. The frequency was selected between 1 and 30 Mc/sec according to the values of the absorption coefficients (mainly about 8 Mc/sec). The frequency dependence of sound absorption in each substance, however, was not determined.

The sound velocity was determined mainly in the purpose of utilizing it in the calculation of the classical absorption coefficient due to viscosity. As any detectable dispersion was not to be expected in this frequency range, the measurement was performed only at one frequency (1.43 Mc/sec). An ultrasonic interferometer with a micrometer screw of 1/1000 mm in accuracy was employed for this purpose. The accuracy of the velocity measurements, however, was rather small and the probable error was presumably of the order of 0.2%, though this accuracy is sufficient enough for our purpose.

Also the values of η/ρ are necessary in calculating the absorption due to viscosity, where η means the viscosity coefficient and ρ the density. This was determined by employing Ostwald's viscosimeters in a water-bath thermostat.

Sample liquids were prepared from commercial pure liquids by fractional distillation under addition of suitable desiccation agents. The samples of ethylene glycol and diethylene glycol, however, were not distilled.

§ 3. Ultrasonic Velocity

Fig. 1 shows the ultrasonic velocity at 1.43 Mc/sec in the sample liquids here investigated (except water) as functions of temperature. The accuracy of the smooth curves is of the order of 2 m/sec, though some of the individual measurements are more scattered. Ultrasonic velocities obtained by some other authors15)−18) are also indicated in the figure. Some of these data are rather scattered, but the velocity data by Weissler *et al.* on glycols are in excellent agreement with our measurements.

§ 4. Ultrasonic Absorption

Now the sound absorption due to viscosity is given by

$$\alpha_{\text{vis}} = \frac{2}{3}\frac{\eta}{\rho}\frac{1}{V^3}\frac{\omega^2}{1+\omega^2\tau^2}, \qquad (1)$$

were ω means the circular frequency ($=2\pi\nu$; ν the frequency), V the sound velocity in the liquid, ρ and η the density and the viscosity of the liquid respectively, and τ the relaxation time. As we have $\omega \ll 1$ for the liquids here investigated and in the frequency range of our experiment—1∼30 Mc/sec, the relaxation time being given by $\tau = \eta/G$, where G means the rigidity modulus of the liquid, we have

$$\alpha_{\text{vis}} = \frac{8\pi^2}{3}\frac{\eta}{\rho}\frac{\nu^2}{V^3}, \qquad (2)$$

as the classical sound absorption. The sound absorption due to thermal conductivity is neglibly small in liquids[19] except in mercury and the molten metals. Classical absorption in each liquid was computed by this formula by employing the measured values of η/ρ and that of V, given in Fig. 1.

Sound absorption decreased with increasing temperature in all the liquids here investigated in a similar manner as in the case of classical absorption due to viscosity (α_{vis}). The experimental absorption coefficient (α_{exp}) was higher than α_{vis} in many of the liquids, but the ratio

$$r = \alpha_{\text{exp}}/\alpha_{\text{vis}}, \qquad (3)$$

was nearly independent of the temperature.

From the temperature dependence of ultrasonic absorption it was concluded that the liquids here investigated, i.e., glycols, cyclohexanol and *m*-cresol belong to that type of liquids in which the sound absorption is mainly due to the shear viscosity and the bulk viscosity, as water and alcohols, but in which the molecular absorption is negligible. The ultrasonic absorption in ethylene glycol can be accounted for by the classical viscosity absorption only.

(i) **Water** (H_2O)

There are some precise measurements on the temperature dependence of ultrasonic absorption in distilled water already (cf. Pinkerton[7], Smith and Beyer[8], Fox and Rock[9], etc.) We performed the absorption measurements in distilled water in order to test the accuracy of our measuring equipments. Fig. 2 gives the ultrasonic absorption coefficient (at 24 Mc/sec) in distilled water as function of temperature. It is in good agreement with the former precise results. As the theoretical interpretation of sound absorption in water has been discussed in detail already (cf. Hall[10]), we reproduce only the experimental result here.

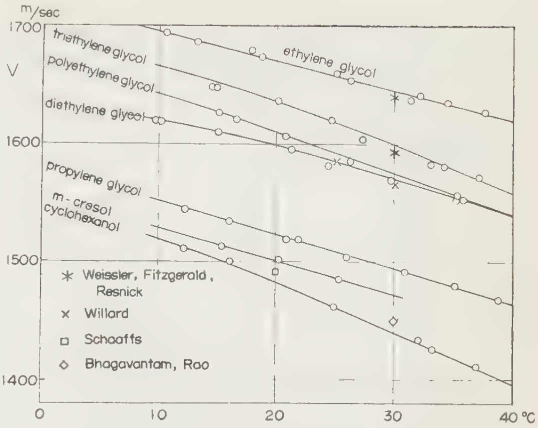

Fig. 1. Temperature dependence of ultrasonic velocity in glycols, cyclohexanol and *m*-cresol (1.43 Mc/sec).

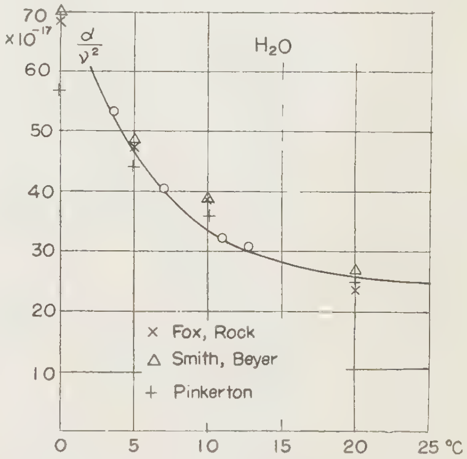

Fig. 2. Temperature dependence of ultrasonic absorption in water.

(ii) **Ethylene glycol** ($HO \cdot CH_2 \cdot CH_2 \cdot OH$, Molecular weight $M = 62.05$)

Fig. 3 shows the ultrasonic absorption in ethylene glycol as function of temperature. The curve in dotted line in the figure shows the classical absorption. It is to be seen that

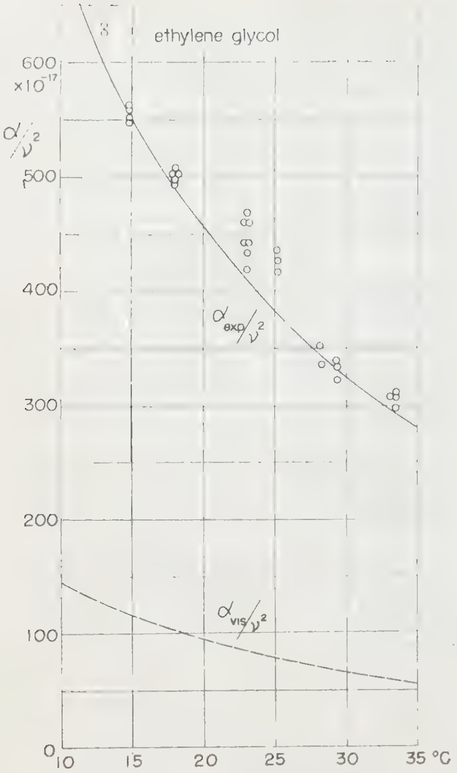

Fig. 3. Temperature dependence of ultrasonic absorption in ethylene glycol.

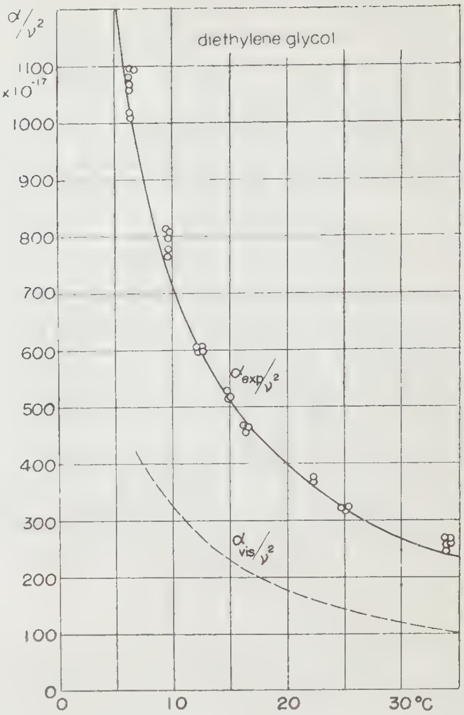

Fig. 4. Temperature dependence of ultrasonic absorption in diethylene glycol.

Table I. Ultrasonic velocity and absorption in ethylene glycol as functions of temperature.

t °C	η/ρ centi-poise/gr/cm³	V m/sec	$\frac{\alpha_{\mathrm{exp}}}{\nu^2}\times 10^{17}$	$\frac{\alpha_{\mathrm{vis}}}{\nu^2}\times 10^{17}$	ratio r
10	26.8	1693		145.2	
15	20.8	1682	550	114.9	4.78
20	16.7	1671	460	94.1	4.88
25	13.7	1660	386	78.7	4.90
30	11.2	1646	325	66.0	4.91
35	9.3	1630	283	54.5	5.00
				mean	4.88

Table II. Ultrasonic velocity and absorption in diethylene glycol as functions of temperature.

t °C	η/ρ centi-poise/gr/cm³	V m/sec	$\frac{\alpha_{\mathrm{exp}}}{\nu^2}\times 10^{17}$	$\frac{\alpha_{\mathrm{vis}}}{\nu^2}\times 10^{17}$	ratio r
5			1050		
10	52	1618	725	322.7	2.24
15	35.4	1610	520	230.0	2·26
20	28.0	1598	400	180.4	2.23
25	22.4	1583	325	143.0	2.26
30	17.8	1567	275	121.6	2.25
35	14.8	1551	237	104.2	2.24
				mean	2.23

the total absorption is about 5 times greater than the classical absorption due to viscosity, but their ratio is almost independent of the temperature. Table I gives the values of η/ρ, V, α_{exp}, α_{vis}, and the ratio $r=\alpha_{\text{exp}}/\alpha_{\text{vis}}$ at various temperatures.

It is reasonable to suppose that the difference between the observed and the classical absorption is due to bulk viscosity, i.e.,

$$\alpha_{\text{exp}}=\alpha_{\text{class}}+\alpha_{\text{bulk vis}}=\alpha_{\text{vis}}+\alpha_{\text{bulk vis}}\ , \tag{4}$$

because the temperature dependence of $\alpha_{\text{bulk vis}}$ must be nearly the same with that of α_{vis} also from theoretical point of view, as is to be discussed later. Also the OH-groups contained in the molecules of this liquid suggest the formation of hydrogen bonds between neighbouring molecules (i.e., association), which may account for the mechanism of bulk viscosity of this liquid. The absorption due to bulk viscosity is given theoretically by

$$\alpha_{\text{bulk vis}}=\frac{1}{2}\frac{\kappa}{\rho}\frac{\omega^2}{V^3}=2\pi^2\frac{\kappa}{\rho}\frac{\nu^2}{V^3}\ , \tag{5}$$

where κ means the bulk viscosity.

(iii) Diethylene glycol

($HO\cdot CH_2\cdot CH_2\cdot O\cdot CH_2\cdot CH_2\cdot OH$, $M=106.08$)

Fig. 4 shows the observed and the classical ultrasonic absorption coefficients (at about 8 Mc/sec) in diethylene glycol in dependence of temperature and Table II shows the values of η/ρ, V, α_{exp}, α_{vis}, and their ration r at various temperatures. The observed absorption is greater than the classical theoretical value by a factor of about 2.25 and this factor is independent of temperature within the accuracy of measurements.

Also this liquid is to be supposed to exhibit bulk viscosity by the OH-groups as in the case of ethylene glycol. The excess absorption due to bulk viscosity, however, is smaller than in the case of ethylene glycol by a factor of about 2/3, while the absorption due to shear viscosity is twice as large as in the case of ethylene glycol. This, presumably, is due to the greater size of the molecule of diethylene glycol as compared to the ethylene glycol.

(iv) Triethylene glycol

($HO\cdot CH_2\cdot CH_2\cdot O\cdot CH_2\cdot CH_2\cdot O\cdot CH_2\cdot CH_2\cdot OH$, $M=150.11$)

Fig. 5, curves *a*, soow the observed and the classical sound absorptions (8 Mc/sec) in this liquid in dependence of temperature and Table III shows the data of η/ρ, V, $\alpha_{\text{exp}}/\nu^2$, $\alpha_{\text{vis}}/\nu^2$, and their ratio r at various temperatures. The observed absorption is nearly the same with the viscosity absorption except at low temperatures, where α_{exp} becomes somewhat higher than α_{vis}.

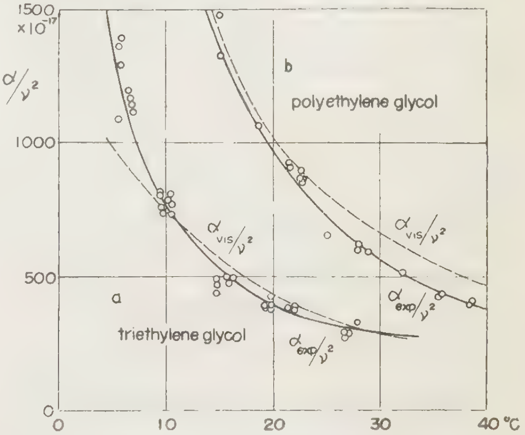

Fig. 5. Temperature dependence of ultrasonic absorption in triethylene glycol (curves *a*) and polyethylene glycol (curves *b*).

(v) Polyethylene glycol

Fig. 5, curves *b*, show the observed and the classical absorption (8 Mc/sec) in this liquid in dependence of temperature, and Table IV

Table III. Ultrasonic velocity and absorption in triethylene glycol as functions of temperature.

t °C	η/ρ centi-poise/ gr/cm³	V m/sec	$\frac{\alpha_{\text{exp}}}{\nu^2}\times10^{17}$	$\frac{\alpha_{\text{vis}}}{\nu^2}\times10^{17}$	ratio r
5			1300		
10	126	1655	760	730.8	1.04
15	95	1641	530	565.2	0.94
20	71	1627	405	433.4	0.935
25	55	1611	325	345.8	0.945
30	44	1594	295	285.6	1.035
				mean	0.98

Table IV. Ultrasonic velocity and absorption in polyethylene glycol as functions of temperature (8.00 Mc/sec).

t °C	η/ρ centi-poise/gr/cm³	V m/sec	$\frac{\alpha_{\text{exp}}}{\nu^2}\times10^{17}$	$\frac{\alpha_{\text{vis}}}{\nu^2}\times10^{17}$	ratio r
15	230	1625	1350	1409	0.95
20	160	1608	950	1011	0.94
25	124	1590	735	810.9	0.90
30	99	1571	570	671.3	0.85
35	78	1553	450	547.4	0.83
				mean	0.89

Table V. Ultrasonic velocity and absorption in propylene glycol as functions of temperature.

t °C	η/ρ centi-poise/gr/cm³	V m/sec	$\frac{\alpha_{\text{exp}}}{\nu^2}\times10^{17}$	$\frac{\alpha_{\text{vis}}}{\nu^2}\times10^{17}$	ratio r
10			2000		
15	127	1537	1420	919.8	1.54
20	91	1523	1060	677.2	1.56
25	68	1509	800	520.3	1.54
30	52	1496	570	408.3	1.40
35	40	1483	435	322.4	1.35
40	32	1470	310	264.8	1.36
				mean	1.46

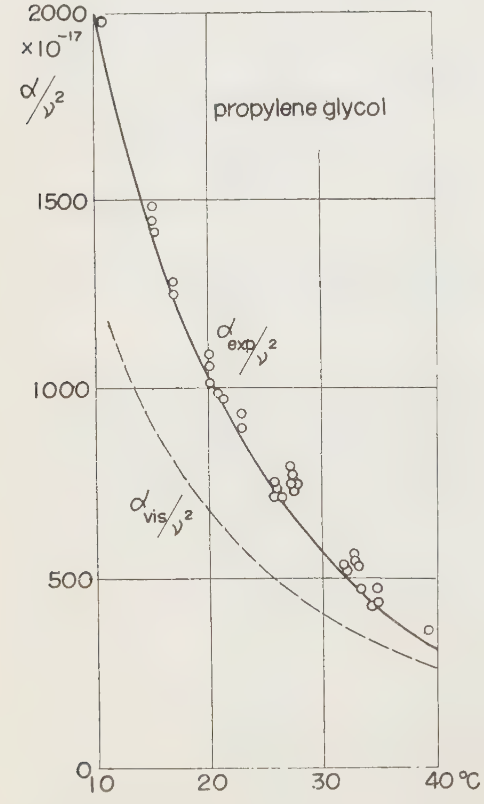

Fig. 6. Temperature dependence of ultrasonic absorption in propylene glycol.

shows the values of η/ρ, V, $\alpha_{\text{exp}}/\nu^2$, $\alpha_{\text{vis}}/\nu^2$, and their ratio r at various temperatures. The observed absorption is somewhat lower than the viscosity absorption in this case. This, however, may presumably be due to experimental errors, because the relaxation of shear viscosity after Eq. (1) is not to be expected at this frequency considering the observed values of the static viscosity. The experimental errors are to be introduced not only in the measurements of α_{exp}, but more probably in the measurements of η/ρ by the Ostwald's viscosimeters. We have noticed that our velosity data for ethylene glycols are in good agreement with those obtained by Weissler, Fitzgerald, and Resnick[17]. This may indicate the accuracy of the velocity measurements as well as the purities of the sample liquids. The viscosity data, on the other hand, are not in good agreement with those of Weissler *et al.* Also the table values (International Critical Tables, etc.) are not in agreement neither with our measurements nor with those of Weissler *et al.* This indicates the uncertainty of viscosity measurements as compared with the measurements of ultrasonic absorption. Therefore, we may suppose the calculated values of α_{vis} more uncertain than the observed values of α_{exp}.

(**vi**) **Propylene glycol** ($CH_3 \cdot CHOH \cdot CH_2OH$, $M=76.06$)

The ultrasonic absorption in propylene glycol is represented in Fig. 6 and Table V. The ratio $r=\alpha_{\text{exp}}/\alpha_{\text{vis}}$ decreases with increasing temperature slightly. The values of α_{exp} and α_{vis} are higher, but that of the ratio r is lower, than are to be expected from the molecular weight only. This is presumably due to the difference in molecular structure.

Table VI. Ultrasonic velocity and absorption in cyclohexanol as functions of temperature.

t °C	η/ρ centi-poise/gr/cm³	V m/sec	$\frac{\alpha_{\text{exp}}}{\nu^2}\times 10^{17}$	$\frac{\alpha_{\text{vis}}}{\nu^2}\times 10^{17}$	ratio r
10	128	1518.0	1140	962	1.18
15	97	1502.5	870	752	1.16
20	71.5	1483.0	670	576	1.15
25	54.0	1462.0	515	454	1.13
30	41.5	1440.0	410	365	1.12
35	32.5	1417.0	335	300	1.12
				mean	1.14

(**vii**) **Cyclohexanol** ($(CH_2)_5COH$, $M=100.09$)

Fig. 7 shows the observed and the classical sound absorption (at ca. 8.6 Mc/sec) in this liquid in dependence of temperature and Table 6 shows the values of η/ρ, V, $\alpha_{\text{exp}}/\nu^2$, $\alpha_{\text{vis}}/\nu^2$, and their ratio r at various temperatures. The observed sound absorption is higher than α_{vis} by about 15% in this case, the ratio r being nearly independent of the temperature. Also this liquid is supposed to exhibit bulk viscosity because of the associating nature of the OH-group. The contribution of bulk viscosity on sound absorption, however, is much decreased in this liquid than in the case of ethylene glycol and diethylene glycol presumably because there is only one OH-group in one molecule of cyclohexanol, while there are two OH-groups in one molecule of glycols.

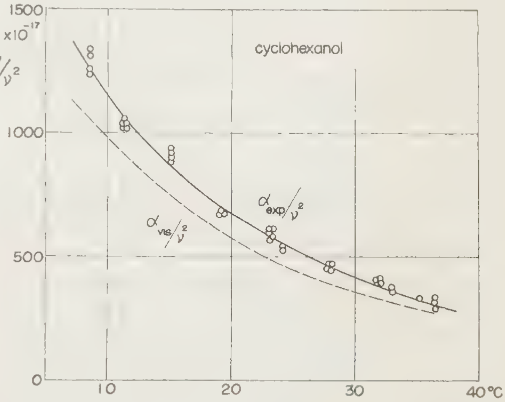

Fig. 7. Temperature dependence of ultrasonic absorption in cyclohexanol.

(**viii**) ***m*-cresol** ($C_6H_4 \cdot CH_3(OH)$, $M=108.06$)

Fig. 8 shows the ultrasonic absorption in *m*-cresol, and Table VII shows the values of η/ρ, V, $\alpha_{\text{exp}}/\nu^2$, $\alpha_{\text{vis}}/\nu^2$, and their ratio r at various temperatures. The experimental absorption is higher than the viscosity absorption by about 30%, the ratio being nearly independent of the temperature. Also this liquid has one OH-group per molecule and presumably exhibits bulk viscosity by hydro-

Table VII. Ultrasonic velocity and absorption in *m*-cresol as functions of temperature (ca. 7.7 Mc/sec).

t °C	η/ρ centi-poise/gr/cm³	V m/sec	$\frac{\alpha_{\text{exp}}}{\nu^2}\times 10^{17}$	$\frac{\alpha_{\text{vis}}}{\nu^2}\times 10^{17}$	ratio r
5	78	(1542)*	750	559.3	1.34
10	51	(1528)*	495	375.8	1.35
15	35	1514	335	265.1	1.27
				mean	1.32

* extrapolated values.

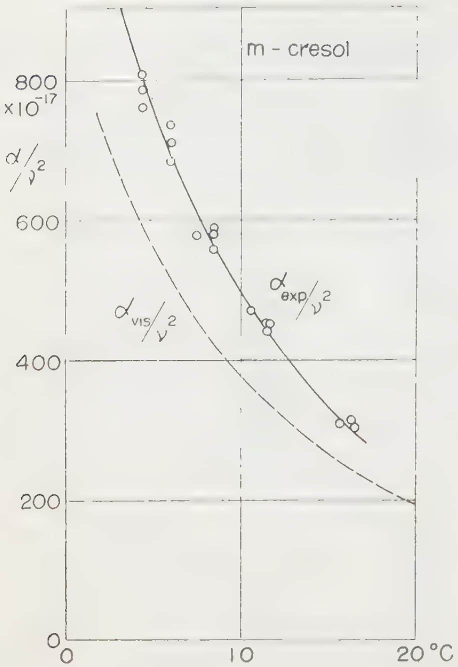

Fig. 8. Temperature dependence of ultrasonic absorption in *m*-cresol.

gen bonds.

§ 5. Activation Energies of the Shear and the Bulk Viscosity

We have already stated that the values of the ultrasonic absorption in glycols, cyclohexanol and *m*-cresol decrease with increasing temperature nearly in the same proportion as the classical sound absorption due to viscosity. This leads us to conclude that the excess absorption, in case it is present, is mainly due to the bulk viscosity, for the temperature dependence of the shear and the bulk viscosity are considered to be nearly the same. In these liquids the both mechanism involves the movement of molecules which requires the breaking of hydrogen bonds.

The activation energy for the shear viscosity E_{vis} and that for the bulk viscosity $E_{\text{bulk vis}}$ were obtained from the temperature dependence of η and κ, the latter being calculated from the excess absorption $\alpha_{\text{bulk vis}}=\alpha_{\text{exp}}-\alpha_{\text{vis}}$ by Eq. (5).

Here we assumed the relations

$$\eta=\eta_0 \exp (E_{\text{vis}}/RT)\ , \tag{6}$$

and

$$\kappa=\kappa_0 \exp (E_{\text{bulk vis}}/RT)\ , \tag{7}$$

where η_0 and κ_0 are the constants, R means the universal gas constant, and T the absolute temperature. As, however, the temperature variation of the density ρ is far smaller than those of η and κ, we neglected the former in this calculation and employed the approximate relations

$$\eta/\rho=(\eta/\rho)_0 \exp (E_{\text{vis}}/RT)\ , \tag{6$'$}$$

and

$$\kappa/\rho=(\kappa/\rho)_0 \exp (E_{\text{bulk vis}}/RT)\ , \tag{7$'$}$$

in place of Eq. (6) and (7).

Fig. 9 shows the curves of η/ρ and κ/ρ *vs.* $1/T$ for the liquids here investigated. These are straight lines, when η/ρ and κ/ρ are plotted in logarithmic scale as in these figures, and this indicates the applicability of (6′) and (7′).

The values of the activation energies are tabulated in Table VIII, together with the molecular weight, and the absorption coefficients at 20°C. As is to be seen in the table, E_{vis} and $E_{\text{bulk vis}}$ are nearly the same for the same liquid; they are of the order of 8∼10 kcal/mole for many of the liquids here investigated, although those for ethylene glycol are somewhat lower and those of *m*-cresol are much higher. They increase with increasing molecular weight in the series: ethylene, diethylene, and triethylene glycol.

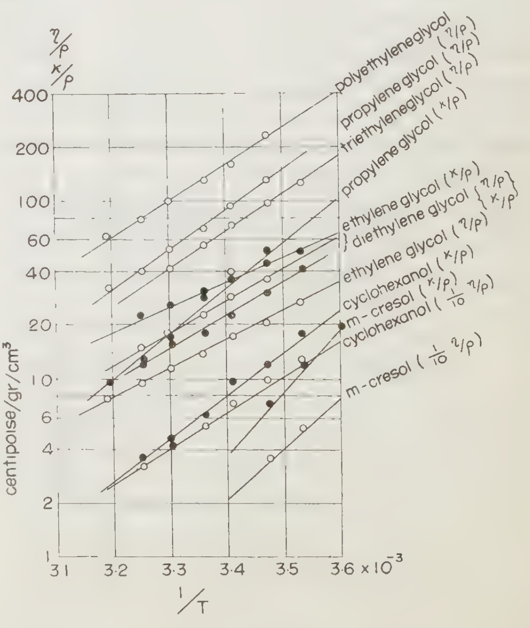

Fig. 9. Temperature dependence of η/ρ and κ/ρ in glycols, cyclohexanol and *m*-cresol.

Table VIII. Ultrasonic absorption and the activation energies of the shear and the bulk viscosity for glycols, cyclohexanol and *m*-cresol.

liquid	molecular weight M	$\frac{\alpha_{\text{exp}}}{\nu^2}\times 10^{17}$	$\frac{\alpha_{\text{vis}}}{\nu^2}\times 10^{17}$	ratio r	activation energies E_{vis}	activation energies $E_{\text{bulk vis}}$
glycols						
ethylene glycol	62.05	460	94.1	4.88	7.5	6.6
diethylene glycol	106.08	400	180.4	2.23	8.2	8.4
triethylene glycol	150.11	405	433.4	0.935	9.7	—
polyethylene glycol		950	1011	0.94	9.6	—
propylene glycol	76.06	1060	677.2	1.56	10.3	11.7
phenol derivatives						
cyclohexanol	100.09	670	576	1.15	9.0	10.6
m-cresol (15°C)	108.06	335	265.1	1.27	13.6	16.0

It is probable that the sound absorption in these liquids may involve a small part of molecular absorption. In general, if the molecular absorption. α_{mol} is also present, the experimental absorption coefficient must be given by

$$\alpha_{\text{exp}}=\alpha_{\text{vis}}+\alpha_{\text{bulk vis}}+\alpha_{\text{mol}}\ . \qquad (8)$$

We can conclude, however, that the molecular sound absorption, if present, is very small for all these liquids. As the molecular absorption is only slightly dependent of temperature, slightly increasing with increasing temperature, any molecular absorption of more than $\alpha_{\text{mol}}/\nu^2=30\sim 60\times 10^{-17}$ in magnitude will affect the values of the ratio $r=\alpha_{\text{exp}}/\alpha_{\text{vis}}$ for most of the liquids here investigated appreciably, and presumably be excluded. The molecular absorption in these liquids are considered to be small also from theoretical points of view. For it is known that the liquids with high molecular absorption consists of molecules with high symmetry such as carbon disulphide and benzene, while liquids constituting of the molecules with low symmetry exhibit low values of (molecular) sound absorption. The molecules of associating liquids as here investigated, are considered to have strong mutual interactions and this may account for the low molecular absorption, *i.e.*, the high efficiency of energy exchange between vibrational and translational degrees of freedoms of the molecules.

Acknowledgements

In conclusion, we express our sincere thanks to Mr. S. Okui, Assistant Professor, Institute of Pharmaceutics, Faculty of Medicine, Tokyo University, for his kind collaboration in distillation and desiccation of the sample liquids.

References

1) T. Kishimoto and O. Nomoto: J. Phys. Soc. Japan **9** (1954) 620.

2) O. Nomoto, T. Kishimoto and T. Ikeda: Bull. Kobayasi Inst. Phys. Res. **2** (1952) 72.

3) I. G. Mikhailov: C. R. (Doklady) Nauk URSS. **89** (1953) 991.

4) T. A. Litovitz: J. Acous. Soc. Amer. **23** (1951) 75.

5) F. E. Fox and T. A. Litovitz: Colloquium over ultrasonore trillingen (Brussels 1951) 38.

6) T. A. Litovitz and D. Sette: J. Chem. Phys. **21** (1953), 17.

7) J. M. M. Pinkerton: Nature **160** (1947) 128.

8) M. C. Smith and R. T. Beyer: J. Acous. Soc. Amer. **20** (1948) 608.

9) F. E. Fox and G. D. Rock: J. Acous. Soc. Amer. **12** (1941), 505; Phys. Rev. **70** (1946) 68.

10) L. Hall: Phys. Rev. **71** (1947) 318.

11) J. R. Pellam and J. Galt: J. Chem. Phys. **14** (1946) 608.

12) Ch. J. Burton: J. Acous. Soc. Amer. **20** (1948) 186.

13) J. M. M. Pinkerton: Proc. Phys. Soc. **B 62** (1949) 129.

14) G. S. Verma: J. Chem. Phys. **18** (1950) 1352.

15) A. Weissler, J. W. Fitzgerald and I. Resnick: J. Appl. Phys. **18** (1947) 434.

16) G. W. Willard: J. Acous. Soc. Amer. **12** (1941) 438.

17) W. Schaaffs: Zeits. Phys. Chem. **194** (1944) 28.

18) S. Bhagavantam and Ch. V. Joga Rao: Proc. Indian Acad. Sci. **8A** (1939) 312.

19) P. Biquard: Annale de physique **6** (1936) 195.

Short Notes

J. Phys. Soc. Japan **9** (1954) 1030~1031

Hall Effect in Cesium Antimonide with Audiofrequency Currents

By Toshimichi Sakata
The Electrical Communication Laboratory, Tokyo

(Received November 25, 1953)

In the previous report[1] the writer has pointed out that there is a linear relation between log R_H or log n and $1/T$, where R_H is the Hall coefficient and n is the number of carriers.

The primary object of this work is to observe changes in the magnitude and phase of Hall effect between 189 and 357°K. The construction of experimental vacuum tube was nearly the same as described in the previous report[1]. Schematic diagram of the entire circuit is shown in Fig. 1. Our results are summarized in Tables I, II and III. (d is the thickness of the sample.)

For all specimens the value of the activation energy derived from the Hall coefficient agrees well with that derived from the temperature variation of resistivity.

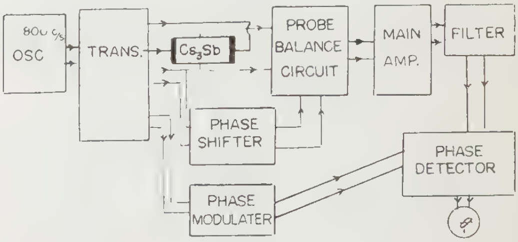

Fig. 1. Schematic diagram of the entire circuit for measuring the Hall effects by a.c methods.

The mobility of holes is 6~11 cm²/volt. Sec., and the mean free path l is $4\sim7\times10^{-8}$ cm from 345 to

Table I. Characteristic properties of Cs_3Sb.

Sample	Temp. °K	Resistance ohm	$E/2$ eV	R_H/d Volt / Gauss. Amp.	Sign of Hall Coeff. R_H
1	296	5.33×10^6	0.27	0.150	+
2	296.4	1.84 〃	0.25	0.010	+
4	295.2	1.01×10^7	0.23	0.051	+
5	297.0	2.10 〃	0.22	0.140	+
6	298	3.00×10^6	〃	0.060	+
7	298.2	1.64×10^5	0.28	0.002	+
8	297.2	4.96×10^6	0.24	0.089	+
9	299	3.26×10^5	0.28	0.006	+

Table II. R_H/d as a function of absolute temperature.

Temp. °K	Resistance ohm	R_H/d Volt / Gauss. Amp.	Temp. °K	Resistance ohm	R_H/d Volt / Gauss. Amp.
	No. 1			No. 5	
209	5.06×10^8	23.00	200	1.25×10^9	12.2
222	2.01 〃	8.61	227	2.70×10^8	2.35
238	7.20×10^7	3.01	250	9.80×10^7	0.79
250	4.01 〃	1.71	273	4.30 〃	0.32
273	1.35 〃	0.44	297	2.10 〃	0.14
296	5.33×10^6	0.15	302	1.75 〃	0.12
306	3.82 〃	0.10_2	306	1.55 〃	0.11
308	3.61 〃	0.09_5	313	1.35 〃	0.09
315	2.85 〃	0.07_5		No. 6	
323	2.32 〃	0.05_6	201	2.05×10^8	4.41
334	1.61 〃	0.03_6	210	1.24 〃	2.60
345	1.22 〃	0.03	228	4.44×10^7	0.97
			244	2.23 〃	0.44
			273	6.81×10^6	0.14
			298	3.02 〃	0.06

Table III.

Tube No.	Temp. °K	R_H Volt cm Gauss. Amp.	Mobility cm²/Volt-sec	n cm⁻³	n_0 cm⁻³	σ Ω⁻¹ cm⁻¹
1	296	1.2×10^{-5}	15	6.16×10^{15}	1.8×10^{21}	1.44×10^{-2}
4	295	2.5×10^{-6}	7	1.10×10^{16}	1.5×10^{20}	1.23 〃
5	303	7.1×10^{-6}	6.7	1.05 〃	1.0 〃	1.17×10^{-2}
6	298	4.2 〃	5.1	1.76 〃	3.0 〃	1.40 〃
7	〃	—	—	—	—	—
8	〃	6.3 〃	6.0	1.10 〃	5.0 〃	1.10 〃

200°K. The mobility varies approximately as $T^{-3/2}$.

Reference

1) T. Sakata: J. Phys. Soc. Japan **8** (1953) 793.

J. Phys. Soc. Japan **9** (1954) 1031～1032

On the Thermoelectric Power of Cesium Antimonide

By Toshimichi Sakata
The Electrical Communication Laboratory, Tokyo

(Received May 8, 1954)

In the impurity range the numbers of intrinsic electrons and holes due to thermal excitation are negligible compared to the number of holes excited from acceptor levels. According to Johnson and Lark-Horovitz(1), the thermoelectic power Q is given by

$$Q=\pm k/e[2-\log nh^3/2(2\pi mkT)^{3/2}]\,. \tag{1}$$

In this case, the chemical potential ζ may be related to the carrier density(n) by the well-known formula

$$\zeta=kT\log nh^3/2(2\pi mkT)^{3/2}\,. \tag{2}$$

Thus the conventional theory predicts the following relation between Q and R_H (Hall coefficient) in the impurity range,

$$Q=\pm\frac{k}{e}(\log \mathrm{R}_H T^{3/2}-5.32)\,. \tag{3}$$

If these expressions are valid, measurement of the thermoelectric power should give approximate values of the Hall coefficient and carrier density of the same sample.

The purpose of this note is to examine the relation between Q and R_H by measuring them for two samples of Cs_3Sb. In order to find the temperature dependence of the effective thermoelectric power of two specimens, measurements were carried out between 220 and 305°K. The thermoelectro-motive forces were determined by means of zero method, operating in conjunction with an electrometer tube.2) Fig. 1 shows relation between Q and $1/T$. Within the limits of experimental error, the lines were straight. The carrier density n. Hall constant R_H and chemical potential ζ are found, for a given temperature, from the

Table I. The calculated characteristics of n, ζ and R_H versus $1/T$.

Tube	$10^3/T$	n (cm⁻³)	$R_H\left(\frac{\text{cm}^3}{\text{Coulomb}}\right)$	ζ (eV)
1	3.28	6.6×10^{16}	1.12×10^{2}	0.15
	3.41	4.0_8 〃	1.81 〃	
	3.53	2.6_8 〃	2.76 〃	
	3.64	2.0 〃	3.70 〃	
	3.80	1.1_7 〃	6.89 〃	
	3.94	$7.2_8\times10^{15}$	1.02×10^{3}	
	4.12	3.8 〃	1.94 〃	
	4.29	2.2_8 〃	3.24 〃	
	4.49	1.1_7 〃	6.89 〃	
2	3.30	1.74×10^{17}	4.25×10	0.13
	3.40	1.38 〃	5.36 〃	
	3.53	1.07 〃	6.91 〃	
	3.66	8.52×10^{16}	8.68 〃	
	3.77	6.46 〃	1.14×10^{2}	
	3.95	4.78 〃	1.54 〃	
	4.10	3.56 〃	2.07 〃	
	4.27	2.64 〃	2.80 〃	
	4.50	1.82 〃	4.06 〃	

Table II.

Tube	$10^3/T$	n (cm⁻³)	$R_H\left(\frac{\text{cm}^3}{\text{Coulomb}}\right)$	$E/2$ (eV)
1	3.29	1.3×10^{16}	5.69×10^{2}	0.23
	3.49	7.3×10^{15}	1.01×10^{3}	
	3.59	5.4 〃	1.37 〃	
	3.78	3.2 〃	2.31 〃	
	3.90	2.3 〃	3.21 〃	
	4.11	1.3 〃	5.70 〃	
	4.30	8.0×10^{14}	9.25 〃	
2	3.31	8.8×10^{16}	8.40×10	0.20
	3.41	6.72 〃	1.10×10^{2}	
	3.60	4.1 〃	1.80 〃	
	3.81	2.45 〃	3.02 〃	
	3.92	1.85 〃	4.00 〃	
	4.15	1.03 〃	7.20 〃	
	4.34	6.37×10^{15}	1.16×10^{3}	

$E/2$: measured activation energy of the conductivity.

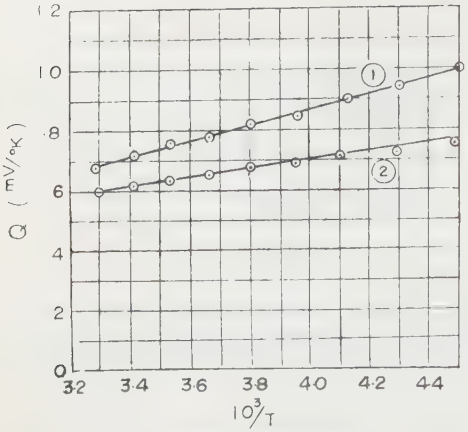

Fig. 1. The measured thermoelectric power plotted against $1/T$.

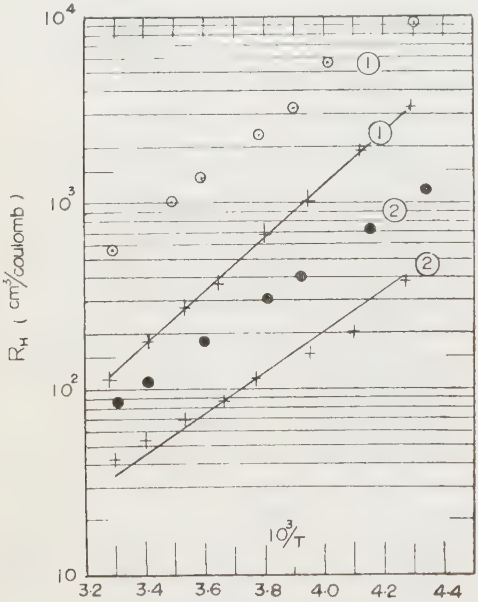

Fig. 2. Comparison of calculated and measured Hall const. for two samples. The circles represent the experimental result and the full curve shows the resultant Eq. (3).

values of Q at that temperature by using the above equations (1), (2) and (3). The calculated values are given in Table I. The conductivity and Hall constant heve been measured on the same specimens in the manner already mentioned[3]. The results obtained are given in Table II. Fig. 2 shows the measured (Table II) and calculated (Table I) Hall constants for two samples.

References

1) V. A. Johnson and K. Lark-Horovitz: Phys. Rev. **92** (1953) 226.
2) T. Sakata: J. Phys. Soc. Japan **8** (1953) 272.
3) T. Sakata: J. Phys. Soc. Japan **8** (1953) 793.

J. Phys. Soc. Japan **9** (1954) 1032~1034

On the Electron Bombardment Effect for Deposited Barium Oxide Films (II)

By T. Imai and Y. Mizushima
Electrical Communication Laboratory,
Nippon Telegraph and Telephone
Public Corporation

(Received August 17, 1954)

In the previous paper[1] the variations of emission caused by the electron bombardment upon the barium oxide films were reported. The films were deposited from the oxide coated cathode and the results showed activation or deactivation phenomena from case to case. The cause of these phenomena was ascribed reasonably to the production of free barium atoms owing to the dissociation of the oxide by the electron bombardment. Thus optimum quantity of the surface barium has been expected to give the maximum value of emission in the deposited film, and the change of emission due to the electron impact has been supposed to be influenced primarily by the quantity of the free barium existed in the film from the beginning. In order to ensure the above supposition, further investigations are undertaken in this paper.

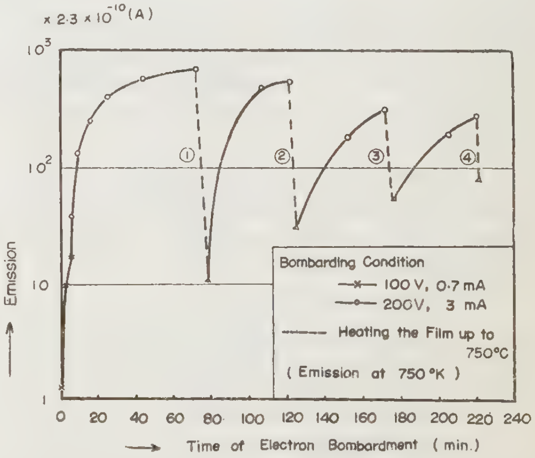

Fig. 1. Increment and Decrement by alternative electron bombardment and heat—treatment.

Two kinds of deposited films are formed on nickel sleeves by flashing the oxide cathodes coated on Pt and Ta sleeve respectively. Deposited film formed from the oxide coating on Pt sleeve contains extremely a small quantity of free barium, while quite large is contained in the film formed from the coating on Ta sleeve.[2] The result of the bombardment showed that the emission of the former film, which is very small initially, increased

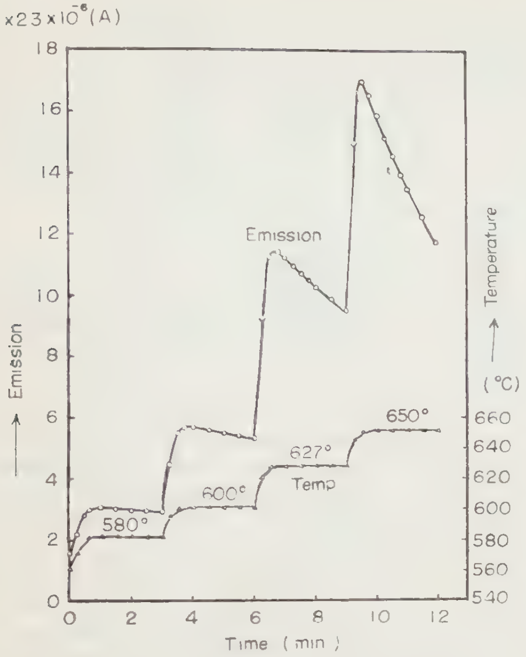

Fig. 2. Rate of emission decay under heat-treatment.

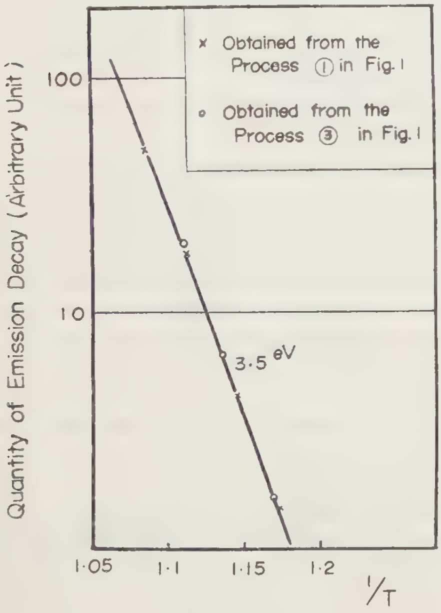

Fig. 3. Logarithmic plot of the rate of decay against inverse temperature.

by a factor of 100 by the electron bombardment, while in the latter, the increase in emission due to the bombardment is scarce and the longer bombardment causes the tendency to deactivation.

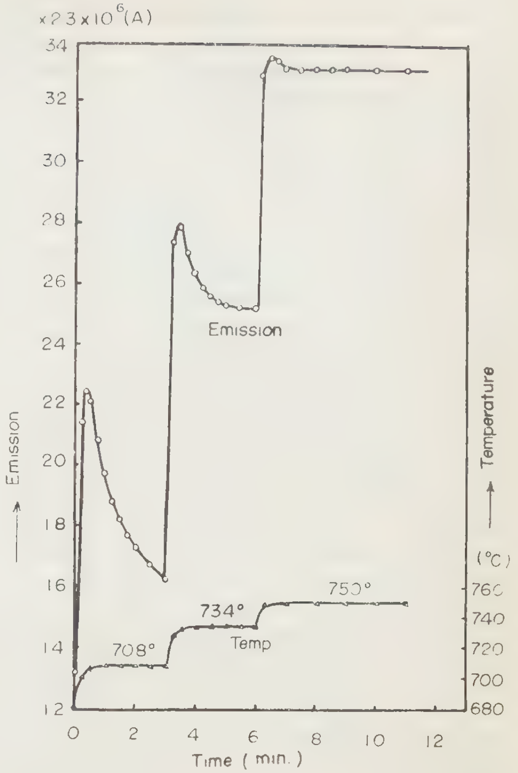

Fig. 4. Disappearance of the temperature effect probably due to the saturation of diffusing agent.

Furthermore, as the extremely inactive thin film, the barium film oxidized completely is taken under investigation in detail. The stoichiometric barium oxide film is formed by heating the evaporated barium film at 500°C in an oxygen atmosphere of 10^{-1} mm Hg. Though the emission of this film is extremely small, electron bombardment causes a marked increase in emission as seen at the left side of Fig. 1. Raising the film temperature after the electron bombardment causes a strong decrease in emission which is intensified as the temperature becomes higher, and the further electron bombardment after the decrease due to the temperature raising again brings about an increment of emission. The feature of the change of emission by the alternative electron bombardment and temperature raising is shown at the right side of Fig. 1. An example of the detailed feature of emission decay process, such as ①, ②, ③, ④ in Fig. 1, caused by the temperature raising is illustrated in Fig. 2 together with the variation of film temperature. Assuming that the decay is linear with time, logarithmic plot of the decay rate against $1/T$ gives a straight line whose slope corresponds to the energy of about 3.5 eV. Fig. 3 indicates such plots obtained for the process ① and ③, and shows good reproducibility of the temperature effect in the decay process. Although in Fig. 2 decrease in emission continues linearly with time during the short-time measurement, the prolonged heating causes breakdown in the linearity of the decay curve to reach an equilibrium. Thus, by heating the film at higher temperature the decrease in emission becomes slight and at about 750°C emission reachs to a final state in a short time as shown in Fig. 4.

This temperature effect may be explained by the diffusion of barium atom through the film. The value of 3.5 eV obtained in Fig. 3 is higher than that obtained in the previous paper (2.0 ev) and this may be due to difficulties in the diffusion of the free barium through the pure barium oxide film which needs larger activation energy compared to the normal oxide cathode material, with many lattice imperfections or impurities. The linearity of the decay curve shown in Fig. 2 represents the constancy of the gradient of barium density inside the film during the short-time measurement. As the gradient of the barium density becomes smaller due to its diffusion, the decay becomes slower and at last emission decay disappears as seen in Fig. 4.

It will be mentioned conclusively, in view of these results, that the smaller the quantity of the free barium existed in the film at the beginning, the more remarkable the activation due to the electron bombardment, and for the film which contains a large number of free barium deactivation may be found by the electron bombardment. It will be concluded further that the barium atoms produced by the electron bombardment are the main cause of emission change of the deposited film suffered by the electron bombardment.

References

1) T. Imai: J. Phys. Soc., Japan **9** (1954) 28.
2) L. T. Aldrich: J. App. Phys. **22** (1950) 1168.

J. PHYS. SOC. JAPAN **9** (1954) 1034～1035

Effect of the Base Metal on the Electron Dissociation of Deposited Barium Oxide Films

By T. IMAI and N. SHIBATA

Electrical Communication Laboratory,
Nippon Telegraph and Telephone
Public Corporation

(Received September 11, 1954)

During the life test of minuature pentode with titanium anode, the contact difference of potential between control grid and cathode was found to decrease remarkably, and gray deposit was observed gradually on the glass wall faced to the window of the anode.1) These phenomena were supposed to be due to the deposition of barium atoms on the grid and glass envelope, which were dissociated by electron bombardment upon barium oxide film evaporated on the titanium anode. As the tube with nickel anode did not indicate such phenomena, it will be expected that the efficiency of dissociation of the barium oxide film by electron bombardment may differ considerably for two films.

In this paper comparisons of pressure of gas evolved from the deposited film and of decrease of barium atoms on the anode both caused by electron bombardment are made for the two films mentioned above.

(1) Measurement of gas pressure

Gas pressures are compared for two valves with the nickel and the titanium anode during electron bombardment, after several depositions of barium oxide from the cathode are made onto these anodes. Fig. 1 (a) shows evolution of gas measured for a valve with the titanium anode, while Fig. 1 (b) indicates that for a valve with the nickel anode. In Fig. 1 (a) the evolution of gas, which disappears after heating the anode at high temperature by electron bombardment, becomes marked as the deposition becomes thicker. In Fig. 1 (b) the evolution of gas is quite small and the increment of pressure is not found appreciable although the depositing and the bombarding condition is same as that for Fig. 1 (a).

(2) Comparision of the quantity of barium on the anodes

By the use of barium isotope, quantities of barium on the titanium and the nickel anodes on which deposition were made are compared after electron bombardment. The results are illustrated in Table 1 together with the result of the blank test for these anodes. Smaller counts for the titanium anodes measured after electron bombardment indicate the larger rate of release of barium atoms from them.

From these results it may be clear that dissociation of the deposited barium oxide film on titanium takes place more markedly by the electron bombardment than of the film on nickel. Thus it may be sure that the released barium atoms deposit onto the control grid and so the work function of the grid is lowered in the valve with the titanium anode.

In the previous paper,2) comparision of gas evolution was made for the nickel and the tantalum anodes both contaminated with evaporating materials from oxide cathode and it was pointed out that the evolution of gas, probably oxygen, caused by electron bombardment was far larger for the latter. Reductive base metal such as tantalum and titanium, therefore, may act effectively for the dissociation due to electron bombardment of barium

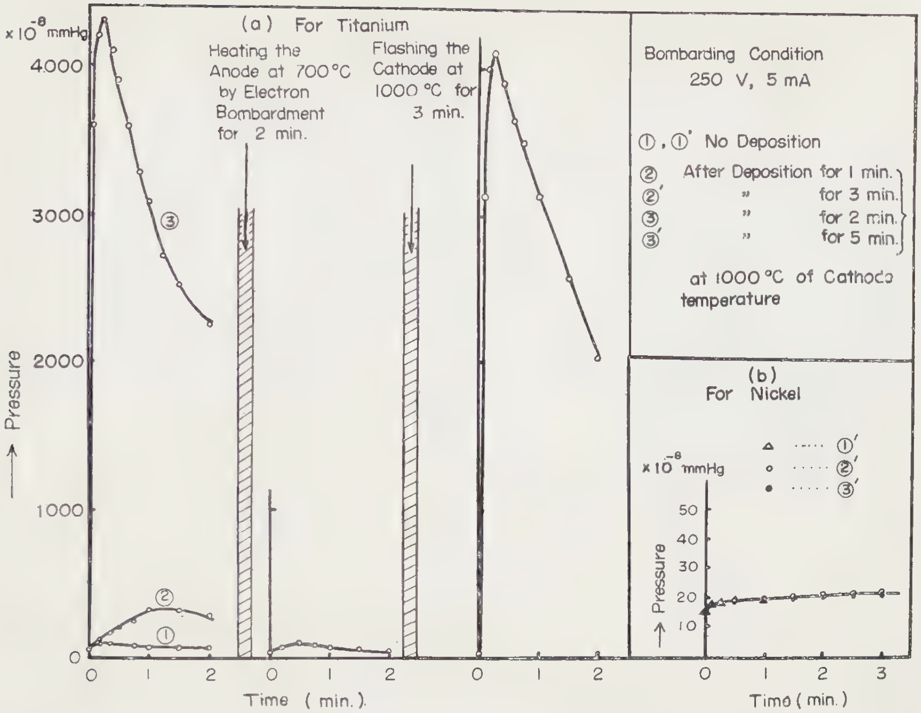

Fig. 1. Gas evolution from the titanium and nickel anodes covered by deposited film.

Table I.

	No.	Conditions of Electron Bombardment	Counts per min. for Ti	Counts per min. for Ni	Ratio of c.p.m. Ti/Ni	Mean (Ti/Ni)
I	1	180 V	906	1688	0.54	0.58
	2	15 mA	814	1237	0.66	
	3	for 15 Min.	204	379	0.54	
II	4	180 V	446	507	0.84	0.84
	5	3 mA	415	646	0.64	
	6	for 120 Min.	639	690	0.93	
III	7	No	768	1022	0.75	0.99
	8	Bombard-	128	103	1.24	
	9	ment	590	595	0.99	

oxide film deposited on it. It is interesting that the evolution of oxygen is quite large in spite of the good affinity of these metal for oxygen.

References

1) Presented by T. Imai at the Joint Meeting of the Tokyo annexes of three Institutes of Electrical Engineers of Japan, Oct., 1954.
2) T. Imai: J. Phys. Soc. Japan **9** (1954) 28.

J. Phys. Soc. Japan **9** (1954) 1035~1036

Multiple Lines in the Energy Spectrum of Electrons Passing through an Mg Foil

By Hiroshi WATANABE

Hitachi Central Research Lab. Kokubunji, Tokyo, Japan

(Received September 27, 1954)

During the course of the experiment of electron velocity analysis, a number of equally spaced and very sharp lines are observed in the energy spectrum of electrons which have passed through an Mg foil. An example is shown in Fig. 1.

The electron velocity analyzer used in this experiment is of the same type as that of Möllenstedt,[1] the details of which is to be published in this Journal.

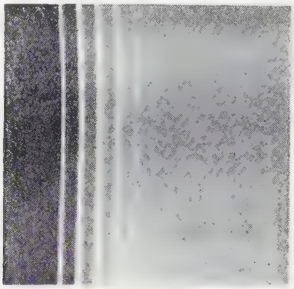

Fig. 1. The energy spectrum of electrons which have passed through an Mg foil of ca. 600Å.

The Mg foil was prepared by evaporating Mg metal onto a collodion film in a highly evacuated belljar, then dissolving the collodion film in 50% ether-alcohol. The estimated thickness of the Mg foil was ca. 600Å, and the foil had a metallic lustre. Electron diffraction patterns of the foil have shown a trace of MgO. It is probable that an oxide film covers the metal foil, but since this Mg foil is sufficiently thick and the rings of MgO are very feeble in the diffraction patterns the author considers with confidence that the sharp lines in the energy spectrum correspond to the energy losses in an Mg foil. It is also known that the energy spectrum of MgO has lines of different energy values.[2]

Fig. 1 shows the energy spectrum of electrons passing through the Mg foil. It contains the undisturbed baseline (the leftmost line) corresponding to the primary energy of 25 kev, and equally spaced lines representing the energy losses of integral multiples of a fairly sharply defined basic unit. Table I gives the energy distances of the sharp lines from the baseline and also the approximate half widths of them.

Ruthemann[3] has reported similar multiple lines observed in the energy spectra of electrons passing through Al and Be foils. Bohm and Pines[4] have considered that these energy losses would be caused by the excitation of a plasma oscillation of the electron gas in the metals. Pines[5] also has calculated the energy quantum of a plasma oscillation in Mg as 10.8 ev, and has proposed the existence of very sharp lines in the energy spectrum of Mg. Since the Mg atom possesses a small ion core and the interaction of plasma oscillation with the core electrons is considered to be quite weak, the energy spectrum of electrons passing through Mg foil would have a number of very sharp lines corresponding to the excitation of undamped plasma oscillation.

Table I. The energy distances and the estimated half widths of the lines in the spectrum.

	1st line	2nd line	3rd line	4th line
Energy Distance	10.3 ev	20.7 ev	31.2 ev	41.5 ev
Half Width	1.5	1.5	2	3

The energy distance of 10.3 ev between two lines in the present experiment agrees fairly well with the calculated value of 10.8 ev. The half widths of the lines are considered to be extremely narrow as compared with those of the other metals.

Recently Marton and Leder[6] have reported the energy losses of electrons in passage through thin films by means of the similar instrument. According to their experimental data the energy spectrum of Mg foil is reported to have two lines at 9.7 and 20.3 ev. Although the values of energy losses are nearly equal to those of the present experiment, the estimated half width of the line at 20.3 ev is remarkably large. The author believes that the line at 20.3 ev found in Marton's experiment may be attributed to some other origin.

It is a pleasure of the author to express his thanks to Dr. B. Tadano and Mr. N. Morito of his laboratory for their encouragement throughout this experiment.

References

1) G. Möllenstedt: Optik **5** (1949) 499.

2) H. Watanabe: to be published in Phys. Rev. (scheduled issue: Sept. 15, 1954).

3) G. Ruthemann: Ann. Physik **2** (1948) 113.

4) D. Pines and D. Bohm: Phys. Rev. **85** (1952) 338.

D. Pines: Phys. Rev. **92** (1953) 626.

5) D. Pines: private communication.

6) L. Marton and Leder: Phys. Rev. **94** (1954) 203.

Errata

On the Electron Bombardment Effect for Deposited Barium Oxide Films

By Tetsuji Imai

J. Phys. Soc. Japan **9** (1954) 28∼37

P. 28	right column line 19	lines	should be read	lies
P. 29	right column lines 9 and 10	enhancement of dissociation as bombarding energy increases.	〃	increment of the gas evolution as the depositing quantity increases.
P. 31	right column line 30	far-	〃	fur-
P. 32	left column line 1	vatirn	〃	vation
P. 34	right column line 23	Fig. 10	〃	Fig. 9
P. 35	in Fig. 10 (b)	20 eV	〃	2.0 eV

PROGRESS OF THEORETICAL PHYSICS

(Founded by H. Yukawa in 1946)

Published for the

Research Institute for Fundamental Physics

The Physical Society of Japan

Progress of Theoretical Physics Vol. 12, No. 2, 1954

The Quantum Statistical Theory of Transport Phenomena, III — Coarsegrained Phase-space Distribution Functions — ....Syu ONO....113
On Equivalent Observers, II ....Hyôitirô TAKENO....129
Reduced Width on Collective Model ....Shiro YOSHIDA....141
On the Construction of Potential in Field Theory ....Nobuyuki FUKUDA, Katuro SAWADA and Mituo TAKETANI....156
The Effects of Heavy Particles on π^--meson-proton Scattering ....Shigeaki HATANO, Tadashi KANENO and Mitsuo SHINDO....167
An Attempt to the Unified Description of Elementary Particles .... Osamu HARA, Toshio MARUMORI, Yoshio OHNUKI and Hajime SHIMODAIRA....177
Wave Equations with New Degree of Freedom ....Ken-iti Goto....208
Upper and Lower Bounds of Born Approximation, I ....Takashi KIKUTA....225
Upper and Lower Bounds of Born Approximation, II ....Takashi KIKUTA....234
Letters to the Editor:
Effect of the Pauli Moment on the γ-decay of Neutral Meson........ .... H. KATSUMORI....241
Meson Production in Meson-nuclear Collisions ....Y. MIYACHI....243
Electronic Structure of Graphite and Boron Nitride ....K. ARIYAMA and S. MASE....244
An Interpretation for the Electronic Conductivity and Diamagnetic Susceptibility of Graphite..................K. ARIYAMA and S. MASE....246
On the Excited States of Even-even Nuclei....M. NAGASAKI and T. TARO....248
Corrigenda: Radiative Corrections to the Anomalous Magnetic Moment of the Nucleon in Pseudoscalar Meson Theory ....K. NAKABAYASHI, I. SATO and T. AKIBA....250

Price $ 1.25 per copy
$ 15.00 per year (postage inclusive)
Annual dues for foreign members (individual subscribers)
$ 12.00 (postage inclusive)
〃 for foreign members of the Physical Society of Japan
$ 10.00 (postage inclusive)

Application for members, subscriptions and orders for back mumbers should be sent, directly or through book-dealers, to

The Publication Office
in

Yukawa Hall, Kyoto University, Kyoto, Japan

CONTENTS

(Vol. 9)

No. 1

Toshio AZUMA: Internal Conversion Coefficient of Ba^{137} ... 1
Toshio KITAGAKI: Higher Order Focusing Pair Spectrometers ... 4
Isao KITA and Osamu MINAKAWA: Nuclear Interactions of Secondary Shower Particles of Cosmic Rays in Lead and Carbon ... 6
Morikazu TODA and Fumihiko TAKANO: Notes on Fermi and Bose Statistics ... 14
Yasumitsu SHIMOMURA and Ichiro TSUBOKAWA: Some Physical Properties of Nickel Oxides ... 19
Shin-ichiro NARITA: External Photo-Emission of Thin Films Deposited by Evaporation from Barium Oxide ... 22
Tetsuji IMAI: On the Electron Bombardment Effect for Deposited Barium Oxide Films 28
Takuzo SHINDO: Transient Phenomenon in the Oxide Cathode Layer ... 38
Einosuke FUKUSHIMA and Akiya OOKAWA: Observation of the Grain Boundary in Soap Bubble Raft Part II. Dynamical Behaviour of the Grain Boundary ... 44
Sigeru NAGAHARA: The Scattering of Slow Electrons by the Diatomic Molecules II. Elastic Scattering by the Hydrogen Molecules ... 52
Shigeru HAYASHI: The Viscoelasticity of Linear Polymeric Substance ... 56
Tadashi KISHIMOTO and Otohiko NOMOTO: On Molecular Sound Velocity of Liquids I. Consideration on the Rao's Relation between the Temperature Coefficient of Sound Velocity in and the Coefficient of Thermal Expansion of Liquids ... 59
Tadashi KISHIMOTO and Otohiko NOMOTO: On Molecular Sound Velocity of Liquids II. Dependence of the Thermal Expansion Coefficient and the Temperature Coefficient of Compressibility of Liquids on the Boiling Point ... 66
Otohiko NOMOTO and Tadashi KISHIMOTO: On Molecular Sound Velocity of Liquids III. Consideration on the Rao's Relation on the Dependence of Molecular Sound Velocity on Critical Constants ... 73
Yasaku WADA and Sotoshi SHIMBO: The Density and the Ultrasonic Velocity in Benzene Solutions of Methyl Methacrylate at Different Polymerization Stages ... 78
Yoshika MASUDA and Teinosuke KANDA: Concentration Shift of Nuclear Magnetic Resonances in Some Concentrated Acids ... 82
Masao SUMI: On the Excitation of Oscillations in a Thermal Plasma ... 88
Kiyoshi MURAKAWA and Shigeki SUWA: Hyperfine Structure of the Spectrum of Pr II 93
Goro KUWABARA: The Optical and Electrical Properties of Cadmium Sulphide Films 97
Isao IMAI: Extension of von Kármán's Transonic Similarity Rule ... 103
Nobuzo TERAO and Shigeo SAKATA: Electromicroscopie de la Surface d'une Cassure de Verre (II) ... 109
Kuniya FUKUDA: Feed-Back Resonance Amplifier for the Infrared Spectrometry Part I ... 115
Kuniya FUKUDA: Feed-Back Resonance Amplifier for the Infrared Spectrometry Part II ... 123

No. 2

Shin-ichi KANEKO, Tadayoshi KUBOZOE and Masaomi TAKAHATA: Frequency of Slow Cosmic-ray μ-Mesons Stopped in the Photographic Emulsions at 23 m.w.e. Underground ... 147
Hatsujiro HASHIMOTO: Study of Thin Crystalline Films by Universal Electron Diffraction Microscope ... 150
Riitsu TAKAGI: Morphology of ZnO Crystals formed on the Surface of Brass or Zinc at High Temperatures ... 162
Jiro KAKINOKI and Yukitomo KOMURA: Intensity of X-ray Diffraction by a One-dimensionally Disordered Crystal (II) General Derivation in the Case of the Correlation Range $s \geq 2$ ... 169
Jiro KAKINOKI and Yukitomo KOMURA: Intensity of X-ray Diffraction by a One-dimensionally Disordered Crystal (III) The Close-packed Structure ... 177

Goro HONJO and Kazuhiro MIHAMA: Fine Structure due to Refraction Effect in Electron Diffraction Pattern of Powder Sample. Part II Multiple Structures due to Double Refraction given by Randomly Oriented Smoke Particles of Magnesium and Cadmium Oxide 184

Takechiyo INOUE and Takehito TAKAHASHI: Inelastic Collisions between Two Molecules 199

H. TAKAKI, S. NAKAMURA, Y. NAKAMURA, J. HAYASHI, K. FURUKAWA and M. ASO: The Production of Single Crystals of Metals and Alloys with any Desired Orientation by Solidification at High Temperature 204

Junkichi ITOH, Riichiro KUSAKA and Yukio YAMAGATA: The Electric Quardrupole Splitting of the Nuclear Magnetic Resonance Lines of Sodium in a Single Crystal of $Na_2S_2O_3 \cdot 5H_2O$ 209

Tadao HORIE and Masamoto OTSUKA: Simultaneous Excitation and Dissociation of Water Molecule by Hydrogen Canal Ray Impact 219

V. VENKATESWARLU and N. A. RAMAIAH: Studies of Light Absorption under Conditions productive of Joshi Effect in Mercury Vapour under Ozoniser Discharge.. 225

Hiroomi FUJIKAWA: The Lift on the Symmetrical Joukowski Aerofoil in a Stream bounded by a Plane Wall 233

Hiroomi FUJIKAWA: Note on the Lift acting on a Circular-arc Aerofoil in a Stream bounded by a Plane Wall 240

Yoshikazu SUGIURA: Experimental Studies on the Force exerted on a Disc placed in a Flow of Rarefied Gas 244

Hakuro OGUCHI: On the Subsonic Flow behind the Bow Wave of a Finite Wedge .. 249

Akira SAKURAI: On the Propagation and Structure of a Blast Wave, II 256

Otohiko NOMOTO: Theory of the Visualization of Ultrasonic Waves I, Theory of the Schlieren Method for Visualizing Ultrasonic Waves 267

Otohiko NOMOTO: Theory of the Visualization of Ultrasonic Waves II, Theory of the Phase-shift Method for visualizing Ultrasonic Waves 279

Chikara HAYASHI: On the Rate of Decomposition of Diffusion Pump Oil 287

No. 3

Obituary Notice of Professor KŌTARO HONDA I

Takeo NAGAMIYA and Noriko TATSUUMA: Theory of Color Centers. III. Continuum Models of F_2^+- and F_2-Centers 307

Takeo NAGAMIYA, Tadanobu KOJIMA and Hisamoto KONDOH: Theory of Color Centers. IV. Energy Levels of Various Complex Centers 310

P. W. ANDERSON: A Mathematical Model for the Narrowing of Spectral Lines by Exchange or Motion 316

Jiro YAMASHITA: Theory of Superexchange Interaction in MnO Crystal 339

Shūichi IIDA: Formation Energy of Superlattice in Ni_3Fe II. Kinetics of the Superlattice in the Stage of Local Ordering 346

Shoichi ANNAKA: X-ray Study of Cold Work in Some Ordered Alloys 354

Mieko TAKAGI: Electron-Diffraction Study of Liquid-Solid Transition of Thin Metal Films 359

Haruo TANAKA and Takakiyo KAKINUMA: Multiple Element Interferometer for Locating Sources of Solar Noise at 4,000 MC 364

H. KUMAGAI, K. ŌNO, I. HAYASHI, H. ABE, J. SHIMADA, H. SHŌNO, H. IBAMOTO and S. TACHIMORI: On Line Widths of Paramagnetic Resonance Absorption 369

H. KUMAGAI, I. HAYASHI, K. ŌNO, H. ABE, J. SHIMADA and H. SHŌNO: Absolute Values of Absorption Coefficients in Paramagnetic Resonance Absorption 376

Koichi SHIMODA: Atomic Clocks and Frequency Standard on an Ammonia Line. I .. 378

Kozo ISHIGURO and Toshiharu HAYASHI: The Change of the Refractive Index of Some Germanium Films Irradiated by Intense Light 387

Kiyoshi MURAKAWA: Quadrupole Moment of La^{139} 391

Tōru KAWAMURA: Contribution of the Change of Entropy to the Directions of Spines of Shock Polar 396

Hiromu WAKESHIMA: Fog Formation due to Self Nucleation 400

Hiromu WAKESHIMA: Fog Formation due to Self Nucleation II 407

Koji SATO, Heinosuke NAKANE, Teruo HIDESHIMA and Shigeo IWAYANAGI: Creep of Polymethyl Methacrylate at Low Temperature 413
Eizō KANAI and Takesi SATOH: On the Transitional Phenomena of Glass............ 417

No. 4

Toshio AZUMA: K-Auger Electrons From Ba137 443
S. TAKEMOTO, T. DAZAI, R. CHIBA, S. ITO, S. SUGANOMATA and Z. WATANABE: The Angular Distribution of Protons from the $C^{12}(d, p)C^{13}$ Reactions 447
Ikuro SHIMOSE: Statistical Theory of Phase Transition, I General Theory for Lattice Gas 451
Ikuro SHIMOSE: Statistical Theory of Phase Transition. II Numerical Calculation for Lattice Gas 457
Akira SUGIYAMA: On the Variational Calculation of the Activation Energy of Dislocation 460
Akio YOSHIMORI and Takeo MATSUBARA: A Method of Treating the Zero-point Vibration of the Crystal of Lighter Molecules 465
Tomoyasu TANAKA: Note on the Partition Function of a Free Rotator.............. 472
Shiro OGAWA and Denjiro WATANABE: Electron Diffraction Study on the Ordered Alloy CuAu 475
Sukeaki HOSOYA: Order-Disorder Transitions in A_2BC Ternary Alloy with the Plane Square or the Body-Centered Cubic Lattice 489
Tokutarō HIRONE, Seijirō MAEDA and Noboru TSUYA: On the Ferrimagnetism of Iron Selenides 496
Tokutarō HIRONE, Seijirō MAEDA, Shu CHIBA and Noboru TSUYA: Thermal Analysis of Iron Sulfides at the Temperature Range of β-transformation 500
Tokutarō HIRONE, Seijirō MAEDA and Noboru TSUYA: Thermal Analysis of Iron Sulfides at the Temperature Range of α-transformation.......................... 503
Hideo TAKAKI and Yoji NAKAMURA: The Magnetostriction Constants of Silicon Steel I 507
Kōzō NONAKA and Kazutake KOHRA: Study on the Crystallization Process of Polished Layers of Metals by Electron Diffraction and Microscopy 512
Yasumitsu SHIMOMURA, Ichiro TSUBOKAWA and Morio KOJIMA: On Nickel Oxides of High Oxygen Content 521
Sukeaki HOSOYA: On the Transition Temperature of Molecular Rotation in Long-Chain Compounds with the Discontinuous Model.................................. 524
Hideji SUZUKI: A Theory of the Formation of Slip Bands in Face-Centred Cubic Crystals 531
Hazimu KAWAMURA, Hiroshi OHKURA and Takeo KIKUCHI: The Statistical Time Lag of the Dielectric Breakdown of Mica, Glass and KCl 541
Sanchi MIZUSHIMA: Thermal Conductivity of Crystals and Liquids................. 546
Masao KOTANI, Eiichi ISHIGURO and Katsunori HIJIKATA: Tables of Integrals Useful for the Calculations of Molecular Energies. IV 553
Koichi SHIMODA: Atomic Clocks and Frequency Standards on an Ammonia Line. II .. 558
Koichi SHIMODA: Atomic Clocks and Frequency Standards on an Ammonia Line. III .. 567
S. R. MOHANTY, J. JAYARAMAN and G. V. G. KRISHNA RAO: The Positive Joshi Effect in Oxygen under Electrodeless Discharge.................................. 576
Sumitada ASANO: On the Infrared-Sensitive Behaviors of Some Doubly Activated ZnS Phosphors 580
Yuzuru OOSHIKA: Absorption Spectra of Dyes in Solution 594
Yukichi UKITA and Jumpei TSUJIUCHI: On the Wave Aberrations of the Decentred Lens System with the Finite Aperture 602
Ken-ichi KUSUKAWA: On the Subsonic Flow of a Compressible Fluid past an Axisymmetric Slender Body.. 605
Hidenori HASIMOTO: Rayleigh's Problem for a Cylinder of Arbitrary Shape........ 611
Tadashi KISHIMOTO and Otohiko NOMOTO: Absorption of Ultrasonic Waves in Organic Liquids I. Liquids with Positive Temperature Coefficients of Sound Absorption.. 620
Tadashi HIBI and Takuji OGAWA: Crystals Habit of Magnesium Oxide Smokes 627

Hide YOSHIOKA: On the Anomalous Absorption of X-rays by Crystals at the Setting of Bragg Reflection ... 636

No. 5

S. HIGASHI, M. ODA, T. OSHIO, H. SHIBATA and K. WATANABE: On the Absorption of Cosmic Rays Underground ... 655
Kiyosi NIU: On the Unstable Heavy Meson Decaying in Flight in the Photographic Emulsion Exposed at High Altitudes ... 659
Makoto KIKUCHI: Long Period Effects in Germanium Crystal Rectifiers ... 665
Eiji HIRAHARA and Miyuki MURAKAMI: Hall Effect and Electrical Conductivity of Lead Selenide ... 671
Taro KIHARA, Yukio MIDZUNO and Toshio SHIZUME: Statistics of Lattices with Many Components ... 681
Taro KIHARA and Saburo KOBA: Second Virial Cofficient between Unlike Molecules 688
Kazutake KOHRA: Simultaneous Reflexion in Electron Diffraction as a Cause of the Failure of Friedel's Law ... 690
Shizuo MIYAKE and Kazuo SUZUKI: X-ray Studies on the Structures of Solid Solutions NaCl-CaCl$_2$ I. Main Results and General Considerations ... 702
Tadami TAOKA and Taiichiro OHTSUKA: The Magnetic Properties and their Temperature Dependence of Ferromagnetic Alloys with an Order-disorder Transformation I. Ni$_3$Fe ... 712
Tadami TAOKA and Taiichiro OHTSUKA: The Magnetic Properties and their Temperature Dependence of Ferromagnetic Alloys with an Order-disorder Transformation II. Ni$_3$Mn ... 723
Ken-ichi HIRANO and Yutaka TAKAGI: On the Solid Solubility of Silver in Aluminium 730
Tokutarō HIRONE, Seijirō MAEDA and Noboru TSUYA: On the Λ-shaped Ferrimagnetism of FeS$_{1.10}$ ... 736
Hiroshi KIHŌ: The Crystallographic Aspect of the Mechanical Twinning in Metals.... 739
Hideo TAKAKI and Yoji NAKAMURA: The Magnetostriction Constants of Silicon Steel II ... 748
Yukito TANABE and Satoru SUGANO: On the Absorption Spectra of Complex Ions I 753
Yukito TANABE and Satoru SUGANO: On the Absorption Spectra of Complex Ions II 766
Nobuhiko SAITŌ: Statistical Mechanics of Flexible Linear Polymers. I. Moments of End-to-End Distance of a Polymer ... 780
Eiichi FUKADA: The Relation between Dynamic Elastic Modulus, Internal Friction, Greep and Stress Relaxation in Polymethyl Methacrylate ... 786
Taiji ARAKAWA: Paramagnetic Resonance Absorption in Manganese Fluosilicate Dilued with Magnesium Ions ... 790
Shoji KOJIMA, Kineo TSUKADA, Akira SHIMAUCHI and Yasushi HINAGA: Zeeman Splitting of Nuclear Quadrupole Resonance Line of Bromine ... 795
Shoji KOJIMA, Kazuo TAKAYAMA and Akira SHIMAUCHI: Noise of Gas Discharge Plasma 802
Shoji KOJIMA, Kineo TSUKADA, Shizuko OGAWA, Akira SHIMAUCHI and Yoshihito ABE: Nuclear Quadrupole Resonances in Arsenic Tribromide and Tri-iodide ... 805
Toshimoto KUSHIDA, Yoshitaka KOI and Yoshiro IMAEDA: Zeeman Splitting of Nuclear Quadrupole Spectra of NaBrO$_3$ ... 809
H. ABE, K. ONO, I. HAYASAI, J. SHIMADA and K. IWANAGA: Paramagnetic Resonance Absorption in K$_2$CuCl$_4$·2H$_2$O ... 814
Tadao HORIE, Kazuo KAWABE and Shozo SAWADA: Optical Behaviours of BaTi$_3$ Multi-domain Single Crystal in Dependence on Temperature ... 823
Masahumi NAGASE: On the Zeros of Certain Transcendental Functions connected with Hankel Function Part I ... 826
Masahumi NAGASE: On the Zeros of Certain Transcendental Functions connected with Hankel Function Part II ... 842
Kinzo HIDA: On the Curved Shock Wave due to an Infinite Wedge placed in a Supersonic Uniform Flow ... 853
Hakuro OGUCHI: On the Attached Curved Shock in Front of an Open-Nosed Axially Symmetrical Body ... 861
Hiroshi FUJITA and Akira KISHIMOTO: The Relaxation of Stress in Undrawn Amilan 867

No. 6

K. HINOTANI, K. SUGA and Y. TANAKA: A Study of Shower Curves with the Multiplate Cloud Chamber 883
Ryogo KUBO and Kazuhisa TOMITA: A General Theory of Magnetic Resonance Absorption........ 888
Hiroshi WATANABE: On the Velocity Analysis of Electrons Scattered by Thin Foils.. 920
Yoichi UCHIDA and Yoshio NAKAI: On the V-centers in Alkali Crystals 928
Ryogo KUBO: Note on the Stochastic Theory of Resonance Absorption........ 935
Jiro YAMASHITA and Tatumi KUROSAWA: Formation Energy of Lattice Difect in Simple Oxide Crystals........ 944
Mario YOKOTA and Shoichiro KOIDE: The Exchange Effects on the Absorption Spectrum by the Paramagnetic Crystal with Anisotropic g-factors........ 954
Joji MIZUNO, Shiro OGAWA and Tokutaro HIRONE: Dependence of the Intermetallic Diffusion Coefficient upon Concentration........ 961
Nahonori MIYATA and Zenya FUNATOGAWA: Magneto-thermoelectric Powers of Nickel Single Crystals.... 967
Koichi SHIMODA, Tetsuji NISHIKAWA and Takashi ITOH: Microwave Spectrum of Methylamine 974
Goro KUWABARA: Optical Properties of Cadmium Sulfide in Glass 992
Kazunori TAKAZAWA and Tosiro TOMOTIKA: On the Optical Absorption of Thin BaO Film in the Ultraviolet Region........ 996
Hisamitu YOSHIMURA and Kuniya FUKUDA: Feed-back Resonance Amplifier for the Infrared Spectrometry Part III........1001
Isao IMAI: On a Refinement of the Transonic Approximation Theory 1009
Tadashi KISHIMOTO and Otohiko NOMOTO: Absorption of Ultrasonic Waves in Organic Liquids (II) Liquids with Negative Temperature Coefficient of Sound Absorption (a) Glycols, Cyclohexanol and Cresol 1021
CONTENTS (Vol. 9.)........ i
AUTHOR INDEX TO Vol. 9 vii

SHORT NOTES

No. 1

Makoto KIKUCHI and Tomio ONISHI: The "Photo-Aftereffect" of Germanium Crystal Rectifiers 130
Yasuo KANAI: On the Electrical Properties of Silicon Single Crystals (I)........ 132
Kenji NUKASAWA: On the Delocalization Energy in Molecules 133
Motoichi SHIBUYA: The Magneto-resistance Effect in a Cubic Semiconductor with the Spheroidal Energy Surfaces........ 134
Akira OKAYA: New Spectra of $H_2C^{12}O$ in 6 mm Wave Range 135
Kikusaburo OSADA: A Filter Transmitting near the Mercury Line, 2537A 136
O. MINAKAWA and J. NISHIMURA: On "An Unusual Star" by Nakagawa et al. 137
Kinzo SATO and Masaharu NAMBA: On the Photocurrent of High Purity SiC Single Crystal 139
Sadabumi ISSIKI and Hiroshi KIMURA: On the Change of Density of Copper Single Crystals by Cold Working........ 139
Toshimichi SAKATA and Seiji MUNESUE: Magneto-Resistance of Cs_3Sb Photo-Cathodes 141
Yutaka SHIGEMITSU: Decay of Shear Trubulence........ 142
Yasuo KANAI: On the A. C. Characteristics of Silicon p-n Junction Alloy Diodes 143
Yoshibumi FUJIKI and Ryoji SUGANUMA: On the Lattice Anomaly of Bismuth Film deposited from its Vapour........ 144

No. 2

Kwai UMEDA: A Measure for Approximation Degree of the Approximate TF Function for Free Neutral Atom 290
Kwai UMEDA: On the Approximate TF Function for Compressed Neutral Atom 291

Yasuo KANAI: Temperature Dependency of the Surface Recombination Velocity in Germanium 292
Shinji KATAOKA: On the Dissociation Constant of Polyelectrolyte 293
Sadao HOSHINO: Anomalous Structure of α-AgI 295
Masahumi NAGASE: Asymptotic Expansions of Bessel Functions in the Transitional Resions 296
Kazuo HUKE and Giiti IWATA: The Effect of Field Bump in a Strong Focusing Synchrotron 297
Yoshiharu TORIZUKA, Yuzo KOJIMA and Tadao FUJIMURA: On the g-Factor and Hi of Nickel Ferrite-Aluminate 298
Kenji MITANI: On the Radial Extent of Glow in Microwave Gas Discharge between Coaxial Cylinders 299
Masahiro KUWAGATA, Eizo OTSUKA and Masao TOMURA: Electrical Resistivity of Polycrystalline Selenium at Higher Fields 300
Mitsuo MIWA and Shoichi ANNAKA: An X-ray Study of Thin Evaporated Films of Metals 302

No. 3

Fumihiko TAKANO: An Attempt to Treat the Interaction between Electrons and Lattice Vibrations 430
Yoshio INUISHI and Tokuo SUITA: On the Breakdown of Colored KCl 431
Makoto HAYASHI and Yasunori MIYOSHI: Temperature Dependence of Fluctuation of Sparking Voltages of a Gas Discharge Tube 432
Junkichi ITOH and Riichiro KUSAKA: Nuclear Quadrupole Interaction in Sodium Chlorate and Sodium Bromate 434
Kin-ichi NOGA and Koji NAKAMURA: Cathodo-Luminescence Study of (BaSr)O 435
Mitsuo SAKAI: A Note on Avoiding Scattered Electrons from the Spectrum obtained by Magnetic Spectrometer 437
Inseun RYU and Hazimu KAWAMURA: On the Thickness Effect of Dielectric Breakdown of Mica and KCl 438
F. J. BLATT: Diffusion on the Fermi-Surface and the Conductivity of Metals 400
Morikazu TODA: Diffusion on the Fermi Surface 400

No. 4

Shigetomo YOSHIDA, Nagao SHIBATA, Yoshitaka IGARASHI and Hikaru ARATA: The Use of Radioactive Isotope in a Study of Evolution of Strontium Oxide under Electron Bombardment 640
Yasaku WADA: On the Relation Between Sound Velocity and Intermolecular Free Length of Liquids 641
Makoto KIKUCHI and Yasuo TARUI: Transient Phenomena in the Backward Direction of Germanium Crystal Rectifiers 642
Noboru TSUYA: On the Internal Field of the Microwave Resonance in Ferrites 644
Kazuo TORIZUKA: Chlorine Pure Quadrupole Spectra in Some Solid Compounds 645
Ryukiti Robert HASIGUTI and Gen-ichi KAMOSHITA: Internal Friction of Alpha-Iron Due to Boron Atoms 646
Kiyoshi ARAKAWA: On the Free Volume Theory of Liquid 647
Hisao MIYASAWA and Suezo SUGAIKE: Photoconductivity of In_2Te_3 and CdTe Single Crystals 648
W. SASAKI, N. SAKAMOTO and M. KUNO: Some Electrical Properties of AlSb 650

No. 5

Kineo TSUKADA: Contribution of Overlap Integral to Nuclear Quadrupole Coupling .. 872
Atsuo NISHIOKA and Kyozo SEKIKAWA: Powder Density Measurement by Gas Burette 873
Osamu SHIMADA: An Evaluation of Plasma-ion Temperature 874
Kiyoshi MURAKAWA: Isotope Shift in the Spectra of Tin and Lead 876
Isao KUMABE and Masateru SONODA: On the External Cathode Proportional Counter .. 877
S. R. MOHANTY: The Electrode Surface-Gas Interface as the Seat of the Joshi Effect Under Silent Electric Discharge 878
Nobuzo TERAO: Sur la Resistance a la Rupture du Verre a la Basse Pression 879

No. 6

Toshimichi SAKATA: Hall Effect in Cesium Antimonid with Audiofrequency Currents..1030
Toshimichi SAKATA: On the Thermoelectric Power of Cesium Antimonide 1031
T. IMAI and Y. MIZUSHIMA: On the Electron Bombardment Effect for Deposited Barium Oxide Films (II)..........1032
T. IMAI and N. SHIBATA: Effect of the Basic Metal on the Dissociation of Deposited Barium Oxide Films 1034
Hiroshi WATANABE: Multipled Lines in the Energy Spectrum of Electrons Passing through an Mg Foil..........1035

Errata

Hidenori HASIMOTO: Application of the Thin-Wing-Expansion Method to the Compressible Flow past an Elliptic Cylinder.......... 145
Hidenori HASIMOTO: On the Flow of a Viscous Fluid past an Inclined Elliptic Cylinder at Small Reynolds Numbers 146
Sadabumi ISSIKI and Hiroshi KIMURA: On the Change of Density of Copper Single Crystals by Cold Working.......... 303
Mitutosi KAWAGUTI: Numerical Solution of the Navier-Stokes Equations for the Flow around a Circular Cylinder at Reynolds Number 40 303
Tadao HORIE and Masamoto OTSUKA: Simultaneous Excitation and Dissociation of Water Molecule by Hydrogen Canal Ray Impact 442
M. KUWAGATA, E. OTSUKA and M. TOMURA: Electrical Resistivity of Poly-Crystalline Selenium at Higher Fields.......... 442
Kiyoshi MURAKAWA: Hyperfine Structure of the Spectrum of Ruthenium. Part II .. 651
Kazuo NIIRA: $\sigma\pi$ Interaction in Benzene 651
Ken-ichi KUSUKAWA: On the Subsonic Flow of a Compressible Fluid past an Axisymmetric Slender Body 881
Tetsuji IMAI: On the Electron Bombardment Effect for Deposited Barium Oxide Films1037

AUTHOR INDEX TO Vol. 9

- ABE H.;
  - H. KUMAGAI, K. ŌNO, I. HAYASHI, ——, J. SHIMADA, H. SHŌNO, H. IBAMOTO and S. TACHIMORI: On Line Widths of Paramagnetic Resonance Absorption 369
  - H. KUMAGAI, I. HAYASHI, K. ŌNO, ——, J. SHIMADA and H. SHŌNO: Absolute Values of Absorption Coefficients in Paramagnetic Resonance Absorption 376
  - ——, K. ŌNO, I. HAYASHI, J. SHIMADA and K. IWANAGA: Paramagnetic Resonance Absorption in $K_2CuCl_4\cdot 2H_2O$ 814
- ABE Yoshihito;
  - S. KOJIMA, K. TSUKADA, S. OGAWA, A. SHIMAUCHI and ——: Nuclear Quadrupole Resonances in Arsenic Tribromide and Tri-iodide 805
- ANNAKA Shoichi;
  - M. MIWA and ——: An X-ray Study of Thin Evaporated Films of Metals 302
  - ——: X-ray Study of Cold Work in Some Ordered Alloys 354
- ANDERSON P. W.: A Mathematical Model for the Narrowing of Spectral Lines by Exchange or Motion 316
- ANNAKA Shoichi: X-Ray Study of Cold Work in Some Ordered Alloys 354
- ARATA Hikaru;
  - S. YOSHIDA, N. SHIBATA, Y. IGARASHI and ——: The Use of Radioactive Isotope in a Study of Evolution of Strontium Oxide under Electron Bombardment 640
- ARAKAWA Kiyoshi: On the Free Volume Theory of Liquids 647
- ARAKAWA Taiji: Paramagnetic Resonance Absorption in Manganese Fluosilicate Diluted with Magnesium Ions 790
- ASO M.;
  - H. TAKAKI, S. NAKAMURA, Y. NAKAMURA, J. HAYASHI, K. FURUKAWA and ——: The Production of Single Crystals of Metals and Alloys with any Desired Orientation by Solidification at High Temperature 204
- ASANO Sumitada: On the Infrared-Sensitive Behaviors of Some Doubly Activated ZnS Phosphors 580
- AZUMA Toshio: Internal Conversion Coefficient of Ba^{136} 1
  - ——: K-Auger Electrons From Ba137 443
- BLATT F. J.: Diffusion on the Fermi-Surface and the Conductivity of Metals 400
- CHIBA R.;
  - S. TAKEMOTO, T. DAZAI, ——, S. ITO, S. SUGANOMATA and Z. WATANABE: The Angular Distribution of Protons from the C^{12}(d, p)C^{13} Reactions 447
- CHIBA Shu.;
  - T. HIRONE, S. MAEDA, —— and N. TSUYA: Thermal Analysis of Iron Sulfides at the Temperature Range of β-transformation 500
- DAZAI T.;
  - S. TAKAMOTO, ——, R. CHIBA, S. ITO, S. SUGANOMATA and Z. WATANABE: The Angular Distribution of Protons from the C^{12}(d, p)C^{13} Reactans 447
- FUJIKAWA Hiroomi: The Lift on the Symmetrical Joukowski Aerofoil in a Stream bounded by a plane Wall 233
- FUJIKI Yoshibumi;
  - —— and R. SUGANUMA: On the Lattice Anomaly of Bismuth Film deposited from its Vapour 144
- FUJITA F. E.;
  - H. SUZUKI and ——: Slip Bands in an α-Brass Crystal 428
- FUJITA Hiroshi;
  - —— and A. KISHIMOTO: The Relaxation of Stress in Undrawn Amilan 867
- FUJIKAWA Hiroomi: Note on the Lift acting on a Circular-arc Aerofoil in a Stream bounded by a Plane Wall 240
- FUKADA Eiichi: The Relation between Dynamic Elastic Modulus, Internal Friction, Greep and Stress Relaxation in Polymethyl Metacrylate 786
- FUKUDA Kuniya: Feed-Back Resonance Amplifier for the Infrared Spectrometry Part I 115

: Feed-Back Resonance Amplifier for the Infrared Spectrometry Part II 123
H. Yosimura and ———: Feed-back Resonance Amplifier for the Infrared Spectrometry Part III 1001

Fukushima Einosuke;
and A. Ookawa: Observation of the Grain Boundary in Soap Bubble Raft Part II. Dynamical Behaviour of the Grain Boundary 44

Funatogawa Zenya;
N. Miyata and : Magneto-thermoelectric Powers of Nickel Single Crystals 967

Furukawa K.;
H. Takaki, S. Nakamura, Y. Nakamura, J. Hayashi, ——— and M. Aso: The Production of Single Crystals of Metals and Alloys with any Desired Orientation by Solidification at High Temperature 204

Hashimoto Hatsujiro: Study of Thin Crystalline Films by Universal Electron Diffraction Microscope 150

Hasiguti Ryukiti:
and G. Kamoshita: Internal Friction of Alpha-Iron Due to Boron Atoms 646

Hasimoto Hidenori: Rayleigh's Problem for a Cylinder of Arbitrary Shape 611

Hayashi Chikara: On the Rate of Decomposition of Diffusion Pump Oil 287

Hayashi I.;
H. Kumagai, K. Ōno, ———, H. Abe, I. Shimada, H. Shōno, H. Ibamoto and S. Tachimori: On Line Widths of Paramagnetic Resonance Absorption .. 369
H. Kumagai, ———, K. Ōno, H. Abe, J. Shimada and H. Shōno: Absolute Values of Absorption Coefficients in Paramagnetic Resonance Absorption .. 376
H. Abe, K. Ono, ———, J. Shimada and K. Iwanaga: Paramagnetic Resonance Absorption in $K_2CuCl_4 \cdot 2H_2O$ 814

Hayashi J.;
H. Takaki, S. Nakamura, Y. Nakamura, ———, K. Furukawa and M. Aso: The Production of Single Crystals of Metals and Alloys with any Desired Orientation by Solidification at High Temperature 204

Hayashi Makoto;
and Y. Miyoshi: Temperature Dependence of Fluctuation of Sparking Voltages of a Gas Discharge Tube 432

Hayashi Shigeru: The Viscoelasticity of Linear Polymeric Substance 56

Hayashi Toshiharu;
K. Ishiguro and ———: The Change of the Refractive Index of Some Germanium Films Irradiated by Intense Light 387

Hibi Tadatosi;
and T. Ogawa: Crystals Habit of Magnesium Oxide Smokes 627

Hida Kinzo: On the Curved Shock Wave due to an Infinite Wedge placed in a Supersonic Uniform Flow 853

Hideshima Teruo;
K. Sato, H. Nakane, ——— and S. Iwayanagi: Creep of Polymethy Methacrylate at Low Temperature 413

Higashi S.;
———, M. Oda, T. Oshio, H. Shibata and K. Watanabe: On the Absorption of Cosmic Rays Underground 655

Hijikata Katsunori;
M. Kotani, E. Ishiguro and ———: Tables of Integrals Useful for the Calculations of Molecular Energies. IV 553

Hinaga Yasushi;
S. Kojima, K. Tsukada, A. Shimauchi and ———: Zeeman Splitting of Nuclear Quadrupole Resonance Line of Bromine 795

Hinotani K.;
, K. Suga and Y. Tanaka: A Study of Shower Curves with the Multiplate Cloud Chamber 883

HIRAHARA Eiji;
——— and M. MURAKAMI: Hall Effect and Electrical Conductivity of Lead Selenide 671
HIRANO Ken-ichi;
——— and Y. TAKAGI: On the Solid Solubility of Silver in Aluminium 730
HIRONE Tokutaro;
———, S. MAEDA and N. TSUYA: On the Ferrimagnetism of Iron Selenides 496
———, S. MAEDA, S. BHIBA and N. TSUYA: Thermal Analysis of Iron Sulfides at the Temperature Range of β-transformation 500
———, S. MAEDA and N. TSUYA: Thermal Analysis of Iron Sulfides at the Temperature Range of α-transformation 503
———, S. MAEDA and N. TSUYA: On the Λ-shaped Ferrimagnetism of $FeS_{1.10}$ 736
HONJO Goro;
——— and K. MIHAMA: Fine Structure due to Refraction Effect in Electron Diffraction Pattern of Powder Sample. Part II Multiple Structures due to Double Refraction given by Randomly oriented Smoke Particles of Magnesium and Cadmium Oxide 184
HORIE Tadao;
——— and M. OTSUKA: Simultaneous Excitation and Dissociation of Water Molecule by Hydrogen Canal Ray Impact 219
———, K. KAWABE and S. SAWADA: Optical Behaviours of $BaTiO_3$ Multidomain Single Crystal in Dependence on Temperature 823
HOSHINO Sadao: Anomalous Structure of α-AgI 295
HOSOYA Sukeaki: Order-Disorder Transitions in A_2BC Ternary Alloy with the Plane Square or the Body-Centered Cubic Lattice 489
———: On the Transition Temperature of Molecular Rotation in Long-Chain Compounds with the Discontinuous Model 524
HUKE Kazuo;
——— and G. IWATA: The Effect of Field Bump in a Strong Focusing Synchrotron 297
IBAMOTO H.;
H. KUMAGAI, K. ŌNO, I. HAYASHI, H. ABE, J. SHIMADA, H. SHŌNO, ——— and S. TACHIMORI: On Line Widths of Paramagnetic Resonance Absorption 369
IGARASHI Yoshitaka;
S. YOSHIDA, N. SHIBATA, ——— and H. ARATA: The Use of Radioactive Isotope in a Study of Evolution of Strontium Oxide under Electron Bombardment 640
IIDA Shūichi: Formation Energy of Superlattice in Ni_3Fe II. Kinetics of the Superlattice in the Stage of Local Ordering 346
IMAEDA Yoshiro;
T. KUSHIDA, Y. KOI and ———: Zeeman Splitting of Nuclear Quadrupole Spectra of $NaBrO_3$ 809
IMAI Isao: Extension of von Kármán's Transonic Similarity Rule 103
———: On a Refinement of the Transonic Approximation Theory 1009
IMAI Tetsuji: On the Electron Bombardment Effect for Deposited Barium Oxide Films 28
IMAI T.;
——— and Y. MIZUSHIMA: On the Electron Bombardment Effect for Deposited Barium Oxide Films (II) 1032
——— and N. SHIBATA: Effect of the Basic Metal on the Dissociation of Deposited Barium Oxide Films 1034
INOUE Takechiyo;
——— and T. TAKAHASHI: Inelastic Collisions between Two Molecules 199
INUISHI Yoshio;
——— and T. SUITA: On the Breakdown of Colored KCl 430
ISHIGURO Eiichi;
M. KOTANI, ——— and K. HIJIKATA: Tables of Integrals Useful for the Calculations of Molecular Energies. IV 553

ISHIGURO Kozo;

——— and T. HAYASHI: The Change of the Refractive Index of Some Germanium Films Irradiated by Intense Light 387

ISSIKI Sadabumi;

and H. KIMURA: On the Change of Density of Copper Single Crystals by Cold Working 139

ITO S.;

S. TAKEMOTO, T. DAZAI, R. CHIBA, ———, S. SUGANOMATA and Z. WATANABE: The Angular Distribution of Protons from the $C^{12}(d, p)C^{13}$ Reactions 447

ITOH Junkichi;

———, R. KUSAKA and Y. YAMAGATA: The Electric Quadrupole Splictting of the Nuclear Magnetic Resonance Lines of Sodium in a Single Crystal of $Na_2S_2O_3 \cdot 5H_2O$ 209

——— and KUSAKA: Nuclear Quadrupole Interaction in Sodium Chlorate and Sodium Bromate 434

ITOH Takashi;

K. SHIMODA, T. NISHIKAWA and ———: Micro wave Spectrum of Methylamine 974

IWANAGA K.;

H. ABE, K. ŌNO, I. HAYASHI, J. SHIMADA and ———: Paramagnetic Resonance Absorption in $K_2CuCl_4 \cdot 2H_2O$ 814

IWATA Giiti;

K. HUKE and ———: The Effect of Field Bump in a Strong Focusing Synchrotron 297

IWAYANAGI Shigeo;

K. SATO, H. NAKANE, T. HIDESHIMA and ———: Creep of Polymethyl Methacrylate at Low Temperature 413

JAYARAMAN J.;

S. R. MOHANTY, ——— and G. V. G. KRISHNA RAO: The Positive Joshi Effect in Oxygen under Electrodeless Discharge 576

KAKINUMA Takakiyo;

H. TANAKA and ———: Multiple Element Interferometer for Locating Sources of Solar Noise at 4,000 MC 364

KAKINOKI Jiro;

——— and Y. KOMURA: Intensity of X-ray Diffraction by a One-dimensionally Disordered Crystal (II) General Derivation in the Case of the Correlation Range $s \geq 2$ 169

——— and Y. KOMURA: Intensity of X-ray Diffraction by a One-dimensionally Disordered Crystal (III) The Close-packed Structure 177

KAMOSHITA Gen-ichi;

R. HASIGUTI and ———: Internal Friction of Alpha-Iron Due to Boron Atoms 646

KANAI Eizō;

——— and T. SATOH: On the Transitional Phenomena of Glass 417

KANAI Yasuo: Temperature Dependency of the Surface Recombination Velocity in Germanium 292

———: On the Electrical Properties of Silicon Single Crystals (I) 132

———: On the A. C. Characteristics of Silicon p-n Junction Alloy Diodes 143

KANDA Teinosuke;

Y. MASUDA and ———: Concentration Shift of Nuclear Magnetic Resonances in Some Concentrated Acids 82

KANEKO Shin-ichi;

———, T. KUBOZOE and M. TAKAHATA: Frequency of Slow Cosmic-ray Mesons Stopped in the Photographic Emulsions at 23 m.w.e. Underground.. 147

KATAOKA Shinji: On the Dissociation Constant of Polyelectrolyte 293

KAWABE Kazuo;

T. HORIE, ——— and S. SAWADA: Optical Behaviours of $BaTiO_3$ Multi-domain Single Crystal in Dependence on Temperature 823

KAWAMURA Hazimu;

I. RYU and ———: On the Thickness Effect of Dielectric Breakdown of Mica

and KCl ... 438
——, H. **Ohkura** and T. **Kikuchi**: The Statistical Time Lag of the Dielectric Breakdown of Mica, Glass and KCl ... 541
Kawamura Tōru: Contribution of the Change of Entropy to the Directions of Spines of Shock Polar ... 396
Kihara Taro;
——, Y. **Midzuno** and T. **Shizume**: Statistical of Lattices with Many Components ... 681
—— and S. **Koba**: Second Virial Coefficient between Unlike Molecules ... 688
Kiho Hiroshi: The Cr Stallographic Aspect of the Mechanical Twinning in Metals 739
Kikuchi Makoto;
—— and T. **Onishi**: The "Photo-Aftereffect" of Germanium Crystal Rectifiers ... 130
—— and Y. **Tarui**: Transient Phenomena in the Backward Direction of Germanium Crystal Rectifiers ... 642
——: Long Period Effects in Germanium Crystal Rectifiers ... 665
Kikuchi Takeo;
H. **Kawamura**, H. **Ohkura** and ——: The Statistical Time Lag of the Dielectric Breakdown of Mica, Glass and KCl ... 541
Kimura Hiroshi;
S. **Issiki** and ——: On the Change of Density of Copper Single Crystals by Cold Working ... 139
Kishimoto Akira;
H. **Fujita** and ——: The Relaxation of Stress in Undrawn Amilan ... 867
Kishimoto Tadashi;
—— and O. **Nomoto**: On Molecular Sound Velocity of Liquids I. Consideration on the Rao's Relation between the Temperature Coefficient of Thermal Expansion of Liquids ... 59
—— and O. **Nomoto**: On Molecular Sound Velocity of Liquids II. Dependence of the Thermal Expansion Coefficient and the Temperature Coefficient of Compressibility of Liquids on the Boiling Point ... 66
O. **Nomoto** and ——: On Molecular Sound Velocity of Liquids III. Consideration on the Rao's Relation on the Dependence of Molecular Sound Velocity on Critical Constants ... 73
—— and O. **Nomoto**: Absorption of Ultrasonic Waves in Organic Liquids I. Liquids with Positive Temperature Coefficients of Sound Absorption ... 620
—— and O. **Nomoto**: Absorption of Ultrasonic Waves in Organic Liquids (II) Liquids with Negative Temperature Coefficient of Sound Absorption (a) Glycols, Cyclohexanol and Cresol ... 1021
Kita Isao;
—— and O. **Minakawa**: Nuclear Interactions of Secondary Shower Particles of Cosmic Rays in Lead and Carbon ... 6
Kitagaki Toshio: Higher Order Focusing Pair Spectrometers ... 4
Koba Saburo;
T. **Kihara** and ——: Second Virial Coefficient Unlike Molecules ... 688
Kohra Kazutake;
K. **Nonaka** and ——: Study on the Crystallization Process of Polished Layers of Metals by Electron Diffraction and Microscopy ... 512
——: Simultaneous Reflexion in Electron Diffraction as a Cause of the Failure of Friedel's Law ... 690
Koi Yoshitaka;
T. **Kushida**, —— and Y. **Imaeda**: Zeeman Splitting of Nuclear Quadrupole Spectra of $NaBrO_3$ ... 809
Koide Shoichiro;
M. **Yokota** and ——: The Exchange Effects on the Absorption Spectrum by the Paramagnetic Crystal with Anisotropic *g*-factors ... 954
Kojima Morio;
Y. **Shimomura**, I. **Tsubokawa** and ——: On Nickel Oxides of High Oxygen

Content 521

KOJIMA Shoji;

———, K. TSUKADA, A. SHIMAUCHI and Y. HINAGA: Zeeman Splitting of Nuclear Quadrupole Resonance Line of Bromine 795

——, K. TAKAYAMA and A. SHIMAUCHI: Noise of Gas Discharge Plasma .. 802

, K. TSUKADA, S. OGAWA, A. SHIMAUCHI and Y. ABE: Nuclear Quadrupole Resonances in Arsenic Tribromide and Tri-iodide 805

KOJIMA Tadanobu;

T. NAGAMIYA, —— and H. KONDOH: Theory of Color Centers. IV. Energy Levels of Various Complex Centers 310

KOMURA Yukitomo;

J. KAKINOKI and ———: Intensity of X-ray Diffraction by a One-dimensionally Disordered Crystal (II) General Derivation in the Case of the Correlation Range $s \geqq 2$ 169

J. KAKINOKI and ———: Intensity of X-ray Diffraction by a One-dimensionally Disordered Crystal (III) The Close-packed Structure 177

KONDOH Hisamoto;

T. NAGAMIYA, T. KOJIMA and ———: Theory of Color Centers. IV. Energy Levels of Various Complex Centers 310

KOTANI Masao;

———, E. ISHIGURO and K. HIJIKATA: Tables of Integrals Useful for the Calculations of Molecular Energies. IV 553

KRISHNA RAO G. V. G.;

S. R. MOHANTY, J. JAYARAMAN and ———: The Positive Joshi Effect in Oxygen under Electrodeless Discharge 576

KUBO Ryogo;

and K. TOMITA: A General Theory of Magnetic Resonance Absorption 888

: Note on the Stochastic Theory of Resonance Absorption 935

KUBOZOE Tadayoshi;

S. KANEKO, — and M. TAKAHATA: Frequency of Slow Cosmic-ray μ-Mesons Stopped in the Photographic Emulsions at 23 m.w.e. Underground .. 147

KUMABE Isao;

and M. SONODA: On the External Cathode Proportional Counter 877

KUMAGAI H.;

———, K. ŌNO, I. HAYASHI, H. ABE, J. SHIMADA, H. SHŌNO, H. IBAMOTO and S. TACHIMORI: On Line Widths of Paramagnetic Resonance Absorption 369

—, I. HAYASHI, K. ŌNO, H. ABE, J. SHIMADA and H. SHŌNO: Absolute Values of Absorption Coefficients in Paramagnetic Resonance Absorption .. 376

KUNO M.;

W. SASAKI, N. SAKAMOTO and ———: Some Electrical Properties of AlSb .. 650

KUROSAWA Tatumi;

J. YAMASHITA and ——: Formation Energy of Lattice Difect in Sliple Oxide Crystals 944

KUSAKA Riichiro;

J. ITOH, ——— and Y. YAMAGATA: The Electric Quadrupole Splitting of the Nuclear Magnetic Resonance Lines of Sodium in a Single Crystal of $Na_2S_2O_3 \cdot 5H_2O$ 209

J. ITOH and ———: Nuclear Quadrupole Interaction in Sodium Chlorate and Sodium Bromate 434

KUSHIDA Toshimoto;

—, Y. KOI and Y. IMAEDA: Zeeman Splitting of Nuclear Quadrupole Spectra of $NaBrO_3$ 809

KUSUKAWA Ken-ichi: On the Subsonic Flow of a Compressible Fluid past an Axi-symmetric Slender Body 605

KUWABARA Goro: The Optical and Electrical Properties of Cadmium Sulphide Films .. 97

———: Optical Properties of Cadmium Sulfide in Glass 992

KUWAGATA Masashiro;

E. OTSUKA and M. TOMURA: Electrical Resistivity of Polycrystalline Selenium at Higher Fields 300

MAEDA Seijiro;

T. HIRONE, ——— and N. TSUYA: On the Ferrimagnetism of Iron Selenides 496

T. HIRONE, ———, S. CHIBA and N. TSUYA: Thermal Analysis of Iron Sulfides at the Temperature Range of β-transformation 500

T. HIRONE, ——— and N. TSUYA: Thermal Analysis of Iron Sulfides at the Temperature Range of α-transformation 503

T. HIRONE, ——— and N. TSUYA: On the Λ-shaped Ferrimagnetism of FeS$_{1.10}$ 736

MASUDA Yoshika;

——— and T. KANDA: Concentration Shift of Nuclear Magnetic Resonances in Some Concentrated Acids 82

MATSUBARA Takeo;

A. YOSHIMORI and ———: A Method of Treating the Zero-point Vibration of the Crystal of Lighter Molecules 465

MIDZUNO Yukio;

T. KIHARA, ——— and T. SHIZUME: Statistical of Lattices with Many Components 681

MIHAMA Kazuhiro;

G. HONJO and ———: Fine Structure due to Refraction Effect in Electron Diffraction Pattern of Powder Sample. Part II Multiple Structures due to Double Refraction given by Randomly Oriented Smoke Particles of Magnesium and Cadmium Oxide 184

MINAKAWA Osamu;

I. KITA and ———: Nuclear Interactions of Secondary Shower Particles of Cosmic Rays in Lead and Carbon 6

——— and J. NISHIMURA: On "An Unusual Star" by Nakagawa et al 137

MIYAKE Shizuo

——— and K. SUZUKI: X-ray Studies on the Structures of Solid Solutions NaCl-CaCl$_2$ I. Main Results and General Considerations 702

MIYASAWA Hisao;

——— and S. SUGAIKE: Photoconductivity of In$_2$Te$_3$ and CdTe Single Crystals 648

MIYATA Nahonori;

- and Z. FUNATOGAWA: Magneto-thermoelectric Powers of Nickel Single Crystals 967

MIYOSHI Yasunori;

M. HAYASHI and ———: Temperature Dependence of Fluctuation of Sparking Voltages of a Gas Discharge Tube 432

MIWA Mitsuo:

——— and S. ANNAKA: An X-ray Study of Thin Evaporated Films of Metals 302

MIZUNO Joji;

-, S. OGAWA and T. HIRONE: Dependence of the Intermatallic Diffusion Coefficient upon Concentration 961

MIZUSHIMA Sanchi: Thermal Conductivity of Crystals and Liquids 546

MIZUSHIMA Y.;

T. IMAI and ———: On the Electron Bombardment Effect for Deposited Barium Oxide Films (II) 1032

MOHANTY S. R.;

———, J. JAYARAMAN and G. V. G. KRISHNA RAO: The Positive Joshi Effect in Oxygen under Electrodeless Discharge 576

: The Electrode Surface-Gas Interface as the Seat of the Joshi Effect Under Silent Electric Discharge 878

MUNESUE Seiji;

T. SAKATA and ———: Magneto-Resistance of Cs$_3$Sb Photo-Cathodes 141

MURAKAWA Kiyoshi;

——— and S. SUWA: Hyperfine Structure of the Spectrum of Pr II 93

———: Quadrupole Moment of La^{139} 391

—: Hyperfine Structure of the Spectrum of Ruthenium II 427

———: Isotope Shift in the Spectra of Tin and Lead 876

MURAKAMI Miyuki;
  E. HIRAHARA and ———: Hall Effect and Electrical Conductivity of Lead Selenide 671
NAGAHARA Sigeru: The Scattering of Slow Electrons by the Deatomic Molecules II. Elastic Scattering by the Hydrogen Molecules 52
NAGAMIYA Takeo;
  ——— and N. TATSUUMA: Theory of Color Centers III. Continuum Models of F_2^+- and F_2-Centers 307
  ———, T. KOJIMA and H. KONDOH: Theory of Color Centers IV. Energy Levels of Various Complex Centers 310
NAGASE Masahumi: Asymptotic Expansions of Bessel Functions in the Transitional Resions 296
  ———: On the Zeros of Certain Transcendental Functions connected with Hankel Function Part I 826
  ———: On the Zeros of Certain Transcendental Functions connected with Hankel Function Part II 842
NAKAI Yoshio;
  Y. UCHIDA and ———: On the V-centers in Alkali Iodide Crystals 928
NAKANE Heinosuke;
  K. SATO, ———, T. HIDESHIMA and S. IWAYANAGI: Creep of Polymethyl Methacrylate at Low Temperature 413
NAKAMURA Koji;
  K. NOGA and ———: Cathodo-luminescence Study of (BaSr)O 435
NAKAMURA S.;
  H. TAKAKI, ———, Y. NAKAMURA, J. HAYASHI, K. FURUKAWA and M. ASO: The Production of Single Crystals of Metals and Alloys with any Desired Orientation by Solidification at High Temperature 204
NAKAMURA Terutaro: Possible Mechanism of Ferroelectric Domain Boundary Movement 425
NAKAMURA Y.;
  H. TAKAKI, S. NAKAMURA, ———, J. HAYASHI, K. FURUKAWA and M. ASO: The Production of Single Crystals of Metals and Alloys with any Desired Orientation by Solidification at High Temperature 204
NAKAMURA Yoji;
  H. TAKAKI and ———: The Magnetostriction Constants of Silicon Steel I .. 507
  H. TAKAKI and ———: The Magnetostriction Constants of Silicon Steel II .. 748
NAMBA Masaharu;
  K. SATO and ———: On the Photocurrent of High Purity SiC Single Crystals 139
NARITA Shin-ichiro: External Photo-Emission of Thin Films Deposited by Evaporation from Barium Oxide 22
NISHIKAWA Tetsuji;
  K. SHIMODA, ——— and T. ITOH: Microwave Spectrum of Methylamine 974
NISHIMURA J.;
  O. MINAKAWA and ———: On "An Unusual Star" by Nakagawa et al 137
NISHIOKA Atsuo;
  ——— and K. SEKIKAWA: Powder Density Measurement by Gas Burette 873
NIU Kiyosi: On the Unstable Heavy Meson Decaying in Flight in the Photographic Emulsion Exposed at High Altitudes 659
NOGA Kin-ichi;
  ——— and K. NAKAMURA: Cathode-luminescence Study of (BaSr)O 435
NOMOTO Otohiko;
  T. KISHIMOTO and ———: On Molecular Sound Velocity of Liquids I. Consideration on the Rao's Relation between the Temperature Coefficient of Sound Velocity in and the Coefficient of Thermal Expansion of Liquids 59
  T. KISHIMOTO and ———: On Molecular Sound Velocity of Liquids II. Dependence of the Thermal Expansion Coefficient and the Temperature Coefficient of Compressibility of Liquids on the Boiling Point 66
  ——— and T. KISHIMOTO: On Molecular Sound Velocity of Liquids III. Con-

sideration on the Rao's Relation on the Dependence of Molecular Sound Velocity on Critical Constants 73

: Theory of the Visualization of Ultrasonic Waves I. Theory of the Schlieren Method for Visualizing Ultrasonic Waves 267

: Theory of the Visualization of Ultrasonic Waves II. Theory of the Phase-shift Method for Visualizing Ultrasonic Waves 279

T. KISHIMOTO and ——: Absorption of Ultrasonic Waves in Organic Liquids I. Liquids with Positive Temperature Coefficients of Sound Absorption 620

NONAKA Kōzō;

and K. KOHRA: Study on the Crystallization Process of Polished Layers of Metals by Electron Diffraction and Microscopy 512

NUKASAWA Kenji: On the Delocalization Energy in Molecules 133

ODA M.;

S. HIGASHI, ——, T. OSHIO, H. SHIBATA and K. WATANABE: On the Absorption of Cosmic Rays Underground 655

OKAYA Akira: New Spectra of $H_2C^{12}O$ in 6 mm Wave Range 135

OGAWA Shiro;

and D. WATANABE: Electron Diffraction Study on the Ordered Alloy CuAu 475

J. MIZUNO, —— and T. HIRONE: Dependence of the Intermatollic Diffusion Coefficient upon Concentration 961

OGAWA Shizuko;

S. KOJIMA, K. TSUKADA, ——, A. SHIMAUCHI and Y. ABE: Muclear Quadrupole Resonances in Arsenic Tribromide and Tri-iodide 805

OGAWA Takuji;

T. HIBI and ——: Crystals Habit of Magnesium Oxide Smokes 627

OGUCHI Hakuro: On the Subsonic Flow behind the Bow Wave of a Finite Wedge .. 249

: On the Attached Curved Shock in Front of an Open-Nosed Axially Symmetrical Body 861

OHKURA Hiroshi;

H. KAWAMURA, —— and T. KIKUCHI: The Statistical Time Lag of the Dielectric Breakdown of Mica, Glass and KCl 541

OHTSUKA Taiichiro;

T. TAOKA and ——: The Magnetic Properties and their Temperature Dependence of Ferromagnetic Alloys with an Order-disorder Transformation I Ni_3Fe 712

T. TAOKA and ——: The Magnetic Properties and their Temperature Dependence of Ferromagnetic Alloys with an Order-disorder Transformation II. Ni_3Mn 723

ONISHI Tomio;

M. KIKUCHI and ——: The "Photo-Aftereffect" of Germanium Crystal Rectifiers 130

ŌNO K.;

H. KUMAGAI, ——, I. HAYASHI, H. ABE, J. SHIMADA, H. SHŌNO, H. IBAMOTO and S. TACHIMORI: On Line Widths of Paramagnetic Resonance Absorption 369

H. KUMAGAI, I. HAYASHI, ——, H. ABE, J. SHIMADA and H. SHŌNO: Absolute Values of Absorption Coefficients in Paramagnetic Resonance Absorption 376

H. ABE, ——, I. HAYASHI, J. SHIMADA and K. IWANAGA: Paramagnetic Resonance Absorption in $K_2CuCl_4 \cdot 2H_2O$ 814

OOKAWA Akira

E. FUKUSHIMA and ——: Observation of the Grain Boundary in Soap Bubble Raft Part II. Dynamical Behaviour of the Grain Boundary 44

OOSHIKA Yuzuru: Absorption Spectra of Dyes in Solution 594

OSADA Kikusaburo: A Filter Transmitting near the Mercury Line, 2537A 136

OSHIO T.;

S. HIGASHI, M. ODA, ——, H. SHIBATA and K. WATANABE: On the Absorption of Cosmic Rays Underground 655

OTSUKA Eizo;
M. KUWAGATA, and M. TOMURA: Electrical Resistivity of Polycrystalline Selenium at Higher Fields 300
OTSUKA Masamoto;
T. HORIE and ——: Simultaneous Excitation and Dissociation of Water Molecule by Hydrogen Canal Ray Impact 219
RAMAIAH N. A.;
V. VENKATESWARLU and ——: Studies of Light Absorption under Conditions Productive of Joshi Efiect in Mercury Vapour under Ozoniser Discharge 225
RYU Inseun;
—— and H. KAWAMURA: On the Thickness Effect of Dielectric Breakdown of Mica and KCl 438
SAKAI Mitsuo: A Note on Avoiding Scattered Electrons from the Spectrum obtained by Magnetic Spectrometer 437
SASAKI W.;
, N. SAKAMOTO and M. KUNO: Some Electrical Properties of AlSb 650
SAKAMOTO N.;
W. SASAKI, —— and M. KUNO: Some Electrical Properties of AlSb 650
SAKATA Shigeo;
N. TERAO and : Electromicroscopie de la Surface d'une Cassure de Verre (II) 109
SAKATA Toshimichi;
and S. MUNESUE: Magneto-Resistance of Cs_3Sb Photo-Cathodes 141
: Hall Effect in Cesium Antimonide with Audiofrequency Currents....1030
——: On the Thermoelectric Power of Cesium Antimonide........1031
SAKURAI Akira: On the Propagation and Structure of a Blast Wave II........ 256
SAITO Nobuhiko: Statistical Mechanics of Flexible Linear Polymers. I. Moments of End-to-End Distance of a Polymer........ 780
SATO Kinzo;
—— and M. NAMBA: On the Photocurrent of High Purity SiC Single Crystal 139
SATO Koji;
——, H. NAKANE, T. HIDESHIMA and S. IWAYANAGI: Creep of Polymethyl Methacrylate at Low Temperature 413
SATOH Takesi;
E. KANAI and : On the Transitional Phenomena of Glass 417
SAWADA Shozo;
T. HORIE, K. KAWABE and : Optical Behaviours of $BaTiO_3$ Multidomain Single Crystal in Dependence on Temperature........ 823
SEKIKAWA Kyozo;
A. NISHIOKA and : Powder Density Measurement by Gas Burette 873
SHIBATA H.;
S. HIGASHI, M. ODA, T. OSHIO, —— and K. WATANABE: On the Absorption of Cosmic Rays Underground 655
SHIBATA Nagao;
S. YOSHIDA, ——, Y. IGARASHI and H. ARATA: The Use of Radioactive Isotope in a Study of Evolution of Strontium Oxide under Electron Bombardment 640
SHIBATA N.;
T. IMAI and : Effect of the Basic Metal on the Dissociation of Deposited Barium Oxide Films........1034
SHIBUYA Motoichi: The Magneto-resistance Effect in a Cubic Semiconductor with the Spheroidal Energy Surfaces 134
SHIGEMITSU Yutaka: Decay of Shear Turbulence........ 142
SHIMADA J.;
H. KUMAGAI, K. ŌNO, I. HAYASHI, H. ABE, ——, H. SHŌNO, H. IBAMOTO and S. TACHIMORI: On Line Widths of Paramagnetic Resonance Absorption 369
H. KUMAGAI, I. HAYASHI, K. ŌNO, H. ABE, —— and H. SHŌNO: Absolute Values of Absorption Coefficients in Paramagnetic Resonance Absorption .. 376

H. Abe, K. Ono, I. Hayashi, ——— and K. Iwanaga: Paramagnetic Resonance Absorption in $K_2CuCl_4 \cdot 2H_2O$ 814

Shimada Osamu: An Evaluation of Plasma-ion Temperature 874

Shimauchi Akira;

S. Kojima, K. Tsukada, ——— and Y. Hinaga: Zeeman Splitting of Nuclear Quadrupole Resonance Line of Bromine 795

S. Kojima, K. Takayama and ———: Noise of Gas Discharge Plasma 802

S. Kojima, T. Tsukada, S. Ogawa, ——— and Y. Abe: Nuclear Quadrupole Resonances in Arsenic Tribromide and Tri-iodide 805

Shimbo Sotoshi;

Y. Wada and ———: The Density and the Ultrasonic Velocity in Benzene Solutions of Methyl Methacrylate at Different Polymerization Stages 78

Shimoda Koichi: Atomic Clocks and Frequency Standard on an Ammonia Line I .. 378

———: Atomic Clocks and Frequency Standards on an Ammonia Line II.... 558

———: Atomic Clocks and Frequency Standards on an Ammonia Line III .. 567

———, T. Nishikawa and T. Itoh: Microwave Spectrum of Methylamine.. 974

Shimomura Yasumitsu;

——— and I. Tsubokawa: Some Physical Properties of Nickel Oxides........ 19

———, I. Tsubokawa and M. Kojima: On Nickel Oxides of High Oxygen Content 521

Shimose Ikuro: Statistical Theory of Phase Transition, I General Theory for Lattice Gas 451

———: Statistical Theory of Phase Transition, II Numerical Calculation for Lattice Gas 457

Shindo Takuzo: Transient Phenomenon in the Oxide Cathode Layer........ 28

Shizume Toshio;

T. Kihara, Y. Midzuno and ———: Statistics of Lattices with Many Components 681

Shōno H.;

H. Kumagai, K. Ōno, I. Hayashi, H. Abe, J. Shimada, ———, H. Ibamoto and S. Tachimori: On Line Widths of Paramagnetic Resonance Absorption.. 369

H. Kumagai, I. Hayashi, K. Ōno, H. Abe, J. Shimada and ———: Absolute Values of Absorption Coefficients in Paramagnetic Resonance Absorption .. 376

Sonoda Masateru;

I. Kumabe and ———: On the External Cathode Proportional Counter 877

Suga K.;

K. Hinotani, ——— and Y. Tanaka: A Study of Schower Curves with the Multiplate Cloud Chamber 883

Sugaike Suezo;

K. Arakawa and ———: Photoconductivity of In_2Te_3 and CdTe single Crystals 648

Sugano Satoru;

Y. Tanabe and ———: On the Absorption Spectra of Complex Ions I 753

Y. Tanabe and ———: On the Absorption Spectra of Complex Ions II...... 766

Suganomata S.;

S. Takemoto, T. Dazai, R. Chiba, S. Ito, ——— and Z. Watanabe: The Angular Distribution of Protons from the $C^{12}(d, p)C^{13}$ Reactions........ 447

Suganuma Ryoji;

Y. Fujiki and ———: On the Lattice Anomaly of Bismuth Film deposited from its Vapour 144

Sugiura Yoshikazu: Experimental Studies on the Force exerted on a Disc placed in Flow of Raredfied Gas 244

Sugiyama Akira: On the Variational Calculation of the Activation Energy of Dislocation 460

Suita Tokuo;

Y. Inuishi and ———: On the Breakdown of Colored KCl 430

Sumi Masao: On the Excitation of Oscillations in a Thermal Plasma........ 88

Suzuki Hideji;

——— and F. E. Fujita: Slip Bands in an α-Brass Crystal........ 428

——: A Theory of the Formation of Slip Bands in Face-Centred Cubic Crystals 531
SUZUKI Kazuo;
S. MIYAKE and ——: X-ray Studies on the Structures of Solid Solutions NaCl-$CaCl_2$ I. Main Results and General Considerations 702
SUWA Shigeki;
K. MURAKAWA and ——: Hyperfine Structure of the Spectrum of Pr II .. 93
TACHIMORI S.;
H. KUMAGAI, K. ŌNO, I. HAYASHI, H. ABE, J. SHIMADA, H. SHŌNO, H. IBAMOTO and ——; On Line Widths of Paramagnetic Resonance Absorption 369
TAKAGI Mieko: Electron-Diffraction Study of Liquids-Solid Transition of Thin Metal Films 359
TAKAGI Riitsu: Morphology of ZnO Crystals fromed on the Surface of Brass or Zinc at High Temperatures 162
TAKAGI Yutaka;
K. HIRANO and ——: On the Solid Solubility of Silver in Aluminium...... 730
TAKAKI Hideo;
——, S. NAKAMURA, Y. NAKAMURA, J. HAYASHI, K. FURUKAWA and M. ASO: The Production of Single Crystals of Metals and Alloys with any Desired Orientation by Solidification at High Temperature 204
—— and Y. NAKAMURA: The Magnetostriction Constants of Silicon Steel I.. 507
—— and Y. NAKAMURA: The Magnetostriction Constants of Silicon Steel II . 749
TAKAHASHI Takehito;
T. INOUE and ——: Inelastic Collisions between Two Molecules 199
TAKAHATA Masaomi;
S. KANEKO, T. KUBOZOE and ——: Frequency of Slow Cosmic-ray μ-Mesons Stopped in the Photographic Emulsions at 23 m.w.e. Underground.. 147
TAKANO Fumihiko;
M. TODA and ——: Notes on Fermi and Bose Statistics 14
——: An Attempt to Treat the Interaction Between Electrons and Lattice Vibrations 430
TAKAYAMA Kazuo;
S. KOJIMA, —— and A. SHIMAUCHI: Noise of Gas Discharge Plasma 802
TAKAZAWA Kazunori;
—— and T. TOMOTIKA: On the Optical Absorption of Thin BaO Film in the Ultraviolet Region 996
TAKEMOTO S.;
——, T. DAZAI, R. CHIBA, S. ITO, S. SUGANOMATA and Z. WATANABE: The Angular Distribution of Protons from the $C^{12}(d, p)C^{13}$ Reactions........ 447
TANABE Yukito;
—— and S. SUGANO: On the Absorption Spectra of Complex Ions I 753
—— and S. SUGANO: On the Absorption Spectra of Complex Ions II 766
TANAKA Haruo;
—— and T. KAKINUMA: Multiple Element Inerferometer for Locating Sources of Solar Noise at 4,000 MC 364
TANAKA Tomoyasu: Note on the Partition Function of a Free Rotator........ 472
TANAKA Y.;
K. HINOTANI, K. SUGA and ——: A Study of Shower Curves with the Multiplate Cloud Chamber 883
TAOKA Tadami;
—— and T. OHTSUKA: The Magnetic Properties and their Temperature Dependence of Ferromagnetic Alloys with an Order-disorder Transformation I Ni_3Fe 712
—— and T. OHTSUKA: The Magnetic Properties and their Temperature Dependence of Ferromagnetic Alloys with an Order-disorder Transformation II. Ni_3Mn 723
TARUI Yasuo;
M. KIKUCHI and ——: Transient Phenomena in the Backward Direction of

Germanium Crystal Rectifiers 642

TATSUUMA Noriko;
 T. NAGAMIYA and ———: Theory of Color Centers III. Continuum Models of F_2^+- and F_2-Centers 307

TERAO Nobuzo;
 ——— and S. SAKATA: Electromicroscopie de la Surface d'une Cassure de Verre (II) 109
 ———: Sur la Resistance a la Rupture du Verre a la Basse Pression 879

TODA Morikazu;
 ——— and F. TAKANO: Notes on Fermi and Bose Statistics 14

TODA Morikazu: Diffusion on the Fermi Surface 400

TOMITA Kazuhisa;
 R. KUBO and ———: A General Theory of Magnetic Resonance Absorption 888

TOMOTIKA Tosiro;
 K. TAKAZAWA and ———: On the Optical Absorption of Thin BaO Film in the Ultraviolet Region 996

TOMURA Masao;
 M. KUWAGATA, E. OTSUKA and ———: Electrical Resistivity of Polycrystalline Selenium at Higher Fields 300

TORIZUKA Kazuo: Chlorine Pure Quadrupole Spectra in Some Solid Compounds 645

TSUBOKAWA Ichiro;
 Y. SHIMOMURA and ———: Some Physical Properties of Nickel Oxides...... 19
 Y. SHIMOMURA, ——— and M. KOJIMA: On Nickel Oxides of High Oxygen Content 521

TSUJIUCHI Jumpei;
 Y. UKITA and ———: On the Wave Aberrations of the Decentred Lens System with the Finite Aperture 602

TSUKADA Kineo;
 S. KOJIMA, ———, A. SHIMAUCHI and Y. HINAGA: Zeeman splitting of Nuclear Quadrupole Resonance Line of Bromine 795
 S. KOJIMA, ———, S. OGAWA, A. SHIMAUCHI and Y. ABE: Nuclear Quadrupole Resonances in Arsenic Tribromide and Tri-iodide 805
 ———: Contribution of Overlap Integral to Nuclear Quadrupole Coupling .. 872

TSUYA Noboru;
 T. HIRONE, S. MAEDA and ———: On the Ferrimagnetism of Iron Selenides .. 496
 T. HIRONE, S. MAEDA, S. CHIBA and ———: Thermal Analysis of Iron Sulfides at the Temperature Range of β-transformation 500
 T. HIRONE, S. MAEDA and ———: Thermal Analysis of Iron Sulfides at the Temperature Range of α-transformation 503
 ———: On the Internal Field of the Microwave Resonance in Ferrites...... 644
 T. HIRONE, S. MAEDA and ———: On the Λ-sharped Ferrimagnetism of $FeS_{1.10}$ 736

UCHIDA Yoichi;
 ——— and Y. NAKAI: On the V-centers in Alkali Iodide Crystals 928

UKITA Yukichi;
 ——— and J. TSUJIUCHI: On the Wave Aberations of the Decentred Lens System with the Finite Aperture 602

UMEDA Kwai: A Measure for Approximation Degree of the Approximate TF Function for Free Neutral Atom 290
 ———: On the Approximate TF Function for Compressed Neutral Atom.... 291

VENKATESWARLU V.;
 ——— and N. A. RAMAIAH: Studies of Light Absorption under Conditions Productive of Joshi Effect in Mercury Vapour under Ozoniser Discharge .. 225

WADA Yasaku;
 ——— and S. SHIMBO: The Density and the Ultrasonic Velocity in Benzene Solutions of Methyl Methacrylate at Different Polymerization Stages 78
 ———: On the Relation between Sound Velocity and Intermolecular Free Length of Liquids 641

WAKESHIMA Hiromu: Fog Formation due to Self Nucleation 400

———: Fog Formation due to Self Nucleation II 407

WATANABE Denjiro;

S. OGAWA and ———: Electron Diffraction Study on the Ordered Alloy CuAu 475

WATANABE Hiroshi: On the Velocity Analysis of Electrons Scattered by Thin Foils 920

———: Multipled Lines in the Energy Spectrum of Electrons Passing through an Mg Foil 1035

WATANABE K.;

S. HIGASHI, M. ODA, T. OSHIO, H. SHIBATA and ———: On the Absorption of Cosmic Rays Underground 655

WATANABE Z.;

S. TAKEMOTO, T. DAZAI, R. CHIBA, S. ITO S. SUGANOMATA and ———: The Angular Distribution of Protons from the C^{12}(d, p)C^{13} Reactions............ 447

YAMAGATA Yukio;

J. ITOH, R. KUSAKA and ———: The Electric Quadrupole Splitting of the Nuclear Magnetic Resonance Lines of Sodium in a Single Crystal of $Na_2S_2O_3 \cdot 5H_2O$.. 209

YAMANAKA Chiyoe: Electret 425

YAMASHITA Jiro: Theory of Superexchange Interaction in MnO Crystal 339

——— and T. KUROSAWA: Formation Energy of Lattice Difect in Sliple Oxide Crystals.. 944

YOKOTA Mario;

——— and S. KOIDE: The Exchange Effects on the Absorption Spectrum by the Paramagnetic Crystal with Anisotropic *g*-factors 954

YOSHIDA Shigetomo;

———, N. SHIBATA, Y. IGARASHI and H. ARATA: The Use of Radioactive Isotope in Study of Evolution of Strontium Oxide under Electron Bombardment 640

YOSHIMORI Akio;

——— and T. MATSUBARA: A Method of Treating the Zero-point Vibration of the Crystal of Lighter Molecules.. 465

YOSHIMURA Hisamitu;

——— and K. FUKUDA: Feed-back Resonance Amplifier for the Infrared Spectrometry Part III 1001

YOSHIOKA Hide: On the Anomalous Absorption of X-rays by Crystals at the Setting of Bragg Reflection 636